Nicholas C. Gourtsoyiannis
Pablo R. Ros
Editors

Radiologic-Pathologic Correlations from Head to Toe

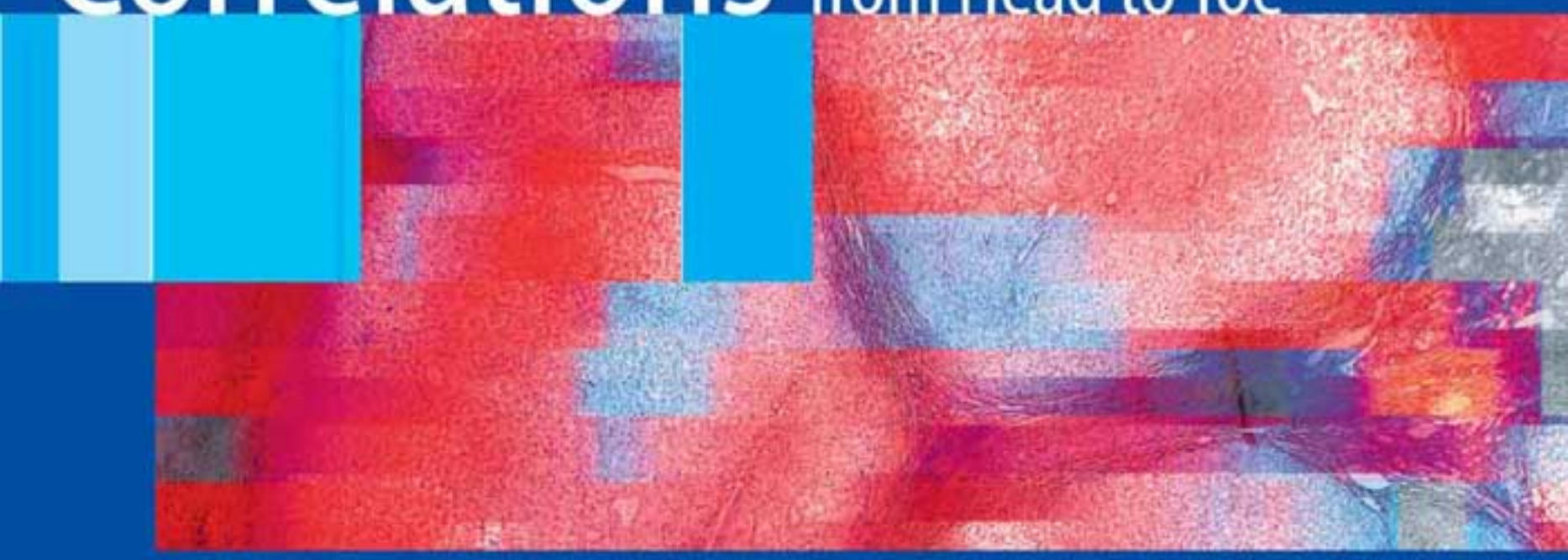

Understanding the Manifestations of Disease

Springer

Nicholas C. Gourtsoyiannis · Pablo R. Ros (Eds.)

Radiologic-Pathologic Correlations
from Head to Toe
Understanding the Manifestations of Disease

Nicholas C. Gourtsoyiannis · Pablo R. Ros (Eds.)

Radiologic-Pathologic Correlations

from Head to Toe

Understanding the Manifestations of Disease

With 794 Figures in 1863 Separate Illustrations, 599 in Colour and 38 Tables

Springer

Professor Nicholas C. Gourtsoyiannis, M.D.
Department of Radiology
University Hospital of Heraklion
P.O. Box 1352
Stavrakia
Heraklion Crete
71110 Greece

Pablo R. Ros, M.D., MPH
Professor of Radiology, Harvard Medical School
Executive Vice Chairman, Department of Radiology
Brigham and Women's Hospital
75 Francis St.
Boston, MA 02115, USA

Library of Congress Control Number 2004114605

ISBN 3-540-04395-0 Springer Berlin Heidelberg New York

Springer-Verlag is a part of Springer Science+Business Media
springeronline.com

Printed in Germany

Editor: Dr. Ute Heilmann
Desk Editor: Wilma McHugh
Production: Marina Litterer, ProEdit GmbH, 69126 Heidelberg, Germany
Cover: Frido Steinen-Broo, EStudio Calamar, Spain
Typesetting: K. Detzner, 67346 Speyer, Germany
Printing and binding: Stürtz, 97080 Würzburg, Germany

Printed on acid-free paper 21/3150 5 4 3 2 1 0

Preface

We are proud to offer this unique textbook, the first in its class presenting state-of-the-art radiologic images of the entire body correlated with underlying pathology. This book is based on a categorical course presented for 3 years at recent European Congresses of Radiology and covers from head to toe, key aspects of human disease lending themselves well to the correlation of modern imaging techniques with microscopic and gross pathology. Obviously, the most suitable candidate for radiologic–pathologic correlation is the study of neoplasms, since they are resected ideally in toto and therefore offer excellent gross–imaging comparisons. Although there is a wealth of educational material based on radiologic–pathologic correlation, not until now has there been a comprehensive textbook that offers in a single source a compendium of topics such as that between these covers.

The concept of radiologic–pathologic correlation was born in 1947 with the establishment of the Radiologic Pathology Department and Registry at the Armed Forces Institute of Pathology in Washington, DC. This method has become a key teaching tool to understand the radiological manifestations of disease, initially on plain films and later with cross-sectional techniques. With the advent of computed tomography and magnetic resonance imaging, precise correlation between imaging and the underlying pathology became possible throughout the entire body. For decades now, generations of radiology residents from North America, and more recently from many other regions of the world, have enjoyed the quiet revolution in radiology teaching offered by radiologic–pathologic correlation, since this method demonstrates not only the "how" but also the "why" of the radiologic findings.

The success of courses on radiologic–pathologic correlations at venues such as the European Congress of Radiology, The International Congress of Radiology, The Radiological Society of North America Assembly, among others made us believe that radiologists, as well as pathologists and other specialists, would enjoy having in a single source the best of class in this educational method. This book is indeed a global effort since it assembles the leading authorities in all major organ systems who use radiologic–pathologic correlation as a research and teaching method. Many of the chapter authors have dedicated the bulk of their professional life to educating radiologists throughout the world using this method. There are experts from 12 European countries and the USA. All the United States authors and many of the European ones have direct or indirect links with the Armed Forces Institute of Pathology, having served there as full-time faculty, distinguished lecturers or researchers in radiologic–pathologic correlation.

This textbook is divided in the main organ systems including neuroradiology, head and neck, chest, abdominal–gastrointestinal, urogenital, musculoskeletal and breast imaging. In each one of these organ systems the topics most salient to radiologic–pathologic correlation are discussed in a systematic fashion, in many cases emphasizing the study of benign and malignant neoplasms. This book is intended to be used as a working guide to assist radiologists in their daily practice when difficult cases are encountered. It should also help physicians in training to learn imaging findings not by memory but through the knowledge of the pathologic basis of disease. Finally, we hope that the readers will enjoy the high-resolution images and the many color prints of the specimens.

Nicholas C. Gourtsoyiannis, MD
Pablo R. Ros, MD, MPH

Acknowledgements. We are indebted to the many people who have made this book possible, starting with our 60 contributing authors. All of them are extremely busy people and generously donated their time, knowledge and experience of many years to write well-constructed chapters.

A very special thanks to Ms. Wilma McHugh from Springer Verlag. She kept us focused during the years it has taken to put this book together and bridged distances and time zones so the project could become reality. Special thanks to our assistants in the Departments of Radiology of the University of Crete (Eve Markaki) and Brigham and Women's Hospital/Harvard Medical School (Mildred Dewire and Linda Pedersen). Without them this would not have been possible.

We are also indebted to the many students, residents, fellows and practicing radiologists that throughout the years have kept alive our interest in radiologic–pathologic correlation with their positive feedback and also have contributed cases for our personal and institutional files.

Finally, special thanks are due to the many pathologists that have interacted with radiologists during the past decades to initially establish and later enhance the teaching and research method of radiologic–pathologic correlation.

Contents

List of Contributors

Gerald F. Abbott
Department of Diagnostic Imaging
Brown Medical School
Rhode Island Hospital
593, Eddy Street
Providence, RI 02903, USA

Cosma F. Andreula
Neuroradiology
Anthea Hospital
Guppo Villa Maria
70124 Bari, Italy

Ingvar Andersson
Department of Diagnostic Radiology
University of Lund
Malmö University Hospital
205 02 Malmö, Sweden

Dominique Artaud
Service de Radiology
Hôpital A. Calmette
C.H.R.U. de Lille
Blvd du Professeur Leclercq
59037 Lille, France

Edward Azavedo
Mammography Section
Department of Diagnostic Radiology
Karolinska Hospital
171 76 Stockholm, Sweden

Zelena Aziz
Department of Radiology
Royal Brompton National Heart and Lung Hospital
Sydney Street
London SW3 6NP, UK

Dimitris Bays
Department of Radiology
Airforces and V.A. Hospital
P. Kanelopoulou 3
11525 Athens, Greece

Minerva Becker
Division of Diagnostic
and Interventional Radiology
University Hospital
24 Rue Micheli-du-Crest
1211 Geneva 4, Switzerland

Johan L. Bloem
Department of Radiology
University Hospital Leiden
Albinusdreef 2
2300 RC, Leiden, The Netherlands

François Bonnel
Service de Radiology
Hôpital A. Calmette
C.H.R.U. de Lille
Blvd du Professeur Leclercq
59037 Lille, France

James L. Buck
Department of Diagnostic Radiology
University of Kentucky
College of Medicine
800 Rose Street
Room hX311
Lexington, KY 40536-0084, USA

Giovanni Carbognin
Department of Radiology
University Hospital G.B. Rossi
Piazzale L.A. Scuro, 1
37134 Verona, Italy

Marie-Christine Copin
Service de Radiology
Hôpital A. Calmette
C.H.R.U. de Lille
Blvd du Professeur Leclercq
59037 Lille, France

A. Mark Davies
MRI Centre
Royal Orthopaedic Hospital NHS Trust
Bristol Road South
Birmingham B31 2AP, UK

Claudia Feldmann
Department of Radiology
Charité University Hospital
Humboldt University Berlin
Schumannstr. 20/21
10098 Berlin, Germany

Marc Fribourg
Service de Radiology
Hôpital A. Calmette
C.H.R.U. de Lille
Blvd du Professeur Leclercq
59037 Lille, France

Bernard Gosselin
Service de Radiology
Hôpital A. Calmette
C.H.R.U. de Lille
Blvd du Professeur Leclercq
59037 Lille, France

Nicholas C. Gourtsoyiannis
Department of Radiology
University of Crete
Faculty of Medicine
P.O. Box 1352
71110 Iraklion, Crete, Greece

Catherine Guettier
Department of Pathology
Hôpital Paul Brousse
94300 Villejuif, France

Bernd Hamm
Department of Radiology
Charité University Hospital
Humboldt University Berlin
Schumannstr. 20/21
10098 Berlin, Germany

David M. Hansell
Department of Radiology
Royal Brompton National Heart and Lung Hospital
Sydney Street
London, SW3 6NP, UK

David S. Hartman
Department of Radiology
Pennsylvania State College of Medicine
University Hershey Medical Center
Hershey, PA 17033, USA

Matthew S. Hartman
Department of Radiology
Emory University School of Medicine
Atlanta, GA 30322, USA

Herwig Imhof
University Clinic for Diagnostical Radiology
AKH Vienna
Waehringer Guertel 18-0
1090 Vienna, Austria

Hoon Ji
Department of Radiology
Harvard Medical School
Brigham and Women's Hospital
75 Francis Street
Boston, MA 02115, USA

Shah H.M. Khan
Department of Radiology
University Hospital Leiden
Ablinusdreef 2
2300 RC Leiden, The Netherlands

Kelly K. Koeller
Department of Radiologic Pathology
Room M-121
Armed Forces Institute of Pathology
14 Street and Alaska Avenue
Washington, DC 20306-6000, USA

Mark J. Kransdorf
Department of Radiologic Pathology
Armed Forces Institute of Pathology
6825 16th Street, NW
Bldg. 54, Room 133A
Washington, DC 20306, USA

Rahel A. Kubik-Huch
Department of Radiology
Cantonal Hospital
5404 Baden, Switzerland

François Laurent
Department of Thoracic and Cardiovascular Imaging
Cardiologic Hospital
Groupe Hospitalier Sud
CHU de Bordeaux
Avenue de Magellan
33604 Pessac, France

Angela D. Levy
Department of Radiology Pathology
Armed Forces Institute of Pathology
Washington, DC 20306, USA

Joel E. Lichtenstein
Department of Radiology
University of Washington School of Medicine
Box 357115
Seattle, WA 98195-7155, USA

Jutta Lüttges
Department of Pathology
University Hospital Kiel
Michaelisstr. 11
24105 Kiel, Germany

David C. Mangham
Department of Pathology
Royal Orthopaedic Hospital NHS Trust
Bristol Road South
Birmingham, B31 2AP, UK

Iain W. McCall
Department of Diagnostic Imaging
The Robert Jones & Agnes Hunt
Orthopaedic and District Hospital NHS Trust
Oswestry, SY101 7AG, UK

Yves Menu
Department of Radiology B
Centre Hospitalier Universitaire de Bicêtre
78, rue du Général Leclerc
94275 Le Kremlin-Bicêtre, France

Paulette Mhawech
Division of Diagnostic and Interventional Radiology
University Hospital
24 Rue Micheli-du-Crest
1211 Geneva 4, Switzerland

Koenraad J. Mortele
Department of Radiology
Harvard Medical School
Brigham and Women's Hospital
75, Francis Street
Boston, MA 02115, USA

Mark D. Murphey
Department of Radiologic Pathology
Armed Forces Institute of Pathology
6825 16th Street, NW
Bldg. 54, Room 133A
Washington, DC 20306, USA

Daniel Joseph Nolan
Department of Radiology
John Radcliffe Hospital Headington
10, Apsley Road, Summertown
Oxford, OX3 9DU, UK

Arantxa Ortega-Aznar
Neuroradiology Section
Hospital Vall d'Hebron
Pg. Vall d'Hebron 119–129
08035 Barcelona, Spain

Anne G. Osborn
Deparment of Radiology
University of Utah
Health Sciences Center
50 N. Medical Drive
Salt Lake City, UT 84132-0001, USA

Raymond H. Oyen
Department of Radiology
University Hospitals KUL Gasthuisberg
Herestraat 49
3000 Leuven, Belgium

Valérie Paradis
Department of Pathology
Hôpital Beaujon
100, Bd du Général Leclerc
92110 Clichy, France

Marie Parrens
Department of Thoracic and Cardiovascular Imaging
Cardiologic Hospital
Groupe Hospitalier Sud
CHU de Bordeaux
Avenue de Magellan
33604 Pessac, France

Lucia Pinali
Department of Radiology
Unit for Morphological and Biomedical Sciences
Policlinic G.B. Rossi
Piazzale L.A. Scuro 1
37134 Verona, Italy

Hendrik Van Poppel
Department of Radiology
University Hospitals KUL Gasthuisberg
Herestraat 49
3000 Leuven, Belgium

Carlo Procacci (†)
Department of Radiology
Unit for Morphological and Biomedical Sciences
Policlinic G.B. Rossi
Piazzale L.A. Scuro 1
37134 Verona, Italy

Jacques W.A.J. Reeders
Department of Radiology
Saint Elisabeth Hospital
Curaçao, Netherland Antilles

Jacques Rémy
Service de Radiology
Hôpital A. Calmette
C.H.R.U. de Lille
Blvd du Professeur Leclercq
59037 Lille, France

Martine Rémy-Jardin
Service de Radiology
Hôpital A. Calmette
C.H.R.U. de Lille
Blvd du Professeur Leclercq
59037 Lille, France

Charles Rohrmann
Department of Radiology
University of Washington
1959 N.E. Pacific
Seattle, WA 98195-7115, USA

Francisco J. Romero-Vidal
Neuroradiology Section
Hospital Vall d'Hebron
Pg. Vall d'Hebron 119-129
08035 Barcelona, Spain

Pablo R. Ros
Department of Radiology
Harvard Medical School
Brigham and Women's Hospital
75, Francis Street
Boston, MA 02115, USA

Melissa L. Rosado de Christenson
Department of Radiology
The Ohio State University Medical Center
630 Means Hall
1654 Upham Drive
Columbus, OH 43210-1228
USA

Tania Roskams
Department of Radiology
University Hospitals Gasthuisberg
Herestraat 49
3000 Leuven, Belgium

Francis J. Scholz
Department of Radiology
Tufts University School of Medicine
Lahey Clinic Medical Center
41, Mall Road
Burlington, MA 01805, USA

Ingrid Schreer
Breast Center
University Hospital Kiel
Michaelisstr. 16
24105 Kiel, Germany

Enrica Segatto
Division of Abdominal Imaging and Intervention
Department of Radiology
Brigham and Women's Hospital
Harvard Medical School
75, Francis Street
Boston, MA 02115, USA

Diane C. Strollo
University of Pittsburgh
UPMC Health System
Department of Radiology
200, Lothrop Street
Pittsburgh, PA 15213-2582, USA

Benoît Terris
Department of Pathology
Hôpital Beaujon
100, Bd du Général Leclerc
92110 Clichy, France

Valérie Vilgrain
Department of Radiology
Hôpital Beaujon
100, Bd du Général Leclerc
92118 Clichy Cedex, France

Iain Watt
8 Parry's Grove
Stoke Bishop
Bristol, BS9 ITT, UK

Part 1
Neuroradiology

Central Nervous System: CNS Infections

Cosma F. Andreula

1.1

Contents

Introduction

The increasing sensitivity and specificity of the latest generations of medical modalities, magnetic resonance imaging (MRI) above all, are filling the gap between pathology and in-vivo imaging. The pathological lesion is always our gold standard, but the contemporary MRI image appears so closely related to it that diagnosis, the probable etiology, the lesion's advance over time, the answer (or missing answer) to medical therapy, timely planning of surgery become possible.

The primary limit to this approach is the relative lack of specificity, above all in terms of etiology. Often we can handle no more than suggestions, most coming from anamnesis, medical examination, clinical considerations, and laboratory reports.

The justification of this phenomenon is a matter of complex understanding.

Although the blood–brain barrier (BBB) protects and serves the CNS very effectively, behind it no factual immune system is present (only a few primitive macrophagic functions are accomplished by microglia). When the BBB discontinues its remarkable action, the CNS sancta sanctorum has almost no resistance to external infectious agents. Invasions are extremely ruinous: many infections can have fatal consequences if they reach the CNS, whereas the same organisms cause banal infections in the rest of the body. The example of polioviruses is classic: they cause anterior poliomyelitis but mild systemic illness.

In most circumstances, when the patient survives, serious sequelae commonly remain after resolution of the acute phase.

Moreover, the deficiency in complex immune responses frequently induces CNS stereotyped responses whose pattern is related to the seriousness of the invasion more than to the specific agent involved.

On the other hand, different reactions to the same agent are commonly observed, according to the patient's immune status.

Only a strict partnership with neurologists and infectious disease specialists can clarify the clinical background, and this must be considered mandatory. Nevertheless, some pathology pictures are so typical that MRI can make the dream of seeing into a living body come true.

Think about MRI's unique ability to show all phases, the morphology, the volume, signal characteristics (the last-named providing inestimable data on water, protein content, BBB consistence, etc.) of the infectious process, e.g., a classic skull base tuberculosis, or a cerebritis evolving toward a mature abscess. If the inner workings are visible the advancement of the process can be stopped, sometimes by simply adopting the right antibiotic drug.

These are the reasons why neuroradiology is a major tool in today's diagnostic and follow-up protocol of the infectious patient.

Classification of Microorganisms

The agents causing CNS diseases are classified into pathogens and opportunists. The first are able to produce illness in immunocompetent people, whereas opportunistic agents affect hosts with some degree of immunodeficiency, from a wide variety of causes, most frequently AIDS.

Microorganisms are living agents, with a simple structure and small size, generally under microscopic resolution.

Protozoa are unicellular agents with nucleus and cytoplasm (they may be low-s spirilla), frequently parasites of other organisms. In unfavorable conditions they produce a defensive wall, forming a cyst effective for their survival.

The most widely known protozoa, *Entamoeba* and *Trypanosoma*, rarely affect the CNS, while *Toxoplasma gondii*, an obligatory intracellular parasite, very frequently infects people of the Western world, staying alive and hidden in the CNS and becoming a pathogen in the case of immunodeficiency.

Mycetes or fungi are infectious for humans and animals as molds with long filaments (hyphae) or yeasts with spherical or ovoid morphology, reproducing by gemmation.

The most frequent pathogenic fungi are *Coccidioides* and *Histoplasma*. The most frequent saprophyte fungi are *Cryptococcus*, *Candida* and *Aspergillus*, pathogenic in immune deficiency.

Bacteria are generally unicellular elements, distinguished in Gram-positive or Gram-negative tests by their color-reaction response. They have different shapes: spherical (cocci are Gram-positive such as streptococci and staphylococci or Gram-negative such as *Neisseria meningitidis*), rod-shaped (such as acid–alcohol-resistant mycobacteria), helical (such as spirilla), and curved (such as vibriones).

Spirochetes differ from bacteria by the presence of flexible coiled filaments: among them are *Borrelia* (the agent of Lyme disease), *Treponema* (the agent of syphilis or lues), pathogens with CNS predilection.

Rickettsiae are visible unicellular microorganisms, obligatoryintracellular parasites, necessarily carried by vectors (arthropods).

Viruses are subcellular agents, with a nucleic acid core wrapped in a proteic envelope. They lack their own energy sources and need host cells to regenerate.

The classification of viruses is in permanent revision: grossly we divide pathogenic viruses into RNA and DNA forms, with families, genera and types.

For example, herpes simplex, the agent of the necrotic hemorrhagic meningoencephalitis, is a DNA virus of the Herpesviridae family, genus *Simplex*, type 1.

Classification of unconventional agents is still not completely understood: they should be formed only by proteic material, such as prions (Creutzfeldt-Jakob disease, kuru) or by nucleic acid, such as viroids.

Apart from microorganisms there are the helminths, whose infestations (the best way to describe of these infections) are very frequent. Cestodes are the most frequent, inducing cysticercosis (*Taenia solium* can conclude its own parasitic cycle in humans, in such a case the definitive host) and echinococcosis (for which humans are an accidental host).

Routes of Infection

Access to the CNS by nonviral infectious agents is difficult. The skull provides an effective shield from outside penetration. Dura mater meninges resist for a considerable period, while the arachnoid membranes act as a barrier, with the outer layer of endothelial cells, and as a cellular immunity complex, by virtue of their lymphocytes and reticuloendothelial cells, disseminated in subarachnoid spaces and perivascular Virchow–Robin spaces (along cerebral vessels). The pia mater covering the cortical surface of the brain is a temporary barrier for germs.

The blood route is the most frequent entrance path, directly through cerebral and meningeal vessels, or indirectly, after a choroid plexus infection.

Today the spread of infection from the paranasal sinuses and the ear's pneumatized cavities, by erosion of the thin bone layer, and the dura, ultimately reaching the brain, is less frequent.

Interruptions of the continuity of the skull by trauma or surgical interventions could allow microorganisms free access to the CNS, but hygienic and aseptic measures prevent such events.

Viruses gain access to the CNS mainly via the hematogenous route or via the neural route through the free terminations of the olfactory nerves in the nasal mucosa. Other neural paths are used by obligatory neurotropic viruses, such as rabies or herpes, traveling along the peripheral nerve up to the ganglion.

In certain diseases (HIV infection), viruses overcome the blood–brain barrier concealed in monocyte–macrophage line cells.

Other diseases, such as immune-mediate-disseminated acute and subacute encephalomyelitis, which are increasing in frequency, have a different pathogenesis: they are related to self-immune reactions.

During fetal life, the access to the CNS is hematogenous through the transplacental circulation and – by continuity – through the amniotic liquid.

Classification of Lesion

Infectious diseases of the CNS are arranged in diffuse and focal forms.

The diffuse lesions are related to the involved compartment: meningitis, meningoencephalitis and encephalitis.

The focal lesions are immature (cerebritis) or mature (granuloma and abscess) forms, and cysts.

Leptomeningitides are caused by many microorganisms, ranging from viruses to bacteria, often producing age-related diseases. In neonates the most common causative agents are B streptococcus, *Escherichia coli*, and *Listeria monocytogenes*. Between 2 months and

10 years of age, the most frequent agent is *Haemophilus influenzae*, whereas in childhood *Neisseria meningitidis* causes epidemic and nonepidemic forms.

The leptomeninges offer little resistance to infection, because the cerebrospinal fluid is an optimal culture tissue for germs.

Grossly (Fig. 1A) the brain surface is congested and the basal cisterns of the brain are filled with creamy pus, covering the vessels passing through. The process diffuses to the adventitia and tunica media of the arteries, causing stretching, deformation, stenosis and sometimes occlusion of the vessel. The arachnoid membrane is rarely covered with pus, whereas the fissures and sulci are filled. The subpial cortex is congested, but not as in encephalitis. Pus is on the choroid plexuses, on the ependymal lining of the ventricular walls or in flakes floating in the CSF.

Histologically there are many polymorphonuclear leukocytes mixed with bacteria, with little evidence of inflammatory reaction of the brain.

In later stages mononuclear cells appear, derived from the histiocytes of the meninges or coming from the blood.

In chronic infections, fibroblasts proliferate and collagen fibers invade the meningeal spaces, causing difficult circulation of the CSF, and consequently unfavorable noncommunicating, extraventricular hydrocephalus.

Invasion of the arterial walls causes thrombosis with malacia of the tributary territories, and/or septic embolism with cerebrovascular disorders at the corticomedullary junctions.

Neuroradiologically (Fig. 1B), acute leptomeningitis is revealed by the obliteration of the fissures and sulci, sometimes dilated, giving a pseudo-atrophy appearance. After contrast administration there is contrast enhancement of the spaces to a certain degree, closely related to the inflammatory reaction. Ventricular walls are lined by contrast enhancement and the choroid plexuses are engulfed, dilated and markedly enhanced.

Ventricles are dilated with periventricular suffusion for the delayed readsorption of the fluid for an unfavorable gradient. Ventricular CSF is hyperproteic.

The vessel walls in the basal cisterns are altered, with enhanced wrapping. If the inflammatory infiltrative vessel process determines thrombosis, an arterial infarct occurs, and if the cortical veins – running in the sulci of the brain surface – are contaminated, venous infarct appears. Cerebral embolisms cause superficial ischemic zones, revealed by a gyriform pattern of the contrast enhancement at the cortex.

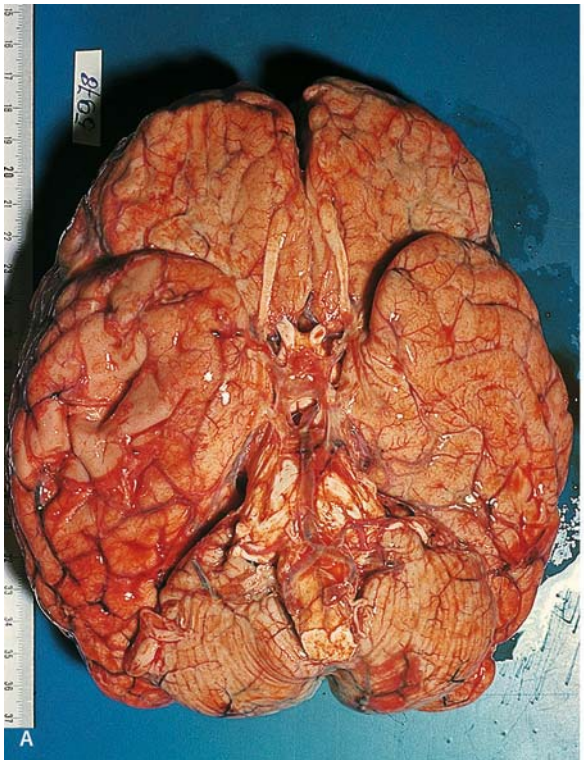

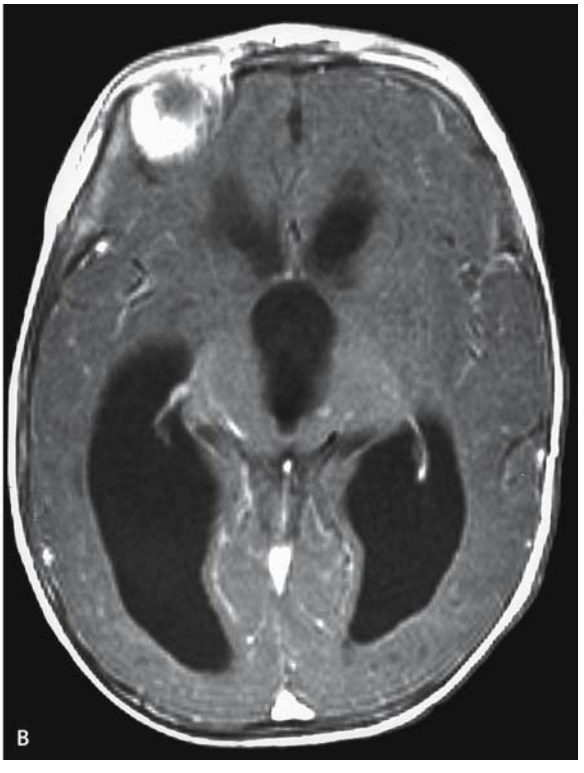

Fig. 1A, B. Bacterial meningitis. **A** Neuropathology: the cisterns at the base are filled with exudate covering cranial nerves and vessels. The cortex appears mildly congested. **B** MRI T1 axial weighted image (w.i.) after contrast administration: leptomeninges appear mildly contrast-enhanced. Difficult CSF circulation because the exudate filling the basal cisterns provokes extraventricular hydrocephalus

A common complication of bacterial meningitis is subdural effusion revealed by a water-like collection around the cerebral hemispheres, frequently with frontal lobes and falx location, without contrast enhancement of the medial border. On the contrary, marked enhancement of the membrane and mass effect should point to subdural empyema.

Viral meningitides are very mild infections, with rare neuroradiological signs. CT and MRI studies are very frequently negative.

Chronic meningitides are caused by mycobacteria (tuberculosis) and fungi (coccidioidomycosis, cryptococcosis).

CNS involvement by *Mycobacterium tuberculosis* or Koch bacillus is almost always related to a pulmonary focus that is frequently uncovered and produces granulomatous leptomeningitis and intracerebral tuberculomas.

The elementary lesion is the granuloma, with a small caseous center, surrounded by lymphocytes and plasma cells, with an intermediate zone containing epithelioid cells and the classic Langhans giant cells. Defensive, adequate response of the host leads to fibrosis and calcifications. Otherwise an unfavorable evolution of the lesion produces an increase in the caseous center, inefficient control of the capsule and diffusion of the process.

If this undesirable situation occurs in the meningeal tubercle, caseous material invades the subarachnoid spaces, producing leptomeningitis.

Macroscopically (Fig. 2A), a grayish, gelatinous exudate fills the basal cisterns (prepontine, quadrigeminal, sylvian spaces), with wrapping of cranial nerves and vessels running in the CSF spaces; nodules, which appear later in the meninges involvement, are very unusual.

Microscopically lymphocytes, plasma cells and large histiocytes are in a matrix of fibrin, with a tendency to form tubercles with caseous center.

The process involves the walls of arteries and veins: necrotizing arteritis is the lesion of the small vessels, while in the medium-sized arteries the entire wall is involved, with necrosis and formation of pseudoaneurysms (and consequent hemorrhage in the case of rupture). Vessel repair occurs with endothelial proliferation and reduction of the diameter of the vessel up to occlusion.

The chronic progression of leptomeningitis determines fibrosis of the exudate with difficult CSF circulation, ventricular dilatation, and slowly increasing extraventricular hydrocephalus.

Neuroradiologically (Fig. 2B), the inflamed meninges are revealed by intense contrast enhancement. Granulomas are small ring-shaped masses, hyperintense in MRI

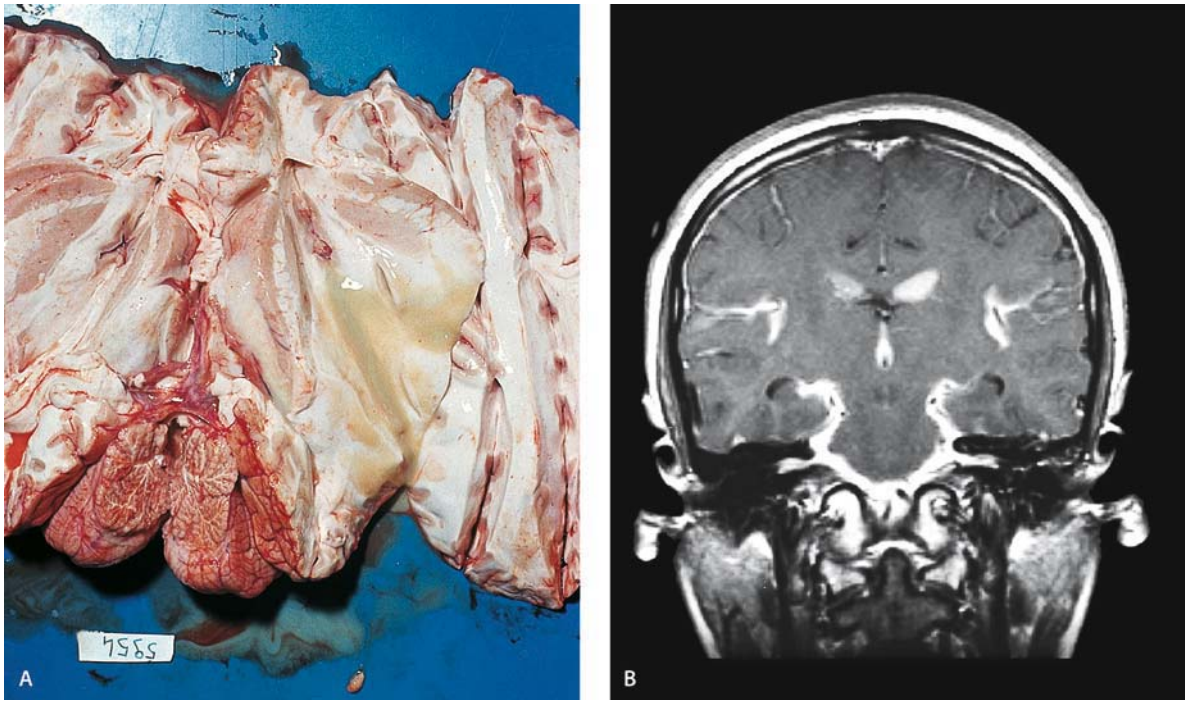

Fig. 2A, B. Tuberculosis: leptomeningitis and ependymitis. **A** Neuropathology: thick exudate covering ependyma of the ventricles with some granulomas implanted on ventricular wall. **B** MRI coronal T1 w.i. after contrast administration: marked contrast enhancement of the subarachnoid spaces and sylvian fissures to the acoustic meatus, and of the ependymal lining. Vessels appear stretched and wrapped by the contrast enhancement

long TR-weighted images (w.i.), iso- to hypointense in T1 w.i., with marked enhancement; the necrotic center is small, inhomogeneously hypo- or isointense in T2 w.i., hypointense in T1, without contrast enhancement. The aspect of the nodules is target-like, with a very small center.

The hematogenous spread to the brain causes intracerebral granuloma, so-called tuberculoma. The most common site for tuberculoma, usually solitary, is the cerebellum.

Tuberculomas are rounded or oval masses, sometimes lobulated by fusion of several smaller nodules. The capsule is gray, gelatinous with a gliotic tissue around it.

Microscopically, the capsule is rich of collagen and surrounds the caseous necrotic center, with a variable number of Langhans giant cells, epithelioid cells, histiocytes and lymphocytes in between.

In older lesions, the proportion of collagen increases while the tubercles almost completely disappear.

In MRI, the capsule is hyperintense in long TR images, iso-hypointense in T1 w.i., with marked enhancement; the necrotic center is large enough, inhomogeneously hyperintense in T2 w.i., hypointense in T1, without contrast enhancement. In the active lesion, around the capsule there is a thin rim of hypointensity in T2 w.i., related to the macrophages' energy-consuming activity, with release of paramagnetic free radicals.

Cryptococcus neoformans is the most common fungus causing chronic meningitis in man, and is almost exclusively found in immunodepressed patients.

The portal of entry of cryptococci is the lung, from where they spread hematogenously, with meninges the preferred site of infection, where protected growth can occur.

Macroscopic examination reveals that the CSF in the leptomeningeal spaces is cloudy, yellowish, with opacity of the meninges and flattening of the convolutions, and the brain is slippery to the touch. Cryptococci grow around the vessel and follow the Virchow–Robin spaces up to the end at the basal ganglia and to the periventricular areas, where they accumulate forming gelatinous pseudocysts (soap-bubbles aspect) (Fig. 3A). They also grow slowly but continuously in the choroid plexuses, sometimes occluding the exit "door" and dilating locally the ventricles (monoventricular hydrocephalus).

The last elementary lesion is the granuloma with the above-described characteristics: a nodule that is hyperintense in long TR images, iso-hypointense in T1 w.i. with mild enhancement; the necrotic center is small, inhomogeneously hypo-isointense in T2 w.i., hypointense in T1, without contrast enhancement.

Histologically, the meningeal lesions consist of an irregular granulomatous thickening of the meninges, with lymphocytes, plasma cells, and capsulated cryptococci. Pseudocysts (distended perivascular spaces) are filled with cryptococci, with less exudate, sometimes breaking out in the surrounding brain, forming pseudogranulomas.

In MRI, leptomeningitis has a less intense contrast enhancement than the tuberculosis form, providing better definition with the use of double or triple doses of contrast media.

The pseudocysts appear as rounded or oval lesions that are hyperintense in long TR images, hypointense in T1 w.i. without enhancement for the very moderately excited inflammatory reaction, with no edema surrounding it (Fig. 3B–E).

Coccidioidomycosis is a chronic fungal granulomatous leptomeningitis caused by *Coccidioides immitis*, a fungus widespread in South America and the desert zone of the United States and Mexico. Inhalation of the spores infects the lung with subsequent hematogenous diffusion. CNS involvement is rare (1%). The neuropathological aspects are quite similar to the tuberculosis form, with small granulomas implanted on the meninges and extension of the process into the subarachnoid spaces, filled with a gelatinous exudate.

Microscopically, lymphocytes and plasma cells form granulomas, with an intermediate zone containing epithelioid and giant cells, which frequently contain organisms, such as large spherical bodies.

Neuroradiologically, meningitis is revealed by obliteration of the basal cisterns and marked contrast enhancement. The process is diffuse and symmetrical, and involvement of the vessels running in the spaces determines arteritis and consequent ischemia and infarcts, but these sequelae fortunately are less common than in tuberculosis.

Difficult CSF circulation and tendency to fibrosis of the leptomeningitis can cause ventricular dilatation, which can lead to hydrocephalus.

Encephalitis is a diffuse inflammatory process, with inflammatory cells infiltrating the nervous tissues and necrosis of neuronal populations. Although viral infections are very common, clinically evident CNS viral illness is fortunately very rare. Viruses are the most common cause of encephalitis, and although etiological diagnosis can be very useful, clinical, laboratory and neuroradiological efforts are frequently in vain.

Pathogenesis of such diffuse forms recognizes different mechanisms:

- Acute forms such as acute viral systemic illness, with brain localization concurrent with other organs or localizations
- Reactivation of latent form, with an acute phenomenon such as in herpes simplex encephalitis
- Reactivation of latent form with chronic phenomena such as subacute sclerosing panencephalitis or progressive multifocal encephalitis
- Chronic forms caused by slow viruses or unconventional viral agents such as prions


A

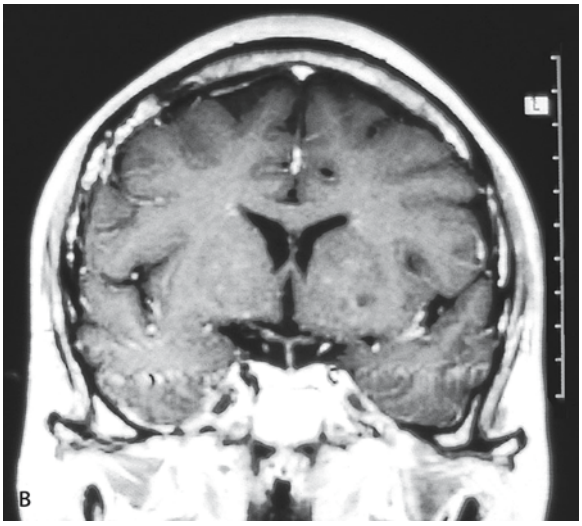
B

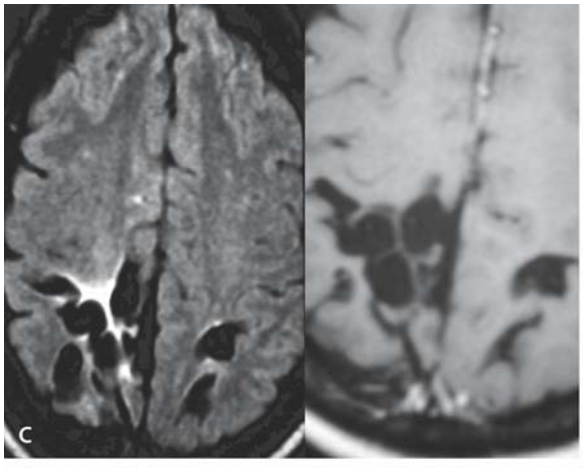
C

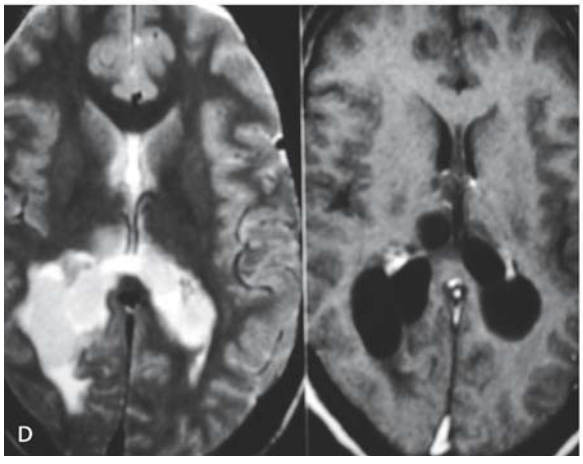
D

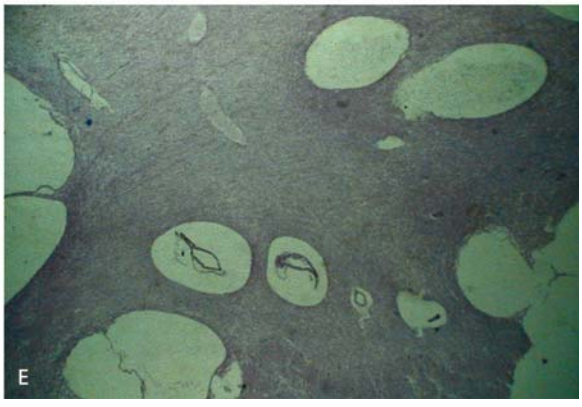
E

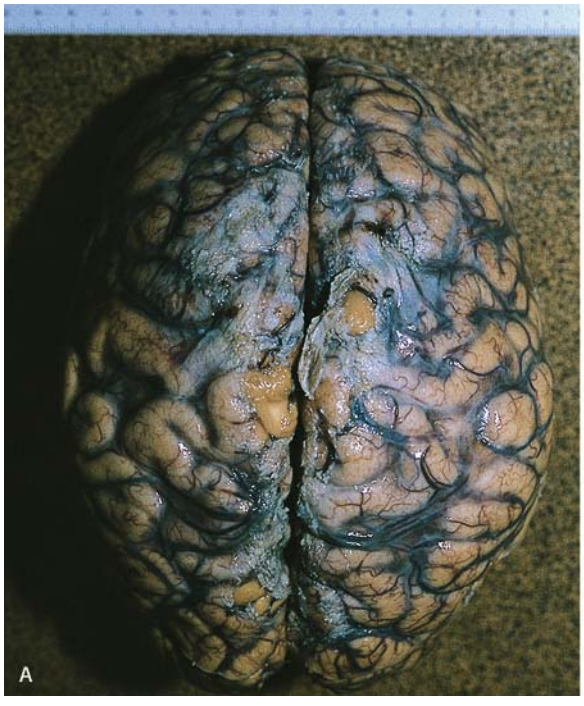

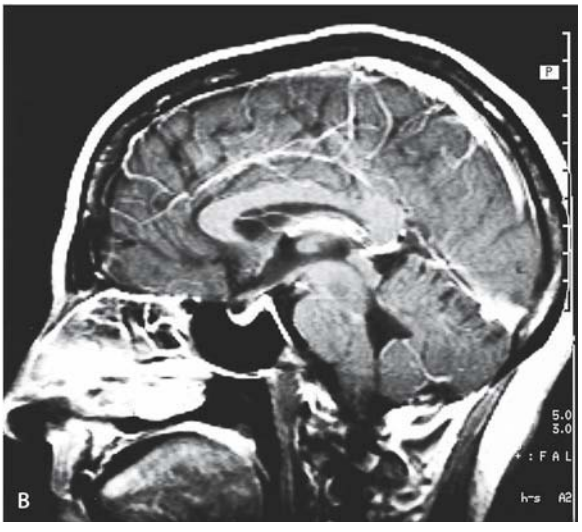

Fig. 4A, B. Meningoencephalitis. **A** Neuropathology: the brain is markedly congested and swollen. An exudate covers the medial surface of the cerebral hemispheres. **B** MRI sagittal T1 w.i. after contrast administration: marked enhancement of the venous vessels (dural sinus and cortical veins), which appear dilated. Initial dilatation of the ventricular system, beginning from the 4th ventricle

- Immune-mediated forms caused by a cross-reaction mechanism, between some viruses and myelin.
- Teratogenic forms caused by agents attaining the fetus during pregnancy

Paths of invasion more likely follow the bloodstream and uncommonly climb along peripheral nerves through olfactory mucosa or along postganglial fibers. Use of cells (lymphocytes or monocyte-macrophage cells) as carriers (the Trojan horse mechanism) is a recent concept, adopted for HIV and other viruses.

Many reasons are postulated to explain the different lesions observed in the brain such as the different susceptibility of the various cellular populations, different effects of viruses on the cells (lysis, latency, fusion, modifications), and the need for viruses of specific receptors on the cells.

The CNS reaction in viral encephalitis is somewhat stereotyped, with no peculiar variations related to different viruses.

Macroscopically (Fig. 4A), nervous tissue involvement ranges from mild edema and minimal softening to large areas of necrosis and encephalomalacia.

Elementary tissue changes, presenting individually or in combination, are:

1. Inflammatory infiltrates, formed by granulocytes in the acute phase, and then by plasma cells and macrophages in perivascular sites
2. Microglial proliferation located around dying neurons (neuronophagia) or clustered in groups in the white matter (glial stars)
3. Astrocyte modifications with hyperplasia of the protoplasmatic cells and hypertrophy of the fibrillar cells, with an increase in fiber production (gliosis)
4. Neuronal alterations from cellular swelling to death
5. Inclusion bodies, mainly intranuclear, related to viral particles

Fig. 3A–E. Fungal disease: cryptococcosis. **A** Neuropathology: distension of the perivascular spaces, filled with mucoid gelatinous material (soap bubbles). **B** MRI coronal T1 w.i. after contrast administration: small, rounded hypointense cysts in the perivascular spaces, which appear dilated and with very mild contrast enhancement, for the poor brain reaction to the yeast colonies. **C** MRI axial FLAIR: multiple cysts in the perivascular Virchow–Robin spaces. **D** MRI axial T2 w.i. and T1 w.i. after contrast administration: multiple periventricular medium-sized cysts with no contrast enhancement after contrast administration. **E** Neuropathology: cryptococcal soap bubbles around vessels

Neuroradiologically (Fig. 4B), MRI features vary widely. In mild forms, some degree of edema is visible, in MRI as initial alteration of the physiological signal of the brain. In severe forms, large symmetrical areas of malacia in the hemispheres appear as zones of hypointensity in T1 w.i., and hyperintensity in long TR w.i.

MRI is more sensitive than CT, revealing more extensive involvement of the gray and white matter. Hemorrhagic complications are well depicted in the acute, subacute and chronic phases of the transformation of hemoglobin, as areas of signal alterations related to the magnetic susceptibility of the breakdown products.

It is typical to find:

- Hypointensity in T1 w.i. and hyperintensity in long TR w.i. in the acute phase of deoxyhemoglobin
- Hyperintensity in T1 w.i. and hypointensity in long TR w.i. in the early subacute phase of intracellular methemoglobin
- Hyperintensity in T1 w.i. and hyperintensity in long TR w.i. in the late subacute phase of extracellular methemoglobin
- Hypointensity in long TR w.i. in the chronic phase of hemosiderin

The most frequent virus responsible for acute viral encephalitides in the adult today is the herpes simplex virus (HSV), type 1, a DNA virus. Despite the ubiquity of the HSV in the population, encephalitis is very uncommon (two to four cases per million every year). One-third of the cases result from primary infection, mostly in young patients less than 18 years old, whereas the remaining two-thirds are presumably related to reactivation of HSV latent in the nervous tissue (trigeminal Gasser ganglion in 50% of cases) after the primary infection. But only 10% of patients have experienced recurrent mucocutaneous infections (herpes labialis), and herpes simplex encephalitis (HSE) is not more common in immunocompromised patients. For these reasons pathogenesis, initially related to situations of immune system dysfunction, is still unclear.

Clinically the patient, generally a young adult, rapidly deteriorates in few days with seizures and behavior disturbances that may include coma.

An accurate and early etiological diagnosis suggests adequate therapy, with a dramatic reduction in the incidence of death (20% of cases) and sequelae (20%).

HSE is a necrotizing hemorrhagic meningoencephalitis, involving the temporal lobe(s) and the orbital surface of the frontal lobe(s), with diffusion of the infectious process by contiguity to the insula (sparing the lenticular nucleus), the cerebral convexity and along the efferent connections of the hippocampus to the cingulate gyrus.

Macroscopically, the temporal lobe involved is soft and swollen: the infective process produces meningeal inflammation and involves asymmetrically the temporal lobes, particularly the medial part, hippocampus, amygdala, cingulate and insular cortex, with cortical areas of edema and necrosis for neurons and astrocyte death related to cell-to-cell spread of the viruses, and softening of the adjacent white matter. Petechial hemorrhages are very common for vessel wall necrosis.

In survivors, necrosis leads to cysts and wrinkles.

Microscopically, areas of neuronophagia and inflammatory infiltrates with lymphocytes and macrophages, oligodendroglial intranuclear bodies are present.

Neuroradiological aspects reflect neuropathology. The necrotic areas are depicted as zones of hypointensity in T1, hyperintensity in proton density and T2 w.i. with fairly infrequent hemorrhagic complications, identified as fairly large areas of signal alteration, which is related to hemoglobin breakdown. Contrast enhancement takes the form of meningeal inflammation, with gyriform patterns and ill-defined linear parenchymal enhancement (Fig. 5A, B).

Dedicated sequences (FLAIR, and diffusion weighted images (DWI) could show subtle tissue alterations (Fig. 5C, D).

Visualization of the leptomeningeal and cortical involvement is more difficult, sometimes disclosed by the sulcal and gyral enhancement after contrast administration, along temporal lobes, the subfrontal area, and insula. This pattern could be enhanced using magnetization transfer images.

In survivors, cerebral destruction is more widespread than that of the initial lesions depicted by neuroradiological studies, with encephalomalacia and dystrophic calcifications of the border zones more common in children.

The imaging modality of choice is MRI, because of its sensitivity to the initially mild degree of edema; when CT becomes positive, in the great majority of cases diagnosis is too late to allow efficient pharmacological treatment.

Subacute sclerosing panencephalitis (SSPE or von Bogaert disease) and progressive multifocal leukoencephalopathy (PML) are classic examples of reactivation of the latent form with chronic phenomena. The first is caused by a persistent measles viral infection. The incidence is rare, decreased after immunization initiation in 1963 (risk, 8.5/million cases of natural measles infection, and now the risk 0.7/million cases after immunization). The age of onset is 5–15 years in 85% of cases. It is very rare in the adults. The suggested pathogenesis involves the accumulation of incomplete measles virus, due to defective synthesis from the guest cell of a viral protein (M), essential to the assemblage of the virus, that cannot be cleared by B- or T-cell mechanisms.

Clinically after a long interval of 8–12 years after the measles or immunization, behavioral changes occur followed by seizures, movement disorders and dementia. Rapid clinical worsening (1–3 years) leads to death.

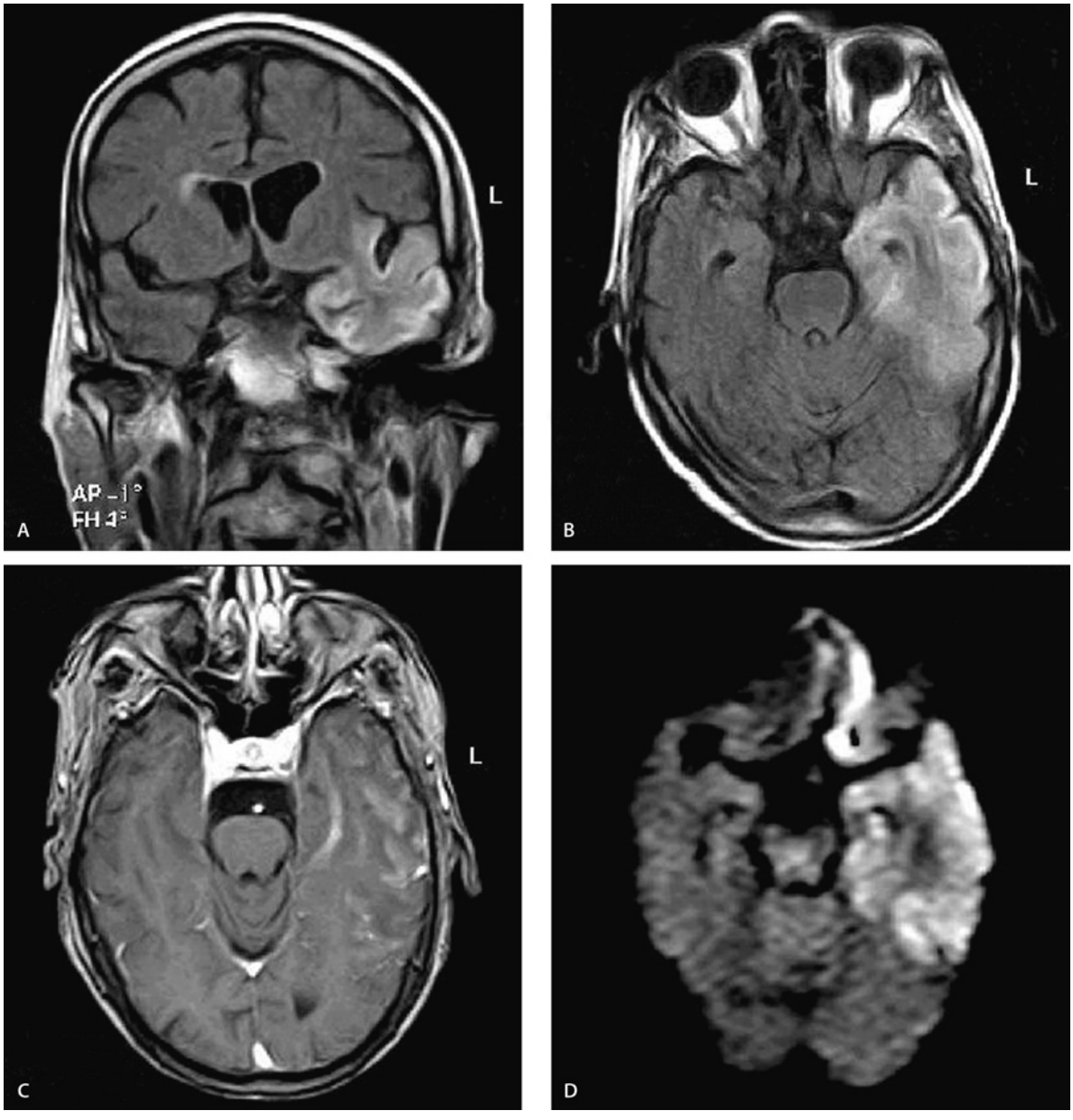

Fig. 5A–D. Herpes simplex virus (type 1) encephalitis (acute stage). **A, B** Axial spin-echo FLAIR. **C** Axial spin-echo T1-weighted MR image after contrast administration. **D** Diffusion-weighted (DW) MR image. Meningoencephalitis involving the left temporal lobe, with contrast enhancement of the meninges and cortical areas. Diffusion of the process to the homolateral frontal lobe, better defined by DWI

The panencephalitis involves the cortical and subcortical gray and white matter and blood vessels, with an increasing number of glial cells beginning in cortical gray matter and further diffusion to subcortical gray and white matter and later to the brainstem. The brain on macroscopic inspection appears normal or with increased consistency. Occipital lobes, hippocampi and medial thalami are the areas that are most severely afflicted.

The particular feature, spongiform encephalopathy, is related to gliosis of the white matter with hypertrophic astrocytes, prevalent on demyelination.Neuronal loss, microglial proliferation, neuronal and oligodendroglial intranuclear inclusion bodies are the other frequent microscopic aspects.

MRI follows neuropathological events and reveals the pathological process with focal, periventricular, high-T2-intensity white matter changes. Severe diffuse

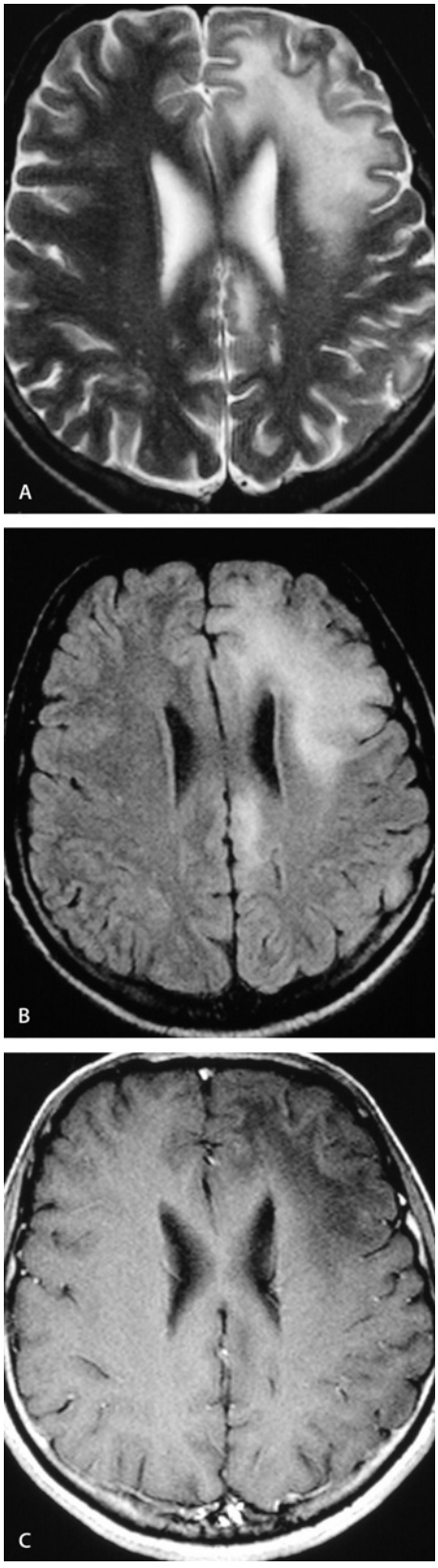

atrophy, predominantly in the white matter, accompanies the progression of the disease. Cortical gray matter changes are infrequent.

PML is caused by JC virus, a polyoma virus of the Papova family. It typically causes a subclinical infection, and the majority of humans worldwide have been infected. Its DNA may be detected in healthy human tissues where it causes a persistent virus infection, reactivated by a situation of immunosuppression. The clinical picture is very severe with poor prognosis (3–9 months until death). Pathologically, the virus attacks subcortical oligodendrocytes leading to demyelination and necrosis. Bizarre, hypertrophic astrocytes bind areas of demyelination. The white matter lesions are typically bilateral (although asymmetrical in their degree of involvement), confluent, and multiple: MRI reveals a multifocal leukoencephalopathy. The lesions are asymmetrical in sites and extension, with a subcortical debut: their external contour is frequently finger-like, and this aspect is very suggestive for diagnosis. The most common sites are the periventricular white matter, centrum semiovale, and subcortical white matter, with a predilection for parietal lobes in AIDS patients; the posterior location suggests PML diagnosis. Posterior fossa locations such as cerebellum and brainstem occur. Sometimes involved areas are confluent, resembling a diffuse leukoencephalopathy.

In MRI the lesions have low signal intensity on T1-weighted images and hyperintense signal on T2-weighted images, generally attributed to demyelination. In follow-up studies, the hypointensity in T1 w.i. could increase because of further myelin destruction culminating in more extensive areas of necrosis, as supported with proton MR spectroscopy in which choline, a marker of cellular membrane integrity, is elevated in PML patients.

The T1 prolongation (necrosis) and the aspect of the edges of the lesions are very useful for the differential diagnosis with HIV encephalitis (Fig. 6A–C).Contrast enhancement of the lesions is extremely rare for the situation of a reactivation inside an intact blood–brain barrier. It may occur in cases of primary infection.

No MR abnormalities significantly correlated with patient survival, with the exception of mass effect, which was significantly associated with shorter survi-

Fig. 6A–C. PML Leukoencephalopathy. **A** Axial spin-echo T2-weighted MR image. **B** Axial FLAIR MR image. **C** Axial spin-echo T1-weighted MR image after contrast administration. Subcortical white matter encephalopathy: low signal intensity on T1-weighted images and high signal on FLAIR and T2-weighted images, with no contrast enhancement. The peripheral edge of the lesion is finger-like. This aspect along with hypointensity in T1 w.i., for demyelination and necrosis, suggests the PML diagnosis

val. The mass effect, however, always minimal, was infrequent.

CT is similarly diagnostic, revealing areas of hypodensity in the white matter, with finger-like peripheral edges, preferentially in the parietal and occipital lobes.

The chronic forms of PML are caused by slow viruses or unconventional viral agents such as prions. A paradigmatic example of a slow virus is HIV infection. HIV belongs to the retrovirus family, a family of RNA viruses, with a reverse transcriptase that transcribes viral RNA into provirus DNA, which is integrated into the host-cell genome. HIV is transported to the brain by infected macrophages, which, after adhesion to endothelial cells, cross the blood–brain barrier. Viral replication occurs within macrophages and microglial cells, and viruses have been detected in astrocytes, vascular endothelial cells, and neurons. Production of neurotoxins (e.g., cytokines, inflammatory mediators, viral proteins) induces excessive calcium influx, leading to neuronal death.

This situation causes a progressive reduction in brain volume (cerebral atrophy) and/or a picture of gradual myelin pallor ending in demyelination (leukoencephalopathy) and perivascular nodules of microglia cells, monohistiocytes, and macrophages (focal encephalitis). Atrophy is disclosed as the progressive expansion of the subarachnoidal spaces and of the ventricular system, with the cortex mainly involved, whereas in non-HIV seropositive older patients atrophy starts centrally.

The brain volume reduction is a valuable predictor of neuropsychological impairment and clinically apparent cognitive/motor dysfunction among HIV-infected persons.

Encephalitis correlated with AIDS dementia complex (ADC) is characterized by multiple discrete foci of high signal intensity described on T2-weighted and FLAIR sequences, with isointensity in T1 w.i. These lesions are in the periventricular and subcortical areas, with a punctuate or nodular aspect, varying in size and number.

Progression of white matter focal lesions due to HIV is seen only in a minority of HIV+ subjects over a 2-year time period, only in those who are neurologically symptomatic, and correlates with clinical deterioration, whereas these nodules do not change in size and number in HIV+ subjects who remain neurologically asymptomatic.

Preliminary studies suggest that the patients with ADC who respond to potent antiretroviral regimens present an improvement of the neurological dysfunction along with neuroimaging findings, indicating that the disease may be at least partly reversible.

Leukoencephalopathy has MR images of T2 elongation starting from the centrum semiovale, and then involving the myelinic projections to the brainstem, with isointensity in T1 w.i. The signal alterations are symmetrically distributed, with edges regular and parallel to the ventricular cast (Fig. 7A, B).

Use of the FLAIR may improve the detection of the HIV lesions.

Creutzfeldt-Jakob disease (CJD)is the most frequently cited example of chronic encephalitides caused by unconventional agents.

CJD occurs worldwide. It is very rare, with an incidence of about one case per million population. While most cases are sporadic, 5%–10% are familial. In the familial form, CJD is inherited as an autosomal dominant condition.

The clinical presentation of the forms affecting humans is progressive dementia and cerebellar dysfunction. The condition is relentlessly progressive and patients usually die within 1 year of presentation.

Lesions involve cortical areas, striatum, medial thalamus, and cerebellum. The brain is almost normal or slightly atrophic. Microscopic alterations are neuronal loss, astrocyte alterations, and spongiform changes. These differ from the spongiform degeneration because the vacuoles are included in the cells.

Although the specificity of routine MR imaging for sporadic CJD may be as high as 93%, the sensitivity in detecting abnormalities is only 67%–79%. When observed, the abnormalities generally appear late in the course of the disease, thus limiting the diagnostic value of routine MR imaging.

MRI showed increased signal intensity in all the sequences in the striatum, thalamus, and cerebral cortex (Fig. 8A–D).

Although approximately 20% of patients did not have MR imaging abnormalities, MR imaging shows signal intensity alterations due to gliosis and spongiform changes early in the course of CJD in the remaining 80%.

In the early stage of the disease, MRI reveals symmetrical or asymmetrical high signal intensity of the basal ganglia in T2 w.i., predominantly in the caudate nuclei and the putamina, a suggestive finding. Recent studies have proposed the high signal in the globus pallidus in T1 w.i. as a new neuroradiological sign for the CDJ diagnosis.

In the terminal stage, the findings are diffuse involvement of the gray and white matter with atrophy and leukoencephalopathy.

Using DWI in patients with suspected CJD, the basal ganglia and/or cortical alterations detected could support an early diagnosis, with the spongiform neuronal degeneration altering the molecular motion of water.

The immune-mediated forms (acute disseminated encephalomyelitis, ADEM) are diseases with many features common to demyelinating syndromes such as multiple sclerosis. The frequency of the disease is uncertain, but certainly underestimated.

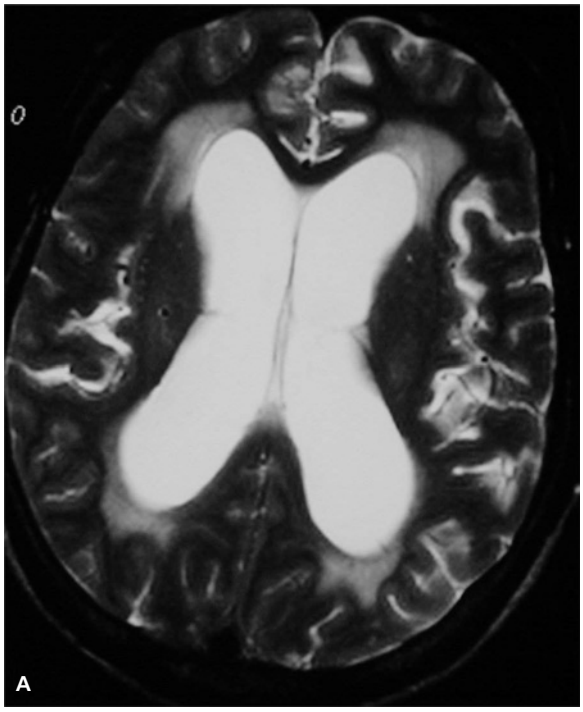

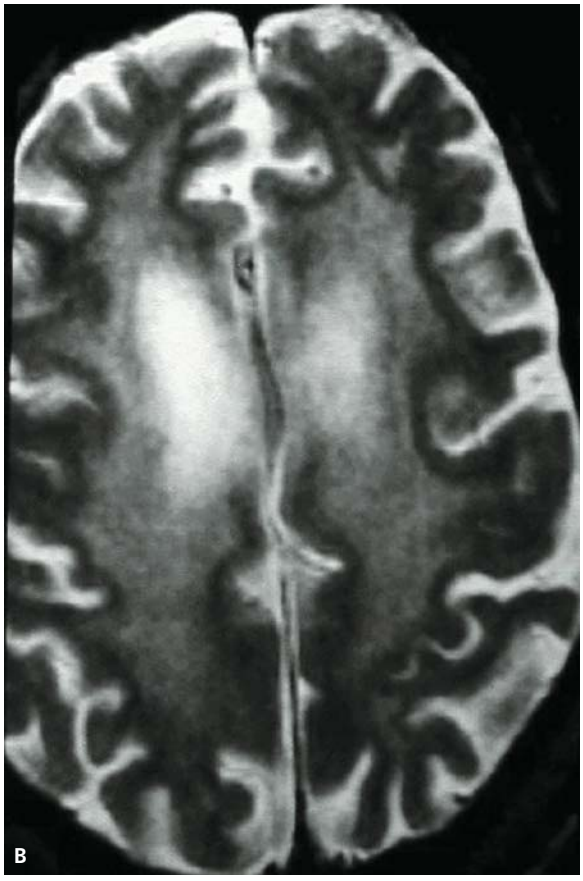

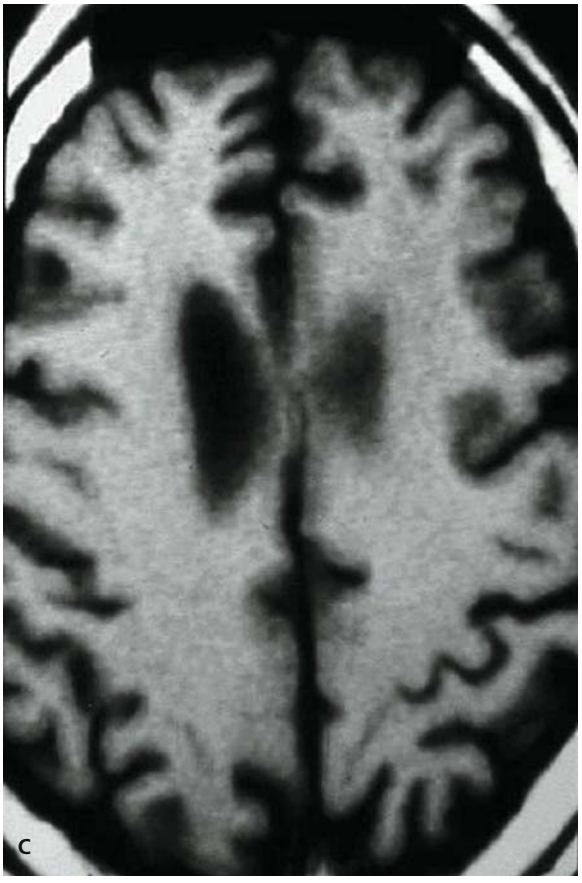

Fig. 7A–C. HIV leukoencephalopathy. **A** Coronal spin-echo T2-weighted MR image. **B** Axial spin-echo T2-weighted MR image. **C** Axial spin-echo T1-weighted MR image. Leukoencephalopathy with hyperintensity in T2-weighted MR image, isointensity in T1-weighted MR image symmetrically distributed, with edges regular and parallel to the ventricular cast

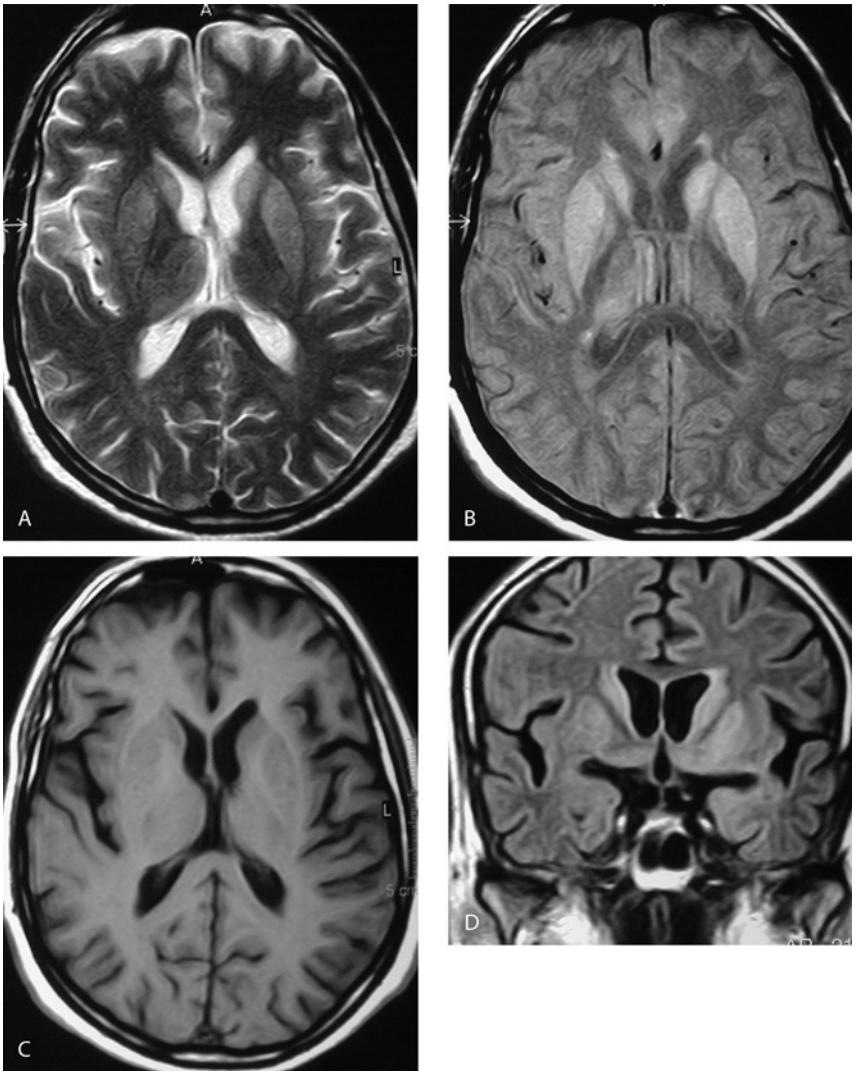

Fig. 8A–D.
Creutzfeldt-Jakob disease. **A** Axial spin-echo T2-weighted MR image. **B** Axial spin-echo proton density-weighted MR image. **C** Axial spin-echo T1-weighted MR image. Symmetrical high signal intensity of the basal ganglia in PD and T2 w.i., predominantly in the striatum

The immune-mediated encephalitides are closely related to mild viral infections, vaccinations, but – not rarely – they can be of unknown origin.

Pathogenesis is surely multifactorial,: it presumably depends on the missed recognition of the myelin as its own component (self-recognition) the liberation of segregated antigens by viral cellular destruction (autoantigens), or cross-reactions among viral components and myelin constituents.

A hemorrhagic, hyperacute variant of ADEM (AHEM/AHLE or Hurst disease) has also been described. The course of ADEM is usually monophasic and affects children more commonly than adults. The process has been established 7–15 days from a viral illness, determining the appearance of neurological multifocal symptomatology, sometimes complicated with stupor and coma.

The myelinoclastic effects of these infections appear to be histologically indistinguishable from that observed in experimental allergic and postvaccinal encephalomyelitides. ADEM is associated with a significant mortality of 10%–30%. About 20%–30% of patients who survive are left with neurological sequelae. In 75% of cases, the illness is self-extinguishing with almost always complete clinical recovery; sometimes mild neurological sequelae remain, with scars that can be seen neuroradiologically.

The neuropathological features are perivascular infiltrates with lymphocytes and plasma cells, demyelination areas along the veins, microglial proliferation and astroglial hypertrophy In MR imaging, ADEM causes multiple sclerosis (MS)-like, but more asymmetrical, white matter lesions.

The ADEM-related changes in MR imaging scans include multiple hyperintense lesions seen in T2-weighted, FLAIR, and proton density PD images, isointense and or hypointense in PD and T2 w.i., with frequent contrast enhancement. The lesions may be large and

confluent, occupying almost all of the white matter, but smaller lesions resembling those of MS are common. The lesions seen in ADEM are often located in the rim of the occipital and parietal regions, including the centrum semiovale, in the thalami, and frequently in the brain stem and spinal cord.

In several reports, these lesions have been documented to show up in the first MR imaging scans performed shortly after the first symptoms. Disappearance of these lesions has been suggested to be associated with clinical recovery.

Although ADEM typically is a monophasic illness, and the lesions would be expected to appear and mature simultaneously; new lesions may be seen on follow-up MR imaging scans. The lesions may or may not enhance with contrast medium, and a mixture of enhancing and nonenhancing lesions, depending on their age, may be seen. They may also resolve gradually up to 18 months after the onset of the symptoms.

In some cases the onset of the symptomatology is of the vascular type: acute and sudden, followed in a few days by multifocal neurological deficits. This clinical pattern represents the vasculo-encephalomyelitis form, sustained by an immune-mediated mechanism consisting in arteritis and demyelinating lesions. MR images reveal an area of ischemia in the territory of an artery of medium caliber (in particular the middle cerebral artery) with multifocal white matter lesions.

In everyday neuroradiological practice, there is often a differential diagnosis problem between these lesions and those of multiple sclerosis, especially in teenagers. The problem of the similarity in MRI pictures between these two diseases is often raised, but not in presence of a clinical picture debut with severe alteration in the state of alertness and convulsions: MS rarely starts out this way. ADEM diagnosis should be suggested by the neuroradiologist considering symmetry in the distribution of the lesions, rhombencephalon and thalamic location, rare involvement of the corpus callosum, simultaneous enhancement of the lesions (all in the same phase of activity), and the clinical support of almost complete recovery. Other elements such as the involvement of the white matter underlying the gray matter (corticomedullary junction) and centrum semiovale, and the lesions' signal characteristics are similar to MS signs and are not suggestive.

On the contrary, in MS the contrast enhancement of the lesions after contrast medium administration occurs in different stages (multiphasic illness), also within the same demyelinating lesion.

Viral infections during the ontogenesis cause congenital malformations of the central nervous system. Viruses considered responsible for such diseases are cytomegalovirus (CMV) and rubeolla virus.

CMV in the first trimester of pregnancy infects germinal matrix cells, producing disorders of neuronal migration, ranging from the very severe forms of lissencephaly to the nonlissencephalic cortical dysplasias. Microencephaly, microcrania, and periventricular calcifications are the most frequent aspects. Otherwise, a late pregnancy CMV infection determines areas of encephalomalacia.

Rubeola virus effects on CNS are closely related to the moment of infection during pregnancy. If fetus–mother contagion occurs early, severe cerebral, visual and auditory system malformations appear, whereas later infections produce meningoencephalitis and vasculitis with cerebrovascular disorders. Delayed, chronic forms quite similar to SSPE are reported, although they are rare.

Focal Lesions

These lesions are divided into immature and mature forms, and cysts. The initial localized parenchymal area of infection is the cerebritis, immature form. Anatomopathologically it is an ill-defined zone of dense, acute inflammatory infiltrate with rare areas of necrosis surrounded by acute inflammatory cells coming from perivascular cuffing.

MRI is, as always, more sensitive than CT and shows a localized area of edema, mildly hypointense in T1 w.i., hyperintense in T2 w.i. In the late stage of cerebritis, contrast enhancement appears, from faint to marked, ill-defined to nodular or ring-like, with diffusion of contrast medium centrifugally and centripetally in delayed scans.

Over time the areas of necrosis become confluent with the border formed by dense granulation tissue. The host becomes able to circumscribe the infection, using fibroblasts to build the capsule. These cells come from vessels and neovascularity plays an important role in this type of defense.

This stage of seclusion represents the mature form: abscess or granuloma. Macroscopically (Figs. 9A, 10A) the mature lesion is a well-defined area of brain softening, with petechial hemorrhages surrounded by a clearly visible wall.

On histological examination, the center of the lesion is formed by necrotic material: around it are granulation tissue and a network of collagen fibers, produced by fibroblasts. Outside the macrophages ring mobilizes the debris, and around it an area of cerebritis with neovessels and gliosis is found.

The capsule increases its thickness in time up to 3 mm: it is located in the white matter at the corticomedullary junction and is thicker in the part facing gray matter for greater vascularity.

Abscess differs from granulomas in the organisms involved, the primarily participating cellular lines, and the necrotic center. The organisms producing abscess

are bacteria, and the types are related to the pathogenetic mechanisms: we have found aerobic staphylococci complicating trauma, anaerobic agents – such as *Bacteroides* – in mastoid and paranasal sinus infections. Other nonbacterial germs implicated are *Nocardia*, mycobacteria, and fungi such as *Candida*.

Daughter abscesses are related to the virulence of the germs. They grow through the weaker part of the capsule.

Polymorphonuclear neutrophils are the involved cells, and therefore the necrotic material is purulent, with a yellowish, creamy aspect.

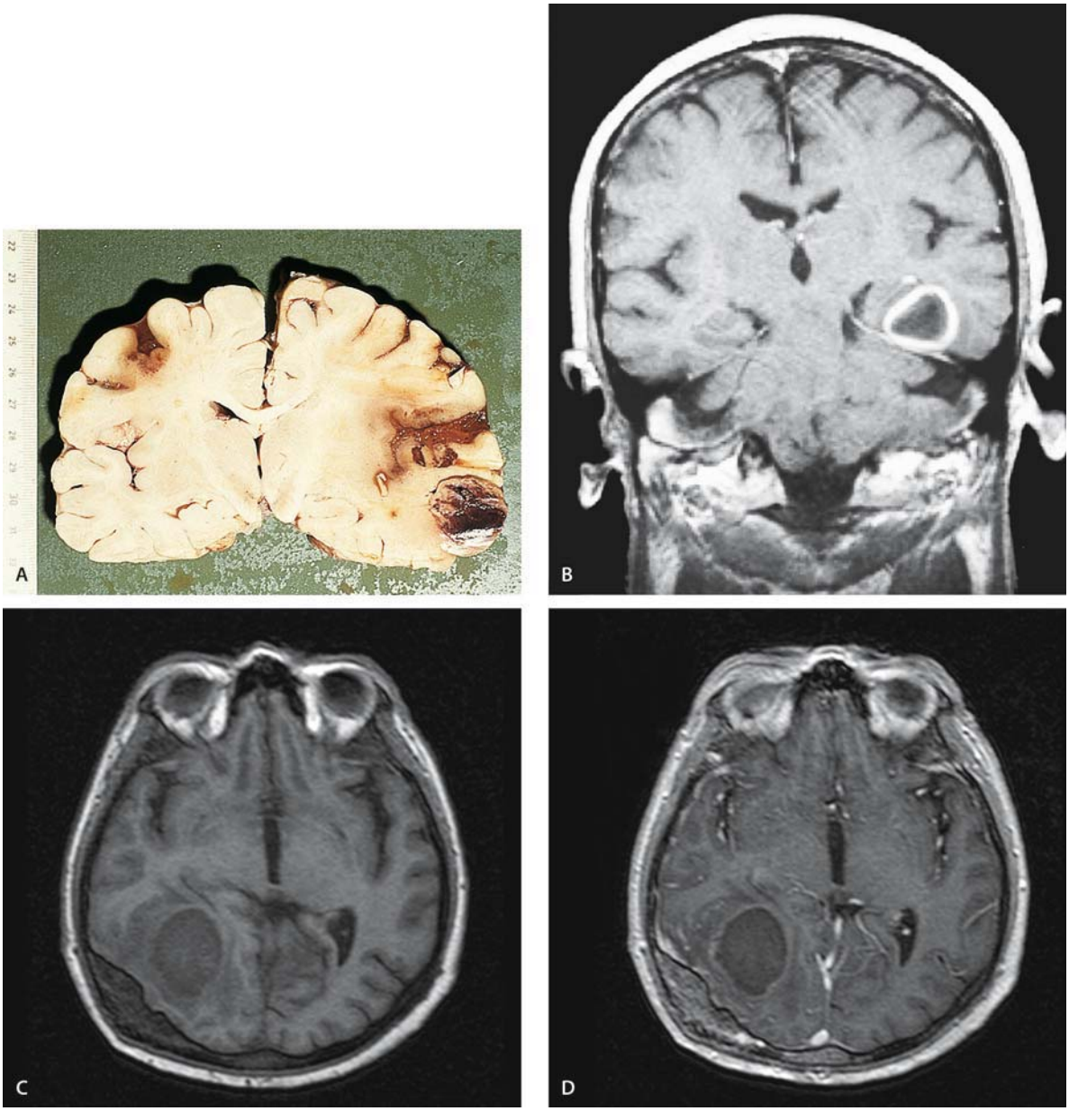

Fig. 9A–J. Two cases of bacterial abscess. First case: **A** Neuropathology: large bacterial abscess in the temporal lobe well defined by a fibrous capsule, surrounding a necrotic purulent center. **B** MRI coronal T1 w.i. after contrast administration: large hypointense necrotic center surrounded by a regular marked contrast enhanced ring, with smooth outer and inner borders, thicker in the part facing gray matter. **C** MRI axial T1 w.i.: oval lesion with hypointense center, and slightly hyperintense ring related to capsule. **D** MRI axial T1 w.i. after contrast administration: the center remains hypointense whereas the capsule becomes ringed contrast enhanced. **E** MRI axial FLAIR: hyperintense center with slightly hypointense ring related to capsule. **F** MRI axial DWI: hypointense center confirming the abscess nature of the lesion. Second case: **G** MRI axial T1 w.i. after contrast administration: hypointense center remains with ring. **H** MRI axial FLAIR: isointense center with hypointense ring related to capsule. **I** MRI axial DWI: hyperintense center confirming the abscess nature of the lesion. **J** MRI axial ADC: hypointense center confirming the abscess nature of the lesion

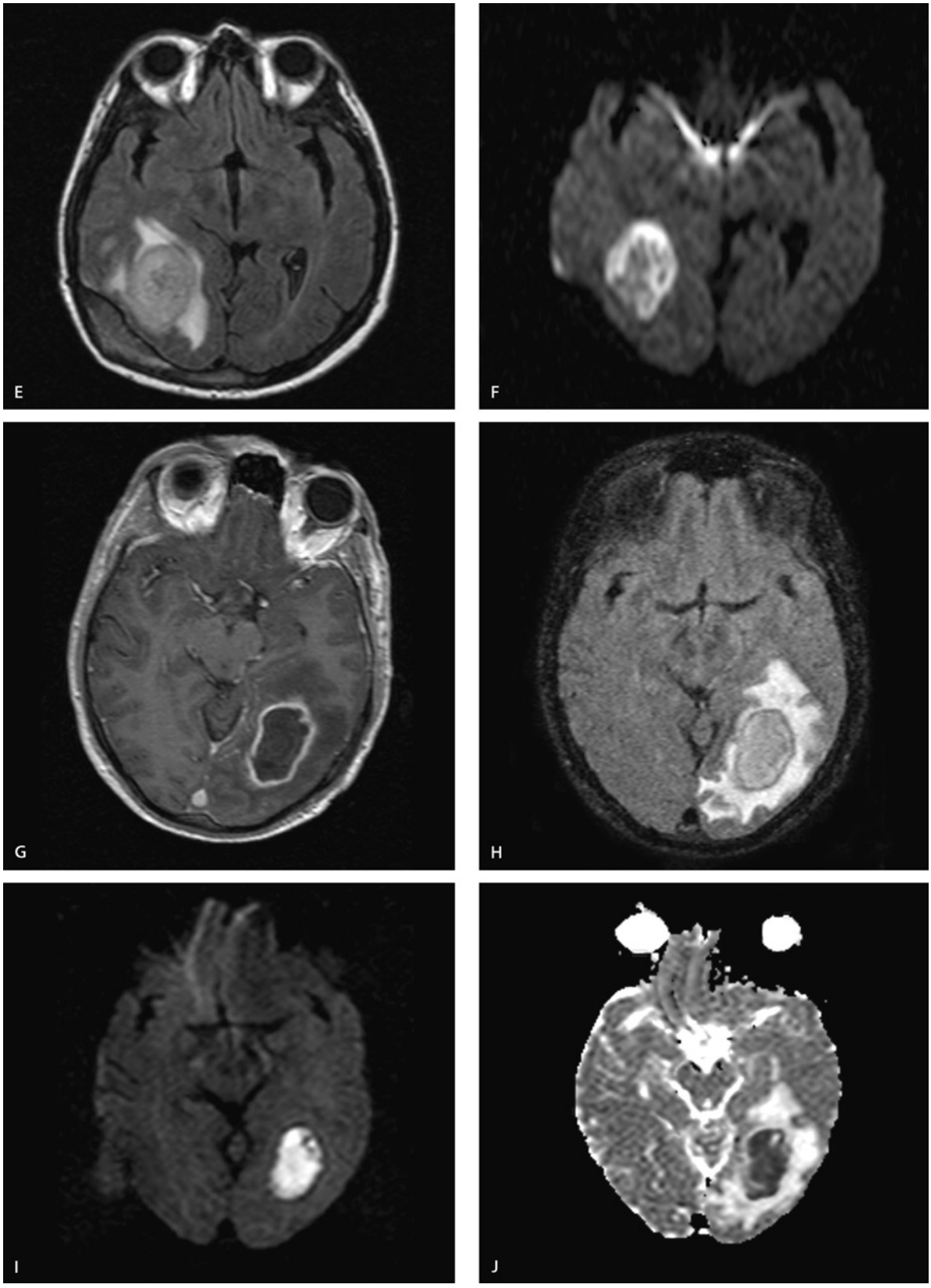

Fig. 9E–J.

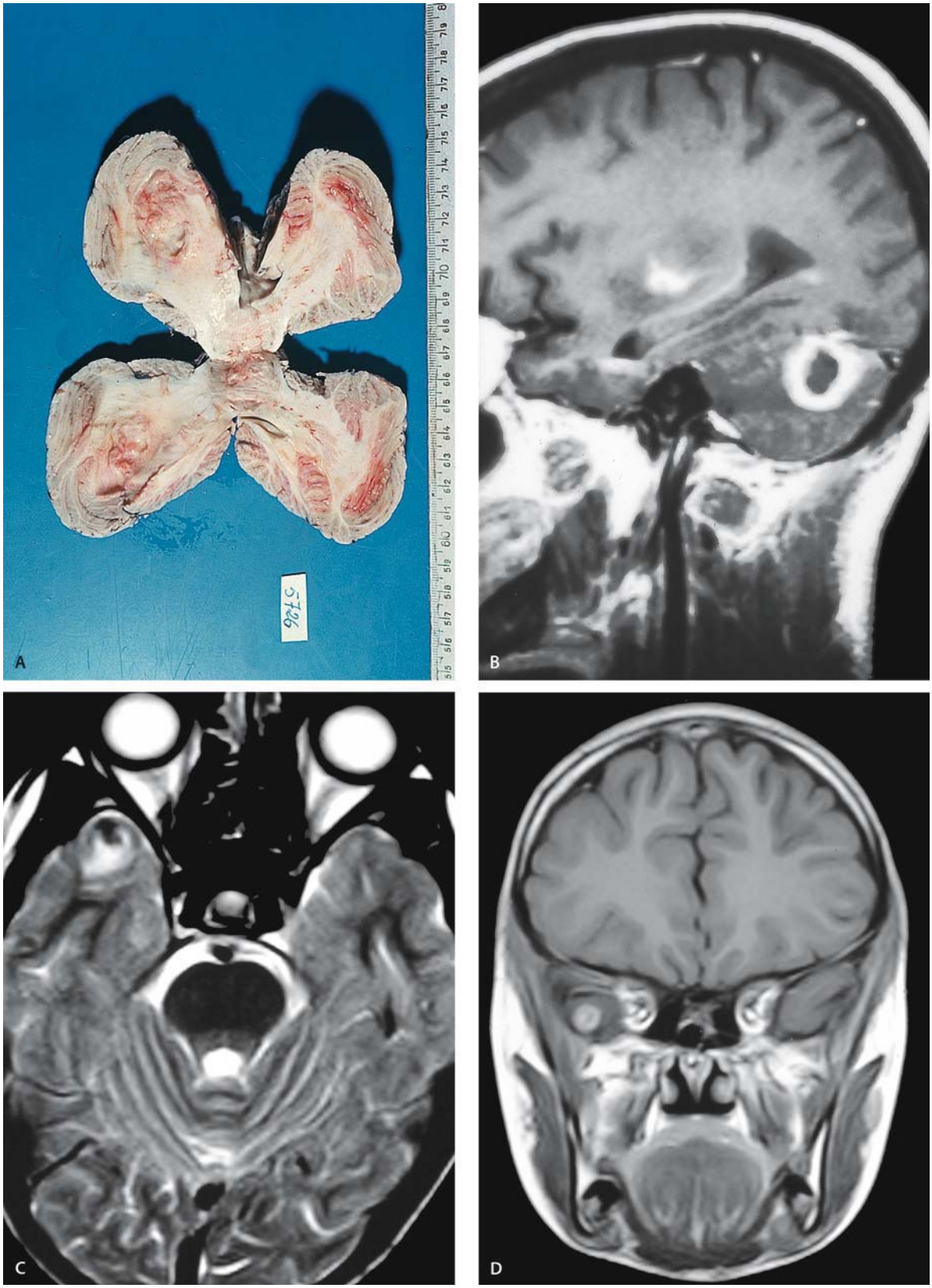

Fig. 10A–D. Granuloma. **A** Neuropathology: central caseated necrosis walled off by fibrosis capsule in cerebellar hemisphere. **B** MRI sagittal T1 w.i. after contrast administration: oval lesion with hypointense center, with a markedly contrasted enhanced thick ring, with smooth outer border and irregular inner border. Perifocal edema. **C** MRI axial T2 w.i.: hypointense center related to caseum. **D** MRI axial T1 w.i. after contrast administration: the punctuate center is hypointense, and the capsule has a thick ring enhancement

The organisms producing granulomas are *Nocardia*, mycobacteria, fungi (*Aspergillus fumigatus*), protozoa (*Toxoplasma gondii*), and parasites (*Schistosoma*).

Epithelioid, giant cells, plasma cells and lymphocytes are the cell lines involved, and consequently the necrotic center is caseous, grayish and firm, with calcium deposition on the capsule at the end-stage.

Neuroradiologically, such differences in the necrotic center are appreciable only by MRI (Figs. 9B, 10B). Necrosis of granulomas is of the caseous type, with an inhomogeneous MRI signal in all sequences, especially in T2 w.i. with prevalence of hypointensity (Fig. 10C, D), whereas in abscess the necrosis is suppurative with a low signal in T1, and a homogeneous high signal in FLAIR, T2 and proton density w.i.(Fig. 9H, E).

Immediately surrounding the mature lesions there is the capsule, which has a slightly hyperintense signal, quite similar to the normal nervous tissue in T1 w.i., but it is better appreciated because of the interposition among the T1 hypointensity of the necrosis and the perifocal edema (Fig. 9C).

In FLAIR and T2 w.i., the macrophage ring appears as a hypointense line thought to stem from the presence of free radicals, produced in the perossidative trial from the macrophages of tissue destruction (Fig. 9H, E).

The external surface of the capsule shows ring enhancement after administration of contrast medium in the T1 w.i., because of the alteration of the BBB on the inflammatory base, with an increase in vascular permeability (Figs. 8B, D, G, 10B).

The surrounding edema with a hypointense signal in T1 w.i. and a hyperintense signal in T2 w.i. shows only rare zones of permeability to the contrast medium.

Diffusion MRI appears to be a sensitive method for differentiating abscesses from necrotic neoplasms in doubtful lesions. An abscess has a high signal on diffusion images and a low signal and low ADC values on ADC maps (Fig. 9C–L). Contrary findings are usual for necrotic cystic tumors, but these features are not pathognomonic.

In the era of antibiotics, focal lesions of the brain are rare, but the worldwide spread of AIDS with many opportunistic diseases has brought such lesions back to the forefront.

The most frequent opportunistic agent during the course of AIDS is *Toxoplasma gondii*, which is an obligatory intracellular parasite. It is widespread in nature and found in the excreta of domestic animals (especially cats) and in the meat of contaminated or infected mammals.

Apart from connatal cerebral toxoplasmosis with characteristics of encephalitis, in adults the first infection is subclinical, and the toxoplasma that survives forms cysts in some organs, brain and muscles, where they can live protected and latent for years. In a condition of immunodepression, the process of multiplication restarts and all the cells of the CNS, the immunologically preferred site, are attacked by a cell-to-cell mechanism. Cell death and focal necrosis are caused by replicating tachyzoites: an intense mononuclear inflammatory response in any tissue or cell type infected. Once the cyst reaches maturity, the inflammatory process can no longer be detected, and the cysts remain immunologically quiescent within the brain matrix until they rupture.

Neuropathologically, various type of lesions are reported: cerebritis, granulomas, abscesses and meningoencephalitis (Figs. 11A, 12A). In the AIDS population polymorphonuclear leukocytes, monocytes, lymphocytes, and plasma cells can be found, whereas in non-AIDS patients necrotizing encephalitis occurs with small, diffuse lesions with perivascular cuffing in contiguous areas.

Granulomas and abscesses are multiple, located in favored sites (basal ganglia, corticomedullary junctions), surrounded by extensive edema with a mass effect.

Meningoencephalitis occurs when the host cannot contain infection: along with immature and mature lesions, quite extensive necrosis with hemorrhages appears, related to toxic invasion of the endothelial cells.

Neuroradiologically (Figs. 11B, C, 12B, C), all the lesions are evident with the features already described: the contrast enhancement varies from a nodular to a ring pattern presenting smooth or irregular margins. Histologically, the area of enhancement corresponds to an intense inflammatory reaction, with many intra- and extracellular tachyzoites; in the edema around the lesion free tachyzoites are rare and encysted forms are present.

Cysts

Cystic lesions of the CNS are characteristic manifestations of cestode infections produced at the larval stage of *Echinococcus* and *Taenia solium.*

Echinococcosis is the infection of the larval form of the cestode *Echinococcus*. In the Mediterranean area, *E. granulosus* is the most infesting form, *E. multilocularis* being a rarer form, typical of Central and South America.

Dogs eat sheep offal infected by *Echinococcus* and thus become the definitive host. Humans become infected via foods polluted by the eggs contained in dog feces, or by inadequate hygiene of the hands.

The cerebral location is very rare (2%) in adults, because of the efficiency of liver and pulmonary filters.

The cysts generally are single, spherical and unilocular, and they determine the appearance of focal symptoms only when they reach conspicuous dimensions (>5 cm).

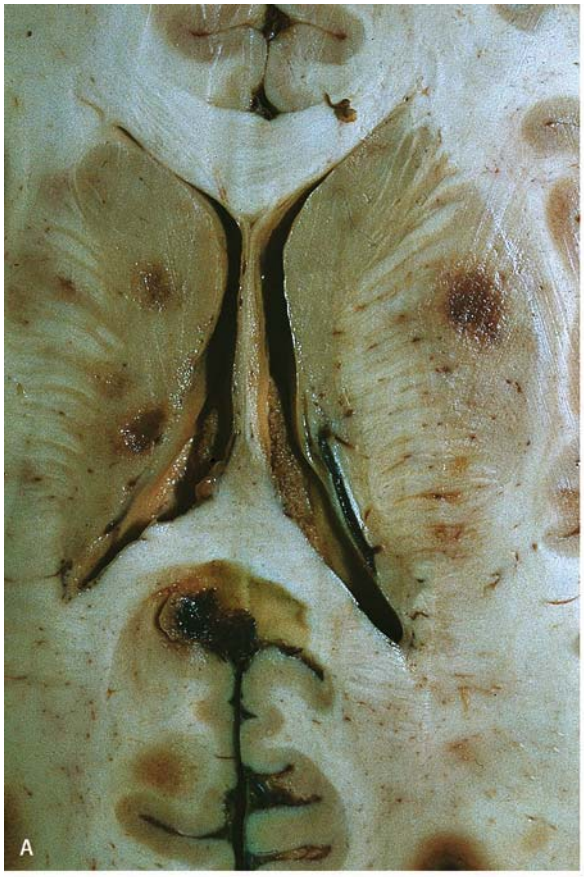

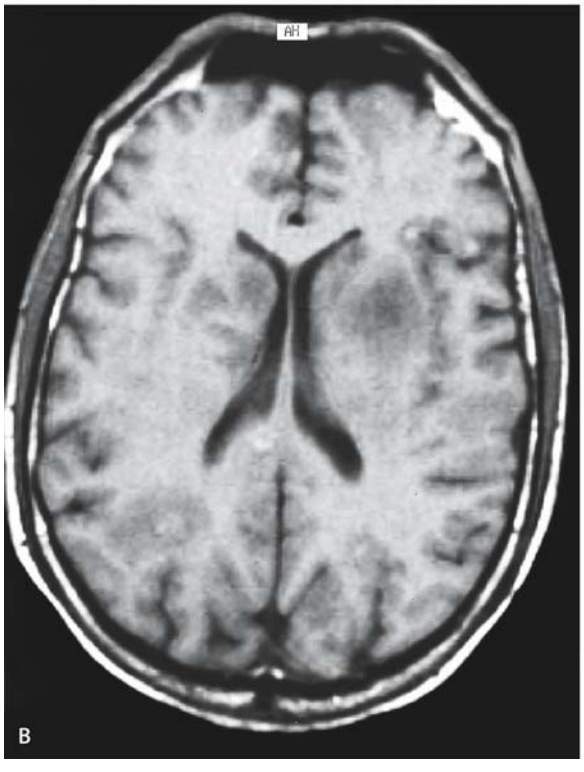

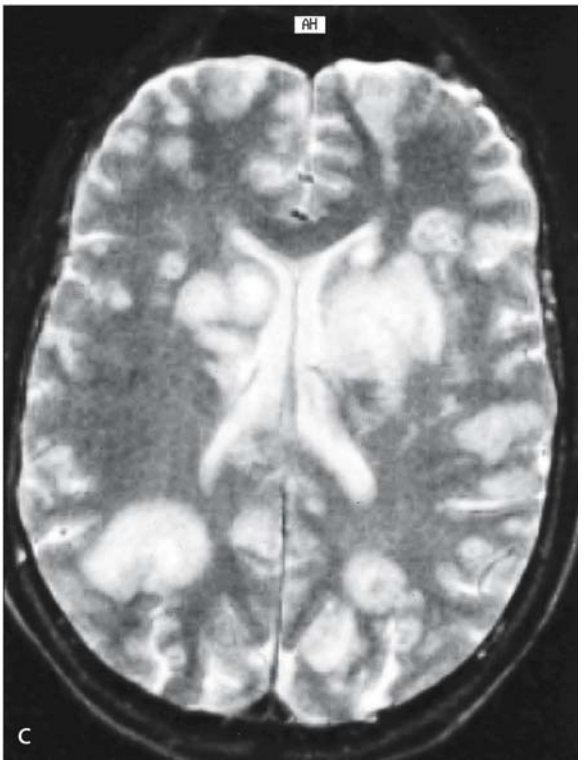

Fig. 11A–C. Toxoplasmosis: cerebritis. **A** Neuropathology: softening and congestion of some localized areas of brain tissue, with small petechial hemorrhage at the basal ganglia and the corticomedullary junctions. **B** MRI T1 w.i. **C** MRI T2 w.i. Multiple areas at the basal ganglia and at the corticomedullary junctions hyperintense in T2 w.i., hypointense in T1 w.i. representing areas of localized edema related to cerebritis

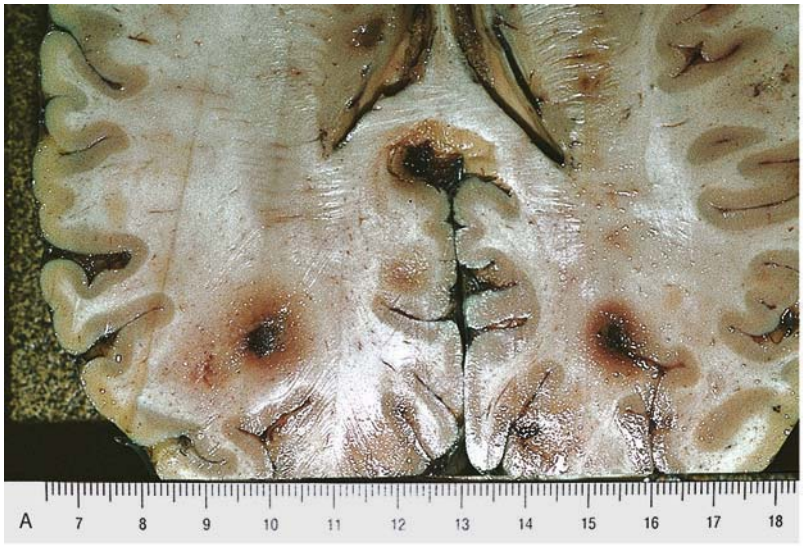

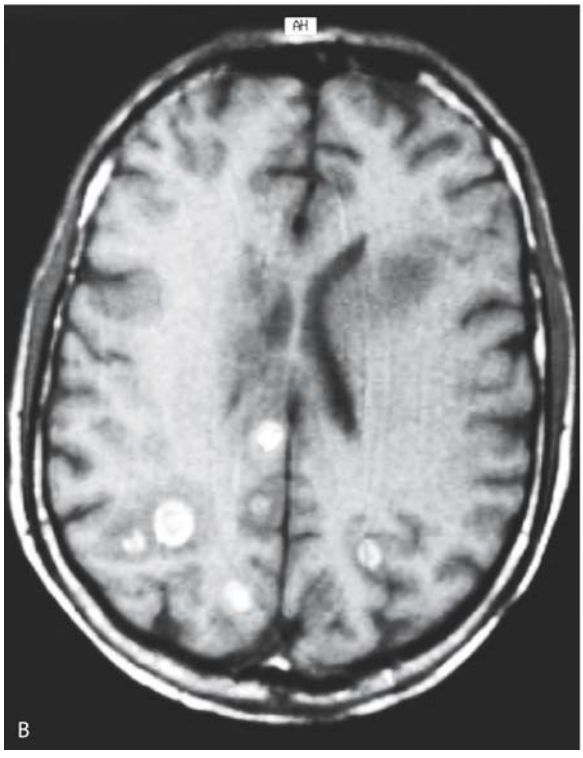

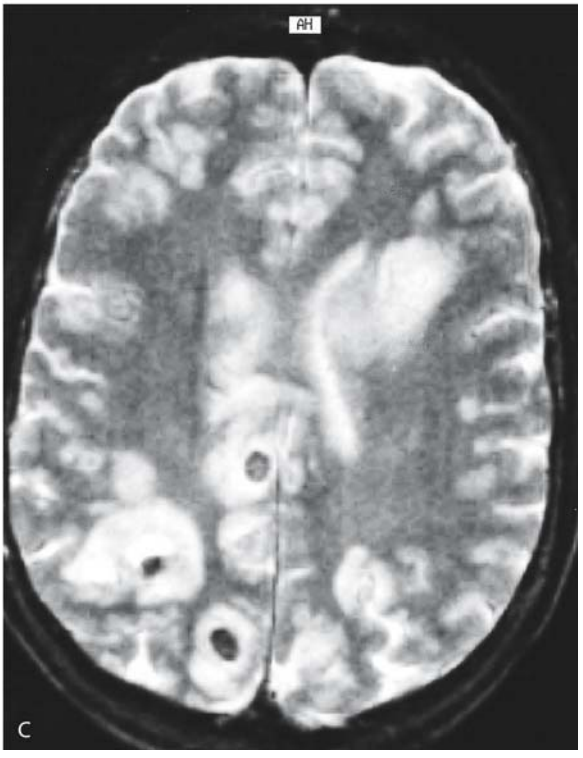

Fig. 12A–C. Toxoplasmosis: hemorrhagic abscesses. **A** Neuropathology: in different locations central hemorrhagic necrosis with a firm concentric capsule of fibrosis, surrounded by a zone of edematous and softened zone in the white matter. **B** MRI T1 w.i. **C** MRI T2 w.i. At the posterior corticomedullary junctions grossly rounded nodules with high signal in T1 w.i., and low signal in T2 w.i. related to hemorrhagic foci in phase of intracellular methemoglobin, in the necrotic center of the abscesses. The capsule is defined by a thin rim of hypointense signal in T2 w.i. slightly beyond the necrosis. Perifocal edema surrounds the areas

Macroscopically, the large size of the cyst flattens the cortex, which appears bluish. The contents are a clear colorless fluid, which usually contains small daughter cysts and scolices. Three layers form the capsule: the inner granular endocyst, the cuticular lamina, and the outer ectocyst formed by fibrous tissue derived from the host. Around it there is poor or no nervous tissue reaction.

On MRI, the lesion appears spherical, large in size, and filled with fluid. It is hyperintense in long TR sequences, hypointense in T1 w.i., with ventricular distortion and a midline shift.

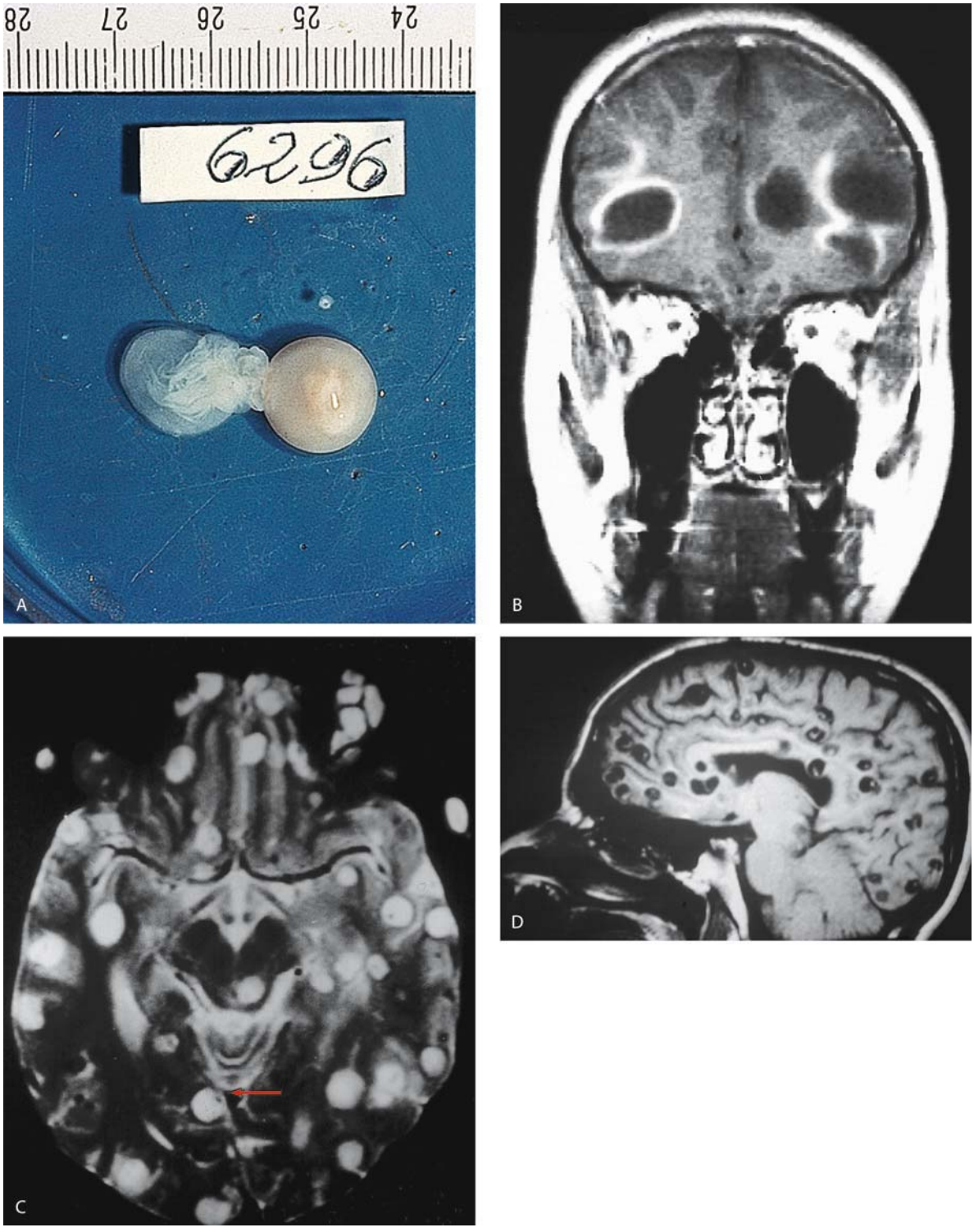

Fig. 13A–D. Neurocysticercosis. **A** Neuropathology: large cyst containing clear fluid, with a tense gray capsule through which a mural, whitish nodule appears where the embryo lives. **B** MRI coronal T1 w.i. after contrast administration: large cysts occupying both the frontal lobes: the right one is completely surrounded by a regular ring of contrast enhancement; in the left lobe two are incompletely circumscribed by the enhanced ring, and the third one has no ring. These different patterns of contrast enhancement represent the various stages of the embryo, which when still alive provokes no brain reaction, and when dying incites acute inflammatory reaction, with capsule formation. **C** MRI axial T2 w.i.: widely diffused multiple cysts. In some of these lesions a hypointense eccentric dot is revealed, corresponding to the scolex (*arrow*)

It is only in the case of partial break-ups of the capsule with transudation of the hydatid liquid, an irritating substance, that a perifocal reaction occurs with edema and a thin rim of enhancement after administration of contrast medium.

The content of the cysts is liquid, with long T1 and T2 but the presence of scolices and hooks (hydatid sand) intensifies the signal in proton density sequences.

Taenia Solium Causes Cysticercosis

Humans are infested with *Taenia solium* by eating contaminated pig meat: the shell of the egg dissolves in the stomach and the embryo penetrates through the intestinal wall, and enters lymphatic vessels and mesenteric venules, disseminating along the hematogenous path.

The dimensions of the cysts, smaller than those found in *Echinococcus*, allow a greater incidence of location in the CNS (up to 10%), with elevated frequency in children (65% with a peak at age 5–10 years). At necropsy the brain may weigh more than normal.

The cysts may be single or in the thousands; they are fluid-filled and lucent with a white spot representing the scolex or the body itself (Fig. 13A). Parenchymal cysts are uncalcified if active or calcified if inactive. Intraventricular and subarachnoid cysts are racemose and are organized as a collection of translucent membranes in the shape of a bunch of grapes.

The cysts – containing living embryos – do not have antigenic action. The nervous system cohabits with such lesions, while the cerebral microglia form only a thin demarcation capsule made up of collagen fibers.

In the first stage of development (vesicular) the parasite is alive and appears as a mural nodule in a small cyst. MRI will disclose the presence of a round lesion with a liquid content (long T1 and long T2), with a thin ring of demarcation, sometimes irregular with an inward propjection (i.e., the nodule). The surrounding tissue will not show signs of inflammatory reaction.

The progressive impairment of the larva will lead to the parasite's death, with liberation of antigenic substances. MRI will follow this process, revealing the variation in the proton density of cysts and the inflammatory response of the surrounding nervous tissue with intense neovascularization and perilesional enhancement after contrast medium administration.

The third phase, in which the parasite is dead, will be disclosed from the appearance of the lesion's degenerative phenomena with consequent precipitation of calcium salts. MRI will show characteristic nodular calcifications.

The locations at the level of corticomedullary junctions, nervous tissue, choroid plexus and subarachnoid spaces are the result of cyst dimensions and the impossibility of further progression.

The simultaneous presence of the three different types of elementary lesions of neurocysticercosis is pathognomonic in the case of repeated episodes of infection (Fig. 13B).

Location to the level of subarachnoid spaces is much rarer, with preferential distribution at the level of basal cisterns. The cysts are racemose and sterile; therefore calcifications are not present. Consequently obstruction of the outflow pathways causes slowly progressive extraventricular hydrocephalus.

Conclusions

Our work constantly refers to MRI as the medical modality of choice in the study of infectious diseases of the CNS, above all if pathology is considered. Why? Because MRI is a more effective response to the complex questions posed by clinicians. The reason relies on a basic concept. A computed tomogram, a plain film, or an echograph is nothing more than a map of a single physical feature of the studied object. For example, a computed tomogram is mainly a map of the densities in a certain slice of the body. MRI is different: it provides three or more maps, of three cardinal parameters, proton density, T1 and T2, and more. The total information emerging from a system (as defined in cybernetics and in system analysis) is more than the sum of its parts.

Other specific magnetic effects (such as magnetic susceptibility or paramagnetic contrast media actions) contribute to MRI's tool box, providing the neuroradiologist with great resources to act as a sort of in-vivo pathologist.

Etiological specificity remains essential, but our hope rests on new perspectives such as functional studies (i.e., diffusion w.i.) and spectroscopy, domains that today are making substantial progress.

References

1. Enzmann DR (1984) Imaging of infection and inflammation of the central nervous system: computed tomography, ultrasound and nuclear magnetic resonance. Raven Press, New York
2. Sheld WM, Whitley RJ, Durack DT (eds) (1991) Infections of the central nervous system. Raven Press, New York
3. Wood M, Anderson M (1988) Acute encephalitis. In: Wood M, Anderson M (eds) Neurological infections. Saunders, Philadelphia, pp 381–486
4. Parker JC Jr, Dyer MC (1985) Neurologic infections due to bacteria, fungi and parasites. In: Davis RL, Robertson DM (eds) Textbook of neuropathology. Williams & Wilkins, Baltimore, pp 632–703
5. Donovan Post MJ (ed) (1997) Neuroimaging of AIDS I and II. Neuroimaging Clin North Am 7
6. Andreula CF, Recchia Luciani ANM (1997) Rationale for the use of contrast media in MR imaging. Neuroimaging of AIDS II. Neuroimaging Clin North Am 7:461–498
7. Cohen WA (1997) Intracranial bacterial infections in AIDS. In: Neuroimaging of AIDS I, Vol 7. Neuroimaging Clin N Am 7: 223–230
8. Bazan MG, Rinaldi R, Rauch JR, Jinkins (1991) Fungal infections of the brain. Neuroimaging Clin North Am
9. Jinkins R, Gupta R, Chang KH (1993) MRI of CNS tuberculosis Radiol Clinic North Am 33:771–786
10. Dastur DK, Lalitha VS (1973) The many facets of neurotuberculosis and epitome of neuropathology. In: Zimmerman HM (ed) Progress in neuropathology, Vol.2, Grune & Stratton, New York, pp 351–408
11. Andreula CF, Burdi N, Carella A (1993) CNS cryptococcosis in AIDS: Spectrum of MR findings J Comput Assist Tomogr 17: 438–441
12. Matthews VP, Alo PL, Glass JD et al (1992) AIDS related cryptococcosis. Am J Neuroradiol 13:1477–1478
13. Boos J, Kim JH (1984) Biopsy histopathology in herpes simplex encephalitis and in encephalitis of undefined etiology. Yale J Biol Med 57:751–755
14. Andreula CF, Tarantino A, Ladisa P, Studio RM (1996) Della meningoencefalite da herpes simplex. Riv Neuroradiol 9: 261–271
15. Tsuchiya K, Katase S, Yoshino A, Hachiya J (1999) Diffusion-weighted MR imaging of encephalitis. AmJ Roentgenol 173: 1097–1099
16. Tien RD, Feldberg GJ, Osumi AK (1993) Herpesvirus infections of the CNS: MR findings. Am J Roentgenol 161: 167–176
17. Burke JW, Mathews VP, Elster AD, Ulmer JL, McLean FM, Davis SB (1996) Contrast-enhanced magnetization transfer saturation imaging improves MR detection of herpes simplex encephalitis. AJNR Am J Neuroradiol 17:773–776
18. Brismar J, Gascon GG, von Steyern KV, Bohlega S (1996) Subacute sclerosing panencephalitis: evaluation with CT and MR. AJNR Am J Neuroradiol 17:761–772
19. Mark A, Atlas SW (1989) Progressive multifocal leukoencephalopathy in patients with AIDS: appearance on MR images. Radiology 173:517–520
20. Whiteman MLH, Post MJD, Berger JR, Tate LG, Bell MD, Limonte LP (1993) Progressive multifocal leukoencephalopathy in 47 HIV-seropositive patients: neuroimaging with clinical and pathogenic correlation. Radiology 187:233–240
21. Wheeler AL, Truwit CL, Kleinschmidt-DeMasters BK, Bryne WR, Hannon RN (1993) Progressive multifocal leukoencephalopathy: contrast enhancement on CT scans and MR images. Am J Roentgenol 161:1049–1051
22. Grant JH, Atkinson JR, Hesselink J (1987) Evidence for early central nervous system involvement in the acquired immunodeficiency syndrome (AIDS) and other immunodeficiency virus (HIV) infections Ann Intern Med 107:828–836
23. Lantos PL, MacLaughlin JE, Sholtz CL et al (1989) Neuropathology of the brain in HIV infection. Lancet 1:309–311
24. Petito E-S, Cho W, Lemann et al (1986) Neuropathology of acquired immunodeficiency syndrome (AIDS): an autopsy review. J Neuropathol Exp Neurol 45:635–646
25. Patel SH, Kolson DL, Glosser G, Matozzo I, Ge Y, Babb JS, Mannon LJ, Grossman RI (2002) Correlation between percentage of brain parenchymal volume and neurocognitive performance in HIV-infected patients. AJNR Am J Neuroradiol 23:543–549
26. Thurnher MM, Schindler EG, Thurnher SA, Pernerstorfer-Schön H, Kleibl-Popov C, Rieger A (2000) Highly active antiretroviral therapy for patients with AIDS dementia complex: effect on MR imaging findings and clinical course. AJNR Am J Neuroradiol 21:670–678
27. Thurnher MM, Thurnher SA, Fleischmann D, Steuer A, Rieger A, Helbich T, Trattnig S, Schindler E, Hittmair K (1997) Comparison of T2-weighted and fluid-attenuated inversion-recovery fast spin-echo MR sequences in intracerebral AIDS-associated disease. AJNR Am J Neuroradiol 18:1601–1609
28. Post MJ (1997) Fluid-attenuated inversion-recovery fast spin-echo MR: a clinically useful tool in the evaluation of neurologically symptomatic HIV-positive patients. AJNR Am J Neuroradiol 18:1611–1616
29. Thurnher M,Thurnher SAA, Schindler E (1997) CNS involvement in AIDS: spectrum of CT and MR findings. Eur Radiol 7: 1091–1097
30. Donovan Post MJ, Tate LJ, Quencer RM et al (1988) CT, MR and pathology in HIV encephalitis and meningitis" Am JNeuroradiol 9:469–476
31. Finkenstaedt M, Szudra A, Zerr I et al (1996) MR imaging of Creutzfeldt-Jakob disease. Radiology 199:793 –798
32. De Priester JA, Jansen GH, de Kruijk JR et al (1999) New MRI findings in Creutzfeldt-Jakob disease: high signal in the globus pallidus on T1-weighted images. Neuroradiology 265–268
33. Mao-Draayer Y, Braff SP, Nagle KJ, Pendlebury W, Penar PL, Shapiro RE (2002) Emerging patterns of diffusion-weighted MR imaging in Creutzfeldt-Jakob disease: case report and review of the literature. AJNR Am J Neuroradiol 23:550–556
34. Del Canto SG, Rabinowitz SG (1982) Experimental models of virus-induced demyelination of the central nervous system. Ann Neurol 11:109–127
35. Andreula CF, Recchia Luciani ANM Acute disseminated encephalitis. Int J Neuroradiol 3:21–34
36. Van Der Knaap MS, Valk J (1995) Acute disseminated encephalomyelitis and acute hemorrhagic encephalomyelitis. In: Van Der Knaap MS, Valk J (eds) Magnetic resonance of myelin, myelination and myelin disorders. Springer-Verlag, Berlin New York Heidelberg, pp 320–326
37. Wang PN, Fuh JL, Liu HC, Wang SJ (1996) Acute disseminated encephalomyelitis in middle-aged or elderly patients. Eur Neurol 36:219–223
38. Singh S, Alexander M, Korah IP (1999) Acute disseminated encephalomyelitis: MR imaging features. AJR Am J Roentgenol 173:1101–1107.
39. Osborn RE, Byrd SE (1991) Congenital infections of the brain. Neuroimaging Clin N Am 1:105–118
40. Britt RH, Enzmann DR, Yaeger AS (1981) Neuropathological and CT findings in experimental brain abscess. J Neurosurg 55:590–603
41. Desprechins B, Stadnik T, Koerts G, Shabana W, Breucq C, Osteaux M (1999) Use of diffusion-weighted MR imaging in differential diagnosis between intracerebral necrotic tumors and cerebral abscesses. Am J Neuroradiol 20:1252–1257
42. Hartmann M, Jansen O, Heiland S, Sommer C, Münkel K Sartor K (2001) Restricted diffusion within ring enhancement is not pathognomonic for brain abscess. Am J Neuroradiol 22: 1738–1742
43. Conley FK, Jenkins KA, Remington JS (1981) *Toxoplasma gondii* infection in the central nervous system. Hum Pathol 12:690–698
44. Ramsey RG, Gean AD (1997) CNS Toxoplasmosis. Neuroimaging of AIDS I. Neuroimaging Clin N Am 7:171–186
45. Bia FJ, Barry M (1986) Parasitic infections of the central nervous system. Neurol Clin 49:408–411
46. Escobar A (1983) The pathology of neurocysticercosis. In: Palacio E, Rodriguez-Carbajal J, Taveras JM (eds) Cysticercosis of the central nervous system. Charles C Thomas, Springfield, IL, pp 27–54
47. Zee HD, Segall W, Boswell W et al (1988) MR imaging of neurocysticercosis. J Comput Assist Tomogr 12:927–934

Extra-Axial Neoplasms, Cysts and Tumor-Like Lesions

Anne G. Osborn

1.2

Contents

Introduction

Extra-axial neoplasms, cysts and tumor-like lesions account for approximately one-third of all intracranial primary neoplasms in adults and about one-quarter of brain tumors in children. The differential diagnosis of an extra-axial mass varies significantly with both patient age and geographic location [1]. In this article we consider the pathology and imaging appearance of intracranial extra-axial masses, subdividing them into supra- and infratentorial lesions by age group. Their more specific differential diagnosis by anatomic region is illustrated graphically. Special attention is given to sellar and parasellar lesions.

Supratentorial Extra-axial Tumors in Adults

Adult supratentorial extra-axial neoplasms occur in several general locations (Fig. 1): (1) The sella and parasellar region; (2) skull and meninges; (3) CSF spaces (subarachnoid cisterns and ventricles); and (4) the pineal region. In this chapter we focus on lesions that involve the sellar region and the skull and its linings.

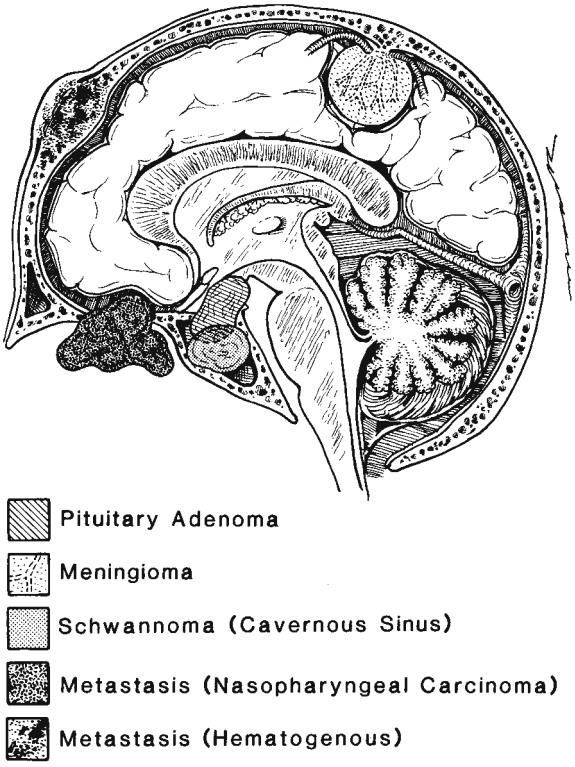

Fig. 1. Sagittal anatomic diagram depicts common locations of supratentorial extra-axial tumors in adults, showing the most important lesions found in each anatomic area

Sella and Parasellar Region

A variety of neoplasms and tumorlike lesions affect the sella and parasellar region. The differential diagnosis of a mass in this anatomically complex area is extensive, with more than thirty different pathologic entities reported in this area. However, just five lesions ("The Big Five") account for the vast majority of masses that occur in and around the sella (Table 1).

Three neoplasms account for the vast majority of sellar and parasellar tumors in adults: (1) pituitary adenoma; (2) meningioma; and (3) schwannoma (in the cavernous sinus). Less common lesions in adults include craniopharyngioma and metastasis. A spectrum of nonneoplastic cysts also can be found in this location [2].

Dividing lesions into intra-, supra-, and parasellar masses is helpful in establishing a more limited diagnosis.

Table 1. Sellar/parasellar masses in adults

Intrasellar
Most common
Microadenoma
Hyperplasia (physiologic, end-organ failure)
Less common
Rathke cleft cyst
Other nonneoplastic cysts
Metastasis to pituitary gland
Rare
Craniopharyngioma
Suprasellar
Most common
Pituitary macroadenoma
Meningioma
Aneurysm
Less common
Astrocytoma
Rathke cleft cyst
Other nonneoplastic cysts (parasitic, arachnoid, epidermoid, dermoid)
Metastasis (infundibular stalk, hypothalamus)
Lymphoma
Hypophysitis
Sarcoid
Lipoma
Rare
Craniopharyngioma
Germinoma
Parasellar (cavernous sinus)
Most common
Meningioma
Schwannoma
Metastasis
Less common
Lymphoma
Aneurysm
Rare
Chordoma
Osteocartilaginous tumor
Infrasellar (basisphenoid)
Most common
Metastasis (hematogenous)
Common
Metastasis (nasopharyngeal carcinoma)
Inflammatory disease (osteomyelitis)
Less common
Plasmacytoma
Lymphoma
Invasive adenoma
Rare
Nonfungal granuloma
Mucocele

Intrasellar Masses

Pituitary microadenomas (by definition, these are 10 mm or less in diameter) and *nonneoplastic cysts* are the most common intrasellar masses. Other lesions (e.g., craniopharyngioma, meningioma, and metastasis) are rare. Dynamic contrast-enhanced MR scans are the best imaging technique for identifying intrasellar masses. Most microadenomas enhance more slowly than the surrounding normal pituitary gland. They are seen as an area of relative hypointensity compared to the intensely enhancing pituitary gland and cavernous sinus.

Suprasellar Masses

Overall, pituitary adenoma is the most common sellar region mass, accounting for at least half of all tumors in this location. As they enlarge, small pituitary adenomas often grow upwards through the diaphragma sellae and acquire a figure of eight appearance. On MR scans, these *pituitary macroadenomas* demonstrate variable signal intensity and strong but heterogenous enhancement following contrast administration. Hemorrhage and cyst formation are not uncommon.

At surgery, microscopic dural invasion is identified with the vast majority of macroadenomas. However, identifying this finding preoperatively is difficult on imaging studies alone. Occasionally macroadenomas attain striking size, extending into the anterior and middle cranial fossae. Some adenomas exhibit frank invasion of the skull base. Despite their aggressive appearance, nearly all of these "invasive adenomas" are histologically benign; true pituitary carcinoma is exceptionally rare [3].

Meningioma is the second most common suprasellar tumor in adults (see below). It may arise from the diaphragma sellae, tuberculum, dorsum, or cavernous sinus and secondarily involve the sella itself.

Craniopharyngiomas are most commonly seen in children. However, a second peak occurs in adults between the fourth and sixth decades. *Metastases* in the

sellar/juxtasellar region most commonly involve the skull base and cavernous sinus (see below). Hematogenous metastases to the pituitary gland may cause an intrasellar mass; metastases that involve the infundibular stalk or hypothalamus are an uncommon but important cause of a suprasellar mass.

Lymphoma (almost always non-Hodgkin type) is another tumor that has a predilection for the sellar region. Any site (pituitary gland, infundibular stalk, hypothalamus, cavernous sinus) may be involved.

A variety of nonneoplastic cysts and tumor-like lesions involve the suprasellar region. These include *Rathke cleft cyst*, *dermoid cyst*, *epidermoid inclusion cyst* and *arachnoid cyst*.

Parasellar Masses

Schwannomas are comparatively rare in intracranial locations other than the cerebellopontine angle cistern (see below). The most common supratentorial site is the cavernous sinus; the trigeminal (cranial nerve V) nerve is most commonly involved. *Meningiomas* and *metastases* often also involve the cavernous sinus.

Skull and Meninges

Meningioma

Meningioma is the second most common primary brain tumor in adults, representing between 15% and 20% of these neoplasms. Most *typical meningiomas* are slowly growing neoplasms that are histologically benign although their location at the skull base may make complete resection difficult.

Three microscopic subtypes of *typical meningioma* are recognized: (1) A meningothelial (or syncytial) type; (2) a fibrous (fibroblastic) type; and (3) a transitional form. *Atypical and anaplastic (malignant) meningiomas* are biologically more aggressive tumors that account for 10%-15% of cases. The rare tumor formerly known as "angioblastic meningioma" is now designated as *hemangiopericytoma of the meninges* [4].

More than three-quarters of meningiomas are supratentorial; the most common locations are the convexity and falx cerebri. Other favored sites include the sphenoid ridges, olfactory grooves, parasellar region (tuberculum, dorsum, diaphragma sellae and the cavernous sinus), and cerebellopontine angles (see below).

Most meningiomas arise from arachnoid cap cells and are firmly attached to the dura. A circumferential collar of reactive thickening accounts for the "dural tail sign" that is seen in approximately 60% of meningiomas. Meningiomas typically invaginate into the brain, displacing the cortex and creating a surrounding cleft of cerebrospinal fluid and vessels that is easily identified on MR imaging.

Metastases

Metastases account for between one-quarter and one-third of all brain tumors in adults. Several varieties are recognized: (1) direct geographic extension of local tumors; (2) hematogenous metastasis; and (3) CSF dissemination from extra- or intracranial neoplasms.

Common regional malignant tumors that may spread directly to the adjacent skull and dura include *squamous cell carcinoma* (of the nasopharynx and paranasal sinuses) and *adenoid cystic carcinomas* (of the salivary or mucous glands). *Scalp carcinomas* (e.g., basal cell carcinoma) occasionally extend through the underlying calvarium and may even involve the dura.

Hematogenous metastases from extracranial primary tumors such as carcinoma of the lung or breast most commonly involve the brain parenchyma. The calvarial vault, central skull base, and dura are also frequently affected.

Supratentorial Extra-axial Tumors in Children

Extra-axial tumors in children are less common than their intra-axial counterparts. The most common location of a supratentorial extra-axial mass in a child is the sella, followed by the pineal region and ventricles (Fig. 2) [5]. The skull and meninges are a less common but nevertheless important site.

Sella and Parasellar Region

Pituitary adenoma, the most common sellar lesion in adults, is very rare in children. Only two sellar lesions commonly occur in the pediatric age group; one (craniopharyngioma) is truly an extra-axial mass whereas the other (an exophytic astrocytoma of the optic chiasm or hypothalamus) is considered an intra-axial neoplasm.

As with adults, dividing lesions into intra-, supra-, and parasellar locations is helpful in establishing an appropriate differential diagnosis (Table 2).

Intrasellar Masses

Craniopharyngiomas that are exclusively intrasellar are rare. Nonneoplastic cysts (such as a *Rathke cleft cyst*) occur but are relatively uncommon in this age group.

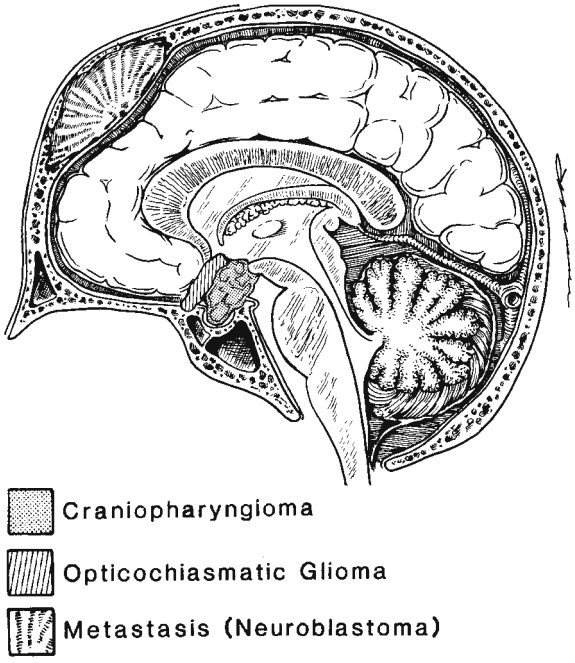

Fig. 2. Sagittal anatomic diagram depicts supratentorial extra-axial tumors in children, showing the important lesions found in the sella/ parasellar region as well as the calvarial vault

Table 2. Supratentorial extra-axial masses in children

Sellar/parasellar
Common
Craniopharyngioma
Astrocytoma (exophytic from chiasm, hypothalamus)
Less common
Germinoma
Lymphoproliferative disorder
Rare
Langerhans' cell histiocytosis (eosinophilic granuloma)
Hypothalamic hamartoma
Skull/meninges
Common
Eosinophilic granuloma
Less common
Metastasis (neuroblastoma)
Lymphoproliferative disorder
Rare
Chordoma

Suprasellar Masses

Craniopharyngiomas are the most common nonglial brain tumor in children. Approximately 80% of craniopharyngiomas are suprasellar, accounting for almost half of all pediatric tumors in this location. Craniopharyngiomas are derived from fetal ectodermal anlage, probably as incomplete involution of an upward evagination of the primitive oral cavity called the stomatodeum, also known as the craniopharyngeal duct (Rathke's pouch).

Between 85% and 90% of all craniopharyngiomas are cystic or are composed of both solid and cystic components. Two histologic types are recognized, namely, the so-called "adamantinomatous" craniopharyngioma (the most common type in children and usually cystic or mixed) and the "papillary" craniopharyngioma (the dominant variant in adults, and more often solid). Most craniopharyngiomas are calcified; their signal intensity on MR scan varies.

Although they are histologically benign tumors and most are very slow-growing lesions, craniopharyngiomas do tend to infiltrate surrounding structures. Malignant transformation is exceedingly rare.

Exophytic astrocytoma of the optic chiasm, optic nerves, and hypothalamus is the second most common suprasellar neoplasm in children. Other less common tumors in children include *germinoma* and *lymphoproliferative disorders*. Nonneoplastic masses in this area include the same spectrum of developmental cysts observed in adults (see above) as well as uncommon lesions such as *Langerhans' cell histiocytosis* and *hypothalamic (tuber cinereum) hamartoma*.

Other less common tumors such as *germinoma* also occur in the suprasellar region.

Skull and Meninges

In the absence of neurofibromatosis type 2 (NF-2), meningioma (the most common adult neoplasm in this location) is rare in children. In contrast to adults, metastases are also rare. The exceptions are *metastatic neuroblastoma* and *lymphoproliferative disorders*. *Eosinophilic granuloma* is a common nonneoplastic calvarial or skull base lesion that may show extensive bony destruction, occasionally mimicking infiltrating tumor.

Chordomas represent less than 1% of all intracranial tumors. Chordomas are derived from notochordal remnants. Their preferred intracranial location is the clivus; the cavernous sinus is a less common site. Although chordomas can occur at any age, they rarely affect individuals less than 20 years of age [3].

Infratentorial Extra-axial Tumors in Adults

Most infratentorial tumors in adults are extra-axial and their most common site is the cerebellopontine angle cistern (Fig. 3). The jugular foramen, foramen magnum, and clivus are also relatively common sites, whereas the occipital squamae are rarely involved by tumors.

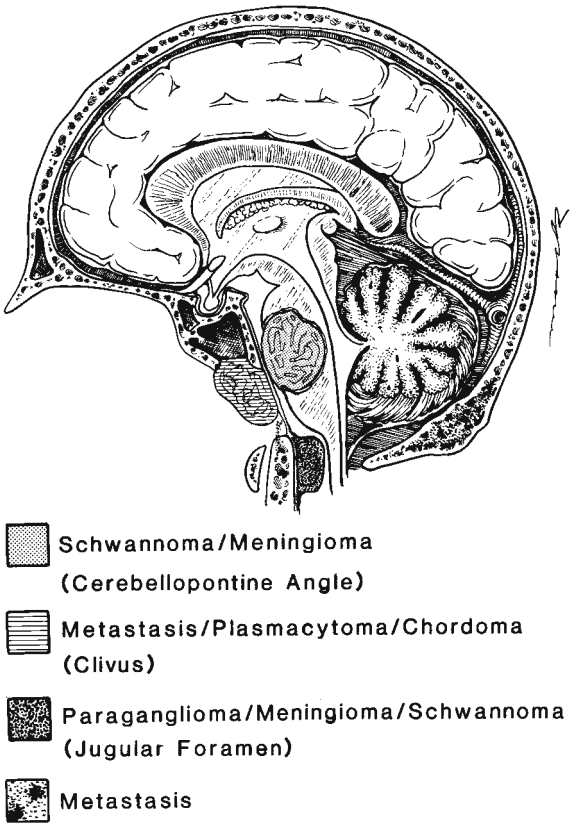

Fig. 3. Sagittal ana-tomic diagram depicts common infratentorial extra-axial tumors in adults, showing the important lesions found in specific locations within the posterior fossa

Table 3. Infratentorial extra-axial masses in adults

Cerebellopontine angle/temporal bone
Most common
Vestibulocochlear ("acoustic") schwannoma
Common
Meningioma
Vascular ectasia (vertebrobasilar)
Less common
Aneurysm
Other schwannomas (e.g., trigeminal)
Nonneoplastic cyst (parasitic, epidermoid, arachnoid)
Metastasis
Paraganglioma
Rare
Cholesterol granuloma
Malignant external otitis
Sarcoid
Idiopathic invasive cranial pachymeningitis
Jugular foramen
Most common
Meningioma
Common
Schwannoma
Paraganglioma
Metastasis
"Pseudotumor" (asymmetric jugular bulb; turbulent flow)
Clivus/foramen magnum
Most common
Metastasis
Common
Meningioma
Less common
Plasmacytoma
Invasive adenoma
Paraganglioma
Rare
Chordoma
Osteocartilaginous tumors

Cerebellopontine Angle

Most cerebellopontine angle (CPA) masses arise as extensions from lesions in the temporal bone (particularly the internal auditory canal). Others occur as primary lesions of the CPA itself (Table 3).

Temporal Bone Tumors

Schwannoma is the most common posterior fossa mass in adults. Intracranial schwannomas account for approximately 8% of all primary intracranial tumors. The vestibulocochlear nerve (cranial nerve VIII; "acoustic schwannoma") is the site of origin in approximately 80%-90% of these tumors. Most arise from the vestibular portion of the nerve.

Small vestibulocochlear schwannomas are initially intracanalicular. As they expand, they extend through the porus acusticus into the CPA cistern. An "ice cream on a cone" appearance on imaging studies is typical. Most schwannomas are isointense with brain on T1-weighted scans and hyperintense on T2-weighted scans. Strong contrast enhancement is typical. Intratumoral cysts and associated arachnoid cysts are common.

Metastases and *endolymphatic duct tumors* may involve the petrous temporal bone and cause a secondary CPA mass.

Cisternal Neoplasms

Meningioma is the second most common posterior fossa mass in adults. Most arise along the petrous temporal bone and exhibit a flat broad-based attachment to the underlying dura. Larger lesions may invaginate into the adjacent cerebellum and usually appear separated from it by an identifiable CSF-vascular cleft. Meningiomas sometimes extend into the internal auditory canal al-

though nonneoplastic dural reaction also occurs in this area.

Less common CPA cisternal masses in adults include *epidermoid, dermoid,* and *arachnoid cysts*. *Tumor mimics* such as malignant otitis, mastoiditis, hemangioma, and idiopathic invasive cranial pachymeningitis may cause bone destruction with thickening of the adjacent dura.

Jugular Foramen

Benign Neoplasms

Several tumors may originate within the jugular foramen and extend intracranially. A *paraganglioma (chemodectoma)* is a benign neoplasm that arises from parasympathetic ganglia adjacent to the jugular bulb adventitia. Paragangliomas are highly vascular tumors that enhance strongly but heterogeneously with contrast administration. "Flow voids" caused by high velocity signal loss often give these lesions a "salt and pepper" appearance on MR scans. Paragangliomas may extend locally into the basal cisterns and cause an extra-axial mass effect. Focal (e.g., jugular spine) as well as more striking, diffuse bone erosion may be present.

Schwannomas of glossopharyngeal, vagus, and spinal accessory nerves (cranial nerves IX, X, and XI) are much less common than their counterparts in the internal auditory canal. When present, schwannomas cause smooth, scalloped expansion of the jugular foramen. Flow voids are uncommon and contrast enhancement is comparatively homogeneous.

Jugular foramen "pseudotumors" (e.g., asymmetric jugular bulb) should not be confused with true masses in this location.

Malignant Neoplasms

Hematogenous *metastases* to the jugular foramen are uncommon. When they occur, irregular permeative bone destruction with an adjacent soft tissue mass is typical.

Clivus and Foramen Magnum

Clivus Masses

Any aggressive or slowly-growing clival tumor may break through the overlying cortex and extend extradurally. In adults, tumors that commonly affect the clivus include *chordoma*, *meningioma, plasmacytoma, metastasis* (either hematogenous or direct spread of regional extracranial neoplasms such as nasopharyngeal squamous cell carcinoma), and *invasive pituitary adenoma* (see above). Because it is formed from enchondral bone, the central skull base may also give rise to a spectrum of *osteocartilaginous tumors* (e.g., enchondroma) that may cause an extra-axial mass effect.

Foramen Magnum Masses

The differential diagnosis of a foramen magnum mass in an adult varies with specific location. Anterior intradural extramedullary masses include *meningioma*, *schwannoma*, and *glomus jugulare tumor*. Less commonly, *nonneoplastic cysts* (such as epidermoid inclusion cyst, arachnoid cyst, neurenteric cyst) are found in this location. Nonneoplastic masses include craniovertebral junction anomalies and proliferative arthropathies with associated degenerative disease (e.g., rheumatoid pannus).

Tumors that are located posterior to the medulla are less common. In adults, *subependymoma* (extending inferiorly from the fourth ventricle) and *metastasis* are the most common neoplasms that occur here. Overall, tonsillar herniation (congenital or acquired) is the most common cause of a mass behind the cervicomedullary junction.

Infratentorial Extra-axial Masses in Children

Most posterior fossa neoplasms in children are intra-axial, arising either from the cerebellum or brainstem (e.g., pilocytic and fibrillary astrocytoma) or from the fourth ventricle and its adjacent structures (e.g., medulloblastoma and ependymoma). Primary infratentorial extra-axial tumors are rare in children. Occasionally an *exophytic astrocytoma* or lateral extension from an *ependymoma* causes a significant extra-axial mass effect (Fig. 4).

Although sporadic cases do occur, *schwannoma* and *meningioma* are rare in the absence of neurofibromatosis type 2 (NF-2). Uncommon tumors such as *choroid plexus papilloma* and nonneoplastic cysts such as an *arachnoid, epidermoid, neurenteric* or *dermoid cyst* are occasionally identified as posterior fossa extra-axial masses in children [6].

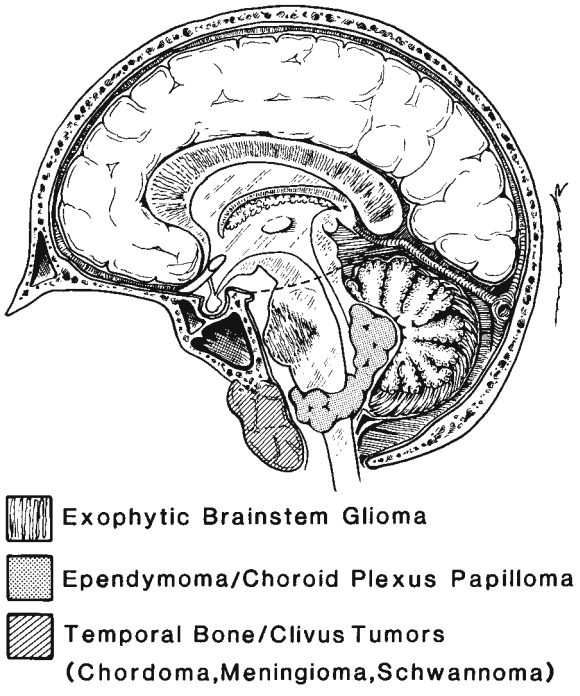

Fig. 4. Sagittal anatomic diagram depicts extra-axial posterior fossa masses in children, showing typical infratentorial lesions in each location

References

1. Osborn AG (1994) Brain tumors and tumorlike masses: Classification and differential diagnosis. In: Diagnostic Neuroradiology. CV Mosby Co, St. Louis, pp 401–528
2. Swallow CE, Osborn AG (1998) Imaging of sella and parasellar disease. Sem US, CT, MR 19:257–271
3. Thapar K, Kovacs K (1998) Neoplasms of the sellar region. In: DD Bigner, RE McLendon, JM Bruner (eds) Russell & Rubinstein's Pathology of Tumors of the Nervous System, 6th ed., vol. 2. Arnold, London, pp 561–677
4. Bruner JM, Tien RD, Enterline DS (1998) Tumors of the meninges and related tissues. In: DD Bigner et al., op. cit., pp 69–139
5. Pfleger MJ, Gerson LP (1993) Supratentorial tumors in children. Neuroimaging Clinics N Amer 3:671–687
6. Zee CS, Segall HD, Nelson M et al. (1993) Infratentorial tumors in children. Neuroimaging Clinics N Amer 3:705–714

Hemispheric Brain Tumors

Francisco J. Romero-Vidal, Arantxa Ortega-Aznar

1.3

Contents

Introduction

The incidence of brain tumors has been estimated at 4.5 per 100,000 inhabitants. In autopsy series, they are found in 2.5% of cases. In this chapter, we will analyze supratentorial hemisphere tumors of the central nervous system (CNS) in the context of the WHO criteria, published in 2000 [1].

The WHO criteria are based on a histological evaluation of the tumor cell types and tissue patterns recognized by conventional optic microscopy and include the related information gleaned from immunohistochemical studies. The importance of this classification is that besides introducing important changes, it substantially clarifies the degree of malignancy. The modifications that have been made can be summarized in the following points:

a. Introduction of new tumoral entities described in recent years such as:
   – Pleomorphic xanthoastrocytoma [2]
   – Central neurocytoma [3]
   – Dysembryoplastic neuroepithelial tumor [4]
b. However, for selective use the term "primitive neuroectodermal tumor" (PNET) is accepted for some embryonal tumors in children.
c. Changes in the consideration of astrocytic tumors and the progression of glioma to malignancy. Basically, a clear a line of separation has been drawn between circumscribed astrocytic lesions (such as pilocytic astrocytoma, pleomorphic xanthoastrocytoma and subependymal giant cell astrocytoma associated with tuberous sclerosis) and diffusely infiltrating astrocytomas, which are typically located in the cerebral hemispheres. This last group alone shows an intrinsic tendency to progress to an anaplastic astrocytoma, and finally to multiforme glioblastoma.
d. Multiform glioblastoma, one of the most frequently occurring malignant tumors in adults, has been displaced from the group of embryonal tumors to group of astrocytic tumors. Presently multiforme glioblastoma is considered to be the extreme of the spectrum of loss of differentiation seen in astrocytic tumors [1].
e. Astroblastoma and ependymoblastoma are considered by some authors as architectural patterns that can occur in gliomas, while others believe them to be true clinical pathological entities. To resolve this problem, they have been included in a group termed "uncertain histogenesis."
f. New histological subtypes have been recognized in the ependymomas group. The majority are not associated with a different biological behavior, but their description helps the pathologist in identifying and classifying them.
g. The entity called monstrocellular sarcoma has been eliminated.
h. Together with the indispensable element of histological typing of central nervous system tumors, a scale of increasing degree of malignancy (I to IV) has been created. In general, each type of tumor corresponds to one of these degrees. Thus, when diagnosis is established, it is not possible to apply different degrees of malignancy to the same tumor.

Tumors of Neuroepithelial Tissue

Low-Grade Diffuse Astrocytomas

Astrocytic tumors are characterized by a high degree of cellular differentiation, slow growth, and diffuse infiltration of the neighboring brain structures. These lesions, corresponding to grade II in the WHO classification, have a tendency to malignant progression [1, 6].

Low-grade fibrillary astrocytomas are neoplasms occurring in children and adults from 20–40 years of age. Fibrillary astrocytomas are found throughout the hemispheres in proportion to the white matter present, and often involve the adjacent cortex as well.

Seizures are a common presenting symptom.

Radiopathological Correlation

Because of their infiltrating nature, these low-grade astrocytomas usually show blurring of the gross anatomical boundaries on microscopy. This feature is due to enlargement and distortion, but not destruction, of the invaded anatomical structures [7].

On CT, low-grade astrocytoma is commonly visualized as a nonenhancing, poorly defined, homogeneous, low-grade density mass. However, calcification, cystic change and even varying degrees of enhancement may be present early. Surrounding edema is minimal or absent [8, 9].

MRI studies usually show hypointensity in the T1-weighted images (T1-W), with enlargement of the areas first affected by the tumor and hyperintensity on T2-W [10] (Fig. 1). Gadolinium enhancement is uncommon in low-grade diffuse astrocytoma, but it can manifest with progression of the tumor.

Anaplastic Astrocytoma

Anaplastic astrocytoma is an infiltrating lesion with local or dispersed anaplasia and a marked proliferative potential. Anaplastic astrocytomas may arise from low-grade astrocytoma, but they can also be diagnosed first, without indication of a less malignant precursor lesion. These tumors are classified as grade III in the WHO system and require two histological criteria, usually nuclear atypia and mitotic activity, to be included in this category [1, 6].

Anaplastic astrocytomas generally appear in a slightly higher age group than low-grade astrocytoma (mean, 41 years) and a predominance of males are affected (2:1). The clinical symptoms are similar to those of low-grade astrocytomas, but with a shorter history.

Radiopathological Correlation

Generally it is not possible to grossly distinguish between low-grade and anaplastic astrocytomas. On the cut surface, the high cellularity of anaplastic astrocytomas produces a discernible tumor mass, which shows a clearer distinction from the surrounding brain struc-

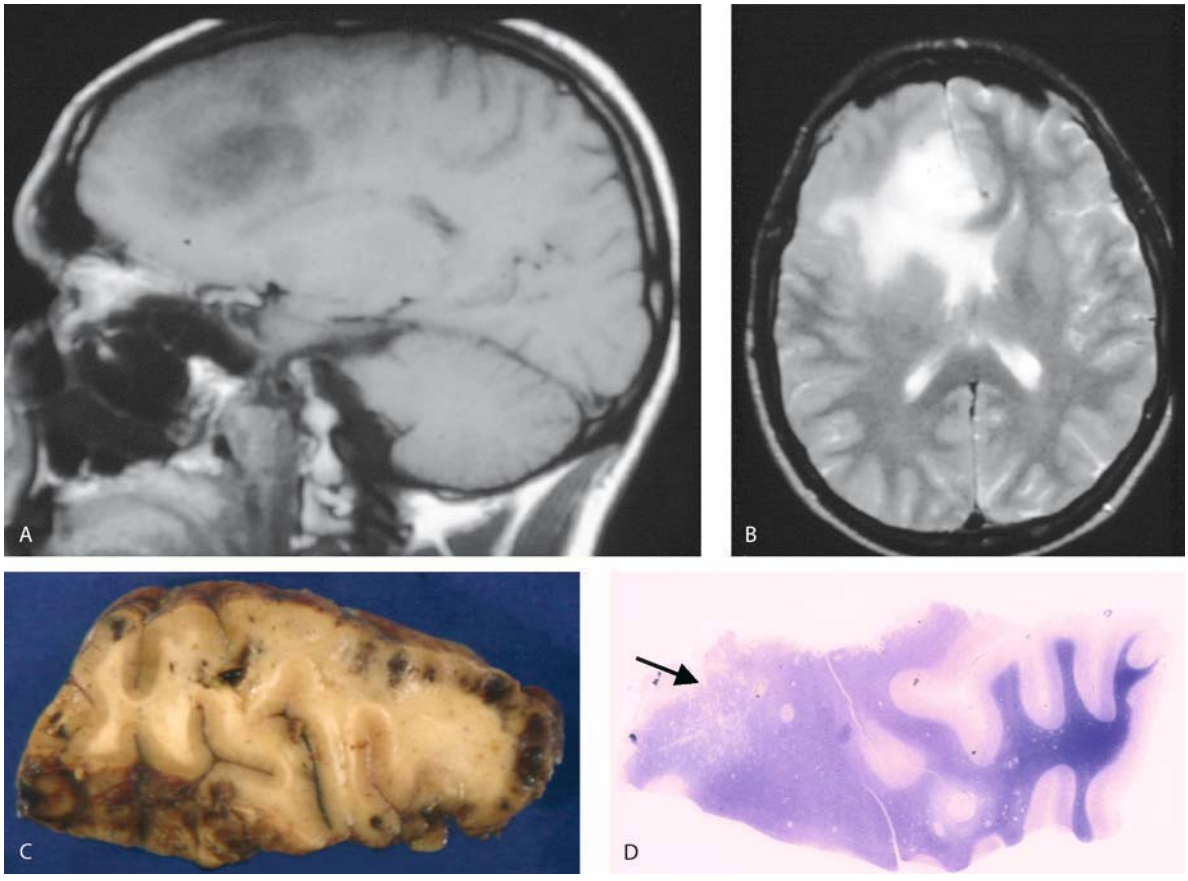

Fig. 1A–D. Low-grade diffuse astrocytoma. **A** MRI T1-W sagittal shows hypointense frontal area. **B** MI T2 W axial scan with hyperintense lesion located on the frontal white matter. **C** Coronal section of frontal lobe with a poorly defined mass and local blurring of the neocortex with focal hemorrhages. **D** Histological picture of the same section shows reduced myelin staining in white matter while the cortex shows increased cellularity with a diffuse infiltration pattern of growth (*arrow*)

tures than does low-grade diffuse astrocytoma. Macroscopic cysts are common, but frequently there are areas of granularity, opacity and a soft consistency.

On CT study, anaplastic astrocytoma tends to be nonhomogeneous and shows a mixed density. Calcifications are infrequent, except in cases of malignant transformation of a low-grade astrocytoma. Contrast uptake is heterogeneous and occasionally irregular ring enhancement is seen because of edema surrounding the lesion [9] (Fig. 2).

MRI shows a heterogeneous intensity on the T1- and T2-weighted images. On T2-W, the lesion often presents as a hyperintense area surrounded by an isointense ring which, in turn, is surrounded by a hyperintensity produced by vasogenic edema (Fig. 2A). Following contrast administration, marked but irregular peripheral ring-like enhancement is usually evident (Fig. 2B), but non-enhancing lesions may be histologically anaplastic [11]. Anaplastic astrocytoma may also spread to the ependyma, leptomeninges and cerebrospinal fluid (CSF).

Glioblastoma Multiforme

Glioblastoma multiforme, composed of poorly differentiated neoplastic astrocytes with areas of vascular proliferation and/or necrosis, is the most malignant astrocytic tumor. Glioblastoma typically affects adults and is mainly found in the cerebral hemispheres [1]. The tumors can develop from low-grade diffuse or anaplastic astrocytoma (secondary glioblastoma) (Fig. 3), but more frequently, they manifest after a short clinical history with no evidence of a less malignant precursor lesion (primary glioblastoma) [(6].

Corresponding to grade IV in the WHO system, glioblastoma requires three or four histological criteria for this classification**:** nuclear atypia, mitotic activity, microvascular proliferation, and/or necrosis.

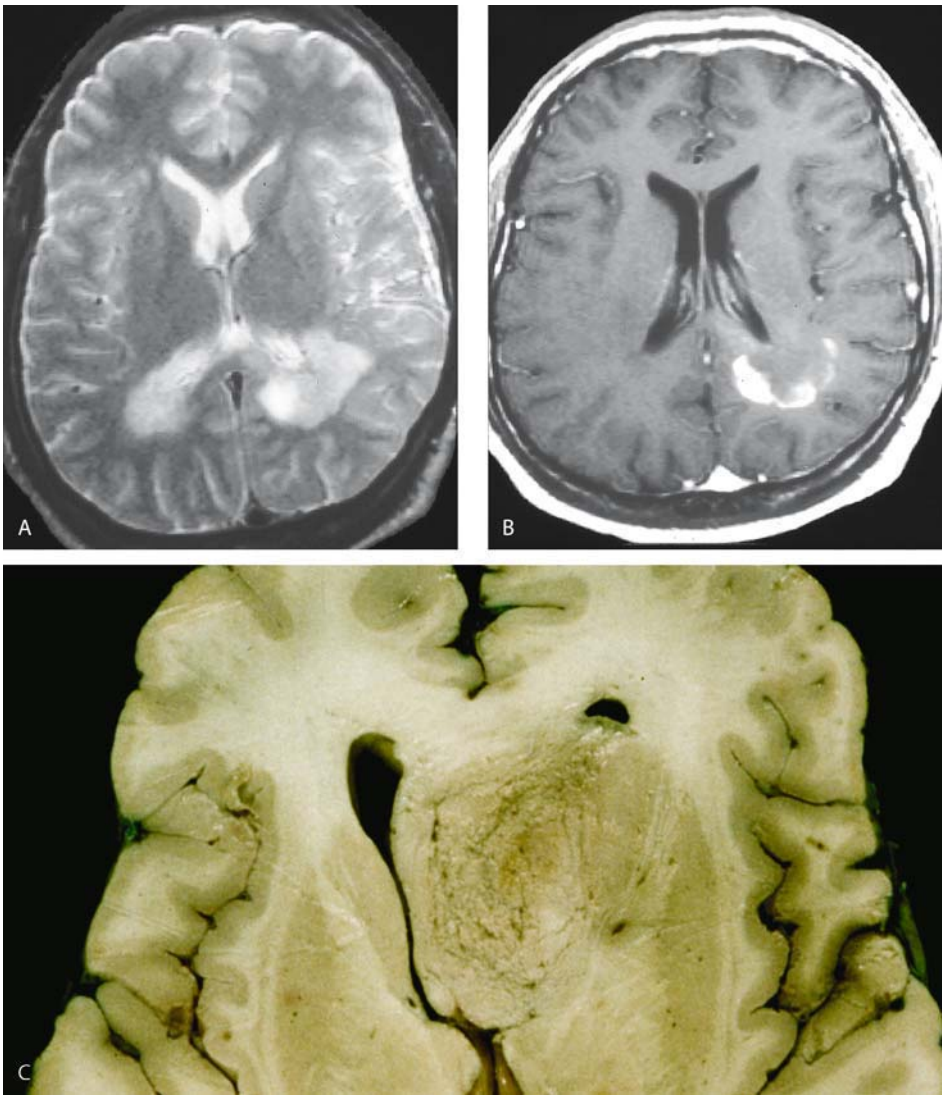

Fig. 2A–C. Anaplastic astrocytoma. **A** Axial T2-W MRI shows left hyperintense periventricular area with compression of occipital horn. **B** Axial postcontrast T1-W with enhancement incomplete ring. **C** Discernible tumor mass produces clear distinction from surrounding brain structures. This lesion infiltrates caudate nucleus, corpus callosum and lateral ventricle

Fig. 3A–C. Progression of low-grade astrocytoma to glioblastoma multiforme **(GBM).** A Baseline axial T2-weighted image shows hyperintense area without contrast enhancement. **B, C** After 2 years, glioblastoma demonstrated

Fig. 4A–C. Glioblastoma. MRI: **A** On axial T2-W the mass shows central high signal intensity due to necrosis. Note also surrounding vasogenic edema extending along the adjacent white matter (*arrows*). **B** Coronal post contrast T1-W shows central necrosis with thick and irregular ring-like enhancement. Significant mass effect. **C** Periventricular GBM in frontal lobe shows an epicenter in the white matter with granular surface and focal cystic necrosis

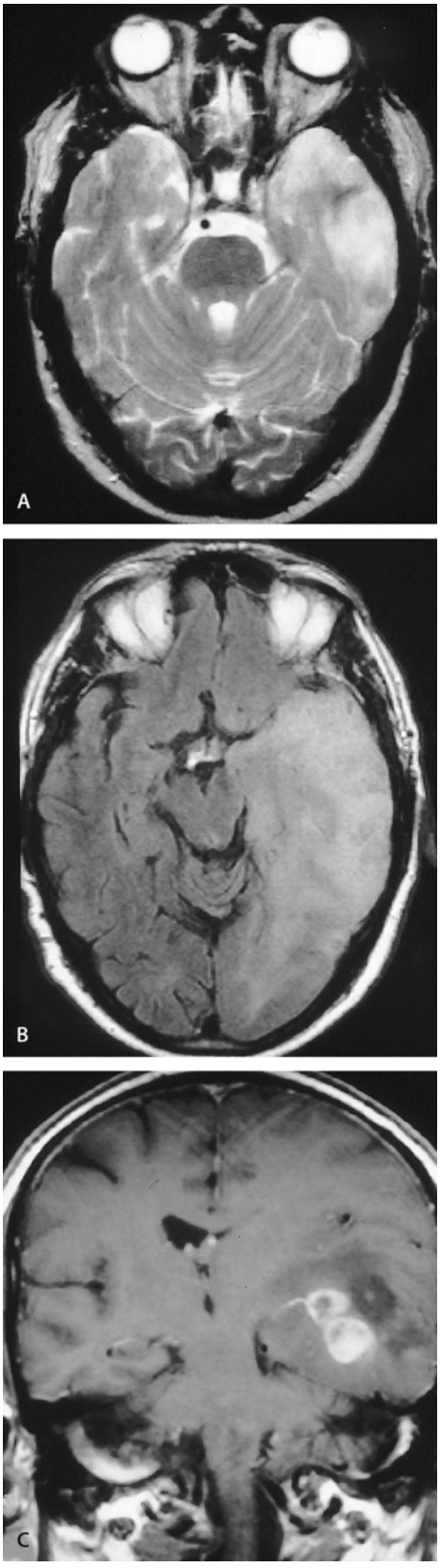

Fig. 3A–C.

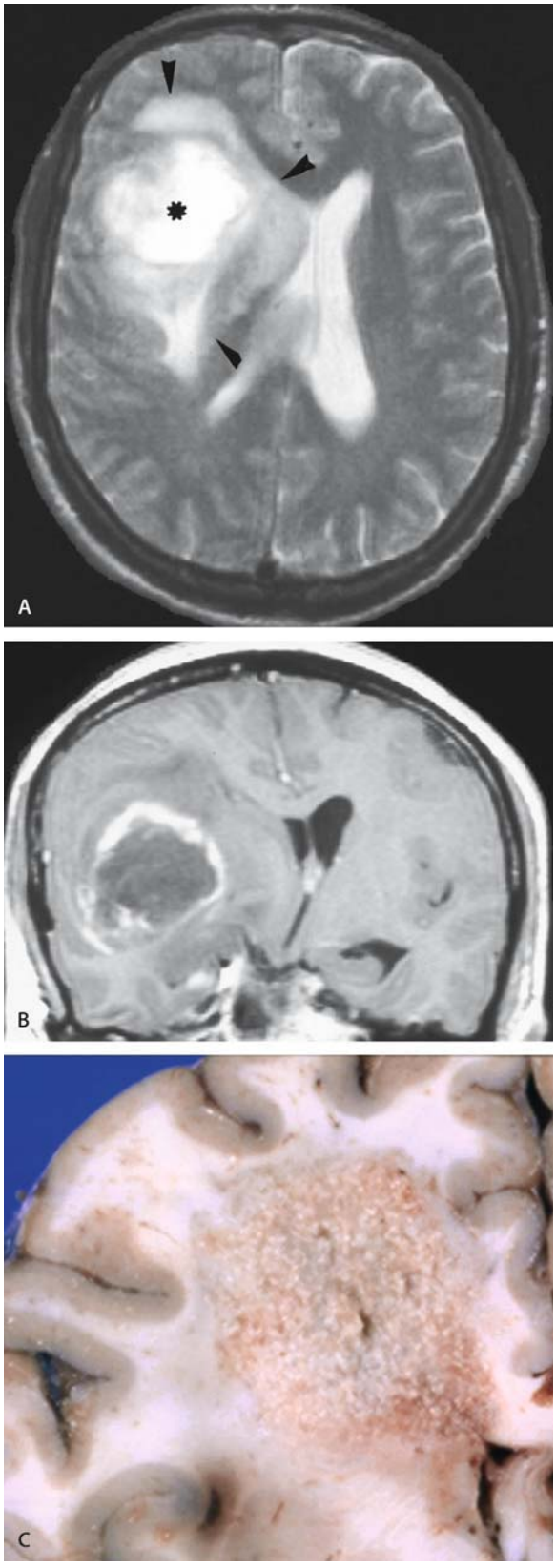

Fig. 4A–C.

Radiopathological Correlation

Glioblastomas occur most often in the cerebral hemispheres, particularly the frontotemporal and parietal regions. They are poorly delineated macroscopically, the cut surface showing a variable color with peripheral grayish tumor masses, yellowish necrosis from membrane breakdown and red and brown stipples from recent and remote hemorrhage. Central necrosis may occupy as much as 90% of the tumor mass. Macroscopic cysts, when present, contain a turbid fluid that represents liquefied necrotic tumor tissue. The lesion is usually unilateral but those in the corpus callosum can be found contralaterally (Fig. 4).

Most glioblastomas of the brain hemispheres are clearly intraparenchymal with the epicenter in the white matte (Fig. 5C); however, some are largely superficial and in contact with the leptomeninges and dura. As these latter neoplasms are frequently rich in collagen, they can be interpreted as metastatic carcinoma or as an extraaxial lesion, such a meningioma.

On CT, glioblastoma typically presents as an irregularly shaped lesion with a peripheral, ring-like zone of contrast enhancement around a dark, usually hypodense central area of necrosis (Fig. 5A, B) [12]. On T1-weighted MR images, the contrast-enhanced ring structure corresponds to the cellular and highly vascularized peripheral area of the neoplasm. Analysis whole brain sections of early untreated glioblastomas has shown that this ring structure is not the outer tumor border – infiltrating glioma cells can be easily identified within, and occasionally beyond, a 2-cm margin. In T2-weighted images, this zone is broader, less well-defined and overlaps the surrounding vasogenic edema [13].

Glioblastoma multiforme that appears as a smooth-walled cyst with a mural nodule is distinctly uncommon. A potential diagnostic pitfall is glioblastoma multiforme that manifests primarily as intraaxial hemorrhage.

Arteriovenous shunting and early filling of draining cerebral veins are commonly seen on angiographic study. Glioblastoma multiforme can be so highly vascular that it may resemble an arteriovenous malformation or a cerebral infarct with luxury perfusion.

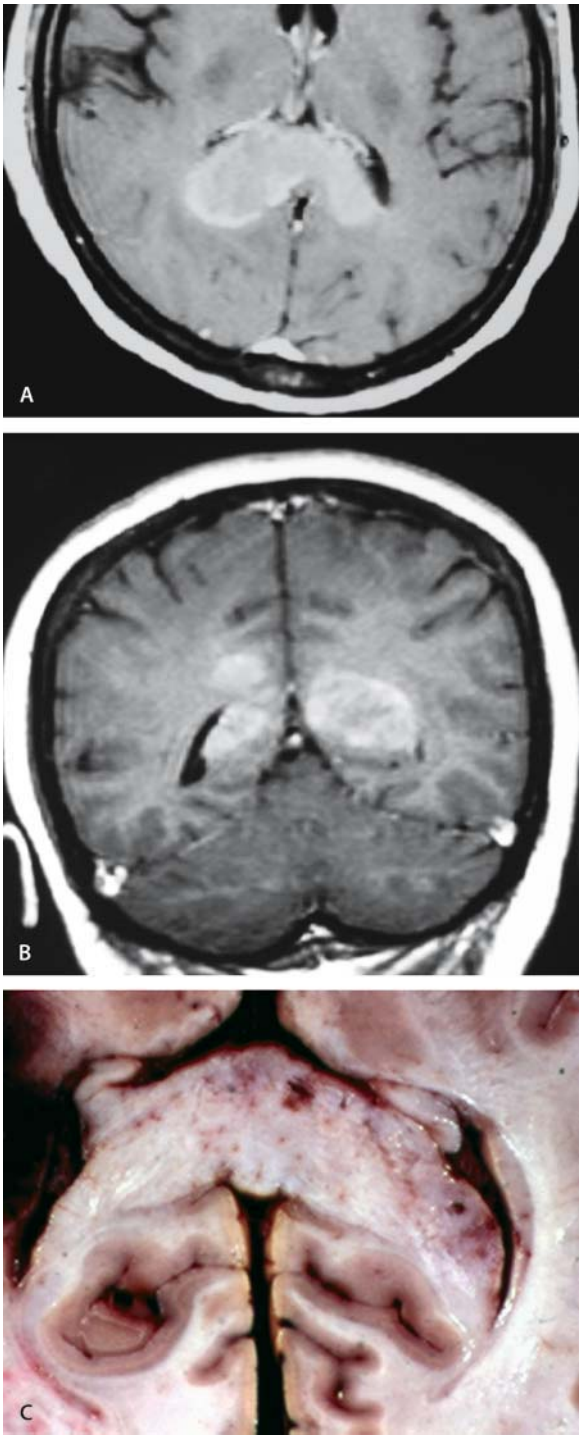

Fig. 5A–C. Glioblastoma multiforme on the splenium of corpus callosum (butterfly glioma). Axial postcontrast T1-W image (**A**) and T1 coronal shows extension of a glioblastoma multiforme through the splenium of the corpus callosum. **C** Severe enlargement of the corpus callosum and fornices. Both structures show distorted growth and granular surface

Multifocal Glioblastoma

The are three pathways that can result in multifocal glioblastoma [13, 14]:

1. primary glioblastoma spread, usually through cerebrospinal fluid pathways or through white matter tracts (Fig. 6)
2. Multiple areas of malignant degeneration occurring in a patient with diffuse, low-grade astrocytoma
3. Multiple areas of glioblastoma arising de novo in a patient with a genetic abnormality and no underlying low-grade lesion (Fig. 7).

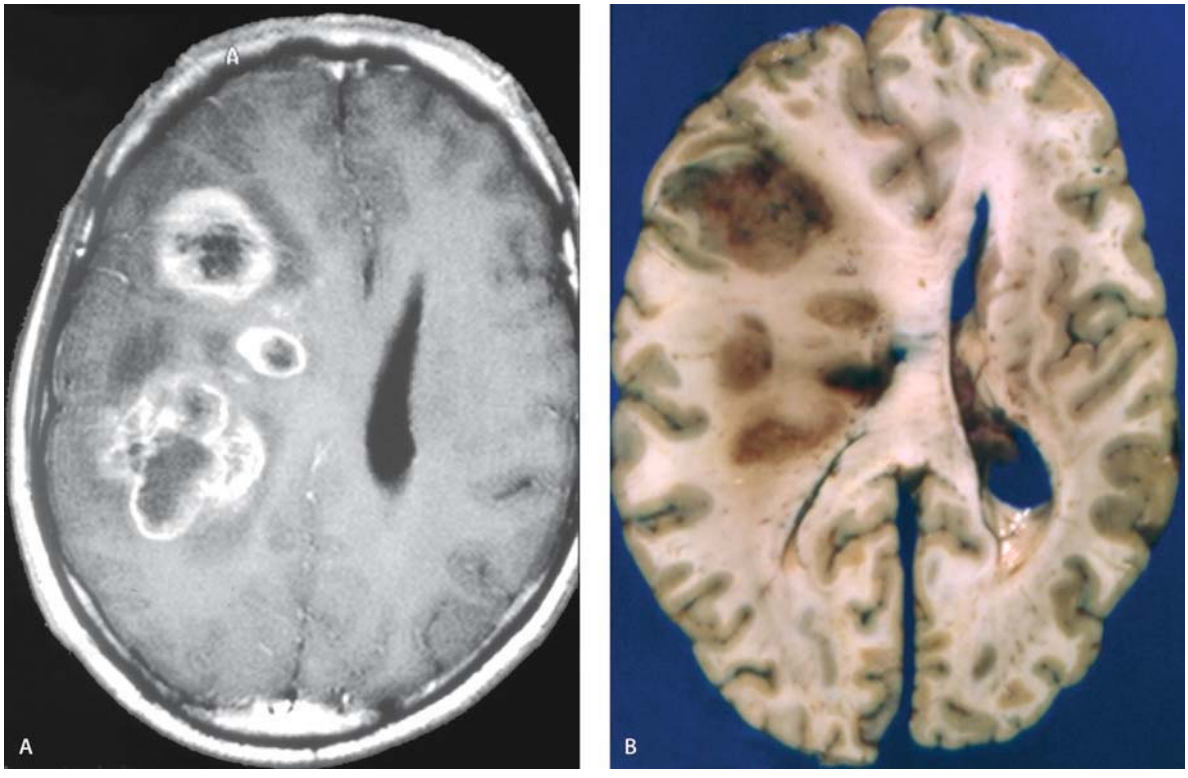

Fig. 6A, B. Multifocal glioblastoma **A** Axial postcontrast T1 MRI demonstrates multiple irregular ring enhancement lesions. **B** Axial brain section shows multiple foci of GBM in the same hemisphere. Gross features are similar in all lesions

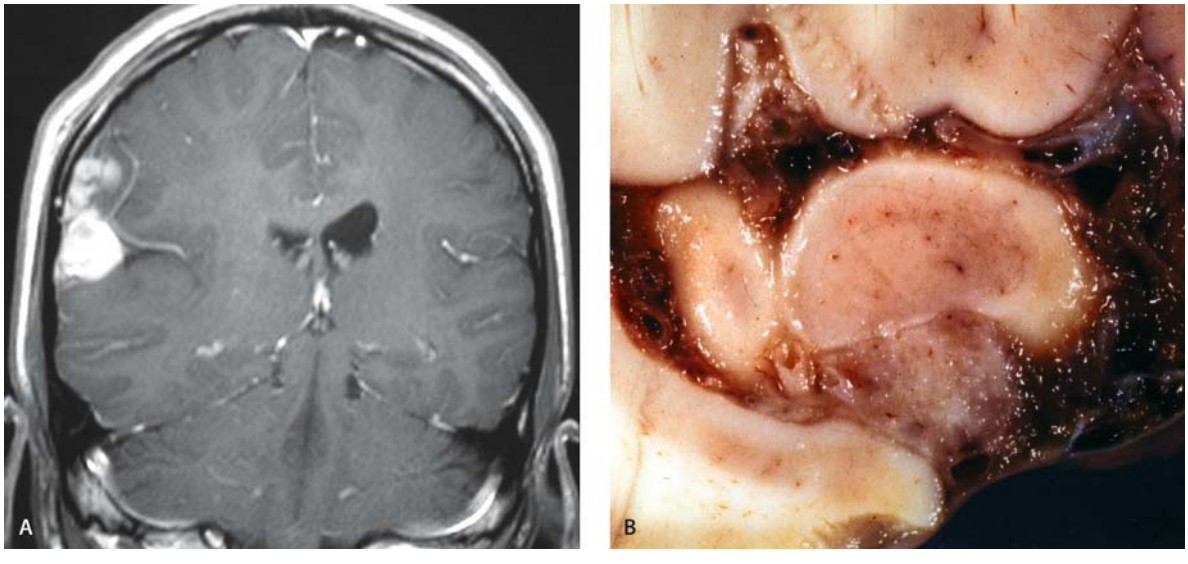

Fig. 7A, B. Patterns of glioblastoma multiforme dissemination through of the cerebrospinal fluid. **A** Coronal postcontrast T1-W image shows enhanced extra-axial mass (*arrow*). **B** Macroscopic brain section with thickened and opaque meningeal areas

Giant-Cell Glioblastoma

Giant-cell glioblastoma is a histological variant of glioblastoma with a marked predominance of bizarre, "monstrous" multinucleated giant cells and, on occasion, an abundant stromal reticulin network. They are categorized histologically as WHO grade IV and are a rare variant (less that 1% of all brain tumors) [1, 6].

Radiopathological Correlation

Giant-cell glioblastomas are distinctive because of their circumscription and firmness caused by production of tumor stroma. They are often subcortically located, in the temporal, frontal and parietal lobes. On CT and MRI, they can mimic a metastatic tumor [6, 15] (Fig. 8).

Gliosarcoma

Gliosarcoma has a sarcomatous component and accounts for approximately 2% of all glioblastomas. It is typically located in the cerebrum, and involves the temporal, frontal, parietal and occipital lobes [1, 6].

Radiopathological Correlation

The sarcomatous component produces a firm, often superficial, rather discrete mass in a lesion that may elsewhere have typical features of glioblastoma.

CT and MRI scans often show features of diffusely infiltrating glioblastoma (Fig. 9A). In cases with a predominant sarcomatous component, the tumor appears as a well-delineated hyperdense mass with homogeneous contrast enhancement, mimicking a meningioma (Fig. 9B) [16, 17]. At angiography, some gliosarcomas reveal a mixed dural and pial vascular supply [18].

Pilocytic Astrocytoma

Occurring in children and young adults, pilocytic astrocytoma is a generally well-circumscribed astrocytoma composed of a variable percentage of spongy, compact tissue [6].

These lesions are classified into WHO grade I and are the most common glioma in children [1].

The thalamus and basal ganglia are the sites of predilection in the cerebral hemispheres. Cerebral pilocytic astrocytomas are uncommon tumors that tend to affect an older group of patients than do those occurring in the cerebellum, optic chiasm or optic nerve. Cerebral hemispheres comprise 3% of cerebral gliomas [19, 20]. The right hemisphere is more commonly affected.

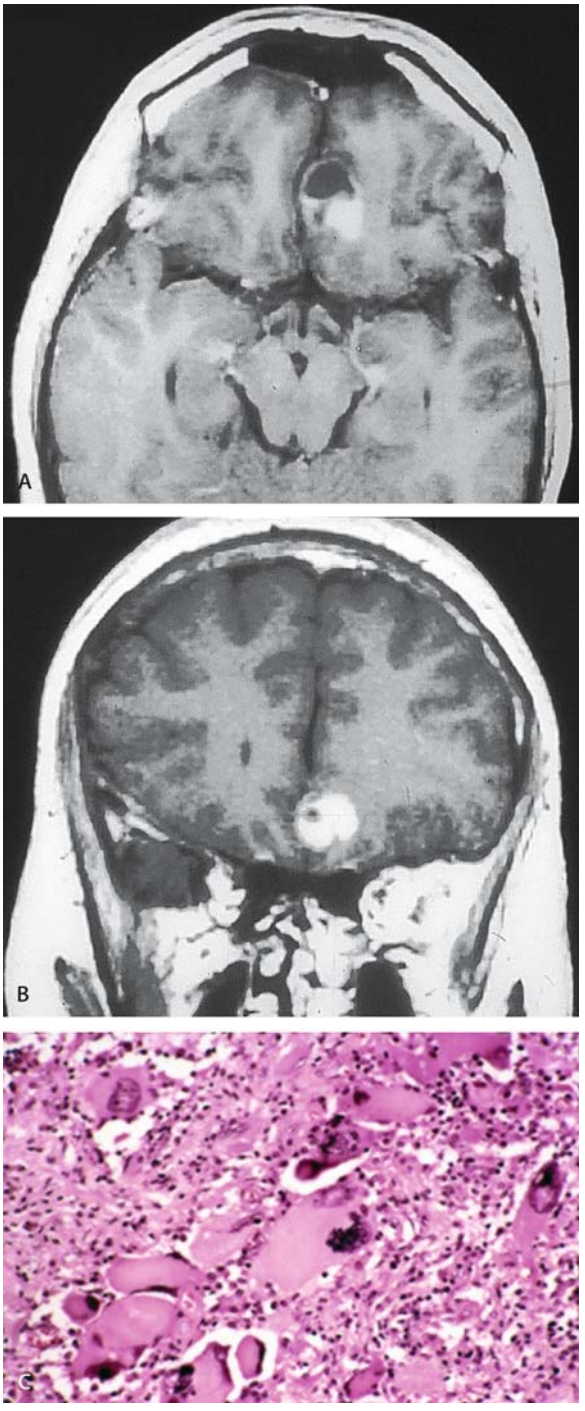

Fig. 8A–C. Giant-cell glioblastoma. Axial (**A**) and coronal (**B**) postcontrast T1-weighted MRI scans show a well-circumscribed superficial located tumor in the left gyrus rectus. **C** Typical bizarre monstrous multinucleated tumor cells are the key component in this GBM

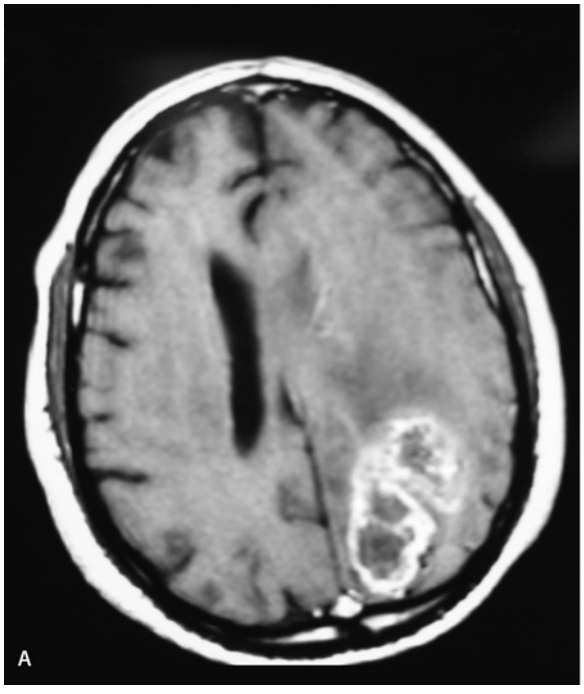

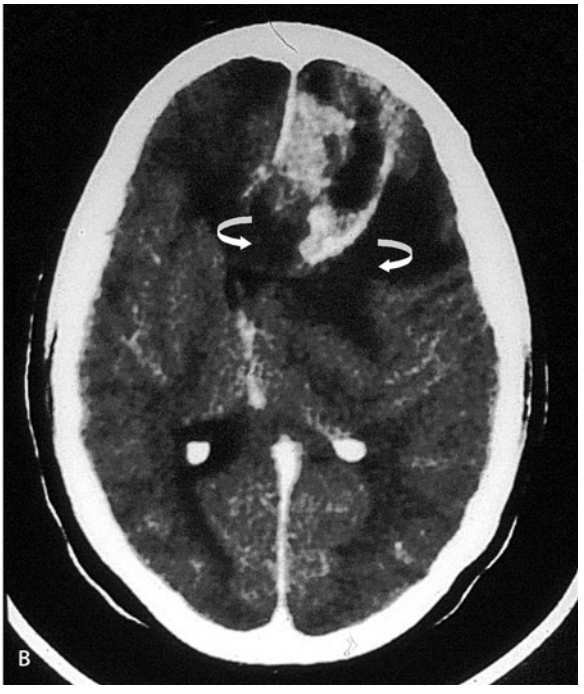

Fig. 9A, B. Gliosarcoma. **A** Axial postcontrast T1-W image. The tumor shows intense heterogeneous ring-like enhancement. **B** Axial contrast-enhanced CT in another case shows a mixed density frontal mass (the hyperdense area represents sarcomatous component). Note dural attachment (*arrow*) and peritumoral edema (*curved arrows*)

Radiopathological Correlation

Pilocytic astrocytoma is a relatively well-circumscribed lesion (Fig. 10D), often showing a heterogeneous consistency with firm or mucoid areas [21]. Focal calcification may be present. Pilocytic astrocytoma sometimes forms a mural nodule associated with cysts [22]. Invasion of the subarachnoid spaces may be evident.

CT and MR images typically show a cystic mass with an enhancing mural nodule (Fig. 10) [23–26]. Calcification occurs in 10% of cases.

Subependymal Giant Cell Astrocytoma

A discrete, large cell astrocytoma arising near the foramen is the Monro, almost always in the setting of tuberous sclerosis (TS). It is WHO grade I [1].

Clinical manifestations of SEGA usually appear during the second decade of life, but congenital examples have been encountered in premature infants. It is not uncommon to document the slow progression of an asymptomatic lesion during routine radiological screening of patients with TS.

Radiopathological Correlation

Whether solitary or bilateral, these contrast enhancing masses are solid and sharply demarcated from the underlying caudate head (Fig. 11). In their obstructive effects at the foramen, the Monro are evident on CT and MRI. The other cerebral components of cerebral tuberous sclerosis are usually evident as well [28]. These include:

1. Calcified subependymal nodules in the lateral ventricles
2. Cortical tubers with ether subjacent rarefaction or cyst formation, evident as hyperintensity on T2-WI
3. Linear abnormalities that reflect hypomyelination of the underlying white mater

Pleomorphic Xanthoastrocytoma

An astrocytic neoplasm with a relatively favorable prognosis, pleomorphic xanthoastrocytoma is typically encountered in children and young adults. It typically shows a superficial location in the cerebral hemispheres, involvement of the meninges and a pleomorphic histological appearance [2, 6]. Classified as WHO grade II, pleomorphic xanthoastrocytoma accounts for less than 1% of all astrocytic neoplasms [1].

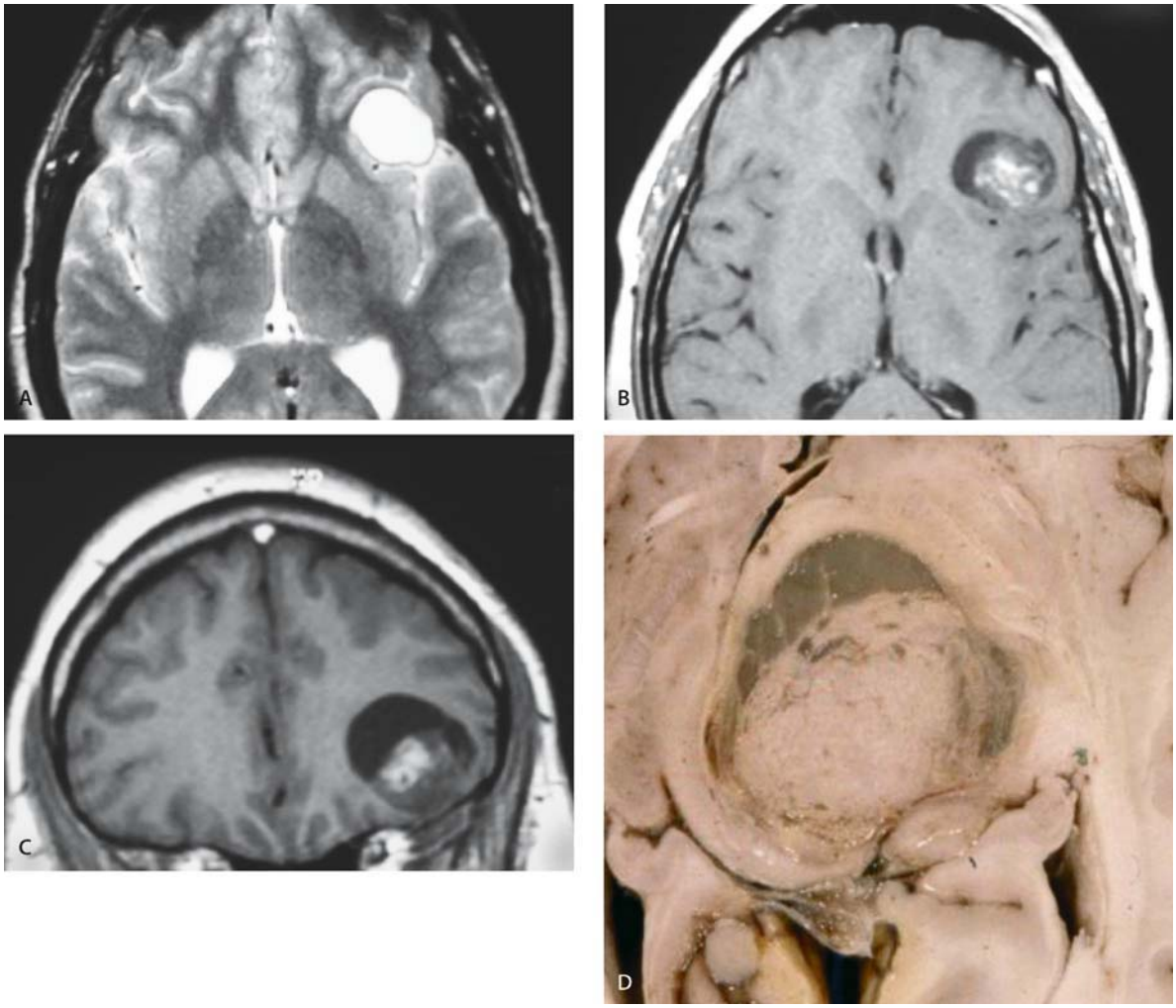

Fig. 10A–D. Pilocytic astrocytoma. Axial T2 (**A**), axial (**B**) and coronal (**C**) postcontrast T1 MRI of a pilocytic astrocytoma centered in the left frontal lobe. **D** In other patient, well-circumscribed, largely solid neoplasm with a cystic component is shown in the hypothalamic and thalamic region. Note the mural nodule (**C**, **D**)

Radiopathological Correlation

The meningocerebral type generally has a superficial location, particularly in the temporal lobe.

Pleomorphic xanthoastrocytomas are attached to the meninges and are frequently accompanied by cysts; sometime a mural nodule forms within the cyst wall. Invasion of the dura matter is exceptional.

CT and MRI scans usually outline the tumor mass and/or the cyst that is present (Fig. 12). Peripheral edema is usually not pronounced. The mural nodule enhances strongly after contrast administration [27, 29, 30].

Oligodendroglioma

Oligodendrogliomas are diffusely infiltrating tumors composed predominantly of cells morphologically resembling oligodendroglia. Histologically, oligodendroglial tumors comprise a continuous spectrum ranging from well-differentiated neoplasms to frankly malignant tumors [6]. The WHO classification system recognizes two malignant grades for oligodendroglial tumors: grade II for well-differentiated tumors, and grade III for anaplastic tumors [1].

Oligodendroglial tumors constitute only 5% of all cerebral gliomas. Although they can occur at any age, they predominate in adults, with a peak incidence in the fifth and sixth decades. The most common signs are epileptic seizures and headache.

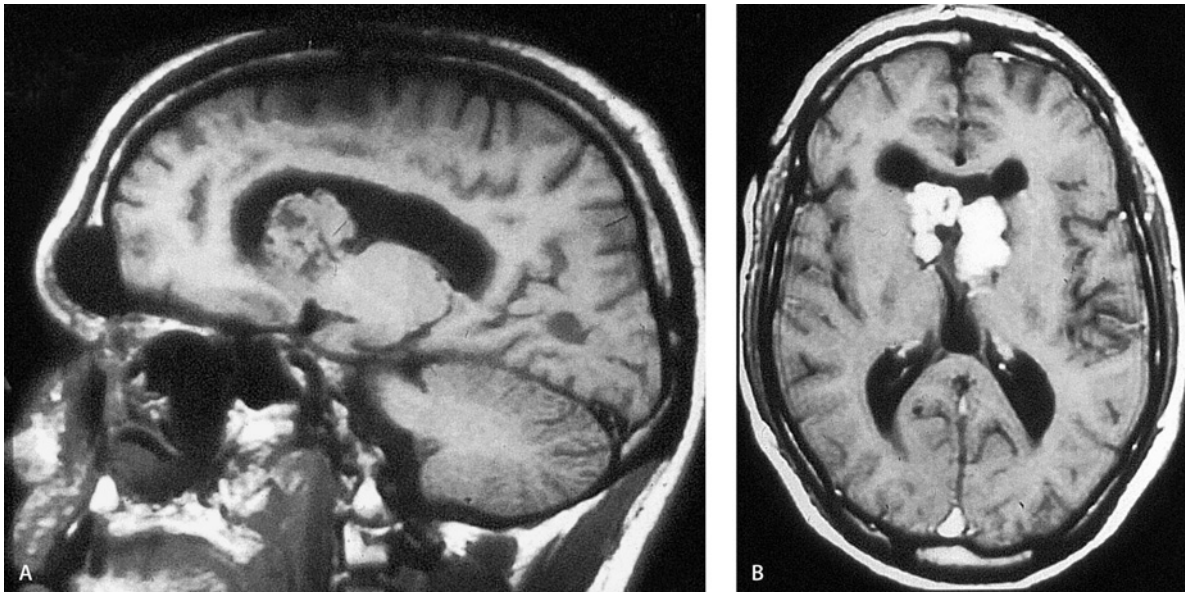

Fig. 11A, B. Subependymal giant-cell astrocytoma in a patient with tuberous sclerosis. **A** Sagittal T1-weigthed image shows a heterogeneous mass in the foramen of Monro. **B** Axial postcontrast T1-weighted image with intense enhancement

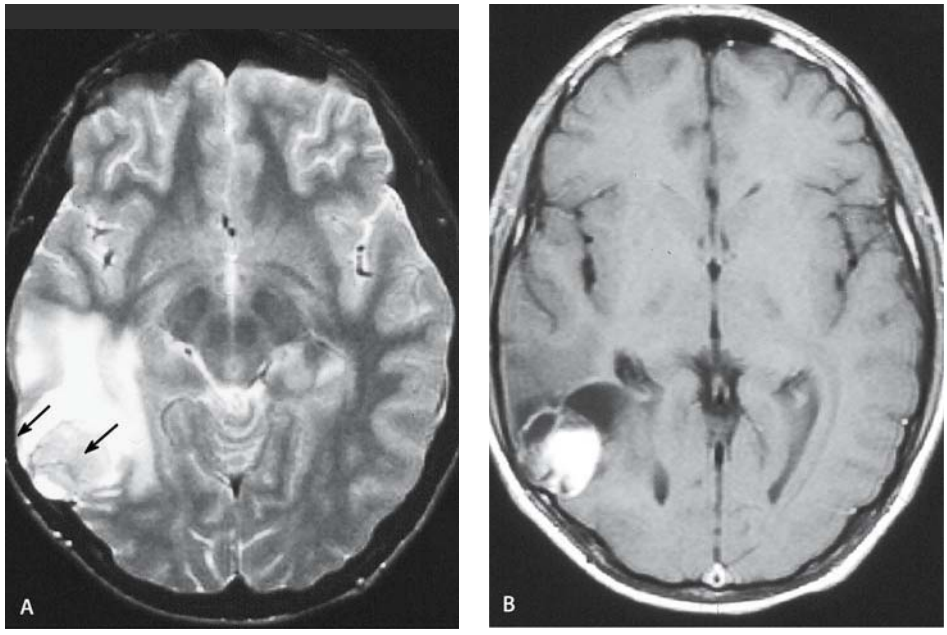

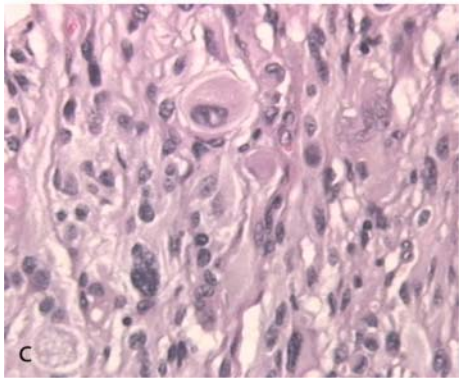

Fig. 12A–C. Pleomorphic xanthoastrocytoma of the right temporal lobe. **A** Axial T2-weighted image shows hyperintense cortical lesion (*arrows*) surrounded by edema. **B** Coronal postcontrast T1-W image shows a cystic lesion with enhanced peripheral nodule (*arrow*). **C** This neoplasm shows marked cytologic pleomorphism. Many cells have abundant cytoplasm and cytoplasmic lipid droplets

Radiopathological Correlation

Macroscopically, they appear as well-defined soft, grayish pink masses. Cyst degeneration and necrosis can occur in large lesions. Typically, oligodendrogliomas affect the cerebral cortex and subcortical white matter of the cerebral frontotemporal regions. Infiltration of the adjacent leptomeninges is common. Anaplastic oligodendrogliomas may demonstrate areas of tumor necrosis.

On CT, the tumors are usually hypo- or isodense in comparison to the normal gray matter. Calcification is common (Fig. 13). Mild contrast enhancement may be seen in a fraction of cases. Peripheral edema is usually mild or not seen. Calvarial erosion occurs in about 17% of cases [31].

MRI studies typically demonstrate a hypointense lesion in the T1-weighted images and a hyperintense lesion in T2. The tumors are well-delineated and show little perifocal edema. However, some may demonstrate heterogeneous images of variable intensities due to intratumoral hemorrhage and/or areas of cystic degeneration. Although enhancement is more frequently identified with MR imaging than with CT, it is usually modest. Anaplastic oligodendrogliomas may show nonhomogeneous patterns and contrast enhancement is usual.

Mixed Gliomas

Mixed gliomas are tumors composed of a conspicuous mixture of two or more distinct neoplasia counterparts of the normal macroglial cell types. By far the most common mixed gliomas are oligoastrocytomas [6].

Oligoastrocytomas are tumors composed of mixture of two different neoplastic cell types morphologically resembling the tumor cells in oligodendroglioma or low-grade diffuse astrocytoma (WHO grade II). The oligodendroglial and astroglial components may be either diffusely intermingled or separated into distinct areas.

Mixed gliomas correspond histologically to WHO grade II and the anaplastic types to grade III [1].

Radiopathological Correlation

Generally, mixed gliomas cannot be differentiated from other WHO grade II or III gliomas by their gross appearance.

On imaging studies, they demonstrate no special features that would provide reliable clues to distinguish them from other gliomas (Fig. 14). In the series published by Shaw et al. [32], calcifications were demonstrated in 14% of these tumors. About half of the oligoastrocytomas evaluated by CT and MRI showed contrast enhancement.

Ependymoma

Ependymoma is a tumor predominantly composed of neoplastic ependymal cells, with preferential manifestation in children and young adults. Anaplastic ependymoma is a variant with histological evidence of advanced anaplasia, including nuclear atypia, marked mitotic activity, high cellular, microvascular proliferation and necrosis [6].

Histologically, ependymoma are low-grade and correspond to WHO grade II. Anaplastic ependymomas are classified as WHO grade III [1]. Ependymomas account for 2%–4% of supratentorial tumors. The age distribution is slightly lower for supratentorial than for infratentorial location and males are affected slightly more frequently than females.

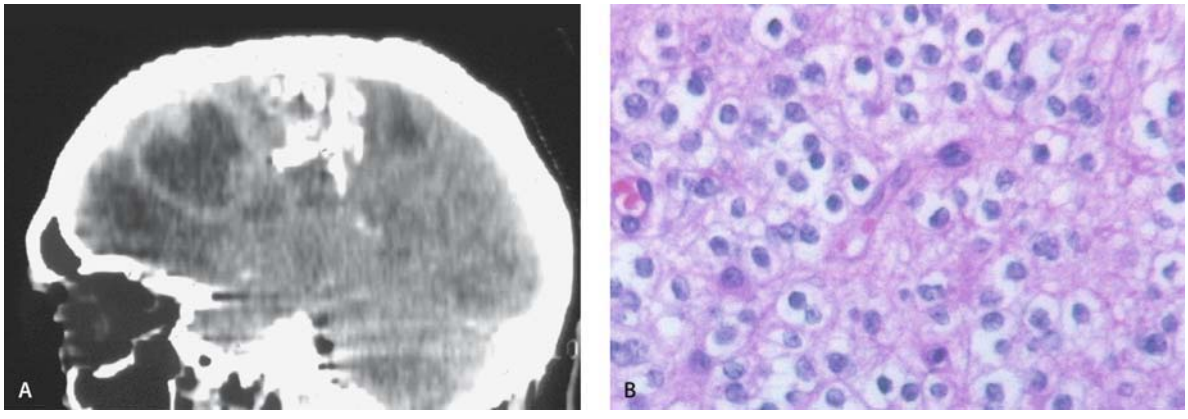

Fig. 13A, B. Oligodendroglioma. **A** CECT sagittal reformation shows frontal tumor with calcification. **B** Classic picture with diffuse pattern of regular round cells with clear perinuclear halo

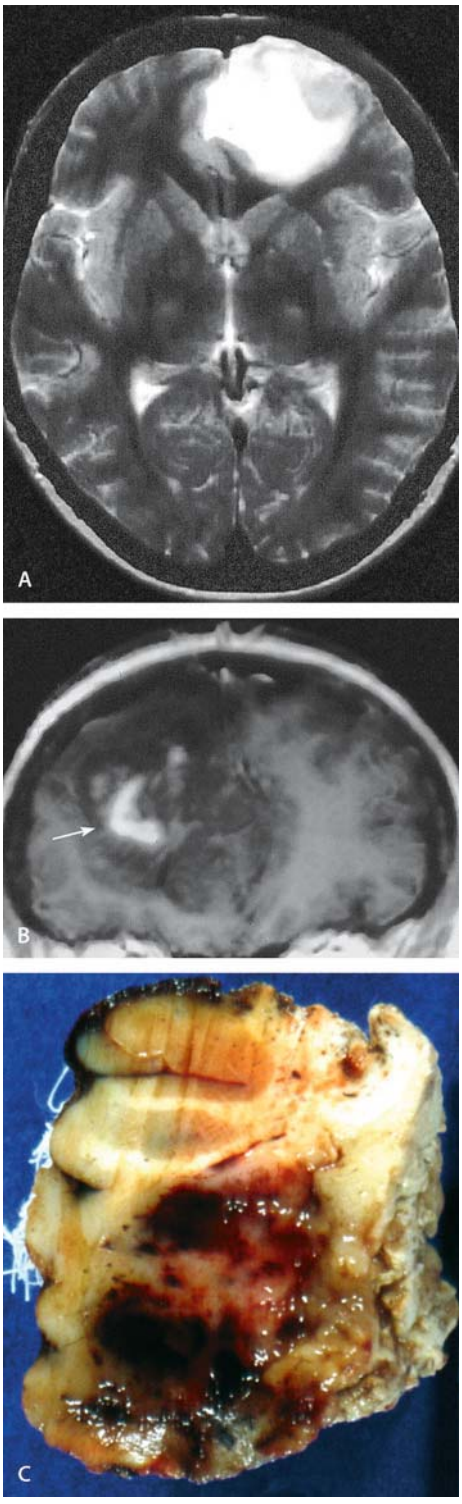

Fig. 14A–C. Oligoastrocytoma. **A** Axial T2-weighted MR scan shows a frontal hyperintense well-demarcated lesion with mild perifocal edema. **B** Coronal postcontrast T1-W image demonstrates a focus of enhancement (*arrow*). **C** Gross appearance of the frontal lobe shows an oligoastrocytoma with recent hemorrhagic component after incomplete removal of tumor

The white matter of the frontal and parietal lobes is most commonly involved, some parts of the cerebral hemispheres can be affected. Cerebrospinal fluid dissemination occurs frequently, especially with recurrence of the tumor.

Radiopathological Correlation

Supratentorial ependymomas intrude upon the ventricular system, but also enlarge centrifugally into the surrounding brain where they present to the surgeon as freshly gray and, most importantly, relatively discrete masses. Since the epicenter in the ventricular zone may not be apparent, the diagnosis may be not suspected when approached laterally. Ependymomas are soft, gray masses with or without cysts, necrotic foci or hemorrhage.

On CT and MRI, these tumors have a variable, heterogeneous appearance [33–35]. They are usually large (>4 cm) and well-demarcated. Cyst formation or necrosis is typical (70%–80%), as is calcification (50%). Hemorrhage into the lesion occurs occasionally [36]. Moderate to intense contrast enhancement is the rule (Fig. 15). CT scan demonstrates a heterogeneously hypodense to isodense mass. Increased density can be seen if hemorrhage has occurred, and anaplastic lesions often have higher attenuation. MRI reveals a heterogeneous lesion that is hypointense to isointense on T1-weighted images and hyperintense on T2. Gadolinium often shows a rather well-circumscribed lesion with varying intensity of contrast enhancement. MRI is particularly useful in determining the relationship to surrounding structures and invasion along cerebrospinal spaces [35, 36].

Subependymoma

Subependymoma is a well-differentiated, nodular, and highly fibrillar ependymal tumor generally situated within a ventricle. It is WHO grade I.

Subependymoma are most often encountered as an incidental finding. The lateral ventricle near the caudate nucleus (40%–75%) and the floor of the fourth ventricle (30%–60%) are the most common locations. Like ependymomas, occasional examples occur near the surface of the brain.. Based on critical location and size, hydrocephalus is the most common presentation [37].

Radiopathological Correlation

As lobulated, flat-based tumors, subependymoma are firmly attached to their site of origin. Although basically soft than solid, the texture of long-standing lesion may be modified by calcification, hemorrhage, or cyst

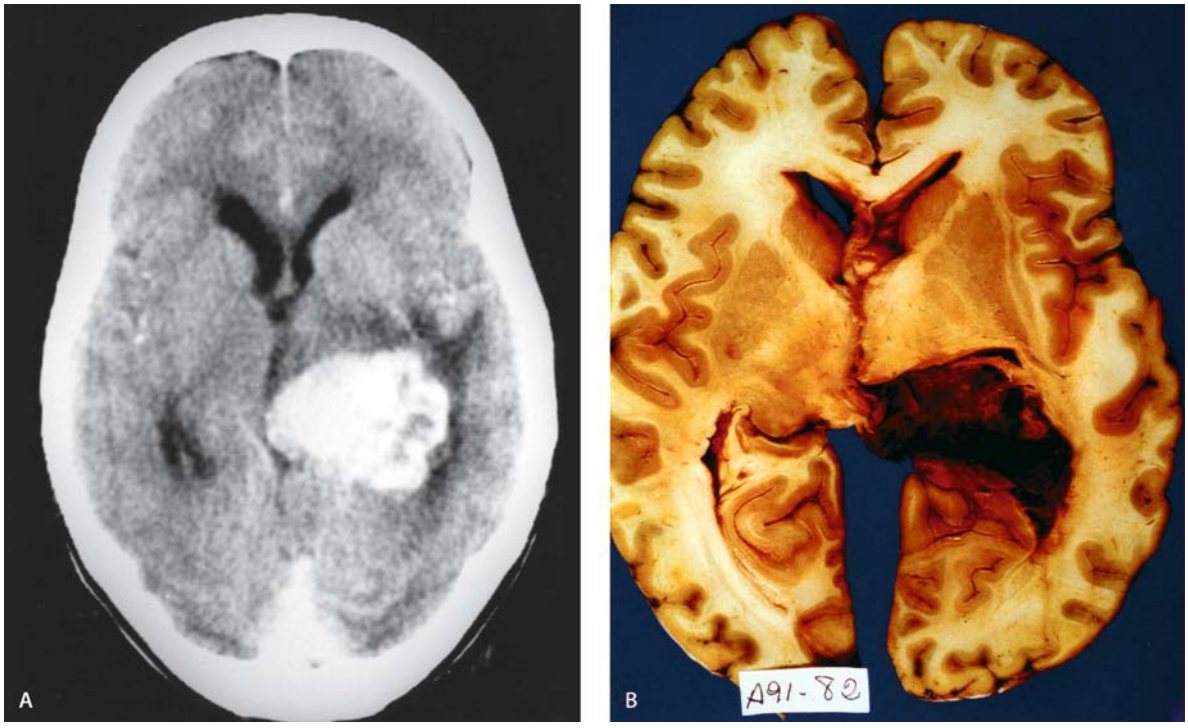

Fig. 15A, B. Ependymoma supratentorial. **A** Axial contrast-enhanced CT demonstrates homogeneous enhancing mass in the atrium of the right lateral ventricle. **B** In this axial section of the brain, the right temporal horn is occupied by a well-defined hemorrhagic granular tumor

formation. The tumor is characterized by small group of ependymal cells in a rather dense, delicately fibrillar stroma. Calcifications, hemorrhage and/or microvascular proliferation may be formed.

Radiological findings show lateral ventricle subependymoma on CT [38], which vary in density, but are more often hypodense, and usually do not enhance. Calcifications are seen in less 10% of cases. On MRI, they are typically hypointense to gray matter on T1-WI and hyperintense on T2-WI (Fig. 16). As with CT, they seldom demonstrate enhancement and are thus readily distinguished from other lateral ventricle tumors, which typically do enhance. Subependymoma do not demonstrate paraventricular extension.

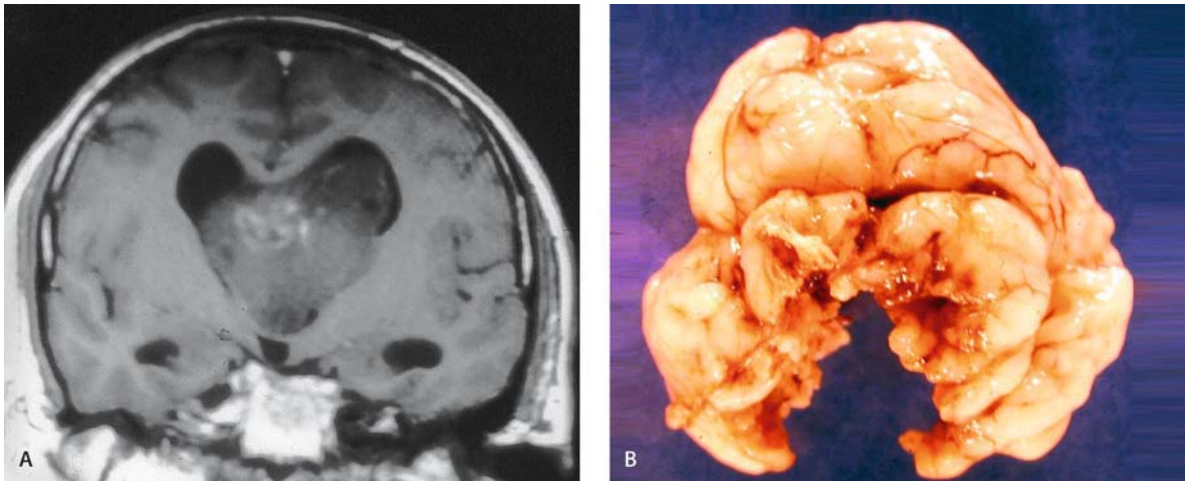

Fig. 16A, B. Lateral ventricle subependymoma. **A** Coronal postgadolinium T1-weighted image. Lack of contrast enhancement discerns this neoplasm from others in the same location. **B** Macroscopic appearance after surgical removal shows nodular surface

Choroid Plexus Tumors

Choroid tumors are papillary neoplasms of the cerebral ventricles derived from choroid plexus epithelium. Choroid plexus papilloma is classified as WHO grade I, whereas choroid plexus carcinoma is histologically malignant (WHO grade III) [1, 6].

Although choroid plexus tumors account for only 0.4%–0.6% of all brain tumors, they represent 2%–4% of those that occur in children and 10%–20% of those manifesting in the 1st year of life. Around 80% of lateral ventricle tumors present in patients under 20 years old. Choroid plexus tumors tend to block cerebrospinal pathways.

Radiopathological Correlation

Choroid plexus papillomas are circumscribed, cauliflower-like masses that adhere to the ventricular wall, but are usually well-delineated in relation to the brain tissue. Choroid plexus carcinomas are invasive tumors that may appear solid, hemorrhagic and necrotic [36].

Choroid plexus papillomas are well-circumscribed, lobulated intraventricular masses. Ventriculomegaly or effacement of the lateral ventricles is often present. The majority are isodense to hyperdense, with about a quarter of the lesion being hypodense, on CT images. They are brightly enhancing tumors that may have calcifications [39].

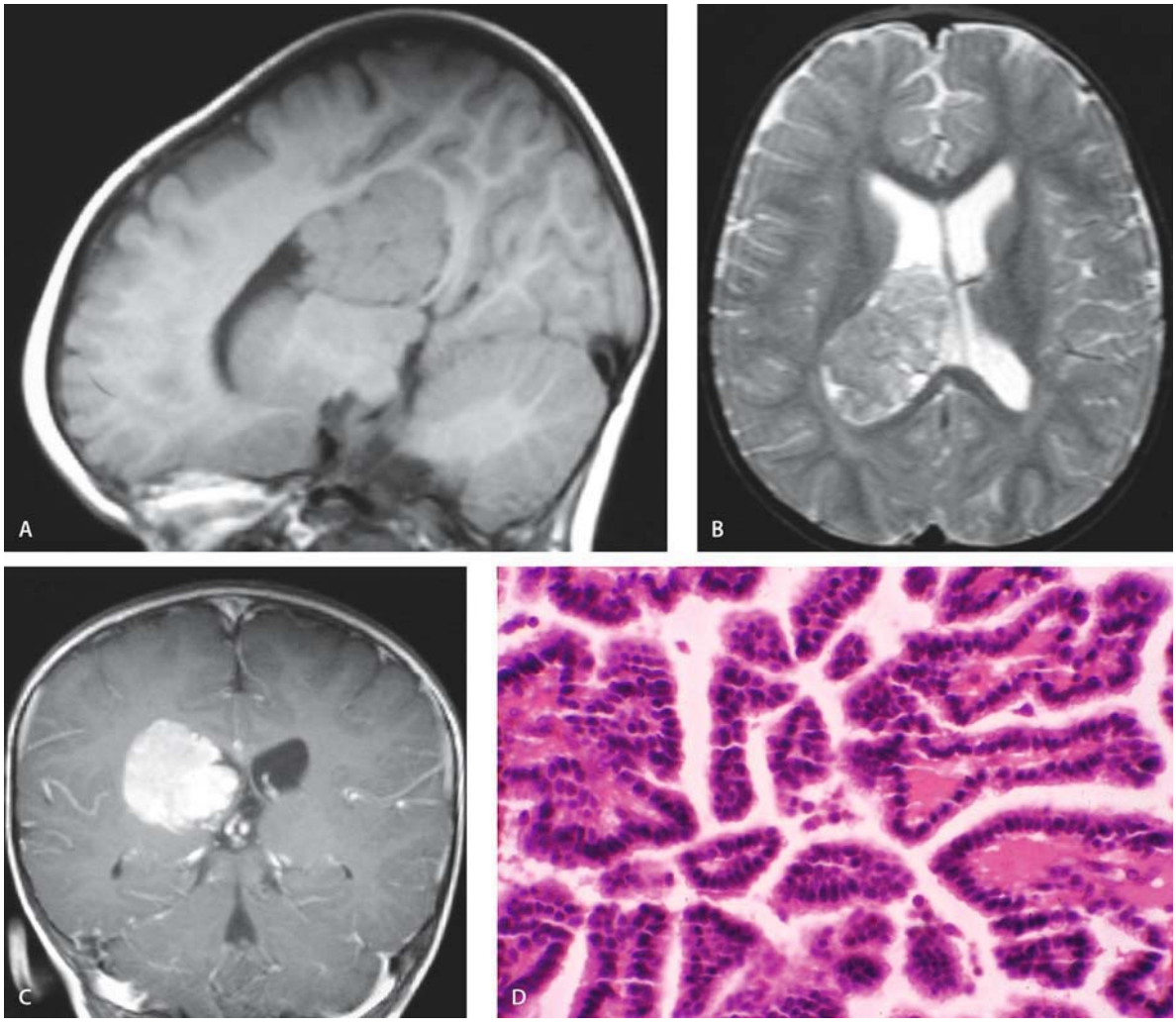

Fig. 17A–D. Choroid plexus papilloma. **A** Sagittal T1-weighted image shows a large, almost isointense intraventricular mass. **B** Axial T2-weighted image shows heterogeneous, high signal intensity mass, causing hydrocephalus. **C** Coronal T2 postcontrast image shows a markedly enhanced intraventricular mass. **D** Obvious papillary architecture is found. The layer of cuboidal cells without atypia is characteristic

On MRI (Fig. 17), choroid plexus papillomas are isointense to hypointense to the brain tissue and hyperintense to the cerebrospinal fluid in T1-weighted images. There are areas of signal void, suggesting increased regional blood flow or calcifications. On T2-weighted images, 60% are hyperintense to the parenchyma. Gadolinium enhancement is uniform [40, 41].

Angiography may demonstrate tumor blush. Lateral ventricular lesions are associated with enlarged choroid arteries [41].

Choroid plexus carcinomas often grow through the ventricular wall and invade the surrounding brain. They are of varied density on precontrast scan and enhance nonhomogeneously on postcontrast CT. Cysts, calcifications and hemorrhages are frequent.

On MRI they show mixed signal intensities on T1-weighted images because of the presence of cysts and hemorrhage. Irregular enhancement is noted after gadolinium.

Choroid plexus carcinomas have a marked propensity to metastasize through the cerebrospinal pathways, sometimes forming large subarachnoid masses [42] (Fig. 18).

Neuroepithelial Tumors of Uncertain Origin

Astroblastoma

Astroblastoma is a glial neoplasm characterized by a typical perivascular pattern of GFAP-positive astrocytic cells with broad, nontapering processes radiating towards central blood vessels [6]. Astroblastoma occurs most frequently in young adults, occasionally in children and rarely in infants. A case of congenital astroblastoma has been reported [43].

Radiopathological Correlation

The cerebral hemispheres are most often affected. Macroscopically, they are usually well-circumscribed solid masses with a homogeneous cut surface, although large examples may show both cyst formation and necrosis [36].

On CT and MRI, they are often enhancing, well-defined lesions (Fig. 19).

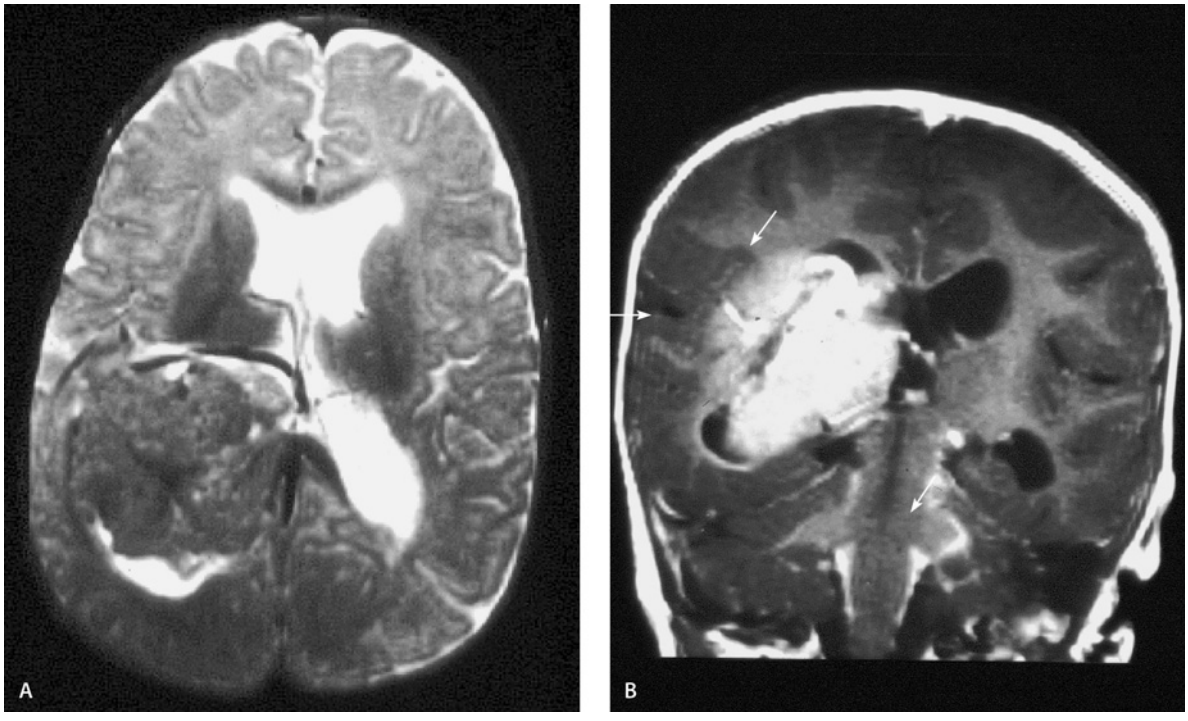

Fig. 18A, B. Congenital choroid plexus carcinoma. Axial T2-weighted (**A**) and coronal T1 postgadolinium images (**B**) of a choroid plexus carcinoma involves the trigone and right lateral ventricle. Note the hydrocephalus, a frequent finding among patients with choroid plexus tumors. This tumor tends to invade adjacent brain (*arrowheads*) and subarachnoid space (*arrow*) more readily, as seen in this case (**B**)

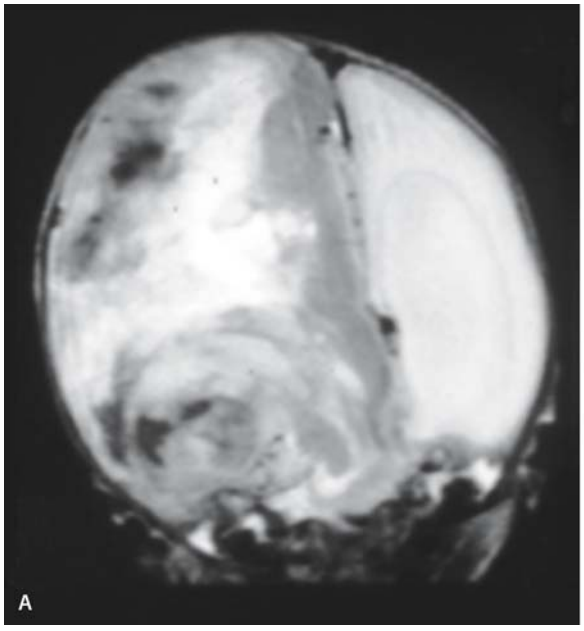

Fig. 19A, B. Astroblastoma. **A** Coronal T2-weighted MRI shows a large mixed-intensity tumoral mass with necrotic focus. **B** Extensive, well-circumscribed extensive hemispheric tumor with hemorrhagic component is a rare case of congenital tumor in a 35-weeksgestation newborn

Gliomatosis Cerebri

Diffuse glial tumors infiltrating the brain extensively so as to involve more than one lobe, gliomatosis cerebri are frequently bilateral and often extend to infratentorial structures and even the spinal cord [6].

Gliomatosis cerebri are malignant lesions, corresponding to grade III or IV in the WHO classification [1]. The term "gliomatosis cerebri" was originally coined by Nevin in 1938 [44] to describe infiltration by glial cells of extensive areas of the brain without formation of an obvious tumor mass.

Radiopathological Correlation

The most commonly affected areas, as defined by postmortem studies and images are: cerebrum (76%), mesencephalon (52%), pons (52%), and thalamus (43%). When the lesion involves the cerebral hemispheres, the centrum semioval is always affected, whereas the cortex is infiltrated in only 19% of such cases.

Macroscopically, two types of gliomatosis cerebri have been distinguished. Type I is the classic lesion, in which there is diffuse neoplastic growth and enlargement of involved existing structures, without the formation of a circumscribed mass. Type II gliomatosis, which may develop from type I, is associated with the presence of an obvious neoplastic mass, usually a malignant glioma [45].

On both on CT and MRI [46, 47], the pattern is infiltrative, with enlargement but not destruction of the involved structure. The gyri are swollen and flattened and the sulci are obliterated. On CT study, the lesion appears as poorly defined areas of low density [45]. In the T1-weighted images, MRI shows hypointense areas, whereas proton-density images and T2 reveal the full extension of the tumor with hyperintensity (Fig. 20). Enhancement is rare but has been seen in type II gliomatosis. We believe that ante-mortem diagnosis is possible by means of the correlation between the radiological findings and brain biopsy

Hemangioblastoma Supratentorial

Supratentorial hemangioblastomas are rare, although less than originally believed, owing to their earlier confusion with vascular meningiomas [1]. They probably represent about 5% of all cases and occur in a variety of locations, including the pituitary stalk, optic nerve and third and fourth ventricles. Proportions are hemispheric and superficial, and may show dural attachment or lie entirely within the leptomeninges. Both posterior fossa and supratentorial hemangioblastomas may be multiple at the time of presentation, especially in the context of von Hippel–Lindau disease (VHL).

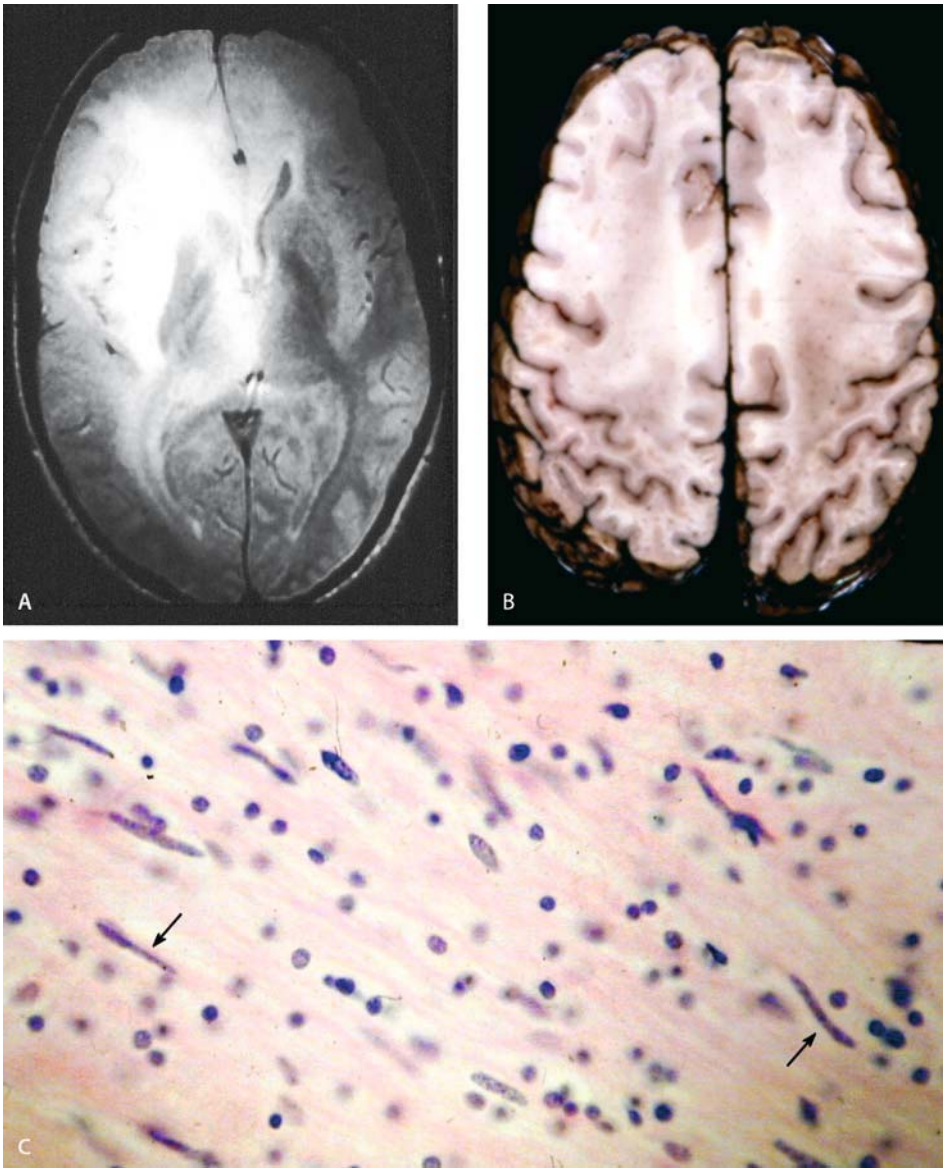

Fig. 20A–C. Gliomatosis cerebri. **A** Axial T2-weighted MRI scan shows extensive infiltration of the white and gray matter in both hemispheres and corpus callosum with obliterated sulci. **B** Axial section of the brain shows diffuse enlargement in the greater part of both centra semiovales. Note widened flattened circumvolutions and obliterated sulci in the left frontal lobe. **C** White matter, in centrum semiovale, shows diffuse infiltration by neoplastic spindle-shape astrocytes

Radiopathological Correlation

Macroscopic features are hemangioblastomas that are well-circumscribed red-brown tumors that may be totally intraparenchymal, partly extraparenchymal or entirely extra-axial. The intraparenchymal tumors usually have a superficial margin at the pial surface, and this is often covered by ecstatic and tortuous superficial blood vessels. Supratentorial hemangioblastomas sometimes have a dural attachment and grossly recable margins, especially when they are predominantly extraparenchymal. Intraventricular examples may appear macroscopically similar to ependymomas. Something over two-thirds of hemangioblastomas at any site take the form of a large cystic lesion with a well-defined, often quite small mural nodule. The cyst usually contains yellow or brown proteinaceous fluid, which coagulates at room temperature. Angiography has been the traditional radiological investigation of choice for intracranial hemangioblastoma (Fig. 21C) and remains an important diagnostic procedure despite the advent of CT and MRI [48]. In addition to establishing the blood supply and

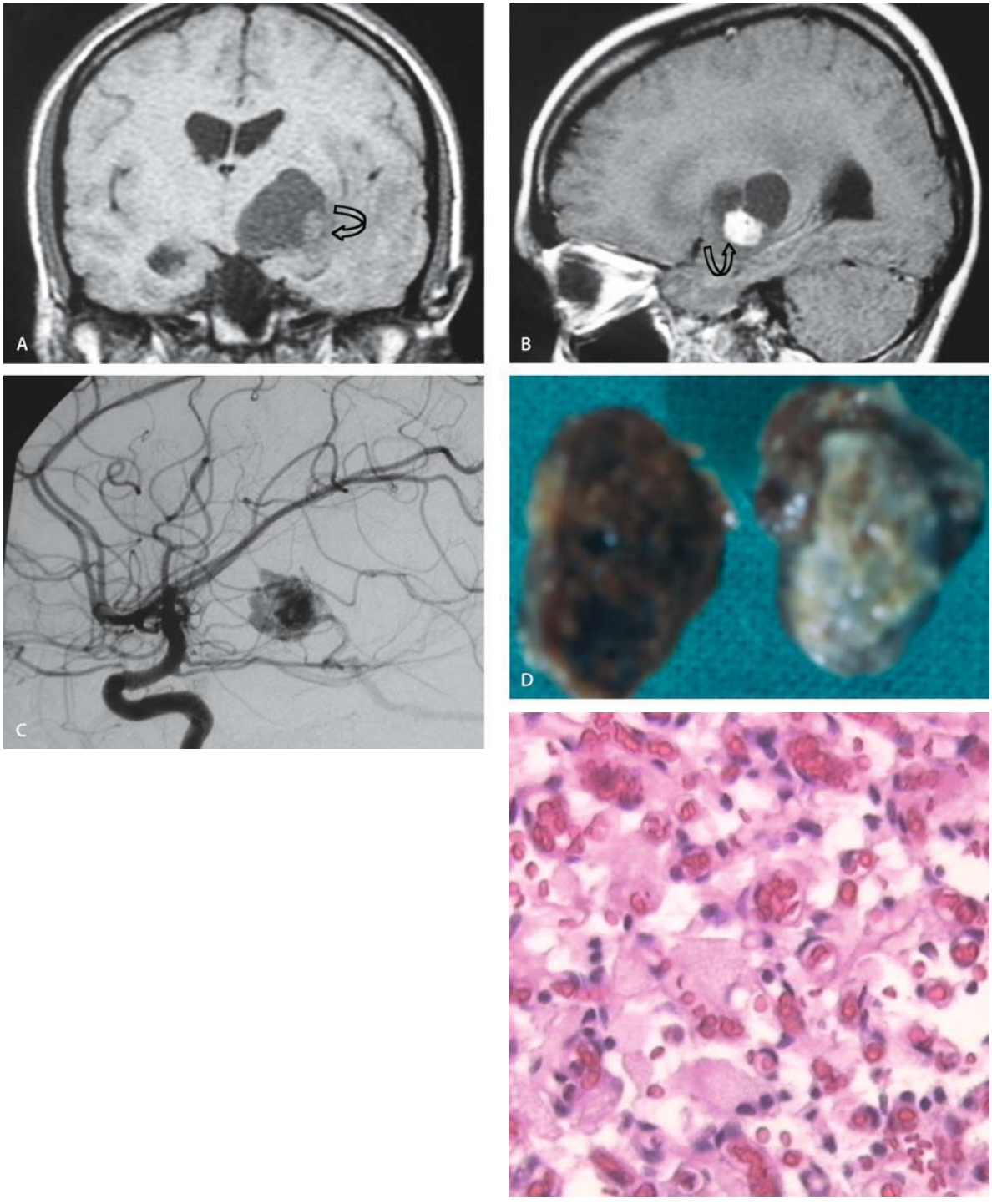

Fig. 21A–E. Supratentorial hemangioblastoma. Coronal T1-weighted image (**A**) and sagittal T1 image after contrast administration show a cystic lesion and an isointense mural nodule (*curved arrow*). Strong enhancement of the mural nodule (**B**). Carotid angiography (**C**) shows a vascular mural nodule. **D** The removed nodule shows in the cutting a cystic and hemorrhagic surface while it is nodular externally. **E** A network of capillary channels with interstitial clear cells are characteristic features

vascular drainage of the tumor, angiography is a sensitive method of locating noncystic examples and allows detection of other unsuspected tumors overlooked by localized scans. For cystic tumors, CT allows precise definition at the cystic cavity and is often used in combination with angiography. Solid tumors and mural nodules are isodense with brain and not well seen in nonenhancement scans, but they show uniform, intense enhancement with intravenous contrast media. MRI again provides a good definition of cystic tumors, which are visible as well-defined low-signal areas, slightly hyperintense to CSF on T2-W. However, gadolinium administration is essential to identify to mural nodules of cystic lesions and to define the extent of solid tumors (Fig. 19). MRI also allow visualization of the large abnormal vessels feeding and draining the tumors, which show as flow void on T2-W [49].

Chordoid Glioma of the Third Ventricle

The lesion presents in adults with the generic symptoms attributable to the obstructing third ventricle mass. Females are more frequently affected.

Radiopathological Correlation

Macroscopic features are the solid lobulated lesion that often distends the third ventricle and adheres to the wall. The lesion has a sharp interface with surrounding brain parenchyma. Its substance consists of ribbons, cords, and lobule of uniform, epithelial-like cells in a faintly basophilic, mucinous matrix [50]

Radiological Features

The lesions are remarkably similar from case to case, all are discrete, smooth-contoured, contrast-enhancing, third-ventricle masses that obstruct CSF flow and produce hydrocephalus [51].

Neuronal and Mixed Neural-Glial Tumors

Gangliocytoma and Ganglioglioma

Tumors are composed of neoplastic, mature ganglion cells, either alone (gangliocytoma) or in combination with neoplastic glial cells (ganglioglioma) [6]. Gangliocytoma is classified into WHO grade I, while ganglioglioma may be grade I or II [1]. These two types represent 1.3% of all brain tumors. Any age can be affected, but 80% occur in individuals under 30 years old.

Patients typically present with seizures or focal neurological signs. These tumors preferentially occur in the temporal lobe, followed by the frontal and parietal lobes.

Radiopathological Correlation

Macroscopically, gangliocytomas and gangliogliomas are solid or cystic tumors that are not usually accompanied by mass effects. Calcification may be present. Hemorrhage and necrosis are rare.

CT shows a well-circumscribed mass, often peripherally located in the cerebral hemispheres. The lesion may be solid or cystic. The tumor is isodense or hypodense and may show calcifications. Surrounding edema is only occasionally noted, and hemorrhage is rarely identified. Contrast is variable and usually of moderate intensity. Scalloping of the calvaria may be seen adjacent to superficially located tumors [52, 53].

On MRI the most common appearance is a well-delineated temporal or frontal lobe mass that is hypointense in T1- and hyperintense in T2-weighted images (Fig. 22). Enhancement varies in intensity from weak to marked, and may be solid, at the rim or nodular [54].

Desmoplastic Infantile Ganglioglioma

Desmoplastic astrocytoma is a clinicopathological entity (WHO grade I), characterized by large tumors that involve the superficial cortex and occur in infants, with a generally good prognosis following surgery [5].

Desmoplastic gangliogliomas are rare supratentorial neuroepithelial neoplasms that present in early infancy, between 1 and 24 months of age (mean, 6.3 months). They invariably arise in the supratentorial region and affect more than one lobe, preferentially the frontal and parietal, followed by the temporal.

The symptoms and signs are of short duration and include increasing head circumference and tense, bulging fontanelles.

Radiopathological Correlation

Macroscopically these tumors are large, measuring up to 13 cm in diameter, and have deep uni- or multiloculated cysts filled with clear or xanthochromic fluid. The solid superficial portion is primarily extracerebral, involving the leptomeninges; the superficial cortex is commonly attached to the dura [55].

Plain skull films show sutural diastasis with or without erosion of the internal table adjacent to the tumor. On CT, the lesion is a large, well-defined cystic region, similar to cerebrospinal fluid, with a solid isodense or slightly hyperdense superficial portion, which shows contrast enhancement (Fig. 23). T1-weighted MR images characteristically show a hypointense cystic mass

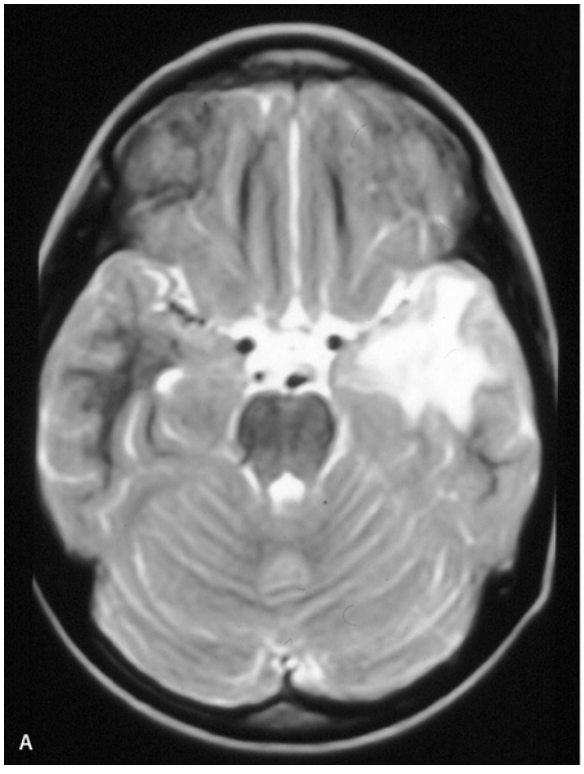

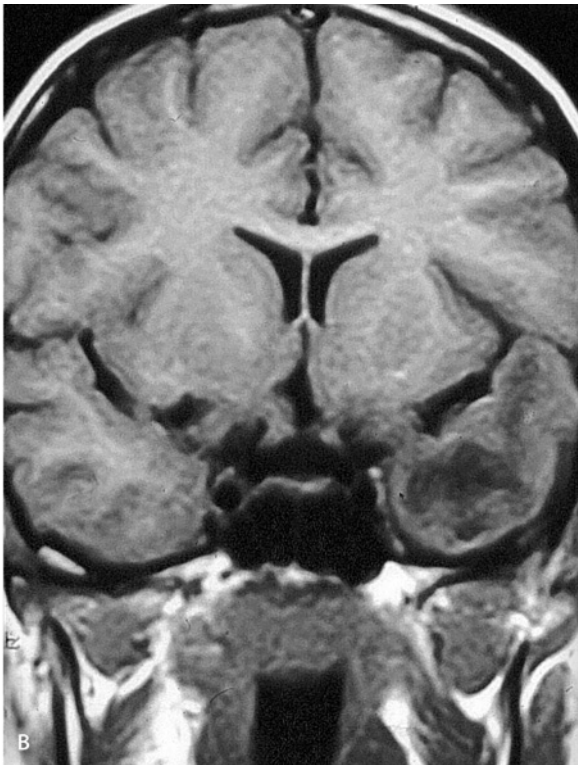

Fig. 22A, B. Ganglioglioma. **A** Axial T2-weighted image demonstrates hyperintense left temporal lobe mass. **B** Coronal T1-weghted image shows low-intensity area

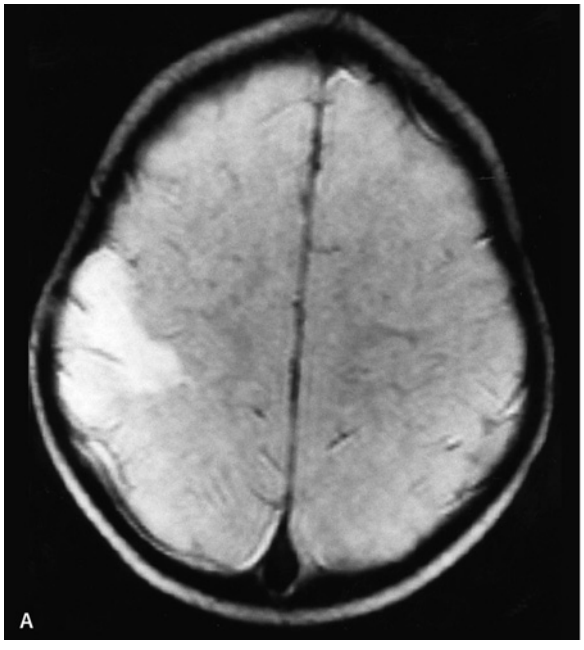

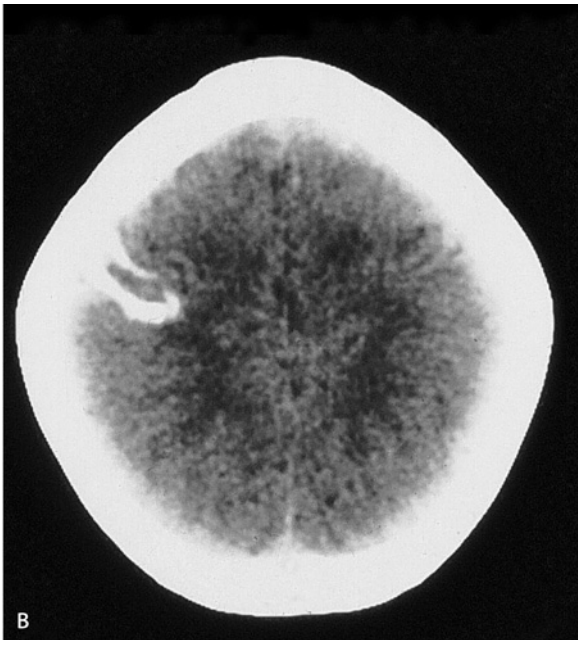

Fig. 23A, B. Dysembryoplastic neuroepithelial tumor. **A** Axial T2-weighted MR image shows a well-demarcated hypersignal. The cortical topography of the lesion, which looks like microgyri, can be seen. **B** CT in the same patient demonstrates gyral calcifications and involvement of the overlying calvaria

with a peripheral solid component that enhances with gadolinium. The solid portion is heterogeneous in T2-weighted images.

Dysembryoplastic Neuroepithelial Tumor

Dysembryoplastic neuroepithelial tumors (WHO grade I) are benign, usually supratentorial mixed glial neuronal neoplasms, characterized by multinodular architecture and a predominantly intracortical location. They may be associated with cortical dysplasia [4, 56].

A large majority of dysembryoplastic neuroepithelial tumors that are identified during surgery for epilepsy are located in the temporal lobe and preferentially involve the mesial structure [57]. However, they may develop in any part of the supratentorial cortex.

Radiopathological Correlation

The gross appearance may reflect the complex histological architecture of the lesion. The most typical feature is the viscous consistency of the ganglioneural component. The affected cortex is often expanded and, although the tumor is predominantly intracortical, the subcortical white matter may also be affected.

On imaging, the cortical topography of the lesion is an important criterion for differentiating between these tumors and gliosis. On CT, definition of the overlying calvaria is often seen, and this finding supports the diagnosis of dysembryoplastic neuroepithelial tumors. Calcifications are often present (Fig. 24B).

Hypointense on the T1-weighted and hyperintense on the T2-weighted MR images, these tumors can resemble macrogyria (Fig. 24A). True cyst formation is seen in a minority of cases. About one-third show contrast enhancement on CT or MRI, which often appears as multiple rings [58, 59].

Central Neurocytoma

A WHO grade I neoplasm composed of uniform round cells with neuronal differentiation, central neurocytoma is typically located in the lateral ventricles, in the region of the foramen of Monro [3, 60]. These tumors affect mainly young adults, and have a favorable prognosis. The incidence of central neurocytoma is estimated at 0.2%–0.5% of all intracranial tumors.

The clinical history is short and the majority of patients present with symptoms of intracranial hypertension.

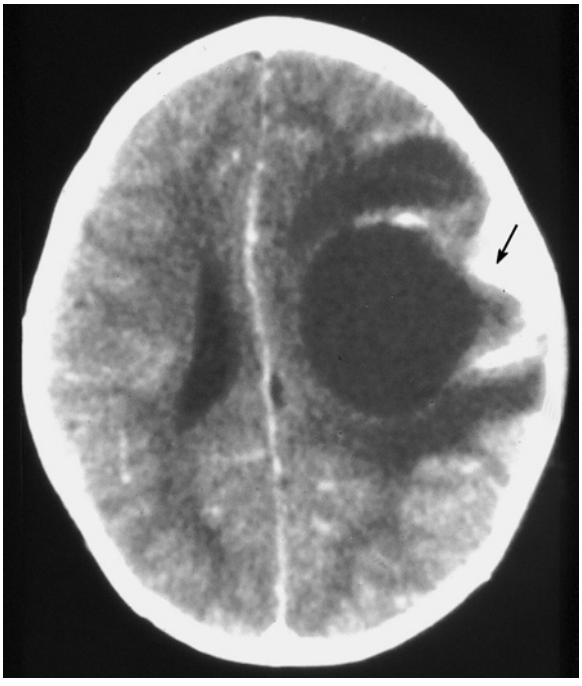

Fig. 24. Desmoplastic infantile ganglioglioma. CT after contrast administration. Cystic and solid (*arrow*) components

Radiopathological Correlation

Macroscopically, central neurocytoma is a soft, well-circumscribed neoplasm that often contains flecks of calcification and occasional hemorrhage.

On CT, the majority are visualized as well-circumscribed nonhomogeneous masses, which are isodense or slightly hyperdense to the parenchyma. Calcifications (52%) and cystic areas (67%) are often seen (Fig. 25A). Contrast enhancement and associated hydrocephalus are present [61, 62].

On MRI, the T1- and T2-weighted images show an essentially isointense lesion with nonhomogeneous regions reflecting areas of calcification and cyst formation. Areas of hypointensity in T1-W images are probably related to focal calcification, and areas of hyperintensity on T2-W to areas of cystic necrosis. Tumor enhancement is moderate to strong after gadolinium administration [61, 62] (Fig. 25B).

Cerebral angiography demonstrates a faint tumor blush persisting into the late venous phase [63].

Cerebral Neuroblastoma

The neuroblastoma is a another small blue cell tumor of presumed neuronal linage that occurs as a tumor of children and young adults: approximately half are diagnosed in the first 5 years of life.

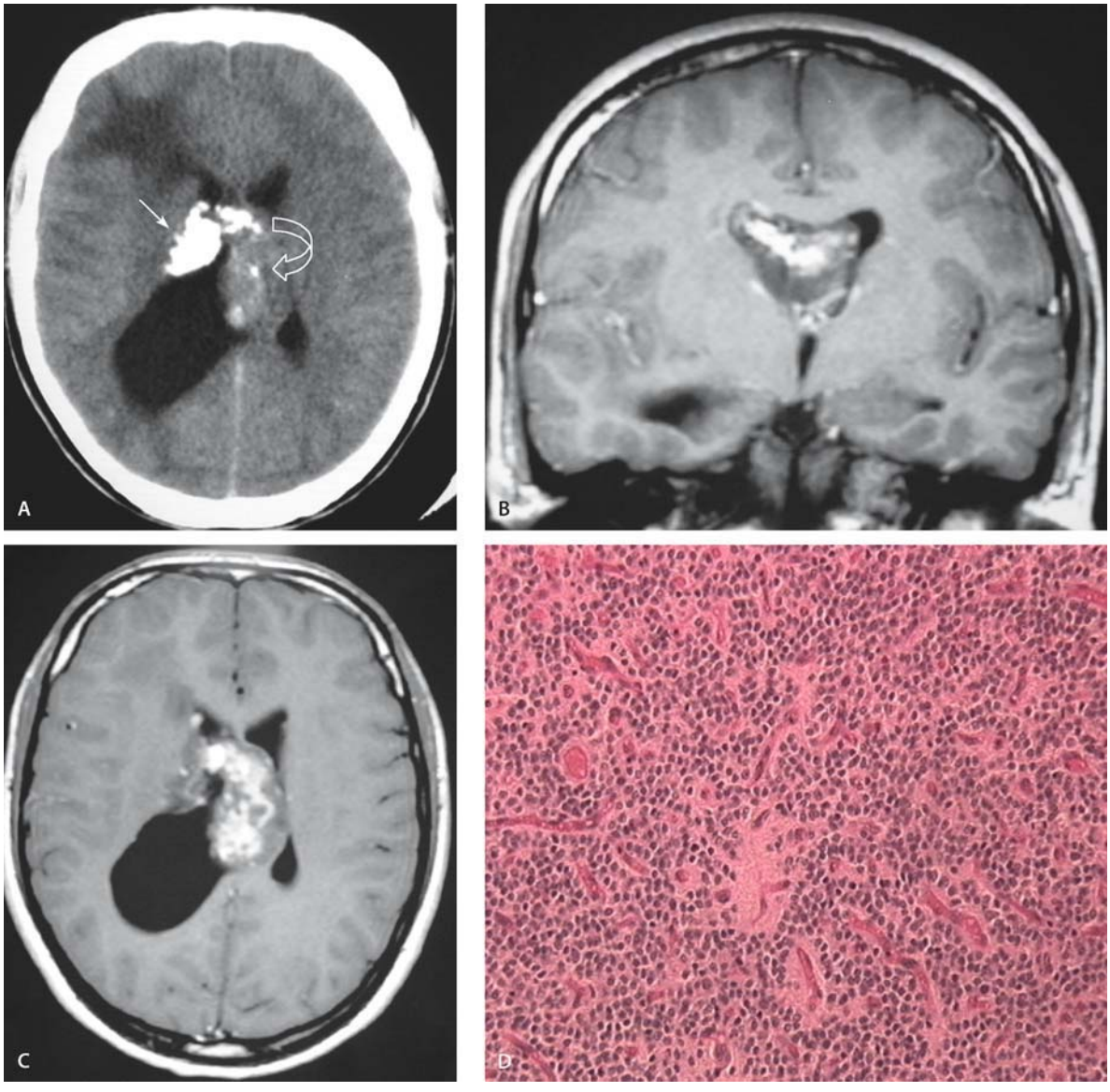

Fig. 25A–D. Central neurocytoma. **A** CT shows mixed calcified (*arrow*) and isodense (*curved arrow*) intraventricular mass. No symmetrical hydrocephalus. Coronal (**B**) and axial (**C**) postcontrast T1-weighted MR image shows a large enhancing tumor occupying the frontal horns of both lateral ventricles with obstruction of the foramen of Monro. **D** A sheet of cells with uniform, round nuclei which have fibrillary cytoplasm

Radiopathological Correlation

The macroscopic appearance shows the neuroblastoma growing as expansile masses, within the brain, typically with gross circumscribed, pushing borders and often has attained a large size (several centimeters in diameter) by time of diagnosis. The tumors tend to be firm and are particularly superficial and desmoplastic. Multilobulation and cyst formation are common, the cyst often as large than the tumor itself. Widespread dissemination along the CSF pathways is a common finding at autopsy.

The unenhanced CT appearance is that of an inhomogeneous mass with hypodense regions due to necrosis and cyst formation and hyperdense regions due to calcification. A large amount of mass effect and edema is commonly present. Inhomogeneous contrast enhancement is typically seen. Dissemination through the subarachnoid space and ventricular system can be seen as foci of abnormal contrast enhancement within such spaces.

The lesions are inhomogeneous on T2-W MRI due to the presence of necrosis and hypointense regions of hemorrhage and calcification. Contrast enhanced MRI

is more sensitive than CT for determining tumor extent, including subarachnoid and meningeal spread.

Supratentorial Primitive Neuroectodermal Tumor

Supratentorial primitive neuroectodermal tumor (WHO grade IV) is an embryonal tumor composed of undifferentiated or poorly differentiated neuroepithelial cells, which have a capacity for divergent differentiation along neuronal astrocytic, ependymal, vascular or melanotic lines. Primitive neuroectodermal tumors are uncommon in the supratentorial compartment [64].

Radiopathological Correlation

The parenchymal tumors are massive growths with or without cysts or hemorrhage. The demarcation between tumor and brain may range from indistinct to clear-cut. They are soft, unless they contain a prominent desmoplastic component.

Imaging typically reveals a large mass deep in the cerebral white matter. Necrosis or cyst formation is seen in 30%–60%, with calcifications in 50%–70%. Hemorrhage is always noted and may be solid, heterogeneous or ring-like, depending on the degree of cystic or necrotic changes (Fig. 26). The lesions are iso- to hyperdense on CT. Surrounding edema is not usually extensive [65, 66].

Lymphomas

Malignant lymphomas of the CNS include: 1) primary CNS lymphomas (PCNSL), defined as extranodal malignant lymphomas arising in the CNS in the absence of obvious lymphoma outside the CNS at the time of diagnosis, 2) secondary involvement of the CNS in systemic lymphoma.

The current annual incidence [61] in immunocompetent patients is 0.3 new cases per 100,000 person–years. In AIDS patients, the incidence of 4.7 per 1000 person–years is about 3,600-fold higher than in the general population. Primary CNS lymphoma is the second most common (following toxoplasmosis) CNS mass lesion in adult AIDS patients and is the most common mass lesion in pediatric AIDS patients. Secondary CNS involvement by systemic lymphoma occurred in approximately 25% of cases before the advent of effective chemotherapy.

Epstein-Barr virus is implicated in the pathogenesis of PCNSL in all immunocompromised patients and 15%–20% of immunocompetent patients.

About 60% of primary CNS lymphoma involve the supratentorial space. The cerebral white matter of the frontal lobes is the most common site for CNS lymphoma, and in the temporal, parietal and occipital lobes in decreasing order of frequency. Approximately 2%–50% are multiple. Secondary meningeal spread is seen in 30%–40% of primary lymphomas. One of the most characteristic features of CNSL is its tendency to spread through the ependyma, the meninges, or both.

Peak incidence is seen in the sixth and seventh decades in immunocompetent patients and in the fourth decade in immunocompromised patients.

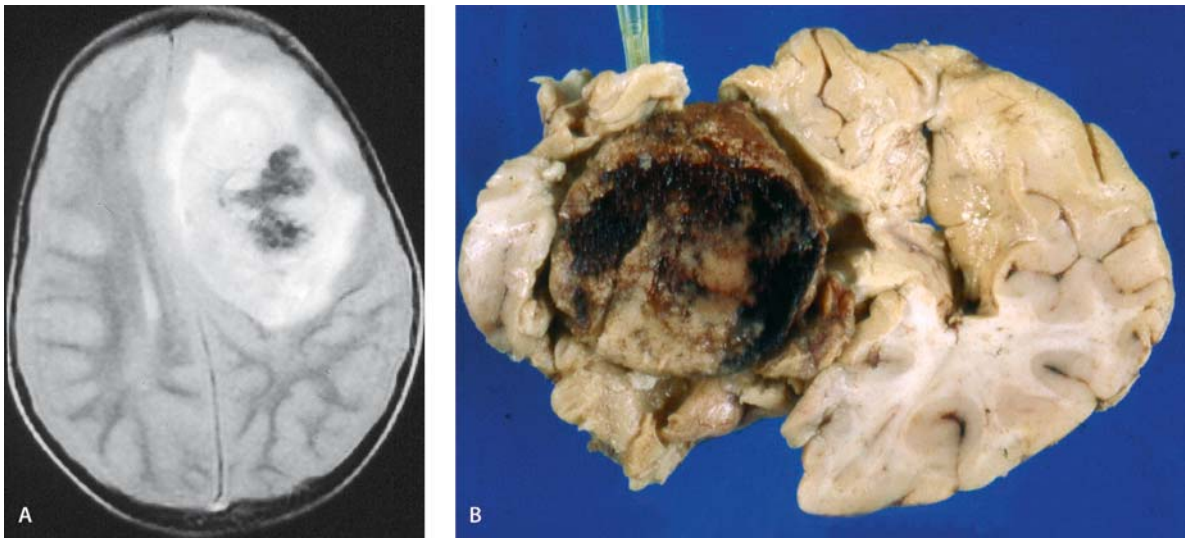

Fig. 26A, B. Primitive neuroectodermal tumor. **A** Axial T2-weighted image MR scan shows heterogeneous left frontal mass with hemorrhage (low-signal areas). **B** A sharply circumscribed and soft tumor in the left frontal lobe occurred in a 6-year-old girl. Terminal intratumoral hemorrhage can be seen

PCNSL present as space-occupying lesions causing raised intracranial pressure, focal neurological deficit or epilepsy.

Radiopathological Correlation

Macroscopically, primary lymphomas appear as simple or multiple masses in the cerebral hemispheres. While they are often deep-seated and adjacent to the ventricular system, superficial tumors are also encountered. The tumors manifest as grayish-tan to pink homogeneous, circumscribed nodular masses with a firm to friable consistency and a granular surface. The lesion is frequently surrounded by edema. Demarcation from the surrounding parenchyma is variable. Some tumors appear well-delineated, as in metastasis. When a diffuse border and architectural effacement is present, the lesions resemble gliomas. It is impossible to grossly determine the extent of the tumor. Focal necrosis is present in AIDS patients.

The infiltrated meninges appear thick, and subependymal intraventricular spread may manifest as areas of irregularity and softening.

Non-AIDS lymphomas appear as hyperdense masses on nonenhanced CT examination because of the cellularity of the lesion, with little associated edema. In AIDS-related CNS lymphoma, the lesion may be hyperdense or hypodense on noncontrast CT. Hypodensity is often related to the high degree of necrosis present in AIDS-related lymphomas. The hypodense lesions often have hyperdense rims where there is less necrosis. Hemorrhage in this lesion is uncommonly seen on CT. Calcification is rare. There is usually a variable degree of mass effect and edema.

Postcontrast CT demonstrates dense enhancement, which is homogeneous in non-AIDS lymphoma but may be homogeneous (Fig. 27), heterogeneous, or show ring enhancement in AIDS-related lymphoma. This again may be related to the greater frequency of necrosis in the latter. Periventricular enhancement suggests subependymal spread and is often a valuable clue in the radiographic diagnosis of CNS lymphoma [67, 68].

The dense cellularity of lymphoma renders these lesions isointense or hypointense to the parenchyma in all MRI sequences. These signal characteristics strongly suggest the diagnosis in the appropriate clinical setting. Administration of gadolinium results in solid or ring-like enhancement. Ring enhancement is more frequently associated with necrotic lesions. Nonenhancing PCNSL has been thought to be extremely rare (Fig. 28) [69, 70].

The recent use of T1 brain SPECT has made it possible to differentiate between these tumors and infec-

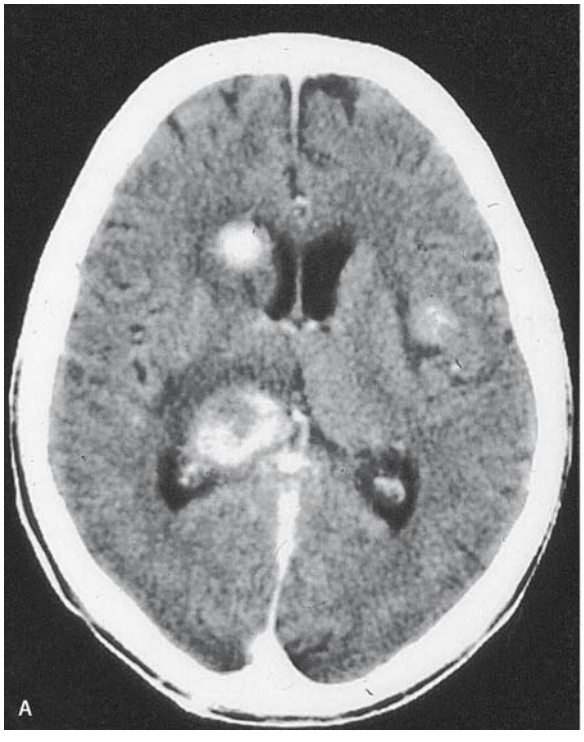

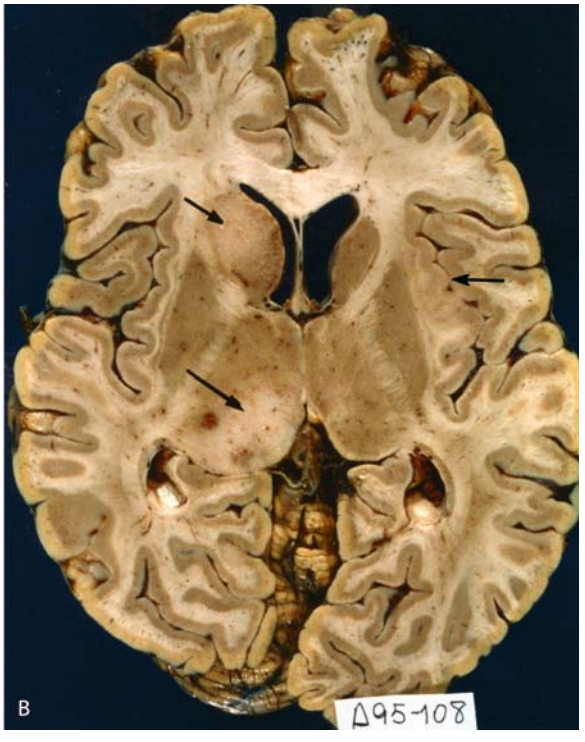

Fig. 27A, B. Primary CNS lymphoma in AIDS patient. **A** Axial contrast-enhanced CECT shows multiples homogeneous enhancing lesions in the right caudate nucleus, left thalamus and left sylvian fissure. **B** Right caudate and thalamus nuclei show a definite pale homogeneous space-occupying mass with ill-defined outlines. Left claustrum is blurred (*arrows*)

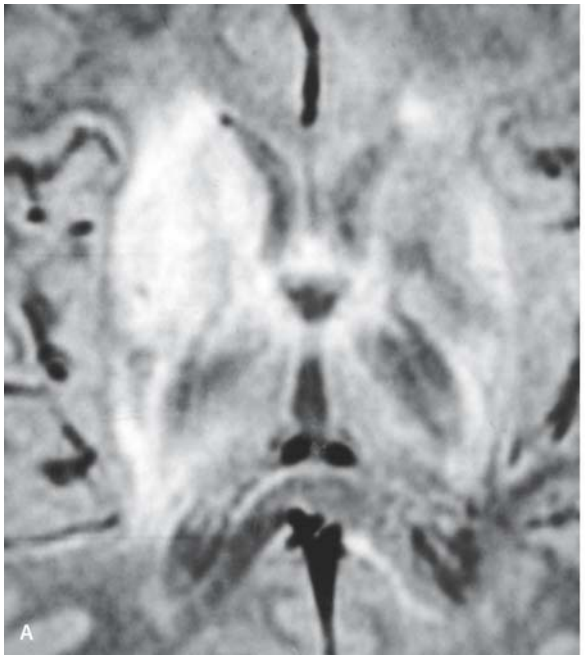

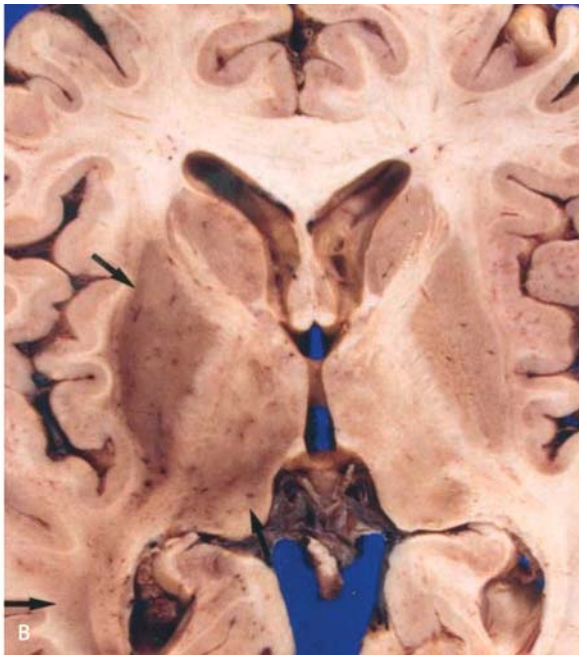

Fig. 28A, B. Nonenhancing primary CNS lymphoma. **A** Axial T2-weighted image shows multiple high-intensity areas in both hemispheres (caudate nucleus, putamen, internal capsula). **B** A rare case of extensive diffuse lymphoma in which the brain appears virtually normal grossly. Left nuclei and deep regions show a darker brownish appearance (*arrow*)

tion (commonly toxoplasma) in AIDS patients. Neoplasms demonstrate increased uptake of thallium, due to their metabolic activity, whereas infection does not. A positive T1 brain SPECT study strongly suggests lymphoma in a patient with AIDS, and biopsy is obtained for confirmation [63].

Radiological studies revealed multiple lesions in 16% of cases, but the true prevalence of multiple lesions proved at pathological examination is 20%–44% [6]).

Metastasis

In the context of this study, metastasis refers to tumors involving the CNS that originate from, but are discontinuous with, primary systemic neoplasms. Solitary or multiple deposits of secondary neoplasms may occur in the CNS parenchyma and cause symptoms of increased intracranial pressure, focal neurological deficit, and epilepsy.

Intracranial spread of tumor is a relatively common occurrence, and metastases are found in approximately 25% of all patients who die from cancer. The initial sources of CNS metastasis are lung, breast, gastrointestinal tract and malignant melanoma. The supratentorial compartment is the most common site, accounting for 80%–85% of metastatic foci. Eighty percent of brain metastases are located in the arterial border zones of the cerebral hemispheres.

Radiopathological Correlation

Metastatic neoplasms form spherical masses in the brain and surrounding edema is evident. The deposit may be firm or have a soft, mucoid or necrotic center. Hemorrhagic deposits are characteristic of melanoma, choriocarcinoma, lung and adenocarcinoma. Malignant melanoma may show obvious pigmentation.

On CT study, the majority of metastases are isodense in comparison to the adjacent brain. Hyperdense metastases are seen with small round cell tumors or hemorrhage (Fig. 29A, B). Cystic metastases are uncommon (Fig. 29E, F). Edema associated with metastasis can be striking and, in some cases, it is the only abnormality seen. After contrast administration, parenchymal metastasis enhances strongly and solid (Fig. 29C, D, G, K) and ring-like patterns are common [71].

On MRI the signal characteristics of metastatic tumors are also variable. Nonhemorrhagic metastases are slightly hypointense in relation to the normal brain tissue on the T1-weighted images. Certain nonhemorrhagic metastatic tumors such as malignant melanoma

Fig. 29A–H. Metastasis. **A**, **B** Acute hemorrhagic metastasis. **C**, **D** Melanoma metastasis. **E**, **F** Intestinal adenocarcinoma metastasis with a cystic mucinous component. **G**, **H** Miliary bronchial carcinoma metastasis

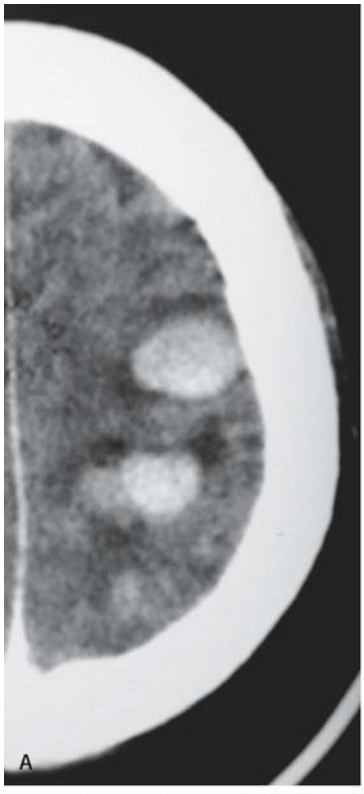
A

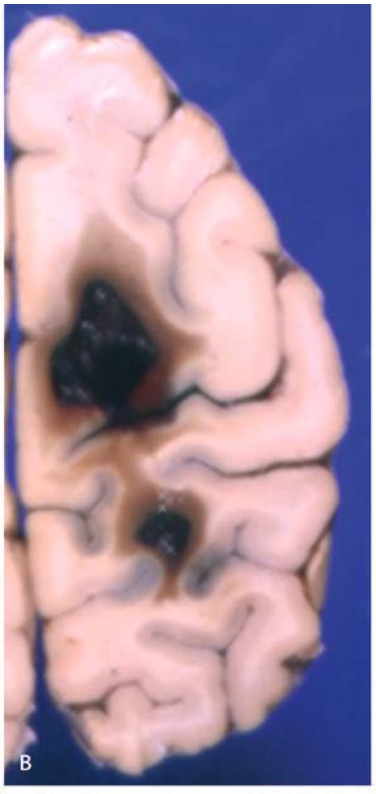
B

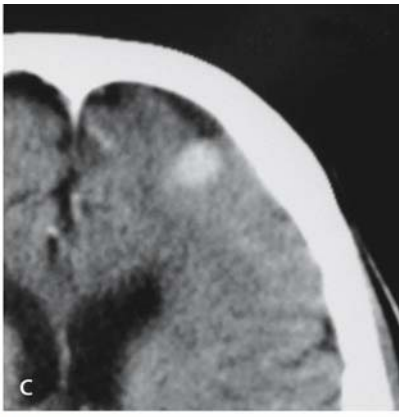
C

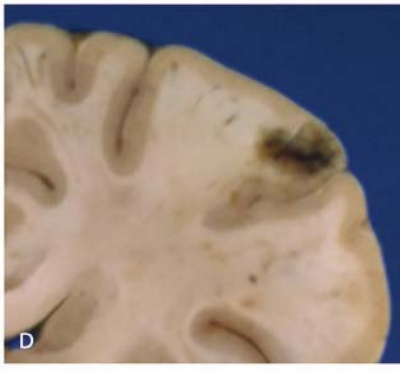
D

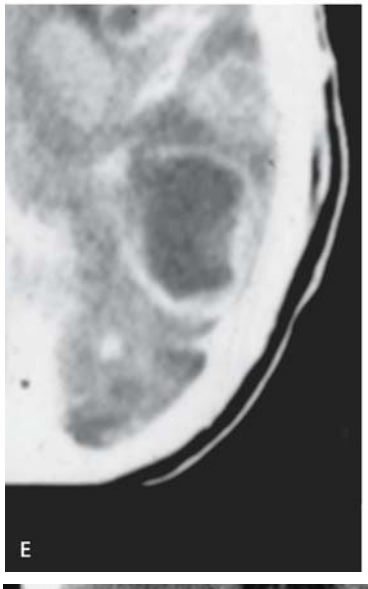
E

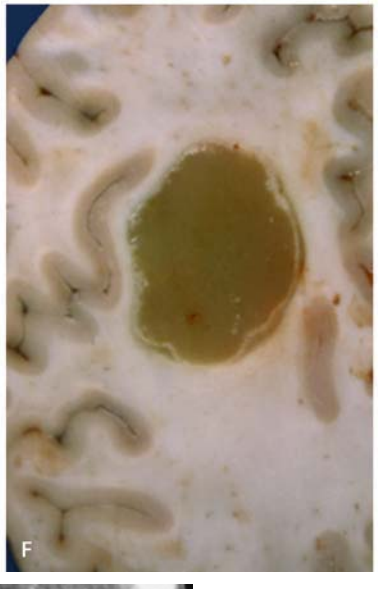
F

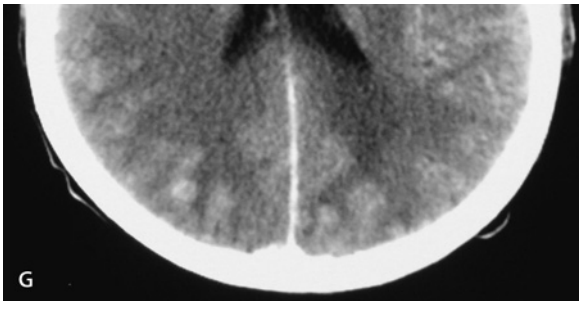
G

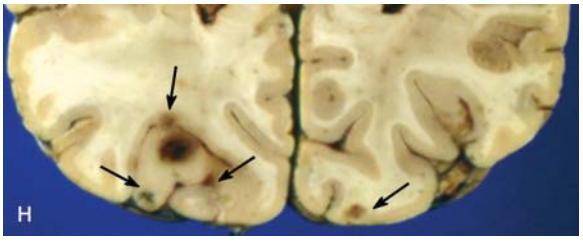
H

are often hyperintense on T1-W. Generally metastases appear as hypointense on T1- and hyperintense on T2-weighted images, with markedly enhanced adjacent parenchymal edema. Solid, rim and mixed patterns occur.

Emerging CNS Neoplasms

Since the appearance in 2000 of the WHO classification for central nervous system neoplasms, numerous descriptions of new entities or variants have appeared in the literature. In the group of neuronal and mixed glioneuronal tumors are lesions with distinctive morphological features that are still not included in a precise classification, including extraventricular neurocytoma, papillary glioneural tumors ad dysembryoplastic-like tumor of the septum pellucidum [72].

Extraventricular Neurocytomas

Extraventricular neurocytomas (EVNS) are mentioned but not formally listed in 2000 WHO classification of tumors of the CNS. Nonetheless, reports of such lesions are increasing and recent studies have better delineated their clinicopathological features [73, 74].

Extraventricular neurocytic neoplasms (Fig. 30) that arise within central nervous system parenchyma share histological features with the most common central neurocytoma, but exhibit a wider morphological spectrum. Neurocytes most often demonstrate finely granular, slight eosinophilic cytoplasm. Less often than their intraventricular counterpart, they exhibit cytoplasmic clearing, which in combination with round nuclei suggest a diagnosis of oligodendroglioma. With regard to biological behavior, like central neurocytoma, most EVNSs are well differentiated and do not recur, especially after complete resection.

Papillary Glioneural Tumors

This uncommon lesion is uniquely characterized by pseudopapillary structures of hyalinized blood vessels surrounded by astrocytic cells.

This tumor occurs in patients of various ages and there is no gender predilection. Occurrence in young children as well as in elderly persons has been observed [13, 14]. The tumors present radiographically as contrast-enhancing cystic masses of variable size, affecting the cerebral hemispheres with no specific location [75].

Follow-up data indicate no evidences of recurrence in tumor totally resected grossly during intervals ranging from 6 months to 7 years [75–77].

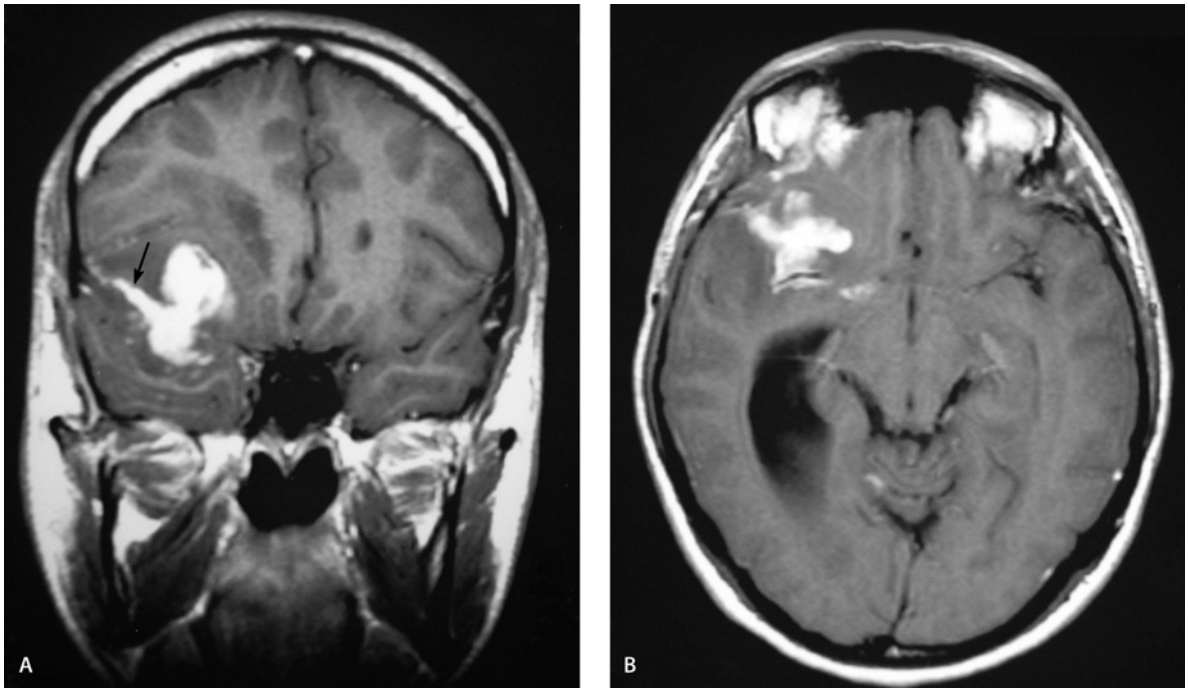

Fig. 30A, B. Extraventricular neurocytoma. Coronal and axial T1-weighted MRI after contrast administration shows enhancing mass arising in the sylvian fissure (*arrow*)

DNT-Like Tumor of the Septum Pellucidum and Caudate Nucleus Area

The DNT tumor is now a well-known, seizure-producing entity that occurs characteristically in the cerebral cortex of children and young adults.

Most recently, DNT-like lesions have been reported to occur in the extracortical locations [78]. The better-characterized location of such DNT-like lesions is the caudate nuclei/septum pellucidum area [79, 80]. As a consequence of this location, the presenting symptoms are those increasing intracranial pressure, in contrast to

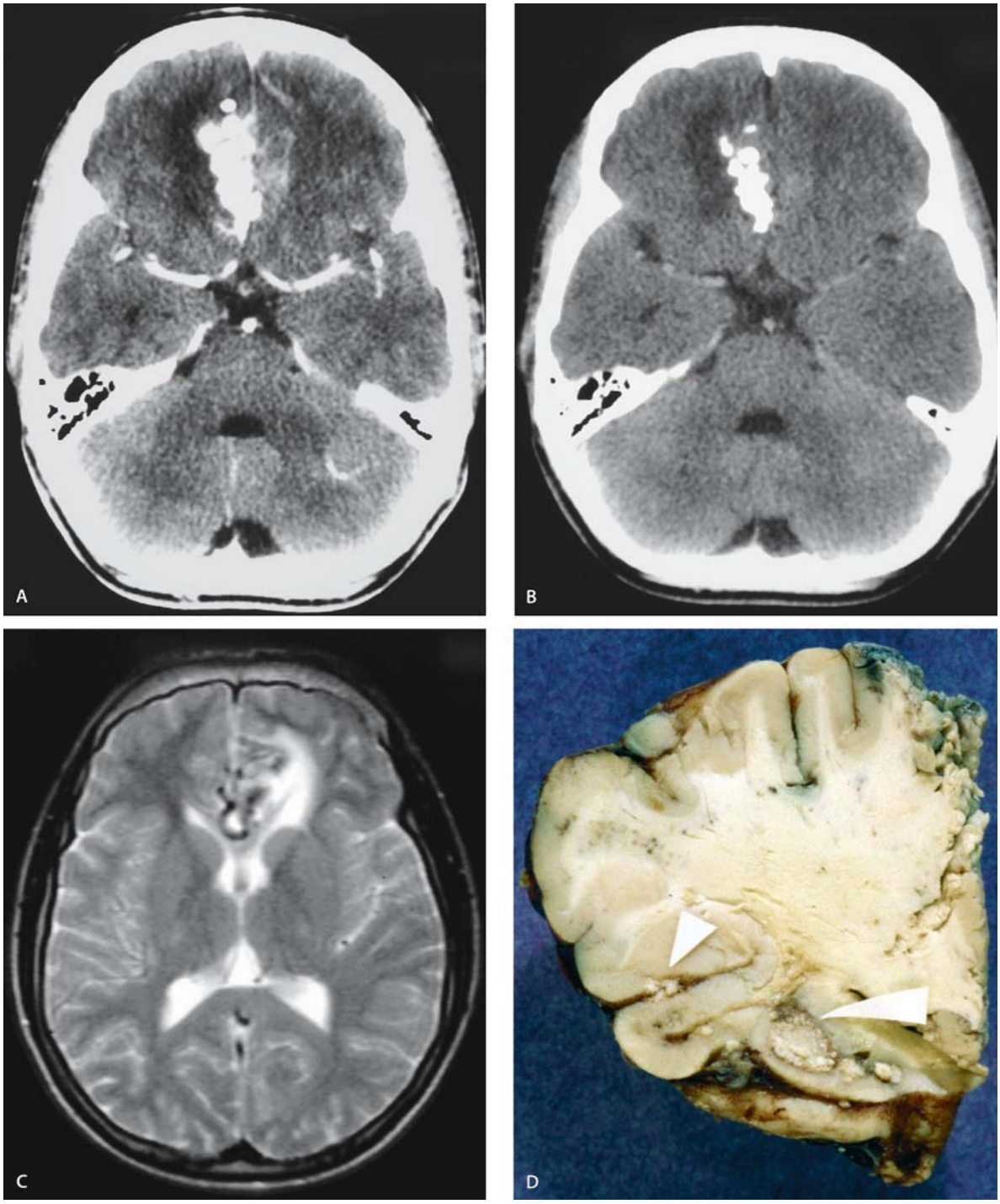

Fig. 31. A–D

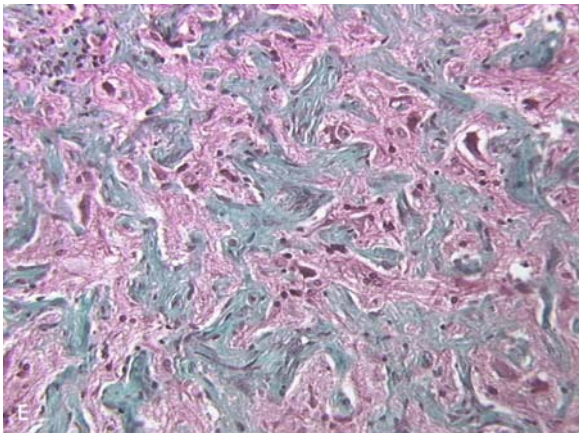

Fig. 31. A–E CT. Gyral calcifications located in frontal cortex of interhemispheric fissure. Hypodense area. **B** Contrast-enhanced CT shows enhancing surrounding area of calcification with invasion of the left frontal lobe. **C** Coronal T1-weighted MRI demonstrates cystic component and areas of flow void. **D** Frontal lobe shows large cortical calcifications (*white arrowheads*). **E** Diffuse cortical meningioangiomatosis. Predominance of meningothelial cells is seen (*green in trichrome staining*)

the seizures observed in the classic intracortical counterpart.

Radiopathological Correlation

Radiographically, the tumors extend in the lateral ventricle from the septal region and obstruct the foramen of Monro, causing varying degrees of hydrocephalus. The lesions are lobular, well-delineated, hypointense on T1-weighted images and hyperintense on T2-weighted images and no enhancing. The histological features include a mucin-rich background, oligodendrocyte-like cells, so-called floating neurons, specific glioneural elements. Distinction from more aggressive neoplasms such as oligodendrogliomas or well-differentiated, diffuse astrocytoma is mandatory because these tumors appear to behave in the benign fashion, similar to that of cortical DNTs [80].

Meningioangiomatosis

Meningioangiomatosis (MA) is a focal lesion of the leptomeninges and underlying cortex, was originally described in association with von Recklinghausen's disease (neurofibromatosis, NF) and has since been known to also occur sporadically [81]. Sporadically MA is fours times more common than MA with NF. MA presents clinically as partial seizures that are difficult to control or as an incidental finding in individuals who are asymptomatic.

Radiopathological Correlation

All patients' MA lesions were confined to the cortex, with variable involvement of the overlying leptomeninges characterized by leptomeningeal and meningovascular proliferation. Cases were classified into those with predominantly cellular and those with predominantly vascular lesions.

Patients with and without NF had similar findings on the various imaging modalities. The commonest finding on CT scan was a calcified enhancing lesion with surrounding low density (Fig. 31) [82]. MRI showed low or mixed central signal on T1 and T2-W in 84% of cases. Gadolinium enhancement is frequently. MA resembled various diseases on MRI, including meningioma, acute hemorrhage, and calcified arteriovenous malformation [81, 83].

Proton MR Spectroscopy (^{1}H MRS) in the Diagnosis of Brain Tumors

Astrocytic Tumors (Low-Grade Astrocytoma, Anaplastic Astrocytoma and Glioblastoma)

In this group, glioblastomas are characterized by the presence of lipids at 0.90 ppm and 1.30 ppm, due to the presence of necrosis [84–87] (Fig. 32). Although a certain amount of lipids can be found in anaplastic astrocytomas, the level of lipids in this group uses to be lower than in glioblastoma. An increase in Cho has been considered to correlate with malignancy in astrocytic tumors. This rule is prevalent for the comparison between anaplastic and low-grade astrocytomas (Figs. 33, 34). Different results are found in the comparison between anaplastic astrocytoma and glioblastoma. Although, in theory, Cho should be higher in glioblastomas, some authors have found lower levels in this group than in anaplastic astrocytomas. A suggested explanation has been a preponderance of necrotic areas over viable proliferative cellular areas in glioblastoma. Lactate has also been considered to correlate with malignancy by some groups; nevertheless values of lactate show a high variability between tumors and cannot be used to differentiate between groups.

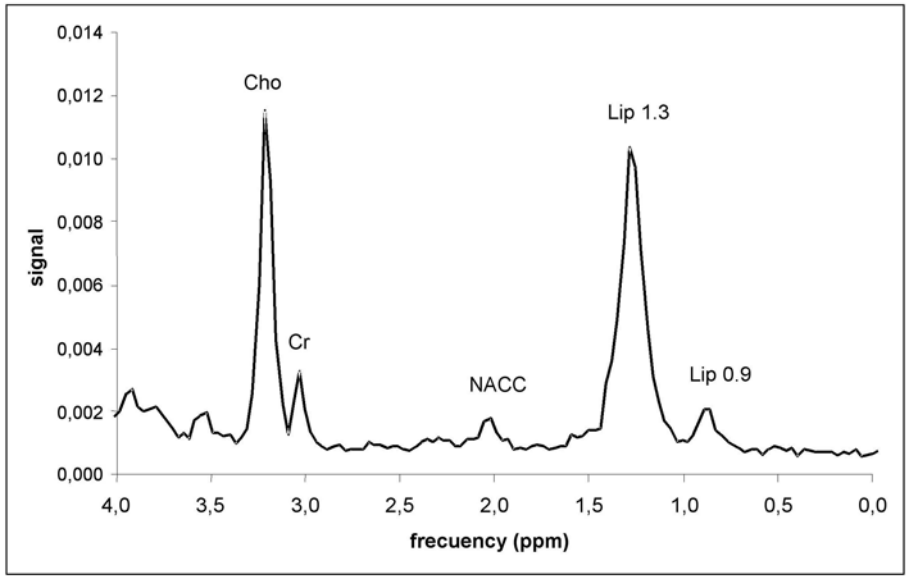

Fig. 32. Mean spectrum of glioblastoma at TE, 136 ms. Lipid resonances correspond to presence of necrosis, characteristic of this tumor

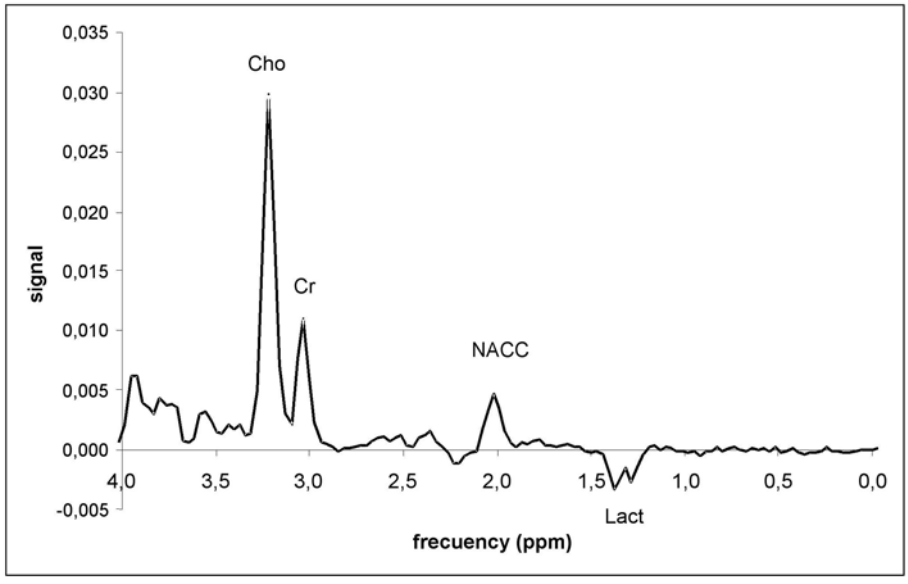

Fig. 33. Mean spectrum of anaplastic astrocytoma at TE, 136 ms. The Cho/Cr ratio is significantly increased. There is also some amount of lactate

Metastasis

Metastases are high-grade brain lesions in which presence of necrosis, represented in the spectrum by broad resonances centered at 0.90 ppm (Lip 0.9) and 1.30 ppm (Lip 1.3) can be found [88]. High values of Cho and low levels of Cr and NACC are also found in this group of tumors (Fig. 35). Differentiation between this group and glioblastoma cannot be confidently made by ^{1}H MRS to date. The origin of metastasis can not be satisfactorily differentiated by ^{1}H MRS either.

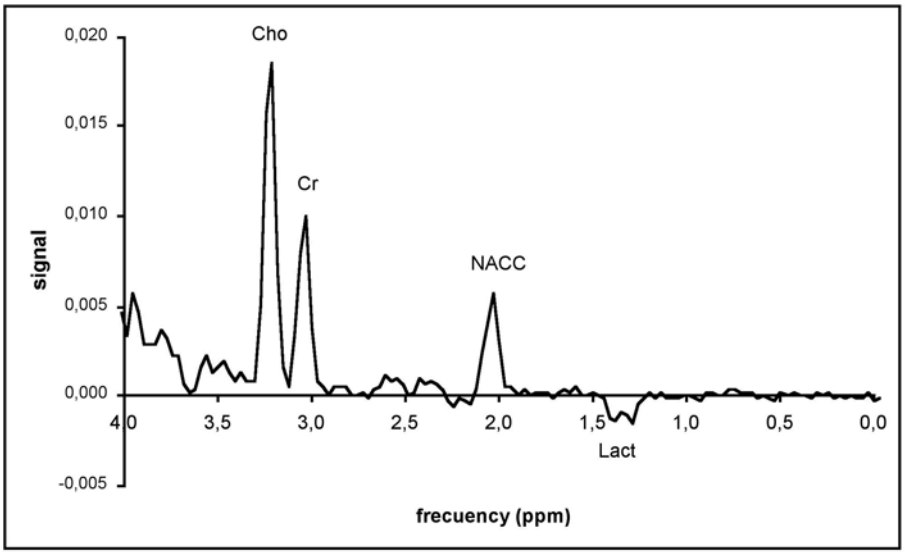

Fig. 34. Mean spectrum of low-grade astrocytoma at TE, 136 ms. There is an increase in the Cho/Cr and Cho/NACC ratios with respect to normal brain, but in lower levels than in anaplastic astrocytoma and meningioma. There is also some amount of lactate

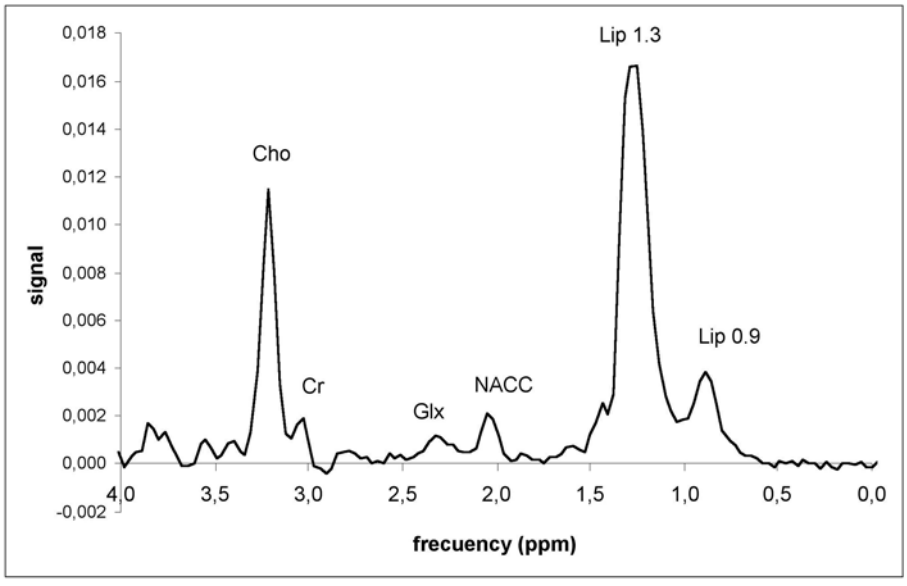

Fig. 35. Mean spectrum of metastasis at TE, 136 ms. The most prevalent findings are high amounts of lipids and Cho, and low levels of NACC and Cr. The spectrum is very similar to glioblastoma

References

1. Kleihues P, Cavance WK (2000) World Health Organization classification of tumours of nervous system. WHO/IARC, Lyon, France
2. Kepes JJ, Rubintein LJ, Enj IE (1979) A distinctive meningocerebral glioma of young subjects with relative favorable prognosis. Cancer 44:1839–1852
3. Housson J, Gambarelli D, Grisoli F, Pellet W, Salomon G, Pellisier J, Toga M (1982) Central neurocytoma. An electron microscopic study of two cases. Acta Neuropathol 56:151–156
4. Daumas-Duport C, Monsaingeon V, Veudoenne C, Munari C, Bancand J, Chodkiewicz JP (1988) Complex neuroepithelial tumors in epilepsy surgery. A series of 20 cases. In: Broggi G, The Rational Basis of Epilepsies, John Libbe, London, pp 149–167
5. Tarauto AL, Monges J, Lylyk P, Leiguatda R (1984) Superficial central astrocytoma attached to dura. Report of six cases in infants. Cancer 54:2505–2512
6. Kleihues P, Cavenee WK (1997) Tumors of the nervous system. IARC Press, Lyon, France, pp 1–225
7. Ellison D, Love S (1998) Astrocytic neoplasms, In Neuropathology, Mosby International, Barcelona, pp 35.1–35.15

8. Dean BL, Drayer , Bird CR et al (1990) Gliomas: Classification with MR imaging. Radiology 174:411–415
9. Castillo M, Seatliff JH, Buldin TW, Sowki K (1992) Radiologic-pathologic correlation: intracranial astrocytomas. AJNR 13: 1609–1661
10. Teronen O, Forbes G, Scheihauter BW, Dietz MJ (1992) Diffuse fibrillary astrocytoma correlation MRI features with histopathologic parameter and tumor grade. Neuroradiology 34: 173–178
11. Barker FG, Chang SM, Huhn SL, Davis RL, Gutin PH, McDermot MW, Wilson CHB (1997) Age and risk of anaplasia in MR nonenhancing supratentorial cerebral tumors. Cancer 80: 936–941
12. Burger PC, Heinz ER, Shih Bata T, Kleihues P (1988) Topographic anatomy and TC correlations in the untreated glioblastoma multiforme. J Neurosurg 68:698–704
13. Rees JH, Smirniotopoulos JG, Jones RV, Wang K (1996) Glioblastoma multiforme: radiopathologic correlations. Radiographic 16:1413–1438
14. Graff PA, Albright AL, Paig D (1992) Dissemination of supratentorial malignant glioma via cerebrospinal fluid in children. Neuroradiology 30:64–71
15. Osborn AG (1994) Brain tumors and tumorlike process. In: Diagnostic neuroradiology. Mosby-Yearbook, St Louis, pp 529–578
16. Hayashi K, Ohara N, Leon HJ, Akagi S, Takahasi , Akagi T, Namiba S (1993) Gliosarcoma with features of chondroblastic osteosarcoma. Cancer 72:850–855
17. Mauri F, Stella L, Benvenuti D, Giamundo A, Pettinati G (1990) Cerebral gliosarcoma: correlation of CT findings, surgical aspect, pathological features, and prognosis. Neurosurgery 26: 261–267
18. Jack CR, Bhausali DT, Chason JL, Boulos RS, Metha BA, Patel SC, Sanders WP (1987) Angiographic features of gliosarcoma. AJNR 8:117–122
19. Clark GB, Hury JM, Mckeever PE (1985) Cerebral pilocytic astrocytoma. Cancer 56:1128–1133
20. Forsth PA, Shaw EG, Schutauer BW, O´Fallon JR, Layton DD Jr, Kazman JA (1993) Supratentorial pilocytic astrocytomas. A clinicopathologic prognosis and flow cytometric study of 51 cases. Cancer 72:1335–1342
21. Katsetos CD, Kristina L (1994) Lobar pilocytic astrocytoma of the cerebral hemispheres: diagnostic and nosology. Clin Neuropathol 13:295–305
22. Palma L, Guidetti B (1985) Cystic pilocytic astrocytomas of the cerebral hemispheres. Surgical experience with 51 cases and long-term results. J Neurosurg 62:811–815
23. Fulhan MJ, Melisi JW, Nishimiya J, Dwyer AJ, Di Chiro G (1993) Neuroimaging of juvenile pilocytic astrocytoma: CT and MRI characteristics. AJNR 152:1263–1270
24. Lee YY, Van Tassel P, Bruner JM, Moser RP, Share JC (1989) Juvenile pilocytic astrocytoma: CT and MRI characteristics. AJR Am J Roentgenol 152:1263–1270
25. Strong JA, Hatlen HP, Brown MT, Debatin JF, Friedman HS, Oakes WJ, Tien R (1993) Pilocytic astrocytoma: correlation between the initial imaging features and clinical aggressiveness. AJR 161:369–372
26. Giannini C, Scheithauer (1997) Classification and grading of low-grade astrocytic tumors in children. Brain Pathol 7: 785–798
27. Russo CP, Frederickson K, Smoker WRK, Ghatok, Naidich TP, Rubin D, Gonzalez-Arias S (1996) Pleomorphic xanthoastrocytoma. J Neuroradiol 2:570–578
28. Turgut M, Akalan N, Ozgen T et al (1996) Subependymal glial cells astrocytoma associated with tuberous sclerosis: diagnosis and surgical characteristics of five cases with unusual features. Clin Neurol Neurosurg 98:217–221
29. Lipper MH, Eberhard DA, Phillips CD (1993) Pleomorphic xanthoastrocytoma, a distinctive astroglial tumor. Neuroradiologic and pathologic features. AJNR 14:1397–1404
30. Romero FJ, Ortega A, Coscojuela P, Rovira A, Ibarra B (1995) Neuroradiological findings in pleomorphic xanthoastrocytoma: report of six cases (abstract). Neuroradiology 37:S88
31. Dolinskas CA, Simeone FA (1982) CT characteristics of intraventricular oligodendrogliomas. AJNR 8:1077–1083
32. Shaw EG, Evans RG, Scheithauer BW, O'Falon JR, Davis DH (1994) Mixed oligoastrocytomas: a survival and prognostic factor analysis. Neurosurgery 24:577–582
33. Armington WG, Osborn AG, Cubberley DA et al (1985) Supratentorial ependymoma: CT appearance. Radiology 175:367–372
34. Swartz JD, Zimmerman RA, Bilaniuk LT (1982) CT of intracranial ependymoma. Radiology 143:97–101
35. Spoto GP, Press GA, Hesselink JR, Salomon (1990) Intracranial ependymoma and subependymoma: MR manifestations AJNR 11:83–91
36. Pleger MJ, Gerson LP (1993) Supratentorial tumors in children. Neuroimaging Clin North Am 3:671–687
37. Maiuri F, Gangemi M, Iaconetta G, (1997) Symptomatic subependymomas the lateral ventricles. Report of eight cases. Clin Neurol Neurosurg 99:17–22
38. Stevens MJ, Kendall BE, Love S (1984) Radiological features of subependymomas with emphasis on computed tomography. Neuroradiology 26:223–228
39. Delfini R, Acqui M, Oppido PA (1991) Tumors of the lateral ventricles. Neurosurg Rev 14:127–133
40. Girardot C, Boukohza M, Lamoureux JP (1990) Choroid plexus papillomas of the posterior fossa in adults: MR imaging and gadolinium enhancement. J Neuroradiol 17:303–318
41. Wagle V, Maclauson D, Eithier R (1987) Choroid plexus papilloma. Magnetic resonance, CT and angiographic observation. Surg Neurol 27:466–468
42. Jeline KJ, Smirniotopoulos JC, Parsi JE, Kanzer M (1990) Lateral intraventricular neoplasms of the brain. AJNR 11:567–574
43. Pizer BL, Moss T, Oakhill A, Webb D, Coakham HB (1995) Congenital astroblastoma: an immunohistochemical study. Case report. J Neurosurg 83:550–555
44. Nevin S (1938) Gliomatosis cerebri. Brain 61:170–191
45. Romero FJ, Ortega A, Titus F, Ibarra B, Navarro C, Rovira M (1988) Gliomatosis cerebri with formation of a glioblastoma multiforme: study and follow-up by MR and CT. J Comput Tomogr 12:253–257
46. Del Carpio OR, Korah I, Salazar A, Melançon D (1996) Gliomatosis cerebri. Radiology 198:830–835
47. Pythien J, Pääkko P (1996) A difficult diagnosis of gliomatosis cerebri: Neuroradiology 38:444–448
48. Ishwar S, Tonoguchi RM, Vogel FS. (1971) Multiple supratentorial hemangioblastomas. Case report and ultrastructural characteristics. J Neurosurg 22:197–203
49. Reyner Y, Baldini M, Hassoun H (1985) Hemangioblastoma of the brain. Computed tomography and angiographic studies in 17 patients. Acta Neurochir 74:12–17
50. Pomper MG, Passer TJ, Burger PC et al (2001) Chordoid glioma: a neoplasm unique to the hypothalamus and anterior third ventricle. AJNR 22:464–469
51. Ricoy JR, Lobato RD, Baez B et al (2000) Suprasellar chordoid glioma. Acta Neuropathol 99:699–703
52. Castillo M, Davis PC, Takei Y, Hoffman JC Jr (1990) Intracranial ganglioglioma: MR, CT and clinical findings in 18 patients. AJNR 11:109–114
53. Tampieri D, Mudgian RM, Melauson D, Either R (1991) Intracranial ganglioglomas in patients with partial complex seizures: CT and MR imaging findings. AJNR 12:749–755
54. Tien RD, Tuosi SL, Pulkinghaums N, Burger PC (1992) Ganglioglioma with leptomeninglial and subarachnoid spread. Result of CT, MR and PET imaging. AJR 159:391–393
55. Vandenberg SR (1993) Desmoplastic infantile ganglioglioma and desmoplastic cerebral astrocytoma of infancy. Brain Pathol 3:275–281
56. Dauma-Duport C (1993) Dysembryoplastic neuroepithelial tumors. Brain Pathol 3:285–295
57. Daumas-Duport C, Scheuthauer BW, Chodkiewicz JP, Laws ER Jr, Vendenne C (1988) Dysembryoplastic neuroepithelial tumor: a surgical curable tumor of young patients with intractable seizures. Report of thirty-nine cases. Neurosurgery 23: 545–556
58. Koeller KK, Dillon WP (1992) Dysembryoplastic neuroepithelial tumors. MR appearance. AJNR 13:1319–1325
59. Kuroiwa T, Bergey GB, Rothman MI, Zoarski LP, Krumholdz A, Barry E (1995) Radiologic appearance of the dysembryoplastic neuroepithelial tumor. Radiology 197:223–238

60. Hassoun J, Söylemezoglu F, Gambarelli D, Figarella-Brauger D, von Amon K, Keihues P (1993) Central neurocytoma: A synopsis of clinical and histological features. Brain Pathol 3:297–306
61. Bolen JW, Lipper MH, Cccano D (1989) Intraventricular neurocytoma. CT and MR findings. A case report. J Comput Assist Tomogr 13:495–497
62. Georgen SK, Gonzañlez MF, McLean CA (1992) Intraventricular neurocytoma. Radiologic features and review of the literature. Radiology 182:787–792
63. Poster-Greenn LM, Silberglest R, Stern H (1991) Intraventricular neuronal neoplasms: CT, MR and angiographic findings. J Comp Assist Tomogr 15.365–368
64. Rorke LB, Trojanowski JO, Lee VMY, Zimmerman RD, Sutlon LN, Biegel JA, Godwein JW, Packer RJ (1997) Primitive neuroectodermal tumors of the central nervous system. Brain Pathol 7:765–784
65. Zimmermam RA (1990) Pediatric supratentorial tumor. Sem Roentgenol 25:225–248
66. Figueroa RE, El Gommal T, Brook BS et al (1989) MR findings on primitive neuroectodermal tumors. J Comput Assist Tomogr 13:773–778
67. Cote TR, Manns A, Hardy CR, Yellin FJ, Harlge P, Yellini FJ (1996) Epidemiology of brain lymphomas among people with or without acquired immunodeficiency syndrome. AIDS/Cancer Study Group. J Natl Cancer Inst 88:675–678
68. Koeller KK, Smirniotopoulous JC, Jones RV (1997) Primary central nervous system lymphoma: radiopathologic correlation. Radiographic 17:1497–1526
69. Whiteman MH, Donovan Post J, Skaler E (1997) Neuroimaging of acquired immunodeficiency syndrome, In: AIDS of the CNS. Lippincott-Raven, Philadelphia
70. Terae S, Ojate A (1996) Nonenhancing primary central nervous system lymphoma. Neuroradiology 38:34–37
71. Osborn AG (1994) Miscellaneous tumors, cysts and metastasis. In: Diagnostic neuroradiology. MosbyYearbook, St Louis, pp 626–670
72. Cenacchi G, Giansgaspero F (2004) Emerging tumor entities and variants of CNS neoplasms. J Neuropathol Exper Neurol 63:185–192
73. Gianspero F, Ceancchi G, Losi L et al (1996) Extraventricular neoplasms with neurocytoma features: a clinicopathological study of 11 cases. Am J Surg Pathol 21:206–212
74. Brat DJ, Scheithauer BW, Eberhart CG, Burger PC (2001) Extraventricular neurocytoma. Pathological features and clinical outcome. Am J Surg Pathol 25:1252–60
75. Komori T, Scheitahauer BW, Anthony DC et al (1998) Papillary glioneural tumor. A new variant of mixed neuronal-glial neoplasm. Am J Surg Pathol 22:1171–1183
76. Payson RA (2000) Papillary glioneural tumours. Arch Pathol Lab Med 20:558–563
77. Broholm H, Madsen FF, Wagner AA, Laursen H (2002) Papillary glioneural tumor. A new tumor entity. Clin Neuropathol 21:1–4
78. Leung SY, Gwi E, Ng HK et al (1994) Dysembryoplastic neuroepithelial tumor. A tumor with small neuronal cells resembling oligodendroglioma. Am J Pathol 18:604–614
79. Cervera-Pierrot P, Varlet P, Chordkiewicz JP, Daumas-Duport C Leung SY, Gwi E, Ng HK et al (1997) Dysembryoplastic neuroepithelial tumor located in the caudate nuclei area: report of four cases. Neurosurgery 40:1065–1070
80. Baiden BL, Brat DJ, Melhem ER, Rosemblum M et al (2001) Dysembryoplastic neuroepithelial tumor-like neoplasm of the septum pellucidum: a lesion often misdiagnosis as glioma. Report of 10 cases. Am Surg Pathol 25:494–
81. Wiebe S, Muñoz DG, Smith S, Lee DH (1999) Meningioangiomatosis. A comprehensive analysis of clinical and laboratory features. Brain 122:709–726
82. Tien RD, Oakes JW, Madden JF, Burger PC (1992) Meningioangiomatosis: CT and MR findings. J Comput Ass Tomograph 16: 361–365
83. Aizpuru RN, Quencer RM, Norenberg M, Altman N, Smirniotopoulus J (1991) Radiology (1991) Meningioangiomatosis: clinical, radiologic and histopathologic correlation. 179: 819–821
84. Majós C, Alonso J, Aguilera C et al (2003) Proton magnetic resonance spectroscopy (^{1}H MRS) of human brain tumours: assessment of differences between tumour types and its applicability in brain tumour categorization. Eur Radiol 13: 582–591
85 Negendank WG, Sauter R, Brown TR et al (1996) Proton magnetic resonance spectroscopy in patients with glial tumors: a multicenter study. J Neurosurg 84:449–458
86. Tien RD, Lai PH, Smith JS et al (1996) Single-voxel proton brain spectroscopy exam (PROBE/SV) in patients with primary brain tumors. AJR Am J Roentgenol 167:201–209
87. Gotsis ED, Fountas K, Kapsalaki E, Toulas P, Peristeris G, Papadakis N (1996) In vivo proton MR spectroscopy: the diagnostic possibilities of lipid resonances in brain tumors. Anticancer Res 16:1565–1568
88. Sijens PE, Knopp MV, Brunetti A et al (1995) 1H MR spectroscopy in patients with metastatic brain tumors: a multicenter study. Magn Reson Med 33: 818–826

Neoplasms of the Posterior Fossa

Kelly K. Koeller

1.4

Contents

The opinions and assertions contained herein are the private views of the author and are not to be construed as official or representing the views of the Departments of the Navy or Defense.

Introduction

Neoplasms of the posterior fossa form a heterogeneous group of tumors that manifest either within the cerebellum, the fourth ventricle, or the cisternal spaces. Using the predominant age group in which each occurs is a convenient method to analyze this group.

Within the pediatric population, medulloblastoma and pilocytic astrocytoma arise within the cerebellum while ependymoma and choroid plexus papilloma occur within the ventricular system. In the adult population, hemangioblastoma is the most common cerebellar tumor, followed by dysplastic cerebellar gangliocytoma (Lhermitte-Duclos disease) and cerebellar liponeurocytoma while the fourth ventricle is the most common location for the subependymoma. In the extra-axial cerebellopontine angle, the vestibular schwannoma is the most common tumor, followed by meningioma.

Pediatric Neoplasms

Medulloblastoma

Incidence and Clinical Presentation

Medulloblastoma is the most common pediatric central nervous system malignancy and the most common (38%) primary tumor of the posterior fossa in children. Following only astrocytoma, it is the second most common pediatric brain neoplasm overall (6–8%) with an incidence of about 1 in 200,000 [1–7]. Males (60%) are slightly more commonly affected [5]. Among children, the mean age is about 7 years with small peaks at 3 years and 7 years [3]. Other cases may manifest between the ages of 20 and 40 years [8, 9].

Nearly all cases occur in the cerebellum (94.4%) and most (>75%) of these arise in the midline cerebellar

vermis [3, 10]. A more lateral location within the cerebellar hemisphere is typical when these tumors manifest in older children, adolescents, and adults, and is likely related to the lateral migration of undifferentiated cells, the putative cell of origin, away from the midline in older children and adolescents [3, 6, 11]. Brain stem infiltration is a common (33%) manifestation [12]. Less common locations include the fourth ventricle (3%), other areas of the brain (2.1%), and spinal cord (0.6%) [3].

The clinical presentation is usually less than 3 months in duration, reflecting the tumor's aggressive biologic behavior [12, 13]. Headache (generalized or localized to the suboccipital region) and persistent vomiting (without or with nausea) are common symptoms [12, 13]. Seizure activity is uncommon and may herald metastatic spread [13]. Truncal ataxia, secondary to destruction of the cerebellar vermis, is the most common objective clinical sign. and is frequently accompanied by spasticity [12, 13]. Other common clinical signs include papilledema (related to hydrocephalus), nystagmus, limb ataxia, and dysdiadochokinesis, the last two findings reflecting a more laterally located mass within the cerebellar hemisphere [12, 13]. Abducens nerve palsy, resulting from compression of the relatively exposed sixth nerve nucleus along the anterior margin of the fourth ventricle, may indicate extraventricular tumor extension [13].

Most patients with medulloblastoma have 5-year survival rates between 50% and 80% [13–19]. Patients with gross total resection of the tumor have improved survival rates compared to those with subtotal resection [12, 18, 20]. Recurrence of medulloblastoma is very common with most occurring within 2 years of initial treatment [21, 22]. Long-term recurrences may also occur in children but are less common with the implementation of chemotherapy in combination with radiation therapy [21–23].

Pathologic Findings

The gross appearance of a medulloblastoma is variable. Some are firm and discrete masses while others may be soft and less well-defined [10]. Four major subtypes of the tumor are recognized in the World Health Organization (WHO) classification of central nervous system (CNS) neoplasms [10]. The most common subtype is the classic subtype, defined by dense, sheet-like growth of cells with hyperchromatic round-to-oval nuclei accompanied by increased mitotic activity and conspicuous apoptosis [10]. Neuroblastic or Homer-Wright rosettes, consisting of neoplastic cell nuclei disposed in a radial arrangement around fibrillary processes, are common features while areas of necrosis are less common [10]. Other less common subtypes include the desmoplastic subtype, characterized by nodular reticulin-free "pale islands" that are surrounded by reticulin-staining collagen fibers, the "medulloblastoma with extensive nodularity and advanced neuronal differentiation" subtype, occurring primarily in children less than 3 years of age and associated with a "grape-like" nodularity seen on imaging studies, and the large cell medulloblastoma subtype [10]. The loss of genetic material from chromosomal arm 17p, site of a suppressor gene, is the most common (35–40%) of many chromosomal abnormalities associated with this disease [24]. Medulloblastoma, a WHO grade IV tumor, is regarded as a distinct entity from primitive neuroectodermal tumor (PNET) in the WHO classification scheme [10].

Imaging Findings

The classic computed tomography (CT) appearance of a medulloblastoma is a hyperattenuated well-defined vermian cerebellar mass with surrounding vasogenic edema, evidence of hydrocephalus, and fairly uniform contrast enhancement on post-contrast images in a child less than 10 years of age [13, 25, 26] (Fig. 1). Most (89–95%) of all medulloblastomas demonstrate at least some hyperattenuation compared to normal cerebellar attenuation on nonenhanced CT and have marginal vasogenic edema [13, 25, 27] Heterogeneity, with cyst formation (59%) and calcification (22%), are commonly

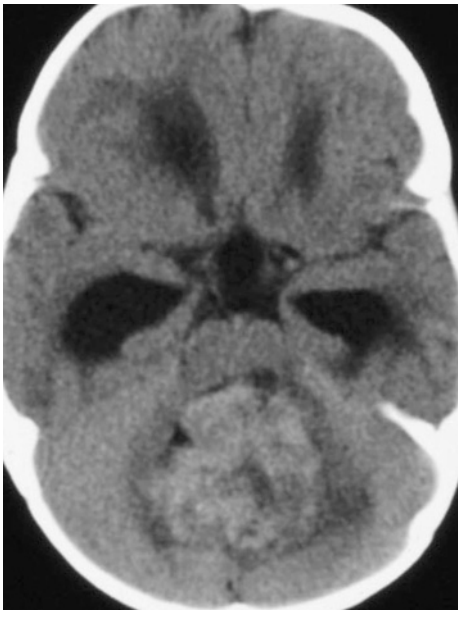

Fig. 1. Medulloblastoma, CT appearance. Axial nonenhanced CT image demonstrates heterogeneous hyperattenuation of a vermian cerebellar mass with surrounding vasogenic edema

seen [27]. Atypical features include ill-defined margins, absence of vasogenic edema or hydrocephalus, hypoattenuation, hemorrhage, absence of enhancement on post-contrast images, and the appearance of "primary" leptomeningeal dissemination [13, 25, 27–29]. The presence of falcine calcification in children with medulloblastoma may be a marker for nevoid basal cell carcinoma [30].

On magnetic resonance (MR) imaging, an even greater degree of heterogeneity among these lesions is noted on MR imaging than on CT [31]. Iso- to hypointensity compared to white matter on T1-weighted images and variable signal intensity compared to white matter on T2-weighted images is typical [31]. Virtually all (97%) show at least some enhancement on post-contrast imaging studies [27] (Fig. 2). MR spectroscopy typically shows a characteristic, albeit not specific, spectrographic signature for a neuroectodermal tumor with elevated choline, reduced N-acetyl aspartate (NAA), and reduced creatine peaks, and occasionally elevated lipid and lactic acid peaks [32]. Striking grape-like nodularity characterizes the CT and MR imaging appearance of the medulloblastoma with extensive nodularity subtype [33].

Subarachnoid seeding is common in medulloblastomas, present in 33% of cases at the time of initial diagnosis and is best assessed before surgical resection takes place [18, 32]. Post-operative evaluation of such spread is hampered by the presence of hemorrhage within the cerebrospinal fluid (CSF) and may lead to false-positive results in the first 2 post-operative weeks, either from the presence of methemoglobin or from leptomeningeal irritation caused by subarachnoid blood [34] Corroboration with clinical and cytopathologic CSF findings is crucial to substantiate the diagnosis of CSF dissemination [35]. In contrast to ependymoma and choroid plexus tumors, foraminal extension by a medulloblastoma from the fourth ventricle to involve the cerebellopontine angle (CPA), cisterna magna, and other cisternal compartments is not common [27, 36].

Recurrence of medulloblastoma most commonly manifests as leptomeningeal enhancement or focal parenchymal nodular enhancement within the brain [22]. Extraneural metastasis is uncommon (7.1%) with the skeletal system as the most common (77%) site of involvement [37].

Medulloblastomas occurring in the adult population tend to manifest as hyperattenuated poorly defined masses located in the cerebellar hemisphere. Cyst-like regions, from either cystic degeneration or necrosis, are more commonly noted (82%) than in those that occur in children [11]. Medulloblastomas in adult patients are also commonly of the desmoplastic histologic type, which is prone to late recurrence and demonstrates an imaging appearance that may mimic that of a meningioma with abnormal intense leptomeningeal enhancement secondary to the desmoplastic reaction [7, 11, 38, 39].

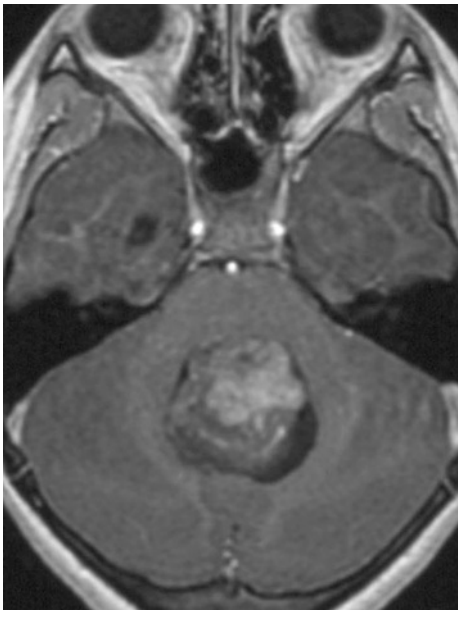

Fig. 2. Medulloblastoma, MR appearance. Axial post-contrast T1-weighted image shows diffuse enhancement of midline posterior fossa mass

Pilocytic Astrocytoma

Incidence and Clinical Presentation

Pilocytic astrocytoma accounts for 5–10% of all cerebral gliomas and 85% of all cerebellar astrocytomas [40, 41]. It is the most common (30%) glial neoplasm to occur in the pediatric population. About half arise within the hypothalamus or optic chiasm and a third originate within the cerebellum [41–44]. Other locations include the brain stem, cerebral hemisphere and spinal cord [41]. Unlike those arising in the optic nerve or chiasm, there is no association with neurofibromatosis for these tumors arising in the posterior fossa [42]. Most cases manifest before the age of 20 years [41] with the peak being between birth and 9 years of age [45]. There is no gender predilection [41].

Truncal ataxia, headache, nausea, and vomiting are common symptoms for those that arise in the cerebellum while brainstem dysfunction heralds a tumor in that location. Seizure activity is infrequent [41]. A prolonged clinical course is typical and correlates with the slow growth of the tumor [41]. The vast majority of patients have an excellent prognosis with 5-year survival rate of 86–100% and some studies report a 25-year-survival rate as high as 90% [46, 47]. Gross surgical resec-

tion is generally considered curative, with the extent of resection directly correlating with the prognosis [48, 49].

Pathologic Findings

Cerebellar pilocytic astrocytoma is typically a discretely circumscribed astrocytoma characterized by slow growth and an often cystic morphology [41]. While most arise in the cerebellar vermis, about 30% extend into a cerebellar hemisphere and 15% are located exclusively in the hemisphere [50]. Histologically, the tumor is characterized by a biphasic pattern of compacted elongated cells with hair-like processes, usually with Rosenthal fibers, and loosely textured astrocytic cells that contain globular aggregates, called eosinophilic granular bodies, and microcystic changes [41]. Prominent glomeruloid vascularity and endothelial proliferation are also commonly noted but are not associated with aggressive biologic behavior [41, 43]. "Open" tight junctions and fenestrations within the endothelial lining of these tumors correlate with prominent enhancement noted on post-contrast imaging studies [51]. Spontaneous regression is possible and malignant transformation is rare [41]. Because of these features and its low mitotic activity, the tumor is considered grade I in the WHO classification scheme [41] Recurrence is uncommonly seen [52].

Imaging Findings

The classic and most common cross-sectional imaging appearance of a cerebellar pilocytic astrocytoma is a well-circumscribed, predominantly cystic mass in a periventricular location [43]. Surrounding vasogenic edema (5–37%) and calcification (11–21%) are occasionally noted [42, 43]. A mural nodule is frequently present and has soft tissue characteristics with iso- to hypoattenuation compared to the cerebellar parenchyma on CT [42] (Fig. 3). On MR, it is hypo- to isointense on T1-weighted images and hyperintense on T2-weighted images compared to the cerebellar parenchyma, reflecting the increased amounts of free water contained within the neoplasm [43]. The nodule is round, oval, or plaque-like in morphology and demonstrates intense homogeneous enhancement on post-contrast CT or MR imaging [42, 50] (Fig. 4). The cyst wall usually does not enhance. When wall enhancement does occur, it suggests but is not definitive for neoplastic involvement [53]. Less commonly, the appearance of a pilocytic astrocytoma may manifest as a solid mass, generally with homogeneous enhancement [54]. Despite the well-demarcated radiologic appearance, histologic evidence of infiltration into the surrounding cerebellum is common [43]. Leptomeningeal dissemination is rare and does not necessarily indicate malignant spread [52].

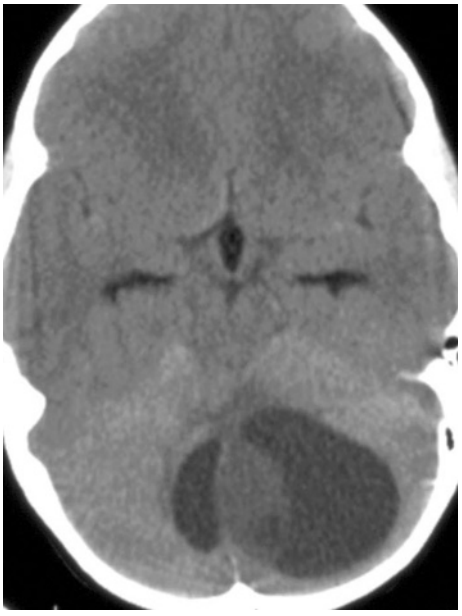

Fig. 3. Pilocytic astrocytoma, CT appearance. Axial nonenhanced CT image reveals cyst-like mass with nodule that is slightly hypoattenuated to the cerebellum

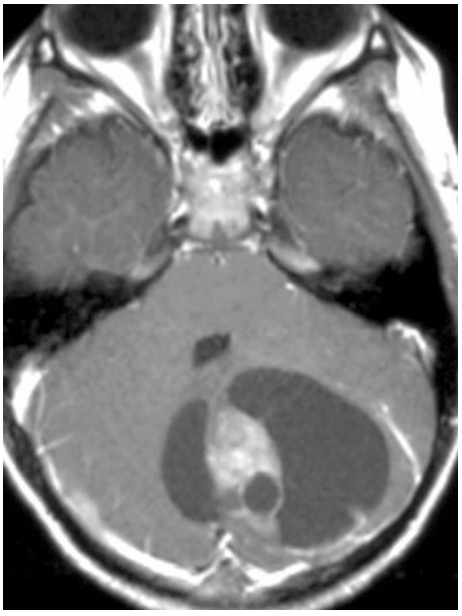

Fig. 4. Pilocytic astrocytoma, MR appearance. Axial post-contrast T1-weighted image demonstrates intense enhancement of soft tissue nodule seen in Fig. 3

Ependymoma

Incidence and Clinical Presentation

Ependymoma comprises 3–9% of all neuroepithelial neoplasms, 6–12% of all pediatric brain tumors, and almost one-third of all brain tumors in patients younger than 3 years [55]. Of those that occur intraventricularly, 58% originate in the fourth ventricle, while the remaining 42% are located in the lateral and third ventricles [56]. When it occurs in the posterior fossa, the tumor typically manifests in children, with a mean age of presentation of about 6 years [55].

Clinical signs and symptoms are largely secondary to the effects of increased intracranial pressure and hydrocephalus [55]. Cerebellar ataxia and paresis are commonly noted [55, 57]. In general, children with ependymomas have a less favorable prognosis than adults, in part from the increased incidence of a fourth ventricle location and the predilection of this group for more anaplastic forms of the disease [55]. The treatment of choice is gross total resection and the degree of resection directly correlates with improved prognosis [58]. Recurrence is common [59, 60]. Post-operative radiation therapy is advocated for partially resected ependymomas [60].

Pathologic Findings

Ependymomas are common neoplasms that arise from differentiated ependymal cells that line the cerebral ventricles and the central canal of the spinal cord [55]. Fourth ventricular ependymomas are well-circumscribed, soft, pliable, grayish-red masses that arise from the floor or roof of the ventricle, usually fill the ventricular lumen, and frequently extend through the foramen of Luschka into the cerebellopontine angle and even the foramen magnum. Occasionally, they may invade into the adjacent brain parenchyma [55].

Histologically, ependymomas are moderately cellular tumors characterized by perivascular pseudorosettes and, less commonly, ependymal rosettes. Mitotic figures are rare. With the exception of some rare variant forms, they are considered WHO grade II lesions [55].

Imaging Findings

On CT, ependymoma is often a heterogeneous mass with a predominant soft tissue component frequently mixed with calcification (40–80%), occasional cystic formation, and hemorrhage [59, 61] (Fig. 5). The soft tissue portion of the tumor is usually hypo- to isoattenuated on unenhanced CT [62]. Contrast enhancement is variable, usually intense within the soft tissue portions but sparing the cyst-like regions [59, 61].

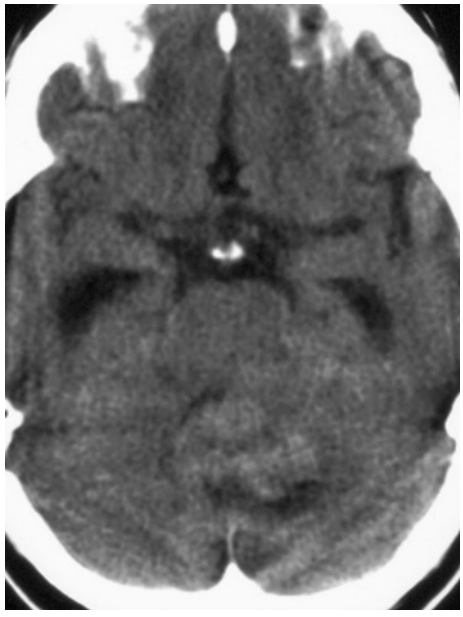

Fig. 5. Ependymoma, CT appearance. Axial nonenhanced CT image shows mild hyperattenuation of fourth ventricular mass

On MR imaging, intraventricular ependymomas typically show isointensity on T1-weighted images and hyperintensity on T2-weighted images compared to gray matter. Heterogeneity is even more conspicuous than on CT and reflects the presence of calcification, hemor-

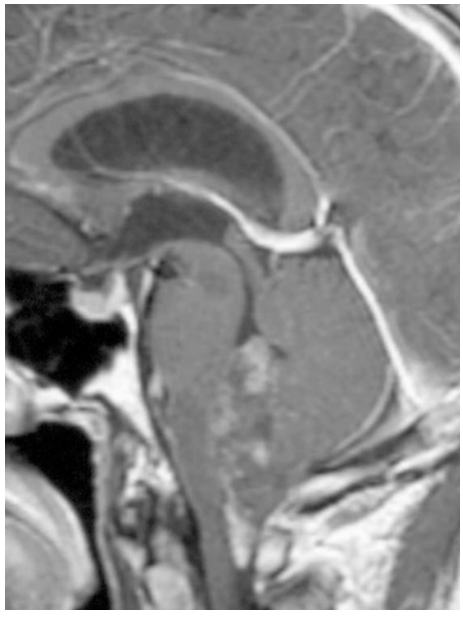

Fig. 6. Ependymoma, MR appearance. Sagittal post-contrast T1-weighted image reveals heterogeneous enhancement of a fourth ventricular mass with inferior extension

rhage, and cystic changes that are often present. There is variable enhancement on post-contrast images (Fig. 6). MR imaging is considered the imaging modality of choice to evaluate these lesions, although CT is superior in the detection of calcification [59]. Post-operative imaging is considered essential in documenting the presence of post-operative residual disease, which has a substantial negative impact on survival [63].

Choroid Plexus Papilloma and Carcinoma

Incidence and Clinical Presentation

Neoplasms of the choroid plexus account for 0.4–0.6% of all intracranial tumors, 2–4% of pediatric brain tumors, and 10–20% of brain tumors before the age of one year [64]. The overall incidence is about 0.3 per 1 million [64]. Most (~80%) choroid plexus tumors occur as the benign slowly growing choroid plexus papilloma, a WHO grade I tumor with a favorable overall prognosis [64]. The other 20% manifest as a much more biologically aggressive WHO grade III tumor, the choroid plexus carcinoma, which is far more common in children than adults [64]. For choroid plexus tumors that arise in the fourth ventricle (the second most common site, following the lateral ventricle), the incidence is fairly evenly distributed through the first five decades and males are more commonly affected [64]. About 5% are multiple [64]. Rarely, they may occur within the cerebellopontine angle and the cerebellum [65]. An embryonic rest of choroid plexus is speculated as the cause of these extraventricular lesions [66].

Symptoms are usually related to hydrocephalus which results from a combination of overproduction of CSF, impaired resorption of CSF secondary to hemorrhage, and obstruction of normal CSF flow by the presence of an intraventricular mass [67–70]. Focal neurologic deficits, cranial nerve palsies, seizures, coma, and even psychosis may also occur [67, 71]. While the prognosis for patients with a choroid plexus papilloma is excellent with 100% 5-year-survival reported in one large series, it is less promising in the presence of a choroid plexus carcinoma [67, 69, 72, 73]. The presence of residual disease on post-operative imaging studies is an especially poor prognostic factor [73].

Pathologic Findings

Grossly, choroid plexus tumors are soft, well-circumscribed, cauliflower-like masses with prominent peripheral lobulations, frequent hemorrhage, and cyst formation [64, 72]. Necrosis and parenchymal invasion are characteristic features for the choroid plexus carcinoma [64]. Fourth ventricle choroid plexus tumors are attached to the posterior medullary velum by a vascular pedicle [70].

Histologic examination of choroid plexus papillomas reveals an appearance quite similar to normal non-neoplastic choroid plexus tissue [64]. Prominent fronds of fibrovascular connective tissue surrounded by columnar or cuboidal cells without significant mitotic activity is typical [64]. In contrast, the choroid plexus carcinoma demonstrates clear signs of malignancy with hypercellularity, nuclear pleomorphism, high nucleus-cytoplasm ratio, conspicuous mitotic activity, and invasion into the adjacent brain parenchyma [64]. Transformation from a choroid plexus papilloma to a choroid plexus carcinoma occurs uncommonly [74]. Rarely, a choroid plexus tumor may be pigmented from either melanin or lipofuscin [75, 76] While CSF seeding may occur in both choroid plexus papilloma and carcinoma, clinically significant seeding leading to frank metastatic spread is much more common in patients with a carcinoma [64, 77, 78].

Imaging Findings

Choroid plexus tumors are generally iso- to hyperattenuated intraventricular masses without brain invasion on nonenhanced CT studies [69, 70]. Hydrocephalus is very common [69]. Calcification is noted in 4–10% of choroid plexus tumors on plain skull x-rays and 24% on CT studies [69, 79, 80] (Fig. 7). The degree of calcification varies widely, from scattered punctate foci to cal-

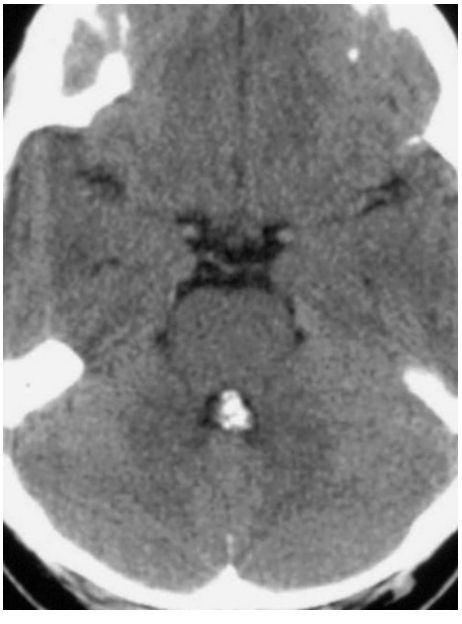

Fig. 7. Choroid plexus papilloma, CT appearance. Axial nonenhanced CT image demonstrates calcified fourth ventricular mass

cification involving the entire mass [81]. Cerebellopontine angle extension is a characteristic feature of a fourth ventricle choroid plexus tumors [82].

On MR imaging, choroid plexus papillomas appear as iso- to hypointense intraventricular masses on T1-weighted images compared to normal brain parenchyma and variable single intensity masses on T2-weighted images [70, 81]. The tumors show intense enhancement on post-contrast imaging studies [69, 70] (Fig. 8). Flow voids, consistent with increased vascularity, are common [70]. Post-contrast MR imaging of the spine is recommended to exclude the possibility of seeding from choroid plexus papillomas on follow-up post-operative studies [83].

Choroid plexus papillomas appear as lobulated uniformly echogenic masses on ultrasonography and demonstrate bi-directional flow continuing throughout diastole and a ragged outline consistent with flow in a chaotic arrangement of many small vessels [84, 85]. Enlargement of a choroidal artery is a common imaging feature on both cross-sectional and angiographic studies [69].

Choroid plexus carcinomas tend to be more heterogeneous on CT and MR than choroid plexus papillomas, reflecting the presence of more necrosis and parenchymal invasion. The findings of extraventricular extension of a choroid plexus tumor into the brain parenchyma, heterogeneity of signal intensity, and the presence of vasogenic edema in the cerebral white matter all favor the imaging diagnosis of a choroid plexus carcinoma [70]. There is often considerable overlap in the imaging appearance between papillomas and carcinomas and the distinction between the two neoplasms is not always possible on imaging studies [81, 86]. Fourth ventricular choroid plexus tumors are usually supplied by choroidal branches of the posterior inferior cerebellar artery and may be amenable to pre-operative embolization [69, 70, 87, 88].

Atypical Teratoid / Rhabdoid Tumor

First described in 1978, the atypical teratoid / rhabdoid tumor (ATRT) has a biologic behavior and some histologic features that mimic that of malignant rhabdoid tumor of the kidney. Various names have also been applied to define this lesion, including rhabdomyosarcomatoid variant of Wilms tumor, embryonal small cell tumor, and, simply, rhabdoid tumor [89].

ATRT accounts for about 2% of all pediatric CNS tumors [89]. The overwhelming majority of patients are less than 5 years of age at the time of presentation. Males are more commonly affected. Clinical symptomatology is non-specific with lethargy and failure to thrive common when it manifests in infants. Head tilt and cranial nerve palsies may be noted in young children [89].

ATRT is a highly malignant neoplasm and is classified as a WHO grade IV tumor. Grossly, the tumor usually manifests as a soft lobulated mass with necrosis and hemorrhage common. Histologically, the tumor is characterized by rhabdoid cells variably mixed with primitive neuroepithelial, epithelial, and mesenchymal ele-

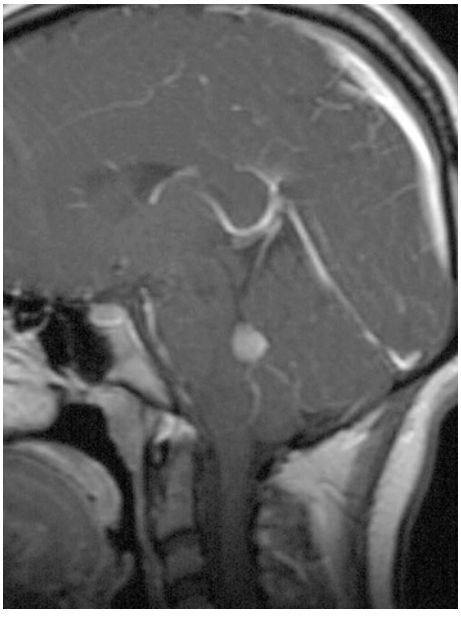

Fig. 8. Choroid plexus papilloma, MR appearance. Sagittal post-contrast T1-weighted image reveals intense enhancement of a small well-defined mass within the fourth ventricle

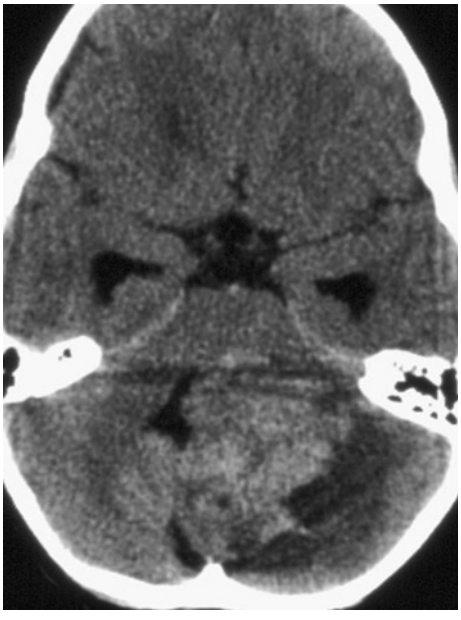

Fig. 9. Atypical teratoid / rhabdoid tumor, CT appearance. Axial nonenhanced CT image shows heterogeneous hyperattenuated mass with surrounding vasogenic edema

ments. Accordingly, it is not a germ-cell tumor. Most patients die from the disease within one year of presentation [89].

About half of ATRT occur in the posterior fossa and commonly extend into the cerebellopontine angle. Nearly 40% are supratentorial in location and may be intraventricular. The pineal region and spinal axis comprise the remaining locations [89]. The combination of a posterior fossa location and characteristic hyperdensity on CT often produces an imaging appearance that mimics a medulloblastoma (Fig. 9). Surrounding vasogenic edema and heterogeneity on both CT and MR are very common, secondary to necrosis and hemorrhage. Heterogeneous enhancement is typical and about 33% of all patients with the disease have subarachnoid seeding at the time of presentation [90].

Adult Tumors

Hemangioblastoma

Incidence and Clinical Presentation

Capillary hemangioblastoma constitutes about 1 to 2.5% of all CNS tumors and 7.3% of those arising within the posterior fossa [91, 92]. The vast majority (75%) of capillary hemangioblastomas arise in the cerebellum, with the spinal cord (20%) and medulla (4%) other common locations [93]. Rarely, they may occur within the cerebral hemispheres (1%), suprasellar region, meninges, and numerous other locations [93–95]. The cerebellar lesions are more commonly found in the hemispheres rather than the vermis and are virtually always located peripherally, near the cerebellar pial surface [93, 96]. Males are slightly more commonly affected [97].

Clinical manifestations of a hemangioblastoma typically reflect increased intracranial pressure and restriction of CSF flow caused by a mass within the cerebellum or spinal cord [98]. Headache, nausea, vomiting, ataxia, and dizziness are common symptoms and a long clinical course (average, 25 weeks) is typical [93, 99]. Pain and sensory deficits are more common in patients with a spinal cord lesion [93]. Polycythemia occurs in about 20% of cases of cerebellar hemangioblastoma, especially those of solid morphology, secondary to increased amounts of erythropoietin secreted by the tumor [93, 100]. Pregnancy appears to exacerbate the clinical course of patients with a cerebellar hemangioblastoma [101].

Capillary hemangioblastoma is the most frequent manifestation of von Hippel-Lindau (VHL) disease, an autosomal dominant phakomatosis with variable penetrance [93]. About one-third of all patients with a capillary hemangioblastoma have other clinical stigmata that establish the diagnosis of VHL disease and up to 80% of all VHL patients will have a CNS hemangioblastoma [93]. The predilection for VHL in a patient with a hemangioblastoma is even stronger (50%) when the tumor is located in the spinal cord [93, 98]. Those that occur in association with VHL disease tend to manifest in younger patients (mean age, 29–32 years) compared to those that occur sporadically (mean age, 44–47 years) [93, 98, 99, 102].

The diagnosis of VHL disease is established when a patient has a hemangioblastoma of either the CNS or the retina and at least one other VHL-associated tumor or a family history of VHL disease [98]. Numerous other manifestations of VHL disease are common and include retinal hemangioblastoma (the von Hippel tumor), benign cysts (renal, pancreatic, and epididymal), benign or low-grade tumors (pheochromocytoma and endolymphatic sac tumor), and malignant tumors (renal cell carcinoma, pancreatic islet cell tumor) [98, 103]. The occurrence of multiple hemangioblastomas is almost always indicative of VHL disease [98].

VHL is classified into two types with Type I patients also having a pheochromocytoma, while type II patients do not [93]. The overall prevalence of VHL disease is estimated at approximately 1:40,000 [98]. A suppressor gene for VHL has been identified on chromosome 3p [104]. The overall prognosis for patients with a capillary hemangioblastoma is good with approximately 85% surviving for at least 5 years, although patients with VHL disease may not fare as well, because of the added burden of renal cell carcinoma [100].

Pathologic Findings

The slowly growing hemangioblastoma is regarded as a grade I tumor in the WHO classification scheme [98]. Grossly, the tumor is typically a well-circumscribed mass but lacks a true capsule [105]. Most lesions are complex masses with a larger cystic component combined with a smaller highly vascular nodule that abuts the pial cerebellar surface [91]. Simple diffusion of the vascular element within the mural nodule likely accounts for the cyst fluid, which is frequently xanthochromic and contains erythropoietin [100, 106]. Occasional yellowish lipid-containing regions may also be noted [98]. The cyst wall is composed of compressed brain parenchyma or reactive neuroglial cells and is not considered part of the neoplasm [100].

On histologic examination, the neoplasm demonstrates both large lipid-filled vacuolated stromal cells, representing the neoplastic component of the lesion that produces a “clear cell” appearance (similar to that of renal cell carcinoma), and an abundant capillary network, accounting for the propensity of these tumors to hemorrhage [98]. Cystic degeneration, low mitotic rate, hyperchromatic nuclei, and nuclear atypia are common

features [93, 98]. Despite intense investigation, the histogenesis of capillary hemangioblastoma remains uncertain, with both mesenchymal and angioblastic origins supported [93, 98].

Imaging Findings

Most (60%) capillary hemangioblastomas manifest as a cystic mass with a mural nodule, which is usually small in size (<1.5 cm diameter) and near the pial surface [96, 107, 108]. This nodule represents the neoplasm itself while a proteinaceous, gelatinous material secreted by the nodule results in the cystic component [107]. The remaining 40% of capillary hemangioblastoma are solid without or with a central "cyst-like" component [96, 107]. Solid lesions have a nonspecific appearance and are more commonly noted in the brain stem and spinal cord [93, 107].

The CT appearance of capillary hemangioblastoma is straight-forward when it is in the cystic form. The peripheral nodule is isodense compared to the surrounding brain and easy to visualize in comparison to the hypodense cystic component [108]. However, when the tumor is in its solid form, it may be difficult to detect on unenhanced studies and, even when it is seen, its appearance is nonspecific [107, 108]. Calcification is not seen in capillary hemangioblastomas [108]. When present, the nodule enhances intensely on post-contrast CT images [107, 108]. Mild enhancement of the cyst wall is also seen on occasion [108].

MR imaging is considered the imaging study of choice for the evaluation of capillary hemangioblastomas [93]. The tumor usually demonstrates hypointensity on T1-weighted images and hyperintensity on T2-weighted images regardless of its morphology [96]. In the classic "cyst with a mural nodule" form, the cystic portion is iso- to hyperintense on T1-weighted imaging and hyperintense on T2-weighted imaging compared to CSF, reflective of its elevated protein content [96]. The nodule is isointense on T1-weighted imaging and hyperintense on T2-weighted imaging compared to gray matter and usually easy to identify contrasted to the hyperintense signal of the cyst fluid [96, 107]. Inherent T1 hyperintensity is occasionally noted and represents either an abundance of lipid within the tumor or the presence of methemoglobin [100]. Prominent vascularity in the form of serpentine flow-voids and hemorrhage are common features [96, 107]. MR enhancement patterns are similar to that seen with CT [96, 107] (Fig. 10).

Angiography of capillary hemangioblastoma demonstrates the nodule as either an intense vascular blush or a grouping of disordered vessels [100]. While it is considered superior to contrast-enhanced CT, angiography has been largely supplanted by non-invasive, multi-planar, contrast-enhanced MR imaging [93, 109].

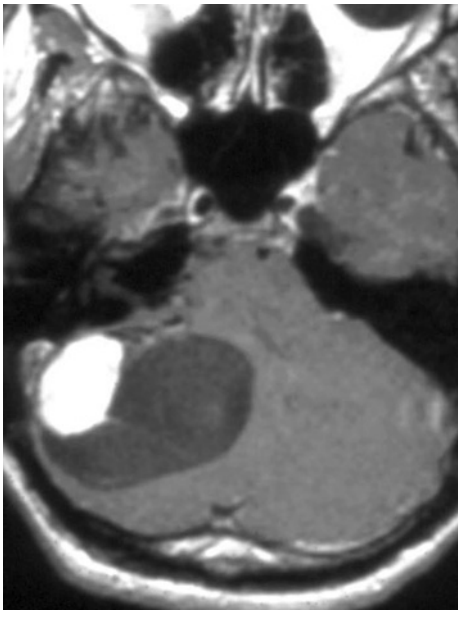

Fig. 10. Hemangioblastoma, MR appearance. Axial post-contrast T1-weighted image demonstrates the classic "cyst-like mass with enhancing mural nodule" form

Dysplastic Cerebellar Gangliocytoma (Lhermitte-Duclos Disease)

Incidence and Clinical Presentation

Originally described in 1920, the entity of dysplastic cerebellar gangliocytoma (Lhermitte-Duclos disease) was not firmly established until many decades later when refinements in histological analysis permitted a more accurate evaluation. While some evidence has supported a neoplastic histogenesis, recent investigations strongly favor a hamartomatous origin [110] Lhermitte-Duclos disease manifests in young adults (average age of presentation: 34 years) in the vast majority of cases with only a few cases reported in children [111, 112]. There is no gender predilection.

Most patients have clinical symptoms related to increased intracranial pressure and hydrocephalus. Less commonly, about 40% of patients present with a slowly progressive cerebellar syndrome. Megalencephaly (seen in 50% of cases) and mental retardation are other common features [112–114]. The natural history of the disease is ill-defined. There is considerable variability in the duration of symptoms (3 to 29 years) and some patients with the disease may be asymptomatic [115, 116].

Decompression of the ventricular system is the immediate goal of therapy in symptomatic cases. The gradual change from normal cerebellar tissue to the abnormal tissue makes visualization of a tissue plane dif-

ficult and impairs a complete resection [112, 117]. While most patients do well following surgical resection, some have recurrence of their disease even after a prolonged disease-free interval [110, 115]. Accordingly, long-term follow-up is recommended [115].

There is a strong association of Lhermitte-Duclos disease with Cowden disease, an autosomal dominant hamartoma syndrome characterized by a variety of mucocutaneous lesions, macrocephaly, and increased frequency of hamartomas and neoplasia in the multiple organ systems (breast, thyroid, colon, genitourinary, and the CNS) [110, 118]. Recent investigations have established a molecular basis for Cowden disease with identification of a susceptibility gene on the long arm of chromosome 10 (10q23) [119]. The combination of Lhermitte-Duclos disease and either breast cancer, thyroid cancer, or macrocephaly is one of the criteria that establishes the diagnosis of Cowden disease [119]. Patients with Cowden disease and family members of patients with Lhermitte-Duclos disease should be screened with brain MR studies [115]. There is a growing body of evidence that perhaps all patients with Lhermitte-Duclos disease also have Cowden disease with identification of Cowden disease made only after the diagnosis of Lhermitte-Duclos disease is established [110, 113].

Pathologic Findings

Histologic analysis of Lhermitte-Duclos disease reveals disruption of the normal cerebellar laminar structure with hypertrophic ganglion cells expanding the granular and molecular layers of the cerebellar cortex and abnormally increased myelination in the molecular layer [120]. A marked reduction in myelination of the central white matter of the cerebellar folia is also common [117]. Mitotic activity, necrosis, and endothelial proliferation – all associated with high-grade brain neoplasms – are not characteristically seen in these lesions. Malignant transformation has not been observed [110].

Imaging Findings

Lhermitte-Duclos disease is usually hypoattenuated on nonenhanced CT studies but may be isoattenuated, making detection difficult [111, 113, 117]. Calcification is uncommon [111–113, 116]. Thinning of the skull may be noted on plain x-rays and on CT [117]. Vertebral angiography reveals an avascular mass [117].

MR is considered the imaging modality of choice for Lhermitte-Duclos [115]. The presence of a "striated" cerebellar mass involving one hemisphere with alternating bands of hyperintensity and isointensity compared to gray matter on T2-weighted images is highly characteristic [112, 113] (Fig. 11). These same bands are isointense and hypointense on T1-weighted images [113, 115, 121]. The hyperintense signal seen on T2-weighted images corresponds to the inner molecular layer, granular cell layer, and loss of central white matter within the folia [115]. The overwhelming majority of these lesions do not enhance [110, 113, 115].

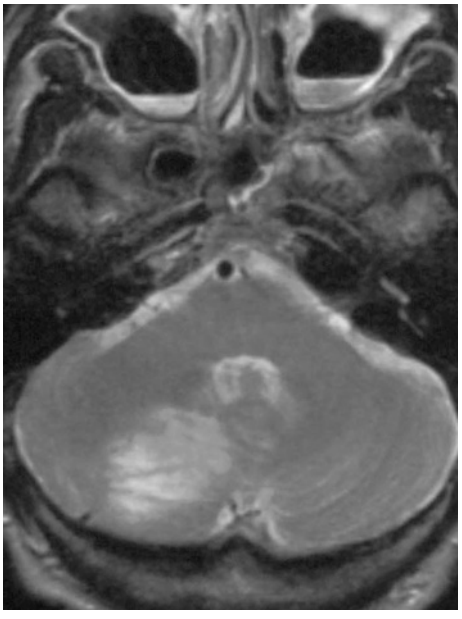

Fig. 11. Dysplastic cerebellar gangliocytoma, MR appearance. Axial T2-weighted image reveals "striated appearance", characteristic for Lhermitte-Duclos disease

Cerebellar Liponeurocytoma

The entity previously known as "lipomatous medulloblastoma" is now designated "cerebellar liponeurocytoma" [122]. It is considered a distinct clinico-pathological entity with a good overall prognosis. In contrast to medulloblastoma, this low-grade neuronal tumor usually occurs in much older patients (range: 36–67 years) and does not require adjuvant post-operative therapy in most, if not all, cases [123]. This lesion has a distinctive imaging appearance with areas of fat attenuation or signal intensity seen within a cerebellar mass on cross-sectional imaging [124].

Subependymoma

Incidence and Clinical Presentation

Subependymoma is a distinct pathologic entity from ependymoma and is so named because it arises from

the subependymal glial layer located immediately adjacent to the ependymal lining of the ventricular system [125]. The true incidence of the tumor is difficult to ascertain as many of the cases occur in asymptomatic patients, being detected only incidentally at autopsy. In one series of 1000 necropsies in asymptomatic patients, the incidence was 0.4% [126]. Males are more commonly affected and most reported cases (82%) have occurred in patients older than 15 years of age [127, 128]. Almost all of these tumors occur within the fourth and lateral ventricles with at least half of the reported cases located in the fourth ventricle and 40–45% arising in the lateral ventricle [65]. It may also rarely occur in the septum pellucidum, the third ventricle, and in the cervical or cervico-thoracic spinal cord [128, 129]. Gross total surgical resection is the goal of therapy [128]. Recurrence following surgical resection is rare [59, 130].

The clinical presentation is usually non-specific. Symptoms are most commonly dependent on its location, size, and the presence of intratumoral hemorrhage [57]. Most symptomatic patients (80%) present with symptoms related to hydrocephalus as a consequence of ventricular obstruction [127, 128]. Less commonly, focal neurologic deficits (27%), seizures (9%), and subarachnoid hemorrhage (4.5%) have been reported [128]. The vast majority of patients have a good prognosis following surgical resection [131].

Pathologic Findings

Grossly, subependymoma is a well-circumscribed mass with a firm texture and a white to grayish color [128]. Attached to the ventricular wall by a narrow pedicle, the tumor grows in a slow deliberate fashion, and is usually avascular [128]. Most of those that arise in asymptomatic patients are smaller than 2 cm in diameter while they tend to be slightly larger when they manifest in symptomatic patients [57, 130, 131].

On histologic examination, the tumor manifests as a dense fibrillary matrix interrupted by numerous small cysts and nests of isomorphic nuclei that resemble subependymal glia [127]. Mitotic activity is usually low or absent [127]. Accordingly, subependymoma corresponds histologically to WHO grade I [127]. About 10% may manifest as an admixture with an ependymoma or other tumor types [57, 127, 128].

Imaging Findings

The typical CT appearance of a subependymoma is a well-circumscribed lobulated intraventricular mass that produces hydrocephalus (85% of cases) and is predominantly iso- to slightly hypoattenuated compared to the brain parenchyma [128, 130] (Fig. 12). Calcification (32%) and cystic degeneration (18%) are common features [128, 130]. Surrounding vasogenic edema is occasionally seen [59, 128]. Hyperattenuation may be an indication of hemorrhage [126, 132]. On post-contrast imaging, most (84%) show at least some enhancement, which is usually focal in nature [128].

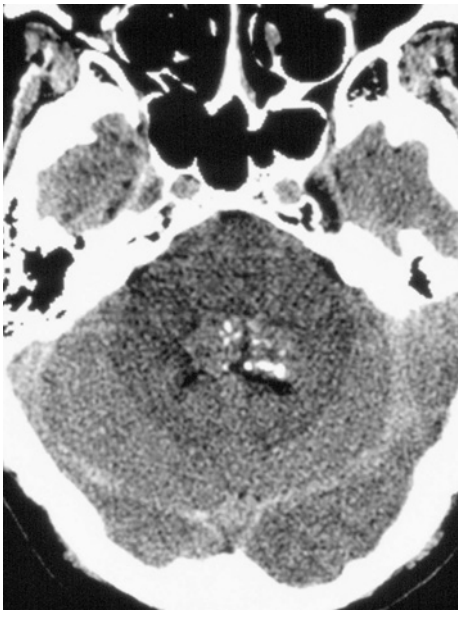

Fig. 12. Subependymoma, CT appearance. Axial nonenhanced CT image reveals heterogeneous midline mass in the posterior fossa with multiple foci of calcification

On MR imaging, subependymoma is heterogeneous partially cyst-like masses, generally hypointense on T1-weighted images and hyperintense on T2-weighted images compared to white matter [129, 130, 133]. Intratumoral hemorrhage occurs occasionally and produces even more heterogeneity [129]. Enhancement is quite variable on post-contrast images. They may not enhance, enhance minimally, or show intense enhancement following the intravenous administration of a contrast agent [129, 130, 133]. In contrast to ependymomas, intense enhancement is usually heterogeneous and extraventricular extension is rare [59, 129, 133, 134]. Most are avascular on angiographic studies [126].

Cerebellopontine Angle Tumors

Vestibular schwannoma

Incidence and Clinical Presentation

Schwannoma accounts for 8% of all intracranial neoplasms and those that involve the eighth cranial nerve

account for 60–90% of all cerebellopontine angle (CPA) masses [135]. It is especially common in patients with neurofibromatosis type 2, in which 96% of patients will have bilateral tumors [136]. The presence of bilateral vestibular schwannomas is pathognomonic for NF2 [137]. Most cases manifest between the ages of 30 and 70 years of age with the peak age of presentation between 40 and 60 years of age [138]. A variety of names have been employed to describe this lesion. To emphasize its origin from the eighth cranial nerve, the term vestibular schwannoma is preferred.

Symptoms typically progress slowly over several months to years and are directly related to pressure effects on the cochlear and vestibular divisions of the eighth cranial nerve within the internal auditory canal (IAC) [138]. Sensorineural hearing loss is the most common presentation and is frequently accompanied by tinnitus and dysequilibrium [139]. Loss of speech discrimination is a classic manifestation often noticed by the patient while using the telephone with the affected ear [140]. As the tumor enlarges, symptoms related to other cranial nerve or brain stem involvement may occur. Decreased sensation in the external auditory canal of the involved ear (Hitselberger's sign) manifests because of pressure on the sensory branch of the facial nerve [140].

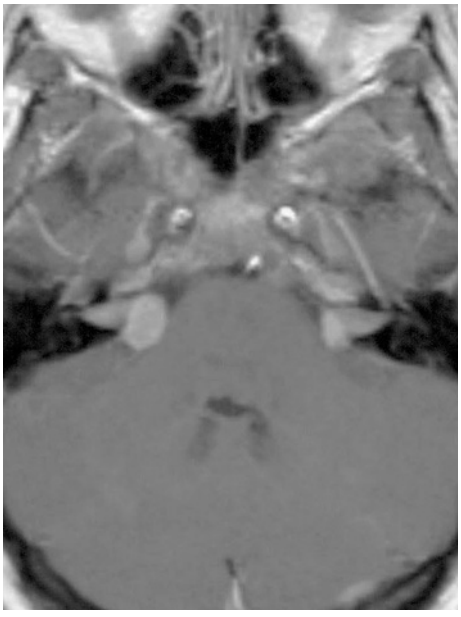

Fig. 13. Vestibular schwannoma, MR appearance. Axial post-contrast T1-weighted image demonstrates intense enhancement of bilateral vestibular schwannomas extending from the internal auditory canals in a patient with neurofibromatosis type 2

Pathologic Findings

Schwannoma is a benign WHO grade I tumor that typically manifests as an encapsulated globoid mass of variable size, ranging from less than 1 centimeter to several centimeters in diameter [137]. Histologically, the neoplasm is composed of spindle-shaped neoplastic Schwann cells in a mixture of either compact areas with elongated cells (Antoni A type) or less cellular, loosely textured areas (Antoni B type) [137]. The Antoni A regions frequently contain nuclear palisading and another histologic hallmark of schwannoma, the Verocay body [137]. CT correlation of these different regions has been noted with the Antoni A regions producing hyperattenuation while the Antoni B regions remain hypoattenuated. Hypercellular, melanotic, and plexiform variants of schwannoma have been documented [137]. Vestibular schwannoma is known for its relative absence of Verocay bodies, the predominance of Antoni B areas, and the presence of lipidized cells [137].

Imaging Findings

The shape of a vestibular schwannoma varies with its location. It tends to be cylindrical in shape and has a convex medial margin when it is confined to the IAC, while it is usually spherical in shape when larger and extends into the cisternal space as it expands the IAC [141]. This second morphology produces the classic "ice-cream cone" or "mushroom" appearance, best appreciated on contrast-enhanced MR. The so-called "giant" schwannoma may be confined to the cisternal space without any extension from the IAC. Most (85%) vestibular schwannomas have acute angles at the bone-tumor interface.

On CT, most (64%) vestibular schwannomas are isoattenuated compared to the cerebellar parenchyma, making detection on nonenhanced studies difficult [142]. Calcification and hemorrhage are rare [143]. The vast majority (90%) enhance on post-contrast imaging [143, 144].

On MR imaging, the tumor is usually iso- to mildly hypointense on T1-weighted images and hyperintense on T2-weighted images compared to white matter [145]. Virtually all vestibular schwannomas demonstrate intense enhancement following intravenous gadolinium contrast administration, although the pattern of enhancement may be heterogeneous in the presence of cystic degeneration, a common feature in larger schwannomas [146] (Fig. 13). Fast-spin echo T2-weighted imaging is also useful to identify small intracanicular tumors [147].

Meningioma

Incidence and Clinical Presentation

Meningioma is the second most common (3%) mass of the cerebellopontine angle [135]. It usually arises from the posterior surface of the petrous bone, is larger compared to the vestibular schwannoma, and rarely directly involves the internal auditory canal [142, 148]. Extension into the middle cranial fossa is common [149]. Symptoms are nonspecific and reflect the presence of mass effect on adjacent structures, such as the brain stem and cranial nerves.

Pathologic Findings

Meningioma arises anywhere arachnoidal cap cells are found, including the jugular foramen and skull base foramina [150]. Dural invasion is very common, as is hyperostosis [150]. Many different subtypes of meningioma have been identified. General histologic features include lobular collections of tumor cells surrounded by thin collagenous septa. Most are classified as WHO grade I tumors [150].

Imaging Findings

As with meningiomas located elsewhere in the CNS, those that arise in the cerebellopontine angle are usually hyperattenuated on CT with a broad dural base. In contrast to the appearance of most vestibular schwannomas, most (75%) CPA meningiomas show an obtuse angle at the bone-tumor interface [149]. Intense homogeneous enhancement is typical on post-contrast studies.

On MR imaging, the tumor is usually isointense compared to the cerebellum on both T1-weighted and T2-weighted images with intense enhancement following intravenous contrast administration (Fig. 14). A "dural tail" is seen in 50–70% of cases and represents simply a reaction of the dura to the presence of the tumor [151]. Prominent flow voids are often noted [152].

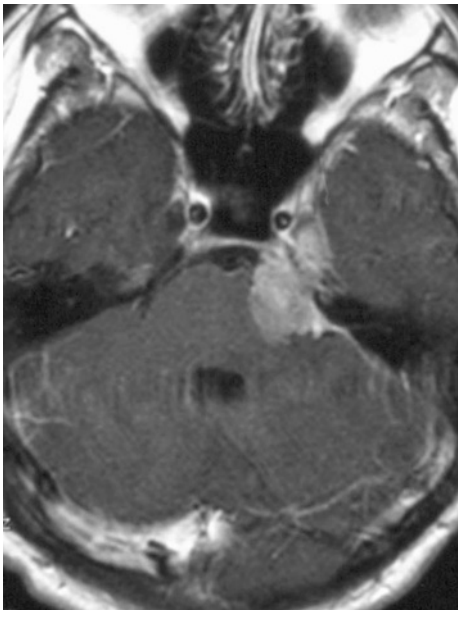

Fig. 14. Meningioma, MR appearance. Axial post-contrast T1-weighted image reveals intense enhancement of a dural-based mass in the left cerebellopontine angle

Other Tumors

Virtually any type of neuroepithelial tumor may arise within the cerebellum. Diffuse astrocytoma, mixed glial tumor, oligodendroglioma, ganglioglioma, and glioblastoma multiforme are just a few of the many such tumors in this location. While not a true neoplasm, epidermoid accounts for about 5% of such masses in the cerebellopontine angle. Although it frequently has an appearance similar to CSF fluid on CT and MR, it is a soft-tissue mass and rarely contains fluid. Diffusion-weighted imaging is ideal for the detection of this lesion, with its characteristic hyperintensity compared to normal CSF. Other schwannomas arising from the facial nerve and other cranial nerves in the cisternal space may also arise in this location.

Conclusion

By combining the imaging appearance with the location of the mass and the patient's age, it is frequently possible to limit the differential diagnosis of neoplasms that arise in the posterior fossa to only a few likely diseases and occasionally one most likely entity. The imaging appearance of many of these lesions is directly related to their gross pathologic and histologic manifestations.

References

1. Arseni C, Ciurea AV (1981) Statistical survey of 276 cases of medulloblastoma (1935–1978). Acta Neurochir 57:159–162
2. Farwell JR, Dohrmann GJ, Flannery JT (1977) Central nervous system tumors in children. Cancer 40:3123–3132
3. Roberts RO, Lynch CF, Jones MP, Hart MN (1991) Medulloblastoma: a population-based study of 532 cases. J Neuropath Exp Neurol 50:134–144
4. Duffner PK, Cohen ME (1986) Recent developments in pediatric neuro-oncology. Cancer 58 (suppl):561–568
5. Farwell JR, Dohrmann GJ, Flannery JT (1984) Medulloblastoma in childhood: an epidemiological study. J Neurosurg 61:657–664

6. Maleci A, Cervoni L, Delfini R (1992) Medulloblastoma in children and in adults: a comparative study. Acta Neurochir 119:62–67
7. Koci TM, Chiang F, Mehringer CM, et al (1993) Adult cerebellar medulloblastoma: imaging features with emphasis on MR findings. AJNR 14:929–939
8. Hubbard JL, Scheithauer BW, Kispert DB, Carpenter SM, Wick MR, Laws ER Jr (1989) Adult cerebellar medulloblastomas: the pathologic, radiographic, and clinical disease spectrum. J Neurosurg 70:536–544
9. Giordana MT, Schiffer P, Lanotte M, Girardi P, Chio A (1999) Epidemiology of adult medulloblastoma. Int J Cancer 80: 689–692
10. Giangaspero F, Bigner SH, Kleihues P, Pietsch T, Trojanowski JQ (2000) Medulloblastoma. In: Kleihues P, Cavenee W (eds) Pathology and genetics of tumours of the central nervous system. Lyon, France: IARC Press, pp 129–137
11. Bourgouin PM, Tampieri D, Grahovac SZ, Leger C, Del Carpio R, Melancon D (1992) CT and MR imaging findings in adults with cerebellar medulloblastoma: comparison with findings in children. AJR 159:609–612
12. Park TS, Hofman HJ, Hendrick EB, Humphreys RP, Becker LE (1983) Medulloblastoma: clinical presentation and management. Experience at the Hospital for Sick Children, Toronto, 1950–1980. J Neurosurg 58:543–552
13. Al-Mefty O, Jinkins JR, El-Senoussi M, El-Shaker M, Fox JL (1985) Medulloblastomas: a review of modern management with a report on 75 cases. Surg Neurol 24:606–624
14. Hope-Stone HF (1970) Results of treatment of medulloblastomas. J Neurosurg 32:83–88
15. Levin VA, Rodriguez LA, Edwards MSB, et al (1988) Treatment of medulloblastoma with procarbazine, hydroxyurea, and reduced radiation doses to whole brain and spine. J Neurosurg 68:383–387
16. Stavrou T, Bromley CM, Nicholson HS, et al (2001) Prognostic factors and secondary malignancies in childhood medulloblastoma. J Pedaitr Hematol Oncol 23:431–436
17. Reddick WE, Russell JM, Glass JO, et al (2000) Subtle white matter volume differences in children treated for medulloblastoma with conventional or reduced dose craniospinal irradiation. Magn Reson Imaging 18:787–793
18. David KF, Casey ATH, Hayward RD, Harkness WFJ, Phipps K, Wade AM (1997) Medulloblastoma: is the 5-year survival rate improving? A review of 80 cases from a single institution. J Neurosurg 86:13–21
19. Packer RJ, Sutton LN, Elterman R, et al (1994) Outcome for children with medulloblastoma treated with radiation and cisplatin, CCNU, and vincristine chemotherapy. J Neurosurg 81:690–698
20. Zeltzer PM, Boyett JM, Finlay JL, et al (1999) Metastasis stage, adjuvant treatment, and residual tumor are prognostic factors for medulloblastoma in children: conclusions from the children's cancer group 921 randomized phase III study. J Clin Oncol 17:832–845
21. Meyers SP, Wildenhain SL, Chang J-K, et al (2000) Postoperative evaluation for disseminated medulloblastoma involving the spine: contrast-enhanced MR findings, CSF cytologic analysis, timing of diease occurrence, and patient outcomes. AJNR 21:1757–1765
22. Meyers SP, Wildenhain SL, Chess MA, Tarr RW (1994) Postoperative evaluation for intracranial recurrence of medulloblastoma: MR findings with gadopentetate dimeglumine. AJNR 15:1425–1234
23. Packer RJ, Goldwein J, Nicholson HS, et al (1999) Treatment of children with medulloblastomas with reduced-dose craniospinal radiation therapy and adjuvant chemotherapy: a Children's Cancer Group Study. J Clin Oncol 17:2127–2136
24. Cogen PH, McDonald JD (1996) Tumor suppressor genes and medulloblastoma. J Neurooncol 29:103–112
25. Sandhu A, Kendall B (1987) Computed tomography in management of medulloblastomas. Neuroradiology 29:444–452
26. Zimmerman RA, Bilaniuk LT, Pahlajani H (1978) Spectrum of medulloblastomas demonstrated by computed tomography. Radiology 126:137–141
27. Nelson M, Diebler C, Forbes WSC (1991) Paediatric medulloblastoma: atypical CT features at presentation in the SIOP II trial. Neuroradiology 33:140–142
28. Zee CS, Segall HD, Miller C, et al (1982) Less common CT features of medulloblastoma. Radiology 144:97–102
29. Ferrara M, Bizzozero L, Fiumara E, D'Angelo V, Corona C, Columbo N (1989) "Primary" leptomeningeal dissemination of medulloblastoma. J Neurosurg Sci 33:219–223
30. Stavrou T, Dubovsky EC, Reaman GH, Goldstein AM, Vezina G (2000) Intracranial calcifications in childhood medulloblastoma: relation to nevoid basal cell carcinoma syndrome. AJNR 21:790–794
31. Meyers SP, Kemp SS, Tarr RW (1992) MR imaging features of medulloblastomas. AJR 158:859–865
32. Barkovich AJ (2000) Pediatric Neuroimaging. 3rd ed. Philadelphia: Lippincott, Williams, and Wilkins
33. Naitoh Y, Sasajima T, Kinouchi H, Mikawa S, Mizoi K (2002) Medulloblastoma with extensive nodularity: single photon emission CT study with iodine-123 metaiodobenylguanidine. AJNR 23:1564–1567
34. Wiener MD, Boyko OB, Friedman HS, Hockenberger B, Oakes WJ (1990) False-positive spinal MR findings for subarchnoid spread of primary CNS tumor in postoperative pediatric patients. AJNR 11:1100–1103
35. Fouladi M, Gajjar A, Boyett JM, et al (1999) Comparison of CSF cytology and spinal magnetic resonance imaging in the detection of leptomeningeal disease in pediatric medulloblastoma or primitive neuroectodermal tumor. J Clin Oncol 17:3234–3237
36. Mueller DP, Moore SA, Sato Y, Yuh WTC (1992) MRI spectrum of medulloblastoma. Clin Imaging 16:250–255
37. Rochkind S, Blatt I, Sadeh M, Goldhammer Y (1991) Extracranial metastases of medulloblastoma in adults: literature review. J Neurol Neurosurg Psychiatry 54:80–86
38. Abacioglu U, Uzel O, Sengoz M, Turkan S, Ober A (2002) Medulloblastoma in adults: treatment results and prognostic factors. Int J Radiat Oncol Phys 54:855–860
39. Levy RA, Blaivas M, Muraszko K, Robertson PL (1997) Desmoplastic medulloblastoma: MR findings. AJNR 18: 1364–1366
40. Osborn AG (1994) Diagnostic neuroradiology. St. Louis: Mosby-Year Book
41. Burger PC, Scheithauer BW, Paulus W, Szymas J, Giannini C, Kleihues P (2000) Pilocytic astrocytoma. In: Kleihues P, Cavenee W (eds) Pathology and genetics of tumours of the nervous system. Lyon, France: IARC Press, pp 45–51
42. Lee YY, Van Tassel P, Bruner JM, Moser RP, Share JC (1989) Juvenile pilocytic astrocytomas: CT and MR characteristics. AJR 152:1263–1270
43. Coakley KJ, Huston J III, Scheithauer BW, Forbes G, Kelly PJ (1995) Pilocytic astrocytomas: well-demarcated magnetic resonance appearance despite frequent infiltration histologically. May Clin Proc 70:747–751
44. Zattara-Cannoni H, Gambarelli D, Lena G, et al (1998) Are juvenile pilocytic astrocytomas benign tumors? A cytogenetic study in 24 cases. Cancer Genet Cytogenet 104:157–160
45. Gjerris F, Klinken L (1978) Long-term prognosis in children with benign cerebcellar astroyctoma. J Neurosurg 49: 179–184
46. Obana WG, Cogen PH, Davis RL, Edwards MSB (1991) Metastatic juvenile pilocytic astrocytoma. J Neurosurg 75: 972–975
47. Nadich TP, Zimmerman RA (1984) Primary brain tumors in children. Semin Roentgenol 19:100–114
48. Hayostek CJ, Shaw EG, Scheithauer BW, et al (1993) Astrocytomas of the cerebellum: a comparative clinicopathologic study of pilocytic and diffuse astrocytomas. Cancer 72: 856–869
49. Schneider JH Jr, Raffel C, McComb JG (1992) Benign cerebellar astrocytomas of childhood. Neurosurgery 30:58–63
50. Barkovich AJ (2000) Pediatric Neuroimaging. 3rd ed. Philadelphia: Lippincott, Williams and Wilkins
51. Sato K, Rorke LB (1989) Vascular bundles and wickerworks in childhood brain tumors. Pediatr Neurosci 15:105–110

52. Morikawa M, Tamaki N, Kokunai T, et al (1997) Cerebellar pilocytic astrocytoma with leptomeningeal dissemination: case report. Surg Neurol 48:49–52
53. Beni-Adani L, Gomori M, Spektor S, Constantini S (2000) Cyst wall enhancement in pilocytic astrocytoma: neoplastic or reactive phenomena. Pediatr Neurosurg 32:234–239
54. Pencalet P, Maixner W, Sainte-Rose C, et al (1999) Benign cerebellar astrocytomas in children. J Neurosurg 90:265–273
55. Wiestler OD, Schiffer D, Coons SW, Prayson RA, Rosenblum MK (2000) Ependymoma. In: Kleihues P, Cavenee W (eds) Pathology and genetics of tumours of the central nervous system. Lyon: IARC Press, pp 72–76
56. Schiffer D, Chio A, Giordana MT, et al (1991) Histologic prognostic factors in ependymoma. Childs Nerv Syst 7:177–182
57. Scheithauer BW (1978) Symptomatic subependymoma: report of 21 cases with review of the literature. J Neurosurg 49:689–696
58. Pollock IF, Gerszten PC, Martinez AJ, et al (1995) Intracranial ependymomas of childhood: long-term outcome and prognostic factors. Neurosurgery 37:655–667
59. Furie DM, Provenzale JM (1995) Supratentorial epedymomas and subependymomas: CT and MR appearance. J Comput Assist Tomogr 19:518–526
60. Palma L, Celli P, Cantore G (1993) Supratentorial ependymomas of the first two decades of life. Long-term follow-up of 20 cases (including two subependymomas). Neurosurgery 32(2):169–175
61. Swartz JD, Zimmerman RA, Bilaniuk LT (1982) Computed tomography of intracranial ependymomas. Radiology 143:97–101
62. McConachie NS, Worthington BS, Cornford EJ, Balsitis M, Kerslake RW, Jaspan T (1994) Review article: computed tomography and magnetic resonance in the diagnosis of intraventricular cerebral masses. Br J Radiol 67:223–243
63. Healey EA, Barnes PD, Kupsky WJ, et al (1991) The prognostic significance of postoperative residual tumor in ependymoma. Neurosurgery 28:666–672
64. Aguzzi A, Brandner S, Paulus W (2000) Choroid plexus tumours. In: Kleihues P, Cavenee W (eds) Pathology and genetics of tumours of the nervous system. Lyon: IARC Press, pp 84–86
65. Koeller KK, Sandberg GA (2002) Cerebral intraventricular neoplasms: radiologic-pathologic correlation. Radiographics
66. Martin N, Pierot L, Sterkers O, Mompoint D, Nahum H (1990) Primary choroid plexus papilloma of the cerebellopontine angle: MR imaging. Neuroradiology 31(6):541–543
67. Ellenbogen RG, Winston KR, Kupsky WJ (1989) Tumors of the choroid plexus in children. Neurosurgery 25(3):327–335
68. Kahn EA, Luros JT (1952) Hydrocephalus from overproduction of cerebrospinal fluid. J Neurosurg 9:59–67
69. Pencalet P, Sainte-Rose C, Lellouch-Tubiana A, et al (1998) Papillomas and carcinomas of the choroid plexus in children. J Neurosurg 88(3):521–528
70. Coates TL, Hinshaw DB, Peckman N, et al (1989) Pediatric choroid plexus neoplasms: MR, CT, and pathologic correlation. Radiology 173(1):81–88
71. Carson BS, Weingart JD, Guarnieri M, Fisher PG (1997) Third ventricular choroid plexus papilloma with psychosis. Case report. J Neurosurg 87(1):103–105
72. McGirr SJ, Ebersold MJ, Scheithauer BW, Quast LM, Shaw EG (1988) Choroid plexus papillomas: long-term follow-up results in a surgically treated series. J Neurosurg 69(6):843–849
73. Berger C, Thiesse P, Lellouch-Tubiana A, Kalifa C, Pierre-Kahn A, Bouffet E (1998) Choroid plexus carcinomas in childhood: clinical features and prognostic factors. Neurosurgery 42(3):470–475
74. Chow E, Jenkins JJ, Burger PC, et al (1999) Malignant evolution of choroid plexus papilloma. Pediatr Neurosurg 31(3):127–130
75. Sarkar C, Sharma MC, Gaikwad S, Sharma C, Singh VP (1999) Choroid plexus papilloma: a clinicopathological study of 23 cases. Surg Neurol 52:37–39
76. Reimund EL, Sitton JE, Harkin JC (1990) Pigmented choroid plexus papilloma. Arch Pathol Lab Med 114(8):902–905
77. Enomoto H, Mizuno M, Katsumata T, Doi T (1991) Intracranial metastasis of a choroid plexus papilloma originating in the cerebellopontine angle region: a case report. Surg Neurol 36(1):54–58
78. Leblanc R, Bekhor S, Melanson D, Carpenter S (1998) Diffuse craniospinal seeding from a benign fourth ventricle choroid plexus papilloma. Case report. J Neurosurg 88(4):757–760
79. van Swieten JC, Thomeer RT, Vielvoye GJ, Bots GT (1987) Choroid plexus papilloma in the posterior fossa. Surg Neurol 28(2):129–134
80. Kendall B, Reider-Grosswasser I, Valentine A (1983) Diagnosis of masses presenting within the ventricles on computed tomography. Neuroradiology 25(1):11–22
81. Vazquez E, Ball WS, Prenger EC, Castellote A, Crone KR (1991) Magnetic resonance imaging of fourth ventricular choroid plexus neoplasms in childhood. A report of two cases. Pediatr Neurosurg 17(1):48–52
82. Hopper KD, Foley LC, Nieves NL, Smirniotopoulos JG (1987) The interventricular extension of choroid plexus papillomas. AJNR Am J Neuroradiol 8:469–472
83. Irsutti M, Thorn-Kany M, Arrue P, et al (2000) Suprasellar seeding of a benign choroid plexus papilloma of the fourth ventricle with local recurrence. Neuroradiology 42(9):657–661
84. Cappe IP, Lam AH (1985) Ultrasound in the diagnosis of choroid plexus papilloma. J Clin Ultrasound 13:121–123
85. Chow P, Horgan J, Burns P, Weltin G, Taylor K (1986) Choroid plexus papilloma: detection by real-time and Doppler ultrasonography. AJNR 7:168–170
86. Levy ML, Goldfarb A, Hyder DJ, et al (2001) Choroid plexus tumors in children: significance of stromal invasion. Neurosurgery 48:303–309
87. Do HM, Marx WF, Khanam H, Jensen ME (2001) Choroid plexus papilloma of the third ventricle: angiography, preoperative embolization, and histology. Neuroradiology 43(6):503–506
88. Nagib MG, O'Fallon MT (2000) Lateral ventricle choroid plexus papilloma in childhood: management and complications. Surg Neurol 54(5):366–372
89. Rorke LB, Biegel JA (2000) Atypical teratoid/rhabdoid tumor. In: Kleihues P, Cavenee W (eds) Pathology and genetics of tumours of the nervous system. Lyon, France: IARC Press, pp 145–148
90. Hanna SL, Langston JW, Parham DM, Douglass EC (1993) Primary malignant rhabdoid tumor of the brain: clinical, imaging, and pathologic findings. AJNR 14:107–115
91. Rubinstein LJ (1972) Tumors of the central nervous system. Washington, DC: Armed Forces Institute of Pathology
92. Olivecrona H (1952) The cerebellar angioreticulomas. J Neurosurg 9:317–330
93. Richard S, Campello C, Taillandier L, Parker F, Resche F (1998) Haemangioblastoma of the central nervous system in von Hippel-Lindau disease. J Int Med 243:547–553
94. McDonnell DE, Pollack P (1978) Cerebral cystic hemangioblastoma. Surg Neurol 10:195–199
95. Grisoli F, Gambarelli D, Raybaud C, Guibout M, Leclercq T (1984) Suprasellar hemangioblastoma. Surg Neurol 22:257–262
96. Lee SR, Sanches J, Mark AS, Dillon WP, Norman D, Newton TH (1989) Posterior fossa hemangioblastomas: MR imaging. Radiology 171:463–468
97. Burger PC, Scheithauer BW (1994) Tumors of uncertain origins. In: Burger P, Scheithauer B (eds) Tumors of the central nervous system. Washington, DC: Armed Forces Institute of Pathology, pp 239–243
98. Bohling T, Plate KH, Haltia MJ, Alitalo K, Neumann HPH (2000) von Hippel-Lindau disease and capillary hemangioblastoma. In: Kleihues P, Cavenee W (eds) Pathology and genetics of tumours of the central nervous system. Lyon, France: IARC Press, pp 223–226
99. Neumann HPH, Eggert HR, Weigel K, Friedburg H, Wiestler OD, Schollmeyer P (1989) Hemangioblastoma of the central nervous system. J Neurosurg 70:24–30
100. Ho V, Smirniotopoulos JG, Murphy FM, Rushing EJ (1992) Radiologic-pathologic correlation: hemangioblastoma. AJNR 13:1343–1352

101. Erdogan B, Sen O, Aydin MV, Bagis T, Bavbek M (2002) Cerebellar hemangioblastoma in pregnancy. A case report. J Reprod Med 47:864–866
102. Huson SM, Harper PS, Hourihan MD, Cole G, Weeks RD, Compston DAS (1986) Cerebellar haemangioblastoma and von Hippel-Lindau disease. Brain 109:1297–1310
103. Manski TJ, Heffner DK, Glenn GM, et al (1997) Endolymphatic sac tumors: a source of morbid hearing loss in von Hippel-Lindau disease. JAMA 277:1461–1466
104. Latif F, Tory K, Gnarra J, et al (1993) Identification of the von Hippel-Lindau disease tumor suppressor gene. Science 260:1317–1320
105. Russell DS, Rubinstein LJ (1977) Pathology of tumors of the nervous system. 4th ed. Baltimore: Williams and Wilkins
106. Cumings JN (1950) The chemistry of cerebral cysts. Brain 73:244–250
107. Elster AD, Arthur DW (1988) Intracranial hemangioblastomas: CT and MR findings. J Comput Asst Tomogr 12:736–739
108. Ganti SR, Silver AJ, Hilal SK, Mawad ME, Sane P (1982) Computed tomography of cerebellar hemangioblastomas. J Comput Asst Tomogr 6:912–919
109. Seeger JF, Burke DP, Knake JE, Gabrielsen TO (1981) Computed tomographic and aniographic evaluation of hemangioblastomas. Radiology 138:65–73
110. Robinson S, Cohen AR (2000) Cowden disease and Lhermitte-Duclos disease: characterization of a new phakomatosis. Neurosurgery 46(2):371–83
111. Ashley DG, Zee CS, Chandrasoma PT, Segall HD (1990) Lhermitte-Duclos disease: CT and MR findings. J Comput Assist Tomogr 14(6):984–987
112. Vieco PT, del Carpio-O'Donovan R, Melanson D, Montes J, O'Gorman AM, Meagher-Villemure K (1992) Dysplastic gangliocytoma (Lhermitte-Duclos disease): CT and MR imaging. Pediatr Radiol 22(5):366–369
113. Cidis-Meltzer C, Smirniotopoulos JG, Jones RV (1995) The "striated cerebellum": an MR imaging sign in Lhermitte-Duclos disease (dysplastic gangliocytoma). Radiology 194:699–703
114. Padberg GW, Schot JD, Vielvoye GJ, Bots GT, de Beer FC (1991) Lhermitte-Duclos disease and Cowden disease: a single phakomatosis. Ann Neurol 29(5):517–23
115. Kulkantrakorn K, Awwad EE, Levy B, et al (1997) MRI in Lhermitte-Duclos disease. Neurology 48(3):725–31
116. Reeder RF, Saunders RL, Roberts DW, Fratkin JD, Cromwell LD (1988) Magnetic resonance imaging in the diagnosis and treatment of Lhermitte-Duclos disease (dysplastic gangliocytoma of the cerebellum). Neurosurgery 23:240–245
117. Milbouw G, Born JD, Martin D, et al (1988) Clinical and radiological aspects of dysplastic gangliocytoma (Lhermitte-Duclos disease): a report of two cases with review of the literature. Neurosurgery 22:124–138
118. Williams DW III, Elster AD, Ginsberg LE (1992) Recurrent Lhermitte-Duclos disease in a child: report of two cases and association with Cowden's disease. AJNR 13:287–290
119. Nelen MR, Padberg GW, Peeters EAJ, et al (1996) Localization of the gene for Cowden disease to chromosome 10q22–23. Nat Genet 13:114–116
120. Wiestler OD, Padberg GW, Steck PA (2000) Cowden disease and dysplastic gangliocytoma of the cerebellum/Lhermitte-Duclos disease. In: Kleihues P, Cavenee W (eds) Pathology and genetics of tumours of the nervous system. Lyon, France: IARC Press, pp 235–237
121. Awwad EE, Levy E, Martin DS, Merenda GO (1995) Atypical MR appearance of Lhermitte-Duclos disease with contrast enhancement. AJNR 16:1719–1720
122. Bechtel JT, Patton JM, Takei Y (1978) Mixed mesenchymal and neuroectodermal tumor of the cerebellum. Acta Neuropathol 41:261–263
123. Kleihues P, Chimelli L, Giangaspero F (2000) Cerebellar liponeurocytoma. In: Kleihues P, Cavenee W (eds) Pathology and genetics of tumours of the central nervous system. Lyon, France: IARC Press, pp 110–111
124. Jackson TR, Regine WF, Wilson D, Davis DG (2001) Cerebellar liponeurocytoma. Case report and review of the literature. J Neurosurg 95:700–703
125. Scheinker IM (1945) Subependymoma: a newly recognized tumor of subependymal derivation. J Neurosurg 2:232–240
126. Matsumura A, Ahyai A, Hori A, Schaake T (1989) Intracerebral subependymomas. Clinical and neuropathological analyses with special reference to the possible existence of a less benign variant. Acta Neurochir (Wien) 96(1–2):15–25
127. Wiestler OD, Schiffer D (2000) Subependymoma. In: Kleihues P, Cavenee W (eds) Pathology and genetics of tumours of the nervous system. Lyon: IARC Press, pp 80–81
128. Lobato RD, Sarabia M, Castro S, et al (1986) Symptomatic subependymoma: report of four new cases studied with computed tomography and review of the literature. Neurosurgery 19(4):594–598
129. Yamasaki T, Kikuchi H, Higashi T, Yamabe H, Moritake K (1990) Two surgically cured cases of subependymoma with emphasis on magnetic resonance imaging. Surg Neurol 33(5):329–335
130. Chiechi MV, Smirniotopoulos JG, Jones RV (1995) Intracranial subependymomas: CT and MR imaging features in 24 cases. AJR Am J Roentgenol 165(5):1245–1250
131. Giordana MT, Wiestler OD (2000) Medullomyoblastoma. In: Kleihues P, Cavenee W (eds) Pathology and genetics of tumours of the central nervous system. Lyon, France: IARC Press, pp 138–139
132. Lindboe CF, Stolt-Nielsen A, Dale LG (1992) Hemorrhage in a highly vascularized subependymoma of the septum pellucidum: case report. Neurosurgery 31(4):741–745
133. Hoeffel C, Boukobza M, Polivka M, et al (1995) MR manifestations of subependymomas. AJNR Am J Neuroradiol 16(10):2121–2129
134. Spoto GP, Press GA, Hesselink JR, Solomon M (1990) Intracranial ependymoma and subependymoma: MR manifestations. AJNR Am J Neuroradiol 11(1):83–91
135. Brackmann DE, Bartels LJ (1980) Rare tumors of the cerebellopontine angle. Otolaryngol Head Neck Surg 88:555–559
136. Casadei GP, Komori T, Scheithauer BW, Miller GM, Parisi JE, Kelly PJ () Intracranial parenchymal schwannoma. A clinicopathological and neuroimaging study of nine cases. J Neurosurg 1993; 79:217–222
137. Woodruff JM, Kourea HP, Louis DN, Scheithauer BW (2000) Schwannoma. In: Kleihues P, Cavenee W (eds) Pathology and genetics of tumours of the nervous system. Lyon, France: IARC Press, pp 164–166
138. Kasantikul V, Netsky MG, Glasscock ME III (1980) Acoustic neurilemmoma. Clinicoanatomical study of 103 patients. J Neurosurg 52:28–35
139. Selesnick SH, Jackler RK (1992) Clinical manifestations and audiologic diagnosis in acoustic neuromas. Otolaryngol Clin North Am 25:521–551
140. Brackmann DE, Green JD Jr (1998) Cerebellopontine angle tumors. In: Bailey B, ed. Head and Neck Surgery – Otolaryngology. 2nd ed. Philadelphia: Lippincott-Raven, pp 2171–2192
141. Solti-Bohman LG, Magaram DL, Lo WW, et al (1984) Gas-CT cisternography for detection of small acoustic nerve tumors. Radiology 150:403–407
142. Maya MM, Lo WWM, Kovanlikaya I (2003) Temporal bone tumors and cerebellopontine angle lesions. In: Som P, Curtin H (eds) Head and Neck Imaging. 4th ed. St. Louis: Mosby, pp 1275–1360
143. Moller A, Hatam A, Olivecrona H (1978) Diagnosis of acoustic neuroma with computed tomography. Neuroradiology 17:25–30
144. Hatam A, Bergstrom M, Moller A, Olivecrona H (1978) Early contrast enhancement of acoustic neuroma. Neuroradiology 17:31–33
145. Press GA, Hesselink JR (1988) MR imaging of cerebellopontine angle and internal auditory canal lesions at 1.5T. AJR 150:1371–1381
146. Curtin HD (1997) Rule out eighth nerve tumor: contrast-emjamced T1-weighted or high-resolution T2-weighted MR? AJNR 18:1834–1838
147. Shelton C, Harnsberger HR, Allen R, King B (1996) Fast spin echo magnetic resonance imaging: clinical application in screening for acoustic neuroma. Otolaryngol Head Neck Surg 114:71–76

148. Gentry LR, Jacoby CG, Turski PA, Houston LW, Strother CM, Sackett JF (1987) Cerebellopontine angle-premastoid lesions: comparative study of diagnosis with MR imaging and CT. Radiology 167:513–520
149. Valavanis A, Schubiger O, Hayek J, Pouliadis G (1981) CT of meningiomas on the posterior surface of the petrous bone. Neuroradiology 22:111–121
150. Louis DN, Scheithauer BW, Budka H, von Deimling A, Kepes JJ (2000) Meningioma. In: Kleihues P, Cavenee W (eds) Pathology and genetics of tumours of the nervous system. Lyon, France: IARC Press, pp 176–184
151. Goldsher D, Litt AW, Pinto RS, Bannon KR, Kricheff II (1990) Dural "tail" associated with meningiomas on Gd-DTPA-enhanced MR images: characteristics, differential diagnosis value, and possible implications for treatment. Radiology 176: 447–450
152. Zimmerman RD, Fleming CA, Saint-Louis LA, Lee BC, Manning JJ, Deck MD (1985) Magnetic resonance imaging of meningiomas. AJNR 6:149–157

Part 2
Head and Neck Radiology

The Infrahyoid Neck: CT and MR Imaging Versus Histopathology

Minerva Becker, Paulette Mhawech

2.1

Contents

Introduction

The term "infrahyoid neck" refers to the anatomical region that extends longitudinally from the hyoid bone to the thoracic inlet. The hyoid bone has been chosen as the landmark structure between the suprahyoid and infrahyoid neck because several fasciae that act as a natural cleavage plane are attached to the hyoid bone. In the transverse plane, the infrahyoid neck contains five distinct spaces that are defined by the deep cervical fascia, namely the visceral space, the carotid space, the retropharyngeal space, the posterior cervical space and the perivertebral space [13, 29, 30, 41] (Fig. 1). These spaces play an important role for the pathways of spread of inflammatory and neoplastic disease in the infrahyoid neck. The relationship between the major anatomical structures and the different spaces is given in Tables 1–5.

Cross-sectional imaging techniques, especially computed tomography (CT) and magnetic resonance (MR) imaging, play an important role for the diagnosis of pathologic conditions affecting the infrahyoid neck. The purpose of the present chapter is to provide an overview of the diagnostic features of a variety of be-

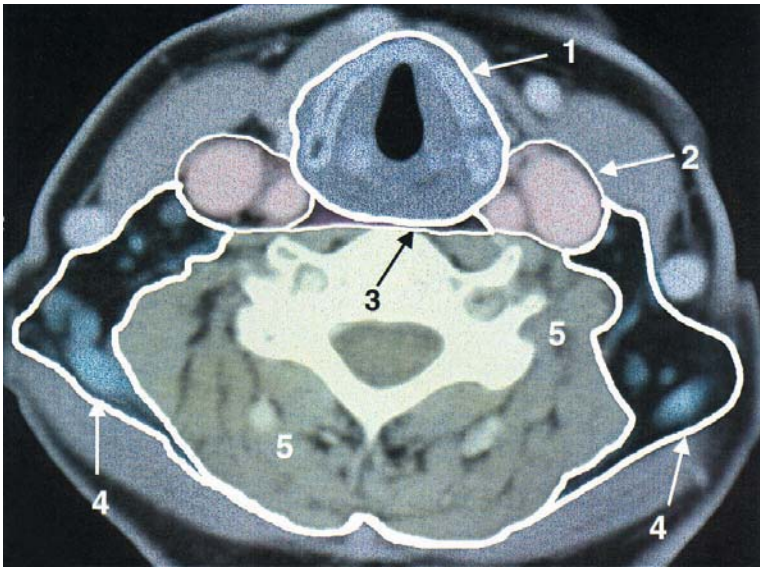

Fig. 1. Schematic representation of the infrahyoid neck spaces at the level of the true vocal cords. *1* visceral space; *2* carotid space, *3* retropharyngeal space; *4* posterior cervical space; *5* perivertebral space; Reproduced with permission from [13]

nign and malignant diseases occurring in the infrahyoid neck as seen on CT and MR images and to correlate the radiologic findings with the underlying pathologic–anatomical changes. An overview of the most common pathologic conditions affecting the different spaces of the infrahyoid neck is given in Tables 1–5.

Table 1. Visceral space: extent, contents and differential diagnosis of the most common pathologic conditions

Extent	Contents	Key pathologies
Hyoid bone to mediastinum	Larynx	Squamous cell carcinoma Chondrosarcoma
	Hypopharynx and cervical esophagus	Squamous cell carcinoma Zenker's diverticulum
	Trachea	Carcinoma (squamous cell and adenoid cystic) Benign stenosis
	Thyroid gland	Goiter Colloid cyst Carcinoma (papillary, follicular, anaplastic) Hashimoto's thyroiditis
	Parathyroid glands	Adenoma
	Remnants of the thyroid/parathyroid anlage	Thyroglossal duct cyst
	Paratracheal lymph nodes	Metastases (squamous cell carcinoma, thyroid carcinoma, lymphoma)
	Recurrent laryngeal nerves	Paralysis (after surgery, lymph node metastases)

Table 2. Carotid space: extent, contents and differential diagnosis of the most common pathologic conditions

Extent	Contents	Key pathologies
Jugular foramen to aortic arch[a]	Common and internal carotid artery	Thrombosis, aneurysm or pseudoaneurysm Dissection
	Internal jugular vein	Thrombosis/thrombophlebitis
	Vagus nerve (cranial nerve X)	Schwannoma, neurofibroma
	Carotid body	Paraganglioma
	Glomus jugulare and vagale	Paraganglioma
	Deep cervical lymph nodes	Metastases (squamous cell carcinoma of the upper aerodigestive tract, lymphoma, thyroid cancer) Suppurative adenopathy, abscess
	Remnants of the second branchial cleft apparatus	Second branchial cleft cyst

[a] Note that the superior portion of the carotid space is situated in the suprahyoid neck, while the inferior portion is situated in the infrahyoid neck

Table 3. Retropharyngeal space: extent, contents and differential diagnosis of the most common pathologic conditions

Extent	Contents	Key pathologies
Skull base to mediastinum[a]	Fat	Channel for infection and tumor to travel from the neck into the mediastinum: Inflammatory conditions (cellulitis, abscess, necrotizing fasciitis) Direct invasion from primary squamous cell carcinoma Lipoma
	Lymph nodes[b]	Metastases (squamous cell carcinoma of the upper aerodigestive tract, lymphoma, thyroid cancer) Reactive adenopathy, tuberculous adenitis, suppurative adenopathy and abscess

[a] Note that the superior portion of the retropharyngeal space is situated in the suprahyoid neck, while the inferior portion is situated in the infrahyoid neck
[b] Note that lymph nodes are found only in the suprahyoid retropharyngeal space

Table 4. Posterior cervical space: extent, contents and differential diagnosis of the most common pathologic conditions

Extent	Contents	Key pathologies
Skull base to clavicle[a]	Fat	Lipoma/liposarcoma
	Spinal accessory nerve (cranial nerve XI)	Schwannoma, neurofibroma
	Brachial plexus (preaxillary portion)	Direct invasion (apical lung carcinoma, breast carcinoma)
		Schwannoma, neurofibroma
	Spinal accessory lymph nodes	Metastases (squamous cell carcinoma of the nasopharynx, lymphoma)
		Reactive adenopathy, tuberculous adenitis, suppurative adenopathy and abscess
	Sequestrations of primitive embryonic lymph sacs	Congenital lesions (cystic hygroma-lymphangioma spectrum)

[a] Note that the superior portion of the posterior cervical space is situated in the suprahyoid neck, while the inferior portion is situated in the infrahyoid neck

Table 5. Perivertebral space: extent, contents and differential diagnosis of the most common pathologic conditions

Extent	Contents	Key pathologies
Skull base to mediastinum[a]	Prevertebral, scalene and paraspinal muscles	Abscess
	Vertebral body and pedicle	Osteomyelitis (pyogenic, tuberculous)
		Metastases
		Direct invasion of squamous cell carcinoma
		Chordoma
		Vertebral body primary tumors
	Brachial plexus roots	
	Phrenic nerve	Schwannoma, neurofibroma
	Vertebral artery and vein	Aneurysm or pseudoaneurysm
		Dissection
		Thrombosis

[a] Note that the superior portion of the posterior cervical space is situated in the suprahyoid neck, while the inferior portion is situated in the infrahyoid neck

Congenital and Developmental Lesions

The most common congenital masses found in the infrahyoid neck include the following entities: branchial cleft cyst, thyroglossal duct cyst, venous malformations and lymphangioma. All masses in this group arise from a rest of tissue left behind after formation of the structures in the neck.

Branchial Cleft Cyst

Of all branchial cleft anomalies, 95% arise from the remnant of the second branchial apparatus. Normally, the second branchial cleft apparatus involutes by the 9th fetal week [29, 30, 33, 38]. When the involution phase is incomplete, the remnant tissue has the potential to grow into a branchial cleft anomaly. The most common form of second branchial cleft anomaly is a cystic mass without sinus or fistula. However, any permutation of cyst, sinus or fistula may be possible. *Second branchial cleft cysts* occur either in infants or in the young adult. Typically, patients with a second branchial cleft cyst present with a painless neck mass. A history of a change in the size of the cyst, usually after an upper respiratory tract infection, is common. The most common location of a second branchial cleft cyst is at the angle of the mandible posterolateral to the submandibular gland, lateral to the carotid artery and anteromedial to the sternocleidomastoid muscle (Fig. 2). When present on the cyst, a beak that points medially between the internal and external carotid artery is pathognomonic of a second branchial cleft cyst. CT typically reveals a unilocular cystic mass essentially isoattenuating with cerebrospinal fluid (CSF). A uniformly thin peripheral capsular enhancement is characteristic. Infection of the cyst may,

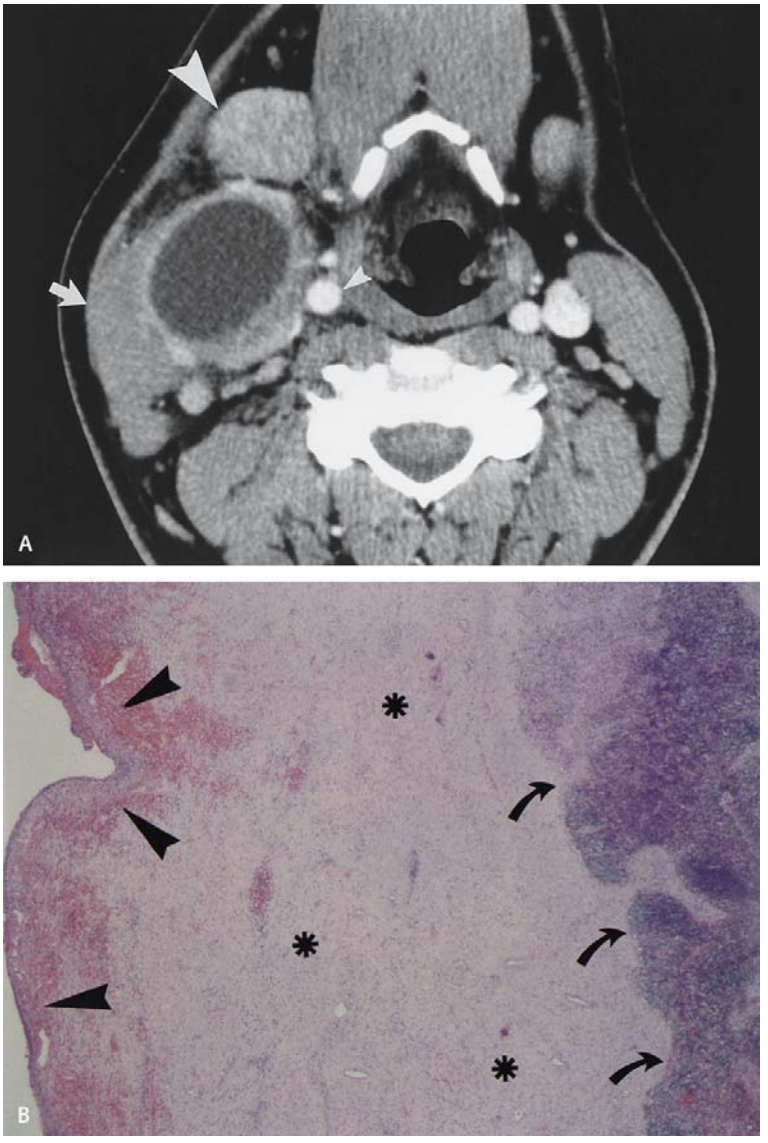

Fig. 2A, B. Classic second branchial cleft cyst. CT scan appearance and microscopic findings. **A** Axial contrast-enhanced CT image at the level of the hyoid bone demonstrates a cystic lesion with significant capsular enhancement. Thickening of the wall of the cyst is caused by inflammation. Note the embryologically defined location of the cyst. Submandibular gland (*large arrowhead*), internal carotid artery (*small arrowhead*), sternocleidomastoid muscle (*arrow*). **B** Photomicrograph demonstrates the characteristic components of the branchial cleft cyst wall: squamous epithelium (*arrowheads*) surrounded by an inflammatory and fibrotic stroma (*asterisks*) and lymphoid tissue with germinal centers (*arrows*). Reproduced with permission from [13]

however, result in thickening and irregular capsular enhancement (Fig. 2) [13]. Depending on the relative protein concentration within the cyst, second branchial cleft cysts are typically isointense to CSF on T2-weighted images, while they have a variable appearance on T1-weighted images. The characteristic histologic features of the branchial cleft cyst are shown in Fig. 2. The differential diagnosis includes necrotic lymph nodes (see "Involvement of Cervical Lymph Nodes by Squamous Cell Carcinoma").

Thyroglossal Duct Cyst

During embryogenesis, the anlage of the thyroid and parathyroid glands descends from the foramen cecum at the tongue base to its final position in the anterior visceral space. During this caudal migration, the anlage passes just anterior to the precursor tissue of the hyoid bone, leaving a tract of epithelial tissue called the thyroglossal duct [13, 29]. The normal thyroglossal duct involutes by the 8th fetal week. Thyroglossal duct remnants may give rise to cysts, fistulae or solid nodules of thyroid tissue. Thyroglossal duct cysts most commonly occur in the region of the hyoid bone; 15% of all cysts are located at the level of the hyoid bone, 65% are located just below the hyoid bone and only 20% are located in the suprahyoid neck. Most patients with a thyroglossal duct cyst present with an asymptomatic mass. CT or MRI typically show a midline or paramedian cystic mass located in the infrahyoid strap muscles at or below the level of the hyoid bone (Fig. 3). The capsule of the

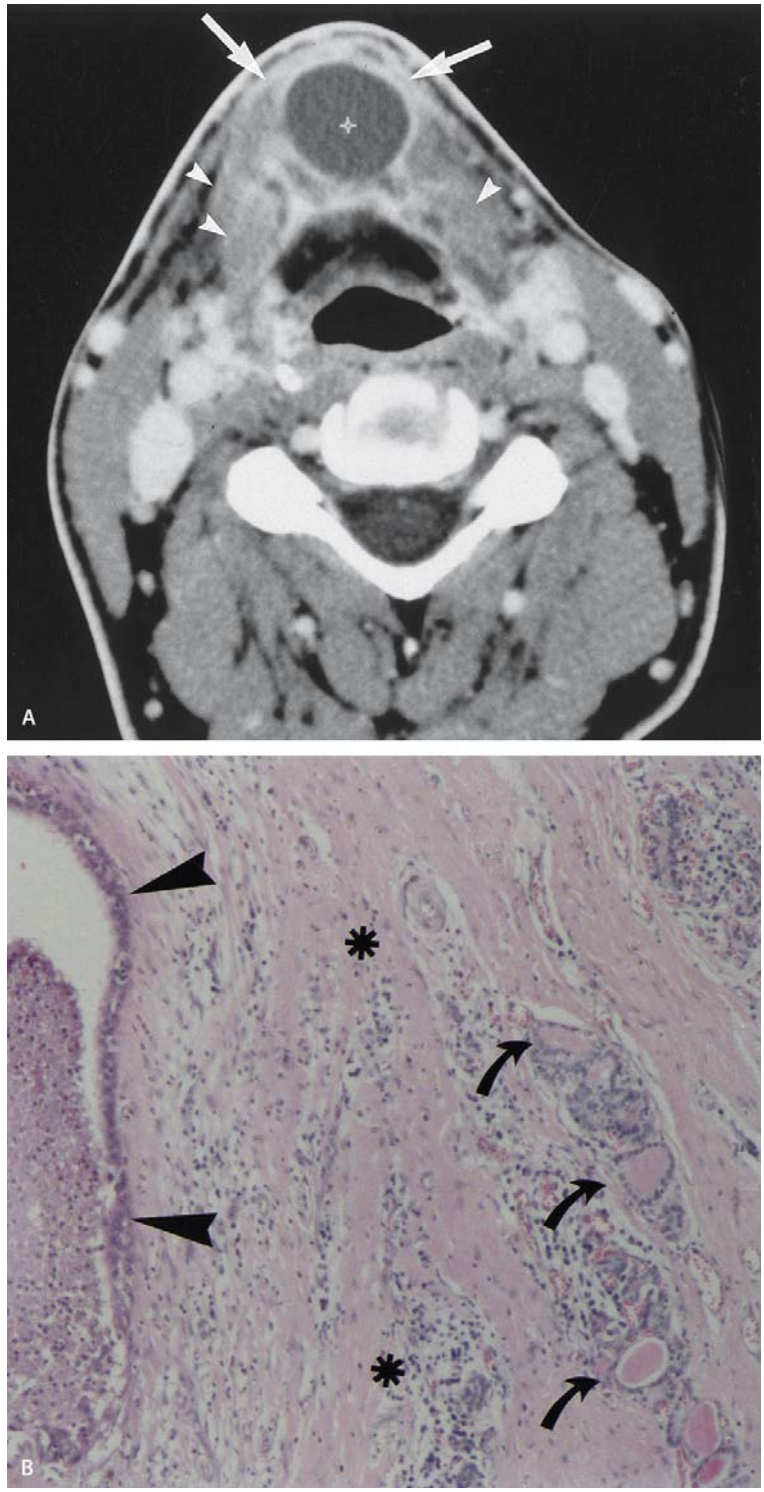

Fig. 3A, B. Thyroglossal duct cyst. Characteristic CT and histologic appearance. **A** Axial contrast-enhanced CT image immediately below the level of the hyoid bone. Key features include midline location and beaking of the strap muscles over the surface of the cyst (*arrows*). Infection of the cyst has resulted in thickening of the cyst wall and significant capsular enhancement. Associated inflammatory changes within the strap muscles have resulted in muscular and fascial enhancement (*arrowheads*). **B** Photomicrograph demonstrates the characteristic components of the thyroglossal duct cyst wall: squamous epithelium (*arrowheads*) surrounded by an inflammatory and fibrotic stroma (*asterisks*) and thyroid follicles (*arrows*). Reproduced with permission from [13]

cyst shows a uniformly thin enhancement. The location of the thyroglossal duct cyst within the strap muscles is the key feature that allows differentiation from other adult neck masses that may have a similar CT or MR appearance, i.e., necrotic anterior cervical nodes and thrombosed anterior jugular veins. The latter are, however, located superficial to the strap muscles [13, 29]. Histologic examination reveals that the wall of the thyroglossal duct cyst is composed of squamous cell mucosa, and thyroid tissue is often present (Fig. 3). Inflamma-

tory changes may obliterate the mucosa of the thyroglossal duct wall, making the pathologic diagnosis difficult.

Vascular Malformations

According to Mulliken and Glowaki, vascular lesions of the head and neck are divided into hemangiomas and vascular malformations [32, 39]. *Hemangiomas* are neoplastic conditions characterized by an increased proliferation and turnover of endothelial cells [4, 32, 39]. They are the most common tumors of the head and neck in infancy and childhood. Hemangiomas typically display a rapid proliferation phase during the 1st year of life followed by an involution phase.

As opposed to hemangiomas, *vascular malformations* are not tumors but true congenital vascular anomalies with a normal proliferation rate of endothelial cells. Typically, they do not regress and may rapidly enlarge in association with trauma or endocrine changes. Vascular malformations are further subdivided into capillary, venous, arterial, and lymphatic malformations [32, 39]. Arterial malformations are high-flow malformations characterized by enlarged, tortuous arteries and draining veins. Capillary and *venous malformations* are low-flow lesions. The characteristic CT appearance is shown in Fig. 4. On MRI, venous malformations are isointense or hyperintense to muscle on T1-weighted images, become very hyperintense on T2-weighted images, and typically enhance significantly following administration of contrast material [13].

Lymphangiomas are benign, nonencapsulated lesions that are believed to arise from sequestrations of primitive embryonic lymph sacs. At approximately the 6th gestational week, the jugular lymphatic sacs open and begin to drain into the adjacent jugular veins. If a communication between the jugular sac and the jugular vein fails to develop, the lymph-filled jugular sac dilates. Ninety per cent of lymphangiomas become clinically apparent by 2 years of age, while the remaining 10% present as neck masses in the young adult. Lymphangiomas are classified into three histologic types on the basis of the size of the abnormal lymphatic spaces. Capillary lymphangioma is composed of small, capillary-sized, thin-walled lymphatic channels. Cavernous lymphangioma is composed of medium-sized dilated lymphatics with a fibrous adventitia, and cystic lymphangioma (cystic hygroma) is composed of large dilated lymphatic vessels that range in diameter from a few millimeters to several centimeters [7, 8] (Fig. 5). Most cystic hygromas arise in the posterior cervical space (Fig. 5) and up to 10% of all cervical cystic hygromas extend into the mediastinum. The characteristic CT and MR appearance includes a multiseptate cystic mass that may insinuate in and around normal structures, making surgical resection very difficult (Fig. 5). On T2-weighted MR images, cystic hygromas are typically isointense to CSF, while they have a variable signal intensity on T1-weighted images because of the variable protein content (Fig. 5). Rapid enlargement of a cervical cystic hygroma is usually caused by hemorrhage into the cystic spaces of the mass. Multiple fluid–fluid levels, representing layering of blood and lymph are characteristic in this clinical setting. Fluid–fluid levels may be identified at CT; however, the conspicuity of this finding is more apparent on MR images [13, 40].

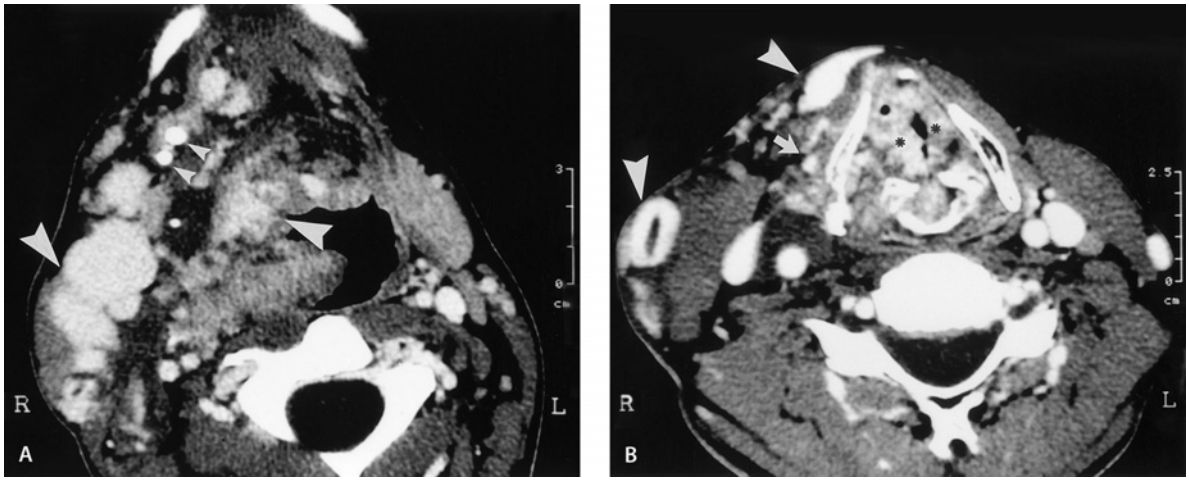

Fig. 4A, B. Venous malformation. Characteristic CT appearance. Axial contrast-enhanced CT images at the suprahyoid (**A**) and infrahyoid (**B**) level demonstrate an extensive cervical venous malformation (*large arrowheads*) with phleboliths (*small arrowheads*). Note also extensive involvement of both vocal cords (*asterisks*) and strap muscles (*arrow*). Reproduced with permission from [14]

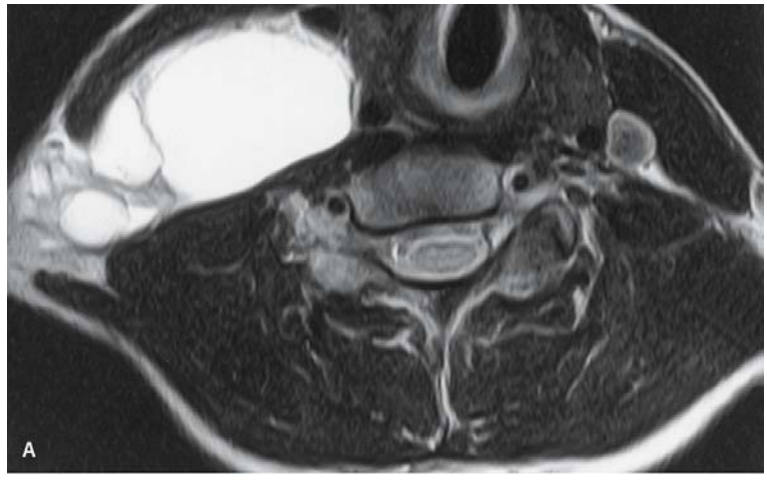

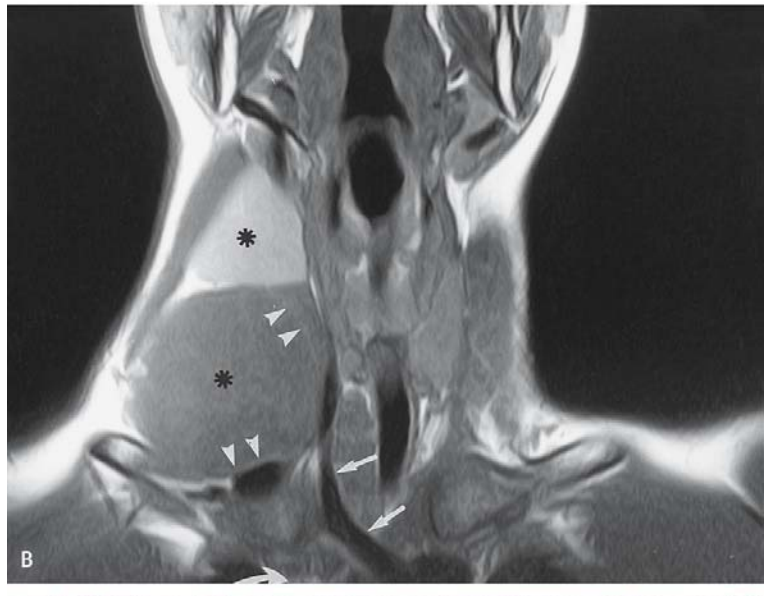

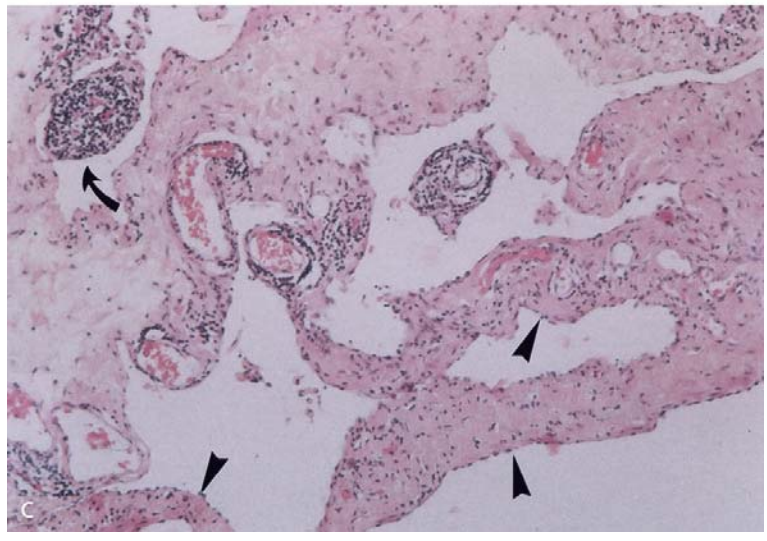

Fig. 5A–C. Cystic hygroma. MR appearance and microscopic findings. **A** Axial T2-weighted FSE image at the level of the cricoid cartilage demonstrates a multiseptate, cystic lesion originating from the right posterior cervical space. **B** Coronal T1-weighted spin-echo (SE) image obtained after injection of Gd-DTPA shows enhancement of the thin septa (*arrowheads*). The cystic spaces have a variable signal intensity (*asterisks*) due to the variable protein content. Note that the cystic hygroma extends into the mediastinum (*curved arrow*) and it insinuates around the common carotid and subclavian arteries (*arrows*). **C** Photomicrograph demonstrates large cystic spaces surrounded by lymphatic channels lined by prominent endothelial cells (*arrowheads*). The lymphatic channels are surrounded by a fibrous stroma containing scattered lymph follicles (*arrow*). Reproduced with permission from [13]

Neoplastic Lesions

This section covers the major neoplastic lesions of the infrahyoid neck that have significant CT and MR imaging findings. Emphasis is placed on radiologic–pathologic correlation discussing gross and microscopic features that are responsible for the imaging findings. The tumors discussed in this section are squamous cell carcinoma and non-squamous cell tumors of the larynx and hypopharynx, nodal and non-nodal neck neoplasms and thyroid gland tumors.

Larynx and Hypopharynx

Squamous Cell Carcinoma

Approximately 95% of laryngeal and hypopharyngeal tumors are squamous cell carcinomas [5–12]. Etiologically, these tumors are related to tobacco and alcohol abuse. With very few exceptions, squamous cell tumors are located at the mucosal surface, and the clinical diagnosis is readily confirmed by endoscopic biopsy. However, submucosal tumor extension cannot be assessed reliably with endoscopy alone. Because the degree of infiltration into the surrounding deep anatomic structures, as well as the presence or absence of lymph node metastases has implications for treatment and prognosis, cross-sectional imaging is required for the diagnostic workup of these tumors. Non-squamous cell tumors of the larynx and hypopharynx, however, are often entirely located submucosally. The origin and extension of these tumors are difficult to diagnose with endoscopy alone, and planning of biopsy and treatment usually depends on imaging findings [9–12].

Imaging Characteristics and Patterns of Tumor Spread

Interpretation of CT and MR imaging studies of patients with laryngeal and hypopharyngeal cancer requires a thorough understanding of the typical pathways of tumor spread from the different primary sites and subsites and knowledge of the criteria for neoplastic invasion of the adjacent structures and spaces, particularly the preepiglottic space, the paraglottic space and the cartilaginous framework of the larynx. Squamous cell carcinoma typically displays a low signal intensity on T1-weighted images and an intermediate signal intensity on T2-weighted images. After intravenous injection of contrast material, moderate enhancement is seen on both CT and MR images. Because of the similar imaging characteristics of tumor and mucosa on both unenhanced and enhanced images, both CT and MR imaging cannot compete with endoscopy for the detection of early cancer. Correlation with endoscopic biopsy is, therefore, indispensable.

Depending on its origin, carcinoma of the larynx may be divided into supraglottic cancer, glottic cancer and subglottic cancer [5, 6, 9–11]. *Supraglottic tumors* originating from the epiglottis primarily invade the preepiglottic space, either through the preexisting natural perforations of the epiglottic cartilage or along its lateral border. The preepiglottic space is a triangular space situated anterior to the epiglottis. It mainly contains fat. According to the TNM classification [42], invasion of the preepiglottic space – which cannot be detected endoscopically – upstages a tumor, which is then classified as T3. Tumors that originate in the region of the caudal portion of the epiglottis (petiole) often invade the low preepiglottic space and tend to spread inferiorly into the glottis or subglottis, thus becoming transglottic tumors. This has major implications for therapy because certain voice-preserving laryngectomy procedures cannot be performed and total laryngectomy – a very mutilating procedure – may become necessary [5, 6, 11]. Both CT and MRI are well suited to demonstrating replacement of fatty tissue normally found within the preepiglottic space by tumor tissue (Fig. 6). The reported sensitivity of CT and MRI to detect invasion of the preepiglottic space is 100%, and the corresponding specificities 93% and 84%–90%, respectively [5, 6, 11, 55, 57]. Supraglottic tumors originating primarily from the laryngeal ventricle typically infiltrate the paraglottic space (Fig. 7). The paraglottic space lies between the mucosa and the laryngeal framework and is paired and symmetrical. In the supraglottic region, it surrounds the laryngeal ventricle and mainly contains fat, whereas at the glottic level the thyroarytenoid muscle, which forms the bulk and shape of the vocal cord, occupies most of the volume of the paraglottic space. Within the paraglottic space, tumors may easily spread in a cephalad or caudad direction to areas that are remote from the site of the primary mucosal lesion. Therefore, these tumors are often diagnosed in an advanced stage. The primary sign of tumor spread to the paraglottic space on both CT and MR images is replacement of fatty tissue by tumor tissue (Fig. 7). Based on radiologic–pathologic correlation studies, neoplastic invasion of the paraglottic space can be equally well detected with both techniques [5, 6, 11, 55, 57]. The reported sensitivities of CT and MRI are 93% and 97%, respectively. The specificity of both CT and MRI is, however, limited because peritumoral inflammatory changes may lead to overestimation of tumor spread with either methods.

Glottic carcinoma typically arises from the anterior half of the vocal cord and primarily spreads into the anterior commissure. Invasion of the anterior commissure is seen on CT and MR images as a soft tissue thickening of more than 1–2 mm (Fig. 8). Once the tumor has reached the anterior commissure, it may easily spread

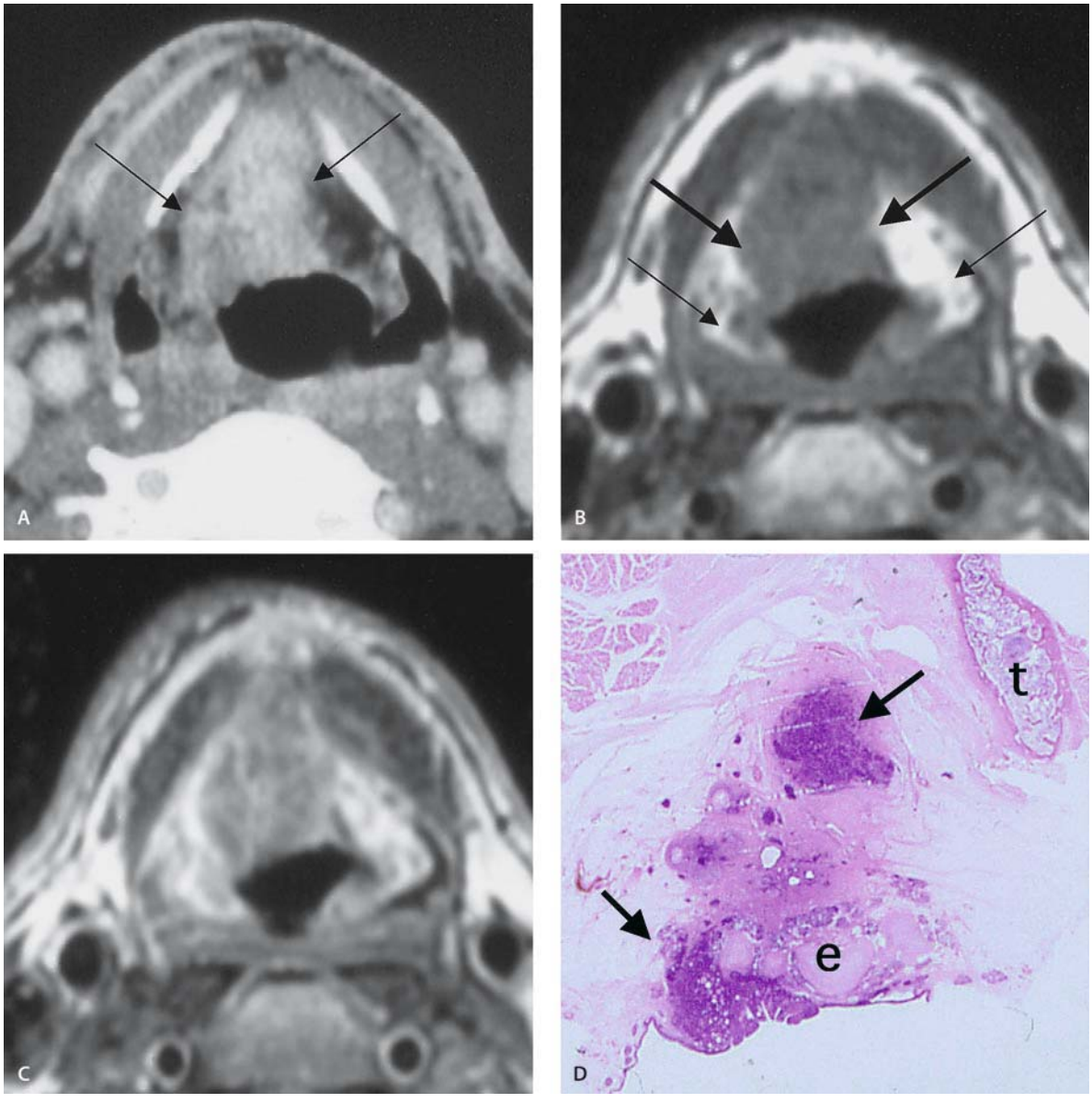

Fig. 6A–D. Neoplastic invasion of the preepiglottic space due to anterior supraglottic cancer. **A** Axial, contrast-enhanced CT image at the supraglottic level shows an enhancing tumor mass as it invades the preepiglottic space (*arrows*). **B** Axial, unenhanced T1-weighted SE image obtained in the same patient at the same level shows a tumor mass with an intermediate signal intensity as it extends into the preepiglottic space (*thick arrows*). Note the high signal intensity of the noninvaded paraglottic space due to the high content of fatty tissue (*thin arrows*). **C** Axial Gd-enhanced T1-weighted SE image at the same level shows enhancement of the tumor mass invading the preepiglottic space. **D** Whole organ, axial histologic slice from supraglottic horizontal laryngectomy specimen confirms tumor invasion of the preepiglottic space (*arrows*). Epiglottis (*e*), thyroid cartilage (*t*). Reproduced with permission from [9]

into the contralateral cord, supraglottis or subglottis. Invasion of the subglottis precludes various types of voice-sparing laryngectomy procedures and total laryngectomy may be required. When the glottic tumor spreads laterally, it may invade the paraglottic space (Fig. 8). Paraglottic tumor spread may be entirely occult clinically and detectable only by means of CT or MR imaging.

Primary *subglottic cancers* are uncommon and tend to spread to the trachea or invade the thyroid gland and the cervical esophagus. Their diagnosis is straightforward on both CT and MR images.

Depending on its origin, carcinoma of the hypopharynx may be divided into piriform sinus carcinoma, postcricoid carcinoma and posterior pharyngeal wall carcinoma [42]. *Carcinoma of the piriform sinus* is read-

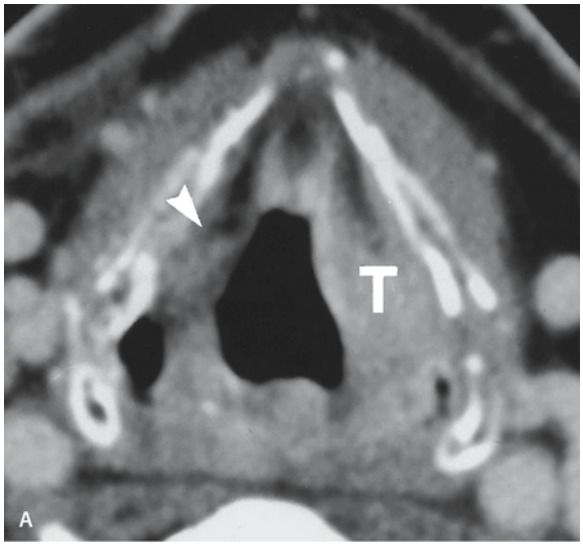

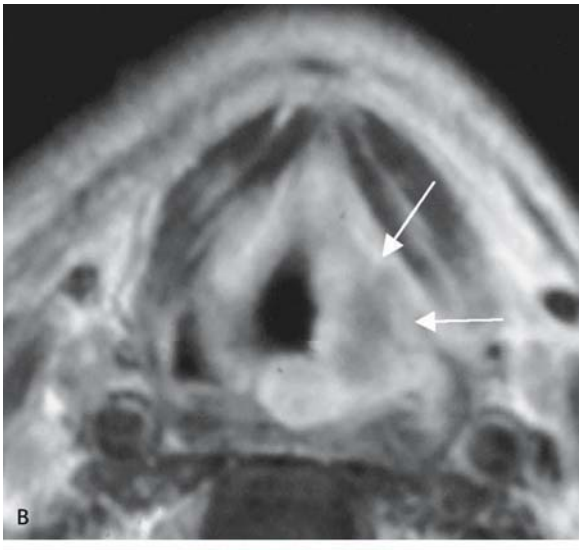

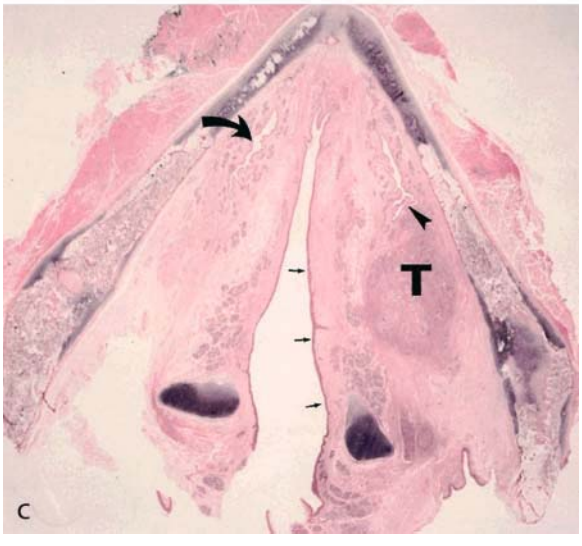

Fig. 7A–C. Neoplastic invasion of the left paraglottic space due to ventricular cancer. Endoscopically only a very small mucosal lesion was present within the left laryngeal ventricle. **A** Axial contrast-enhanced CT image at the supraglottic level shows an enhancing tumor mass (*T*) obliterating the left paraglottic fat. Note for comparison the normal aspect of the right paraglottic space (*arrowhead*). **B** Axial contrast-enhanced T1-weighted SE image obtained in the same patient at the same level shows an enhancing tumor mass (*arrows*) invading the left paraglottic fat. **C** Whole-organ axial slice from specimen confirms extensive paraglottic space invasion by a predominantly submucosal tumor mass (*T*). The tumor mass originates from the left laryngeal ventricle (*arrowhead*). *Curved arrow* points to the right laryngeal ventricle. Note the normal aspect of the laryngeal mucosa overlying the tumor mass (*thin arrows*). Reproduced with permission from [9]

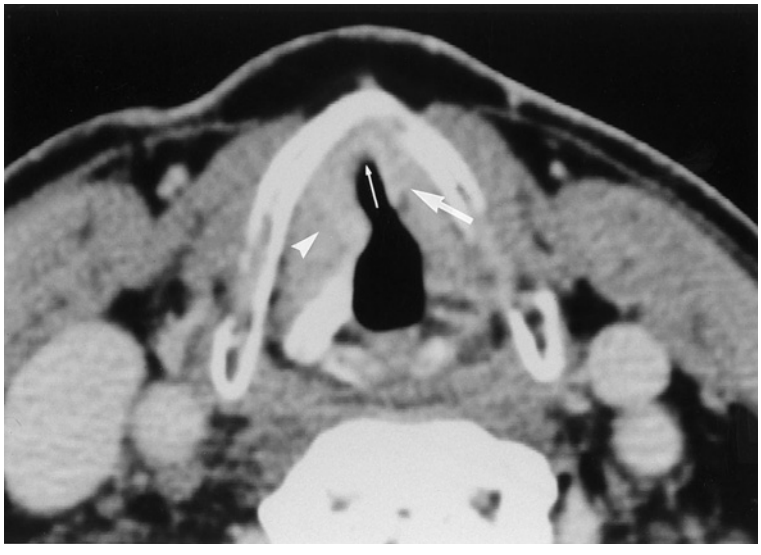

Fig. 8. Glottic cancer with invasion of the anterior commissure. Characteristic CT appearance. Axial, contrast-enhanced CT image obtained at the glottic level shows a tumor mass arising from the right vocal cord invading the anterior commissure (*thin arrow*) and the contralateral vocal cord (*thick arrow*). Note also invasion of the right thyroarytenoid muscle (*arrowhead*), which occupies most of the paraglottic space at this level. Reproduced with permission from [6]

ily detected with endoscopy, while early superficial spreading tumors may be invisible on CT and MR images. In many cases, however, patients with piriform sinus tumors initially present with advanced lesions and diagnosis with CT or MRI is straightforward (Fig. 9). Tumors originating from the lateral wall of the piriform sinus have a tendency to infiltrate the soft tissues of the neck very early. Tumors originating from the medial wall of the piriform sinus may infiltrate the larynx by growing anteriorly into the paraglottic space or they may spread to the postcricoid region and cervical esophagus (Fig. 10). Piriform sinus carcinoma frequently invades the laryngeal framework (see "Neoplastic Cartilage Invasion).

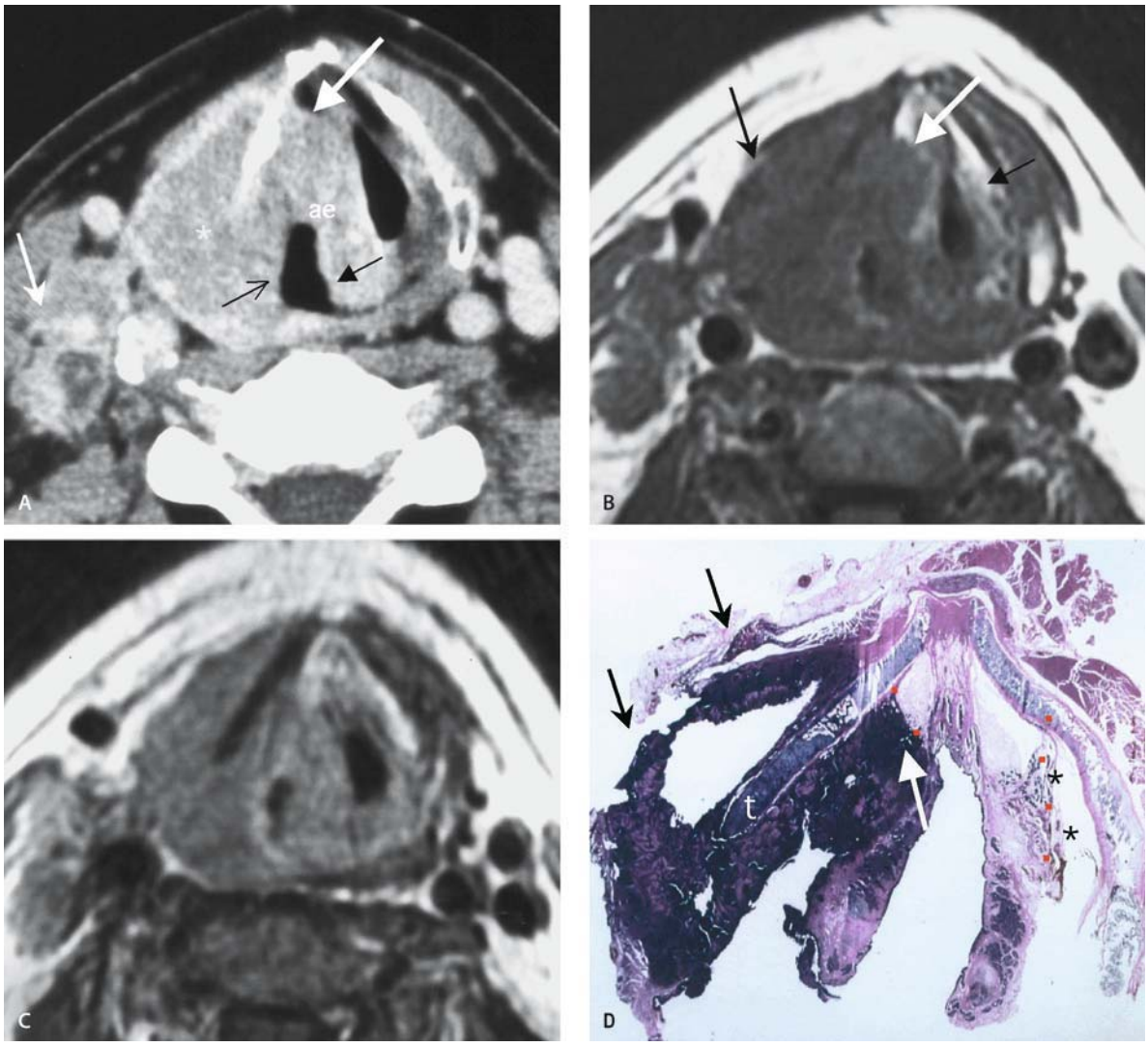

Fig. 9A–D. Invasion of the paraglottic space and lateral neck by piriform sinus cancer. **A** Axial, contrast-enhanced CT image at the supraglottic level shows a hypopharyngeal tumor mass involving the medial wall (*arrow*) and the lateral wall (*open arrow*) of the piriform sinus, and the entire right aryepiglottic fold (*ae*). Invasion of the paraglottic space (*thick arrow*), destruction of the posterior thyroid lamina (*asterisk*) and invasion of the prelaryngeal muscles. A large lymph node metastasis with central nodal necrosis (*stealth arrow*) is seen on the right. **B** Axial, unenhanced T1-weighted SE image obtained in the same patient at the same level shows a tumor mass with an intermediate signal intensity as it extends into the right paraglottic space (*thick arrow*) and into the soft tissues of the neck (*stealth arrow*). Note the high signal intensity of the noninvaded left paraglottic space due to the high content of fatty tissue (*thin arrow*). **C** Axial Gd-enhanced T1-weighted SE image at the same level shows enhancement of the tumor mass invading the right paraglottic space, the thyroid cartilage and the soft tissues of the neck. **D** Whole organ, axial histologic slice from specimen confirms tumor invasion of the right paraglottic space (*thick arrow*) and of the soft tissues of the neck (*stealth arrows*). Thyroid cartilage (*t*), normal left paraglottic space (*asterisks*). The right and left thyroglottic ligaments, which separate the paraglottic from the preepiglottic space, are indicated by *dots*. Note massive anterior displacement of the right thyroglottic ligament by the tumor mass. Reproduced with permission from [19]

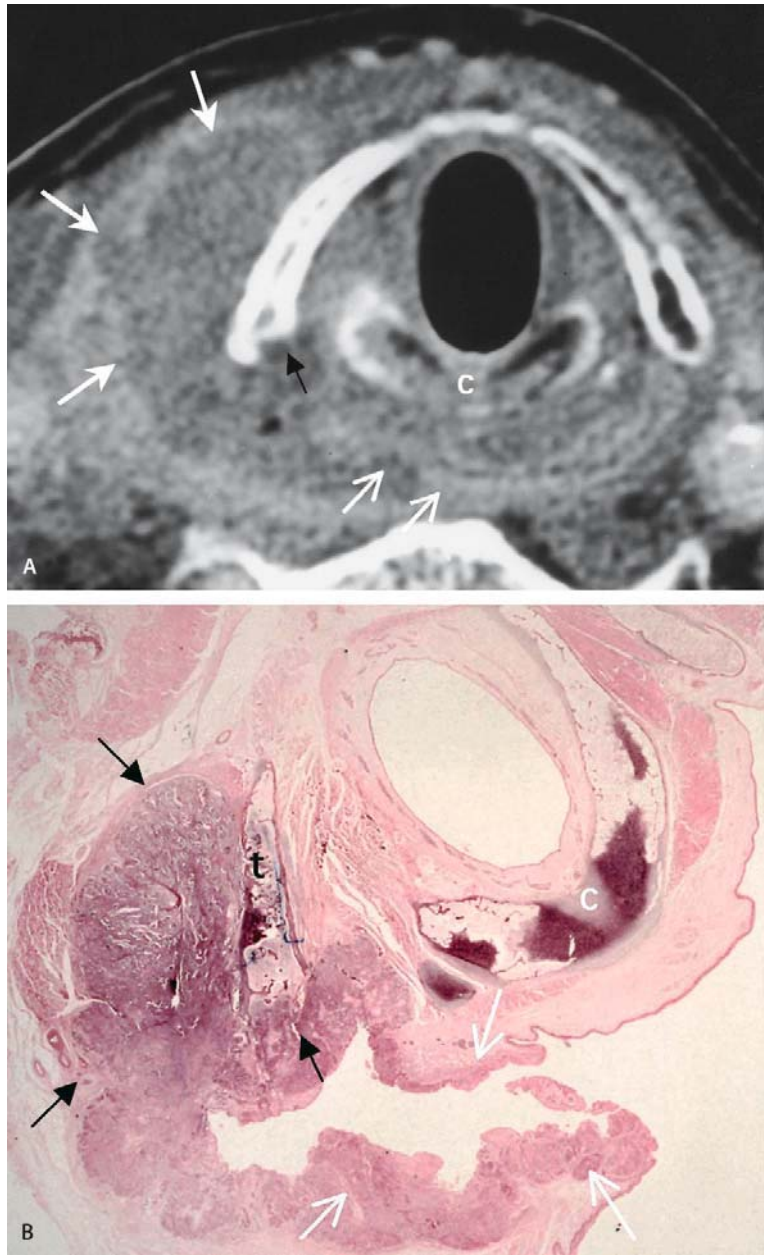

Fig. 10A, B. Invasion of the esophageal verge in a piriform sinus cancer. **A** Axial, contrast-enhanced CT image at the subglottic level shows a piriform sinus tumor invading the posterior thyroid lamina (*arrow*), the soft tissues of the neck (*stealth arrow*) and the esophageal verge submucosally (*thin arrows*). Cricoid cartilage (*c*). **B** Whole-organ, axial histologic slice from specimen confirms submucosal tumor invasion of the esophageal verge (*white arrows*) and invasion of the thyroid cartilage and of the soft tissues of the neck (*black arrows*). Thyroid cartilage (*t*), cricoid cartilage (*c*). Reproduced with permission from [13]

Postcricoid carcinoma is uncommon in general but observed in certain groups at risk such as patients with the Plummer-Vinson syndrome. These tumors spread submucosally most often toward the cervical esophagus. The key diagnostic features on axial CT and MR images include thickening of the postcricoid region and anterior displacement of the arytenoid and cricoid cartilages (Fig. 11).

Carcinoma of the posterior pharyngeal wall commonly involves both the oropharynx and hypopharynx. On axial CT and MR images, these tumors appear as asymmetrical thickening of the posterior pharyngeal wall. Invasion of the retropharyngeal space is common. However, invasion of the prevertebral muscles is unusual at initial presentation (see Tables 3 and 5).

Neoplastic Cartilage Invasion

Invasion of the hyaline laryngeal cartilage by squamous cell carcinoma alters tumor stage (leading automatically to a T4 classification), prognosis and, in most centers, the therapeutic approach [17, 19, 22, 24, 25, 42]. Neoplastic invasion of cartilage is associated with a lower re-

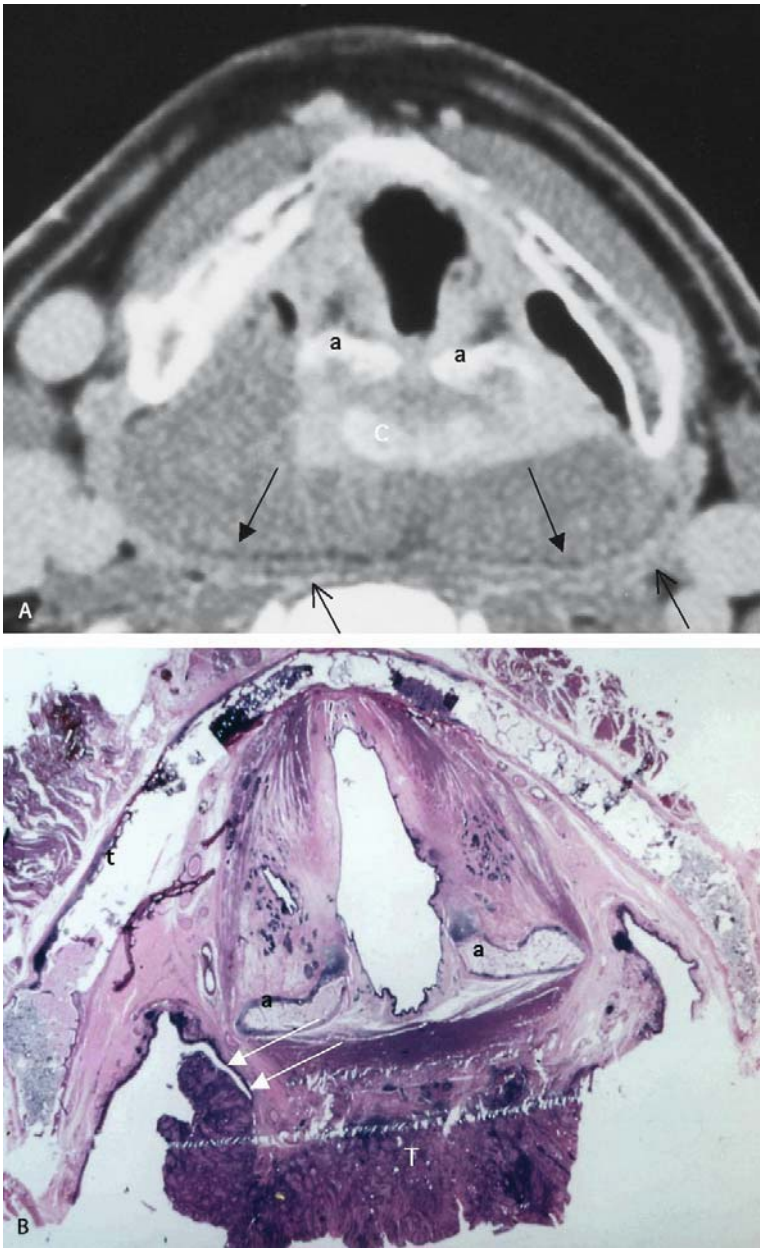

Fig. 11A, B. Postcricoid carcinoma of the hypopharynx. **A** Axial, contrast-enhanced CT scan at the glottic level demonstrates a large tumor arising from the postcricoid region and extending into the right piriform sinus. The lumen of the hypopharynx is collapsed (*arrows*). Note strong enhancement of the normal mucosa over the posterior pharyngeal wall (*open arrows*). *c* Cricoid cartilage, *a* arytenoid cartilage. **B** Whole-organ, axial histologic slice from specimen confirms postcricoid tumor (*T*) with invasion of the medial wall of the piriform sinus (*arrows*). Thyroid cartilage (*t*), arytenoid cartilage (*a*). Reproduced with permission from [5]

sponse rate to radiation therapy and a higher risk of tumor recurrence than involvement of soft tissue, and may also result in radiation-induced necrosis [16]. Invasion of the cartilaginous framework of the larynx by tumor tissue also precludes various voice-sparing laryngectomy procedures and total laryngectomy is eventually required.

The normal thyroid, cricoid and arytenoid cartilages of adults consist of three tissue components: nonossified hyaline cartilage, cortical bone, and a marrow cavity containing fatty tissue and scattered bone trabeculae. On CT, ossified cartilage shows a high-attenuating outer and inner cortex and a central low-attenuating medullary space while nonossified hyaline cartilage has the attenuation value of soft tissue. Normal nonossified hyaline cartilage has a low signal intensity on both T1- and T2-weighted images. Cortical bone has a very low signal intensity on T1- and T2-weighted images, whereas the medullary cavity of ossified cartilage has a high signal intensity on T1-weighted images and an intermediate signal intensity on T2-weighted images because of the high content of fatty tissue [19, 22]. Cortical bone, fatty marrow and nonossified hyaline cartilage show no contrast material enhancement.

The suggested mechanism of laryngeal cartilage invasion by neoplastic tissue involves an osteoblastic phase in which hyaline cartilage is transformed into metaplastic bone followed by an osteoclastic phase in which the newly formed bone is eroded [5, 17, 28]. Osteoclasts are stimulated by prostaglandins and interleukin-1 released by tumor cells. This process is not bound to the direct presence of tumor cells within cartilage but occurs also as a reaction within cartilage in the vicinity of tumor. Therefore, increased osteoblastic activity and new bone formation are seen prior to actual tumor invasion. The process of neoplastic invasion of laryngeal cartilage thus involves three distinct phases, namely (a) inflammatory changes and new bone formation within cartilage prior to actual tumor invasion, (b) osteolysis of bone trabeculae and (c) frank invasion by tumor cells [11, 19].

Until recently, the presence of tumor on both sides of a laryngeal cartilage was the only accepted diagnostic sign for tumor invasion on CT [17]. Because this sign is positive only in an advanced stage, CT was long considered to be insensitive to cartilage invasion. Results of our recent radiologic–pathologic correlation study indicate, however, that four different diagnostic signs and their combinations can be recommended to detect neoplastic invasion of laryngeal cartilage on CT, namely extralaryngeal tumor spread, sclerosis, erosion and lysis [11, 17] (Fig. 12). Each of these CT signs corresponds to distinct histologic findings [17]. Sclerosis corresponds histologically to tumor-induced inflammation and new bone formation. New bone formation is the first step in the process of neoplastic cartilage invasion and is associated with invasion of cartilage in approximately 50% of cases (Figs. 12, 13). Therefore, sclerosis enables diagnosis of early intracartilaginous tumor spread. However, the overall specificity of this sign is relatively low (65%) [19]. As a consequence, if a tumor mass is seen adjacent to a sclerotic cartilage, this does not automatically imply that tumor cells are found within the remodeled marrow cavity (Fig. 14). As the process of cartilage invasion progresses, minor and major osteolysis is seen within the areas of newly formed (metaplastic) bone. Minor areas of osteolysis correspond to the CT criterion of erosion, while major areas of osteolysis correspond to the CT criterion of lysis (Figs. 12, 15). Histologically, erosion and lysis correspond to destruction of bone trabeculae. Therefore, erosion and lysis can be considered specific criteria for the detection of neoplastic cartilage invasion. The overall specificity of erosion and lysis is 93% [17]. However, both of these criteria are not very sensitive as they are bound to the presence of more advanced invasion of laryngeal cartilage [11, 17]. Extrala-

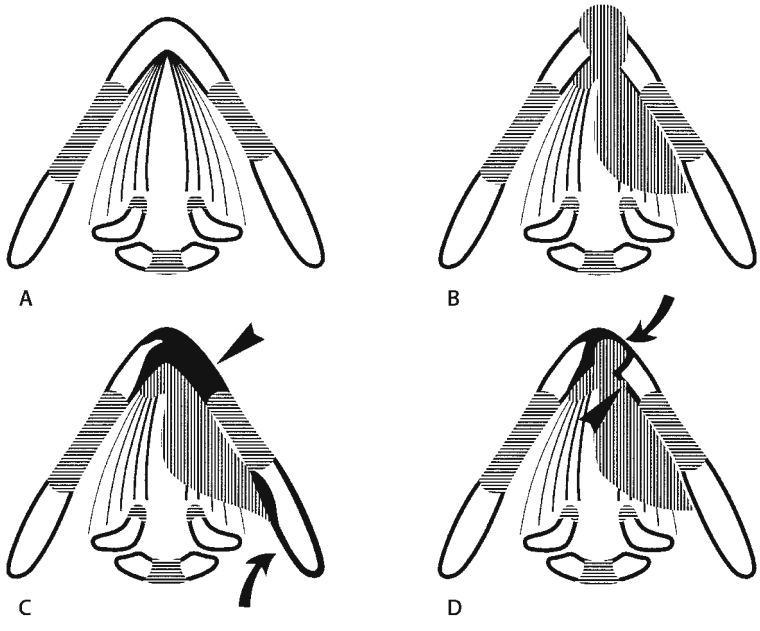

Fig. 12A–D. Criteria for CT diagnosis of neoplastic cartilage invasion. **A** Schematic representation of normal ossified and nonossified laryngeal cartilages as seen at the glottic level on contrast-enhanced CT. Cortical bone is represented as solid black lines, fatty marrow cavity as white areas, and nonossified cartilage as horizontal black lines. The diagnostic criteria of tumor invasion are illustrated using the thyroid cartilage as an example **(B–D)**. In analogy, these criteria can be applied to the cricoid and arytenoid cartilage. Tumor is represented throughout by vertical black hatches to suggest an attenuation value similar to that of nonossified cartilage. **B** Extralaryngeal tumor spread: tumor is seen on the inner and outer aspect of a cartilage, including extralaryngeal soft tissues. **C** Sclerosis: thickening of cortical layers (*arrow*) or increased ossification of marrow cavity (*arrowhead*). **D** Lysis: punched-out lesion or focal lytic defect within sclerotic marrow comparable to osteolysis in a bone structure (*arrow*). Erosion: localized form of lysis limited to a sclerotic cortex (*arrowhead*). Modified with permission from [17]

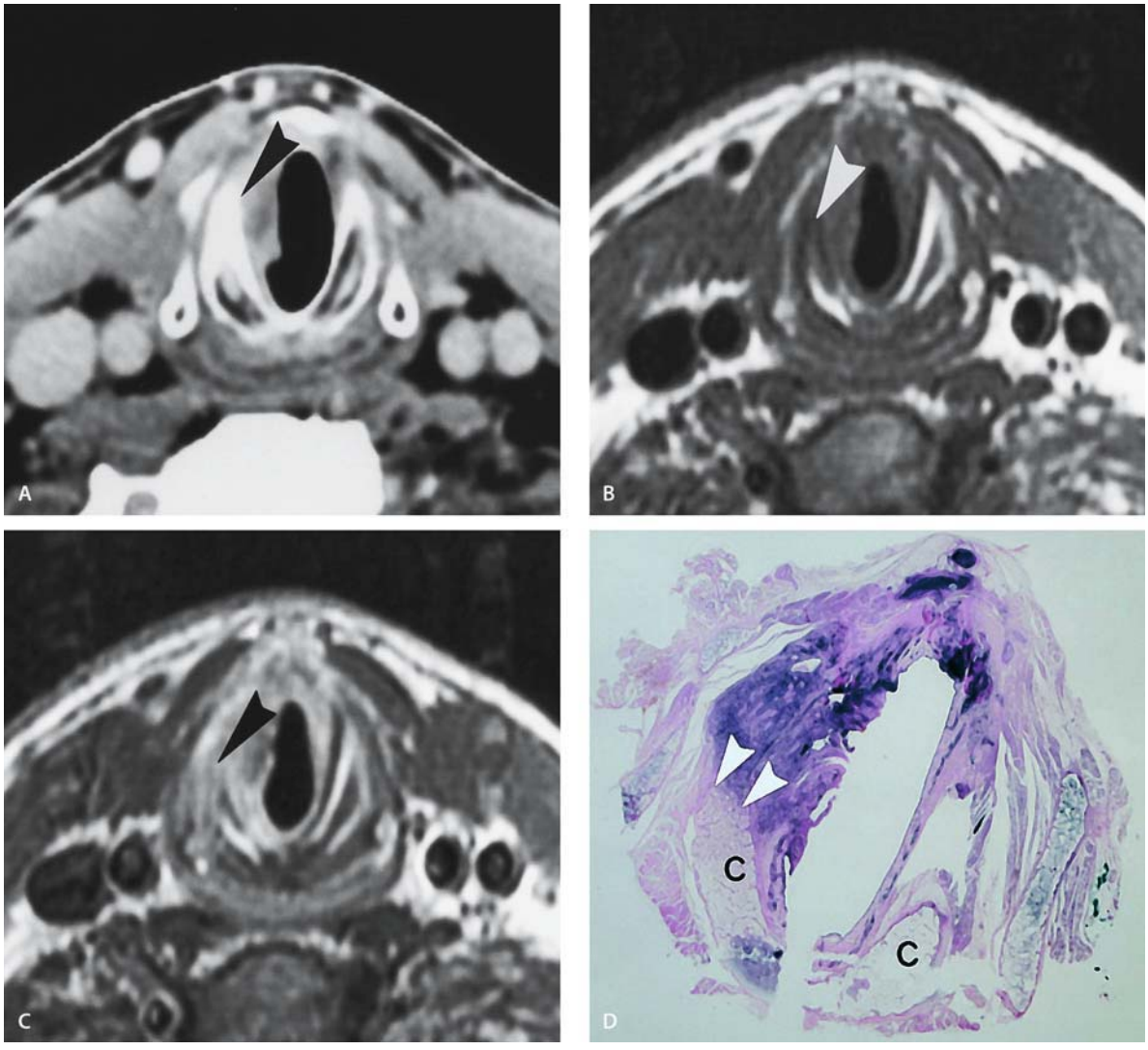

Fig. 13A–D. Neoplastic invasion of the cricoid cartilage detected by both CT and MRI. Glottosubglottic carcinoma of the larynx in a 46-year-old male patient. **A** Axial, contrast enhanced CT scan at the subglottic level. A mass with homogeneous contrast enhancement is infiltrating the right subglottic region. The cricoid cartilage shows asymmetric sclerosis (*arrowhead*), indicating cartilage invasion. Note preservation of the inner margin of the cricoid cartilage. **B** Axial T1-weighted SE image. A mass with intermediate signal intensity infiltrates the right subglottic region. The right cricoid cartilage shows a decreased signal intensity (*arrowhead*). **C** Contrast-enhanced axial T1-weighted SE image shows extensive contrast enhancement of the right subglottic tumor mass, as well as of the adjacent cricoid cartilage. The extensive enhancement of the right cricoid cartilage (*arrowhead*) suggests tumor invasion. **D** Axial slice from specimen at the same level shows a large subglottic tumor mass invading the right cricoid cartilage (*arrowheads*). *C* cricoid cartilage. Hematoxylin-eosin stain. Reproduced with permission from [19]

ryngeal spread occurs due to tumor invasion through a cartilage into the extralaryngeal soft tissues (Figs. 9, 10). This CT criteria is highly specific (overall specificity, 95%), but because it is only seen very late in the disease process its sensitivity is as low as 44%. Using the combination of extralaryngeal tumor, sclerosis, and erosion/lysis applied to all cartilages an overall sensitivity as high as 91% may be obtained. Because the negative predictive value of this combination is 95%, CT may be considered as an excellent test to exclude cartilage invasion prior to treatment. However, the associated overall specificity of only 68% appears quite low because it is very difficult and impractical to confirm cartilage invasion by means of biopsy.

The reported sensitivity of MRI for the detection of neoplastic cartilage invasion is 89%–94%, the specificity 74%–88%, and the negative predictive value 92%–96% [19, 22]. Extensive tumor invasion involving both inner and outer aspects of the cartilage (extralaryngeal spread) can be diagnosed with a high accuracy with

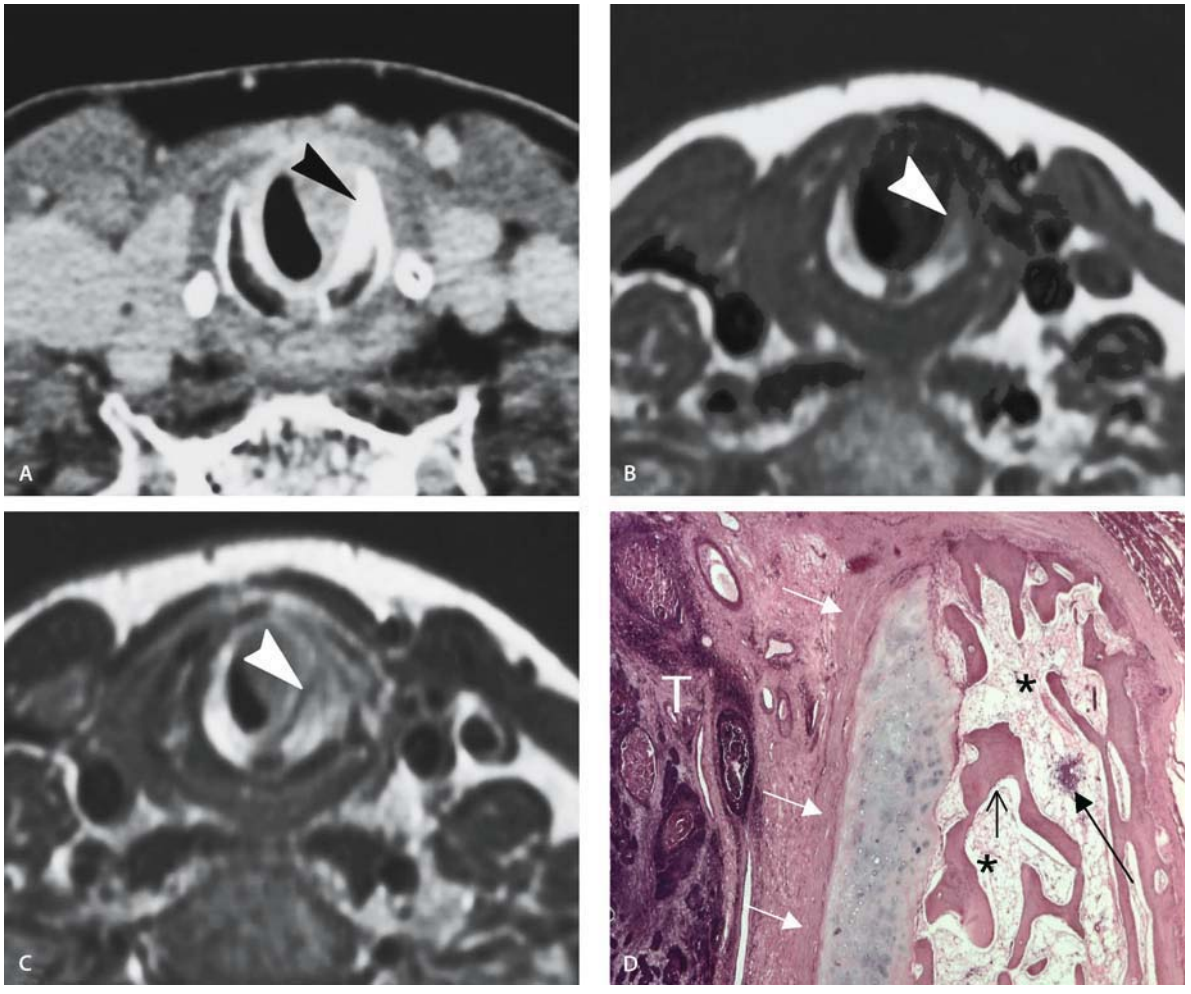

Fig. 14A–D. CT and MRI false positive for neoplastic cartilage invasion due to inflammatory changes in the noninvaded cricoid cartilage. Glottosubglottic carcinoma of the larynx in a 71-year-old female patient. **A** Axial contrast enhanced CT scan at the subglottic level. A mass with homogeneous contrast enhancement is infiltrating the left subglottic region. The left cricoid cartilage shows extensive sclerosis in tumor vicinity (*arrowhead*) suggestive of cartilage invasion. **B** T1-weighted axial SE image. A mass with low signal intensity infiltrates the left subglottic region. The adjacent left cricoid cartilage shows a decreased signal intensity (*arrowhead*). **C** Contrast-enhanced T1-weighted SE image. Contrast enhancement is seen within the left cricoid cartilage (*arrowhead*) as well as within the subglottic tumor mass. **D** Axial slice from specimen shows a large, left-sided subglottic tumor mass (*T*) but no evidence of cartilage invasion. The cricoid cartilage shows extensive inflammatory changes with lymph follicles (*black arrow*), fibrosis (*asterisks*), bone resorption (*open arrows*) but with an intact perichondrium (*white arrows*). Reproduced with permission from [19]

MRI. If tumor is present only adjacent to the inner aspect of a cartilage, the radiologist can differentiate between tumor and noninvaded cartilage by comparing the different MR pulse sequences. Cartilage invaded by tumor displays a low signal intensity on T1-weighted images, an intermediate signal intensity on T2-weighted images and enhancement within the cartilage adjacent to the tumor after injection of gadolinium chelates (Fig. 13). If these signs are absent, cartilage infiltration can be ruled out with a high level of confidence, since the negative predictive value of MR imaging is very high [11, 17] (Fig. 16). Unfortunately, the MR findings suggesting neoplastic cartilage invasion are not as specific as expected initially, but may be false positive in a considerable number of instances [19]. This is because reactive inflammation in the vicinity of the tumor may display similar diagnostic features as cartilage infiltrated by tumor (Fig. 14).

In summary, due to their high negative predictive value, both CT and MRI may be used to exclude cartilage invasion quite reliably. However, false positive results are inevitable with both imaging modalities. This may be explained by the fact that the underlying pathologic process leading to overestimation of neoplastic cartilage invasion is the same, namely reactive inflammation.

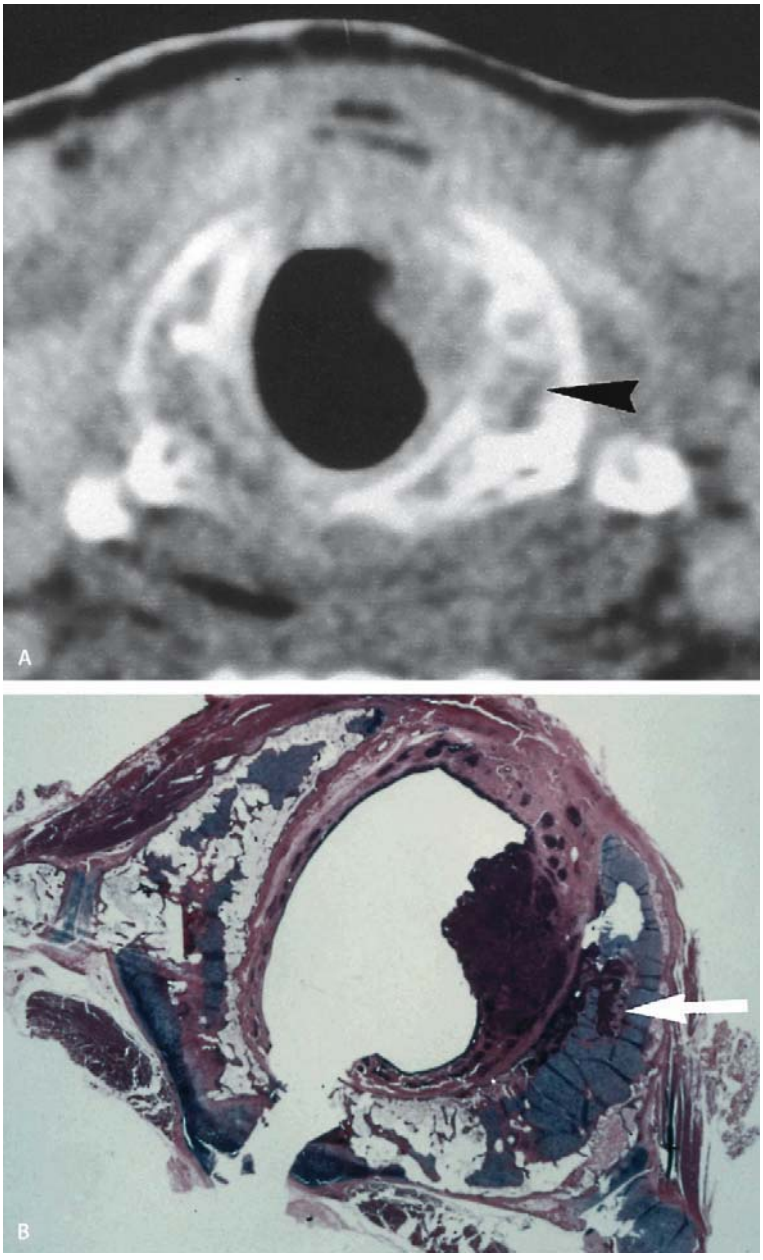

Fig. 15A, B. Lysis and sclerosis of the cricoid cartilage in a glottic-subglottic cancer. **A** Contrast-enhanced CT scan obtained at the subglottic level shows a tumor mass that abuts the cricoid cartilage. The left cricoid lamina demonstrates an area of lysis (*arrowhead*) surrounded by extensive sclerosis. **B** Corresponding axial slice from surgical specimen at the same level confirms major intracartilaginous tumor spread (*arrow*) corresponding to lysis seen on CT. Reproduced with permission from [5]

TNM Classification of Laryngeal and Hypopharyngeal Carcinoma

Laryngeal and hypopharyngeal carcinoma is staged according to the criteria recommended by the International Union Against Cancer UICC [11, 35, 42]. The degree of invasion of the primary tumor is most accurately reflected in the postsurgical (pT) classification, which is based on histopathologic analysis of the resected specimen. The clinical or pretherapeutic (T) classification is based on all information available prior to treatment (i.e., physical examination, endoscopy, biopsy and cross-sectional imaging). The guidelines of the UICC recommend the use of cross-sectional imaging and several studies, as well as the experience at our institution, have shown that the use of CT or MRI greatly improves the accuracy of the pretherapeutic T-classification of laryngeal and hypopharyngeal tumors. Using the pT classification as gold standard, the staging accuracy of clinical examination combined with endoscopic biopsy is only 58%; however, it is increased significantly when combined with either CT (accuracy, 80%) or with MR imaging (accuracy, 85%) [5, 11, 55, 57].

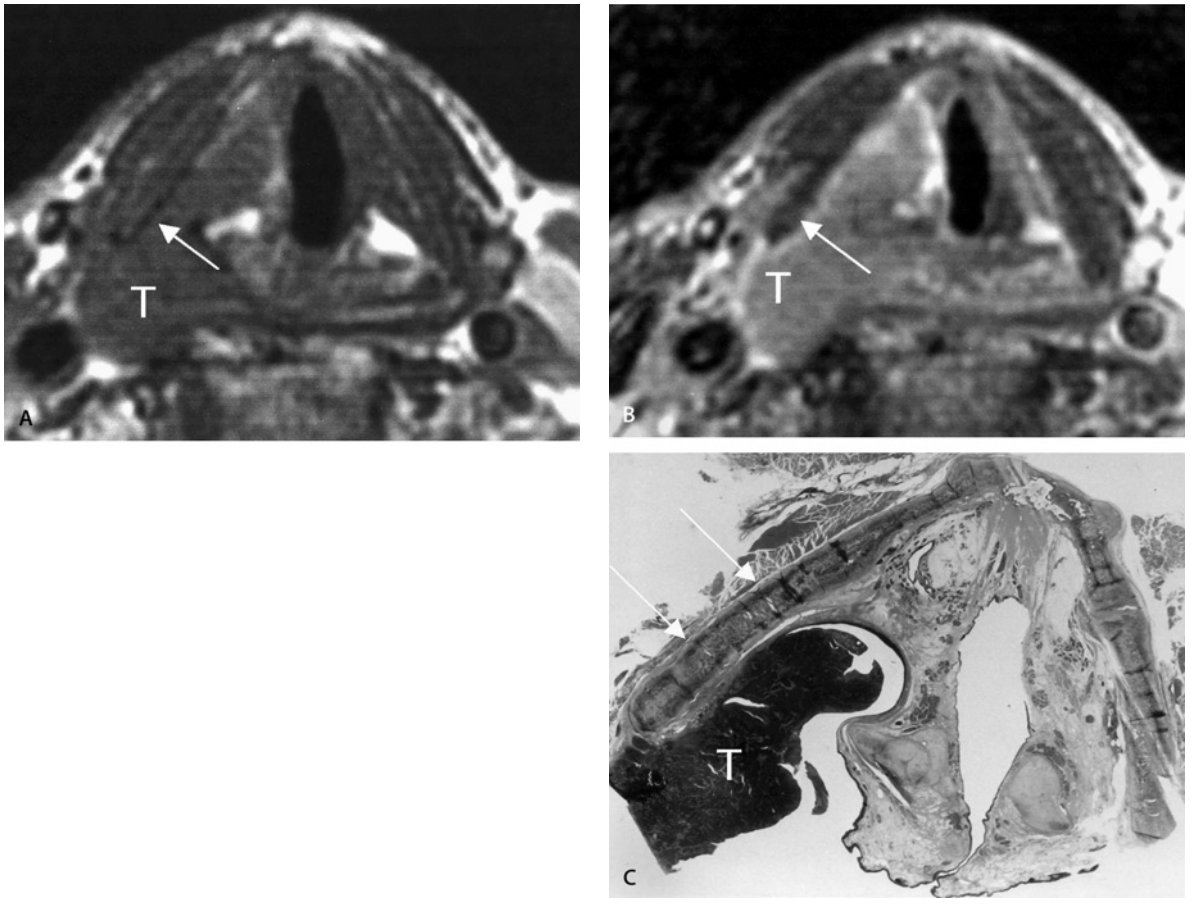

Fig. 16A–C. MRI findings true negative for neoplastic invasion of the thyroid cartilage. **A** T1-weighted SE image obtained at the supraglottic level shows a right-sided piriform sinus tumor with intermediate to low signal intensity (*T*). The adjacent right thyroid lamina shows an intermediate to low signal intensity as well (*arrow*). **B** T1-weighted SE image obtained after intravenous administration of contrast material shows contrast enhancement of the tumor mass (*T*), however, no enhancement of the adjacent thyroid lamina (*arrow*). This suggests that the thyroid cartilage is composed of nonossified hyaline cartilage and that no intracartilaginous tumor spread is present. **C** Corresponding axial slice from surgical specimen at the same level confirms that the right thyroid lamina is composed of nonossified hyaline cartilage (*arrows*). No cartilage invasion was found at histology. The tumor (*T*) arises from the lateral wall of the right piriform sinus. Hematoxylin-eosin stain. Reproduced with permission from [5]

Non-squamous Cell Neoplasms of the Larynx and Hypopharynx

Non-squamous cell neoplasms of the larynx and hypopharynx constitute less than 5% of all tumors of this region. They are typically located extramucosally, and the endoscopist may see nothing but an asymmetry or a bulge beneath an intact mucosa. Therefore, the diagnosis of these submucosal tumors is difficult with endoscopy alone, and sampling errors may occur if only traditional superficial biopsies are performed [14, 15]. The discrepancy between an intact mucosa at endoscopic examination and an obvious mass at CT or MRI should, therefore, raise the suspicion of a tumor with an unusual histology. In such cases, both CT and MR imaging may serve not only to assess the degree of tumor spread, but also to direct the endoscopist to the appropriate site where deep, aggressive biopsies are to be done, which are necessary to establish the correct histologic diagnosis [14, 15].

The following submucosal neoplasms can be further characterized with regard to their etiology: chondrosarcoma, lipoma, hypervascular tumors and metastases from malignant melanoma. *Chondrosarcoma* is the most frequent sarcoma of the larynx (Fig. 17). It predominantly affects males in their 6th or 7th decade and more commonly originates from the cricoid than from the thyroid cartilage. As in chondrogenic tumors of other locations, the tumor matrix has a very high signal intensity on T2-weighted images, corresponding to hyaline cartilage with its low cellularity and high water content. Small areas of low signal intensity correspond to stippled calcifications; these changes are, however, not as well demonstrated as with CT. Although the injection

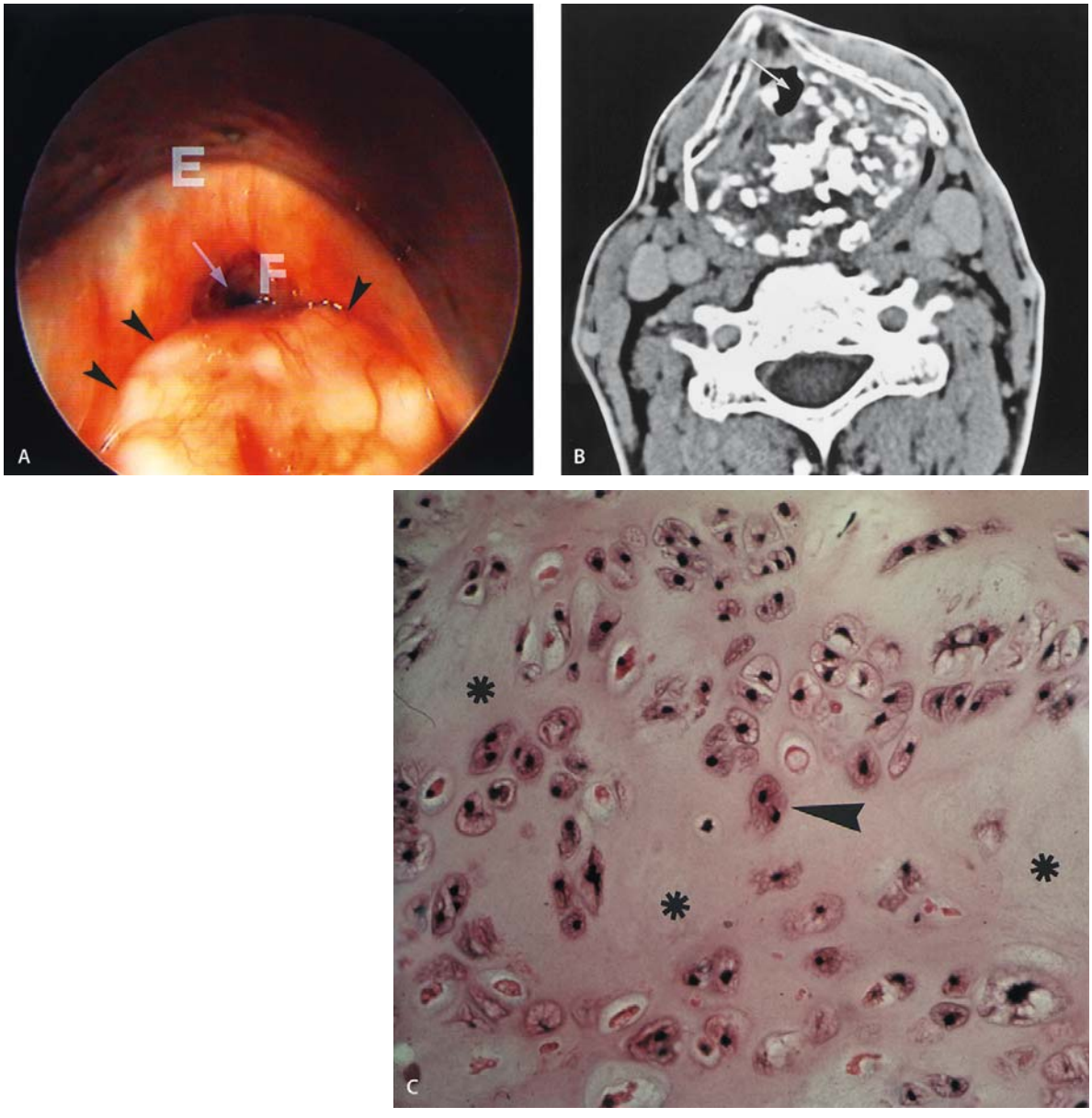

Fig. 17A–C. Chondrosarcoma of the cricoid cartilage. Characteristic endoscopic, CT and histologic appearance. A 70-year-old male patient presenting with dyspnea and dysphagia. **A** Endoscopic view shows a large tumor mass (*arrowheads*) covered by intact mucosa. *E* epiglottis. *F* false cord. Note significant airway obstruction (*arrow*). **B** Axial contrast-enhanced CT scan shows a large, hypodense mass with coarse calcifications characteristic of chondrosarcoma. The mass arises from the cricoid cartilage and leads to significant airway obstruction (*arrow*). **C** Photomicrograph shows the characteristic features of low-grade chondrosarcoma. Lobular growth pattern with multinucleated chondrocytes (*arrowhead*) surrounded by chondroid intercellular substance (*asterisks*). Figure 17a and 17b reproduced with permission from [14]

of gadolinium chelates may lead to a diffuse central or peripheral enhancement, these findings are nonspecific and do not help in differentiating low-grade chondrosarcomas from benign chondroma. The characteristic gross and microscopic features of laryngeal chondrosarcoma are shown in Fig. 17.

The radiologic diagnosis of *laryngeal and hypopharyngeal lipoma* is straightforward. The typical CT features are those of a homogeneous, nonenhancing lesion with attenuation values from –65 to –125 HU [14, 58] (Fig. 18). On MRI, lipoma has the same signal intensity as subcutaneous fat and shows no significant enhancement after administration of intravenous contrast material.

The differential diagnosis of strongly vascularized laryngeal tumors includes hemangioma, paraganglio-

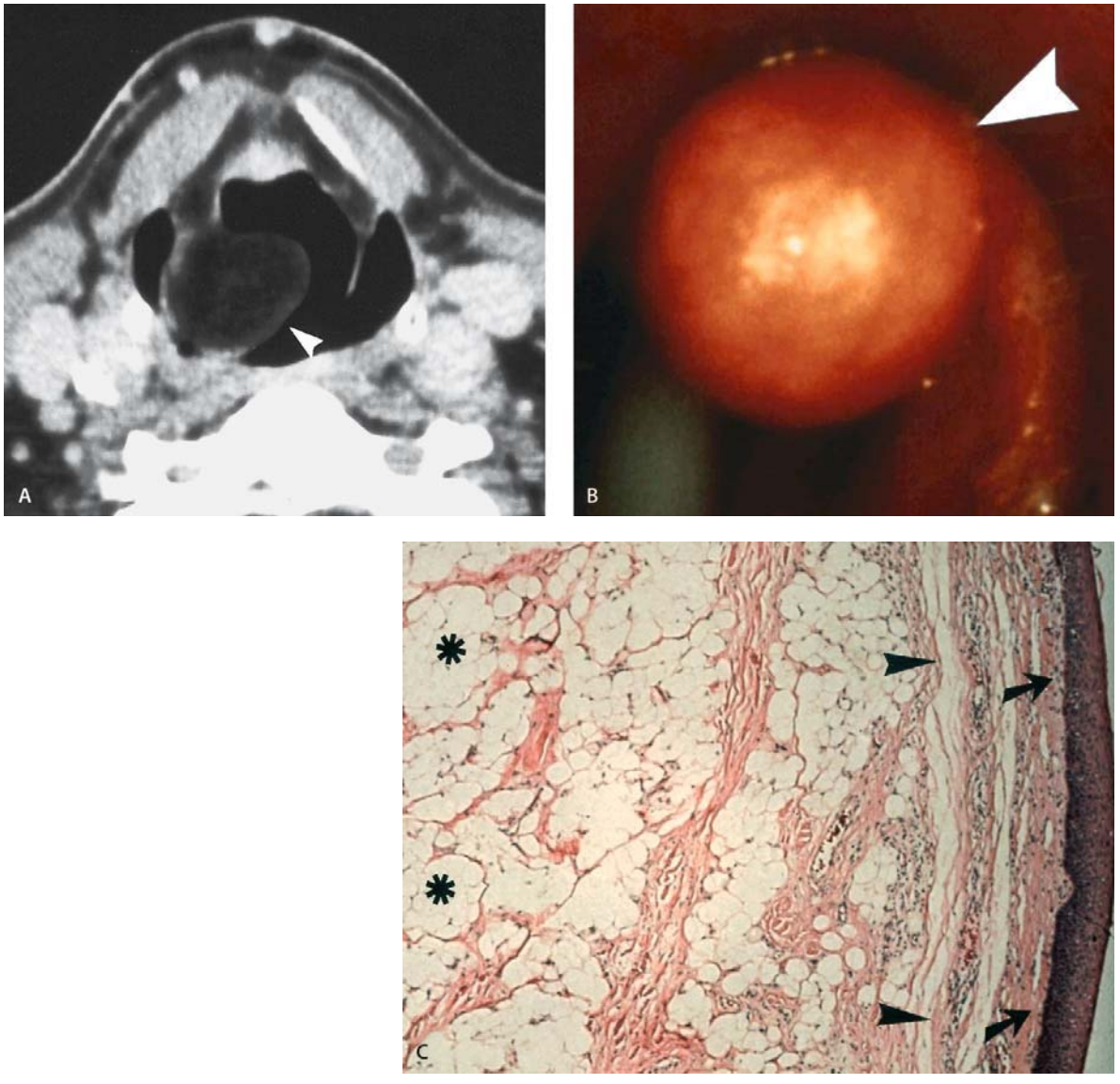

Fig. 18A–C. Lipoma. A 77-year-old male patient with a foreign body sensation, episodes of suffocation and change in quality of voice. **A** Axial, contrast-enhanced CT scan at the supraglottic level. A homogeneous, nonenhancing lesion with the density of fat is seen at the level of the right aryepiglottic fold (*arrowhead*). **B** Endoscopic view: a pedunculated mass covered by intact laryngeal mucosa arises from the right aryepiglottic fold (*arrowhead*). **C** Low-power micrograph showing intact overlying squamous epithelium (*arrows*). Lobulated laryngeal lipoma composed of mature adipocytes (*asterisks*) and fibrous pseudocapsule (*arrowheads*). The patient underwent endoscopic resection and is free of recurrence 5 - years later. Reproduced with permission from [14]

ma and metastases from hypervascular tumors, such as renal cell carcinoma. On CT, hemangioma, paraganglioma and metastases from hypervascular tumors appear as well-circumscribed soft tissue masses that display uniform, intense contrast enhancement [9]. On MRI, laryngeal hemangiomas display a very high signal intensity on T2-weighted sequences and strong contrast material enhancement on T1-weighted images [8]. Laryngeal paragangliomas and laryngeal metastases from renal cell carcinoma may display multiple curvilinear signal voids on both T1- and T2-weighted images (see "Paraganglioma"). Laryngeal metastases from *melanotic melanoma* display the signal characteristics of melanotic melanoma elsewhere in the body, namely a high signal intensity on T1-weighted images and an intermediate to low signal intensity on T2-weighted images due to the paramagnetic properties of melanin [14].

Nodal Masses

The most common neoplasms involving the cervical lymph node groups are metastases from head and neck squamous cell carcinoma, thyroid gland cancer, and lymphoma.

Involvement of Cervical Lymph Nodes by Squamous Cell Carcinoma

The incidence of nodal disease in squamous cell carcinoma of the head and neck depends on the primary tumor site. The incidence of metastatic adenopathy at initial presentation varies between less than 10% in glottic cancer and up to 75% in hypopharyngeal cancer [3, 10, 44, 47, 48]. Although there is some variation with tumor site and with the various reports in the literature, the presence of lymph node metastases in patients with squamous cell carcinoma of the head and neck is associated with a 50% reduction in the long-term survival if there is a solitary ipsilateral cervical node, a solitary contralateral node or extracapsular neoplastic spread in either of these lymph nodes [44, 47, 48]. Initially, the assessment of cervical lymph nodes was based purely on clinical evaluation. However, when considering clinically negative (N0) necks, histologically positive lymph nodes have been reported in 20%–40% of cases. Therefore, cross-sectional imaging techniques (CT, MRI and US) are used widely to search for lymph node metastases. Anatomically, all lymph nodes in the neck are located within fatty tissue. This fact accounts for the excellent ability of CT to depict lymph nodes as small as a few millimeters.

Anatomic Considerations

Infrahyoid nodal groups of importance in the staging of squamous cell carcinoma of the head and neck include the deep lateral cervical group and the anterior cervical group [10, 41, 47, 48]. The deep lateral cervical group is divided into three subgroups: (a) deep cervical chain or internal jugular chain (found along the internal jugular vein within the carotid space, Fig. 1, Table 2), (b) spinal accessory chain (found along the cranial nerve XI in the posterior cervical space, Fig. 1, Table 4) and (c) transverse cervical or supraclavicular chain (running parallel to the clavicle). When deciding whether a node is in the internal jugular chain or the spinal accessory chain, one has to decide whether the node is located beneath (medial) or dorsal to the sternocleidomastoid muscle. If a node is dorsal to the posterior border of the sternocleidomastoid muscle, it can be classified as a spinal accessory node, whereas if a node is located anteriorly or lateroposteriorly to the internal jugular (i.e., anterior or deep to the sternocleidomastoid muscle), it can be classified as an internal jugular node. Important nodes found within the internal jugular chain include the jugulodigastric node (i.e., highest node found at the angle of the mandible) and Virchow's node (i.e., lowest node among the inferior internal jugular nodes).

The anterior cervical group is divided into three subgroups: (a) the pretracheal chain (found along the external jugular vein and lying external to the strap muscles), (b) the prelaryngeal or delphian node chain (found in immediate proximity of the anterior portion of the thyroid cartilage) and (c) the paratracheal chain (found in the tracheoesophageal groove within the visceral space).

The most commonly used classifications for lymph nodes are the ones of the International Union Against Cancer (UICC) and the American Joint Committee on Cancer (AJCC) [42]. Recently, a new imaging-based nodal classification [47, 48] has been proposed in an effort to standardize descriptions of node location between imaging and physical examination (Fig. 19). Level I nodes are located above the hyoid bone, below the mylohyoid muscle and anterior to a transverse line drawn through the posterior edge of the submandibular glands. Level IA nodes (previously classified as submen-

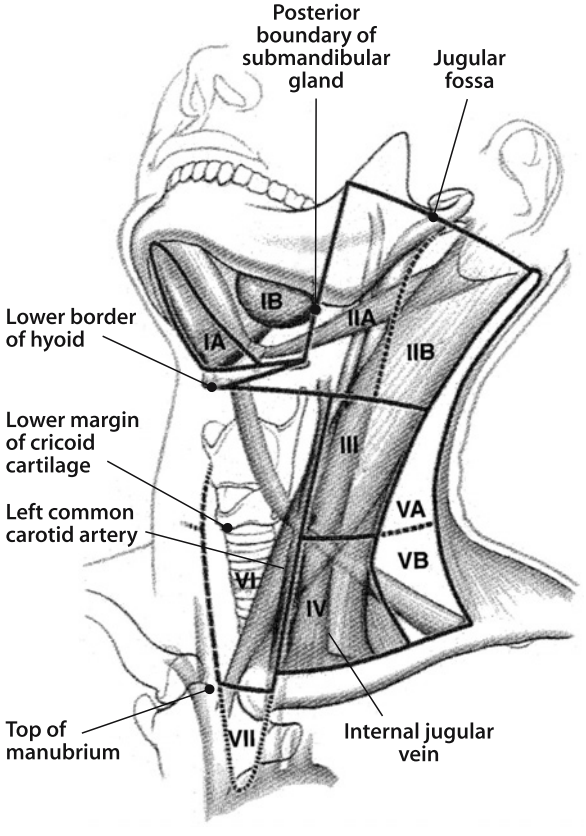

Fig. 19. The imaging based nodal classification. The neck as seen from the left anterior view outlines the levels of the classification. Reproduced with permission from [47]

tal nodes) are located between the medial margins of the anterior bellies of the digastric muscles. Level IB nodes (former submandibular nodes) represent the nodes that lie lateral to the medial edge of the anterior belly of the digastric muscle. Level II (upper jugular) nodes extend from the skull base to the lower body of the hyoid bone. Level II nodes lie anterior to a transverse line drawn on each axial image through the posterior edge of the sternocleidomastoid muscle and posterior to a transverse line through the posterior edge of the submandibular gland. Level IIA nodes are inseparable from the internal jugular vein or they lie anterior, lateral or medial to the internal jugular vein. Level IIB nodes (previously classified as upper spinal accessory nodes) lie posterior to the internal jugular vein with a fat plane separating the nodes and the vein. Retropharyngeal nodes lie medial to the internal carotid artery. Level III (middle jugular) nodes lie between the lower body of the hyoid and the lower margin of the cricoid cartilage. These nodes lie anterior to the transverse line drawn on each axial image through the posterior edge of the sternocleidomastoid muscle. Level IV (lower jugular) nodes lie between the lower margin of the cricoid cartilage and the clavicle. Level V (posterior triangle) nodes extend from the skull base to the level of the clavicle. All level V nodes lie anterior to a transverse line drawn on each axial image through the anterior edge of the trapezius muscle. Above the lower margin of the cricoid ring, level V nodes (also named upper level V nodes or VA nodes) lie posterior to a transverse line drawn on each axial image through the posterior edge of the sternocleidomastoid muscle. Below the lower margin of the cricoid ring, level V nodes (also named lower level V nodes or VB nodes) lie posterior and lateral to an oblique line through the posterior edge of the sternocleidomastoid muscle and the lateral edge of the anterior scalene muscle. Level VI (anterior compartment) nodes are located between the hyoid bone and the top of the manubrium, and between the medial margins of the carotid arteries. They include the juxtavisceral, anterior cervical, and external jugular nodes. Level VII nodes are located between the top of the manubrium and the innominate vein. Level VII nodes are superior mediastinal nodes. Supraclavicular nodes are the low level IV or V nodes that are seen on the images that contain a portion of the clavicle. For all levels, if the transverse or oblique lines drawn on the axial images for dividing the levels transect a node, the node is classified into the level in which most of its cross-sectional area is located [47, 48].

Normal lymph nodes enhance slightly more than muscle on both CT and MR imaging. Normal lymph nodes have well-defined borders and are usually oval. The ratio of the maximum longitudinal length to the maximum transverse length should be greater than 2 [49]. They have a fatty hilum, which can often be visualized on CT.

Imaging Issues and Pathologic Considerations

When imaging the neck, size-based criteria, nodal shape criteria and internal nodal architecture criteria are applied to both CT and MR imaging. Regardless of which criteria are used, the overall error rates for both false-positive and false-negative diagnoses are in the range of 10%–20%. The currently applied size criteria include a minimal axial diameter of 11 mm in the jugulodigastric region and 10 mm elsewhere in the neck [10, 43, 44, 50–52] (Fig. 20). More recently, it has been sug-

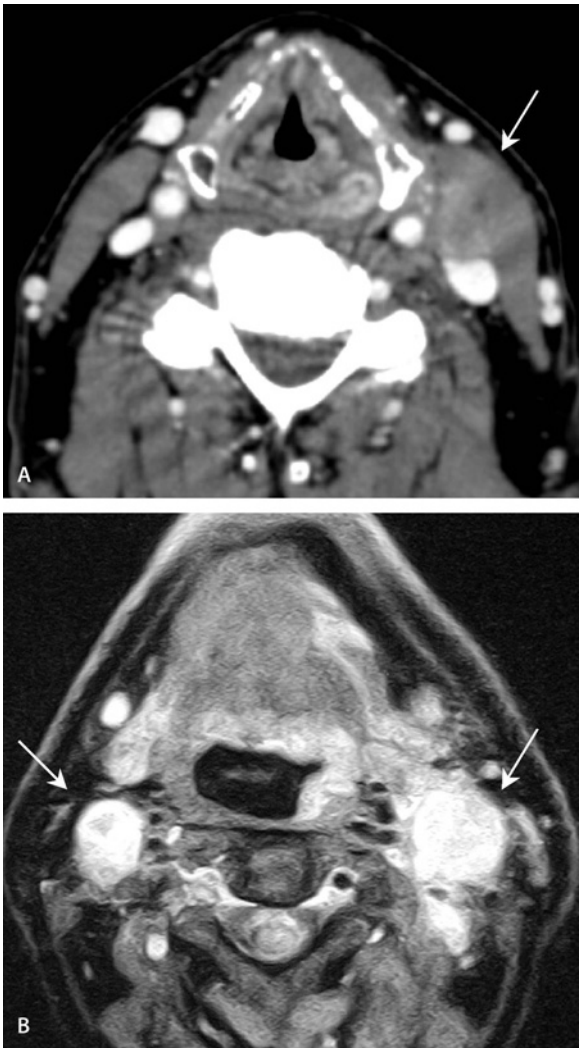

Fig. 20A, B. Metastatic lymph nodes detected using the size-criterion on both CT and MRI. **A** Patient presenting with a small left-sided piriform sinus squamous cell carcinoma and with a 17-mm large upper jugular lymph node metastasis (level II). **B** Homogenously enhancing enlarged lymph nodes (*arrows*) as seen on a fat suppressed T2-weighted MR image of a patient with a base of the tongue squamous cell carcinoma. The minimal axial diameter was 17 mm on the left (upper jugular or level II) and 13 mm on the right (upper jugular or level II). Histology confirmed the radiologic findings in both patients

gested that the ratio of the maximal longitudinal nodal length to the nodal width should be greater than 2 for normal hyperplastic nodes and less than 2 for metastatic lymph nodes. This approach is based on the concept that a normal lymph node tends to be oblong, whereas a metastatic lymph node is often spherical in shape (Fig. 21). Groups of three or more lymph nodes with a minimal axial diameter of 9–10 mm in the jugulodigastric region and 8–9 mm in the remaining neck are suggestive of metastatic lymph nodes, provided that they are in the drainage chains of the primary tumor site. All of these criteria apply to homogenous, sharply delineated nodes. Regardless of the lymph node size, the most reliable imaging finding of metastatic disease is the presence of *central nodal necrosis*. Central nodal necrosis is seen as an area of low density on contrast-enhanced CT images or low intensity on contrast-enhanced fat-suppressed T1-weighted images (Fig. 22). On T2-weighted images, central nodal necrosis appears as an area of high signal intensity. When comparing CT and MR images in the same patient, the areas of central nodal necrosis appear larger at CT than at MRI. This discrepancy may be explained by the underlying pathologic process [43, 44]. Invasion of lymph nodes by cancer cells first occurs within the marginal sinuses of the nodal cortex. Proliferation of the tumor cells then leads to invasion of the nodal medulla, resulting in blockage of the flow of lymph through the node. While the medulla undergoes necrosis, spread of tumor cells to other nodes may occur either via lymphatico-lymphatic or lymphatico-venous pathways. Although it is common practice to refer to such a lymph node as being necrotic, pathologically the nodal medulla contains both tumor cells and interstitial fluid. The necrotic appearance at CT contains both tumor cells and interstitial fluid, whereas at MR only the truly necrotic zones will have signal intensities similar to water. Central nodal necrosis has to be differentiated radiologically from *fatty hilar metaplasia*, which occurs almost exclusively at the periphery of the node. *Extranodal tumor spread* is found histologically in 40% of lymph nodes smaller than 2 cm and in 23% of lymph nodes smaller than 1 cm in diameter [43, 44]. On contrast-enhanced CT and MR images, extranodal tumor spread is seen as an enhancing nodal rim with infiltration of the adjacent fatty tissue or of the adjacent sternocleidomastoid muscle (Fig. 23).

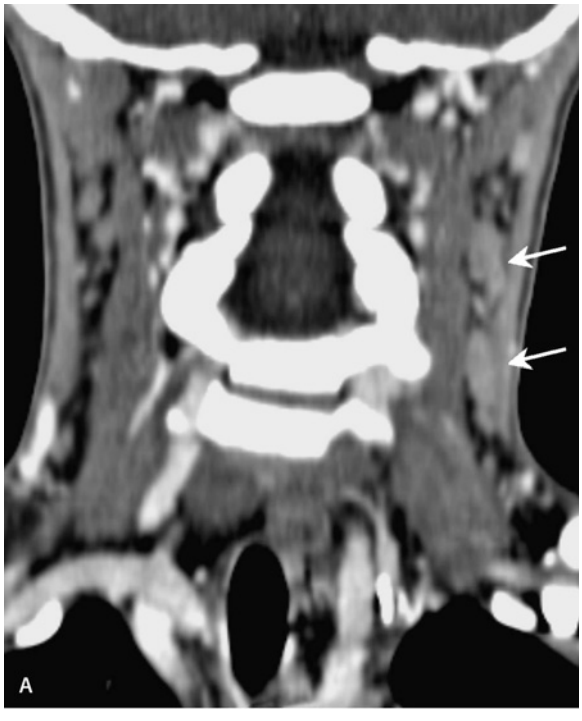

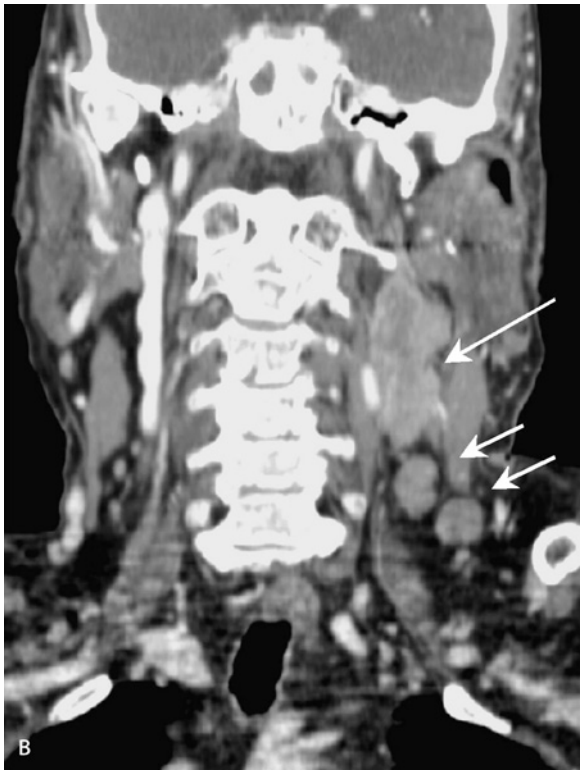

Fig. 21A, B. Nodal size and shape as an indicator of metastatic lymph node involvement as seen on contrast-enhanced CT. **A** Patient with left-sided enlarged lymph nodes (level II–IV). Note the oblong shape (*arrows*) characteristic for benign, reactive nodes. **B** Different patient with a squamous cell carcinoma of the ethmoid sinuses and with left-sided level II–IV lymph node metastases. Note an enlarged node (*long arrow*), as well as nodes with a spherical shape rather than elliptical shape (*short arrows*). In addition, there is inhomogeneous lymph node enhancement of all nodes. Neck dissection confirmed metastatic involvement of all described lymph nodes. Figure 21b reproduced with permission from [10]

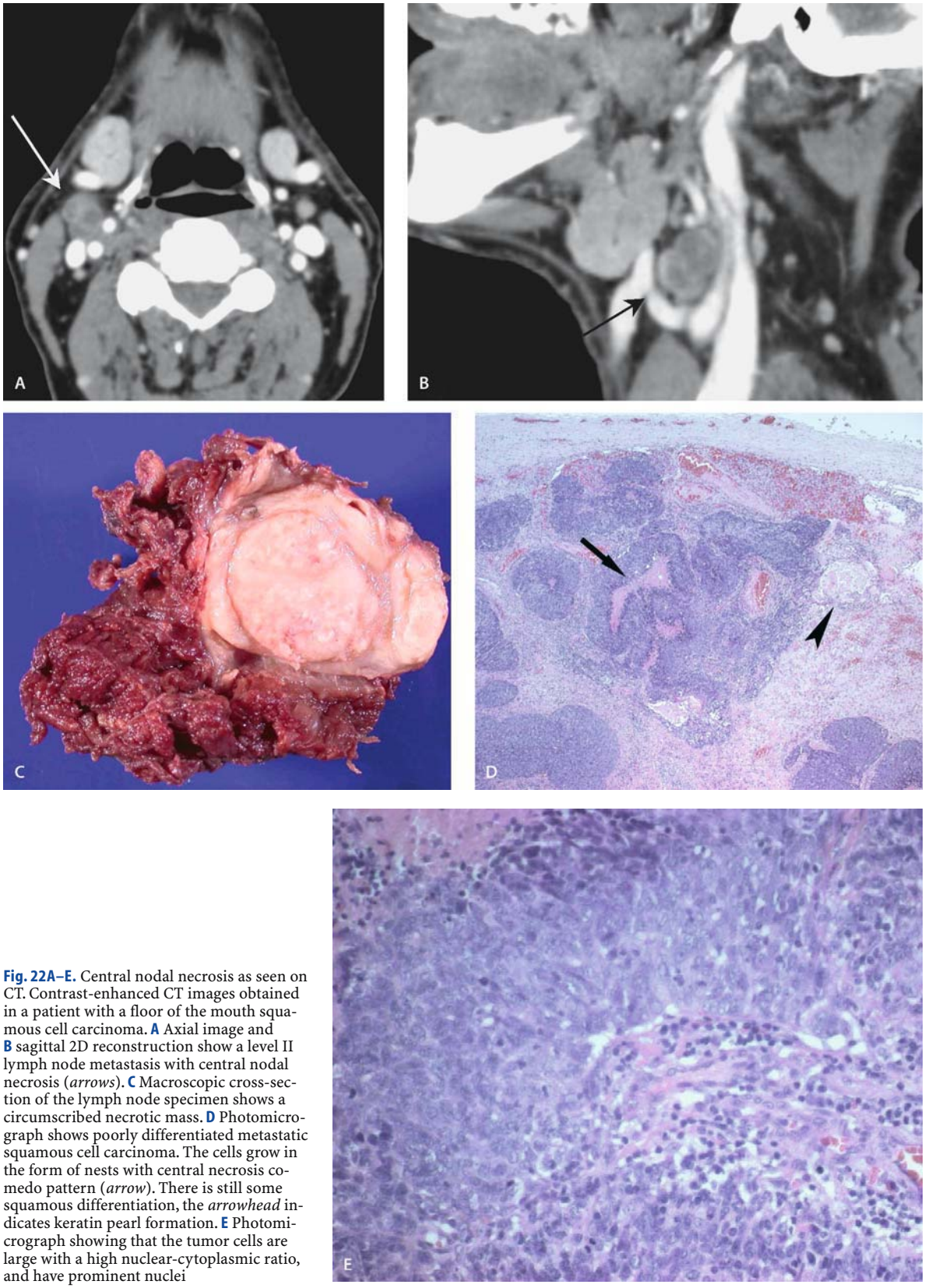

Fig. 22A–E. Central nodal necrosis as seen on CT. Contrast-enhanced CT images obtained in a patient with a floor of the mouth squamous cell carcinoma. **A** Axial image and **B** sagittal 2D reconstruction show a level II lymph node metastasis with central nodal necrosis (*arrows*). **C** Macroscopic cross-section of the lymph node specimen shows a circumscribed necrotic mass. **D** Photomicrograph shows poorly differentiated metastatic squamous cell carcinoma. The cells grow in the form of nests with central necrosis comedo pattern (*arrow*). There is still some squamous differentiation, the *arrowhead* indicates keratin pearl formation. **E** Photomicrograph showing that the tumor cells are large with a high nuclear-cytoplasmic ratio, and have prominent nuclei

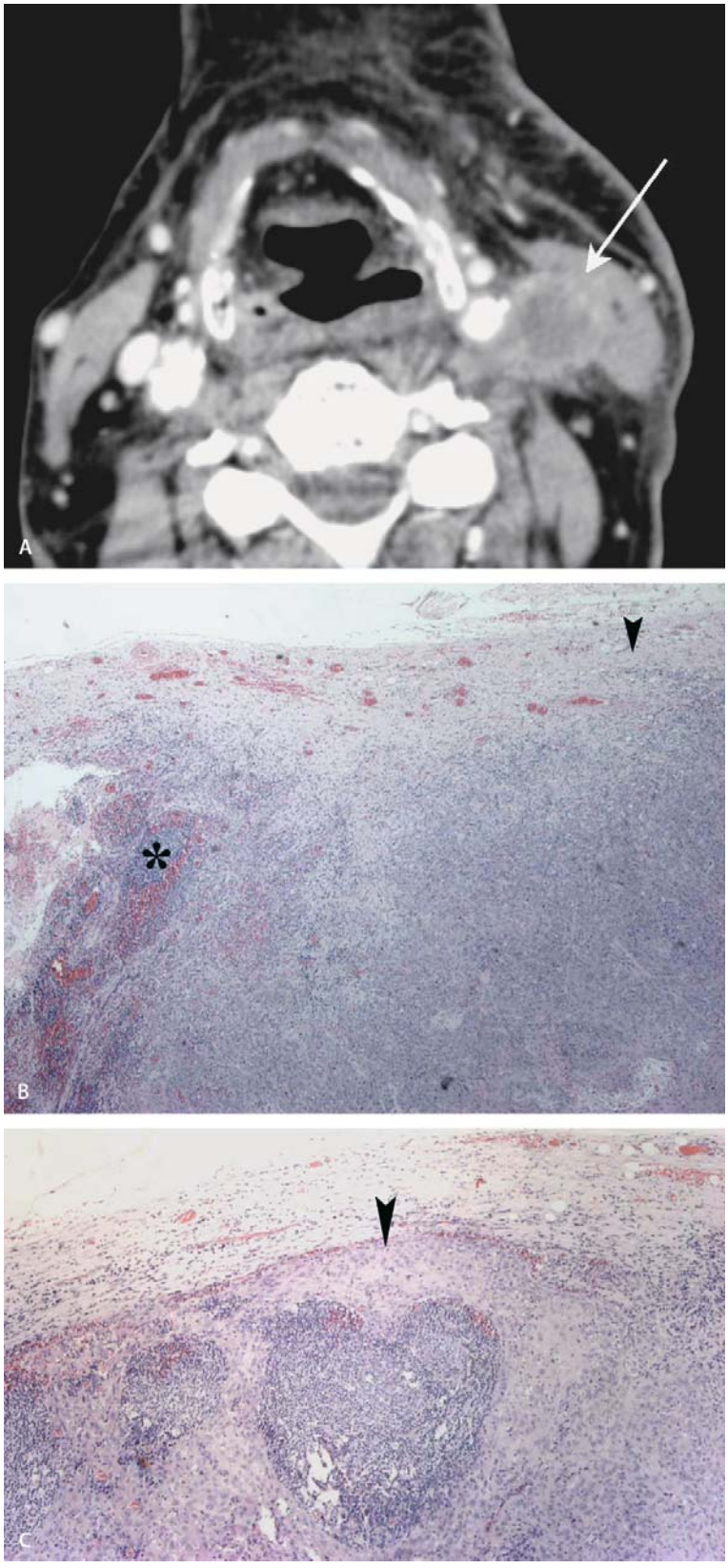

Fig. 23A–C. Extranodal spread as seen on CT and histology. **A** Middle jugular (level III) lymph node metastasis with central nodal necrosis, invasion of the sternocleidomastoid muscle (*arrow*) and enhancement of the surrounding perinodal fat, which has a streaky appearance, suggesting extranodal spread. The patient underwent neck dissection, which confirmed the findings. Photomicrographs show squamous cell carcinoma with sinusoidal invasion (*asterisk* in **B**) and capsular invasion of the lymph node (*arrowheads* in **B** and **C**). A few residual lymphoid follicles are still present in the lymph node (**C**)

Lymphoma

Both Hodgkin's and non-Hodgkin's lymphoma commonly involve the cervical lymph node groups. The characteristic CT appearance includes fairly large nodal neck masses with a homogenous low density and with a thin nodal capsule (Fig. 24). Nodal necrosis may occur; however, it is much less frequent than with metastatic squamous cell carcinoma or metastatic thyroid cancer (Fig. 25). Extranodal involvement – most often at the level of Waldeyer's ring – may be seen in up to 23% of patients with non-Hodgkin's lymphoma; it is, however, unusual in patients with Hodgkin's lymphoma (only 4%) [10, 40, 41]. Intranodal calcification may be seen after radiation therapy or chemotherapy of both Hodgkin's and non-Hodgkin's lymphoma. Rarely it may be seen prior to therapy.

Non-nodal Masses

The most common non-nodal neck masses include neurogenic tumors, lipomas and paragangliomas.

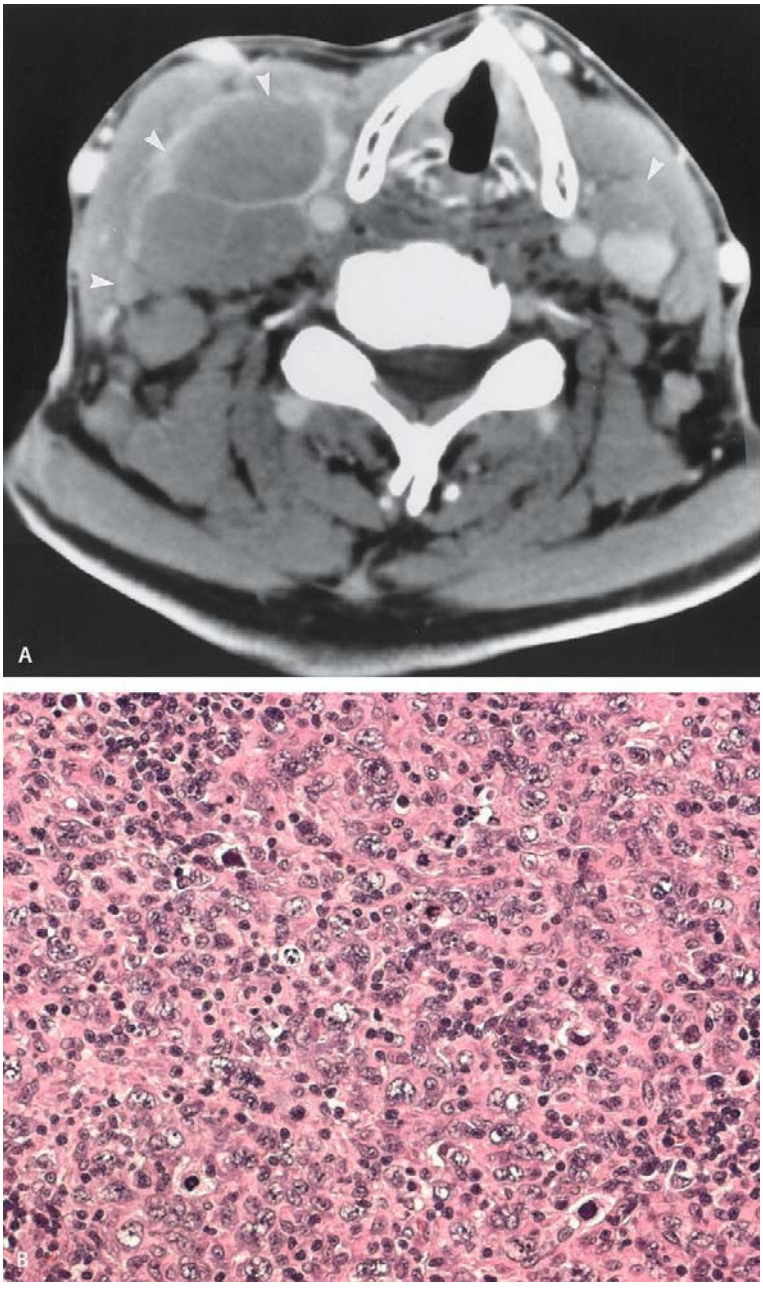

Fig. 24A, B. Characteristic CT appearance of lymph node involvement by lymphoma. **A** Axial, contrast-enhanced CT scan shows bilateral huge nodal masses (*arrowheads*) with a homogenous low density and with a thin, enhancing nodal capsule. Typically, the attenuation value of the involved lymph nodes is higher than that of fat and lower than that of muscle. Histology revealed diffuse large B cell lymphoma. **B** Photomicrograph shows that the lymph node is diffusely infiltrated by medium-sized to large cells with irregular nuclei, dense chromatin and small nucleoli. Small lymphocytes are seen intermingling with the large lymphoma cells

Neurogenic Tumors

Neurogenic tumors include schwannoma, neurofibroma, ganglioneuroma, granular cell tumors and malignant peripheral nerve sheath tumors. Schwannomas and neurofibromas are the most common types of neurogenic tumors found in the infrahyoid neck [10, 26, 31, 53, 56]. They typically involve the vagus nerve (Fig. 26), the cervical nerve roots or the brachial plexus. Clinical findings are inconstant and include motor dysfunction or pain in the distribution of a sensory nerve. Without a clinical history of neurofibromatosis it is impossible to distinguish between schwannomas and neurofibromas with cross-sectional imaging. Schwannomas and neurofibromas display typical features on MRI (Fig. 27). Nearly 75% of all nerve sheath tumors have the same signal intensity as the spinal cord on T1-weighted sequences, more than 95% have a high signal intensity on T2-weighted sequences, and nearly all nerve sheath tumors enhance following intravenous administration of contrast material [10, 31]. The enhancement pattern of neurogenic tumors is highly variable. A target appearance (hyperintense rim and hypointense center) may be seen on contrast-enhanced MR images or contrast-enhanced CT images, and is caused by central areas of cystic or necrotic degeneration. Most schwannomas are a mixture of two histologic types of tissue: the cell-rich Antoni type A tissue with chromatin-rich cells arranged in characteristic palisades and in onion rings (Verocay

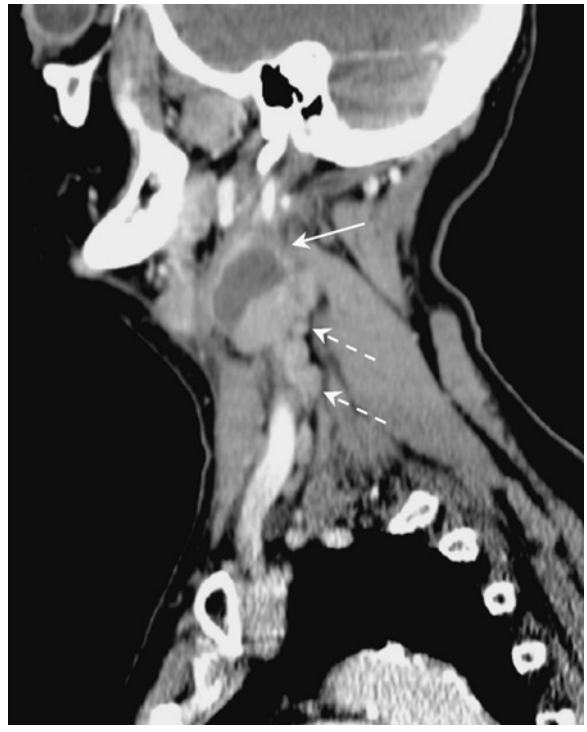

Fig. 25. Nodal necrosis seen in non-Hodgkin lymphoma. Sagittal 2D reconstruction from a volumetric, contrast-enhanced CT data set shows a level III lymph node with nodal necrosis (*arrow*), as well as several enlarged level III and IV lymph nodes (*dashed arrows*). Histology revealed anaplastic-large cell lymphoma (Ki-1 lymphoma)

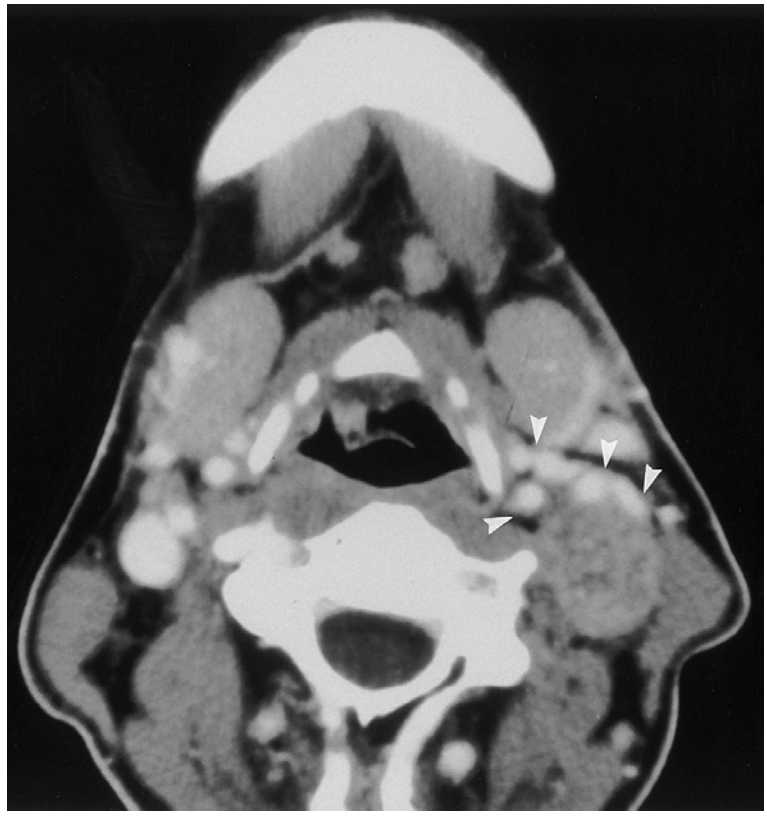

Fig. 26. Schwannoma of the vagus nerve: Characteristic CT appearance. Axial, contrast-enhanced CT image demonstrates a mass with inhomogeneous enhancement situated within the carotid space. It displaces the internal and external carotid artery and the internal jugular vein anteriorly (*arrowheads*). CT images obtained at multiple levels showed that the mass was located along the vagus nerve. Reproduced with permission from [13]

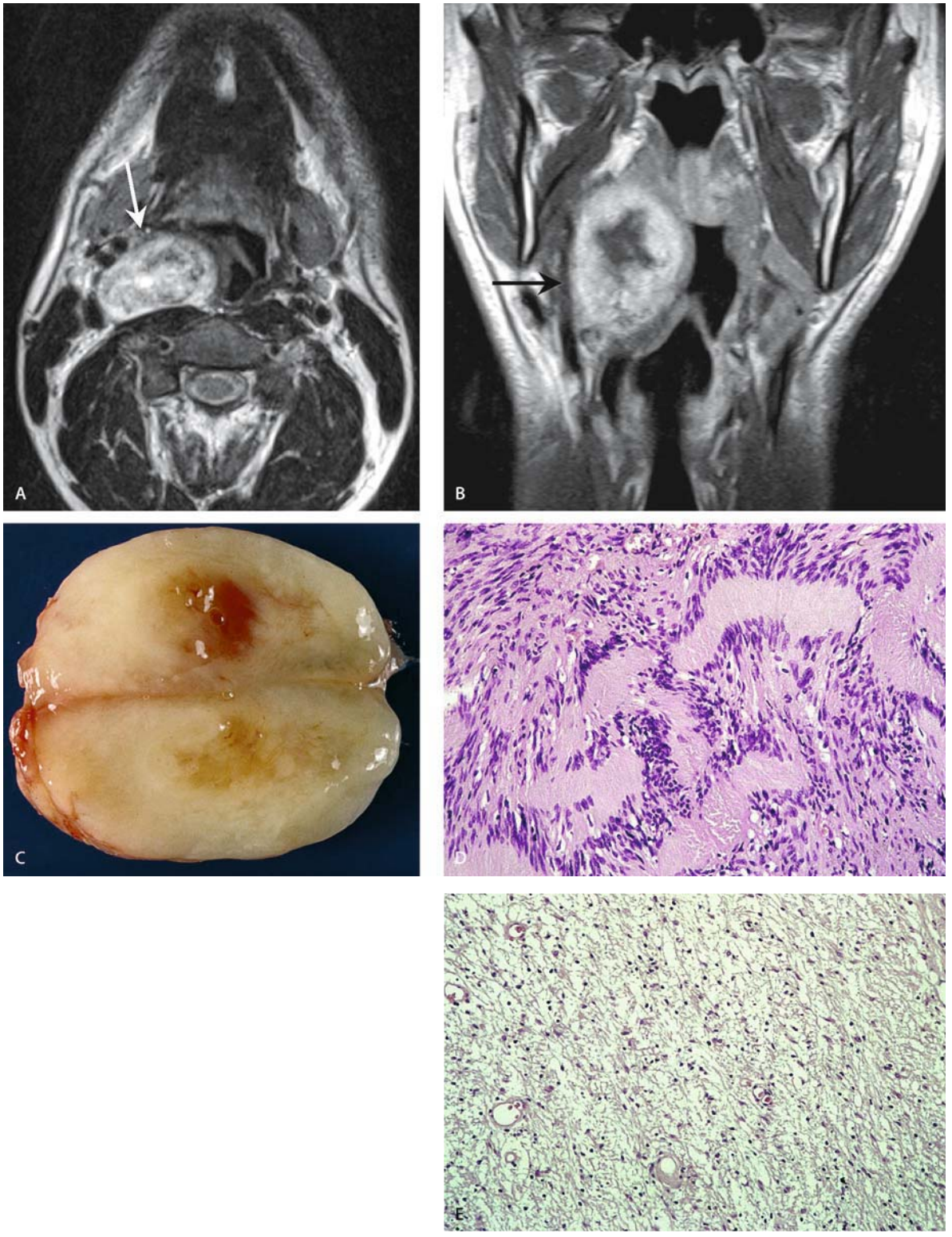

Fig. 27A–E. Schwannoma of the sympathetic chain: characteristic MRI and histologic appearance. **A** Axial T2-weighted MR image obtained in a young female with dysphagia shows a well-delineated mass (*arrow*) located in the parapharyngeal space and with inhomogeneous signal intensity. **B** Coronal, contrast-enhanced T1-weighted image shows a characteristic target appearance (*arrow*) with peripheral enhancement and central areas of necrosis. The mass displaces the epiglottis towards the left. **C** Macroscopic view of the resected specimen shows a well-circumscribed tumor. The cut surface shows cyst formation and areas of hemorrhage. **D** Photomicrograph showing Antoni type A areas of the schwannoma with prominent spindle cells palisading and with formation of Verocay bodies. **E** Photomicrograph showing Antoni type B areas of the schwannoma which are characterized by loose, less cellular myxoid areas where the spindle cells are arranged in a haphazardly fashion

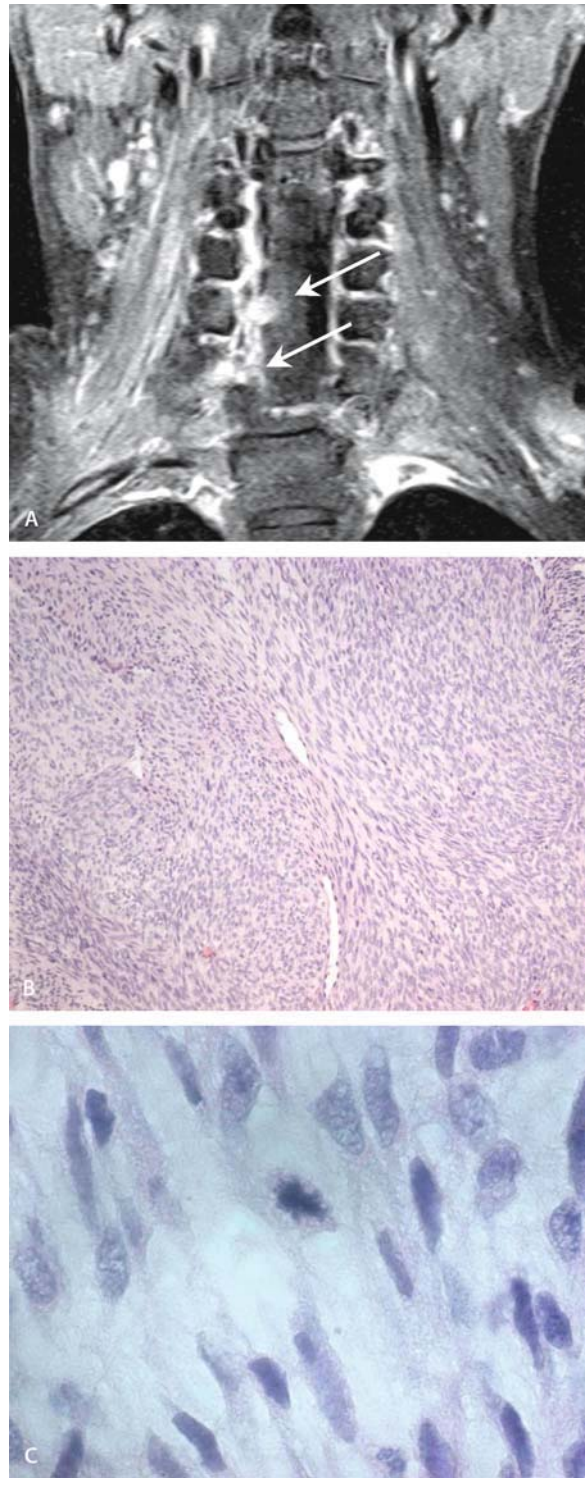

Fig. 28A–C. MPNST in a young male without NF1. The patient was complaining of pain as well as motor and sensory deficits at the level of C7. **A** Coronal contrast-enhanced, fat-saturated T1-weighted image shows a small, poorly delineated, homogenously enhancing tumor (*arrows*) involving the C6 and C7 nerve roots on the right. MR imaging suggested the diagnosis of a neurogenic tumor of the brachial plexus. Surgery revealed a MPNST. **B** Photomicrograph shows a hypercellular tumor which is composed of spindle cells in form of fascicles. **C** The tumor cells are spindle-shaped, with hyperchromatic nuclei, prominent nucleoli and eosinophilic abundant cytoplasm. Numerous mitoses are present

bodies) and the relatively acellular cystic Antoni type B tissue (Fig. 27). The Antoni type B pattern is commonly intermixed with the Antoni type A, but an entire tumor may have this arrangement. Regressive changes, including necrosis, cystic degeneration and lipidization may be prominent and do not bear relation to the size or location of the tumor.

Malignant peripheral nerve sheath tumors (MPNST) is the new name adopted by the World Health Organization to unify the previously designated entities of ma-

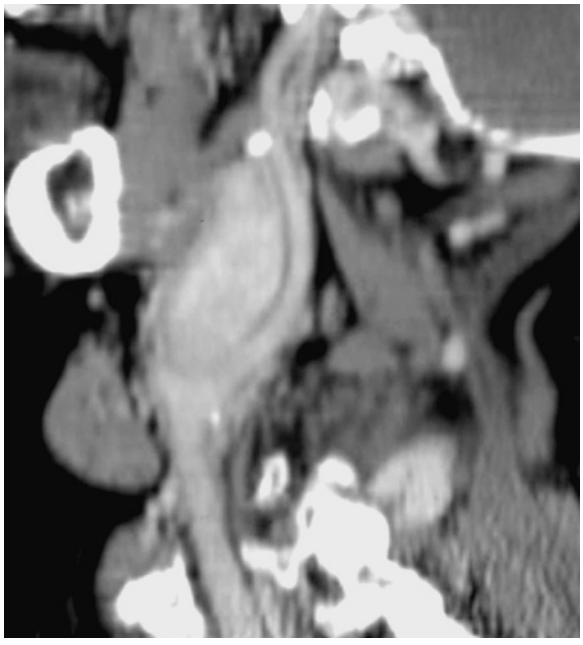

Fig. 29. Carotid body paraganglioma: characteristic CT appearance. Contrast-enhanced 2D parasagittal reconstruction at the level of the carotid bifurcation from a multislice volumetric data set shows a hypervascular mass that displaces the external carotid artery anteriorly and the internal carotid artery posteriorly. Note the characteristic splaying of the carotid bifurcation

lignant schwannoma, neurofibrosarcoma and neurogenic sarcoma [53]. These tumors arise de novo (Fig. 28) or from malignant transformation of a plexiform neurofibroma. As many as 11% of MPSTs are induced by radiation therapy. Most tumors are seen between 30 and 50 years of age, but in a younger age group in patients with NF1 [53]. The imaging findings in MPNST (are nonspecific and include a large fusiform and invasive tumor, which spreads along nerve trunks and sometimes presents with areas of necrosis and hemorrhage.

Paraganglioma

Paragangliomas arise from neural crest cell derivates within vessel walls. In the infrahyoid neck, paragangliomas occur in the carotid body, which is situated in the carotid bifurcation (carotid body tumor, Table 2). Occasionally, a large glomus vagale tumor may extend into the infrahyoid neck and present as a carotid space lesion. Carotid body tumors typically present in women, in the 4th decade of life, and may be multiple in as many as 30% of patients with a family history of paraganglioma [10, 13, 34]. On contrast-enhanced CT images, paragangliomas appear as highly enhancing lesions found medial to the sternocleidomastoid muscle (Fig. 29). They typically display multiple curvilinear signal voids on both T1- and T2-weighted images (Fig. 30). The conspicuity of these signal void areas increases with tumor size and increasing vessel diameter. This MR appearance is not pathognomonic for paragangliomas and it has been reported in other hypervascular lesions, i.e., vascular malformations, hemangiomas and metastases from renal cell carcinoma [3, 8]. The key to the radiologic diagnosis of carotid body paraganglioma is splaying of the proximal internal and external carotid arteries around the mass at the carotid bifurcation (Figs. 29, 30). Histologic analysis of paragangliomas reveals non-encapsulated lesions with ill-defined margins. Chief cells arranged in clusters and round cell nests (Zellballen) are surrounded by a delicate stroma containing numerous vascular channels. Invasion of the adventitia of the carotid wall is common.

Lipomatous Tumors

Although *lipomas* are the most common tumors of mesenchymal origin in the body, only 13% arise in the extracranial head and neck. Most head and neck lipomas are located subcutaneously or in the posterior cervical triangle. In rare instances, they may arise in the retropharyngeal space or they may insinuate around the common carotid artery and internal jugular vein. Subcutaneous tumors are most often asymptomatic. Lipomas arising in the deep spaces of the neck may present with symptoms related to mass effect on the pharynx, larynx or esophagus, such as dysphagia, sleep apnea syndrome and dyspnea. Histologically, lipoma is composed of mature adipose tissue arranged in lobules, separated by fibrous tissue septa (Fig. 31). Most tumors are well circumscribed and encapsulated, although infiltrating non-encapsulated lipomas have been reported.

The radiologic diagnosis of lipoma is straightforward. Both CT and MRI provide a definitive diagnosis in virtually all cases (Figs. 31, 32). The typical CT characteristics are a homogeneous and nonenhancing lesion with attenuation values from –65 to –125 HU (Fig. 31) On MRI, lipoma has the same signal intensity as subcutaneous fat on all pulse sequences (hyperintense on T1-weighted images, decrease in intensity on T2-weighted images and very low intensity on fat-suppressed T1-weighted images (Fig. 32). As in other parts of the body, if portions of the lipoma have the attenuation value or signal intensity characteristics of soft tissue on CT or MRI, and if contrast enhancement is observed within these strands of connective tissue, the diagnosis of a liposarcoma should be considered [27].

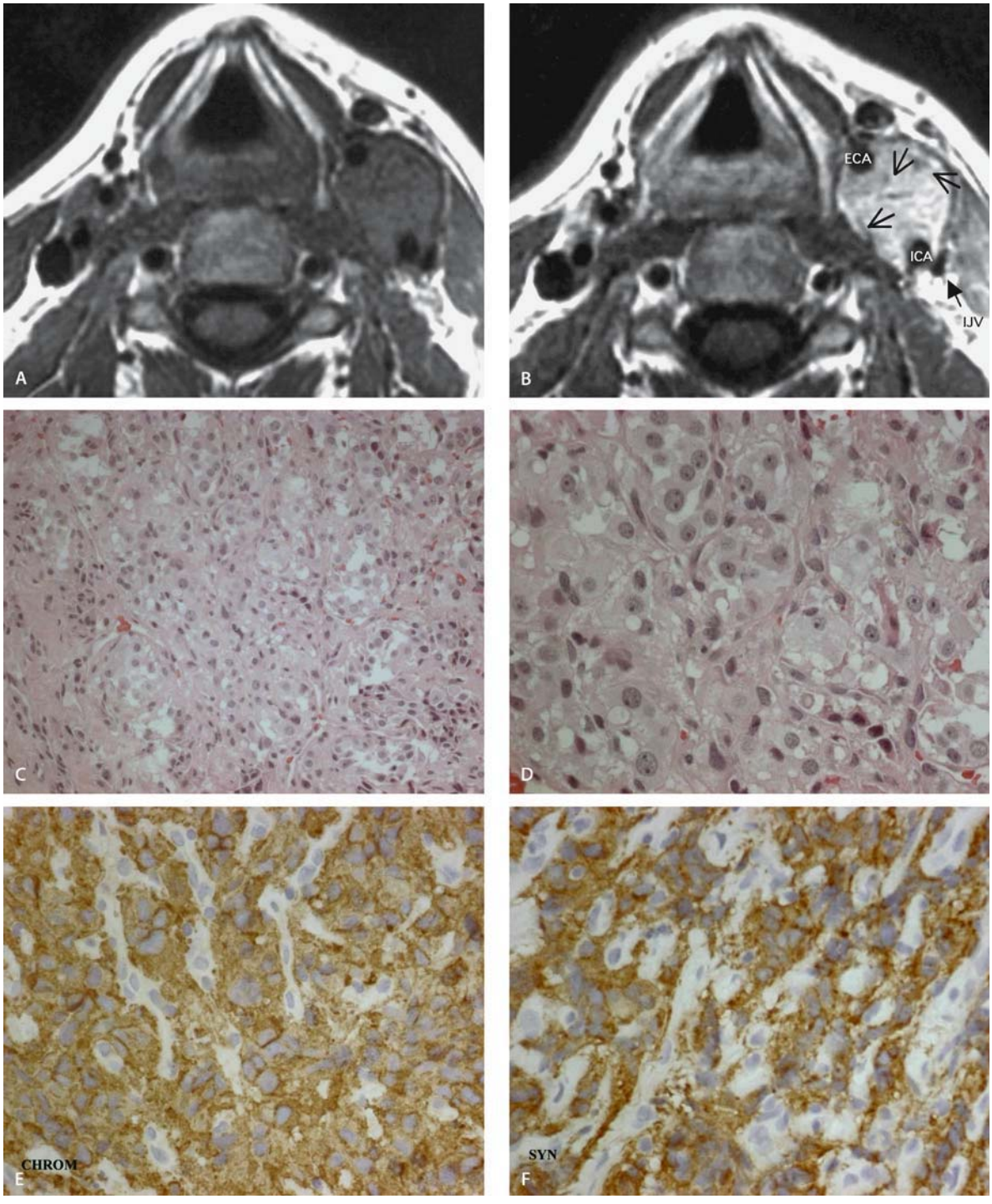

Fig. 30A–F. Carotid body paraganglioma: characteristic MR and histologic findings. **A** Axial, nonenhanced and **B** axial contrast-enhanced T1-weighted MR images demonstrate an enhancing lesion containing signal voids (*black arrows*). The mass displaces the internal carotid artery (*ICA*) and the internal jugular vein (IJV) posterolaterally and the proximal external carotid artery (*ECA*) anteriorly. **C** Characteristic histologic aspect of paraganglioma: organoid nesting pattern – *Zellballen* – of neoplastic cells. **D** These cells are medium to large in size. They have round nuclei, small inconspicuous nucleoli and ample eosinophilic cytoplasm. Mild nuclear pleomorphism can be seen. **E** and **F** Paragangliomas are neuroendocrine tumors where the neoplastic cells are positive for neuroendocrine markers such as chromogranin and synaptophysin

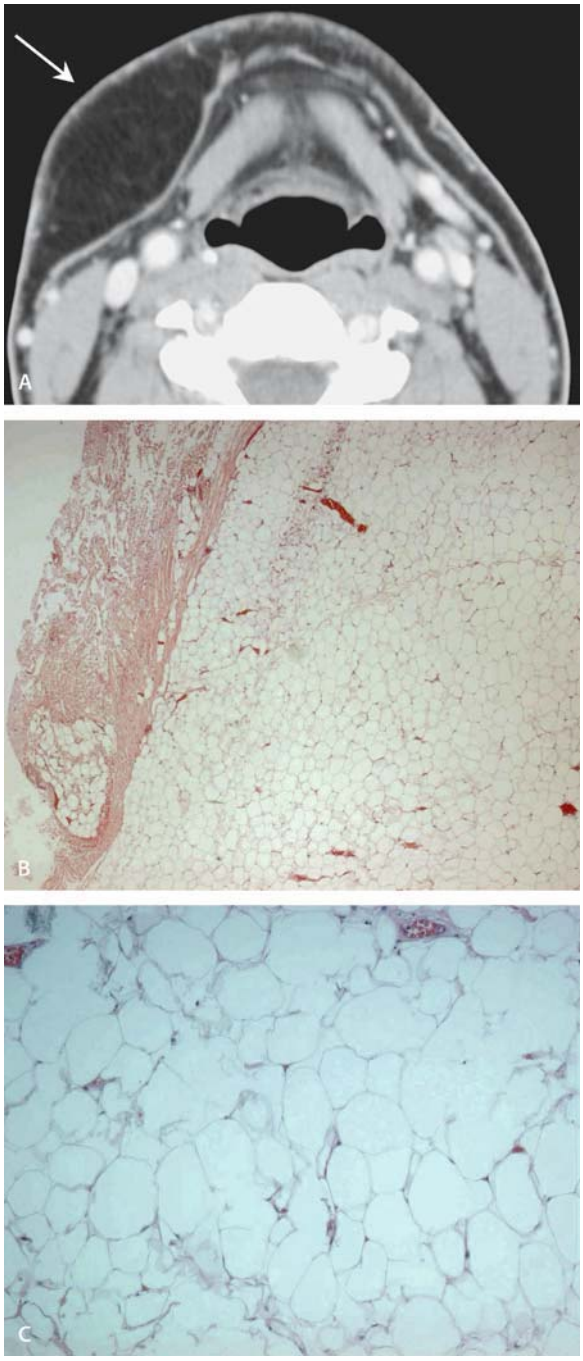

Fig. 31A–C. Lipoma: characteristic CT and histologic appearance. **A** Axial, contrast-enhanced image below the hyoid bone shows a subcutaneous mass with attenuation values, suggesting a lipoma (*arrow*). **B** Photomicrograph of the resected specimen reveals an encapsulated lesion. **C** The tumor is composed of mature adipose tissue with no cellular atypia nor necrosis

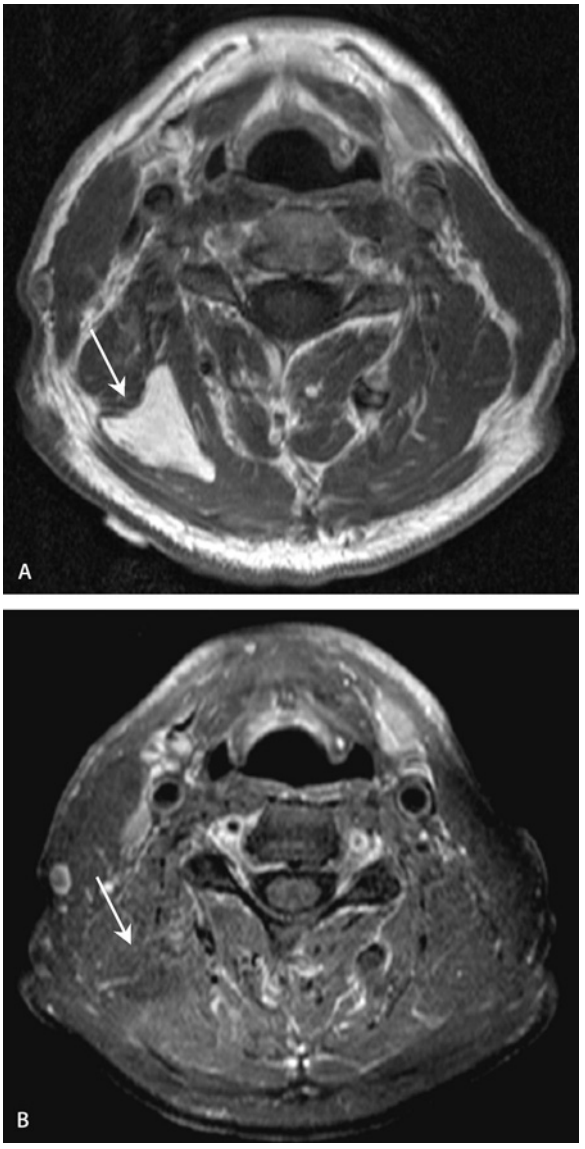

Fig. 32A, B. Lipoma: characteristic MRI appearance. **A** T1-weighted axial image shows a hyperintense mass located within the prevertebral space (*arrow*). **B** Contrast-enhanced, fat-suppressed axial MR image shows that the mass is composed of adipose tissue and that it does not enhance (*arrow*), therefore suggesting the diagnosis of a lipoma. Surgery confirmed the findings

Thyroid Gland Nodules

Thyroid nodules are common and comprise adenomas, cysts, multinodular goiter and malignant tumors [1, 2, 36]. Thyroid nodules are estimated to occur in 4%–8% of the adult population when palpable nodules are involved. Thyroid nodules may be either single (one-third) or multiple (two-thirds). The differentiation between a gland with a single nodule from a gland with multiple nodules is essential because the incidence of malignancy in a single nodule is 10%–15%, and the incidence of malignancy in a multinodular goiter is 4%–7.5% [36]. It is generally accepted that a ^{99}mTc-pertechnetate visualized "hot" thyroid nodule is almost invariably a benign lesion, while the probability of malignancy varies from 10%–25% in ^{99}mTc-pertechnetate visualized "cold" nodules. Therefore, fine-needle aspiration biopsy (FNAB) with or without US guidance, is always required to rule out malignancy. FNAB has been found to be a safe and inexpensive procedure, and in several clinical studies this technique has shown a high diagnostic accuracy [36].

Adenomas are benign thyroid neoplasms that may occur in all age groups. They are more common in women than men. Adenomas are usually solitary and are smaller than 3 cm in diameter. They often display degenerative changes, such as cyst formation, hemorrhage, fibrosis or calcification. On CT and MRI, adenomas are either solid and enhancing or they reveal cystic degeneration and calcification. Thyroid adenomas are either functioning (hot nodule) or nonfunctioning (cold nodule) on radionuclide scans.

Multinodular goiter has an incidence of 3%–5% in the general population with a higher incidence in endemic goiter regions. Patients usually present with either palpable neck masses or tracheoesophageal compression and displacement. Goiters may be seen with hyperthyroidism, euthyroidism or hypothyroidism. Histologically, multinodular goiters are composed of either colloid nodules or true adenomas. These nodules are multiple, their size is variable and they are partly encapsulated. Areas of fibrosis, necrosis and calcifications are common at histopathology. Therefore, on CT and MRI, the findings are variable depending on the underlying histology. Calcifications, which are commonly seen in multinodular goiters, are optimally visualized on CT. On ^{99}mTc-pertechnetate scans, a multinodular goiter appears enlarged and heterogeneous with hot, cold, and spared areas. This characteristic aspect will usually obviate the need for biopsy of a palpable nodule. However, a large, dominant, or growing mass amidst a goiter will most probably be biopsied.

Thyroid cancer is uncommon, accounting for around 1.6% of all cancers. The role of imaging in thyroid cancer depends to a large extent on the histology of the tumor. Because the vast majority of thyroid nodules are benign, a major role of imaging is to try to differentiate between benign and malignant lesions. Most thyroid cancers present as cold nodules on radionuclide scans. Nuclear medicine thyroid scans performed with ^{99}mTc-pertechnetate or radioactive iodine and ultrasound combined with fine-needle aspiration biopsy are used as a first-line approach, whereas CT and MRI are used only in selected cases to determine the extent of the tumor preoperatively, as well as the presence or absence of metastases [36, 46]. One must be cautious regarding CT scanning and the administration of contrast-enhanced iodinated compounds, since these agents will interfere with thyroid function tests for up to 6 weeks.

Follicular carcinoma typically occurs in females in their 5th decade. Although macroscopically, they may resemble an adenoma; microscopic evaluation clearly shows that these tumors have features of vascular and capsular invasion. These aggressive tumors typically invade the surrounding tissue, including the airway. Lymph node metastases are rare; however, hematogenous metastases to lung, liver, bone and brain are common. Differentiated tumor forms and their metastases may take up radioiodine, which can be used to detect and treat metastases. The CT and MR imaging findings are variable, ranging from a well-delineated nodule to an ill-defined tumor with necrosis and calcification (Fig. 33).

Papillary carcinoma has a peak incidence in the 3rd and 4th decades. Females are affected more often than males. The prognosis is usually excellent (>90% at 20 - years), provided that the size of the lesion does not exceed 5 cm and that the capsule of the thyroid gland is preserved [36]. As many as 20% of papillary carcinomas are multifocal. Most often the tumor is smaller than 1.5 cm in size. However, aggressive forms may invade the larynx and trachea or the cervical esophagus [4, 10, 36] (Fig. 34). Histology reveals papillae with a fibrovascular core with epithelial lining, nuclear atypia, and psammoma bodies (laminated calcific spherules) in 50% of cases. Follicular elements in a papillary carcinoma are common, and this has led to the histologic classification of a follicular variant or mixed papillary-follicular carcinoma. However, this mixed cancer ultimately behaves like a papillary carcinoma. Psammomatous calcifications are easily seen on CT. They are punctate and in some instances appear as cloudy calcifications. Amorphous calcifications may also be observed in papillary thyroid carcinoma (Fig. 34). On CT and MR imaging, a malignant lesion should be expected when the margins are ill defined, when there is extraglandular tumor spread, lymph node involvement, or invasion of the larynx or trachea. In up to 50% of papillary carcinoma cases, lymph node metastases in the neck may precede the clinical recognition of a tumor in the thyroid gland.

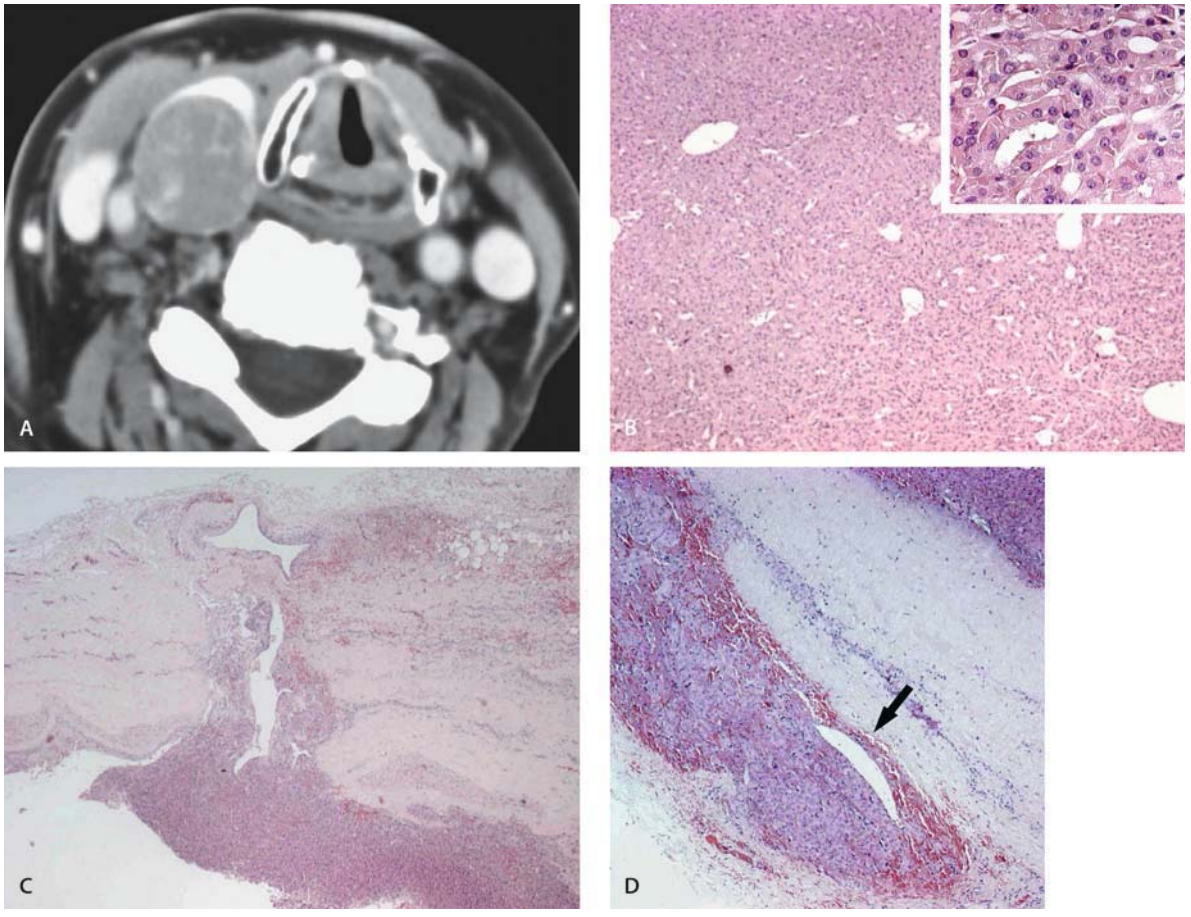

Fig. 33A–D. Follicular carcinoma: CT and histologic aspect. **A** Contrast-enhanced CT image obtained in an elderly female with a palpable neck mass demonstrates a single, well-delineated thyroid nodule on the right. No metastatic lymph nodes were seen on the CT examination. **B** Photomicrograph of the surgical specimen revealed a tumor that is composed of small, round, closely packed follicles. The *inset* shows tumor cells with hyperchromatic nuclei and prominent nucleoli. **C** The same tumor shows infiltration of the capsule. **D** Also there is blood vessel invasion by tumor cells (*arrow*). Fig. 33a reproduced with permission from [10]

However, as opposed to squamous cell cancer where the prognosis is tremendously influenced by the presence or absence of lymph node metastases, cervical lymph node metastases do not significantly affect prognosis of patients with papillary carcinoma. Lymph node metastases from papillary carcinoma may have a variable aspect on imaging: solid and hypervascular, solid and cystic, cystic, and cystic and calcified. In general, any lymph node seen in a patient with papillary carcinoma should be suspected of being malignant, no matter what the size, because of the relatively high rate of lymphatic spread.

Anaplastic carcinoma is the most aggressive neoplasm in the thyroid gland. It is seen in patients over 50 years of age and the mean survival is 6–12 months. In almost 50% of cases, the anaplastic carcinoma develops within a goiter or it may arise from papillary and follicular thyroid cancers. At diagnosis, the tumor usually demonstrates invasion into the neighboring soft tissue structures, larynx, trachea, esophagus, carotid arteries and internal jugular vein. Lymph node metastases, extension into the mediastinum and distant hematogenous metastases are common. The imaging features on CT and MRI do not allow differentiation from other advanced thyroid carcinomas.

Medullary carcinoma arises from the parafollicular, or C cells of the thyroid. The C cells appear to be derived from neural crest tissue in the ultimobranchial bodies of the branchial pouch system. These cells secrete thyrocalcitonin, which decreases serum calcium. Most patients with a medullary carcinoma present with a well-circumscribed solid nodule that is usually nonencapsulated. Histologically, a highly vascularized stroma may be seen, as well as amyloid deposition, hemorrhage and hyalinized collagen. Seventy per cent of medullary carcinomas arise sporadically; the remaining 30% are seen

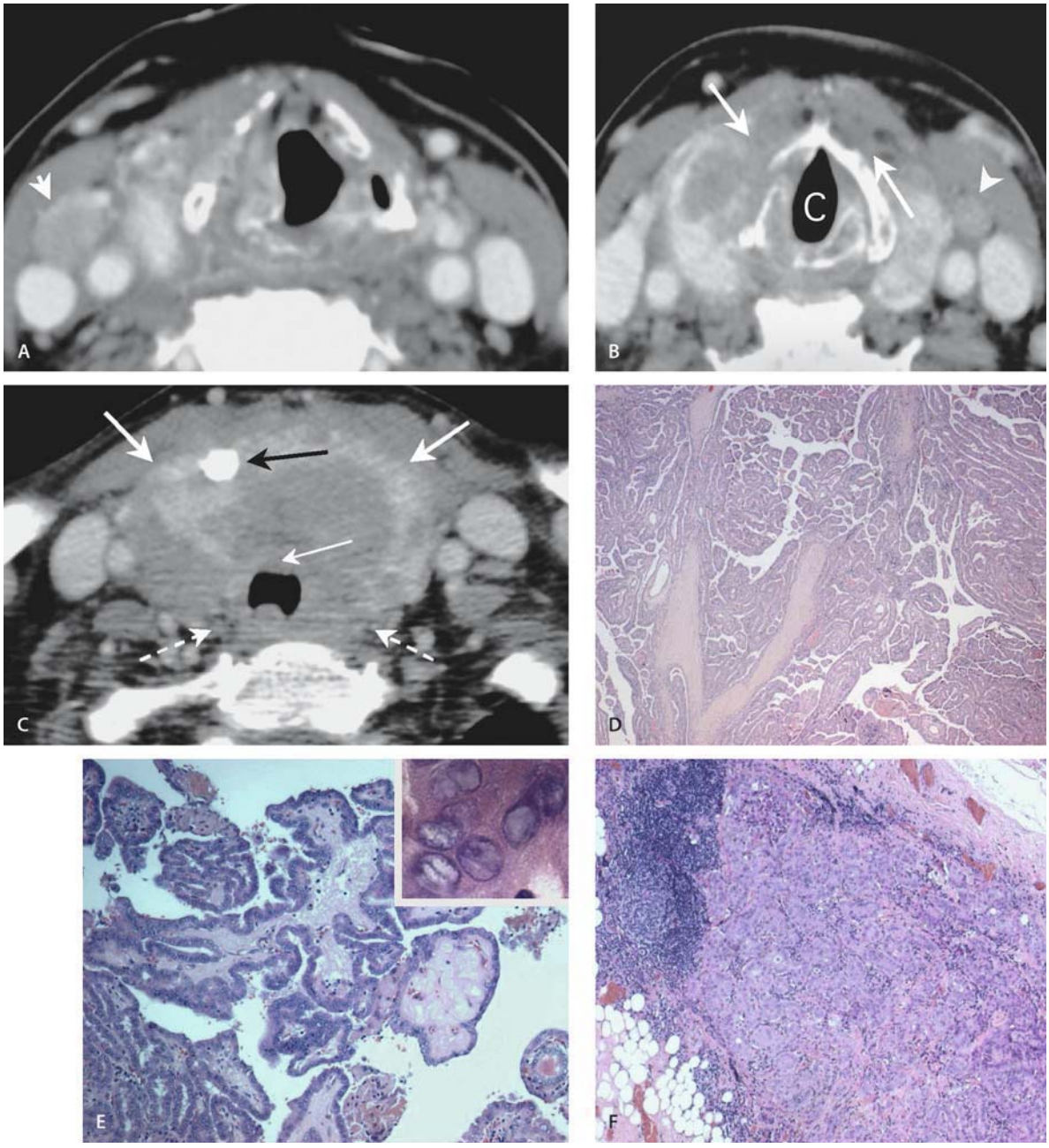

Fig. 34A–F. Advanced papillary carcinoma with extraglandular spread and metastatic lymph nodes. Axial contrast-enhanced CT images at the level of the supraglottic larynx (**A**), subglottis (**B**) and cervical trachea (**C**) show a thyroid tumor extending beyond the thyroid gland. Invasion of the prelaryngeal strap muscles (*arrows*), trachea (*thin arrow*) and both tracheoesophageal groves (*dashed arrows*). Bilateral level III lymph node metastases (*short arrows*). Note a paramedian position of the left false cord, suggesting recurrent laryngeal nerve paralysis caused by invasion of the left tracheoesophageal grove. A large amorphous calcification (*black arrow*) is present within the tumor. The level of the cricoid is indicated by *C*. **D** Photomicrograph shows the typical appearance of papillary carcinoma at low magnification with complex branching papillae. **E** The papillae have a central fibrovascular core. They are lined by cuboidal cells showing the typical features of a papillary carcinoma. *Inset*, two nuclei present longitudinal nuclear grooves, coffee bean, and two others a ground glass egg-basket appearance. **F** A level III lymph node metastasis with tumor cells replacing the normal lymph node architecture

in the familial form without MEN (multiple endocrine neoplasia) and in the familial form associated with MEN. Patients with MEN syndrome may have elevated serum levels of calcitonin, which can be used as a screening test in families with the genetic trait. On CT and MRI, the tumor may be solid, it may demonstrate psammomatous or coarse calcifications, extraglandular spread, lymph node and distant metastases to the lungs, liver, and bone.

Infectious and Inflammatory Conditions

Inflammatory and infectious lesions of the infrahyoid neck may be classified into two groups: (a) cervical chain nodal inflammation and (b) soft tissue infections. For practical reasons (quick availability, high diagnostic performance), CT is still the modality of choice in evaluating inflammatory and infectious diseases of the infrahyoid neck.

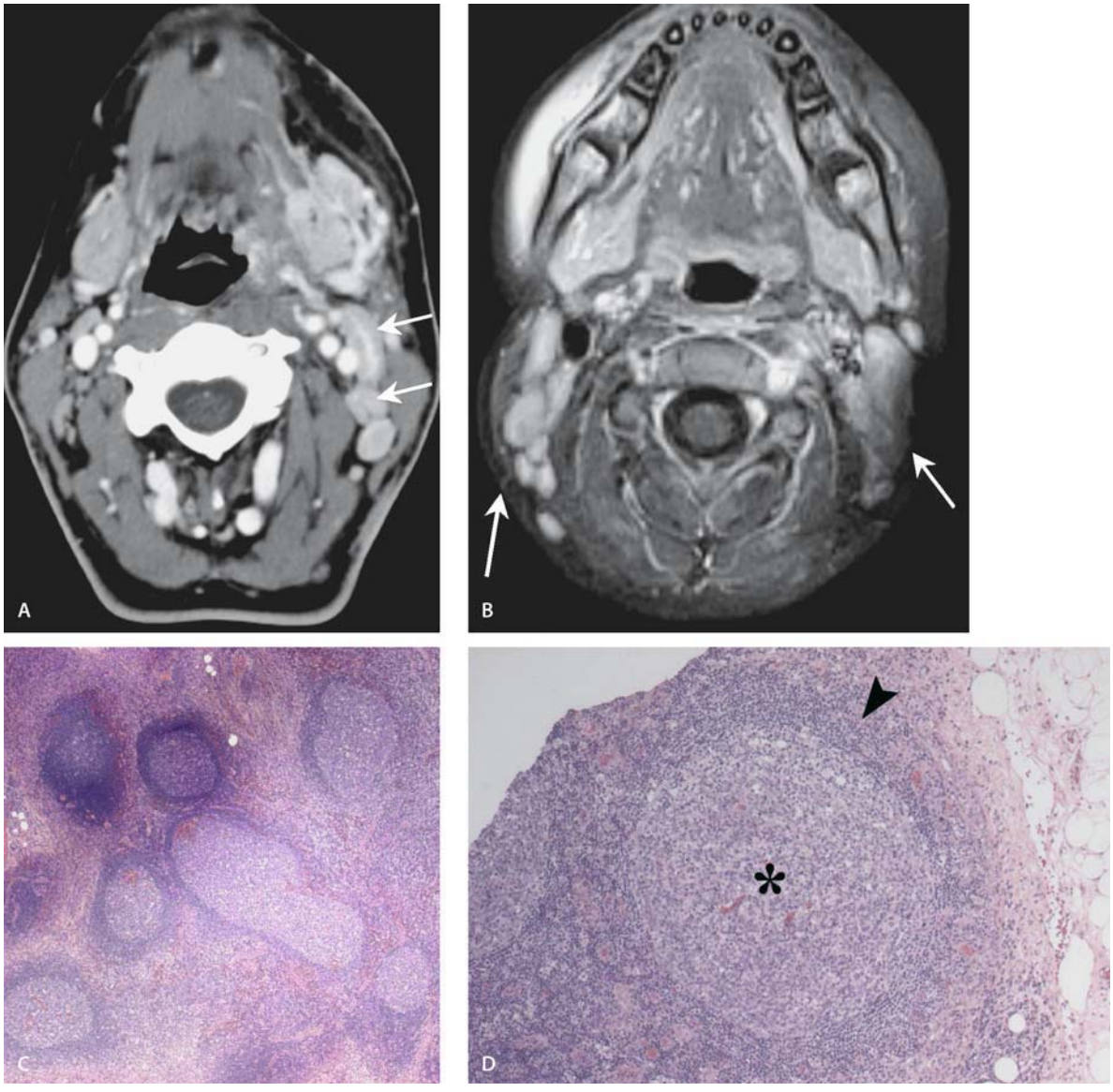

Fig. 35A–D. Reactive lymph nodes as seen on CT, MRI and histology. Two different patients with enlarged cervical nodes. **A** Axial, contrast-enhanced CT in a 23-year-old male shows marked enlargement of the left superior internal jugular nodes (level II). The enlarged nodes are homogenously enhancing (*arrows*). **B** Axial fat6suppressed T1-weighted image obtained after injection of contrast material in a 9-year-old girl shows bilateral enlargement of the upper jugular nodes (level II). The nodes are homogenously enhancing (*arrows*) and have an elliptical shape. **C** Photomicrograph obtained from a resected node in patient A shows follicular lymphoid hyperplasia (reactive lymph node). The lymphoid follicles are increased in number and in size with wide variation in size and shape. **D** The hyperplastic follicular center (*asterisk*) present numerous tangible body macrophages. The marginal zone (monocytoid cells) is preserved (*arrowhead*)

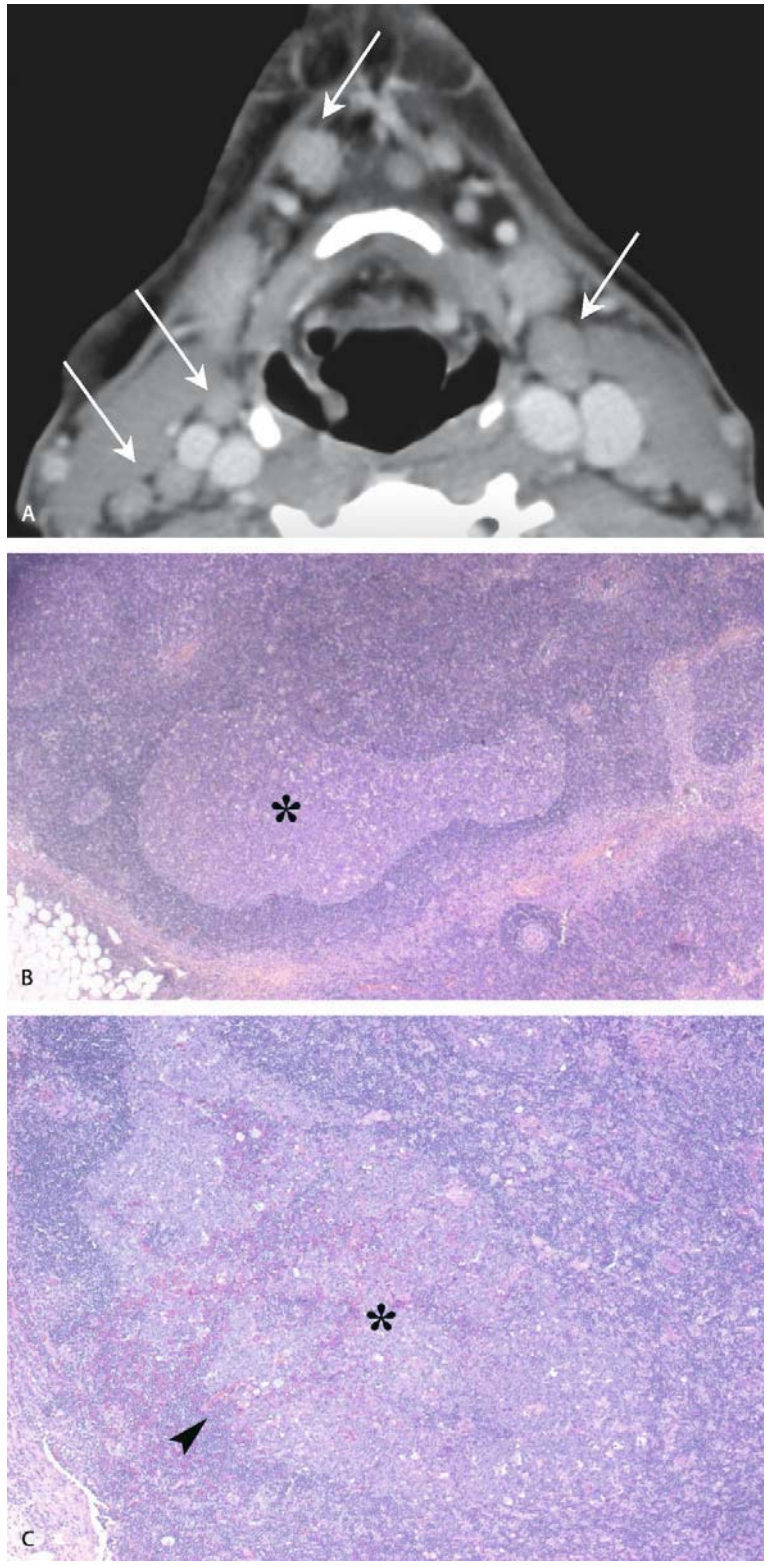

Fig. 36A–C. Persistent generalized lymphadenopathy in HIV-positive patients. **A** Axial contrast-enhanced CT image at the level of the hyoid bone in an HIV-positive patient shows multiple, slightly enlarged lymph nodes involving level I and II on both sides (*arrows*). **B** Photomicrograph of a cervical node shows large and irregular follicles with a map-like configuration (*asterisk*). **C** Persistent generalized lymphadenopathy showing folliculosis where the follicular center (*asterisk*) is invaded by small mantle-cell lymphocytes (*arrowhead*)

Cervical Chain Nodal Inflammation

When cervical lymph nodes react to inflammation, they enlarge and are referred to as *reactive adenopathy* [4, 10, 13, 43, 44]. This term is used for nodes less than 1.5 cm in maximum dimension, oval, with homogenous internal architecture and with variable enhancement (Fig. 35). Nodal enhancement may also be seen in a variety of inflammatory diseases [37, 45] (i.e., any type of acute infection, Castleman disease, Kikuchi disease).

In HIV infection, bilateral diffuse lymph node enlargement may be seen on either CT or MRI (Fig. 36). This imaging finding is non-specific and may be observed in a variety of viral infections, such as Epstein-Barr virus and cytomegalovirus. However, in the presence of lymphoepithelial cysts within the parotid glands, large adenoid tissue and diffuse lymph node enlargement, HIV infection should be strongly suggested.

If there is an acute virulent infection (i.e., staphylococcus), nodal necrosis may be seen at both CT or MR imaging. In this context, nodal necrosis corresponds histologically to an intranodal abscess, and the term "suppurative adenopathy" is used (Fig. 37). Suppurative adenopathy and malignant adenopathy can be radiologically indistinguishable (see also "Imaging Issues and Pathologic Considerations"). Extracapsular spread of infection from the suppurative lymph nodes results in *abscess* formation (Fig. 38). If the internal jugular chain

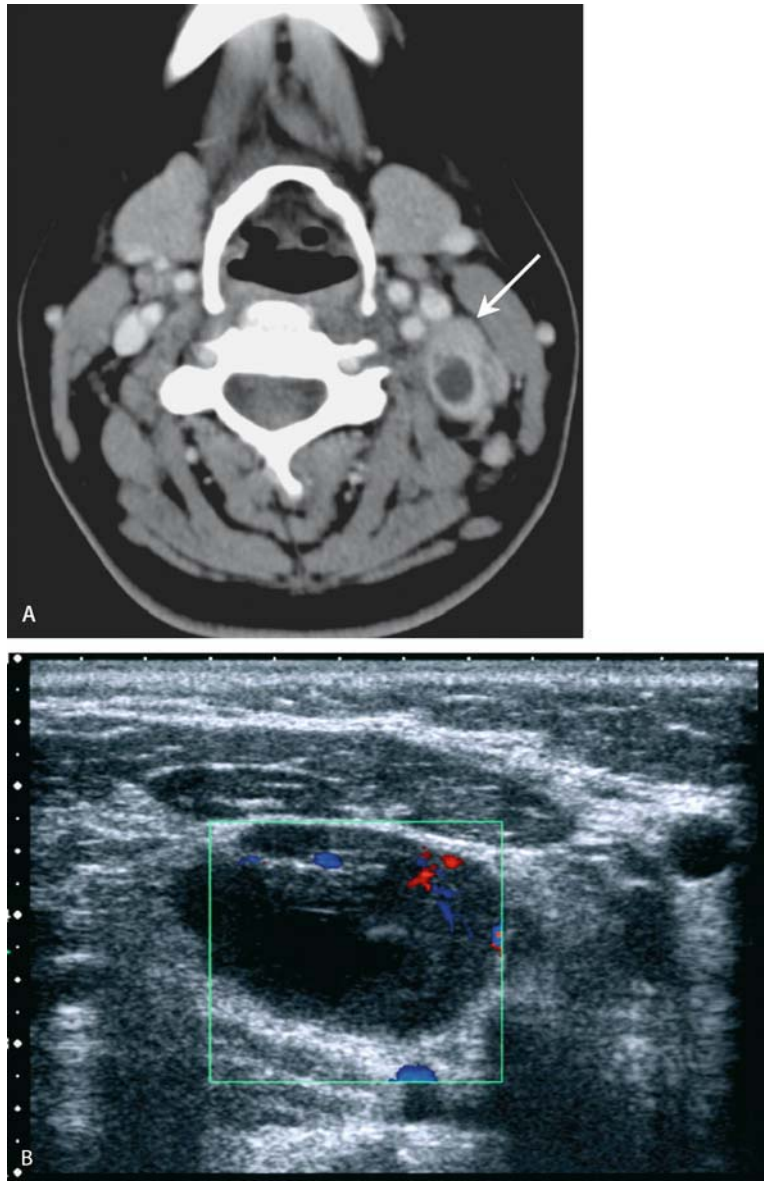

Fig. 37A, B. CT and US appearance of suppurative lymphadenitis in an 19-year-old girl. **A** Axial, contrast-enhanced CT image obtained at the level of the hyoid bone shows an enlarged level II lymph node with a central area of necrosis (*arrow*). **B** US performed in the same patient shows a lymph node with an anechoic central area. Fine-needle aspiration cytology performed under US guidance revealed suppurative lymphadenitis caused by *staphylococcus aureus*

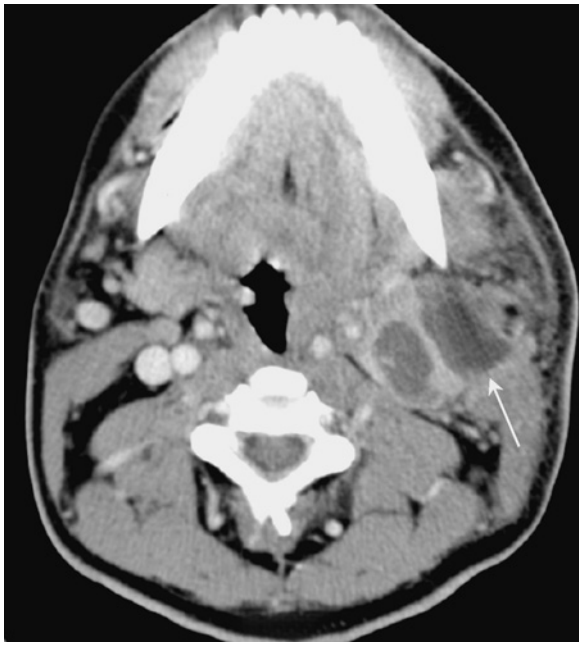

Fig. 38. Neck abscess: characteristic CT appearance. A multiloculated area of fluid density without gas collections and with thick, peripheral rim enhancement (*arrow*) displaces the neck vessels medially. Note compression of the internal jugular vein

is primarily affected the resulting abscess is located within the carotid space, whereas if the spinal accessory chain is primarily involved the abscess is located within the posterior cervical space. An abscess appears as a single or multiloculated area of fluid density with or without gas collections, usually expands the compartment that is involved, and typically demonstrates a peripheral rim enhancement. The abscess wall is usually thick (Fig. 38).

Tuberculous adenitis occurs when mycobacteria involve the nodes of the infrahyoid neck chains [37]. Tuberculous nodes have a characteristic CT appearance: they are multiple in presentation, with variable enhancement, areas of central nodal necrosis and globular calcifications (Fig. 39). Although nodal calcifications are most commonly seen in cervical tuberculous adenitis, metastatic papillary thyroid carcinoma, healed irradiated carcinomatous and lymphomatous nodes and healed necrotic abscessed nodes may also calcify. Egg-shell type calcifications are typically seen in silicosis, sarcoidosis, tuberculosis and amyloidosis.

Soft Tissue Infections

Bacterial soft-tissue infections may be classified, according to their invasive behavior, as (a) erysipelas (affecting the more superficial layers of the skin and cutaneous lymphatics), (b) cellulitis (extending more deeply into the subcutaneous tissue but sparing fascias), (c) necrotizing fasciitis (destruction of fasciae and fat, with or without skin necrosis, and with or without myonecrosis), and (d) myositis and myonecrosis [18, 20, 21]. The different above-defined forms of infectious soft-tissue inflammation have particular features on CT. The characteristic CT aspect of *cellulitis* includes thickening of the cutis and subcutis and increased density of fatty tissue with streaky, irregular enhancement. *Fasciitis* appears as thickening or enhancement of fasciae. *Myositis* appears as thickening and enhancement of cervical muscles, and myonecrosis may become visible as a hypodense area within enhancing portions of a muscle or as frank muscle disruption.

Necrotizing fasciitis of the head and neck is a severe, acute, and potentially life-threatening streptococcal or mixed bacterial soft tissue infection with a very rapid clinical evolution [3, 18, 20, 21]. It affects both immunocompetent and immunocompromised patients and, unless immediate surgical treatment is given, leads invariably to mediastinitis and fatal sepsis [30]. Radiologic–pathologic correlation studies have shown that four constant features are identified at CT [18, 20]. These radiographic features include: (a) cellulitis, (b) multiple fluid collections with or without gas in various neck compartments, (c) fasciitis (diffuse enhancement of neck fasciae) and (d) myositis (enhancement and thickening of cervical musculature) (Figs. 40, 41). Three additional features are found in two-thirds or less of patients with cervical necrotizing fasciitis at initial CT, namely gas collections, streaky enhancement of mediastinal fat and mediastinal fluid collections, and pleural and pericardial effusions. Because necrotizing fasciitis is often complicated by mediastinitis, which may be very difficult to detect on clinical grounds alone, CT of the chest as well as the neck should be performed when assessing cervical necrotizing fasciitis. The postoperative use of CT also has tremendous value. The identification of persistent fluid collections or progressing infection may only be possible with this modality, and findings on cervicothoracic CT often guide further treatment [18]. The characteristic histologic features of cervical necrotizing fasciitis include infiltration of the deep dermis, fasciae and muscular planes with bacteria and polymorphonuclear cells, and necrosis of fatty and muscular tissue with fragmentation and secondary degeneration of muscle fibers. Necrosis of fasciae is a characteristic feature. Correlation between histologic findings and CT scans reveals that most of the fluid collections seen in the cervical compartments correspond with liquefied necrotic tissue rather than with true abscesses [18]. Vasculitis and thrombosis of small vessels are seen histologically not only in areas that are obviously involved macroscopically on CT, but also in apparently healthy tissue adjacent to inflammatory lesions.

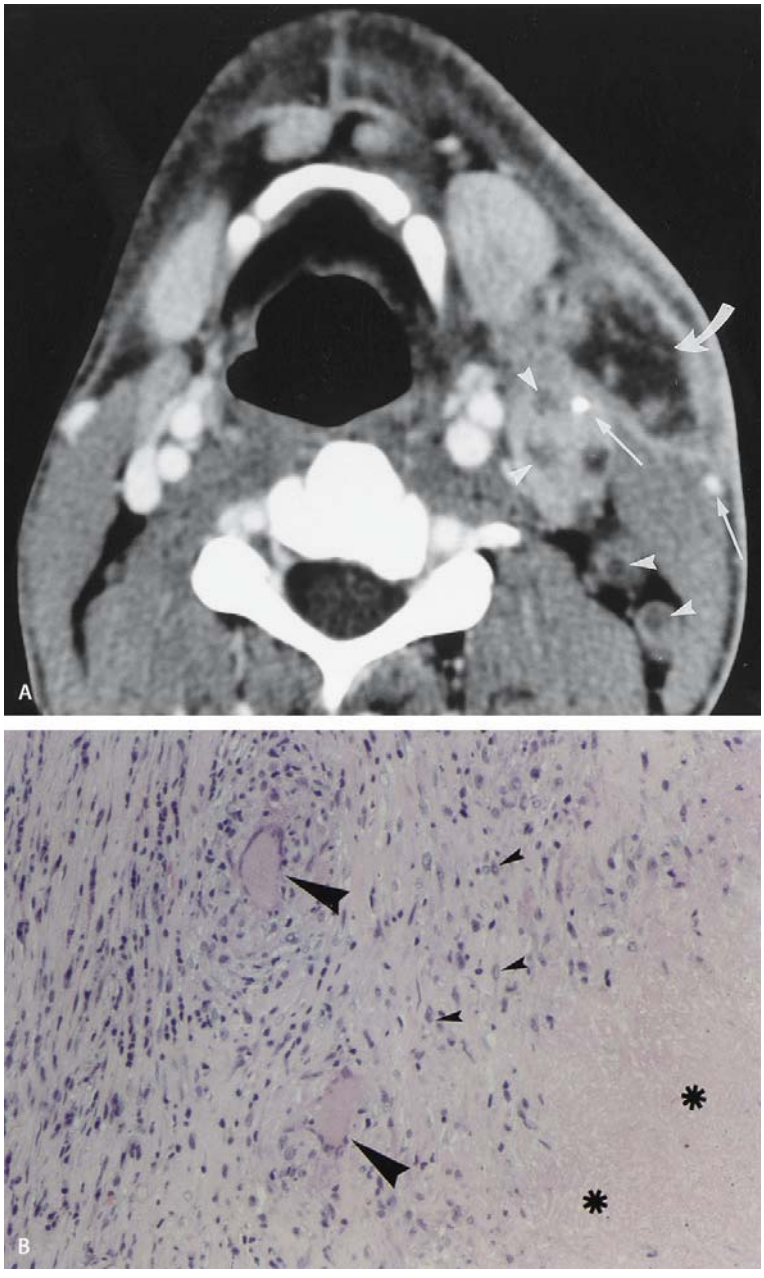

Fig. 39A, B. Tuberculous lymphadenitis: characteristic CT and histologic appearance. **A** Axial, contrast-enhanced CT image demonstrates multiple lymph nodes with inhomogeneous contrast enhancement, areas of nodal necrosis (*arrowheads*) and calcifications (*arrows*). Extracapsular spread of infection from the suppurative lymph nodes has resulted in abscess formation (*curved arrow*). **B** Photomicrograph of a tuberculous lymph node obtained by excisional biopsy demonstrates caseous necrosis (*asterisks*) surrounded by an inflammatory stroma containing fibrous tissue, epithelioid cells and Langhans giant cells (*arrowheads*)

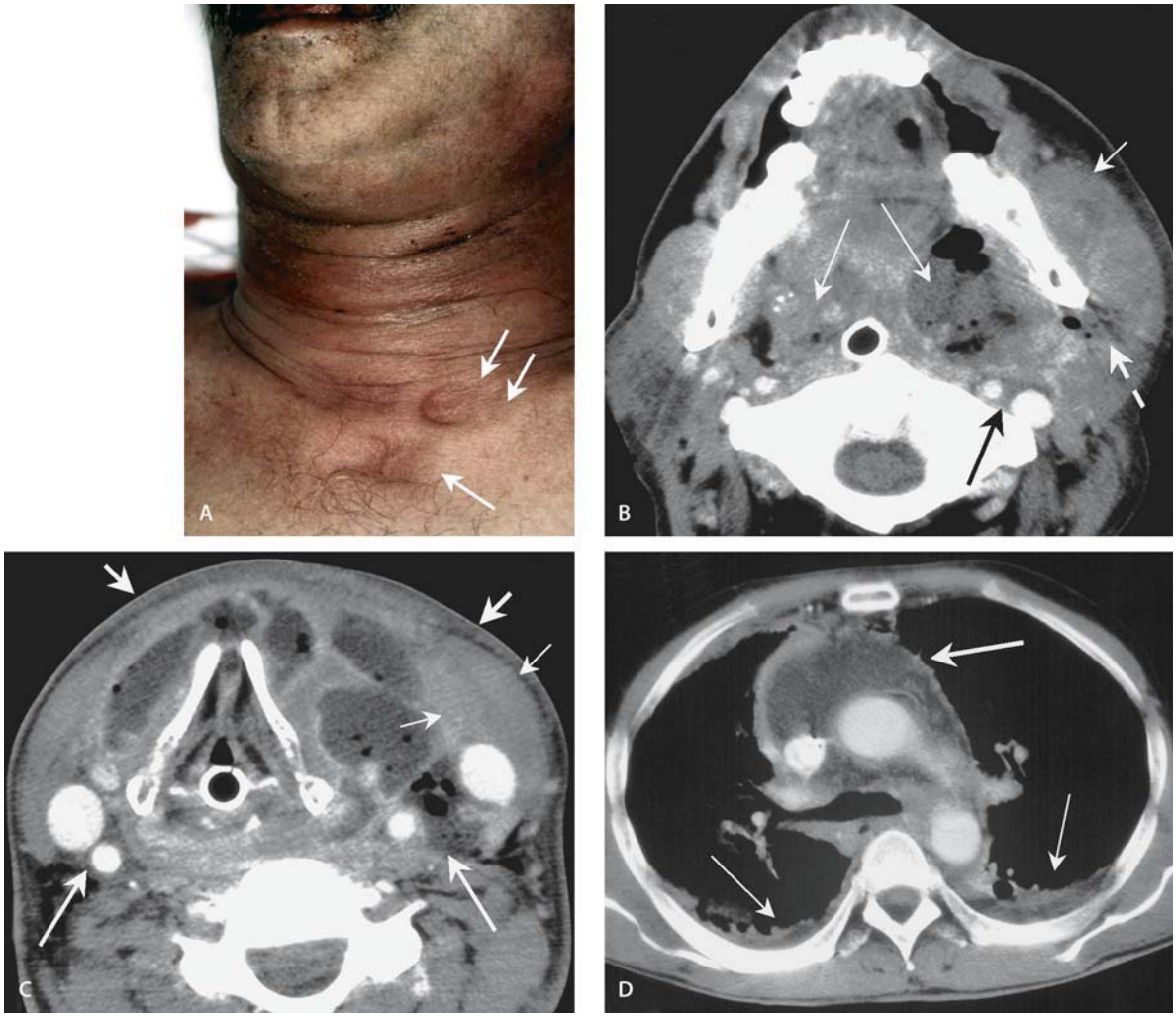

Fig. 40A–D. Necrotizing fasciitis of the neck caused by anaerobes: characteristic CT appearance. 58-year-old male with a history of dental treatment 7 days earlier presenting with fever, bilateral erythema of the neck with swelling and induration. Dyspnea necessitated intubation and mechanical ventilation at admission. Photograph of the neck at admission obtained prior to intubation (**A**) shows diffuse neck erythema and edema indicated by thumb prints (*arrowheads*). Contrast-enhanced CT images at the level of the oropharynx (**B**), supraglottic larynx (**C**), and tracheal bifurcation (**D**) in intubated patient show diffuse thickening of the cutis and subcutaneous fat, which has an increased density (*short arrows*). There is enhancement of the superficial layer of the deep cervical fascia along the left masticatory space and left sternocleidomastoid muscle (*thin short arrows*). Enhancement and inflammatory swelling of the left masseter muscle (in **B**) and left sternocleidomastoid muscle (in **C**), indicate myositis. Extensive fluid collections with gas within the strap muscles correspond with myonecrosis (**C**). Multiple fluid collections with gas are seen in both parapharyngeal spaces (*long arrows* in **B**), left masticator space (*dashed arrow* in **B**) and both carotid spaces (*long thick arrows* in **B** and **C**). A large fluid collection is seen in the anterior mediastinum (*thick arrows* in **D**) and there are bilateral pleural effusions (*thin arrows*). Cervicotomy and thoracotomy performed immediately after CT revealed necrotizing fasciitis and necrotizing mediastinitis. Reproduced with permission from [18]

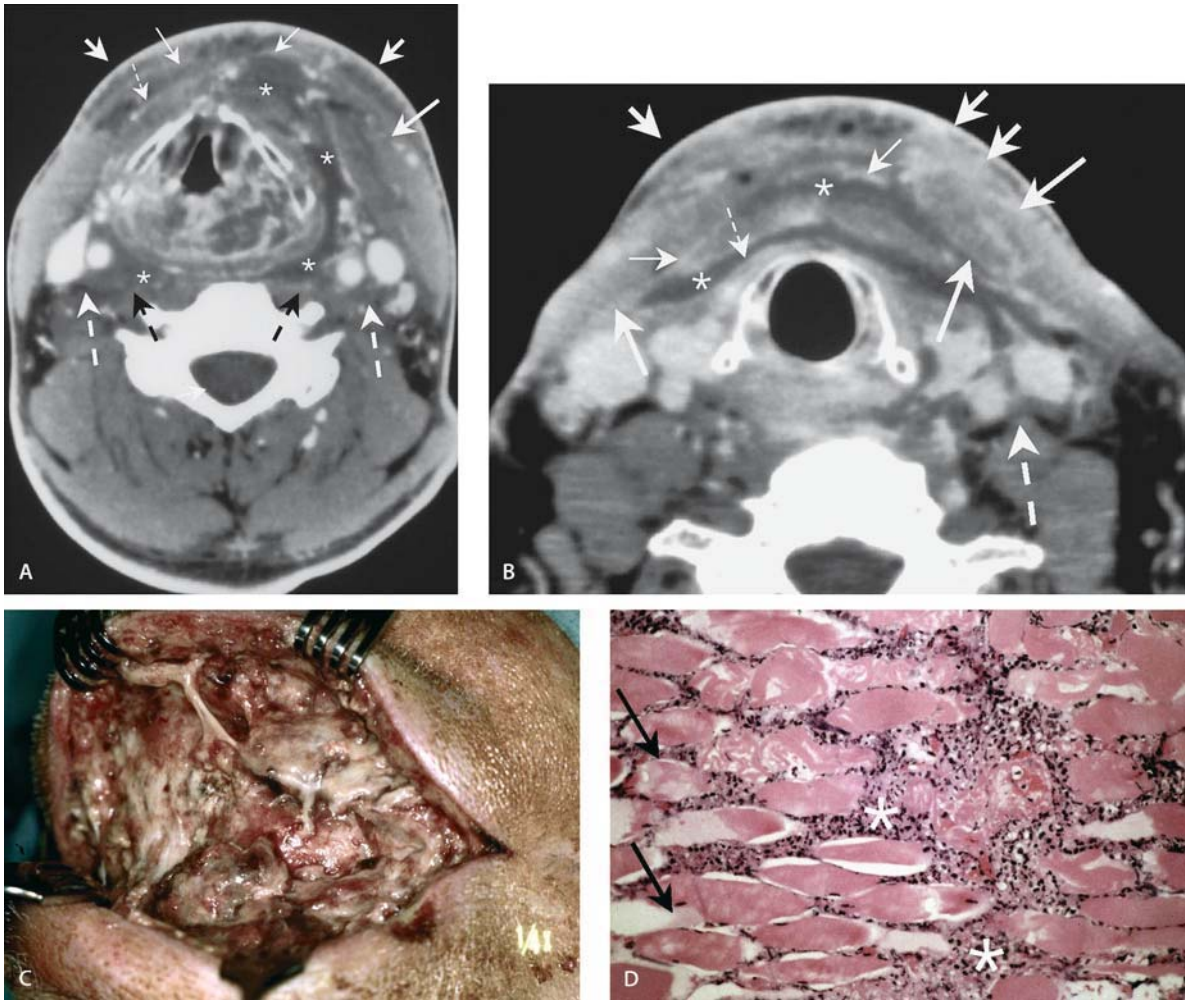

Fig. 41A–D. Necrotizing fasciitis of the neck: characteristic CT, surgical and histologic findings. 54-year-old male treated for tonsillitis 3 days earlier, presenting with dysphagia and diffuse, noncrepitant neck swelling without erythema or fever. Contrast-enhanced CT images at the level of the supraglottis (**A**) and subglottis (**B**) show diffuse, massive thickening of the skin (*short arrows*) and there is marked edema and a dirty appearance of the subcutaneous fat and platysma. Note enhancement of the investing fascia along the sternocleidomastoid muscles (*long white arrows*) and strap muscles (*short thin white arrows*), enhancement of visceral fascia (*short, thin dashed arrows*) and of the prevertebral fascia (*black dashed arrows*). Multiple fluid collections are seen along the inner border of the left sternocleidomastoid muscle, within the retropharyngeal space and along the strap muscles (*asterisks*). Note also inflammatory involvement of the left and right carotid space (*long, white dashed arrows*) and marked myositis of the left sternocleidomastoid muscle with diffuse swelling and irregular contrast enhancement. There is extensive inflammatory edema of the aryepiglottic folds. Photograph of the neck as seen during surgery (**C**) shows pus covering all fascia and neck muscles, which show diffuse swelling and diminished perfusion. Microscopic evaluation of surgical biopsy specimen of various muscles, subcutaneous fat and fascial layers revealed cervical necrotizing fasciitis. Microphotograph of a biopsy specimen from the strap muscles (**D**) shows fragmentation of muscle fibers (*arrows*) and severe inflammatory infiltrates with polymorphonuclear leukocytes and plasma cells between necrotic muscle fibers (*asterisks*). Reproduced with permission from [18]

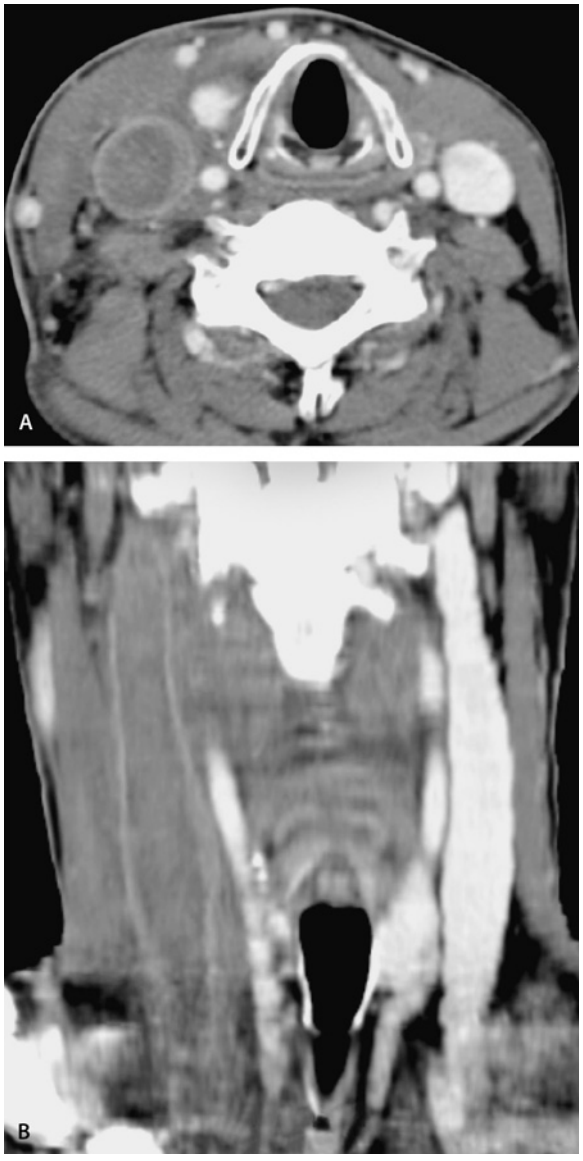

Fig. 42A, B. Septic thrombosis of the internal jugular vein: characteristic CT appearance. Axial contrast-enhanced CT image through the infrahyoid neck (**A**) and coronal 2D reconstruction from the volumetric data set (**B**) show complete thrombosis of the internal jugular vein, which is surrounded by inflammatory changes within the posterior cervical space and carotid space (note obliteration of fat)

Septic Thrombosis of the Internal Jugular Vein

Septic thrombosis of the internal jugular vein is the most common complication of deep neck infection. Patients typically present with fever, tenderness and swelling along the course of the internal jugular vein. Septic emboli may settle at distant sites, resulting in thrombosis of the lateral sinus, meningitis and pulmonary infarcts. Lemierre syndrome is a form of septic internal jugular vein thrombosis that occurs after tonsillitis. This disease was common in the preantibiotic era, leading often to sepsis and death. On CT, septic thrombosis of the internal jugular vein has a characteristic appearance: the low attenuation luminal thrombus is surrounded by an enhancing wall (Fig. 41). The perivascular soft tissues of the neck show an inflammatory reaction (cellulitis and myositis) of various intensity.

References

1. Ashcraft M, VanHerle A (1981) Management of thyroid nodules, I. Head Neck Surg 3:216–227
2. Ashcraft M, VanHerle A (1981) Management of thyroid nodules, II. Head Neck Surg 3:297–322
3. Bahna M, Canalis RF (1980) Necrotizing fasciitis (streptococcal gangrene) of the face. Arch Otolaryngol 106:648 - 651
4. Batsakis JG (1979) Tumors of the head and neck. Clinical and pathologic considerations. 2nd edition, Williams and Wilkins, Baltimore
5. Becker M (1988) Larynx and hypopharynx. Radiologic Clinics North Am 36:891–920
6. Becker M (1998) Diagnose und Stadieneinteilung von Larynxtumoren mittels CT und MRT. Der Radiologe 38:93–100
7. Becker M (2000) Oral cavity, oropharynx and hypopharynx. Seminars Roentgenol 35:21–30
8. Becker M (2000) Neoplastic invasion of laryngeal cartilage: radiologic diagnosis and therapeutic implications. Eur J Radiol 33:216–229
9. Becker M (2002) Malignant lesions of the larynx and hypopharynx. In: Hermans R, Baert AL, Sartor K (eds) Imaging of the larynx, diagnostic imaging series. Springer, Berlin Heidelberg New York pp 57–84
10. Becker M (2004) Other infrahyoid neck lesions. In: Mafee MF, Valvassori GE, Becker M (eds) Imaging of the head and neck. Thieme, New York, Stuttgart, pp 780–842
11. Becker M (2004) Larynx and hypopharynx. In: Mafee MF, Valvassori GE, Becker M (eds) Imaging of the head and neck. Thieme, New York, Stuttgart, pp 731–777
12. Becker M, Hasso AN (1996) Imaging of malignant neoplasms of the pharynx and larynx. In: Taveras JM, Ferruci JT (eds) Radiology: diagnosis-imaging, intervention, Lippincott, Philadelphia, pp 1–16
13. Becker M, Kurt AM (1999) Infrahyoid neck: CT and MR imaging versus histopathology. Eur Radiol 9 [Suppl 2]:53–68
14. Becker M, Moulin G, Kurt AM et al (1998) Non-squamous cell neoplasms of the larynx: radiologic-pathologic correlation. Radiographics 18:1118–1209
15. Becker M, Moulin G, Kurt AM et al (1998). Atypical squamous cell carcinoma of the larynx and hypopharynx: radiologic features and pathologic correlation. Eur Radiol 8:1541–1551
16. Becker M, Schroth G, Zbären P et al (1997) Long-term changes induced by high-dose irradiation of the head and neck region: imaging findings. Radiographics 17:5–26
17. Becker M, Zbären P, Delavelle J et al (1997) Neoplastic invasion of the laryngeal cartilage: reassessment of criteria for diagnosis at CT. Radiology 203:521–532

18. Becker M, Zbären P, Hermans R et al (1997) Necrotizing fasciitis of the head and neck: role of CT in diagnosis and management. Radiology 202:471–476
19. Becker M, Zbären P, Laeng H et al (1995) Neoplastic invasion of the laryngeal cartilage: comparison of MR imaging and CT with histopathologic correlation. Radiology 194:661–669
20. Becker M, Zbären P, Stoupis C, Marré S, Vock P, Rüfenacht DA (1996) Necrotizing fasciitis of the neck: radiologic-pathologic correlation. Radiographics 16:1527
21. Bisno AL, Stevens DL (1996) Streptococcal infections of skin and soft tissues. Current concepts. New Engl J Med 334: 240–245
22. Castelijns JA, Gerritsen GJ, Kaiser MC et al (1988) Invasion of laryngeal cartilage by cancer: comparison of CT and MR imaging. Radiology 167:199–206
23. Castelijns JA, Becker M, Hermans R (1996) The impact of cartilage invasion on treatment and prognosis of laryngeal cancer. Eur Radiol 6:156–169
24. Castelijns JA, van den Brekel MWM, Tobi H et al (1996) Laryngeal carcinoma after radiation therapy: correlation of abnormal MR imaging signal patterns in laryngeal cartilage with the risk of recurrence. Radiology 198:151–155
25. Curtin HD (1989) Imaging of the larynx. Current concepts. Radiology 173:1–11
26. Ducatman BS, Scheithauer BW, Piepgras DG, Reiman HM, Ilstrup DM (1986) Malignant peripheral nerve sheath tumors. A clinicopathologic study of 120 cases. Cancer 57:2006–2021
27. Einarsdottir H, Soderlund V, Larson O, Jenner G, Bauer HC (1999) MR imaging of lipoma and liposarcoma. Acta Radiol 40:64–68
28. Gallo A, Mocetti P, De Vincentiis M et al (1992) Neoplastic infiltration of laryngeal cartilages: histocytochemical study. Laryngoscope 102:891–895
29. Harnsberger HR (1995) Handbook of head and neck imaging. Mosby-Year Book, St. Louis
30. Harnsberger HR, Mancuso AA, Muraki AS et al (1984) Branchial cleft anomalies and their mimicks: CT evaluation. Radiology 152:739–748
31. Hu HP, Huang QL(1992) Signal intensity correlation of MRI with pathological findings in spinal neurinomas. J Comput Assist Tomogr 34:98–102
32. Kaban L, Mulliken JB (1986) Vascular anomalies of the maxillofacial region. J Oral Maxillofac Surg 44:201–213
33. Koeller KK, Alamo L, Adair CF, Smirniotopoulos JG (1999) Congenital cystic masses of the neck: radiologic-pathologic correlation. Radiographics 19:121–146
34. Mafee MF, Raofi B, Kumar A et al (2000) Glomus faciale, glomus jugulare, glomus tympanicum, glomus vagale, carotid body tumors and simulating lesions. Role of MR imaging. Radiol Clin N Am 38:1059–1076
35. Mancuso AA (1991) Evaluation and staging of laryngeal and hypopharyngeal cancer by computed tomography and magnetic resonance imaging. In: Silver CE (ed) Laryngeal cancer. Thieme, New-York, pp 46–94
36. Mazzaferri EL (1992) Thyroid cancer in thyroid nodules: finding a needle in the haystack. Am J Med 93:359–362
37. Moon WK, Han MH, Chang KH et al (1997) CT and MR imaging of head and neck tuberculosis. Radiographics 17: 391–402
38. Mukherji SK, Fatterpekar G, Castillo M, Stone JA, Chung CJ (2000) Imaging of congenital anomalies of the branchial apparatus. Neuroimaging Clin N Am 10:75–93
39. Mulliken J B, Glowacki J (1982) Hemangiomas and vascular malformations in infants and children: a classification based on endothelial characteristics. Plast Reconstr Surg 69:412–420
40. Reede DL (1996) Nodal and non-nodal neck masses. 2. Non-nodal neck masses. In: Som PM, Curtin HD, Holliday RA (eds) A special course in head and neck radiology. Radiological Society of North America, Chicago, pp 75–85
41. Sigal R (1998) Infrahyoid neck. Radiol Clin North Am 36: 781–99
42. Sobin LH, Wittekind C (2002) TNM classification of malignant tumors. UICC. 6th edn. Wiley-Liss, pp 30–41
43. Som PM (1996) Non-nodal neck masses. 1. Imaging cervical lymph nodes In: Som PM, Curtin HD, Holliday RA (eds) A special course in head and neck radiology. Radiological Society of North America, Chicago, pp 65–74
44. Som PM (1992) Update on imaging metastatic cervical lymph nodes: criteria and differential diagnosis. AJR Am J Roentgenol 158:961–969
45. Som PM, Biller H (1992) Kimura disease involving parotid gland and cervical lymph nodes. CT and MR findings. J Comput Assist Tomogr 16:320–322
46. Som PM, Brandwein M, Lidov M et al (1994) The varied presentations of papillary thyroid carcinoma cervical nodal disease: CT and MR findings. AJNR Am J Neuroradiol 15: 1123–1128
47. Som PM, Curtin HD, Mancuso AA (1999) An imaging-based classification for the cervical nodes designated as an adjunct to clinically based nodal classifications. Arch Otolaryngol Head and Neck Surg 125:388–396
48. Som PM, Curtin HD, Mancuso AA (2000) Imaging-based nodal classification for evaluation of neck metastatic adenopathy. AJR Am J Roentgenol 174:837–844
49. Steinkamp HJ, Hosten N, Richter C, Schedel H, Felix R (1994) Enlarged cervical lymph nodes at helical CT. Radiology 191: 795–798
50. Van den Brekel MWM (2000) Lymph node metastases: CT and MRI. Eur J Radiol 33:230–238
51. Van den Brekel MWM, Castelijns JA, Snow GB (1996) Imaging of cervical lymphadenopathy. Neuroimaging Clin North Am 6: 417–434
52. Van den Brekel MWM, Castelijns JA, Stel HV et al (1990) Detection and characterization of metastatic cervical adenopathy by MR imaging: comparison of different MR techniques. J Comput Assist Tomogr 14:581–589
53. Weber AL, Montandon C, Robson CD (2000) Neurogenic tumors of the neck. Radiol Clin N Am 38:1077–1090
54. Zadvinskis DP (1992) Congenital malformations of the cervicothoracic lymphatic system: embryology and pathogenesis. Radiographics 12:1175–1189
55. Zbären P, Becker M, Laeng H (1996) Pretherapeutic staging of laryngeal cancer: clinical findings, computed tomography and magnetic resonance imaging versus histopathology. Cancer 77:1263–1273
56. Zbären P, Becker M (1996) Schwannoma of the brachial plexus. Annf Otol Rhinol Laryngol 105:748–750
57. Zbären P, Becker M, Egger C (1997) Staging of laryngeal cancer: endoscopy, computed tomography and magnetic resonance versus histopathology. Eur Arch Otolaryngol 254: 117–122
58. Zbären P, Laeng H, Becker M (1995) Rare benign neoplasms of the larynx: rhabdomyoma and lipoma. ORL J Otorhinolaryngol Relat Spec 57:351–355

Part 3
Chest Radiology

HRCT – Pathologic Correlations in Chronic Diffuse Infiltrative Lung Disease

Martine Rémy-Jardin, Jacques Rémy, Dominique Artaud, Marc Fribourg, François Bonnel, Marie-Christine Copin, Bernard Gosselin

3.1

Contents

Introduction

The introduction of high-resolution computed tomography (HRCT) has revolutionized the radiologic approach to patients with suspected diffuse infiltrative lung disease (DILD). The requirements for performing HRCT include a current technology scanner, thin slices (1–2 mm), and reconstruction using a high spatial frequency algorithm. The scans are performed during breath holding at end-inspiration, and images are reconstructed using a matrix of 512 pixels with a 35–40 cm field of view. When necessary, a smaller field of view (12–24 cm) is used to further improve spatial resolution and expiratory scans may be indicated in order to identify air trapping.

An accurate interpretation of HRCT scans requires a detailed understanding of normal lung anatomy and of the pathological alterations in normal lung that occur in the presence of disease. Over the last 10 years, this technique has enabled precise analysis of the morphological changes occurring at the level of the lung parenchyma as well as better understanding of the distribution of abnormalities. On the basis of close correlations between HRCT findings and pathological lung abnormalities, it has been possible to clarify the terminology used to describe abnormal CT findings and thus to avoid nonspecific terms. In addition to the main categories of HRCT findings in DILD, the distribution of parenchymal abnormalities must be integrated when attempting to reach a diagnosis or differential diagnosis of diffuse lung disease using CT.

Among the predominant patterns of lung infiltration, ground glass opacity is one of the most difficult to diagnose and is particularly influenced by the CT technique used. The goals of this chapter are to review the CT criteria for accurate recognition of ground glass opacity, to describe the potential pitfalls in the recognition of this CT sign, and to clarify the significance of increased lung attenuation in DILD.

Patterns of Lung Infiltration in DILD

A number of HRCT findings may indicate the presence of DILD and they are usually divided into six main categories [1–10].

Abnormal Interfaces

This is a common manifestation of DILD. Abnormal interfaces between vessels, bronchi and visceral pleura with the surrounding parenchyma can be detected along the bronchovascular structures and in the subpleural areas. The subpleural areas are represented by the lung parenchyma immediately beneath the visceral pleura along the concavity of the chest wall and along the fissures and mediastinum.

Abnormal interfaces include regular thickening but also nodular and linear irregularity of the interfaces.

This CT sign reflects involvement of the axial and peripheral interstitium by the disease process.

Ground Glass Opacity

Areas of ground glass attenuation are defined as areas (a) of hazy and amorphous increased lung attenuation, (b) without obscuration of the underlying vascular markings and bronchial walls, (c) identified on thin HRCT sections, (d) taken at deep inspiration, and (e) photographed with wide window settings [11]. They can be diffuse, disseminated, or focalized in distribution, and of low or high attenuation values, leading to various difficulties in their CT identification. As underlined in the above definition, areas of ground glass attenuation are differentiated from airspace consolidation in that vessels and bronchi remain distinguishable throughout the areas of increased attenuation.

Linear Pattern

Two main categories of linear opacities can be isolated, namely septal and nonseptal lines. Septal thickening is best appreciated in the subpleural and juxtadiaphragmatic regions where septa are anatomically well developped. Thickened interlobular septa are identified as fine linear opacities or as a pattern of multiple polygonal lines when several secondary pulmonary lobules are involved. These linear or polygonal patterns must be in close contact with the centrilobular pulmonary artery, the distance from the vessel to the corresponding lobular border ranging from 3 to 5 mm. In lymphangitic carcinomatosis, the septa have a nodular or beaded appearance, whereas interstitial infiltration may also lead to regular septal thickening.

Nonseptal lines and numerous linear opacities can be identified in a large number of cases of DILD, according to their width, length, and location. The most frequently described are the so-called "subpleural curvilinear opacities," which are thin curvilinear lines observed within 1 cm of the pleural surface, paralleling the chest wall. Initially described in patients with asbestosis, they can also occur in idiopathic pulmonary fibrosis and many fibrotic forms of DILD.

Nodular Pattern

According to the size of these rounded opacities, they are usually described as micronodules (≤3 mm), nodules (3–20 mm), or masses (≥20 mm). Although CT recognition of nodules and masses is similarly obtained by conventional and HRCT scans, the identification of micronodules requires HRCT scans. It should be underlined that spiral CT may help solve interpretive difficulties with regard to the identification of ill-defined micronodules for low attenuation. This is a unique indication for a recently introduced technique called STS-MIP, i.e., sliding thin slice maximum intensity projection [12].

Among the various potential locations of micronodules, their predominant distribution in the subpleural regions on transverse CT scans is worth considering. Three main diagnoses are usually suggested by such a distribution: pneumoconiosis (silicosis and coal worker's pneumoconiosis), sarcoidosis, and pulmonary lymphangitic carcinomatosis [12]. This sign has no diagnostic value when observed as an isolated finding in the upper lung zones as it can be observed in 14% of healthy young adults. It should be emphasised that it is a common feature in smoker's lung due to the accumulation of anthracotic pigment at the base of interlobular septa [13].

Honeycombing

The HRCT findings consist of numerous thin or thick walled, cystic airspaces of various sizes. These lesions are related to parenchymal destruction by fibrosis of various etiologies. The cystic lesions can be surrounded either by normal lung parenchyma, such as in pulmonary lymphangioleiomyomatosis, or by abnormal lung infiltration, as usually observed in idiopathic pulmonary fibrosis.

From time to time, honeycomb cysts are too small to be identified on thin CT scans. In such circumstances, parenchymal fibrosis can only be suspected by indirect signs such as traction bronchiectases and/or bronchiolectases.

HRCT Features of Small Airway Disease

Inflammation of the bronchioles, also called bronchiolitis, results in two main categories of HRCT abnormalities: those resulting from thickening of the bronchiolar wall by inflammation and fibrosis and those resulting from obstruction of the bronchiolar lumen. Thickening of the bronchiolar wall may be identified on HRCT as centrilobular linear or branching opacities when seen along their long axis or as centrilobular nodular opacities when seen in cross-section. Obstruction of the bronchiolar lumen leads to reflex vasoconstriction, decreased attenuation, and air trapping. Blood flow redistribution to uninvolved lung leads to a pattern of mosaic attenuation and mosaic perfusion. The HRCT findings in any individual case depend on the relative degree of bronchial wall thickening and narrowing of the

bronchial lumen, and on the presence of other associated abnormalities.

Optimal assessment of bronchiolar abnormalities requires the use of HRCT technique. It may be recommended to select narrow window settings (window width, 1000 HU; window level: –800 HU) to facilitate the detection of focal areas of air trapping. Whenever the inspiratory scans do not provide sufficient morphological information, care should be taken to complete the inspiratory CT examination by additional expiratory scans, which can be obtained every 30 mm. An additional technical option is to perform STS-MinIP, which enables confident assessment of mild heterogeneity in lung attenuation whenever the latter finding is only suspected on HRCT scans [14].

Pathological Basis for Ground Glass Opacities

Several diseases may produce ground glass opacity or airspace consolidation as primary HRCT abnormalities, including interstitial pneumonias associated with active alveolitis, pulmonary edema, adult respiratory distress syndrome, viral, bacterial, tuberculous, fungal, and *Pneumocystis carinii* pneumonia, radiation pneumonitis, infarction and bronchoalveolar cell carcinoma. As pointed out by Webb et al. [15], the clinical findings and plain chest radiographic appearances of many of these diseases are often sufficient for diagnosis. However, in select cases, HRCT may contribute to patient management by detecting abnormalities when the chest radiographs are normal, or by clarifying confusing or equivocal radiographic findings, or by delineating the true extent of disease.

Assessment of Lung Density

The attenuation coefficient for a CT lung scan is a blended value that results from the complex interplay between tissues with highly differing densities including the airways and alveoli, soft tissues (bronchi, vessels, blood, and interstitium), and interstitial fluid. CT lung density measurements are also markedly influenced by physiologic patient-related and machine-related factors. The two most important physiologic patient-related parameters influencing lung density are the amount of air in the lung and the blood volume (Fig. 1).

Moreover, the CT technique used for parenchymal analysis may also influence recognition of abnormal lung density, as underlined by Zwirevich et al. who observed that low dose HRCT technique failed to identify ground glass opacities that were evident but subtle on the high dose scans [16].

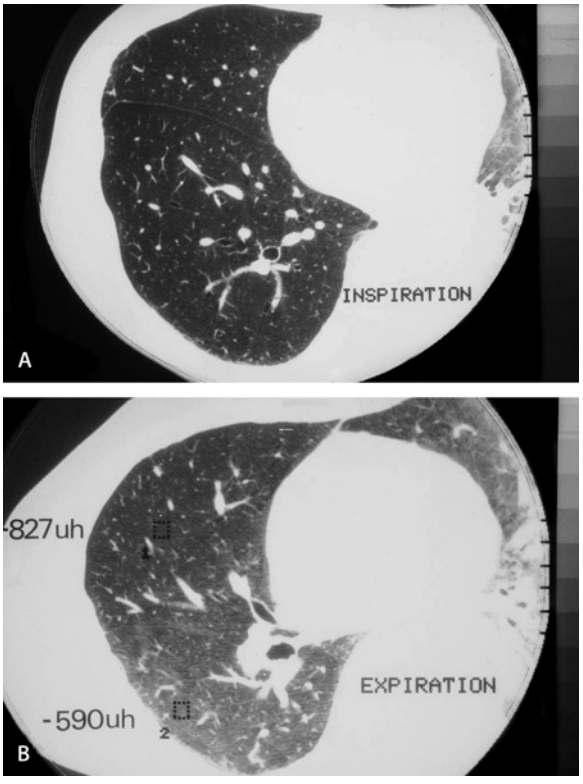

Fig. 1A, B. Target reconstructions of 1-mm HRCT sections through the right lower lobe in a normal patient. **A** The section is taken at deep inspiration and illustrates the HRCT appearance of normal lung parenchyma. **B** A diffuse ground glass opacity is a constant finding on normal HRCT scans at expiration, more pronounced in the gravity-dependent portion of the lung

Pitfalls in ground glass pattern recognition

A false interpretation of ground glass appearance may result from inadequate CT technique, incorrect interpretation of HRCT images, and/or physiologic variations.

Pitfalls Related to Technique

A ground glass pattern is a CT sign that can only be confidently diagnosed on HRCT images. Although abnormal lung density can be suspected on 5–10 mm collimation scans, only thin sections (1–2 mm) allow distinction of ground glass opacity from haziness, due to volume averaging of fine parenchymal abnormalities such as linear or micronodular opacities. Optimal assessment of ground glass opacities also requires the use of a large window width (range, 1500–2000 HU) and a high window level (range, –500 to –700 HU) for analysis of the lung parenchyma on HRCT images. By reducing window level and width, higher contrast is achieved

with subsequent magnification of vascular sections, bronchial walls (whether normal or not), and fissural thickening. The preferential magnification of small structures that is observed when using low window settings can create a pseudo-ground glass appearance that may lead the unwary observer to overdiagnose abnormal lung density.

Pitfalls Related to Interpretation

■ **Micronodular pattern.** Poorly marginated, small rounded opacities are readily recognized on cross-sectional images and should be differentiated from ground glass opacities by their nodular shape. Nevertheless, the distinction between diffusely distributed micronodules with poor margination and ground glass opacity may sometimes be difficult.

■ **Airspace consolidation.** Airspace consolidation is characterized by increased lung density with obscuration of the surrounding vascular markings and the presence of air bronchogram. Consolidation is observed when the pulmonary parenchyma is completely or almost completely airless as a result of complete filling of the alveolar spaces with liquid, cells, or tissue or secondary to atelectasis.

■ **Parenchymal density analysis.** In cases of mild and heterogenously distributed gradients of density in the lung parenchyma, it may be difficult or impossible to distinguish a pattern of normal lung intermingled with areas of ground glass attenuation from a pattern of areas of abnormally low attenuation against normal lung. To provide optimal assessment, the HRCT images must be interpreted in the context of clinical history, physical data, and pulmonary function tests. It should be noted that this interpretive difficulty may be solved by expiratory scans on which a homogeneous increase in lung attenuation is expected in normal lung.

Pitfalls Due to Physiologic Variations

■ **Ground glass opacity and expiratory scans.** Several investigators have demonstrated an attenuation coefficient gradient, related primarily to the influence of gravity on blood flow, that is normally present between the nondependent and dependent portions of the lung in the supine, prone, and lateral decubitus positions. Since a diffuse ground glass opacity is a constant CT finding on normal scans taken at or near end-expiratory volumes, any mild parenchymal abnormality can be easily overlooked or obscured by this physiological feature; therefore, CT scans must be performed during breath holding at end-inspiration.

■ **Dependent ground glass pattern.** Aberle et al. demonstrated subpleural dependent density on inspiratory scans in 17% of cases of a control group [17]. These abnormalities result from an increased amount of blood flow in dependent lung and from a gravity-dependent variation in the size of alveoli, which accounts for the decreased amount of air in the posterior lung.

Significance of Ground Glass Pattern

Because lung density results from the relative proportions of blood, gas, extravascular water, and pulmonary tissue, increased lung density may result from changes in the airspaces or the extravascular interstitial tissue (as in DILD) or from an increase in capillary blood volume.

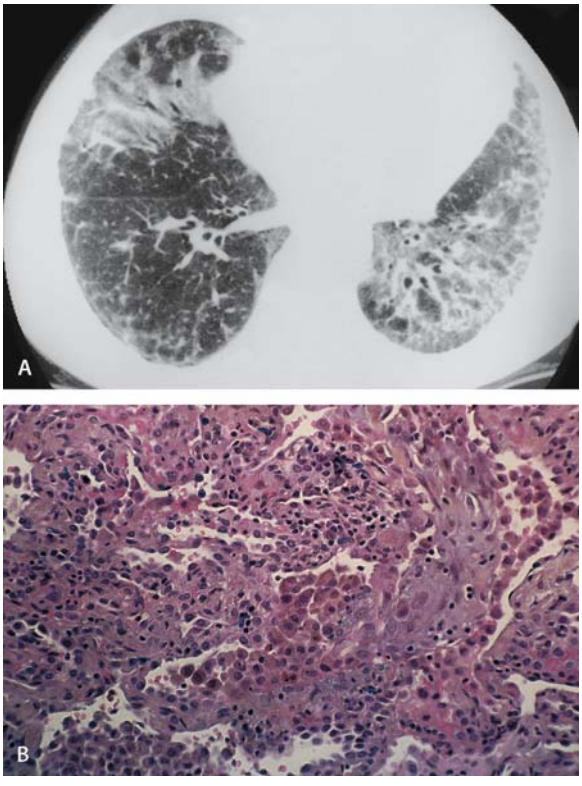

Fig. 2A, B. CT-pathology correlation in a patient with idiopathic pulmonary fibrosis and active alveolitis. (From [11], with permission.) **A** HRCT scan obtained through the lower lobes shows extensive ground glass pattern that preferentially involves the left lower lobe and the right middle lobe. Also note irregular linear opacities demonstrating the presence of fibrosis. An open lung biopsy sample was obtained in the lateral segment of the left lower lobe. **B** Photomicrograph of the corresponding histological section shows interstitial fibrosis and chronic inflammation, alveolar lining cell hypertrophy, and hyperplasia in association with enlarged macrophages filling alveolar spaces in a desquamative pattern. (Hematoxylin-eosin stain, original magnification × 400)

Pathological Basis

The infiltrative lung diseases are a heterogenous group of disorders of varied etiologies sharing similar histological features. These diseases usually involve the lung, in a multifocal rather than diffuse manner, beginning with an accumulation of inflammatory cells in the alveolar septa and airspaces and often culminating in severe fibrosis of the interstitium, the supporting structure of the lung [18]. Although the ground glass pattern is not a specific sign of DILD as further developed, there is considerable interest in demonstrating its presence on HRCT images in patients with suspected or known DILD because it often reflects mild parenchymal alterations, unsuspected on the radiographs, and it may provide information about disease activity and prognosis.

The best known significance of ground glass opacity is as a reflection of an active inflammatory process, representing the acute phase of lung injury often related to alveolitis. During this phase, two main pathological features are observed, involving both the interstitium and the airspaces in the majority of chronic DILD: abnormal thickening of the alveolar wall interstitium and incomplete filling of the alveolar spaces with inflammatory cells, cellular debris, and edema. Changes occurring during this phase of injury reduce the amount of air in affected areas without any architectural destruction, thus resulting in areas of increased lung density or "ground glass pattern" (Fig. 2). This CT pattern may sometimes reflect isolated mural inflammation without airspace filling (Fig. 3).

Ground glass opacity may also result from the chronic changes that are known to occur following the acute phase of lung injury in the absence of complete healing corresponding to lung fibrosis with or without lung distortion (Fig. 4). This CT interpretation is based on the

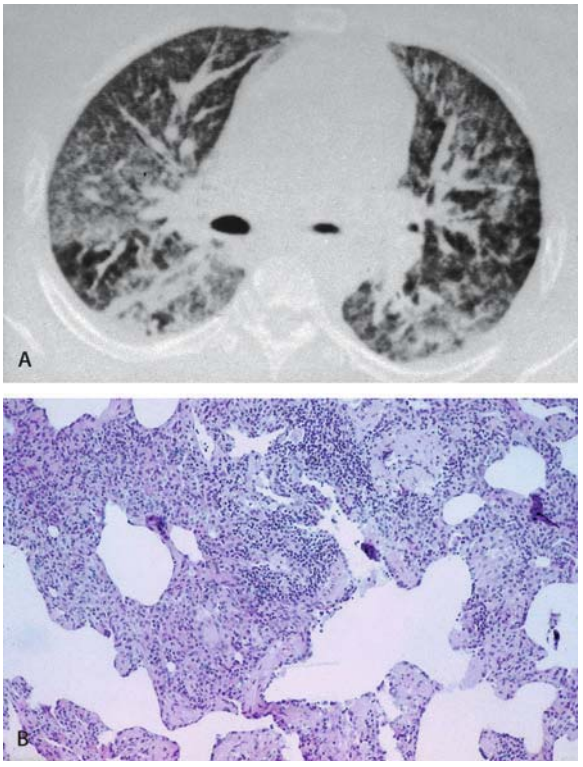

Fig. 3A, B. CT-pathology correlation in a 17-year-old patient with idiopathic pulmonary fibrosis and severe dyspnea (From [11], with permission.) **A** HRCT scan through the upper lobes demonstrates bilateral multifocal distribution of ground glass opacity and areas of airspace consolidation, posteriorly situated. Open lung biopsy sample was obtained in the anterior segment of the right upper lobe. **B** Photomicrograph of the corresponding histological section shows interstitial fibrosis associated with an intense infiltrate of lymphocytes and plasma cells. Ground glass opacities in this patient were due to purely interstitial changes. (Original magnification × 400)

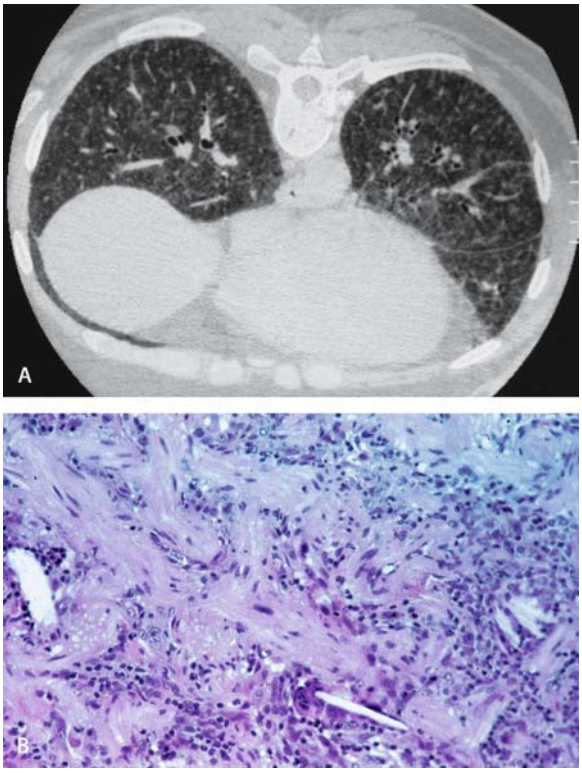

Fig. 4A, B. CT-pathology correlation in a patient with idiopathic pulmonary fibrosis (From [11], with permission.) **A** HRCT scan obtained in the prone position through the lower lobes shows diffuse and uniform ground glass opacity associated with a few ill-defined micronodules. Open lung biopsy sample was obtained in the posterior segment of the left lower lobe. **B** Photomicrograph of the corresponding histological section demonstrates parenchymal collapse in association with intense smooth muscle proliferation and cellular infiltration by multinucleate giant cells with cholesterol deposits and numerous macrophages. Ground glass opacities in this patient were mainly due to chronic changes. (Original magnification × 400)

knowledge of pathological changes observed during the chronic forms of DILD [18–20]. The fibroblastic reaction associated with residual alveolar infiltrates and debris leads to reduction of the amount of air. By similar mechanisms as previously described in the acute phase of lung injury, these changes can be responsible for ground glass opacity. In the latest stages of lung response to injury, the alveolar structure is destroyed and the interstitium is no longer recognizable as a distinct entity. Healing by fibrosis leads to formation of dense areas of collagen interspersed with regions of parenchymal destruction; the resultant cystic and destructive changes constitute the hallmarks of late-phase lung disease. When cystic changes are within the resolution capabilities of HRCT, a classic honeycomb pattern appears in which cystic airspaces and traction bronchiectasis are identified. When cystic changes are too small to be detected by thin HRCT images, volume averaging of the tiny parenchymal cysts that characterize the microcystic honeycomb pattern may lead to ground glass opacity. Bronchi in areas of lung distortion appear dilated and deformed secondary to this underlying destructive process, which involves the peribronchial connective tissue sheaths [20].

The presence of so-called traction bronchiectasis and bronchiolectasis is a reliable indirect sign of lung destruction on CT images even in the absence of typical honeycombing. In the absence of open lung biopsy and subsequent CT-pathology correlation, the only possibility that allows the radiologist to assess lung fibrosis is to identify traction bronchiectasis within areas of ground glass attenuation, a direct result of the fibrotic process (Fig. 5).

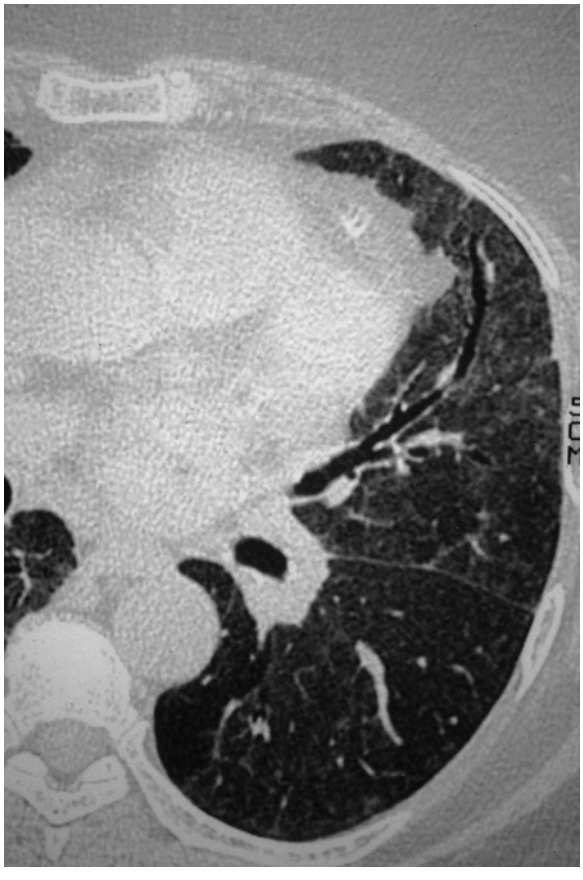

Fig. 5. Target reconstruction of 1-mm HRCT section through the lingula in a patient with systemic sclerosis. Note the presence of a homogeneous increase in lung attenuation in the left lung, more pronounced in the lingula, with the concurrent presence of bronchiolectasis. Ground glass opacities in this patient result from a fibrotic process

Clinical Impact

Ground glass opacity, as an isolated CT finding or in association with other parenchymal abnormalities, has been reported in various chronic DILDs, including alveolar proteinosis, sarcoidosis, fibrosing alveolitis, bronchiolitis obliterans with organizing pneumonia (BOOP), chronic eosinophilic pneumonia, and radiation pneumonitis. Grenier et al. demonstrated that ground glass opacity was among the discriminant radiographic and CT findings for the correct diagnosis in five groups of DILDs, including sarcoidosis, histiocytosis X, silicosis, and a fifth group of miscellaneous diseases [21]. However, ground glass appearance has only a moderate discriminant value in differentiating among the five groups when considering radiographic and CT findings ranked by stepwise discriminant analysis.

The most important clinical application of ground glass identification in chronic DILD is the assessment of disease activity. Evaluating the cellularity and degree of fibrosis of the pulmonary parenchyma pathologically is the foundation on which the prognosis and response to treatment are based. The cellular alveolar reaction is not only the earliest finding in many DILDs but it is also the "active" inflammatory lesion. Information about the presence of alveolitis helps stage disease activity and predict the likelihood of reversal of functional impairment and response to therapy. A patient with extensive interstitial lung disease composed of active alveolitis and mild fibrosis has a better chance of benefiting from therapy than a patient with disease of similar radiographic extent but composed of extensive fibrosis and little residual alveolitis.

Open lung biopsy is an invasive procedure not routinely indicated in chronic DILD. In most cases, a noninvasive approach is used to evaluate disease activity, such as bronchoalveolar lavage (BAL), gallium scanning, and/or CT scanning [22–24]. Although gallium scanning is of limited use in fibrosing alveolitis, BAL has been reported to be useful in characterizing this finding. However, discrepancies between BAL results and open lung bi-

opsies suggest that the cellular sampling obtained by BAL does not systematically reveal what happens in the alveolar spaces but may reflect the inflammatory reaction occurring in the bronchiolar and peribronchiolar areas [25]. In patients with interstitial lung disease of unknown etiology, there are insufficient data to suggest that BAL provides information that can be used to determine the need for therapy, to predict response to therapy, and to determine when therapy can be discontinued [26].

Since disease activity is reflected by interstitial and intra-alveolar cellularity, it was postulated that such activity might result in opacification of airspaces on CT scans and that the degree of increased density compared with the surrounding parenchyma might indicate the degree of inflammatory disease activity [27]. The role of CT as predictor of disease activity has been reported mainly with reference to fibrosing alveolitis and sarcoidosis [27–29]. Muller et al. demonstrated among patients with fibrosing alveolitis that when there was marked disease activity seen pathologically, there was patchy, predominantly peripheral, opacification of airspaces; all patients evaluated by HRCT with marked or mild disease activity pathologically were correctly categorized by these observers [28]. In sarcoidosis, the pathological correlate of focal increase in lung density on HRCT is not clear, possibly due to widespread interstitial granulomata of a size below the limits of resolution of the HRCT technique or to interstitial and alveolar inflammation. Because ground glass opacity may also reflect the presence of extensive parenchymal fibrosis with minimal alveolitis, this sign has limited specificity. As CT accurately reflects the changes seen macroscopically on the lung specimen, identification of areas of ground glass attenuation is potentially useful in guiding the surgeon to the biopsy site.

Retrospective assessment of disease activity remains possible on follow-up CT scans when decrease or complete resolution of ground glass opacity is observed spontaneously or after treatment [29, 30]. Conversely, stability of ground glass opacity after steroid treatment allows retrospective assessment of fibrosis. When follow-up CT scans demonstrate sequential replacement of ground glass opacity by typical honeycombing, the initial CT finding may correspond to pathological changes observed in the acute phase of lung injury, or it may be due to partial volume averaging with thickened interstitial tissue or a microcystic honeycomb pattern on HRCT images.

Because macrophage alveolitis is a constant finding in the smoker's lung, it is not surprising to identify areas of ground glass attenuation on CT scans of smokers. In a study designed to assess lung changes in apparently healthy smokers on CT scans, Remy-Jardin et al. observed areas of ground glass attenuation in 21% of smokers but failed to identify this CT sign in nonsmokers [31] (Fig. 6). Although increased lung attenuation is related to increased cellularity within alveoli in smokers [32] (Fig. 7), its pattern also reflect areas of disparate lung perfusion resulting from air trapping in patients with bronchiolitis, especially when disseminated. Increased regional differences in lung attenuation on expiratory CT scans help demonstrate this interpretaion of heterogenous lung attenuation in smokers.

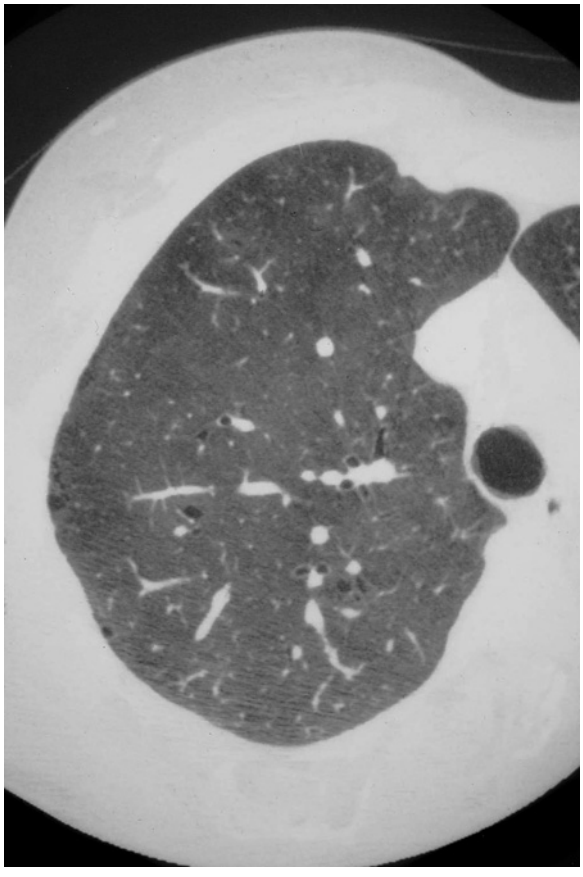

Fig. 6. HRCT scan at the level of the right upper lobe in a 25-year-old smoker shows areas of ground glass attenuation diffusely distributed through the lung and responsible for the darker air bronchogram. Note the small emphysematous areas in the subpleural axillary region and the central part of the lung. (From [31], with permission)

Differential Diagnosis of Ground Glass Pattern

Ground Glass Pattern in Acute Lung Infiltration

Ground glass opacity may be observed in all situations characterized by acute lung infiltration in acutely or subacutely ill patients. This CT sign is thus considered to represent mild to moderate alveolar filling, preceding the stage of completely airless alveoli that leads to airspace consolidation. HRCT can detect a ground glass pattern (i.e., airspace processes) before it becomes ap-

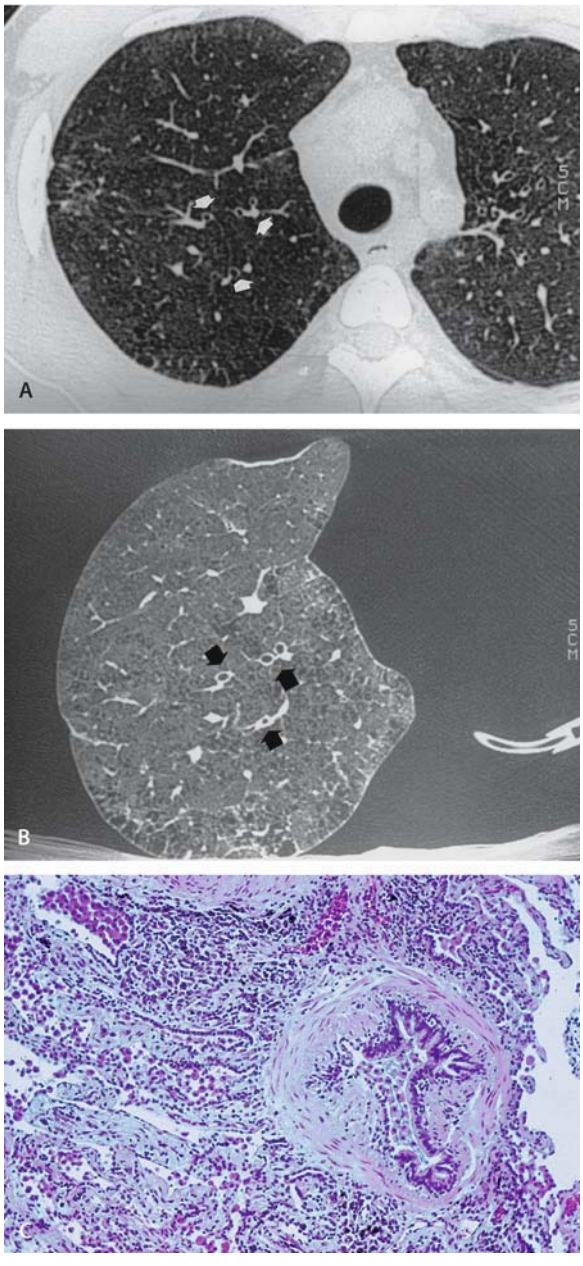

Fig. 7A–C. Areas of ground glass attenuation: CT-pathologic correlation in a 48-year-old male smoker (45 pack-years) in whom surgery was indicated for lung carcinoma (From [31], with permission). **A** Targeted CT scan at the level of the right upper lobe demonstrates minimal diffuse attenuation alterations, interpreted as mild and homogeneous increase in lung density, diffusely distributed through the lung, with adjacent emphysematous changes. Note axillary infiltrate corresponding to the upper part of the tumor (*arrows* indicate subsegmental bronchovascular sections in the apical and posterior segments). **B** Targeted CT scan of the inflated right upper lobe obtained at the same level as in a confirms the presence of diffuse ground glass lesions and emphysema, the latter observed to a higher extent throughout the entire section (*arrows* indicate subsegmental bronchovascular sections in the apical and posterior segments). **C** Photomicrograph of the corresponding histological section shows bronchiolar and alveolar abnormal filling, with brown pigmented macrophages. (Hematoxylin-eosin stain; original magnification × 80)

parent on plain films, providing extra time compared to eventual detection by plain films and accurately pinpointing abnormal areas for possible bronchoscopic sampling.

In immunocompromised patients, various infectious processes may cause increased lung attenuation from mild ground glass pattern to dense consolidation according to the level of lung infiltration. The greater sensitivity of CT compared to chest radiography in detecting parenchymal changes at a time when the patient has significant respiratory dysfunction and a normal chest radiograph may lead to consideration of CT as an effective monitoring tool to guide diagnostic and therapeutic decisions.

Pulmonary hemorrhage may also be a cause of ground glass opacity on HRCT images, demonstrated either clinically by means of bronchoalveolar lavage-CT correlation or experimentally. In the early CT evaluation of patients with hemoptysis, detection of ground glass opacity may help localize the bleeding site, which may be of value when fiberoptic bronchoscopy is noncontributory.

A segmental or lobar distribution of ground glass attenuation should suggest the possibility of recent bronchoalveolar lavage, especially if it is observed in the right middle lobe.

Ground Glass Pattern of Hemodynamic Origin

Regional alterations in pulmonary blood flow and subsequent changes in regional blood volume are common hemodynamic factors shared by various clinical situations in which ground glass opacity can be seen on HRCT images. In most cases, adjacent areas of hyper- or hypoperfused lung have great differences in attenuation, and the presence of increased vascular diameters through the abnormal lung density will help identify ground glass opacity of hemodynamic origin.

■ **Redistribution of blood flow in pulmonary diseases.** Ground glass opacity identified in patients with chronic obstructive lung disease (COPD) may be the result of regional increased blood flow secondary to widespread narrowing of vessel lumina in the pulmonary arterial bed due to vascular smooth muscle contraction and/or structural changes in vessel walls [32]. Alterations in regional blood flow affect lung attenuation by increasing and decreasing blood volume in the capillary bed, a phenomenon previously described as mosaic oligemia [33]. Moreover, the denser areas representing hyperperfused lung may appear with even higher contrast than the surrounding lung when destructive changes, air trapping and oligemic changes act as cofactors responsible for areas of abnormally low attenuation. These regional differences in lung attenuation in patients with COPD are increased on expiratory scans.

■ **Chronic thromboembolic disease.** Ground glass opacity in patients with chronic thromboembolic disease is often sharply demarcated with lobular borders; increased vascular sections through the abnormal lung density have been a constant feature. When branches of the arterial bed are occluded, there is a constant increase in blood flow in the remaining patent areas in order to maintain the cardiac output. There are two additional but usually transient factors that explain the regional increase in lung attenuation immediately after pulmonary arterial occlusion: edema and pulmonary hemorrhage. These are known to occur in the occluded area with subsequent resolution, except when pulmonary embolism is followed by parenchymal infarction. A third element potentially responsible for increased lung density in occluded areas is the development of systemic collateral supply in the occluded area that enters the pulmonary circulation distal to the site of obstruction, angiographically observed as antegrade systemic-to-pulmonary arterial shunts [34].

■ **Postcapillary pulmonary hypertension.** In addition to the enlargement of proximal pulmonary arterial branches, CT may help identify morphological changes suggestive of postcapillary pulmonary hypertension. This is usually suggested by the identification of CT features of interstitial and/or alveolar edema, including septal lines and abnormal lung attenuation varying from ground glass opacities to consolidation. These parenchymal abnormalities are observed with the concurrent presence of enlarged pulmonary veins, sometimes associated with pleural effusion.

Over the last few years, several studies have shown that a mosaic pattern of lung attenuation can be seen in patients with pulmonary hypertension of various causes [35]. In attempting to determine whether infiltrative, airway, or vascular lung disease is the cause of mosaic attenuation on thin-section CT scans of the lung, one may pay attention to the size of the pulmonary vascular sections within the areas of ground glass attenuation and search for air trapping. The areas of increased lung attenuation can be attributed to blood flow redistribution when the size and number of vessels in the areas of increased attenuation are increased compared with those in the areas with normal or decreased attenuation in the absence of air trapping [11, 36-38]. As recently demonstrated by Worthy et al. [38], it should be emphasized that, while the diagnoses of infiltrative lung disease and airway disease are frequently correct and confident, vascular disease is more difficult to suggest on thin-section CT scans as the cause of areas of ground glass attenuation.

■ **Pulmonary edema.** Detection of subclinical forms of pulmonary edema has been aided by understanding the findings on CT of the chest in experimental pulmonary edema [39]. In patients with raised pulmonary venous pressure due to left heart failure but no auscultatory signs, CT may detect pulmonary edema by demonstrating pulmonary extravascular lung water either in the interstitial tissue (i.e., interlobular septal thickening) or in the alveoli (i.e., featureless or sharply demarcated areas of ground glass opacity); there may also be dilated vessels through the abnormal lung density due to hemodynamic changes. The distribution is usually bilateral and almost symmetrical, but distribution of parenchymal abnormalities must be interpreted in the context of the presence or absence of capillary hypertension, since obstructive arterial changes are known to interfere with regional distribution of blood flow.

Identical CT findings are expected to be found in pulmonary edema of any etiology, that is, in all situations where the capacity of the lung lymphatics to drain capillary transudate is exceeded, including venous and lymphatic obstruction, increased capillary permeability, and hypoproteinemia.

In patients with acquired left heart disorders, CT can demonstrate several parenchymal abnormalities reflecting an abnormal accumulation of extravascular lung water secondary to elevated pressure in the pulmonary circulation, i.e., hydrostatic pulmonary edema. Abnormalities related to interstitial edema visible on HRCT scans include interlobular septal thickening and peribronchovascular interstitial thickening, whereas centrilobular areas of ground glass attenuation or consolidation reflect underlying pulmonary edema, both categories of lung changes variably associated with increased pulmonary vascular caliber, pleural effusions, or thickening of fissures [11, 40]. Although hydrostatic pulmonary edema can have a predominantly central and gravitational distribution, this is not always the case as lung infiltration is influenced by preexisting pleural and/or parenchymal disorders [41, 42].

As recently underlined by Storto et al. [40], the diagnosis of hydrostatic pulmonary edema is usually based on clinical information, conventional chest radiographic findings, and response to treatment and does not require HRCT. However, recognizing the appearance of hydrostatic pulmonary edema on HRCT can be important as the edema can mimic other diseases or can occur as an unsuspected finding in patients undergoing HRCT for other indications [43, 44].

Conclusion

The accurate evaluation of DILD requires interpretation of the radiological features in the light not only of the clinical, functional, biological, but also of pathological data, whether these derive from routine light microscopy, bronchoalveolar lavage material, or ultrastructural or immunological studies.

The radiologist must be aware of the pathological changes commonly encountered, and only close cooperation between radiologists and pathologists can ensure improvement in HRCT descriptions.

References

1. Muller NL (1991) Differential diagnosis of chronic infiltrative lung disease on HRCT. Sem Roentgenol 26:132–142
2. Murata K, Khan A, Rojaska, Herman PG (1988) Optimization of computed tomography technique to demonstrate the fine structure of the lung. Invest Radiol 23:170–175
3. Remy-Jardin M, Remy J, Dupont S, Chabanne B, Duhamel A (1991) Diffuse infiltrative lung diseases: comparison between conventional 10 mm and 1.2 mm HRCT. Radiology 181: 157–162
4. Austin JM, Muller NL, Friedman JP, Hansell DM, Naidich DP, Remy-Jardin M, Webb WR, Zerhouni EA (1996) Glossary of terms for computed tomography of the lungs: recommendations of the Nomenclature Committee of the Fleischner Society. Radiology 200:327–331
5. Remy-Jardin M, Giraud F, Remy J, Copin MC, Gosselin B, Duhamel B (1993) Importance of ground glass attenuation in chronic diffuse infiltrative lung disease: pathologic-CT correlation. Radiology 189:693–698
6. Stein MG, Mayo JR, Muller NL, Aberle DR, Webb WR, Gamsu G (1988) Pulmonary lymphangitic spread of carcinoma: appearance on CT scans. Radiology 151:371–375
7. Remy-Jardin M, Beuscart R, Sault MC, Marquette CH, Remy J (1990) Subpleural micronodules in diffuse infiltrative lung diseases: evaluation with thin section CT scans. Radiology 177:133–139
8. Myers JL, Colby TV (1993) Pathologic manifestations of constrictive bronchiolitis, cryptogenetic organizing pneumonia and diffuse panbronchiolitis. Clin Chest Med 14:611–622
9. Muller NL, Miller RR (1995) Diseases of the bronchioles: CT and histopathologic findings. Radiology 196:3–12
10. Gruden JF, Webb WR, Warnock M (1994) Centrilobular opacities in the lung on high-resolution CT: diagnostic considerations and pathologic correlation. AJR 162:569–574
11. Remy-Jardin M, Remy J, Giraud F, Wattinne L, Gosselin B (1993) Computed tomography assessment of ground glass opacity: semiology and significance. J Thorac Imaging 8: 249–264
12. Remy-Jardin M, Remy J, Aartaud D, Deschildre F, Duhamel A (1996) Diffuse infiltrative lung disease: clinical value of sliding thin-slab-maximum intensity projection CT scans in the detection of mild micronodular patterns. Radiology 200: 333–339
13. Remy-Jardin M, Remy J, Gosselin B, Becette V, Edme JL (1993) Lung parenchymal changes secondary to cigarette smoking: Pathologic-CT correlations. Radiology 186:643–651
14. Remy-Jardin M, Remy J, Gosselin B, Copin MC, Wurtz A, Duhamel A (1996) Sliding thin-slab minimum intensity projection technique in the diagnosis of emphysema: histologic-CT correlation. Radiology 200:665–671
15. Webb WR, Muller NL, Naidich DP (eds) (1992) Diseases characterized primarily by increased lung opacity. In: High Resolution CT of the Lung. Raven Press, New York, pp 88-110
16. Swirevich CV, Mayo JR, Muller NL (1991) Low-dose high resolution CT of the lung parenchyma. Radiology 180:413-417
17. Aberle DR, Gamsu G, Ray SC, Feurstein IM (1988) Asbestos-related pleural and parenchymal fibrosis: detection with high-resolution CT. Radiology 166:729–734
18. Colby TV, Carrington CB (1988) Infiltrative lung disease. In: Thurlbeck WM (ed) Pathology of the lung. Thieme, Stuttgart New York
19. Flint A (1988) Pathologic features of interstitial lung disease. In: Schwartz MI, King TE (eds) Interstitial lung disease. Dekker, Toronto
20. Wescott JL, Cole SR (1986) Traction bronchiectasis in end-stage pulmonary fibrosis. Radiology 161:665–669
21. Grenier P, Valeyre D, Cluzel P et al (1991) Chronic diffuse interstitial lung disease: diagnosis value of chest radiography and high resolution CT. Radiology 179:123–132
22. Keogh BA, Crystal RG (1982) Alveolitis: the key to the interstitial lung disorders. Thorax 37:1–10
23. Niederman MS, Matthay RA (1983) New techniques for assessment of interstitial lung disease. Radiol Clin North Am 21:667–681
24. Whitcomb ME, Dixon GF (1984) Gallium scanning, bronchoalveolar lavage and the national debt. [Editorial.] Chest 85:719–721
25. Walters EH, Gardiner PV (1991) Bronchoalveolar lavage as a research tool. Thorax 46:613–618
26. Helmers RA, Hunninghake GW (1989) Bronchoalveolar lavage in the immunocompromised patient. Chest 96:1184–1190
27. Muller NL, Miller RR, Webb WR, Evans KG, Ostrow DN (1986) Fibrosing alveolitis: CT-pathologic correlation. Radiology 160:585–588
28. Muller NL, Staples C, Miller RR, Vedal S, Thurlbeck WM, Ostrow DN (1987) Disease activity in idiopathic pulmonary fibrosis: CT and pathologic correlation. Radiology 165:731–734
29. Lynch DA, Webb WR, Gamsu G et al (1989) Computed tomography in pulmonary sarcoidosis. J Comput Assist Tomogr 13: 405–410
30. Vedal S, Welsch EV, Miller RR, Muller NL (1988) Desquamative interstitial pneumonia: computed tomographic findings before and after treatment with corticosteroids. Chest 93:215–217
31. Remy-Jardin M , Remy J, Boulenguez C, Sobaszek A, Edme JL, Furon D (1993) Morphologic effects of cigarette smoking on airways and pulmonary parenchyma in healthy adult volunteers: CT evaluation and correlation with pulmonary function tests. Radiology 186:107–115
32. Rounds S, Hill NS (1989) Pulmonary hypertensive diseases. Chest 85:397–405
33. Martin KW, Sagel SS, Siegel BA (1986) Mosaic oligemia simulating pulmonary infiltrates on CT. AJR 147:670–673
34. Remy-Jardin M, Wattinne L, Remy J (1991) Transcatheter occlusion of pulmonary arterial circulation and collateral supply: failures, incidents and complications. Radiology 180:699–705
35. Sheerick AD, Swensen SJ, Hartman TE (1997) Mosaic pattern of lung attenuation on CT scans: frequency among patients with pulmonary artery hypertension of different causes. AJR 169:79–82
36. Primack SL, Muller NL, Mayo JR, Remy-Jardin M, Remy J (1994) Pulmonary parenchymal abnormalities of vascular origin: high-resolution CT findings. Radiographics 14:739–746
37. Stern EJ, Muller NL, Swensen SJ, Hartman TE (1995) CT mosaic pattern of lung attenuation: etiologies and terminology. J Thorac Imaging 10:294–297
38. Worthy SA, Muller NL, Hartman TE, Swensen SJ, Padley SPG, Hansell DM (1997) Mosaic attenuation pattern on thin-section CT scans of the lung: differentiation among infiltrative lung, airway and vascular diseases as a cause. Radiology 205: 465–470
39. Hedlung LW, Vock P, Effman EL, Lischko MM, Putman CE (1984) Hydrostatic pulmonary edema: an analysis of lung density changes by computed tomography. Invest Radiol 19: 254–262
40. Storto ML, Kee ST, Golden JA, Webb WR (1995) Hydrostatic pulmonary edema: high-resolution CT findings. AJR 165: 817–820
41. Forster BB, Muller NL, Mayo JR, Okazawa M, Wiggs BJ, Pare PD (1992) High-resolution computed tomography of experimental hydrostatic pulmonary edema. Chest 101:1434–1437
42. Ketai LH, Godwin JD (1998) A new view of pulmonary edema and acute respiratory distress syndrome. J Thorac Imaging 13:147–171
43. Kato S, Nakamoto T, Iizuka M (1996) Early diagnosis and estimation of pulmonary congestion and edema in patients with left-sided heart diseases from histogram of pulmonary CT number. Chest 109:1439–1445
44. Brasiliero FC, Vargas FS, Kawakama JI, Leite JJ, Cukier A, Prefaut C (1997) High-resolution CT scan in the evaluation of exercise-induced interstitial pulmonary edema in cardiac patients. Chest 111:1577–1582

HRCT – Pathologic Correlations in Small Airways Diseases

Zelena Aziz, David M. Hansell

3.2

Contents

Introduction

Abnormalities of the small airways are found in a wide variety of disorders. The pathologic type of inflammation, extent of involvement, and underlying cause all contribute to the final clinical presentation. Identification of small airways disease has been hampered by the non-specificity and insensitivity of plain chest radiography and conventional pulmonary function tests. Furthermore, because the small airways are a "silent zone" of the lungs, clinical presentation is often late so that lung biopsy may not be feasible because of severe airflow obstruction. The detection of small airways has undergone a renaissance as a result of increased understanding of the high-resolution computed tomographic (HRCT) appearance of the various pathologic types of small airways disease. In contrast to the numerous studies on HRCT-pathologic correlations in interstitial lung disease, there is relatively little similar literature on small airways diseases, probably because of the relative rarity of the individual conditions that make up this heterogeneous group, and the reluctance of clinicians to submit patients with suspected small airways disease to lung biopsy.

The greatest difficulty in reaching an understanding of diseases of the small airways is the problem of classification. The apparently simple term *small airways disease* is defined differently by pathologists, physiologists and physicians. Each of these groups has its own understanding of the term and use it variously in a morphological or functional sense. Further confusion arises when the term is used synonymously with inflammation of the distal bronchioles, that is, "bronchiolitis" [1] The generic terms bronchiolitis and the more specific obliterative bronchiolitis (alternatively bronchiolitis obliterans) have been used to describe a variety of clinico-pathological conditions [2]. The increasing array of reported causes and associations prohibits a manageable clinical classification. Although pathologists categorise small airways diseases according to their histopathologic subtypes, the difficulty with this classical approach is that there are not always obvious clinical or imaging (HRCT) correlates. One of the more comprehensive histopathologic schemes, described by Myers and Colby, is shown in Table 1 [3]. Many other schemes are loosely based on the classification of Myers and Colby, for example an abbreviated version by Worthy and Muller [4] includes the following five histopathological entities: 1) cellular bronchiolitis, 2) panbronchiolitis, 3) respiratory bronchiolitis, 4) constrictive bronchiolitis and 5) bronchiolitis obliterans with intraluminal polyps. A simpler approach is to divide small airways disease into "exudative" and "constrictive" types based on the fundamental difference between the indirect HRCT signs of constrictive bronchiolitis and the direct visualisation on HRCT of exudative forms of bronchio-

Table 1. Classification of small airways disease by pathological features

Constrictive bronchiolitis Obliterative bronchiolitis Bronchiolitis obliterans
Cryptogenic organising pneumonia Bronchiolitis obliterans organising pneumonia
Proliferative bronchiolitis
Acute bronchiolitis Infectious bronchiolitis
Small airways disease Adult bronchiolitis
Respiratory bronchiolitis Smoker's bronchiolitis Respiratory bronchiolitis-associated interstitial lung disease
Mineral dust airways disease Early pneumoconiosis
Follicular bronchiolitis
Diffuse panbronchiolitis

litis (typified by diffuse panbronchiolitis). These two patterns of small airways disease account for most that are encountered in clinical practice.

The confusion surrounding the concept of bronchiolitis obliterans organising pneumonia (BOOP) is diminishing with the realisation that this distinctive clinicopathological entity is primarily a disease of the air spaces (Fig. 1) [5–7], and the term 'organising pneumonia' without the bronchiolitis obliterans prefix, is therefore more appropriate. Although the terms BOOP/ proliferative bronchiolitis/bronchiolitis obliterans with intraluminal polyps /organising pneumonia are encountered in the pathological literature on small airways disease, BOOP/COP will not be further considered in this review.

This review will explore some of the radiologic and pathologic features relevant to the two main types of small airways disease: 'constrictive' and 'exudative'. Individual conditions characterised by small airways disease, including those which have components of both interstitial and small airways disease will then be discussed.

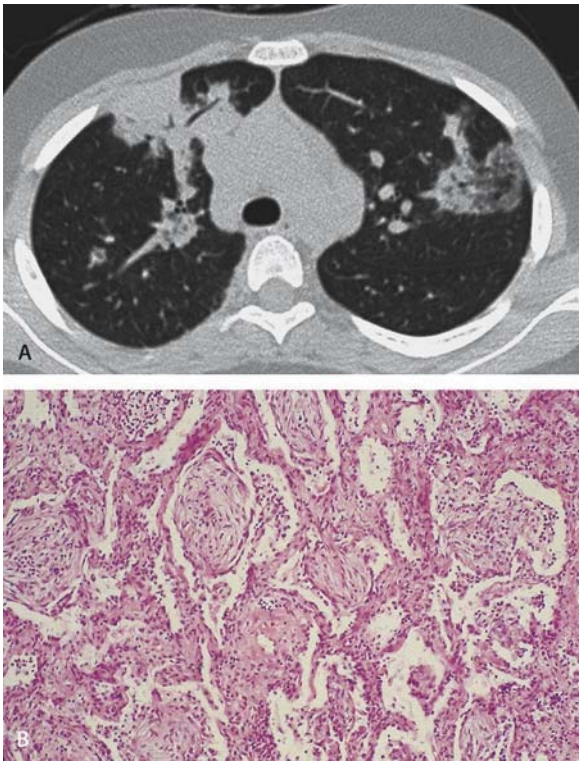

Fig. 1 A CT through the mid-zones of a patient with organising pneumonia. There is ground glass opacification and areas of parenchymal consolidation in a predominantly peripheral distribution. **B** At a pathological level there are buds of granulation tissue (immature, potentially reversible, fibrosis) occupying the air spaces

Anatomic Definition of the Bronchioles

The branching pattern of airways is one of asymmetric dichotomy so that each bronchus gives rise to two daughter bronchi of differing lengths. There is a thirty-fold difference in diameter between the trachea and the terminal bronchiole (approximate diameter of 0.5 mm). The distal airways are generically called bronchioles, one morphologic definition being all those airways that do not contain cartilage; this occurs after between six to twenty divisions. However, there is no precise distinction between bronchi and bronchioles because cartilage may be found in some peripheral airways less than 1 mm in diameter [8]. Although there cannot be an exact division between "small airways" (those with an internal diameter of less than 2 mm) and the remainder of the bronchial tree, it may be useful to consider conditions as affecting "large" or "small" airways because of their distinctive clinical and physiological abnormalities (provided the reality of anatomical and physiological continuity of the bronchial tree is remembered) [9].

The bronchioles are classified as terminal (membranous) bronchioles or respiratory bronchioles [10]. The terminal or membranous bronchioles are considered to be the furthest reaches of the conducting airways since they are defined by a complete fibromuscular wall (that is, no alveoli arise directly from them). In man, the terminal bronchioles are found between the sixth and twenty third generations of branching [11] and have been variously estimated to number between 25,000 and 65,000 [12, 13]. The terminal bronchioles vary in length from 0.8 to 2.5 mm and have an internal luminal diameter of 0.6 mm which appears to be relatively constant along the length of the bronchiole [14]. Downstream from these airways is the transitional zone that denotes a change in functional characteristics from gas

conduction to gas exchange. The respiratory bronchioles which appear in this transitional zone have alveoli arising directly from their walls. The distinction between terminal and respiratory bronchioles at a microscopic level on the basis of diameter alone is not always straightforward, because of variations in inflation pressure at the time of specimen fixation. A single terminal bronchiole supplies a gas-exchange unit – the pulmonary acinus (Fig. 2). The acinus comprises numerous alveolar sacs which communicate through alveolar ducts with the respiratory bronchioles [11].

The secondary pulmonary lobule consists of approximately ten (range 3–24) acini and is defined as the smallest portion of lung that is surrounded by a connective tissue septum [15]. An important feature of the secondary pulmonary lobule is the "core structure" comprising the supplying bronchiole and homologous pulmonary artery. At the level at which the centrilobular bronchiole enters the lobule, the bronchiole is approximately 1 mm in diameter and has a wall thickness of less than 100 μ [16], below the limits of HRCT spatial resolution.

Pathologic Considerations in Constrictive (Obliterative) Bronchiolitis

Constrictive (obliterative) bronchiolitis represents an attempt to repair bronchiolar damage caused by a wide variety of agents [8] and the most frequently encountered are shown in Table 2. The term constrictive bronchiolitis is specific in a pathologic sense because it refers to lesions characterised by scarring leading to obliteration of the bronchiolar lumen; it has the secondary advantage of implying a functional effect, namely limitation of air flow through the bronchioles. The histopathologic findings in constrictive obliterative bronchiolitis may be patchy and in established cases only short

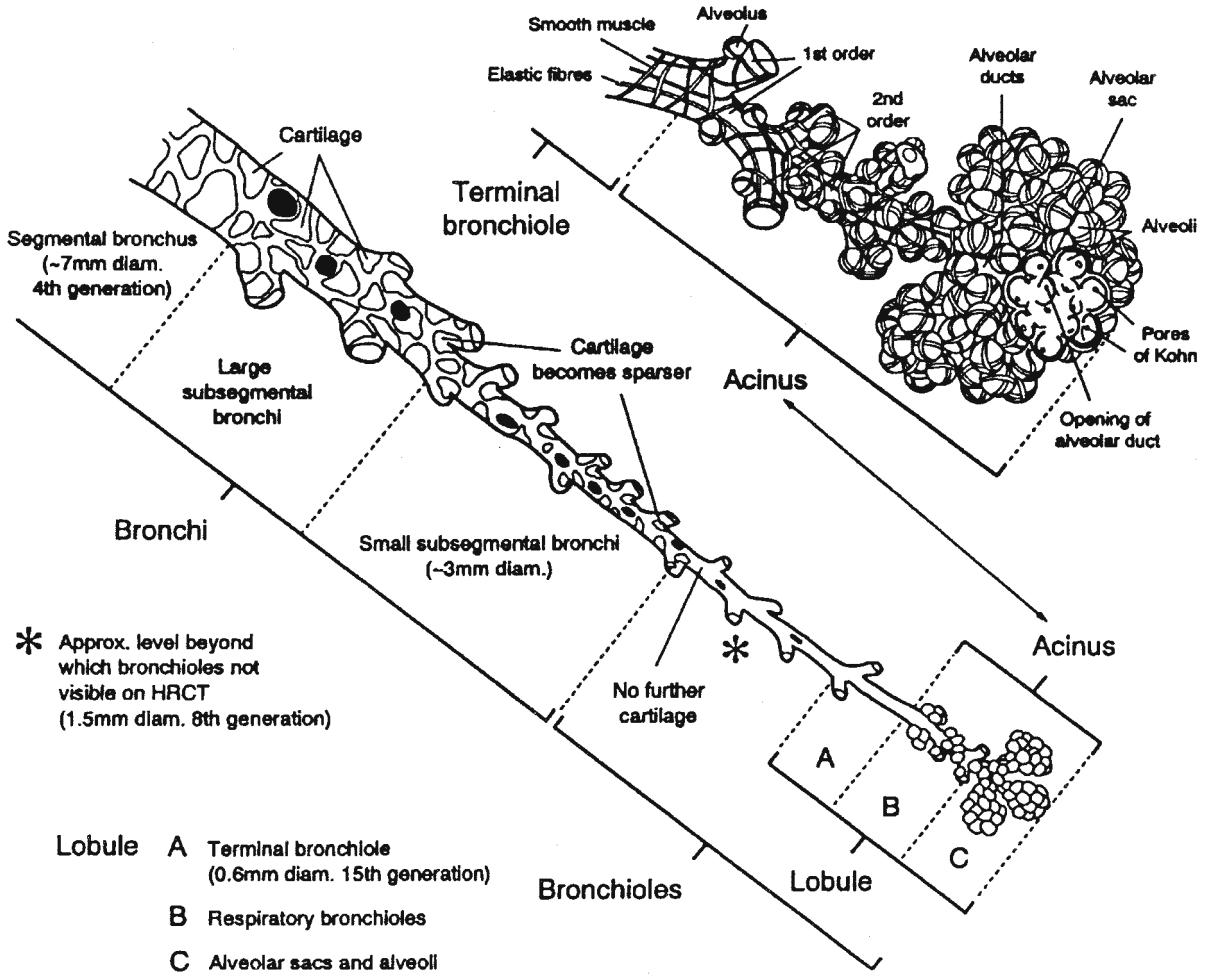

Fig. 2. Normal bronchial and bronchiolar anatomy and schematic representation of an acinus. Note the level (*) at which normal airways are no longer visible on HRCT

Table 2. Some causes and associations of constrictive (obliterative) bronchiolitis

Postinfectious (usually viral)
Adenovirus
Respiratory syncytial virus
Influenza
Mycoplasma pneumoniae
Inhalational injury
Nitrogen dioxide (silo-filler's disease)
Sulfur dioxide
Ammonia
Phosgene
Hot gases
Connective tissue disorders
Rheumatoid arthritis
Sjögren's syndrome
Transplant recipients
Bone marrow transplant
Heart-lung or lung transplant
Drugs
Penicillamine
Lomustine
Other conditions
Inflammatory bowel diseases
Bronchiectasis including cystic fibrosis
Hypersensitivity pneumonitis
Microcarcinoid tumourlets
Paraneoplastic pemphigus

segments of the bronchioles may be affected, necessitating careful step-sectioning to ensure the obliteration is fully demonstrated [17]. Patients with obliterative bronchiolitis caused by a known insult, such as a viral infection, seem to have widely spaced or "skip" lesions with eccentric or focal damage to bronchiolar epithelium whereas in immunopathological forms of bronchiolitis, for example chronic rejection post-lung transplant, widespread circumferential epithelial damage is more usual. The cardinal feature of constrictive obliterative bronchiolitis is submucosal and peribronchiolar fibrosis, resulting in narrowing and obliteration of the bronchiolar lumen (Fig. 3).

The inflammatory process that leads to fibrosis and cicatrisation is centred mainly on the terminal and respiratory bronchioles. The initial inflammatory infiltrate is composed of polymorph neutrophils, lymphocytes and plasma cells. The polymorphs tend to traffic into the bronchiolar lumen, while the mononuclear cells reside in the peribronchiolar interstitium [3]. In some cases, there may be necrosis and sloughing of the bronchiolar epithelium which ultimately results in mucosal scarring. There is disagreement about the degree of involvement of the epithelial lining in bronchiolitis: one authority states that fibrosis is laid down between the muscularis mucosa and an intact epithelium [18]; however, epithelial denuding is probably the rule in most cases of obliterative bronchiolitis [19]. Smooth muscle hyperplasia occurs in the bronchiolar walls and where there is submucosal fibrosis, the bronchiolar lumen narrows in either a concentric or irregular manner. The lumen is progressively reduced, becoming slit-like and finally totally obliterated [10]; van Gieson staining of the durable mural elastin fibres may be the only evidence of the bronchiolar remnant [17]. Elsewhere bronchioles appear distorted and ectatic and may contain mucus plugs and cellular debris. The natural history of the inflammatory process within the bronchiolar walls is unknown but persistent inflammation may be found in the specific circumstance of post-viral bronchiolitis obliterans in children [20, 21]. Because of the relative lack of pathological studies in adult constrictive bronchiolitis [22] (and because longitudinal pathologic studies are impossible), the evolution of obliterative bronchiolitis remains relatively uncharted. In adults however there appears to be temporal compartmentalisation between the inflammatory and fibrotic bronchiolar changes; the subepithelial bronchiolar lesions being either primarily fibrotic or inflammatory. It is suggested that inflammation and fibrosis occur at different time points in the course of the disease, or alternatively, that patients with

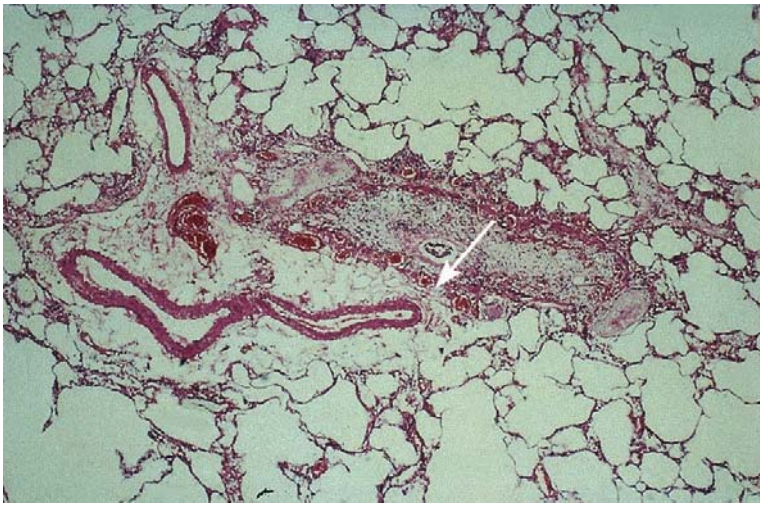

Fig. 3. The end stage of constrictive obliterative bronchiolitis with complete loss of the bronchiolar lumen by circumferential fibrosis. In the normal state, the lumen of the airway is approximately the same as that of the accompanying pulmonary artery (courtesy of Prof. B Corrin)

one type of presentation usually do not show transition to another type of bronchiolar pathology [23]. The lack of clinical response by patients with constrictive bronchiolitis to immunosuppressive treatment suggests that on-going bronchiolar mural inflammation is, at most, a minor feature.

Whether there is a temporal relationship between constrictive bronchiolitis and the so-called proliferative (organising pneumonia end of the spectrum) bronchiolitis is unclear. There is little in the literature to suggest that immature intraluminal fibrosis, or granulation tissue in the membranous bronchioles is transfigured to produce the lesion of established constrictive bronchiolitis [3]. Nevertheless, in particular situations such as heart-lung transplantation [24] and silo filler's disease [25] it is possible that intraluminal granulation tissue in the terminal bronchioles progresses over time to a pathological picture indistinguishable from constrictive bronchiolitis. This sequence should be regarded as exceptional and it seems that constrictive bronchiolitis is not necessarily preceded by a proliferative phase.

In pathologic studies of constrictive bronchiolitis, reference is rarely made to the state of the larger airways. In vivo studies using high-resolution computed tomography suggest that there is often abnormality of the larger airways and sometimes frank bronchiectatic change, particularly in conditions in which a pure constrictive bronchiolitis is the dominant feature, for example, lung allograft rejection [26–28] and MacLeod's (Swyer-James) syndrome [29]. A recent histological study of childhood constrictive obliterative bronchiolitis [20] describes bronchiectasis in 30% of open lung biopsy specimens and in a 100% of lobectomy and autopsy specimens. Other exceedingly rare cases of coexisting inflammatory obliteration of the bronchioles and the larger cartilaginous bronchi have been reported in association with Stevens-Johnson syndrome [30] and Castleman's disease [31]. In diffuse panbronchiolitis, ectatic dilatation of both the bronchioles and bronchi occurs, the former being filled with a combination of inflammatory exudate and foamy macrophages [3, 32, 33]. Apart from this singular entity, the relationship between large and small airways involvement is uncertain; specifically, whether obliterative bronchiolitis ultimately leads to damage of the larger airways, or vice versa, remains contentious.

High-Resolution Computed Tomography of Constrictive Obliterative Bronchiolitis

The signs of small airways disease on chest radiography are indirect [34]: widespread bronchiolar obstruction that characterises constrictive obliterative bronchiolitis results in areas of lung that are under-ventilated with attenuation of the pulmonary vasculature and increased transradiancy. The sensitivity of chest radiography in detecting anything other than very severe small airways disease is low and is further diminished if there is coexisting interstitial lung disease: the visual "noise" of additional parenchymal disease obscures these relatively subtle indirect signs of small airways disease. The radiographic features of cryptogenic constrictive obliterative bronchiolitis described by Breatnach and Kerr can be summarised as diminished pulmonary vasculature and mild over-inflation of the lungs [35]. However, even these non-specific abnormalities are not present in all patients finally diagnosed as having obliterative bronchiolitis [34, 36, 37].

In one of the first CT studies of constrictive bronchiolitis, 15 patients who fulfilled the criteria of Turton et al. [38] were examined with conventional and thin section computed tomography (contiguous 10 mm sections and interspaced 3 mm sections) [39]. Chest radiographs were regarded as normal in five out of the fifteen patients; the remaining ten patients showed "limited vascular attenuation and hyperinflation". In thirteen out of fifteen patients (87%) a pattern of "patchy irregular areas of high and low attenuation in variable proportions, accentuated in expiration" was noted. This, and a report of two cases by Eber et al. [40] were the first reports to identify regional inhomogeneity of the density of the lung parenchyma as the key CT feature of constrictive bronchiolitis.

Subsequent descriptions have confirmed and refined the HRCT signs of constrictive obliterative bronchiolitis [41–44]. The HRCT features comprise areas of reduced density of the lungs (the patchy density differences giving rise to the term "mosaic attenuation pattern"), constriction of the pulmonary vessels within areas of decreased lung density, bronchial abnormalities and lack of change of cross-sectional area of affected parts of the lung on scans obtained at end-expiration [45–47]. These individual CT signs of constrictive obliterative bronchiolitis are now considered on more detail.

Areas of Decreased Density of the Lung Parenchyma

Regions of decreased attenuation ("black lung") usually have poorly defined margins (Fig. 4a), but sometimes have a sharp geographical outline (representing a collection of affected secondary pulmonary lobules) (Fig. 4b). The relatively higher attenuation regions of lung represent relatively increased perfusion of the normally ventilated lung. When severe, the lung may be of homogeneously decreased attenuation (so that the patchy density difference, or mosaic pattern, is lost) (Fig. 5).

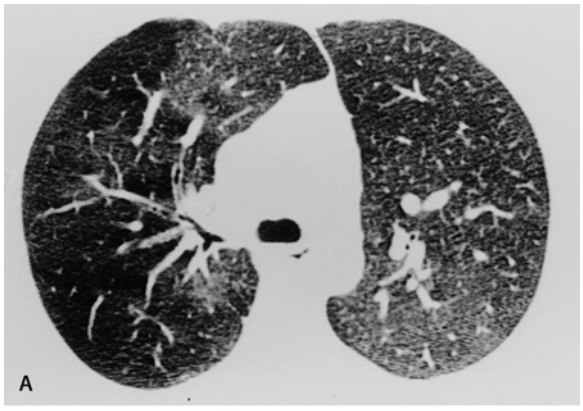

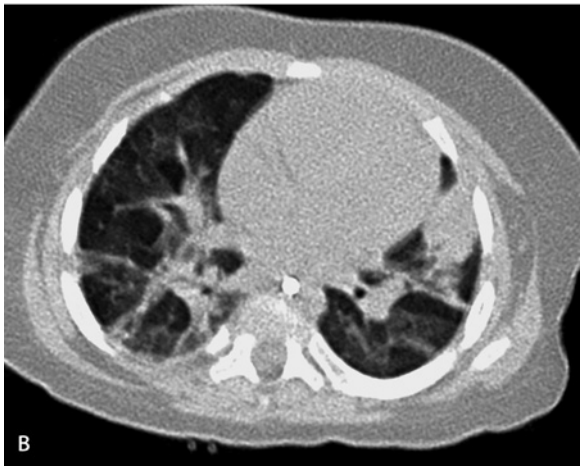

Fig. 4 A HRCT of patient with post-viral constrictive obliterative bronchiolitis, predominantly affecting the right lung, showing areas of decreased attenuation with poorly defined margins. Within the areas of decreased attenuation the vessels are or reduced calibre. **B** HRCT of another patient with post-viral constrictive obliterative bronchiolitis. In this case the areas of decreased attenuation have a more geographical margin, representing individually affected secondary pulmonary lobules

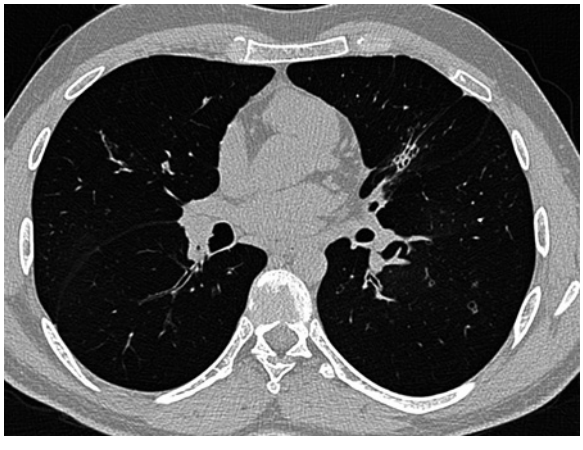

Fig. 5. Patient with severe "end stage" constrictive obliterative bronchiolitis. The lungs are of uniformly decreased attenuation and the mosaic pattern is absent because of the widespread involvement of the small airways. The main features are decreased calibre of the pulmonary vessels and bronchiectatic changes

Reduction in Calibre of the Macroscopic Pulmonary Vessels

In the areas of decreased attenuation, pulmonary perfusion is reduced. In acute bronchiolar obstruction this represents physiologic reflex of hypoxic vasoconstriction [48] but in the chronic state there is vascular remodelling and the reduced perfusion becomes irreversible. In some instances the inflammatory process that causes bronchiolar scarring may synchronously affect the adjacent pulmonary artery, thus leading to vascular obliteration (Fig. 6). Although the vessels within areas of decreased attenuation on HRCT may be of markedly reduced calibre they are not distorted.

Abnormalities of the Macroscopic Airways

The severity of bronchial dilatation and wall thickening is highly variable from one case to another: in immunologically mediated constrictive bronchiolitis (e.g. post-transplant or rheumatoid arthritis associated), marked dilatation of the bronchi is a frequent finding [49, 50]. Some degree of bronchial thickening and dilatation abnormality is the rule in most patients with constrictive bronchiolitis [43].

Air Trapping at Expiratory CT

The regional inhomogeneity of the lung density is accentuated and small or subtle areas of air trapping may be revealed on CT performed at end-expiration [51–54]. The cross-sectional area of the affected parts of the lung does not decrease in size on expiratory CT [47]. Expiratory CT may be helpful in differentiating between the three main causes of a mosaic pattern (infiltrative lung disease, small airways disease, and occlusive pulmonary vascular disease) which may be problematic on inspiratory CT [55, 56]. An important caveat is that in patients with widespread small airways disease, end-expiratory CT sections may appear virtually identical to the standard inspiratory CT sections, simply because of the severity of the air trapping (i.e. there is no mosaic pattern or change in cross-sectional area of the lungs).

The individual HRCT signs listed above may be encountered in other conditions characterised by chronic obstructive pulmonary disease. Patients with asthma show widespread, usually minor, bronchial abnormalities and the HRCT appearances may be confused with those of obliterative bronchiolitis [57]. A mosaic attenuation pattern is also seen commonly in severe asthma, but the inspiratory and expiratory decreased attenuation demonstrated tends to be more extensive in obliterative bronchiolitis than in asthma [58]. In patients with centrilobular emphysema, the HRCT features of permeative destruction of the lung parenchyma and

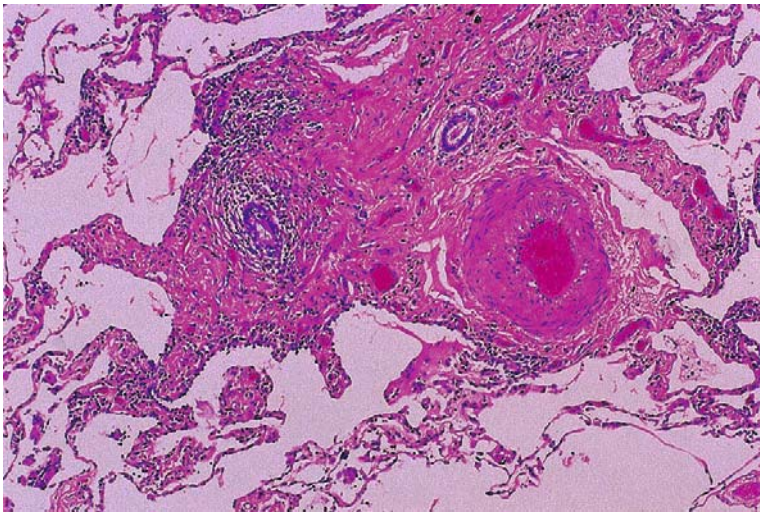

Fig. 6. Adjacent to the two scarred bronchioles the pulmonary artery shows mural fibrosis and intimal hyperplasia suggesting involvement with the initial inflammatory process that resulted in the obliterative bronchiolitis (Courtesy of Prof. T Colby)

distortion of the pulmonary vasculature within areas of decreased attenuation are usually sufficiently distinctive to prevent confusion with constrictive obliterative bronchiolitis. The differentiation between panacinar emphysema and advanced constrictive obliterative bronchiolitis may be less straightforward, but a recent study evaluating the use of thin-section CT in distinguishing between causes of obstructive pulmonary disease revealed surprisingly few misdiagnoses between these two groups [57]. An explanation for this being that the degree of parenchymal destruction is usually greater in patients with panlobular emphysema.

The mosaic pattern is a non-specific HRCT sign and can reflect the presence of small airways disease, occlusive vascular disease, or infiltrative lung disease [55, 56, 59, 60]. In a study of 70 patients with a mosaic pattern as the dominant HRCT abnormality, Worthy et al. showed that infiltrative lung disease and small airways disease were readily identified but the mosaic pattern caused by occlusive vascular disease was frequently misinterpreted [61]. A recent study by Arakawa [62] has shown that air trapping is common (seen in 60%) on expiratory scans in acute pulmonary embolism, highlighting that expiratory air trapping may not be as helpful as previously thought in distinguishing a mosaic pattern caused by small airways disease and occlusive vascular disease. In practice the differentiation between the various causes of a mosaic pattern is less problematic if the clinical and functional picture, particularly the gas diffusing capacity, are taken into account.

The density differences that make up the mosaic pattern may be extremely subtle on inspiratory CT and simple image processing of adjacent thin sections may improve detection. Spiral CT can be used to acquire a "slab" of anatomically contiguous thin-sections (for example, a 5 mm slab consisting of five adjacent 1 mm sections); a simple image processing algorithm is applied whereby only the lowest attenuation value of the five adjacent pixels is projected on the final image, producing a so-called "minimum intensity projection (MinIP) image". This technique improves the detection of subtle areas of low attenuation, encountered in small airways disease and emphysema [63, 64].

Specific Forms of Small Airways Disease

It has been suggested that inflammation of the bronchioles with or without subsequent obliteration is the most common lesion within the lungs [65], so that while clinically identifiable "pure" obliterative bronchiolitis may be rare in practice, milder obliterative bronchiolitis, sometimes masked by a more familiar disease, is often overlooked. Over the years pathological studies have drawn attention to frequent involvement of the small airways in a wide variety of diffuse interstitial and airway diseases [66–70]. What follows is a consideration of specific types of bronchiolitis that have been classified as clinically recognisable entities [71].

Cryptogenic Obliterative Bronchiolitis

Cryptogenic obliterative bronchiolitis (idiopathic bronchiolitis obliterans) is, by definition, applied to those patients with evidence of obliteration of the small airways, with no identifiable cause or disease known to be associated with obliterative bronchiolitis. The clinical diagnosis is thus therefore largely one of exclusion. In an early pathological study of 42,038 consecutive post mortems over forty two years, LaDue identified only one patient as having bronchiolitis obliterans of no

known cause [72]. Later, Turton et al. identified ten patients out of 2,094 individuals with chronic flow obstruction and an FEV_1 of less than 60% in whom the obstructive deficit was irreversible and no cause could be isolated. The rigorous exclusion criteria applied by these authors are detailed below; such patients were considered to have a distinct disease entity and were labelled as having "cryptogenic obliterative bronchiolitis" [38].

Exclusion Criteria for the Diagnosis of Cryptogenic Obliterative Bronchiolitis [38]

- Diurnal peak respiratory flow rate (PEFR) variability >50L/min
- Increase in PEFR of >50L/min or 20% after oral corticosteroid therapy
- Rise in FEV_1 or FVC of <15% after inhaled $beta_2$-agonist therapy
- History of episodic wheezing
- Personal/family history of atopy
- Chronic bronchitis (Medical Research Council criteria)
- Emphysema
- Known cause of chronic airflow obstruction

Five of the ten patients reported by Turton et al. had associated rheumatoid arthritis and two had had a preceding chest infection (viral?), leaving a total of three patients. Thus, using the most stringent criteria, less than 1% of cases in this series can be considered truly idiopathic, highlighting the extreme rarity of cryptogenic obliterative bronchiolitis. Nevertheless, the obligatory inclusion criterion of an FEV_1 of less than 60% undoubtedly reduces the apparent prevalence of the disease because pathologically bona fide but less severe cases are excluded.

In a remarkable descriptive study of seventy "unselected" hospital patients, McLean examined 20,000 sections from blocks of lung tissue from seventy patients. McLean found, through his painstaking analysis, that pathological evidence of bronchiolitis obliterans, although relatively slight, was extensive and increased with age; quantitative data on the profusion and severity of small airway lesions is not given but McLean states: *"in all such patients aged over forty years (however normal their lungs appeared to be on superficial inspection) diffuse damage to the smaller bronchioles was regularly found"* [73].

The clinical course of patients thought to have cryptogenic obliterative bronchiolitis is variable: in the series reported by Turton et al., half the patients survived for more than ten years [38] and in a smaller series of four patients there did not appear to be any disease progression over a five year follow-up period [22]. Although it is convenient to exclude smokers when describing patients with cryptogenic obliterative bronchiolitis for study, this may is a potential source of selection bias: Kindt et al. studied sixteen patients, nine of whom were smokers, with mild chronic airflow obstruction and found that five of these individuals had an obliterative bronchiolitis [74]. The authors considered the smoking history in these patients insufficient to account for the severity of these bronchiolar lesions, suggesting that bronchiolitis in smokers may not always be due to tobacco smoke.

Post-viral Obliterative Bronchiolitis

The epidemiological and pathological consequences of lower respiratory tract viral infections are difficult to study because of the wide range of potential infective agents, the extreme variability of lung injury, and the lack of satisfactory pathological data. Given that most

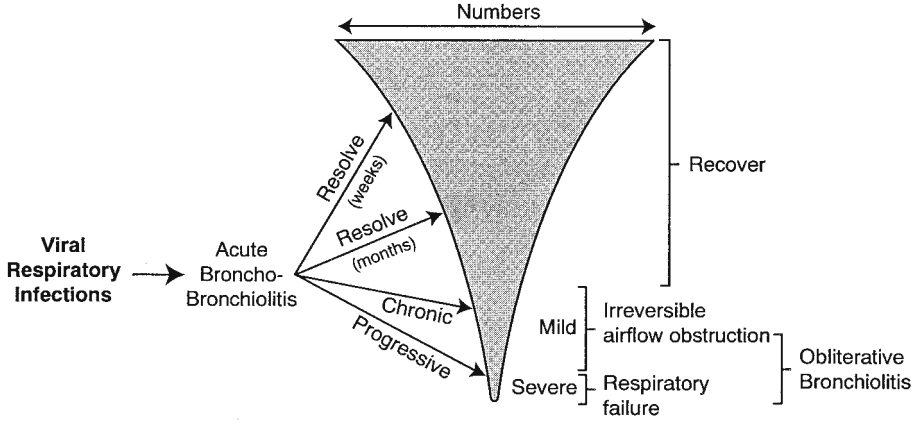

Fig. 7. Natural history of viral lower respiratory tract infections: potential outcomes (modified from [9])

individuals are likely to suffer repeated viral respiratory tract infections in a lifetime, in numerical terms post-viral bronchiolitis is by far the commonest cause of obliterative bronchiolitis. However, the severity or extent of post-viral obliterative bronchiolitis is highly variable and in the vast majority, the resulting functional deficit is slight or non-existent. Although exact figures are not available, the scheme shown in (Fig. 7) provides some idea of the likely outcome of viral infection of the airways [9].

Infectious agents known to be capable of causing an obliterative bronchiolitis are the DNA viruses such as adenovirus, cytomegalovirus and varicella; of the RNA viruses the most commonly recognised are influenza A and B, parainfluenza 2 and 3 and the respiratory syncytial virus. Occasionally a severe viral lower respiratory tract infection in childhood results in Swyer-James' (or MacLeod's) syndrome in which, in addition to an obliterative bronchiolitis, there is arrest of the normal increase in number of alveoli in the developing lung; involvement is often asymmetrical resulting in the characteristic "hyperlucent lung" [29] (Fig. 8). *Mycoplasma pneumoniae*, which has a particular predilection for ciliated cells, is a potent cause of obliterative bronchiolitis [75]. In the developing world pertussis and measles remain common causes of obliterative bronchiolitis.

Many factors determine the differences in type of micro-organism responsible for lower respiratory tract infections in adults and children – most obviously pre-existing immunity to specific viral agents. In children, acute viral lower respiratory tract infections may result in a lymphocytic infiltrate around the airways, so called follicular bronchiolitis (see section on small airways disease associated with connective tissue diseases) (Fig. 9). By adulthood, most lower respiratory tract infections are bacterial. However, no bacterium has definitely been incriminated as a cause of obliterative bronchiolitis. Although some authors have listed bacteria such as *Haemophilus influenzae* and *Nocardia asteroides* as causes of obliterative bronchiolitis [76], firm evidence for these, or other bacteria, as causative agents is scant. *Nocardia asteroides* and *Legionella pneumophila* have both been reported as causes of obliterative bronchiolitis [77, 78]. However, the pathology described in both reports is clearly of an organising pneumonia, rather than a constrictive obliterative bronchiolitis.

In a study of patients with bronchiectasis, Miszkiel et al. showed that patients colonised with *Pseudomonas aeruginosa* had features consistent with obliterative bronchiolitis on computed tomography significantly more often than non-colonised control patients [79]. However, this link does not necessarily imply that *Pseu-*

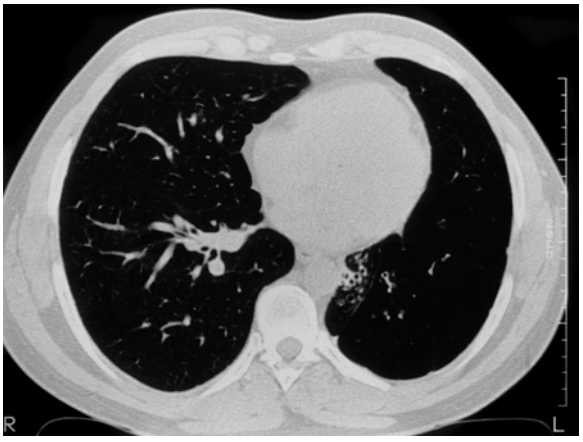

Fig. 8. HRCT of a patient with Swyer-James' (MacLeod's) syndrome. The asymmetrical (if not unilateral) lung involvement is characteristic. In addition to the features of constrictive obliterative bronchiolitis, the left lung is of small volume (partly due to the collapsed bronchiectatic left lower lobe) and on higher sections the main pulmonary artery was small

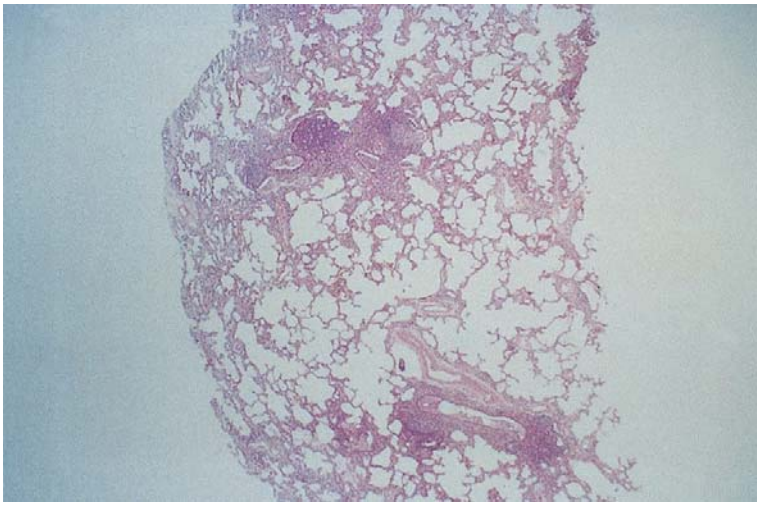

Fig. 9. Low power photomicrograph of a lung biopsy taken from a child with a slow to resolve lower respiratory tract infection. Note the inflammation and follicles of lymphocytes centred on the airways (Courtesy of Dr A Nicholson)

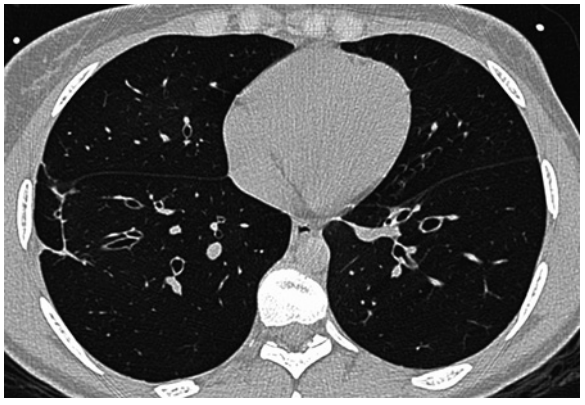

Fig. 10. HRCT of a patient who had had a severe viral lower respiratory infection nine years earlier. In the middle lobe and both lower lobes there are features of bronchiectasis and coexisting obliterative bronchiolitis

domonas aeruginosa is the causative agent of obliterative bronchiolitis; the relationship may merely reflect the fact that patients with severe bronchiectasis and associated obliterative bronchiolitis are more likely to have their airways colonised by *Pseudomonas aeruginosa*. A similar relationship between *Mycobacterium avium intracellulare* and small airways disease has been described. Kubo et al. [80] found both radiological and physiological evidence of small airways disease in patients with MAI infection who were not known to have preexisting lung disease which suggests that infection by MAI may directly cause small airway pathology.

Although it is recognised that a variety of infective agents may result in both bronchiectasis and obliterative bronchiolitis, the relationship between the two has not been fully elucidated. In a study of the sequel of childhood infection by adenovirus type 21, Becroft showed that in addition to an obliterative bronchiolitis, bronchiectasis also occurred [81]. Whether this was the result of synchronous damage to the large and small airways, or bronchiectasis developing as a consequence of the obliterative bronchiolitis is not clear (Fig. 10). The converse idea that bronchiectasis may ultimately lead to obstruction of the small airways is sometimes implied: "...bronchiolitis obliterans is often found *beyond* chronic suppurative bronchial disease, such as bronchiectasis or cystic fibrosis" [8] and "Longstanding obstruction may lead to deletion of small airways, which are replaced by relatively acellular fibrotic strands" [82].

Small Airways Disease Associated with Connective Tissue Diseases

The connective tissue diseases are collectively characterised by immunologically mediated chronic inflammatory damage to a variety of tissues. Obliterative bronchiolitis associated with rheumatoid arthritis was first reported in 1956 [83], but attention became sharply focussed on small airways involvement in connective tissue diseases following the report by Geddes et al. [17]. The pathogenesis of obliterative bronchiolitis in the connective tissue diseases remains uncertain [84]; there is no clear autoimmune basis and other possibilities such as an increased susceptibility to airways infections or complications of therapy have been postulated, but these remain unproven.

Small airways involvement in connective tissue diseases may be cryptic because of the panoply of other possible pathologies which have the potential to mask the functional effects of small airways disease. Despite the recognition that the multi-system connective tissue diseases are associated with various lung complications, there is little quantitative data on their prevalence, severity and natural history. Knowledge of bronchiolar involvement is largely based on anecdotal clinical descriptions of severe cases [85]. A pathological study that reviewed forty one open lung biopsies of patients with rheumatoid arthritis [86] did not include any cases of "pure" obliterative bronchiolitis, highlighting the variable recognition of bronchiolar involvement in rheumatoid arthritis.

A histopathological diagnosis of obliterative bronchiolitis may not be readily established even when an open lung biopsy is undertaken: small airways involvement needs to be distinguished from involvement of the airways by a background fibrosing process – this phenomenon is described in lone cryptogenic fibrosing alveolitis [87] and in fibrosing alveolitis associated with systemic sclerosis [88]. In one CT study of eighty four patients with rheumatoid arthritis, twenty three individuals (30%) showed features of bronchiectasis and/or bronchiolectasis [50]; again, whether these abnormalities reflect small airways disease is uncertain.

The role of penicillamine in inducing obliterative bronchiolitis in patients with rheumatoid arthritis has been widely debated. In one large study which examined this specific question, rheumatoid arthritis patients treated with penicillamine had a significantly higher prevalence of obliterative bronchiolitis (3 out of 133) than untreated patients (0 out of 380) [89]. Furthermore, there was a close temporal relationship between the onset of small airways disease and starting penicillamine treatment, suggesting an underlying predisposition to obliterative bronchiolitis, triggered by penicillamine treatment. Nevertheless, these observations do not exclude the possibility of a spurious link between penicillamine and obliterative bronchiolitis: the use of one and the development of the other both reflecting more progressive and severe rheumatoid arthritis.

A separate pathological entity termed follicular bronchiolitis is more commonly associated with rheu-

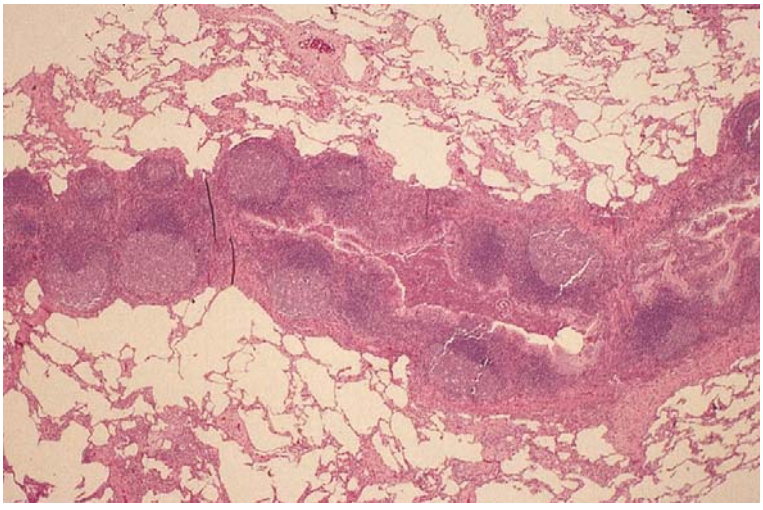

Fig. 11. Lung biopsy from a patient with Sjögren's syndrome showing hyperplastic lymphoid follicles ranged along a bronchiole causing compression of the lumen. The surrounding lung parenchyma is normal

matoid arthritis, often accompanied by Sjögren's syndrome, than with the other connective tissue diseases [90, 91]. Follicular bronchiolitis refers to a form of bronchiolar disease characterised histologically by the presence of abundant lymphoid tissue, frequently with prominent germinal centres, situated in the walls of bronchioles, and to some extent, bronchi. The characteristic lesion is external compression of the bronchioles by hyperplastic lymphoid follicles (Fig. 11); this external compression may be accompanied by lymphocytic infiltration of the adjacent bronchiolar wall. The most common HRCT finding in follicular bronchiolitis are small (1 to 12 mm) nodules located predominantly in a centrilobular distribution (Fig. 12). Peribronchial nodules and patchy non-segmental areas of ground glass have also been described [92]. The CT pattern of nodular attenuation is not surprising considering the predominant histological findings of peribronchiolar inflammation with coalescent germinal centres [92]. Although coexisting follicular and obliterative bronchiolitis have been reported [93, 94], the link between the two is unclear. More diffuse lymphocytic infiltration of the bronchiolar walls has been reported in patients with Sjögren's syndrome [95]. It seems likely that these specific forms of lymphocytic bronchiolitis are rare except in connective tissue diseases and thus should not be regarded as a precursor to constrictive obliterative bronchiolitis.

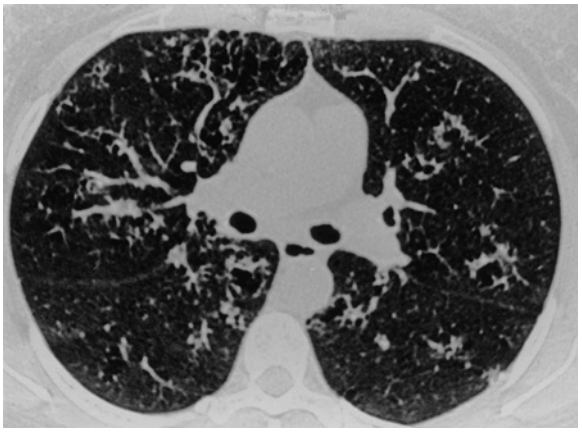

Fig. 12. HRCT of a patient with rheumatoid arthritis and biopsy proven follicular bronchiolitis. The unusual irregular opacities appear to be centred on the airways, as would be expected from the pathology (see Fig. 11). There are also focal areas of lung destruction (pathogenesis unknown) resembling emphysema

Interstitial fibrosis is an extremely common association of systemic sclerosis and the occurrence of independent small airways disease in systemic sclerosis is thus difficult to define. Although standard lung function tests have suggested the presence of small airways disease in up to 42% of patients with systemic sclerosis [85], this high prevalence is questionable. In another study which used sophisticated lung function tests, no evidence of small airways disease was found in non-smoking patients with systemic sclerosis [96].

Post-transplant Obliterative Bronchiolitis

Obliterative bronchiolitis is a well-recognised and serious complication in patients who have received a heart-lung or lung transplant. Burke et al. first reported the frequent occurrence and grave consequences of obliterative bronchiolitis in heart-lung recipients in 1984 [97]. The pathogenesis of this specific form of obliterative bronchiolitis has been the subject of much study [24] [98, 99]. The general consensus is that obliterative bronchiolitis reflects chronic rejection and is due to immunologically mediated injury to the pulmonary endothelium and bronchial epithelium with possible contribu-

tions from intercurrent infection and vascular insufficiency. However, there are reports suggesting that the number of early or "acute" rejection episodes correlates with the later development of obliterative bronchiolitis [100, 101].

Bronchiolitis obliterans in the post-transplant patient progresses through a sequence of lymphohistiocytic-mediated cytotoxicity directed at the respiratory epithelium. The initial process is a lymphocytic infiltrate of the sub-mucosa of the airways with migration of lymphocytes through the basement membrane into the epithelium [102]. At this site, epithelial cell necrosis occurs with denudation of the mucosa. The subsequent secondary cascade of inflammatory mediators eventually leads to the migration of fibroblasts and myofibroblasts into the luminal exudate. Intraluminal plugs of fibrous tissue may occur and it has been postulated that this latter feature is more likely to reflect a response to infection or aspiration [24].

The diagnostic fibrous scarring can be eccentric with formation of a fibrous plaque in the wall of the airway, concentric with the interposition of a 'donut' of collagen tissue, or the granulation tissue may completely obliterate the lumen of the airway, reducing the air passages to stenotic cords of scar tissue [103]. Generally the development of obliterative bronchiolitis is thought to mirror the progression of chronic lung transplant rejection [104]. It has been estimated using a variety of diagnostic criteria, that obliterative bronchiolitis occurs in at least 40% of individuals surviving at least three months following transplantation [105]. The reported incidence of obliterative bronchiolitis after lung transplantation reflects the mean follow-up periods of the different groups of survivors, those with longer follow-up having higher rates of obliterative bronchiolitis. For example, in one large series of patients who had heart-lung transplantation for cystic fibrosis, the incidence of obliterative bronchiolitis at one, two and three years was 17%, 28% and 48% respectively [106]. Most cases are identified clinically between six and eighteen months post-transplantation.

The reported sensitivity and specificity of HRCT for the diagnosis of established constrictive bronchiolitis in post-lung transplant patients has been variable, largely due to patient selection and the HRCT feature evaluated [26, 49, 107–111]. Early studies concentrated on bronchiectasis [26, 27], but more recently attention has turned to the mosaic attenuation pattern on inspiratory CT and, more particularly, on expiratory CT. In a study by Leung et al. [108], air trapping on expiratory CT was the most sensitive sign (sensitivity 91%) of obliterative bronchiolitis in 11 patients with transbronchial biopsy confirmation. In a recent prospective study that included 111expiratory CT scans in 38 heart-lung transplant recipients, the presence of air trapping occupying more than 32% of lung parenchyma had a sensitivity of 83% and a specificity of 89% for the diagnosis of bronchiolitis obliterans syndrome, and in some patients this preceded the spirometric criteria for BOS [111]. However Lee et al. have questioned the sensitivity and specificity of expiratory CT. In their study [109], the air trapping score in patients with biopsy proven bronchiolitis obliterans was not significantly different to biopsy negative patients with airflow limitation.

Obliterative bronchiolitis also occurs following autologous bone marrow transplantation [112]. In this setting, other complications (including a variety of infections, pulmonary oedema and drug toxicity) are equally problematic in these patients [106]. In general, the obliterative bronchiolitis which is a presumed manifestation of graft-versus-host disease occurs in only a small proportion of patients following allogenic bone marrow transplant (probably less than 10%) and is usually less severe than that seen following lung transplantation [113].

Diffuse Panbronchiolitis

Exudative bronchiolitis is responsible for the other basic HRCT pattern of small airways disease and is typified by diffuse panbronchiolitis. Diffuse (Japanese) panbronchiolitis is a sinobronchial disease and was initially thought to be confined to Asian countries, but sporadic cases have been reported in every continent [114]. Nevertheless, most of the definitive pathological and imaging studies originate from Japan [32, 33, 115]. The pathology is characterised by thickening of the walls of the respiratory bronchioles with infiltration by lymphocytes, plasma cells and histiocytes and bronchiolectasis, with secretions and foamy macrophages filling the chronically inflamed airways and immediately adjacent alveoli (Fig. 13). The inflammatory process may extend from the centrilobular airways to involve the adjacent interstitium, but the air-spaces are not affected. The bronchiolocentric lesions are visible macroscopically as yellow nodules. As the disease progresses, an element of fibrotic bronchiolar constriction supervenes.

In the absence of longitudinal histopathological studies, it is not clear the extent to which the basic "exudative" pathology progresses to constrictive bronchiolar obliteration.

HRCT appearances reflect the pathologic process. There is a nodular pattern and small branching opacities (tree-in-bud pattern) can be identified in a predominantly centrilobular distribution, corresponding to the plugged small airways (Figs. 14, 15]. These features are reversible and most patients respond to erythromycin (although the mechanism for this response is unclear: there is no obvious bacterial cause). Mild cylindrical bronchiectasis is an almost invariable accompa-

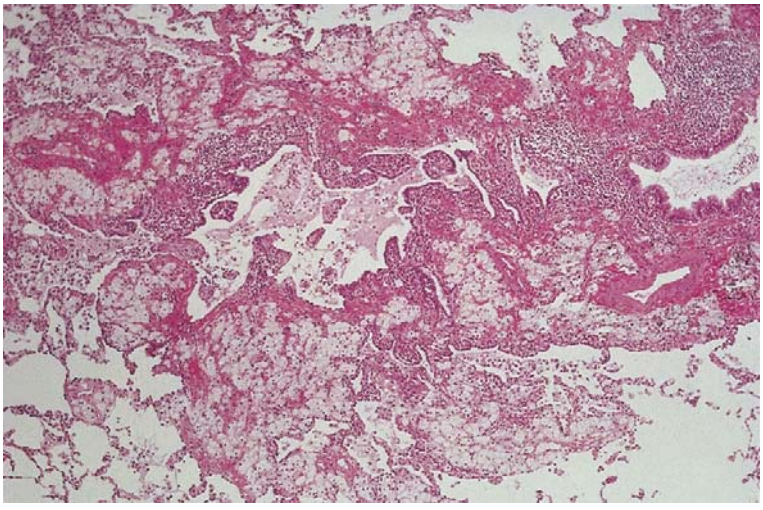

Fig. 13. Pathology of diffuse panbronchiolitis: the bronchiolar wall is thickened by a chronic inflammatory infiltrate and the surrounding alveoli are filled with foamy macrophages (Courtesy of Prof M. Kitaichi)

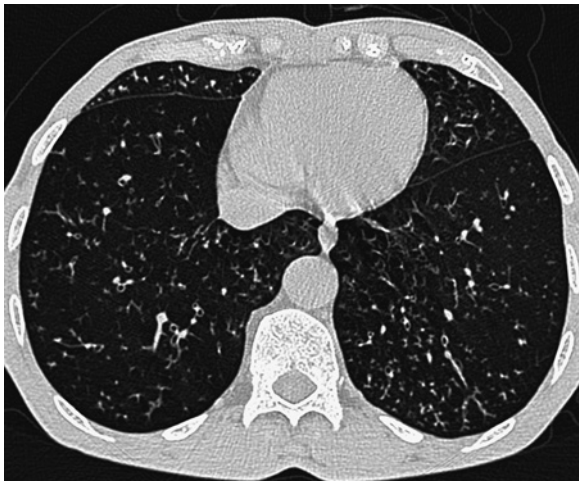

Fig. 14. HRCT of a patient with diffuse panbronchiolitis showing a combination of mild cylindrical bronchiectasis and peripheral branching structures; the latter represent thickened and plugged bronchioles

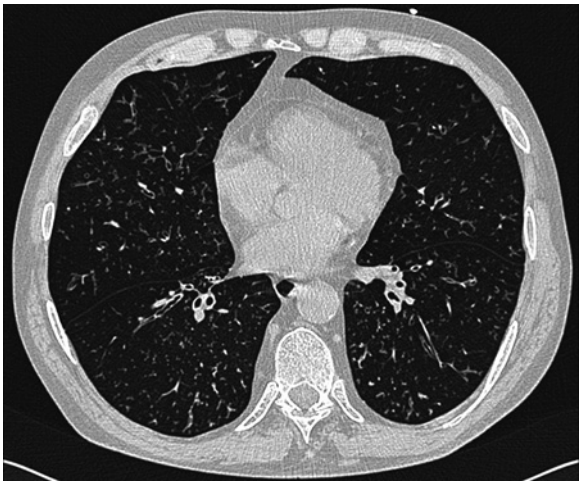

Fig. 15. A patient with diffuse panbronchiolitis showing a predominantly nodular pattern in association with the tree-in-bud pattern

niment and progression of bronchiectasis occurs in severe cases. Even in those who respond to treatment with erythromycin, follow-up CT scans do not demonstrate any appreciable change in the severity of bronchiectasis [115]. Interestingly, although mosaic attenuation may be identified in some cases, it is not usually a major feature; furthermore, regional inhomogeneity of the density of the lung parenchyma on expiratory CT, reflecting air trapping, maybe surprisingly unimpressive. The HRCT features, in the appropriate clinical setting, are virtually pathognomonic. However, other conditions may rarely cause an identical pattern on HRCT and these include invasive aspergillosis centred on the airways [116] and primary pulmonary lymphoma [117]. Other conditions characterised by a tree-in-bud pattern are listed in Table 3.

Table 3. Conditions characterised by tree-in-bud pattern on high-resolution computed tomography

Major feature
Diffuse panbronchiolitis
Bronchiectasis (idiopathic and known cause e.g. cystic fibrosis)
Mycobacterial infection
Aspiration and bronchopneumonia
Acute infectious bronchiolitis (e.g. *Mycoplasma pneumoniae*)
Invasive aspergillosis centred on the airways
Occasional or rare feature
Sjögren's syndrome (follicular bronchiolitis)
Allergic bronchopulmonary aspergillosis
Pneumocystis carinii pneumonia
Leukaemia

Interstitial Lung Diseases with a Component of Small Airways Disease

In contrast to the occurrence of small airways involvement in chronic obstructive airways disease [118], disease of the small airways was not considered part of the concept of "interstitial" lung disease until more recently [119]. One explanation is the stereotyping of interstitial lung disease as functionally restrictive: the heterogeneous group of conditions classically regarded as interstitial are typified by reduced lung volume and compliance (restriction) with no evidence of airflow obstruction. In contradistinction, chronic obstructive pulmonary disease is characterised by an obstructive defect with normal or increased lung volume. It is now widely recognised that diffuse lung pathology cannot always be compartmentalised into processes that affect the small airways or alveolar interstitium exclusively.

Perhaps the earliest acknowledgement of small airways involvement as a constituent of an interstitial lung disease was by Hamman and Rich in their description of fulminant pulmonary fibrosis [66] The pathological features of the condition documented by Hamman and Rich are now thought to resemble an acute interstitial pneumonia with diffuse alveolar damage and hyaline membrane formation, rather than an accelerated usual interstitial pneumonia [120].

An early suggestion that small airways were functionally involved in interstitial pulmonary disease was made by Ostrow and Cherniack in 1973 [121]. Further morphological and physiological studies confirmed that peribronchiolar fibrosis can cause narrowing of the small airways in fibrosing alveolitis and have a measurable effect on physiological indices of small airways function [87, 122]. These studies used dynamic compliance and maximum expiratory flow-volume curves to detect small airways obstruction; the validity of these and other esoteric tests when there is coexisting interstitial lung disease is controversial. In one study which used closing volume and upstream conductance to identify small airways obstruction in a nine patients with fibrosing alveolitis, the authors concluded that there was no evidence of narrowing of (functional) small airways in ventilated parts of the lung [123]. This study highlights the difficulty in functional evaluation of what is likely to be patchy and variable bronchiolar involvement. The prevalence of small airways disease in patients with fibrosing lung disease depends heavily whether it is sought in terms of pathological, functional or clinical terms. In summary, although bronchiolar involvement by interstitial fibrosis can occur, its prevalence and significance remain a source of debate [119].

Respiratory Bronchiolitis – Interstitial Lung Disease

Respiratory bronchiolitis is a common incidental histologic finding in heavy smokers [124] but such cases were thought to be asymptomatic until Myers et al. described 6 patients, all heavy smokers, who had clinical, radiological and physiologic evidence of chronic interstitial lung disease but only respiratory bronchiolitis on open lung biopsy [125]. The term "Respiratory bronchiolitis – interstitial lung disease (RB-ILD)" was later coined in a further series that described the histologic differences between the incidental changes of smoking, RB-ILD and DIP [126]. Almost all patients with RB-ILD are cigarette smokers [127–129], although occasional patients have occupational exposure to irritant fumes [129] and a few patients are described as never smokers [128].

Histologically, respiratory bronchiolitis is characterised by an accumulation of alveolar macrophages within the respiratory bronchioles spilling into neighbouring alveoli. These macrophages typically have glassy eosinophilic cytoplasm with variably intense light brown pigmentation that most likely represent metabolites of cigarette smoke, (hence the term 'smokers macrophages') given that the degree of cytoplasmic pigmentation of macrophages has been shown to correlate with the number of pack-years smoked [128]. Their accumulation may be associated with peribronchiolar alveolar septal thickening by fibroblasts and collagen deposition, characteristically radiating from the bronchiole and there is usually an accompanying chronic inflammatory cell infiltrate in the wall of the bronchiole and the surrounding alveolar walls (Fig. 16). Again, the presence of peribronchiolar fibrosis has been shown to correlate with the number of pack-years smoked, but no correlation was found between pulmonary function tests and pathologic findings [128]. The interstitial fibrosis is of variable severity but is usually a minor component.

The typical HRCT features include: patchy ground-glass opacification (Fig. 17) [130] [131], poorly defined centrilobular nodules (upper zone predominant) [131] and a limited reticular pattern with some thickening of the interlobular septa (probably due to interstitial fibrosis). A recent study of 21 patients with pathologically proven RB-ILD also documented patchy areas of decreased attenuation, a mosaic attenuation pattern (most probably reflecting small airways dysfunction) in 38% [127] (Fig. 18). Associated emphysematous changes are often present (57%) (Fig. 19) and interestingly, the majority of patients showed wall thickening of both proximal and distal airways, presumably analogous to chronic bronchitis. The extent of centrilobular nodules has been found to correlate with the extent of macrophages in respiratory bronchioles and with the extent of chronic inflammation of respiratory bronchioles. Ground

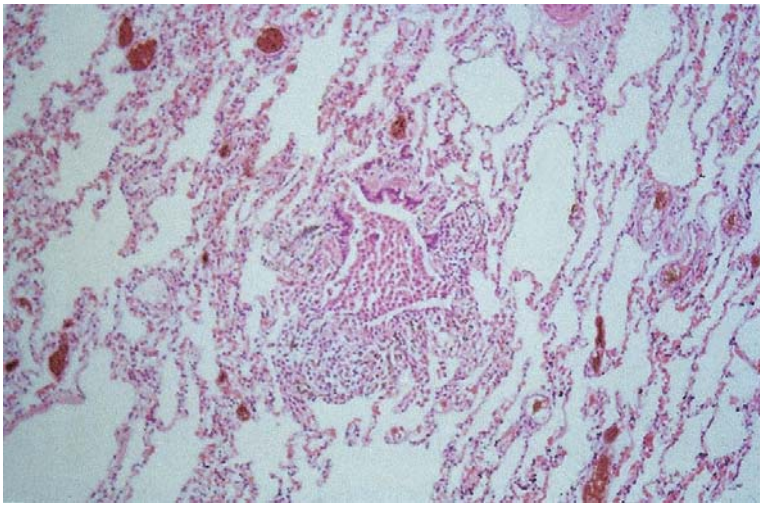

Fig. 16. Pathology of respiratory bronchiolitis–interstitial lung disease (RB-ILD). The lumen of the bronchiole in the centre of the field is full of pigmented macrophages. The bronchiolar wall is disrupted and there is some peribronchiolar fibrosis (Courtesy of Dr A Nicholson)

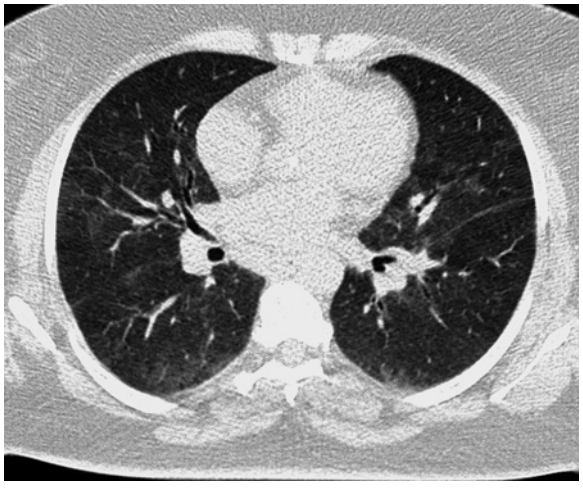

Fig. 17. Areas of ground glass opacification in a patient with RB-ILD

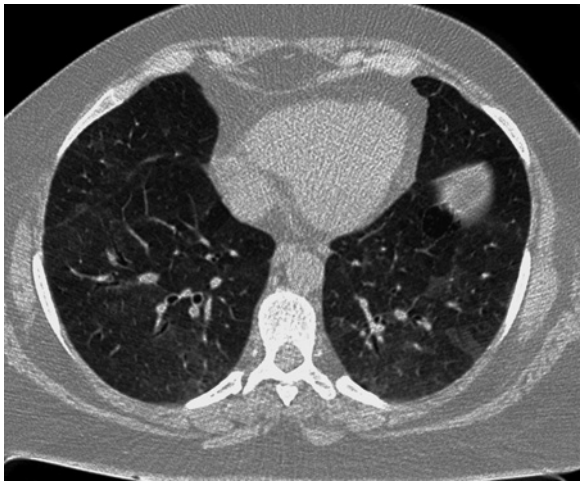

Fig. 18. Patient with RB-ILD showing a subtle mosaic attenuation pattern on HRCT

glass opacity correlates with macrophage accumulation in the alveolar space and alveolar ducts [127].

The features on HRCT of an infiltrative process in combination with small airways disease are remarkably reminiscent of the HRCT appearances of subacute hypersensitivity pneumonitis, and the differential diagnosis between these two conditions is an important one for radiologists. The constellation of HRCT features seen in RB-ILD in approximate order of frequency are summarised below:

- Poorly defined centrilobular nodules
- Areas of ground-glass opacity
- Bronchial wall thickening
- Areas of decreased attenuation reflecting small airways disease
- Emphysema (paraseptal and centrilobular) – limited
- Thickened interlobular septa
- Features of established interstitial fibrosis

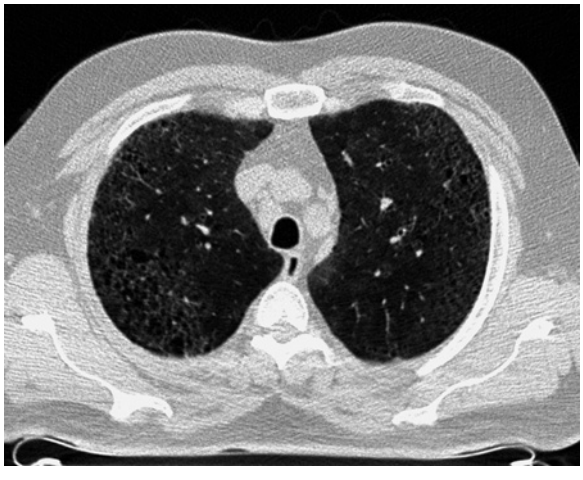

Fig. 19. HRCT of a patient with RB-ILD showing patchy areas of ground glass on a background of emphysema

Extrinsic Allergic Alveolitis (Hypersensitivity Pneumonitis)

In extrinsic allergic alveolitis, deposition of organic dusts in the terminal and respiratory bronchioles may cause an inflammatory bronchiolitis of variable pathological [132], clinical [133] and functional [134] severity. The potential for varying degrees of involvement of the airways and interstitium, and the coexistence of more than one phase of the disease explains the complex abnormalities found on pulmonary function testing [135]. The HRCT features of subacute extrinsic allergic alveolitis consist of varying proportions of ground glass opacification, poorly defined centrilobular nodules, and areas of decreased attenuation [136–138] (Fig. 20A, B). There is a strong correlation between the CT feature of decreased attenuation (mosaic pattern) and lung function indices of air trapping. The airflow obstruction has been ascribed to the coexisting bronchiolitis which is readily apparent in lung biopsy specimens of some patients with extrinsic allergic alveolitis [138] (Fig. 21).

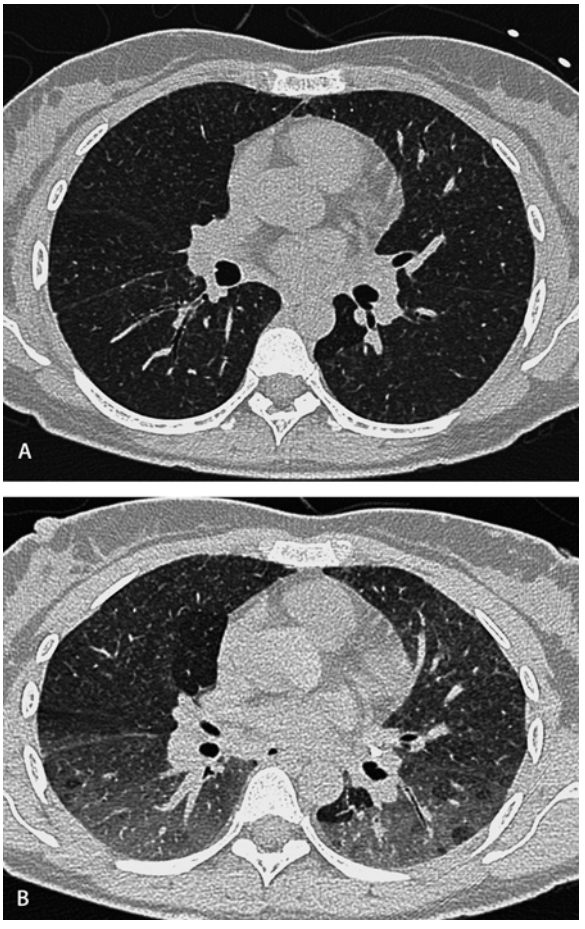

Fig. 20A, B. Patient with suspected extrinsic allergic alveolitis. **A** On a conventional CT performed at end there is regional inhomogeneity of the density of the lung parenchyma in addition to centrilobular nodules. **B** A section taken at approximately the same level, performed at end expiration, reveals extensive air trapping in numerous secondary pulmonary lobules

Sarcoidosis

Granulomatous interstitial lung disease, notably sarcoidosis, by virtue of its peri-lymphatic distribution is concentrated around both large and small airways (Fig. 22). The combination of airways and interstitial involvement may result in complex pulmonary function abnormalities which do not correlate consistently with radiographic, CT or histological indices [68, 139–141]. Studies using sophisticated lung function tests have suggested that airflow limitation ascribable to the small airways dysfunction may be a feature of early pulmonary sarcoi-

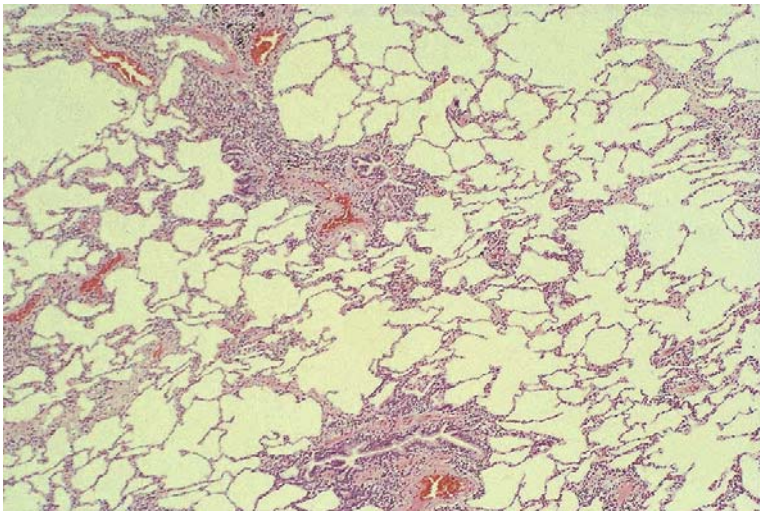

Fig. 21. Lung biopsy of a patient with subacute extrinsic allergic alveolitis highlighting the intense inflammation centred on the airways (cellular bronchiolitis)

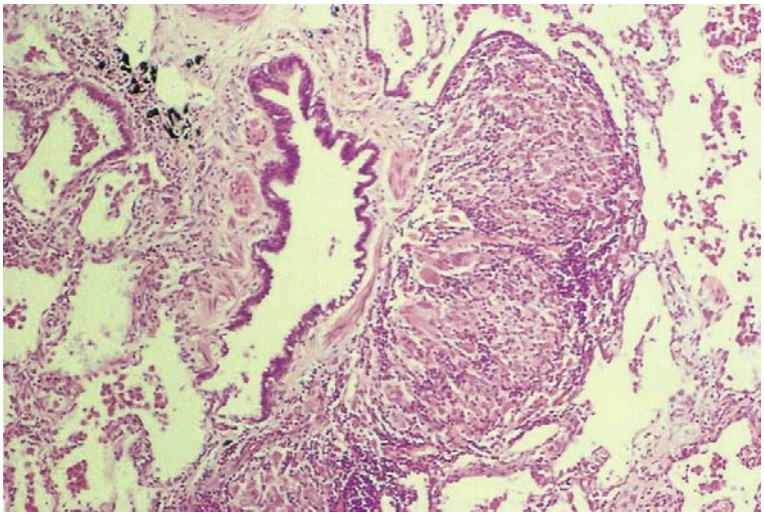

Fig. 22. Typical peri-lymphatic distribution of a granuloma in pulmonary sarcoid. Because the lymphatic channels lie within the bronchovascular connective tissue sheath, sarcoid granulomas have a bronchocentric distribution

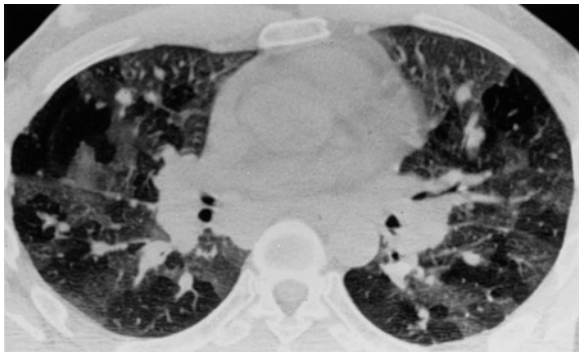

Fig. 23. Expiratory CT of a patient with transbronchial biopsy proven sarcoidosis (there was no obvious endobronchial disease). In addition to the hilar lymphadenopathy and scattered 8 mm diameter nodules, there are obvious areas of air trapping, presumably due to bronchiolar obstruction by sarcoid granulomas

dosis [142, 143]. In support of this, is a report of three cases in which expiratory CT demonstrated areas of decreased attenuation, thought to represent small airways involvement [144] (Fig. 23).

References

1. Thurlbeck WM (1982) The pathology of small airways in chronic airflow limitation. Eur J Respir Dis 63 (suppl 121): 9–18
2. Epler GR, Colby TV (1983) The spectrum of bronchiolitis obliterans. Chest 83:161–162
3. Myers JL, Colby TV (1993) Pathologic manifestations of bronchiolitis, constrictive bronchiolitis, cryptogenic organizing pneumonia, and diffuse panbronchiolitis. Clin Chest Med 14(4):611–622
4. Worthy SA, Muller NL (1998) Small airway diseases. Radiol Clin North Am 36(1):163–173
5. Sulavik SS (1989) The concept of "organizing pneumonia". Chest 96:967–968
6. Geddes DM (1991) BOOP and COP. Thorax 46:545–547
7. Hansell DM (1992) What are bronchiolitis obliterans organizing pneumonia (BOOP) and cryptogenic organizing pneumonia (COP)? Clin Radiol 45:369–370
8. Corrin B (1990) Diseases characterised by airflow limitation. In: Symmers WS (ed) Systemic Pathology: The Lungs. Edinburgh: Churchill Livingstone, pp 167–196
9. Green M, Turton CW (1982) Bronchiolitis and its manifestations. Eur J Respir Dis 63:36–42
10. Wright JL, Cagle P, Churg A, Colby TV, Myers J (1992) Diseases of the small airways. Am Rev Respir Dis 146(1):240–262
11. Plopper CG, Ten Have-Opbroek AAW (1994) Anatomical and histological classification of the bronchioles. In: Epler GR (ed) Diseases of the bronchioles. New York: Raven Press, pp 15–25
12. Horsfield K, Cumming G (1968) Morphology of the bronchial tree in man. J Appl Physiol 24:373–383
13. Weibel ER (1963) Morphometry of the human lung. Berlin: Academic Press
14. Hansen JE, Ampaya PE, Bryant GH, Navin JJ (1975) Branching pattern of airways and airspaces of single human terminal bronchiole. J Appl Physiol 38:983–989
15. Miller WS (1947) The lung. 2 ed. Springfield, Ilinois: C C Thomas
16. Kuhn C (1995) Normal anatomy and histology. In: Thurlbeck WM, Churg AM (eds) Pathology of the Lung. New York: Thieme Medical Publishers Inc, pp 1–36
17. Geddes DM, Corrin B, Brewerton DA, Davies RJ, Turner-Warwick M (1977) Progressive airway obliteration in adults and its association with rheumatoid arthritis. Q J Med 46(184): 427–444
18. Fraser RG, Paré JAP, Paré PD, Fraser RS, Genereux GP (1991) Diseases of the airways. Diagnosis of Diseases of the Chest. Philadelphia: WB Saunders Company, pp 2221–2224
19. Colby TV (1994) Bronchiolar pathology. In: Epler GR (ed) Diseases of the bronchioles. New York: Raven Press, pp 77–100
20. Mauad T, Dolhnikoff M (2002) Histology of childhood bronchiolitis obliterans. Pediatr Pulmonol 33(6):466–474
21. Milner AD, Murray M (1989) Acute bronchiolitis in infancy: treatment and prognosis. Thorax 44:1–5
22. Kraft M, Mortenson RL, Colby TV, Newman L, Waldron JA, King TE (1993) Cryptogenic constrictive bronchiolitis: a clinicopathologic study. Am Rev Respir Dis 148:1093–1101
23. Markopoulo KD, Cool CD, Elliot TL, Lync DA, Newell JD, Jr, Hale VA, Brown KK, Schwarz MI, Tuder RM (2002) Obliterative bronchiolitis: varying presentations and clinicopathological correlation. Eur Respir J 19:20–30
24. Abernathy EC, Hruban RH, Baumgartner WA, Reitz BA, Hutchins GM (1991) The two forms of bronchiolitis obliterans in heart-lung transplant recipients. Hum Pathol 22(11): 1102–1110

25. Douglas WW, Hepper N, Colby TV (1989) Silo filler's disease. Mayo Clin Proc 64:291–304
26. Morrish WF, Herman SJ, Weisbrod GL, Chamberlain DW (1991) Bronchiolitis obliterans after lung transplantation: findings at chest radiography and high-resolution CT. The Toronto Lung Transplant Group. Radiology 179(2):487–490
27. Lentz D, Bergin CJ, Berry GJ, Stoehr C, Theodore J (1992) Diagnosis of bronchiolitis obliterans in heart-lung transplantation patients: importance of bronchial dilatation on CT. AJR Am J Roentgenol 159:463–467
28. Loubeyre P, Revel D, Delignette A, Loire R, Mornex JF (1995) High-resolution computed tomographic findings associated with histologically diagnosed acute lung rejection in heart-lung transplant recipients. Chest 107(1):132–138
29. Moore ADA, Godwin JD, Dietrich PA, Verschakelen JA, Henderson WR (1992) Swyer-James syndrome: CT findings in eight patients. AJR Am J Roentgenol 158:1211–1215
30. Tsunoda N, Iwanaga T, Saito T, Kitamura S, Saito K (1990) Rapidly progressive bronchiolitis obliterans associated with Stevens-Johnson syndrome. Chest 98(1):243–245
31. Kondo M, Matsuda N, Chiyotani A, Inuo G, Kawakami M, Konno K, Takizawa T, Hamano K, Kasajima T (1989) A case of bronchobronchiolitis obliterans with Castleman's lymphoma. Jap J Thorac Dis 27:735–741
32. Nishimura K, Kitaichi M, Izumi T, Itoh H (1992) Diffuse panbronchiolitis: correlation of high-resolution CT and pathologic findings. Radiology 184:779–785
33. Homma H, Yamanaka A, Shinichi T, et al (1983) Diffuse panbronchiolitis: a disease of the transitional zone of the lung. Chest 83:63–69
34. Friedman PJ (1986) Radiology of the airways with emphasis on the small airways. J Thorac Imag 1 (2):7–22
35. Breatnach E, Kerr I (1982) The radiology of cryptogenic obliterative bronchiolitis. Clin Radiol 33:657–661
36. Lynch DA (1993) Imaging of small airways diseases. Clin Chest Med 14(4):623–634
37. Wilson AG (1995) Diseases of the Airways. In: Armstrong P, Wilson AG, Dee P, Hansell DM (eds) Imaging of Diseases of the Chest. St Louis: Mosby, pp 817–868
38. Turton CW, Williams G, Green M (1981) Cryptogenic obliterative bronchiolitis in adults. Thorax 36:805–810
39. Sweatman MC, Millar AB, Strickland B, Turner-Warwick M (1990) Computed tomography in adult obliterative bronchiolitis. Clin Radiol 41(2):116–119
40. Eber CD, Stark P, Bertozzi P (1993) Bronchiolitis obliterans on high-resolution CT: a pattern of mosaic oligemia. J Comput Assist Tomogr 17(6):853–856
41. Muller NL, Miller RR (1995) Diseases of the bronchioles: CT and histopathologic findings. Radiology 196:3–12
42. Hartman TE, Swensen SJ, Muller NL (1994) Bronchiolar diseases: computed tomography. In: Epler GR (ed) Diseases of the bronchioles. New York: Raven Press, pp 43–58
43. Hansell DM, Rubens MB, Padley SPG, Wells AU (1997) Obliterative bronchiolitis: individual CT signs of small airways disease and functional correlation. Radiology 203:721–726
44. Hwang JH, Kim TS, Lee KS, Choi YH, Han J, Chung MP, Kwon OJ, Rhee CH (1997) Bronchiolitis in adults: pathology and imaging. J Comput Assist Tomogr 21:913–919
45. Padley SP, Adler BD, Hansell DM, Muller NL (1993) Bronchiolitis obliterans: high resolution CT findings and correlation with pulmonary function tests. Clin Radiol 47:236–240
46. Marti-Bonmati L, Ruiz Perales F, Catala F, Mata JM, Calonge E (1989) CT findings in Swyer-James syndrome. Radiology 172:477–480
47. Stern EJ, Frank MS (1994) Small-airways disease of the lungs: findings at expiratory CT. AJR Am J Roentgenol 163:37–41
48. Guckel C, Wells AU, Taylor DA, Chabat F, Hansell DM (1999) Mechanism of mosaic attenuation of the lungs on computed tomography in induced bronchospasm. J Appl Physiol 86:701–708
49. Loubeyre P, Revel D, Delignette A, Wiesendanger T, Philit F, Bertocchi M, Loire R, Mornex JF (1995) Bronchiectasis detected with thin-section CT as a predictor of chronic lung allograft rejection. Radiology 194(1):213–216
50. Remy-Jardin M, Remy J, Cortet B, Mauri F, Delcambre B (1994) Lung changes in rheumatoid arthritis: CT findings. Radiology 193(2):375–382
51. Arakawa H, Webb WR (1998) Air trapping on expiratory high-resolution CT scans in the absence of inspiratory scan abnormalities: correlation with pulmonary function tests and differential diagnosis. AJR Am J Roentgenol 170:1349–1353
52. Desai SR, Hansell DM (1997) Small airways disease: expiratory computed tomography comes of age. Clin Radiol 52:332–337
53. Lucidarme O, Coche E, Cluzel P, Mourey-Gerosa I, Howarth N, Grenier P (1998) Expiratory CT scans for chronic airway disease: correlation with pulmonary function test results. AJR Am J Roentgenol 170:301–307
54. Verschakelen JA, Scheinbaum K, Bogaert J, Demedts M, Lacquet LL, Baert AL (1998) Expiratory CT in cigarette smokers: correlation between areas of decreased lung attenuation, pulmonary function tests and smoking history. Eur Radiol 8:1391–1399
55. Arakawa H, Webb WR, McCowin M, Katsou G, Lee KN, Seitz, RF (1998) Inhomogeneous lung attenuation at thin-section CT: diagnostic value of expiratory scans. Radiology 206(1):89–94
56. Stern EJ, Swensen SJ, Hartman TE, Frank MS (1995) CT mosaic pattern of lung attenuation: distinguishing different causes. AJR Am J Roentgenol 165:813–816
57. Copley SJ, Wells AU, Muller NL, Rubens MB, Hollings NP, Cleverley JR, Milne DG, Hansell DM (2002) Thin-section CT in obstructive pulmonary disease: discriminatory value. Radiology 223:812–819
58. Jensen SP, Lynch DA, Brown KK, Wenzel SE, Newell JD (2002) High-resolution CT Features of Severe Asthma and Bronchiolitis Obliterans. Clin Radiol 57:1078–1085
59. Remy-Jardin M, Remy J, Giraud F, Wattinne L, Gosselin B (1993) Computed tomography (CT) assessment of ground-glass opacity: semiology and significance. J Thorac Imag 8:249–264
60. Austin JHM, Muller NL, Friedman PJ, Hansell DM, Naidich DP, Remy-Jardin M, Webb WR, Zerhouni EA, Austin JH (1996) Glossary of terms for CT of the lungs: recommendations of the nomenclature committee of the Fleischner Society. Radiology 200(2):327–331
61. Worthy SA, Muller NL, Hartman TE, Swensen SJ, Padley SP, Hansell DM (1997) Mosaic attenuation pattern on thin-section CT scans of the lung: differentiation among infiltrative lung, airway, and vascular diseases as a cause. Radiology 205(2):465–470
62. Arakawa H, Kurihara Y, Sasaka K, Nakajima Y, Webb WR (2002) Air trapping on CT of patients with pulmonary embolism. AJR Am J Roentgenol 178:1201–1207
63. Remy-Jardin M, Remy J, Gosselin B, Copin MC, Wurtz A, Duhamel A (1996) Sliding thin slab, minimum intensity projection technique in the diagnosis of emphysema: histopathologic-CT correlation. Radiology 200(3):665–671
64. Bhalla M, Naidich DP, McGuinness G, Gruden JF, Leitman BS, McCauley DI (1996) Diffuse lung disease: assessment with helical CT – preliminary observations of the role of maximum and minimum intensity projection images. Radiology 200:341–347
65. Thurlbeck WM (1995) Chronic airflow obstruction. In: Thurlbeck WM, Churg AM (eds) Pathology of the lung. New York: Thieme Medical Publishers Inc, pp 739–825
66. Hamman L, Rich AR (1944) Acute diffuse interstitial fibrosis of the lungs. Bull Johns Hopkins Hosp 74:177–212
67. Hapke EJ, Seal RME, Thomas GO, Hayes WM, Meek JC (1968) Farmer's lung: a clinical, radiographic, functional and serological correlation of acute and chronic stages. Thorax 23:451–468
68. Carrington CB, Gaensler EA, Mikus JP, Schachter AW, Burke GW, Goff AM (1978) Structure and function in sarcoidosis. Ann N Y Acad Sci 29:265–283
69. Whitwell F (1952) Study of the pathology and pathogenesis of bronchiectasis. Thorax 7:213–239
70. Culiner MM (1963) Obliterative bronchitis and bronchiolitis with bronchiectasis. Dis Chest 44:351–361

71. Epler GR (1994) A clinician's classification of the diseases of the bronchioles. In: Epler GR (ed) Diseases of the bronchioles. New York: Raven Press, pp 101–112
72. LaDue JS (1941) Bronchiolitis fibrosa obliterans. Arch Intern Med 68:663–673
73. McLean KH (1957) The pathology of acute bronchiolitis: a study of its evolution. II: The repair phase. Australas Ann Med 6:29–43
74. Kindt GC, Weiland JE, Davis WB, et al (1989) Bronchiolitis in adults: a reversible cause of airway obstruction associated with airway neutrophils and neutrophil products. Am Rev Respir Dis 140:483–492
75. Prabhu MB, Barber D, Cockcroft DW (1991) Bronchiolitis obliterans and Mycoplasma pneumonia. Respir Med 85(6): 535–537
76. Penn CC, Liu C (1993) Bronchiolitis following infection in adults and children. Clin Chest Med 14(4):645–654
77. Camp M, Mehta JB, Whitson M (1987) Bronchiolitis obliterans and Nocardia asteroides infection of the lung. Chest 92(6):1107–1108
78. Sato P, Madtes DK, Thorning D, Albert RK (1985) Bronchiolitis obliterans caused by Legionella pneumophila. Chest 87: 840–842
79. Miszkiel KA, Wells AU, Rubens MB, Cole PJ, Hansell DM (1997) Effects of airway infection by Pseudomonas aeruginosa: a computed tomographic study. Thorax 52:260–264
80. Kubo K, Yamazaki Y, Masubuchi T, Takamizawa A, Yamamoto H, Koizumi T, Fujimoto K, Matsuzawa Y, Honda T, Hasegawa M, Sone S (1998) Pulmonary infection with Mycobacterium avium-intracellulare leads to air trapping distal to the small airways. Am J Respir Crit Care Med 158(3):979–984
81. Becroft DMO (1971) Bronchiolitis obliterans, bronchiectasis, and other sequelae of adenovirus type 21 infection in young children. J Clin Pathol 24:72–82
82. Barker AF, Bardana EJ (1988) Bronchiectasis: update of an orphan disease. Am Rev Respir Dis 137:969–978
83. Price TML, Skelton MD (1956) Rheumatoid arthritis with lung lesions. Thorax 11:234–240
84. Halpin DMG, Geddes DMG (1994) Rheumatoid arthritis and connective tissue disease related bronchiolitis obliterans. In: Epler GR (ed) Diseases of the bronchioles. New York: Raven Press, pp 231–240
85. Wells AU, Du Bois RM (1993) Bronchiolitis in association with connective tissue disorders. Clin Chest Med 14:655–666
86. Yousem SA, Colby TV, Carrington CB (1985) Lung biopsy in rheumatoid arthritis. Am Rev Respir Dis 131:770–777
87. Fulmer JD, Roberts CW, von Gal ER, Crystal RG (1977) Small airways in idiopathic pulmonary fibrosis: comparison of morphologic and physiologic observations. J Clin Invest 60: 595–610
88. Spain DM, Thomas AG (1950) The pulmonary manifestations of scleroderma: an anatomic-physiological correlation. Ann Intern Med 32:152–161
89. Wolfe F, Schurle DR, Lin JJ, et al (1983) Upper and lower airway disease in penicillamine treated patients with rheumatoid arthritis. J Rheumatol 10:406–410
90. Fortoul TI, Cano-Valle F, Oliva E, et al (1985) Follicular bronchiolitis in association with connective tissue diseases. Lung 163:305–314
91. Yousem SA, Colby TV, Carrington CB (1985) Follicular bronchitis/bronchiolitis. Hum Pathol 16:700–706
92. Howling SJ, Hansell DM, Wells AU, Nicholson AG, Flint JD, Muller NL (1999) Follicular bronchiolitis: thin-section CT and histologic findings. Radiology 212(3):637–642
93. Epler GR, Snider GL, Gaensler EA, et al (1979) Bronchiolitis and bronchitis in connective tissue disease: a possible relationship to the use of penicillamine. JAMA 242:528–532
94. Hayakawa H, Sato A, Imokawa S, Toyoshima M, Chida K, Iwata M (1996) Bronchiolar disease in rheumatoid arthritis. Am J Respir Crit Care Med 154:1531–1536
95. Newball HH, Brahim SA (1977) Chronic obstructive airway disease in patients with Sjögren's disease. Am Rev Respir Dis 115:295–304
96. Bjerke RD, Tashkin DP, Clements PJ (1979) Small airways in progressive systemic sclerosis. Am J Med 66:201–209
97. Burke CM, Theodore J, Dawkins KD (1984) Post-transplant obliterative bronchiolitis and other late sequelae in human heart-lung transplantation. Chest 86:824–829
98. Yousem S, Burke C, Billingham M (1985) Pathologic pulmonary alterations in long-term human heart-lung transplantation. Hum Pathol 16:911–923
99. Reinsmoen NL, Bolman RM, Savik K, Butters K, Hertz MI (1993) Are multiple immunopathogenetic events occurring during the development of obliterative bronchiolitis and acute rejection? Transplantation 55(5):1040–1044
100. Yousem SA, Dauber JA, Keenan R, Paradis IL, Zeevi A, Griffith BP (1991) Does histologic acute rejection in lung allografts predict the development of bronchiolitis obliterans? Transplantation 52(2):306–309
101. Scott JP, Higenbottam TW, Sharples L, Clelland CA, Smyth RL, Stewart S, Wallwork J (1991) Risk factors for obliterative bronchiolitis in heart-lung transplant recipients. Transplantation 51(4):813–817
102. Yousem SA (1993) Lymphocytic bronchitis/bronchiolitis in lung allograft recipients. Am J Surg Pathol 17(5):491–496
103. Yousem SA, Duncan SR, Griffith BP (1992) Interstitial and airspace granulation tissue reactions in lung transplant recipients. Am J Surg Pathol 16(9):877–884
104. Cagle PT, Brown RW, Frost A, Kellar C, Yousem SA (1995) Diagnosis of chronic lung transplant rejection by transbronchial biopsy. Modern Pathol 8(2):137–142
105. Cooper JD, Billingham M, Egan T, Hertz MI, Higenbottam T, Lynch J, Mauer J, Paradis I, Patterson GA, Smith C, et al (1993) A working formulation for the standardization of nomenclature and for clinical staging of chronic dysfunction in lung allografts. International Society for Heart and Lung Transplantation. J Heart Lung Transplant 12(5):713–716
106. Madden BP, Hodson ME, Tsang V, Radley-Smith R, Khagani A, Yacoub MY (1992) Intermediate term results of heart-lung transplantation for cystic fibrosis. Lancet 339:1583–1587
107. Ikonen T, Kivisaari L, Taskinen E, Piilonen A, Harjula ALJ (1997) High-resolution CT in long-term follow-up after lung transplantation. Chest 111:370–376
108. Leung AN, Fisher K, Valentine V, Girgis RE, Berry GJ, Robbins RC, Theodore J (1998) Bronchiolitis obliterans after lung transplantation: detection using expiratory HRCT. Chest 113(2):365–370
109. Lee ES, Gotway MB, Reddy GP, Golden JA, Keith FM, Webb WR (2000) Early bronchiolitis obliterans following lung transplantation: accuracy of expiratory thin-section CT for diagnosis. Radiology 216:472–477
110. Lau DM, Siegel MJ, Hildebolt CF, Cohen AH (1998) Bronchiolitis obliterans syndrome: thin-section CT diagnosis of obstructive changes in infants and young children after lung transplantation. Radiology 208(3):783–788
111. Bankier AA, Van Muylem A, Knoop C, Estenne M, Gevenois PA (2001) Bronchiolitis obliterans syndrome in heart-lung transplant recipients: diagnosis with expiratory CT. Radiology 218:533–539
112. Paz HL, Crilley P, Patchefsky A, Schiffman RL, Brodsky I (1992) Bronchiolitis obliterans after autologous bone marrow transplantation. Chest 101(3):775–778
113. Breuer R, Lossos IS, Berkman N, Or R (1993) Pulmonary complications of bone marrow transplantation. Respir Med 87(8):571–579
114. Fitzgerald JE, King TE, Jr., Lynch DA, Tuder RM, Schwarz MI (1996) Diffuse panbronchiolitis in the United States. Am J Respir Crit Care Med 154(2 Pt 1):497–503
115. Akira M, Higashihara S, Sakatani M, Hara H (1993) Diffuse panbronchiolitis: follow-up CT examination. Radiology 189: 559–562
116. Logan PM, Primack SL, Miller RR, Muller NL (1994) Invasive aspergillosis of the airways: radiographic, CT, and pathologic findings. Radiology 193(2):383–388
117. Hwang JH, Kim TS, Han J, Lee KS (1998) Primary lymphoma of the lung simulating bronchiolitis: radiologic findings [letter]. AJR 170:220–221
118. Hogg JC, Macklem PT, Thurlbeck WM (1968) Site and nature of airway obstruction in chronic obstructive lung disease. N Engl J Med 268:1355–1360

119. Fulmer JD, Roberts WC (1980) Small airways disease and intersititial pulmonary disease. Chest 77:470–472
120. Askin FB (1993) Acute interstitial pneumonia: histopathologic patterns of acute lung injury and the Hamman-Rich syndrome revisited. Radiology 188:620–621
121. Ostrow D, Cherniack RM (1973) Resistance to airflow in patients with diffuse interstitial lung disease. Am Rev Respir Dis 108:205–210
122. Yernault JC, Dejoinghe M, De Coster A, et al (1975) Pulmonary mechanics in diffuse fibrosing alveolitis. Bull Eur Physiopathol Respir 11:231–244
123. Schofield NC, Davies RJ, Cameron IR, et al (1976) Small airways in fibrosing alveolitis. Am Rev Respir Dis 113: 729–735
124. Niewoehner DE, Kleinerman J, Rice DB (1974) Pathologic changes in the peripheral airways of young cigarette smokers. N Engl J Med 291:775–777
125. Myers JL, Veal CF, Shin MS, Katzenstein ALA (1987) Respiratory bronchiolitis causing interstitial lung disease: a clinicopathologic study of six cases. Am Rev Respir Dis 135: 880–884
126. Yousem SA, Colby TV, Gaensler EA (1989) Respiratory bronchiolitis – associated interstitial lung disease and its relationship to desquamative interstitial pneumonia. Mayo Clin Proc 64:1373–1380
127. Park JS, Brown KK, Tuder RM, Hale VA, King Jr TE, Lynch DA (2002) Respiratory bronchiolitis-associated interstitial lung disease: radiologic features with clinical and pathologic correlation. J Comput Assist Tomogr 26:13–20
128. Fraig M, Shreesha U, Savici D, Katzenstein AL (2002) Respiratory bronchiolitis: a clinicopathologic study in current smokers, ex-smokers, and never-smokers. Am J Surg Pathol 26: 647–653
129. Moon J, Du Bois RM, Colby TV, Hansell DM, Nicholson AG (1999) Clinical significance of respiratory bronchiolitis on open lung biopsy and its relationship to smoking related interstitial lung disease. Thorax 54(11):1009–1014
130. Holt RM, Schmidt RA, Godwin JD, Raghu G (1993) High resolution CT in respiratory bronchiolitis-associated interstitial lung disease. J Comput Assist Tomogr 17:46–50
131. Remy-Jardin M, Remy J, Boulenguez C, Sobaszek A, Edme JL, Furon D (1993) Morphologic effects of cigarette smoking on airways and pulmonary parenchyma in healthy adult volunteers: CT evaluation and correlation with pulmonary function tests. Radiology 186:107–115
132. Sutinen S, Reijula K, Huhti E, Karkola P (1983) Extrinsic allergic bronchiolo-alveolitis: serology and biopsy findings. Eur J Respir Dis 64:271–282
133. Harries MG, Heard B, Geddes D (1984) Extrinsic allergic broncholitis in a bird fancier. Br J Ind Med 41:220–223
134. Sovijarvi AR, Kuusisto P, Muittari A, Kauppinen-Walin K (1980) Trapped air in extrinsic allergic alveolitis. Respiration 40(2):57–64
135. Warren CP, Tse KS, Cherniack RM (1978) Mechanical properties of the lung in extrinsic allergic alveolitis. Thorax 33(3): 315–321
136. Silver SF, Muller NL, Miller RR, Lefcoe MS (1989) Hypersensitivity pneumonitis: Evaluation with CT. Radiology 173: 441–445
137. Remy-Jardin M, Remy J, Wallaert B, Muller NL (1993) Subacute and chronic bird breeder hypersensitivity pneumonitis: sequential evaluation with CT and correlation with lung function tests and bronchoalveolar lavage. Radiology 189(1): 111–118
138. Hansell DM, Wells AU, Padley SPG, Muller NL (1996) Hypersensitivity pneumonitis: correlation of individual CT patterns with functional abnormalities. Radiology 199:123–128
139. Young RL, Krumholtz RA, Harkleroad LE (1966) A physiologic roentgenographic disparity in sarcoidosis. Dis Chest 50: 81–86
140. Remy-Jardin M, Giraud F, Remy J, Wattinne L, Wallaert B, Duhamel A (1994) Pulmonary sarcoidosis: role of CT in the evaluation of disease activity and functional impairment and in prognosis assessment. Radiology 191(3):675–680
141. Muller NL, Mawson JB, Mathieson JR, Abboud R, Ostrow DN, Champion P (1989) Sarcoidosis: correlation of extent of disease at CT with clinical, functional, and radiographic findings. Radiology 171:613–618
142. Kaneko K, Sharma OP (1977) Airway obstruction in pulmonary sarcoidosis. Bull Eur Physiopathol Respir 13(2): 231–240
143. Levinson RS, Metzger LF, Stanley NN, et al (1977) Airway function in sarcoidosis. Am J Med 62:51–59
144. Gleeson FV, Traill ZC, Hansell DM (1996) Expiratory CT evidence of small airways obstruction in sarcoidosis. AJR 166: 1052–1054

Neoplasms of the Lung, Pleura and Chest Wall

Melissa L. Rosado-de-Christenson,
Gerald F. Abbott, Diane C. Strollo

3.3

Contents

Introduction

Benign and malignant neoplasms may affect the lung, the pleura and the chest wall. Malignant neoplasms in these anatomic locations may represent primary or secondary lesions. Radiologists play an important role in the diagnosis and staging of these tumors. Imaging allows correct prospective localization of a mass in one of the anatomic compartments of the thorax, a crucial first step in the formulation of an appropriate differential diagnosis. Common neoplasms of the lung, pleura and chest wall will be discussed with emphasis on radiologic-pathologic correlation.

Neoplasms of the Lung

Lung Cancer

Lung cancer is the leading cause of cancer mortality in the United States (US) for both men and women [1]. While lung cancer deaths in men had steadily declined after the mid 1990s, the recorded number of lung cancer deaths increased in the year 2000 in both men and women. It is expected that in 2003 there will be 171,900 new cases of lung cancer and 157,200 deaths from lung cancer in the US alone [1]. Because of its high frequency and case fatality rate, lung cancer represents the principal cancer worldwide based on number of cases and deaths [2]. Cigarette smoking is a major risk factor and is responsible for approximately 87% of all cases of lung cancer (90% in men; 79% in women) [3]. However, the etiology of lung cancer is probably multifactorial with evidence of an association with occupational and environmental exposures, underlying diseases and genetic susceptibility [4]. The prognosis of patients with lung cancer is poor; the five-year survival rate is 15% [5].

The vast majority (over 90%) of patients with lung cancer are symptomatic. Presenting symptoms may relate to central obstruction by the primary tumor, invasion of adjacent extrapulmonary structures, distant metastases or paraneoplastic syndromes. Approximately 6% of affected patients have no symptoms and are diagnosed incidentally because of an abnormal chest radiograph [6]. Symptoms and signs related to bronchial obstruction include cough, dyspnea and hemoptysis. Local invasion of the pleura, chest wall and mediastinum may manifest with pleuritic chest pain, Pancoast syndrome, superior vena cava obstruction, and neurologic dysfunction secondary to recurrent laryngeal nerve, phrenic nerve, sympathetic chain and/or stellate ganglion involvement. Symptoms may also relate to extrathoracic metastases, which may affect the lymph nodes, adrenal glands, central nervous system, liver, bones and skin. Paraneoplastic syndromes are systemic disorders associated with malignancy but not directly related to the primary neoplasm or its metastases and occur in up to

10% of patients with lung cancer. They include: hypercalcemia, inappropriate secretion of antidiuretic hormone, Cushing syndrome, digital clubbing and osteoarthropathy, and neurologic syndromes [6].

According to the most recent (1999) World Health Organization (WHO) classification, there are four major cell types of lung cancer: adenocarcinoma, squamous cell carcinoma, small cell carcinoma, and large cell carcinoma [7]. Lung cancers are classified based on their most differentiated components and are graded based on their least differentiated elements. However, it is recognized that lung cancers commonly demonstrate histologic heterogeneity with almost 50% of neoplasms exhibiting more than one cell type. Some primary pulmonary malignancies are considered neuroendocrine neoplasms based on light microscopy features of organoid nesting, palisading, and rosette and trabeculae formation. These neoplasms include: small cell carcinoma, carcinoid tumor and large cell neuroendocrine carcinoma [7]. Pre-invasive pulmonary lesions which may progress to invasive pulmonary malignancy are currently recognized [8].

Adenocarcinoma

Adenocarcinoma is the most frequently diagnosed cell type of lung cancer and is characterized by its slow local growth and its propensity for early metastases. It has a weak association with cigarette smoking and is the most common cell type of lung cancer that affects women and non-smokers [9]. Grossly, adenocarcinoma manifests as a peripheral subpleural nodule or mass that preferentially affects the upper lobes (Fig. 1A) and often exhibits central fibrosis and spiculated borders. Peripheral adenocarcinomas may invade and diffusely involve the pleura [10, 11]. Atypical adenomatous hyperplasia is an incidental microscopic finding that is often seen adjacent to resected lung cancers and probably represents a pre-invasive lesion that may progress to bronchioloalveolar carcinoma and ultimately to invasive adenocarcinoma [8]. Adenocarcinoma is characterized microscopically by glandular differentiation (Fig. 1B) and mucin production and may display acinar, papillary (Fig 1B), bronchioloalveolar, and solid with mucin formation growth patterns or a mixture of these [7]. Adenocarcinomas are associated with focal and diffuse pulmonary fibrosis. While fibrosis may antedate the development of neoplasia, as in cases of progressive systemic

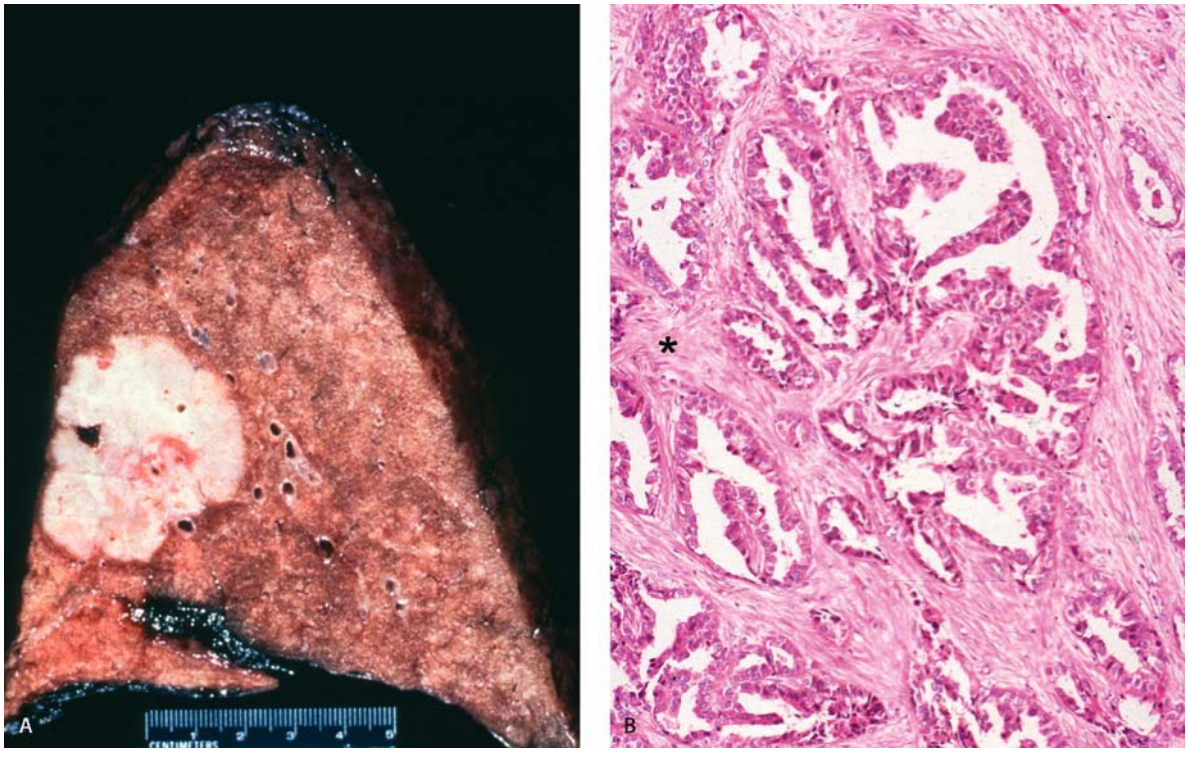

Fig. 1A, B. Adenocarcinoma, pathologic features. **A** Cut surface of a resected right upper lobe demonstrates a well-defined lobular subpleural mass with foci of internal hemorrhage and necrosis. **B** High power photomicrograph [hematoxylin and eosin (H-E) stain] shows a well-differentiated adenocarcinoma forming glands and papillary structures. Note fibrosis (*) surrounding the glandular elements of the tumor

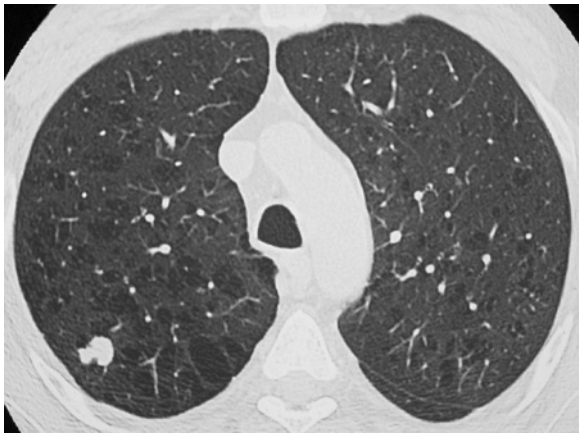

Fig. 2. Adenocarcinoma in an asymptomatic 64-year-old man. Unenhanced chest CT (lung window) demonstrates a 1 cm lobular right upper lobe solitary nodule and mild centrilobular emphysema

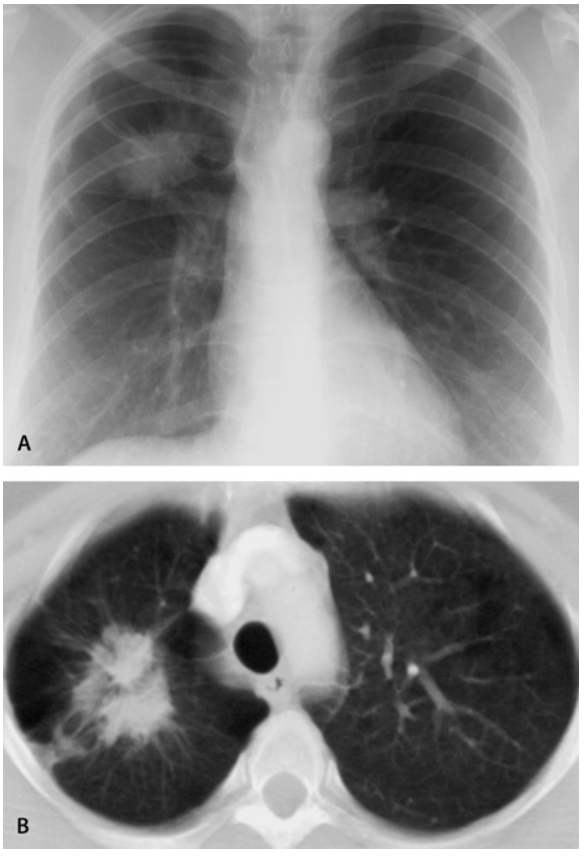

Fig. 3A, B. Adenocarcinoma in an asymptomatic 48-year-old woman. **A** Posteroanterior (PA) chest radiograph demonstrates a spiculated right upper lobe mass. **B** Chest CT (lung window) demonstrates a peripheral mass with spiculated borders and a pleural tag with adjacent focal pleural thickening

sclerosis and idiopathic pulmonary fibrosis, it more commonly represents a desmoplastic reaction to the tumor (Fig. 1B) [8, 9]. Adenocarcinoma typically manifests radiologically as a peripheral solitary pulmonary nodule (Fig. 2) or mass (Fig. 3). The tumor borders may be lobular (Fig. 2) and well-defined or spiculated (Fig. 3) and ill-defined. Peripheral adenocarcinomas may invade the adjacent pleura and chest wall. Rarely, pleural involvement progresses to diffuse and circumferential thickening that may mimic malignant pleural mesothelioma (Fig. 4) [4]. Adenocarcinoma often metastasizes to regional lymph nodes and/or distant sites.

Bronchioloalveolar carcinoma is a well-differentiated subtype of adenocarcinoma that arises beyond a recognizable bronchus. Grossly, it may manifest as a peripheral solitary nodule or consolidation (Fig. 5A), but may also exhibit bronchial dissemination resulting in multifocal pulmonary nodules, masses and/or consolidations [12]. Bronchioloalveolar carcinoma exhibits a characteristic growth pattern in which neoplastic cells line the air spaces without destroying the underlying pulmonary interstitium and use it as "scaffolding" for their growth (Fig. 5B) [9]. The histologic diagnosis requires absence of stromal, vascular or pleural invasion. As a result, the diagnosis cannot be established on small biopsy samples, and complete surgical excision and thorough tumor sampling is required as invasive adenocarcinomas may exhibit a bronchioloalveolar growth pattern [7, 13]. Bronchioloalveolar carcinoma, like other adenocarcinomas manifests radiologically as a peripheral solitary nodule (Fig. 6) or mass. It may also manifest as a parenchymal consolidation (Fig. 7) or as multifocal lung nodules, masses or consolidations [9]. Computed tomography (CT) and high-resolution computed tomography (HRCT) demonstrate focal ground glass at-

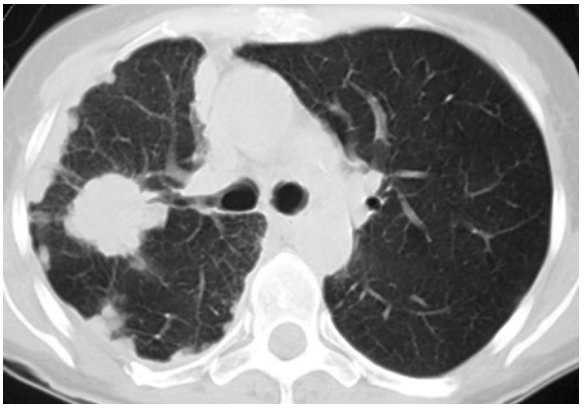

Fig. 4. Adenocarcinoma in a 43-year-old woman with advanced lung cancer. Unenhanced chest CT (lung window) demonstrates a peripheral lobular right upper lobe mass with associated ipsilateral circumferential nodular pleural thickening

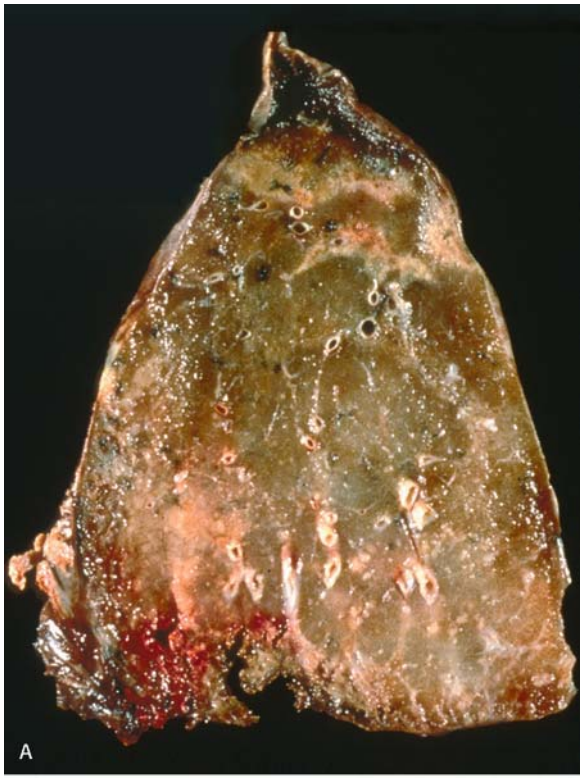

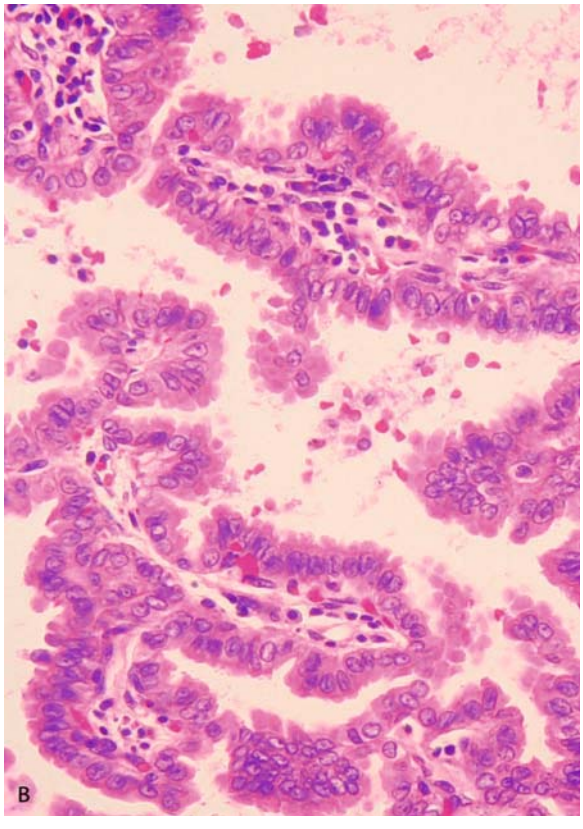

tenuation or nodules with components of ground glass opacity. Other appearances include focal consolidation and centrilobular opacities [14, 15]. Bronchioloalveolar carcinomas that manifest with consolidation may also exhibit the "CT angiogram" sign in which enhancing normal pulmonary vessels are identified within the tumor. Diffuse bronchioloalveolar carcinoma may manifest with multifocal ground glass opacities, consolida-

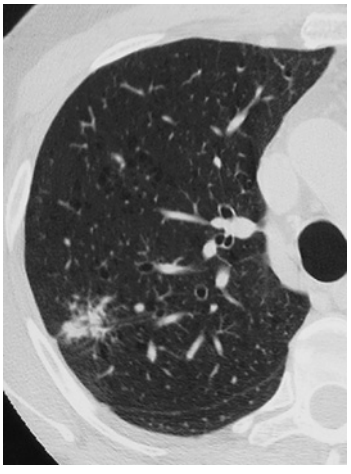

Fig. 6. Bronchioloalveolar carcinoma in an asymptomatic adult. Unenhanced chest CT (lung window) demonstrates an irregular right upper lobe nodule of heterogeneous attenuation with intrinsic air bronchiolograms

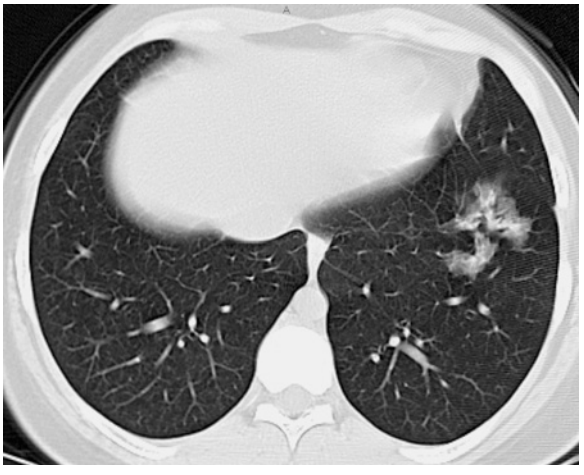

Fig. 7. Bronchioloalveolar carcinoma in a 44-year-old man with cough. Unenhanced chest CT (lung window) demonstrates a patchy subsegmental left lower lobe consolidation with internal air bronchiolograms

Fig. 5A, B. Bronchioloalveolar carcinoma, pathologic features. **A** Cut specimen of a resected left lower lobe demonstrates diffuse bronchioloalveolar carcinoma manifesting as homogeneous consolidation. **B** High-power photomicrograph (H-E stain) demonstrates columnar peg-like neoplastic cells lining the alveolar walls without destroying the underlying pulmonary interstitium

tions, and nodules which may exhibit a centrilobular distribution [16]. While air bronchograms, air bronchiolograms (Fig. 6) and cystic changes may occur, the latter may be more characteristic of adenocarcinoma [13, 15, 16].

Squamous Cell Carcinoma

Squamous cell carcinoma exhibits rapid local growth and late metastases and is strongly related to cigarette smoking [9]. It is typically a central neoplasm that arises from the mucosa of large bronchi as an irregular polypoid tumor, which often produces bronchial wall invasion and irregular narrowing of the bronchial lumen (Fig. 8A). However, peripheral squamous cell carcinomas are increasingly reported [17]. The postulated pre-invasive lesions for squamous cell carcinoma are squamous dysplasia and carcinoma *in situ* [8]. Squamous cell carcinomas are characterized by keratinization and intercellular bridges. These features are characteristic of well-differentiated neoplasms which may also form squamous pearls (individual cells with markedly eosinophilic cytoplasm) (Fig. 8B) [7]. Because of their central location, squamous cell carcinomas often manifest radiologically as hilar or perihilar masses (Fig. 9). Early lesions may produce focal bronchial wall

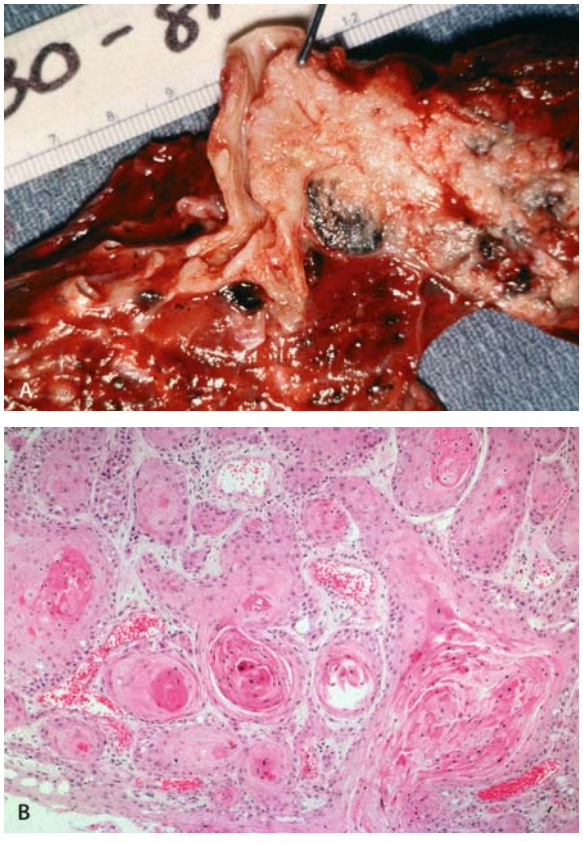

Fig. 8A, B. Squamous cell carcinoma, pathologic features. **A** Gross specimen of a squamous cell carcinoma of the right main stem bronchus demonstrates a lobular endobronchial mass partially obstructing the bronchial lumen. The mass invades the bronchial wall, an adjacent lymph node, and the surrounding lung parenchyma. **B** High-power photomicrograph (H-E stain) of a well-differentiated squamous cell carcinoma demonstrates flattened neoplastic cells with moderate amounts of eosinophilic cytoplasm. Rounded collections of eosinophilic material represent squamous pearls, seen in typical of well-differentiated neoplasms. Figure 8a is reproduced with permission from [9]

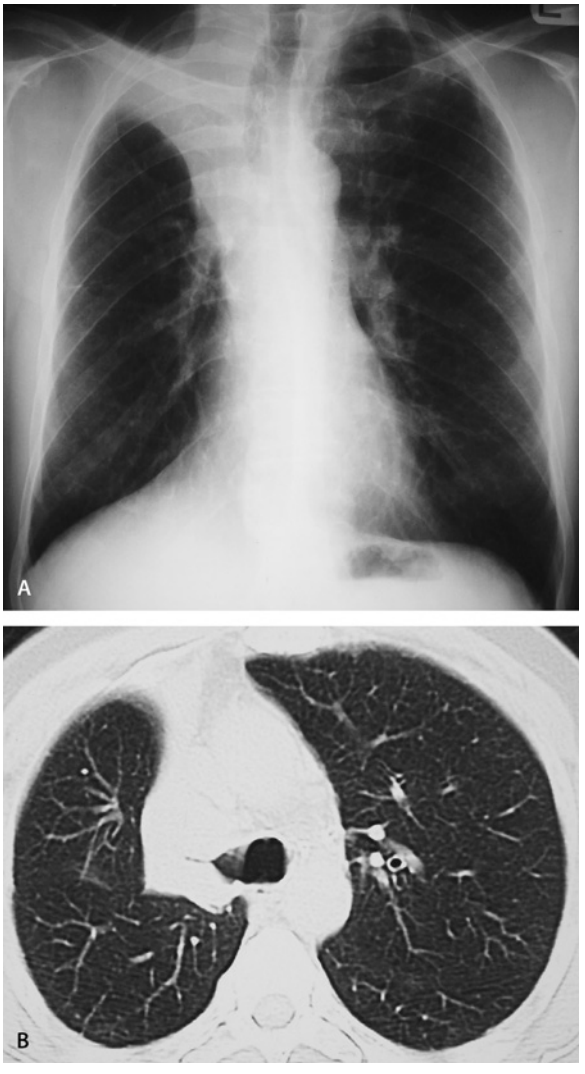

Fig. 9A, B. Squamous cell carcinoma in an elderly man with cough and hemoptysis. **A** PA chest radiograph demonstrates marked volume loss of the right upper lobe with associated ipsilateral tracheal deviation and a central convexity at the hilum. The findings are consistent with a central mass with associated atelectasis producing the S-sign of Golden. **B** Unenhanced chest CT (lung window) demonstrates irregular narrowing of the right main stem bronchus by an adjacent central mass with resultant right upper lobe atelectasis. Endoscopic biopsy revealed squamous cell carcinoma

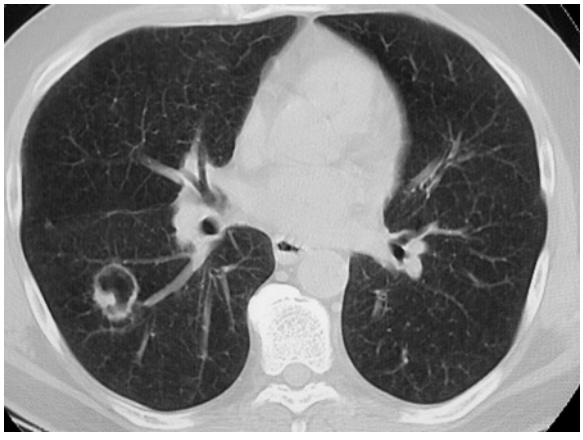

Fig. 10. Peripheral squamous cell carcinoma in an asymptomatic middle aged man. Unenhanced chest CT (lung window) demonstrates a peripheral right lower lobe cavitary mass with an irregular and nodular cavity wall

thickening. Bronchial obstruction is common and may result in atelectasis or post-obstructive pneumonia. In these cases, the central neoplasm manifests as a focal convexity in continuity with the distal concavity formed by the fissure adjacent to the collapsed lung (the radiographic "S-sign of Golden") (Fig. 9). Peripheral squamous cell carcinomas (and adenocarcinomas) may exhibit cavitation (Fig. 10) or may manifest as Pancoast tumors. The latter arise in the pulmonary apex and may invade adjacent osseous and soft tissue structures (Fig. 11). Affected patients may present with the Pancoast syndrome: ipsilateral shoulder or arm pain which may be associated with atrophy of upper extremity muscles and Horner syndrome [4, 9].

Small Cell Carcinoma

Small cell carcinoma is a highly aggressive malignant neuroendocrine neoplasm that is strongly related to cigarette smoking and typically exhibits rapid local growth and early metastases. In fact, the majority of affected patients have metastatic disease at presentation. A small number of patients present with a clinical hormone syndrome such as ectopic production of adrenocorticotropic hormone (ACTH) characterized by weakness, muscle wasting, drowsiness, confusion, edema, hypokalemic alkalosis and hyperglycemia [6]. Small cell carcinoma is a central lung cancer that often manifests as a hilar or perihilar mass associated with extensive lymph node metastases. Tumor growth is typically submucosal resulting in smooth stenosis of the bronchial lumen with rare endobronchial growth. Extensive necrosis is characteristic [9, 18]. A pre-invasive lesion for small cell carcinoma has not been identified [7]. Microscopically, small cell carcinoma is characterized by

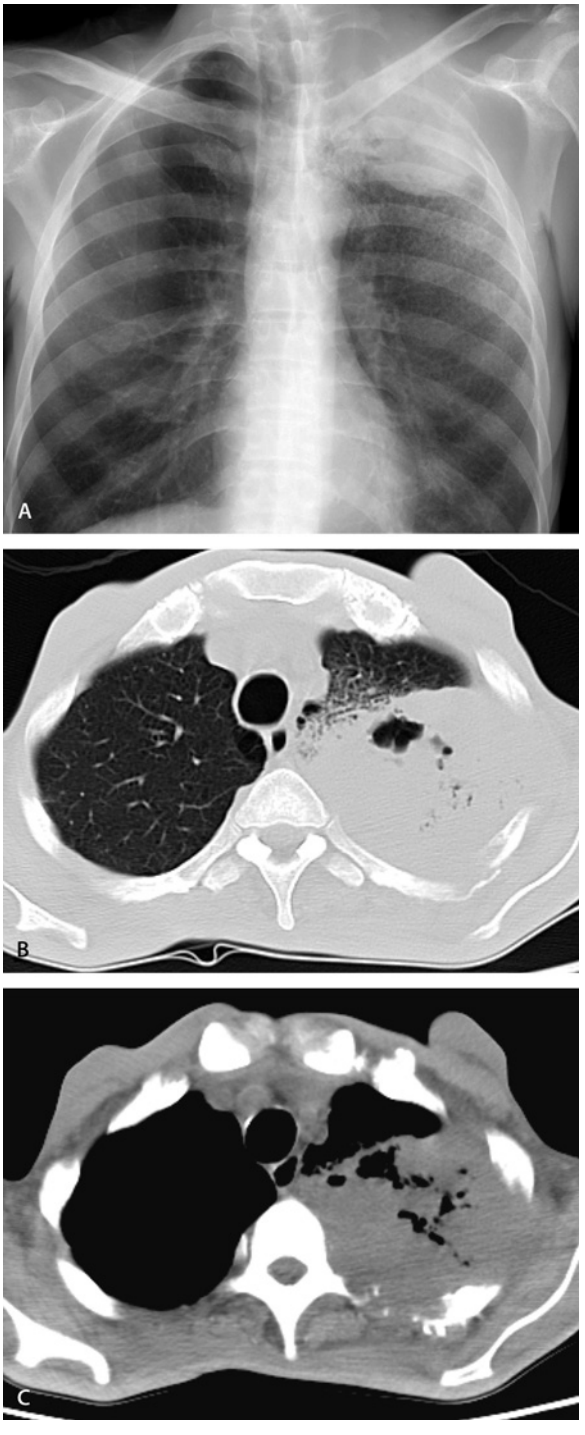

Fig. 11A–C. Peripheral squamous cell carcinoma in an elderly man who presented with Pancoast syndrome. **A** PA chest radiograph demonstrates a left apical lung mass with extensive destruction of the posterior aspects of the first four left ribs. **B**, **C** Unenhanced chest CT (lung and mediastinal window) demonstrates the large left apical cavitary mass with associated rib destruction

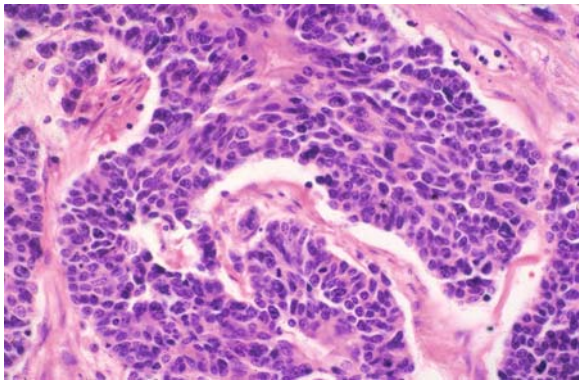

Fig. 12. Small cell carcinoma, microscopic features. High-power photomicrograph (H-E stain) of a small cell carcinoma demonstrates small cells with round-to-oval nuclei, absent nucleoli, and scant cytoplasm

small cells with scant cytoplasm and small round or oval nuclei with finely granular chromatin and absent nucleoli (Fig. 12). Mitotic rates are high with 11 or more mitoses per ten high power fields (HPF) and an average of 60 to 70 mitoses per 10 high power fields (HPF) [7]. Radiologically, there is usually a large hilar or perihilar mass with extensive mediastinal lymphadenopathy (Fig. 13). In fact, the primary pulmonary tumor may not be evident, and the principal finding may be hilar and/or mediastinal metastatic lymph node enlargement. Small cell carcinoma produces little desmoplastic reaction, violates tissue planes and readily invades adjacent structures. It is the most common cause of superior vena cava obstruction (Fig. 13). Rarely, small cell carcinoma manifests as a peripheral solitary nodule or mass [4, 9].

Large Cell Carcinoma

Large cell carcinoma is an undifferentiated primary lung cancer that lacks the histologic features of the above mentioned cell types of lung cancer [7]. Grossly, it manifests as a large peripheral lung mass [9]. Microscopy demonstrates large cells with large nuclei and prominent nucleoli [7]. Radiologic imaging typically shows a large pulmonary mass which may exhibit cavitation and central low attenuation corresponding to tumor necrosis [9].

Carcinoid

Carcinoid is an uncommon primary malignant neuroendocrine neoplasm of the lung and accounts for approximately 2% of lung tumors. Affected patients are typically adult males and females who are generally younger than patients with lung cancer. Carcinoid is the most common primary lung neoplasm of childhood.

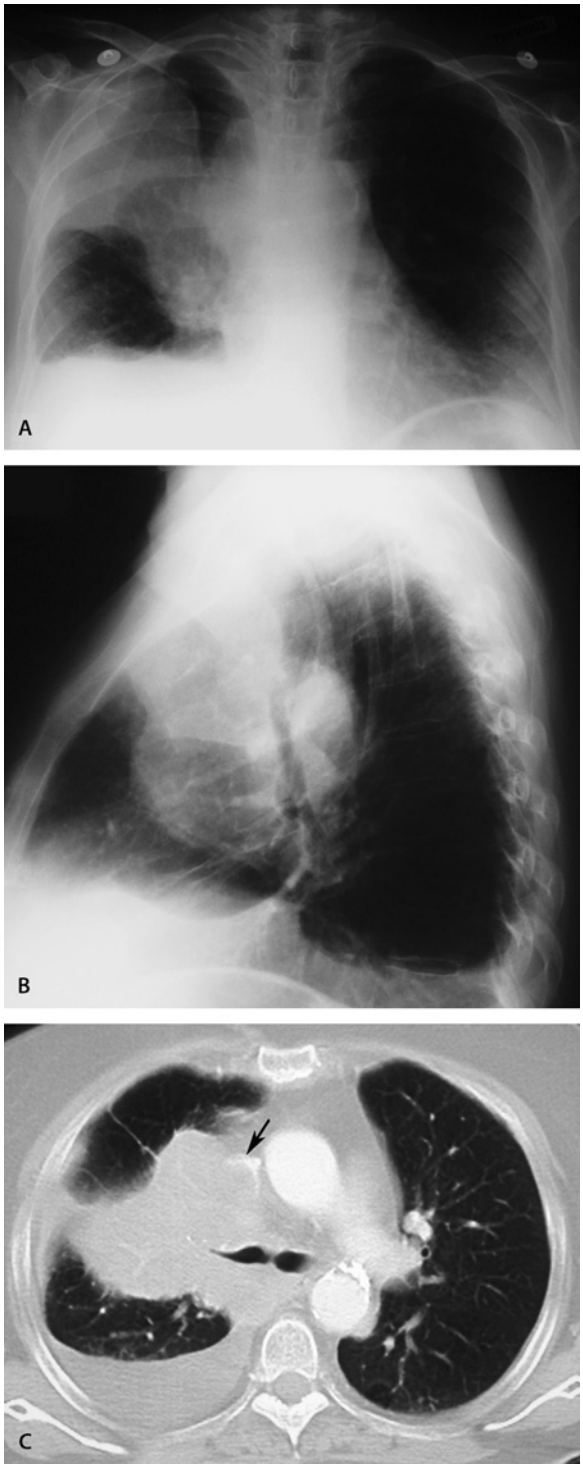

Fig. 13A–C. Small cell carcinoma in a 69-year-old man with neck swelling, dyspnea and weight loss. **A**, **B** PA and lateral chest radiographs demonstrate a large right perihilar mass with ipsilateral mediastinal lymphadenopathy, right upper lobe volume loss and right pleural effusion. **C** Contrast-enhanced chest CT (lung window) demonstrates a large soft tissue mass which encases the right main stem bronchus, produces smooth narrowing of the bronchial lumen and invades the superior vena cava (arrow). Note the large right pleural effusion

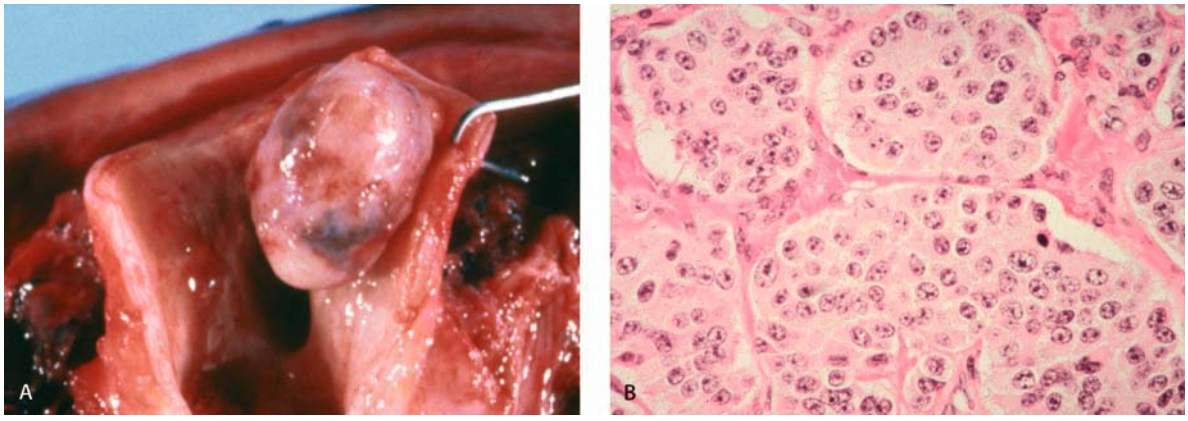

Fig. 14A, B. Bronchial carcinoid, pathologic features. **A** Gross specimen of a carcinoid tumor demonstrates a well-defined endobronchial ovoid and lobular polypoid mass. The metallic hook holds open one of the walls of the bisected bronchus. **B** High-power photomicrograph (H-E stain) of a typical bronchial carcinoid demonstrates uniform cells distributed in an organoid pattern. The cells have moderate amounts of granular cytoplasm and nuclei with a finely stippled chromatin. Fig 14a is reproduced with permission from [19]

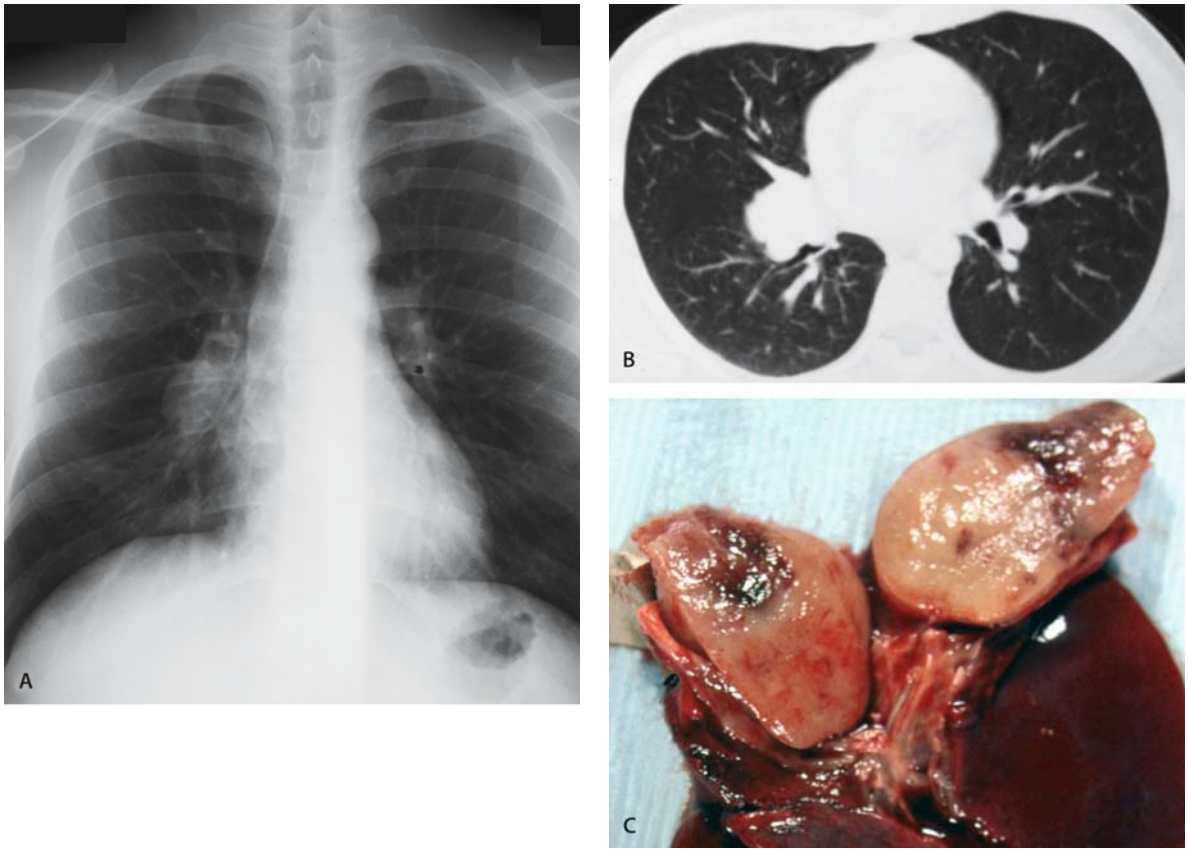

Fig. 15A–C. Bronchial carcinoid in a 35-year-old man with fever, hemoptysis and recurrent pneumonia. **A** PA chest radiograph demonstrates right upper lobe atelectasis and suggests a central hilar mass. **B** Contrast-enhanced chest CT (lung window) demonstrates a central mass that produces bronchial obstruction. Note the endoluminal component of the lesion. While the lesion could represent lung cancer, the diagnosis of carcinoid is more likely in this young patient. **C** Cut section through the tumor demonstrates a well-defined lobular ovoid soft tissue mass with focal hemorrhage which almost completely obstructs the bronchial lumen. Figs. 15a and 15b are reproduced with permission from [19]

There is no documented association between carcinoid and cigarette smoking or exposure to other carcinogens. Affected patients often present with symptoms of central airway obstruction: cough, recurrent pulmonary infection and hemoptysis. However, a significant number of patients are asymptomatic. Approximately 2% of patients present because of ectopic ACTH production [19]. Grossly, carcinoids are well-circumscribed central masses that frequently display a polypoid endobronchial component (Fig. 14A) and bronchial wall invasion. Carcinoids may be partially or completely endobronchial, may abut an adjacent bronchus, or may manifest as peripheral solitary nodules or masses [19, 20]. Microscopically there are uniform neoplastic cells with eosinophilic cytoplasm and nuclei with a finely-stippled chromatin (Fig. 14B). Carcinoids are classified as typical or atypical based on the number of mitoses seen at microscopic evaluation. Typical carcinoids exhibit fewer than 2 mitoses per 10 high power fields (HPF) and no necrosis, and atypical carcinoids demonstrate 2 to 10 mitoses per 10 HPF and/or areas of necrosis [7]. While both typical and atypical carcinoids may produce lymph node metastases, atypical carcinoids are more aggressive neoplasms with a higher propensity for metastatic spread [19]. Radiologically, carcinoid is a central well-marginated lobular mass, which commonly demonstrates an endobronchial component (Fig. 15) and is often associated with distal consolidation, atelectasis, bronchiectasis and/or mucoid impaction. Peripheral carcinoid often manifests as a well-defined spherical nodule or mass of lobular contours. CT typically demonstrates a well-defined nodule or mass and may show an associated endobronchial component or bronchial relationship (Fig. 15B) and is useful in demonstrating and characterizing post-obstructive sequelae such as consolidation, atelectasis, and bronchiectasis. In addition, CT allows detection of enlarged hilar and mediastinal lymph nodes which may result from metastatic involvement [19]. Although carcinoid is a malignant neoplasm, the prognosis of patients with typical carcinoid is excellent with 92.4% five-year survivals following surgical excision. Patients with atypical carcinoids have a less favorable prognosis [19]

Hamartomas

Hamartomas are the most common benign lung neoplasms and represent approximately 8% of all pulmonary neoplasia [21]. Affected patients are typically middle-aged or elderly adults with a peak incidence in the sixth or seventh decades of life. Males are more commonly affected than females with a male-to-female ratio of 3:1. The overwhelming majority of patients are asymptomatic [22]. While hamartomas are composed of an abnormal mixture of tissues that are normally found in the lung, the 1999 WHO classification characterizes them as benign lung neoplasms [7]. Hamartomas are usually solitary, well-circumscribed nodules which commonly exhibit a cartilaginous consistency (Fig. 16A). The majority of lesions occur in the lung periphery, but approximately 10% are endobronchial [23]. Microscopically they are composed of connective tissue including cartilage, fibrous tissue and adipose tissue (Fig. 16B), intersected by epithelial clefts [7, 24]. Radiography usually demonstrates a well-defined solitary pulmonary nodule which exhibits calcification in less than 10% of cases. Popcorn-like calcification may be identified in hamartomas and is a reliable indicator of benignity [24]. Classic CT features that allow a confident prospective diagnosis are the presence of areas of fat attenuation (seen in up to 50% of cases) with or without foci of calcification within a well-defined pulmonary nodule (Fig. 17) [24, 25]. Hamartomas do not undergo malignant transformation, and affected patients have an excellent prognosis.

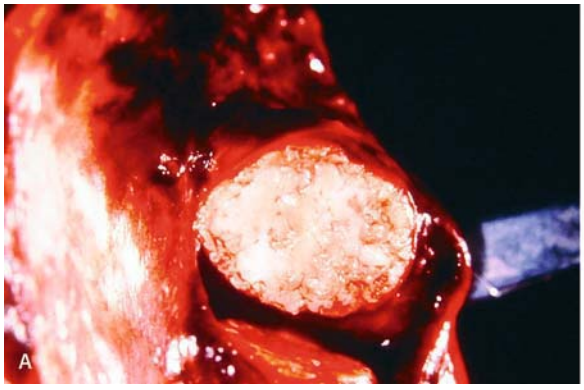

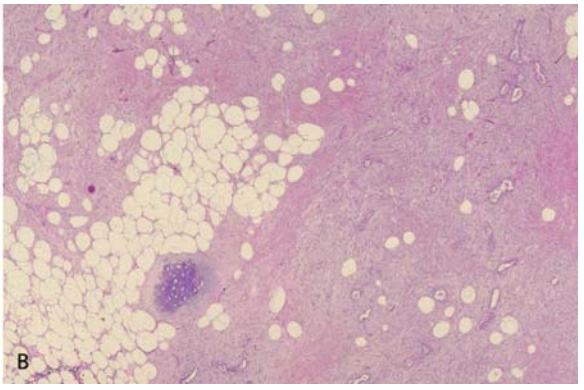

Fig. 16A, B. Hamartoma, pathologic features. **A** Cut section of a hamartoma demonstrates a well-defined lobular pulmonary nodule with a glistening cut surface consistent with its cartilaginous content. **B** High-power photomicrograph (H-E stain) demonstrates fibrous tissue, adipose tissue and a focal area of cartilage. Fig 16b is reproduced with permission from [24]

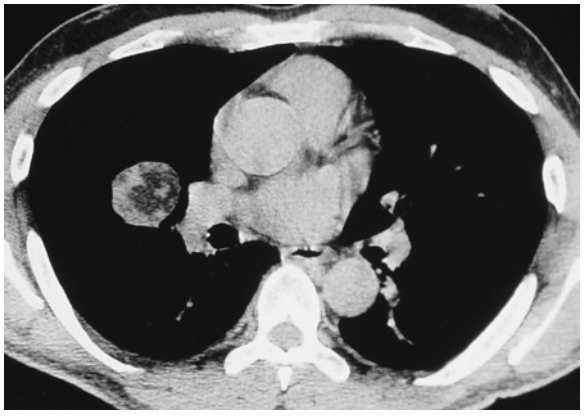

Fig. 17. Hamartoma in a 48-year-old man who presented with hemoptysis. Unenhanced chest CT (mediastinal window) demonstrates a well-defined lobular solitary pulmonary nodule with internal fat and soft tissue attenuation

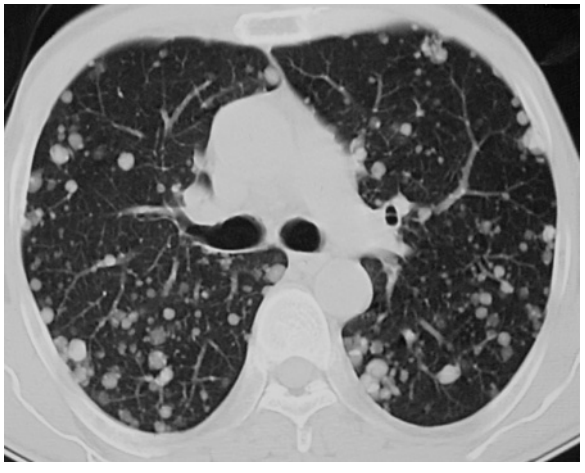

Fig. 18. Pulmonary metastases in a young man who presented with dyspnea and metastatic carcinoma of unknown origin. Unenhanced chest CT (lung window) demonstrates multifocal pulmonary nodules of various sizes and well-defined borders. Note that the nodules are more profuse in the lung periphery, have a spherical morphology and bear a relationship to adjacent pulmonary arteries (angiocentric distribution)

Pulmonary Metastases

Pulmonary metastases represent the most common neoplasms of the lung and typically result from hematogenous dissemination of extrapulmonary malignancies. Lung metastases may also occur via lymphatic dissemination [26]. Primary pulmonary neoplasms rarely exhibit tracheobronchial dissemination which results in multifocal lung lesions [4]. Radiologically, metastases are usually multiple spherical nodules or masses with well-defined borders and an angiocentric distribution (a pulmonary vessel entering the medial aspect of the lung nodule). Metastases are more numerous in peripheral subpleural locations and the lower lobes (the latter reflects the preferential pulmonary blood flow to the lung bases) (Fig. 18). Hemorrhagic metastases may exhibit ill-defined borders [26]. Unusual radiologic manifestations of metastatic disease include solitary lesions, calcification, cavitation, and lymphangitic carcinomatosis [27].

Neoplasms of the Pleura

Primary pleural neoplasms are rare; most pleural neoplasms are secondary to metastatic disease. Pleural masses that form obtuse angles with the adjacent pleural surface typically exhibit "clasic" radiographic features of extrapulmonary lesions and display "incomplete" borders on radiography. This discrepancy in margin visualization results when some portions of a lesion are imaged in profile while others are imaged en face (Fig. 20A). Cross-sectional imaging is helpful in excluding chest wall involvement, identifying multifocal disease and determining extent of involvement.

Localized Fibrous Tumor of the Pleura

Localized fibrous tumor of the pleura is a rare primary pleural neoplasm that typically affects adults in the fifth through eighth decades of life. Patients typically present with symptoms which relate to large tumor sizes and include dyspnea, chest pain and cough. Patients rarely present with clubbing, hypertrophic osteoarthropathy and/or episodic hypoglycemia. However, a significant number of patients, usually those with small-to-moderate-sized tumors, may be entirely asymptomatic. Grossly, localized fibrous tumors are solitary, encapsulated, and often pedunculated lobular masses that typically arise from the visceral pleura. The cut surface often shows a whorled nodular pattern (Fig. 19A) and may exhibit necrosis, hemorrhage or cystic degeneration particularly in large masses [28]. Microscopy demonstrates low-grade neoplasms of variable cellularity composed of spindle-shaped cells with round-to-oval nuclei arranged in a haphazard pattern amid abundant collagen bundles (Fig. 19B). While most localized fibrous tumors are benign, malignant lesions also occur. Microscopic criteria for malignancy include high cellularity, pleomorphism and more than four mitoses per 10 HPF. Radiography demonstrates well-defined lobular solitary masses which may reach enormous sizes and rarely exhibit features of a pleural (extraparenchymal) location. A fissural location and mobility within the thorax with positional changes may suggest the correct diagnosis (Fig. 20). The majority of localized fibrous tumors are located in the mid and inferior hemithorax and, when in contiguity with the diaphragm, may mimic diaphrag-

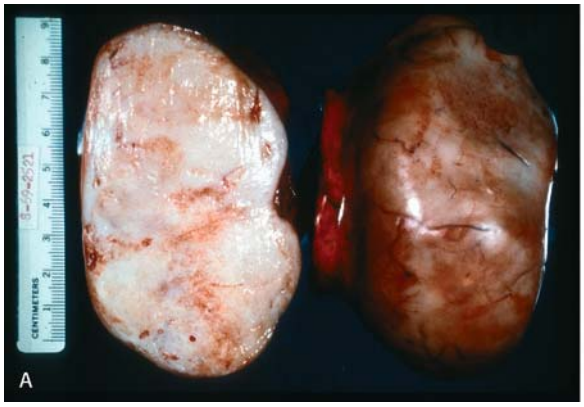

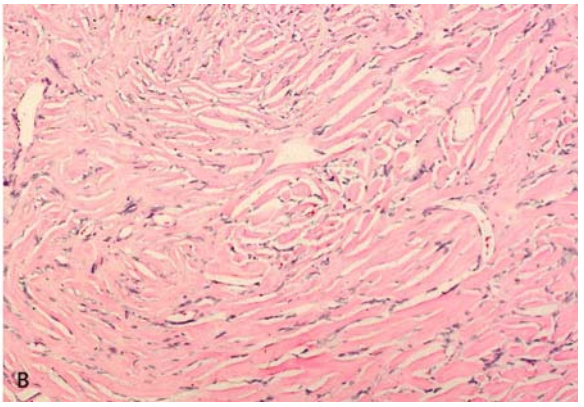

Fig. 19A, B. Localized fibrous tumor of the pleura, pathologic features. **A** Photograph of the cut and external surfaces of a resected localized fibrous tumor of the pleura demonstrates an encapsulated ovoid mass with a whorled fibrous internal appearance. Note the broad pedicle that connected the lesion to the visceral pleura. **B** High power photomicrograph (H-E stain) demonstrates a haphazard arrangement of effaced elongate cells amid strands of ropy collagen

matic elevation on radiography (Fig. 21). CT typically demonstrates a heterogeneous soft tissue mass that usually forms acute angles with the adjacent pleural surfaces (Fig. 22). Contrast enhancement is common and highlights the heterogeneous attenuation of these lesions (Fig. 22). Calcification occurs in approximately 26% of cases. Most patients (88%) are cured by complete surgical excision although both benign and malignant lesions may recur locally [28].

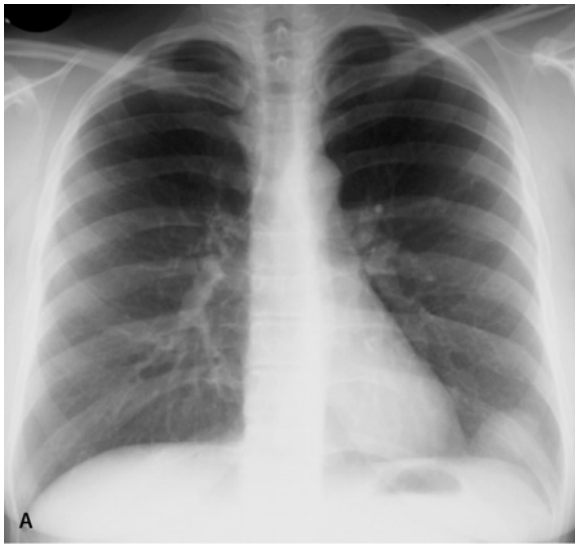

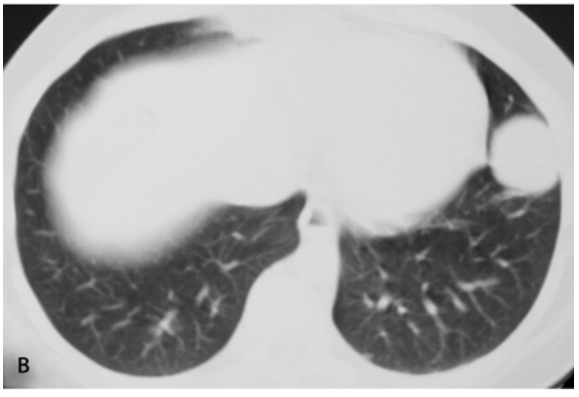

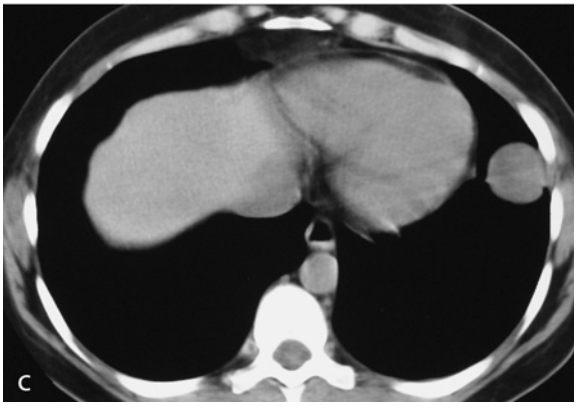

Fig. 20A–C. Localized fibrous tumor of the pleura in an asymptomatic 52-year-old woman. **A** PA chest radiograph demonstrates a rounded mass at the left inferior hemithorax. Note that some of the lesion borders are poorly visualized. **B**, **C** Unenhanced chest CT (lung and mediastinal window) demonstrates a spherical homogeneous mass located in the left major fissure. At surgery, a pedunculated histologically benign localized fibrous tumor was resected

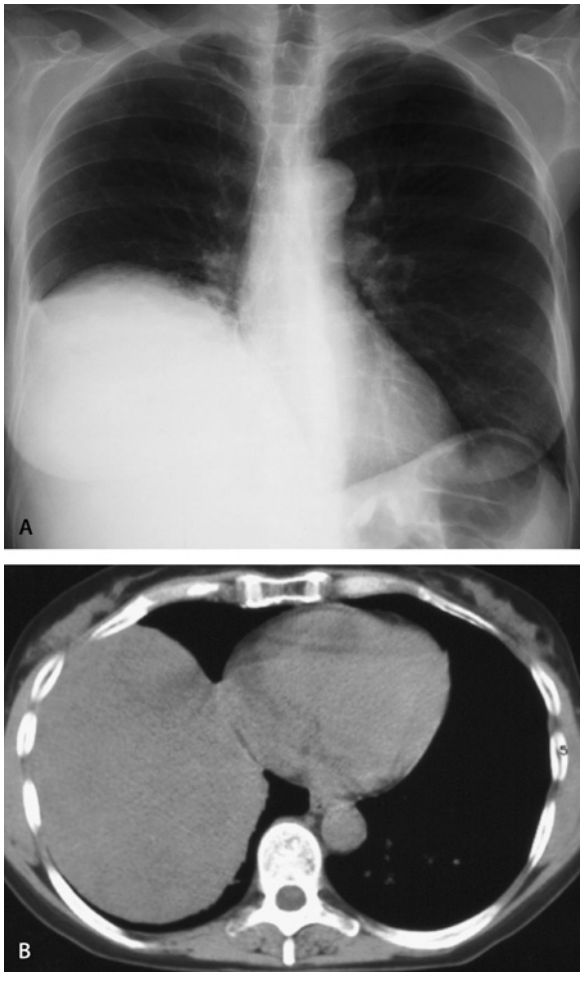

Fig. 21A, B. Localized fibrous tumor of the pleura in a 64-year-old woman with confusion and hypoglycemia. **A** PA chest radiograph demonstrates a large soft tissue mass with a well-defined superior border occupying the right inferior hemithorax. Note that the mass mimics diaphragmatic elevation. **B** Unenhanced chest CT (mediastinal window) demonstrates a large mass of homogeneous soft tissue attenuation

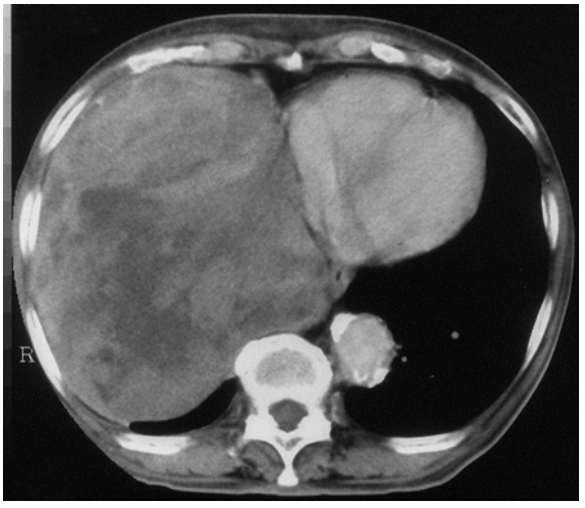

Fig. 22. Localized fibrous tumor of the pleura in a 74-year-old woman who presented with hypoglycemia. Contrast-enhanced chest CT (mediastinal window) demonstrates a large lobular mass of heterogeneous enhancement which occupies most of the right hemithorax and produces mass effect on the mediastinum. Note that the lesion forms acute angles with the adjacent pleural surfaces

Malignant Mesothelioma

Malignant mesothelioma is the most common primary neoplasm of the pleura and is related to occupational exposure to asbestos. Approximately 3,000 cases are reported annually in the US [29]. Affected patients are typically in the sixth and seventh decades of life and present with an insidious onset of chest pain, progressive dyspnea, constitutional symptoms, cough, and/or weight loss. Men are more frequently affected than women [29]. Grossly, mesotheliomas manifest as diffuse pleural masses that affect both the visceral and parietal surfaces and circumferentially encase the lung (Fig. 23A). Characteristically there is greater involvement of the parietal pleura (Fig. 23b) and the inferior hemithorax [29, 30]. Early mesothelioma may manifest with multifocal pleural nodules or masses [7]. Advanced mesothelioma may invade the adjacent lung, mediastinum, chest wall and diaphragm and may metastasize to distant sites [29, 30]. Mesothelioma exhibits several histologic patterns including epithelioid, sarcomatoid and biphasic types (Fig. 23B). Epithelioid malignant mesotheliomas must be distinguished from lung adenocarcinomas with diffuse pleural involvement. This is accomplished with immunohistochemistry [7]. Radiography of patients with mesothelioma typically demonstrates unilateral diffuse circumferential pleural thickening or masses (Fig. 24) with or without an associated pleural effusion, but unilateral pleural effusion may be the only finding. There may be volume loss in the affected hemithorax and mediastinal fixation. CT demonstrates circumferential nodular pleural thickening with frequent involvement of the interlobar fissures (Fig.

Fig. 23A, B. Diffuse malignant mesothelioma, pathologic features. **A** Cut surface of an extrapleural pneumonectomy lung specimen demonstrates circumferential nodular lung encasement by tumor, growth into the fissure and focal invasion of the lung parenchyma. **B** Low-power photomicrograph (H-E stain) of a biphasic malignant mesothelioma demonstrates tumor involvement of both the visceral and parietal pleural surfaces. Note that the bulk of the tumor affects the parietal pleura. Figure 23b is reproduced with permission from [29]

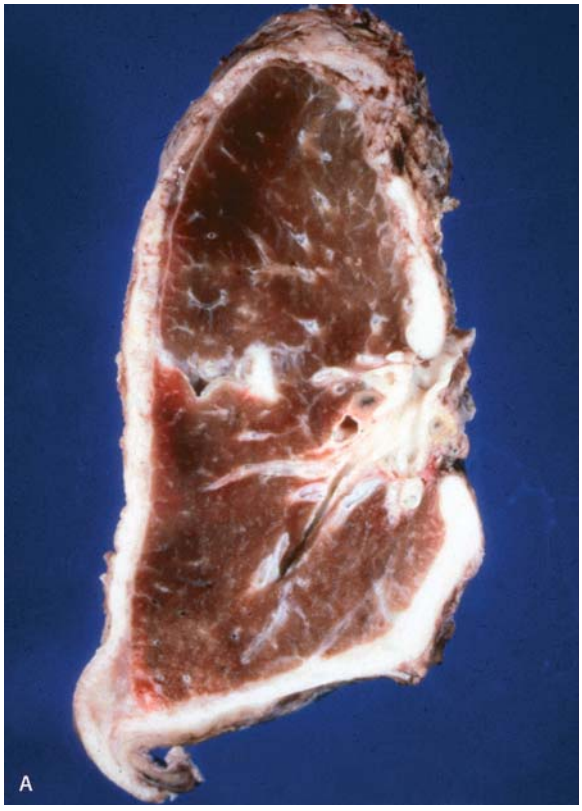

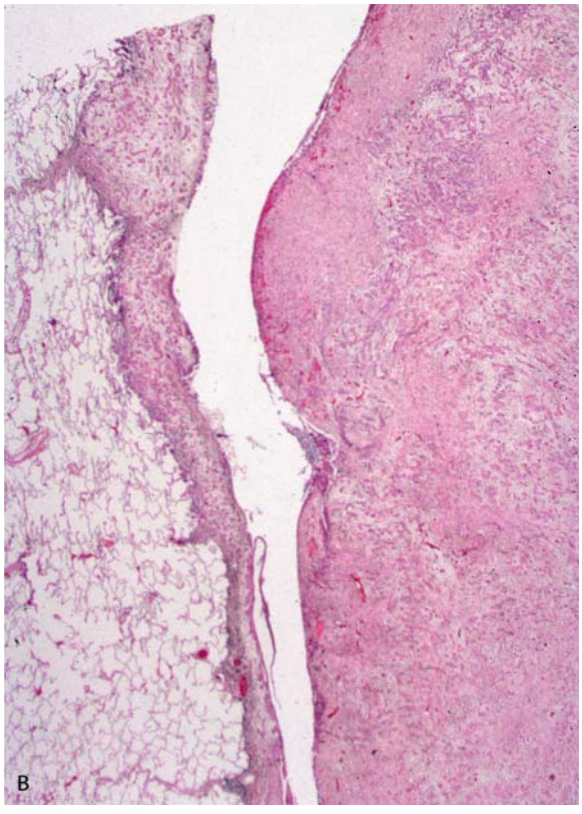

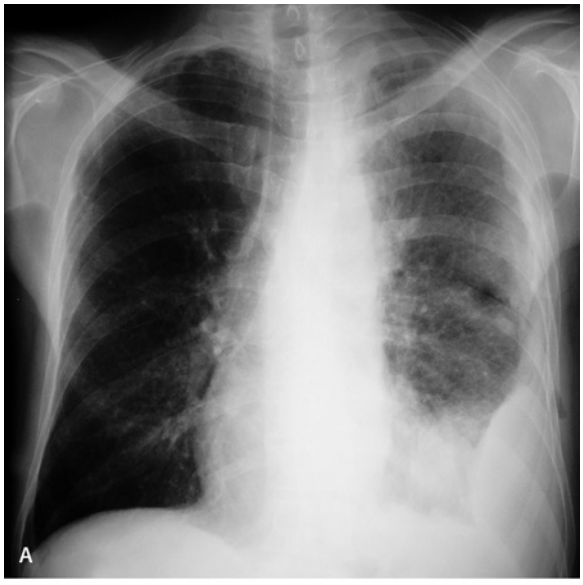

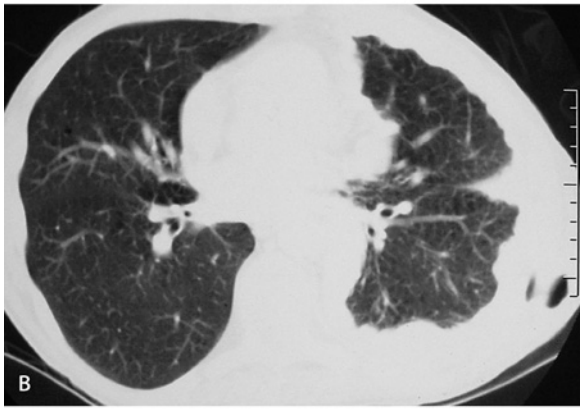

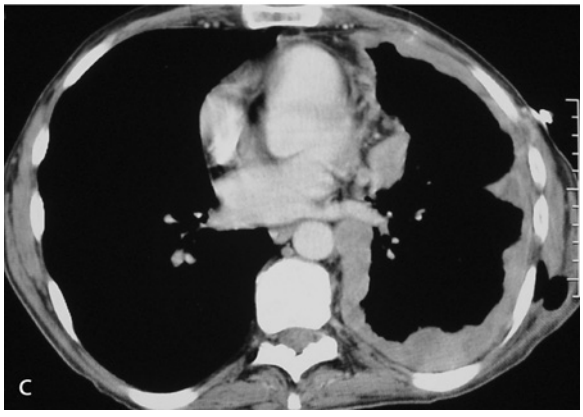

Fig. 24A–C. Malignant mesothelioma in a 56-year-old man with progressive dyspnea, weight loss and chest pain. **A** PA chest radiograph demonstrates circumferential nodular pleural thickening that encases the left lung and reduces its volume. **B, C** Contrast-enhanced chest CT (lung and mediastinal window) demonstrates nodular circumferential pleural thickening that affects the mediastinal pleura, encases the lung and extends into the major fissure. The chest wall defect resulted from a prior biopsy

24B, C). Pleural effusion is common. Ipsilateral volume loss (Fig. 24) is more common than ipsilateral increase in lung volume. Pleural calcification occurs in only 20% of patients [31]. While CT findings are very suggestive of malignant pleural thickening, mesothelioma cannot be differentiated from pleural metastases [32]. CT and MR are used in preoperative staging to exclude invasion of local structures, contralateral disease and intraabdominal involvement [33]. Although some patients with mesothelioma undergo extrapleural pneumonectomy for cure, most have advanced disease at presentation and invariably succumb to their disease [29, 33].

Pleural Metastases

Pleural metastases typically manifest as unilateral or bilateral pleural effusions. The most common primary neoplasms associated with malignant pleural effusions are lung cancer and breast cancer. Pleural metastases may also manifest as pleural masses (Fig. 25) and may exhibit circumferential pleural involvement, fissural growth and lung encasement, mimicking malignant mesothelioma. Circumferential pleural thickening may be seen in advanced lung cancer (Fig. 4), pleural metastases from other malignancies, invasive thymoma, and lymphoma. CT features of malignant pleural thickening include nodular pleural thickening, pleural thickening greater than 1 cm, and thickening of the mediastinal pleura [32].

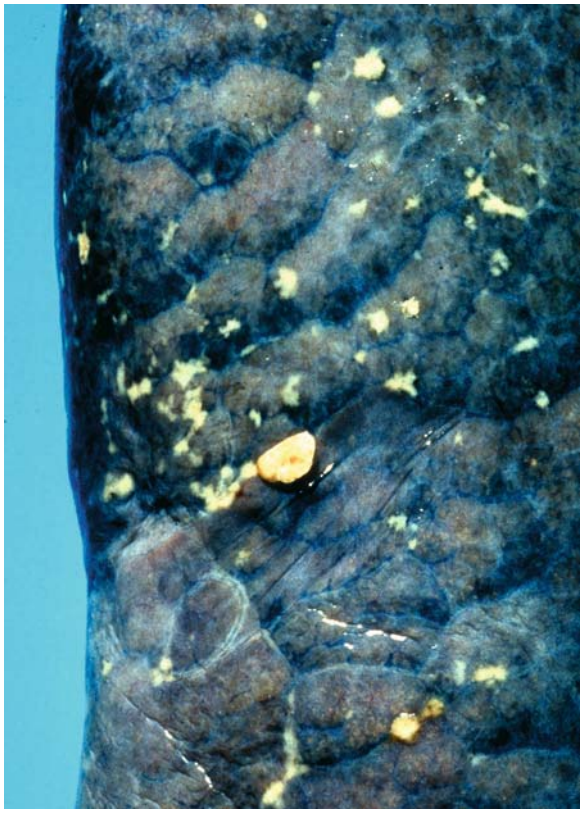

Fig. 25. Solid pleural metastases, gross features. Autopsy photograph of the lung surface of a patient who died of metastatic breast carcinoma demonstrates multiple pleural metastases manifesting as nodules of various sizes distributed over the visceral pleura

Neoplasms of the Chest Wall

Chest wall neoplasms may originate in the soft tissues or osseous structures and may represent primary or secondary lesions. Primary malignant chest wall neoplasms typically affect adults and include chondrosarcoma, myeloma, lymphoma, fibrosarcoma, and malignant fibrohistiocytoma. Metastases are common chest wall malignancies. Malignant chest wall neoplasms that affect children and adolescents include lymphoma and primitive neuroectodermal tumors (metastatic neuroblastoma, Ewing sarcoma, and Askin tumor) [34, 35]. Malignant chest wall neoplasms typically produce symptoms including focal chest pain, a palpable mass, or a pathologic fracture.

Benign soft tissue neoplasms include lipomas, neurogenic neoplasms, fibromas, angiofibromas and desmoid tumors. Benign osseous neoplasms include osteochondromas and enchondromas. Benign chest wall neoplasms typically affect asymptomatic adults who are diagnosed because of an incidental radiographic abnormality.

Chest wall masses (like pleural masses) exhibit incomplete visualization of lesion margins on radiography, an indication of their extrapulmonary location. The “incomplete border” sign, together with radiographic evidence of adjacent soft tissue or osseous involvement indicates a chest wall location. Cross-sectional imaging further refines lesion localization, permits lesion characterization and the evaluation of adjacent structures and facilitates the formulation of a focused differential diagnosis.

Lipomas

Lipomas are neoplasms of mature adipose tissue and represent the most common benign lesions of the chest wall (Fig. 26). Affected patients are generally asymptomatic, although subcutaneous lesions may be palpable. Chest wall lipomas may affect only the soft tissues, may arise near the parietal pleura and exhibit intrathoracic growth, or may grow in a dumbbell fashion extending into both compartments. The diagnosis is typically made prospectively when CT (or MR) demonstrates a chest wall lesion of fat attenuation (Fig. 27) (or signal). Chest wall lipomas may exhibit intrinsic calcification in areas of fat necrosis [34].

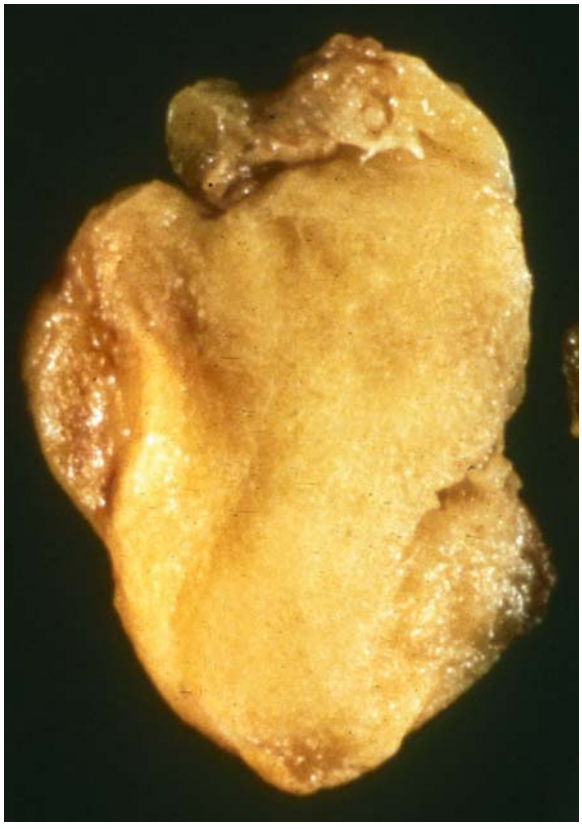

Fig. 26. Chest wall lipoma, gross features. Cut section of a chest wall lipoma resected at the time of right upper lobectomy for lung cancer demonstrates a lobular yellow mass of fatty consistency

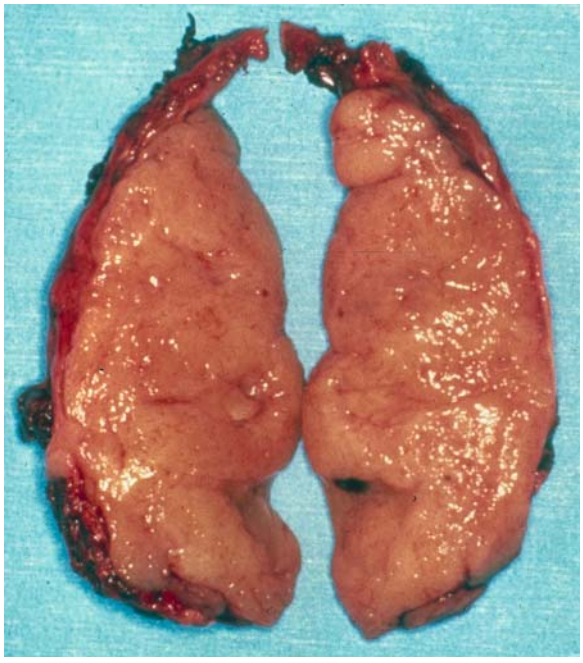

Fig. 28. Neurofibroma, gross features. Cut section of a chest wall neurofibroma that was resected from a young patient with neurofibromatosis demonstrates an elongate lobular soft tissue mass that bears a close relationship to the undersurface of an adjacent rib which was resected en block with the lesion

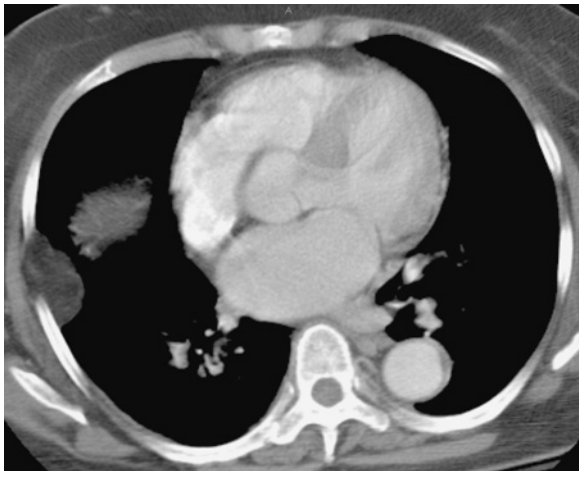

Fig. 27. Chest wall lipoma in an asymptomatic middle-aged woman. Contrast-enhanced chest CT (mediastinal window) demonstrates a heterogeneous well-defined right chest wall mass of predominant fat attenuation. The bulk of the lesion is intrathoracic but there is mild involvement of the soft tissues of the chest wall. The imaging findings are diagnostic for a chest wall lipoma

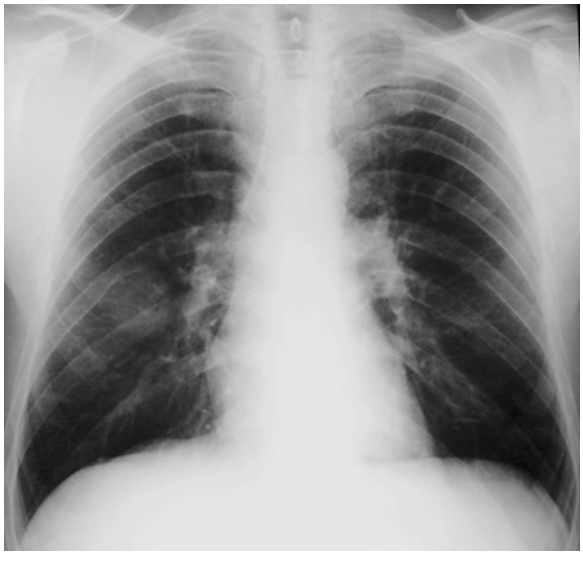

Fig. 29. Chest wall schwannoma in an asymptomatic young man. PA chest radiograph demonstrates an ill-defined mass that projects over the right mid lung and produces pressure erosion and sclerosis on the inferior aspect of the right posterior eight rib

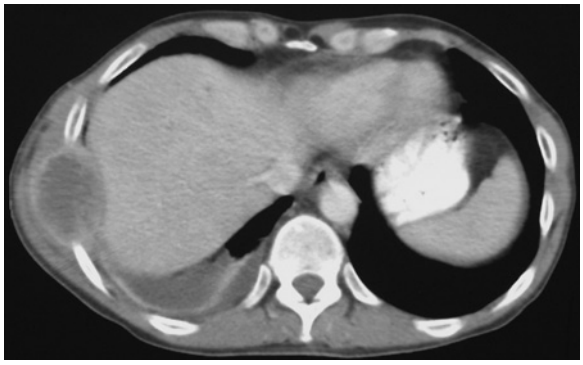

Fig. 30. Malignant tumor of nerve sheath origin in a young patient with a painful palpable chest wall mass. Contrast-enhanced chest CT (mediastinal window) demonstrates a peripherally-enhancing low-attenuation right chest wall soft tissue mass with an associated right pleural effusion

Neurogenic Neoplasms

Neurogenic neoplasms (neurofibromas and schwannomas) may arise from the thoracic nerve roots, the sympathetic chain or the intercostal nerves. Neurofibroma is a well-circumscribed unencapsulated firm neoplasm (Fig. 28) composed of Schwann cell cylinders and axons in a mucinous matrix. Schwannoma is an encapsulated neoplasm composed of compact collections of spindle cells arranged in interlacing fascicles with interspersed areas of decreased cellularity [36]. Neurogenic neoplasms are slow-growing lesions and commonly produce benign pressure erosion, notching and sclerosis of adjacent ribs (Fig. 29). Multifocal neurogenic neoplasms may occur in patients with neurofibromatosis. CT usually demonstrates well-defined cylindrical masses of homogeneous or heterogeneous attenuation and shows

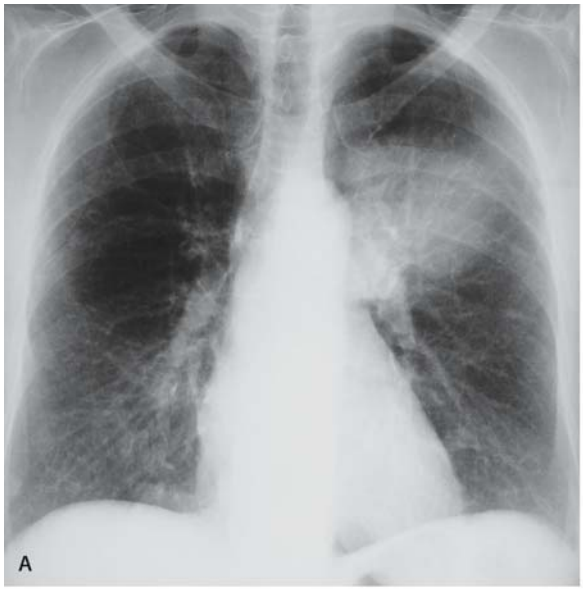

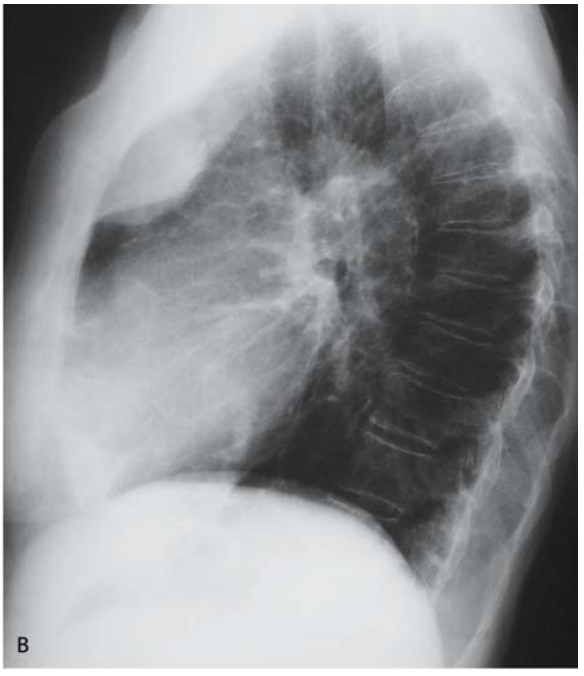

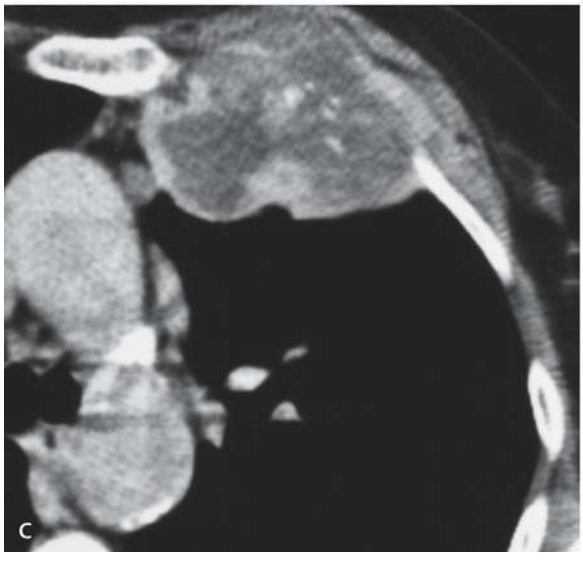

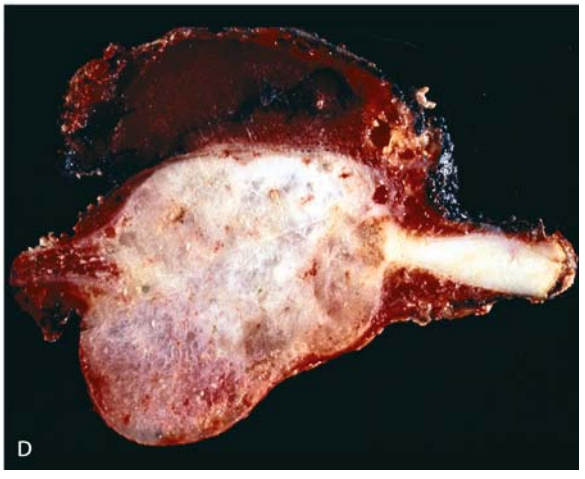

pressure effects on adjacent osseous structures. Contrast studies typically show heterogeneous enhancement. MR demonstrates low-to-intermediate signal intensity on T1-weighted images and high signal intensity on T2-weighted images. Neurogenic neoplasms of the chest wall may undergo malignant transformation [34, 36] (Fig. 30).

Chondrosarcoma

Chondrosarcoma is the most common primary malignant neoplasm of the chest wall. Affected patients are typically middle-aged or elderly adults (although young patients may also be affected) who present with chest wall pain and a palpable mass [21, 35]. Chondrosarcomas often arise in the anterior portion of the rib (characteristically ribs 1 to 5) near the costal cartilage (Fig. 31) or in the sternum. They typically exhibit radiographic characteristics of chest wall masses with indistinct margins and soft tissue extension (Fig. 31). CT demonstrates a heterogeneous soft tissue mass with occasional internal foci of chondroid calcification in a pattern of rings and arcs (Fig. 31C) [21, 34]. MR imaging shows non-specific findings of intermediate signal intensity on T1-weighted images and heterogeneity with foci of high signal intensity on T2-weighted images [34].

Multiple Myeloma

Multiple myeloma affects elderly individuals and males more commonly than females. Focal or multifocal lesions occur and manifest with soft tissue masses and osseous involvement of the ribs or the sternum with osseous expansion or destruction as well as pathologic fractures. Multiple myeloma is also characterized by absence of activity on scintigraphy in spite of significant osseous involvement [34, 35].

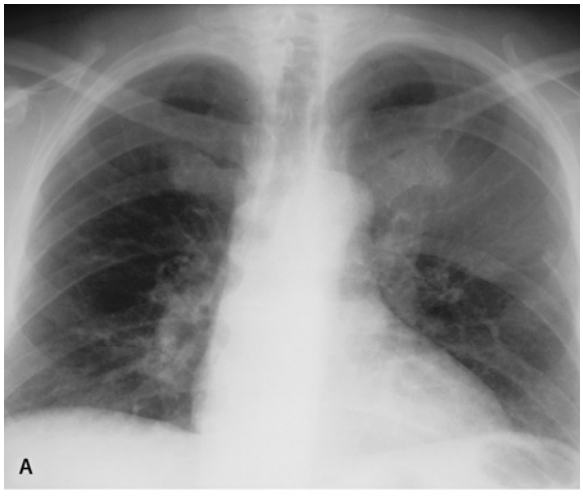

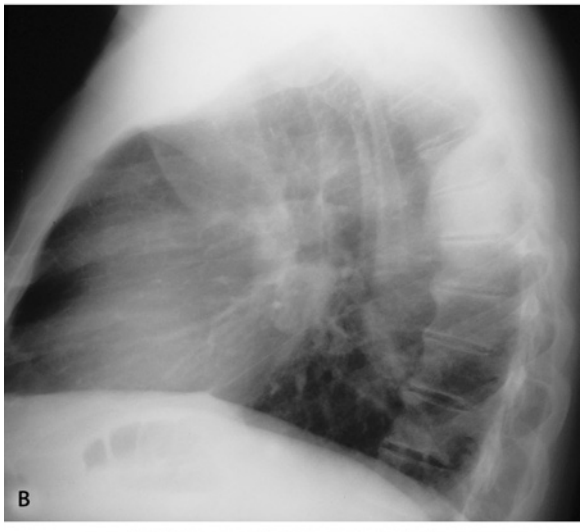

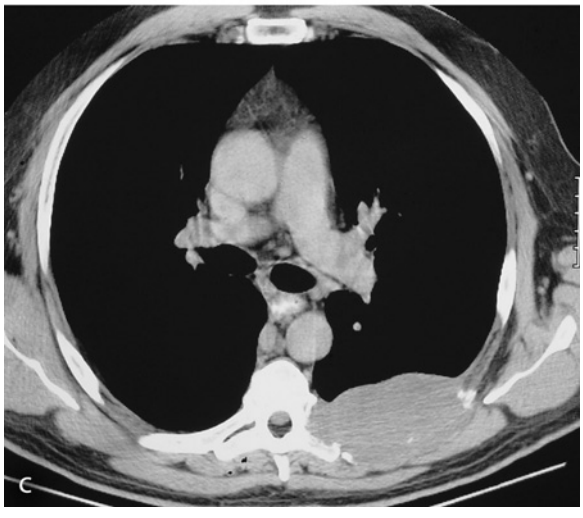

Fig. 31A–D. Chest wall chondrosarcoma in a 45-year-old woman who presented with a painful palpable left chest wall mass. **A**, **B** PA and lateral chest radiographs demonstrate a left anterior chest wall mass. Note the incomplete visualization of the lesion borders on the frontal radiograph (**A**) indicating its extrapulmonary location. **C** Contrast-enhanced chest CT (mediastinal window) shows a lobular chest wall mass centered on the cartilaginous portion of an anterior rib with internal heterogeneous attenuation and linear, punctate and arcuate foci of calcification. **D** Cut section of the resected neoplasm demonstrates the lobular cartilaginous lesion replacing the anterior aspect of the rib. Note the associated soft tissue mass

Fig. 32A–C. Chest wall metastasis in a 58-year-old woman with known thyroid carcinoma who presented with left chest wall pain. **A**, **B** PA and lateral chest radiographs demonstrate destruction of the left fifth posterior rib by a large soft tissue mass. Note that the lesion borders are not visible on the frontal radiograph (**A**), but are well-defined on the lateral radiograph (**B**), indicating the extrapulmonary location of the mass. **C** Contrast-enhanced chest CT (mediastinal window) demonstrates a large chest wall soft tissue mass with associated destruction of an adjacent posterior rib

Chest Wall Metastases

Chest wall metastases may manifest as solitary or multifocal chest wall masses in patients with known malignancies. Common primary neoplasms include carcinomas of the lung, breast and prostate. These lesions manifest with osseous destruction, pathologic fractures and soft tissue masses (Fig. 32).

Conclusion

Lung neoplasms display a wide range of radiologic characteristics that reflect the underlying gross and microscopic features of these lesions as well as their biological behavior. Lung cancer has multiple radiologic manifestations that include solitary nodules, masses or consolidations and atelectasis or consolidation secondary to central obstructing lesions. Advanced lung cancer may manifest with invasion of extrapulmonary structures, multifocal nodules, masses and consolidations, or diffuse pleural involvement (with or without malignant pleural effusion). Carcinoid tumors manifest as well-defined central nodules or masses with a bronchial relationship and frequent post obstructive complications. Hamartomas are peripheral pulmonary nodules that may be diagnosed prospectively based on the presence of internal fat attenuation on CT. Pulmonary metastases manifest as multifocal well-defined nodules or masses with a predilection for the lower lobes and the lung periphery.

Benign pleural neoplasms are rare, but always manifest as focal pleural masses. While malignant pleural neoplasms may also manifest as focal masses, they more commonly exhibit diffuse pleural involvement. The differentiation between primary and metastatic malignant pleural neoplasms cannot be made on the basis of imaging features.

Benign chest wall neoplasms are typically focal chest wall lesions that may exhibit benign pressure effects on adjacent ribs and soft tissue involvement, but do not destroy adjacent osseous structures. Malignant chest wall neoplasms are typically metastatic tumors that may be focal or multifocal and frequently produce bone destruction and soft tissue masses. Malignant primary chest wall neoplasms exhibit imaging features similar to those of secondary chest wall malignancies.

Radiologic imaging plays an important role in the localization and characterization of lung, pleural and chest wall neoplasms. Knowledge of the pathologic characteristics of these lesions and their radiologic manifestations allows the formulation of an appropriate and focused differential diagnosis. Recognition of benign conditions such as hamartoma and chest wall lipoma based on their imaging features permits conservative management of these lesions.

References

1. Jemal A, Murray T, Samuels A, Ghafoor A, Ward E, Thun MJ (2003) Cancer statistics, 2003. CA Cancer J Clin 53:5–26
2. Parkin DM, Pisani P, Ferlay J (1999) Global cancer statistics. CA Cancer J Clin 49:33–64
3. Ahuja R, Weibel SB, Leone FT (2003) Lung cancer: The oncologist's role in smoking cessation. Semin Oncol 30: 94–103
4. Fraser RS, Müller NL, Colman N, Paré PD (1999) Pulmonary Carcinoma. In: Fraser RS, Müller NL, Colman N, Paré PD (eds) Fraser and Paré's Diagnosis of Diseases of the Chest. Fourth edition. WB Saunders, Philadelphia, pp 1069–1228
5. Alberts WM. Lung cancer guidelines. Introduction (2003) Chest 123:1S-2S
6. Beckles MA, Spiro SG, Colice GL, Rudd RM (2003) Initial evaluation of the patient with lung cancer. Symptoms, signs, laboratory tests, and paraneoplastic syndromes. Chest 123: 97S–104S
7. Travis WD, Colby TV, Corrin B, et al (1999) Histological Typing of Lung and Pleural Tumours. International Histological Classification of Tumours. Third edition. Springer-Verlag, Berlin
8. Kerr KM (2001) Pulmonary preinvasive neoplasia. J Clin Pathol 54:257–271
9. Rosado-de-Christenson ML, Templeton PA, Moran CA (1994) Bronchogenic carcinoma: Radiologic-pathologic correlation. RadioGraphics 14:429–446
10. Colby T, Koss M, Travis WD (1995) Adenocarcinoma of the lung (excluding bronchioloalveolar carcinoma). In: Colby T, Koss M, Travis WD (eds). Atlas of Tumor Pathology: Tumors of the Lower Respiratory Tract, fasc 13, ser 3. Armed Forces Institute of Pathology, Washington, DC, pp 179–202
11. Tang P, Vatsia SK, Teichberg S, Kahn E (2001) Pulmonary adenocarcinoma simulating malignant mesothelioma. Arch Pathol Lab Med 125:1598–1600
12. Colby T, Koss M, Travis WD (1995) Bronchioloalveolar carcinoma. In: Colby T, Koss M, Travis WD (eds). Atlas of Tumor Pathology: Tumors of the Lower Respiratory Tract, fasc 13, ser 3. Armed Forces Institute of Pathology, Washington, DC, pp 203–257
13. Strollo DC, Rosado-de-Christenson ML, Franks TJ (2003) Reclassification of cystic bronchioloalveolar carcinomas to adenocarcinomas based on the revised World Health Organization classification of lung and pleural tumors. J Thorac Imaging 18:59–66
14. Kuriyama K, Seto M, Kasugai T, et al (1999) Ground-glass opacity on thin-section CT: Value in differentiating subtypes of adenocarcinoma of the lung. AJR 173:465–469
15. Mihara N, Ichikado K, Johkoh T, et al (1999) The subtypes of localized bronchioloalveolar carcinoma: CT-pathologic correlation in 18 cases. AJR 173:75–79
16. Akira M, Atagi S, Kawahara M, Iuchi K, Johkoh T (1999). High-resolution CT findings of diffuse bronchioloalveolar carcinoma in 38 patients. AJR 173:1623–1629
17. Colby TV, Koss MN, Travis WD (1995) Squamous cell carcinoma and variants. In: Colby TV, Koss MN, Travis WD (eds) Atlas of tumor pathology: Tumors of the lower respiratory tract, fasc 13, ser 3. Armed Forces Institute of Pathology, Washington, DC, pp 287–317
18. Zakowski MF (2003) Pathology of small cell carcinoma of the lung. Semin Oncol 30:3–8
19. Rosado-de-Christenson ML, Abbott GF, Kirejczyk WM, Galvin JR, Travis WD (1999) Thoracic carcinoids: Radiologic-Pathologic Correlation. RadioGraphics 19:707–736.
20. Colby TV, Koss MN, Travis WD (1995) Carcinoid and other neuroendocrine tumors. In: Colby TV, Koss MN, Travis WD (eds) Atlas of Tumor Pathology: Tumors of the Lower Respiratory Tract, fasc 13, ser 3. Armed Forces Institute of Pathology, Washington, DC, pp 287–317.
21. Meyer CA, White CS. Cartilaginous disorders of the chest (1998) RadioGraphics 18:1109–1123
22. Gjevre JA, Myers JL, Prakash UBS. Pulmonary hamartomas (1996) Mayo Clin Proc; 71:14–20.

23. Colby TV, Koss MN, Travis WD (1995) Hamartoma. In: Colby TV, Koss MN, Travis WD (eds) Atlas of Tumor Pathology: Tumors of the Lower Respiratory Tract, fasc 13, ser 3. Armed Forces Institute of Pathology, Washington, DC, pp 319–325
24. Erasmus JJ, Connolly JE, McAdams HP, Roggli VL (2000) Solitary pulmonary nodules: Part I. Morphologic evaluation for differentiation of benign and malignant lesions. RadioGraphics 20:43–58
25. Fraser RS, Müller NL, Colman N, Paré PD (1999) Mesenchymal neoplasms. In: Fraser RS, Müller NL, Colman N, Paré PD (eds) Fraser and Paré's Diagnosis of Diseases of the Chest. Fourth edition. WB Saunders, Philadelphia, pp 1331–1362
26. Coppage L, Shaw C, Curtis AM (1987) Metastatic disease to the chest in patients with extrathoracic malignancy. J Thorac Imaging 2:24–37
27. Seo JB, Im J-G, Goo JM, Chung MJ, Kim M-Y (2001) Atypical pulmonary metastases: Spectrum of radiologic findings. RadioGraphics 21:403–417
28. Rosado-de-Christenson ML, Abbott GF, McAdams HP, Franks TJ, Galvin JR (2003) Localized fibrous tumor of the pleura. RadioGraphics 23:759–783
29. Miller BH, Rosado-de-Christenson ML, Mason AC, Fleming MV, White CC, Krasna MJ (1996) Malignant pleural mesothelioma: Radiologic-pathologic correlation. RadioGraphics 16: 613–644
30. Battifora H, McCaughey WTE. Diffuse malignant mesothelioma (1995) In: Battifora H, McCaughey WTE (eds) Atlas of Tumor Pathology: Tumors of the Serosal Membranes, fasc 15 ser 3. Armed Forces Institute of Pathology, Washington, DC, pp 15–88 and 101–109
31. Kawashima A, Libshitz HI (1990) Malignant pleural mesothelioma: CT manifestations in 50 cases. AJR 155:965–969
32. Leung AN, Müller NL, Miller RR (1990) CT in differential diagnosis of diffuse pleural disease. AJR 154:487–492
33. Heelan RT, Rusch VW, Begg CB, Panicek DM, Caravelli JF, Eisen C. Staging of malignant pleural mesothelioma: Comparison of CT and MR imaging (1999) AJR; 172:1039–1047
34. Fraser RS, Müller NL, Colman N, Paré PD (1999) The chest wall. In: Fraser RS, Müller NL, Colman N, Paré PD (eds) Fraser and Paré's Diagnosis of Diseases of the Chest. Fourth edition. WB Saunders, Philadelphia, pp 3011–3042
35. Fechner RE, Mills SE (1993) Atlas of tumor pathology: tumors of the bones and joints, fasc 8, ser 3. Armed Forces Institute of Pathology, Washington, DC, pp 79–128.
36. Harkin JC, Reed RJ. Solitary benign nerve sheath tumors (1969) In: Harkin JC, Reed RJ (eds) Atlas of Tumor Pathology: Tumors of the Peripheral nervous system, fasc 3 ser 2. Armed Forces Institute of Pathology, Washington, DC, pp 29–65

Mediastinal Masses

François Laurent, Marie Parrens

3.4

Contents

Introduction

The wide variety of tissues within the mediastinum is reflected in the many forms of neoplastic, developmental and inflammatory masses that can be seen as a localized mass in the mediastinum. This review will emphasize the imaging and pathological features of primary tumours and cysts of the mediastinum. Metastases, most often associated with primary bronchogenic carcinoma, and vascular lesions, particularly aortic aneurysms, are also common but not usually considered in reviews of mediastinal masses and therefore not within of the scope of this chapter.

General Considerations

According to two large series, thymoma, neurogenic tumours and benign cysts, taken together represent 60% of patients with mediastinal masses. Significant differences exist between adults and children concerning the respective frequency of various histological types. Neurogenic tumours, germ cell neoplasms and foregut cysts represent 80% of childhood lesions whereas primary thymic neoplasms, thyroid masses and lymphomas are the most frequent in adults. In two large series collecting more than 200 cases of primary tumours of the mediastinum, thymic tumours represent 20%–25%, lymphomas 15%–20% and neurogenic tumours 20%–25% [1, 2]. These proportions are nevertheless thought to be biased because they are retrospective and exclude non-operated patients. There are significant differences between children and adults. Neurogenic tumours, germinal tumours, bronchogenic and neuroenteric cysts representing 80% of lesions in childhood whereas thymic tumours, tumours of thyroid origin and lymphomas are more frequent in adults [1, 3]. In a large series from the Mayo clinic, tumours were malignant in 25% of cases and 75% were resectable [4].

Most patients with mediastinal lesions are usually chronically asymptomatic and 83% of incidentally discovered masses are benign. Approximately one-third of mediastinal masses are malignant and are more often symptomatic. Symptoms relate to invasion or obstruction of nearby structures and can include dyspnoea, dysphagia, cough from airway compression, superior vena cava syndrome, hoarseness from laryngeal nerve involvement or symptoms resulting from spinal cord compression. Myasthenia gravis or less frequently Cushing syndrome can also reveal mediastinal masses.

Imaging Studies and Differential Diagnosis of Mediastinal Masses

Computed tomography and magnetic resonance imaging today play a powerful role in evaluating the medias-

tinum. While plain film gives limited results, a specific diagnosis is sometimes possible with these techniques and if not, at least a limited differential diagnosis can be made. Ultrasound can be used in specific situations, especially in children and nuclear medicine techniques; in particular PET may have specific indications discussed in the dedicated section. The general trends of the radiological diagnosis of mediastinal masses are presented below.

Posteroanterior and lateral views of chest radiographs remain the first and simplest method for detecting a mediastinal mass. Typical findings include changes in mediastinal contours and lines. The sensitivity of chest film, however, is much lower than that of CT or MRI and the former tomographic technique is mandatory in case of clinical suspicion of a mediastinal mass when the chest film is unremarkable. On the lateral view, a rough but useful classification of mediastinal masses according to their topography can be obtained. Anterior mediastinal masses are those projecting in front of a virtual line following the anterior aspect of the trachea, posterior masses those situated below a virtual line running 1 cm below but parallel to the anterior aspect of the vertebral bodies of the thoracic spine and medial masses those located between these two limits. Although a specific type of tumour may arise from several compartments of the mediastinum, and despite that large tumours are often located within several compartments, a first approach of the differential diagnosis can be obtained from the very simple observation of these findings. Radiographic findings related to anatomical variants, vascular masses and masses arising from the digestive tract (hiatal herniae, oesophageal masses) are of primary importance to avoid unnecessary extensive imaging evaluation and invasive procedures but are not within of the scope of this chapter. Chest film is often suggestive but in clinical practice, CT can only be avoided in case of typical hiatal herniae. Tissue components, as shown by CT or MR scans, together with size, shape and precise location according to the situation within mediastinal compartments, are today the leading edge of the diagnosis of a mediastinal mass. Attenuation values at CT and signal intensity at MRI give much more detailed information than chest film concerning the tissular composition of the mass. The diagnosis can be at least partly suggested based on the identification of the major components of a mass: fatty, cystic or solid tissue. Calcifications can also be detectable, but this pattern is not as useful as the former in the differential diagnosis. Additional information can also be obtained from the degree and type of vascularity of the lesion visible according to the degree of contrast enhancement after intravenous injection of contrast media.

A very useful finding for the differential diagnosis is identification of fat. Normal fat is unencapsulated and does not affect the normal contours of the mediastinum. True lipomatous tumours are much less common than herniation of abdominal fat or diffuse lipomatosis. So, in the majority of cases, discovery of the fatty nature of a mass indicates benignancy. Mediastinal diffuse lipomatosis is an overabundant amount of histologically normal fat. Homogeneity and absence of compression of surrounding structures differentiate this benign condition from multiple lipomas. This condition may be part of a generalized obesity, or is seen in patients suffering from Cushing disease or those treated with steroid therapy. Omental fat can herniate through the foramen of Morgagni or Larrey and create the appearance of a cardiophrenic angle mass. Therefore primary fatty tumours of the mediastinum are rare, including lipomas, liposarcomas and thymolipomas. However, some tumours other than true lipomatous lesions may contain some fat. The most common is teratoma, but fat has also been reported in hemangiomas, angiolipomas, lipoblastomas in infants and extramedullary hematopoiesis. The fatty tissue component may be part of a complex mesenchymal sarcoma with various tissues of mesenchymal origin, i.e. fibrous, osseous or vascular components.

Typical cysts appear on chest radiograph as smooth, sharply marginated mediastinal lesions. On CT, they have a similar attenuation to that of water and do not enhance [5, 6]. Any cyst may have a higher attenuation than that of water due to its calcic, proteinaceous, mucus, or hemorrhagic content. Such lesions may be indistinguishable from solid soft tissue neoplasms, although the complete absence of enhancement after administration of intravenous contrast material may be a clue to their recognition. On MRI, typical cysts have a high signal intensity on T2-weighted images but show a variable T1-weighted appearance [7]. Those filled in with serous fluid have a low signal intensity and those with a viscous proteinaceous or bloody content have a signal which varies from intermediate to very high intensity. Absence of enhancement after gadolinium chelate injection is a useful additional feature to assess the cystic composition. True cystic lesions should be differentiated from the cystic degenerative changes observed in many solid tissular tumours and nodes. Areas of low attenuation may be present secondary to necrosis, old haemorrhage, or the intrinsic properties of the neoplasm. On CT, identification of these degenerative cystic changes is based on the visualization of an inhomogeneous low-density mass with thick wall, sometimes in conjunction with other CT findings such as lymphadenopathy, pulmonary or pleural abnormalities. Goitres, thymomas, mature cystic teratomas, nerve root tumours, seminomas, lymphangiomas and enlarged nodes from any origin may show this type of finding. Mediastinal abscess may also show as a low attenuation mass surrounded by an enhancing rim and sometimes are filled in with gas or

the air–fluid level. Clinical features and associated CT findings such as gas bubbles, or communication with an empyema, usually permit differentiation from true cysts [5]. Mediastinal pancreatic pseudocyst is the encapsulated collection of pancreatic secretion, blood and necrotic material. The lesion gains access to the posterior and inferior part of the mediastinum through the oesophageal or aortic hiatus. A recent pancreatitis and the compression or splaying of the diaphragmatic crura are suggestive features [8].

Most mediastinal masses, especially in an adult population, are solid. Among tissular masses, two types of CT attenuation may restrict the differential diagnosis to a limited number of possibilities: the spontaneously hyperattenuated mass and masses with a strong enhancement on enhanced CT. Spontaneous hyperattenuation is an uncommon finding which can be simply defined by a mass that has a higher attenuation than muscles on unenhanced CT. Apart from calcified nodes or tumour calcifications, and some cysts that have been previously mentioned, this feature is frequently seen in thyroid goitres and recent hematomas [9]. Ninety percent of haematomas have areas of high attenuation during the first 72 h, reflecting the high haemoglobin concentration of clotted blood. At this stage, the MR signal intensity is low on T1 and T2. When the haematoma ages, its attenuation decreases at CT in a centripetal fashion, creating a low-attenuation peripheral halo that increases over time. At MRI, the signal intensity on T1WI increases and gives a more typical appearance of the haemorrhagic content. Other spontaneously hyperattenuated masses include foreign bodies, fresh clots in aneurysms, residual lymphangiographic contrast material, retained surgical sponges and orally opacified oesophageal diverticula.

Masses that are known to possibly enhance strongly at CT after contrast media injection are goitres, medullary cancer of the thyroid, parathyroid masses, vascular tumours (haemangiomas), Castleman disease, thymic carcinoid, metastasis of sarcomas and melanomas [10]. In clinical practice, the assessment of a strong enhancement is simply obtained by comparing the degree of enhancement of the mass to that of vessels.

The vast majority of solid masses which arise in the mediastinum enhance less strongly than the vascular structures. Apart from clinical findings, the location of the mass within a mediastinal compartment is therefore the leading thread of the diagnosis. In the anterior mediastinum, tumours of thymic origin, lymphomas and germ cell tumours are the most common. Neurogenic tumours most frequently arise from the posterior mediastinum and primary cysts and tumours of mesenchymal origin can be found in any mediastinal compartment.

Primary Cysts

Primary cysts represent 15%–20% of all primary mediastinal tumours and occur in all compartments of the mediastinum [11]. Most are developmental in origin and the distinction between these cysts is not always easy. Identification of the original tissue is often provided only by histological examination. Cysts containing cartilage are classified as bronchogenic, whereas those with gastric epithelium are neuroenteric. Primary cysts include bronchogenic cysts, oesophageal duplication cysts, neuroenteric cysts, pericardial cysts, thymic cysts and cysts of the thoracic canal.

Bronchogenic cysts result from abnormal ventral budding or branching of the tracheobronchial tree during embryological development. The formation of a bronchogenic cyst, rather than other bronchopulmonary foregut malformation, i.e. cystic adenomatoid malformation or bronchopulmonary sequestration, seems to be a matter of exact timing of the event which involves the lung bud. Although bronchogenic cysts could be found within the lung, the mediastinum is by far the most common location in large series [12]. They have a fibrous capsule, often contain cartilage, smooth muscle and mucous glands, and are lined by respiratory epithelium (Fig. 1). They may be filled with clear serous fluid or contain remarkably viscid mucoid material and are stable in size except when complicated by infection or haemorrhage. They do not usually communicate with the bronchial tree, unlike intraparenchymal cysts, and therefore an air–fluid level is very uncommon. The majority of bronchogenic cysts are asymptomatic but symptoms secondary to compression of adjacent structures causing bronchiectasis, haemoptysis, pulmonary artery stenosis or airway obstruction, or due to a complication such as infection or haemorrhage may occur [12].

The gradual improvement and use of antenatal ultrasound has led to an increase in prenatal detection. Bronchogenic cysts tend to appear as single cystic structures with a thin wall [13]. On conventional radiographs, a bronchogenic cyst appears as a well-defined solitary mass of the mediastinum or hilum in close proximity of the major airways. On CT scan, a smooth, round or elliptic mass with an imperceptible wall and a uniform attenuation is found. Half of them are of water density and the others have a CT density which varies depending on the cyst content [14, 15] (Fig. 2). On rare occasions bronchogenic cysts show an extremely high density related to a milk of calcium content or a fluid–fluid content [16] (Fig. 3). On MR imaging, the signal intensity on T2-weighted images is very high and homogeneous, suggesting a cystic lesion; bronchogenic cysts frequently show a signal intensity higher than that of muscle on T1-weighted images because of their high proteinaceous content (Fig. 4) [17]. Because this finding may

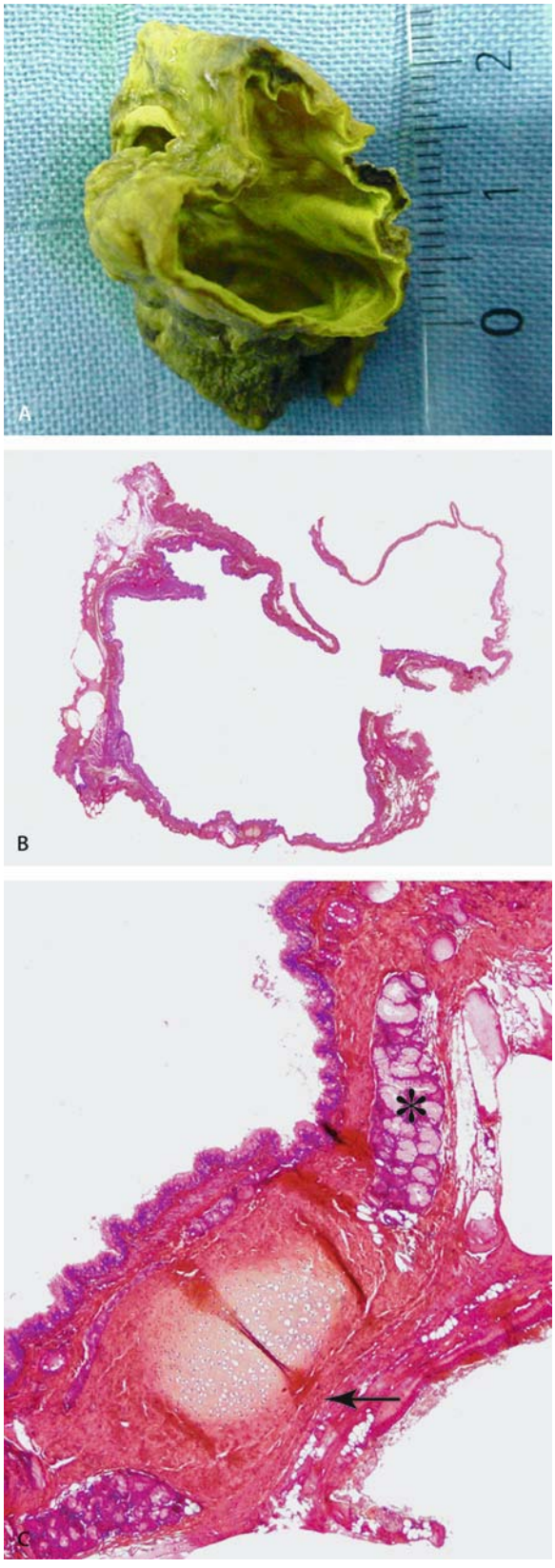

Fig. 1A–C. Bronchogenic cyst. Gross view: Unilocular well-defined cyst (**A**). **B, C** Microscopy: the cystic wall is lined with a respiratory epithelium and contains bronchial glands (*asterisk*) and cartilage (*arrow*)

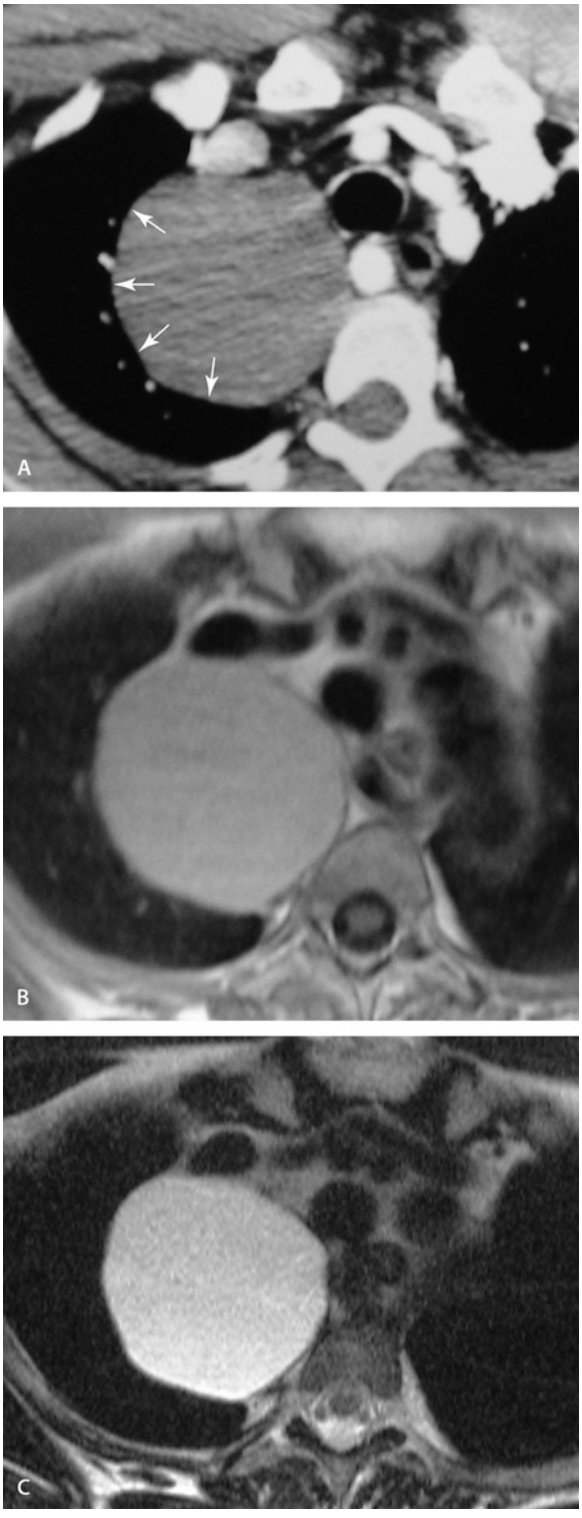

Fig. 2A, B. Bronchogenic cyst, typical appearance. **A** Enhanced CT: low-attenuation (25 HU) homogeneous mass located at the right lateral aspect of the trachea. The cystic wall (*arrows*) is very thin. No enhancement was observed compared with the unenhanced scan (not shown). **B, C** T1 (**B**) and T2 (**C**)-weighted MRI: the lesion is of slightly higher intensity than muscular wall tissue on T1 (**B**) and very intense on T2 (**C**), a signal intensity characterizing a cystic fluid of high protein content

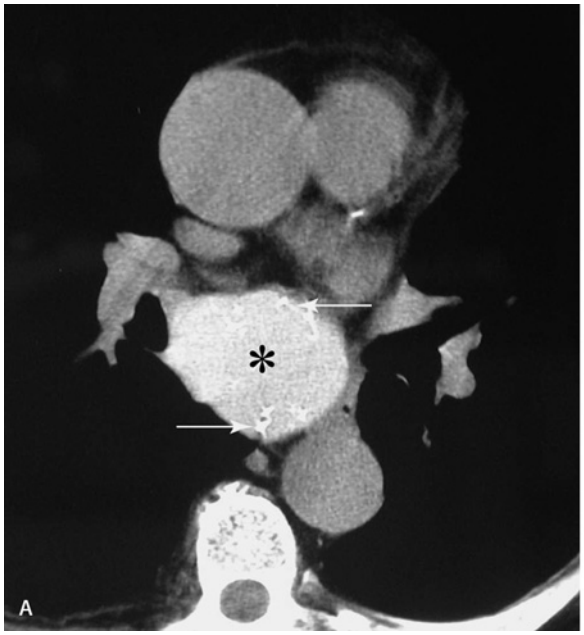

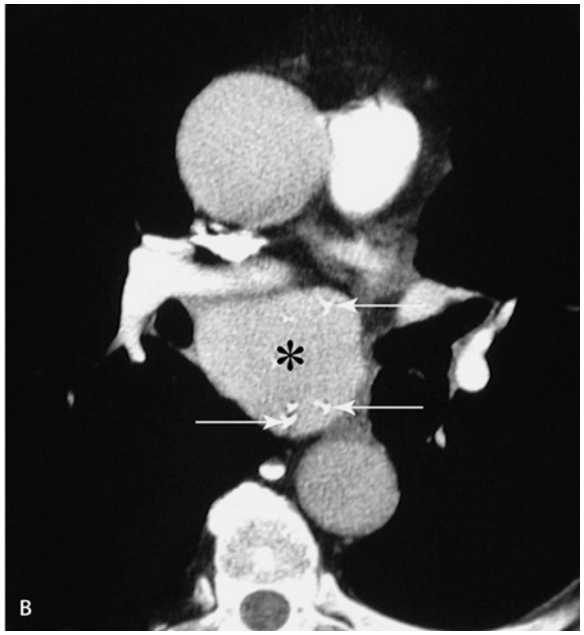

Fig. 3A, B. Bronchogenic cyst, atypical appearance. Unenhanced (**A**) and enhanced (**B**) CT. High attenuation mass (*asterisk*) without enhancement and with a thin wall. Some calcifications (*arrows*) are visible). Pathological examination (not shown) revealed a "milk of calcium" content

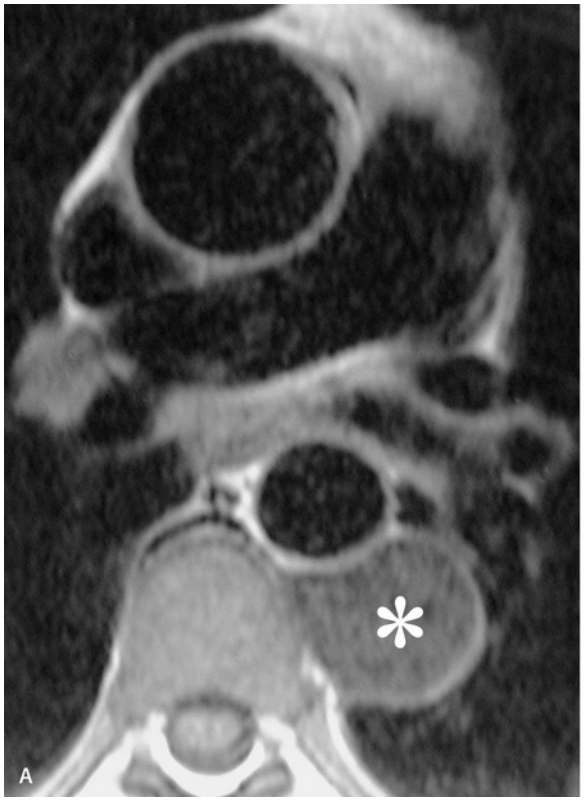

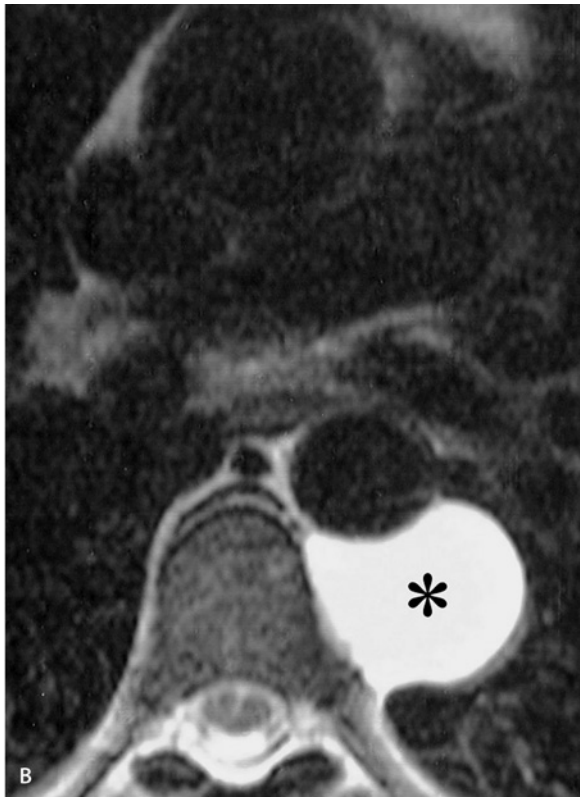

Fig. 4A, B. Bronchogenic cyst, atypical location. MRI showing a low-intensity T1 (**A**) and a high-intensity T2 (**B**) well-defined homogeneous mass (*asterisk*) within the posterior mediastinum with no perceptible wall and therefore suggesting a primary cyst. Pathological examination revealed a bronchogenic cyst

be seen in some solid tumours, gadolinium injection is recommended, as bronchogenic cysts do not enhance. Atypical features of bronchogenic cysts have been described in rare situations: high protein concentrations in cysts produce a low signal intensity on T2-wieghted images [18]; a nonspecific fluid–fluid level has also been shown [19]. Most bronchogenic cysts are located adjacent to the major airways along the paratracheal wall, near the carina or in the posterior mediastinum, but they may occur in any part of the mediastinum. The first suggested diagnosis at imaging studies is that of another primary cystic tumour in those cases (Fig. 5).

Oesophageal duplication cysts result from failure of the originally solid oesophagus to vacuolate completely to produce a hollow tube [20]. Although most often asymptomatic, the majority are detected in infants and children, usually adjacent to the oesophageal wall. They are lined with a stratified squamous epithelium, supported by a lamina propria with oesophageal glands and surrounded by a double layer of smooth muscle. Ectopic mucosa may cause haemorrhage, perforation or infection. Their appearance at CT or MRI is identical to that of bronchogenic cysts [21] except that the wall may be thicker and in a more intimate contact with the oesophagus, which results in an intramural compression aspect on barium examination [22]. Radionuclide scans with Tc-99m sodium pertechnetate may be helpful to detect those that contain ectopic gastric mucosa. Neuroenteric or gastroenteric cysts arise from a gut anlage that has herniated through a split in the notochord. They occur in the posterior mediastinum and are distinguished from the others by their usual association with spinal malformations of the cervical and thoracic vertebrae such as hemivertebrae, posterior spina bifida and scoliosis. Symptoms can be caused by compression of nerves or surrounding structures or peptic ulceration of the epithelium.

Pericardial cysts are the result of anomalous outpouchings of the parietal pericardium in contrast with

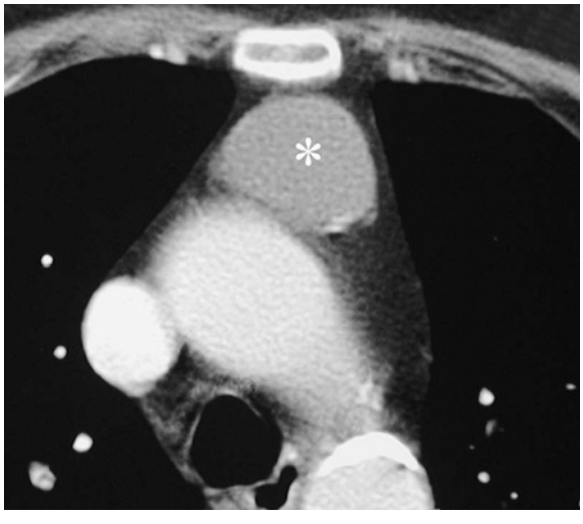

Fig. 5. Bronchogenic cyst, atypical location. Low-attenuation well defined mass (*asterisk*) of the anterior mediastinum suggesting a thymic or a pericardial cyst. Pathological examination revealed a bronchogenic cyst

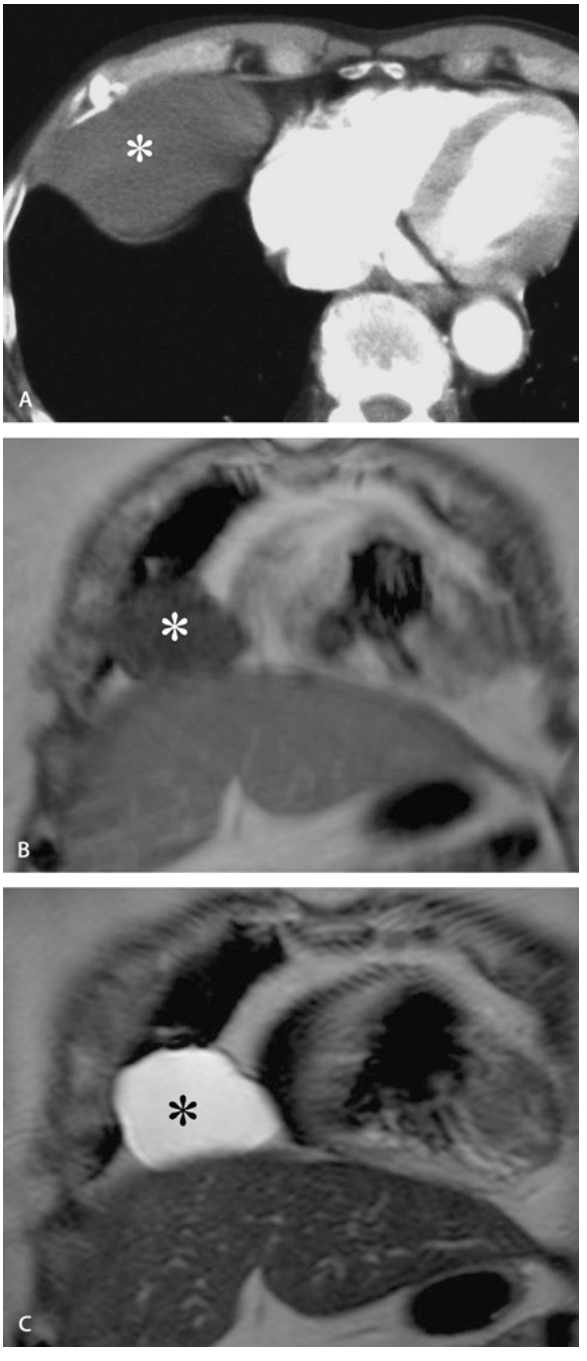

Fig. 6A–C. Pleuropericardial cyst, typical appearance: on enhanced CT (**A**), the lesion (*asterisk*) is low-attenuated, homogeneous, circumscribed by a very thin wall and typically situated in the anterior cardiophrenic angle. T1 (**B**) and T2 (**C**) coronal MRI slices show the typical signal of a cystic lesion filled by a water-like fluid

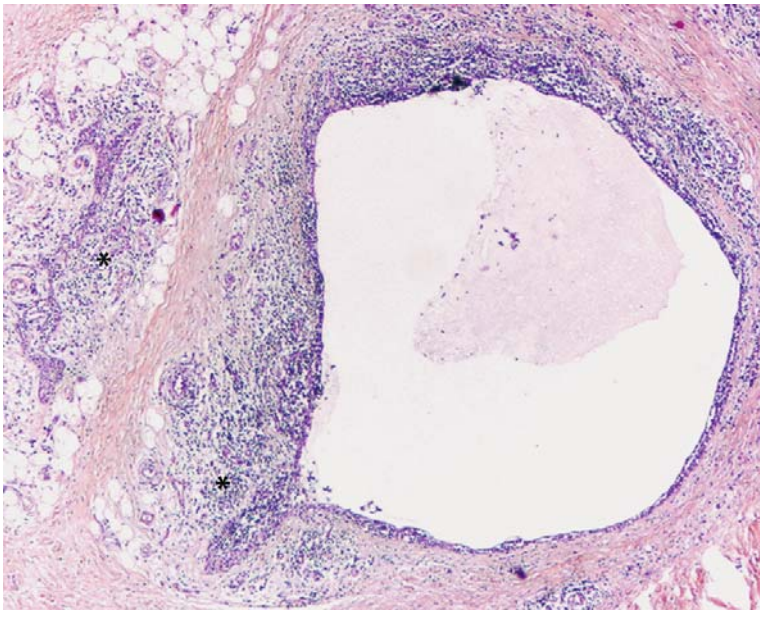

Fig. 7. Thymic cyst: unilocular thin walled cyst lined with epithelial cells attached to fatty thymic tissue

pericardial diverticula that communicate with the pericardial sac. The cyst wall is composed of a single layer of mesothelial cells and connective tissue and contains a clear fluid. Although constant at surgery, the connection to the pericardial sac is barely visible preoperatively. Most pericardial cysts are unilocular and occasionally they are pedunculated. They are commonly located in the right cardiophrenic angle, although they may occur anywhere in relation to the pericardium, the posterior cardiophrenic angle, the superior retroaortic pericardial recess. On imaging studies, they are seen as smooth, well-defined, oval or round masses in contact with the heart [23], without a perceptible wall at CT and with a water-attenuation content (Fig. 6). They may demonstrate different shapes at different times of examination and have a pointed appearance at CT [24].

Thymic cysts are uncommon and represent 1% of all mediastinal masses [25]. Two distinct forms of thymic cysts are described: congenital and acquired. The congenital cyst tends to be unilocular (Fig. 7), derives from remnants of the thymopharyngeal duct and occurs anywhere along the course of the embryonic thymus gland from the angle of the mandible to the manubrium [26]. Thymic cysts can also be acquired lesions following thymic inflammation and they tend to be multilocular. They are known to occur occasionally in patients after radiation therapy for mediastinal Hodgkin disease [27], in association with thymic tumours [28] and after thoracotomy. Large multilocular cysts are seen in about 1% of children with HIV infection [29]. Grossly, thymic cysts may be unilocular or multilocular with a thin wall with attached fatty thymic tissue. The content is generally a straw-coloured fluid or brown due to previous haemorrhage. The lining is made up of flattened or columnar epithelium and thymic tissue should be identified to assess the diagnosis of thymic cyst [30]. Careful examination is necessary to exclude a cystic thymic neoplasm, a seminoma or Hodgkin disease. At CT, a congenital cyst appears as a well-defined water-attenuation mass with imperceptible walls (Fig. 8), whereas a multilocular cyst is more heterogeneous with a more clearly visible wall [31]. Curvilinear calcification of the wall may be visible [32].

Cysts of the thoracic duct are rare, thin-walled and unilocular, lined by flat endothelial cells. A location

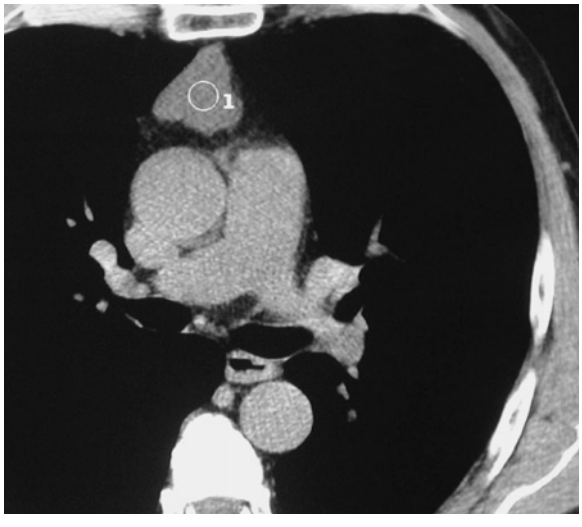

Fig. 8. Thymic cyst, nonenhanced CT: low-attenuation mass (*circle*) of the anterior mediastinum with no enhancement (not shown), a very thin wall and the typical triangular shape of the thymus

strictly medial to the spine at CT mat is suggestive but connection with the thoracic duct can be proved by CT lymphangiography obtained by injection of iodized oil into the patient's foot [33].

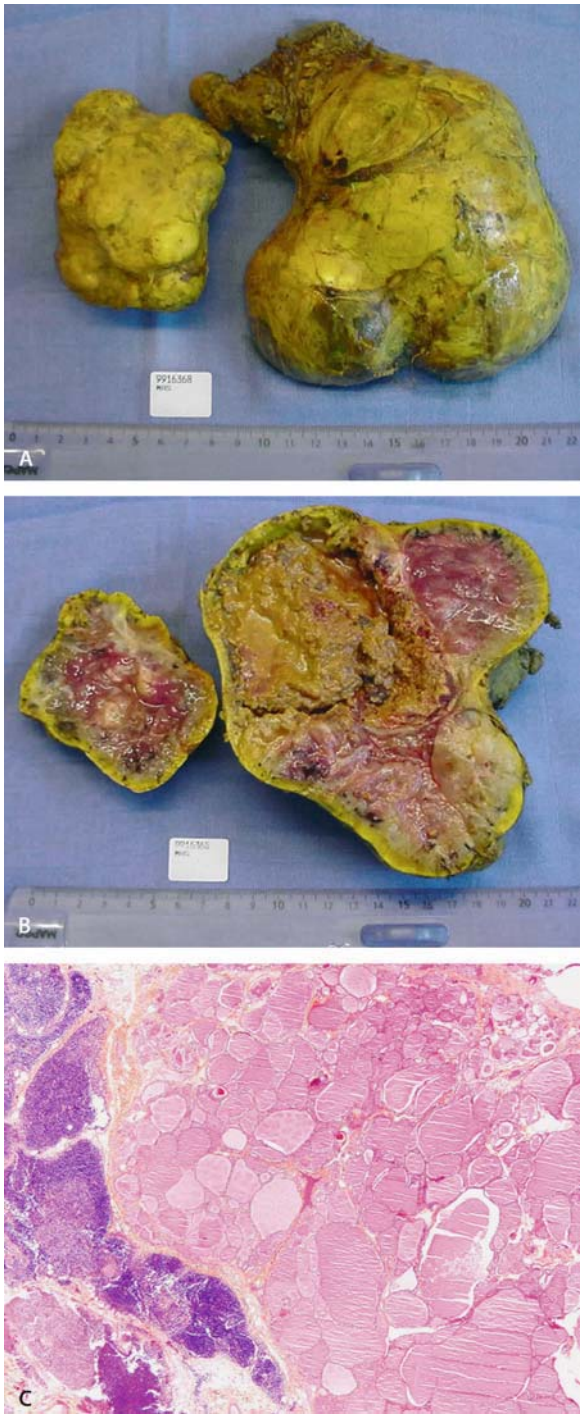

Fig. 9A–C. Thyroid goitre. Gross specimen: asymmetrical enlargement and bilateral nodularity (**A**, **B**). Microscopy: hyperplastic nodule composed of vesicles of various sizes (**C**)

Goitres and Parathyroid Masses

Thyroid and parathyroid are not mediastinal organs but the frequency of mediastinal thyroid goitres and of ectopic parathyroid tumours led to considering these lesions in the list of common mediastinal masses. Mediastinal goitres constitute 5%–10% of all resected mediastinal masses. An intrathoracic thyroid mass is usually a benign multinodular colloid goitre or an adenoma and rarely a carcinoma. Considering malignancy, small foci of degeneration are frequent while massive malignant transformation remains very rare, and malignancy in thoracic goitres is not more frequent that within the neck. Patients are generally older women and present with neck mass or tracheo-oesophageal compression and displacement. Intrathoracic thyroid masses are almost always a downward extension of a thyroid mass that originates in the neck and very rarely arises from ectopic thyroid tissue. Therefore the continuity between the mediastinal mass and the thyroid is a major diagnostic feature. Occasionally, the only connection is a narrow fibrous or vascular pedicle not visible on axial CT slices. In 80% of cases, the thyroid extends into the prevascular spaces, but posterior extension behind the aortic arch vessels along the trachea represents 20% of cases [25]. Histologically, a multinodular goitre is an aggregate of multiple discrete nodules, either colloid or true adenomas. The nodules are partially encapsulated, numerous, and the size can vary greatly with one nodule being dominant. The cysts are lined with a low cuboidal epithelium with abundant colloid in variable-sized follicles (Fig. 9). Within a goitre; areas of haemorrhage, fibrosis and calcifications are often visible.

On chest radiographs, a thyroid mass is spherical or lobular, well defined, and very frequently displaces the trachea. The pattern of displacement depends on the location of the mass, usually anterior or lateral to the trachea but possibly posterior to it, separating the trachea from the oesophagus. Considering the diagnosis of a goitre, the combination of findings on CT is characteristic in most instances: communication between the cervical thyroid gland and the mass by contiguous slices, a mass of inhomogeneous attenuation with cystic and high-attenuation areas, calcifications of various shapes (Fig. 10), marked and prolonged contrast enhancement [9, 34]. Occasionally, goitres may compress the brachiocephalic veins or the superior vena cava. Calcifications are more frequently seen the longer the goitre is present. Dense, amorphous with a nodular, curvilinear or circular configuration, cysts are seen in the benign goitre but also in medullary carcinomas, whereas calcifications made up of cloud-like or fine dots that are found in papillary and follicular carcinomas. Distinguishing between benign and malignant goitres at CT is not possible unless the tumour clearly invades beyond the thyroid gland. On MR, multinodular goitres have

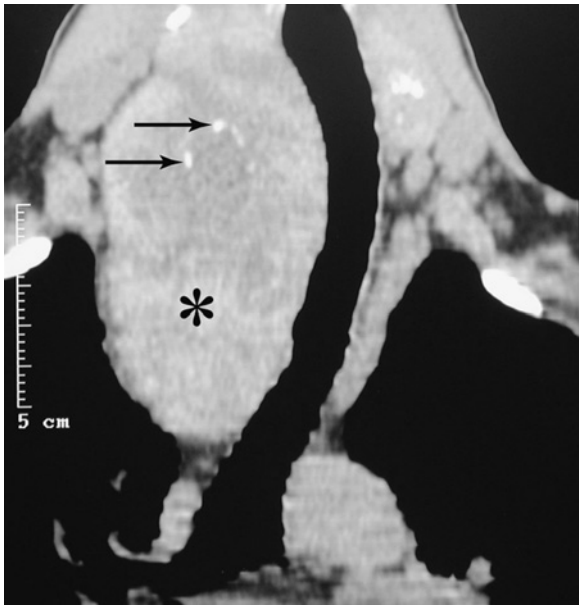

Fig. 10. Thyroid goitre, unenhanced CT. Coronal 2D reconstruction showing the mass (*asterisk*) growing down from the right thyroid lobe. The lesion is slightly heterogeneous and calcified (*arrows*)

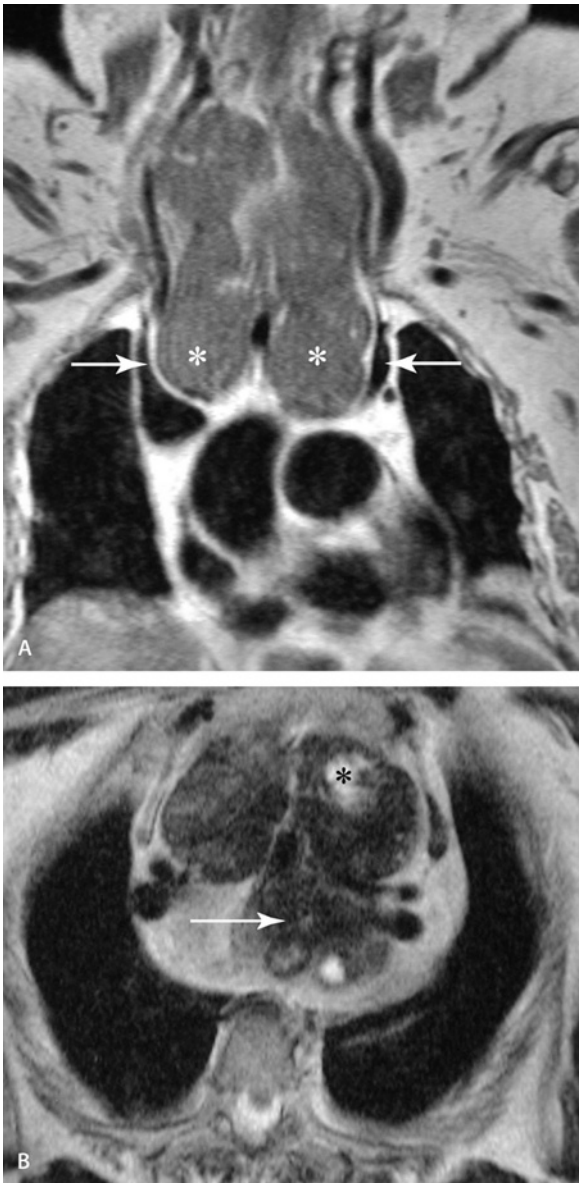

Fig. 11A, B. Thyroid goitre MRI, T1 (**A**) coronal slice showing the goitre developed from both thyroid lobes (*asterisks*) compressing the trachea and the innominate veins (*arrows*) and the T2 axial slice (**B**) showing high-intensity cystic areas (*asterisk*) and the posterior extent of the goitre (*arrow*) behind the trachea

been shown to be relatively hypointense compared with normal thyroid tissue on T1-weighted images, except foci of haemorrhage and cysts that may be hyperintense. T2-weighted images show a typically heterogeneous appearance with high signal intensity throughout most of the gland [35]. The MR imaging signal intensity is a depiction of the different tissue components, including follicular colloid (low or high T1 and high T2), fibrosis (low T1 and low T2), blood (variable T1 and T2) and calcium (signal void) (Fig. 11). Displacement of mediastinal vessels, trachea, oesophagus and relationships between the cervical and thoracic components of the goitre are exquisitely demonstrated by multiplanar imaging whatever the technique, spiral CT or MRI (Fig. 12). The dimension of a goitre and the locus of extension should be assessed preoperatively to guide the surgeon in the preoperative approach [36]. Radionuclide imaging of the thyroid shows some functioning thyroid tissue in almost all intrathoracic goitres.

Because of the likely common origin of the thymus and the inferior parathyroid glands from the third branchial pouch, ectopic parathyroid gland may be found in the anterior mediastinum near or within the thymus. The frequency of a mediastinal parathyroid tumour increases in patients requiring repeat surgery for persistent or recurrent hyperparathyroidism. Adenoma arising from ectopic parathyroid glands in the mediastinum is common and carcinoma exceedingly rare. The tumour is well defined and consists of trabeculae, small follicles and tubules consisting of polygonal cells. The lesion may be cystic due to necrosis (Fig. 13). These patients may have four parathyroid glands in their normal position in the neck [37]. The most common location is lateral to the oesophagus [38]. They may also occur in or near the thymus and an aortopulmonary window location is possible [39–41]. They are often less than 2 cm in diameter and their detection at CT drops considerably below this size, because they are the same size as normal lymph nodes. A marked contrast enhancement is therefore a useful feature but not constant. Sestamibi radio-

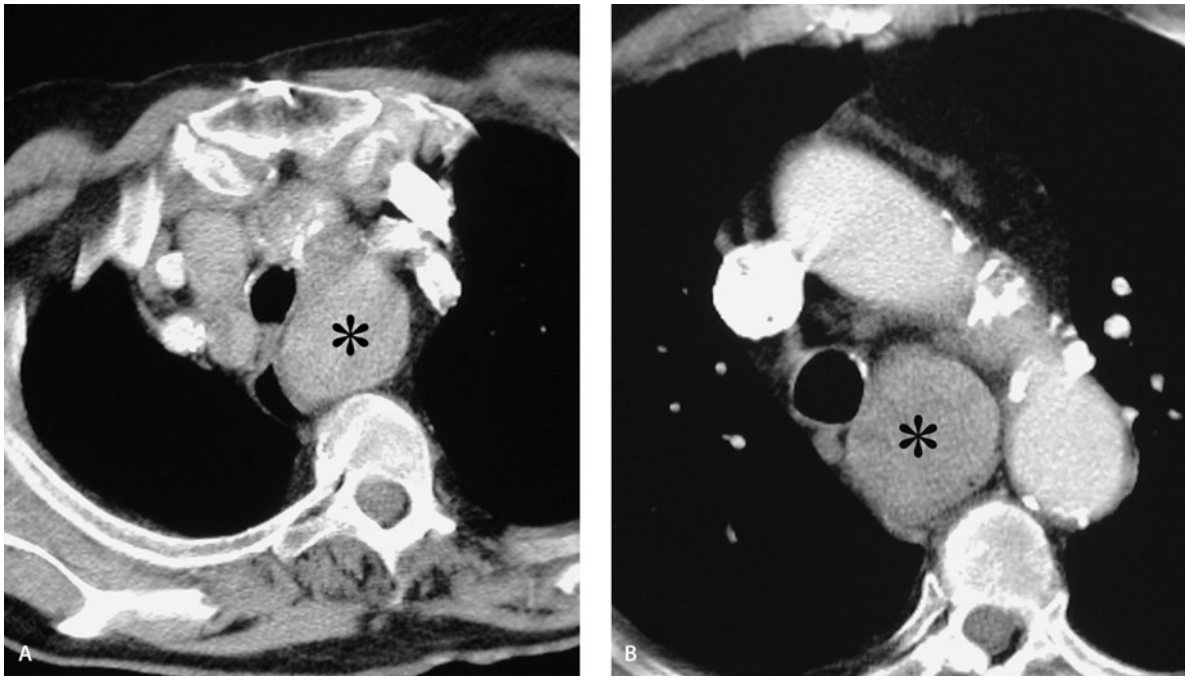

Fig. 12A, B. Thyroid goitre with retrotracheal extent. Enhanced CT showing (**A**) the origin from the left thyroid lobe (*asterisk*) and a posterior extension behind the trachea compressing the oesophagus and growing down between the aortic arch (*asterisk*) and the trachea (**B**)

Fig. 13A, B. Parathyroid cystic adenoma: the cystic wall is composed of parathyroid cells (*asterisk*) (**B**) attached to ectopic parathyroid tissue (*arrows*) (**A**)

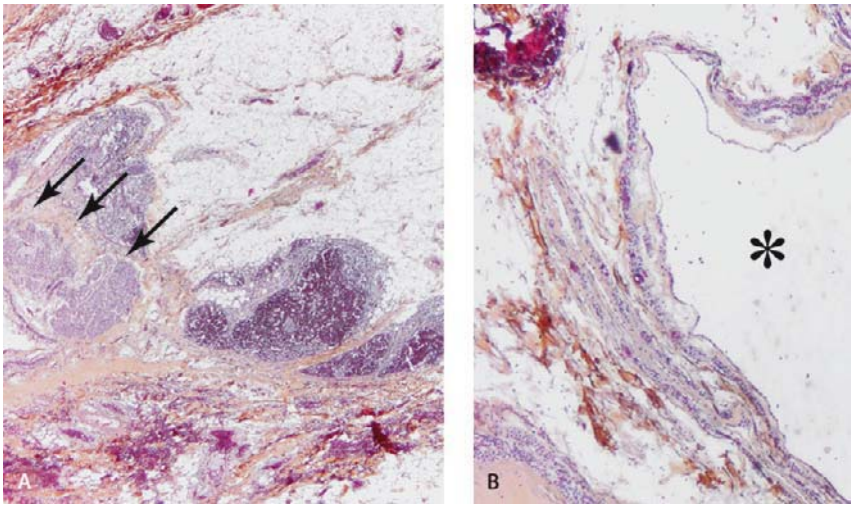

nuclide imaging, SPECT and MRI (Fig. 14) are the best techniques to demonstrate mediastinal parathyroid glands [42–44]. On MR imaging, the mass is usually of low signal on T1, a bright signal on T2-weigthed images, but any type of signal can be seen [36]. Mediastinal parathyroid cysts are rare and discovered incidentally with imaging findings that do not differ from other cysts of the mediastinum [45].

Thymic Masses

Epithelial Tumours of the Thymus

The term "thymoma" was used for many years to designate any type of involvement of the thymus. Today this term is strictly reserved for tumours composed of thymic epithelial cells and with a variable proportion of reactive lymphocytes, excluding mesenchymatous, en-

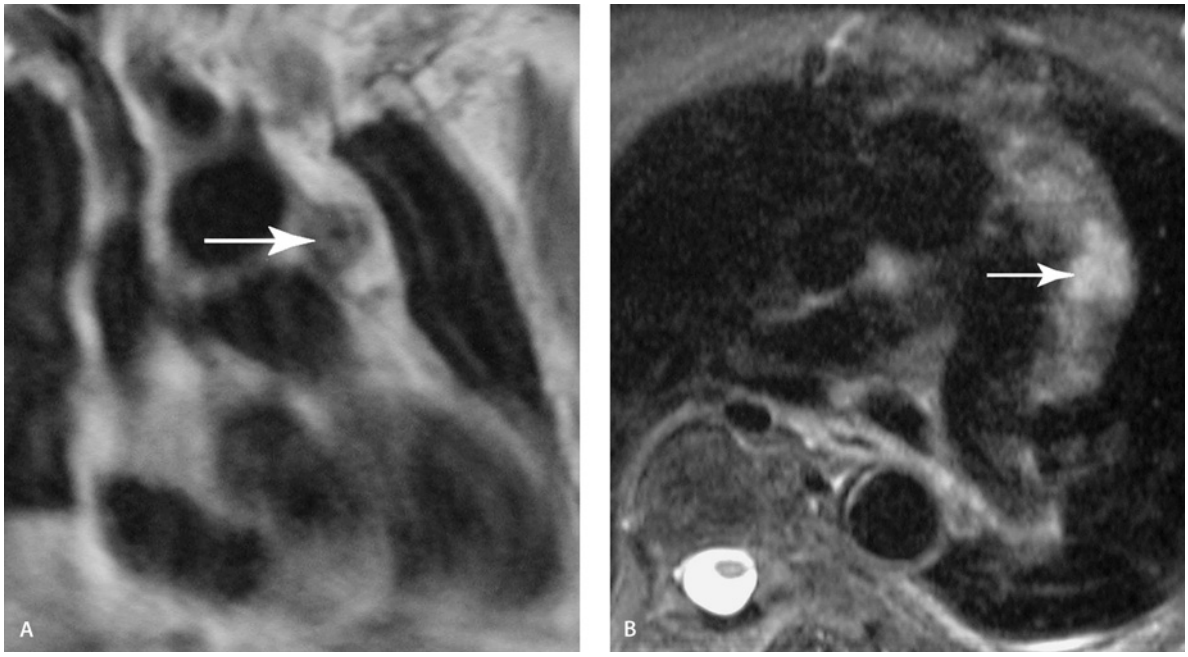

Fig. 14A, B. Parathyroid ectopic adenoma. MRI T1-weighted (**A**) coronal and T2-weighted (**B**) axial slices showing an intermediate on T1, high signal intensity on T2 located within the aortopulmonary window (*arrow*). A central area of low signal intensity (**A**) indicates necrosis

docrine, germinal neoplasms and lymphomas. Thymoma is the most common neoplasm of the anterosuperior mediastinum and the most common primary tumour of the thymus. Seventy percent are found in the 5th and 6th decades of life, with no gender predilection.

Thymomas are characterized by an admixture of neoplastic epithelial cells with mature lymphocytes (Fig. 15). Most are homogeneous but areas of necrosis, haemorrhage or cystic changes occur in one-third of cases. Most thymomas are encapsulated but one-third show various degrees of invasion of the capsule or of surrounding fat, pleura, pericardium and vascular structures. Lymphatic and haematogenous metastases are rare. The term "invasive thymoma" is used to designate a capsular invasion. The staging system proposed by Masoaka takes into account a capsular breakthrough, contiguous involvement of surrounding tissues, implants, and metastases [46]. Stage I shows no capsular invasion; stage II microscopic invasion of the capsule, surrounding fat or pleura, stage III invasion of surrounding organs; stage IVa pleural or pericardial dissemination and IVb lymphatic or haematogenous metastases. The histological classification of thymomas still remains controversial. Initially two major classifications were proposed, one by Levine and Rosaï and the other by Marino and Müller-Hermelink. Levin and

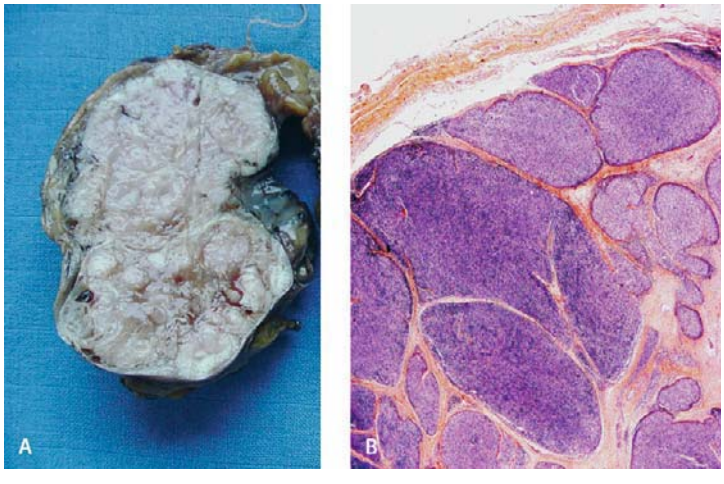

Fig. 15A, B. Thymoma. Gross anatomy showing an encapsulated tumour with a faintly lobulated ivory-coloured surface (**A**) and a lobulated appearance at low-power microscopy (**B**)

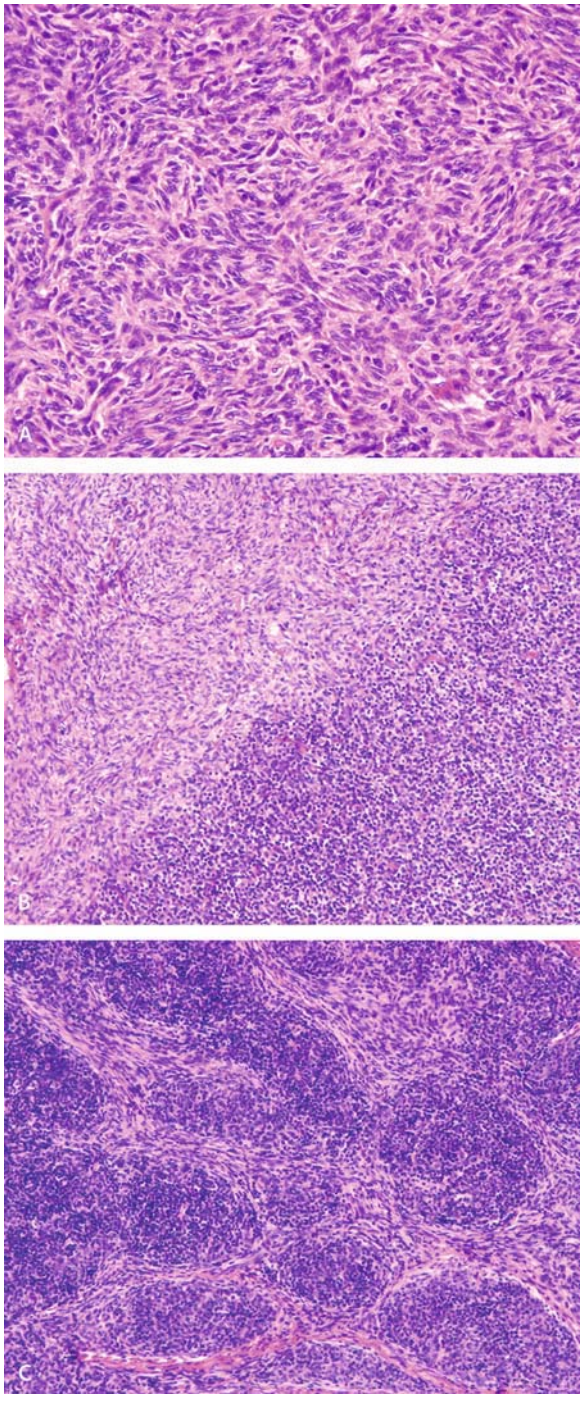

Fig. 16A–C. Thymoma. Cytological characteristics of A and AB types. Type A: tumour composed of neoplastic spindle, oval-shaped epithelial cells without nuclear atypia (**A**). Type AB: tumour showing foci of type A and admixed foci rich in lymphocytes (**B**, **C**)

Rosaï distinguished morphologically benign thymomas (noninvasive) from malignant thymomas type 1 (histologically malignant but cytologically benign) and type 2 malignant thymomas (thymic carcinomas) [47]. Marino and Müller-Hermelink proposed a classification based on the histological resemblance with the cortex or medulla of the normal thymus [48]. According to this last criterion, thymomas were classified in six categories, medullary, mixed, predominantly cortical (organoid), cortical, well-differentiated carcinoma and high-grade carcinomas. Compared with the previous results, this system would have prognostic significance, independent of tumour stage, the prognosis being worse with cortical and carcinomatous features. Nevertheless, some lesions remained difficult to classify. Therefore, a WHO classification has been suggested recently, retaining aspects from the two previously described, based on the degree of invasion and histology [49]. In this last classification, thymomas are divided into six groups: A, AB (Fig. 16), B (1, 2, 3) (Fig. 17) and C (Fig. 18). Type A (for atrophic) are thymomas with epithelial cells identical to subcapsular normal cells in thymic remnants in adults. Type B (for bioactive) is divided into three groups (1, 2 and 3) according to the increasing number of cellular atypical epithelial cells and has morphological features close to those of the cortical cells of a child. Type C are thymic carcinomas with obvious cellular atypia and loss of lobulated architecture. Various types of type C can be described: epithelial, sarcomatoid, basaloid, and clear cell. The main advantages of the WHO classification are its reproducibility and prognostic significance. Because these types are similar to primary carcinomas outside the thymus, metastases from another primary site, especially the lung, need to be excluded [32]. There is a strong correlation between stage and histological type, most A, AB and B1 being encapsulated tumours with a 10-year survival of more than 90%, whereas B2 and B3 are often infiltrative with an only 40% 10-year survival [50]. The latter and type C tumours are those requiring additional therapeutic actions when they are resectable. However, there is no doubt that the staging and the extent of the surgical resection (complete vs partial) are major prognostic factors. Therefore stage, as previously mentioned, is essential for the therapeutic decision.

Patients with thymomas are asymptomatic in 20%–50% of cases. Patients may complain of dyspnoea, chest pain, respiratory infection, hoarseness, dysphagia and cough, which are produced by compression of adjacent structures. Superior vena cava syndrome and sudden death due to right atrial compression are rare. Pure red-cell aplasia, hypogammaglobulinaemia, endocrine, connective and cutaneous disorders have been reported associated with thymomas. Myasthenia gravis is associated with thymomas in 10%–15% and one-third of patients with thymomas have myasthenia gravis, although

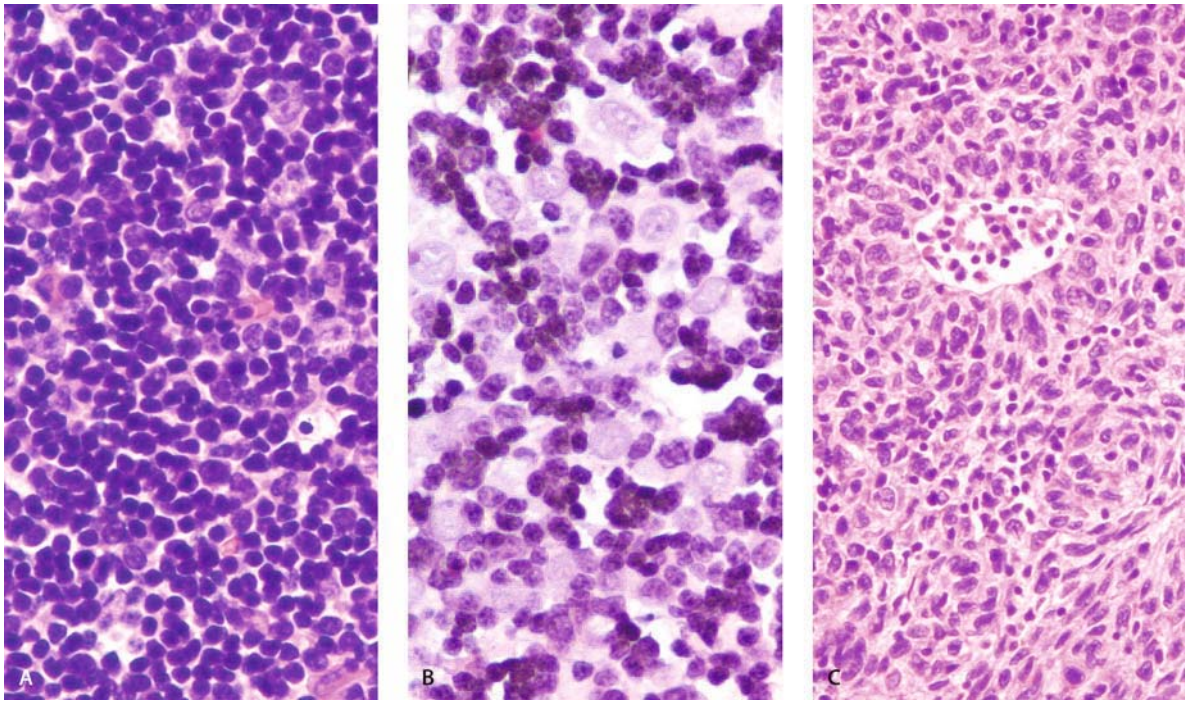

Fig. 17A–C. Thymoma. Cytological characteristics of B1 (**A**), B2 (**B**), B3 (**C**) types. B1: mixture of thymocytes and of epithelial cells with inconspicuous nuclei (**A**). B2: mixture of thymocytes and large epithelial tumour cells with vesicular nuclei (**B**). B3: predominant epithelial tumour cells with round or polygonal shape and rare lymphocytes (**C**)

these two conditions are not necessarily synchronous. The most frequent thymic abnormality associated with myasthenia gravis, however, is follicular thymic hyperplasia, which is a non-neoplastic condition [51].

The most frequent radiographic appearance of thymoma is a soft tissue mass of the anterior mediastinum, with smooth margins and lobulated borders against the lung, adjacent to the junction of great vessels or pericardium. Cardiophrenic angles, neck or other compartments are possible locations. On lateral projection, a soft-tissue opacity is often visible in the retrosternal clear space. Various patterns of calcifications may be visible. Invasive thymomas may be revealed by pleural disease, usually unilateral and nonspecific. Twenty-five percent of thymomas remain invisible on plain film and therefore clinical suspicion should lead to a CT examination when plain film remains unremarkable . The spectrum of CT findings in patients with thymoma has

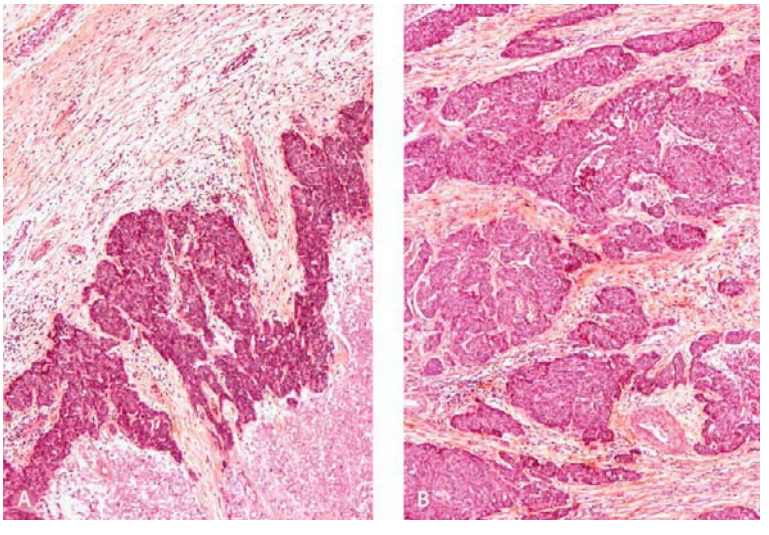

Fig. 18A, B. Thymoma type C (thymic carcinoma). Microscopy: low-power magnification showing necrosis and ill-defined nonencapsulated islets of irregular contours with epidermoid differentiation

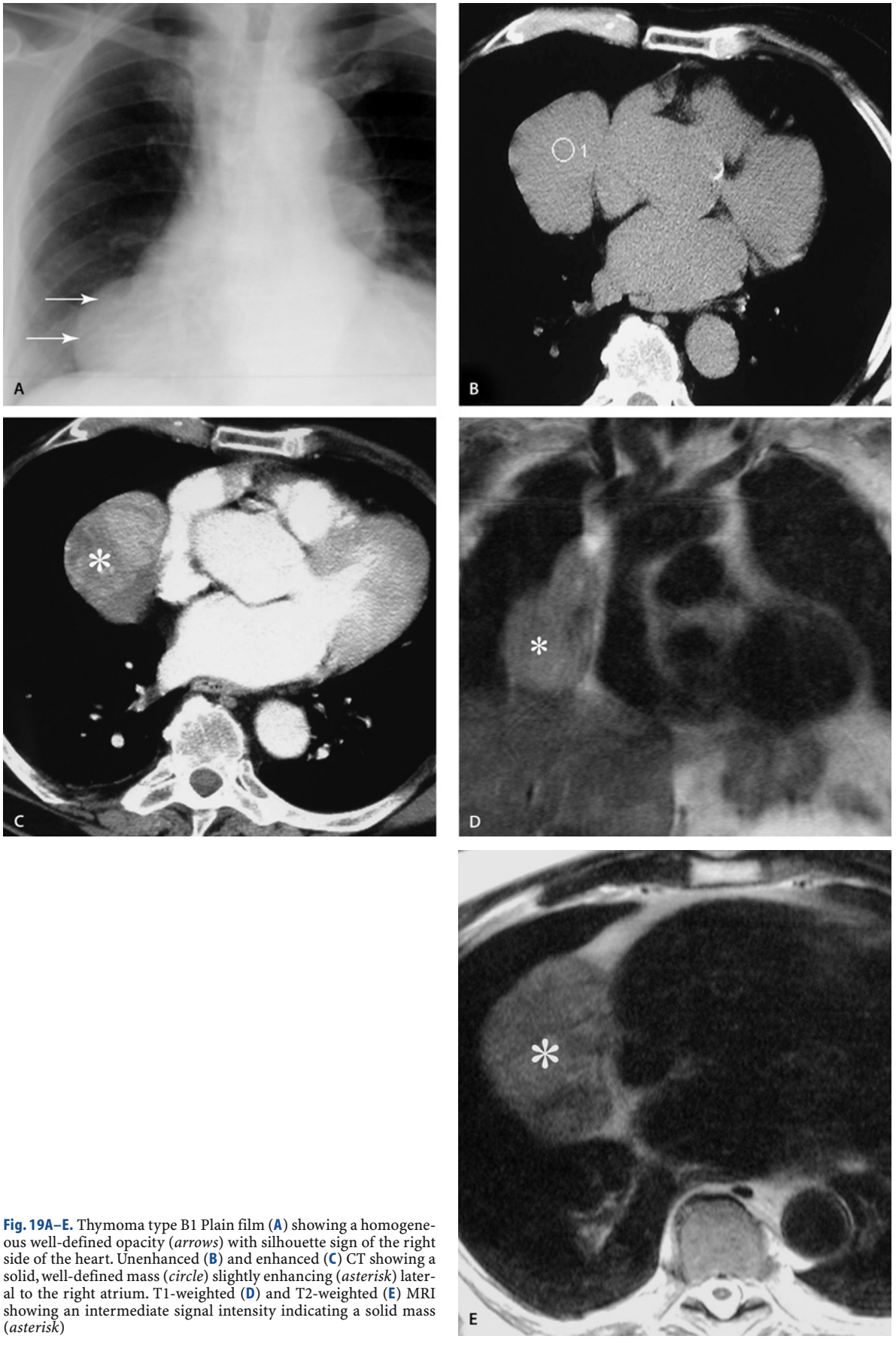

Fig. 19A–E. Thymoma type B1 Plain film (**A**) showing a homogeneous well-defined opacity (*arrows*) with silhouette sign of the right side of the heart. Unenhanced (**B**) and enhanced (**C**) CT showing a solid, well-defined mass (*circle*) slightly enhancing (*asterisk*) lateral to the right atrium. T1-weighted (**D**) and T2-weighted (**E**) MRI showing an intermediate signal intensity indicating a solid mass (*asterisk*)

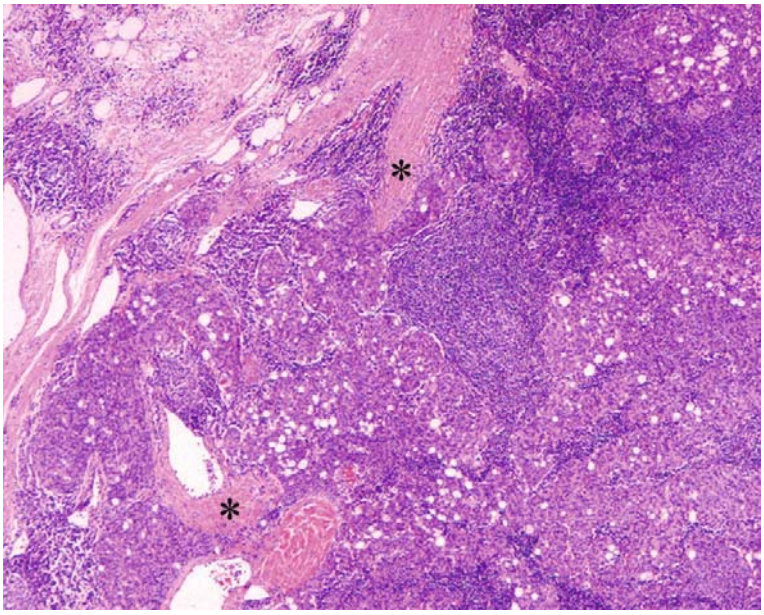

Fig. 20. Thymoma, minimally invasive type (micronodular variant) showing the rupture of the capsule (*asterisk*) with extension into the surrounding tissues

been extensively described [51]. Noninvasive thymomas appear as round or oval, well-circumscribed masses of variable size, growing asymmetrically to one side of the anterior mediastinum (Fig. 19). Lobular septations separated by thick septa can be visible. The mass may be partially outlined by fat or may replace fat completely, but the latter finding does not inform on local invasion. Direct contact and absence of cleavage planes are not strictly reliable criteria to predict invasion, which should not be overdiagnosed. On the other hand, clear delineation of fat planes surrounding a tumour should be interpreted as indicating an absence of extensive local invasion (Figs. 20, 21). The CT density is similar to that of a normal young thymus and slightly increases with administration of contrast material. Curvilinear capsular calcifications of solid tumours or cyst wall or amorphous central calcifications can be detected; areas of cystic degeneration are also common. Sometimes the cystic part is dominant and the tumour arises from the cyst wall. The tumour can occur in the prevascular

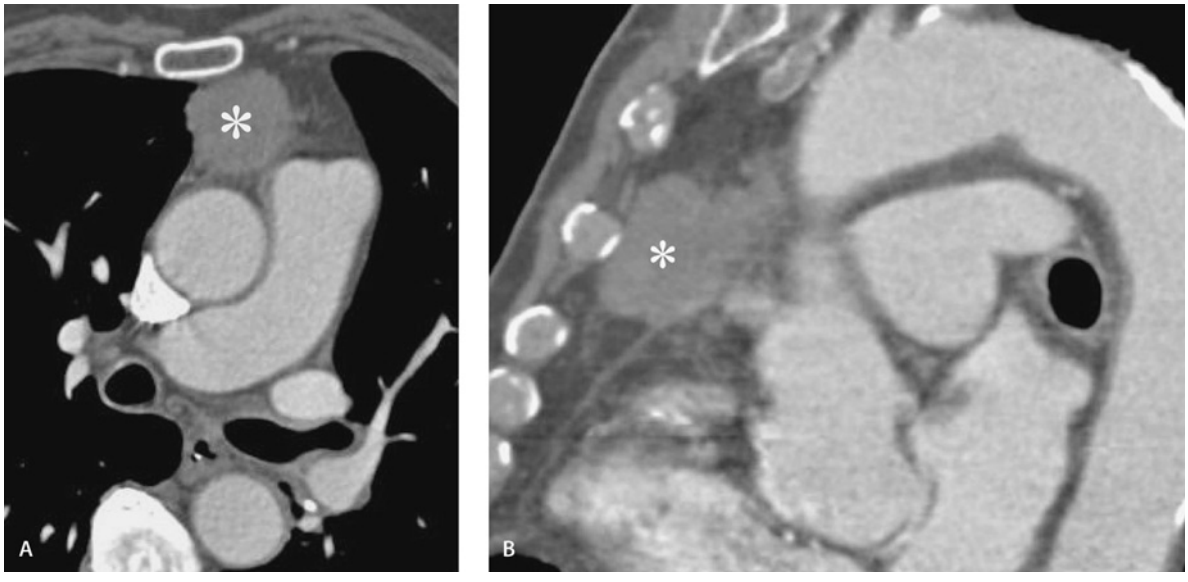

Fig. 21A, B. Minimally invasive thymoma. CT, axial (**A**) and sagittal (**B**) 2D reconstruction, showing a homogeneous, well-defined solid mass (*asterisk*) of the anterior mediastinum. Contours and relationships with pericardium and great vessels are nicely evaluated by multiplanar CT

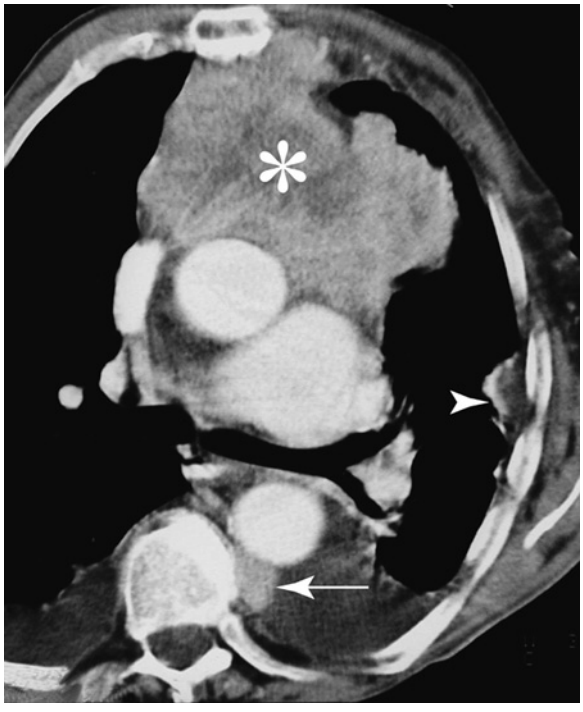

Fig. 22. Invasive thymoma. The main lesion is situated in the anterior mediastinum, is heterogeneous and irregular in shape, with ill-defined contours on the left mediastinum–lung interface, suggesting lung invasion. The lesion grows posteriorly along the descending aorta (*arrow*). A bilateral pleural effusion and pleural implants (*arrowhead*) without apparent connection to the main lesion indicate pleural invasion

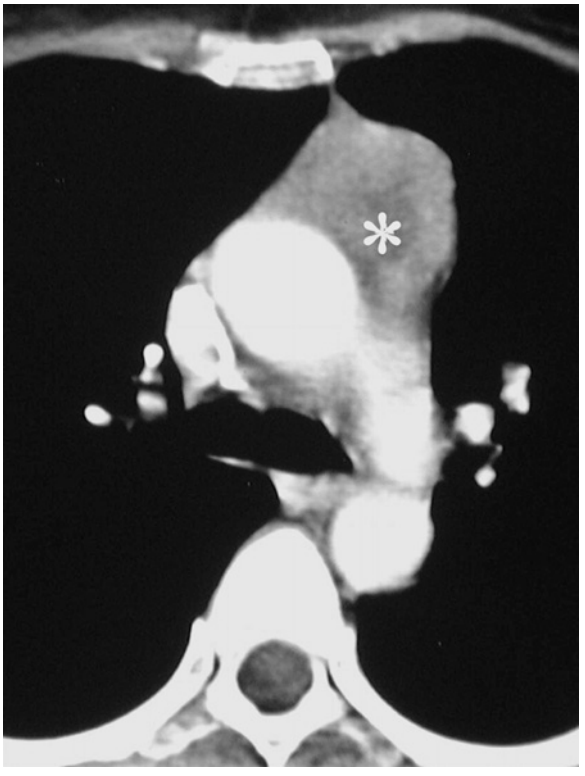

Fig. 23. Thymic carcinoma. CT showing a heterogeneous anterior mass (*asterisk*) without specific features but ill-defined contours suggesting an invasive lesion

space of the mediastinum but also at a lower level around the base of the heart and anywhere between the lower pole of the thyroid gland and the anterior surface of the pericardium. A sensitivity of 91% and a specificity of 97% of CT in the diagnosis of a thymic mass have been reported [52]. The main difficulty for the radiologist is to distinguish thymoma from thymic lymphoid follicular hyperplasia, because the latter may manifest as a diffuse enlargement of the thymus but also as a focal mass [53]. This distinction is even more complicated in young patients, who may have residual thymic tissue, but is more reliable in those older than 40, whose thymus has undergone a fatty involution. Somatostatin receptor scintigraphy with somatostatin analogue, indium-111 and thallium-201 scintigraphy are more reliable in distinguishing thymomas from follicular hyperplasia or thymomas from scar tissue [54].

Invasive thymomas appear on CT as an irregular ill-defined mass. Most often, they tend to show lobulated or irregular contours, to have a higher prevalence of low attenuation areas within the tumour, as well as multifocal calcifications [55]. They grow along pleural surfaces and can reach the posterior mediastinum and extend downwards along the aorta to involve the crus of the diaphragm and the retroperitoneum. A full CT examination in these patients should extend to the upper abdomen. Pleural extension as droplet spread without continuity with the primary tumour can be seen (Fig. 22). Drop metastases may coalesce to encase the lung and simulate a malignant mesothelioma. Invasion of the thoracic wall, mediastinal vessels, trachea, pericardium and lung parenchyma is frequent. Metastatic involvement of liver, kidney, bone and brain is infrequent. Despite a more aggressive appearance and lymphatic and metastatic dissemination more frequent in thymic carcinomas (type C) than in other types of thymomas at presentation [56], there is so far no correlation between histological subtypes and imaging features, nor with associated neoplasm (Fig. 23). Recent reports have shown that smooth contours and a round shape are most suggestive of type A, whereas irregular contours are more likely to occur in type C. Calcification is suggestive of type B. However, CT is of limited value in differentiating types AB, B1, B2 and B3 tumours [57].

MR has a limited role in the evaluation of thymomas because it does not add significant information to CT in most cases. This technique, however, is very useful when CT appearance is equivocal and when CT cannot be performed with contrast material to assess vascular and cardiac involvement. Thymomas show a signal intensity

close to skeletal muscle on T1-weighted images and an increased signal relative to muscles on T2-weighted images [58]. Radiological–pathological correlations have shown that the signal on T2-weighted images is heterogeneous in malignant thymomas and show a lobulated appearance in about half of the cases [59, 60].

The treatment of choice of a thymoma is complete surgical resection with en-bloc removal of the thymus and neighbouring adipose tissue. Patients with stage I encapsulated tumour are almost always cured by complete surgical resection. Postoperative radiation therapy is used in patients with stage II invasive thymomas and in stage III and IVa. It may also control residual disease and provide long term free-survival. Patients with stage IV disease, invasive incompletely excised or recurrent thymomas are candidates for chemotherapy.

Other Thymic Tumours and Non-neoplastic Conditions of the Thymus

Carcinoid tumour is a well-differentiated neuroendocrine tumour of low-grade malignancy. Carcinoid occupies lies opposite to small cell carcinoma on the spectrum of neuroendocrine tumours, intermediate types called atypical carcinoid and large cell neuroendocrine tumours. The thymus is an uncommon location, the gastrointestinal tract and the respiratory tract being the most commonly affected. The histology of carcinoid tumour of the thymus is similar to its bronchial and gastrointestinal counterpart, regardless of the frequency of mitotic figures and foci of necrosis. They are composed of solid nests of relatively large cells with finely granular cytoplasm, arranged in a pattern suggestive of endocrine tumour, often with argyrophilia. As in other locations, the tumour cells immunostain for neuron-specific enolase and chromogranin A with variable intensity, sometimes with somatostatin and ACTH (Fig. 24). Thymic carcinoid may secrete ACTH and present with ectopic ACTH Cushing syndrome, rarely a multiple endocrine neoplasia type I (Wermer syndrome) [61]. The carcinoid syndrome has not been described in patients with carcinoid tumour. The tumour affects patients within a wide age range who present with symptoms of compression or invasion of adjacent structures, complain of chest pain or dyspnoea or have metastases at presentation. One-third are asymptomatic. CT features are indistinguishable from thymomas (Fig. 25) [62, 63]. Indium DTPA is accumulated in thymic carcinoid as well as in other thymic neoplasms and has been used for anatomical localization of occult hormonally active tumours [64, 65].

Thymolipoma is a rare slow-growing tumour, thought to represent a hamartomatous lesion. It occurs in both sexes in relatively young patients. The tumour enlarged the thymus, which often remains normal in

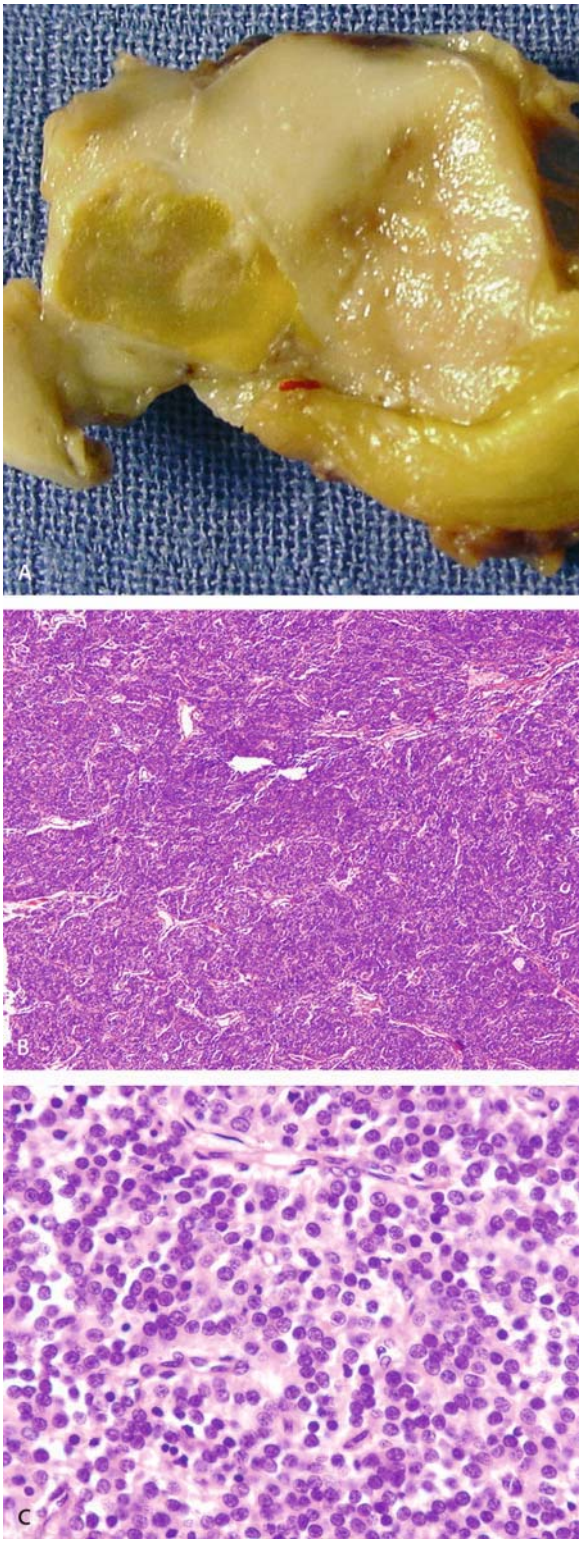

Fig. 24A–C. Carcinoid tumour of the thymus. Gross anatomy: pale to yellow solid cut surface with scattered areas of necrosis (**A**). Microscopy: cellular tumour admixed with scantly and microvascular stroma (**B**). High-power magnification: ribbons and nets of small to medium-sized polygonal cells with eccentric nuclei (**C**)

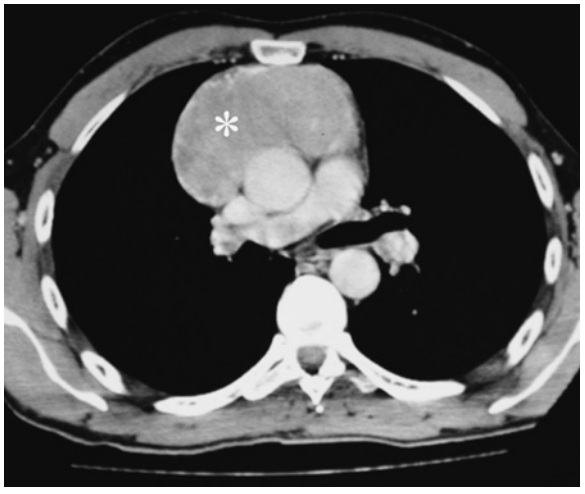

Fig. 25. Thymic carcinoid. CT showing a well-defined anterior mediastinal mass (*asterisk*) without specific features. The patient had no symptoms that would arouse suspicion of the endocrine nature of the lesion

shape and may be attached to the thymus by a pedicle. Histologically, it is composed of normal fat and thymic tissue, the latter appearing normal [66]. When they are large, thymolipomas may extend downwards on the diaphragm, leaving the superior mediastinum relatively clear, as the result of their soft and pliable consistency. They are composed of a mixture of fatty and tissular components of nearly equal proportions, although some are predominantly composed of fat mimicking a lipoma [67].

Thymic lymphoid (follicular) hyperplasia is characterized by expansion of the medulla at the expense of the cortex, due to the proliferation of medullary B-cell lymphoid follicles with active germinal centres and accelerated production of antibodies to acetylcholine receptors [32]. It affects young adults and is frequently associated with myasthenia gravis and account for 85% of thymic abnormalities associated with myasthenia gravis [68]. Thymic hyperplasia can also be associated with thyrotoxicosis, Addison disease, a variety of connective tissue and autoimmune disorders, and other nonthymic neoplasms [47]. Thymic shape is normal and its size can either be normal or enlarged. CT may show a grossly normal thymus, a diffuse enlargement or a focal nodule. On MRI, the signal intensity is similar to the thymus of normal subjects [53].

Lymphoid hyperplasia should be distinguished from true thymic hyperplasia, which shows an increase in size and weight with a normal microscopic appearance. This condition results from rebound growth after an acute illness, corticosteroid administration or thymic radiation therapy or chemotherapy, mainly lymphoma and germ cell tumour, for usually during the year following its cessation. Young subjects are predominantly affected. Imaging features are those of an enlarged normal-shaped thymus of homogeneous attenuation or signal similar to that of a normal gland [32].

Lymphoma

The term "lymphoma" refers to a primary tumour of the immune system and encompasses a spectrum of diseases among which Hodgkin disease (HD), and a group of lymphoproliferative disorders termed non-Hodgkin lymphomas (NHL) are distinguished. HD accounts for approximately 0.5%–1% of newly diagnosed cancers in adults, whereas NHLs are four times more common. However, HD more commonly affects the mediastinum and is confined to the thymus in 10%–40%, whereas 15%–25% of patients with NHL have mediastinal or hilar lymph nodes at presentation, and the disease is limited to the mediastinum in less than 10% of the cases [32]. HD shows a characteristic bimodal peak in the 3rd and 6th decades and the median age of diagnosis of NHL is 55 years [69]. Improvement in histopathology and immunology have led to the development of the REAL/WHO (Revised European and American Lymphoma/World Health Organization) classification system based on morphology, immunology, cell differentiation, aetiology and clinical behaviour [70]. The clinical staging uses the Cotswold classification, a modification of the Ann Arbour classification [71].

Hodgkin Disease

Pathologically, HD is characterized by the presence of the Reed-Sternberg cell (Fig. 26). The pathological classification of HD relies on the RYE system which is still accepted and divides four subtypes: lymphocyte predominance, nodular sclerosis, mixed cellularity and lymphocyte depletion, the nodular sclerosis type being the most frequent and the most frequently affecting the mediastinum. A fifth histological type, nodular lymphocyte predominance Hodgkin lymphoma, has been added to this histological categorization but its tendency is to spare the mediastinum [72]. HD spreads predictably from one lymph node group to the contiguous one. Staging, based on a systemic evaluation of the disease, is a critical step for treatment decisions [69]. Radiotherapy suffices in early stages (IA and IIA), whereas combination chemotherapy is indicated in more advanced disease [73]. Prognosis depends on the stage of the disease, cure being obtained in 90% of patients with localized disease and in 60% in those with extensive disease.

Radiographic evidence of intrathoracic disease is seen at presentation in 70% of patients, of whom the mediastinum is frequently involved but rarely isolated. Only 15% of patients have lymphadenopathy confined

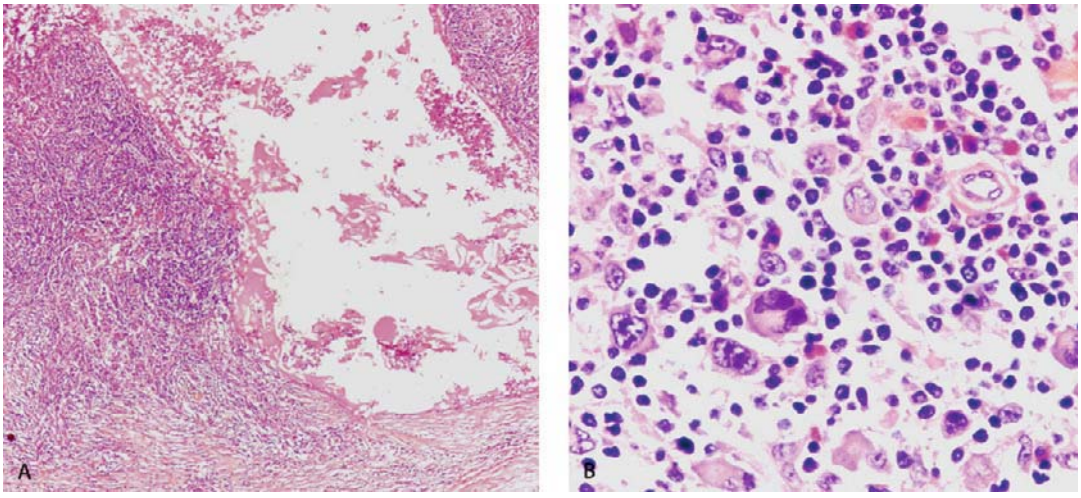

Fig. 26A, B. Hodgkin disease. Lymphoid nodular proliferation in the setting of thymic cyst (**A**). High power: Sternberg neoplastic cells and Hodgkin cells mixed with lymphocytes plasma cells and eosinophilic granular cells (**B**)

to a single lymph node group [74, 75]. Posteroanterior and lateral chest films can detect most intrathoracic abnormalities [73] and are important at baseline and for periodic surveillance. A diffuse mediastinal widening with lobulated contours and varying degrees of mass effect are the main features. CT and PET are, however, more sensitive and specific. CT can add additional information in 8% of patients whose radiograph is normal and globally in 15% of cases and is therefore recommended [74]. Mediastinal HD typically manifests as

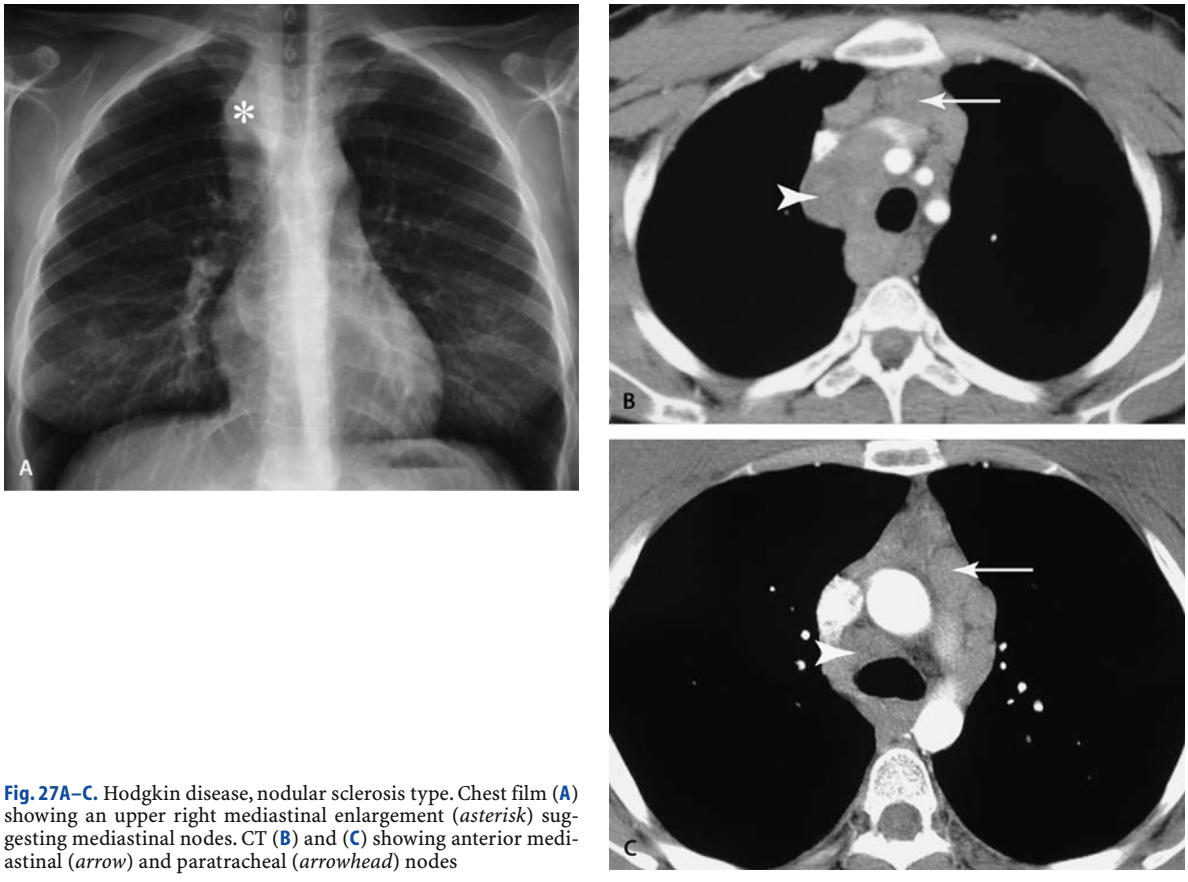

Fig. 27A–C. Hodgkin disease, nodular sclerosis type. Chest film (**A**) showing an upper right mediastinal enlargement (*asterisk*) suggesting mediastinal nodes. CT (**B**) and (**C**) showing anterior mediastinal (*arrow*) and paratracheal (*arrowhead*) nodes

multiple rounded lymph nodes. The anterior and paratracheal lymph nodes are the most frequently involved [76]. The other group and hilar nodes are less frequently involved (Fig. 27). Lung parenchymal evaluation is almost always associated with mediastinal involvement. Mediastinal HD may also manifest as a dominant bulky mass of lymph nodes, and mass effect or invasion of adjacent pleura, lung or chest wall is possible. Thymic involvement is difficult to distinguish from adenopathy on CT alone but the thymus is considered as a lymph node and therefore its involvement does not affect the staging [77]. Pleural effusion is usually a consequence of lymphatic or venous obstruction rather than a lymphomatous involvement, and parietal extension may be seen at presentation [74, 75]. The paracardiac nodes are not commonly involved at the initial presentation but are a common finding of relapse [78]. Masses typically show homogeneous soft tissue attenuation but large tumours may show fluid-filled cystic changes corresponding to haemorrhage and necrosis. Calcifications are rare before therapy but could be seen in residual masses and nodes after treatment (Fig. 28). On MR, masses and nodes exhibit homogeneous low signal intensity similar to that of muscle on T1-weighted images and a greater or equal signal than fat on T2-weighted images. Tumoral oedema, immature fibrosis, areas of necrosis and cyst formations may show high signal, whereas dense fibrosis shows low signal intensity [79]. After treatment, a residual fibrotic mass cannot be differentiated from a viable tumour in the first 6 months after therapy [80]. However, recurrent disease tends to exhibit one or more increased signal intensities or heterogeneous high signal when compared with baseline studies, independent of tumour size [80, 81]. A close follow-up should is required. A new or enlarging mediastinal mass that develops after therapy may represent recurrence, post-therapeutic cyst or hyperplasia. Although MR shows advantages over CT in the detection of occult bone-marrow involvement, it is less accurate in evaluating the lung parenchyma and usually employed for evaluating important anatomical issues raised by CT and not as the initial test after chest X-ray. Gallium scanning has been employed for several decades and has declined in popularity since its results and utility remains ambiguous. In contrast, fluorodeoxyglucose PET has been proved to be more sensitive than CT and to be able to modify the initial staging [82]. Today PET and CT would appear to be the examinations of choice.

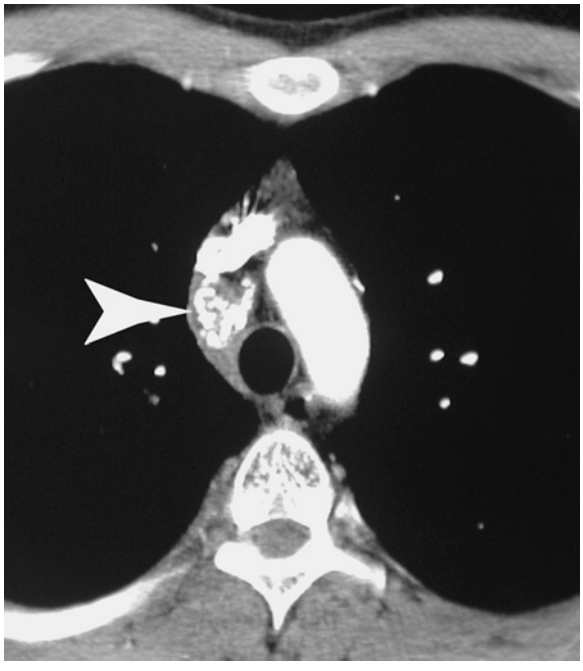

Fig. 28. Hodgkin disease, nodular sclerosis type. CT following treatment showing a residual calcified lateral tracheal node (*arrowhead*)

Non-Hodgkin Lymphoma

NHL accounts for approximately 3% of all cancers in adults. This group of diseases is more heterogeneous than Hodgkin disease, with a wider spectrum of clinical manifestations and pathological characteristics [83]. Treatment strategy and prognosis strongly depend on the histology subtype. The working formulation classifies NHL into low, intermediate, and high grades on the basis of morphology. In general, NHL presents at a more advanced stage than HD, with constitutional symptoms, generalized lymphadenopathy or extensive extranodal disease [32]. NHL in adults is rarely localized solely to the mediastinum, but primary mediastinal large B-cell type and lymphoblastic lymphoma arise preferentially as anterior mediastinal or thymic masses.

Lymphoblastic lymphoma represents 40% of childhood lymphomas and 15% of acute leukaemias. Males are predominantly affected and it is considered as a form of acute lymphoblastic leukaemia. Patients frequently show widespread disease at presentation and the rapid growth and high degree of invasion are responsible for superior vena cava syndrome and airway compromise, a true oncological emergency. Other clinical presentations are subacute. The tumour is composed of small immature lymphocytic T cells (Fig. 29). Internal fibrous bands are absent. Radiologically, patients have large lobulated anterior masses, often measuring over 10 cm. Compression of thoracic vessels, trachea and oesophagus and invasion of pericardium, lung and chest wall and pleural effusion are common (Fig. 30).

Primary large B-cell lymphoma occurs in adolescents or young adult females who present with a rapid onset of constitutional symptoms or superior vena cava syndrome. Grossly, this an unencapsulated bulky inva-

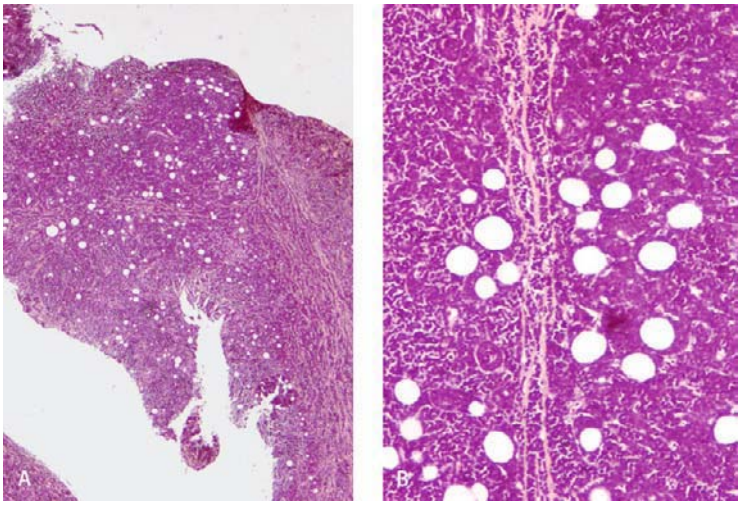

Fig. 29A, B. Lymphoblastic lymphoma. Microscopy: diffuse infiltration (**A**) of the mediastinal fat (seen as isolated vacuoles) surrounded b y lymphoblasts (**B**)

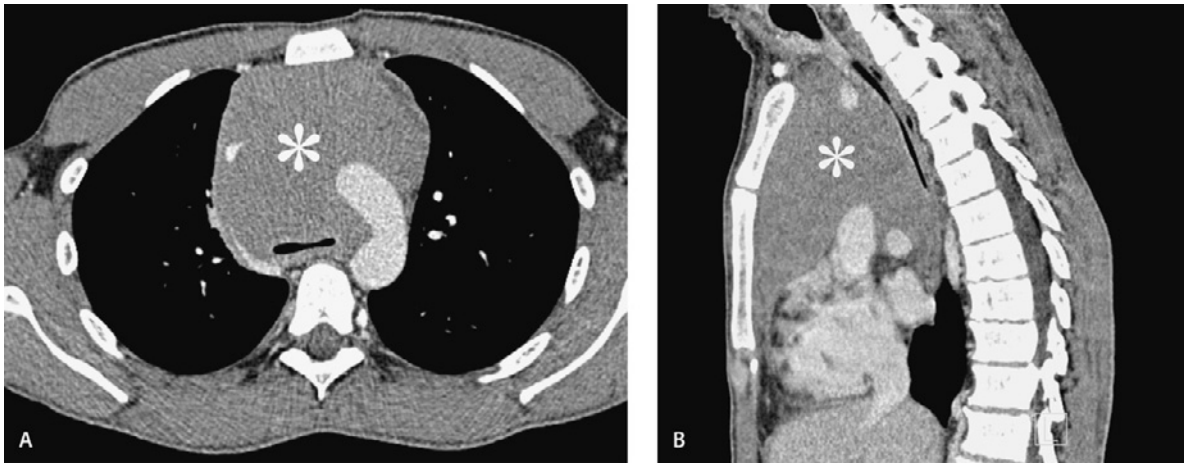

Fig. 30A, B. Lymphoblastic lymphoma in a 22-year-old man revealed by a superior vena cava syndrome. CT axial (**A**), sagittal (**B**) 2D reformations. Invasive solid anterior mass (*asterisk*) compressing the mediastinal vessels and the trachea

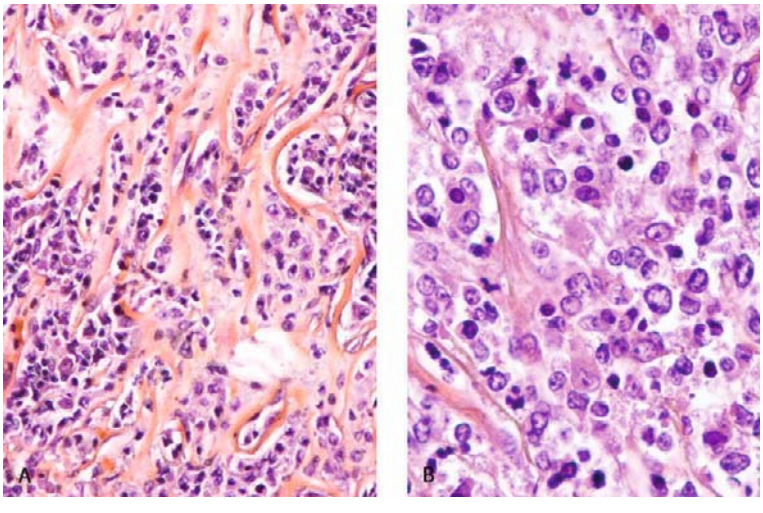

Fig. 31A, B. Diffuse large B-cell lymphoma (sclerosing variant). The tumour is characterized by fibrohyaline bands incompletely dividing the lymphomatous cells into nets (**A**, **B**)

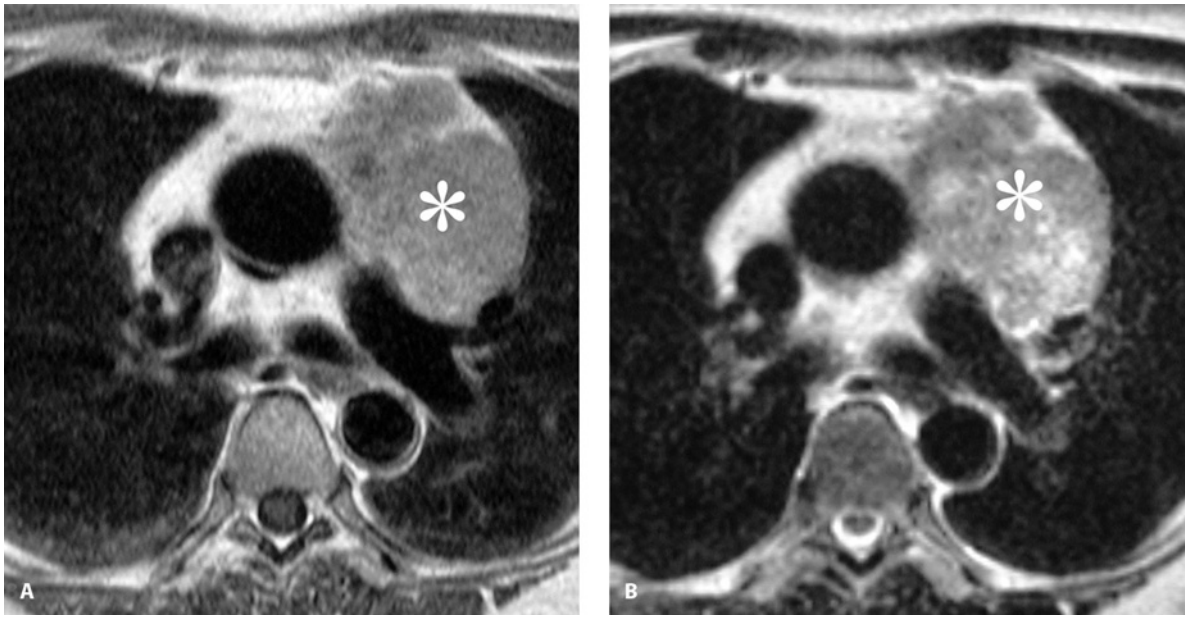

Fig. 32A, B. Diffuse large B-cell lymphoma (sclerosant variant). T1-weighted (**A**) and T2-weighted (**B**) MRI showing a solid mass (*asterisk*) of the anterior mediastinum with ill-defined contours

sive soft tissue mass which consists of clear cells with indistinct borders and prominent fibrosis and is thought to arise from thymic medullary B cells (Fig. 31). Imaging features are similar to the others, with involvement of the thymus and/or mediastinal nodes. CT constitutes the principal modality for initial staging of thoracic lymphoma, providing a baseline staging evaluation that is useful for follow-up. Ultrasound can be employed in case of pericardial or cardiac involvement but MRI is, in this particular case, as well as in vascular compromise, the preferred method (Fig. 32). Today the use of gallium scintigraphy has declined at the expense of PET. Although PET has limitations in detecting uptake in low-grade lymphomas, its improved sensitivity over CT suggests that this technique has an important role in both staging and in predicting prognosis and relapse of residual masses [84, 85].

Germ Cell Tumours

Germinal-cell tumours account for roughly 10%–0% of primary mediastinal tumours in adults. Extragonadal germ cell tumours arise from tumoral transformation of multipotential primitive germ cells that are displaced along midline structures during their migration from the yolk endoderm to the gonad during early embryogenesis. Most arise in the anterior mediastinum between the 2nd and 4th decade of life, particularly the anterosuperior portion, with only 3% of them being found in the posterior mediastinum. Seventy-five percent are benign teratomas, mature or immature, which occur with equal frequency in men and women. Malignant varieties have a strong male predominance and include teratoma with malignant transformation, seminoma, the most common accounting for 40% of the malignant varieties, but also embryonal cell carcinomas (teratocarcinoma), endodermal sinus tumour, choriocarcinomas, and mixtures of these various cell types [86–88].

Teratomas

Mature teratomas are rare slow-growing primary germ cell neoplasms composed of well-differentiated tissues derived from more than one of the three embryonic germ cell layers that occurs near or within the thymus gland. A teratoma with immature neuroectodermal and mesenchymal tissue is called an immature teratoma. Those that contains foci of carcinoma, sarcoma or malignant germ cell tumours are called teratoma with malignant components. Grossly, it is a lobulated, encapsulated, multicystic neoplasm (Fig. 33) that exhibits a variety of components ranging from lipid-rich fluid and cheese-like material to well-formed tissues, usually consisting of ectodermal elements such as skin, sebaceous material, hair (ectodermal elements), bone, cartilage and smooth muscle (mesodermal elements) and gastrointestinal or respiratory epithelium (endodermal elements). Pancreatic tissue may be present and as though it were the cause of a noninfective pancreatitis explaining acute events due to inflammation (Fig. 33). Rupture into the bronchial tree, pleural or pericardial

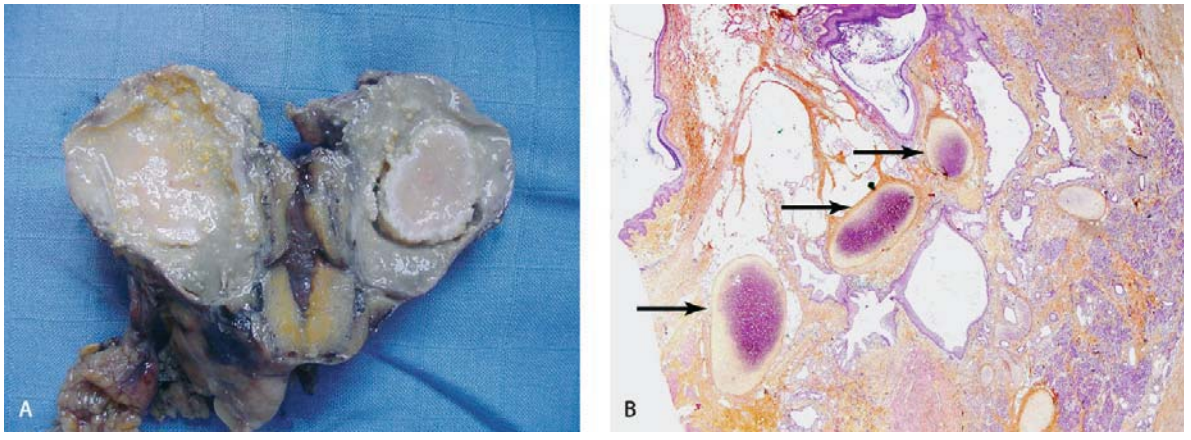

Fig. 33A, B. Mature cystic teratoma. Gross specimen (**A**): well-defined encapsulated cystic tumour filled with sebaceous material. Microscopy (**B**): presence of mature cartilage (*arrows*), cutaneous and islets of well-differentiated pancreatic tissue on the right part of the image

space or lung may occur. The term "dermoid cyst" is commonly applied because of the frequent expression of the ectodermal component of the teratoma. Cyst formation is typical, the cyst being lined by mucus-secretin epithelial cells [32, 86].

Mature teratomas affect children and young adults. Half to 75% of the cases complain of chest pain, dyspnoea and cough, caused by local compression. Expectoration of hair (trichoptysis) or sebum is rare but characteristic clinical findings of a ruptured teratoma. They grow slowly and rapid increase of size may occur because of haemorrhage.

Radiographically, the typical appearance is that of a sharply marginated lobulated anterior mediastinal mass which projects beyond the boundaries into adjacent lung fields. Calcification of the wall, the substance or ossification of mature bone or a tooth within the tumour have been reported in 20%–43% of cases [89]. On CT, teratomas may contain one loculus or be or be multiloculated; and the most typical appearance is a mass containing a mixture of CT fatty, tissular and water densities (Fig. 34). Fatty and cystic components are present in more than half the cases. Soft tissue attenuation is not usually the dominant component and is frequently limited to the thin peripheral capsule, although enhancement is frequently seen. Calcification in the wall or small spherical or irregular calcifications within the mass, sometimes suggesting dental material, may be seen. A fat–fluid level within a cyst strongly suggests the diagnosis [90]. Complications such as rupture into the lung, pleural space, bronchial tree and pericardial or pleural space can be observed on CT examinations. In cases of rupture within the pleura, a fat–fluid level has been reported [91, 92]. At MRI, the appearance is that of a heterogeneous lesion (Fig. 34), with solid elements with a similar signal intensity to muscle, while cystic

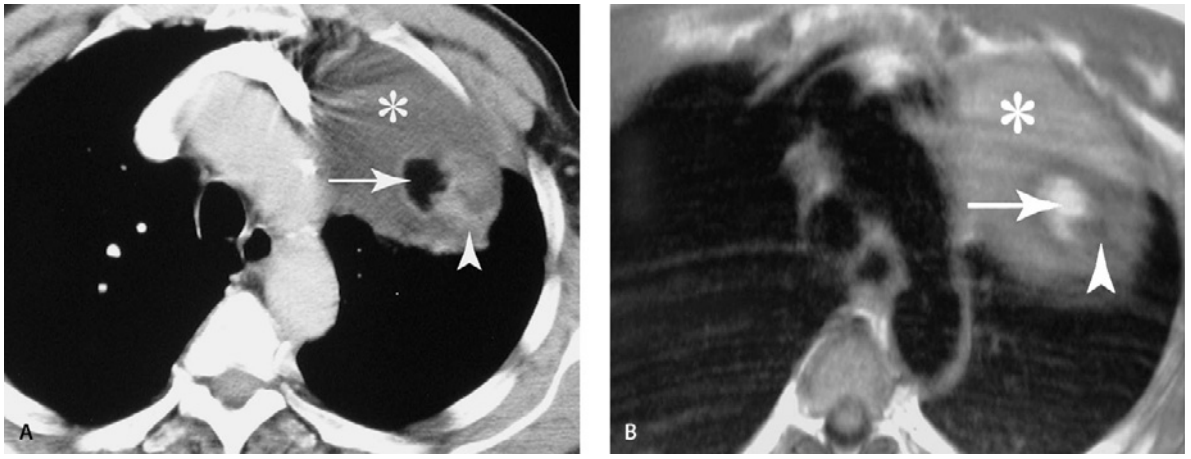

Fig. 34A, B. Mature cystic teratoma. CT (**A**): a small central area of fat (*arrow*) surrounded by a rim of enhancing solid tissue (*arrowhead*) and a large low-attenuation low-intensity area is characteristic of a teratoma. Similar characterization is possible with T1 (**B**) and T2 MRI

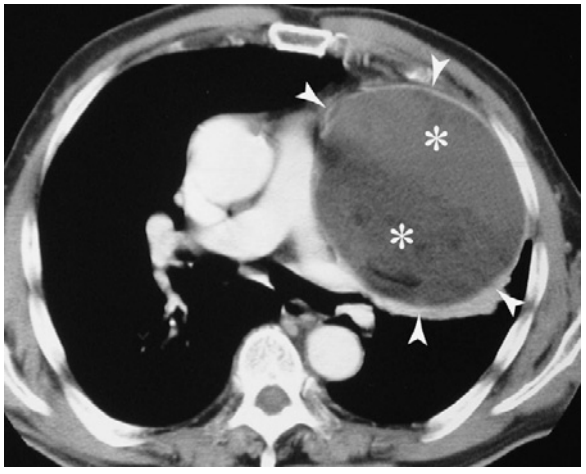

Fig. 35. Cystic teratoma with foci of teratocarcinoma. Enhanced CT shows the cystic content with two layers of slightly different attenuation values (*asterisk*) and a thick wall (*arrowhead*)

components are of high intensity on T2 but from low to moderately high intensity on T1-weighted images, depending on the fluid content. Visualization of fat is useful in determining the diagnosis [93]. Malignant transformation of a teratoma may occur in the mediastinum without any detectable finding leading to suspect this malignant transformation (Fig. 35).

Seminomatous and Non Seminomatous Germ Cell Tumours

Seminoma is the most common primary malignant germ cell occurring in the mediastinum, occurring typically in the 3rd to 4th decades of life in men exclusively and frequently symptomatic at presentation. Patients with pure seminomas may have a slightly elevated B-chorionic gonadotropin level but never an elevated serum alpha-foetoprotein [87]. Grossly, the tumour is large, soft, well-circumscribed and often homogeneous. Histologically, the tumour is identical to its gonadal counterpart, made of sheets of large polygonal cells with a fine granular cytoplasm containing glycogen and centrally located round nuclei, with prominent nucleoli within a loose stroma (Fig. 36). The differential diagnosis includes epithelioma-like carcinoma of the thymus and large cell lymphoma [87]. On CT, the lesion appears as a large solid mass, rarely partly or almost totally cystic, with sharply marginated borders and homogeneous attenuation, enhancing slightly after contrast medium administration (Fig. 37) [94, 95]. The low attenuation areas are due to necrosis, cyst or haemorrhage. Calcifications are uncommon. These tumours are highly sensitive to radiation therapy and systemic chemotherapy, the current therapeutic options. Prognosis is good when the diagnosis is established early and 60%–80% long-term survival has been reported [87]. The tumour may spread to bone, lung and liver.

Malignant nonseminomatous germ cell tumours include yolk sac tumour (endodermal sinus), embryonal carcinoma, choriocarcinoma and malignant germ cell tumours with more than one germ cell histology. Confirmation of the primary nature of these tumours requires that there is no evidence of testicular or retroperitoneal tumour. Malignant nonseminomatous germ cell tumour lesions affect almost exclusively men, 20% having Klinefelter syndrome. They also have a risk of developing a concurrent haematological malignancy unrelat-

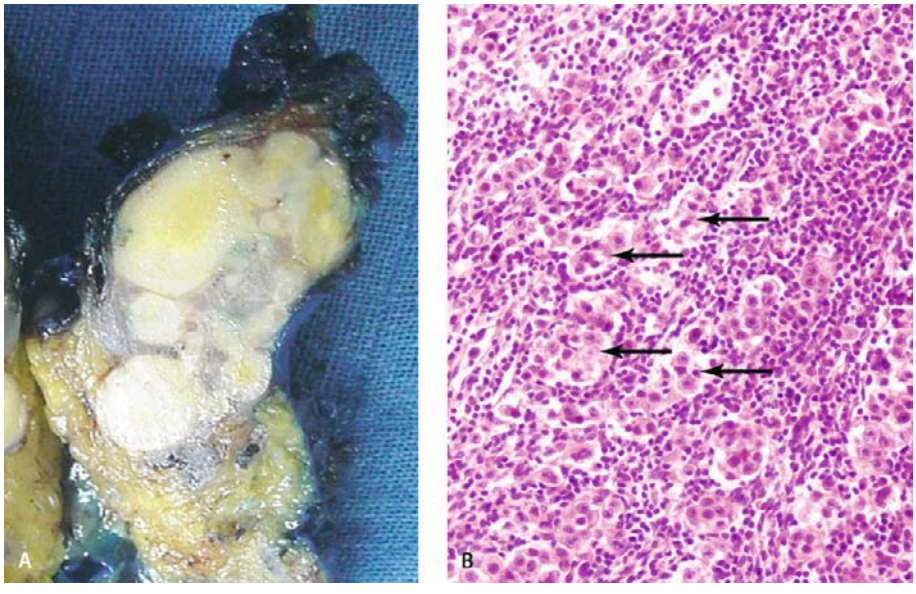

Fig. 36A, B. Seminoma. Gross anatomy: large soft and well-circumscribed tumour (**A**). Microscopy: sheets of large polygonal cells (*arrows*) with a loose stroma densely infiltrated by lymphocytes (**B**)

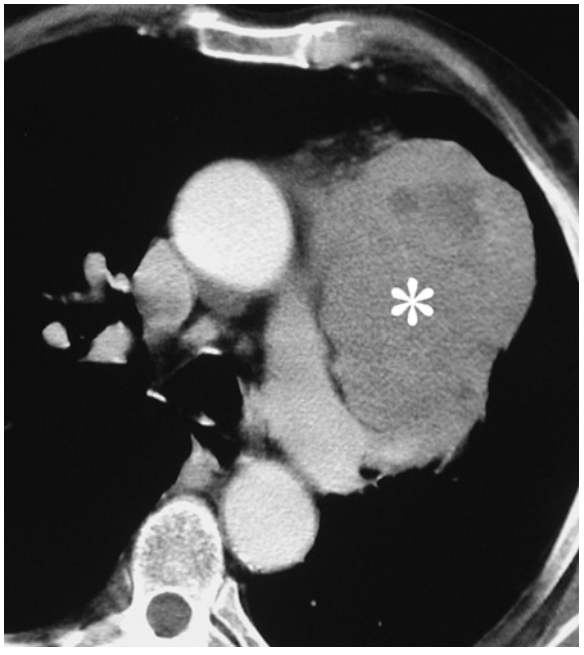

Fig. 37. Seminoma. Large anterior mediastinal mass with well-defined borders (*asterisk*)

ed to chemotherapy, which occurs simultaneously or within the 1st year after the diagnosis of germ cell tumour. They are highly malignant lesions, large and invasive at presentation, often with symptoms of superior vena cava syndrome. Gynecomastia is frequent in choriocarcinomas. The serological markers alpha-foetoprotein and β-human chorionic gonadotropin (HCG) are elevated in yolk sac or embryonal carcinoma and choriocarcinoma, respectively. They are of primary importance in establishing the diagnosis. Serum lactate dehydrogenase is elevated in 60% of cases and correlates with tumour burden [88].

Grossly, the tumour is largely occupied by areas of coagulation necrosis and haemorrhage. Embryonal carcinoma is composed of sheets of polygonal cells with frequent mitotic figures. Yolk sac tumour is characterized by a reticular pattern with various-sized spaces lined with flattened cells (Figs. 38, 39). Choriocarcinoma consists of mononuclear cytotrophoblastic cells and giant syncytiotrophoblastic cells that are beta-HCG-positive (Fig. 40). They grow rapidly and metastases may be seen in the lung, pleura or bone.

Malignant germ cell tumours have CT and MR features similar to other primary malignant tumours arising within the anterior mediastinum [32]. The tumour appears as a large lobulated anterior mass, often with irregular margins and spiculated interface due to lung invasion, extending on both sides of the mediastinum. Extensive areas of low attenuation indicating necrosis or haemorrhage are almost always visible and tissue

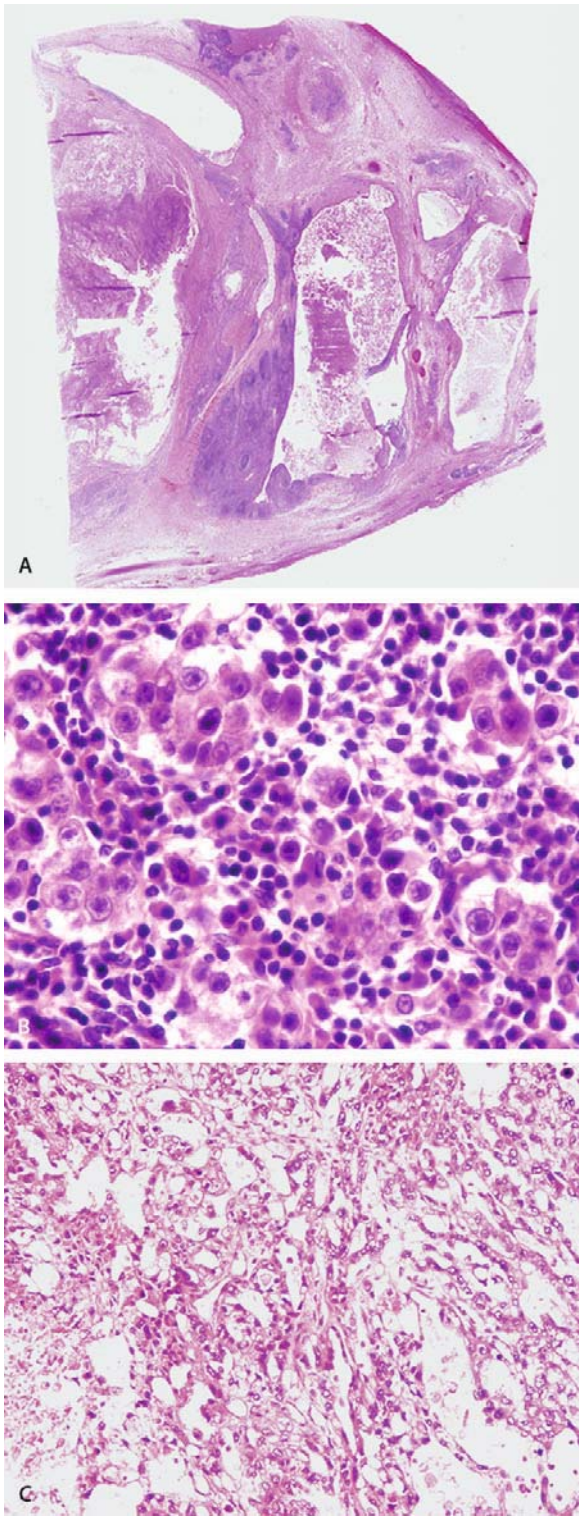

Fig. 38A–C. Complex seminomatous and nonseminomatous germinal tumour. At low magnification, the tumour is large and heterogeneous with necrotic and hemorrhagic changes (**A**). At high-power magnification, seminomatous (**B**) and yolk sac or endodermal sinus tumour (**C**) components are visible

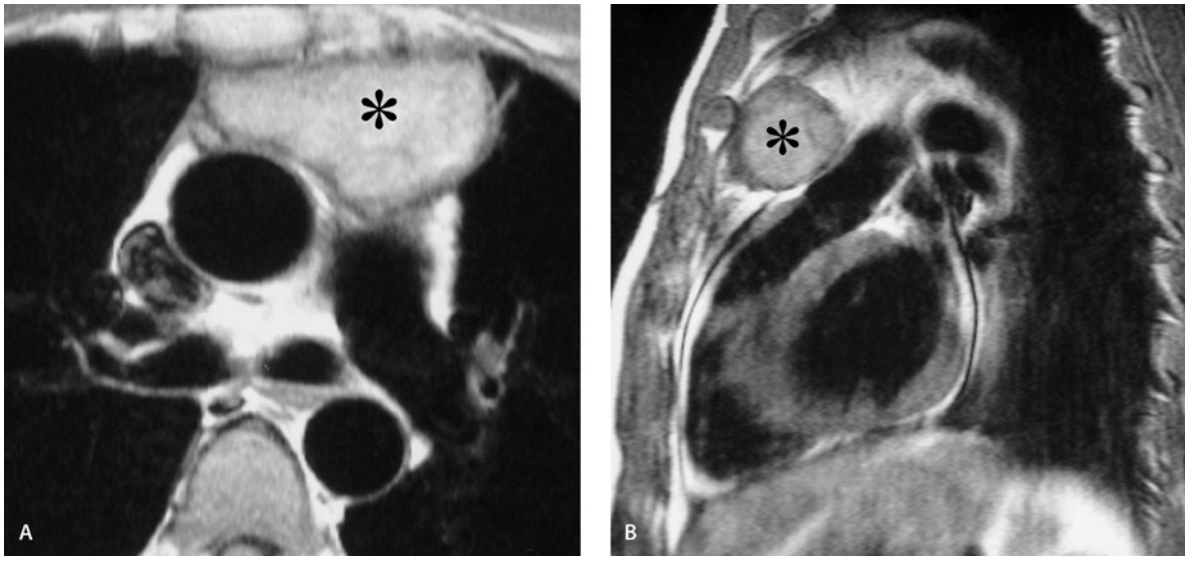

Fig. 39A, B. Nonseminomatous germinal tumour. Gadolinium-enhanced T1-weighted axial (**A**) and sagittal (**B**) MRI show a nonspecific enhancing ill-defined solid mass (*asterisk*) of the anterior mediastinum

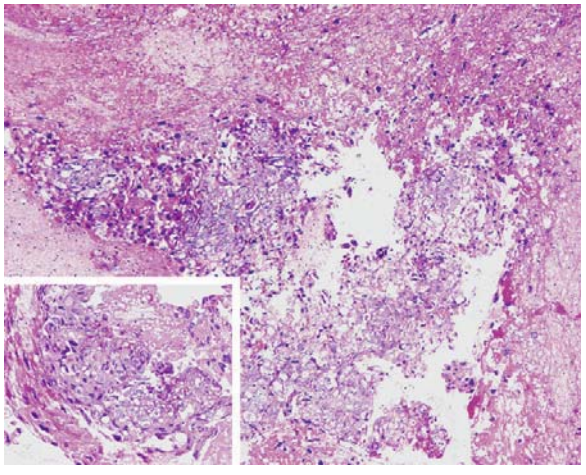

Fig. 40. Choriocarcinoma. Low magnification: extensive areas of haemorrhage surrounded by cytotrophoblastic cells and syncytiotrophoblastic cells (*inset*)

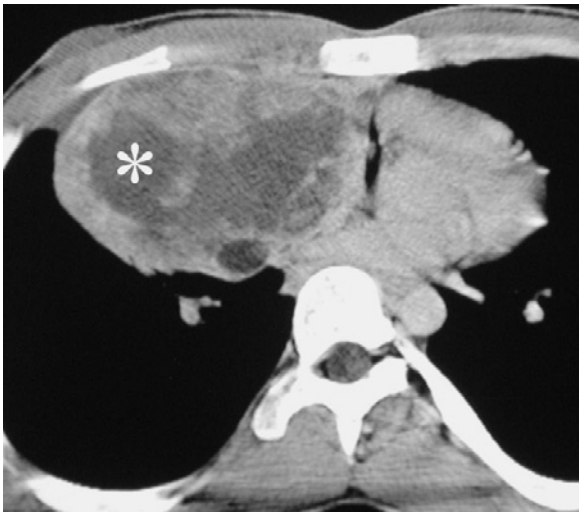

Fig. 41. Choriocarcinoma. Anterior mediastinum mass with large areas of low attenuation (*asterisk*) suggesting necrosis and haemorrhage

planes are frequently obliterated [96] (Figs. 39, 41). Pleural and pericardial effusions are common. The role of imaging modalities is to define disease extent and to monitor response to therapy, together with serum markers. Chemotherapy is given first, often followed by resection of a residual tumour, manifesting as peripheral solid and enhancing masses. A residual mass may also be seen after complete eradication of malignant cells and normalization of serum markers. This mass may be cystic, and may be histologically mature teratoma and growing even though it is benign. This has been reported under the term of "growing teratoma syndrome" [97]. The benign or malignant nature of the mass cannot be stated with certainty on imaging criteria and therefore surgical removal is often undertaken.

Neurogenic Tumours

Neural tumours can arise from nerve sheath, ganglion cell and paraganglionic cells. The nerve sheath tumours comprise benign neoplasms including schwannomas (also known as neurilemmoma, or neurinoma), neurofibromas and their malignant counterparts, frequently

described under a confusing multitude of names such as malignant schwannoma, malignant neurilemmoma, nerve sheath fibrosarcoma, neurogenic sarcoma, or neurofibrosarcoma, and today designated under the generic term of "malignant peripheral nerve sheath tumours" (MPNST). Schwannomas, neurofibromas and MPNST can occur in patients with neurofibromatosis type 1 (NF-1). A variety of neurofibromas called plexiform neurofibromas, which show the greatest propensity for malignant degeneration, is the hallmark of NF-1. Between 3% and 13% of patients with NF-1 develop MPNST, usually after a long latent period of 10–20 years [98].

Schwannomas and Neurofibromas

Schwannomas occur sporadically at any age, but are uncommon in children except when associated with neurofibromatosis. They most commonly involve the major nerve trunk of the head, neck and limbs, but when deeply situated are predominantly found in the posterior mediastinum and retroperitoneum. Schwannomas are benign, slow-growing neoplasms composed of Schwann cells in a collagenous matrix, originating in a nerve but eccentric with no nerve fibres passing through it. They are round or ovoid, with a tan or grey cut surface, sometimes cystic and filled with a watery fluid or partially haemorrhagic. According to the morphology and spatial arrangement of tumour cells, two types of tissue are distinguished, Antoni type-A and type-B tissue. In Antoni type-A, the texture is composed of compactly arranged spindle cells with a pale cytoplasm, their nuclei being aligned in rows separated by clear hyaline bands, a pattern called Verocay nodules. Antoni type-B tissue, commonly but not invariably associated, has a less cellular pattern, a looser texture, with mucinous and microcystic changes presumably resulting in cysts when confluent (Fig. 42). The tumours have a rich vascular supply and calcifications are rarely seen [98].

Small schwannomas are asymptomatic and when symptoms occur, this is because of increasing size and impingement on neighbouring structures. A posterior mass on chest film suggests the possibility of a neurogenic tumour in 30% of these lesions. Rib notching can be seen in schwannomas of the intercostal nerves, and widening of vertebral foramina is a frequent findings in schwannoma occurring along exiting spinal nerves [98]. On unenhanced CT scans, schwannomas are well-circumscribed, homogeneous lesions that are hypodense or isodense relative to muscle. On enhanced scans, most become isodense or hyperdense (Fig. 43). Nonenhancing necrotic or cystic areas are typically found, given a very frequent inhomogeneous appearance [8, 99]. On T1-weigthed MR images, the tumours have an identical or slightly higher signal intensity as muscle and a marked increased signal on T2-weighted images (Fig. 44). Cystic lesions display a low signal on T1 and high signal on T2 (Fig. 45). MRI is superior to any imaging technique in depicting intratumoral inhomogeneities that reflect the histological nature of the lesion (Fig. 46) [100, 101]. The detection of a capsule could have been a useful criterion for differentiating schwannomas from neurofibromas if the finding had been proven to be reliable on imaging studies [98]. Since schwannomas develop peripheral to the nerve, the relationships between the lesion and the nerve could also be a valuable feature but assessment requires high-resolution images. Small schwannomas tend to enhance brightly and uniformly after gadolinium injection. The MR characteristics are not specific and can be mimicked by other neoplasms, most commonly myxofibrosarcomas (formerly known as malignant fibrous histiocytomas) and metastases.

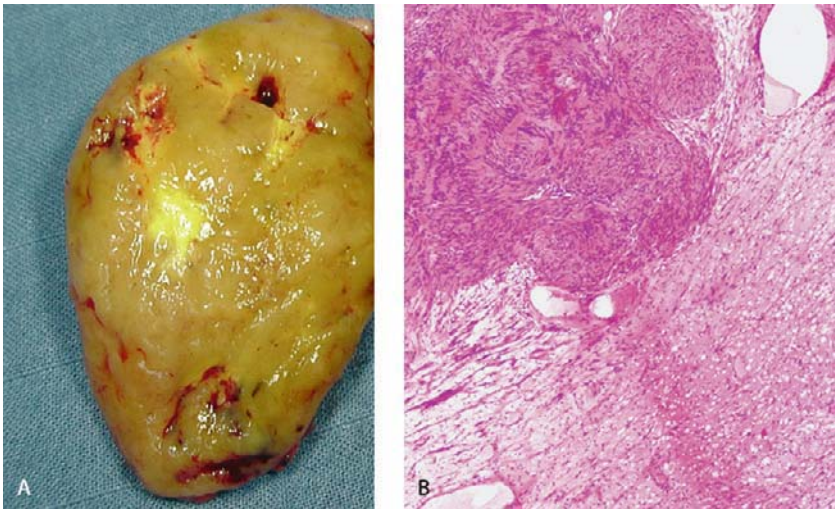

Fig. 42A, B. Schwannoma gross anatomy: spherical tumour with central microcystic degenerative changes (**A**) Histology: Antoni type A in the upper left and type B in the lower right part of the image (**B**)

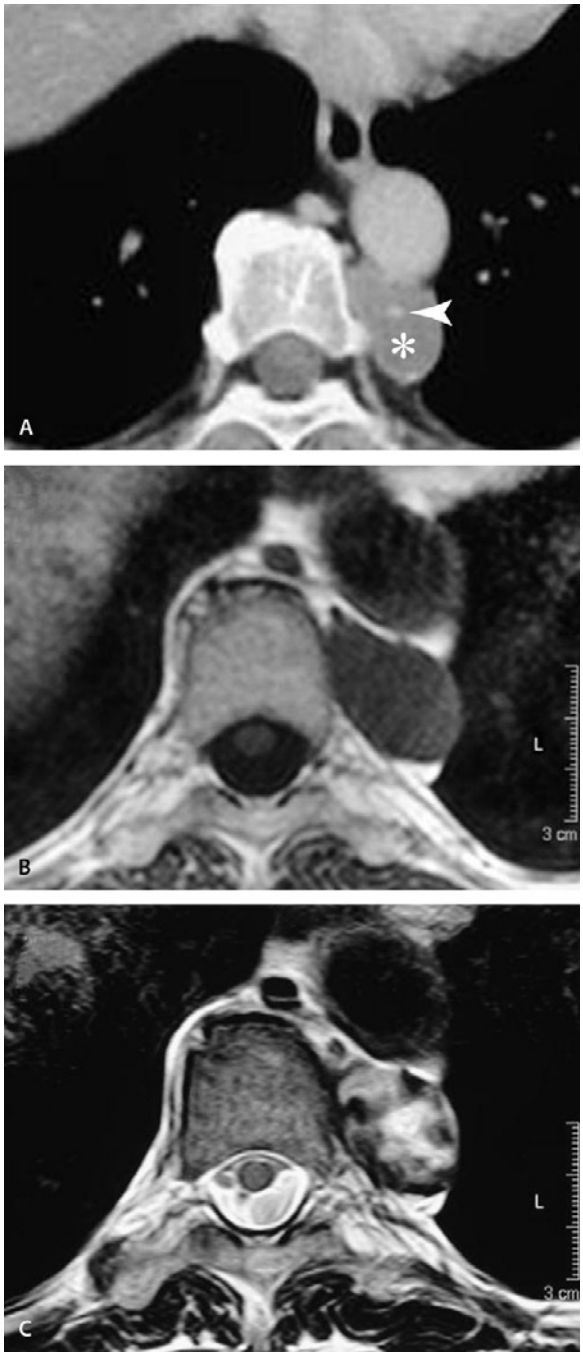

Fig. 43A–C. Schwannoma. CT (**A**): well-defined homogeneous low-attenuated mass (*asterisk*) with a small calcification (*arrowhead*). T1-weighted (**B**) and T2-weighted (**C**) MRI slices showing the low on T1 and heterogeneous signal intensity on T2

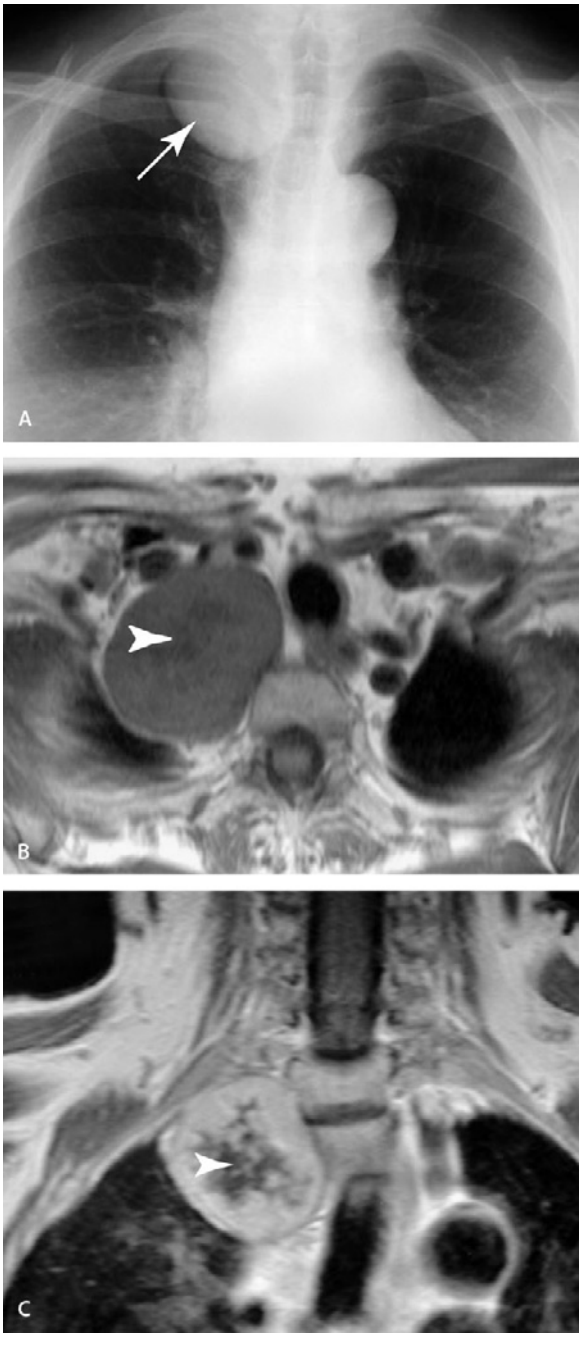

Fig. 44A–C. Schwannoma. Chest film (**A**) showing a well-defined opacity (*arrow*) projecting above the clavicle indicating its posterior mediastinal situation. T1-weighted (**B**) and gadolinium-enhanced T1-weighted (**C**) MRI showing the central necrosis (*arrowhead*) and strong enhancement of the lesion

Solitary neurofibromas develop mostly between the ages of 20 and 30, affecting both sexes equally and all ethnic groups. In 60%–90% of cases, they occur in patients who do not have NF-1. The major nerves of the trunk, including the sympathetic system and its ganglia, can be involved. Typically, it is a benign slow-growing tumour, variably encapsulated, originating in a nerve with nerve fibres scattered throughout the lesion. As opposed to schwannomas, the lesions are homogeneous, with no areas of cystic degeneration, haemorrhage or xanthomatous material but more frequently calcified than schwannomas. They are composed of a central zone of tightly packed eosinophilic fibres with a highly cellular component. The peripheral zone is composed of

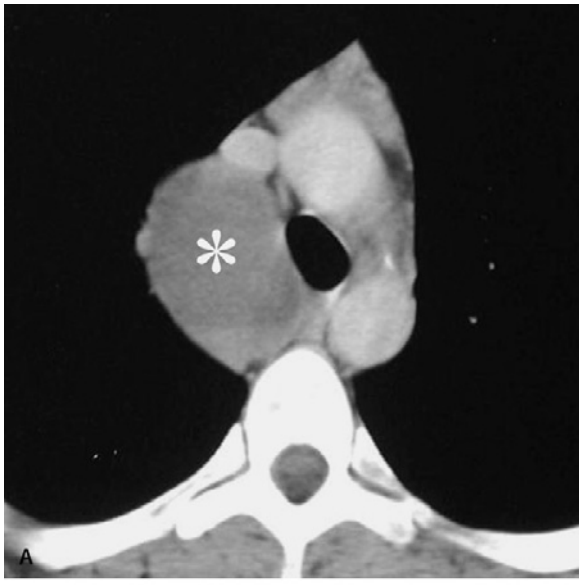

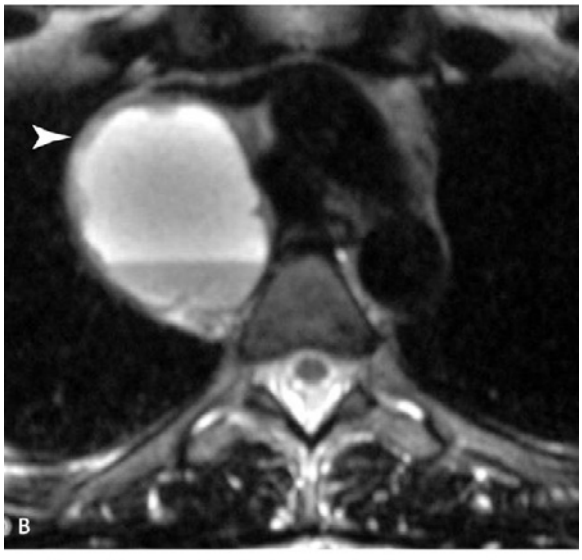

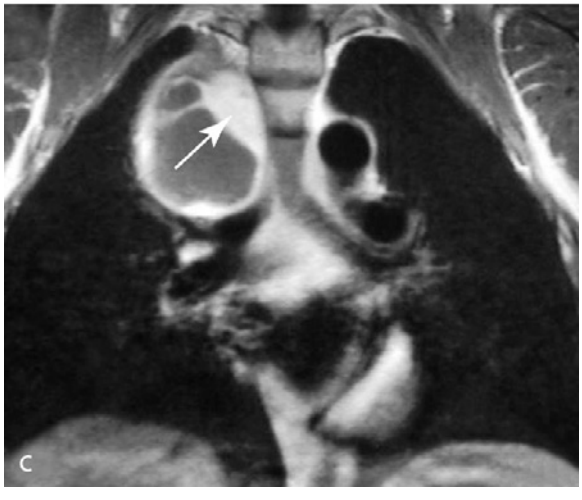

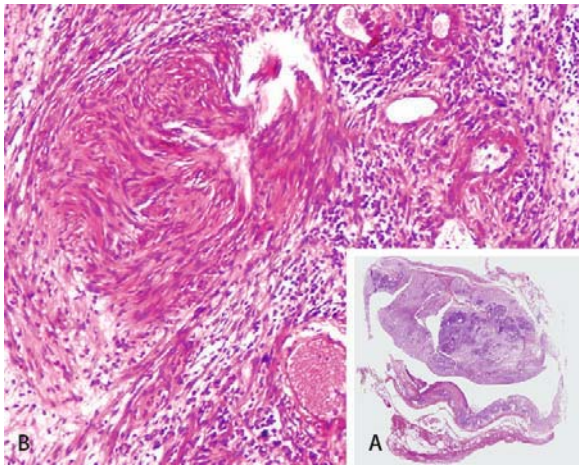

Fig. 46A, B. Cystic schwannoma. **A** cystic tumour with a nodular component of the cystic wall. Microscopy: typical "Verocay nodule" within the nodular component of the cystic wall

loosely arranged fibres and an abundant nonfibrillary stromal material [98]. This zonal distinction is presumed to be the correlate of the so-called target appearance of neurofibromas on CT and MR studies. Neurofibromas have a similar appearance on plain film to that of schwannomas. On unenhanced CT, they mostly appear as hypodense lesions, owing to the presence of Schwann cells, neural elements and adipocytes. On enhanced CT, they usually show little or no enhancement [102, 103]. On T1-weighted MR images they have an intermediate signal intensity and are hyperintense on T2-weighted images, sometimes a salt and pepper appearance. Their pattern after enhancement is variable, bright and uniform or inhomogeneous. On T2-weighted images, they can have a target appearance, characterized by a peripheral rim of increased intensity, while the central part of the tumour is less hyperintense. This pattern corresponds to the zonal histological appearance [104]. The central zone enhances more intensively after gadolinium injection (Fig. 47). The target appearance is not seen in malignant MPNST and is very rare in schwannomas, but it is not seen in small lesions and in cystic lesions although it is rare in neurofibromas [105].

Plexiform neurofibroma relates to a diffuse enlargement and distortion of a major nerve trunk. Multiple masses are found along the course of the nerve, sometimes giving rise to massive growth or conversely to a

Fig. 45A–C. Cystic schwannoma. CT (**A**) showing a paratracheal mass (*asterisk*) of low attenuation. T2-weighted MRI (**B**) showing a fluid–fluid level and a thick wall (*arrowhead*) suggesting a necrotic lesion. Gadolinium-enhanced coronal MRI (**C**) shows a strongly enhanced nodule (*arrow*) and multiloculations

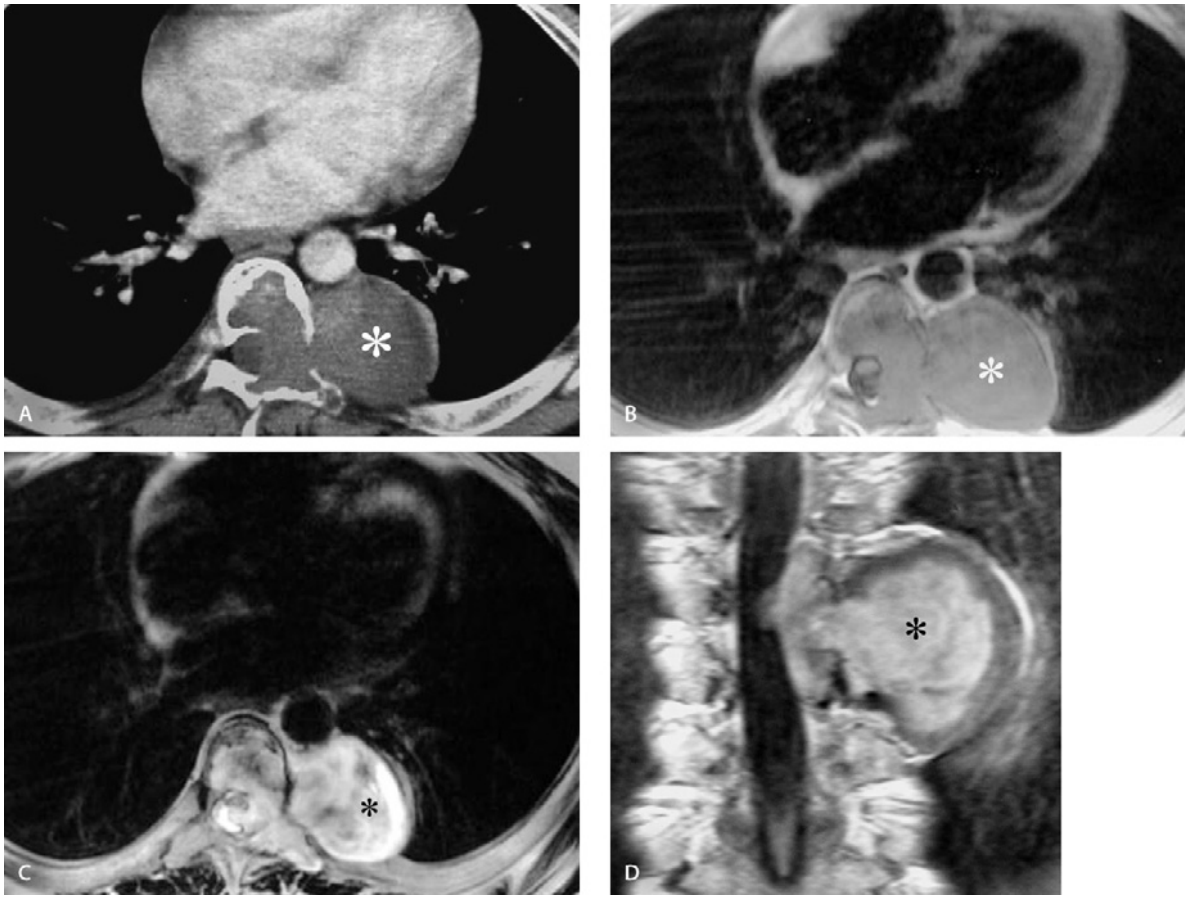

Fig. 47A–D. Neurofibroma CT (**A**) T1-weighted (**B**) and T2-weighted (**C**) axial and gadolinium-enhanced T1-weighted coronal MRI (**D**) showing a heterogeneous mass (*asterisk*) with the target appearance on T2 (**C**) and a dumbbell extension through the vertebral foramina within the subarachnoidal spaces

moniliform enlargement. It may involve any of the cranial and spinal nerve roots and ganglia, the major nerves of neck, trunk and limbs, including the sympathetic system and its ganglia, the subcutaneous branches of major nerves and the visceral plexuses (Fig. 48) [106].

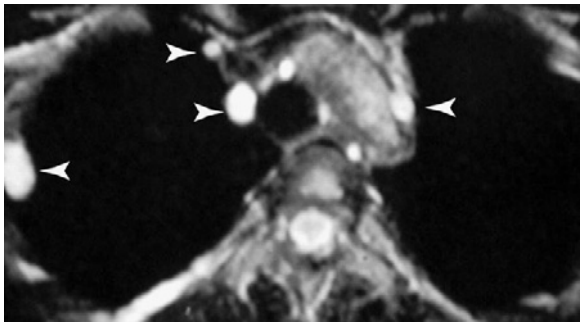

Fig. 48. Neurofibroma (plexiform type). T2-weighted axial MRI showing the multiple high-intensity nodular tumours (*arrowheads*) along the intercostals and mediastinal nerves

Malignant Peripheral Nerve Sheath Tumours

MPNST accounts for about 6% of malignant soft tissue tumours. They are four times more frequent in women of middle age and are associated with NF-1 in up to 50% of cases. They typically affect the large nerves and can develop in an unaltered nerve or in a neurofibroma, with between 5% and 13% estimated as becoming malignant. They are microscopically well-circumscribed to multinodular formations and commonly show areas of necrosis. Divergent differentiation may lead to bone cartilage and epithelial material. As other soft tissue sarcomas, the present as enlarging masses with a specific sarcomatous degeneration, and pain is not an indicator of malignancy. The sudden enlargement of a known pre-existing mass in the setting of NF-1 should lead to immediate diagnostic imaging. The tumour carries a poor 5-year survival rate of 15%–30% compared with the 75% survival rate of the solitary form when it occurs in NF-1. They tend to recur locally after resection and to metastasize within 2 years to lung, liver, skin and bone [107, 108]. CT and MRI offer little help in attempts

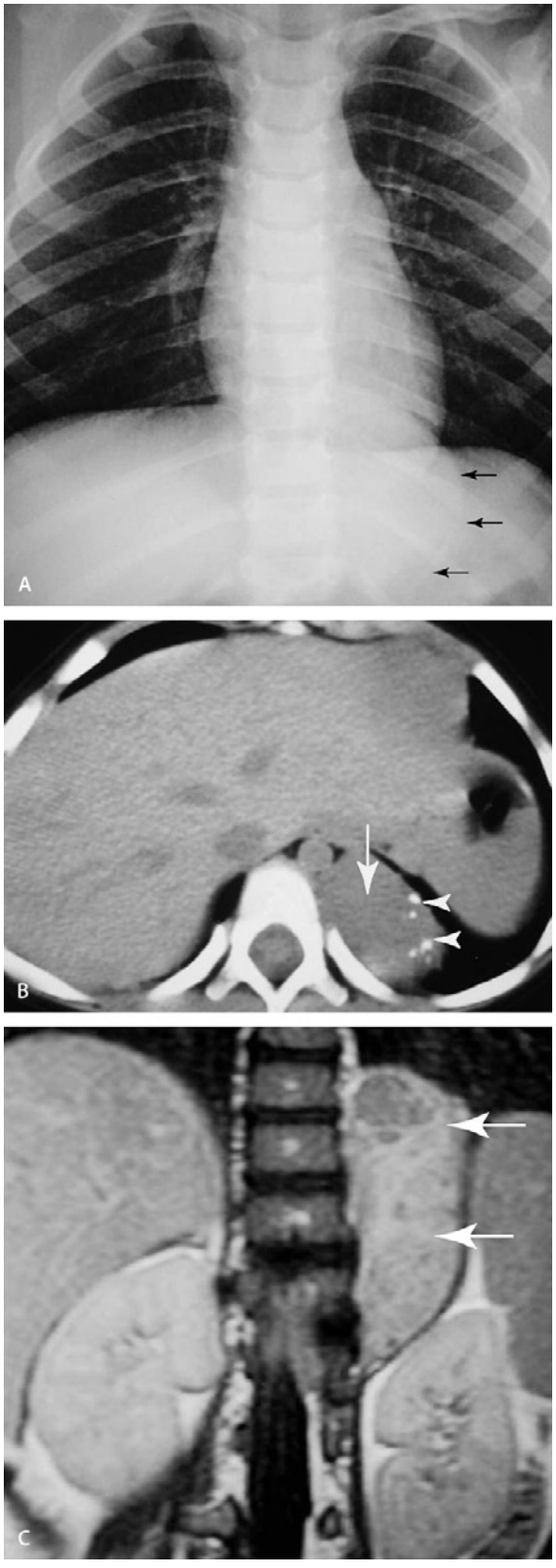

Fig. 49A–C. Neuroblastoma of a 6-year-old boy. Chest film (**A**), CT (**B**) and Gd-enhanced MRI (**C**) showing a enhancing posterior mediastinal mass (*arrows*) with small calcifications on CT (*arrowheads*). Courtesy Prof. J.F. Chateil

at demonstrating the malignant nature of the lesion and they can be very similar to benign nerve sheath tumours at imaging studies. The criteria that can be of help in establishing the diagnosis are a large mass with compression of adjacent structures, an inhomogeneous internal architecture, invasion of fat planes, bone destruction, perilesional oedema, pleural effusion, and involvement of lymph nodes. These features, however, are not sufficiently specific to distinguish them from other malignant soft tissue tumours [95, 109–111].

Ganglion Cell Tumours

Ganglion cell tumours form a spectrum – with neuroblastoma at the malignant end and ganglioneuroma at the benign end, ganglioneuroblastoma being an intermediate form. The mediastinum is the second most common location of these tumours after the adrenal gland. One-third of neuroblastomas are primarily from the mediastinum; the remainder are secondary to lymph node metastases or to thoracic spread. Neuroblastomas (Fig. 49) and ganglioneuroblastomas are essentially childhood tumours; less than 10% are seen in patients older than 20 years of age. Ganglioneuromas shows a wider age distribution: from 1 to 50 years. Increased level of plasma and urinary catecholamines may be encountered and are therefore a useful marker. Ganglioneuromas may show a whorl appearance corresponding to whorls of collagenous fibrous tissue and neural tissue (Figs. 50, 51). Ganglioneuroma is often large and encapsulated, with a pale tan and finely trabeculated cut surface, composed of mature ganglial cells with Nissl granules, Schwann cells and nerve fibres. Neuroblastoma is often large, encapsulated and soft, with areas of haemorrhage on cut sections, and can be well or poorly differentiated. Ganglioneuroblastomas consist of neuroblasts, ganglion cells and interme-

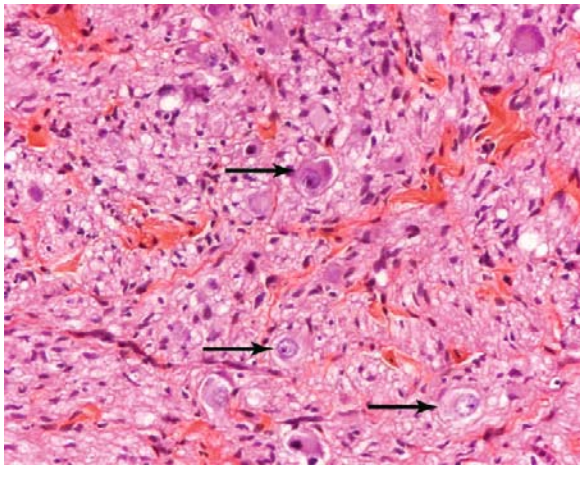

Fig. 50. Ganglioneuroma. Tumour composed of mature ganglion cells (*arrows*), nerve fibres and Schwann cells

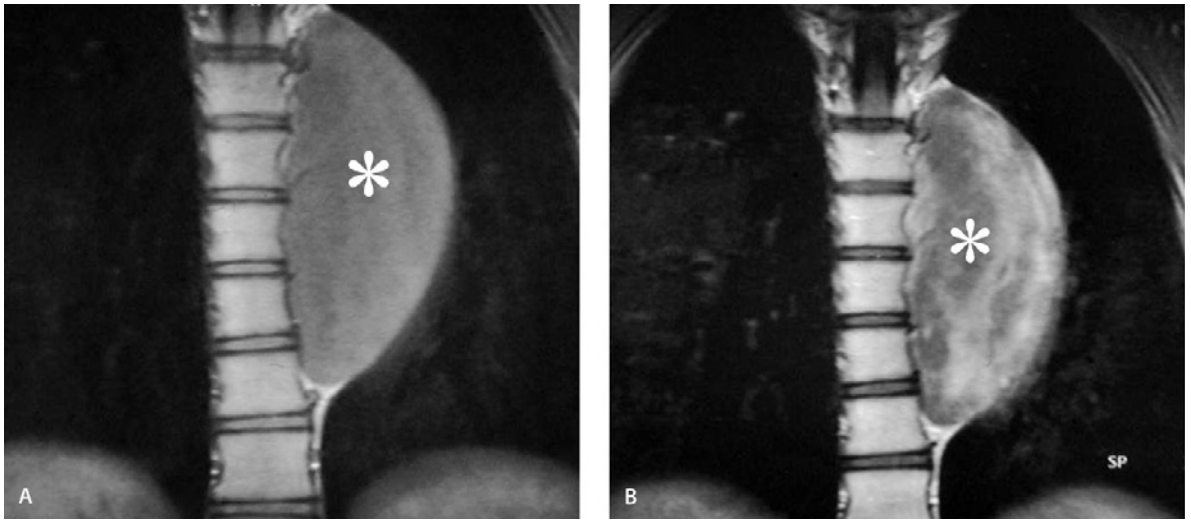

Fig. 51A, B. Ganglioneuroma of a 17-year-old boy. T1-weighted (**A**) and T2-weighted (**B**) coronal MRI showing a heterogeneous well-defined elongated mass (*asterisk*)

diate cells in various proportions. PNET (primitive neuroectodermal tumour) is rare in the mediastinum. Ganglial cell tumours tend to arise more anteriorly, with their epicentre against the vertebral body. Approximately 10% of neuroblastomas are calcified on plain radiograph, usually finely stippled, whereas coarse and denser calcifications are seen in other histological types. Bone changes are frequently encountered. Franck destruction of bone and pleural effusion are signs of malignancy. CT findings are nonspecific but CT detects calcifications more accurately than MRI, which is even better than CT in demonstrating or excluding spinal involvement.

Paragangliomas originate from aorticopulmonary paraganglia present in the mediastinum and from aorticosympathetic paraganglia in the posterior mediasti-

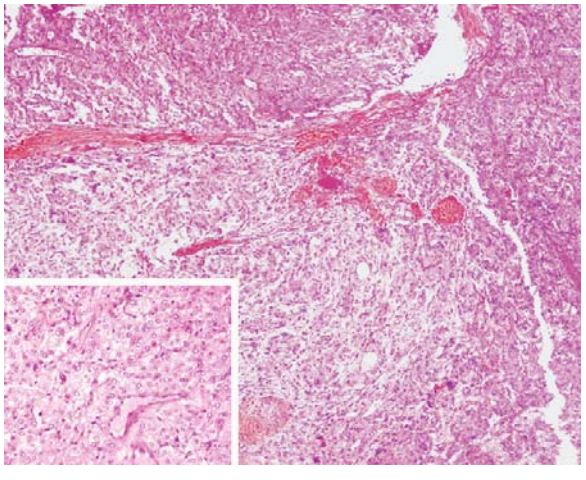

Fig. 52. Paraganglioma. Microscopy at low magnification: dense cellular tumour with vascular stroma composed of Zellballen bordered by capillaries

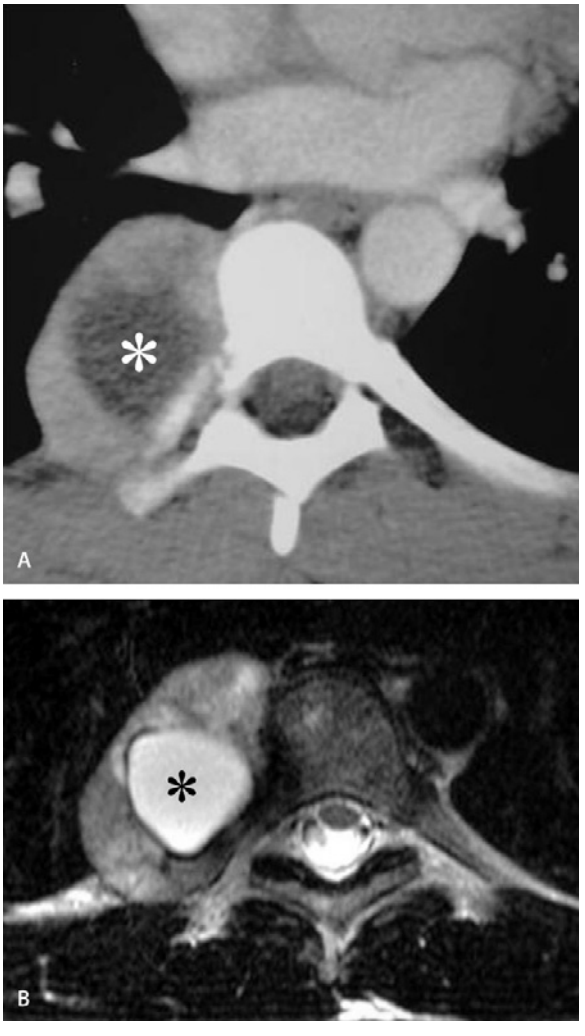

Fig. 53A, B. Paraganglioma CT (**A**) and T2-weighted MRI (**B**) showing a tumour of the paravertebral gutter with a necrotic centre (*asterisk*)

num. They are characterized by zellballen of polygonal tumour cells bordered by capillaries (Figs. 52, 53). Chemodectomas are aortic body tumours and are seen as masses of the aortopulmonary window. Functioning paragangliomas occur rarely in the chest and mostly in the posterior mediastinum [112, 113], although other locations are possible [114–117]. These masses are usually extremely vascular and enhance brightly at enhanced CT or MR [10]. On MR imaging, they may show high signal intensity on T2-weighted images (Fig. 52). Functional imaging with various markers and PET are valuable techniques because they can show increased activity into the mass [118–120].

A diverse group of entities different from neurogenic tumours may also involve the posterior mediastinum, including lipomatosis, lymphadenopathies, aortic aneurysm, cystic masses, thoracic spinal inflammatory or neoplastic lesions and extramedullary haematopoiesis. This entity is a presumed physiological compensatory mechanism for the disturbed medullary haematopoiesis that often accompanies congenital haemoglobinopathies, sickle cell disease and spherocytosis or acquired marrow replacement disorders such as leukaemia, lymphoma and myelofibrosis. The classic appearance at CT is a homogeneous enhancing soft-tissue mass in the paravertebral region.

Mesenchymal Tumours

Mesenchymal tumours, either benign or malignant are rare lesions with protean imaging features. The cell of origin, adipocytes, pericytes, mesothelial cells, fibroblasts and muscle cells, defines the histological type. The malignant counterpart are sarcomas, extremely rare lesions, sometimes constituted by undifferentiated malignant mesenchymal cells.

Lipomatous Tumours

Mediastinal lipomas and liposarcomas represent only 1% of all primary mediastinal tumours. Adipose tissue is classified into two types, white fat (lipocytes) and brown fat, an immature form of white fat more common in hibernating animals (hibernoma), chiefly found in the human body. Lipomas are encapsulated masses, composed of mature fat, differing very little from the surrounding fat. They may contain other mesenchymal elements, fibrous connective tissue, cartilaginous or smooth muscle and are named appropriately. Fibrous connective tissue is the most common, often with the configuration of septa. Benign lipomas do not compress surrounding structures unless they are very large. The moulding to the mediastinal contour can be so marked that a large lipoma may mimic a cardiomegaly [120]. On CT and MRI, lipomas also present circumscribed masses of fatty nature without enhancement. Regular and thin septations of soft tissue density and signal can be visible, and are slightly enhancing [121]. Larger areas of nonfatty tissue are detectable in lipomas that contain connective tissue. Other types of benign lipomatous tumours such as hibernoma, arising from brown fat, and lipoblastomas, that have developed in children younger than 3 years, show indistinct imaging features.

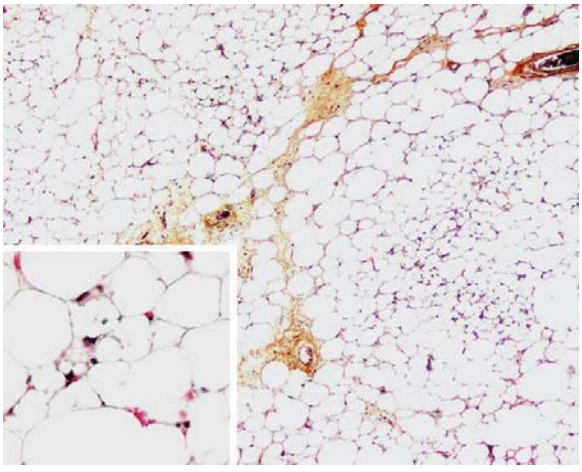

Fig. 54. Well-differentiated liposarcoma. On microscopy the tumour is composed of adipocytes including lipoblasts (*insert*)

Liposarcomas are classified into five histological subtypes, well-differentiated, myxoid, round-cell, pleomorphic and dedifferentiated, the last three types hav-

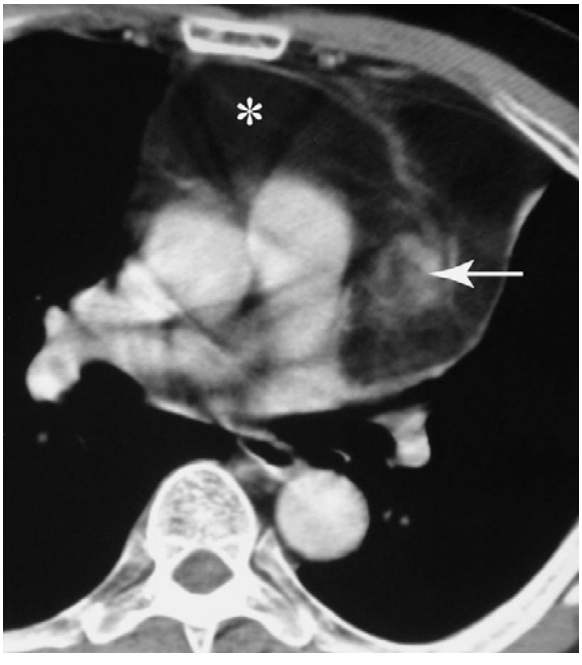

Fig. 55. Liposarcoma. CT: large fatty mass (*asterisk*) with a central nodular tissular component (*arrow*)

ing a strong tendency to recur and metastasize (Fig. 54). The mediastinum is a rare location of this soft-tissue neoplasm. The imaging features depend on the histological type and tend to reflect the degree of differentiation. Well-differentiated liposarcomas are composed of more than 75% fat (Fig. 55) and therefore sometimes cannot be distinguished from a lipoma based on imaging features, or even from normal overabundant fat [122, 123]. In this case, CT shows uniform fat density except for a few strands of soft tissue. Calcifications are possible. Conversely, other types of liposarcomas show inhomogeneity of the fat on CT and often contain large areas of soft tissue density [124, 125]. The poorly differentiated category may not demonstrate any visible fatty component on imaging studies.

Tumours and Tumour-like Lesions of Blood Vessels

Blood vessel tumours in the mediastinum are rare, with an incidence of less than 0.5% among mediastinal masses. The tumours are categorized as haemangiomas (mainly capillary, cavernous, or venous types according to the size of their vascular spaces), vascular tumours of intermediate malignancy (haemangiopericytoma, epithelioid haemangioendothelioma) and malignant vascular tumours (angiosarcomas). Ninety per cent are capillary or cavernous haemangiomas [126]. They tend to be well-circumscribed lesions without a true capsule. Phleboliths, which are visible as punctuate calcifications, are seen in 10% on chest X-ray or CT. On enhanced CT, four distinct patterns of enhancement have been reported, in decreasing order of frequency: central, mixed central and peripheral, or peripheral. However, the majority do not enhance or enhance slightly [127–133]. Haemangiopericytomas are extremely rare within the mediastinum and when this diagnosis is proposed, the tumour should be thoroughly examined in order not to overlook features characteristic of thymomas, since a haemangiopericytoma-like thymoma is more common. Very few cases of haemangioendothelioma have been reported. The lesion is thought to have an intermediate malignant potential between that of haemangioma and angiosarcoma. A low-attenuation lesion with peripheral and nodular enhancement mimicking a liver haemangioma, although nonspecific, may suggest the diagnosis [132].

Lymphatic Tumours

There is growing evidence that soft tissue tumours of lymphatic origin are very rare and that the majority of these lesions are hamartomas or developmental lymphangiectasias rather than true neoplasms. They include lymphangiomas, lymphangiomatosis and lymphangioleiomyomatosis. Lymphangiomatosis is a systemic disorder in children and lymphangioleiomyomatosis involves the lung parenchyma and mediastinal lymph nodes in young women

Lymphangiomas are not rare lesions of the mediastinum. They are tumour-like congenital malformations of

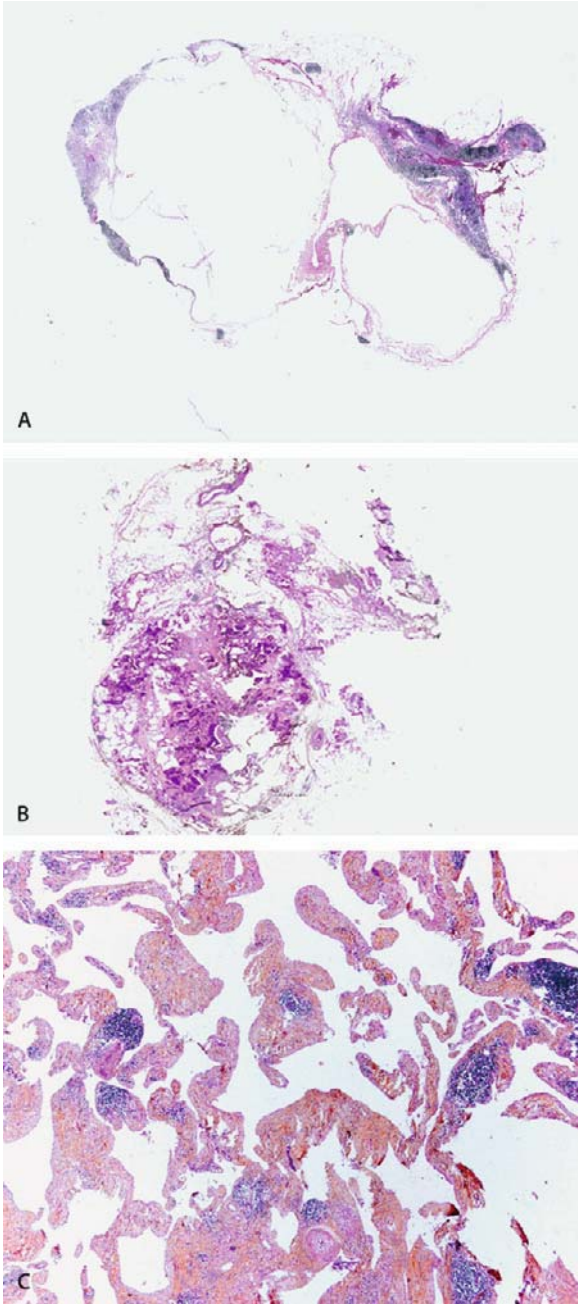

Fig. 56A–C. Cystic lymphangiomas. Low magnification: unilocular (**A**) and multilocular cystic lymphangioma (**B**). High magnification: spongy tumour composed of interconnecting channels whose walls are variably fibrotic and focally infiltrated by lymphocytes (**C**)

the lymphatic system, consisting of lymph channel or cystic lymph spaces lined with endothelium. Their walls are formed by fibrous tissue and smooth muscle. Three types have been described: capillary, cavernous and cystic (Fig. 56). Capillary lymphangioma is composed of small, capillary-sized endothelium-lined lymphatics. Cavernous lymphangioma is made up of larger lymphatic channels with adventitial coats. Cystic lymphangiomas or hygromas are constituted of large macroscopic lymphatic spaces that possess investitures of collagen and smooth muscle. When confined to the mediastinum, they are usually asymptomatic and may be discovered in children or adults in the anterior or superior mediastinum. Fewer than 10% occur in the posterior mediastinum. The CT or MRI appearance is that of a cystic mass, most commonly unilocular, sometimes multilocular or septate (Figs. 57, 58), which mould or envelop adjacent mediastinal vessels [134, 135] (Fig. 59). When attenuation is slightly higher than that of water, this may evidence elevated protein content of the fluid. However, a partial-volume effect caused by the mixture of low-density fluid and higher-density lymphatic vessel walls below the resolution of CT may also be an explanation. Septa are sometimes seen within the lesion and may enhance [135]. Unilateral or bilateral effusion may occur and in invasive forms chylothorax is possible [6]. Findings on MR have been reported to be variable, with a signal similar to or greater than that of muscle on T1-weighted images and a marked increase in signal on T2-weighted images. However, low signal intensity on

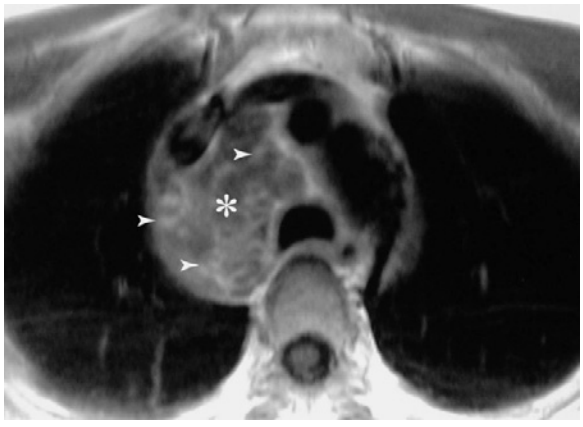

Fig. 58. Cystic lymphangioma, multilocular type. Gd-enhanced T1 MRI showing a heterogeneous loculated mass with enhanced septa. Pathologically, the tumour was composed of multiple small cysts separated by small septations visible with the enhancement (*arrowheads*) but responsible for the enhancement pattern of the lesion

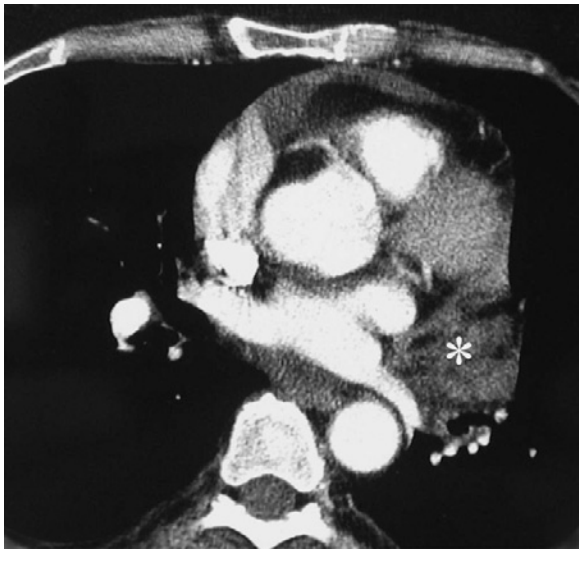

Fig. 57. Cystic lymphangioma, multilocular type. CT showing a heterogeneous, slightly enhancing mass lateral to the left atrium. Pathologically, the tumour was composed of multiple small cysts separated by small septations hardly visible but responsible for the enhancement pattern of the lesion

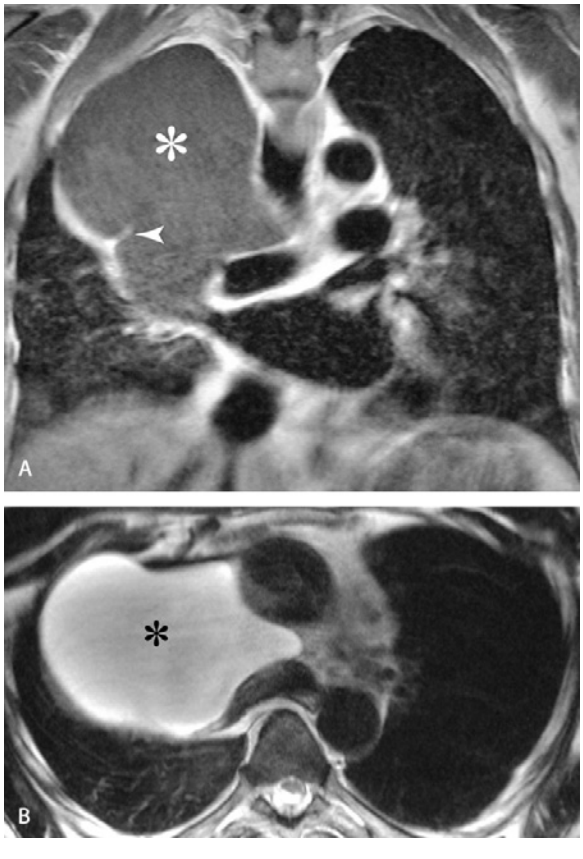

Fig. 59A, B. Cystic lymphangioma. Gd-enhanced T1-weighted (**A**) and axial T2-weighted (**B**) MRI showing a large cystic mass (*asterisk*). A small septation is visible (*arrowhead*)

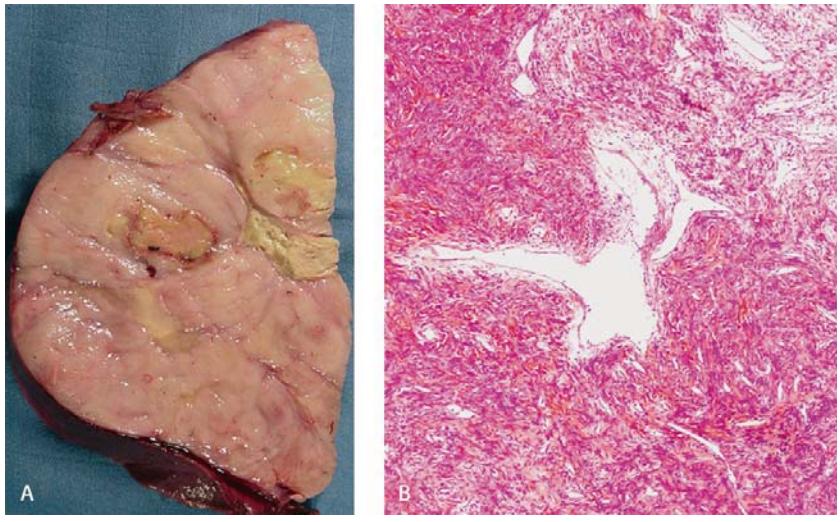

Fig. 60A, B. Fibrous tumour. Gross anatomy: lobulated well-defined pale to pink homogeneous cut surface (**A**). Microscopy: mesenchymal tumour composed of spindle cells of fibroblastic appearance separated by dense collagen (**B**)

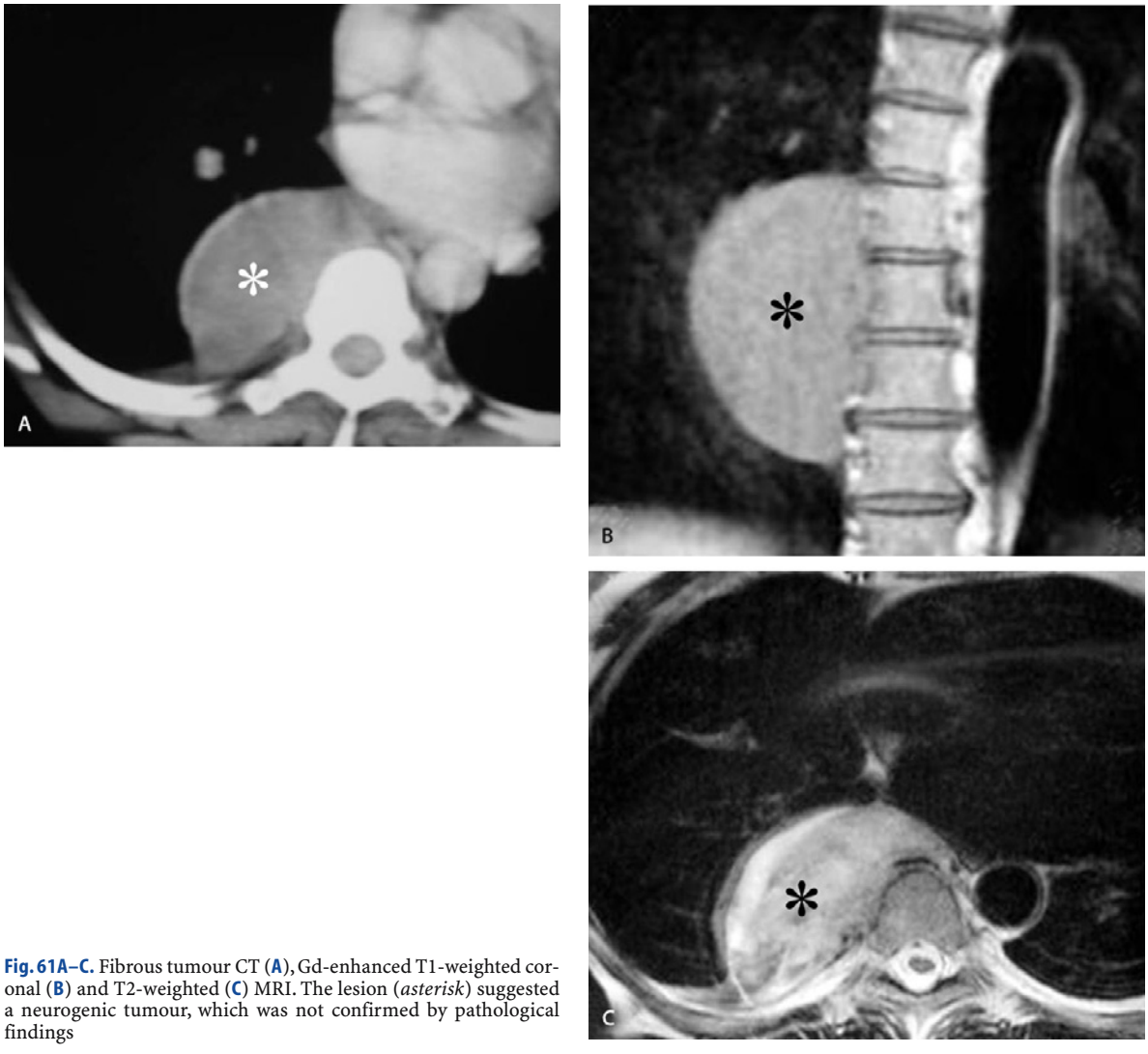

Fig. 61A–C. Fibrous tumour CT (**A**), Gd-enhanced T1-weighted coronal (**B**) and T2-weighted (**C**) MRI. The lesion (*asterisk*) suggested a neurogenic tumour, which was not confirmed by pathological findings

T2-weighted images that can be explained either by haemorrhagic or fibrous changes has been reported [134]. A particular pattern consists of small, numerous linear structures of low signal intensity representing septa, which are better demonstrated on gadolinium-enhanced images and are thought to correspond to pathological findings of the cavernous type [135, 136]. Mixed lymphatic and blood vessel lesions such as lymphangiohaemangiomas, haemangioendotheliomas, and haemangiosarcomas have occasionally been encountered [137, 138].

Tumours of Fibrous Tissue and Fibrohistiocytic Tumours, and Miscellaneous Malignant Sarcomas

Solitary benign fibrous tumours are less commonly reported in the mediastinum than in pleura [139]. Nonspecific features have been reported on CT or MR imaging, mimicking the usual lesions that are found in a specific location (Figs. 60, 61) [140].

Primary malignant mesenchymal tumours of the mediastinum are very unusual lesions with protean imaging features [141]. They may also occur in the lung and pleura, and their compartment of origin is sometimes difficult to specify because of their large volume. The cells of origin can be smooth or striated muscle, fibroblasts or undifferentiated mesenchymal cells in addition to those arising from adipocytes, pericytes, and mesothelial cells as previously described. Leiomyosarcomas and malignant fibrous histiocytomas [142–145] are the least uncommon, rhabdosarcomas, liposarcomas and osteosarcomas being extremely rare. Most tumours are bulky at presentation and show no specific feature. However, chondrosarcomas and extraosseous osteogenic sarcomas, densely calcified or ossified, can be suggested by imaging studies [146].

Conclusion

Detection of a mediastinal mass essentially remains the role of chest radiography. CT is the next logical step and is often sufficient to suggest a limited differential diagnosis adequate for a further invasive procedure and therapeutic decisions. MR imaging provides additional information in selected cases.

References

1. Cohen AJ, Thompson L, Edwards FH, Bellamy RF (1991) Primary cysts and tumours of the mediastinum. Ann Thorac Surg 51:378–384
2. Benjamin SP, McCormack LJ, Effler DB, Groves LK (1972) Primary tumours of the mediastinum. Chest 62:297–303
3. Azarow KS, Pearl RH, Zurcher R, Edwards FH, Cohen AJ. (1993) Primary mediastinal masses. A comparison of adult and pediatric populations. J Thorac Cardiovasc Surg 106: 67–72
4. Wychulis AR, Payne WS, Clagett OT, Woolner LB (1971) Surgical treatment of mediastinal tumours: a 40-year experience. J Thorac Cardiovasc Surg 62:379–392
5. Glazer HS, Siegel MJ, Sagel SS (1989) Low-attenuation mediastinal masses on CT AJR Am J Roentgenol 152:1173–7
6. Jeung MY, Gasser B, Gangi A, Bogorin A, Charneau D, Wihlm JM et al (2002) Imaging of cystic masses of the mediastinum. Radiographics 22:S79–S93
7. Murayama S, Murakami J, Watanabe H, Sakai S, Hinaga S, Soeda H et al (1995) Signal intensity characteristics of mediastinal cystic masses on T1-weighted MRI. J Comput Assist Tomogr 19:188–191
8. Kawashima A, Fishman EK, Kuhlman JE, Nixon MS (1991) CT of posterior mediastinal masses. Radiographics 11: 1045–1067
9. Glazer HS, Molina PL, Siegel MJ, Sagel SS (1991) High-attenuation mediastinal masses on unenhanced CT. AJR Am J Roentgenol 156:45–50
10. Spizarny DL, Rebner M, Gross BH (1987) CT evaluation of enhancing mediastinal masses. J Comput Assist Tomogr 11: 990–993
11. Oldham HN Jr (1971) Mediastinal tumours and cysts. Ann Thorac Surg 11:246–275
12. St-Georges R, Deslauriers J, Duranceau A, Vaillancourt R, Deschamps C, Beauchamp G et al (1991) Clinical spectrum of bronchogenic cysts of the mediastinum and lung in the adult. Ann Thorac Surg 52:6–13
13. Barnes NA, Pilling DW (2003) Bronchopulmonary foregut malformations: embryology, radiology and quandary. Eur Radiol 13:2659–2673
14. Suen HC, Mathisen DJ, Grillo HC, LeBlanc J, McLoud TC, Moncure AC et al (1993) Surgical management and radiological characteristics of bronchogenic cysts. Ann Thorac Surg 5:476–481
15. Yernault JC, Kuhn G, Dumortier P, Rocmans P, Ketelbant P, De Vuyst P (1986) "Solid" mediastinal bronchogenic cyst: mineralogic analysis. AJR Am J Roentgenol 146:73–74
16. McAdams HP, Kirejczyk WM, Rosado-de-Christenson ML, Matsumoto S (2000) Bronchogenic cyst: imaging features with clinical and histopathologic correlation. Radiology 217: 441–446
17. Nakata H, Egashira K, Watanabe H, Nakamura K, Onitsuka H, Murayama S et al MRI of bronchogenic cysts. J Comput Assist Tomogr 1993;17:267–70
18. Gaeta M, Vinci S, Minutoli F, Mazziotti S, Ascenti G, Salamone I et al (2002) CT and MRI findings of mucin-containing tumours and pseudotumours of the thorax: pictorial review. Eur Radiol 12:181–189
19. Lyon RD, McAdams HP (1993) Mediastinal bronchogenic cyst: demonstration of a fluid-fluid level at MR imaging. Radiology 186:427–428
20. Fitch SJ, Tonkin IL, Tonkin AK (1986) Imaging of foregut duplication cysts. Radiographics 6:189–201
21. LeBlanc J, Guttentag AR, Shepard JA, McLoud TC (1994) Imaging of mediastinal foregut cysts. Can Assoc Radiol J 45: 381–386
22. Salo JA, Ala-Kulju KV (1987) Congenital esophageal cysts in adults. Ann Thorac Surg 44:135–138
23. Feigin DS, Fenoglio JJ, McAllister HA, Madewell JE (1977) Pericardial cysts. A radiologic-pathologic correlation and review. Radiology 125:15–20
24. Demos TC, Budorick NE, Posniak HV (1989) Benign mediastinal cysts: pointed appearance on CT. J Comput Assist Tomogr 13:132–133
25. Brown LR, Aughenbaugh GL (1991) Masses of the anterior mediastinum: CT and MR imaging. AJR Am J Roentgenol 157:1171–1180
26. Strollo DC, Rosado-de-Christenson ML, Jett JR (1997) Primary mediastinal tumours: part II. Tumours of the middle and posterior mediastinum. Chest 112:1344–1357

27. Lewis JE, Wick MR, Scheithauer BW, Bernatz PE, Taylor WF (1987) Thymoma. A clinicopathologic review. Cancer 60: 2727–2743
28. Graeber GM, Thompson LD, Cohen DJ, Ronnigen LD, Jaffin J, Zajtchuk R (1984) Cystic lesion of the thymus. An occasionally malignant cervical and/or anterior mediastinal mass. J Thorac Cardiovasc Surg 87: 295–300
29. Avila NA, Mueller BU, Carrasquillo JA, Kontny HU, Jaffe ES, Pizzo PA (1996) Multilocular thymic cysts: imaging features in children with human immunodeficiency virus infection. Radiology 201: 130–134
30. Suster S, Rosai J (1991) Multilocular thymic cyst: an acquired reactive process. Study of 18 cases. Am J Surg Pathol 15: 388–398
31. Choi YW, McAdams HP, Jeon SC, Hong EK, Kim YH, Im JG et al (2001) Idiopathic multilocular thymic cyst: CT features with clinical and histopathologic correlation. AJR Am J Roentgenol 177: 881–885
32. Strollo DC, Rosado-de-Christenson ML (1999) Tumours of the thymus. J Thorac Imaging 14: 152–171
33. Tsuchiya R, Sugiura Y, Ogata T, Suemasu K (1980) Thoracic duct cyst of the mediastinum. J Thorac Cardiovasc Surg 79: 856–859
34. Glazer GM, Axel L, Moss AA (1982) CT diagnosis of mediastinal thyroid. AJR Am J Roentgenol 138: 495–498
35. Gefter W, Spritzer CE, Eisenberg H et al (1987) Thyroid imaging with high-field-strength surface-coil MR. Radiology 164: 483–490
36. Weber AL, Randolph G, Aksoy FG (2000) The thyroid and parathyroid glands. CT and MR imaging and correlation with pathology and clinical findings. Radiol Clin North Am 38: 1105–1129
37. Russell CF, Edis AJ, Scholz DA, Sheedy PF, van Heerden JA (1981) Mediastinal parathyroid tumours: experience with 38 tumours requiring mediastinotomy for removal. Ann Surg 193: 805–809
38. Doppman JL, Krudy AG, Brennan MF, Schneider P, Lasker RD, Marx SJ (1982) CT appearance of enlarged parathyroid glands in the posterior superior mediastinum. J Comput Assist Tomogr 6: 1099–1102
39. Doppman JL, Skarulis MC, Chen CC, Chang R, Pass HI, Fraker DL et al (1996) Parathyroid adenomas in the aortopulmonary window. Radiology 201: 456–462
40. Clark OH, Okerlund MD, Moss AA, Stark D, Norman D, Newton TH et al (1985) Localization studies in patients with persistent or recurrent hyperparathyroidism. Surgery 98: 1083–1094
41. Clark OH (1988) Mediastinal parathyroid tumours. Arch Surg 123: 1096–1100
42. MacFarlane SD, Hanelin LG, Taft DA, Ryan JA Jr, Fredlund PN (1984) Localization of abnormal parathyroid glands using thallium-201. Am J Surg 148: 7–13
43. Ishibashi M, Nishida H, Hiromatsu Y, Kojima K, Uchida M, Hayabuchi N (1997) Localization of ectopic parathyroid glands using technetium-99m sestamibi imaging: comparison with magnetic resonance and computed tomographic imaging. Eur J Nucl Med 24: 197–201
44. Krubsack AJ, Wilson SD, Lawson TL, Kneeland JB, Thorsen MK, Collier BD et al (1989) Prospective comparison of radionuclide, computed tomographic, sonographic, and magnetic resonance localization of parathyroid tumours. Surgery 106: 639–644
45. Kuriyama K, Ikezoe J, Morimoto S, Arisawa J, Akira M, Tomoda K et al (1986) Functioning parathyroid cyst extending from neck to anterior mediastinum. Diagnosis by sonography and computed tomography. Diagn Imaging Clin Med 55: 301–305
46. Masaoka A, Monden Y, Nakahara K, Tanioka T (1981) Follow-up study of thymomas with special reference to their clinical stages. Cancer 48: 2485–2492
47. Levine GD, Rosai J (1978) Thymic hyperplasia and neoplasia: a review of current concepts. Hum Pathol 9: 495–515
48. Marino M, Muller-Hermelink HK (1985) Thymoma and thymic carcinoma. Relation of thymoma epithelial cells to the cortical and medullary differentiation of thymus. Virchows Arch A Pathol Anat Histopathol 407: 119–149
49. Okumura M, Miyoshi S, Fujii Y, Takeuchi Y, Shiono H, Inoue M et al (2001) Clinical and functional significance of WHO classification on human thymic epithelial neoplasms: a study of 146 consecutive tumours. Am J Surg Pathol 25: 103–110
50. Okumura M, Ohta M, Tateyama H, Nakagawa K, Matsumura A, Maeda H et al (2002) The World Health Organization histologic classification system reflects the oncologic behavior of thymoma: a clinical study of 273 patients. Cancer 94: 624–632
51. Rosado-de-Christenson ML, Galobardes J, Moran CA (1992) Thymoma: radiologic–pathologic correlation. Radiographics 12: 151–168
52. Chen JL, Weisbrod GL, Herman SJ (1988) Computed tomography and pathologic correlations of thymic lesions. J Thorac Imaging 3: 61–65
53. Nicolaou S, Muller NL, Li DK, Oger JJ (1996) Thymus in myasthenia gravis: comparison of CT and pathologic findings and clinical outcome after thymectomy. Radiology 201: 471–474
54. Higuchi T, Taki J, Kinuya S, Yamada M, Kawasuji M, Matsui O et al (2001) Thymic lesions in patients with myasthenia gravis: characterization with thallium 201 scintigraphy. Radiology 221: 201–206
55. Tomiyama N, Muller NL, Ellis SJ, Cleverley JR, Okumura M, Miyoshi S et al (2001) Invasive and noninvasive thymoma: distinctive CT features. J Comput Assist Tomogr 25: 388–393
56. Do YS, Im JG, Lee BH, Kim KH, Oh YW, Chin SY et al (1995) CT findings in malignant tumours of thymic epithelium. J Comput Assist Tomogr 19: 192–197
57. Tomiyama N, Johkoh T, Mihara N, Honda O, Kozuka T, Koyama M et al (2002) Using the World Health Organization Classification of thymic epithelial neoplasms to describe CT findings. AJR Am J Roentgenol 179: 881–886
58. Kushihashi T, Fujisawa H, Munechika H (1996) Magnetic resonance imaging of thymic epithelial tumours. Crit Rev Diagn Imaging 37: 191–259
59. Molina PL, Siegel MJ, Glazer HS (1990) Thymic masses on MR imaging. AJR Am J Roentgenol 155: 495–500
60. Sakai S, Murayama S, Soeda H, Matsuo Y, Ono M, Masuda K (2002) Differential diagnosis between thymoma and non-thymoma by dynamic MR imaging. Acta Radiol 43: 262–268
61. Birnberg FA, Webb WR, Selch MT, Gamsu G, Goodman PC (1982) Thymic carcinoid tumours with hyperparathyroidism. AJR Am J Roentgenol 139: 1001–1004
62. Rosado de Christenson ML, Abbott GF, Kirejczyk WM, Galvin JR, Travis WD (1999) Thoracic carcinoids: radiologic-pathologic correlation. Radiographics 19: 707–736
63. Parra I, Remacha A, Costilla S, Calderon JA (2002) Thymic carcinoid tumours. Can Respir J 9: 215–216
64. Cadigan DG, Hollett PD, Collingwood PW, Ur E (1996) Imaging of a mediastinal thymic carcinoid tumour with radiolabeled somatostatin analogue. Clin Nucl Med 21: 487–488
65. Lastoria S, Palmieri G, Muto P, Lombardi G (1999) Functional imaging of thymic disorders. Ann Med 31[Suppl 2]: 63–69
66. Moran CA, Rosado-de-Christenson M, Suster S (1995) Thymolipoma: clinicopathologic review of 33 cases. Mod Pathol 8: 741–744
67. Rosado-de-Christenson ML, Pugatch RD, Moran CA, Galobardes J (1994) Thymolipoma: analysis of 27 cases. Radiology 193: 121–126
68. Drachman DB (1994) Myasthenia gravis. N Engl J Med 330: 1797–1810
69. Bonomo L, Ciccotosto C, Guidotti A, Merlino B Storto ML (1997) Staging of thoracic lymphoma by radiological imaging. Eur Radiol 7: 1179–1189
70. Harris NL (1994) A revised European-American classification of lymphoid neoplasms: a proposal from the International Lymphoma Study Group. Blood 84: 1361–1392
71. Lister TA (1989) Report of a committee. J Clin Oncol 7: 1630–1636
72. Ekstrand BC, Horning SJ (2002) Lymphocyte prominent Hodgkin's disease. Curr Oncol Rep 4: 424–433
73. Castellino RA (1986) Hodgkin disease: practical concept for the diagnostic radiologist. Radiology 159: 305–310
74. Castellino RA, Blank N, Hope RT, Cho C (1986) Hodgkin's disease: contribution of chest CT in the initial staging evaluation. Radiology 160: 603–605

75. Filly R, Blank N, Castellino RA (1976) Radiographic distribution of intrathoracic disease in previously untreated patients with Hodgkin's disease. Radiology 120:277–281
76. Heron CW, Husband JE, Williams MP (1988) Hodgkin disease: CT of the thymus. Radiology 167:647–651
77. Hopper KD, Diehl LF, Cole BA, Lynch JC, Meilstrup JW, McCauslin MA (1990) The significance of necrotic mediastinal lymph nodes on CT in patients with newly diagnosed Hodgkin disease. AJR Am J Roentgenol 155:267–270
78. Heron CW, Husband JE, Williams MP, Cherryman GR (1988) The value of thoracic computed tomography in the detection of recurrent Hodgkin's disease. Br J Radiol 61:567–572
79. Negendank WG, al-Katib AM, Karanes C, Smith MR (1990) Lymphomas: MR imaging contrast characteristics with clinical-pathologic correlations. Radiology 177:209–216
80. Rahmouni A, Divine M, Lepage E, Jazaerli N, Belhadj K, Gaulard P et al Mediastinal lymphoma: quantitative changes in gadolinium enhancement at MR imaging after treatment. Radiology 219:621–628
81. Spiers AS, Husband JE, MacVicar AD (1997) Treated thymic lymphoma: comparison of MR imaging with CT. Radiology 203:369–376
82. Menzel C, Dobert N, Mitrou P, Mose S, Diehl M, Berner U et al (2002) Positron emission tomography for the staging of Hodgkin's lymphoma–increasing the body of evidence in favor of the method. Acta Oncol 41:430–436
83. Castellino RA (1991) The non-Hodgkin's lymphomas: practical concepts for the diagnostic radiologist. Radiology 178:315–321
84. Kostakoglu L, Coleman M, Leonard JP, Kuji I, Zoe H, Goldsmith SJ (2002) PET predicts prognosis after 1 cycle of chemotherapy in aggressive lymphoma and Hodgkin's disease. J Nucl Med 43:1018–1027
85. Kostakoglu L, Leonard JP, Kuji I, Coleman M, Vallabhajosula S, Goldsmith SJ (2002) Comparison of fluorine-18 fluorodeoxyglucose positron emission tomography and Ga-67 scintigraphy in evaluation of lymphoma. Cancer 94:879–888
86. Moran CA, Suster S (1997) Primary germ cell tumours of the mediastinum: I. Analysis of 322 cases with special emphasis on teratomatous lesions and a proposal for histopathologic classification and clinical staging. Cancer 80:681–690
87. Moran CA, Suster S, Przygodzki RM, Koss MN (1997) Primary germ cell tumours of the mediastinum: II. Mediastinal seminomas–a clinicopathologic and immunohistochemical study of 120 cases. Cancer 80:691–698
88. Moran CA, Suster S, Koss MN (1997) Primary germ cell tumours of the mediastinum: III. Yolk sac tumour, embryonal carcinoma, choriocarcinoma, and combined nonteratomatous germ cell tumours of the mediastinum–a clinicopathologic and immunohistochemical study of 64 cases. Cancer 80:699–707
89. Lewis BD, Hurt RD, Payne WS, Farrow GM, Knapp RH, Muhm JR (1983) Benign teratomas of the mediastinum. J Thorac Cardiovasc Surg 86:727–731
90. Moeller KH, Rosado-de-Christenson ML, Templeton PA (1997) Mediastinal mature teratoma: imaging features. AJR Am J Roentgenol 169:985–990
91. Sasaka K, Kurihara Y, Nakajima Y, Seto Y, Endo I, Ishikawa T et al (1998) Spontaneous rupture: a complication of benign mature teratomas of the mediastinum. AJR Am J Roentgenol 170:323–328
92. Choi SJ, Lee JS, Song KS, Lim TH (1998) Mediastinal teratoma: CT differentiation of ruptured and unruptured tumours. AJR Am J Roentgenol 171:591–594
93. Landwehr P, Schulte O, Lackner K (1999) MR imaging of the chest: mediastinum and chest wall. Eur Radiol 9:1737–1744
94. Shin MS, Ho KJ (1983) Computed tomography of primary mediastinal seminomas. J Comput Assist Tomogr 7:990–994
95. Lee KS, Im JG, Han CH, Han MC, Kim CW, Kim WS (1989) Malignant primary germ cell tumours of the mediastinum: CT features. AJR Am J Roentgenol 153:947–951
96. Drevelegas A, Palladas P, Scordalaki A (2001) Mediastinal germ cell tumours: a radiologic-pathologic review. Eur Radiol 11:1925–1932
97. Afifi HY, Bosl GJ, Burt ME (1997) Mediastinal growing teratoma syndrome. Ann Thorac Surg 64:359–362
98. Parizel PM, Simoens WA, Martos C, Verstaete K (eds) Tumours of peripheral nerves. 2nd edn, Springer, Berlin New York Heidelberg
99. Cohen LM, Schwartz AM, Rockoff SD (1986) Benign schwannomas: pathologic basis for CT inhomogeneities. AJR Am J Roentgenol 147:141–143
100. Sakai F, Sone S, Kiyono K, Maruyama Y, Oguchi K, Imai N et al (1996) Magnetic resonance imaging of neurogenic tumours of the thoracic inlet: determination of the parent nerve. J Thorac Imaging 11:272–278
101. Kiryu T, Ohashi N, Hoshi H, Iwata H, Shimokawa K, Kawaguchi S (2003) Mediastinal schwannoma: MR imaging findings of an unusual case presenting as a lobulated mass with internal fibrous septa. Clin Radiol 58:652–655
102. Kumar AJ (1983) CT of extracranial nerve sheath tumours with pathological correlation. J Comput Assist Tomogr 7:857–865
103. Kawashima A, Fishman EK, Kuhlman JE (1992) CT and MR evaluation of posterior mediastinal masses. Crit Rev Diagn Imaging 33:311–367
104. Suh JS, Abenoza P, Galloway HR, Everson LI, Griffiths HJ (1992) Peripheral (extracranial) nerve tumours: correlation of MR imaging and histologic findings. Radiology 183:341–346
105. Simoens WA, Wuyts FL, De Beuckeleer LH, Vandevenne JE, Bloem JL, De Schepper AM (2001) MR features of peripheral nerve sheath tumours: can a calculated index compete with radiologist's experience? Eur Radiol 11:250–257
106. Bourgouin PM, Shepard JO, Moore EH, McLoud TC (1988) Plexiform neurofibromatosis of the mediastinum: CT appearance. AJR Am J Roentgenol 151:461–463
107. Mulvihill JJ, Parry DM, Sherman JL, Pikus A, Kaiser-Kupfer MI, Eldridge R (1990) NIH conference. Neurofibromatosis 1 (Recklinghausen disease) and neurofibromatosis 2 (bilateral acoustic neurofibromatosis). An update. Ann Intern Med 113:39–52
108. Ducatman BS, Scheithauer BW, Piepgras DG, Reiman HM, Ilstrup DM (1986) Malignant peripheral nerve sheath tumours. A clinicopathologic study of 120 cases. Cancer 57:2006–2021
109. Burk DL Jr, Brunberg JA, Kanal E, Latchaw RE, Wolf GL (1987) Spinal and paraspinal neurofibromatosis: surface coil MR imaging at 1.5 T1. Radiology 162:797–801
110. Coleman BG, Arger PH, Dalinka MK, Obringer AC, Raney BR, Meadows AT (1983) CT of sarcomatous degeneration in neurofibromatosis. AJR Am J Roentgenol 140:383–387
111. Murphey MD, Smith WS, Smith SE, Kransdorf MJ, Temple HT (1999) From the archives of the AFIP. Imaging of musculoskeletal neurogenic tumours: radiologic-pathologic correlation. Radiographics 19:1253–1280
112. Moran CA, Albores-Saavedra J, Wenig BM, Mena H (1997) Pigmented extraadrenal paragangliomas. A clinicopathologic and immunohistochemical study of five cases. Cancer 79:398–402
113. Moran CA, Suster S, Fishback N, Koss MN (1993) Mediastinal paragangliomas. A clinicopathologic and immunohistochemical study of 16 cases. Cancer 72:2358–264
114. Shirkhoda A, Wallace S (1984) Computed tomography of juxtacardiac pheochromocytoma. J Comput Tomogr 8:207–209
115. Shapiro B, Sisson J, Kalff V, Glowniak J, Satterlee W, Glazer G et al (1984) The location of middle mediastinal pheochromocytomas. J Thorac Cardiovasc Surg 87:814–820
116. Blandino A, Salvi L, Faranda C, Spadaro P, Perrotta F, Maiello F et al (1992) Unusual malignant paraganglioma of the anterior mediastinum: CT and MR findings. Eur J Radiol 15:1–3
117. Andrade CF, Camargo SM, Zanchet M, Felicetti JC, Cardoso PF (2003) Nonfunctioning paraganglioma of the aortopulmonary window. Ann Thorac Surg 75:1950–1951
118. Argiris A, Mellott A, Spies S (2003) PET scan assessment of chemotherapy response in metastatic paraganglioma. Am J Clin Oncol 26:563–566
119. Neumann DR, Basile KE, Bravo EL, Chen EQ, Go RT (1996) Malignant pheochromocytoma of the anterior mediastinum: PET findings with [18F]FDG and 82Rb. J Comput Assist Tomogr 20:312–316

120. Klimstra DS, Moran CA, Perino G, Koss MN, Rosai J (1995) Liposarcoma of the anterior mediastinum and thymus. A clinicopathologic study of 28 cases. Am J Surg Pathol 19: 782–791
121. Viamonte M Jr, Viamonte M (1981) Radiology and pathology of fat. Crit Rev Diagn Imaging 16: 93–123
122. Laurino L, Furlanetto A, Orvieto E, Del Tos AP (2001) Well-differentiated liposarcoma (atypical lipomatous tumours). Semin Diagn Pathol 18: 258–262
123 Eisenstat R, Bruce D, Williams LE, Katz DS (2000) Primary liposarcoma of the mediastinum with coexistent mediastinal lipomatosis. AJR Am J Roentgenol 174: 572–573
124. Dogan R, Ayrancioglu K, Aksu O (1989) Primary mediastinal liposarcoma. A report of a case and review of the literature. Eur J Cardiothorac Surg 3: 367–370
125. Munden RF, Nesbitt JC, Kemp BL, Chasen MH, Whitman GJ (2000) Primary liposarcoma of the mediastinum. AJR Am J Roentgenol 175: 1340
126. Mineo TC, Biancari F, Cristino B, D'Andrea V (1995) Benign vascular tumours of the mediastinum: presentation of three cases and review of the literature. Thorac Cardiovasc Surg 43: 361–364
127. Ishii K, Maeda K, Hashihira M, Miyamoto Y, Kanegawa K, Kusumoto M et al (1990) MRI of mediastinal cavernous hemangioma. Pediatr Radiol 20: 556–557
128. Schurawitzki H, Stiglbauer R, Klepetko W, Eckersberger F (1991) CT and MRI in benign mediastinal haemangioma. Clin Radiol 43: 91–94
129. Cohen AJ, Sbaschnig RJ, Hochholzer L, Lough FC, Albus RA (1987) Mediastinal hemangiomas. Ann Thorac Surg 43: 656–659
130 Tarr RW, Page DL, Glick AG, Shaff MI (1986) Benign hemangioendothelioma involving posterior mediastinum: CT findings. J Comput Assist Tomogr 10: 865–867
131. Seline TH, Gross BH, Francis IR (1990) CT and MR imaging of mediastinal hemangiomas. J Comput Assist Tomogr 14: 766–768
132. McAdams HP, Rosado-de-Christenson ML, Moran CA (1994) Mediastinal hemangioma: radiographic and CT features in 14 patients. Radiology 193: 399–402
133. Rubinowitz AN, Moreira AL, Naidich DP (2000) Mediastinal hemangioendothelioma: radiologic–pathologic correlation. J Comput Assist Tomogr 24: 721–723
134. Shaffer K, Rosado-de-Christenson ML, Patz EF Jr, Young S, Farver CF (1994) Thoracic lymphangioma in adults: CT and MR imaging features. AJR Am J Roentgenol 162: 283–289
135. Charruau L, Parrens M, Jougon J, Montaudon M, Blachere H, Latrabe V et al (2001) Mediastinal lymphangioma in adults: CT and MR imaging features. Eur Radiol 10: 1310–1314
136. Kobayashi H, Furuse M, Yamada T, Mukai M (1994) Cavernous lymphangioma of the thorax: MRI findings. J Thorac Imaging 9: 64–66
137. Toye R, Armstrong P, Dacie JE (1991) Lymphangiohaemangioma of the mediastinum. Br J Radiol 64: 62–64
138. Riquet M, Briere J, Le Pimpec-Barthes F, Puyo P (1997) Lymphangiohemangioma of the mediastinum. Ann Thorac Surg 64: 1476–1478
139. Hanau CA, Miettinen M (1995) Solitary fibrous tumour: histological and immunohistochemical spectrum of benign and malignant variants presenting at different sites. Hum Pathol 26: 440–449
140. Lee KH, Song KS, Kwon Y, Lee I, Lee JS, Lim TH (2003) Mesenchymal tumours of the thorax: CT findings and pathological features. Clin Radiol 58: 934–944
141. Gladish GW, Sabloff BM, Munden RF, Truong MT, Erasmus JJ, Chasen MH (2002) Primary thoracic sarcomas. Radiographics 22: 621–637
142. Murakawa T, Nakajima J, Fukami T, Tanaka M, Takeuchi E, Takamoto S (2001) Malignant fibrous histiocytoma in the anterior mediastinum. Jpn J Thorac Cardiovasc Surg 49: 722–727
143. Morshuis WJ, Cox AL, Lacquet LK, Mravunac M, Barentsz JO (1990) Primary malignant fibrous histiocytoma of the mediastinum. Thorax 45: 154–155
144. Besznyak I, Svastits E, Krasznai G, Szentirmay Z (1985) Malignant fibrous histiocytoma of the mediastinum. Thorac Cardiovasc Surg 33: 106–108
145. Chen W, Chan CW, Mok C (1982) Malignant fibrous histiocytoma of the mediastinum. Cancer 50: 797–800
146. Stark P, Smith DC, Watkins GE, Chun KE (1990) Primary intrathoracic extraosseous osteogenic sarcoma: report of three cases. Radiology 174: 725–726

Part 4
Abdominal and Gastrointestinal Radiology

Neoplastic and Non-neoplastic Tumors of the Esophagus

James L. Buck

4.1

Contents

Non-neoplastic Tumors

Duplication cysts of the esophagus are often completely surrounded by the muscularis propria and therefore appear as intramural masses [1]. Since they are foregut malformations, the lining of the cysts will be either gastrointestinal or bronchial epithelium and they may even contain cartilage. Although the lesions are congenital, they are often found in asymptomatic older patients as incidental findings [2]. On barium examinations, the lesions are indistinguishable from other mural masses such as leiomyomas (Fig. 1) [2]. On CT and MR, the luminal contents typically appear like water, i.e., low attenuation on CT with low signal on T1-and high signal on T2 weighted MR images. However, like bronchogenic cysts, the complex fluid may be of soft tissue density on CT and have a high signal on T1-weighted images [3]. In some cases, duplication cysts of the esophagus, so called "neurenteric cysts," are associated with vertebral anomalies. Typically, the vertebral anomalies occur at a higher level in the spine due to differential growth between the neural axis and the gastrointestinal (GI) tract during embryologic development.

The *fibrovascular polyp* of the esophagus is a fascinating tumor. It is comprised of submucosal fibrovascular tissue and a variable amount of fat [4]. Other names for the lesion include angiolipoma and fibrolipoma. In almost all cases, the tumor originates in the proximal cervical esophagus. Although it is initially an intramural mass, because of the vigorous peristaltic waves traversing this area, the lesion is dragged into the lumen and eventually becomes a long polyp extending down as far as the gastroesophageal junction. Patients typically present with dysphagia. In some cases, the duration of dysphagia is long and the patents are clinically suspected to have achalasia. Occasionally, the patients regurgitate the long polyp from the esophagus into or even out of the mouth and, in rare instances, aspiration of the polyp into the airway has lead to the patient's demise [5].

The radiographic findings are those of a filling defect within the esophagus that may extend as far as the gastroesophageal (GE) junction. Careful evaluation will demonstrate a stalk that extends up to the cervical esophagus. Frequently, the esophagus is distended by the large intraluminal mass and the dilated esophagus can easily be seen on plain radiographs of the chest. On barium examinations, if the filling defect is not appreciated and the distension extends to the GE junction, an incorrect diagnosis of achalasia can be made. The surface of the lesion is typically smooth due to the intact mucosa covering the lesion, but lobulation of the intraluminal mass is also seen and may be extensive. CT imaging with oral contrast demonstrates the intraluminal mass and frequently shows areas of low attenuation due to the fat within the tumor (Fig. 2). When the fat is seen, a confident diagnosis of fibrovascular polyp can be made. Without the appearance of fat, the identical radiographic appearance can rarely be caused by other tumors originating in the submucosal or muscular layers of the esophagus [6].

Benign Neoplasms

Papilloma is a benign neoplasm of the squamous epithelium. Although more often solitary, when lesions are multiple, the term "papillomatosis" is used. The etiology is controversial. Approximately half of papillomas appear to be related to human papilloma virus (HPV) infection [7]. This is especially true of the multiple lesions seen in the proximal esophagus. However, in other cases there seems to be no association with HPV and the distal lesions may be related to the irritation of gastroesophageal reflux. Typically, the papillomas remain benign [8], but there are rare cases of malignant transformation into squamous cell carcinoma. Radiographically, papillomas appear as an esophageal polyp(s), often with

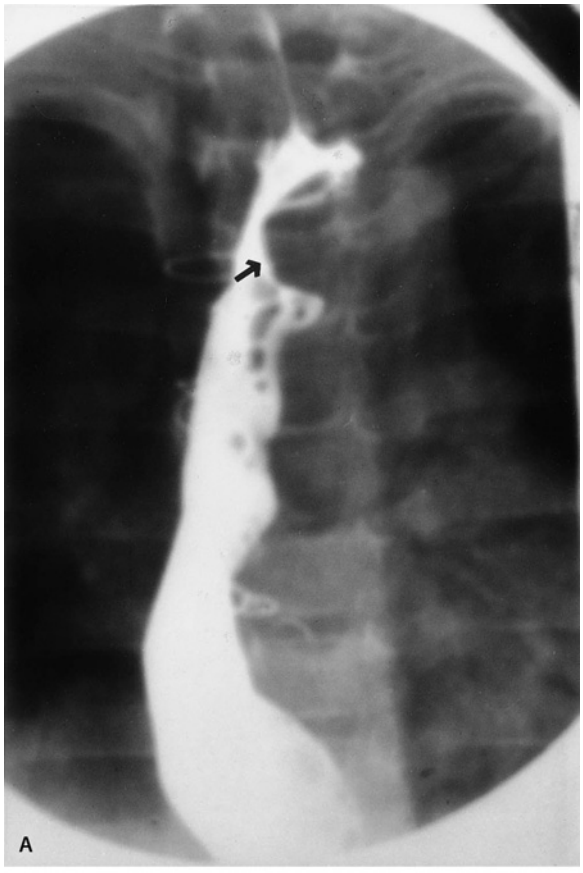

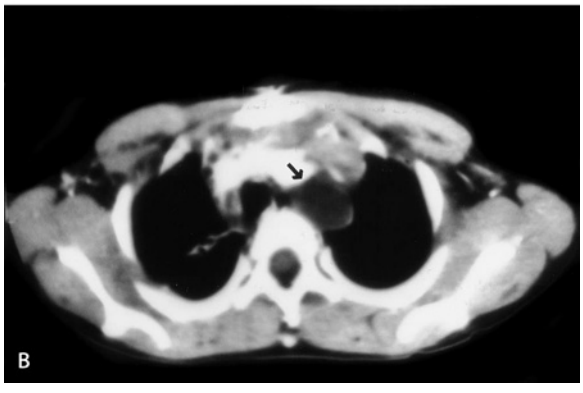

Fig. 1A, B. Duplication cysts. The single contrast esophagram (**A**) demonstrates a smoothly marginated filling defect (*arrow*) in the proximal thoracic esophagus. The sternotomy wires are from an unrelated procedure. A CT scan through the same level, performed with intravenous contrast (**B**), demonstrates a water density mass (*arrow*) just to the left of the air filled esophagus. The thin wall of the cyst is seen laterally

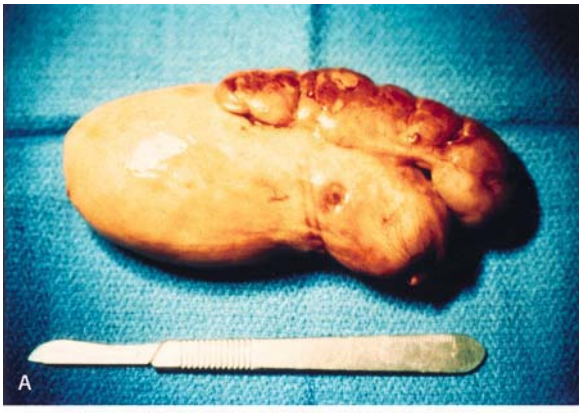

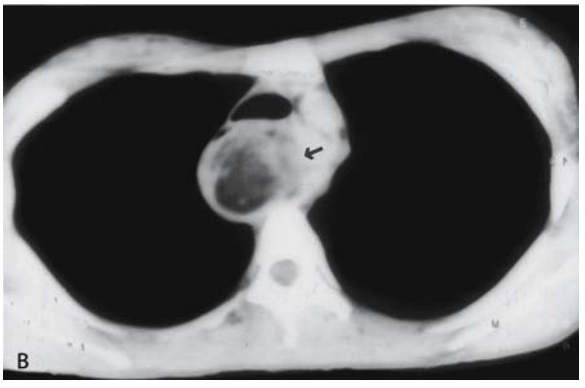

Fig. 2A, B. Fibrovascular polyp. The gross surgical specimen (**A**) demonstrates a smooth surface of the lesion due to the overlying intact mucosa. Lobulation of the lesion is also demonstrated. A CT scan performed with oral and intravenous contrast (**B**) demonstrates the large intraluminal mass (*arrow*) corresponding to the fibrovascular polyp. Note the fat attenuation within the lesion, allowing a confident diagnosis

with an irregular surface. When they are tiny, they are likely to be missed radiographically, especially on single contrast exams [9]. Larger lesions may be indistinguishable from squamous cell carcinoma (Fig. 3).

The most common site of *granular cell tumors* in the GI tract is the esophagus. Although granular cell tumors in other locations are frequently seen in black females, there does not appear to be any racial or sexual predilection for gastrointestinal granular cell tumors. Patients are typically asymptomatic and the granular cell tumors, located within the submucosa, are incidental findings [10]. Radiographically, these small mural masses, typically located in the distal esophagus, are indistinguishable from leiomyomas. They may be multifocal. Although the granular cell tumor, itself, is benign, occasional reports of squamous hyperplasia and even squamous cell carcinoma in the mucosa overlying the granular cell tumor have been reported [11].

By far the most common benign tumor of the esophagus is the *leiomyoma*, although it is more common for smooth muscle tumors to involve the stomach or small bowel. There may be symptoms of dysphagia or chest pain, and rarely hypertrophic osteoarthropathy occurs. However, the lesions are often discovered as incidental findings on radiographic examinations performed for other reasons [12].

Esophageal leiomyomas are, typically, very well differentiated tumors arising from the muscle layer of the esophagus. Although no true capsule is present, a pseu-

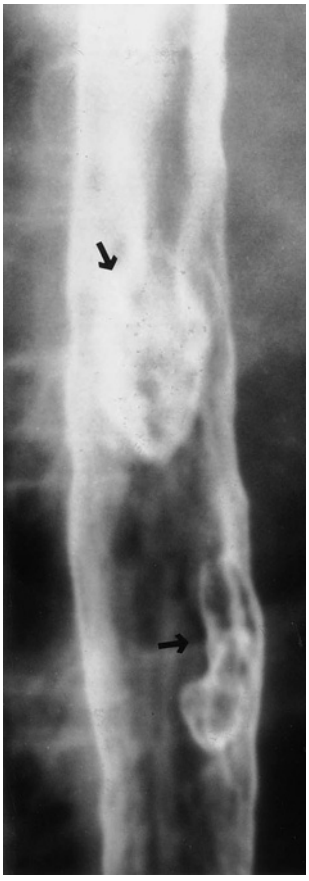

Fig. 3. Papillomas. The air contrast esophagram demonstrates two polypoid masses in the mid esophagus (*arrows*). An irregular surface is noted on both lesions

docapsule of compressed muscle surrounds the tumors and allows them to be bluntly dissected out of the esophageal wall by the surgeon (Fig. 4). Necrosis and ulceration is very uncommon. Unlike in other areas of the GI tract, leiomyomas of the esophagus appear to have minimal malignant potential [13].

The lesions typically occur in the mid or distal esophagus. Radiographically, leiomyomas appear as sharply marginated filling defects arising from the esophageal wall which may be somewhat elongated along the long axis of the esophagus and may be lobulated (Fig. 4). In some cases, lesions extend out the advential side of the esophagus and have relatively little mass effect on the lumen. On CT, esophageal leiomyomas are homogeneous tumors of soft tissue density that enhance after contrast [14]. By endoscopic US the muscular layer of origin of the tumor can be very well demonstrated [15].

In cases of "leiomyomatosis," the growth pattern is circumferential and often extensive (Fig. 5). Such cases are typically seen in the distal esophagus and affected patients are likely to have severe dysphagia requiring

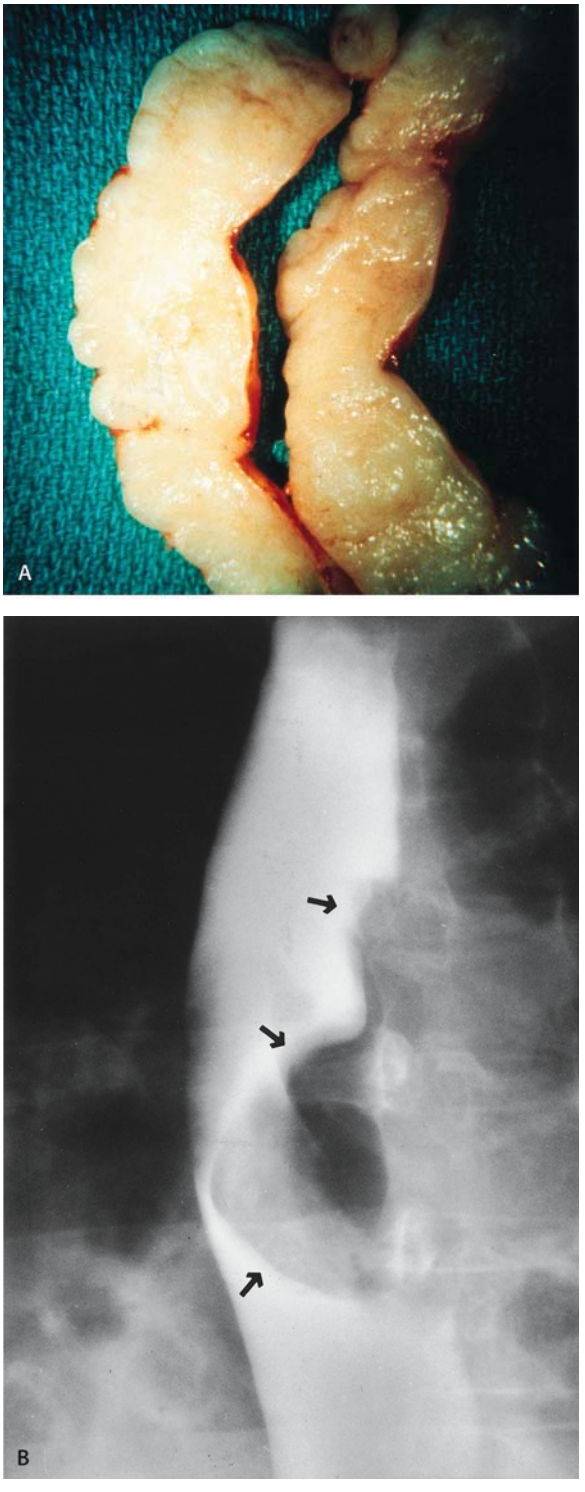

Fig. 4A, B. Leiomyoma. The bivalved gross surgical specimen (**A**) demonstrates the characteristically sharp borders due to a pseudocapsule and the homogeneous appearance of the tumor. Slight lobulation on the surface of the tumor is also seen. A single contrast esophagram (**B**) demonstrates the smoothly marginated filling defect (*arrows*) originating from the wall of the esophagus. The mass is somewhat elongated along the vertical axis of the esophagus and has slight lobulation

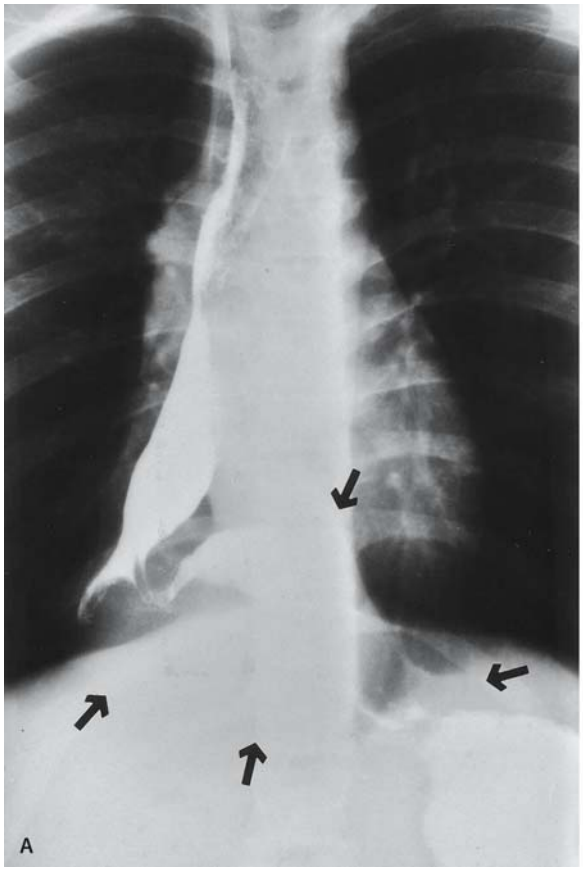

Fig. 5A, B. Leiomyomatosis. The single contrast barium examination (**A**) shows a bizarre course and caliber of the distal esophagus with a surrounding soft tissue mass (*arrows*) that extends into the proximal stomach. Due to significant dysphagia, a surgical resection was performed. The surgical specimen (**B**) demonstrates the extensive and circumferential involvement of the smooth muscle tumor around the distal esophagus

surgical correction [16]. Leiomyomatosis may be inherited and associated with Alport syndrome (i.e., congenital neural deafness and renal insufficiency) [17].

Malignant Neoplasms

Hematogenous *metastases* to the esophagus are rare. However, secondary involvement from mediastinal spread of bronchogenic carcinoma is relatively common. Such involvement of the esophagus by lung cancer may result in fistulae between the esophagus and tracheo-bronchial tree [18]. In gay men with AIDS, *Kaposi sarcoma* will produce nodules and thickened folds [19].

The esophagus is the least common site in the GI tract for *lymphoma*, and when lymphoma occurs it is usually in the setting of widespread disease that began in lymph nodes [20]. However, in immunocompromised patients, such as patients with AIDS or organ transplants, high grade lymphomas of the esophagus may occur primarily (Fig. 6). The radiographic appearance of lymphoma is quite variable and includes mural mass(es), multiple nodules, thickened folds and both smooth and irregular strictures [21].

The most common malignancy of the esophagus probably remains *squamous cell carcinoma*, although the incidence is decreasing. Affected patients are typically men between 50 and 70 years of age [22]. In the US, African-Americans are relatively more commonly affected. The etiology is multifactorial, but clearly involves the combination of alcohol and tobacco abuse. Not surprisingly, there is a strong association between squamous cell carcinoma of the esophagus and squamous cell carcinoma of the head and neck. Other predisposing conditions include lung cancer, lye stricture, achalasia, celiac disease, Plummer-Vinson syndrome, and tylosis palmaris et plantaris [23-27].

Fig. 7 A, B. Squamous cell carcinoma in a patient with achalasia. On the frontal view (**A**) of the air contrast esophagram, barium outlines the inferior border of a large, sessile polypoid mass at the junction of the cervical and thoracic esophagus (*arrows*). On the lateral view (**B**), the soft tissue density of the mass can be seen (*asterisk*) indenting the trachea

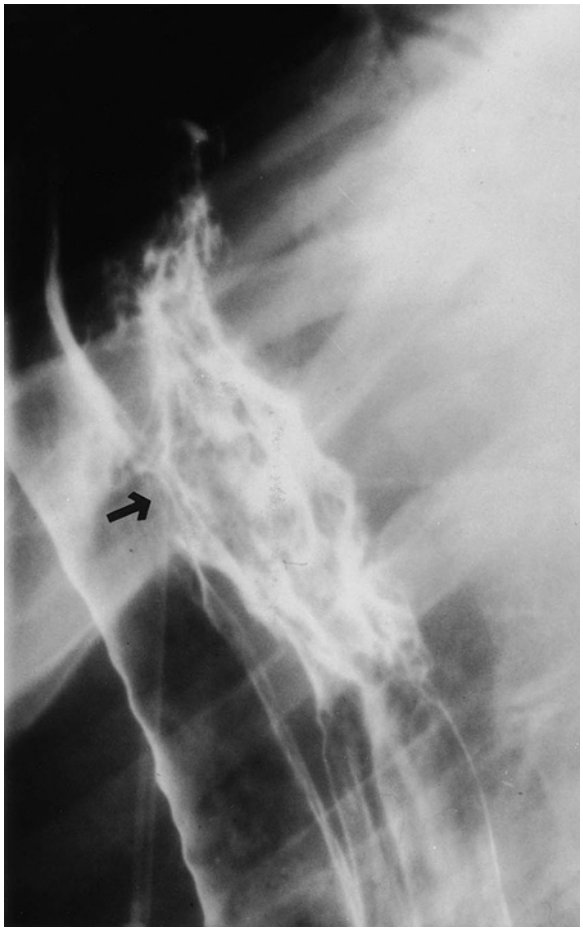

Fig. 6. Esophageal lymphoma in a patient with AIDS. The air contrast esophagram shows a markedly irregular stenosis involving the cervicothoracic esophagus. The lesion is associated with a wide fistula to the adjacent trachea (*arrow*)

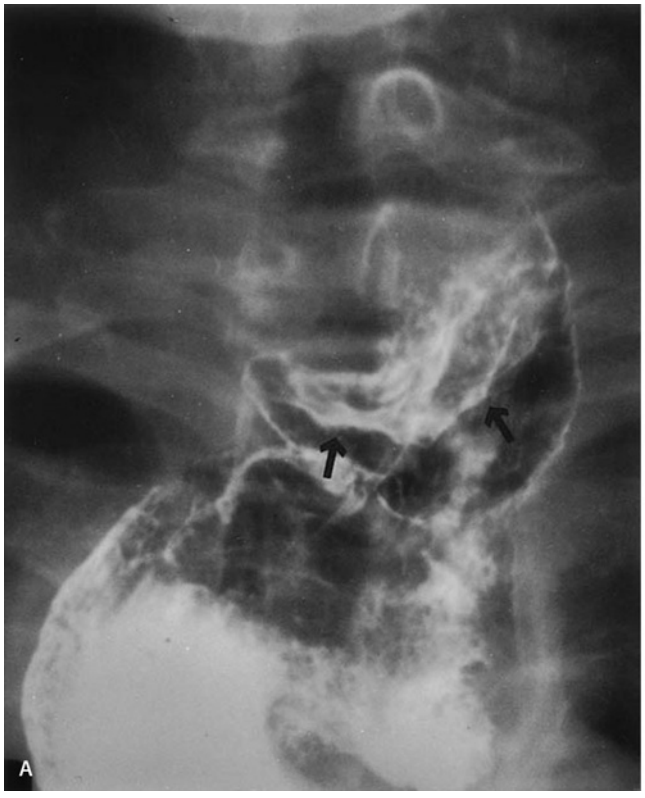

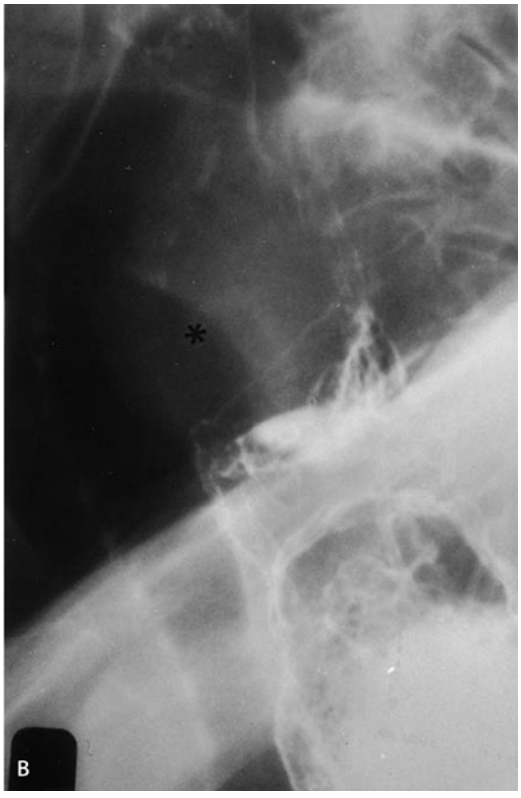

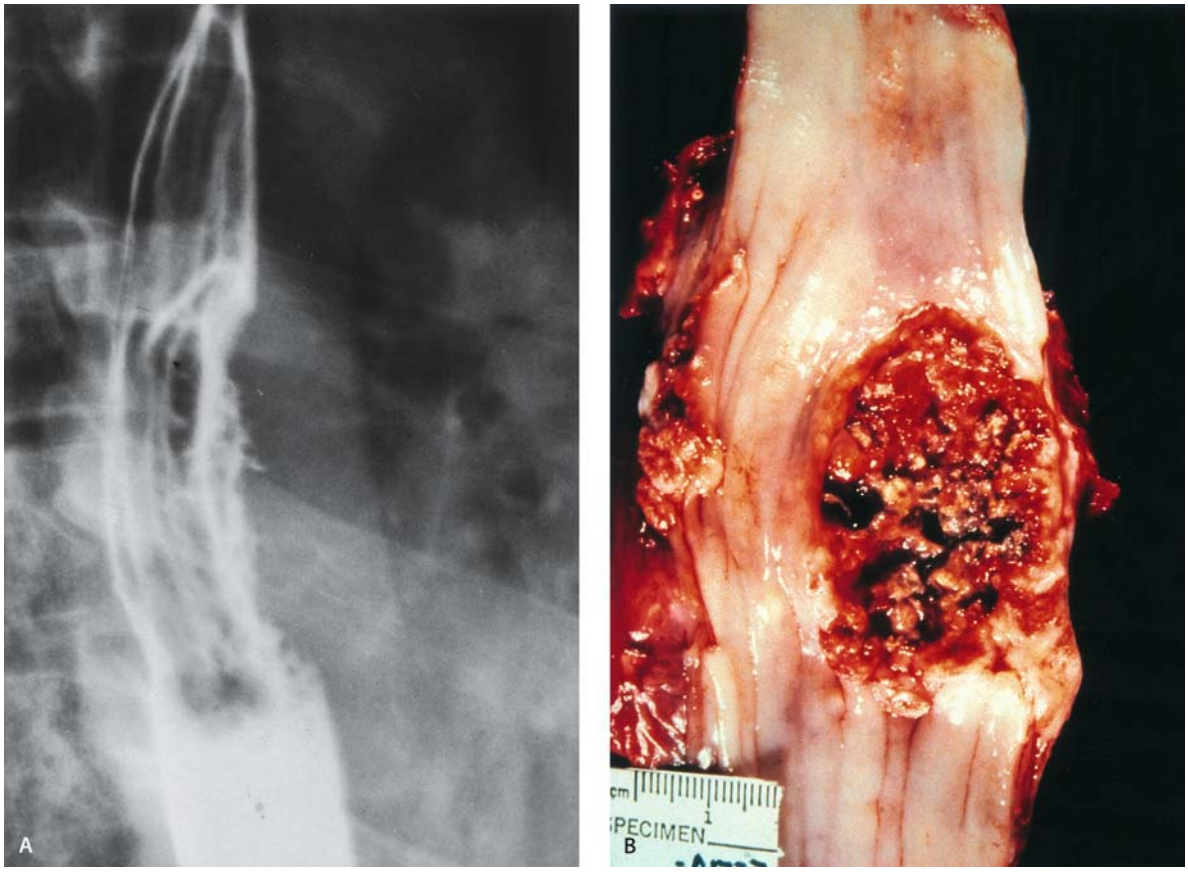

Fig. 8A, B. Squamous cell carcinoma. An air contrast esophagram (**A**) reveals an irregular mass with extensive surface ulceration in the mid esophagus. The corresponding surgical specimen (**B**) confirms the marked ulceration of the tumor

Squamous cell carcinoma, of course, originates from the squamous epithelium. However, infiltration into the esophageal wall almost always occurs. Within the submucosal space, the cancer can spread for a long distance up or down the esophagus. Rarely, so much of the tumor is submucosal that a mucosal biopsy will fail to make a diagnosis.

The lesions are most commonly seen within the thoracic esophagus, especially its mid portion [28]. When the distal esophagus is involved by squamous cell carcinoma, direct spread into the proximal stomach is unusual. Cervical esophageal involvement is uncommon. The tumor may appear as a fungating polypoid mass (Fig. 7) [29], an ulcerating mass (Fig. 8) [30], and, most commonly, an irregular stricture (Figs. 9, 10). Frequently, these malignant strictures are very tight and they often prevent the passage of an endoscope without a risky dilatation [31]. Submucosal extension of tumor may produce the appearance of a varicoid carcinoma. Unlike true varices, the filling defects of varicoid carcinoma will not change in appearance with Valsalva maneuvers or varying amounts of esophageal distention [32]. The least common appearance is "superficial spreading" carcinoma, in which the subtle small filling defects can be seen only on good air contrast examinations [33].

Because of the lack of a serosal barrier and the close proximity of the esophagus to the pericardium, tracheobronchial tree, and aorta, local extension of squamous cell carcinoma to these mediastinal structures is common (Figs. 9, 10). Some authors have reported limited success in determining the extent of local disease with CT and MRI, but endoscopic US is clearly the superior modality in this regard [34-37]. Lymphatic metastases are also common. Small periesophageal nodes are usually unapparent on CT even when involved by tumor [38], but endoscopic US is relatively sensitive [37]. Cervical and/or mediastinal nodes are more likely to be enlarged and are best imaged with conventional cross-sec-

Fig. 10A, B. Squamous cell carcinoma. The single contrast examination (**A**) shows an irregular stricture involving the mid esophagus with a large surrounding soft tissue mass. The CT scan of the chest, performed with intravenous contrast (**B**), demonstrates the extensive soft tissue mass seen on the barium examination

Fig. 9. Squamous cell carcinoma. An air contrast esophagram demonstrates an irregular ulcerated stricture involving the mid esophagus. The surrounding soft tissue mass of tumor is seen indenting the left main stem bronchus (*arrow*)

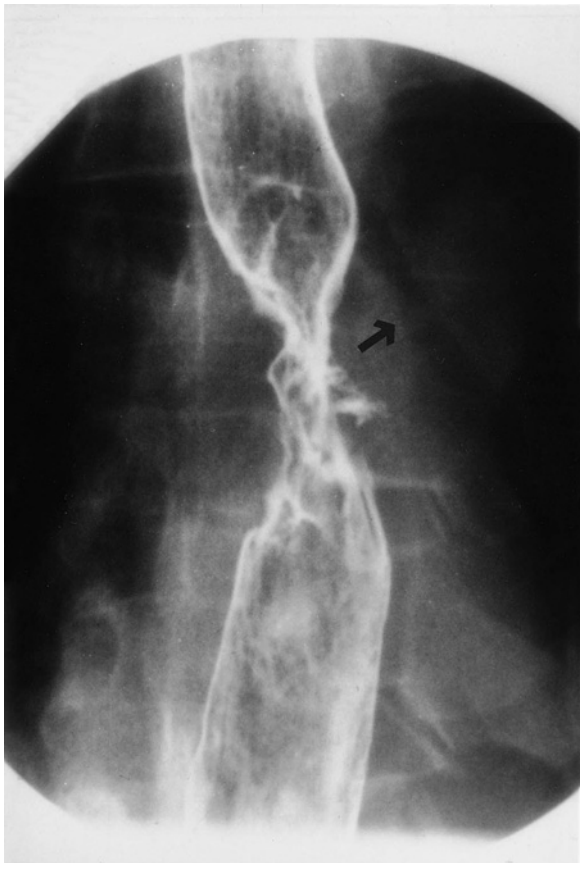

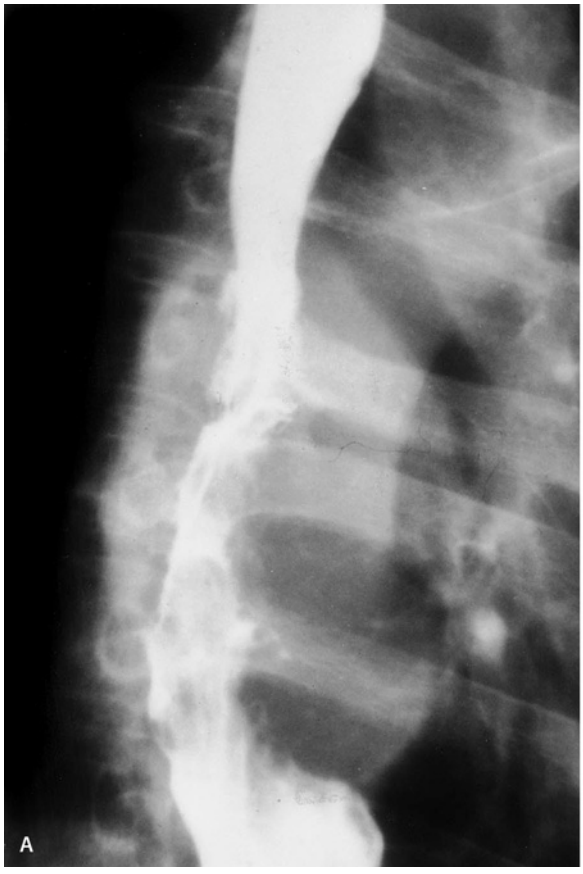

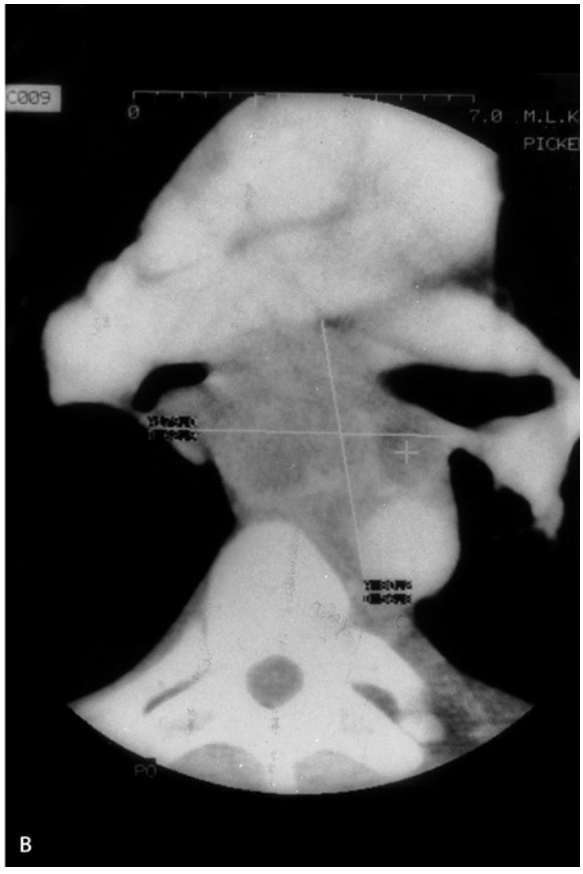

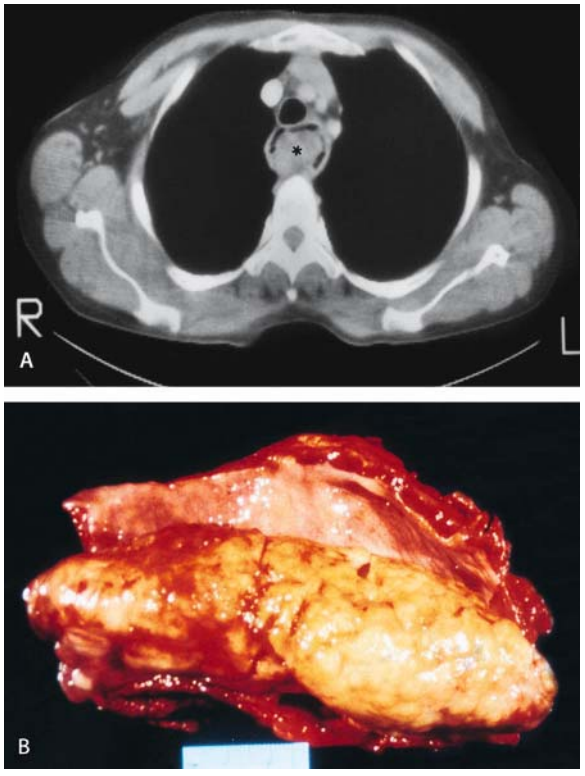

Fig. 11A, B. Spindle cell carcinoma. The CT scan, performed with intravenous contrast (**A**), reveals a large, sessile, polypoid mass arising from the posterior wall of the esophagus. The air filled lumen surrounds the tumor on three sides. The corresponding resected specimen (**B**) correlates with the CT findings

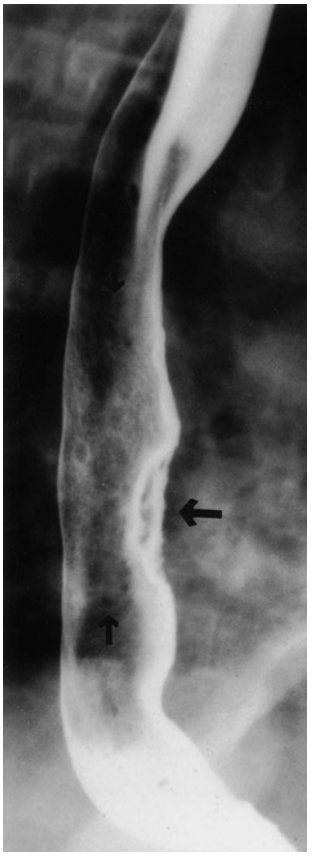

Fig. 12. Adenocarcinoma, secondary to Barrett esophagus. An air contrast esophagram demonstrates an ulcerating mass (*arrow*) along the anterolateral aspect of the esophagus. The surrounding reticular mucosal pattern (between the smaller arrows) is indicative of the pre-existing Barrett esophagus

tional imaging. Staging examinations should always include the upper abdomen. Lymphatic drainage of distal and even mid esophageal tumors is often to nodes in the gastrohepatic ligament and celiac axis area. Occasionally, esophageal squamous cell carcinoma will metastasize, apparently via lymphatics, to the wall of the gastric cardia. Hematogenous metastases may also be seen within the liver. Such intra-abdominal spread of disease may be better detected by laparoscopy than by CT [40]. Likewise, PET imaging with fluorodeoxyglucose has been shown to be superior to CT for the detection of regional and distal metastases [41].

Spindle cell carcinoma (also called "carcinosarcoma") is a biphasic tumor with both carcinomatous and sarcomatous elements. The carcinomatous elements are typically squamous cell carcinoma, although adenocarcinomas may be seen [42, 43]. The sarcomatous elements are now felt to be derived from the epithelial malignancy [42]. Spindle cell carcinomas are typically large, sessile, polypoid masses arising in the mid esophagus (Fig. 11) [42, 44].

Adenocarcinoma of the esophagus, like adenocarcinoma of the gastric cardia, is rising in incidence rapidly. Just over a decade ago, approximately one-third of carcinomas in the white population of the United States were adenocarcinomas. Now, in some series, they account for the majority of esophageal malignancies [45, 22]. Adenocarcinoma may rarely arise from congenital rests of columnar epithelium in the cervical esophagus, but, in the vast majority of cases, it arises from areas of columnar metaplasia due to Barrett esophagus. Barrett esophagus is seen predominately in middle aged and older white men, and adenocarcinoma has an identical demographic pattern [45]. Approximately 10% of patients with Barrett esophagus will develop adenocarcinoma and affected patients, therefore, must be followed with annual endoscopic surveillance [46].

Since Barrett esophagus most commonly occurs in the distal esophagus, adenocarcinoma is usually a distal esophageal tumor [47]. Mid esophageal adenocarcinomas are seen when Barrett metaplasia is extensive, but

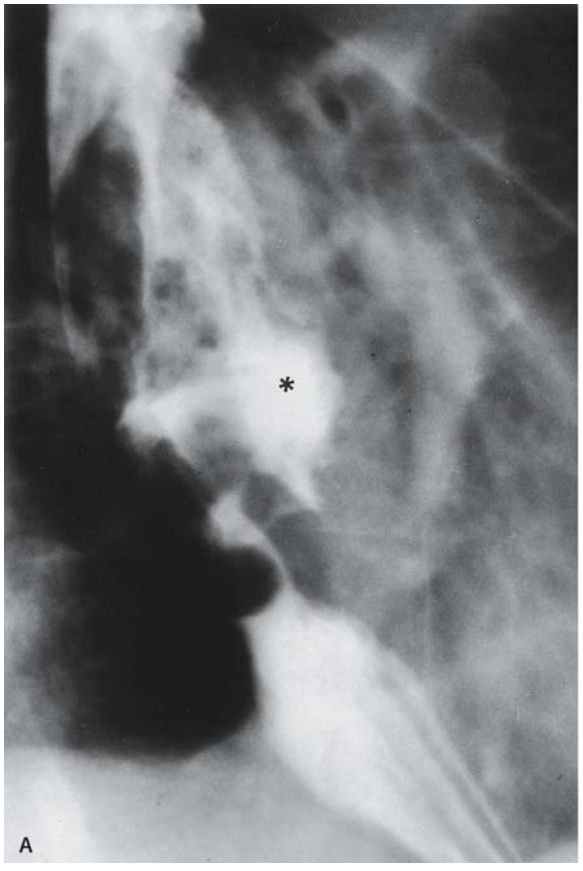

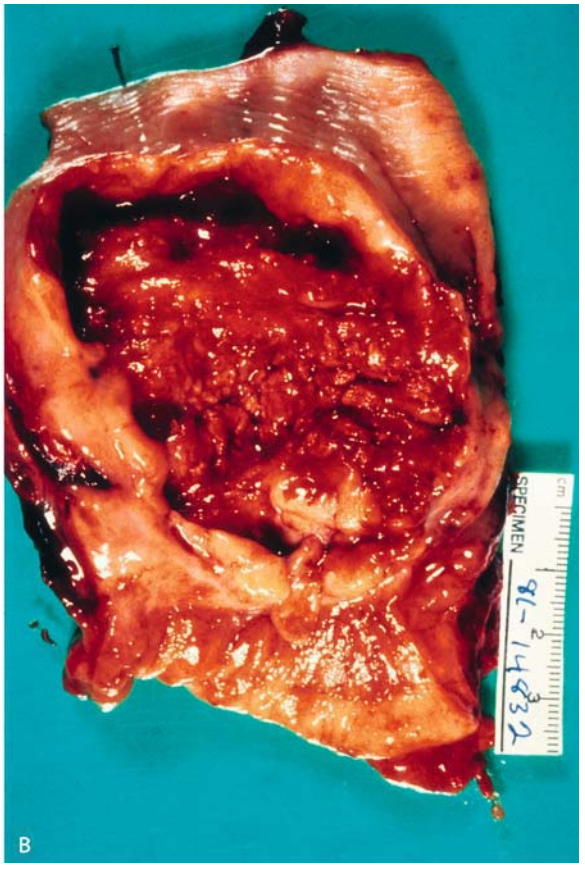

Fig. 13A, B. Leiomyosarcoma. A single contrast examination (**A**) demonstrates a large ulcerating mass (*asterisk* indicates part of the ulcer) in the distal esophagus. The corresponding gross specimen (**B**) shows the extensive ulceration of the mass which is located just above the gastroesophageal junction

cervical esophageal adenocarcinoma is rare and is more likely to arise from congenital rests of columnar epithelium rather than Barrett metaplasia.

When a patient is known to have Barrett esophagus or has a history of reflux esophagitis, adenocarcinoma should, of course, be suspected when an esophageal malignancy is noted. When a reticular mucosal pattern, a characteristic but uncommon feature of Barrett esophagus [48], is seen in association with an esophageal malignancy, a confident diagnosis of adenocarcinoma can be made (Fig. 12). Also, hiatal hernia is very frequently seen in patients with adenocarcinoma [47, 49]. Otherwise, the appearances of adenocarcinoma are indistinguishable from squamous cell carcinoma with polypoid, ulcerative, stenotic and even varicoid appearances noted. Superficial spreading adenocarcinoma, however, is not reported.

Adenocarcinoma of the esophagus may extend into the proximal stomach just as gastric cardia tumors can extend into the distal esophagus [49]. Patterns of local spread and metastatic disease are otherwise similar to that of squamous cell carcinoma.

Leiomyosarcoma is probably the most common of the other malignant neoplasms of the esophagus. Typically these lesions appear as large ulcerating masses, but in some cases the masses are smoothly marginated and difficult to differentiate from a benign leiomyoma [50]. Primary *malignant melanoma*, *small cell carcinoma*, and *salivary gland tumors* (e.g., adenoid cystic carcinoma and mucoepidermoid carcinoma) are also seen, but infrequently [51-53].

References

1. Bhutani MS, Hoffman BJ, Reed C (1996) Endosonographic diagnosis of an esophageal duplication cyst. Endoscopy 28(4): 396–397
2. Bondestam S, Salo JA, Salonen OLM, Lamminen AE (1990) Imaging of congenital esophageal cysts in adults. Gastrointest Radiol 15:279–281
3. Mendelson DS, Rose JS, Efremidis SC, Kirschner PA, Cohen BA (1983) Bronchogenic cysts with high CT numbers. AJR 140:463–465
4. Levin MS, Buck JL, Pantongrag-Brown L, Buetow PC, Hallman JR, Sobin LH (1996) Fibrovascular polyps of the esophagus: clinical, radiographic, and pathologic findings in 16 patients. AJR 166:781–787

5. Cochet B, Hohl P, Sans M, Cox JN (1980) Asphyxia caused by laryngeal impaction of an esophageal polyp. Arch Otolaryngol 106:176–178
6. Eberlein TJ, Hannan R, Josa M, Sugarbaker DJ (1992) Benign schwannoma of the esophagus presenting as a giant fibrovascular polyp. Ann Thorac Surg 53:343–345
7. Odze R, Antonioli D, Shocket D, Noble-Topham S, Goldman H, Upton M (1993) Esophageal squamous papillomas: a clinicopathologic study of 38 lesions and analysis for human papillomavirus of the polymerase chain reaction. Am J Surg Pathol 17:803–812
8. Politoske EJ (1992) Squamous papillomas of the esophagus associated with the human papillomavirus. Gastroenterology 102:668–673
9. Montesi A, Pesaresi A, Graziani L, Salmistraro D, Dini L, Bearzi I (1983) Small benign tumors of the esophagus: radiological diagnosis with double-contrast examination. Gastrointest Radiol 8:207–212
10. Johnston J, Helwig EB (1981) Granular cell tumors of the gastrointestinal tract and perianal region: a study of 74 cases. Dig Dis Sci 26:807–816
11. Rubesin S, Herlinger H, Sigal H (1985) Granular cell tumors of the esophagus. Gastrointest Radiol 10:11–15
12. Seremetis MG, Lyons WS, DeGuzman VC, Peabody JW Jr (1976) Leiomyomata of the esophagus. Cancer 38:2166–2177
13. Ueyama T, Guo K-J, Hashimoto H, Daimaru Y, Enjoji M (1993) A clinicopathologic and immunohistochemical study of gastrointestinal stromal tumors. Cancer 69:947–955
14. Megibow AJ, Balthazar EJ, Hulnick DH, Naidich DP, Bosniak MA (1985) CT evaluation of gastrointestinal leiomyomas and leiomyosarcomas. AJR 144:727–731
15. Massari M, Lattuada E, Zappa MA, et al. (1997) Evaluation of leiomyoma of the esophagus with endoscopic ultrasonography. Hepatogastroenterology 44(15):727–731
16. Levins MS, Buck JL, Pantongrag-Brown L, Buetow PC, Lowry MA, Sobin LH (1996) Esophageal leiomyomatosis. Radiology 199(2):533–536
17. Rabushka LS, Fishman EK, Kuhlman JE, Hruban RH (1991) Diffuse esophageal leiomyomatosis in a patient with Alport syndrome: CT demonstration. Radiology 179:176–178
18. Agha FP (1987) Secondary neoplasms of the esophagus. Gastrointest Radiol 12:187–193
19. Rose HS, Balthazar EJ, Megibow AJ, et al. (1982) Alimentary tract involvement in Kaposi sarcoma: radiographic and endoscopic findings in 25 homosexual men. AJR 139:661–666
20. Agha FP, Schnitzer B (1985) Esophageal involvement in lymphoma. Am J Gastroenterol 80(6):412–416
21. Carnovale RL, Goldstein HM, Zornoza J, Dodd GD (1977) Radiologic manifestations of esophageal lymphoma. AJR 128:751–754
22. Swisher SG, Hunt KK, Holmes C, Zinner MJ, McFadden DW (1995) Changes in the surgical management of esophageal cancer from 1970 to 1993. Am J Surg 169:609–614
23. Goldstein HM, Zornoza J (1978) Association of squamous cell carcinoma of the head and neck with cancer of the esophagus. AJR 131:791–794
24. Appelqvist P, Salmo M (1980) Lye corrosion carcinoma of the esophagus. Cancer 45:2655–2658
25. Hankins JR, McLaughlin JS (1975) The association of carcinoma of the esophagus with achalasis. J Thorac Cardiovasc Surg 65:355–360
26. Collins SM, Hamilton JD, Lewis TD, Laufer I (1978) Small-bowel malabsorption and gastrointestinal malignancy. Radiology 126:603–609
27. Yesudian P, Premalatha S, Thambiah AS (1980) Genetic tylosis with malignancy: a study of a south Indian pedigree. Br J Dermatol 103:597–600
28. Wolfman NT, Scharling ES, Chen MY (1994) Esophageal squamous carcinoma. Radiol Clin North AM 32(6):1183–1201
29. Mori M, Mimori K, Sadanaga N, Watanabe M, Kuwano H, Sugimachi K (1994) Polypoid carcinoma of the esophagus. Jpn J Cancer Res 85(11):1131–1136
30. Gloyna RE, Zornoza J, Goldstein HM (1977) Primary ulcerative carcinoma of the esophagus. AJR 129:599–600
31. Catalano MF, Van Dam J, Sivak MV Jr (1995) Malignant esophageal strictures: staging accuracy of endoscopic ultrasonography. Gastrointest Endosc 41: 535–539
32. Yates CW Jr., LeVine MA, Jensen KM (1977) Varicoid carcinoma of the esophagus. Radiology 122:605–608
33. Itai Y, Kogure T, Okuyama Y, Akiyama H (1978) Superficial esophageal carcinoma. Radiology 126:597–601
34. Thompson WM, Halvorsen RA, Foster WL, Jr., Williford ME, Postlethwait RW, Korobkin M (1983) Computed tomography for staging esophageal and gastroesophageal cancer: reevaluation. AJR 141:951–958
35. Quint LE, Glazer GM, Orringer MB, Gross BH (1985) Esophageal carcinoma: CT findings. Radiology 155:171–175
36. Takashima S, Takeuchi N, Shiozaki H, et al. (1991) Carcinoma of the esophagus: CT vs MR imaging in determining resectability. AJR 156:297–302
37. Holscher AH, Dittler HJ, Siewert JR (1994) Staging of squamous esophageal cancer: accuracy and value. World J Surg 18(3):312–320
38. Picus D, Balfe DM, Koehler RE, Roper CL, Owen JW (1983) Computed tomography in the staging of esophageal carcinoma. Radiology 146:433–438
39. Glick SN, Teplick SK, Levin MS, Caroline DF (1986) Gastric cardia metastasis in esophageal carcinoma. Radiology 160:627–630
40. Bonavina L, Incarbone R, Lattuada E, Segalin A, Cesana B, Peracchia A (1997) Preoperative laparoscopy in management of patients with carcinoma of the esophagus and of the esophagogastric junction. J Surg Oncol 65(3):171–174
41. Flanagan FL, Dehdashti F, Siegel BA, et al. (1997) Staging of esophageal cancer with 18F- fluorodeoxyglucose positron emission tomography. AJR 168(2):417–424
42. Agha FP, Keren DF (1985) Spindle-cell squamous carcinoma of the esophagus: a tumor with biphasic morphology. AJR 145:541–545
43. Dworak O, Koerfgen HP (1993) Carcinosarcoma in Barrett's oesophagus: a case report with immunohistological examination. Virchows Arch A Pathol Anat Histopathol 422(5):423–426
44. Olmsted WW, Lichtenstein JE, Hyams VJ (1983) Polypoid epithelial malignancies of the esophagus. AJR 140:921–925
45. Blot WJ, Devesa SS, Kneller RW, Fraumeni JF, Jr (1991) Rising incidence of adenocarcinoma of the esophagus and gastric cardia. JAMA 265:1287–1289
46. Haggett RC (1992) Adenocarcinoma in Barrett's esophagus: A new epidemic? Hum Pathol 23:475–476
47. Agha FP (1985) Barrett carcinoma of the esophagus: clinical and radiographic analysis of 34 cases. AJR 145:41-46
48. Levin MS, Kressel HY, Caroline DF, Laufer I, Herlinger H, Thompson JJ (1983) Barrett esophagus: reticular pattern of the mucosa. Radiology 147:663–617
49. Levin MS, Caroline DF, Thompson JJ, Kressel HY, Laufer I, Herlinger H (1984) Adenocarcinoma of the esophagus: relationship to Barrett mucosa. Radiology 150:305–309
50. Levine MS, Buck JL, Pantongrag-Brown L, Buetow PC, Hallman JR, Sobin LH (1996) Leiomyosarcoma of the esophagus: radiographic findings in 10 patients. AJR 167(1):27–32
51. DeMatos P, Wolfe WG, Shea CR, Prieto VG, Seigler HF (1997) Primary malignant melanoma of the esophagus. J Surg Oncol 66(3):201–206
52. Levine MS, Pantongrag-Brown L, Buck JL, Buetow PC, Lowry MA, Sobin LH (1996) Small-cell carcinoma of the esophagus: radiographic findings. Radiology 199:703–705
53. Bell-Thomson J, Haggitt RC, Ellis FH (1980) Mucoepidermoid and adenoid cystic carcinomas of the esophagus. J Thorac Cardiovasc Surg 79:438–446

Neoplastic and Non-neoplastic Diseases of the Stomach

Angela D. Levy

4.2

Contents

The opinions and assertions contained herein are the private views of the author, and are not to be construed as official, or as reflecting the view of the Department of the Army or Defense.

Introduction

Nonneoplastic and neoplastic diseases of the stomach are commonly encountered in clinical practice. Peptic ulcer disease is one of the most common causes of acute and chronic epigastric pain, while gastric cancer is one of the leading causes of cancer mortality worldwide. Over the past decade, it has been shown that the gram-negative, spiral-shaped bacillus, *Helicobacter pylori* is the major etiologic force behind the most common gastric diseases (peptic ulcer disease, acute and chronic gastritis, gastric carcinoma, and primary gastric lymphoma). Knowledge of the radiologic and pathologic manifestations of this disease spectrum is vital to the initial diagnosis and management of these patients. Currently, management is based not only upon imaging and endoscopic appearance, but also the presence or absence of *H. pylori* infection. In this chapter, the diseases of the stomach associated with *H. pylori* infection are discussed, as well as other disorders in the spectrum of neoplastic and nonneoplastic diseases affecting the stomach.

Part I: Neoplastic Diseases

Gastric Carcinoma

Incidence and Clinical Features

Gastric carcinoma is a worldwide health problem, second only to lung cancer in incidence and mortality worldwide [1]. The highest rates are reported from Japan, China, and other East Asian countries, as well as the countries of Eastern Europe and tropical South America. The lowest rates are in North America, South Central Asia, and North Africa. In the United States, there has been a progressive decline in the incidence of gastric carcinoma since the early 1930's. Currently, gastric carcinoma is the eleventh most common cancer in men and thirteenth in women in the United States [2].

The striking geographic variation in the incidence of gastric carcinoma has traditionally led to the hypothe-

sis that environmental and dietary factors play a leading role in pathogenesis. However, there is convincing scientific and epidemiological evidence that *H. pylori* is the major causative agent in the development of gastric carcinoma, and that chronic inflammation leading to atrophic gastritis is the precursor lesion [3]. In this model, atrophic gastritis leads to metaplasia, dysplasia, and ultimately, carcinoma [4, 5]. The ultimate development of carcinoma is thought to be a multifactorial process that involves infection with *H. Pylori*, genetics, and dietary substances such as *N*-nitroso compounds and salts. Gastric carcinoma also occurs with increased incidence in patients with pernicious anemia that have autoimmune atrophic gastritis. However, in these patients, *H. pylori* is not necessary for the development of carcinoma [6].

As the incidence of gastric carcinoma has been decreasing in the United States, there has been a gradual change in the distribution of carcinoma within the stomach. In the first quarter of the twentieth century, two-thirds of gastric carcinomas were located in the antrum and prepyloric region and 10% or less in the cardia [7]. The frequency of carcinomas in the cardia and proximal third of the stomach has been increasing since the late 1960's, accounting for up to 50% of gastric carcinomas in recently published series [8]. The change in distribution of gastric carcinomas, as well as the decreasing incidence, suggests that the etiology for proximal tumors is probably different from that of distal tumors.

Typically, patients with gastric carcinoma do not develop symptoms until the disease is advanced stage. Early satiety, epigastric fullness, anorexia, and weight loss are common initial symptoms in patients with infiltrating tumors that diminish gastric capacity. Patients with ulcerative tumors may present with pain, fatigue from anemia, melena, or hematemesis. Occasionally, metastatic spread to the left supraclavicular node (Virchow's node) or to the pelvis in female patients (Krukenburg ovarian metastases) will bring a patient to medical attention. Asymptomatic, early stage tumors are more commonly seen in Japan, where vigorous screening programs are in place due to the marked prevalence of gastric carcinoma in the population.

Pathologic Features

Ninety-five percent of gastric carcinomas are adenocarcinomas. Histologically, these are either gland forming or composed tumor cells that have a combination of glandular, trabecular, or solid structures. There are several histologic classifications for gastric adenocarcinoma. The World Health Organization (WHO) and Lauren classifications are the most widely used. The WHO classification divides gastric adenocarcinoma into four histologic subtypes: tubular, papillary, mucinous, and signet-ring cell carcinomas [9].

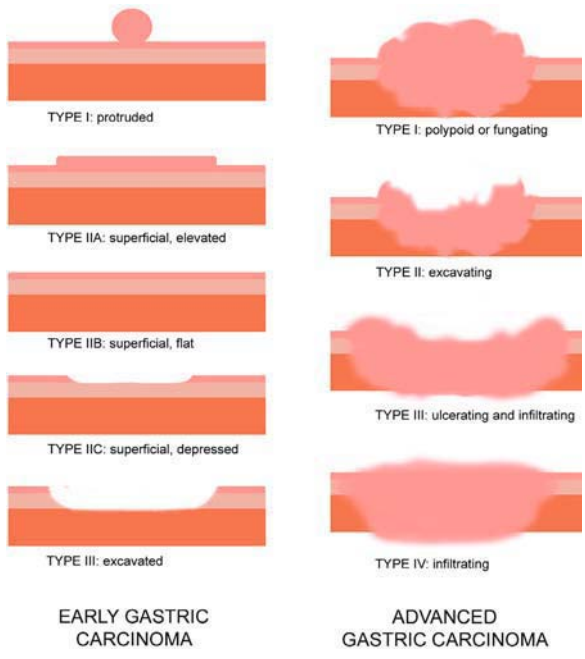

Fig. 1. Macroscopic classification of early and advanced gastric carcinoma

The Lauren classification separates gastric adenocarcinoma into an intestinal and diffuse type. The intestinal type is characterized by well-defined glandular structures histologically and a polypoid or fungating gross morphology. The diffuse type is histologically a poorly differentiated adenocarcinoma with or without signet ring cells. It has an ulcerative or diffusely infiltrating gross morphology [10, 11].

The gross morphologic features of gastric adenocarcinoma have been described for early and advanced gastric carcinoma (Fig. 1). The Japanese Research Society for Gastric Carcinoma established a classification system based upon the macroscopic appearance of early gastric carcinoma at endoscopy [12]. Early carcinoma is defined as tumor limited to the submucosa or mucosa, irrespective of nodal metastasis. Borrmann initially classified the gross morphology of advanced gastric carcinoma. Four patterns were described: polypoid or fungating, excavating, ulcerating and infiltrating, or diffusely infiltrative (Fig. 1) [13]. Patients with advanced carcinomas are usually symptomatic at the time of diagnosis. Infiltrative tumors may elicit a desmoplastic response in the gastric wall, which produces marked rigidity of the stomach. These carcinomas are referred to as scirrhous carcinomas, and have a morphologic appearance that is termed *linitis plastica*.

Radiologic Features

The radiologic appearance of gastric adenocarcinoma parallels the gross morphology of the tumor. Tumors that form polypoid masses (Borrmann type I) typically have acute angles with the gastric wall when visualized on barium or CT evaluation of the stomach (Fig. 2). On barium examination of the stomach, polypoid masses may be smooth, lobulated, or irregular in contour. On single contrast studies, they are filling defects in the barium pool. On air contrast studies, they are intraluminal masses that are etched in barium [14]. When ulceration is the predominant feature (Borrmann type II and III), the ulcer craters are usually irregular with a rind of nodular neoplastic tissue (Fig. 3). Small malignant ulcers may have scalloped, angular, or stellate borders [15]. CT evaluation of these lesions usually reveals a soft-tissue component that is either a focal mass or an infiltrative lesion.

Diffusely infiltrating adenocarcinoma (Borrmann type IV) that is associated with desmoplasia produces a diffusely thickened gastric wall and narrowed lumen. This appearance has been likened to a leather bottle, and is most often referred to as linitis plastica (Fig. 4). Most of these tumors involve the gastric antrum; however, the entire stomach may be involved in severe cases [16, 17]. Rugal fold thickening, mucosal nodularity, ul-

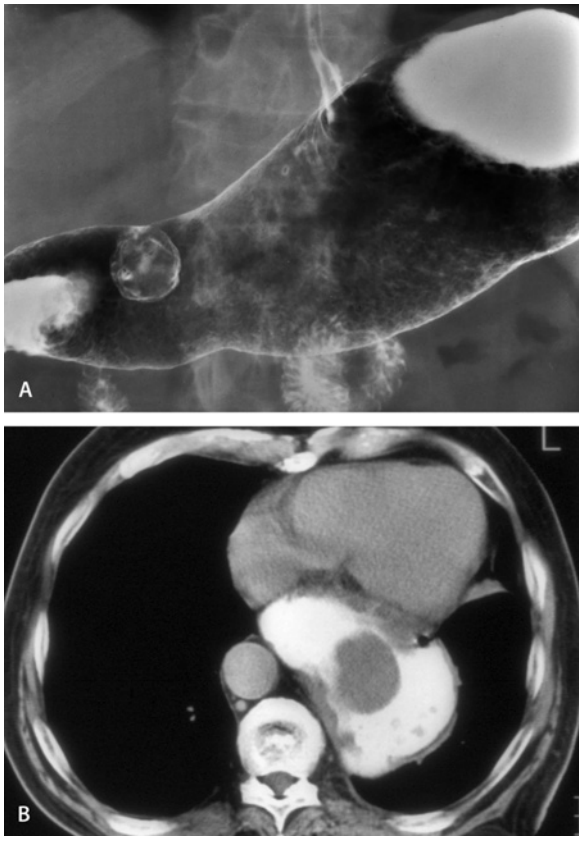

Fig. 2A, B. Polypoid gastric adenocarcinoma. **A** Air-contrast barium examination of the stomach in a 55-year-old man with occult gastrointestinal bleeding shows a 3-cm intraluminal polypoid adenocarcinoma arising from the lesser curvature of the antrum. **B** Intravenous and oral contrast-enhanced CT scan in a 60-year-old man with epigastric pain shows a large hiatal hernia containing a 4.0-cm intraluminal polypoid adenocarcinoma

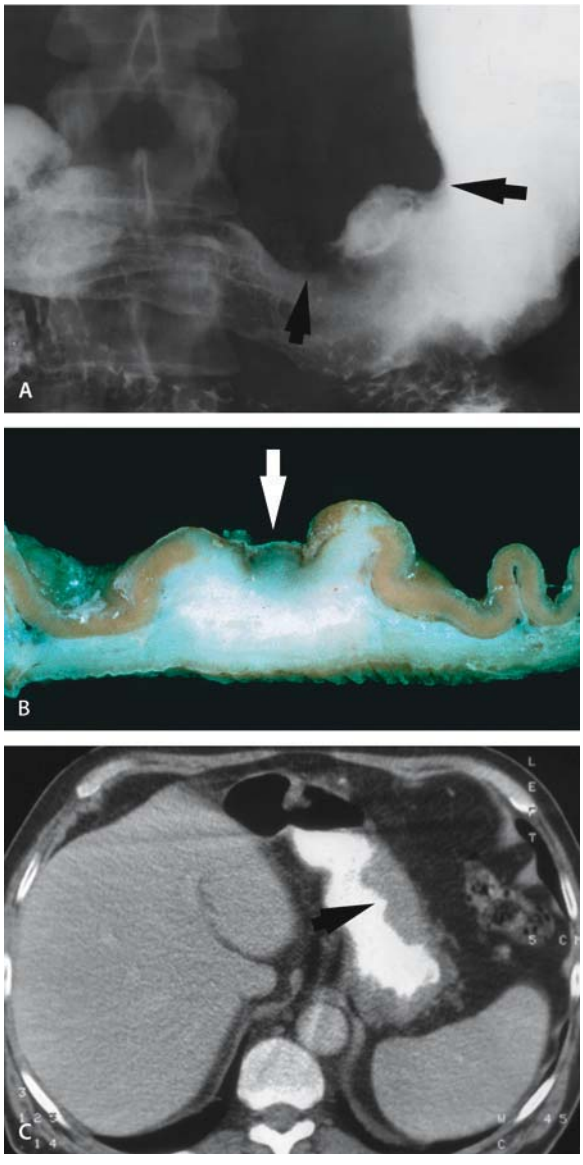

Fig. 3A–C. Ulcerative gastric adenocarcinoma. **A** Single-contrast barium examination of the stomach in a 65-year-old man with hematemesis shows a large irregular ulcer crater on the lesser curvature of the stomach. There is mass effect surrounding the ulcer (*arrows*). **B** Photograph of the resected surgical specimen shows the ulcerative adenocarcinoma in cross-section. The central ulcer crater (*arrow*) is surrounded by white tumor that infiltrates through the adjacent mucosa and submucosa. **C** Intravenous and oral contrast-enhanced CT scan in a 50-year-old male with melena shows an irregularly marginated soft-tissue mass along the greater curvature of the stomach that contains a central ulcer crater (*arrow*)

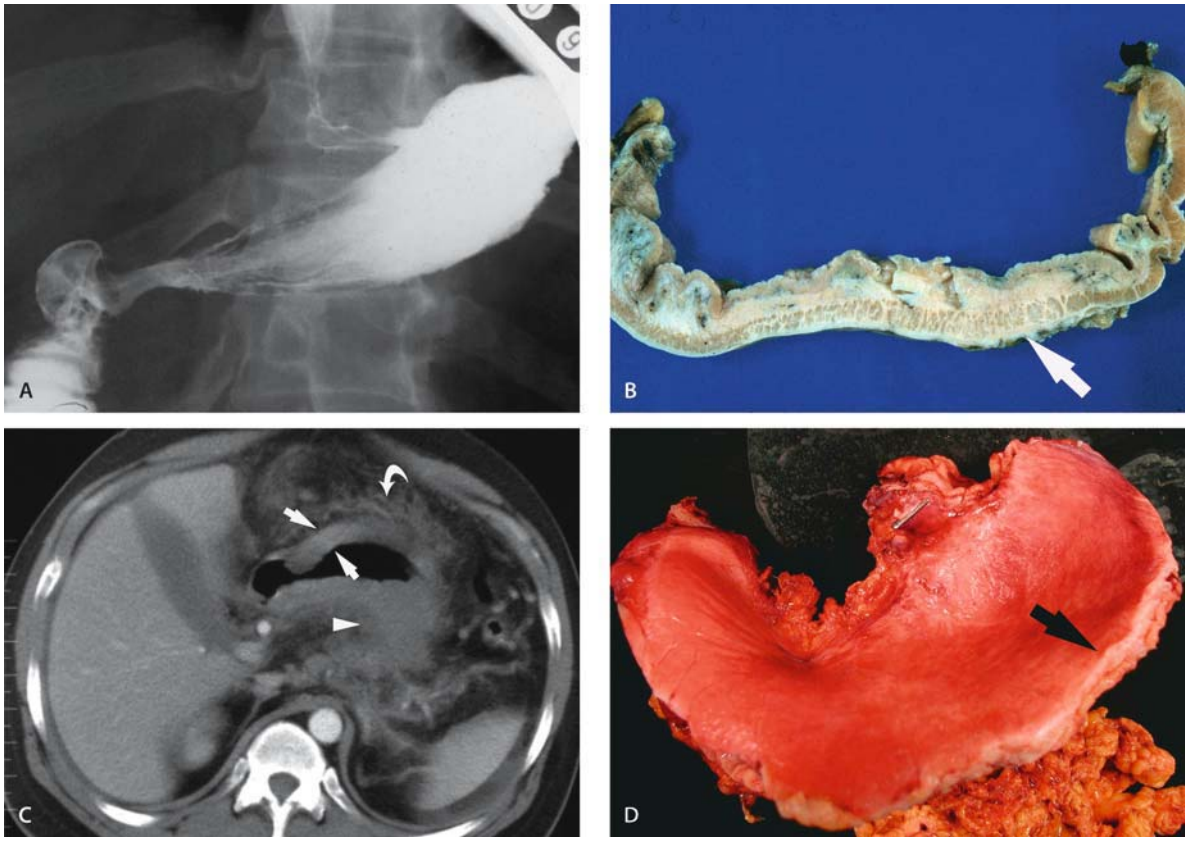

Fig. 4A–D. Infiltrating gastric adenocarcinoma. **A** Air-contrast barium examination of the stomach in a 67-year-old man with early satiety shows poor gastric distension and diffuse, circumferential narrowing the body and antrum of the stomach. There is obliteration of the pylorus. **B** Photograph of the resected surgical specimen shows the gastric wall in cross-section. Pale yellow tumor infiltrates through the mucosa, submucosa, and muscularis propria. Subserosal tumor is also evident (*arrow*). **C** Intravenous contrast-enhanced CT scan in a 77-year-old woman with early satiety shows soft-tissue thickening of the gastric wall (*arrows*). Extraserosal spread of tumor into the greater omentum (*curved arrow*) and lesser sac (*arrowhead*) is shown by soft-tissue density within the perigastric fat. A small lymph node is also present in the greater omentum. **D** Photograph of the resected surgical specimen shows the opened stomach that has effaced rugal folds from tumor that has infiltrated throughout the wall (*arrow*)

ceration, and fold distortion may be the predominant features of a scirrhous carcinoma that involves the proximal stomach [18]. On CT, these tumors appear as diffuse mural thickening (Fig. 4C).

Helical CT technology has greatly improved preoperative evaluation of patients with gastric adenocarcinoma. Adequate distention the stomach with water (500–750 ml) optimizes visualization of the gastric wall during the arterial phase of contrast enhancement [19]. Although CT is useful in identifying hematogenous liver metastasis and spread to adjacent organs such as the omentum, pancreas, and spleen, CT has not been proven to be accurate in preoperative staging. The major limitations of CT include the following: identifying the degree of gastric wall involvement; identifying small foci of peritoneal metastasis; and, identifying tumor in normal sized nodes [15].

Gastric Lymphoma

Incidence and Clinical Features

The incidence of gastric lymphoma has been steadily increasing over the past two decades, approaching 10% of all gastric neoplasms in recent published series [20]. The rising incidence reflects the improved identification and understanding of gastric lymphoma and the recognition that many of the lesions previously diagnosed as pseudolymphoma are neoplastic [21]. In addition, there is an increased incidence of lymphoma in the growing population of immunosuppressed individuals. The stomach is the most common location for gastrointestinal lymphoma in western countries, whereas the small bowel is the most common site in the Middle East and Mediterranean [22]. Gastrointestinal lymphoma is almost exclusively non-Hodgkin lymphoma. It is considered to be primary when the patient presents with

the bulk of disease confined to the gastrointestinal tract. The gastrointestinal tract is also one of the most frequent sites of secondary involvement in patients with primary nodal lymphoma.

There is a wide age range at presentation for gastric lymphoma, however most patients are over the age of 50 years [20]. Patients with low-grade gastric lymphoma typically have a long history of nonspecific symptoms such as dyspepsia, nausea, and vomiting [20]. In general, the presenting signs and symptoms in patients with high-grade lymphoma parallel tumor morphology. Patients with ulcerating tumors have gastrointestinal bleeding or anemia, and those with infiltrating tumors have pain, nausea, vomiting, early satiety, anorexia, or weight loss.

Pathologic Features

Lymphomas are currently classified according to the WHO classification of lymphoid neoplasms introduced in 2000 [23, 24]. The majority of gastric lymphoma is high-grade B-cell lymphoma that develops from low-grade mucosal-associated lymphoid tissue (MALT) lymphoma. Low-grade gastric lymphomas are almost always MALT lymphomas, which account for 20% to 30% of all gastric lymphomas [25, 26]. Although there has been conflicting evidence in the literature, most authors agree that gastric MALT lymphoma is derived from MALT that accumulates in response to *H. pylori* infection [27]. Treatment to eradicate *H. pylori* causes tumor resolution or regression in 75% of cases [28].

Gastric lymphoma is most commonly found in the antrum. Low-grade MALT lymphoma is a superficial, infiltrating lesion that produces a nodular gastric mucosa. Histologically, the neoplastic cells of MALT lymphoma infiltrate between pre-existing lymphoid follicles and may be difficult to differentiate from a florid gastritis [20]. High-grade B-cell lymphoma destroys the normal gastric glandular architecture and may infiltrate throughout the gastric wall. High-grade B-cell lymphoma may form polypoid masses, infiltrative lesions with focal ulceration, or, occasionally, annular lesions [11].

Radiologic Features

The features of low-grade MALT lymphoma on barium evaluation of the stomach includes mucosal nodularity, mucosal ulceration, rugal fold thickening, prominent areae gastricae, and focal masses (Fig. 5) [29, 30]. The lesions of MALT lymphoma most commonly involve the gastric antrum and may be multifocal [31, 32]. In most cases, the radiologic features of MALT lymphoma are indistinguishable from *H. pylori* gastritis and early gastric carcinoma. CT may demonstrate segmental or diffuse gastric wall thickening (Fig. 6A).

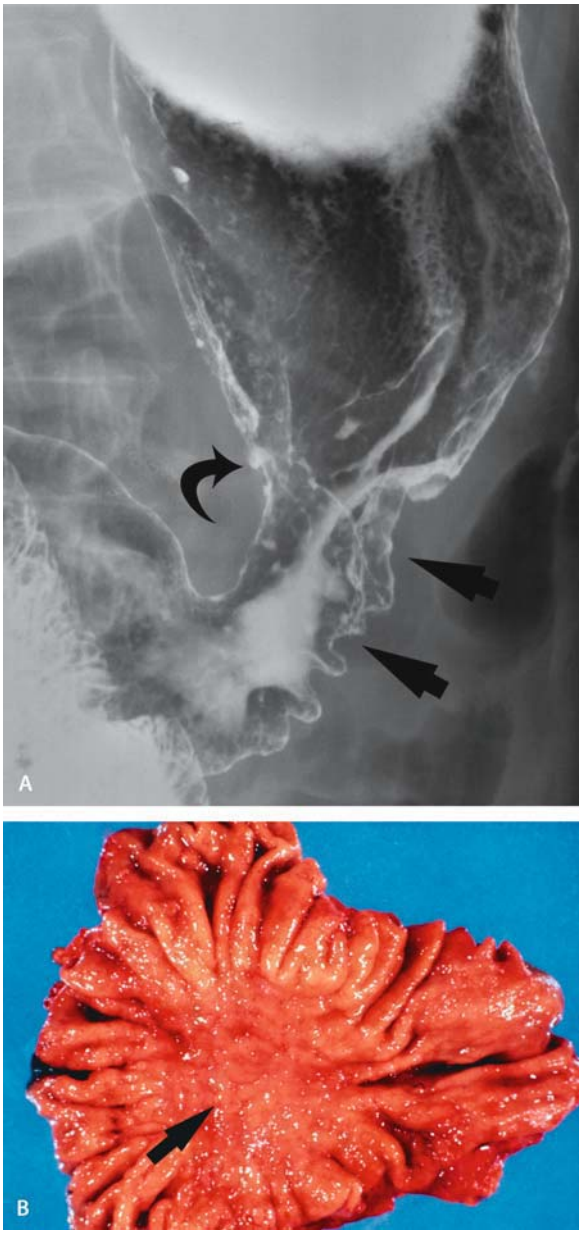

Fig. 5A,B. Low-grade MALT lymphoma in a 52-year-old woman with epigastric pain. **A** Air-contrast barium examination of the stomach shows nodularity and fold thickening along the greater curvature of the antrum. Small ulcers are present along the lesser curvature (*curved arrow*). **B** Photograph of the resected surgical specimen rugal fold thickening and nodular effacement of the gastric mucosa (*arrow*)

High-grade gastric lymphomas are infiltrative, polypoid, ulcerative, or nodular masses [33]. Infiltrative lymphomas most commonly manifest as enlarged lobulated rugal folds on barium or CT examination of the stomach (Fig. 6B). Rigidity and narrowing resulting in linitis plastica has been reported as a manifestation of infiltrating gastric lymphoma [34]. On CT, the attenuation of lymphoma is typically homogeneous. Rarely, low

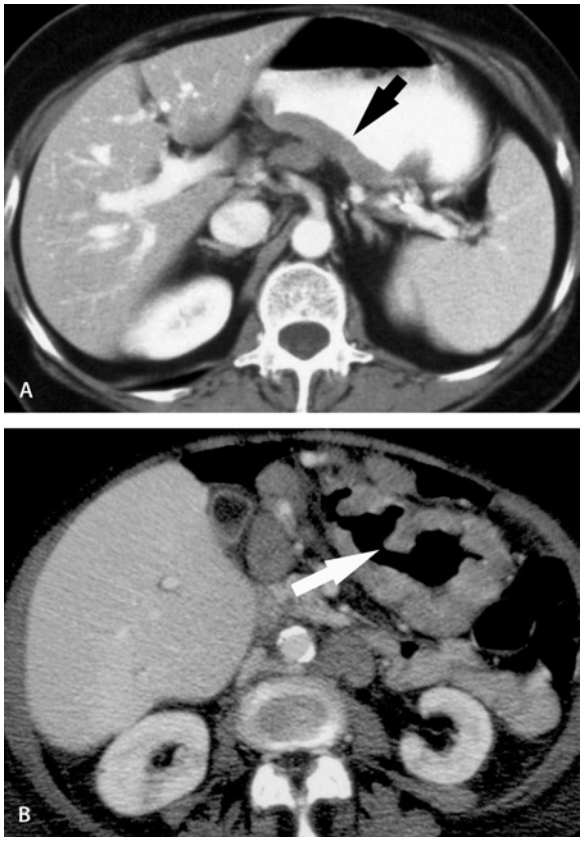

Fig. 6A, B. CT features of gastric lymphoma. **A** Low-grade MALT lymphoma in a 45-year-old woman with epigastric pain. Intravenous and oral contrast-enhanced CT scan shows focal wall thickening along the posterior gastric body (*arrow*). There is an adjacent perigastric lymph node. **B** High-grade diffuse B-cell lymphoma in a 60-year-old man with anorexia and weight loss. Intravenous and oral contrast-enhanced CT scan shows diffuse wall thickening and rugal fold thickening (*arrow*). There are multiple perigastric and retroperitoneal lymph nodes

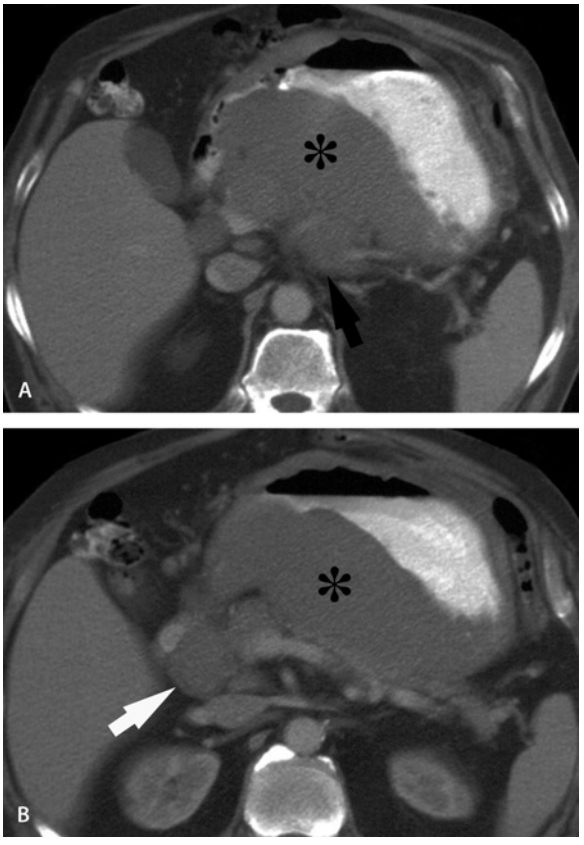

Fig. 7A,B. High-grade diffuse B-cell lymphoma in a 62-year-old woman with abdominal pain, anorexia, and weight loss. (**A**, **B**) Intravenous and oral contrast-enhanced CT scan shows diffuse gastric wall thickening that is marked along the posterior body of the stomach (*asterisk*). There is bulky perigastric and retroperitoneal adenopathy (*arrows*)

attenuation regions may be present in lymphoma that has an aggressive histology. Perigastric, omental, and retroperitoneal adenopathy is frequently identified in patients with high-grade and advanced staged lymphoma (Fig. 7). It may difficult to differentiate gastric lymphoma from gastric adenocarcinoma on imaging studies alone because they have similar morphologic features. CT features that suggest the diagnosis of lymphoma include marked gastric wall thickening, exceeding 4 cm, bulky adenopathy, and adenopathy that extends below the renal hilum (Fig. 7) [35].

Gastrointestinal Stromal Tumor

Incidence and Clinical Features

Gastrointestinal stromal tumors (GISTs) are the most common mesenchymal neoplasms of the gastrointestinal tract. They occur most frequently in the stomach and account for 2% to 3% of gastric malignancies. The best defining feature of GISTs is their immunohistochemical expression of KIT (CD117), a tyrosine kinase growth factor receptor. KIT immunoreactivity distinguishes GISTs from other mesenchymal neoplasms such as leiomyomas, leiomyosarcomas, schwannomas, and neurofibromas. The expression of KIT by GISTs has led some authors to postulate that GISTs arise from primitive stem cells that phenotypically resemble the native KIT-positive gut pacemaker cell or interstitial cell of Cajal [36].

Most patients with GISTs are over the age of 50 years at the time of diagnosis [37]. Some studies in the medical literature show a slight increased incidence of GISTs in the male population, but others show no gender predilection. The presenting signs and symptoms depend upon the anatomic location and size of the tumor [38]. Patients with gastric GISTs may present with evidence

of bleeding or anemia from mucosal ulceration. Other signs and symptoms include abdominal pain, nausea, vomiting, abdominal distension, and a palpable epigastric mass.

Pathologic Features

The majority of GISTs arise from the muscularis propria of the stomach wall and have a propensity for exophytic growth. Therefore, most tumors will have an dominant extramural component that projects into the abdominal cavity [39]. Smaller sized tumors may be primarily intramural in location, or have a component that extends into the gastric lumen. On gross pathology, focal areas of hemorrhage, cystic degeneration, and necrosis are commonly present. Occasionally, extensive hemorrhage and degeneration may result in cavitation, a large fluid component within the tumor, and fluid-fluid levels. At light microscopy, the majority gastric GISTs are composed of spindle cells (70% to 80%), and the remaining are composed of epithelioid cells (20% to 30%) [40]. By definition, GISTs are positive for KIT (CD 117) on immunohistochemical staining. Many are also positive for CD34.

An estimation of biologic behavior (benign versus malignant) is made based upon tumor size and mitotic rate. It is generally accepted that gastric GISTs that are less than 5-cm in largest dimension and have five or fewer mitoses per 50 consecutive high power fields (HPF) have low risk for metastasis and are probably benign. Those that are larger than 10-cm with more than five mitoses per 50 HPF are considered malignant, while those that fall in between these categories have uncertain malignant potential or intermediate risk for metastasis or recurrence. GISTs with marked mitotic activity (more than 50 mitoses per 50 HPF) are considered high-grade malignancies with an extremely aggressive clinical behavior [41]. In the stomach, benign GISTs are approximately three times more common than malignant GISTs [37].

Radiologic Features

The majority of gastric GISTs are located in the body of the stomach (75%), followed by the cardia and fundus (14%), and antrum (11%) [42]. On barium examination of the stomach, GISTs demonstrate the classic features of a mural mass: obtuse or right angles with the gastric wall when viewed in profile (Fig. 8) and a smoothly circumscribed mass when viewed en face. Focal ulceration on the surface of the tumor may be present.

CT shows extragastric extension in 86% of cases [42]. The tumor may extend to involve the perigastric fat, gastrohepatic ligament, gastrosplenic ligament, greater

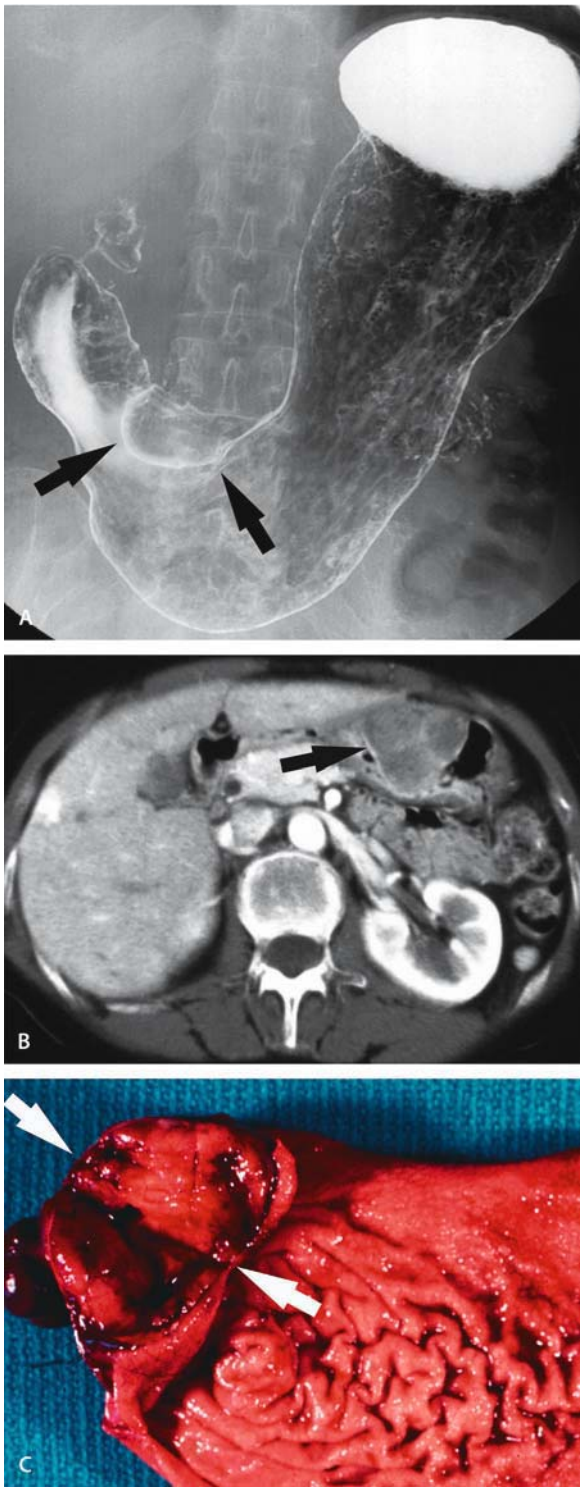

Fig. 8A–C. Malignant GIST in a 65-year-old woman with epigastric pain. **A** Air-contrast barium examination of the stomach shows a smoothly marginated mural mass (*arrows*) arising from the lesser curvature of the gastric body producing obtuse angles with the gastric wall. **B** Intravenous contrast-enhanced CT scan shows a heterogeneously low attenuation mass (*arrow*) arising from the gastric wall. **C** Photograph of the opened resected surgical specimen shows the intramural GIST with focal hemorrhage on its cut surface

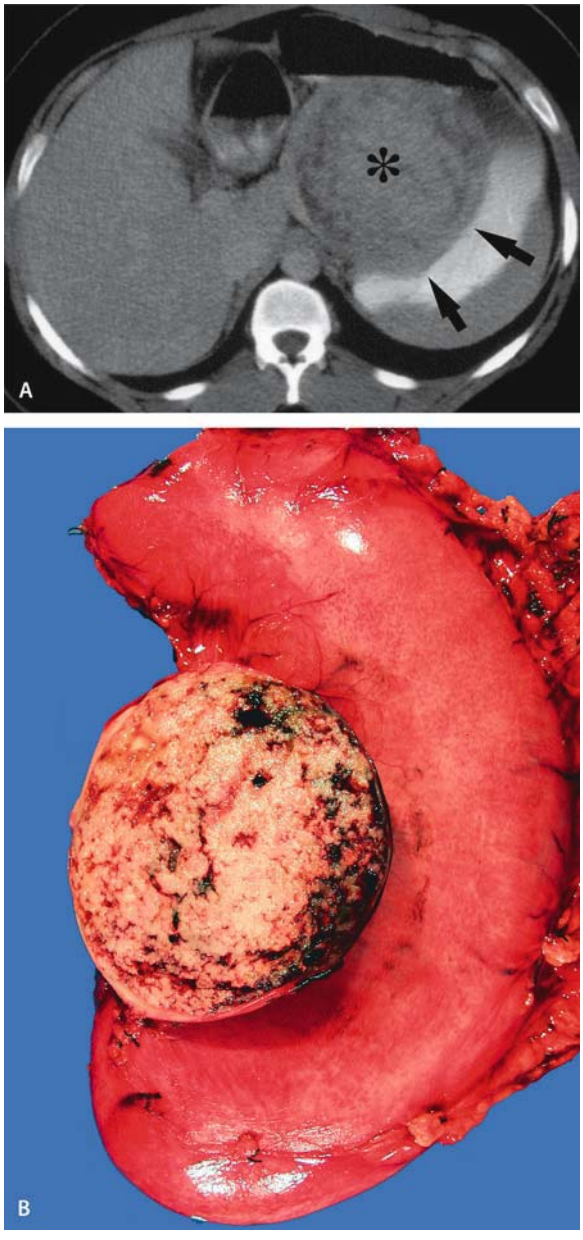

Fig. 9A, B. Malignant GIST in a 54-year-old woman with anorexia and a palpable epigastric mass. **A** Unenhanced CT scan with oral contrast shows a well-circumscribed heterogeneous mass (*asterisk*) adjacent to the lesser curvature of the stomach. Mural thickening along the lesser curvature (*arrows*) proves its gastric origin. **B** Photograph of the resected surgical specimen shows foci of hemorrhage on cut surface of the GIST adjacent to the unopened stomach

omentum, or posteriorly into the lesser sac. A gastric origin may be difficult to appreciate on CT of large, predominantly exophytic GISTs. Subtle gastric wall thickening may be the clue to its origin (Fig. 9). Heterogeneous enhancement is typically identified because focal areas of hemorrhage and necrosis are commonly present (Fig. 10). When cavitation occurs, there is usually communication of the tumor with the gastric lumen such that air and/or oral contrast are present within the tumor cavity. Metastatic lymphadenopathy is not a feature of malignant GISTs. Metastasis, if present, will be to the liver or peritoneal cavity [38].

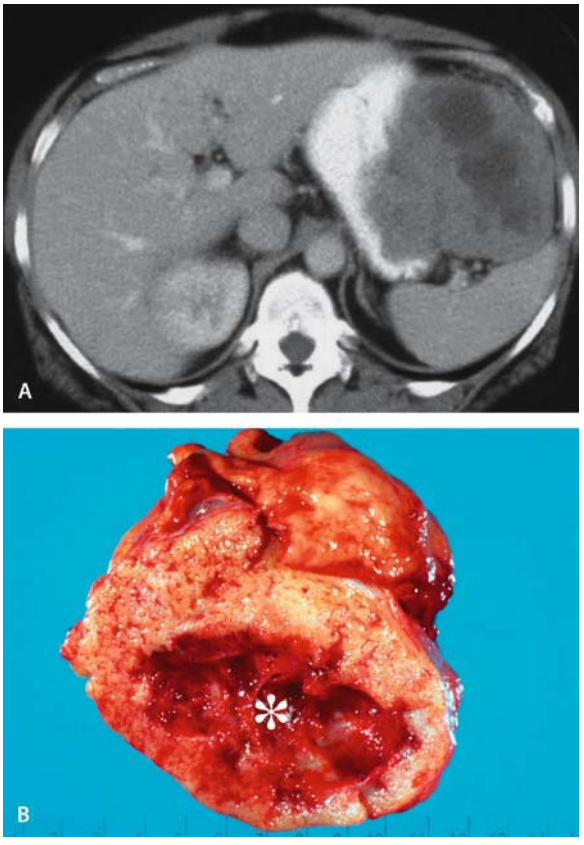

Fig. 10A, B. Malignant GIST in a 59-year-old man who present gastrointestinal bleeding and a palpable left upper quadrant mass. **A** Intravenous and oral contrast enhanced CT scan shows a large left upper quadrant mass with containing focal areas of low attenuation. The mass arises from the gastric wall and has intraluminal and extramural components. **B** Photograph of the cut surface of the resected surgical specimen shows a large area of hemorrhage within the tumor (*asterisk*)

Carcinoid

Incidence and Clinical Features

Gastric carcinoids are rare, accounting for 2% to 3% of all gastrointestinal carcinoids and 0.3% of all gastric neoplasms [43]. Three distinct types of gastric carcinoid have been recognized. Type I gastric carcinoid is associated with autoimmune chronic atrophic gastritis and occurs more commonly in women (M:F, 1:2.5). Type II gastric carcinoid is associated with Multiple Endocrine Neoplasia Type I (MEN-I) and Zollinger-Ellison syndrome, and has no gender predilection. Type III

gastric carcinoid is sporadic, and is not associated with hypergastrinemia or autoimmune chronic atrophic gastritis. Type III gastric carcinoids are more common in men than women (M: F, 2.8:1) [44].

The clinical presentation and biologic behavior of gastric carcinoids varies depending on the underlying etiology and the presence or absence of chronic atrophic gastritis. Carcinoids associated with chronic atrophic gastritis and hypergastrinemia (Type I and II) are usually small, multiple, and typically have benign biologic behavior. Solitary, sporadic carcinoids have a more aggressive clinical course, often presenting with clinical features similar to carcinoma: gastrointestinal hemorrhage, gastric outlet obstruction, and metastatic disease [11].

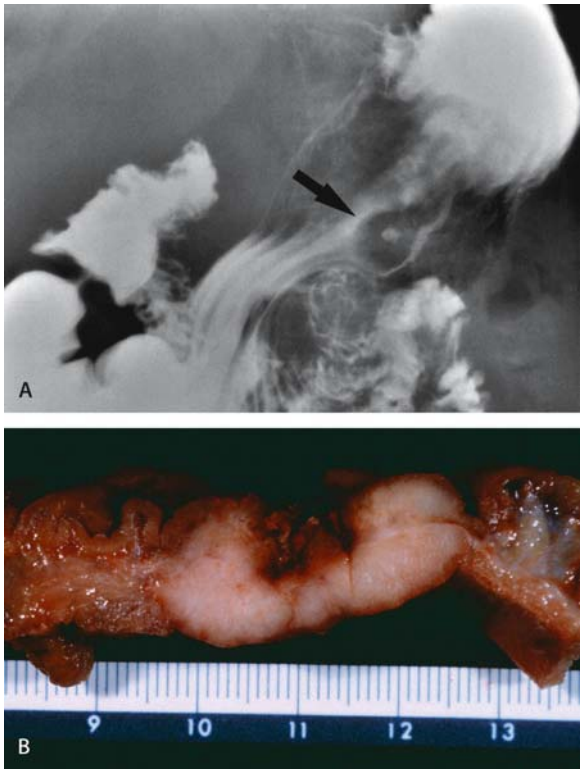

Fig. 11A, B. Solitary carcinoid in a 54-year-old man with melena. **A** Air-contrast barium examination of the stomach shows a smoothly circumscribed "bull's-eye" lesion in the body of the stomach (*arrow*). **B** Photograph of the resected surgical specimen shows the intramural mass of carcinoid cut in cross-section. Central ulceration is present along the mucosal surface

Pathologic Features

Gross pathology reveals carcinoids to be submucosal masses that often extend into the gastric lumen with attenuation of the overlying mucosa. As they enlarge, an erythematous depression or ulceration forms on the mucosal surface of the tumor [11]. Type I and II carcinoids are often frequently small (1 to 3 mm) and multiple with extensive thickening of the gastric wall due to a hypertrophic-hypersecretory gastropathy that is secondary to hypergastrinemia. Histologically, gastric carcinoids are composed of small round or polygonal neuroendocrine cells that form ribbons, festoons, rosettes, or trabecular patterns.

Radiologic Features

Carcinoids have a variety of radiologic appearances. Classically, they manifest as smoothly marginated submucosal masses on barium evaluation of the stomach. If central ulceration is present, they may have a "bulls-eye" appearance (Fig. 11). However, they may be single or multiple pedunculated polypoid lesions (Fig. 12) or large ulcerative masses [45]. CT may demonstrate en-

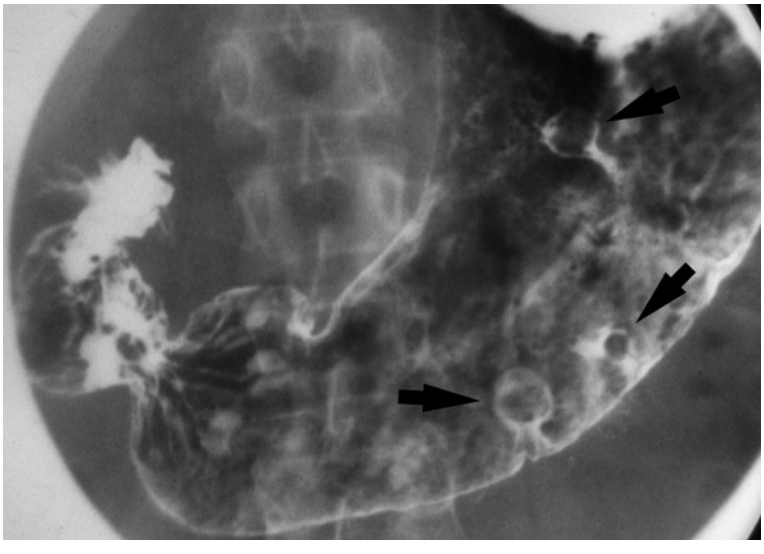

Fig. 12. Multiple gastric carcinoids in a 40-year-old woman with chronic atrophic gastritis. Air-contrast barium examination of the stomach shows multiple, intraluminal pedunculated, polypoid masses (*arrows*)

hancing nodular masses and polypoid thickening of the gastric wall in those patients with hypergastrinemia [46, 47].

Metastasis

Gastric metastases are uncommon. The incidence at autopsy in cancer patients is 1.7% [48]. Metastasis may be secondary to hematogenous dissemination or direct extension from adjacent organs. In the case of hematogenous metastasis, gastric involvement generally represents a late stage of disease when there is evidence of hematogenous metastasis to multiple organs. Melanoma, lung, and breast cancer are common primary sites. Clinically, patients may present with bleeding, pain, vomiting, or anorexia. Gross pathology and radiologic evaluation of the stomach show gastric metastases as infiltrative lesions producing a linitis plastica pattern, ulcerating masses, or polypoid masses [49]. Primary carcinomas of the colon, esophagus, and pancreas may involve the stomach by direct extension or lymphatic spread. Occasionally, omental metastases from carcinomas of the gastrointestinal tract or pelvis may encase the stomach.

Miscellaneous Neoplasms

Benign polypoid tumors of the stomach are common. These are most often found incidentally during radiologic or endoscopic evaluation of the stomach. Hyperplastic polyps are the most common benign epithelial neoplasms of the stomach. Hyperplastic polyps are typically found in the antrum in the setting of *H. pylori* gastritis [9]. On double contrast barium examination of the stomach, hyperplastic polyps are usually 5 mm to 10 mm in size, smooth, round, sessile, or pedunculated polyps [50]. Other benign polypoid lesions include adenomas and fundic gland polyps. Gastric adenomas may undergo malignant transformation to adenocarcinoma.

Leiomyomas, leiomyosarcomas, gastrointestinal autonomic nerve tumors, schwannomas, and neurofibromas are mesenchymal neoplasms that are rarely seen within the stomach. Radiologically, these are intramural tumors that have an appearance identical to GISTs. Histologically, they are distinctly different tumors and should be differentiated from GISTs because clinical and surgical management differs. Rarely, other mesenchymal neoplasms such glomus tumors, lipomas, granular cell tumors, hemangiomas, and lymphangiomas may be found in the stomach.

In the setting of human immunodeficiency virus (HIV) infection, the rare vascular neoplasm, Kaposi sarcoma may involve the gastrointestinal tract. The stomach and duodenum are the most common sites of involvement. Single or multiple submucosal masses are typically present. They may have central ulceration, which results in a bull's eye appearance on air-contrast barium examination of the stomach. Rarely, an infiltrative form may manifest as thick, nodular rugal folds.

Part II: Nonneoplastic Diseases

Peptic Ulcer Disease

Incidence and Clinical Features

Peptic ulcer disease is very common, affecting 10% of adults in western countries. *H. pylori* infection and the use of nonsteroidal anti-inflammatory drugs (NSAIDS) are the two principal etiologies of peptic ulcers. Less commonly, peptic ulcers occur in the setting of hypergastrinemia, such as Multiple Endocrine Neoplasia Type I and Zollinger-Ellison syndrome. *H. pylori* infects in the mucous layer of the gastric and/or duodenal mucosa, preferring the gastric antrum and duodenal bulb. The prevalence of *H. pylori* infection increases with age and lower socioeconomic status. Approximately 10% of the United States population under the age of 30 is infected with *H. pylori*, whereas 60% of the population over the age of 60 is infected [51]. *H. pylori* is found in 90% of patients with duodenal ulcers, 80% of patients with gastric ulcers, and 100% of patients with chronic active gastritis [52, 53].

The mechanism for gastric ulceration in the setting of NSAIDS is two-fold. Principally, NSAIDS produce ulceration because they block the production of prostaglandin, which has a cytoprotective effect on the gastric mucosa. NSAIDS are also local irritants to the gastric mucosa producing direct mucosal injury (erosions, hemorrhage, and ulcers) in 15% to 20% of patients who use them chronically [54].

The most consistent clinical symptom of peptic ulcer disease is epigastric pain. Commonly, the pain occurs at night, several hours after meals, and may be relieved by food intake. Some patients may complain of right upper quadrant, chest, or back pain. Other signs and symptoms include bloating, nausea, and vomiting. Bleeding develops in approximately 20% of patients. Occasionally, patients will present with signs and symptoms of gastric outlet obstruction from localized edema or peritonitis secondary to perforation.

Pathologic Features

Benign peptic ulcers usually have circumscribed, round, or oval ulcer craters on gross inspection. Edematous, congested folds radiate toward the ulcer crater. In con-

trast, malignant gastric ulcers tend to have irregular margins, rolled edges, and radiating folds that are nodular, clubbed, and do not converge toward the crater. Histologically, acute benign ulcers are characterized by an inflammatory infiltrate and granulation tissue replacing the denuded gastric epithelium. Chronic benign ulcers typically have a zone of inflammation, coagulation necrosis, granulation tissue, and fibrosis in the ulcer base [55].

Radiologic Features

The majority of benign gastric ulcers are located on the lesser curvature and the posterior wall of the body and antrum of the stomach. Ulcers vary in size and shape. Giant ulcers are those greater than 3 cm. Ulcer craters may be round, oval, linear, or serpiginous. When viewed in profile, on double contrast barium evaluation of the stomach, ulcer craters fill with barium and project beyond the mucosal margin of the stomach. Other features of benign ulcers include: Hampton line, ulcer mound, ulcer collar, and smooth radiating folds (Fig. 13) [56]. Hampton line is produced from the undermining of the mucosa surrounding the ulcer crater (Fig. 13B). The ulcer mound is a thick radiolucent ring surrounding the ulcer that is produced by edema (Fig. 13D).

Although there is a trend to perform endoscopy and biopsy on all ulcers that are detected radiographically, it has been demonstrated that almost all ulcers that have a radiographically benign appearance are benign [57, 58], therefore radiographic follow up is appropriate for these patients. Malignant ulcers generally show one or more of the following features: irregular crater in a mass, nodular or clubbed radiating folds, projection of the ulcer crater inside a mass, nodular ulcer margins (Fig. 14). Equivocal features on double contrast examinations are ulcers that have an irregular shape, asymmetry of mass effect, enlarged areae gastricae, and a location on the greater curvature. Patients that have ulcers with malignant or equivocal features should proceed to endoscopic biopsy for definitive diagnosis.

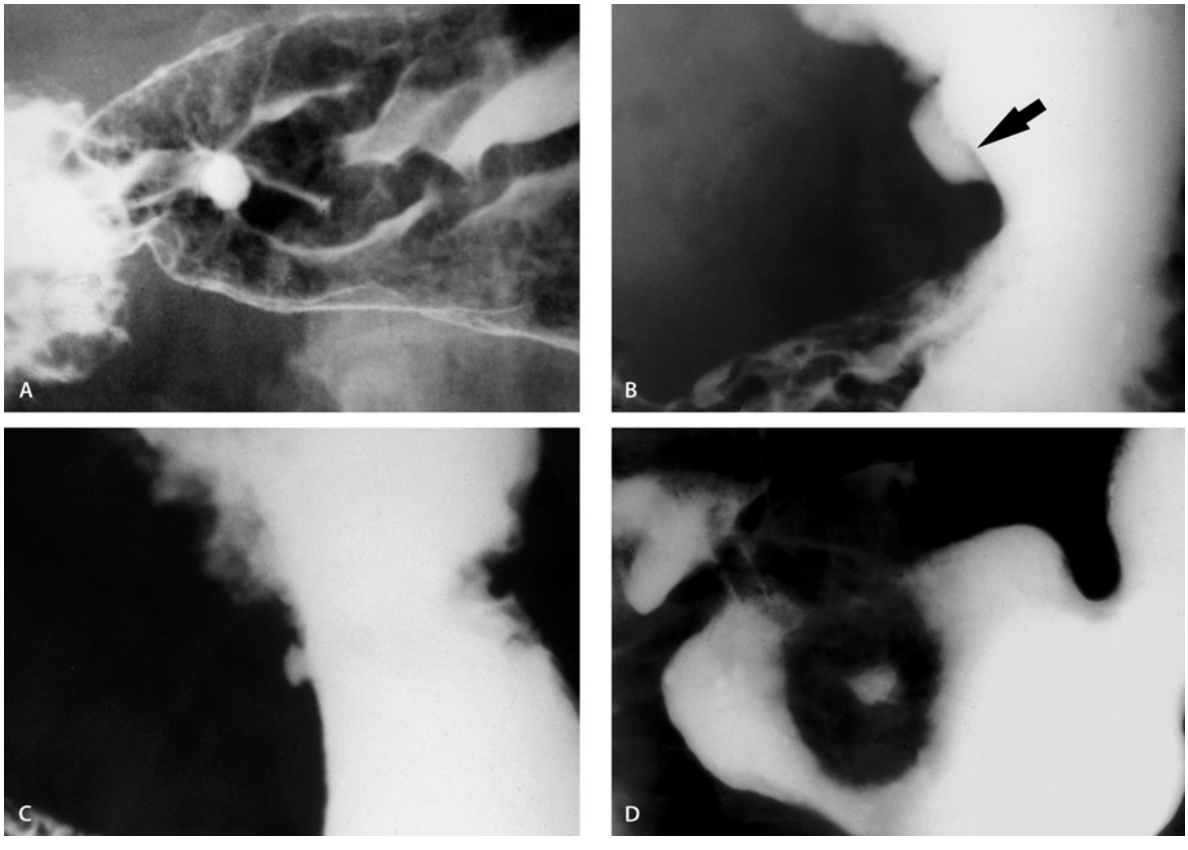

Fig. 13A–D. Features of benign gastric ulcers on barium examination of the stomach. **A** Benign antral ulcer with smooth, radiating folds. **B** Benign lesser curvature ulcer shown in profile reveals a radiolucent Hampton line (*arrow*). **C** Benign lesser curvature ulcer shown in profile reveals collar-button morphology. **D** Benign antral ulcer shows a large radiolucent edema mound surrounding the ulcer crater. (Courtesy of Dr. Charles Rohrmann, University of Washington, Seattle, WA)

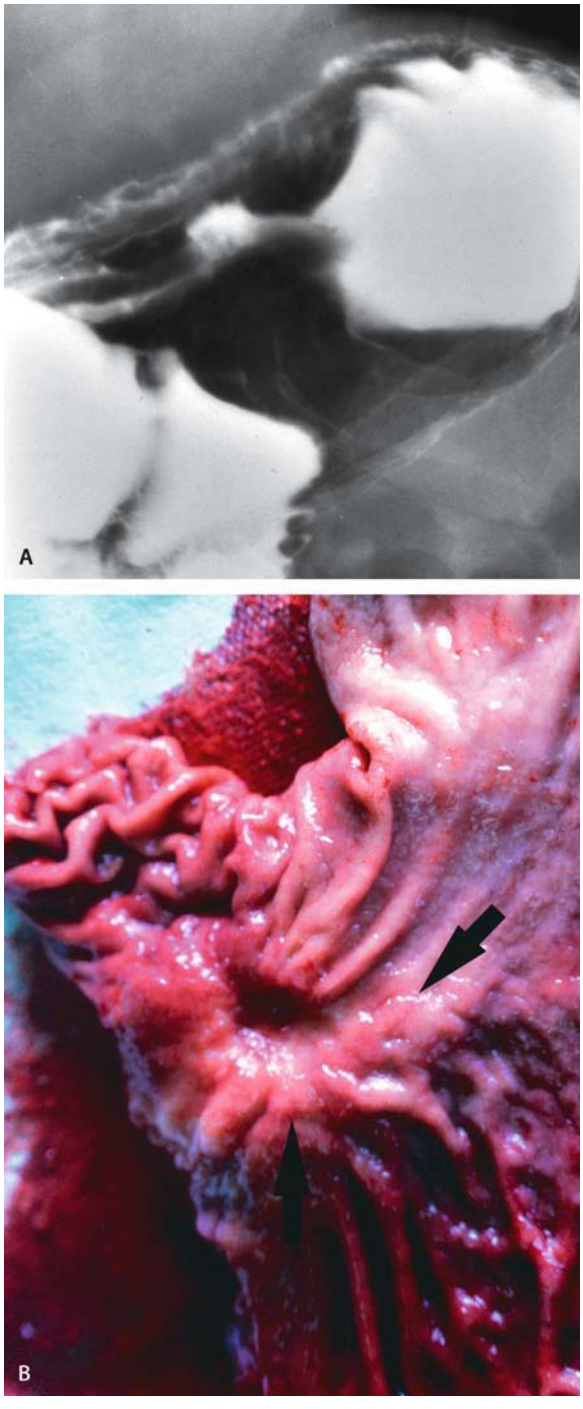

Fig. 14A, B. Malignant gastric ulcer in a 65-year-old male with epigastric pain. **A** Air-contrast barium examination of the stomach shows an irregular ulcer crater in the proximal stomach. **B** Photograph of the resected surgical specimen shows thick, nodular folds and a nodular tumor margin surrounding the ulcer (*arrows*)

Zollinger-Ellison Syndrome

Incidence and Clinical Features

Zollinger-Ellison syndrome (ZES) is the clinical syndrome produced by a gastrin-secreting neuroendocrine tumor (gastrinoma). Patients typically have elevated gastrin levels and one or more benign peptic ulcers of the stomach, duodenum, or proximal small intestine. Approximately 0.1 to 1.0% of peptic ulcer disease in the United States is due to ZES [59]. The most common presenting symptom in patients with ZES is epigastric pain from peptic ulcers. Persistent, severe diarrhea secondary to hypergastrinemia occurs in 30% of patients [59].

Zollinger-Ellison syndrome is most commonly associated with sporadic gastrinomas, but is also seen in the setting MEN-I syndrome. Gastrinomas occurring in the sporadic form of Zollinger-Ellison syndrome are most commonly primary to the pancreas (75%), but may be

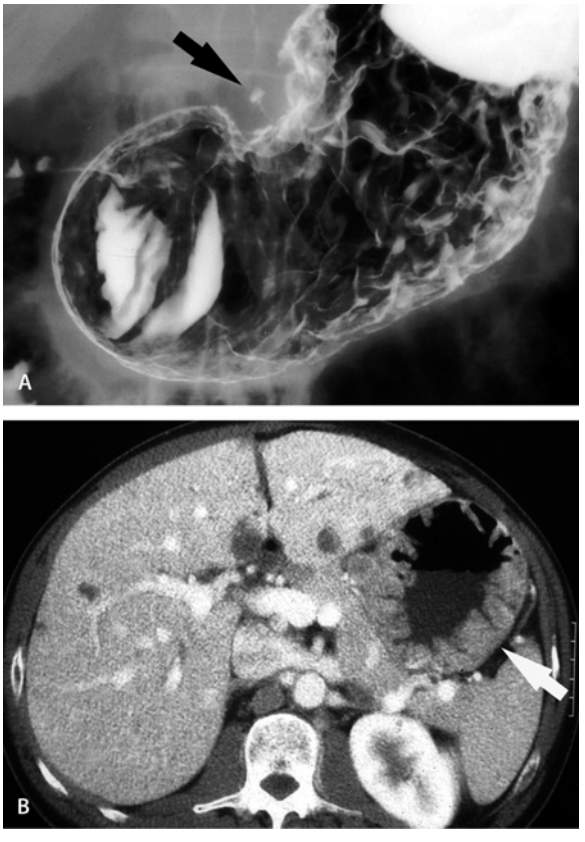

Fig. 15A, B. Zollinger-Ellison syndrome secondary to a malignant gastrinoma in a 39-year-old male with abdominal pain and a history of recurrent peptic ulcers. **A** Air-contrast barium examination of the stomach shows thick gastric folds and a peptic ulcer (*arrow*) with surrounding edema on the lesser curvature of the stomach. **B** Intravenous contrast-enhanced CT scan shows a thickened gastric wall (*arrow*) and liver metastasis. The primary gastrinoma is not shown in this image

found in extrapancreatic locations such as the duodenum (15%), liver, ovary, and lymph nodes [60]. The incidence of malignancy in gastrinomas is 60%. Surgery is the most effective therapy for these patients if they do not have evidence of metastatic disease. Gastrinomas in MEN-I syndrome are frequently multiple. The management of MEN-I patients is controversial since these patients are rarely cured by surgery and the gastrinomas of MEN-I have a lower rate of malignancy [59].

Radiologic Features

Gastric and duodenal ulcers, excessive gastric secretions, and thick gastric and duodenal folds are radiologic findings that may be seen in patients with ZES. However, one of the most important indications for radiologic evaluation of patients with ZES is preoperative localization of the gastrinoma and screening for metastatic disease (Fig. 15). CT and magnetic resonance imaging (MR) are useful modalities in the preoperative evaluation of ZES patients [61]. Somatostatin receptor scintigraphy has been shown to be a very effective tool for localization of the primary tumor and detection of occult metastatic disease preoperatively [62, 63].

Ménétrier Disease

Incidence and Clinical Features

Ménétrier disease is an uncommon and irreversible idiopathic disorder characterized by hypertrophy of the gastric folds. Ménétrier disease is most commonly seen in adult men, aged 50 to 70 years [55]. Epigastric pain, bloating, vomiting, anorexia, and weight loss are the most common presenting complaints. Severe hypoproteinemia and malnutrition may result from hyposecretion of gastric acids and hypersecretion of mucous in severe cases. Ménétrier disease is rare in the pediatric population. When it occurs, the disease is often reversible. Autoimmune reaction, CMV infection, and allergy are thought to play a role in the pediatric form of the disease.

Pathologic Features

Ménétrier disease is characterized by hypertrophy and elongation of the foveolar compartment of the gastric mucosa. The foveolar cells produce excessive mucin. Usually, there is concomitant atrophy of the glandular compartment. At gross pathology, the mucosal fold enlargement resembles the convolutions of the cerebral cortex [55].

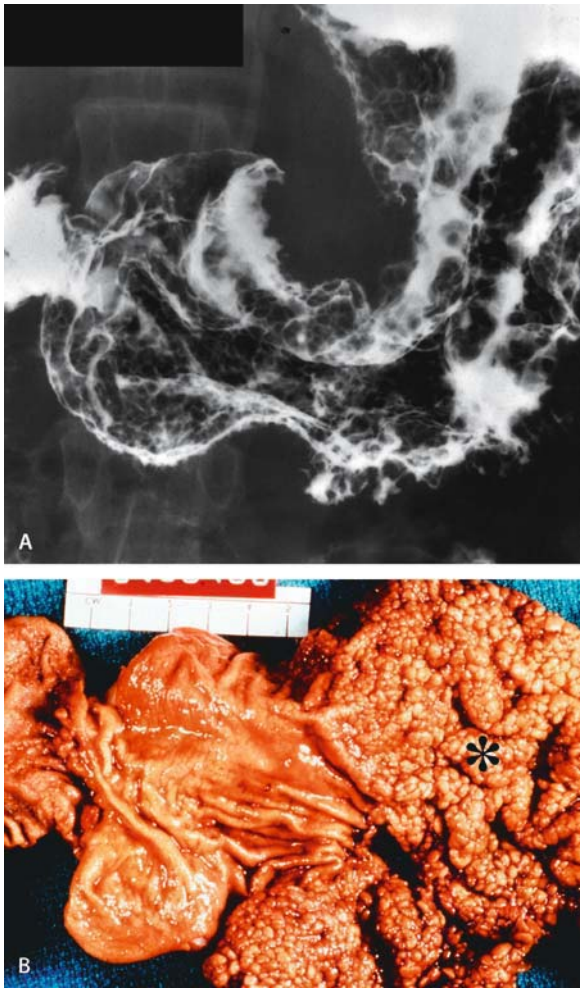

Fig. 16A, B. Ménétrier disease in a 70-year-old man with pedal edema and hypoalbuminemia. **A** Air-contrast barium examination of the stomach shows thickened, nodular gastric folds. There is spiculation of the fold pattern along the greater curvature. **B** Photograph of the opened, resected surgical specimen shows marked rugal hypertrophy in the proximal stomach (*asterisk*) and normal antral mucosa

Radiologic Features

Rugal fold enlargement is the radiologic hallmark of the disease. Classically, the proximal stomach is involved with sparing of the antrum. However, the entire stomach may be affected. The folds are typically nodular, irregular, and tortuous. Barium examination of the stomach may show a spiculated appearance of the greater curvature due to small amounts of barium that become trapped between the thickened folds (Fig. 16A).

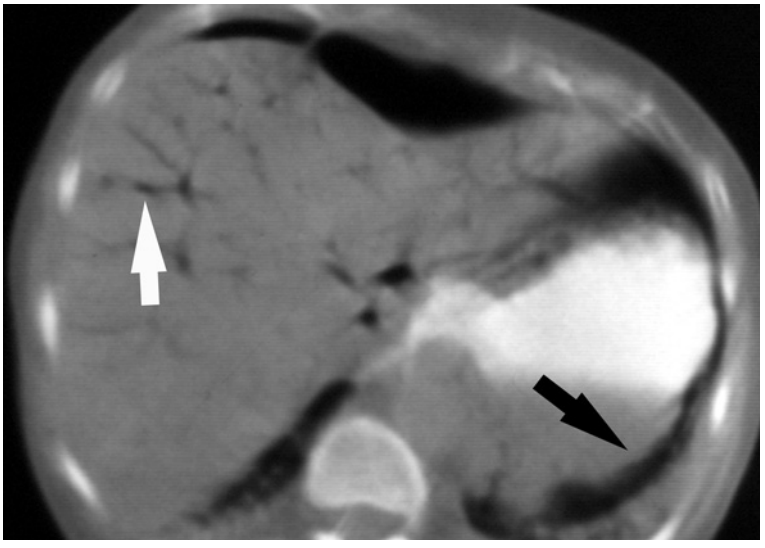

Fig. 17. Emphysematous gastritis in a 69-year-old woman who presented with hypovolemia and metabolic acidosis. Unenhanced CT scan with oral contrast shows gas within the stomach wall (*black arrow*) and portal venous air (*white arrow*)

Emphysematous Gastritis

Emphysematous gastritis is an uncommon suppurative bacterial infection caused by gas forming organisms. Ingestion of corrosives, chronic alcohol abuse, malnutrition, trauma, and underlying malignancy are often predisposing factors. Patients may present with overwhelming sepsis, acute gastrointestinal hemorrhage, or rarely, with purulent emesis [64]. *Clostridium*, *E. coli*, *Streptococcus*, *Enterobacter*, and *Pseudomonas aeruginosa* are the most common offending organisms [55]. The mortality rate is high (60% to 80%) and those that survive usually have long-term sequelae such as gastric fibrosis and stricture formation [65, 66].

Gas within the stomach wall is the radiographic hallmark. CT is the imaging modality of choice and may show intramural gas and fold thickening, as well as complications such as pneumoperitoneum and portal venous gas (Fig. 17) [64].

References

1. Parkin DM, Pisani P, Ferlay J (1999) Global cancer statistics. CA Cancer J Clin 49:33–64
2. Jemal A, Murray T, Samuels A, Ghafoor A, Ward E, Thun M (2003) Cancer statistics, 2003. CA Cancer J Clin 53:5–26
3. Parsonnet J (1993) Helicobacter pylori and gastric cancer. Gastroenterol Clin North Am 22:89–104
4. Parsonnet J, Friedman GD, Vandersteen DP, et al (1991) Helicobacter pylori infection and the risk of gastric carcinoma. N Engl J Med 325:1127–1131
5. Correa P (1992) Human gastric carcinogenesis: a multistep and multifactorial process–First American Cancer Society Award Lecture on Cancer Epidemiology and Prevention. Cancer Res 52:6735–6740
6. Sipponen P, Marshall BJ (2000) Gastritis and gastric cancer. Western countries. Gastroenterol Clin North Am 29:579–592, v–vi
7. Longmire WP, Jr. (1993) A current view of gastric cancer in the US. Ann Surg 218:579–582
8. Blot WJ, Devesa SS, Kneller RW, Fraumeni JF, Jr. (1991) Rising incidence of adenocarcinoma of the esophagus and gastric cardia. Jama 265:1287–1289
9. Fenoglio-Presier C, Munoz N, Carneiro F, et al (2000) Gastric carcinoma. In: Hamilton SR, Aaltonen LA (ed) World health organization classification of tumours: pathology and genetics of tumours of the digestive system. Lyon, IARC Press, pp 38–52
10. Lauren T (1965) The two histologic main types of gastric carcinoma: diffuse and so-called intestinal-type carcinoma. An attempt at histo-clinical classification. Acta Pathol Microbiol Scand 64:31–49
11. Lewin KJ, Appleman HD (1996) Tumors of the esophagus and stomach, third series, fascicle 18. Washington, DC: Armed Forces Institute of Pathology
12. Murakami T (1971) Pathomorphological diagnosis. Definition and gross classification of early gastric cancer. In: Murakami T (ed) Early gastric cancer. Gann Monogr Cancer Res, no. 11. Tokyo, University of Tokyo Press, pp 53–55
13. Borrmann R (1926) Geshwulste des magens und duodenums. In: Henke F, Lubarsch O (ed) Handbuch der speziellen pathologischen anatomie und histologie. Berlin, Springer-Verlag, pp 865
14. Levine MS, Megibow AJ, Kochman ML (2000) Carcinoma of the stomach and duodenum. In: Gore RM, Levine MS (ed) Textbook of gastrointestinal radiology. 2nd ed. Philadelphia, Saunders, pp 601–626
15. Gore RM, Levine MS, Ghahremani GG, Miller FH (1997) Gastric cancer. Radiologic diagnosis. Radiol Clin North Am 35:311–329
16. Balthazar EJ, Rosenberg H, Davidian MM (1980) Scirrhous carcinoma of the pyloric channel and distal antrum. AJR Am J Roentgenol 134:669–673
17. Balthazar EJ, Siegel SE, Megibow AJ, Scholes J, Gordon R (1995) CT in patients with scirrhous carcinoma of the GI tract: imaging findings and value for tumor detection and staging. AJR 165:839–845
18. Levine MS, Kong V, Rubesin SE, Laufer I, Herlinger H (1990) Scirrhous carcinoma of the stomach: radiologic and endoscopic diagnosis. Radiology 175:151–154
19. Horton KM, Fishman EK (1998) Helical CT of the stomach: evaluation with water as an oral contrast agent. AJR 171:1373–1376
20. Wotherspoon A, Chott A, Gascoyne RD, Muller-Hermelink HK (2000) Lymphoma of the stomach. In: Aaltonen LA (ed) World health organization classification of tumours: pathology and genetics of tumours of the digestive system. Lyon, IARC Press, pp 57–61

21. Abbondanzo SL, Sobin LH (1997) Gastric "pseudolymphoma": a retrospective morphologic and immunophenotypic study of 97 cases. Cancer 79:1656–1663
22. Isaacson PG (1994) Gastrointestinal lymphoma. Hum Pathol 25:1020–1029
23. Jaffe ES, Harris NL, Stein H, Vardiman JW, eds (2001) World health organization classification of tumours: pathology and genetics of tumours of haematopoietic and lymphoid tissues. Lyon: IARC Press,
24. Harris NL, Jaffe ES, Diebold J, et al (2000) The World Health Organization classification of neoplasms of the hematopoietic and lymphoid tissues: report of the Clinical Advisory Committee meeting–Airlie House, Virginia, November, 1997. Hematol J 1:53–66
25. Nakamura S, Akazawa K, Yao T, Tsuneyoshi M (1995) A clinicopathologic study of 233 cases with special reference to evaluation with the MIB-1 index. Cancer 76:1313–1324
26. Montalban C, Castrillo JM, Abraira V, et al (1995) Gastric B-cell mucosa-associated lymphoid tissue (MALT) lymphoma. Clinicopathological study and evaluation of the prognostic factors in 143 patients. Ann Oncol 6:355–362
27. Passaro DJ, Chosy EJ, Parsonnet J (2002) Helicobacter pylori: consensus and controversy. Clin Infect Dis 35:298–304
28. Wotherspoon AC (2000) A critical review of the effect of helicobacter pylori eradication on gastric MALT lymphoma. Curr Gastroenterol Rep 2:494–498
29. An SK, Han JK, Kim YH, et al (2001) Gastric mucosa-associated lymphoid tissue lymphoma: spectrum of findings at double-contrast gastrointestinal examination with pathologic correlation. RadioGraphics 21:1491–1502, discussion 1502–1494
30. Kim YH, Lim HK, Han JK, et al (1999) Low-grade gastric mucosa-associated lymphoid tissue lymphoma: correlation of radiographic and pathologic findings. Radiology 212: 241–248
31. Kessar P, Norton A, Rohatiner AZ, Lister TA, Reznek RH (1999) CT appearances of mucosa-associated lymphoid tissue (MALT) lymphoma. Eur Radiol 9:693–696
32. Choi D, Lim HK, Lee SJ, et al (2002) Gastric mucosa-associated lymphoid tissue lymphoma: helical CT findings and pathologic correlation. AJR 178:1117–1122
33. Levine MS, Rubesin SE, Pantongrag-Brown L, Buck JL, Herlinger H (1997) Non-Hodgkin's lymphoma of the gastrointestinal tract: radiographic findings. AJR Am J Roentgenol 168: 165–172
34. Levine MS, Pantongrag-Brown L, Aguilera NS, Buck JL, Buetow PC (1996) Non-Hodgkin lymphoma of the stomach: a cause of linitis plastica. Radiology 201:375–378
35. Buy JN, Moss AA (1982) Computed tomography of gastric lymphoma. AJR 138:859–865
36. Kindblom LG, Remotti HE, Aldenborg F, Meis-Kindblom JM (1998) Gastrointestinal pacemaker cell tumor (GIPACT): gastrointestinal stromal tumors show phenotypic characteristics of the interstitial cells of Cajal. Am J Pathol 152:1259–1269
37. Miettinen M, Lasota J (2001) Gastrointestinal stromal tumors–definition, clinical, histological, immunohistochemical, and molecular genetic features and differential diagnosis. Virchows Arch 438:1–12
38. Burkill GJ, Badran M, Al-Muderis O, et al (2003) Malignant gastrointestinal stromal tumor: distribution, imaging features, and pattern of metastatic spread. Radiology 226: 527–532
39. Suster S (1996) Gastrointestinal stromal tumors. Seminars in Diagnostic Pathology 13:297–313
40. Fletcher CD, Berman JJ, Corless C, et al (2002) Diagnosis of gastrointestinal stromal tumors: A consensus approach. Hum Pathol 33:459–465
41. Miettinen M, El-Rifai W, Sobin LH, Lasota J (2002) Evaluation of malignancy and prognosis of gastrointestinal stromal tumors: a review. Hum Pathol 33:478–483
42. Levy AD, Remotti HE, Thompson WM, Sobin LH, Miettinen M (2003) From the Archives of the AFIP: Gastrointestinal stromal tumors: radiologic features with pathologic correlation. RadioGraphics 23:283–304
43. Capella C, Solcia E, Sobin LH, Arnold R (2000) Endocrine tumours of the stomach. In: Hamilton SR, Aaltonen LA (ed) World health organization classification of tumours: pathology and genetics of tumours of the digestive system. Lyon, IARC Press, pp 53–57
44. Rindi G, Bordi C, Rappel S, La Rosa S, Stolte M, Solcia E (1996) Gastric carcinoids and neuroendocrine carcinomas: pathogenesis, pathology, and behavior. World J Surg 20:168–172
45. Balthazar EJ, Megibow A, Bryk D, Cohen T (1982) Gastric carcinoid tumors: radiographic features in eight cases. AJR Am J Roentgenol 139:1123–1127
46. Ho AC, Horton KM, Fishman EK (2000) Gastric carcinoid tumors as a consequence of chronic hypergastrinemia: spiral CT findings. Clin Imaging 24:200–203
47. Berger MW, Stephens DH (1996) Gastric carcinoid tumors associated with chronic hypergastrinemia in a patient with Zollinger-Ellison syndrome. Radiology 201:371–373
48. Menuck LS, Amberg JR (1975) Metastatic disease involving the stomach. Am J Dig Dis 20:903–913
49. Niederau C, Sobin LH (2000) Secondary tumors of the stomach. In: Hamilton SR, Aaltonen LA (ed) World Health Organization Classification of Tumours: Pathology and Genetics of Tumours of the Digestive System. Lyon, IARC Press, pp 66–67
50. Feczko PJ, Halpert RD, Ackerman LV (1985) Gastric polyps: radiological evaluation and clinical significance. Radiology 155:581–584
51. Cello JP (1995) Helicobacter pylori and peptic ulcer disease. AJR 164:283–286
52. Saita H, Murakami M, Yoo JK, et al (1993) Link between Helicobacter pylori-associated gastritis and duodenal ulcer. Dig Dis Sci 38:117–122
53. Peterson WL (1991) Helicobacter pylori and peptic ulcer disease. N Engl J Med 324:1043–1048
54. Larkai EN, Smith JL, Lidsky MD, Graham DY (1987) Gastroduodenal mucosa and dyspeptic symptoms in arthritic patients during chronic nonsteroidal anti-inflammatory drug use. Am J Gastroenterol 82:1153–1158
55. Fenoglio-Preiser CM, Noffsinger AE, Stemmermann GN, Lantz PE, Listrom MB, Rilke FO (1999) Gastrointestinal pathology: an atlas and text. 2nd ed. Philadelphia: Lippincott-Raven
56. Levine MS (1994) Erosive gastritis and gastric ulcers. Radiol Clin North Am 32:1203–1214
57. Thompson G, Somers S, Stevenson GW (1983) Benign gastric ulcer: a reliable radiologic diagnosis? AJR Am J Roentgenol 141:331–333
58. Levine MS, Creteur V, Kressel HY, Laufer I, Herlinger H (1987) Benign gastric ulcers: diagnosis and follow-up with double-contrast radiography. Radiology 164:9–13
59. Meko JB, Norton JA (1995) Management of patients with Zollinger-Ellison syndrome. Annu Rev Med 46:395–411
60. Wolfe MM, Jensen RT (1987) Zollinger-Ellison syndrome. Current concepts in diagnosis and management. N Engl J Med 317:1200–1209
61. Tjon ATRT, Falke TH, Jansen JB, Lamers CB (1989) CT and MR imaging of advanced Zollinger-Ellison syndrome. J Comput Assist Tomogr 13:821–828
62. Lebtahi R, Le Cloirec J, Houzard C, et al (2002) Detection of neuroendocrine tumors: 99mTc-P829 scintigraphy compared with 111In-pentetreotide scintigraphy. J Nucl Med 43: 889–895
63. Termanini B, Gibril F, Reynolds JC, et al (1997) Value of somatostatin receptor scintigraphy: a prospective study in gastrinoma of its effect on clinical management. Gastroenterology 112:335–347
64. Grayson DE, Abbott RM, Levy AD, Sherman PM (2002) Emphysematous infections of the abdomen and pelvis: a pictorial review. RadioGraphics 22:543–561
65. Moosvi AR, Saravolatz LD, Wong DH, Simms SM (1990) Emphysematous gastritis: case report and review. Rev Infect Dis 12:848–855
66. Kussin SZ, Henry C, Navarro C, Stenson W, Clain DJ (1982) Gas within the wall of the stomach report of a case and review of the literature. Dig Dis Sci 27:949–954

Duodenum: Basics of Radiologic-Pathologic Correlations

Joel E. Lichtenstein, Francis J. Scholz

4.3

Contents

Introduction

The duodenum is one of the most unique and dynamic parts of the body. It has both intra- and retro-peritoneal portions. Being centrally located in the abdomen, it is often affected by diseases in neighboring organs. It is a battleground of acids and alkali relating to drainage from three of the body's major sources of digestive chemicals: the liver via the biliary tree, the pancreas draining alkaline secretions and powerful enzymes through the major and minor papillae, and the stomach producing caustic acids. It has a complex embryology involving development of adjacent organs and numerous anomalies. As a consequence of location, embryology, histology, surrounding structures and the adjacent organs draining into it, the pathology of the duodenum differs from that of other alimentary tract organs. Inch for inch and ounce for ounce, more distinct pathologies occur here than in any other abdominal organ [1].

Developmental phenomena give rise to annular pancreas, webs and choledochoceles, and account for ectopias. Anatomy dictates patterns of obstruction and spread of disease from adjacent organs as well as patterns of rupture and hematoma formation in blunt trauma. Exposure to gastric acid leads to ulcers and hyperplasias. Influx of bile and pancreatic juice is thought to determine some types and sites of mucosal neoplasia.

In common with the rest of the bowel, the duodenum is a stratified tube that is organized into four main layers: mucosa, submucosa, muscularis propria and an outer adventitial covering. The mucosa, in turn, has three layers. The luminal lining of squamous or columnar epithelial cells provides a protective surface involved in absorption and mucus production. The lamina propria is a supportive layer of mesenchyme containing capillaries and nerves. A thin layer of smooth muscle, the muscularis mucosae, separates the mucosa from the submucosa. A unique feature of the proximal duodenum are Brunner glands which are found in the lamina propria and submucosa bridging across the muscularis mucosae.

"Adventitia" is a general term for whatever surrounds the gut. Much of the GI tract is surrounded by delicate fibrofatty mesenchyme supporting a continuous thin fibrous layer, the serosa. In common with the esophagus and part of the colon, the retroperitoneal portions of the duodenum lack a defined serosa. The direct continuity of the duodenal wall with surrounding tissue is important in spread of disease.

Developmental Lesions

Annular Pancreas

Annular pancreas provides a classic example of a duodenal stricture due to compression by an extrinsic encircling mass. The pancreas is formed normally by the fusion of dorsal and ventral embryologic precursors. The ventral portion arises as a bud from the common bile duct and normally rotates with the bile duct, traveling behind the duodenum. It accounts for most of the head and uncinate process of the mature pancreas after fusing with the inferior aspect of the dorsal precursor which becomes the body and tail of the gland. The pancreatic ducts normally join to form a kink or genu. Usually the main pancreatic drainage is via a common ampulla and papilla with the CBD on the medial wall of the descending duodenum. A variable accessory drainage from the dorsal component often extends from the region of the genu to the minor papilla slightly more anterior and cephalad on the wall of the duodenum, although a wide spectrum of variations occur.

Annular pancreas is a result of anomalous rotation of the ventral pancreatic precursor anteriorly around the duodenum. It fuses in a nearly normal relationship to the dorsal component but leaves a trailing band of pancreatic tissue and duct around the anterior and lateral aspects of the second part of the duodenum. The duod-

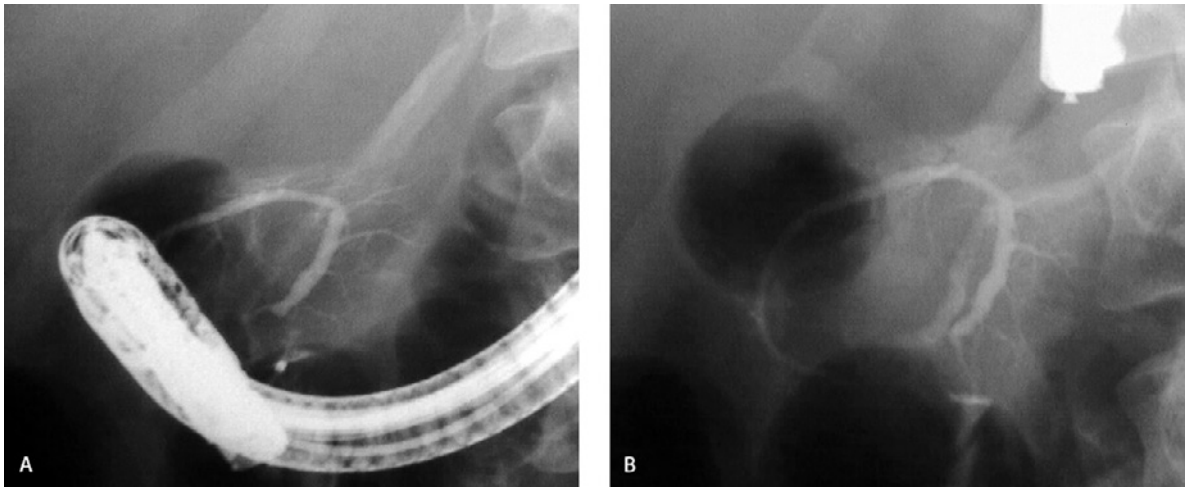

Fig. 1A, B. ERCP demonstrating annular pancreas. **A** Pancreatic duct extending laterally around endoscope. **B** Pancreatic ducts seen encircling the duodenum as endoscope is withdrawn

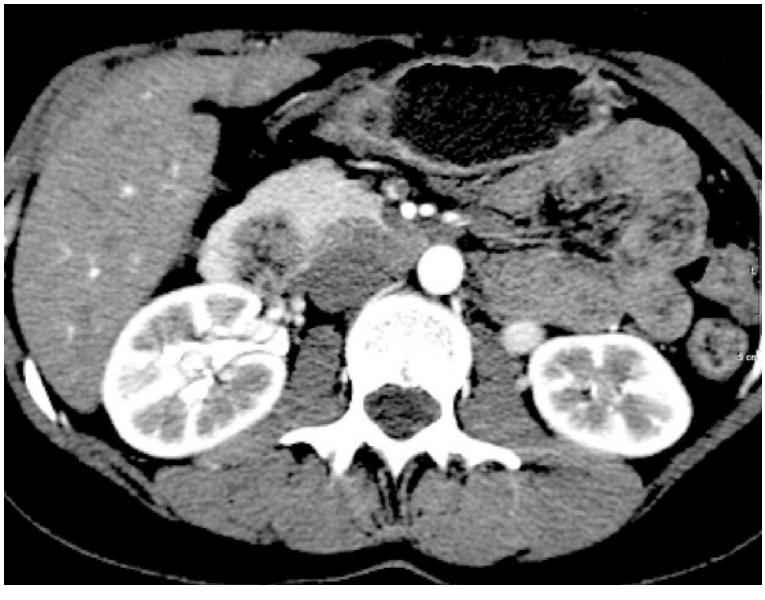

Fig. 2. Contrast-enhanced CT in annular pancreas showing enhancing rim of gland wrapping around descending duodenum

enal lumen passing through the resulting ring or collar varies in diameter. It may be tight enough to obstruct in the newborn or wide enough to be asymptomatic. The mucosa and submucosa are unaffected except for being stretched over the lesion, providing a smooth contour. A pancreatogram demonstrating a duct surrounding the duodenum or a CT demonstrating the gland wrapping around the duodenum may be diagnostic [2] (Figs. 1, 2).

As both the pancreas and the duodenum enlarge with increasing patient age, a ring, which caused no problem initially, may increasingly compromise the lumen and become symptomatic in adulthood [3, 4]. Pancreatitis may precipitate obstruction when the edematous pancreatic collar further narrows the duodenal lumen.

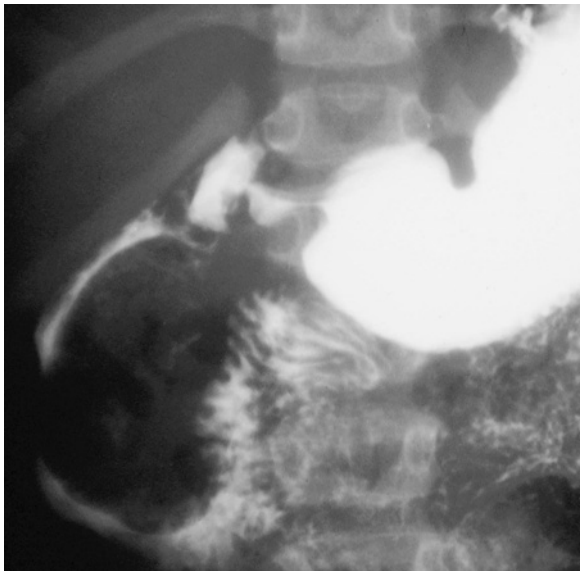

Fig. 3. Duodenal duplication widening and causing a smooth impression upon the inner aspect of the descending duodenum

Duplication

Duplication cysts are developmental lesions which contain both muscular and mucosal elements. They probably begin embryologically during the sixth to tenth fetal week. At this stage, the entire hollow enteric canal undergoes rapid growth, and the core fills with rapidly proliferating cells that obliterate the entire intestinal lumen. By the tenth week, numerous discontinuous vacuoles from in the gastrointestinal tract and eventually coalesce to form one continuous gastrointestinal lumen. If a vacuole fails to coalesce into the enteric lumen, it remains a blind cyst that may gradually enlarge as lining cells are shed into the lumen of the cyst. The lining epithelium is often a complex combination of tissues, commonly including respiratory and pancreatic acinar epithelium. The cysts are usually named according to the organ with which they share a muscular wall, rather than by the histology of the lining epithelium. Duplication cysts can be located anywhere within the GI tract. The terminal ileum is the most common site, but the duodenum is a relatively common location, especially along the medial aspect of the descending portion (Figs. 3, 4). The majority of duplication cysts are ovoid, and do not communicate with bowel.

Patients with duplication cysts may present in infancy or early childhood with obstruction. However, presenting symptoms depend on both the location of the duplication cyst and whether the cyst is complicated. Abdominal pain may occur due to cyst distention, intussusception, infection, or ulceration and bleeding, especially if gastric mucosa is present and pancreatitis is another potential complication [5, 6].

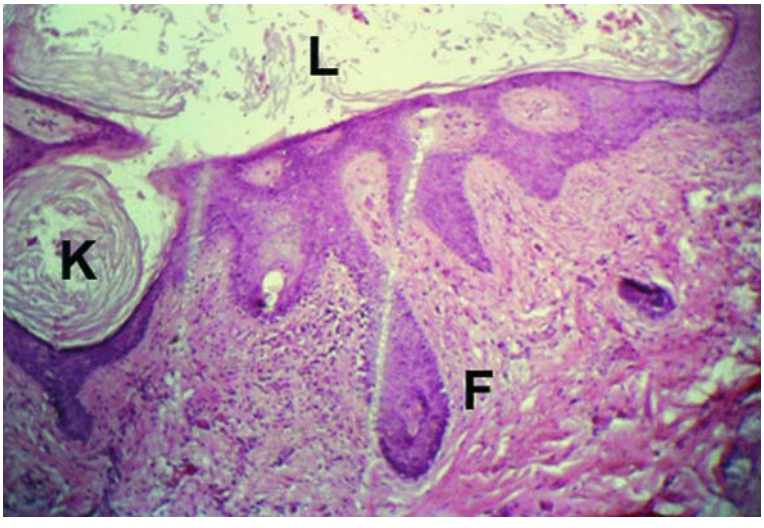

Fig. 4. Photomicrograph demonstrating varied tissue lining a duodenal duplication some of which in this case resembles skin. *L*, lumen; *F*, hair follicle; *K*, keratin whorl

Ultrasonography can be highly suggestive of duplication cyst. Typically, there is a hypoechoic cystic structure with an echogenic mucosal layer surrounded by a sonolucent muscular layer [7–9]. CT may be helpful in problem cases by showing a low attenuation center and an enhancing wall. Wall calcification is rare.

Choledochocele

Cystic dilations of the distal common bile duct are considered congenital anomalies. They typically protrude into the duodenal lumen forming soft deformable masses at, or surrounding, the papilla of Vater. They are often classified as type 3 choledochal cysts, but seem unrelated in embryologic origin, having normal pancreatic duct junctions and no documented increased incidence of carcinoma. They contain bile and are visualized cholangiographically but do not fill with ingested luminal gut contrast which instead they displace. They may become quite large and prolapse into the more distal duodenum [10].

Diverticula

Duodenal diverticula are very common and are almost always acquired "false" diverticula, consisting of only a mucosal layer herniated through the muscular wall at sites of weakness near the papilla. The ampullary "window" is the channel through which the common ampulla or the separate pancreatic and biliary ducts normally pass. It is the weakest part of the duodenal wall and a frequent site of diverticulum formation. The diverticulum usually arises parallel to the ampulla. With progressive enlargement of the diverticulum, the adjacent duodenal mucosa containing the ampulla itself sometimes herniates and the diverticulum contains the ampulla.

Diverticula may be multiple and may occur elsewhere in the duodenum, at sites where major feeding arteries penetrate the muscular wall, sometimes attaining considerable size. Rarely, an acquired diverticulum contains all layers of the duodenal wall and is secondary to traction from an adjacent inflammatory process.

Considerable uncertainty exists about the clinical significance of insertion of the common bile duct and pancreatic ducts into the duodenal diverticulum. Disagreement exists about whether this anomaly plays any significant role in clinical disease, choledocholithiasis, cholangitis, or pancreatitis.

Intraluminal Diverticulum

A rare form of duodenal web forms at or very near the papilla of Vater and may develop a classic radiographic

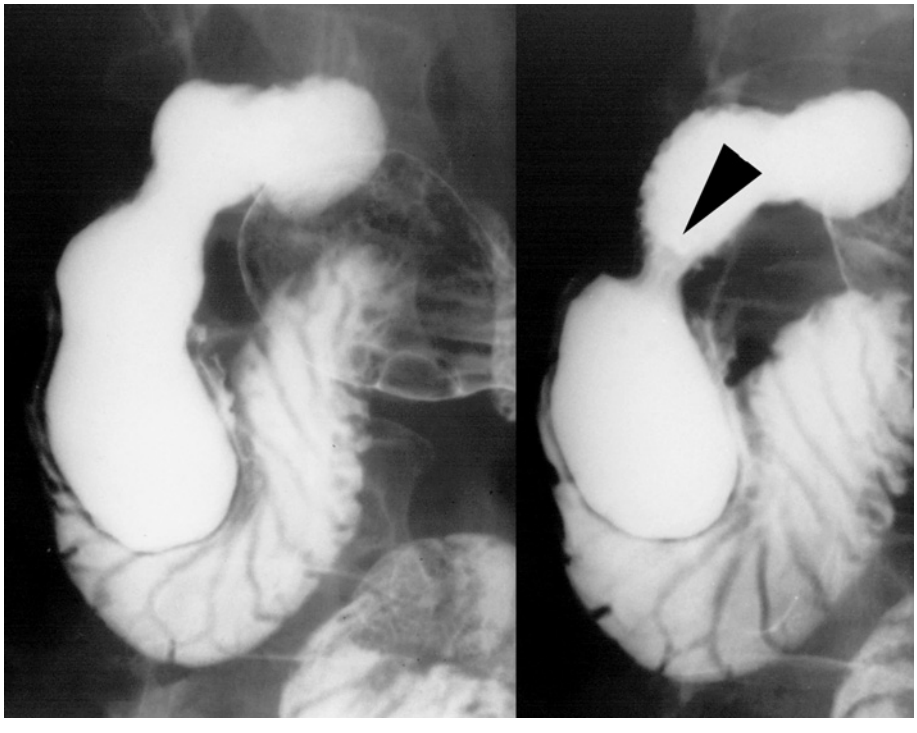

Fig. 5. Intraluminal pseudodiverticulum. Spot images from upper GI series show contrast accumulating in a classic sac-like intraluminal structure in the descending duodenum outlined by a thin lucent wall. The *arrowhead* indicates the opening of the sac but the presence of contrast distally implies an adjacent, eccentric opening which prevents total obstruction

appearance [11–13]. Its origin is probably related to the period of vacuole coalescence in early embryologic life. If a transverse portion of the wall between major duodenal vacuoles fails to disappear, a duodenal diaphragm remains [14]. If this is complete, the neonate will have complete duodenal obstruction requiring immediate surgical correction. If the diaphragm is incomplete, an opening permitting passage of food is present. Gradual peristaltic pressure on the intact portion of the diaphragm causes progressive invagination. The diaphragm may be stretched and drawn downstream. If the opening remains central the configuration resembles an airport "wind sock". More commonly the opening is eccentric with the mouth near the papilla and the diaphragm protrudes downstream like a condom or the finger of a glove (Fig. 5).

As opposed to a duplication, which has a muscular wall, the intraluminal diverticulum is lined on both sides by duodenal mucosa and lacks a muscularis propria, consistent with its origin from a mucosal web (Fig. 6).

Symptoms usually do not occur until adulthood, when the diverticulum has attained considerable size. An increased incidence in Down's syndrome is reported [15]. The pain, nausea, and vomiting may be due not only to degrees of duodenal obstruction but also to peristaltic pressure pulling or stretching the intraluminal diverticulum. The fundus of the diverticulum may

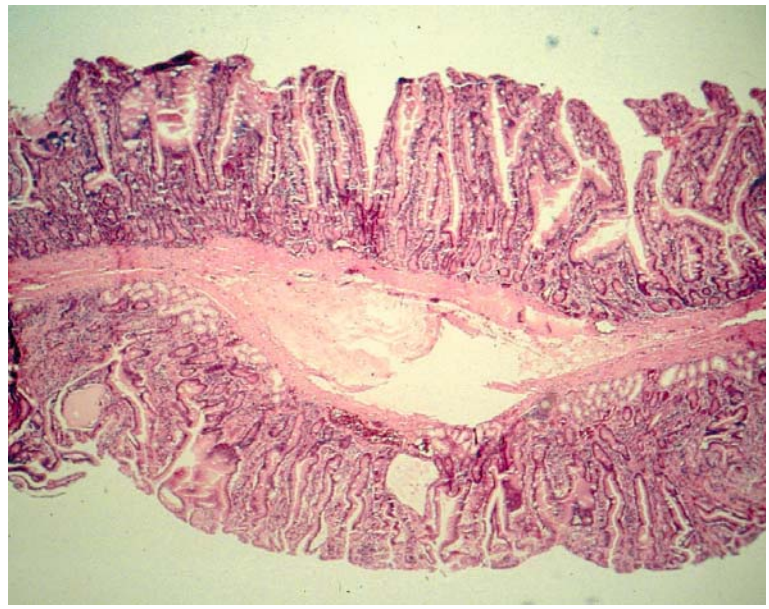

Fig. 6. Photomicrograph of wall of intraluminal pseudodiverticulum (H&E original magnification ×40). It is composed of two layers of apposed mucosa with no intervening submucosa or muscularis propria confirming its origin as a mucosal web rather than a duplication

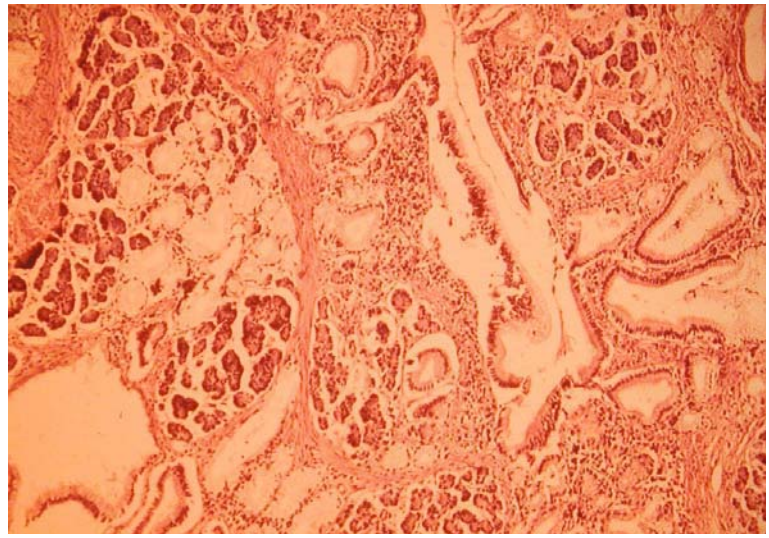

Fig. 7. Ectopic pancreas: medium-power photomicrograph. Note the wide variety of glandular tissue and ducts with relatively sparse intermixed strands of muscle in a hamartomatous arrangement. (H&E x70 original magnification)

stretch to the ligament of Treitz because of chronic peristaltic traction. Ingested material, such as fruit pits, may become trapped within the sac.

Ectopic Pancreas (Pancreatic Rest or Myoepithelial Hamartoma)

Polypoid lesions containing pancreatic acini are relatively common in the wall of the gut adjacent to the pancreas and apparently are embryologic anomalies. In spite of the common appellation, they are seldom rests of normal appearing pancreas. Usually they are complex hamartomatous accumulations of epithelial and muscular tissue in the mucosa and submucosa. The epithelial components are quite variable including a variety of glandular elements including gastric and Brunner gland- like cells. Pancreatic islets may be present but often are not (Fig. 7). The glandular tissue drains to the gut lumen through a central duct whose orifice is usually in a central dimple or umbilication in the mucosa which is stretched over the lesion (Fig. 8). Contrast tends to accumulate in the dimple sometimes suggesting an ulcer, but very rarely actually enters the ducts which are usually microscopic [16]. The lesions are usually innocuous incidental findings, but inflammation, carcinoma and islet cell tumors have been reported rarely within them.

Inflammatory Conditions

Duodenitis

Duodenal inflammation is very common but the radiographic findings, such as spasm and irritability and fold

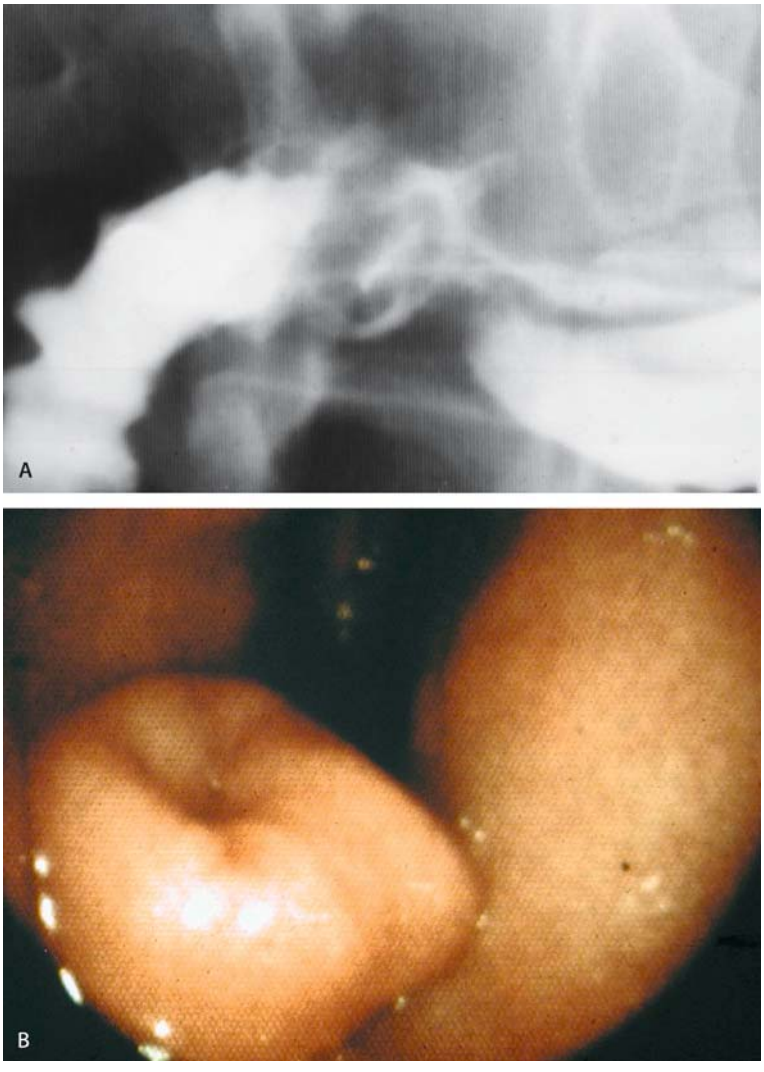

Fig. 8. A Radiograph of nodule of ectopic pancreas in the duodenal bulb. The central, somewhat elongated, contrast accumulation marks the orifice of duct entrance into the lumen. **B** Endoscopic view of a similar lesion from another patient

irregularity and thickening are often nonspecific and difficult to distinguish from normal variation when relatively mild. Erosions through the epithelium which do not breach the muscularis mucosae, which separates mucosa from submucosa, may be detected with double contrast technique. Aphthous lesions suggest granulomatous disease, especially Crohn disease but are not specific [17–19].

Ulcers

Ulcers are holes in the normal protective mucosal barrier lining the gut. They result in protrusions of contrast beyond the expected margin of the lumen of the organ. They may be caused by noxious agents in the bowel lumen or by insults such as mucosal ischemia or inflammation in the mucosa itself. Infection with *Helicobacter pylori* is now recognized as the etiology for most upper GI tract ulceration (see below). Once the surface is breached, the erosion can extend more deeply. In a benign ulcer, the surrounding epithelium remains relatively resistant and intact even though inflamed. Destruction of the less resistant submucosa undermines the mucosa, which tends to overhang the crater edge. The firm, rubbery muscularis mucosae is relatively resistant and forms a temporary barrier. The resulting flat-bottomed defect has a characteristic "collar button" shape. Surrounding mucosal folds extend all the way in to the edge of the ulcer [20, 21].

In contrast, adenocarcinoma by definition arises in dysplastic epithelium and typically produces a nodular, irregular mucosa. An ulcer in this abnormal tissue usually has irregular edges that tend to be eroded along with underlying tissue without undermining. Erosion into an extensive tumor mass produces an irregular, saucer-shaped hole rather than a flat bottom. Ulceration into a submucosal tumor such as a leiomyoma or lymphoma nodule produces a variably shaped crater, but because the epithelium is not primarily involved, it's edge is often sharply defined.

Zollinger-Ellison Syndrome is a classic entity in which an ectopic gastrin source stimulates gastric acid production and marked hyperplasia of parietal cells in the deep mucosal glands of the gastric fundus. The resulting excess highly acidic fluid causes inflammation and ulcers, often more distal in the duodenum than in more ordinary hyperacidity (Fig. 9) [22]. Almost a quarter of patients have multiple endocrine neoplasia type 1 (MEN-1), often with associated hyperparathyroidism and renal calculi. Despite publicity and improved testing and treatment methods, the diagnosis often remains difficult and delayed [23].

In contrast to the inflammation caused by excess acid in Zollinger-Ellison syndrome, duodenitis also may be seen in patients with normal acid production but who have diminished mucosal defense. Patients taking NSAIDs have decreased mucosal defense. Patients with active celiac sprue have mucosal atrophy predisposing to ulcers and inflammation of the duodenum and the jejunum (Fig. 10) [24–26].

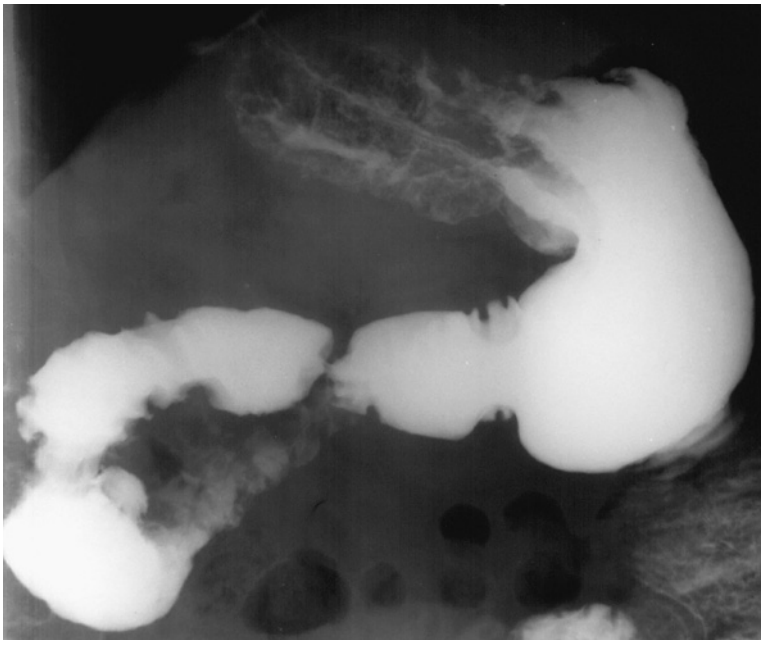

Fig. 9. Zollinger-Ellison syndrome. Duodenal folds are thick and irregular and there is a deep ulcer at the junction of second and third parts. Gastric folds are also thick especially in the fundus reflecting parietal cell hyperplasia

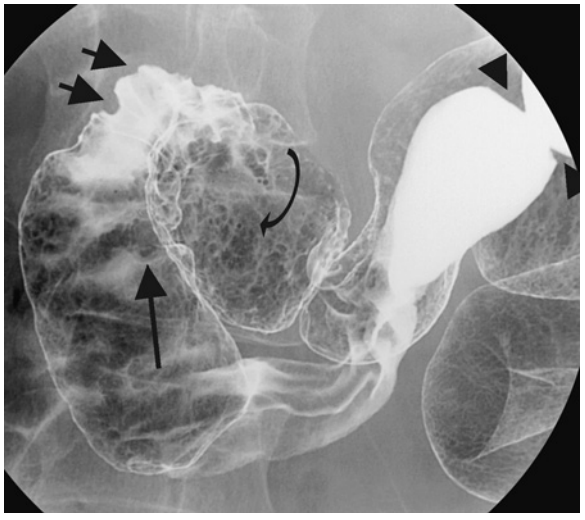

Fig. 10. A patient with symptomatic sprue with weight loss, diarrhea and anemia shows typical changes of active sprue which can be seen in the duodenum. Arrows show fold thickening. The curved arrow shows nodules in the bulb, called the foamy bulb [24] representing glandular hypertrophy, and arrowheads show a ring stricture from healed ulceration. The folds in the more distal duodenum are flat. All findings are due to loss of mucosal protection from mucosal atrophy allowing gastric acid to produce inflammation

Regional Enteritis (Crohn Disease)

Duodenal involvement with Crohn's disease is relatively uncommon and rarely the only site affected. It may precede or follow the diagnosis of Crohn's disease elsewhere in the gastrointestinal tract. Concurrent involvement of the gastric antrum and duodenal bulb is more common than is isolated involvement of either the stomach or the duodenum. Involvement of the antrum, pylorus, and duodenal bulb often leads to obliteration of the normal pyloric canal. In these instances, the antrum is narrowed, the pylorus is widened, and the duodenal bulb is narrowed, yielding a uniform tubular appearance that has been called a pseudo post-Billroth I appearance.

The radiographic findings in the duodenum include thickened folds, ulceration, pseudodiverticula, and short- or long-segment strictures (string sign) [27, 28]. Involvement in or about the papilla of Vater may lead either to a patulous, incompetent sphincter of Oddi or to a fistula with reflux of barium into the common bile duct or pancreatic duct. Hepatic abscess and pancreatitis are reported complications [29, 30]. A duodenocolic fistula between the descending portion of the duodenum and the proximal transverse colon may cause a short bowel or blind loop syndrome or both. The colon, the duodenum, or both may be the diseased organ from which the fistula originates.

Infection

A very common, gram negative, spiral bacterium, *Helicobacter pylori* (formerly called *Campylobacter*), is now recognized as an etiologic agent for inflammation, erosions, ulcers and metaplasia leading to neoplasm in the stomach and proximal duodenum [31, 32]. Tuberculosis may mimic Crohn's disease in the upper GI tract and may be more common world wide although primary duodenal TB is very rare [33].

Strongyloides stercoralis is a microscopic nematode parasite which tends to invade the superficial layers of the duodenum. Resulting acute and chronic inflammation commonly resembles the classic findings of Crohn's disease, especially stenosis of the 2nd and 3rd portions of the duodenum [34, 35]. Involvement of the major papilla may lead to reflux of barium into the pancreatic duct and biliary tree through a patulous sphincter [36]. It is very common in south east Asia and in the Caribbean, but there are also endemic foci in the United States. Its unusual life cycle, including an autoinfection pathway, eliminating the need for repeat environmental exposure, makes it difficult to eradicate. Intense peripheral eosinophilia may be a diagnostic clue. Treatment with steroids may lead to systemic hyperinfestation and be disastrous.

Primary Duodenal Tumors

Tumors are usually seen as combinations of filling defects and strictures [37, 38]. As in the rest of the gut, determining the layer of the wall from which a tumor arises is helpful in differential diagnosis. The histologic components found normally in the wall vary with the region of the gut and so do their tendencies for pathologic growth. One must know the local "track record" for successful prediction. Polyps in the duodenum are likely to be hyperplasias of Brunner glands or hamartomas including pancreatic tissue. Such lesions would be rare elsewhere and similar gross morphology would prompt different considerations.

The radiographic morphology of lesions almost always gives important clues about the pathologic diagnosis [19, 39–42]. Overgrowths of the luminal surface epithelium can cause hyperplasias, adenomas, or carcinomas, depending on the degree of histologic atypia. Epithelial polyps and tumors tend to protrude into the lumen, have irregular surface texture, form acute angles with the surrounding surface, and usually do not displace the centerline of the gut until quite large. Hamartomas are mixed arrangements of otherwise normal tissues. They are generally benign and usually contain both epithelial and mesenchymal elements. Benign lesions tend to grow slowly, are often small, rounded and,

if growing into the lumen, have time to be drawn out onto stalks by peristaltic action. Aggressive lesions spread out and involve adjacent structures. They are likely to be broad-based and tethered to deeper mural structures. They become large sooner and are more likely to outgrow blood supply and become necrotic. Nonuniform, multicentric growth tends to cause irregular contours and lobulation.

The incidence of benign tumors is difficult to define since, if they are small or produce little effect on the lumen they are often asymptomatic and escape attention [43]. They are relatively uncommon among clinically evident tumors, but the absolute incidence is probably much higher and may exceed that of malignancy. Epithelial hyperplasias and adenomas may be sessile or pedunculated nodules. Mesenchymal tumors arise in the deeper layers. Thus, initially, the overlying epithelial layer of the mucosa is intact. Its smooth luminal surface provides a convenient means of predicting the nature of such tumors. Other aspects of appearance depend upon the consistency of the tumor tissue and its site of origin within the wall. Virtually any type of mesenchymal cell found in the bowel wall may rarely give rise to neoplastic or hamartomatous tumors, but only a very few occur frequently enough to warrant serious consideration.

Epithelial Lesions

Benign hyperplastic and adenomatous tumors also arise in the epithelium and this is reflected in their roentgen appearance, often allowing their differentiation.

Brunner Gland Lesions

Brunner glands are unique features of the histology of the proximal duodenum. They form acini of distinctive pale cells located in the mucosa and submucosa bridging across the muscularis mucosae. They produce a watery alkaline fluid which begins the neutralization of gastric acid and which drains into the lumen through microscopic ducts that are not seen grossly or on contrast studies. They frequently become hyperplastic, presumably in response to hyperacidity. Mild hyperplasia results in subtle coarsening of duodenal fold patterns difficult to distinguish from normal or duodenitis. Further enlargement gives a mammillated, nodular appearance to the duodenal bulb and proximal post bulbar duodenum (Fig. 11).

Occasionally polypoid Brunner gland tumors occur and, being formed of glandular tissue, have frequently been called adenomas. However, they resemble hyperplastic lesions histologically and rarely, if ever, demonstrate the cellular dysplasia needed to define an adenoma. They usually have some element of smooth muscle proliferation suggesting a hamartomatous lesion. The polyps typically arise in the proximal duodenum and are small and either sessile or pedunculated [44, 45]. Rarely, they can become very large and extend into the distal duodenum, usually retaining a proximal stalk [46] (Fig. 12). Malignancy has not been reported regardless of size.

Adenomas

Adenomas are neoplastic, usually polypoid, excrescences due to proliferation of dysplastic epithelial cells. As in the rest of the GI tract, they may be sessile or pedunculated. They are uncommon in the duodenum and, excluding polyposis syndromes, are usually solitary and found most commonly near the papilla. It is tempting to speculate that the dysplasia results from the irritating effect of bile or pancreatic secretions.

Villous tumors imply more severe dysplasia, with more aggressive growth. The lesions tend to be more sessile, larger and have more irregular surface texture. Barium trapped in the interstices of the villous surface gives a striated, reticulated, or “soap bubbly” appearance. They are usually found near the papilla and frequently harbor foci of carcinoma, especially if large [47–49] (Fig. 13).

Adenocarcinoma

Carcinoma is, by definition, an epithelial lesion. Its mucosal origin is generally reflected by ulcers and luminal nodules. Its poor prognosis can be explained, in part, by its propensity for submucosal extension and for spread through the wall.

Duodenal carcinoma is rare, accounting for less than 1 percent of GI malignancy. They typically arise in the periampullary and post ampullary second portion of the duodenum. Carcinomas arising remotely from the ampullary region show characteristics similar to those of carcinomas in the remainder of the gastrointestinal tract. As noted above, they often have villous components and appear to arise as anaplastic transitions from preceding dysplastic villous adenomas (Fig. 14). By the time they become markedly symptomatic, the tumors are often advanced and beyond cure [50]. The role of the radiologist, at that point, is one of locating and staging the tumor. However, the upper GI study performed for other reasons, provides the potential for detection of relatively early carcinoma.

Often epithelial malignancy will grow into the lumen as a mainly cellular, polypoid mass of tissue with little fibrosis. Such a lesion is often well differentiated. Typi-

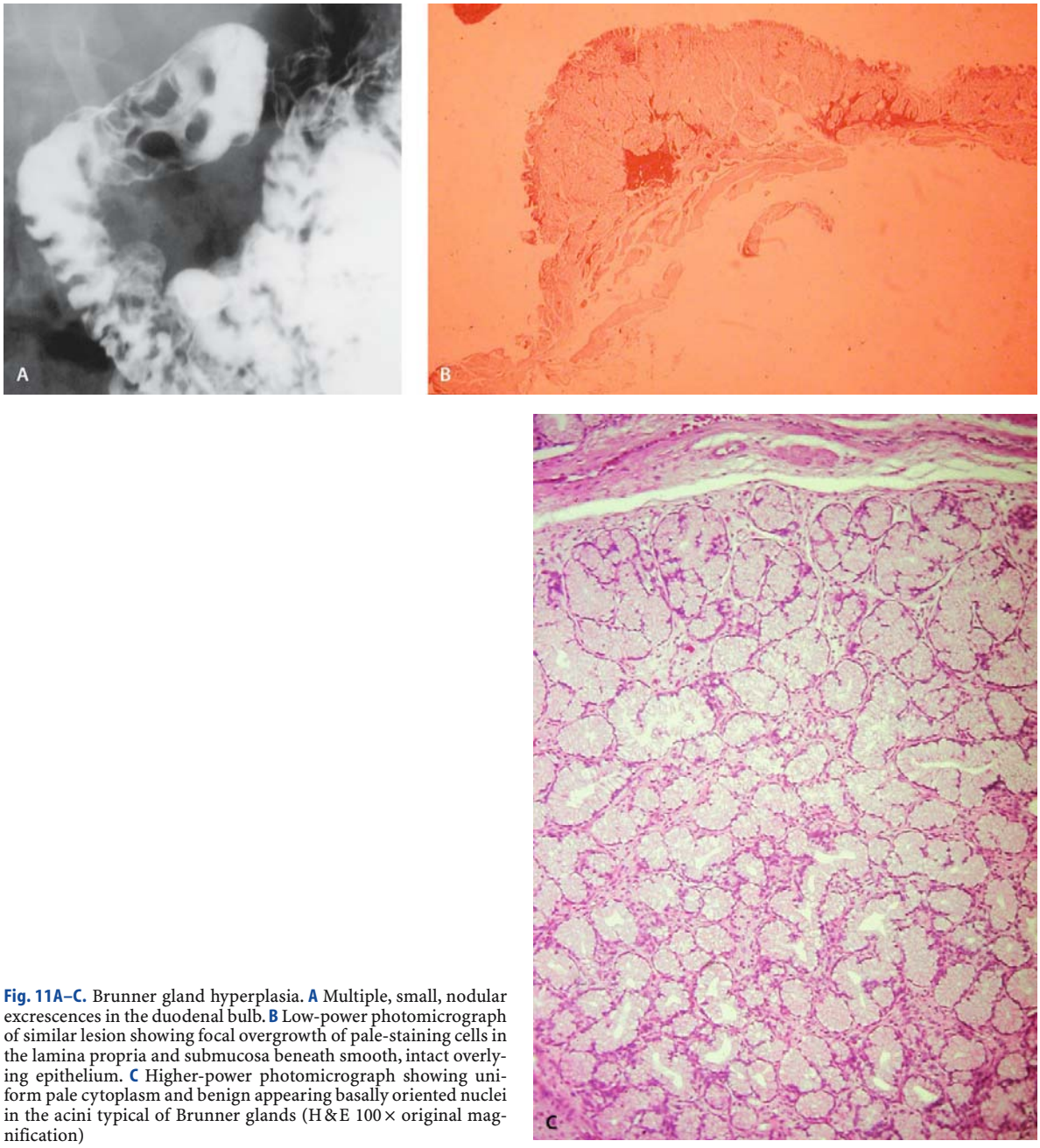

Fig. 11A–C. Brunner gland hyperplasia. **A** Multiple, small, nodular excrescences in the duodenal bulb. **B** Low-power photomicrograph of similar lesion showing focal overgrowth of pale-staining cells in the lamina propria and submucosa beneath smooth, intact overlying epithelium. **C** Higher-power photomicrograph showing uniform pale cytoplasm and benign appearing basally oriented nuclei in the acini typical of Brunner glands (H&E 100× original magnification)

cally, the surface is lobulated or ulcerated as opposed to the usual smooth surface of benign lesions [51, 52].

Mucin producing tumors have a tendency to infiltrate widely and incite a great deal of fibrotic reaction. Fold thickening may result. Often the wall will be thickened and appear stiff and constricted producing the classic "leather bottle" appearance. The lesion may extend around the lumen in an annular manner (Fig. 15).

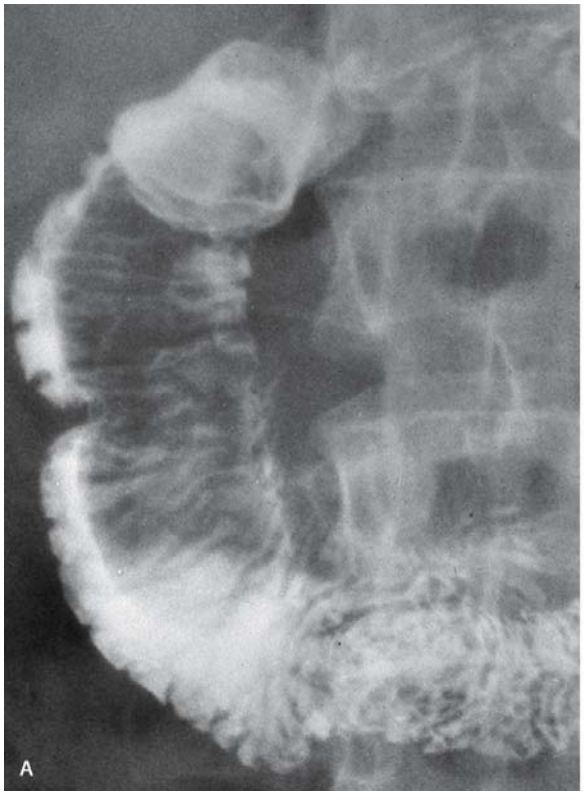

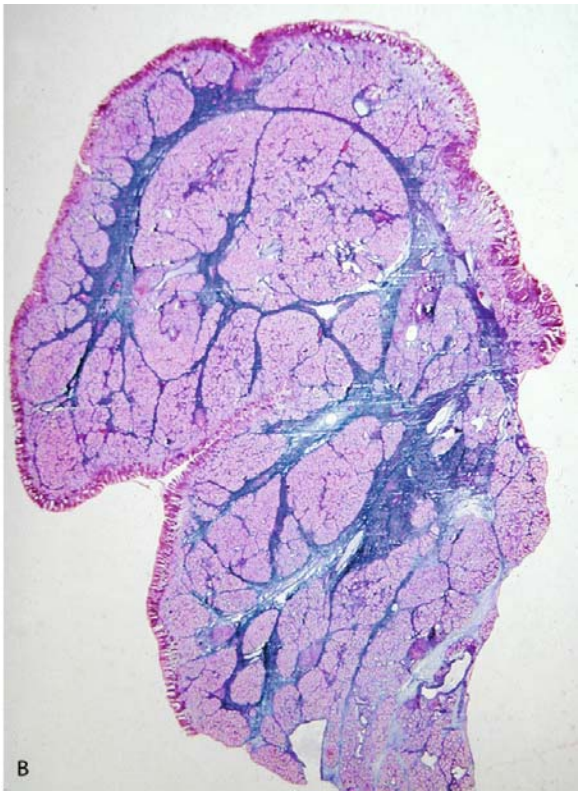

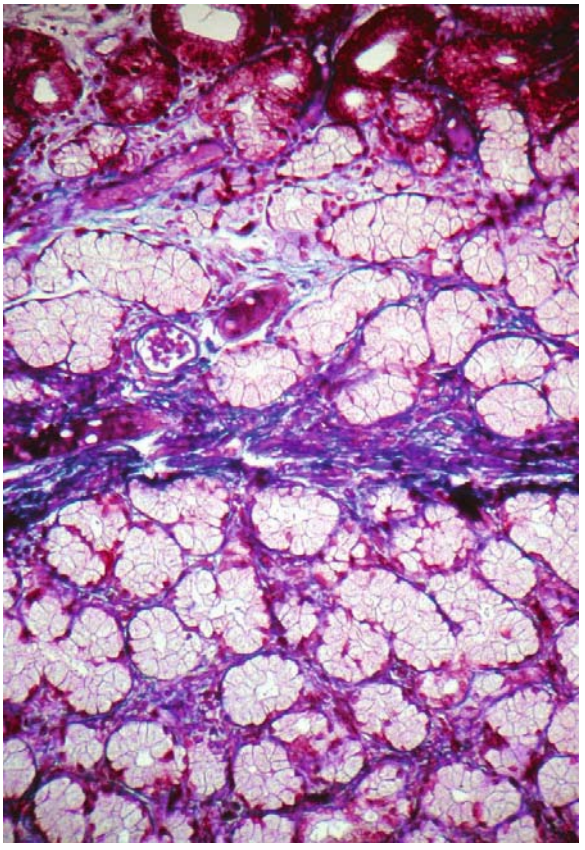

Fig. 12. A Radiograph of Brunner gland tumor presenting as large polypoid mass in descending part of duodenum. **B** Low-power photomicrograph using trichrome stain of such a polyp. Note the dark bands of fibrous tissue and muscle suggesting a hamartomatous lesion. **C** Higher-power photomicrograph from same polyp showing acini of normal appearing Brunner glands

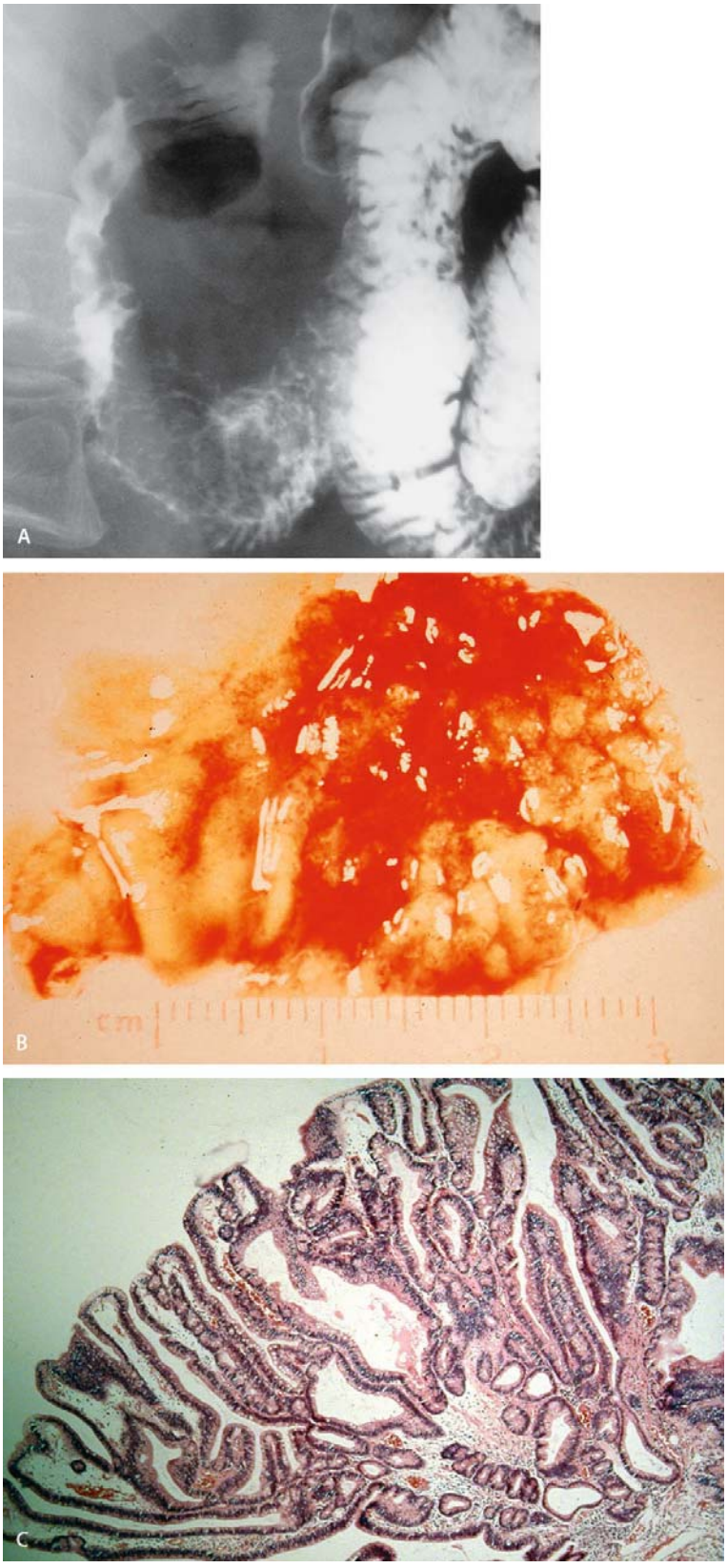

Fig. 13. A Villous adenoma arising near papilla and prolapsing distally. Configuration suggests relatively soft consistency and surface texture appears irregular. **B** Gross specimen of a similar lesion showing the typical features. **C** Low-power photomicrograph showing the branching mucosal pattern and dark-staining, pleomorphic, dysplastic cells which define the lesion histologically

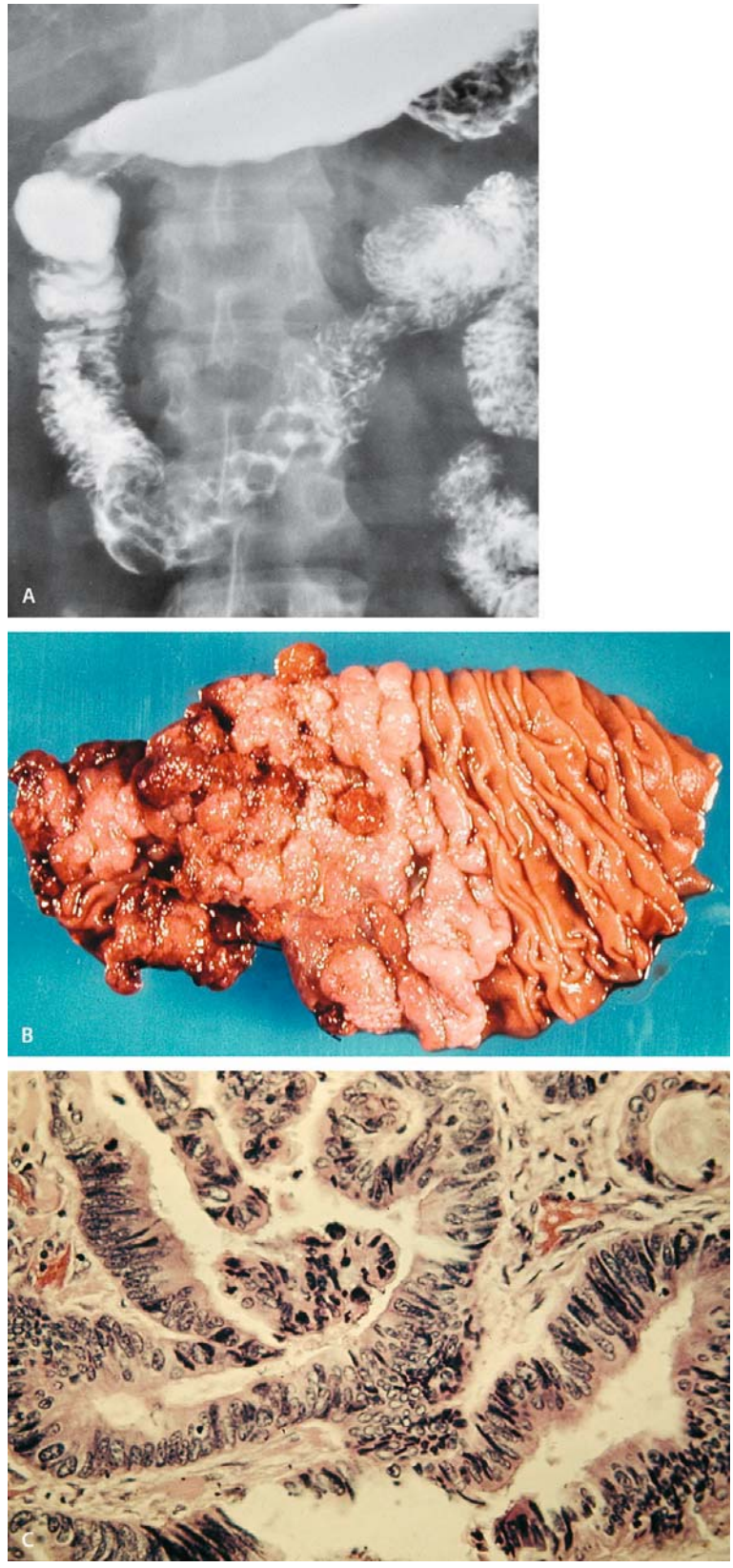

Fig. 14A–C. **A** Radiograph from upper GI series of lobulated villous adenocarcinoma arising at junction of second and third parts of duodenum. **B** Gross specimen shows irregularity of surface texture. **C** High-power photomicrograph showing marked pleomorphism of cells typical of severely anaplastic adenocarcinoma

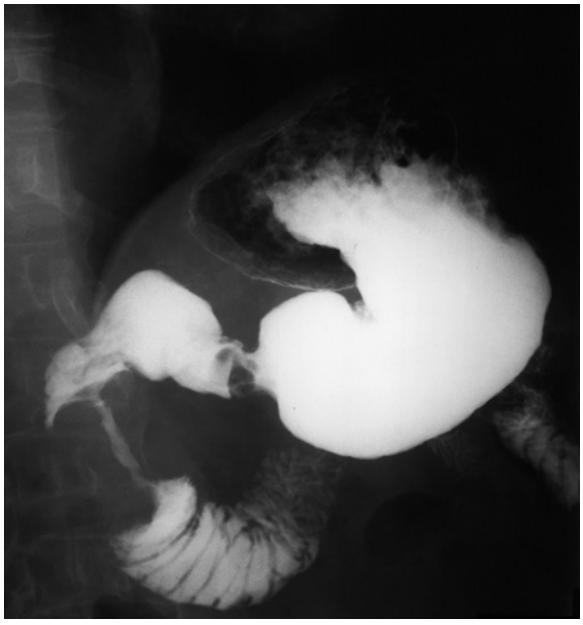

Fig. 15. Spot image of adenocarcinoma of the duodenum presenting as a classic tight annular "apple core" lesion in the second part of the duodenum

Tumors of the Papilla

"Periampullary cancer" is a term that includes tumors arising from the ampullary region of the duodenum or the closely adjacent pancreatic or common bile ducts and whose organ of origin cannot always be differentiated clinically, radiographically, or pathologically [53]. Radiographically, early periampullary tumors may show only a prominent papilla, especially if the growth of the tumor is still within the ampulla itself. Wide variability of normal papilla size and in the configuration of the intrapapillary portion of the common bile duct makes early diagnosis more difficult by conventional studies and by cholangiography. Endoscopic ultrasound may be useful in such cases [54].

More advanced tumors show nodularity, ulceration, and finally, circumferential encasement of the duodenum like that seen in the apple-core lesion common in the colon. Local spread can easily involve the adjacent organs, especially the pancreas. Familial adenomatous polyposis patients are particularly likely to develop tumors in the papilla and periampullary region which may be either adenomas or carcinomas [55].

Tumors arising from the cuboidal cell epithelium of the distal bile duct tend to be locally invasive, hypovascular and incite fibrotic reaction. Being strategically placed, they often come to attention early by obstructing the bile and /or adjacent pancreatic duct while still quite small. Thus, jaundice and a prominent papilla re-

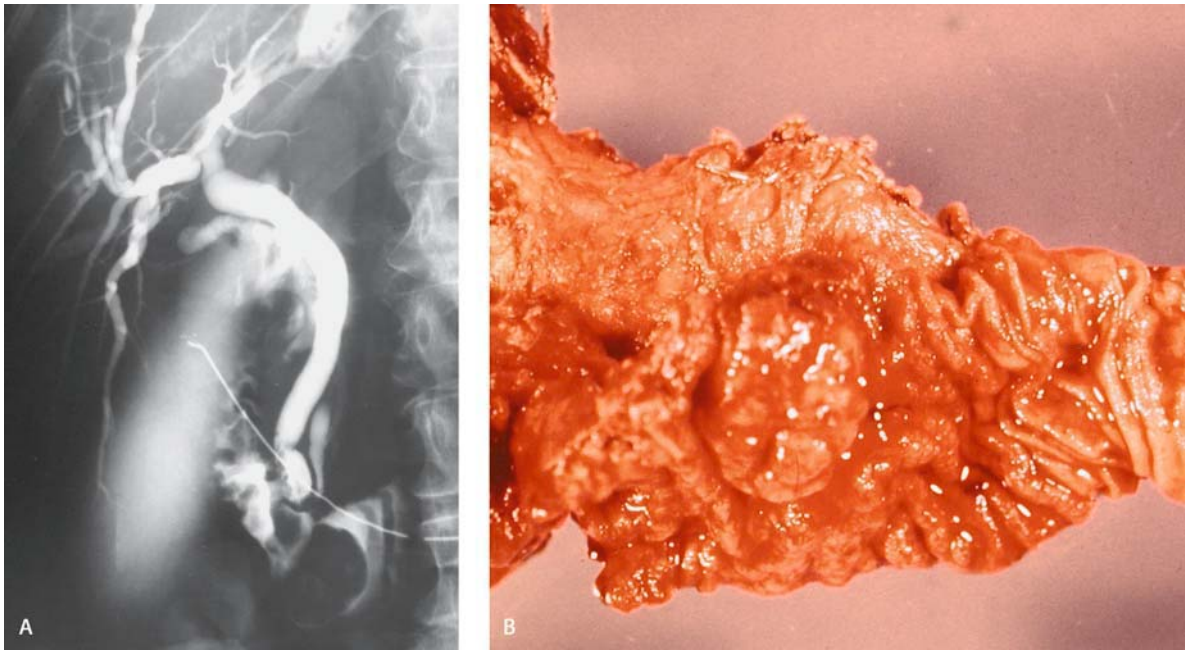

Fig. 16A, B. Peripapillary adenocarcinoma of duodenum. Elderly patient thought to have ascending cholangitis and mildly dilated biliary tree on ultrasound. **A** Transhepatic cholangiogram shows irregular distal CBD and contrast in duodenum outlines component of tumor involving adjacent duodenal lumen. **B** Gross photograph showing tumor in opened duodenum

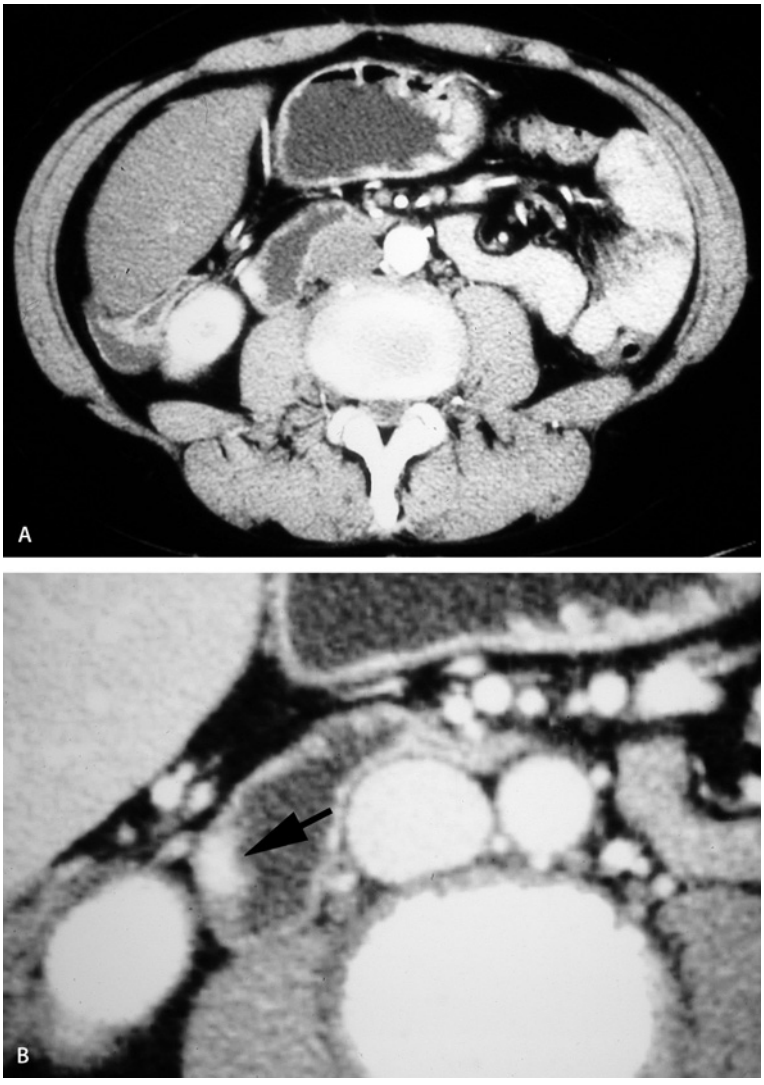

Fig. 17A, B. Gastrinoma. **A** CT showing sessile enhancing lesion on the wall of the second portion of the duodenum. **B** Magnified view of same lesion (*arrow*)

quire such additional diagnostic procedures as endoscopic retrograde cannulation and percutaneous transhepatic cholangiography (Fig. 16).

Endocrine Tumors

Benign and malignant endocrine tumors are more commonly encountered in the duodenum, especially in the descending second portion, than in most of the rest of the bowel. Carcinoid and pancreatic islet cell tumors are the most common but paragangliomas and other neuroendocrine tumors are occasionally found [55–57]. Gastrinomas associated with the Zollinger-Ellison Syndrome are particularly likely to occur in the wall of the proximal duodenum (Fig. 17). These tumors are often small and difficult to detect (Fig. 18). They tend to be vascular and may be seen with multidetector CT scanning with intravenous contrast administration as well as with angiography. If they produce active hormones, those not seen by CT or Angiography sometimes may be localized by venous sampling technique.

Subepithelial Lesions

Tumors may arise in the submucosal mesenchymal tissue of the GI tract. Many of these are slow growing and benign. They often grow toward the lumen being restrained in the opposite direction by the firm, rubbery muscularis propria. The displaced mucosal surface tends to be smooth with rounded edges. Such tumors typically present radiographically as rounded intramural lesions with smooth overlying mucosa. As such lesions become large, however, the epithelium may ulcerate. The malignant counterparts of mesenchymal le-

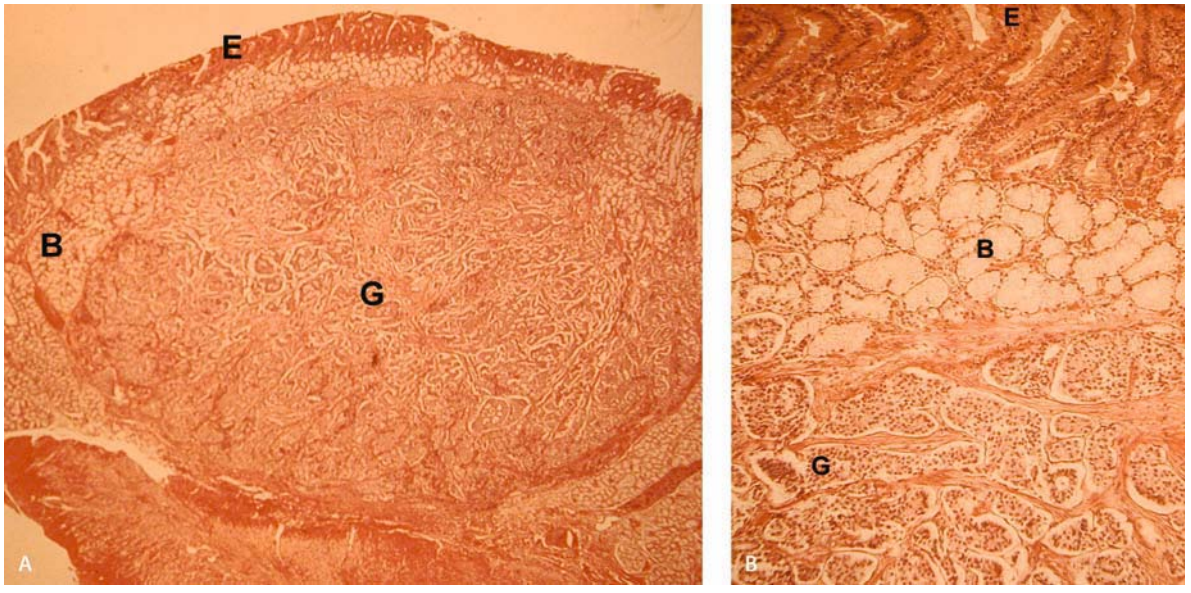

Fig. 18. A Photomicrograph of gastrinoma (*G*) presenting as a tiny nodule in submucosa of duodenum. Note the intact overlying mucosal epithelium (*E*) and normal paler-staining Brunner glands (*B*). **B** Higher-power view of same lesion showing acini of grossly normal appearing pancreatic islet cells intermixed with strands of muscle but infiltrating into the Brunner glands in the lamina propria

sions are termed sarcomas and tend to grow larger, invade adjacent tissue and metastasize.

Masses arising in the muscle wall (e.g., stromal cell tumors and leiomyomas and leiomyosarcomas etc.) may grow either toward the lumen (endoenteric) or away (exoenteric) or in a combination of both patterns. Extrinsic masses sometimes bulge into the lumen, but they typically have very obtuse angles at the margins and tend to displace the lumen centerline earlier than do intrinsic lesions.

Stromal Tumors

Gastrointestinal stromal tumors (GIST) are by far the most common benign mesenchymal tumors of the GI tract, although relatively uncommon in the duodenum [58]. In the past these tumors were generally called leiomyomas and leiomyosarcomas and were thought to arise usually from the smooth muscle of the wall. It has now been determined that only a minority of such lesions demonstrate smooth muscle characteristics. The majority are now considered to arise from stem cells similar to the pacemaker cells of the bowel wall, the interstitial cells of Cajal. They are characterized by expression of a tyrosine kinase growth factor receptor KIT (CD117) [59]. While often small and difficult to detect, these tumors may occasionally become huge but they tend to grow slowly.

The pathological criteria for malignancy in GISTs and smooth muscle lesions are somewhat arbitrary. They depend upon averaging the number of mitotic figures in multiple high-power microscopic fields and an assessment of cellularity and pleomorphism. Malignancy in smooth muscle and GISTs correlates well with size, except in the esophagus where the vast majority are benign, even when very large.

Stromal tumors tend to grow as firm, rubbery, rounded masses of compact intertwined bundles of spindle cells. The tumors have no true capsules but usually easily shell out from surrounding compressed tissue. Their radiographic appearance depends upon their site of origin, size and direction of growth. Tumors arising in the outer layers of the wall tend to grow outward into the surrounding tissue. If small, they cause no symptoms and the majority are probably never detected. When larger, they may appear as extrinsic masses. Lesions arising on the inner aspect of the muscle wall or muscularis mucosae more easily displace the pliable submucosa and mucosa than the firmer muscle wall. Thus they grow toward the lumen and tend to cause symptoms relatively early. Ordinarily the epithelium is stretched smoothly over such submucosal masses, often with obtuse angles at the periphery (Fig. 19). If such lesions become large enough, however, they may protrude into the lumen and develop short pedicles. In that case the mucosa will be tucked around the lesion with acute angles at the boarders, a limitation of the so-called "sulcus sign" sometimes used to distinguish mucosal from submucosal or extrinsic lesions. While the covering mucosa is initially intact, the protruding submucosal mass exposes it to trauma from luminal contents and may

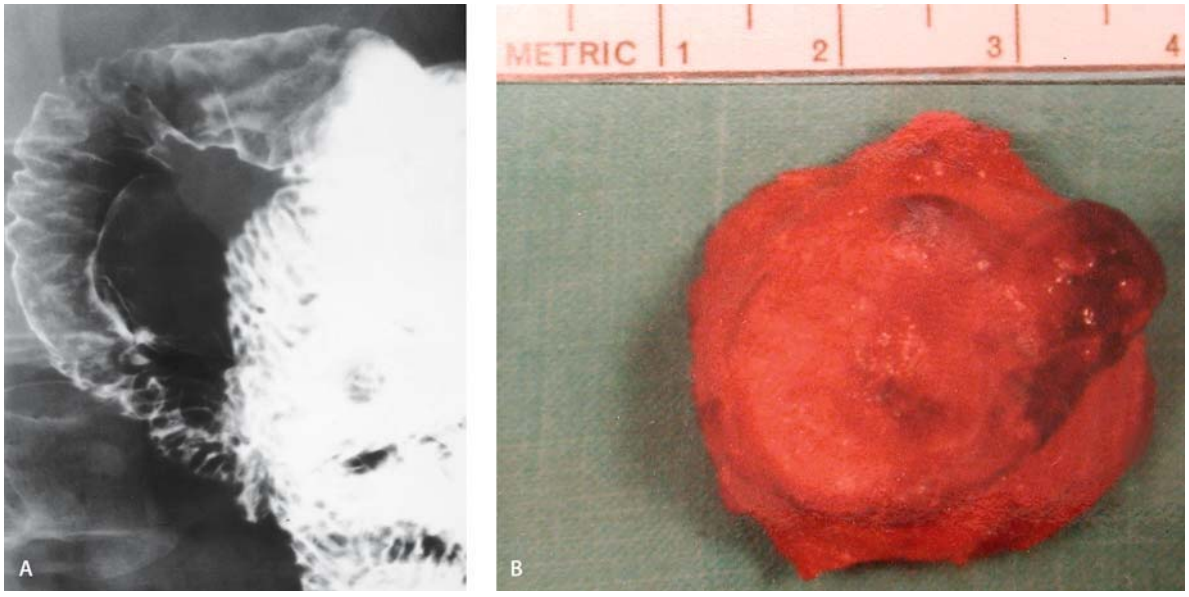

Fig. 19A B. Spindle cell stromal tumor in patient presenting with intermittent GI bleeding. **A** Upper GI study showing smooth submucosal-appearing mass impinging on lumen of descending duodenum. **B** Photograph of gross specimen. (Case courtesy of Robert Tallaksen, MD)

compromise its blood supply. Superficial ulceration, is an expected complication of any such lesion and may be its mode of presentation. Vascularity within stromal tumors is variable, often being rather sparse. Frequently, however, there are prominent arteries in the superficial layers of such tumors and these can be the source of sudden, dramatic hemorrhage when eroded by ulcers. Such behavior is well known with gastric lesions where the luminal contents are ulcerogenic and where the lesions can become larger without luminal compromise.

Stromal tumors are usually solitary, but are multiple in a small percentage of cases. Calcification is rare in GI tract leiomyomas, as opposed to the situation in the uterus. When it occasionally occurs, it can be a useful radiographic clue to the diagnosis.

Lipoma

Lipomas are, uniformly benign, localized proliferations of submucosal fat (Fig. 20). The low attenuation of the

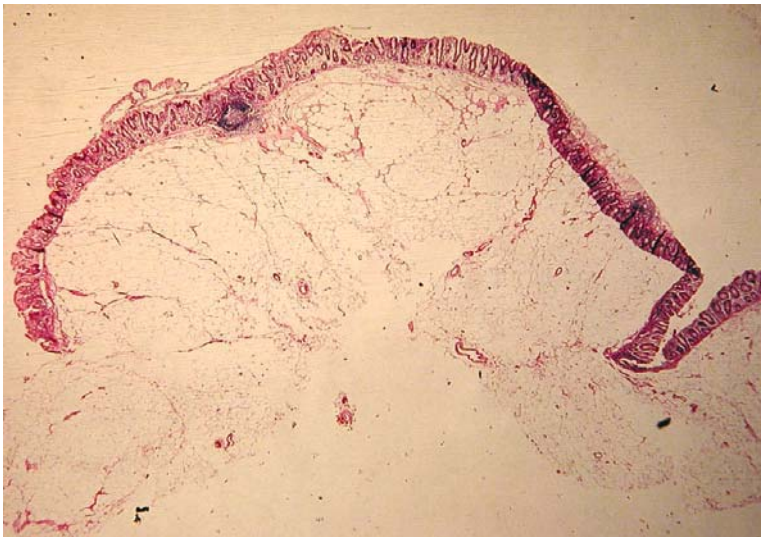

Fig. 20. Lipoma. Low-power photomicrograph shows mass of normal lipocytes beneath intact mucosa. The cells appear clear because the organic solvents used to prepare the slide has removed the lipid cytoplasm

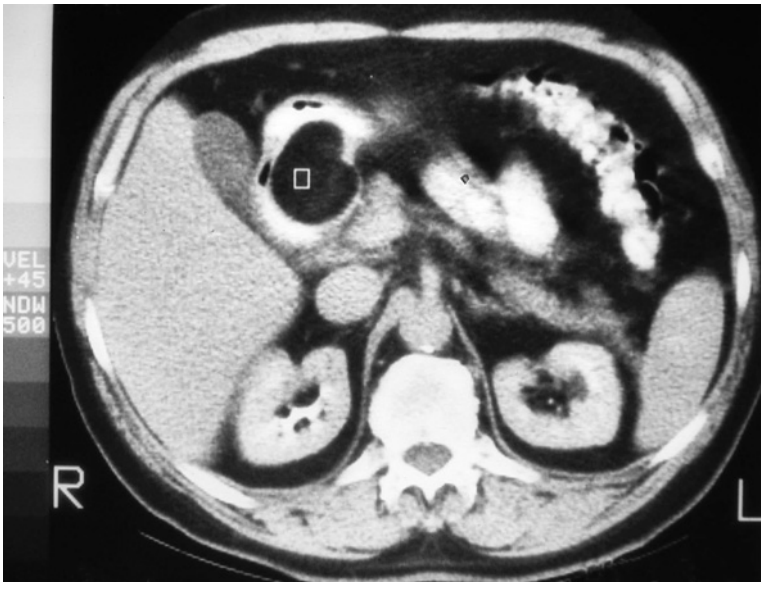

Fig. 21. CT of lipoma in duodenal bulb showing very low attenuation in smooth intraluminal filling defect

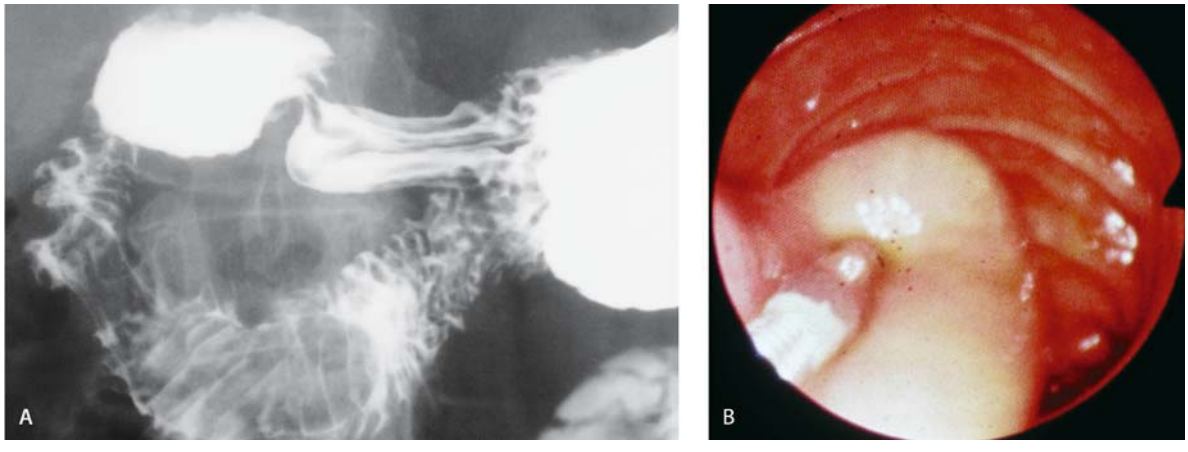

Fig. 22. A Large lipoma arising in descending duodenum and prolapsing distally. **B** Endoscopic photograph of the same lesion being indented by the instrument, demonstrating its characteristic pliability

fat is usually diagnostic on CT imaging [60, 61] (Fig. 21). Like leiomyomas, they grow by slow compression of surrounding tissue and usually no true capsule can be defined. The soft texture and submucosal origin dictate that the tumors grow almost entirely into the lumen with relatively little effect on the muscle wall. As they become large they may form pedunculated, intraluminal, polypoid masses and may cause intussusception (Fig. 22A). At endoscopy they appear smooth and characteristically they can be indented by the endoscope (Fig. 22B). The overlying mucosa is initially intact but may eventually breakdown and ulceration is one means of presentation.

Lymphoma may arise in the mesenchymal lymphoid tissue of any part of the bowel but primary lymphoma in the duodenum is very rare. Lymphoma involving the duodenum is generally part of a more widespread process including the periduodenal lymph nodes. As is true elsewhere in the bowel, lymphoma may have many varied appearances. It may be finely nodular, grossly polypoid, infiltrative with mucosal fold changes, such as fold thickening, flattening, constriction or involve extrinsic mesenteric tissue (with extrinsic mass effect). Typically lobulated lesions result. The mucosa may be intact until late, but ulceration into the soft, cellular adjacent tumor masses is often extensive, causing an ulcerated, dilated segment. Extensive infiltration of the wall, with or without ulceration, may cause weakening of the wall. Upstream peristaltic pressure balloons out the diseased segment creating so call “aneurysmal dilatation, a finding more common in the pediatric than the adult patient. Lymphoma may mimic other, more common, du-

odenal deformities, such as those due to hyperplasia of Brunner's glands, pancreatitis, Crohn's disease, and peptic ulceration.

Secondary Tumors

Metastatic involvement of the duodenum is more often by invasion from contiguous organs than by hematogenous or lymphatic spread from distant sites. Almost the entire length of the duodenum is contiguous to the pancreas, and pancreatic carcinoma is the most frequent invading neoplasm. Carcinoma of the gallbladder, or kidneys may also directly invade the contiguous duodenum. The duodenal bulb and immediate postbulbar portion may be deformed or even invaded by metastatic nodes in the liver hilum. The changes of metastatic disease in the duodenum are typical of metastatic invasion anywhere in the gastrointestinal tract and include fixation of mucosal folds, spiculation, nodularity, and ulceration. Primary tumors such as melanoma and lung and breast carcinoma, which commonly metastasize via blood and lymphatic pathways, involve the duodenum in common with the rest of the bowel (Fig. 23). Metastases from remote primaries are frequently multiple but can have many appearances depending upon the primary type and whether the tumor deposits are submucosal or serosal. Breast cancer, in particular has a tendency to resemble sclerosing mucin-producing adenocarcinoma. Annular constricting and obstructing metastatic lesions may be indistinguishable from primary duodenal carcinoma.

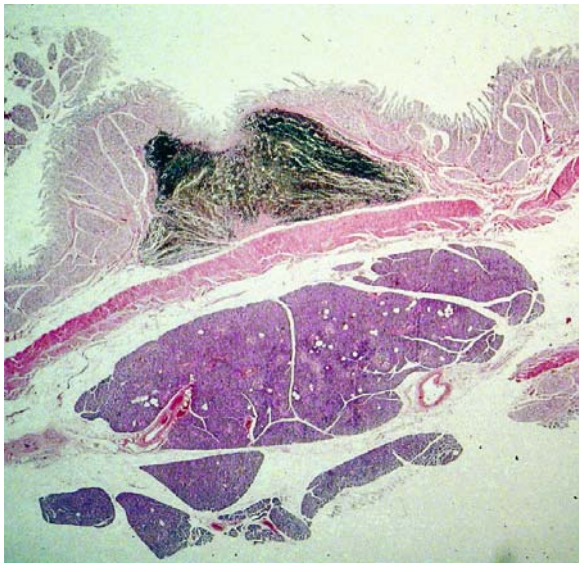

Fig. 23. Metastatic melanoma deposit in the descending duodenum. Low-power photomicrograph (H&E x6 original magnification) showing dark melanin-containing cells in the submucosa surrounded by normal Brunner glands between the intact, but deformed mucosa and the muscularis propria. The mass of darker-staining tissue on the other side of the muscularis is normal pancreas

References

1. Scholz FJ (1981) Duodenum in Surgical Radiology: a complement in radiology and imaging to the Sabiston Davis Christopher Textbook of Surgery. Teplick JG, Haskin ME. Philadelphia, Saunders, pp 502–537
2. Jayaraman MV, Mayo-Smith WW, et al (2001) CT of the duodenum: an overlooked segment gets its due. Radiographics 21:S147–S160
3. Chen YC, Yeh CN, Tseng JH (2003) Symptomatic adult annular pancreas. J Clin Gastroenterol 36(5):446–450
4. Ladd AP, Madura JA (2001) Congenital duodenal anomalies in the adult. Arch Surg 136(5):576–584
5. Stelling T, von Rooij WJ, Tio TL, Reeders JW,et al (1987) Pancreatitis associated with congenital duodenal duplication cyst in an adult. Endoscopy 19(4):171–173
6. Procacci C, Portuese A, Fugazzola C, Pederzoli P, Caudana R, Gallo E, Bergamo Andreis IA, Spiller M, Zonta L, Graziani R, et al (1988) Duodenal duplication in the adult: its relationship with pancreatitis. Gastrointest Radiol 13(4):315–322
7. Barr LL, Hayden CK Jr, Stansberry SD, et al (1990) Enteric duplication cyst in children: Are their ultrasonic wall characteristics diagnostic? Ped Rad 20:326–328
8. Bender TM, Ledesma-Medina J, Ooh KS (1991) Radiographic manifestations of anomalies of the gastrointestinal tract. Rad Clin North Amer 29:335–344
9. Teele RL, Henschke CT, Tapper D (1980) The radiographic ultrasonographic evaluation of enteric duplication cysts. Ped Rad 10:9–13
10. Scholz FJ, Carrera GF, Larsen CR (1976) The choledochocele: correlation of radiological, clinical and pathological findings. Radiology 118(1):25–28
11. Laudan JC, Norton GI (1963) Intraluminal Duodenal Diverticulum. Am J Roentgenol Radium Ther Nucl Med 90:756–760
12. Yang TS, Greenspan A, Farber M, et al (1974) Intraluminal duodenal diverticulum. Arch Surg 109(1):113–115
13. Fidler JL, Saigh JA, Thompson JS, Habbe TG (1998) Demonstration of intraluminal duodenal diverticulum by computed tomography. Abdom Imaging 23(1):38–39
14. Pratt AD Jr (1971) Current concepts of the obstructing duodenal diaphragm. Radiology 100(3):637–643
15. Sampliner J, Kollins SA, Hermann RE (1976) Intraluminal duodenal diverticulum associated with trisomy 21. Am J Roentgenol 127(4):677–679
16. Thoeni RF, Gedgaudas RK (1980) Ectopic pancreas: usual and unusual features. Gastrointest Radiol 5(1):37–42
17. Gelfand DW (1994) Radiological diagnosis of duodenitis. Radiol Clin North Am. 32(6):1253–1258
18. Levine MS, Turner D, Ekberg O, et al (1991) Duodenitis: a reliable radiologic diagnosis? Gastrointest Radio 16:99
19. Lichtenstein JE (1993) Inflammatory conditions of the stomach and duodenum. Radiology Clinics of North America 31:1315–1333
20. Glick SN (1994) Duodenal ulcer. Radiol Clin North Am 32(6):1259–1274
21. Lichtenstein JE, Madewell JE, Feigin DS (1979) The collar button ulcer. Gastrointest Radiol 4:79–84
22. Nelson SW, Lichtenstein JE (1983) Zollinger-Ellison Syndrome. In: Marshak R, Maklansky D (eds) Radiology of the Stomach. Philadelphia, WB Saunders
23. Roy PK, Venzon DJ, Shojamanesh H, Abou-Saif A, Peghini P, Doppman JL, Gibril F, Jensen RT (2000) Zollinger-Ellison syndrome. Clinical presentation in 261 patients. Medicine (Baltimore) 79(6):379–411
24. Jones B, Bayless TM, Hamilton SR, Yardley JH (1984) "Bubbly" duodenal bulb in celiac disease: radiologic-pathologic correlation. AJR Am J Roentgenol 142(1):119–122

25. Marn CS, Gore RM, Ghahremani GG (1986) Duodenal manifestations of non-tropical sprue. Gastrointest Rad 11(1): 30–35
26. Schweiger GD, Murray JA (1998) Postbulbar Duodenal Ulceration and Stenosis with Celiac Disease; Abdominal Imaging 23(4): 347–349
27. Levine MS (1989) Crohn's disease of the upper gastrointestinal tract. Radiol Clin North Am 25: 79–91
28. Poggioli G, Stocchi L, Laureti S, Selleri S, Marra C, Salone MC, Cavallari A (1997) Duodenal involvement of Crohn's disease: three different clinicopathologic patterns. Dis Colon Rectum 40(2): 179–183
29. Legge DA, Hoffman HN 2nd, Carlson HC (1971) Pancreatitis as a complication of regional enteritis of the duodenum. Gastroenterology 61(6): 834–837
30. Zarnow H, Grant TH, Spellberg M, Levin B (1976) Unusual complications of regional enteritis. Duodenobiliary fistula and hepatic abscess. JAMA 235(17): 1880–1881
31. Graham DY (1989) *Campylobacter pylori* and peptic ulcer disease. Gastroenterology 96: 615–625
32. Peterson WL (1991) Helicobacter pylori and peptic ulcer disease. N Engl J Med 324: 1043–1048
33. Agrawal S, Shetty SV, Bakshi G (1999) Primary hypertrophic tuberculosis of the pyloroduodenal area: report of 2 cases. J Postgrad Med 45(1): 10–12
34. Berkmen YM, Rabinowitz J (1972) Gastrointestinal manifestations of the strongyloidiasis. Am J Roentgenol Radium Ther Nucl Med 115(2): 306–311
35. Medina LS, Heiken JP, Gold RP (1992) Pipestem appearance of small bowel in strongyloidiasis is not pathognomonic of fibrosis and irreversibility. AJR Am J Roentgenol 159(3): 543–544
36. Dallemand S, Waxman M, Farman J (1983) Radiological manifestations of Strongyloides stercoralis. Gastrointest Radiol 8(1): 45–51
37. Michelassi F, Erroi F, Dawson PJ, et al (1989) Experience with 647 consecutive tumors of the duodenum, ampulla, head of the pancreas, and distal common bile duct. Ann Surg 210(4): 544–54; discussion 554–556
38. Kazerooni EA, Quint LE, Francis IR (1992) Duodenal neoplasms: predictive value of CT for determining malignancy and tumor resectability. AJR Am J Roentgenol 159(2): 303–309
39. Theros E (1969) The value of radiologic-pathologic correlation in the education of the radiologist. AJR 107: 235–257
40. Valdes-Dapena AM, Stein GN (1970) Morphologic Pathology of the Alimentary Canal. Philadelphia, WB Saunders
41. Lichtenstein JE (1986) Basics of Radiologic-Pathologic Correlation in the GI Tract. Chapter in Tavaras JM, Ferrucci JT Jr, Eds., Radiology: Diagnosis/Imaging/Intervention, Philadelphia, JB Lippincott Co, Vol. 4, Chapter 4, pp 1–19. (Revised 1991 and again revised by Gore R. 1994)
42. Reeders JWAJ, Rosenbusch G (1994) Radiology of benign and malignant diseases of the duodenum. In: Freeny PC, Stevenson GW (eds) Margulis and Burhenne's Alimentary Tract Radiology. St. Louis, CV Mosby Co, pp 467–511
43. Perez A, Saltzman JR, Carr-Locke DL, Brooks DC, Osteen RT, Zinner MJ, Ashley SW, Whang EE (2003) Benign nonampullary duodenal neoplasms. J Gastrointest Surg 7(4): 536–541
44. Fuller JW, Cruse CW, Williams JW (1977) Hyperplasia of Brunner's glands of the duodenum. Am Surg 43(4): 246–250
45. Merine D, Jones B, Ghahremani GG, Hamilton SR, Bayless TM (1991) Hyperplasia of Brunner glands: the spectrum of its radiographic manifestations. Gastrointest Radiol 16(2): 104–108
46. Saida Y, Matsueda K, Itai Y (2002) Distal migration of duodenal tumors: simple prolapse or intussusception? Abdom Imaging 27(1): 9–14
47. Ring EJ, Ferrucci JT Jr, Eaton SB Jr, Clements JL (1972) Villous adenomas of the duodenum. Radiology 104(1): 45–48
48. Kutin ND, Ranson JH, Gouge TH, Localio SA (1975) Villous tumors of the duodenum. Ann Surg 181(2): 164–168
49. Bjork KJ, Davis CJ, Nagorney DM, Mucha P Jr (1990) Duodenal villous tumors. Arch Surg 125(8): 961–965
50. Alwmark A, Andersson A, Lasson A (1980) Primary carcinoma of the duodenum. Ann Surg 191(1): 13–18
51. Bosse G, Neely JA (1969) Roentgenologic findings in primary malignant tumors of the duodenum. Report of 27 cases. Am J Roentgenol Radium Ther Nucl Med 107(1): 111–118
52. Spira IA, Ghazi A, Wolff WI (1977) Primary adenocarcinoma of the duodenum. Cancer 39(4): 1721–1726
53. Jean M, Dua K (2003) Tumors of the ampulla of Vater. Curr Gastroenterol Rep 5(2): 171–175
54. Chen CH, Tseng LJ, Yang CC, Yeh YH (2001) Preoperative evaluation of periampullary tumors by endoscopic sonography, transabdominal sonography, and computed tomography. J Clin Ultrasound 29(6): 313–321
55. Buck JL, Elsayed AM (1993) Ampullary tumors: radiologic-pathologic correlation. Radiographics 13(1): 193–212
57. Attanoos R, Williams GT (1991) Epithelial and neuroendocrine tumors of the duodenum. Semin Diagn Pathol 8(3): 149–162
56. Evans WE, Armstrong RG, Schulte W, Garancis JC (1972) Ulcerogenic tumor of the duodenum. Am J Surg 124(5): 596–599
58. Serraf A, Klein E, Schneebaum S, Davidson B, et al (1988) Leiomyomas of the duodenum. J Surg Oncol 39(3): 183–186
59. Levy AD, Remotti HE, Thompson WM, et al (2003) Gastrointestinal stromal tumors: Radiologic features with pathologic correlation. Radiographics 23: 283–304
60. Megibow AJ, Redmond PE, Bosniak MA, et al (1979) Diagnosis of gastrointestinal lipomas by CT. AJR 133: 743–745
61. Whetstone MR, Zuckerman MJ, Saltzstein EC, Boman D (1985) CT diagnosis of duodenal lipoma. Am J Gastroenterol 80(4): 251–252

Primary Tumors of the Small Intestine

Nicholas C. Gourtsoyiannis, Dimitris Bays

4.4

Contents

Introduction

Primary small intestinal neoplasms are universally and surprisingly rare. Although the small intestine represents more than 75% of the length and 90% of the mucosal surface area of the gastrointestinal tract, it is estimated that they account for 3%–6% of all gastrointestinal tract neoplasms [1].

Documented rarity complicated further by nonspecific clinical presentation and a small index of clinical suspicion makes the detection of these tumors a challenge for both the physician and the radiologist. A mean delay of up to 3 years, from first symptoms to diagnosis, has been reported for benign tumors and 18 months for malignant neoplasms [2]. Inadequate radiological studies or incorrect interpretation of radiological findings are estimated to account for an average 12 months of delay in diagnosing primary malignancies of the small intestine [3].

The cornerstone of preoperative diagnosis is contrast radiology. The radiological characteristics of these neoplasms as shown by enteroclysis and computed tomography (CT) correlate almost perfectly with the morphological changes seen in the gross pathology specimens [4]. This ability to accurately image small intestinal neoplasms, independently of their size, anatomic localization and growth tendency, represents a major improvement in their diagnosis and management.

Benign Neoplasms

Benign small intestinal neoplasms are reported to account for approximately 0.5%–2% of all gastrointestinal tract neoplasms. Their histopathological variety includes more than 12 types, among which leiomyomas and adenomas appear to be the most common and the only two with definite malignant predisposition [5]. Lipomas, vascular and neurogenic tumors, hamartomas and heterotopias are less frequently encountered.

Gastrointestinal stromal tumors (GISTs) are a unique type of mesenchymal tumor that may occur anywhere in the gastrointestinal tract. They exhibit a wide spectrum of clinical behavior from benign, small incidentally detected nodules to frank malignant tumors [6]. Until recently GISTs were categorized as smooth muscle tumors including leiomyomas and leiomyosarcomas. The best defining feature of GISTs is their expression of KIT (CD 117), a tyrosine kinase growth factor receptor. Immunoreactivity for KIT distinguishes GISTs from leiomyomas, leiomyosarcomas, schwannomas and neurofibromas [7]. However, radiological criteria to separate GISTs from other mesenchymal, nonepithelial tumors have not yet been developed [8].

Clinical presentation of benign small intestinal neoplasms is often minimal, intermittent and nonspecific and depend on their extension and growth pattern rather than their histological type. Occult gastrointestinal bleeding or anemia and abdominal pain are the most common presenting symptoms, while intestinal obstruction, intussusception, a palpable abdominal mass and weight loss are less frequently present. Nearly 50% of patients remain asymptomatic.

The radiological characteristics of benign neoplasms are directly related to the type of growth, which may be intraluminal, extraluminal or a combination of both. The radiographic features most commonly encountered are filling defects of different sizes, either solitary or

multiple. A combination of morphology and certain clinical data such as location predilection, growing tendency, and size and number of lesions may be of considerable help in reaching a more specific diagnosis [5].

Leiomyomas (Benign GISTs)

Leiomyomas are the most frequently encountered symptomatic benign small intestinal neoplasms, originating in the circular or longitudinal muscle coats and rarely in the muscularis mucosa. They are mostly solitary lesions, distributed throughout the jejunum and ileum in over 80% of cases.

Three distinctive radiological appearances mirroring the type of growth have been described [9]. Intraluminal tumors appear as punched-out, round or semilunar filling defects, demarcated by sharp angles to the intestinal wall. Subserosal leiomyomas frequently grow larger and produce a mass effect outside the intestinal wall or a "blank space" between neighbouring loops of intestine (Fig. 1). Displacement or smooth indentation of the intestinal wall, or a tending deformity (Fig. 2) indicative of the neoplastic attachment, may also be shown. Dumbbell leiomyomas combine features of both, an intraluminal protrusion and an extraintestinal mass (Fig. 3). Ulceration is frequently present in leiomyomas and may be demonstrated radiologically in up to one-third of cases. When seen, ulcerations are usually single, small, well defined, and round or linear in shape (Fig. 4). Ulceration occurs much more frequently in leiomyosarcomas, largely in the form of cavitation.

Besides enteroclysis, CT may also contribute to the preoperative diagnosis. Ancillary CT findings include a round or semilunar, smoothly outlined, homogeneous, soft tissue mass, associated with the intestinal wall, showing marked homogeneous or rim contrast enhancement (Fig. 5) and absence of metastases or mesenteric changes [10].

Small intestinal leiomyomas need to be differentiated from neurogenic and carcinoid tumors, but even

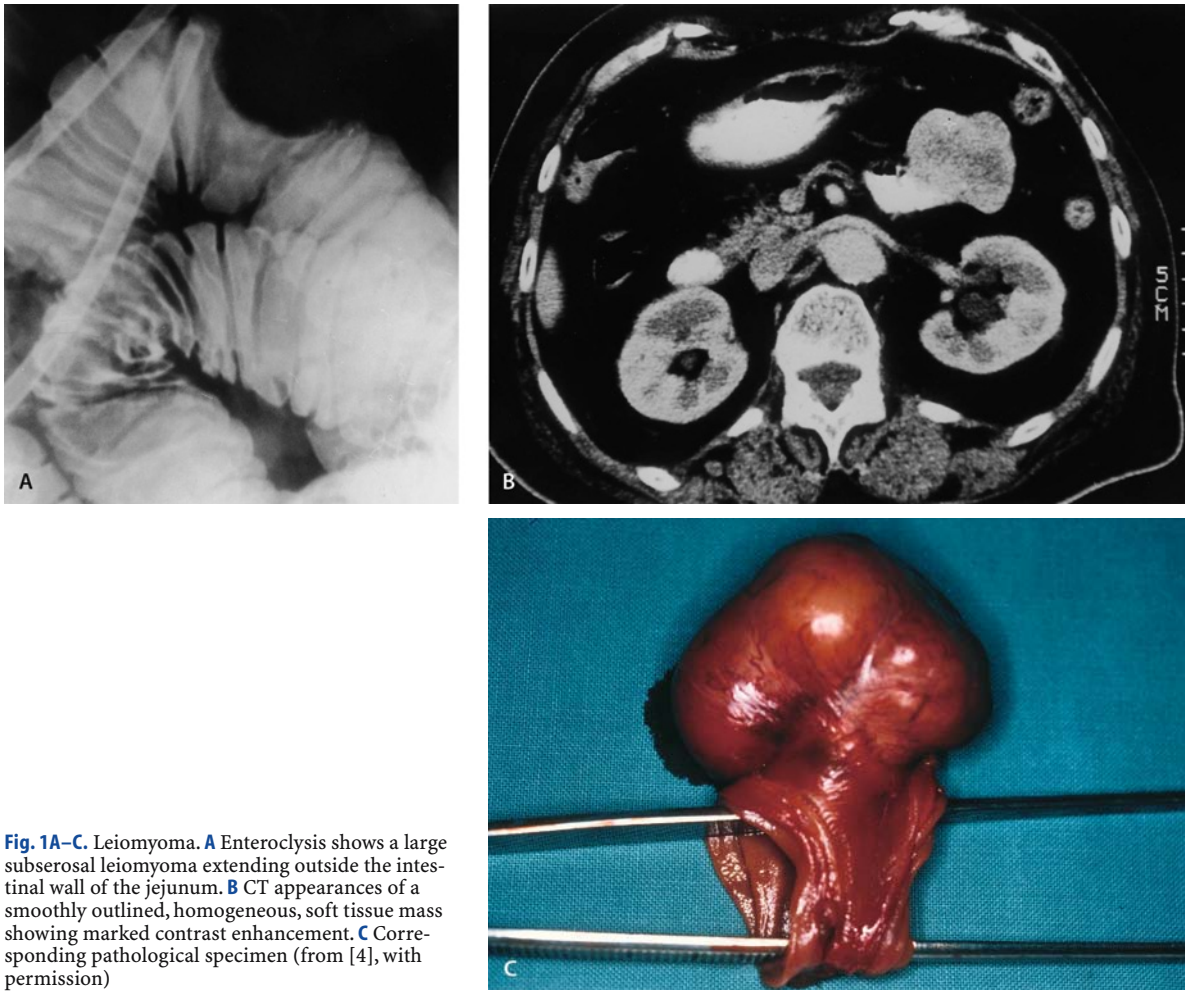

Fig. 1A–C. Leiomyoma. **A** Enteroclysis shows a large subserosal leiomyoma extending outside the intestinal wall of the jejunum. **B** CT appearances of a smoothly outlined, homogeneous, soft tissue mass showing marked contrast enhancement. **C** Corresponding pathological specimen (from [4], with permission)

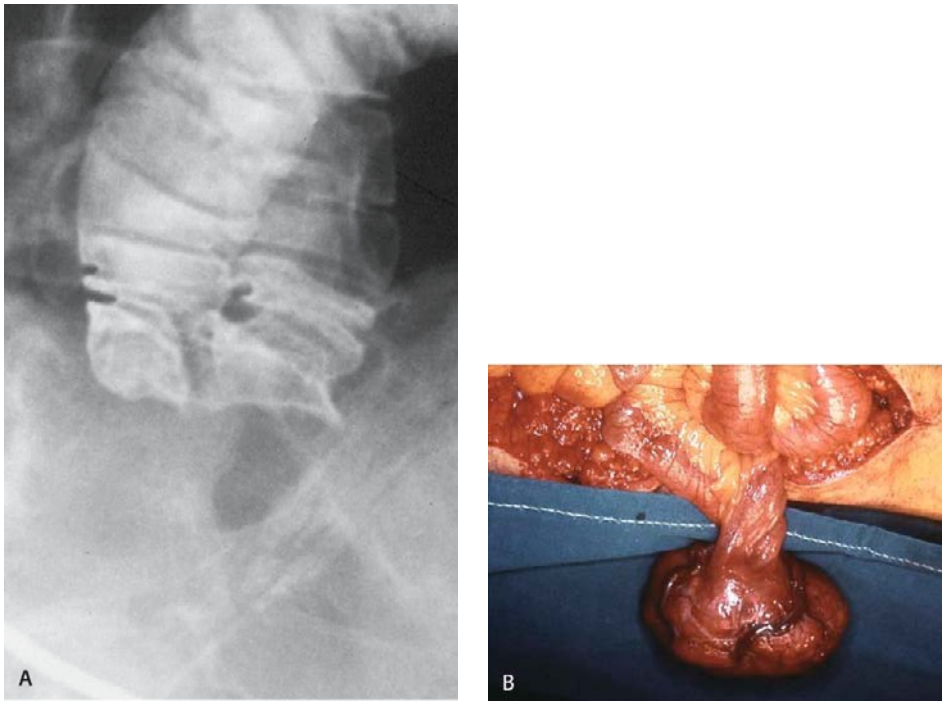

Fig. 2. A Enteroclysis study of an extraluminal leiomyoma. Local traction of an ileal loop causing tenting deformity with a biconcave contour on the intestinal wall. **B** Corresponding view of the neoplasm and its attachment to the intestine, on the operating table (from [9], with permission)

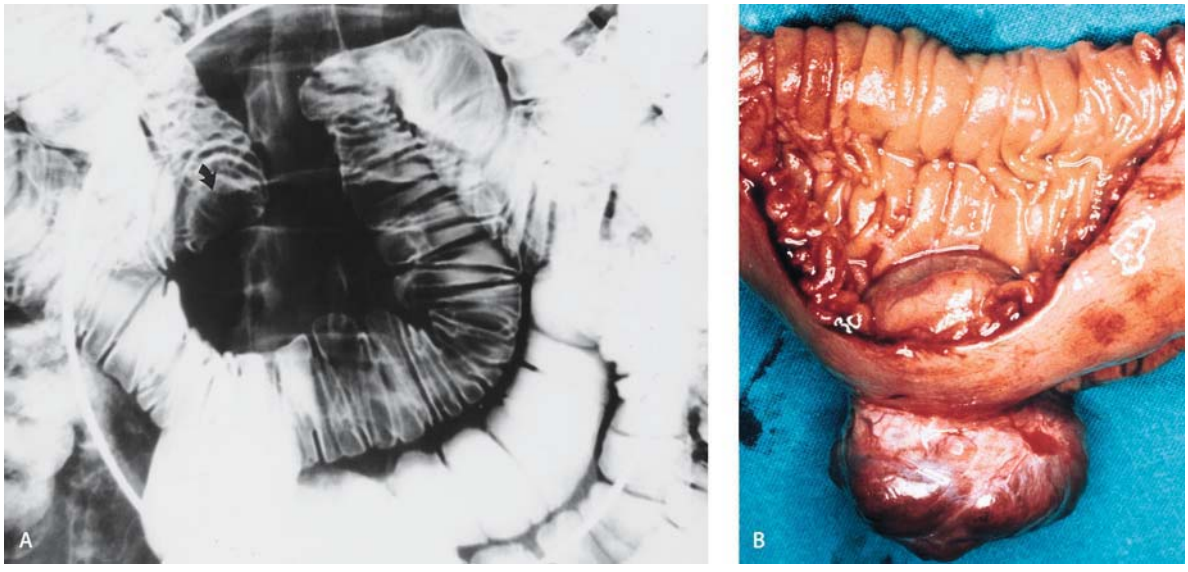

Fig. 3. Dumbbell leiomyoma. **A** Enteroclysis shows a small, semilunar, intraluminal filling defect (*arrow*) and displacement of adjacent intestinal loops by the extraluminal portion of the neoplasm causing a so-called blank space. **B** Resected specimen demonstrates both portions of leiomyoma (from [4], with permission)

more from their malignant counterparts. No radiological differences have been found between leiomyomas and leiomyosarcomas. It appears however, that the above-described features in neoplasms smaller than 6 cm, in the absence of lymph node enlargement or liver metastases, large ragged ulceration, excavation or fistula formation, indicate that the neoplasm in benign [9].

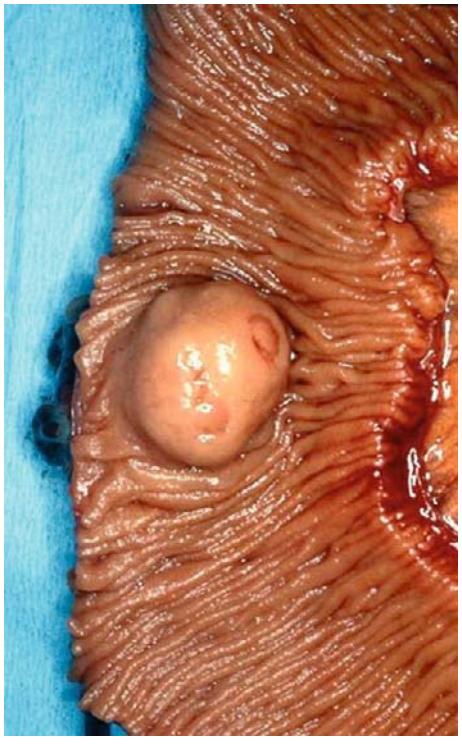

Fig. 4. Resected pathology specimen outlines a dumbbell leiomyoma with two shallow oval-shaped ulcers (from [13], with permission)

Adenomas

Adenomas are estimated to account for up to 20% of benign small intestinal neoplasms. They consist of glandular epithelium exhibiting definite malignant predisposition and are currently classified histologically as tubular, tubulovillous and villous [11]. "Adenomatous polyps" and "villous adenomas" are two terms widely used to designate their growth pattern and gross morphological appearance.

Adenomatous polyps feature as intraluminal filling defects of small size, averaging less than 2 cm. They are smoothly outlined, round, oval or slightly lobulated in shape, and they are often solitary and sessile. When multiple, they usually affect a single segment, are of different sizes and may be pedunculated. This latter appearance is in contrast with familiar polyposis, where filling defects are mostly distributed throughout the entire small intestine and colon, are sessile and mostly of equal size.

Villous adenomas are larger lesions, over 3 cm in size, are invariably broad-based and radiographically present as lobulated, cauliflower-like filling defects, exhibiting multiple radiolucent striations interspersed with frond-like projections [12].

The CT appearance may be helpful in depicting such lesions. A sharply demarcated soft tissue mass, well confined within the boundaries of the intestinal lumen may

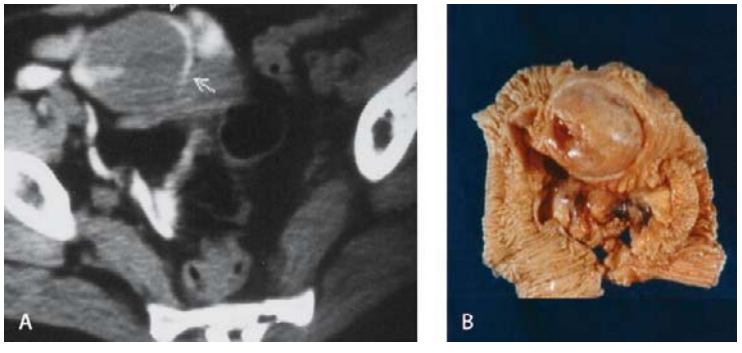

Fig. 5. A Postcontrast CT scan of a leiomyoma demonstrates a homogeneous, smoothly outlined, soft tissue mass with a discrete ulceration and rim contrast enhancement (*arrow*). **B** Corresponding resected specimen (courtesy of Dr. E. Mako)

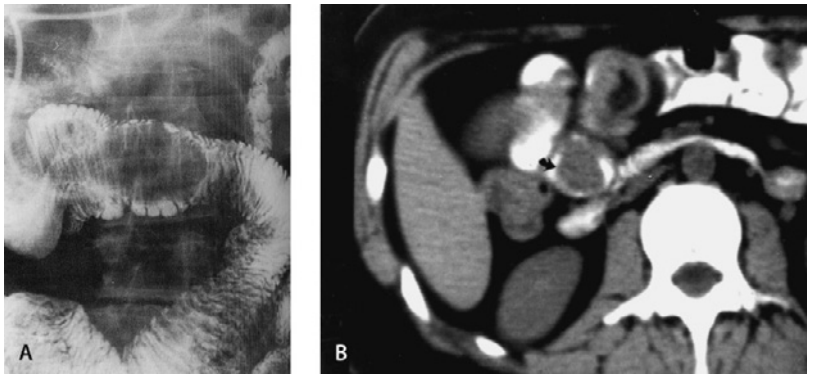

Fig. 6A, B. Adenomatous polyp. **A** Enteroclysis shows a large, solitary, oval shaped, finely demarcated, intraluminal filling defect in the duodenum. **B** CT examination of the same patient demonstrates a homogeneous, intraluminal, well marginated mass in the third portion of the duodenum (*arrow*) (from [4], with permission)

be demonstrated, with homogeneous, moderate contrast enhancement (Fig. 6).

The radiological diagnosis of adenomas can be difficult. The differential diagnosis may include polypoid adenocarcinoma of the duodenum, Brunner's gland adenoma, hamartomatous polyps seen with the Peutz-Jeghers syndrome, inflammatory fibroid polyp and rarely myoepithelial hamartoma or hemangioma [13]. Brunner's gland adenomas present as solitary, smoothly lobulated, usually pedunculated, large filling defects in the second portion of the duodenum. Peutz-Jeghers hamartomas are shown as multiple polyps of different sizes exhibiting coarse lobulation, broad distribution and coalescence, with possible synchronous similar lesions in the stomach and colon. Inflammatory fibroid polyps usually appear as a solitary, round or elongated filling defect, 2–6 cm in size, predominantly located in the ileum.

Lipomas

Lipomas are estimated to be the third most common benign neoplasm. In the majority of cases they arise in the submucosa and are encapsulated, mostly solitary, well circumscribed, ovoid or lobulated, homogeneous and yellowish colored masses of adult adipose tissue.

On barium studies, lipomas are demonstrated as sharply marginated, solitary, sessile, intraluminal filling defects, averaging 3–4 cm in diameter. Their shape conforms to that of the small intestine and is easily deformed by peristalsis, compression or palpation during fluoroscopy [14]. On CT, features of a smooth, ovoid or spherical mass, homogeneous in density, exhibiting attenuation values of –40 to –100 HU, are considered characteristic (Fig. 7).

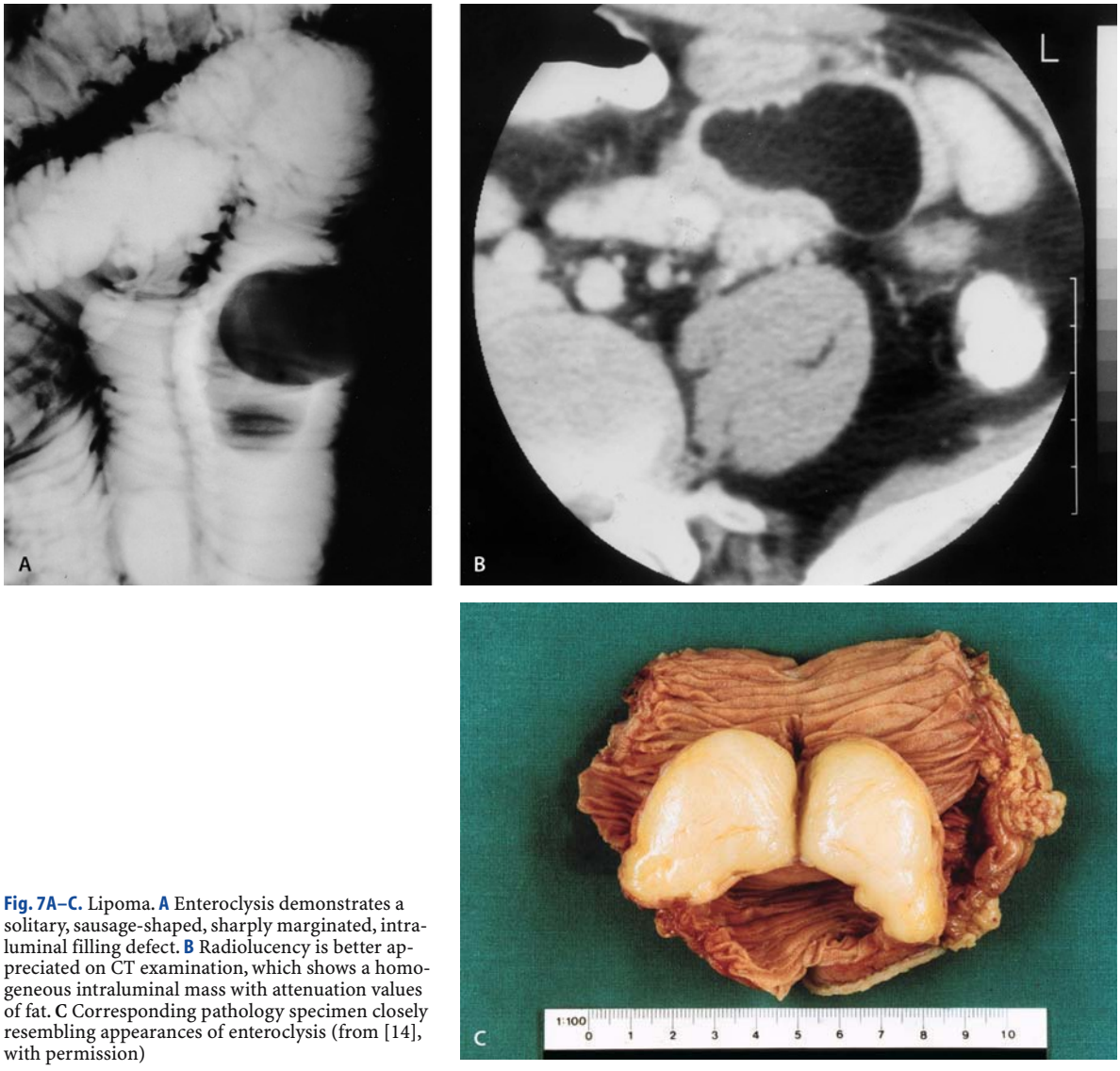

Fig. 7A–C. Lipoma. **A** Enteroclysis demonstrates a solitary, sausage-shaped, sharply marginated, intraluminal filling defect. **B** Radiolucency is better appreciated on CT examination, which shows a homogeneous intraluminal mass with attenuation values of fat. **C** Corresponding pathology specimen closely resembling appearances of enteroclysis (from [14], with permission)

Neurogenic Tumors

Neurogenic tumors account for 2%–6% of all benign small intestinal neoplasms. They arise from subserosal nerve sheaths or cells of the plexus of Auerbach and Meissner and result in polypoid masses, mostly subserosal along the antimesenteric border, rarely exhibiting malignant potential. Neurilemmoma (schwannoma), a mostly solitary and encapsulated tumor, and neurofibroma, which is characteristically multiple in cases of neurofibromatosis (von Recklinghausen disease), are the most frequent types encountered. Solitary neurogenic tumors are located in the jejunum in approximately 50% of cases and average less the 5 cm in diameter.

It may be difficult to distinguish these tumors radiologically. They appear as smoothly surfaced, well-defined, occasionally ulcerated polypoid masses. Intraluminally protruding lesions are easily detected (Fig. 8), while subserosal or small-sized lesions may be elusive or poorly depicted. Dumbbell-type tumors, may be also encountered (Fig. 9) [13]. Preoperative differential diagnosis of solitary neurogenic tumors from intestinal leiomyomas is extremely difficult, since their presenting symptoms, type of growth and radiological appearances are similar [9].

Malignant Neoplasms

Primary malignant small intestinal neoplasms account for less than 2% of primary gastrointestinal malignancies. It is estimated that they are perhaps the most devastating neoplasms of the gastrointestinal tract, since at the time of diagnosis less than 50% are amenable to resection [14]. Despite major advances, both in surgery and diagnostic imaging, survival rates from these tumors have not improved during the past four decades. Universal experience reinforces the need for early detection [3].

The most common primary malignancies include adenocarcinoma, carcinoid tumor, lymphoma and leiomyosarcoma. Their distribution along the small intestine varies according to the specific type. The majority of adenocarcinomas occur in the duodenum and jejunum; carcinoid and lymphomas are usually located in the ileum and leiomyosarcomas arise with equal frequency in the jejunum and ileum.

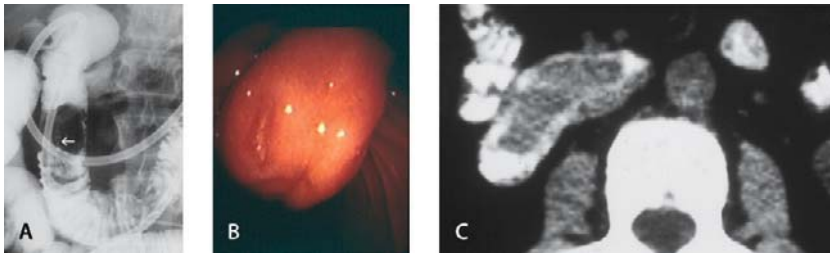

Fig. 8A–C. Neurilemmoma. **A** Enteroclysis shows a smoothly outlined intraluminal filling defect in the second portion of the duodenum with a linear ulceration (*arrow*). **B** Endoscopy confirms the presence of a polypoid intraluminal mass with a superficial longitudinal ulcer. **C** CT demonstrates a homogeneous soft tissue mass confined within the boundaries of the lumen of the duodenum

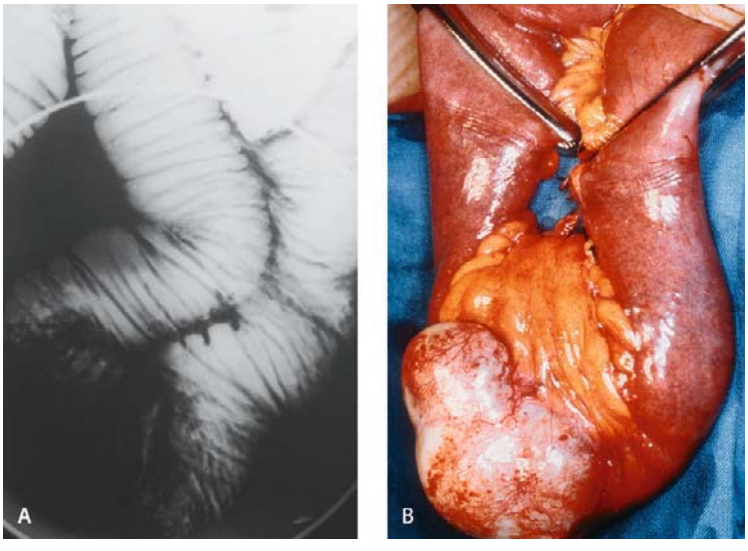

Fig. 9A, B. Dumbbell-type neurilemmoma. **A** Enteroclysis study showing broad-based indentation and encroachment of the lumen of a jejunal loop with dilation proximally. **B** Corresponding view of the extraluminal portion of the tumor and its attachment to the bowel, on the operating table (from [13], with permission)

Adenocarcinoma

In most documented series adenocarcinoma appears to be the most common malignant neoplasm of the small intestine. It is a solitary lesion mostly located in the proximal small intestine. Adenocarcinomas are almost always symptomatic. However, clinical presentation is nonspecific and usually related to intestinal obstruction or chronic blood loss. The overall prognosis is dismal, comparatively the worst of all primary small intestinal malignancies.

Adenocarcinomas arise typically from glandular epithelium composed of tubular or villous structures. Gland formation and production of mucin are criteria for their classification as mucinous, signet-ring cell or undifferentiated adenocarcinomas [11]. Most often, they are moderately to well-differentiated carcinomas. On gross pathology, they most frequently appear as infiltrative, annular, constrictive lesions; polypoid intraluminal masses are a less common presentation. The majority has metastasized to regional lymph nodes, liver, or the peritoneal surface by the time of diagnosis.

The radiological appearance is similar to that of carcinoma of the colon. It reflects the pattern of growth and includes annular narrowing or stricture formation, filling defects, polypoid or ulcerated masses or a combination of these.

Infiltrating adenocarcinomas invariably appear as short, sharply demarcated, circumferential narrowing of the lumen with shouldering of the margins and mucosal destruction (Fig. 10). Adenocarcinomas may initiate a local desmoplastic reaction, less frequently leading to complete obstruction. Annular constricting lesions in the distal ileum, resembling primary adenocarcinomas, need to be considered carefully, as in most cases they represent secondary involvement from primary lesions in the cecum or lymphomatous infiltration. Polypoid-type adenocarcinoma is not unusual in the duodenum, presenting as a large, solitary polypoid filling defect with irregular margins and mucosal destruction. Even larger or multiple polypoid masses may less frequently be seen in the mesenteric small intestine (Fig. 11). Ulceration is a frequent feature of adenocarcinoma. Single or multiple ulcers of variable sizes are often present in infiltrating or polypoid-type adenocarcinomas and cases with large, bulky ulcerated masses are indistinguishable from cavitating intestinal lymphomas. Combined features corresponding to infiltrat-

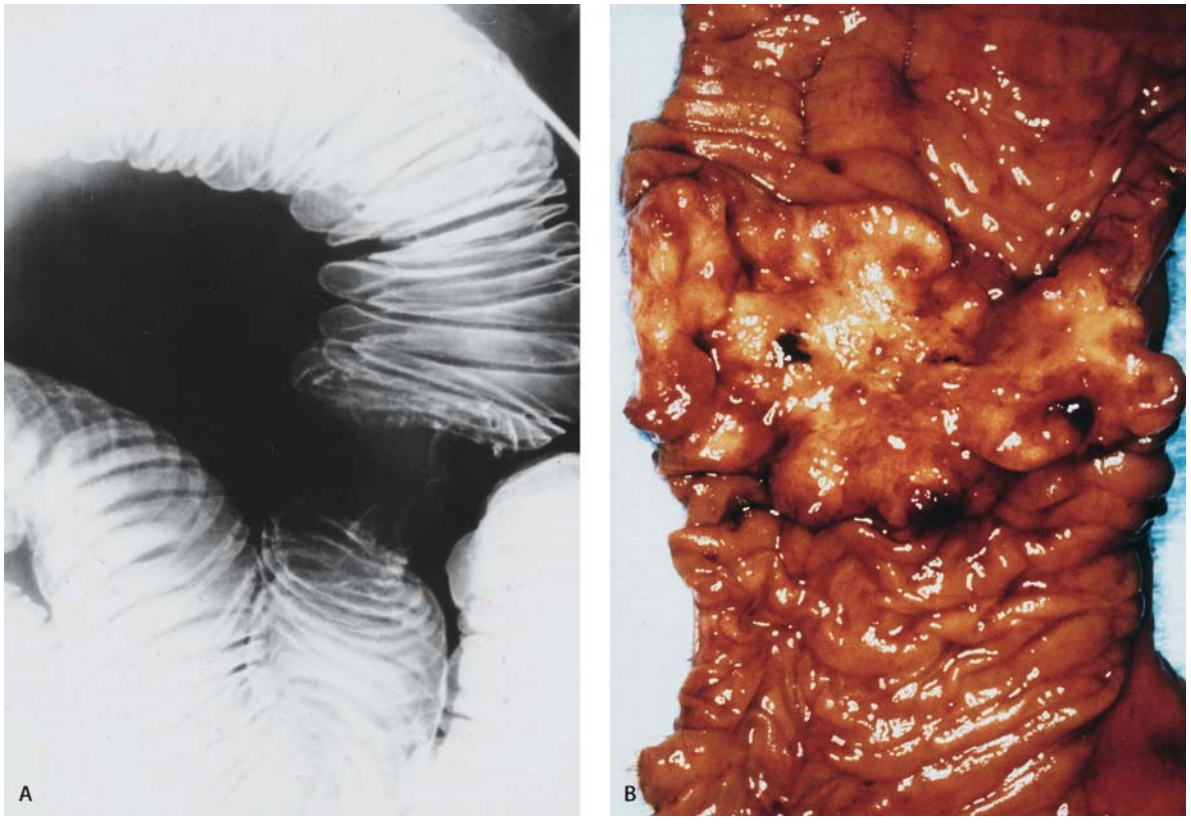

Fig. 10A, B. Infiltrative adenocarcinoma of the jejunum. **A** Enteroclysis demonstrates a short, annular, constricting lesion with mucosal destruction. Proximal dilatation is also present. **B** Corresponding pathology specimen (from [4], with permission)

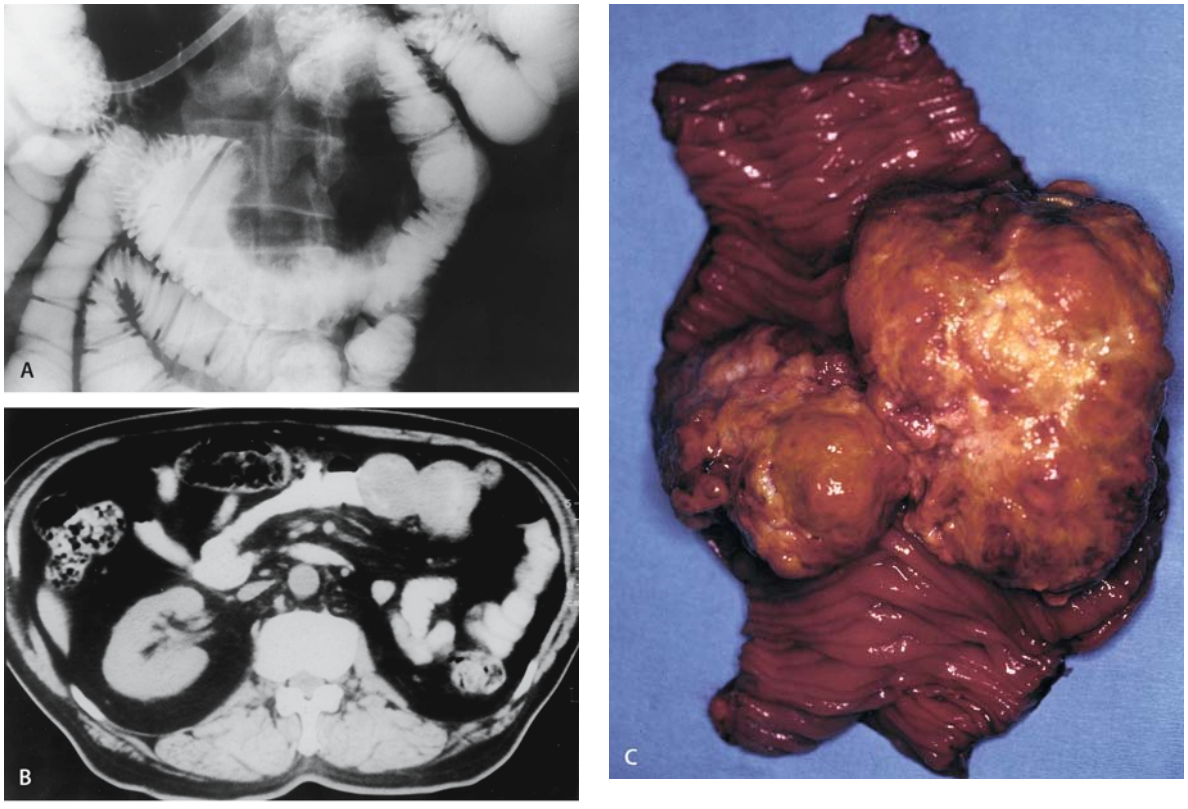

Fig. 11A–C. Polypoid adenocarcinoma of the jejunum. **A** Enteroclysis showing indentation and encroachment of the lumen of the jejunal loop by a bilobed mass, displacing adjacent loops. **B** CT demonstrates a bilobed, polypoid mass. There is no evidence of extraintestinal involvement or lymph node enlargement. **C** The pathology specimen of the lesion (from [4], with permission)

ing, polypoid and ulcerating lesions are rarely encountered, and indicate an advanced stage of disease [4].

Adenocarcinoma appears on CT as a solitary, focal, sharply outlined mass, causing thickening of the intestinal wall, usually not exceeding 1.5 cm, and narrowing of its lumen. The tumor mass may be homogeneous or heterogeneous when ulcerated and shows moderate contrast enhancement. Infiltration of the surrounding mesentery is seen with advanced disease, whereas associated lymph node enlargement, in the form of microadenopathy, is found in less than 50% of patients (Fig. 12).

The variety of radiological appearances of adenocarcinoma makes its differential diagnosis a difficult one, especially when lesions are located in the distal intestine or when the disease is advanced. Predominately ulcerated adenocarcinomas may simulate lymphomas, leiomyosarcomas or metastatic melanomas. Moreover, annular-type lesions will need to differentiate from secondary adenocarcinoma, carcinoid or Crohn's disease. In our experience, comparative characteristics favoring the diagnosis of primary adenocarcinoma include that this is a solitary obstructive lesion, it is most frequently located proximally, it involves shorter segments of

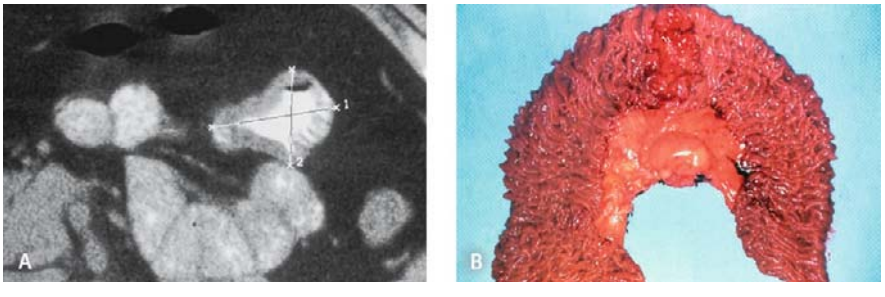

Fig. 12A, B. Adenocarcinoma. **A** CT scan demonstrates a focal lesion 1 cm in size, featuring as asymmetrical bowel wall thickening. **B** Corresponding resected specimen shows the small infiltrating adenocarcinoma and metastasis to regional lymph nodes

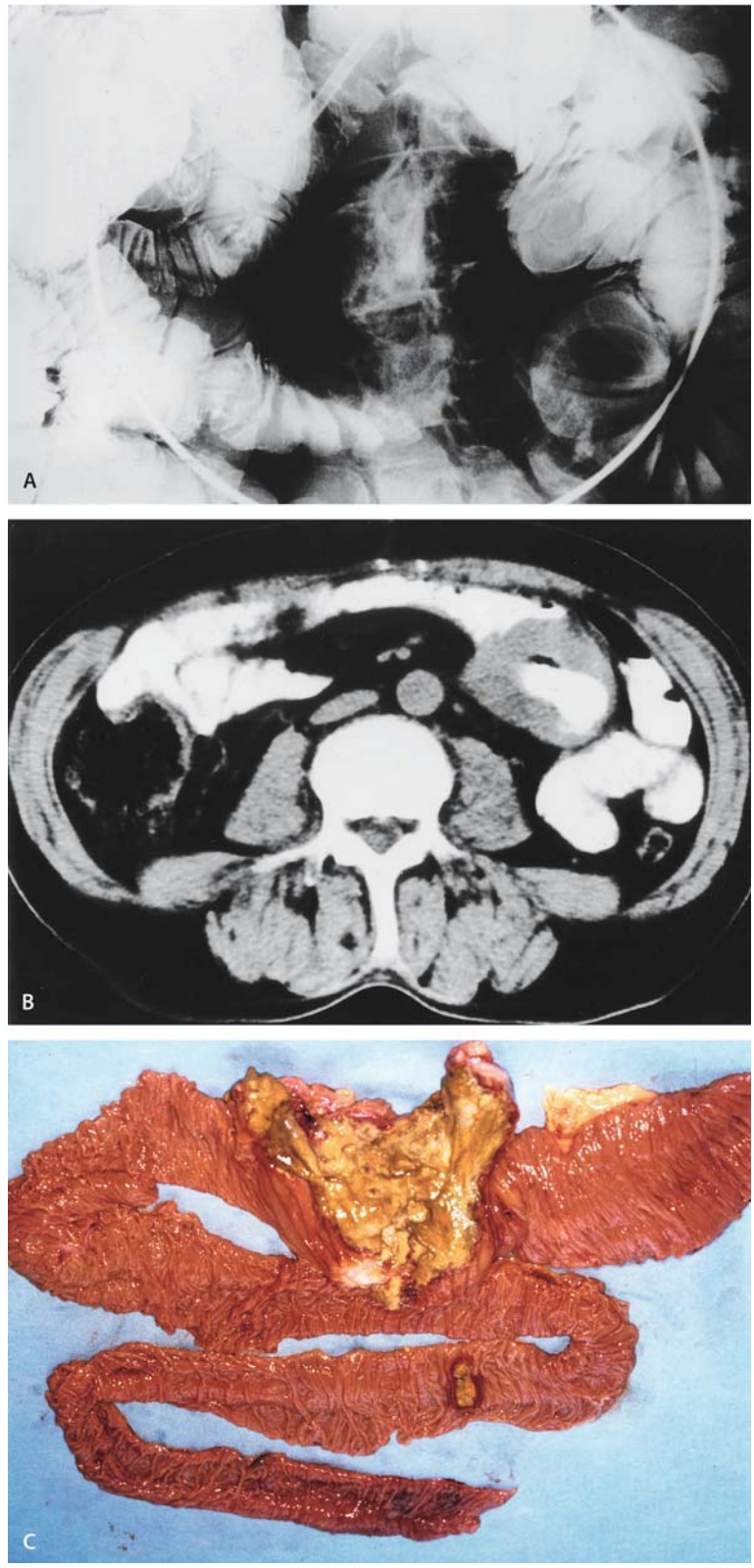

Fig. 13A–C. Ulcerated lymphoma. **A** Amorphous barium collection in a jejunal loop representing a large ulcer. **B** CT examination shows segmental infiltration and distortion of the barium-filled lumen. **C** Corresponding pathology specimen (from [4], with permission)

bowel and it is rarely associated with bulky adenopathy [4].

Lymphoma

Primary lymphoma accounts for 20% of primary small intestinal malignancies. Predisposing factors that may alert the radiologist to the likelihood of intestinal lymphoma include previous extraintestinal lymphoma, chronic lymphatic leukemia, immunoproliferative small intestinal (α-heavy chain) disease, and immunological dysfunction including acquired immunodeficiency syndrome (AIDS). It is mostly located in the ileum, it has a bimodal age distribution, with peaks below the age of 10 and above the age of 50 years, and a variable clinical presentation, including abdominal pain, diarrhea, weight loss, anemia or gastrointestinal bleeding. Small intestinal lymphoma carries a poor prognosis, which depends mainly on the extent of spread at presentation.

The majority of primary intestinal lymphomas are non-Hodgkin lymphomas, arising form mucosa-associated lymphoid tissue (MALT). They are typically low-grade, small-cell lymphomas, mostly of B-cell origin and may exhibit a diffuse histological pattern [11]. However, their gross morphology appears to be unrelated to the histology.

A broad spectrum of radiological pictures is encountered mirroring the pattern of growth, which includes infiltrating, ulcerating, cavitating, nodular, aneurysmal, mesenteric or combined forms. Multifocal involvement in the same or widely separated segments is seen in 10%–40% of patients. Narrowing of the lumen, usually nonobstructing, is a common finding. When it represents the only feature of lymphoma it may be indistinguishable from adenocarcinoma, except that it is mostly

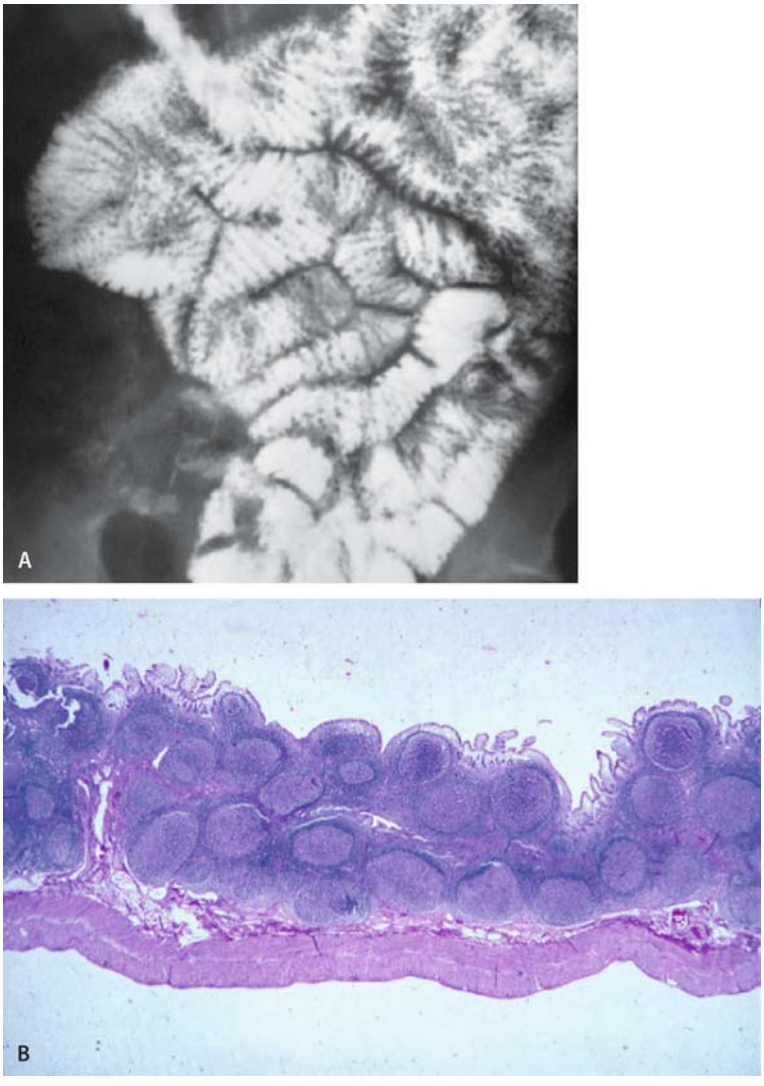

Fig. 14A, B. Diffuse small-intestinal lymphoma. **A** Enteroclysis demonstrates diffuse nodular thickening of folds of the small intestine. **B** Microscopy demonstrates diffuse submucosal involvement of lymphoma (from [6], with permission)

located distally. Discrete, broad-based ulceration is an underestimated but fairly valid feature, while a large cavitating lesion, secondary to central necrosis of a large neoplastic mass, is highly characteristic (Fig. 13). Focal aneurysmal dilatation, featuring as an aperistaltic, ballooned, thick-walled segment, filled with amorphous barium collection is another valid feature of lymphoma [15]. Discrete, usually multiple mucosal or intraluminal nodules of varying size and shape, featuring as filling defects, may affect variable lengths of the small intestine (Fig. 14). Thickening of the valvulae conniventes is a less frequent and nonspecific finding of lymphoma, and in the absence of other manifestations the diagnosis may not be suspected.

Unlike other forms of lymphoma, thickening of the valvulae conniventes, often nodular, involving long segments of the jejunum, and usually accompanied by progressive narrowing of the lumen and confluent or nonconfluent lymph node enlargement, are features invariably seen with Mediterranean-type lymphoma [16] (Fig. 15).

CT appearances of intestinal lymphoma are also variable. Mural infiltration presents as intestinal wall thickening, relatively homogeneous, nodular or concentric (Fig. 16), with moderate peripheral enhancement, after intravenous contrast administration. Dilatation of the bowel lumen is characteristic of intestinal involvement and is recognized as a central or eccentric collection of gas or contrast within a usually ulcerated mass. Mesenteric involvement is frequently present. It may appear as bulky mesenteric or retroperitoneal adenopathy, ill-defined confluent mesenteric masses encasing loops of bowel, and less often, as a conglomerate mantle of mesenteric/retroperitoneal tissue or a sandwich-like configuration, due to encasement of vessels from enlarged mesenteric lymph nodes (Fig. 17) [10].

Complementary use of detailed barium and CT examinations enables a diagnosis to be made in most cases. The differential diagnosis mainly includes Crohn's disease and adenocarcinoma and less frequently metastatic melanoma or leiomyosarcoma. Features favoring the diagnosis of intestinal lymphoma include that it is usually located distally, it involves longer segments, it causes larger lesions, and it is not accompanied by desmoplastic reaction, which allows changes in shape with compression (Fig. 18), while it prevents the development of significant intestinal obstruction and is associated with mesenteric involvement and bulky adenopathy [4].

Carcinoid

Carcinoid is the most common neoplasm of the small intestine found at autopsy or incidentally during laparotomy, while it accounts for nearly one-fourth of primary malignant small intestinal neoplasms. Almost 90% of the lesions are located distally, they are multiple in approximately one-third of cases and they may coexist with other primary malignant neoplasms in another third of cases [17].

The primary carcinoid tumor is invariably small, usually less than 1.5 cm in size. A definite correlation has been established between the size of the lesion at

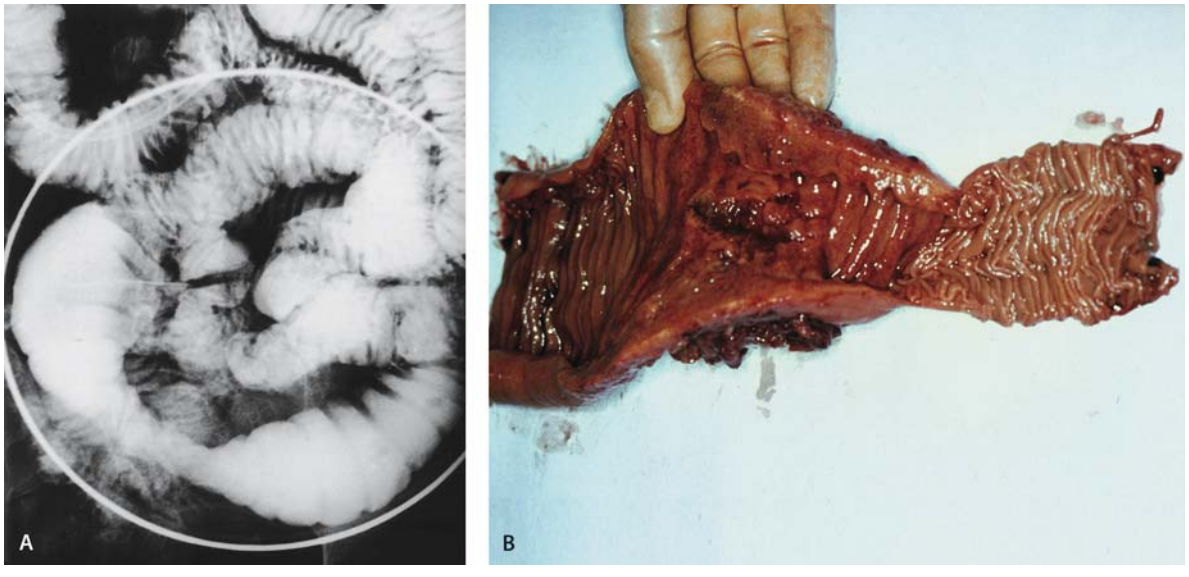

Fig. 15A, B. Mediterranean-type lymphoma. **A** Thickening of the valvulae conniventes and a short circumferential narrowing of a jejunal segment accompanied by pre-and poststenotic dilatation. **B** Corresponding pathological specimen showing the intestinal and mesenteric involvement (from [4], with permission)

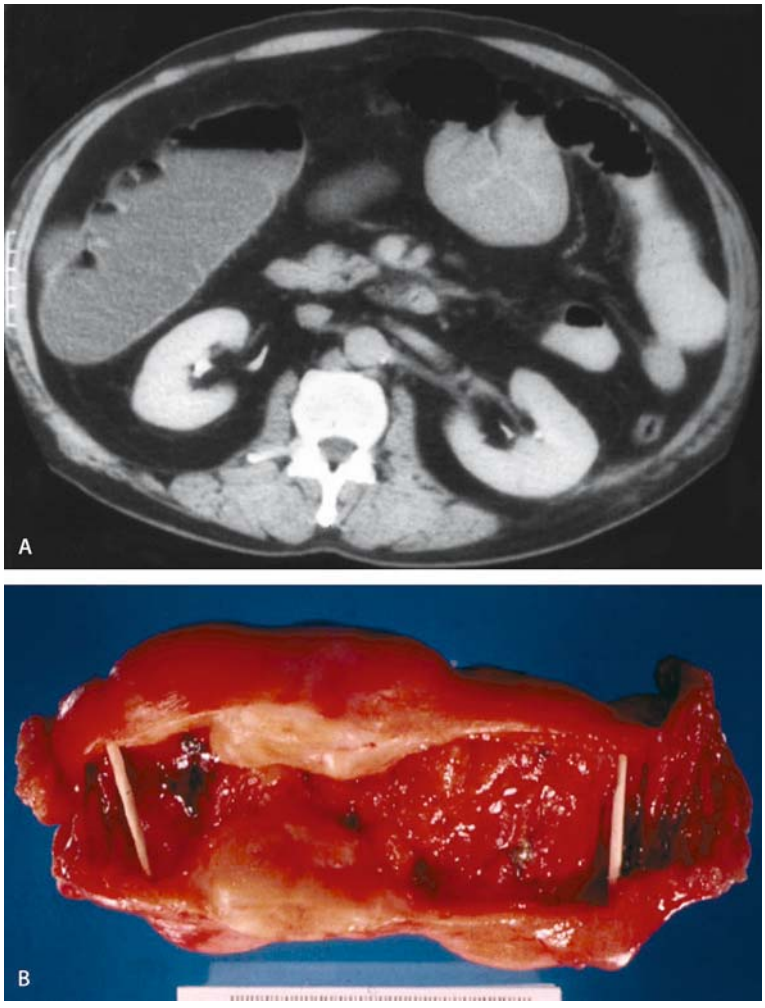

Fig. 16A, B. Localized annular infiltrating lymphoma. **A** CT shows marked thickening of localized small bowel. The attenuation of the thickened wall is relatively homogeneous, which suggests the diagnosis of lymphoma. **B** Gross specimen demonstrates annular infiltration of lymphoma (from [6], with permission)

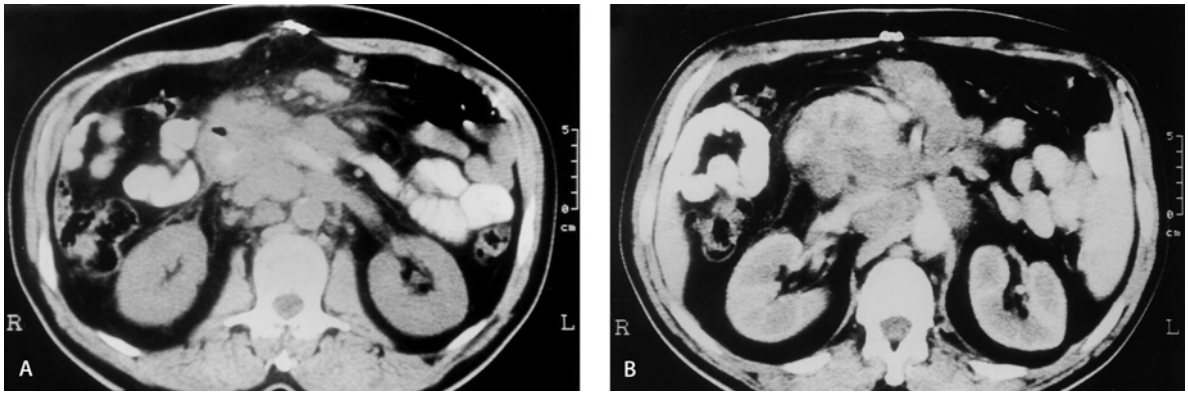

Fig. 17A, B. Lymphoma. Mesenteric involvement. **A** CT shows confluent mesenteric masses encasing loops of barium-filled intestine. **B** In the same patient, mesenteric vessels are sandwiched between lymphomatous mesenteric nodal masses (from [4], with permission)

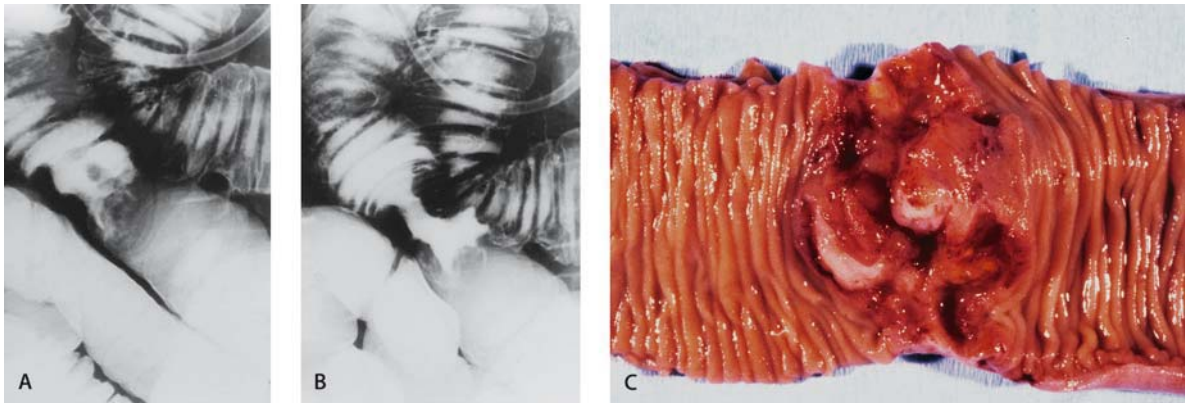

Fig. 18A–C. Lymphoma resembling adenocarcinoma. **A**, **B** Enteroclysis showing focal annular stenosis with mucosal destruction, simulating infiltrative adenocarcinoma. Compression view (**A**) allows for some distensibility and changing of the shape of the stenosed segment due to lack of desmoplastic reaction. **C** Corresponding pathology specimen (from [4], with permission)

presentation, muscle invasion and metastases, with carcinoids smaller than 1 cm exhibiting malignant behavior only occasionally and those sized 2 cm or larger being consistently malignant [18]. Histological features distinguishing benign from malignant carcinoids have not been described. The tumor is considered malignant in the presence of metastases.

Carcinoids arise among the endocrine cells within the basal portion of the mucosa, superficial to the muscularis mucosa. They are composed of small cells with uniform, round nuclei without prominent nucleoli, and they exhibit the typical insular growth pattern of midgut carcinoids [19]. They have a distinctive tendency to grow into the submucosa and infiltrate the intestinal wall and serosa. Invasion of the muscle coats of the intestinal wall may result in spread to regional lymph nodes or distant metastases. It may also stimulate an intense desmoplastic response in the surrounding submucosa, mesentery and adjacent mesenteric vessels. Less frequently intraluminal growth may result in a polypoid lesion, which also can invade the muscle layer, serosa and mesentery in a stepwise process [4].

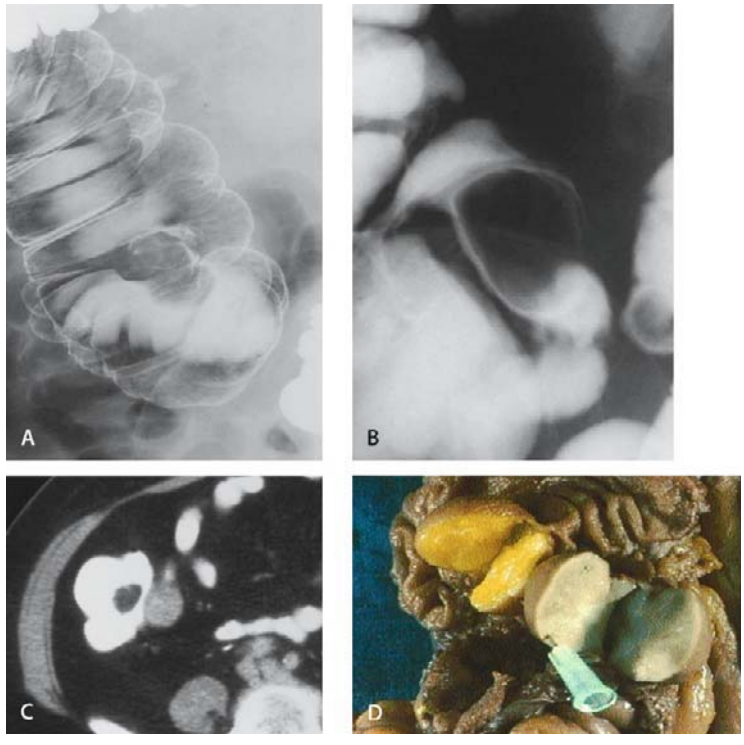

Fig. 19A–D. Carcinoid tumor. **A** Barium enema shows a mass effect to the cecal pole, adjacent to the ileocecal valve, which is exhibiting features of lipomatosis. **B** Enteroclysis study demonstrating an ovoid, sharply demarcated, intraluminal filling defect in the terminal ileum. **C** CT confirms the presence of ileocecal valve lipomatosis and a small, ovoid, homogeneous soft tissue mass in the terminal ileum. **D** Corresponding pathology specimen showing both entities

The primary tumor rarely produces symptoms, due to its small size and deep mucosal site of origin. Abdominal pain and diarrhea are the most common clinical presentation, while gastrointestinal bleeding is extremely rare. The carcinoid syndrome is an uncommon initial presentation and it is reported to occur in one-third of jejunoileal carcinoids that have metastasized to the liver [17].

Careful barium examination is essential, since it often provides the first and perhaps the only opportunity to suggest the diagnosis preoperatively. The radiological signs shown on enteroclysis mirror the stage that the pathological process has reached at the time of examination. They may be those of the primary lesion, featuring as solitary (Fig. 19) or multiple (Fig. 20), round, smoothly outlined, intramural or intraluminal filling defects encroaching the intestinal lumen; those of a secondary mesenteric mass, causing stretching, rigidity and fixation of ileal loops; those due to interference with the ileal blood supply, resulting in thickening of the valvulae conniventes and chronic ischemic intestinal changes; or to the effects of fibrosis associated with the tumor spread, presenting as sharp angulation of a loop or a stellate or spoke-like arrangement of adjacent intestinal loops [20].

Carcinoid tumors are best recognized on CT on the basis of mesenteric findings. Due to its relatively small size, the primary tumor is rarely visualized as a soft tissue mass projecting into optimally opacified intestinal lumen or as focal wall thickening [21]. Secondary mesenteric changes include a discrete, unifocal, soft tissue mass associated, or not, with linear soft tissue strands radiating into the surrounding fat in a stellate pattern, while displacing adjacent intestinal loops. Segmental, intestinal wall thickening, indicative of chronic ischemia, may also be seen. Hypervascular liver metastases, usually hypodense on precontrast scans, mesenteric lymph node enlargement, ascites secondary to peritoneal seeding and occasionally dystrophic calcification in metastatic nodes or in liver metastases may be additionally encountered [10].

The radiological features of carcinoid tumor are nonspecific, but are nearly always diagnostic in the presence of carcinoid syndrome (Fig. 21). Primary carcinoid needs to be differentiated from benign intraluminally protruding lesions such as leiomyomas. Radiographic findings of carcinoid-induced mesenteric infiltration may be mimicked by inflammatory or neoplastic disorders or chronic ischemia. Perhaps the single most important differential diagnosis of an ileal carcinoid is

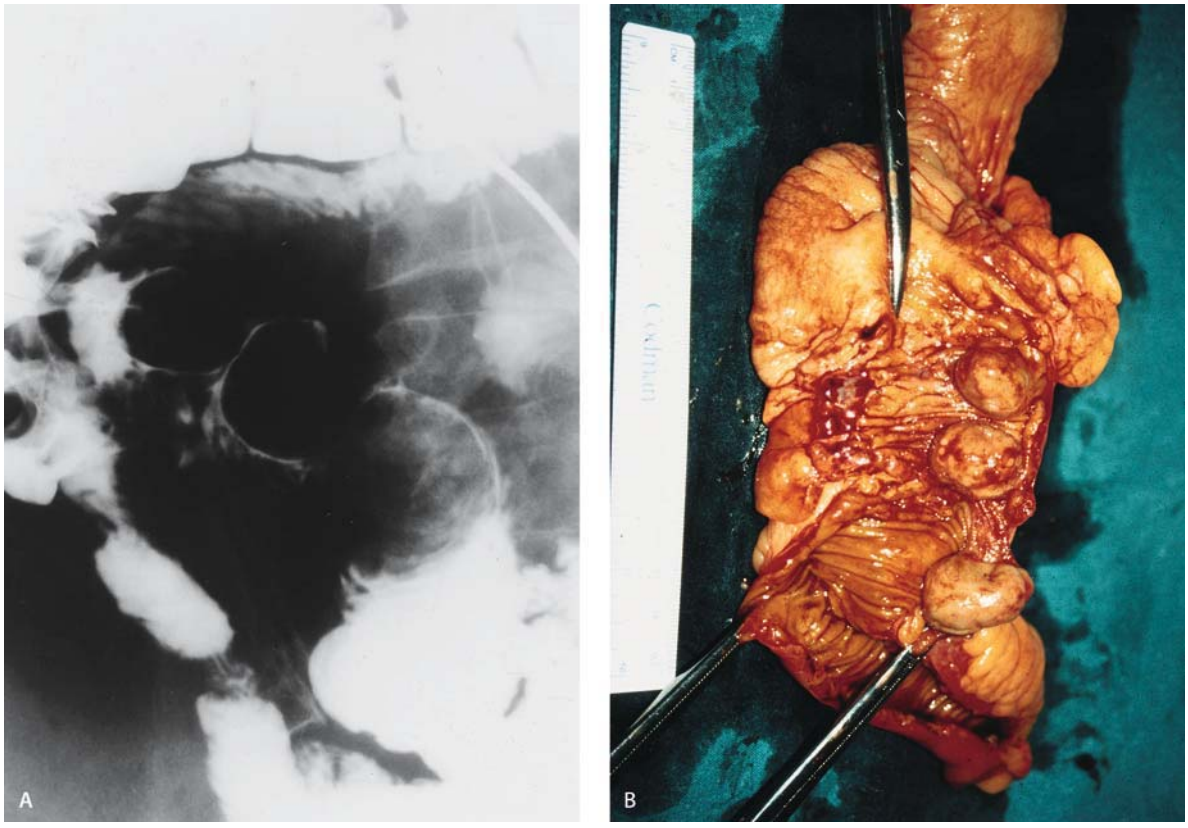

Fig. 20A, B. Multiple ileal carcinoids. **A** Enteroclysis shows three adjacent, finely demarcated filling defects in the terminal ileum. **B** Corresponding pathology specimen (courtesy of Dr. E. Lambrakos)

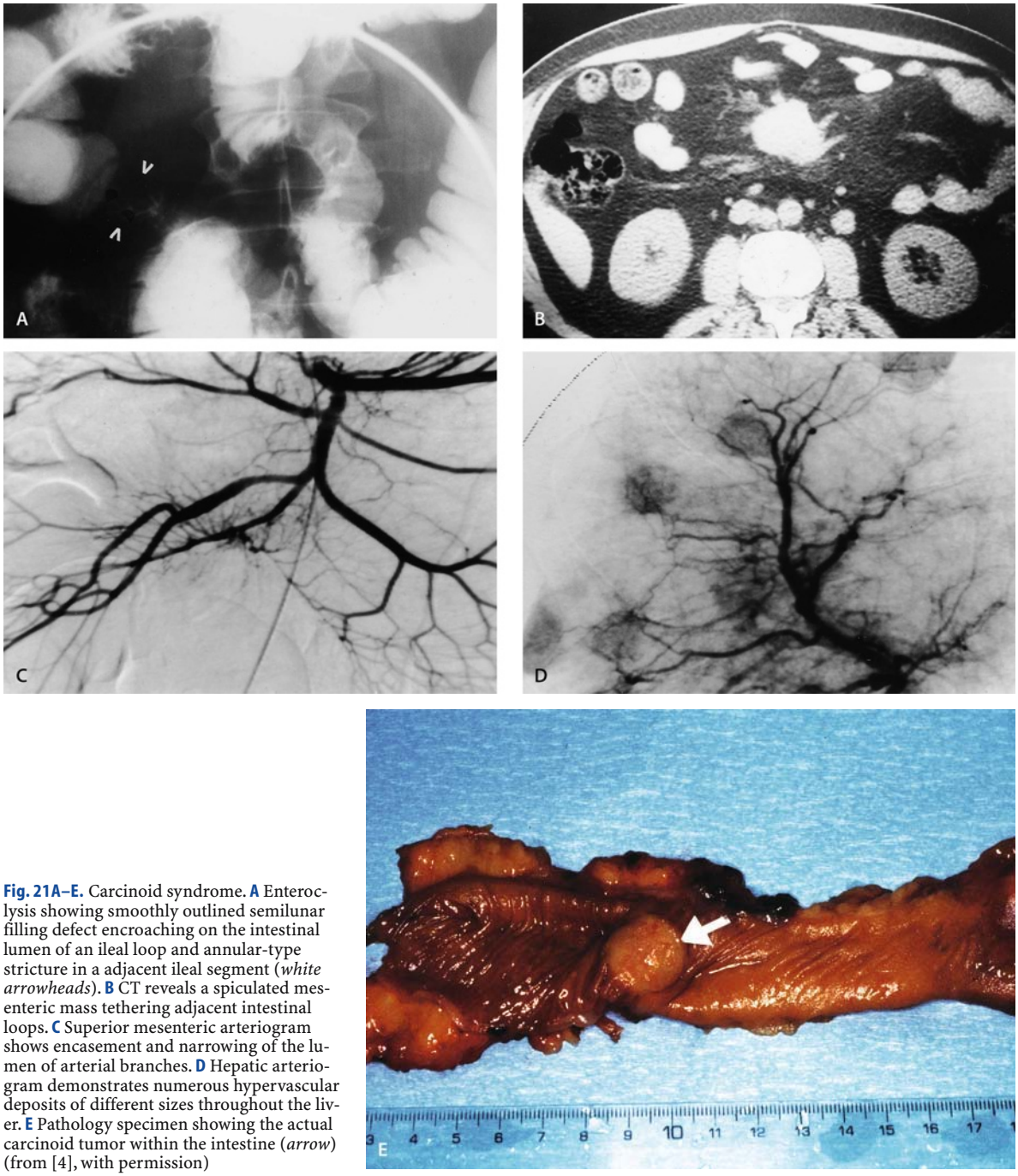

Fig. 21A–E. Carcinoid syndrome. **A** Enteroclysis showing smoothly outlined semilunar filling defect encroaching on the intestinal lumen of an ileal loop and annular-type stricture in a adjacent ileal segment (*white arrowheads*). **B** CT reveals a spiculated mesenteric mass tethering adjacent intestinal loops. **C** Superior mesenteric arteriogram shows encasement and narrowing of the lumen of arterial branches. **D** Hepatic arteriogram demonstrates numerous hypervascular deposits of different sizes throughout the liver. **E** Pathology specimen showing the actual carcinoid tumor within the intestine (*arrow*) (from [4], with permission)

Crohn's disease. Comparative characteristics that should alert the radiologist to the possibility of a carcinoid tumor include multiple or diverse lesions, sharp angulation, kinking, spoke-like arrangement of intestinal loops, predominantly ileal involvement with absence of ulceration, and a desmoplastic mesenteric mass with or without radiating linear strands [4].

Leiomyosarcoma (Malignant GISTs)

Leiomyosarcomas account for less than 15% of primary intestinal malignancies, yet they are the most common malignant soft tissue neoplasms of the small intestine.

Leiomyosarcomas are, as a rule, single lesions, most commonly located in the jejunum and ileum. Patients

are almost always symptomatic with abdominal pain and bleeding being the most common presenting complaints. A palpable abdominal mass may be encountered in nearly 50% of cases. However, partial or complete obstruction is infrequent despite the large size they usually attain.

Leiomyosarcomas arise from intestinal smooth muscle of the wall or the small intestinal blood vessels, and they are considered as sarcomatous degeneration of benign smooth muscle neoplasms. Histological distinction between leiomyosarcomas and leiomyomas may be quite difficult, especially in well-differentiated, low-grade tumors [11]. In general, leiomyosarcomas are histologically more disorganized, while exhibiting marked cellularity and more mitoses, ten per high power field or more.

Leiomyosarcomas grow slowly, predominately extraluminally and eccentrically, and are prone to developing degenerative changes such as necrosis, hemorrhage, calcification, fistula or secondary infection. On barium

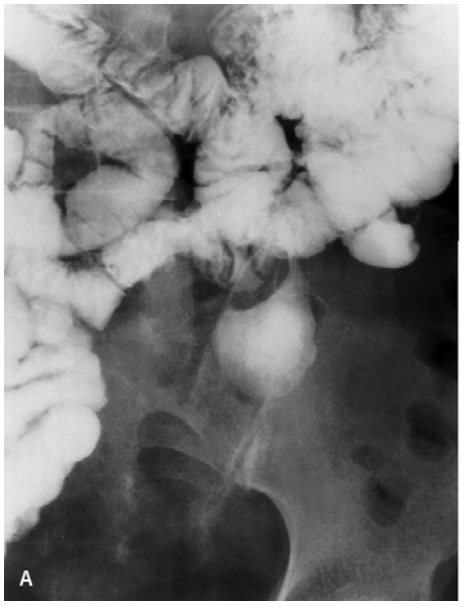

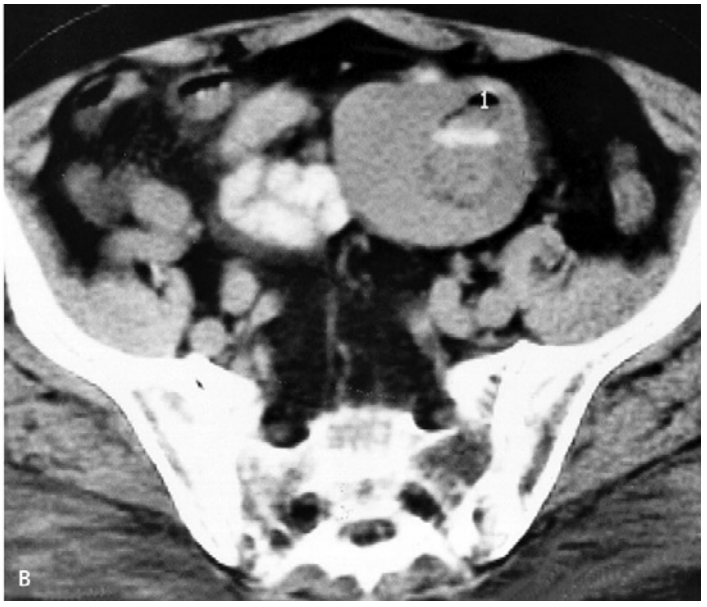

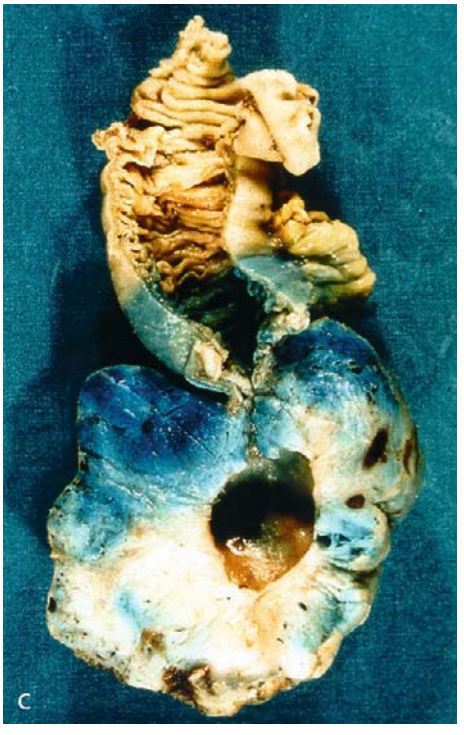

Fig. 22A–C. Malignant gastrointestinal stromal tumor (GIST). **A** Enteroclysis showing a large, nonobstructing, largely excavated mass, displacing adjacent barium-filled loops of intestine. **B** CT demonstrates a large, extraintestinal, inhomogeneous mass. There is no evidence of enlarged lymph nodes. **c** Corresponding pathology specimen (from [6], with permission)

studies, their main feature is usually a large extrinsic mass, displacing or distorting adjacent loops of intestine. This may be associated with ulceration, cavitation or fistula formation. Less often leiomyosarcoma may appear as large cavity filled with barium and it may be difficult to identity the connection between the small intestine and the cavity (Fig. 22) [4].

CT examination may add considerably to the evaluation of leiomyosarcomas. It can accurately demonstrate the size, shape and extent of the lesion, and it can depict the presence of liver, peritoneal or other metastases. In comparison to their benign counterpart, CT criteria favoring malignancy include a large size (greater than 6 cm), necrotic or heterogeneous tissue density and extensive ulceration or fistula formation [22]. Liver metastases from leiomyosarcoma are large, necrotic or cystic in nature, with peripheral or rim enhancement, whereas peritoneal metastases may appear as widely distributed multiple, round, smoothly outlined, homogeneous satellite masses [23].

Largely excavated leiomyosarcomas need to be differentiated from lymphomas and metastatic melanomas. In addition, there are no valid radiological criteria to differentiate leiomyoma from leiomyosarcoma. However, leiomyosarcomas are distinctive from other malignant small intestinal neoplasms in that they have a greater tendency to develop large ulcers and therefore to bleed, they attain a large size without obstruction, regional lymph node metastases are unusual and they are associated with higher survival rates, despite metastases [4].

References

1. Good CA (1963) Tumors of the small intestine. AJR Am J Roentgenol 89:685–705
2. Gupta S, Gupta S (1982) Primary tumors of the small bowel: a clinico-pathological study of 58 cases. J Surg Oncol 20: 161–167
3. Maglinte DDT, O' Connor K, Bassette J, Gernish SM, Kelvin FM (1991) The role of physician in the late diagnosis of primary malignant tumors of the small intestine. Am J Gastroenterol 86:304–308
4. Gourtsoyiannis N, Mako E (1997) Imaging of primary small intestinal tumours by enteroclysis and CT with pathological correlation. Eur Radiol 7:625–642
5. Olmsted WW, Ros PR, Hjermstad BM, McCarthy MJ, Dachman AH (1987) Tumors of the small intestine with little or no malignant predisposition: a review of the literature and report of 56 cases. Gastrointest Radiol 12:231–239
6. Gourtsoyiannis NC, Odze HJRD, Ros PR (2002) Malignant small intestinal neoplasms. In: Gourtsoyiannis NC (ed) Radiological imaging of the small intestine. Springer, Berlin Heidelberg New York, pp 399–428
7. Miettinen M, Lasota (2001) Gastrointestinal stromal tumors – definition, clinical, histological, immunohistochemical, and molecular genetic features and differential diagnosis. Virchows Arch 438:1–12
8. Levy AD, Remotti HE, Thompson WM, Sobin LH, Miettinen M (2003) Gastrointestinal stromal tumors: radiologic features with pathologic correlation. Radiographics 23:283–304
9. Gourtsoyiannis NC, Bays D, Malamas M, Barouxis G, Liasis N (1992) Radiological appearances of small intestinal leiomyomas. Clin Radiol 45:94–103
10. Megibow A (1997) Computed tomography. In: Gourtsoyiannis NC, Nolan DJ (eds) Radiology of small intestinal tumours. Elsevier, Amsterdam, pp 347–371
11. Elsayed AM, Sobin LH (1997) Pathology of small intestinal neoplasms. In: Gourtsoyiannis NC, Nolan DJ (eds) Imaging of small intestinal neoplasms. Elsevier, Amsterdam, pp 31–64
12. Cho KC (1997) Neoplasms specific to the duodenum. In: Gourtsoyiannis NC, Nolan DJ (eds) Imaging of small intestinal neoplasms. Elsevier, Amsterdam, pp 249–282
13. Gourtsoyiannis NC, Bays D, Papaioannou N, Theotokas J, Barouxis G, Karabelas T (1993) Benign tumors of the small intestine: preoperative evaluation with a barium infusion technique. Eur J Radiol 16:115–125
14. Hadjidakis AA, Raissaki MT, Bays D, Gourtsoyiannis NC (1995) Blutende lipome des jejunums: diagnose mit Hilfe des Enteroclysis und der CT. Röfo 162:356–357
15. Gourtsoyiannis NC, Nolan DJ (1988) Lymphoma of the small intestine: radiological appearances. Clin Radiol 39:639–645
16. Ramos L, Marcos J, Illanas M, Hernandez-Mora M, Perez-Paya F, Picouto JL, Santana P, Chantar C (1978) Radiologic characteristics of primary intestinal lymphoma of the "Mediterranean" type: observations on twelve cases. Radiology 126: 379–385
17. Moertel CG, Sauer WG, Dockerty MB, Baggenstoss AH (1961) Life history of the carcinoid tumor of the small intestine. Carcer 14:901–912
18. Moertel CG (1987) An odyssey in the land of small tumors. J Clin Oncol 5:1503–1522
19. Buck JL, Sobin LH (1990) Carcinoids of the gastrointestinal tract. Radiographics 10:1081–1095
20. Jeffree MA, Barter SJ, Hemingway AP, Nolan DJ (1984) Primary carcinoid tumors of the ileum: the radiologic appearances. Clin Radiol 35:451–454
21. Gourtsoyiannis NC (1998) Diagnosis and staging of small bowel malignancies In: Meyers AM (ed) Neoplasms of the digestive tract: imaging, staging and management. Lippincott-Raven, Philadelphia, pp 179–201
22. Megibow AJ, Baltazar EJ, Hulnick DH, Naidich DP, Bosniak MA (1985) CT evaluation of gastrointestinal leiomyomas and leiomyosarcomas AJR 144:727–731
23. Choi BY, Lee WWJ, Chi JG, Han JK (1990) CT manifestations of peritoneal leiomyosarcomatosis. AJR Am J Roentgenol 155: 799–803

Nonneoplastic Conditions of the Small Intestine

Nicholas C. Gourtsoyiannis, Daniel J. Nolan

4.5

Contents

Introduction

The mesenteric small intestine is a difficult organ to examine. Long-term experience has shown that there are no shortcuts in achieving a reliable examination and several parameters need to be respected if a confident diagnosis is to be made. These would include selection of patients, closely supervised studies, background data, image quality, familiarity with imaging findings and utilization of radiologic–pathologic correlations.

Thoughtful *selection of patients* by clinicians is essential to make radiologic examination cost effective. *Closed supervised studies*, incorporating an adequate index of clinical suspicion, cooperation between a focused radiologist and a keen physician, expertise and time are important. *Familiarity with imaging findings* and *image quality*, to guarantee demonstration of fine surface mucosal detail and transitional morphological changes are necessary. Applying the principles of *radiologic–pathologic correlation* to the interpretation of radiological findings offers a certain advantage and in association with the *background data* available, including localization and distribution of changes, extent of involvement, the solitary or multiple nature of the lesions present and the clinical history, provide a confident differential diagnosis.

Enteroclysis is widely recognized as a most reliable method for imaging evaluation of the small intestine. Adequate distension of the entire small-bowel lumen by barium contrast medium makes a detailed demonstration of the anatomy easier and results in a more confident identification of morphological and functional abnormalities present [1, 2]. In long-term follow-up studies, enteroclysis has been shown to be a highly accurate method with a sensitivity of 93.1% and a specificity of 96.9% [3, 4]. The main limitation of enteroclysis remains its inability to demonstrate exoenteric pathology associated with small intestinal diseases. In parallel, an increasing role has been established for computed tomography (CT) in evaluating mural and extramural lesions and in assessing mesenteric involvement associated with inflammatory or neoplastic small intestinal diseases [5].

CT enteroclysis was recently introduced to combine advantages of both techniques [6]. Distension of small bowel lumen and cross-sectional display are proven imaging principles incorporated into CT enteroclysis. It is used selectively to answer specific clinical questions. Two different approaches have been adopted concerning the choice of the contrast medium that should be used for luminal opacification. The first includes a negative contrast agent in the form of 4%–15% water-soluble methylcellulose solution in combination with intravenous contrast enhancement, which is mainly used to assess inflammatory activity and complications of small-bowel Crohn disease [7]. The second approach makes use of a positive contrast agent in the form of 1% barium solution, and is mainly applied when small-bowel obstruction [8] or the possibility of internal extraintestinal fistula are the clinical indications.

MR enteroclysis (MRE), a combined functional and morphological imaging method, has only recently been introduced into clinical practice [9, 10]; it combines the

benefits of volume challenge with adequate image quality. Administration of 1.5–2 l of iso-osmotic water solution through a nasojejunal catheter ensures bowel distension and facilitates identification of bowel wall abnormalities. True fast imaging with steady-state precision (FISP), half-Fourier acquisition single-shot turbo spin echo (HASTE) and postgadolinium T1-weighted 3D FLASH sequences can be employed in a comprehensive and integrated MRE examination protocol [11].

Results so far have shown that the functional information provided by MR enteroclysis equals that of conventional enteroclysis, while the inherent advantages of the technique include detailed morphological evaluation of the bowel wall and the mesenteries, lack of radiation exposure and excellent soft tissue contrast based on different mechanisms [12].

Crohn disease is by far the most common disorder to cause morphological changes in the intestine. Coeliac disease is also common, but the radiological appearances are unreliable and jejunal biopsy is the technique of choice for making the diagnosis. Other disorders that are clearly shown by enteroclysis include tuberculosis, chronic radiation enteritis, acute ischaemia, chronic ischaemia, ischaemic strictures, NSAID diaphragm strictures, Meckel's diverticulum, systemic sclerosis, intestinal lymphangiectasia and Whipple disease.

Goldblum and Petras [13] state that the gross pathological examination of surgically resected specimens of Crohn disease gives important information on the precise location, extent and distribution of the disease and

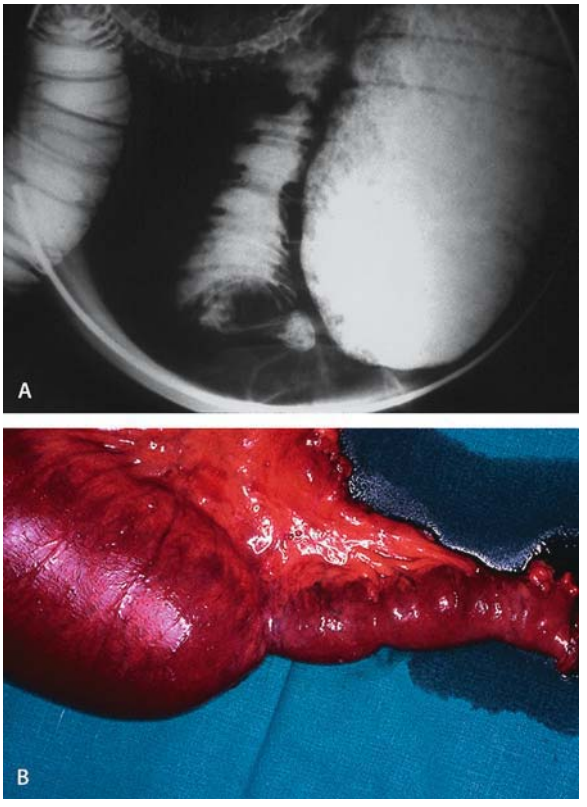

Fig. 1. A Crohn disease involving the jejunum. A tight stricture is accompanied by a pronounced proximal dilatation. **B** Corresponding pathology specimen

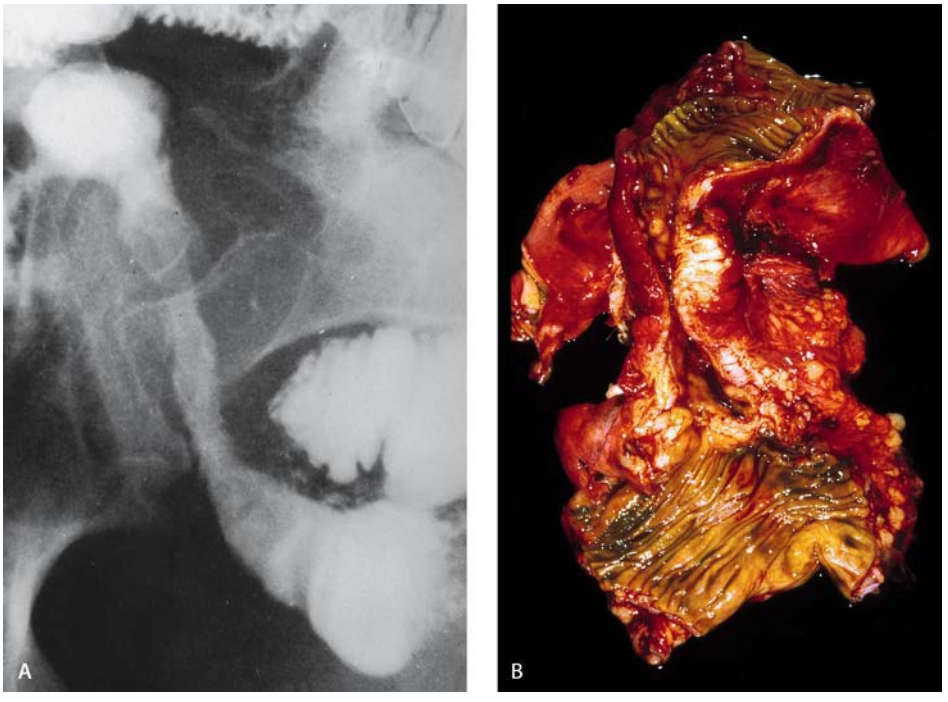

Fig. 2A, B. Crohn disease. **A** A long, tight stricture of the terminal ileum characteristic of Crohn disease shown by enteroclysis. **B** The resected specimen shows normal ileum and normal ascending colon separated by the stricture (from [17], with permission)

that in most cases these features will enable an accurate diagnosis to be made. By applying these criteria to abnormal findings at enteroclysis complemented by cross-sectional techniques, it is possible to make the correct diagnosis, not only in cases of Crohn disease, but in most other disorders that cause morphological changes in the small intestine.

Crohn Disease

The most characteristic feature of Crohn disease of the small intestine is the variety of its radiological appearances and the multiplicity of radiological features often present in the majority of patients. Categorization of these radiological features has been defined in terms of stenotic and nonstenotic forms, active and chronic, early and late or advanced, or into superficial, transmural and extramural changes.

Most information on the sequence of progression of the pathological lesions in Crohn disease is derived from radiological descriptions [14, 15]. The early lesions of Crohn disease are blunting, flattening, thickening, distortion and straightening of the valvulae conniventes. These changes are followed by discrete ulcers and by longitudinal and transverse ulcers. The stenotic phase eventually develops (Fig. 1) and the involved segment is transformed into a rigid, cast-like tube (Fig. 2); fistulae may be seen at this stage (Fig. 3). Deep ulcers precede sinuses and fistulae to other organs.

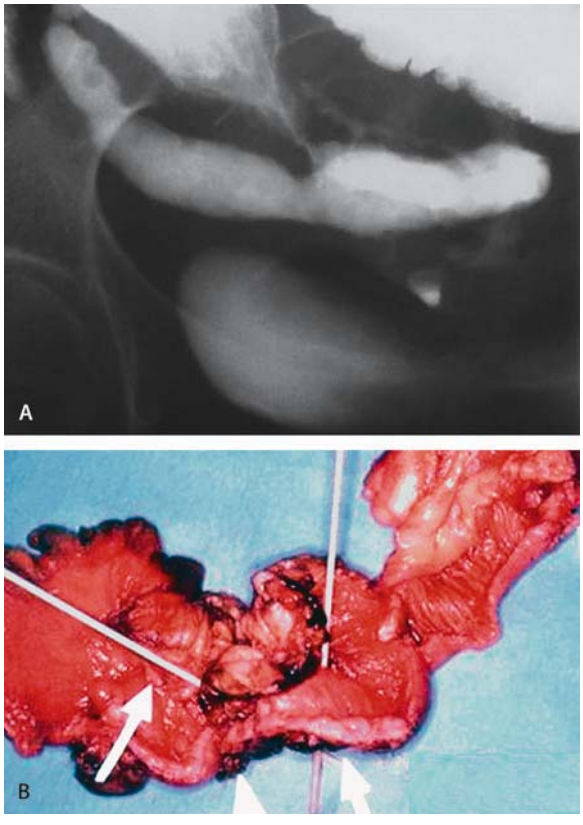

Fig. 3A, B. Fistulizing Crohn disease. **A** Two fistulous tracts connect a markedly narrowed and severely affected segment of ileum with the bladder. **B** Corresponding pathology specimen

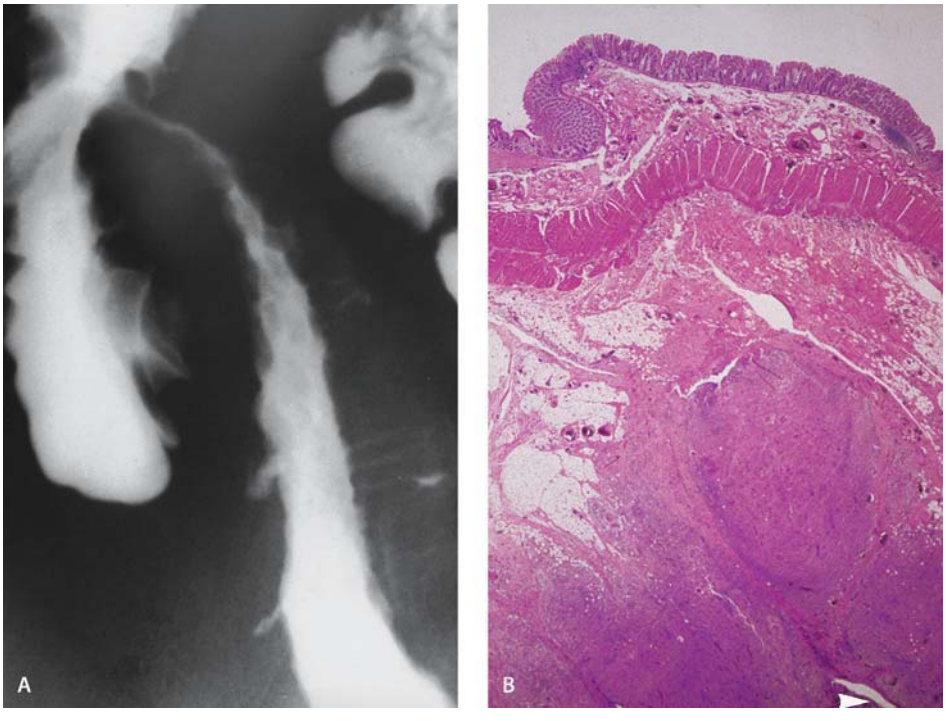

Fig. 4A, B. Crohn disease. **A** The terminal ileum is severely involved with Crohn disease. The wall is markedly thickened and a number of fissure ulcers are seen. Barium has formed collections in small abscess cavities in the fissure ulcers. **B** A histological view showing a subserosal abscess. The end of a fissure ulcer can also be seen (*arrowhead*) (from [17], with permission)

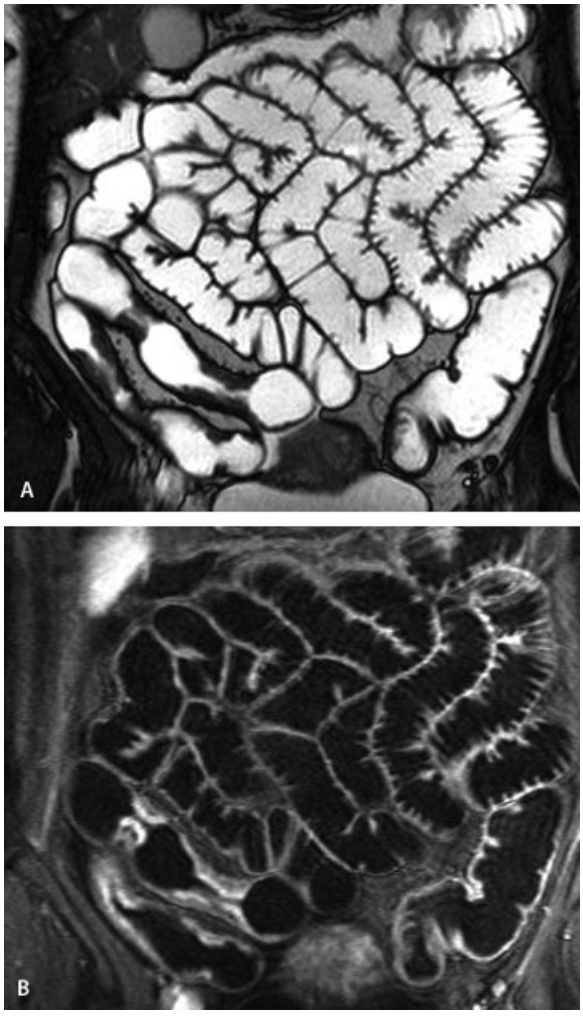

Fig. 5A, B. MR enteroclysis in a patient with Crohn disease. **A** Coronal true FISP image showing skip lesions in distal ileal loops. **B** Postgadolinium 3D FLASH image with fat saturation demonstrating marked gadolinium uptake by the thickened wall indicative of active inflammation (from [12], with permission)

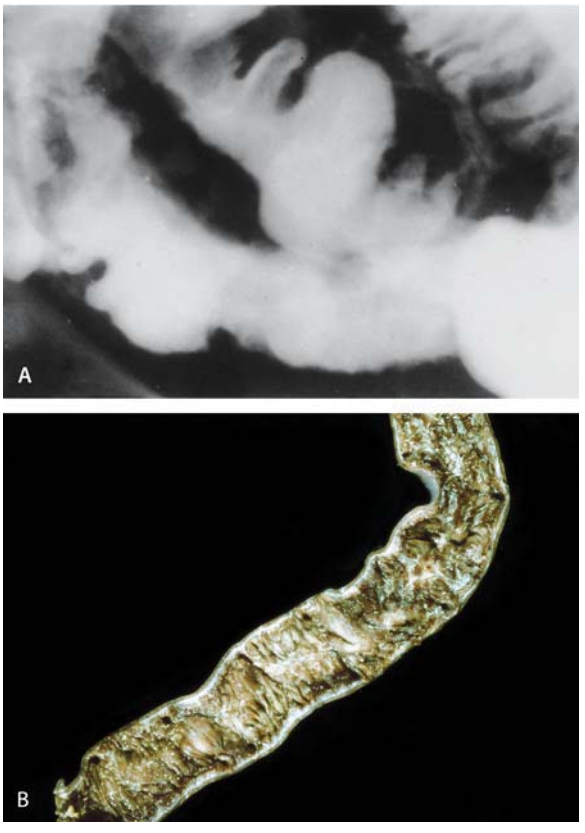

Fig. 6A, B. Crohn disease. **A** Pseudodiverticula attributable to asymmetrical involvement. **B** The pseudodiverticula are seen on a view of the resected specimen (from [17], with permission)

Discrete ulcers are seen as small collections of barium with surrounding radiolucent margins [16]. Fissure ulcers are seen in profile and may penetrate deep into the thickened intestinal wall (Fig. 4); small abscess cavities are occasionally seen at the base of deep fissure ulcers [17]. Longitudinal ulcers running along the mesenteric border of the ileum are a characteristic feature of Crohn disease, although they are only occasionally present. Cobblestoning is caused mostly by a combination of longitudinal and transverse ulceration. Discontinuous involvement of the intestinal wall is shown either as skip lesions (Fig. 5) or asymmetry. Asymmetrical involvement of the intestinal wall produces the characteristic pseudodiverticula appearance. The pseudodiverticula represent small patches of normal intestine in an otherwise severely involved segment (Fig. 6): the involved segment contracts and the normal areas become pseudodiverticula. Inflammatory polyps (pseudopolyps) are occasionally seen in Crohn disease and are shown as small discrete filling defects in a severely involved segment (Fig. 7).

Cross-sectional imaging modalities offer an important complementary diagnostic perspective in patients with Crohn disease, because of their ability to directly image the intestinal wall and surrounding mesentery and therefore to determine the extramucosal extent and spread of the disease process.

Computed tomography has shown to be extremely valuable in documenting mesenteric disease, including fibrofatty proliferation, abscess or phlegmon formation, microadenopathy (Fig. 8) and in adequately evaluating perirectal and/or perianal extension of Crohn disease [5]. In addition, the ability of CT to simultaneously evaluate extraintestinal organs may allow the detection of concurrent hepatobiliary, urinary or musculoskeletal complications, which may well lead to significant changes in the management of the individual patient.

MR enteroclysis is an emerging technique for the evaluation of small bowel in patients with Crohn dis-

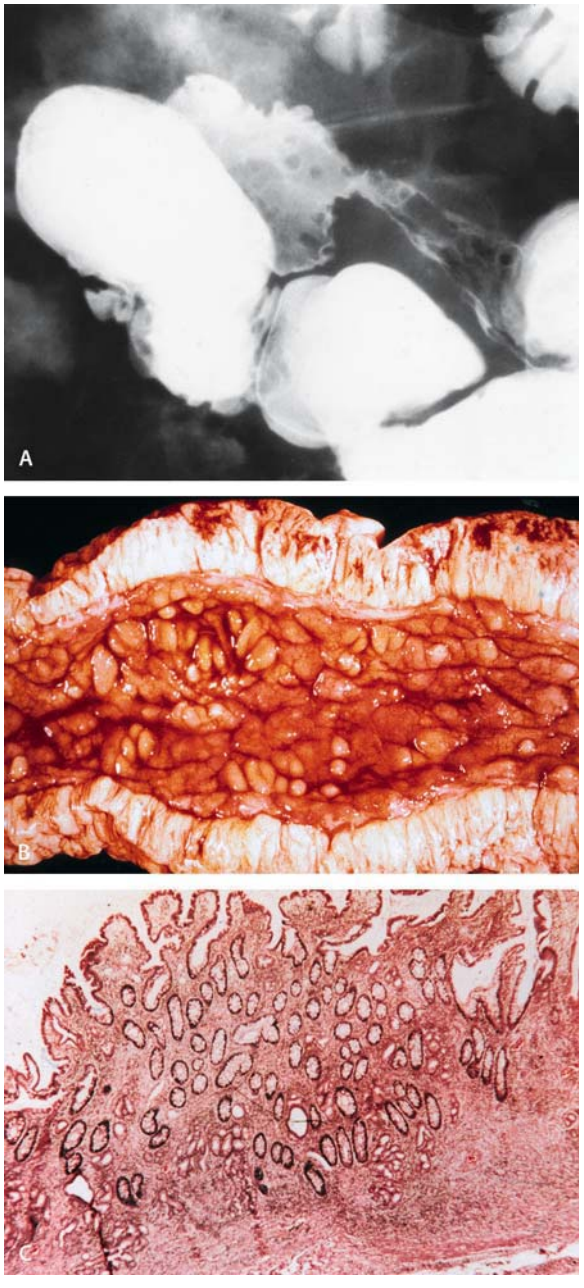

Fig. 7A–C. Crohn disease. **A** Inflammatory polyps are shown as multiple small round filling defects in a patient with severe Crohn disease. **B** The resected specimen showing the inflammatory polyps. **C** Histological section through one of the inflammatory polyps showing the disorganized mucosal pattern and redundant folds of glandular epithelium (from [17], with permission)

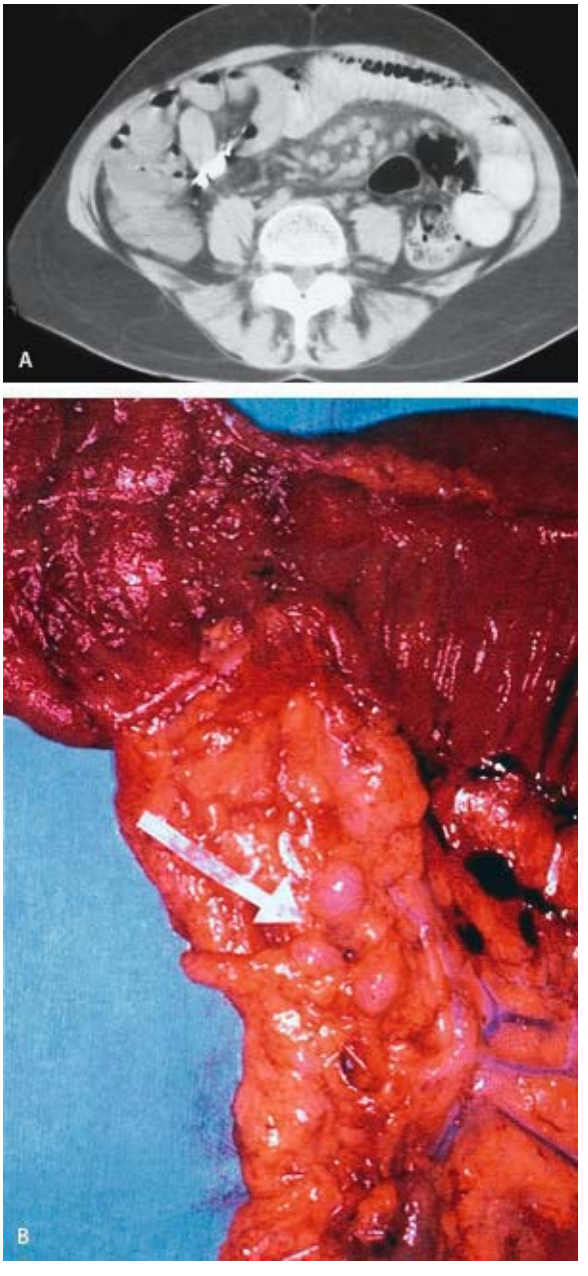

Fig. 8A, B. Crohn disease. **A** CT shows a large number of small and medium-sized mesenteric lymph nodes, adjacent to affected loops of bowel. **B** Pathology specimen of lymph node enlargement in Crohn disease

ease. The characteristic transmural lesions of Crohn disease such as bowel wall thickening, linear and fissure ulcers, and cobblestoning are accurately depicted by MRE, especially when using the true FISP sequence. MRE is of equal value with conventional enteroclysis in assessing the number and extent of involved small-bowel segments and in disclosing luminal narrowing and/or prestenotic dilatation [12, 18]. MRE has a clear advantage over conventional enteroclysis in demonstrating extramural manifestations and/or complications of Crohn disease, including fibrofatty proliferation (Fig. 9), mesenteric lymphadenopathy (Fig. 10), sinus tracts and fistulae or abscesses [18]. Disease activity may be accurately appreciated [19].

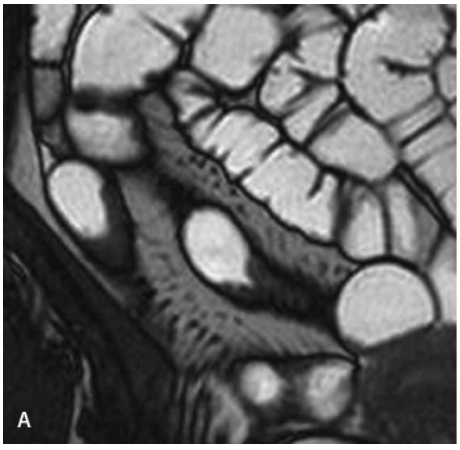

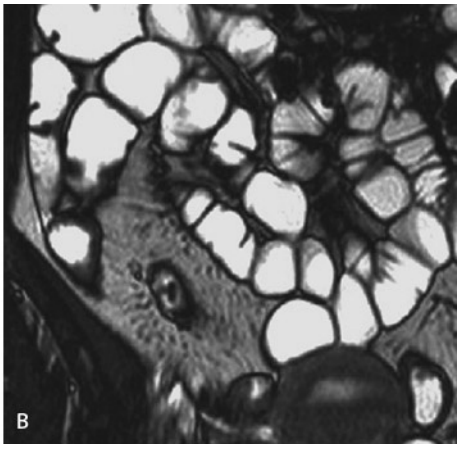

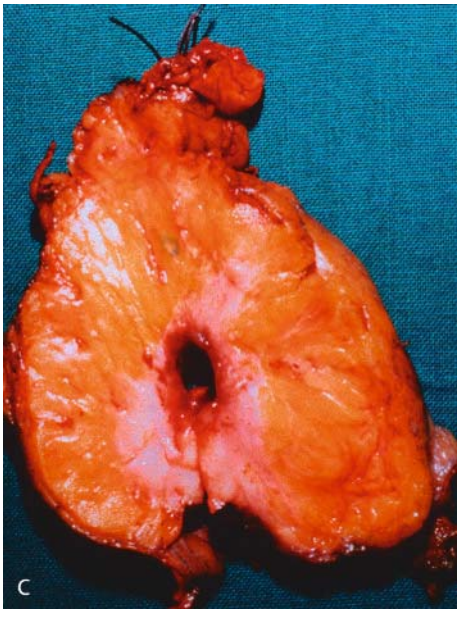

Fig. 9A–C. MR enteroclysis in a patient with Crohn disease. **A**, **B** Two consecutive coronal true FISP images demonstrating fibrofatty proliferation separating ileal bowel loops (from [12], with permission). **C** Mesenteric involvement. Pathology specimen of a resected small bowel segment, surrounded by abundant fibrofatty tissue

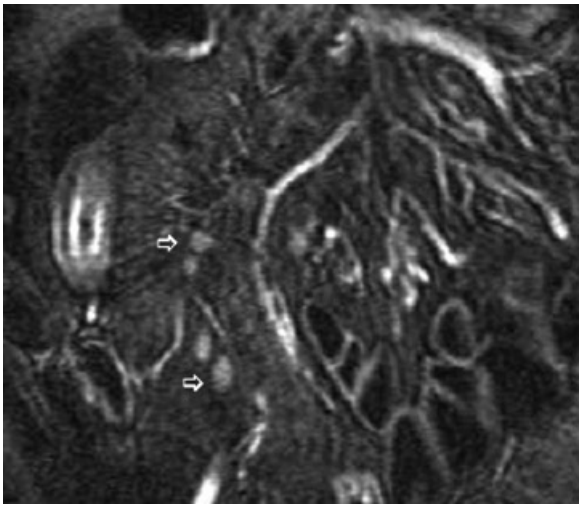

Fig. 10. MR enteroclysis: Coronal 2-mm postgadolinium 3D FLASH section with fat saturation in a patient with active Crohn disease. Small mesenteric lymph nodes measuring a few millimetres in diameter exhibiting contrast enhancement (from [12], with permission)

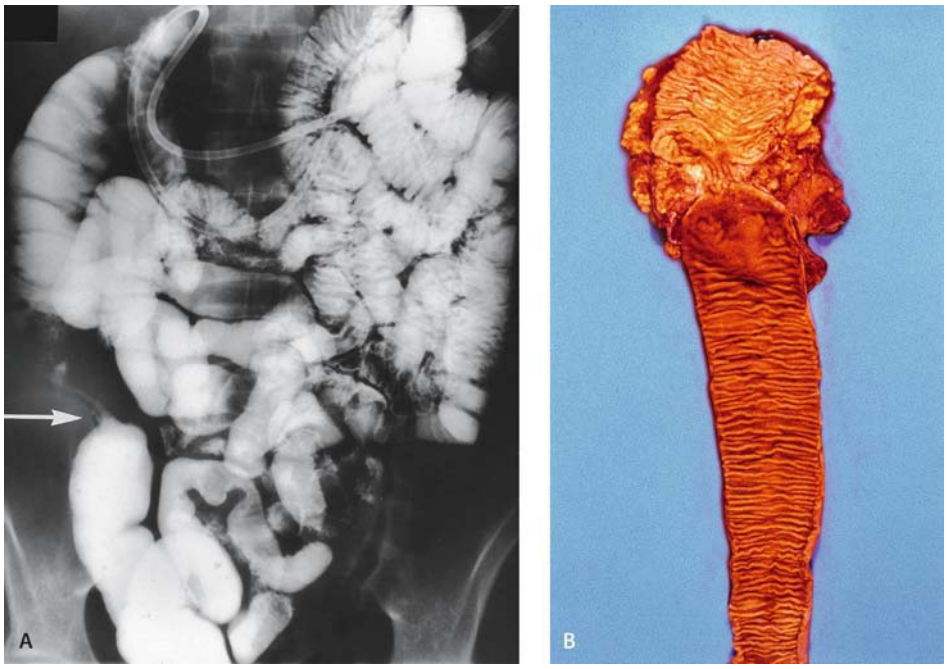

Fig. 11A, B. Tuberculosis. **A** A short stricture of the terminal ileum (*arrow*) is shown causing obstruction. **B** A view of the resected specimen shows a short ileal stricture

Tuberculosis

Intestinal tuberculosis is rare in Europe. In the past, when it was more common, involvement of the small intestine was usually caused by infection with bovine tuberculosis. Most cases are now secondary to active pulmonary tuberculosis [20]. The lesions are often multiple and mostly involve the ileum, particularly the terminal ileum and ileocaecal junction. Strictures may be short (Fig. 11) or long, single or multiple and may be indistinguishable from those seen in Crohn disease. In ileocaecal tuberculosis, the length of terminal ileum involved is normally shorter than in Crohn disease. Tuberculosis may be seen as a segment of severe ileal ulceration. Features of Crohn disease not seen in tuberculosis include cobblestoning, asymmetry and longitudinal ulceration.

Chronic Radiation Enteritis

Chronic radiation enteritis is a form of intestinal ischaemia resulting from damage to vascular endothelial cells that results in endarteritis obliterans [21]. Previous laparotomy with the development of adhesions increases the risk of developing chronic radiation enteritis. The distal ileum, particularly the pelvic loops, is the most frequent site of intestinal damage. The time interval between the radiation therapy and the development of symptoms varies considerably and may be a long as 25 - years [22]. The typical clinical presentation of patients with chronic radiation enteritis is colicky abdominal pain, diarrhoea, malabsorption and intermittent small intestinal obstruction.

The radiological features of chronic enteritis are well shown by enteroclysis [22] and include thickening of the valvulae conniventes, mural thickening, mucosal tacking, fixity and angulation of small intestinal loops, loss of the normal mucosal pattern, strictures (Fig. 12) and ulceration. Sinuses and fistulae are an uncommon finding. The pool of barium appearance, only occasionally seen, is caused by matted loops of closely adherent small intestine. Mural thickening is the result of a combined wall thickness of greater than 2 mm when adjacent adherent loops are parallel for a distance of at least 4 cm under compression. Mucosal tacking is seen as spiking and distortion of the mucosal folds on the antemesenteric border of the intestine caused by adhesions to the inflamed and thickened mesentery [23].

Acute Ischaemia

Patients with acute intestinal ischaemia only rarely have barium studies, as they normally present as acute abdominal emergencies investigated with plain radiographs, ultrasound or computed tomography (CT). On enteroclysis, acute ischaemia is shown as marked thickening of the valvulae conniventes with no significant luminal narrowing that resolves over 6–8 weeks, with the intestine returning to normal or a stricture developing at the site of ischaemia.

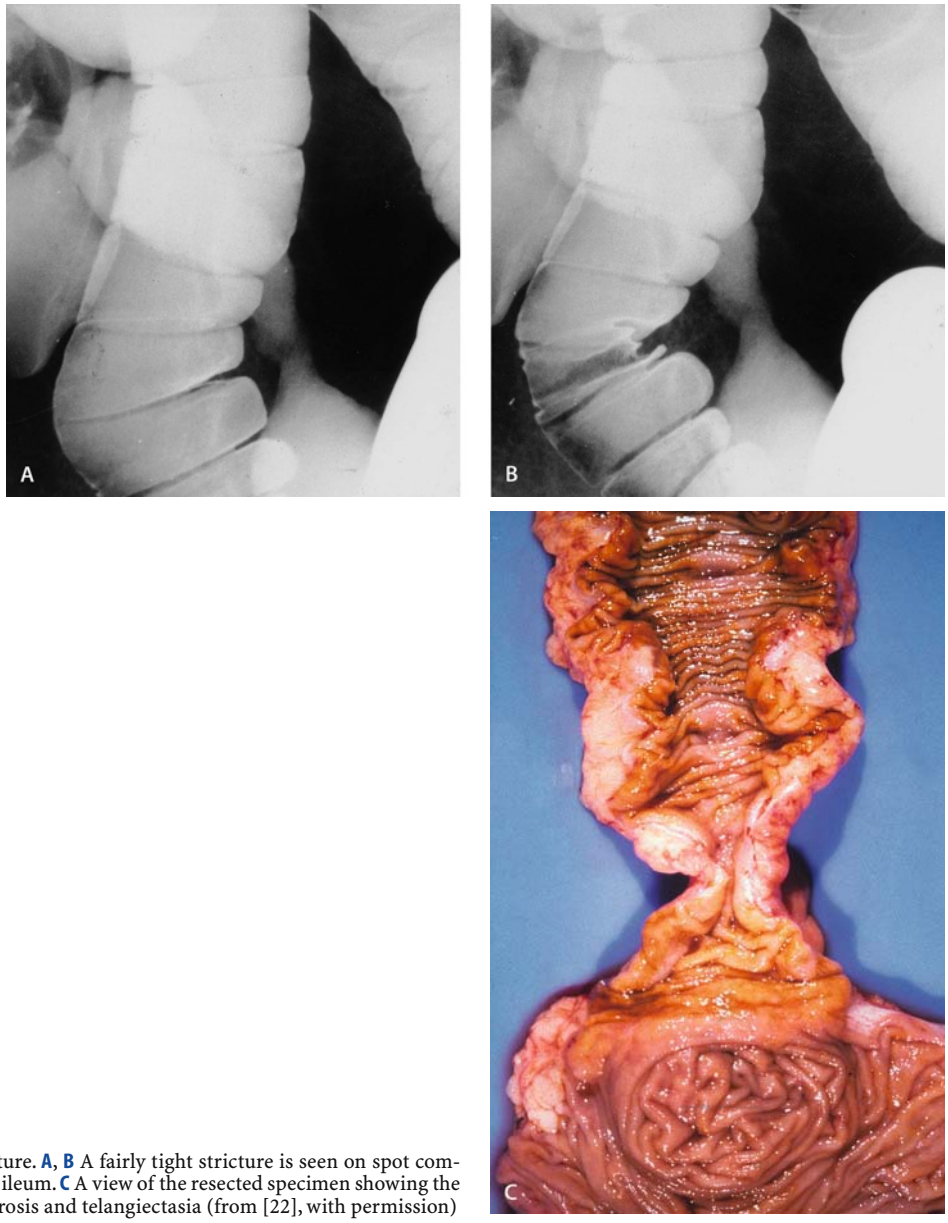

Fig. 12A–C. Radiation stricture. **A**, **B** A fairly tight stricture is seen on spot compression views of the distal ileum. **C** A view of the resected specimen showing the stricture with extensive fibrosis and telangiectasia (from [22], with permission)

Chronic Ischaemia

Chronic ischaemia due to mesenteric venous occlusion in an uncommon but clearly recognized disorder that mostly results from compression of the mesenteric veins by metastatic lymph glands. Patients normally present with obstructive symptoms and enteroclysis shows gross thickening of the valvulae conniventes with narrowing of the intestinal lumen [24].

Ischaemic Strictures

Short intestinal strictures resulting from a previous ischaemic episode are uncommon and develop following ischaemia caused by localized mesenteric vascular embolus, a short segment of strangulation or trauma. Ischaemic strictures resulting from trauma are caused either by a short mesenteric tear (Fig. 13), direct trauma to the intestinal wall (Fig. 14) [25] or a small perforation caused by acute compression of a segment of gas-filled intestine.

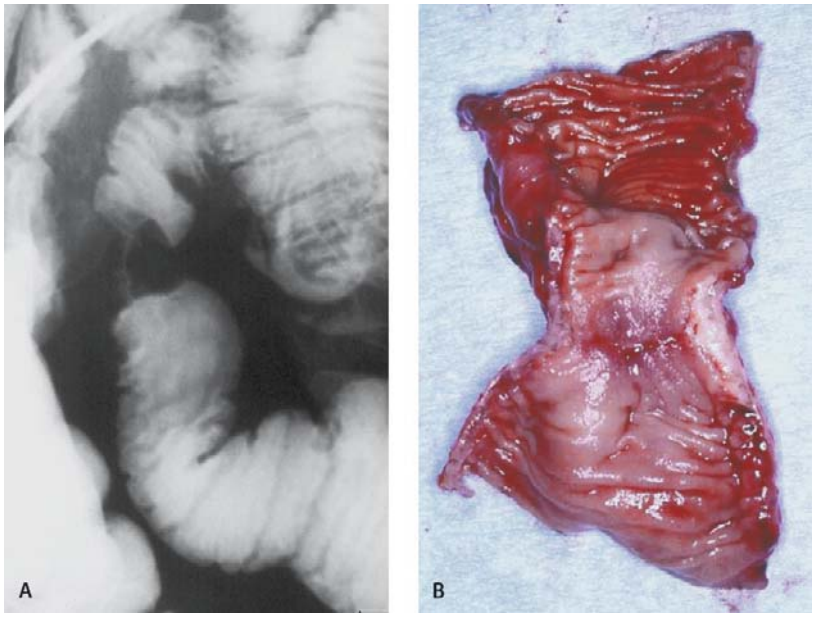

Fig. 13A, B. Focal ischemia with stricture formation. **A** Short, tight stricture in an ileal loop, following iatrogenic, focal, mesenteric injury. **B** The resected specimen shows fibrotic tissue as a result of healing of the vascular insult to this short bowel segment

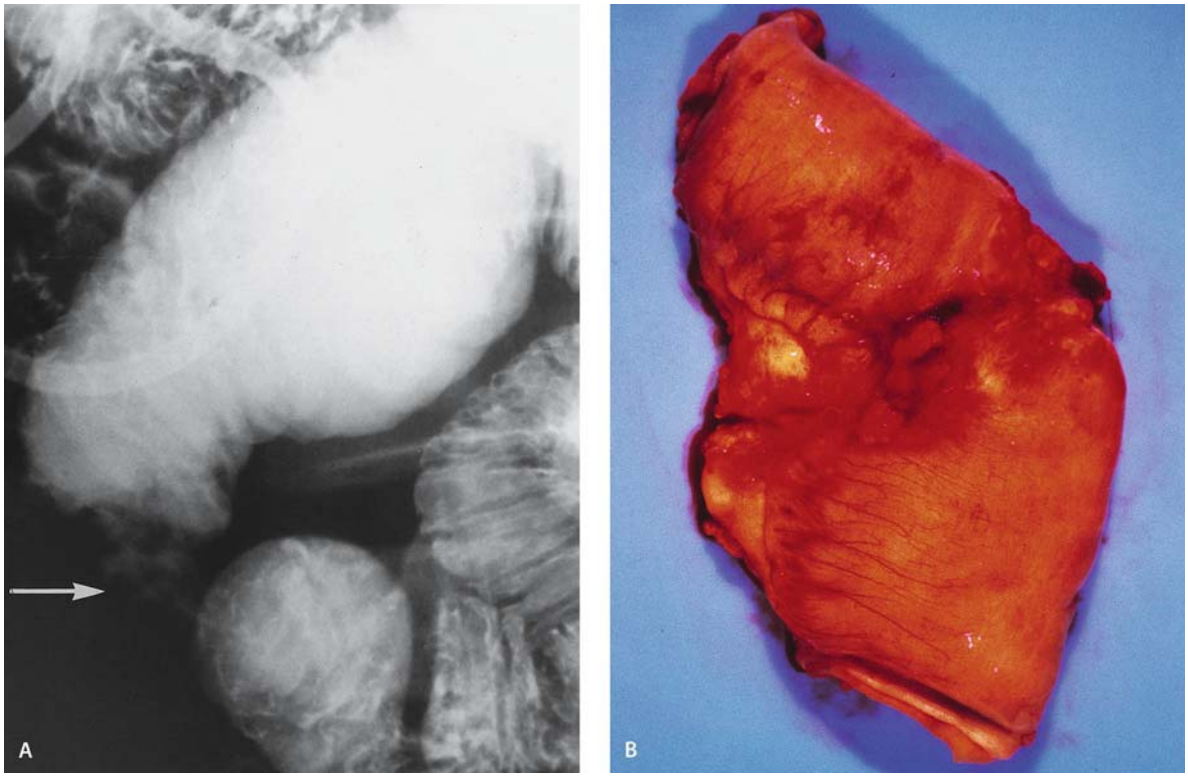

Fig. 14A, B. Ischaemic stricture due to trauma. **A** A short tight jejunal stricture is seen overlying the spine (*arrow*) in a patient who sustained blunt abdominal trauma 10 weeks earlier. Note the dilatation of the proximal jejunum. **B** A view of the resected specimen shows a very short localized stricture (from [25], with permission)

Systemic Sclerosis

Systemic sclerosis is a systemic disease characterized by widespread collagen deposition that results in tissue fibrosis. It involves the small intestine in up to 50% of cases. The replacement of smooth muscle by fibrous tissue [26] is responsible for the radiological changes.

The two most characteristic radiological features of systemic sclerosis of the small intestine are the hide-bound appearance (Fig. 15) and pseudodiverticula formation (Fig. 16). The hide-bound appearance, mostly seen in the jejunum and proximal ileum, describes a narrow separation between valvulae conniventes of normal thickness, despite dilatation of the bowel lumen [27]. This is probably caused by asymmetric smooth muscle atrophy and fibrosis of the inner circular layer of the tunica muscularis, relative to the outer longitudinal layer. Foreshortening of the bowel caused by longitudinal smooth muscle contraction results in packing of the valvulae conniventes, which is further accentuated by the associated dilatation of the affected loops. Wide-mouthed intestinal diverticula or sacculations are also related to smooth muscle fibrosis and atrophy.

Hypomotility from smooth muscle atrophy and fibrosis may also lead to stasis, dilatation and pseudo-obstruction, in cases with systemic sclerosis. Similar radiographic findings may be attributed to mechanical obstruction, or pseudo-obstruction, because of visceral

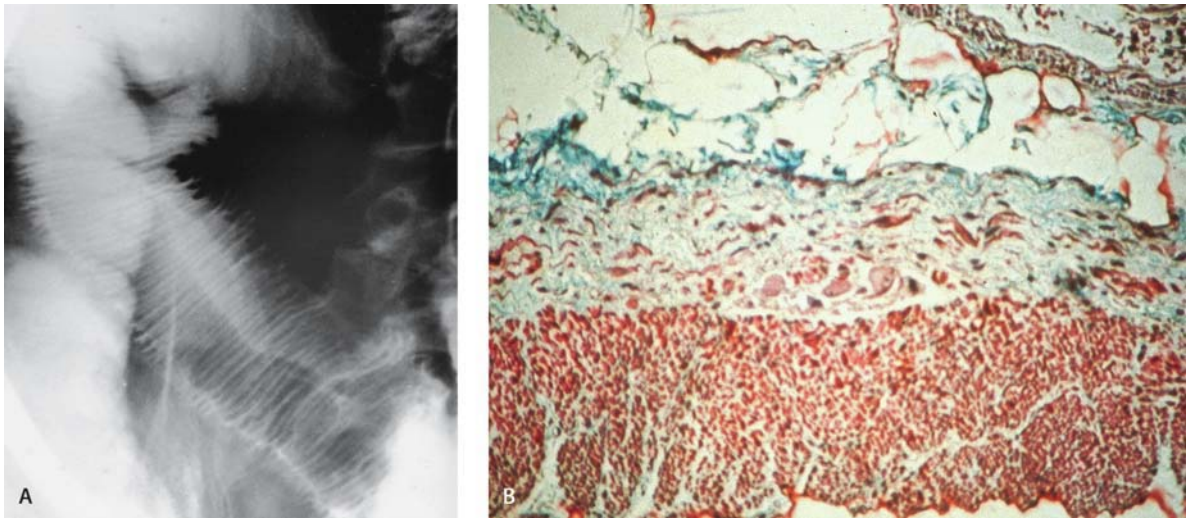

Fig. 15A, B. Systemic sclerosis. **A** A spot radiograph shows increased number of thin folds in a segment of mid small intestine – the hidebound appearance. **B** A histological section from a full-thickness biopsy shows marked fibrosis of the inner circular layer of smooth muscle with relative sparing of the outer longitudinal fibres (**A** from [2], with permission; **B** courtesy of Dr Charles A. Rohrmann)

Fig. 16A, B. Systemic sclerosis. **A** Squared sacculations at the antemesenteric border of the jejunum with hidebound folds at the mesenteric border. **B** Gross sacculations in another patient

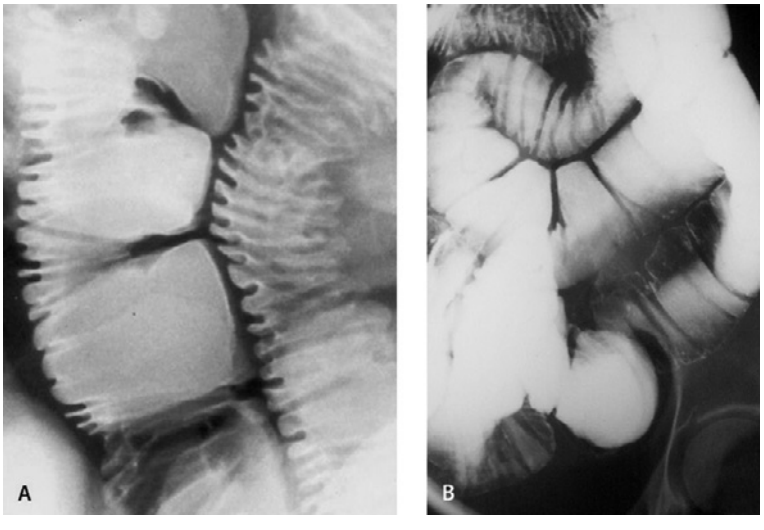

myopathies or neuropathies or celiac disease. Lack of the hide-bound bowel sign in these later conditions in a useful sign for the differential diagnosis.

Whipple Disease

Whipple disease is an uncommon disease that affects the small bowel in the majority of cases [28]. It is caused by a Gram-positive bacillus, *Tropheryma whippelii,* and characteristically involves middle-aged men who present with hepatosplenomegaly, chronic diarrhoea, sometimes ascites and a chronic debilitating syndrome and arthralgias [29].

Small-bowel barium studies may demonstrate abnormalities indicative of Whipple disease. These are related to inflammation of the intestinal villi, which results in thickening and occasionally nodularity of the valvulae conniventes, caused by severe swelling of the villi (Fig. 17). Findings are more prominent in the jejunum. Variable dilatation of the intestinal loops and moderate flocculation and dilution of the contrast material may be also present. Pseudo-Whipple disease, a disseminated infection by nontuberculous mycobacteria, may be seen in patients with malignancies or immunodeficiencies. Barium studies are also helpful in excluding other abnormalities such as celiac and Crohn disease, which may appear with similar clinical features. Lymph node involvement occurs in more than 50% of patients with Whipple disease. Noncontrast CT will show discrete mesenteric or retroperitoneal adenopathy of low attenuation, because of high fat content within the nodes (Fig. 17) [29, 30]. Abdominal ultrasound will also show unusually echogenic abdominal lymphadenopathy. Metastatic testicular neoplasms, treated lymphomas or tuberculous lymphadenopathy may also appear similar; however they will be accompanied by a relevant history.

Although the hallmark of Whipple disease is the histological demonstration of Sudan-negative and period-

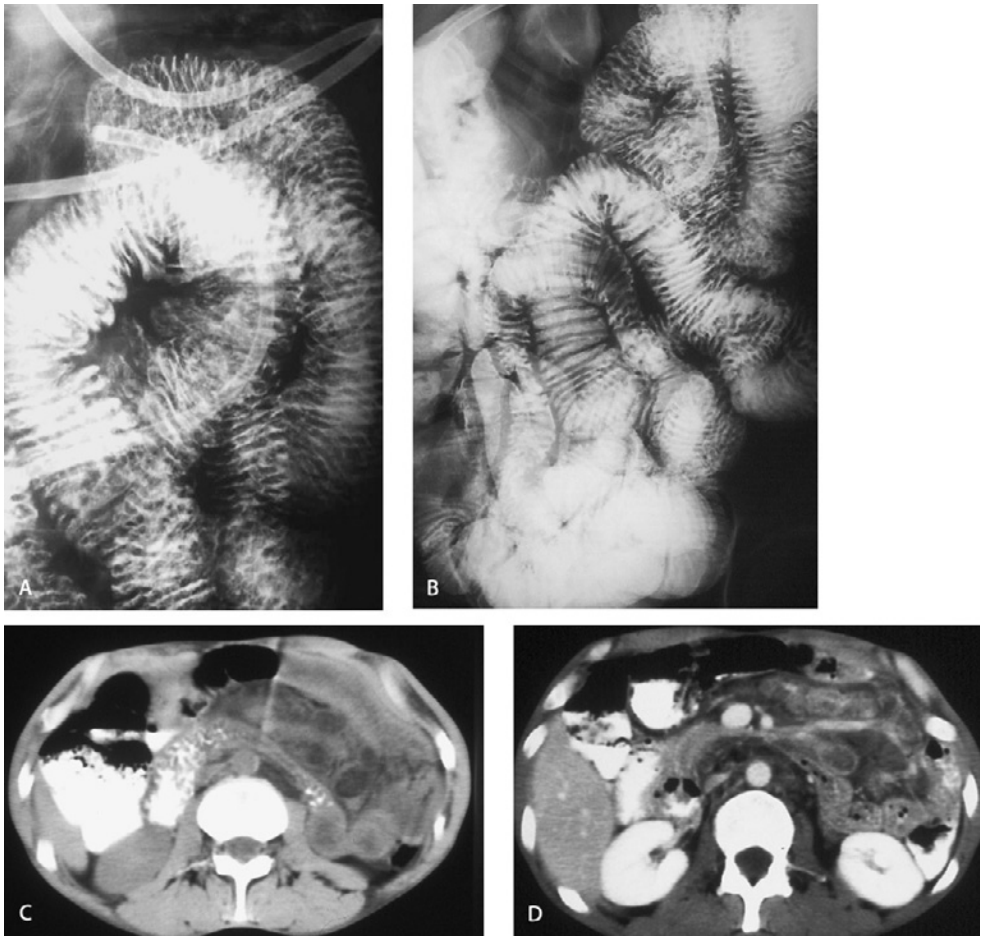

Fig. 17A–D. Whipple disease. **A**, and **B** Thickened folds with a diffuse micronodular pattern, predominantly in the proximal small bowel. **C**, **D** Pre- and postcontrast CT show nonenhancing, low attenuation, mesenteric and retroperitoneal lymph nodes

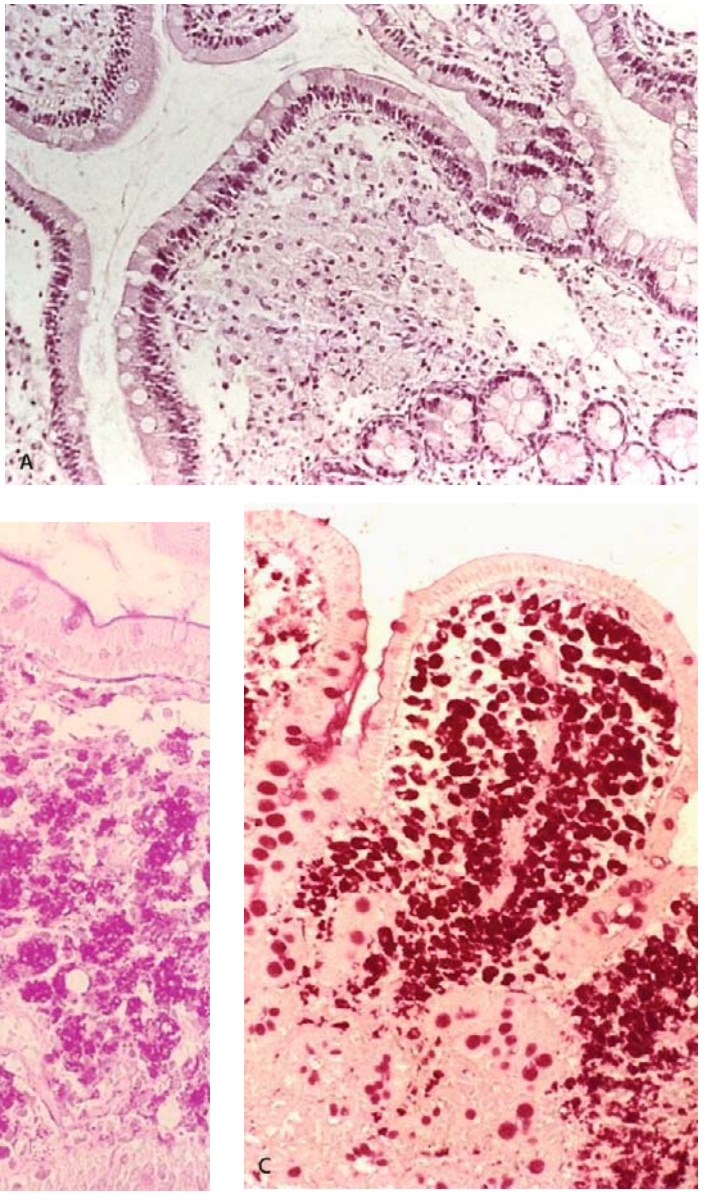

Fig. 18A–C. Whipple disease. Histological sections of the same patient as in Fig. 17. **A** Diffuse infiltration of the mucosa and submucosa with foamy macrophages. Macrophages are **B** periodic acid–Schiff (PAS) positive and **C** PAS diastase resistant

ic acid-Schiff-positive macrophages (Fig. 18), definitive diagnosis will require the demonstration of the characteristic bacilliform bodies by electron microscopy.

Intestinal Lymphangiectasia

Intestinal lymphangiectasia is part of a generalized congenital abnormality of the lymphatic system [31]. Patients present with hypoproteinaemia, enteric loss of plasma protein, lymphoedema, severe steatorrhoea and malabsorptive state. The diagnosis is confirmed by finding dilated lymph vessels in the submucosa of the jejunum (Fig. 19).

Nonsteroidal Anti-inflammatory Drug (NSAID) Enteritis

Nonsteroidal anti-inflammatory drugs are known to cause small intestinal damage. Characteristic findings are seen at histopathology as mucosal diaphragms encircling the intestine and reducing the lumen to as small as 1 mm. These diaphragm-like strictures are usually multiple and comprise only mucosa and submucosa [32]. The number of these strictures varies considerably. Radiologically the strictures are seen as a very short diaphragm-like narrowing, similar to those seen at histopathology (Fig. 20) [33].

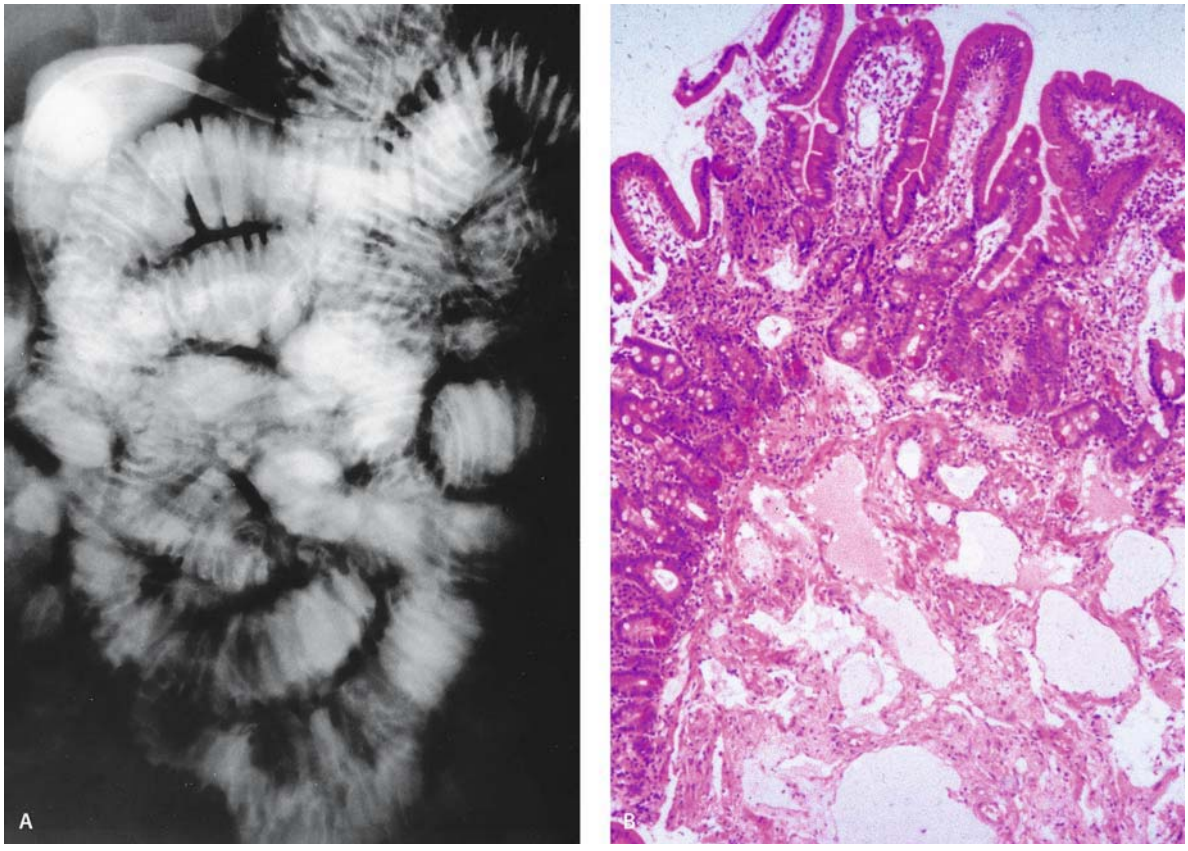

Fig. 19A, B. Intestinal lymphangiectasia. **A** There is thickening of the valvulae conniventes through the jejunum. **B** A histological section showing dilatation of the lymphatics in the submucosa

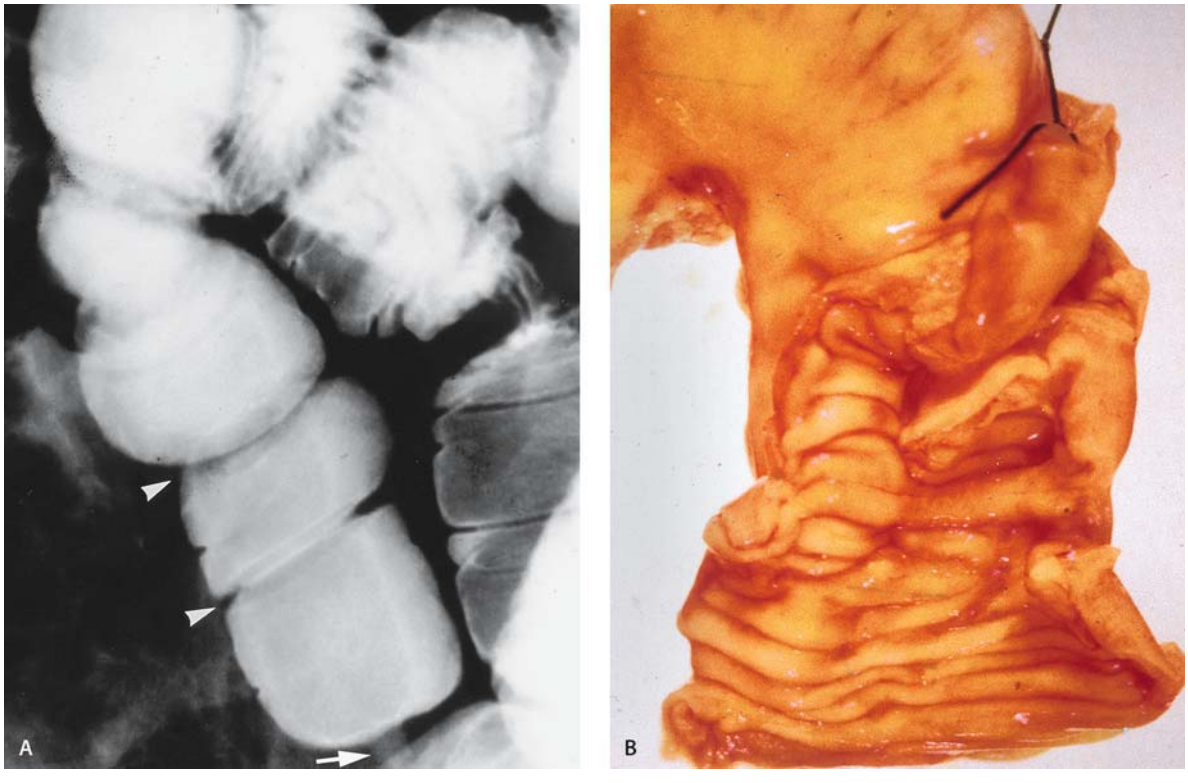

Fig. 20A, B. NSAID stricture. **A** The characteristic diaphragm-like strictures (*arrowheads*) are seen on a spot view of the terminal ileum. A further stricture is seen more proximally (*arrow*). **B** A view of the resected specimen

Meckel's Diverticulum

Meckel's diverticulum is the most common congenital anomaly of the small intestine, occurring in 1%–3% of the population. It is mostly asymptomatic. Lower gastrointestinal bleeding, acute, life-threatening, chronic or intermittent, mostly due to ectopic gastric mucosa and peptic ulceration is one of the most common complications. Ectopic gastric mucosa is found in about 15%–20% of cases. It occurs in 90% of children with a Meckel's diverticulum presenting with bleeding and in 67% of adults with a similar presentation.

Preoperative radiological diagnosis of Meckel's diverticulum ranges from difficult to very difficult. Radionuclide imaging, the Meckel's scan, based on the affinity of the isotope technetium 99m pertechnetate for functioning ectopic gastric mucosa, has long been considered a more sensitive study [34]. However, sensitivity varies with technique and age, and it is estimated to be around 60% for adults. False-positive results do occur in a number of conditions, whereas false-negative results usually occur with symptomatic diverticula without ectopic gastric mucosa or acutely haemorrhaging diverticula.

Enteroclysis has also been suggested as a most reliable imaging technique for their preoperative diagnosis. It usually shows a blindly ending sac of variable size, arising from the antemesenteric border of ileum (Fig. 21). Additional characteristic findings include a gastric rugal pattern or a triangular fold pattern at the base of the diverticulum (Fig. 22) [35]. Careful fluoroscopy with compression is essential. However, unsuccessful demonstration of a Meckel's diverticulum on enteroclysis is not unusual and reasons, despite a detailed examination, will include stenosis of the ostium, filling with intestinal contents, rapid emptying or small size. CT has been reported to be of value in Meckel's diverticulitis and infarcted Meckel's diverticulum.

Selective angiography is a well-established method for both nonhaemorrhaging-negative scintigraphic, and in massively bleeding diverticula. Extravasation of contrast into the bowel lumen is an expected angiographic finding in a patient with active bleeding. Very recently, the importance of visualization and identification of the vitelline artery for the diagnosis of Meckel's diverticulum, with or without active haemorrhage, has again been stressed [36]. Characteristic angiographic findings of selective or superselective catheterization will include a) an abnormal elongated vessel originating from the ileal artery, without anastomotic branches to the ileal artery branches and b) a group of dilated tortuous vessels at the distal portion of the artery (Fig. 23).

Conclusion

The radiological signs seen at enteroclysis, complemented with cross-sectional imaging, are similar to the gross pathological changes, and by analysing the radiological appearances, it is possible to suggest the correct diagnosis in a high percentage of patients.

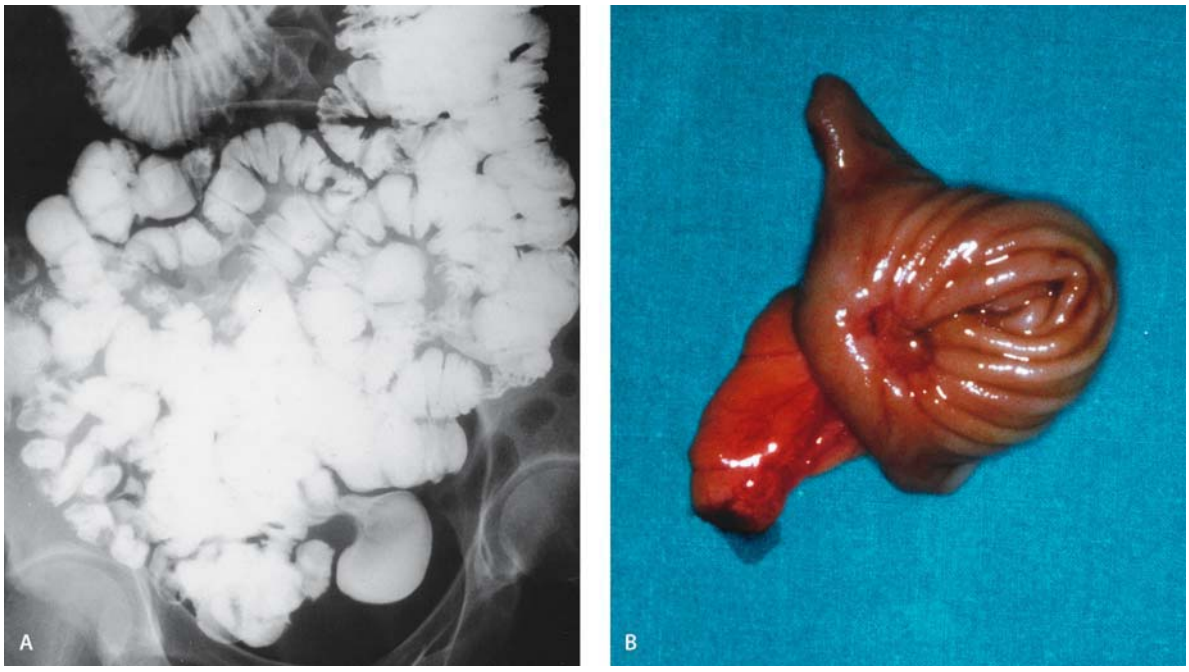

Fig. 21A, B. Meckel's diverticulum. **A** A fairly large sac-like structure is outlined with barium. **B** A view of the resected specimen (**a** from [2], with permission)

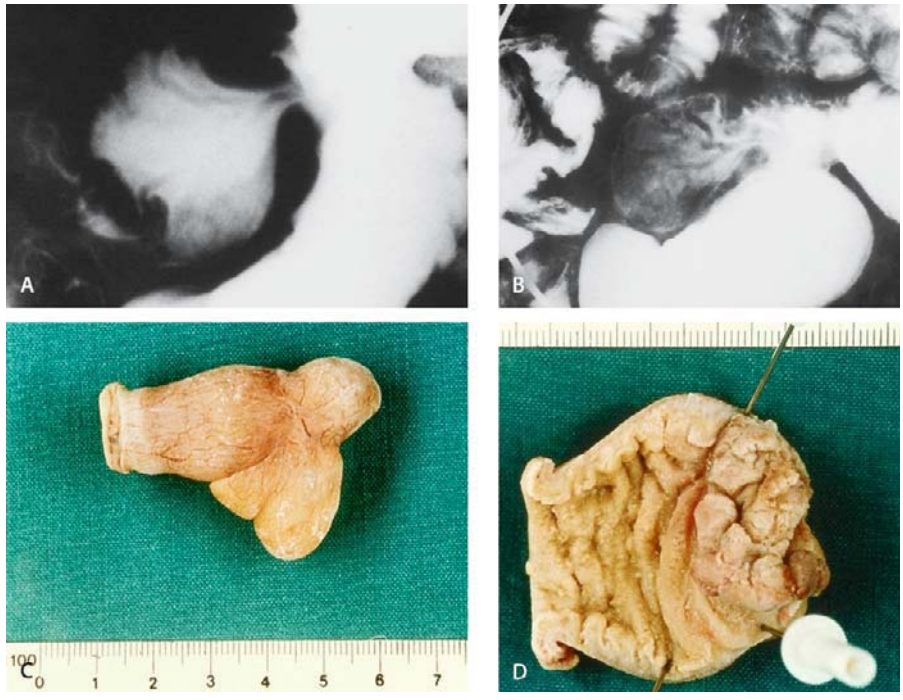

Fig. 22A–D. Meckel's diverticulum **A**, **B** Enteroclysis shows a single blind sac attached to antemesenteric border, junctional fold pattern at its base and appearances simulating gastric rugae **C**, **D** Corresponding pathology specimens, confirming the radiological findings

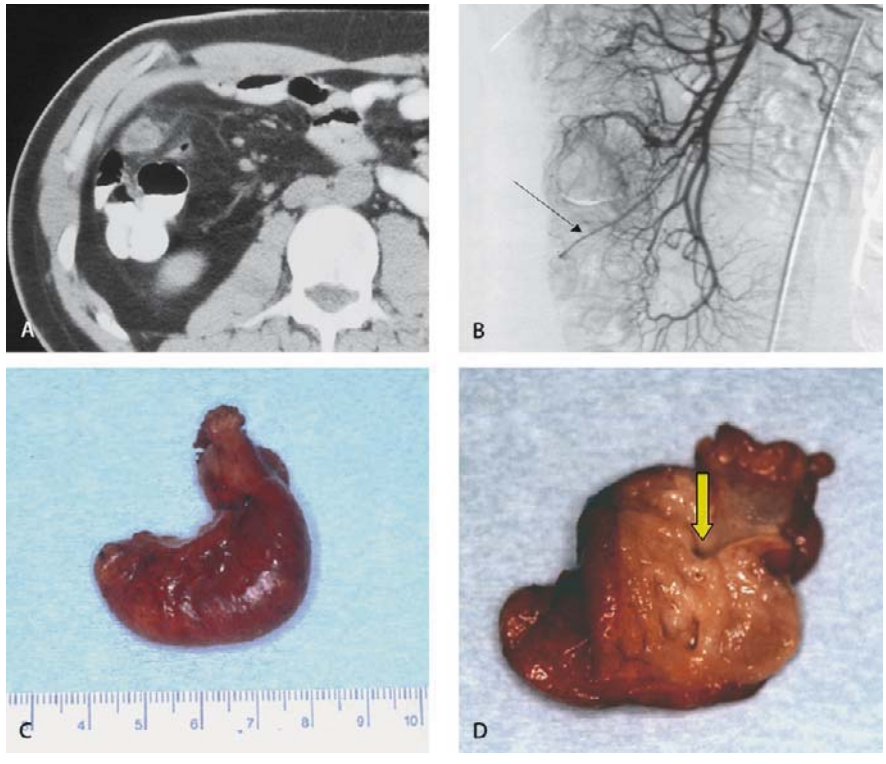

Fig. 23A–D. Meckel's diverticulum. **A** CT shows a small, well-demarcated soft tissue mass attached to the distal small bowel in a patient who presented with episodes of intermittent intestinal bleeding and a negative enteroclysis study. **B** Mesenteric angiography reveals an abnormal, elongated, nonbranching artery with tortuous vessels at its distal portion. Features consistent with the vitelline artery. **C**, **D** Corresponding pathology specimens shows stenosis of the ostium (*arrow*) of the diverticulum, which caused unsuccessful demonstration by enteroclysis (from [35], with permission)

References

1. Theoni RF (1987) Radiography of the small bowel and enteroclysis: a perspective. Invest Radiol 22:930–936
2. Nolan DJ, Cadman PJ (1987) The small bowel enema made easy. Clin Radiol 38:295–301
3. Barloon TJ, Lu CC, Honda H et al (1994) Does a normal small bowel enteroclysis exclude small bowel disease? A long-term follow-up of consecutive normal studies. Abdom Imaging 19: 113–115
4. Dixon PM, Roulston ME, Nolan DJ (1993) The small enema: a 10-year review. Clin Radiol 4:46–48
5. Balthazar EJ (2003) Evaluation of the small intestine by computed tomography. In: Gourtsoyiannis N (ed) Radiological imaging of the small intestine. Springer, Berlin Heidelberg New York, pp 87–130
6. Bender GN, Maglinte DT, Kloeppel VR, Timmons JH (1999) CT- enteroclysis: a superfluous diagnostic procedure or valuable when investigating small bowel disease. AJR Am J Roentgenol 172: 373–378
7. Maglinte DT, Gourtsoyiannis N, Rex D, Howard TJ, Kelvin FM (2003) Classification of small bowel Crohn subtypes based on multimodality imaging. Radiol Clin North Am 41:285–303
8. Maglinte DT, Heitkamp DE, Howard TJ, Kelvin FM, Lappas JC (2003) Current concepts in imaging of small bowel obstruction. Radiol Clin North Am 41:263–283
9. Gourtsoyiannis N, Papanikolaou N, Grammatikakis J, Maris T, Prassopoulos P (2000). MR Imaging of the small bowel with a true-FISP sequence after enteroclysis with water solution. Investigat Radiol 35:707–711
10. Umschaden HW, Szolar D, Gasser J, Umschaden M, Haselbach H (2000) Small-bowel disease: comparison of MR enteroclysis images with conventional enteroclysis and surgical findings. Radiology 215:717–7125
11. Gourtsoyiannis N, Papanikolaou N, Grammatikakis J, Maris T, Prassopoulos P (2001) MR enteroclysis protocol optimization: comparison between 3D FLASH with fat saturation after intravenous gadolinium injection and true FISP sequences. Eur Radiol 11:908–913
12. Gourtsoyiannis N, Papanikolaou N, Rieber A, Brambs HJ, Prassopoulos P (2002) Evaluation of the small intestine by MR imaging. In: Gourtsoyiannis N (ed) Radiological imaging of the small intestine. Springer, Berlin Heidelberg New York, pp 157–170
13. Goldblum JR, Petras RE (1997) Histopathology of Crohn disease. In: Alan RN, Rhodes JM, Hanauer SB, Keightly MRB, Alexander-Williams J, Fazio VW (eds) Inflammatory bowel diseases. Churchill Livingstone, New York, pp 311–316
14. Kelly JK, Sutherland LR (1988) The chronological sequence in the pathology of Crohn disease. J Clin Gastroenterol 10: 28–33
15. Marshak RH, Lindner AE (1976) Radiology of the small intestine. Saunders, Philadelphia
16. Nolan DJ, Gourtsoyiannis NC (1980): Crohn disease of the small intestine: a review of the radiological appearances in 100 consecutive patients examined by a barium infusion technique. Clin Radio 31:597–603
17. Nolan DJ, Piris J (1980) Crohn disease of the small intestine: a comparative study of the radiological and pathological appearances. Clin Radiol 31:591–596
18. Prassopoulos P, Papanikolaou N, Grammatikakis J, Rousomoustakaki M, Maris T, Gourtsoyiannis N (2001) MR enteroclysis imaging of Crohn disease. Radiographics 21:S161–172
19. Gourtsoyiannis N, Papanikolaou N, Grammatikakis J, Papamastorakis G, Prassopoulos P, Roussomoustakaki M (2004) Assessment of Crohn disease activity in the small bowel with MR and conventional enteroclysis: preliminary results. Eur Radiol 14:1017–1024
20. Morson BC, Dawson IMP (1979) Gastrointestinal pathology, 2nd edn. Blackwell Scientific, Oxford
21. Hasleton PS, Carr N, Schofield PF (1985) Vascular changes in radiation bowel disease. Histopathology 9:517–534
22. Mendelson RM, Nolan DJ (1985) The radiological features of chronic radiation enteritis. Clin Radiol 36:141–148
23 Mason GR, Dietrich P, Friedland GW, Hanks GE (1970) The radiological findings in radiation-induced enteritis and colitis. A review of 30 cases. Clin Radiol 21:232–247
24. Nolan DJ, Traill ZC (1997) Metastatic oesophageal carcinoma presenting as small intestinal ischemia: imaging findings. Eur Radiol 7:341–343
25. Nolan DJ (1983) Radiological atlas of gastrointestinal disease. John Wiley, Chichester and New York
26. Rohrmann CA Jr, Ricci MT, Krishnamurthy S, Schuffler MD (1984) Radiologic and histologic differentiation of neuromuscular disorders of the gastrointestinal tract, visceral myopathies, visceral neuropathies, and progressive systemic sclerosis. AJR Am J Roentgenol 143:933–941
27. Horowitz AL, Meyers MA (1973) The "hide-bound" small bowel of scleroderma: characteristic mucosal fold pattern. AJR Am J Roentgenol 119:332–334
28. Ramaiah C, Boynton RF (1998) Whipple disease. Gastroenterol Clin North Am 27:683–695
29. Horton KM, Fishman EK (1998) Uncommon inflammatory diseases of the small bowel: CT findings. AJR Am J Roentgenol 170:385–388
30. Rijke AM, Falke THM, De Vries RRP (1983) Computed tomography in Whipple disease. J Comput Assist Tomog 7: 1101–1102
31. Mistilis SP, Skyring AP, Stephens DD (1965) Intestinal lymphangiectasia. Mechanism of enteric loss of plasma-proteins and fat. Lancet i:77–80
32. Bjarnason I, Price AB, Zanelli J, Smethurst P, Burke M, Gumpal JM, Levi AG (1988) Clinical pathological features of nonsteroidal anti-inflammatory drug-induced small intestinal strictures. Gastroenterology 94:1070–1074
33. Levi S, de Lacey G, Price AB, Gumpel MJ, Levi AJ, Bjarnason I (1990) "Diaphragm-like" strictures of the small bowel in patients treated with non-steroidal, anti-inflammatory drugs. Br J Radiol 63:186–189
34. Sfakianakis GN, Conway JJ (1981) Detection of ectopic gastric mucosa in Meckel's diverticulum and in other aberrations by scintigraphy: I. Pathophysiology and 10-year clinical experience. J Nucl Med 22:647–654
35. Rossi P, Gourtsoyiannis N, Bezzi M, Raptopoulos V, Massa R, Capanna G, Pedicini V, Coe M (1996) Meckel's diverticulum: imaging diagnosis. AJR Am J Roentgenol 166:567–573
36. Okazaki M, Higashihara H, Saida Y, Minami M, Yamasaki S, Sato S, Nagayama H (1993) Angiographic findings of Meckel's diverticulum: the characteristic appearance of vitelline artery. Abdom Imaging 18:15–19

Neoplastic and Inflammatory Diseases of the Colon

Jacques W.A.J. Reeders

4.6

Contents

Introduction

This chapter discusses both neoplastic and inflammatory diseases of the colon. Emphasis is also placed on discussing different techniques to study the colon by imaging such as virtual colonoscopy (CT and MRI colonography). In addition, other topics of interest to the diagnosis of the colon, such as comparing double-contrast barium edema and colonoscopy, PET, and monoclonal antibody imaging, are treated.

Neoplastic Diseases of the Colon

Polyps

Because adenomas almost always represent the primary stage in the development of colorectal carcinoma, diagnosis and appropriate therapy of polyps are of crucial importance in the prevention of colonic cancer [1–3].

A polyp is any circumscribed protrusion of normal mucosa into the lumen, whether originating from the mucosa or situated submucosally. Therefore the term "-polyp" is a microscopic description and not a histologic diagnosis.

Genuine polyps are lesions arising from the epithelium of the mucosa. According to Morson [4], there are two main groups of polyps:

- Neoplastic (adenomatous) polyps
- Nonneoplastic polyps

Both groups include a broad histopathologic spectrum, the neoplastic polyps being particularly important, due to their precancerous potential.

- Neoplastic polyps are polyps arising from new tissue, whose growth is autonomic and progressive; they can be benign or malignant. Neoplastic polyps can be classified as tubular adenoma, villous adenoma, or tubulovillous adenoma.
- Nonneoplastic polyps are tumor-like lesions with autonomic and progressive growth. In principle they have no invasive or metastatic potential. This group can be classified as hamartomatous polyps, inflammatory polyps and unclassified polyps (metaplastic, hyperplastic).

Neoplastic Polyps (Adenomas)

Colorectal adenomas, according to the World Health Organization (WHO) definition, are benign, pedunculated or sessile neoplastic lesions of the glandular epithelium with varying degrees of cellular atypia. When ten or fewer polyps are present, they are termed solitary.

When ten or more are present, polyposis syndrome is suggested. In autopsy series, the incidence is 11%–51% and in the general population it is 3%–15%. There is an increased incidence with increased age, particularly above 40 years of age (males:females, 2:1) [4].

In 8%–25% of cases there are synchronous adenomas (primary multiple), increasing with age. Where a rectal adenoma or carcinoma is present, 35%–55% of patients will have adenomas in the proximal colon. Synchronous adenomas are more common in groups. In 22%, adenomas are metachronous (secondary multiple). After removal of one polyp, there is an increased risk of development of one or more new polyps; after removal of a solitary adenoma, 5 years later, 20% will have a new adenoma and 10 years later 40% will have a new one. After removal of several adenomas, 5 years later 40% will have a new adenoma and 10 years later 75% will [2].

■ **Location.** There is great variation in reports concerning the distribution of these lesions. The largest proportional distribution of the various adenomas throughout the colon can be found in the rectosigmoid. In old age, the incidence is relatively higher on the right side; in younger persons it is higher on the left side. In

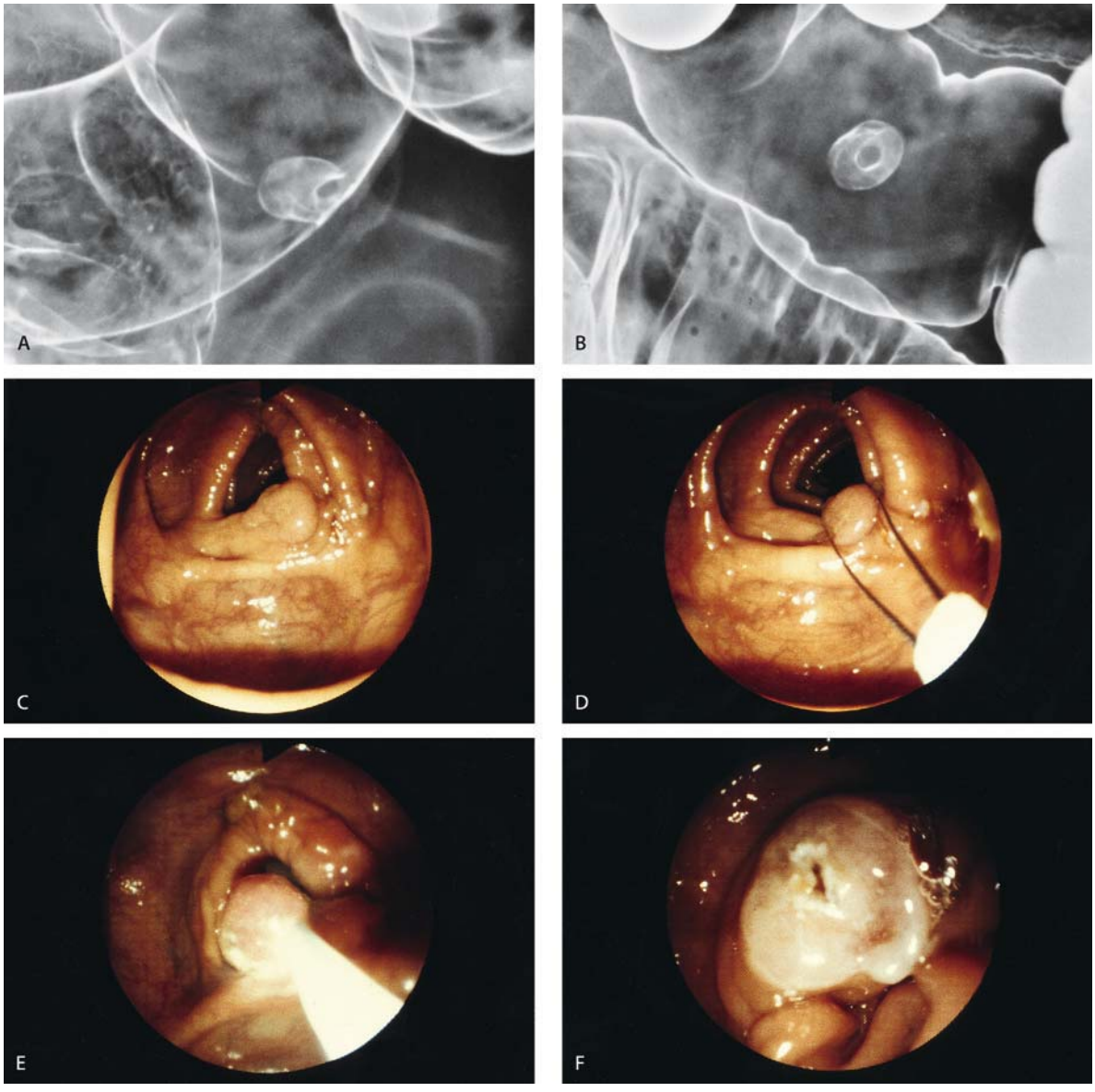

Fig. 1A–F. Intermediate polyp; histologically a benign tubular adenoma. **A** Oblique view, **B** En face view. "Mexican hat" appearance: the central ring is formed by the narrow base, the outer ring by the large head of the polyp. **C–F** Polypectomy procedure. **C** Intermediate polyp in the transverse colon; **D** a snare is placed around the polyp; **E** the sheath is advanced for transection, nearer to the head than to the base and current is applied; **F** white appearance indicates coagulation of tissue

the more recent literature, there have been reports of an increase in right-sided and a decrease in left-sided adenomas; this may be due to improved examination techniques and increased use of endoscopy [2].

■ **Etiology.** The etiology is unknown. Low-fiber diets, high in meat, high-fat diets, genetic factors (recessive gene) may be a cause. Slower passage provides the opportunity for synthesis of carcinogenic substances and provides time for interaction between possible carcinogens and the colonic mucosa.

■ **Clinical Presentation.** Small adenomas (<1 cm) are usually an incidental finding and are asymptomatic. Larger adenomas may lead to general bowel complaints and occult bleeding. Obstruction can occur if they are large. When they are pedunculated, an anal prolapse is possible.

Large, sessile villous adenomas are usually found in the rectum but can also be found in the sigmoid. There may be passage of mucus with diarrhea. Hyponatremia, hypokalemia and hypochloremia and/or bleeding may occur.

■ **Morphology.** The polyps may be sessile, pedunculated or intermediate (Figs. 1–3).

Tubular adenomas can be several millimeters to 1 cm. They are spherical, round or oval with a smooth, lobulated, reddish surface. They contain highly branched glandular ducts, separated by a normal lamina propria. Cystic dilatation, secondary ulceration, infection, and hemorrhage may occur.

Villous adenomas (>75% villous structures) are larger than tubular adenomas, up to 10 cm or more. The surface is irregular, nodular, and covered in a carpet-like fashion by mucus (Fig. 4). They are often very soft. Larger villous adenomas are sessile and may rarely be pedunculated. Many finger-like structures may be found oriented perpendicular to the colonic wall, consisting of lamina propria with epithelial cells extending the muscularis mucosa [5].

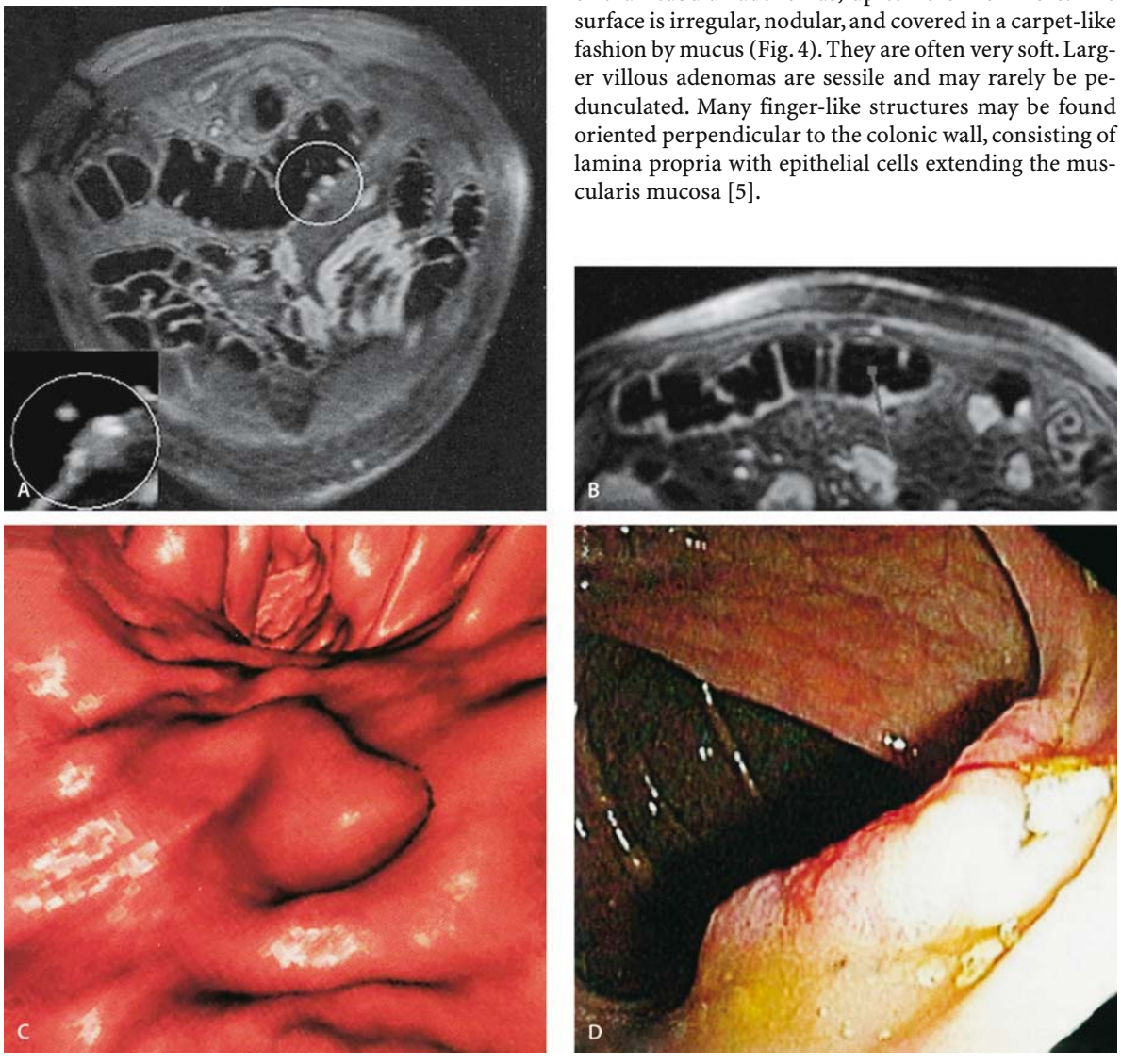

Fig. 2A–D. Sessile intermediate polyp of the transverse colon; **A–C** virtual MR colonoscopy. **A** Coronal 3D VIBE sequence colonoscopy. **B** Transverse reconstruction. **C** 3D reconstruction. **D** Endoscopic view (adapted from [99])

Tubulovillous adenomas are a combination of tubular and villous structures. With increasing size, more villous elements can be found. The surface is smooth or lobulated and central indentation is possible. Central ulceration is an indication of malignancy. If the adenoma is hard, this is an indication of previous hemorrhage, inflammation or carcinoma.

■ **Malignant Transformation in Adenomas.** According to most authors, it is generally believed that nearly all carcinomas of the colon arise from adenomas. There is an increasing incidence of carcinoma with increasing size of polyps: an adenoma smaller than 1 cm has a 1% malignant potential; an adenoma between 1–2 cm has a 10% malignant potential and an adenoma greater than 2 cm a 50% malignant potential [2, 4].

Diagnostic Imaging

■ **Double-contrast barium enema.** The radiologic appearances of the various polyps (broad-based, sessile, pedunculated or intermediate) are summarized in Table 1 [2].

■ **Interval between proctosigmoidoscopy/colonoscopy and barium enema.** If endoscopy and air/contrast enema require the same preparation, the following applies: the radiographic examination can follow immedi-

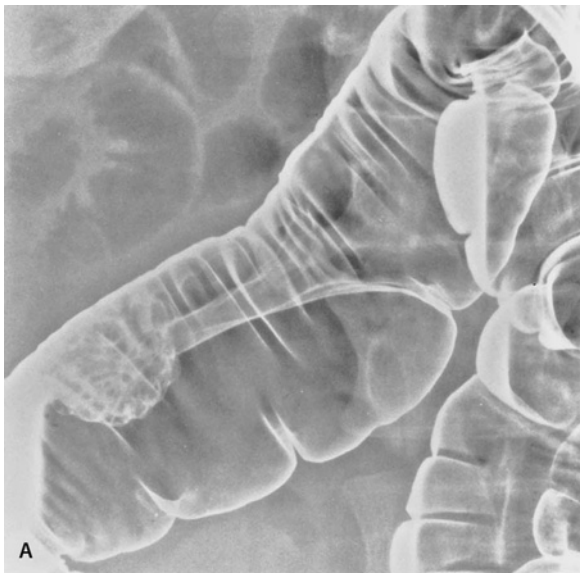

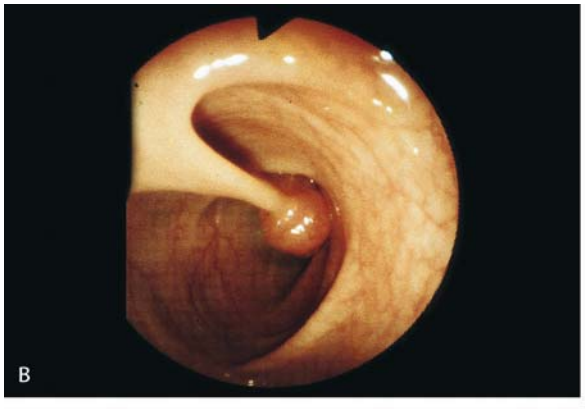

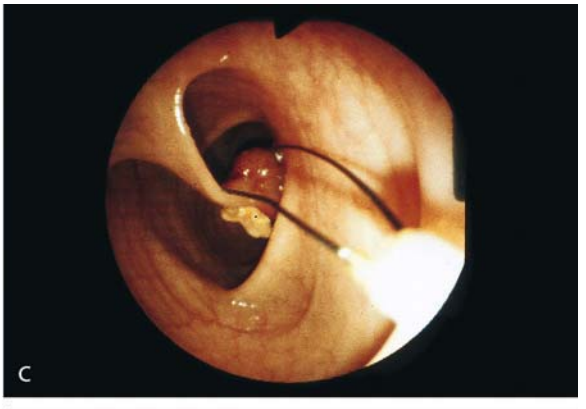

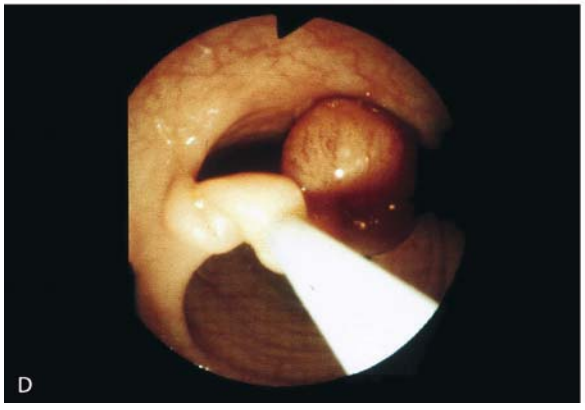

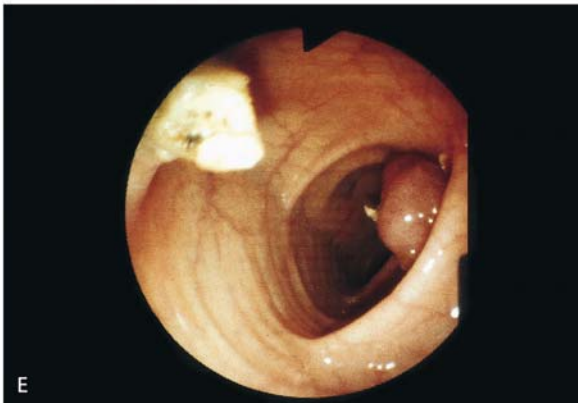

Fig. 3A–G. Benign pedunculated polyp. **A** Long pedicle and smooth, round head. **B–E** Pedunculated polyp; polypectomy procedure. **B** Pedunculated polyp in the descending colon; **C** a snare is placed around the polyp; **D** the sheath is advanced for transection nearer to the head than to the base. Current is applied; white appearance indicates coagulation of tissue. **E** The coagulated base of the pedicle (*upper left*) and the separated polyp (in lumen) can both be seen. **F**, **G** Macroscopy/microscopy: mucosa of the pedicle is normal, nonmalignant

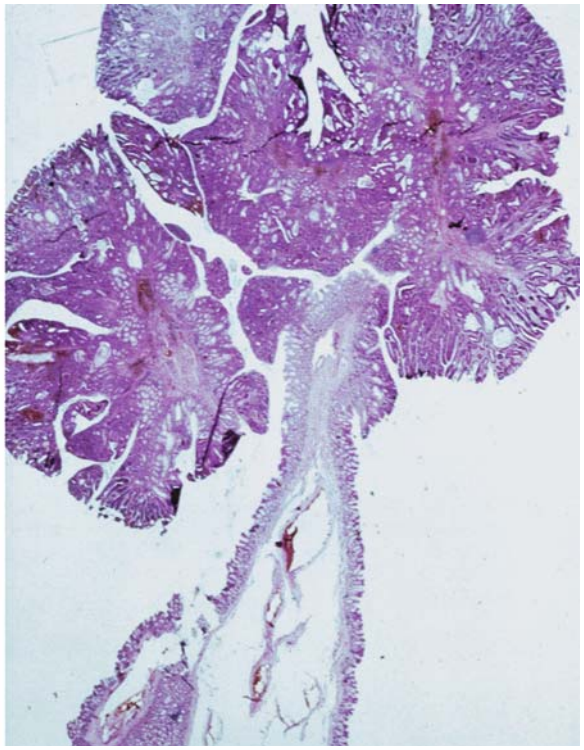

Fig. 3F, G.

Table 1. Roentgenographic appearance of various polyps (from [2])

	Wide-based or sessile adenoma	Intermediate form or suggestive of pedunculated adenoma	Pedunculated adenoma
Definition	Height < 50% width of base; immobile; size a few millimeters to many centimeters, usually 0.5-1 cm	Height > 50% width of base	Head, ≥ 1 cm; pedicle often several centimeters long; position of head and pedicle vary with respect to one another
Projection frontal/ en face	Dense circle = ring shadow ("meniscus" sign), also oval or polycyclic dense ring shadows. The center is less dense, inside sharp and regular; only with larger polyps is the center irregular and the periphery unclear. Polyp denser than surroundings. Appears as as filling defect in the barium collection. Barium droplets may adhere to the polyp (hanging drops)	Two more or less concentric rings. Between the rings the polyp looks denser ("target" sign)	"Target" sign (two more or less concentric rings, the inner ring representing the thinner pedicle)
Three-quarter view	Oval- or ring-shaped, sometimes denser area around base caused by superimposition of polyp head	Pedicle eccentric, "bowler hat" appearance	Depending on angle, denser head, peripheral, cylindrical density, projecting on or outside (or partially in or outside) the polyp head
Profile/ tangential	Hemispherical protrusion denser than surroundings. Tangential image of the polyp base: – Flat – Pitted – Irregular	Base appears smaller than the head, base smooth or slightly indented, "bowler hat" appearance	
Mobility			Upright view: Polyp head caudal Trendelenburg: Polyp head cranial

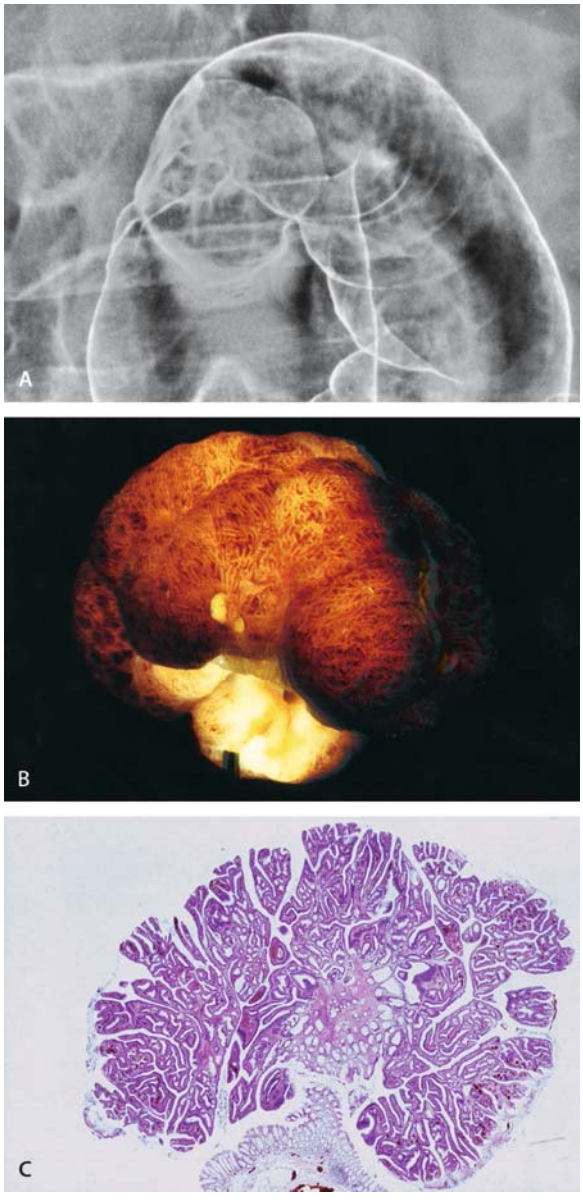

Fig. 4A–C. Villous adenoma in the sigmoid. **A** Double-contrast study, **B** gross specimen and **C** histological section of the excised adenoma showing typical villous structures

ately if the proctosigmoidoscopy or colonoscopy was performed without biopsy or with superficial biopsy (small biopsy forceps). The radiographic examination should be postponed for 40 days if a deep biopsy (large biopsy forceps) was performed during a proctosigmoidoscopy or colonoscopy. Likewise, a polypectomy requires a latent period of 14 days to allow for adequate reepithelialization at the biopsy site. If the barium study immediately follows a deep biopsy, the following complications can be seen: intramural extravasation or venous intravasation of contrast medium and/or perforation. The risk of perforation increases if the biopsy is taken from diseased mucosa. The forceps used in fiberoptic endoscopy does not penetrate the muscularis propria. The forceps used with a ridged endoscope can reach the muscularis propria. If the endoscope was performed following preparation with oral irrigation a double-contrast enema cannot be performed immediately, since the increased fluid content of the colon interferes with adequate adhesion of the contrast medium along the mucosa. The waiting period is at least 3 h. If a barium study is scheduled immediately after sigmoidoscopy (colonoscopy), the endoscopist should be asked whether a deep biopsy was performed. Even days after a deep biopsy, the double contrast enema may show a small ulcer (ring density, small collection).

■ **Double-contrast Examination Versus Colonoscopy.** In polyps larger than 1 cm, the diagnostic accuracy has been reported as up to 95%; for polyps of 5–10 mm the accuracy is up to 90% and for polyps less than 5 mm the diagnostic accuracy is less than 70%. Polyps that are less than 3 cm often cannot be described with respect to malignancy on the basis of radiological findings [2].

■ **Colonoscopy.** Polyps 1 cm in diameter and larger are detected colonoscopically in 90% of cases and on barium enema in 50%–85% of cases. The advantage of colonoscopy is that it allows simultaneous biopsy and polypectomy. The limitations are deeply situated flexures, fixation, inflammatory or other stenoses, marked haustration or a long colon, which may render it difficult to reach the proximal colonic segments. Suboptimal examinations result from poor cleansing of the colon, superficial or small lesions, fast retrieval of the endoscope, and lack of experience on the part of the examiner [6].

The complementary character of double-contrast examination and colonoscopy has been emphasized by several authors [7–11]. Right-sided polypoid lesions were diagnosed with an accuracy of 80% using colonoscopy; the reliability of double-contrast examination was 82%. Using both methods together, a diagnostic accuracy of 97% was attained. Kewenter et al. suggest the combination of proctosigmoidoscopy and double-contrast examination when screening for carcinoma (i.e., having discovered polyps >0.5–1 cm, with a positive Guaiac test) [12]. Flexible proctosigmoidoscopy and double-contrast examination in one sitting has been advocated, both performed by radiologists, whereby the reliability of the diagnosis of polyps in the rectosigmoid increased markedly, particularly for polyps less than 1 cm in diameter [13]. As such, approximately half of all adenomas are the target of this examination, i.e., are a potential risk for development of carcinoma. In our institution we have performed double-contrast examinations immediately following biopsy and polypectomy without complications.

Usually colonoscopy is considered as the gold standard for the reliability of radiologic examinations. However, when a radiologic examination has been performed previously, the endoscopic examiner has had the advantage of being the second examiner. Even colonoscopy misses 3%–13% of lesions. The 15% false-negative rate for colonoscopy in the study by Gelfand et al. is similar to the false-negative rate for barium enema examinations performed in the same institution [1]. A previous review of radiologic accuracy in the detection of 234 colonic polyps using colonoscopy as the comparison standard indicated an overall false-negative rate of 13%. As with colonoscopy, most lesions undetected radiologically were less than 1 cm in size, with a false-negative rate of 5% for lesions measuring 1 cm or more and 18% for lesions less than 1 cm in size.

■ **Technical Reasons for Failure to Detect Polyps in Double-contrast Examinations.** Air bubbles, overlapping loops of bowel, feces, diverticula, poor film quality, spasm, excess of barium and poor adhesion of barium to the colon if the colon is too wet, are the main technical reasons for failure to detect polyps in double contrast examinations. According to Markus et al., independent evaluation of double-contrast examination of the colon increases the sensitivity: with two independent examiners from 70% to 83%; with three independent examiners to 89% [14]. We believe that false-negative interpretation is a larger problem in interpretation of the double-contrast examination and regard evaluation by more than one examiner as necessary to reduce this error.

■ **Cross-sectional Imaging.** In CT, only larger polyps can be seen. In solid tumors (HU >0), surrounded by remaining contrast medium or seen as a filling defect within contrast medium, subtle blurring or an irregular surface is seen.

Nonneoplastic Polyps

Hamartomatous Polyps

Hamartomatous polyps are the most common form of polyps in children. They are usually seen in the 4th–6th year of life. In adults the incidence is 0.5%–3.3% of all endoscopically removed polyps. The male : female ratio is 1.5 : 1.

■ **Location.** More than 80% are found in the rectosigmoid, usually in the rectum, with a decrease in number proximally.

■ **Morphology.** The size of the polyp is 0.3–5 cm; they are commonly pedunculated, but can occasionally also be sessile. They can be round, smooth and, rarely, lobulated.

■ **Histopathology.** There is excessive stroma content in the lamina propria with inflammatory infiltrate, edema, capillaries, fibroblasts, and lymph follicles. Cystically widened crypts with mucus are seen. There may be epithelial defects (ulceration/erosion); the pedicle of the polyp contains many wide vessels.

Inflammatory Polyps

The definition of inflammatory polyps is confusing. Usually they are divided in two main categories:

- Mucosal islands are equal to pseudopolyps, which are the same as polypoid mucosal remnants. These arise through ulceration of surrounding tissues, usually with undermining of the muscularis mucosae, so those islands of mucosa and submucosa remain. They are 0.3–1.5 cm high.

Cobblestones are longitudinal and transverse ulcerations that communicate with each other and surround polypoid islands of mucosa. These islands show at most minor involvement in the inflammatory process. These mounds of mucosa are relatively large in comparison to the ulcerations and are typically irregularly polygonal or round. They are commonly seen in Crohn colitis (see Fig. 15). Reepithelialization of the ulcers may take place; a cobblestone pattern, however, persists.

- Mature inflammatory polyps are the same as postinflammatory polyps. These pseudopolyps are surrounded by regenerating mucosa, which arise from spared mucosal islands and consist predominantly of granulation tissue (see Figs. 15, 16).

■ **Incidence:** Common. Location: Polyps occur in locations where the primary disease is or was localized and are diffuse, segmental, and focal. They are usually seen multiply, i.e., more than ten.

■ **Etiology and Pathogenesis.** As a result of acute disease or earlier disease we find ulcerative colitis, Crohn colitis, amebic colitis, schistosomiasis, ischemic colitis, tuberculosis, pseudomembranous colitis and Behçet colitis.

Unclassified Polyps

Metaplastic (hyperplastic) polyps can be seen very frequently in 75% in subjects aged over 40 years. These polyps are usually multiple. They are often so small that they may be missed even on sigmoidoscopy. Radiographically and endoscopically metaplastic polyps account for approximately 11%–16% of small (2–5 mm) polyps. The male : female ratio is 1 : 1.

■ **Location.** The metaplastic polyps can be found in rectum, sigmoid and proximal colon. Most commonly

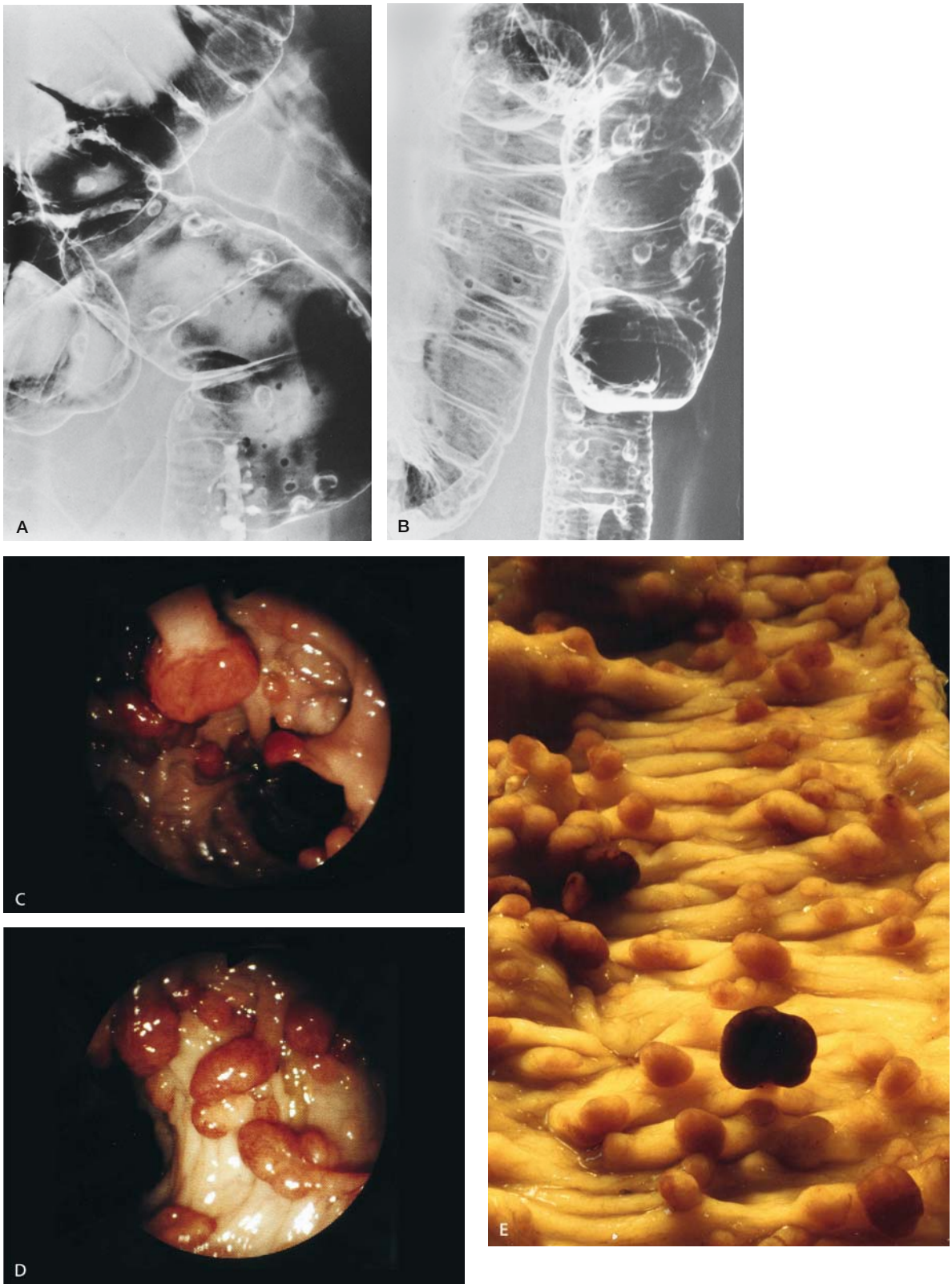

Fig. 5A–E. Familial polyposis. Countless sessile or slightly pedunculated polyps of varying size carpet the entire colonic wall. **A** Rectum, **B** splenic flexure and proximal descending colon. **C**, **D** Endoscopy, **E** Resection specimen

they are solitary; however, multiple polyps can also be found. The polyps are often seen on mucosal folds.

■ **Etiology/Pathogenesis:** There may be an ischemic or inflammatory origin; it may be caused by a disturbed maturation process of cells in the crypts without a known cause or it may be caused by hypertrophy of the crypts due to excessive epithelial cells.

■ **Associated Illnesses.** Hyperplastic polyps are seen more frequently in populations with an increased risk for colorectal carcinoma. In 40% of patients with hyperplastic polyps, adenomas occur.

■ **Morphology.** Sessile, flat and rarely pedunculated polyps are usually up to 5 mm in size; only in 13%–16% are they larger than 5 mm. They cannot be differentiated from adenomas.

■ **Histopathology.** Elongated crypts; reduced goblet cell count, sawtooth-like rows of epithelium crypts, hypermature cells on the surface. There is no dysplasia and no malignant potential. However, combination forms with adenomatous polyps are not rare.

Diagnostic Imaging

On contrast enema they cannot be differentiated from adenomas. They are often located on the mucosal folds; for this reason and because of their small size they are seen less frequently on radiologic film, but more easily on colonoscopy.

Inflammatory Fibroid Polyp

Inflammatory fibroid polyps are nonneoplastic cellular proliferations that originate primarily in the submucosa and are composed of fibroblasts, blood vessels and inflammatory cells within an edematous and collagenous stroma. They are uncommon in the gastrointestinal tract and very rare in the colon.

Polyposis Syndromes

The intestinal polyposis syndromes (Fig. 5) are usually hereditary; some forms must be considered as obligate precancers, others as facultative precancers. The discovery of intestinal polyposis in a patient has important consequences because when an obligate precancer is present, early colectomy is necessary, and where heredity plays a role, relatives must be examined and genetic counseling must be considered. Screening also reduces the colorectal cancer rate in families with hereditary nonpolyposis colorectal cancer (HNPCC) [15].

■ **High Risk.** HNPCC families have a high preponderance of right-sided tumors, possibly of flat adenomas and probably of mucinous tumor. Screening should begin at 10 years younger than the youngest affected family member, and not later than 40 years of age. Some recommend starting colonoscopy screening every 2 years starting at age 25; others are reconsidering recommending prophylactic colectomy in HNPCC families. Barium enema is probably not the ideal way to screen HNPCC families, since the incidence of adenoma is high, perhaps double that of the general population, and many will need to return for colonoscopy. In addition, flat lesions are harder to detect radiologically. However, it is even more important in this group that failed or incomplete colonoscopy be followed by CT/MR colonography or barium enema to assess the right colon.

■ **Moderate Risk.** This includes first degree relatives of colon cancer patients, especially those with two colon cancers in the family, or relatives of patients under 55 but who are not HNPCC families. Such individuals have about five times the chance of developing colorectal cancer as other members of the general population. Colonoscopy, double-contrast barium enema, or full preparation with flexible sigmoidoscopy should be done, followed immediately by barium enema if the sigmoidoscopy is negative or shows polyps under 5 mm in diameter, but followed instead by immediate colonoscopy if the sigmoidoscopy shows polyps larger than 5 mm.

■ **Low Risk.** There are no data that permit the unequivocal recommendation of any form of imaging for screening of the normal risk population, though there are data supporting the use of both fecal occult blood testing and flexible sigmoidoscopy. Radiologists have provided no data to support the theoretical advantages of barium enema as a screening tool.

Radiographically, polyposis syndrome is suggested when:

- A polyp is found in the gastrointestinal tract of a younger person.
- Several polyps are detected in a patient.
- Colon carcinoma is found in a relatively young patient (<40 years).
- Certain typical cutaneous changes are found that are known to be associated with a polyposis syndrome.

For the different syndromes (familial polyposis, flat adenomas syndrome, Gardner syndrome, Peutz-Jeghers syndrome, Turcot syndrome, Cronkhite-Canada syndrome, juvenile polyposis coli, etc.) we refer to the literature.

Colorectal Carcinoma

Colorectal neoplasm is the third most common cancer, the second most common tumor in the United States and the most common cancer in the gastrointestinal tract; it is even the most common malignant tumor after bronchial carcinoma in males and breast carcinoma in females. Every year, 155,000 new cases are seen and in a large percentage of these cases colonic and hepatic surgery is performed for palliation or possible cure. Widely published data indicate the importance of screening for colorectal cancer after the age of 40 and improved survival rates for patients in whom colorectal cancer is detected at an early stage [16–22].

Although the average lifetime risks of a diagnosis of and dying of colorectal cancer are 5.6% and 2.5%, respectively [24], and although a majority of cases of colorectal cancer can be prevented with colonoscopic removal of the precursor adenomatous polyp [25], compliance with full structural colon examinations, such as colonoscopy and double-contrast barium enema, is abysmal.

Unfortunately, the more attractive tests, such as fecal occult blood testing (FOBT) and sigmoidoscopy appear ineffective. The broad literature clearly indicates that FOBT is too unspecific and misses a substantial proportions of cancers [26, 27].

In the search for an adequate screening method, CT colonography and MR colonography have emerged relatively quickly as rapid, noninvasive and full structural colon examinations.

They have the potential to be highly accurate and reproducible, highly acceptable to the patient and can display extra colonic findings [28, 29].

■ **Incidence.** It must be expected that the incidence of colorectal carcinoma continues to increase. It rarely occurs in persons younger than 35 years of age (except in familial polyposis). In children, rare cases have been reported. There is an increased incidence above 50 years of age. The male : female ratio is = 1–2 : 1. Rectal carcinoma is, however, more prevalent in men and colon carcinoma is more prevalent in women. In some families there is an increased incidence of colon carcinoma, particularly of the right colon. In these cases, carcinoma typically occurs earlier (approximately 40 years of age).

■ **Location.** The majority of carcinomas arise in the rectum (36%–59%) and sigmoid (17%–30%) [2].

■ **Etiology and Pathogenesis.** There is no clear known cause. Hypotheses include diet: reduced consumption of high-fiber foods allows a greater concentration of carcinogenic and cocarcinogenic substances to accumulate in the colon. Iatrogenic factors include cholecystectomy: absence of the gallbladder allows continuous passage of bile acids into the colon, leading to increased bacterial enzyme activity, with production of carcinogenic metabolites, epitheliolysis and increased cell turn over.

■ **Risk Factors.** The risk of colon carcinoma is 20–30 times higher in patients with ulcerative colitis than in the general population and depends on the duration and extent of the disease. The risk in Crohn colitis patients is approximately six to seven times higher. Risk factors for colon carcinoma (precancerous lesions) are summarized in Table 2.

■ **Clinical Presentation.** In the early phase, there are nonspecific symptoms or occult bleeding. Clinical symptoms in the late stage are dependent on the size, rate of growth and location of the tumor.

■ **Morphology.** Table 3 shows the classification of colon carcinoma according to Borrmann:

- Circumscribed solitary polypoid carcinoma: Borrmann I
- Ulcerated carcinoma with elevated margins: Borrmann II, the most common type, represents approximately two-thirds of all colon carcinomas
- Ulcerated carcinoma with elevated or diffuse margins (intermediate type): Borrmann III
- Diffuse infiltrating carcinoma (linitis plastica): Borrmann IV infiltration with hardening, often leading to severe stenosis. Poor prognosis, often seen in secondary colon carcinoma.

■ **Histologic Grading and Spread.** There are three histologic grades of malignancy: low grade (20%), medium grade (60%) and high grade (20%) [4, 19, 30]. The 5-year survival rates are 80%, 60% and 25% respectively. A combined histologic and cytologic examination is necessary to assess the degree of malignancy.

Particularly larger, advanced carcinomas spread along the tissue layers that provide the least resistance, e.g., submucosa, through vascular gaps in the muscular propria, along the myenteric plexus, between layers of

Table 2. Risk factors for colon carcinoma (precancerous lesions)

Adenoma ⩾1 cm
Familial polyposis coli (100%)
Other polyposis syndromes
Ulcerative colitis > (10)–20 years
Crohn colitis
Ureterosigmoidostomy
Cholecystectomy
"Family cancer syndrome" (Lynch I-S)
Familial colon carcinoma (Lynch II-S)
Family history of colorectal carcinoma
Hereditary colon cancer
Colon carcinoma
Synchronous second primary of colon
Metachronous second primary of colon
Radiation colitis
Age > 40 years

Table 3. Classification of colon carcinoma according to Borrmann

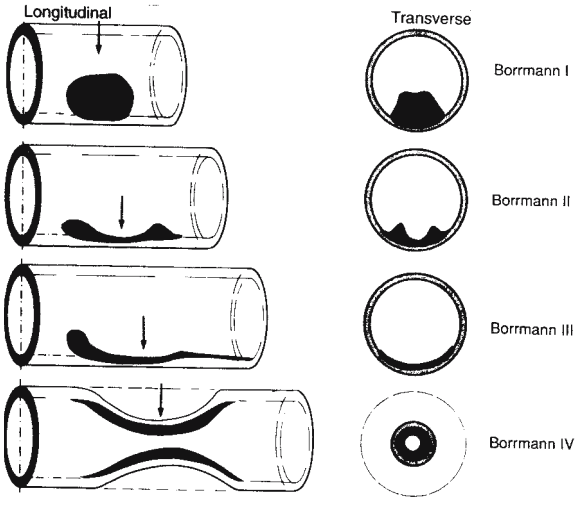

muscle, and along the connective tissue of the serosa or the mesocolon. Only rarely does direct spread to neighboring intraperitoneal organs occur because the peritoneum represents a relative barrier. In these cases, the small intestine, liver, bladder and prostate may be involved. Highly malignant rectal carcinoma may show inferiorly directed intramural spread.

Lymphogenous spread is not possible until the muscularis mucosa has been penetrated; at first, regional lymph nodes are involved; later, the more centrally located nodes. Generally, no skipping of nodes is observed. Retrograde metastases may, however, occur through blockage of lymph vessels, allowing metastases to atypical locations, for example, the ovaries. Lymph node metastases may affect the paracolic, para-aortic, iliac, and inguinal (rectal carcinoma) nodes. The prognosis worsens with increasing number of involved lymph nodes: one lymph node: 60% 5-year survival; two to five lymph nodes: 35% 5-year survival; >six lymph nodes 20% 5-year survival.

■ **Intraperitoneal Seeding.** If the serosa is reached, which may also occur during surgery, dissemination of tumor cells may occur. In the peritoneal cavity, in particular in the pouch of Douglas, it can intraperitoneally seed to the ovaries and to other intestinal segments; in 10% of patients peritoneal metastases will develop after resection of colon carcinoma.

■ **Venous (Hematogenous) Spread.** Infiltration of the intramural veins is observed at histopathologic examination in more than 50%; in 35% the extramural veins are invaded. Submucosal involvement of veins does not effect the prognosis. When extramural veins are involved, metastases to other organs are common.

■ **Spread by Implantation.** Implantation of tumor cells that have become separated from the primary mass of tumor during the course of growth, or that have been released due to surgical manipulation, may cause tumor recurrence in the wound, in anal fistulas, at the colostomy, peritoneum, rectovaginal septum, anastomosis or in the pelvis.

■ **Staging and Classification.** There is a variety of classification and staging systems for colorectal carcinoma: TNM classification, Staging Systems of the American Joint Committee (AJC), the Astler-Collier classification and the Dukes classification [31]. The Dukes classification, as a surgical pathologic staging system for colorectal cancer, has been the most widely used, but many modifications have been introduced since the seminal article appeared in 1932. The TNM system, introduced in 1954, has increased in use in recent years because it more clearly defines the extent of tumor within and beyond the bowel wall.

Diagnostic Imaging

■ **Abdominal Plain Film.** Sometimes dilatation of the colon and small intestine and "thumbprinting" (ischemic colitis) can be seen proximal to the obstructing colon carcinoma.

Free intra-abdominal air may be present in case of perforation.

■ **Double-Contrast Barium Enema.** Barium enema (double contrast) can detect up to 98% of colorectal cancers, but detection rates between 76% and 95% are often reported. Colonoscopy also has high potential sensitivity, but detection rates as low as 85% have been reported. Barium enema examination has a diagnostic yield of 3.2% for neoplastic lesions larger than 1 cm in the nonvisualized colon after incomplete colonoscopy [32]. The mortality from colonoscopy is about three times higher than with barium enema. If barium enema discloses a significant polyp, colonoscopy will also be required. The choice between these two principal methods of detection therefore depends on both local skills of practitioners and the patient or subject population mix.

- Polypoid carcinoma (Borrmann I type). Polypoid and or shaggy surface, larger than 1 cm at the base, up to 15 cm. Almost exclusively sessile, broad-based with intraluminal growth.
  When larger, there may be circumferential growth. The surface may be smooth or irregular. Occasionally only linear opacities are seen when slightly obliquely orientated tumors are seen in en face projection.
- Ulcerated carcinoma (Borrmann II and III types) (Fig. 6). Protruding lesion with minimal to marked deformation of the colonic wall. There may be partial

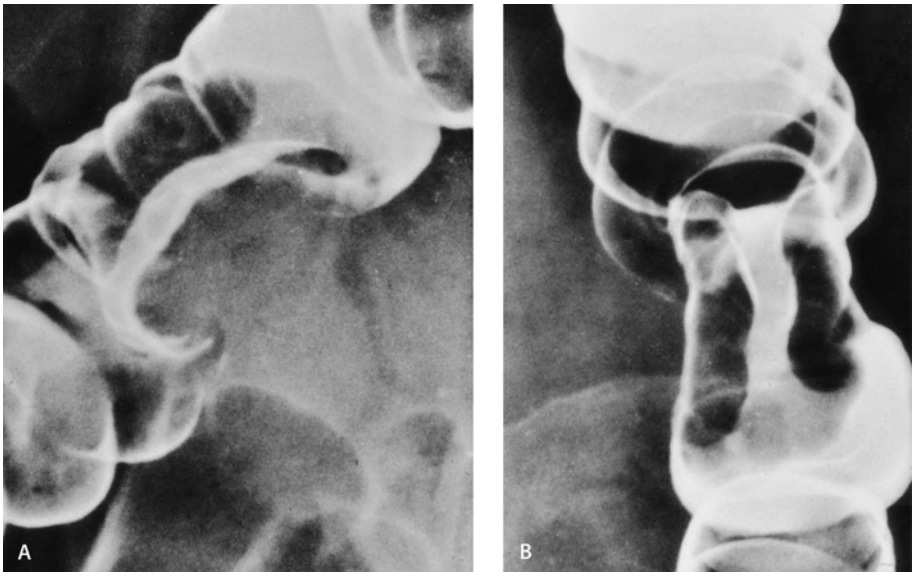

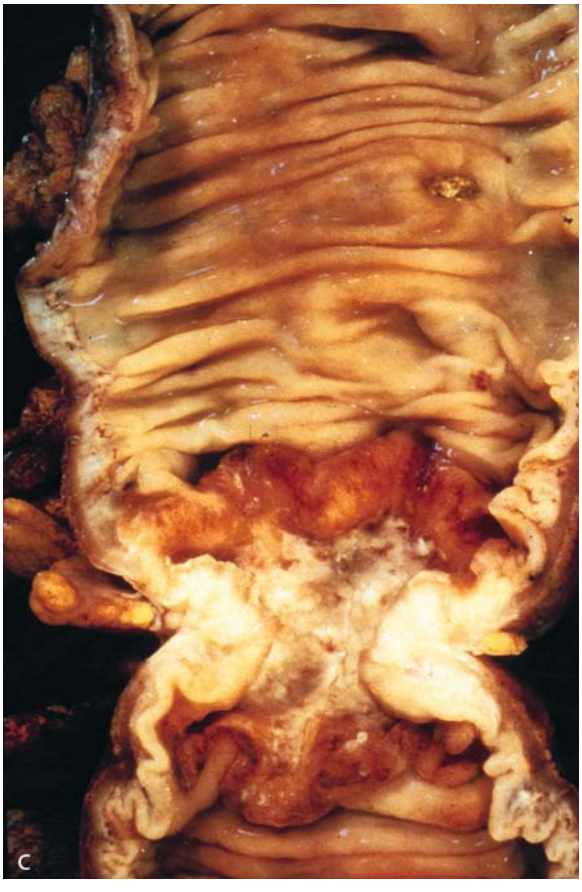

Fig. 6A–C. Semicircumferential polypoid carcinoma (Borrmann II). **A** Tangential projection, **B** en face projection, **C** resection specimen

or complete circumferential narrowing of the colonic lumen, with an irregular surface. Often central indentations due to ulceration are seen.

- Diffuse infiltrating carcinoma (Borrmann IV type). Symmetric or, rarely, asymmetric narrowing of the lumen. The length of distribution may be several centimeters or may involve the entire segment and occasionally the entire colon (linitis plastica). There is often shortening of the involved colonic segment. There is a slight irregularity of the mucosal surface, because the carcinoma grows primarily submucosally. There is often a conical transition to normal colon.

The most frequent errors of perception [33–35] are failure to recognize a filling defect in a pool of barium (the margin of a barium pool is convex; any concave margin should suggest carcinoma) and the failure to recognize the mucosal surface of carcinoma in en face projections.

Many lesions are only seen in en face projection in the double-contrast examination, and therefore, assessment should not be restricted to the contour of the intestine. The en face appearance in double-contrast examination is often very subtle if the carcinoma shows only a slight protrusion, the so-called white line.

Technical factors in missed diagnoses are incomplete evacuation, overexposed films, insufficient distention of the colon with multiple contractions, the hidden loop of intestine is not projected freely, incompletely cleansed colon, poor barium adherence or artifacts caused by gross movement of the intestines.

The most common errors in interpretation are simultaneous presence of diverticula (in patients with less than 15 diverticula, 3.1% of carcinomas are missed, in patients with more than 15 diverticula more than 20% of carcinomas are missed); strictures in other diseases (ulcerative colitis) and/or polypoid lesions (hemorrhoids) are not recognized as carcinoma; insufficient knowledge of the differential diagnosis; in diagnosing a colon carcinoma a second synchronous colon carcinoma is easily missed.

■ **Computed Tomography.** Routine CT examination of the abdomen seldom visualizes gastrointestinal lesions adequately, and a particular effort is required to detect and examine such lesions.

Principles to follow include:

- Intestinal cleansing, opacification and distension
- Imaging during the arterial phase of an intravenous injection of contrast material
- Liberal use of thin section (5 mm) scans over the area of interest

Both spiral CT and intravenous glucagon or scopolamine (Buscopan, Boehringer Ingelheim, Germany) facilitate good CT imaging of intestinal lesions. Three-dimensional spiral CT has the potential to replace barium enema (and colonoscopy) for detection of polypoid colonic lesions. CT is reliable for confirming spread of advanced tumors through the bowel wall, but less useful in excluding such spread. In staging colorectal cancer the sensitivity of CT for detection of local extension is between 55% and 61%. Most errors are in understaging local infiltration. Sensitivities are between 26% and 73% for nodal metastases and between 73% and 79% for hepatic metastases. The early enthusiasm for CT in preoperative staging has not been sustained because of poor accuracy in identifying lymph node metastases and inability to determine local spread. Particular caution should be exercised in describing local invasion in cachectic patients. Conversely, scarring and inflammation may mimic the precolonic fat streaking that is the hallmark of early extracolonic spread.

The indications for CT are:

- Preoperative staging (local spread, metastasis).
- Pre- and postoperative complications; hematoma, abscess, fistulas, recurrent tumor.
- Intraluminal, space-occupying lesions can be seen, sharply or poorly demarcated (40–60 HU). Often there is a local or circumferential thickening of the colonic wall; diffuse calcifications and a central region of lower density can be seen due to necrosis: pericolic infiltration by tumor may be evident.

■ **CT of Colorectal Carcinoma with Respect to TNM Classification.**

- T (tumor):
  - T1 Infiltration of mucosa and submucosa: colonic wall thickening
  - T2 Muscularis propria infiltrated: thickening of the colonic wall, local or circumferential
  - T3 Spread beyond the colonic wall: thickening of the colonic wall, poorly demarcated outer wall contours, spiculated or dentate contour
  - T4 Surrounding fat tissue is infiltrated: increased absorption of pericolic fat tissue (i.e., streaky densities in fat tissue). Infiltration of musculature or skeletal structures; thickening of the rectal/extraperitoneal fascia (differential diagnosis: inflammatory bowel disease, hematoma, radiogenic edema, fibrosis); infiltration of the ureters (hydronephrosis), perforation, abscesses, fistulas.
- N (nodes): Normal lymph nodes should not be larger than 1 cm. Enlargement of lymph nodes does not necessarily prove the existence of metastases because such changes may also be the result of inflammatory reaction. Oblique cross-sections of vascular structures or sections through nonopacified intestines may be mistaken for enlarged lymph nodes. The correlation between lymphadenopathy and tumor involvement in colorectal carcinoma is, in general, poor. Lymph node metastases are often not recognized on CT.
- M (metastasis): The sensitivity of CT in the detection of hepatic metastases depends on the size and density of the lesions, as well as on the technique used. In 5%–29% metastases may be occult.

■ **CT findings in rectal carcinoma.**

- Thickening of the rectal wall to 0.5–0.8 cm, circumferentially or locally.
- Infiltration of perirectal adipose tissue. Poor delineation of tumor from neighboring organs (vagina, uterus, prostate, seminal vesicles, musculature, bone) is an indication of infiltration; however, partial volume effects must be taken into consideration.
- Enlarged lymph nodes (1–1.5 cm), suggestive of metastases.

CT findings of local extent and regional spread of tumor correlate well with surgical and histopathologic findings, and accuracy rates between 77% and 100% (sensitivity ranging from 54% to 100% and specificity ranging from 93% to 100%) have been reported in early studies. Later studies [36–38] showed much lower accuracy rates (41%–64%), largely owing to low sensitivity for detection of lymph node metastases (22%–73%) and of local tumor extent (53%–77%). The accuracy may increase from 17% for Dukes B lesions to 81% for Dukes D lesions [39]. Refinement of CT techniques, such as colonic preparation, prone positioning of the patient, air distension of the rectum and dynamic multidetector/multislice-helical CT may increase the accuracy of assessing local tumor extent by CT [40].

In general CT cannot detect microscopic invasion of the serosa, normally sized lymph nodes affected by the tumor or peritoneal metastases less than 1 cm and hepatic metastases less than 1 cm in size (Fig. 7).

■ **Ultrasonography.** Ultrasonography can be used to assess the size of the tumor, to assess infiltration into the surrounding tissues and to detect hepatic metastases. Colon carcinoma may be an incidental finding in sonographic examination of the abdomen. The findings are dependent on growth and spread. Hypoechoic or

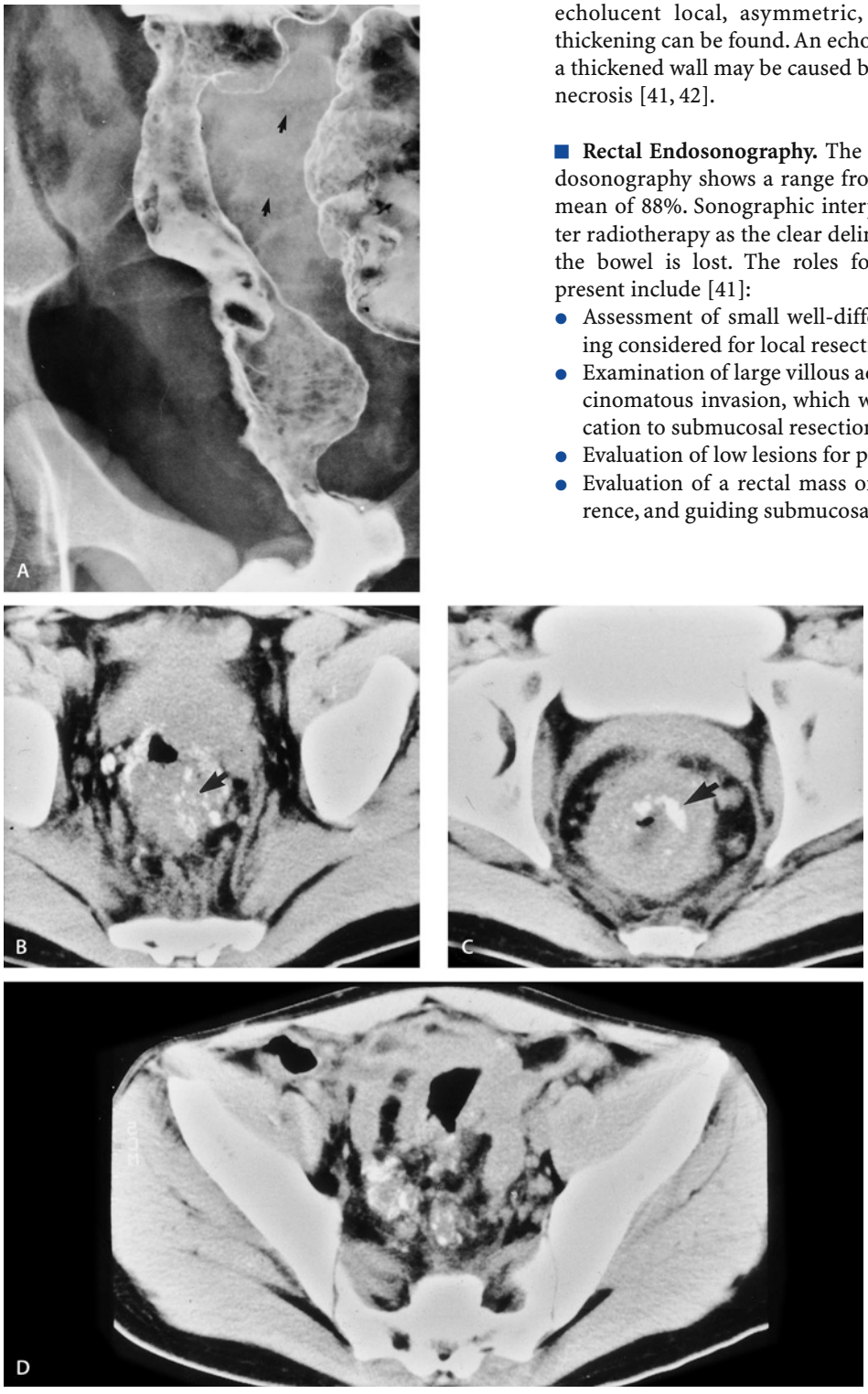

Fig. 7A–D. Schistosomiasis. Malignant changes of the rectosigmoid. Multiple calcifications can be seen both in the double-contrast enema (**A**) and on CT (**B–D**) (*arrows*)

echolucent local, asymmetric, circumferential wall thickening can be found. An echogenic central area and a thickened wall may be caused by mucosa, gas, feces or necrosis [41, 42].

■ **Rectal Endosonography.** The accuracy of rectal endosonography shows a range from 81% to 93%, with a mean of 88%. Sonographic interpretation is harder after radiotherapy as the clear delineation of the layers of the bowel is lost. The roles for endosonography at present include [41]:

- Assessment of small well-differentiated cancers being considered for local resection
- Examination of large villous adenomas to detect carcinomatous invasion, which would be a contraindication to submucosal resection
- Evaluation of low lesions for prostatic invasion
- Evaluation of a rectal mass or possible local recurrence, and guiding submucosal biopsy

For detection of lymph node metastases and other extrahepatic metastases, endorectal ultrasonography has limitations, as it can assess only perhaps half the lymph nodes removed at surgery for rectal cancer and cannot distinguish reactive from malignant enlarged nodes (sensitivity, 50%–57%).

■ **Magnetic Resonance Imaging.** As in CT, the TNM staging can be used. MRI appears to have overall the same limitations as CT, but multiplanar imaging may often have special advantages. MRI seems more effective in staging (accuracy up to 100%) [42–44]. Local tumor extent is particularly well shown on T1-weighted images. Direct invasion of tumor into bone or muscle such as the levator ani and piriform muscles may be better shown by MRI. The depth of tumor infiltration in the bowel wall and the presence of metastatic foci in lymph nodes cannot be accurately determined by MR imaging. The reported overall staging accuracy is between 74% and 96%. MR results are in flux as new contrast agents (Ferristene, Abdoscan, Nycomed, Oslo), new coils and pulse sequences are developed. Endorectal coils in particular are producing spectacular images, and can show the layers of the bowel wall.

- T1-weighted image: tumor tissue shows low signal intensity, similar to musculature.
- Proton-density image: tumor tissue shows intermediate signal intensity, higher than musculature.
- T2-weighted image: tumor tissue shows high signal intensity; however, this is dependent on the type of tumor (mucus production) (Fig. 8).

CT/MR Colonography and Virtual Colonoscopy

With increasing emphasis on the early diagnosis of colonic polyps and diagnosis and preoperative stages of colorectal cancer, interest has grown rapidly in CT/MR colonography (virtual colonoscopy), developing techniques to challenge existing methods such as barium enema and conventional colonoscopy.

Virtual colonoscopy is the term used to describe thin-section CT of the prepared colon with the volumetric data set reviewed both as two dimensional and three dimensional endoluminal images of the colonic mucosa [29].

First introduced in 1994 and since the initial clinical colonographic studies published 6 years ago [45], over 160 peer-reviewed articles and several international symposia have focused on colonography.

CT and MR colonography have experienced dramatic improvements in both hardware and software capabilities, resulting in shorter scanning time, dose reduction, greater user friendliness and promising performance statistics [46].

The improved spatial resolution and lower number of artifacts, associated with multislice CT, the use of intravenous contrast in CT/MR colonography and increasing familiarity with the technique by radiologists should continue to improve test performance [47–50].

Innovation in image reconstruction and manipulation (computed-aided detection) have optimized and simplified study interpretation [51–54].

Current interest has focused on improving patient acceptance of the technique through the development of dietary fecal tagging agents to avoid full bowel catharsis [55–57].

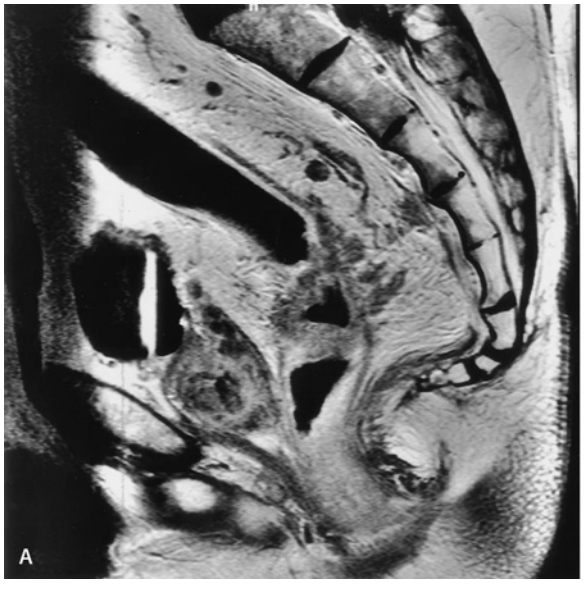

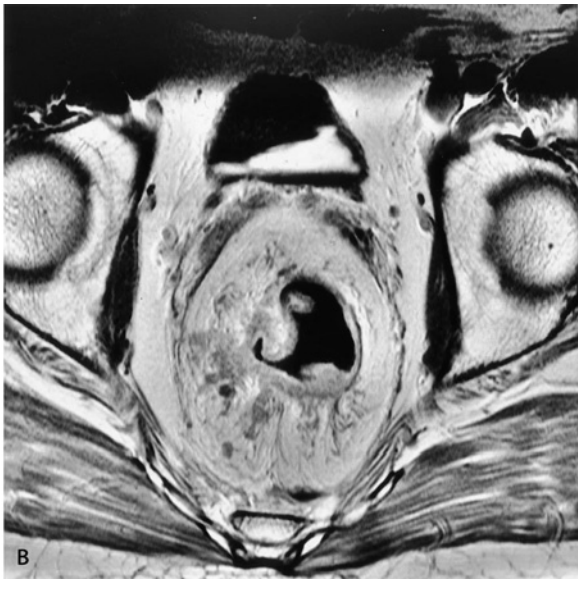

Fig. 8A, B. MRI after rectal contrast (Ferristene, Abdoscan, Nycomed, Oslo) application and intravenous contrast injection (gadopentetate dimeglumine, Magnevist, Schering, Berlin): large T4 rectal carcinoma with dorsal infiltration into perirectal tissue and sacral bone. **A** Sagittal view, **B** transverse view

Multislice CT appears to be currently more suitable for colorectal and possibly combined lung-abdomen screening than MRI, given the speed of performing the examination, increased spatial resolution and robustness in image quality.

MR colonography avoids ionizing radiation but currently fails to demonstrate the colonic wall in a spatial resolution comparable to that of multislice CT colonography.

Virtual Colonoscopy and Polyp Detection

The accuracy of colonoscopy for polyp detection in patients at high risk for colorectal neoplasia has been reported in many studies (Table 4). Virtual colonoscopy was first described by Vining et al. in 1994 [45], but the first clinical trial was not reported until 1996, when Hara et al. described a proprietary method of CT colonography to evaluate 30 endoscopically proven polyps in ten patients [58]. They found that this technique detected 100% of all polyps larger than 1 cm in diameter, 71% of polyps between 0.5 and 0.9 cm, and up to 28% of polyps 0.5 cm in diameter.

Several studies have compared the sensitivity and specificity of interpreting axial images alone compared with the combination of axial images and 3D virtual reconstructions. Hara et al. found that the interpretation of axial images alone had a lower sensitivity and speci-

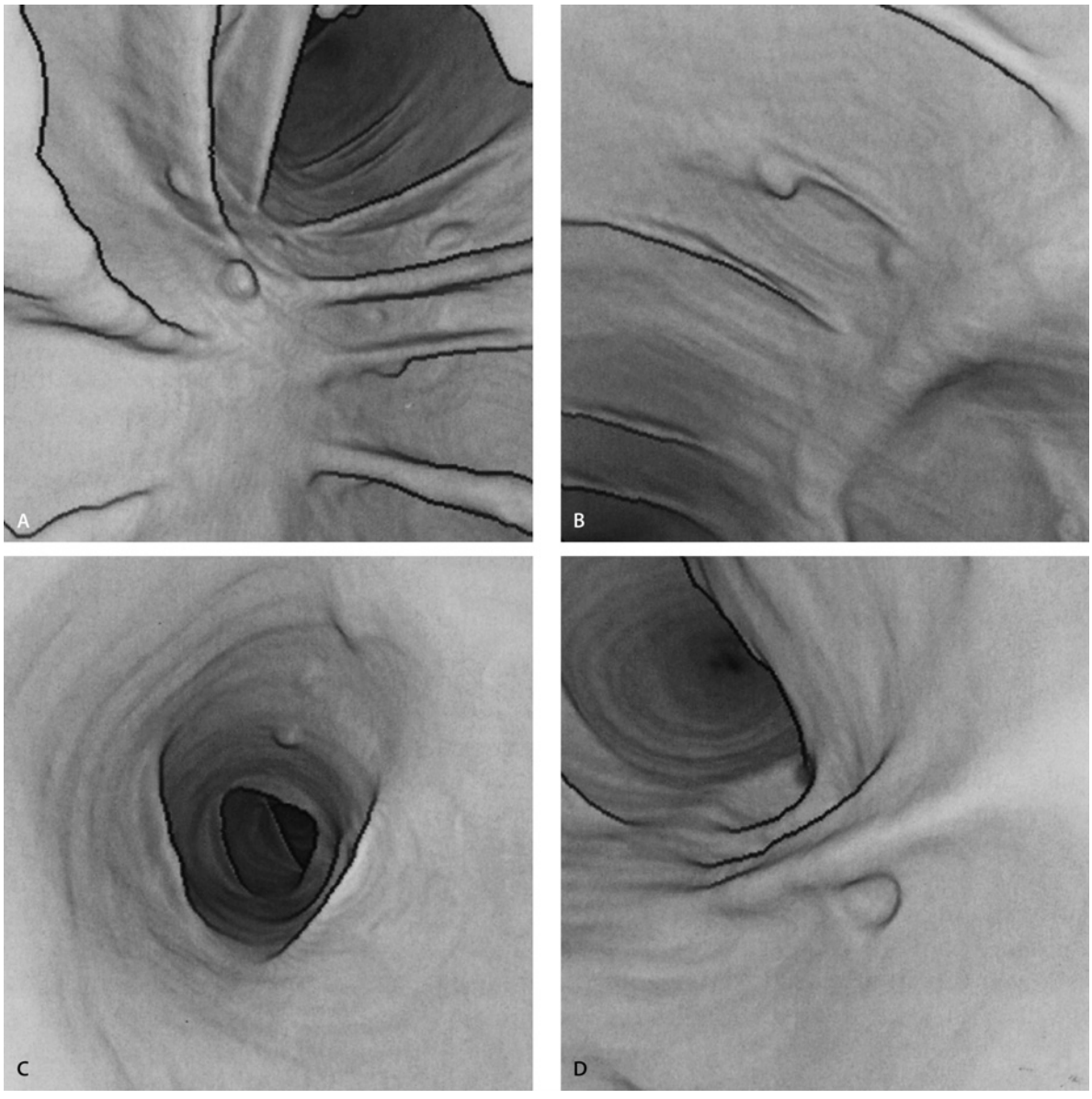

Fig. 9A–D. Performance of multislice CT in a patient with attenuated polyposis coli. The high spatial resolution inherent to multislice CT enables detection of diminutive polyps down to 1–3 mm in size. Adapted from [28]

ficity compared with virtual colonoscopy (58% and 74% vs 75% and 90%, respectively, for adenomas >10 mm in diameter) [59].

Other authors have also found the two techniques to be complimentary [60, 61].

Larger, more recent studies on the accuracy of CT/MR colonoscopy in the detection of colonic polyps are consistent with reported sensitivities of 50%–100% for lesions larger than 1 cm in diameter, 16%–100% for lesions between 6 and 9 mm in diameter and 61%–68% for lesions under 0.5 cm [28, 29, 53, 62–79].

Table 4 summarizes the performance of colonography in the detection of colorectal masses on a per-lesion and per-patient basis [28].

The sensitivity and specificity of virtual colonoscopy have consistently been shown to be dependent on polyp size, with a low reported accuracy for polyps under 5 mm in diameter; however, the importance of removing polyps smaller than 5 mm in diameter may be neither clinically justified nor cost-effective.

The risk of malignancy in such polyps is less than 0.1% [80] and the likelihood of these being invasive in 10 years is less than 5%.

The sensitivity of virtual colonoscopy for polyps larger than 5 mm in diameter reported in recent studies is equal to or exceeds that of conventional colonoscopy [79].

Virtual Colonoscopy and Colorectal Carcinoma

Between 1.5% and 9% of patients with colorectal carcinomas have a second synchronous cancer [81].

CT colonography can be used for the search of (pre)cancer in case of significant weight loss, elevated tumor markers, a paraneoplastic syndrome or metastasis of an unknown primary tumor, as well as for staging and surveillance.

When occlusive colorectal carcinomas prohibit a complete endoscopic review, CT colonography can detect synchronous carcinomas [79, 82]. If intravenous contrast is employed, CT colonography can be an accurate method for predicting local tumor invasion. In addition, CT colonography can be combined with liver and lung imaging to diagnose metastatic spread.

Virtual colonoscopy is an immediately appealing tool for the diagnosis and staging of colorectal cancer through its ability to evaluate all segments of the colon in addition to imaging the peri-colic tissues and liver (Figs. 9–12). Conventional colonoscopy fails to reach the

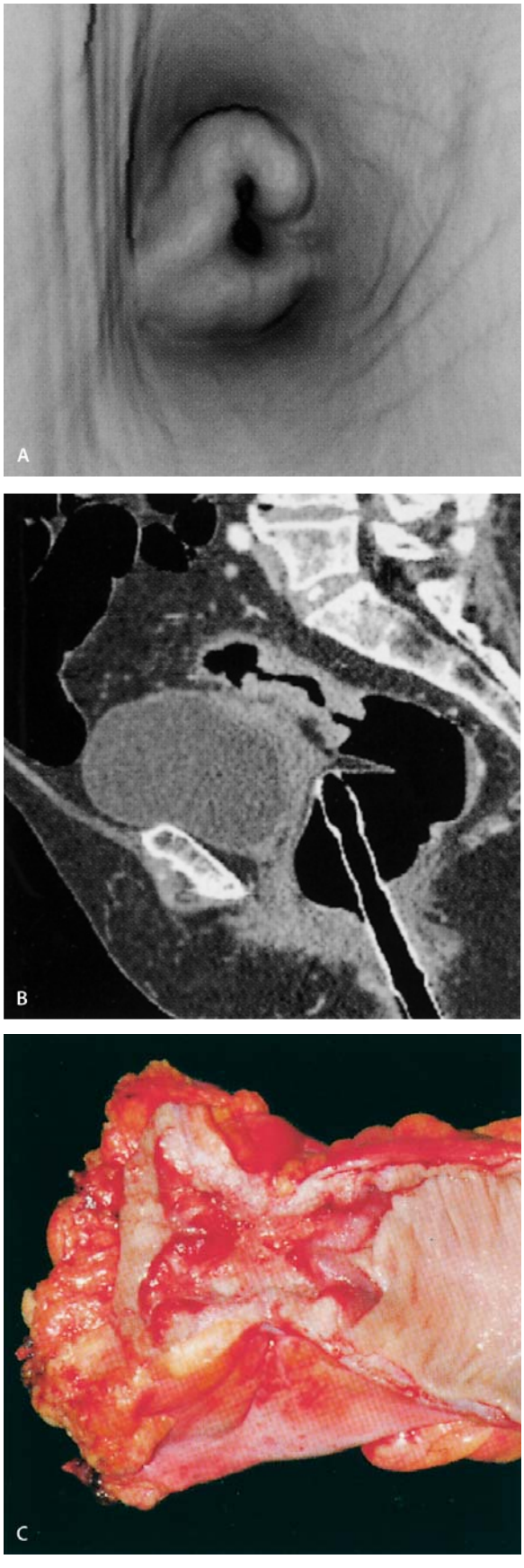

Fig. 10A–C. Occlusive carcinoma as clinical indication for CT colonography: occlusive carcinoma often renders conventional colonoscopy and, consequently, the assessment of the proximal colon impossible. CT colonography can be used in these cases and simultaneously combined with staging. In the case of rectal carcinoma, sagittal reconstructions can help in deciding whether continence-preserving surgery can be performed. Adapted from [28]. **A** CT-3D colonography, **B** sagittal CT colonography, **C** resection specimen

Table 4. Performance of CT/MR colonography in the detection of colorectal masses on a per-lesion and per-patient basis [28]

Reference	Year	No. of patients	Per lesion			Per patient (cut-off=10 mm)	
			Sensitivity			Sensitivity	Specificity
			<5 mm	6–9 mm	>10 mm		
CT colonography							
Hara [59]	1997	70	26%	66%	73%	75%	90%
Dachman [67]	1998	44	15%	33%	83%	–	–
Fenlon [79]	1999	100	55%	82%	92%	96%	96%
Rex [68]	1999	46	–	43%	50%	80%	89%
Fletcher [65]	2000	180	–	47%	75%	85%	93%
Miao [69]	2000	201	11%	16%	74%	73%	94%
Mendelson [70]	2000	53	–	22%	73%	–	–
Kay [71]	2000	38	–	38%	91%	90%	82%
Macari [83]	2000	42	20%	60%	100%	100%	100%
Pescatore [72]	2000	50	–	–	–	51%	74%
Spinizi [73]	2001	99	–	56%	71%	–	100%
Yee [74]	2001	300	59%	80%	90%	100%	–
Macari [53]	2002	95	12%	70%	–	93%	97%
Neri [78]	2002	29	68%	100%	100%	100%	96%
Single and multidetector CT							
Morrin [66]	2000	81	33%	65%	94%	87%	100%
Hara [75]	2001	237	–	–	68%	86%	92%
Total		**1649**	**44%**	**59%**	**80%**	**86%**	**93%**
MR colonography							
Luboldt [76]	2000	132	6%	61%	96%	93%	99%
Pappalardo [77]	2000	70	33%	96%	100%	96%	93%
Total		**202**	**8%**	**97%**	**99%**	**96%**	**98%**

cecum in up to 15% of cases. Virtual colonoscopy has been shown to successfully evaluate all segments of the colon not examined either at colonoscopy or by barium enema [66, 69, 79, 82].

Virtual Colonoscopy and Population Screening

Current recommended screening strategies for low-to-average-risk people include annual fecal occult blood testing (FOBT), flexible sigmoidoscopy every 5 years, double-contrast barium enema every 5–10 year or colonoscopy every 10 years [20, 84].

The double-contrast barium enema examination has also been approved as a reimbursable option for colorectal cancer screening both for average-risk and for high-risk individuals under recent Medicare guidelines [85].The rationale for the use of screening barium enema examination is supported by cost-effectiveness models that have shown that a double-contrast barium enema examination at 5-year intervals is competitive with other strategies for colorectal cancer screening [86, 87].

Compared with sigmoidoscopy, FOBT has a poor sensitivity for detecting rectosigmoid cancers and polyps [88]. Flexible sigmoidoscopy is highly sensitive and specific but visualizes only the distal colon, where only 50%–60% of polyps and cancer reside, and entails some discomfort, risk and inconvenience for the patient [20].

In high-risk patients, the reported sensitivity of barium enema for polyps greater than 5–7 mm is approximately 70%, whereas its specificity is approximately 90% [86].

The wide range in sensitivity with CT/MR colonography for the detection of polyps as shown in Table 1 may be in part explained by the different techniques used in data acquisition and analysis. With increasing spatial resolution, faster computer platforms and greater reader experience, better results are expected.

Neri et al. [78]) found that CT colonography in preoperative evaluation after incomplete colonoscopy provided complete information to properly address surgery of colorectal cancer and treatment of liver metastases [78].

No large studies have directly compared CT/MR colonoscopy with double contrast barium enema, but indirect evidence suggests that the predictive value of virtual colonoscopy and high-risk patients exceeds that of barium enema and conventional colonoscopy.

Currently the application of CT/MR colonoscopy as a screening tool is limited not only by a lack of multicenter data, but also by logistical and financial constraints.

FDG PET and Monoclonal Antibody Imaging

Fluoro-deoxy-glucose positron emission tomography (FDG PET) is sensitive for primary colorectal carcinoma; however, the main role of FDG PET in staging colorectal cancer is the assessment of regional lymph node involvement and distal metastases (sensitivity of both

FDG PET and CT is 29% and specificity is 96% vs 85%, respectively [89].

FDG PET is superior to CT for identification of hepatic metastases, with a sensitivity of 88% vs 38% and a specificity of 100% vs 97% [89].

The sensitivity and specificity of FDG PET for demonstration of local pelvic recurrences of colorectal cancer are 95% and 97%, respectively [90].

The sensitivity and specificity of FDG PET in detection of recurrences in the liver are 96% and 97%, respectively, and are therefore higher than conventional imaging modalities [89].

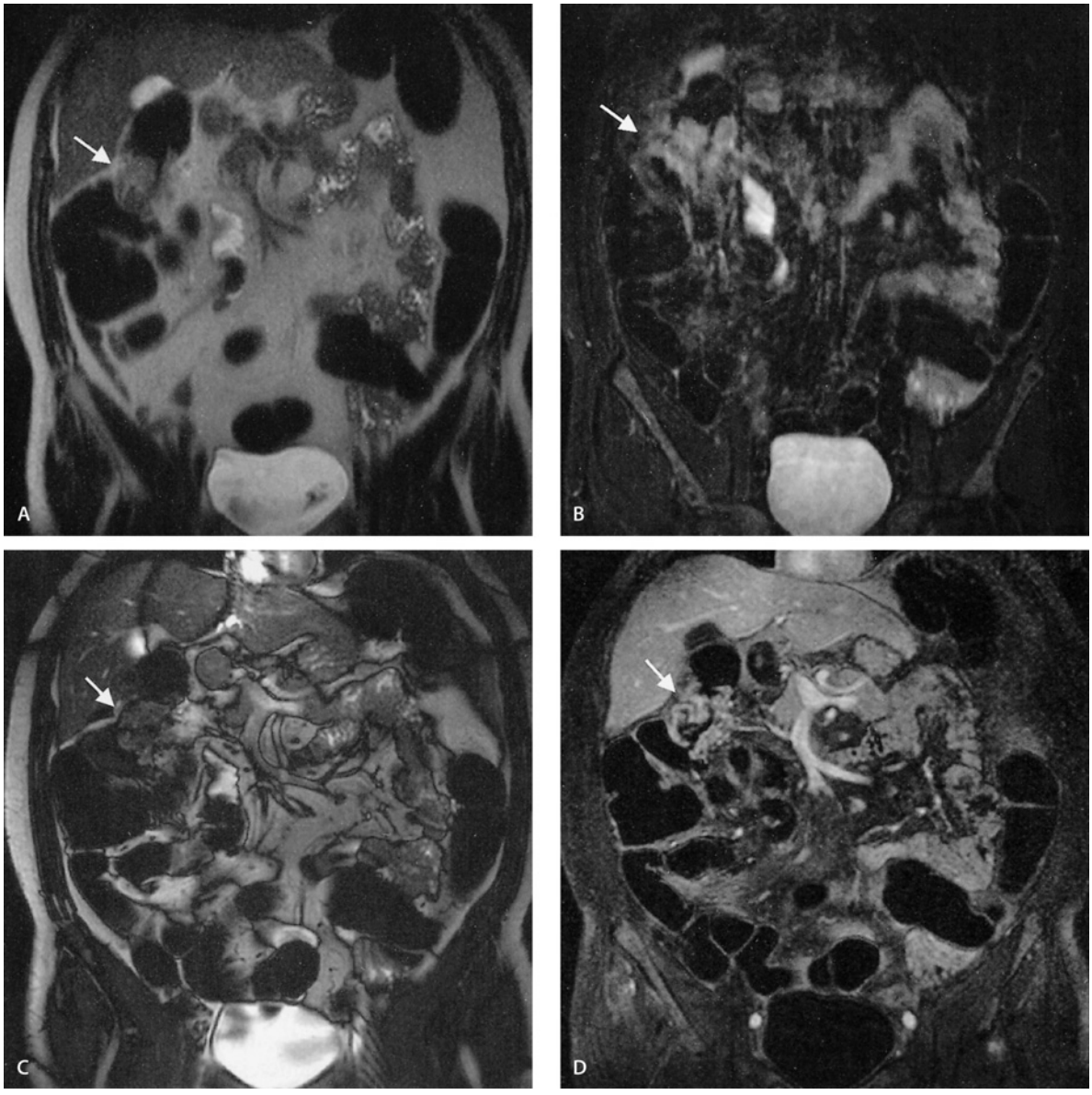

Fig. 11A–D. Alternative protocol in MR colonography with an air enema: **A** HASTE/SSFSE sequence, **B** non-breath-hold T2-weighted IR-TSE sequence, **C** TrueFISP sequence, and **D** contrast-enhanced heavily T1-weighted 3D-GRE (VIBE) sequence. The HASTE/SSFSE sequence shows **A** carcinoma in the ascending colon (*arrow*) without artifacts but with low signal (**A**). As suggested by the delineation of the bladder wall, on HASTE/SSFE images water appears superior to air as enema for the delineation of the colonic wall. The non-breath-hold T2-weighted IR-TSE sequence (**B**) is susceptible to motion artifacts but provides a brighter signal for colorectal masses than the HASTE/SSFE sequence, which speaks for the use of a dark enema in the T2-weighted IR-TSE. In comparison to the HASTE/SSFSE and T2-weighted I-TSE sequence, the TrueFISP sequence appears to be of minor diagnostic value, particularly if used in combination with an air enema (**C**). On the contrast-enhanced VIBE (**D**) colorectal masses show a higher enhancement than in contrast-enhanced CT – suggesting that relevant masses can already be detected on multiplanar reconstructions as in CT colonography without the help of virtual colonoscopy – which is limited in this approach. The distortions, as seen here at the upper part of the liver, resulting from the smaller field of view of dedicated powerful gradient scanners can be corrected by software (adapted from [28])

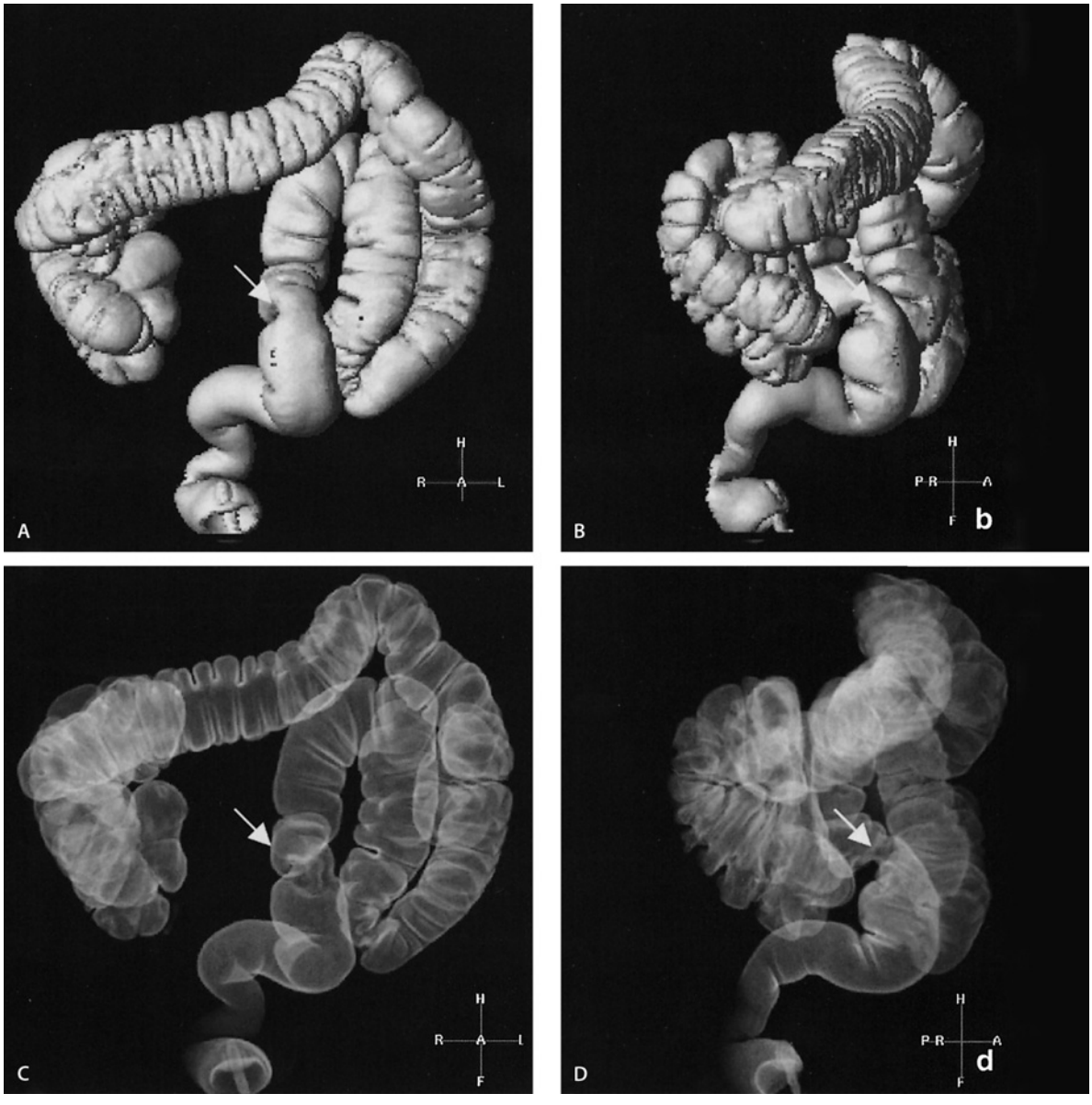

Fig. 12A–D. Sigmoid carcinoma (*arrow*) shown with surface-shaded (**A**, **B**) and virtual double-contrast (**C**, **D**) displays rendered on the basis of MR colonography data: surface shaded and virtual double-contrast displays provide a comprehensive overview of the colon and can be analyzed from any perspective in space due to their 3D nature. Rotation around the z-axis improves the detection of cancer. The virtual double-contrast display appears to be superior to the shaded-surface display. Due to the transparency, tumor-related irregularities in the colonic wall are displayed in every perspective, similar to the barium double-contrast enema, with the difference that the virtual contrast is based on 3D data and thus can be interactively rotated around any arbitrary axis in space independent from the patient. Adapted from [28]

The sensitivity and specificity of FDG PET in whole body FDG PET in the evaluation of distant metastases in patients with resected colorectal carcinoma are 97% and 77%, respectively [90].

Monoclonal antibody scanning (immunoscintigraphy) also shows great promise. Fortunately, its strengths appear to be in areas where CT and MRI are weak: thus, extrahepatic and extraintestinal metastases are clearly shown. The main use of this technology may therefore be in patients in whom carcinoembryonic antigen levels are rising, but initial evaluations with ultrasound, CT or MRI are negative or equivocal. Immunoscintigraphy seems more sensitive than either CT or MRI for nodal metastases.

Double and Multiple Carcinomas

Double and multiple colonic carcinomas concern carcinomas of multicentric origin. Criteria for double or multiple carcinoma are:

- Pathologic-anatomic evidence of the malignancy of each tumor
- Normal tissue between the tumors
- The possibility that the tumor is a metastasis or has arisen by means of local spread is ruled out

■ **Synchronous Double and Multiple Carcinomas.** In 2%–9% of patients, a second or more than one additional carcinoma is detected simultaneously or within 6 months after detection of the first, usually in the rectosigmoid.

■ **Metachronous Double and Multiple Carcinomas.** In 1.3%–2% of patients, one or more additional carcinomas arise in the colon 6 months or more after detection of the first carcinoma (metachronous, asynchronous, interval carcinoma).

Nonpolypoid Colorectal Cancers

Recent studies [15, 37, 38] have noted the existence of small flat colon carcinomas, but their clinicopathologic features have not been fully delineated. Early flat and depressed carcinomas are defined as colorectal adenocarcinoma confined to the mucosa or submucosa, macroscopically characterized as slightly elevated, often nearly flat and sometimes with central shallow depressions. Barium enema radiographs may show covering folds, a deep depression, an irregular surface of central depression, tumor on en face views and semilunar deformity on profile views. These characteristic findings are useful for determining the depth of invasion and therapy in early nonpolypoid colorectal cancer [37, 38].

Follow-up and Detection of Disease Recurrence

Follow-up after resection of colorectal cancer is for three purposes:

- Early detection of a second primary is by barium enema or colonoscopy. This follow-up should be early and repeated to ensure that the colon is clear, and then every 5 years to detect metachronous tumors.
- Detection of recurrence. Ninety-three per cent of all recurrences present within 4 years, and distant recurrence is more common than local disease. The liver is affected in 13% of cases, lymph nodes in 4%, lung in 3%, peritoneum in 2%, bones in 0.9% and brain in 0.7%. What data there are on the value of routine postoperative CT are not promising. However, radiologists would like to see every rectal cancer patient have CT 3 months after surgery to provide a base line. This is because the CT scan at 9 months in a patient with pelvic symptoms is often difficult to interpret, as an apparent pelvic mass may be either postoperative scarring or recurrent tumor. A 3-month base line CT scan, it is argued, will expedite the management of those patients who present with symptoms later. There are now data that do show better diagnostic accuracy for interpretation of pelvic findings when there has been an early postoperative CT scan. Apart from this single base-line CT after resection of rectal cancer, there appears to be consensus that initial follow-up should be clinical, supplemented by carcinoembryonic antigen and perhaps liver function tests.
- Assessment of possible resectable hepatic metastasis. The aim of investigation is to spare the majority of patients unnecessary radiofrequency (RF) ablation of (up to 4) liver metastases or surgery by demonstrating absence of extrahepatic disease and that two contiguous segments of the liver can be left in place after resection surgery. If MRI is readily available it should be used. If not, then a graded approach to CT and preoperative assessment may be considered, and can be offered on a 1-day outpatient basis. Immunoscintigraphy can demonstrate extrahepatic lesions overlooked by CT or MRI, though this is still a controversial area.

Inflammatory Bowel Disease

The diagnosis of inflammatory bowel disease is based on the contrast enema and is supported by the patient's history, the abdominal and digital rectal examination and endoscopy.

Ulcerative colitis and Crohn colitis (Crohn disease) comprise 90% of all cases of chronic inflammatory bowel disease and are classed as the most important considerations in differential diagnosis.

Both diseases are classed as idiopathic since neither etiology nor pathogenesis is completely understood. Each condition is associated with a rather specific but overlapping constellation of clinical, pathologic, endoscopic and radiographic findings. Socioeconomic factors do not appear to contribute to the epidemiology or etiology of either condition.

Increased familial occurrence is found in both conditions, with a range of from 0.6% to 16% for ulcerative colitis and approximately 9% for Crohn colitis. Colonoscopy plays an established role in the evaluation of patients with inflammatory disorders of the large bowel. The indications for the diagnostic evaluation of inflammatory bowel disease are:

- Determination of the extent and/or grade of activity
- To rule out cancer or in follow-up after surgery for cancer
- Differentiation from other inflammatory diseases

Detecting these colonic processes by visualizing the full extent of the pathoanatomic changes is the primary goal of the radiographic examination. Thorough bowel preparation and good double contrast technique are mandatory, as is adequate contrast resolution. Recognizing and distinguishing the two conditions is of therapeutic and prognostic consequence. Although ulcerative colitis and Crohn colitis are the inflammatory diseases most frequently identified by endoscopy or radiography, underlying infections or identifiable causes of the colitis should be excluded.

Ulcerative Colitis

Ulcerative colitis is an idiopathic acute or chronic mural inflammatory/ulcerative disease of the rectum and/or colon, with acute exacerbations and remissions.

■ **Incidence.** The incidence of ulcerative colitis has remained largely unchanged within the last 20 years. The first age peak is between 15 and 35 years and the second shallow peak is between 50–60 years; the greatest prevalence is in the period between 20 and 30 years. Men and women are equally affected; in the adult age group only, the ratio is women:men 3:2. There is a positive family history in 0.6%–16% of cases.

■ **Location.** Involvement of the entire colon can be seen in 36%–47% of cases; most commonly a left-sided colitis is found (15%–88%). Rectosigmoid colitis can be found in 10%–18%, subtotal colitis with backwash ileitis in 5%–11% and proctitis in 3%.

■ **Etiology.** The disease is considered to be idiopathic. The hypothesis is that there might be an infectious genesis from cytomegalovirus. It may be influenced by immunologic and genetic factors (a polygenic [multifactorial] inherited disease), and psychosomatic factors, although the causal role of psychological problems is still undetermined.

■ **Clinical Presentation.** Four types can be distinguished, although overlapping is frequent:
- Acute fulminant type (50%–10%)
- Subacute recurrent type (50%–60%)
- Recurrent type with progression to a chronic course
- Chronic course with intermittent exacerbation (10%–25%)

■ **Clinical Findings.** Clinical bleeding (90%–100%) with diarrhea and bloody mucus may be found as well as abdominal pain, fever and weight loss. Possible systemic extraintestinal complications are skin abnormalities, conjunctivitis, iritis, pericholangitis, sclerosing cholangitis and arthritis.

■ **Morphology and Histopathology.** The microscopic and histologic features depend on the stage and severity of the disease [93]. Mucosal vascular congestion with areas of fibrosis are seen. Inflammatory lymphadenopathy is usually found.

In the active phase, an irregular mucosal surface with pus may be seen with loss of the mucosal epithelium; penetrating ulcers with granulation tissue can be found. Focal polymorphonuclear infiltration of the muscularis mucosae with crypt abscesses of the nonulcerative epithelium is present in 70% of cases. There may be a depletion of goblet cells with mucin depletion. The muscularis mucosae and subserosa remain spared and are only involved in fulminant colitis. Occasionally foreign body giant cells are present.

In cases of beginning remission there is decreased hyperemia with slow disappearance of the polymorphonuclear infiltration and crypt abscesses; reepithelialization of the ulcerations will take place, leading to restoration of the epithelial continuity. There will be a regeneration of epithelium in the crypts and a decrease in lymphocytes and plasma cells without epithelioid granulomas.

In cases of complete remission (inactive, quiescent colitis), there is distortion of the structure and arrangement of the crypts, which do not extend to the muscularis mucosae. There is a flattened epithelium and an atrophic mucosa with a decreased number of crypts. Furthermore, fat in the lamina propria, metaplasia of the goblet cells and thickening of the muscularis mucosae can be found.

In the chronic phase, in cases of chronic stricturing ulcerative colitis, there is marked hypertrophy of the muscularis mucosae, often by a factor of up to 40-fold, due to chronic inflammation and diarrhea. Forceful contraction of this longitudinally oriented, hypertrophied muscular layer both shortens the colon and pulls the mucosa away from the muscularis propria, producing diffuse segmental narrowing of the lumen. The muscularis propria is often thin and relaxed. The lamina propria is often thickened with round cell infiltration and widening of the submucosa due to fat deposition, which further compromises lumen diameter blunted by a completely lost haustral pattern.

Diagnostic Imaging

The essential radiologic elements suggestive or diagnostic of ulcerative colitis include fine granularity, superficial and deep ulcerations, development of inflammatory pseudopolyps, loss of haustration, tubular narrowing, shortening and presacral widening. Most characteristic is the diffuse, symmetrical nature of involvement of the left side of the colon, in particular the rectum. Endoscopically, excessive mucus discharge,

Table 5. Ulcerative colitis: stages and findings on endoscopy and contrast enema. (From [2])

Ulcerative colitis	Stages	Endoscopy	Contrast enema
Active disease (bleeding)	Early stage (preulcerative stage) (congestive stage)	• Altered or absent (sub)mucosal vascular pattern (edema, hyperemia) • Diffuse erythema (edema, hyperemia) • Solitary petechiae, erosions • Solitary regions of granularity or appearance of striations	• Loss of bowel transparancy • Fine granularity, maculae, cystoid appearance, "powdered sugar" appearance (hyperemia/edema of (sub)mucosa • Irregular, blurred mucosal contours • Reduced distensibility • Thickened, blunt semilunar folds (flattening of haustra) • Erosions, but no ulcerations
	Ulcerative stage (progressive phase)	• Altered or absent (sub)mucosal vascular pattern, granular mucosa • Symmetric ulcerations of varying depth, linear, serpiginous, round, ellipsoid, solitary, or coalescing • Undermining of mucosa within altered region (< 5 mm) (collar-button or T-shaped ulcers) • Within a 10-cm segment of colon, as a rule less than 10 ulcers • Marked, extensive, or focal erythema • Friability • Blunting of haustra and transverse rectal folds	• Coarsely granular appearance of colon • Blunting of haustra and transverse rectal folds • Serrated contours • Widening of the retrorectal space • Superficial and deep collar-button or T-shaped ulcers
Regression (healing)	Recovery stage (proliferative phase)	• Extensive, severe ulceration (collar-button or T-shaped) (< 5 mm), surrounded by markedly erythematous mucosa • Within a 10-cm segment of colon, more than 10 ulcers • Friability • Sloughing of mucosa • Mucoid, purulent exudate • Atropic mucosa, beginning of tubular narrowing of colon • Postinflammatory polyps (pseudopolyps) (broadbased, sessile, or pedunculated, fernlike or filiform), covered with whitish exudate; giant polyps, may also be seen • Patchy or diffuse erythema in terminal ileum ("backwash" ileitis)	• Fine "sawtooth" contour of colonic wall • Deep ulcerations, "tangential" collar-button or T-shaped, "en face" solitary specks of barium on background of diffusely changed mucosa ("speckled gas" pattern) • Postinflammatory polyps (pseudopolyps) (broadbased, sessile, or pedunculated, fernlike or filiform) • Contour indentations • Widening of the retrorectal space • "Backwash" ileitis
Reversible			
Recurrence during remission (no massive bleeding)	Irreversible		
	Chronic stage (fibrosis and atrophy)	• Ulcerations and pseudopolyps regress • Atrophic mucosa • Reduced interhaustral foids (hypertrophy, contraction of the muscularis propria) • Tubular narrowing with induration • Postinflammatory polyps, solitary, diffuse, or in groups (pseudopolyps) (pedunculated, filiform), with or without mucosal bridging ("colitis polyposa")	• Reduction in ulcerations and finely granular or coarsely nodular patterns • Loss of haustra • Beginning formation of tubular stenosis • Filling defects: postinflammatory polyps (pseudopolyps) (sessile, filiform), reduced in size and number • Interconnections via mucosal folds or bridges, solitary, diffuse, or in groups • Widening of the retrorectal space
	Late stage	• Loss of haustra • Rigidity, reduction of caliber • Colonic shortening, smooth contours • Symmetric short or long tubular stenosis (hypertrophy of the muscularis propria) • Tubular, indurated ileum with loss of normal folds • Gaping ileocecal valve • Macroscopic dysplasia (DALM) (polypoid lesions with irregular, nonulcerated surface)	• Loss of haustra • Rigidity, smooth contours • Symmetric short or long tubular stenosis ("leadpipe" colon) • Shortening with inferiorly displaced flexures • Tubular terminal ileum with simultaneous reduction of normal folds • Gaping ileocecal valve • Macroscopic dysplasia (polypoid lesions with irregular, nonulcerated surface)
Characteristic changes of the colon • Disease activity increases with decreasing distance from rectum • Polymorphic • Continuous and symmetric • Mural (mucosa and submucosa) • Concentric, affecting the entire circumference • Sharp demarcation between healthy and diseased portions • Tendency to "total" colitis rather than to "segmental" colitis • Remissions and exacerbations	Complications	• Toxic megacolon (1.6–2.5%) • Extensive bleeding (1–2.5%) • Free perforation (rare) • Walled-off perforation (1–3%) • Postinflammatory polyps (12.5%) • Strictured (solitary or multiple) Rectum alone (3.6%) Rectum & left colon (7.5%) Rectum & entire colon (17.1%) • Rectovaginal fistulas (2.2%) • Perianal inflammation (18–20%) • Shortening of colon • Coprostasis • Dysplasia (5.7–88%) • Synchronous colon carcinoma (0.5–13.1%) • Portal venous thrombosis • Systemic complications	• Linear lucencies in colonic wall (pneumatosis) • Toxic megacolon • Tubular colon with ulcerations • Strictures • Perforation • Gas-fluid levels (ileus) • Polypoid filling defects • Postinflammatory polyps (pseudopolyps)

edema, erythema, irregularity and disappearance of the vascular pattern, friability with punctiform petechial bleeding, overt contact bleeding, spots or flecks of mucopurulent exudate, fine granularity, superficial or confluent and deep ulcerations, development of inflammatory pseudopolyps, luminal narrowing and retraction are the essential elements in the diagnosis. Again, most characteristic is the diffuse, symmetrical nature of involvement.

The most important features observed at the different stages of ulcerative colitis with double-contrast barium enema and endoscopy are shown in Table 5 and Figs. 13–18 [2, 10].

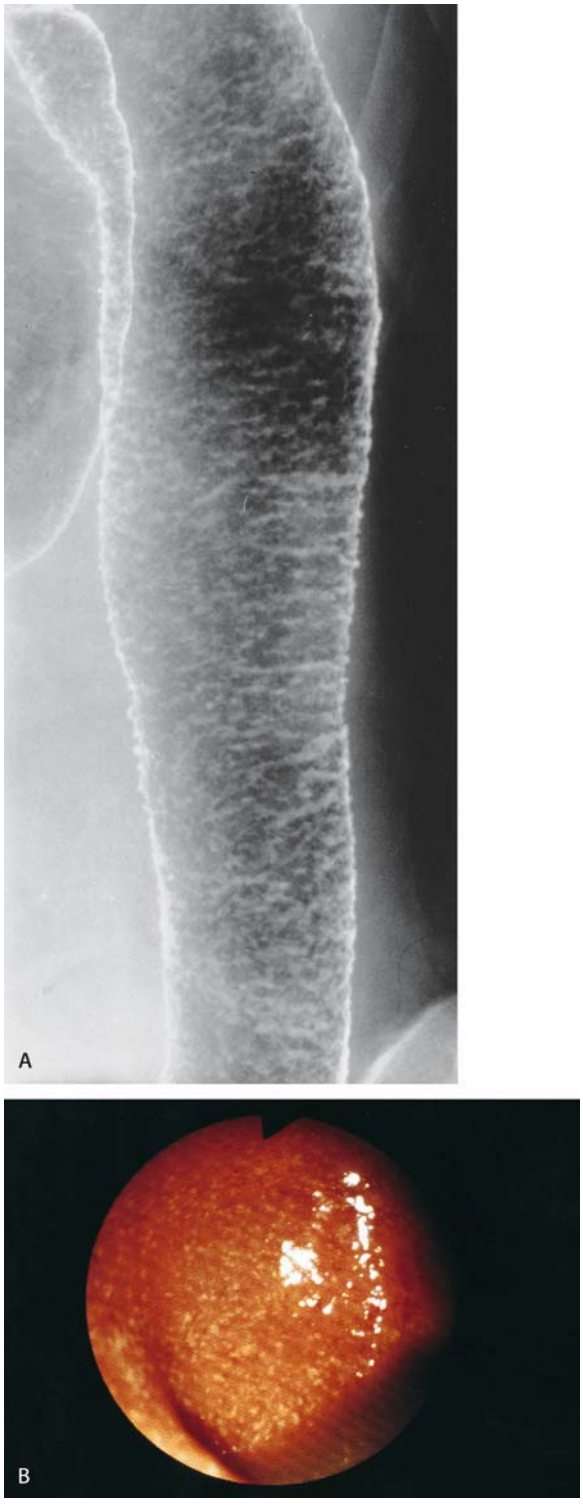

Fig. 13A, B. Early ulcerative colitis. **A** Barium enema: granularity of mucosal surface. **B** Endoscopy: fine mucosal granularity, blurred vascular markings

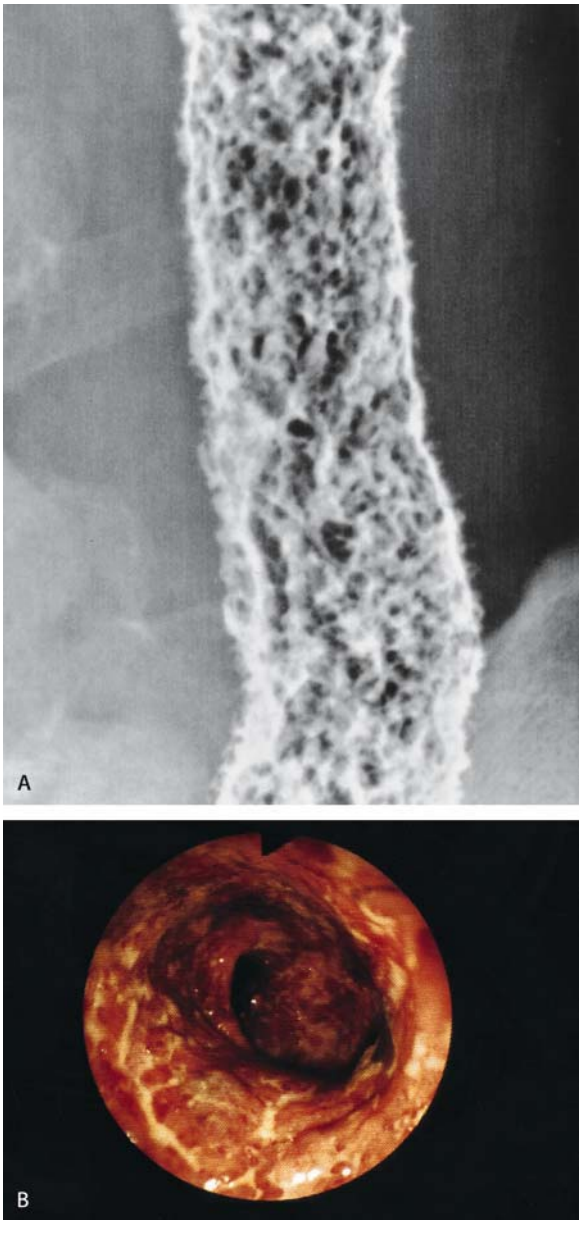

Fig. 14A, B. Remission (proliferative stage) in ulcerative colitis. **A** Barium enema: extensive severe ulceration (collar-button form) with postinflammatory polyps (pseudopolyps). **B** Endoscopy: extensive ulceration with mucopurulent exudate

■ **Complications.** The most important complications of ulcerative colitis are shown in Table 5.

Segmental fibrotic strictures do not occur in ulcerative colitis. The strictures observed in ulcerative colitis are generally caused by focal muscular hypertrophy or retraction.

■ **Course and Prognosis.** The risk of malignant degeneration is none if there is an 8- to 10-year disease duration: the risk is increased 23-fold in a 10- to 20-year du-

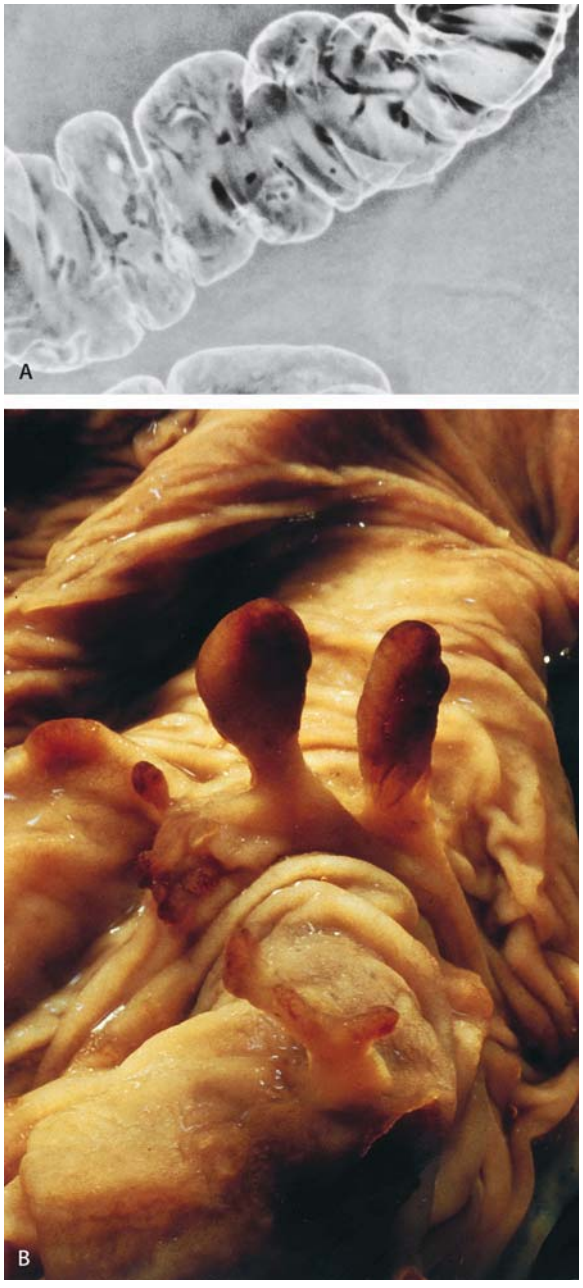

Fig. 15A, B. Postinflammatory polyposis. **A** Barium enema: multiple inflammatory, mostly filiform polyps surrounded by otherwise normal mucosa: ulcerative colitis. **B** An excised specimen shows the filiform structure of the polyps

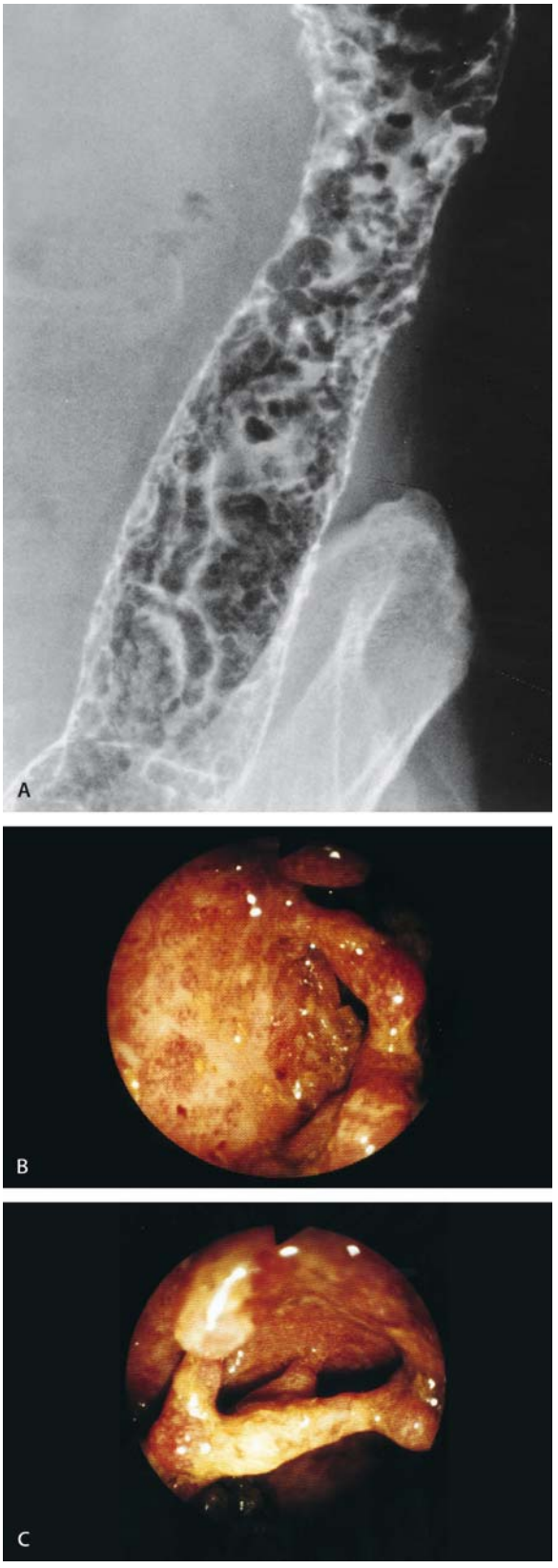

Fig. 16A–C. Giant filiform pseudopolyps, some showing branching or bridging, in ulcerative colitis. **A** Barium enema: benign stricture in the distal transverse colon. **B**, **C** Endoscopy

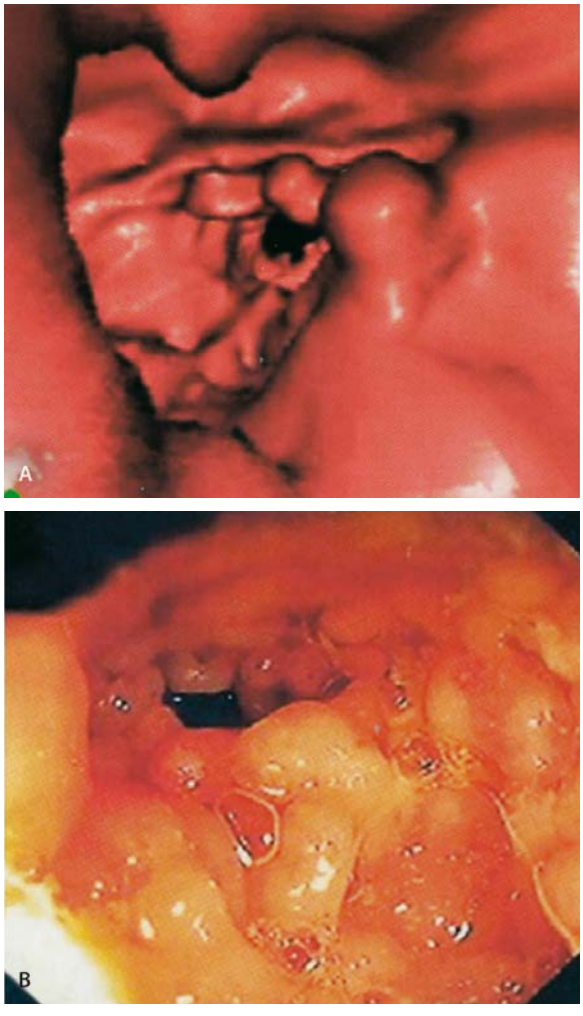

Fig. 17A, B. Pseudopolyps in a 45-year-old patient with known ulcerative colitis. **A**, **B** Virtual colonoscopy. **A** 3D reconstruction. **B** endoscopic view (adapted from [99])

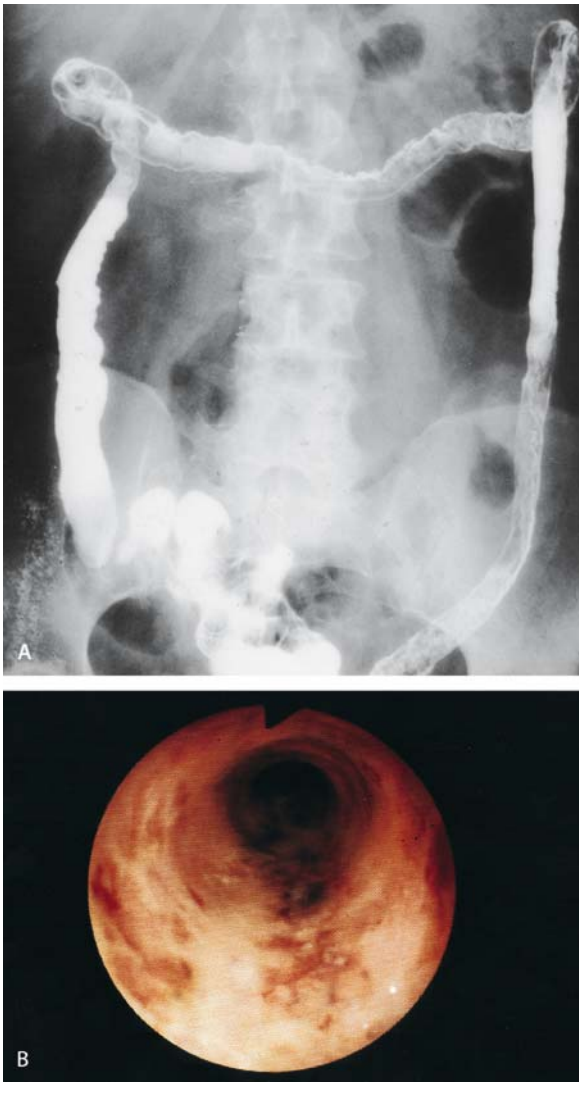

Fig. 18A, B. Chronic ulcerative colitis. **A** Barium enema: tubular, rigid colon with loss of normal folds. Filiform polyps in transverse and descending colon. **B** Endoscopy: tubular colon with spotty exudates and petechial bleeding

ration and 24-fold (30%–40%) in a duration of more than 20 years. The exact risk is uncertain, since most reports are from special centers with patient populations that are often skewed toward the most severe cases. In 1% of colorectal cancers, a history of previous ulcerative colitis can be found [94].

More than 50% of early cancers in ulcerative colitis are proximal to the splenic flexure. The carcinomas associated with ulcerative colitis are often infiltrating and highly malignant [95]. The growth patterns are annular infiltrating, nodular polypoid, annular polypoid (apple core) and villous.

The total mortality is 1%–7%. The recurrence rate following bowel resection is 15%–20% and depends on the extent of colonic involvement. The prognosis of pancolitis is considerably worse than that of colitis confined to the left hemicolon. The prognosis is better following proctocolectomy (ileoanal anastomosis) with a histopathologic examination of the specimen that is negative for carcinoma.

■ **Differential Diagnosis.** The differential diagnosis of ulcerative colitis is summarized in Table 6.

Table 6. Differential diagnosis of ulcerative colitis

Infectious diarrhea
– Salmonella enterocolitis
– Dysentery
– Campylobacter enterocolitis
– Staphylococcal enterocolitis
– Gonococcal proctitis
– Tuberculous enterocolitis
– Amebic enteritis
Pseudomembranous colitis
Hemorrhoids
Carcinoma, polyposis, lymphoma of colon or rectum
Irritable bowel disease
Laxative abuse
Crohn colitis
Ischemic colitis
Radiation enteritis
Diverticulitis
Metastatic lymphoma
Schistosomiasis
Behçet syndrome
Rectal ulcer
Uremic colitis
Polyarthritis
Scleroderma
Amyloidosis
Malabsorption syndrome

Crohn Colitis

Crohn disease of the colon is an idiopathic, chronic, transmural, inflammatory/ulcerative disease of the gastrointestinal tract, affecting particularly the terminal ileum and characterized by acute exacerbations and remissions.

■ **Incidence.** The first peak incidence is between the ages of 15 and 35 years, with a second, less prominent peak incidence between the ages of 50 and 60 years. The highest frequency is between the ages of 20 and 50 years. Both sexes are equally affected. There is a positive family history in 26%–38% of the patients.

■ **Location.** The disease has a segmental pattern. The oral cavity can be diseased in 6%–20%; the esophagus, stomach and duodenum are rare locations. It will be found in the small intestine alone in 30%–43%; in the small intestine and colon in 31%–60%, and in the colon alone in 20%–35%. Isolated anorectal disease can be found in 3%–6%. The perianal region will be diseased in 43%–94%.

■ **Etiology.** Crohn colitis is considered to be idiopathic. The hypothesis is that there may be an infectious cause: bacterial, viral or parasitic. Dietary factors, allergic reactions, sarcoidosis, tuberculosis and immunologic and genetic factors may also have an influence.

■ **Clinical Findings.** Four individual stages can be recognized in Crohn disease:

- Early
- Intermediate
- Proliferative
- Advanced

The different stages of disease may be present simultaneously in separate segments of the colon. The clinical symptoms are most commonly diarrhea without bleeding (66%–90%). In contrast to ulcerative colitis, the presence of blood, pus, or mucus in the stool is atypical. Occult blood may be seen in up to 50% of patients. Extensive bleeding is very rare.

Gradual, progressive development of epigastric or right lower-quadrant abdominal pain may be found in 45%–95% of cases. Weight loss may occur. Systemic extraintestinal complications may occur in Crohn disease of the colon similar to what is seen in ulcerative colitis.

■ **Morphology.** Intestinal changes may be found in various stages simultaneously. Small erythematous plaques and/or aphthoid ulcers may be seen, together with a small erythematous margin with absence of raised margins and a gray-yellow central indentation; discontinuous linear ulcers can occur. There is a coarse nodular mucosa. Typical is the cobblestone pattern with an irregular, coarsely nodular contour, possibly with stricture or ulceration. Parallel longitudinal or transverse, fissure-like ulcerations, a thickened, edematous mucosa and inflammatory pseudopolyps can be found.

■ **Histopathology.** Mucosal bleeding, focal crypt abscesses and destruction of crypt epithelium are common findings. At times, complete destruction of crypts and surrounding epithelium in regions of former inflammation can be found. Small, noncaseating epithelioid cell granulomas with or without giant cells of the Langhans type can occur. Largely intact goblet cell populations in crypts can be seen with focal aggregations of lymphocytes with or without germinal centers at the mucosa/submucosa interface. Submucosal tissue may be seen in the connective tissue of the muscularis propria and beneath the serosal surface.

There may be a transmural inflammation with fissure formation.

The inflammatory infiltration is often disproportionate, i.e., more marked in the submucosa than in the mucosa. Fibrotic strictures may develop with deep ulcerations and fissures into the submucosa.

Diagnostic Imaging

The essential radiologic elements suggestive of Crohn colitis include aphthoid erosions, small and large, linear, longitudinally aligned and serpiginous ulcers, cobblestones, development of inflammatory pseudopolyps, stricturing, retraction and deformity of the contours

Table 7. Crohn colitis: stages and findings on endoscopy and contrast enema. (From [2])

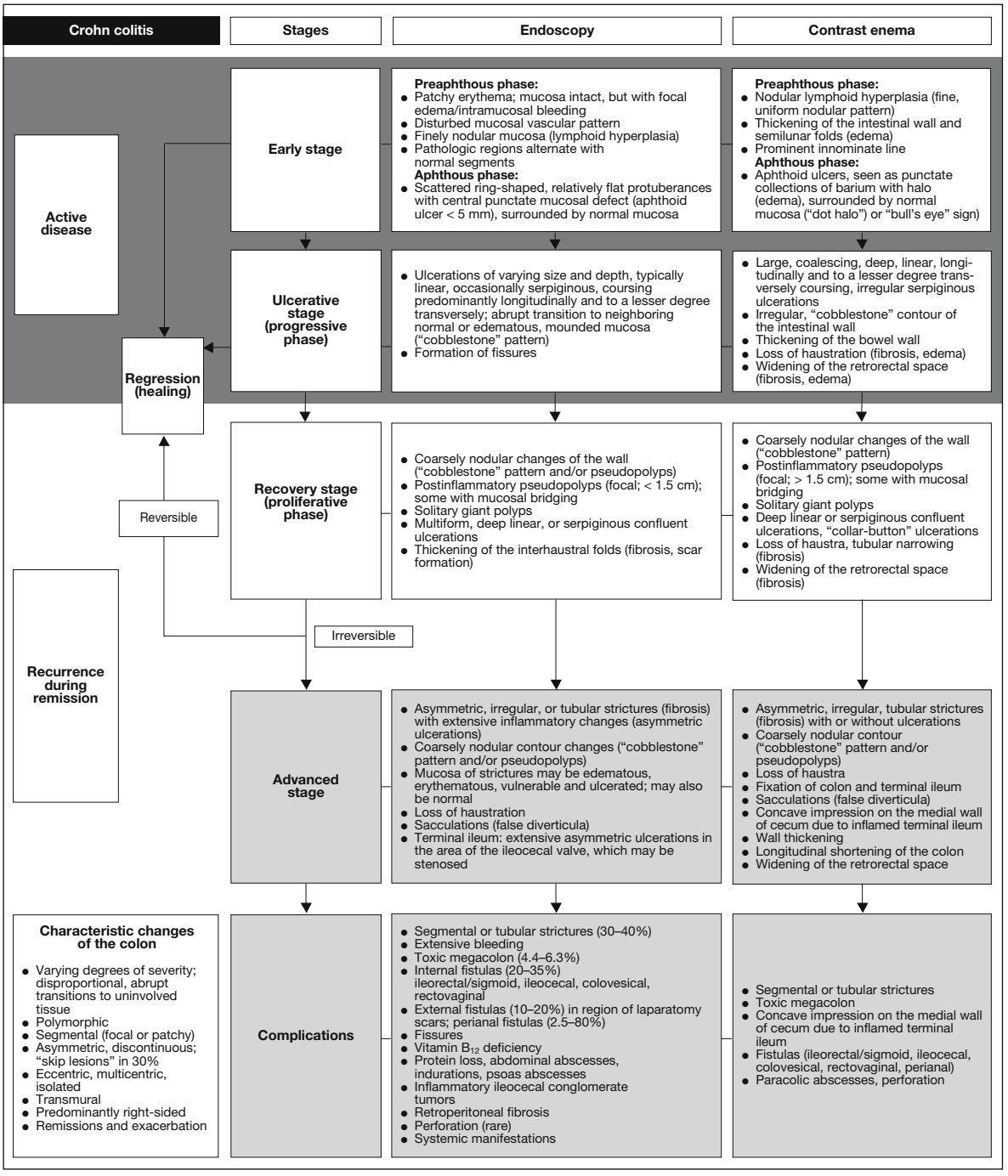

and fistulation. A striking feature of Crohn colitis is the asymmetrical, discontinuous distribution of the lesions.

The essential endoscopic elements suggestive or diagnostic of Crohn colitis include focal preaphthoid red spots, aphthoid erosions, superficial small, linear, confluent, serpiginous or longitudinally aligned ulcers, cobblestones, development of inflammatory pseudopolyps, stricturing and fistulation. A striking feature of Crohn colitis is the focal patchy discontinuous, asymmetrical nature of the endoscopic abnormalities.

The most important features observed at the different stages of Crohn colitis by endoscopy and double

contrast barium enema are shown in Table 7 and Figs. 19–24 [2, 10].

■ **Complications.** The most important complications of Crohn colitis are shown in Table 7 [2, 10].

■ **Course and Prognosis.** The risk of colorectal carcinoma is increased by a factor of six to seven in patients with Crohn colitis, particularly when they have extensive colonic involvement, after surgery (bypass operation) and in cases where there is colorectal stricture [96].

Colon carcinoma can appear multifocally, typically arising 16–45 years after the diagnosis of Crohn colitis is made.

Carcinoma (infiltrating, nodular, polypoid: flat/plaque-like polyps) appears in relatively young patients and is usually right-sided and in the vicinity of fistulas. The chronic morphologic changes that have taken place due to underlying disease (stricture, cobblestoning or ulceration) may cause great difficulty in diagnosing the cancer. The precancerous dysplastic epithelial changes are largely similar to those seen in ulcerative colitis.

The recurrence rate after colon resection is 14%–94% and depends on age, tumor location (recurrence higher in ileitis than in colitis), the duration of postoperative recurrence-free period and the extent of the operation. The total mortality is 3.3%–18%. The death rate in patients with Crohn disease is increased by a factor of 1.5–5.

■ **Differential Diagnosis.** The differential diagnosis of Crohn colitis is summarized in Table 8.

Table 8. Differential diagnosis of Crohn colitis

Specific infections:
Bacterial infections
Salmonellosis
Shigellosis
Tuberculous colitis
Gonorrheal proctitis
Staphylococcal enterocolitis
Fungal infections
Histoplasmosis
Viral infections
Lymphogranuloma venereum
Parasitic infections
Amebic dysentery
Schistosomiasis
Other specific diseases:
Ulcerative colitis
Radiation proctitis
Diverticulitis
Ischemic colitis
Pseudomembranous colitis
Postantibiotic proctocolitis
Neoplasms and illnesses associated with premalignancies:
Carcinoma
Lymphoma
Familial intestinal polyposis
Other:
Suppurative appendicitis
Behçet syndrome
Hemorrhoids
Irritable colon
Laxative abuse
Caustic colitis
Solitary rectal ulcer
Polyarteritis
Scleroderma
Secondary amyloidosis
Mercury poisoning
Uremic colitis
Malabsorption syndrome

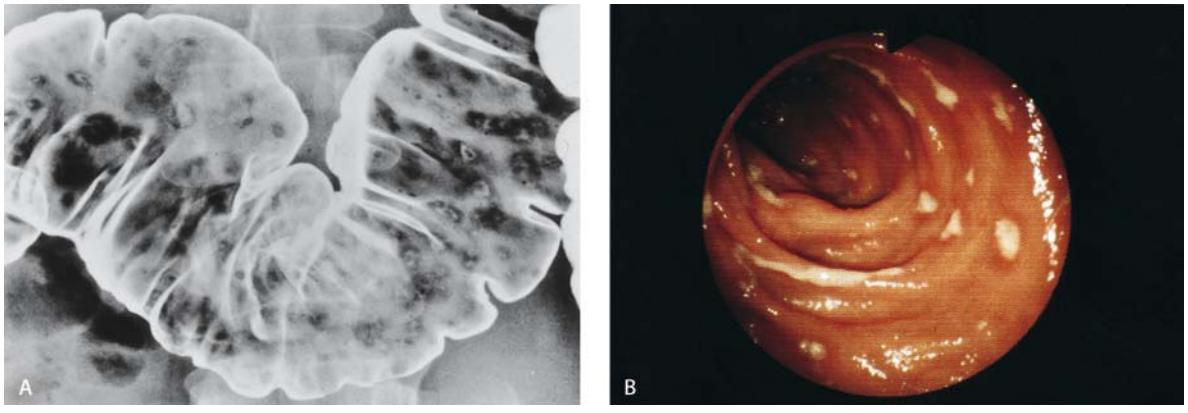

Fig. 19A, B. Crohn colitis. **A** Barium enema: aphthous phase with scattered ring-like, relatively flat prominences with subtle central mucosal defects (aphthoid ulcers <5 mm), surrounded by normal mucosa (early stage). **B** Endoscopy: characteristic aphthoid ulcers, interspersed within normal mucosa (early stage)

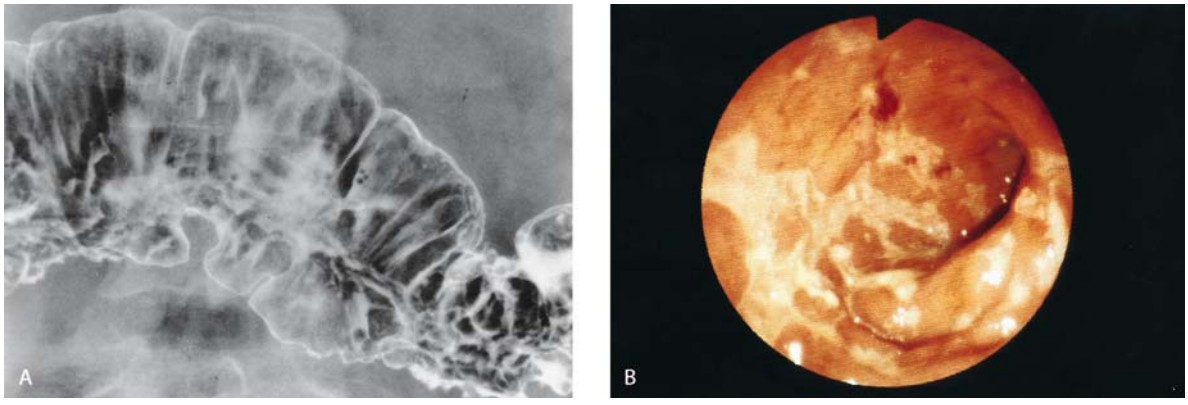

Fig. 20A, B. Crohn colitis. **A** Barium enema: extensive confluent serpiginous ulcerations, covering approximately half the circumference of the colon. **B** Endoscopy: longitudinal arrangement of the ulceration, producing a track-like appearance

Radiology Versus Endoscopy

Diagnostic methods, essential for the management of patients, should be evaluated critically. The usefulness of lower gastrointestinal radiology and endoscopy in the diagnosis and differential diagnosis of inflammatory bowel disease is well established. Since a true diagnosis cannot be obtained systematically, the accuracy of a radiological or endoscopic diagnosis is difficult to determine.

Double-contrast barium enema and colonoscopy share common problems, including patient preparation and cooperation, technical difficulties in reaching the cecum and the terminal ileum and variables relating to the expertise of the physician performing the procedure. The strength of endoscopy is its superior accuracy in the diagnosis of mucosal disease and the facility for biopsy and (when necessary) endoscopic therapy. On the other hand, completeness and safety are qualities of the double-contrast barium enema that cannot be matched by colonoscopy.

Numerous reports have compared the diagnostic accuracy of colonoscopy with that of double-contrast barium enema and the results have been variable. Usually a variable time interval was present between the two examinations and the preparatory cleansing regimens were different. Controversy about the relative diagnostic accuracy of colonoscopy compared with double-contrast barium enema persists and may be the result of errors in the design of previously reported trials. Most discussions have been written by gastroenterologists overemphasizing the endoscopic point of view. As a result, few reliable data are available from comparative studies of state of the art double-contrast barium enema and colonoscopy. Additional major criticism of these studies includes bias in patient selection, retrospective analysis, failure to use state of the art techniques, use of trainees to perform procedures, use of the endoscopic diagnosis as the gold standard, failure to blind investigators to results of previous studies, unequal availability of clinical information to the investigators and lack of documentation or confirmation of the endoscopic diagnosis. We have compared the relative diagnostic accuracy of double-contrast barium enema and colonoscopy in a prospective study in which approximately 100 patients were examined within the same period by double-contrast barium enema and colonoscopy by experienced, blinded examiners using state of the art techniques [10]. The determination of accuracy was then made by a third, independent and infallible criterion such as a resection specimen or autopsy.

We have found that double-contrast barium enema and colonoscopy are complementary imaging modalities: each test has its own intrinsic advantages and merits. Colonoscopy and biopsy remain the most sensitive imaging modalities to identify mucosal involvement (small and superficial lesions, abnormal mucosa surrounding ulcers); double-contrast barium enema remains the cornerstone in the detection of structural abnormalities (fistulas, strictures, perforations) and in estimating the depth of ulceration [10]. Since the pioneer studies that identified and categorized ulcerative and Crohn colitis, the problems in discriminating between these two conditions have given rise to considerable controversy. As a result, the proportion of patients with unclassifiable or indeterminate inflammatory bowel disease has been estimated to be as high as 10%.

In a given patient, distinguishing features may be more apparent by one method of examination than by the other. Therefore a compilation of radiological and endoscopic features is often useful, particularly in ileocolic disease.

Meticulous, systemic study of colonoscopic and radiologic findings, the use of a standard evaluation sheet or a diagnostic scoring system and repeated observations should provide a valuable contribution in classifying patients with inflammatory bowel disease: this should increase diagnostic accuracy and facilitate the differential diagnosis of ulcerative and Crohn colitis. The main clinically relevant discrepancies between double-contrast barium enema and colonoscopy con-

sist of inflammatory lesions without distortion of the mucosal relief and inflammation in the form of small, superficial erosions and ulcers.

Cross-sectional Imaging

Although double-contrast radiographs and endoscopy provide a wealth of information regarding the mucosa (e.g., the presence of aphthoid lesions, cobblestoning, pseudopolyps, ulcerations, etc.), ultrasound, CT and MRI may provide an important additional diagnostic perspective [97]. These modalities have proven to be superior in recognizing intramural, serosal and mesenteric changes, including thickening of the intestinal wall or serosa, fibrofatty proliferation of the mesenteric adipose tissue, inflammatory changes of the surrounding mesentery, and mesenteric lymphadenopathy. Clinically these modalities are very helpful in assessing space-occupying masses or displacement of intestinal segments. In approximately 10%–15% of patients with inflammatory bowel disease, clinical and colonoscopic findings, pathologic characteristics or changes seen in contrast enema studies do not provide sufficient information to distinguish between ulcerative colitis and Crohn colitis. Such cases are occasionally termed undetermined colitis.

■ **Ultrasonography and CT.** The most important characteristics of inflammatory bowel disease that can be assessed with ultrasonography and CT are listed in Table 9.

Diagnostic ultrasound is an inexpensive alternative diagnostic modality in detection of Crohn colitis and

Table 9. Ultrasound and CT in ulcerative colitis and Crohn colitis. (From [2])

Pathologic changes	Ulcerative colitis	Crohn colitis
Changes in the mucosa and lumen:		
Narrowing of the lumen	+	±
Thickening of the bowel wall	+	+
Mural involvement:		
Mural thickening	± < 1 cm	+ > 1 cm
Terminal ileum	–	+
Small intestine	–	+ (Symmetric)
Colon	± (Average 8 mm)	+ (Average 13 mm–3 cm)
Transmural involvement:		
Transmural ulceration	–	+
Thickness of wall on CT	Homogeneous	Inhomogeneous
Irregular contour:		
Inner contour	+	+
Outer contour	–	+
"Thumbprint"	–	+
Submucosal edema ("bull's eye sign")	+	–
Changes in the mesentery:		
Fibrofatty proliferation of the mesentery	–	+
Mesenteric abscess/phlegmon	–	+
Inflammatory reaction of the mesentery	–	+
Increased and enlarged mesenteric lymph nodes	±	+
Fistulas and recesses	–	+ (Peri-, ischiorectal)
Changes in the rectum:		
"Bull's eye sign"	+	–
Significant thickening of the rectum	± (Average 11 mm)	+ (Average 27 mm)
Narrowing of the lumen	±	+
Perirectal fat layer	–	+
Extraperitoneal fat tissue	–	+
Perirectal changes:		
Perirectal abscess formation	–	+
Normal fat tissue	+	+
Increased fat deposits	+	–
Increased density (CT)	+	+
Increased fat mass in presacral and perirectal areas	+	+a
Abscesses:		
Iliopsoas muscle	–	+
Periluminal	–	+
Subcutaneous	–	+
Intramusular	–	+
Liver	–	+
Perirectal	–	–
Free fluid in peritoneum/seroma:		
Extraintestinal manifestations:		
Fatty infiltration of the liver	–	±
Hydronephrosis	–	+

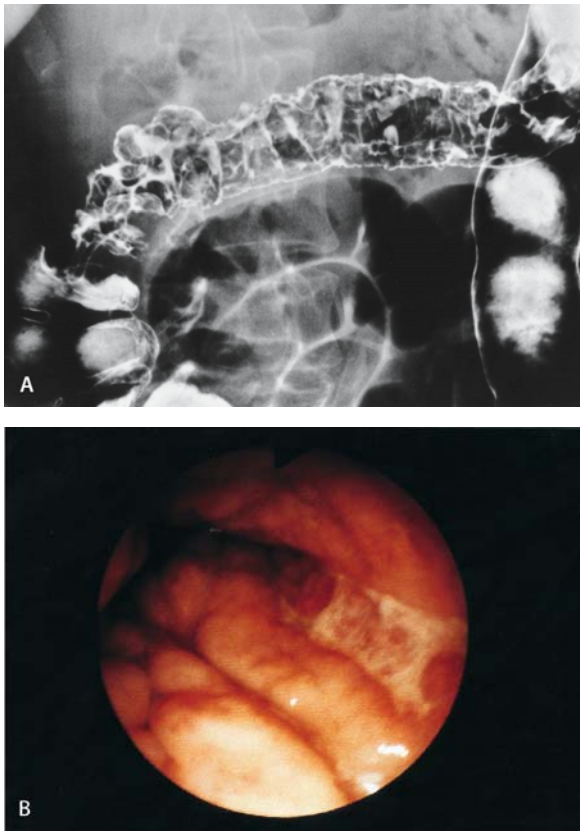

Fig. 21A, B. Crohn colitis. **A** Barium enema: marked cobblestone pattern and rigid tubular narrowing of the transverse colon with a proximal abrupt transition to normal mucosa. Additionally, multiple filiform pseudopolyps can be seen at the right side of the colon. **B** Endoscopy: typical cobblestone appearance with railroad track ulcerations

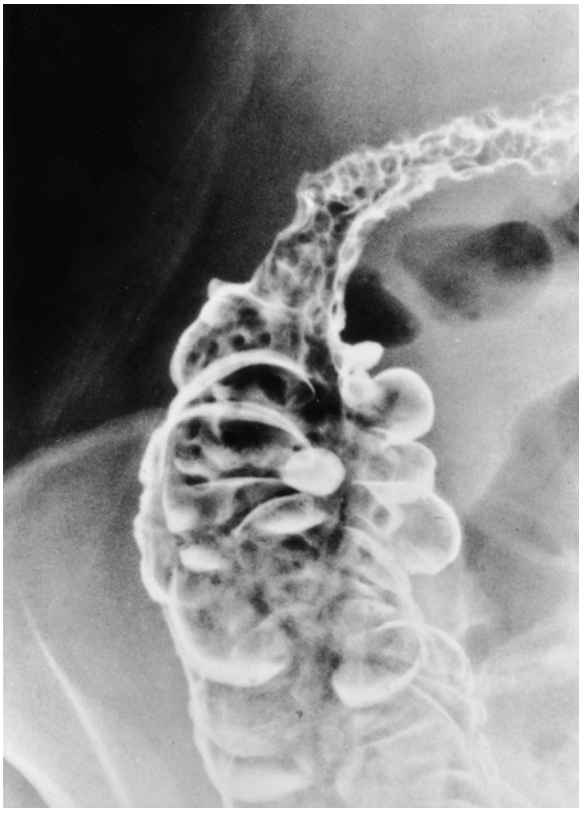

Fig. 22. Crohn colitis; advanced stage. Barium enema: extensive small postinflammatory pseudopolyps in a tubular section of the colon; several ulcerations. Sacculations in the ascending colon

the degree of radiation exposure. Depending on the ultrasound unit, the examiner and patient characteristics, inflammatory bowel wall changes, stenosis as well as abscesses and fistulae can be reliably diagnosed.

Because of the gas overlay, an exact determination of the length of the transmural affected segments is impossible with ultrasound. Findings by different examiners using different units, together with the difficulties involved with standardization of data, may lead to divergent interpretations of the ultrasound status [100, 101].

For the diagnosis of stenoses in Crohn ileocolitis, US showed a sensitivity of 58%–100% and a specificity of 91%–100%.

For the diagnosis of Crohn abscesses, US showed a sensitivity of 83%–100% and a specificity of 92%–94%.

For fistulae, US showed a sensitivity of 31%–87% and a specificity of 90%–100% [100, 102].

Bowel wall ultrasound is an elegant method for clinical follow-up in patients with Crohn colitis. It has been recommended that US be supplemented in both the primary diagnosis and follow-up with methods as colonoscopy and – if required – with MRI/CT [100].

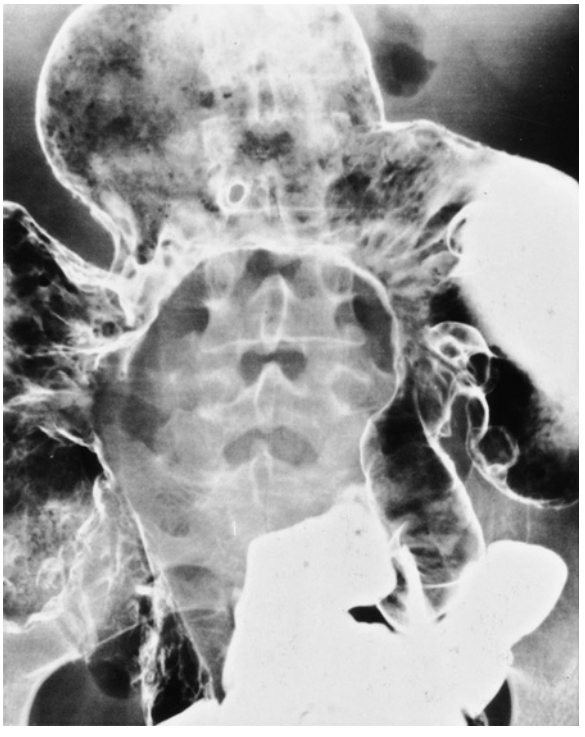

Fig. 23. Crohn ileocolitis. Barium enema: extreme shrinkage of the mesenteric site of the colon giving a rise to the "omega sign"

Computed tomography of the abdomen is an additional diagnostic method for identifying the intra- and extraluminal changes of Crohn colitis. As with ultrasound, diagnosis depends on visualization of bowel wall thickening, which in acute disease can be seen in 100% of patients [100].

Whereas CT is capable of reliably identifying moderate to high-grade stenoses and their causes, its capability in the diagnosis of less severe stenoses is limited, due to incomplete contrasting of the lumen of the colon, poor tissue contrast and the exclusively axial images.

These limitations with the associated radiation exposure have nowadays restricted the application of CT as a primary diagnostic procedure in the evaluation of Crohn colitis [100].

■ **Magnetic Resonance Imaging.** Several reports [100, 103–110] have described MR Imaging of Crohn disease with use of a combination of unenhanced and gadolinium-enhanced imaging. With faster breath-hold pulse sequences, MR evaluation of the Crohn disease involvement of the colon has become feasible [100] (Figs. 25, 26). In a MRI study by Low et al. [103] of Crohn disease with endoscopic correlations, gadolinium-enhanced fat-suppressed spoiled GRE-MR imaging better depicted the extent of mural colonic changes and severity of disease compared with single-shot fast SE imaging, be-

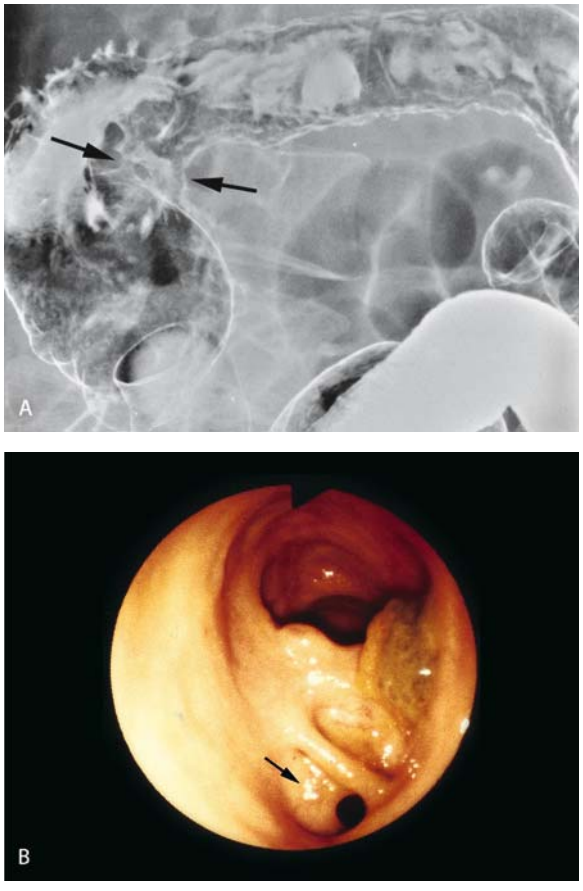

Fig. 24A, B. Colocolic fistula. **A** Barium enema shows two fistulas at the hepatic flexure (*arrows*). The hepatic flexure shows marked ulceration and foreshortening of the ascending colon. **B** Endoscopy, showing the colocolic fistula at the hepatic flexure in Crohn colitis

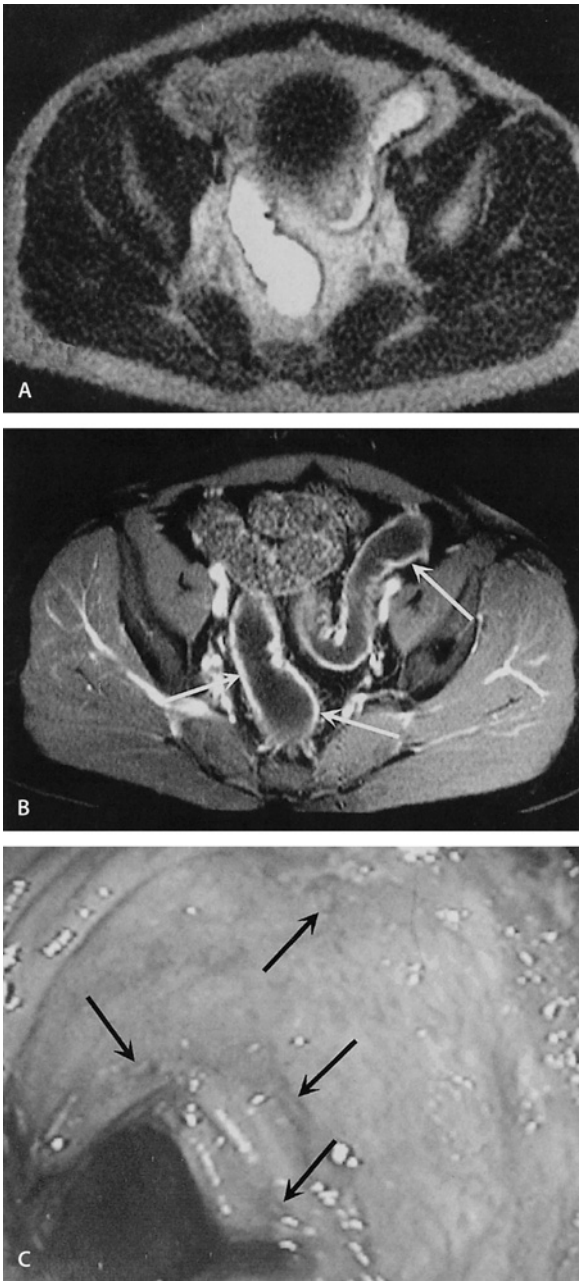

Fig. 25A–C. Images obtained through the pelvis in a 37-year-old man with recently diagnosed Crohn disease. **A** Transverse breath-hold single-shot fast SE MR image (00/94, 30° flip angle) is unremarkable. Rectal water distends the rectosigmoid colon without evidence of mural thickening. **B** Transverse fat-suppressed gadolinium-enhanced spoiled GRE MR image (165/2, 70° flip angle) shows mild mural thickening and marked enhancement of the rectosigmoid colon (*arrows*). Similar changes are noted throughout the colon and at the terminal ileum. **C** Colonoscopic image shows scattered linear ulcerations (*arrows*) involving the entire colon and the terminal ileum (adapted from [103])

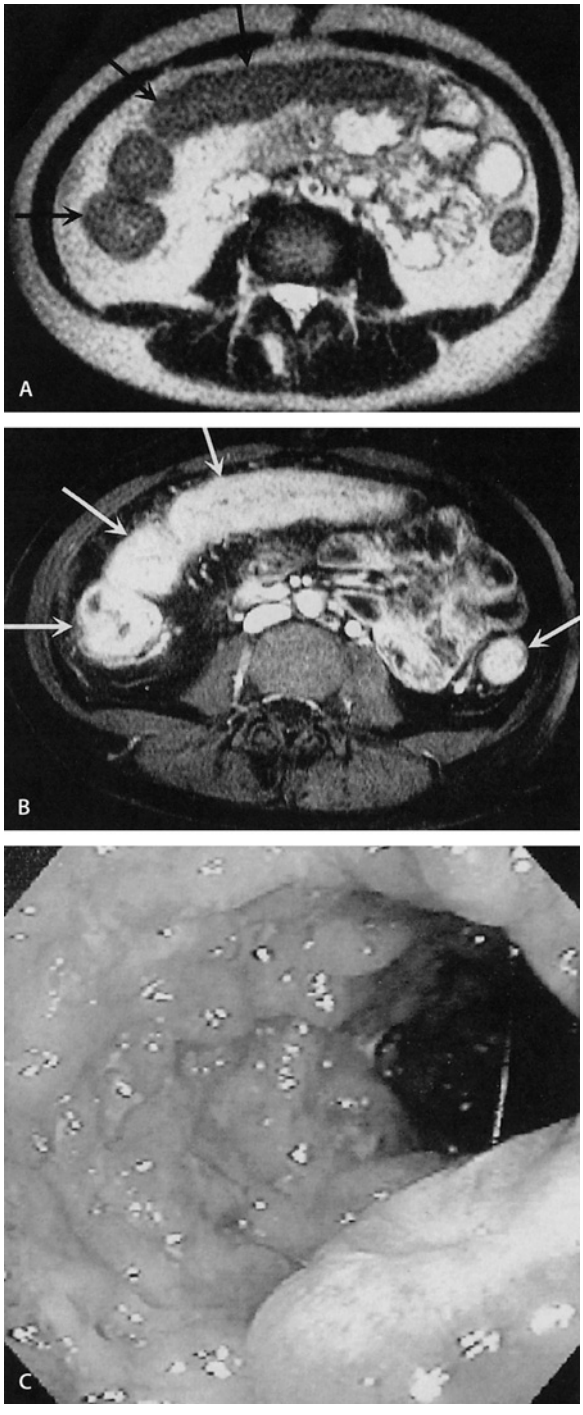

Fig. 26A–C. Transverse fat-suppressed gadolinium.enhanced spoiled GER MR image. **A** Transverse single-shot fast SE MR image (00/90, 90° flip angle) shows the colon (*arrows*). Administration of rectal water was limited by the patient's acute perirectal symptoms. Marked mural thickening is present but is difficult to distinguish from intraluminal stool. **B** Transverse gadolinium-enhanced fat-suppressed spoiled GRE MR image (165/2.1, 70° flip angle) shows pancolitis (*arrows*) with marked mural thickening and enhancement. Severe luminal narrowing is present. **C** Colonoscopic image confirms marked changes in the Crohn disease with edematous, inflamed, and friable mucosa. Heaped folds of abnormal mucosa produce a cobblestone appearance, which results in luminal narrowing (adapted from [103])

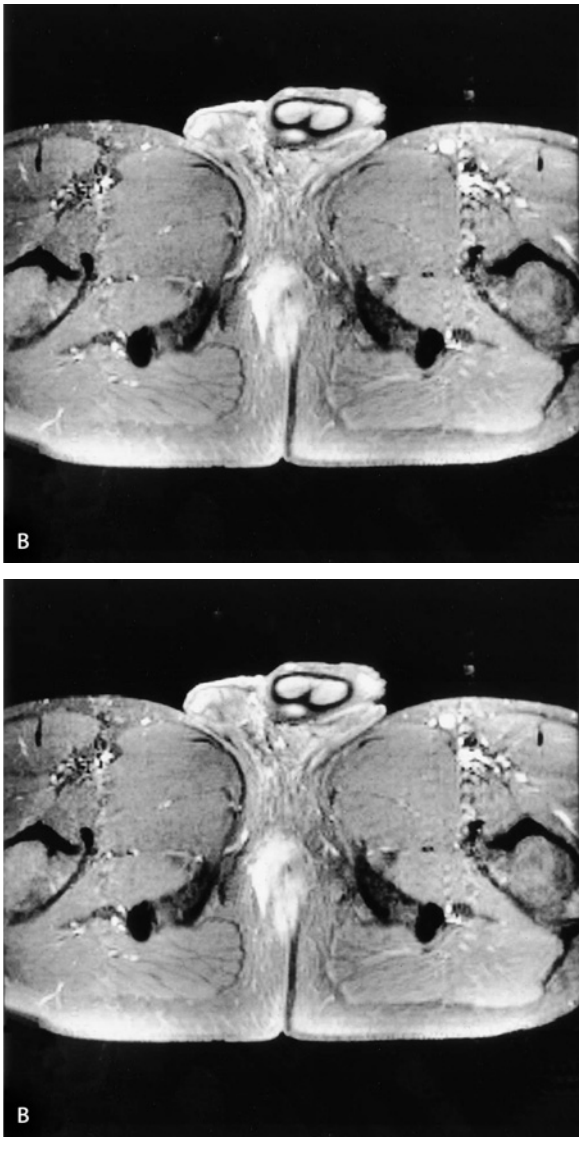

Fig. 27A, B. Crohn fistula: MRI showing a right-sided ischiorectal fistula. **A** Coronal view, **B** transverse view

cause of better enhancement of the diseased colonic segments, with a sensitivity of 85%–89% and 51%–52% respectively, and specificity of 94%–96% and 96%–98% respectively [103].

For the diagnosis of stenoses, MRI shows a sensitivity of 100% and a specificity of 96% [100].

For the diagnosis of abscesses in Crohn disease, MRI shows a sensitivity of 100% and a specificity of 97%.

For the diagnosis of Crohn fistulae, MRI (Fig. 27) shows a sensitivity of 98% and a specificity of 93% [100].

MRI of the abdomen should be obtained to clarify clinical and sonographic findings in Crohn colitis. Despite its higher cost, MRI of the abdomen is justified in patients in whom Crohn colitis is known or suspected and in cases with suspicion of fistulae and abscesses.

References

1. Gelfand DW, Chen YM, Ott DJ (1987) Detection of colonic polyps on single-contrast barium enema study: emphasis on the elderly. Radiology 164:333–337
2. Rosenbusch G, Reeders JWAJ (1993) Kolon, Klinische Radiologie-Endoscopie. Thieme, Stuttgart
3. Ott DJ (1996) Barium enema: colorectal polyps and carcinoma. Semin Roentgenol 31:125–141
4. Morson BC, Dawson IMP (1979) Gastrointestinal pathology, 2nd edn. Blackwell, Oxford
5. Teoh SK, Whitman GJ, Chew PS (1996) Villous adenoma of the colon. Am J Roentgenol 167:1146
6. Van Der Werken BS, Wu WC (1996) Endoscopic evaluation of colon polyps. Semin Roentgenol 31:118–124
7. Thoeni RF, Menuck L (1977) Comparison of barium enema and colonoscopy in the detection of small colonic polyps. Radiology 124:631–635
8. Miller RE, Lehman G (1978) Polypoid colonic lesions undetected by endoscopy. Radiology 129:295–297
9. Thoeni RF, Petras A (1982) Double-contrast barium-enema examination and endoscopy in the detection of polypoid lesions in the cecum and ascending colon. Radiology 144:257–260
10. Dijkstra J, Reeders JWAJ, Tytgat GNJ (1995) Idiopathic inflammatory bowel disease: endoscopic-radiologic correlation. Radiology 197:369–375
11. Rex DK, Cummings OW, Helper DJ et al (1997) 5-year incidence of adenomas after negative colonoscopy in asymptomatic average-risk persons (abstract). Radiology 203:885
12. Kewenter J, Jensen J, Boijsen M et al (1987) Perception errors with double-contrast enema after a positive guaiac test. Gastrointest Radiol 12:79–82
13. Saito Y, Slezak P, Rubio C (1989) The diagnostic value of combining flexible sigmoidoscopy and double contrast barium enema on a one stage procedure. Gastrointest Radiol 14:357–359
14. Markus JB, Somers S, O'Malley BP et al (1990) Double-contrast barium enema studies: effect of multiple reading on perception error. Radiology 175:155–156
15. Järvinen HJ, Mecklin JP, Sistonen P (1995) Screening reduces colorectal cancer rate in families with hereditary nonpolyposis colorectal cancer. Gastroenterology 108:1405–1411
16. Thoeni RF (1997) Colorectal cancer: radiologic staging. Radiol Clin North Am 35:457–485
17. Gore RM (1997) Colorectal cancer: clinical and pathologic features. Radiol Clin North Am 35:403–429
18. Gelfand DW (1997) Colorectal cancer: screening strategies. Radiol Clin North Am 35:431–438
19. Buetow PC, Buck JL, Carr NJ et al (1995) Colorectal adenocarcinoma: radiologic-pathologic correlation. Radiographics 15:640–648
20. Winawer SJ, Fletcher RH, Miller L et al (1997) Colorectal cancer screening: clinical guidelines and rationale. Gastroenterology 112:594–642
21. Okizuka H, Sugimura K, Shinozaki N et al (1995) Colorectal carcinoma: evaluation with ultrafast CT. Clin Imaging 19:247–251
22. Ott DJ, Wolfman NT (1996) Integrated imaging in colorectal cancer. Semin Roentgenol 31:166–169
23. Levine MS, Glick SN, Rubesin SE, Laufer I (2002) Double-contrast barium enema examination and colorectal cancer: a plea for radiologic screening (editorial). Radiology 22:313–315
24. Greenlee RT, Murray T, Bolden S, Wingo PA (2000) Cancer statistics, 2000. CA Cancer J Clin 50:7–33
25. Winawer SJ, Zauber AG, Ho MN et al (1993) Prevention of colorectal cancer by colonoscopic polypectomy. The National Polyp Study Workgroup. N Engl J Med 329:1977–1981
26. Ahlquist D, Wieland H, Moertel C et al (1993) Accuracy of fecal occult blood screening for colorectal neoplasia. JAMA 269:1262–1267
27. Simon JB (1998) Should all people over the age of 50 have regular fecal occult-blood tests? Postpone population screening until problems are solved. N Engl Med 338:1151–1152
28. Luboldt W, Fletcher JG, Vogl TJ (2002) Colonography: current status, research directions and challenges. Update 2002 Eur Radiol 12:502–524
29. Bruzzi JF, Moss AC, Fenlon HM (2001) Clinical Results by CT colonoscopy. Eur Radiol 11:2188–2194
30. McCarthy PA, Rubesin SE, Levine MS et al (1995) Colon cancer: morphology detected with barium enema examination versus histopathologic stage. Radiology 197:683–687
31. Johnson RD, Geisinger KR (1996) Colorectal adenocarcinoma: staging and histopathology. Semin Roentgenol 31:94–102
32. Chong A, Shah JN, Levine MS et al (2002) Diagnostic yield of barium enema examination after incomplete colonoscopy. Radiology 223:620–624
33. Rex DK, Rahmani EY, Haseman JH et al (1997) Relative sensitivity of colonoscopy and barium enema for detection of colorectal cancer in clinical practice. Radiology 203:885
34. Bach DB (1995) Missed diagnosis of colorectal carcinoma at barium enema examination (letter to the editor). Radiology 194:580
35. Brady AP, Stevenson GW, Stevenson I (1994) Colorectal cancer overlooked at barium enema examination and colonoscopy: a continuing perceptual problem. Radiology 192:373–378
36. Cohan RH (1985) Computed tomography of epithelial neoplasms in the anal canal. Am J Roentgenol 145:569
37. Thompson WM (1989) Computed tomography of the rectum. Radiographics 7:773–779
38. Rifkin MD, Ehrich SM, Rahs G (1989) Staging of rectal carcinoma: prospective comparison of endorectal US and CT. Radiology 170:319–322
39. Balthazar EJ, Rejibon AJ, Hulmick D, Nadich DP (1988) Carcinomas of the colon: detection and preoperative staging by CT. Am J Roentgenol 150:301–306
40. Thoeni RF (1981) Detection and staging of primary rectal and rectosigmoidal carcinoma by computed tomography. Radiology 141:135–138
41. Goldman S, Arvidson H, Norming U, Lagerstad F et al (1991) Transrectal ultrasound and computed tomography in preoperative staging of lower rectal adenocarcinomas. Gastrointest Radiol 16:259–263
42. De Lange EE (1987) Evaluation of primary rectal cancer with MRI: MR histopathologic correlation (abstract). Radiology 165:174
43. De Lange EE, Fechner RE, Spaulding CA, Edge SB (1992) Rectal carcinoma treated by preoperative irradiation: MR imaging and histopathologic correlation. Am J Roentgenol 150:287–292
44. De Lange EE, Fechner RE, Wanebo HJ (1989) Suspected rectosigmoid carcinoma after abdominoperineal resection: MR imaging and histopathologic findings. Radiology 170:323–328
45. Vining DJ, Gelfland DW (1994) Non-invasive colonoscopy using helical CT scanning, 3D reconstruction, and virtual reality. Presented at the 1994 meeting of the Society of gastrointestinal Radiologists, Maui, Hawaii; 13–18 February 1994
46. Van Gelder RE, Venema HW, Serlie IWO et al (2002) CT colonography at different radiation dose levels: feasibility of dose reduction. Radiology 224:25–33
47. Whiting BR, McFarland EG, Brink JA (2002) Influence of image acquisition parameters on CT artefact and polyp depiction in spiral CT colonography: in vitro evaluation. Radiology, 217:165–172
48. Gluecker T, Meuwly JY, Percaore P et al (2002) Effect of investigator experience in CT colonography. Eur Radiol 12:1405–1409
49. Mc Farland EG, Brink JA, Pilgram TK (2000), Spiral CT colonography: reader agreement and diagnostic performance with two-and three dimensional image-display techniques. Radiology 218:375–383
50. Luboldt W, Bauerfeind P, Steiner P, Fried M, Krestin GP, Debatin JF (1997) Preliminary assessment of three-dimensional magnetic resonance imaging for various colonic disorders. Lancet 349:1288–1291
51. Morrin MM, Farrell RJ, Keogam MT et al (2002) CT colonography: colonic distention improved by dual position but not intravenous glucagon. Eur Radiol 12:525–530
52. McFarland EG, Pilgram TK, Brink JA et al (2002) CT colonography: multiobserver diagnostic performance. Radiology 225:380–390
53. Macari M, Bini EJ, Xue Xiaonan et al (2002) Colorectal neoplasms: prospective comparison of thin section low dose multi-detecter row CT colonography and conventional colonoscopy for detection. Radiology 224:383–392
54. Summers RM, Jeretko AK, Franaszek M, Malley JD, Johnson CD (2002) Colonic polyps: complementary role of computer-aided detection in CT colonography. Radiology 225:291–399
55. Thomeer M, Bielen D, Vanbeckevoort D et al (2002) Patient acceptance for CT colonography. What is the real issue? Eur Radiol 12:1410–1415
56. Lefere PA, Gryspeerdt SS, Dewyspelaere J et al (2002) Dietary fecal tagging as a cleansing method before CT colonography: initial results – polyp detection and patient acceptance. Radiology 224:390–403
57. Lauwenstein TC, Gobhde SC, Ruehn SG et al (2002) MR colonography with barium-based fecal tagging. Initial clinical experience. Radiology 223:248–254
58. Hara AK, Johnson CT, Reed JE et al (1996) Detection of colorectal polyps by computed tomographic colography: feasibility of a novel technique. Gastroenterology 110:284–290
59. Hara AK, Johnson CD, Reed JE, Ahlquist DA, Nelson H, MacCarty Rl, Harmsen WS, Ilstrup DM (1997) Detection of colorectal polyps with CT colography: initial assessment of sensitivity and specificity. Radiology 205:59–65
60. Royster AP, Fenlon HM, Clarke PD, Nunes DP, Ferrucci JT (1997) CT colonoscopy of colorectal neoplasms: two-dimensional and

three-dimensional virtual-reality techniques with colonoscopic correlation. Am J Roentgenol 169:1237–1242
61. Morra A, Medure S, Ammar L, Ukmar M, Pozzi Muscelli R (1999) Colonoscopy with computed tomography with volume reconstruction. The results and a comparison with endoscopy and surgery. Radiol Med (Torino) 98:162–167
62. Yee J, Hung RK, Akerkar GA, MCQuaid K, Wall SD, Steinauer-Gebauer AAM (2000) Performance of CT colonography for colorectal polyp detection in screening patients. ESGAR 2000. Eur Radiology 10:D1
63. Foster N, Wood C, Rosenberg M, Forbes G, Mendelson R (2000) A comparison of CT virtual colonoscopy in the detection of colorectal polyps and cancer. ESGAR 2000. Eur Radiol 10:D2
64. Lefere P, Van Holsbeeck B, Baekelandt M, Gryspeerdt S (2000) Virtual CT colonoscopy: initial results. ESGAR 2000. Eur Radiol 10:D3
65. Fletcher JG, Johnson CD, Welch TJ et al (2000) Optimization of CT colonography technique: prospective trial in 180 patient. Radiology 216:704–711
66. Morrin MM, Farrell RJ, Kruskal JVB, Reynolds K, McGee JB, Raptopoulos V (2000) Utility of intravenously administered contrast material at CT colonography. Radiology 217:765–771
67. Dachman AH, Kuniyoshi JK, Boyle CM et al (1998) CT colonography with three-dimensional problem solving for detection of colonic polyps. Am J Roentgenol 171:989–995
68. Rex DK, Vining D, Kopecky KK (1999) An initial experience with screening for colon polyps using spiral (virtual colonoscopy), Gastrointest Endosc 50:309–313
69. Miao YM, Amin Z, Healy J et al (2000) A prospective single center study comparing computed tomography pneumocolon against colonoscopy in the detection of colorectal neoplasms. Gut 47:832–837
70. Mendelson RM, Foster NM, Edwards JT, Wood CJ, Rosenberg MS, Forbes GM (2000) Virtual colonoscopy compared with conventional colonoscopy: a developing technology. Med J Aust 173:472–475
71. Kay CL, Kulling D, Hawes RH, Young JW, Cotton PB (2002) Virtual endoscopy: comparison with colonoscopy in the detection of space-occupying lesions of the colon. Endoscopy 32:226–130
72. Pescatore P, Glucker T, Delarive J et al (2000) Diagnostic accuracy and inter-observer agreement of CT colonography (virtual colonoscopy). Gut 46:126–130
73. Spinizi G, Belloni G, Martegani A, Sangiovanni A, Del Favero C, Minoli G (2001) Computed tomographic colonography and conventional colonoscopy for colon diseases: a prospective, blinded study. Am J Gastroenterol 96:394–400
74. Yee J, Akerkar GA, Hung RK, Steinauer-Gebauer AM, Wall SD, McQuaid KR (2001) Colorectal neoplasia: performance characteristics of CT colonography for detection in 300 patients. Radiology 219:685–692
75. Hara AK, Johnson CD, MacCarty RL, Welch TJ, McCollough CH, Harmsen WS (2001) CT colonography: single-versus multi-detector row imaging. Radiology 219:461–465
76. Luboldt W, Bauerfeind P, Wildermuth S, Marincek B, Fried M, Debatin JF (2000) Colonic masses: detection with MR colonography. Radiology 216:383–388
77. Pappalardo G, Polettini E, Frattarol FM et al (2002) Magnetic resonance colonography versus conventional colonoscopy of the detection of chronic endoluminal lesions. Gastroenterology 119:300–304
78. Neri E, Giusti P, Batolla L et al (2002) Colorectal cancer: role of CT colonography in preoperative evaluation after incomplete colonoscopy. Radiology, 223:615–619
79. Fenlon HM, Nunes DP, Schroy PC III, Barish MA, Clarke PD, Ferrucci JT (1999) A comparison of virtual and conventional colonoscopy for the detection of colorectal polyps. N Engl J Med 342:1496–1503
80. Waye JD, Lewis BS, Frankel A, Geller SA (1998) Small colon polyps, Am J Gastroenterol 83:120–122
81. Dasmahapatra KS, Lopyan K (1989) Rationale for aggressive colonoscopy in patients with colorectal neoplasia. Arch Surg 124:63–66
82. Morrin MM, Kruskal JB, Ferrell RJ, Goldberg SN, McGee JB, Raptopoulos V (1999) Endoluminal CT colonography after incomplete endoscopic colonoscopy. Am J Roentgenol 172:913–918
83. Macari M, Milano A, Lavelle N, Bernan P, Megibow AJ (2000) Comparison of time-efficient CT colonography with two and three dimensional colonic evaluation for detecting colorectal polyps. Am J Roentgenol 174:1543–1549
84. Smith RA, von Eschenbach AC, Wender R et al (2001) American Cancer Society guidelines for the early detection of cancer update of early detection guidelines for prostate, colorectal and endometrial cancer. Ca Cancer J Clin 51:28–75
85. Levine MS, Glick SN, Rubersin SE, Laufer I (2002), Double contrast barium enema examination and colorectal cancer: a plea for radiologic screening. Radiology 222:313–315
86. Glick S, Wagner JL, Johnson CD (1998) Cost-effectiveness of double-contrast barium enema in screening for colorectal cancer. Am J Roentgenol 170:629–636
87. McMahon PM, Bosch JL, Gleason S, Halpenn EF et al (2001) Cost-effectiveness of colorectal cancer screening. Radiology 219:44–50
88. Mandel JS, Bond JH, Church TR et al (1993) Reducing mortality from colorectal cancer by screening for fecal occult blood. N Engl J Med 328:1365–1371
89. Kostakoglu L, Agress H, Goldsmith SJ (2003) Clinical role of FDG PET in evaluation of cancer patients. Radiographics 23:315–340
90. Huebner RF, Park KC, Shepherd JE, Schwimmer J, Czernin J (2000) A meta-analysis of the literature for whole body FDG-PET detection of recurrent colorectal cancer. J Nucl Med 41:1177– 1189
91. Watari J, Saitoh Y, Obara T et al (1997) Early nonpolypoid colorectal cancer: radiographic diagnosis of depth of invasion. Radiology 205:67–74
92. Tada S, Yao T, Iida M et al (1994) Clinicopathologic study of small flat colorectal carcinoma. Cancer 74:2430–2435
93. Ridell RH, Goldman H, Ransohoff DF, Ähren C et al (1983) Dysplasia in inflammatory bowel disease. Standardized classification with provisional clinical applications. Hum Path 14:931–968
94. Giardiello FM, Bayles TM (1996) Colorectal cancer and ulcerative colitis. Radiology 199:28–30
95. Matsumoto T, Iida M, Kuroki F et al (1996) Dysplasia in ulcerative colitis: is radiography adequate for diagnosis? Radiology 199:85–90
96. Ribeiro MB, Greenstein AJ, Sachar DB et al (1996) Colorectal adenocarcinoma in Crohn's disease. Ann Surg 233:186–193
97. Gore RM (1992) Colonic contour changes in chronic ulcerative colitis: reappraisal of old concepts. Am J Roentgenol 158:59–61
98. Reeders JWAJ, Rosenbusch G (1994) Clinical radiology and endoscopy of the colon. Thieme, Stuttgart
99. Hartmann D, Bazzler B, Zindler C, Rings S, Breer H, Schilling D, Adamek HE, Riemann JF, Layer G (2003) MR kolonographie in einem interdisziplinären Kooperationsproject – Erste Erfarungen am Klinikum Ludwigshafen, Electromedica 71 Heft 1:73–78
100. Potthast S, Rieber A, von Tirpitz C, Wruk D, Adler G, Brambs HJ (2002) Ultrasound and magnetic resonance imaging in Crohn's disease: a comparison. Eur Radiol 12:1416–1422
101. Bozkur T, Richter F, Lux G (1994) Ultrasonography as a primary diagnostic tool in patients with inflammatory bowel disease and tumors of the small intestine and large bowel. J Clin Ultrasound 22:85–91
102. Maconi G, Bollani S, Bianchi, Porro G (1996) Ultrasonographic detection of intestinal complications in Crohn's disease. Dig Dis Sci 41:1643–1648
103. Low RN, Sebrechts CP, Politoske DA, Bennett MT, Flores S, Snyder RJ, Pressman JH (2002) Crohn disease with endoscopic correlation: single-shot fast spin-echo and gadolinium-enhanced fat-suppressed spoiled gradient-echo MR imaging. Radiology 222:652–660
104. Low RN, Francis IR, Politoske D, Bennett M (2000) Crohn's disease evaluation: comparison of contrast-enhanced MR imaging and single phase helical CT scanning. J Magn Reson Imaging 11:127–135
105. Low RN, Francis IR (1997) MR imaging of the gastrointestinal tract with IV gadolinium and diluted barium oral contrast media compared with unenhanced MR imaging and CT. Am J Roentgenol 169:1051–1059
106. Maccioni F, Viscido A, Broglia L et al (2000) Evaluation of Crohn disease activity with magnetic resonance imaging. Abdom Imaging 25:219–228
107. Semelka RC, Shoenut JP, Silverman R, Kroeker MA, Yaffe CS, Micflikier AB (1991) Bowel disease: prospective comparison of CT and 1.5-T pre- and postcontrast MR imaging with T1-weighted fat-suppressed and breath-hold FLASH, sequences. J Magn Reson Imaging 1:625–632
108. Schunk K, Kern A, Oberholzer K et al (2000) Hydro-MRI in Crohn's disease: appraisal of disease activity. Invest Radiol 35:431–437
109. Ernst O, Asselah T, Casblan X, Sergent G (1998) Breath-hold fast spin-echo MR imaging of Crohn's disease. Am J Roentgenol 10:1465–1469
110. Marcos HB, Semelka RC (2000) Evaluation of Crohn's disease using half-Fourier RARE and Gadoliniumn-enhanced SGE sequences: initial results. Magn Reson Imaging 18:263–268
111. Madsen SM, Thomsen HS, Schlichting P, Dorph S, Munkholm P (1991) Evaluation of treatment response in active Crohn's disease by low-field magnetic resonance imaging. Abdom Imaging 24:232–239

Benign Liver Tumors

Hoon Ji, Pablo R. Ros

4.7

Contents

Introduction

The liver is a large and vital organ of the abdomen and is often studied for evaluation of many surgical or nonsurgical conditions. The study of liver lesions is particularly challenging, because many adults have benign, nonsurgical hepatic lesions, such as hemangioma or simple cyst. In many cases, a preoperative diagnosis may be achieved with the appropriate combination of imaging techniques in a purely noninvasive fashion. For many tumors, each imaging technique provides a piece of the puzzles. It consists of pathological characteristics of the tumor. Appreciation of pathological features of the tumor must be combined with imaging findings as well as clinical information to achieve a diagnosis.

Each of the cellular components of the liver can give rise to benign tumors and some heterotopic tissues may result in benign tumor-like lesions (Table 1). In this

Table 1. Benign liver tumors and tumor-like conditions

Hepatocellular origin
Hepatocellular adenoma
Hepatocellular hyperplasia:
Focal nodular hyperplasia
Nodular regenerative hyperplasia
Macroregenerative nodule
Dysplastic nodules
Cholangiocellular origin
Hepatic cysts:
Simple hepatic cysts
Congenital hepatic fibrosis/polycystic liver disease
Biliary hamartoma
Biliary cystadenoma
Bile duct adenoma
Mesenchymal origin
Mesenchymal hamartoma
Hemangioma
Infantile hemangioendothelioma
Lymphangioma
Lipoma/ Angiomyolipoma/ myelolipoma
Leiomyoma
Fibroma
Heterotopic tissue
Adrenal rests
Pancreatic rests

Modified from [6]

chapter, the benign liver lesions are discussed with emphasis on the microscopic and gross findings that have radiologic impact.

Benign Hepatocellular Lesions

Hepatocellular Adenoma

HCA is a rare primary benign liver tumor of hepatocellular origin. Oral contraceptives as well as androgen steroid therapy have been identified as definite causative agents and its incidence has increased dramatically with the widespread use of these medications [1, 2]. HCA can also occur spontaneously or be associated with underlying metabolic disease, such as type I glycogen storage disease and diabetes mellitus [3].

The diagnosis of this entity is clinically relevant because it can be associated with life-threatening hemorrhage [4] and because it has a small potential for malignant transformation into hepatocellular carcinoma.

Withdrawal of estrogen compounds may result in regression of the HCA, which can require a period of several months [5].

Pathologic Findings

Hepatocellular adenoma (HCA) presents as a solitary lesion in 80% of cases, and it is typically a well-circumscribed, encapsulated tumor. The presence of large subcapsular vessels accounts for its frequent hypervascular nature. Pedunculation is seen in approximately 10% of cases [6].

Histologically, it is composed of cords of hepatocytes. Although the hepatocytes can produce bile, there are no bile ductules present to enable biliary excretion. The architecture also lacks portal venous tracts and terminal hepatic veins like all other liver tumors. The hepatocytes contain large amounts of fat and glycogen. The tumor receives its vascular supply from hepatic arterial branches. As the tumor grows it has a propensity to outgrow its vascular supply, resulting in hemorrhage and necrosis, and occasionally rupture (Fig. 1).

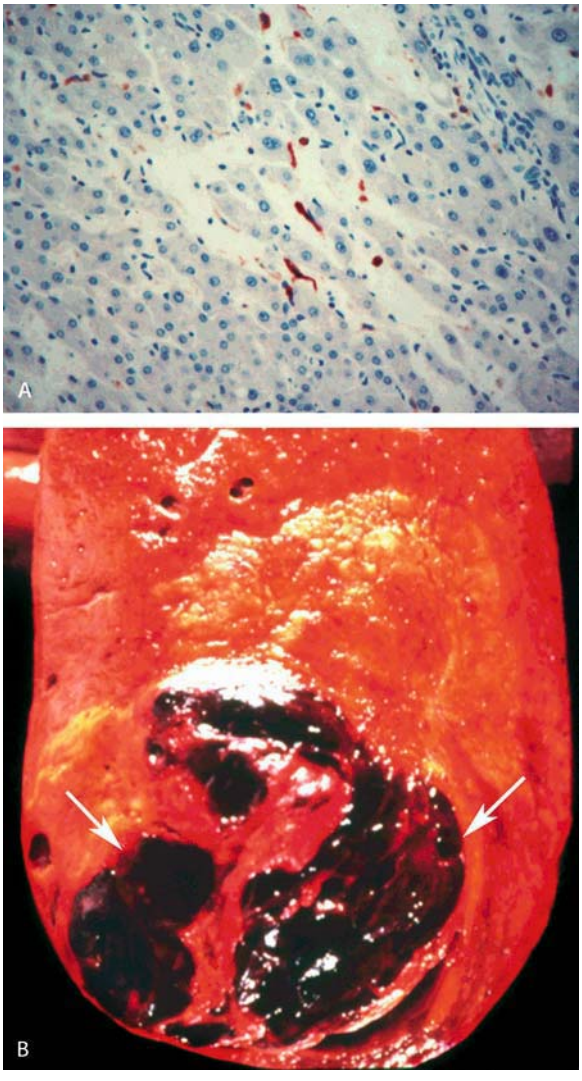

Fig. 1A, B. Hepatocellular adenoma, pathology. **A** Photomicrograph demonstrates the pale hepatocytes of the adenoma, indicating presence of fat and glycogen within the tumor. Lysozyme stain demonstrates multiple Kupffer cells within the adenoma. **B** Cut-section of a liver resection demonstrates an adenoma with well-defined margin and of lighter color than the liver due to presence of fat. Note central areas of hemorrhage within the adenoma (*arrows*)

Imaging Features

The sonographic appearance of HCA is nonspecific and can be mimicked by other benign and malignant lesions. The high lipid content of hepatocytes within HCA results in a common appearance as a hyperechoic mass (Fig. 2). Internal hemorrhage can also result in increased echogenicity in the acute setting, whereas older hemorrhage is hypo- to anechoic. Color Doppler ultrasound demonstrates peripheral arteries and veins. In addition, color Doppler may identify intratumoral veins [7, 8]. This finding is absent in FNH and may be a useful discriminating feature for HCA [7].

Unenhanced CT usually demonstrates a hypodense mass due to the presence of fat and glycogen within the tumor [9]. However, hyperdense areas corresponding to fresh hemorrhage can be identified. With contrast-enhanced CT, peripheral enhancement may be seen as a reflection of the large subcapsular feeding vessels, with a centripetal pattern of enhancement (Fig. 3). Small HCAs enhance rapidly and are of increased attenuation relative to the liver [10]. The enhancement does not per-

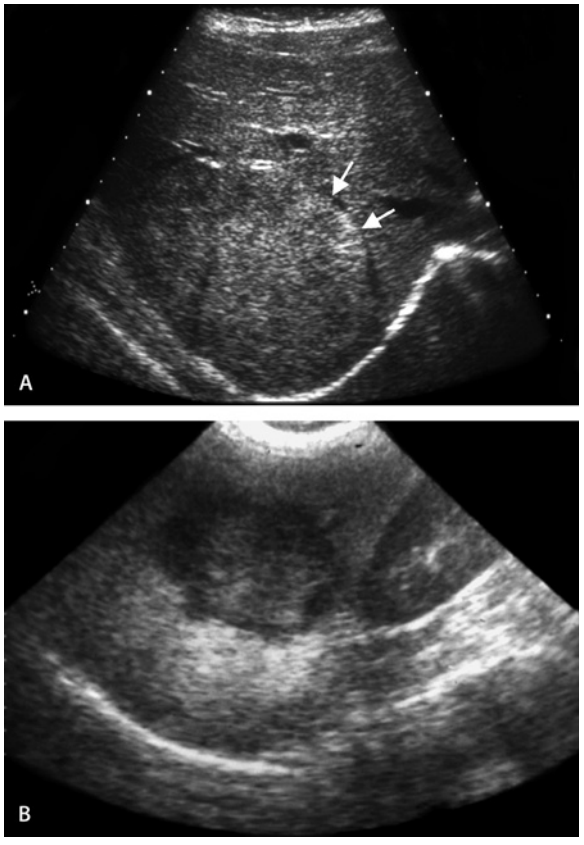

Fig. 2A, B. Ultrasound findings of hepatocellular adenoma. **A** Ultrasound demonstrates a homogeneous, large echogenic mass in the liver. Thin hypoechoic rim surrounding the lesion suggests capsule (*arrows*). **B** Ultrasound shows a lobulated mass lesion seen in the right lobe of liver. Surrounding parenchyma shows fatty change. Note echogenic center of lesion suggesting hemorrhage or necrosis

sist in adenomas because of arteriovenous shunting [11]. Larger HCAs may be more heterogeneous than smaller lesions and the CT appearance is nonspecific [10].

On MR studies, adenomas are heterogeneous in appearance and contain areas of increased signal intensity on T1-weighted images (Fig. 3). This results from the presence of fat and hemorrhage and low-signal areas corresponding to necrosis [12, 13]. One-third of HCAs have a peripheral rim corresponding to a fibrous capsule [14]. In most cases the rim is of low signal intensity on both T1-and T2-weighted images [14].

Adenomas in some cases may take up SPIO, resulting in a decreased signal on T2-weighted images. Dynamic gadolinium-enhanced gradient echo imaging can be used to demonstrate the early arterial enhancement that results from the presence of subcapsular feeding vessels [15] (Fig. 4). Although the diagnosis of a hemorrhagic HCA can be suggested by the imaging features and the clinical setting of a young woman on oral contraceptives, the nonspecific nature of the imaging findings makes tissue diagnosis a necessity.

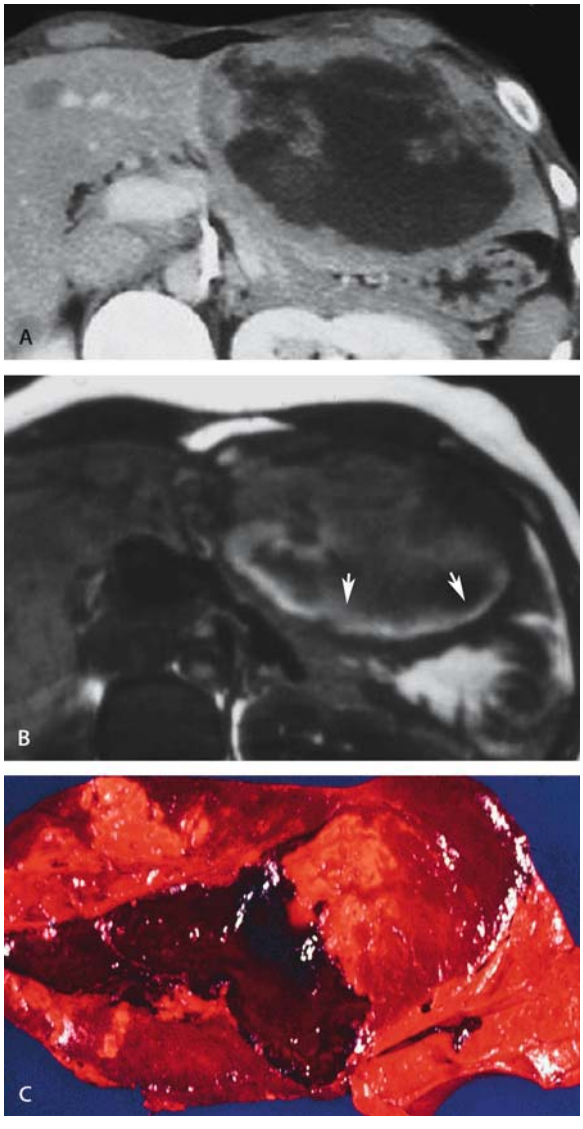

Fig. 3A–C. CT/MRI of hepatocellular adenoma in a 29-year-old woman with history of using oral contraceptives. **A** Contrast-enhanced CT scan demonstrates a large hypoattenuating mass of complex nature corresponding to a large adenoma with massive internal bleeding. Note other smaller adenomas within the liver. **B** T1-weighted imaging shows a mass in the left lobe of the liver. High signal intensity rim (*arrows*) in the mass suggests intratumoral hemorrhage. **c** Corresponding cut section of the specimen demonstrates the hemorrhage in this mass

Multiple Hepatocellular Adenomas, or Adenomatosis

This rare entity is characterized by the presence of multiple (greater than four) HCAs, usually present in both hepatic lobes [16] (Fig. 4). This entity should not be confused with other hyperplastic hepatocellular conditions, such as nodular regenerative hyperplasia or macroregenerative/dysplastic nodules of cirrhosis (Table 2).

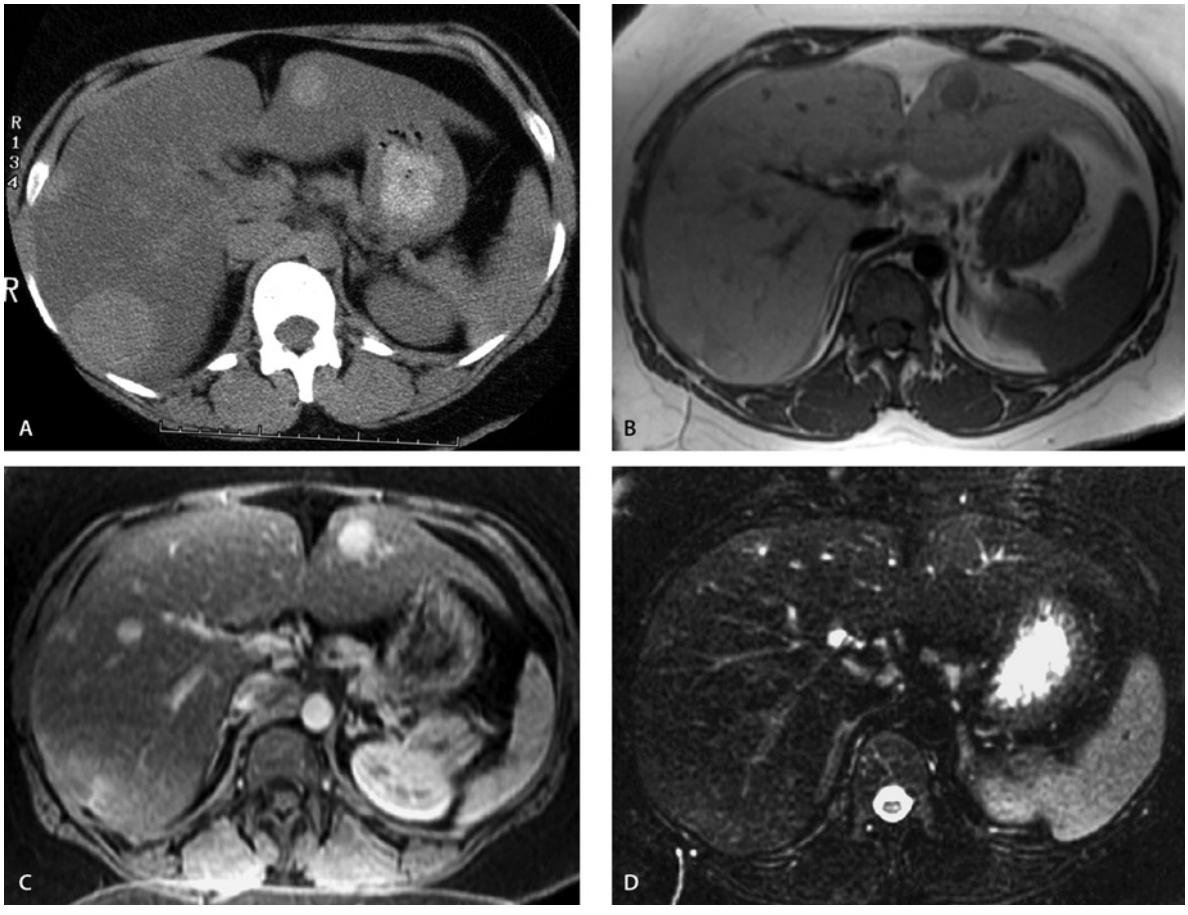

Fig. 4A–D. Multiple hepatocellular adenomas. **A** On noncontrast enhanced CT scan, multiple masses with slightly high attenuation are seen in liver with relatively low attenuation due to fatty change. **B** On T1-weighted MR image, lesions demonstrate hypointense signal to liver. **C** Gadolinium-enhanced fat suppression T1-weighted image demonstrates intense enhancement of the lesions. Note heterogeneous enhancement of the lesion in right lobe of the liver. **D** On T2-weighted image the lesions are isointense to liver and are not detectable

Table 2. Comparison of hepatocellular lesions

Criteria	Hepatocellular Adenoma	Hepatocellular adenomatosis	Focal Nodular Hyperplasia	Nodular Regenerative Hyperplasia	Macroregenerative Nodule
Gross	Hemorrhage, necrosis	Bulging nodules	Scar	Bulging nodules	Bulging nodules
Number of lesions	1 (90%)	Many	1 (90%)	Many	Many or few
Size (average range)	4–12 cm	2–9 cm	1–6 cm	<1.5 cm	1–6 cm
Key feature	Neohepatocytes	Normal cords	Pseudoductules	Small nodules	Portal tracts
Prior liver disease	None	None	None	None	Hepatic necrosis or cirrhosis
Associated etiology	Estrogen, anabolic steroids	None	None	Vascular disease	None

Modified from [6]

Focal Nodular Hyperplasia

FNH accounts for approximately 8% of all primary hepatic tumors [6] and is the second most common benign liver tumor. Most are seen in women (80–95%) in the third to fifth decades of life. It is thought to arise as a localized hepatocyte response to an underlying congenital vascular malformation [17, 18]. Although oral contraceptive use is associated with FNH, the real influence is still controversial; unlike their behavior with hepatocellular adenoma, oral contraceptives do not induce its formation [19].

Clinically, FNH is usually asymptomatic, but less than one-third of cases are discovered with symptoms, such as right upper quadrant or epigastric pain.

Pathologic Findings

Focal nodular hyperplasia (FNH) is defined microscopically as a tumor-like condition characterized by a central fibrous scar with surrounding nodules of hyperplastic hepatocytes and small bile ductules [6].

Grossly, FNH is a well-circumscribed, solitary mass (95%) that is often located on the surface of the liver or pedunculated [6]. The majority of FNHs are smaller than 5 cm and have a mean diameter of 3 cm at the time of diagnosis [17]. Occasionally. FNH replaces an entire lobe of the liver (lobar FNH) [6]. The tumor does not usually have internal hemorrhage or necrosis (Fig. 5). This is due to the fact that the growth of FNH remains proportional to its blood supply, rather than exceeding it, and thus necrosis usually does not occur.

Most FNH are well-defined, sharply marginated lesions that lack the presence of a true capsule. They have a central scar with prominent vessels. The vessels extend outward, through fibrous septa, to the periphery of the tumor, and provide efficient vascularity. Essentially, FNH is a hyperplastic process in which all of the components of normal liver are present, but abnormally organized.

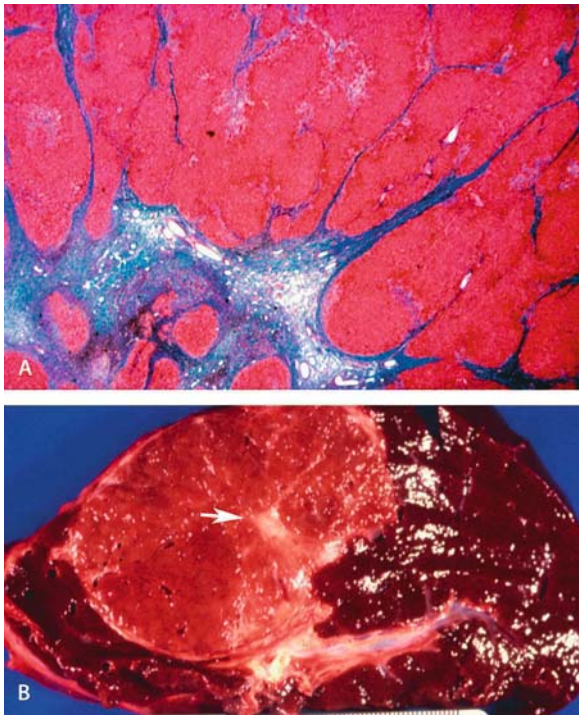

Fig. 5A, B. Focal nodular hyperplasia (FNH), pathology. **A** Microscopic appearance. Photomicrograph demonstrates lobular nature of FNH with multiple, fibrous septa that radiate from a large central scar. Note that within the central scar there are multiple vascular structures that radiate to the surface along the fibrous septa. **B** Gross appearance. Cut-section demonstrates whitish stellate scar (*arrow*) that extends to the periphery of the tumor. Note the lack of large areas of necrosis or hemorrhage

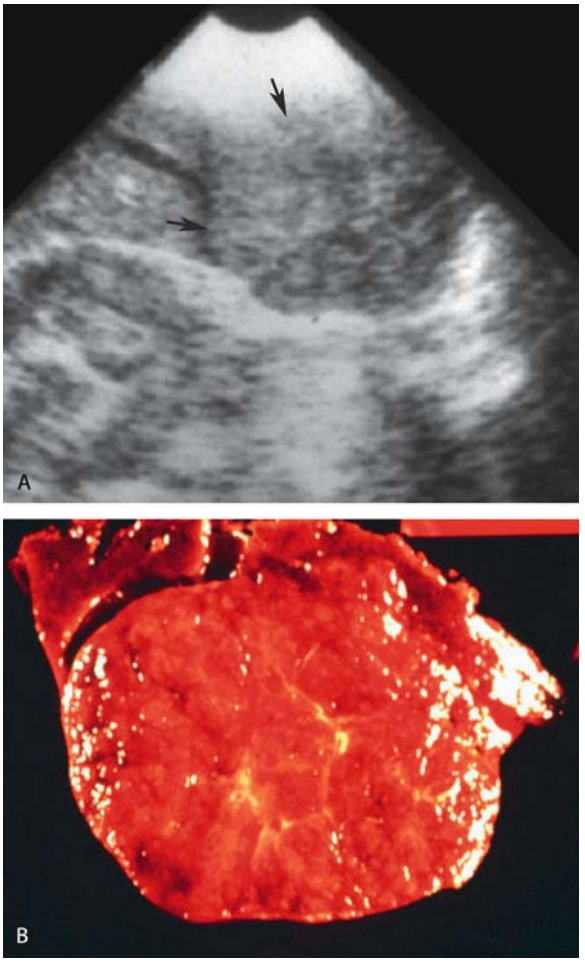

Fig. 6A, B. Pedunculated focal nodular hyperplasia, ultrasound findings. **A** Sonogram demonstrates the homogeneous isoechoic nature of this tumor that arises from the edge of the liver (*arrows*). **B** Gross specimen shows a focal nodular hyperplasia with the stellate scar and a large peripheral draining vein

Imaging Features

Ultrasonogram (US) shows a well-demarcated homogeneous mass that can either be hyperechoic or isoechoic to normal liver. The central scar is not demonstrable in many cases, and is seen as a linear hyperechoic band in only 20% of cases [9] (Fig. 6). On color Doppler sonography, FNH shows increased blood flow and a pattern of blood vessels radiating peripherally from a central feeding artery [20].

The optimal evaluation of FNH by CT scan is obtained by using helical imaging with a triple-phase examination: noncontrast, hepatic arterial-phase imaging and portal venous-phase imaging. In unenhanced CT studies, FNH usually appears as a homogeneous, hypodense mass. In a third of cases, a low-density central area is seen, corresponding to the scar [9]. During the arterial phase of contrast-enhanced CT, FNH enhances rapidly and becomes hyperdense relative to normal liver because it receives its vascularity from the hepatic arterial system [21] (Fig. 7). The low attenuation scar appears conspicuous against the hyperdense tissue and foci of enhancement may be seen within the scar representing arteries [21]. In the portal venous phase of enhancement the difference in attenuation between FNH and normal liver decreases and the FNH may become isointense with normal liver [21].

The appearance of FNH on MR can be mimicked by benign and malignant lesions, such as hepatocellular adenoma and fibrolamellar carcinoma. MR imaging can, however, aid in narrowing the differential diagnosis.

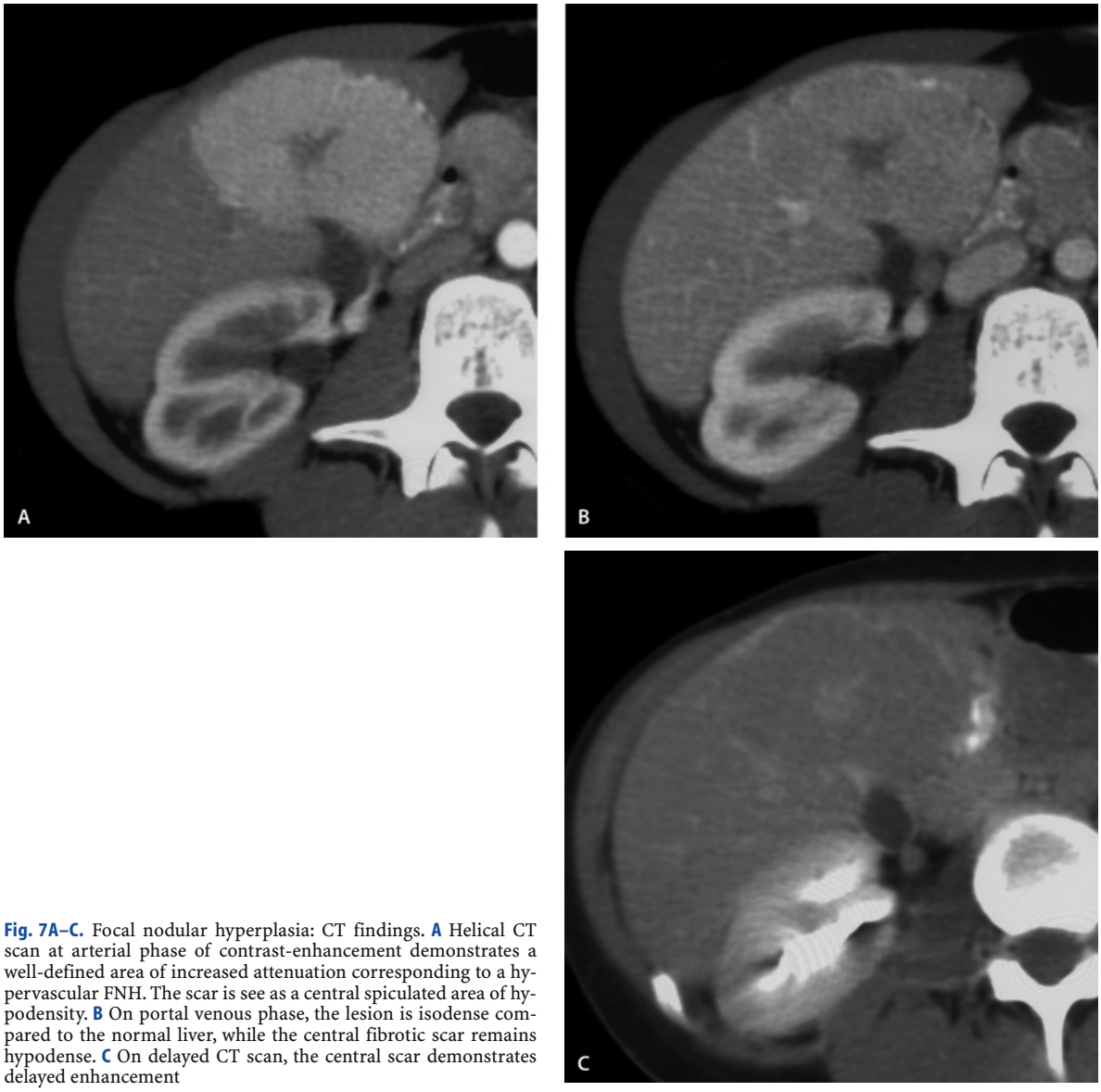

Fig. 7A–C. Focal nodular hyperplasia: CT findings. **A** Helical CT scan at arterial phase of contrast-enhancement demonstrates a well-defined area of increased attenuation corresponding to a hypervascular FNH. The scar is see as a central spiculated area of hypodensity. **B** On portal venous phase, the lesion is isodense compared to the normal liver, while the central fibrotic scar remains hypodense. **C** On delayed CT scan, the central scar demonstrates delayed enhancement

Because the lesion is composed of normal hepatic elements with an abnormal architecture, the signal characteristics of the lesion are not very different from those of normal liver. FNH is isointense or hypointense to normal liver on T1 weighted image, with the central scar being hypointense. Similarly, on T2 weighted image, it is isointense or mildly hyperintense compared with normal liver, with the central scar being hyperintense [22, 23] (Fig. 8).

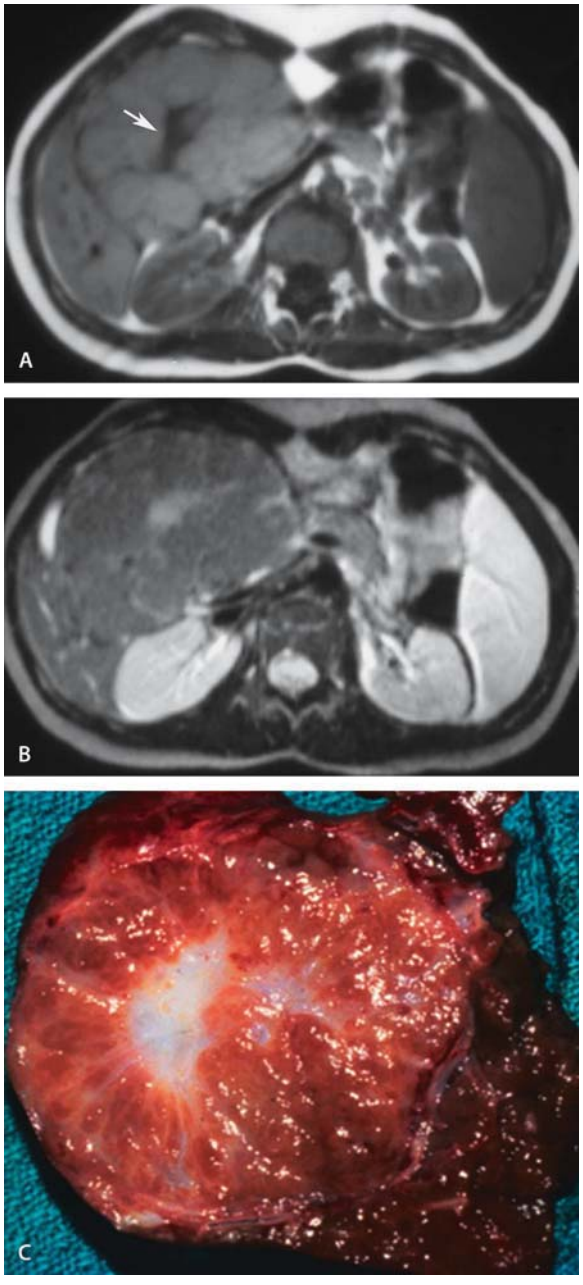

Fig. 8A–C. Focal nodular hyperplasia: MRI appearance. **A** A large mass replaces the left lobe of the liver on this axial T1-weighted image. The low signal stellate area in the center (*arrow*) corresponds to the scar. **B** T2-weighted image of the same patient demonstrates a hyperintense scar and mild hyperintensity of the entire mass. **C** Cut section of the FNH specimen correlates nicely with the CT and MRI features with homogeneity of the mass except for the central scar

Using dynamic Gd-DTPA-enhanced MR imaging, early homogeneous enhancement of FNH is seen followed by late enhancement of the central scar [24]. Recently, use of reticuloendothelial MR contrast agents such as SPIO and USPIO has greatly expanded the role of MRI in the diagnosis of FNH. On T2-weighted images with SPIO administration, FNH shows loss of signal due to uptake of iron oxide particles by Kupffer cells within the lesion [25]. The degree of signal loss seen in FNH lesions using SPIO-enhanced T2-weighted sequences is significantly greater than in other focal liver lesions such as metastases and hepatocellular adenoma [26]. This feature may be useful in the characterization of hepatic lesions as FNH [26]. Use of hepatobiliary agents such as Mn-DPDP and Gd-EOB-DTPA is helpful in the characterization of FNH. The hepatocytes of FNH can take up these agents, resulting in hyperintensity of the lesion relative to the liver on T1-weighted image [27].

Nodular Regenerative Hyperplasia

Nodular regenerative hyperplasia (NRH) is defined as diffusely distributed monoacinar regenerative nodules that are not associated with fibrosis. NRH has been referred to by many names in the literature including *nodular transformation, noncirrhotic nodulation,* and *partial nodular transformation.*

Various systemic diseases and drugs are often associated with NRH [28]: myeloproliferative syndromes (polycythemia vera, chronic myelogenous leukemia, and myeloid metaplasia), lymphoproliferative syndromes (Hodgkin's and non-Hodgkin's lymphoma, chronic lymphocytic leukemia, and plasma cell dysplasias), chronic vascular disorders (rheumatoid arthritis), Felty's syndrome, polyarteritis nodosa, scleroderma, calcinosis cutis, Raynaud's phenomenon, sclerodactyly and telangiectasia, lupus erythematosus, steroids, and antineoplastic medication [29, 30]. Familial cases have also been described [31]. Up to 50% of cases are associated with portal hypertension [32]. NRH is common in non-cirrhotic portal hypertension in the Western world and is often associated with esophageal varices and ascites. Recently NRH has been used to describe the benign hepatocellular nodules in patients with Budd-Chiari syndrome [33]. But they are larger and often have histologic hepatic fibrosis between the nodules [34].

Pathologic Findings

Grossly, NRH is characterized by the presence of multiple bulging nodules and affects the periportal areas (Fig. 9). The nodules vary in size from a few millimeters to several centimeters, but are mostly small and diffusely scattered [35, 36].

The regenerative nodules of NRH are composed of hyperplastic hepatocytes. The hyperplastic reaction may result in portal triads becoming entrapped within the nodules. The nodular proliferation of NRH lacks a fibrotic reaction and thus is distinguishable from cirrhosis. Because the process is benign and contains the same elements as HCA, it may be very difficult or impossible to distinguish the two entities based on a biopsy. NRH is a diffuse or multinodular process and HCA is a solitary process (or occasionally several solitary lesions) in which the remainder of the liver is normal.

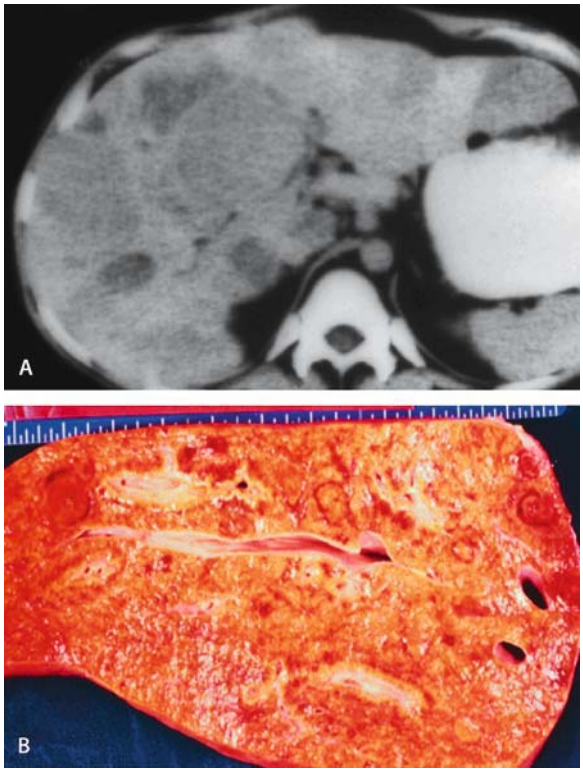

Fig. 9A, B. Nodular regenerative hyperplasia. **A** CT scan of the same patient demonstrates diffuse involvement of the liver, which has a heterogeneous appearance with multiple areas of decreased density. Note associated ascites. **B** Cut-section of a hepatectomy specimen demonstrates multiple nodules of nodular regenerative hyperplasia of varying size, which replace the entire liver

Imaging Features

NRH can present as tiny nodules diffusely involving the liver or as focal larger nodules producing a spectrum of radiologic findings. The findings range from a normal-appearing liver with associated portal hypertension to multiple hepatic masses [37, 38] (Table 2). NRH must be differentiated from other hepatocellular lesions. Unfortunately, the imaging characteristics of the individual nodules are nonspecific and similar to those seen with other benign and malignant lesions. The diffuse nature of the involvement, the associated presence of portal hypertension, and the appropriate clinical story, however, are all features that allow the distinction of this entity from others.

Sonographically, the nodules are isoechoic to normal liver, because they contain normal hepatic elements. They become focally hypoechoic or anechoic as a result of hemorrhage [39].

On CT scans, the appearance of NRH ranges from that of a normal liver to that of a liver with focal nodules of varying attenuation that are primarily hypodense [28, 40] (Fig. 9). They may have focal hyperdense areas representative of areas of hemorrhage.

There are a few reports of the MRI findings of NRH. Lesions are described as isointense to normal liver on T2-weighted images and contain foci of high signal, compatible with hemorrhage, on T1-weighted scans [40, 41].

Macroregenerative and Dysplastic Nodules

The macroregenerative nodule (MRN), also acceptably known as large regenerative nodule, has also been described as adenomatous hyperplasia, or type I macroregenerative nodule. MRNs are often noted incidentally in patients with cirrhosis or Budd-Chiari syndrome, and on examination of the explanted liver at the time of liver transplantation [33].

The dysplastic nodule has also been known as atypical adenomatous hyperplasia, type II macroregenerative nodule, or atypical macroregenerative nodule. The International Working Party has designated two types of dysplastic nodules [42]. The low-grade dysplastic nodule is microscopically similar to the description above for macroregenerative nodules. Although in these cases, the proliferation is thought to be a clonal one rather than reactive in nature. As with the MRN, the dysplastic nodule almost always occurs in the setting of cirrhosis. It is generally considered to be a premalignant change or stage in the transformation to HCC [43]. With MRN or dysplastic nodules, serum AFP is normal or in the range seen with the background chronic liver disease or cirrhosis.

Pathologic Findings

MRNs generally are found in the setting of cirrhosis or Budd-Chiari syndrome. MRNs are larger than typical cirrhotic nodules, measuring 0.8 to 1 cm as the lower size limit and only rarely larger than 3 cm. The nodules may be different in color than other nodules. The borders are distinct and rounded due to alterations in bile or fat content. Presence of central scar has been described in large nodules [44] (Fig. 10). Histologically, MRNs are similar to cirrhotic nodules, with cell plates of 1–2 cells thick and an intact reticulin framework. Likewise, the hepatocytes have similar cytologic features as seen in normal or cirrhotic liver with some mild variations in size and nuclear features. Occasional focal or diffuse fatty change, clear cell cytoplasmic change, and/or iron may be present. Portal tracts and/or fibrous septa without ducts are commonly seen within the nodule.

Grossly, the dysplastic nodule usually has a similar appearance to the macroregenerative nodule. Its size is usually within 10–20 mm. Microscopically, the atypical features seen often include zones of small cell change with increased nuclear/cytoplasmic ratio. This finding has also been described as increased nuclear density, which is defined as the estimated number of hepatocyte nuclei per microscopic field compared to that found in the normal liver [45]. Other common features are a focal decrease in the reticulin framework; focal zones of cell plates up to three cells thick; mild dilation of sinusoids; the presence of portal tracts within the nodule; and/or focal cells containing Mallory bodies, bile, cytoplasmic clear cell change, fatty change, and/or iron deposition.

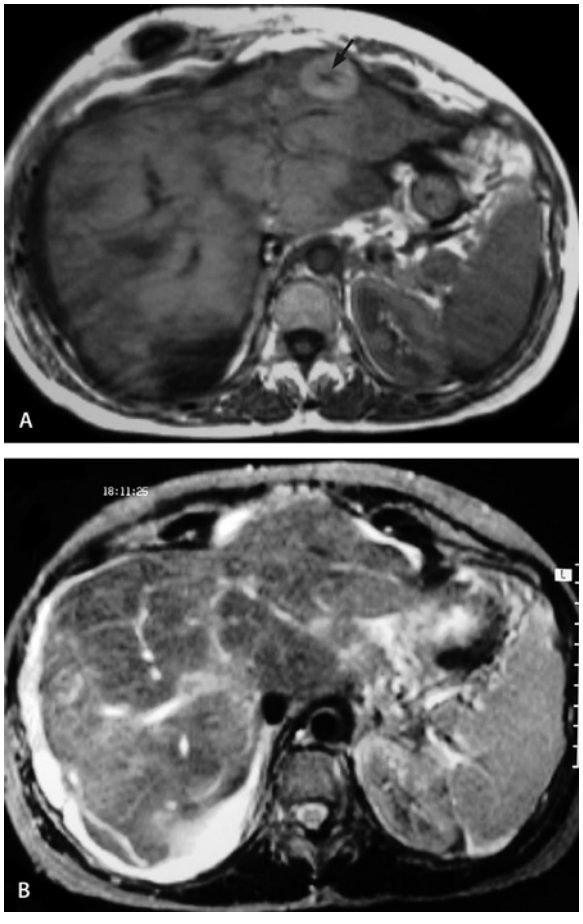

Fig. 10A, B. Regenerative nodule in a patient with Budd-Chiari syndrome. **A** An axial T1-weighted image shows a mass in the left lobe of liver. The lesion exhibits hyperintense than the liver (*arrow*). There is distinct central lower signal area within the lesion. **B** An axial T2-weighted image shows that the mass has heterogeneously iso-signal intensity. Note the heterogeneous signal intensity of liver and tortuous intrahepatic vessels compatible to known history of Budd-Chiari syndrome

Imaging Features

On sonograms, MRN and dysplastic nodules show diverse echogenicity patterns including hyper-, iso-, or hypoechoic, and sonographic findings are similar to those of small HCCs [46].

On CT scans, MRN and dysplastic nodules may show high attenuation on precontrast CT scan probably due to increased cellularity of the lesions. The majority of MRN and dysplastic nodules show low attenuation on arterial phase CT scans. This is probably due to poor vascular supply form the hepatic artery [46, 47]. MRNs in Budd-Chiari syndrome, however, are usually multiple and hypervascular [34, 44].

Typically, regenerative nodules show low signal intensity on T2-weighted images, variable signal intensity on T1-wighted images, and no enhancement on arterial phase dynamic gadolinium-enhanced images (Fig. 10).

The signal intensity and enhancement characteristics of dysplastic nodules are not yet established. Owing to a gradual stepwise transition from a regenerative nodule to a low-grade dysplastic nodule, a high-grade dysplastic nodule, and eventually to a small HCC, the hepatocytes within hepatic nodules undergo numerous changes that might not be reflected in their signal intensity or vascularity. Thus, current MR imaging sequences might not allow differentiation of regenerative nodules from dysplastic nodules [48]. Some MR imaging features of a high-grade dysplastic nodules and small HCC have been described [46, 49]. A majority of high-grade dysplastic lesions (formerly known as adenomatous hyperplasia) and well-differentiated small HCCs (Edmondson grade I or II) have high signal intensity on T1-weighted images [49] (Fig. 11).

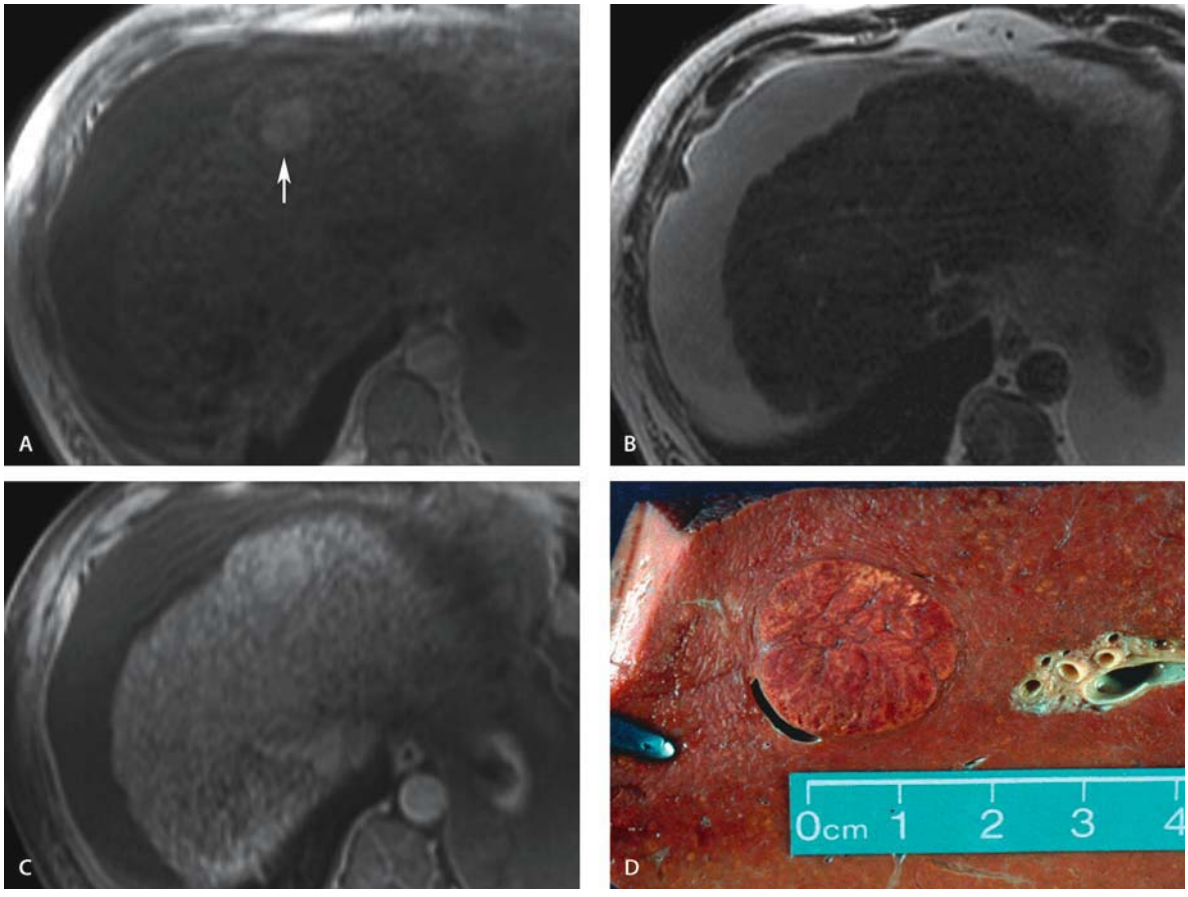

Fig. 11A–D. Dysplastic nodules. **A** T1-weighted image shows a small hyperintense nodule of the left lobe of the liver (*arrow*). **B** T2-weighted image demonstrates the dysplastic nodule of the left lobe of the liver to be of slightly hyper signal intensity. **C** Gadolinium-enhanced dynamic MR image shows no remarkable enhancement during arterial phase of enhancement. **D** Gross specimen demonstrates a well-demarcated lesion in cirrhotic liver

Benign Biliary Lesions

Hepatic Cyst

Hepatic cysts are very common and occur most frequently as solitary (or several solitary), simple, and asymptomatic cysts. They also occur in association with adult polycystic kidney disease.

Simple hepatic (bile duct) cysts range in incidence from 1% to 14% in autopsy series and appear to occur more commonly in women than in men (5:1) [6]. Most hepatic cysts are asymptomatic. Large cysts (>10 cm) may become symptomatic from extrinsic compression on adjacent structures, patients presenting with abdominal fullness, nausea, vomiting, or obstructive jaundice. Other more common complications include hemorrhage, rupture, or occasionally torsion of the cysts. Liver function remains intact, because the overall functioning volume of hepatic parenchyma remains unchanged.

Asymptomatic cysts are not usually treated unless complicated by hemorrhage or infection. The treatment for symptomatic cysts is wide incision and drainage. Percutaneous aspiration and sclerotherapy with alcohol are often useful [50].

Pathologic Findings

A simple hepatic (bile duct) cyst is defined as a single, unilocular cyst lined by a single layer of cuboidal, bile duct epithelium. The wall is a thin layer of fibrous tissue and the adjacent liver is normal. The wall is approximately 1 mm or less in thickness and typically occurs just beneath the surface of the liver, although some may occur deeper. The simple hepatic cyst is considered to be of congenital, developmental origin.

Imaging Features

Ultrasound is the best way to confirm the cystic nature of a hepatic mass. Sonographically, uncomplicated simple (bile duct) cysts present as anechoic masses, with smooth borders, nondetectable walls, no septations, and no mural calcification. They present increased through-transmission and back wall enhancement.

Cysts complicated by infection or hemorrhage may have septations and/or internal debris, as well as enhancement of the wall (Fig. 12).

The CT features of an uncomplicated hepatic cyst are (1) a well-defined intrahepatic mass; (2) water attenuation; (3) round or oval shape; (4) smooth, thin walls; (5) absence of internal structures; and (6) no enhancement after administration of contrast material [51] (Fig. 12).

Simple cysts of the liver are usually solitary but can number fewer than ten. When more than ten cysts are seen, one of the fibropolycystic diseases should be considered.

MR imaging shows the cysts to be classically hypointense on T1 weighted image and hyperintense on T2 weighted image. Hemorrhagic cysts are hyperintense on both T1 and T2 weighted images. It is impossible in some cases to differentiate a cyst from a typical hemangioma on MR images [52].

Congenital Hepatic Fibrosis and Polycystic Liver Disease

Clinically, the majority of patients present in childhood, when congenital hepatic fibrosis predominates, with

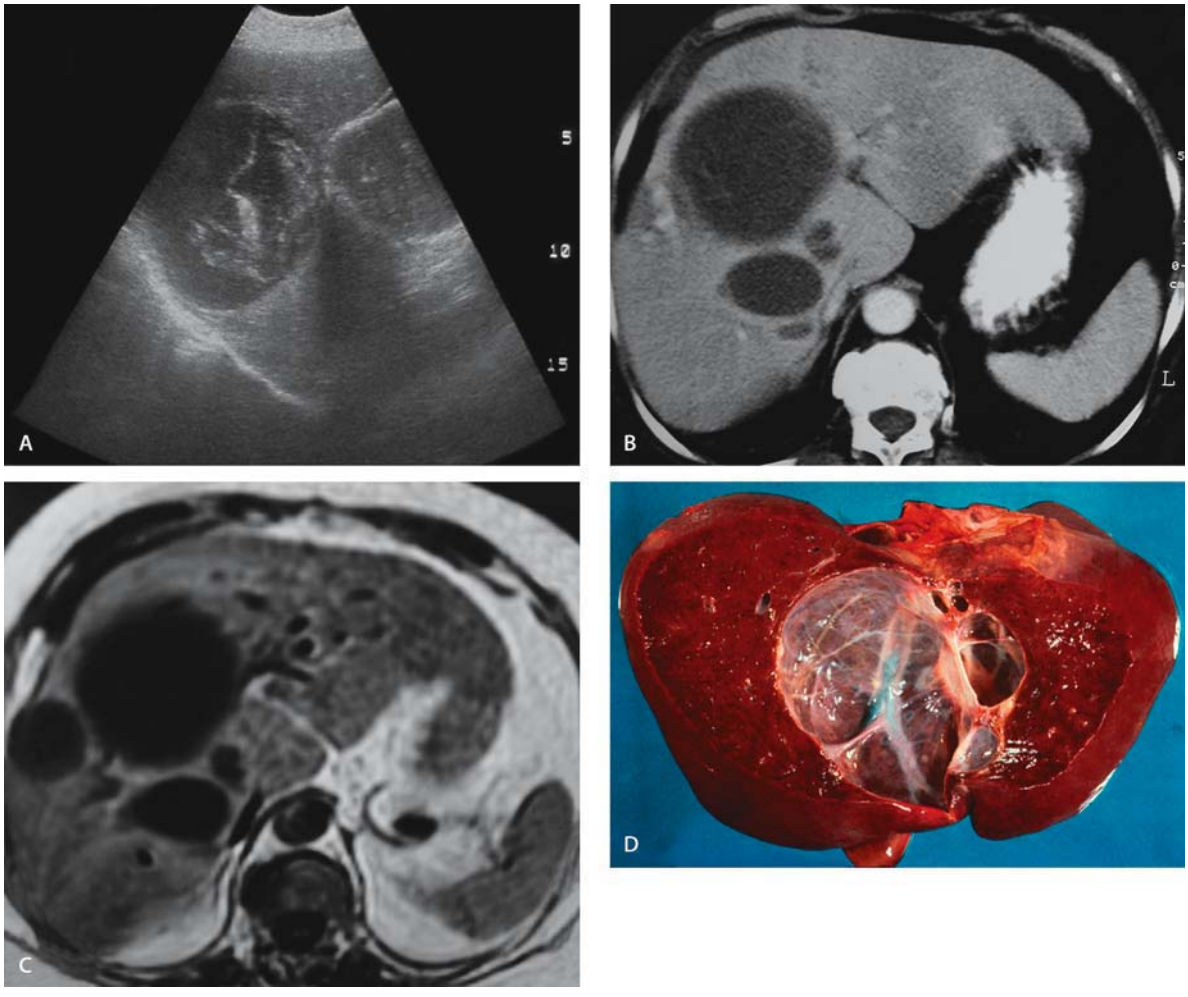

Fig. 12A–D. Complicated cyst of the liver. **A** Transverse ultrasound indicates a complex cystic mass with multiple septations in the left upper quadrant. **B** Correlative CT scan demonstrates uniformly hypodense well-circumscribed lesion. Note how there is no evidence of septations in CT. **C** T1-weighted coronal image demonstrates marked uniform hyperintensity of the cyst, indicating a hemorrhagic nature. Coronal imaging helps to determine that the origin of the cyst is the liver. **D** Gross photograph shows a large cyst with septations. Clotted blood was removed at section

bleeding varices and other manifestations of portal hypertension. Congenital hepatic fibrosis is also related to Caroli's disease. In patients with polycystic liver disease, the lesions are usually identified incidentally at radiologic examination. Approximately 70% of patients with polycystic liver disease also have renal involvement.

Pathologic Findings

Congenital hepatic fibrosis is part of the spectrum of hepatic cystic diseases. It is characterized by aberrant bile duct proliferation and periductal fibrosis [6]. In typical congenital hepatic fibrosis, cysts are not visible without a hand lens. However, in the polycystic liver disease variant, numerous large and small cysts coexist with fibrosis. In cases of polycystic liver and/or kidney disease, the liver surrounding the cysts is not due to increased fibrous tissue [6].

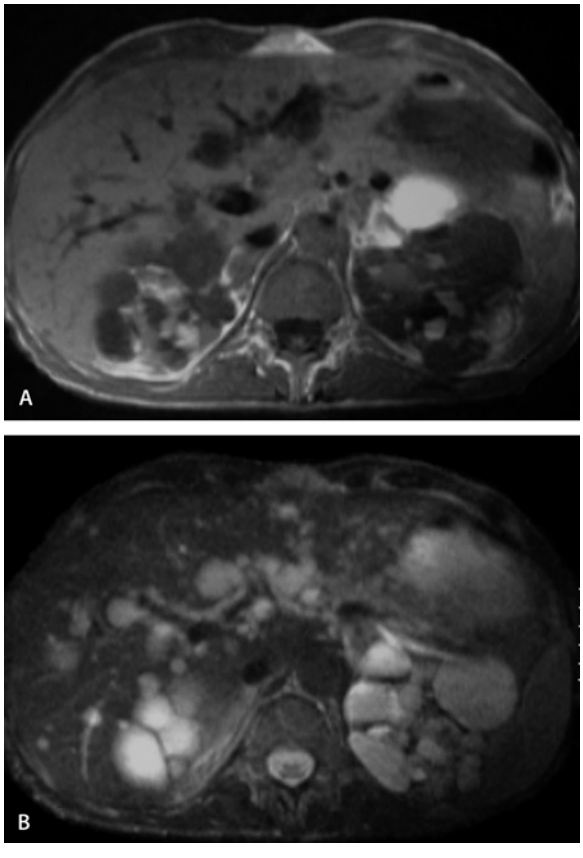

Fig. 13A, B. Polycystic disease of the liver and kidney. **A** T1-weighted image demonstrates multiple thin-walled cysts in the liver, as well as the typical appearance of multicystic kidney disease in both kidneys. Note some of the cysts show high signal intensity probably due to hemorrhage. **B** T2-weighted image again demonstrates the involvement of both liver and kidney by multiple cysts

Imaging Features

Cross-sectional imaging shows multiple cysts in the liver, frequently associated with multiple renal cysts (Fig. 13). Calcification in the cyst wall is occasionally seen and the cysts may contain blood and fluid levels [51]. These hepatic cysts are pathologically identical to simple or bile duct cysts.

Biliary Hamartoma (von Meyenburg Complex)

Biliary hamartoma (BH), also designated as von Meyenburg complex, is thought to represent a focal congenital defect in the formation of the ductal plates. It is often seen as part of the spectrum of polycystic disease, and so may be associated with the presence of polycystic disease in other organs and/or benign biliary cysts of the liver [53, 54].

Pathologic Findings

Biliary hamartoma is an irregularly shaped, whitish lesion, usually measuring less than 0.5 cm in greatest diameter; multiple lesions in the same liver are common [55]. They are stable and without significant growth over time. Microscopically, the hamartoma consists of numerous small to medium-sized ductular structures located within the portal zone. The shape of the ductules is more irregular than that of normal ducts (Fig. 14). They are also dilated to variable degrees, separated by dense collagen, and may contain proteinaceous (eosinophilic) debris or inspissated bile.

Imaging Features

Ultrasonographic findings of biliary hamartoma are not specific [55], and described as hypoechoic, hyperechoic, or anechoic small nodules with acoustic enhancement. Unenhanced CT images usually show hypodense small hepatic nodules scattered throughout both liver lobes [56]. Most of these nodules measure less than 0.5 to 1.0 cm in diameter. In most cases there is no enhancement after intravenous administration of contrast material (Fig. 14).

On MR imaging, biliary hamartoma is usually hypointense compared with liver parenchyma on T1-weighted images and is strongly hyperintense on T2-weighted images [57]. Biliary hamartoma does not exhibit a characteristic pattern of enhancement after intravenous administration of gadolinium. Some authors have reported a homogeneous enhancement of these lesions. In some cases, a thin rim of enhancement, correlating pathologically with the compressed liver parenchyma that surrounds the lesions, can be seen [58].

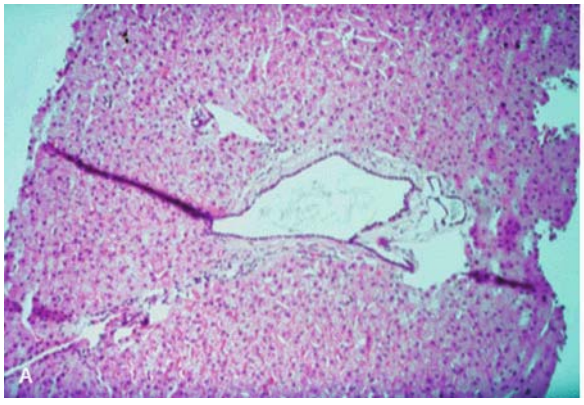

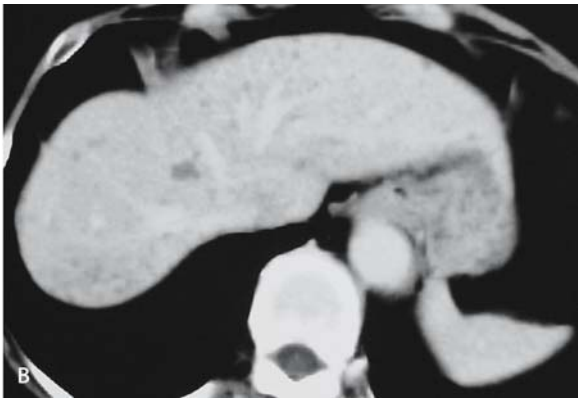

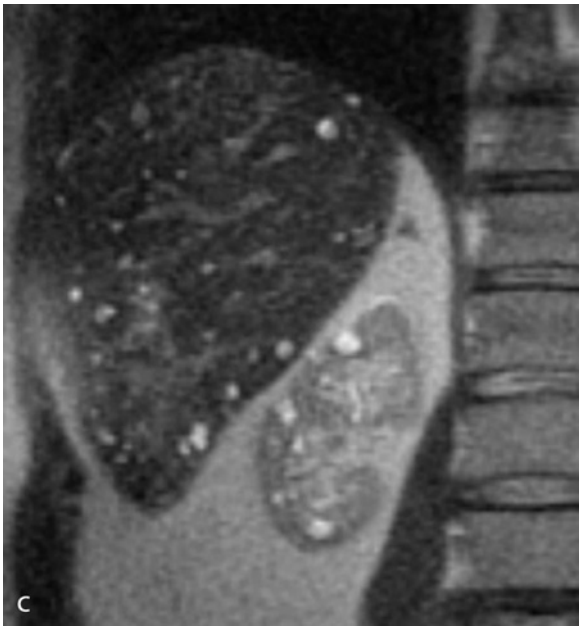

Fig. 14A–C. Biliary hamartoma (von Meyenburg complex). **A** Low power photomicrograph demonstrates a small cyst lined by biliary epithelium in portal zone. **B** Contrast-enhanced CT image in a woman demonstrates numerous nonenhancing cystic nodules scattered throughout the liver parenchyma. The size of the lesions (all less than 1 cm) is a major suggestive feature for biliary hamartoma. **C** T2-weighted image shows the multiple tiny high signal intensity hepatic nodules

Biliary Cystadenoma

Cystadenoma is a rare cystic biliary epithelial neoplasm. Cystadenomas are considered to be premalignant lesions. They are viewed on a continuum with cystadenocarcinomas.

Pathologic Findings

Cystadenomas are large cystic neoplasms with internal septations and internal nodularity (less than in cystadenocarcinoma) and a surrounding fibrous capsule (Fig. 15). They are lined with columnar epithelium and resemble mucinous cystic neoplasms of the ovary and pancreas. The wall may contain areas of hemorrhage.

Imaging Features

Sonographically, biliary cystadenoma is an anechoic lesion with internal septations, having a multilocular (rarely unilocular), septate appearance. Hemorrhage and nodular areas are apparent as focal hyperechoic regions (mural nodules) within the anechoic mass [59].

On CT scan, the locules are usually of water density and the nodular areas are evident as focal regions of soft tissue attenuation, which enhance after contrast material administration [60].

The MRI descriptions of biliary cystadenoma are limited [59–61]. The appearance given is that of a lesion that is hyperintense on T2 weighted image and hypointense on T1 weighted image (Fig. 15).

The global imaging characteristics are those of a cystic mass with varying degrees of internal septations and nodularity within the cyst wall. Biliary cystadenomas

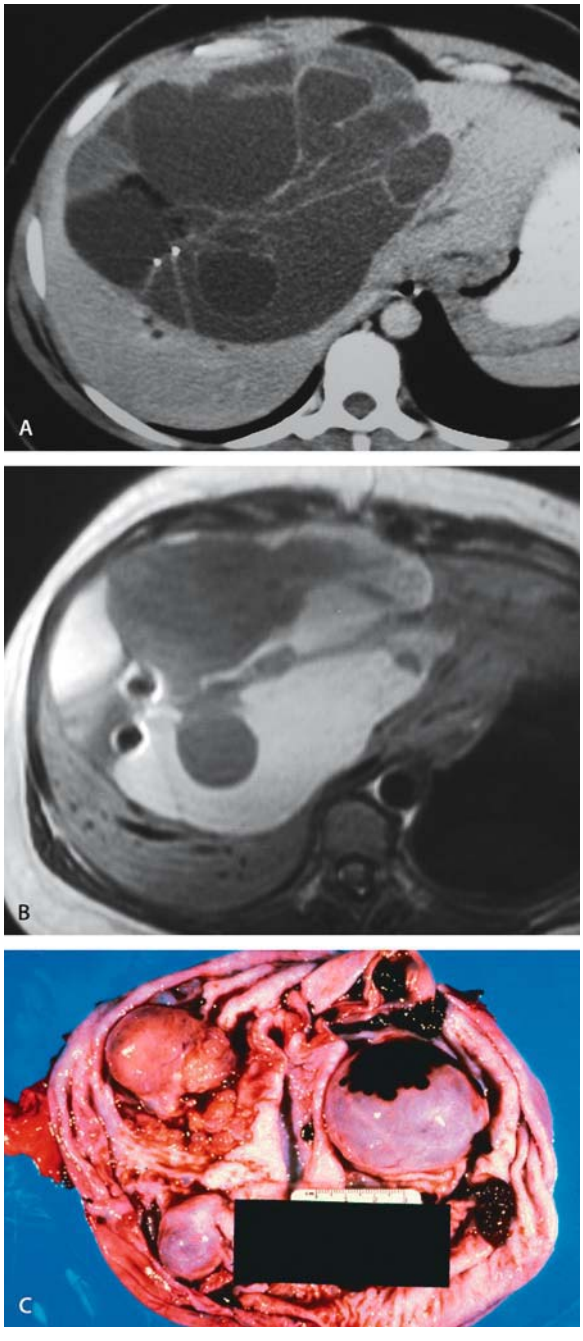

Fig. 15A–C. Biliary cystadenoma. **A** Contrast-enhanced CT scan shows the large, predominately cystic attenuation, multiloculated intrahepatic lesion to contain several surgical clips from a previous resection. **B** T2-weighted image shows the mass to consist of varied signal, predominately hyperintense as a result of the protein content of the locules. **C** Gross specimen demonstrates large cystic neoplasms with internal septations and internal nodularity

cannot be distinguished from cystadenocarcinoma by imaging characteristics alone, but this distinction is not paramount, because the treatment of choice for both is surgical resection.

Bile Duct Adenoma

This benign, solitary, small (<2 cm) mass is composed of small bile ducts and is discovered incidentally at autopsy [2]. It has been suggested that this represents a scar reaction at a site of injury or a hamartoma of peribiliary glands rather than a true benign neoplasm [62, 63].

Microscopically, the glands in the lesion are closely packed and uniform in size. The glands may contain mucin but not bile. Focal dense zones of collagen (scar) may be present.

Bile duct adenoma is shown as a small mass located in the peripheral region of the liver. The lesion demonstrates a mass with early nodular enhancement, which is disproportionately evident compared with their small size and distinct delayed or prolonged enhancement on CT [64].

Benign Mesenchymal Lesions

Hemangioma

Hemangioma is the most common benign tumor of the liver, with a reported incidence ranging from 1% to 20% [11]. They are usually asymptomatic (85%) and are thus incidentally detected. They can produce symptoms as a result of rupture, hemorrhage, thrombosis, or extrinsic compression of adjacent structures. Hemangiomas are more common in women (female/male ratio of 5:1). Although hemangiomas may be present at all ages, they are seen more commonly in postmenopausal women. Hemangiomas may occur in conjunction with focal nodular hyperplasia (FNH) [6].

Pathologic Findings

Hemangiomas consist of multiple vascular channels lined by a single layer of endothelial cells supported by a thin, fibrous stroma [6]. The channels are separated by thin fibrous septa, which may form finger-like protrusions into the channels (Fig. 16). Hemangioma is frequently solitary, well circumscribed, and blood filled and ranges in size from a few millimeters to more than 20 cm [65]. Hemangiomas larger than 10 cm are defined as giant hemangiomas. Hemangiomas may be multiple in up to 50% of cases. On cut sections, areas of fibrosis, thrombosis, cystic degeneration, and occasional calcification may be present [65, 66] (Fig. 16).

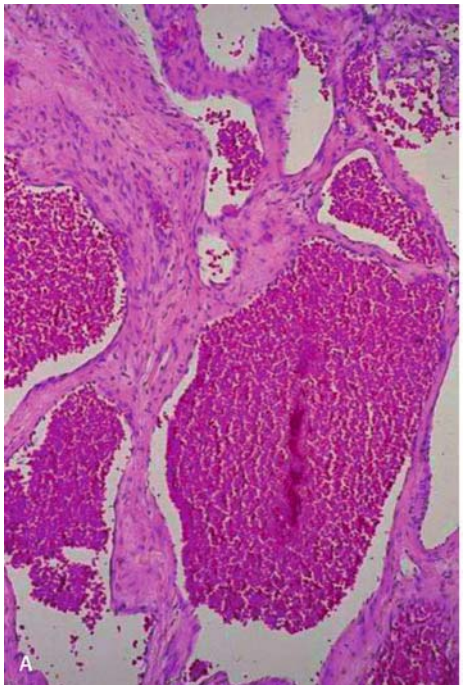

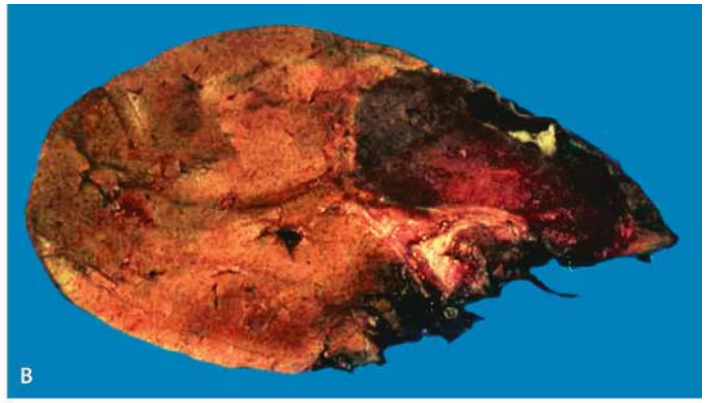

Fig. 16A, B. Hemangioma, pathology. **A** Microscopic appearance. Note presence of red blood cells within vascular channels, as well as thin fibrous septations. **B** Gross appearance. Cut-section of a hemangioma demonstrates its well-defined borders, as well as preservation of liver contour

Imaging Features

Sonographically, hemangiomas are typically hyperechoic, well delimited, and exhibit faint acoustic enhancement. The echogenicity may vary because these tumors may contain cystic and fibrotic regions [67] (Fig. 17). Color Doppler ultrasound demonstrates filling vessels in the periphery of the tumor but no significant color Doppler flow deep within the hemangioma [68].

Hemangiomas appear as low-attenuation masses with well-defined, lobulated borders on unenhanced computed tomography (CT) scans. Calcification is observed in 10–20% of cases [11]. Using repeated scanning at a single level over 2–15 min following administration

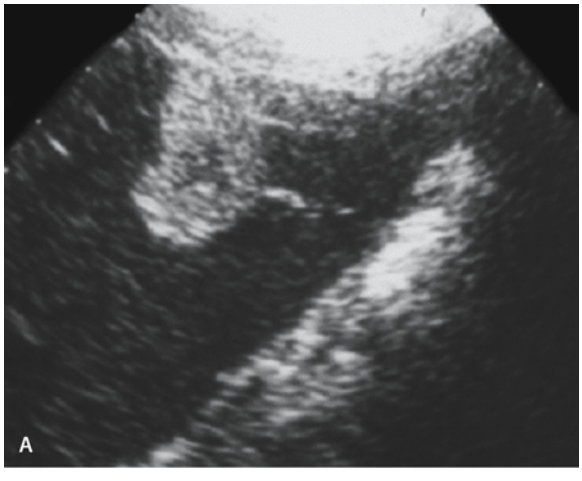

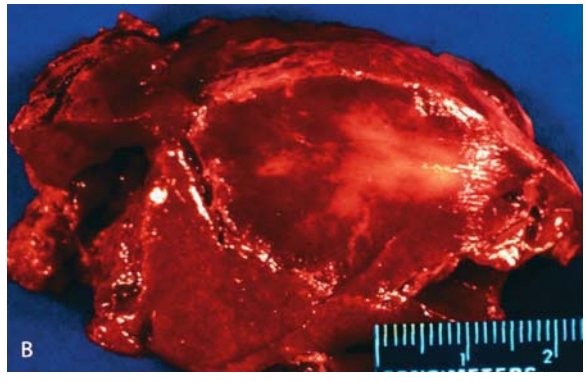

Fig. 17A, B. Hemangioma: ultrasound findings. **A** Longitudinal ultrasound through the right upper quadrant demonstrates a markedly echogenic, well-delimited tumor in the liver. Note central area of decreased echogenicity, as well as faint acoustic enhancement. **B** Gross specimen demonstrates the well-defined borders of this hemangioma there is central area of fibrosis

of intravenous contrast, hemangiomas demonstrate initial peripheral enhancement which progresses centrally (Fig. 18). On delayed scans the lesion becomes isointense with the liver. Using helical CT scanning, hemangiomas may demonstrate early globular peripheral enhancement corresponding to large peripheral feeding vessels [10]. In a recent study the presence of globular enhancement isodense with the aorta was found to be 67% sensitive and 100% specific in differentiating hemangiomas from hepatic metastases [69]. Therefore if a lesion demonstrates globular peripheral enhancement isodense with the aorta during the early phase of contrast-enhanced helical scanning, a diagnosis of hemangioma can be confidently made. Smaller lesions may uniformly enhance on early phase imaging, while larger hemangiomas with discernible fibrotic scars show corresponding persistent areas of nonenhancement.

The study of hemangiomas of the liver is one of the major applications of abdominal magnetic resonance (MR). Hemangiomas characteristically demonstrate marked hyperintensity on T2-weighted images, which may contain low-intensity areas correlating with zones of fibrosis [65, 70–73]. The hyperintensity is secondary to their high water content and subsequent prolonged T2 relaxation time. After gadolinium diethylenetriaminepentaacetic acid (Gd-DTPA) injection, three patterns of enhancement may be seen, depending on the size of the lesion [74]: uniform early enhancement (<1.5 cm), peripheral nodular enhancement progressing centripetally to uniform enhancement (1.5–5 cm), and peripheral nodular enhancement while the center of the lesion remains hypointense (>5 cm) [74]. Peripheral nodular enhancement is a useful discriminating feature in the differential diagnosis of hemangiomas and metastases [75]. In the majority of cases the combination of T2-weighted images [76] and serial dynamic post gadolinium images allows a confident diagnosis of hemangioma to be made [77–79] (Fig. 19).

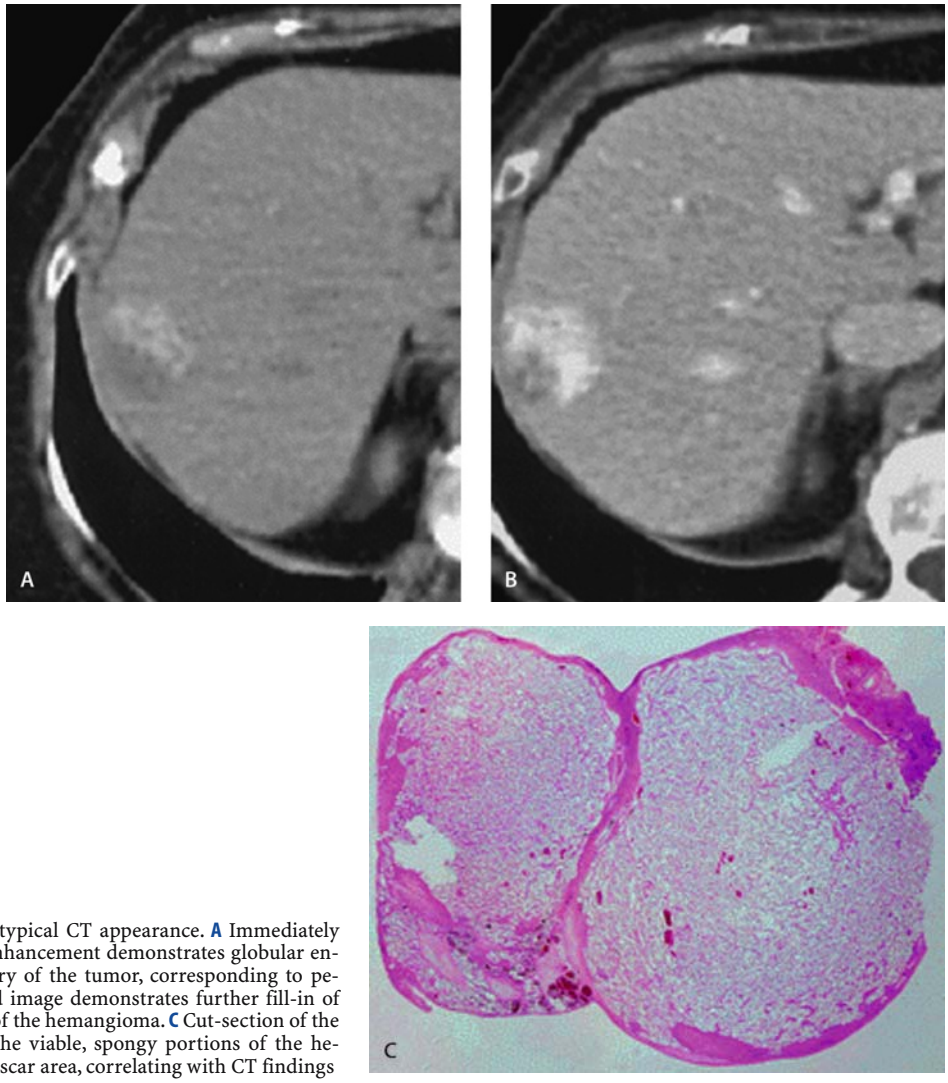

Fig. 18A–C. Hemangioma, typical CT appearance. **A** Immediately after intravenous iodine enhancement demonstrates globular enhancement in the periphery of the tumor, corresponding to peripheral feeders. **B** Delayed image demonstrates further fill-in of contrast on the periphery of the hemangioma. **C** Cut-section of the specimen demonstrating the viable, spongy portions of the hemangioma and the central scar area, correlating with CT findings

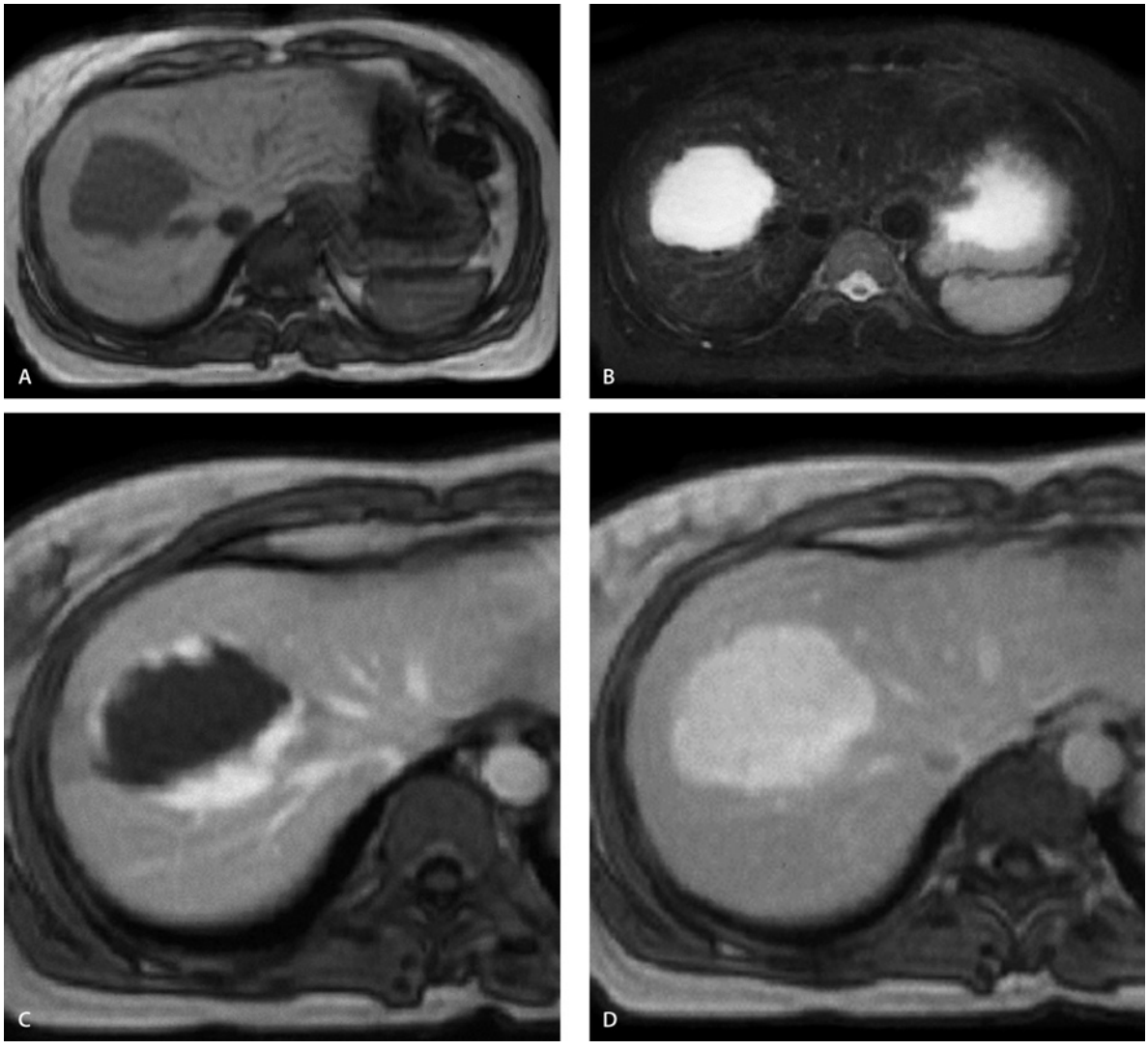

Fig. 19A–D. Hemangioma, MRI appearance. **A** Typical hypointense appearance of two hemangiomas of the right lobe of the liver in this unenhanced T1-weighted spin-echo image. **B** Marked hyperintensity in the T2-weighted appearance. **C** Immediately after injection of Gd-DTPA, there is peripheral enhancement similar to that seen in CT. **D** Ten minutes after contrast injection, there is complete filling of the hemangiomas

Ultrasmall superparamagnetic iron colloid (USPIO) is an agent which is ultimately cleared by the reticuloendothelial system but resides in the intravascular compartment ("blood pool") immediately after injection [80]. On T1 -weighted images hemangiomas enhance immediately due to their vascularity and become isointense to a normal liver. On T2-weighted scans, hemangiomas demonstrate decreased signal intensity and may become isointense to the liver at higher doses of USPIO [80]. Hemangiomas do not have uptake of superparamagnetic iron oxide particles (SPIO) or manganese dipyridoxyl-ethylenediamine-diacetate-(bis)phosphate (Mn-DPDP) because they do not contain Kupffer cells or normal hepatocytes [81].

Infantile Hemangioendothelioma

IHE is relatively common and accounts for 12% of all childhood hepatic tumors. It is the most common liver tumor during the first 6 months of life. Ninety percent of IHEs are discovered within this period, and females are affected more often than males [82]. Clinical findings include hepatomegaly, congestive heart failure (present in Up to 25% of cases), thrombocytopenia caused by trapping of platelets by the tumor, and occasional rupture with hemoperitoneum. In up to 40% of patients, cutaneous hemangiomas are commonly present in the multinodular form of IHE [83].

Pathologic Findings

Infantile hemangioendothelioma (IHE) is a vascular tumor derived from endothelial cells that proliferate and form vascular channels [82]. IHEs are usually multiple and diffuse; a solitary lesion is an uncommon variant.

Microscopically, IHEs are composed of a proliferation of small vascular channels lined by endothelial cells. Cavernous areas, as well as zones of hemorrhage, thrombosis, fibrosis, and calcification, are common [83].

Imaging Features

Typically there is a complex liver mass with large draining hepatic veins. Single or multiple lesions may be seen, and the lesions may range from hypo- to hyperechoic. During a period of months, these lesions tend to involute slowly and develop increased echogenicity [84] (Fig. 20).

On precontrast CT scans, IHE appears as a hypodense mass with or without calcifications [85]. After administration of contrast agent, there is early enhancement of the edge of the mass with variable delayed central enhancement [83, 85] (Fig. 20).

On MRI, IHE has a nonspecific appearance and is predominantly hypointense on T1-weighted images and hyperintense on T2-weighted images. Foci of hyper- or hypointense signal on T1-weighted scans correspond to areas of hemorrhage and fibrosis [85]. After intravenous gadolinium administration, IHE may show an early rim-like pseudocapsular enhancement followed by progressive fill-in of the lesion on delayed imaging [86].

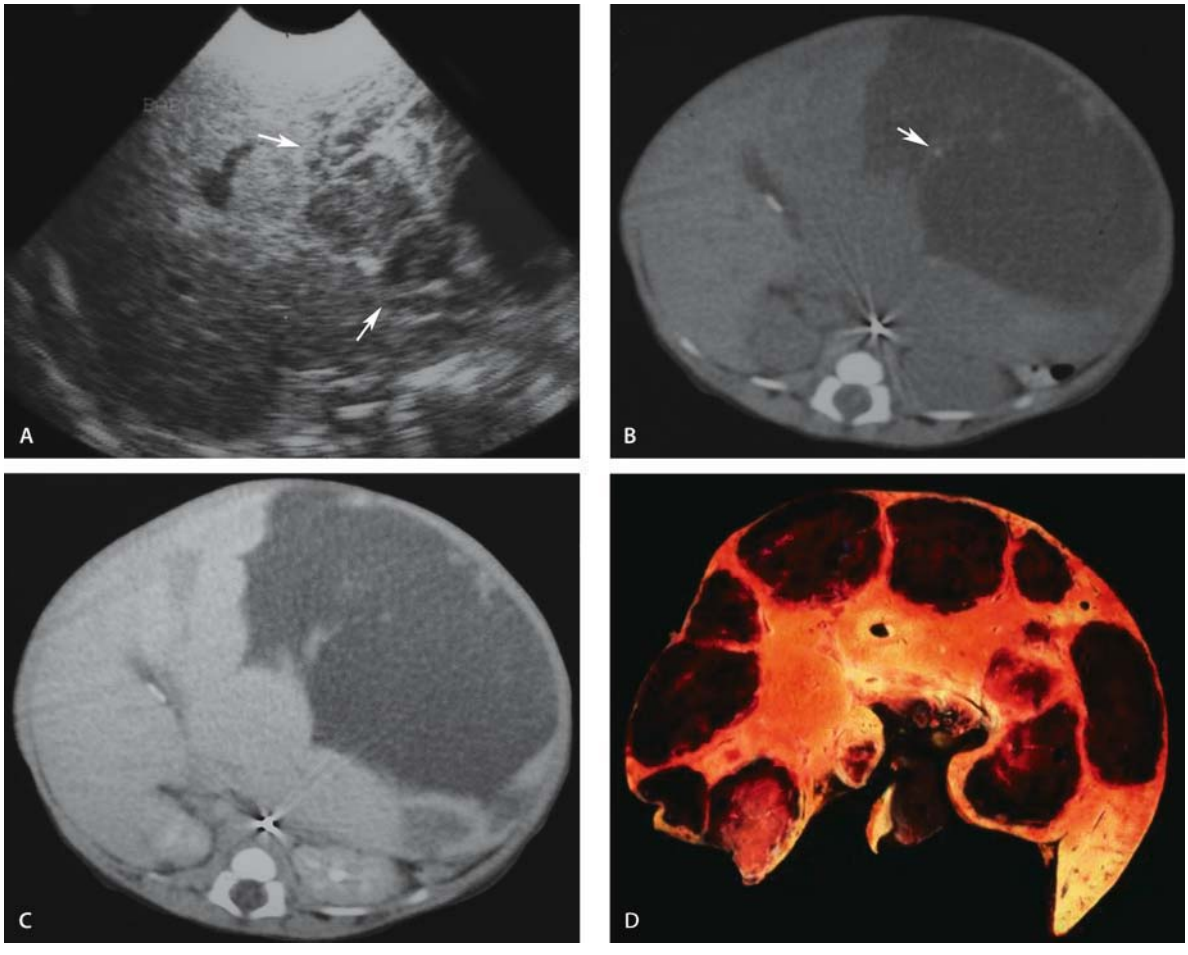

Fig. 20A–D. Infantile hemangioendothelioma in a two day-old baby. **A** Transverse sonographic image demonstrates a large heterogeneously echogenic lesions in left lobe of the liver (*arrows*). **B** On the unenhanced CT, there is a large hypodense lesion in the left lobe with a punctate calcification (*arrow*). **C** After contrast administration, there is peripheral enhancement, similar to that of a hemangioma. **D** Gross specimen demonstrates multiple dark lesions suggesting vascular origin

Mesenchymal Hamartoma

Mesenchymal hamartoma is an uncommon lesion, accounting for 8% of all childhood liver tumors. The majority of cases occur during the first 3 years of life and there is a slight male predominance [87]. Hepatoblastoma and IHE have a similar age presentation but are solid, whereas mesenchymal hamartomas are predominantly cystic. Clinically, slow, progressive, painless abdominal enlargement is seen. Sometimes rapid enlargement may occur because of rapid accumulation of fluid in the cyst. This may occasionally cause respiratory distress and edema of the lower extremities.

Pathologic Findings

Mesenchymal hamartoma is a benign cystic developmental lesion and is not considered a true neoplasm. It is composed of gelatinous mesenchymal tissue with cyst formation, as well as remnants of normal hepatic parenchyma [87]. It is a large, soft, predominantly cystic mass measuring 15 cm or more in largest diameter at the time of diagnosis. The tumors are well defined and encapsulated or pedunculated [88]. Histologically, the tumor consists of cysts, remnants of portal triads, hepatocytes, and fluid-filled mesenchyme.

Imaging Features

Sonography demonstrates either large cysts within internal septa (cystic predominance) or, less commonly, smaller cysts with thick septa (mesenchymal predominance) [88, 89] (Fig. 21).

On CT scans, these tumors appear as well-defined masses with central hypodense areas and internal septa [88] (Fig. 21).

The MR appearance of mesenchymal hamartoma depends on whether an individual lesion is predominantly stromal or cystic. For lesions with stromal predominance, the intensity on T1-weighted images is low-

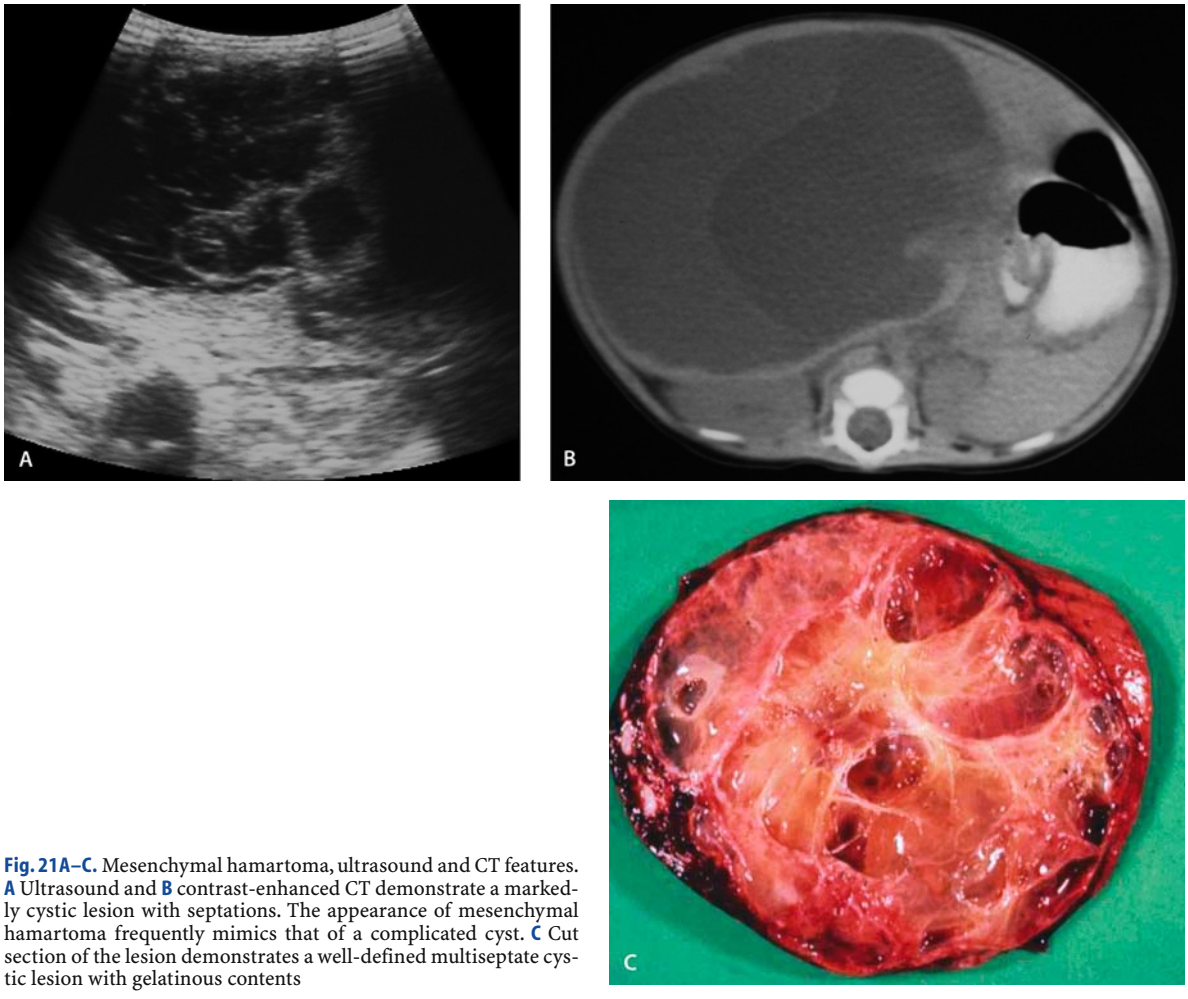

Fig. 21A–C. Mesenchymal hamartoma, ultrasound and CT features. **A** Ultrasound and **B** contrast-enhanced CT demonstrate a markedly cystic lesion with septations. The appearance of mesenchymal hamartoma frequently mimics that of a complicated cyst. **C** Cut section of the lesion demonstrates a well-defined multiseptate cystic lesion with gelatinous contents

er than that of the normal liver because of increased fibrosis. Conversely, if there is cystic predominance, the mesenchymal hamartoma is predominantly hypointense on T1-weighted images and markedly hyperintense on T2-weighted images. On T2-weighted images, multiple septa can be seen traversing the tumor, indicating that the mass is not a simple cyst [83] (Fig. 22).

Lipomatous Tumors

Benign hepatic tumors composed of fat include lipoma, hibernoma, and combined tumors such as angiomyolipoma (fat and blood vessels), myelolipoma (fat and hematopoietic tissue), or angiomyelolipoma [90].

Pathologic Findings

Grossly, lipomatous tumors are usually solitary, well circumscribed, round and most commonly occur in a noncirrhotic liver [91]. There is no sex predilection and they have been reported in a broad age range (24–70 years) [6].

Approximately 10% of patients with tuberous sclerosis and renal angiolipomas have hepatic fatty tumors, either lipoma or angiomyolipoma [92]. Most lipomatous tumors of the liver are asymptomatic and are incidental findings. The lipomatous tumors can grow to be quite large. When enlarged the tumor has increased propensity for hemorrhage, occasionally bleeds causing abdominal pain.

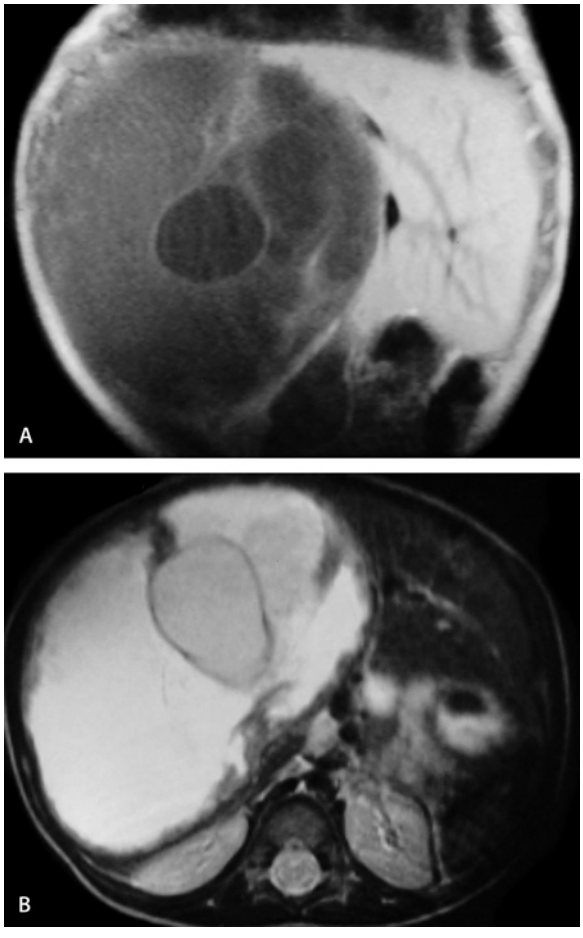

Fig. 22A, B. MRI appearance of a mesenchymal hamartoma. **A** T1-weighted coronal image shows a hypointense mass extending from the inferior aspects of the right lobe of the liver. Draining vessels are noted leading to the hepatic veins confirming the hepatic origin of this tumor. **B** T2-weighted image demonstrates a markedly hyperintense mass, in keeping with the cystic nature of mesenchymal hamartoma. Internal septations, that remain hypointense since they are fibrous, can be seen. This is the typical appearance of mesenchymal hamartoma with cystic predominance

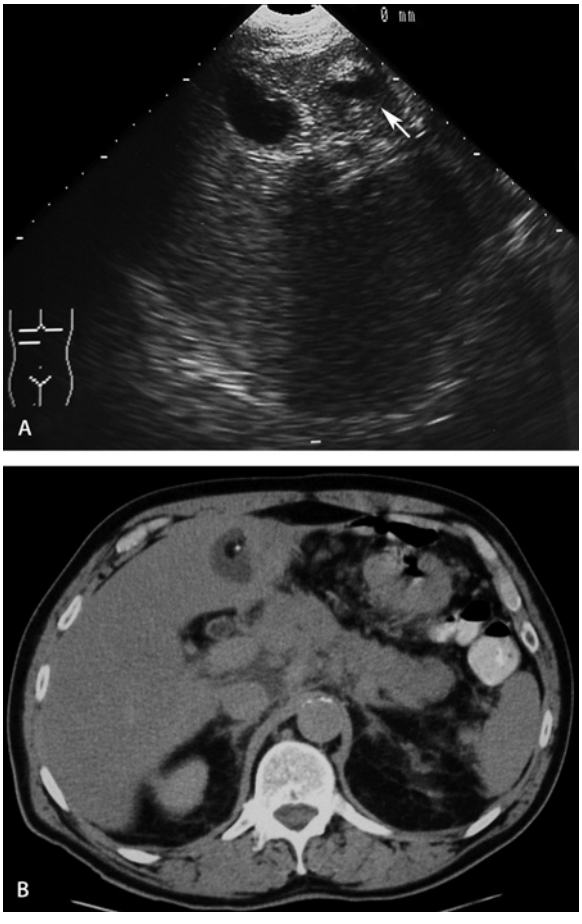

Fig. 23A, B. Angiomyolipoma of the liver, ultrasound and CT appearance. **A** Longitudinal section by ultrasound demonstrates a very echogenic mass with few small, hypoechoic areas within it (*arrow*). **B** Correlative CT in the same patient demonstrates a well-defined, round mass in the liver of fat density with small areas within it that are of higher density that correspond to muscular portions in these tumors. The areas of increased density in CT correspond to the hyperechoic areas seen by ultrasound

Imaging Features

Angiomyolipomas are highly echogenic on sonography and indistinguishable from hemangiomas [92] (Fig. 23). On CT scans, these tumors appear as well-defined masses with attenuation values in the range of those of fat [92]. On MRI scans the fatty component of angiomyolipomas is of high signal on T1- and T2-weighted images (Fig. 24). The early phase of contrast-enhanced dynamic CT or MRI may be useful in discriminating between angiomyolipomas and hepatocellular carcinomas with fat. The fatty areas of angiomyolipomas are well vascularized and enhance early. Conversely, the areas of fatty change in hepatocellular carcinoma are relatively avascular and enhancement is less obvious. MRI using fat suppression shows lesions that appear hypointense to liver (Fig. 24). The presence of large intratumoral vessels ("macroaneurysms") is a classic feature of large angiomyolipomas. Color Doppler ultrasound, CT and MRI are useful techniques in the detection of mac-

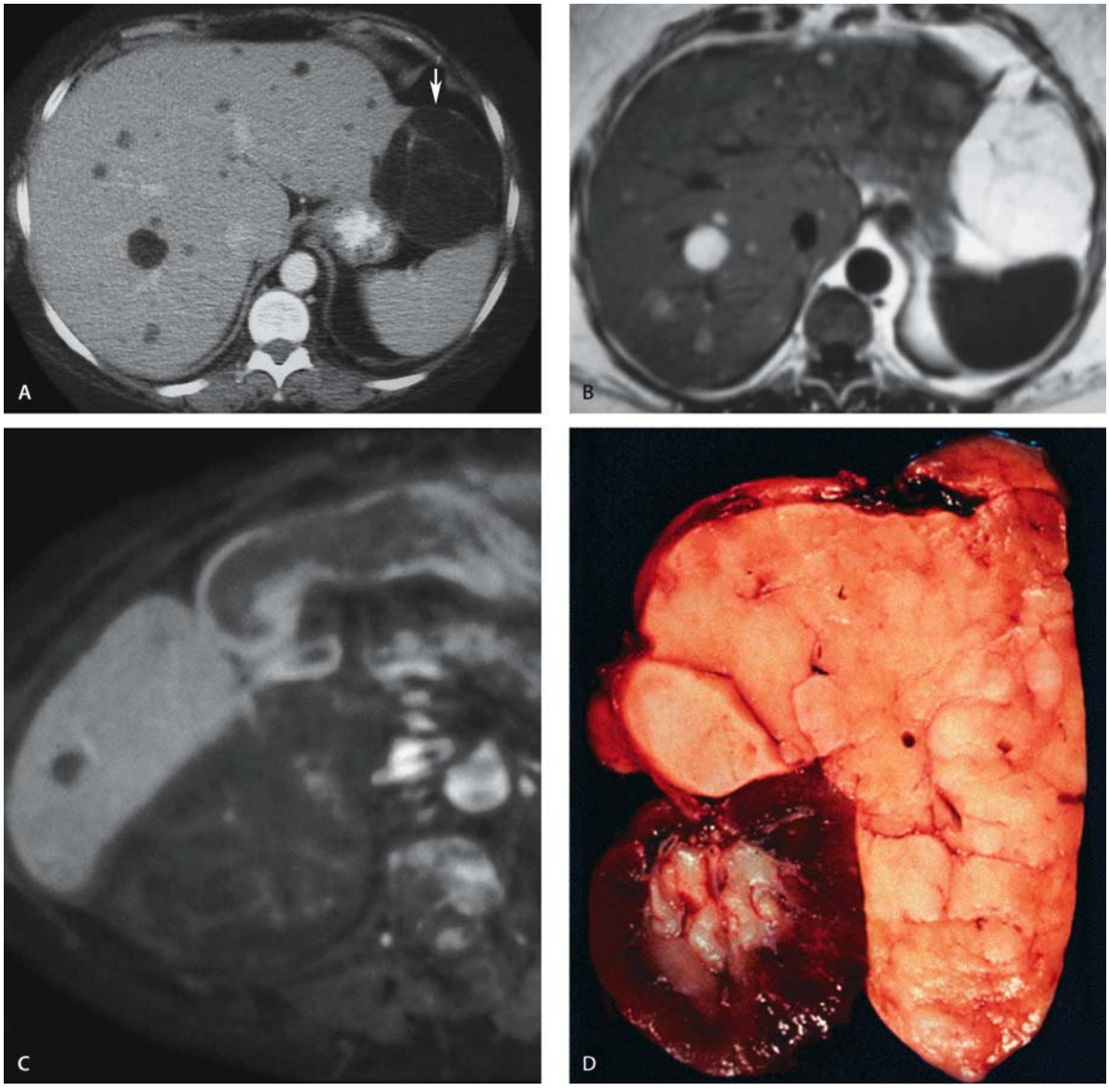

Fig. 24A–D. Woman with tuberous sclerosis having angiomyolipomas of the liver and kidneys. **A** Contrast-enhanced CT scan demonstrates multiple lipomatous lesions of the liver having fat attenuation. A large pedunculated angiomyolipoma (*arrow*) is present in the lateral segment of the left lobe of the liver. **B** T1-weighted image demonstrates the multiple lipomatous tumors of the liver to be of increased signal intensity similar to that of the subcutaneous and retroperitoneal fat. Fibrous septa of the angiomyolipoma of the left lobe of the liver have low signal intensity. **C** Fat-suppression T1-weighted image of the kidney demonstrates the fatty lesions in right kidney similar to that of liver. **D** Gross specimen demonstrates typical angiomyolipoma featuring as a large lipomatous mass involving liver and kidney

roaneurysms [93, 94]. Other focal fatty lesions of the liver include pseudolipoma and focal fatty change.

Other Uncommon Benign Lesions

Some uncommon benign tumors of the liver are mentioned here for completeness. They are of marginal radiologic importance and have been described primarily in case reports.

Lymphangioma

Hepatic lymphangioma is defined by the presence of a mass or multiple masses (lymphangiomatosis) composed of prominent lymphatic channels that compress the normal hepatic parenchyma [6]. Lymphangiomatosis usually is part of a systemic syndrome which involves other organs, including the spleen, skeleton, soft tissues, lung, and/or brain [95].

Leiomyoma

This extremely rare lesion is a well-circumscribed smooth muscle tumor arising in the liver with nonspecific radiologic characteristics. Several cases of leiomyoma have recently been reported in adults and children infected with HIV. This suggests that there may be a clinical association between these two entities [96]. On ultrasound examination the lesion may appear solid or hypoechoic with internal echoes [97]. Leiomyomas are of low attenuation relative to the liver on noncontrast CT scans and display two distinct enhancement patterns: peripheral rim enhancement similar to abscesses or homogeneous enhancement resembling hemangioma [97]. On MRI scans leiomyomas are hypointense relative to the liver on T1-weighted images and hyperintense on T2-weighted images [97].

Fibroma (Fibrous Mesothelioma)

Fibrous mesotheliomas are rare tumors that localize on the surface of the liver. They are usually large and consist histologically of spindle cells and collagen [98].

Adrenal Rest Tumor

Adrenal rest tumors are derived from ectopic adrenal tissue that is histologically identical to that in adrenocortical tumors. They are extremely rare [99].

Pancreatic Heterotopia

Ectopic pancreas in the liver has been rarely described [100].

References

1. Rooks JB, Ory HW, Ishak KG, et al (1979) Epidemiology of hepatocellular adenoma, the role of oral contraceptive use. JAMA 242:644–648
2. Rabe T, Feldmann K, Grunwald K, et al (1994) Liver tumours in women on oral contraceptives. Lancet 344:1568–1569
3. Labrune P, Trioche P, Duvaltier I, et al (1997) Hepatocellular adenomas in glycogen storage disease type I and III: A series of 43 patients and review of the literature. J Pediatr Gastroenterol Nutr 24:276–279
4. Meissner K (1998) Hemorrhage caused by ruptured liver cell adenoma following long-term oral contraceptives: A case report. Hepatogastroenterology 45:224–225
5. Kawakatsu M, Vilgrain V, Erlinger S, et al (1997) Disappearance of liver cell adenoma: CT and MR imaging. Abdom Imaging 22:274–276
6. Craig GR, Peters RL, Edmonson HA (1989) Tumors of the liver and intrahepatic bile ducts. In: Atlas of tumor pathology (2nd series). Armed Forces Institute of Pathology, Washington, DC
7. Golli M, Nhieu JTV, Mathieu D, et al (1994) Hepatocellular adenoma: color Doppler US and pathologic correlations. Radiology 190:741–744
8. Bartolozzi C, Lencioni R, Paolicchi A, et al (1997) Differentiation of hepatocellular adenoma and focal nodular hyperplasia of the liver: Comparison of power Doppler imaging and conventional color Doppler sonography. Eur Radiol 7:1410–1415
9. Shamsi K, De Schepper A, Degryse H, Deckers F (1993) Focal nodular hyperplasia of the liver: radiologic findings. Abdom Imaging 18:32–38
10. Bluemke DA, Soyer P, Fishman EK (1995) Helical (spiral) CT of the liver. Radiol Clin North Am 33:863–886
11. Ros PR (1990) Computed tomography-pathologic correlations in hepatic tumors. In: Ferrucci JT, Mathieu DG (eds) Advances in hepatobiliary radiology. St Louis, CV Mosby, pp 75–108
12. Paulson EK, McClellan JS, Washington K, et al (1994) Hepatic adenoma: MR characteristics and correlation with pathologic findings. AJR 163:113–116
13. Powers C, Ros PR, Stoupis C, et al (1994) Primary liver neoplasms: MR imaging with pathologic correlation. Radiographics 14:459–482
14. Arrive L, Flejou J-F, Vilgrain V, et al (1994) Hepatic adenoma: MR findings in 51 pathologically proved lesions. Radiology 193:507–512
15. Chung KY, Mayo-Smith WW, Saini S, et al (1995) Hepatocellular adenoma: MR imaging features with pathologic correlation. AJR Am J Roentgenol 165:303–308
16. Chen KT, Bocian JJ (1983) Multiple hepatic adenomas. Arch Pathol Lab Med 107:274–275
17. Nguyen BN, Flejou JF, Terris B, et al (1999) Focal nodular hyperplasia of the liver: A comprehensive pathologic study of 305 lesions and recognition of new histologic forms. Am J Surg Pathol 23:1441–1454
18. Kondo F (2000) Focal nodular hyperplasia of the liver: Controversy over etiology. J Gastrcenterol Hepatol 15:1229–1231
19. Mathieu D, Kobeiter H, Maison P, et al (2000) Oral contraceptive use and focal nodular hyperplasia of the liver. Gastrcenterology 118:560–564
20. Nisenbaum HL, Rowling SE (1995) Ultrasound of focal hepatic lesions. Semin Roentgenol 30:324–346
21. Buetow PC, Pantongrag-Brown L, Buck JL, et al (1996) Focal nodular hyperplasia of the liver: radiologic-pathologic correlation. Radiographics 16:369–388

22. Lee M, Hamm B, Saini S (1991) Focal nodular hyperplasia of the liver: MR findings in 35 proved cases. AJR Am J Roentgenol 156:317–320
23. Shirkhoda A, Farah MC, Bernacki E, et al (1994) Hepatic focal nodular hyperplasia: CT and sonographic spectrum. Abdom Imaging 19:34–38
24. Mahfouz A-E, Hamm B, Taupiz M, et al (1993) Hypervascular liver lesions: differentiation of focal nodular hyperplasia from malignant tumors with dynamic gadolinium-enhanced MR imaging. Radiology 186:133–138
25. Grandin C, Van Beers BE, Robert A, et al (1995) Benign hepatocellular tumors: MRI after superparamagnetic iron oxide administration. J Comput Assist Tomogr 19:412–418
26. Paley MR, Mergo PJ, Ros PR (1997) Characterization of focal liver lesions with SPIO-enhanced T2WI: patterns of signal intensity and liver lesion contrast change. Radiology 205(P): 455–456
27. Mathieu D, Vilgrain V, Mahfouz A-E, et al (1997) Benign liver tumors. MRI Clin North Am 5:255–258
28. Dachman AH, Ros PR, Goodman ZD, et al (1987) Nodular regenerative hyperplasia of the liver: clinical and radiologic observations. AJR 148:717–722
29. Naber AH, Van Haelst U, Yap SH (1991) Nodular regenerative hyperplasia of the liver: An important cause of portal hypertension in non-cirrhotic patients. J Hepatol 12:94–99
30. Portmann B, Stewart S, Higenbottam TW et al (1993) Nodular transformation of the liver associated with portal and pulmonary arterial hypertension. Gastroenterology 104: 616–621
31. Dumortier J, Boillot O, Chevallier M, et al (1999) Familial occurrence of nodular regenerative hyperplasia of the liver: A report on three families. Gut 45:289–294
32. Stomeyer FW, Ishak KG (1981) Nodular transformation (nodular "regenerative" hyperplasia) of the liver. A clinico-pathologic study of 30 cases. Hum Pathol 12:60–71
33. Vilgrain V, Lewin M, Vons C, et al (1999) Hepatic nodules in Budd-Chiari syndrome: imaging features. Radiology 210: 443–450
34. Brancatelli G, Federle MP, Grazioli L, Golfieri R, Lencioni R (2002) Large regenerative nodules in Budd-Chiari syndrome and other vascular disorders of the liver: CT and MR imaging findings with clinicopathologic correlation. *AJR Am J Roentgenol* 178:877–883
35. Nakanuma Y, Hoso M, Sasaki M, et al (1996) Histopathology of the liver in non-cirrhotic portal hypertension of unknown aetiology. Histopathology 28:195–204
36. Nakanuma Y (1990) Nodular regenerative hyperplasia of the liver: Retrospective survey in autopsy series. J Clin Gastroenterol 12:460–465
37. Casillas C, Marti-Bonmati L, Galant J (1997) Pseudotumoral presentation of nodular regenerative hyperplasia of the liver: Imaging in five patients including MR imaging. Eur Radiol 7: 654–658
38. Clouet M, Boulay I, Boudiaf M, et al (1999) Imaging features of nodular regenerative hyperplasia of the liver mimicking hepatic metastases. Abdom Imaging 24:258–261
39. Siegelman ES, Outwater EK, Furth EE, et al (1995) MR imaging of hepatic nodular regenerative hyperplasia. J Magr Reson Imaging 5:730–732
40. Rha SE, Lee MG, Lee YS, et al (2000) Nodular regenerative hyperplasia of the liver in BuddChiari syndrome: CT and MR features. Abdom Imaging 25:255–258
41. Goodman ZD (1987) Benign tumors of the liver. In: Okuda K. Ishak KG (eds) Neoplasms of the liver. Springer. Tokyo, pp 105–125
42. International Working Party (1995) Terminology of nodular hepatocellular lesions. Hepatology 25:983–993
43. Sakamoto M, Hirohashi S, Shimosato Y (1991) Early stages of multistep hepatocarcinogenesis: Adenomatous hyperplasia and early hepatocellular carcinoma. Hum Pathol 22:172–178
44. Maetani Y, Itoh K, Egawa H, et al (2002) Benign hepatic nodules in Budd-Chiari syndrome: radiologic-pathologic correlation with emphasis on the central scar. *AJR Am J Roentgenol* 178:869–875
45. Ferrell LD, Crawford JM, Dhillon AP, Scheuer PJ, Nakanuma Y (1993) Proposal for standardized criteria for the diagnosis of benign, borderline, and malignant hepatocellular lesions arising in chronic advanced liver disease. Am J Surg Pathol 17:1113–1123
46. Choi BI, Han JK, Hong SH, et al (1999) Dysplastic nodules of the liver: imaging findings. *Abdom Imaging* 24:250–257
47. Rode A, Bancel B, Douek P, et al (2001) Small nodule detection in cirrhotic livers: evaluation with US, spiral CT, and MRI and correlation with pathologic examination of explanted liver. *J Comput Assist Tomogr* 25:327–336
48. Efremidis SC, Hytiroglou P (2002) The multistep process of hepatocarcinogenesis in cirrhosis with imaging correlation. *Eur Radiol* 12:753–764
49. Earls JP, Theise ND, Weinreb JC, et al (1996) Dysplastic nodules and hepatocellular carcinoma: thin-section MR imaging of explanted cirrhotic livers with pathologic correlation. *Radiology* 201:207–214
50. Murphy BJ, Casillas J, Ros PR, et al (1989) The CT appearance of cystic masses of the liver. RadioGraphics 9:307–322
51. Buetow PC, Buck JL, Pantongrag-Brown L, et al (1995) Biliary cystadenoma and cystadenocarcinoma: Clinical-imaging-pathologic correlation with emphasis on the importance of ovarian stroma. Radiology 196:805–810
52. Mathieu D, Paret M, Mahfouz AE, et al (1997) Hyperintense benign liver lesions on spinecho Tl-weighted MR images: Pathologic correlations. Abdom Imaging 22:410–417
53. Desmet VJ (1998) Ludwig Symposium on Biliary Disorders-part I. Pathogenesis of ductal plate abnormalities. Mayo Clin Proc 73:80–89
54. Principe A, Lugaresi ML, Lords RC, et al (1997) Bile duct hamartomas: Diagnostic problems and treatment. Hepatogastroenterology 44:994–997
55. Lev-Toaff AS, Bach AM, Wechsler RJ, et al (1995) The radiologic and pathologic spectrum of biliary hamartomas. AJR Am J Roentgenol 165:309–313
56. Cooke JC, Cooke DA (1987) The appearances of multiple biliary hamartomas of the liver (von Meyenberg complexes) on computed tomography. Clin Radiol 38:101–102
57. Slone HW, Bennett WF, Bova JG (1993) MR findings of multiple biliary hamartomas. AJR Am J Roentgenol 161:581–583
58. Semelka RC, Hussain SM, Marcos HB, et al (1999) Biliary hamartomas: Solitary and multiple lesions shown on current MR techniques including gadolinium enhancement. J Magn Reson Imaging 10:196–201
59. Choi BI, Lim HJ, Han MC, et al (1989) Biliary cystadenoma and cystadenocarcinoma: CT and sonographic findings. Radiology 171:57–61
60. Stoupis C, Ros PR, Dolson DJ (1994) Recurrent biliary cystadenoma: MR imaging appearance. J Magn Reson Imaging 4: 99–101
61. Dachman AH, Lichenstein JE, Friedman AC, et al (1983) Infantile hemangioendothelioma of the liver: a radiologicpathologic-clinical correlation. AJR 140:1091–1096
62. Allaire GS, Rabin L, Ishak KG, Sesterhenn IA (1988) Bile duct adenoma: A study of 152 cases. Am J Surg Pathol 12:708–715
63. Bhathal PS, Hughes NR, Goodman ZD (1996) The so-called bile duct adenoma is a peribiliary gland hamartoma. Am J Surg Pathol 20:858–864
64. Tajima T, Honda H, Kuroiwa T, et al (1999) Radiologic features of intrahepatic bile duct adenoma: a look at the surface of the liver. *J Comput Assist Tomogr* 23:690–695
65. Ros PR, Lubbers PR, Olmsted WW, et al (1987) Hemangioma of the liver: magnetic resonance – gross morphologic correlation. AJR 149:1167–1170
66. Karhunen PJ (1986) Benign hepatic tumors and tumor-like conditions in men. J Clin Pathol 39:183–188
67. Gandolfi L, Leo P, Solmi L, et al (1991) Natural history of hepatic haemangiomas: Clinical and ultrasound study. Gut 32: 677–680
68. Kim TK, Han JK, Kim AY, et al (1999) Limitations of characterization of hepatic hemangiomas using a sonographic contrast agent (Levovist) and power Doppler ultrasonography. J Ultrasound Med 18:737–743

69. Leslie DE, Johnson CD, Johnson CM, et al (1995) Distinction between cavernous hemangiomas of the liver and hepatic metastases on CT: value of contrast enhancement patterns. AJR 164:625–629
70. Itai Y, Ohtomo K, Furui S, et al (1985) Noninvasive diagnosis of small cavernous hemangioma of the liver: advantage of MRI. AJR 145:1195–1199
71. Ferrucci JT (1986) MR imaging of the liver. AJR 147: 1103–1116
72. Yoshida H, Itai Y, Ohtomo K, et al (1989) Small hepatocellular carcinoma and cavernous hemangioma: differentiation with dynamic FLASH MR imaging with Gd-DTPA. Radiology 171: 339–342
73. Ohtomo K, Itai Y, Yoshikawa K, et al (1987) Hepatic tumors: dynamic MR imaging. Radiology 163:27–31
74. Semelka RC, Brown ED, Ascher SM, et al (1994) Hepatic hemangiomas: a multi-institutional study of appearances on T2-weighted and serial gadolinium-enhanced gradient-echo MR images. Radiology 192:401–406
75. Whitney WS, Herfkens RJ, Jeffrey RB, et al (1993) Dynamic breath-hold multiplanar spoiled gradient-recalled MR imaging with gadolinium enhancement for differentiating hepatic hemangiomas from malignancies at 1.5 T. Radiology 189: 863–870
76. McFarland EG, Mayo-Smith WW, Saini S, et al (1994) Hepatic hemangiomas and malignant tumors: improved differentiation with heavily T2-weighted conventional spin-echo MR imaging. Radiology 193:43–47
77. Semelka RC, Sofka CM (1997) Hepatic hemangiomas. MRI Clin North Am 5:241–253
78. Mitchell DG, Saini S, Weinreb J, et al (1994) Hepatic metastases and cavernous hemangiomas: distinction with standard and triple-dose Gadoteridol-enhanced MR imaging. Radiology 193:49–57
79. Soyer P, Gueye C, Somerveille E, et al (1995) MR diagnosis of hepatic metastases from neuroendocrine tumors versus hemangiomas: relative merits of dynamic gadolinium chelate-enhanced gradient-recalled echo and unenhanced spin-echo images. AJR Am J Roentgenol 165:1407–1413
80. Saini S, Edelman RR, Sharma P, et al (1995) Blood-pool MR contrast material for detection and characterization of focal hepatic lesions: initial clinical experience with ultra-small superparamagnetic iron oxide (AMI-227). AJR 164:1147–1152
81. Ros PR (1991) Focal liver masses other than metastases. In: Gore RM (ed) Syllabus for categorical course on gastrointestinal radiology. American College of Radiology. Reston, Va. pp 159–169
82. Mortele KJ, Mergo PJ, Urrutia M, et al (1998) Dynamic gadolinium-enhanced MR findings in infantile hepatic hemangioendothelioma. J Comput Assist Tomogr 22:714–717
83. Helmberger TK, Ros PR, Mergo PJ, Tomczak R, Reiser MF (1999) Pediatric liver neoplasms: a radiologic-pathologic correlation. *Eur Radiol* 9:1339–1347
84. Pobiel RS, Bisset GS 3rd. (1995) Pictorial essay: imaging of liver tumors in the infant and child. Pediatr Radiol 25: 495–506
85. Stocker JT, Ishak KG (1983) Mesenchymal hamartoma of the liver: report of 30 cases and review of the literature. Pediatr Pathol 1:245–267
86. Mortele KJ, Vanzieleghem B, Mortele B, Benoit Y, Ros PR (2002) Solitary hepatic infantile hemangioendothelioma: dynamic gadolinium-enhanced MR imaging findings. *Eur Radiol* 12:862–865
87. Ros PR, Goodman ZD, Ishak KG, et al (1986) Mesenchymal hamartoma of the liver: radiologic-pathologic correlation. Radiology 158:619–624
88. O'Neill J, Ros PR (1989) Knowing hepatic pathology aids MRI of liver tumors. Diagn Imaging 19:558–67
89. Sato M, Ishida H, Konno K, et al (2000) Liver tumors in children and young patients: sonographic and color Doppler findings. *Abdom Imaging* 25:596–601
90. Goodman ZD, Ishak KG (1984) Angiomyolipomas of the liver. Am J Surg Pathol 8:745–750
91. Roberts JL, Fishman EK, Hartman DS, et al (1986) Lipomatous tumors of the liver: evaluation with CT and US. Radiology 158:613–617
92. Ros PR (1994) Hepatic angiomyolipoma: is fat in the liver friend or foe? Abdom Imaging 19:552–553
93. Hogemann D, Flemming P, Kreipe H, Galanski M (2001) Correlation of MRI and CT findings with histopathology in hepatic angiomyolipoma. *Eur Radiol* 11:1389–1395
94. Murakami T, Nakamura H, Hori S, et al (1993) Angiomyolipoma of the liver. Ultrasound, CT, MR imaging and angiography. *Acta Radiol* 34:392–394
95. O'Sullivan DA, Torres VE, de Groen PC, Batts KP, King BF, Vockley J (1998) Hepatic lymphangiomatosis mimicking polycystic liver disease. *Mayo Clin Proc* 73:1188–1192
96. Wachsberg RH, Cho KC, Adekosan A (1994) Two leomyomas of the liver in an adult with AIDS: CT and MR appearance. J Comput Assist Tomogr 18:156–157
97. Mobini J, Krouse TB, Cooper DR (1974) Intrahepatic pancreatic heterotopia. Review and report of a case presenting as an abdominal mass. Am J Dis 19:64–70
98. Lecesne R, Drouillard J, Le Bail B, Saric J, Balabaud C, Laurent F (1998) Localized fibrous tumor of the liver: imaging findings. *Eur Radiol* 8:36–38
99. Tajima T, Funakoshi A, Ikeda Y, et al (2001) Nonfunctioning adrenal rest tumor of the liver: radiologic appearance. *J Comput Assist Tomogr* 25:98–101
100. Ros PR (1998) Hepatic imaging. Radiol Clin North Am 36: 237–246

Primary Hepatic Malignant Neoplasms: Radiologic-Pathologic Correlations

Valérie Vilgrain, Valérie Paradis, Yves Menu, Koenraad J. Mortele, Benoît Terris, Pable R. Ros

4.8

Contents

Introduction

Primary hepatic malignant neoplasms are less common than metastatic liver neoplasms. Primary hepatic malignant neoplasms may develop from hepatocytes, bile duct epithelium, endothelial cells, lymphoid cells. Most of the primary malignant hepatic neoplasms are epithelial in origin with hepatocellular carcinoma and cholangiocarcinoma. Mesenchymal tumors such as epithelioid hemangioendothelioma and angiosarcoma, primary lymphoma and other sarcomas are rare and represent about 1% of primary hepatic neoplasms. This chapter will review primary hepatic malignant neoplasms observed in adult patients with a special focus on radiologic-pathologic correlation.

Hepatocellular Carcinoma

Hepatocellular carcinoma (HCC) is the most common primary malignant hepatic neoplasm and is a tumor derived from the hepatocyte. It usually occurs in association with chronic liver disease. Conditions associated with the development of hepatocellular carcinoma are mainly chronic viral hepatitis, alcoholic cirrhosis, and hemochromatosis. Patients with chronic hepatitis B without underlying cirrhosis may develop hepatocellular carcinoma due to a direct oncogenic effect of the virus. Other causes are more rare such as Wilson disease, biliary cirrhosis, Thorotrast exposure, Budd-Chiari disease, hereditary tyrosinemia, and glycogen storage disease. Due to the high number of patients with C viral infection, and to the high propensity of hepatitis C to become chronic and leading to cirrhosis, this will be a major cause of hepatocellular carcinoma in the future.

The diagnosis of hepatocellular carcinoma is usually made during the follow-up of patients with chronic liver disease or more rarely the diagnosis hepatocellular carcinoma and the underlying liver disease are made simultaneously. The follow-up of these patients is based on liver ultrasonography and serum alfa-fetoprotein every four to six months. There are two possible mechanisms of development of HCC: development de-novo or from a progressive temporal progression in cirrhotic

livers from regenerative nodules to dysplastic nodules to well-differentiated hepatocellular carcinoma.

The prognosis of HCC varies and depends on the tumor characteristics (number, size, capsular effraction, vascular effraction, tumor differentiation) as well as the underlying liver disease (cause, severity, degree of portal hypertension). That is why many different therapeutic procedures are applied from percutaneous treatments to chemoembolization or surgical procedures (surgical resection, liver transplantation).

Pathology

There are two common gross patterns of HCC in livers: expanding pattern and spreading pattern [1]. More rarely, HCC has a multifocal growth pattern. The expanding pattern compresses and displaces the liver parenchyma (Figs. 1A, 2A). Expanding HCC may be encapsulated or not. The capsule is usually observed in medium-sized HCC and very small HCC are unencapsulated. The pedunculated HCC belongs to this catego-

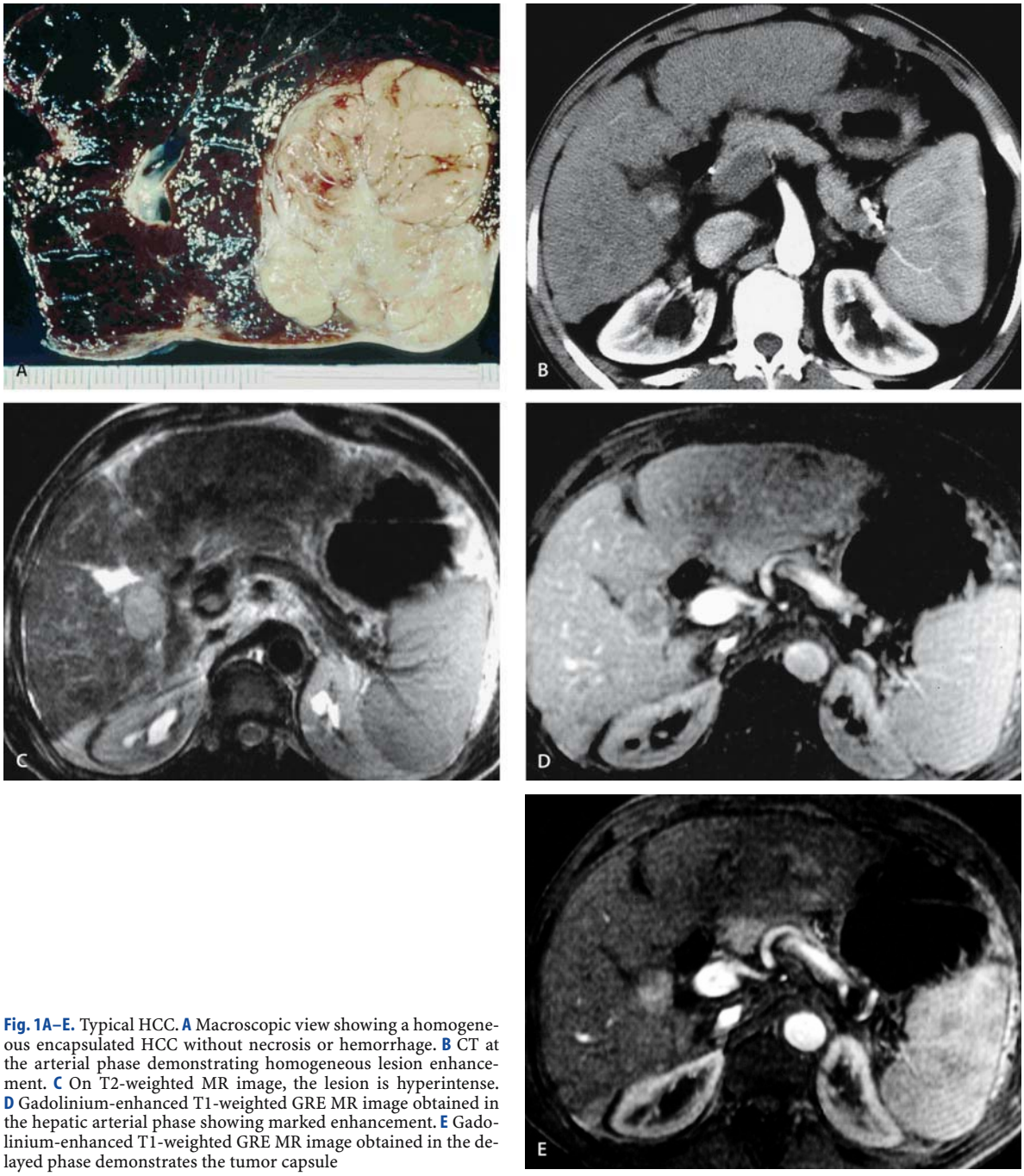

Fig. 1A–E. Typical HCC. **A** Macroscopic view showing a homogeneous encapsulated HCC without necrosis or hemorrhage. **B** CT at the arterial phase demonstrating homogeneous lesion enhancement. **C** On T2-weighted MR image, the lesion is hyperintense. **D** Gadolinium-enhanced T1-weighted GRE MR image obtained in the hepatic arterial phase showing marked enhancement. **E** Gadolinium-enhanced T1-weighted GRE MR image obtained in the delayed phase demonstrates the tumor capsule

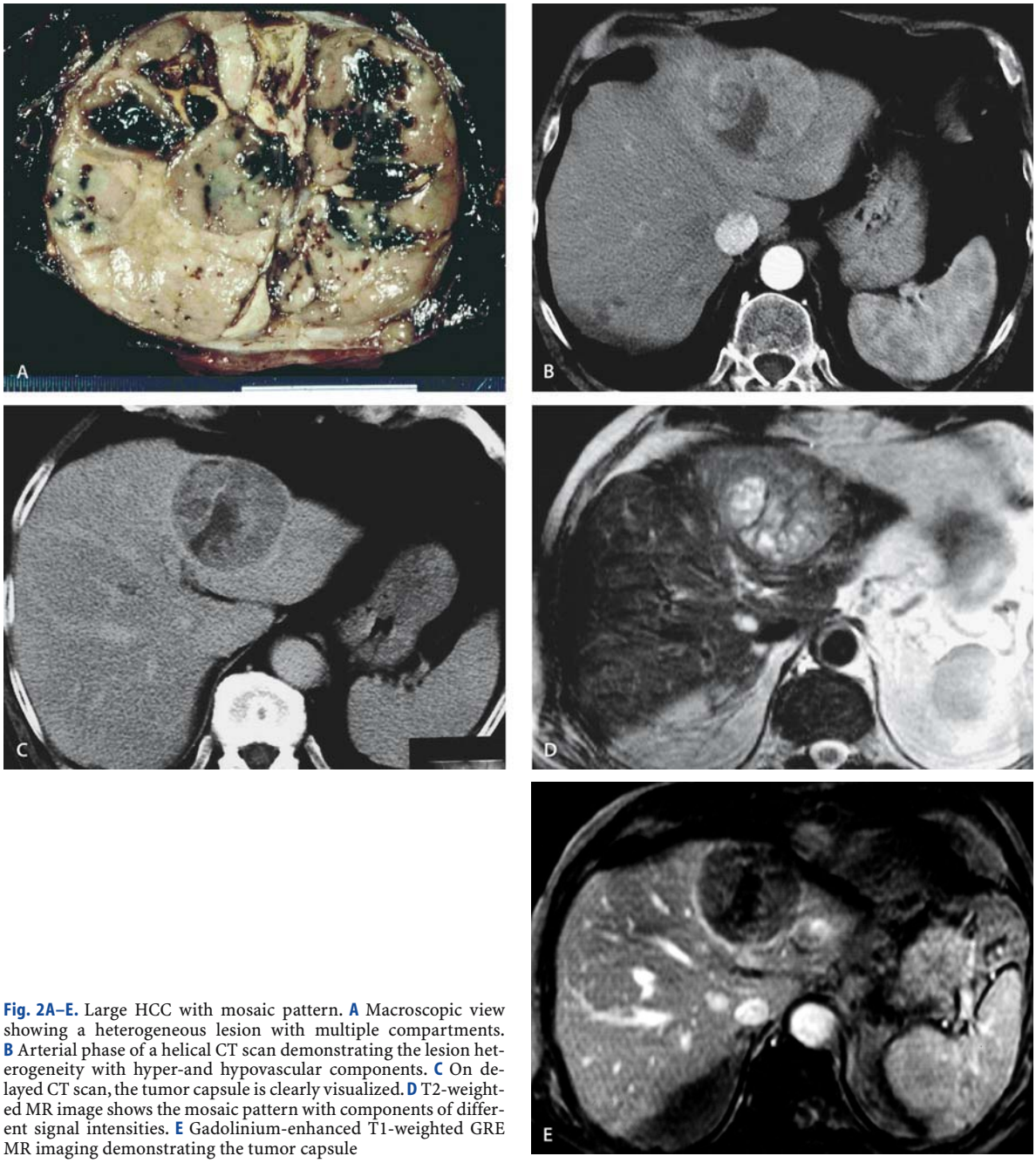

Fig. 2A–E. Large HCC with mosaic pattern. **A** Macroscopic view showing a heterogeneous lesion with multiple compartments. **B** Arterial phase of a helical CT scan demonstrating the lesion heterogeneity with hyper-and hypovascular components. **C** On delayed CT scan, the tumor capsule is clearly visualized. **D** T2-weighted MR image shows the mosaic pattern with components of different signal intensities. **E** Gadolinium-enhanced T1-weighted GRE MR imaging demonstrating the tumor capsule

ry. The spreading HCC usually corresponds to larger tumors with indistinct margins (Fig. 3). Little compression of the liver by the tumor is noted. Multifocal growth pattern represents about 10% of the HCC and is characterized by numerous tumor foci.

At macroscopy the lesions may be homogeneous when of small size or may have necrotic and hemorrhagic changes as well as scar-like areas due to fibrosis. Portal invasion by the tumor is often seen especially in large, spreading HCC or in HCC with multifocal growth pattern (Fig. 4).

The microscopic appearance of HCC is variable between tumors and within the same tumor. Prognosis of a mixed-pattern tumor depends on the most malignant component [1]. The grading of HCC, based on the architecture of the tumor and cellular atypia, has been correlated with prognosis, clinical parameters and laboratory tests. Grade 1 HCC is the most differentiated HCC with a trabecular architecture. The nuclear/cytoplasmic ratio is nearly normal. Its diagnosis could be difficult with an atypical adenoma. Grade 2 HCC shows few cellular atypia and a trabecular and or acinar pat-

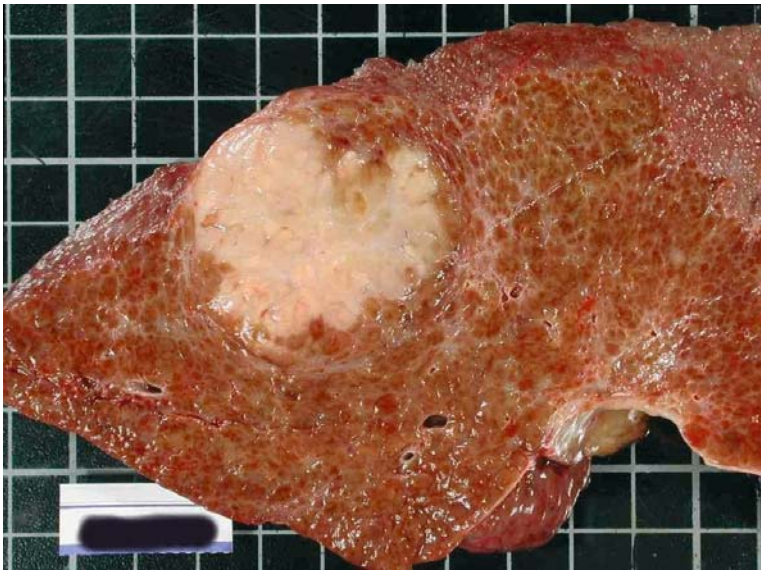

Fig. 3. Macroinfiltrative form of HCC. Macroscopic view shows a ill-limited tumor unencapsulated developed on liver cirrhosis

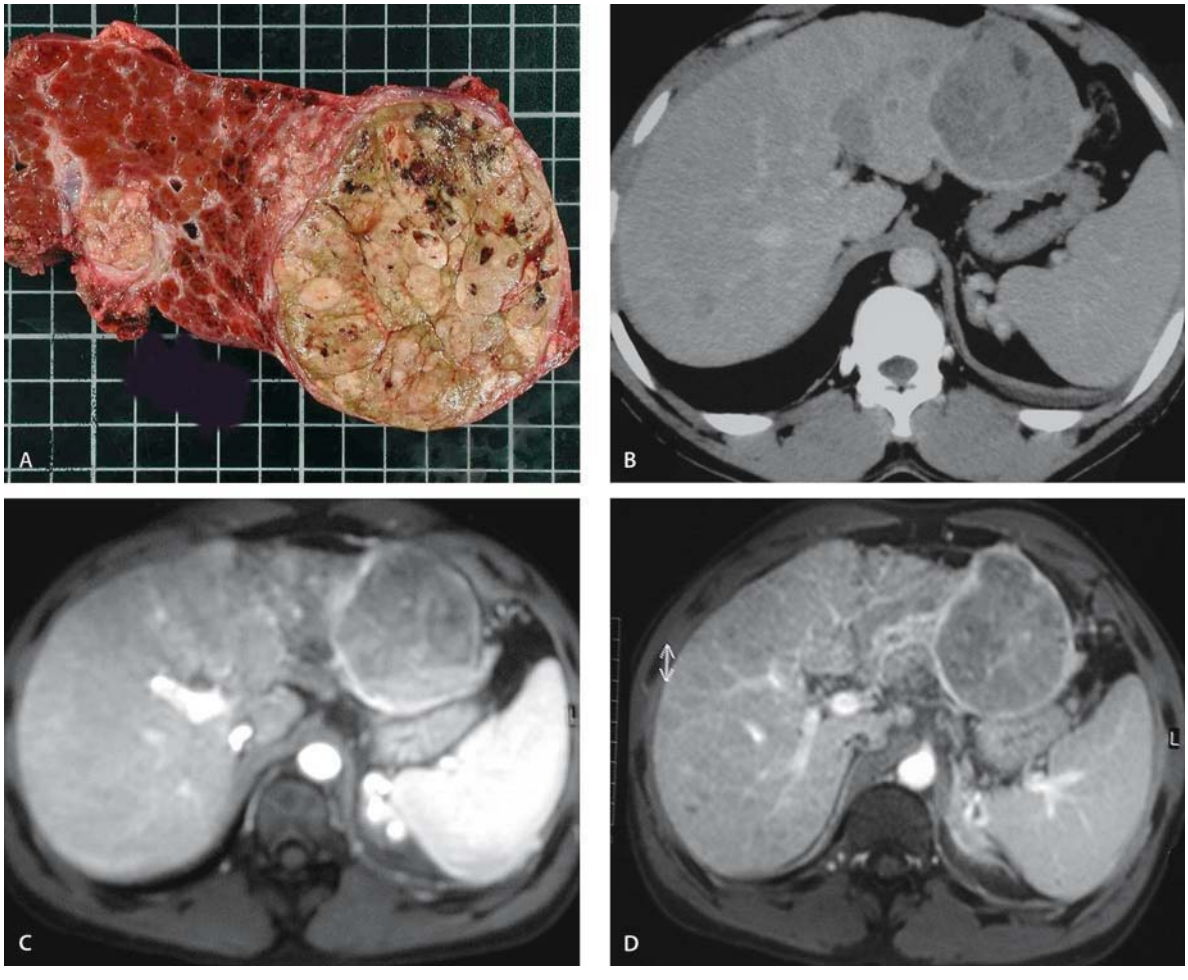

Fig. 4A–D. HCC with portal invasion. **A** macroscopic view shows both the main tumoral nodule and the extension of the tumor into the portal branch. **B** portal-venous phase of a helical CT scan demonstrates a large encapsulated HCC of the left lobe invading the left portal branch. **C**, **D** dynamic post-gadolinium T1-weighted images show lack of enhancement of the left portal branch in the portal-venous (**C**) and delayed phase (**D**)

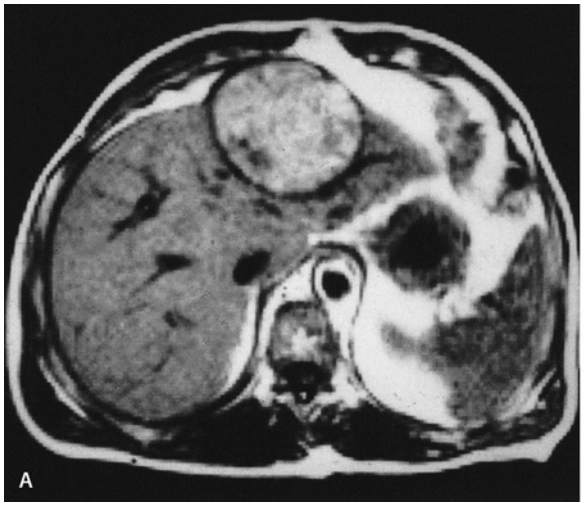

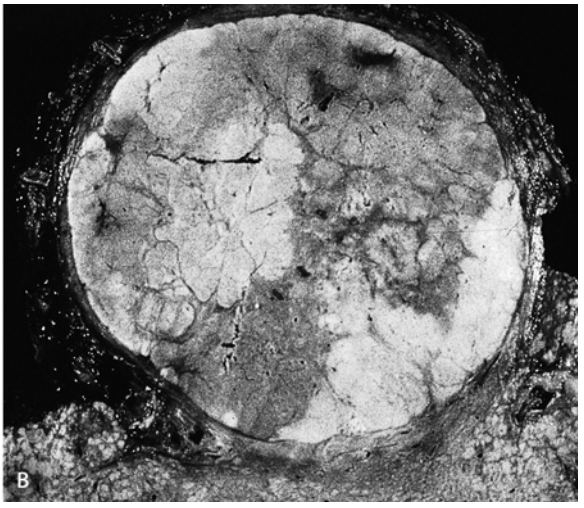

Fig. 5A, B. HCC with fatty changes. **A** Macroscopic view showing a protruding encapsulated HCC with fatty changes. **B** On T1-weighted SE MR image, the lesion is strongly hyperintense and is surrounded by a hypointense rim corresponding to tumor capsule at pathology

tern. Grade 3 HCC has larger hyperchromatic and more variable nuclei with multiple nucleoli and less cytoplasm. A macrotrabecular arrangement is encountered. In Grade 4, the trabecular pattern is lost and the cancer cells demonstrate high atypia. The vascular supply of HCC is abundant in most tumors and the trabeculae are sheathed by endothelial cells. The surrounding space carries arterial blood. Intracellular inclusions such as Mallory bodies and globular hyalin bodies may be seen in HCC. Calcifications are rare. Variants of histologic pattern include fatty HCC and prominent bile production HCC (Fig. 5A). Fatty HCC is composed of cells with a clear cytoplasm containing fat and a eccentrically located nucleus. Fatty change is most frequent in small tumors (<2 cm). Sarcomatous changes may also be observed, characterized by the proliferation of spindle cells. Portal vein involvement is more common that hepatic vein involvement and typically is represented by an enlarged lumen filled with hepatocellular carcinoma. HCC may develop within intrahepatic bile ducts and this form often demonstrates hemobilia.

Imaging Features

Sonography plays an important role because it is used worldwide as a screening test in patients with chronic liver disease in association with serologic testing for alfa-fetoprotein. The sonography appearance is variable and often nonspecific. Small tumors (less than 3 cm in diameter) are mainly hypoechoic and uniform in appearance, and may resemble other lesions developing in chronic liver disease such as cirrhotic nodules, dysplastic nodules or other lesions. Large masses are usually heterogeneous with a mixed hyper- and hypoechogenicity. Some features may suggest the diagnosis: 1° peripheral hypoechoic rim that corresponds to a fibrous capsule at pathology, 2° target appearance with a hypoechoic halo, 3° mosaic pattern, 4° lateral shadowing. Doppler studies are interesting when pulsatile or continuous flows are detected within the lesion and to differentiate clot from malignant thrombus in the portal veins. In rare cases, HCC appears as strongly hyperechoic lesion due to fatty deposition. This appearance can mimic that of hemangioma.

On unenhanced CT scans, HCCs are seen mainly as hypoattenuating lesions. Focal hyperattenuations due to calcifications or diffuse hyperattenuations related to iron overload are rarely observed. The optimal CT protocol is a multiphasic examination on multidetector row helical CT. The most common appearance of HCC on arterial phase is a hyperattenuating or mixed attenuation lesion (Fig. 1B). However, hypoattenuating HCC are observed in about 10% of the cases. The hyperattenuation is related to the prominent arterial blood supply. Other findings are frequently observed:

1 a mosaic pattern is seen in about 40–60% of cases and is consisted of multiple nodular areas of different CT attenuations on contrast-enhanced scans (Fig. 2B) [2]. This pattern is more common in large tumors and does not seem correlated to the histologic tumor grade,
2 a portal or hepatic venous invasion is comprised between 33 to 48% of cases [2]. It appears as unenhancing intraluminal material in portal veins, hepatic veins or the inferior vena cava. Venous invasion is more common in lesions larger than 5 cm in diameter, and in high grade tumors [2],
3 a tumor capsule is a thick rim of tissue surrounding all or part of tumor. The capsule appears iso- or hy-

poattenuating relative to the liver at the arterial phase on the enhancement, and enhances on delayed CT images (Fig. 2C). Tumor capsule is seen in 30 to 67% of tumors and is correlated to encapsulated expanding HCC at pathology. Capsules are found more often in lower grade than in higher grade tumors and in medium-sized tumors (from 3 to 10 cm in diameter) [2, 3],

4 a central scar may be identified as a central linear or stellate low-attenuation region within the tumor without enhancement of contrast material. The scar may have at pathology an inflammatory predominance with a large number of inflammatory cells, extensive necrosis and/or edema, or a collagenous predominance with dense, sclerotic collagen [4],

5 a fatty metamorphosis is recognized at CT as an area within the tumor that had CT attenuation similar to subcutaneous fat. It occurs in 2–21% of cases and is more evident at MR imaging that at CT [2, 5],

6 arterioportal shuntings are detected at contrast-enhanced CT if one of the following features is present: early and prolonged enhancement of the portal vein, abnormally dilated portal vein with irregular intraluminal or periportal vessels, and a wedge shaped area of hepatic parenchymal enhancement distal to the tumor [5]. Arterioportal shunting are best detected on multiphasic helical CT and may be observed in 11 to 60% of cases [2].

HCC may vary in signal intensity on both T1- and T2-weighted MR images. However the most common combination is a hypointensity on T1-weighted images and a hyperintensity on T2-weighted images. This finding represents 54% of HCCs in 113 patients (Fig. 1C) [6]. Other combinations are observed such as isointensity on both T1- and T2-weighted images (16%), hypointensity on T1-weighted images and isointensity on T2-weighted images (10%), hyperintensity on both T1- and T2-weighted images (6.8%) and isointensity on T1-weighted images and hyperintensity on T2-weighted images (6.2%) [6]. Other combinations are very rarely encountered. On immediate gadolinium-enhanced images, the lesions exhibit a diffuse homogeneous or heterogeneous enhancement in 84% of the cases (Fig. 1D). Some lesions enhance with a more prominent peripheral rim. The MR appearance of HCC greater than 1.5 cm or 2 cm and those that are less than or equal to 1.5 cm or 2 cm are significantly different [6, 7]. Ninety-one percent of the isointense lesions on both T1- and T2-weighted images are ≤1.5 cm in diameter in the study reported by Kelekis et al [6]. In the study published by Kadoya et al, on T2-weighted images the lesions smaller than 2 cm in diameter or greater than 2 cm were hyperintense in 88% and 100%, respectively [7]. On T1-weighted images the lesions smaller than 2 cm in diameter or greater than 2 cm were iso- or hyperintense in 64% and 48%, respectively [7]. Also most of the lesions ≤1.5 cm in diameter exhibit diffuse homogeneous enhancement.

Some lesions may contain localized foci with marked hyperintensity on T2-weighted images. This finding has been observed up to 44% of HCCs and correspond mostly to peliotic change of intratumoral sinusoid [7]. HCCs that are undetected or hypointense on T2-weighted images are well differentiated with replacing growths and portal tracts [8].

Other findings are frequently observed at MR imaging:

1 a high signal intensity on T1-weighted images is observed in 12 to 50%. This signal intensity is often related to fatty metamorphosis, and tumors that contain fat in all or most of the tumor cells are hyperintense on T1-weighted images (Fig. 5B). However, fatty metamorphosis is not the unique cause for hyperintensity on T1-weighted images. Other substances may be responsible such as copper-binding protein, hemorrhage, other protein and glycogen [9]. There is still a controversy regarding the respective role of metallic factors contributing to the signal intensities of HCC on T1-weighted images. For some authors copper accumulation within tumor alone may be the cause whereas some authors have demonstrated that the various signal intensities are reflections of copper in HCC and iron in liver and HCC [9, 10]. Intratumoral hemorrhage may give foci of iso- or hyperintensity on T1-weighted images and hyper or hypointensity on T2-weighted images. Usually, hemorrhagic areas occupy only a portion of the tumor (Fig. 6). It is known also that hyperintensity on-T1 weighted images is more frequently observed in grade 1 HCC than in grade 2 and 3 HCC. This finding is similar to that reported in dysplastic nodules and it may be suggested in these cases that hyperintensity on T1-weighted images is a feature of hyperplastic changes of the hepatocytes [7],

2 a mosaic pattern may be identified in about 50% of the cases at MR imaging and is mostly observed in tumors greater than 3 cm in diameter. Depiction of the mosaic pattern on T1-weighted imaging is rare and most tumors appear homogeneous. Conversely, T2-weighted imaging is closely correlated to the macroscopic configuration that is composed of confluent nodules separated by thin septa [11]. On T2-weighted images, the mosaic pattern appears when the tumor shows nonuniform signal intensity or when linear-like structures of hypointensity are seen within the tumor (Fig. 2D) [7],

3 a portal or venous invasion is seen in about 1/3 of patients. Involvement of branches of portal vein is more common than that of hepatic veins. Confidence in the diagnosis is increased when transient increased enhancement of the area of liver correspond-

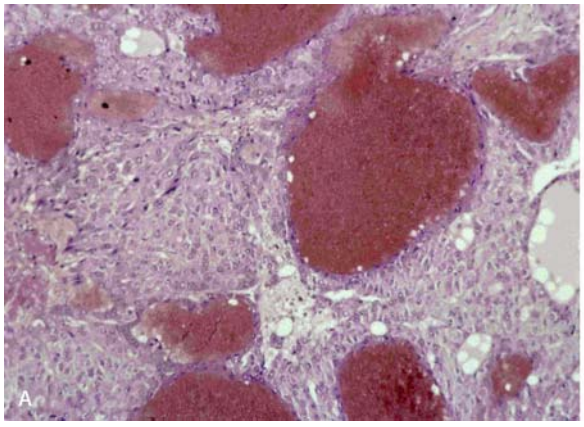

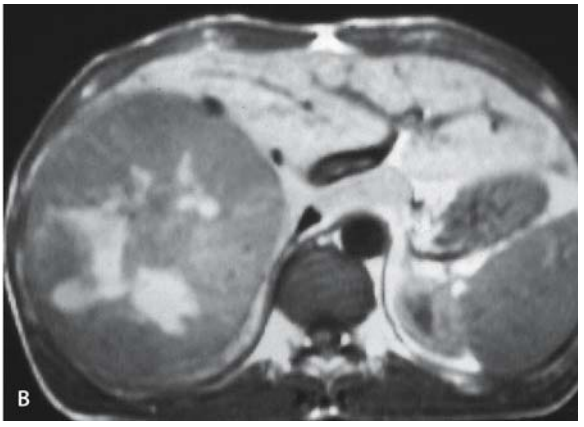

Fig. 6A, B. HCC with hemorrhagic foci. **A** Microscopic view of a resected specimen showing hemorrhage within the lesion. **B** On T1-weighted SE MR image, the lesion is heterogeneous and hyperintense areas correspond to hemorrhagic foci at pathology

ing to portal obstruction or when enhancement of the intravascular tumor thrombus itself is demonstrated,

4 a tumor capsule is a ring-like structure around the lesion. The capsule is mostly seen as hypointense ring on T1-weighted images and can be visualized as hypointense rim on T2-weighted images. More rarely, capsules are seen as double-layered rings (hypointense inner layer and hyperintense outer layer) on T2-weighted images [7]. Capsule detection rate with T1-weighted images is higher than that of with T2-weighted images [7]. Tumor capsule is mainly observed at MR imaging in HCC larger than 2 cm in diameter, and the capsule tends to become thicker as tumor size increases (Figs. 1E, 2E). MR imaging is considered superior to CT in demonstrating capsule, however in a MR-pathologic correlation study, a capsule was detected only in 66% of the cases of encapsulated HCC [7]. MR imaging and especially T1-weighted imaging is also superior to CT imaging in detecting extracapsular invasion by showing a partial tumor capsule [12],

5 a central scar may be identified in HCC as a central stellate area that is hypointense on T1-weighted images and hypo- or hyperintense on T2-weighted images. The first pattern is more frequent and corresponds to collagenous scar mostly composed of dense sclerotic collagen at pathology [4].

In summary, the most common appearance of HCC is a hyperattenuating lesion on the arterial phase at CT examination and a combination of hypointensity on T1-weighted images, hyperintensity on T2-weighted images and diffuse heterogeneous enhancement on immediate gadolinium-enhanced images. However, other appearances are not infrequent and tumors ≤1.5 cm in diameter are frequently isointense on both T1-and T2-weighted images. Knowledge of underlying chronic liver disease and lesion enhancement on immediate contrast medium-enhanced images at CT or MR examination help to establish the diagnosis.

Distinctive Hepatocellular Carcinoma Variants

Infiltrative HCC

Infiltrative HCC represents about 10%–13% of all patients with HCC. Imaging findings appear as permeative, diffuse pattern with ill-defined borders and no evidence of convex margination.

Infiltrative HCCs have a variable appearance on arterial-phase CT or MR images: patchy enhancement, miliary enhancement or even minimal enhancement. Most lesions show heterogeneous washout on portal-phase or delayed phase imaging [13]. Portal venous tumor thrombosis is a common finding.

Infiltrative HCC are mainly hypointense on T1-weighted MR images and heterogeneous and hyperintense on T2-weighted MR images [13].

Early HCC

HCC may develop independently of regenerative or dysplastic nodules or may develop within these nodules. Areas of regenerative or dysplastic nodules with malignant foci have been called early HCC. The cancerous areas can be seen or not at macroscopy. A characteristic feature is a nodule of HCC within a benign or dysplastic nodule at gross examination. Early HCCs have an iso- or hyperintense pattern on T1-weighted images and a isointense pattern with or without partial hyperintensity on T2-weighted images. A nodule in nodule appearance at gross examination is usually responsible of mixed signal intensity on T2-weighted images [14].

Rupture HCC

About 10% of patients with HCC have spontaneous rupture of the tumor resulting hemoperitoneum in most cases. Different characteristics of the rupture and non-rupture groups were observed [15, 16]: increased tumor size, extent of extrahepatic protrusion and decreased thickness of peritumoral liver parenchyma are associated with an increased risk for rupture of HCC. Emergency embolization is an effective treatment in ruptured cases.

Hepatocellular Cholangiocarcinoma

This tumor as been classified into three types: two separate masses of HCC and cholangiocarcinoma in the same liver (double tumor), continuous but independent masses of HCC and cholangiocarcinoma (collision tumor), and a mass of intermingling HCC and cholangiocarcinoma components (mixed tumor). The collision tumor type should not be included into the group at hepatocellular-cholangiocarcinoma.

Hepatocellular-cholangiocarcinoma constitutes about 3% to 5% of all primary hepatic malignant tumors. This tumor may be observed in patients with cirrhosis. Serum alpha-fetoprotein is elevated in most of cases whereas serum carcinoembryonic antigen is elevated in one half of patients [17]. The tumor followed an aggressive clinical course with actuarial five year survival of 24% [18].

At pathology, both tumor components are seen (Fig. 7A, B): HCC component with a green-yellow appearance and cholangiocarcinoma component including a white infiltrative mass with irregular margins. The diagnosis of combined hepatocellular-cholangiocarcinoma is based on histologic evidence of both tumor types: one of hepatocellular differentiation and one of cholangiocellular differentiation. Either cell type may predominate although cholangiocarcinoma is the most predominant in the largest series [17, 18].

Microscopically, special stainings (mucus staining) and immunohistochemistry may help to demonstrate the presence of both components [19].

Imaging shows various findings corresponding to the predominant component. Some areas demonstrate tumor enhancement on arterial-phase CT or MR imaging suggestive of HCC whereas other show delayed enhancement and capsular retraction similar to that observed in cholangiocarcinoma (Fig. 7) [17].

Fibrolamellar Carcinoma

Fibrolamellar carcinoma accounts for 1%–9% of cases of HCC overall [20]. Fibrolamellar hepatocellular carcinoma is a slowly growing tumor with septate fibrosis arising in normal liver and is characterized by eosinophilic neoplastic hepatocytes separated into cords by lamellar fibrous strands. Fibrolamellar hepatocellular carcinoma is generally a malignancy of young adults and the mean age of diagnosis is 22 years [21]. There is no gender predominance. The most common complaint is abdominal pain and the physical findings are non specific. Conversely to most HCCs, fibrolamellar carcinoma does not occur in the setting of chronic liver disease. Tumor markers are usually absent however mild elevation of alpha-fetoprotein (less than 200 ng/µl) may occur in up to 10% of patients. Elevated neurotensin and vitamin B 12 binding capacity have been described in patients with fibrolamellar carcinoma. Patients with fibrolamellar carcinoma have a better survival rate than those with HCC. Overall median survival of patients with fibrolamellar carcinoma is between 28 and 32 months [21]. With surgical resection, the five-year survival is between 56 and 65% [21]. The better survival rate for fibrolamellar carcinoma than that of non fibrolamellar carcinoma is attributed to a more favorable prognosis or to an increased resection rate in the former [22]. This is why aggressive surgical treatment such as subtotal hepatectomy or transplantation is proposed. In a series of 41 patients who had aggressive treatment the cumulative survival at 5 and 10 years was 66% and 47%, respectively [23].

Fibrolamellar carcinoma usually appears as a large focal tumor and measures a mean of 12 cm in diameter [21]. At gross examination, the tumor is bulging, brown, well demarcated from the adjacent liver and often lobulated. Necrosis and hemorrhage are seen in large specimens. The tumors are mostly solitary (80%–90% of cases). Multicentric tumors are composed of a dominant mass with smaller lesions in adjacent parenchyma. Some tumors have typical "focal nodular hyperplasia-type" lesions with a central fibrous scar (Fig. 8A) [1]. The microscopic pattern is composed of two distinctive components (Fig. 8B, C). The epithelial component consists of large, polygonal and deeply eosinophilic cells "oncocytic cells" with coarsely granular cytoplasm and distinct nuclei. Pale bodies and eosinophilic globules are frequently present in the cytoplasm of tumoral cells. The fibrous component is made of hyalinized collagen bundles with a characteristic lamellar pattern. In large tumors, these fibrous areas may design large central scars containing only a few residual tumoral epithelial cells.

In some cases the diagnosis is more difficult because tumors may be composed of separate fibrolamellar and non fibrolamellar components [24] or because the distinction between fibrolamellar carcinoma and sclerosing hepatocellular carcinoma is not evident. Fibrolamellar carcinoma may be heterogeneous in primary cell type and degree of differentiation. Vascular invasion by

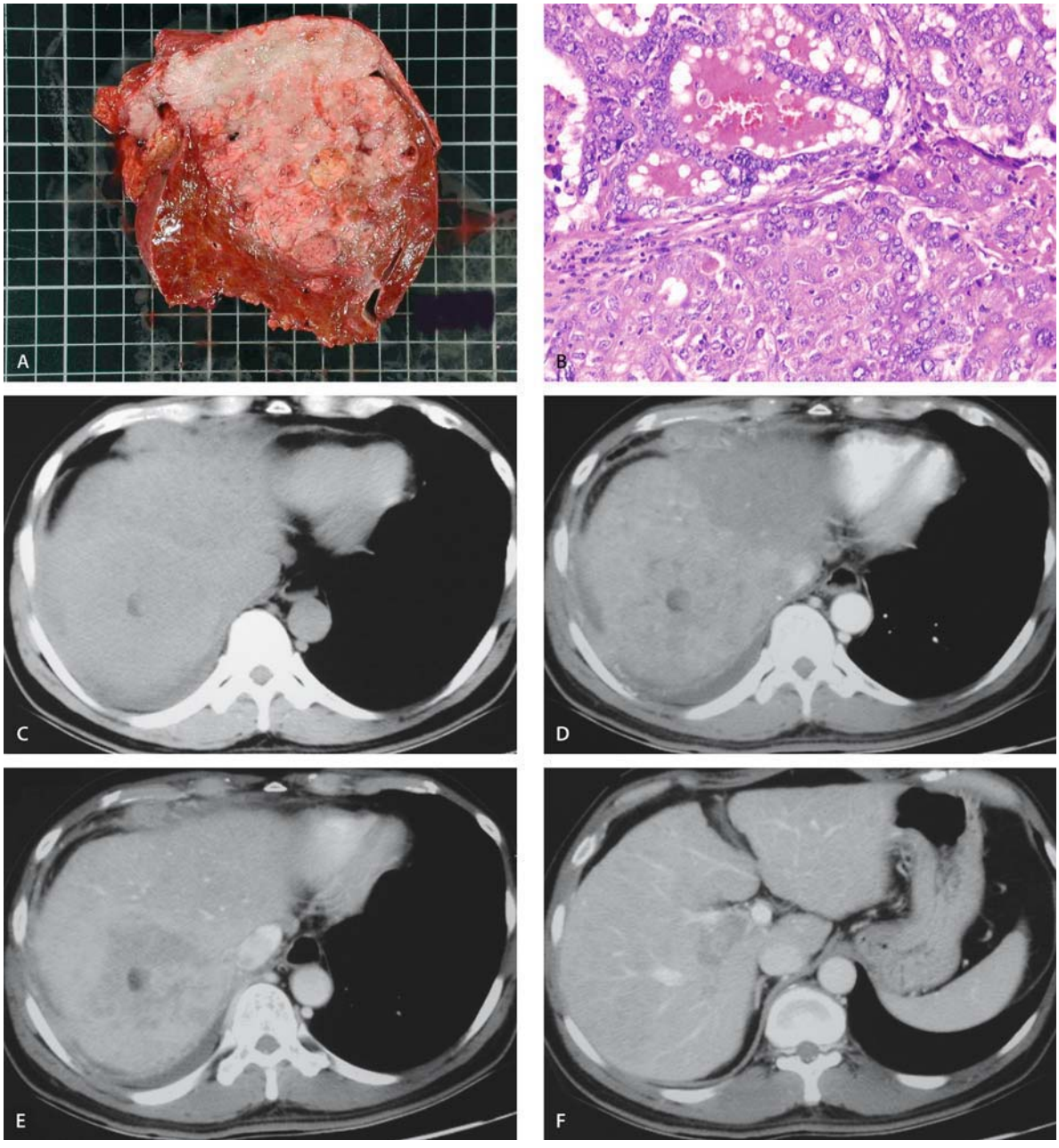

Fig. 7A–F. Hepatocholangiocarcinoma. **A** Macroscopic view of a large and heterogeneous tumor. Contours are ill-defined. **B** Microscopic view clearly shows two distinct components, one displaying a glandular differentiation with carcinomatous glands lined by cuboidal cells (*top*), and one displaying a trabecular pattern of hepatocellular carcinoma composed of large polygonal eosinophilic cells (*bottom*). **C** Unenhanced CT scan demonstrating a large tumor of the right liver. **D, E** Arterial and portal venous-phase helical CT images show a large, ill-defined lesion which enhances moderately. **F** More caudally, the right branch of the portal vein is invaded by the tumor

the tumor is uncommon [20]. Regional adenopathy occurs in 50%–70% of patients. Also, in some cases, fibrolamellar carcinoma may resemble focal nodular hyperplasia. Some authors have called this tumor "the malignant counterpart of focal nodular hyperplasia with oncocytic change" [25]. Moreover fibrolamellar carcinoma has been described in association with focal nodular hyperplasia. In all the reported cases, the lesions were composed of a central area of fibrolamellar carcinoma and a peripheral zone consisted of nodular hyperplastic parenchyma resembling the changes seen in focal nodular hyperplasia [26, 27]. Hepatocellular hyperplasia as-

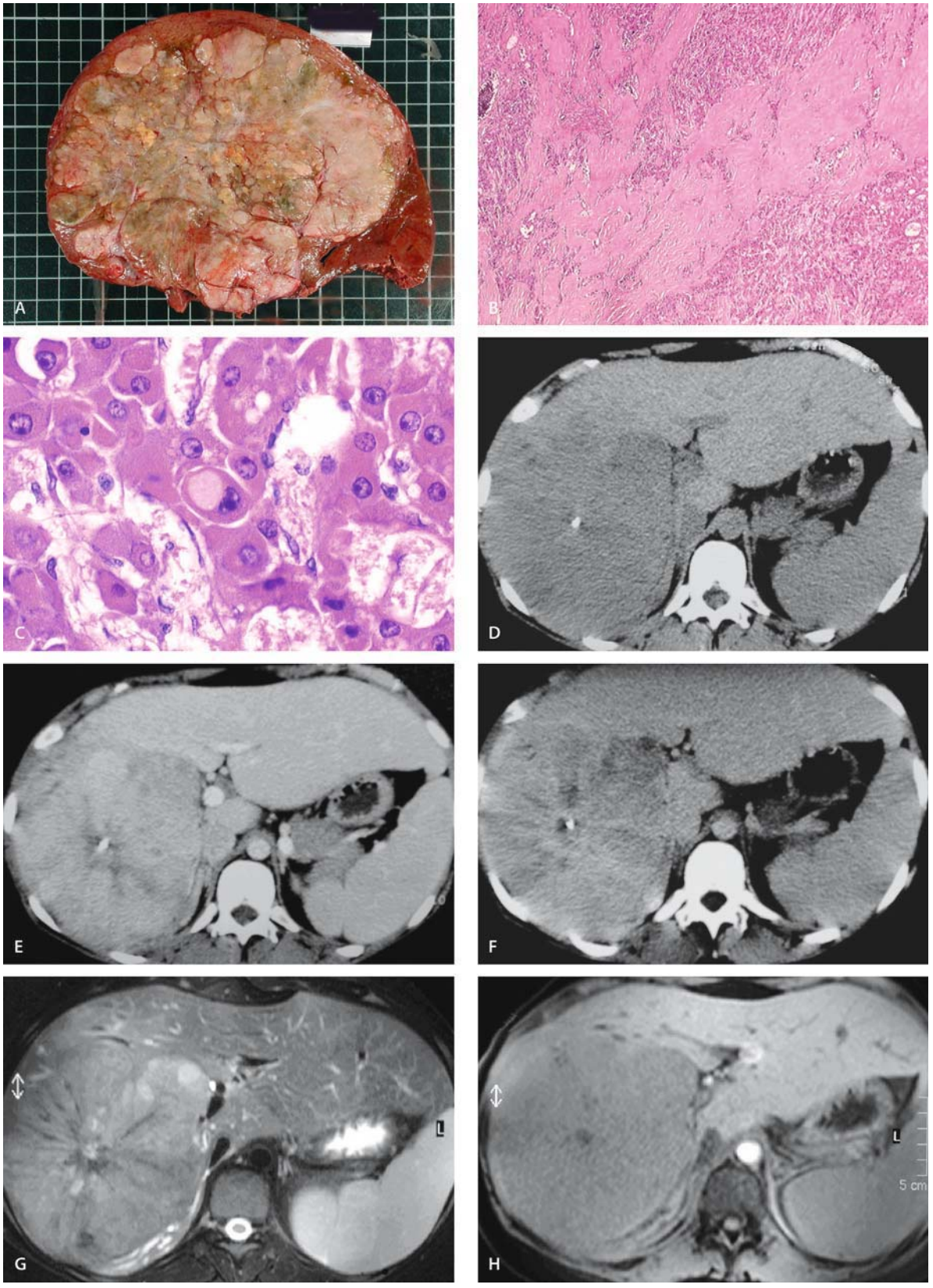

Fig. 8A–H.

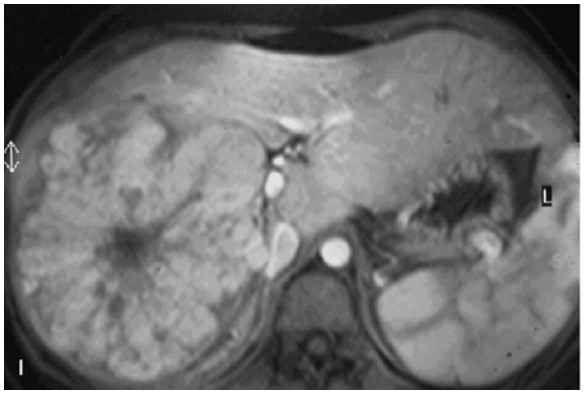

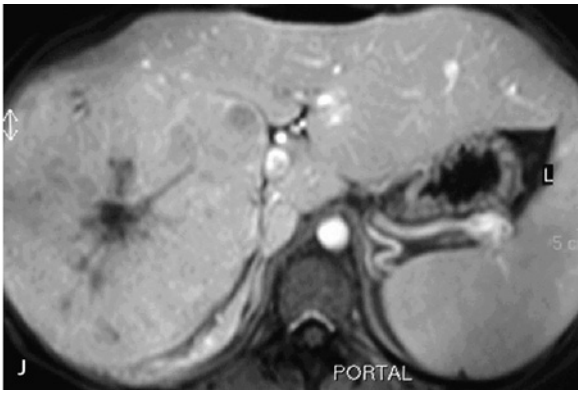

Fig. 8A–J. Fibrolamellar hepatocellular carcinoma. **A** Macroscopic view of the lesion with a "focal nodular-like" appearance; a central scar is evident. Some necrotic foci are seen within the tumor. **B** At low magnification, histologic analysis shows the fibrous hyalinized stroma surrounding sheaths of tumoral cells. **C** At higher magnification, pale bodies are seen in the cytoplasm of tumoral cells. **D** Unenhanced CT shows a large tumor containing a central calcification. **E**, **F** Lesion enhancement is heterogeneous in the portal-venous (**E**) and delayed phase (**F**) imaging. **G**, **H** On MRI the lesion is heterogeneous and contains an hypointense scar on both T2 (**G**) and T1 (**H**) images. **I**, **J** Lesion enhancement mimics that of focal nodular hyperplasia on arterial (**I**) and portal-venous (**J**) phase images

sociated with fibrolamellar carcinoma is probably a response to locally increased blood flow.

At sonography, fibrolamellar hepatocellular carcinoma may be either isoechoic, hyperechoic or hypoechoic [28–30]. Surface lobulations are frequently observed. Central scars are seen in about half of the cases as hyperechoic linear bands. Calcifications are seen in some cases and are located in the center.

On unenhanced CT scans, the tumor appears as a hypoattenuating and solitary mass [31]. Central calcifications are seen in 40% to 68% of the cases (Fig. 8D) [29, 32]. The lesions are hypervascular at the arterial phase and are heterogeneous in 90% of the cases [31] (Fig. 8E, F). Hypoattenuating areas correspond mostly to necrosis. On delayed-CT scans after contrast medium injection, central scars demonstrate delayed enhancement in 25% of the cases [20]. Lymphadenopathy is seen in 50%–70% of cases.

At MR imaging, fibrolamellar carcinoma is heterogeneous and is predominantly hypointense on T1-weighted images and hyperintense on T2-weighted images. The central scar is characteristically of low signal on both T1- and T2-weighted images (Fig. 8G, H) [28]. On dynamic-enhanced images, the tumor demonstrates immediate diffuse heterogeneous enhancement (Fig. 8I) [33]. The central scar may or not enhance on delayed images (Fig. 8J). MR imaging demonstrates the central scar and fibrous septa more reliably than does CT, whereas CT is better to demonstrate calcifications [31]. These findings are distinct from those of focal nodular hyperplasia, however a case of fibrolamellar hepatocellular carcinoma that fulfills MR criteria proposed as diagnostic of focal nodular hyperplasia has been reported [34].

Scirrhous HCC

This uncommon type observed in small tumor, is characterized by marked fibrosis along the sinusoid-like blood spaces with varying degrees of atrophy of tumor trabeculae.

Sclerosing HCC

Sclerosing hepatocellular carcinoma is a rare but distinctive variant of hepatocellular carcinoma characterized by abundant, diffusely distributed fibrous stroma and acinar transformation of the tumor cells. Such tumor tends to occur in an older age group, affecting men and women equally, and be associated with hypercalcemia. Macroscopically, they appear as large, firm, gray-white masses, usually occurring in a noncirrhotic background. Histologically, trabecular cords and nests of tumor cells are segregated by dense paucicellular connective tissue. Individual tumor cells, especially at the periphery of the mass, correspond to those of the usual hepatocellular carcinoma. At the center of the mass, the sclerosis is especially pronounced, frequently obliterating the cellular component.

HCC in Noncirrhotic Liver

HCC usually occurs in the setting of cirrhosis with a known cause such as chronic viral hepatitis or alcoholism. More rarely HCC may develop in a noncirrhotic liver, but some degree of fibrosis may be observed. Association between HCC and cirrhosis is considered less fre-

quent in the USA than that in Japan [35]. Studies have shown that HCC occurring in the noncirrhotic liver has several distinguishing features. Patients are younger, have a single or dominant mass (72%–82%) [35, 36]. Furthermore, tumors are large (mean diameter, 12 cm) and commonly have a scar [35].

It has been suggested that some of these characteristics were also observed in fibrolamellar HCC. However, most patients with conventional HCC are male, and have positive serum tumor markers. Conversely to fibrolamellar HCC, calcifications and lymphadenopathy are rarely observed.

Cholangiocarcinoma

Cholangiocarcinoma is a malignant tumor arising from bile duct epithelium, that can develop in a small intrahepatic bile duct branch (intrahepatic cholangiocarcinoma), at the level of the hilum (hilar cholangiocarcinoma) or within extrahepatic bile ducts (extrahepatic cholangiocarcinoma). All of these tumors are adenocarcinomas. We will only discuss in this chapter the intrahepatic cholangiocarcinoma which accounts for 10% of all cholangiocarcinomas. Intrahepatic cholangiocarcinoma is mainly observed in elderly women. Several predisposing factors are known and the most frequent are primary sclerosing cholangitis, cholangitis secondary to intrahepatic calculi and *Clonorchis sinensis* and *Opisthorchis viverrini* infections. The other factors are congenital hepatic fibrosis, Caroli disease, von Meyenburg complexes, choledochal cysts, and Thorotrast exposure. The incidence of cholangiocarcinoma in association with hepatolithiasis ranges from 2.4 to 10% [37]. The relationship between hepatolithiasis and cholangiocarcinoma is not well explained. Common factors could be bile stasis and repeated cholangitis leading to development of periductal inflammation, mucosal hyperplasia, adenomatous hyperplasia and bile duct carcinoma.

Patients may have abdominal pain, mass, anorexia, weight loss or even be asymptomatic. The serum alkaline phosphatase level is usually elevated but patients are seldom jaundiced. The clinical features also vary according to the mucin production and in some cases mucobilia is observed. In a series of 170 cases of peripheral cholangiocarcinoma, 22 cases (12.9%) were found to have mucin-producing cholangiocarcinoma [37]. These authors have reported that presence of fever and weakness are more frequently encountered in patients with mucin-producing cholangiocarcinoma [37]. Serum alpha-fetoprotein is increased in a few patients with cholangiocarcinoma and serum carcinoembryonic antigen is elevated in 75% of the cases [1]. Usually intrahepatic cholangiocarcinoma presents as a large mass because the tumor causes no or few symptoms in its early stages.

According to the Liver Cancer Study Group of Japan, cholangiocarcinoma is classified in three types: mass-forming, periductal-infiltrating, and intraductal-growing. The prognosis of intraductal-growing cholangiocarcinoma is much better after surgical resection than the two others.

Pathology

At macroscopy, the appearance of intrahepatic cholangiocarcinoma has three patterns: a single large mass, multiple confluent mass, and a diffuse form. The two first appearances are more frequent that the latter. At cut section, the tumor is well limited and non-encapsulated. In about half of the cases, lobulated contours are seen (Fig. 9A). The tumor is firm, white-colored due to dense fibrosis and may have a scar-like at the center.

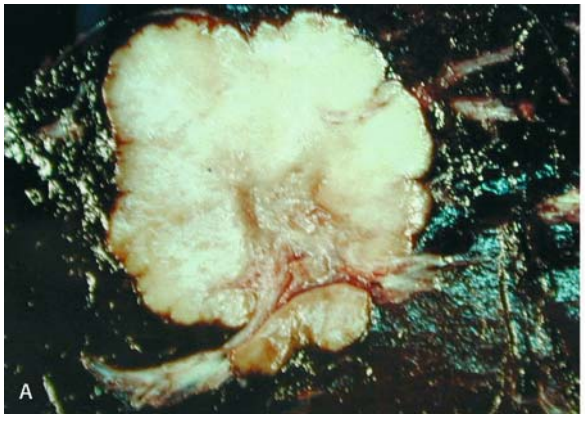

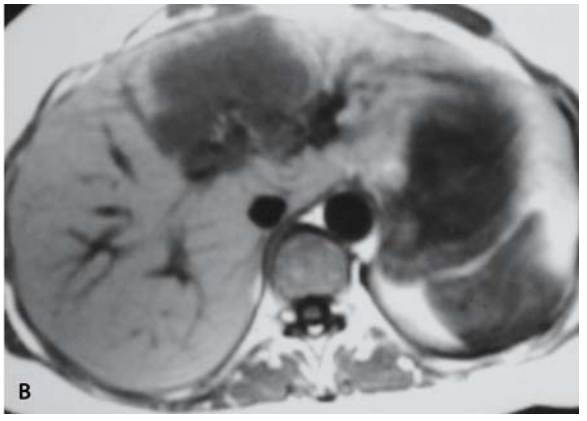

Fig. 9A, B. Peripheral cholangiocarcinoma. **A** macroscopic view of a lobulated non-encapsulated lesion. Note the encasement of a portal branch. **B** T1-weighted SE MR image shows a homogeneously hypodense lesion. Portal branch encasement is seen at the posterior part

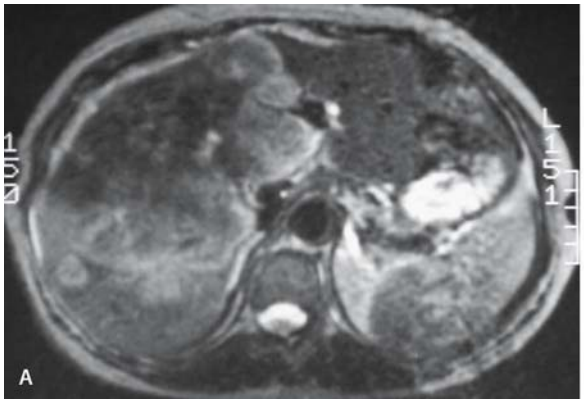

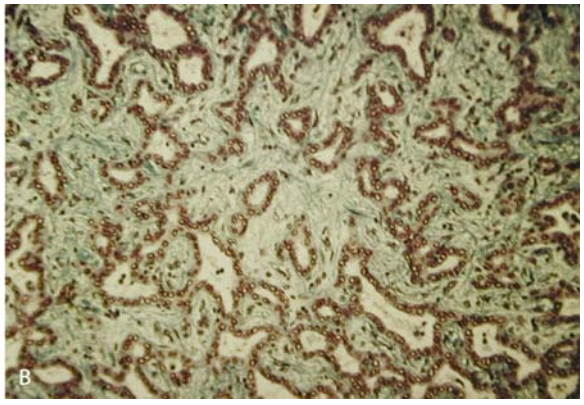

Fig. 10A, B. Peripheral cholangiocarcinoma. **A** Microscopic view of the resected specimen showing marked fibrosis and low components of necrosis or mucus. **B** T2-weighted SE MR image demonstrates isointensity of the lesion which is explained by abundant fibrosis seen at pathology

At microscopy, intrahepatic cholangiocarcinoma is a glandular adenocarcinoma with abundant sclerosis (Fig. 10A). Secretion of mucin from the glands and presence of necrosis vary from one lesion to the other (Fig. 11A). The glandular epithelium is composed of small cuboidal cells with round nuclei. In rare cases, papillary growth in bile duct is observed. Different morphological variants can be observed, at least focally inside the tumor: papillary pattern, mucoid change, squamous differentiation. Histologically, differential diagnosis may be difficult with a metastatic adenocarcinoma. As the carcinoma grows and obstructs bile ducts or involves portal branches, the ipsilateral hepatic lobe undergoes atrophy and the contralateral hepatic lobe becomes hypertrophied.

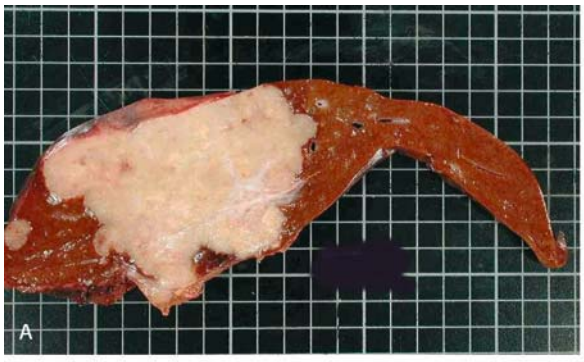

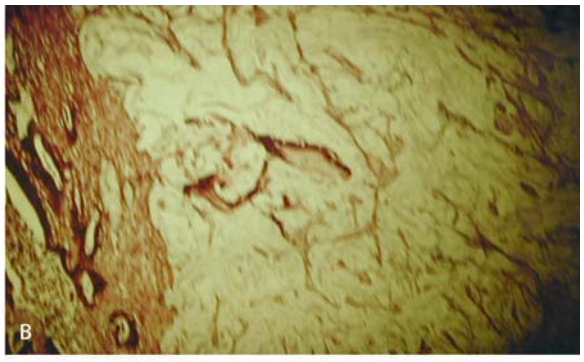

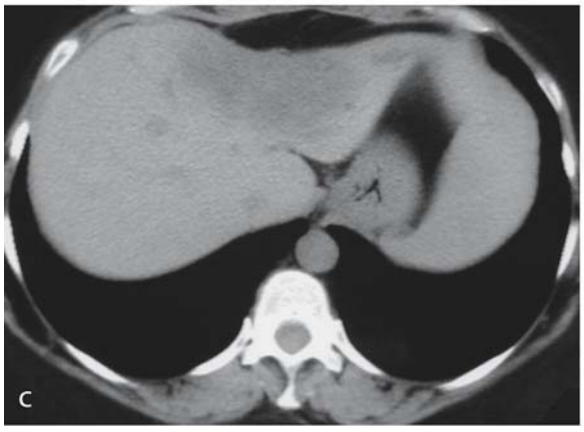

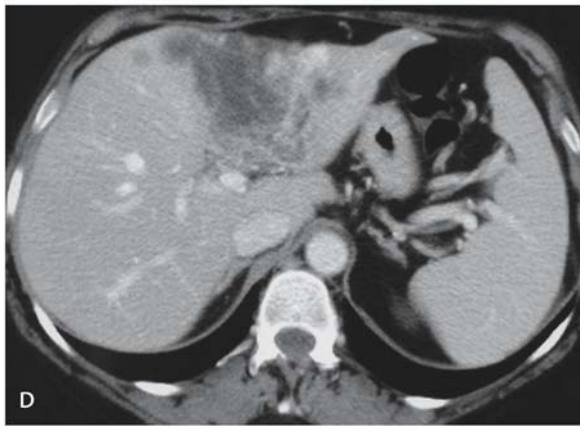

Fig. 11A–D.

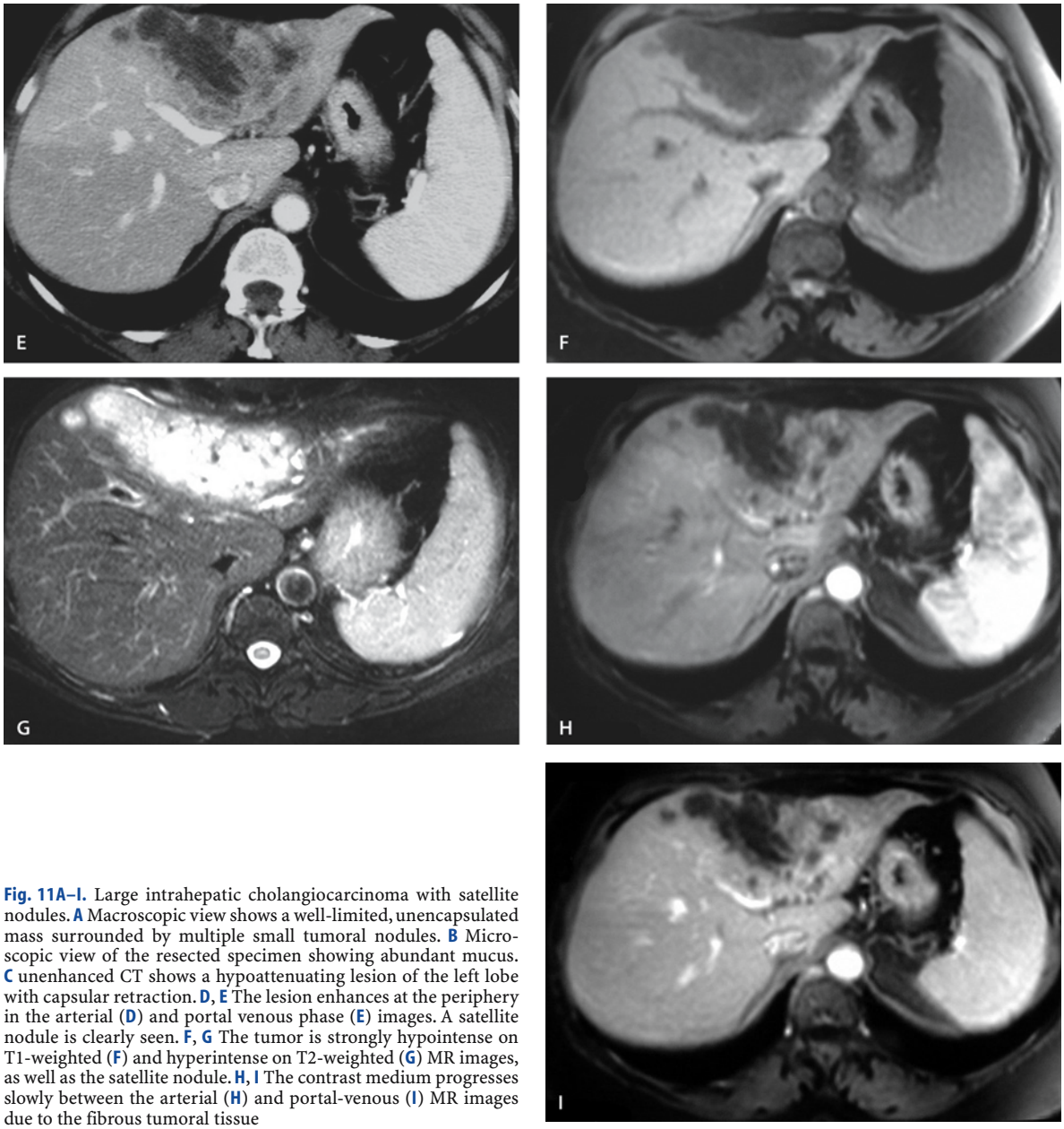

Fig. 11A–I. Large intrahepatic cholangiocarcinoma with satellite nodules. **A** Macroscopic view shows a well-limited, unencapsulated mass surrounded by multiple small tumoral nodules. **B** Microscopic view of the resected specimen showing abundant mucus. **C** unenhanced CT shows a hypoattenuating lesion of the left lobe with capsular retraction. **D**, **E** The lesion enhances at the periphery in the arterial (**D**) and portal venous phase (**E**) images. A satellite nodule is clearly seen. **F**, **G** The tumor is strongly hypointense on T1-weighted (**F**) and hyperintense on T2-weighted (**G**) MR images, as well as the satellite nodule. **H**, **I** The contrast medium progresses slowly between the arterial (**H**) and portal-venous (**I**) MR images due to the fibrous tumoral tissue

Intrahepatic cholangiocarcinoma often spreads along the ducts wall and adjacent to nerves. Portal vein involvement is frequent and has been demonstrated in 52% of the cases of a histopathologic study (Fig. 9A) [38].

More than one half of the mass-forming intrahepatic cholangiocarcinomas are poorly differentiated, whereas most periductal-infiltrating cholangiocarcinomas are well differentiated. Most intraductal-growing cholangiocarcinomas are papillary adenocarcinomas [39].

Imaging Features

Mass-forming Type

The most frequent appearance of mass-forming cholangiocarcinoma is a single and usually large mass up 15 cm in diameter. Multicentricity especially around the main tumor is common. More rarely the lesions are multiple and disseminated. The tumor echogenicity is mainly hyperechoic in lesions larger than 3 cm in diam-

eter [40] and hypo- or isoechoic in lesions of 3 cm or less in diameter. The tumors are clearly separated from the normal liver parenchyma and irregular margins are seen in approximately half of the cases [40]. In most lesions of cholangiocarcinoma, there is an absence of signal at Doppler studies. Other findings may be seen at sonography such as intrahepatic bile duct dilatation (30%) or portal venous encasement.

On unenhanced CT scans, intrahepatic cholangiocarcinoma is usually a solitary non-encapsulated hypoattenuating lesion with irregular margins (Fig. 11C). Hyperattenuating foci within the lesion may be seen and correspond to calcifications [41]. On both hepatic arterial phase and portal-venous phase, the most common pattern of contrast enhancement is a peripheral area of thin, mild, incomplete rim-like contrast enhancement (Fig. 11D, E) [42]. Absence of change between the two phases is due to the slow progression of contrast enhancement within the tumorous tissue. On delayed CT-images, characteristically there is an incomplete or complete fill-in of the contrast medium.

At MR imaging, the pattern of intrahepatic cholangiocarcinoma is related to the microscopic changes. Lesions are usually hypointense on T1-weighted images, however the lesions may be predominantly iso-, slightly hyper-, or strongly hyperintense on T2-weighted images (Figs. 9, 11). Comparison with pathologic examination shows that the iso- or slightly hyperintense lesions contain abundant fibrosis and have a low content of mucous secretion or necrosis, whereas the hyperintense lesions contain low or moderate fibrosis and prominent mucous secretion and/or necrosis (Figs. 10, 11) [43]. After gadolinium-enhanced images, there is a initial rim enhancement with progressive, concentric fill-in in all cases (Fig. 11H, I). On delayed contrast-enhanced T1-weighted images, the fill-in is usually incomplete and heterogeneous, but the entire mass may be enhanced rarely [39].

Intrahepatic cholangiocarcinomas are hypervascular in 30% of the cases. Angiography shows neovascularity in these cases and discloses no arteriovenous fistula but may demonstrate stenosis or occlusion of intrahepatic portal branch.

Other findings that are not characteristic of mass-forming cholangiocarcinoma but may suggest the diagnosis are observed on different imaging modalities such as: 1° lobulated contour and absence of capsule, 2° intratumoral septum like linear structures or central scar. This finding has been reported in both CT and MR studies and did not correspond to a central scar on gross pathologic examination but may represent part of fibrous component [42, 43], 3° capsular retraction seen in about 20% of the cases on CT or MR examinations. Capsular retraction is probably due to the fibrotic nature of the tumor as well as the bile duct or portal involvement (Fig. 11), 4° dilatation of the peripheral portion of the intrahepatic bile ducts seen in 20 to 68% of the cases [42, 43], 5° narrowing or obstruction of the portal vein due to invasion or extrinsic compression by the tumor in 47 to 50% of the cases [42, 43], 6° morphologic changes of the liver with or without transient hyperattenuated areas. Segmental or lobar atrophy of the tumorous lobe is seen in 40% of the cases, whereas transient hyperattenuation peripheral to the tumor is seen in 7 to 21% on CT or MR images [42, 43], 7° extrahepatic spread: lymph node involvement, invasion of adjacent organs.

In summary, mass-forming cholangiocarcinoma usually appears as a solitary non-encapsulated intrahepatic lesion. Associated findings may strengthen the diagnosis at imaging.

Periductal-infiltrating Type

Periductal-infiltrating type grows along the bile ducts. This intrahepatic tumor is radiologically similar to hilar cholangiocarcinoma but is located between the small intrahepatic ducts and the secondary confluence. On imaging, the bile ducts proximal to the cholangiocarcinoma are dilated and the involved bile ducts are narrow or not seen [39]. In the early stage, it is difficult to depict the tumor. In the later stage, the tumor invades the hepatic parenchyma and hepatic hilum [44].

Intraductal-growing Type

Intraductal intrahepatic cholangiocarcinoma constitutes 8%–18% of all resected intrahepatic cholangiocarcinoma. The tumors are usually small, sessile or polypoid, often spreading along the mucosa, and resulting in multiple tumors (papillomatosis) [39]. Bile ducts are dilated because of obstruction by a tumor, by debris or by profuse amount of mucus. Imaging shows dilated bile ducts of the involved segment or lobe. At sonography, the mass appears as echogenic. At CT, characteristic features of the tumor include a focal dilatation of intrahepatic bile duct with higher attenuation than that of bile which enhances on portal-venous phase and delayed phase imaging. The tumor may not be depicted when it is small and isoattenuating to the liver [39].

Unusual Manifestations

Mucin-hypersecreting Cholangiocarcinoma

Cholangiocarcinoma produces variable amounts of mucin which is retained in the tumor in most cases. Some papillary tumors produce so much mucin that it enters the bile duct resulting in bile stasis, and obstructive

jaundice. Imaging shows marked dilatation of the intra and extrahepatic ducts both proximal to and distal from the tumor. The tumor usually is small and may not be seen. Endoscopic retrograde cholangiopancreaticography can demonstrate large, amorphous filling defects caused by mucin [39].

Cholangiocarcinoma Arising from Preexisting Bile Duct Diseases

Cholangiocarcinoma is associated with preexisting bile duct disease. Due to associated imaging findings, the diagnosis of cholangiocarcinoma may be more difficult or done at a later stage. For instance, the diagnosis of a cholangiocarcinoma complicating primary sclerosis cholangitis remains a challenge at imaging.

Cholangiocarcinoma Developing from Benign Biliary Tumors

Rarely cholangiocarcinoma can develop from papilloma and adenoma which are now known as premalignant lesions [45].

Cystic Degeneration of Peripheral Cholangiocarcinoma is Very Rare

All imaging modalities demonstrate a large intrahepatic cystic neoplasm often containing enhancing portion.

Angiosarcoma

Angiosarcoma is a rare hepatic tumor, although it is one of the most frequent mesenchymal malignancy in the liver. This tumor is originating from the endothelial cells. In 40% of the cases, angiosarcomas are related to one of several environmental carcinogens including: Thorotrast, vinyl chloride, arsenic ingestion [1]. More rarely, angiosarcomas have been associated with radium implant and hemochromatosis. This tumor occurs predominantly in men between the sixth and the seventh decade.

Patients usually present with non specific symptoms, including abdominal pain, weakness, weight loss and anorexia. Hematologic abnormalities such as anemia, thrombocytopenia, and microangiopathic hemolytic anemia are seen in most cases.

At the time of the diagnosis, most patients have distant metastases, most often to the lung or the spleen. Angiosarcoma may be revealed by a spontaneous intraperitoneal hemorrhage (15% of the cases) [46], or by acute or subacute hepatic failure. Tumor markers (alfafetoprotein and carcinoembryonic antigen) are not elevated. The prognosis of angiosarcoma is very poor with a mean life duration of six months. The course of the disease may be altered by percutaneous liver biopsy which may increase the risk of massive hemorrhage, however, in a recent series percutaneous biopsies yielded diagnostic specimens without substantial bleeding [47].

Treatment of hepatic angiosarcoma is based on surgical resection in patients with limited intra- or extrahepatic extent, and on chemotherapeutic drugs in non-surgical patients.

Pathology

At macroscopy, a variety of patterns has been described and may be classified in four types: diffuse micronodular, diffuse multinodular, massive, and mixed. The two first types are the most frequent. The tumors are predominantly located at the surface of the liver. They are nodular, ill-defined, and may contain thrombosis, necrosis, and hemorrhage. Cirrhosis may be observed in patients exposed to Thorotrast.

At microscopy, different serial aspects may be observed: first the endothelial lining cells increase in number, become enlarged and have large hyperchromatic nuclei. Then, an increase in endothelial tumoral cells is observed inside the sinusoids leading to the formation of tumoral nodules (Fig. 12A). Multiple mitoses are seen. Immunohistochemical studies show a positive staining of vascular markers such as factor VIII (Fig. 12B). Adjacent liver tissue may display significant fibrosis, especially in the context of Thorotrast, vinyl chloride exposure.

Imaging Studies

All presentations are observed between a solitary liver mass to multiple disseminated intrahepatic lesions associated with splenic tumors.

At ultrasonography the tumors may be either hyperechoic or mixed hypo-hyperechoic due to hemorrhagic or necrotic changes. In Thorotrast-related cases, some hyperechoic foci represent Thorotrast accumulation.

On unenhanced CT scans, angiosarcoma appears mainly as a hypoattenuating lesion, however, hyperattenuating areas are sometimes observed within the lesions (due to hemorrhage) or in the non-tumorous liver (due to Thorotrast deposit). Thorotrast accumulation may be observed as well in lymph nodes and spleen. In case of rupture of hepatic angiosarcoma, the diagnosis is ascertained by demonstrating free intraperitoneal fluid and focal high-density area adjacent to the tumor consistent with acute clot (Fig. 12C) [46]. After contrast

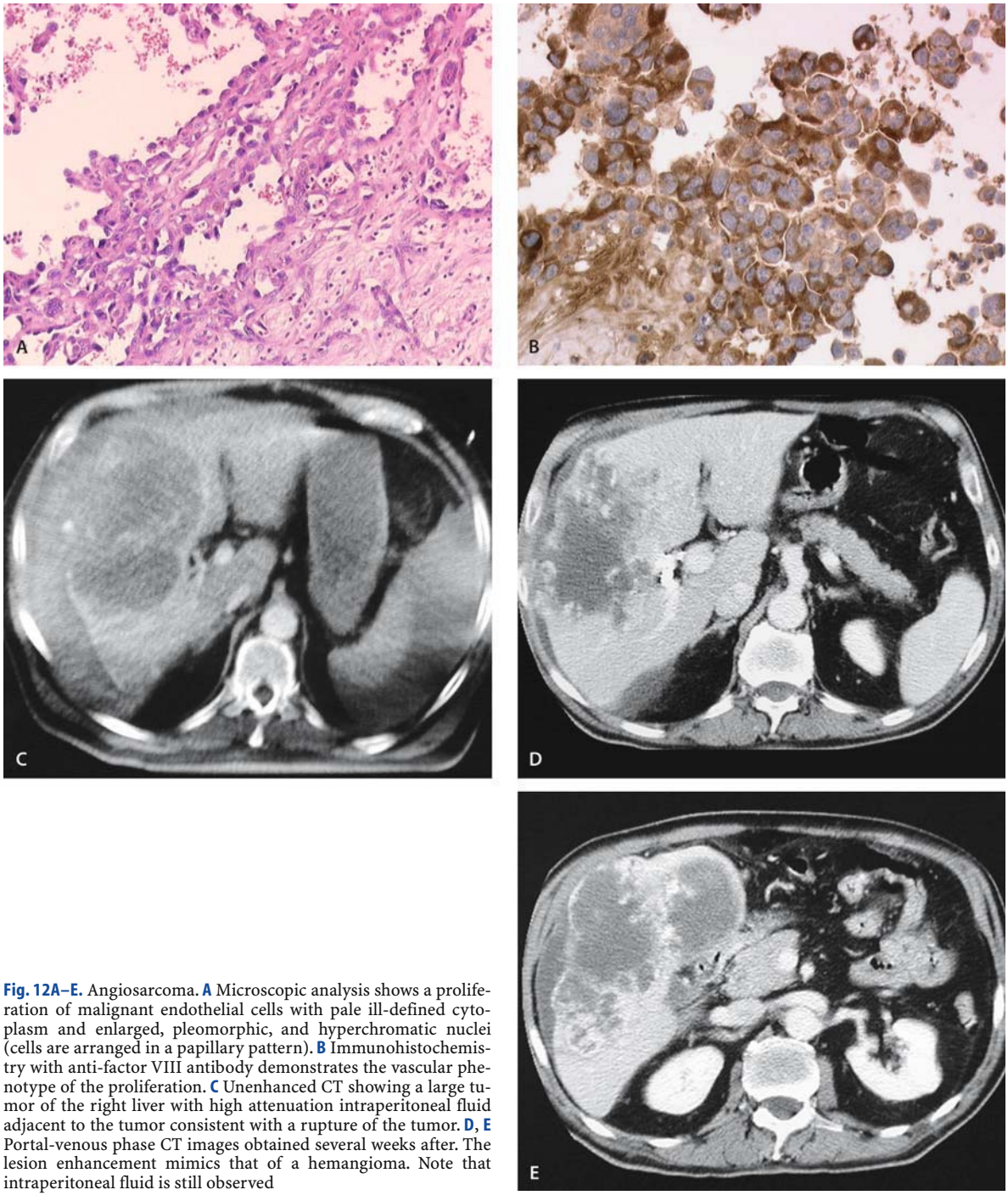

Fig. 12A–E. Angiosarcoma. **A** Microscopic analysis shows a proliferation of malignant endothelial cells with pale ill-defined cytoplasm and enlarged, pleomorphic, and hyperchromatic nuclei (cells are arranged in a papillary pattern). **B** Immunohistochemistry with anti-factor VIII antibody demonstrates the vascular phenotype of the proliferation. **C** Unenhanced CT showing a large tumor of the right liver with high attenuation intraperitoneal fluid adjacent to the tumor consistent with a rupture of the tumor. **D**, **E** Portal-venous phase CT images obtained several weeks after. The lesion enhancement mimics that of a hemangioma. Note that intraperitoneal fluid is still observed

medium injection, angiosarcoma may mimic hepatic angioma with progressive spreading enhancement (Fig. 12D, E) [48]. But in most cases angiosarcomas do not resemble benign cavernous hemangiomas because most lesions are hypoattenuating compared with normal liver tissue or because enhancing lesions have focal areas of enhancement that show less attenuation than the aorta or demonstrate peripheral ring-shaped enhancement [47].

At MR imaging, the tumor is strongly hyperintense and heterogeneous on T2-weighted images and has a more variable appearance on T1-weighted images. Areas of hyperintensity on T1-weighted images are related to hemorrhage. Other features have been described on

T2-weighted images: fluid-fluid levels that reflect the hemorrhagic nature and marked heterogeneity with focal areas of high intensity along with septum like or rounded areas of low intensity [47]. On dynamic contrast-enhanced MR images, lesions show heterogeneous enhancement with progressive enhancement at delayed imaging due to abundant vascular channels and dilated vascular spaces [47].

Angiographic findings have been rarely reported and are consistent with intense peripheral tumor stain appearing late in the arterial phase and persisting for 30–40 s.

Angiosarcoma has various appearance at imaging that reflect the different histologic compositions. A specific diagnosis of this entity is difficult. Acute onset of the disease, exposure to chemical carcinogens, characteristic hematologic abnormalities and a hypervascular and hemorrhagic dominant mass or multiple liver lesions with splenic metastases are highly suggestive of hepatic angiosarcoma [49].

Epithelioid Hemangioendothelioma

Hepatic epithelioid hemangioendothelioma (EHE) is a rare, slowly growing tumor of vascular origin. It arises also in soft tissue, lung and there is still a controversy whether multiple localizations are metastases or multicentric tumors. In most cases, no causative factor is found, however oral contraceptive use and a possible linkage to vinyl chloride exposure have been suggested [1, 50]. EHE is mainly observed in women at a mean age of 50 years. Most patients have no specific symptoms, but in rare cases Budd-Chiari syndrome or liver failure can reveal the tumor in a late stage [51]. Other patients may be asymptomatic [52]. Tumor markers are negative.

The prognosis of patients with EHE is considerably better than that of angiosarcoma, but survival may vary from several months to two or three decades. Treatment depends on the intrahepatic extent and involvement of other organs. When possible, liver transplantation is the treatment of choice.

Pathology

EHE is composed of epithelioid and dendritic cells originating from endothelial cells, abundant sclerosis, and myxoid stroma [1]. This tumor differs histopathologically from infantile hemangioendothelioma which is most often present before six months of age and later regresses spontaneously.

Macroscopically, EHE is characterized by the presence of multiple, solid, firm nodules, with a predominantly peripheral location [53, 54]. The external surface of the liver may appear irregular. The diameter of the nodules varies from 1 to more than 10 cm. With progression of the disease, the nodules often coalescence in the periphery of the liver and cause capsular retraction that is due to the tumor fibrous reaction (Fig. 13A) [53]. On the other hand, EHE enlarges slowly over years and compensatory hypertrophy of uninvolved portions of the liver are often seen. At cut section, typically the le-

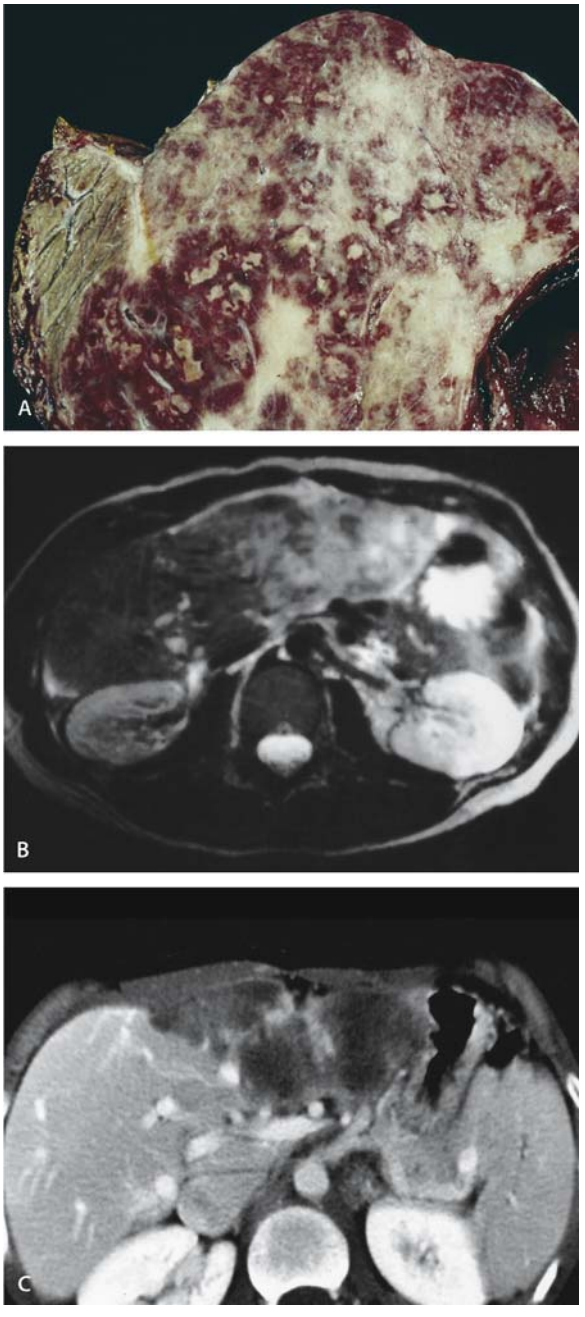

Fig. 13A–C. Epithelioid hemangioendothelioma. **A** Macroscopic view of a large tumor of the left lobe with capsular retraction. **B** Portal-venous phase of a CT demonstrating a hypodense lesion with capsular retraction. **C** On T2-weighted FSE MR image, the lesion is heterogeneous

sion contains a central dense fibrous scar tissue surrounded by a hyperemic periphery.

At microscopy, the pattern of the tumor varies. The center of the nodules are densely fibrotic with remnants of portal areas. Occasionally, dendritic cells and dystrophic calcifications are observed. At the periphery of the mass, there is an increased cellularity mainly composed of epithelioid cells that contain eosinophilic cytoplasm. At the margin of the nodules, tumor cells invade the hepatic sinusoids and small portal branches and adjacent hepatocytes become atrophic. The vascular origin of EHE is demonstrated by positive staining for factor VIII-related antigen, CD 34 or CD 31, or both. At electron microscopy, tubular structures called Weibel-Palade bodies are seen within tumorous cells.

EHE frequently is confused with other lesions. In a series of 137 patients with EHE, a diagnosis was made correctly by the pathologist in 25% [52]. The most common misdiagnoses were cholangiocarcinoma and angiosarcoma. Features of EHE that are helpful in differential diagnosis are the infiltrative pattern, the vascular invasion of portal branches and hepatic venules, and the positive endothelial marker.

Imaging Studies

In nodular lesions, sonography shows multiple peripheral tumor nodules with a variable appearance. The lesions may be homogeneously hypoechoic, hyperechoic, or mixed: hypo- and isoechoic. Some lesions appear as "bull's-eye" nodules [55]: hyperechoic or isoechoic masses with a peripheral hypoechoic rim [53]. There is no correlation between sonographic pattern and the size of the lesions. In diffuse lesions, US studies show the lesions to be areas of overall decreased echogenicity [53] that contain in some cases hyperechoic foci corresponding to calcifications.

In nodular lesions, unenhanced CT demonstrates multiple, round or oval areas of low attenuation. Calcifications within tumors may be observed. It is generally considered that lesion conspicuity is better on unenhanced scans than that on enhanced scans [53]. On postcontrast CT images, there is a moderate contrast enhancement and incomplete filling of the lesions may be seen on delayed images in tumors with a high content of fibrosis. In some cases, lesions have a second more peripheral hypoattenuating rim that correlate with a avascular rim seen at pathology [53]. In diffuse lesions, precontrast CT scans show large and diffuse areas of overall low attenuation. The vascularity of diffuse lesions is moderate but delayed fill-in of contrast medium is consistent with fibrosis (Fig. 13B).

Changes in hepatic contours are more often observed in diffuse lesions than in nodular lesions. These changes include: 1° capsular retraction which may be seen in more than one half of the cases [53]. Capsular retraction is always centered over a peripheral mass and is suggestive of EHE but is not a specific finding and could be encountered in other malignant tumors such as peripheral cholangiocarcinoma, hepatocellular carcinoma, or metastases (Fig. 13B), 2° compensatory hypertrophy of the unaffected segments mainly observed in the left lobe or the caudate lobe in patients with predominant lesions located in the right lobe.

The lesions have various signal characteristics at MR imaging. On T1-weighted images, the lesions may be either homogeneously hypointense, either may contain central areas of lower signal intensity than the remainder of the lesion or are surrounded by a thin dark rim [53, 54]. On T2-weighted images, the lesions are moderately hyperintense. Some lesions may have a target appearance [51]. The center of the lesion itself may contain one or several concentric zones of various intensity. The hyperintense periphery correspond at pathology to viable tumor, the hypointense rim correspond with the peripheral avascular zone and the central areas are related to connective tissue admixed with calcifications or coagulation necrosis. After intravenous administration of gadolinium, the tumor demonstrates a moderate peripheral enhancement and delayed central enhancement [54]. MR imaging as well as CT is able to detect capsular retraction and compensatory hypertrophy of the normal liver (Fig. 13C). Furthermore, additional signs may be detected at MR imaging such as tumor invasion in portal branches, obliteration of hepatic veins and signs of portal hypertension.

Hepatic arteriography shows hypovascular lesions with a moderate, predominantly peripheral staining on the hepatogram phase [54]. The portal phase of superior mesenteric angiography may detect portal obstruction.

Extrahepatic involvement includes the peritoneal lymph nodes, omentum and mesentery and may be associated with calcification. Thoracic disease (intrapulmonary or pleural) and cutaneous or intramuscular metastases may be observed as well.

Although the diagnosis cannot be established firmly at imaging, some imaging findings are highly characteristic: (1) predominant distribution at the periphery of the liver, (2) intratumorous calcifications, (3) changes of the liver contour (capsular retraction and compensatory hypertrophy of the normal liver), (4) invasion of portal and hepatic veins, (5) tumors composed of concentric zones, (6) changes of nodular lesions to large coalescent masses.

Biliary Cystadenocarcinoma

Biliary cystadenocarcinoma is a malignant tumor and is usually a papillary adenocarcinoma. It is a rare neo-

plasm that develops mostly in biliary cystadenoma. Most of the reported cases (83%) have been in middle-aged women (mean age, 59 years) [56]. Clinical symptoms are abdominal pain, mass and intermittent jaundice. Biliary cystadenocarcinomas arise mostly from intrahepatic bile ducts (85%). Among intrahepatic cystadenomas, 55% occur in the right lobe, 29% occur in the left lobe, and 16% occur in both lobes [57].

Very rarely, biliary cystadenocarcinoma may arise in a congenital cyst [58]. The prognosis of the patients with cystadenocarcinoma depends on the possibility of surgical resection. In patients who had complete surgical resection, most of them are free of disease.

Pathology

The lesions are usually multilocular and large with a range of 5 to 14 cm [1]. They frequently contain mucoid fluid. Large papillary masses as well as solid areas of gray-white tumor may occur in a thickened wall (Fig. 14A, E). The cyst is bloody in one-third of the cases. At microscopy, we may see a variety of epithelium including columnar, stratified cuboid and purely squamous epithelium. Most cases have invasive tubulopapillary epithelial components [56]. Areas of preexisting benign cystadenoma are found in about one third of the cases suggesting that benign lesions may evolve into malignant ones [56]. The levels of CA 19–9 and carcinoembryonic antigen in the cystic fluid are high.

Most tumor cells are positive on immuno-histochemical staining with antibodies to cytokeratin, epithelial membrane antigen and carcinoembryonic antigen. It seems that two types of cystadenocarcinomas exist, one developing in female patients with an "ovarian-like" stroma and the other seen in males, lacking the distinctive cellular stroma with a more aggressive course [56].

Imaging Features

At sonography, cystadenocarcinoma appears mostly as a multilocular cystic mass. Associated nodularity is observed in half of the patients [59]. The fluid-filled spaces may be either anechoic or hypoechoic.

CT usually shows a multilocular lesion with water-attenuation or both water and soft tissue attenuation locules surrounded by a well-defined thick fibrous capsule (Fig. 14B, F) [57]. Calcifications may be observed and are typically thick [60]. At MR imaging, the lesions are multiseptate with predominantly high signal intensity on T2-weighted imaging and mixed high or low signal intensity on T1-weighted images (Fig. 14C, D) [59]. Lesions with hemorrhagic components or protein content demonstrate areas of increased signal intensity on T1-weighted images.

Although the distinction between cystadenoma and cystadenoma is difficult, the presence of septation and nodularity is suggestive of biliary cystadenocarcinoma. The two types of cystadenocarcinomas cannot also be distinguished with imaging studies.

Primary Lymphoma of the Liver

Although the liver is often secondarily involved in the late stages of lymphoma, primary lymphoma of the liver is extremely rare, representing 0.4% of extranodal non-Hodgkin's lymphoma and 0.016% of all non-Hodgkin's lymphomas. Primary lymphoma of the liver is defined as a liver involvement with no lymphadenopathy or splenomegaly, normal abdominal and thoracic CT scans, normal bone marrow and blood count for at least six months after the biopsy.

Most cases are non-Hodgkin's lymphoma of "large-cell" subtype, B cell-phenotype [61]. Hepatitis C virus prevalence is found between 9% to 42% which suggests a potential pathogenic role of HCV in primary lymphoma of the liver.

This tumor predominantly occurs in men during the fifth decade [62]. The circumstances of diagnosis are various: abdominal pain, poor general condition, fever and inflammatory syndrome. The clinical examination shows a hepatomegaly in half of the cases [61]. The primary lymphoma of the liver is multinodular in half of the patients, uninodular in one third of the patients and diffuse in the other patients [61].

Abnormal blood liver tests are seen in most patients, whereas an inflammatory syndrome and elevation of lactate dehydrogenase are observed in one third of patients [61]. Tumor markers are not elevated. Most patients have complete response after chemotherapy.

Pathology

The gross appearance of primary lymphoma of the liver varies from a large solitary mass with necrosis to multiple white nodules and to diffuse hepatomegaly without distinct mass lesions.

At microscopy, large cells with large nuclei and large nucleoli are mixed with small lymphocytes and proliferate around bile ducts and portal structures. Immunochemical studies to demonstrate lymphoid markers are required to prove the lymphoid origin. Most of them display CD 20 marker consistent with B-phenotype. Relation with EBV infection should be checked in these cases.

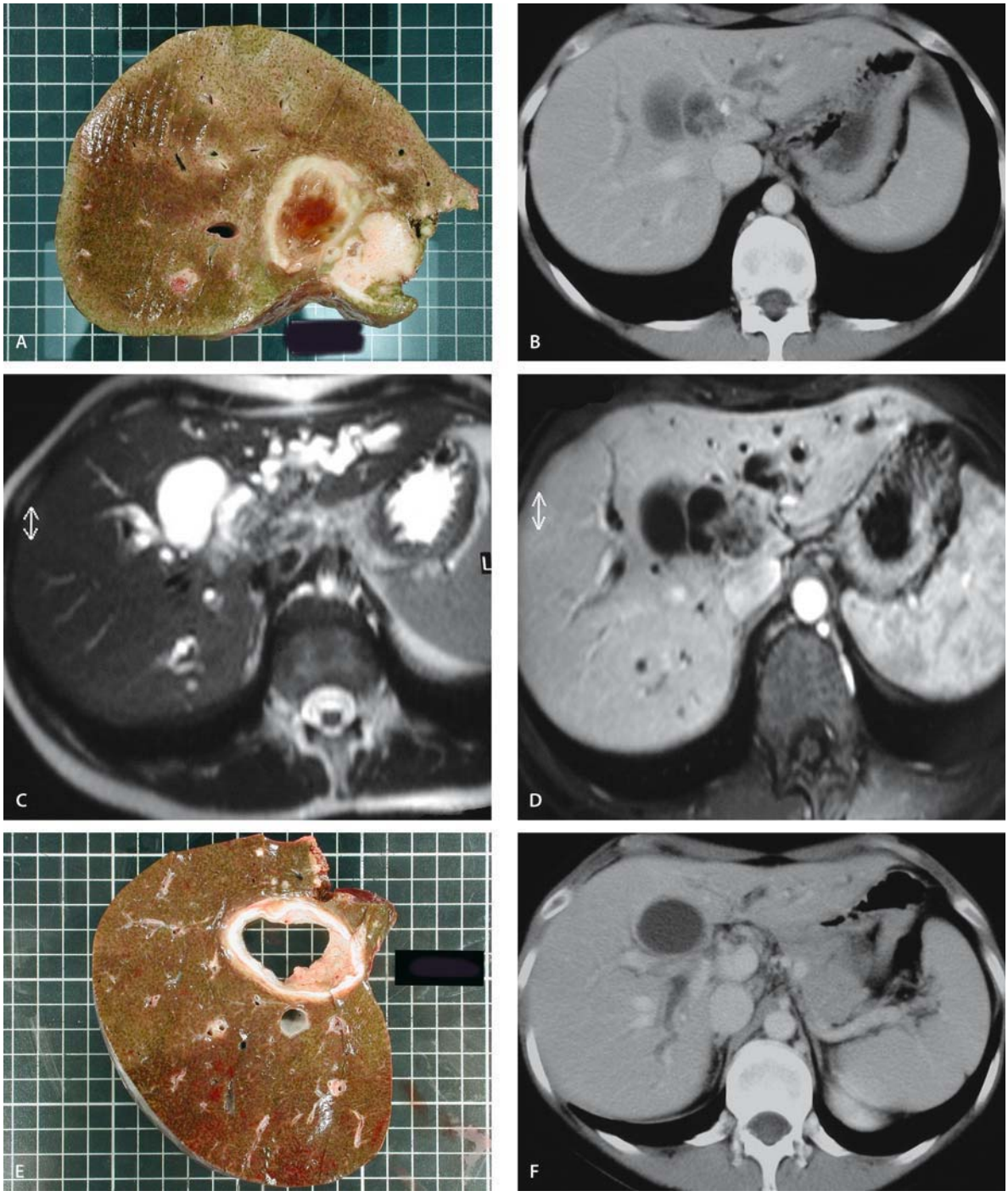

Fig. 14A–F. Cystadenocarcinoma. **A** Macroscopic view shows a liver mass displaying both cystic and massive infiltrative patterns. **B** Portal-venous phase of helical CT scan demonstrates a cystic and solid mass. Calcifications are seen within the solid portion. **C** The tumor is strongly hyperintense on T2-weighted MR image. **D** Dynamic MR image shows mild lesion enhancement of the solid portion in the arterial phase. **E** Macroscopic view (more caudally) exhibits only the cystic pattern. **F** Portal-venous phase of helical CT scan at the same level demonstrates the cystic component surrounded by a thick capsule. Note diffuse dilatation of intrahepatic bile ducts

Imaging

Primary lymphoma of the liver mostly appears as multiple hypoechoic lesions at sonography and hypoattenuating lesions at unenhanced CT. Lesion enhancement after contrast medium injection is usually minimal [61]. Depiction of tumor infiltration is difficult in diffuse involvement of the liver.

Other Primary Hepatic Malignant Neoplasms

Other primary malignant neoplasms such as other types of sarcoma, malignant schwannoma, malignant fibrous histiocytoma are very rare and will not be emphasized in this chapter.

References

1. Craig JR, Peters RL, Edmondson HA (1988) Tumors of the liver and intra-hepatic bile ducts. AFIP, Washington.
2. Stevens WR, Johnson CD, Stephens DH, Batts KP (1994) CT findings in hepatocellular carcinoma: correlation of tumor characteristics with causative factors, tumor size, and histologic tumor grade. Radiology 191:531–537
3. Honda H, Ochiai K, Adachi E et al. (1993) Hepatocellular carcinoma: correlation of CT, angiographic, and histopathologic findings. Radiology 189:857–862
4. Rummeny E, Weissleder R, Sironi S et al. (1989) Central scars in primary liver tumors: MR features, specificity and pathologic correlation. Radiology 171:323–326
5. Freeny PC, Baron RL, Teefey SA (1992) Hepatocellular carcinoma: reduced frequency of typical findings with dynamic contrast–enhanced CT in non-Asian population. Radiology 182:143–148
6. Kelekis NL, Semelka RC, Worawattanakul S et al (1998) Hepatocellular carcinoma in North America: A multiinstitutional study of appearance on T1-weighted, T2-weighted, and serial Gadolinium-enhanced gradient-echo images. AJR 170:1005–1013
7. Kadoya M, Matsui O, Takashima T, Nonomura A (1992) Hepatocellular carcinoma: correlation of MR imaging and histopathologic findings. Radiology 183:819–825
8. Honda H, Kaneko K, Maeda T et al (1997) Small hepatocellular carcinoma on magnetic resonance imaging. Relation of signal intensity to angiographic and clinicopathologic findings. Invest Radiol 32:161–168
9. Ebara M, Watanabe S, Kita K et al (1991) MR imaging of small hepatocellular carcinoma: effect of intratumoral copper content on signal intensity. Radiology 180:617–621
10. Honda H, Kaneko K, Kanazawa Y et al (1997) MR imaging of hepatocellular carcinomas: effect of Cu and Fe contents on signal intensity. Abdom Imaging 22:60–66
11. Choi BI, Lee GK, Kim ST (1990) Mosaic Pattern of Encapsulated Hepatocellular Carcinoma: Correlation of Magnetic Resonance Imaging and Pathology. Gastrointest Radiol 15:238–240
12. Imaeda T, Kanematsu M, Mochizuki R, Goto H, SAJI S, SHIMOKAWA K (1994) Extracapsular invasion of small hepatocellular carcinoma: MR and CT findings. J Comput Assist Tomogr 18:755–760
13. Kanematsu M, Semelka RC, Leonardon P, Mastropasqua M, Lee JK (2003) Hepatocellular carcinoma of diffuse type: MR imaging findings and clinical manifestations. J Magn Reson Imaging ; 18:189–195
14. Muramatsu Y, Nawano S, Takayasu K et al (1991) Early hepatocellular carcinoma: MR imaging. Radiology 181:209–213
15. Chen CY, Lin XZ, Shin JS et al (1995) Spontaneous rupture of hepatocellular carcinoma. A review of 141 Taiwanese cases and comparison with non-rupture cases. J Clin Gastroenterol 21:238–242
16. Kanematsu M, Imaeda T, Yamawaki Y et al (1992) Rupture of hepatocellular carcinoma: predictive value of CT findings. AJR 158:1247–1250
17. Ebied O, Federle MP, Blachar A (2003) Hepatocellular cholangiocarcinoma: helical computed tomography findings in 30 patients. J Comput Assist Tomogr 27:117–124
18. Jarnagin WR, Weber S, Tickoo SK (2002) Combined hepatocellular and cholangiocarcinoma. Cancer 94:2040–2046
19. Tickoo SK, Zee SY, Obieckwe S et al (2000) Combined hepatocellular-cholangiocarcinoma: a histopathology, immunohistochemical, and in-situ hybridization study. Am J Surg Pathol 26:989–997
20. Mc Larney JK, Rucker PT, Bender GN, Goodman ZD, Kashitari N, Ros PR (1999) Fibrolamellar carcinoma of the liver: radiologic-pathologic correlation. Radiographics 19:453–471
21. Saab S, Yao F (1996) Fibrolamellar hepatocellular carcinoma. Case reports and a review of the literature. Dig Dis Sci 41:1981–1985
22. Stevens WR, Johnson CD, Stephens DH, Nagorney DM (1995) Fibrolamellar hepatocellular carcinoma: stage at presentation and results of aggressive surgical management. AJR 164:1153–1158
23. Pinna AD, Iwatsuki S, Lee RG et al (1997) Treatment of fibrolamellar hepatoma with subtotal hepatectomy or transplantation. Hepatology 26:877–883
24. Nagorney DM, Adson MA, Weiland LH, Knight CD, Smalley SR, Zinsmeister AR (1985) Fibrolamellar hepatoma. The American Journal of Surgery 149:113–119
25. Vecchio FM, Fabiano A, Ghirlanda G, Manna R, Massi G (1984) Fibrolamellar carcinoma of the liver: the malignant counterpart of focal nodular hyperplasia with oncocytic change. Am J Clin Pathol 81:521–526
26. Saul SH, Titelbaum DS, Gansler TS et al (1987) The fibrolamellar variant of hepatocellular carcinoma. Cancer 60:3049–3055
27. Saxena R, Humphreys S, Williams R, Portmann B (1994) Nodular hyperplasia surrounding fibrolamellar carcinoma: a zone of arterialized liver parenchyma. Histopathology 25:275–278
28. Titelbaum DS, Hatabu H, Schiebler ML, Kressel HY, Burke DR, Saul SH (1988) Fibrolamellar hepatocellular carcinoma: MR appearance. J Comput Assist Tomogr 12:588–591
29. Friedman AC, Lichtenstein JE, Goodman Z, Fishman EK, Siegelman SS, Dachman AH (1985) Fibrolamellar hepatocellular carcinoma.Radiology 157:583–587
30. Brandt DJ, Johnson CD, Stephens DH, Weiland LH (1988) Imaging of fibrolamellar hepatocellular carcinoma. AJR 151:295–299
31. Ichikawa T, Federle MP, Grazioli L, Madariaga J, Nalesnik M, Marsh W (1999) Fibrolamellar hepatocellular carcinoma: imaging and pathologic findings in 31 recent cases. Radiology 213:352–361
32. Soyer P, Roche A, Levesque M, Legmann P (1991) CT of fibrolamellar hepatocellular carcinoma. J Comput Assist Tomogr 15:533–538
33. Corrigan K, Semelka RC (1995) Dynamic contrast-enhanced MR imaging of fibrolamellar hepatocellular carcinoma. Abdom Imaging 20:122–125
34. Hamrick-Turner JE, Shipkey FH, Cranston PE (1994) Fibrolamellar hepatocellular carcinoma: MR appearance mimicking focal nodular hyperplasia. J Comput Assist Tomogr 18:301–304
35. Winston CB, Schwartz LH, Fong Y, Blumgart LH, Panicek DM (1999) Hepatocellular carcinoma: MR imaging findings in cirrhotic livers and noncirrhotic livers. Radiology 210:75–79
36. Brancatelli G, Federle MP, Grazioli L, Carr BI (2002) Hepatocellular carcinoma in noncirrhotic liver: CT, clinical, and pathologic findings in 39 US residents. Radiology 222:89–94
37. Chen MF, Jan YY, Chen TC (1998) Clinical studies of mucin-producing cholangiocellular carcinoma. Ann Surg 227:63–69

38. Nakajima T, Kondo Y, Miyazaki M, Okui K (1988) A histopathologic study of 102 cases of intrahepatic cholangiocarcinoma: histologic classification and modes of spreading. Hum Pathol 19:1128–1234
39. Lim JH (2003) Cholangiocarcinoma: morphologic classification according to growth pattern and imaging findings. AJR 181:819–827
40. Wibulpolprasert B, Dhiensiri T (1992) Peripheral cholangiocarcinoma: sonographic evaluation. J Clin Ultrasound 20: 303–314
41. Ros PR, Buck JL, Goodman Z, Ros AMV, Olmsted WW (1988) Intrahepatic cholangiocarcinoma: radiologic-pathologic correlation. Radiology 167:689–693
42. Kim TK, Choi BI, Han JK, Jang HJ, Cho SG, Han MC (1997) Peripheral cholangiocarcinoma of the liver: two phase spiral CT findings. Radiology 204:539–543
43. Vilgrain V, Van Beers B, Flejou JF et al (1997) Intrahepatic cholangiocarcinoma: MRI and pathologic correlation in 14 patients. JCAT 21:59–65
44. Han JK, Choi BI, Kim AY et al (2002) Cholangiocarcinoma: pictorial essay of CT and cholangiographic findings. Radiographics 22:173–187
45. Lee WJ, Lim HK, Jang KM (2001) Radiologic spectrum of cholangiocarcinoma: emphasis or unusual manifestations and differential diagnosis. Radiographics 21:S 97-S 116
46. Mahony B, Jeffrey RB, Federle MP (1982) Spontaneous rupture of hepatic and splenic angiosarcoma demonstrated by CT. AJR 138:965–966
47. Koyama T, Fletcher JG, Johnson CD, Kuo MS, Notohara K, Burgart LJ (2002) Primary hepatic angiosarcoma: findings at CT and MR imaging. Radiology 222:667–673
48. Itai Y, Teraoka T (1989) Angiosarcoma of the liver mimicking cavernous hemangioma on dynamic CT. JCAT 13:910–912
49. Tordjman R, Eugene C, Clouet O, Wesenfelder L, Collet C, Bergue A (1995) Angiosarcome hépato-splénique compliqué d'hémopéritoine et de coagulation intravasculaire disséminée. Traitement par embolisation artérielle et chimiothérapie. Gastroentérol Clin Biol 19:625–628
50. Shin MS, Carpenter JT, Ho KJ (1991) Epithelioid hemangioendothelioma: CT manifestations and possible linkage to vinyl chloride exposure. JCAT 15:505–507
51. Lyburn ID, Torreggiani WC, Harris AC (2003) Hepatic epithelioid hemangioendothelioma: sonographic, CT, and MR imaging appearances. AJR 180:1359–1364
52. Makhlouf HR, Ishak KG, Goodman ZD (1999) Epithelioid hemangioendothelioma of the liver. Cancer 85:562–582
53. Miller WJ, Dodd III GD, Federle MP, Baron RL (1992) Epithelioid hemangioendothelioma of the liver: imaging findings with pathologic correlation. AJR 159:53–57
54. Van Beers B, Roche A, Mathieu D et al (1992) Epithelioid hemangioendothelioma of the liver: MR and CT findings. JCAT16:420–424
55. Furui S, Itai Y, Ohtomo K et al (1989) Hepatic epithelioid hemangioendothelioma: report of five cases. Radiology 171: 63–68
56. Devaney K, Goodman ZD, Ishak KG (1994) Hepatobiliary cystadenoma and cystadenocarcinoma. A light microscopic and immunohistochemical study of 70 patients. Am J Surg Pathol 18:1078–1091
57. Mortelé KJ, Ros PR (2001) Cystic focal liver lesions in the adult: differential CT and MR imaging features. Radiographics 21:895–910
58. Devine P, Ucci AA (1985) Biliary cystadenocarcinoma arising in a congenital cyst. Hum Pathol 16:92–94
59. Buetow PC, Buck JL, Pantongrag-Brown L et al (1995) Biliary cystadenoma and cystadenocarcinoma: clinical-imaging-pathologic correlations with emphasis on the importance of ovarian stroma. Radiology 196:805–810
60. Korobkin M, Stephens DH, Lee JKT et al (1989) Biliary cystadenoma and cystadenocarcinoma: CT and sonographic findings. AJR 153:507–511
61. Bronowicki JP, Bineau C, Feugier P et al (2003) Primary lymphoma of the liver: clinical-pathological features and relationship with HCV infection in French patients. Hepatology 37:781–787
62. Emile JF, Azoulay D, Gornet JM (2001) Primary non-Hodgkin's lymphomas of the liver with nodular and diffuse infiltration patterns have different prognoses. Ann Oncol 7: 1005–1010

Radiologic-Pathologic Correlations in Diffuse Liver Diseases

Yves Menu, Catherine Guettier

4.9

Contents

Introduction

Diffuse liver diseases are very common. Fatty liver and cirrhosis are routinely seen in every day practice and will be detailed in this chapter. Progress in imaging has allowed radiologists to participate not only in the diagnosis but also in the staging of chronic liver diseases such as chronic viral hepatitis. Other diseases are less common worldwide, but might present with a very high prevalence in selected populations and areas, as is the case for hemochromatosis. Other diffuse diseases are far less common, such as vascular liver diseases, diffuse cystic diseases or diffuse infiltrating tumors, but nevertheless they are characterized by a number of significant imaging features. Diffuse liver diseases with no characteristic imaging features such as Wilson's disease or liver amyloidosis will not be detailed in this chapter.

Fatty Liver Diseases

Alcoholic fatty liver disease is a very common condition. Almost all patients with alcohol abuse have an increased deposit of fat in the liver. On liver biopsy, it ap-

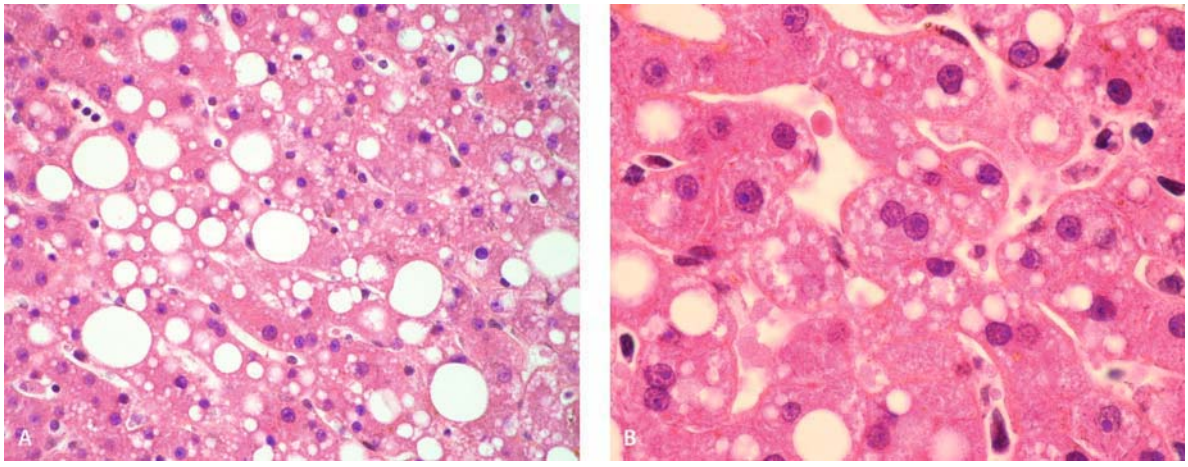

Fig. 1. A Macrovesicular steatosis. Large fat droplet displacing the nucleus to the periphery of the cell (HES 400×). **B** Microvesicular steatosis. Small fat droplets surrounding the centrally situated nucleus (HES 1,000×)

pears as a macrovesicular and/or microvesicular steatosis (Fig. 1). The main purpose of imaging is to stage the disease and to recognize other conditions associated with alcohol abuse. Great interest has now arisen the identification of fatty liver not related to alcohol abuse.

NAFLD and NASH – Definition

For years, fat deposition in the liver has been regarded as an ancillary finding, mostly seen in patients with heavy alcohol intake, with no significant consequence. Fatty liver was observed in patients without alcohol abuse, especially patients with diabetes mellitus and overweight persons, but this has not produced any special interest for a long time.

Recently, renewed interest was brought through the NAFLD and NASH classification [[1, 2]. It is now considered as a significant form of chronic liver disease in adults and children, and should be identified by the clinician as well as the radiologist.

NAFLD (nonalcoholic fatty liver disease) is a generic term. It can be defined as fatty infiltration of the liver exceeding 5%–10% by weight. NAFLD represents a broad spectrum of pathological conditions ranging from simple steatosis to steatohepatitis (NASH), advanced fibrosis and cirrhosis with the risk of hepatocellular carcinoma. The clinical importance of this classification is obvious. NASH might be also the explanation of most cases labeled as cryptogenic cirrhosis. In up to one-third of patients, NASH might lead to cirrhosis. A special preoccupying population is the obese child, who is dramatically exposed to NASH. It has been observed that in patients treated by liver transplantation, NASH may recur during follow-up.

However, in most cases, simple steatosis, also called nonprogressive NAFLD, does not appear to be evolutive and requires no special attention in itself. Nonprogressive NAFLD accounts for the vast majority of cases seen on imaging modalities.

The prevalence of NAFLD is high, reaching 20% of the population. Conversely, prevalence of NASH is much lower but remains at a 2% level in the United States, which still is very common. Because of associated conditions such as overweight, it may be anticipated that NASH prevalence is lower in other countries. Nevertheless, NAFLD is perhaps the most common liver disease. The pathogenesis of NAFLD consists of hepatic fat accumulation that triggers lipid peroxidation by oxidative stress with formation of free radicals and mitochondrial dysfunction. It is part of a metabolic syndrome characterized by obesity, insulin resistance, type II diabetes, hypertension and hyperlipidemia.

The clinical diagnosis relies on the presence of the insulin resistance syndrome and mainly aims to exclude alcohol abuse as well as viral, autoimmune, genetic, and drug-induced liver diseases.

There is no biological profile that favors the diagnosis. Liver enzymes are insensitive and cannot be used reliably to confirm the diagnosis or stage the extent of fibrosis. The elevation of transaminases and phosphatases is a common and nonspecific finding.

Finally, it should be remembered that the NAFLD encompasses two different entities, one a usual and benign condition, requiring no special treatment, the other a potentially severe liver disease that should be carefully staged and treated.

A considerable amount of work in progress is devoted to the identification of histological and/or clinical markers of progression, allowing the clinician to evaluate the severity of the disease. As this condition has been recently described, it is not surprising that some topics dealing with the prognosis of the disease are still controversial and subject to major changes in the coming years, with increasing experience in a large population and better follow-up of patient cohorts.

Treatment is aimed at correcting the risk factors for NAFLD, although it can sometimes be disappointing. Another treatment process consists in using potentially hepatoprotective agents that are included in encouraging trials [3].

NAFLD and NASH – Pathology

Liver biopsy is the main tool for diagnosis and is considered the gold standard for diagnosis [4]. Debate continues on the accuracy of histological criteria, but overall, the main features of NASH are steatosis, hepatocyte ballooning degeneration, mild inflammatory infiltration consisting of lymphocytes and neutrophils located mainly in the lobule and perisinusoidal fibrosis around terminal hepatic veins (Fig. 2). Hepatocyte ballooning degeneration, which is a sign of hepatocellular injury, is mandatory for the diagnosis of NASH. Other findings are very common but not constantly observed, such as Mallory bodies, glycogenated nuclei in periportal hepatocytes, lipogranulomas, and abnormal giant mitochondria. The lesions in NASH are close to those of alcoholic steatohepatitis, but with less inflammatory intensity and smaller and fewer Mallory bodies. In biopsy specimens from children, portal inflammation may be more prominent than in adults. Fibrosis may progress with the appearance of portal and periportal fibrosis and progressive formation of fibrous bridges leading finally to constituted cirrhosis. Steatohepatitis may be seen concurrently with other forms of chronic liver disease. Standardized reporting of liver biopsy with grading and staging systems is being developed, in order to provide a better comparison from patient to patient.

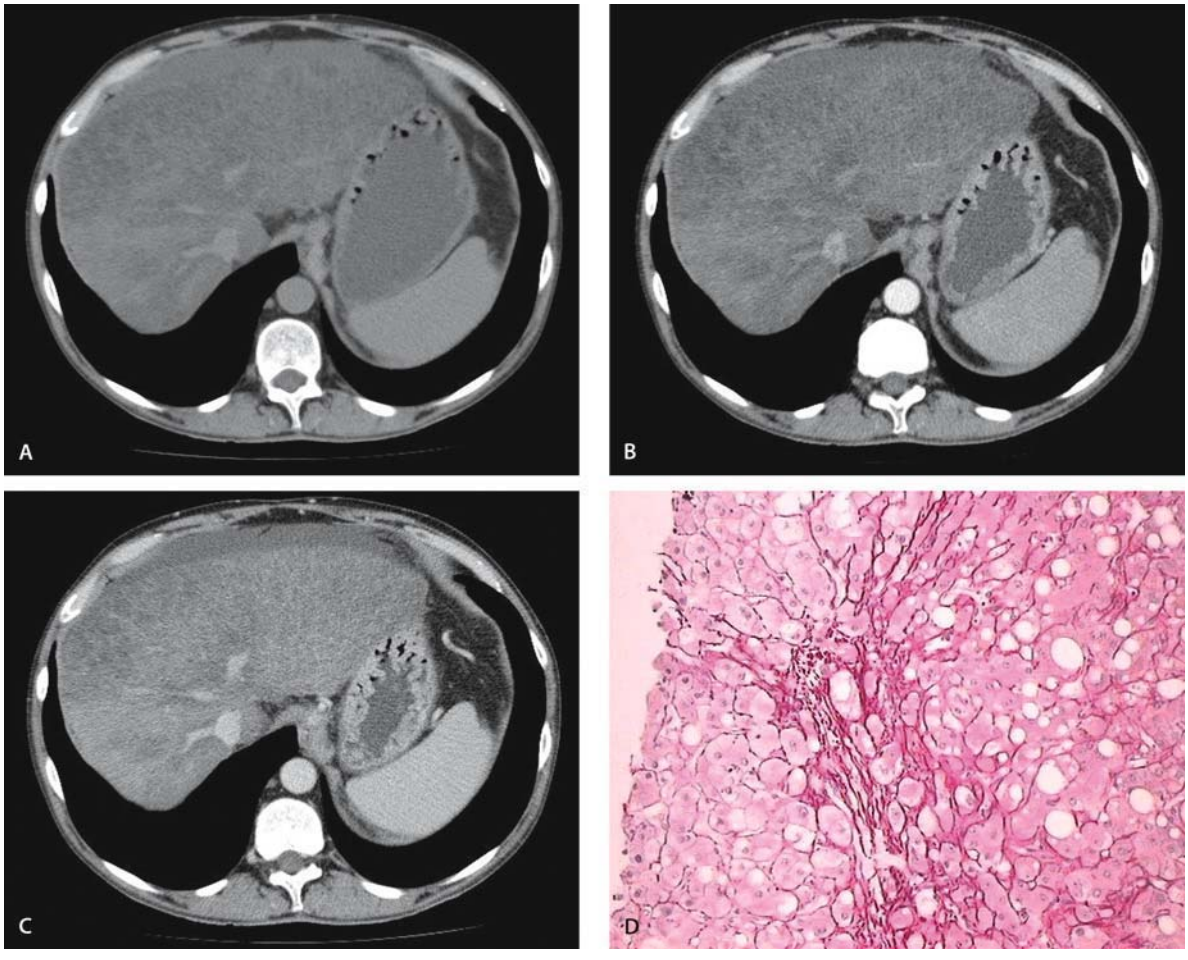

Fig. 2A–D. Steatofibrosis: CT and biopsy. Plain CT (**A**) shows heterogeneous liver with relatively hyperdense nonenhanced vessels. Iodine-enhanced CT at arterial phase (**B**) and portal phase (**C**) shows that there is a parallel enhancement of areas containing a larger or a smaller amount of fat. Moderate ascites is also seen. On liver biopsy (**D**), pericellular fibrosis in the perivenular area and steatosis (HES 200×) can be observed

Focal Fatty Liver – Physiopathology

Fatty infiltration is also highly related to local oxygen pressure [5]. In case of ischemia or a local low level of blood oxygen, the glucose metabolism in the liver cell is reoriented towards fatty acid formation. This is the one of the explanations for fat accumulation during alcohol intake, as alcohol in the blood will prevent oxygen from entering the hepatocyte. When the arterial flow is impaired, blood oxygen pressure is lower, and the local liver metabolism is reoriented to fat accumulation. Conversely, in case of portal vein local obstruction, arterial blood flow increases, as a natural balance phenomenon. The oxygen pressure increases, and this acts as a protector against fat accumulation. If this patient is exposed to fatty liver, the arterialized portion of the liver will be spared.

Another explanation is related to portal venous variants [6]. Some areas of the liver are naturally irrigated by accessory portal radices. This is the case of the liver surrounding the gallbladder bed, the liver hilum and the transverse ligaments. All these areas do not receive portal blood coming from the intestine, but from organs or areas with a low oxygen uptake such as the gallbladder and biliary tree. The oxygen level in these portal radices is significantly higher than in the superior mesenteric blood, because of high intestinal oxygen uptake. These areas are thus protected again fatty deposition. These findings are extremely common and easy to recognize.

Fatty Liver – Imaging Features

The mechanisms for hyperechogenicity associated with fatty infiltration may be explained by histological considerations. Fatty overload of the liver cells is seen as intracytoplasmic droplets. Each droplet will provide two echoes, one when the beam enters the droplet, the other one at the exit. The level of echogenicity is related to the number of droplets and not to their size. The fat content of the droplet is echo free, as is liquid fat. One may imagine that several small droplets will produce several echoes, thus a high level of ultrasonographic signal. Conversely, a single large droplet, though containing more fat than several small ones, will not produce as many echoes. This may explain in part the observed discrepancy between histological evaluation of fat and ultrasonographic appearance. This may also explain that CT and ultrasound do not seem to be correlated in the evaluation of fat, as CT measures the overall quantity of fat, when ultrasound evaluates the number of tissue interfaces [7]. Another explanation is that liver biopsy is only a small sample of the liver in a selected area, which may not represent the whole appearance of the liver. Whatever the exact mechanism, it appears that ultrasonography is not a routine tool for the quantitative evaluation of liver fatty infiltration.

Since radiologists have discovered that imaging methods could detect fatty liver, it has always been reported as a potential source of errors [8, 9]. Today, as fatty liver is better known, and given the impact of MRI, imaging provides acceptable tools to detect the presence of fat in the liver. On the other hand, if NASH or alcohol intake has lead to cirrhosis, gross morphological abnormalities are seen. Nevertheless, few authors have reported on the role of imaging to stage the severity of the disease. Ultrasound and CT have benefited from a great deal of work between 1980 and 1990, but since that time, few reports have been published, meaning that nothing really new has been found with ultrasonography and CT of fatty liver.

Ultrasound

Ultrasound was the first imaging method reported to be able to detect fatty liver infiltration [10–12]. Hepatic steatosis produces high amplitude echo patterns on ultrasound scanning, known as the bright liver. Ultrasound carries a high sensitivity to detect fatty liver infiltration, as high as 94% [11], and the specificity is high also (84%) according to the same authors. In normal patients, the liver and the kidney have a similar level of signal, but in case of steatosis, the level of liver echoes is much higher, creating a gradient between the liver and the kidney.

When focal areas of fat are present in otherwise normal liver parenchyma, the fatty area may mimic a mass, leading to further imaging evaluation and sometimes even biopsy. Some features are highly suggestive of the fatty nature of the masses. These signs are angulated, geometric margins between normal and fatty tissue and interdigitating margins with slender fingers of normal or fatty tissue. Vessels if any cross the area without any distortion. Focal areas may be spared spots, appearing darker than the surrounding liver. In other cases, there are focal areas of steatosis, appearing as hyperechoic spots as compared with the normal liver. Attention should be given to the term „normal“ as in most cases the whole liver is involved with steatosis. The so-called spared areas are only parts of the liver with a smaller amount of fat. Biopsy in these areas would also show some level of fatty infiltration. Thus, it is not recommended to perform a biopsy for diagnostic purposes only. In some cases, the appearance of focal steatosis is problematic, as it presents like a hyperechoic nodule (Fig. 3), or even like a ring-shaped lesion, mimicking liver metastases [13].

Besides the diagnostic role of ultrasound, it appears that there is no clear relationship between the level of echoes and the amount of fat in the liver, or between ultrasound findings and the association of fat and fibrosis. It is only grossly true that a highly reflective liver is a commonly associated with a high degree of fatty infiltration. Posterior attenuation was thought to be related to fibrosis, but it is clear that either fibrosis or heavy fatty infiltration may explain this beam attenuation.

Computed Tomography

As stated previously, CT more objectively measures the overall density of the liver. When the amount of fat is significant, the average density is lower (Fig. 4). In very severe cases, the liver density might be near 0 Hounsfield units (HU), similar to water density, or even negative. It is very unusual that the liver density is lower than 10 HU. In a large cohort of 1,425 adult patients, El-Hassan [14] found evidence of fatty infiltration of the liver in 138 patients (9.7%). Images showed diffuse changes related to fatty infiltration in 68% of patients. Conversely, focal areas were seen in 32% of the patients. The authors reported significant problems in the diagnosis of a possible focal liver tumor in 14%, leading to additional and possibly invasive examinations. The diagnosis of fatty liver infiltration relies on the decreased density of the liver parenchyma. As in ultrasonography, focal steatosis, or conversely focal spared areas may mimic tumor. Iodine injection helps in distinguishing these entities, as in fatty infiltration; the enhancement of the fatty area is strictly parallel to that of the normal liver

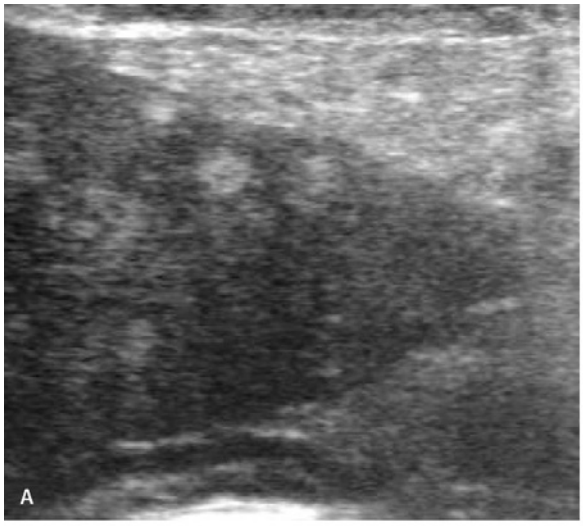

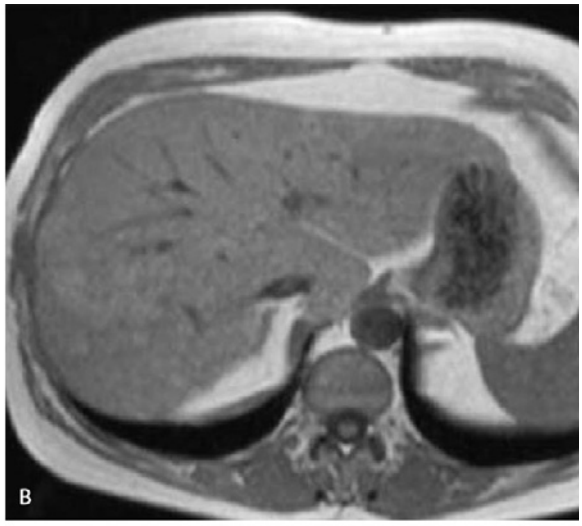

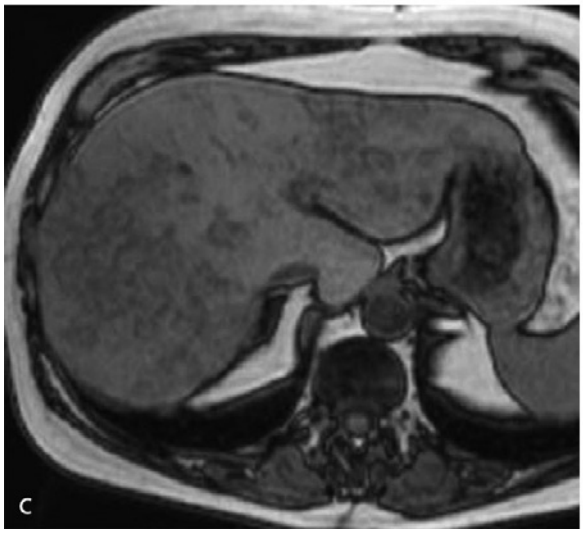

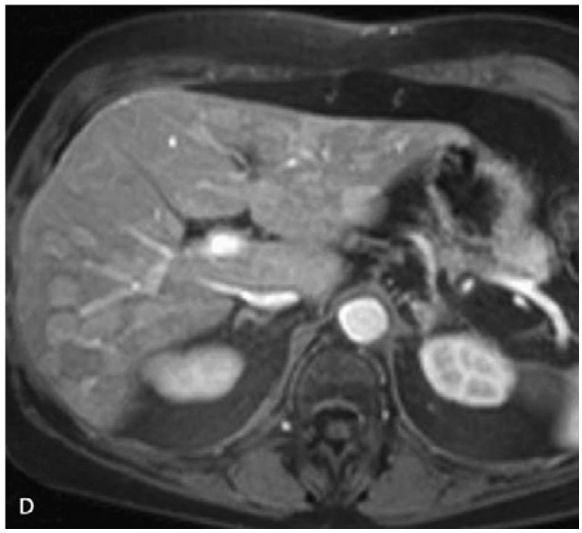

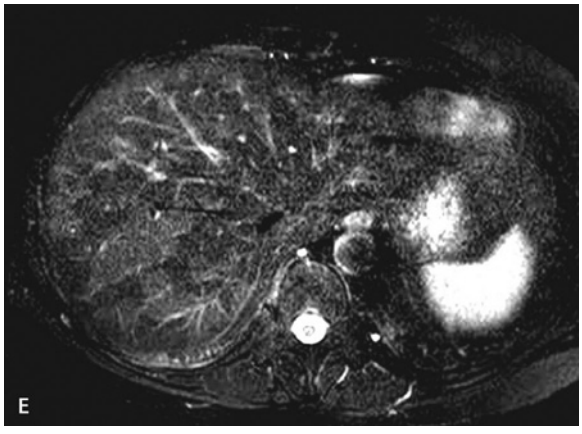

Fig. 3A–E. Pseudo metastatic steatosis. **A** Ultrasound. Multiple hyperechoic small nodules can be seen throughout the liver, with a main predominance in the right liver lobe, some with a hypoechoic central dot, mimicking malignant disease. **B** MRI. In-phase T1 image: the liver is only slightly heterogeneous. Hyperintense areas are seen mainly in the right liver lobe. **C** MRI. Opposed-phase T1 image: multiple areas presenting with a bull's eye appearance, mimicking liver metastases. Comparison with in-phase images shows that the hypointense areas are fat-containing. **D** T1-weighted images after gadolinium chelate injection (portal phase) showing some nodular enhancement that might be misleading. **E** T2 fat-suppressed images show heterogenous liver parenchyma

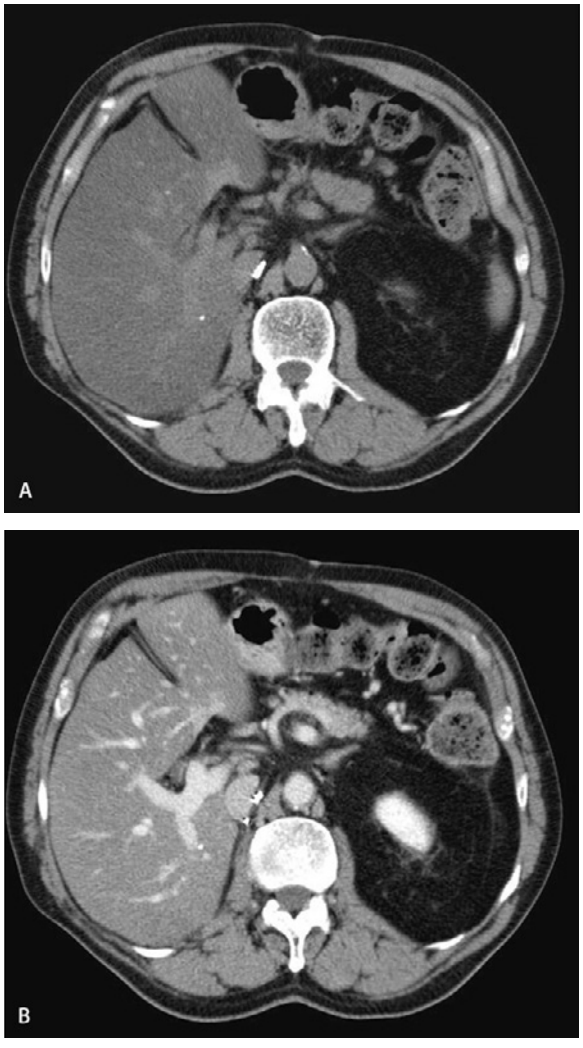

Fig. 4A, B. Liver steatosis. CT. On plain CT (**A**), the liver parenchyma is hypodense, as compared with the vessels, which appear with an unusual higher density. The average density of the liver parenchyma is 20 HU. There is a slightly hyperdense area at the posterior aspect of segment IV, anterior to the portal vein, representing a usual location of spare liver. After iodine injection (**B**), enhancement of the liver is normal, and the preportal area remains hyperdense as compared with the rest of the liver

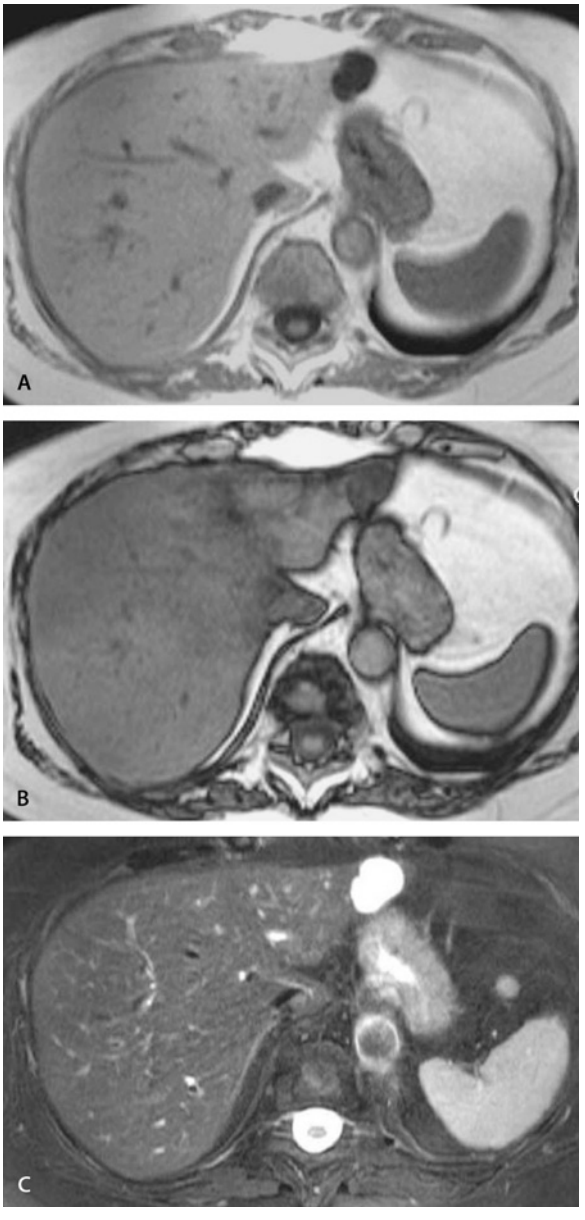

Fig. 5A–C. Liver steatosis in a patient with an hemangioma. Comparison of in-phase T1 images (**A**), out-phase images (**B**) and T2 fat-suppressed images (**C**) show that there is an overall but heterogeneous decrease in liver intensity between in-phase and out-phase images. Comparing with the intensity of the hemangioma, which is not supposed to be different on the two images, the right lobe of the liver becomes more markedly hypointense, signifying that the left lobe contains a lesser amount of fat. T2 images show the hemangioma, but fat-suppressed images prove to be insensitive to fatty liver detection

(Figs. 2, 4). There is no arterial hypervascularization. Some cases are more difficult to assess because heterogeneity of the fatty deposition in the liver is related to the scattered vascular distribution, areas with a higher arterial perfusion being protected against fatty deposition.

Magnetic Resonance Imaging

Initial reports had stated that MRI could show fatty deposition as hyperintense on T1-weighted images and T2-weighted images [15]. Clues were also a lack of a mass effect, vessels traversing the area with no distortion,

very similar to ultrasound and CT reports, but it appeared that MRI would be obviously of limited value if restricted to these signs.

Since Mitchell et al. [16] reported on chemical shift imaging, a broad spectrum of imaging sequences has been evaluated. HASTE images show fatty areas as hyperintense, but there is no difference with metastases, thus the clinical utility is low. Fat suppression techniques may be helpful.

Since MRI allows selective suppression of fatty areas, however, it works in areas with a high fat content. The signal loss is not as clear with mild infiltration, which might nevertheless be the cause of ultrasonographic mass-like lesions. The most sensitive MR method for detecting liver fat deposition in liver cells is the combination of in phase (IP) and opposed phase (OP) sequences (Figs. 3, 5). On modern devices, the two images may be acquired within a single dual-echo sequence. This sequence is a regular T1-weighted gradient echo sequence. The two echoes' echo times are set to meet the spin position of water and fat together (IP) or at a 180° shift (OP). The echo time is dependent on field strength. Registering both images during the same apnea means that there is no risk for slice misregistration. All IP images have a corresponding OP image in the same data set. On the IP images, the resulting signal is the sum of fat and water signals. On OP images, the final signal is a subtraction of the fat signal from the water signal, voxel by voxel. This leads to a very strong difference in intensity between the two images when a voxel contains both water and fat, which is the case in patients with intracellular fat droplets. As this sequence provides convincing and accurate T1-weighted images, a routine T1 sequence for all liver examinations is strongly suggested.

Quantitative evaluation would be the next step for MRI imaging. One may anticipate that the contrast between IP and OP images may be related to the quantity of fat. Preliminary reports are encouraging, especially in populations such as liver donors, where the quantitative evaluation of fatty infiltration is meaningful, while both the patient and the physician are reluctant to perform a biopsy [17].

Hemochromatosis

Pathology

Hemochromatosis is an inherited autosomal recessive disease characterized by progressive iron overload of multiple organs. In the liver, iron overload starts early in the life and can be detected on liver biopsy by Perls staining (Fig. 6); considerable amounts of iron are already present by the mid-teens. Young males are generally more affected than females of the same age. The overload in genetic hemochromatosis mainly involves the hepatocytes, first in the periportal areas, and then progresses through the entire lobule. With the accumulation of still more iron, increasing fibrosis develops around portal tracts leading to irregular and incomplete cirrhosis and at the very final stage to a micronodular pattern. This condition is associated with a high risk of hepatocellular carcinoma. In overloaded livers, iron-free nodules are considered as precancerous lesions. Iterative phlebotomies result in the disappearance of stored iron from the liver.

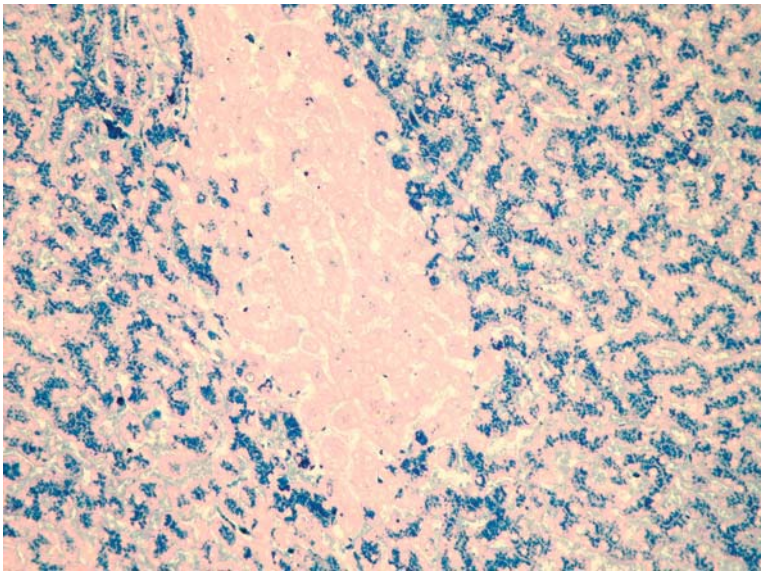

Fig. 6. Hemochromatosis. Iron overload with an iron-free focus in genetic hemochromatosis (Perls staining 200×)

Computed Tomography

CT is not commonly used for hemochromatosis detection. Sensitivity and specificity are low. It should be recalled that an increased density of the nonenhanced liver may be observed in three different conditions: iron overload, amiodarone intake, and glycogen-storage disease. A gradient greater than 10 UH between the spleen and the liver on plain CT is considered as abnormal. Nevertheless, the gradient may not always be related to increased liver density. In many instances, the spleen may be hypodense (portal hypertension, lymphoma, any spleen enlargement), and this explains the increased difference in liver-spleen density. For this reason, and also because there is only a gross relationship between liver iron concentration and liver density, CT is not a recommended tool for detection and follow-up of patients with iron overload.

Magnetic Resonance Imaging

In iron overload, MRI is an easy-to-perform procedure for the detection and quantification of increased liver iron concentration. Evaluation of the iron overload could be performed on standardized sequences, comparing the liver to the muscle ratio on MRI images. Several sequences have been tested, but the best sequence is a highly T2-weighted gradient echo sequence (Figs. 7, 8). Eighty-nine percent sensitivity and 80% specificity was obtained using a liver-to-muscle ratio intensity below 0.88. This threshold allowed the authors to detect all liver iron overload greater than 60 µmol/g (the normal value is lower than 36 µmol/g) [18]. This sequence is not dedicated to precise anatomical delineation of the liver, and should not replace conventional MRI examination of the liver, in order to detect hepatocellular carcinoma.

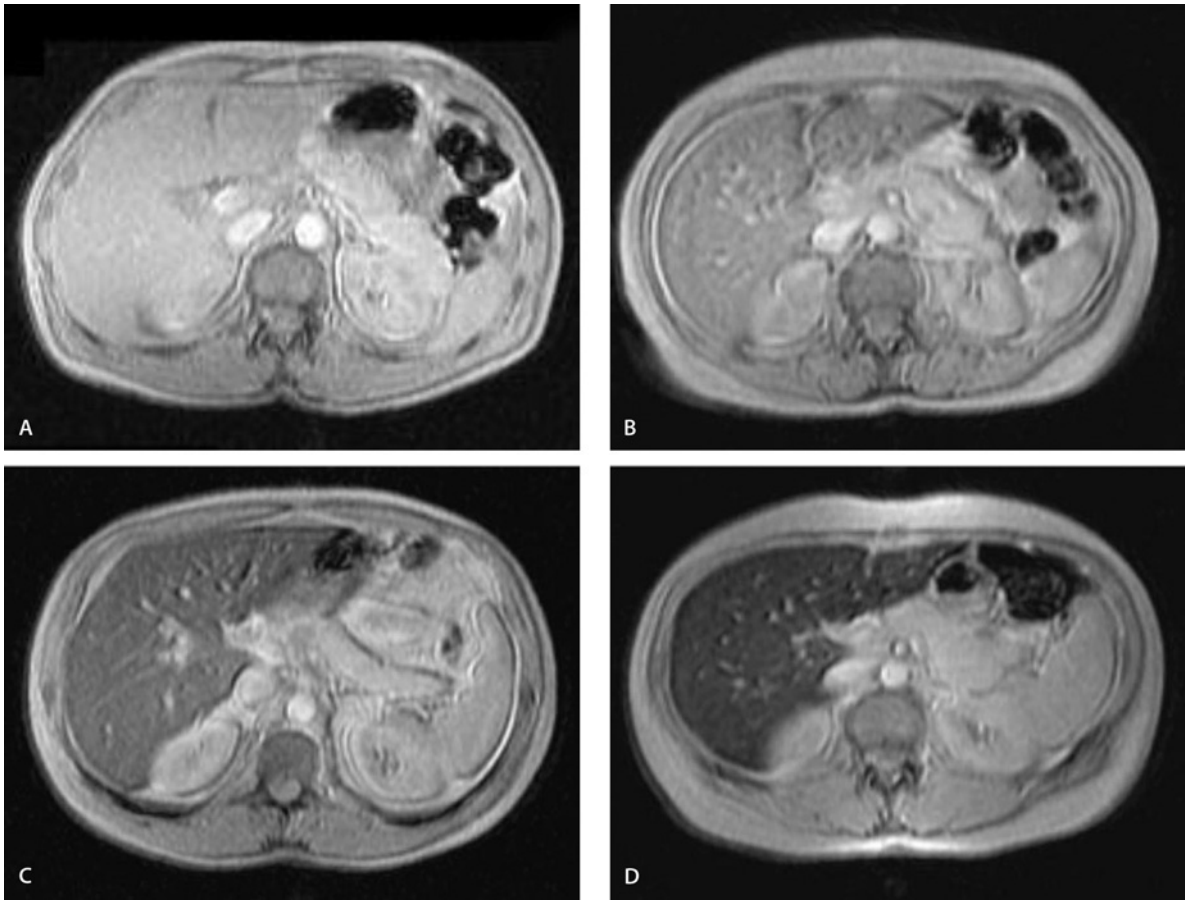

Fig. 7A–D. Hemochromatosis. T2-weighted gradient echo sequence with a TE at 4 ms. Four different cases: a normal (**A**) case and three patients with mild (**B**), intermediate (**C**) and severe (**D**) iron overload. Compare the gradient between liver and muscle. With this sequence, detection of mild iron overload is difficult, but any clinically significant situation is detected. Courtesy of Prof. Yves Gandon

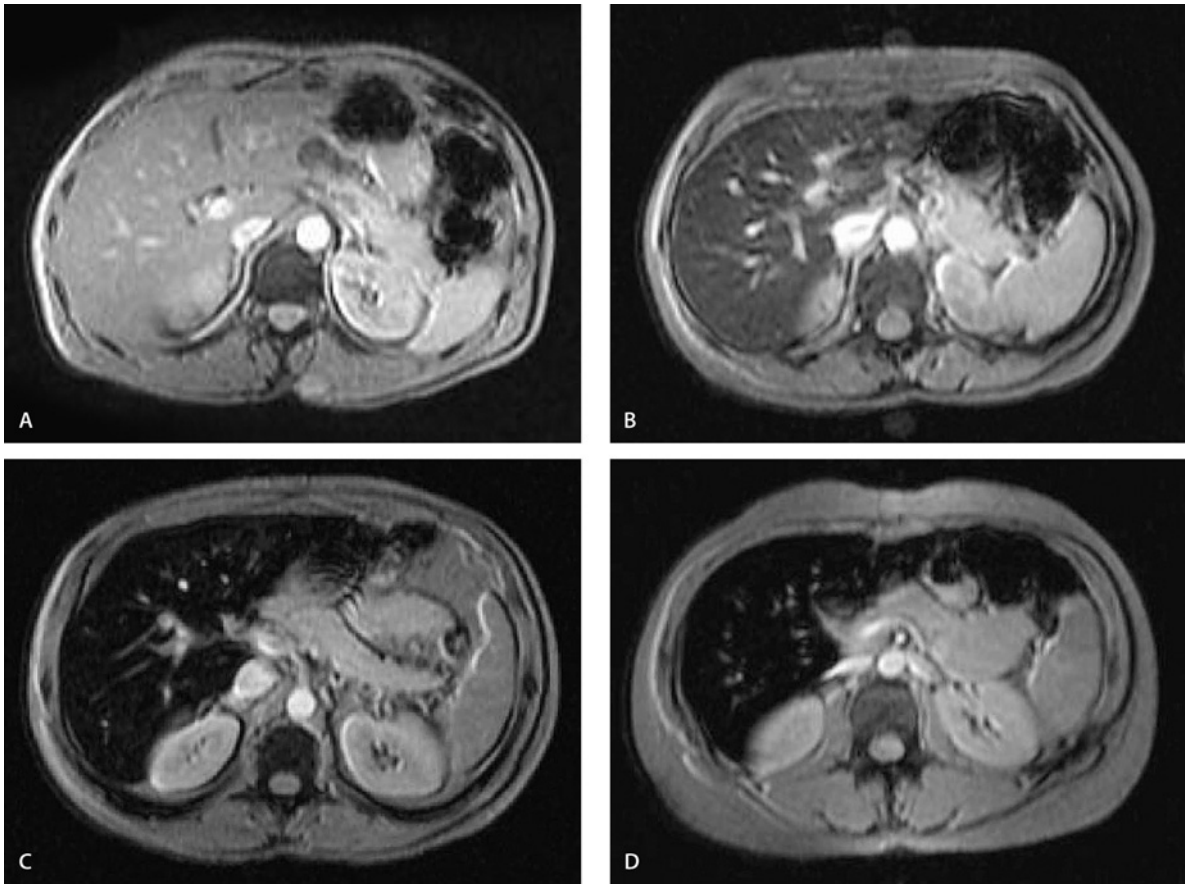

Fig. 8A–D. Hemochromatosis. T2-weighted gradient echo sequence with a TE at 14 ms. The same cases as in Fig. 6: normal case (**A**), and three patients with mild (**B**), intermediate (**C**) and severe (**D**) iron overload. With this sequence, signal drop is more readily visible, even, for mild cases. Sensitivity increases Courtesy of Prof. Yves Gandon

At the end-stage disease, liver atrophy is moderate. Usually the liver presents with a micronodular pattern. During the entire course of the disease, there is no clear correlation between the amount of iron deposition and the severity of the cirrhosis. Fibrosis may partially regress while correcting the iron overload. Finally, hepatocellular carcinoma may appear in both treated and untreated patients.

Fibrosis and Cirrhosis

With fibrosis as its end-point, cirrhosis is the main consequence of every chronic liver disease, whether it develops from the portal tracts as in chronic viral hepatitis or from the centrilobular area as in NASH or alcoholic liver disease. The assessment of liver fibrosis is essential for the evaluation of the severity of the disease and for therapeutic decisions. Liver histology has been the gold standard for fibrosis assessment for many years but noninvasive methods including imaging are now under investigation for assessing fibrosis.

Pathology

Schematically, fibrosis during chronic liver disease progresses through two mechanisms either following collapse and condensation of the reticulin meshwork of the parenchyma in an area of confluent or bridging necrosis, or resulting from a more active process of injury and repair. Fibrous septa form and extend within the parenchyma linking portal tracts or portal tracts to central veins. Cirrhosis characterized by annular fibrosis and nodules of regeneration represents the end-point of this phenomenon. In the early stage, there is little fibrosis, and the amount of remaining liver cells is sufficient. Cell regeneration is limited. With time liver cell loss continues and increases in part due to the phenomenon of parenchymal extinction secondary to vascular occlusion;

thus, small islands of remaining cells will try to regenerate, but will be soon limited by the extensive fibrosis. As an equilibrium between the growing bunch of new cells and the resistance of surrounding fibrosis, the result is a spherical nodule containing regenerating normal cells, surrounded by a circular network of fibrosis. This is the explanation of the fundamental annular fibrosis, a distinctive feature of cirrhosis. Mechanical pressure increases as well as disruption of global liver architecture. As a consequence, the centrolobular vein, which has a very thin wall, will be the first vessel to be obstructed, leading to intrahepatic hypertension and an upstream increase in portal vein pressure. When the cause of liver cell injury stops, remodeling of the cirrhosis occurs with resorption of the fibrous septa and expansion of adjacent nodules as well as the development of new micronodules from buds.

Microscopically, the nodules show a distortion of the trabecular architecture. The portal tracts and central veins are engulfed within the fibrotic septa or have lost their regular spacing.

Fibrosis contains fine or dense collagen fibers, with a varying vascular density, depending on the duration of the cirrhotic process. This may explain the various appearances of fibrotic tissue on imaging. Gross appearance of the liver is different depending on the stage of the disease. In the early phase, the inflammatory process is abundant, fibrosis is not prominent. In most cases, the liver is enlarged. As the disease progresses, the fibrosing process increases and the liver volume decreases. At the end stage, the liver is very small, meaning that fibrosis is substantial and the number of liver cells is limited. The patient has portal hypertension and liver failure. Association of these symptoms may vary from one case to another, but in most patients, a small liver volume is an indicator of a poor prognosis.

A nodular pattern is different from one patient to another. Pathological classification distinguishes macronodular and micronodular cirrhosis. In the latter, the nodules are approximately the same size, and usually less than 3 mm (Figs. 9, 10). In the former, the nodules are larger, up to 1 cm or even larger, and nodules may vary in size (Figs. 11–13). Mixed types are also observed. It appears that the value of this classification is doubtful, because the correlation between the gross appearance and the etiology of the liver disease is poor. In the end-stage liver, the distinctive morphological features have usually disappeared.

Association of hypertrophic and hypotrophic areas is a common finding (Fig. 14). As a rule, segment IV of the liver shrinks (Figs. 13, 14), as well as the posterior part of the right liver (segments VI and VII). Conversely, hypertrophy of the left lobe and caudate lobe is common. Not all patients follow this rule; the left lobe might be atrophic in some instances. Early demonstration of morphological changes should also incite caution be-

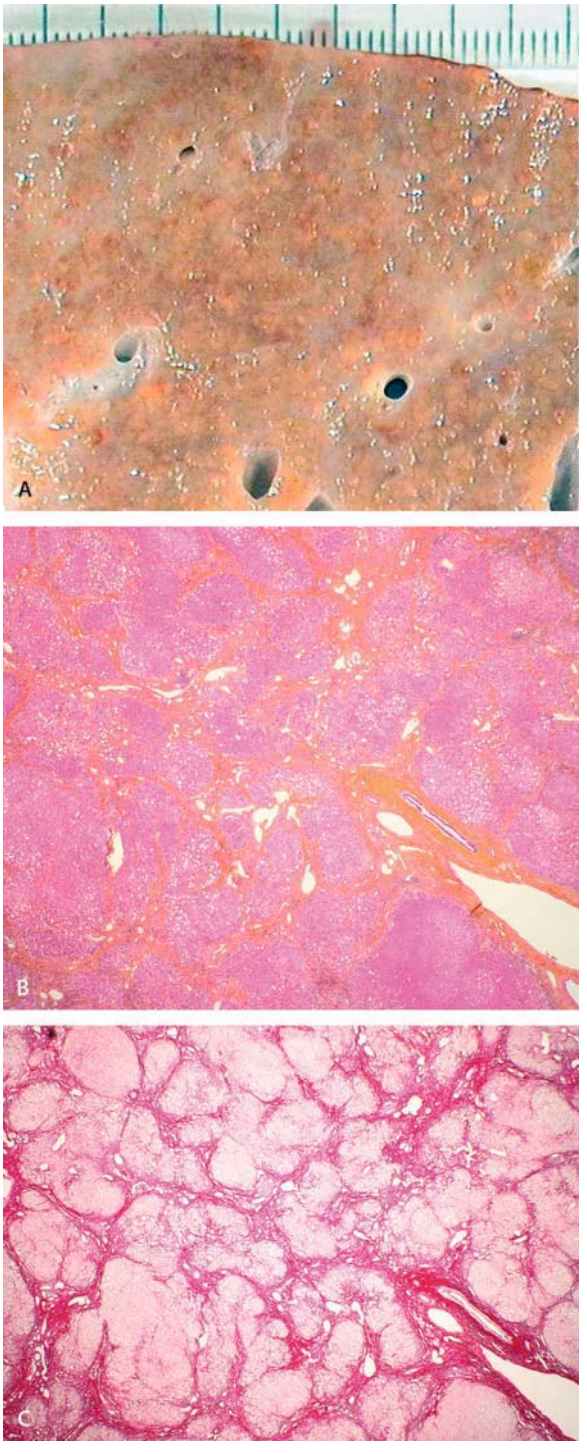

Fig. 9A–C. Micronodular cirrhosis. **A** Gross aspect of the cut section from a micronodular cirrhosis. **B** Histology of macronodular cirrhosis (HES 400×). **C** Histology of macronodular cirrhosis (Picrosirius staining 400×)

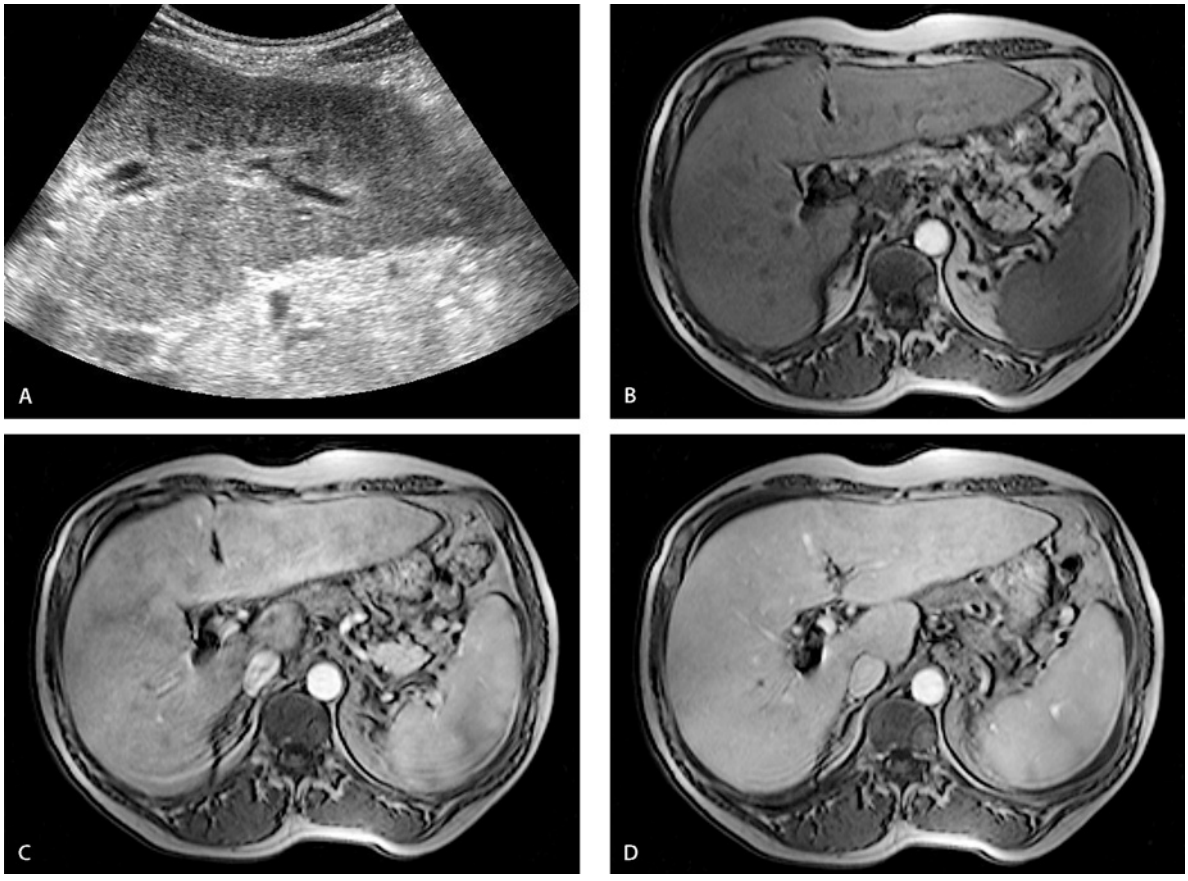

Fig. 10A–D. Micronodular cirrhosis. **A** Ultrasonography in a patient with micronodular cirrhosis: the liver contour is moderately nodular, and liver parenchyma is diffusely coarse, with no discrete nodules. Plain (**B**), arterial phase (**C**) and portal phase (**D**) T1 MRI images after gadolinium chelate injection show hypertrophy of the left lobe, diffuse irregularity of vascularization, but no special nodular pattern

cause of interindividual congenital variations, especially concerning the size of the segment IV. The reason why some areas are hypertrophic while others shrink is not fully understood. This heterogeneity could be in part related to blood flow phenomenon. Flow in the left portal vein may favor the left lobe, which could be detrimental to segment IV, but this remains nothing more than a hypothesis. Experimental work in animals shows some differences in sinusoidal perfusion depending on the liver area [19], which may be a lead for investigating this process.

Space-occupying small nodules (0.5–2.5 cm) are present in15%–37% of cirrhotic livers. They include large regenerative (Figs. 11–14), dysplastic (Figs. 15–17) and malignant hepatocellular nodules (Fig. 17) and can be detected by imaging. Recent studies have established the precancerous nature of dysplastic nodules in the cirrhotic liver. Dysplastic nodules show evidence of architectural and cytological atypia; according to the degree of these atypia they are graded as low or high grade. The continuum from dysplastic nodules to hepatocellular carcinoma is well documented and is morphologically illustrated by the progressive acquisition of the following features: increased cell density, thickening of the hepatocyte plates, presence of acini with bile plugs, an increased number of unpaired arteries, reduction of the reticulin framework and sinusoidal capillarization detected by CD34 staining of endothelial cells. It has been claimed that 40% of high-grade dysplastic nodules may progress to a hepatocellular carcinoma [20]. Small hepatocellular carcinoma is defined by a size up to approximately 15 mm and is classified into two types: small hepatocellular carcinoma of the distinctly nodular type and hepatocellular carcinoma with indistinct margins. Vascularity of this lesion varies, but there is a clear tendency of a higher vascularity in small hepatocellular carcinoma than in dysplastic nodules.

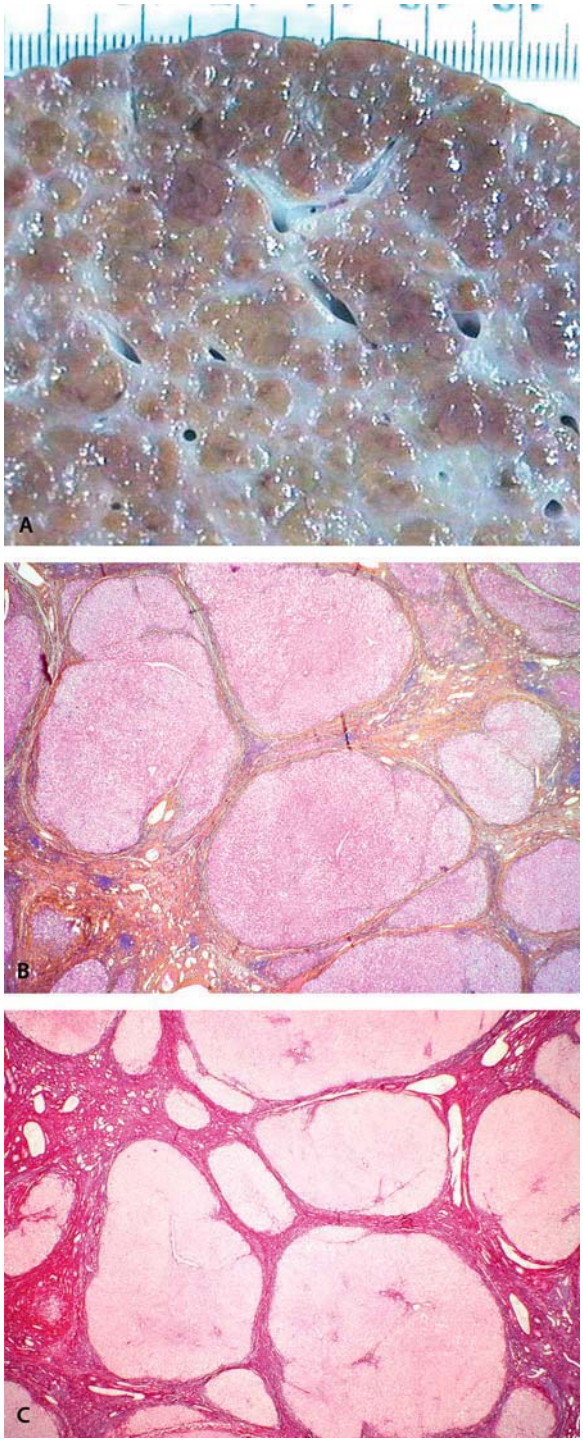

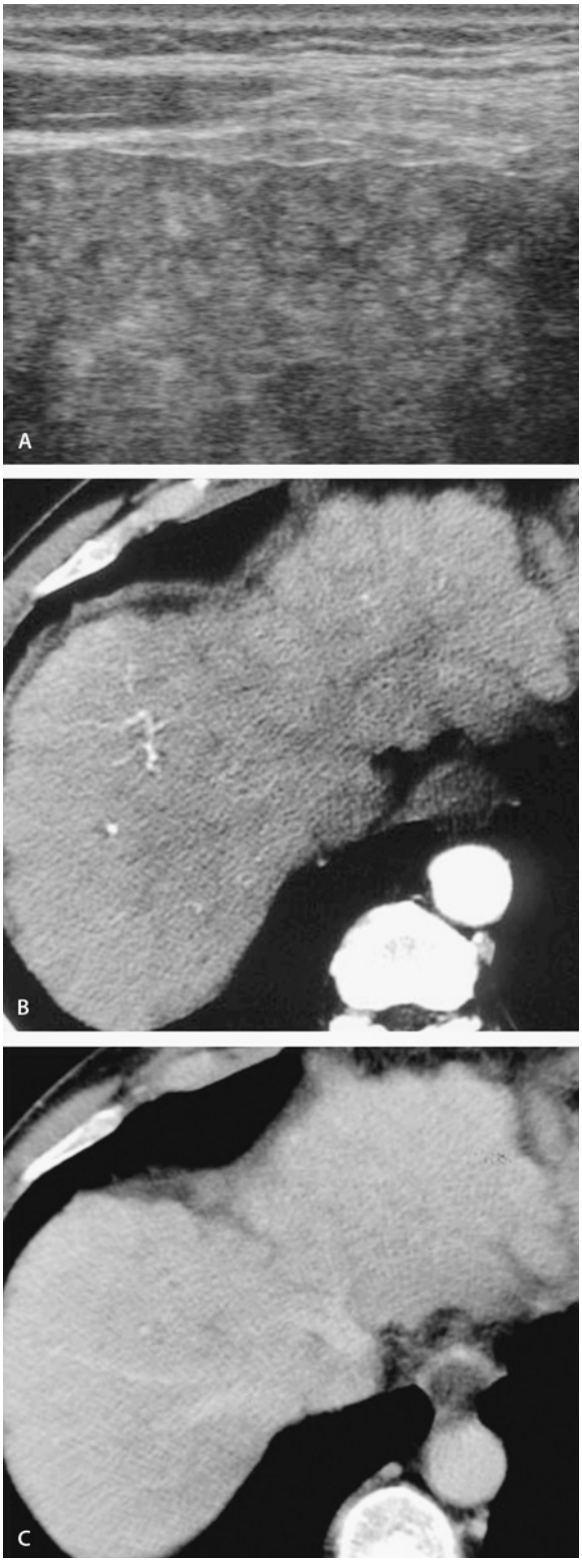

Fig. 11A–C. Macronodular cirrhosis. **A** Gross aspect of the cut section from macronodular cirrhosis. **B** Histology of macronodular cirrhosis (HES 400×). **C** Histology of macronodular cirrhosis (Picrosirius staining 400×).

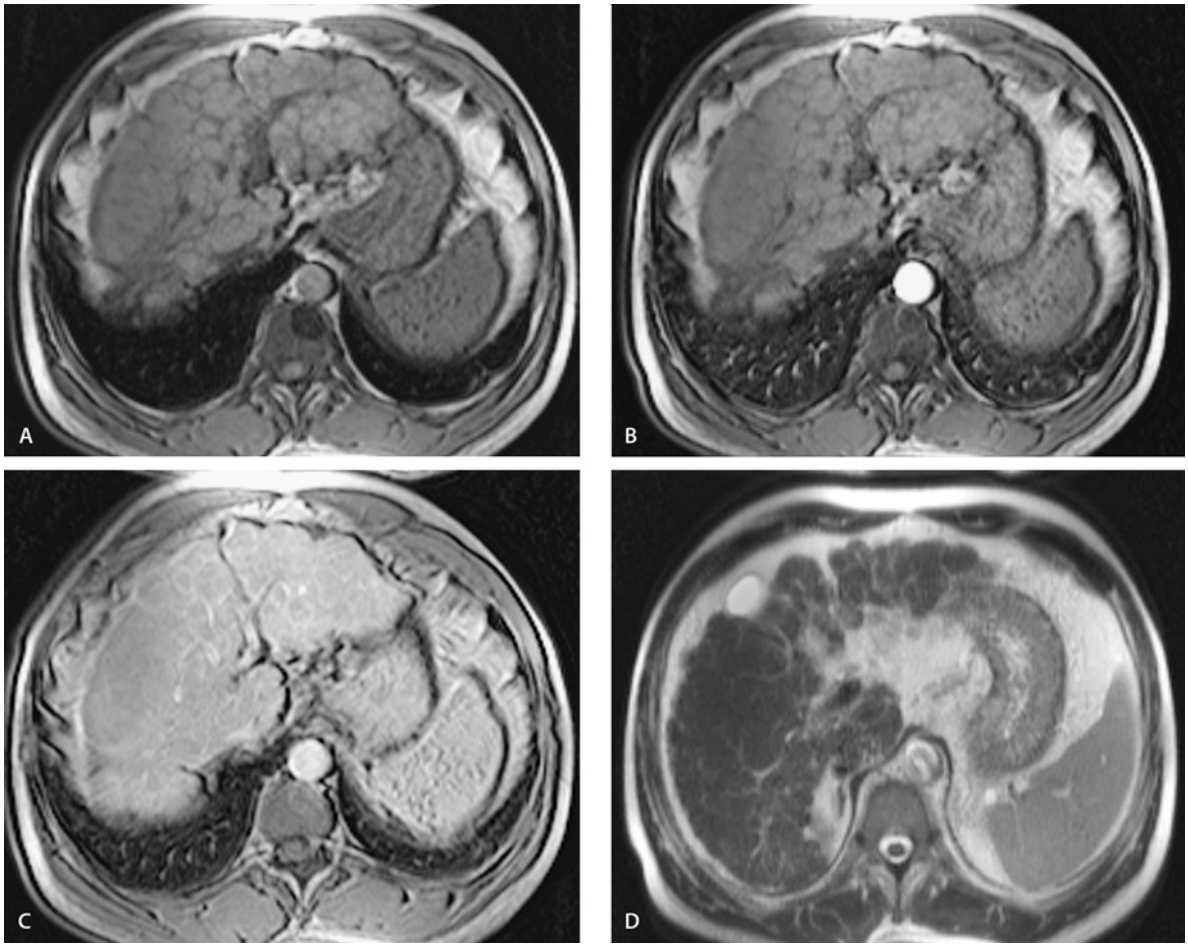

Fig. 13A–D. Macronodular cirrhosis. MRI. Plain T1 (**A**) arterial phase (**B**) and equilibrium phase (**C**) after gadolinium chelate injection (**D**) show the nodular pattern and annular fibrosis. Nodules do not enhance at arterial phase. Enhancing fibrosis sometimes delineates a hyperintense pseudocapsule surrounding some nodules. On T2 images, the nodules are hypointense, sometimes delineated by hyperintense fibrosis. Atrophy of segment IV is obvious

Fig. 12A–C. Macronodular cirrhosis. **A** Ultrasonography with a high-resolution probe shows nodularity of the liver anterior aspect, as well as nodular heterogeneity of the parenchyma. **B** CT at arterial phase and **C** portal phase after iodine injection. On the arterial phase image, the regeneration nodules are seen as nonenhancing masses surrounded by annular hypodense fibrosis. The appearance would be similar on plain CT. On portal phase images, fibrosis enhances and there is no gradient between the nodules and surrounding fibrosis. The liver seems to be more homogeneous

Imaging

Imaging is an interesting tool for the evaluation of cirrhosis. The role of imaging is to provide clues for the evaluation of liver damage and its consequences such as portal hypertension. Another aim is to detect small hepatocellular carcinoma as early as possible. In selected cases such as hemochromatosis, imaging gathers etiological information and helps in the evaluation of the disease severity.

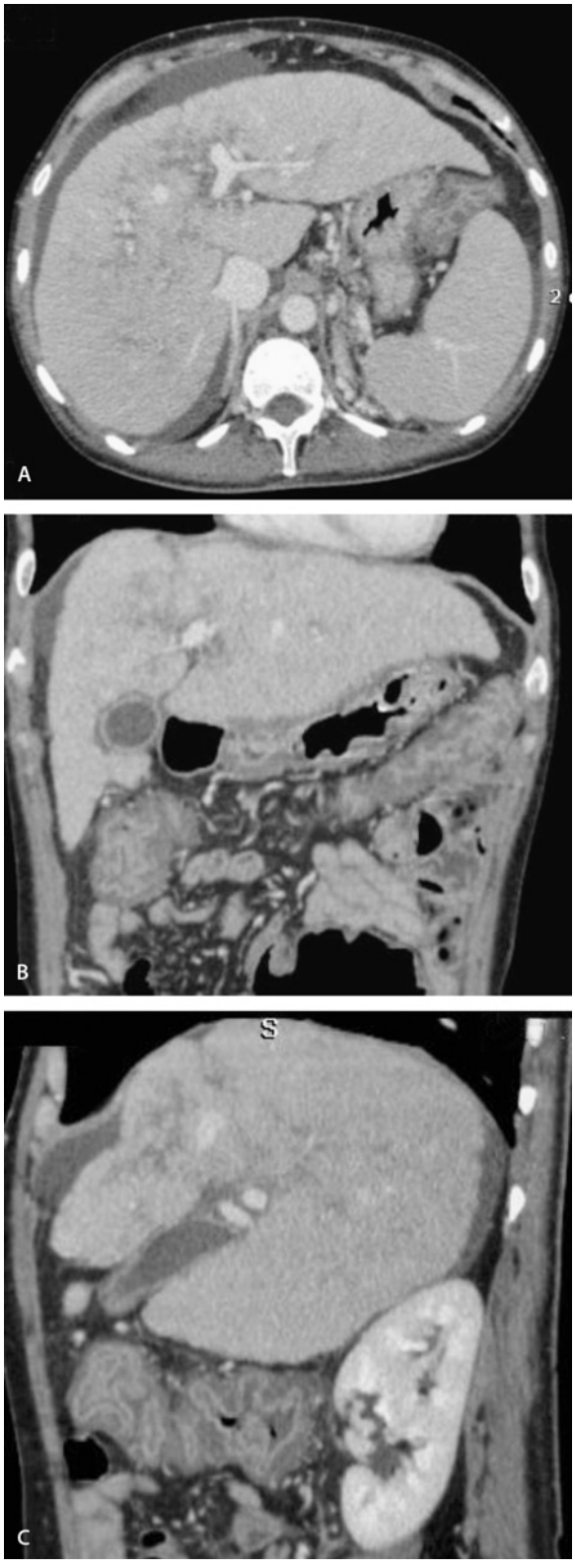

Fig. 14A–C. Macronodular cirrhosis. Morphological changes. On CT, axial transverse (**A**), coronal (**B**) and sagittal (**C**) planes show the association of nodular contour, left lobe enlargement, right lobe atrophy, segment IV atrophy, and confluent fibrosis within segment IV. This is the most common association in patients with cirrhosis. Mild ascites is visible

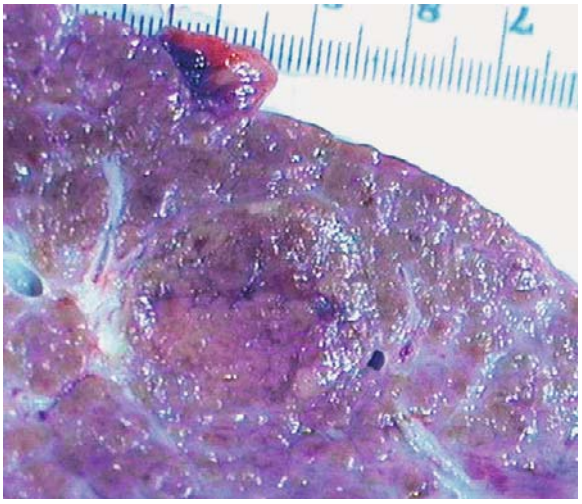

Fig. 15. High-grade dysplastic nodule in C virus cirrhosis

Ultrasound

In the early stage, the liver commonly shows fatty infiltration, at least in alcohol-related liver disease and NAFLD. When cirrhosis progresses, the liver pattern seems to be scattered and irregular (a coarse pattern). This is not specific at all. Liver contours are nodular (Fig. 12). Sometimes, a high resolution probe will be helpful to examine the anterior or lateral aspect of the liver. This nodular appearance is almost specific for the cirrhosis.

Liver morphological changes are also common, as described in „Pathology." Many measurements have been described in order to facilitate the diagnosis, but it should be stated that most teams dealing with chronic liver disease never take these measurements, as the morphological changes are usually quite obvious at a glance. The simplest measurements, and maybe the most useful, could be the transverse diameter of segment IV. If smaller than 3 cm, atrophy is likely. If greater than 4 cm, segment IV is normal in size. Between 3 and 4 cm, it is not possible to conclude.

Regeneration nodules appear as small rounded iso- or hypoechoic areas. Most of them have a similar size. Nevertheless, ultrasound has a very low sensitivity and specificity to detect and differentiate regeneration nodules, dysplastic nodules and small hepatocellular carcinoma. Recent reports have shown that contrast-enhanced Doppler US might help in differentiating benign and malignant lesions [21]. In this study, some premalignant lesions such as high-grade dysplastic nodules showed increased vascularity, like hepatocellular carcinoma. However, there is not substantial agreement on this question, and some authors doubt that it could be possible to differentiate benign, premalignant and malignant lesions when equal or smaller to 1 cm in diameter [22].

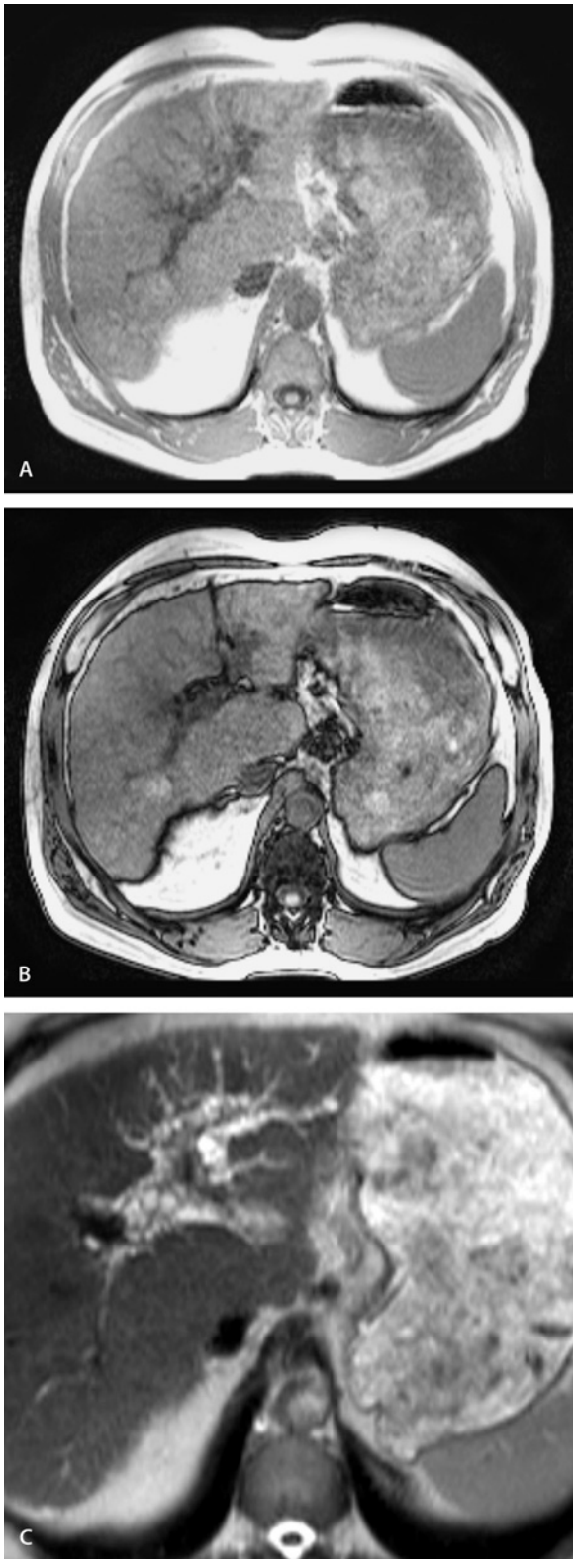

Fig. 16A–C. Cirrhosis with dysplastic nodule. In this patient, a hyperintense nodule in seen in the posterior aspect of the right liver lobe. The nodule is more conspicuous on the opposed-phase T1 image (**A**) than on the in-phase T1 image (**B**). On T2 images (**C**), the nodule is isointense. In this patient, there are numerous peribiliary cysts, which is a rather common finding in liver cirrhosis, sometimes mimicking bile ducts dilatation

Computed Tomography

CT is adequate to show gross morphological changes and the nodular contours (Fig. 14). Atrophy of segment IV is the cause of a coalescence of the gallbladder and the transverse ligament. Besides the measurements of segment IV, as in ultrasonography, calculating the ratio between the caudate lobe and the right lobe of the liver has been proposed. If greater than 0.65, the sensitivity is 96% for the diagnosis of cirrhosis [23]. Once again, not many teams really rely on these measurements to conclude the diagnosis.

Iodine uptake of the cirrhotic liver may be heterogeneous (Figs. 10, 14). The hepatic artery is usually enlarged and the liver enhances more than a normal liver at the arterial phase. The enhancement is sometimes heterogeneous, which could be interpreted as a hypervascular tumor. Fibrosis may also be a pitfall, when arterial vascularity is increased, as occurs in young fibrosis. In most cases, these hypervascular areas are not nodular, have fuzzy or geometric contours, and the liver becomes homogeneous on the portal phase. Nevertheless, in some cases interpretation might be challenging.

Regeneration nodules may appear as hyperdense round areas on plain slices. The nodules are not really hyperdense, but they are surrounded by annular hypodense fibrosis, which underlines the nodule. At the arterial phase, no hypervascularization is seen, while at the portal phase, the fibrosis and the nodule itself become isodense. Dysplastic nodules are not specifically seen on CT.

Magnetic Resonance Imaging

As in US and CT, gross morphological changes are clearly seen. The overall signal of the liver parenchyma is of little interest. Diffusion sequences and chemical shift images are not really prominent methods. MRI does not provide additional information as compared with US and CT in usual cases.

MRI has clear advantages in the evaluation of hemochromatosis and the characterization of liver nodules.

The characterization of liver nodules, although not perfect, is better with MRI than with other techniques [24]. Regeneration nodules are usually hypointense on T2 images and also hypointense on T1 images [25]. Conversely, dysplastic nodules are mainly hyperintense on T1-weighted images and hypointense or isointense on T2-weighted images (Figs. 16, 17). This means that one should be cautious when hyperintense nodules are seen in a cirrhotic liver, even if this finding is not specific. Small hepatocellular carcinomas are mainly hypo- or hyperintense on T1-weighted images and hypo- to hyperintense on T2-weighted images (Fig. 17). Hypervascularization is not always found in malignant tumors, but when present, it is an indicator of severe dysplasia and more likely of hepatocellular carcinoma. Neverthe-

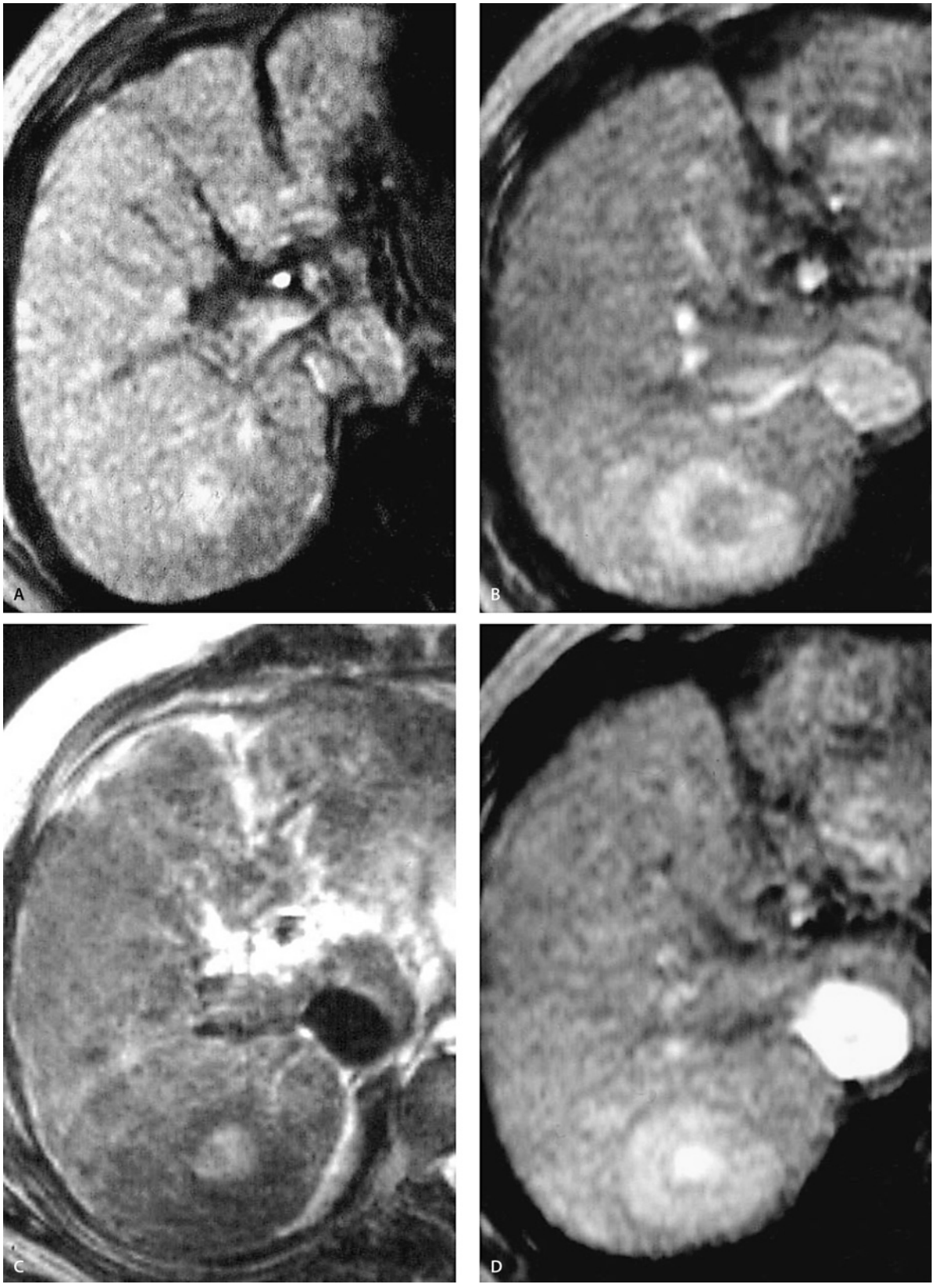

Fig. 17A–D. Progression of a dysplastic nodule. A small hyperintense nodule was seen on T1 images in this patient (**A**). Four years later, the nodule increased in size and became heterogeneous with a hypointense center on T1 image (**B**), hyperintense on T2 images (**C**), with a central enhancement after gadolinium injection (**D**). This is an example of the development of a small hepatocellular carcinoma within a dysplastic nodule, which is the so-called nodule in the nodule appearance

less, absence of vascularity does not rule out a malignant or premalignant lesion.

These results are still confusing and should be ascertained, if possible by further studies. Positron emission tomography is not useful as sensitivity for HCC diagnosis is low. Further studies will hopefully provide evidence of prominent features for each case, or more likely define clear rules to follow-up these and undetermined nodular-pattern cirrhosis, in order to detect hepatocellular carcinoma as soon as possible

References

1. Brunt EM (2004) Nonalcoholic steatohepatitis. Semin Liver Dis 24:3–20
2. Brunt EM (2001) Nonalcoholic steatohepatitis: definition and pathology. Semin Liver Dis 21:3–16
3. Neuschwander-Tetri BA, Brunt EM, Wehmeier KR, Oliver D, Bacon BR (2003) Improved nonalcoholic steatohepatitis after 48 weeks of treatment with the PPAR-gamma ligand rosiglitazone. Hepatology 38:1008–1017
4. Neuschwander-Tetri BA, Caldwell SH (2003) Nonalcoholic steatohepatitis: summary of an AASLD Single Topic Conference. Hepatology 37:1202–1219
5. Brawer MK, Austin GE, Lewin KJ (1980) Focal fatty change of the liver, a hitherto poorly recognized entity. Gastroenterology 78:247–252
6. Itai Y, Matsui O (1999) 'Nonportal' splanchnic venous supply to the liver: abnormal findings on CT, US and MRI. Eur Radiol 9:237–243
7. Scatarige JC, Scott WW, Donovan PJ, Siegelman SS, Sanders RC (1984) Fatty infiltration of the liver: ultrasonographic and computed tomographic correlation. J Ultrasound Med 3: 9–14
8. Wilson SR, Rosen IE, Chin-Sang HB, Arenson AM (1982) Fatty infiltration of the liver – an imaging challenge. J Can Assoc Radiol 33:227–232
9. Halvorsen RA, Korobkin M, Ram PC, Thompson WM (1982) CT appearance of focal fatty infiltration of the liver. AJR Am J Roentgenol 139:277–281
10. Foster KJ, Dewbury KC, Griffith AH, Wright R (1980) The accuracy of ultrasound in the detection of fatty infiltration of the liver. Br J Radiol 53:440–442
11. Saverymuttu SH, Joseph AE, Maxwell JD (1986) Ultrasound scanning in the detection of hepatic fibrosis and steatosis. Br Med J (Clin Res Ed) 292:13–15
12. Quinn SF, Gosink BB (1985) Characteristic sonographic signs of hepatic fatty infiltration. AJR Am J Roentgenol 145: 753–755
13. Kemper J, Jung G, Poll LW, Jonkmanns C, Luthen R, Moedder U (2002) CT and MRI findings of multifocal hepatic steatosis mimicking malignancy. Abdom Imaging 27:708–710
14. El-Hassan AY, Ibrahim EM, al-Mulhim FA, Nabhan AA, Chammas MY (1992) Fatty infiltration of the liver: analysis of prevalence, radiological and clinical features and influence on patient management. Br J Radiol 65:774–778
15. Thu HD, Mathieu D, Thu NT, Derhy S, Vasile N (1991) Value of MR imaging in evaluating focal fatty infiltration of the liver: preliminary study. Radiographics 11:1003–1012
16. Mitchell DG (1992) Focal manifestations of diffuse liver disease at MR imaging. Radiology 185:1–11
17. Rinella ME, McCarthy R, Thakrar K et al (2003) Dual-echo, chemical shift gradient-echo magnetic resonance imaging to quantify hepatic steatosis: implications for living liver donation. Liver Transpl 9:851–856
18. Gandon Y, Olivie D, Guyader D et al (2004) Non-invasive assessment of hepatic iron stores by MRI. Lancet 363:357–362
19. Niggemann P, Murata S, Naito Z, Kumazaki T (2004) A comparative study of the microcirculatory changes in the developing liver cirrhosis between the central and peripheral parts of the main lobe in mice. Hepatol Res 28:41–48
20. Eguchi A, Nakashima O, Okudaira S, Sugihara S, Kojiro M (1992) Adenomatous hyperplasia in the vicinity of small hepatocellular carcinoma. Hepatology 15:843–848
21. Fracanzani AL, Burdick L, Borzio M et al (2001) Contrast-enhanced Doppler ultrasonography in the diagnosis of hepatocellular carcinoma and premalignant lesions in patients with cirrhosis. Hepatology 34:1109–1112
22. Gritzmann N (2003) Small hepatocellular carcinomas in patients with liver cirrhosis: potentials and limitations of contrast-enhanced power Doppler sonography. Eur J Gastroenterol Hepatol 15:881–883
23. Harbin WP, Robert NJ, Ferrucci JT Jr (1980) Diagnosis of cirrhosis based on regional changes in hepatic morphology: a radiological and pathological analysis. Radiology 135: 273–283
24. Hussain SM, Zondervan PE, IJzermans JNM, Schalm SW, de Man RA, Krestin GP (2002) Benign versus malignant hepatic nodules: MR imaging findings with pathologic correlation. Radiographics 22:1023–1036
25. Earls J, Theise N, Weinreb J et al (1996) Dysplastic nodules and hepatocellular carcinoma: thin-section MR imaging of explanted cirrhotic livers with pathologic correlation. Radiology 201:207–214

Pancreatic Neoplasms and Tumor-like Conditions

Giovanni Carbognin, Lucia Pinali, Carlo Procacci (†)

4.10

Contents

Introduction

The new WHO classification of pancreatic tumors, based on histological type and grade, has recently been proposed [1]. Unfortunately, with the exception of functioning endocrine tumors characterized by a specific clinical picture, the other pancreatic tumors manifest with either nonspecific symptoms, or symptoms similar to pancreatitis. Moreover, some tumors, particularly cystic tumors, which may long be asymptomatic, are occasionally encountered.

The great technical evolution in imaging techniques has led to an ever more precise depiction of the macroscopic structural characteristics of pancreatic tumors. This, in some cases, has led to the differentiation of tumor types and has helped in distinguishing other pancreatic diseases. The current interest in obtaining precise classification of pancreatic tumors by imaging is a result of the substantially different therapeutic approach and prognosis related to the specific tumor type.

In this chapter, both the macro- and microscopic pathological aspect of pancreatic tumors and tumor-like conditions are reviewed, and particular focus is given to those features that affect the findings at ultrasound (US), computed tomography (CT), and magnetic resonance imaging (MRI). For this reason the lesions are subdivided, following the prevalent radiological aspect, into two categories: (1) solid pancreatic tumors (Table 1), and (2) cystic pancreatic tumors (Table 2).

Table 1. Classification of solid pancreatic tumors (according to WHO) [1, 4]

Exocrine pancreas
Borderline (uncertain malignant potential)
Solid-pseudopapillary
Malignant
Ductal adenocarcinoma
Mucinous noncystic carcinoma
Signet-ring cell carcinoma
Adenosquamous carcinoma
Undifferentiated (anaplastic) carcinoma
Mixed ductal–endocrine carcinoma
Osteoclast-like giant cell tumor
Acinar cell carcinoma
Mixed acinar–endocrine carcinoma
Pancreatoblastoma
Solid-pseudopapillary carcinoma
Miscellaneous carcinomas
Endocrine pancreas
Benign
Insulinoma
Nonfunctioning adenoma
Borderline (uncertain malignant potential)/ low-grade malignant/high-grade malignant
Functioning or nonfunctioning tumors
Nonepithelial tumors
Benign soft tissue tumors
Malignant soft tissue tumors
Malignant lymphomas
Secondary tumors
Tumor-like lesions of the exocrine pancreas
Chronic pancreatitis
Miscellaneous inflammatory changes
Heterotopic pancreas
Heterotopic (ectopic) spleen
Hamartoma and pseudotumor

Table 2. Classification of cystic pancreatic tumors (according to WHO) [1, 4]

Exocrine pancreas
Benign
Serous cystadenoma
Mucinous cystadenoma
Intraductal papillary-mucinous adenoma
Mature cystic teratoma
Borderline (uncertain malignant potential)
Mucinous cystic tumor with moderate dysplasia
Intraductal papillary-mucinous tumor with moderate dysplasia
Solid-pseudopapillary tumor
Malignant
Ductal adenocarcinoma
Undifferentiated (anaplastic) carcinoma
Serous cystadenocarcinoma
Mucinous cystadenocarcinoma: noninvasive or invasive (papillary-mucinous carcinoma)
Acinar cell cystadenocarcinoma
Solid-pseudopapillary carcinoma
Endocrine pancreas
Functioning and nonfunctioning islet cell tumors
Secondary tumors
Cystic tumor-like lesions of the exocrine pancreas
Pseudocyst
Retention cyst
Parasitic cyst
Congenital cyst
Para-ampullary duodenal wall cyst
Enterogenous cyst
Lymphoepithelial cyst
Endometrial cyst

Solid Pancreatic Tumors

Ductal Adenocarcinoma

Although ductal cells account for only 10%–30% of the normal pancreatic parenchyma, ductal adenocarcinoma comprises between 80% and 90% of all tumors of the exocrine pancreas [2]. Pancreatic adenocarcinoma is one of the most aggressive of human malignancies. Because of its silent course, late clinical manifestation and rapid growth, it is known as the silent killer [3].

The incidence of this tumor is increasing. It ranks as the fourth cause of cancer-related death, and the second cause, after colorectal cancer, when considering digestive cancers alone. The tumor is prevalent in the male gender, manifesting after the age of 60 in 80% of cases [4].

The technical development in imaging techniques over the last 30 years has led to a slight reduction in the incidence of stage IV tumors, with a consensual increase in stage I tumors. Nevertheless, the prognosis of this disease still remains dismal, with no particular change over the past few years [5, 6]. As opposed to the high sensitivity of imaging techniques, early diagnosis is practically impossible to achieve, since the tumor remains asymptomatic until surrounding structures are involved [7]. Moreover, it has been demonstrated that a tumor 2 cm or less in diameter is not always an early cancer. Finally, a tumor less than 1 cm could be an early cancer but does not necessarily mean long-term survival [8]. Thus we conclude that the current status of imaging and tumor markers does not lead to an early diagnosis of adenocarcinoma of the pancreas. The development of improved early detection methods for pancreatic cancer is essential; however, at the present time, it should be limited to high-risk individuals to give a better chance of success [9].

Even when treated with radical surgery, the incidence of recurrence is high [7]. This may depend on the intrinsic characteristics of the tumor and, in particular, the infiltrative pattern of growth, the strong neurotropism, the lack of a capsule, and the rich vascular, lymphatic, and neurological network surrounding the gland.

From a clinical standpoint, the earliest clinical sign is jaundice. In fact, a tumor in the pancreatic head can infiltrate the choledochus and cause obstruction before encasing the peripancreatic vessels. Unfortunately, the same jaundice is quite often associated with an advanced tumor stage. Persistent epigastric pain, weight loss, asthenia, the recent onset of diabetes, nausea and vomiting are additional clinical signs and symptoms [10]. They are usually associated with unresectable tumors.

Laboratory tests, in addition to elevated levels of serum alkaline phosphatase and bilirubin, demonstrate a high concentration of the nonspecific tumor marker CA 19–9.

■ **Gross Findings.** Ductal adenocarcinomas are mainly located in the head of the pancreas; they account for 80%–90% in the surgical series and 60%–70% in the autopsy series. The prevalence of the head in the surgical series results from their earlier detection and better resectability. The average size of tumors of the head (2–3 cm) is considerably smaller than tumors of the body and tail (5–7 cm). On cut surface, the tumor usually appears as a solid mass with infiltrating margins, whitish color and a hard consistency (Fig. 1A). The tumor can rarely appear with cystic-degenerative changes (necrosis and hemorrhage), cyst formation, papillary (intraductal) tumor components or ectatic, mucin-filled duct segments. Such features can favor the erroneous diagnosis of special types of pancreatic tumors with a generally better prognosis, such as mucinous cystic tumor or intraductal papillary tumor [4].

Carcinomas of the head of the pancreas, with the exception of those arising in the uncinate process, almost always infiltrate the common bile duct (CBD) and the duct of Wirsung (main pancreatic duct, MPD). More

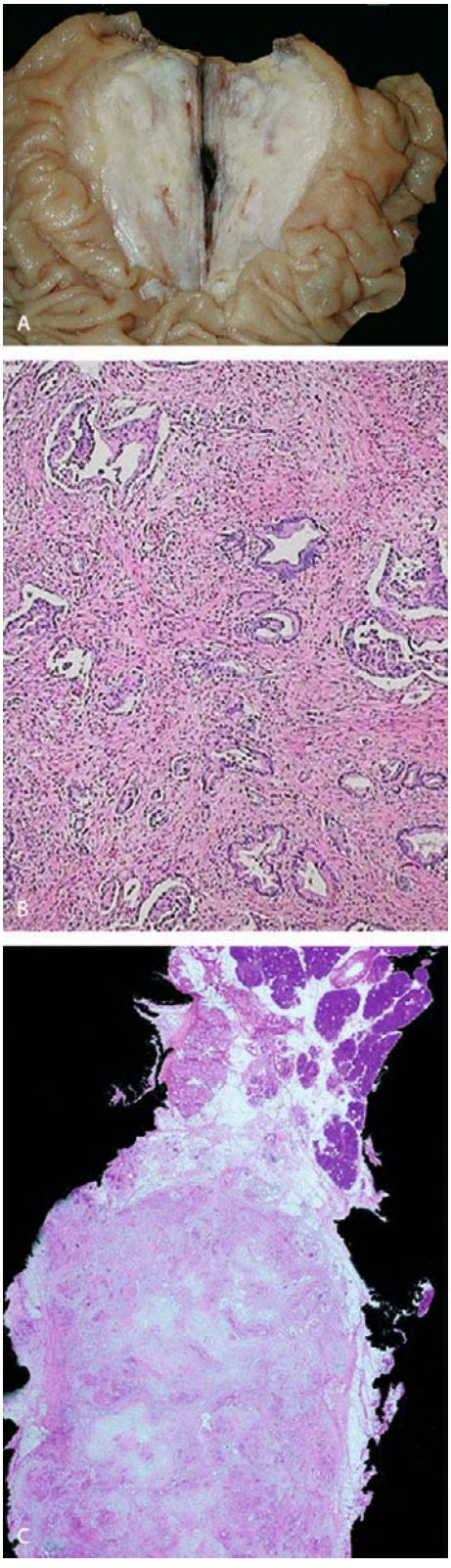

Fig. 1A–C. Ductal adenocarcinoma. **A** Whipple resection specimen showing ill-demarcated tumor in the head of the pancreas. **B** Duct-like and tubular structures of various shapes and arrangements embedded in dense fibrous stroma. **C** Whole-mount macrosection of the tumor showing firm mass with necrotic areas merging imperceptibly with the surrounding pancreatic tissue

frequently, the infiltration of the ducts causes variable degrees of stenosis and ultimately results in complete stenosis, leading to their dilation. A minute carcinoma may only rarely manifest with abdominal pain and mild dilatation of the MPD without mass. In this case the MPD stricture, demonstrated with endoscopic retrograde cholangiography (ERCP) or magnetic resonance cholangiopancreatography (MRCP), can be caused by periductal elastosis and fibroblast proliferation [11].

The obstruction of the CBD causes jaundice, while obstruction of the MPD results in an obstructive chronic pancreatitis with fibrosis and atrophy of the pancreatic parenchyma. The involvement of the ampulla of Vater causes retraction of the wall, and eventually mucosal ulceration. Retroperitoneal tissue infiltration with neural, lymphatic and vascular (portal vein and/or mesenteric vessels) invasion is considered a relatively early event. In pancreatoduodenectomy specimens, the pathological evaluation of involvement of the retroperitoneal resection margin provides the most important information about local recurrence and patient survival. This margin is defined as the peripancreatic fat plane behind the head of the pancreas that is located dorsal and lateral to the superior mesenteric artery. In advanced cases, the tumor infiltrates the stomach, gallbladder and peritoneum, leading to carcinomatosis and ascites. Carcinoma of the head of the pancreas metastasizes more frequently in the lymph nodes removed in the usual Whipple procedure (group I and II of the Japanese classification). The more frequently involved nodes are those of the superior head and posterior pancreaticoduodenal group.

Carcinomas of the body and tail of the pancreas have the same macroscopic appearance as those arising in the head, with the exception of their usually larger size (more space for tumors to grow before they become symptomatic). The extrapancreatic invasion of the tumor involves the mesocolon, transverse colon with encasement of the celiac trunk and splenic vessels, the peritoneum, the stomach, spleen and left adrenal gland. Hematological spread via the portal vein explains the frequent metastasis in the liver, which is sometimes large and centrally located and sometimes small and superficial (under Glisson's capsule).

Microscopically, ductal adenocarcinoma is composed of neoplastic tubules or glands lined with cuboidal or cylindrical cells, characteristically embedded in fibrous stroma (Fig. 1B), which gives the macroscopic scirrhous appearance (Fig. 1C). Perineural infiltration is present in most cases [3]. Ductal adenocarcinomas are distinguished into well, moderately or poorly differentiated, according to WHO criteria. The tumor presents a considerable diminution of the vascular bed with respect to the normal parenchyma (potentially useful in the radiological detection of the carcinoma). Nevertheless, this phenomenon is less evident for the develop-

ment of a marked peritumoral fibrotic reaction (obstructive chronic pancreatitis). Most importantly, ductal carcinoma of the pancreatic head has to be differentiated from ampullary carcinoma (which has a better prognosis). Unfortunately, the two lesions have similar microscopic features and the unequivocal establishment of ampullary origin is only possible in small lesions by applying strict topographical criteria. This bias may reflect the marked heterogeneity of epidemiological data.

■ **Imaging Findings.** Transabdominal US often represents the first imaging technique in the study of ductal

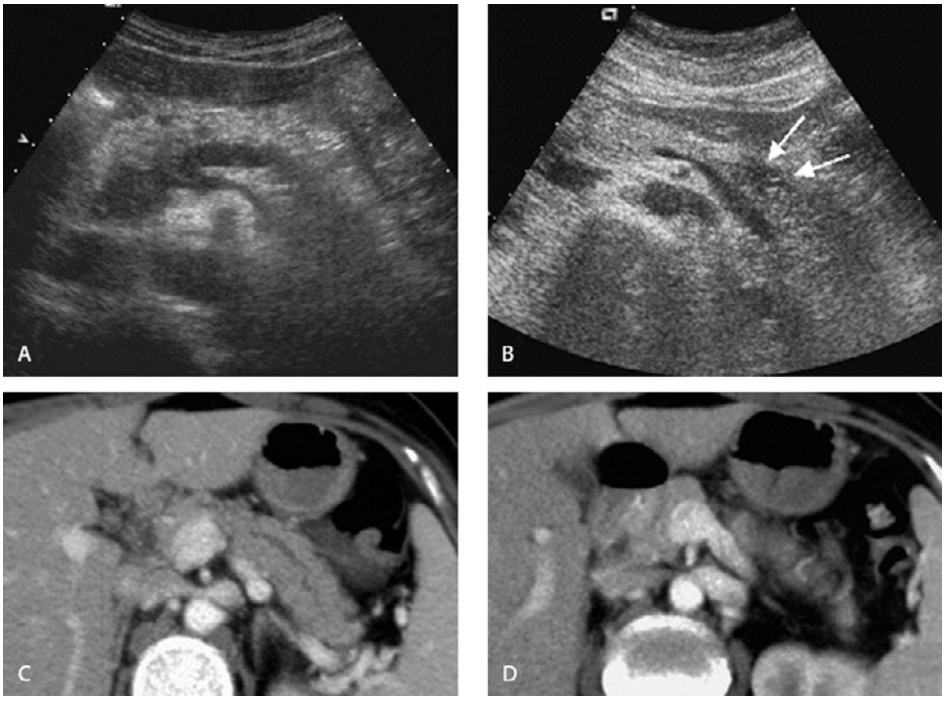

Fig. 2A–D. Ductal adenocarcinoma. **A** US image shows a hypoechoic mass with marked dilation of the main duct upstream. **B–D** Another case. US transverse image demonstrates a small hypoechoic mass in the body of the pancreas (*arrows*), isolated from the splenic vein (**B**). In the same patient during contrast medium (CM) administration, CT shows dilation of the main pancreatic duct in the body-tail of the pancreas, while the small tumor is not recognizable (**C**, **D**)

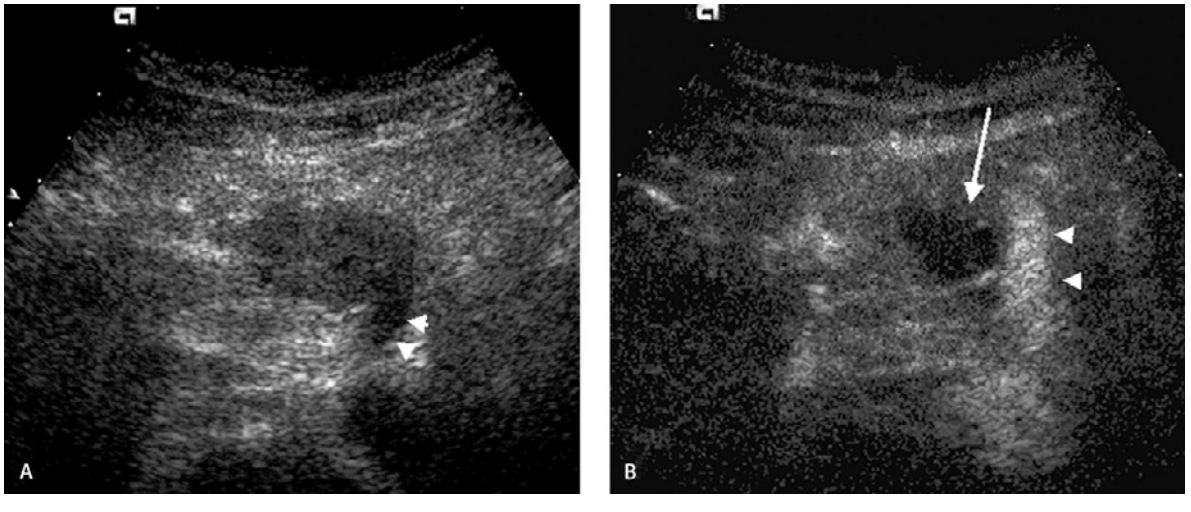

Fig. 3A, B. Ductal adenocarcinoma. **A** US image shows a large hypoechoic mass adhering to the superior mesenteric artery (*arrowheads*). **B** In the same patient during contrast medium administration, the tumor (*arrow*) appears definitely hypoechoic in comparison to the enhanced normal parenchyma. The image obtained during the pancreatic phase shows hyperechogenicity of the aorta and the superior mesenteric artery (*arrowheads*)

adenocarcinoma, especially when the tumor suddenly manifests with jaundice. In this case, the issue is to make a differential diagnosis among the possible causes of obstructive jaundice. At US, the lesion appears as a hypoechoic nodule, usually responsible for the abrupt amputation of the CBD, the MPD or both (Fig. 2A). Contrast-enhanced CT has a higher sensitivity than US, but some small pancreatic tumors are better resolved by US (Fig. 2B–D) than by CT because of the texture changes [12]. Using the new contrast agent for sonography in association with pulse inversion harmonic imaging increases lesion detectability [13]. Ductal adenocarcinoma shows less enhancement than the normal pancreatic parenchyma and its margins become well demonstrated (Fig. 3A, B). The enhancement characteristic thus narrows down the differential diagnosis indicating the vascularity of the lesions. The limitation of this method is that it is applicable only when the pancreatic tumor and parenchyma can be clearly observed in a single view [13].

Large tumors in the body-tail may show inhomogeneous echotexture because of the presence of intratumoral foci of necrosis. US, associated with the Doppler technique, is able to show the vascular encasement, in particular of the porto-mesenteric axis, especially in advanced stage [14, 15]. The US multiplanar approach can distinguish between the neoplastic foci and the peritumoral lymph nodes. The identification of liver metastases is quite easy, particularly when both second harmonic technique and contrast media (CM) are utilized [16, 17].

Peritoneal carcinomatosis is documented only indirectly because of ascites. In the clear case of either local spread and/or distant metastases, theoretically the diagnostic protocol could end up with US-guided core biopsy.

To date, CT represents the imaging technique of choice in the study of ductal adenocarcinoma [18, 19, 20]. The optimization of intravenous CM administration, besides giving an overall better demonstration of the gland, also allows for a better evaluation of peripancreatic vessels by spiral CT [21]. While waiting for the expected refinements in the multi-slice technique, spiral CT gives a consistent increase in sensitivity in the detection of the disease, and, at the same time, a better evaluation of its extent [22].

The objective of a precontrastographic study is to exclude the presence of calcifications and thereby contribute to the differential diagnosis of chronic pancreatitis. In this phase, the tumor is recognizable only when its conspicuous dimensions alter the morphology of the gland (Fig. 4A).

The early contrastographic phase (dynamic CT), or rather the arterial or pancreatic phase (spiral CT), is optimal for the identification of the tumor [23], since the maximum difference of contrast is reached between the

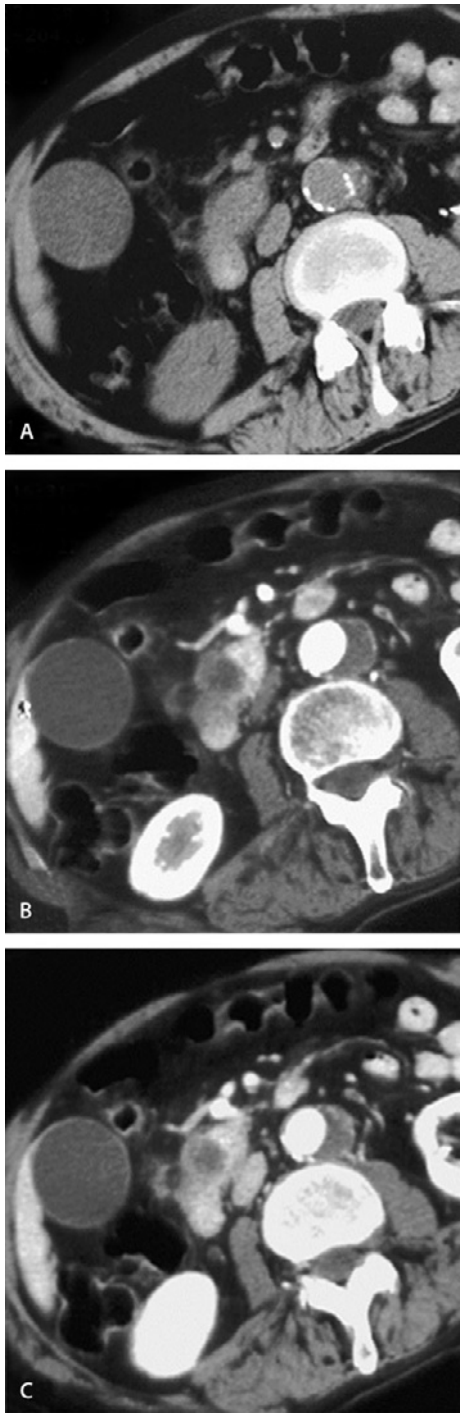

Fig. 4A–C. Ductal adenocarcinoma of the pancreatic head. In the unenhanced scan (**A**), CT shows an enlargement of the head, within which a hypodense mass is recognizable after contrast medium (**B**). The tumor looks smaller in the venous phase due to the peripheral enhancement (**C**)

healthy hyperdense parenchyma and the neoplastic focus, which is markedly hypodense because of its reduced vascularization (Fig. 4B). In this phase, using a reduced slice thickness (3 mm), the optimal evaluation of the connections of the tumor with the arterial vessels is also achieved [24, 25] with the consequently easy demonstration of their encasement (Fig. 5A, B). In reality the CT evaluation of the contact between the mass and the vessel is less accurate in demonstrating arterial involvement in comparison to the venous involvement. The most advanced grade of arterial involvement, detected with CT, may in fact simply correspond to perivascular fibrosis, neointimal hyperplasia or thrombosis [26].

In the late (dynamic CT) or venous (spiral CT) contrastographic phase, the difference in the density between the normal parenchyma and the neoplastic focus is reduced (Fig. 4C); at the same time, the marginal enhancement of the tumor can show up, so that its dimensions can appear inferior in comparison to those documented in the early/arterial phase [27]. In the venous phase, the connections of the neoplastic lesion with the peripancreatic venous vessels are accurately evaluated. The involvement of the superior mesenteric vein (SMV) can be revealed with stenosis of its lumen up to its complete obstruction (Fig. 5C), but also with widespread adhesion of the tumor to the vessel (Fig. 5D). Recently it has been confirmed that involvement of the venous system exceeding half of the vessel's circumference is suggestive of venous involvement [26]. More subtle findings are the dilation of either the pancreaticoduodenal veins or the gastrocolic trunk upstream of the tumor [28]. Unfortunately in personal experience, determination of nonresectability based on the pattern of venous collateral branches has led to overestimation of nonresectability with the consequent risk of denying some patients the chance of surgery [29]. The so-called tear-drop aspect, consistent with the stretching of the vessel toward the tumor, has been reported to be a reliable sign of infiltration of the SMV [30]. The venous phase, for which a greater slice thickness (5 mm) is employed, allows for the exploration of the middle and superior abdominal quadrants with the consequent possible demonstration of either foci of peritoneal carcinomatosis and/or liver metastases. CT, despite the reduced slice thickness, can sometimes miss the identification of enlarged peritumoral lymph nodes, not distinguishable from the primitive tumor.

Recently a single phase, acquired caudocranially (from the inferior hepatic margin to the diaphragm), starting 50 s after IV contrast administration, has been suggested for studying pancreatic carcinoma [31]. The authors demonstrated that, for tumor detection and assessment of resectability in patients with pancreatic carcinoma, dual-phase and single-phase helical CT

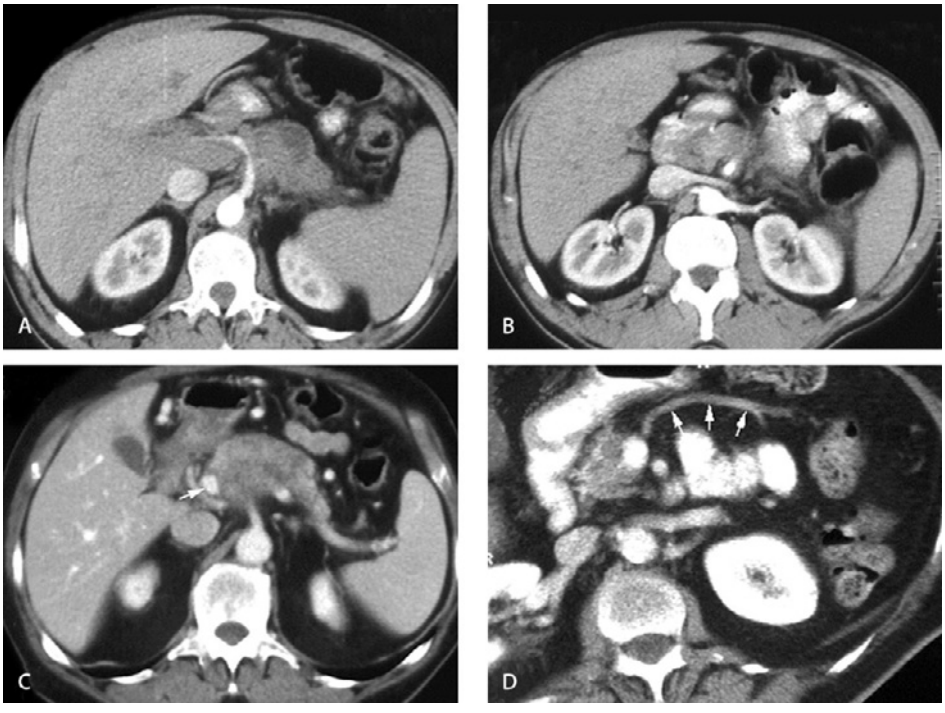

Fig. 5A–D. Ductal adenocarcinoma. **A**, **B** Large necrotic mass of the body with encasement of the celiac trunk (**A**) and of the superior mesenteric artery (**B**), embedded in the neoplastic tissue. **C** Tumor of the body obstructing the splenomesenteric venous confluence. Marked dilation of the posterior superior pancreaticoduodenal vein (*arrow*). **D** Small tumor of the head jutting into the superior mesenteric vein of normal diameter; the dilation of a collateral vein (*arrows*) must arouse suspicions

show comparable diagnostic accuracy. Advantages of the single-phase helical CT are the lower radiation dose and fewer images to film and store [31].

Spiral CT has proved to be highly specific for the determination of nonresectability, while the accuracy for predicting resectability is between 70%–80%, partly because of its lower specificity [20, 25]. CT does, in fact, perform poorly in the detection of small peritoneal implants, small hepatic surface and parenchymal metastases, and lymph node metastases in normal-sized nodes. Lastly, high-resolution helical CT is accurate in demonstrating the venous encasement when the involvement of the vessel exceeds half of the circumference, but arterial involvement is less frequent with this criterion. Nontumorous changes, such as perivascular fibrosis and atherosclerotic change, may cause the same pattern [26].

Recently, multidetector CT (MDCT) has been introduced providing incomparable capabilities for fast data acquisition and narrow collimation. The improved quality of 3D vascular maps of the peripancreatic vessels, obtained with MDCT, helps to detect vascular encasement [32]. Multidetector CT angiography provides a comprehensive display, not only of the major arteries [33], but also of the small peripancreatic arteries such as the pancreatic arcades or the dorsal pancreatic artery [34]. The use of 3D imaging has improved the evaluation of the venous pancreatic system (Fig. 6), since the vascular maps that can be created often provide more information than the sum of the axial images [35]. Thus

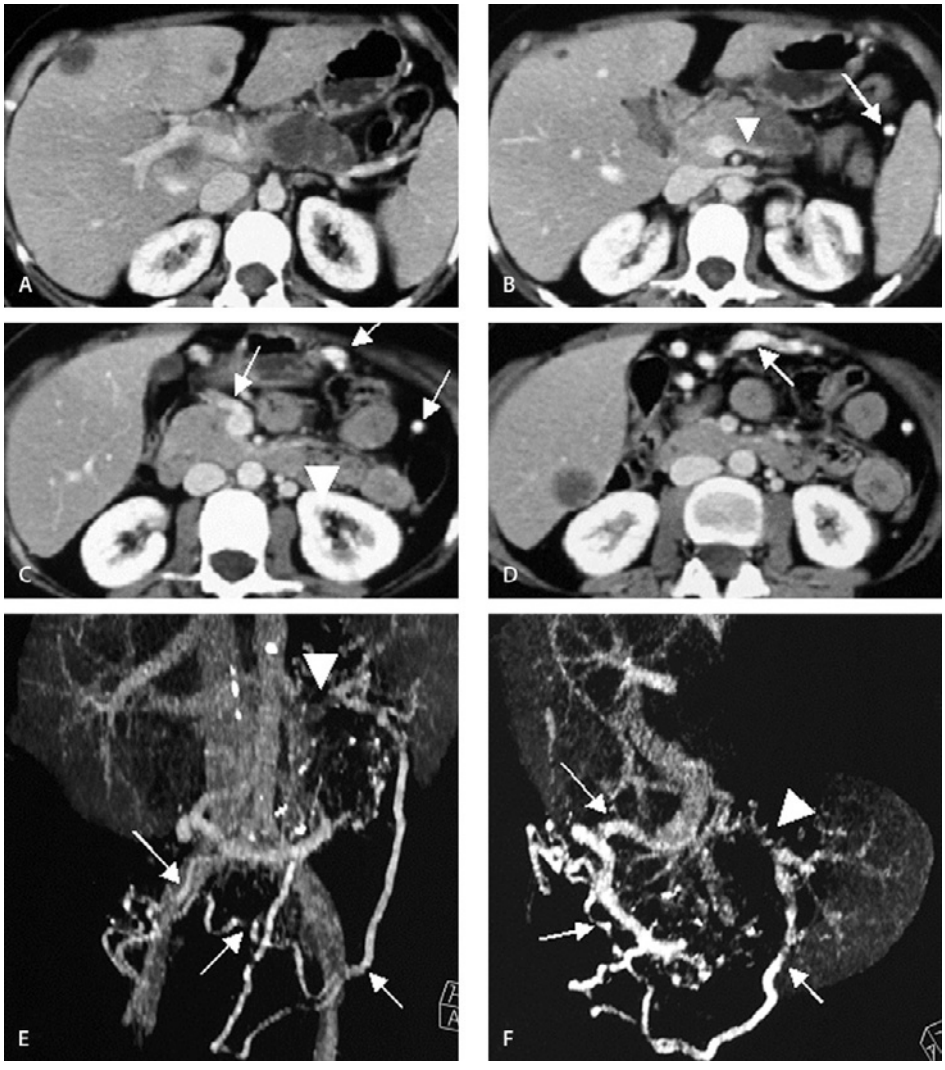

Fig. 6A–F. MDCT evaluation of ductal adenocarcinoma of the body of the pancreas. **A**, **B** Large hypodense mass in the body with encasement of the splenic vein (*arrowhead*) and liver metastases. In the lower scans (**C**, **D**) the collateral network through the gastroepiploic veins and the gastrocolic trunk (*arrows*) is evident. Maximum-intensity projection (MIP) confirms the obstruction of the splenic vein (*arrowhead*) and the collateral network (*arrows* in **E**, **F**).

we can assume that these techniques may someday improve CT accuracy in staging pancreatic neoplasms [32].

Either maximum-intensity-projection (MIP) or volume-rendering CT is utilized in studying the pancreatic vessels because each one provides specific advantages [33]. On current workstations, it is easy to go back and forth between the two techniques. In reality, volume rendering is preferable to MIP because it requires no preprocessing of data and both the soft tissues and the vessels can be evaluated in a single view [32, 34]. Moreover, it is possible to determine the organ from which a tumor arises by tracing arteries that run on the surface of the organs [34]. By using thin collimation and fast scanning techniques, high-quality multiplanar reformations can be obtained. Curved planar reformations allow for single two-dimensional image display of pancreatic and common bile ducts in their entirety [36, 37]. Some authors have suggested that the main value of curved planar reformations (Fig. 7) is the additional diagnostic information provided on the extent of local invasion [36]. More recently, after a more accurate evaluation, the same authors have affirmed that they were unable to detect a significant difference between curved planar reformations and transverse images for detection and local staging of pancreatic carcinoma [37]. Other limitations of this time-consuming technique is that trained personnel and a three-dimensional workstation are necessary [36]. Thus this technique should only be used in selected patients. Curved planar reformation is a useful tool for depicting the secondary signs of an isoattenuating pancreatic carcinoma. With no visible tumor–pancreas contrast, indirect signs such as mass effect, atrophic distal parenchyma, and an interrupted duct sign, easily detected with curved planar reformations (Fig. 7), are important indicators of tumor [38].

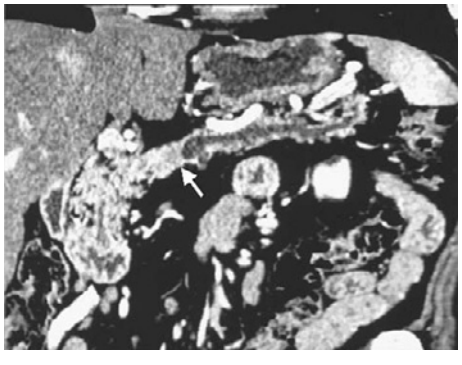

Fig. 7. MDCT evaluation of ductal adenocarcinoma of the body of the pancreas. After CM administration in the pancreatic phase, curved planar reformation of the pancreatic gland shows a small hypodense mass in the body (*arrow*). The parenchyma upstream is atrophic and hypodense, and the main duct markedly dilated. Downstream the normal parenchyma is regularly enhanced

MRI has been increasingly used in the study of ductal adenocarcinoma, hand in hand with technological progress. The recent possibility of a dynamic MRI study after contrast administration has made this technique (Fig. 8) competitive with, and for some authors, even superior to spiral CT [39–45]. In spin echo (SE) sequences, the tumor usually appears hypointense on both T1- and T2-weighted images. Obviously, the difference in signal intensity between the normal parenchyma and the neoplastic focus increases significantly

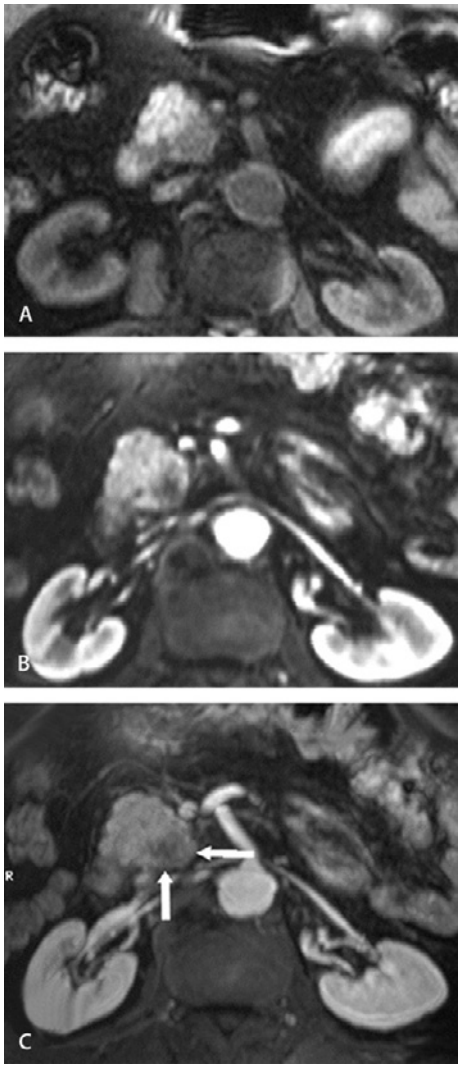

Fig. 8A–C. MR evaluation of small ductal adenocarcinoma in the uncinate process of the pancreas. **A** The gradient recalled echo fat-suppressed (GRE FS) T1-weighted image confirms the presence of a small mass, definitely hypointense in comparison to the normal parenchyma. **B** The GRE FS T1-weighted image, obtained during the pancreatic phase after CM administration demonstrates the small hypointense mass, easily distinguishable from the normal enhanced parenchyma. **C** The thin MIP of the GRE FS T1-weighted images (thickness: 5 cm) shows the small mass (*arrows*), which is isolated from the surrounding vessels

whenever CM is administered, particularly if the sequence is carried out with suppression of the signal of fat [46]. The tumor can appear inhomogeneous due to necrosis; in particular, the necrotic area is slightly hyperintense on T2-weighted sequences. On gradient recalled echo T1-weighted fat-suppressed (GRE T1WFS) images, the tumor appears markedly hypointense with respect to the adjacent normal parenchyma (Fig. 8b), especially when the latter shows no signs of fibrosis secondary to ductal obstruction, which may sometimes occur. When the dynamic technique is adopted, the MRI and CT features of ductal adenocarcinoma are superimposable [47]. Small tumors may occasionally be encountered with MR (Fig. 9). The tumor, usually isointense or slightly hypointense with respect to the normal parenchyma, appears clearly hypointense after CM administration (Figs. 8C, 9A, B), especially in the pancreatic phase (Figs. 8C, 9B). This signal difference tends to weaken in the following phases, depending on the slow impregnation of the tumor. Unfortunately, many authors have demonstrated that there is no statistically significant difference in T1 and T2 between chronic pancreatitis and pancreatic carcinoma [48]. The abundant fibrosis in both pathological conditions justifies the gradual progressive enhancement of the pancreatic parenchyma involved when a dynamic gadolinium-enhanced multiplanar fast spoiled GRE sequence is utilized. Consequently the similar gradual pattern of enhancement and overlap in peak enhancement preclude distinction of the two entities on the basis of gadolinium-enhanced MR findings [49]. The demonstration of the neoplastic lesion can also be achieved using manganese-DPDP (manganese-N,N'-bis(pyridoxal-5-phosphate)ethylenediamine-N,N'-diacetic acid). Initially used in the study of the liver, this CM is also effective for the pancreas, since it is ultimately and selectively accumulated in the normal pancreatic parenchyma, with the consequent demonstration of even very small tumors, which appear as hypointense foci [50–53]. Mn DPDP-enhanced MR imaging is as accurate as contrast-enhanced helical CT for the detection of pancreatic cancer [52].

MRI also allows for an accurate evaluation of the tumoral extension, especially when the breath-hold technique is used. The retroperitoneal spread is characterized by the irregular aspect of the tumoral margins and, at the same time, by the progressive cancellation of the peripancreatic fat plane (Fig. 10A, B), hyperintense on both T1- and T2-weighted sequences without fat suppression. The connections of the tumor with the peripancreatic vessels are more accurately evaluated by the MR-angiography (MRA) technique (Figs. 10C, 11), with optimal visualization at different times and from many angles of both the arterial and venous vascular tree [41–43, 54]. Right anterior coronal oblique images are particularly useful for showing the relationship of the lesion with the mesenteric and portal vein and for assessing the length of vascular involvement [43]. MR imaging is even better than spiral CT for the detection of liver metastases when Mn DPDP or benzyloxypropionictetra-acetate (BOPTA) is utilized [52, 55]. In both cases the huge delayed enhancement of the liver parenchyma leads to the identification of very small focal liver lesions on T1-weighted MR images. Finally, MRI, with the MRCP technique, which relies on rapid-acquisition relaxation enhancement (RARE) single-shots and half-Fourier acquisition single-shot turbo spin echo

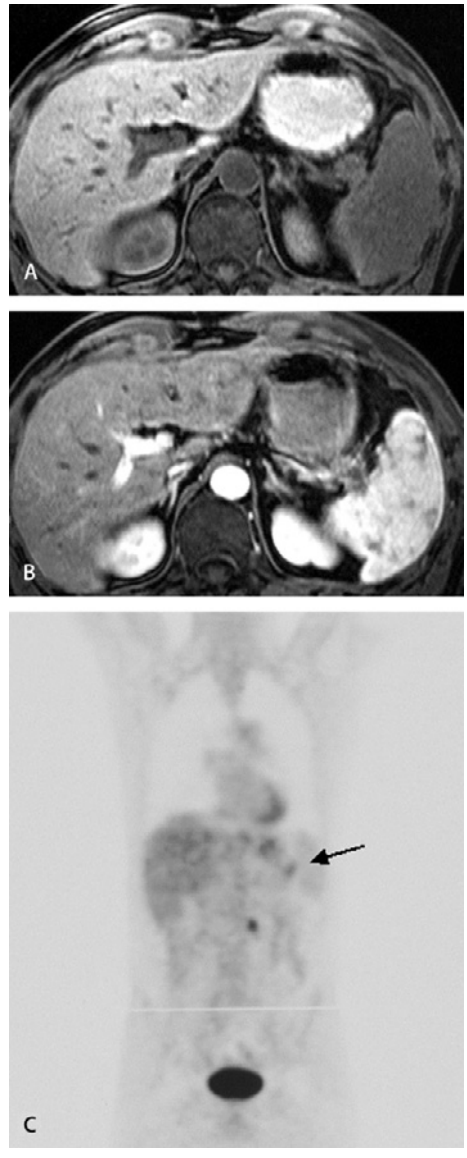

Fig. 9A–C. MR evaluation of small ductal adenocarcinoma of the tail of the pancreas **A** The GRE FS T1-weighted image shows a small round mass in the splenic hilum. **B** The GRE FS T1-weighted image during the pancreatic phase after CM administration shows the small hypointense mass. **C** Fluorodeoxyglucose (FDG) positron emission tomography (PET) confirms the small lesion (*arrow*)

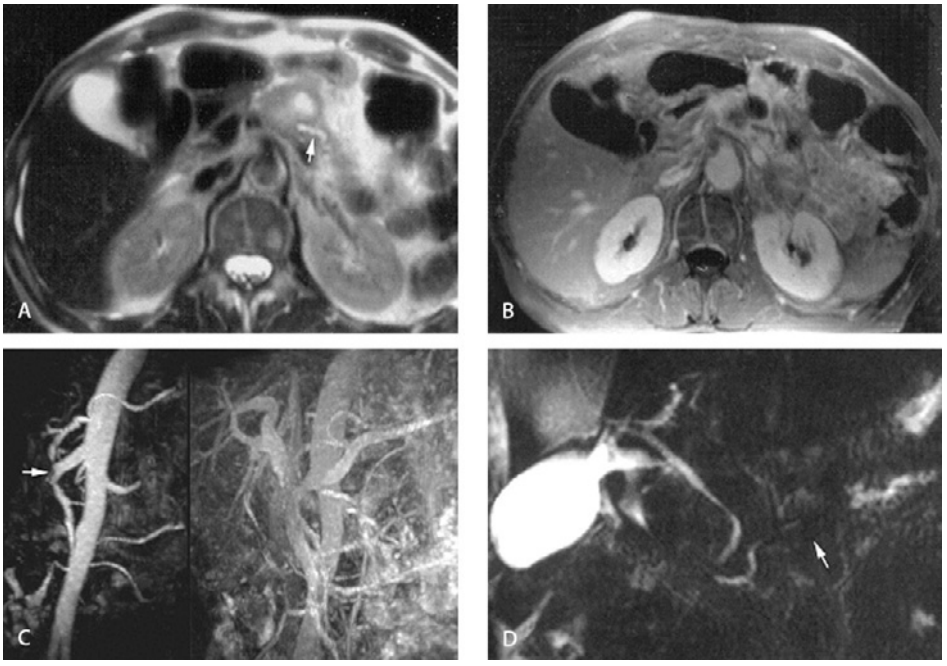

Fig. 10A–D. Ductal adenocarcinoma. **A** On the half-Fourier acquisition single shot turbo spin echo (HASTE) T2-weighted image, the tumor of the body appears inhomogeneous with a central hyperintense necrotic area. The dilated main duct is recognizable upstream (*arrow*). **B** On the GRE T1 FS image, obtained after CM administration in the venous phase, the mass is hypointense. **C** The magnetic resonance angiography (MRA) in the arterial phase shows the encasement of the superior mesenteric artery (*arrow*) and in the venous phase, the obstruction of the splenomesenteric confluence. **D** MRCP shows the stenosis of the main duct at the tumor site (*arrow*) with dilation of the tract upstream

(HASTE) multi-slice sequences, allows for the analysis of the biliopancreatic tree (Fig. 10D). MRCP is as sensitive as ERCP when detecting pancreatic carcinomas [56]. The MRCP evaluation of the main duct can be particularly useful in order to distinguish an inflammatory pancreatic mass from a conventional pancreatic carcinoma [57]. In reality, the CT or MR characterization of a focal mass of the pancreas is definitely difficult when typical signs of chronic pancreatitis (calcifications) or of ductal adenocarcinoma (vascular involvement, distant metastases) are absent. In fact the contrast enhancement of the mass is almost the same in both cases. In particular the heterogeneous hypoattenuation or hypointensity of inflammatory mass is indistinguishable from that of ductal adenocarcinomas. On the contrary, the duct-penetrating sign on MRCP images – a smoothly stenotic or normal MPD penetrating a mass – was seen more frequently in inflammatory mass than in pancreatic neoplasm (Fig. 12) [41, 42, 57]. The double-duct sign can be easily detected with MRCP (Fig. 13). Although it is highly suggestive of malignancy, it is not diagnostic [58]. Recently with MRCP, it was demonstrated that, in pancreatic head carcinoma, the most distal parts of the pancreatic and bile ducts may be relatively spared from tumor infiltration, thus resulting in the so-called four-segment sign (proximal dilation of the biliary and pancreatic ducts and regularity of their distal parts).

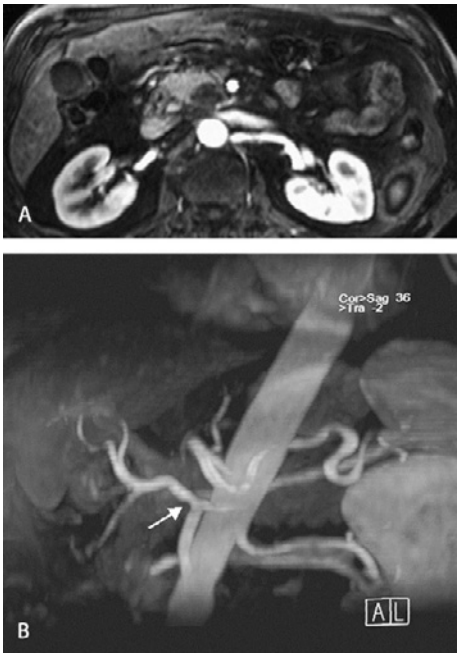

Fig. 11A, B. MR evaluation of ductal carcinoma of the uncinate process. **A** The GRE FS T1-weighted image during the contrast-enhanced pancreatic phase shows a small hypointense mass in the uncinate process near the superior mesenteric artery. **B** The MRA in the arterial phase shows the normal caliber of the superior mesenteric artery and the anomalous origin of the hepatic artery from the former vessel (*arrow*)

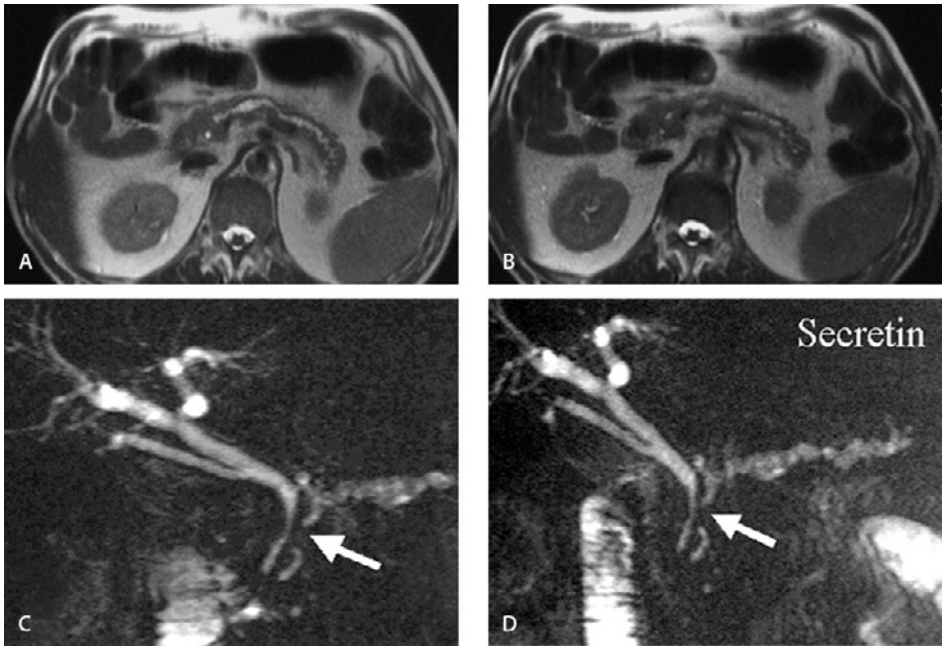

Fig. 12A–D. MRCP evaluation of ductal adenocarcinoma of the head of the pancreas. **A**, **B** The turbo spin-echo (TSE) T2-weighted images show dilation of the main duct with a stricture in the pancreatic head. A mass is not recognizable. **C**, **D** Magnetic resonance cholangiopancreatography (MRCP) before and after secretin administration shows a marked stenosis which does not change after secretin (negative duct-penetrating sign (*arrow*)). After 3 months a mass was demonstrated at the site of stenosis

This sign, almost always absent in other types of periampullary carcinomas or in chronic pancreatitis, leads to suspicion of a ductal adenocarcinoma [59]. Another sign, which can be considered specific of focal chronic pancreatitis, is the presence of dilated collateral branches within the mass [60].

In conclusion, the dynamic MRI study with a single imaging technique gives information otherwise achievable with CT (study of the parenchyma), angiography (study of the vessels) and ERCP (study of the biliopancreatic tree). For this reason, it has been defined as the "all-in-one" or "one-stop-shopping" technique (Fig. 10).

Fig. 13. MRCP evaluation of ductal adenocarcinoma of the head of the pancreas. The typical double-duct sign is easily demonstrated

Variants of Ductal Adenocarcinoma

Variants of ductal carcinoma are those neoplasms that present a specific histological differentiation pattern associated with a typical ductal adenocarcinoma component. These tumors, whose incidence ranges from 2% to 10%, show similar clinical and biological features to those of ductal adenocarcinoma.

■ **Mucinous Noncystic Carcinoma.** This carcinoma is composed of well-differentiated glands floating in abundant (>50%) extracellular mucin and is macroscopically characterized by a gelatinous mass, better demarcated than the ductal adenocarcinoma. Its incidence is 1%–3% of all pancreatic cancers; sex and age at onset are similar to those of ductal carcinoma. This tumor is associated with a significantly better prognosis than ordinary ductal adenocarcinoma [61]. At CT, the tumor appears centrally hypodense in the contrastographic phase and slightly hyperintense in the T2-weighted MRI sequence, in relation to the rich mucinous component. In cases of clinical suspicion of mucinous noncystic carcinoma, the possibility of an incisional biopsy contributing to thromboembolic complications or even dissemination of the tumor, needs to be considered [61].

■ **Adenosquamous carcinoma** is a rare subtype, accounting for 1%–4% of exocrine malignancies, and is

composed of a mixture (>30%) of two neoplastic components: a glandular and a squamous cell component [62]. It shows a high metastatic potential and the prognosis is worse than that of conventional adenocarcinoma. Macroscopically, it does not present significant differences to a ductal adenocarcinoma and therefore, the two cannot be distinguished by imaging [63].

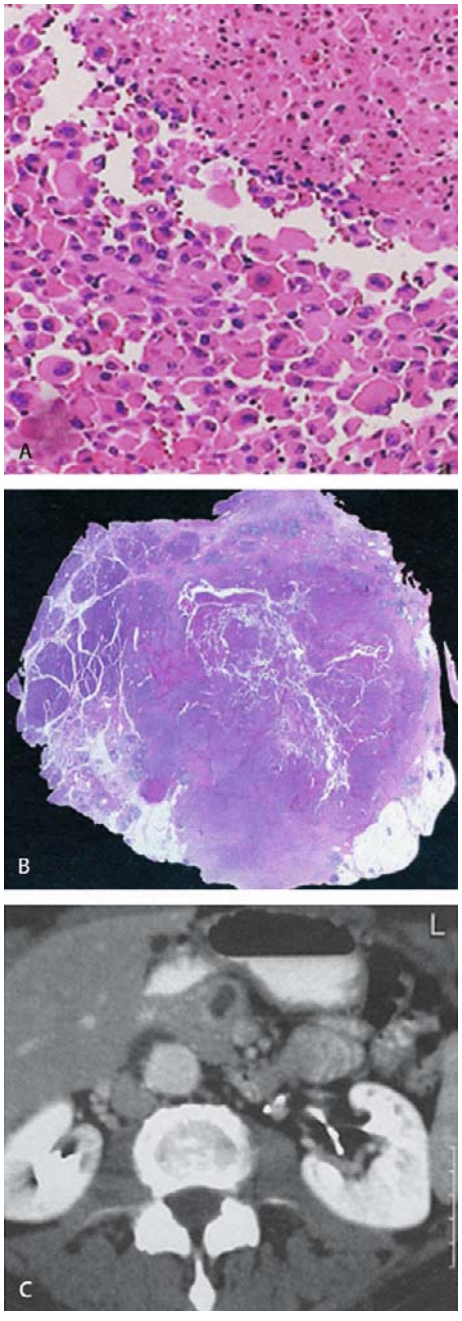

Fig. 14A–C. Anaplastic carcinoma. **A** Large undifferentiated cells showing extreme anaplasia and growing in poorly cohesive sheets supported by scanty fibrous tissue **B** Ill-demarcated tumor mass with areas of hemorrhagic necrosis. **C** At the CT exam (venous phase of contrast enhancement), a well-defined round mass can be seen in the neck of the pancreas. The tumor shows a thick hyperdense solid wall with central hypodense necrotic area

■ **Undifferentiated (Anaplastic) Carcinoma.** This carcinoma is composed of pleomorphic large cells, giant cells and/or spindle cells (Fig. 14A). Its incidence is 5%–7% of all pancreatic tumors; its prognosis is poorer than that of conventional adenocarcinoma, with distant metastases frequently present at the time of the diagnosis. The preferential location is in the tail of the pancreas. Macroscopically, it is characterized by a voluminous mass (mean diameter of around 6 cm), with a variegated aspect on cut section because of the presence of degenerative changes (necrosis and hemorrhage, Fig. 14B). At imaging, in addition to the larger dimensions and the frequent presence of lymphatic or liver metastases, the more significant differential finding compared to that of the adenocarcinoma is in the marked enhancement of the tumor [64, 65], with the exception of the areas of necrosis (Fig. 14C). Lymphadenopathy and liver metastases are usual.

■ **Osteoclast-like Giant Cell Carcinoma.** This carcinoma is composed of malignant undifferentiated epithelial cells with round or spindle-shaped cells associated with nonneoplastic osteoclast-like giant cells. The clinical course is extremely aggressive and most patients do not survive 1 year. The macroscopic aspect is identical to that of anaplastic carcinoma [4, 66].

Other extremely rare histological subtypes of carcinoma, with macroscopic features similar to those of adenocarcinoma, are signet-ring cell carcinoma, clear cell carcinoma, ciliated cell carcinoma and mixed ductal–endocrine carcinoma.

Acinar Cell Carcinoma

Acinar cell carcinoma is an epithelial tumor made up of neoplastic cells with acinar differentiation, occasionally associated with endocrine differentiation. It is rare, constituting 1%–2% of the tumors of the exocrine pancreas, with lymphatic and liver metastases in 50% of the cases at the time of diagnosis [67, 68, 69]. It is prevalent in males and in advanced age, with a peak incidence in the seventh decade [68, 69], even if sporadic cases have been described in children. The clinical picture is mostly nonspecific, identical to that of ductal adenocarcinoma, with the only exception of jaundice, which is rather rare even in large tumors involving the pancreatic head. In around 15% of cases, the manifestation of a quite specific clinical picture can occur, which is characterized by polyarthralgia-polyarthritis, disseminated (mainly subcutaneous) focuses of fat necrosis and peripheral eosinophilia induced by the activity of the lipase enzyme [68, 69].

Macroscopically, the pancreatic head (Fig. 15) and tail are common sites of occurrence of acinar cell carcinoma, accounting for 56% and 36% of cases, respectively [68, 69]. Although cystic variants have been described, the majority of the lesions are solid. It presents as a well-circumscribed, soft mass (Fig. 15A), with an average size of 10 cm. The cut surface demonstrates the presence of many bands of dense connective tissue that separate the tumor nodules, which can appear with necrotic foci. The tumor can grow exophytically into the duodenum.

Histologically, the carcinoma shows solid proliferation of acinar cells (Fig. 15B), characterized by round nuclei and abundant eosinophilic, granular cytoplasm (PAS-positive). Immunohistochemical analysis shows acinar differentiation, with variable positivity for the pancreatic enzymes, trypsin, amylase, lipase and chymotrypsin. The expression of endocrine markers is usually negative or restricted to single cells [70]. When the endocrine component exceeds 30% of the entire lesion, the tumor is classified as a mixed acinar–endocrine carcinoma.

At imaging, the tumor appears both more notable and more voluminous compared to ductal adenocarcinoma. Despite the conspicuous dimensions of the tumor, the Wirsung duct can appear normal upstream. Marked hypodensity or T1 hypointensity after CM administration, compared to the normal pancreatic tissue, is usually reported for this tumor, relating to its poor vascularization [65]. In personal experience and in that of other authors [71, 72], acinar carcinoma of the head has been documented as markedly hyperdense after CM administration (Fig. 15C, D). Recently the MR features of acinar cell carcinoma have been described. There was avid uptake of Mn-DPDP by the tumor, which appeared hyperintense in post-contrast T1-weighted fat-saturated gradient echo (GRE) images [69]. Therefore, this tumor is distinguishable from ductal adenocarcinoma given its greater dimensions and more defined contours, while the differential diagnosis in both the pancreatoblastoma and the solid-pseudopapillary tumor (when the acinar carcinoma is poorly vascularized) or the endocrine nonhyperfunctioning tumor (when highly vascularized) cannot be proposed [70, 73].

The prognosis is midway between that of ductal adenocarcinoma and that of the endocrine tumors; however, only 6% have a 5-year survival [65, 68]. Favorable prognostic factors are: less than 60 years of age, resectability and absence of metastases at intervention.

Pancreatoblastoma

Pancreatoblastoma is a malignant tumor composed of epithelial elements with acinar differentiation, squamoid corpuscles and occasional endocrine cells and nonepithelial components. It is a rare tumor, prevalent in males, representing the most common pancreatic tumor in children. Nevertheless, the increase in reported cases has shown a bimodal distribution in relation to

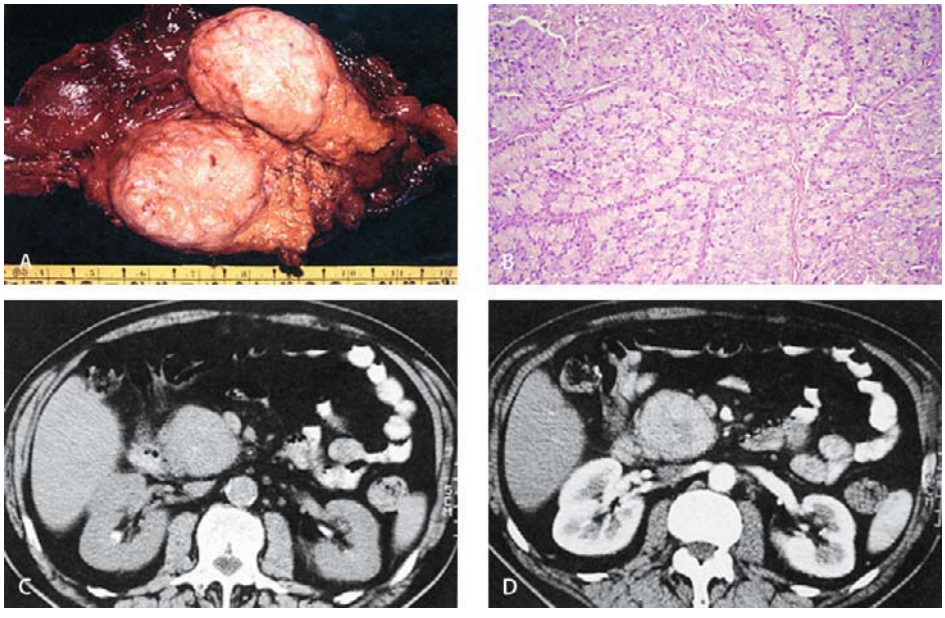

Fig. 15A–D. Acinar cell carcinoma. **A** Whipple resection specimen showing well-circumscribed tumor composed of nodules separated by thin fibrous strands. **B** Trabecular pattern: uniform tumor cells with nuclei showing a polarized arrangement reminiscent of normal pancreatic acinar tissue. **C**, **D** CT shows a well-demarcated, round mass in the head of the pancreas, with conspicuous enhancement after CM administration.

age, with one group of mean age around 3–5 years and the other around 25–30 years [73, 74]. Its incidence appears to be relatively high in East Asia [75]. Clinically, symptoms are nonspecific, usually late, when the tumor has reached conspicuous dimensions, with a consequent mass effect on the adjacent structures. However, obstructive jaundice is infrequent. Alpha-fetoprotein levels are reported to be high in 25%–55% of patients [75].

Macroscopically, these tumors are solitary, large and well circumscribed and have no preferential location in the pancreas (Fig. 16A); the entire organ can be involved [75]. In the late stage, the tumor extensively infiltrates the peripancreatic soft tissue, the adjacent organs, and the margins are no longer clearly demarcated [76].

Histologically, the neoplasm consists of lobules of relatively uniform cells, separated by dense fibrous tissue and blended with the characteristic squamoid corpuscles (Fig. 16B). The pattern of growth can be solid, trabecular or acinar. The tumor may show foci of necrosis or hemorrhage [65] as well as, in rare cases, the presence of a conspicuous mesenchymal component with chondroid and osseous differentiation.

At imaging the lesion appears as a voluminous and well-circumscribed mass, with a homogeneous structure. Hypoechoic at US, the tumor shows no significant staining at contrast-enhanced CT (Fig. 16C) and/or MRI (Fig. 16D). The greater part of these tumors shows low or intermediate signal on T1-weighted MR images and high signal on T2-weighted images. Calcifications are sometimes present [65]. Distinguishing pancreatoblastoma from other pediatric abdominal masses can be difficult, particularly when the tumor is large and when its origin is uncertain. In such cases, the differential diagnosis, as with other pancreatic tumors (e.g., endocrine tumors, solid-pseudopapillary neoplasms), includes the consideration of any large intra- or retroperitoneal mass, such as a neuroblastoma, non-Hodgkin lymphoma, or Wilms tumor.

The prognosis of this tumor is variable. Metastases, above all in the liver, have been described in up to one-third of patients [74]. The reported survival rate is only 18 months for adult patients, and 50% (mean follow-up of 8 years) for children.

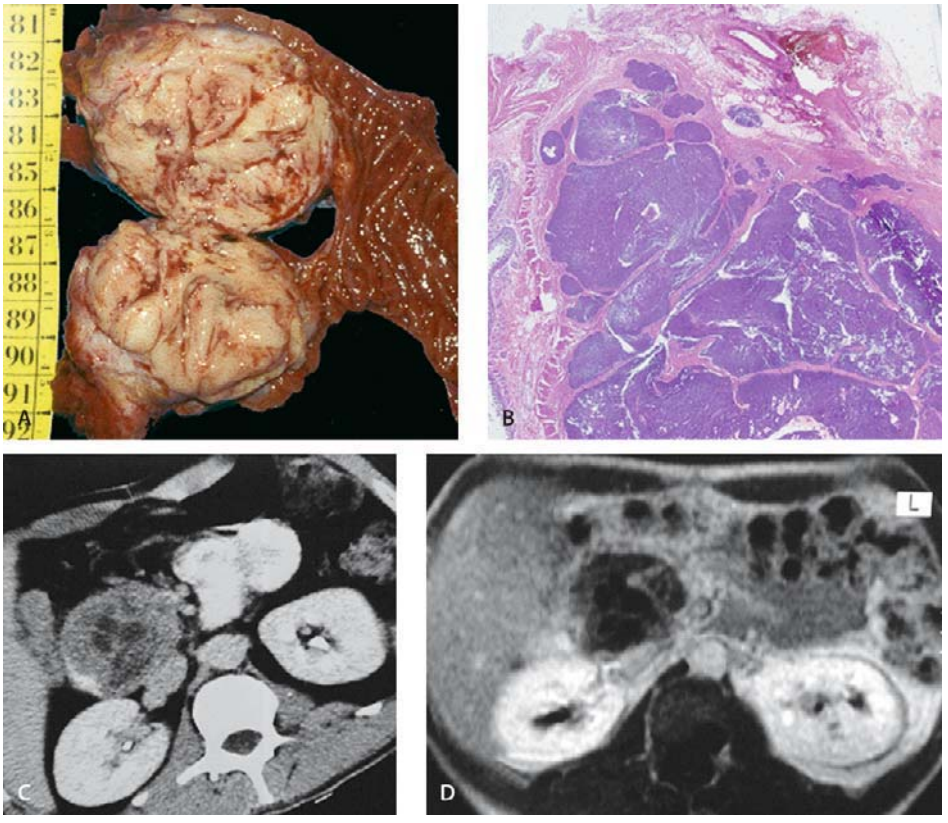

Fig. 16A–D. Pancreatoblastoma in an adult male. **A** Gross specimen showing solid well-demarcated mass. **B** Macrosection of the tumor displays large nodules separated by thin fibrous strands like acinar cell carcinoma. **C** At the contrast enhanced CT exam, the mass appears well demarcated, hypodense and inhomogeneous. **D** The Gd-DTPA-enhanced GRE T1-weighted MR image confirms the poor vascularization of the mass

Solid-Pseudopapillary Tumor

Solid-pseudopapillary tumor (SPT) of the pancreas, also known as Frantz tumor, is a distinctive low-grade malignancy that primarily occurs in girls and young women and is composed of monomorphous cells variably expressing epithelial, mesenchymal, and endocrine markers. It represents 1%–2% of all exocrine tumors of the pancreas. It has rarely been reported in older women, males and in extrapancreatic sites [4]. SPT seems to have a predilection for Asians [77]. Its identification is usually incidental or justified by nonspecific symptoms. Jaundice is very rare.

Macroscopically, SPT appears as a large (size range, 2–20 cm; average 10 cm), round, well-circumscribed mass (Fig. 17A), which exhibits variable proportions of solid and cystic areas filled with hemorrhagic fluid and necrotic debris. The "pure" solid and cystic forms are prevalent in the smaller and larger tumors, respectively. The tumors occur with a slight predilection for the head of the pancreas [77].

Microscopically, the tumors are composed of a mixture of solid, pseudopapillary and cystic areas, usually surrounded by a fibrous capsule that is often calcified. The tumor cells are monomorphous, with round to oval nuclei and eosinophilic, granular cytoplasm. PAS-positive globules, stromal myxoid degeneration, necrotic changes and hemorrhage are characteristically present. Mitotic figures are virtually absent. SPTs show strong immunoreactivity for neuron-specific enolase, vimentin, α-1-antitrypsin and α-1-antichimotrypsin, and only focal positivity for keratin markers [78].

Although the histogenesis remains obscure, the immunohistochemical and ultrastructural findings favor the hypothesis of a ductular cell origin with divergent differentiation [79, 80]. The pathogenetic role of sex hormones is suggested by the predilection of SPT for young, fertile women and by the immunohistochemical presence of progesterone receptors in the large majority of neoplastic cells [78].

The most important differential diagnosis is with nonfunctioning islet cell tumors, pancreatoblastoma and acinar cell tumor. Preoperative diagnosis may frequently be obtained using fine needle aspiration biopsy under ultrasound guidance. Cytological smears are quite characteristic because of the presence of branching papillae, formed by delicate central fibrovascular stalks covered by one or more layers of monomorphic tumor.

The clinical course is usually favorable, although some cases of invasion of vital structures and metastases have been reported [81, 82, 83]. The complete removal of the tumor is considered the most appropriate therapy. Metastases and recurrent tumors were more frequently noted in elderly patients. For this reason, children with SPT generally have a better prognosis than adults [77].

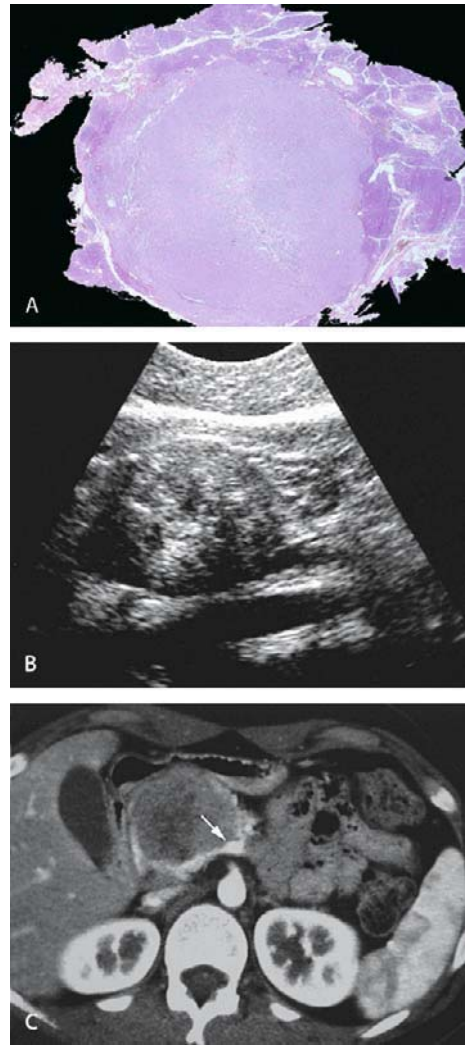

Fig. 17A–C. Solid-pseudopapillary tumor. **A** Whole-mount macrosection of the tumor displays round, solid, homogeneous mass well demarcated from the remaining pancreas. **B**, **C** US (**B**) and CT (**C**) examinations demonstrate homogeneous solid mass in the head of the pancreas. At CT an adhesion to the superior mesenteric vein (*arrow*) is demonstrated

At US the tumor appears well circumscribed, homogeneously hypoechoic when small (Fig. 17B), and with inhomogeneous echotexture when voluminous (Fig. 18A). At both CT and MRI, the peripheral thick capsule, which shows moderate enhancement especially in the late contrastographic phase, is clearly recognizable (Figs. 17C, 18C). At CT lamellar calcifications can be recognized within the mass. Centrally, the tumor, which appears hypodense at CT and T1 hypointense/T2 hyperintense at MRI, does not show significant enhancement after CM administration (Figs. 17C, 18C). At MRI, the foci of subacute hemorrhage (Fig. 18B) appear hyperintense on the unenhanced T1-weighted sequence [84].

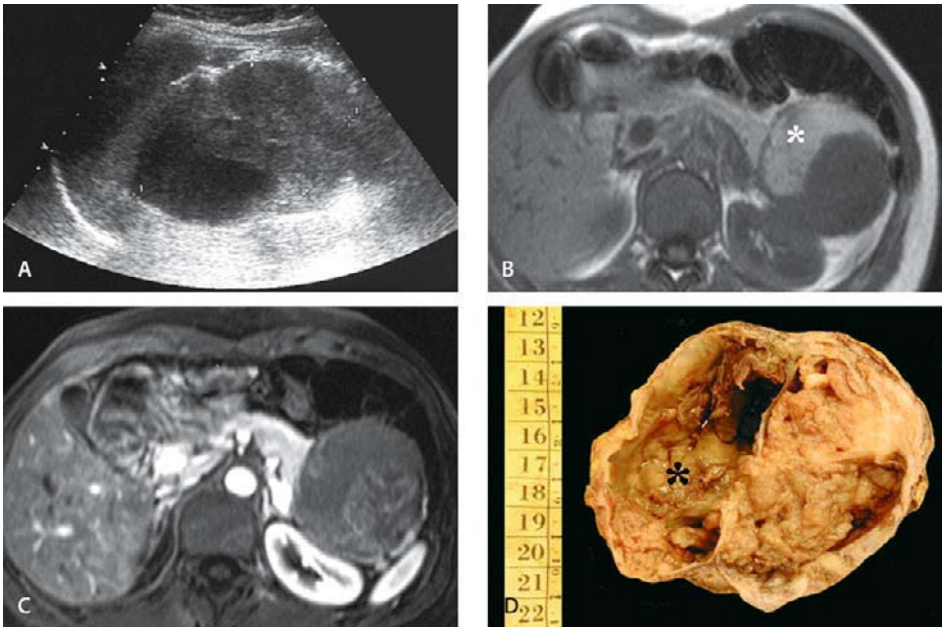

Fig. 18A–D. Solid-pseudopapillary tumor. **A** US examination demonstrates a large inhomogeneous solid and fluid mass in the tail of the pancreas. **B** The GRE T1-weighted image confirms the inhomogeneous content of the mass with a fluid, hyperintense, hemorrhagic area (*asterisk*) and solid hypointense component. The latter shows a slight enhancement after gadolinium in the GRE FS T1-weighted sequence (**C**). **D** Gross specimen showing well-demarcated mass with thick capsule and solid and fluid (*asterisk*) areas

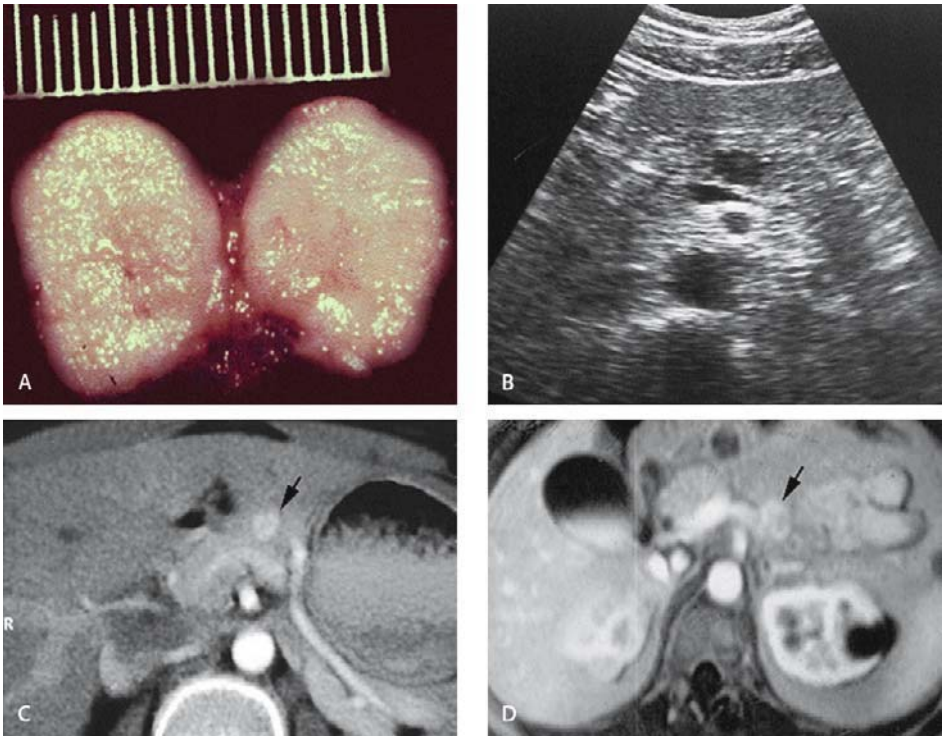

Fig. 19A–D. Endocrine hyperfunctioning tumor (insulinoma). **A** Small (2 cm in diameter) intrapancreatic tumor, showing a homogeneous appearance. **B** At US a small hypoechoic nodule is located in the body of the pancreas. **C** CT scan during the arterial phase of contrast enhancement shows a small hyperdense tumor in the body of the pancreas (*arrow*). **D** Another case. In Gd-DTPA-enhanced T1-weighted MR image, a small hyperintense nodule (*arrow*) is seen in the tail of the pancreas

Endocrine Tumors

Endocrine tumors comprise benign or malignant epithelial neoplasms, that show morphological and immunohistochemical evidence of endocrine cell differentiation. Their incidence is very low, accounting for about 1%–2% of all pancreatic tumors, with a frequency of 1 case per 2,000,000 inhabitants in the surgical series [85, 86]. Endocrine tumors can be encountered at any age, although they are rare in childhood. There is no notable difference in gender distribution. The tumors can be sporadic (usually single) or in association with multiple endocrine neoplasm syndrome like MEN-1 (frequent presence of multiple pancreatic lesions). Pancreatic endocrine tumors are an unusual manifestation of Von Hippel-Lindau disease. These lesions are typically nonfunctional and therefore do not cause symptoms [87]. Their histopathological classification is based on the degree of differentiation and on the type of hormone produced (inferred by the immunohistochemical findings on tissue samples) [88]. The presence of one or more hormone demonstrated with immunohistochemical methods does not implicate the presence of a clinical syndrome. A neoplasm should be defined as functioning only when the clinical syndrome is present in association with elevated hormonal title in the serum.

Endocrine tumors are clinically subdivided into two groups, which raise significantly different diagnostic problems. Functioning endocrine tumors manifest specific symptoms, closely correlated with hormone secretion, so that the main diagnostic problem is represented by their location. Nonfunctioning endocrine tumors manifest later, with nonspecific symptoms correlated with their mass effect. In this case, the principal diagnostic problem is the identification of this tumor, with a more favorable prognosis than that for other tumors of the pancreas. Malignant neoplasms may grow slowly and thus survival may be long, despite metastatic diseases. The main metastatic sites are lymph nodes, liver and bones. The lungs, mediastinum, peritoneum and the brain may also be involved [89].

Endocrine tumors do not present particular topographical predilection in the pancreas, although the insulinomas show a slight prevalence in the body-tail [90], while the nonfunctioning tumors prefer the head. The dimensions can range from 0.5–1 cm to 10 cm. Generally, nonfunctioning tumors are diagnosed in the more advanced phase (greater dimensions and often already with lymphatic and liver metastases).

Macroscopically, most tumors appear as well-circumscribed, rounded masses (Figs. 19A, 20A). On cut sections, a fibrous pseudocapsule frequently divides the

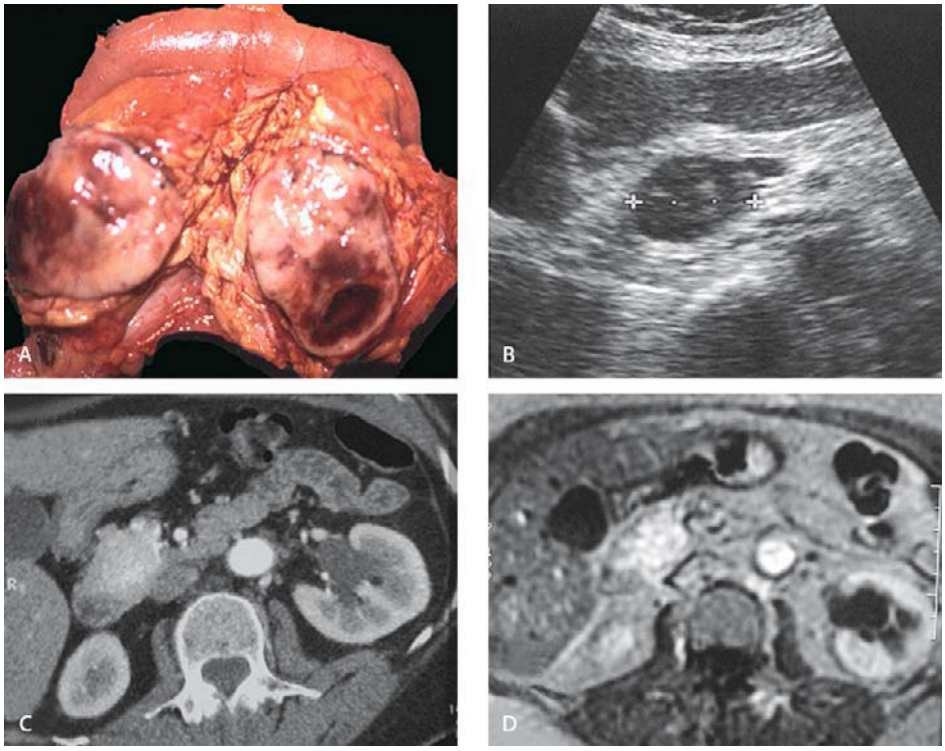

Fig. 20A–D. Endocrine nonfunctioning tumor. **A** Whipple resection specimen showing a well-demarcated tumor with a focus of hemorrhage. **B** US demonstrates a round, homogeneously hypoechoic mass in the head of the pancreas. **C**, **D** Enhanced CT (**C**) and MR (**D**) images demonstrate a solid homogeneous, well-vascularized tumor in the head of the pancreas

lesion from the surrounding parenchyma. Hemorrhagic and necrotic areas are prevalent in malignant tumors; a purely cystic aspect is rarely found. Malignant cases show infiltration of the peripancreatic soft tissue and direct invasion of the surrounding organs.

Microscopically, the majority of tumors present sufficient distinctive features to be recognized as endocrine. They are represented by a solid, trabecular, or glandular pattern of growth and by the presence of round, regular and mild to moderate atypical cells. Special or immunohistochemical stain for general endocrine markers and specific hormonal products are needed for better tumor identification (morphofunctional classification). It is extremely difficult to predict the biological behavior of these tumors using classic histopathological criteria. Invasion of the peripancreatic organs, and hepatic and distant lymph node metastases are considered the only unequivocal evidence of malignancy. Negative prognostic factors include large locally invasive tumors, high-grade cellular atypia, increased mitotic index/proliferative activity (Ki-67 index above 5%), the presence of tumor necrosis and vascular invasion. In the recent WHO classification, pancreatic neoplasms are typed in three different prognostic categories: well-differentiated endocrine tumors, well-differentiated endocrine carcinoma and poorly differentiated endocrine carcinoma [88].

Insulinoma, the most frequent among the functioning endocrine tumors, is benign in the majority of cases. Clinically, it appears with the Whipple triad (starvation attacks, hypoglycemia after periods of fasting, resolution of the latter with intravenous administration of dextrose). The prevalence within the clinical picture of a psychiatric syndrome sometimes justifies a diagnostic delay. Its association with MEN-1 is common. Among the endocrine tumors, insulinoma has the smallest dimensions (50% of the tumors have a diameter <15 mm). This tumor is more frequently located in the body-tail of the pancreas.

Macroscopically, the neoplastic nodule is well circumscribed. It is often at least partially encapsulated (Fig. 19A). It is identified through imaging techniques by its rich vascularization [91, 92].

At US, the tumor appears as an intrapancreatic, sharply marginated hypoechoic nodule (Fig. 19B). The sensitivity of CT is currently high [93], thanks to the spiral technique, which can identify the tumor in the arterial phase of contrast enhancement (Figs. 19C, 21). Because of its ability to demonstrate the lesion in different planes (Fig. 21), MDCT leads to a better differentiation of the tumors with regard to the other structures (e.g., vessels) that may mimic it. Moreover, MDCT can precisely locate the tumor within the pancreatic gland. In the venous phase the tumor can either persist as hyperdense or become isodense with the consequent impossibility of differentiation from the normal pancreatic parenchyma [94]. Liver metastases, very rare, show similar vascular architecture to that of the primitive tumor, and are also well documented in the arterial contrastographic phase. The sensitivity of MRI seems to be slightly superior to that of spiral CT (Fig. 22), since the identification of the tumor, in addition to a dynamic contrast-enhanced study (Figs. 19D, 22A), for which fat suppression is particularly useful, can also be achieved on the T2-weighted images (hyperintensity of the neoplastic nodule: Fig. 22B) [95–97]. Atypical presentations of insulinomas have been described as cystic, calcified or hypodense in relation to the surrounding parenchyma during the arterial phase images on contrast-enhanced CT and hypointense on dynamic contrast-enhanced MR images. In this case, a hypercellular tumor with poor vascularization and amyloid deposits can be demonstrated [98].

Gastrinoma is the second most common endocrine tumor. Unlike insulinoma, it is characterized by an elevated incidence of malignancy. At the moment of diagnosis liver metastases are frequently shown. This tumor can also be linked to MEN-1. The clinical picture is highly specific, represented by Zollinger-Ellison syndrome (multiple gastric ulcers and diarrhea) because of the excessive secretion of gastric acid (unregulated hypergastrinemia).

The tumor, whose macro- and microscopic features are both similar to those of insulinoma, is prevailingly located in the so-called gastrinoma triangle, formed by the pancreatic head, the duodenum and the junction of

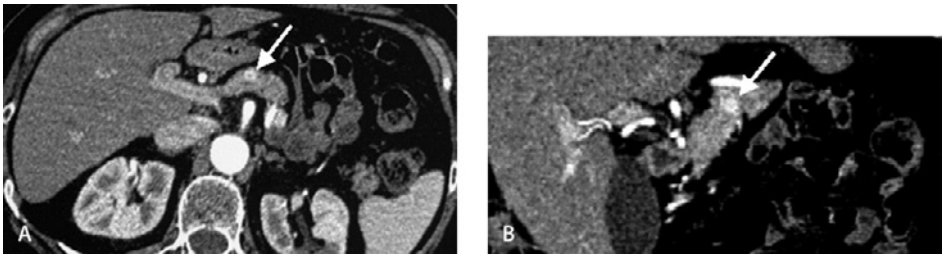

Fig. 21A, B. Endocrine hyperfunctioning tumor (insulinoma), multidetector CT (MDCT) study. **A** During the pancreatic phase of contrast enhancement a small hyperdense nodule (*arrow*) is recognizable in the neck of the pancreas. **B** In the paracoronal 2D MPR reconstruction of the images, the intrapancreatic site of the nodule is confirmed (*arrow*)

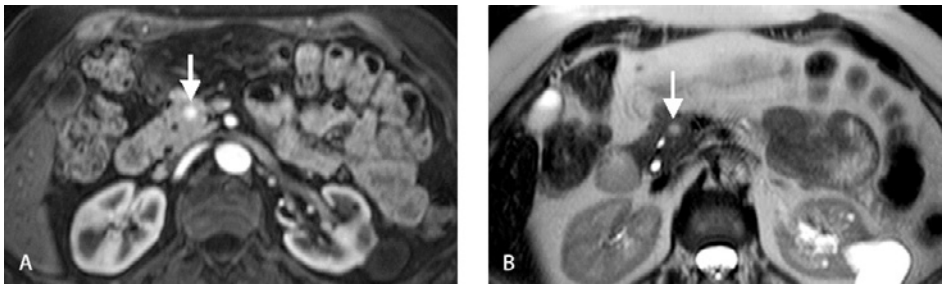

Fig. 22A, B. Endocrine hyperfunctioning tumor (insulinoma), MR study. **A** In Gd-DTPA-enhanced T1-weighted VIBE sequence a very small hyperintense nodule (*arrow*) is identifiable in the head of the pancreas. **B** The same lesion is demonstrated by TSE T2-weighted image, where it appears hyperintense (*arrow*)

the cystic and common bile duct. The identification of lymph nodes or liver metastases is not infrequent, even when the primitive tumor has not been identified.

The imaging features of this tumor are very similar to those of the insulinoma. However, its identification is more difficult considering the possibility of extrapancreatic location. In some cases, faced with negative US, CT and MRI results, nuclear medicine with [^{111}In]-pentetreotide (OctreoScan) is diagnostic [99].

The other functioning endocrine tumors (glucagonoma, vipoma, somatostatinoma) are rare, and are characterized by a less specific clinical picture compared to that of both insulinoma and gastrinoma. For this reason, there is usually a delay in their identification, as is confirmed by the mean dimensions (4–10 cm), which are clearly greater than those of the other functioning endocrine tumors. The imaging features of these tumors are similar to those already described; they can sometimes be cystic.

Nonfunctioning endocrine tumors, whose histological aspect is analogous to that of the functioning ones, account for roughly 30% of endocrine tumors, with an incidence ranging from 15% to 41%. The lack of a specific clinical picture justifies the notable diagnostic delay. In fact, they manifest when, having reached conspicuous dimensions, they either involve the digestive or biliary tract. At diagnosis, the mean diameter of these tumors is greater than that of functioning tumors (Fig. 20A). The incidence of malignant degeneration is high, manifesting with both infiltration of the peripancreatic structures and distant metastases. The prognosis of these tumors is somewhat better compared to that of ductal adenocarcinoma, and therefore warrant a more aggressive therapeutic approach, even in the presence of distant metastases.

At US, the tumor has a homogeneous hypoechoic structure (Fig. 20B); the liver metastases are also hypoechoic. The distinction between the nonfunctioning en-

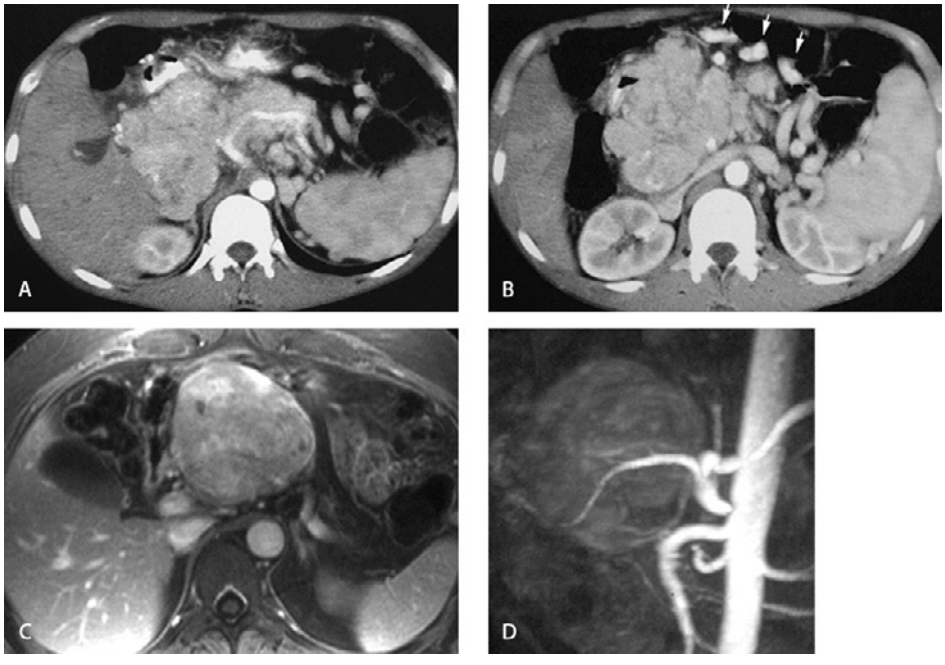

Fig. 23A–D.

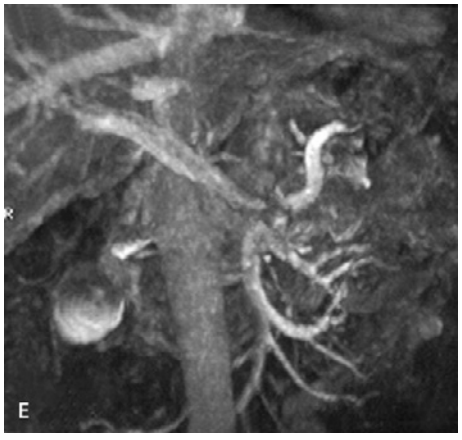

Fig. 23A–E. Endocrine nonfunctioning tumor. **A**, **B** CT scans, performed during the pancreatic phase of contrast enhancement, demonstrate a huge, multilobulated, hyperdense mass, occupying the head and the body of the pancreas, with encasement of the splenic artery and obstruction of the superior mesenteric vein. An important collateral venous network (*arrows*) is present. **C–E** Different MR study. **C** On fat-suppressed Gd-DTPA-enhanced T1-weighted MR image, a large, well-circumscribed, hyperintense mass in the body of the pancreas is present. **D** MRA in the arterial phase demonstrates the normal aspect of the arterial vessels; "nest" pattern of the small arterial vessels at the periphery of the tumor. **E** In the venous phase, the superior mesenteric vein and the portal vein appear compressed

docrine tumor and ductal adenocarcinoma is easier to obtain with CT and MRI, because of the frequent hypervascularization of both the tumor (Fig. 20C, D) and its metastases, as documented in the arterial contrastographic phase. In reality, not all nonfunctioning endocrine tumors are hypervascularized; in some cases, the aspect of both the primitive tumor and the metastases, hypovascularized, is in practice indistinguishable from that of ductal adenocarcinoma. Therefore, in all cases histological proof by fine-needle core biopsy is mandatory. CT and MRI have the task of evaluating the diffusion of the tumor, and particularly its connection with the peripancreatic vessels (Fig. 23).

Nonepithelial Tumors of the Pancreas

Nonepithelial tumors may present a solid pattern. Of these, primitive mesenchymal tumors, both benign and malignant, should be mentioned. These tumors are extremely rare in the pancreas and present features that are identical to those observed in the other organs [4, 100].

The benign soft tissue tumors are extremely rare, represented by benign schwannomas, hemangioendotheliomas, and fibrous histiocytomas. In the radiology literature, some cases of pancreatic lipoma have been reported. The tumor, usually located in the head of the pancreas, is hypoechoic on US, and isodense and isointense to the fat tissue on CT and T1- and T2-weighted MR images, respectively [100]. Fat-suppressed MRI can confirm that the lesion is composed of fat. It is in truth quite difficult to distinguish by imaging a pancreatic lipoma from the focal fatty infiltration of the gland. Furthermore, this distinction, obtainable histologically (the lipoma has a capsule and central septation, while the fatty infiltration includes small foci of atrophic parenchyma), has no clinical significance, since surgical intervention is not needed in either case. This is why the core biopsy can be avoided [101].

The inflammatory myofibroblastic tumor, also known as inflammatory pseudotumor, is a rare mass lesion composed of a variety of inflammatory or other mesenchymal cells. The prognosis of this tumor is generally considered to be favorable, with only a rare incidence of malignant transformation. The most common clinical presentation is generally an incidentally discovered mass. Less frequently a palpable abdominal mass,

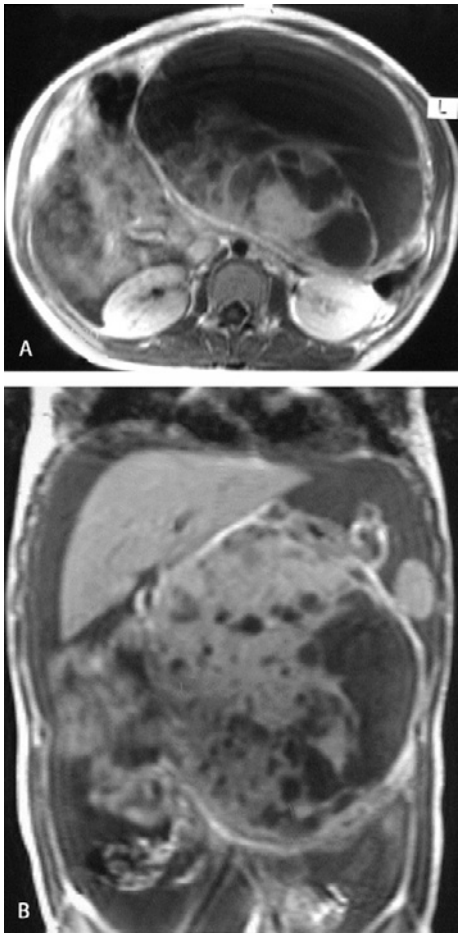

Fig. 24A, B. Pancreatic primitive neuroectodermal tumor (PNET). On the Gd-DTPA-enhanced GE T1-weighted axial (**A**) and coronal (**B**) MR images, a huge mass originating from the body of the pancreas occupies the abdomen. The tumor has a mixed solid and cystic content

abdominal pain, jaundice and anemia are present. In these patients the preoperative diagnosis is usually pancreatic carcinoma because it resembles malignant neoplasms on the radiological examination [102].

Malignant soft tissue tumors are often hardly distinguishable from primitive retroperitoneal tumors secondarily involving the gland, considering their conspicuous dimensions. Cases of leiomyosarcoma, fibrosarcoma, liposarcoma, etc., have been reported in the literature. We observed a huge primitive neuroectodermal tumor (PNET), identified in pediatric age [103]. The mass, particularly voluminous, presented a mixed solid and liquid pattern and was associated with ascites (Fig. 24). A very rare malignant tumor is carcinosarcoma, composed of malignant mixed epithelial and mesenchymal elements. Its prognosis appears dismal [104].

Lymphomas and Leukemias

Malignant lymphomas rarely manifest as primitive lesions. They represent less than 0.5% of pancreatic tumors [105] and 2% of extranodal non-Hodgkin's lymphomas [106]. More frequently they are an expression of secondary involvement; the pancreatic gland is involved in more than 30% of patients with non-Hodgkin's lymphoma [4, 105–107]. In many cases, both clinical presentation and imaging findings do not significantly differ from those of tumors of the exocrine pancreas. Jaundice is an infrequent finding. The most common findings were abdominal pain and weight loss [106].

At US primary pancreatic lymphoma usually appears as a bulky homogeneous hypoechoic mass with multiple isoechogenic peripancreatic lymph nodes. At CT, two different patterns of pancreatic involvement are detectable: a well circumscribed solid mass or diffuse enlargement of the gland. In both cases the enhancement after administration of IV CM is poor and homogeneous. The focal lesion appears as a low-signal-intensity homogeneous mass on T1-weighted images with slight enhancement after IV administration of CM. On T2-weighted images, the mass has an intermediate signal, higher than that of the residual gland but much lower than the signal intensity of fluid. The diffuse infiltrating type of the lesion shows similar characteristics. MR imaging is equivalent to CT regarding information about the peripancreatic vessels and enlarged lymph nodes [106, 108]. The clinical features and imaging findings are not specific and, in all cases, the final diagnosis must be made by pathological examination. The small amount of tissue obtained by FNA may not distinguish between a lymphoma and an anaplastic carcinoma or identify the subclasses of non-Hodgkin lymphoma [105].

From the clinical, therapeutic and prognostic viewpoint, the most important aspect is their differential diagnosis with the poorly differentiated (small cell) carcinoma and the endocrine tumors.

Immunohistochemical analysis to demonstrate specific differentiation markers is extremely important, highlighting the positivity for leukocyte antigens in lymphomas and for keratins and endocrine markers in carcinomas and endocrine tumors, respectively.

Secondary extramedullary plasmacytoma involving the pancreas is rare. In fact, only 18 cases have been reported in literature. The mass can involve the entire pancreas or may have a focal aspect. At CT extramedullary plasmacytoma of the pancreas is usually demonstrated as a homogeneously enhanced solid mass, in contrast to the irregular low-density mass of pancreatic adenocarcinoma. Given the high enhancement, it is very difficult to radiologically differentiate extramedullary plasmacytoma of the pancreas from other hypervascular tumors of the pancreas such as endocrine cell tumors and acinar cell carcinoma. To obtain a definite diagnosis, percutaneous biopsy may be useful [109].

Metastases

Even if direct invasion of the gland is possible, metastases in the pancreas are much more likely to be the expression of a hematogenous spread [4]. From a clinical and radiological standpoint, metastases can mimic a long-hidden primitive carcinoma before revealing itself in the late stage with jaundice, weight loss, abdominal pain, digestive hemorrhage or pancreatic insufficiency [110, 111]. An accurate diagnosis is extremely important since most of these patients must undergo different chemotherapy or radiotherapy than needed in the case of primitive tumors of the pancreas. Tumors that more frequently metastasize in the pancreas are breast carcinoma, anaplastic carcinoma of the lung, melanoma, renal carcinoma, hepatocarcinoma, and colon carcinoma [110–113]. Adenocarcinoma of the stomach is the most frequent primary site of metastatic pancreatic tumors in Japan [114]. Late metastases of renal carcinoma are not infrequent; the mean time lag is around 11 years [115].

In most cases, identification is incidental during an investigation for either staging (synchronous metastases) or follow-up (metachronous metastases) of the primitive tumor.

The metastases, single or multiple, present definite margins and hypoechoic texture at US [111]; after CM administration, they are hypodense and hypointense at CT and MRI, respectively, (Fig. 25A). The only exception is the metastases which originate from a hypervascularized tumor of the kidney (Fig. 25B), with a pattern that is identical to that of the primitive tumor [110].

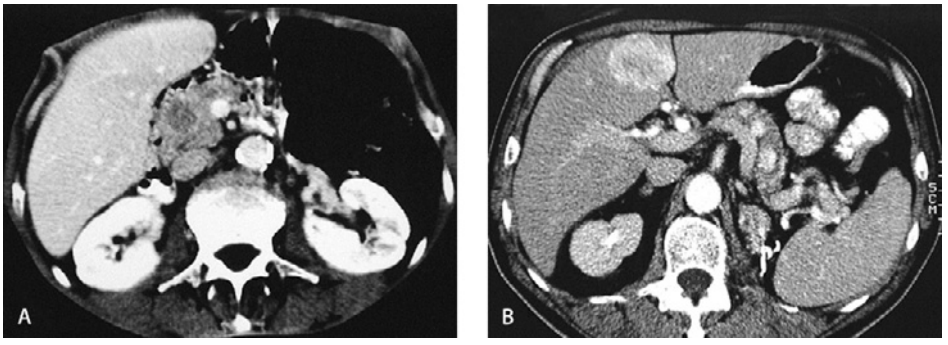

Fig. 25A, B. Metastases. **A** Metastasis of primitive lung carcinoma: at CT during the venous phase of contrast enhancement a small, well circumscribed, hypodense mass is recognizable in the head of the pancreas. **B** Metastases from primitive renal conventional carcinoma: at enhanced CT multiple hyperdense nodules are located in the body of the pancreas; a large hepatic hyperdense metastasis coexists

Morphological evidence of a metastatic neoplasm can be obtained with fine needle aspiration cytology. The diagnostic clues rely on the presence of both distinctive features (e.g., presence of bile thrombi for hepatic carcinoma) and being aware of the primitive neoplasm (e.g., renal cell carcinoma vs clear cell carcinoma of the pancreas). The immunohistochemical analysis may play a crucial role in the final diagnosis: positivity for melanocyte markers S-100 or HMB-45 for the diagnosis of metastatic melanoma.

Lesions Mimicking Solid Tumors of the Pancreas

Focal chronic pancreatitis, mainly located in the pancreatic head, in the absence of any signs of the advanced stage of the disease, such as calcifications, ductal ectasia, and pseudocysts, can simulate the ductal adenocarcinoma of the pancreas. In some cases, fine needle aspiration biopsy cytology may be useful in the differential diagnosis. Among the multiple manifestations of chronic pancreatitis there are two conditions where, at first glance, the pattern of the lesion can simulate an adenocarcinoma.

Cystic dystrophy of the duodenal wall (also known as groove pancreatitis), is characterized by inflammation of the heterotopic pancreatic tissue located within the duodenal wall (Fig. 26A). In the solid variant, CT and MRI show a solid hypodense/hypointense mass after contrast enhancement (Fig. 26B, C), embedded in the duodenal wall, frequently associated with dilation of MPD. In this case, the duodenal origin of the lesion can be shown thanks to dislocation to the left of both the gastroduodenal artery and the CBD. Furthermore, the inflammatory nature of the lesion is confirmed by the absence of infiltration of these structures [116].

Autoimmune pancreatitis, only recently identified as a distinct entity, in association with other immune-mediated disorders such as sialoadenitis or sclerosing cholangitis, can involve the pancreas focally [117, 118]. Both the reduced vascularization of the pancreatic area involved and its volumetric increase explain the pseudotumoral aspect at imaging (Fig. 26D). In this event, the clinical picture (either acute relapsing or chronic pancreatitis), and the young age of the patient arouse the suspicion of this type of lesion, which needs to be confirmed by a fine-needle biopsy. In the early stages of autoimmune pancreatitis, the prompt introduction of steroid treatment ensures the rapid regression of the disease with final *restitutio ad integrum*.

Peripancreatic fat necrosis, which may be found even long after an episode of pancreatitis, may appear as a well-defined mass on CT and MR imaging, mimicking pancreatic cancer. In patients with a history of pancreatitis, in the absence of an infiltrative appearance of the mass, the diagnosis of peripancreatic fat necrosis should be considered. However, the definitive diagnosis can be obtained with FNAB of the mass [119].

Heterotopic spleen, embedded in the pancreatic tail, can simulate an endocrine tumor of the pancreas at imaging [120]. In this case, an accurate diagnosis can be achieved either with fine needle biopsy or with nuclear medicine, which will show an uptake of the radiotracer in the ectopic nodule analogous to that of the splenic parenchyma [121].

Cystic Pancreatic Tumors

Cystic lesions of the pancreas (Table 2) are detected in 1.4% of all the abdominal US investigations [122]. Traditionally considered rare lesions (1% of all the tumors of the pancreas and 10% of all the cysts of the pancreas), they are ever more frequently diagnosed in routine clinical practice [123–126]. Although an exact estimation of their true prevalence is difficult, they probably represent approximately 5% of all pancreatic tumors.

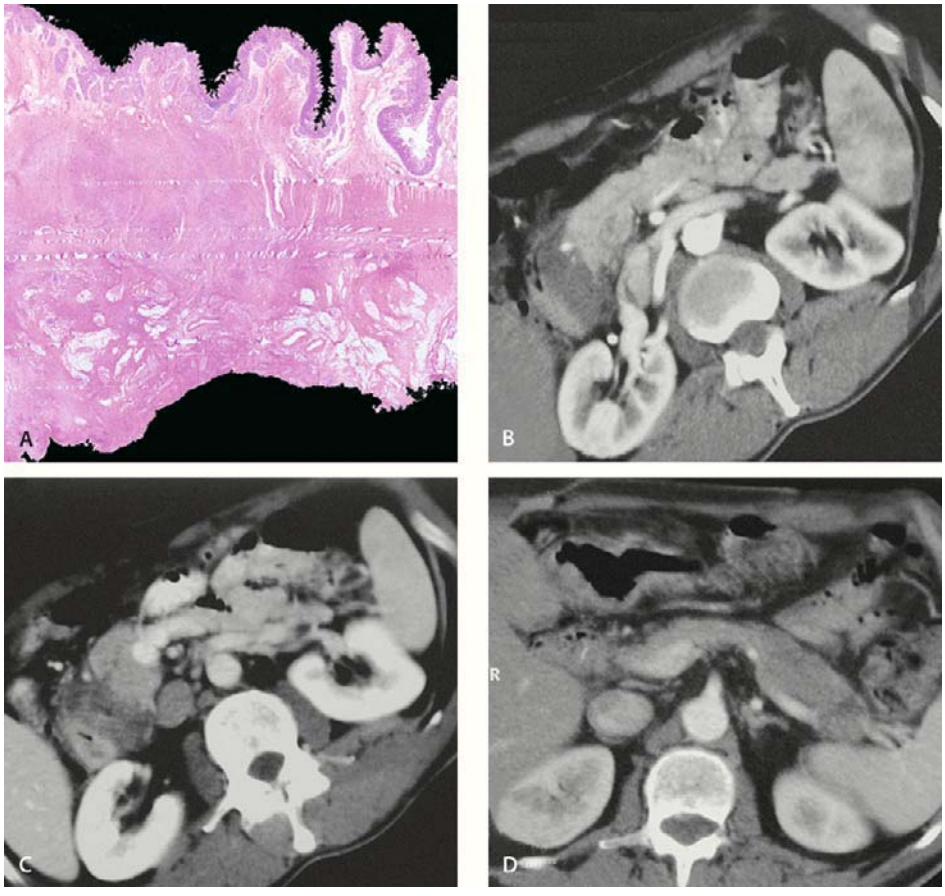

Fig. 26A–D. Tumor-like conditions. **A–C** Solid dystrophy of the duodenal wall. Whole-mount macrosection of duodenum showing a thickened duodenal wall and an enlarged groove region occupied by dense fibrous tissue without macrocysts (**A**). At arterial (**B**) and venous (**C**) enhanced CT scans a thick solid sheet-like mass is recognizable between the duodenum and the head of the pancreas; the gastroduodenal artery is displaced to the left side. The fibrotic tissue is clearly hypodense in comparison to the pancreatic parenchyma. **D** Focal autoimmune pancreatitis: at arterial-enhanced CT a round hypodense mass is present in the body of the pancreas, without encasement of the adjacent splenic vein

The spectrum of pancreatic tumors with cystic features is broad, and includes serous microcystic or oligocystic (macrocystic) tumor, mucinous cystic tumor, intraductal papillary mucinous tumor, acinar cell cystadenocarcinoma, solid-pseudopapillary tumor with cystic degeneration (i.e., solid cystic tumor), and endocrine tumor with cystic degeneration [4]. Recently a new entity, acinar cell cystadenoma, was proposed as the benign counterpart of the well-recognized acinar cystadenocarcinoma [127].

Preoperative diagnosis of cystic lesions is of paramount importance in planning appropriate surgical treatment. A misdiagnosis may result in inappropriate therapy, which, in some instances, may favor the malignant transformation and spread of the disease [4].

The current sensitivity of imaging in detecting pancreatic cystic mass is very high. The prevalence of pancreatic cysts detected with MR imaging, especially those with a diameter of less than 10 mm, is similar to that of pancreatic cysts detected at autopsy [128]. The difficulties in diagnosis are well known and persist in spite of the wonderful technical progress in imaging. Knowledge of clinical, laboratory and imaging information can be used to make a diagnosis or to narrow down the differential diagnosis [129]. Differentiation between serous cystic tumors and mucinous neoplasms can usually be made on the basis of imaging. However, when the distinction is not clear, aspiration of intracystic fluid is recommended [130]. In reality, in some cases, the only reliable way to differentiate benign cystic tumors from malignant ones is to investigate the cyst wall following resection [131]. Unfortunately, when the cystic wall is totally denuded, the correct diagnosis is not achieved, even pathologically.

Serous Cystadenoma

Serous cystadenomas (SCA), occasionally called microcystic adenoma or glycogen-rich cystadenoma, is a benign tumor made up of nonatypical epithelial cells, which produce serous fluid. The serous cystadenoma is usually a large lesion typically occurring in women aged between 50 and 70 years [4, 132].

Clinically, it can be sporadic or associated with von Hippel-Lindau syndrome (the lesions are frequently diffuse or multifocal) [133–135].

SCA differs from the mucinous cystic tumors in many aspects, the most important of which is represented by the indolent clinical course [136]. However, there are few exceptions: the local destructive growth with progressive involvement of the entire organ and the minimal risk of malignant transformation. Since the description of Compagno and Oertel in 1978 [136], only a few malignant cases have been reported [137–141].

Except for their metastasizing behavior, serous cystadenocarcinomas are histologically, and presumably also cytologically, indistinguishable from typical SCA [142]. For this reason, the tumor can be monitored, especially when the location of the tumor requires a high-risk surgical intervention taking into consideration either the advanced age or the poor clinical conditions of the patients.

Approximately 30% of these tumors are incidentally encountered during a radiological investigation undertaken for other reasons. In the other two-thirds of patients, the clinical picture is nonspecific and is related to the conspicuous dimensions of the tumor, which is responsible for local pressure effect on adjacent structures. Despite the frequent location in the pancreatic head, the tumor is seldom associated with jaundice.

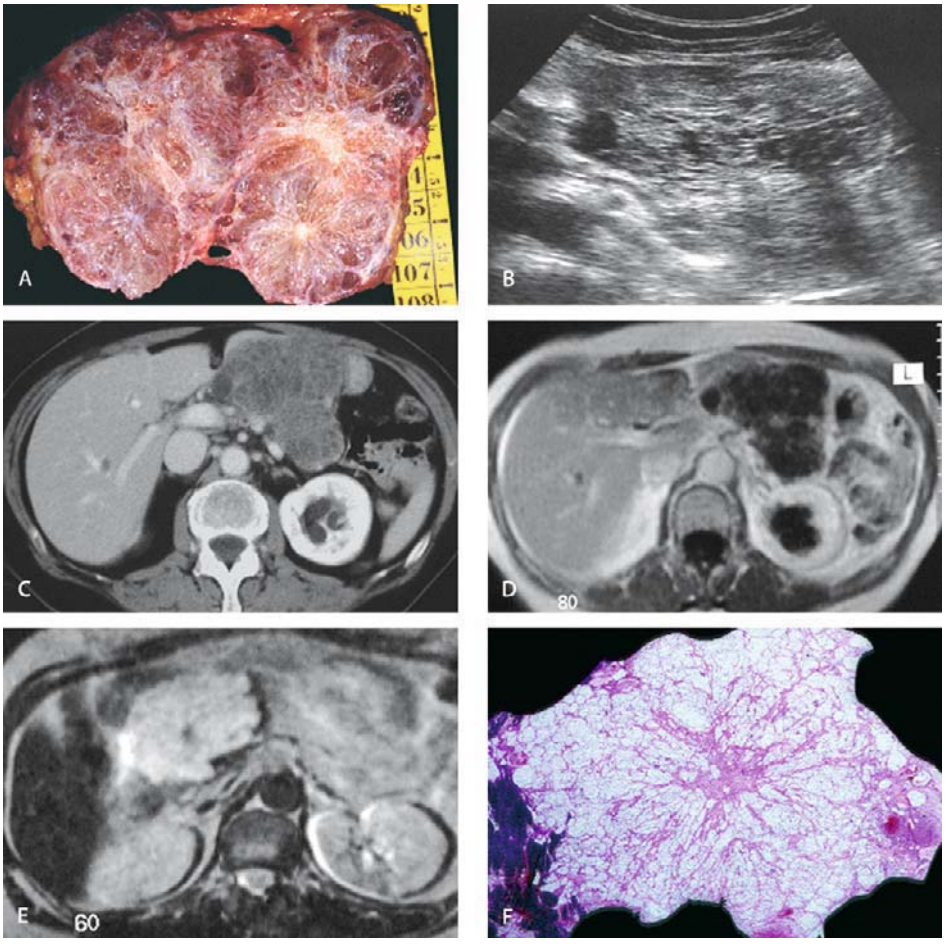

Fig. 27A–F. Serous microcystic adenoma. **A–D** First case. **A** The specimen demonstrates a well-demarcated microcystic lesion, displaying two central star-shaped scars. **B** The axial US scan shows a large echoic mass with multiple tiny cysts. At CT (**C**) and MR (**D**) after CM administration, the microcystic pattern of the mass is clearly evident. **E, F** Second case. On the spin echo (SE) T2-weighted MR image (**E**), a hyperintense microcystic mass with a central hypointense scar is present; the aspect is analogous to that of a whole-mount macrosection (**F**) displaying a microcystic mass with multiple septa radiating from a central scar

SCA is frequently associated with diabetes mellitus, probably in relation to islet cell damage caused by the tumor. In reality, the association could merely be coincidental and related to patient age [134, 136].

Macroscopically, two principal types are recognized. The classic or microcystic variant, with definite borders, is related to the expansive type of growth, and is characterized by tiny cysts (<2 cm), conferring a spongy appearance to the lesion (Fig. 27A). A central scar is characteristically present (Fig. 27A). The macrocystic or oligocystic type (Fig. 28A) is characterized by the presence of one or more cysts (>2 cm), the lack of a central scar, and ill-demarcated growth margins, related to the extension of the cysts and the supporting fibrous tissue into the adjacent pancreatic tissue. One of these cysts can reach conspicuous dimensions (up to 10–15 cm). In a discrete percentage of cases, lesions with mixed (micro- and macrocystic) pattern can be observed.

Microscopically, in both variants, the cysts are lined with a single layer of cuboidal epithelial cells with roundish nuclei and a pale-to-clear, glycogen-rich cytoplasm (PAS-positive following diastase digestion). They are delimited by highly vascularized fibrous septa, sometimes showing a spoke-wheel aspect converging toward a central scar (in the microcystic type) within which calcifications can be present.

At US, the microcystic variant can show a solid aspect; on the other hand, the coexistence of microcystic and macrocystic areas can help in the diagnosis (Fig. 29). CT easily shows either the central calcified scar or the possible presence of calcification within the internal septa wall with a linear, arcuate or globular pattern [143]. After CM administration, both CT and MRI are able to document the enhancement of the microcystic mass (Fig. 27C, D), which sometimes mimics a solid tumor. On T2-weighted MR images, the liquid content of the tumor is constantly found (Figs. 27E, 29A, 30B). On T1-weighted precontrastographic MR images, some cysts may appear hyperintense because of their increased protein content. In particular, macrocystic SCA usually displays intracystic hemorrhage or debris deriving from the denuded or necrotic epithelium lining the cystic cavity [144].

No matter which technique is adopted, imaging gives the correct diagnosis of serous cystadenoma whenever the microcystic pattern (Fig. 27), at times associated with macrocysts (Fig. 30), is demonstrated [145]. On the contrary, the oligocystic serous adenoma (Fig. 28) presents features indistinguishable from those of other macrocystic tumors of the pancreas [146, 147].

The most conspicuous masses involving the pancreatic head may sometimes have a compression effect on adjacent structures such as the CBD. Such findings are easily demonstrated with MR (Fig. 29B).

Preoperative (fine needle aspiration biopsy) or intraoperative (frozen section) diagnosis of macrocystic serous adenoma is of the utmost importance, since conservative procedures (i.e., biliary bypass or cystojejunostomy) may be considered in patients at high surgical risk.

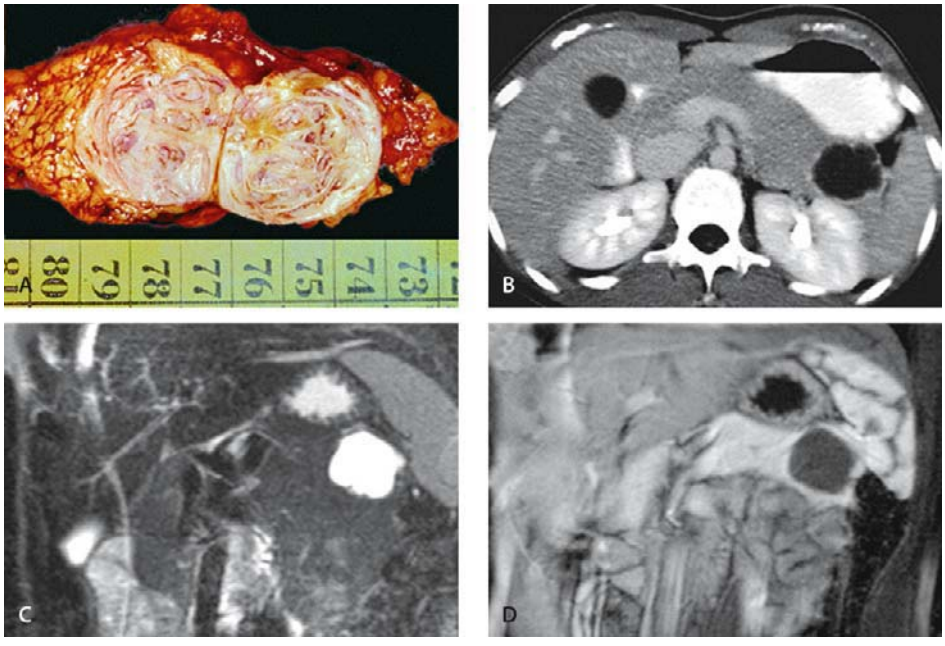

Fig. 28A–D. Serous oligocystic adenoma. **A** Serous oligocystic adenoma presenting as unilocular cystic lesion. **B** Enhanced CT shows a unilocular macrocystic mass in the tail of the pancreas. HASTE T2-weighted (**C**) and Gd-DTPA-enhanced T1-weighted (**D**) coronal MR images confirm the fluid content and the absence of septa into the mass

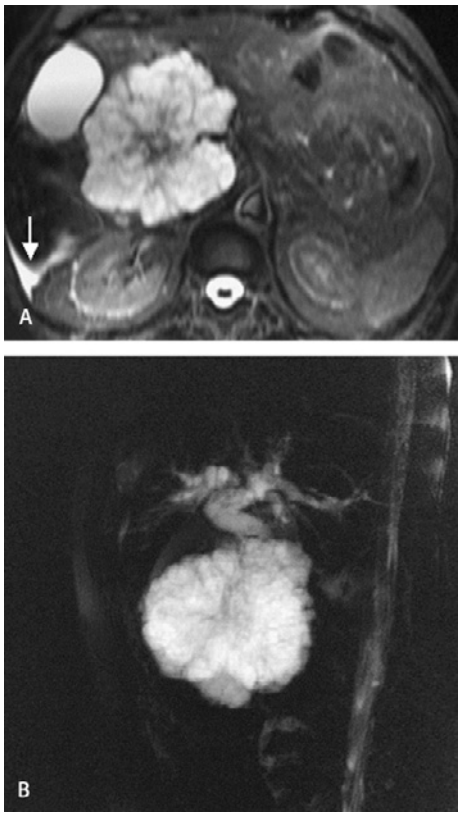

Fig. 29A, B. Serous microcystic adenoma. Axial TSE T2-weighted MR image (**A**) and MRCP (**B**) demonstrate that the head of the pancreas is occupied by a large microcystic mass with central fibrous scar, responsible for dilation of the biliary tree upstream (**B**). Ascites is present (*arrow* in **A**)

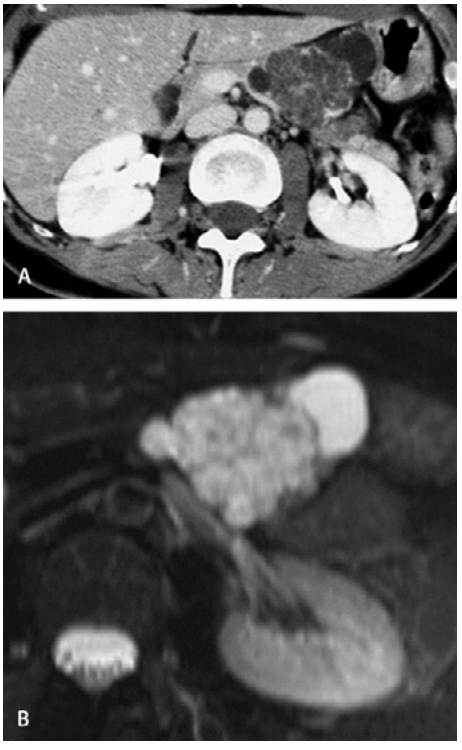

Fig. 30A, B. Mixed (micro- and macrocystic) serous cystadenoma. At contrast-enhanced CT (**A**) and turbo spin-echo T2-weighted fat-suppressed (TSE T2-WFS) MR image (**B**), the mixed, micro- and macrocystic pattern of the mass is evident. The macrocysts are located peripherally

Mucinous Tumors

Originally, mucinous tumors were considered to be a homogeneous group of lesions, characterized by mucin-producing columnar epithelium [148]. Today, a cystic structure and the presence of mucin-secreting epithelium are not sufficient to classify these neoplasms. At the moment, two distinct groups of tumors are considered separately [1, 4, 149]:

1. Mucinous cystic tumor: unilocular or multilocular cysts with no connection with the main pancreatic duct, lined by mucin-secreting epithelium supported by ovarian-type stroma [150];
2. Intraductal papillary-mucinous tumor, characterized by intraductal growth with dilatation of the main and/or branch ducts, and mucus hyperproduction [151–153].

According to the grade of epithelial dysplasia, as suggested by the WHO classification, these tumors are subdivided into adenoma (atypia of a low grade), borderline (atypia of a moderate grade) and adenocarcinoma (severe atypia), invasive and noninvasive forms [1]. A variable degree of dysplastic change is present in the same lesion, with foci of high-grade dysplasia frequently restricted to tumor areas that grossly show papillation or nodules. Therefore it is important to emphasize the necessity of appropriate sampling of the lesion for detecting small foci of invasive carcinoma and for making the right diagnosis. It is conceivable that limited tumor sampling might explain the presence of metastases reported in an apparently noninvasive tumor.

■ **Mucinous Cystic Tumor.** Mucinous cystic tumor (MCT) is a uni- or multilocular cystic tumor formed by mucin-secreting epithelium supported by ovarian-type stroma, which shows no connection to the main pancreatic duct. This tumor, which accounts for 2% of all exocrine pancreatic tumors, occurs almost exclusively in women, aged from 20–80 years. It is likely that most of the MCT reported in the past in males should be considered as intraductal papillary-mucinous tumors (IPMTs) [1, 4, 150, 154].

Clinically, when the tumor is small, it is almost always encountered incidentally. The most voluminous tumors can be revealed as palpable masses or by symptoms correlated with the compressive effect on the adjacent structures. In the malignant forms, a significant increase in the tumoral markers, such as CEA or CA 19-9, may be present.

Macroscopically, MCT shows a marked predilection for the body and tail of the pancreas [154–156]. Most of the tumors are round with a smooth surface and a fibrous pseudocapsule with focal calcification. On cut section, the multilocular (Fig. 31A) or unilocular (Fig. 31E) cystic space contains mucinous, hemorrhagic or necrotic material; the individual cystic space ranges from a few millimeters to 30 cm.

The tumor lacks any connection with the main duct of Wirsung or the secondary ducts. The malignancy of the tumors correlates significantly with the presence of

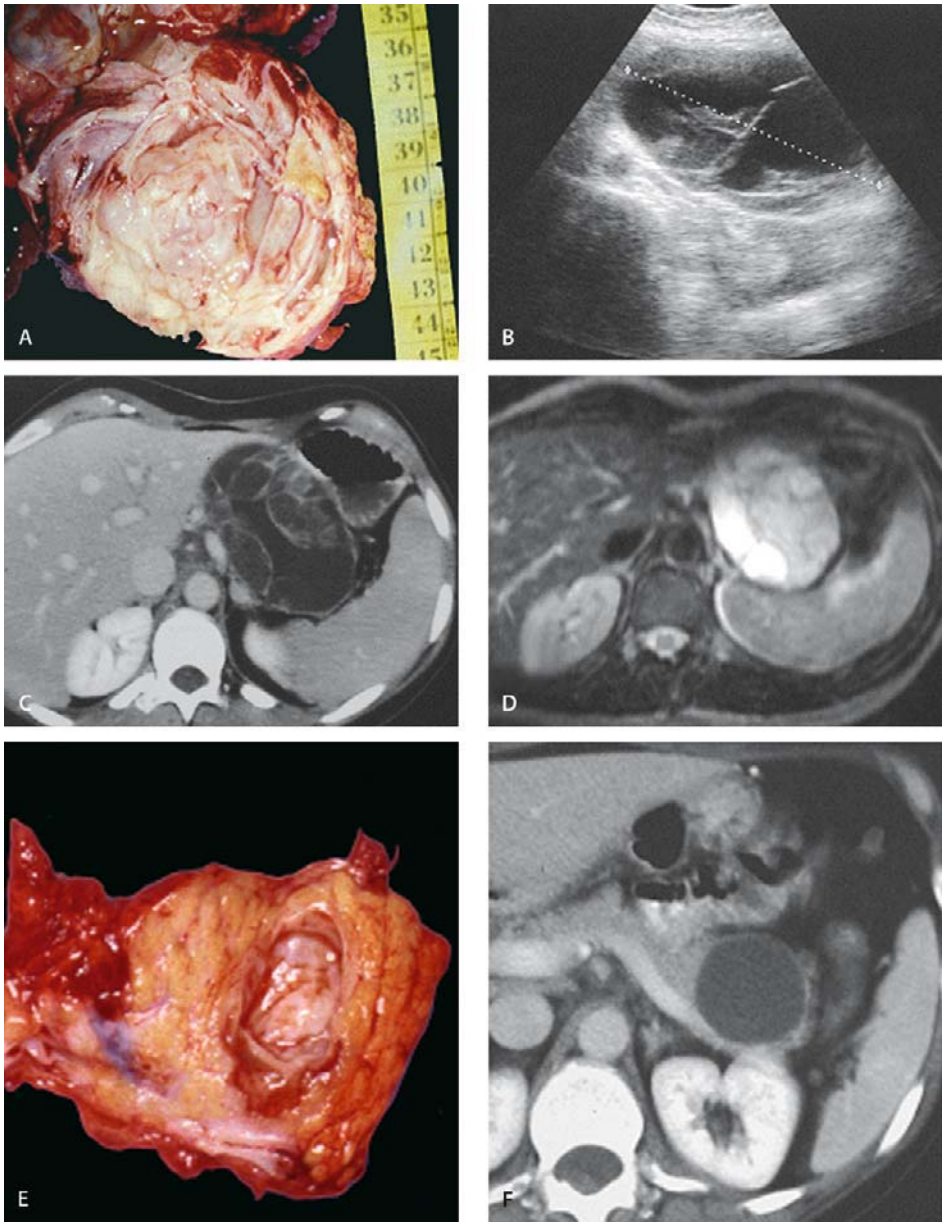

Fig. 31A–G. Mucinous cystic tumor. **A–D** Multilocular mass. **A** Gross specimen. Multilocular tumor showing thick fibrous wall and cysts of varying size separated by numerous septa. US axial scan (**B**), venous contrast-enhanced CT image (**C**) and SE T2-weighted MR image (**D**) display a large, ovoid, well-demarcated cystic lesion with a multilocular pattern due to the presence of multiple septa. **E**, **F** Unilocular mass. Left pancreatectomy specimen (**E**) and enhanced CT image (**F**) demonstrate a unilocular cystic mass with thin wall. **G** Photomicrograph of the lesion shows cystic spaces lined by tall, columnar, mucin-producing cells with basally located single nuclei, supported by ovarian-type stroma, with focal luteinization

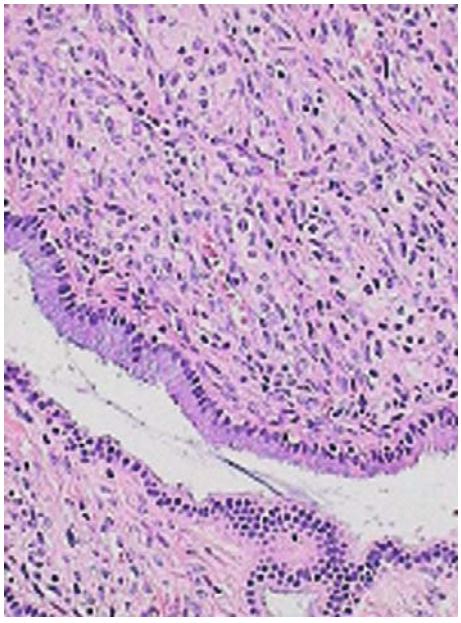

Fig. 31G.

papillary projections and/or mural nodules and multilocularity as well as location in the head [150].

Microscopically, the cysts present two distinct elements: an inner epithelium and an outer densely cellular ovarian-type stromal layer. The epithelium, which may display metaplastic differentiation, presents a variable degree of dysplastic changes within the tumor. On the basis of the most severe atypia, the tumors are classified as adenoma, borderline tumor and carcinoma. Although all these tumors should be considered as potentially malignant [123, 148, 149, 157–159], the most significant prognostic factor is the presence and the extent of invasive carcinoma (i.e., the infiltration of the tumor capsule and the surrounding tissue) [150]. In these cases, the outlook is similar to that of ductal carcinoma [154].

Although it is usually easy to differentiate MCT from the other cystic tumors, with the exception of intraductal papillary-mucinous tumors, it may be more difficult to distinguish it from a pancreatic pseudocyst. It is not only a clinical and radiological problem, but also a morphological one because the tumor epithelium may be denuded and the contents may be hemorrhagic. It is mandatory in such cases to extensively sample the lesion in search of the diagnostic features, i.e., epithelium and/or ovarian stroma.

The importance of a correct preoperative diagnosis lies in the fact that all mucinous tumors should be submitted, whenever possible, to radical surgical resection. Whichever technique is used, diagnosis is possible at imaging [145] when the tumor presents multilocular architecture (Fig. 31B–D) and/or parietal nodules [157]. The diagnosis is almost certain when identification is incidental, yet not justified by a clinical picture of acute or chronic pancreatitis, a situation where exclusion of the inflammatory nature of the lesion (pseudocyst) is difficult. At MRI, the content of the tumor can show high signal intensity in the T1-weighted sequence, because of the presence of hemorrhage or a proteinaceous element. On T2-weighted sequences, the fluid component has a high signal intensity and the internal septations are more conspicuous than on the T1-weighted scan showing as low-signal-intensity curvilinear septa [156]. There are no reliable features of malignancy; nevertheless, the coexistence of multilocular architecture with thick wall and septa with calcifications correlates with malignancy [160]

A unilocular architecture without nodules (Fig. 31E, F) does not lead to a specific diagnosis, since the same finding could be encountered in all cystic masses of the pancreas.

■ **Intraductal Papillary-mucinous Tumor.** This is an intraductal pancreatic tumor, made up of columnar mucin-producing epithelial cells, primarily ectatic or papillary. Described for the first time in 1980 [161], the intraductal papillary-mucinous tumor (IPMT) has long been underestimated, often wrongly diagnosed as chronic pancreatitis, or included in the mucinous cystic tumors. In the literature, numerous reports describing this entity under different names have appeared [149, 151, 152, 163, 164]. Traditionally considered a rare lesion, it has recently been reported with increasing frequency. It is likely that some of these tumors have been incorrectly interpreted as sequela of chronic obstructive pancreatitis because of the macroscopic features of the tumor and the clinical history of the patient [165].

The peculiarities of this tumor are:

1. Slight prevalence in males, unlike other cystic tumors, with a mean age bracket of around 60 years
2. Characteristic aspect at ERCP, with both dilation of the main duct and/or of the collateral branches in absence of stenosis, and presence of filling defects representing mucin plugs or intraductal papillary proliferations
3. Dilated major and/or minor papilla with mucin leakage
4. Symptoms like those of either chronic pancreatitis or relapsing acute pancreatitis, related to the presence of excessive production of mucin, which hinders the outflow of pancreatic secretion, accompanied by a high serous amylase level

Macroscopically, the distinctive element is the intraductal growth with segmental or diffuse dilation of the main or secondary ducts in the absence of stenosis. Two main types can be distinguished: the ductectatic mucin-hypersecreting type in which the dilated ducts are filled

with thick mucin and the epithelial linings are flat or present tiny, microscopic papillae, and the papillary-villous type, which is characterized by polypoid-papillary proliferations associated with mucous material within the dilated pancreatic duct. Precise tumor localization can only be made when a neoplasm is small. In the early phase of the disease, exclusive recognition of the tumor localization in the main duct or in the secondary ducts is possible. In the first case it appears as a diffuse and regular dilatation of the main duct and in the second case as a round macro/microcystic lesion, frequently located in the uncinate process. In the advanced stage, the cystic ectasia of the main duct is often associated with grape-like cystic dilatations of the branch ducts and tumoral involvement of the papilla of Vater, which appears dilated and protrudes into the duodenal lumen.

Wirsung biliary or Wirsung duodenal fistulas and intraperitoneal mucus dissemination (pseudomyxoma peritonei) are rare.

Microscopically, IPMTs show flat or papillary proliferations of mucin-producing cells originating from the ductal epithelium.

The tumor cells show a large spectrum of dysplastic changes, ranging from benign-appearing epithelium to carcinoma. The dysplastic changes are multifocal, with high-grade and carcinomatous changes more likely to be detected in the wide-spectrum lesion showing extensive papillary growth and/or nodules. The tumors may be benign (adenoma), borderline and malignant (carcinoma) according to the varying degrees of epithelial differentiation. Invasive carcinoma may show either tubular or muconodular pattern, characterized by the presence of tubular structures and mucin pools containing floating neoplastic cells, respectively.

The main differential diagnoses of IPMT are with MCT, ductal carcinoma and chronic pancreatitis. The cystic changes in a segmental form of IPMTs may occasionally be so extensive that they can be confused with a MCT. However, MCTs almost exclusively affect women, frequently involve the tail, do not communicate with the duct system, which consequently appears normal, and characteristically present the ovarian-type stroma at pathology.

Differential diagnosis with ductal carcinoma is not usually difficult because of the prevalence of the solid growth over the intraductal involvement. Although chronic pancreatitis presents ectasia of the main duct, it is usually irregular, contains distortion, and histologically the papillary proliferation is never the dominant lesion. Moreover, demonstration of the herniation of the papilla into the duodenal lumen helps differentiate IPMT from chronic pancreatitis [166].

In the past, this tumor was diagnosed almost exclusively with ERCP because of the endoscopic demonstration of a dilated papilla, bulging into the duodenal lumen, with mucin leaking from the patulous orifice. In the pancreatographic phase, dilation of the main duct or the collateral branches, within which multiple filling defects due to mucin globs or papillary proliferations, is an additional finding. Nowadays, diagnosis can easily be

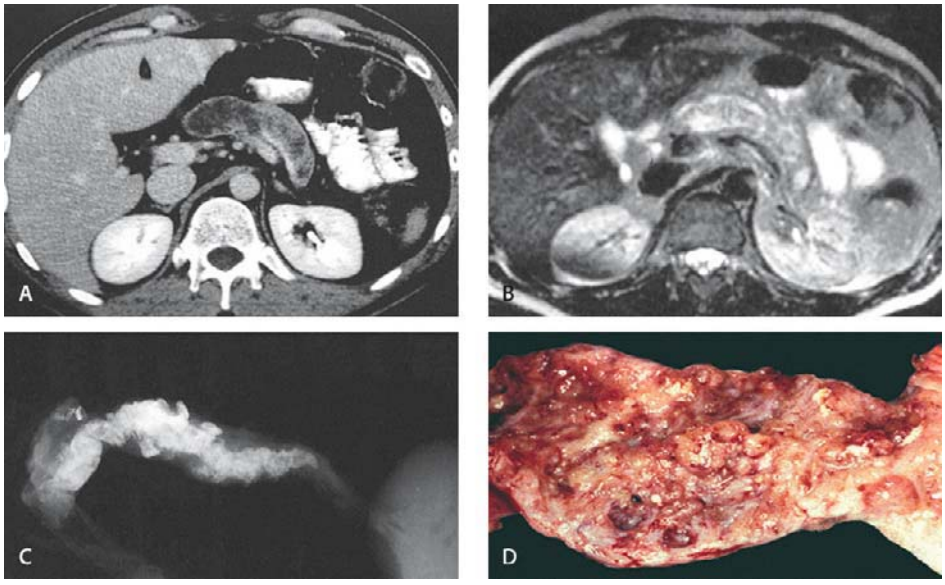

Fig. 32A–D. Intraductal papillary mucinous tumor of the main duct. **A** At CT the main duct appears uniformly and markedly dilated with parenchymal atrophy; many papillary growths are present on the wall of the duct. **B** On TSE T2-weighted MR image, the dilated main duct is shown as prevailingly hypointense due to the presence of the papillary projections. **C** The pancreatography, performed on the total pancreatectomy specimen, shows the irregular pattern of the ductal walls due to the presence of parietal nodules, clearly recognizable on the gross specimen (**D**)

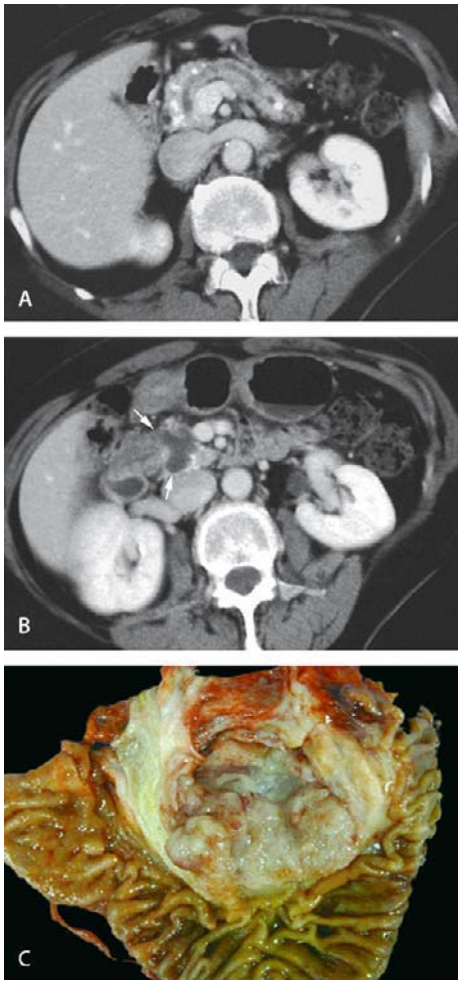

Fig. 33A–C. Intraductal papillary mucinous tumor of the main duct. **A**, **B** On the enhanced CT scans, calcified chronic pancreatitis of the body-tail, with mild dilation of the main duct (**A**) and intraductal papillary mucinous tumor of the cephalic segment (**B**), which appears markedly dilated, are present. The huge dilation of the minor and major papillae (*arrows*) is also present. **C** Whipple resection specimen displaying the marked dilation of pancreatic main duct

made with both CT and MRI (Figs. 32–34) since these imaging techniques, as well as showing the dilation of the main pancreatic duct (Fig. 32A, B) also present in chronic obstructive pancreatitis, are able to document the typical aspects of this tumor such as the protrusion of the dilated papilla into the duodenal lumen (Fig. 33b), the cystic ectasia of the collateral branches and the endoluminal filling defects (Fig. 32A, B), the origin of which is sometimes possible to define [154, 156, 168]. The papillary proliferations can be demonstrated in the non-gravity-dependent position, while the mucin globs, which can be mobilized, are collected in the gravity-dependent portion of the ducts [170, 171]. In addition, intraductal mucin, as a result of its high signal intensity, is indistinguishable from pancreatic juice at MRCP, whereas mural nodules are seen as filling defects [172]. Lastly, at CT and MR imaging, mural nodules enhance after contrast material administration, whereas mucin does not [166].

In order to differentiate IPMTs from peripheral mucinous tumors, MRCP is of fundamental importance thanks to both the three-dimensional (3D) and HASTE images which, taken at different planes, provide documentation of the communication between the tumor and the main duct. Administration of intravenous secretin can sometimes improve the detection of the ductal communication between the lesion and the main duct on cross-sectional imaging, particularly MRCP [166].

A greater accuracy of the MRCP over ERCP has been reported [174–176], since, in performing the latter, dense mucin can prevent the opacification of either the main duct or the communicating duct between the main duct and the cystic tumor of the collateral branches (Fig. 34).

The prognosis of this tumor depends upon the presence of malignant transformation and the diffused involvement of the entire gland [178]. IPMTs of the main duct have a higher grade of malignancy than IPMTs of the collateral branches [179]. In patients with an IPMT,

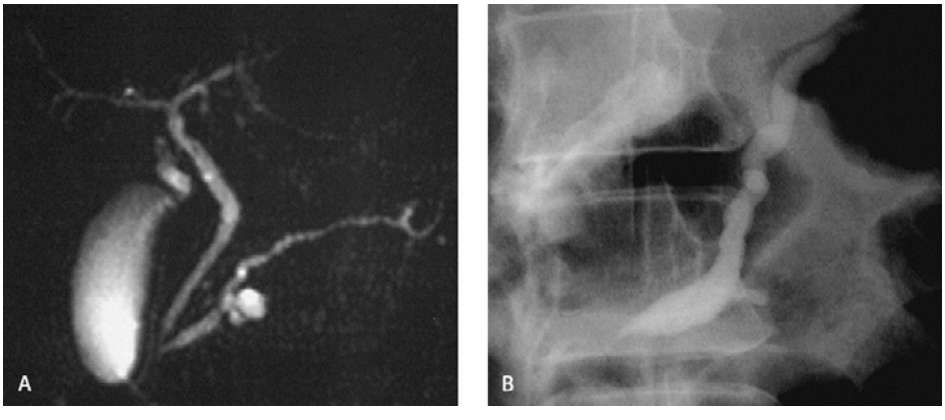

Fig. 34A, B. Intraductal papillary mucinous tumor of the collateral branches. **A** MRCP shows the cystic dilation of a side branch of the neck of the pancreas; the communicating duct is also clearly identifiable. **B** On endoscopic retrograde cholangiography (ERCP), only the initial tract of the communicating duct is visible because of the presence of thick mucin hampering the passage of CM into the cystic lesion

filling defects are indicative of malignancy. However, absence of mural nodules does not indicate that the tumor is benign. Diffuse main pancreatic duct dilation greater than 15 mm (main duct type), or any main pancreatic duct dilation (branch duct type), is strongly associated with malignancy [179].

Furthermore, the prognosis depends on the type of surgical intervention. In the case of diffuse involvement, total pancreatectomy is the best treatment, depending on the clinical conditions of the patient [180]. A partial resection is advocated in the case of segmental involvement. Extreme care must be taken, however, to ensure the radical removal of the lesion. The intervention must be guided by the analysis of frozen sections from the surgical margins, in order to exclude microscopic foci of dysplasia [177].

In recent years, refinement in imaging techniques and the radiologist's better understanding of the many aspects of this tumor have led to a notable increase in the number of observations. In particular, thanks to MRCP, the reported number of small localized or multicentric tumors of the collateral branches has drastically increased, especially in patients of an advanced age. In these instances, when the diameter of the lesion is smaller than 2.5 cm, no endoluminal filling defects are present and the MPD is regular, it is preferable, especially in very elderly subjects, to monitor the patient through imaging, preferably with MRCP, rather than proceed to high-surgical-risk demolition [166, 168, 179].

Solid-Pseudopapillary Tumor

As previously reported, besides the homogeneously solid tumor, this type can more frequently manifest a cystic pattern. The process of cyst formation in SPT is probably related to hemorrhage and necrosis in an essentially solid and hypovascular tumor. Moreover, regressive degeneration may occur with the apoptotic process [181].

In some cases coexistence within the encapsulated mass of both solid and liquid areas can be observed (Fig. 35). This aspect, particularly evident with MRI, which can reveal the presence of hemorrhage [156], gives rise to the suspicion of solid-pseudopapillary tumor, especially if encountered in a very young woman, since this tumor is found most commonly in young females. SPT has a higher incidence of malignancy in the elderly [156]. In other cases, both necrosis and hemorrhage can transform the tumor into a uni- or rarely multilocular cystic mass with thick wall, which some-

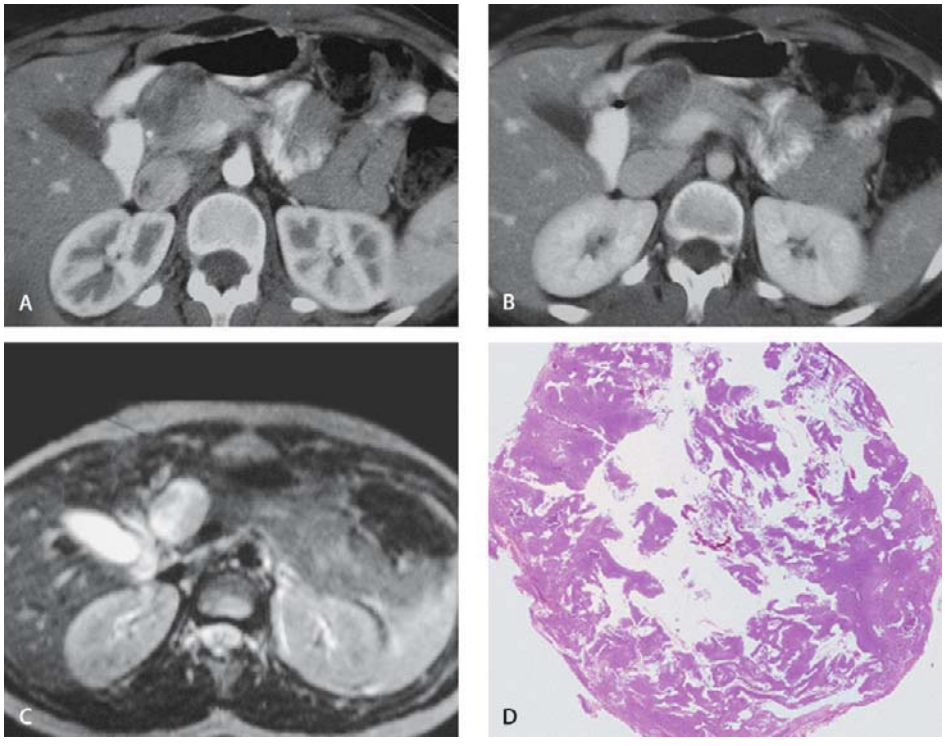

Fig. 35A–D. Solid-pseudopapillary tumor (cystic variant). On enhanced CT, in the pancreatic (**A**) and venous (**B**) phases, a round, capsulated mass is located in the head of the pancreas; centrally, a mixed solid and fluid pattern is present. On SE T2-weighted (**C**) MR image, the mass presents a inhomogeneous hyperintense content. The whole-mount macrosection (**D**) shows a round, thinly capsulated mass. The tumor is partly necrotic

times calcifies. In this case, imaging cannot make a differential diagnosis with the other cystic masses of the pancreas [145, 156, 182]

Other Cystic Tumors

■ **Acinar Cell Cystadenoma.** Recently a new entity, acinar cell cystadenoma (ACA) has been reported, possibly the benign counterpart of the well-recognized acinar cell cystadenocarcinoma. The cystic lesion, whose nonneoplastic nature cannot be excluded, is composed of mature acinar cells and is unrelated to the major ductal system. The imaging pattern of this tumor is definitely nonspecific because of its macrocystic multilocular or unilocular structure (Fig. 36). In the ten cases studied, the preoperative diagnosis, mainly on the basis of CT, was either wrong (IPMT, serous cystic adenoma) or nonspecific. On the contrary, the pathological differential diagnosis vs the cystic variant of acinar cell carcinoma and the other cystic tumors of the pancreas is easy [127].

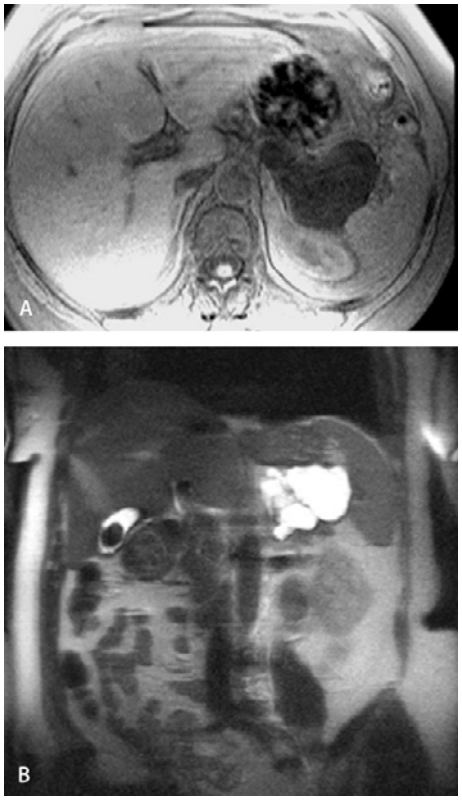

Fig. 36A, B. Acinar cell cystadenoma, MR evaluation. **A** At GRE FS T1-weighted image a large fluid hypointense mass occupies the tail of the pancreas. **B** In the coronal HASTE T2-weighted image, the mass has a macrocystic multilocular pattern, analogous to that of other cystic lesions of the pancreas

■ **Lymphangioma.** The histogenesis of lymphangioma of the pancreas is uncertain (congenital malformation of the lymphatic system vs true neoplasm) [183]. This lesion, common in pediatric patients in the soft tissue of the neck and the axilla, is very rare in the abdomen, especially in the pancreas [184]. Lymphangiomas are considered to be of pancreatic origin if they are in the pancreatic parenchyma or connected to the organ by a pedicle [185]. Imaging shows a macrocystic multilocular mass with septa, which enhance after IV contrast injection. Rarely phlebolith-like calcifications may be present. Consequently, imaging does not usually distinguish between the numerous cystic masses of the pancreas. Fine needle aspiration may suggest a diagnosis of lymphangioma, however, the definitive diagnosis can only be made by excision and histopathological examination [184].

■ **Mature Teratoma.** The mature teratoma (dermoid cyst) of the pancreas is an extremely rare tumor, probably originating from aberrant germ cells arrested in migration toward the gonads early in embryonic life [167, 186]. They are composed of tissue deriving from any of the three germinal lines. The radiological appearance of these lesions, similar to those seen elsewhere in the body, depends on the proportions of the various tissues of which they are composed. The combination of fat with fat–fluid levels and calcifications is suggestive of mature teratoma. Computed tomography is better than sonography in characterizing teratomas. MR shows the typical high signal intensity on T1-weighted images and on T2-weighted turbo spin echo (TSE) images of fat-containing lesions, but fat-suppression images are recommended in order to differentiate the fat tissue from a hemorrhagic content of the lesion. Differential diagnosis includes tumors with abundant amounts of fat such as lipomas and myelolipomas [186].

■ **Schwannoma.** Schwannoma of the pancreas is an extremely rare tumor, which often shows cystic features, mimicking pseudocyst or other cystic tumors. Definitive diagnosis can only be established by pathological examination. Macroscopically, the mass shows a well-circumscribed, septate, cystic pattern with a thick fibrous capsule. Microscopically the peripheral portion of the mass, partially solid, is composed of sheets of spindle cells [187].

Cystic Forms of Typically Solid Pancreatic Tumors

The ductal adenocarcinoma can show cystic degeneration, which generally occurs in large tumors with central necrosis. In other cases, a peripancreatic fluid collection from ductal disruption or decompression related to malignant involvement may mimic a mucinous

cystic neoplasm. Finally, an intraductal papillary mucinous tumor is mimicked by the markedly dilated main pancreatic duct because of neoplastic obstruction or by the predominantly intraductal growth of a pancreatic carcinoma [154].

The mucinous adenocarcinoma (colloid carcinoma), an uncommon variant of adenocarcinoma, produces a large volume of mucin that results in a cystic appearance on imaging [129].

The anaplastic carcinoma, in which necrosis is almost constant, can sometimes show a cystic aspect.

The acinar carcinoma can sometimes assume the multilocular cystic aspect, as a result indistinguishable from the other cystic tumors at imaging. However, histological classification is easy.

Endocrine tumors, hyperfunctioning and not, in less than 10% of cases can present cystic architecture due to previous necrosis. Septations are sometimes present along with wall calcifications. The pattern is nonspecific, analogous to that of the other cystic masses of the pancreas. In these cases, the most frequent radiological diagnosis is mucinous cystadenoma or cystadenocarcinoma, because of the macrocystic appearance of the lesion and the presence of features suggestive of intratumoral septa or vegetation. The diagnosis of cystic endocrine tumor can be considered only when the pancreatic cystic mass is discovered in a patient with a history of MEN-1 syndrome or with clinical features suggestive of this syndrome [188].

Tumor-like Cystic Lesions

The pseudocyst is the most frequent cystic mass encountered in the pancreatic gland; it has a fibrous wall without epithelial lining. The lesion can be located outside the pancreas (especially when it represents the development of acute necrotizing pancreatitis) or within the pancreas (more frequently in association with chronic pancreatitis). The pseudocyst can sometimes communicate with the duct of Wirsung. Additionally, the compression related to its presence can erode the nearby vessels and cause venous thrombosis or arterial pseudoaneurysms. Fatal hemorrhages can sometimes occur.

At imaging, whenever septations are present, the pseudocyst is indistinguishable from cystic tumors, particularly where the mucinous cystic tumor and the solid-pseudopapillary tumor (cystic variant) are concerned. The differential element is obviously represented by the clinical picture which, in the case of the pseudocyst, corresponds to that of acute and chronic pancreatitis, while it can be nonspecific or even absent in the case of tumor.

The most deceitful clinical situation, which frequently leads to diagnostic error, is that in which the pseudocyst complicates the presence of a ductal adenocarcinoma which has created an obstruction of the duct of Wirsung with superimposed pancreatitis. In this case, the tumor can be easily underestimated at imaging, resulting in the wrong diagnosis of pseudocyst or cystic tumor [145].

An abscess can also be differentiated from the tumor by considering the clinical history (previous acute pancreatitis), the clinical picture (fever) and sometimes the imaging features (presence of gas bubbles within the lesion).

The congenital cyst, usually small, does not communicate with the ductal tree and shows a flat epithelial lining.

Most of the time it is an incidental finding. The lesions are single or multiple; multiple locations are more often associated with Von Hippel-Lindau disease or, rarely, with inherited polycystic kidney disease or cystic fibrosis [129, 156].

In the case of a single cyst, the differential diagnosis should consider a small IPMT of the collateral branches. The correct diagnosis is obtainable with ERCP, and more recently with MRCP, which is able to recognize whether communication with the main duct is present or not.

The lymphoepithelial cyst, usually an incidental finding, can often stick out from the contour of the gland, resulting in a fluid-filled mass with thin wall, indistinguishable from other cystic lesions of the pancreas. Since lymphoepithelial cysts may develop in females and are frequently located in the tail of the organ, they should be considered in the clinical differential diagnosis of mucinous cystic neoplasms [189]. Its real nature can be documented only histologically, thanks to the presence of squamous epithelium supported by a small layer of lymphoid tissue.

The mucinous nonneoplastic cyst of the pancreas has been recently reported as a nonneoplastic cystic change of the pancreas, distinct from mucinous cystic neoplasm. On the whole, these masses appear as uniocular or multilocular thin-walled cysts that contain turbid fluid or blood, isolated from the duct system. The imaging features are consequently analogous to those of many other cystic masses of the pancreas. The differential diagnosis of mucinous nonneoplastic cysts vs pancreatic retention cysts and mucinous cystic neoplasms is challenging because both of these lesions are lined with epithelium similar to that of mucinous nonneoplastic cysts [189].

The other cystic lesions that can significantly raise differential problems regarding cystic pancreatic tumors are the parasitic cyst, the enterogenous cyst and the endometrial cyst. In such instances, the diagnosis is usually acquired by histology [4, 129].

References

1. Klöppel G, Solcia E, Longnecker DS, Capella C, Sobin LH (1996) Histological typing of tumors of the exocrine pancreas. International histological classification of tumors, 2nd edn. Springer, Berlin Heidelberg New York
2. Paker SL, Tong T, Bolden S (1997) Cancer statistics. CA Cancer J Clin 47:5–27
3. Pour PM (1991) The silent killer. Int J Pancreatol 10:103–104
4. Solcia E, Capella C, Klöppel G (1997) Tumors of the pancreas. Atlas of Tumor Pathology, 3rd Series, No. 20. Armed Forces Institute of Pathology, Washington, DC
5. Trede M, Schwall G, Saeger H (1990) Survival after pancreaticoduodenectomy. Ann Surg 211:447–458
6. Yeo CJ, Cameron JL, Sohn TA, Lillemoe KD, Pitt HA, Talamini MA, Hruban RH, Ord SE, Sauter PK, Coleman J, Zahurak ML, Grochow LB, Abrams RA (1997) Six hundred and fifty consecutive pancreaticoduodenectomies in the 1990s: pathology, complications, and outcomes. Ann Surg 226:248–257
7. Kayahara M, Nagakawa T, Ueno K, Ohta T, Takeda T, Miyazaki I (1993) An evaluation after radical resection for pancreatic cancer based on the mode of recurrence as determined by autopsy and diagnostic imaging. Cancer 72:2118–2123
8. Tsuchiya R, Tajima Y, Matsuzaki S, Onizuka S, Kanematsu T (2001) Early pancreatic cancer. Pancreatology 1:597–603
9. Brand R (2001) The diagnosis of pancreatic cancer. Cancer J 7:287–297
10. DiMagno EP, Reber HA, Tempero MA (1999) AGA technical review on the epidemiology, diagnosis, and treatment of pancreatic ductal adenocarcinoma. Gastroenterology 117:1464–1484
11. Yachida S, Fukushima N, Nakanishi K, Shimada K, Kosuge T, Sakamoto M (2002) Minute pancreatic adenocarcinoma presenting with stenosis of the main pancreatic duct. Pathol Int 52:607–611
12. Martínez-Noguera A, Montserrat E, Torrubia S, Monill JM, Estrada P (2001) Ultrasound of the pancreas: update and controversies. Eur Radiol 11:1594–1606
13. Oshikawa O, Tanaka S, Ioka T, Nakaizumi A, Hamada Y, Mitani T (2002) Dynamic sonography of pancreatic tumors: comparison with dynamic CT. Am J Roentgenol 178:1133–1137
14. Wang C (1997) Gray-scale and color flow sonography of pancreatic ductal adenocarcinoma. J Clin Ultrasound 415:473–480
15. Morrin MM, Kruskal JB, Raptopoulos V, Weisinger K, Farrel RJ, Steer ML, Kane RA (2001) State of the art ultrasonography is as accurate as helical computed tomography and computed tomographic angiography for detecting unresectable periampullary cancer. J Ultrasound Med 20:481–490
16. Koito K, Namieno T, Nagakawa T, Morita K (1997) Inflammatory pancreatic masses: differentiation from ductal carcinomas with contrast-enhanced sonography using carbon dioxide microbubbles. Am J Roentgenol 169:1263–1267
17. Skjoldbye B, Pedersen MH, Struckmann J, Burcharth F, Larsen T (2002) Improved detection and biopsy of solid liver lesions using pulse-inversion ultrasound scanning and contrast agent infusion. Ultrasound Med Biol 28:439–444
18. Nishiharu T, Yamashita Y, Abe Y, Mitsuzaki K, Tsuchigame T, Nakayama Y, Takahashi M (1999) Local extension of pancreatic carcinoma: assessment with thin-section helical CT versus with breath-hold fast MR imaging – ROC analysis. Radiology 212:445–452
19. Megibow AJ, Zhou XH, Rotterdam H, Francis IR, Zerhouni EA, Balfe DM, Weinreb JC, Aisen A, Kuhlman J, Heiken JP (1995) Pancreatic adenocarcinoma: CT versus MR imaging in the evaluation of respectability – report of the Radiology Diagnostic Oncology Group. Radiology 195:327–332
20. Bluemke DA, Cameron JL, Hruban RH, Pitt HA, Siegelman SS, Soyer P, Fishman EK (1995) Potentially resectable pancreatic adenocarcinoma: spiral CT assessment with surgical and pathologic correlation. Radiology 197:381–385
21. Chong M, Freeny PC, Schmiedl UP (1998) Pancreatic arterial anatomy: depiction with dual-phase helical CT. Radiology 208:537–542
22. Demachi H, Matsui O, Kobayashi S (1997) Histological influence on contrast-enhanced CT of pancreatic ductal adenocarcinoma. J Comput Assist Tomogr 21:980–985
23. Lu DSK, Vedantham S, Krasny RM, Kadell B, Berger WL, Reber HA (1996) Two-phase helical CT for pancreatic tumors: pancreatic versus hepatic phase enhancement of tumor, pancreas, and vascular structures. Radiology 199:697–701
24. Raptopoulos V, Steer ML, Sheiman RG, Vrachliotis TG, Gougoutas CA, Movson JS (1997) The use of helical CT and CT angiography to predict vascular involvement from pancreatic cancer: correlation with findings at surgery. Am J Roentgenol 168:971–977
25. Diehl SJ, Lehmann KJ, Sadick M, Lachmann R, Georgi M (1998) Pancreatic cancer: value of dual-phase helical CT in assessing resectability. Radiology 206:373–378
26. Nakayama Y, Yamashita Y, Kadota M, Takahashi M, Kanemitsu K, Hiraoka T, Hirota M, Ogawa M, Takeya M (2001) Vascular encasement by pancreatic cancer: correlation of CT findings with surgical and pathologic results. J Comput Assist Tomogr 25:337–342
27. Choi BI, Chung MJ, Han JK, Han MC, Yoon YB (1997) Detection of pancreatic adenocarcinoma: relative value of arterial and late phases of spiral CT. Abdom Imaging 22:199–203
28. Novick SL, Fishman EK (1998) Three-dimensional CT angiography of pancreatic carcinoma: role in staging extent of disease. Am J Roentgenol 170:139–143
29. Procacci C, Biasiutti C, Carbognin G, Bicego E, Graziani R, Franzoso F, Pesci A, Megibow AJ (2002) Spiral computed tomography assessment of resectability of pancreatic ductal adenocarcinoma: analysis of results. Digest Liver Dis 34:739–747
30. Hough TJ, Raptopoulos V, Siewert B, Matthews JB (1999) Teardrop superior mesenteric vein: CT sign for unresectable carcinoma of the pancreas Am J Roentgenol 173:1509–1512
31. Imbriaco M, Megibow AJ, Camera L, Pace L, Mainenti PP, Romano M, Selva G, Salvatore M (2002) Dual-phase versus single-phase helical CT to detect and asses resectability of pancreatic carcinoma. Am J Roentgenol 178:1473–1479
32. Fishman EK, Horton KM, Urban BA (2000) Multidetector CT angiography in the evaluation of pancreatic carcinoma: preliminary observations. J Comput Assist Tomogr 24:849–853
33. Horton KM, Fishman EK (2002) Multidetector CT angiography of pancreatic carcinoma: part 1, evaluation of arterial involvement. Am J Roentgenol 178:827–831
34. Shioyama Y, Kimura M, Horihata K, Masuda M, Hagihira T, Okumura T, Yoshimi F, Amemiya R, Kishi K, Terada M, Sato M (2001) Peripancreatic arteries in thin-section multislice helical CT. Abdom Imaging 26:234–242
35. Horton KM, Fishman EK (2002) Multidetector CT angiography of pancreatic carcinoma: part 2, evaluation of venous involvement. Am J Roentgenol 178:832–836
36. Nino-Murcia M, Jeffrey RB, Beaulieu CF, Li KCP, Rubin GD (2001) Multidetector CT of the pancreas and bile duct system: value of curved planar reformations. Am J Roentgenol 176:689–693
37. Prokesch RW, Chow LC, Beaulieu CF, Nino-Murcia M, Mindelzun RE, Bammer R, Huang J, Jeffrey RB (2002) Local staging of pancreatic carcinoma with multi-detector row CT: use of curve planar reformations – initial experience. Radiology 225:759–765
38. Prokesch RW, Chow CL, Beaulieu CF, Bammer R, Jeffrey RB (2002) Isoattenuating pancreatic adenocarcinoma at multidetector row CT: secondary signs. Radiology 224:764–768
39. Semelka RC, Kelekis NL, Molina PL, Sharp TJ, Calvo B (1996) Pancreatic masses with inconclusive findings on spiral CT: is there a role for MRI? J Magn Reson Imaging 6:585–588
40. Ichikawa T, Haradome H, Hachiya J, Nitatori T, Ohtomo K, Kinoshita T, Araki T (1997) Pancreatic ductal adenocarcinoma: preoperative assessment with helical CT versus dynamic MR imaging. Radiology 202:655–662
41. Hänninen EL, Amthauer H, Hosten N, Ricke J, Böhmig M, Langrehr J, Hintze R, Neuhaus P, Wiedenmann B, Rosewicz S, Felix R (2002) Prospective evaluation of pancreatic tumors: accuracy of MR imaging with MR cholangiopancreatography and MR angiography. Radiology 224:34–41

42. Fisher U, Vosshenrich R, Horstmann O, Becker H, Salamat B, Baum F, Grabbe E (2002) Preoperative local MRI-staging of patients with a suspected pancreatic mass. Eur Radiol 12: 296–303
43. Sheridan MB, Ward J, Guthrie JA, Spencer JA, Craven CM, Wilson D, Guillon PJ, Robinson PJ (1999) Dynamic contrast-enhanced MR imaging and dual-phase helical CT in the preoperative assessment of suspected pancreatic cancer: a comparative study with receiver operating characteristic analysis. Am J Roentgenol 173: 583–590
44. Irie H, Honda H, Kaneko K, Kuroiwa T, Yoshimitsu K, Masuda K (1997) Comparison of helical CT and MR imaging in detecting and staging small pancreatic adenocarcinoma. Abdom Imaging 22: 429–433
45. Robinson PJA (2002) The role of MRI in pancreatic cancer. Eur Radiol 12: 267–269
46. Gabata T, Matsui O, Kadoya M, Yoshikawa J, Miyayama S, Takashima T, Nagakawa T, Kayahara M, Nonomura A (1994) Small pancreatic adenocarcinomas: efficacy of MR imaging with fat suppression and gadolinium enhancement. Radiology 193: 683–688
47. Spencer JA, Ward J, Guthrie JA, Guillou PJ, Robinson PJ (1998) Assessment of resectability of pancreatic cancer with dynamic contrast-enhanced MR imaging: technique, surgical correlation and patient outcome. Eur Radiol 8: 23–29
48. Jenkins JP, Braganza JM, Hickey DS, Iserwood I, Machin M (1987) Quantitative tissue characterization in pancreatic disease using magnetic resonance imaging. Br J Radiol 60: 333–341
49. Johnson PT, Outwater EK (1999) Pancreatic carcinoma versus chronic pancreatitis: dynamic MR imaging. Radiology 212: 213–218
50. Wang C (1998) Mangafodipir trisodium (MnDPDP)-enhanced magnetic resonance imaging of the liver and pancreas. Acta Radiol Suppl 415: 1–31
51. Schima W, Függer R (2002) Evaluation of focal pancreatic masses: comparison of mangafodipir-enhanced MR imaging and contrast-enhanced helical CT. Eur Radiol 12: 2998–3008
52. Schima W, Függer R, Schober E, Oettl C, Wamser P, Grabenwöger F, Ryan JM, Novacek G (2002) Diagnosis and staging of pancreatic cancer: comparison of mangafodipir trisodium-enhanced MR imaging and contrast-enhanced helical hydro-CT Am J Roentgenol 179: 717–724
53. Gehl HB, Urhahn R, Bohndorf K, Klever P, Hauptmann S, Lodemann KP, Matern S, Schumpelick V, Gunther RW (1993) Mn-DPDP in MR imaging of pancreatic adenocarcinoma: initial clinical experience. Radiology 186: 795–798
54. Kanematsu M, Shiratori Y, Hoshi H, Kondo H, Matsuo M, Moriwaki H (2000) Pancreas and peripancreatic vessels: effect of imaging delay on gadolinium enhancement at dynamic gradient-recalled-echo MR imaging. Radiology 215: 95–102
55. Caudana R, Morana G, Pirovano GP, Nicoli N, Portuese A, Spinazzi A, Di Rito R, Pistolesi GF (1996) Focal malignant hepatic lesions: MR imaging enhanced with gadolinium benzyloxypropionictetra-acetate (BOPTA)-preliminary results of phase II clinical application. Radiology 199: 513–520
56. Adamek HE, Albert J, Breer H, Weitz M, Schilling D, Riemann JF (2000) Pancreatic cancer detection with magnetic resonance cholangiopancreatography and endoscopic retrograde cholangiopancreatography: a prospective controlled study. Lancet 356: 190–193
57. Ichicawa T, Sou H, Araki T, Arbab AS, Yoshikawa T, Ishigame K, Haradome H, Hachiya J (2001) Duct-penetrating sign at MRCP: usefulness for differentiating inflammatory pancreatic mass from pancreatic carcinomas. Radiology 221: 107–116
58. Fulcher AS, Turner MA (1999) MR pancreatography: a useful tool for evaluating pancreatic disorders. Radiographics 19: 5–24
59. Kim JH, Kim MJ, Chung JJ, Lee WJ, Yoo HS, Lee JT (2002) Differential diagnosis of periampullary carcinomas at MR imaging. Radiographics 22: 1335–1352
60. Haven F, Bloemen H, Van Hoe L (1999) Chronic pancreatitis with enlargement of the pancreatic head: new specific signs on cross-sectional and projective magnetic resonance cholangio-pancreatography. Eur Radiol 9[Suppl 1]: S143
61. Adsay NV, Pierson C, Abrams J, Sarkar F, Weaver D, Conlon KC, Brennan MF, Klimstra DS (2001) Colloid (mucinous noncystic) carcinoma of the pancreas. Am J Surg Pathol 25: 26–42
62. Kardon DE, Thompson LD, Przygodzki RM, Heffess CS (2001) Adenosquamous carcinoma of the pancreas: a clinicopathologic series of 25 cases. Mod Pathol 14: 443–451
63. Makiyama K, Takuma K, Zea Iriarte WL, Ikuno N, Kawatomi M, Mori N, Ishino T, Yonemitsu N (1995) Adenosquamous carcinoma of the pancreas. J Gastroenterol 30: 798–802
64. Motoo Y, Kawashima A, Watanabe H, Su SB, Okai T, Sawabu N (1997) Undifferentiated (anaplastic) carcinoma of the pancreas showing sarcomatous change and neoplastic cyst formation. Int J Pancreatol 21: 243–248
65. Ros PR, Mortelé KJ (2001) Imaging features of pancreatic neoplasms. JBR-BTR 84: 239–249
66. Nojima T, Nakamura F, Ishikura M, Inoue K, Nagashima K, Kato H (1993) Pleomorphic carcinoma of the pancreas with osteoclast-like giant cells. Int J Pancreatol 14: 275–281
67. Hoorens A, Lemoine N, Mc Lellan E, Morohoshi T, Kamisawua T, Heitz P, Stamm B, Ruschoff J, Wiedenmann B, Kloppel G (1993) Pancreatic acinar cell carcinoma. An analysis of cell lineage markers, p53 expression and Ki-ras mutation. Am J Pathol 143: 685–698
68. Klimstra DS, Heffes CS, Oertl J, Rosai J (1992) Acinar cell carcinoma of the pancreas. Clinicopathologic study of 28 cases. Am J Surg Pathol 16: 815–837
69. Sahani D, Prasad SR, Maher M, Warshaw AL, Hahn PF, Saini S (2002) Functioning acinar cell pancreatic carcinoma: diagnosis on mangafodir trisodium (Mn-DPDP)-enhanced MRI. J Comput Assist Tomogr 26: 126–128
70. Hartman GG, Ni H, Pickleman J (2001) Acinar cell carcinoma of the pancreas. Arch Pathol Lab Med 125: 1127–1128
71. Mustert BR, Stafford-Johnson DB, Francis IR (1998) Appearance of acinar cell carcinoma of the pancreas on dual-phase CT. Am J Roentgenol 171: 1709
72. Ishizaki A, Koito K, Namieno T, Nagakawa T, Murashima Y, Suga T (1995) Acinar cell carcinoma of the pancreas: a rare case of an alpha-fetoprotein-producing cystic tumor. Eur J Radiol 21: 58–60
73. Horie A, Haratake J, Jimi A, Matsumoto M, Ishii N, Tsutsumi Y (1987) Pancreatoblastoma in Japan with differential diagnosis from papillary cystic tumor (ductuloacinar adenoma) of the pancreas. Acta Pathol Jpn 37: 47–63
74. Klimstra DS, Wring B, Adair CF, Heffess CS (1995) Pancreatoblastoma: a clinicopathologic study and review of the literature. Am J Surg Pathol 16: 371–389
75. Roebuck DJ, Yuen MK, Wong YC, Shing MK, Lee CW, Li CK (2001) Imaging features of pancreatoblastoma. Pediatr Radiol 31: 501–506
76. Mergo PJ, Helmberger TK, Buetow PC, Helmberger RC, Ros PR (1997) Pancreatic neoplasms: MR imaging and pathologic correlation. Radiographics 17: 281–301
77. Zhou H, Cheng W, Lam KY, Chan GCF, Khong PL, Tam PKH (2001) Solid-cystic papillary tumor of the pancreas in children. Pediatr Surg 17: 614–620
78. Zamboni G, Bonetti F, Scarpa A, Pelosi G, Doglioni C, Iannucci A, Castelli P, Balercia G, Aldovini D, Bellomi A, Iacono C, Serio G, Mariuzzi GM (1993) Expression of progesterone receptors in solid-cystic tumour of the pancreas: a clinicopathological and immunohistochemical study of ten cases. Virchows Archiv A 423: 425–431
79. Balercia G, Zamboni G, Bogina G, Mariuzzi GM (1995) Solid-cystic tumor of the pancreas. An extensive ultrastructural study of fourteen cases. J Submicrosc Cytol Pathol 27: 331–340
80. Matsunou H, Konishi F, Yamamichi N, Takayanagi N, Mukai M (1990) Solid, infiltrating variety of papillary cystic neoplasm of the pancreas. Cancer 65: 2747–2757
81. Cappellari JO, Geisinger KR, Albertson DA, Wolfman NT, Kute TE (1990) Malignant papillary cystic tumor of the pancreas. Cancer 66: 193–198
82. Nishihara K, Nagoshi M, Tsuneyoshi M, Yamaguchi K, Hayashi I (1990) Papillary cystic tumors of the pancreas. Assessment of their malignant potential. Cancer 71: 82–92

83. Sclafani LM, Reiter VE, Coit DG, Brennan MF (1991) The malignant nature of papillary and cystic neoplasm of the pancreas. Cancer 68:153–158
84. Buetow PC, Buck JL, Pantongrag-Brown L, Beck KG, Ros PR, Adair CF (1996) Solid and papillary epithelial neoplasm of the pancreas: imaging-pathologic correlation on 56 cases. Radiology 199:707–711
85. Klöppel G, Heitz PU (1988) Pancreatic endocrine tumors. Pathol Res Pract 183:155–168
86. Buetow PC, Miller DL, Parrino TV, Buck JL (1997) Islet cell tumors of the pancreas: clinical, radiologic, and pathologic correlation in diagnosis and localization. Radiographics 17: 453–472
87. Marcos HB, Libutti SK, Alexander HR, Lubensky IA, Bartlett DL, Walther MM, Linehan WM, Glenn GM, Choyke PL (2002) Neuroendocrine tumors of the pancreas in Von Hippel-Lindau disease: spectrum of appearances at CT and MR imaging with histopathologic comparison. Radiology 225: 751–775
88. Solcia E, Klöppel G, Sobin LH (2000) Histological typing of endocrine tumours. 2nd edn. Springer, Berlin Heidelberg New York
89. Debray MP, Geoffroy O, Laissy JP, Lebtahi R, Silbermann-Hoffman O, Henry-Feugeas MC, Cadiot G, Mignon M, Schouman-Claeys E (2001) Imaging appearances of metastases from neuroendocrine tumors of the pancreas. Br J Radiol 74: 1065–1070
90. Buetow PC, Parrino TV, Buck JL, Pantongrag-Brown L, Ros PR, Dachman AH, Cruess DF (1995) Islet cell tumors of the pancreas: pathologic-imaging correlation among size, necrosis and cysts, calcification, malignant behavior and functional status. Am J Roentgenol 165:1175–1179
91. Schein S, De Lellis RA, Kahn CR (1973) Islet cell tumors: current concepts and management. Ann Intern Med 79:239–257
92. Namieno T, Koito K, Uchino J (1995) Doppler color flow imaging for assessment and localization of pancreatic insulinoma. Eur J Radiol 20:208–209
93. Stafford-Johnson DB, Francis IR, Eckhauser FE, Knol JA, Chang AE (1998) Dual-phase helical CT of nonfunctioning islet cell tumors. J Comput Assist Tomogr 22:335–339
94. Van Hoe L, Gryspeerdt S, Marchal G, Baert AL, Mertens L (1995) Helical CT for the preoperative localization of islet cell tumors of the pancreas: value of arterial and parenchymal phase images. Am J Roentgenol 165:1437–1439
95. Semelka RC, Cumming MJ, Shoenut JP, Magro CM, Yaffe CS, Kroeker MA, Greenberg HM (1993) Islet cell tumors: comparison of dynamic contrast-enhanced CT and MR imaging with dynamic gadolinium enhancement and fat suppression. Radiology 186:799–802
96. Ichikawa T, Peterson MS, Federle MP, Baron RL, Haradome H, Kawamori Y, Nawano S, Araki T (2000) Islet cell tumor of the pancreas: biphasic CT versus MR imaging in tumor detection. Radiology 216:163–171
97. Owen NJ, Sohaib SAA, Peppercorn PD, Monson JP, Grossman AB, Besser GM, Reznek RH (2001) MRI of pancreatic neuroendocrine tumors. Br J Radiol 74:968–973
98. Iglesias A, Arias M, Casal M, Páramo C, Fiaño C, Brasa J (2001) Unusual presentation of a pancreatic insulinoma in helical CT and dynamic contrast-enhanced MR imaging: case report. Eur Radiol 11:926–930
99. Shi W, Johnston CF, Buchanan KD, Ferguson WR, Laird JD, Crothers JG, McIlrath EM (1998) Localization of neuroendocrine tumours with [^{111}In] DTPA-octreotide scintigraphy (Octreoscan): a comparative study with CT and MR imaging. QJM 91:295–301
100. Baructu O, Cihangiroglu M, Yildirim T, Kayaselcuk F, Noyan T (2002) Fat containing unusual tumor of the pancreas. Eur Radiol 12:770–773
101. Matsumoto S, Mori H, Miyake H, Takaki H, Maeda T, Yamada Y, Oga M (1995) Uneven fatty replacement of the pancreas: evaluation with CT. Radiology 194:453–458
102. Yamamoto H, Watanabe K, Nagata M, Tasaki K, Honda I, Watanabe S, Soda H, Takenouti T (2002) Inflammatory myofibroblastic tumor (IMT) of the pancreas. J Hepatobiliary Surgery 9:116–119
103. Luttges J, Pierre E, Zamboni G, Weh G, Lietz H, Kussmann J, Kloppel G (1997) Malignant non-epithelial tumors of the pancreas. Pathologe 18:233–237
104. Darvishan F, Sullivan J, Teichberg S, Basham K (2002) Carcinosarcoma of the pancreas. Arch Pathol Lab Med 126: 1114–1117
105. Boni L, Benevento A, Dionigi G, Cabrini L, Dionigi R (2002) Primary pancreatic lymphoma. Surg Endosc 16:1107–1108
106. Merkle EM, Bender GN, Brambs HJ (2000) Imaging findings in pancreatic lymphoma: differential aspects. Am J Roentgenol 174:671–675
107. Bernardeu M, Auroux J, Cavicchi M, Haioun C, Tsakiris L, Delchier JC (2002) Secondary pancreatic involvement by diffuse large B-cell lymphoma presenting as acute pancreatitis: treatment and outcome. Pancreatology 2:427–430
108. Sheth S, Fishman EK (2002) Imaging of uncommon tumors of the pancreas. Radiol Clin North Am 40:1273–1287
109. Hirata S, Yamaguchi K, Bandai S, Izumo A, Chijiiwa K, Tanaka M (2002) Secondary extramedullary plasmacytoma involving the pancreas. J Hepatobiliary Pancreat Surg 9:111–115
110. Scatarige JC, Horton KM, Sheth S, Fishman EK (2001) Pancreatic parenchymal metastases: observations on helical CT. Am J Roentgenol 176:695–699
111. Sato M, Ishida H, Konno K, Hamashima Y, Naganuma H, Komatsuda T, Ishida J, Watanabe S (2001) Pancreatic metastasis: sonographic findings. Abdom Imaging 26:72–75
112. Cubilla AL, Fitzgerald PJ (1984) Tumors of the exocrine pancreas. Atlas of Tumor Pathology, 2nd Series, part 19. Armed Forces Institute of Pathology, Washington DC
113. Charnsangavej C, Whitley NO (1993) Metastases to the pancreas and peripancreatic lymph nodes from carcinoma of the right side of the colon: CT findings in 12 patients. Am J Roentgenol 160:49–52
114. Nakamura E, Shimizu M, Itoh T, Manabe T (2001) Secondary tumors of the pancreas: clinicopathological study of 103 autopsy cases of Japanese patients. Pathol Int 51:686–690
115. Butturini G, Bassi C, Falconi M, Salvia R, Caldiron E, Iannucci A, Zamboni G, Graziani R, Procacci C, Pederzoli P (1998) Surgical treatment of pancreatic metastases from renal cell carcinoma. Dig Surg 15:241–246
116. Procacci C, Graziani R, Zamboni G, Cavallini G, Pederzoli P, Guarise A, Bogina G, Biasiutti C, Carbognin G, Bergamo-Andreis IA, Pistolesi GF (1997) Cystic dystrophy of the duodenal wall: radiologic findings. Radiology 205:741–747
117. Irie H, Honda H, Baba S, Kuroiwa T, Yoshimitsu K, Tajima T, Jimi M, Sumii T, Masuda K (1998) Autoimmune pancreatitis: CT and MR characteristics. Am J Roentgenol 170:1323–1327
118. Van Hoe L, Gryspeerdt S, Ectors N, Van Steenbergen W, Aerts R, Baert AL, Marchal G (1998) Nonalcoholic duct-destructive chronic pancreatitis: imaging findings. Am J Roentgenol 170: 643–647
119. Thurnher MM, Schima W, Turetschek K, Thurnher SA, Fugger R, Oberhuber G (2001) Peripancreatic fat necrosis mimicking pancreatic cancer. Eur Radiol 11:922–925
120. Churei H, Inoue H, Nakajo M (1998) Intrapancreatic accessory spleen: case report. Abdom Imag 23:191
121. Paterson A, Frush DP, Donnelly LF, Foss JN, O'Hara SM, Bisset GS III (1999) A pattern-oriented approach to splenic imaging in infants and children. Radiographics 19:1465–1485
122. Parienty RA, Ducellier R, Lubrano JM, Piccard JD, Pradel J, Solarski N (1980) Cystadenomas of the pancreas: diagnosis by computed tomography. J Comput Assist Tomogr 4: 364–367
123. Hodgkinson DJ, ReMine WH, Weiland LH (1978) A clinicopathologic study of 45 cases of pancreatic cystadenocarcinoma. Ann Surg 188:679–684
124. Zamboni G, Scarpa A, Franzin G, Capelli P, Bogina G, Iannucci A, Bassi C, Pederzoli P, Iacono C, Serio G, Procacci C, Mariuzzi GM (1994) Pathology of cystic tumors of the pancreas. In: Pederzoli P, Bassi C, Cavallini G, Falconi M (eds) Facing the pancreatic dilemma. Springer, Berlin Heidelberg New York, pp 368–397
125. Gibson JB, Sobin LH (1978) Histological typing of tumor of the liver, biliary tract and pancreas No. 20. World Health Organization, Geneva

126. Wheeler DA, Edmonson HA (1985) Cystadenoma with mesenchymal stroma (CMS) in the liver and bile ducts. A clinicopathologic study of 17 cases, 4 with malignant changes. Cancer 56:1434–1445
127. Zamboni G, Terris B, Scarpa A, Kosmahl M, Capelli P, Klimstra DS, Lam PW, Klöppel G (2002) Acinar cell cystadenoma of the pancreas: a new entity? Am J Surg Pathol 26:698–704
128. Zhang XM, Mitchell DG, Dohke M, Holland GA, Parker L (2002) Pancreatic cysts: depiction on single-shot fast spin-echo MR images. Radiology 223:547–553
129. Demos TC, Posniak HV, Harmath C, Olson MC, Aranha G (2002) Cystic lesions of the pancreas Am J Roentgenol 179:1375–1388
130. Sarr MG, Kendrick ML, Nagorney DM, Thompson GB, Farley DR, Farnell MB (2001) Cystic neoplasms of the pancreas: benign to malignant epithelial neoplasms. Surg Clin North Am 81:497–509
131. Gasslander T, Arnelo U, Albiin N, Permert J (2001) Cystic tumors of the pancreas. Dig Dis 19:57–62
132. Le Borgne J, de Calan L, Partensky C (1999) Cystadenomas and cystadenocarcinomas of the pancreas: a multiinstitutional retrospective study of 398 cases. Ann Surg 230:152–161
133. Horton WA, Wong V, Eldridge R (1976) Von Hippel-Lindau disease: clinical and pathological manifestations in nine families with 50 affected members. Arch Int Med 136:769–777
134. Yasuhara Y, Sakaida N, Uemura Y, Senzaki H, Shikata N, Tsubura A (2002) Serous microcystic adenoma (glycogen-rich cystadenoma) of the pancreas: study of 11 cases showing clinicopathological and immunohistochemical correlations Pathol Int 52:307–312
135. Masatsugu T, Yamaguchi K, Chijiiwa K, Nishiyama K, Tanaka M (2002) Serous cystadenoma of the pancreas associated with pancreas divisum. J Gastroenterol 37:669–673
136. Compagno J, Oertel J (1978) Microcystic adenomas of the pancreas (glycogen-rich cystadenomas): a clinicopathological study of 34 cases. Am J Clin Pathol 69:289–298
137. George DH, Murphy F, Michalski R, Ulmer BG (1989) Serous cystadenocarcinoma of the pancreas: a new entity? Am J Surg Pathol 13:61–66
138. Kamei K, Funabiki T, Ochiai M, Amano H, Marugami Y, Kasahara M, Sakamoto T (1992) Some considerations on the biology of pancreatic serous cystadenoma. Int J Pancreatol 11:97–104
139. Yoshinmi N, Sugie S, Tanaka T, Aijin W, Bunai Y, Tatematsu A, Okada T, Mori H (1992) A rare case of serous cystadenocarcinoma of the pancreas. Cancer 69:2449–2453
140. Zirinsky K, Abiri M, Baer JW (1984) Computed tomography demonstration of pancreatic microcystic adenoma. Am J Gastroenterol 79:139–142
141. Abe H, Kubota K, Mori M, Miki K, Minagawa M, Noie T, Kimura W, Makuuchi M (1998) Serous cystadenoma of the pancreas with invasive growth: benign or malignant? Am J Gastroenterol 93:1963–1966
142. Rampy BA, Waxman I, Xiao SY, Logrono R (2001) Serous cystadenoma of the pancreas with papillary features: a diagnostic pitfall on fine-needle aspiration biopsy Arch Pathol Lab Med 125:1591–1594
143. Smart JM, Blaquiere RM (2002) Synchronous serous cystadenomas of the pancreas. Clin Radiol 57:532–534
144. Kobayashi T, Kawabe A, Uenoyama S, Kazui T, Takehara Y, Kosugi I (2001) Macrocystic serous cystadenoma of the pancreas: case report. Abdom Imaging 26:69–71
145. Procacci C, Biasiutti C, Carbognin G, Accordini S, Bicego E, Guarise A, Spoto E, Andreis IA, De Marco R, Megibow AJ (1999) Characterization of cystic tumors of the pancreas: CT accuracy. J Comput Assist Tomogr 23:906–912
146. Procacci C, Graziani R, Bicego E, Bergamo-Andreis IA, Guarise A, Valdo M, Bogina G, Solarino U, Pistolesi GF (1997) Serous cystadenoma of the pancreas: report of 30 cases with emphasis on the imaging findings. J Comput Assist Tomogr 21:373–382
147. Curry CA, Eng J, Horton KM, Urban B, Siegelman S, Kuszyk BS, Fishman EK (2000) CT of primary cystic pancreatic neoplasms: can CT be used for patient triage and treatment? Am J Roentgenol 175:99–103
148. Compagno J, Oertel JE (1978) Mucinous cystic neoplasms of the pancreas with overt and latent malignancy (cystadenocarcinoma and cystadenoma): a clinicopathologic study of 41 cases. Am J Clin Pathol 69:573–580
149. Yamada M, Kozuka S, Yamano K, Nakazawa S, Naitoh Y, Tsukamoto Y (1991) Mucin-producing tumor of the pancreas. Cancer 68:159–168
150. Zamboni G, Scarpa A, Bogina G, Iacono C, Bassi C, Talamini G, Sessa F, Capella C, Solcia E, Rickaert F, Mariuzzi GM, Kloeppel G (1999) Mucinous cystic tumors of the pancreas: clinicopathological features, prognosis and relationship to other mucinous tumors. Am J Surg Pathol 23:410–422
151. Morohoshi T, Kanda M, Asanuma K, Klöppel G (1989) Intraductal papillary neoplasms of the pancreas. A clinicopathologic study of six patients. Cancer 64:1329–1335
152. Rickaert F, Cremer M, Deviére J, Tavares L, Lambilliotte JP, Schröder S, Wurbs D, Klöppel G (1991) Intraductal mucin-hypersecreting neoplasms of the pancreas. A clinicopathologic study of eight patients. Gastroenterology 101:512–519
153. Sessa F, Solcia E, Capella C, Bonato M, Scarpa A, Zamboni G, Pellegata NS, Ranzani GN, Rickaert F, Klöppel G (1994) Intraductal papillary-mucinous tumours represent a distinct group of pancreatic neoplasms: an investigation of tumour cell differentiation and K-ras, p53 and c-erbB-2 abnormalities in 26 patients. Virchows Archiv 425:357–367
154. Grogan JR, Saeian K, Taylor AJ, Quiroz F, Demeure MJ, Komorowski RA (2001) Making sense of mucin-producing pancreatic tumors. Am J Roentgenol 176:921–929
155. Balci NC, Semelka RC (2001) Radiologic features of cystic, endocrine and other pancreatic neoplasms. Eur J Radiol 38:113–119
156. Hammond N, Miller FH, Sica GT, Gore RM (2002) Imaging of cystic diseases of the pancreas. Radiol Clin North Am 40:1243–1262
157. Albores-Saavedra J, Angeles-Angeles A, Nadji M, Henson ED, Alvarez L (1987) Mucinous cystadenocarcinoma of the pancreas. Morphologic and immunohistochemical observations. Am J Surg Pathol 11:11–20
158. Albores-Saavedra J, Gould EW, Angeles-Angeles A, Henson DE (1990) Cystic tumors of the pancreas. Pathol Annu 25:19–50
159. Warshaw AL, Compton CC, Lewandrowsk KB, Cardenosa G, Mueller PR (1990) Cystic tumors of the pancreas. New clinical, radiologic, and pathologic observations in 67 patients. Ann Surg 4:432–445
160. Procacci C, Carbognin G, Accordini S, Biasiutti C, Guarise A, Lombardo F, Ghirardi C, Graziani R, Pagnotta N, De Marco R (2001) CT features of malignant mucinous cystic tumors of the pancreas. Eur Radiol 11:1626–1630
161. Ohashi K, Takagi K (1980) ERCP and imaging diagnosis of pancreatic cancer. Gastroenterol Endoscopy 20:1439–1495 [in Japanese]
162. Itai Y, Ohhashi K, Nagai H, Murakami Y, Kokubo T, Makita K, Ohtomo K (1986) Ductectatic mucinous cystadenoma and cystadenocarcinoma of the pancreas. Radiology 161:697–700
163. Obara T, Maguchi H, Saitoh Y, Ura H, Koike Y, Kitazawa S, Namiki M (1991) Mucin-producing tumor of the pancreas: a unique clinical entity. Am J Gastroentrol 86:1619–1625
164. Ohashi K, Murakami Y, Maruyama M, Takekoskhi T, Ohta H, Ohashi I, Takagi K, Kato Y (1982) Four cases of mucous secreting pancreatic cancer. Prog Dig Endosc 348–351 [in Japanese]
165. Kimura W, Kuroda A, Makuuchi M (1998) Problems in the diagnosis and treatment of a so-called mucin-producing tumor of the pancreas. Pancreas 16:363–369
166. Procacci C, Megibow AJ, Carbognin G, Guarise A, Spoto E, Biasiutti C, Pistolesi GF (1999) Intraductal papillary mucinous tumor of the pancreas: a pictorial essay. Radiographics 19:1447–1463
167. Procacci C, Megibow AJ (2003) Imaging of the pancreas. Cystic and rare tumors. Springer-Verlag, Berlin Heidelberg New York
168. Lim JH, Lee G, Oh YL (2001) Radiologic spectrum of intraductal papillary mucinous tumor of the pancreas. Radiographics 21:323–340

169. Itoh S, Ishiguchi T, Ishigaki T, Sakuma S, Maruyama K, Senda K (1992) Mucin-producing pancreatic tumor: CT findings and histopathologic correlation. Radiology 183:81–86
170. Procacci C, Graziani R, Bicego E, Bergamo-Andreis IA, Mainardi P, Zamboni G, Pederzoli P, Cavallini G, Valdo M, Pistolesi GF (1996) Intraductal mucin-producing tumors of the pancreas: imaging findings. Radiology 198:249–257
171. Fukukura Y, Fujiyoshi F, Sasaki M, Inoue H, Yonezawa S, Nakajo M (2000) Intraductal papillary mucinous tumors of the pancreas: thin-section helical CT findings. Am J Roentgenol 174:441–447
172. Irie H, Honda H, Aibe H, Kuroiwa T, Yoshimitsu K, Shinozaki K, Yamaguchi K, Shimada M, Masuda K (2000) MR cholangiopancreatographic differentiation of benign and malignant intraductal mucin-producing tumors of the pancreas. Am J Roentgenol 174:1403–1408
173. Koito K, Namieno T, Ichimura T, Yama N, Hareyama M, Morita K, Nishi M (1998) Mucin-producing pancreatic tumors: comparison of MR cholangiopancreatography with endoscopic retrograde cholangiopancreatography. Radiology 208:231–237
174. Peters HE, Vitellas KM (2001) Magnetic resonance cholangiopancreatography (MRCP) of intraductal papillary-mucinous neoplasm (IPMN) of the pancreas: case report. Magn Reson Imaging 19:1139–1143
175. Megibow AJ, Lavelle MT, Rofsky NM (2001) Cystic tumors of the pancreas: the radiologist. Surg Clin North Am 81:489–495
176. Irie H, Honda H, Kuroiwa T, Yoshimitsu K, Aibe H, Shinozaki K, Masuda K (2002) Measurement of the apparent diffusion coefficient in intraductal mucin-producing tumor of the pancreas by diffusion-weighted echo-planar MR imaging. Abdom Imaging 27:82–87
177. Falconi M, Salvia R, Bassi C, Zamboni G, Talamini G, Pederzoli P (2001) Clinicopathological features and treatment of intraductal papillary mucinous tumour of the pancreas. Br J Surg 88:376–381
178. Maire F, Hammel P, Terris B, Paye F, Scoazec JY, Cellier C, Barthet M, O'Toole D, Rufat P, Partensky C, Cuillerier E, Levy P, Belghiti J, Ruszniewski P (2002) Prognosis of malignant intraductal papillary mucinous tumours of the pancreas after surgical resection. Comparison with pancreatic ductal adenocarcinoma. Gut 51:717–722
179. Yamaguchi K, Ogawa Y, Chijiiwa K, Tanaka M (1996) Mucin-hypersecreting tumors of the pancreas: assessing the grade of malignancy preoperatively. Am J Surg 171:427–431
180. Traverso LW, Peralta EA, Ryan JA Jr, Kozarek RA (1998) Intraductal neoplasms of the pancreas. Am J Surg 175:426–432
181. Uchimi K, Fujita N, Noda Y, Kobayashi G, Kimura K, Matsunaga A, Yuki T, Nomura M, Sato T, Ishida K, Seno S, Ito K, Okubo K, Suzuki T, Hirasawa D, Sugawara T, Horaguchi J, Tada T, Takazawa O (2002) Solid cystic tumor of the pancreas: report of six cases and a review of the Japanese literature. J Gastroenterol 37:972–980
182. Procacci C, Graziani R, Bicego E, Zicari M, Bergamo Andreis IA, Zamboni G, Iacono C, Mainardi P, Valdo M, Pistolesi GF (1996) Papillary cystic neoplasm of the pancreas: radiological findings. Abdom Imaging 21:554–558
183. Schneider G, Seidel R, Altmeyer K, Remberger K, Pistorius G, Kramann B, Uder M (2001) Lymphangioma of the pancreas and the duodenal wall: MR imaging findings. Eur Radiol 11:2232–2235
184. Koenig TR, Loyer EM, Whitman GJ, Raymond AK, Charnsangavej C (2001) Cystic lymphangioma of the pancreas. Am J Roentgenol 177:1090
185. Paal E, Thompson LD, Heffess CS (1998) A clinicopathologic and immunohistochemical study of ten pancreatic lymphangiomas and a review of the literature. Cancer 1;82:2150–2158
186. Strasser G, Kutilek M, Mazal P, Schima W (2002) Mature teratoma of the pancreas: CT and MR findings. Eur Radiol 12 Suppl 4: S56–S58
187. Lee JS, Kim HS, Jung JJ, Han SW, Kim YB (2001) Ancient schwannoma of the pancreas mimicking a cystic tumor. Virchows Arch 439:697–699
188. Ligneau B, Lombard-Bohas C, Partensky C, Valette PJ, Calender A, Dumortier J, Gouysse G, Boulez J, Napoleon B, Berger F, Chayvialle JA, Scoazec JY (2001) Cystic endocrine tumors of the pancreas: clinical, radiologic, and histopathologic features in 13 cases. Am J Surg Pathol 25:752–760
189. Kosmahl M, Egawa N, Schröder S, Carneiro F, Lüttges J, Klöppel G (2002) Mucinous nonneoplastic cyst of the pancreas: a novel nonneoplastic cystic change? Mod Pathol 15:154–158

Tumors of the Mesentery and Omentum

Hoon Ji, Pablo R. Ros

4.11

Contents

Introduction

Cross-sectional imaging techniques (ultrasound (US), computed tomography (CT) and magnetic resonance imaging (MRI)) will depict abdominal lesions in the connecting folds of tissue that constitute the mesentery (including small bowel mesentery, mesocolon, mesosigmoid and mesoappendix) and omentum (including both greater omentum or epiploon) and lesser omentum or gastrohepatic ligament. All of these folds of tissue are covered by peritoneum.

Although uncommon, mesenteric/omental tumors are encountered in all age groups from infancy to the very elderly. These tumors should be considered as possible causes for a palpable abdominal mass, but they are most commonly brought into the differential diagnosis of abdominal pathology once discovered by a radiologic study. An increased awareness of both neoplastic and non-neoplastic processes resulting in mesenteric masses aids the clinical radiologist in differentiating these diseases.

Cross-sectional imaging techniques are able to clearly depict mesenteric and omental masses and determine if they are cystic or solid. To make this determination, a practical approach involving both cystic and solid patterns is used, highlighting the radiologic-pathologic features that may allow a specific diagnosis.

Cystic Masses

Once it is determined that a cystic abdominal mass arises from the mesentery or omentum rather than a solid abdominal organ, the differential diagnosis includes primary mesenteric/omental cyst, mesenteric teratoma, cystic mesothelioma, cystic spindle cell tumor (cystic leiomyoma/leiomyosarcoma), pseudomyxoma peritonei, pancreatic pseudocyst, mycobacterium avium-intracellulare (MAI) adenopathy and complicated ascites (Table 1) [1, 2].

Mesenteric/Omental Cysts

Mesenteric/omental cysts are rare: the incidence is about 1 per 140,000 general hospital admissions and about 1 per 20,000 pediatric hospital admissions [3–5]. In a study from Egleston Children's Hospital at Emory University from 1965–1994, 14 patients were treated for mesenteric or omental cysts, which represents a prevalence of about 1 case per 11,250 admissions [6]. Approximately one third of cases occur in children younger than 15 [7]. Mesenteric cysts are 4.5 times more common than omental cysts [8].

Table 1. Mesenteric/Omental Cystic Masses[a]

I.	Mesenteric/Omental Cyst
	Lymphangioma
	Enteric duplication cyst
	Enteric cyst
	Mesothelial cyst
	Nonpancreatic pseudocyst
II.	Neoplasms
	Teratoma
	Cystic mesothelioma
	Cystic spindle cell tumor (leiomyoma/leiomyosarcoma)
	Pseudomyxoma peritonei
III.	Miscellaneous
	Pancreatic pseudocyst
	MAI adenopathy
	Complicated ascites

[a] Modified from references 1 and 10

Table 2. Histologic Classification of Mesenteric/Omental Cysts[a]

Diagnosis	Histologic Features
Lymphangioma	Endothelial lining
Enteric duplication cyst	Enteric lining, double muscle layer with neural elements
Enteric cyst	Enteric lining, no muscle layer
Mesothelial cyst	Mesothelial lining
Pseudocyst (nonpancreatic)	No lining, fibrous wall

[a] From reference 3

A classification of mesenteric/omental cysts based essentially on histopathological features should include the following six groups: (1) cysts of lymphatic origin (simple lymphatic cyst and lymphangioma); (2) cysts of enteric origin (enteric cyst and enteric duplication cyst); (3) cysts of mesothelial origin (simple mesothelial cyst, benign cystic mesothelioma, and malignant cystic mesothelioma); (4) cysts of urogenital origin; (5) mature cystic teratoma (dermoid cysts), and (6) pseudocysts (infectious and traumatic cysts) (Table 2).

Lymphangioma

Lymphangioma is the most common subtype of mesenteric/omental cyst and represents a congenital malformation of the lymphatic vessels arising from the bowel [4]. Ninety-five percent of lymphangiomas are found in the neck and axilla [9]. In cases with the mesenteric/omental lymphangioma, abdominal distention with a palpable mass is the most common clinical presentation [10].

Pathologic Findings

Lymphangiomas are large, thin-walled multiloculated cystic masses lined with endothelium (Fig. 1). The contents may be chylous or hemorrhagic. Prominent stromal myxoid degeneration may occur rarely [11]. Lymphangiomas are intimally attached to the bowel wall and are the only type of mesenteric/omental cyst that routinely requires bowel resection for removal [10].

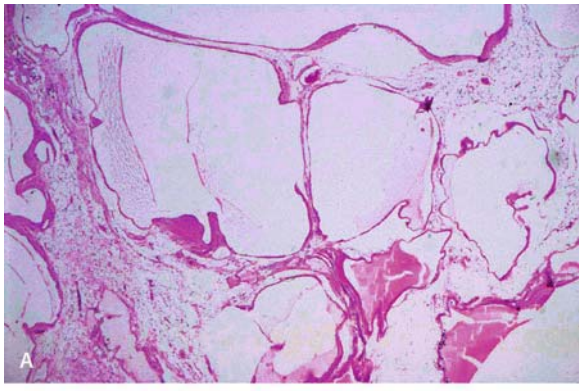

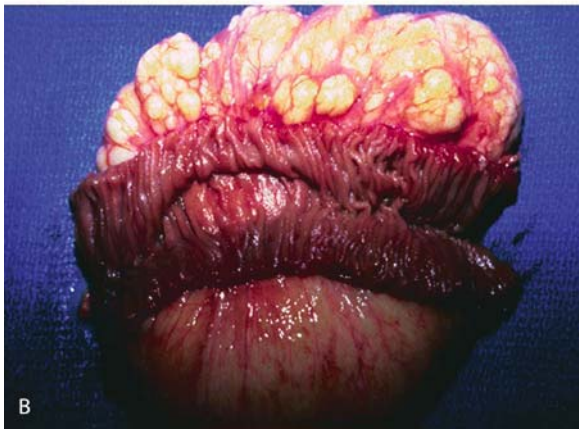

Fig. 1A, B. Lymphangioma: pathology. **A** Photomicrograph demonstrates a typical lymphangioma consisting of multiloculated cystic lesion with endothelial cell lining. **B** Resected specimen shows the large mass intimately attached to bowel

Imaging Features

Plain radiograph and barium studies may demonstrate a small bowel obstruction (frequently partial) and possibly a noncalcified soft-tissue mass or displaced bowel loops [10]. US demonstrates lymphangiomas to be anechoic, multiseptate masses (Fig. 2). On CT, they are multiloculated, frequently seen surrounding or tethered by a loop of bowel from where they originate and with Hounsfield units ranging from water (if the contents are serous) to fat (if the contents are chylous) attenuation [12]. CT allows differentiation of lymphangioma from ascites with separation of bowel loops, absence of fluid

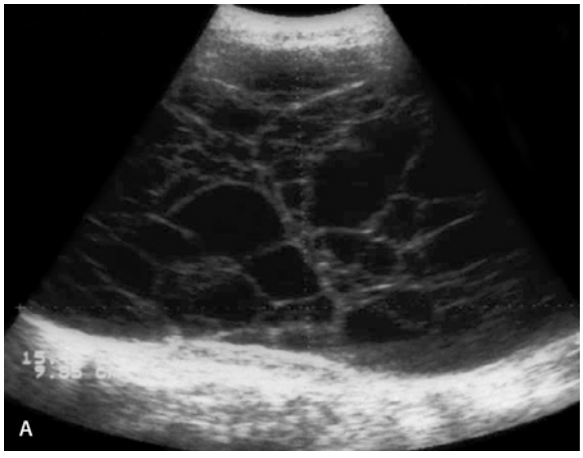

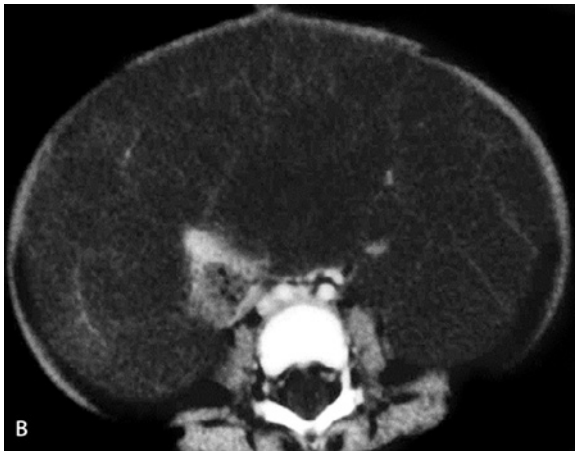

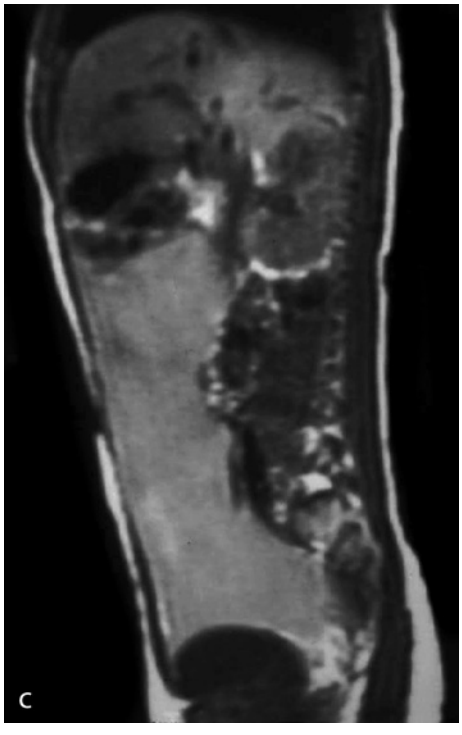

Fig. 2A–C. Lymphangioma: imaging features. **A** Ultrasonogram (US) demonstrates a large multilocular cystic mass in abdomen. **B** Enhanced CT scan of the abdomen demonstrates a multilocular cystic mass containing fluid of water attenuation. **C** T1-weighted MR image of the entire abdomen in the sagittal plane demonstrates a large mass centered in the mesentery. The high-intensity of the fluid corresponds to the fat seen in the chylous material typically contained in lymphangiomas

in the perihepatic spaces and cul-de-sac, and focal septations [13]. MRI is helpful to characterize the chylous (fatty nature) of the contents due to high signal intensity in T1-weighted images [14].

Enteric Duplication Cyst

Duplications of the alimentary tract are uncommon congenital abnormalities. When an enteric duplication (usually attached to the bowel) migrates into the mesentery, it becomes a mesenteric cyst [10]. Duplications are usually observed early in life, but a minority remains unsuspected until adulthood [15]. The clinical presentation may depend on the location of the duplication and adjacent structures, and includes abdominal distention, vomiting, bleeding, and a palpable abdominal mass. The symptoms and signs produced by duplications, however, are often vague [16]. Complications such as perforation, intussusception, volvulus, and associated malignancy may occur [17].

Pathologic Findings

Enteric duplication cysts are usually small, thick-walled and unilocular with predominantly serous contents. The wall "reduplicates" the normal wall of the bowel and contains all layers, including mucosa, circular and longitudinal muscular layers and mesenteric plexus (Fig. 3). Gastric mucosa can be present in 17%–36% of duplication cysts [18–20], and which may cause gastrointestinal bleeding.

Imaging Features

By US, enteric duplication cysts have a thick wall similar in composition to the normal bowel wall. It contains multiple layers, typically including an echogenic inner mucosal layer and a hypoechoic outer muscular layer (Fig. 4). Enteric duplication cysts containing gastric mucosa may be demonstrated with uptake of technetium-

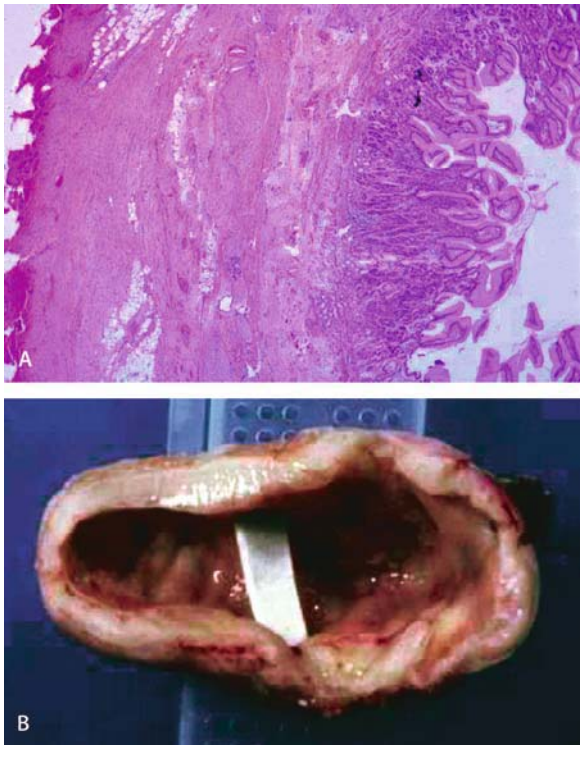

Fig. 3A, B. Enteric duplication cyst: pathology. **A** Photomicrograph demonstrates a typical enteric duplication cyst with thick wall lined by enteric epithelium. **B** Gross specimen shows a thick-walled unilocular cystic mass with serous contents

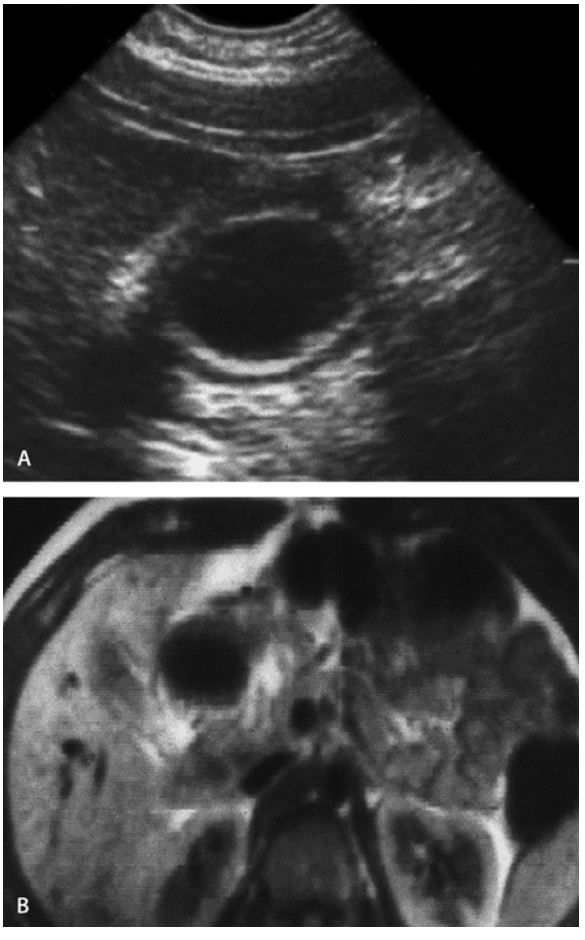

Fig. 4A, B. Enteric duplication cyst: imaging features. **A** US demonstrates a small unilocular cystic lesion with multilayered wall. **B** Axial T1-weighted MR image demonstrates a low signal intensity lesion with thick wall (*arrow*)

99m sodium pertechnetate [19]. CT and MRI reveal a cystic mass in the mesentery with a thick wall that enhances after administration of contrast material. Attenuation of the lesion on CT scans may be high due to the mucoid-rich viscous fluid within the cyst [1, 20].

Enteric Cyst

Enteric cysts are lined with enteric (gastrointestinal tract) mucosa, and have a thin fibrous wall (without reduplication of the bowel wall as in enteric duplication cysts) [10, 21]. They are usually unilocular with serous contents and a thin, smooth wall that cannot be visualized by CT or MRI [1, 10] (Fig. 5).

Mesothelial Cyst

Mesothelial cysts are the rarest type of mesenteric/omental cyst and are the result of a failure in the coalescence of the mesothelially lined peritoneal surfaces [10]. The reported incidence varies between 1 in 30,000 and 1 in 200,000 admissions [22]. Clinical presentation includes an asymptomatic abdominal mass, vague chronic abdominal complains, nausea, vomiting or diarrhea [23].

Pathologic Findings

Mesothelial cysts are thin-walled with a characteristic mesothelial lining of the inner surface (Fig. 6). Although they may occur in the mesentery, they are more common in the greater omentum and mesocolon [4, 10].

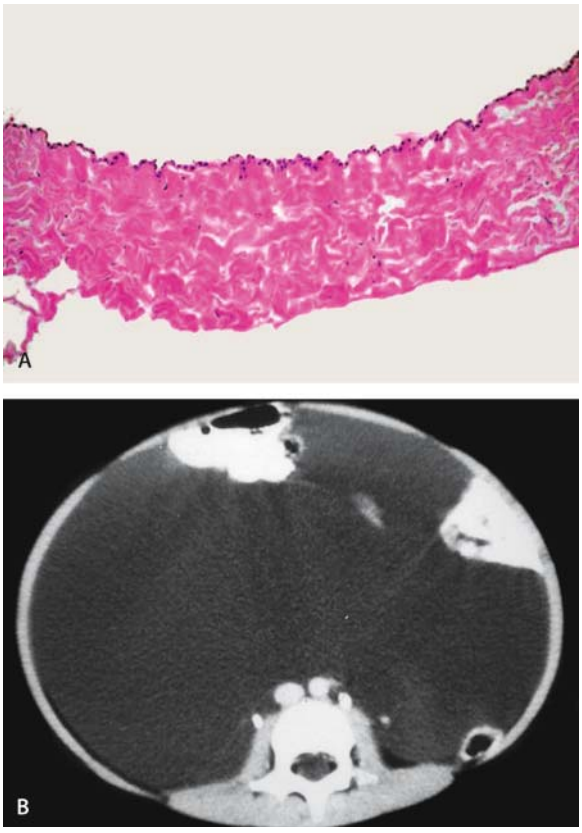

Fig. 6A, B. Mesothelial cyst. **A** Photomicrograph demonstrates a thin-walled cystic mass with mesothelial lining of the inner surface. **B** CT scan shows a large cystic mass displacing bowel loops

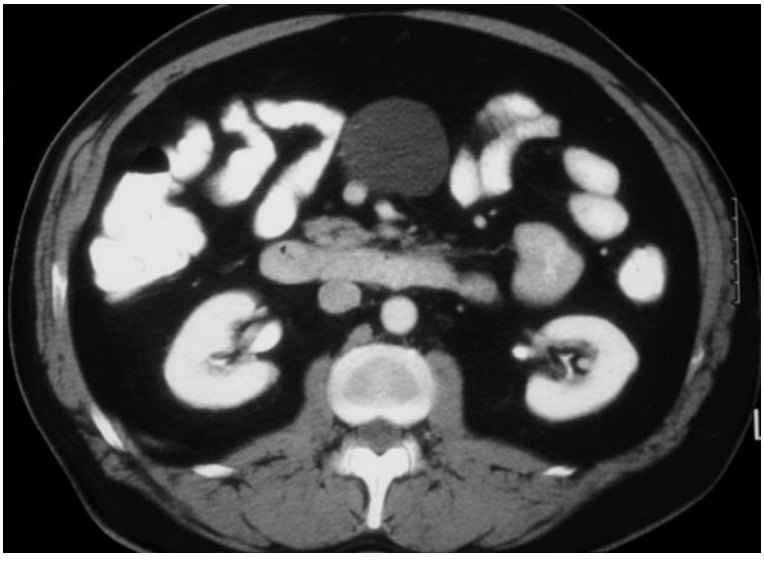

Fig. 5. Enteric cyst: CT appearance. A well-defined cystic mass with attenuation in the range of water is seen in the mesentery, near the superior mesenteric vessels. Note that the wall is not perceptible by CT

Imaging Features

US and CT demonstrate unilocular, thin-walled cystic mass (Fig. 6). They are indistinguishable radiologically from enteric cysts [1, 10, 22].

Nonpancreatic Pseudocyst

By definition, nonpancreatic pseudocysts have no inner cellular lining and are thought to be the sequelae of either a mesenteric/omental hematoma or abscess [10].

Pathologic Findings

They are thick-walled cystic masses with no lining epithelium, usually septate and contain hemorrhagic or purulent debris.

Imaging Features

Radiologically, nonpancreatic pseudocysts have a thick wall and may contain fluid-fluid levels corresponding to hemorrhagic or purulent contents [1, 10] (Fig. 7).

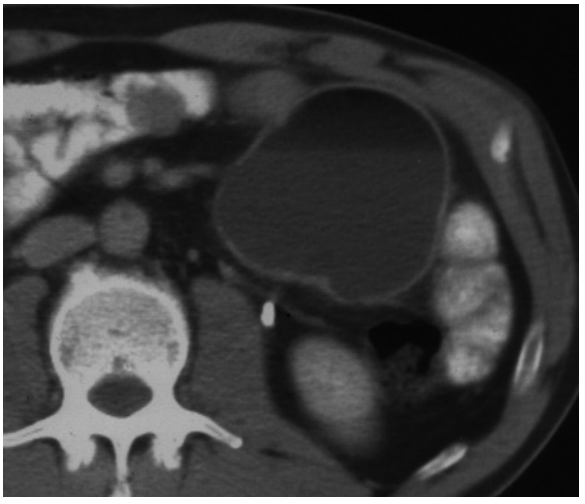

Fig. 7. Nonpancreatic pseudocyst, CT appearance. Enhanced CT of the abdomen demonstrates a thick-walled cystic mass with a fluid-fluid level, typical of pseudocyst containing hemorrhagic debris

Teratoma

This uncommon benign cystic neoplasm of the mesentery or omentum occurs primarily in infancy or childhood but rarely in adult [24–26]. Implantation of ovarian teratoma in the mesentery or omentum has been proposed for an explanation of its pathogenesis [27]. Clinical presentation is usually a palpable mass with associated manifestations, depending on its location.

Pathologic Findings

Grossly, teratomas of the mesentery/omentum are predominantly cystic with solid areas that contain fat or calcification. Histologic components include three germinal layer elements such as skin appendages, cartilage, bone, adipose tissue, and glial/glandular tissue [10, 24] (Fig. 8).

Imaging Features

Radiographically, calcifications are frequently present. Sonography reliably demonstrates the mixed cystic and solid nature of the teratoma (Fig. 9). The cystic component shows an anechoic area in the tumor. The solid

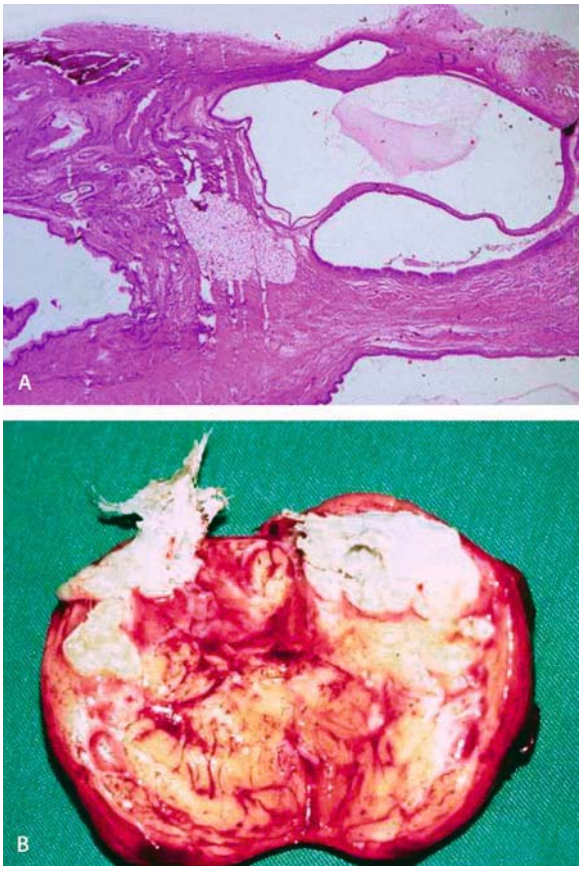

Fig. 8A, B. Mesenteric teratoma, pathologic findings. **A** Photomicrograph demonstrates a typical teratoma consisting of cartilage, skin appendages, and fat. **B** Gross specimen shows a well-demarcated cystic mass with heterogeneous internal contents

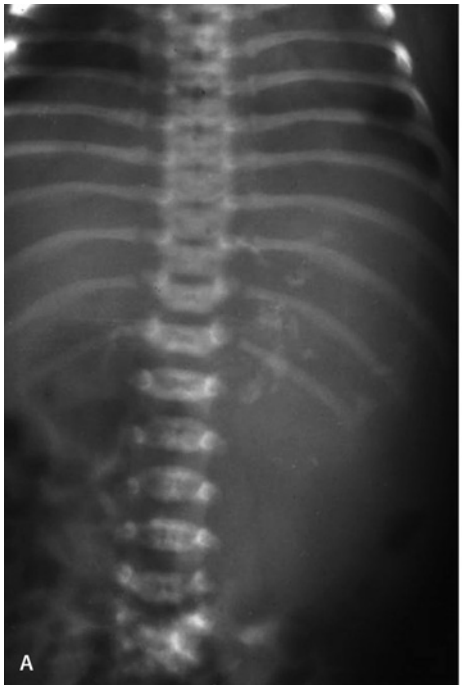

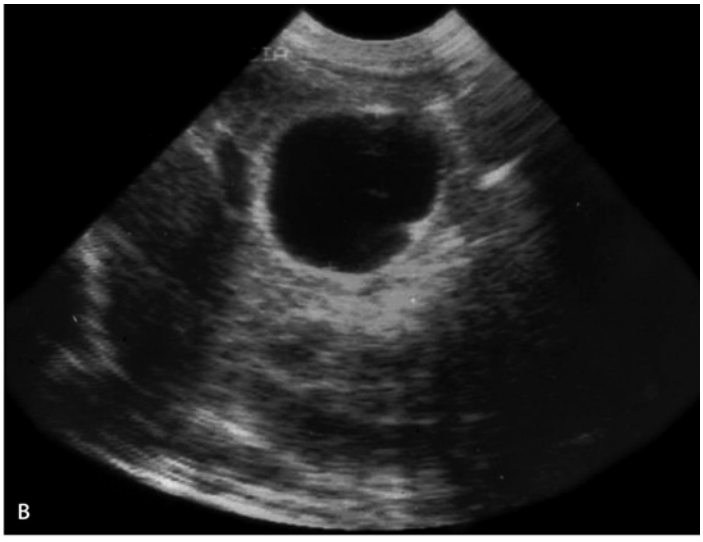

Fig. 9A, B. Mesenteric teratoma, plain film and US findings. **A** Supine film of the abdomen in an infant demonstrates multiple dystrophic calcifications in the left upper quadrant. **B** US shows a well-demarcated mass and cystic nature of the lesion

component shows homogeneous moderate-intensity echoes, and sometimes even higher echogenic areas characteristic of fat and calcification [24]. CT demonstrates a predominantly cystic tumor with attenuation in the range of water except for peripheral areas in the fat attenuation range [24, 26] (Fig. 10). Calcifications may be identifiable as well.

Cystic Mesothelioma

Cystic mesothelioma is a rare benign neoplasm of the peritoneum, unrelated to malignant peritoneal mesothelioma. Cystic mesothelioma is not a malignant mesothelioma that has undergone necrosis and cystic transformation. It is unrelated to asbestos exposure [2]. Cystic

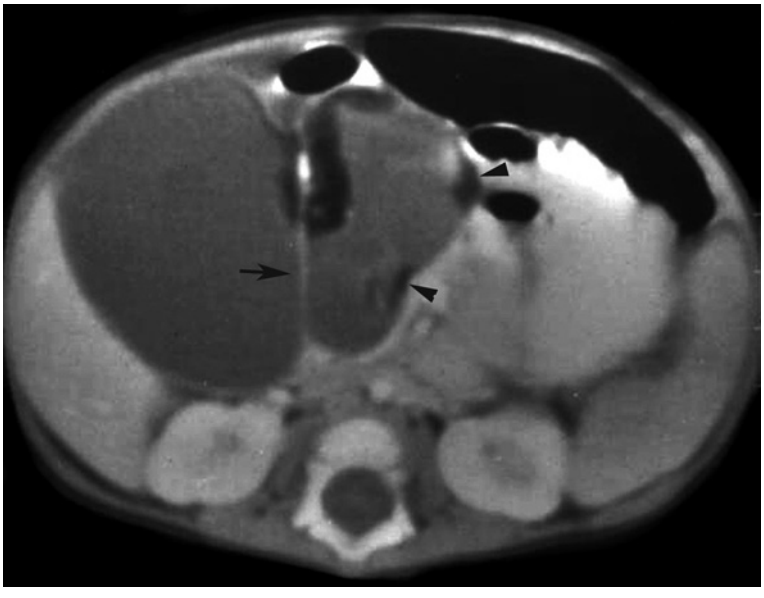

Fig. 10. Teratoma of the lesser omentum, CT appearance. A bilobed cystic mass is seen with attenuation in the range of water. A focus of calcification is seen in the central septation (*arrow*). Areas of fat are seen peripherally (*arrowheads*)

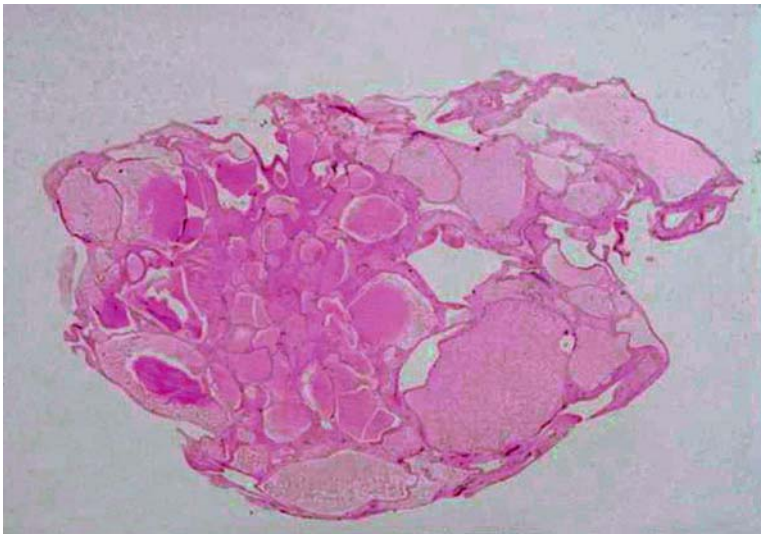

Fig. 11. Cystic mesothelioma, pathologic finding. Photomicrograph demonstrates typical findings of a cystic mesothelioma composed of mesothelium-lined cysts surrounded by a fibrovascular stroma

mesothelioma is almost always encountered in middle-aged women who present with abdominal pain and/or a palpable mass. It is considered a low-grade malignancy because it recurs locally, although generally it does not metastasize [28]. Although it may involve any peritoneal or omental surface, it is much more frequently seen in the pelvis.

Pathologic Findings

The tumor is composed of multiple cysts, ranging in size from a few millimeters (mm) to six centimeters (cm) and containing clear watery fluid. Histopathologic finding shows multiple mesothelium-lined cysts surrounded by a fibrovascular stroma [29] (Fig. 11).

Imaging Features

By ultrasound, they appear as multiloculated cystic masses, usually large. CT demonstrates a well-defined, non-calcified mass, although a few cases with calcification have been reported [30, 31]. Cystic mesothelioma compresses and surrounds bowel loops, but typically does not cause bowel obstruction (Fig. 12). MRI shows the cystic masses that have hypointensity on T1-weighted images and intermediate or hyper signal on T2-weighted images, correlating with their watery-like contents [1, 32] (Fig. 13).

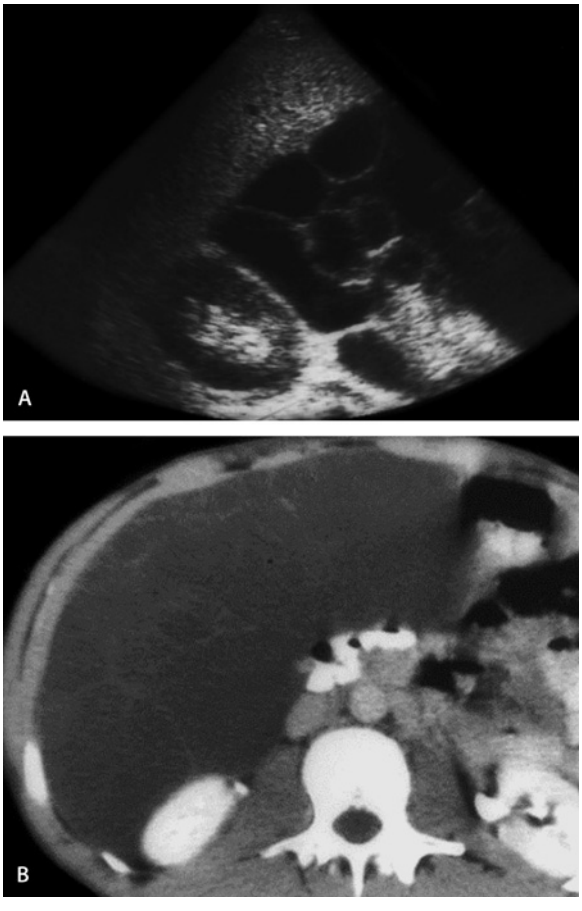

Fig. 12A, B. Cystic mesothelioma, US and CT features. **A** US of the upper abdomen demonstrates a multiple cystic mass with septations. **B** On CT scan, multiple water-density masses are seen in the abdomen, displacing loops of bowel without obstructing them

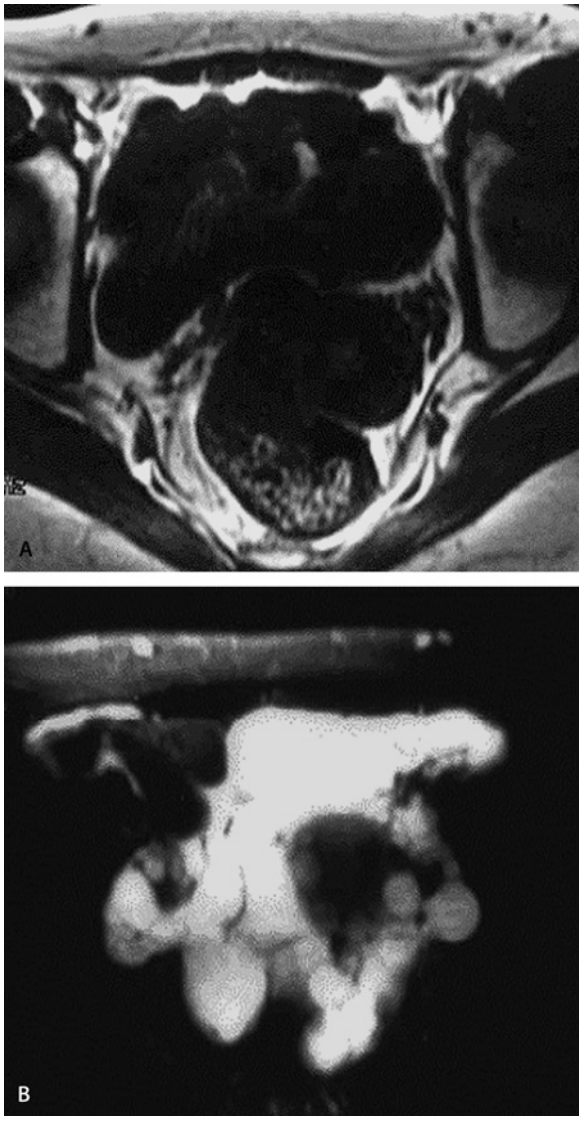

Fig. 13A, B. Cystic mesothelioma, MRI appearance. **A** T1-weighted MR image demonstrates a multilocular low signal intensity lesion in pelvic cavity. **B** T2-weighted MR image shows high signal intensity of the lesion correlating of watery contents

Cystic Spindle Cell Tumor

Spindle cell tumors in the mesentery/omentum and gastrointestinal tract (i.e., gastrointestinal stromal tumor, leiomyoma/leiomyosarcoma, schwannomas) can undergo central liquefactive necrosis and hemorrhage, appearing as complex cystic mesenteric/omental masses on US or CT [1, 33, 34].

Pathologic Findings

Grossly, cystic mesenchymal tumors are large masses with internal debris and hemorrhage. They may invade the surrounding structures such as the bowel or solid abdominal organs. Microscopic examination may reveal foci of myxoid degeneration, microcyst formation epithelioid or spindle cells with prominent cytoplasmic vacuolization. Immunohistochemical studies enable differential diagnosis of subsets of mesenchymal tumors [34, 35].

Imaging Features

US demonstrates a complex mass with large amounts of internal echoes [33] (Fig. 14). By CT, the mass has a low-attenuation central zone surrounded by irregular walls

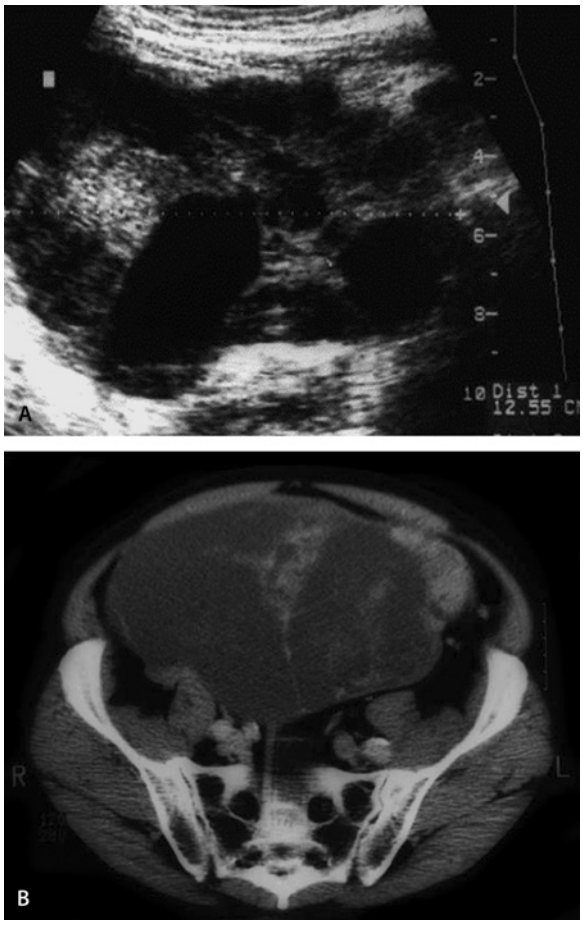

Fig. 14A, B. Cystic spindle cell tumor (leiomyosarcoma), imaging features. **A** US demonstrates a large complex cystic mass with heterogeneous internal echoes. **B** Axial CT scan shows a large, well-defined cystic mass with solid portion, corresponding to viable portions of the tumor

and a high-attenuation peripheral rim, corresponding to viable tumor [1, 34, 36].

Pseudomyxoma Peritonei

Pseudomyxoma peritonei is defined as massive and diffuse involvement of the peritoneal cavity by a low-grade metastatic mucinous adenocarcinoma originating in the ovary, appendix, or colon. It is most common in women aged between 50–70 [37]. Clinically the main complaints of pseudomyxoma include abdominal pain, abdominal distention, partial bowel obstruction, and fistula formation [38].

Pathologic Findings

Typically pseudomyxoma peritonei manifests as multiple discrete nodules containing mucin on the peritoneum (Fig. 15). It may have solid and hemorrhagic areas and septal calcifications. Microscopically pseudomyxoma nodules are characterized by multifocal pools of mucin with scant strips of mucinous epithelium or varying proportion of glandular and signet ring cell components [1, 2].

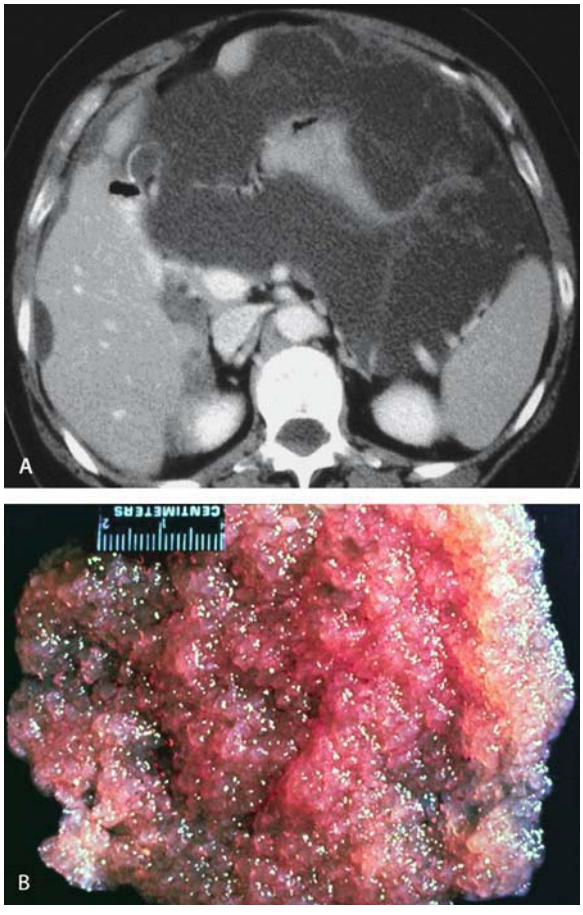

Fig. 15A, B. Pseudomyxoma peritonei. **A** Enhanced CT scan of the abdomen demonstrates multiple cystic masses encasing the stomach and producing scalloping of the liver. **B** Gross specimen shows the multiple discrete nodules containing mucin on the peritoneum

Imaging Features

Ultrasonography is useful to detect hypoechoic cysts or ascites with scalloping of hepatic or splenic margins due to extrinsic pressure of adjacent peritoneal implants [39]. CT scans demonstrates myxomatous tumor collections that are of low attenuation (Fig. 15). Areas of high attenuation or solid component can be seen within it. Calcifications may also be present. Pseudomyxoma peritonei may mimic ascites, but it should not be confused with the latter, Pseudomyxoma peritonei, unlike ascites, produces scalloping of the liver and spleen, as well as encasement with displacement of the gastrointestinal tract [2, 38]. Spread of mucinous material to the pleural cavity may occur, presumably through the congenital pleuroperitoneal communication [40]. MRI may be useful in assessment of small bowel obstruction in patients with pseudomyxoma peritonei [41].

Miscellaneous Cystic Mesenteric/ Omental Lesions

Pancreatic Pseudocyst

Pancreatic pseudocysts are common cystic masses, sequelae of acute pancreatitis. The clinical history, laboratory findings and classic CT appearance are usually diagnostic of this entity.

Mycobacterium avium-intracellulare Adenopathy

Mesenteric adenopathy may have marked low attenuation by CT, mimicking the appearance of multiple cystic masses, such as those caused by infection with *Mycobacterium avium-intracellulare* (MAI) [42].

Pathologic Findings

Multiple conglomerated nodular masses are found in the mesentery and/or omentum, often adherent to bowel and other solid organs. Cross-sectional specimens show that caseous or liquefactive substances in the center of the enlarged lymph nodes are surrounded by inflammatory lymphatic tissue and preserved blood vessels [43].

Imaging Features

MAI lymphadenopathy has extremely low attenuation by CT with an enhancing rim [44]. The anatomic distribution and specific enhancement patterns of lymphadenopathy seen on contrast-enhanced CT or MRI can be useful in differentiating between tuberculosis and untreated lymphomas of the abdominal lymph nodes [44, 45] (Fig. 16). Enlarged lymph nodes with a low-attenuation center can also be seen in pyogenic infection and Whipple's disease [44, 46].

Complicated Ascites

Complicated ascites (hemorrhagic or infected) will appear as a multiseptate pseudomass mimicking a lymphangioma or cystic mesothelioma (Fig. 17).

Solid Masses

While the cystic masses involving the mesentery and omentum are mainly benign (teratoma, mesenteric cyst) or malignant with low-aggressiveness (cystic mesothelioma), solid masses are overtly malignant (mesothelioma, leiomyosarcoma) or characterized by highly aggressive behavior (fibromatosis). There is a wide range of solid masses involving the mesentery and omentum [47] (Table 3).

Infectious Diseases

Tuberculosis

In the developing world, tuberculosis continues to be an endemia, while in the West it has experienced a recent

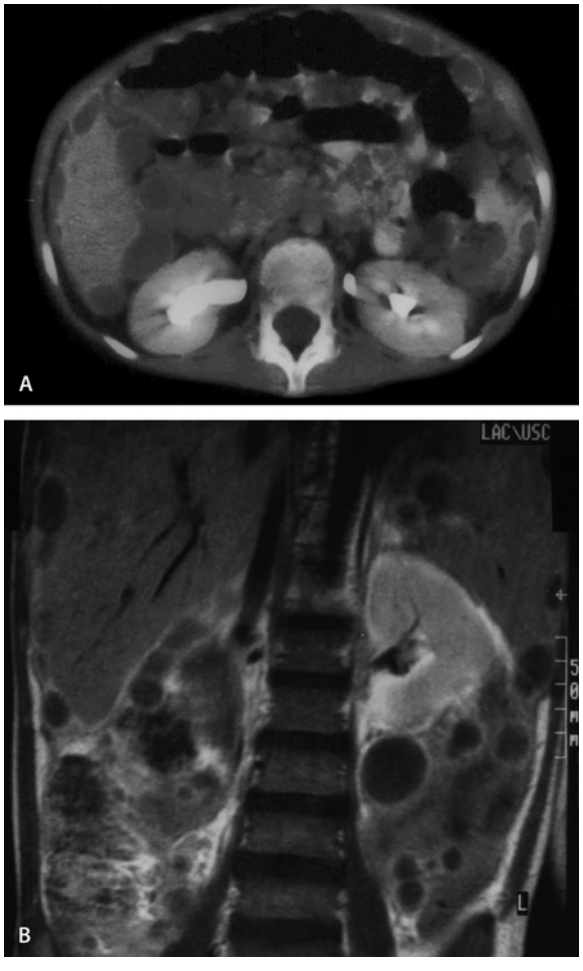

Fig. 16A, B. MAI mesenteric lymphadenopathy. **A** CT scan and **B** T1-weighted MR image of a patient with HIV and MAI infection show multiple well-circumscribed, almost cystic-appearing masses with enhancing rims

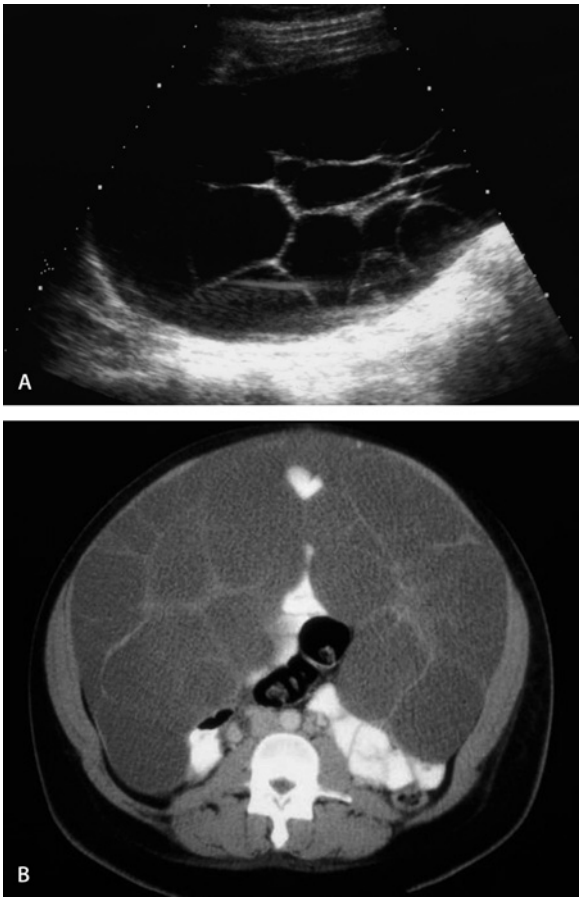

Fig. 17A, B. Infected ascites mimicking a multiseptate mass. **A** US and **B** CT scan demonstrate multi-septate cystic lesions that proved to be infected ascites

Table 3. Mesenteric/Omental Solid Masses[a]

I.	Infectious Diseases
	Tuberculosis
II.	Neoplasms
	Primary benign tumors
	– Lipoma
	– Neural tumors (neurofibroma, schwannoma, paraganglioma, ganglioneuroma)
	Primary malignant tumors
	– Malignant mesothelioma
	– Malignant fibrous histiocytoma
	– Spindle cell tumors (leiomyoma/leiomyosarcoma)
	– Liposarcoma
	Secondary tumors
	– Peritoneal carcinomatosis
	– Mesentery/omental metastases (carcinoid tumor)
	– Lymphoma
III.	Miscellaneous
	Fibrosing mesenteritis
	Fibromatosis or desmoid tumor
	Castleman's disease
	Splenosis

[a] Modified from [2] and [47]

resurgence. The increased incidence of tuberculosis has been attributed to several causes, including the AIDS epidemic, intravenous drug abuse, and increased immunocompromised patients [48].

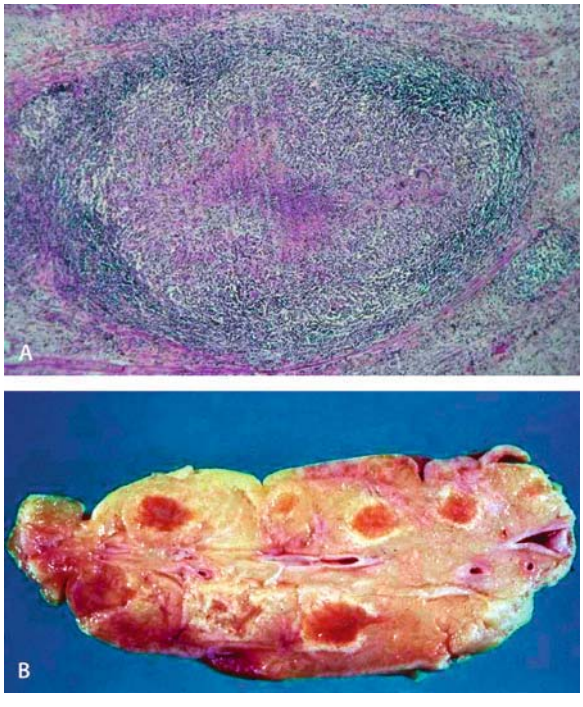

Fig. 18A, B. Tuberculosis: pathologic findings. **A** Microscopic finding of a tuberculous nodule demonstrates an inflammatory granuloma with typical caseous necrosis in the center. **B** Gross specimen shows multiple indurated nodules in the omentum

Mesenteric/omental tuberculosis occurs most frequently in immunocompromised patients. Tuberculosis within the abdomen can potentially infect all abdominal organs. Possible mechanisms in development of abdominal tuberculosis include hematogenous or lymphatic dissemination from a distant focus, usually in the lung, and ingestion of infected milk or sputum [49].

Pathologic Findings

The causative organism is usually *M. tuberculosis hominis*, or atypical mycobacteria (*M. avium-intracellulare*). As elsewhere in the body, tuberculosis in the abdomen forms granulomas with typical caseous necrosis (Fig. 18). These may present clinically as ulcers or masses (tuberculoma).

Grossly, tuberculous granulomas aggregate to confluent masses, replacing the fat in the greater omentum and forming the so-called "omental cake pattern" [50].

Imaging Features

Abdominal tuberculosis may mimic a large variety of conditions such as lymphoma, inflammatory bowel diseases, or other gastrointestinal tumors. Lymphadenopathy in mesentery or omentum is a common manifestation of abdominal tuberculosis.

CT demonstrates mesenteric and omental tuberculous masses with replacement of the normal fat by enhancing, high-attenuation masses that may contain small islands of normal fat (Fig. 19). Tuberculous adenopathy is often identified in the mesentery. Contrast enhanced CT most commonly demonstrates peripherally enhancing lymph nodes with low-density centers reflecting the usual findings of a peripheral inflammatory reaction and central caseous necrosis [40, 48, 49].

On MRI, tuberculous adenopathy shows T1 iso- or hypointensity and central T2 hyperintensity [45] (Fig. 16). Similar patterns, however, may be seen with metastases of malignant neoplasms, Whipple's disease, and lymphoma [46, 51].

Tuberculous peritonitis is the most common presentation of abdominal tuberculosis. The several patterns of tuberculous peritonitis are described: wet, fibrotic, and dry types. The wet type, characterized by large amounts of free or loculated viscus fluid, is most common. CT demonstrates the nonspecific appearance of ascitic fluid with high Hounsfield units (25–45 HU) [52] (Fig. 20). The fibrotic-fixed type is less common and characterized by omental masses, matted and tethered bowel loops and mesentery. The dry type is unusual and characterized by caseous nodules, fibrous calcified or noncalcified peritoneal reaction, and dense adhesions. Similar peritoneal features may occur with carcinomat-

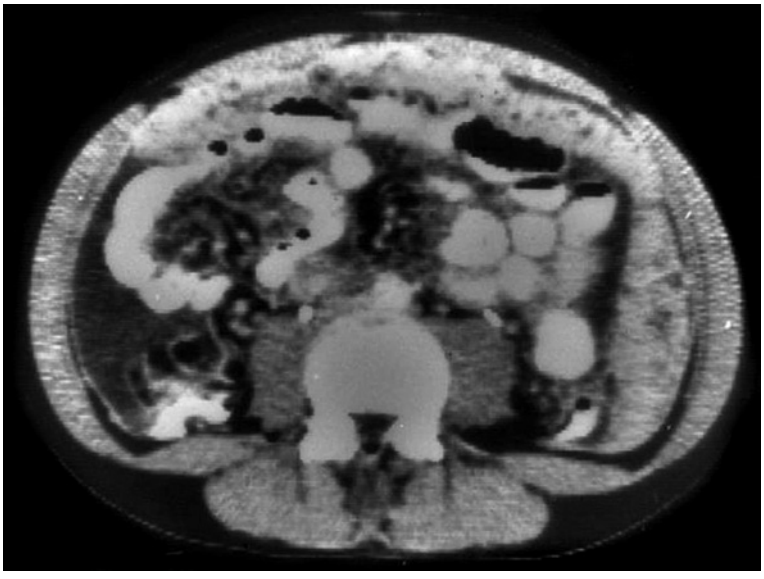

Fig. 19. Tuberculosis. Axial CT scan demonstrates mesenteric and omental high-attenuation masses that may contain small islands of normal fat

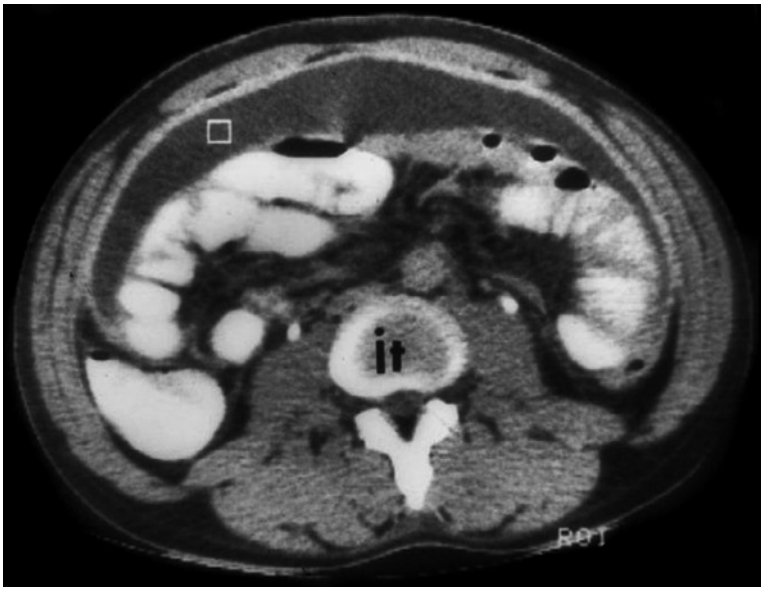

Fig. 20. Tuberculous peritonitis. Contrast-enhanced CT scan of abdomen shows nonspecific ascitic fluid with high Hounsfield units. Note the enhancement of thickened peritoneum

osis, mesothelioma, and non-tuberculous peritonitis. Although there are occasionally difficulties of a differential diagnosis, a high degree of clinical suspicion and the imaging features may allow early diagnosis of mesenteric and omental tuberculosis.

Neoplasms

Lipoma, liposarcoma

Lipoma/liposarcoma arises from adipose tissue and is the most common soft tissue tumor. While in the retroperitoneum liposarcomas are the most common neoplasms, in the mesentery lipomas are much more common. Lipoma is the second most frequent mesenteric primary tumor after fibromatosis [2].

Pathologic Findings

Histologically, liposarcomas are classified as well-differentiated, myxoid, pleomorphic, and round-cell subtypes. Prognosis for patients with liposarcoma varies on the basis of the histologic subtype [53, 54].

Imaging Features

Although the site of origin cannot be determined before surgery, the diagnosis of lipoma is made relatively easily with US, CT, or MRI. Well-differentiated liposarcomas can have two subtypes: fatty or lipoma-like and fibrous or sclerosing liposarcoma. Lipoma and lipoma-like liposarcoma demonstrate a well-defined mass, with negative attenuation values on CT images or with hyperintensity in T1-weighted MR images. It may be impossible to differentiate this type of liposarcoma from benign lipoma, although internal septations are unusual for lipoma [55]. The sclerosing type of liposarcoma demonstrates the CT attenuation or MR signal intensity that approximate the characteristics of muscle, and enhances homogeneously on contrast enhanced CT or MR images. Less differentiated liposarcomas have myxoid and pleomorphic subtypes. Myxoid components show CT attenuation and MR signal intensity similar to that of water. After contrast enhancement, gradual reticular enhancement can be seen within the myxoid components. Some areas of myxoid liposarcoma may enhance markedly. Pleomorphic components show similar attenuation than muscle on CT images and signal intensity on T1-weighted MR images (Fig. 21). On T2-weighted MR images, however, they have signal intensity equal to that of fat (Fig. 22). Thus the pleomorphic component differs from the sclerosing component in MR signal intensity.

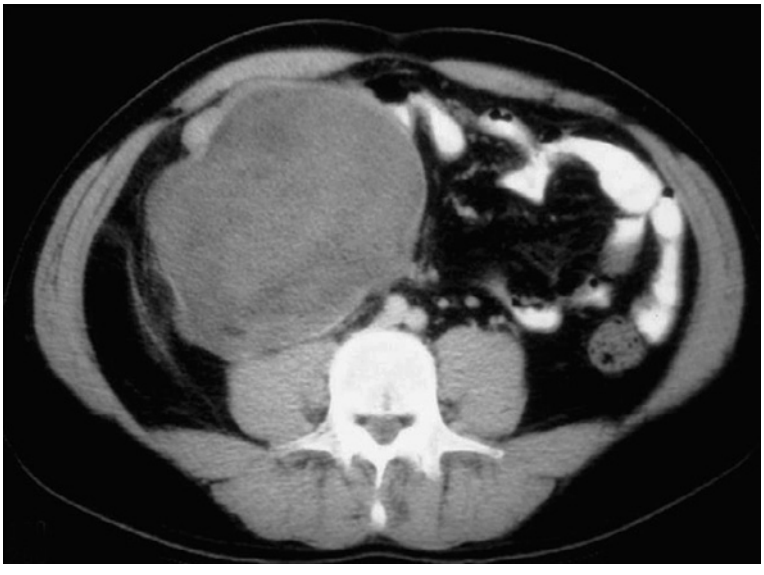

Fig. 21. Pleomorphic liposarcoma. Axial CT scan demonstrates a large mesenteric mass with mainly solid in density

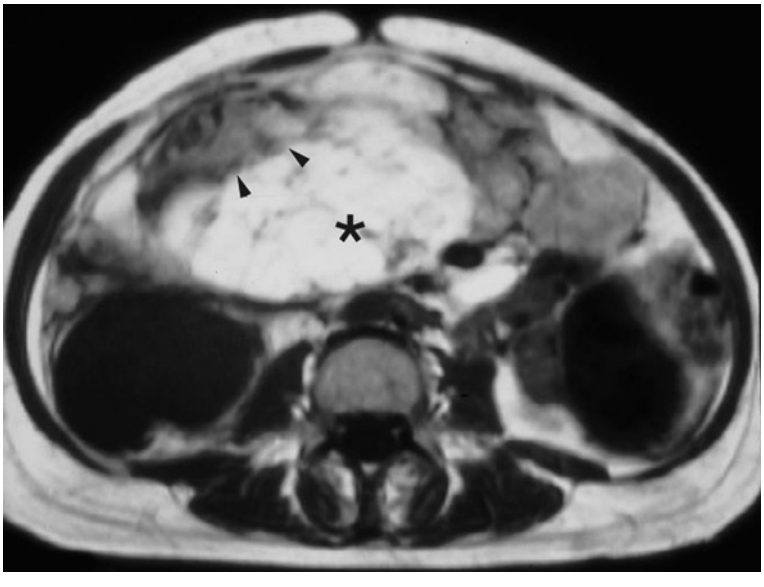

Fig. 22. Liposarcoma, MRI appearance. T1-weighted spin-echo image demonstrates a large mass in the mesentery with predominantly high signal intensity (*). There are peripheral components of lower signal intensity corresponding to areas with sarcomatous contents (*arrowheads*). Note multiple fibrous septa

The round-cell type liposarcoma demonstrates similar attenuation and signal intensity to that of muscle. It appears heterogeneous, while the sclerosing component is relatively homogeneous on contrast-enhanced CT images [54].

The combination of two or more histologic components in a tumor occurs commonly and results in the combined characteristics of the individual subtypes.

Neural Tumors (Neurofibroma, Schwannoma)

Most benign nerve sheath tumors are either schwannoma or neurofibroma [56]. Schwannoma arises from Schwann cell of the peripheral nerve sheaths. Schwannoma is a slow-growing benign tumor with favorable prognosis. It occurs without sex predominance in the 30–60-year age group [57]. They generally occur as a solitary mass located in the deep soft-tissue commonly in the head and neck, mediastinum, retroperitoneum, pelvis, presacral location or in an extremity [58]. The patient presents with a slowly expanding mass that may or may not be symptomatic, depending on its location.

Neurofibroma is a benign neoplasm consisting of fibroblasts, Schwann cells and nerve's elements that expand and diffusely infiltrate the nerve. Neurofibromas may appear sporadically, or in patients with neurofibromatosis without a sex predilection. They rarely can degenerate into a neurofibrosarcoma.

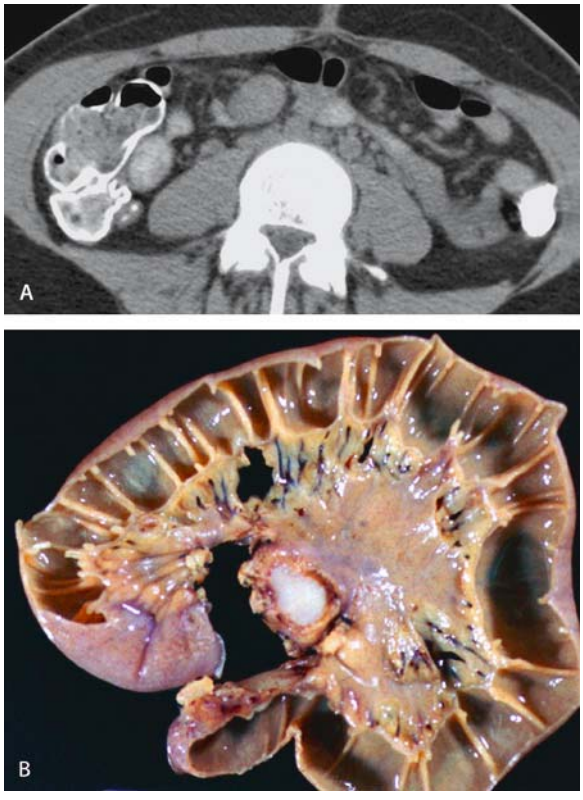

Fig. 23A, B. Schwannoma. **A** Axial CT scan demonstrates a small well-circumscribed, homogeneous soft tissue mass in the mesentery. **B** Cut section of resected specimen shows whitish mass with no necrosis

Pathologic Findings

Schwannomas are composed of Antoni type A (cellular pattern) and B (sparsely cellular pattern) areas. These lesions begin as solid tumors but as they become larger, they undergo spontaneous degeneration with areas of hemorrhage and cystic changes.

Typically in the abdomen, neurofibromas are massive and plexiform (involving multiple continuous nerves), or forming discrete masses along the same nerve. They are gelatinous in consistence and homogeneous in composition.

Imaging Features

On CT they appear as well-circumscribed masses. Although the presence of calcification on histology is common, on CT calcification is not usually evident (Fig. 23). The majority of these tumors are hypervascular, showing an intense contrast enhancement. Schwannomas are often heterogeneous and are generally isointense to muscle on T1-weighted images and hyperintense on T2-weighted images. The presence of a low-signal capsule is more suggestive of a schwannoma than of a neurofibroma [59].

On CT, neurofibromas appear of low-density because of their myxoid matrix. They displace vessels and involve the root of the mesentery without producing bowel obstruction or biliary dilatation (Fig. 24). Simple neurofibromas are usually smooth, well-demarcated, homogeneous, hypodense masses relative to muscle. They enhance homogeneously with contrast material. Low CT density less than muscle is related to the high lipid and water content in the mucinous matrix, entrapment of perineural adipose tissue, and cystic degeneration [57].

On MRI a target pattern with peripheral hyperintense rim and central low intensity has been described in 50% of peripheral nerve sheath tumors but this distinguishing feature is unlikely to be present in schwannomas due to degenerative changes [60–62]. The high T2 signal, enhanced peripheral component of the tumor represents myxomatous tissue, whereas the central low T2 signal, hypovascular area represents fibrous and collagenous material [62] (Fig. 25). This zonal pattern does not correlate histologically with the proportion of Antoni-A and Antoni-B type tissue present [63].

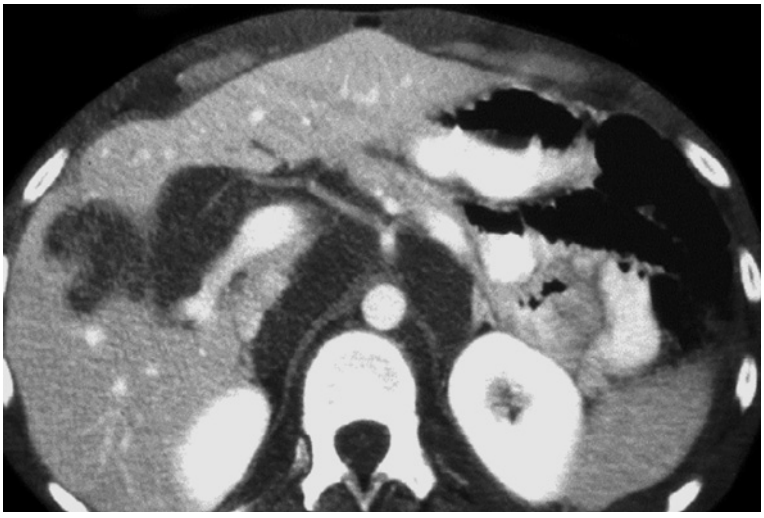

Fig. 24. Neurofibroma. Contrast enhanced CT scan demonstrates low attenuation mass involving mesenteric root and porta hepatis

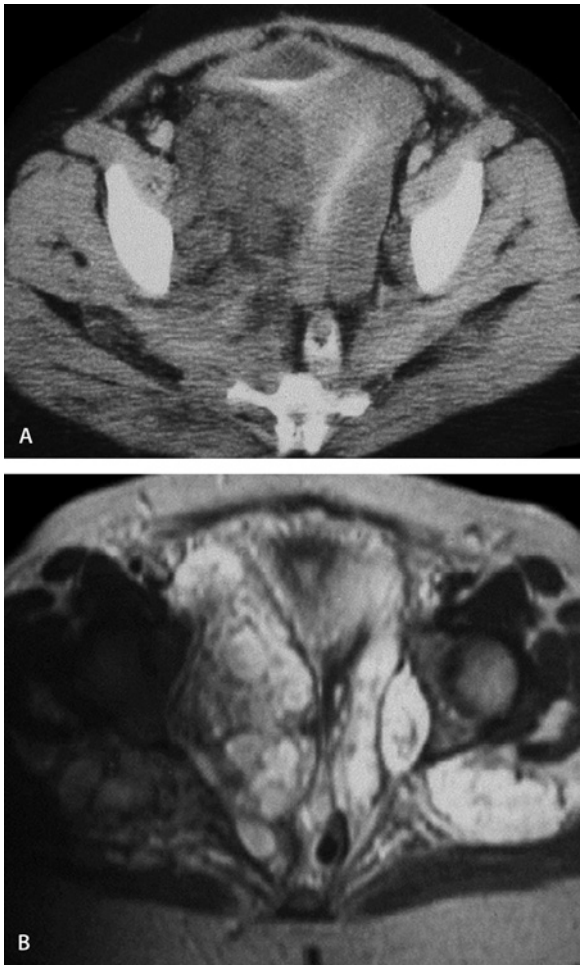

Fig. 25A, B. Neurofibroma, MRI appearance. **A** Axial CT shows low attenuation soft tissue mass in right pelvic cavity. **B** T2-weighted MR image demonstrates the high signal intensity of the lesion due to myxoid component

Malignant Mesothelioma

Malignant mesothelioma is the primary malignancy of the peritoneum. While the majority originate in the pleura, 25% of cases arise in the peritoneum. The association of asbestos exposure is higher with peritoneal than with pleural mesothelioma. The prognosis is extremely poor. It presents usually in men with a history of prior asbestos exposure.

Pathologic Findings and Imaging Features

Three different types of peritoneal malignant mesothelioma are recognized histologically with different growth patterns and radiological appearance: (1) carcinomatous, (2) sarcomatous, and (3) biphasic or mixed. The carcinomatous type appears as diffuse thickening of the peritoneum with small nodular plaques in the mesentery, producing crowning, fixation and diffuse thickening of the small bowel (Fig. 26). Both parietal and visceral peritoneum are involved. Sarcomatous, peritoneal mesothelioma presents as a large encapsulated mass, similar in appearance to spindle cell tumors (leiomyoma/leiomyosarcoma) (Fig. 27). The biphasic or mixed type presents as both a band of tissue involving the peritoneal surfaces and masses. Regardless of the histological subtype, pleural plaques and calcification due to asbestos exposure can be present in approximately 70% of cases [64] (Fig. 27). Gadolinium enhanced breath hold fat-saturated MRI may reveal more peritoneal tumors than CT, especially when ascites is present.

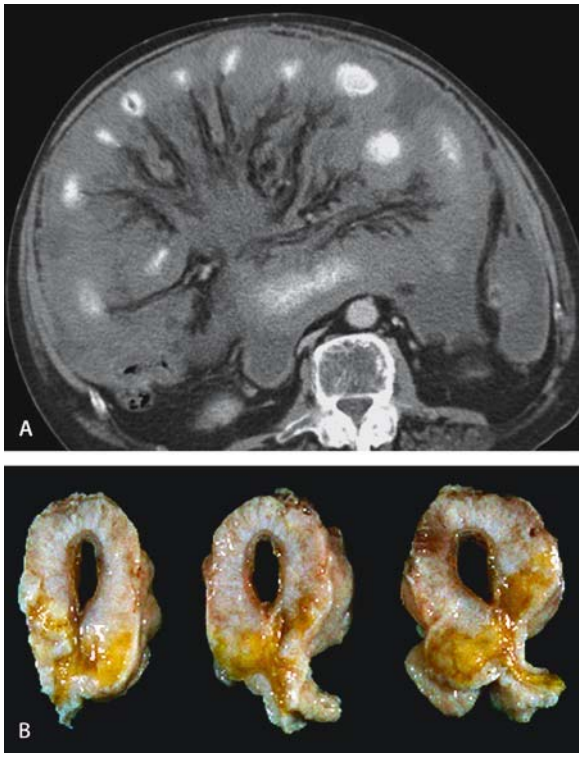

Fig. 26A, B. Malignant mesothelioma (carcinomatous form). **A** CT scan demonstrates thickening of both parietal and visceral peritoneum. Note how mesothelioma surrounds multiple loops of bowel and extends into the mesentery. **B** Cut sections of the specimen show the diffuse tumor infiltration and bowel wall thickening

Malignant Fibrous Histiocytoma

Malignant fibrous histiocytoma (MFH) is one of the most common sarcomas appearing in late adult life. Typically it appears in the fifth and sixth decades of life. It frequently occurs in the soft tissue of the extremities, the retroperitoneum and in the bone [65–69]. Despite this ubiquity, involvement of the peritoneal cavity is uncommon.

Pathologic Findings

MFH is typically manifested as a broad range of histopathological appearances and is currently classified into four subtypes: storiform-pleomorphic, myxoid, giant cell, and inflammatory. Microscopically MFH consists of areas of spindle cells arranged in a storiform pattern, and pleomorphic areas with haphazardly arranged sheets of fibroblasts and histiocytes [66, 67]. Calcification is common [68–71].

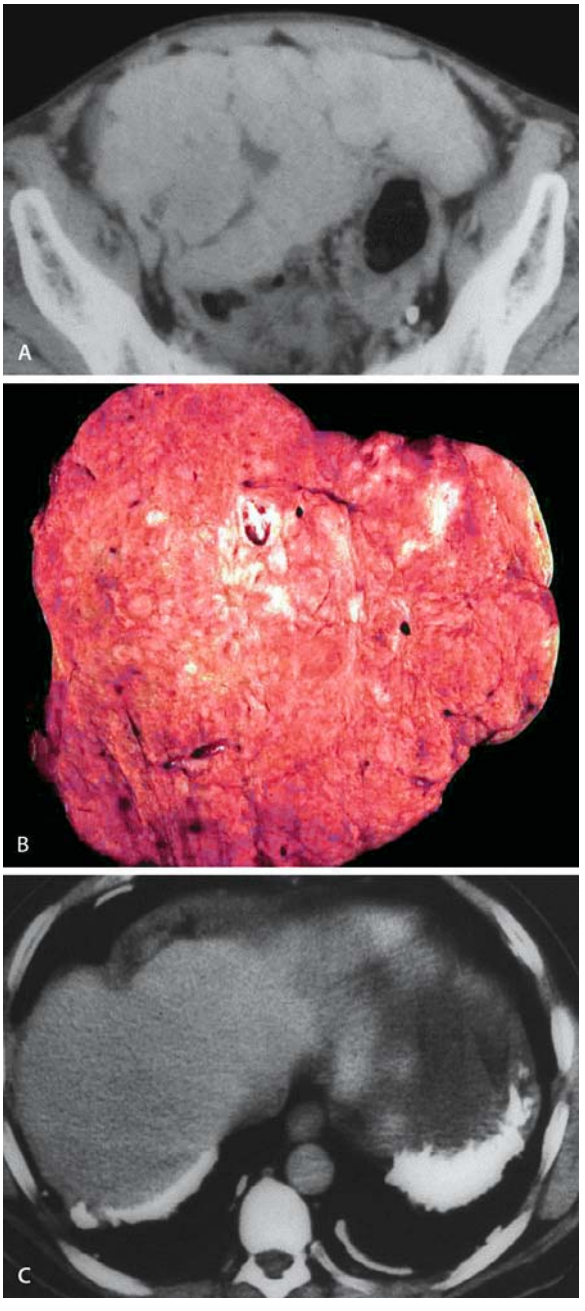

Fig. 27A–C. Malignant mesothelioma (sarcomatoid form). **A** Axial CT scan and **B** resected specimen demonstrate large mass with similar imaging features to stromal cell tumor. **C** CT shows pleural calcification plaque suggestive of asbestos exposure

Imaging Features

Imaging features of MFH are nonspecific and most examples of MFH appear as heterogeneous solid masses with areas of necrosis [68–71]. A variety of patterns have been reported on ultrasound, including hypoechoic, mixed (due to tumor necrosis) or predominantly an-

echoic with thick septa. MFH generally presents as a hypoechoic or heteroechoic solid mass [69, 70].

On CT, MFH typically presents as a poorly marginated or well-circumscribed mass, with a density similar to or slightly less than that of normal muscle and with hypodense areas due to necrosis [68–71]. Eccentrically located lumpy and ring-like calcifications due to osteoid and chondroid metaplasia have been reported on CT in 16% of abdominal MFH [71]. Tumor invasion of contiguous organs are common [68]. Occasionally MFH with extensive necrosis may be manifested as a cystic tumor [72, 73]. Extensive intratumoral hemorrhage may occur, creating a cyst-like tumor that may be confused with hematoma [67, 74].

MRI demonstrates the tumor usually of intermediate to low signal intensity on T1-weighted images. With T2-weighted images, the tumors tend to be of high signal intensity, although often quite inhomogeneous centrally [75].

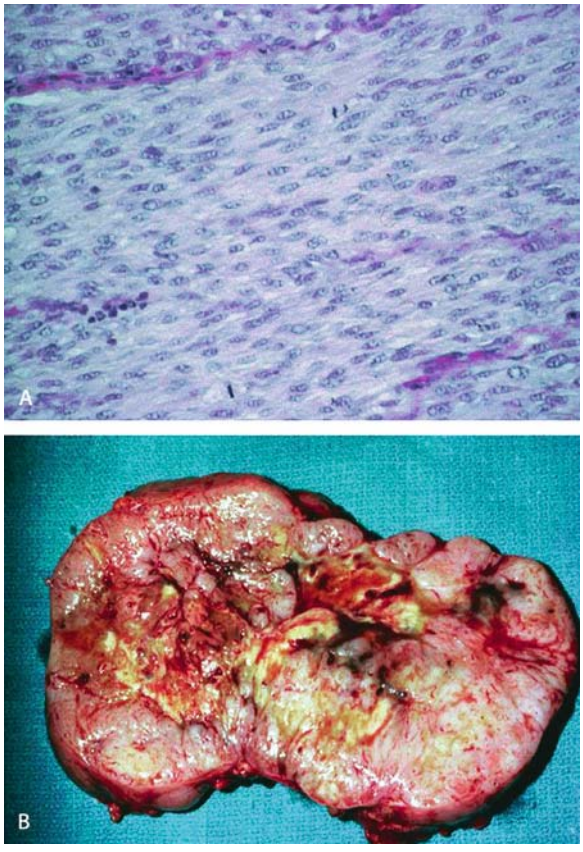

Fig. 28A, B. Spindle cell tumor (leiomyosarcoma): pathology. **A** Photomicrograph demonstrates tumors with spindle cells in bundles. **B** Gross specimen shows a large solid mass lesion with multiple cystic spaces suggesting central necrosis

Spindle Cell Tumor (Leiomyoma/Leiomyosarcoma)

Spindle cell tumor or smooth muscle tumor are preferred terms for mesenteric/omental leiomyoma/leiomyosarcoma. Leiomyosarcoma is more common in the mesentery than leiomyoma [76].

Pathologic Findings

Grossly, spindle cell tumors usually have central areas of necrosis, adenoma and hemorrhage (Fig. 28). Leiomyosarcomas are usually large, with invasion of surrounding structures. They often contain no fat or calcification [77, 78].

Imaging Features

By US and CT, leiomyosarcomas usually appear as large and heterogeneous masses. They are predominantly

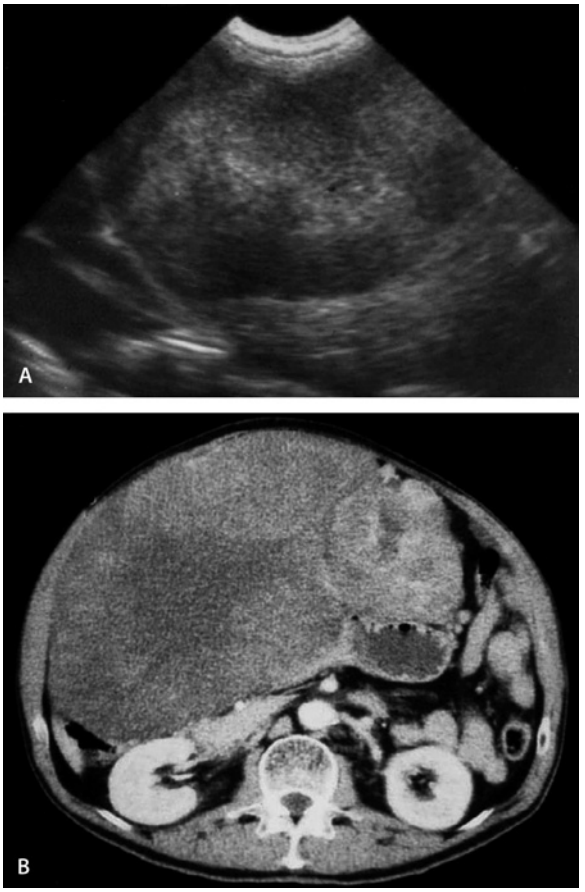

Fig. 29A, B. Spindle cell tumor (leiomyosarcoma). **A** Ultrasonogram and **B** contrast enhanced CT scan demonstrate a huge solid mass with heterogeneous center

solid with internal cystic spaces, correlating with areas of necrosis grossly [79] (Fig. 29).

On MRI the mass is usually heterogeneous with low to intermediate signal intensity on T1-weighted images and with intermediate to high signal intensity on T2-weighted images. Intratumoral necrosis is evident as a high intensity central zone on T2-weighed images, without enhancement [77, 78].

Lymphoma, Metastasis

Peritoneal carcinomatosis, carcinoid metastases and lymphoma are three common secondary malignancies that may involve the mesentery and omentum.

Primary mesenteric lymphoma, usually non-Hodgkin lymphoma, is a disease of the mesenteric lymph nodes that may appear as a localized process or a component of a more disseminated pattern of disease. A few cases of mesenteric lymphomas observed in association with AIDS, immune thrombocytopenia, and dermatitis herpetiformis have been reported [80]. The clinical presentation of mesenteric lymphoma is much like that of other mesenteric tumors, with abdominal pain and a palpable mass as the principal findings.

The vast majority of metastatic lesions of the mesentery consist of mesenteric lymph nodes that have become secondarily involved in a neoplastic process of the tubular gastrointestinal tract. Distinguishing this pattern of tumor growth from primary mesenteric tumors usually presents no difficulty because the gastrointestinal primary tumor is usually readily identifiable.

Pathologic Findings

The appearance is variable, with lymphoma and carcinomatosis frequently appearing as multiple masses with variable degrees of involvement and carcinoid metastases seen typically as a mesenteric mass producing kinking and retraction of adjacent bowel loops and with frequent calcification [81]. This is due to the notable desmoplastic reaction seen with carcinoid tumors.

Imaging Features

CT is the preferred imaging modality for evaluation of the mesentery in patients presenting with lymphoma. With lymphoma, bulky paraaortic lymphadenopathy is common (Fig. 30). Enlarged lymph nodes may appear as discrete masses or as confluent soft tissue obliterating the mesenteric fat, resulting in loss of definition of fat planes between the other organs. Many other lymph node groups, such as retrocrural, gastrohepatic, paraceliac, periportal, peripancreatic, posterior iliac crest, and pelvic chains are frequently involved [82]. CT scans can characterize the lesion from the standpoint of size and mesenteric location and can raise the probability of the lymphoma diagnosis [83].

Carcinoid metastases are seen typically as mesenteric masses producing kinking and retraction of adjacent bowel loops and with frequent calcification [81]. This is due to the notable desmoplastic reaction seen with carcinoid tumors (Fig. 31).

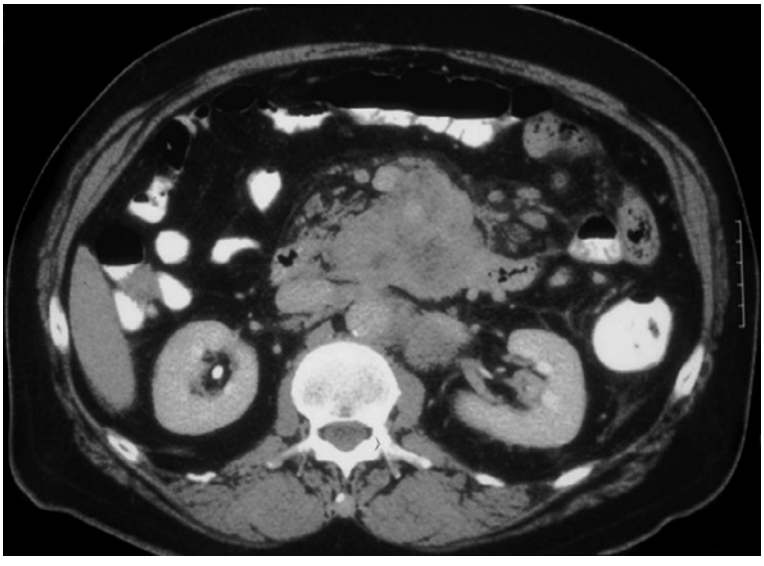

Fig. 30. Lymphoma. Axial CT scan demonstrates an irregular marginated soft tissue nodule in mesentery. Note the para-aortic lymphadenopathy

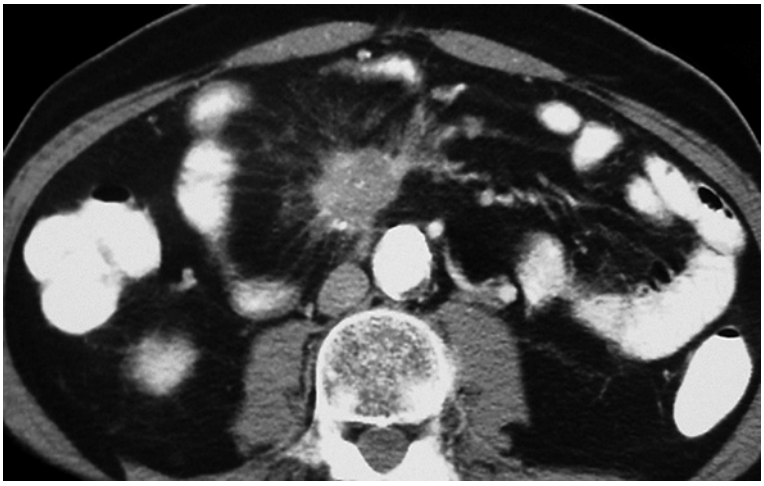

Fig. 31. Carcinoid tumors involving mesentery. Axial CT scan demonstrates a soft tissue mass with peripheral radiating strands in mesentery. Note the calcification in the mass and mural thickening of adjacent small bowel

MRI is able to demonstrate similar findings in carcinoid tumors, including the primary tumor, mesenteric metastases, and liver metastases. Liver metastases are commonly hypervascular on postgadolinium images [84].

Miscellaneous Solid Mesenteric/Omental Lesions

Fibrosing Mesenteritis (Mesenteric Panniculitis)

Fibrosing mesenteritis is a rare condition that can be mistaken for a mesenteric neoplasm based on clinical, radiologic, and gross characteristics. Fibrosing mesenteritis is part of the same process that includes other terms such as mesenteric lipodystrophy, sclerosing (retractile) mesenteritis, and mesenteric panniculitis. They

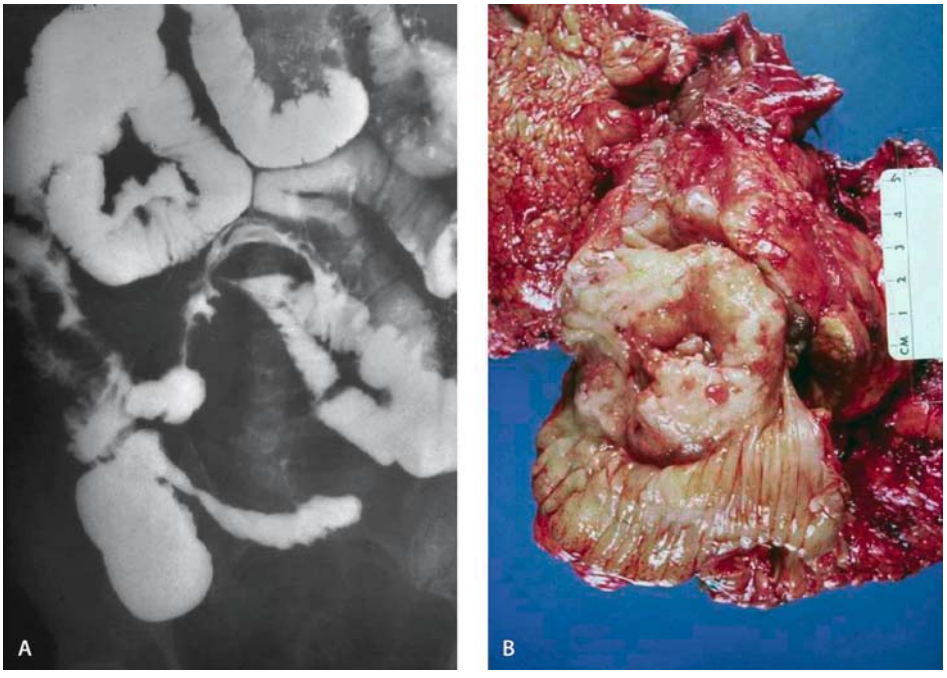

Fig. 32A, B. Sclerosing mesenteritis. **A** Barium follow-thorough demonstrates kinking and displacement of ileum due to the mass. **B** Gross specimen shows mesenteric mass formation with encasing small bowel segments

are all infiltrative mesenteric processes, with fatty, inflammatory and fibrosing components. The causative agents are unknown, although an association with lymphoma has been reported. The likely cause for fibrosing mesenteritis is trauma or other injury to the mesentery [85, 86]. Fibrosing mesenteritis has a self-limited course, with resection only necessary when there is mechanical bowel obstruction.

Its presenting symptom is abdominal pain in most patients, although it has been anecdotally reported in association with fever, mesenteric calcifications, and protein-losing enteropathy.

Pathologic Findings

Grossly, fibrosing mesenteritis shows a firm, rubbery, fibrous mass that can be either focal or diffuse within the small intestinal mesentery. The root of the mesentery and the tissues surrounding the superior mesenteric vessels are invariably involved (Fig. 32).

Histologically it consists of hypertrophied fatty tissue, dense fibrous tissue, fat necrosis, or combinations of these, along with a nonspecific chronic inflammatory infiltrate with possible calcification.

Imaging Features

Barium study may demonstrate kinking or displacement of bowel loops due to mesenteric fibrous mass formation within the intestinal mesentery (Fig. 32).

By CT, fibrosing mesenteritis may appear as a soft tissue density or heterogeneous mass, with possible calcifications [87, 88] (Fig. 33). Puckering of adjacent small bowel loops are seen. In MRI, fibrosing mesenteritis appears as a low signal intensity mass in all sequences, suggesting mature fibrotic tissue [89–91].

Fibromatosis (Desmoid Tumor)

Fibromatosis (desmoid tumor) is a non-neoplastic locally aggressive growth of fibroblastic tissue. Mesenteric fibromatosis (MF) is considered the most common primary solid mass of the mesentery. These tumors are areas of progressive fibroblastic and fibrous proliferation within the mesentery (and less frequently, the retroperitoneum or omentum) that can locally involve vascular structures and can constrict and obstruct the bowel. Although described as histologically benign lesions, their infiltrative pattern of growth can ultimately lead to life-threatening patterns of visceral involvement [92].

Although MF occurs sporadically, it may be associated with familial adenomatous polyposis (FAP). MF is identified in 20 percent of asymptomatic FAP patients [93]. MF was originally reported as a component of Gardner syndrome, a phenotypic pattern of FAP that, in addition to intestinal adenomatous polyps, is also associated with bony abnormalities, pigmented ocular fundus lesions, and cutaneous epidermoid cysts and fibromas. Prior surgery and local trauma are also frequently noted preceding the formation of mesenteric fibromatosis [94]. Although a causative relationship in fibromatosis formation has not been firmly established, various mutations of the *APC* gene have been identified in these tumors [95].

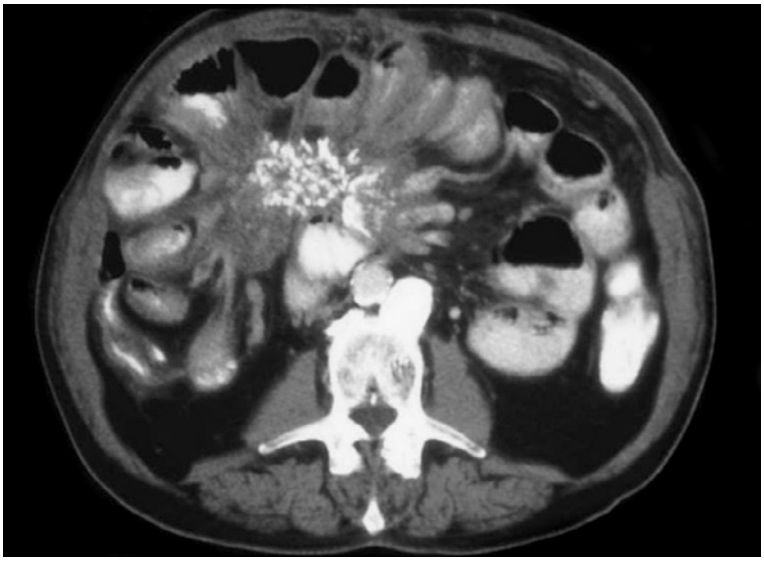

Fig. 33. Sclerosing mesenteritis, CT appearance. Enhanced CT of the abdomen demonstrates a mass in the mesentery with multiple calcifications. Note also the retraction and puckering of multiple loops of small and large bowel

Pathologic Findings

Fibromatosis is usually a large mass with no capsule. It may have whitish scar tissue within it. It rarely has areas of necrosis or hemorrhage because it is a mass with benign histologic features. Histologic specimen shows orderly arrangement of fibroblasts with uniform spine-shaped nuclei admixed to a variable amount of collagen and mucoid matrix [93] (Fig. 34).

Imaging Features

Ultrasonography demonstrates homogeneous hypoechoic mass with no signs compatible with cystic degeneration or areas of diminished echogenicity suggestive of necrosis [96] (Fig. 35). By CT imaging, a mass with sharply defined margins is seen with homogeneous density that has variable attenuation or en-

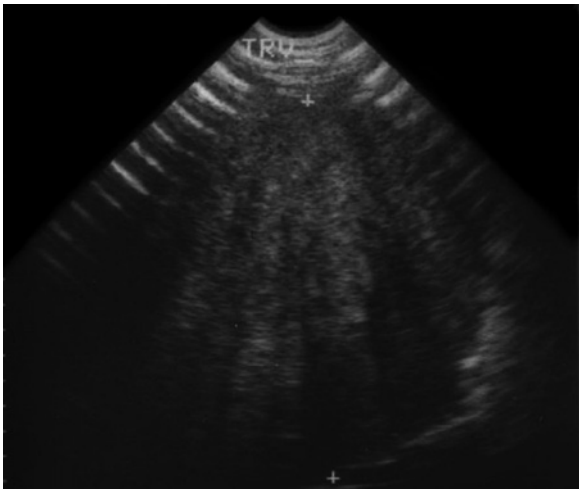

Fig. 35. Fibromatosis, US finding. Ultrasonogram demonstrates a homogeneous soft tissue mass with no areas of diminished echogenicity suggestive of necrosis

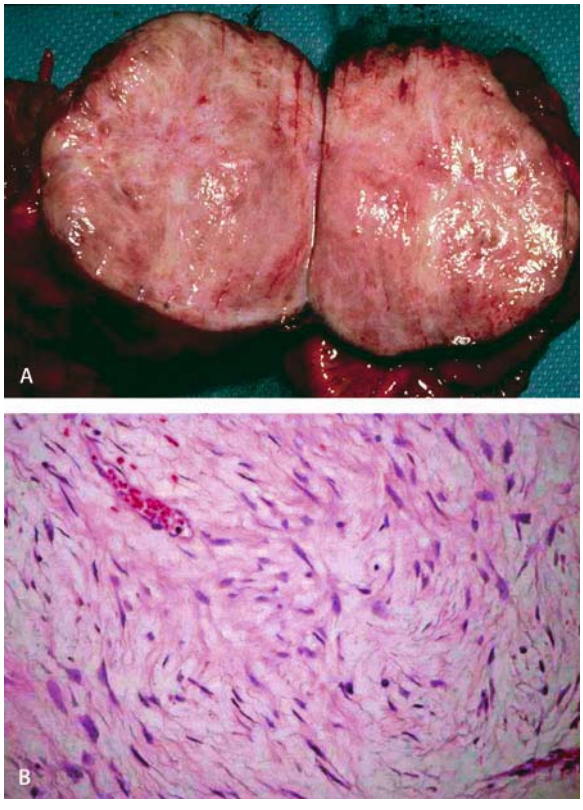

Fig. 34A, B. Pathologic findings of fibromatosis. **A** Gross specimen of fibromatosis shows a solitary fibrotic mass with no internal necrosis or hemorrhage. **B** The lesion reveals benign collagenous myxoid histologic components of typical fibromatosis

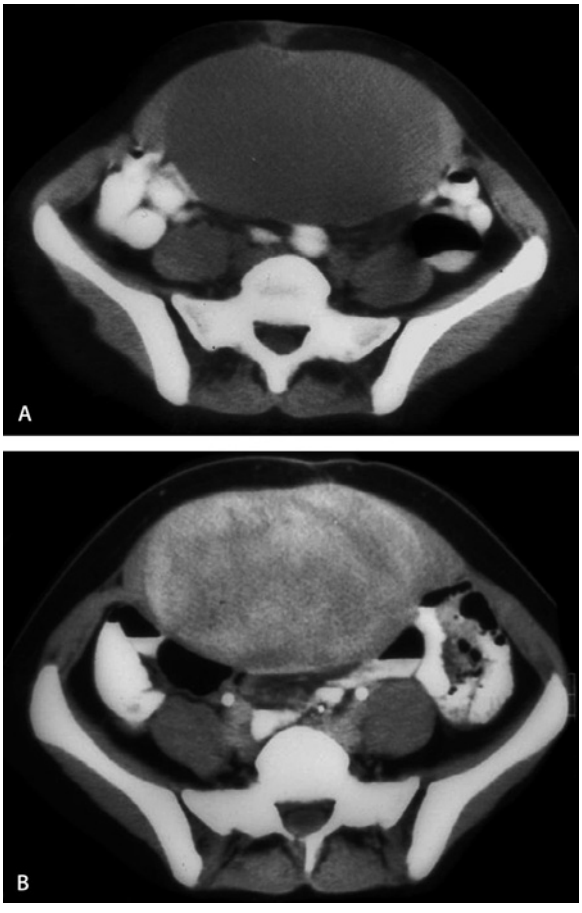

Fig. 36A, B. Fibromatosis, CT appearance. **A** Enhanced CT of the abdomen demonstrates a very large homogeneous mass. **B** After administration of contrast, there is marked enhancement of the mass, correlating with its hypervascular nature. The lack of areas of hemorrhage or necrosis is typical of mesenteric fibromatosis

hancement after contrast administration [97] (Fig. 36). MRI demonstrates fibromatosis as a mass with low signal intensity relative to muscle on T1-weighted images and variable signal intensity on T2-weighted images [98]. High signal intensity on T2-weighted images may be seen from rapidly growing fibromatosis [99] (Fig. 37).

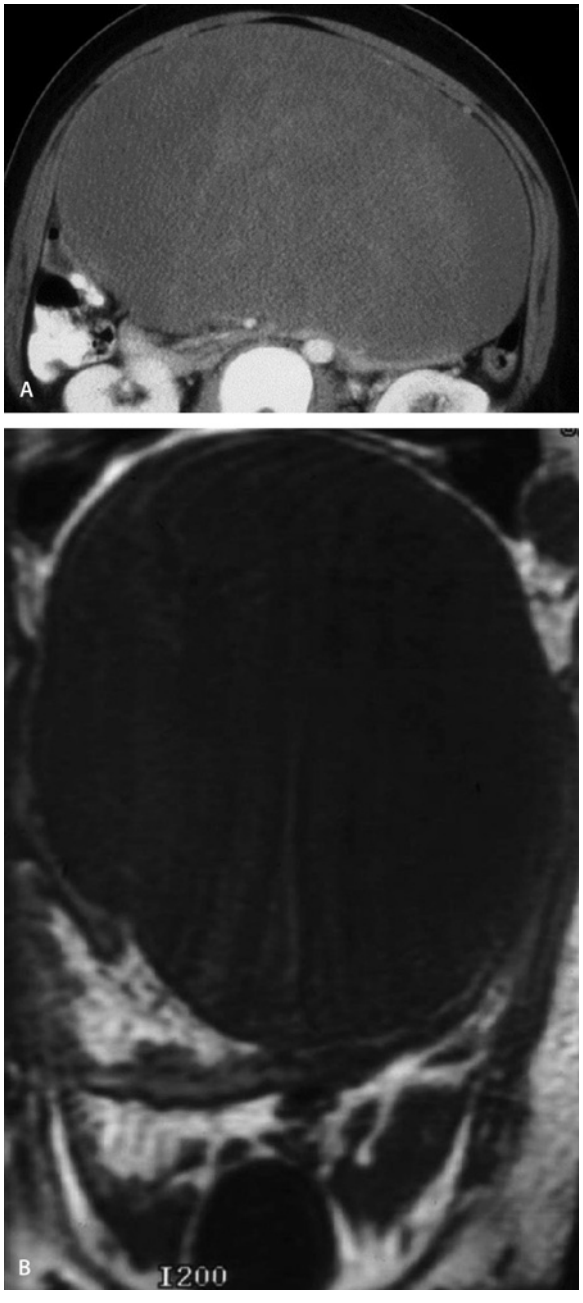

Fig. 37A, B. Fibromatosis, MRI appearance. **A** Axial CT image demonstrates a homogeneously low attenuation mass in the mesentery. **B** Coronal T1-weighted spin-echo image demonstrates a large mass in the mesentery with muscle intensity and lack of areas of necrosis or hemorrhage

Castleman's Disease

Castleman's disease is an uncommon benign lymphoproliferative disorder characterized by hyperplasia of lymphoid follicles [100]. Castleman's disease may occur anywhere along the lymphatic chain, but the mediastinum is the most common location (70%). Extrathoracic sites have been reported in the neck, axilla, pelvis, pancreas, adrenal, mesentery, and retroperitoneum [101]. Clinically, patients are usually asymptomatic, although sometimes associated with systemic manifestations such as fever, anemia, weight loss, night sweat, and polyclonal hypergammaglobulinemia [102]. Castleman's disease with systemic symptoms is usually bad in prognosis.

Pathologic Findings

There are two major histologic variants: The hyaline-vascular type, which is more frequent, is characterized by small hyaline-vascular follicles and interfollicular capillary proliferation; the plasma cell type is characterized by large follicles with intervening sheets of plasma cells [101].

Calcification and central stellate fibrosis is not uncommon in hyaline-vascular Castleman disease [102].

Imaging Features

The characteristic feature of localized Castleman disease at CT is a well-defined, homogeneous, single mass of soft tissue attenuation with or without satellite nodules (Fig. 38). The degree of enhancement may vary from mild to strong according to the histologic type [103]. Typically dynamic CT reveals the early strong enhancement and delayed washout in hyaline-vascular type [104]. Plasma cell type does not show strong enhancement. Small lumpy calcifications may be seen in the center of the mass.

The central fibrosis in hyaline-vascular type may be demonstrated as interspersed area of low attenuation on CT and hypointense on both T1- and T2-weighted MR images [105].

No radiologic finding is pathognomonic for disseminated Castleman's disease [101, 106].

Splenosis

Splenosis is the autotransplantation of residual fragments of splenic tissue in the abdomen and occasionally in the pelvis or thorax, following splenectomy typically performed for traumatic splenic injury. The most commonly involved site is the peritoneal cavity. These

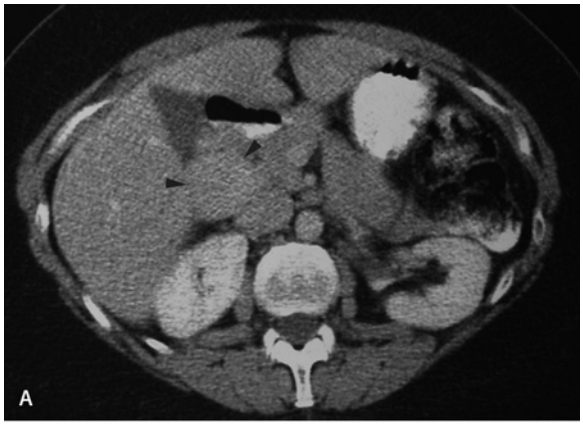

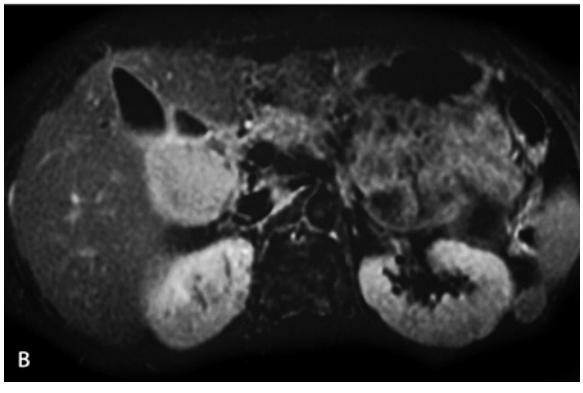

Fig. 38A, B. Castleman disease. **A** Axial CT scan demonstrates a soft tissue mass (*arrowheads*) in peripancreatic portion. **B** Gadolinium-enhanced axial T1-weighted image illustrates a large mass displacing the IVC posteriorly. The mass shows intense enhancement (nearly equal to kidneys)

foci of splenic tissue subsequently grow and regenerate nodules of functional splenic tissue [107]. Splenosis rarely becomes symptomatic in cases with infarction or spontaneous hemorrhage of intraperitoneal nodule, gastrointestinal wall implant, or recurrence of hematologic diseases (congenital hemolytic anemia, idiopathic thrombocytopenic purpura, etc) [108].

Pathologic Findings

Peritoneal splenosis may exhibit multiple round or oval peritoneal nodules. Nodules of splenosis do not exhibit a well-defined hilus. Most are up to 3 cm across but nodules up to 7 cm in greatest dimension have been reported [107].

Histological finding of splenosis may vary, but it may exhibit read and white pulp that appears histologically and immunohistochemically indistinguishable from normal or accessory spleen [109].

Imaging Features

The characteristic feature of splenosis at ultrasound, CT, and MRI is multiple well-defined, round or oval, homogeneous masses of soft tissue attenuation [110]. They enhance uniformly with intravenous contrast medium.

MRI usually demonstrates hypointense signal of the nodules on both T1- and T2-weighted MR images, identical to those of the normal spleen [111].

If necessary, their splenic origin can be confirmed with Tc-99m-tagged, heat-damaged red blood cells or sulfur colloid scintigraphy [112].

Conclusion

A wide range of entities may involve the mesentery and omentum. The radiologist must be aware of the pathological changes commonly encountered, not only for ensuring improvement in interpretation of imaging features but also for formulating a reasonable differential diagnosis.

CT, US, or MR imaging allows detecting the origin of an abdominal mass as mesenteric/omental and whether it is solid or cystic in nature. If the mass is cystic, the differential diagnosis should include benign mesenteric/omental cysts, such as cystic teratoma, cystic mesothelioma, and pseudocyst. However, it is important to remember that some malignant neoplasms, such as spindle cell tumors, can occasionally have massive cystic change and appear cystic by imaging.

Although there is substantial overlap in imaging features, it should be remembered that most solid masses involving the mesentery/omentum are neoplastic and most are secondary malignant tumors. It is also important to consider the possibility of tuberculosis or lymphoma, since these entities are usually treated with medical therapy, and surgery should be avoided.

■ **Acknowledgements.** The authors are grateful to Seth Levine for editorial assistance in preparing the manuscript.

References

1. Stoupis C, Ros PR, Abbitt PL, Burton SS, Gauger J (1994) Bubbles of the belly: imaging of cystic mesenteric or omental masses. RadioGraphics 14:729–737
2. Hamrick-Turner JE, Chiechi MV, Abbitt PL, Ros PR (1992) Neoplastic and inflammatory processes of the peritoneum, omentum, and mesentery: diagnosis with CT. RadioGraphics 12:1051–1068
3. Kurtz R, Heimann T, Holt J (1986) Mesenteric and retroperitoneal cysts. Ann Surg 203:109–112
4. Takiff H, Calabria R, Yin L (1985) Mesenteric cysts and intra-abdominal cystic lymphangiomas. Arch Surg 120:1266–1269

5. Vanek V, Phillips A (1984) Retroperitoneal, mesenteric, and omental cysts. Arch Surg 119:838–842
6. Egozi E, Ricketts R (1997) Mesenteric and omental cysts in children. Am Surg 63:287–290
7. Bliss DJ, Coffin C, Bower R (1994) Mesenteric cysts in children. Surgery 115:571–577
8. Walker A, Putnam T (1973) Omental, mesenteric, and retroperitoneal cysts: a clinical study of 33 new cases. Ann Surg 178:13–19
9. Singh S, Baboo ML, Pathak IC (1971) Cystic lymphangioma in children: report of 32 cases including lesions atrrare sites. Surgery 69:947–951
10. Ros PR, Olmsted WW, Moser RP Jr, Dachman AH, Hjermstad BH, Sobin LH (1987) Mesenteric and omental cysts: histologic classification with imaging correlation. Radiology 164: 327–332
11. Ko SF, Ng SH, Shieh CS, Lin JW, Huang CC, Lee TY.1995) Mesenteric cystic lymphangioma with myxoid degeneration: unusual CT and MR manifestations. Pediatr Radiol 25:525–527
12. Davidson AJ, Hartman DS (1990) Lymphangioma of the retroperitoneum: CT and sonographic characteristic. Radiology 175:507–510
13. Lugo-Olivieri CH, Taylor GA (1993) CT differentiation of large abdominal lymphangioma from ascites. Pediatr Radiol 23:129–130
14. Stoupis C, Ros PR, Williams JL (1993) Hemorrhagic lymphangioma mimicking hemoperitoneum: MR imaging diagnosis. J Magn Reson Imaging 3:541–542
15. Forshall I (1961) Duplication of the intestinal tract. Postgrad Med J 37:570–589
16. Anderson MC, Silberman WW, Shields TW (1962) Duplications of the alimentary tract in the adult. Arch Surg 85: 94–108
17. Otter MI, Marks CG, Cook MG (1996) An unusual presentation of intestinal duplication with a literature review. Dig Dis Sci 41:627–629
18. Royle SG, Doig CM (1988) Perforation of the jejunum secondary to a duplication cyst lined with ectopic gastric mucosa. J Pediatr Surg 23:1025–1026
19. Lecouffe P, Spyckerelle C, Venel H, Meuriot S, Marchandise X (1992) Use of pertechnetate 99mTc for abdominal scanning in localising an ileal duplication cyst: case report and review of the literature. Eur J Nucl Med 19:65–67
20. Tong SC, Pitman M, Anupindi SA (2002) Best cases from the AFIP. Ileocecal enteric duplication cyst: radiologic-pathologic correlation. Radiographics 22:1217–1222
21. de Perrot M, Brundler M, Totsch M, Mentha G, Morel P (2000) Mesenteric cysts. Toward less confusion? Dig Surg 17: 323–328
22. Gourtsoyiannis NC, Bays D, Malamas M, Mouchtouris A (1993) Mesothelial cyst complicated by torsion: preoperative imaging evaluation. Hepatogastroenterology 40:509–512
23. Sardi A, Parikh KJ, Singer JA, Minken SL (1987) Mesenteric cysts. Am Surg 53:58–60
24. Bowen B, Ros PR, McCarthy MJ, Olmsted WW, Hjermstad BM (1987) Gastrointestinal teratomas: CT and US appearance with pathologic correlation. Radiology 162:431–433
25. Whang SH, Lee KS, Kim PN, Bae WK, Lee BH (1990) Omental teratoma in an adult: a case report. Gastrointest Radiol 15: 301–302
26. Ralls PW, Hartman B, White W, Radin DR, Halls J (1987) Computed tomography of benign cystic teratoma of the omentum. J Comput Assist Tomogr 11:548–549
27. Moon W, Kim Y, Rhim H, Koh B, Cho O (1997) Coexistent cystic teratoma of the omentum and ovary: report of two cases. Abdom Imaging 22:516–518
28. O'Neil JD, Ros PR, Storm BL, Buck JL, Wilkinson EJ (1989) Cystic mesothelioma of the peritoneum. Radiology 170: 333–337
29. Weiss SW, Tavassoli FA (1988) Multicystic mesothelioma. An analysis of pathologic findings and biologic behavior in 37 cases. Am J Surg Pathol 12:737–746
30. Hasan AK, Sinclair DJ (1993) Case report: calcification in benign cystic peritoneal mesothelioma. Clin Radiol 48:66–67
31. Ozgen A, Akata D, Akhan O, Tez M, Gedikoglu G, Ozmen MN (1998) Giant benign cystic peritoneal mesothelioma: US, CT, and MRI findings. Abdom Imaging 23:502–504
32. Bui-Mansfield LT, Kim-Ahn G, O'Bryant LK (2002) Multicystic mesothelioma of the peritoneum. AJR Am J Roentgenol 178:402
33. Volk BA, Scholmerich J, Farthmann E, Gerok W, Wenz W (1983) Leiomyoblastoma of the stomach–a case report on ultrasonographic differential diagnosis of cystic lesions in the abdomen. Hepatogastroenterology 30:33–35
34. McFadden DW, Hiyama D, Moulton JS, Biddinger P (1993) Primary mesenteric leiomyosarcoma masquerading as a pancreatic pseudocyst. Pancreas 8:647–9
35. Miettinen M, Monihan JM, Sarlomo-Rikala M, Kovatich AJ, Carr NJ, Emory TS, Sobin LH (1999) Gastrointestinal stromal tumors/smooth muscle tumors (GISTs) primary in the omentum and mesentery: clinicopathologic and immunohistochemical study of 26 cases. Am J Surg Pathol 23:1109–1118
36. Lee JT, Kim MJ, Yoo KS, Suh JH, Leong HJ (1991) Primary leiomyosarcoma of the greater omentum: CT findings. J Comput Assist Tomogr 15:92–94
37. Jivan S, Bahal V (2002) Pseudomyxoma peritonei. Postgrad Med J 78:170–172
38. Sulkin TV, O'Neill H, Amin AI, Moran B (2002) CT in pseudomyxoma peritonei: a review of 17 cases. Clin Radiol 57: 608–613
39. Lersch C, Frimberger E, Ott R, Classen M (2001) Gray-scale sonographic findings in a patient with pseudomyxoma peritonei. J Clin Ultrasound 29:186–191
40. Pestieau SR, Wolk R, Sugarbaker PH (2000) Congenital pleuroperitoneal communication in a patient with pseudomyxoma peritonei. J Surg Oncol 73:174–178
41. Gollub MJ, DeCorato D, Schwartz LH (2000) MR enteroclysis: evaluation of small-bowel obstruction in a patient with pseudomyxoma peritonei. AJR Am J Roentgenol 174:688–690
42. Pantongrag-Brown L, Krebs TL, Daly BD, Wong-You-Cheong JJ, Beiser C, Krause B, Brown AE (1998) Frequency of abdominal CT findings in AIDS patients with M. avium complex bacteraemia. Clin Radiol 53:816–819
43. Klatt EC, Jensen DF, Meyer PR (1987) Pathology of Mycobacterium avium-intracellulare infection in acquired immunodeficiency syndrome. Hum Pathol 18:709–714
44. Yang ZG, Min PQ, Sone S, He ZY, Liao ZY, Zhou XP, Yang GQ, Silverman PM (1999) Tuberculosis versus lymphomas in the abdominal lymph nodes: evaluation with contrast-enhanced CT. AJR Am J Roentgenol 172:619–623
45. Kim SY, Kim MJ, Chung JJ, Lee JT, Yoo HS (2000) Abdominal tuberculous lymphadenopathy: MR imaging findings. Abdom Imaging 25:627–32
46. Horton KM, Corl FM, Fishman EK (1999) CT of nonneoplastic diseases of the small bowel: spectrum of disease. J Comput Assist Tomogr 23:417–428
47. Nicolas AI, Ros PR (1995) Marbles in the belly: imaging-pathologic correlation of solid mesenteric/omental masses. Postgrad Radiol 15:51–73
48. Jadvar H, Mindelzun RE, Olcott EW, Levitt DB.1997) Still the great mimicker: abdominal tuberculosis. AJR Am J Roentgenol 168:1455–1460
49. Hulnick DH, Megibow AJ, Naidich DP, Hilton S, Cho KC, Balthazar EJ (1985) Abdominal tuberculosis: CT evaluation. Radiology 157:199–204
50. Demir K, Okten A, Kaymakoglu S, Dincer D, Besisik F, Cevikbas U, Ozdil S, Bostas G, Mungan Z, Cakaloglu Y (2001) Tuberculous peritonitis–reports of 26 cases, detailing diagnostic and therapeutic problems. Eur J Gastroenterol Hepatol 13: 581–585
51. Yilmaz T, Sever A, Gur S, Killi RM, Elmas N (2002) CT findings of abdominal tuberculosis in 12 patients. Comput Med Imaging Graph 26:321–325
52. Ha HK, Jung JI, Lee MS, Choi BG, Lee MG, Kim YH, Kim PN, Auh YH (1996) CT differentiation of tuberculous peritonitis and peritoneal carcinomatosis. AJR Am J Roentgenol 167: 743–748
53. Jelinek JS, Kransdorf MJ, Shmookler BM, Aboulafia AJ, Malawer MM (1993) Liposarcoma of the extremities: MR and CT findings in the histologic subtypes. Radiology 186:455–459

54. Kim T, Murakami T, Oi H, Tsuda K, Matsushita M, Tomoda K, Fukuda H, Nakamura H (1996) CT and MR imaging of abdominal liposarcoma. AJR Am J Roentgenol 166:829–833
55. Munk PL, Lee MJ, Poon PY, Goddard KJ, Knowling MA, Hassell PR (1996) Computed tomography of retroperitoneal and mesenteric sarcomas: a pictorial essay. Can Assoc Radiol J 47: 335–341
56. Enzinger FM, Weiss SM (1995) Benign tumors of peripheral nerves. In: Enzinger FM, Weiss SW (eds) Soft tissue tumors. St Louis, Mosby
57. Pui MH, et al (1998) Computed tomography of abdominal neurogenic tumours. Australas Radiol 42(3):183–187
58. Kim SH, Choi BI, Han MC, et al (1992) Retroperitoneal neurilemnoma: CT and MR findings. Am J Roentgenol 159: 1023
59. Cerofolini E, Landi A, DeSantis G, et al (1991) MR of benign peripheral nerve sheath tumors. J Comput Assist Tomogr 15:593
60. Loke TKL, Yuen NWF, Lo KKL, et al (1998) Retroperitoneal ancient schwannoma: Review of clinico-radiological features. Australas Radiol 42(2):136–138
61. Suh JS, Abenoza P, Galloway HR, et al (1992) Peripheral (extracranial) nerve tumors: correlation of MR imaging and histologic findings. Radiology 183:341
62. Varma DG, Moulopoulos A, Sara AS, et al (1992) MR imaging of extracranial nerve sheath tumors. J Comput Assist Tomogr 16:448
63. Friedman DP, Tartaglino LM, Flanders AE (1992) Intradural schwannomas of the spine: MR findings with emphasis on contrast-enhancement characteristics. Am J Roentgenol 158:1347
64. Ros PR, Yuschok TJ, Buck JL, et al (1991) Peritoneal mesothelioma: radiologic appearances correlated with histology. Acta Radiol 32:355–358
65. O'Brien JE, Stout AP (1964) Malignant fibrous xanthomas. Cancer 17:1445–58
66. Enzinger FM, Weiss SW (1995) Malignant fibrohistiocytic tumors. In: Enzinger FM, Weiss SW (eds) Soft tissue tumors. St Louis, MO: Mosby Year Book, pp 351–380
67. Weiss SW, Enzinger FM (1978) Malignant fibrous histiocytoma: an analysis of 200 cases. Cancer 41:2250–2266
68. Goldman SM, Hartman DS, Weiss SW (1986) The varied radiographic manifestations of retroperitoneal malignant fibrous histiocytoma revealed through 27 cases. J Urol 135: 33–38
69. Ros PR, Viamonte M Jr, Rywlin AM (1984) Malignant fibrous histiocytoma; mesenchymal tumor of ubiquitous origin. AJR 142:753–759
70. Bruneton JN, Drouillard J, Rogopoulos A, Laurent F, Normand F, Balu-Maestro C, et al (1988) Extraretroperitoneal abdominal malignant fibrous histiocytoma. Gastrointest Radiol 13:299–305
71. Ko SF, Wan YL, Lee TY, Ng SH, Lin JW, Chen WJ (1998) CT features of calcifications in abdominal malignant fibrous histiocytoma. Clin Imaging 22:408–13
72. Castillo M, Davis PC, Takei YD, Schwartzberg DG, Hoffman JC Jr (1990) Intracranial cystic malignant fibrous histiocytoma in a child: sonographic and CT findings. Pediatr Radiol 20:194–5
73. Berry AD III, Reintjes SL, Kepes JJ (1988) Intracranial malignant fibrous histiocytoma with abscess-like tumor necrosis. J Neurosurg 69:780–784
74. Panicek DM, Casper ES, Brennan MF, Hajdu SI, Heelan RT (1991) Hemorrhage simulating tumor growth in malignant fibrous histiocytoma at MR imaging. Radiology 181:398–400
75. Munk PL, Sallomi DF, Janzen DL, et al (1998) Malignant fibrous histiocytoma of soft tissue imaging with emphasis on MRI. J Comput Assist Tomogr 22:819–826
76. Fenoglio-Preiser CM, Pascal RR, Perzin KH (1990) Mesenchymal tumors. In: Leiomyosarcomas; tumors of the intestines. 2nd series. Washington, DC: Armed Forces Institute of Pathology, 433–441
77. Arakawa A, Yasunaga T, Yano S, et al (1993) Radiological findings of the retroperitoneal leiomyosarcoma: report of two cases. Comput Med Imaging Graph 17:125
78. Hartman DS, Hayes WS, Choyke PL, et al (1992) From the archives of the AFIP: leiomyosarcoma of the retroperitoneum and inferior vena cava: radiologic-pathologic correlation. Radiographics 12:1203
79. Lane RH, Stephens DH, and Reiman HM (1989) Primary retroperitoneal neoplasms: CT findings in 90 cases with clinical and pathologic correlation. Am J Roentgenol 152: 83
80. Maya MM, Fried K, Gendal ES (1993) AIDS-related lymphoma: an unusual cause of omental caking. AJR Am J Roentgenol 160:661
81. Pantongrag-Brown L, Buetow PC, Carr NJ, Lichtenstein JE, Buck JL (1995) Calcification and fibrosis in mesenteric carcinoid tumor: CT findings and pathologic correlation. AJR Am J Roentgenol 164:387–391
82. Einstein DM, et al (1991) Abdominal lymphadenopathy: spectrum of CT findings. Radiographics 11: 457
83. Kim Y, Cho O, Song S, Lee H, Rhim H, Koh B (1998) Peritoneal lymphomatosis: CT findings. Abdom Imaging 23:87–90
84. Bader TR, Semelka RC, Chiu VC, Armao DM, Woosley JT (2001) MRI of carcinoid tumors: spectrum of appearances in the gastrointestinal tract and liver. J Magn Reson Imaging 14: 261–269
85. Emory TS, Carr NJ, Sobin LH (1997) Sclerosing mesenteritis, mesenteric panniculitis and mesenteric lipodystrophy: a single entity? Am J Surg Pathol 21:392–398
86. Katz ME, Heiken JP, Glazer HS, Lee JKT (1985) Intraabdominal panniculitis: clinical, radiographic, and CT features. AJR 145:293–296
87. Mata JM, Inaraja L, Martin J, et al (1987) CT features of mesenteric panniculitis. J Comput Asst Tomogr 11:1021–1023
88. Lawler LP, McCarthy DM, Fishman EK, Hruban R (2002) Sclerosing mesenteritis: depiction by multidetector CT and three-dimensional volume rendering. AJR Am J Roentgenol 178:97–99
89. Kronthal AJ, Kang YS, Fishman EK, Jones B, Kuhlman JE, Tempany CM (1991) MR imaging in sclerosing mesenteritis. AJR Am J Roentgenol 156:517–519
90. Kakitsubata Y, Umemura Y, Kakitsubata S, Tamura S, Watanabe K, Abe Y, Hatakeyama K (1993) CT and MRI manifestations of intraabdominal panniculitis. Clin Imaging 17: 186–188
91. Fujiyoshi F, Ichinari N, Kajiya Y, Nishida H, Shimura T, Nakajo M, Matsunaga Y, Furoi A, Imaguma M (1997) Retractile mesenteritis: small-bowel radiography, CT, and MR imaging. AJR Am J Roentgenol 169:791–793
92. Dalen BP, Bergh PM, Gunterberg BU (2003) Desmoid tumors: a clinical review of 30 patients with more than 20 years' follow-up. Acta Orthop Scand 74:455–459
93. Middleton SB, Clark SK, Matravers P, Katz D, Reznek R, Phillips RK (2003) Stepwise progression of familial adenomatous polyposis-associated desmoid precursor lesions demonstrated by a novel CT scoring system. Dis Colon Rectum 46: 481–485
94. Al Jadaan SA, Al Rabeeah A (1999) Mesenteric fibromatosis: case report and literature review. J Pediatr Surg 34:1130–1132
95. Tolg C, Poon R, Fodde R, Turley EA, Alman BA (2003) Genetic deletion of receptor for hyaluronan-mediated motility (Rhamm) attenuates the formation of aggressive fibromatosis (desmoid tumor). Oncogene 22:6873–6882
96. Maconi G, Cristaldi M, Vago L, Rovati M, Elli M, Sampietro GM, Nebuloni E, Sainaghi M, Taschieri AM, Bianchi Porro G (1998) Clinical, ultrasonographic and tomographic features on the natural evolution of primary mesenteric fibromatosis: a case report. Hepatogastroenterology 45:1663–1666
97. Kawashima A, Goldman SM, Fishman EK, Kuhlman JE, Onitsuka H, Fukuya T, Masuda K (1994) CT of intraabdominal desmoid tumors: is the tumor different in patients with Gardner's disease? AJR Am J Roentgenol 162:339–342
98. Quinn SF, Erickson SJ, Dee PM, et al (1991) MR imaging in fibromatosis: results in 26 patients with pathologic correlation. AJR 156:539–542
99. Healy JC, Reznek RH, Clark SK, Phillips RK, Armstrong P (1997) MR appearances of desmoid tumors in familial adenomatous polyposis. AJR Am J Roentgenol 169:465–472

100. Castleman B, Iverson L, Mercedez VP (1956) Localized mediastinal lymph node hyperplasia resembling thymoma. Cancer 9:822–830
101. Keller AR, Hochholzer L, Castleman B (1976) Hyaline vascular and plasma-cell types of giant lymph node hyperplasia of the mediastinum and other locations. Cancer 29:670–681
102. Kim TJ, Han JK, Kim YH, Kim TK, Choi BI (2001) Castleman disease of the abdomen: imaging spectrum and clinicopathologic correlations. J Comput Assist Tomogr 25:207–214
103. Meador TL, McLarney JK (2000) CT features of Castleman disease of the abdomen and pelvis. AJR Am J Roentgenol 175:115–118
104. Singletary LA, Karcnik TJ, Abujudeh H (2000) Hyaline vascular-type Castleman disease: a rare cause of a hypervascular retroperitoneal mass. Abdom Imaging 25:207–209
105. Irsutti M, Paul JL, Selves J, Railhac JJ (1999) Castleman disease: CT and MR imaging features of a retroperitoneal location in association with paraneoplastic pemphigus. Eur Radiol 9:1219–1221
106. Johnson WK, Ros PR, Powers C, Stoupis C, Segel KH (1994) Castleman disease mimicking an aggressive retroperitoneal neoplasm. Abdom Imaging 19:342–344
107. Livingston CD, Levine BA, Lecklitner ML, Sirinek KR (1983) Incidence and function of residual splenic tissue following splenectomy for trauma in adults. Arch Surg 118:617–620
108. Katz DS, Moshiri M, Smith G, Meiner EM, Fruauff AA (1998) Spontaneous hemorrhage of abdominal splenosis. J Comput Assist Tomogr 22:725–727
109. Carr NJ, Turk EP (1992) The histological features of splenosis. Histopathology 21:549–553
110. Delamarre J, Capron JP, Drouard F, Joly JP, Deschepper B, Carton S (1988) Splenosis: ultrasound and CT findings in a case complicated by an intraperitoneal implant traumatic hematoma. Gastrointest Radiol 13:275–278
111. Lin WC, Lee RC, Chiang JH, Wei CJ, Chu LS, Liu RS, Chang CY (2003) MR features of abdominal splenosis. AJR Am J Roentgenol 180:493–496
112. Castellani M, Cappellini MD, Cappelletti M, Fedriga E, Reschini E, Cerino M, Gerundini P (2001) Tc-99m sulphur colloid scintigraphy in the assessment of residual splenic tissue after splenectomy. Clin Radiol 56:596–598

Spleen

Enrica Segatto, Koenraad J. Mortele, Pablo R. Ros

4.12

Contents

Introduction

The spleen is generally not considered a challenge to the radiologist and it is also true that the spleen is an uncommon site of primary disease; however, it may be involved by a variety of different diseases including generalized hematopoietic and lymphopoietic disorders, systemic infections, neoplasms, and immunologic-inflammatory disorders. Some of these conditions have no clinical significance but familiarity with their existence is nevertheless important in order to avoid interpretative pitfalls. Computer tomography and ultrasonography are screening modalities for the spleen. For problem solving, magnetic resonance imaging may be helpful, especially given its free choice of the imaging plane and because of the high contrast resolution. The purpose of this chapter is to present a review of imaging findings of a vast array of splenic diseases, correlated with underlying gross and microscopic pathologic features.

Neoplasms

Cyst

Definition

Cysts of the spleen may be divided into primary (or true) cysts, which possess a cellular lining, and secondary (or false) cysts, which are without a cellular lining [1]. Primary cysts are either parasitic (echinococcal) or nonparasitic (epithelial). Parasitic cysts, most common in endemic areas where the spleen is affected in less then 5% of cases, are caused by infection with *Echinococcus granulosus* [2]. Nonparasitic epithelial-lined cysts of the spleen (typically epidermoid) account for 10%–25% of all cystic lesions and may be a manifestation of a genetic defect of mesothelial migration [3]. Non-epithelial-lined cysts are thought to be secondary to traumatic splenic injuries, and it is reported that they arise from encapsulation of subcapsular or intrasplenic hematomas [4]. They can also result from prior infarctions or infections.

Pathology

At histopathologic analysis, echinococcal cyst (parasitic) is composed of three layers: (1) the outer pericyst, which corresponds to compressed and fibrosed splenic tissue; (2) the endocyst, an inner germinal layer; and (3) the ectocyst, a translucent thin interleaved membrane. Maturation of a cyst is characterized by the development of daughter cysts in the periphery as a result of endocyst invagination. Peripheral calcifications are not uncommon in viable or nonviable cysts [5].

True, nonparasitic (epidermoid) cysts are distinguished from false cysts by their epithelial lining and may have following possible causes, including 1) peritoneal mesothelium infolded after rupture of the splenic capsule, 2) aggregates of peritoneal mesothelial cells trapped in splenic sulci, or (3) dilatation of normal lymphatic spaces [4] (Fig. 1).

Secondary or false cysts tend to have a smoother surface with fibrous tissue lining. They presumably are the residua of previous trauma, splenic infarction or infection. The contents of the cysts can be serous, hemorrhagic, or inflammatory [6, 7].

Radiologic Findings

Sonographically, splenic cysts are anechoic lesions with well-defined walls and increased transmission [8]. Epidermoid cysts may appear as anechoic cystic lesions or may have low-level internal echoes and good through transmission. False cysts usually are reported to be ane-

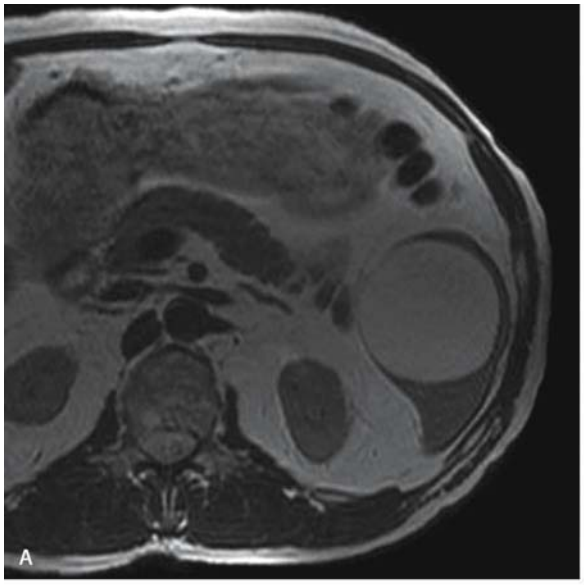

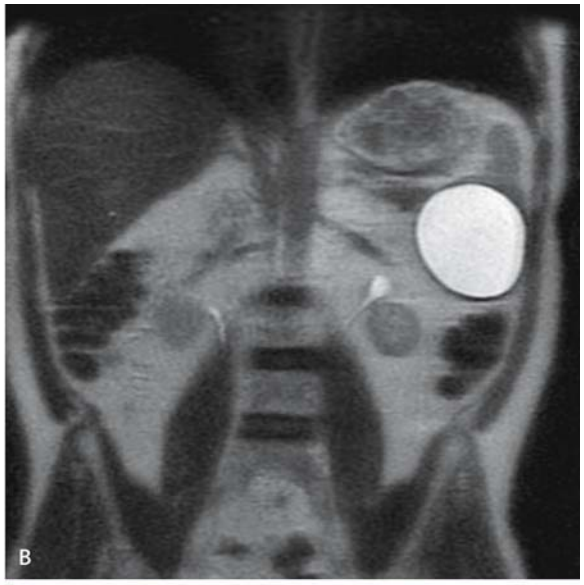

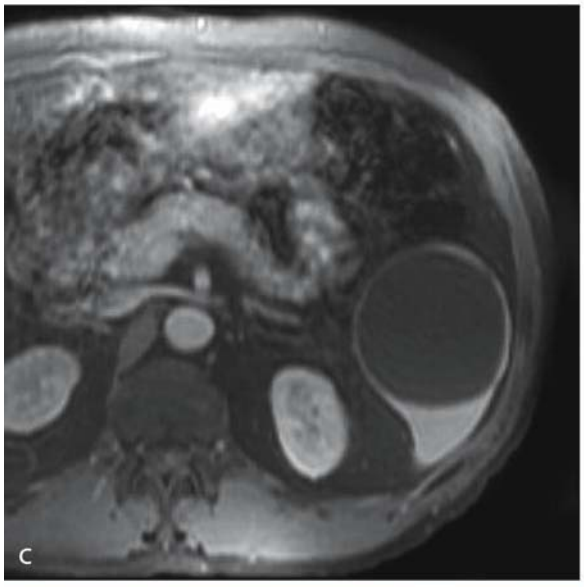

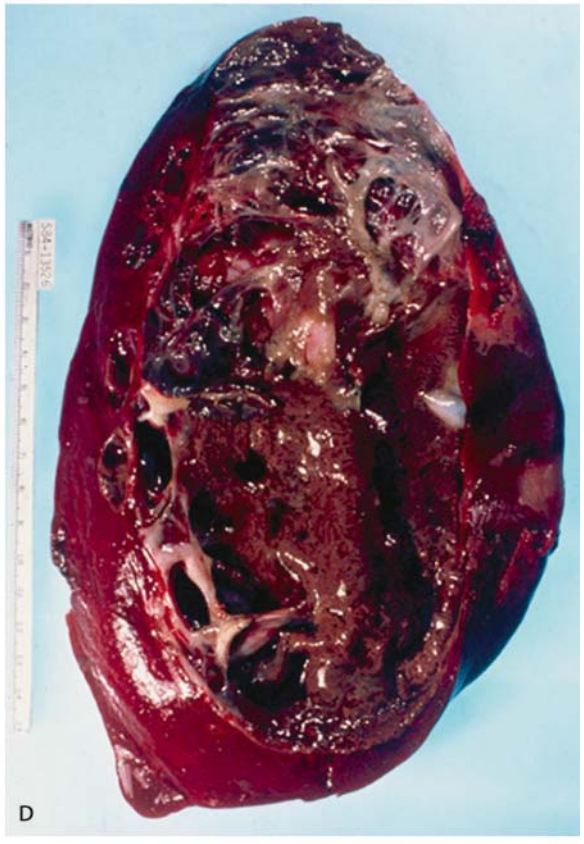

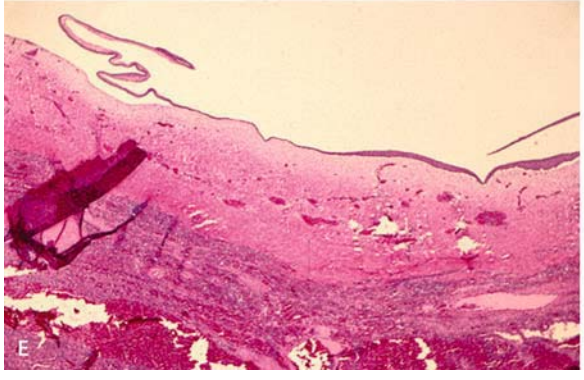

Fig. 1A–H. Splenic cyst. **A** True cyst. T2-weighted axial MR image shows a large, well-defined cystic mass, arising from the spleen. **B** Heavily T2-weighted coronal image confirms the cystic nature of the lesion. **C** Contrast-enhanced T1-weighted image shows lack of enhancement of the lesion. **D** Gross specimen clearly demonstrates the unilocular, trabeculated structure of the true cyst. **E** Photomicrograph of the wall of the cyst shows the epithelial lining, characteristic for the true cysts. **F** False cyst. Ultrasound image shows complex cystic lesion in the spleen with curvilinear peripheral calcifications. **G** Contrast-enhanced CT shows a rounded, low-density lesion, with parietal calcifications. **H** Gross specimen confirms the smoother surface with fibrous tissue lining typical of the false cyst.

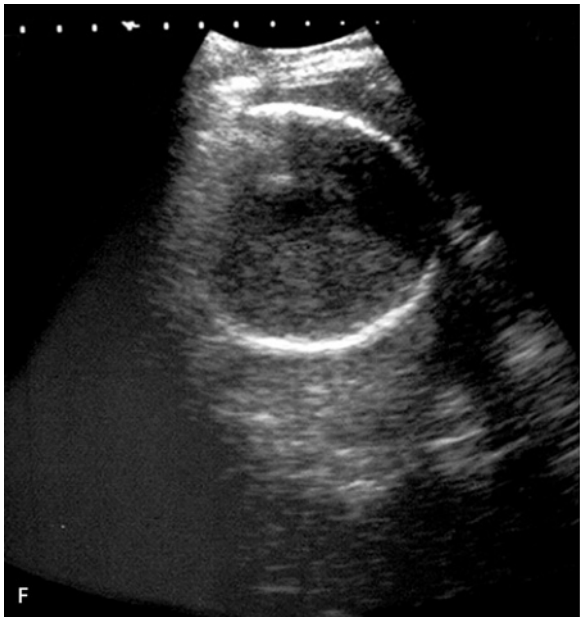

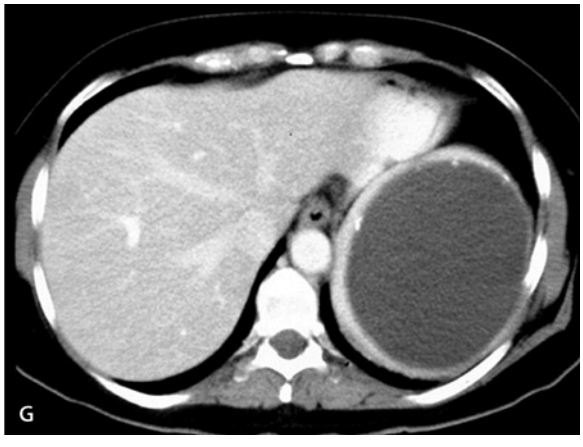

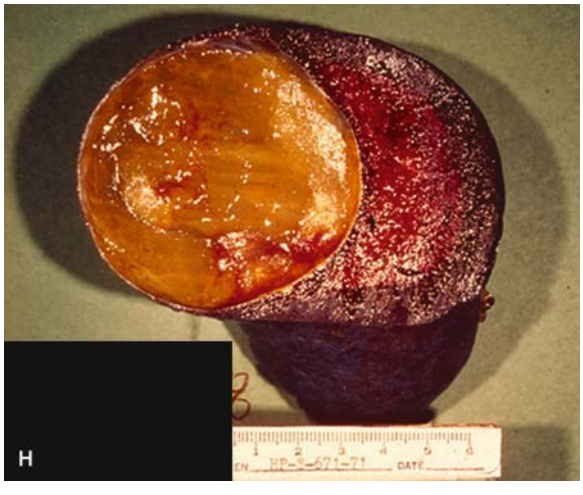

Fig. 1F–H.

choic; in 15% of cases they show a mixed pattern with solid components and anechoic spaces. Intracystic hemorrhage or debris from inflammation is responsible for the internal echogenicity within the mass [7, 9].

On CT, both true and false cysts appear as thin-walled, unilocular, spherical intrasplenic masses of water density without rim enhancement after contrast material administration (Fig. 1). Cyst wall trabeculation or peripheral septa may be found in either type of cyst, but rim calcification is more common in false cyst. Debris or high-density material may be noted in either type of cyst secondary to intracystic hemorrhage or in the case of false cyst caused by resolving hematoma [4, 10].

MR shows a well-defined, rounded mass with high signal intensity on T2-weighted images and a variable intensity on T1-weighted images depending on the protein or hemorrhagic component of the cystic fluid [11, 12]. Peripheral rim of hypointensity may be caused by the presence of a calcified wall or hemosiderin deposits at the cyst wall.

Hemangioma

Definition

Hemangioma is the most common primary benign neoplasm of the spleen and primarily affects adults aged 35–55 years. Hemangiomas are often detected incidentally on radiologic or pathologic studies [13]. In Klippel-Trenaunay-Weber syndrome, they are often multiple [14].

Pathology

Histologically, hemangiomas are composed of a proliferation of vascular channels of variable size, capillary to cavernous, lined with a single layer of endothelium and filled with red blood cells in an otherwise normal spleen [13] (Fig. 2). Hemangiomas of the spleen may be homogeneously solid or may demonstrate multiple cystic spaces of various sizes within the larger solid tumor mass [13].

Radiologic Findings

On sonography, hemangiomas may appear as discrete echogenic masses with areas of complex echoes, representing blood pools within the proliferating vascular channels or as complex masses with solid and cystic areas [15, 16] (Fig. 2).

On unenhanced CT scans, these lesions may present as homogeneously solid masses (Fig. 2) or as multiple cystic masses [15, 17]. The cystic areas demonstrate a

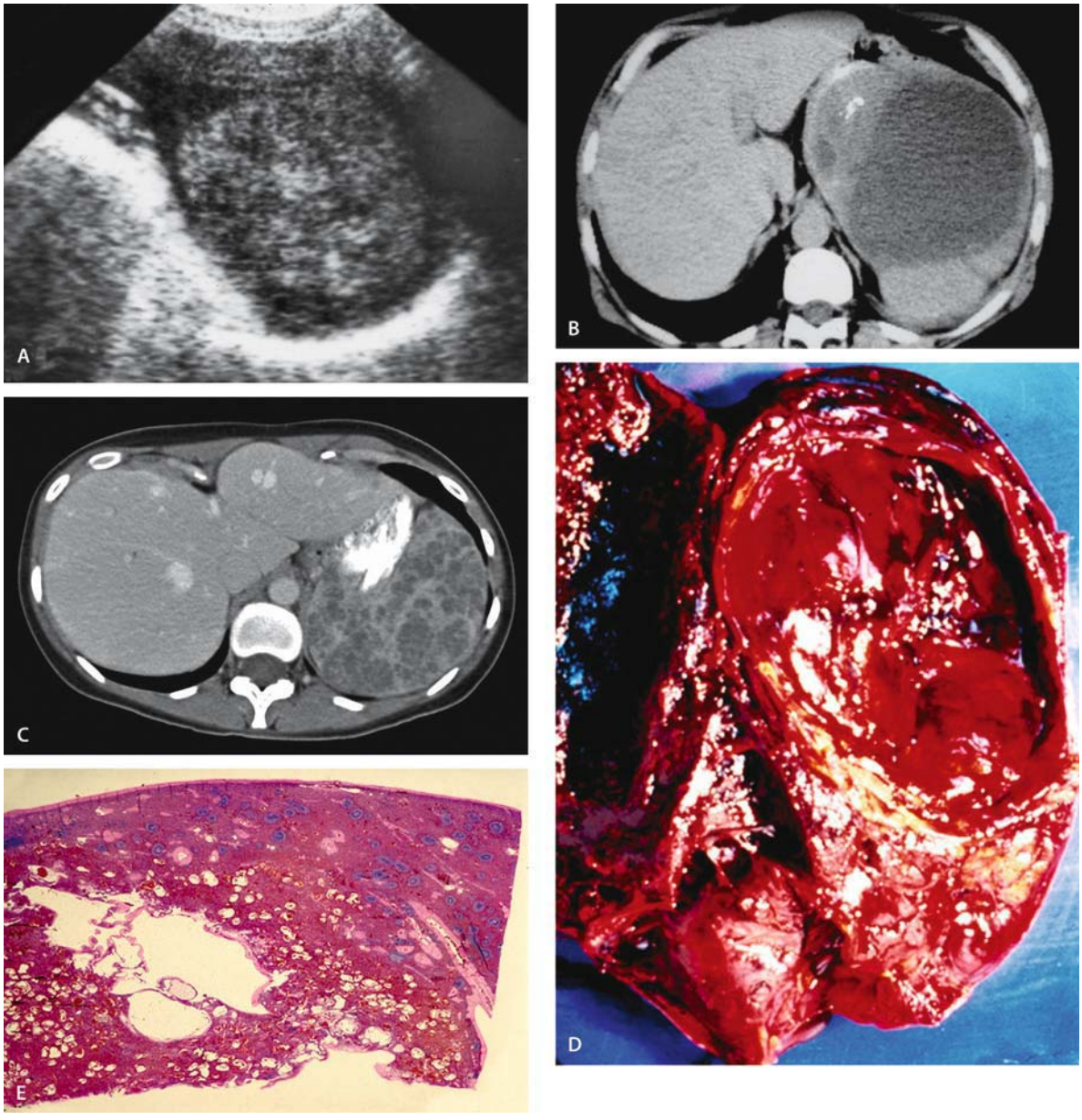

Fig. 2A–E. Splenic hemangioma. **A** Ultrasound shows a discrete echogenic 6-cm mass in the spleen. **B** Unenhanced CT shows splenic hemangioma as a hypodense partially cystic mass with calcifications. **C** Contrast-enhanced CT image in a patient with hemangiomatosis shows multiple predominantly cystic lesions in an enlarged spleen. **D** Gross appearance. Cut section demonstrates a well-circumscribed mass with predominantly solid appearance. **E** Photomicrograph of splenic hemangioma shows a vascular channel lined with a single layer of endothelium

density similar to water and lie within a mass that is isodense with normal spleen [15]. Central and punctate or peripheral and curvilinear calcifications may be demonstrated [17]. Peripheral enhancement after intravenous contrast medium administration, with delayed central enhancement, similar to hepatic hemangioma, has been described. In the multicystic type of lesion, the solid portion will enhance following intravenous contrast [15].

On MR examination, splenic hemangiomas typically present low signal intensity on T1-weighted images and higher signal intensity on T2-weighted images, whereas the latter may show heterogeneity representing previous infarction, hemorrhage, or vascular pooling [15, 18]. Dynamic scanning following a rapid bolus of Gd-DTPA may demonstrate three different patterns of enhancement: 1) immediate, homogeneous, persistent enhancement; 2) early peripheral enhancement with uni-

form delayed enhancement; 3) peripheral enhancement with centripetal progression but persistent enhancement of a central fibrous scar [19]. In case of cystic hemangioma, contrast enhancement within the mass may be heterogeneous [20].

Lymphangioma

Definition

Lymphangiomas of the spleen are benign neoplasms that are either solitary or multiple (lymphangiomyo-

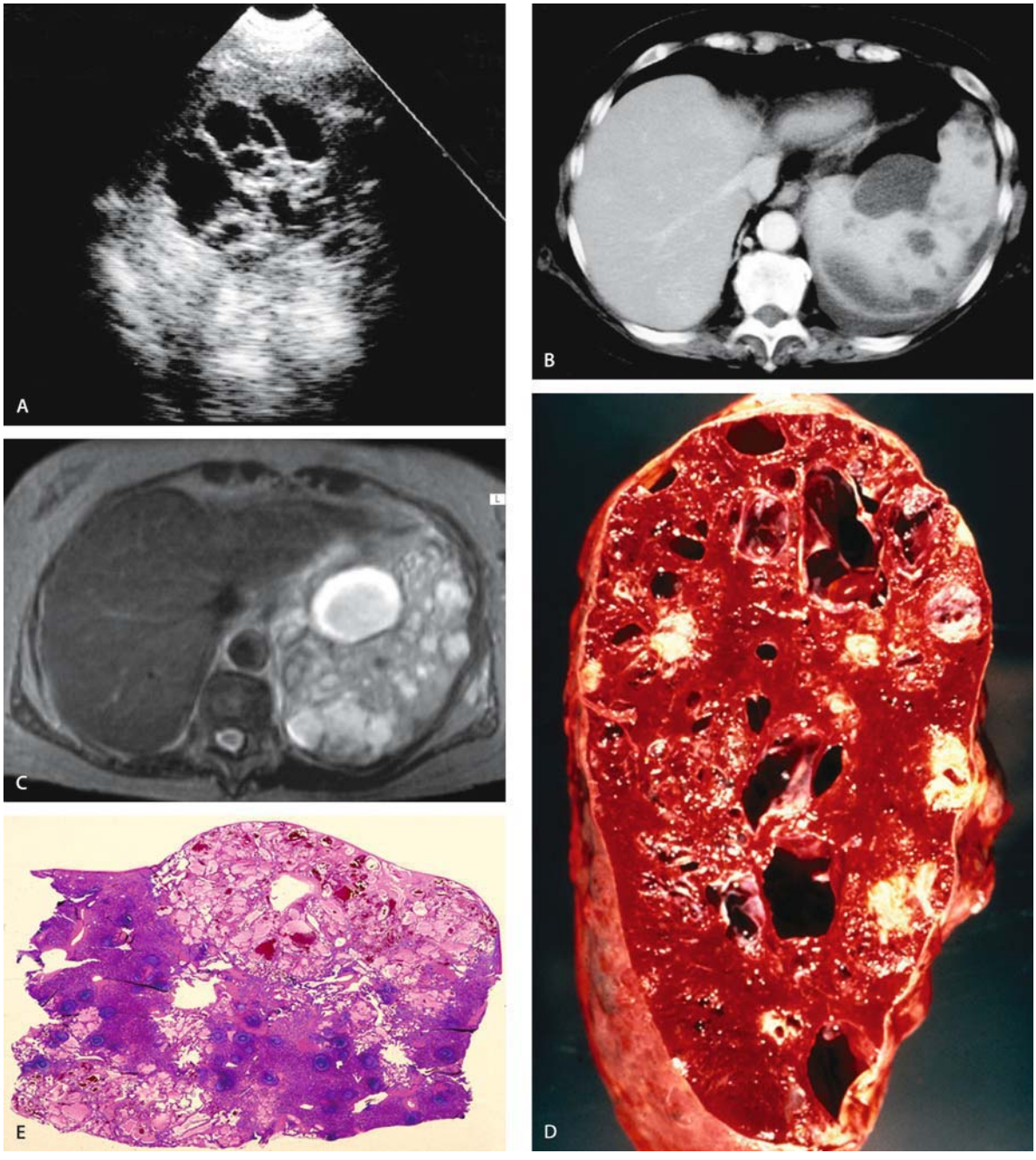

Fig. 3A–E. Splenic lymphangioma. **A** Sonography demonstrates the typical multicystic appearance of lymphangioma, with the presence of multiple anechoic cysts separated by septations, representing lymphatic spaces. **B** Contrast-enhanced CT scan shows multiple low-density, nonenhancing, thin-walled cysts, which appear, on MRI (**C**), markedly hyperintense on T2-weighted images, with hypointense structures representing septations. **D** Gross pathology. Cut section of specimen demonstrates a multilocular cystic mass. **E** Low-power microphotograph demonstrates endothelium-lined cysts

matosis) [21], usually subcapsular and mostly occurring in childhood. Like hemangiomas, they are also composed of endothelial-lined spaces containing lymph instead of red blood cells [22].

Pathology

Lymphangiomas are usually divided into three types: capillary, cavernous and cystic, depending on the size of the dilated lymphatic channels. Lymphangioma of the spleen can be of any of the three above-mentioned types [23].

Histologically, lymphangiomas are composed of endothelium-lined cysts of the lymphatic system and classified as capillary, cavernous or cystic depending on the size of the lymphatic channels (Fig. 3). Occasionally the cystic spaces of a lymphangioma contain red blood cells, secondary to hemorrhage. Gross pathology classically shows a unilocular or multilocular cystic mass [24].

Radiologic Findings

On sonography, cystic lymphangiomas usually occur with a multicystic appearance in an enlarged spleen (Fig. 3). The cysts may appear anechoic or hypoechoic. The presence of internal echoes within cysts depends on the size of the lymphatic spaces and the presence of septa and proteinaceous material [23, 25]. If the cystic spaces are small and below the resolution of the US technique, then portions of the mass may appear hyperechoic due to the existence of numerous reflecting interfaces [23].

CT shows a mass made up of multiple low-density, nonenhancing, sharply marginated, thin-walled cysts, usually subcapsular with or without mural calcifications [26–28] (Fig. 3). After intravenous injection of iodinated contrast the cystic fluid does not enhance, while the septations present moderate enhancement [23].

On MR, lymphangiomas appear as multiple, well-defined cysts, hypointense on T1-weighted images and markedly hyperintense on T2-weighted images [27], with hypointense internal structures on T2-weighted images, representing septations (Fig. 3). On T1-weighted images, the cysts may rarely be hyperintense, due to the proteinaceous nature of the fluid or internal hemorrhage [23].

Hamartoma

Definition

Hamartomas of the spleen are rare benign tumors, classically composed of anomalous mixtures of normal elements of splenic tissue, with red pulp predominating [29]; they may also contain cystic or necrotic components and small calcifications [30] . They are usually less than 3 cm in diameter, but can reach up to 18 cm in size [31] .

Pathology

Histologically, hamartomas are classified into the red pulp (vascular) type, the white pulp (lymphomatous) type, and the mixed type [32]. Grossly, they appear as discrete, circumscribed nodules of various sizes without encapsulation and may be solitary or multiple (Fig. 4). Splenic hamartomas are usually solid lesions but may have a cystic component [32].

Radiologic Findings

Sonographically, hamartoma may appear as a well-defined, homogeneous, echogenic mass, which may contain cystic areas [32, 33]. In a reported case of splenic hamartoma, gray-scale sonogram showed a hypoechoic, homogeneous splenic mass, whereas color Doppler sonography demonstrated multiple radial blood-flow signals inside the mass, and spectral analysis confirmed arterial and venous flow [34].

On unenhanced CT scan, these tumors may be isodense or hypodense and, when they become larger, may show a central area of low attenuation, representing a star-like scar or a region of necrosis with focal calcification (Fig. 4).

MRI demonstrates a well-defined mass, isointense on T1-weighted images, and hypointense to hyperintense on T2-weighted images. After contrast medium administration, both CT and MRI show, on delayed images, more uniform contrast enhancement [20, 35].

Hemangiopericytoma

Definition

Hemangiopericytomas are rare vascular tumors apparently arising from Zimmerman's pericytes [36]. They are most frequently described in the muscles of the lower extremities and subcutaneous tissue [37], with a parenchymatous origin being extremely infrequent, but especially aggressive [38].

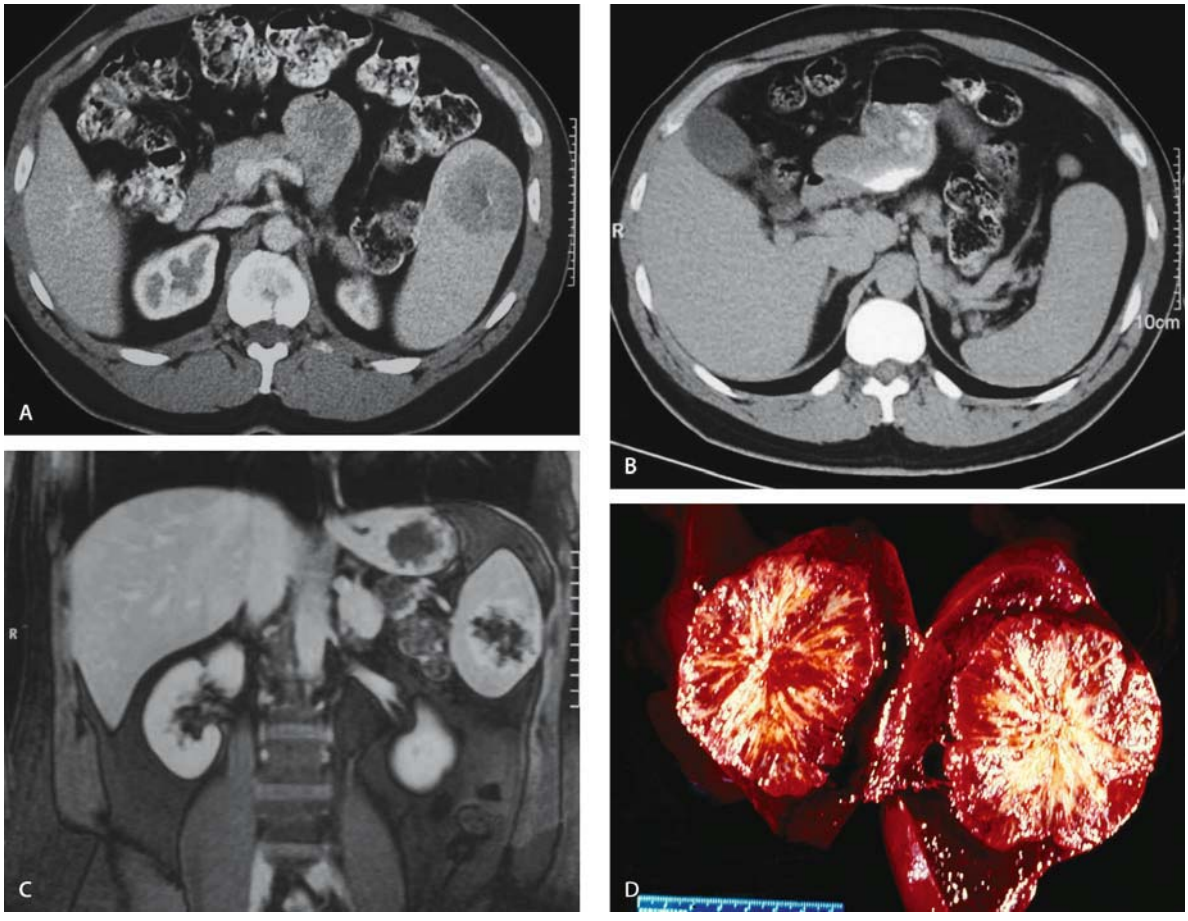

Fig. 4A–D. Splenic hamartoma. **A** Arterial phase contrast-enhanced axial CT scan shows a rounded, well-demarcated, splenic mass with a central scar formation. **B** Delayed-phase contrast-enhanced axial CT scan shows gradual fill in of the lesion with contrast. **C** Coronal gadolinium-enhanced MR image shows the heterogeneous enhancement of the lesion during the early phase of splenic enhancement. **D** Cut section of the gross specimen nicely demonstrates the central scar

Pathology

This kind of tumor originates from pericytes. Histologically, hemangiopericytomas consist of numerous capillary channels lined with epithelium and surrounded by and enclosed by nests and masses of spindle cells, which occasionally can be ovoid or even round. Silver impregnation can be used to confirm that these cells are outside the basement of the endothelium and hence are pericytes rather than endothelial cells [39].

Radiologic Findings

On CT scan, reported findings include the presence of a large mass with polylobular contour, along with numerous other smaller lesions disseminated throughout the whole spleen. Hyperattenuation of the solid portions and internal septations after contrast medium administration reflects the vascularity of this tumor [40].

Epithelioid Vascular Tumor

Definition

Epithelioid vascular tumors are unusual vascular neoplasms ranging from epithelioid hemangioma (histiocytoid hemangioma, angiolymphoid hyperplasia with eosinophilia) to malignant epithelioid angiosarcoma [41].

Pathology

Epithelioid vascular tumors are characterized by the proliferation of epithelioid (histiocytoid) endothelial cells accompanied by an infiltrate of lymphocytes and eosinophils [41].

Radiologic Findings

Reported radiologic findings are nonspecific and often make the diagnosis difficult, especially when fibrosis, calcification, thrombosis or necrosis is present [42]. On CT, these tumors usually appear as focal, rounded or irregular areas of heterogeneous low attenuation [43]. Occasionally, cystic or necrotic portions may be demonstrated. MR may demonstrate a well-defined mass, with heterogeneous texture and hypointense radial streaks representing fibrosis on both T1- and T2-weighted images [42].

Littoral Cell Angioma

Definition

Littoral cell angioma is a very rare splenic tumor that arises from splenic sinus-lining cells or littoral cells [44].

Pathology

Grossly, the presence of an enlarged spleen with multiple small nodules is typical. These nodules are histologically characterized by the presence of multiple vascular spaces similar to the venous sinuses of the spleen and covered by high endothelial cells that show hematophagocytosis. With the typical littoral cell angioma, no recurrent or metastatic disease is demonstrated [45]. A malignant type, termed littoral cell angiosarcoma, possesses cytologically atypical cells and malignant morphologic features, including invasion of surrounding organs [46].

Radiologic Findings

Sonography may demonstrate mainly isoechogenic lesions, with anechogenic foci representing prominent, cavernous blood-filled spaces [47, 48]. Splenomegaly with a mottled echo texture of the spleen, but no presence of discrete focal masses, has also been described [46].

CT scan shows an enlarged spleen containing multiple, ovoid low-attenuation nodular masses [48, 49].

On MR, the lesions show a characteristic signal intensity, hypointense on both T1- and T2-weighted images, which is caused by the presence of hemosiderin in these entities due to the hematophagocytic capacity of the neoplastic cells [47, 50].

Lymphoma

Definition

Lymphoma is the most common malignant tumor involving the spleen and may be categorized into primary splenic lymphoma (without evidence of nodal disease) or lymphomatous involvement as a part of disseminated disease [11, 51]. The spleen is involved in approximately 23%–40% of patients with Hodgkin's disease (HD) or non-Hodgkin lymphoma (NHL) at the time of initial diagnosis [52] .

Although splenomegaly is found in 80% of cases, its presence alone is not a reliable sign of lymphomatous involvement; on the other hand, one-third of normal-sized spleens exhibit tumors in patients with Hodgkin's disease [2].

Pathology

Four distinct gross pathologic patterns of splenic involvement in lymphoma have been described: 1) homogeneous enlargement without masses; 2) miliary masses (<5 mm in diameter); 3) multiple masses of various sizes (1–10 cm); and 4) a large solitary mass (>5 cm) [53] (Fig. 5). High-grade NHL (e.g., large cell lymphoma) and HD in an advanced stage commonly produce the last two patterns of disease. Lymphocytic lymphomas most likely show a miliary pattern, and low-grade lymphomas typically cause homogeneous involvement [54]. Primary splenic lymphoma usually presents with a mass or masses rather than splenomegaly alone [55].

Radiologic Findings

On ultrasound, splenic lymphoma typically shows a diffuse or focal hypoechoic pattern [56]. Four patterns of involvement have been reported: 1) diffuse heterogeneity (37%); 2) focal, small nodular hypoechoic lesions smaller then 3 cm in diameter (39%); 3) focal, large nodular hypoechoic lesions larger than 3 cm in diameter (23%) (Fig. 5); and 4) bulky mass lesions (2%) [57]. Patients with low-grade HD and NHL commonly present diffuse infiltration of the splenic parenchyma with small nodules. High-grade NHL usually shows focal lesions greater than 3 cm in diameter. Hyperechoic lesions have also been described.

The CT appearance of splenic lymphoma mirrors the variety of pathologic appearances, including 1) homogeneous enlargement without a discrete mass; 2) a solitary mass (Fig. 5); 3) multifocal lesions; and 4) diffuse infiltration [11]. The focal lesions are typically low attenuating and usually range from less than 1 up to 10 cm. The infiltrative pattern and small tumor foci less

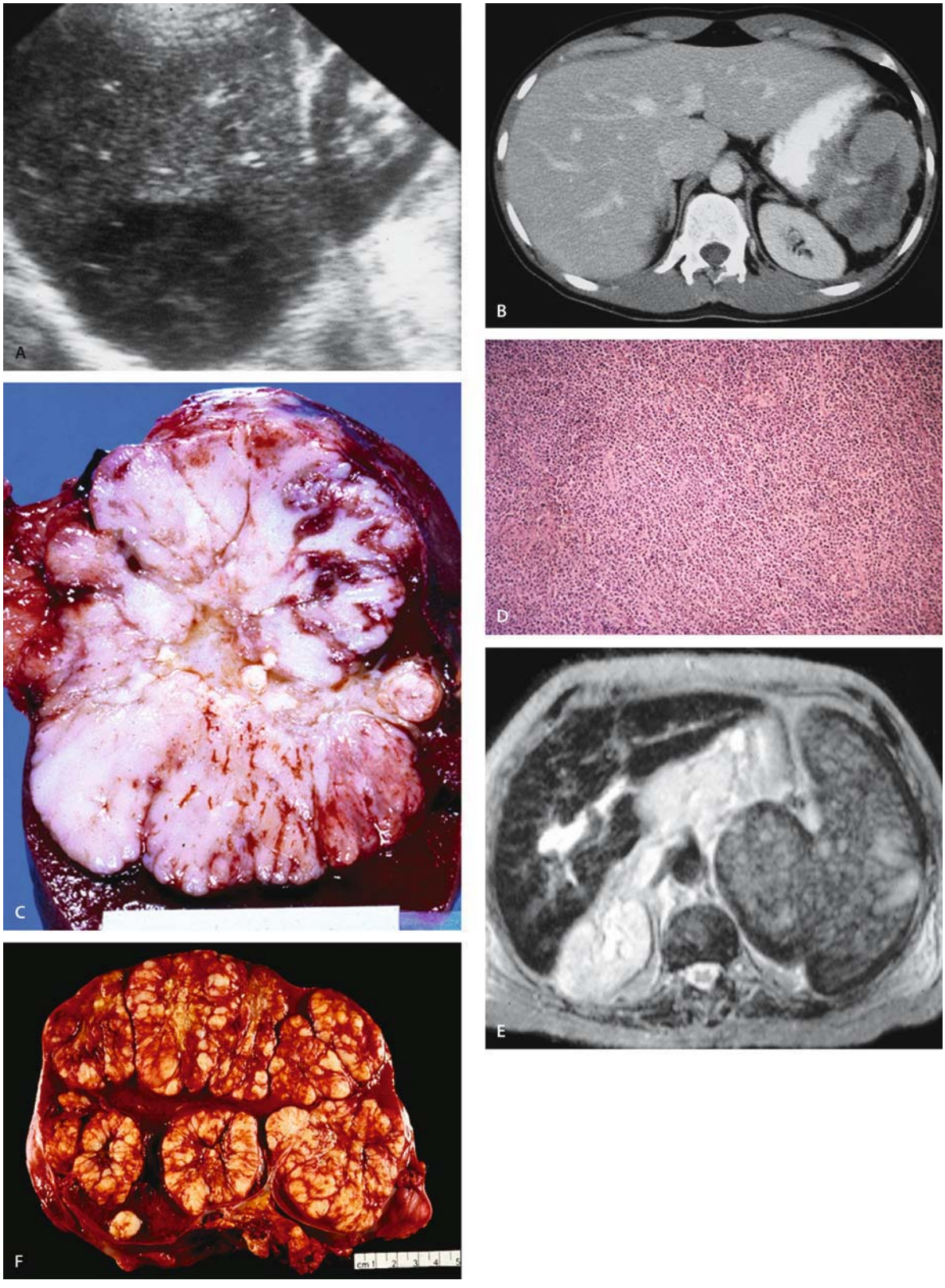

Fig. 5A–F. Splenic lymphoma. **A** Ultrasonography shows a focal large nodular, hypoechoic lesion (pattern type 3). **B** Contrast-enhanced CT demonstrates a focal, low-attenuation lesion in the spleen. **C** Gross pathology. Cut section of specimen shows the large solitary mass appearance of splenic lymphoma. **D** Low-power microphotograph demonstrates the presence of lymphatic tumor cells. **E** T2-weighted images show multiple small nodular hyperintense lesions scattered throughout the spleen. **F** Gross pathology as appears on the corresponding cut section of specimen

than 1 cm in size may be difficult to detect on CT [58]. It is rare to show a rim of contrast enhancement in lymphoma [59]. Primary splenic lymphoma may be bulky, transgress the splenic capsule and involve adjacent organs such as the diaphragm, stomach, pancreas, and abdominal wall [60]. After intravenous contrast administration, these masses enhance only minimally and appear hypodense with respect to the surrounding spleen [61]. Calcifications in splenic lymphoma may be occasionally detected, but probably represent dystrophic calcification secondary to hemorrhage, necrosis, and subsequent fibrosis [59].

On MR, the T1 and T2 relaxation and proton-density values of lymphoma and normal splenic parenchyma are unfortunately similar [62]. However, by using fast pulse sequences (e.g., double-phase multisection dy-

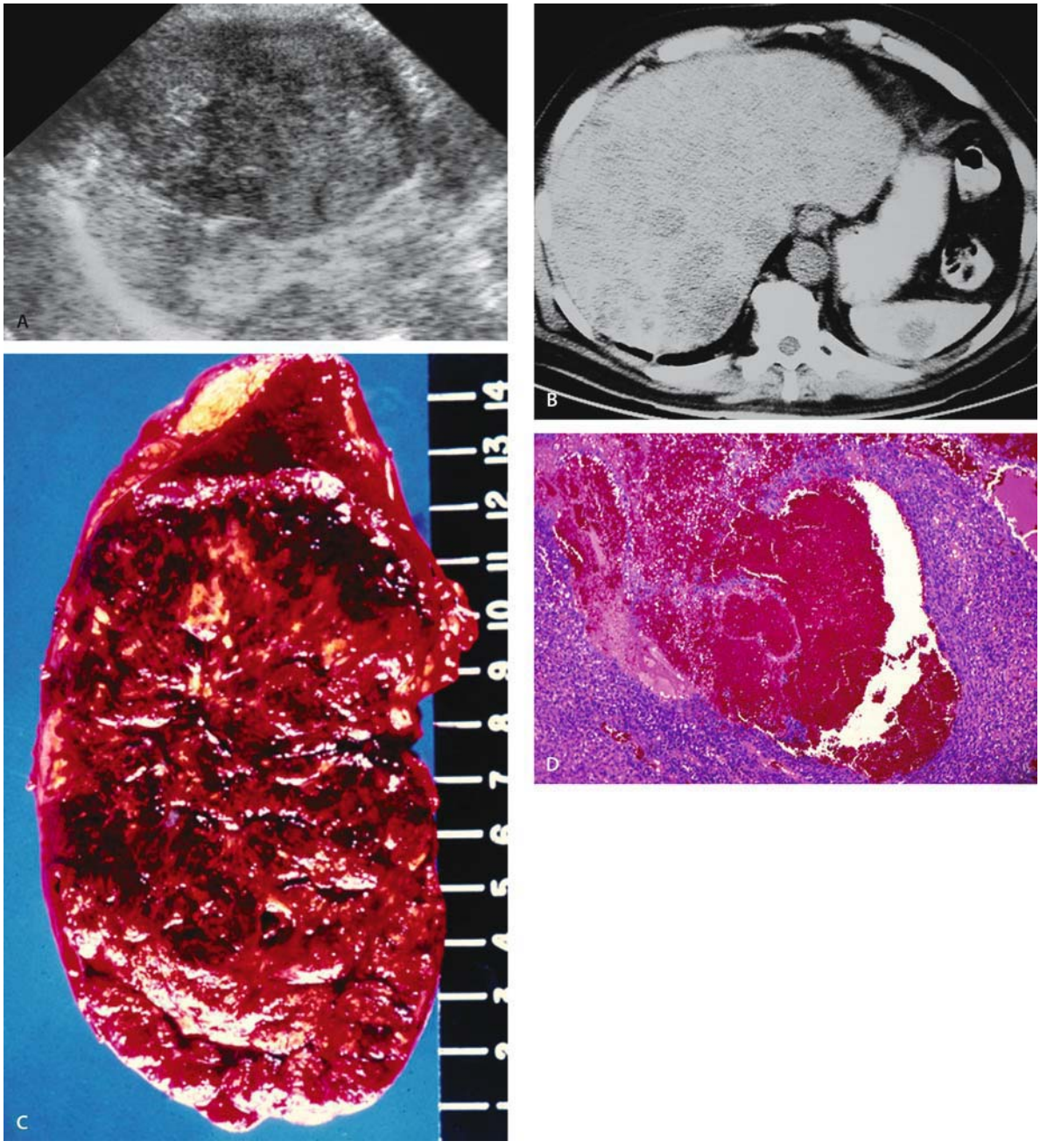

Fig. 6A–D. Splenic angiosarcoma. **A** Ultrasound shows a large splenic, discrete echogenic mass. **B** Unenhanced CT scan shows a focal, poorly defined lesion of low attenuation in the spleen. Note the presence of multiple, similar low-density lesions scattered throughout the hepatic parenchyma. **C** A cut section of gross splenic specimen shows multiple hemorrhagic nodules varying in size. **D** Low-power microphotograph demonstrates vascular channels and sarcomatous stroma

namic MR imaging) lymphoma may appear clearly as hypointense areas compared with enhanced normal parenchyma [62]. Furthermore, when the lesions are cystic, necrotic or hemorrhagic, they are easier to detect [63] (Fig. 5). Also, use of MR contrast media such as superparamagnetic iron oxide, or AMI-25, has improved detection of splenic lymphoma [54].

Angiosarcoma

Definition

Angiosarcoma, although exceedingly rare, is the most common primary nonlymphoid vascular malignant tumor of the spleen, with a poor prognosis and early widespread metastases.

Pathology

Angiosarcoma is a malignant neoplasm of vascular origin, characterized by masses of endothelial cells displaying cellular atypia and anaplasia.

Grossly, the spleen is enlarged and typically contains multiple hemorrhagic nodules varying in size, frequently associated with hemorrhage, infarction, and necrosis [64]. Microscopically, all degrees of differentiation of these tumors may be found, but two main features have been described: the formation of vascular channels and a sarcomatous stroma [6] (Fig. 6). Various patterns are recognized, including a spindle cell variant, papillary type, and undifferentiated sarcomatous variety; in this more malignant variant, pleomorphism, tumor giant cells, and mitoses are characteristic.

Radiologic Findings

Ultrasound may show a mildly enlarged spleen with multiple hyperechoic masses or a solitary mass with a complex echo pattern [65] (Fig. 6).

CT may demonstrate a diffuse, poorly defined focal mass of heterogeneous or low attenuation in an enlarged spleen with occasional intratumoral necrosis and subcapsular or extracapsular blood collections [40, 66] (Fig. 6). Areas of high attenuation on unenhanced CT may represent acute hemorrhage or hemosiderin deposits. Contrast enhancement of angiosarcoma may be similar to that of cavernous hemangioma, although the pattern of enhancement is variable, ranging from the presence of multiple low-attenuation masses within the spleen to a mottled nodular enhancing appearance [66].

MRI, on all pulse sequences, may exhibit multiple nodular masses with low signal rims, caused by hemosiderin deposition [11]. The signal intensity of central portion on T1-weighted images may vary, depending on the degree of necrosis and hemorrhage [11, 67]. Hyperintense areas encountered in T1- and T2-weighted images may be considered as regions of subacute hemorrhage [67] . Enhancement of the tumor with gadolinium is intense [66].

Metastases

Definition

Splenic metastases are uncommon and occur only in a few percent of patients with widespread malignant disease, usually resulting from hematogenous spread from primary tumors, e.g., in breast, lung, ovary, stomach, prostate, and malignant melanoma [11]. However, solitary splenic metastases have been described, without evidence of involvement of other organs [68].

Pathology

One-third of intrasplenic metastases appear as microscopic nodules, and the other two-thirds are grossly visible at autopsy [69]. Splenic metastases may be solitary (31.5%) (Fig. 7) or multiple (60%) nodular lesions or diffuse infiltrating lesions (8.5%) and can appear as discrete nodules or as confluent tumor masses [70].

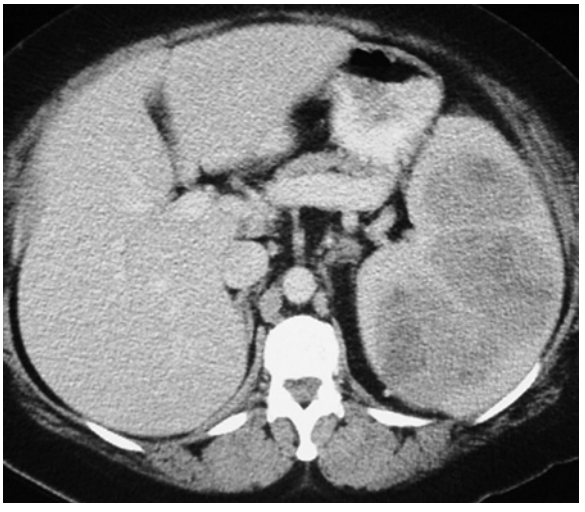

Fig. 7A–C. Splenic metastases. **A** Contrast-enhanced CT scan demonstrates a low-attenuating mass in the spleen. **B** A cut section of the spleen demonstrates a large solitary and heterogeneous lesion. **C** Photomicrograph shows the presence of metastatic cells

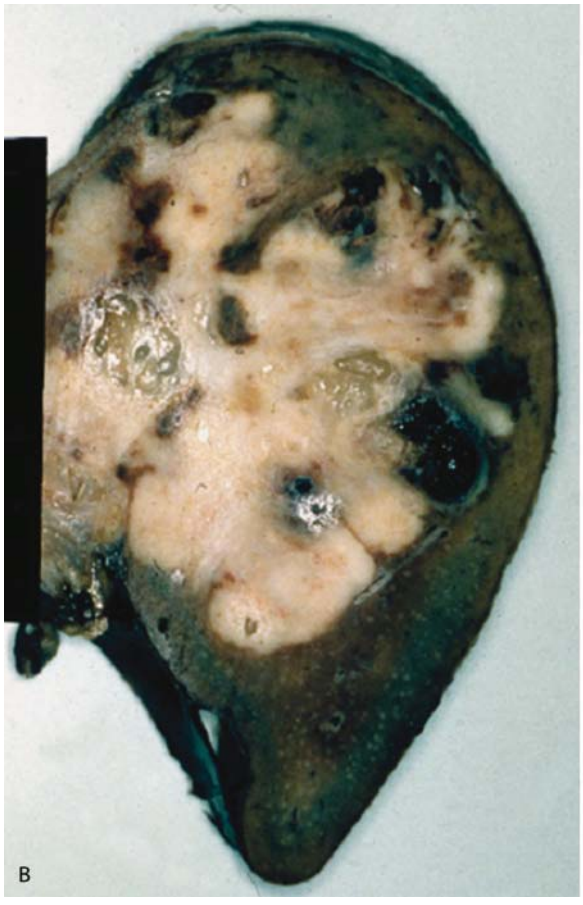

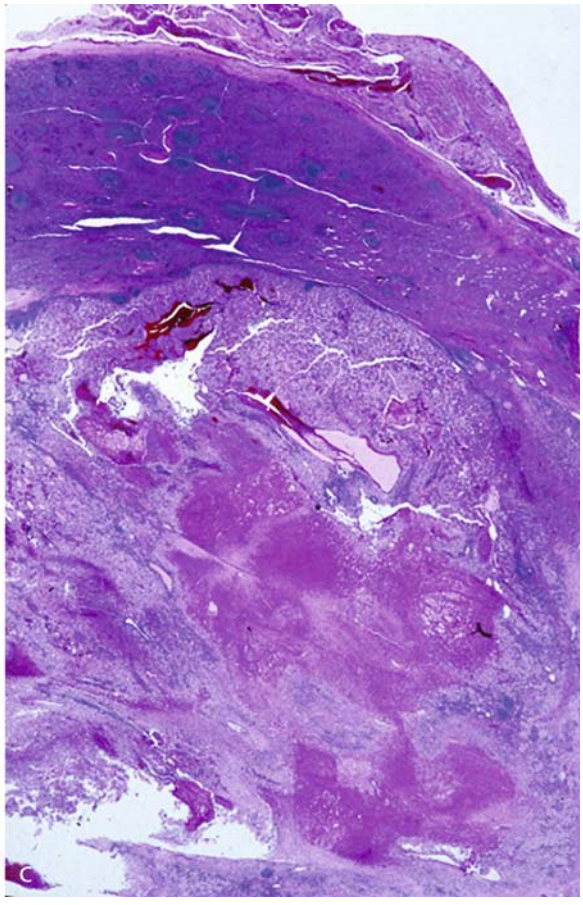

Fig. 7B, C.

Radiologic Findings

On ultrasound, splenic metastases are predominantly hypoechoic, but may display a mixed or hyperechoic appearance [11]. Larger lesions tend to be more complex than smaller ones, and diffuse involvement of the spleen may be seen in 10% of cases [71].

On CT, splenic metastases typically appear as low-attenuating solid or cystic masses with homogeneous or occasionally heterogeneous contrast enhancement [11] (Fig. 7).

MRI is accurate to demonstrate splenic metastases with necrosis or hemorrhage, which appear hyperintense on T2-weighted images. Detection of smaller metastases is harder without intravenous contrast medium administration, because they usually have, like lymphoma, the same MR tissue characteristics as the normal splenic parenchyma [63]. The use of ferrumoxides has been shown to improve detection of splenic metastases among patients with widespread malignancy [72].

Infectious Disorders

Bacterial Abscess

Definition

Splenic pyogenic abscesses are uncommon, with a reported incidence less than 1% in large autopsy series [73]. However, their frequency is growing as a result of an increasing number of immunosuppressed or chronically debilitated patients because of aggressive chemotherapy regimen, hematological disorders, diabetes, and AIDS [74, 75]. Immunosuppressed patients account for 25% of patients with splenic abscess [76]. The most common pathogens are streptococci, staphylococci and salmonella, but every pyogenic organism may be involved.

Pathology

Histologically, an abscess consists of dead leucocytes (pus) surrounded by a highly vascularized fibrous capsule, the wall of the abscess (Fig. 8).

Radiologic Findings

On US, splenic pyogenic abscesses typically appear as focal hypo- or anechoic lesions or as lesions with a solid and cystic component [77] (Fig. 8). They may also appear similar to cysts, often with a thick and irregular wall, and they may show echoes due to debris, septations or gas bubbles [77]. Gas is uncommon but, if it is present, increased echogenicity combined with "dirty" shadowing can be demonstrated [22].

CT may show the presence of a focal low-attenuating well-defined lesion, with an attenuation ranging from 20 HU to 40 HU [78]. Minimal peripheral contrast enhancement may be present when a capsule has developed, although it is less common in splenic than in he-

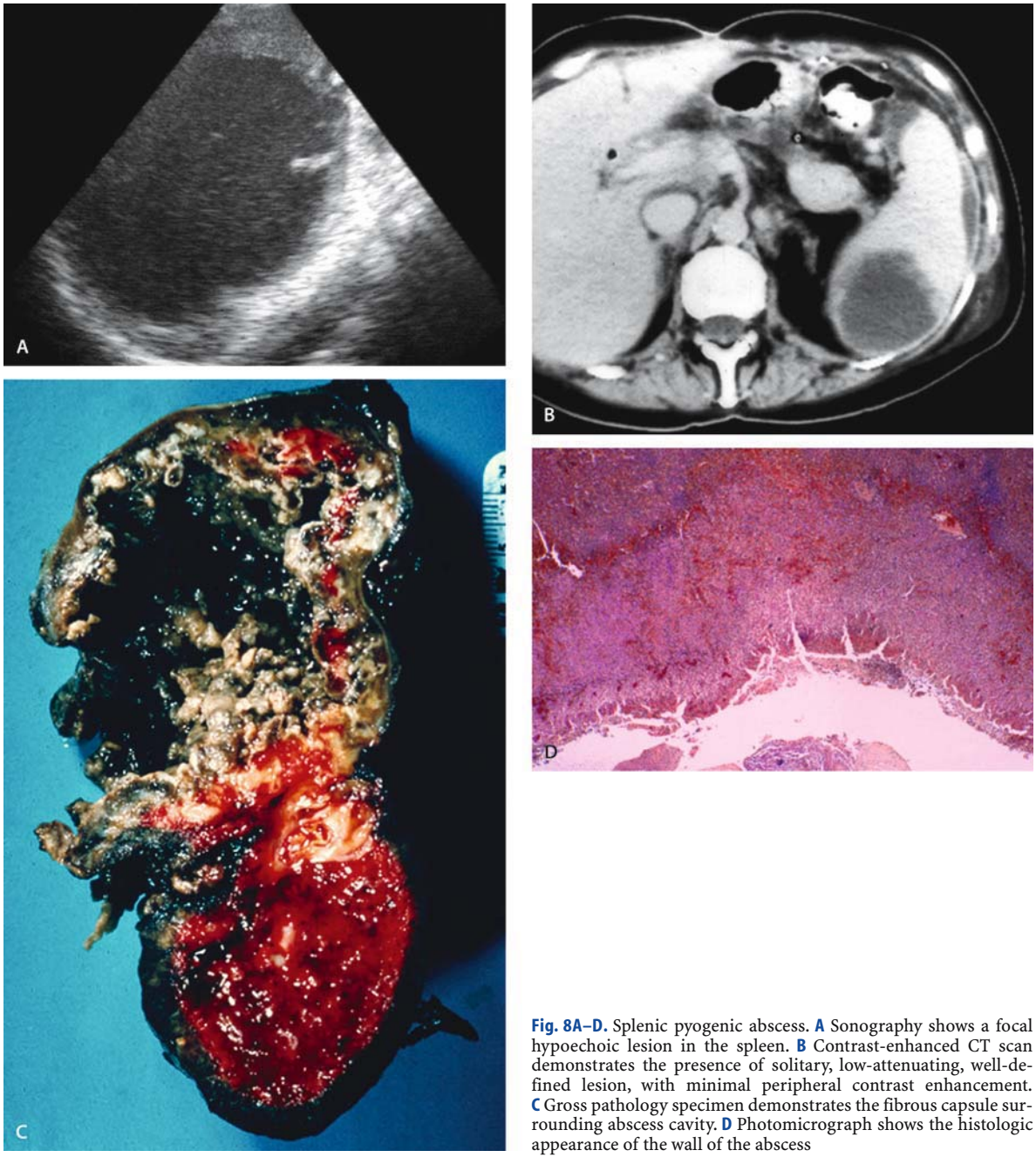

Fig. 8A–D. Splenic pyogenic abscess. **A** Sonography shows a focal hypoechoic lesion in the spleen. **B** Contrast-enhanced CT scan demonstrates the presence of solitary, low-attenuating, well-defined lesion, with minimal peripheral contrast enhancement. **C** Gross pathology specimen demonstrates the fibrous capsule surrounding abscess cavity. **D** Photomicrograph shows the histologic appearance of the wall of the abscess

patic abscesses (Fig. 8). The presence of gas is usually diagnostic; unfortunately, only the minority of splenic abscesses contain gas [11, 74]. CT is very sensitive in detecting splenic abscesses but is not specific. There are several differential diagnoses, including splenic infarct, cysts, tumors, and hematomas, so fine-needle aspiration may be useful to confirm the diagnosis [79].

At MR imaging, splenic abscesses usually appear as low signal intensity on T1-weighted images, with high signal on T2-weighted images, but may have some low signal representing necrotic debris [80].

Fungal Infection

Definition

Fungal abscesses have been reported to account for up to 26% of splenic abscesses [81]. The most common pathogen is *Candida albicans*, and is usually diagnosed in immunocompromised patients on therapy for leukemia. Other fungi include *Aspergillus* and *Cryptococcus* fungi.

Pathology

Histologically, concentric rings with central necrotic hyphae can be seen; these rings are surrounded by viable hyphae and a rim of peripheral inflammation [82]. Grossly, the entire spleen may demonstrate multiple small (less than 5 mm in size) fungal deposits (Fig. 9).

Radiologic Findings

Ultrasound may demonstrate the presence of multiple, small, rounded, hypoechoic areas scattered throughout the spleen or a diffusely hypoechoic spleen [83].

Similarly, on CT, multiple small lesions of relatively low attenuation, typically ranging from a few millimeters to 2 cm in diameter, are seen (Fig. 9). Occasionally, a central area of higher attenuation or a wheel-within-a-wheel pattern may be demonstrated [22].

At MR imaging, splenic fungal abscesses appear as multiple small lesions, which are hypointense on T1-weighted images and hyperintense on T2-weighted images [11] (Fig. 9). The use of fat saturation with T2-weighted images may improve detection of these small lesions, as well as the use of gadolinium [71].

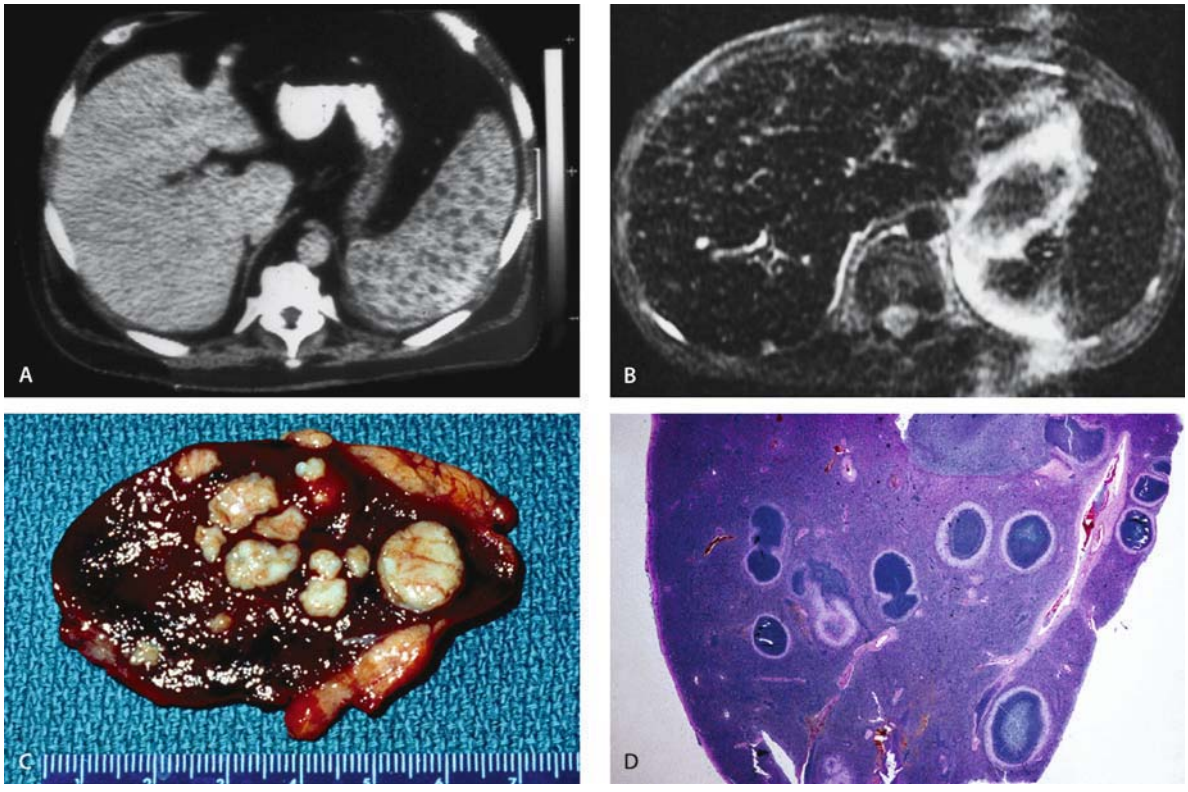

Fig. 9A–D. Candidiasis. **A** Contrast-enhanced CT scan shows multiple, tiny (<1 cm), low-attenuation lesions scattered throughout the spleen. **B** The T2-weighted MR image demonstrates the presence of diffuse small hyperintense lesions in the spleen and in the liver. **C** Gross pathology specimen of the spleen shows multiple, small, white nodules throughout the parenchyma. **D** Low-power view of splenic specimen shows multiple candidiasis microabscesses, with a peripheral zone of fibrosis and a central area of necrosis

Tuberculosis

Definition

Tuberculosis is a chronic bacterial infection caused by *Mycobacterium tuberculosis* and characterized by the formation of granulomas in infected tissues and by cell-mediated hypersensitivity. The usual site of disease is the lung, but other organs may be involved. The rate of extrapulmonary involvement increased with the onset of the HIV epidemic [84]. TB of the spleen is extremely common in patients with disseminated disease; however, it is not usually identified at initial presentation [85]. When present, there usually is miliary hepatosplenic dissemination in association with miliary pulmonary TB [86]. Miliary TB may manifest only as mild to moderate splenomegaly [11].

Pathology

Histologically, a TB granuloma consists of giant cells and epithelioid cells and is characterized by a tendency for fibrosis and caseation, a unique form of nonliquefying necrosis [87]. Caseous necrosis of the tubercle begins after 2–4 weeks, and fibrous scarring may ensue (tuberculoma).

Radiologic Findings

In the miliary form, US may demonstrate the bright-spleen pattern, consisting of a diffuse increase in echogenicity or the presence of small hypoechoic lesions. On CT, tiny, low-density foci scattered throughout the spleen may be seen (Fig. 10); when the lesions are larger, they may appear as small, focal splenic nodules of low attenuation. Occasionally, small peripheral wedge-shaped areas of low attenuation may be present, which represent infarcts from septic emboli [87].

In the macronodular form, occurring less commonly, US may demonstrate the presence of round and hypoechoic areas. On CT, the disease appears as a diffuse spleen enlargement containing multiple, low-density, 1- to 3-cm round lesions or a single mass. This feature may evolve to an abscess with single or multiple low-density, septate, or honeycomb-like lesions. These lesions have irregular, ill-defined margins, and show, after intravenous contrast medium administration, minimal or slight central enhancement. With further evolution of the disease, the lesion typically appears as an abscess with single or multiple low densities with ring-like enhancement [88]. MRI may demonstrate a hypointense lesion with a less hypointense rim on T1-weighted images, which appears hyperintense with a less hyperintense rim on T2-weighted images.

Echinococciasis

Definition

Splenic infection by *Echinococcus* is uncommon and is usually associated with liver and/or lung involvement; *Echinococcus* is the only parasite to produce splenic cysts [71]. The most common organism is *Echinococcus granulosus*; less commonly, hydatid disease is caused by *Echinococcus multilocularis*. The cysts, solitary or multiple, may cause a focal mass effect or splenic enlargement and they may demonstrate aspecific, peripheral, ring-like calcification [71].

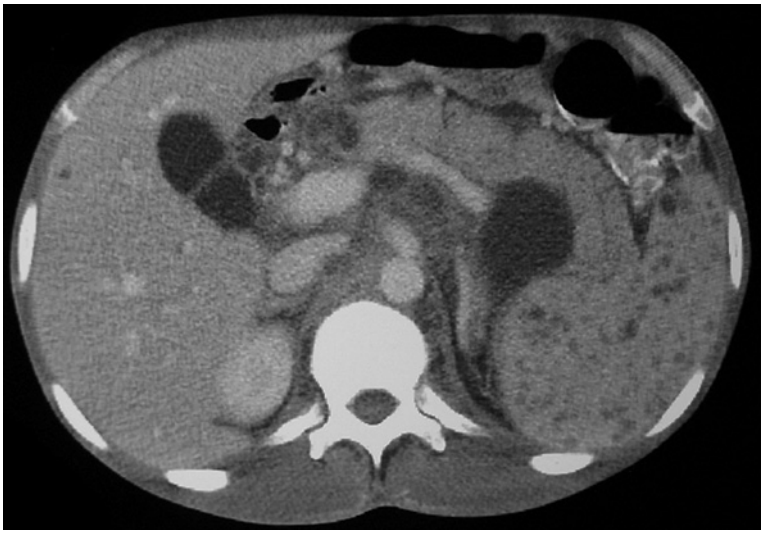

Fig. 10. Tuberculosis. Contrast-enhanced CT scan shows multiple, small, low-density lesions throughout the spleen

Pathology

Histologically, an *Echinococcus* cyst appears as a three-layered structure consisting of the inner germinal layer, the endocyst of hyaline and the pericyst, which is a thin band of vascularized, fibrotic compressed spleen (Fig. 11). Daughter cysts develop from germinal layers and are responsible for the multilocular form on gross pathologic examination. Scolices and fragments of the germinal layer constitute the so-called hydatid sand within the cyst [87].

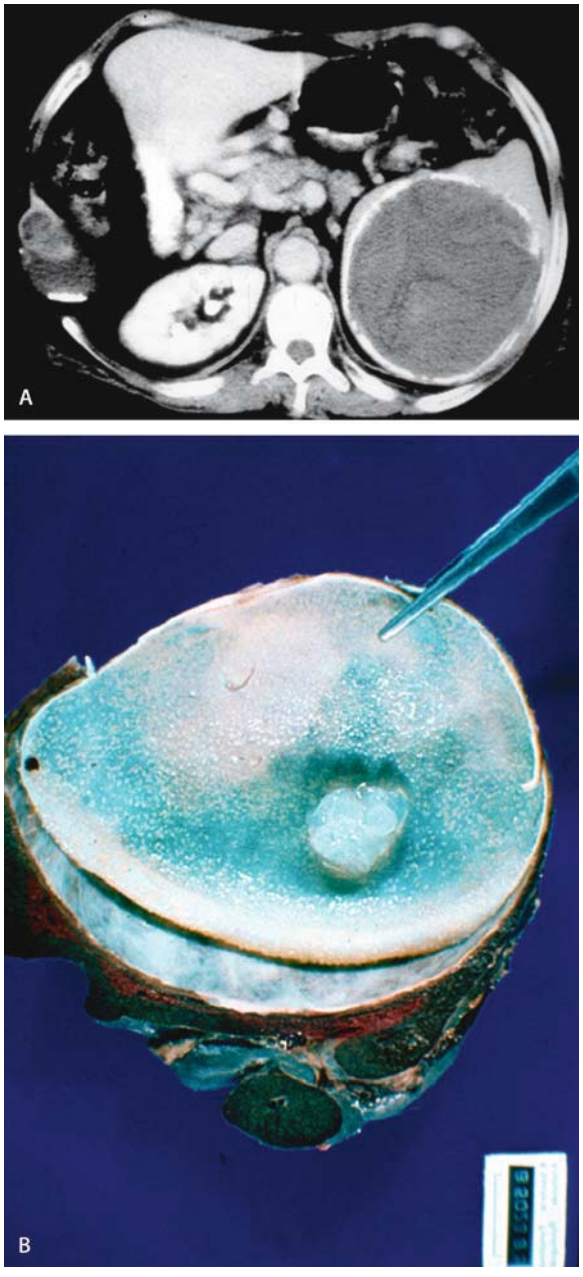

Fig. 11A, B. Echinococciasis. **A** Contrast-enhanced CT scan shows a round, low attenuating, cystic splenic mass with discontinuous rim calcifications. **B** Gross pathology of splenic specimen demonstrates the three-layered structure of the echinococcal cyst

Radiologic Findings

On sonography, anechoic lesions with daughter cysts and calcifications or occasionally a solid mass with fine internal echoes, representing debris, infolded membranes, scolices, or hydatid sand, may be seen [89]. Separation of the membrane produces a pathognomonic appearance for hydatid disease: the water-lily sign, resulting from the detachment and collapse of the inner germinal layer from the ectocyst. The collapsed germinal layer is seen as an undulating, linear collection of echoes either floating in the cyst or lying in the most dependent portion [90].

Unenhanced CT is sensitive in depicting subtle cyst wall calcifications [22]. The CT attenuation of the cyst depends on intracystic content, which usually shows water attenuation values. The presence of debris, hydatid sand and inflammatory cells may determine high CT values [91]. No enhancement is seen after the administration of contrast material, except for the possible ring-like enhancement of the external cyst wall and the enhancement of the internal trabeculae [92] (Fig. 11).

On MRI, typically a well-defined, rounded mass with signal intensity of water is seen on both T1- and T2-weighted sequences. The presence of protein or hemorrhage content in the cystic fluid may vary the signal intensity on T1-weighted images, whereas signal intensity on T2 images remains quite high [11]. The presence of a hypointense rim on T1-weighted and T2-weighted images, corresponding to wall calcification, and a multiloculated appearance are considered to be distinctive features of this lesion [93].

Pneumocystis carinii

Definition

Pneumocystis carinii infection is becoming more common with the increasing prevalence of an immunosuppressed population, and there is an increasing incidence of extrapulmonary disease. This infection affects 80% of patients with AIDS and is one of the major causes of morbidity and mortality [94].

Pathology

Histologically, splenic *P. carinii* infection causes necrotizing granulomas that eventually develop dystrophic calcification within the granulomas [94].

Radiologic Findings

In the early phase of the disease process, US typically shows tiny, highly reflective, nonshadowing foci and small hypoechoic lesions with cystic components. In later stages, calcification develops and acoustic shadowing is seen [95].

On CT, there is mild splenomegaly, and the spleen presents multiple low-attenuation lesions, which may enlarge and become progressively calcified in either a rim-like or a punctate fashion [11].

Cat-scratch Disease

Definition

Cat-scratch disease is an infection that usually affects children and adolescents after being scratched by a domestic cat [96] and it has been attributed to *Bartonella henselae*. The patient typically has had intimate exposure to a cat and presents with unilateral regional lymphadenitis and a site of inoculation.

Pathology

The lesions of the spleen may be distinguished in one or two distinct types on the basis of the histopathologic findings: vascular proliferative lesions (bacillary peliosis splenitis) or necrotizing granulomatous lesions [97].

Radiologic Findings

Sonographically, splenic granulomata generally appear as hypoechoic lesions, ranging from well defined and homogeneous to indistinct and heterogeneous; enhanced through-transmission may occur [98]. On CT, multiple scattered areas of low attenuation, ranging from 3 mm to 2 cm in size, in the spleen may be seen [96]. On MRI, the lesions appear hypointense on T1-weighted images and hyperintense on T2-weighted images [99]. Resolution of the lesions detected on imaging may take 4–6 weeks.

Systemic Disorders

Collagen Vascular Diseases

Definition

Collagen vascular diseases include a group of disorders of immune regulation, which, therefore, may involve the spleen, since it is an organ of the immune system. The function and structure of the spleen can be affected through lymphoid hyperplasia in the white-pulp area and through dysfunction of phagocytic red-pulp areas, which are responsible for the destruction of cells. This red-pulp dysfunction results from autoimmune cytopenias [100]. The most important collagen vascular diseases include: rheumatoid arthritis (RA) and Felty's syndrome, systemic lupus erythematosus, Wegener's granulomatosis and polyarteritis nodosa.

Rheumatoid arthritis (RA) is a chronic multisystem disease of unknown origin, characterized by persistent inflammatory synovitis of peripheral joints in a symmetric distribution and by variable extra-articular manifestations. Felty's syndrome consists of a triad of chronic RA, splenomegaly, neutropenia, and, occasionally, anemia and thrombocytopenia [101]. It occurs preferentially in the fifth to seventh decade of life and after long-standing RA (of more than 10 years); 70% of Felty's syndrome patients are female [100].

Systemic lupus erythematosus (SLE) is a multisystemic disease of unknown etiology in which tissues and cells are damaged by pathogenic autoantibodies and immune complexes, occurring in 90% of cases in women [102]. The spleen is involved in 15%–45% of patients; splenomegaly and lymphadenopathy are the most commonly reported findings. Possible complications are splenic infarction, spontaneous splenic rupture, functional asplenia and hyposplenia [100].

Wegener's granulomatosis is also a systemic disease of unknown origin, characterized by a clinicopathologic complex of necrotizing granulomatous vasculitis of the upper and lower respiratory tract, glomerulonephritis and variable degrees of vasculitis of small arteries and veins. The disease can affect any organ and system. Splenic involvement, however, generally is considered to be rare [103].

Polyarteritis nodosa (PAN) is a systemic inflammatory disease that causes a necrotizing vasculitis of medium-sized arteries and is also characterized by aneurysm formation [104].

Pathology

In Felty's syndrome, the enlargement of the spleen is caused by expansion of the red pulp and sinuses, which contain many macrophages [105].

Systemic lupus erythematosus is characterized, histologically, by the presence of large-and small-vessel necrotizing vasculitis with an onion-skin pattern.

In Wegener's granulomatosis, grossly, a central area of infarction surrounded by a red peripheral zone of splenic parenchyma has been reported [103]. Microscopically, granulomatous vasculitis of small and medium-sized arteries and veins, with thrombotic occlusion and hemorrhage, which causes infarction, may be seen [106].

In Polyarteritis nodosa, similarly to Wegener's granulomatosis, a necrotizing vasculitis of medium-sizes arteries may be seen; the disease is also characterized by aneurysm formation [104].

Radiologic Findings

Generally, in rheumatoid arthritis (RA), Felty's syndrome, and systemic lupus erythematosus, all the different imaging modalities (US, CT, and MRI) may be used to assess the presence of splenomegaly, splenic calcification, and splenic atrophy or for detection of complications such as rupture or splenic abscess [100].

In Wegener's granulomatosis, ultrasound may show a heterogeneous parenchymal architecture [107] or multiple hypoechoic intrasplenic nodules [108], with patency of the splenic artery and veins [107]. On CT, a diffuse pattern of splenic infarction has been reported in addition to a pattern of rim enhancement around a large central area of low attenuation [103]. MRI may demonstrate the presence of diffuse low signal intensity on T1-weighted images and high signal intensity on T2-weighted images, which represent the diffuse infarction pattern [109].

In polyarteritis nodosa, ultrasound and CT scans may be useful in the detection of splenic rupture or abscess formation [100].

Storage Diseases

Definition

In storage diseases, splenic dysfunction and anatomic distortion are the result of deposition of abnormal substances into the reticuloendothelial system (red-pulp area). The most common storage disorders involving the spleen are: Gaucher's disease, Niemann-Pick disease, Langerhans cell histiocytosis, amyloidosis, and iron-overload diseases.

Gaucher's disease is a metabolic disorder in which glucocerebroside accumulates in the reticuloendothelial system because of a deficit of the enzyme glucocerebrosidase and is characterized by the presence of focal nodules in different organ systems. The disease most often follows a chronic, progressive course, characterized by hepatosplenomegaly, anemia, thrombocytopenia, and erosion of the endosteum of long bones [1].

Niemann-Pick disease consists of a group of recessive autosomal diseases that are clinically and biochemically heterogeneous [110]. The basic defect is a disorder of sphingomyelin metabolism, leading to lipid deposition in certain organs such as brain, liver, and spleen. Four clinical forms of Niemann-Pick disease have been described by Schubert [111] on the basis of differences in the age of onset and the presence of neurological symptoms.

Langerhans cell histiocytosis (LCH) is a rare disorder of the bone-marrow-derived histiocytes, which may manifest in a single-system disease or in a multisystemic disorder [100]. Many organs may be affected, including bone, skin, bone marrow, liver, spleen, lungs, lymph nodes, pancreas, intestine, brain, pituitary gland, and buccal involvement.

Amyloidosis is the deposition of eosinophilic proteinaceous material (amyloid substance) in different organs. Splenic involvement is common, as the cells of the reticuloendothelial system play a major role in the formation of amyloid [112].

Iron-overload diseases consist of two different groups of disorders, depending on the location of iron deposition [113]. Primary hemochromatosis is a common inherited autosomal recessive disorder, consisting of abnormal parenchymal iron deposition, which occurs mainly in the hepatocytes but also in the pancreas, heart and synovium [100]. This parenchymal iron deposition may cause damage and organ dysfunction such as cirrhosis of the liver and development of hepatocellular carcinoma. Hemosiderosis is the term used for iron deposition in the reticuloendothelial system of the liver, spleen, lymph nodes and bone marrow; it most commonly develops after multiple blood transfusions (transfusional iron overload) and has little clinical significance [1].

Pathology

Gaucher's disease is pathologically characterized by the presence of focal nodules consisting of focal homogeneous clusters of Gaucher's cells (reticuloendothelial cells laden with glucocerebroside) and fibrosis or infarction [114].

In Niemann-Pick disease, the metabolic defect leads to the storage of lipids (sphingomyelin and cholesterol) in the histiocytes. These multivacuolated, lipid-laden cells (or foam cells) are mainly found in the reticuloendothelial system of the spleen and the liver, the lymph nodes, bone marrow and lungs. In certain types of the disease, they are also found in the central nervous system.

Langerhans cell histiocytosis of the spleen is characterized, histologically, by a diffuse splenic red-pulp infiltration by Langerhans cells, with the typical Birbeck granule within their cytoplasm on electron microscopic examination. Grossly, splenomegaly and splenic rupture have been described, and less commonly, the presence of a solitary nodular lesion [115].

Splenic amyloidosis is pathologically characterized by the presence of amyloid deposits in the splenic parenchyma and in the splenic vasculature [116].

Histologic features of the spleen in iron-overload diseases are iron deposition in the reticuloendothelial system in hemosiderosis and splenomegaly in association with symptomatic liver involvement in hemochromatosis [100].

Radiologic Findings

In Gaucher's disease, ultrasound, CT, and MR studies show marked splenomegaly and the resultant mass effect on adjacent structures. Ultrasound may also reveal multiple discrete hypoechoic lesions or hyperechoic lesions, depending on different histopathologic features of the nodules [100]. Aspestrand et al. [117] reported a case with multiple hypoechoic lesions surrounded by hyperechoic rims (the target appearance). CT may show multiple hypodense lesions, which, after intravenous contrast material administration, enhance to a lesser degree than the surrounding splenic parenchyma [118, 119] (Fig. 12). On MR, the spleen may demonstrate increased signal intensity on T1-weighted images as a result of shortening of the T1 relaxation time, which seems to result from accumulation of glucocerebroside in the spleen [120] (Fig. 12). The presence of splenic nodules, with variable signal intensity and variable size has also been described [121, 122]. Most splenic nodules are isointense on T1-weighted images and hypointense on T2-weighted images, while some lesions are hyperintense on T2-weighted images. A minority of lesions are hyperintense on T1-weighted images.

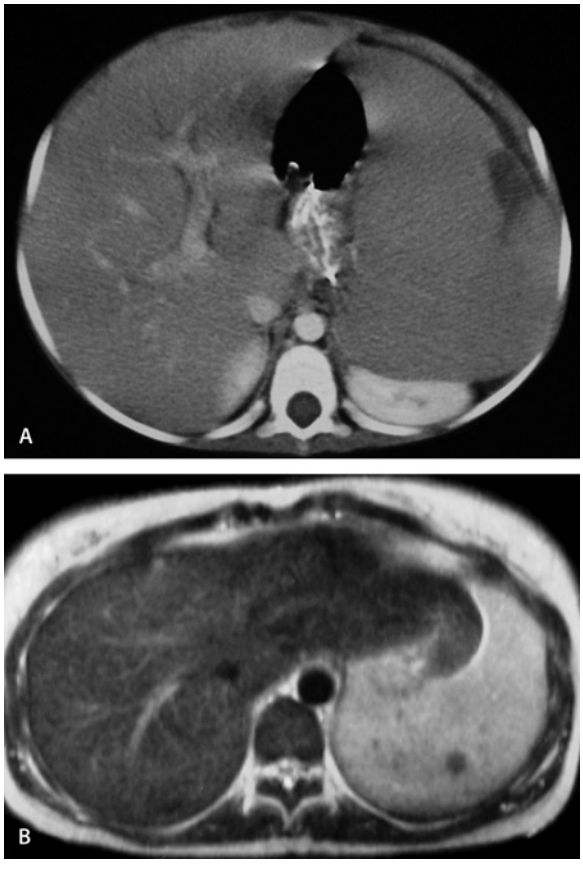

Fig. 12A, B. Gaucher's disease. **A** Contrast-enhanced CT scan demonstrates a subcapsular, wedge-shaped, low-density area, in an enlarged spleen. **B** On MRI the spleen shows increased signal intensity. Note the presence of splenic hypointense nodules

In Niemann-Pick Disease, ultrasound may show nodular splenomegaly with multiple, well-defined hyperechogenic nodules, which appear hypodense on a contrast-enhanced CT scan, probably due to the diminished blood flow [110]. On MR, a diffuse increase in signal intensity of the spleen on T1-weighted images and on T2-weighted-images has been reported, probably caused by the lipid infiltration of the splenic parenchyma. The presence of nodular lesions within the spleen, isointense on T1-weighted images and hyperintense on T2-weighted images has also been described [110].

Few cases of imaging findings of Langerhans cell histiocytosis have been reported. On sonography, the presence of multiple, round, hypoechoic lesions of varying sizes in an enlarged spleen have been described [123], as also a case of a solitary hypoechoic lesion within the spleen [124].

Cross-sectional imaging is rarely performed in patients with amyloidosis of the spleen, because most patients have no clinical symptoms related to splenic amyloid infiltration. No characteristic features that distinguish amyloidosis from other infiltrative disorders have been reported. Rarely, extensive visceral calcifications involving both the liver and the spleen have been described in primary amyloidosis [125]. Sonography and emergency CT may also be useful to confirm hemoperitoneum and an enlarged heterogeneous spleen in cases of acute splenic rupture [100].

In iron-overload diseases, CT shows diffuse increased attenuation values in the liver [1]. However, this finding is not specific and very insensitive for moderate degrees of iron deposition [100]. MRI is a more sensitive and a specific method to detect iron deposition because of the magnetic-susceptibility effect caused by the accumulated iron. This demonstrates a markedly decreased signal intensity (compared with that seen in skeletal muscle) in involved organs on T2-weighted images, especially on T2*-weighted gradient-echo images. In hemochromatosis, a low signal intensity on T2- and T2*-weighted images is found in the liver, pancreas, myocardium and endocrine glands, but the spleen remains normal [126]. In hemosiderosis, spleen, liver and bone marrow reveal decreased intensity on MR studies and the pancreas tends to be spared [1].

Sarcoidosis

Definition

Sarcoidosis is a systemic disease of unknown etiology that primarily affects the mediastinal and hilar lymph nodes, lung parenchyma, skin and eyes [1]. It is characterized by the presence of noncaseating granulomas in almost any organ [30]. Abdominal sarcoidosis is common and splenic involvement is microscopically demonstrated in approximately 24%–59% of patients, but its clinical significance is uncertain and splenic dysfunction is rare [127]. Mild splenomegaly occurs in 11%–42% of patients with sarcoid. The radiologic features in the abdomen are nonspecific, and most often the diagnosis is made by biopsy of peripheral nodes, liver, or skin [1].

Pathology

Histologically, sarcoidosis is characterized by noncaseating granulomas, frequently less than 2 mm in size, that consist of aggregates of Langerhans-type giant cells surrounded by necrotic or fibrotic tissues [128] (Fig. 13).

Radiologic Findings

Ultrasound may demonstrate the presence of splenomegaly and nonspecific diffusely increased echoes in the splenic parenchyma. However, Kessler et al. [129] reported, in a series of 17 patients with biopsy-proven sarcoidosis, eight patients to have normal splenic echogenicity and a normal spleen size. Focal hypoechoic or mixed echogenic lesions may also be present [1].

On CT, splenic sarcoidosis is usually not detected or abdominal involvement appears as nonspecific hepatosplenomegaly and retroperitoneal lymphadenopathy [130]. Multiple low-density intrasplenic lesions are present in 11%–33% of cases [131], ranging from 1 mm to 30 mm (Fig. 13). When nodules increase in size, a more coalescent hypodense nodular pattern is seen [132].

MRI may demonstrate splenomegaly and diffuse, heterogeneity with decreased signal intensity on T2-weighted images, representing chronic fibrosis [133].

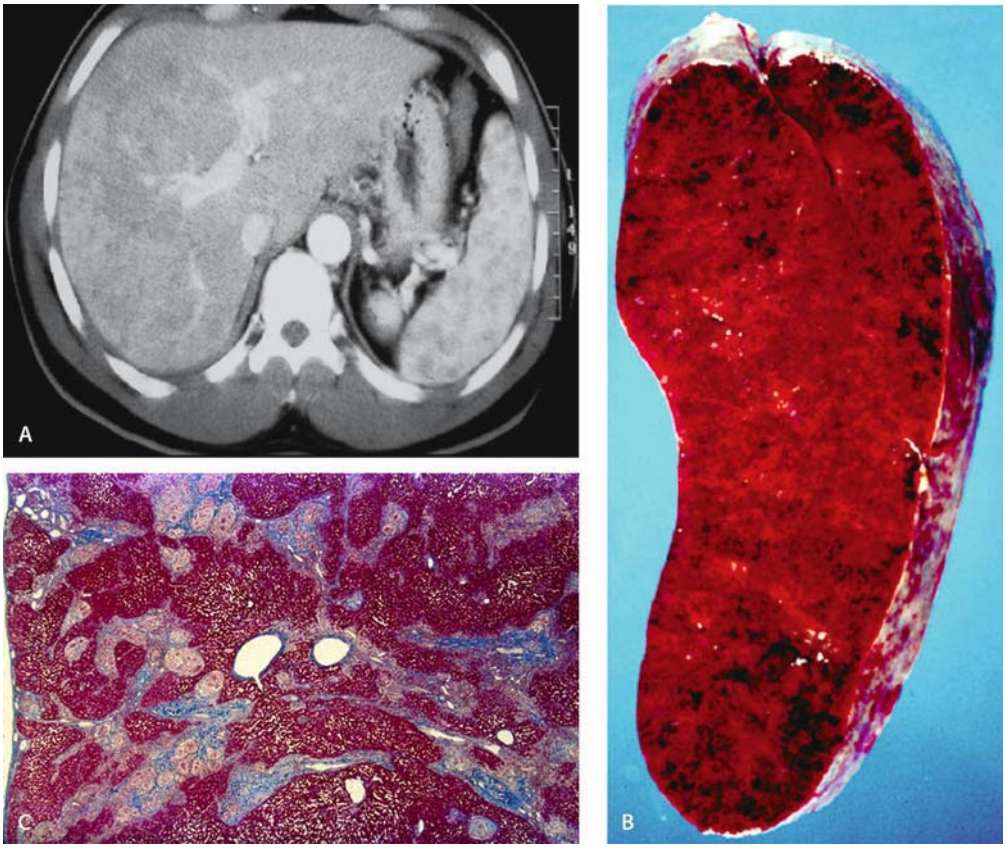

Fig. 13A–C. Sarcoidosis. **A** Contrast-enhanced CT scan shows numerous low-density lesions throughout the spleen. **B** Sarcoidosis of the spleen as it appears grossly. **C** Masson stain low-power view shows coalescing nonspecific granulomas

Hematologic Disorders

Sickle Cell Disease

Definition

Sickle cell disease is a common hereditary disorder caused by hemoglobinopathy and characterized by the destruction of abnormal shaped erythrocytes in the spleen, when the abnormal hemoglobin is desaturated. This situation leads to chronic microthrombosis in the microcirculation. Characteristic of this disease are infarction of the spleen and typical periodic vaso-occlusive crises [134]. In the homozygous subjects, a complete loss of spleen function occurs because of repetitive splenic infarction, while in heterozygous treated patients, the spleen may be damaged without function loss.

Pathology

Grossly, splenomegaly, secondary to sequestration of red blood cells, but also abscess or infarction, may be demonstrated. In older homozygous patients, a fibrotic, end-stage spleen with diffuse or patchy punctate or stippled calcification may be seen [71].

Radiologic Findings

Ultrasound may demonstrate, in an enlarged spleen, the presence of infarction, abscess, and other complications of the disease, but it is less adequate to detect the small, fibrotic, end-stage spleen in homozygous patients.

On unenhanced CT, the presence of splenic calcification and an increased density of the spleen due to calcification and iron deposition may be seen [135] (Fig. 14).

On MRI, the spleen shows a diffusely reduced signal, initially because of hemosiderin deposition, and subsequently because of calcification and fibrosis. In sequestration, areas of abnormally high signal, with dark rim, may be seen on T1-weighted images, as a result of the presence of subacute hemorrhage. Areas of infarction are seen as peripheral wedge-shaped areas of increased signal, on T2-weighted images, against the background of a low-intensity spleen [136].

Thalassemia

Definition

Thalassemia includes a group of congenital disorders characterized by a defect in synthesis of one or more subunits of hemoglobin. This leads to ineffective globin-chain and red-cell production, hemolysis, and anemia.

Pathology

In patients with beta-thalassemia major, the most severe form, deposition of iron complexes into the reticuloendothelial system of the spleen and other organs

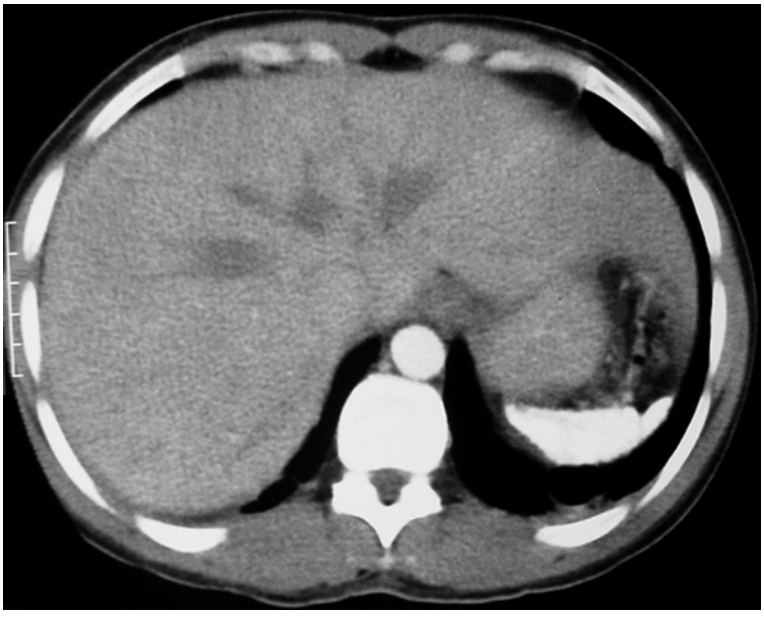

Fig. 14. Sickle cell disease. Early phase contrast-enhanced CT scan shows an increased density of the spleen due to extensive calcification

may be demonstrated and, often, the predominant hemosiderosis results in parenchymal damage [137].

Radiologic Findings

CT can demonstrate iron deposition as increased attenuation of the spleen [138]. MR is a more sensitive technique for detection of iron deposition due to iron's paramagnetic effects and may easily reveal the presence of iron with T2-weighted or T2*-weighted sequences. The possibility to quantify the amount of iron by using these sequences has been reported [139].

Acquired Hemolytic Anemia

Definition

Autoimmune hemolytic anemia is an acquired disorder, which may be idiopathic or secondary to other disorders, characterized by red-cell destruction, frequently intravascular. Shortened erythrocyte life and the presence of erythrocyte-specific antibodies have to be demonstrated for the diagnosis. Mild to severe splenomegaly may be seen. Paroxysmal nocturnal hemoglobinuria (PNH) is a subcategory of hemolytic anemia, characterized by chronic hemolysis with hemoglobinuria, iron-deficiency anemia, and venous thrombosis.

Pathology

These hemolytic disorders are histologically characterized by the presence of mild to marked splenomegaly resulting from reticuloendothelial cell hyperplasia, secondary to active erythrophagocytosis.

Radiologic Findings

MR imaging is a useful modality for demonstrating iron overload. In patients affected by PNH, MR usually shows normal signal intensity of the spleen similar to that of the liver on T1-weighted images and high signal intensity on T2-weighted images; eventually, the presence of iron deposition may be demonstrated after several blood transfusions (transfusional hemosiderosis)

Idiopathic Thrombocytopenic Purpura

Definition

Idiopathic thrombocytopenic purpura (ITP) is a hemorrhagic disorder characterized by a decreased platelet count despite the presence of normal or increased megakaryocytes in the bone marrow. The spleen is the major site of platelet destruction and is a site of production of anti-platelet antibodies.

Pathology

Histologically, the spleen in ITP frequently shows normal appearance even though its production of platelet antibodies may be considerable.

Radiologic Findings

Typically, splenomegaly is not demonstrated in most cases, being the unique characteristic of ITP. Imaging studies are not useful for the diagnosis of ITP, because of the absence of characteristic imaging features. However, imaging modalities may be used in the follow-up examination after splenic resection to evaluate for the eventual presence of accessory spleen.

Polycythemia Vera

Definition

Polycythemia vera is a disorder of unknown etiology characterized by a marked and persistent elevation in the total number of circulating red blood cells in association with cyanosis, leukocytosis, and thrombocytosis.

Pathology

Grossly, mild to moderate splenomegaly is seen in three-quarters of patients with polycythemia vera at the time of diagnosis [140]. Dense streaks of calcification have been occasionally described in the enlarged spleen.

Radiologic Findings

CT may demonstrate the presence of splenic infarcts with typical appearance, but also as large hypodense lesions [141]. When liquefactive necrosis and intraparenchymal gas formation are present, the differential diagnosis with splenic abscess may be difficult [142]. A case of focal extramedullary hematopoiesis in polycythemia vera, detected by MRI, has been reported [143]. This finding, which appeared as a focal mass-like lesion, showed homogeneous hyperintense signal on T2-weighted images, with progressive enhancement on dynamic studies after bolus injection of gadolinium.

Myelogenous Leukemia

Definition

This hematologic disease often involves the spleen, which appears increased in size in more than 90% of untreated cases.

Pathology

Leukemic spleens microscopically show diffuse and focal infiltration of leukemic cells and may present numerous infarcts throughout the parenchyma. With progression of disease, there is an obliteration of the underlying architecture.

Radiologic Findings

Sonography may demonstrate an enlarged spleen associated with increased echogenicity [144]. On CT, the spleen usually maintains a homogeneous, normal attenuation value. Generally, cross-sectional imaging modalities are useful to evaluate the size of the spleen and, therefore, the activity of disease.

Myelofibrosis

Definition

Myelofibrosis is a myeloproliferative state with defects of the bone-marrow matrix and myeloid metaplasia (proliferation of the neoplastic myeloid stem cells) occurring primarily in the spleen and liver. Fibrosis of the bone marrow may represent the ultimate histologic stage of a number of different bone-marrow actions [134].

Pathology

The spleen appears markedly enlarged, sometimes up to 4,000 g. On section, it is firm, red to gray; multiple subcapsular infarcts may be present. Histologically, there is proliferation affecting normoblasts, granulocyte precursors, and megakaryocytes; however, megakaryocytes are usually prominent owing to their large size and nuclear morphology. Sometimes, disproportional activity of any one of the three major cell lines is seen. Initially, the extramedullary hematopoiesis is confined to the sinusoids, but later it may extend to involve the cords.

Radiologic Findings

On sonography, the involved spleen presents markedly increased echogenicity similar to that of the liver, probably due to the dominating red pulp, which is diffusely infiltrated by hematopoietic elements [145].
CT may demonstrate splenomegaly with homogeneous enhancement. Hemosiderosis resulting from repeated transfusion can sometimes be seen together with infarction and hemorrhage [145].

Castleman's Disease

Definition

Castleman's disease is an uncommon benign lymphoproliferative disorder characterized by hyperplasia of lymphoid follicles [146]. It more commonly occurs within the mediastinum but can rarely involve abdominal organs [147] and may present clinically as either a localized form or a disseminated (multicentric) form, which is more aggressive.

Pathology

There are two major histologic variants, depending on the different type of cells: hyaline-vascular Castleman's disease (90% of cases) and plasma cell Castleman's disease (10% of cases).

Radiologic Findings

Imaging findings are generally nonspecific for this disease and may show the presence of splenomegaly with homogeneous appearance, retroperitoneal and mesenteric lymphadenopathy, and ascites. Therefore, the diagnosis of Castleman's disease can only be made on the basis of histologic examination [134]

Vascular Pathology

Splenic Vein Thrombosis

Definition

The pathophysiology of splenic vein thrombosis includes compression, encasement, and inflammation of the splenic vein. In most cases, thrombosis is related to pancreatic carcinoma or pancreatitis, but is also seen in cirrhosis of the liver, after liver transplantation, after splenectomy or it can be idiopathic [148, 149]. Splenic vein thrombosis causes development of gastric varices.

Pathology

Venous thrombi are formed by pale strands of aggregated platelet and fibrin with admixture of erythrocytes, and unlike those originating within a cardiac chamber or the aorta, do not present well-defined laminations.

Radiologic Findings

On US, splenic vein thrombosis may often appear echogenic. A relatively hypoechoic clot is difficult to identify without the use of color flow sonography. Doppler sonography may show no flow in case of complete splenic vein obstruction, whereas a detectable residual flow with an elevated and stenotic flow velocity may be detected in case of incomplete obstruction.

In acute thrombosis of the splenic vein, CT scan may demonstrate an intraluminal, low-density filling defect. CT scan is also particularly useful in demonstrating gastric varices that accompany splenic vein occlusion.

On MRI, the thrombosed splenic vein shows hyperintensity on T2-weighted images and the gastric varices are seen as multiple, tortuous structures with a signal void on T2-weighted images [150].

Splenic Artery Aneurysm

Definition

Splenic artery aneurysm is the most common abdominal visceral artery aneurysm, representing approximately 60% of visceral arterial aneurysms [150]. Various causes and predisposing conditions may lead to splenic artery aneurysm, including portal hypertension, pregnancy and history of multiparity, pancreatitis, arteriosclerotic disease, penetrating gastric ulcer, trauma, and vasculitis.

Pathology

Splenic aneurysms are most often saccular, and over 75% occur at the distal third of the splenic arteries. They are multiple in 20% of cases and range in size from less than 1 cm to 3 cm.

Radiologic Findings

Splenic artery aneurysms are usually diagnosed by the presence of ring calcification in the left upper quadrant on plain film, CT or US.

On US, the aneurysm usually appears as a hypoechoic mass, showing, on color Doppler examination, a weak, turbulent, pulsatile flow [151].

On CT, splenic aneurysm appears as a well-defined, low-density mass with or without calcifications; after intravenous contrast medium administration, marked and early arterial enhancement within the residual patent lumen may be demonstrated [150].

On MRI, splenic aneurysm may demonstrate a well-defined ring of low signal intensity at the periphery, corresponding to the aneurysmal wall, while the signal intensity within the aneurysm depends on the presence and the velocity of flowing blood and the presence and age of the thrombus. Fast-flowing blood within the patent lumen produces usually a signal void, which persists on all spin-echo sequences [150].

Splenic Arteriovenous Fistula

Definition

Splenic arteriovenous fistula is a rare finding, congenital or acquired, which is accompanied by dilated vein or aneurysmal splenic vein that can cause portal hypertension. Acquired causes of arteriovenous fistula include fistulization of a splenic aneurysm into the adjacent splenic vein, local trauma, chronic pancreatitis and splenectomy [152]. Early diagnosis is mandatory, because life-threatening complications may occur if the disease is not treated.

Pathophysiology

A fistula following blunt abdominal trauma is from rupture into the adjacent vein from a preexisting splenic artery aneurysm or posttraumatic pseudoaneurysm. Iatrogenic splenic arteriovenous fistulas have been noted following splenectomy. These are thought to be secondary to the use of ligature for the control of the splenic artery and vein. Following placement of such ligature, it is presumed that an initial small communication enlarges under the force of systemic arterial pressure, leading to substantial increase in arterial venous flow [153].

The fistula is usually located at the splenic hilum or on the main splenic artery. The connection between artery and vein may consist of a well-formed vessel, a vascular channel formed by the canalization of a thrombus, or an aneurysmal sac.

Radiologic Findings

Sonography is noninvasive and can be rapidly performed in emergency conditions. Doppler sonography of the splenic arteriovenous fistula may demonstrate a twofold or threefold increase of the flow velocity in the fistula with dilatation, elongation or loop formation in the afferent artery, and a fairly pulsatile and high-velocity venous flow immediately distal to the fistula [154].

On CT, varices and a tortuous, dilated, splenic vein may be seen. Multiplanar reconstructions are useful in displaying the anatomy of the fistula. Angio-CT confirms the diagnosis of fistula, showing early and intense enhancement of the splenic vein.

MR and angio-MR also contribute to the diagnosis demonstrating the fistula, the possible associated aneurysms and the venous dilatation [1].

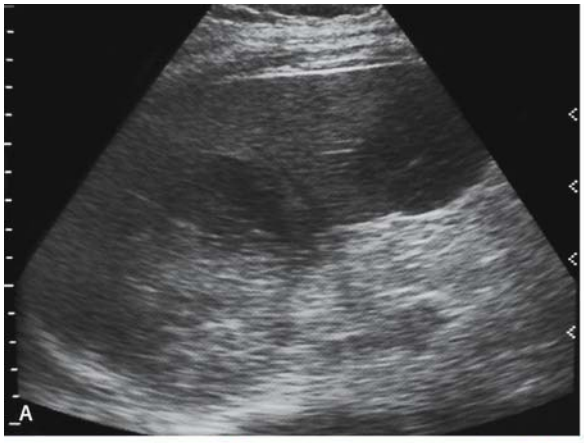

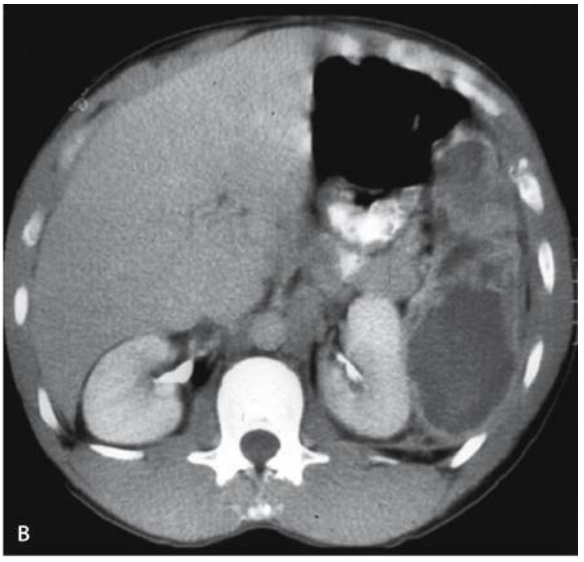

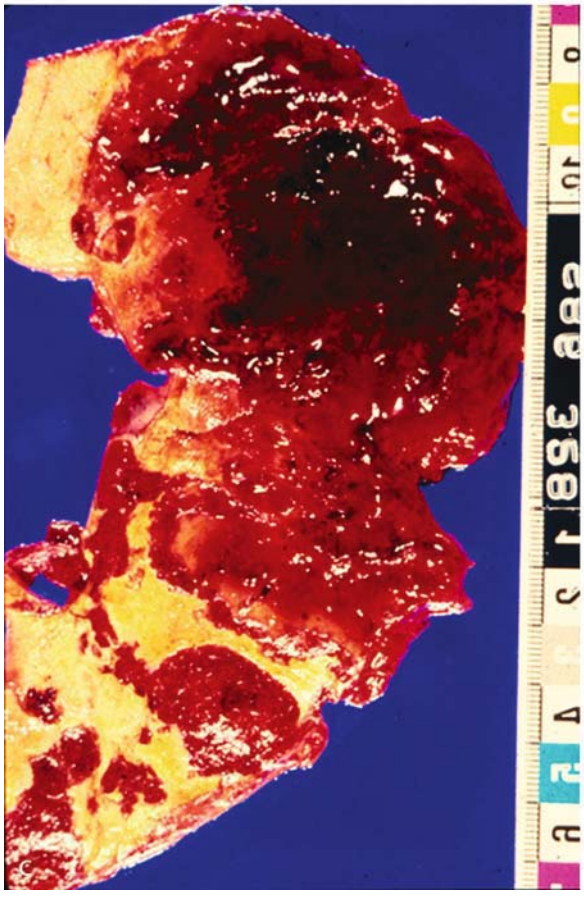

Fig. 15A–C. Splenic infarction. **A** Ultrasound demonstrates a well defined, partially hyperechoic lesion in the spleen. **B** Delayed phase contrast-enhanced CT scan shows wedge-shaped, well-demarcated low-density areas in the spleen. **C** Gross specimen of the spleen shows the wedge-shaped appearance of infarct

Splenic Infarction

Definition

Numerous causes may lead to splenic infarction, including embolic, hematologic, vascular disease, anatomic abnormalities, and nonhematologic malignancy. The most common cause is embolic, from cardiovascular disease, followed by local thrombosis resulting from hematologic diseases [155]. In patients younger than 40 - years, an associated hematologic disorder is most frequent, whereas in older patients the cause most often is an embolic event [1].

Pathology

Pathologically, infarcts are characteristically pale and wedge shaped, with their bases at the periphery where the capsule is often covered with fibrin (Fig. 15). In the course of healing of splenic infarcts, depressed scars may occur. When the thrombus contains bacteria, the infarct becomes soft and filled with pus [1].

Radiologic Findings

On US, an acute splenic infarct typically appears as a wedge-shaped, hypoechoic, and well-demarcated lesion. In the course of several days, the demarcation between the lesion and the surrounding spleen is better defined, probably due to a proliferative fibroblastic response in the preserved margins [156]. In the chronic stage, splenic infarcts appear as areas of increasing echogenicity because of fibrosis and scarring (Fig. 15).

Unenhanced CT scans may show the presence of wedge-shaped, peripheral hypodense lesions in only one-third of cases [141]. After contrast enhancement, these areas become markedly more distinct (Fig. 15). Areas of splenic infarction may also appear as heterogeneous, poorly marginated, and mass-like hypodense areas, which may mimic other splenic lesions such as tumors, hematomas, and abscesses [141]. In the acute phase, areas of increased attenuation may be demonstrated, representing hemorrhagic infarcts. Moreover, infarcts tend to be more focal and better demarcated in the acute and subacute phases, and tend to be isodense and atrophic in chronic phases [141].

On MRI, infarcted areas typically appear hyperintense with a dark rim on T2-weighted images. After intravenous administration of gadolinium, they appear as perfusion defects with sharp marginated zones of hypointensity; capsular contrast enhancement may be seen [62].

Peliosis of the Spleen

Definition

Peliosis is a rare disorder of the reticuloendothelial system that may involve the liver, spleen, and bone marrow, characterized by multiple blood-filled cysts (1–10 mm in diameter) scattered throughout the affected organ [106]. Splenic peliosis can be associated with hematologic malignancy, infection (e.g., tuberculosis, Bartonella infections, HIV), and anabolic and contraceptive steroids [22]

Pathology

Histologically, the cystic areas consist of irregular blood-filled lakes ranging from less than 0.1 to greater than 1 cm in diameter. Microscopically, the lesions consist of irregular cystic spaces with or without endothelial lining [22].

Radiologic Findings

Imaging findings consist of hepatosplenomegaly and multiple small hepatosplenic lesions. On US, multiple hypoechoic or hyperechoic areas with irregular margins may be seen [157]. On contrast-enhanced CT, some lesions may not enhance, probably due to thrombosis, while others may present the target appearance, with central enhancing foci [106]. MR imaging demonstrates areas of hyperintensity on T2-weighted images and of hypointensity to hyperintensity on T1-weighted images [158].

Trauma

Definition

Classically, abdominal trauma is divided into blunt and penetrating categories, which differentiate the mechanism of injury [159].

Penetrating trauma (e.g., gunshot and stab wounds) has an incidence of organ involvement approximately proportional to the cross-sectional area of the organ in question.

Blunt abdominal trauma has increased with the advent of high-speed transportation during recent decades and mechanisms of damage include direct compression, avulsion of vascular attachments by sudden deceleration forces or laceration by fractured adjacent skeletal structures [160].

Splenic Injury in Abdominal Trauma

The spleen is known to be the most frequently injured intraperitoneal organ in cases of blunt abdominal trauma. Other less common causes include iatrogenic etiologies (e.g., abdominal surgery, colonoscopy), penetrating abdominal trauma, spontaneous rupture (Fig. 16), and pancreatitis [30]. The main concern following trauma of the spleen is the possibility of splenic rupture, which is associated with a mortality in more than 75% of cases if surgery is not performed promptly [161].

Assessment of the splenic injury represents one of the most common challenges in diagnostic imaging of the spleen, not only to determine the presence of injury, but also the exact extent of the damage, to allow conservative surgical management, considering the important role of the spleen in preventing infection.

In adults, the incidence of splenic involvement in blunt abdominal trauma is 25% of cases, whereas in penetrating abdominal trauma it accounts for approximately 7% of cases [162]. In children, incidence of splenic injury is preceded by hepatic involvement [163]. Clinically, in addition to the manifestations related to associated injury of other abdominal organs, signs of splenic trauma usually result from hypovolemia, blood loss or local or referred symptoms of hemoperitoneum [164]. Generalized abdominal pain is common, whereas localized left upper quadrant pain is seen in 30% of cases.

Management of these patients depends of the patient's clinical condition [165]. Hemodynamically unstable patients proceed immediately to surgery, whereas the other patients undergo imaging tests to assess potential splenic damage.

Delayed splenic rupture is defined as bleeding occurring more than 48 h after trauma in previously hemodynamically stable patients, with no injury or minor injury detected at initial imaging. Its reported frequency varies between 1% and 14%, with mortality rates higher than in acute splenic injury (5%–15% vs 1% [165]).

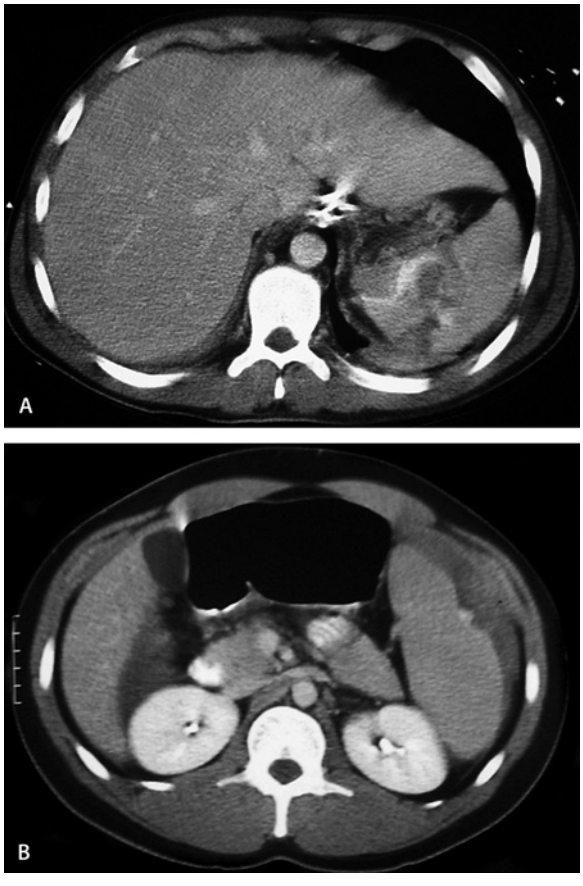

Fig. 16A, B. Splenic trauma. **A** On contrast-enhanced CT scan, the splenic laceration is seen as low-density intrasplenic hematoma with pooling of contrast material. **B** Spontaneous rupture. Contrast-enhanced CT scan demonstrates the presence of a subcapsular hematoma in a patient with spontaneous rupture of the spleen consequent to mononucleosis

Pathophysiology

The susceptibility of the spleen to injury after blunt trauma depends either on its complex ligamentous attachments (lienorenal and phrenicolienal; gastrolienal and cololienal) or on its spongy parenchymal consistency, with minimal connective tissue to allow maximal interface between blood elements and reticuloendothelial cells [166]. The spleen is divided into four or six segments by arterial supply, whereas the venous system is highly anastomotic and does not follow any predictable segmental anatomy. The spleen is enclosed within a thin capsule derived from the peritoneum, which in pediatric patients is relatively thicker and contains more elastic and contractile elements [167].

In blunt abdominal trauma, as described above, possible mechanisms of splenic damage are deceleration and compression. In deceleration injuries, ligamentous-capsular avulsions or vascular injury to the pedicle or short gastric vessels may occur. Blunt compression usually results in parenchymal injuries and venous bleeding along segmental anatomic lines, but, in case of high-energy blows, stellate fractures with extensive arterial and venous bleeding may be seen [166].

Injuries that result in parenchymal hematomas with an intact capsule are less common than was originally believed but may account for the 1%–2% incidence of delayed splenic rupture [168].

Penetrating trauma usually does not respect segmental anatomy and tends to have more vascular disruption.

Radiologic Findings

Ultrasound, when performed by a skilled operator, can be accurate in the diagnosis of splenic trauma and very useful, especially in situations in which CT is not immediately available. However, sonography is often limited by rib fractures, chest tubes, dressings, and the insensitivity of ultrasound to other sites of injury. The echo pattern of a blood collection depends on the time of examination, relative to the time of injury. Fresh splenic lesions may vary from anechoic to hyperechoic poorly marginated areas [169]. Unfortunately, the B-mode US may show no change in echogenicity in intraparenchymal splenic lesions during the 1st day after the trauma. A more accurate detection of small hematomas by using power Doppler has been reported [170]. When chronic, hematomas usually become hypoechogenic prior to complete disappearance [171]. Recently, Catalano et al. [172] reported a preliminary experience in the assessment of splenic trauma by using contrast-coded sonography and a second-generation contrast medium. In this study, 120 patients with suspected splenic trauma underwent sonography, contrast-enhanced harmonic sonography and contrast-enhanced helical computed tomography, as the gold standard. Contrast-enhanced sonography showed an appreciably better correlation than unenhanced sonography in detecting injuries and in estimating their extent.

CT has definitely become the imaging modality of choice in the evaluation of patients with suspected splenic trauma [173], with an accuracy exceeding 95%. Splenic injuries can be classified on CT scans as subcapsular or intraparenchymal hematomas, lacerations, fractures, or vascular pedicles injuries [174]. Intrasplenic hematomas typically appear as hypodense areas within the splenic parenchyma after administration of contrast medium [175] (Fig. 16), but in some cases they may be nearly isodense. Subcapsular hematomas usually appear as crescentic fluid collection along the lateral aspect of the spleen, which may be difficult to distinguish from perisplenic fluid [176]. Splenic lacerations appear as linear, low-attenuation lesions that do not cross the spleen completely and may be single, multiple and stellate [177]. Splenic fractures are lacerations that extend completely across the splenic parenchyma and frequently involve the splenic hilum [175]. Fractures may result in devascularized segments, frequently the superior or inferior polar region. Severe disruption of the splenic parenchyma results in a shattered spleen. Vascular pedicle injuries may result in significant hemorrhage and cardiovascular instability; therefore they are usually not referred for CT evaluation. These patients may characteristically show an unenhanced lower spleen with preservation of upper pole perfusion via the short gastric arteries [174].

Other useful findings that are indicators of splenic injury, well detected by CT, are the presence of hemoperitoneum, perisplenic fluid or clot (sentinel clot), and thickening of the anterior renal fascia and the left lateroconal fascia [178, 179].

MRI is seldom employed in the acute setting of splenic trauma, although it is recognized that it shows high sensitivity for the detection of blood and blood breakdown products [62]. The signal intensity of hematomas depends on the age of the extravascular bleed. During the first 48 h following extravasation, blood undergoes transformation into deoxyhemoglobin and other paramagnetic products. With high-field-strength magnets, deoxyhemoglobin within red blood cells may be identified on T2-weighted images, within a few hours after trauma. Subacute hematomas are of high signal on T1-weighted images, because of paramagnetic effect of the extracellular methemoglobin, which shortens T1 relaxation times [180].

Conclusion

This chapter demonstrates the imaging appearance of the various processes involving the spleen, which include benign and malignant focal disease, infections, systemic and hematologic disorders, vascular pathology, and trauma. A systematic approach reviewing the radiological findings by US, CT, and MRI and correlation of these findings with underlying gross and microscopic pathologic features is used.

References

1. Kawashima A, Urban BA, Fishman EK (2000) Benign lesions of the spleen. In: Gore RM, Levine MS (eds) Textbook of gastrointestinal radiology, 2nd edn. WB Saunders, Philadelphia, pp 1879–1903
2. Grumbach K, McDowell R (1994) The spleen. In: Haaga JR, Lanzieri CF, Sartoris DJ, Zerhami EA (eds) Computed tomography and magnetic resonance imaging of the whole body, 3rd edn. Mosby, St Louis, pp 1131–1150
3. Ragozzino MW, Singletary H, Patrick R (1990) Familial splenic epidermoid cyst. AJR 155:1233–1234
4. Dachman AH, Ros PR, Marari PJ et al (1986) Nonparasitic splenic cysts: a report of 52 cases with radiologic-pathologic correlation. AJR 147:537–542
5. Mortele KJ, Ros PR (2001) Cystic focal liver lesions in the adult: differential CT and MR imaging features. Radiographics 21:895–910
6. Garvin DF, King FM (1981) Cysts and nonlymphomatous tumors of the spleen. Pathol Annu 16:61–80
7. Dawes LG, Malangoni MA (1986) Cystic masses of the spleen. Am Surg 52:333–336
8. Ross ME, Ellwood R, Yang S et al (1977) Epidermoid splenic cysts. Arch Surg 112:596–599
9. Costello P, Kane RA, Oster J et al (1985) Focal splenic disease demonstrated by ultrasound and computed tomography. J Can Assoc Radiol 36:22–28
10. Faer MJ et al (1980) RPC from the AFIP. Radiology 134: 371–376

11. Rabushka LS, Kawashima A, Fishman EK (1994) Imaging of the spleen: CT with supplemental MR examination. Radiographics 14:307–332
12. Shirkoda A, Freeman J, Armin AR et al (1995) Imaging features of splenic epidermoid cysts with pathologic correlation. Abdom Imaging 20:449–451
13. Husni EA (1961) The clinical course of splenic hemangioma: with emphasis on spontaneous rupture. Arch Surg 83: 681–688
14. Parkter RL, Fishman EK, Nussbaum A et al (1987) CT findings in splenic hemangiomas in the Klippel-Trenaunay-Weber syndrome. J Comput Assist Tomogr 11:88–91
15. Ros PR, Moser RPJ, Dachman AH et al (1987) Hemangioma of the spleen: radiologic-pathologic correlation in ten cases. Radiology 162:73–77
16. Rose SC, Kumpe DA, Manco-Johnson ML (1986) Radiographic appearance of diffuse splenic hemangiomatosis. Gastroint Radiol 11:342–345
17. Duddy MJ, Calder CJ (1989) Cystic hemangioma of the spleen: findings on ultrasound and computed tomography. Br J Radiol 62:180–182
18. Disler DG, Chew FS (1991) Splenic hemangioma. AJR 157:44
19. Kelekis NL, Burdeny DA, Semelka RC (1997) Spleen. In: Semelka RC, Ascher SM, Reinhold C (eds) MRI of the abdomen and pelvis. A text atlas. Wiley-Liss, New York, pp 239–256
20. Ramani M, Reinhold C, Semelka RC et al (1997) Splenic hemangiomas and hamartomas: MR imaging characteristics of 28 lesions. Radiology 202:166–172
21. Barrier A, Lacaine F, Callard P et al (2002) Lymphangiomatosis of the spleen and 2 accessory spleens. Surgery 131: 114–116
22. Urrutia M, Mergo PJ, Ros LH et al (1996) Cystic masses of the spleen: radiologic-pathologic correlation. Radiographics 16: 107–129
23. Bezzi M, Spinelli A, Pierleoni M et al (2001) Cystic lymphangioma of the spleen: US-CT-MRI correlation. Eur Radiol 11: 1187–1190
24. Taylor AJ, Dodds WJ, Erickson SJ et al (1991) CT of acquired abnormalities of the spleen. AJR 157:1213–1219
25. Rao BK, AuBuchon J, Lieberman LM et al (1981) Cystic lymphangiomatosis of the spleen: a radiologic-pathologic correlation. Radiology 141:781–782
26. Pistoia F, Markowitz SK (1988) Splenic lymphangiomatosis: CT diagnosis. AJR 150:121–122
27. Wadsworth DT, Newman B, Abramson SJ et al (1997) Splenic lymphangiomatosis in children. Radiology 202:173–176
28. Solomou EG, Patriarheas GV, Mpadra FA et al (2003) Asymptomatic adult cystic lymphangioma of the spleen: case report and review of the literature. Magn Reson Imaging 21: 81–84
29. Lam KY, Yip KH, Pe WC (1999) splenic vascular lesions: unusual features and review of the literature. Aust N Z J Surg 69: 422–425
30. Robertson F, Leander P, Ekberg O (2001) Radiology of the spleen. Eur Radiol 11:80–95
31. Thompson SE, Walsh EA, Cramer BC et al (1996) Radiological features of a symptomatic splenic hamartoma. Pediatr Radiol 26:657–660
32. Brinskley AA, Lee JK (1981) Cystic hamartoma of the spleen: CT and sonographic findings. J Clin Ultrasound 9:136–138
33. Norowitz DG, Morehouse HT (1989) Isodense splenic mass: hamartoma, a case report. Comput Med Imaging Graph 13: 347–350
34. Tang S, Shimizu T, Kikuchi Y et al (2000) Color Doppler sonographic findings in splenic hamartoma. J Clin Ultrasound 28:249–253
35. Fernandez-Canton G, Capelastegui A, Merino A et al (1999) A typical MRI presentation of a small splenic hamartoma. Eur Radiol 9:883–885
36. Stout AP, Murray MR (1942) Hemangiopericytoma: a vascular tumor featuring Zimmerman's pericytes. Ann Surg 16: 26–33
37. Stout AP, Lattes R (1967) Tumors of the soft tissues. Armed Forces Institute of Pathology, Washington, DC, pp 67–72
38. Binder SC, Wolfe HJ, Deterling RA (1973) Intra-abdominal hemangiopericytoma. Report on four cases and review of the literature. Arch Surg 107:536–543
39. Jurado JG, Turegano F, Garcia C et al (1989) Hemangiopericytoma of the spleen. Surgery 106:575–577
40. Ferrozzi F, Bova D, Draghi F et al (1996) CT findings in primary vascular tumors of the spleen. AJR 166:1097–1101
41. Tsang WYW, Chan JKC (1993) The family of epithelioid vascular tumors. Histol Histopathol 8:187–212
42. Vilanova JC, Capdevila A, Aldoma et al (1994) Splenic epithelioid hemangioma: MR findings. AJR 163:747–748
43. Tiu CM, Chou YH, Wang HT et al (1992) Epithelioid hemangioendothelioma of the spleen with intrasplenic metastasis: ultrasound and computed tomography appearance. Comput Med Imaging Graph 16:287–290
44. Falk S, Stutte HG, Frizzera G (1991) Littoral cell angioma. A novel splenic vascular lesion demonstrating histiocytic differentiation. Am J Surg Pathol 15:1023–1033
45. Mortele KJ, Mergo PJ, Kunnen M, Ros PR (2000) Tumoral pathology of the spleen. In: De Shepper AM, Vanhoenacker F (eds) 1st edn. Springer, Berlin Heidleberg New York pp 101–122
46. Kinoshita LL, Yee J, Nash SR (1999) Littoral cell angioma of the spleen: imaging features. AJR 174:467–469
47. Oliver-Goldaracena JM, Blanco A, Miralles M et al (1998) Littoral cell angioma of the spleen: US and MR imaging findings. Abdom Imaging 23:636–639
48. Goldfeld M, Cohen I, Loberant N et al (2002) Littoral cell angioma of the spleen: appearance on sonography and CT. J Clin Ultrasound 30:510–513
49. Grantham M, Einstein D, McCarron K et al (1998) Littoral cell angioma of the spleen. Abdom Imaging 23:633–635
50. Schneider G, Uder M, Altmeyer K et al (2000) Littoral cell angioma of the spleen: CT and MR imaging. Eur Radiol 10: 1395–1400
51. Kehoe J, Straus DJ (1988) Primary lymphoma of the spleen: clinical features and outcome after splenectomy. Cancer 62: 1433–1438
52. Strijk SP, Wagener DJT, Bogman MJJT et al (1985) The spleen in Hodgkin disease: diagnostic value of CT. Radiology 154: 753–757
53. Ahmann DL, Kiely JM, Harrison EGJ et al (1966) Malignant lymphoma of the spleen: a review of 49 cases in which the diagnosis was made at splenectomy. Cancer 19:461–469
54. Warshauer DM, Koehler RE (1998) Spleen. In: Lee JK, Sagel SS, Stanley RG, Heiken JP (eds) Computed body tomography with MR correlation, 3rd edn. Lippencott-Raven, Philadelphia, pp 845–872
55. Runge VM, Williams NM (1998) Dynamic contrast-enhanced magnetic resonance imaging in a model of splenic metastasis. Invest Radiol 33:45–50
56. Solbiati L, Bossi MC, Bellotti E et al (1983) Focal lesions in the spleen: sonographic patterns and guided biopsy. AJR 140: 59–65
57. Goerg C, Weide R, Schwerk WB (1997) Malignant splenic lymphoma: sonographic patterns, diagnosis and follow-up. Clin Radiol 52:535–540
58. Siniluoto TMJ, Tikkakoski TA, Lahde ST et al (1994) Ultrasound or CT in splenic disease? Acta Radiol 35:597–605
59. Dachman AH, Buck JL, Krishnan J et al (1998) Primary non-Hodgkin's splenic lymphoma. Clin Radiol 53:137–142
60. Meyer JE, Harris NL, Elman A et al (1983) Large-cell lymphoma of the spleen: CT appearance. Radiology 148:199–202
61. Urban BA, Fishman EK (1998) Helical CT of the spleen. AJR 170:997–1003
62. Ito K, Mitchell DG, Honjo K et al (1997) MR imaging of acquired abnormalities of the spleen. AJR 168:697–702
63. Hahn PF, Weissleder R, Stark DD et al (1988) MR imaging of focal splenic tumors. AJR 150:823–827
64. Falk S, Krishnan J, Meis JM (1993) Primary angiosarcoma of the spleen: a clinicopathologic study of 40 cases [see comments]. Am J Surg Pathol 17:959–970
65. Ha HK, Kim HH, KimBK et al (1994) Primary angiosarcoma of the spleen: CT and MR imaging. Acta radiol 35:455–458

66. Vrachliotis TG, Bennett WF, Vaswani KK et al (2000) Primary angiosarcoma of the spleen CT, MR, and sonographic characteristics: report of two cases. Abdom Imaging 25:283–285
67. Karakas HM, Demir M, Ozyilmaz F et al (2001) Primary angiosarcoma of the spleen: in vivo and in vitro MRI findings. Clin Imaging 25:192–196
68. Federle MP, Moss AA (1983) Computed tomography of the spleen. Crit Rev Diagn Imaging 19:1–16
69. Berge T (1974) Splenic metastases: frequencies and patterns. Acta Pathol Microbial Scand 82:499–506
70. Rappaport H (1986) Tumors of the hematopoietic system. In: Atlas of tumor pathology, section3, fascicle 8. Armed Forces Institute of Pathology, Washington, DC, p 91
71. Paley MR, Ros PR (2002) Imaging of spleen disorders. In: Bowdler AJ (ed) The complete spleen: structure, function, and clinical disorders, 2nd edn. Humana Press, Totowa, NJ, pp 259–280
72. Weissleder R, Hahn P, Stark DD et al (1988) Superparamagnetic iron oxide: enhanced detection of focal splenic tumors with MR imaging. Radiology 169:399–403
73. Chun CH, Raff MJ, Contreras L et al (1980) Splenic abscess. Medicine 59:50–65
74. Ng KK, Lee TY, Wan Yl et al (2002) Splenic abscess: diagnosis and management. Hepatogastroenterol 49:567–571
75. Green BT (2001) Splenic abscess: report of six cases and review of the literature. Am Surg 67:80–85
76. Caslowitz PL, Labs JD, Fishman EK et al (1989) The changing spectrum of splenic abscess. Clin Imaging 13:201–207
77. Gupta RK, Pant CS, Ganguly SK (1987) Ultrasound demonstration of amebic splenic abscess. J Clin Ultrasound 15:555–557
78. Freeman JL, Jafri SZH, Roberts JL et al (1993) CT of congenital and acquired abnormalities of the spleen. Radiographics 13:597–610
79. Tikkakoski T, Siniluoto T, Paivansalo M et al (1992) Splenic abscess: imaging and intervention. Acta Radiol 33:561–565
80. Shirkoda A (1993) Spleen. In: Ros PR, Bidgood WD (eds) Abdominal magnetic resonance imaging, Mosby-Year Book, St Louis, MO
81. Nelken N, Ignatius J, Skinner M et al (1987) Changing clinical spectrum of splenic abscess: a multicenter study and review of the literature. Am J Surg 154:27–33
82. Henry K, Symmer W (1992) Systemic pathology, 3rd edn. Churchill Livingstone, New York, pp 574–603
83. Goerg C, Schwerk WB, Goerg K (1991) Pictorial essay: sonography of focal lesions of the spleen. AJR 156:949–953
84. Hopewell PC (1995) A clinical view of tuberculosis. Radiol Clin North Am 33:641–653
85. Thoeni RF, Margulis AR (1979) Gastrointestinal tuberculosis. Semin Roentgenol 14:283–294
86. Leder AR, Low VHS (1995) Tuberculosis of the abdomen. Radiol Clin North Am 33:691–705
87. Drevelengas A (2000) The spleen in infectious disorders. In: De Shepper AM, Vanhoenacker F (eds) 1st edn. Springer, Berlin Heidelberg New York, pp 67–80
88. Buxi TBS, Vohra RB, Sujatha Y et al (1992) CT appearances in macronodular hepatosplenic tuberculosis: a review with five additional new cases. Comput Med Imaging Graph 16:381–387
89. Schulman A, van Jaarsvelt J, Loxton AJ et al (1983) Pseudolipid appearance of simple echinococcal cysts on ultrasonography. A report of 2 cases. S Afr Med J 63:905–906
90. Niron EA, Ozer H (1981) Ultrasound appearances of liver hydatid disease. Br J Radiol 54:335–338
91. Lewall DB, Bailey TM, McCorkell SJ (1987) Echinococcal matrix: computed tomographic, sonographic and pathologic correlation. J Ultrasound Med 5:33–35
92. Itzchuk Y, Rubinstein Z, Shilo R (1983) Ultrasound in tropical diseases. In: Sanders RC, Hill MC (eds) Ultrasound annual. Raven, New York
93. Hoff FL, Aisen AM, Walden ME et al (1987) MR imaging in hydatid disease of the liver. Gastrointest Radiol 12:39–42
94. Radin DR, Baker EL, Klatt EC et al (1990) Visceral and nodal calcification in patients with AIDS-related *Pneumocystis carinii* infection. AJR 154:27–31
95. Spouge AR, Wilson SR, Gopinath N et al (1990) Extrapulmonary *Pneumocystis carinii* in a patient with AIDS: sonographic findings. AJR 155:76–78
96. Rappaport DC, Cumming WA, Ros PR (1991) Disseminated hepatic and splenic lesions in cat-scratch disease: imaging features. AJR 156:1227–1228
97. Callen PW, Filly RA, Marcus FS (1980) Ultrasonography and computed tomography in the evaluation of hepatic microabscesses in the immunosuppressed patient. Radiology 136:433–434
98. Larsen CE, Patrick LE (1992) Abdominal (liver, spleen) and bone manifestations of cat-scratch disease. Pediatr Radiol 22:353–355
99. Dangman BC, Albanese BA, Kacica MA et al (1995) Cat scratch disease in two children presenting with fever of unknown origin: imaging features and association with a new causative agent, *Rochalimaea henselae*. Pediatrics 95:767–771
100. Vanhoenacker F, De Schepper AM (2000) The spleen in systemic disorders. In: De Shepper AM, Vanhoenacker F (eds) 1st edn. Springer, Berlin Heidelberg New York, pp 49–66
101. Lipsky PE (1994) Rheumatoid arthritis. In: Isselbacher KJ, Braunwald E, Wilson JD et al (eds) Harrison's principle of internal medicine, 13th edn. McGraw-Hill, New York, pp 1648–1653
102. Hahn BH (1994) Systemic lupus erythematosus. In: Isselbacher KJ, Braunwald E, Wilson JD et al (eds) Harrison's principle of internal medicine, 13th edn. McGraw-Hill, New York, pp 1643–1648
103. Fonner BT, Nemcek AA, Bochman C (1995) CT appearance of splenic infarction in Wegener's granulomatosis. AJR 164:353–354
104. Fishman D, Isenberg DA (1997) Splenic involvement in rheumatic diseases. Semin Arthritis Rheum 27:141–155
105. Van Krieken JHJM, Breedveld FC, Te Velde J (1988) The spleen in Felty's syndrome: a histological, morphometrical, and immunohistochemical study. Eur J Haematol 40:58–64
106. Venbrux AC, Dachman AH, Fishman EK (1993) Vascular disease. In: Dachman AH, Friedman AC (eds) Radiology of the spleen. Mosby Year Book, St. Louis, pp 171–205
107. McHugh K, Manson D, Eberhard BA et al (1991) Splenic necrosis in Wegener's granulomatosis. Pediatric Radiol 21:588–589
108. Gregorini G, Campanini M, Tira P et al (1990) Spleen involvement in Wegener's granulomatosis: two case reports. APMIS Suppl 19:23
109. Kalaitzoglou I, Drevelengas A, Palladas P et al (1998) MRI appearance of pulmonary Wegener's granulomatosis with concomitant splenic infarction. Eur Radiol 8:367–370
110. Omarini LP, Frank-Burkhardt SE, Seemayer TA et al (1995) Nieman-Pick disease type C: nodular splenomegaly. Abdom Imaging 20:157–160
111. Schubert (1994)
112. Kozicky OJ, Brandt LJ, Lederman M et al (1987) Splenic amyloidosis: a case report of spontaneous splenic rupture with a review of the pertinent literature. Am J Gastroenterol 82:582–587
113. Yoon DY, Choi BI, Han JK et al (1994) MR findings of secondary hemochromatosis: transfusional vs erythropoietic. J Comput Assist Tomogr 18:416–419
114. Hill SC, Reinig JW, Barranger JA et al (1986) Gaucher disease: sonographic appearance of the spleen. Radiology 160:631–634
115. Lam KY, Chan ACL, Wat MS (1996) Langerhans' cell histiocytosis forming an asymptomatic solitary nodule in the spleen. J Clin Pathol 49:262–264
116. Cubo T, Ramia JM, Pardo R et al (1997) Spontaneous rupture of the spleen in amyloidosis. Am J Emerg Med 15:443–444
117. Aspestrand et al (1996)
118. Aspestrand F, Charania B, Scheel B et al (1989) Focal changes of the spleen in one case of Gaucher's disease-assessed by ultrasonography, CT, MRI and angiography. Radiologe 29:569–571
119. Poll LW, Koch JA, vom Dahl S et al (2000) Gaucher disease of the spleen: CT and MR findings. Abdom Imaging 25:286–289

120. Lanir A, Hader H, Cohen I et al (1986) Gaucher disease: assessment with MR imaging. Radiology 161:239–244
121. Hill SC, Damaska BM, Ling A et al (1992) Gaucher's disease: abdominal MR imaging findings in 46 patients. Radiology 184:561–566
122. Terk MR, Esplin J, Lee K et al (1995) MR imaging of patients with type-1 Gaucher's disease: relationship between bone and visceral changes. AJR 165:599–604
123. Muwakkit S, Gharagozloo A, Souid AK et al (1994) The sonographic appearance of lesions of the spleen and pancreas in an infant with Langerhans' cell histiocytosis. Pediatr Radiol 24:222–223
124. Williams PH, Fairhust JJ (1995) Sonographic and radiographic appearance of lesions in an infant with Langerhans' cell histiocytosis. Pediatr Radiol 25:401–402
125. Jacobs JE, Birnbaum BA, Furth EE (1997) Abdominal visceral calcification in primary amyloidosis: CT findings. Abdom Imaging 22:519–521
126. Siegelman ES, Mitchell DG, Rubin R et al (1991) Parenchymal versus reticuloendothelial iron overload in the liver: distinction with MR imaging. Radiology 179:361–366
127. Taavitsainen M, Koivuniemi A, Helminen J et al (1987) Aspiration biopsy of the spleen in patients with sarcoidosis. Acta Radiol 28:723–725
128. Hoeffel C, Bokemeyer C, Hoeffel JC et al (1996) CT hepatic and splenic appearances with sarcoidosis. Eur J Radiol 23: 94–96
129. Kessler A, Mitchell DG, Israel HL et al (1993) Hepatic and splenic sarcoidosis: ultrasound and MR imaging. Abdom Imaging 18:159–163
130. Warshauer DM, Molina PL, Hamman SM et al (1995) Nodular sarcoidosis of the liver and spleen: analysis of 32 cases. Radiology 195:757–762
131. Folz SJ, Johnson CD, Swensen SJ (1995) Abdominal manifestations of sarcoidosis in CT studies. J Comput Assist Tomogr 19:573–579
132. Scott GC, Berman JL, Higgins JL Jr (1997) CT patterns of nodular hepatic and splenic sarcoidosis: a review of the literature. J Comput Assist Tomogr 21:369–372
133. Bach DB, Vellet AD (1991) Retroperitoneal sarcoidosis. AJR 156:520–522
134. Ito K, Mitchell DG (2000) The spleen in hematologic disorders. In: De Shepper AM, Vanhoenacker F (eds) 1st edn. Springer, Berlin Heidelberg New York, pp 37–48
135. Lonergan GF, Cline DB, Abbondanzo SL (2001) Sickle cell anemia. AFIP Radiographics 21:971–994
136. Adler DD, Blane CE, Coran AG et al (1986) Splenic trauma in the pediatric patients: integrated roles of ultrasound and computed tomography. Pediatr 78:576–580
137. Jacobs A (1977) Iron overload-clinical and pathologic aspects. Semin Hematol 14:89–113
138. Mitnick JS, Bosniak MA, Megibow A et al (1981) CT in b-thalassemia: iron deposition in the liver, spleen, and lymph nodes. AJR 136:1191–1194
139. Ernst O, Sergent G, Bonvarlet P et al (1997) Hepatic iron overload: diagnosis and quantification with MR imaging. AJR 168:1205–1208
140. Correidora JC, Gonzales M, Perez R et al (1990) A clinical and biological study of 33 cases of polycythemia vera. Rev Clin Esp 186:378–382
141. Balcar J, Seltzer SE, Davis S et al (1984) CT patterns of splenic infarction: a clinical and experimental study. Radiology 151:723–729
142. Downer WR, Peterson MS (1993) Massive splenic infarction and liquefactive necrosis complicating polycythemia vera. AJR 161:79–80
143. Gabata T, Kadoya M, Mori A et al (2000) MR imaging of focal splenic extramedullary hematopoiesis in polycythemia vera: case report. Abdom Imaging 25:514–516
144. Siler J, Hunter TB, Weiss J et al (1980) Increased echogenicity of the spleen in benign and malignant disease. AJR 134: 1011–1014
145. Hunter TB, Haber K (1977) Unusual sonographic appearance of the spleen in a case of myelofibrosis. AJR 128:138–139
146. Castleman B, Iverson L, Mecendez VP (1956) Localized mediastinal lymph node hyperplasia resembling thymoma. Cancer 9:822–830
147. Cirillo RL, Vitellas KM, Deyoung BR et al (1998) Castleman disease: mimicking a hepatic neoplasm. Clin Imaging 22: 124–129
148. Petit P, Bret P, Atri M et al (1994) Splenic vein thrombosis after splenectomy: frequency and role of imaging. Radiology 190:65–68
149. Balthazar EJ, Megibow A, Naidich et al (1984) Computed tomographic recognition of gastric varices. AJR 142:1121–1125
150. Hoeffel CC (2000) Vascular pathology of the spleen. In: De Shepper AM, Vanhoenacker F (eds) 1st edn. Springer, Berlin Heidelberg New York, pp 89–100
151. Derchi LE, Biggi E, Cicio GR et al (1984) Aneurysms of the splenic artery: non-invasive diagnosis by pulsed Doppler sonography. J Ultrasound Med 3:41–44
152. Sarioglu A, Tanyel FC, Ariyurek M et al (1995) Aneurysmatic arteriovenous fistula complicating splenic injury. Eur J Pediatr Surg 6:183–185
153. Gartside R, Gamelli RL (1987) Splenic arteriovenous fistula. J Trauma 27:671–673
154. Piscaglia F, Valgimigli M, Serra C et al (1998) Duplex Doppler findings in splenic arteriovenous fistula. J Clin Ultrasound 26:103–105
155. Nores M, Philips EH, Morgenstern L et al (1998) The clinical spectrum of splenic infarction. Am Surg 64:182–188
156. Maresca G, Mirk P, De Gaetana AM et al (1986) Sonographic patterns in splenic infarct. J Clin Ultrasound 14:23–28
157. Tsuda K, Nakamura H, Murakami T et al (1993) Peliosis of the spleen with intraperitoneal hemorrhage. Abdom Imaging 18: 283–285
158. Torres GM, Terry NL, Mergo PJ et al (1995) MR imaging of the spleen. Magn Reson Imaging Clin North Am 3:39–50
159. Newton EJ, Parisky YR (1992) Abdominal trauma. In: Rosen P, Doris PE, Barkin RM, Barkin SZ, Markovchick VJ (eds) Diagnostic radiology in emergency medicine. Mosby Year Book, St. Louis, pp 101–141
160. Corthouts B, Degryse H (2000) Trauma of the spleen. In: De Shepper AM, Vanhoenacker F (eds) 1st edn. Springer, Berlin Heidelberg New York, pp 81–88
161. Delaney HM, Jason RS (1981) Abdominal trauma: surgical and radiological diagnosis, Springer-Verlag, Berlin Heidelberg New York
162. Anderson CB, Ballinger WF (1985) Abdominal injuries. In: Zuidema GD, Rutheford RB, Ballinger WF (eds) the management of trauma. Saunders, Philadelphia, pp 101–131
163. Sivit CJ, Bulas DI (1993) Diagnostic imaging. In: Eichelberger MR (ed) Pediatric trauma: prevention, acute care and rehabilitation. Mosby, St Louis, pp 226–288
164. Roberts JL (1996) CT of abdominal and pelvic trauma. Semin Ultrasound CT MR 17:142–169
165. Emery KH (1997) Splenic emergencies. Radiol Clin North Am 35:831–843
166. Witte CL, Esser MJ, Rappaport WD (1992) Updating the management of salvageable splenic injury. Ann Surg 215:261–265
167. Benya EC, Bulas DI (1996) Splenic injuries in children after blunt abdominal trauma. Semin Ultrasound CT MR 17: 170–180
168. Black JJ, Sinow RM, Wilson SE et al (1992) Subcapsular hematoma as a predictor of delayed splenic rupture. Am Surg 12:732–735
169. Siniluoto TMJ, Paivansalo MJ, Lanning FP et al (1992) Ultrasonography in traumatic splenic rupture. Clin Radiol 46: 391–396
170. Nilsson A, Loren I, Nirhov N et al (1999) Power Doppler ultrasonography: alternative to computed tomography in abdominal trauma patients. J Ultrasound Med 18:669–672
171. Adler DD, Glazer GM, Aisen AM (1986) MRI of the spleen: normal appearance and findings in sickle-cell anemia. AJR 147:843–845
172. Catalano O, Lobianco R, Sandomenico F et al (2003) Splenic trauma: evaluation with contrast-specific sonography and a second-generation contrast medium: preliminary experience. J Ultrasound Med 22:467–477

173. Mirvis SE, Whitley NO, Gene D (1989) CT-based injury classification system: correlation with prognosis and management of blunt splenic trauma. Radiology 171:33–39
174. Gavant ML, Schurr M, Flick PA et al (1997) Predicting clinical outcome of nonsurgical management of blunt splenic injury: using CT to reveal abnormalities of splenic vasculature. AJR 168:207–212
175. Federle MP (1984) CT of upper abdominal trauma. Semin Roentgenol 19:269–280
176. Umlas SL, Cronan JJ (1991) Splenic trauma: can CT grading systems enable prediction of successful nonsurgical treatment? Radiology 178:481–487
177. Mall JC, Kaiser JA (1980) CT diagnosis of splenic laceration. AJR 134:265–269
178. Sutton CS, Haaga JR (1987) CT evaluation of limited splenic trauma. J Comput Assist Tomogr 11:167–169
179. Yao DC, Jeffrey RB Jr, Mirvis SE et al (2002) Using contrast-enhanced helical CT to visualize arterial extravasation after blunt abdominal trauma: incidence and organ distribution. AJR 178:17–20
180. Gomori JM, Grossman RI, Goldbeg HI et al (1985) Intracranial hematomas: imaging by high field MR. Radiology 157:87–93

Diseases of the Gallbladder and Bile Ducts

Angela D. Levy, Charles A. Rohrmann

4.13

Contents

The opinions and assertions contained herein are the private views of the author, and are not to be construed as official, or as reflecting the view of the Department of the Army or Defense.

Introduction

Over the past decade, technological advances in ultrasound, computed tomography (CT), and magnetic resonance imaging (MR) have expanded the application and versatility of these techniques to more accurately identify and characterize diseases of the gallbladder and bile ducts. Precise definition of the underlying pathologic process and extent of disease is now feasible with noninvasive imaging techniques. In this chapter, the radiologic features of the diseases of the gallbladder and bile ducts will be discussed with pathologic correlation.

Part I: Gallbladder

Inflammatory Diseases

Emphysematous Cholecystitis

Incidence and Clinical Features

Emphysematous cholecystitis is a rare variant of acute cholecystitis characterized by the presence of gas in the gallbladder wall, lumen, or pericholecystic tissues. The majority of patients are between 50 and 70 years of age and have underlying chronic medical conditions such as diabetes mellitus or atherosclerotic peripheral vascular disease [1]. Emphysematous cholecystitis is more common in men. Patients may present with signs and symptoms of acute cholecystitis or vague, insidious symptoms. Vascular compromise of the cystic artery is thought to play a role in the pathogenesis of gas formation [2]. *Clostridium welchii* and *Escherichia coli* are organisms that are commonly isolated from the infected gallbladders.

Radiologic Features

The radiologic diagnosis of emphysematous cholecystitis is made by the identification of gas within the gallbladder lumen, wall, or pericholecystic tissues. Abdom-

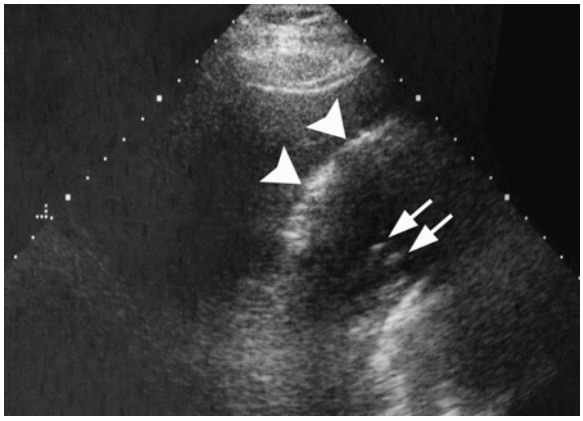

Fig. 1. Emphysematous cholecystitis in a 49-year-old diabetic man with a history of pain and fever. Longitudinal ultrasound image of the gallbladder shows a diffusely echogenic gallbladder wall due to intramural gas (*arrowheads*). Intraluminal gas (*arrows*) is shown as echogenic reflectors within the gallbladder lumen

inal radiography may demonstrate clear demarcation of the gallbladder by intramural gas collections or may show hyperlucency in the right upper quadrant.

The most common sonographic feature of intramural gas is highly echogenic reflectors within the gallbladder wall producing low-level posterior acoustic shadowing and reverberation artifact. The echogenic reflectors in the gallbladder wall may change position and configuration when the position of the patient is changed. Intramural gas may also appear as a highly reflective gallbladder wall [3]. Less commonly, real-time scanning will show gas in the lumen of the gallbladder as a band of highly reflective echoes or small, nonshadowing echogenic foci rising up from the dependent portions of the gallbladder lumen (Fig. 1). The latter appearance has been termed the "effervescent gallbladder" because it resembles the appearance of effervescent bubbles rising in a champagne glass [4, 5]. Careful attention to the appearance of suspected intramural and intraluminal gas should be made because other highly reflective entities such as calcification in the gallbladder wall, a contracted gallbladder with stones, or adenomyomatous hyperplasia may be mistaken for intramural or intraluminal gas.

CT is the most sensitive and specific imaging modality for identifying gas within the gallbladder lumen or wall (Fig. 2). The presence of pneumoperitoneum, pneumobilia, and portal venous gas are readily identified as well.

Xanthogranulomatous Cholecystitis

Incidence and Clinical Features

Xanthogranulomatous cholecystitis is an uncommon form of chronic cholecystitis characterized by the presences of xanthomatous histiocytes, chronic inflammatory cells, and scarring in the gallbladder wall [6]. The inflammatory process produces a tumor-like appearance in the gallbladder that may simulate malignancy radiologically and pathologically [7].

Xanthogranulomatous cholecystitis is most frequently observed in women between the ages of 60 and 70 years [6]. Patients usually present to medical attention with complaints of right upper quadrant pain, nausea, and vomiting. A positive Murphy sign may be present on physical examination. A tender, palpable, right upper quadrant mass is found in less than 50% of patients [8]. Complications such as perforation, abscess formation, fistulous tracts, and extension of the inflammatory process to adjacent organs are present in 32% of cases [9].

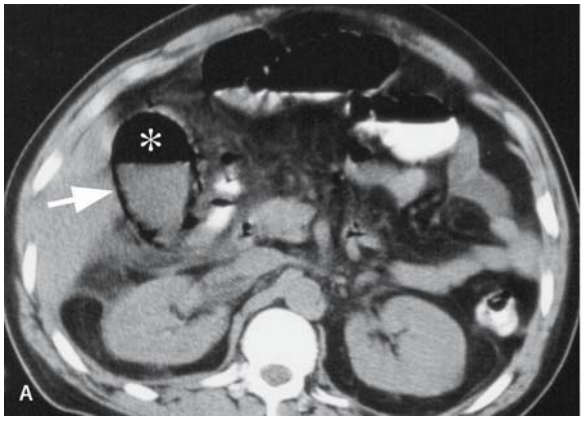

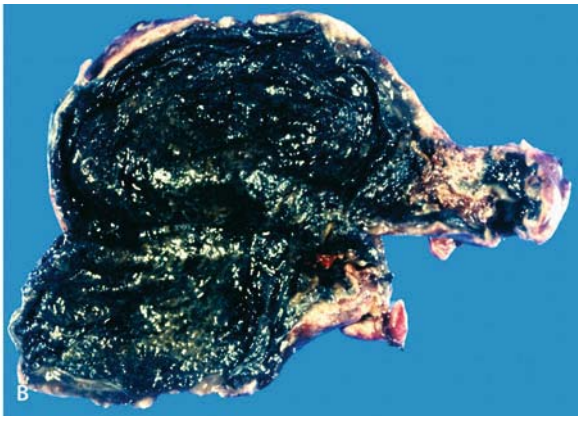

Fig. 2A, B. Emphysematous cholecystitis. **A** Unenhanced CT in a 56-year-old man who presented with right upper quadrant pain and fever shows mural (*arrow*) and intraluminal (*asterisk*) gas within the gallbladder. There are inflammatory changes in the adjacent fat. **B** Opened cholecystectomy specimen from a different patient shows a black, necrotic gallbladder mucosa

Pathologic Features

The pathogenesis of xanthogranulomatous cholecystitis is poorly understood. It has been postulated that the inflammatory process is the result of intravasated bile into the gallbladder wall. Bile may enter the gallbladder wall through mucosal ulceration or rupture of Rokitansky-Aschoff sinuses when there is cystic duct obstruction and increased intraluminal pressure within the gallbladder [6].

A poorly-defined, infiltrating, yellow nodular mass is typically identified on gross inspection of the gallbladder. Lithiasis is frequently present. Histologically, foamy histiocytes, lymphocytes, plasma cells, polymorphonuclear leukocytes, fibroblasts, and foreign body giant cells characterize the inflammatory process (Fig. 3). Histiocytes may contain bile or ceroid pigment. Bands of collagen and cholesterol clefts may be present in the gallbladder wall [10].

Radiologic Features

Focal or diffuse gallbladder wall thickening is the most prominent imaging feature of xanthogranulomatous cholecystitis. Foci of xanthogranulomatous inflammation may appear as hypoechoic bands or nodules on ultrasound, or low attenuation nodules on CT (Fig. 3) [11, 12]. Other features that may be identified on sonography and CT include disruption of the gallbladder wall, indistinct liver margin, pericholecystic fluid, hepatoduodenal ligament adenopathy, and cholelithiasis. CT more effectively demonstrates adjacent organ involvement and extension of the inflammatory process into the adjacent fat planes than sonography. It is well known that xanthogranulomatous cholecystitis may coexist with gallbladder and biliary malignancies and the imaging features overlap with those of gallbladder carcinoma [6]. Therefore, the preoperative distinction between these xanthogranulomatous cholecystitis and gallbladder carcinoma is virtually impossible.

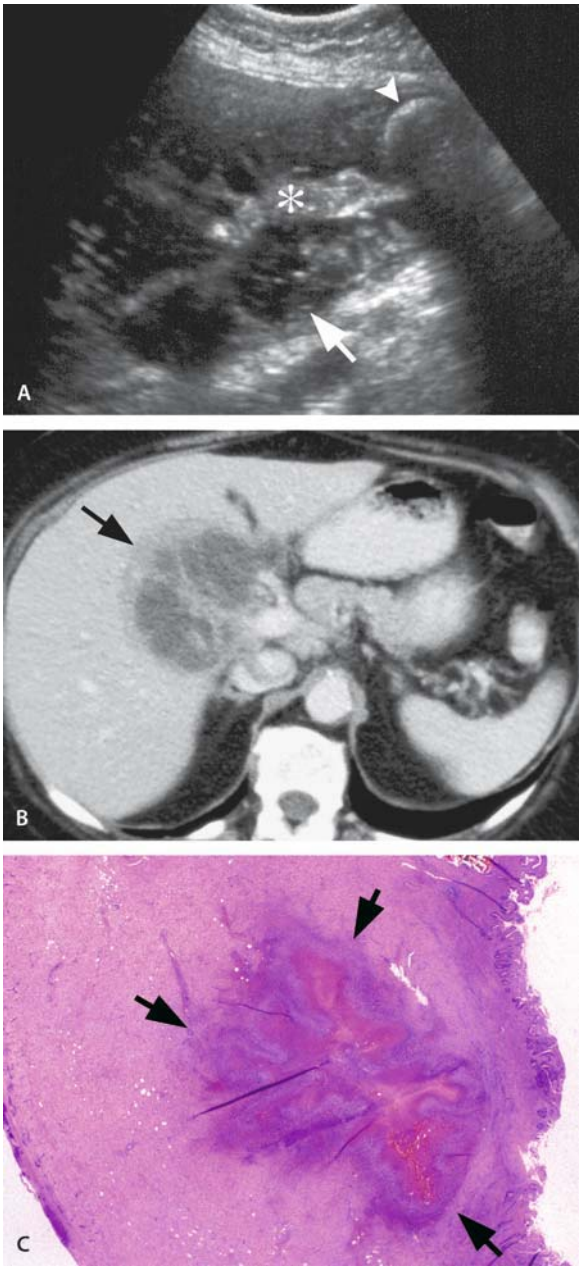

Fig. 3A–C. Xanthogranulomatous cholecystitis. **A** Longitudinal ultrasound image in a 55-year-old man with pain, fever, and leukocytosis shows marked gallbladder wall thickening with prominent hypoechoic nodules (*arrows*). The gallbladder lumen is compressed (*asterisk*) and there is a shadowing stone near the neck of the gallbladder (*arrowhead*). **B** Intravenous contrast-enhanced CT scan in the same patient shows hypoattenuating nodular areas in the thickened gallbladder wall. There is hypoattenuation in the adjacent liver parenchyma (*arrow*). **C** Photomicrograph (original magnification, x2; hematoxylin-eosin stain) shows a thick, fibrotic gallbladder wall with a xanthogranulomatous lesion (*arrows*) containing foamy histiocytes, bile pigment, and inflammatory cells

Tumor-like Lesions

Adenomyomatous Hyperplasia

Incidence and Clinical Features

Adenomyomatous hyperplasia is a common benign condition found in 9% of cholecystectomy specimens [13]. Epithelial and smooth muscle proliferation of the gallbladder wall may result in localized, segmental, or diffuse disease. Throughout the medial literature a variety of names have been applied to this condition including adenomyomatosis, adenomyoma, diverticular

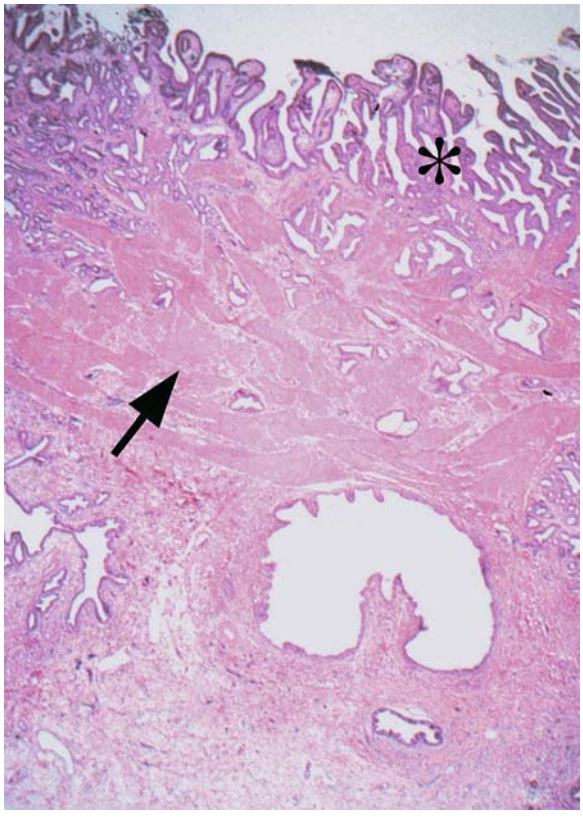

Fig. 4. Adenomyomatous hyperplasia. Photomicrograph (original magnification, x2, hematoxylin-eosin stain) shows papillary hyperplasia of the gallbladder mucosa (*asterisk*). The wall contains penetrating glands and smooth muscle proliferation

disease, intramural diverticulosis, cholecystitis cystica, and cholecystitis glandularis proliferans.

Adenomyomatous hyperplasia is more common in women than men. Most patients complain of chronic right upper quadrant pain, and 90% have coexistent cholelithiasis.

Pathologic Features

Adenomyomatous hyperplasia is histologically characterized by epithelial and smooth muscle proliferation. Normal epithelial structures may invaginate into the gallbladder wall, subserosa, and serosa. The epithelial invaginations (intramural diverticula) may contain inspissated bile, mucus, or stones. Hyperplastic smooth muscle cells accompany the epithelial invaginations (Fig. 4). Inflammatory and fibrotic changes may accompany the proliferative process [14].

There are three variants of adenomyomatous hyperplasia: localized (or fundal), segmental, and diffuse. The localized variant is the most common and is characterized on gross pathology by a well-formed mass in the gallbladder fundus. The fundal mass is often referred to as an adenomyoma. Multiple, small cystic spaces representing hyperplastic glands may be present on sectioning of the mass. The segmental variant is characterized by focal, circumferential thickening of the gallbladder wall, which may result in an hourglass shaped gallbladder. Diffuse adenomyomatous hyperplasia is characterized by diffuse gallbladder wall thickening with small cystic spaces on the cut surface.

Radiologic Features

Sonographically, adenomyomatous hyperplasia manifests as focal, segmental, or diffuse gallbladder wall thickening. Narrowing of the gallbladder lumen may be seen in the diffuse and segmental variants. Intramural diverticula appear as anechoic or echogenic foci in the gallbladder wall. Diverticula that contain bile are anechoic, and those that contain biliary sludge, cholesterol, or stones are echogenic [15]. The sonographic hallmark of adenomyomatous hyperplasia is a "comet-tail" or "V-shaped" reverberation artifact that emanates from the

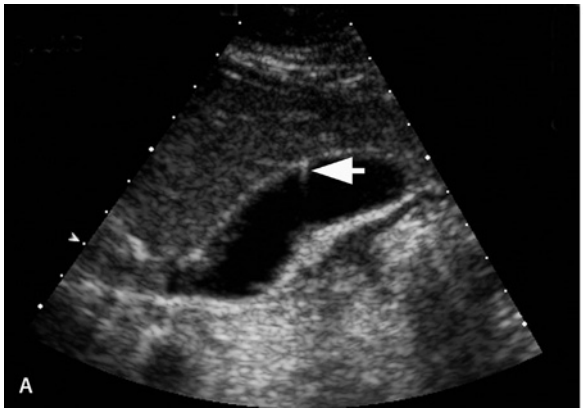

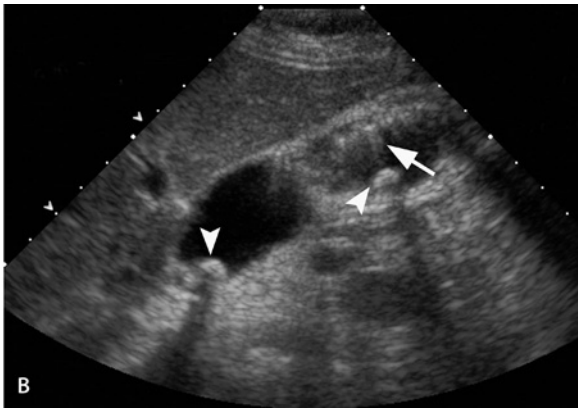

Fig. 5A, B. Adenomyomatous hyperplasia. **A** Longitudinal ultrasound image of the gallbladder show a V-shaped reverberation artifact emanating from the anterior gallbladder wall (*arrow*). **B** Longitudinal ultrasound image of the gallbladder shows mural thickening in the fundus that contains echogenic foci with reverberation artifact in a patient with segmental adenomyomatous hyperplasia. There are stones present (*arrowheads*)

small echogenic foci in the gallbladder wall (Fig. 5) [14]. The localized (fundal) variant manifests as a mass in the gallbladder fundus. It may be difficult to distinguish this form of adenomyomatous hyperplasia from a neoplastic process such as primary gallbladder carcinoma or metastasis. In difficult cases, MR imaging may be helpful for the diagnosis of adenomyomatous hyperplasia. Intramural diverticula are high signal intensity on T2-weighted images [16, 17].

Cholesterol Polyps

Incidence and Clinical Features

Cholesterol polyps are the most common polypoid lesions of the gallbladder; representing 50% of all gallbladder polyps [18]. Cholesterol polyps are nonneoplastic and have no malignant potential. They are three times more common in women than men, and are frequently seen in women between the ages of 40 and 50 years. Although they are typically seen in patients who are being evaluated for epigastric pain, they are rarely found in association with cholelithiasis [19].

Pathologic Features

Grossly, cholesterol polyps are single or multiple, small, yellow, polypoid projections on the mucosal surface of the gallbladder (Fig. 6). Histologically, they are composed of lipid-laden macrophages that stain positive for oil red O stain, and covered with normal gallbladder epithelium [10]. Most cholesterol polyps are less than 10 mm in diameter, although larger polyps up to 20 mm are occasionally encountered [20].

Radiologic Features

Sonographically, cholesterol polyps are usually round, slightly lobulated echogenic nodules projecting into the gallbladder lumen (Fig. 6). They may extend from the gallbladder wall on a thin pedicle. They do not produce a posterior acoustic shadow or reverberation artifact. A small gallstone may have a similar appearance, but can be distinguished from a cholesterol polyp since the latter is adherent to the gallbladder wall. Larger cholesterol polyps are generally less echogenic and therefore may be difficult to differentiate from an adenoma or small adenocarcinoma. The finding of echogenic aggregates within the polyp has been reported to be a feature of cholesterol polyps that is helpful in distinguishing them from neoplastic lesions [20].

In general, unenhanced CT is not helpful in the evaluation of small polypoid lesions of the gallbladder because the attenuation values of polyps and bile are similar. Intravenous contrast-enhanced CT may demonstrate cholesterol polyps as small enhancing mucosal nodules.

Neoplastic Diseases

Gallbladder Adenomas

Incidence and Clinical Features

Gallbladder adenomas are uncommon. They are found in 0.3% to 0.5% of gallbladders removed for cholecystitis or cholelithiasis [21]. Gallbladder adenomas are more common in women, with a reported female to male ratio of 2.4:1 [22]. Most patients with gallbladder adenomas are asymptomatic. Small adenomas are usu-

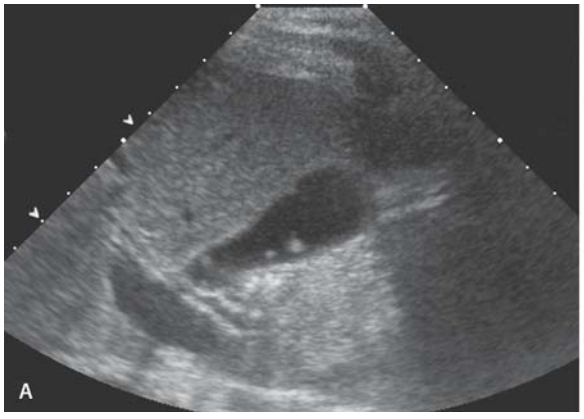

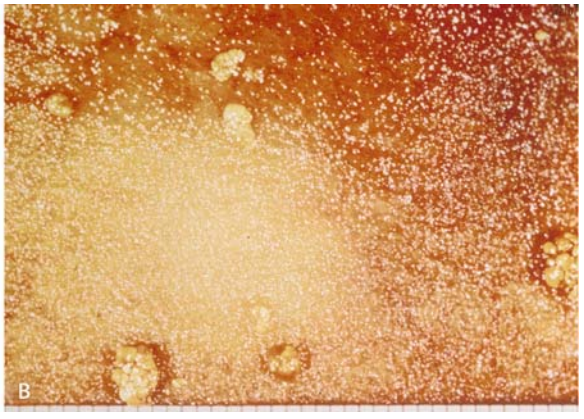

Fig. 6A, B. Cholesterol polyps. **A** Longitudinal ultrasound image of the gallbladder shows several echogenic nodules protruding into the gallbladder lumen from the posterior wall. **B** Photograph of an opened resected gallbladder shows multiple, yellow polyps attached to the gallbladder mucosa

ally discovered incidentally during the radiologic evaluation of the abdomen or at cholecystectomy. Large adenomas may produce symptoms if they obstruct the gallbladder neck or cystic duct [10].

Pathologic Features

Gallbladder adenomas are classified as tubular, papillary, or tubulopapillary. Tubular adenomas are most common and are composed of pyloric- or intestinal-type glands. Papillary adenomas are composed of papillary structures lined by cuboidal or columnar cells [10].

On gross pathologic examination, gallbladder adenomas are polypoid masses that protrude into the gallbladder lumen (Fig. 7). Tubular adenomas are usually lobular in contour, whereas papillary adenomas tend to have a cauliflower-like surface. Multiple adenomas are present in 10% of cases [10]. Cholelithiasis is present in 50% to 65% of cases [19].

Radiologic Features

Sonographically, adenomas are smooth, lobulated, or cauliflower-like polypoid masses within the gallbladder lumen (Fig. 7). They may be sessile or pedunculated. The adjacent gallbladder wall is normal in thickness (<3 mm). The echotexture of adenomas is variable, however most reported cases are homogeneously hyperechoic with respect to the adjacent liver parenchyma [20].

Gallbladder adenomas are difficult to distinguish from carcinoma on imaging studies. Intravenous contrast-enhanced CT may be helpful in the evaluation of patients with polypoid gallbladder lesion. Adenomas have been reported to appear as iso-or hypoattenuating masses [23]. Gallbladder adenomas have malignant potential and may develop into carcinomas through the adenoma to carcinoma sequence. However, most authors believe that adenomas play a minor role in the pathogenesis of gallbladder carcinoma [10]. CT is useful for the detection of lymphadenopathy, and subtle adjacent organ invasion that would typically accompany gallbladder carcinoma.

Gallbladder Carcinoma

Incidence and Clinical Features

Gallbladder carcinoma is an uncommon, but highly lethal malignancy. It is the sixth most common gastrointestinal tract malignancy worldwide and in the United States. Worldwide, gallbladder carcinoma follows carcinoma of the stomach, colorectum, liver, esophagus, and pancreas in incidence [24]. Gallbladder carcinoma is three times more common in women than men. Gallstones are present in 74% to 92% of affected patients [25]. The pathogenesis of gallbladder carcinoma is postulated to begin with chronic mucosal irritation and inflammation, which leads to mucosal dysplasia and subsequent carcinoma [26]. Other risk factors include: increased body mass, cigarette smoking [27], chronic *Salmonella typhi* infection [28]; exposure to chemicals used in the rubber, automobile, wood finishing, and metal fabricating industries [29]; primary sclerosing cholangitis [30]; and congenital anatomic abnormalities of the biliary tree such as choledochal cyst, anomalous pancreaticobiliary junction, and low insertion of the cystic duct [31, 32]. There is a 10% to 25% incidence of gallbladder carcinoma in patients with diffuse calcification of the gallbladder wall (porcelain gallbladder) [33].

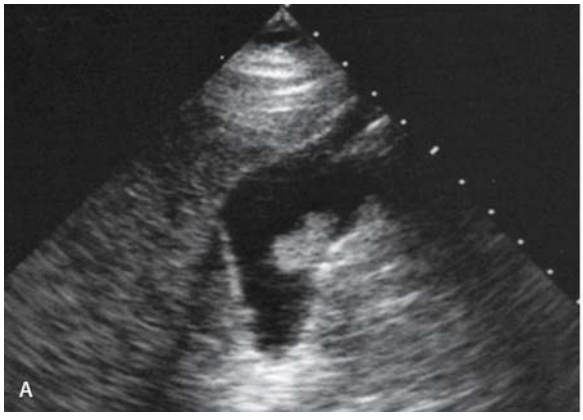

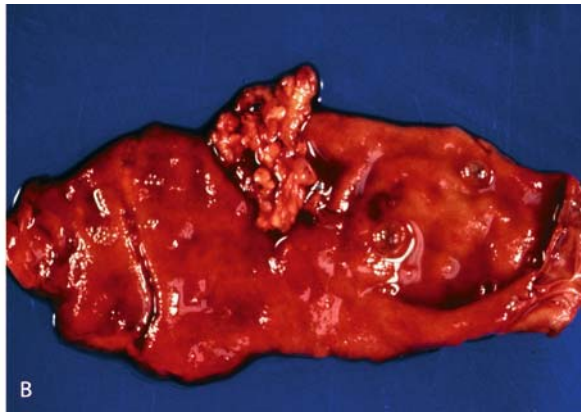

Fig. 7A, B. Gallbladder adenoma in a 45-year-old asymptomatic woman. **A** Longitudinal ultrasound of the gallbladder show an echogenic, lobulated gallbladder polyp. **B** Opened cholecystectomy specimen shows a multilobulated mass on the mucosal surface of the gallbladder

Early stage gallbladder carcinoma is typically asymptomatic. The majority of patients with gallbladder carcinoma develop symptoms when the tumor is advanced in stage. Chronic abdominal pain, weight loss, and anorexia are common initial complaints. On physical examination, hepatomegaly, palpable right upper quadrant mass, and jaundice may be present.

Pathologic Features

Two gross pathologic patterns typify gallbladder carcinoma: infiltrating lesions and intraluminal polypoid masses. The infiltrating pattern (68% of cases) is encountered most commonly, and is secondary to submucosal spread of tumor, which may manifest as focal or diffuse wall thickening (Fig. 8). Thirty-two percent of cases exhibit intraluminal polypoid growth [34]. Sixty percent of tumors originate in the gallbladder fundus, 30% in the body, and 10% in the neck [21]. Those tumors that arise in the neck of the gallbladder not only lead to gallbladder obstruction (hydrops), but also commonly infiltrate the adjacent extrahepatic bile ducts [10].

The majority (98%) of gallbladder malignancies are epithelial in origin. Sarcomas, lymphomas, carcinoid, and metastasis account for the remainder. Adenocarcinoma accounts for 90% of the epithelial malignancies and is characterized histologically by neoplastic glands lined by columnar or cuboidal cells. There are several well-recognized variants of adenocarcinoma: papillary, intestinal, mucinous, signet ring, and clear cell. Papillary carcinomas are usually sessile, polypoid, or cauliflower-like masses that project into the gallbladder lumen. Mucinous and signet-ring cell carcinomas have a gelatinous appearance on cut surface due to intra- and extracellular mucin [10].

Radiologic Features

The cross-sectional imaging features of gallbladder carcinoma are described as a mass replacing the gallbladder, focal or diffuse gallbladder wall thickening, and an intraluminal polypoid mass [35, 36]. Carcinomas that completely replace the gallbladder account for 40% to 65% of cases. Sonographically, these carcinomas are typically heterogeneous in echotexture, reflecting varying degrees of necrosis and hemorrhage within the tumor. Calcification associated with the tumor may be secondary to tumoral calcification, gallbladder wall calcification, or, most commonly, coexistent gallstones [37]. Intravenous contrast-enhanced CT shows a heterogeneously hypoattenuating mass in the gallbladder fossa. The tumor mass is contiguous with the adjacent liver in many cases. Areas of viable tumor may enhance, whereas foci of tumor necrosis show focal hypoattenuation.

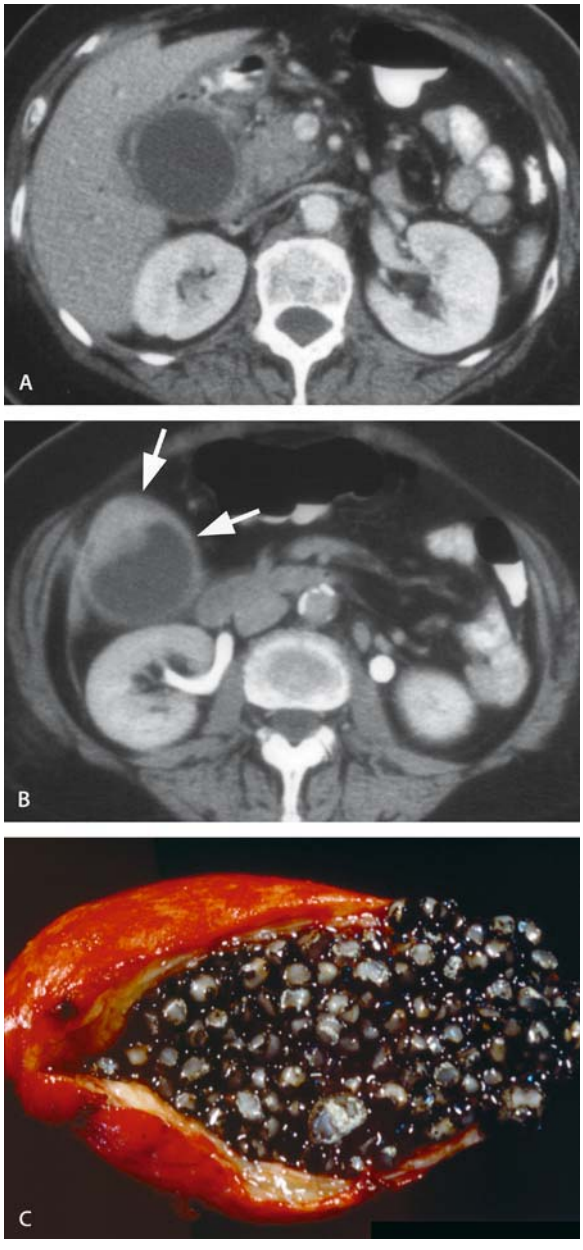

Fig. 8A–C. Gallbladder carcinoma in a 65-year-old woman with abdominal pain. **A**, **B** Intravenous contrast-enhanced CT scans show mural thickening (*arrow*) that is more prominent along the anterior wall. There is tumor infiltration of the hepatoduodenal ligament (*arrow*) and hepatic invasion (*curved arrow*). **C** Opened resected specimen shows neoplastic mural thickening and pigment stones

Gallbladder carcinoma will manifest as focal or diffuse gallbladder wall thickening in 20% to 30% of cases. Sonographically, wall thickening is the most diagnostically challenging pattern because it mimics more common inflammatory conditions of the gallbladder. Fea-

tures such as mural irregularity, marked asymmetry, or extension of the process beyond the limits of the gallbladder wall should raise concerns for malignancy [38, 39]. Use of intravenous contrast-enhanced CT is helpful for distinguishing complicated cholecystitis from gallbladder carcinoma. The CT demonstration of hepatoduodenal ligament or peripancreatic adenopathy, soft-tissue extension in the adjacent liver, or evidence of hematogenous metastasis favors the diagnosis of gallbladder carcinoma (Fig. 8).

Intraluminal polypoid mass is the least common imaging manifestation of gallbladder carcinoma, occurring in 15% to 25% of cases [36]. Sonography or CT may identify a well-defined, oval or round mass. Subtle extension beyond the gallbladder wall may be more apparent on intravenous contrast-enhanced CT than sonography.

Extension of gallbladder carcinoma to adjacent structures is facilitated by the normally thin gallbladder wall, which lacks a substantial lamina propria and muscular layer [37]. Furthermore, the perimuscular connective tissue of the gallbladder is continuous with the interlobular connective tissue of the liver. The liver is the most common site for direct extension of gallbladder carcinoma (65% of cases), followed by the colon (15%), duodenum (15%), and pancreas (6%) [34]. Use of helical CT in the preoperative assessment of local spread has recently been shown to have an accuracy of 83% to 86% [40].

Biliary dilatation occurs in 38% of patients with gallbladder carcinoma [41]. Infiltrative tumor growth into the extrahepatic bile ducts, lymph node enlargement, and intraductal spread of tumor may account for biliary obstruction [37]. Cholangiography may show malignant strictures of the extrahepatic bile duct, confluence of the right and left ducts, or the right intrahepatic duct.

The radiologic differential diagnosis of gallbladder carcinoma manifesting as a mass replacing the gallbladder includes aggressive malignancies in or near the gallbladder such as hepatocellular carcinoma, cholangiocarcinoma, and metastatic disease to the gallbladder fossa. The differential diagnosis for carcinomas producing diffuse gallbladder wall thickening includes inflammatory conditions such as acute and chronic cholecystitis and xanthogranulomatous cholecystitis. Congestive heart failure, hepatitis, hypoproteinemia, and renal failure may also produce chronic gallbladder wall thickening. Adenomyomatous hyperplasia is a common tumor-like condition of the gallbladder wall that produces focal or diffuse wall thickening indistinguishable from gallbladder carcinoma. Sonographic demonstration of echogenic foci in the gallbladder wall with ring-down reverberation artifact, or the MR finding of Rokitansky-Aschoff sinuses is helpful to distinguish adenomyomatous hyperplasia from gallbladder carcinoma.

The differential diagnosis for an intraluminal polypoid mass in the gallbladder includes cholesterol polyps, adenomas, carcinoid, and metastatic disease to the gallbladder.

Part II: Bile Ducts

Congenital Disorders

Caroli Disease

Incidence and Clinical Features

Caroli disease, or communicating ectasia of the intrahepatic bile ducts [42], is a rare and complex autosomal recessive disorder that is part of the clinicopathologic spectrum of ductal plate malformations [43]. The ductal plate is the embryologic precursor to intrahepatic bile ducts. The ductal plate malformation is the result of developmental arrest or derangement of the ductal plate during embryogenesis. If the large intrahepatic bile ducts are affected, the result is Caroli disease, whereas abnormal development of the small intrahepatic bile ducts results in congenital hepatic fibrosis. If all levels of the intrahepatic biliary system are involved, the result is Caroli syndrome. Caroli syndrome has features of both congenital hepatic fibrosis and Caroli disease.

The clinical presentation of Caroli disease is related to biliary stasis. Therefore, patients may present to clinical attention at any age. Patients complain of symptoms such as abdominal pain, fever, and chills that are related to cholangitis, stone formation, or hepatic abscesses that are secondary to biliary stasis [44]. Portal hypertension and liver failure may occur in patients that have significant hepatic fibrosis.

Pathologic Features

The histologic hallmark of Caroli disease is the ductal plate malformation, which is characterized by tortuous, dilated dysplastic intrahepatic bile ducts with surrounding fibrosis and inflammation (Fig. 9). Bilirubin calculi may be present within dilated bile ducts. Gross pathologic specimens show saccular or fusiform duct dilatation, periductal fibrosis, and stone formation [44].

Radiologic Features

The pathologic features of duct dilatation, fibrosis, and inflammation result in a wide spectrum of radiologic features. The unifying radiologic feature in all patients is nonobstructive intrahepatic duct dilatation. The majority of patients (82%) with Caroli disease have only

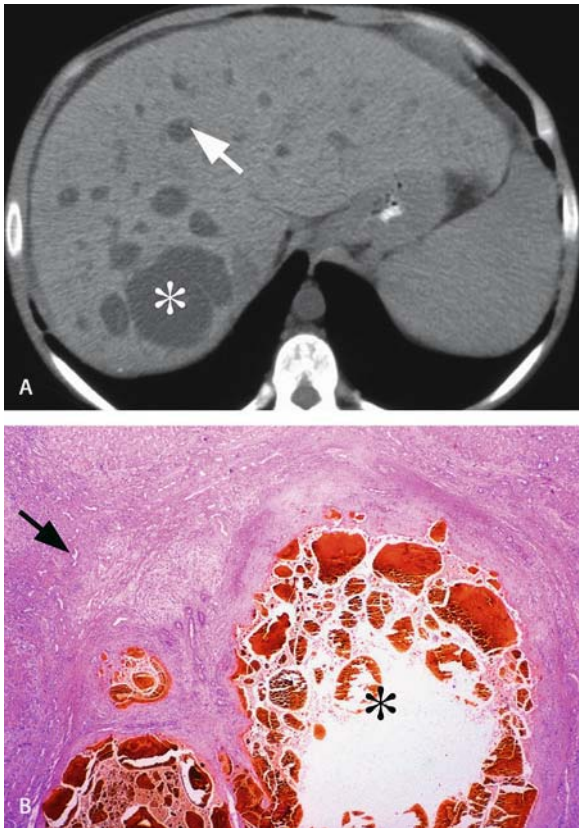

Fig. 9A, B. Caroli disease. **A** Unenhanced CT scan in a 26-year-old man with portal hypertension and end-stage liver disease shows diffuse saccular biliary dilatation and the central-dot sign (*arrow*). There is a hepatic abscess in the right lobe (*asterisk*). **B** Photomicrograph (original magnification, x20; hematoxylin-eosin stain) from a patient with Caroli syndrome shows bilirubin calculi in a dilated bile duct (asterisk) surrounded by fibrosis and embryonic ductal structures (*arrow*)

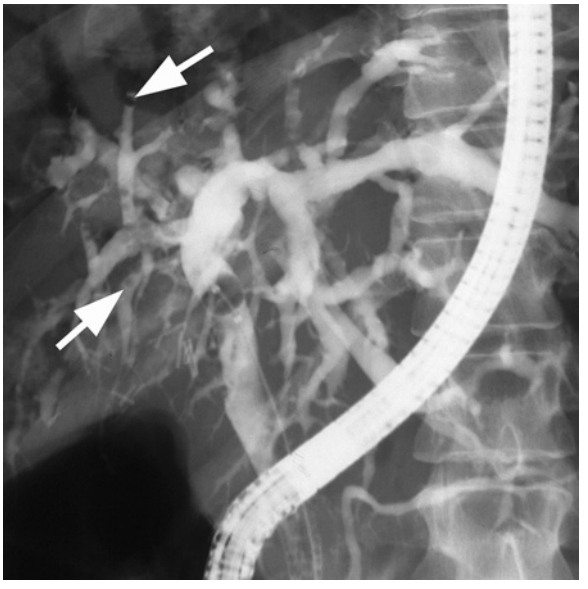

Fig. 10. Caroli disease in a 38-year-old woman with fever and right upper quadrant pain. Endoscopic retrograde cholangiopancreatography (ERCP) image shows fusiform dilatation of the intrahepatic ducts with multiple calculi (*arrows*). The ducts show beading and mural irregularity

segmental involvement of the intrahepatic ducts [44]. Cross-section imaging shows saccular or fusiform biliary dilatation. Fusiform biliary dilatation alternating with strictures may have a beaded appearance. Fibrovascular bundles within or along the edge of the dilated ducts has been termed the "central-dot sign" (Fig. 9) [45]. The cholangiographic features of Caroli disease include saccular dilatation, irregular bile duct walls, strictures, and stones (Fig 10) [46]. Magnetic resonance cholangiopancreatography has been shown to accurately identify the diagnostic features of Caroli disease [47]. The diagnostic challenge with MR is accurate identification of communicating cystic biliary dilatation.

Extrahepatic biliary dilatation occurs in 21% to 53% of patients [44, 48]. Extrahepatic dilatation is usually mild and fusiform, resulting from recurrent cholangitis and stone passage.

Biliary stasis predisposes patients with Caroli disease to the development of adenocarcinoma. The incidence of adenocarcinoma in Caroli disease is 7% [31]. The cholangiographic features of adenocarcinoma (focal hepatic mass, intraductal mass, and biliary stricture) overlap with the disease. Therefore, the diagnosis of biliary adenocarcinoma in Caroli disease may be difficult.

Choledochal Cyst

Incidence and Clinical Features

Choledochal cysts are congenital dilatations of the extrahepatic bile duct. Although uncommon, most cases are reported from Japan, where the incidence is estimated to be 1:1000 persons [49]. The incidence in western countries is estimated to be 1:100,000 to 1:150,000 persons [50].

Choledochal cysts are three times more common in females than males [51]. Although patients may present at any age, the majority present during infancy or childhood with signs and symptoms of biliary obstruction, abdominal pain, or a palpable abdominal mass. During adulthood, pain is the most frequent presenting symptom [50]. Cholelithiasis, choledocholithiasis, cystolithiasis, cholangitis, biliary cirrhosis, portal hypertension, and malignancy may complicate choledochal cysts. The risk of malignancy increases with age and is reported to range from 2.5% to 28% [52–54].

Pathologic Features

The diagnosis of choledochal cyst is based upon the gross appearance of saccular or fusiform dilatation of the extrahepatic bile duct. The distribution of duct dilatation and classification of the cyst is based upon radiologic and intraoperative features. Histologically, the wall of the cyst is composed of dense fibrous tissue with scattered smooth muscle fibers and elastic tissue. The cyst wall is typically thicker than that of a normal bile duct wall. The lining of the cyst is composed of a single layer of normal biliary epithelium.

The proposed etiology of choledochal cysts is anomalous arrangement of the pancreaticobiliary junction [55–58]. In an anomalous pancreaticobiliary junction, the union of the pancreatic duct and common bile duct occurs proximal to the sphincter of Oddi. Consequently, there is reflux of pancreatic enzymes into the common bile duct during sphincter contraction. Recurrent inflammation creates weakness and fibrous thickening of the bile duct wall that results in dilatation of the bile duct lumen, and in some cases, distal duct narrowing with stricture formation.

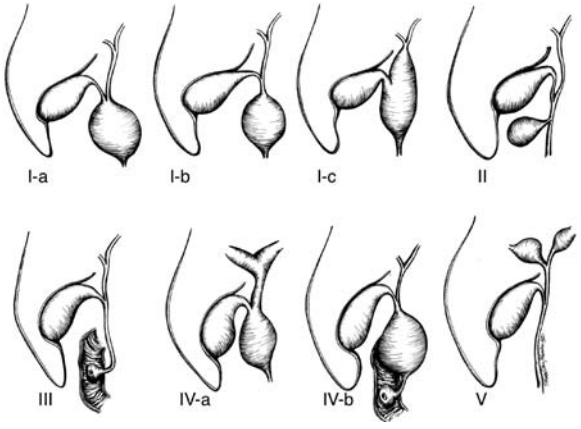

Fig. 11. Todani classification of choledochal cysts

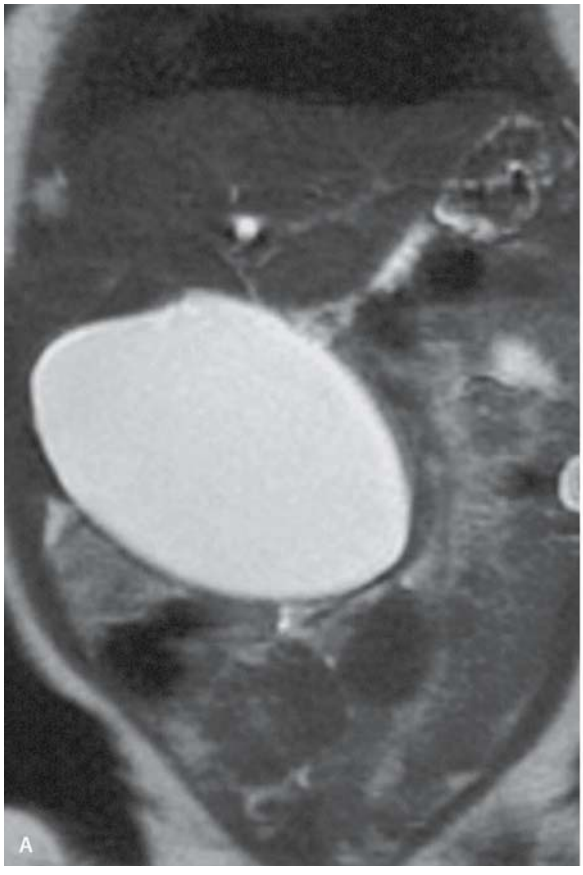

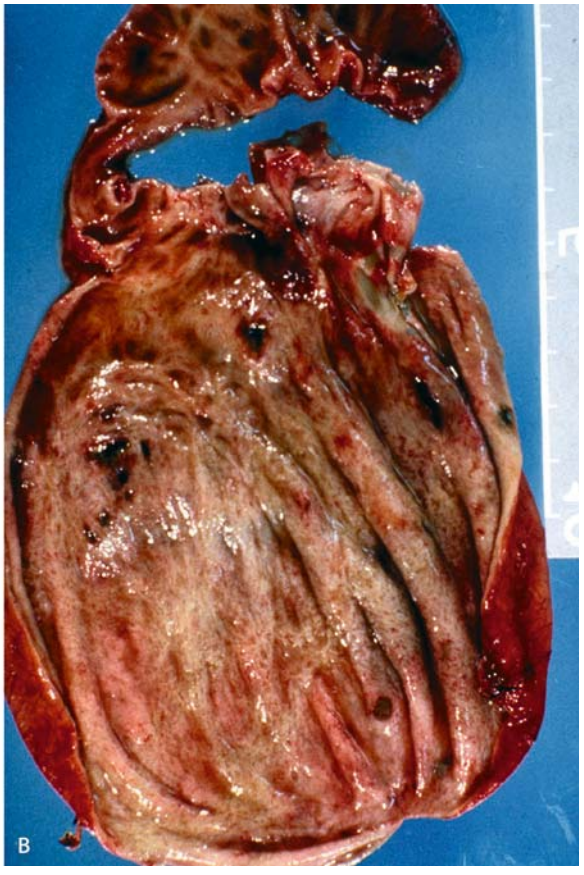

Fig. 12A, B. Todani type I choledochal cyst. **A** A 3-month old infant girl who had abdominal distension and a palpable abdominal mass. Coronal T2-weighted MR shows cystic dilatation of the extrahepatic bile ducts. There is no intrahepatic bile duct dilatation. **B** Opened resected type I choledochal cyst from a different patient shows mild trabeculation of the mucosal surface. The cystic duct enters directly into the cyst

Radiologic Features

Todani et al classified the spectrum of choledochal cysts (Fig. 11) [59]. Cross-sectional imaging studies show saccular or fusiform dilatation of the extrahepatic bile duct with or without extension into the intrahepatic bile ducts (Fig. 12). Inflammatory mural thickening, echogenic sludge, or stones may be shown sonographically. Cholangiography, CT, and MRCP are effective imaging modalities to provide detailed anatomy of the biliary tract and pancreaticobiliary junction (Fig. 13) [60–62]. The margins of the dilated bile ducts are typically smooth. Filling defects within the bile ducts or irregularity in the cyst wall may be secondary to inflammation, stones, tumefactive sludge, or neoplasia.

Choledochocele

Incidence and Clinical Features

Choledochocele is focal cystic dilatation of the intramural segment of the distal common bile duct and was originally classified as a Todani Type III choledochal cyst [59]. The etiology and pathogenesis are uncertain. It has been suggested that they occur secondary to inflammatory obstruction of the papilla of Vater [63], sphincter of Oddi dysfunction [64], or that they may represent an enteric duplication cyst [65]. Choledochoceles are rare, and usually manifest during adulthood. Patients may present with episodes of abdominal pain, nausea and vomiting, or signs and symptoms of obstructive jaundice and pancreatitis [66].

Radiologic Features

Cross-sectional imaging studies may show a fluid-filled cyst protruding into the duodenal lumen that is contiguous with the distal common bile duct. Cholangiographic studies show smoothly marginated saccular dilatation of the intramural portion of the distal common bile duct (Fig. 14). Endoscopic evaluation of patients with suspected choledochoceles is warranted to exclude periampullary neoplasms that may obstruct the papilla of Vater creating the appearance of a choledochocele.

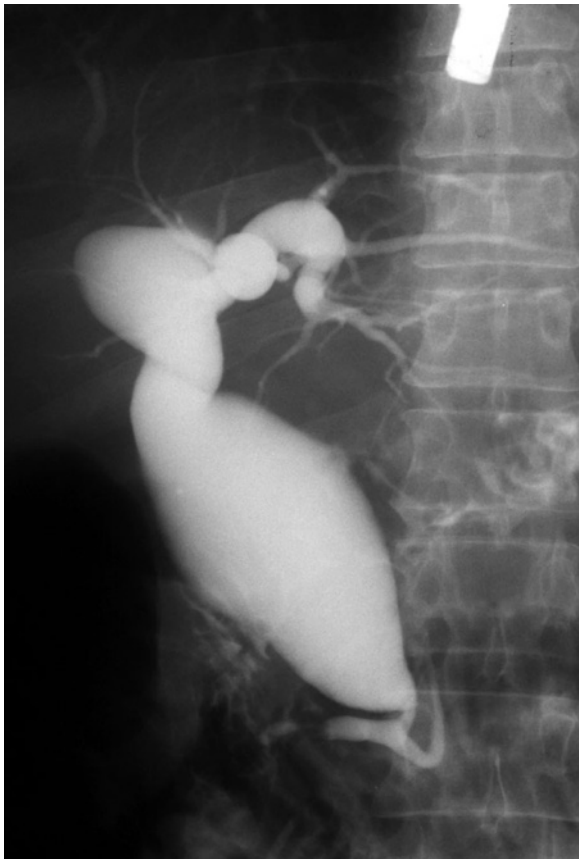

Fig. 13. Todani type IVA choledochal cyst in a 54-year-old man with epigastric pain. ERCP image shows fusiform enlargement of the extrahepatic and central intrahepatic bile ducts. There is an anomalous pancreaticobiliary junction

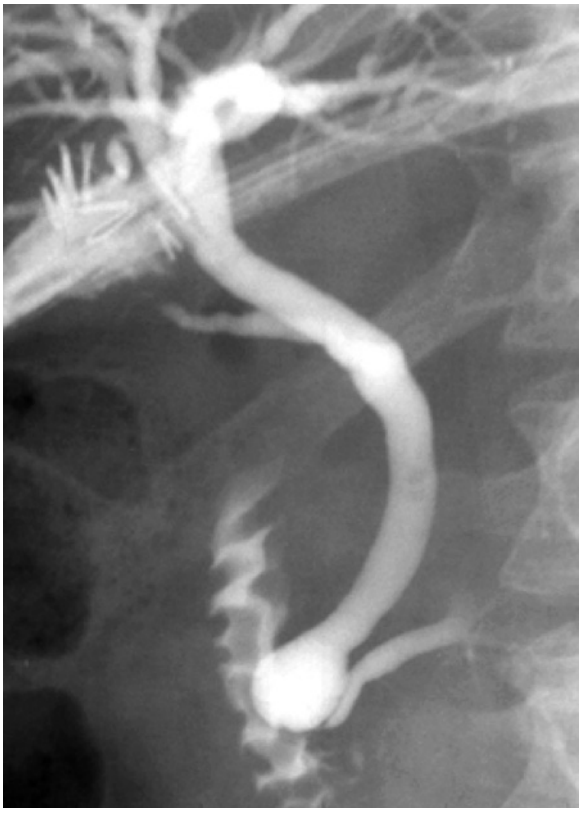

Fig. 14. Choledochocele. Delayed image from an ERCP in a 45-year-old woman post cholecystectomy shows dilatation of the intramural segment of the distal common bile duct

Biliary Diverticulum

Incidence and Clinical Features

Congenital biliary diverticula (Todani Type II) are localized areas of pathologic dilatation in an otherwise normal bile duct. A well-defined neck connects the diverticulum to the bile duct. Given their rarity, diverticular cysts are the most difficult congenital biliary abnormalities to classify and propose an etiology. Biliary diverticula occur ant any age and have no gender predilection.

Radiologic Features

Diverticular cysts may arise from the extrahepatic bile duct as well as the right and left hepatic ducts. Therefore, cross-sectional imaging studies may show a fluid-filled cyst in and around the porta hepatis that is separate from the gallbladder. Traditional cholangiographic techniques as well as MRCP are excellent imaging modalities to identify the relationship of the normal bile duct to the cyst. The diagnosis requires the identification a well-defined neck connecting the cyst to the adjacent bile duct.

Inflammatory Disorders

Acute Pyogenic Cholangitis

Incidence and Clinical Features

Acute pyogenic cholangitis, also known as bacterial or ascending cholangitis, is almost always a complication of bile duct obstruction by choledocholithiasis. Less likely, acute cholangitis may occur in the context of obstructing neoplasm, trauma, surgery, pancreatitis, with papillary stenosis, or as a component of AIDS-related cholangiopathy. Patients usually have fever, right upper quadrant pain, and obstructive liver function abnormalities [67]. Those more severely affected may have hypotension and systemic sepsis, requiring aggressive antibiotic and interventional therapy to recover [68]. Complications of inadequately treated acute cholangitis include emphysematous cholecystitis and cholangitis, liver abscess, gallbladder perforation with abscess, and chronic (secondary sclerosing) cholangitis.

Pathologic Features

Bacteria originating in either the intestine or the portal vein infect the obstructed biliary system. As infection progresses, bacterial invasion of the biliary mucosa and duct wall is enhanced by increased intraductal pressure. Sepsis occurs as the bacteria invade the bloodstream [69].

Radiologic Features

Ultrasound and computed tomography will usually identify bile duct dilatation, intraductal debris, and stones. Direct cholangiography can be expected to confirm the cause of obstruction, as well as portray the ductal morphologic manifestations of cholangitis. These include mucosal edema, duct irregularity, and intraductal debris (Fig. 15) [70].

Primary Sclerosing Cholangitis

Incidence and Clinical Features

Primary sclerosing cholangitis is an idiopathic cholestatic syndrome that affects both the intra- and extrahepatic ducts, and progresses invariably to liver failure

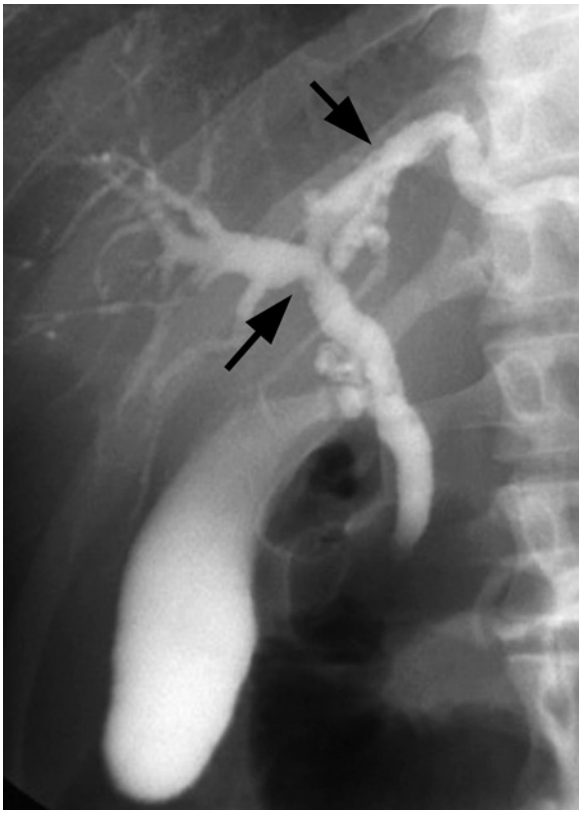

Fig. 15. Ascending cholangitis in a 43-year-old woman with choledocholithiasis. ERCP images show an obstructing stone in the common bile duct. There is mural irregularity (*arrows*) and debris throughout the visualized ducts

with death or transplantation at approximately 12–18 years after diagnosis. Although the cause is unknown, it is most likely an autoimmune condition. It is frequently (70% to 90% of cases) associated with ulcerative colitis; and, 6% to 10% of affected patients develop cholangiocarcinoma [71–73].

Pathologic Features

Primary sclerosing cholangitis always affects the intrahepatic bile ducts and usually involves the extrahepatic ducts as well. A rare variant of the condition only involves interlobular bile ducts. This is termed *small duct primary sclerosing cholangitis*, and the microscopic

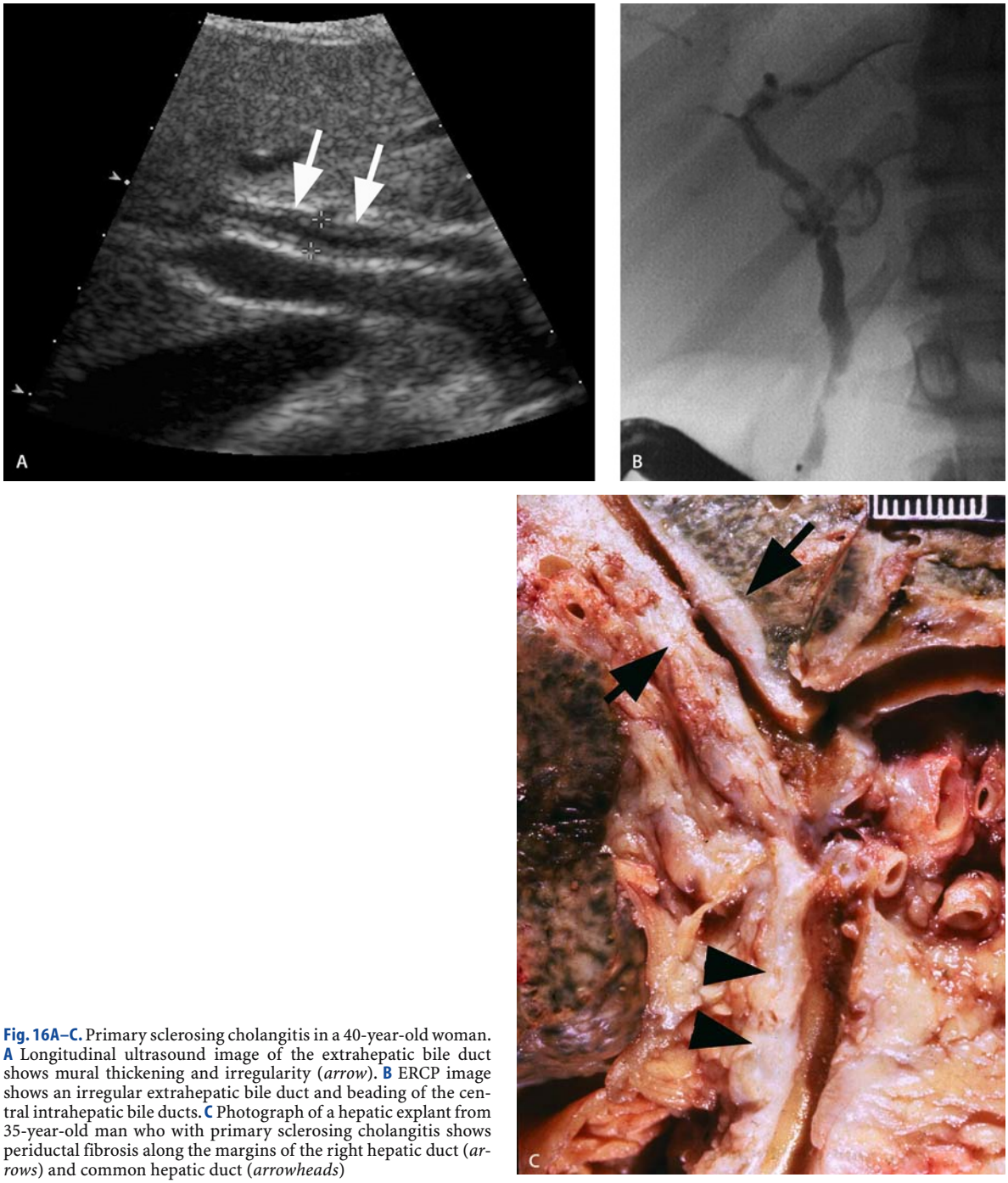

Fig. 16A–C. Primary sclerosing cholangitis in a 40-year-old woman. **A** Longitudinal ultrasound image of the extrahepatic bile duct shows mural thickening and irregularity (*arrow*). **B** ERCP image shows an irregular extrahepatic bile duct and beading of the central intrahepatic bile ducts. **C** Photograph of a hepatic explant from 35-year-old man who with primary sclerosing cholangitis shows periductal fibrosis along the margins of the right hepatic duct (*arrows*) and common hepatic duct (*arrowheads*)

manifestations of the disease are below the resolution of radiologic imaging [74].

The gross and histologic features of primary sclerosing cholangitis are nonspecific. On gross inspection, there may be mucosal ulceration, fibrous duct wall thickening, stenosis, focal or diffuse obstruction, and duct obliteration (Fig. 16). If the disease is focal, differentiation from carcinoma is difficult. Histologic signs include pericholangitis, periductal fibrosis with "onion-skin" appearance, intrahepatic duct loss, and obstruction (Fig. 16C). Extrahepatic duct distortion and ectasia correlate with the cholangiographic findings of diverticula or sacculations [10].

Radiologic Features

Because of the nonspecific pathologic features of primary sclerosing cholangitis, direct cholangiography has traditionally been considered the gold standard for diagnosis. Except for the few patients with small duct primary sclerosing cholangitis, all patients with the disease will have radiographically defined intrahepatic duct abnormalities. Approximately three quarters will have extrahepatic duct findings as well. High resolution CT and MRCP are contributing more to the primary diagnosis of primary sclerosing cholangitis and in some centers have supplanted ERCP as the standard for diagnosis [75].

Although duct stenosis and obliteration are the essential radiographic findings, frequently there is marked duct inflammation with irregularity, nodularity, and ulceration (Fig. 17). Cholangiography will show characteristic alternating stenotic and ectatic duct segments with pruning of duct branches. Theses features establish the diagnosis. The extrahepatic ducts also show segmental or diffuse stenosis, and frequently demonstrate sacculation or ectasia of the biliary glands, a finding characteristic of this disorder.

Computed tomography and MR cholangiography features include alternating intrahepatic duct ectasia and stenosis producing the "beaded" appearance. The manifestations may be diffuse or focal. Since the ducts proximal to obstruction, may not be visualized by ERCP, CT and MRCP have potential to provide a more complete depiction of the involved ducts. The extrahepatic duct wall may be thickened and show echogenic mural thickening on sonography and CT enhancement with intravenous contrast administration (Figs. 16A, 17A). Intramural sacculations may be seen if of adequate size. Cross-sectional imaging studies show advanced liver manifestations, which include periportal fibrosis, liver margin lobulation, atrophy of the lateral or posterior hepatic segments, and enlargement of the caudate lobe [76].

Differential diagnosis of primary sclerosing cholangitis includes those processes causing cirrhosis and secondary sclerosing cholangitis. Considerations include AIDS cholangiopathy, chronic pyogenic cholangitis, recurrent pyogenic cholangiohepatitis, chemotherapy-induced cholangitis, ischemic cholangitis of any cause, radiation cholangitis, rejection following hepatic transplantation, amyloidosis, diffuse cholangiocarcinoma, metastases, and lymphoma [75].

Primary Sclerosing Cholangitis and Adenocarcinoma

Diagnosis of bile duct adenocarcinoma complicating primary sclerosing cholangitis presents a difficult diag-

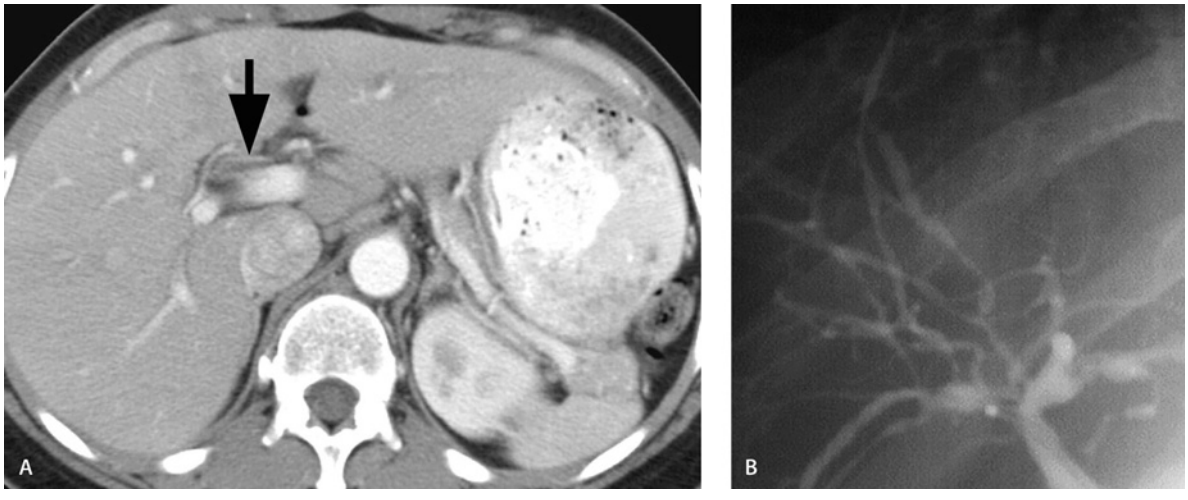

Fig. 17A, B. Primary sclerosing cholangitis in a 35-year-old man. **A** Oral and intravenous contrast-enhanced CT scan shows mural enhancement of the central intrahepatic ducts (*arrow*). **B** ERCP image shows beading and mural irregularity of the intrahepatic ducts

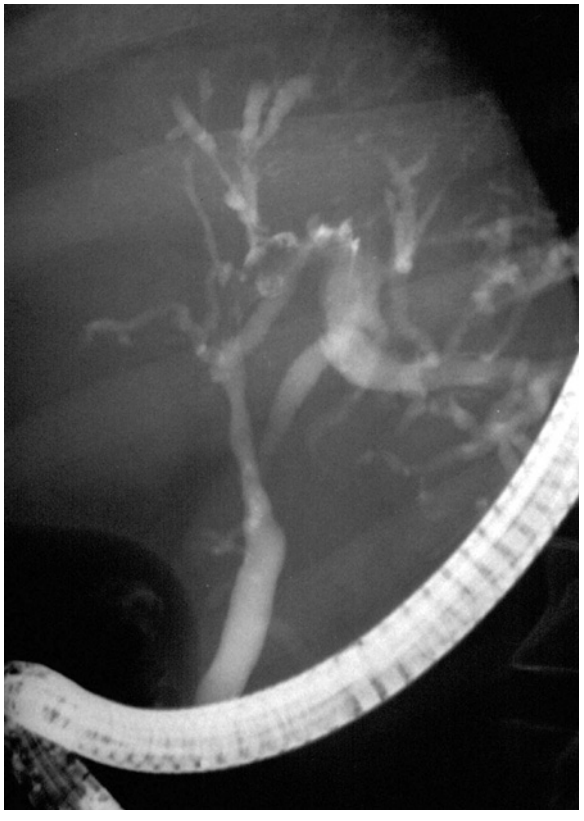

Fig. 18. Hilar cholangiocarcinoma complicating primary sclerosing cholangitis in a 54-year-old man. ERCP image shows intrahepatic ductal changes of primary sclerosing cholangitis and a long segment malignant stricture involving the confluence and proximal extrahepatic duct

nostic challenge. Both conditions produce bile duct stenosis and obstruction; therefore, the appearance of the lesions can be similar. High-grade stenotic lesions that progress rapidly, demonstrate a dominant stricture with shouldered margins, or intraductal mass suggest carcinoma (Fig. 18) [77]. CT accuracy is improved if a neoplastic mass is identified surrounding the duct stenosis or obstruction [78].

Secondary Sclerosing Cholangitis

Definition and Differential Diagnosis

When chronic fibrosing or sclerosing biliary inflammation is associated with, or secondary to an underlying biliary disease, it is termed secondary sclerosing cholangitis. This condition is distinguished therefore from primary sclerosing cholangitis where there is no predisposing biliary condition. The most common cause of secondary sclerosing cholangitis is chronic or recurrent infection, almost always due to untreated or recurrent stone disease. Recurrent pyogenic cholangiohepatitis, also known as oriental cholangiohepatitis, is a disease illustrative of chronic stone formation and infection as a cause of secondary sclerosing cholangitis. AIDS-related cholangiopathy is another example of chronic biliary infection that may or may not have associated lithiasis. Untreated stricture or partial obstruction, due to surgical or traumatic bile duct injury, benign neoplasm, or papillary sphincter dysfunction can cause chronic cholangitis resulting in a progressive fibrosing or sclerosing process. Bile duct ischemia from hepatic arterial infusion chemoembolic therapy, radiation, primary hepatic arterial damage or hepatic transplantation rejection may also lead to secondary sclerosing cholangitis [79].

Radiologic Features

The radiologic findings of acute cholangitis noted above may be present in patients with secondary sclerosing cholangitis. In addition, these patients will generally have radiologic features that will not distinguish among etiologies of the chronic cholangitis. Some of the findings can be very similar to those of primary sclerosing cholangitis. Cross sectional imaging may demonstrate focal duct dilatation and stenosis, intraductal debris and calculi, and signs of cirrhosis. Cholangiography typically shows ductal obstruction by stone or stenosis, irregularities of mucosal lining, duct caliber alterations, and diminished arborization or pruning of duct branches. Imaging features more characteristic of specific diseases leading to secondary sclerosing cholangitis are noted below.

Recurrent Pyogenic Cholangitis

Incidence and Clinical Features

Also known as oriental cholangiohepatitis, recurrent pyogenic cholangiohepatitis is a chronic or recurrent bacterial bile duct infection leading to intrahepatic and extrahepatic calculi, duct ectasia, progressive inflammatory strictures, abscess formation, bile duct sclerosis, and liver failure. Bile duct carcinoma can also result. The syndrome is most prevalent in Asia and the Indian subcontinent, but is found also in recent immigrants from endemic areas. It is associated with a variety of biliary parasites, especially liver flukes (e.g., *Clonorchis sinensis*) and *Ascaris lumbricoides* [80].

Pathologic Features

Parasites, inflammatory debris, and desquamated bile duct cells form the nidus for development of primary or

pigment (calcium bilirubinate) choledocholithiasis. Intrahepatic and especially left hepatic duct stones are typical. As the disease progresses into chronic cholangitis, periductal inflammation results in fibrosis, duct loss, cirrhosis, and hepatic parenchymal atrophy [80].

Radiologic Features

The imaging features of recurrent pyogenic cholangiohepatitis reflect the pathology of this syndrome. Cross sectional imaging and direct cholangiography is complimentary, as each may demonstrate different regions or components of the process. Dilated ducts filled with inflammatory debris, parasites, and calculi characterize the cross-sectional imaging and cholangiographic examinations (Fig. 19). The findings are typically more evident in the left hepatic and extrahepatic ducts. Inflammatory strictures may affect both intra and extrahepatic ducts. As periductal inflammation progresses, intrahepatic branch ducts are obliterated, producing the appearance characterizing this process as a type of secondary sclerosing cholangitis. Severe infection may result in choledochoduodenal fistula, cholecystitis and liver abscess [80].

AIDS-Related Cholangiopathy

Incidence and Clinical Features

The most common AIDS-associated complication of the biliary tree is AIDS-related cholangiopathy. A type of secondary sclerosing cholangitis, it is caused by a varie-

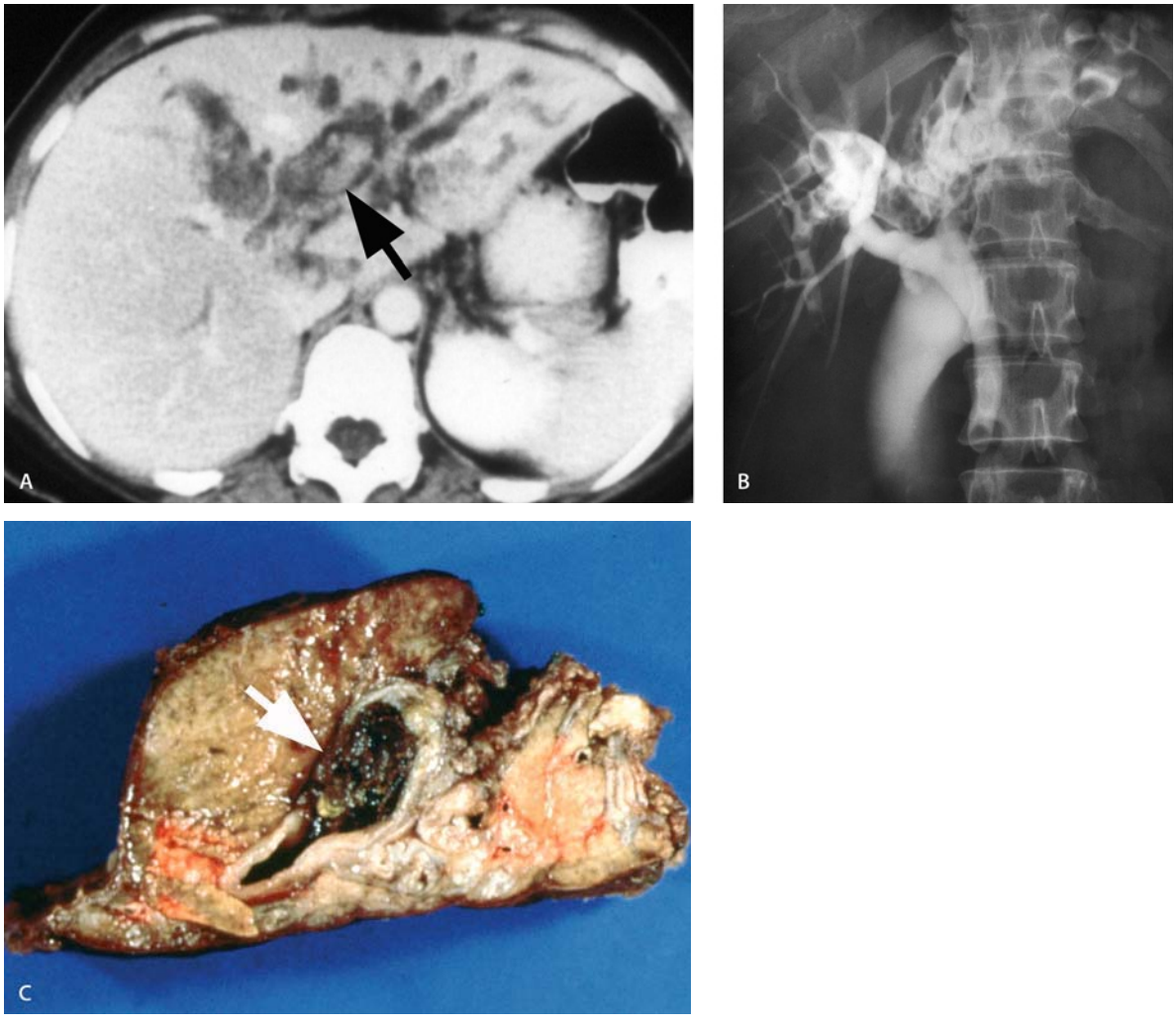

Fig. 19A–C. Recurrent pyogenic cholangitis in a 39-year-old woman. **A** Oral and intravenous contrast-enhanced CT scan shows dilated left intrahepatic bile ducts containing calculi (*arrow*). **B** Percutaneous transhepatic cholangiogram shows multiple filling defects from intrahepatic lithiasis involving the left hepatic ducts. There is a stone impacted in the common bile duct. **C** Photograph of the cut surface of a partial left hepatectomy specimen shows a pigmented stone (*arrow*) in dilated, fibrotic bile duct

ty of opportunistic organisms, and occurs predominately in patients with late stage acquired immunodeficiency syndrome and low (<200/mm^3) CD4 lymphocyte counts. The patients present with right upper quadrant pain, fever, and abnormal liver function tests indicating cholestasis [81, 82].

Pathologic Features

Cryptosporidium is the most commonly associated pathogen, but various others, including *Cytomegalovirus*, *Campylobacter*, *Candida*, *Giardia*, and *Microsporidium* have been found in biliary infections of patients with AIDS-related cholangitis [83]. These organisms invade the duct epithelium producing cell necrosis and periductal inflammation and fibrosis [84].

Radiologic Features

Although the findings of AIDS-related cholangiopathy closely simulate those of primary sclerosing cholangitis, certain features can serve to suggest AIDS-related disease. Papillary stenosis is a feature of AIDS-related cholangiopathy not usually found in primary sclerosing cholangitis (Fig. 20). Extrahepatic duct stenosis (except for the papillary segment) and sacculations, both common in primary sclerosing cholangitis are unusual in AIDS-related cholangitis. Inflammatory nodules, identified frequently in AIDS patients are rarely seen in other types of sclerosing cholangitis. CT and MR can show the beaded pattern of alternating intrahepatic duct stenosis and ectasia. Mural thickening of the bile duct and gallbladder may enhance with intravenous contrast, indicating mural inflammation.

Ischemic Cholangiopathy

Incidence and Clinical Features

A variety of clinical circumstances and conditions may lead to ischemic damage to the biliary tract. These include primary vascular diseases: atherosclerosis; vasculitis such as Henoch-Schönlein purpura; iatrogenic causes such as radiation, chemoembolization, hepatic transplantation complications including hepatic artery

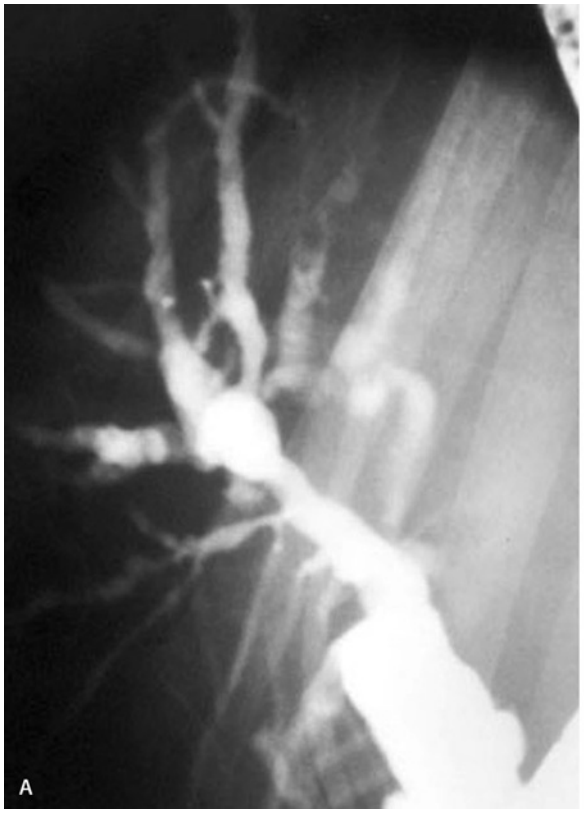

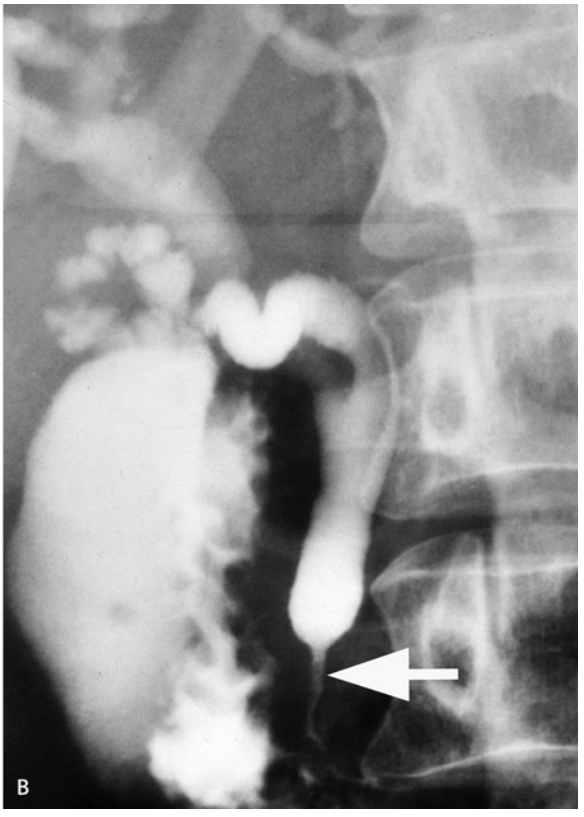

Fig. 20A, B. Cholangiographic features of AIDS-related cholangitis. **A** ERCP image in a 25-year-old man shows diffuse ductal irregularity, beading, and intraductal filling defects. **B** ERCP image in a 35-year-old man shows smooth concentric narrowing of the distal common bile duct from papillary stenosis

thrombosis and rejection; and arterial infusion of chemotherapeutics, especially floxuridine (FUDR) [85–87].

Pathologic Features

Ischemic cholangitis includes a variety of pathologic processes and differing etiologies. Ischemia may result from vasculitis of the peribiliary capillaries of the bile ducts as well as major artery occlusion. These processes may result in cholangitis due to ischemic effect without necrosis, ischemic fibrosis, or frank necrosis. The central intrahepatic and proximal extrahepatic ducts are the most prominently affected. The pathologic features encompass the spectrum of duct necrosis, fibrosis with stricture, and duct ectasia. Complications can include bacterial cholangitis and abscess. A high index of clinical suspicion is often necessary to make the diagnosis because histologic features may be nonspecific and biopsy may be misleading [88, 89].

Radiologic Features

Although the strictures associated with ischemic cholangitis are usually perihilar, they may be diffusely intrahepatic or involve more of the extrahepatic system if there is major vascular occlusion. Total necrosis may result in bile extravasation and biloma formation. The findings by computed tomography and cholangiography may simulate the stenosing and obstructive characteristics of primary sclerosing cholangitis (Fig. 21) [90].

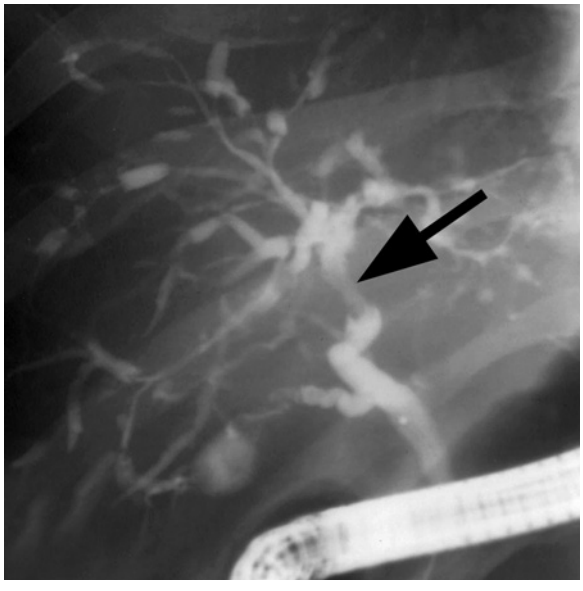

Fig. 21. Ischemic cholangitis from intraarterial chemotherapy in a 61-year-old man who developed hepatocellular carcinoma in a transplanted liver. ERCP image shows a central stricture in the common hepatic duct (*arrow*) and diffuse ischemic changes in the intrahepatic ducts

Neoplastic Diseases

Adenomas and Papillomatosis

Incidence and Clinical Features

Bile duct adenomas are rare; our current knowledge is based on case reports. The most common locations in descending order of frequency are the common bile duct, common hepatic duct, cystic duct, and intrahepatic bile ducts [10]. Patients present to medical attention with signs and symptoms of bile duct obstruction.

Biliary papillomatosis is characterized by multiple and recurrent papillary adenomas of the biliary tract. Most commonly, the extrahepatic ducts are involved, but the intrahepatic bile ducts, cystic duct, gallbladder, and pancreatic duct may also be affected [91, 92]. Patients with biliary papillomatosis present to medical attention between the ages of 50 and 60 years with signs and symptoms of biliary obstruction or cholangitis.

Pathologic Features

The majority of bile duct adenomas are tubular adenomas composed of intestinal-type glands. The adenomas in biliary papillomatosis are composed of a fibrovascular core that supports an epithelium of mucin-secreting columnar or cuboidal cells. Some authors regard biliary papillomatosis as a low-grade intraductal carcinoma since features of in situ or invasive carcinoma are occasionally present [10].

On gross inspection, solitary adenomas are lobulated, intraluminal masses. The adenomas of biliary papillomatosis are typically soft, friable polyps [92]. Tumors that produce a significant amount of mucin may have a jelly-like consistency or may be accompanied by abundant intraluminal mucin within the bile ducts.

Radiologic Features

Sonographically, solitary bile duct adenomas manifest as intraluminal nonshadowing masses that are isoechoic to liver parenchyma [93]. Proximal intra- and extrahepatic biliary dilatation may be present. In the setting of biliary papillomatosis, multiple, nonshadowing, intraluminal masses may be visualized. However, biliary dilatation is the most common sonographic feature [94]. Irregular bile duct walls with multiple filling defects are the characteristic cholangiographic features.

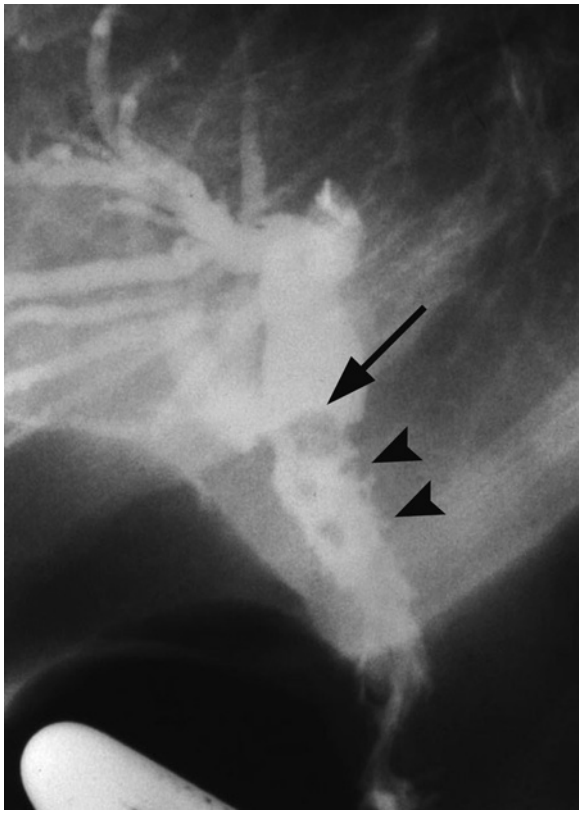

Fig. 22. ERCP image in a 75-year-old man with biliary papillomatosis shows multiple filling defects in a dilated common bile duct (*arrow*) and mural irregularity (*arrowheads*)

The irregular or shaggy appearance of the bile duct wall may be secondary to numerous small adenomas or inflammatory changes from secondary cholangitis (Fig. 22).

Biliary Adenocarcinoma

Incidence and Clinical Features

Biliary adenocarcinoma, or cholangiocarcinoma, is the most common malignancy of the bile ducts. Even so, it is a very unusual tumor, with approximately one case for every 200,000 population. There is a slight male predilection, but no race preponderance [10, 95]. Several associations and predispositions have been identified. The most common are primary sclerosing cholangitis where 10% to 20% can be expected to develop bile duct carcinoma, choledochal cyst (including Caroli disease), a 10% risk, and anomalous pancreatic bile duct junction, a 15% risk. Lesser but definite risk is associated with ulcerative colitis, familial polyposis coli, liver fluke infestation, *Salmonella typhi* infection, and anomalous pancreaticobiliary junction [96, 97]. Even with this consideration, greater than 80% of cases are sporadic and an association or predisposition cannot be identified. Patients usually present with cholestasis in their seventh or eighth decade. The clinical findings also include fever, chills, vomiting, weight loss, and right upper quadrant pain. Those with ulcerative colitis and other predispositions are generally much younger in age, frequently presenting in the third to sixth decades of life with biliary adenocarcinoma.

Pathologic Features

Adenocarcinoma and its subtypes account for over 95% of bile duct malignancies. Other tumors such as lymphoma, metastases, carcinoid tumor, and various sarcomas, make up the remainder. Approximately one-half of cholangiocarcinomas occur in hilar region or proximal portion of the extrahepatic bile ducts. Approximately 20% occur in each of the middle and distal portions. The remainder may be diffuse or involve only the intrahepatic ducts. Although the neoplasm will usually show an infiltrating, polypoid, or a stenosing appearance, a specific tumor may combine all of these pathologic features. Less than 5% will be mucus hypersecreting adenocarcinomas [10].

Radiologic Features

Ultrasound and computed tomography are highly accurate in identifying bile duct obstruction due to bile duct carcinoma. The site can be specified and the etiology suggested, especially if a mass is demonstrated. The direct cholangiogram will identify a stenosis or obstruction (Fig. 23), an intraductal mass (Fig. 24), or suggest a mucus-hypersecreting type of adenocarcinoma if mobile filling defects are identified. MR features of cholangiocarcinoma are characterized by high signal intensity on T2-weighted sequences and low intensity on T1-weighted sequences [98]. CT diagnosis of intrahepatic cholangiocarcinoma is improved by identification of an ill-defined mass, capsular retraction, and delayed enhancement with intravenous contrast administration [99].

Metastases

Incidence and Clinical Features

Metastases account for less than 5% of malignancies of the bile ducts. Common sites of origin are breast, lung, renal cell, stomach, colon, and prostate carcinoma [10, 100]. Gallbladder carcinoma may invade the extrahepatic bile duct as it grows along the cystic duct [37]. Pa-

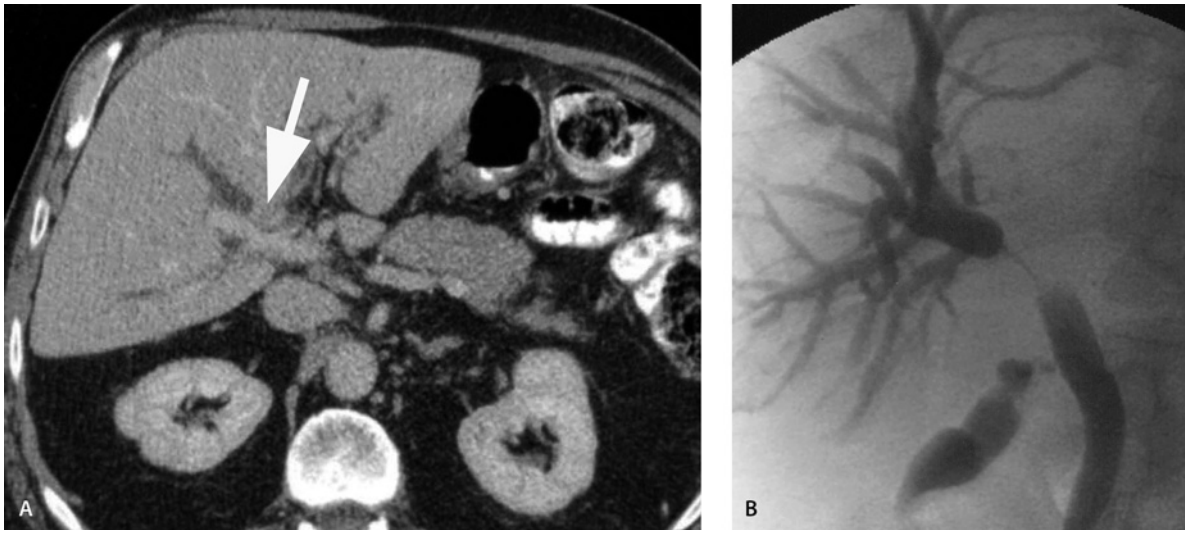

Fig. 23A, B. Adenocarcinoma of the common hepatic duct in an 81-year-old man with jaundice. **A** Contrast-enhanced CT scan shows intrahepatic duct dilatation and a soft-tissue attenuation mass at the level of the common hepatic duct (*arrow*). **B** Delayed image from an ERCP shows an annular stenosis in the common hepatic duct

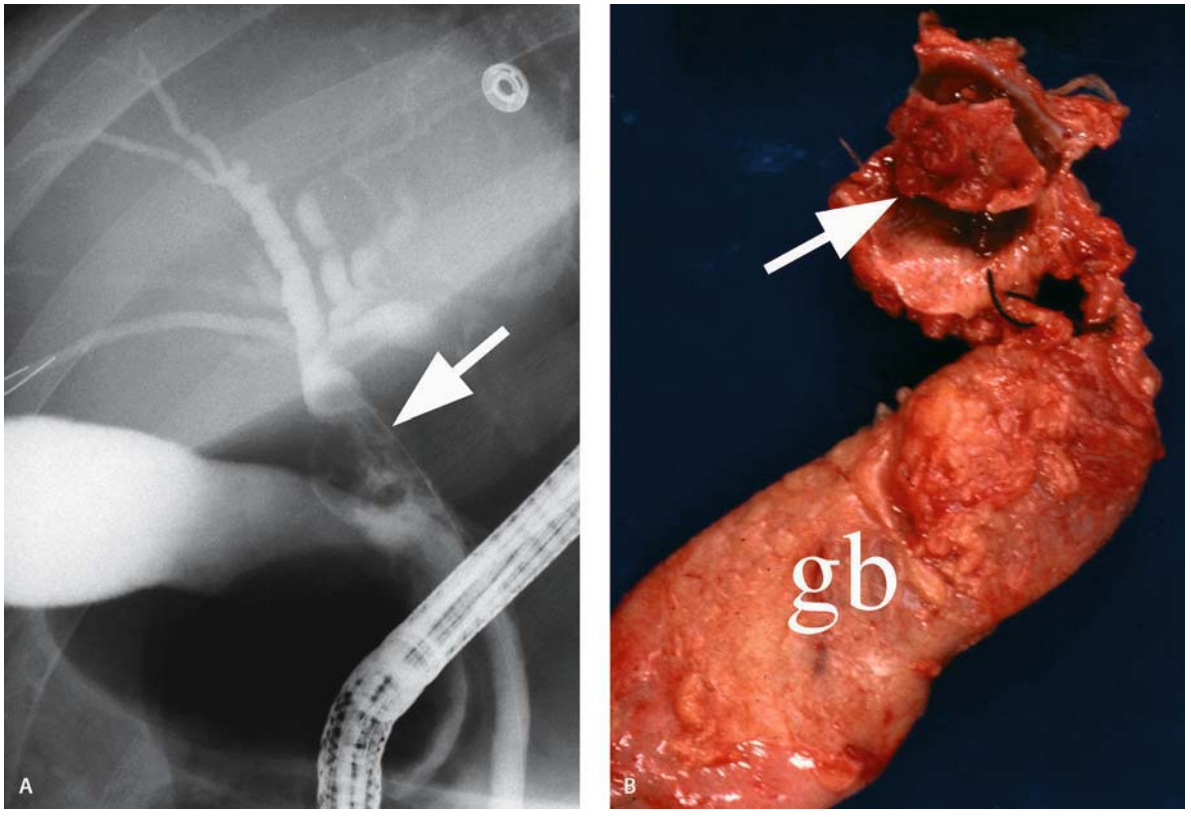

Fig. 24A, B. Papillary adenocarcinoma of the common hepatic duct in a 51-year-old man. **A** ERCP image shows a lobulated intraductal filling defect (*arrow*). **B** Photograph of the resected surgical specimen shows an intraductal polypoid mass (*arrow*) in the opened common hepatic duct. The gallbladder (*gb*) is also shown

tients typically present with obstructive jaundice, gastrointestinal hemorrhage and history of primary neoplasm.

Pathologic Features

Bile duct metastases appear at gross inspection similar to other malignancies of the biliary system. Obstructing masses, duct wall infiltration, and enlarged lymph nodes are common features.

Radiologic Features

The CT features of metastases to the bile ducts include biliary obstruction by high-attenuation masses that may be stenosing, intraductal, or extrinsic compression from intrahepatic, intrapancreatic, or nodal masses. The obstructing lesions are classified as hilar (36%), proximal extrahepatic bile duct (40%), distal extrahepatic bile duct (10%) and periampullary (14%) [100]. Cholangiography may demonstrate focal, multifocal or diffuse stenosis of the bile duct (Fig. 25). The lesions may

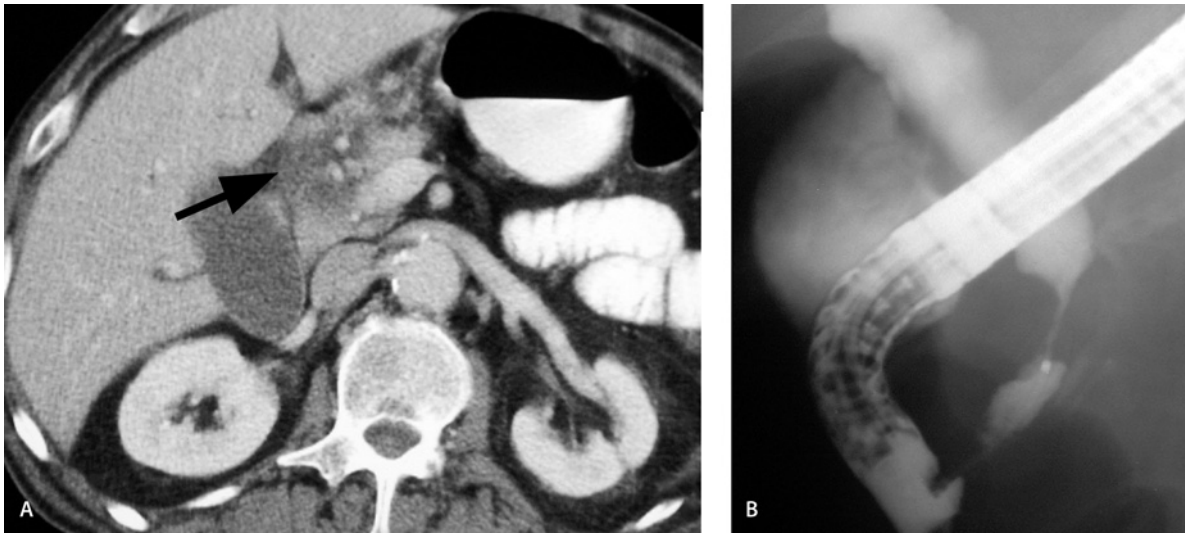

Fig. 25A, B. Gastric adenocarcinoma metastatic to the bile ducts in an 80-year-old man with early satiety and jaundice. **A** Intravenous contrast-enhanced CT scan shows a hypoattenuating mass near the head of the pancreas. **B** ERCP image shows a focal stricture in the distal common bile duct

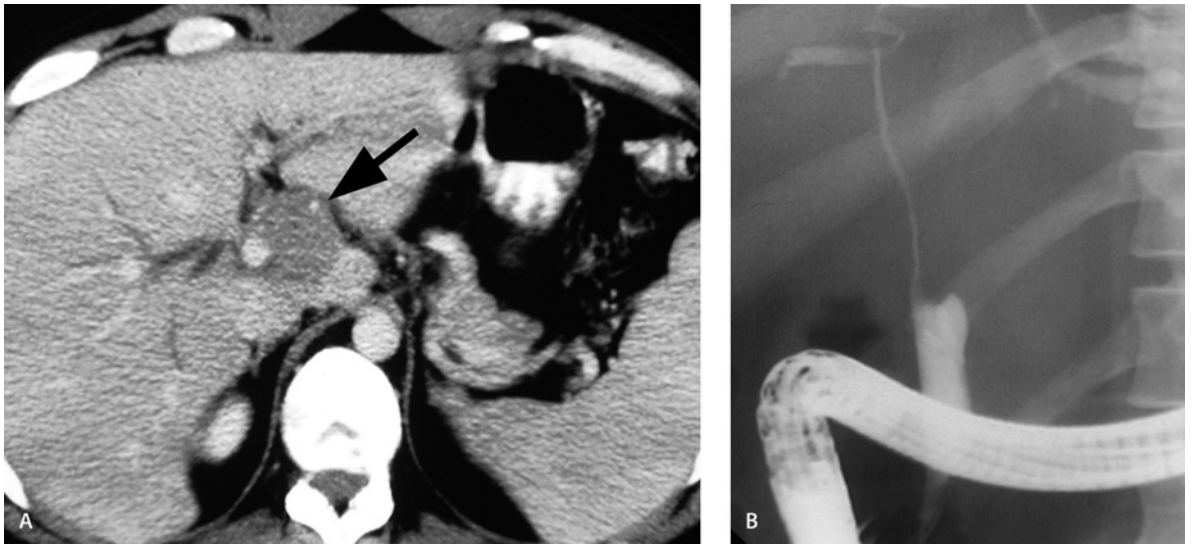

Fig. 26A, B. Non-Hodgkin lymphoma in a 35-year-old man with jaundice. **A** Intravenous contrast-enhanced CT scan shows a hypoattenuating mass in the porta hepatis. **B** ERCP image shows a long segment stricture of the proximal extrahepatic bile duct

progress to total obstruction. If the metastasis infiltrates and stenoses the duct, the appearance may simulate primary sclerosing cholangitis.

Lymphoma

Incidence and Clinical Features

Primary bile duct lymphoma is extremely rare, accounting for less than 1.0% of bile duct malignancies [10]. The patients present with obstructive jaundice, and can have a rapidly deteriorating course [101].

Pathologic Features

Malignant lymphoma of the bile ducts is commonly of the B-cell type, and is frequently at pathologic inspection indistinguishable from primary or metastatic biliary malignancies [102].

Radiologic Features

Biliary lymphoma may be focally stenosing, multifocal, or diffuse. The CT and cholangiographic appearance may simulate primary sclerosing cholangitis or cholangiocarcinoma (Fig. 26). If diffuse and associated with mass, lymphoma is more likely than primary sclerosing cholangitis. Cavitation may be a more specific sign similar to aneurysmal dilatation of the luminal gut [103].

References

1. Grayson DE, Abbott RM, Levy AD, Sherman PM (2002) Emphysematous infections of the abdomen and pelvis: a pictorial review. Radiographics 22:543–561
2. Mentzer RM, Jr., Golden GT, Chandler JG, Horsley JS, 3rd (1975) A comparative appraisal of emphysematous cholecystitis. Am J Surg 129:10–15
3. Bloom RA, Libson E, Lebensart PD, et al (1989) The ultrasound spectrum of emphysematous cholecystitis. J Clin Ultrasound 17:251–256
4. Nemcek AA, Jr., Gore RM, Vogelzang RL, Grant M (1988) The effervescent gallbladder: a sonographic sign of emphysematous cholecystitis. AJR Am J Roentgenol 150:575–577
5. Wu CS, Yao WJ, Hsiao CH (1998) Effervescent gallbladder: sonographic findings in emphysematous cholecystitis. J Clin Ultrasound 26:272–275
6. Goodman ZD, Ishak KG (1981) Xanthogranulomatous cholecystitis. Am J Surg Pathol 5:653–659
7. Ros PR, Goodman ZD (1997) Xanthogranulomatous cholecystitis versus gallbladder carcinoma. Radiology 203:10–12
8. Reed A, Ryan C, Schwartz SI (1994) Xanthogranulomatous cholecystitis. J Am Coll Surg 179:249–252
9. Houston JP, Collins MC, Cameron I, Reed MW, Parsons MA, Roberts KM (1994) Xanthogranulomatous cholecystitis. Br J Surg 81:1030–1032
10. Albores-Saavedra J, Henson DE, Klimstra DS (2000) Tumors of the gallbladder, extrahepatic bile ducts, and ampulla of vater. In: Atlas of tumor pathology, fasc 27, ser 3. Washington, DC: Armed Forces Institute of Pathology
11. Chun KA, Ha HK, Yu ES, et al (1997) Xanthogranulomatous cholecystitis: CT features with emphasis on differentiation from gallbladder carcinoma. Radiology 203:93–97
12. Kim PN, Ha HK, Kim YH, Lee MG, Kim MH, Auh YH (1998) US findings of xanthogranulomatous cholecystitis. Clin Radiol 53:290–292
13. Ootani T, Shirai Y, Tsukada K, Muto T (1992) Relationship between gallbladder carcinoma and the segmental type of adenomyomatosis of the gallbladder. Cancer 69:2647–2652
14. Levy AD, Murakata LA, Abbott RM, Rohrmann CA, Jr. (2002) From the archives of the AFIP. Benign tumors and tumorlike lesions of the gallbladder and extrahepatic bile ducts: radiologic-pathologic correlation. Armed Forces Institute of Pathology. Radiographics 22:387-413
15. Raghavendra BN, Subramanyam BR, Balthazar EJ, Horii SC, Megibow AJ, Hilton S (1983) Sonography of adenomyomatosis of the gallbladder: radiologic-pathologic correlation. Radiology 146:747–752
16. Haradome H, Ichikawa T, Sou H, et al (2003) The Pearl Necklace Sign: An Imaging Sign of Adenomyomatosis of the Gallbladder at MR Cholangiopancreatography. Radiology 227:80–88
17. Yoshimitsu K, Honda H, Jimi M, et al (1999) MR diagnosis of adenomyomatosis of the gallbladder and differentiation from gallbladder carcinoma: importance of showing Rokitansky-Aschoff sinuses. AJR Am J Roentgenol 172:1535–1540
18. Terzi C, Sokmen S, Seckin S, Albayrak L, Ugurlu M (2000) Polypoid lesions of the gallbladder: report of 100 cases with special reference to operative indications. Surgery 127:622–627
19. Christensen AH, Ishak KG (1970) Benign tumors and pseudotumors of the gallbladder. Report of 180 cases. Arch Pathol 90:423–432
20. Sugiyama M, Atomi Y, Kuroda A, Muto T, Wada N (1995) Large cholesterol polyps of the gallbladder: diagnosis by means of US and endoscopic US. Radiology 196:493–497
21. Albores-Saavedra J, Henson DE (1986) Tumors of the gallbladder and extrahepatic bile ducts: Atlas of tumor pathology. Fasc 22, ser 2. Washington, DC: Armed Forces Institute of Pathology
22. Albores-Saavedra J, Vardaman CJ, Vuitch F (1993) Non-neoplastic polypoid lesions and adenomas of the gallbladder. Pathol Annu 28 Pt 1:145–177
23. Furukawa H, Takayasu K, Mukai K, et al (1995) CT evaluation of small polypoid lesions of the gallbladder. Hepatogastroenterology 42:800–810
24. Greenlee RT, Murray T, Bolden S, Wingo PA (2000) Cancer Statistics 2000. CA Cancer J Clin 50:7–33
25. Nagorney DM, McPherson GAD (1988) Carcinoma of the Gallbladder and Extrahepatic Bile Ducts. Semin Oncol 15:106–115
26. Albores-Saavedra J, Alcantra-Vazquez A, Cruz-Ortiz H, Herrera-Goepfert R (1980) The precursor lesions of invasive gallbladder carcinoma. Hyperplasia, atypical hyperplasia and carcinoma in situ. Cancer 45:919–927
27. Khan ZR, Neugut AI, Ahsan H, Chabot JA (1999) Risk factors for biliary tract cancers. Am J Gastroenterol 94:149–152
28. Welton JC, Marr JS, Friedman SM (1979) Association between hepatobiliary cancer and typhoid carrier state. Lancet 1:791–794
29. Bond GG, McLaren EA, Sabel FL, Bodner KM, Lipps TE, Cook RR (1990) Liver and biliary tract cancer among chemical workers. Am J Ind Med 18:19–24
30. Brandt DJ, MacCarty RL, Charboneau JW, LaRusso NF, Wiesner RH, Ludwig J (1988) Gallbladder disease in patients with primary sclerosing cholangitis. AJR 150:571–574
31. Bloustein PA (1977) Association of carcinoma with congenital cystic conditions of the liver and bile ducts. Am J Gastroenterol 67:40–46
32. Yoshida T, Shibata K, Matsumoto T, Sasaki A, Hirose R, Kitano S (1999) Carcinoma of the gallbladder associated with anomalous junction of the pancreaticobiliary duct in adults. J Am Coll Surg 189:57–62
33. Berk RN, Armbuster TG, Saltzstein SL (1973) Carcinoma in the porcelain gallbladder. Radiology 106:29–31

34. Sons HU, Borchard F, Joel BS (1985) Carcinoma of the gallbladder: autopsy findings in 287 cases and review of the literature. J Surg Oncol 28:199–206
35. Franquet T, Montes M, Ruiz de Azua Y, Jimenez FJ, Cozcolluela R (1991) Primary gallbladder carcinoma: imaging findings in 50 patients with pathologic correlation. Gastrointest Radiol 16:143–148
36. Lane J, Buck JL, Zeman RK (1989) Primary carcinoma of the gallbladder: a pictorial essay. RadioGraphics 9:209–228
37. Levy AD, Murakata LA, Rohrmann CA, Jr (2001) Gallbladder carcinoma: radiologic-pathologic correlation. Radiographics 21:295–314; questionnaire, 549–255
38. Weiner SN, Koenigsberg M, Morehouse H, Hoffman J (1984) Sonography and computed tomography in the diagnosis of carcinoma of the gallbladder. AJR Am J Roentgenol 142:735–739
39. Smathers RL, Lee JK, Heiken JP (1984) Differentiation of complicated cholecystitis from gallbladder carcinoma by computed tomography. AJR Am J Roentgenol 143:255–259
40. Yoshimitsu K, Honda H, Shinozaki K, et al (2002) Helical CT of the local spread of carcinoma of the gallbladder: evaluation according to the TNM system in patients who underwent surgical resection. AJR Am J Roentgenol 179:423–428
41. Rooholamini SA, Tehrani NS, Razavi MK, et al (1994) Imaging of gallbladder carcinoma. Radiographics 14:291–306
42. Caroli J, Soupault R, Kossakowski J, Plocker L, Paradowska M (1958) La dilatation polykystique congénitale des voies biliaires intrahépatiques: essai de classification. Sem Hop Paris 34:128–135
43. Desmet VJ (1992) Congenital diseases of intrahepatic bile ducts: variations on the theme "ductal plate malformation". Hepatology 16:1069–1083
44. Levy AD, Rohrmann CA, Jr., Murakata LA, Lonergan GJ (2002) Caroli's disease: radiologic spectrum with pathologic correlation. AJR 179:1053–1057
45. Choi BI, Yeon KM, Kim SH, Han MC (1990) Caroli disease: central dot sign in CT. Radiology 174:161–163
46. Lucaya J, Gomez JL, Molino C, Atienza JG (1978) Congenital dilatation of the intrahepatic bile ducts (Caroli's disease). Radiology 127:746
47. Guy F, Cognet F, Dranssart M, Cercueil JP, Conciatori L, Krause D (2002) Caroli's disease: magnetic resonance imaging features. Eur Radiol 12:2730–2736
48. Barros JL, Polo JR, Sanabia J, Garcia-Sabrido JL, Gomez-Lorenzo FJ (1979) Congenital cystic dilatation of the intrahepatic bile ducts (Caroli's disease): report of a case and review of the literature. Surgery 85:589–592
49. McDuffie SR, Nelson JB, Scobey MW (1995) Unusual presentation of an unusual type of choledochal cyst. Am J Gastroenterol 90:1884–1885
50. De Vries JS, De Vries S, Aronson DC, et al (2002) Choledochal cysts: Age of presentation, symptoms, and late complications related to Todani's classification. J Pediatr Surg 37:1568–1573
51. Yamaguchi M (1980) Congenital choledochal cyst. Analysis of 1,433 patients in the Japanese literature. Am J Surg 140:653–657
52. Todani T, Toki A (1996) Cancer arising in choledochal cyst and management. Nippon Geka Gakkai Zasshi 97:594–598
53. Nagorney DM, McIlrath DC, Adson MA (1984) Choledochal cysts in adults: clinical management. Surgery 96:656–663
54. Rossi RL, Silverman ML, Braasch JW, Munson JL, ReMine SG (1987) Carcinomas arising in cystic conditions of the bile ducts. A clinical and pathologic study. Ann Surg 205:377–384
55. Komi N, Kuwashima T, Kuramoto M, Udaka H, Ogasahara K (1976) Anomalous arrangement of the pancreaticobiliary ductal system in choledochal cyst. Tokushima J Exp Med 23:37–48
56. Jona JZ, Babbitt DP, Starshak RJ, LaPorta AJ, Glicklich M, Cohen RD (1979) Anatomic observations and etiologic and surgical considerations in choledochal cyst. J Pediatr Surg 14:315–320
57. Babbitt DP (1969) Congenital choledochal cysts: new etiological concept based on anomalous relationships of the common bile duct and pancreatic bulb. Ann Radiol (Paris) 12:231–240
58. Babbitt DP, Starshak RJ, Clemett AR (1973) Choledochal cyst: a concept of etiology. AJR 119:57–62
59. Todani T, Watanabe Y, Narusue M, Tabuchi K, Okajima K (1977) Congenital bile duct cysts: Classification, operative procedures, and review of thirty-seven cases including cancer arising from choledochal cyst. Am J Surg 134:263–269
60. Dinsmore JE, Murphy JJ, Jamieson D (2001) Pediatric surgical images: MRCP evaluation of choledochal cysts. J Pediatr Surg 36:829–830
61. Sugiyama M, Baba M, Atomi Y, Hanaoka H, Mizutani Y, Hachiya J (1998) Diagnosis of anomalous pancreaticobiliary junction: value of magnetic resonance cholangiopancreatography. Surgery 123:391–397
62. Kim SH, Lim JH, Yoon HK, Han BK, Lee SK, Kim YI (2000) Choledochal cyst: comparison of MR and conventional cholangiography. Clin Radiol 55:378–383
63. Wheeler W (1940) An unusual case of obstruction of the common bile duct (choledochocele?). Br J Surg 27:446–448
64. Kagiyama S, Okazaki K, Yamamoto Y (1987) Anatomic variants of choledochocele and manometric measurements of pressure in the cele and the orifice zone. Am J Gastroenterol 82:641–649
65. Scholz FJ, Carrera GF, Larsen CR (1976) The choledochocele: correlation of radiological, clinical and pathological findings. Radiology 118:25–28
66. Sarris GE, Tsang D (1989) Choledochocele: case report, literature review, and a proposed classification. Surgery 105:408–414
67. Hanau LH, Steigbigel NH (2000) Acute (ascending) cholangitis. Infect Dis Clin North Am 14:521–546
68. Sinanan MN (1992) Acute cholangitis. Infect Dis Clin North Am 6:571–599
69. Hanau LH, Steigbigel NH (1995) Cholangitis: pathogenesis, diagnosis, and treatment. Curr Clin Top Infect Dis 15:153–178
70. Silvis SE, Rohrmann CA, Ansel HA (1995) Text and atlas of ERCP. New York, Tokyo: Igaku-Shoin
71. Ponsioen CY, Vrouenraets SM, Prawirodirdjo W, et al (2002) Natural history of primary sclerosing cholangitis and prognostic value of cholangiography in a Dutch population. Gut 51:562–566
72. Ponsioen CI, Tytgat GN (1998) Primary sclerosing cholangitis: a clinical review. Am J Gastroenterol 93:515–523
73. Larusso NF (1999) The Fifth Carlos E. Rubio Memorial Lecture. Sclerosing cholangitis: pathogenesis, pathology, and practice. P R Health Sci J 18:11–17
74. Ludwig J (1991) Small-duct primary sclerosing cholangitis. Semin Liver Dis 11:11–17
75. Vitellas KM, Keogan MT, Freed KS, et al (2000) Radiologic manifestations of sclerosing cholangitis with emphasis on MR cholangiopancreatography. Radiographics 20:959–975; quiz 1108–1109, 1112
76. Dodd GD, 3rd, Baron RL, Oliver JH, 3rd, Federle MP (1999) End-stage primary sclerosing cholangitis: CT findings of hepatic morphology in 36 patients. Radiology 211:357–362
77. MacCarty RL, LaRusso NF, May GR, et al (1985) Cholangiocarcinoma complicating primary sclerosing cholangitis: cholangiographic appearances. Radiology 156:43–46
78. Campbell WL, Peterson MS, Federle MP, et al (2001) Using CT and cholangiography to diagnose biliary tract carcinoma complicating primary sclerosing cholangitis. AJR Am J Roentgenol 177:1095–1100
79. Tranter SE, Maddern GJ, Berry DP (2000) Inflammatory conditions of the common bile duct. Aust N Z J Surg 70:95–97
80. Lim JH (1991) Oriental cholangiohepatitis: pathologic, clinical, and radiologic features. AJR Am J Roentgenol 157:1–8
81. Wilcox CM, Monkemuller KE (1998) Hepatobiliary diseases in patients with AIDS: focus on AIDS cholangiopathy and gallbladder disease. Dig Dis 16:205–213
82. Keaveny AP, Karasik MS (1998) Hepatobiliary and pancreatic infections in AIDS: Part II. AIDS Patient Care STDS 12:451–456
83. Alvarez OA, Vanegas F, Maze GL, Gross GW, Lee M (2000) Polymicrobial cholangitis and liver abscess in a patient with the acquired immunodeficiency syndrome. South Med J 93:232–234

84. Chen XM, LaRusso NF (2002) Cryptosporidiosis and the pathogenesis of AIDS-cholangiopathy. Semin Liver Dis 22: 277–289
85. Hasegawa K, Kubota K, Aoki T, et al (2000) Ischemic cholangitis caused by transcatheter hepatic arterial chemoembolization 10 months after resection of the extrahepatic bile duct. Cardiovasc Intervent Radiol 23: 304–306
86. Viola S, Meyer M, Fabre M, et al (1999) Ischemic necrosis of bile ducts complicating Schonlein-Henoch purpura. Gastroenterology 117: 211–214
87. Barnett KT, Malafa MP (2001) Complications of hepatic artery infusion: a review of 4580 reported cases. Int J Gastrointest Cancer 30: 147–160
88. Batts KP (1998) Ischemic cholangitis. Mayo Clin Proc 73: 380–385
89. Ludwig J, Batts KP, MacCarty RL (1992) Ischemic cholangitis in hepatic allografts. Mayo Clin Proc 67: 519–526
90. Clark RA, Gallant TE (1987) Bile duct strictures associated with hepatic arterial infusion chemotherapy. Gastrointest Radiol 12: 148–151
91. Caroli J, Soupault R, Champeau M, Eteve J, Hivet M (1959) Papillomas and papillomatosis of the common bile duct. Rev Med Mal Foie 34: 191–230
92. Okulski EG, Dolin BJ, Kandawalla NM (1979) Intrahepatic biliary papillomatosis. Arch Pathol Lab Med 103: 647–649
93. Cardoza J, Schrumpf J, Skioldebrand C, Gordon P, Richards V (1988) Biliary obstruction caused by a papilloma of the common hepatic duct. J Ultrasound Med 7: 467–469
94. Khan AN, Wilson I, Sherlock DJ, DeKretser D, Chisholm RA (1998) Sonographic features of mucinous biliary papillomatosis: case report and review of imaging findings. J Clin Ultrasound 26: 151–154
95. Torok N, Gores GJ (2001) Cholangiocarcinoma. Semin Gastrointest Dis 12: 125–132
96. Tanaka K, Ikoma A, Hamada N, Nishida S, Kadono J, Taira A (1998) Biliary tract cancer accompanied by anomalous junction of pancreaticobiliary ductal system in adults. Am J Surg 175: 218–220
97. Chapman RW (1999) Risk factors for biliary tract carcinogenesis. Ann Oncol 10 Suppl 4: 308–311
98. Maetani Y, Itoh K, Watanabe C, et al (2001) MR imaging of intrahepatic cholangiocarcinoma with pathologic correlation. AJR Am J Roentgenol 176: 1499–1507
99. Freeny PC (1999) Computed tomography in the diagnosis and staging of cholangiocarcinoma and pancreatic carcinoma. Ann Oncol 10 Suppl 4: 12–17
100. Moon SG, Han JK, Kim TK, Kim AY, Kim TJ, Choi BI (2003) Biliary obstruction in metastatic disease: thin-section helical CT findings. Abdom Imaging 28: 45–52
101. Maymind M, Mergelas JE, Seibert DG, Hostetter RB, Chang WW (1997) Primary non-Hodgkin's lymphoma of the common bile duct. Am J Gastroenterol 92: 1543–1546
102. Eliason SC, Grosso LE (2001) Primary biliary malignant lymphoma clinically mimicking cholangiocarcinoma: a case report and review of the literature. Ann Diagn Pathol 5: 25–33
103. Tartar VM, Balfe DM (1990) Lymphoma in the wall of the bile ducts: radiologic imaging. Gastrointest Radiol 15: 53–57

Part 5
Urogenital Radiology

MRI and CT of the Female Pelvis

Bernd Hamm, Rahel A. Kubik-Huch, Claudia Kluner

5.1

Contents

Introduction

Each diagnostic modality used for assessing gynecologic disorders has its strengths and limitations. The use of all imaging modalities available in a serial diagnostic procedure is time-consuming and does not help to reduce health care spending. Proper selection of imaging modalities can improve management of gynecologic disorders and preclude unnecessary procedures. In general, sonography is the diagnostic modality of first choice in most benign gynecologic disorders, whereas MR imaging and CT are best used for gynecologic malignancies (Table 1).

To make optimal use of the diagnostic potential of CT and above all of MR imaging in the evaluation of gynecologic disorders, the radiologist needs a thorough knowledge of the pathologic-anatomic changes and how they affect imaging. This article discusses the use of MR imaging and CT of benign and malignant tumors of the uterus and ovaries with special emphasis on radiologic-pathologic correlation.

Leiomyomas

Leiomyomas are the most common tumors of the uterus. They are benign and are present in 30%–40% of women of child-bearing age. They consist of smooth muscle and varying amounts of connective tissue. Leiomyomas may occur as single or multiple lesions and are most typically located in the uterine corpus (90%) and only rarely in the cervix (5%) or uterine ligaments and vagina. They are distinguished by location as either submucosal, intramural, or subserosal leiomyomas. Five to 10% of leiomyomas arise submucosally or protrude into the uterine cavity. Subserosal leiomyomas may occasionally mimic a solid mass of the ovaries.

Typically, a myomatous uterus is diagnosed by the gynecologic examination and leiomyomas are detected by ultrasound. MR imaging is currently considered the most accurate imaging technique for the detection, characterization and localization of leiomyomas (Table 2). The high spatial resolution with visualization of even the smallest leiomyomas (e.g., at the angle of a fallopian tube), reliable characterization (e.g., subserosal leiomyoma), and not least the precise morphologic depiction make MR imaging an excellent modality prior to organ-preserving surgical or nonsurgical interventions and also for lesion characterization [1–3].

Table 1. Imaging modalities for various gynecologic disorders

Disorder	1st Modality	2nd Modality
Endometrial carcinoma	TVUS	MRI
Cervical carcinoma	MRI	
Leiomyoma/adenomyosis	TVUS	MRI
Adnexal masses	TAUS/TVUS	MRI
Ovarian cancer	TVUS	CT/MRI

TVUS transvaginal ultrasound, *TAUS* transabdominal ultrasound

Table 2. Sensitivity of imaging modalities for benign disorders of the uterus

Disorder	Sensitivity	
	MRI	TVUS
Adenomyosis	0.73	0.59–0.74
Leiomyoma	0.97–1.0	0.49–0.83
Polyps	0.48	0.48

TVUS transvaginal ultrasound
From [2, 3]

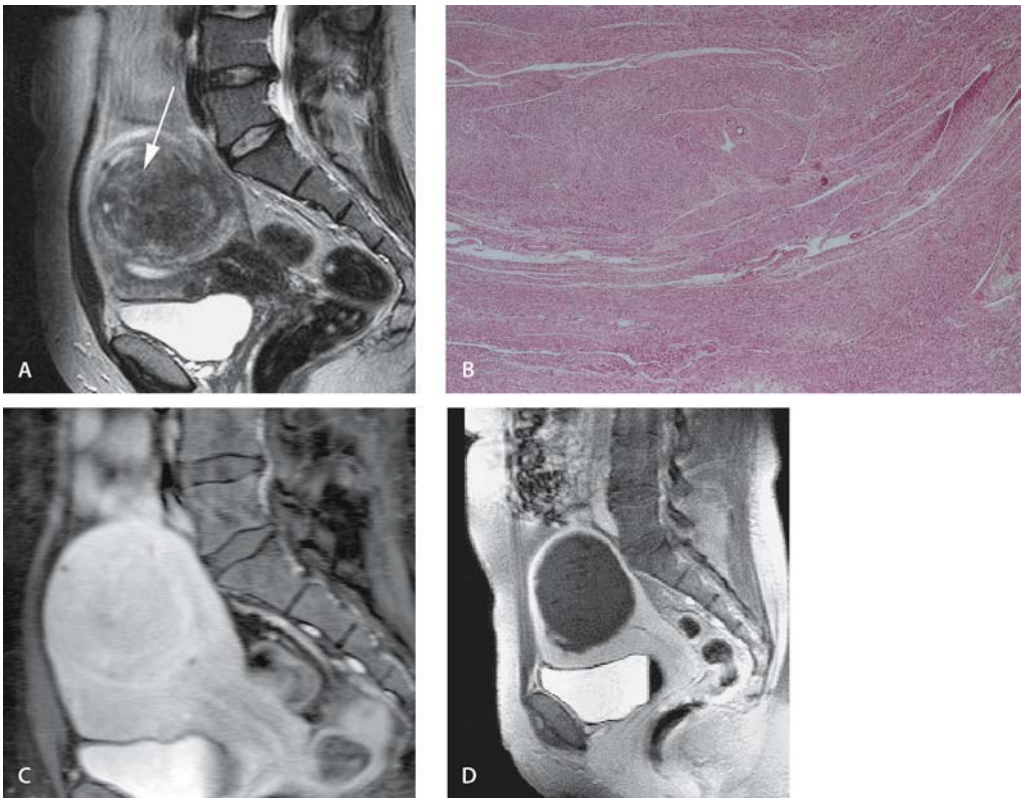

Fig. 1A–D. Intramural leiomyoma (*arrow*) in the posterior wall of the uterus. **A** Transverse T2-weighted fast spin-echo (FSE) image depicting the large leiomyoma. The intranodular hyperintense areas indicate degenerative changes. **B** Histologic specimen (H&E staining) with densely packed cellular bundles of smooth muscle without degenerative changes (not taken from this case). **C** Transverse T1-weighted contrast-enhanced spin-echo image before uterine artery embolization showing well-perfused leiomyoma without any perfusion deficit. **D** Transverse T1-weighted contrast-enhanced spin-echo image 3 months after uterine artery embolization. Significant volume reduction and loss of perfusion

Lesion characterization and assessment of the morphologic relationship is best achieved on T2-weighted pulse sequences, which should be obtained in two planes, whereas T1-weighted images are particularly useful in demonstrating hemorrhage. Contrast-enhanced MR imaging does not add to the characterization of leiomyomas but is a useful diagnostic tool for assessing the degree of infarction after treatment by uterine artery embolization (Fig. 1) [4, 5].

Leiomyomas of the uterus have a typical appearance at MR imaging. On T2-weighted images, they are depicted as roundish lesions of low signal intensity (in contrast to malignant tumors) with smooth borders and are clearly demarcated from the higher signal intensity of the myometrium (Figs. 1–3) [6, 7]. The lesions are sur-

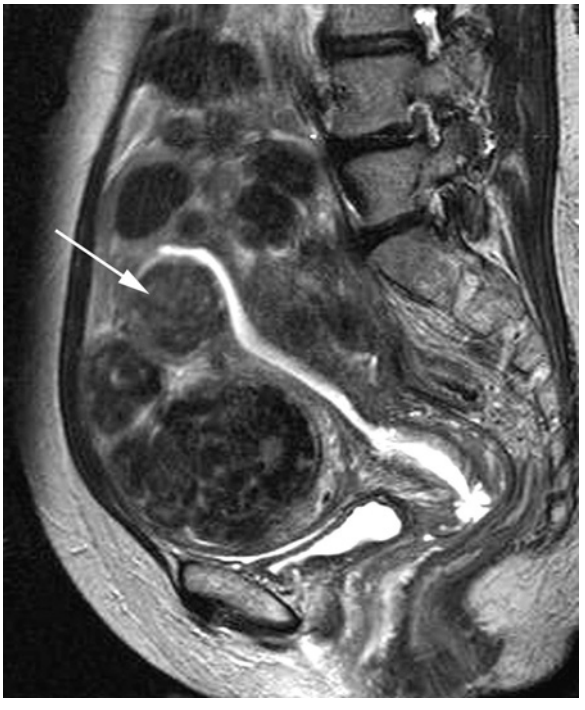

Fig. 2. Multiple leiomyomas of the uterus. Sagittal T2-weighted spin-echo (SE) image. The largest leiomyoma is of intramural location, the smaller submucosal one protrudes into the uterine cavity (*white arrow*). Submucosal, intramural, and subserosal leiomyomas in one patient

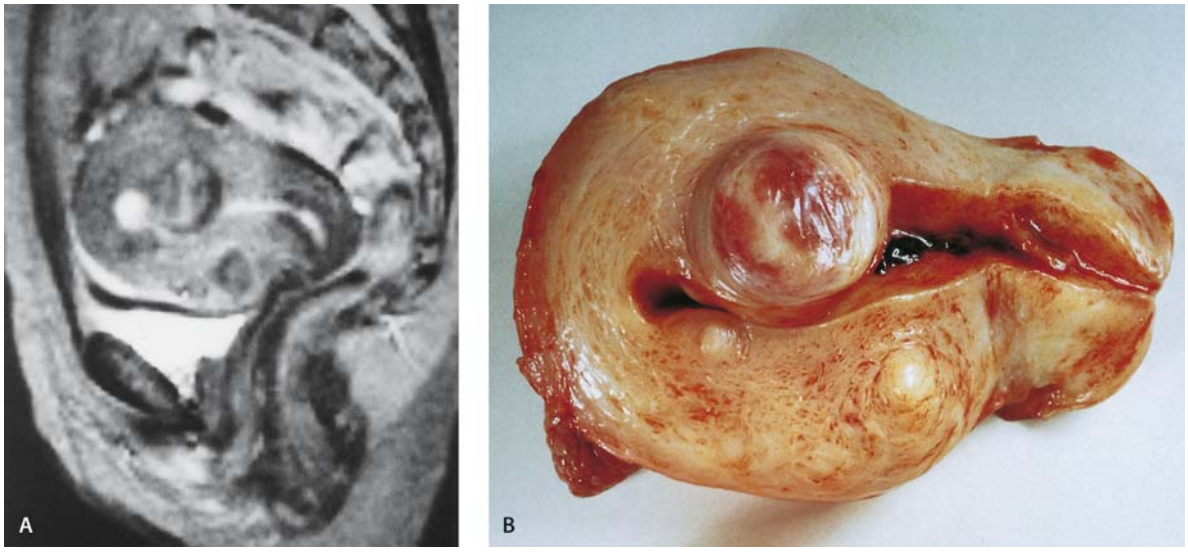

Fig. 3A, B. Multiple leiomyomas of the uterus. **A** Sagittal T2-weighted spin-echo (SE) image of small leiomyomas in the anterior wall and one large myoma in submucosal location with protrusion into the uterine cavity. **B** Gross specimen. Note the good morphologic correlation between MR imaging and the resected specimen

rounded by a pseudocapsule of compressed neighboring tissue. The rim surrounding a leiomyoma may occasionally show dilated lymphatic clefts and veins as well as slight edema. These changes produce a narrow hyperintense rim around the otherwise hypointense lesion on T2-weighted images. Such a rim is present in about one-third of patients with leiomyomas [8]. T1-weighted images only show an enlarged uterus and do not visualize the leiomyomas, which are isointense relative to the surrounding uterus.

The anatomic localization of leiomyomas by MR imaging is straightforward. Submucosal leiomyomas elevate the endometrium or they may be stalked and protrude into the uterine cavity (Fig. 4). Due to their low

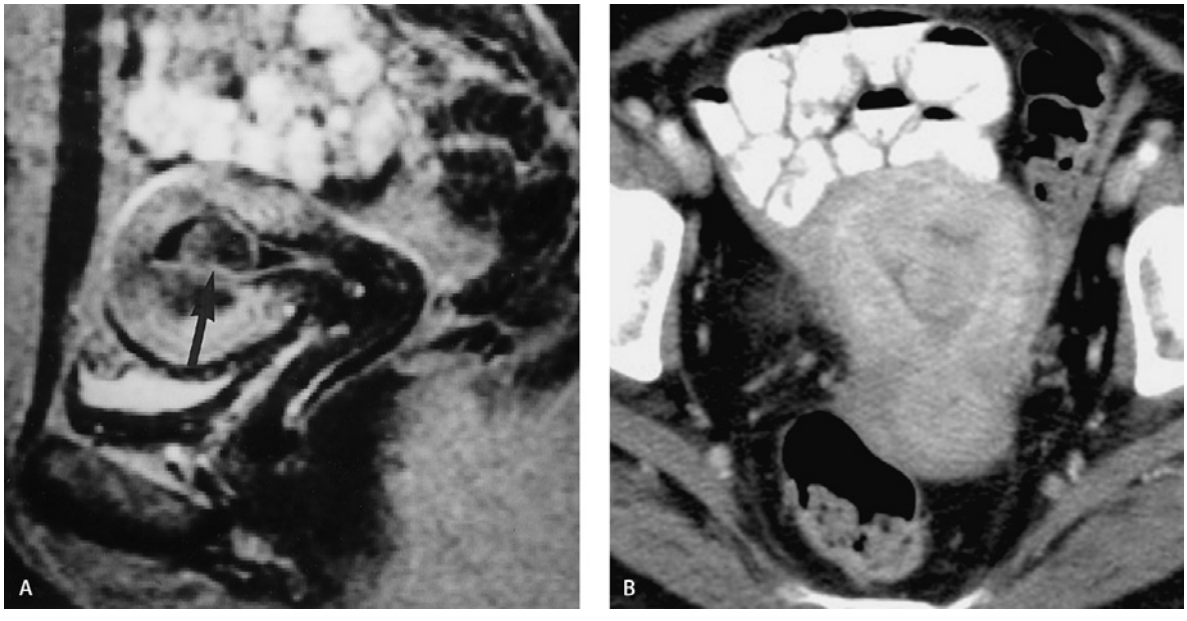

Fig. 4A–C. Submucosal leiomyomas in patients presenting with dysmenorrhea. **A** Sagittal T2-weighted spin-echo (SE) image. The low signal intensity suggests a leiomyoma rather than an endometrial polyp. **B** Contrast-enhanced CT shows a submucosal lesion but one cannot say whether it is a submucosal leiomyoma or an endometrial polyp. **C** Gross specimen with large leiomyoma protruding into the uterine cavity

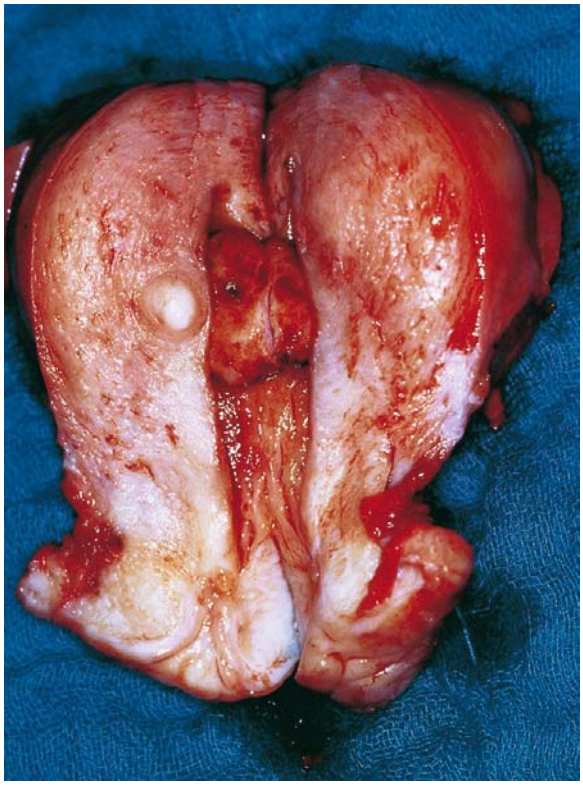

Fig. 4C.

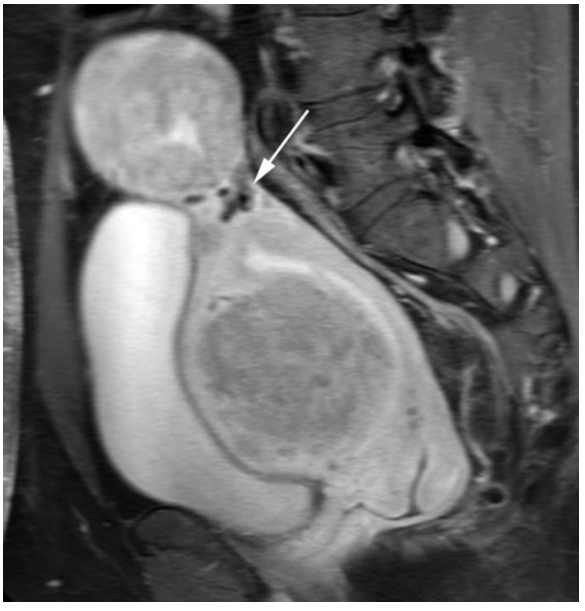

Fig. 5. Subserosal leiomyoma. Sagittal T1-weighted contrast-enhanced image. The stalk-like connection to the uterus and the signal void vascular structures between the mass and the uterus (bridging vascular sign) (*white arrow*) proves the lesion to be a subserosal leiomyoma rather than an ovarian tumor

signal intensity, leiomyomas are reliably distinguished from endometrial polyps or endometrial cancer. Intramural leiomyomas are easily demarcated from the high-intensity myometrium. Larger subserosal leiomyomas may initially be seen as pelvic masses. Their low signal intensity, however, should give rise to the suspicion of a leiomyoma (differential diagnosis: ovarian fibroma). The demonstration of a stalk-like connection to the uterus (T2-weighted image) makes the diagnosis (Fig. 5).

Besides their location, leiomyomas may be distinguished by the presence or absence of degenerative changes. Nondegenerated leiomyomas are of nearly ho-

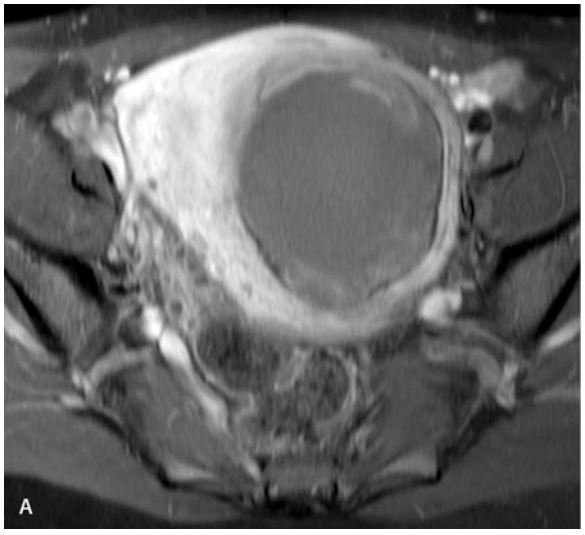

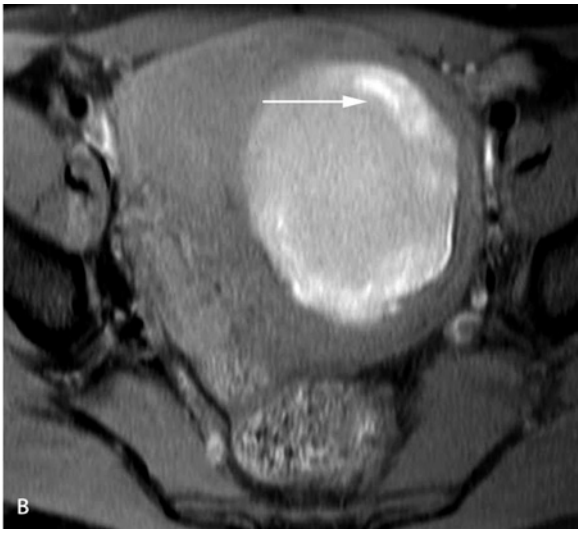

Fig. 6A, B. Leiomyoma with red degeneration. **A** Transverse T1-weighted contrast-enhanced FSE image of an intramural leiomyoma 24 days after uterine artery embolization detects no perfusion of the leiomyoma. **B** Transverse unenhanced T1-weighted FSE image of the same lesion demonstrates hemorrhages as areas of high signal intensity (*arrow*)

mogeneous hypointensity on T2-weighted images. Degenerative changes are depicted as hyperintense intratumoral areas (T2-weighted image) (Fig. 2). Such changes are seen in up to 60% of all leiomyomas, particularly in large ones. The most common types of degeneration seen in leiomyomas are hyalinization (hypointense on T2-weighted image), cystic and myxoid degeneration (hyperintense on T2-weighted image) [9]. Hemorrhages are less common (so-called red degeneration) and can be identified as areas of high signal intensity on T1-weighted images with high or varying signal intensity on T2-weighted images – depending on the time of bleeding (Fig. 6). The demonstration of typical calcifications within the hypointense lesion is rather difficult by MR imaging, but this is irrelevant for the differential diagnosis given the characteristic appearance of leiomyomas as described above.

Adenomyosis

Adenomyosis is defined as the presence of aberrant endometrium within the myometrium. Since the ectopic endometrium in adenomyosis consists nearly exclusively of tissue of the basal layer, it is not affected by hormonal stimulation and, as a rule, does not contain blood (in contrast to endometriosis, which is characterized by the aberrant occurrence of functional endometrial tissue). The incidence of adenomyosis of the uterus is higher than would be expected on clinical grounds; it is demonstrated histologically in up to 25% of all hysterectomies [10, 11]. In a quarter of all cases, adenomyosis is associated with leiomyomas.

Symptoms typically manifest in the fourth to fifth decade of life, with a higher incidence in multiparous women. The physical examination demonstrates an enlarged uterus, which is of a lower consistency compared to a myomatous uterus.

It is important to reliably differentiate adenomyosis from leiomyomas, since the latter can be removed by myomectomy with preservation of the uterus, whereas hysterectomy is the treatment of first choice in symptomatic adenomyosis, though uterine artery embolization seems to be a promising nonsurgical alternative [12].

Differentiation of adenomyosis and leiomyomas by MR imaging is no problem. Adenomyosis is diagnosed on T2-weighted images. The decisive diagnostic criterion is a pathologic thickening of the low-intensity junctional zone to over 12 mm (Figs. 6, 7) [13, 14]. A thickening of the junctional zone to 5 mm – as initially proposed – should no longer be used as the threshold for diagnosing adenomyosis, since such thickening may also be present in the normal uterus (e.g., transient contractions) and thus produce false-positive findings [15]. The thickened junctional zone frequently contains punctiform areas of hyperintensity (Fig. 7). If the latter are depicted on T2-weighted images only, they most likely correspond to cystic glandular tissue. If such small hyperintense foci are present on both T1- and T2-weighted images, they typically represent small hemorrhages. Adenomyosis may be focal or diffuse. In the diffuse form, the changes affect the entire uterus (Fig. 7), which may show pronounced enlargement. The focal form is characterized by a circumscribed thickening of the junctional zone and blurring of its border towards the myometrium (Fig. 8).

Contrast-enhanced MR imaging does not yield any additional information for the diagnostic assessment of adenomyosis or for differentiation from leiomyomas [10].

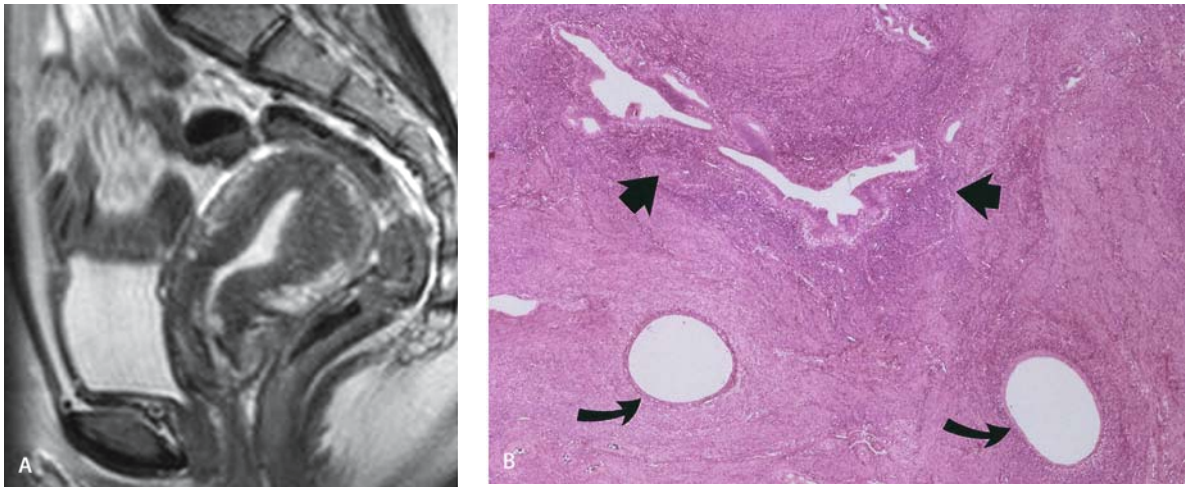

Fig. 7A, B. Diffuse adenomyosis of the fundus uteri. **A** Sagittal T2-weighted SE image. Generalized thickening of the junctional zone with isolated hyperintense spots. **B** Histologic specimen (H&E staining, not taken from this case) with ectopic endometrial tissue in the myometrium showing glandular (*arrow*) and cystic portions (*curved arrow*), which appear hyperintense on T2-weighted images

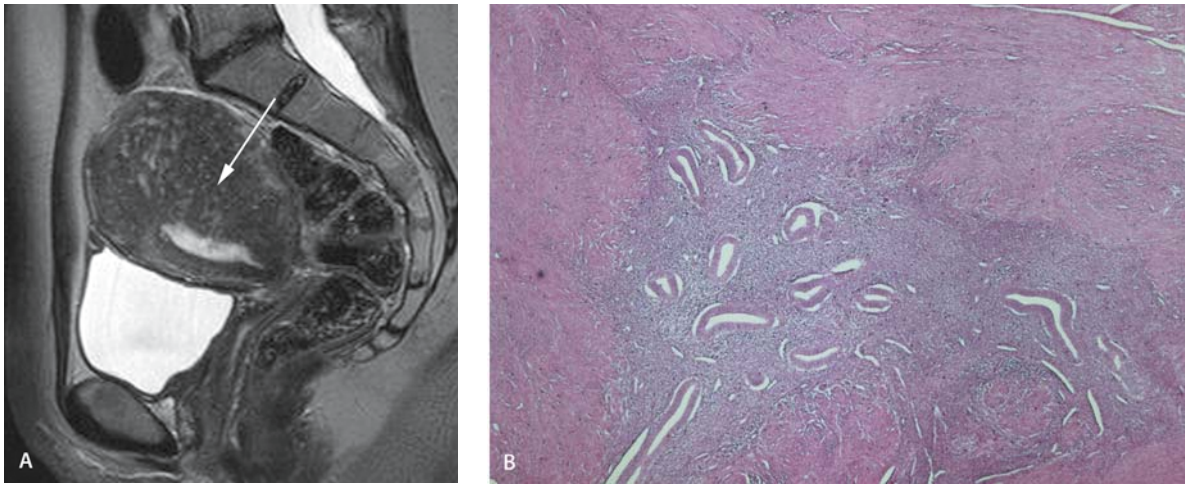

Fig. 8A, B. Focal adenomyosis. **A** Sagittal T2-weighted SE image. Focal thickening (*arrow*) of the junctional zone of the uterus. **B** Histologic specimen (H&E staining, not taken from this case) with ectopic endometrial tissue in the myometrium

Endometrial Polyps

Polyps of the endometrium are seen in about 10% of all uteri – typically in postmenopausal women. The majority of polyps arise in the fundus. Less than 1% of endometrial polyps show malignant transformation in the form of endometrial cancer. Symptoms are irregular or persistent bleeding. Postmenopausal bleeding is caused by endometrial polyps alone in over 20% of the cases. In many instances, however, endometrial polyps cause no symptoms at all.

Polyps are again best diagnosed on T2-weighted MR images, ideally in two planes (sagittal and transverse). On T2-weighted images, polyps are isointense or slightly hypointense relative to the surrounding endometrium (Fig. 9); large polyps may distend the uterine cavity. Polyps are not depicted on T1-weighted images. Following intravenous administration of a contrast agent, endometrial polyps show pronounced enhancement, comparable to the surrounding endometrium [10]. Endometrial polyps are differentiated from submucosal leiomyomas on the basis of their different signal inten-

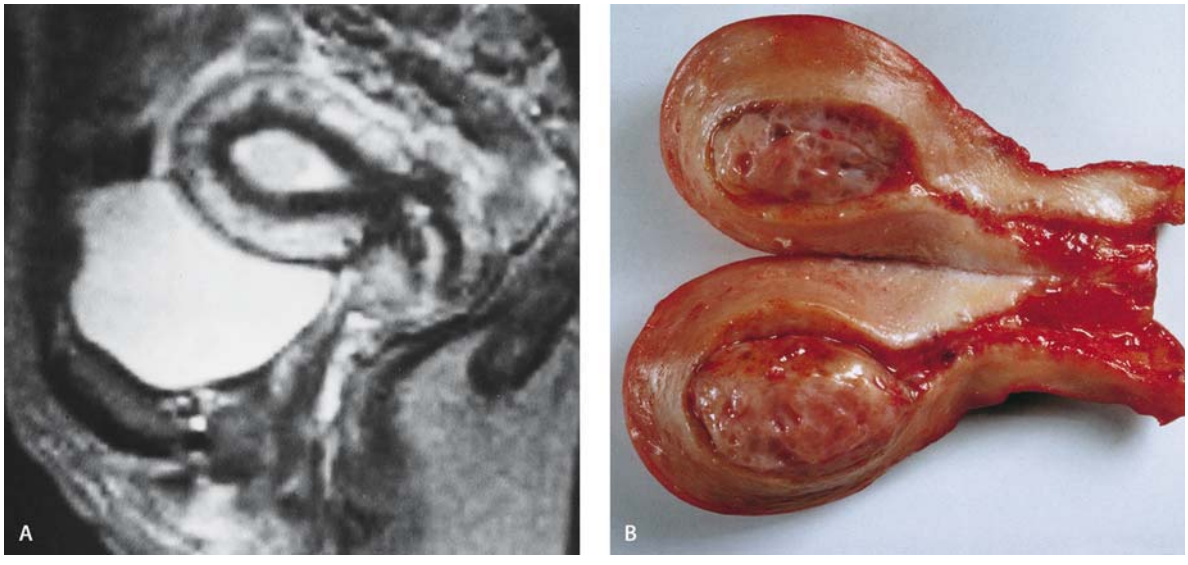

Fig. 9A, B. Endometrial polyp. **A** Sagittal T2-weighted SE image. The endometrial polyp is of slightly lower signal intensity compared to the endometrium. MR imaging does not permit distinction of an endometrial polyp from a polypous endometrial carcinoma. Regular and intact junctional zone of the myometrium. **B** Gross specimen

sities on T2-weighted images (leiomyoma: hypointense). In inconclusive cases, the differentiation is further facilitated by a contrast-enhanced study (leiomyoma: slighter enhancement).

Endometrial Carcinoma

Endometrial cancer is the most frequent malignancy of the female genital tract. The majority of patients are postmenopausal women; the incidence in women below the age of 40 years is only 2%–5%. The most common symptom of endometrial carcinoma is the occurrence of postmenopausal bleeding, which is often its only manifestation.

Endometrial carcinoma invades the myometrium but rarely extends through the serosa into the abdominal cavity. The cervix is involved in about 10% of cases. Lymphatic and hematogenous spread of endometrial cancer occurs later than in cervical carcinoma. There is a close correlation between lymphatic spread and the depth of myometrial invasion [16, 17]. Superficial infiltration of the myometrium (stage Ib) is associated with lymph node metastases in 3% of cases only, whereas over 40% of patients with deep myometrial invasion (stage Ic) have lymph node metastases. Thus, the extent of myometrial invasion is an important prognostic factor.

The most important examination for confirmation of endometrial cancer is fractional abrasion (fractionation in order to exclude or confirm involvement of the endocervix, corresponding to stage II disease). Transvaginal ultrasound reliably depicts the depth of myometrial infiltration in stage I endometrial cancer but is unsuitable for general tumor staging (e.g., extension of the tumor to the uterine cervix) [18, 19].

Because of the excellent depiction of myometrial infiltration and tumor staging as a whole, contrast-enhanced MR imaging performs best in the pretreatment evaluation of endometrial carcinomas compared to ultrasonography and CT [20]. The MR imaging findings provide an optimal basis for therapeutic decision-making (e.g., hysterectomy with or without lymphadenectomy, chemotherapy, or gestagen treatment).

T2-weighted images depict endometrial carcinomas as hyperintense masses, typically seen as pathologic thickening of the endometrium (Fig. 10), which may occasionally contain heterogeneous areas of decreased signal intensity. Since these changes are not specific for endometrial cancer but are also seen in endometrial hyperplasia, endometrial polyps or coagulated blood, the diagnosis is based on the histologic findings [21]. A hyperintense disruption of the junctional zone is indicative of myometrial infiltration, and the depth of infiltration can likewise be assessed by MR imaging. T2-weighted imaging in two planes is essential for precisely determining the depth of myometrial invasion. Demarcation of the tumor from surrounding myometrium may occasionally cause problems on T2-weighted images. Errors in the staging of endometrial carcinoma primarily occur in large polypous endometrial carcinomas (which only rarefy the myometrium but do not invade it) and large leiomyomas, in the presence of congenital anomalies, if the uterus is small and atrophic and when the zonal anatomy is missing [22]. Intravenous administration of a contrast agent is generally indicated for MR imaging of endometrial carcinoma [4, 23–26]. The cancer shows less pronounced enhancement than the surrounding myometrium, which improves the determination of the tumor borders (Fig. 10). Contrast-enhanced imaging furthermore improves the differentiation of vital tumor portions from areas of necrosis or fluid accumulation (e.g., hematometra or pyometra).

Staging of endometrial cancer by MR imaging is based on the International Federation of Gynecology and Obstetrics (FIGO) classification.

In stage I disease, the tumor is confined to the uterine corpus. Since there is considerable variation in prognosis, stage I is further subdivided as follows:

Ia Tumor confined to the endometrium
Ib Tumor infiltration of the inner half of the myometrium (relative to the thickness of the myometrium)
Ic Tumor extension to the outer half of the myometrium

Stage Ia disease is suggested when the hypointense junctional zone is intact. If there is insufficient delineation of the junctional zone, which is typically the case in an atrophic uterus, a stage Ia tumor can be assumed when the lesion is smoothly and clearly demarcated from the myometrium. In stage Ib tumors, there is disruption of the junctional zone or the border between the tumor and myometrium becomes irregular, with confinement of the pathologic process to the inner half of the myometrium (Fig. 10). Stage Ic disease is characterized by deep myometrial involvement extending to the outer half of the myometrium. Assessment of myometrial tumor infiltration is facilitated by contrast-enhanced T1-weighted imaging.

In stage II disease, the tumor has invaded the cervix or endocervix.

Stage III and IV endometrial cancer can likewise be assessed by MR imaging. Both stages are characterized by extension of the tumor beyond the uterus (stage III: tumor confined to the pelvis; stage IV: tumor invasion extending beyond the true pelvis or infiltration of the mucosa of the urinary bladder or rectum). An infiltration of the wall of the bladder or rectum is seen on T2-weighted images as a focal and hyperintense disruption of the otherwise hypointense muscular layer. Further criteria for tumor growth beyond the uterus are an irregular uterine surface and the presence of ascites.

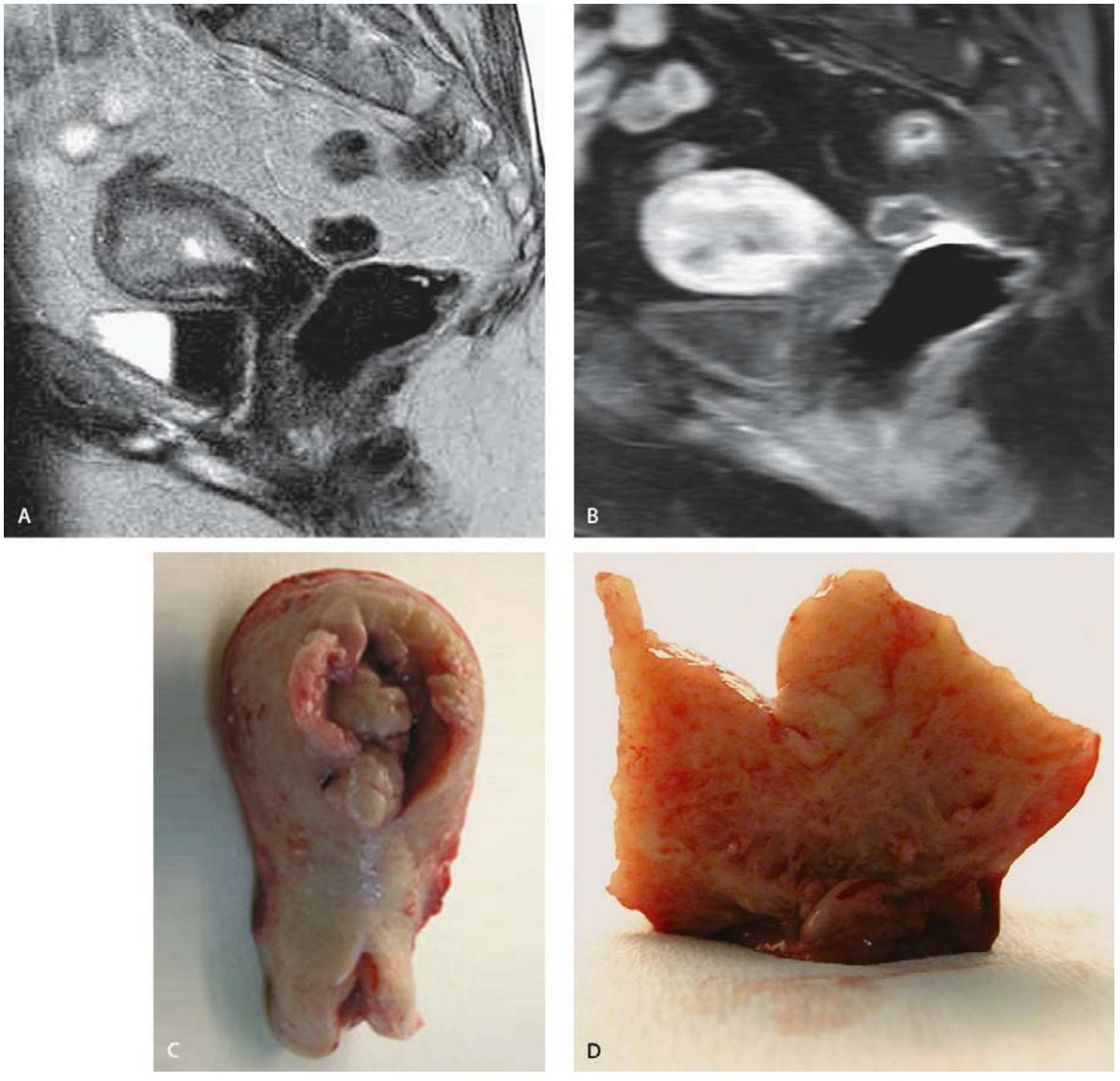

Fig. 10A–D. Endometrial carcinoma; stage Ib. **A** Sagittal T2-weighted SE image. Generalized pathologic thickening of the endometrium. Additionally hyperintense mass in the anterior wall of the uterus, which disrupts the narrow hyperintense junctional zone and invades the inner half of the myometrium. **B** Sagittal T1-weighted contrast-enhanced SE image. Significantly better demarcation of the hypointense invading carcinoma relative to the hyperintense intact myometrium. **C**, **D** Gross specimen confirms the involvement of the inner half of the myometrium

Lymph node assessment by MR imaging uses the same criteria as computed tomography and relies solely on an enlarged transverse nodal diameter (>1 cm). However, MR imaging has a slight advantage over CT in that it is far better in T-stage assessment, from which indirect conclusions can be drawn for differentiating reactive from tumorous lymph node enlargement.

Cervical Carcinoma

The incidence of cervical carcinoma shows two peaks, the first between 35 and 45 years of age and the second between 65 and 75 years. Invasive cervical carcinoma occurring in women younger than 35 years frequently is of a highly aggressive type. It is now commonly assumed that cervical carcinoma develops in several steps (dysplasia – carcinoma in situ – microinvasive carcinoma). Dysplasia and carcinoma in situ together are

termed cervical intraepithelial neoplasia (CIN). Microcarcinoma (stage Ia2: invasion depth <5 mm and surface extension <7 mm) is already associated with lymph node metastases in up to 10% of cases [16].

The initial symptoms are bleeding outside menstruation and vaginal discharge. Regular screening is very helpful for detecting cervical cancer since no other gynecological tumor is that easily accessible to physical examination.

Imaging is not used for detecting cervical carcinoma but for staging of already proven carcinoma. Because of the high soft-tissue contrast and the free selection of imaging planes, MR imaging is far superior to CT in staging cervical carcinoma. Most information is provided by T2-weighted imaging. On T2-weighted images, a cervical carcinoma is depicted as a lesion of high signal intensity, which is clearly seen against the low signal intensity of the cervical stroma (Fig. 11). On T1-weighted images, cervical cancer is not delineated adequately since it is of the same signal intensity as the cervical stroma, the myometrium, and the vagina. T1-weighted imaging, however, is suitable for assessment of larger tumor masses in the parametria and for lymph node staging. In contrast to endometrial cancer, intravenous administration of a contrast agent yields only little additional information for the detection and staging of cervical carcinoma [27–30]. However, dynamic contrast-enhanced MR imaging seems to be a useful tool

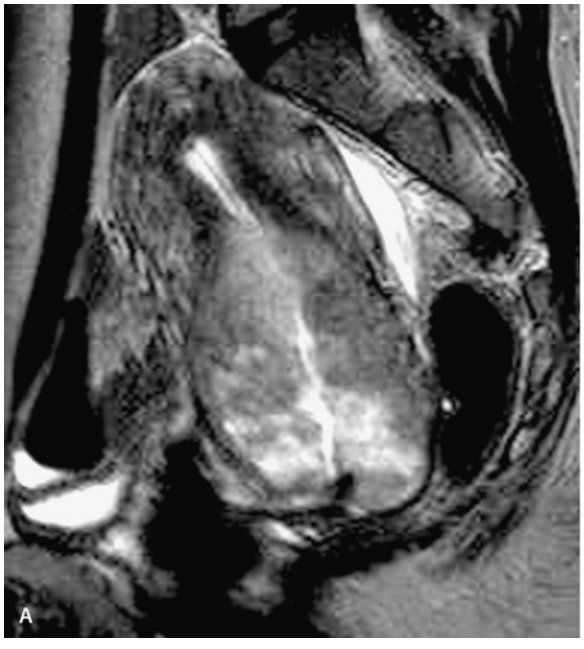

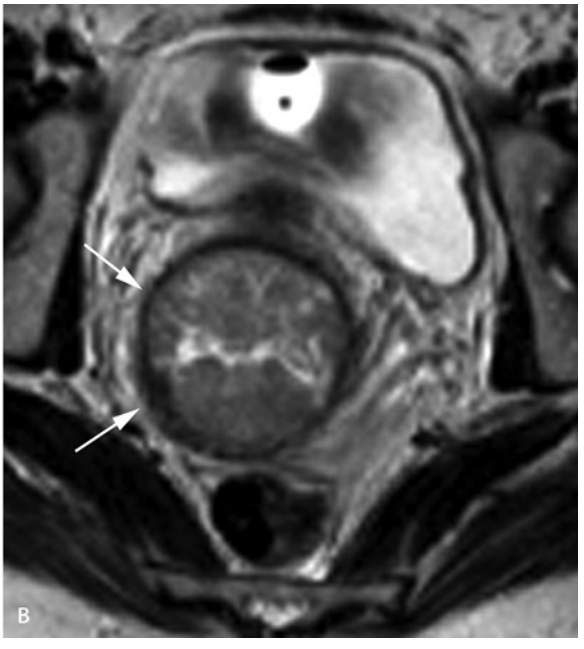

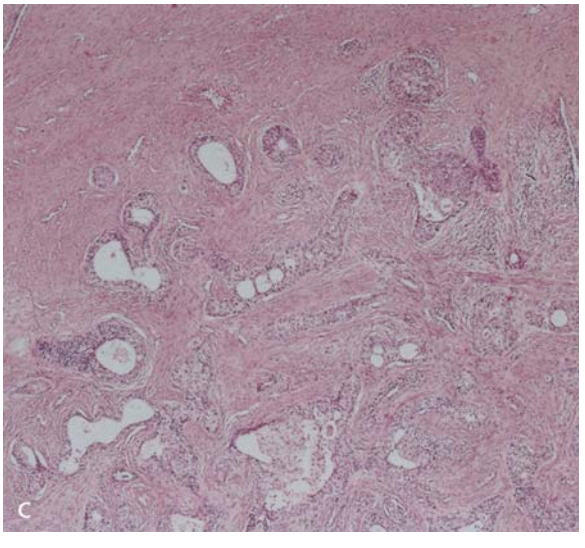

Fig. 11A–C. Cervical carcinoma, stage Ib. **A**, **B** Sagittal and transverse T2-weighted FSE images. The cervical carcinoma is depicted as a hyperintense mass invading the cervix and uterine corpus. Despite the huge size, both the sagittal and the transverse image show that the cancer is still surrounded by a hypointense rim of cervical stroma (*arrows*). Normal appearance of the hypointense vaginal wall without signs of tumor infiltration. **C** Histologic specimen (H&E staining, not taken from this case), lateral border of the carcinoma surrounded by normal myometrium

for predicting and objectively assessing the outcome of radiotherapy [31, 32].

Staging of cervical carcinoma by MR imaging is based on the FIGO criteria. The preclinical form (stage Ia) can only be demonstrated microscopically and is not seen on MR images. Stage Ib carcinoma is restricted to the cervix (with or without involvement of the corpus uteri). The most important criterion on T2-weighted MR images is a fully preserved hypointense rim of normal cervical stroma surrounding the tumor (Fig. 11b). Assessment of the preserved normal cervical stroma is facilitated by T2-weighted imaging in two planes. In addition, the parametrial tissue appears inconspicuous and the normal border relative to the surrounding fatty

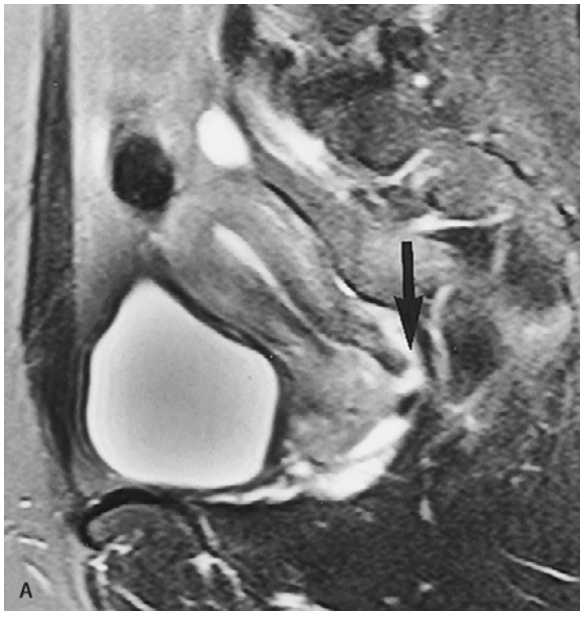

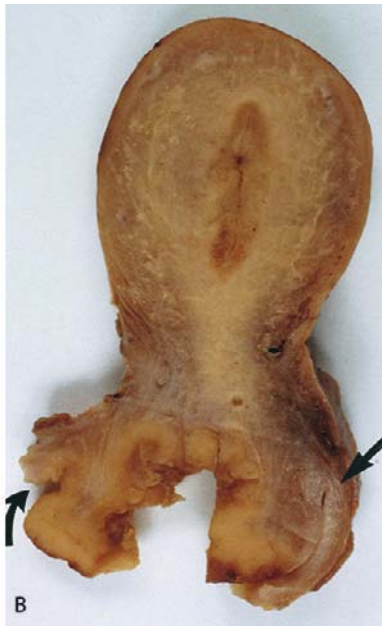

Fig. 12A, B. Cervical carcinoma, stage IIa. **A** Sagittal T2-weighted FSE image. Hyperintense mass, predominantly located in the anterior part of the cervix with obliteration of the anterior vaginal fornix. Normal appearance of the posterior vaginal fornix. **B** Gross specimen: ulcerated cervical carcinoma infiltrating the anterior vagina (*curved arrow*), no infiltration of the posterior vaginal fornix (*arrow*)

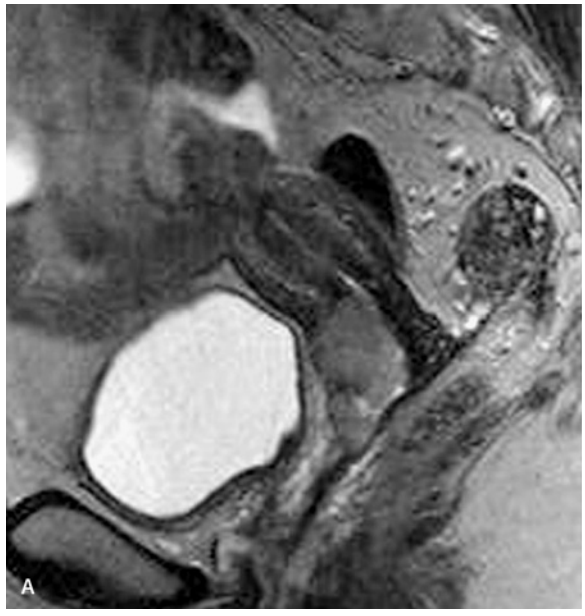

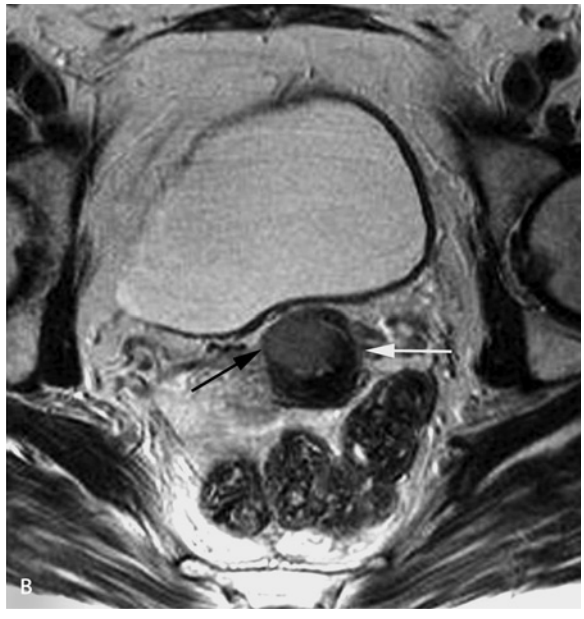

Fig. 13A, B. Cervical carcinoma; stage IIb. **A, B** Sagital and transverse T2-weighted FSE images. The tumor has completely invaded the cervical stroma on the right but leaves a narrow rim of hypointense cervical stroma on the left (*white arrow*). Besides the carcinoma invades the cranial two-thirds of the anterior vagina meanwhile the posterior vaginal fornix seems to bee intact

tissue is preserved. In stage IIa disease, the tumor involves the upper and/or middle third of the vagina. Infiltration of the vaginal wall is visualized on T2-weighted images as a hyperintense disruption of the otherwise hypointense muscle layer (Fig. 12). Stage IIb cervical carcinoma is characterized by infiltration of the parametria. Advanced parametrial invasion is depicted on both T2- and T1-weighted images as a mass within the parametria. The most important criterion of possible parametrian infiltration is the complete disruption of the low-intensity cervical stroma by (hyperintense) tumor tissue (Fig. 13) [33].

In stage IIIa, the hyperintense tumor extends to the lower third of the vagina (because lymphatic drainage is different in this area, the inguinal lymph nodes should be examined as well in these cases!). Infiltration of the pelvic wall or obstruction of one or both ureters by the tumor corresponds to stage IIIb disease (Fig. 14). Involvement of the muscle tissue of the pelvic wall can best be demonstrated on T2-weighted images as a hyperintense infiltration.

Invasion of the urinary bladder and/or rectum (stage IVa) is seen on T2-weighted images as a hyperintense disruption of the otherwise hypointense muscle of the wall of the urinary bladder or rectum (Fig. 15). If the findings are inconclusive with regard to bladder or rectum infiltration, an additional contrast-enhanced study will show contrast enhancement in areas of tumor involvement. The FIGO classification only takes into account involvement of the mucosa of the urinary bladder or rectum, since only this can be assessed endoscopically. MR imaging, on the other hand, can also demonstrate tumorous infiltration in the underlying muscular layers.

In addition to allowing for T-stage assessment, MR imaging is able to depict lymph nodes, peritoneal seeding, and organ metastases (Fig. 16).

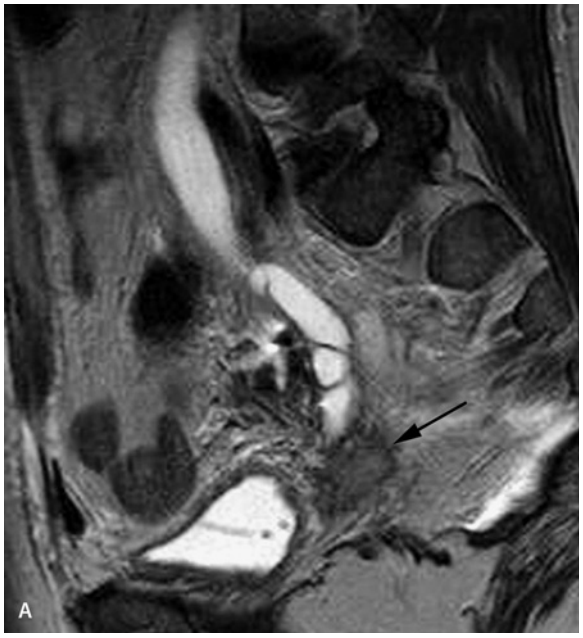

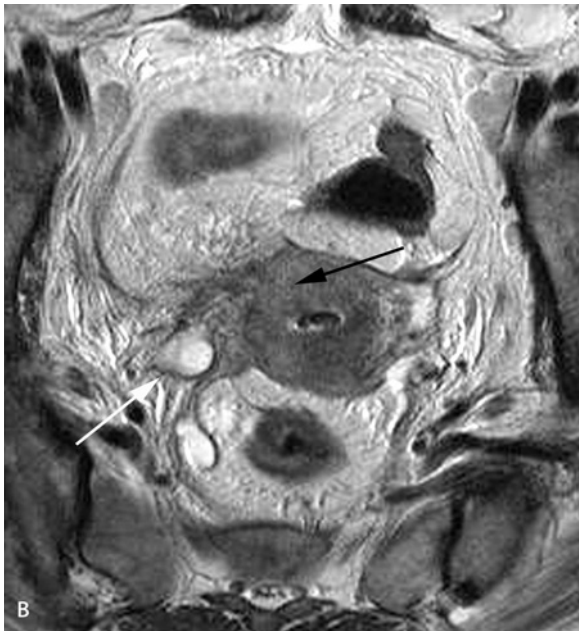

Fig. 14A, B. Cervical carcinoma, stage IIIb. **A**, **B** Sagittal and transverse T2-weighted FSE image. The tumor (*black arrow*) has invaded the right parametrium and caused obstruction of the right ureter (*white arrow*)

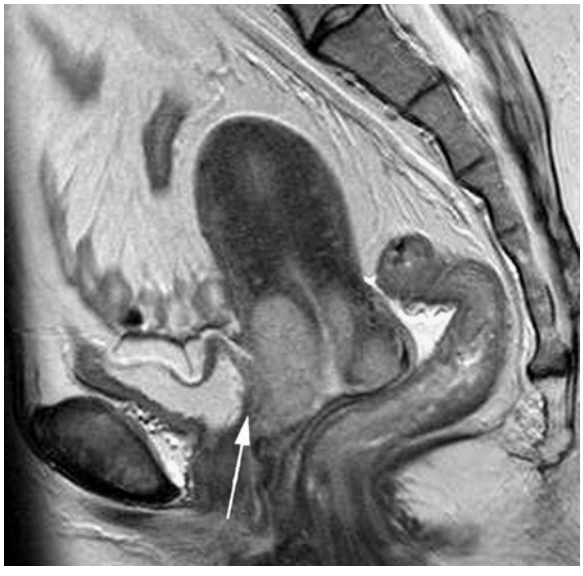

Fig. 15. Cervical carcinoma, stage IVa. Sagittal T2-weighted FSE image. The cervical carcinoma has infiltrated the muscular layers of the urinary bladder, depicted as a hyperintense disruption of the otherwise hypointense muscle wall (*arrow*)

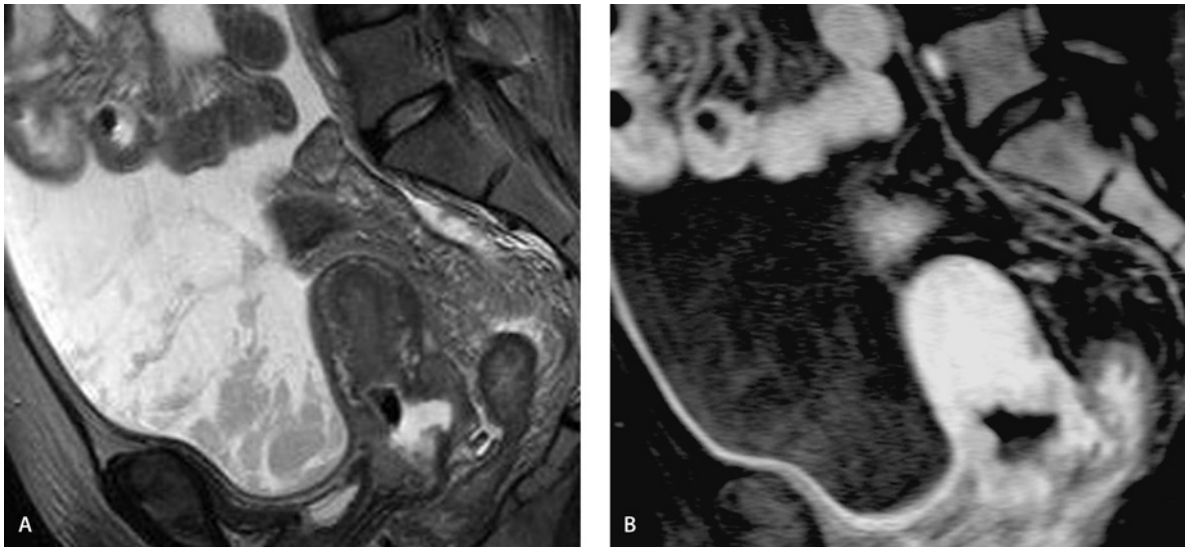

Fig. 16A, B. Cervical carcinoma with peritoneal spread. **A** Sagittal T2-weighted FSE image depicting a large volume of ascites. **B** Sagittal T1-weighed contrast-enhanced image depicts peritoneal spread as generalized; pronounced enhancement of the thickened peritoneal layer

Benign Adnexal Masses

The ovaries are divided into a cortex containing the follicle at different stages of maturation, and a medulla. In young women, the average ovary weighs 8 g and shrinks from age 30 to less than 2 g after menopause [24]. The ovaries can be visualized in virtually all premenopausal women by MR imaging with adequate spatial resolution. The cortex shows lower signal intensity than the medulla on T2-weighted images. Single functional cysts in the cortex are hypointense on T1-weighted images and hyperintense in T2-weighted sequences [34].

Pelvic inflammatory disease is a largely clinical, bacteriological and sometimes sonographic diagnosis, typically made in women of childbearing age. Half of the cases result from ascending infection by sexually trans-

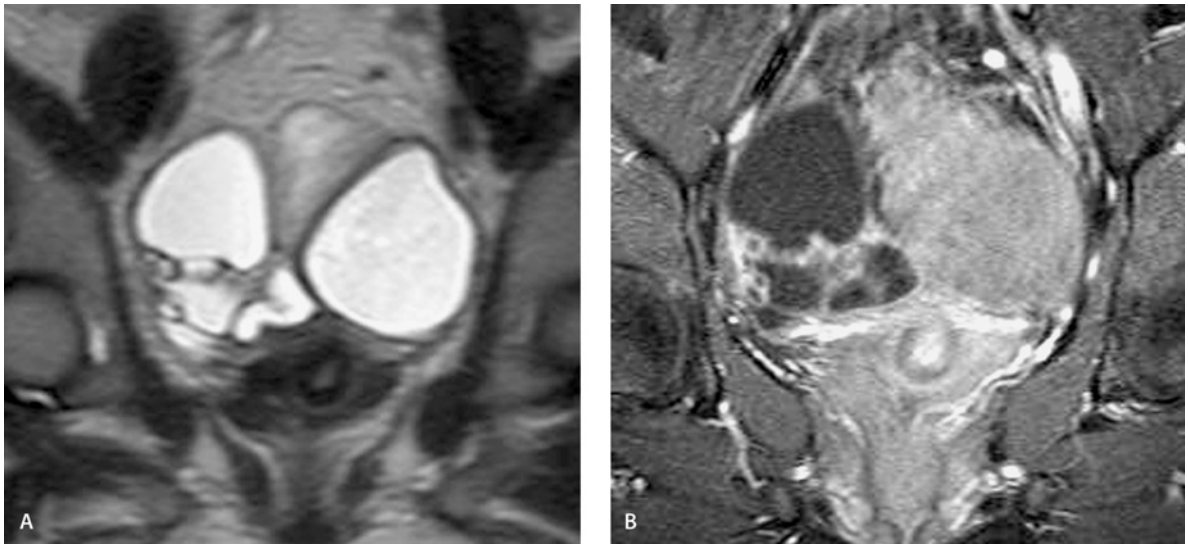

Fig. 17A, B. Pyosalpinx. **A**, **B** Coronal T2-weighted SE and T2-weighted contrast-enhanced SE image depicts a fluid collection at the right pelvic wall with contrast enhancement of surrounding thickened adnexal wall. Two months later (after antibiotic therapy) the lesion was no longer detectable by MR imaging

mitted pathogens such as *Neisseria gonorrhoeae* and *Chlamydia trachomatis*, which migrate into the peritoneum from the cervix via the endometrium and fallopian tube [35, 36]. Known risk factors include multiple partners and use of an intrauterine contraceptive device (IUD). Women with an IUD have a three to seven times higher risk of acute salpingitis [37].

A pyosalpinx arises from infundibular adhesion and pus retention in a patient with salpingitis. Liquefaction and the pooling of pus between the organs of the true pelvis lead to abscesses of the pelvis, adnexa, and pouch of Douglas; suppurative infection of the fallopian tube and ovary results in the tubo-ovarian abscesses [38, 39] seen in up to one-third of admissions for acute salpingitis [40]. Tubo-ovarian abscess is clinically almost indistinguishable from adnexitis and is normally diagnosed by ultrasound [41–43].

The typical CT image of an ovarian abscess is that of central liquefaction (i.e., fluid-equivalent density) surrounded by a rim of increased contrast uptake; inflammation may also involve the surrounding fatty tissue [43] (Fig. 18). The MR image is heterogeneous, generally showing iso- or slight hypointensity compared to urine in T1-weighted sequences [44] and hyperintensity on T2-weighted images (Fig. 17). However, if the abscess contains blood or high protein levels, it may be visualized with varying signal intensities, even on T1-weighted images. Delineation of the abscess border is usually unclear, though the wall shows increased signal intensity on contrast-enhanced images. Edema and inflammatory infiltration give a heterogeneous appearance to the surrounding fat. A chronic untreated or antibiotic-resistant abscess leads to an increase in the number of visible blood vessels [45].

A benign ovarian cyst, whether a functional follicular cyst, single cyst, cystadenoma, dermoid (mature teratoma), endometrioma or polycystic ovary, is typically thin-walled and sharply delineated (Figs. 19–21). The purpose of CT and MRI is to differentiate these lesions from ovarian carcinoma. The primary criteria of malignancy are a diameter greater than 4 cm, intralesional solid elements or septations, wall thickening, and necrosis; ancillary criteria include lymph node hypertrophy, ascites and infiltration of surrounding structures [46].

CT or MRI evidence of intralesional fat is indicative of a dermoid cyst, accounting for 10%–25% of all ovarian neoplasms. On MRI, the fat component can be distinguished from hemorrhage – both are hyperintense

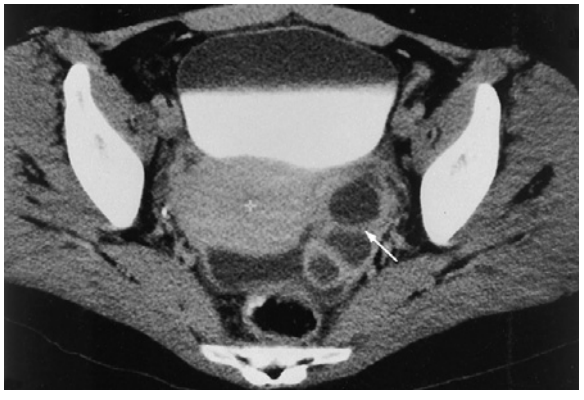

Fig. 18. Tubo-ovarian abscess. Contrast-enhanced CT: multiloculated left adnexal lesion with central liquefaction and contrast-enhancing thickened wall (*arrow*). There is a fluid collection in the pouch of Douglas. (+: uterine cavity)

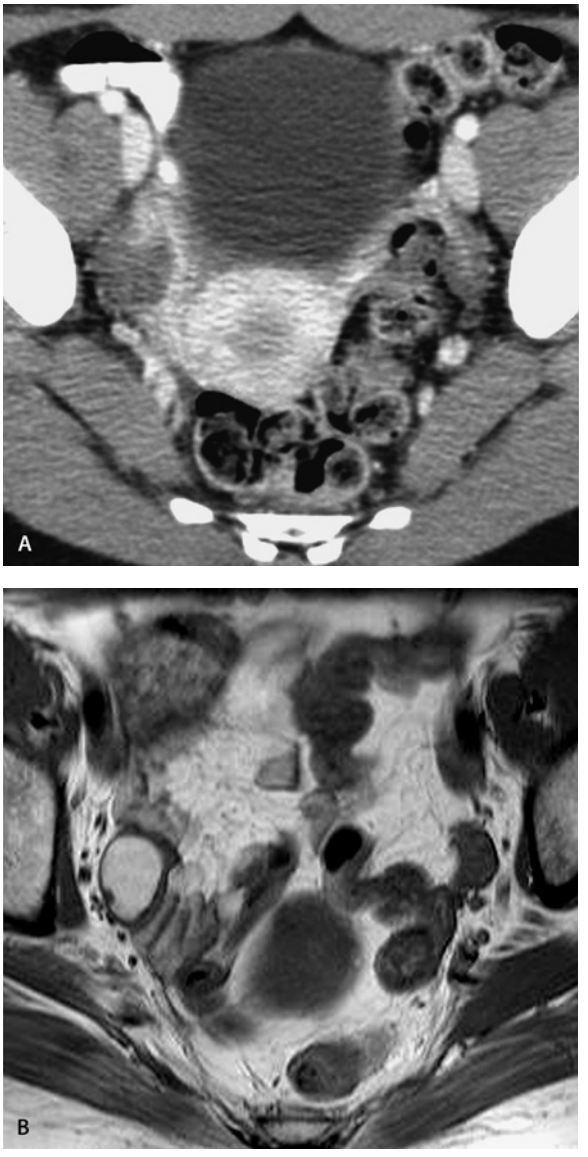

Fig. 19A, B. Functional hemorrhagic ovarian cyst. **A** Contrast-enhanced CT. Small cystic, thin-walled lesion of the right ovary without septations. **B** Axial T1-weithted SE image: small circumscribed thin-walled cystic adnexal lesion on the left with hyperintense content

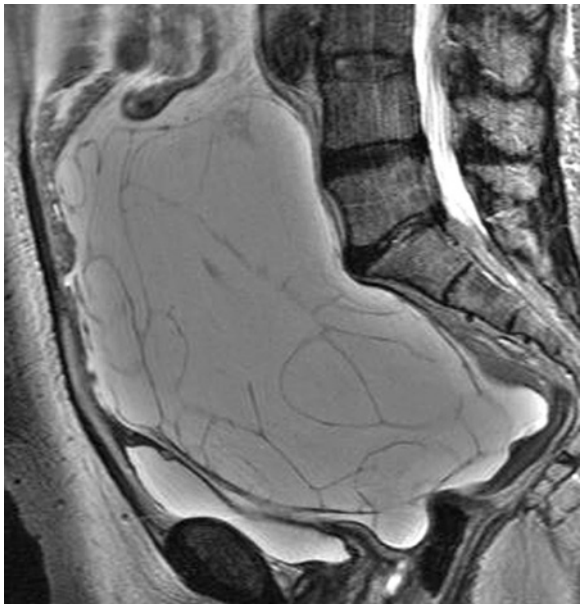

Fig. 20. Benign cystadenoma of the ovary. Sagittal T2-weighted FSE image showing a large, thin-walled adnexal cystic structure with numerous septations. Pathology after surgery confirmed the diagnosis of benign cystadenoma

on T1-weighted images – by using fat suppression. Fat–fluid levels may be visualized, together with a solid nodule arising from the tumor wall (Rokitansky nodule or dermoid plug) [45]. The protuberance contains mature differentiated tissue such as hair, fat, and teeth or other calcifications, the latter being clearer on CT than MRI (Fig. 21).

Ovarian Carcinoma

Carcinoma of the ovary is the third most common malignancy of the female genital tract after carcinoma of the cervix and endometrium. However, its poor prognosis means that it accounts for approximately half of all deaths from gynecologic malignancy [47, 48]. Management of clinically suspected disease involves a staging laparotomy with histologic confirmation of the diagnosis, identification of tumor spread, and debulking prior to chemotherapy. The latter is usually followed by a second-look laparotomy to assess the response.

The strength of MRI lies in its ability, first, to determine the origin of a pelvic mass using multiplanar imaging and high soft-tissue contrast and, secondly, to differentiate between malignant and benign lesions with a

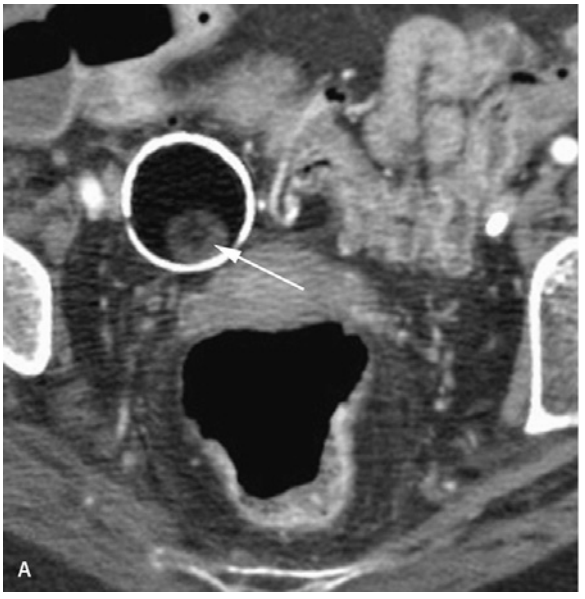

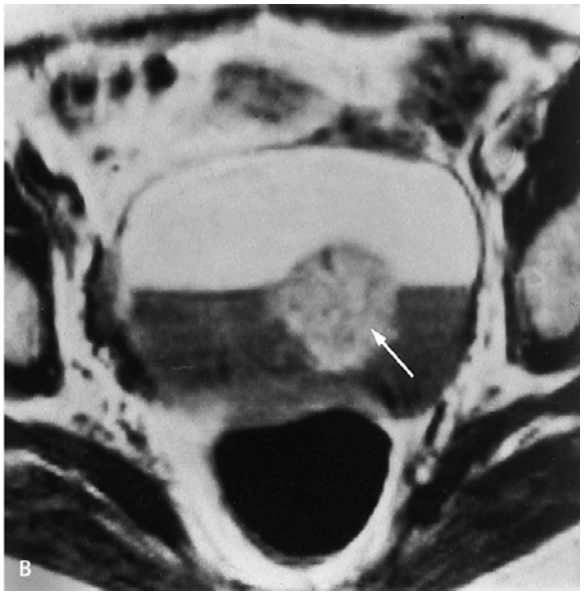

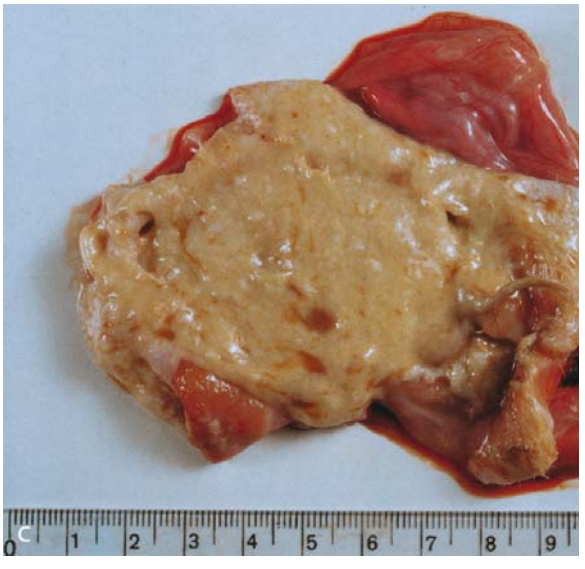

Fig. 21A–C. Mature teratomas. **A** Contrast-enhanced CT clearly demonstrates a fat-containing pelvic mass with surrounding calcifications and a solid, contrast-enhancing nodule (*arrow*), the so-called Rokitansky nodule or dermoid plug. **B** Axial contrast-enhanced T1-weighted SE image: adnexal lesion with a fat–fluid level and the so-called Rokitansky nodule. **C** Macroscopic specimen of a mature teratoma containing fat and hair

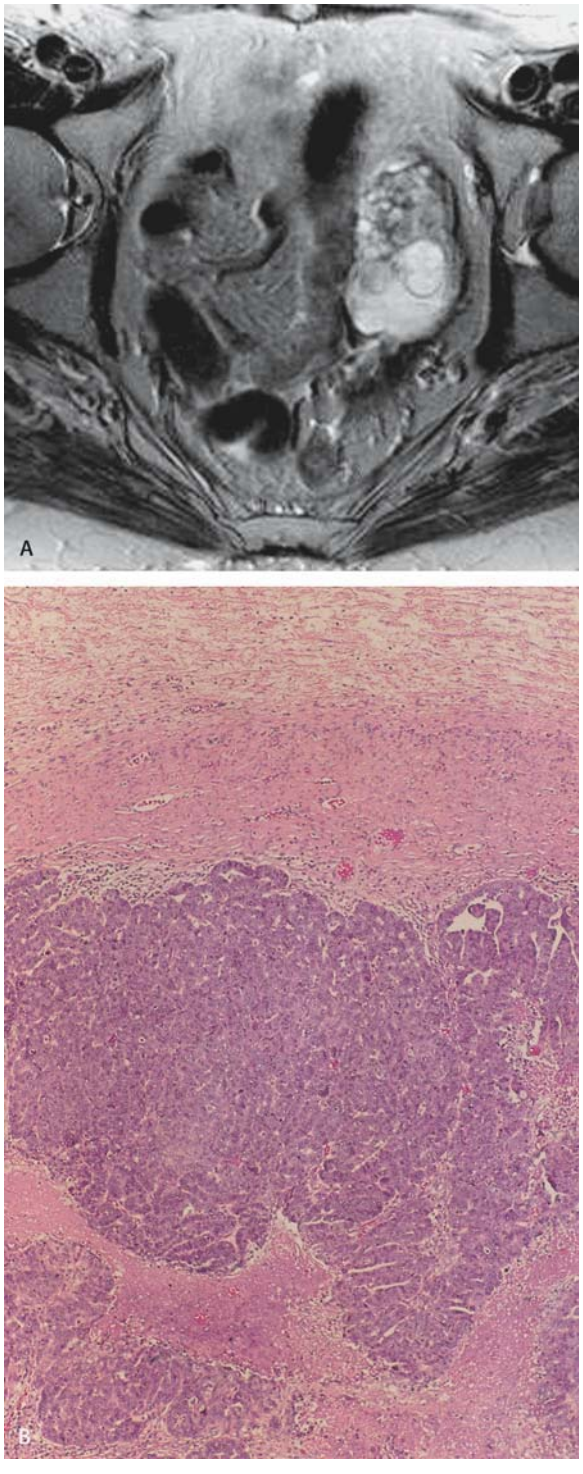

Fig. 22A, B. Serous papillary ovarian carcinoma. **A** Transverse T2-weighted FSE image showing an adnexal semi-solid cystic mass of the left ovary. The diagnosis of a malignant serous papillary ovarian adenocarcinoma was confirmed by the histologic examination. **B** Histologic specimen (H&E staining) of a malignant serous papillary ovarian carcinoma (not taken from this case)

60%–99% accuracy [49–55] using the above primary and ancillary criteria. MRI findings are not specific for the cell types of ovarian carcinoma, although some features are more typical of one histology rather than another. Mucinous tumors, for example, may mimic multiple simple cysts, but frequently display imaging features similar to those of other mucin-laden tumors, i.e., an intermediate to high signal intensity on T1- and T2-weighted images [56].

Imaging does not yet have a clearly defined place in the staging and management of ovarian carcinoma, since many centers still view surgical exploration as the diagnostic gold standard in both primary and recurrent disease. However, surgery can be avoided in cases where the laparoscopic and/or imaging diagnosis is unambiguously benign. Imaging also helps in preoperative planning and follow-up of chemotherapy by providing accurate information on tumor spread (Figs. 22–24).

In our view, CT is the modality of choice alongside transvaginal and abdominal ultrasound in staging ovarian carcinoma, as it is less expensive and more widely available than MRI. However, ovarian cancer metastasizes directly via peritoneal seeding and lymphatic para-aortic and peritoneal spread. Compared to solid viscera, imaging of peritoneal seeding presents particular problems due to the extensive area of the peritoneum, anatomic variation, low tissue contrast, and motion artifacts. Gadolinium-enhanced MRI has proven superior to nonenhanced MRI and CT in demonstrating peritoneal metastases with reported sensitivities of 62%–86% [57–61]. However, MRI is not only more expensive, but also more demanding on the often weakened patients as well as time-consuming. Its advantages are that it can be used in renal failure and situations in

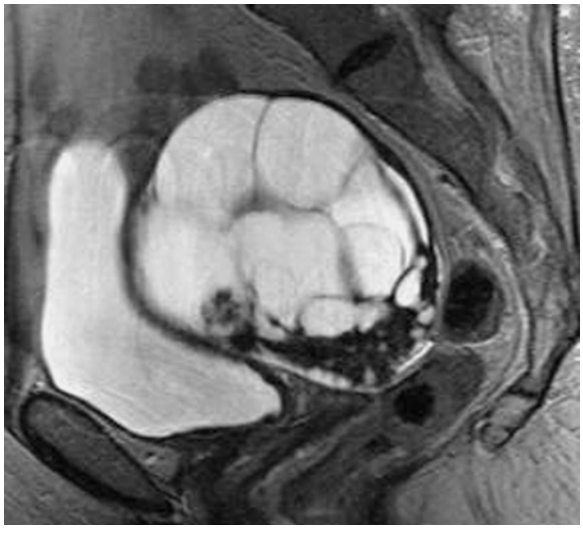

Fig. 23. Serous ovarian carcinoma sagital T2-weighted FSE image showing an adnexal semi-solid/cystic structure, confirmed as a serous cystadenocarcinoma

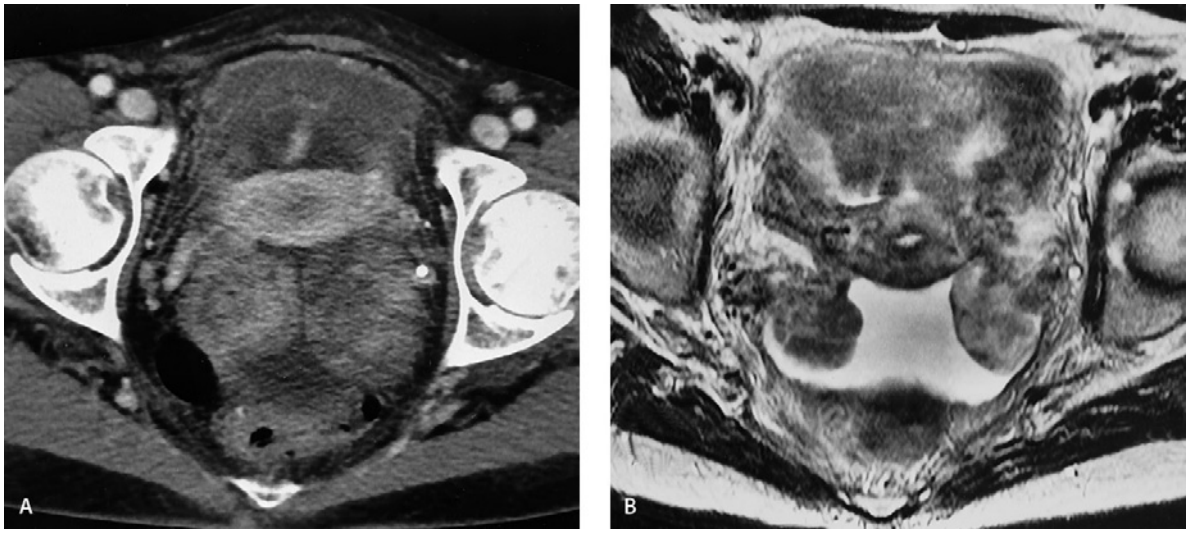

Fig. 24A, B. Bilateral ovarian metastases (Krukenberg's tumor). CT (**A**) and MR imaging (**B**, T2-weighted FSE image) show a solid, inhomogeneous mass in the area of both ovaries and ascites. The patient had been operated on for stomach cancer 1 year previously

which the radiation exposure associated with CT is contraindicated, e.g., during pregnancy.

Up to 10% of ovarian tumors are metastatic with primaries typically in the gastrointestinal tract, breast, uterus, or thyroid. Metastases containing a significant amount of signet-ring cells are termed Krukenberg's tumors. Bilateral contrast-enhanced lesions are generally seen on CT or MR imaging (Fig. 24). Prognosis is poor with a 1-year post-detection mortality of 90% [35, 44].

References

1. Dueholm M, Lundorf E, Hansen ES et al (2002) Accuracy of magnetic resonance imaging and transvaginal ultrasonography in the diagnosis, mapping and measurement of uterine myomas. Am J Obstet Gynecol 186:409–415
2. Dueholm M, Lundorf E, Sorensen JS et al (2002) Reproducibility of evaluation of the uterus by transvaginal sonography, hysterosonographic examination, hysteroscopy and magnetic resonance imaging. Hum Reprod 17:197–200
3. Dueholm M, Lundorf E, Hansen ES et al (2001) Evaluation of the uterine cavity with magnetic resonance imaging, transvaginal sonography, hysterosonograhic examination and diagnostic hysteroscopy. Fertil Steril 76:350–357
4. Hricak H, Kim BK (1993) Contrast-enhanced MR imaging of the female pelvis. JMRI 3:297–306
5. Katsumori T, Nakajima K, Tokuhiro M (2001) Gadolinium-enhanced MR imaging in the evaluation of uterine fibroids treated with uterine artery embolization. AJR 177:303–307
6. Hamlin DJ, Petersson H, Fitzsimmons J Morgan LS (1985) MR imaging of uterine leiomyomas and their complications. JCAT 9:902–907
7. Hricak H, Tscholakoff D, Heinrichs L et al (1986) Uterine leiomyoma correlation by magnetic resonance imaging: clinical symptoms and histopathology. Radiology 158:385–391
8. Mittl RL, Yeh I-T, Kressel HY (1991) High-signal-intensity rim surrounding uterine leiomyomas on MR images: pathologic correlation. Radiology 180:81–83
9. Murase E, Siegelmann ES, Outwater EK et al (1999) Uterine leiomyomas: histopathologic features, MR imaging findings, differential diagnosis and treatment. Radiographics 1179–1197
10. Hricak H, Finck S, Honda G et al (1992) MR imaging in the evaluation of benign uterine masses: value of gadopentetate dimeglumine-enhanced T1-weighted images. AJR 158:1043–1250
11. Reinhold C, Atri M, Mehio A, Zakarian R, Aldis AE, Bret PM (1995) Diffuse uterine adenomyosis: morphologic criteria and diagnostic accuracy of endovaginal sonography. Radiology 197:609–614
12. Siskin GP, Tublin ME, Stainken BF et al (2001) Uterine artery embolization for the treatment of adenomyosis: clinical response and evaluation with MR imaging. AJR 177:297–302
13. Togashi K, Nishimura K, Itho K et al (1988) Adenomyosis: diagnosis with MR imaging. Radiology 166:111–114
14. Togashi K, Ozasa H, Konishi I et al (1989) Enlarged uterus: differentiation between adenomyosis and leiomyoma with MR imaging. Radiology 171:531–534
15. Kang S, Turner DA, Foster GS, Rapoport MI, Spencer SA, Wang J-Z (1996) Adenomyosis: specificity of 5 mm as the maximum normal uterine junctional zone thickness in MR images. AJR 166:1145–1150
16. Martius G, Breckwoldt M, Pfleiderer A (1996) Lehrbuch der Gynäkologie und Geburtshilfe. Georg Thieme Verlag, Stuttgart
17. Chen SS, Lee L (1983) Retroperitoneal lymph node metastases in stage I carcinoma of the endometrium: correlation with risk factors. Gynecol Oncol 16:319–325
18. DelMaschio A, Vanzulli A, Sironi S et al (1993) Estimating the depth of myometrial involvement by endometrial carcinoma: efficacy of transvaginal sonography vs MR imaging. AJR 160:533–538
19. Yamashita Y, Mizutani H, Torashima M et al (1993) Assessment of myometrial invasion by endometrial carcinoma: transvaginal sonography vs contrast-enhanced MR imaging. AJR 161:595–599
20. Frei KA and Kinkel K (2001) Staging endometrial cancer: role of magnetic resonance imaging. J Magn Reson Imaging 13:850–855
21. Grasel RP, Outwater EK, Siegelman ES et al (2000) Endometrial polyps: MR imaging features and distinction from endometrial carcinoma. Radiology 214:47–52
22. Scoutt, LM, McCarthy SM, Flynn SD et al (1995) Clinical stage I endometrial carcinoma: pitfalls in preoperative assessment with MR imaging. Radiology 194:567–572

23. Hricak H, Hamm B, Semelka R et al (1991) Carcinoma of the uterus: use of gadopentetate dimeglumine in MR imaging. Radiology 181:95–106
24. Sironi S, Colombo E, Villa G et al (1992) Myometrial invasion by endometrial carcinoma: assessment with plain and gadolinium-enhanced MR imaging. Radiology 185:207–212
25. Yamashita Y, Harada M, Sawada T, Takahashi M, Miyazaki K, Okamura H (1993) Normal uterus and FIGO stage I endometrial carcinoma: dynamic gadolinium-enhanced MR imaging. Radiology 186:495–501
26. Savci G, Ozyaman T, Tutar M, Bilgin T, Erol O, Tuncel E (1998) Assessment of depth of myometrial invasion by endometrial carcinoma: comparison of T2-weighted SE and contrast-enhanced dynamic GRE MR imaging. Eur Radiol 8:218–223
27. Sironi S, DeCobelli F, Scarfone G et al (1993) Carcinoma of the cervix: value of plain and gadolinium-enhanced MR imaging in assessing degree of invasiveness. Radiology 188:797–801
28. Hawighorst H, Knapstein PG, Weikel W et al (1996) Cervical carcinoma: comparison of standard and pharmacokinetic MR imaging. Radiology 201:531–539
29. Scheidler J, Heuck A, Wencke K, Kimmig R, Müller-Lisse U, Reiser M (1997) Parametrial invasion of cervical cancer: value of contrast-enhanced fat-suppressed T_1-weighted SE-sequences at 1.5 Tesla. Fortschr Röntgenstr 166:312–316
30. Scheidler J, Heuck AF, Steinborn M, Kimmig R, Reiser MF (1998) Parametrial invasion in cervical carcinoma: evaluation of detection at MR imaging with fat suppression. Radiology 206:125–129
31. Loncaster JA, Carrington BM, Sykes JR et al (2002) Prediction of radiotherapy outcome using dynamic contrast MRI of carcinoma of the cervix. Int J Radiat Oncol Biol Phys 54:759–767
32. Ohara K, Tanaka Y, Tsunoda H, Nishida M, Sugahara S, Itai Y (2002) Assessment of cervical cancer radioresponse by serum squamous cell carcinoma antigen and magnetic resonance imaging. Obstet Gynecol 100:781–787
33. Sironi S, Belloni C, Taccagni GL, DelMaschio A (1991) Carcinoma of the cervix: value of MR imaging in detecting parametrial involvement. AJR 156:753–756
34. Zaloudek C (1994) The ovary. In: Compel C, Silverberg SG (eds) Pathology in gynecology and obstetrics, Lippincott, Philadelphia, pp 313–413
35. Outwater EK, Duntion CJ (1995) Imaging of the ovary and adnexa. Clinical issues and applications of MR imaging. Radiology 194:1–18
36. Gross B, Moss A, Mihara K, Goldberg H, Glazer G (1983) Computed tomography of gynecologic diseases. Am J Roentgenol 141:765–773
37. Weström L, Bengston LO, Mardh PA (1976) The risk of pelvic inflammatory disease in women using intrauterine contraceptive devices compared to non-users. Lancet 2:221–224
38. Hirsch HA (1978) Die akute Salpingitis: Pathogenese, Aetiologie, Diagnose und Prognose. Gynäkologe 11:176–184
39. Wulf KH, Schmidt-Matthiesen H (1988) Gutartige gynäkologische Erkrankungen I. In: Klinik der Frauenheilkunde und Geburtshilfe, Mestwerdt W (ed) Urban und Schwarzenberg, Munich
40. Berland L, Lawson T, Foley D, Albarelli J (1982) Ultrasound evaluation of pelvic infections. Radiol Clin North Am 20:367–383
41. Wilbur A (1992) Computed tomography of tuboovarian abscesses. J Comp Assist Tomogr 14:625–628
42. Wilbur A, Aizenstein R, Napp T (1992) CT findings in tuboovarian abscess. Am J Roentgenol 159:575–579
43. Huch Böni RA, Haldeman Heusler R, Hebisch G, Krestin GP (1994) CT und MRT bei Entzündungen der weiblichen Genitalorgane. Radiologe 34:390–396
44. Mitchell D, Mintz M, Spritzer Ch, Gussman D, Arger P, Coleman B, Axel L, Kressel H (1987) Adnexal masses: MR imaging observations at 1.5 T, with US and CT correlation. Radiology 162:319–324
45. Hricak H, Carrington B (1991) MRI of the pelvis. Deutscher Ärzte-Verlag, Cologne, pp 43–249
46. Mawhinney RR, Powell MC, Worthington BS, Symonds EM (1988) Magnetic resonance imaging of benign ovarian masses. Br J Radiol 723:179–186
47. Einhorn W, Nilsson B, Stovall K (1985) Factors influencing survival in carcinoma of the ovary. Cancer 55:2015–2019
48. Boring CC, Squires TS, Tong T, Montgomery S (1994) Cancer statistics, 1994. CA Cancer J Clin 44:7–26
49. Yamashita Y, Torashima M, Hatanaka Y et al (1995) Adnexal masses: accuracy of characterization with transvaginal US and precontrast and postcontrast MR imaging. Radiology 194:557–565
50. Komatsu T, Konishi I, Mandai M, Togashi K, Kawakami S, Konishi J, Mori T (1996) Adnexal masses: transvaginal US and gadolinium-enhanced MR imaging assessment of intratumoral structure. Radiology 198:109–115
51. Smith FW, Cherryman GR, Bayliss AP et al (1988) Comparative study of the accuracy of ultrasound imaging, X-ray computerized tomography and low field MRI diagnosis of ovarian malignancy. Magn Reson Imaging 6:225–227
52. Ghossain MA, Buy JN, Ligneres C et al (1991) Epithelial tumors of the ovary: comparison of MR and CT findings. Radiology 181:863–870
53. Stevens SK, Hricak H, Campos Z (1993) Teratomas versus cystic hemorrhagic adnexal lesions: differentiation with proton-selective fat-saturation MR imaging. Radiology 186:481–488
54. Huber S, Medl M, Baumann L, Czembirek H (2002) Value of ultrasound and magnetic resonance imaging in the preoperative evaluation of suspected ovarian masses. Anticancer Res 22:2501–2507
55. Kubik-Huch RA, Dorffler W, von Schulthess GK et al (2000) Value of (18F)-FDG positron emission tomography, computed tomography, and magnetic resonance imaging in diagnosing primary and recurrent ovarian carcinoma. Eur Radiol 10:761–767
56. Ascher SM, Outwater EK, Reinhold C (1997). Adnexa. In: Semelka RC, Ascher SM, Reinhold C (eds) MRI of the abdomen and pelvis. Wiley-Liss, New York, pp 661–716
57. Low RN, Carter WD, Saleh F, Sigeti JS (1995) Ovarian cancer: comparison of findings with perfluorocarbon-enhanced MR imaging, In-111-CYT-103 immunoscintigraphy, and CT. Radiology 195:391–400
58. Low RN, Sigeti JS (1994) MR imaging of peritoneal disease: comparison of contrast-enhanced fast multiplanar spoiled gradient-recalled and spin-echo imaging. Am J Roentgenol 163:1131–1140
59. Low RN, Barone RM, Lacey C, Sigeti JS, Alzate GD, Sebrechts CP (1997) Peritoneal tumor: MR imaging with dilute oral barium and intravenous gadolinium-containing contrast agents compared with unenhanced MR imaging and CT. Radiology 204:513–520
60. Stevens SK, Hricak H, Stern JL (1991) Ovarian lesions: detection and characterization with gadolinium-enhanced MR imaging at 1.5 T. Radiology 181:481–488
61. Semelka RC, Lawrence PH, Shoenut JP, Heywood M, Kroeker MA, Lotocki R (1993) Primary ovarian cancer: prospective comparison of contrast-enhanced CT and pre- and postcontrast, fat-suppressed MR imaging with histologic correlation. J Magn Reson Imaging 3:99–106

Radiologic-Pathologic Correlations of the Male Genital Tract

Rahel A. Kubik-Huch, Bernd Hamm

5.2

Contents

Introduction

Technical advances in computed tomography (CT) and magnetic resonance imaging (MRI) opened up new diagnostic applications in male pelvic pathology. Cross-sectional imaging modalities thus play an increasing role in the diagnosis, staging, and follow-up of a variety of diseases of the male pelvis.

However, ultrasound (US), nowadays often considered an extension of the physical examination, remains the imaging modality of choice for initial assessment of a pathologic condition of the male genital organs. In many cases, it already supplies sufficient information for the correct diagnosis. CT and MRI are indicated in all cases in which US findings are equivocal or a discrepancy between clinical and sonographic findings exists. Furthermore, a major indication of MRI is the preoperative local tumor staging of prostate cancer. In addition, CT and MRI are important tools for N- and M-staging of malignant disease, e.g., in prostate and testicular cancer.

This chapter attempts to give an overview of the potential and limitations of these imaging modalities in diagnosing and staging disorders of the male genital organs, with special emphasis on radiologic–pathologic correlation.

The Prostate

High spatial resolution and high soft tissue contrast are prerequisites for any imaging modality aimed at the centimeter-wide target of prostate and seminal vesicles. MRI is superior to computed tomography (CT) in this regard and supplements urological transrectal ultrasound, particularly if combination of endorectal coil and pelvic phased-array coil imaging is used [1]. Whereas high resolution axial and coronal T2-weighted imaging is used for assessment of the prostate and seminal vesicles, supplemental T1-weighted imaging through the pelvis should be performed to assess for lymphadenopathy. Additional fat-suppressed T2-weighted imaging of the pelvic bones and lumbar spine is helpful in detection of osseous metastases in patients with prostate carcinoma. Contrast-enhanced imaging should be reserved for patients with suspected recurrent prostate cancer [1–3].

Normal Anatomy of the Prostate and Seminal Vesicles

The normal prostate gland is divided into three different anatomic zones: a posterolateral peripheral zone that accounts for most of the gland's volume, a central zone forming the bulk of the prostate base and accounting for approximately 25% of the volume, and a transition zone enclosing the prostatic urethra and accounting for some 5%–10 % of the volume in the young adult.

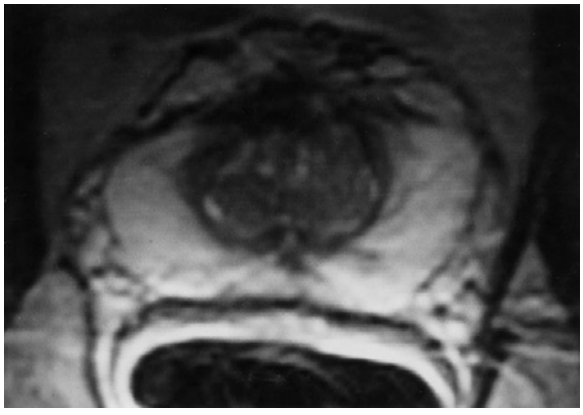

Fig. 1. Normal prostate gland. Axial endorectal T2-weighted fast spin-echo image. The hyperintense peripheral zone can be distinguished from the hypointense central and transitional zone

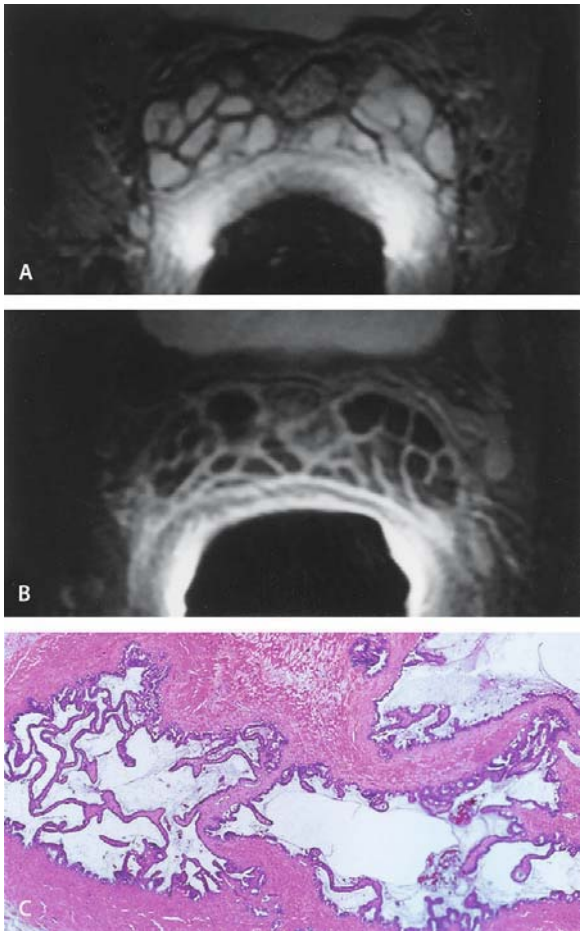

Fig. 2A–C. Normal seminal vesicles: **A**, **B** MRI: the content of seminal vesicles presents hyperintense on the axial endorectal T2-weighted FSE image (**A**) and hypointense on the contrast-enhanced T1-weighted image (**B**), the septa show avid contrast-enhancement. The midline structure of intermediate signal intensity on both sequences represents the ductus deferens. **c** Hematoxylin eosin stain (magnification 35×): normal seminal vesicles

The latter zone is the tissue responsible for the benign prostate hyperplasia (BPH), which in elderly men compromises the other structures and urinary function [4, 5].

On T1-weighted MR images, the prostate is homogeneously hypointense, and zonal anatomy is not demonstrable. The different zones described above can be identified only on T2-weighted images, which show the peripheral zone as hyperintense because of its glandular elements. The central and transition zones are both hypointense in the young male. Differentiation cannot be made by MR imaging features but is primarily based on anatomic location (Fig. 1).

The seminal vesicles are paired glands lying above the prostate. Their contents are homogeneous and isointense to muscle on T1-weighted sequences, whereas the signal intensity is increased on T2-weighted images. The vesicle walls enhance on gadolinium administration (Fig. 2).

Disease Entities of the Prostate and Seminal Vesicles

The main indication for MRI in prostate disease is the pretreatment work-up of carcinoma. In benign disease it is indicated only in isolated cases, but as benign conditions are a frequent incidental finding during MR investigation of the male pelvis, radiologists need to be familiar with their features.

Benign Disease of the Prostate and Seminal Vesicles

Diagnosis of congenital prostate cysts has increased in parallel with the use of transrectal ultrasound and MRI in prostate diagnosis. The incidence of cysts is variously reported as 1%–7.9% [6, 7]. Their characteristic midline location makes them readily identifiable on MRI. They comprise utricular and Müllerian duct cysts. The two differ in embryonic origin. Utricular cysts are more common and of endodermal origin [6, 8–10], while Müllerian duct cysts are of mesodermal origin. Further differentiating features are that utricular cysts often communicate with the prostatic urethra, which is best demonstrated on sagittal MR images and may therefore contain spermatozoa, while Müllerian duct cysts, which tend to project cranially above the prostate, never communicate with the posterior urethra and often contain calcifications [3–12]. Utricular cysts can be associated with hypospadias, pseudohermaphroditism, cryptorchidism and unilateral renal agenesis. For this reason, they are often diagnosed in childhood. The contents are hyperintense on T2-weighted images. Smaller cysts are mostly incidental findings. However, both types of cyst can cause symptoms such as dysuria, urinary tract infections, prostatitis or even infertility [3–13] (Figs. 3, 4).

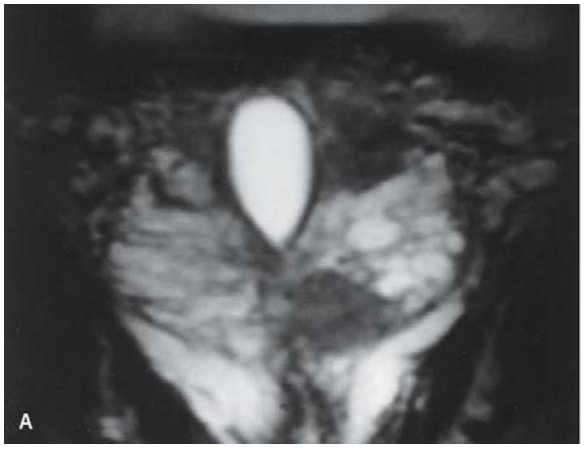

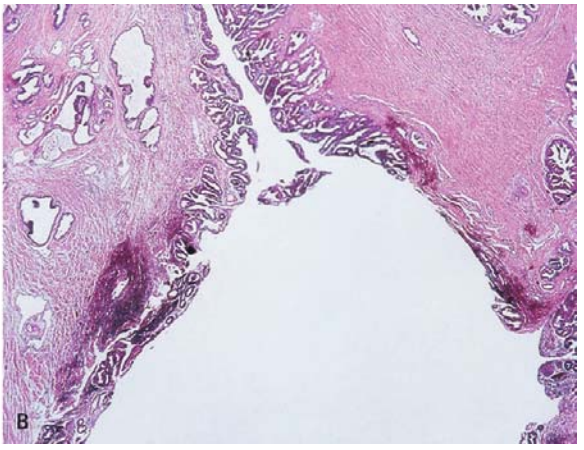

Fig. 3A, B. Incidental diagnosis of congenital prostate cyst in a 58-year-old patient with multifocal stage T2 prostate carcinoma. **A** Coronal endorectal T2-weighted fast spin-echo (FSE) image. The normally hyperintense peripheral zone contains two hypointense foci on the left side compatible with infiltrating carcinoma Midlinc cyst. **B** Hematoxylin eosin stain (magnification25×): The hyperintense midline cyst seen on MRI is consistent with cystic dilatation of the utriculus

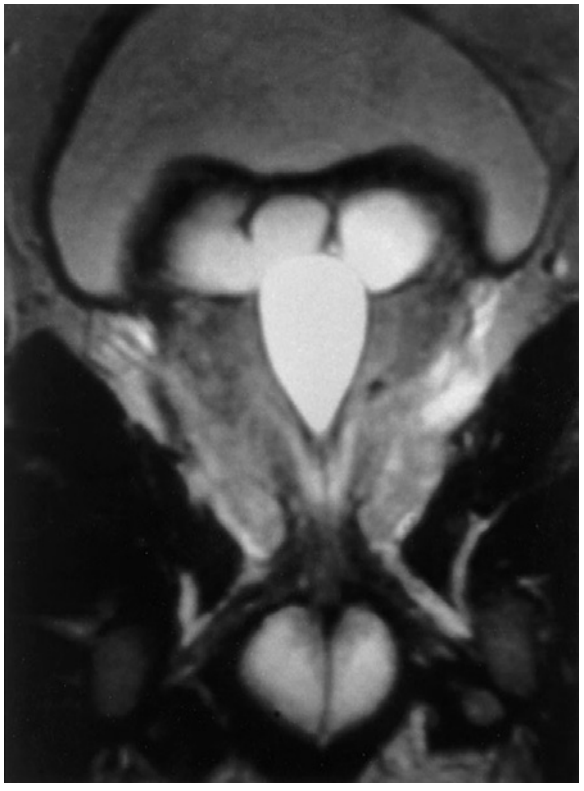

Fig. 4. Coronal endorectal T2-weighted FSE image in a 30-year-old patient with primary infertility. The hyperintense cystic lesion in the dorsal midline of the prostate is compatible with a congenital cyst, associated with obstructed and markedly enlarged seminal vesicles bilaterally. The sperm count returned to normal following cyst incision under ultrasound guidance

Benign prostate hyperplasia (BPH) impairs micturition in half of all men over 50. BPH is not an indication for MRI but is a frequent incidental finding in patients investigated for other reasons such as local staging of prostate carcinoma. Glandular hyperplasia of the transitional zone results in enlargement of the central aspect of the gland with often heterogeneous medium to high signal intensity on T2-weighted imaging (Fig. 5). The surrounding peripheral zone may become compressed, resulting in a hypointense band referred to as pseudocapsule.

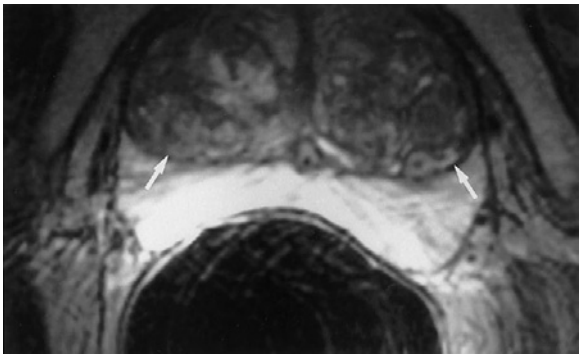

Fig. 5. Axial endorectal T2-weighted FSE image in a patient with benign prostatic hyperplasia. Enlarged transitional zone of inhomogeneous medium signal intensity (*arrows*). Normal hyperintense peripheral zone

Of American men over 60, 20%–40% are likely to require prostatectomy at current surgery rates [14, 15]. The conventional therapy is transurethral resection of the prostate (TURP), with open prostatectomy reserved for very large adenomas. The value of minimally invasive therapeutic approaches in treatment of patients with benign prostate hyperplasia, such as the isolated visual ablation of the prostate (VLAP), is still a matter of debate. MRI makes it possible to monitor the effect of laser ablation in this patient population, which might be of clinical significance in selected cases regarding the considerable interindividual difference of tissue reaction that has been observed in laser treatment [16].

Prostatic Abscess

Nowadays, because of early antibiotic treatment and the decreased incidence of gonococcal urethritis, prostatic abscess has become a rare disease entity. Predisposing factors are prostatitis, diabetes mellitus, prior instrumentation, and an immunocompromised state. The differentiation between acute bacterial prostatitis and prostatic abscess can be difficult based on clinical findings alone. Imaging techniques, i.e., transrectal ultrasound or cross-sectional imaging modalities, are useful for early recognition of abscess formation and assessment of the extent of inflammation [17] (Fig. 6).

Amyloidosis

Amyloid deposits in the seminal vesicles are a fairly common finding at histopathology in elderly males, with rates of 34% at autopsy in >75-year-olds [18–21]. Senile amyloidosis can narrow the lumen and decrease the normally hyperintense vesicle content signal on T2-weighted imaging, prompting a mistaken diagnosis of tumor infiltration of the seminal vesicles [22–24]. Contrast-enhanced sequences may be helpful in distinguishing amyloidosis from tumor invasion. In amyloidosis, only the septa enhance, whereas in tumor invasion, the content within the vesicles will enhance as well. It might be difficult, however, to exclude early tumor invasion with focal thickening of septa and in case of doubt, TRUS-guided biopsies of the seminal vesicles may be needed to establish the correct diagnosis (Fig. 7).

Prostate Adenocarcinoma

Prostate adenocarcinoma is, after lung cancer, the most frequent cancer in men in the industrialized world, with its incidence continuing to increase [25, 26]. Since early stages in general do not present any symptoms, most

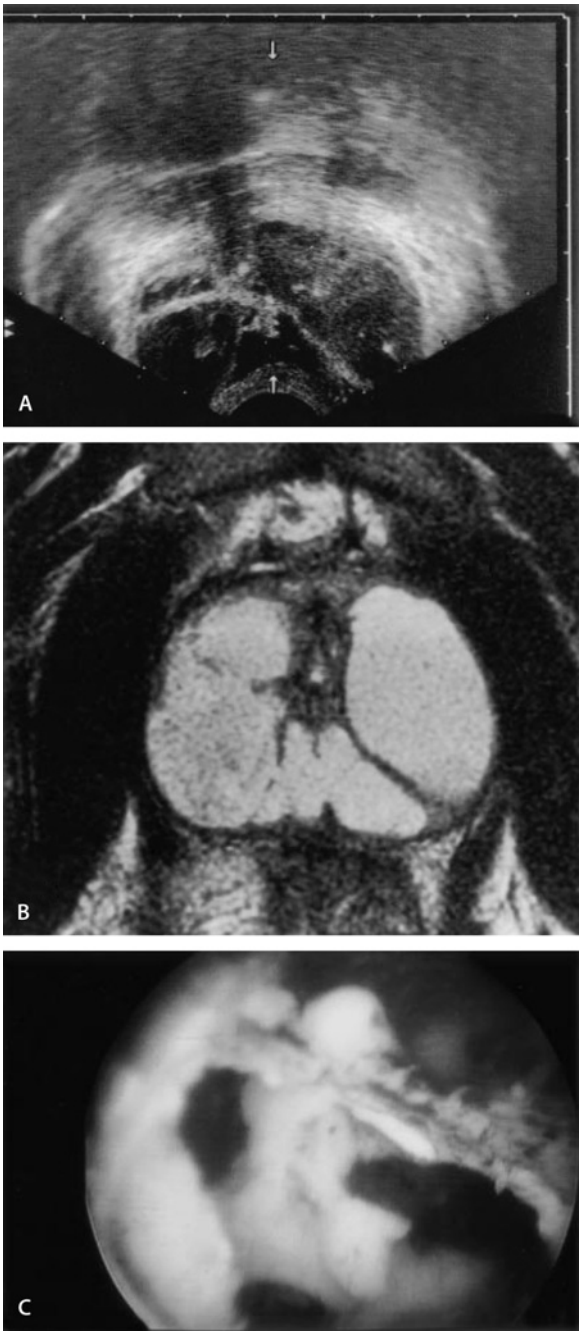

Fig. 6A–C. Prostatic abscess in a 35-year-old HIV-positive patient. **A** Transrectal US: multiple fluid collections in both lobes as well as in the periurethral central zone. Few remaining septa are seen as hyperechoic structures between the necrotic abscess cavities. **B** MRI, axial T2-weighted FSE image: multiple hyperintense fluid collections, separated by a hypointense fibromuscular band. Normal signal intensity of adjacent tissue. **C** Video documentation of transurethral resection: complete destruction of the normal architecture of the glandular tissue.([17] with permission)

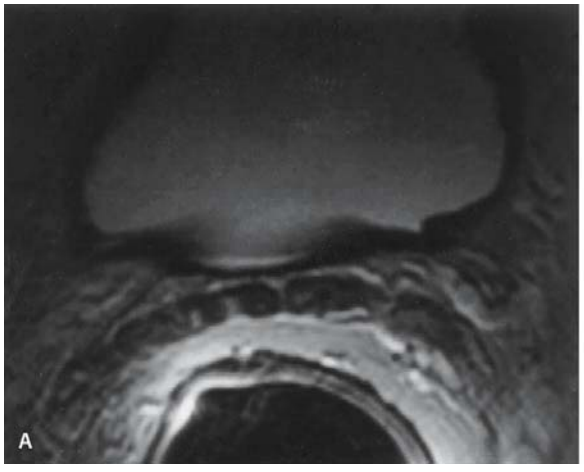

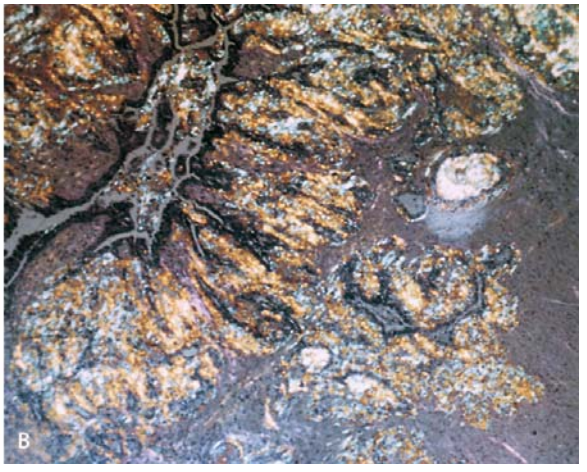

Fig. 7A, B. Preoperative work-up in a 70-year-old man with histologically confirmed prostate carcinoma (from [16]). **A** Axial endorectal T2-weighted FSE image: the normally hyperintense seminal vesicle content is homogeneously decreased, compatible with tumor infiltration. **B** Congo red stain (magnification 100×) of the seminal vesicles showing homogeneous red-brown subepithelial and intraluminal amorphous eosinophilic deposits that appear apple-green under polarized light, compatible with seminal vesicle amyloidosis

cancers are revealed by an elevated prostate specific antigen (PSA) value and/or positive digital rectal examination and are subsequently confirmed by ultrasound-guided biopsy. Prostate carcinoma may also be diagnosed as an incidental finding at the occasion of transurethral resection for benign prostate hyperplasia. Histologic grade is, next to tumor volume, one of the strongest predictors of biologic behavior in prostatic carcinoma, including invasiveness and metastatic potential. Next to the grade, other prognostic factors are included in therapeutic decision making, including patient age and health, accurate clinical stage and serum PSA level [27, 28].

Tumors spread first to penetrate the prostatic capsule and will then extend to the neurovascular bundles and seminal vesicles. Bladder wall invasion is commonly seen in advanced-stage tumors.

The value of high-resolution MRI as an addition to transrectal ultrasound for local staging of prostate cancer remains a matter of debate. In localized tumors, the detection of the tumor by MRI is limited primarily to those approximately 70% of lesions that arise from the peripheral zone.

In localized prostate cancer (stages T1 and T2), life expectancy after radical prostatectomy is similar to that in age-matched controls. However, in advanced local disease (T3 and T4), benefit is questionable. Accurate pretreatment work-up is thus of utmost importance in determining management. The task of imaging is to differentiate stages localized to the prostate from advanced tumor spread. Microcapsular invasion is a gray area in this context. However, it appears not to worsen the prognosis provided the resection margins are free of tumor [29].

For this purpose, the accuracy of endorectal MRI is approximately 80% [30–39]. However, the Radiology Diagnostic Oncology Group study shows considerable interindividual differences in interpretation. Accuracy rates for experienced radiologists were 79% vs 54% for less experienced colleagues [36]. Contrast-enhanced T1-weighted endorectal sequences in addition to T2-weighted images do not generally improve the results, but may be valuable in isolated cases, for example if the image quality of the T2-weighted sequence is impaired by motion artifacts [32, 36, 40, 41] (Figs. 8–10).

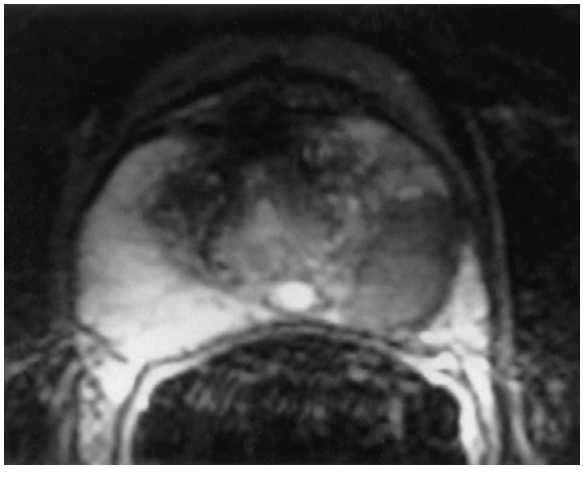

Fig. 8. Axial endorectal T2-weighted FSE image: The normally hyperintense peripheral zone of the prostate shows decreased signal intensity on the left side, compatible with infiltrating tumor. No evidence of capsule invasion. Histology: stage pT2 adenocarcinoma. Coincidental finding: small congenital prostate cyst

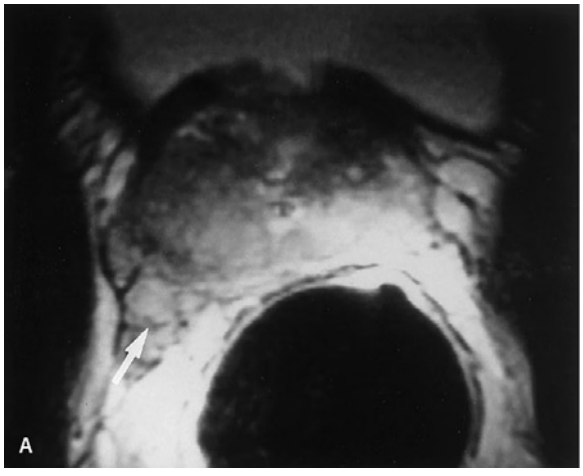

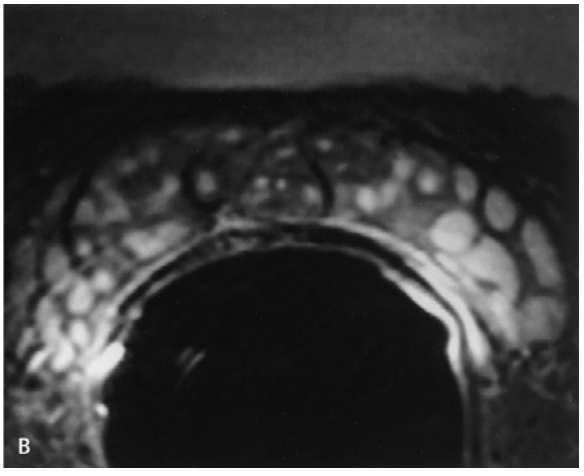

Fig. 9A, B. Histologically confirmed prostate carcinoma stage pT3. **A** Axial endorectal T2-weighted FSE image: tumor infiltration of the entire prostate gland and extension into the right neurovascular bundle (*arrow*). **B** Axial endorectal T2-weighted FSE image: hypointense tumor invades the normally hyperintense seminal vesicle

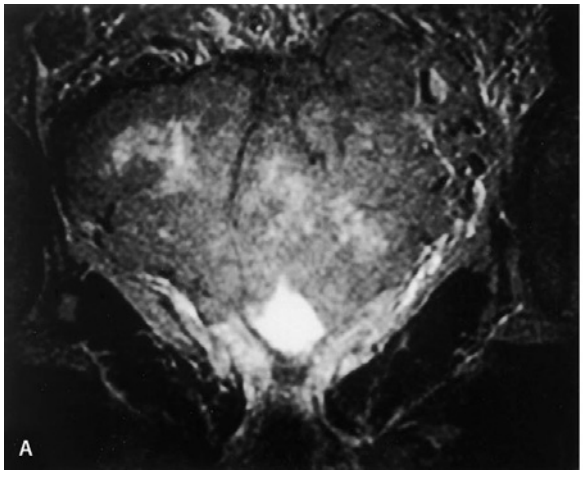

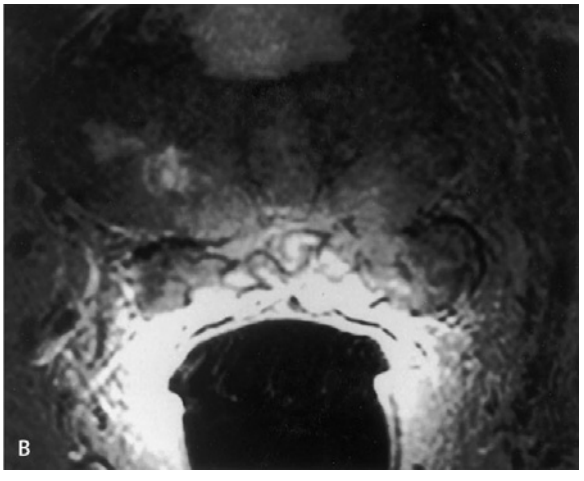

Fig. 10A, B. Histologically confirmed high-grade prostate carcinoma stage pT4 in a patient with normal PSA-values. Axial (**A**) and coronal (**B**) endorectal T2-weighted FSE image: tumor infiltration of the entire prostate gland with capsular penetration and invasion of the seminal vesicles and urinary bladder

Lymph node metastases are a major determinant of prognosis and therapy in prostatic carcinoma [42]. Rates of lymph-borne metastasis depend on tumor volume, histologic differentiation and stage [43]. The main criteria on cross-sectional imaging for malignant lymph nodes is a size exceeding 1.5 cm in small diameter. The literature on lymph node staging with both MRI and CT is disappointing, with sensitivities of 50%–60%, no doubt because of the high number of micrometastases in normal-sized nodes [43–47].

While bone scintigraphy is still the generally accepted method for excluding bone metastases, MRI has nowadays become an alternative imaging technique in this regard [48].

Locally Recurrent Prostate Carcinoma

The frequency of local recurrence after radical prostatectomy is approximately 10% [49]. If detected in its early stages by clinical examination and serial PSA, it can often be controlled by radiation or systemic therapy [50, 51]. PSA is a highly sensitive posttreatment tumor marker. However, it can be elevated in both local recurrence and distant metastasis [52]. Transrectal ultrasound is the imaging modality of choice for visualizing the prostatic bed. However, residual prostate tissue is found anterior to the vesicourethral anastomosis in up to 80% of patients. For this reason it can be difficult to differentiate between a small local recurrence, residual

normal prostate tissue and scar tissue, particularly given the postoperative changes in anatomic relationships [50, 51].

The advantage of MRI is high soft-tissue contrast, enabling it to view the prostatic fossa in each desired plane. Tissues can be differentiated by taking a global view of the data from the various sequences: on T2-weighted images residual prostate tissue is hyperintense, while local recurrence and scar tissue are hypointense. Contrast permits further differentiation: tumor tissue generally enhances, while scar tissue, except in the first 3–6 postoperative months, generally does not [53–56] (Fig. 11).

Endorectal MRI may therefore be a valuable backup to ultrasound. Body coil MRI can scan the regional lymph nodes and bony pelvis. However, this has only limited clinical significance, as distant metastases are rare in this preselected group of patients with generally low PSA values and small tumor volume.

Other Malignant Prostate Tumors

Uncommon primary prostate tumors include leiomyoma, lymphoma, squamous cell carcinoma as well as sarcomas. They account for less than 5% of malignant tumors. Prostate metastasis due to hematogenous tumor spread is also only a rare finding [57] (Fig. 12).

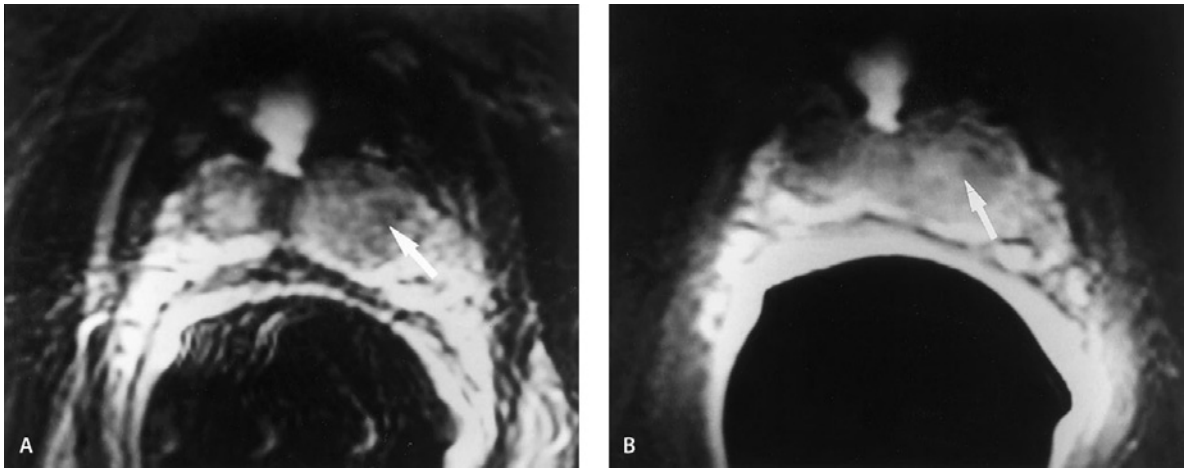

Fig. 11A, B. Histologically confirmed recurrent prostate carcinoma. **A** Axial endorectal T2-weighted FSE image: lobulated mass in the prostatic fossa of medium signal intensity (*arrow*). **B** Axial endorectal contrast-enhanced T1-weighted image: the mass shows avid contrast-enhancement indicative of tumor recurrence rather than scar tissue (*arrow*)

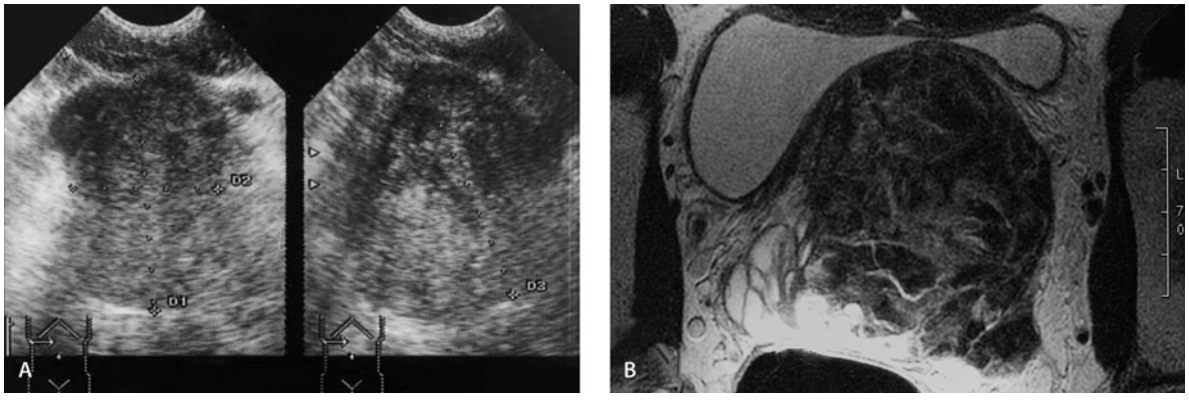

Fig. 12A, B. Prostate metastasis of colorectal carcinoma. **A** Transabdominal US: enlarged, inhomogeneous prostate. **B** Axial endorectal T2-weighted MR image: loss of normal prostatic architecture and replacement by a large nodular inhomogeneously hypointense mass. ([57] with permission)

The Scrotum

Although the scrotum is a superficial structure, its clinical examination frequently fails to provide a specific diagnosis because the clinical history and physical findings are similar in many conditions. Scrotal ultrasound, considered an extension of the physical examination, confirms the presumptive clinical diagnosis and provides relevant additional information. In most clinical problems, ultrasound (US) supplies sufficient information for the correct diagnosis. Significant improvements in US were achieved with the introduction of color-coded duplex sonography (CCDS) and of power Doppler US, which provide information on blood flow over the entire area of the gray-scale image. A CCDS or power Doppler examination is indicated in any situation in which additional information on perfusion is needed to establish the diagnosis, particularly in testicular torsion, inflammation, scrotal trauma, and varicocele [58–61]. Other imaging modalities, except in the staging of testicular cancer, should be used only as problem-solving approaches. Besides ultrasound, MR imaging is a particularly useful modality. The latter is primarily used when the ultrasound findings are equivocal or suboptimal or when there is a discrepancy between clinical and US findings.

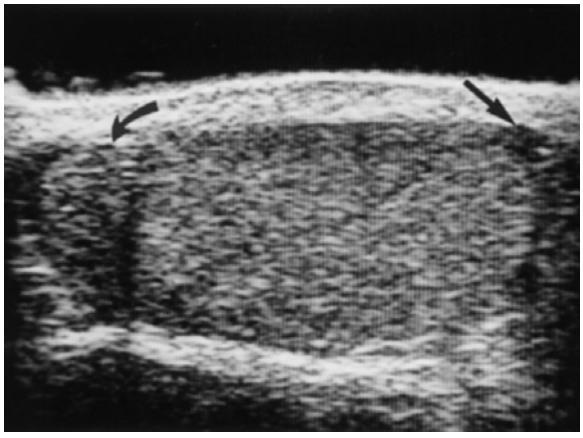

Fig. 13. Normal testis and epididymis. The testis has a homogeneous echo pattern and there is good differentiation between the testis and the head (*curved arrow*) and tail (*arrow*) of the epididymis

Normal Anatomy

The scrotum is divided by a midline septum. Each half of the scrotum contains a testis and its associated structures. The size of the testis depends on age and stage of sexual development. US depicts the normal (postpubescent) testicle as a fine-grained structure of homogeneous texture and medium echogenicity (Fig. 13), which is typically interrupted only by the hyperechoic mediastinum testis representing the posterior surface of the tunica albuginea projecting into the interior of the testis [61] (Fig. 14). The mediastinum testis shows wide interindividual variation in width and may also differ intraindividually between the right and left testis. The epididymis, a tubular structure consisting of head, body and tail, can best be differentiated from the testis on a longitudinal scan. Its thickest part is the head, which is visualized as a small cap-like structure situated on the upper pole of the testis. It may vary in shape and its diameter ranges from 5 to 12 mm. The body of the epididymis is a very delicate and flat structure with a diameter of approximately 2–4 mm and is thus not always delineated from adjacent tissue. The tail of the epididymis is also very flat (approximately 2–5 mm) and surrounds

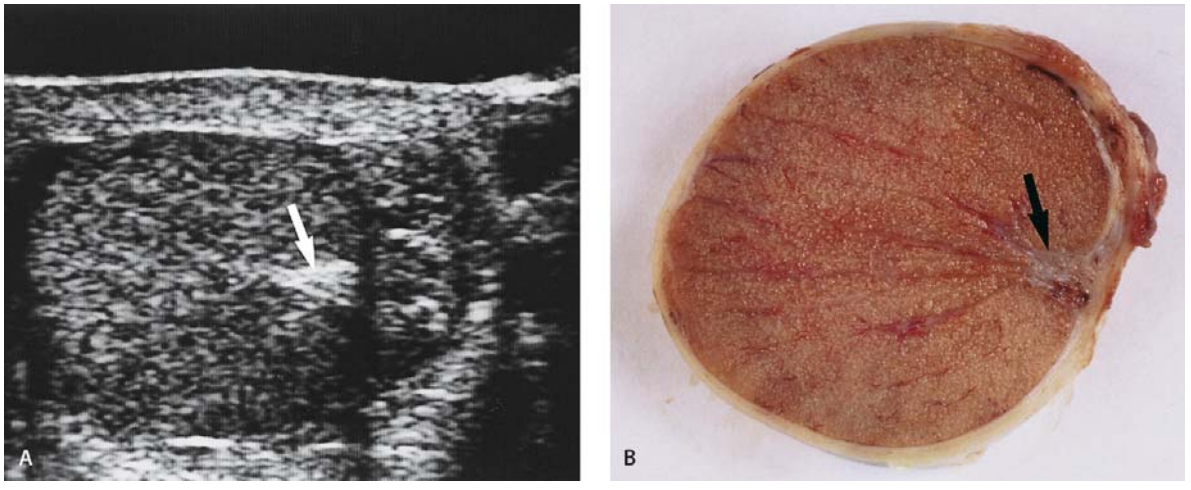

Fig. 14A, B. The mediastinum testis (*arrow*) is shown as a hyperechoic area. It lies eccentrically in the testis (**A**, **B**), facing the epididymis. The septa run toward the mediastinum testis (**B**) and are typically not seen on ultrasound

the lower testicular pole in a crescent-shaped manner. The testicular and epididymal appendages are usually too small to be always visualized on US scans. The testis and epididymis are surrounded by a cleft-like space, the so-called cavum serosum testis. This space may be filled with a small amount of fluid, even under physiologic conditions, and may thus be depicted as a thin anechoic margin (1–3 mm in width), typically around the epididymal head.

On MR imaging, the testes are homogeneous and isointense to muscle on T1-weighted images and higher in signal intensity on T2-weighted images. The tunica albuginea is best seen as a low-intensity line on T2-weighted images, the mediastinum testis can also be identified as a low-intensity band. On T1-weighted images, the signal intensity of the epididymis is slightly heterogeneous and hypo- to isointense relative to the testis. The epididymis is more clearly differentiated from the testis on T2-weighted images because of its lower signal intensity compared to the adjacent testis. Intravenous administration of gadolinium compounds results in hyperintensity of the epididymis relative to the testis [3, 62].

Mass Lesions

Malignant masses

Testicular cancer is the most common malignancy of the scrotum, while malignant tumors of the epididymis and of the spermatic cord are extremely rare. Cancer of the testis constitutes 1% of all malignancies in men; however, it is the most frequent cancer in the 15- to 34-year age group [63]. Testicular tumors comprise germ cell tumors, tumors originating in the gonadal stroma, tumors of the lymphoid and hematopoietic system, and secondary tumors (metastases). Germ cell tumors are by far the most frequent type (about 95%) [64, 65]. In addition, tumor-like lesions may be seen in the testes.

Testicular cancer is typically noted as a lump or painless swelling of the testis. The presence of pain does not exclude testicular cancer: it is present in about 25% of patients with testicular cancer.

The homogeneous parenchyma of the normal testis provides an excellent background for the depiction of intratesticular lesions by both US and MRI (Fig. 15). Small tumors are visualized as focal lesions, while larger ones may alter the entire testicular structure. The margins of testicular tumors may be smooth or irregular. On US, testicular tumors are typically hypoechoic, but may also be hyperechoic or of mixed echogenicity [66, 67]. Intratumoral necroses, hemorrhages, or cysts are depicted as liquid areas (Fig. 16). On MR imaging, testicular tumors most commonly show a signal intensity similar to that of the normal testis on T1-weighted images. On T2-weighted images, they are mostly hypointense relative to the normal testis, with a homogeneous or heterogeneous signal pattern, and only rarely demonstrate a signal intensity resembling that of

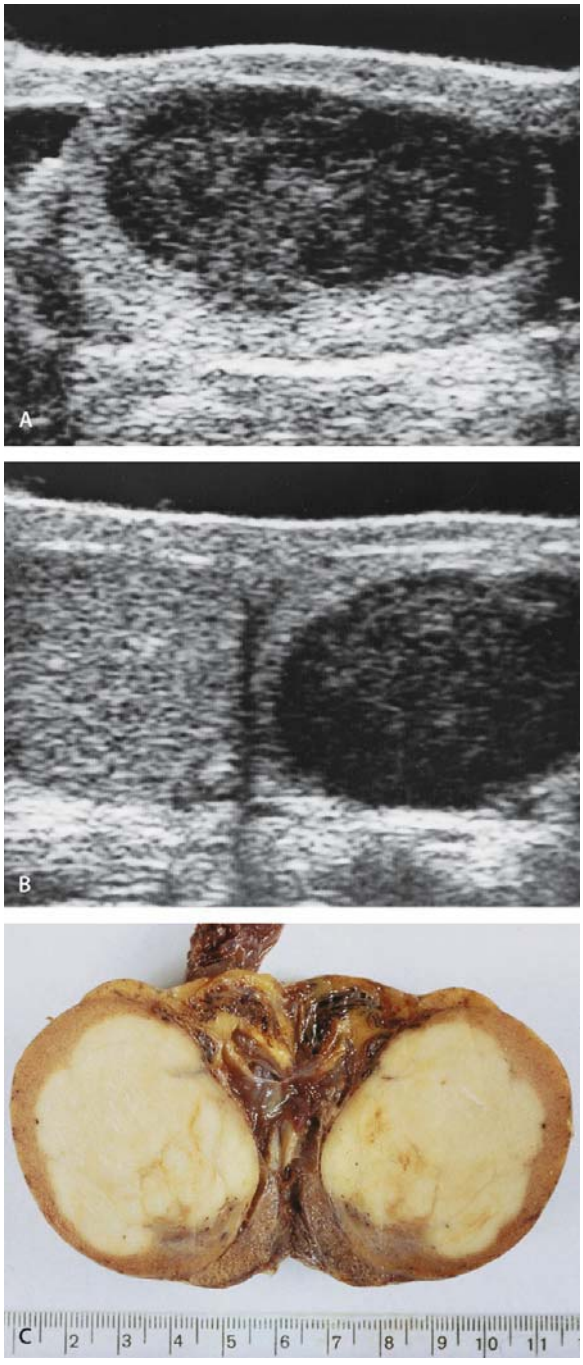

Fig. 15A–C. Seminoma of the left testicle. Longitudinal scan of the left testis (**A**) and transverse scan of both testes (**B**). Ultrasound demonstrates a hypoechoic intratesticular mass surrounded by a small rim of remaining testicular tissue. Gross specimen (**C**) (from [36])

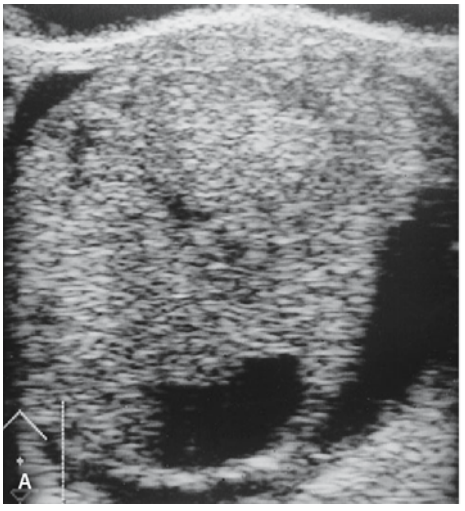

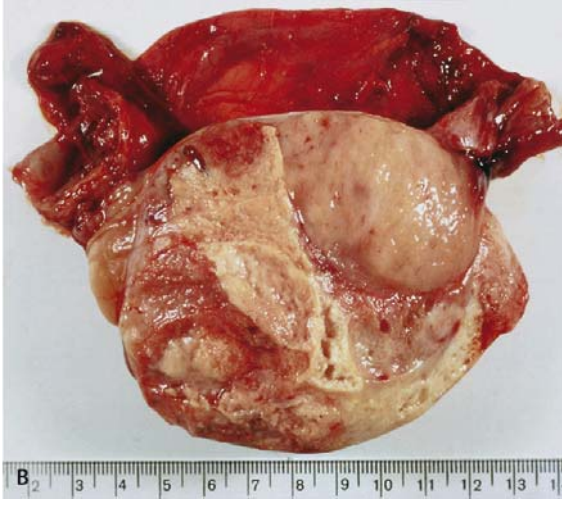

Fig. 16A, B. Seminoma, with extensive, partly liquefied necrosis. Transverse ultrasound (**A**) demonstrates an enlarged testis with irregular, partly cystic alterations. Small amount of fluid around the testicle corresponding to a small hydrocele. Gross specimen (**B**) (from [67], with permission)

healthy testicular tissue [68]. Color-coded duplex sonography depicts testicular tumors as areas of increased, reduced or mixed perfusion and thus does not add any information for lesion characterization [67]. The same also holds for dynamic gadolinium-enhanced MR imaging [68, 69] (Fig. 17).

Seminomas typically have a hypoechoic and homogeneous texture on ultrasound (Fig. 15) and are of homogeneously low signal intensity on T2-weighted MR images [66, 68–70]. Heterogeneous areas within a seminoma are produced by regressive processes such as necrosis (Fig. 16).

Nonseminomatous tumors (e.g., embryonal carcinoma, choriocarcinoma, teratoma) are characterized by an inhomogeneous appearance [66, 71]. Marked heterogeneity in nonseminomatous tumors results from hemorrhage, fibrosis, calcification, or cartilage [66, 72]. Ultrasound depicts such structures (apart from hemorrhage) as dense echogenic foci (Fig. 18). Cystic spaces predominantly occur in teratomas [71]. Since these tumors frequently display a higher signal intensity on T2-weighted images, they may be isointense or slightly hyperintense relative to the normal testicular tissue. Therefore, an additional clinical examination is of particular importance for not missing such isointense testicular tumors.

Testicular intraepithelial neoplasia [TIN] is regarded as the common precursor of all germ cell tumors according to the uniform histogenesis theory [73]. This theory postulates that all germ cell tumors arise from identical precursor cells, namely testicular intraepithelial neoplasia. These changes at the cellular level, which

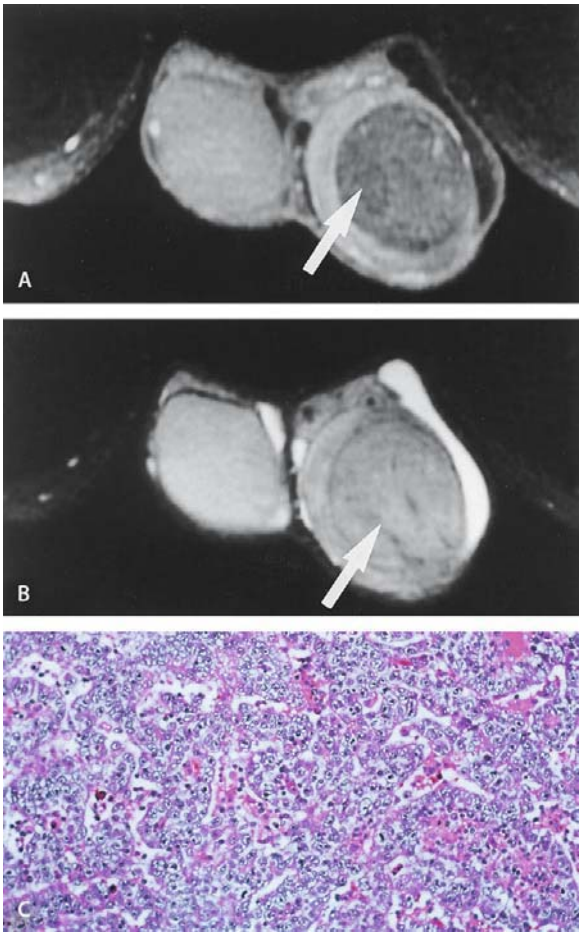

Fig. 17A–C. Malignant nonseminomatous germ cell tumor (embryonal carcinoma). **A** Axial endorectal contrast-enhanced T1-weighted image: the mass in the left testis (*arrow*) shows decreased contrast-enhancement compared to the normal testicular tissue. **B** Axial endorectal T2-weighted FSE image of the testis: well-defined isointense mass in the left testis (*arrow*), hydrocele. **C** Hematoxylin eosin stain (magnification 50×): undifferentiated epithelial-like tumor cells with high mitotic activity and pleomorphic nuclei

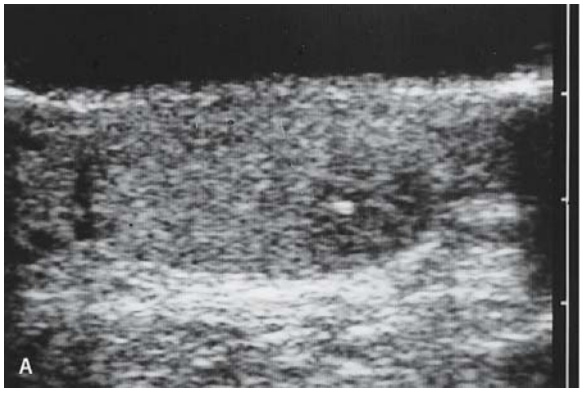

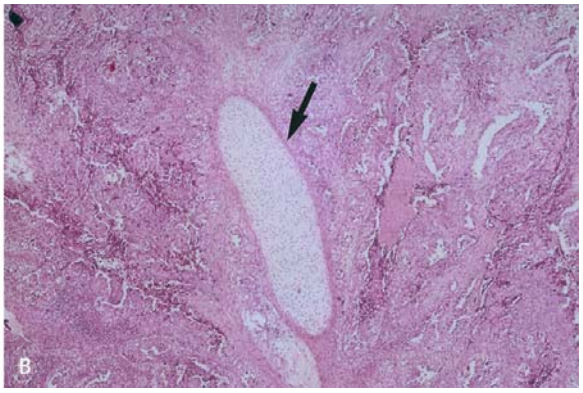

Fig. 18A, B. Small malignant teratoma of the testicle. The patient had undergone left-sided orchiectomy for embryonal carcinoma 10 years previously. Ultrasound (**A**) demonstrates a focal intratesticular lesion in the lower pole of the right testis. The lesion is slightly hypoechoic, has poorly defined borders, and contains isolated small echogenic foci (from [67], with permission). Histologic specimen (**B**) shows a cartilaginous portion (*arrow*) within the malignant teratoma. Patients with a testicular tumor are at an increased risk of developing a second tumor in the remaining testis. Dense echogenic areas in a tumor may correspond to fibrotic foci, calcifications, or cartilaginous structures

may also be regarded as precancerosis, cannot be identified by either ultrasound or MR imaging. In patients with unilateral testicular cancer, ultrasound can be used to check for a contralateral nonpalpable tumor. An irregular testicular tissue or coarse echogenic spots in these patients should give rise to the suspicion of a carcinoma in situ (CIS) [74].

Benign Masses

Benign neoplasms of the testis account for only about 5% of all testicular neoplasms. They may arise from Leydig cells, Sertoli cells, or connective tissue stroma. These tumors typically have a homogeneous appearance and are smoothly demarcated. Neither ultrasound nor MR imaging can reliably distinguish these tumors from malignant neoplasms of the testis.

Epidermal cysts are tumor-like lesions of the testis. They are benign and filled with horny tissue. Enucleation of the lesion is required since only histology allows differentiation from teratoma. This intervention is nowadays performed with preservation of the remaining testicular tissue. On US, some epidermal cysts actually resemble cysts in that they may show a markedly hyperechoic contour, but their distinctive feature is the presence of additional internal echoes and a posterior acoustic shadow (Fig. 19) [71].

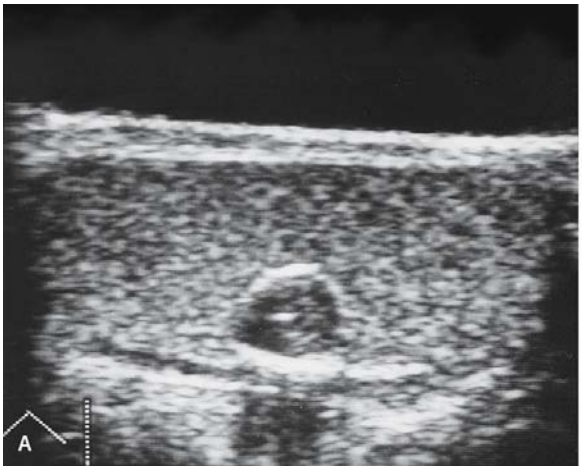

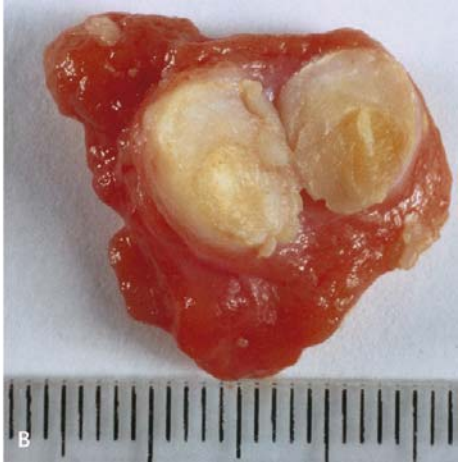

Fig. 19A, B. Epidermoid cyst. Ultrasound (**A**) shows an intratesticular, echo-poor lesion with hyperechoic anterior and posterior margins. The lesion has a cyst-like appearance but contains internal echoes and shows posterior acoustic shadowing. Gross specimen (**B**) (from [33], with permission)

Adenomatoid tumors are the most common extratesticular neoplasms. They most frequently arise in the epididymis but may also be found in the spermatic cord or tunica albuginea. Adenomatoid tumors are depicted as round lesions, typically demarcated by smooth borders. On ultrasound, they are usually hyperechoic and homogeneous in appearance [75] but may also be hypoechoic or heterogeneous [76]. They are typically located in the tail of the epididymis (Fig. 20). Adenomatoid tumors may be difficult to distinguish from epididymal granuloma (or sperm granuloma). A history of previous inflammation, trauma, or surgery (vasectomy) helps to establish the diagnosis of epididymal granuloma.

Simple testicular cysts are rare, and reliable distinction of these benign cysts from malignant cystic tumors is of primary importance. The correct diagnosis can nearly always be made by palpation in combination with ultrasound (Fig. 21). Sonographically, cystic por-

Fig. 20A, B. Adenomatoid tumor of the epididymis. Solid, hypoechoic mass in the area of the tail of the epididymis (**A**). The tumorous lesion is clearly differentiated from the testis. Surgical specimen (**B**), excised epididymis (from [33], with permission)

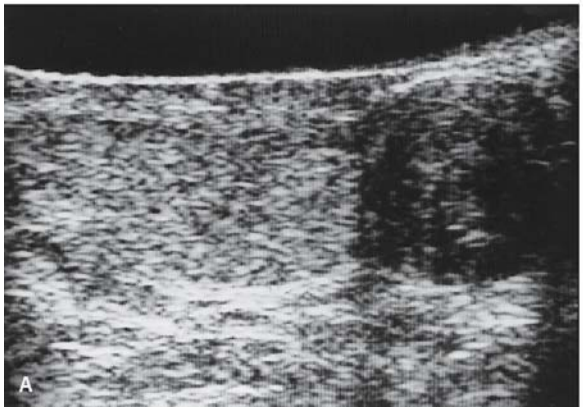

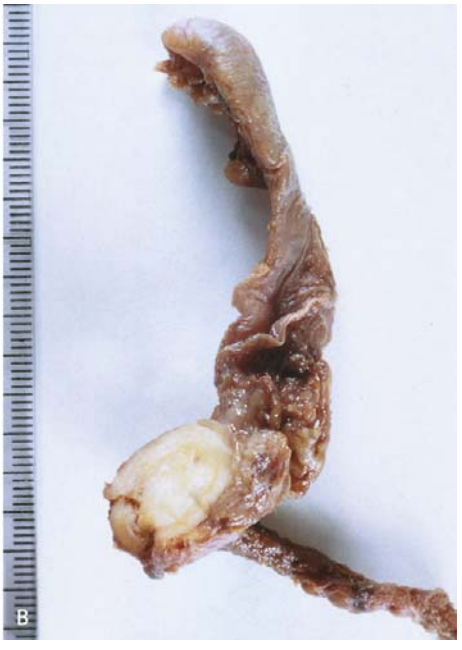

Fig. 21A, B. Simple testicular cyst. Palpation findings were normal and the cyst was discovered only at ultrasound (**A**). The surrounding testicular parenchyma is of a homogeneous appearance. Histologic specimen (**B**) demonstrating a regular cystic wall lined with epithelium (*arrow*)

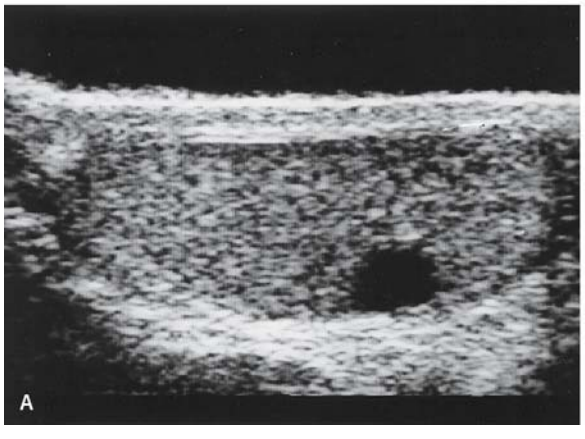

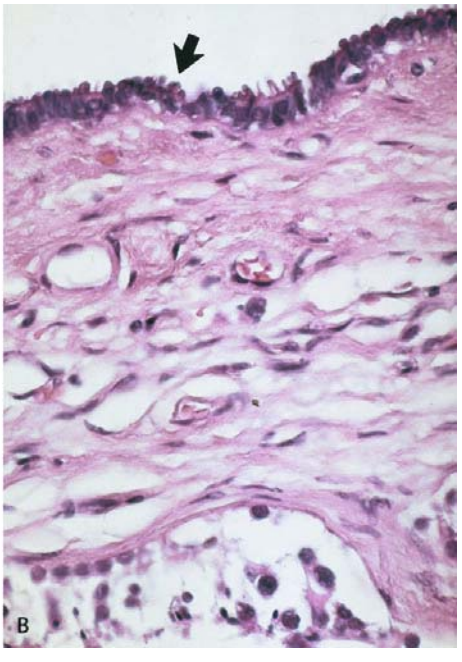

tions of malignant neoplasms are seen as multiple cysts disseminated within an inhomogeneous lesion, which is palpated as a firm mass. In contrast, a simple intratesticular cyst is never discovered as a palpable mass [71]. Rather, it is an incidental finding on ultrasound and located close to the mediastinum testis. It is a solitary lesion in the majority of cases, but multiple lesions are also seen. Histologic examinations have shown that simple intratesticular cysts originate from the rete testis. MR imaging typically depicts testicular cysts as sharply demarcated lesions showing the characteristic signal intensity of fluid. Their relationship to the mediastinum testis can easily be demonstrated.

Spermatoceles are rather common cysts of the epididymis. Their lumen is lined with an epithelial layer and filled with fluid in which sediments of detritus, immobile spermatozoa, and lipids can be identified. Clinically, spermatoceles manifest as palpable, moderately painful masses at the upper pole of the testis. US and MRI clearly depict a cystic, smoothly demarcated lesion typically located in the epididymal head. Spermatoceles may be unilateral, bilateral, solitary or multiple in location. In most cases, ultrasound reliably distinguishes spermatoceles from solid tumors. A spermatocele can, however, be associated with a dilatation of the rete testis and this condition may occasionally mimic a testicular tumor [77].

Hydroceles are pathologic fluid accumulations located between the two layers of the tunica vaginalis testis. They may be idiopathic in origin or develop in association with inflammation (epididymitis or orchitis), secondary to trauma or testicular torsion, and in the presence of a testicular tumor. Clinically, hydroceles are usually painless but frequently prevent palpation of the underlying testis. They are reliably diagnosed by ultrasound as an anechoic fluid collection with smoothly demarcated borders. Ultrasound thus yields a definitive diagnosis of a hydrocele and excludes underlying pathologic conditions of the testis or epididymis. Chronic hydroceles frequently develop septa and their wall becomes thickened. They may compress or deform the testicle (Fig. 22).

MR imaging is hardly ever indicated for diagnosing a hydrocele. On MR images, hydroceles show the characteristic features of fluid and typically represent an incidental finding.

Acute Scrotum

The term "acute scrotum" comprises all disease entities that are characterized by the sudden onset of scrotal symptoms such as pain, swelling, and reddening. These symptoms may occur alone or in combination. From a clinical perspective, it is important to rapidly decide which patients presenting with an acute scrotum require immediate emergency surgery (e.g., testicular torsion or rupture) and which require initial drug treatment only (e.g., inflammation). Physical examination of the acute scrotum is limited by swelling and/or pain; therefore imaging may play a crucial role in identifying the cause of an acute scrotum. CCDS has a central role in the differential diagnosis of an acute scrotum since inflammatory processes are associated with hypervascularization, while testicular torsion is characterized by the absence of perfusion [60, 61, 68].

Epididymitis and Orchitis

Of all pathologic conditions affecting the epididymis, epididymitis is the most frequent cause of an acutely swollen and painful scrotum in adult men. Acute unspecific epididymitis is nearly always caused by descending, intracanalicular spread of pathogens in patients with prostatitis, urethritis, or other urinary tract infec-

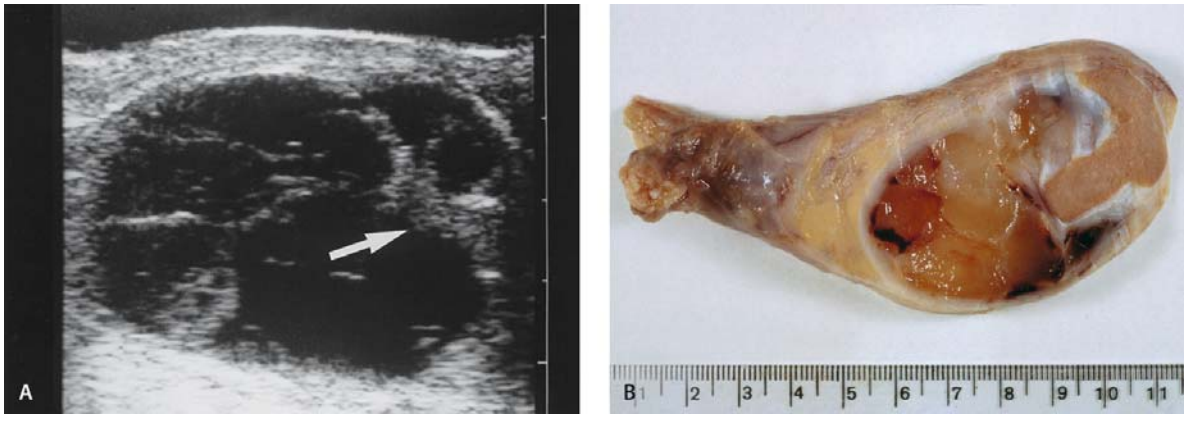

Fig. 22A, B. Chronic inflammatory hydrocele secondary to recurrent epididymitis. Thick-walled, septate hydrocele (**A**). The testicle (*arrow*) is small and deformed. Surgical specimen (**B**)

tions. Concomitant orchitis is found in up to 20% of patients with epididymitis. Isolated orchitis is rare except when caused by a viral infection such as mumps.

During the acute stage, the epididymis is markedly enlarged (Fig. 23) and, depending on the extent of the inflammatory process, swelling may either affect the entire organ or be confined to the tail. On clinical examination, the testis and epididymis usually cannot be palpated separately; however, differentiation should always be possible on ultrasound or MR imaging. An acutely inflamed epididymis usually has an inhomogeneous echotexture with a coarse distribution of echoes (Fig. 23). Compared with the normal testis, the echogenicity of the epididymis is typically reduced but may occasionally be increased (possibly because of epididymal hemorrhages) [78, 79]. On MR imaging, the affected epididymis is enlarged and demonstrates a heterogeneous, mostly high signal intensity on T2-weighted images. Acute epididymitis may be complicated by hemorrhages, producing varying signal intensities on T1- and T2-weighted images. T1-weighted images depict inflammatory infiltration and multiple engorged vessels with signal void due to hypervascularity. Inflammatory areas are markedly enhanced on gadolinium-enhanced T1-weighted images.

The diagnosis of epididymo-orchitis is suggested by the sonographic demonstration of an area of decreased echogenicity in the testis [68]. The involved area (typically in the upper pole of the testis), or even the entire organ, most commonly demonstrates a homogeneous decrease in echogenicity. The hypervascularization associated with inflammation can most easily be demonstrated by CCDS, which thus has a key role in differentiating inflammation from testicular torsion (Fig. 23). In severe orchitis, the testis is hypoechoic and its echotexture becomes more heterogeneous, and early abscess formation may be overlooked. Therefore, such patients require sonographic follow-up while patients with uncomplicated epididymitis do not. On T2-weighted MR images, testicular inflammation appears as a homogeneous or heterogeneous hypointense lesion, which – unlike a testicular tumor – usually does not produce a mass effect. The testicular septula remain well-defined but are thickened, a finding that is in contrast to the loss of normal architecture frequently observed with invasive neoplastic disease [69]. Abscess formation may occur (Fig. 24).

Granulomatous orchitis poses a particular diagnostic problem, both on US and MR imaging. Fever and pain are often absent, and palpation may reveal a firm mass, mimicking a testicular tumor. Sonographically, granulomatous orchitis is characterized by enlargement of the organ and an echopenic, inhomogeneous structure, which does not allow distinction from a testicular tumor. The same holds for MR imaging.

Testicular Torsion

The term "testicular torsion" denotes the rotation of the testis around the longitudinal axis of the spermatic cord (Fig. 25). It requires immediate emergency surgery to prevent irreversible damage of testicular tissue. About 65% of cases occur in young males (between 12 and 18 years of age). Too much emphasis, however, should not be put on age, since the three most frequent causes of an acute scrotum (epididymitis and torsion of a testicle or an appendage) occur in all age groups. Testicular torsion may occur in an otherwise completely healthy individual and manifests itself by a sudden onset of scrotal pain followed by swelling.

The sonographic appearance of testicular torsion is unspecific and diagnostic information from gray-scale ultrasound is limited [60, 80–82]. Therefore, ultrasound

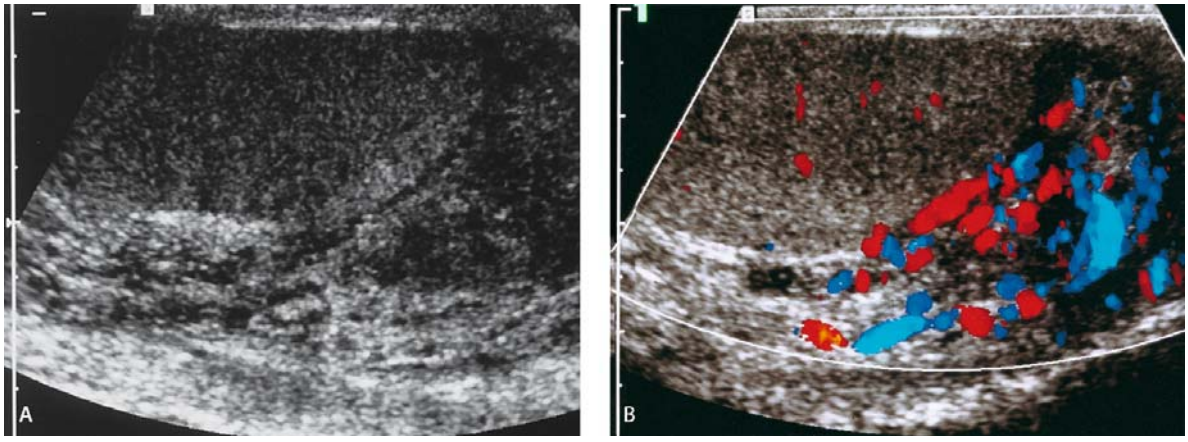

Fig. 23A, B. Epididymitis. Pronounced enlargement and inhomogeneity of the epididymis (**A**). CCDS (**B**) demonstrates increased blood flow in the inflamed epididymis

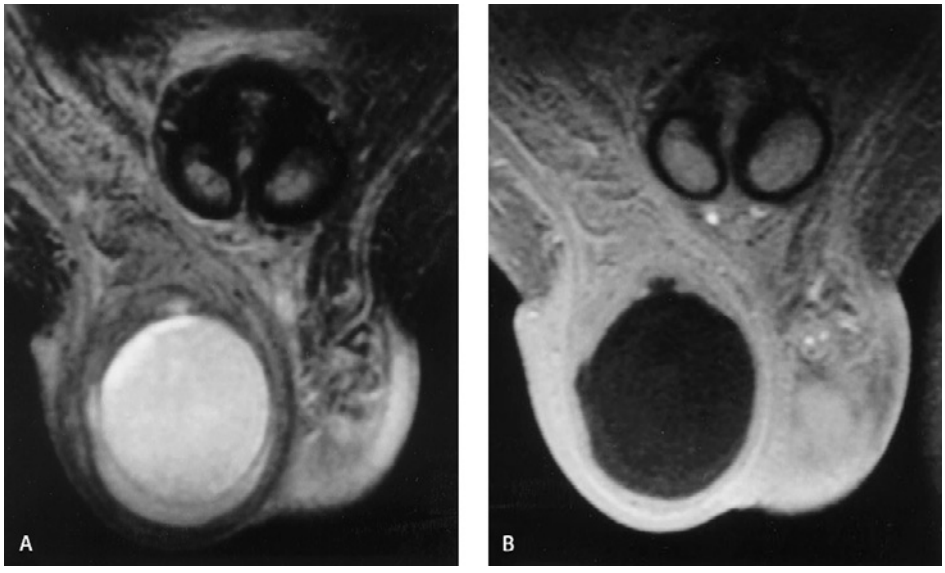

Fig. 24. Testicular abscess formation. The abscess presents as hyperintense on the coronal T2-weighted FSE (**A**) and hypointense on the contrast-enhanced T1-weighted image (**B**) of the testis. Inflammatory changes of the surrounding tissue

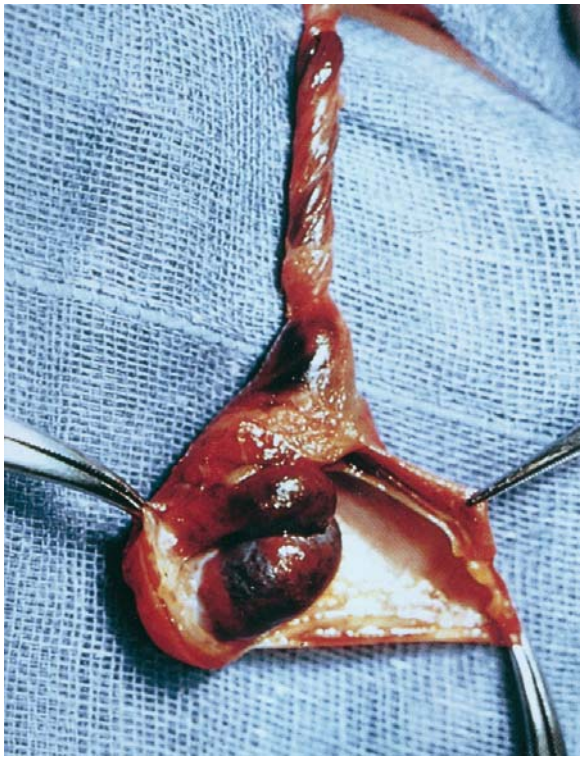

Fig. 25. Testicular torsion in a four-day-old newborn with hemorrhagic necrosis of the testis and epididymis (intraoperative finding)

examination of the scrotum should include CCDS studies. No changes in intrascrotal structures are seen on gray-scale ultrasound at early stages of testicular torsion. Ultrasound only depicts changes resulting from hemorrhagic infarction at later stages – when it is too late in most instances for surgical correction [80]. With the advent of CCDS, it has now become possible to already identify testicular torsion at an early stage [60, 83–86]. Whereas the normal testis and epididymis are characterized by the depiction of isolated flow signals, flow signals are significantly diminished in partial torsion and absent in complete torsion (Fig. 26). However, reactive hyperemia of the scrotal skin can be seen. It is important to bear in mind that the demonstration of blood flow in the testis does not exclude the possibility of partial torsion. In general, the reduction of blood flow to the testis is not immediate or complete; rather, there is a gradual decrease as the edema increases. Therefore, not only the absence of blood flow is an important diagnostic finding but also a decrease compared to the normal contralateral side. Overall, CCDS has a sensitivity ranging from 82% to 90%, while its specificity in diagnosing testicular torsion reaches 100% [86].

MR imaging is only rarely performed in patients with suspected testicular torsion, not least of all because of the rather long examination times and logistic problems. Findings on MR imaging include an enlarged spermatic cord with diminished flow, diffusely decreased signal intensity of the testis, and mild to moderate thickening of the tunica albuginea and epididymis [87]. A twisted cord can be seen as multiple low-inten-

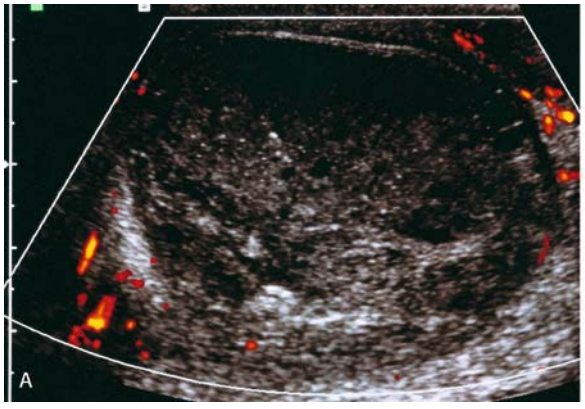

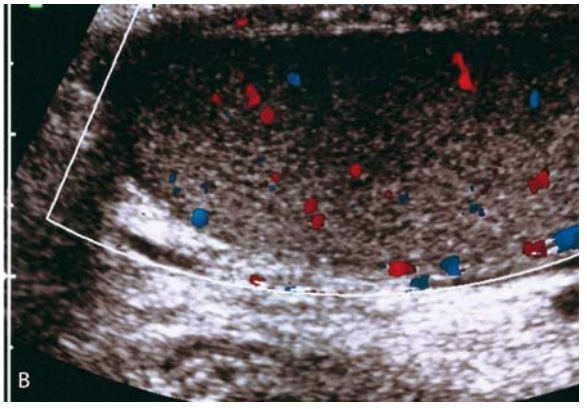

Fig. 26A, B. Testicular torsion. Power Doppler ultrasound (**A**) demonstrates absence of blood flow from the enlarged and inhomogeneous testicle and epididymis; increased blood flow in the peritesticular tissue. Regular intratesticular blood flow in a normal testicle on CCDS (**B**), shown for comparison

sity curvilinear structures radiating in a whirlpool pattern, which is best depicted in a plane perpendicular to its axis. The point of the twist may be identified as an area of signal void (torsion knot). High-signal intensity areas on T1-weighted images indicate diffuse intraparenchymal hemorrhage of the testis or epididymis.

Trauma

In patients with traumatic injuries to the testis, hematoma, hematocele, and intratesticular bleeding or testicular rupture have to be distinguished. Palpation is extremely restricted by severe pain and pronounced swelling.

Ultrasound easily depicts a soft-tissue hematoma as an echopenic lesion and additional CCDS can exclude traumatic testicular torsion (Figs. 27, 28). The diagnosis of a hematocele is established by the sonographic demonstration of a hydrocele-like fluid accumulation that contains numerous small internal echoes (Fig. 30). On MR imaging, most hematoceles initially exhibit medium signal intensity on T1-weighted images and high signal intensity on T2-weighted images [3, 69]. Chronic hematoceles usually demonstrate high signal intensity on both T1- and T2-weighted images.

Intratesticular hemorrhages are depicted as lesions of low echogenicity on US, mostly with sharply demarcated borders and occasionally with a heterogeneous appearance (Fig. 28). A small tear of the tunica albuginea may be overlooked on ultrasound but advanced testicular rupture is always visualized. The latter is associated with irregularities of the testicular contour and either hypo- or hyperechoic heterogeneous areas in the organ (Fig. 29). On MR imaging, the diagnosis of testicular rupture is facilitated by the excellent depiction of

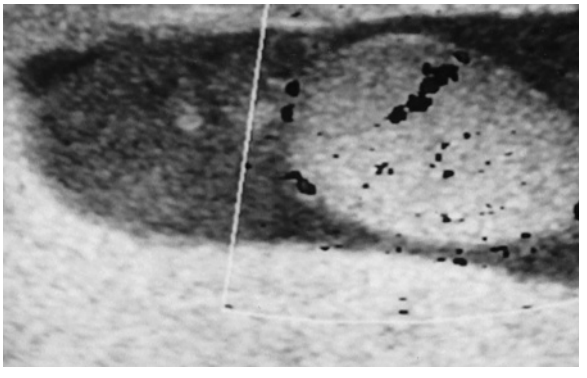

Fig. 27. Posttraumatic hematocele in a 10-year-old boy. The power Doppler mode shows normal perfusion of the testicle and thus excludes traumatic testicular torsion

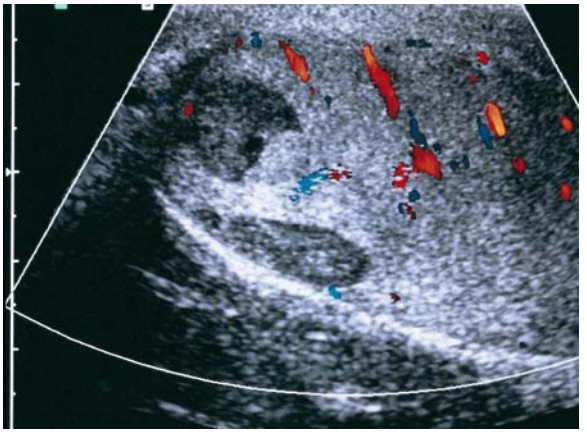

Fig. 28. Posttraumatic intratesticular hematomas. The hematomas are depicted as hypoechoic areas. The testicular contour is preserved. The power Doppler mode shows normal testicular perfusion and thus excludes traumatic testicular torsion

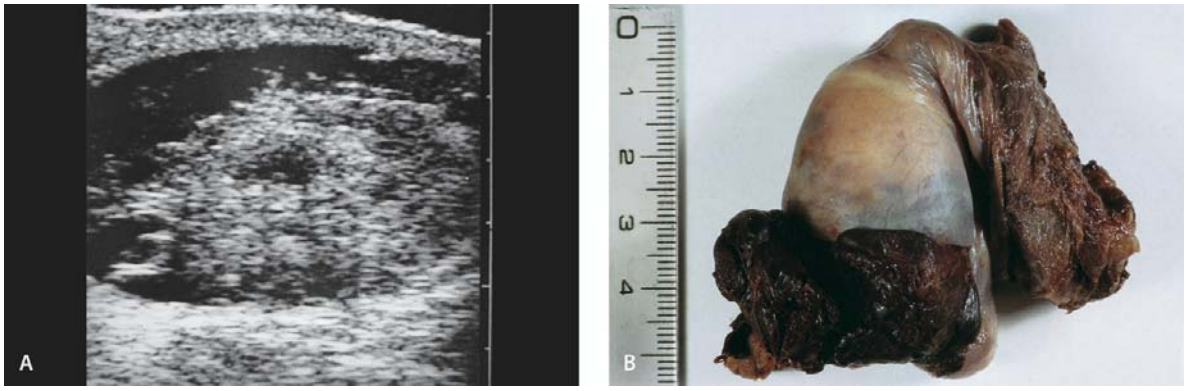

Fig. 29A, B. Traumatic testicular rupture. US (**A**) shows an irregular testicular contour with hypoechoic, ill-defined intratesticular areas and an accompanying hematocele. Surgical specimen (**B**). (from [67], with permission)

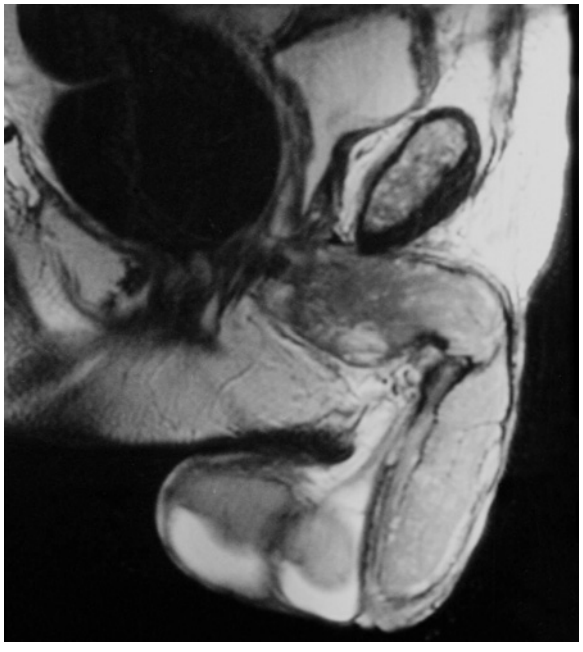

Fig. 30. A 73-year-old patient with a penile metastasis of urinary bladder carcinoma. Sagittal T2-weighted MR image: hyperintense tumor of the corpus cavernosum

the tunica albuginea. The integrity of the tunica albuginea is best judged on T2-weighted or contrast-enhanced T1-weighted images. However, multiple planes of imaging are often needed for thorough evaluation. On T2-weighted images, the signal intensity of the injured testis is lower (!) than that of the normal contralateral testis [69]. On contrast-enhanced T1-weighted images, the injured testis demonstrates less pronounced enhancement. The signal intensity of intratesticular hematoma depends on the time interval elapsed between bleeding and MR imaging. In the acute phase, low or medium signal intensity is seen on T1-weighted images and high signal intensity on T2-weighted images. In the chronic phase, high signal intensity occurs on both T1- and T2-weighted images [88].

The Penis

Normal Anatomy

The penis is divided into a ventral compartment comprising the bulbous and penile portion of the urethra and the corpus spongiosum and the dorsal compartment containing the paired corpora cavernosa [3]. The corpus spongiosum and the corpora cavernosa are cylindrical bodies of endothelium-lined cavernous spaces.

MR signal intensities vary dependent on the rate of blood flow in these cavernous spaces, which in general shows intermediate signal intensity on T1-weighted and high signal intensity on T2-weighted images [89].

The penile arterial supply originates from both internal pudendal arteries, which arise from the internal iliac arteries. Each internal pudendal artery gives rise to the perineal and common penile arteries and its branches. Whereas the larger arteries can be easily visualized by MR angiography, the smaller end arteries of the penis can only be visualized by selective angiography [89].

Disease Entities

US is widely used by the urologist as a primary imaging modality for the penis. If clinical questions, however, remain unanswered by US, high-resolution MRI provides an opportunity to advance imaging evaluation of this organ.

MRI may be used to characterize congenital abnormalities, detect and stage penile and urethral cancers, identify benign penile masses, diagnose penile fracture and evaluate the cause of impotence [3, 89–91] (Fig. 30). Furthermore, it was shown to be helpful in the postoperative evaluation of penile prostheses [3, 89].

References

1. Hricak H, White S, Vigneron D et al (1994) Carcinoma of the prostate gland: MR imaging with pelvic phased-array coils versus integrated endorectal-pelvic phased-array coils. Radiology 1193:703–709
2. Kubik-Huch RA, Hailemariam S, Hamm B (1999) CT and MRI of the male genital tract: radiologic-pathologic correlation. Eur Radiol 9:16–28
3. Noone TC, Semelka RC, Kubik-Huch RA, Braga L (2002) Male pelvis. In: Semelka R (ed) Abdominal-pelvic MRI. Wiley-Liss, New York, pp 981–1019
4. Kirby RS, Christmas TJ, Brawer M (1998) Prostate cancer. In: Anatomical and pathological considerations. Mosby Times Mirror International pp 2–21
5. Nunes LW, Scheibler MS, Rauschning W, Schnall MD, Tomaszewski JE, Pollack H, Kressel H (1995) The normal prostate and periprostatic tissue: correlation between MR images made with endorectal coil and cadaveric microtome sections. Am J Roentgenol 164:923–927
6. Dik P, Lock TMWT, Schrier BP, Zeijlemaker BYW, Boon TA (1996) Transurethral marsupialization of a medial prostatic cyst in patients with prostatitis-like symptoms. J Urology 155:1301–1304
7. Mayersak JS, Kuchenbecker DA (1993) Mullerian duct cyst. Uroradiology 41:176–180
8. McDermott VG, Meakem TJ 3rd, Stolpen AH, Schnall MD (1995) Prostatic and periprostatic cysts: findings on MR imaging. Am J Roentgenol 64:123–127
9. Schwartz JM, Bosniak BA, Hulnick DA, Megibow AJ, Raghavendra BN (1998) Computed tomography of midline cysts of the prostate. J Comput Assist Tomogr 12:215–218
10. Gevenois PA, Van Sinoy ML, Sintzoff SA Jr, Stallenberg B, Salmon I, Van Regemorter G, Struyven J (1990) Cysts of the prostate and seminal vesicles: MR imaging findings in 11 cases. Am J Roentgenol 155:1021–1024
11. Thurnher S, Hricak H, Tanagho E (1988) Mullerian duct cyst: diagnosis with MR Imaging. Radiology 168:25–28
12. Wachsberg RH, Sebastiano L, Sullivan BC, Irwin R (1995) Posterior urethral diverticulum presenting as a midline prostatic cyst: sonographic and MRI appearance. Abdom Imaging 20:70–71
13. Aalame NM, Sulser T, Egli U, Krestin GP, Kubik-Huch RA (1998) Primary male infertility caused by a congenital prostatic cyst: sonographic and MRI findings. Urol Int 61:58–61
14. Barry MJ (1990) Epidemiology and natural history of benign prostatic hyperplasia. Urol Clin North Am 17:495–507
15. Doll HA, Black NA, McPherson K, Flood AB, Williams GB, Smith JC (1992) Mortality, morbidity and complications following transurethral resection of the prostate for benign prostatic hypertrophy. J Urol 147:1566–1573
16. Huch Böni RA, Sulser T, Jochum W, Romanowski B, Debatin JF, Krestin GP (1997) Monitoring of laser ablation induced changes of the prostate by endorectal MRI and correlation to histology. Radiology 202:232–236
17. Bertschinger K, Trinkler F, Reili I, Kubik-Huch RA (1999) Sonographic and MR findings of an extensive, HIV-related prostatic abscess. J Magn Reson Imaging 9:488–490
18. Bursell S (1942) Beitrag zur Kenntnis der Paraamyloidose im urogenitalen Trakt unter besonderer Berücksichtigung der sogenannten senilen Amyloidose in den Samenbläschen und ihres Verhältnis zum Samenblasenpigment. Uppsala Läkaref Förh 47:313–331
19. Fujihara S, Glenner GG (1981) Primary localized amyloidosis of the genitourinary tract: immunohistochemical study on eleven cases. Lab Invest 44:55–60
20. Goldman H (1963) Amyloidosis of the seminal vesicles and vas deferens: primary localized cases. Arch Pathol 75:94–98
21. Pitkanen P, Westermark P, Cornwell GG, Murdoch W (1983) Amyloid of the seminal vesicles: a distinctive and common localized form of senile amyloidosis. Am J Pathol 110:64–69
22. Hutter B, Huch Böni RA, Hawelski S, Maurer R, Krestin GP (1995) Durch Amyloidose vorgetäuschte Tumorinfiltration der Samenblasen. RöFo Fortschr Röntgenstr 163:184–185
23. Yasushi K, Sugimura K, Nagaoka S, Ishida T (1992) Amyloid deposition in seminal vesicles mimicking tumor invasion from bladder cancer: MR findings. J Comput Assist Tomogr 16:989–991
24. Ramschandi P, Schnall MD, LiVolsi VA, Tomaszewski JE, Pollack HM (1993) Senile amyloidosis of the seminal vesicles mimicking metastatic spread of prostatic carcinoma on MRI. Am J Roentgenol 161:99–100
25. American Cancer Society (1994) Cancer, facts and figures. American Cancer Society, Atlanta
26. Levi F, La Vecchia C, Lucchini F, Boyle P (1993) Cancer incidence and mortality in Europe, 1984–1987. Soz Präventivmed 38 [Suppl 3]:S155–S229
27. Epstein JI, Pizor G, Walsh PC (1993) Correlation of logic findings with progression following radical retropubic prostatectomy. Cancer 71:3582–3593
28. Oesterling JE, Brendler CB, Epstein JI et al (1987) Correlation of clinical stage, serum prostatic acid, phosphatase and preoperative Gleason grade with final pathological stage in 275 patients with clinically localized adenocarcinoma of the prostate. U Urol 128:92–98
29. Carter H, Coffey D (1988) Prostate cancer: the magnitude of the problem in the United States. In: Coffey DS, Resnick MI, Dorr FA, Karr JP (eds) A multidisciplinary analysis of controversies in the management of prostate cancer. Plenum Press, New York, pp 1–75
30. Huch Böni RA, Boner JA, Debatin JF, Trinkler F, Knönagel H, von Hochstetter A, Helfenstein U, Krestin GP (1995) Optimization of prostate carcinoma staging: comparison of imaging and clinical strategies. Clin Radiol 50:593–600
31. Huch Böni RA, Hutter B, Trinkler F, Jochum W, Pestalozzi D, Krestin GP (1996) Präoperatives T-Staging des Prostatakarzinoms: Vergleich der endorektalen MRT mit bildgebenden und klinischen Methoden. RöFo Fortschr Röntgenstr 165:152–158
32. Chelsky M, Schnall M, Seidmon E, Pollack H (1993) Use of endorectal surface coil magnetic resonance imaging for local staging of prostate cancer. J Urol 150:391–395
33. Hricak H, White S, Vigneron D et al (1994) Carcinoma of the prostate gland: MR imaging with pelvic phased-array coils versus integrated endorectal-pelvic phased-array coils. Radiology 193:703–709
34. Nicolas V, Beese M, Keulers A, Bressel M, Kastendieck H, Huland H (1993) MR-Tomographie des Prostatakarzinoms – Vergleich konventionelle und endorektale MRT. RöFo Fortschr Röntgenstr 161:319–326
35. Schiebler M, Schnall M, Pollack H et al (1993) Current role of MR imaging in the staging of adenocarcinoma of the prostate. Radiology 189:339–352
36. Tempany N, Zhou X, Zerhouni E et al (1994) Staging of prostate cancer: results of Radiology Diagnostic Oncology Group project comparison of three MR imaging techniques. Radiology 192:47–54
37. Quinn S, Franzini D, Demlow T et al (1994) MR imaging of prostate cancer with an endorectal surface coil technique: correlation with whole-mount specimens. Radiology 190:323–327
38. Jager G, Ruijter E, Kaa CVD et al (1996) Local staging of prostate cancer with endorectal MR imaging: correlation with histopathology Am J Roentgenol 166:845–852
39. Yu K, Hricak H, Alagappan R, Chernoff D, Bachetti P, Zaudek C (1997) Detection of extracapsular extension of prostate carcinoma with endorectal and phased-array coil MR imaging: multivariate feature analysis. Radiology 202:697–702
40. Huch Böni RA, Boner JA, Lütolf UM, Trinkler F, Pestalozzi D, Krestin GP (1995) Contrast-enhanced, endorectal coil MR imaging in local staging of prostate carcinoma. J Comp Assist Tomogr 19:232–237
41. Mirowitz S, Brown J, Heiken J (1993) Evaluation of the prostate and prostatic carcinoma with gadolinium-enhanced endorectal coil MR imaging. Radiology 186:153–157
42. Gervasi LA, Mata J, Easley JD, Wilbanks H, Seale C, Hawkins H, Calron CE, Scardino PT (1989) Prognostic significance of lymph node metastases in prostatic cancer. J Urol 142:332–336

43. Kastendieck H, Bressel M, Henke A, Hüsselmann H (1980) Häufigkeit regionärer Lymphknotenmetastasen beim operablen Prostatakarzinom. Dtsch Med Wschr 105:1348–1354
44. Nicolas V, Beese M, Keulers A, Bressel M, Kastendieck H, Huland H (1994) MR-Tomographie des Prostatakarzinoms – Vergleich konventionelle und endorektale MRT. RöFo Fortschr Röntgenstr 161:319–326
45. McLaughlin A, Ill P, Salzstein SL, McCullough DL, Gittes RF (1996) Prostatic carcinoma: incidence and location of unsuspected lymphatic metastases. J Urol 115:89–94
46. Levine MS, Arger PH, Coleman BG, Mulhern CB, Pollack HM, Wein AJ (1981) Detecting lymphatic metastases from prostatic carcinoma: superiority of CT. Am J Roentgenol 137: 207–211
47. Jager GJ, Barentsz JO, Oosterhof GO, Witjes JA, Ruijs SJH (1996) Pelvic adenopathy in prostatic and urinary bladder carcinoma: MR imaging with a three-dimensional T1-weighted magnetization-prepared-rapid gradient-echo sequence. Am J Roentgenol 167:1503–1507
48. Barkhausen J, Quick HH, Lauenstein T, Goyen M, Ruehm SG, Laub G, Debatin JF, Ladd ME (2001) Whole-body MR imaging in 30 seconds with real-time true FISP and a continuously rolling table platform: feasibility. Radiology 220:252–256
49. Robey EL, Schellhammer PF (1987) Local failure after definitive therapy for prostatic cancer. J Urol 137:613–619
50. Wassermann NF, Kapoor DA, Hildebrandt WC et al (1992) Transrectal ultrasound in evaluation of patients after radical prostatectomy. Part I. Normal postoperative anatomy. Radiology 185:361–366
51. Wassermann NF, Kapoor DA, Hildebrandt WC et al (1992) Ultrasound in evaluation of patients after radical prostatectomy. Part II. Transrectal US and biopsy findings in the presence of residual and early recurrent prostatic cancer. Radiology 185:367–372
52. Lange PH, Ercole CH, Lightner EJ et al (1989) The value of serum prostate specific antigen determinations before and after radical prostatectomy. J Urol 141:873–879
53. Ebner F, Ranner G, Flückiger F (1994) Differenzierung von Narbengewebe und Tumorrezidiv nach Therapie von Tumoren des weiblichen Beckens. Radiologe 34:384–389
54. Schiebler M, Schnall M, Pollack H et al (1993) Current role of MR imaging in the staging of adenocarcinoma of the prostate. Radiology 189:339–352
55. Quinn S, Franzini D, Demlow T et al (1994) MR imaging of prostate cancer with an endorectal surface coil technique: correlation with whole-mount specimens. Radiology 190: 323–327
56. Huch Böni RA, Meyenberger C, Pok Lundquist J, Trinkler F, Lütolf U, Krestin GP (1996) Value of endorectal coil versus body coil MRI for diagnosis of recurrent pelvic malignancies. Abdom Imaging 21:345–352
57. Unterweger M, Marincek B, Hailemariam S, Reilly I, Kubik-Huch RA (2001) Bladder outflow obstruction caused by prostate metastasis in a young male. Eur Radiol 11:2099–2101
58. Fobbe F, Heidt P, Hamm B, Koennecke HC, Hauck G, Dieckmann KP, Wolf KJ (1989) Improved diagnosis of scrotal disorders by color-coded duplex sonography. Fortschr Röntgenstr RöFo 150:629–634
59. Mitchell DG (1990) Color Doppler imaging: principles, limitations, and artifacts. Radiology 177:1–10
60. Herbener TE (1996) Ultrasound in the assessment of the acute scrotum. J Clin Ultrasound 24:405–421
61. Dogram VS, Gottlieb RH, Oka M, Rubens DJ (2003) Sonography of the scrotum. Radiology 227:18–36
62. Müller-Leisse C, Bohndorf K, Stargardt A et al (1994) Gadolinium-enhanced T1-weighted imaging of scrotal disorders: is there an indication for MR imaging? J Magn Reson Imaging 4:389–395
63. Silverberg E (1982) Cancer in young adults (ages 15–34). CA Cancer J Clin 32:32–42
64. Mostofi FK (1973) Proceedings: testicular tumors, epidemiologic, etiologic, and pathologic features. Cancer 32:1186–1201
65. Skakkebaek NE, Berthelsen JG, Giwercman A, Müller J (1987) Carcinoma in situ of the testis: possible origin from gonocytes and precursor of all types of germ-cell tumours except spermatocytoma. Int J Androl 10:19–28
66. Schwerk WB, Schwerk WN, Rodeck G (1987) Testicular tumors: prospective analysis of real-time US patterns and abdominal staging. Radiology 164:369–374
67. Hamm B (1997) Differential diagnosis of scrotal masses by ultrasound. Eur Radiol 7:668–679
68. Hricak H, Hamm B, Kim B (1995) Imaging of the scrotum. Raven Press, New York
69. Cramer BM, Schiegel E, Thuroff J (1991) MR imaging in the differential diagnosis of scrotal and testicular disease. Radiographics 11:9–21
70. Johnson JO, Mattrey RF, Philipson J (1990) Differentiation of seminomatous from nonseminomatous testicular tumors with MR imaging. Am J Roentgenol 154:539–543
71. Hamm B (1994) Sonography of the testis and epididymis. Andrologia 26:193–210
72. Grantham JG, Charboneau JW, James EM, Kirschling RJ, Kvols LK, Segura JW, Wold LE (1985) Testicular neoplasms: 29 tumors studied by high-resolution US. Radiology 157:775–780
73. Skakkebaek NE, Berthelsen JG, Giwercman A, Müller J (1987) Carcinoma in situ of the testis: possible origin from gonocytes and precursor of all types of germ-cell tumours except spermatocytoma. Int J Androl 10:19–28
74. Lenz S, Skakkebaek NE, Hertel NT (1996) Abnormal ultrasonic pattern in contralateral testes in patients with unilateral testicular cancer. World J Urol 14:S55–S58
75. Leonhardt WC, Gooding GA (1992) Sonography of intrascrotal adenomatoid tumor. Urology 39:90–92
76. Frates MC, Benson CB, DiSalvo DN, Brown DL, Laing FC, Doubilet PM (1997) Solid extratesticular masses evaluated with sonography: pathologic correlation. Radiology 204: 43–46
77. Older R, Watson L (1994) Tubular ectasia of the rete testis: a benign condition with a sonographic appearance that may be misinterpreted as malignant. J Urol 152:477–478
78. Benson CB, Doubilet PM, Richie JP (1989) Sonography of the male genital tract. Am J Roentgenol 153:705–713
79. Rifkin MD (1987) Scrotal ultrasound. Urol Radiol 9:119–126
80. Middleton WD, Middleton MA, Dierks M, Keetch D, Dierks S (1997) Sonographic prediction of viability in testicular torsion: preliminary observations. J Ultrasound Med 16:23–27
81. Hricak H, Jeffrey RB (1983) Sonography of acute scrotal abnormalities. Radiol Clin North Am 21:595–603
82. Martin B, Conte J (1987) Ultrasonography of the acute scrotum. J Clin Ultrasound 15:37–44
83. Kass EJ, Stone KT, Cacciarelli AA, Mitchell B (1993) Do all children with an acute scrotum require exploration? J Urol 150:667–669
84. Erden MI, Ozbek SS, Aytac SK, Adsan O, Suzer O, Safak SM (1993) Color Doppler imaging in acute scrotal disorders. Urol Int 50:39–42
85. Fitzgerald SW, Erickson S, DeWire DM et al (1992) Color Doppler sonography in the evaluation of the adult acute scrotum. J Ultrasound Med 11:543–548
86. Wilbert DM, Schaerfe CW, Stern WD, Strohmaier WL, Bichler KH (1993) Evaluation of the acute scrotum by color-coded Doppler ultrasonography. J Urol 149:1475–1477
87. Trambert MA, Mattrey RF, Levine D, Berthoty DP (1990) Subacute scrotal pain: evaluation of torsion versus epididymitis with MR imaging. Radiology 175:53–56
88. Hamm B (1991) Sonographische Diagnostik des Skrotalinhalts – Lehrbuch und Atlas. Springer, Berlin Heidelberg New York
89. Pretorius ES, Siegelman ES, Ramchandani P, Banner MP (2001) MR imaging of the penis. Radiographics 21:S283–S299
90. Wolfensberger U, Bagot A, Hailemariam S, Garzoli E, Kubik-Huch RA (2001) Penismetatase bei Blasenkarzinom. Schw Rundsch Med (Praxis) 90:69–71
91. Matter LE, Hailemariam S, Huch RA, Hauri D, Sulser T (1998) Primary erectile dysfunction in combination with congenital malformation of the cavernous bodies. Urol Int 60:175–177

Benign Renal and Adrenal Tumors

David S. Hartman, Matthew S. Hartman

5.3

Contents

Benign Renal Tumors

Introduction

Benign tumors of the kidney and adrenal constitute a heterogeneous group with different clinical and radiological implications depending on the organ of origin.

In the kidney, benign neoplasms are rare relative to malignant ones. However, in some cases such as angiomyolipoma and multilocular cystic nephroma, an imaging diagnosis is possible.

In the adrenal, benign tumors are the majority and a daily challenge in clinical practice. Again, imaging is capable in many cases to achieve a definitive diagnosis differentiating them from malignancy, particularly metastasis, both in the kidney and adrenal knowledge of the underlying pathology is helpful in understanding the key imaging findings.

Angiomyolipoma

Definition

Angiomyolipoma is a neoplasm consisting of three tissue elements: blood vessels, smooth muscle and fat, hence the name ***angiomyolipoma*** [1].

Pathology

On gross examination, most angiomyolipomas are smoothly rounded or ovoid and circumscribed but lack a tumor capsule (Fig. 1A). The size ranges from less than a centimeter to over 20 cm. The tumor compresses and distorts the renal parenchyma and collecting system but does not invade it. It is not uncommon that a large portion of the mass projects into the perirenal space with only a small intrarenal component. Intratumoral hemorrhage and necrosis are common.

Although every angiomyolipoma is composed of all three cellular constituents, their relative amounts vary tremendously. Those composed primarily of fat will be yellow, while those composed primarily of muscle will be tan or gray.

Small angiomyolipomas are a common finding in the kidney at autopsy or as an incidental finding on computed tomography, ultrasonography, and magnetic resonance imaging. These small angiomyolipoma usually are clinically silent, and do not distort the kidney.

Histologically aggregates of abnormal thick-walled vessels are admixed with varying amounts of adipose tissue and smooth muscle. Fat cells vary considerably in size but otherwise resemble normal adipose tissue. The smooth muscle component is pleomorphic, but mitotic figures are uncommon. The vascular component is the most characteristic feature of the angiomyolipoma (Fig. 1B). The smaller arteries are devoid of elastica. Smooth muscle forms a collar about the periphery of a vessel often exhibiting a perpendicular orientation to the vessel lumen. This abnormal morphology may result in the aneurysms.

Because of the frequency of hemorrhage, perirenal extension and pleomorphism of the myomatous elements, these tumors may lead to an erroneous pathologic diagnosis, usually liposarcoma, leiomyosarcoma, or spindle cell carcinoma. Although there have been case reports of angiomyolipomas engulfing adjacent lymph nodes and extending into the inferior vena cava, distant metastases are extremely rare.

Clinical Setting

Most angiolipoma occur as an isolated finding and not associated with tuberous sclerosis. In the majority of these cases, the angiomyolipoma is clinically silent. Discovery often occurs during the radiological evaluation of the abdomen for unrelated symptoms. Less commonly, patients may present with pain, hematuria and or a mass. Hemorrhage within or around the tumor may produce flank pain, hypotension, and hematuria. Angiomyolipoma is discovered in women more often than in men. Most symptomatic angiomyolipomas occur as, a solitary renal mass in otherwise normal individuals. Lesions larger than 4 cm in diameter may hemorrhage more frequently than smaller tumors. Approximately 80 percent of patients with tuberous sclerosis have angiomyolipoma which are usually multiple and bilateral.

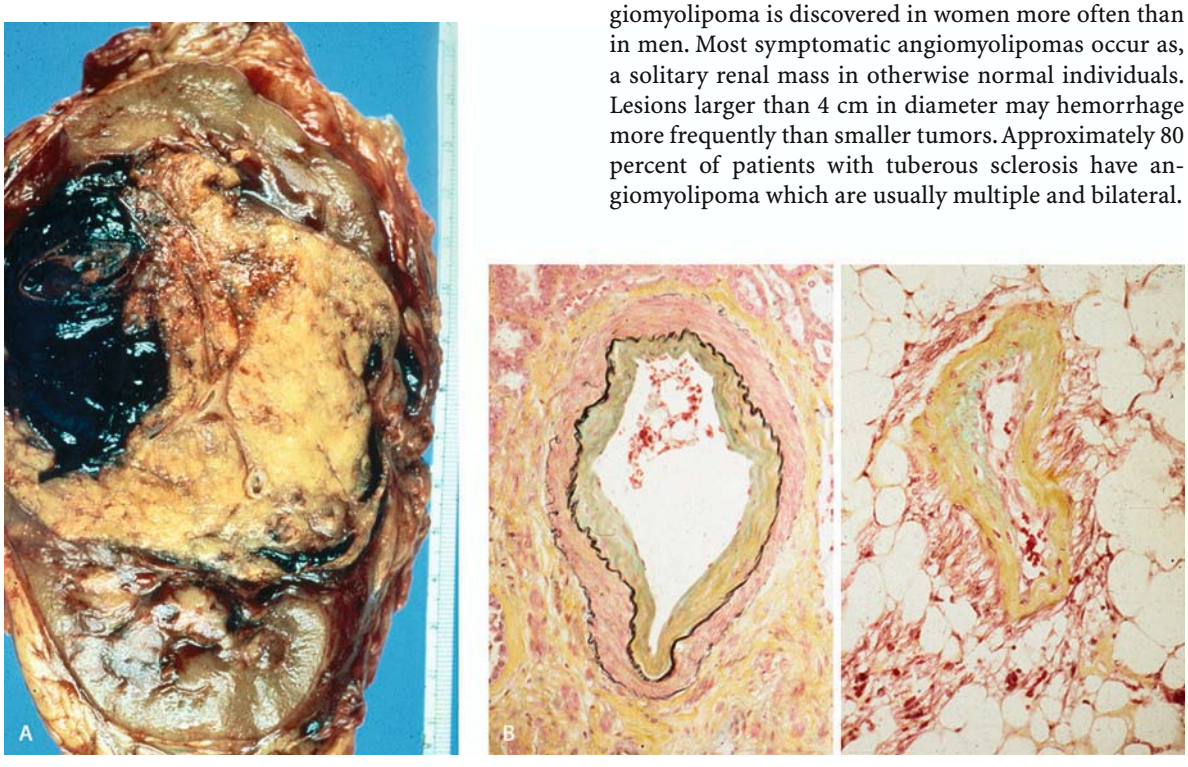

Fig. 1A, B. Angiomyolipoma pathology. **A** Gross specimen. The tumor measures 9 cm and compresses the kidney. The yellow area represents intratumoral fat. A large area of hemorrhage is conspicuous. **B** Normal vessel *left*, angiomyolipoma *right*. The vessel is devoid of elastica. The smooth muscle forms a collar about the periphery of the vessel exhibiting a perpendicular orientation to the vessel lumen

Radiologic Findings

■ **Overview.** The presence of a fatty renal mass is *very suggestive* of angiomyolipoma. The best radiologic techniques to detect this fat are computed tomography and magnetic resonance imaging [2, 3]. Unfortunately this finding is not specific, as renal cell carcinoma *very rarely* will also contain fat.

■ **Excretory Urography.** In sporadic cases, angiomyolipoma causes a unilateral, unifocal renal mass. When associated with tuberous sclerosis, there are typically multiple, bilateral masses. Rarely the angiomyolipoma will demonstrate a radiolucency within the mass when a large component of fat is present. This lucency is significant only on films obtained before administration of contrast material, since any radiolucency seen within a tumor following contrast material more likely represents necrosis or diminished perfusion rather than fat. This fat-related radiolucency on the KUB is an infrequent radiographic observation, being reported in less than 10 per cent of patients. Other urographic features of angiomyolipoma are related to the mass effect of the lesion.

■ **Computed Tomography.** Fat in a renal tumor is a finding that is very suggestive of angiomyolipoma (Fig. 2). As the angiomyolipoma may be largely extrarenal, the fatty component may be easily confused with a primary retroperitoneal tumor such as liposarcoma. Computed tomography is extremely valuable in detecting the nephrographic defect that indicates the true renal origin of the mass. Sagittal and coronal images are especially useful for tumors, which arise, in the upper or lower pole. Intermixed with the fat are muscle and blood vessels, with attenuation values similar to those of renal parenchyma. Large aneurysms can occasionally be recognized as foci of intense enhancement similar to the renal artery. Recent hemorrhage can be recognized by higher attenuation values. Computed tomography is also of value in documenting perinephric blood, which may be massive, and life threatening. It there is a small fatty component; pixel mapping may be very helpful in establishing the diagnosis (Fig. 3). If the fatty component is not detectable, the computed tomographic findings are those of other solid tumors (e.g. renal cell carcinoma). Calcification is uncommon in angiomyolipoma.

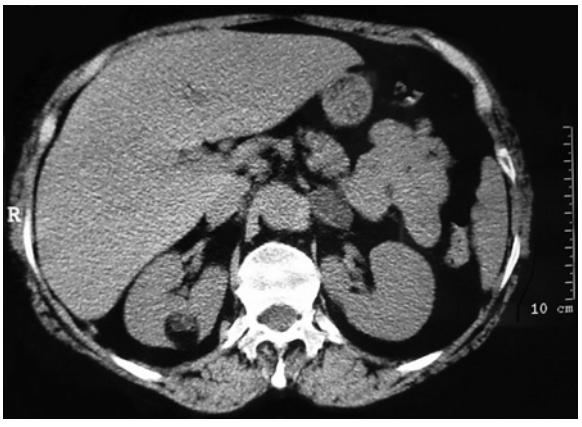

Fig. 2. Angiomyolipoma, CT findings. Computed tomogram, unenhanced. There is a 1.5 cm fatty mass with a density similar to adjacent retroperitoneal fat. The ventral portion of the tumor is of tissue density and probably represents hemorrhage or myomatous elements

■ **Ultrasonography.** The typical angiomyolipoma has an echogenicity similar to that of perirenal or renal sinus fat (Fig. 4). As a result of the hyperechogenicity, small angiomyolipomas may be quite conspicuous. It is to be emphasized, however that this finding of an echogenic renal mass is not specific to angiomyolipoma, since adenocarcinoma may yield a similar image When the fatty component is minimal, or obscured by hemorrhage, the angiomyolipoma is typically less echogenic than the renal sinus fat and may be isoechoic with the renal parenchyma. Especially if small, these nonfatty angiomyolipomas are more difficult to detect and impossible to differentiate from other renal tumors. Most of the angiomyolipoma may be extrarenal and simulate a retroperitoneal soft tissue origin rather than a renal origin.

■ **Magnetic Resonance Imaging.** As with CT, it is the identification of the fatty component on MR that enables confident diagnosis. The fatty components of angiomyolipoma have a similar signal to that of renal sinus and retroperitoneal fat. Fat-suppressed images are extremely helpful and demonstrate signal loss within the mass (Fig. 5). Areas if muscle, blood vessel and hemorrhage will have a less characteristic signal. If fat cannot be identified with certainty, a presumptive diagnosis of angiomyolipoma cannot be made. In exophytic tumors, especially those arising from the upper or lower pole, coronal or sagittal images may be of value in differentiating an angiomyolipoma from a primary retroperitoneal tumor. As the fat within an angiomyolipoma is adipose tissue and not intracellular lipid, chemical shift imaging is not definitive in the MR diagnosis of angiomyolipoma.

■ **Angiography.** Typically, the angiomyolipoma is hypervascular. Suggestive features include one dominant feeding artery with a circumferential arrangement of vessels around the tumor and multiple aneurysms. Unlike renal cell carcinoma, arteriovenous shunting is typically absent. Since these angiographic features are nonspecific and may be seen in renal adenocarcinoma, angiography is not used for diagnosis. The primary utility of angiography is in preoperative embolization, and in those cases with active tumoral bleeding.

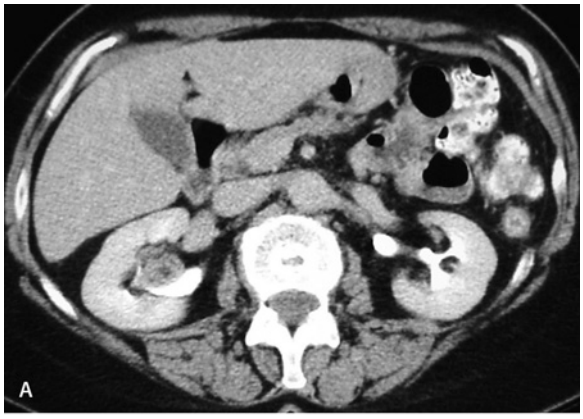

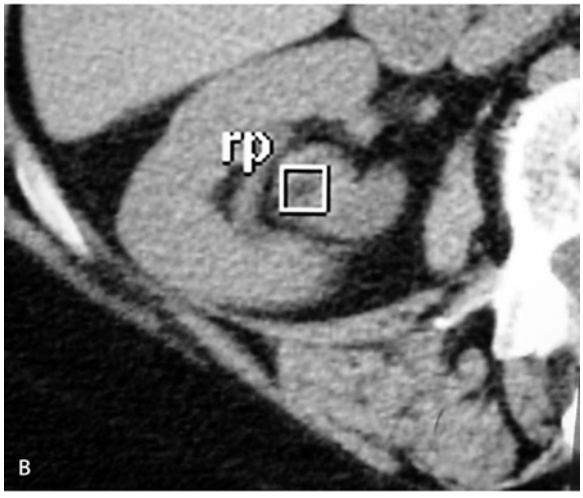

	I	165	166	167	168	169	170	171	172	173	174	175
312	I	43	33	39	5	0	8	20	22	14	26	46
313	I	38	25	54	50	28	18	7	5	13	34	15
314	I	35	35	32	21	3	15	23	11	0	0	-16
315	I	37	40	2	-24	-16	-29	-27	-26	-7	13	0
316	I	-6	1	-26	-3	-11	-50	-33	-24	-17	-10	15
317	I	-14	-11	-31	-35	-34	-43	-19	-30	-38	-7	45
318	I	-23	-13	-18	-37	-58	-50	-31	-33	-8	35	41
319	I	-15	-10	-7	-35	-43	-8	3	18	22	20	9
320	I	11	2	-26	-1	19	11	-12	17	26	21	47
321	I	4	9	-10	9	10	-9	-31	2	34	47	49
C	I	6	15	10	20	35	18	6	26	23	9	27

Fig. 3A–C. Value of pixel mapping in angiomyolipoma with a small amount of fat. **A** Contrast-enhanced computed tomogram. There is a well-defined mass compressing the renal pelvis. Although the mass is heterogeneous, fat is not clearly apparent. **B** Computed tomogram, unenhanced. Individual pixels within the square will be displayed. **C** Quantitative values for each pixel. Note that the center of the mass has values indicative of fat (–58, –50 and –43 Hounsfield units). Case courtesy Brent Wagner, M.D. Reading, PA

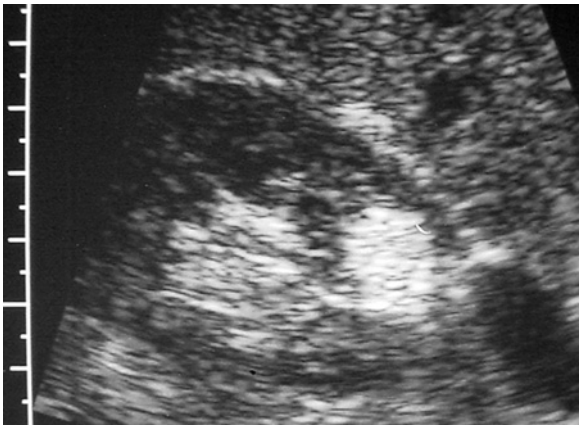

Fig. 4. Angiomyolipoma, ultrasound features. Longitudinal sonogram through the right kidney. The hyperechoic mass is very suggestive, although not diagnostic for angiomyolipoma

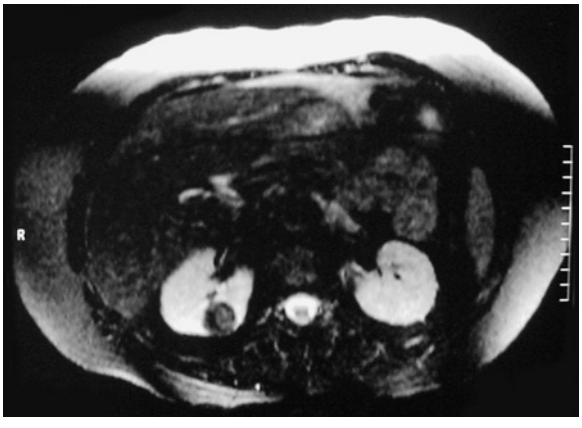

Fig. 5. Angiomyolipoma, MR findings. T2 weighted, fat suppressed scan. There is a 2 cm angiomyolipoma in the right kidney with the same signal of that of adjacent retroperitoneal fat which is black

Multilocular Cystic Nephroma

Definition

Multilocular cystic nephroma is an uncommon, nonfamilial renal neoplasm composed of a well circumscribed encapsulated mass that contains multiple, noncommunicating fluid-filled locules [2, 4]. It is usually although not invariably benign.

Pathology

On gross examination, the multilocular cystic nephroma is well circumscribed by a thick capsule. Typically the tumor compresses the adjacent renal parenchyma.

These tumors can vary from several centimeters to greater than 30 cm. The average size in one large series was 10 cm [5]. Extension of the mass through the renal capsule into the perinephric space is frequent.

On cut sections, the individual locules are variable in size, contain nonhemorrhagic fluid and do not communicate with each other (Fig. 6A) Most locules vary in size from several millimeters to 2.5 cm. Occasionally, however, an individual locule may measure 8 cm in diameter. The locules are separated by thin, translucent septa. Hemorrhage and necrosis are uncommon. Occasionally a portion of the tumor will herniate into the renal pelvis and may obstruct portions of the collecting system.

Microscopically multilocular cystic nephroma is well circumcised by a dense fibrous capsule composed of collagen. The cysts are lined by flattened or cuboidal epithelial cells. In many cases this epithelium projects into the lumen of the locule to create "hob-nail" or "teardrop" appearance (Fig. 6B). The septal stroma is composed of small spindle cells with sparse cytoplasm.

Very rarely the multilocular cystic nephroma will have a stroma that is sarcomatous. Metastases may be histologically similar to the stromal component of the renal lesion. The epithelial elements are not present in the metastases.

Clinical Setting

Multilocular cystic nephroma has a biphasic age and sex distribution: One peak in prevalence occurs in infants and young children with a second peak in middle-aged adults. In children, boys are more commonly affected than girls. In the adult, the multilocular cystic nephroma is more common in women. In infants this lesion is usually discovered as a palpable mass. In the adult most present with pain, a palpable mass or with hematuria (especially those with pelvic herniation). Occasionally the multilocular cystic nephroma is discovered incidentally when imaging is being performed for unrelated symptoms.

Radiologic Findings

■ **Overview.** The multiloculated appearance is readily identifiable on CT, ultrasound, or MRI (Fig. 7). Although the findings of pelvic herniation and lack of hemorrhage and venous invasion favor its diagnosis, the multilocular cystic nephroma is indistinguishable from cystic renal cell in the adult and cystic Wilms tumor in the child. The ultimate differentiation is microscopic.

■ **Excretory Urography.** The typical case demonstrates a large renal mass that distorts the renal contour and the collecting system. Curvilinear or punctate calcification may be detectable in the walls of the locules. Faint linear opacification within the mass may be detectable because of the contrast in the vascularity of the septa. The interface between the lesion and the adjacent renal tissue is sharply defined confirming the renal origin. Herniation of one or more locules into the pelvis presents as a well-defined, nonopaque filling defect. Obstruction of the collecting system may occur. Rarely there is nonvisualization of the collecting system secondary to extensive pelvic herniation.

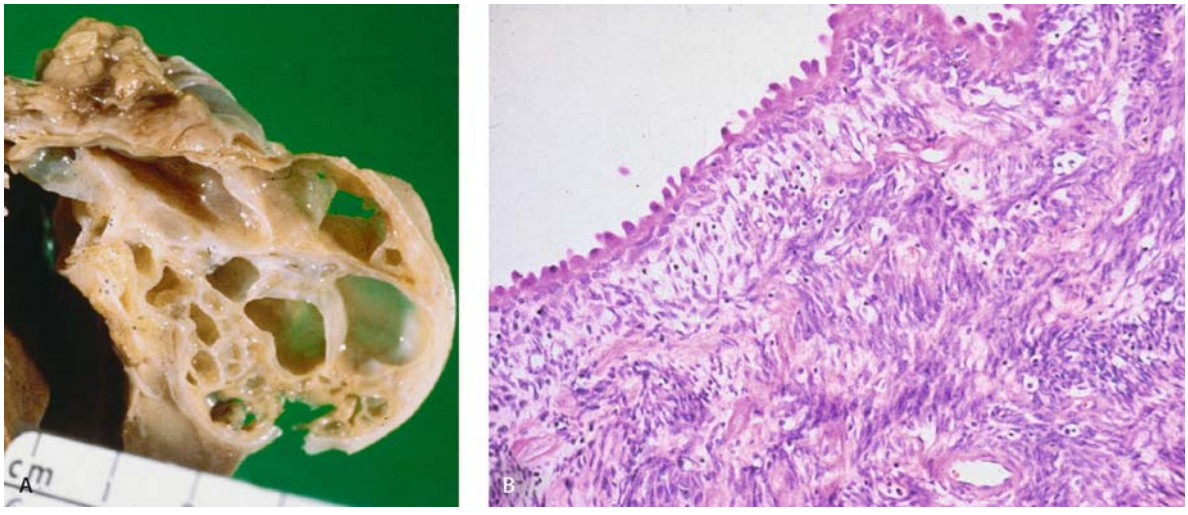

Fig. 6A, B. Multilocular cystic nephroma, pathology. **A** Cut gross specimen. The individual locules vary in size and do not communicate with one another. **B** Photomicrograph. The epithelial cells project into the lumen of the locule ("hob-nail" appearance). The stroma is composed of small spindle cells with sparse cytoplasm

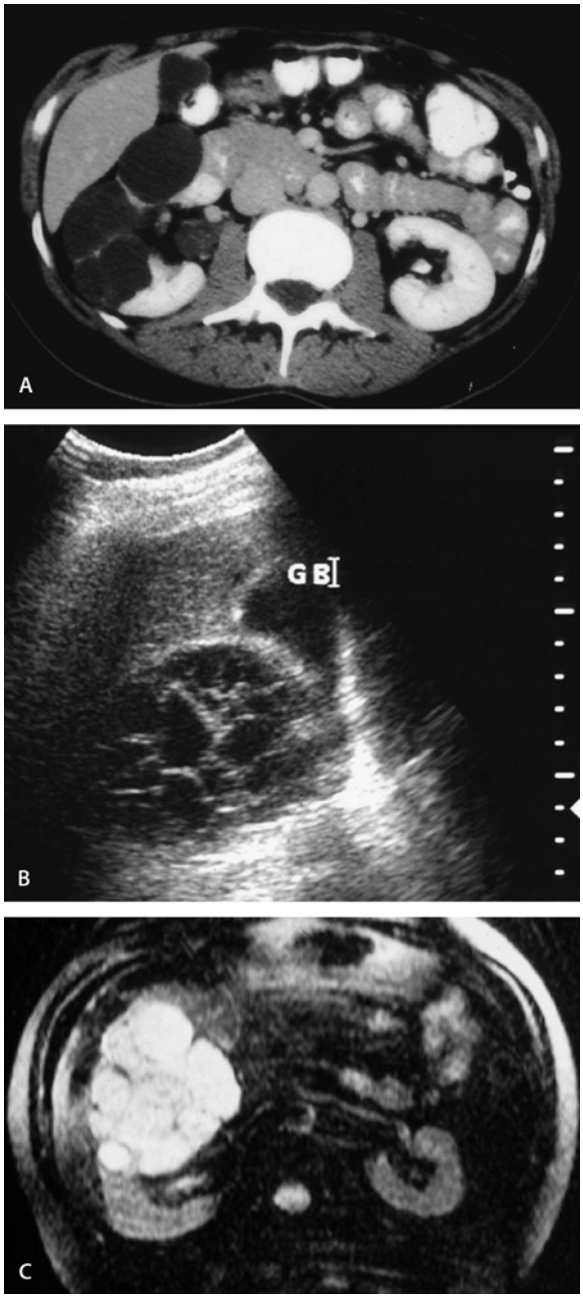

Fig. 7A–C. Multiloculated mass, typical imaging features. **A** Computed tomogram, contrast medium enhanced. There is a large multiloculated mass arising from the right kidney. Each locule is of water density. The septa show prominent enhancement. **B** Longitudinal sonogram, right upper abdomen. Typically the tumor will consist of larger echo free cysts separated by echogenic septa. **C** T2-weighted, fat suppression MR scan of the right kidney. Typically the tumor will consist of high signal, fluid-filled locules and low signal septa

■ **Computed Tomography.** On computed tomographic images (Fig. 7A), multilocular cystic nephroma is a well-defined mass arising from the kidney. The locules vary greatly in size, with variation in attenuation values from that of water to slightly higher. The portion of the tumor that has prolapsed into the pelvis may be identified by the adjacent contrast material in the collecting system. The enhancing septa are much more apparent after contrast material is administered. The fluid-filled locules do not enhance. Computed tomography detects calcium in the septa much more often than does the plain abdominal film.

■ **Ultrasonography.** The ultrasonographic appearance is that of a well-defined, sharply marginated complex cystic mass. (Fig. 7B) The larger cysts are echo free while the septa are echogenic. Extremely small cysts, each too small to be individually resolved, may be imaged as an echogenic foci which paradoxically appear to be solid portions of the mass.

■ **Magnetic Resonance Imaging.** Signal intensity of the fluid within the locules is similar to that of water, (hypointense on T1-weighted images and hyperintense on T2-weighted images) (Fig. 7C). As with enhanced CT, the septations enhance after gadolinium administration are more apparent than on the nonenhanced images. Increased signal intensity within one or more locules, most likely represents increased protein content or less likely hemorrhage within the locule.

■ **Angiography.** Angiography is seldom required, but may reveal neovascularity traversing the septa and around the mass. The septa can be seen during the nephrographic phase as bands of radiodensity coursing through and surrounding radiolucent, the fluid-filled locules. These angiographic findings are indistinguishable from neovascularity in other tumors.

Oncocytoma

Definition

Renal oncocytoma, a subgroup of renal adenoma, is a benign neoplasm that arises from tubular epithelial cells of the kidney [1, 2]. The renal oncocytoma is unrelated to oncocytomas in other organ systems.

Pathology

Oncocytomas are usually solitary, occasionally multiple, and rarely bilateral. They may be familial. They may coexist with renal cell carcinoma in the same kidney. Rarely, a single renal mass will be comprised predomi-

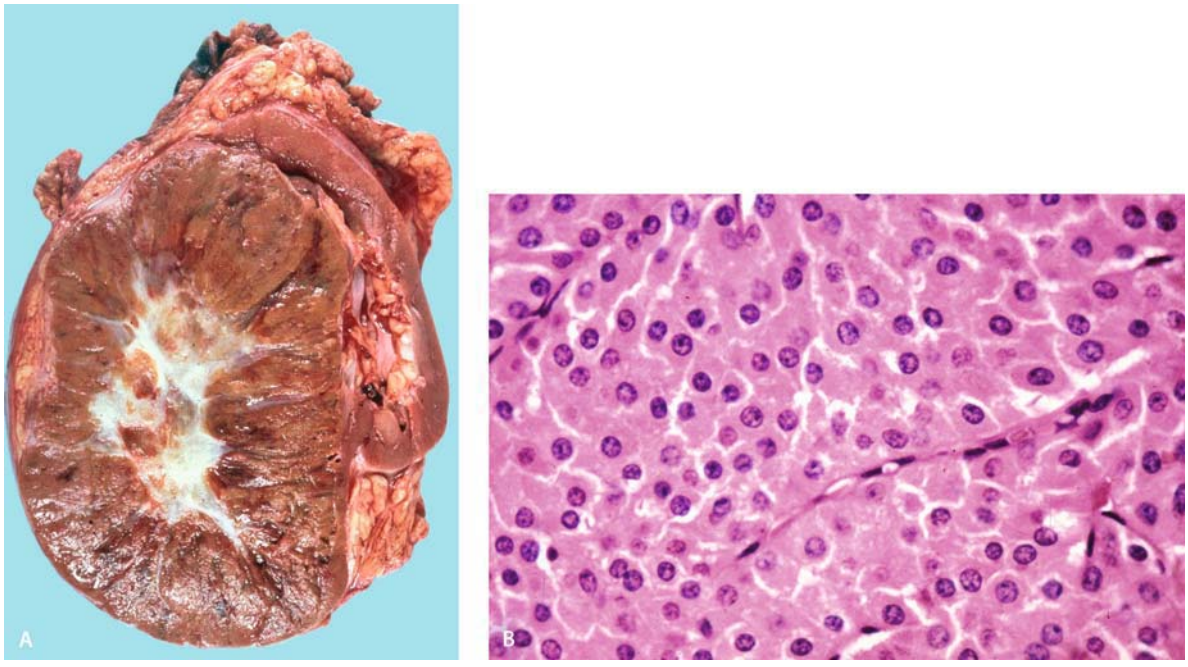

Fig. 8A, B. Oncocytoma, pathology. **A** Cut gross specimen. The tumor is well circumscribed with a color similar to normal kidney. Centrally there is a prominent stellate scar. **B** Photomicrograph. The cells exhibit intense, uniform eosinophilic staining. The nuclei are small without nuclear pleomorphism or mitotic figures

nantly of oncocytes yet have a small focus of renal cell carcinoma.

Oncocytomas may grow to a large size and are usually, but not invariably homogeneous in consistency. On cut surface, they are well circumscribed and have a uniform mahogany brown or beefy red color. The central portion of the cut surface frequently shows a characteristic whitish stellate scar (Fig. 8A). Necrosis, hemorrhage and vascular invasion are very uncommon.

Although this gross is very suggestive of oncocytoma, the diagnosis is made utilizing light microscopy. The tumor is characterized by uniform finely granular eosinophilic cytoplasm and-round-to oval, small nuclei (Fig. 8B). The intense eosinophilic staining is a result of the large number of mitochondria typically present Nuclear pleomorphism is either absent or present focally. Very few mitotic figures are present. Cells near the stellate scar form small nests, which are separated by loose, hyalinized, edematous stroma. Peripherally, cells are arranged in solid sheets with delicate fibrovascular stroma. Dystrophic calcification is uncommon, but may occur.

Clinical Setting

Oncocytomas are usually seen in middle and old age. Men are more commonly affected than women (ratio 1.7:1). Most are detected as an asymptomatic renal mass. Oncocytomas may grow to a size large enough to be palpable, painful, and cause gross or microscopic hematuria.

Radiologic Findings

■ **Overview.** Although historically it was felt that radiologic diagnosis of oncocytoma was possible by detecting the central scar, or a "spoke wheel" arterial supply, it has been found that all of these findings are nonspecific [6]. Confident differential from renal cell carcinoma is impossible [7].

■ **Excretory Urography.** Urographic features of oncocytoma are related to the mass effect of the mass. Depending upon size, there may be alteration of the renal contour with or without displacement or dilatation of the collecting system. Calcification is uncommon, but may be seen in the region of the central scar.

■ **Computed Tomography.** An oncocytoma appears as a focal, ball-shaped, homogeneous mass. On noncontrast enhanced scans, the area isodense or very slightly less dense than normal renal tissue. Contrast enhancement is usually homogeneous and less than that of the normal renal parenchyma.

The most suggestive feature of oncocytoma is a central, stellate area, representative of a central scar (Fig. 9).

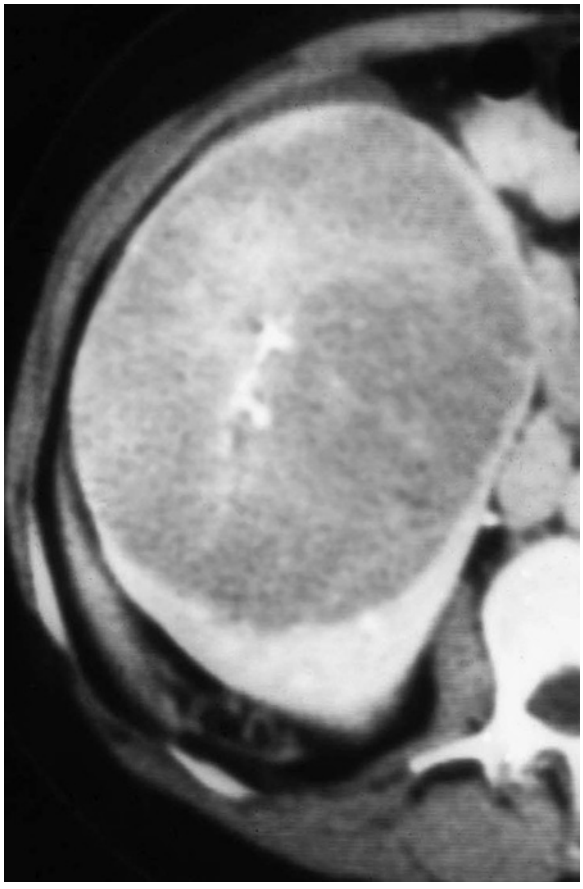

Fig. 9. Renal cell carcinoma. Computed tomogram, contrast medium enhanced. There is a large right renal mass with a well-defined central density which resembles the scar of an oncocytoma. Oncocytoma cannot be confidently differentiated radiologically from renal cell carcinoma

Unfortunately, this pattern overlaps the appearance of central necrosis seen with some adenocarcinomas, and cannot be used as a reliable indicator for the diagnosis of oncocytoma.

The presence of a homogeneous mass without a scar cannot be distinguished from nonnecrotic renal cell carcinoma (Fig. 10). An even less suggestive appearance of the oncocytoma is that of a heterogeneous mass on unenhanced and /or enhanced CT scans. This pattern is clearly indistinguishable from that of renal cell carcinoma.

■ **Ultrasonography.** The typical oncocytoma will be recognized as an evenly echogenic solid mass. The central scar has been described both as an area of increased or decreased echogenicity. In either case the sonographic appearance is not specific enough to confidently distinguish it from a malignant tumor.

■ **Magnetic Resonance Imaging.** The most suggestive features of oncocytoma are a homogeneously enhancing solid tumor with a central scar. The scar may be either hyperintense or hypointense. The absence of hemorrhage, necrosis, adenopathy, or venous tumor thrombus is noteworthy, but do not distinguish an oncocytoma from a renal cell carcinoma or other malignancies.

■ **Angiography.** Oncocytoma is usually a vascular, encapsulated mass that has neovascularity and a homogeneous nephrogram. The scar is typically avascular and may be seem in the angiographic nephrogram. There is no characteristic arrangement of the feeding arteries

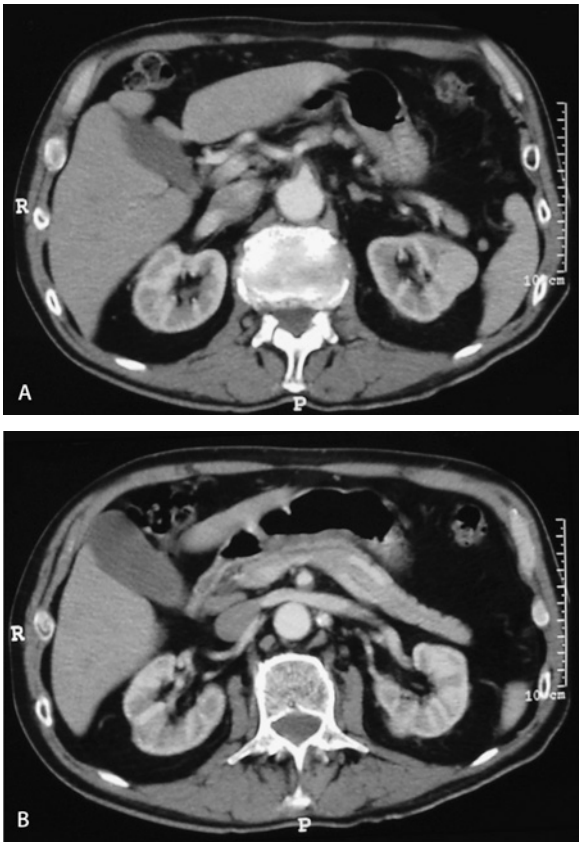

Fig. 10A, B. Coexistent oncocytoma and renal cell kidney in the same kidney. **A** Computed tomogram, contrast medium enhanced. There is a well-defined, homogeneous 2 cm mass, which enhanced 68 Hounsfield units. **B** Section through the lower pole shows a 1.2 cm mass. The larger mass was an oncocytoma, the smaller mass a renal cell carcinoma

that distinguishes this tumor from other tumors. Arterial encasement, arterio-venous shunting, and venous invasion are absent.

Mesoblastic Nephroma

Definition

Mesoblastic nephroma a rare benign renal neoplasm that usually presents in the neonate and is composed primarily of connective tissue [1, 8].

Pathology

The typical tumor is a solid, yellow-tan, unencapsulated mass of 8–30 cm replacing most of the kidney parenchyma. The cut surface has a whorled appearance resembling a uterine leiomyoma. The tumor is unencapsulated with its margins blending imperceptibly with normal renal parenchyma (Fig. 11A). Hemorrhage and necrosis are uncommon. Typically the tumor does not invade the renal pedicle, extend into the renal pelvis or metastasize.

Two types of cysts may be present. There may be discrete areas of cystic degeneration (pseudocyst). There may be small fluid-filled epithelial-lined cysts located near the junction of the tumor and uninvolved parenchyma ("trapped nephrons" vs. benign epithelial differentiation).

Microscopically the tumor consists of interlacing bundles of benign mesenchymal cells. At the renal interface, the spindle cells grow between intact nephrons (Fig. 11B). Within the tumor small numbers of tubules and nephrons may be discovered.

Clinical Findings

The mesoblastic nephroma is the most common solid renal mass discovered in the newborn or neonate. There is no predilection for race or gender. Mesoblastic nephroma is rarely discovered in older children or adults.

Mesoblastic nephroma is usually discovered either in utero during an obstetric sonographic examination or in the newborn as a large, nontender abdominal mass. Polyhydramnios, which may be acute and give rise to premature labor, is a well-recognized complication of mesoblastic nephroma. The large size of the mass in the fetus may also cause dystocia.

Radiologic Findings

■ **Overview.** Mesoblastic nephroma is best evaluated utilizing ultrasonography.

■ **Excretory Urography.** Although seldom utilized, the urographic features of mesoblastic nephroma include large, non-calcified renal mass with distortion of the remaining parenchyma.

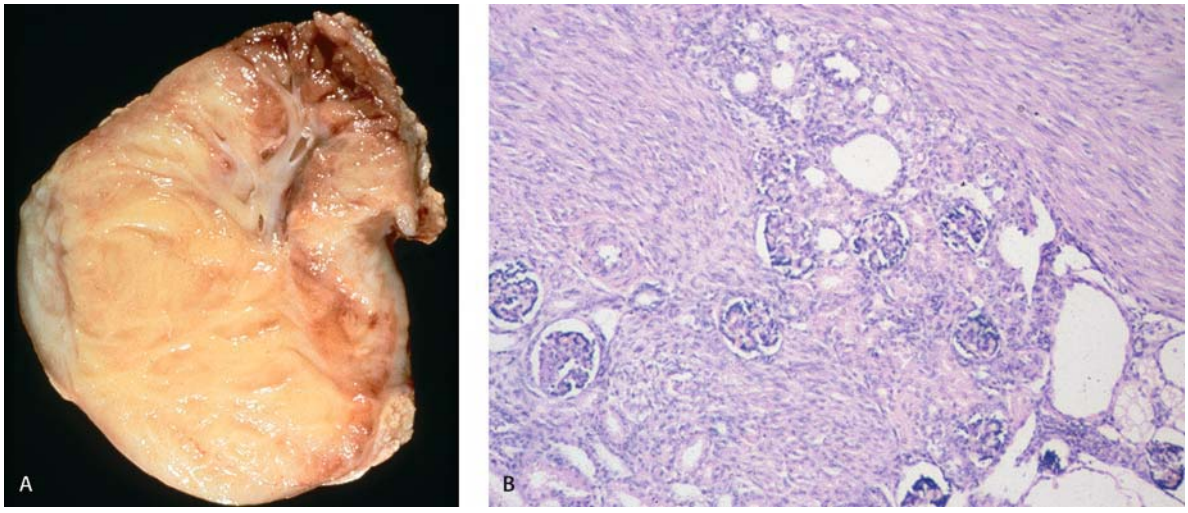

Fig. 11A, B. Mesoblastic nephroma replacing the right kidney. **A** Cut gross specimen. The tumor replaces almost the entire right kidney. The reniform shape is maintained. **B** Photomicrograph. The tumor is comprised of interlacing bundles of benign mesenchymal cells, which infiltrate between intact nephrons

■ **Computed Tomography.** Mesoblastic nephroma is characteristically large and of homogeneous tissue attenuation both before and after contrast material enhancement. Like other renal masses enhancement is less than normal renal tissue. Hemorrhage, necrosis, cyst formation, and calcification are uncommon.

■ **Ultrasonography.** Mesoblastic nephroma is usually typically evenly echogenic with low-level echoes. Cystic areas within the tumor may be identified as small, dilated, fluid-filled structures. Necrosis, although uncommon, is seen as focal hypoechoic areas within the echogenic mass. In utero diagnosis is suggested with the combination of polyhydramnios and a solid abdominal mass (Fig. 12).

■ **Magnetic Resonance Imaging.** Mesoblastic nephroma is usually imaged as a large reniform mass, which enhances less than normal renal parenchyma (Fig. 13).

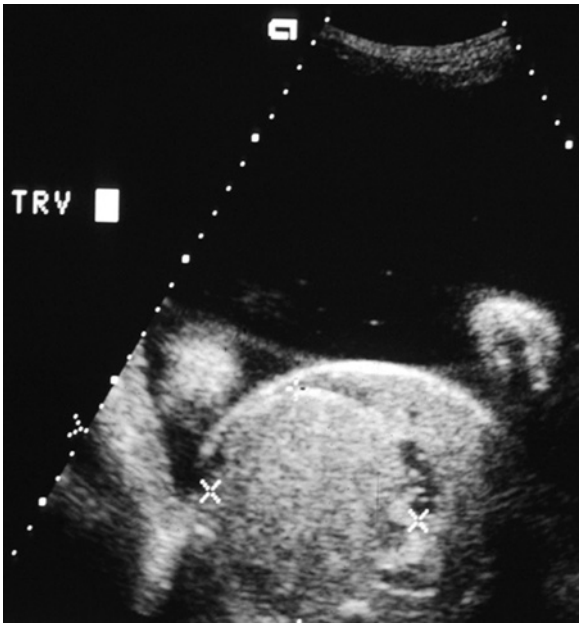

Fig. 12. Mesoblastic nephroma detected on a maternal sonogram. Transverse scan through the fetal abdomen demonstrates a 7.5 cm solid, echogenic mass. Note also the presence of polyhydramnios

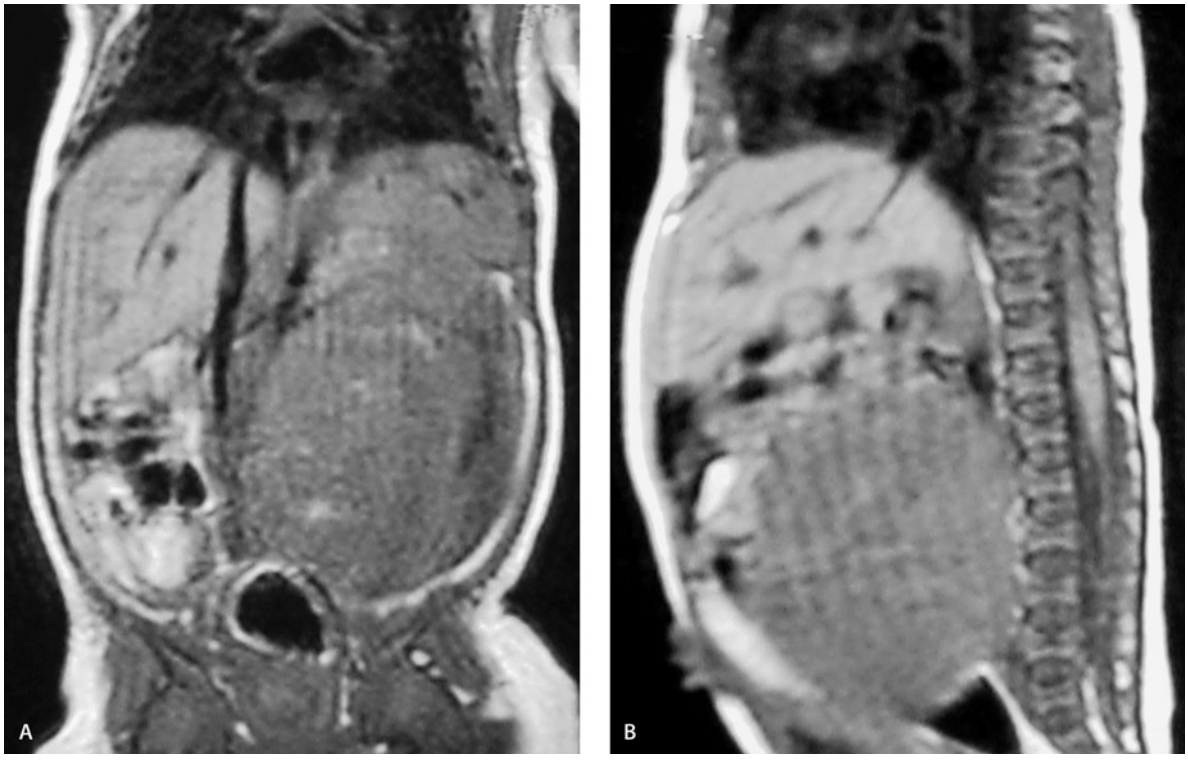

Fig. 13A, B. Mesoblastic nephroma. T1-weighted coronal (**A**) and sagittal (**B**) scans show a large solid mass within the left kidney. Note that the reniform shape is maintained

Juxtaglomerular Tumor

Definition

Juxtaglomerular tumor is a benign renal tumor, which secretes renin and is rare but curable cause of significant hypertension [1, 9].

Pathology

The tumor is usually small, solitary, and confined to the kidney. The average tumor size is small, usually because affected patients come to medical attention because of their symptoms. Most are located just beneath the renal capsule. On gross inspection, the juxtaglomerular cell tumor is usually tan or gray, sharply marginated, and often demarcated from the surrounding parenchyma by a pseudocapsule (Fig. 14A). Small foci of hemorrhage within the tumor are common. Like other peripherally located renal tumors, they may present with massive perinephric hemorrhage.

Microscopically, these tumors are composed of sheets and/or cords of cells associated with numerous blood vessels. The cells resemble smooth muscle cells and form eddies about minute vascular channels. The media of small arteries may be composed of numerous cells identical to those of the tumor, thus recapitulating the morphology of the juxtaglomerular apparatus (Fig. 14B). Cytoplasmic granules can be demonstrated with PAS or Bowie stains. The tumor may contain 30,000 times as much renin as the adjacent renal cortex.

Clinical Setting

Juxtaglomerular tumor often presents in teenagers or young adults and women are more frequently involved than men. The most frequent presenting symptoms include moderate to severe headache (hypertension), polydipsia polyuria, including enuresis (kaliopenic nephropathy), and intermittent neuromuscular complaints (hypokalemia). Hypertension, frequently moderate to severe, is invariably present and may be accompanied by retinopathy. Hypertension is often present for many years, uncontrolled by antihypertensive medication. An abdominal or flank bruit is absent.

The peripheral renin level is usually elevated, with evidence of secondary aldosteronism that persists even if the hypertension is controlled medically. Renal function is usually normal unless complicated by hypertensive nephropathy.

Radiologic Findings

■ **Overview.** The radiologic findings of juxtaglomerular cell tumor are nonspecific. Like other hormone secreting tumors, the diagnosis is made clinically and the radiologic findings are confirmatory.

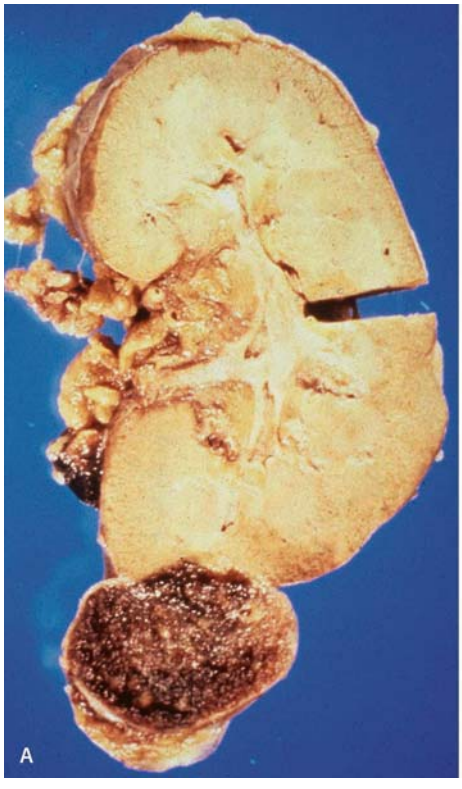

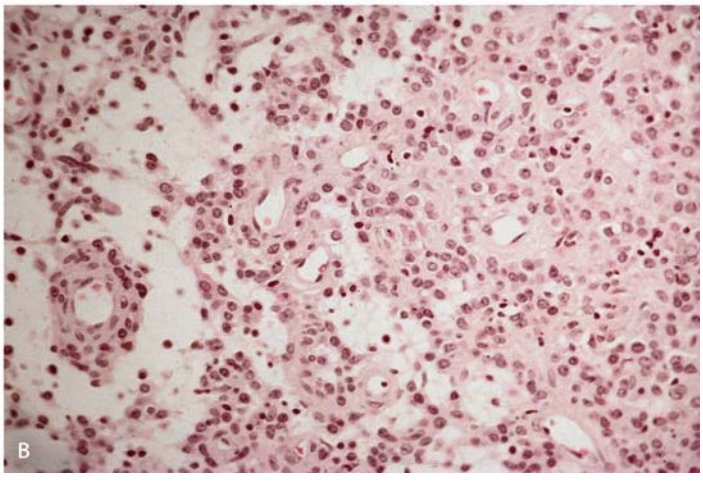

Fig. 14A–C. Juxtaglomerular tumor arising from the lower pole of the left kidney. **A** Gross specimen. A 4 cm mass arises exophytically from the lower pole of the kidney. **B** Photomicrograph. The walls of blood vessels are composed of tumor cells. **C** Excretory urogram, left posterior oblique. There is a 4 cm mass originating from the lower pole of the left kidney

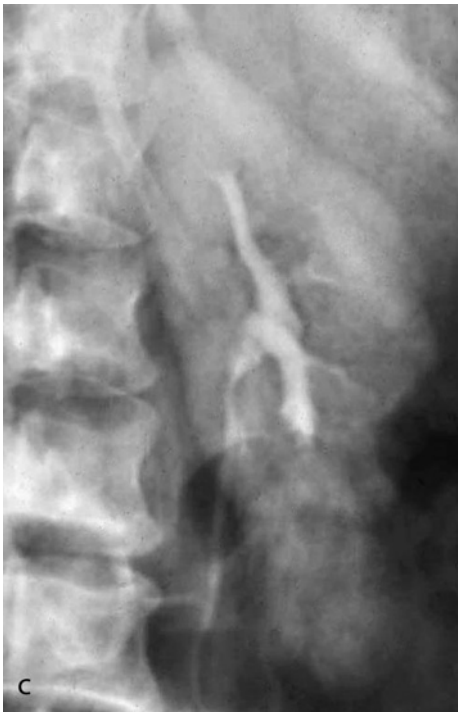

Fig. 14C

■ **Excretory Urography.** The excretory urogram may demonstrate a small, well-defined mass that is often peripheral (Fig. 14C). Because the mass is frequently small, the urogram is often normal.

■ **Computed Tomography.** The juxtaglomerular cell tumor is usually hypodense or isodense with normal renal parenchyma. Especially when the tumor is small it may not be detected on unenhanced scans and be very subtle on enhanced scans. CT may also be helpful in identifying the extent of the tumor as well as detecting intratumor hemorrhage or necrosis.

■ **Ultrasonography.** The juxtaglomerular cell tumor is usually more echogenic than normal renal parenchyma, possibly because of the numerous interfaces between the juxtaglomerular cells and the abundant small vascular channels within the tumor. Hemorrhage and necrosis may are typically hypoechoic areas within the mass. Less commonly, a hypoechoic solid tumor without evidence of necrosis is encountered.

■ **Angiography.** In some cases of juxtaglomerular cell tumor patients are misdiagnosed clinically as renal vascular stenosis. The former will have normal renal arteries whereas the latter will have renal artery stenosis.

When a case of suspected renal artery stenosis has normal renal arteries, careful evaluation for juxtaglomerular cell tumor is warranted. Despite the presence of abundant microscopic vascular spaces within the tumor, arteriography demonstrates a hypovascular mass since the vessels are so small.

Mesenchymal Tumors

Definition

Mesenchymal tissue gives rise to fibroma, lipoma, myoma, angioma, and lymphangioma [2].

Pathology

Tumors of mesenchymal origin are usually small and do not distort either the internal architecture or the contour of the kidney. They are most often incidental findings at nephrectomy or autopsy. Less commonly they present as a large intrarenal mass (Fig. 15). Microscopically they are identical to similar tumors elsewhere in the body.

Clinical Setting

Benign mesenchymal tumors of the adult kidney become symptomatic only when they grow large enough to cause pain or hematuria, or both. Those which are small often escape clinical detection and are discovered at autopsy or when there is a nephrectomy for another disease.

Radiologic Findings

■ **Overview.** A specific radiologic diagnosis of mesenchymal tumors is impossible. Even a rare renal lipoma cannot be distinguished from the more common angiomyolipoma. The radiologic findings are nonspecific. Confident differential from other benign or malignant tumors is impossible.

■ **Excretory Urography.** Urographic features of mesenchymal tumors are the same as those of any other solid tumor, either benign or malignant, and are related to the mass effect of the lesion. These include focal collecting system attenuation and displacement or focal caliectasis due to local pressure on a draining infundibulum.

■ **Computed Tomography and Magnetic Resonance Imaging.** Mesenchymal tumors usually are homogeneous expansive masses that enhance following administration of contrast material, Like other renal tumors, the enhancement is less than surrounding normal renal parenchyma (Fig. 15).

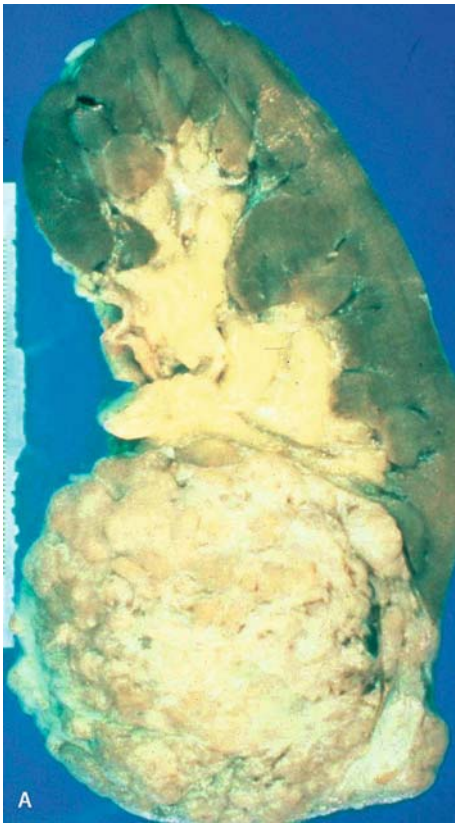

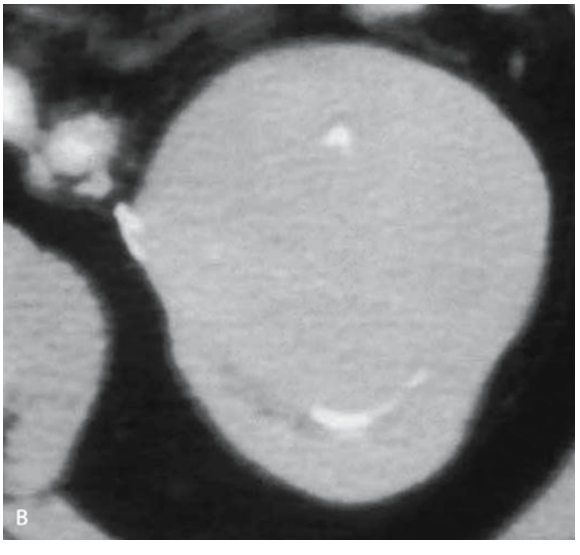

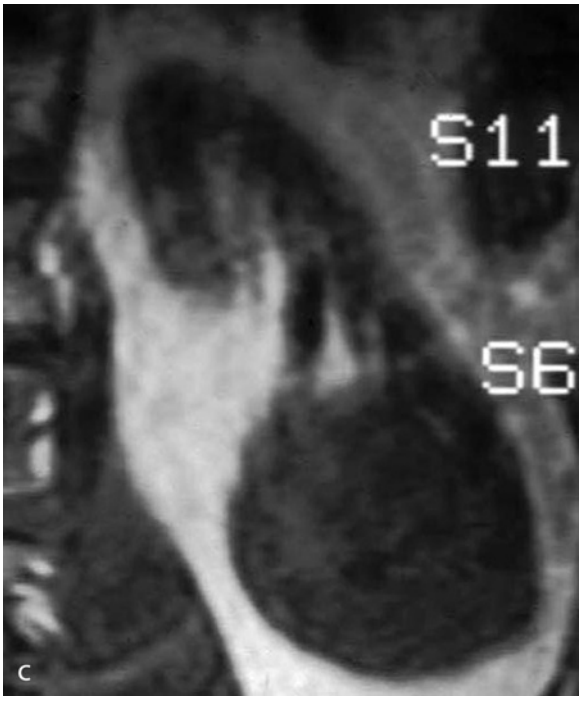

Fig. 15A–C. Large leiomyoma originating from the lower pole of the left kidney. **A** Gross specimen. A 7 cm nonnecrotic tumor arises from the lower pole of the left kidney. **B** Computed tomogram, contrast medium enhanced, pyelographic phase. The tumor is homogeneous, ball-shaped and distorts the collecting system and contour. **C** Coronal MR image, T1-weighted. The mass is homogeneous and has a signal similar to the kidney

■ **Ultrasonography.** Most mesenchymal tumors are echogenic solid masses either deep within the parenchyma or on the surface of the kidney.

■ **Angiography.** Mesenchymal neoplasms of the kidney are usually hypovascular. Angiography could provide valuable information for surgical planning if nephron-sparing surgery is to be performed.

Benign Adrenal Tumors

Adenoma

Definition

Adrenal cortical adenoma is a benign neoplasm arising from adrenal cortical cells that resemble normal adrenal cells histologically.

Pathology

Adrenal adenomas show considerable variation in gross appearance. They vary in size from barely visible to 10 cm. Larger adenomas more commonly seen in patients with virilizing syndromes where the average size is 5 cm. Adenomas which have abundant intracellular lipid (lipid-rich) are typically yellow (Fig. 16A). Those with less intracellular lipid (lipid-poor) may be red, brown or black (Fig. 16B). Tumor necrosis is uncommon. Approximately 70% of adenomas are lipid-rich.

Microscopically, the cells tend to be fairly uniform. Pleomorphism is uncommon. Tumor necrosis is un-

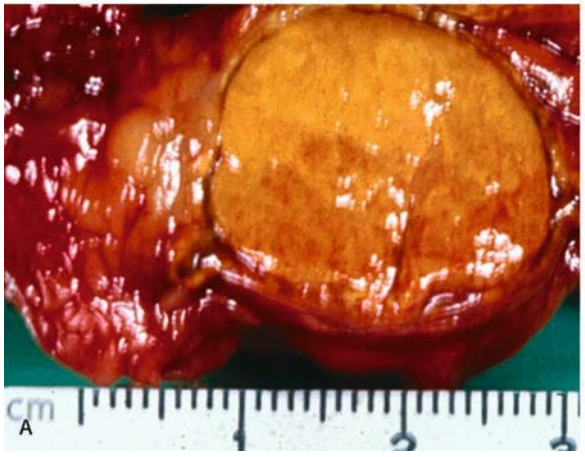

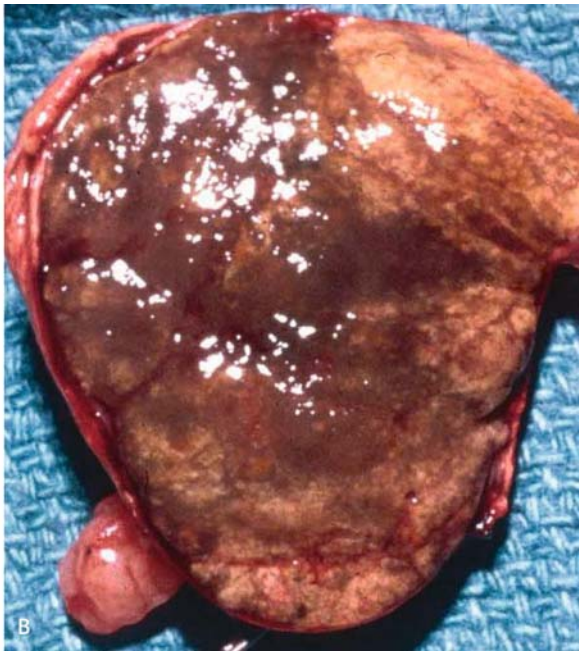

Fig. 16A, B. Adrenal adenoma, pathology. **A** Lipid rich adrenal adenoma, gross specimen, cut section. The yellow color results from the abundant lipid within the tumor. The tumor measures 2 cm, is sharply circumscribed and is nonnecrotic. **B** Lipid poor adrenal mass, gross specimen, cut section. The tumor is brownish-red color is more typical of an adenoma which does may contain abundant lipid. The adenoma is well-defined and nonnecrotic

common and often a complication of thrombosis. Adenomas causing the adrenogenital syndrome are the most difficult to separate from malignancy, especially when the tumor is large. Features that favor malignancy include nuclear pleomorphism, mitotic activity and tumor necrosis.

Clinical Setting

Adrenal adenomas may produce hormones resulting in hypercortisolism, hyperaldosteronism, masculinization and feminization. More commonly, however, cortical adenomas do not hyperfunction and are detected as an incidental mass (incidentaloma). Cortical hormones are synthesized but not in excessive quantities, hence, the term non***hyper***functioning rather than nonfunctioning adenoma. . Functioning and nonfunctioning tumors often have an identical gross and radiologic appearance Functioning adenoma may suppress normal adrenal function result in some degree of atrophy of normal adrenal tissue. Nonhyperfunctioning adenomas greater than 3 cm in diameter occur in approximately 3 per cent of autopsied. Prevalence increases with age.

An increased prevalence of adenoma has been reported in patients with diabetes, hypertension, renal adenocarcinoma, and hereditary colonic adenomatosis.

Radiologic Findings

■ **Overview.** The identification of adenoma in a patient with adrenal hyperfunction (e.g. hypercortisolism, hyperaldosteronism) is usually straightforward. The most challenging task of adrenal imaging is to distinguish the nonhyperfunctioning adenoma from metastasis. This is best accomplished by detecting intracellular lipid (CT or MR) or by evaluating the CT washout dynamics after administration of contrast media [10–12].

■ **Computed Tomography.** Lipid-rich adenomas will appear as a homogeneous mass, with a diameter less than 5 cm, and an attenuation value between –5 and +10 Hounsfield units on an unenhanced scans (Fig. 17A).

Lipid-poor adenomas are typically homogeneous, less than 5 cm but have an attenuation value of greater than 10 Hounsfield units on an unenhanced scan (Fig. 17B). In these cases, adrenal washout is very helpful in differentiating adenoma from metastasis.

Upon immediate administration of intravenous contrast material (60 s), adrenal adenomas and metastases will have nearly identical attenuation values. However, adenomas will lose their enhancement more quickly than metastases. This rapid wash out of enhancement can be measured and can be used to confidently differentiate adenomas from metastases. An attenuation cut-

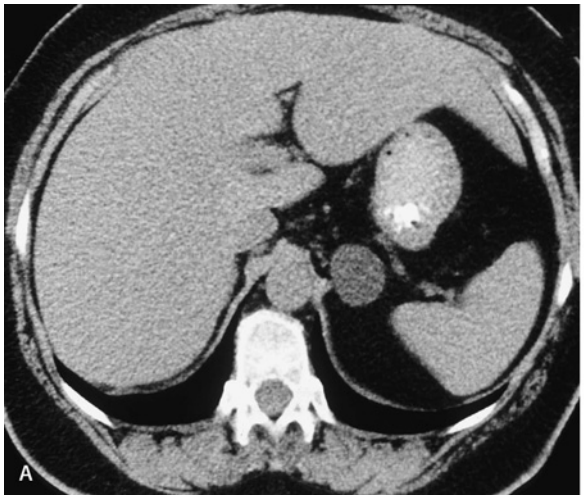

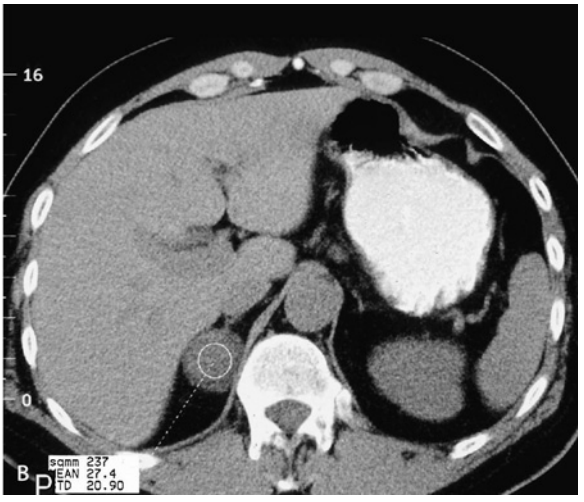

Fig. 17A, B. Adrenal adenoma spectrum of CT findings. **A** Lipid rich. CT scan, nonenhanced. There is a well-defined, homogeneous, 3 cm left adrenal mass, which measures–7 Hounsfield units. **B** Lipid poor. CT scan, nonenhanced. There is a well-defined, homogeneous, 3 cm right adrenal mass that measures 27 Hounsfield units. This appearance is nonspecific and may represent an adenoma, a pheochromocytoma or a metastasis. In these cases, adrenal washout may be helpful

off of 24 HU on enhanced CT performed 12 to 18 minutes after contrast administration can differentiate adenomas (24 HU) from metastases (>24 HU) with a very high sensitivity and specificity [10].

A delayed CT attenuation value can be used to calculate the percentage of relative enhancement washout, which can also be used to differentiate adenomas from metastases.

Percentage of relative enhancement washout = [(E-D)/E] × 100, where E is the enhanced attenuation value and D is the delayed enhanced value. A threshold value of more than 50% contrast washout on 15-minute delayed CT has been used to differentiate adenomas from metastases with a sensitivity and specificity near 100% [10, 13](Fig. 18).

If both of these techniques produce an intermediate result, and if differentiation is critical for patient management, biopsy may be required. This is especially true in patients with a known primary tumor, in which management would be altered if an adrenal metastasis were present.

■ **Magnetic Resonance Imaging.** An adenoma is typically isointense or mildly hypointense to liver on T1- and T2-weighted spin-echo sequences. On an opposed-phase gradient-echo scan, the lipid-rich adenoma demonstrates signal dropout relative to spleen (Fig. 19). This technique is very sensitive at differentiating adenoma from metastasis. The lipid-poor adenoma typically will not demonstrate signal dropout. In these cases, CT adrenal washout should be performed [14].

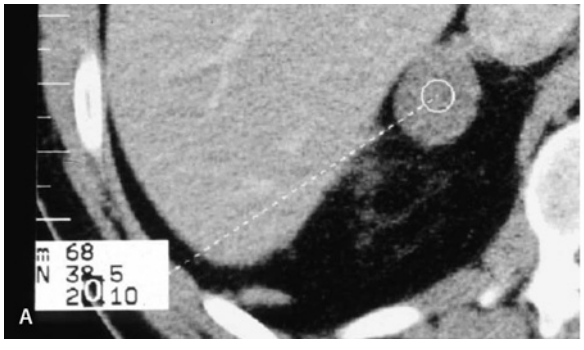

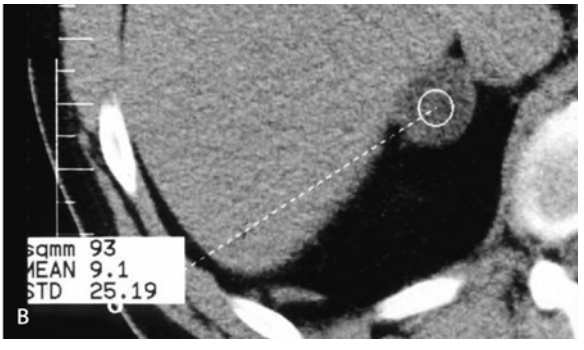

Fig. 18A, B. Adrenal washout study. This study may be very helpful in evaluating adrenal masses which measure greater than 10 Hounsfield units on an nonenhanced scan, or in those cases performed only with a contrast material enhanced scan. **A** On the immediate enhanced scan a well-defined adrenal mass measures 38.5 Hounsfield units. **B** On the delayed scan the mass measures 9.1 Hounsfield units. The washout is 76%, which is indicative of adenoma. Note that on the delayed scan the mass measures less than 10 Hounsfield units, confirming that the mass is a lipid rich adenoma

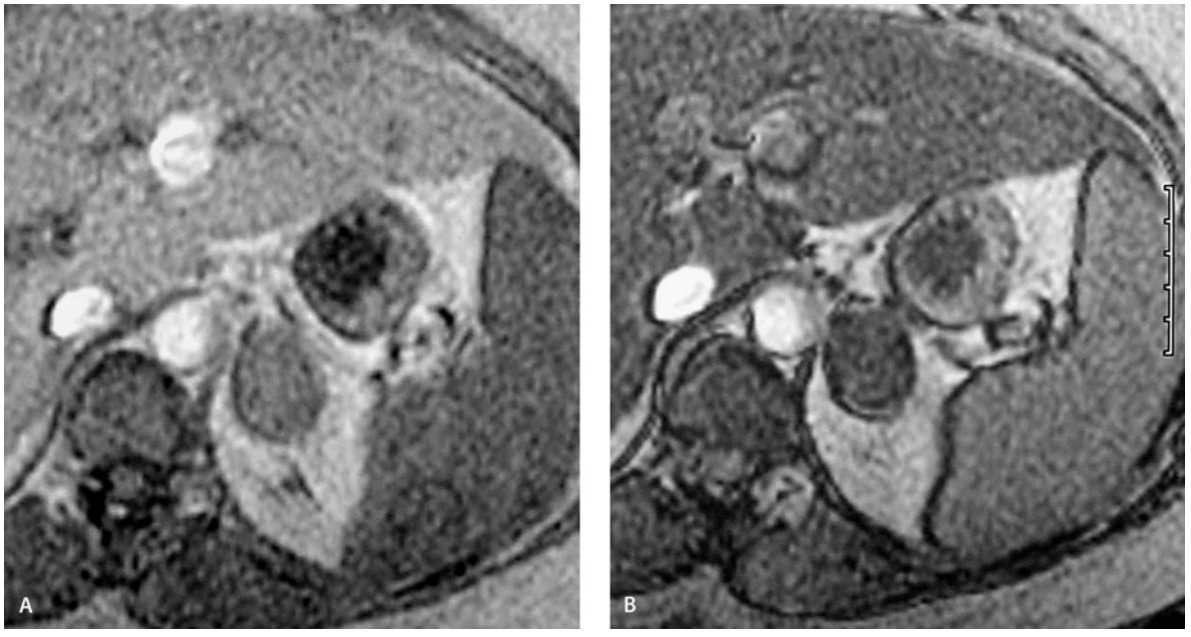

Fig. 19A, B. Opposed-phase gradient-echo scan. **A** On the in-phase scan, the left adrenal mass has a similar signal to that of spleen. **B** On the out-of-phase scan, the adrenal mass demonstrate signal dropout and is of lower signal than the spleen. This signal dropout indicates the presence of intracellular lipid, thus a lipid rich adenoma

Pheochromocytoma

Definition

Pheochromocytoma is a neoplasm of the adrenal medulla composed of paraganglionic cells. Most tumors produce catecholamines. The term pheochromocytoma should be restricted to tumors that arise within the adrenal gland. The same tumor arising outside the adrenal gland should be referred to as a paraganglioma rather than an extra-adrenal pheochromocytoma.

Pathology

Most pheochromocytomas measure from 3–5 cm in diameter. They are typically round to ovoid. Large tumors are demarcated from the normal adrenal by a pseudocapsule of compressed adrenal tissue (Fig. 20A). Small tumors are not encapsulated (Fig. 20B). The tumor is gray pink and has a soft consistency. Multiple tumors are not uncommon (Fig. 20B) Hemorrhage, necrosis and cyst formation are common in large tumors.

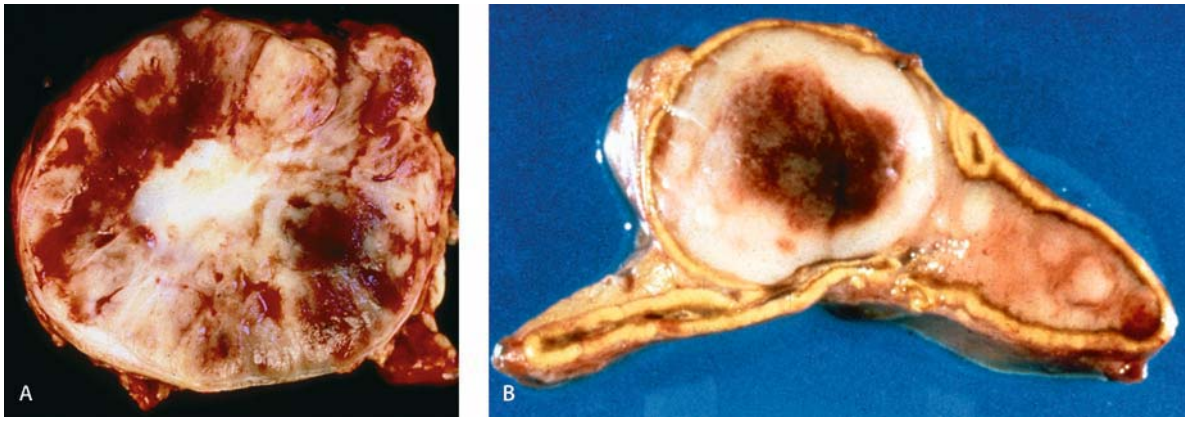

Fig. 20A, B. Pheochromocytoma, gross pathology, two different cases. The tumor may be large (**A**) or small (**B**). Large tumors are often hemorrhagic and necrotic with prominent cystic areas. There are at least four distinct tumors in the specimen (**B**)

Microscopically, the pheochromocytoma resembles normal adrenal medullary tissue and is composed of pheochromocytes. Adjacent groups of tumor cells are separated by a rich fibrovascular stroma. The walls of areas of cystic necrosis may be calcified. The nuclear pleomorphism that may be present in some tumors does not correlate with biologic behavior.

Clinical Setting

Excess catecholamine production causes hypertension (labile or sustained) combined with episodes of palpitations, perspiration, and anxiety. The 24-hour urine vanillylmandelic acid (VMA) level is elevated in 90 per cent of patients. The presence of free norepinephrine in a 24-hour urine specimen is a sensitive indicator of functioning paraganglioma. A urine assay is more sensitive than plasma catecholamine measurement. Approximately 10 per cent of cases are associated with extra-adrenal paragangliomas or are bilateral.

Pheochromocytoma may be associated with Type IIA and Type IIB multiple endocrine neoplasia (MEN) syndromes, neurofibromatosis, von Hippel-Lindau disease and Carney's triad. Patients with MEN syndromes frequently have asymptomatic pheochromocytoma.

Radiologic Findings

■ **Overview.** The radiologic findings of pheochromocytoma are nonspecific, but correlate with the tumor's variable gross pathologic findings. Like other hormone secreting tumors, however, the diagnosis is made clinically and the primary role of imaging is to localize and to determine if there are multiple tumors [1, 11, 14].

■ **Computed Tomography.** Computed tomography has a high sensitivity (>90 per cent) in the detection of pheochromocytoma. Contrast material is rarely required but if nonionic contrast material is utilized, no subsequent increase in epinephrine or norepinephrine levels has been demonstrated. Small tumors are usually homogeneous, whereas large tumors often contain areas of diminished attenuation reflecting necrosis. Those with extensive cystic necrosis may be confused radiologically with a complex adrenal cyst, hemorrhage or abscess (Fig. 21A).

There are, however, several limitations of computed tomography. It is impossible to distinguish pheochromocytoma from other adrenal tumors by computed tomography alone. Computed tomography is less reliable than magnetic resonance imaging studies for very small nodules and less sensitive than magnetic resonance and radionuclide studies for extra-adrenal tumors and metastatic disease. Despite these limitations, computed tomography is the most commonly utilized technique for initial evaluation of a patient with clinical evidence of a catecholamine-producing tumor.

■ **Magnetic Resonance Imaging.** Magnetic resonance imaging is especially useful: (1) in detecting extra-adrenal paragangliomas, especially those arising in the wall of the bladder and paracardiac region; (2) in evaluating the postoperative patient; (3) in patients with hypertension and only mildly elevated catecholamine levels; (4) and in evaluating patients at increased risk for developing paraganglioma (e.g., von Hippel-Lindau syndrome).

On T1-weighted images pheochromocytoma typically has a signal intensity that is lower than or equivalent to that of liver, kidney, or muscle. In many cases the signal intensity is high on T2-weighted images (Fig.

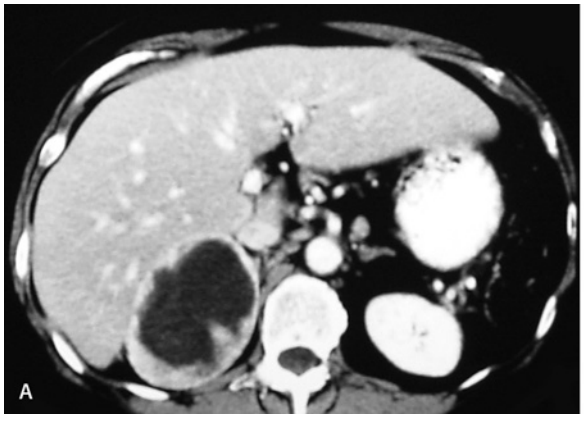

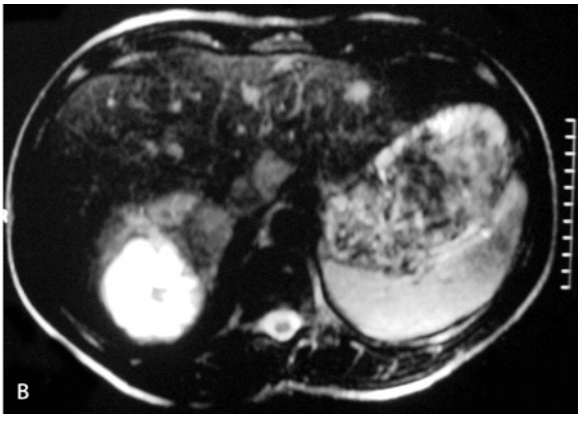

Fig. 21A, B. Pheochromocytoma, 2 different cases. **A** Computed tomogram, contrast material enhanced. There is a 7 cm thick-walled, cystic mass which originated above the right kidney. **B** T 2-weighted axial MR scan with fat saturation. A portion of the tumor has a very high signal (compare to adjacent CSF)

21B). These signal characteristics support the diagnosis of pheochromocytoma but are in no way pathognomonic.

Less commonly, however, a pheochromocytoma may demonstrate atypical signal characteristics, which emphasizes the importance of correlating radiologic abnormalities with clinical and laboratory findings.

■ **Nuclear Medicine.** Metaiodobenzylguanidine (MIBG) is a norepinephrine analogue accumulates at sites of norepinephrine synthesis. It may be especially helpful in detecting medullary hyperplasia, recurrence, metastases, or extra-adrenal paragangliomas. MIBG has the advantage of imaging the entire body with one dose. Disadvantages of MIBG include limited availability, poor spatial resolution, and the length of the procedure (1 to 3 days). MIBG imaging is not specific and may be positive in cases of neuroblastoma, carcinoid, medullary thyroid carcinoma, choriocarcinoma, and atypical schwannoma.

Myelolipoma

Definition

Myelolipoma is an uncommon, benign, metabolically inactive tumor composed of mature fat and bone marrow.

Pathology

On gross examination, the myelolipoma is usually pale yellow with areas of red or pink that represents hematopoietic components and hemorrhage (Fig. 22). Occasionally the hemorrhage is massive. Large lesions are often lobulated. The myelolipoma may be multiple and bilateral.

Microscopically, the lesion is composed of mature fat and proliferating hematopoietic tissue. The hematopoietic tissue resembles bone marrow and contains the cell lines in different stages of maturation. Foci of hemorrhage and calcification are common.

Clinical Setting

Myelolipoma is usually detected as an incidental finding in adults undergoing a radiologic examination for unrelated clinical indications. Autopsy prevalence is less than 0.2 per cent and there is an equal sex distribution. Most adrenal myelolipomas originate in the adrenal cortex and are 10 cm in diameter or larger. Approximately 10 per cent of cases are bilateral. Myelolipomas

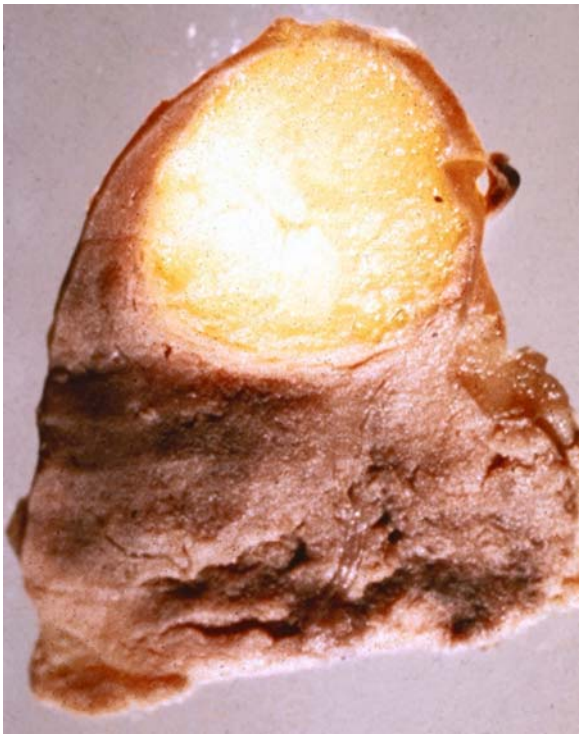

Fig. 22. Myelolipoma, gross pathology. The tumor is well defined and sharply marginated. Its yellow color is a result of the abundant adipose tissue

contain fat as adipose tissue and bone marrow elements in variable proportions. Most have sufficient fat to be detected by computed tomography or magnetic resonance imaging.

The vast majority of patients have otherwise normal adrenal glands. Myelolipoma can coexist with Cushing's syndrome, congenital adrenal hyperplasia, and nonhyperfunctioning adenoma. Very rarely, a myelolipoma arises in an extra-adrenal site, such as the retroperitoneum, thorax, or pelvis. Hemorrhage is a significant complication of myelolipoma; spontaneous bleeding can cause acute flank pain or rarely hypovolemic shock.

Radiologic Findings

■ **Overview.** The presence of a fatty adrenal mass is *very suggestive* of myelolipoma. The best radiologic techniques to detect this fat are computed tomography and magnetic resonance imaging [15, 16]. Differentiation from angiomyolipoma is dependent upon determination of tumor origin. Theoretically, a well-differentiated supra-renal liposarcoma could not be distinguished from a large myelolipoma.

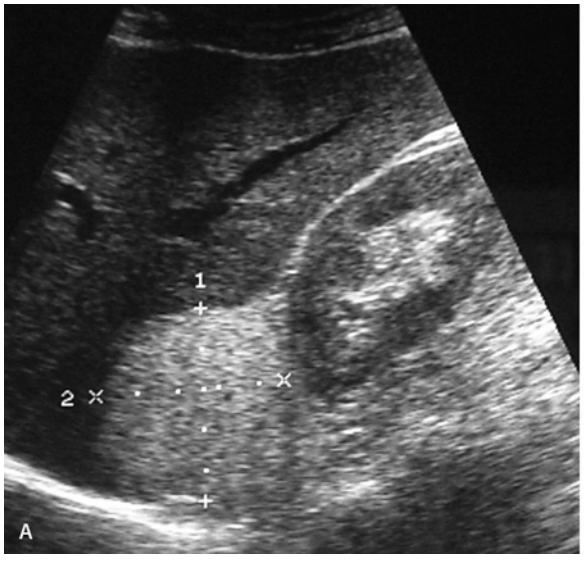

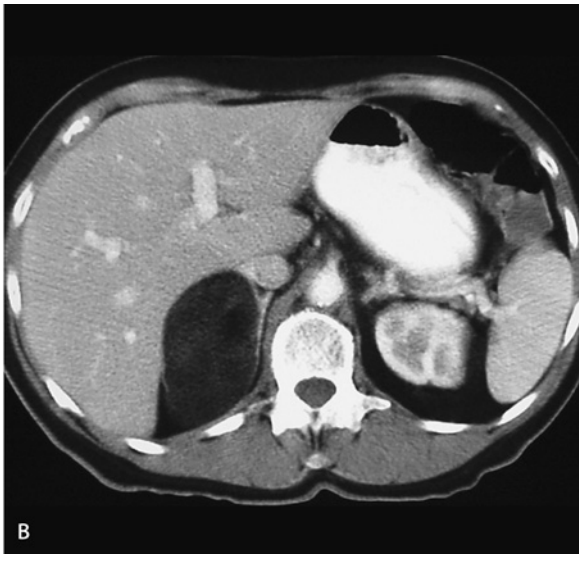

Fig. 23A, B. Myelolipoma, ultrasound and computed tomographic findings. **A** Longitudinal sonogram, right upper abdomen. There is a 4.8 cm by 4.6 cm mass in the region of the right adrenal. **B** Computed tomogram, contrast material enhanced. The tumor measured –40 Hounsfield units, indicative of adipose tissue, hence a myelolipoma

■ **Computed Tomography.** Fatty areas within the tumor will have attenuation values less than –30 Hounsfield units (Fig. 23). Hemorrhage and marrow elements will be recognized as foci of soft tissue density within the tumor. The margins of a hemorrhagic myelolipoma may be irregular, owing to blood dissecting into the adjacent retroperitoneal fat. Very rarely the hemorrhage is so extensive that it obliterates all of the fat. Confident diagnosis in these cases is impossible. Calcification is readily apparent and commonly seen on computed tomography.

■ **Magnetic Resonance Imaging.** As with CT, it is the identification of the fatty component on MR that enables confident diagnosis. The fatty components of myelolipoma have a similar signal to that of renal sinus and retroperitoneal fat. Fat-suppressed images are extremely helpful and demonstrate signal loss within the mass. As the fat within a myelolipoma is adipose tissue and not intracellular lipid, chemical shift imaging is not helpful in MR diagnosis. Bone marrow elements and hemorrhage will have a variable and a less characteristic signal. Coronal or sagittal images are valuable in differentiating a myelolipoma from an upper pole angiomyolipoma.

Ganglioneuroma

Definition

Ganglioneuroma is a benign neoplasm composed of sympathetic ganglion cells with variable numbers of Schwann cells, and collagen.

Pathology

There is considerable variation in size. They are typically sharply marginated, but not encapsulated. On cut section, the ganglioneuroma is gray-white and firm thus resembling a leiomyoma (Fig. 24A). There may be extensive areas of cystic degeneration. They may be bilateral. Very rarely, ganglioneuroma is discovered with pheochromocytoma or with a peripheral nerve sheath tumor.

On microscopic examination, the ganglion cells are often clustered within the tumor mass. Less commonly, they are distributed diffusely throughout the tumor. The stroma may appear edematous or compact. Schwann cells are often arranged in bundles within the ganglioneuroma.

Clinical Setting

Ganglioneuroma occurs at all ages and is typically asymptomatic. Ganglioneuroma is rarely associated with hypertension despite the fact that levels of urinary catecholamines and their metabolites may be elevated. Rarely a patient with ganglioneuroma will present with watery diarrhea, hypochlorhydria, and alkalosis (WDHA), the Verner-Morrison syndrome. This condition results from the secretion of a vasoactive intestinal polypeptide by the tumor. Likewise, very rarely, ganglioneuroma may result from the maturation of a neuroblastoma or a ganglioneuroblastoma.

Radiologic Findings

■ **Overview.** Ganglioneuroma can be suggested in a nonhypertensive patient with an adrenal mass and an elevated level of catecholamine and/or catecholamine metabolites or with Verner-Morrison syndrome. In asymptomatic patients, specific diagnosis requires either biopsy or surgical removal (Fig. 24) [1, 11].

■ **Excretory Urography.** A large ganglioneuroma may compress and displace the upper pole of the kidney. Calcification is uncommon.

■ **Computed Tomography.** On the unenhanced scan, a ganglioneuroma has attenuation slightly less than that of muscle. There may be faint enhancement.

■ **Magnetic Resonance Imaging.** On T1-weighted magnetic resonance images, the tumor is homogeneous with low signal intensity. On T2-weighted images the tumor is heterogeneous with predominantly high signal intensity.

Very Rare Benign Adrenal Tumors

Mesenchymal tumors, such as leiomyoma, and hemangioma are very rare. Affected patients present as a large adrenal mass with normal adrenal function. Although the presence of phleboliths and contrast material pooling on angiography has been reported with hemangioma, an accurate diagnosis is rarely made prospectively. Likewise, a specific radiologic diagnosis is rarely possible in cases of other mesenchymal adrenal tumors [2].

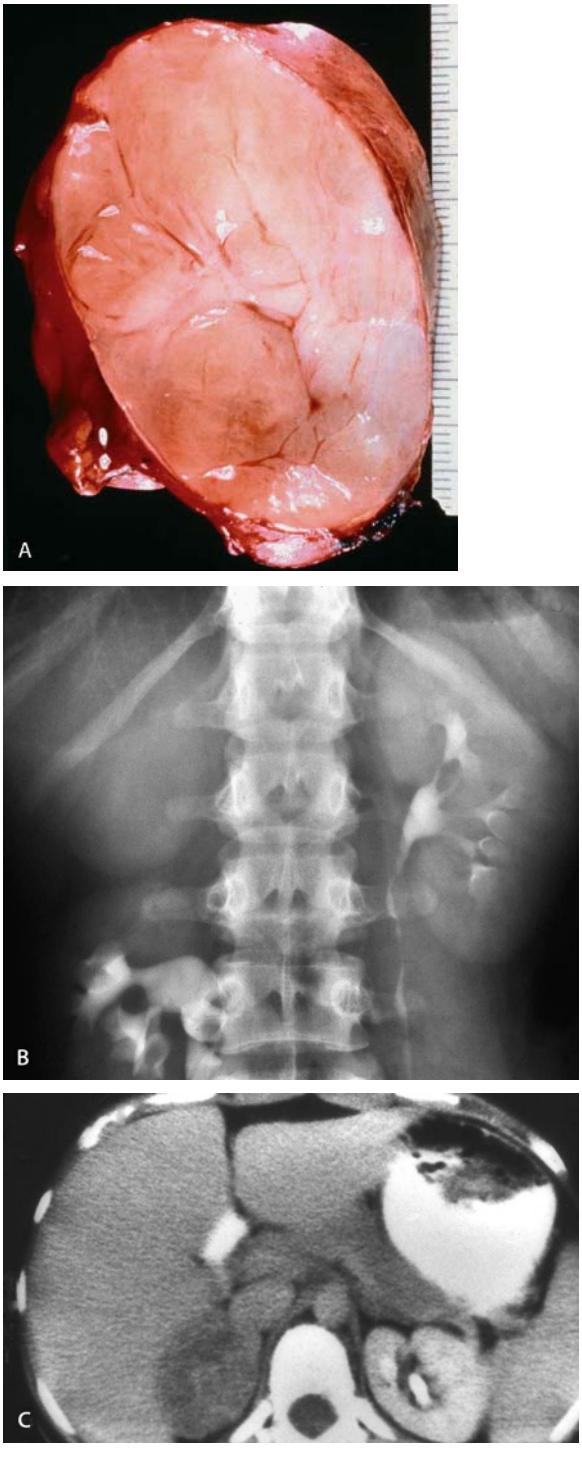

Fig. 24A–C. Ganglioneuroma. **A** Gross pathology, cut section. The tumor is sharply marginated and nonnecrotic. **B** Excretory urogram, pyelographic phase. There is a large mass displacing the right kidney inferiorly. **C** Computed tomogram, contrast material enhanced. The mass is well defined and has a density slightly less than adjacent muscle

References

1. Hartman DS (2000) Benign renal and adrenal tumors. European Radiology 10 (Supplement 2) 5221–5230
2. Davidson AJ, Hartman DS, Choyke PL, Wagner BJ (1999) Davidson's radiology of the kidney and genitourinary tract, Third Edition. W B Saunders Company, Philadelphia
3. Wagner BJ, Wong-You-Cheong JJ, Davis CJ, Jr (1997) Adult renal hamartomas. RadioGraphics 17 : 155–169
4. Agrons GA, et al (1995) Multilocular cystic renal tumor in children: radiologic-pathologic correlation. RadioGraphics 15 : 653–669
5. Madewell JE, Stanford MG, Davis CJ Jr et al (1983) Multilocular Cystic Nephroma: A radiographic-pathologic correlation of 58 patients : Radiology 146: 309–321
6. Quinn MJ, Hartman DS, Friedman AC et al (1984) Renal Oncocytoma: new observations: Radiology 153: 49–53
7. Davidson et al (1993) Renal oncocytoma and carcinoma: Failure of differentiation with CT. Radiology 186 : 693–696.
8. Hartman DS, Lesar MSL, Madewell JE et al (1981) Mesoblastic Nephroma: Radiologic-pathologic correlation of 20 cases: AJR 136 : 69–74
9. Dunnick NR, Hartman DS, Ford KK et al (1983) The radiology of juxtaglomerular tumors: Radiology 147: 321–326
10. Dunnick NR, Korobkin M (2002) Imaging of adrenal incidentalomas: current status. AJR 179 : 559–568.
11. Kawashima A, Sandler CM, Fishman EK, et al (1998) Spectrum of CT findings in nonmalignant disease of the adrenal gland. RadioGraphics 18: 393–412.
12. Szolar DH, Kammerhuber FH (1998) Adrenal adenomas and nonadenomas: assessment of washout at delayed contrast-enhanced CT. Radiology 207 : 369–375
13. Peña CS et al (2000) Characterization of indeterminate (lipid poor) adrenal masses: use of CT washout characteristics at contrast enhanced CT. Radiology 217: 798–802
14. Krebs TL, Wagner BJ (1998) MR imaging of the adrenal gland: radiologic-pathologic correlation. RadioGraphics 18 : 1425–1440
15. Kenney PJ, Wagner BJ, Rao P, Heffess CS (1998). Myelolipoma: CT and pathologic features. Radiology 208 : 87–95.
16. Rao P, Kenney PJ, Wagner BJ, Davidson AJ (1997) Imaging and pathologic features of myelolipoma. RadioGraphics 17 : 1373–1385

Primary Malignant Renal Parenchymal Epithelial Neoplasms in Adults

Raymond Oyen, Hendrik Van Poppel, Tania Roskams

5.4

Contents

Introduction

Primary malignant renal epithelial neoplasms account for 3% of adult malignancies [1]. US, CT and MRI all contribute to the increased detection of all types of renal parenchymal mass lesions, including those that require surgery and those where surgery has to be avoided. Malignant tumors are detected at earlier stages. Earlier detection and more accurate diagnosis improve the cure rate of renal carcinoma. Radiological characterization of these tumors from their benign masses (i.e., angiomyolipoma and complicated cysts) is a continuous challenge and an essential prerequisite for appropriate management [2]. Radical nephrectomy is the treatment of choice, regardless of size. Alternative treatment strategies are available now, in particular for smaller tumors (<4 cm), and include open or laparoscopic tumorectomy, partial nephrectomy, radiofrequency ablation, and cryotherapy [3–6].

Understanding the underlying gross pathology and histological correlates provides an essential substrate for explaining the radiological characteristics of these masses. Many pathologists still rely on hematoxylin- and eosin-stained preparations of surgical specimens to achieve the histological diagnose of renal cell carcinoma (RCC) [7, 8]. From clinicopathological observations, it has been observed that a neoplasm may change its pattern of differentiation in time and that it does not necessarily retain the phenotype of its presumed progenitor cell. Thus it can be explained that in the past, lectin and immunohistochemical studies using markers for different parts of the adult renal tubular system yielded conflicting results regarding the proximal versus distal tubular origin of renal cell tumors. Furthermore, renal cell carcinomas may be composed of admixtures of clear and granular cells or clear and chromophilic cells. Such observations would suggest that a transition between phenotypes occurs during progression.

During the last decades, it has become increasingly clear that the initiation and progression of solid tumors is governed by alterations of genes that control growth and differentiation. Tumor development is based on

specific and separate molecular mechanisms in different cells, and therefore they are almost completely different. There is a specific combination of chromosomal and mitochondrial DNA alterations marking distinct types of tumor genes or putative tumor suppressor genes [9].

Primary Malignant Renal Epithelial Neoplasms

The morphological classification of renal cell neoplasm in adults relies on three essential criteria: (1) the aspect of the tumor cells (i.e., clear cells, chromophilic cells [basophilic or eosinophilic], chromophobic cells, oncocytes, collecting duct cells, and sarcomatoid or fusiform cells); (2) the architecture (solid [acinar], tubulopapillary, tubular, tubulocystic); and (3) nuclear grade, based on increasing numbers of nuclear and nucleolar atypia. Based on these morphological criteria, classification of the majority of renal cell neoplasms is feasible, with few exceptions only. This morphology-based classification is now supported by cytogenetic analysis. Five major groups of malignant renal epithelial neoplasms are distinguished (Table 1) [10–13].

Tumor genesis is driven by genetic changes including not only classic point mutations, but also deletions removing entire genes, as well as gross chromosomal abnormalities at specific sites in the genome. Molecular cytogenetic techniques enable the identification of genetically homogeneous groups of malignant renal parenchymal tumors. Each subgroup is characterized by a combination of genetic changes affecting different sites within the chromosomal and mitochondrial DNA [16].

Careful analysis of CT and/or MR images allows for preoperative characterization of the histological subtypes in the majority of cases. The criteria include size, shape, location, number, contrast enhancement pattern (including the angiographic or corticomedullary phase), presence and site of hemorrhage and necrosis, patency of renal vein, and lymph node status. Categorizing neoplasms may be helpful in designing appropriate therapeutic strategies and predicting the likelihood of progression. Furthermore, the absence of the typical radiological features warrants additional investigation to exclude lesions for which surgery should be avoided (i.e., benign lesions, metastases, lymphoma).

Table 1. Classification of renal epithelial neoplasms (Heidelberg Classification) [14, 15]

Malignant renal epithelial neoplasms
Renal carcinoma conventional (clear cell) type
Papillary renal carcinoma
Chromophobic carcinoma
Collecting duct carcinoma
Medullary carcinoma
Unclassified renal carcinoma
Benign renal epithelial neoplasms
Adenoma
Metanephric adenoma
Oncocytoma

Renal Cell Carcinoma of the Clear Cell Type

Pathology

The clear cell subtype is the most common subtype, accounting for approximately 70%–80% of RCCs. It is also referred to as classic or conventional RCC. The majority occurs sporadically as a solitary tumor and is randomly distributed in the renal cortex. There is a male predominance (1.5–2:1). Multicentricity in the same kidney occurs in approximately 4% of cases, whereas bilaterality occurs in 0.5%–3%. Synchronous (75%) or metachronous multifocality may occur. Multicentricity and bilaterality are often associated with conditions such as von Hippel-Lindau disease [17]. Clear cell carcinomas can become very large but the frequency of small lesions has increased because of earlier detection with US, CT and MRI.

RCC of the clear cell type protrudes from the renal cortex as a rounded, bosselated mass. The interface of the tumor with the kidney is usually well demarcated. Yet the presence of a clear pseudocapsule depends on the nuclear grading: well-differentiated lesions are more likely to have such a pseudocapsule. Rarely, RCC may be diffusely infiltrative and then become difficult to distinguish from urothelial carcinoma or other infiltrating tumors.

On section, clear cell RCCs have a yellowish-golden appearance, due to the abundant cytoplasmic lipid content, mucolipids (Figs. 1–5). Thus the cells are markedly similar to that of the proximal convoluted tubules. The typical lesion is composed of varying mixtures of cells with clear and/or granular cytoplasm in nonpapillary formations, often arranged in sheets of broad trabeculae, separated by a richly vascular fibrous stroma with thin-walled blood vessels (owing to high levels of vascular growth factors) (solid growth pattern), around central spaces to resemble tubules (tubular growth pattern), or line cyst-like spaces (cystic growth pattern). Occasionally, areas with tubulopapillary or papillary growth may also be observed. Granular cells are eosinophilic and the granules correspond to mitochondria. The granular cells usually have a higher nuclear grade compared with the clear cells, and necrosis and hemorrhage are even more likely to be present. The surface of predominantly granular cell tumors is brown because of the phospholipid content of the numerous cytoplasmic organelles. Predominant granular RCCs are most often single tumors with a male predominance (2:1). Many high-grade RCCs of the clear cell type contain granular

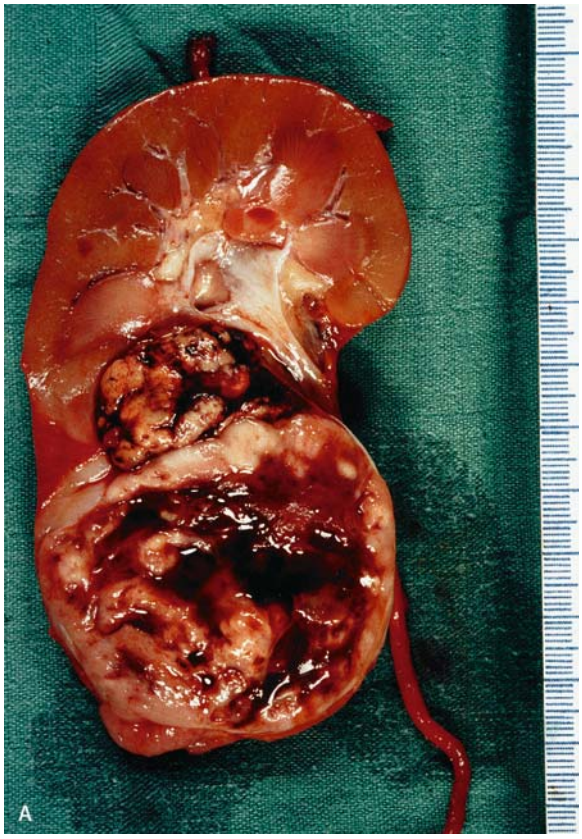

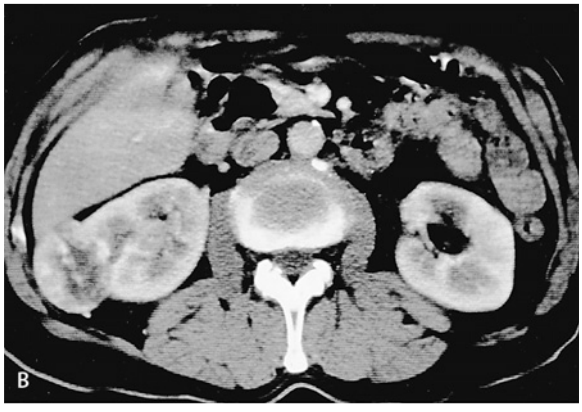

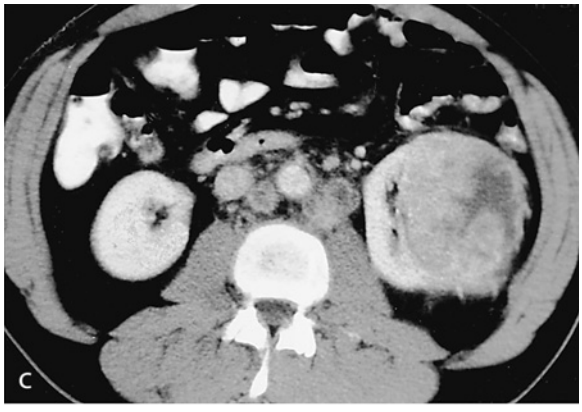

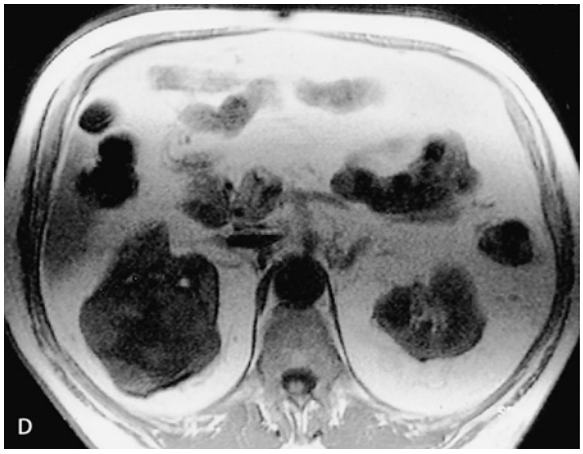

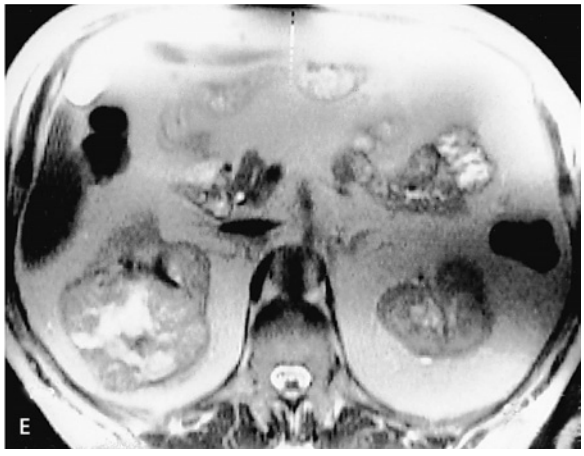

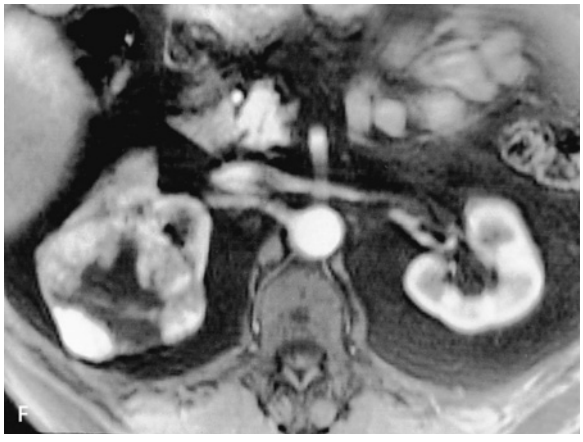

Fig. 1. A Typical RCC of the clear cell type protruding from the renal cortex as a rounded, bosselated mass. The interface of the tumor and the kidney is well demarcated. Note the eccentric hemorrhagic necrosis of the tumor. **B** Contrast-enhanced CT, early vascular phase and **C** nephrographic phase in two different patients. Irregular, hypervascular peripheral rim and predominant eccentric necrosis are typical features. Note retroperitoneal lymph adenopathy with similar characteristics as the primary tumor (**C**). **D** Axial T1-weighted and **E** T2-weighted image in another patient. The tumor is almost isointense on the T1-weighted image; the eccentric necrosis and the irregular border are clearly visible on the T2-weighted image, an almost exclusive feature for this histological subtype of RCC. **F** Axial T1-weighted image with fat saturation and after IV contrast: nodular and hypervascular border and with eccentric necrosis

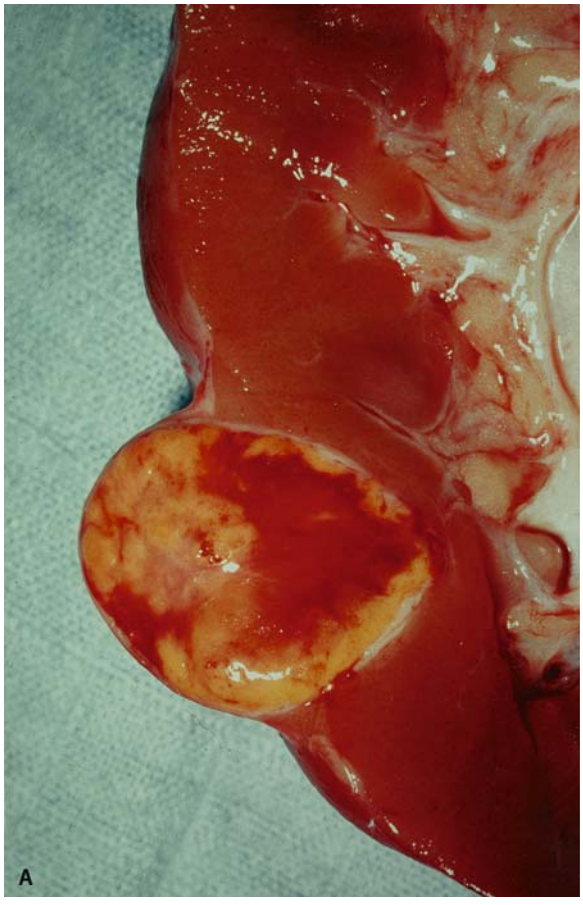

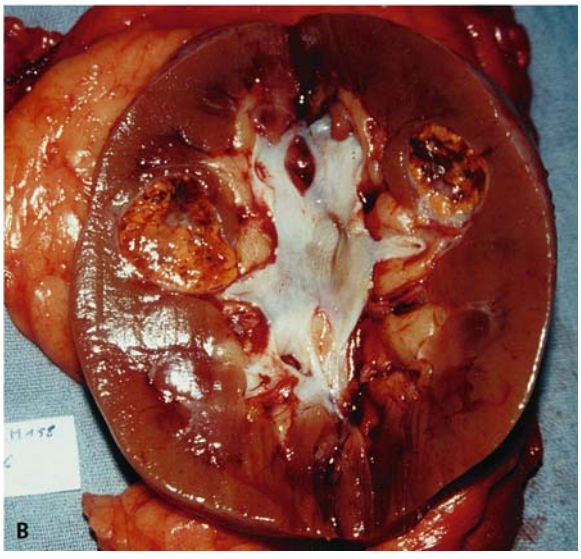

cell components. In some tumors, a highly malignant spindle cell or sarcomatous transformation may be observed. Areas of necrosis, cystic degeneration, hemorrhage and calcification (sometimes even with ossification) are seen. Extensive necrosis occurs predominantly in fast-growing neoplasms of high-grade malignancy. Distinct areas of fat may be present as well [18, 19]. The latter is most frequently seen with extensive calcification. In practice, a calcified, fat-harboring lesion should be considered a RCC until proven otherwise. Angiomyolipomas, in general, do not contain calcifications. In RCC, cystic changes may be so predominant that the tumor resembles a benign cystic mass. Approximately 10% of clear cell RCC is completely cystic [20]. Cystic RCCs tend to be large, rounded or polylobular lesions. They tend to be solitary and predominately on the right side (75%), more frequently in the interpolar area. There is a clear male predominance (2:1).

RCC extends in the venous system in 4%–9% of cases and is associated with worse characteristics.

The cytogenetic abnormality characterizing clear cell RCC is the deletion of the short arm of chromosome 3 (–3p), which is present in 96% of sporadic as well as in hereditary cases, and is considered as the trigger genetic event in the tumor development. Trisomy 5q occurs in 50% of cases. Additional chromosomal abnormalities are acquired during progression (–14q, –8p, –9, –6q, trisomy 7) and the frequency increases with the cytological grade and size of the tumor. The frequency of deletion of 14q increases with the presence of metastases (no metastases –14q: 30%; with metastases –14q: 73%). The loss of the Y chromosome has been observed in 26% of nonpapillary RCC in males. This figure is consis-

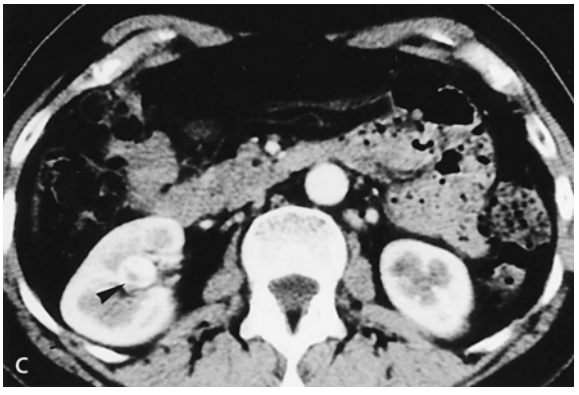

Fig. 2A–C. Smaller RCCs of the clear cell type (2–3 cm), one protruding outside the renal border and sharply demarcated (**A**), the other with intrarenal origin (**B**). Note again the typical eccentric necrosis of both tumors. The contrast-enhanced CT (**C**, same patient as in **B**) in the early corticomedullary phase shows the intrarenal lesion with its eccentric necrosis. This lesion was hypodense in the nephrographic phase (not shown) and could have been erroneously interpreted as a cyst or complicated cyst

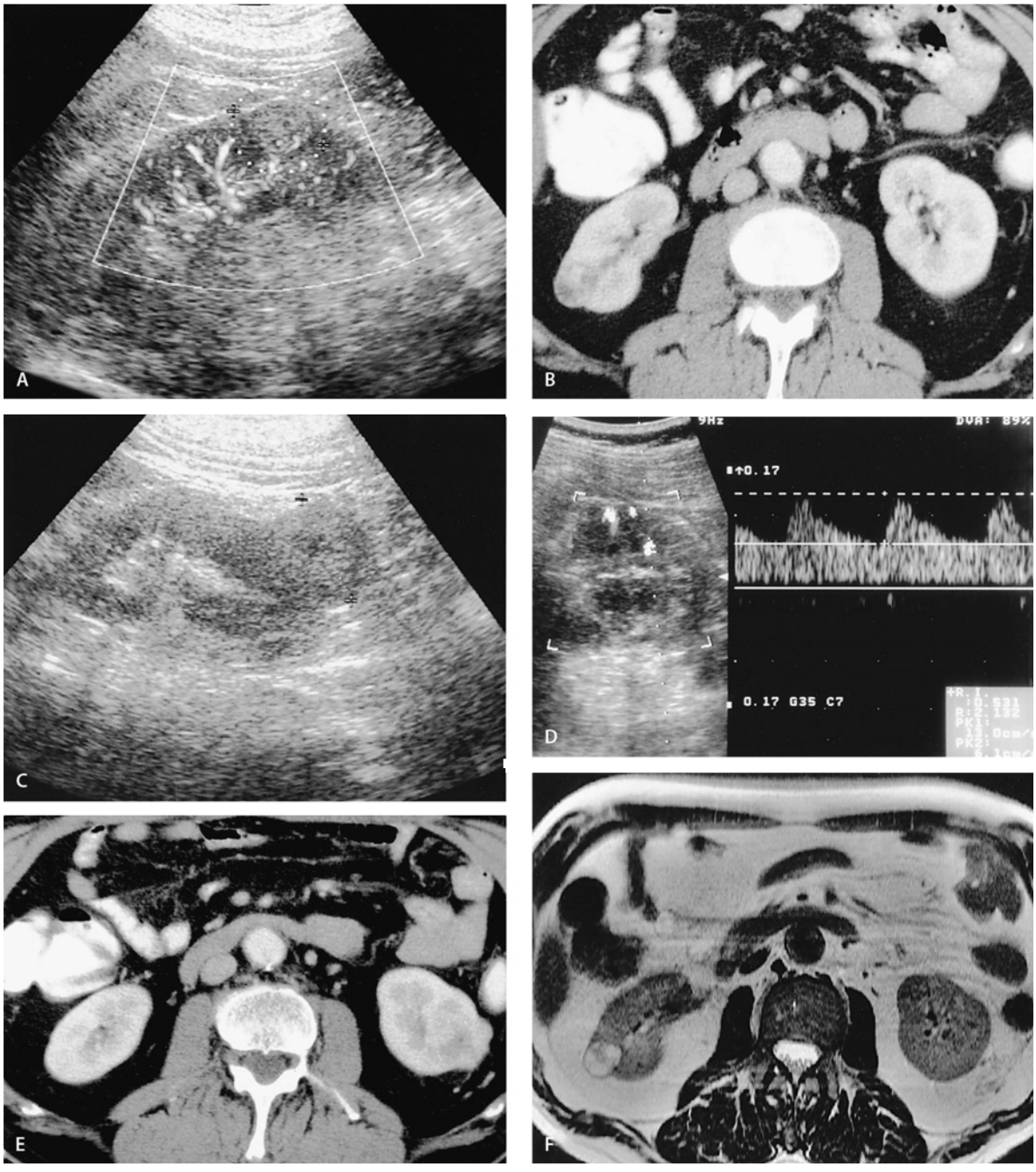

Fig. 3A–H. Bilateral synchronous renal cell carcinoma of the clear cell type. **A** US: slightly hyperechoic lesion at the lower pole of the right kidney (*arrow*). There is only some vascularity at the implantation base. **B** Contrast-enhanced CT, early corticomedullary phase, showing the typical characteristics of a classic clear cell carcinoma: peripheral hypervascular border of viable tumor and eccentric hypodense area due to necrosis (*arrow*). **C** At the lower pole of the left kidney, an almost isoechoic mass lesion is seen on ultrasound (*arrow*). **D** On color-Doppler ultrasound low-resistance flow (0.60) is found in the lesion, suggesting its malignant nature. **E** Again, the characteristics of this classic clear cell RCC are clearly shown on the vascular phase of the contrast-enhanced CT (*arrow*). **F–H** Axial (**F**, **G**) and coronal (**H**) T2-weighted images from the same patient illustrating the irregular viable peripheral border and the necrosis of both lesions in the lower pole of the kidneys

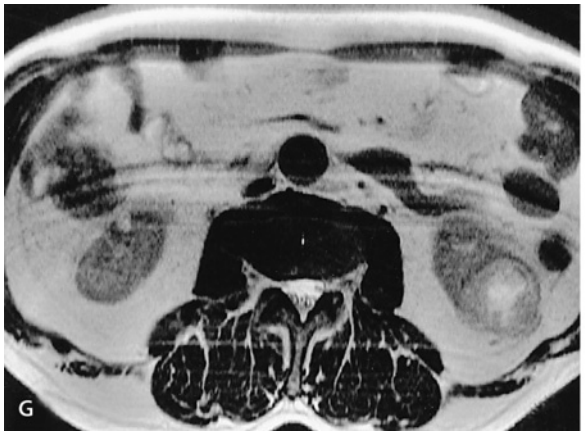

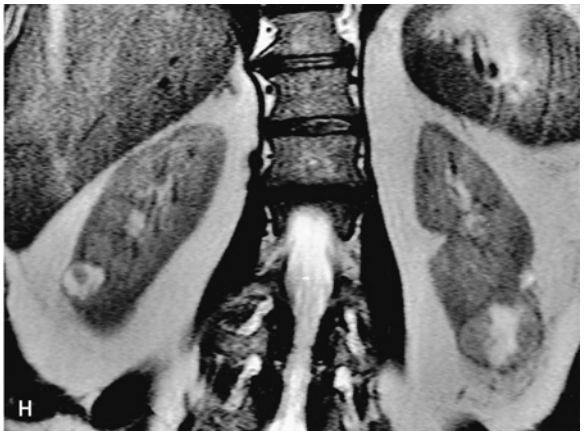

Fig. 3G–H.

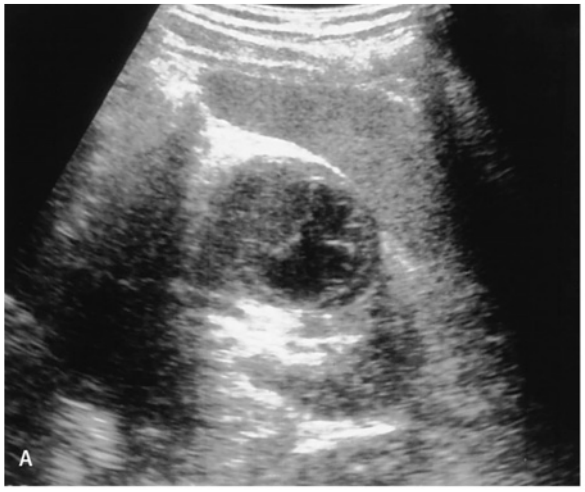

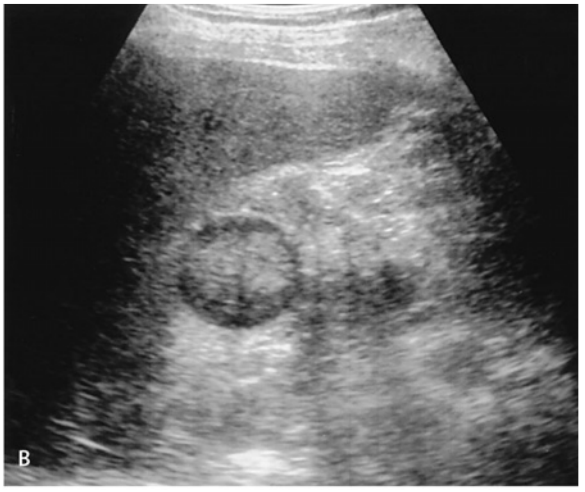

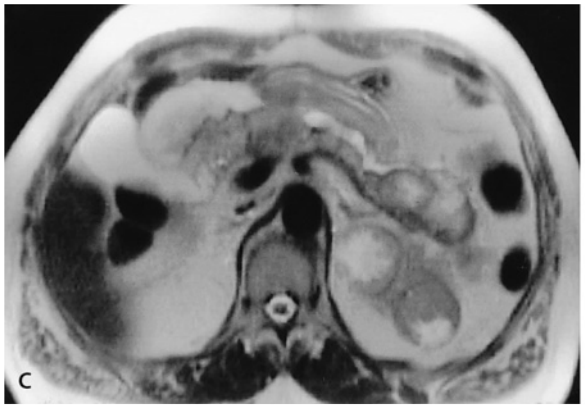

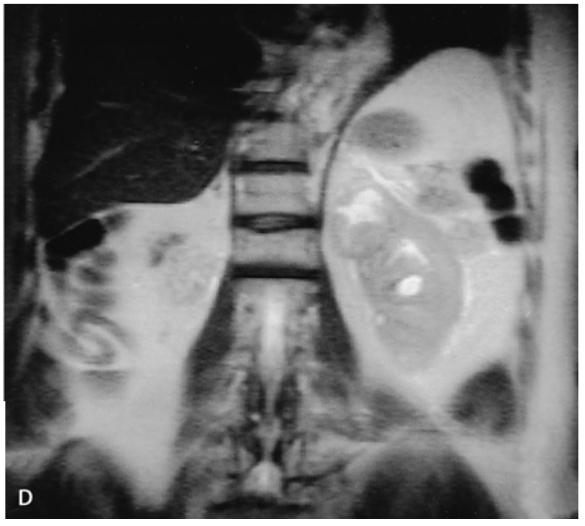

Fig. 4A–D. Multifocal metachronous renal cell carcinoma, clear cell type in the left kidney, after right radical nephrectomy, 16 months earlier. US shows a necrotic lesion in the upper pole of the left kidney (**A**), whereas another one is isoechoic with a hypoechoic rim (**B**). **C**, **D** On MRI, axial (**C**) and coronal (**D**) T2-weighted images, both lesions have almost similar signal characteristics, with extensive necrosis extending to the pseudocapsule of the lesions

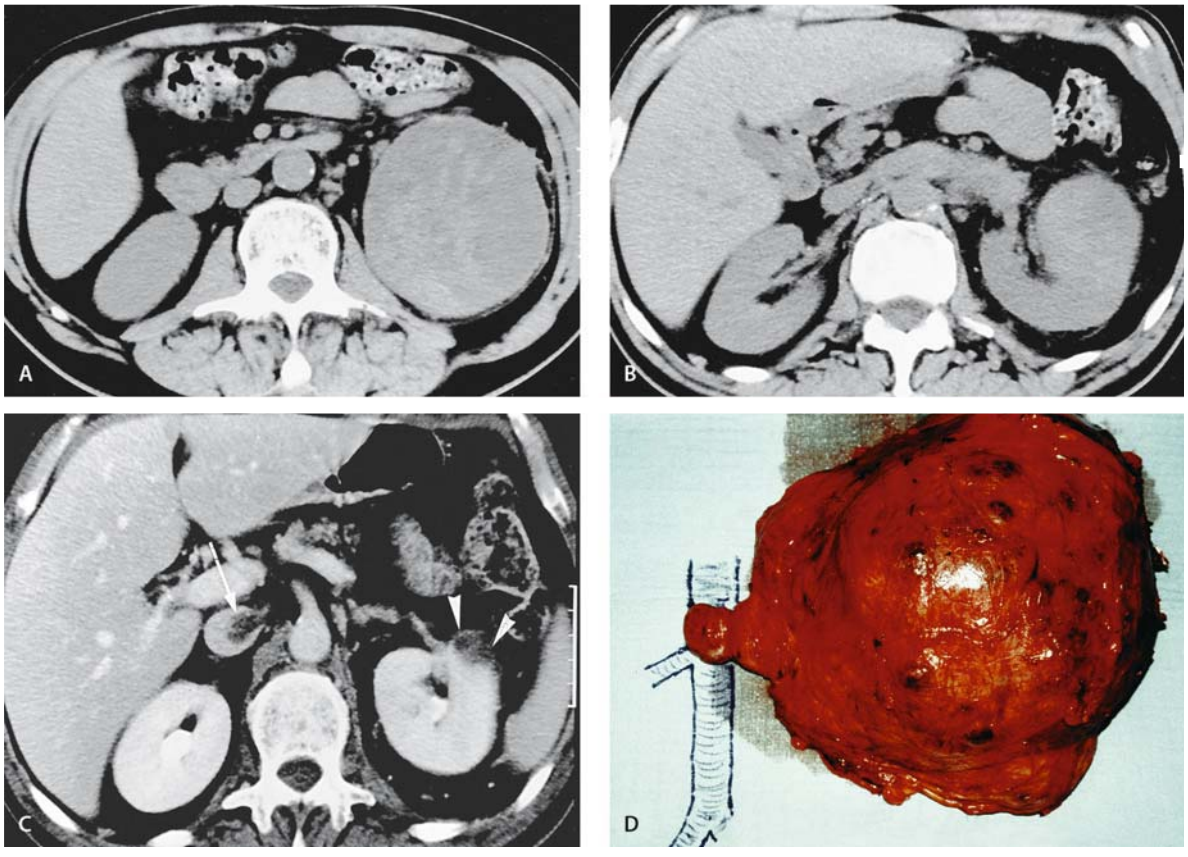

Fig. 5A–D. Clear cell carcinoma invading the left renal vein. **A**, **B** Precontrast CT showing a large necrotic tumor in the lower pole of the left kidney (**A**) and a widened and left renal vein (**B**). **C** The thrombus extends in the inferior vena cava (*arrow*); the implantation base of the carcinoma is visible (*arrowheads*) on this contrast-enhanced CT. **D** The nephrectomy specimen shows the tumor and the extension to the major veins

tent with that of other types of malignant tumors arising in elderly patients. It has been reported to be the only genetic abnormality in tumors as small as 1 mm in diameter, as well as in tumors up to 8 cm in diameter with metastatic growth. The loss of the 3p segment is a highly specific chromosomal anomaly occurring early on in the development of RCC.

A detailed histological analysis of entire kidneys failed to detect any microscopic precursor lesions with the notable exception of some hereditary cases. Microscopic precursor lesions are characterized by susceptibility to develop multiple or bilateral carcinomas, and are associated with a germ line balanced translocation involving the chromosome 3p13–14.2 region. In familial clear cell carcinomas not associated with von Hippel-Lindau disease, the genetic abnormalities include translocations t(3;8) and t(3;6). In von Hippel-Lindau disease, clear cell carcinomas are bilateral (frequently showing a cystic growth pattern) and associated with cystic lesions (lined by clear or sometimes granular cells) [17]. Such tumors develop in approximately 25%–55% of von Hippel-Lindau patients. Lesions tend to be bilateral and multicentric, are often associated with cysts and angiomyolipomas, and occur at an earlier age than sporadic RCC. The genetic defect is situated on segment *3p* (*3p25–26*) and codes for a protein that links with elongins) and is found in over 50% of individuals with von Hippel-Lindau disease. The gene of von Hippel-Lindau disease is muted in the great majority of sporadic clear cell carcinomas.

RCCs are often associated with cysts. In most cases, the cyst is a cortical retention cyst, but associations with both acquired and hereditary polycystic disease have been well documented. The renal neoplasms associated with acquired polycystic kidney disease in patients on chronic hemodialysis generally occur after dialysis for several years (mean, 3.5 years) and the frequency of RCC varies directly with the primary renal disease process and both the duration of dialysis and the incidence of cysts.

Imaging

Ultrasound

There is nothing specific about the US diagnosis of typical clear cell RCC: lesions may be isoechoic, hypoechoic, hyperechoic or complex (Figs. 3, 4). Areas of necrosis may be present, yet sometimes hardly recognizable. Calcifications may be present as well. It is estimated that the small RCC (<3 cm), in almost 50% of the cases, is isoechoic. This explains why many lesions are invisible on US. Isoechoic lesions can only be detected when the inner or outer renal outline is deformed. Furthermore, isoechoic lesions may mimic normal anatomic structures or anatomic variants such as hypertrophy of the septal cortex (Bertin's column). Color or power Doppler may be helpful in such cases to illustrate the normal vasculature in the suspicious area. Whenever there is any doubt about the diagnosis, further imaging with CT is warranted.

With hyperechoic lesions, the differential diagnosis includes angiomyolipoma (AML) and other rare benign and malignant tumors. Angiomyolipomas are rare in males, and therefore, as a rule, hyperechoic masses in males warrant further investigation. Some features may be helpful in distinguishing hyperechoic RCC from AML. Cystic areas due to hemorrhage or necrosis are almost never seen in AML; a hypoechoic rim or halo encircling the lesion is a feature of RCC. The vascular pattern on power Doppler has been suggested to add important information to gray-scale US findings for differential diagnosis of small solid renal lesions [21]. Because of considerable overlap in the vascular pattern between AML and RCC, this criterion is not very useful in the individual patient. Since lesion discrimination is essential for further management, a plain CT scan is proposed to enable the detection of intralesional fat. Whatever the echogenicity of the renal mass lesion, low resistive flow (resistive index <0.6) is more likely to be found in RCC than AML [22].

On US, the cystic clear cell RCC may appear almost completely cystic. Most often, however, diffuse wall thickening, or mural nodular thickening and multiple internal echoes will be seen. Mural nodes virtually exclude the radiological diagnosis of a benign neoplasm. These protrusions are most commonly found near the implantation base of the mass in the kidney. Searching for these protrusions is far more important than putting efforts in measuring the actual size of the lesion. At times (numerous and thick) septations are present. Then, the multicystic RCC resembles a benign neoplasm known as the benign multilocular cystic nephroma [23]. This benign neoplasm is very rare (virtually nonexistent) in adult males: a multilocular cystic mass in adult males, therefore, must be considered as a clear cell RCC. In middle-aged women, however, the radiologist may be faced with the differential diagnosis between a benign multilocular cystic nephroma and RCC. There are no reliable criteria to distinguish these two types of renal masses. Multilocular cystic nephroma is characteristically situated in the upper pole of the kidney and tends to protrude into the renal hilum, even into the collecting system. This lesion is almost always solitary and unilateral and the cysts multiloculated. On color Doppler, in clear cell cystic RCC, the septations are well vascularized, whereas in multilocular cystic nephroma there is almost no vascularity in the septations. Both lesions are considered as surgical lesions (i.e., indication for surgical intervention).

Computed Tomography

On plain CT series, the lesions are iso-, hypo-, or hyperattenuation masses compared to the renal parenchyma; a heterogeneous appearance is a common feature of larger lesions [24]. Coarse calcifications may be present at the periphery of the lesion, near the center, or calcifications may be spread throughout the lesion.

In the arterial phase (corticomedullary phase) after intravenous injection of iodinated contrast, at least three-quarters of the clear cell RCCs are hypervascular, while approximately 20% appear almost isovascular and only few are hypovascular [25]. The enhancement pattern is heterogeneous with a somewhat patchy and nodular pattern in the periphery encircling unenhanced areas (Figs. 1–3). In the venous (nephrographic) and/or excretory phase, RCCs become hypodense compared to the renal parenchyma, the thick peripheral rim remaining clearly visible.

Nephrographic phase scans enable greater lesion detection and better characterization of small renal masses than corticomedullary scans only. Nephrographic phase series should be obtained when only monophasic scanning is used to detect small renal masses [26].

Intralesional necrosis is virtually always present and is frequently characterized by its eccentric location: the necrosis extends to the periphery, most often at the opposite side of the renal parenchyma. Tumor necrosis is independent of the size of the lesion. Therefore, tumor necrosis is the key criterion for imaging-based lesion characterization. Extension into major renal veins and inferior vena cava may occur (Fig. 5).

On plain CT series, most cystic RCCs are hypodense [23]. Typically, the content has attenuation numbers ranging between 10 and 30 Hounsfield units (HU). After IV injection of contrast, the thick wall of cystic RCC enhances with mural nodes, near the renal parenchyma (Figs. 6–8). Calcification in a cystic renal mass is not as important in diagnosis as is the presence of associated enhancing soft tissue elements [27]. It may be impossible to differentiate septate cystic RCCs from multiloc-

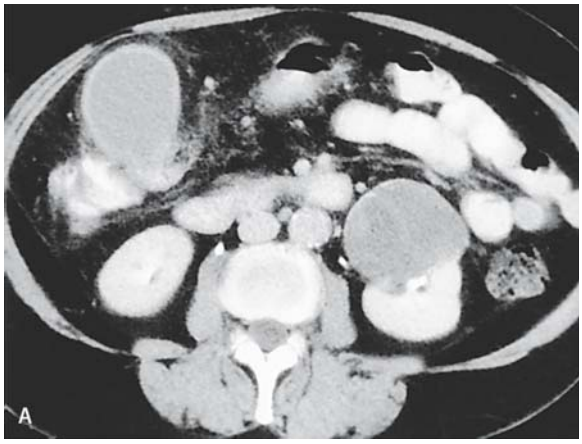

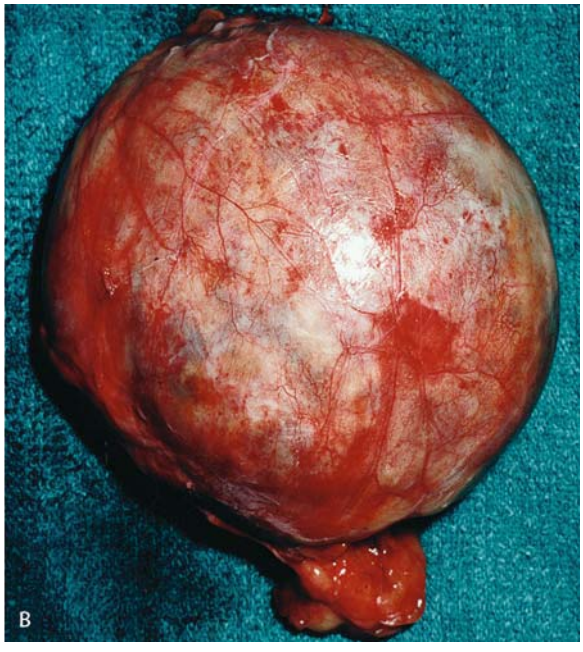

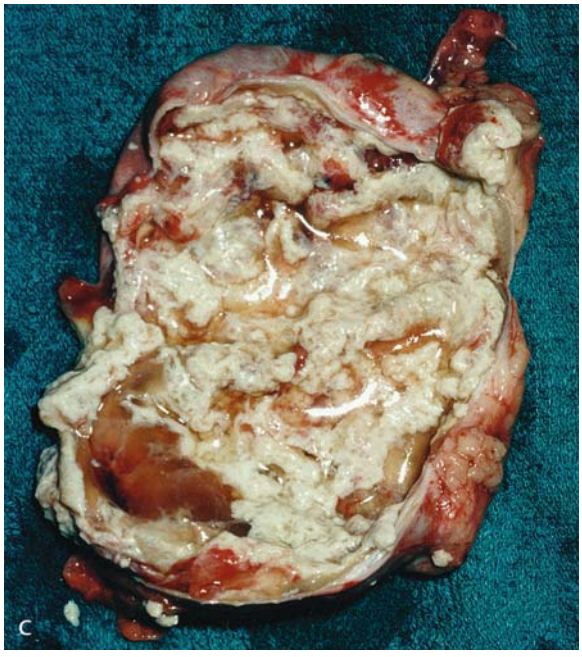

Fig. 6A–C. Cystic renal cell carcinoma. **A** Contrast-enhanced CT shows a predominately cystic mass in the left kidney. The mural nodes (*arrow*) exclude the diagnosis of a benign mass. **B**, **C** The outer surface of the tumor is smooth (**B**), but at cross-section, the inner surface is irregular (**C**)

Fig. 7A–F. Cystic renal cell carcinoma, clear cell type. **A** Precontrast CT shows a rounded mass lesion in the right kidney, with cystic portions. **B** The contrast-enhanced CT shows the multinodular enhancing mass and the anterior cyst-like component. **C**, **D** The lesion is isointense on T1-weighted image (**C**), and heterogeneous on T2-weighted image (**D**). **E** Contrast-enhanced MR with fat saturation displays the heterogeneity of the tumor including a solid area with necrosis and a cyst-like area. Note the striking resemblance with the contrast enhanced CT in **B**. **F** The surgical specimen after nephron-sparing surgery shows the heterogeneity of this renal cell carcinoma of the clear cell type

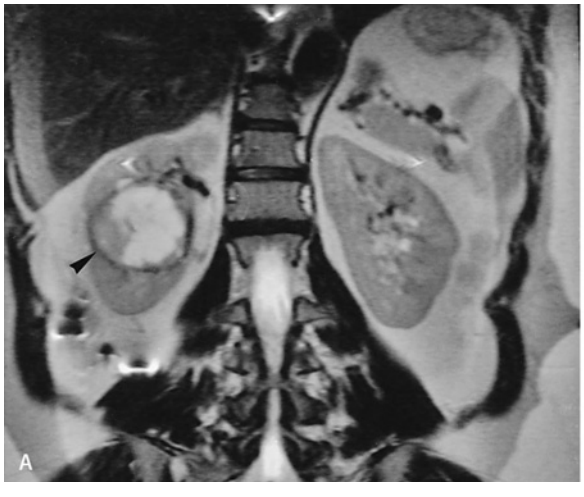

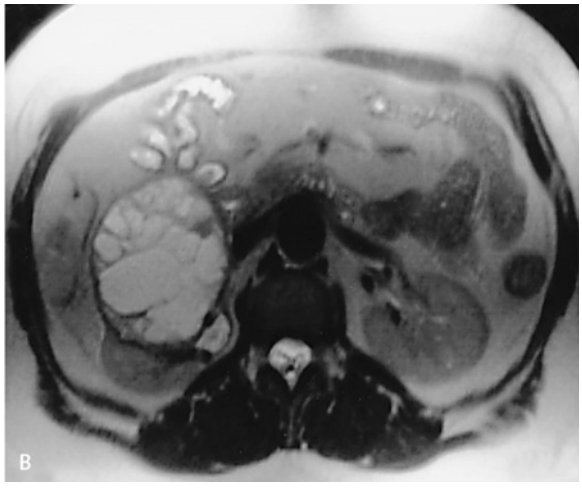

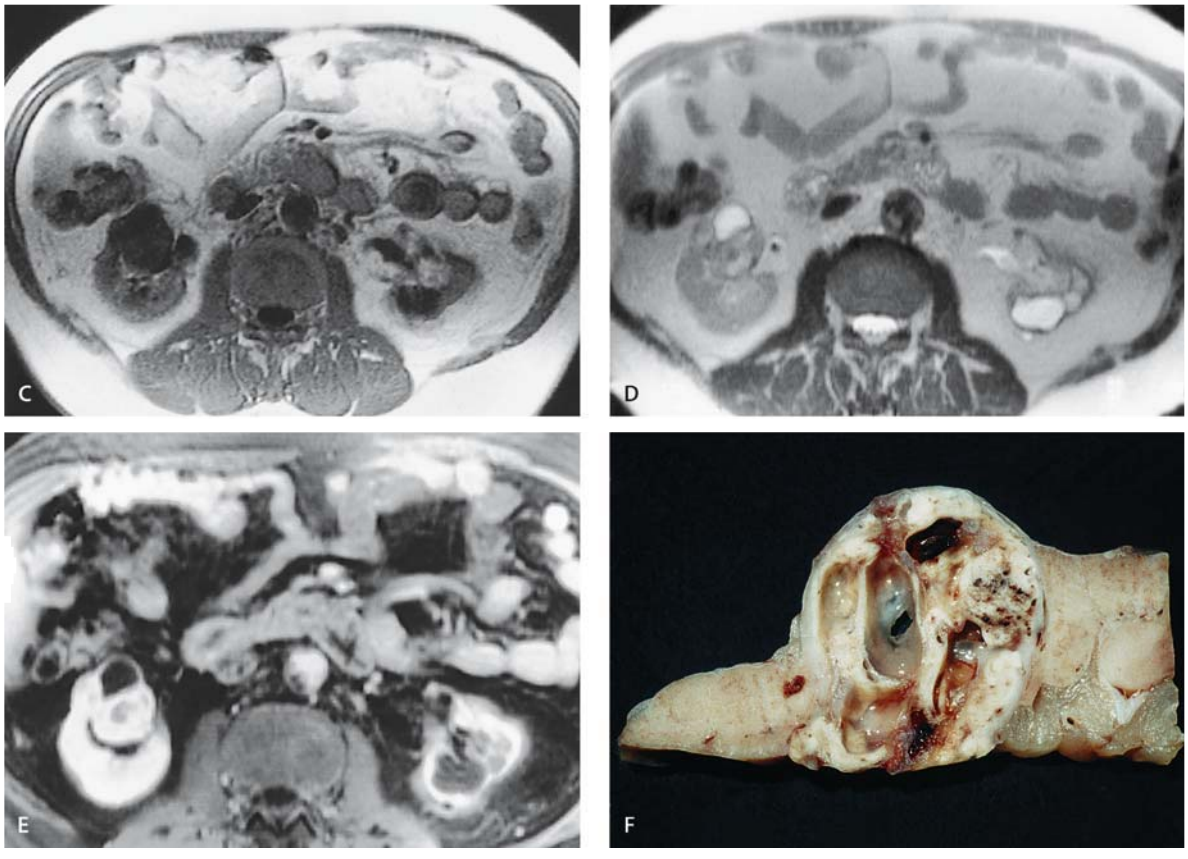

Fig. 7C–F.

ular cystic nephroma. Both neoplasms may have very similar features on CT (Fig. 9). Therefore, secondary signs (gender, location, protrusion in renal hilum, regional lymph nodes, and renal vein patency) may contribute to the radiological diagnosis.

Thrombosis of the renal vein is expected in approximately 10% of cases of cystic RCC. Regional lymph node metastases are detected in 10% of patients at the time of diagnosis. Few patients will have ipsilateral or contralateral adrenal metastases at the time of presentation.

Magnetic Resonance Imaging

Similar to CT, the key to the MR diagnosis of clear cell RCC is the presence of necrosis. Necrosis is hypointense on predominately T1-weighted images and hyperintense on predominately T2-weighted images, and is easily recognized without further intravenous injection of contrast (Figs. 3, 4).

After intravenous administration of contrast, the enhancement pattern is comparable to that of CT: enhancing viable tumor enveloping a hemorrhagic–necrotic, nonenhancing area, which extends to near the pseudocapsule [28].

On MRI cystic RCCs tend to be isointense on T1-weighted images, with extensive hyperintense areas on T2-weighted images [23]. As with CT, the peripheral nodules of viable tissue may be hardly recognizable (Figs. 7, 9). The enhancement pattern again is similar to that of CT lesions [29].

Fig. 8A–C. Cyst-like papillary carcinoma, type A. **A** This contrast-enhanced CT shows a cystic mass lesion with a hardly recognizable mural node at the anterior surface (*arrow*). **B**, **C** The opened surgical specimen shows the yellowish tumor in the deep area of the cyst (**B**) and the nodular tumor at the implantation base on the kidney (**C**)

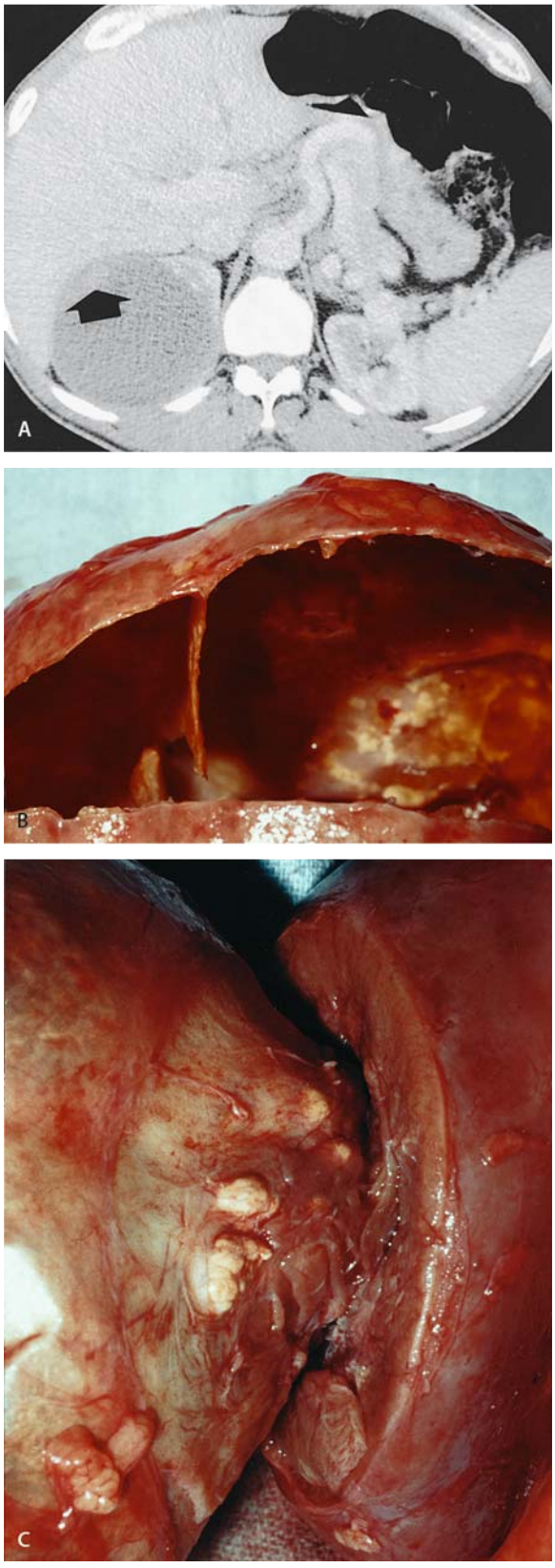

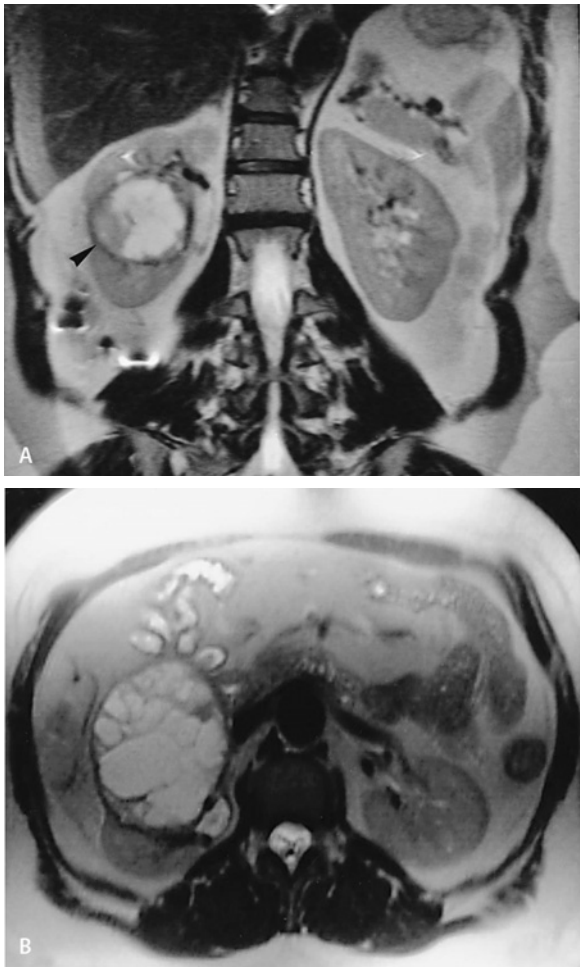

Fig. 9A, B. Cystic renal cell carcinoma, clear cell type. Axial (**A**) and coronal (**B**) T2-weighted images of an almost completely cystic and multilocular renal cell carcinoma. The intralesional protrusions are more readily visible on the axial image, whereas the septations are better recognized on the coronal image. Such a lesion should not be confused with benign multilocular cystic nephroma

Papillary Renal Carcinoma or Chromophilic Cell Carcinoma

Pathology

Papillary RCC constitutes approximately 10%–15% of all RCCs and are predominant among tumors smaller than 3 cm. The current definition is based on the histological finding of vascularized connective tissue stalks invested by neoplastic cells [30]. Nevertheless, at contrast-enhanced imaging studies, virtually all papillary carcinomas are hypovascular. Some investigators require that the papillary areas compose at least 50% (or

even 70%) of the tumor. There is male-female ratio of approximately 2.5–5:1. The mean age is in the 6th decade, but there is a wide age range. The rate of calcification is reported to be higher than in clear cell RCC.

Two subgroups can be distinguished. Type B (one-quarter of cases) consists of multicentric lesions (100%), often bilateral (two-thirds), usually with one large mother lesion (approximately 3 cm in diameter) and with other multiple, small daughter lesions (ranging from microscopic to subcentimeter size) (Figs. 10, 11) [31, 32]. The largest lesion shows a complete or at least partial exorenal growth. Multicentricity may occur

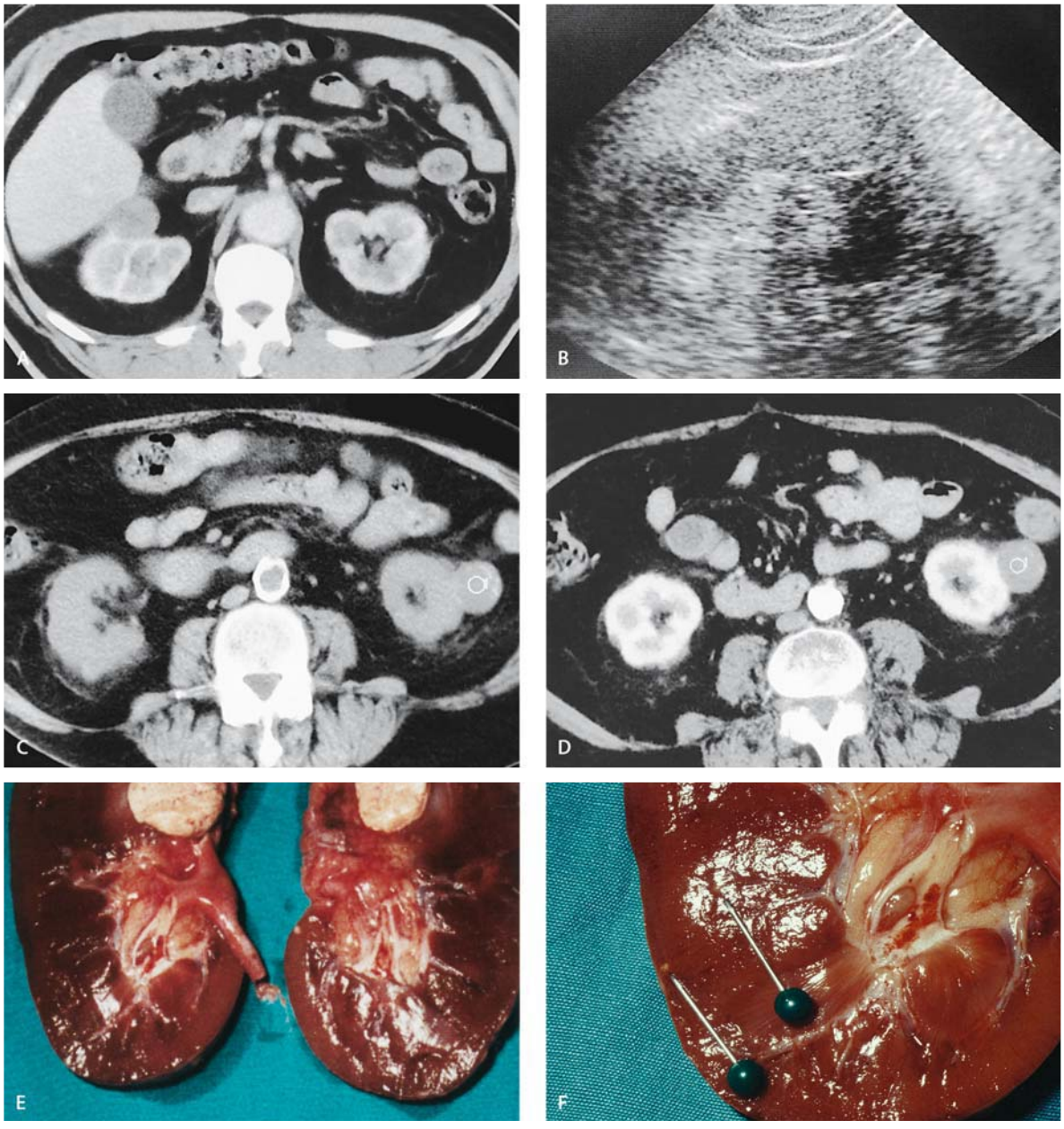

Fig. 10A–G. Papillary RCC carcinoma (chromophilic cell carcinoma). **A** Hypovascular mass with extrarenal growth at the anterior surface of the right kidney on the contrast enhanced CT, vascular phase. **B–D** Another patient with a slightly hyperechoic mass at the lower pole of the left kidney with some calcifications (US in **B**), isodense and with some coarse calcifications on the precontrast CT (**C**) and without increased attenuation on contrast-enhanced CT (**D**). The attenuation numbers though increase from 25 to 46 HU, suggesting a solid hypovascular tumor, rather than an avascular cyst. **E, F** The nephrectomy specimen of the first patient shows a mother lesion (**E**) and multiple daughter lesions (**E, F**). **G** A nephrectomy specimen of another patient with multifocal papillary carcinoma is shown. Note the grayish aspect of the tumors, some of them protruding from the kidney; other smaller lesions are flat

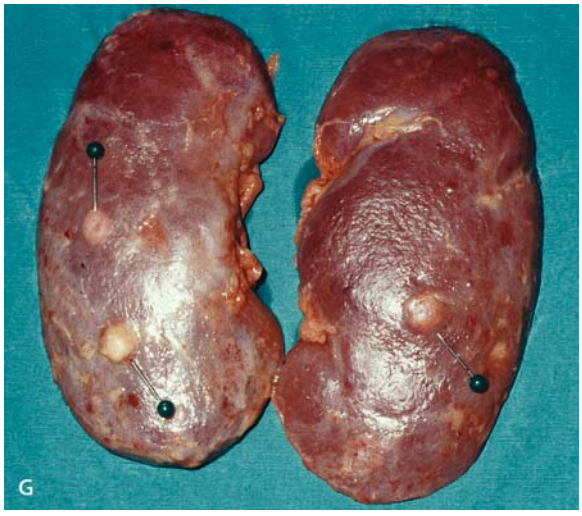

Fig. 10G

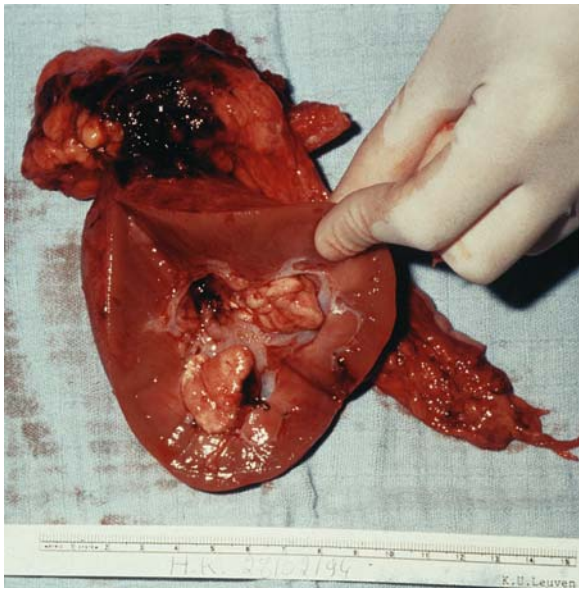

Fig. 11. Rarely, a papillary carcinoma develops intrarenally. On radiological studies, it mimics other tumors, anatomic variants and pseudotumors

either synchronously ipsilateral or contralateral to the largest lesion, or both iso- and contralateral to the largest tumor, with an almost equal frequency. Pathological examination often reveals more tumoral (small microscopic) foci than suspected by imaging. The other type (type A, three-quarters of cases), is more aggressive, and constitutes a single and usually bulky tumor, either multinodular solid or almost completely cystic, with a ratio of approximately 2:1.

On section, the surface of papillary RCC varies in color from light gray to golden yellow. The color depends on the amount of lipid-laden macrophages in the stroma. Tumor necrosis may liberate large amounts of lipid, and cholesterol crystals may form. Intralesional hemorrhage and necrosis are observed in many cases (half to two-thirds) [33].

Adrenal metastases or distant metastases may be seen at the time of diagnosis in type A papillary carcinoma. Invasion of the renal vein or liver metastases is only rarely seen. Lymph node and distant metastases are rare in type B papillary carcinoma.

Multiple, nephrogenic, cyst-like precursor lesions are often seen in the apparently normal part of the tumor-bearing kidney. The potential role of reactivation of nephrogenic rests or regeneration of tubules is investigated in the etiogenesis of tubulopapillary neoplasms. Detailed examination shows multifocal and bilateral development of papillary renal cell tumors in nearly all cases. The carcinomas are usually low stage, with 85% of cases pT1 and only 12% in pathologic pT3.

Papillary neoplasm has only recently been found to have a unique constellation of cytogenetic abnormalities [34, 35]. There is evidence that there is a benign precursor lesion (tubulopapillary adenoma). Regardless of size, both the adenoma and the carcinoma tend to show a loss of the Y chromosome. In papillary renal adenomas, the anomalies are further characterized by trisomy of chromosomes 7 and 17 (+7; +17). The finding that this constant combination of alteration of three chromosomes (–Y, +7 and +17) occurs in very small as well as in large tumors suggests stability of these genetic changes during growth. In papillary RCC the same abnormalities can be found along with other abnormalities (+3q; +8; +12; +16; +20). Most of these tumors show invasive or metastatic growth. Some tumors may acquire complex genetic alterations early during their growth, while others undergo changes at a later stage of development only. Thus it can be explained that papillary renal cell tumors of different size may have a different aggressive biological behavior or, in other words, that the size of papillary tumors does not correlate with their actual biological behavior.

Imaging

Ultrasound

On US, type B papillary RCCs are hypoechoic masses in approximately 60% of cases, or isoechoic or hyperechoic (approximately 20% each) (Fig. 10) [36]. Calcifications are reported in a minority of cases (less than 20%). As can be expected from the gross morphology, almost 40% of papillary RCCs are avascular on color Doppler US (i.e., no intralesional flow detectable).

Solid type A papillary RCCs appear as a hypoechoic, isoechoic or even as a hyperechoic mass. Cystic lesions

have a complex US pattern, 25% appearing as avascular on color Doppler US.

Computed Tomography

In type B papillary RCC, all lesions are isodense on unenhanced CT series (Fig. 10). Sometimes calcifications may be seen. These tumors are hypovascular compared to the renal parenchyma on corticomedullary and delayed-phase images and sharply marginated [31, 32, 37], resembling cortical cysts. Enhancement of renal neoplasms is time-dependent and may not be evident in hypovascular lesions analyzed during the early corticomedullary phase [24]. Therefore, measuring attenuation numbers is essential to prove enhancement and thus to differentiate between a cortical cyst and a papillary RCC. Multiple measurements in different phases with similar parameters (same area, same slice thickness, same pixel area) are required [24]. An increase in the attenuation numbers of at least 20 HU between unenhanced and enhanced series is conclusive for contrast enhancement and, therefore, for a solid lesion (Fig. 10). When no plain CT is available, and CT is only performed during a late venous phase, as in many screening examinations, attenuation numbers over 70 HU indicate contrast enhancement and reliably allow differentiation between a cyst and a solid (vascularized) lesion [36, 38, 39].

Particularly with multifocal papillary RCC the differential diagnosis with renal metastases and lymphoma may be difficult. At times, this may be an indication for percutaneous ultrasound or CT-guided biopsy to differentiate between a surgical renal neoplasm and nonsurgical metastases or lymphoma.

On unenhanced CT, type A papillary RCC is isodense or slightly hypodense. Calcifications are generally punctiform and located near the periphery of the tumor. After IV contrast, the majority of the mass becomes hypodense compared to the renal parenchyma; few tumors are isodense (Fig. 8). All lesions are hypodense on late-phase images and all have a sharp border. The solid lesions show areas of necrosis near the center, unlike carcinomas of the clear cell type that show eccentric necrosis. Lymph node metastases, adrenal metastases and distant metastases may occur. Soft tissue metastases (i.e., corpus cavernosum) may be the presenting symptom. Invasion of the renal vein or liver metastases are not frequently seen at the time of diagnosis.

Magnetic Resonance Imaging

On MR, these tumors appear hypointense or isointense (three-quarters) on T1-weighted images and hypoin-

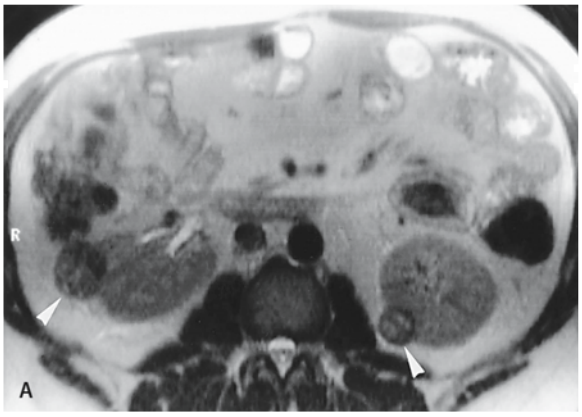

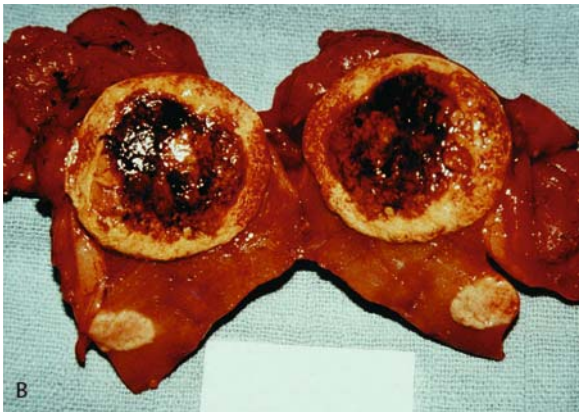

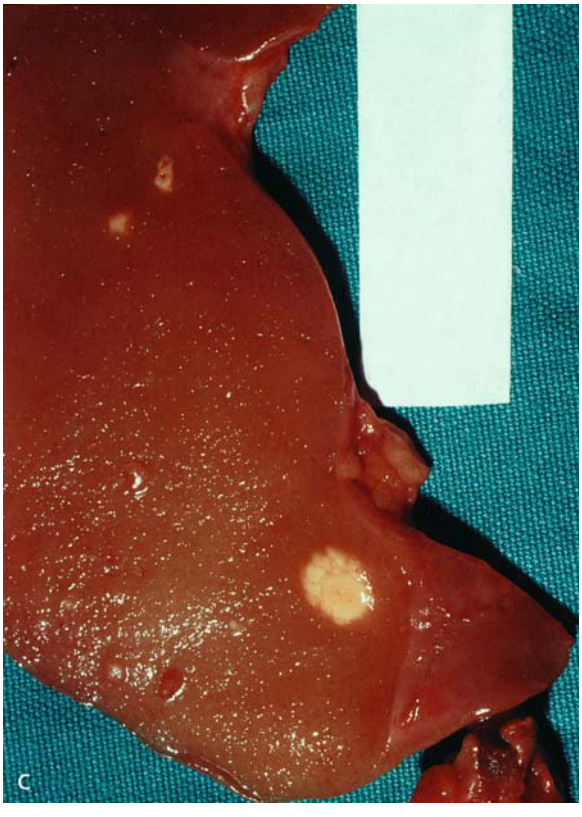

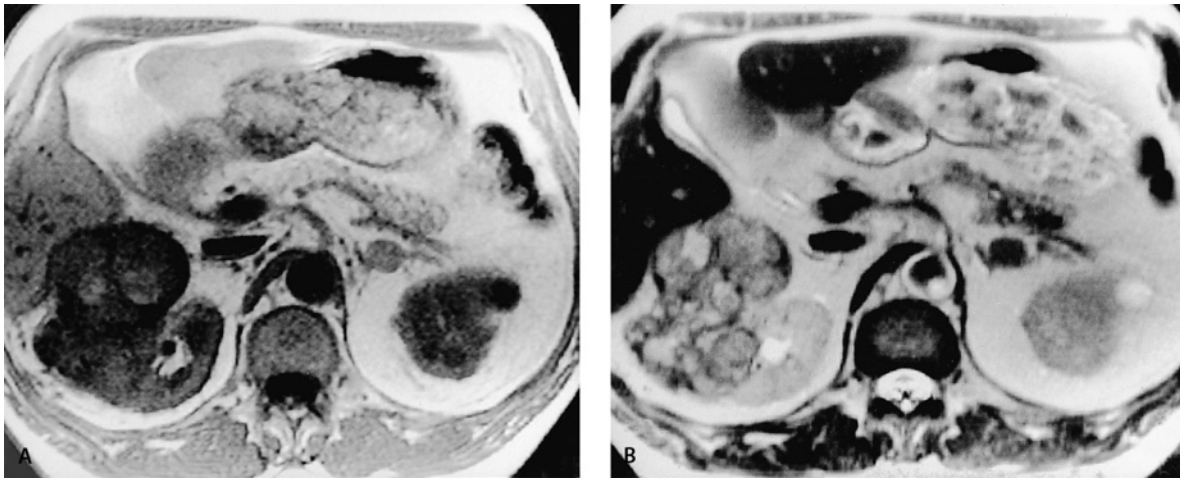

Fig. 13A, B. Multinodular papillary carcinoma, type A. T1-weighted (**A**) and T2-weighted MR (**B**) showing a multinodular mass lesion in the right kidney. This mass lacks the typical eccentric necrosis of the clear cell type. The nodule in the left adrenal gland was proven to be an adenoma

tense on T2-weighted images in all tumors (Fig. 12). All lesions are hypovascular to the renal parenchyma after administration of gadolinium [40]. Here again, appropriate measurement of the lesion signal intensities before and after contrast injection is essential. Larger papillary RCCs show heterogeneous signal intensities (Fig. 13).

Chromophobic Renal Carcinoma

Pathology

Chromophobic carcinoma is a relatively recently (1985) described neoplasm characterized ultrastructurally by cells with abundant cytoplasm. The cells may be related to the normal intercalated cells (type B) of the collecting duct [41]. This subgroup accounts for about 4%–5% of renal cell neoplasms and its median incidence is in the 6th decade (range, 31–75 years). The lesions are most frequently located near the pole of the kidney (Fig. 14). For some reason, the tumor is more frequently observed in rather young females (40–50 years) and in old males. Chromophobic cell carcinoma tends to be large, ranging from 1.3 to 22 cm (mean diameter 8 cm) in their greatest dimension (Fig. 14) [41, 42].

Fig. 12A–C. Papillary carcinomas, type B. **A** T2-weighted MR showing bilateral tumors, hypointense with hyperintense areas (*arrowheads*) in this 36-year-old male. Bilateral nephrectomy was performed. **B** Two lesions of the right kidney, one solid and one with hemorrhagic necrosis. **C** Typical multifocal papillary carcinoma on the cut surface of the left kidney

Grossly, it resembles conventional RCC: they are well circumscribed and solitary, with a gray to brown appearance and typically lacking hemorrhage or necrosis [42, 43]. Most tumors are pathologic stage pT2 or pT3 at the time of resection. Some are associated with conventional RCCs.

The chromophobic carcinoma has a solid architecture, with large cellular blocks and only limited stroma. The lesion consists of large cells, the pale cytoplasm crowded with microvesicles and a variable number of mitochondria, and a fairly typical perinuclear halo. The cells contain little or no glycogen or lipids, but stain with Hale's acid iron colloid, which allows differentiation from oncocytomas. The electron microscopic findings are unequivocal, with cytoplasm containing numerous 150- to 300-nm microvesicles.

Cytogenetic analysis shows a combination of allelic losses, which do not occur in other types of epithelial neoplasms [44]. These genetic losses involve seven chromosomes including –1 (100%); –2 (95%); –6 (80%); –10 (86%); –13 (95%); –17 (70%); and –18 (21%). DNA analysis of one case revealed allelic losses at chromosome *3p*, *5q* and 17 with variable frequency and in a combination, which does not occur in other types of kidney tumors. Along with this chromosomal loss, there are rearrangements in the mitochondrial DNA that are under further investigation.

Follow-up studies have suggested that chromophobic carcinoma has a more favorable prognosis compared to the classic RCC. Nevertheless it can be highly aggressive and must certainly be considered malignant. A sarcomatous transformation of chromophobic cells is only rarely seen.

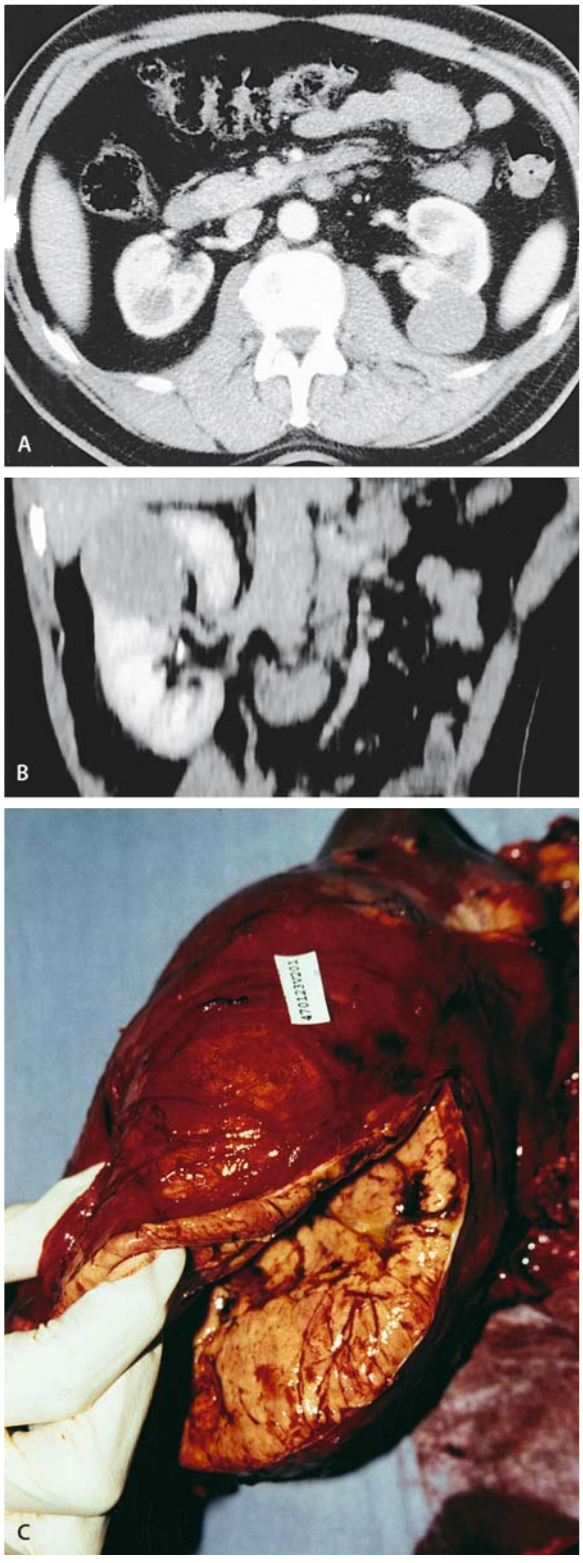

Fig. 14A–C. Chromophobic renal cell carcinoma. Hypovascular mass lesions in the left kidney (**A**) and in the right kidney on the parasagittal reformatted contrast-enhanced CT (**B**). The masses are solid with a grayish aspect at cross section (**C**). In general, these lesions are solitary and have already large dimensions at the time of detection. Compared to chromophilic cell carcinomas (papillary carcinoma), chromophobic cell carcinomas are solitary and larger (larger than 3 cm)

Imaging

Ultrasound

Chromophobic carcinomas are hypo- or isoechoic and heterogeneous or hypovascular on color Doppler.

Computed Tomography

Chromophobic RCCs are homogeneously isodense on unenhanced CT images. Tiny punctiform calcifications may be observed near the periphery. All lesions appear homogeneous and hypovascular on contrast-enhanced CT and are sharply demarcated (Fig. 14A, B). Necrosis is not seen and metastases or invasion of the renal vein in general do not occur [45].

Magnetic Resonance Imaging

Since this subtype is rather rare, experience with MR is limited. The lesion is isointense on T1-weighted images and hypointense on T2-weighted images. A hyperintense peripheral rim may be seen on heavily T2-weighted images. After administration of contrast there is hypovascularity of the lesion compared to the renal parenchyma.

Collecting (Bellini) Duct Renal Carcinoma

Pathology

Bellini duct RCC, a rare tumor, constitutes less than 1% of primary malignant renal parenchymal epithelial neoplasms. Bellini duct carcinomas appear to be aggressive, often with metastatic disease at manifestation and rapid progression despite surgery, with an almost uniformly fatal outcome [46]. Hematuria is the most common symptom. Since this variant seems to originate in the medulla and has a predominately tubular configuration, a collecting duct dedifferentiation is suggested. The cells contain the higher molecular weight keratin characteristic of the collecting ducts compared with the low molecular weight keratins of renal tubular epitheli-

um. The mass is usually localized to the renal medulla, with distortion of the pelvicaliceal system and often with infiltration into the adjacent renal cortex. The shape of the kidney is usually more or less preserved (Fig. 16C) [47]. The tumors are generally firm and white or grayish (not yellow) because of an accompanying desmoplasmic reaction (usually no necrosis or hemorrhage) (Fig. 16). Extension into the renal vein does not occur. Very rarely only, the tumors are cystic with endophytic papillary projections. The intermingling of clear cells, basophilic and eosinophilic cells contribute to a fairly typical aspect. The tumoral architecture is usually tubulopapillary. In general, there is considerable pleomorphism, especially in the invasive component, and mitotic figures are frequent. Associated atypical changes are often seen in adjacent collecting duct epithelium.

The small number of these that have been studied by genetic methods showed monosomies of chromosomes 1, 6, 14, 15 and 22 [48]. Chromosome *3p*, 7, 17 and Y abnormalities were not encountered.

A variant of collecting duct carcinoma, called medullary carcinoma, has been identified in patients suffering from sickle cell trait [49, 50].

Imaging

Ultrasound

The tumor is slightly hypoechoic or almost isoechoic, poorly marginated, and typically centrally located on US.

Computed Tomography

Bellini duct RCC appears homogeneous and isodense compared to the renal parenchyma on unenhanced CT. After intravenous contrast administration, the tumor is hypovascular [51] (Fig. 15A, B). There may be central low attenuation areas, due to the extensive reactive fibrotic reaction (not necrosis), which accompanies the infiltrative growth of this neoplasm, rather than necrosis or hemorrhage.

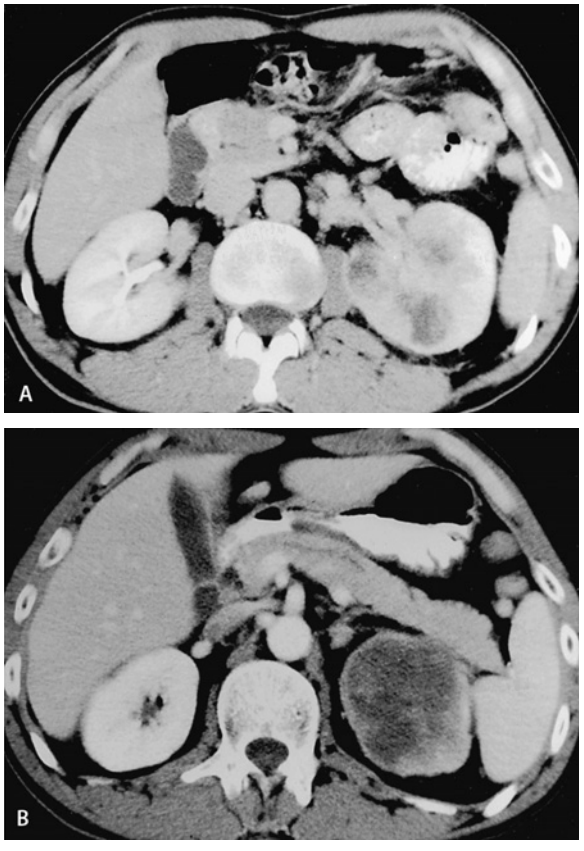

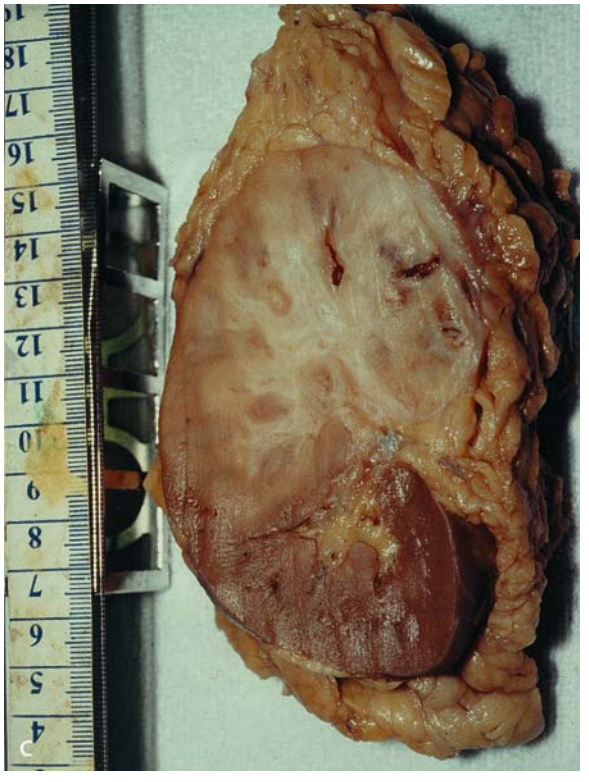

Fig. 15A–C. Collecting (Bellini) duct renal cell carcinoma. **A** Contrast-enhanced CT, excretory phase. Infiltrating tumor in the left kidney with hypodense areas. Note that the renal shape is largely preserved. **B** In the upper pole, the tumor mimics a predominately cystic carcinoma. The hypodense areas are not due to hemorrhage or necrosis, but are explained by reactive fibrosis. Note retroperitoneal lymph node metastases. **C** Nephrectomy specimen of a similar case (*right kidney*) with infiltrating fibrotic tumor involving the upper half of the kidney

Unclassified Renal Carcinoma

There is an increasing number of renal carcinomas, which are not readily classified. They may be observed in patients treated for carcinomas during childhood. Such tumors contain an odd mixture of components, tumors with an unrecognizable architectural or cytological pattern, or sarcomatoid carcinoma in which the original epithelium element cannot be identified or classified properly.

Observations on Sarcomatoid Neoplasms

Pathology

The sarcomatoid RCC is a particularly poorly differentiated, anaplastic variant comprising approximately 1% of cases and has an unfavorable prognosis. In fact, they represent a poorly differentiated, high-grade and invasive (infiltrative) type derived from any of the other cell types (clear cell, papillary, chromophobic, Bellini duct) [52]. They do no constitute a different subgroup per se; any tumor of the histological subtypes may become sarcomatoid. Most frequently they are derived from the conventional clear cell carcinoma. The presence of clear, granular or chromophilic cell areas within spindle cell or sarcomatous RCC is an important distinguishing feature from true sarcomas. When the sarcomatoid portion predominates, the neoplasm appears firm and fibrous without hemorrhage or necrosis; the carcinoma part is heterogeneous with areas of necrosis and hemorrhage. The upper pole seems to be more often affected than lower pole (ratio, 3:1). They are frequently bulky and advanced at presentation, with (atypical) distant metastases and may be inoperable (Fig. 16).

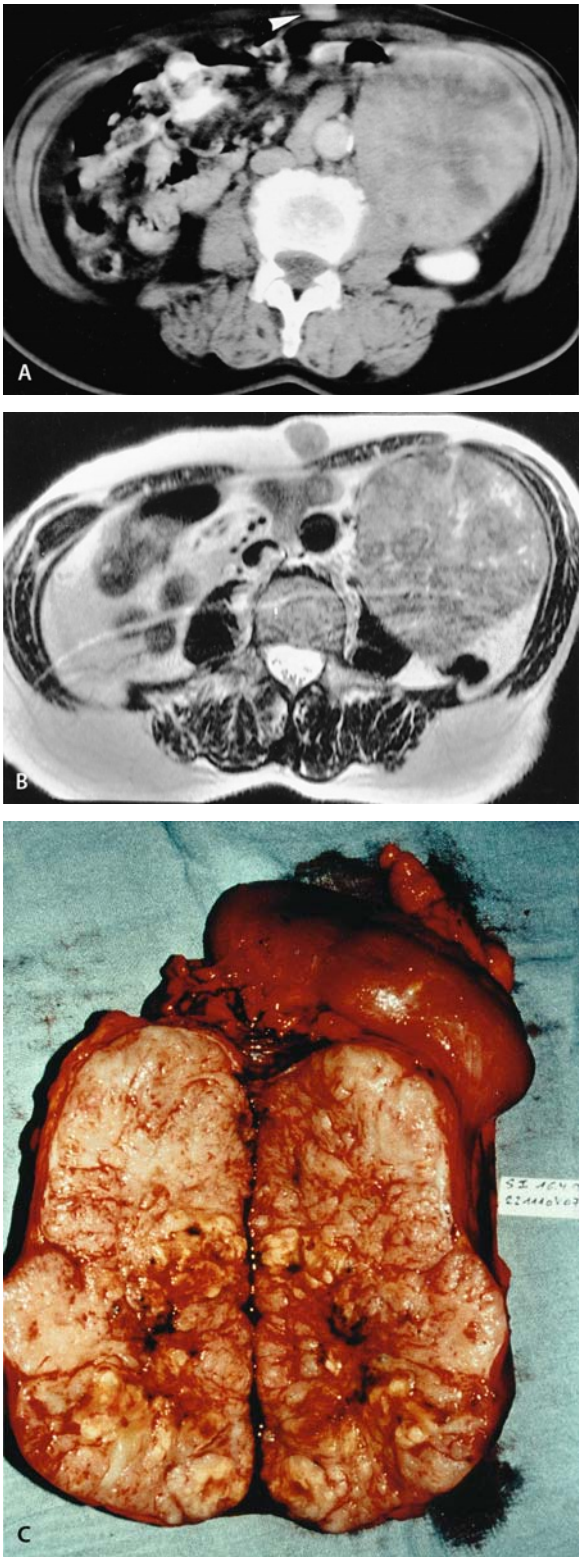

Fig. 16A–C. Sarcomatoid renal cell carcinoma. **A** Contrast-enhanced CT, nephrographic phase. Huge heterogeneous neoplasm at the lower pole of the left kidney. Soft tissue metastases in the subcutaneous fat of the anterior abdominal wall. **B** Axial T2-weighted MR showing similar imaging characteristics. Note that the tumor is predominately solid. Again the subcutaneous metastasis is clearly seen. **C** Surgical specimen showing the homogeneous solid mass extending of the surface of the left kidney

Imaging

Ultrasound

US shows a heterogeneous predominantly hyperechoic, isoechogenic or hypoechogenic mass. Calcifications may be seen quite often. The majority of sarcomatoid RCCs are hypovascular on color Doppler.

Computed Tomography

Sarcomatoid RCCs are iso- or hypodense on unenhanced scans. The tumors are heterogeneously hypervascular in the cortical phase. A hypodense and heterogeneous appearance is seen on late scans (Fig. 16A). Necrosis is always diffusely spread throughout the lesion, reaching the outer border of the lesion.

Lymph node metastases or adrenal or liver metastases are present in the majority of cases. These tumors may be very aggressive to adjacent organs (invasion of liver, spleen, pancreas, abdominal wall), and have atypical metastatic deposits.

Magnetic Resonance Imaging

The solid component of the lesion is either hypo- or isointense on T1-weighted images, heterogeneous and predominantly isointense on T2-weighted images (Fig. 16B). After Gd-DTPA administration, sarcomatoid RCCs are heterogeneously hypo- or hyperintense.

Observations on Renal Adenoma

For many years, size has been used as the main criterion to divide renal cell tumors into benign and malignant. This assumption has been based largely on the work of Bell in 1950 [53]. He suggested that renal tumors of less than 3 cm in maximum diameter should be called adenomas, yet two of his adenomas metastasized! A generally used limit is 3 cm in diameter for diagnosing a well-differentiated renal cell tumor as an adenoma. However, tumors smaller than 3 cm with metastases have been described on several occasions. Furthermore, adenomas share many phenotypic features with RCCs. Therefore, all renal cell tumors should be considered as malignant. The classic clear cell carcinoma and chromophobic RCCs develop as carcinomas, irrespective of grade and size. As already mentioned above, the natural history of papillary renal cell tumors is quite different from that of other types and their appearances are unique. Cortical adenomas are almost always papillary tumors, with a diameter less than or equal to 5 mm, and may transform to papillary carcinoma (Fig. 10) [54]. Tumors with a constant combination of trisomy 7 and 17 as well as loss of the Y chromosome may be diagnosed as a papillary renal cell adenoma. Such tumors may reach a large size without any sign of malignancy, but malignant transformation accompanied by additional complex genetic alterations may occur in small adenomas. It is not the size, but the accumulation of genetic alterations, especially acquired trisomies 16, 12 or 20, that are associated with malignant behavior.

Observations on Renal Oncocytoma

Pathology

Renal oncocytoma is a benign neoplasm and accounts for approximately 2%–5% of renal cell neoplasms [55]. Renal oncocytoma was first described by Klein and Valensi [56]. Incidental coexistence with RCC or angiomyolipoma has been reported. The majority remains asymptomatic and they are discovered incidentally. Most patients are elderly with a median age of about 65 years and a male-female ratio of approximately 2.5 : 1. Contrary to RCC, there is no association with von Hippel-Lindau disease, tuberous sclerosis, or chronic dialysis. Oncocytomas are characteristically single, well demarcated, uniformly expansile masses occurring at any renal site (Fig. 17). Multiple oncocytomas have been reported (oncocytomatosis). Occasionally, oncocytomas become very large (i.e., giant oncocytoma). In one review, the average tumor diameter was 7.4 cm, but reported sizes range from 0.3 to 20 cm. Whatever the size, oncocytomas should be considered as a benign neoplasm.

The tumors are tan (Fig. 15A, B) because of the lipochrome pigment associated with mitochondrial filling of the cytoplasm, circumscribed, with or without a capsule and often surrounded by a rim of dilated blood vessels. Larger tumors tend to have a central myxoid-fibrotic stellate scar that can become calcified. Foci of hemorrhage are commonly seen, but cystic change and necrosis are unusual. The cells are arranged in solid, tubular, or trabecular rests. A predominant extrarenal growth can be expected in 50% of cases. Metastases or invasion of the renal vein do not occur.

Microscopically, cells have abundant, granular eosinophilic cytoplasm; no clear cytoplasm is seen. The tumor cells probably derive from intercalated cells (type A) from the collecting ducts. Nuclei are generally low grade (I or II) and uniform, but focal areas may have marked nuclear atypia (oncocytomas are not graded). Mitotic activity is not seen, and foci of necrosis are uncommon. Ultrastructural examination reveals numerous round mitochondria larger than the mitochondria of other renal cell neoplasms and with a membrane particularly rich in cristae.

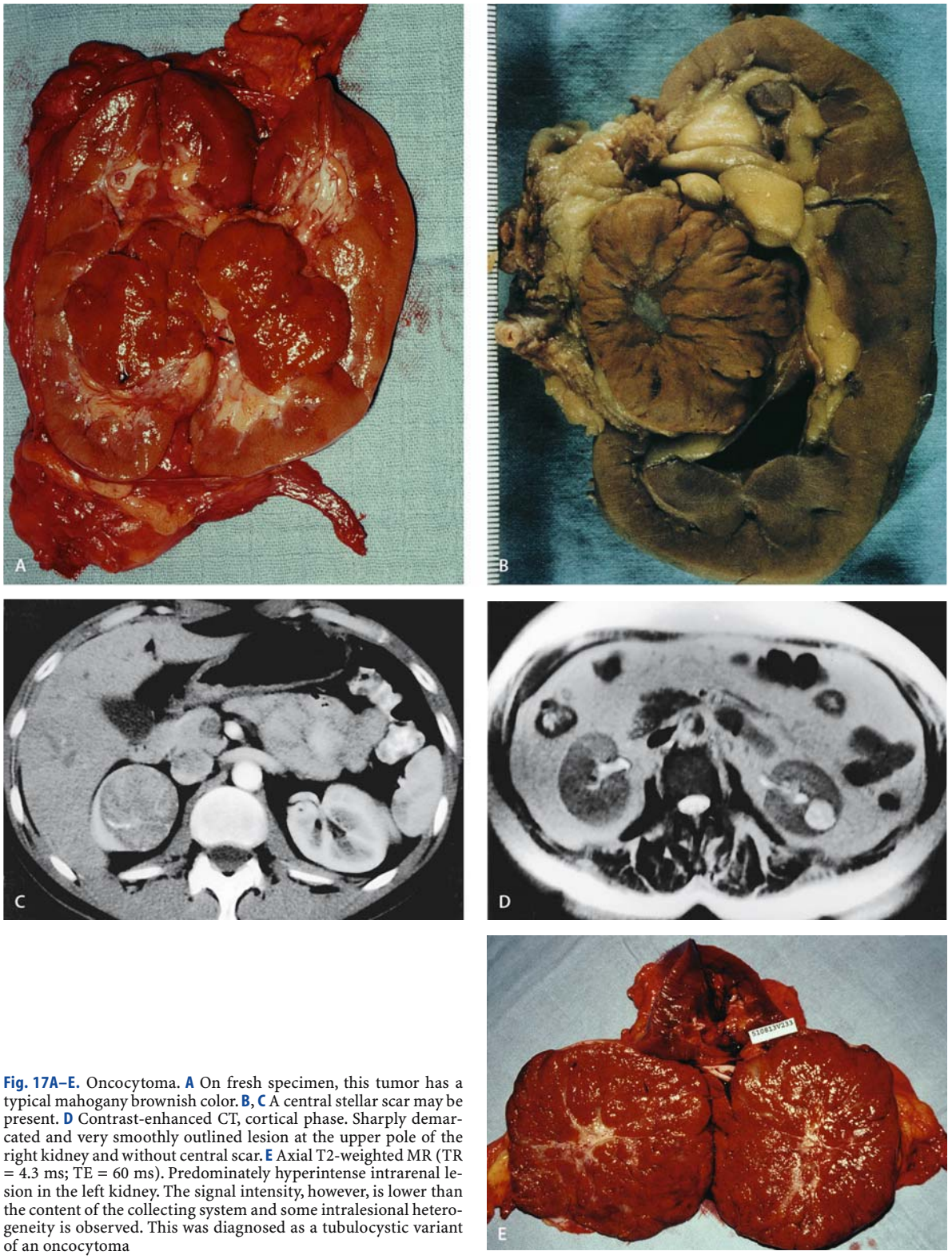

Fig. 17A–E. Oncocytoma. **A** On fresh specimen, this tumor has a typical mahogany brownish color. **B**, **C** A central stellar scar may be present. **D** Contrast-enhanced CT, cortical phase. Sharply demarcated and very smoothly outlined lesion at the upper pole of the right kidney and without central scar. **E** Axial T2-weighted MR (TR = 4.3 ms; TE = 60 ms). Predominately hyperintense intrarenal lesion in the left kidney. The signal intensity, however, is lower than the content of the collecting system and some intralesional heterogeneity is observed. This was diagnosed as a tubulocystic variant of an oncocytoma

Cytogenetic studies show normal or abnormal karyotypes including a translocation *t(11q;13)*, or loss of chromosome 1 or Y. The development of oncocytoma is initiated by typical abnormalities of the mitochondrial DNA structure.

Most reported oncocytomas have a benign behavior, but local or distant metastases have been reported. However, it is now felt that most, if not all, malignant oncocytomas described in the older literature are nonpapillary, papillary or chromophobic RCCs with eosinophilic granular cytoplasm. In addition, these tumors would be expected to display a deletion of 3p or trisomy 17 or mitochondrial alterations at genetic analysis. Yet oncocytomas may have the capacity to become malignant since they can contain chromophobic cells. This raises the possibility that oncocytomas and chromophobic carcinomas represent two ends of the same spectrum.

Imaging

Ultrasound

Most oncocytomas are slightly hypoechoic compared to the renal cortex on US. A central scar, reported as an anechoic center, is only seen in the minority of cases.

Computed Tomography

Oncocytomas are homogeneous and isodense on unenhanced CT. The majority is isodense (75% of cases) on cortical phase images and hypodense on late scans (Fig. 17C). Although a central scar is commonly seen on gross morphology, it can only be expected to be detected in 50% of cases by CT. Furthermore, this scarring is not exclusive for oncocytoma [57–59]. A sharp and very smooth demarcation with the adjacent parenchyma is always seen. A predominant extrarenal location can be expected in 50% of cases.

Many authors focused on the possibility of differentiating oncocytoma and RCC based on CT criteria (or angiography) and that differences would become more apparent as tumors enlarge. On contrast-enhanced scans, homogeneous attenuation throughout the tumor and a central, sharply marginated stellate area of low attenuation were considered predictors of oncocytoma. Any area of decreased attenuation in the tumor except for a stellate, central area was used as a predictor of carcinoma. Among oncocytomas larger than 3 cm in diameter, 67% exhibited criteria for oncocytoma and 33% met the features of carcinoma; among smaller oncocytomas, the respective results were 82% and 18%. Among carcinomas larger than 3 cm in diameter, 84% fulfilled the criterion for malignancy and 16% were incorrectly predicted to be oncocytomas; among smaller carcinomas, the respective results were 58% and 42%. Therefore, CT criteria used are poor predictors of the diagnosis of oncocytoma or carcinoma regardless of tumor size.

A likely explanation for the lack of homogeneity of oncocytomas on contrast-enhanced CT scans is an inhomogeneous perfusion as a result of ischemia. The pattern of growth of oncocytomas in which cells accumulate in more or less rounded, solid cell nests that become smaller, fewer, and farther apart toward the center of the tumor probably favors the ischemic events. Eventually these ischemic tumor cells are replaced by fibroblasts that give the classic gross specimen the pathologic and radiologic finding of a central scar. These same evolutionary changes of ischemia and fibrosis also occur in regions other than the center of an oncocytoma. This is the most likely explanation for the observations of heterogeneity in the enhancement pattern of oncocytoma noted in several studies. In addition to hemorrhage and necrosis, ischemia must also be considered as a cause of low tumor attenuation.

Magnetic Resonance Imaging

Oncocytoma is isointense on T1-weighted images and hyperintense on T2-weighted images (Fig. 17D) [60]. After injection of contrast, lesions are iso- to slightly hypovascular compared to the renal parenchyma and without evidence of necrosis or hemorrhage. A central stellate may occasionally be seen.

Indications for Lesional Biopsy

Needle aspiration puncture or biopsy has a limited role in the evaluation of the renal mass in the CT/MR era and has been abandoned as a routine procedure. Biopsy or needle aspiration has occasional value in the evaluation of the cystic indeterminate mass. In the setting in which a lesion is highly suspicious for neoplasm in a patient who is a very poor surgical risk, the technique could be performed to help establish a diagnosis and determine the treatment approach [61].

There are many occasions in which needle aspiration or biopsy is definitely indicated. These include differentiating a chronic abscess from a cystic carcinoma, differentiating a new primary renal neoplasm from a metastatic one in a patient who has had a previous primary tumor in another organ, and differentiating a primary renal neoplasm from renal lymphoma in a patient with lymphoma, particularly when the lesion does not regress with treatment whereas the rest of the disease does [62].

Conclusion

General agreement exists in the current literature on the importance of early detection of renal parenchymal neoplasms since (a) small lesions grow and then large tend to metastasize, (b) early detection implies earlier treatment and improved survival rate, and (c) it improves the possibility of elective or mandatory renal-sparing surgery [63–65]. Besides earlier detection, subtyping of RCCs may be valuable and useful for the surgeon, especially in centers where elective nephron-sparing surgery is performed. In a study by Van Poppel et al. [65], it has been shown that the most important requirements for this surgery are: (1) tumor is easily resectable, and (2) selection of candidates is based not only on tumor size. Therefore, if a tumor is suspected of being a papillary RCC or when a renal lesion does not fit in any of the above categories, further studies and possibly biopsy are indicated to avoid surgery in nonsurgical lesions such as metastases and lymphoma.

References

1. Murphy WM, Beckwith JB, Farrow GM (1994) Tumors of the kidney. In: Murphey WM, Beckwith JB, Farrow GM (eds) Atlas of tumor pathology. Tumors of the kidney, bladder and related urinary structures. Armed Forces Institute of Pathology, Washington DC, pp 92–145
2. Barbaric ZL (1996) Imaging work-up: is it renal carcinoma and is it operable? Semin Urol Oncol 14:196–202
3. Pavlovich CP, Walther MM, Choyke PL, Pautler SE, Chang R, Linehan WM, Wood BJ (2002) Percutaneous radio frequency ablation of small renal tumors: initial results. J Urol 167: 10–15
4. Uzzo RG, Novick AC (2001) Nephron-sparing surgery for renal tumors: indication, techniques and outcomes. J Urol 166: 6–11
5. Zucchi A, Mearini L, Mearini E, Constantini E, Vivacqua C, Porena M (2003) Renal cell carcinoma: histological findings on surgical margins after nephron sparing surgery. J Urol 169:905–908
6. Novick AC (1998) Nephron-sparing surgery for renal cell carcinoma. Br J Urol 82:321–324
7. Weiss LM, Gelb AB, Medeiros LJ (1995) Adult renal epithelial neoplasms. Am J Clin Pathol 103:624–635
8. Cohen C, McCue PA, Derose PB (1988) Histogenesis of renal cell carcinoma and oncocytoma. An immunohistochemical study. Cancer 62:1946–1951
9. Fleming S, O'Donnell M (2000) Surgical pathology or renal epithelial neoplasms: recent advantages and current status. Histopathology 36:195–202
10. Thoenes W, Störkel ST, Rumpelt HJ (1986) Histopathology and classification of renal cell tumors. Pathol Res Pract 181: 125–143
11. Kovacs G (1993) Molecular differential pathology of renal cell tumors. Histopathology 22:1–8
12. Dal Sin P, Polito P, Van den Berghe H (1998) Genetics of renal tumors. Pathologica 90:101–107
13. Hughson MD, Johnson LD, Silva FG, Kovacs G (1993) Nonpapillary and papillary renal cell carcinoma: a cytogenetic and phenotypic study. Mod Pathol 6:449–456
14. Kovacs G, Akhtar M, Beckwith BJ, Bugert P, Cooper CS, Delahunt B, Eble JN, Fleming S, Ljungberg B, Medeiros LJ, Moch H, Reuter VE, Ritz E, Roos G, Schmidt D, Srigley JR, Störkel S, Van Den Berg E, Zbar B (1997) The Heidelberg classification of renal cell tumours. J Pathol 183:131–133
15. Fleming S, O'Donnell M (2000) Surgical pathology of renal epithelial neoplasms: recent advantages and current status. Histopathology 36:195–202
16. Fleming S (1993) The impact of genetics on the classification of renal carcinoma. Histopathology 22:89–92
17. Choyke PL, Glenn GM, Walther MM, Zbar B, Linehan WM (2003) Hereditary renal cancers. Radiology 226:33–46
18. Takahashi K, Honda M, Okubo R, Hyodo H et al (1993) CT pixel mapping in the diagnosis of small angiomyolipomas of the kidneys. J Comput Assist Tomogr 17:98–101
19. Curry NS, Schnabel SI, Garvin AJ, Fish G (1990) Intratumoral fat in a renal oncocytoma mimicking angiomyolipoma. AJR 154:307–308
20. Hartman DS (1990) Overview of renal cystic disease. In: Pollack HM (ed) Clinical urography, vol 2. Saunders, Philadelphia, pp 1059–1062
21. Jinzaki M, Ohkuma K, Tanimoto A, Mukai M, Hiramatsu K, Murai M, Hata J (1998) Small solid renal lesions: usefulness of power Doppler US. Radiology 209:543–550
22. Ascenti G, Gaeta M, Magno C, Mazziotti S, Blandino A, Melloni D, Zimbaro G (2004) Contrast-enhanced second-harmonic sonography in the detection of pseudocapsule in renal cell carcinoma. AJR 182:1525–1530
23. Israel GM, Hindman N, Bosniak MA (2004) Evaluation of cystic renal masses: comparison of CT and MR imaging by using the Bosniak classification system. Radiology 231:365–371
24. Soyer P, Dufresne AC, Klein I, Barbagelatta M, Herve JM, Scherrer A (1997) Renal cell carcinoma of clear type: correlation of CT features with tumor size, architectural patterns and pathologic staging. Eur Radiol 7:224–229
25. Birnbaum BA, Jacobs JE, Ramchandani P (1996) Multiphasic renal CT: comparison of renal mass enhancement during the corticomedullary and nephrographic phases. Radiology 200: 753–758
26. Szolar DH, Kammerhuber F, Altziebler S, Tillich M, Breinl E, Fotter R, Schreyer HH (1997) Multiphasic helical CT of the kidney: increased conspicuity for detection and characterization of small (<3-cm) renal masses. Radiology 202:211–217
27. Israel GM, Bosniak MA (2003) Calcification in cystic renal masses: is it important in diagnosis? Radiology 226:47–52
28. Walter C, Heindel W, Kreussell M, Kugel H, Jung G, Gindele A (2001) Fast sequences with fat suppression in breath-hold mode: new standard in contrast-enhanced T1-weighted MR imaging of renal tumors? Eur Radiol 11:2092–2098
29. Oto A, Herts BR, Remer EM, Novick AC (1998) Inferior vena cava tumor thrombus in renal cell carcinoma: staging by MR imaging and impact on surgical treatment. AJR 171: 1619–1624
30. Mancilla-Jimenez R, Stanley RJ, Blath RA (1976) Papillary renal cell carcinomas. Cancer 38:2469–2480
31. Amin MB, Corless CL, Renshaw AA, Tickoo SK, Kubus J, Schultz DS (1997) Papillary (chromophil) renal cell carcinoma: histomorphologic characteristics and evaluation of conventional pathologic prognostic parameters in 62 cases. Am J Surg Pathol 21:621–635
32. Lager DJ, Huston BJ, Timmerman TG, Bonsib SM (1995) Papillary renal tumors. Cancer 76:669–673
33. Lesavre A, Correas JM, Meran S, Grenier N, Vieillefond A, Hélénon O (2003) CT of papillary renal cell carcinomas with cholesterol necrosis mimicking angiomyolipomas. AJR 181: 143–145
34. Kovacs G (1989) Papillary renal cell carcinoma: a morphologic and cytogenic study of 11 cases. Am J Pathol 134:27–34
35. Kovacs G, Fuzesi L, Emmanuel A, Kung H (1991) Cytogenetics of papillary renal cell tumors. Genes Chromosom Cancer 3: 249–255
36. Lemaître L, Provost M, Sault MC (1990) Tumeurs papillaires du parenchyme rénal: particularités de l'imagerie. A propos de 18 observations. Rev Im Med 2:615–623
37. Oyen RH (1997) Renal parenchymal tumors. Presented on the NICER course on gastrointestinal and urogenital radiology. World Trade Center, Seville, Spain 1997

38. Macari M, Bosniak MA (1999) Delayed CT to evaluate renal masses incidentally discovered at contrast-enhanced CT: demonstration of vascularity with deenhancement. Radiology 213:674–680
39. Suh M, Coakley FV, Qayyum A, Yeh BM, Breiman RS, Lu Y (2003) Distinction of renal cell carcinomas from high-attenuation renal cysts at portal venous phase contrast-enhanced CT. Radiology 228:330–334
40. Shinmoto H, Yassa Y, Tanimoto A, Narimatsu Y, Jinzaki M, Hiaramatsu K, Mukai M (1998) Small renal cell carcinoma: MRI with pathologic correlation. J Magn Reson Imaging 8: 690–694
41. Thoenes W, Störkel ST, Rumpelt HJ (1985) Human chromophobic cell renal carcinoma. Virchows Arch B 48:207
42. Crotty TB, Farrow GM, Lieber MM (1995) Chromophobic cell renal carcinoma: clinicopathological features of 50 cases. J Urol 154:964–967
43. Akhtar, Kardar H, Linjawi T, McClintock J, Ali MA (1995) Chromophobic cell carcinoma of the kidney: a clinicopathologic study of 21 cases. Am J Surg Pathol 19:1245–1256
44. Kovacs A, Storkel S, Thoenes W, Kovacs G (1992) Mitochondrial and chromosomal DNA alterations in human chromophobe renal cell carcinomas. J Pathol 167:273–277
45. Renshaw AA, Henske EP, Loughlin KR, Shapiro C, Weinberg DS (1996) Aggressive variants of chromophobic renal cell carcinoma. Cancer 78:1756–1761
46. Fleming S, Lewi HJE (1986) Collecting duct carcinoma of the kidney. Histopathology 10:1131–1141
47. Matz L, Latham B, Fabian VA, Vivian JB (1997) Collecting duct carcinoma of the kidney: a report of three cases and a review of the literature. Pathology 29:354–359
48. Füzesi L, Cober M, Mittermayer C (1992) Collecting duct carcinoma: cytogenetic characterization. Histopathology 21: 155–160
49. Swartz MA, Karth J, Schneider DT, Rodriguez R, Beckwith JB, Perlman EJ (2002) Renal medullary carcinoma: clinical, pathologic, immunohistological, and genetic analysis with pathogenetic implications. Urology 60:1083–1089
50. Dimashkieh H, Choe J, Mutema G (2003) Renal medullary carcinoma. A report of 2 cases and review of the literature. Arch Pathol Lab Med 127:e135–e138
51. Fukuya T, Honda H, Goto K, Ono M et al (1996) Computed tomographic findings of Bellini duct carcinoma of the kidney. J Comput Assist Tomogr 20:399–403
52. De Peralta-Venturina M, Moch H, Amin M, Tamboli P, Hailemariam S, Mihatsch M, Javidan J, Stricker H, Ro JY, Amin MB (2001) Sarcomatoid differentiation in renal cell carcinoma. A study of 101 cases. Am J Surg Pathol 25:275–284
53. Bell ET (1950) Renal disease. 2nd edn. Lea & Febiger, Philadelphia
54. Grignon DJ, Eble JN (1998) Papillary and metanephric adenoma of the kidneys. Semin Diagn Pathol 15:41–53
55. Davis CJ, Sesterhenn IA, Mostofi FK, Ho CK (1992) Renal oncocytoma; clinicopathological study of 166 patients. J Urogenital Pathol 1:41–52
56. Klein MJ, Valensi QJ (1976) Proximal tubular adenoma of the kidney with so-called oncocytic features. Cancer 38:906–914
57. Zagoria RJ (1998) Renal masses. Diagnostic imaging features. Presented at the annual meeting of the Society of Uroradiology. Hamilton, Bermuda 1998
58. Amin MB, Crotty TB, Tickoo SK, Farrow GM (1997) Renal oncocytoma: a reappraisal of morphologic features with clinicopathologic findings in 80 cases. Am J Surg Pathol 21:1–12
59. Davidson AJ, Hayes WS, Hartman DS, McCarthy WF, Davis CJ (1993) Renal oncocytoma and carcinoma: failure of differentiation with CT. Radiology 186:693–696
60. Harmon WJ, King BF, Lieber MM (1996) Renal oncocytoma: magnetic resonance imaging characteristics. J Urol 155: 863–867
61. Rybicki FJ, Shu KM, Cibas ES, Fielding JR, van Sonnenberg E, Silverman SG (2003) Percutaneous biopsy of renal masses: sensitivity and negative predictive value stratified by clinical setting and size of masses. AJR 180:1281–1287
62. Neuzillet Y, Lechevallier E, Andre M, Daniel L, Coulange C (2004) Accuracy and clinical role of fine needle percutaneous biopsy with computerized tomography guidance of small (less than 4.0 cm) renal masses. J Urol 171:1802–1805
63. Thompson IM, Peek M (1988) Improvement in survival of patients with renal cell carcinoma: the role of serendipitously detected tumor. J Urol 140:487–490
64. Pronet J, Tessler A, Brown J, Golimbu M, Bosniak M, Morales P (1991) Partial nephrectomy for renal cell carcinoma: indications, results and implications. J Urol 145:472–476
65. Van Poppel H, Bamelis B, Oyen R, Baert L (1998) Partial nephrectomy for renal cell carcinoma can achieve long-term tumor control. J Urol 160:674–678

Retroperitoneal Tumors

Giovanni Carbognin, Lucia Pinali, Carlo Procacci (†)

5.5

Contents

Table 1. Histologic classification of PRT (modified from [12])

Tissue of origin	Tumor
Connective (fibrous, myofibroblastic, and fibrohistiocytic tumors)	Fibroma, fibrosarcoma, malignant fibrous histiocytoma
Fat	Lipoma, liposarcoma
Smooth muscle	Leiomyoma, leiomyosarcoma
Skeletal muscle	Rhabdomyosarcoma
Vascular (blood vessels, lymph vessels) and perivascular tumors	Lymphangioma, lymphangiosarcoma, hemangioma, angiosarcoma, hemangiopericytoma
Neurogenic	Neurofibroma, neurofibrosarcoma, neurilemmoma, malignant schwannoma, ganglioneuroma, ganglioneuroblastoma, neuroblastoma, paraganglioma (inactive), pheochromocytoma
Tumors of uncertain differentiation	Peripheral primitive neuroectodermal tumor (PPNT), Ewing's sarcoma, synovial sarcoma
Miscellaneous	Castleman's disease

Introduction

Primitive retroperitoneal tumors (PRT) include masses that originate in the retroperitoneal space, independently of the organs present therein, and are thus histologically primitive. They derive from tissues contained in the retroperitoneal space (adipose, muscular, vessel and nerve tissue), from embryonic remnants or heterotopies coming from one or more embryonic layers (ectoderm, mesoderm and endoderm) or from totipotent embryonic germs. They do not include any growing lesions belonging to the retroperitoneal organs (kidneys, adrenal glands, excretory tract, pancreas and colon) or secondary invasive organs such as systemic masses (lymphomas) and metastases [1, 2]. PRTs are relatively rare (0.01%–0.3% of all tumors [3–6] in adults, 5% in infants [3, 7]), and they are rather different in histogenesis, structure and evolutionary potential. The only common feature is the site of development.

The average age for the appearance of PRTs is around 50 years even if no age is exempt. The percentage distribution of the various forms differs considerably depending on the age. The tumors are mostly malignant in both adults and infants (62%–86%) [2, 7–11].

In this chapter, following a short discussion on the radiological semiotics necessary to define the exact location of the lesions being examined, the macro- and microscopic aspects of the most common primitive retroperitoneal tumors recently dealt with in the WHO classification (2002) (Table 1) will be reviewed, focusing more on the characteristics that influence the appearance at imaging rather than the purely histological and cytogenetic aspects [12].

Radiological Semiotics of Primitive Retroperitoneal Tumors

In order to define a PRT as such, it is absolutely necessary to exclude its origin from retroperitoneal organs [13]. Many radiological signs have been described to assist in making a differential diagnosis. These include

valid signs common to every imaging method used and other specific signs depending on the study technique. The following are among the common signs:

- The beak sign (positive when the mass causes the edge of an adjacent organ to become beak shaped, meaning that the mass arises from that organ) (Fig. 1A–D).
- The phantom organ sign (positive when a huge mass arises from a small organ that then becomes undetectable) (Fig. 1E, F).
- The embedded organ sign (positive when part of a hollow organ appears embedded in the tumor) (Fig. 1G, H).
- The prominent feeding artery sign (particularly useful for hypervascular lesions supplied by arteries which are prominent enough to be visualized at CT or MR).

Apart from these general signs, there are others that can be specifically found with CT and MR. Specific diagnoses can be suggested with CT when the following are present:

- Calcifications (ganglioneuroma; malignant fibrohistiocytoma)
- Adipose tissue (homogeneous: lipoma (Fig. 2A); heterogeneous: liposarcoma (Fig. 2B)
- Necrotic areas (tumors with high grade malignancy such as leiomyosarcoma (Fig. 2C)
- Hypervascularization (hemangioma, hemangiopericytoma)
- Areas of low homogeneous density (neurofibroma) (Fig. 2D) [14]

MR, which is becoming the main method for examining soft tissues, is not able to give specific information in all cases, but the presence of some histological components can be suggested by evaluating the signal characteristics (intensity and enhancement) of the lesion. In the first place, determination of the dominant histological component can help narrow down the differential diagnosis possibilities [15].

The myxoid stroma is hyperintense in T2- and hypointense in T1-weighted images. After contrast medium (CM) administration, the enhancement is slower. This is common with ganglioneuroma (Fig. 3A–D), schwannoma, neurofibroma, myxoid liposarcoma, malignant fibrohistiocytoma, ganglioneuroblastoma and malignant tumor of the peripheral nerve sheaths.

The collagen fibers are hypointense in T1- and T2-weighted images. After CM, the dense areas of the collagen fibers enhance more slowly. Lesions that contain collagen fiber include neurofibroma, ganglioneuroma (Fig. 3A–D), leiomyosarcoma, malignant fibrohistiocytoma, malignant tumor of the peripheral nerve sheaths, fibrosarcoma and retroperitoneal fibrosis.

Although better seen with CT, calcifications, especially when large (ganglioneuroma, hemangioma, neuroblastoma) appear as markedly hypointense areas with MR.

Fat is rather hyperintense in T1, moderately hyperintense in T2 (fast or turbo spin-echo sequences) and hypointense in fat-suppressed images. Lesions made up of or often containing fat are lipoma, myelolipoma, angiomyolipoma and well-differentiated liposarcoma (Fig. 3E).

Studying the signal behavior after CM administration also gives important information. Four enhancement patterns have been described [15]:

- No enhancement (benign lesions)
- Early enhancement with rapid washout (benign lesions, Castleman's disease)
- Early enhancement with slow or no evident washout (mostly malignant)
- Delayed enhancement (benign masses (Fig. 3A–C) and some malignant tumors with a myxoid component such as myxoid liposarcoma, leiomyosarcoma)

There are other signs that are specifically appreciable with MR [15]:

- Target sign: central area with a low or intermediate signal surrounded by a hyperintense ring in T2. Histologically it corresponds to fibrous tissue centrally and myxoid tissue around the edge. It is frequently seen in neurofibromas and schwannomas.
- Bowl of fruit sign: low intensity mosaic, intermediate and high signal in T2-weighted images due to a combination of solid components, cystic degeneration, hemorrhage, myxoid stroma and fibrous tissue. This is often seen in malignant fibrohistiocytoma, synovial sarcoma (Fig. 3F) and Ewing's sarcoma.
- Whorled appearance: a linear or curvilinear structure appearing hypointense in T2. It corresponds to a band of Schwann cells and collagen fiber in the mass. It is commonly seen in ganglioneuroma (Fig. 3d) and neurofibroma.
- Flow void: this is often seen in hemangiopericytoma, arteriovenous hemangioma and alveolar sarcoma of the soft tissues.
- Speckled enhancement: this can be found in T1-weighted images after CM and corresponds to intratumoral structures similar to septa. It is more frequently seen in leiomyosarcoma and rhabdomyosarcoma.

Fig. 1A–H. Origin of the mass. Positive beak sign: diagram (**A**) and CT scan after CM administration (**B**). The appearance is supported by parenchymal tokens that "envelop" the tumor. The lesion originates from the organ (renal mass). Negative beak sign: diagram (**C**) and CT scan after contrast medium administration (**D**). The tumor does not originate from the organ, which is also compressed. An acute angle forms at the contact points between the resident organ and the lesion as shown in (**c**) (retroperitoneal mass). **E, F** Phantom organ sign: diagram (**E**) and CT scan after CM administration (**F**). The tumor's originating organ (right kidney) appears totally incorporated by the tumor and is no longer recognizable (**F**). Negative embedded organ sign: diagram (**G**) and CT scan after CM administration (**H**). The wall of a hollow viscus is compressed extrinsically from the tumor creating a crescent shape (*arrowheads*)

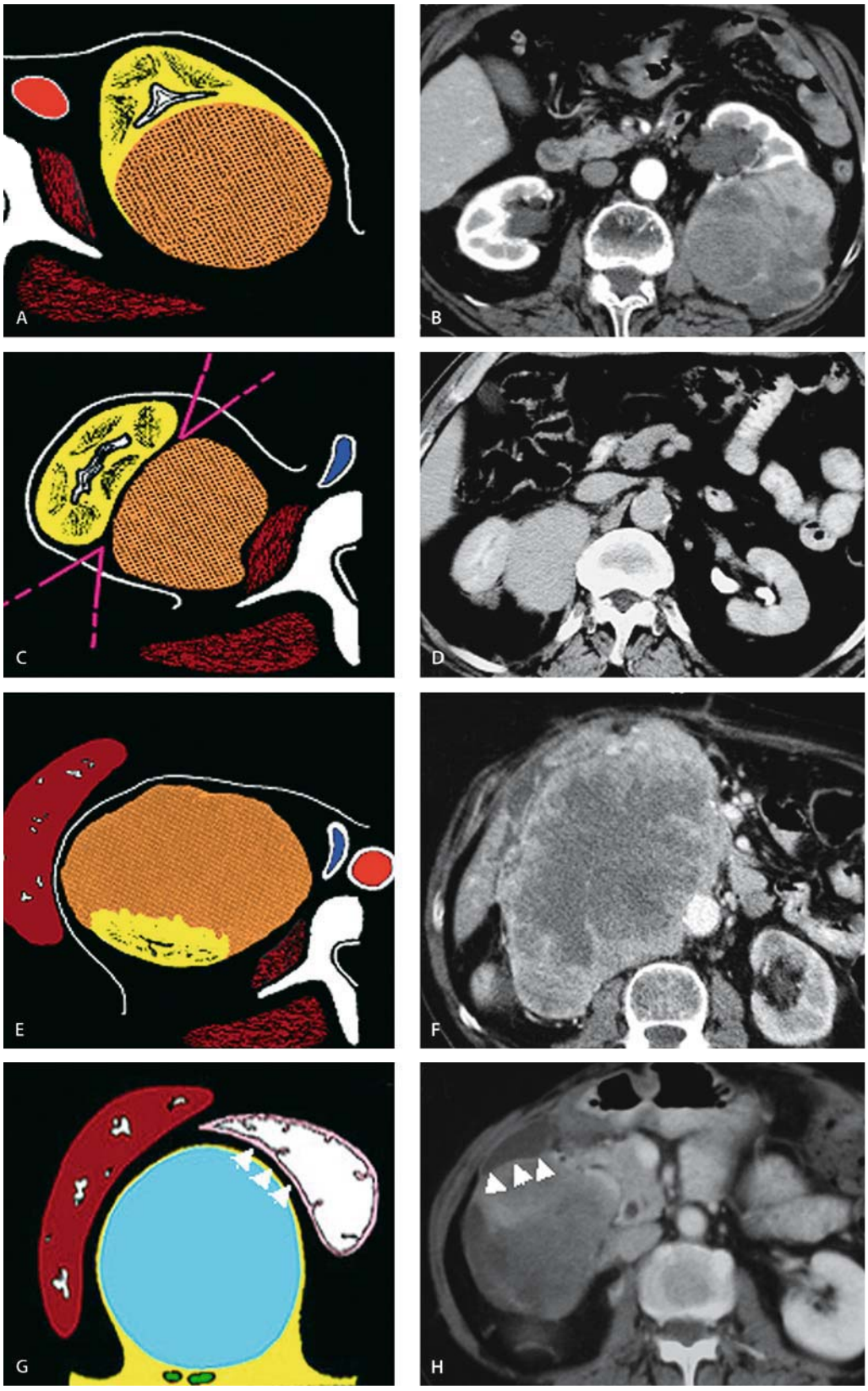
A
B
C
D
E
F
G
H

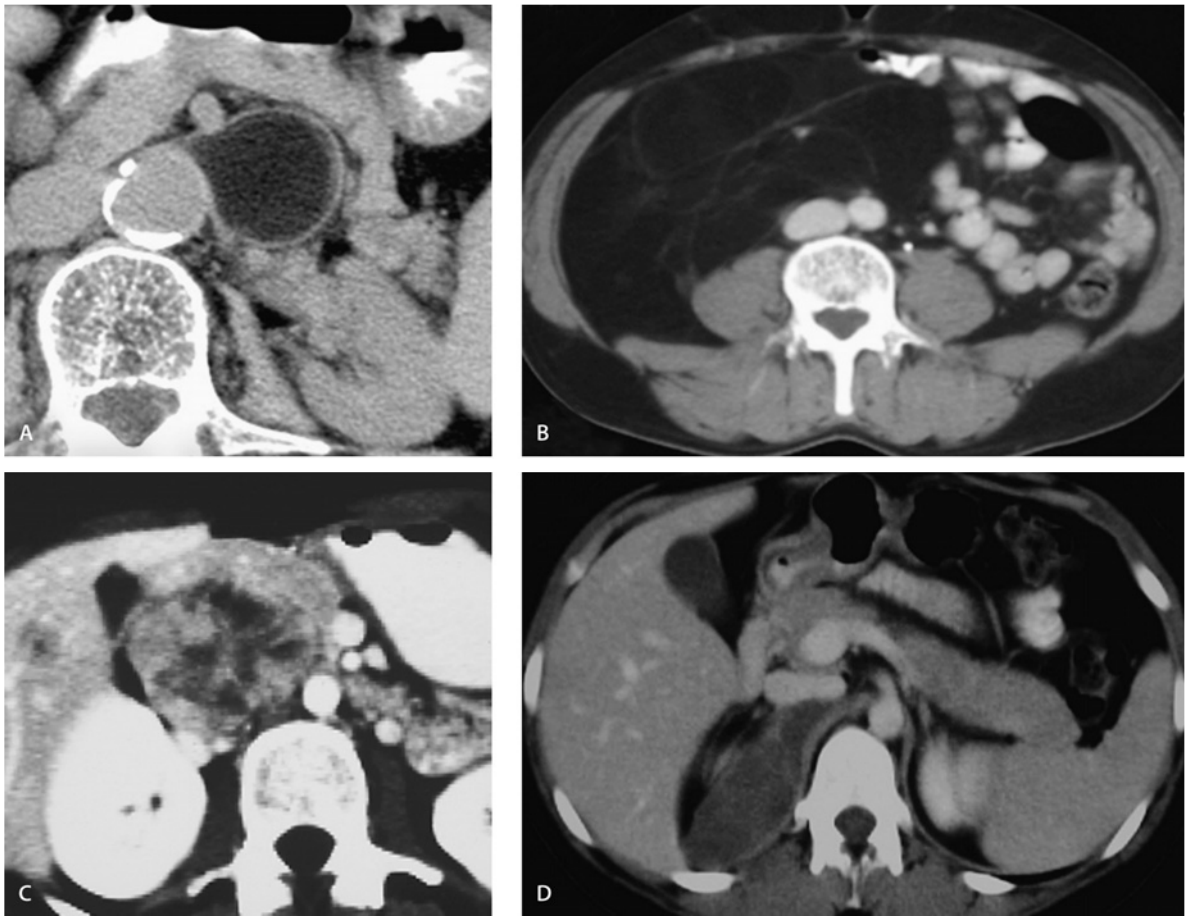

Fig. 2A–D. Densitometric characteristics of retroperitoneal tumors. CT examinations before (**A**) and after (**B–D**) CM administration. **A** Lipoma. Well-circumscribed lesion with homogeneous fat density. **B** Liposarcoma. Voluminous lesion, displacing the intestinal loops toward the left with fat density and within which fibrous septa are visible. **C** Leiomyosarcoma. Voluminous lesion originating from the wall of the vena cava and within which necrotic areas can be seen. **D** Ganglioneurofibroma. Solid lesion with clear margins and low density (myxoid stroma)

Fig. 3A–F. MR aspects of retroperitoneal tumors. **A–D** Ganglioneuroma. In the dynamic contrast-enhanced study (**A–C**), the lesion shows delayed enhancement. In the T2-weighted axial scan (**D**), the lesion has a whorled appearance due to the abundance of collagen fibers. **E** Liposarcoma. In the turbo spin-echo (TSE) T2-weighted coronal scan, the lesion shows a signal hyperintensity due to the fatty content. The hollow organs appear prevalently displaced upward. An embedded sign can be seen in the right hypochondrium (*arrow*). **F** Synovial sarcoma. In the T2-weighted sagittal scan, the lesion has a heterogeneous pattern with areas of high signal intensity (necrosis) and low signal intensity (solid tissue): bowl of fruit sign. The lesion appears well defined

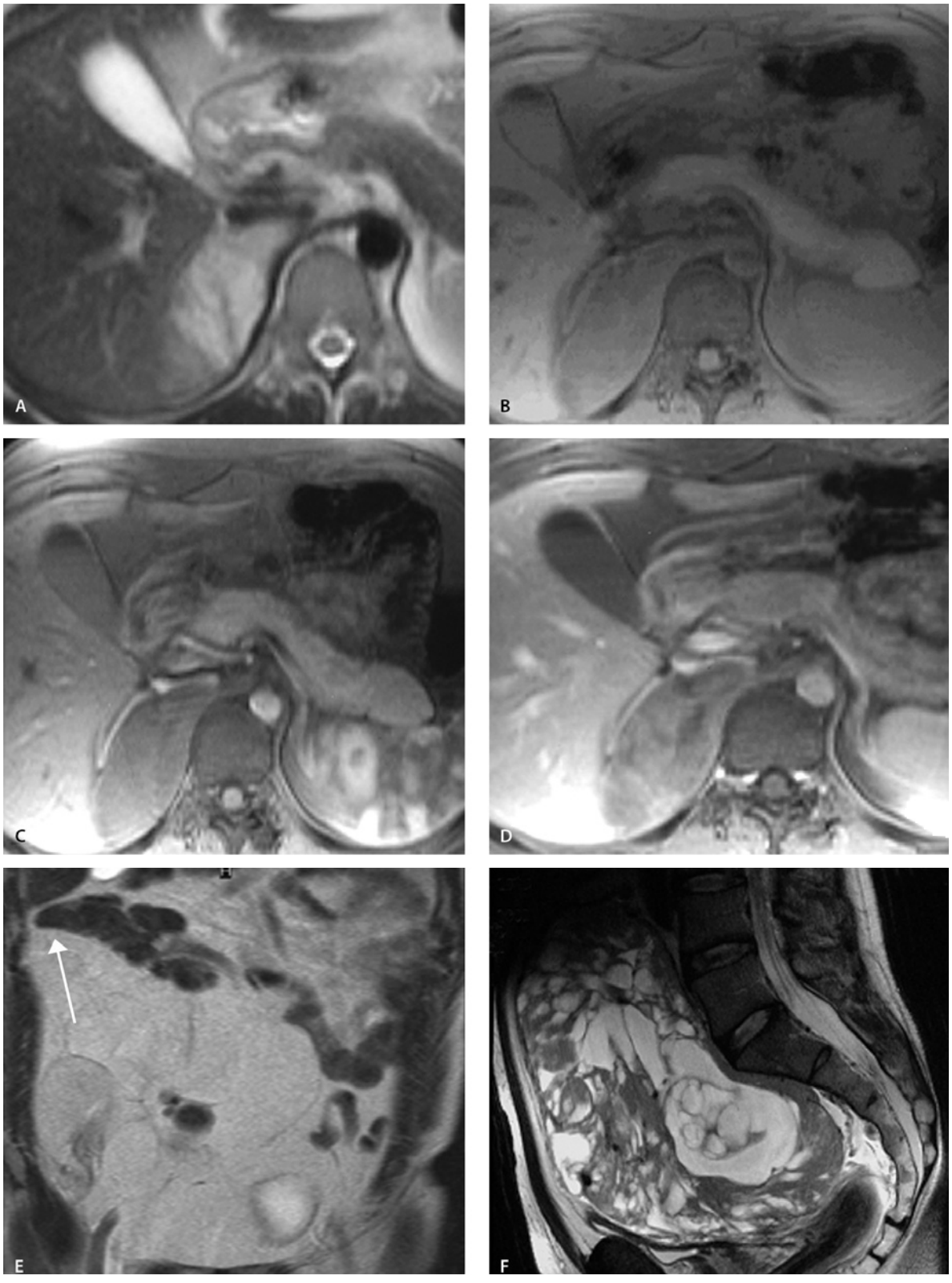
A
B
C
D
E
F

Tumors Originating from Connective Tissue (Fibrous, Myofibroblastic and Fibrohistiocytic)

The retroperitoneum is affected by border-line masses, typically retroperitoneal fibromatosis and malignant forms such as fibrosarcoma in adults.

Retroperitoneal fibromatosis is a group of benign fibrous tissue proliferations, with no sign of inflammation or tumor [14, 16]. The biological behavior is somewhere between benign fibrous lesions and fibrosarcoma: the proliferations tend to be locally aggressive and can relapse locally but do not metastasize [17]. They can be primarily retroperitoneal or, more frequently, extensions of mesenteric fibromatosis [17]. This disease can occur at any age between 10 and 80 years (40 being the average) and usually affects adults [17, 18]. However, these lesions are rare: 10%–15% of cases are associated with familial polyposis syndrome or Gardner syndrome [19]. Macroscopically, the lesion appears as a solid mass of variable size (1–30 cm) [18]. There is no real capsule [19]. Microscopically, it is an infiltrating fibroproliferative process sustained by fibroblasts and myofibroblasts. Collagen with myxoid deposits can be found in proximity to the fibroblasts. At US, fibromatosis shows variable but generally low echotexture and smooth, clear outlines [17, 20, 21].

At CT, it can have a homogeneous pattern and the margins are usually well-defined. After CM administration, enhancement slows down because of the poor vascularization. More particularly, the lesion appears generally isodense (47%) or hyperdense (41%) compared to the muscle [18].

At MR the lesions appear hypointense compared to the muscle in T1-weighted sequences while in T2-weighted sequences the intensity is variable but generally low [19, 21].

Fibromatosis must be distinguished from idiopathic retroperitoneal fibrosis (Ormond's disease), which is a rare pathological condition (1/100,000–200,000) characterized by fibrous proliferation along the posterior part of the retroperitoneum (Fig. 4) [22, 23].

The fibrosarcoma is a collagen-producing malignant tumor deriving from cancerous fibroblast proliferation. It can show variable degrees of cellularity, anaplasia and mitotic index. It occurs more frequently in middle age, typically develops in the more internal soft tissues and is rarely located in the retroperitoneal [12] and mediastinal areas, with the exception of the so called inflammatory subtype, more recently defined as inflammatory myofibroblastic tumor. This is usually a large, well-defined tumor within which necrotic focuses, which are associated with aggressive biological behavior, can often be found (Fig. 5) [12, 24]. There are no further distinct characteristics from the radiological aspect.

Up to now, the malignant fibrohistiocytoma (MFH) has been the most common soft tissue tumor in adults,

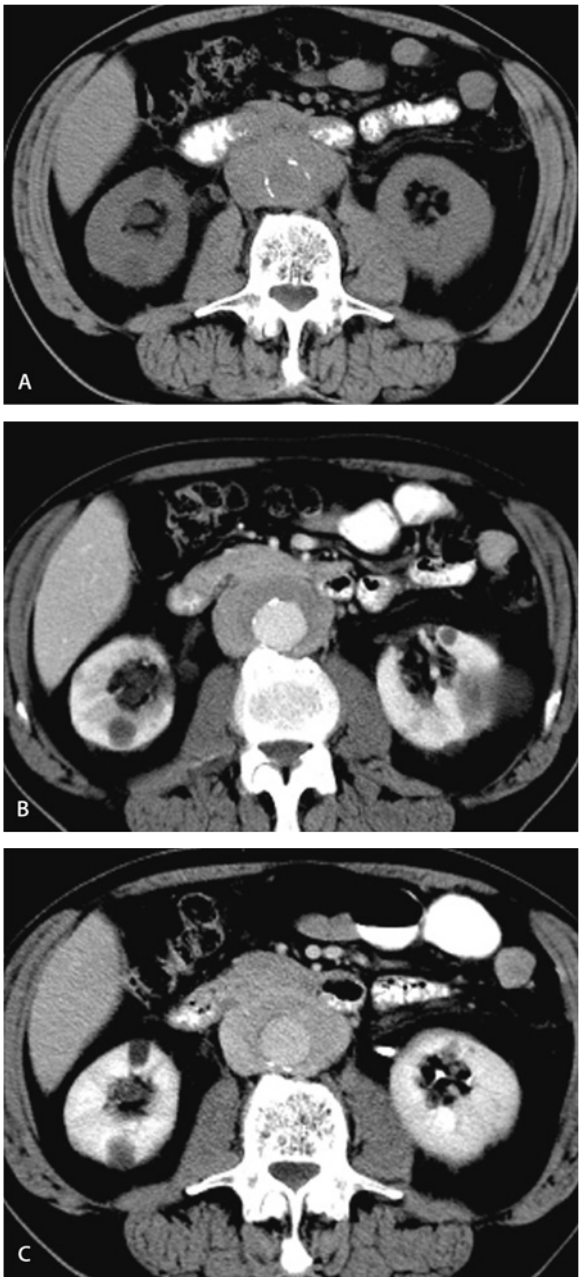

Fig. 4A–C. Retroperitoneal fibrosis (Ormond's disease). CT examination in the pre- (**A**) and post- (**B, C**) contrastographic phases. Solid tissue is visible with homogeneous density in the precontrastographic phase (**A**), surrounding the aorta outlined by lamellar calcifications. In the dynamic contrast-enhanced phase (**B, C**) lesion enhancement is slow

also in view of the fact that, so far, the morphologic pattern known as the pleomorphic MFH may be shared by a wide variety of poorly differentiated malignant masses [12]. However, this lesion appears in the retroperitoneum only in about 16% of cases. It is clinically nonspecific. Sometimes patients complain of indisposition, fe-

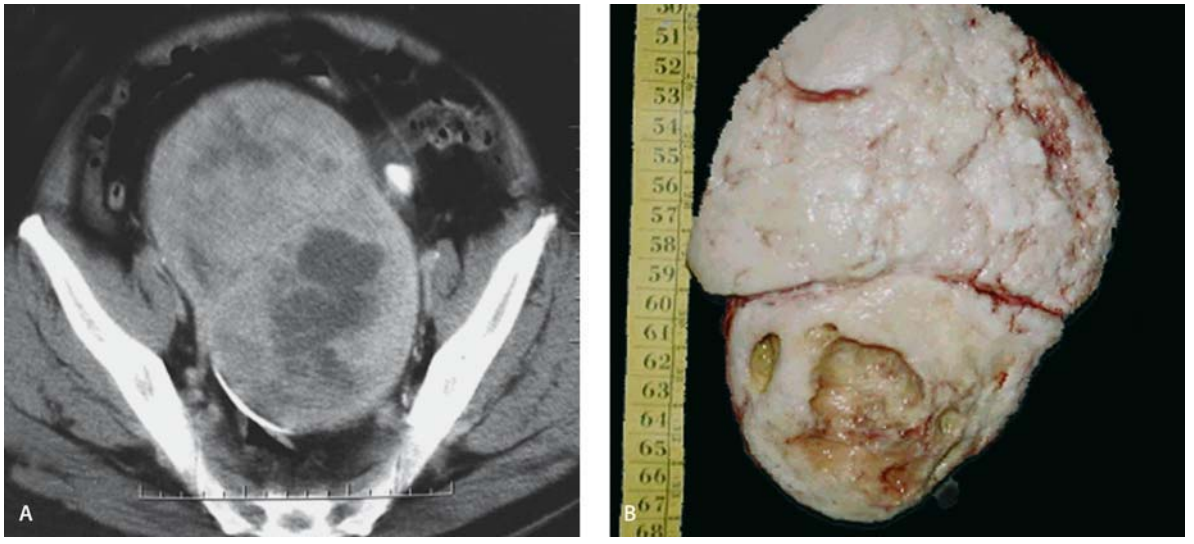

Fig. 5A, B. Fibrosarcoma. CT examination after CM administration (**A**) and macroscopic section (**B**). At CM-enhanced CT (**A**) the lesion shows clear margins and inhomogeneous enhancement due to the presence of necrotic spaces within it, confirmed by the resected specimen (**B**)

ver, weight loss and abdominal pain. Hypoglycemia can be present but is very rare [25].

Macroscopically, it appears as a lobulated, gelatinous mass and is usually more than 5 cm in diameter. There are five different subtypes, depending on the main component, but the most useful to recognize are the myxoid MFH and the pleomorphic MFH, as they have characteristics that can assist diagnosis.

The myxoid MFH has an abundant amount of fundamental and mucopolysaccharide substance. It is biologically less aggressive and hardly ever leads to metastatic spread. With the MR examination, the myxoid component, hypointense in T1- and considerably hyperintense in T2-weighted images, is particularly useful in assisting diagnosis [26].

The pleomorphic variety generally affects areas that have previously undergone radiotherapy. Macroscopically, it is a multilobulated, large mass (about 10 cm). Microscopically, it shows a complex structure with multiple hemosiderin deposits and numerous gigantic cells similar to osteoclasts [27]. The signal intensity at MR is the same as that of the muscular tissue in both T1- and T2-weighted sequences, and enhancement is poor after administration of gadolinium. But the anamnestic findings of previous radiotherapy in the area of a mass with the above characteristics can lead to the correct diagnosis [28].

At imaging, the malignant fibrohistiocytoma is not easily distinguished from other soft tissue sarcomas. The combined use of the various methods, especially MR, together with clinical evaluations, can be useful in making a differential diagnosis, particularly in the case of a large lesion that extensively infiltrates the adjacent structures (Fig. 6).

Lipomatous Tumors

Adipose tissue tumors are common and represent about half of soft tissue tumors in the surgical series [29], and about 6% of all soft tissue tumors in children. They can be divided into benign (lipoma and hibernoma) and malignant (liposarcoma in its different variants) tumors.

The lipoma is the most common benign soft tissue tumor. Nevertheless, its location in the retroperitoneum is so rare that some authors do not take it into consideration at all [12]. It arises at different ages but is more frequently found in Patients of between 40 and 60 years of age while it is very rarely found in children. It involves women more than men with a ratio of 1:2 and causes a large increase in abdominal volume, with dislocation of the contiguous abdominal structures [30, 31]. It is easily removed and usually does not degenerate or relapse.

Histologically, it is a tumor of the white adipose tissue with no lobulation composed of mature adipocytes with a fibromembranous or fibrous capsule and tends to expand without infiltrating the nearby organs. It can be difficult to make a differential diagnosis with other adipose tissue tumors such as the hibernoma and lipoblastoma and especially the well-differentiated liposarcoma [21].

At imaging it appears with the typical characteristics of a fatty, hypovascularized mass: homogeneously ra-

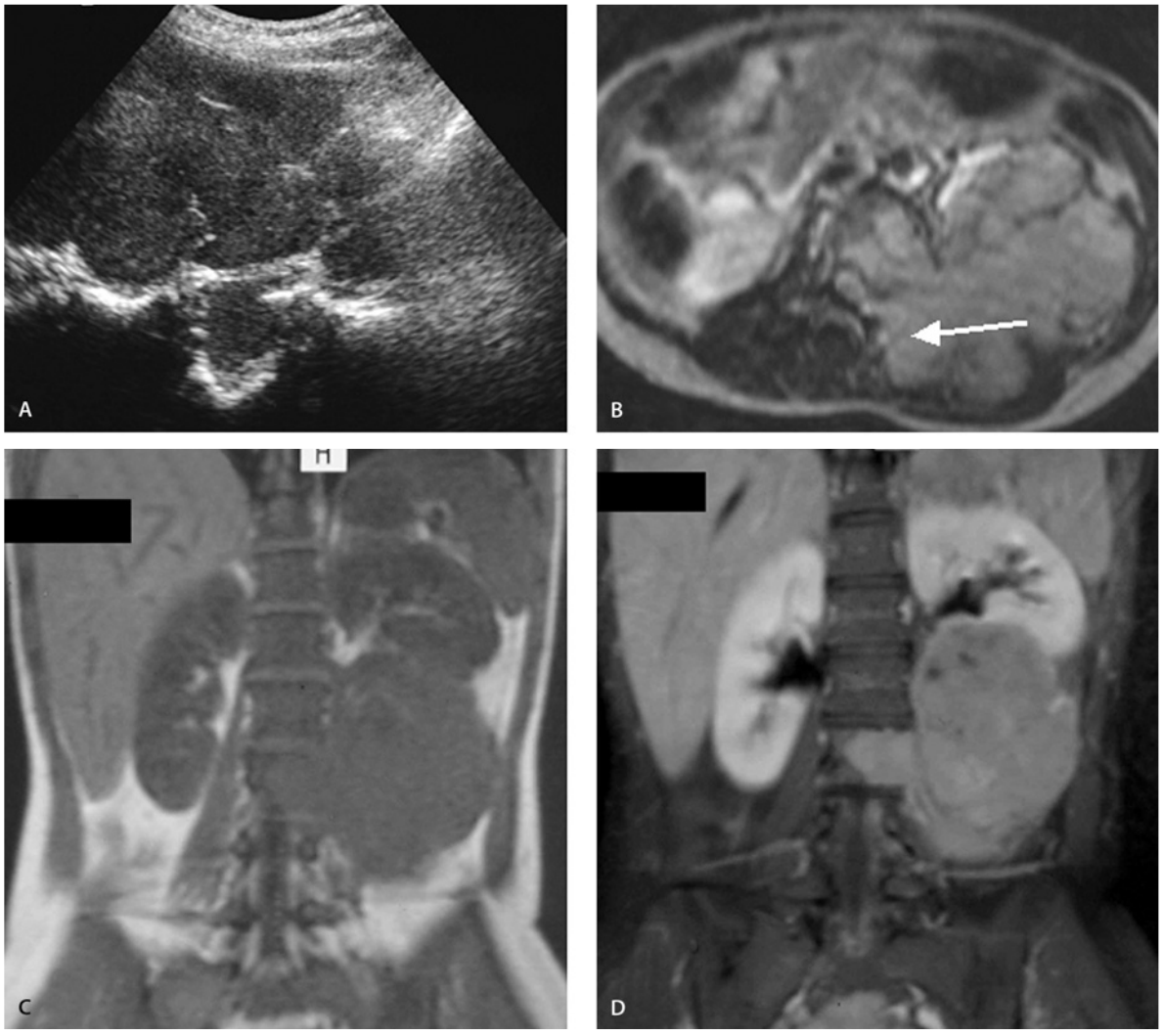

Fig. 6A–D. Giant cell malignant fibrous histiocytoma. At US examination, the paracoronal scan on the left flank (**A**) shows a solid and quite homogeneous mass with a multilobular appearance in strict contiguity with the spine. At MR examination, in the SE T2-weighted scan (**B**), the lesion appears inhomogeneously hyperintense; its medial portion infiltrates the paravertebral muscles and the spine, invading the canal (*arrow*). In the T1-weighted scans before (**C**) and after (**D**) CM, the marked vascularization of the mass is confirmed infiltrating the L2 body and cranially displacing the left kidney

diolucent in conventional radiograms, hyperechogenic at US, and with low intensity at CT (Figs. 2A, 7), where it displays well-defined outlines and the occasional intralesional fibrous septa, which appear with greater density as internal linear stria. There is no enhancement after contrast medium administration (Fig. 7). At MR the lipoma is hyperintense on T1- and hypointense on T2-weighted images. The T1 sequence with selected fat suppression leads to a definite diagnosis, especially when the lesion shows a homogenous aspect [26].

Hibernomas are extremely rare tumors of the brown adipose tissue. Only two of the 100 cases that have been described in the literature were found in the retroperitoneal region. They appear at any age with an incidence peak in the 30s. Clinically, it is a slow-growing, benign tumor that can reach considerable dimensions. Macroscopically, it appears as a mass that is well circumscribed by a reddish-brown capsule, which may be due to the high degree of vascularization. Imaging findings are generally nonspecific and a differential diagnosis between the other adipose soft tissue tumors is difficult to make. A biopsy is therefore necessary for classifying the mass. At CT, the density of the hibernoma can appear somewhere between that of the adipose tissue and the muscle, with clear enhancement in the arterial contrast phase because of the rich vascularization. At MR, a signal hyperintensity in both T1- and T2-weighted images has been described [32].

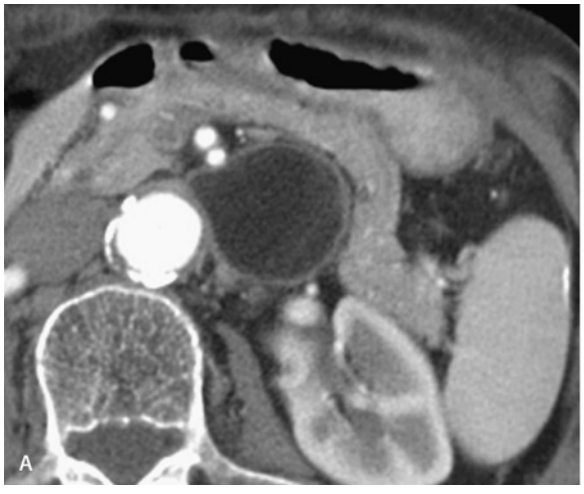

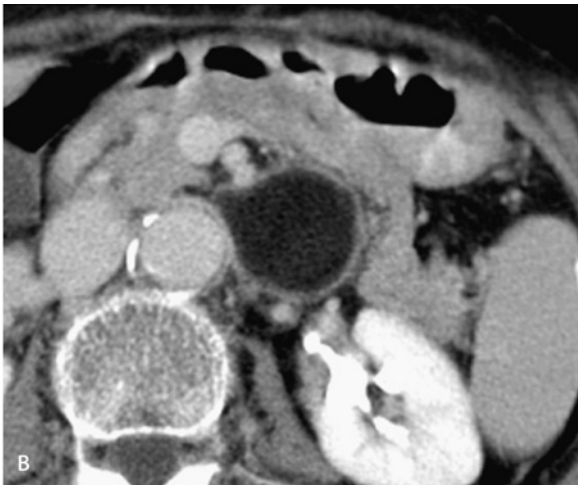

Fig. 7A, B. Lipoma, same case as Fig. 2a. CT examination in the early (**A**) and late (**B**) phases after CM. At enhanced CT, an encapsulated lesion can be seen, considerably hypointense in all the phases of enhancement, which displaces, without infiltrating, the body of the pancreatic gland and the superior mesenteric artery (**A**)

The liposarcoma is a mesenchymal tumor with an uncertain pathogenesis that takes on an adipose differentiation pattern. It represents about 16%–18% of all sarcomas of the soft tissue in adults and is the second most common tumor after malignant fibrohistiocytoma. Although it is the most frequent retroperitoneal tumor, only 14% of cases can be found at this level, since it prefers to locate around the kidneys [33]. It is slightly more common in men than in women [34]. It affects people of all ages but occurs more frequently in the 50s and 60s.

Clinical symptoms are the same as those of other retroperitoneal tumors, i.e., nonspecific and ambiguous, and usually in the advanced stage: vague and diffuse abdominal pain, weight loss, abdominal growth with palpable mass, gastroenteric or genitourinary symptoms. The clinical outcome depends on the size, site and histological variant. Only 50% of tumors at the moment of diagnosis can be completely removed, so an early diagnosis with imaging is therefore of great importance. The best treatment is still surgery since neither radiotherapy nor chemotherapy have proved to have any influence on the prognosis so far [33].

The anatomopathologic aspect is variable, with widespread overlapping between the benign and malignant characteristics with the possibility of identifying five different subtypes: the well-differentiated (Fig. 8), myxoid, pleomorphic, undifferentiated and round cell forms [34–37].

Macroscopically, the liposarcoma appears well-circumscribed, encapsulated, typically multilobulated (Fig. 8B); fibrous septa can be seen internally [38]. Microscopically, the well-differentiated form is made up of lipoblasts, irregularly shaped cells with hyperchromatic nuclei and adipocytes (Fig. 8C), which are often situated along the fibrous septa. The myxoid variant has three main tissue components: lipoblasts in proliferation, a delicate plexiform capillary pattern and a mucopolysaccharide myxoid matrix. The extracellular mucin often forms large lakes (lake-like aspect). Pleomorphic liposarcomas are more aggressive and tend to metastasize early. There is a high degree of cellular pleomorphism, including giant cells, with areas of necrosis and hemorrhage. If there are no characteristic lipoblasts, the anatomopathologic differential diagnosis with malignant fibrohistiocytoma can be difficult [35]. The round cell liposarcoma is extremely aggressive from a clinical and a biological standpoint [35]. The undifferentiated form derives from a dedifferentiation of a well-differentiated liposarcoma, a previous retroperitoneal tumor that was treated with chemo- or radiotherapy. It can also recur as a slow-developing, spontaneous process. This variant is highly malignant. Its cellular population is mixed and heterogeneous and reflects the origin of the mesenchymal tumor from which it has dedifferentiated. This population not only includes multinucleated cells and large pleomorphic cells with abundant cytoplasm, but also nests of smaller cellular elements with a high nucleus/cytoplasm ratio (Fig. 9) [39].

Imaging, traditionally CT and MR, plays a key role in the diagnosis of liposarcomas, so much so that today, MR is considered as the gold standard in their study. Ultrasound is usually used more to define the extent of the tumor than to diagnose its nature. It is, however, very useful during follow-up as it can recognize any cancerous recurrence early. Recurrence arises in 90% of cases within 10 years of surgical intervention. Since pleomorphic liposarcomas recur more often than the well-

differentiated forms, it is good to follow these patients up with frequent ultrasound examinations. The majority of well-differentiated liposarcomas have high echogenicity but they are sometimes very large and have a complex internal structure in which the internal echoes are difficult to recognize. Only well-differentiated liposarcomas have a particularly suggestive echogenic pattern with a wavy aspect stemming from hyperechoic horizontal or concentric lines, depending on whether a linear or curved probe is used. These correspond anatomopathologically to the fibrous septa inside the liposarcoma [37]. The absence of cystic degeneration can be indicative of the liposarcomatous nature of a retroperitoneal lesion even if it is a rather nonspecific sign. Color Doppler examination can often highlight compressed vessels but it does not give any further information in terms of diagnosis [37].

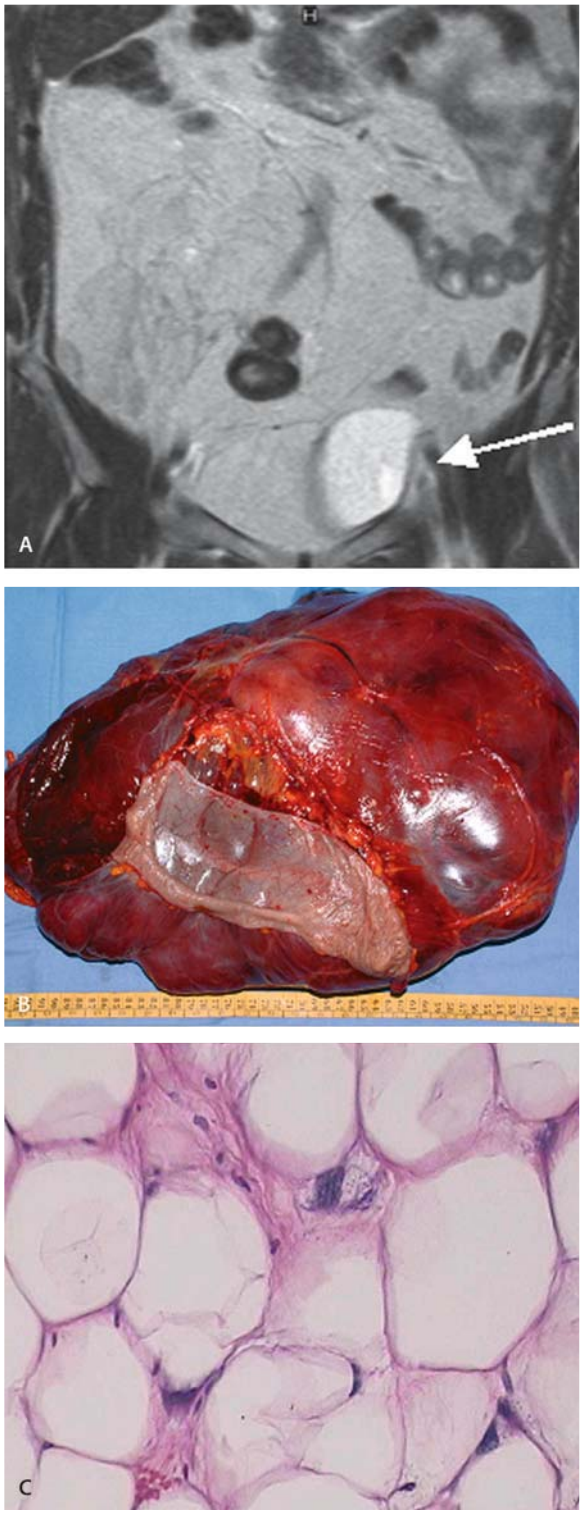

Fig. 8A–C. Lipoma-like liposarcoma. In the T2-weighted coronal scan, a voluminous expansive mass occupies the right flank displacing the intestinal loops and the bladder to the left (*arrow* in **A**). At the subsequent intervention, the lesion was resected (**B**) and proved to have quite clear, multilobular margins. Histologically, the mass appears to be made up of adipoblasts with hyperchromic nuclei and adipocytes (**C**)

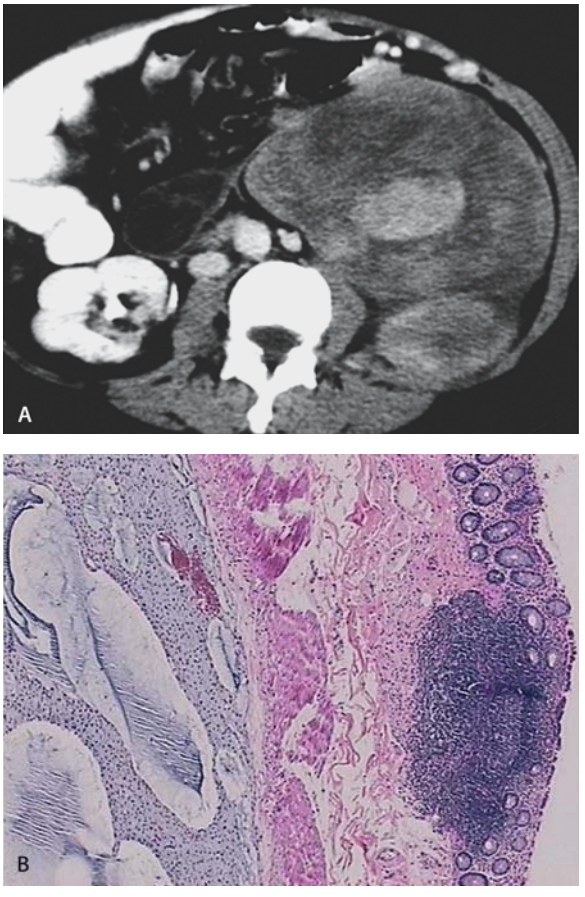

Fig. 9A, B. Dedifferentiated liposarcoma. The contrast-enhanced CT scan (**A**) shows an inhomogeneously dense mass in the front left pararenal space. The irregular aspect is due to the presence of necrotic areas. In the low-magnified histologic section (**B**), the dedifferentiated component is appreciable, heralded by a hypercellular fibrous area

At CT, the liposarcoma appears as a large mass, which displaces, compresses and distorts the outlines of the contiguous organs. It has a negative attenuation coefficient and can have large internal fibrous septa. The well-differentiated forms are hypodense (Fig. 2B), while the pleomorphic forms have a rather inhomogeneous appearance (Fig. 9A).

At MR the mass shows up with a typically thick peripheral ring and linear septa with internal nodules. The adjacent structures are preserved. The signal intensity of the well-differentiated liposarcoma is identical to that of subcutaneous adipose tissue in all the sequences (Fig. 3E). It is largely composed of fat and thin or thick fibrous septa, as well as intralesional nodules. The septa are hypointense in T1-weighted images. After CM administration, there is no noticeable enhancement, only a weak signal increase compared to the unenhanced phase, which is better seen in the fat-suppressed sequences [35, 38]. The myxoid variant is isodense compared to the muscle in MR sequences. It can appear cystic in the unenhanced phase (Fig. 10), but has a solid aspect after CM administration. Furthermore, after CM administration, the pattern of the lesion is heterogeneous with areas that do not enhance, which histologically correspond to mucin accumulation, and others that enhance more, corresponding to areas of greater cellular concentration. The pleomorphic subtype has a poor adipose content and appears inhomogeneous in T1 and T2 sequences, often with areas of hemorrhage and necrosis. It is hypointense compared to the adipose tissue in T1 and hyperintense in T2 with an internal structure that is quite heterogeneous [35, 38].

Tumors Originating from Smooth Muscle Tissue

These tumors originate from smooth muscle, particularly that of the retroperitoneal vessel walls.

The leiomyoma is a lesion that is only occasionally found in the retroperitoneum. It is a small mass (less than 5 cm), usually located in the female pelvis. Microscopically, it is well differentiated and neither presents mitosis or pleomorphism. At imaging it is difficult to distinguish from the malignant counterpart when small [25].

The leiomyosarcoma represents about 15% of soft tissue sarcomas in adults and 2% in children. It more often arises in the gastroenteric and genitourinary tracts and in the retroperitoneum where 30% of cases occur and where its frequency is second only to liposarcoma. Quite often retroperitoneal tumors originate from the wall of the inferior vena cava, under the kidneys or at the mid-upper third of the hepatic segments [40]. The pelvic location is rather rare and differential diagnosis with other pelvic masses is a problem, especially with gynecological, uterine or adnexal masses [41].

Occurrence is usually in adults aged between 50 and 70 years. Females are more commonly affected, and, perhaps due to the influence of estrogens, locations are more frequently retroperitoneal and at the vena cava [40].

At diagnosis, the leiomyosarcoma is already usually in the advanced stage and considerably large, with a diameter of 5–35 cm. Therefore the clinical signs and symptoms resolve little and are nonspecific. Weight loss, pain and the appearance of an abdominal mass are

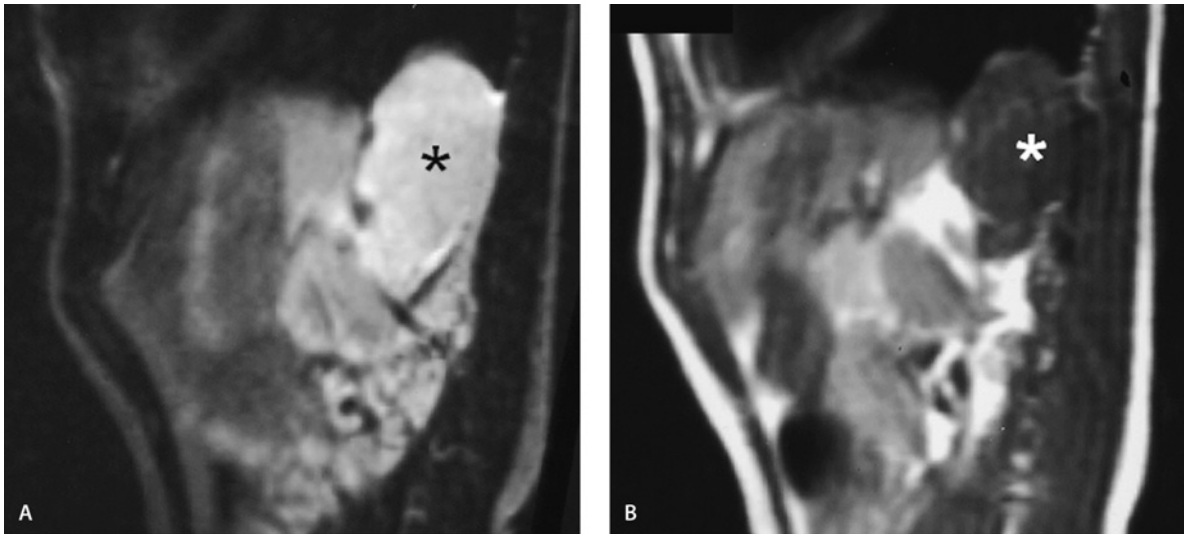

Fig. 10A, B. Myxoid liposarcoma. T2- (**A**) and T1- (**B**) weighted parasagittal scans. The mixed appearance of the lesion with cystic component, T2 hyperintense and T1 hypointense (*asterisk*), can be seen, located cranially

often reported, and the clinical result is sometimes of intestinal obstruction. Among the complications is obstruction of the vena cava with the development of collateral circulation.

Macroscopically, it is a well-circumscribed tumor that tends to grow in size rather than invade the adjacent structures, with the exception of the vessels, particularly the inferior vena cava [42]. The lesion may also spread by means of local or hematogenous dissemination. Microscopically, it is composed of spindle cells with eosinophilic cytoplasm and a spindle aspect, or the nucleus may be cigar-shaped. It contains many hyalinized and necrotic areas, hemorrhage and areas of stroma with myxoid tissue, fibrosis or inflammation. Three different variants can be distinguished: the totally extravascular form (extraluminal), the intravascular form (intraluminal) and the more common mixed variant, both intra- and extraluminal [41, 42].

Intravascular leiomyosarcomas are subdivided on the basis of their origin: intimal or tunica media leiomyosarcoma. The former has limited dimensions and can mimic a parietal thrombus or a dissected aneurysm at imaging.

The leiomyosarcoma usually appears at imaging as a voluminous tumor with a nonadipose, partially necrotic central area, that takes up the CM unevenly both at CT and MR. The periphery of the tumor has clear outlines and is clearly distinguishable from the adjacent structures. The tumor rarely extends to the intraspinal area [40], but a voluminous retroperitoneal mass can originate from vessels or invade them, and often, proximity to the adrenal glands and the displacement of the vena cava can lead to the mistaken suspicion of the suprarenal origin of the tumor [43]. US shows a solid content (Figs. 11A, 12A, B) or cystic lesion and is the method of choice for carrying out a needle biopsy, which is useful

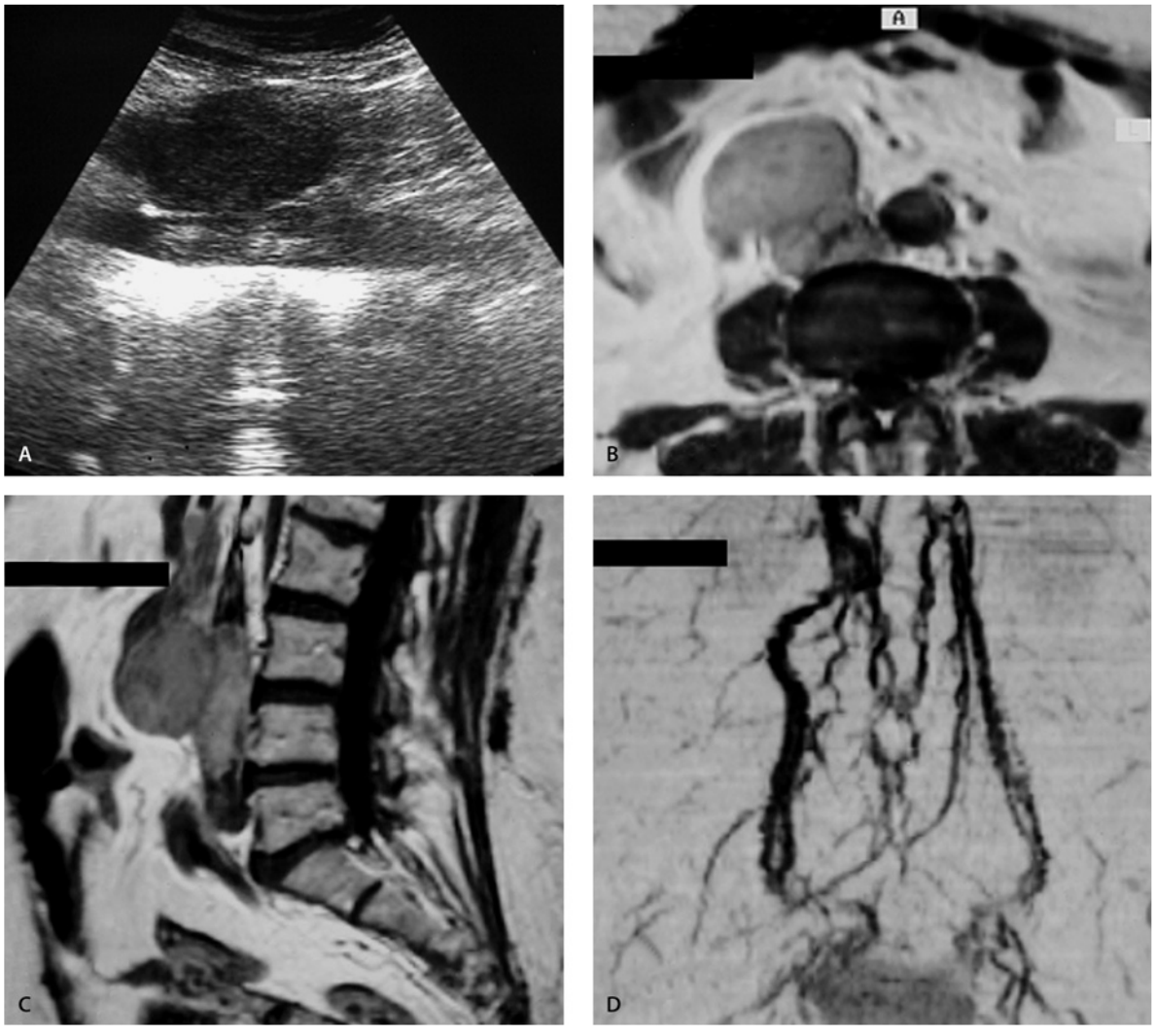

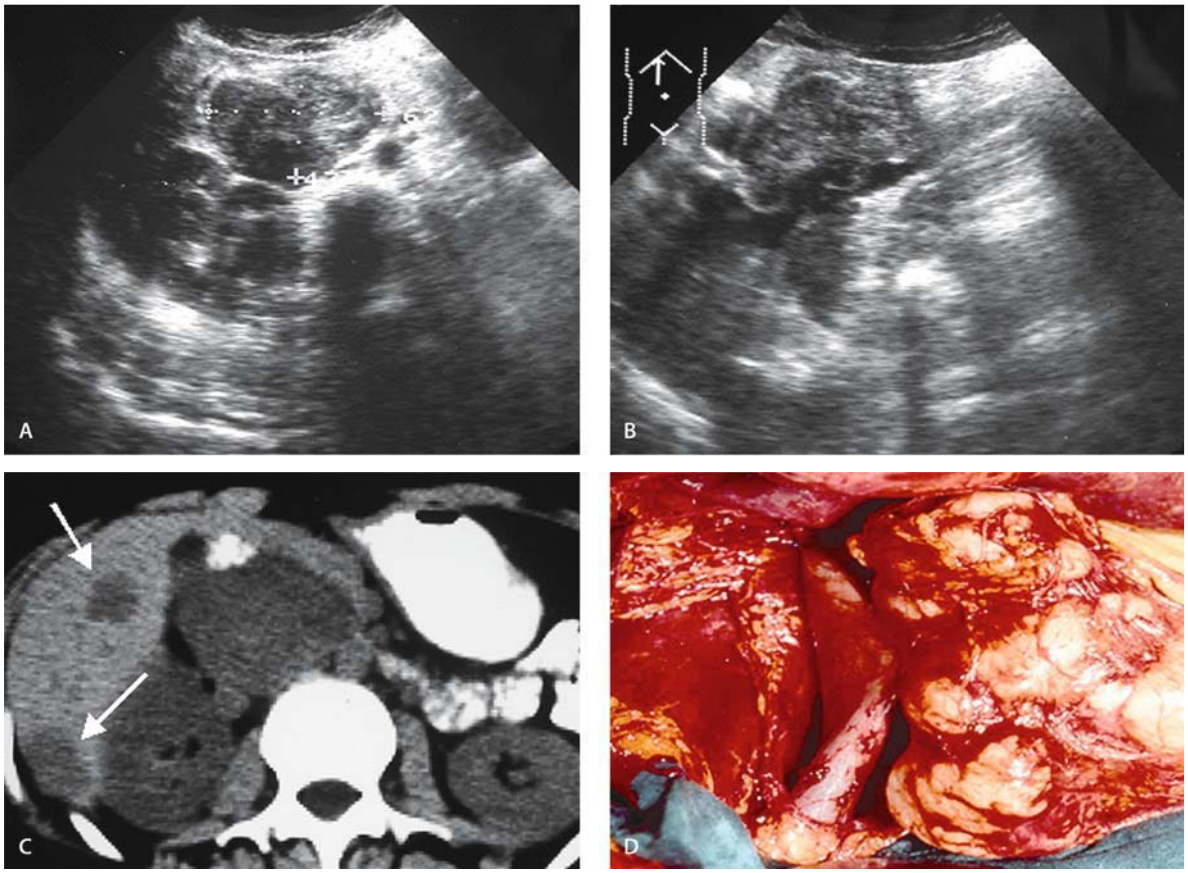

Fig. 12A–D. Leiomyosarcoma with extra- and intraluminal pattern (type 3). At US, axial (**A**) and parasagittal (**B**) scans on the left flank show a solid mass with heterogeneous echotexture occupying the lumen of the vena cava and extending outside of it. CT examination in the unenhanced phase (**C**) highlights a clear-marginated, hypodense lesion that replaces the vessel lumen. There are two hypodense hepatic metastases (*arrows*). Surgery (**D**) demonstrates the lesions origin from the vessel wall

for diagnosis. Both angiography (Fig. 11B) and color Doppler sonography can be used to examine the vascular flow. CT is a sensitive method for diagnosis and follow-up, as it highlights the relationship of the mass with the adjacent structures and the involvement of the retroperitoneal vessels (Fig. 12). The leiomyosarcoma appears as a solid, lobular retroperitoneal mass with cystic areas caused by necrosis. Calcifications are rarely found within it and seldom is it completely cystic [44]. MR is preferable to the other methods for classifying the tumor, as it can highlight the different signal intensities of the individual tissues and carry out a dynamic contrastographic study [40]. Retroperitoneal leiomyosarcomas are hypointense with intermediate intensity in T1- and hyperintense with intermediate intensity in T2-weighted images. Enhancement of the lesion after CM administration mainly involves the muscular or fibrous content of the lesion but it is usually delayed (thus the differential diagnosis with other hypervascularized retroperitoneal tumors such as the hemangiopericytoma, the rhabdomyosarcoma and the extraskeletal Ewing's sarcoma is easier) [41] (Fig. 11C, D).

Fig. 11A–D. Leiomyosarcoma with extra- and intraluminal pattern (type 3). At US examination, the parasagittal scan on the left flank (**A**), shows a solid and quite homogeneous mass, which partially develops inside the vena cava. The T1-weighted axial (**B**) and sagittal (**C**) scans confirm the presence of a rounded mass with extensions both external and internal of the vena cava. The angio-MR (2D time-of-flight, (**D**) highlights a rich network of collateral circulation resulting from the caval obstruction

Tumors Originating from Skeletal Muscle Tissue

The rhabdomyosarcoma is the most common soft tissue tumor in children and adolescents, accounting for roughly 60% of sarcomas. It is however, relatively rare in adults. The PRT rhabdomyosarcoma accounts for about 5% of all rhabdomyosarcomas and has the worst prognosis [45]. There are three variants: the embryonic and alveolar, which are more common in children, and the pleomorphic, which is more common in adults. Macroscopically, this tumor appears well circumscribed, usually large (5–15 cm) [12, 25], lobular and often surrounded by a fibrous pseudocapsule. On dissection, it appears grayish white with a compact appearance and variable amounts of hemorrhage. Sometimes necrotic focuses can be found.

Definite diagnosis is immunohistochemical. Diagnosis is nonspecific at imaging, especially when the lesion is smaller than 2.5 cm. At US it appears as a well-circumscribed, solid, hypoechogenic lesion. At CT, the lesion's density is identical to that of the skeletal muscle tissue. Sometimes, low-density foci are recognizable, suggestive of necrosis. At MR, the lesion appears hypo- to isodense compared to the muscle tissue in T1- and irregularly hyperintense in T2-weighted images, depending on the presence or absence of necrotic foci [26]. As with the other PRTs, the treatment of choice is resection. Nevertheless, the tumor is also highly sensitive to chemotherapy [45].

Vascular and Perivascular Tumors

The lymphangioma is a rare, benign, vascular tumor that typically extends into spaces between preexisting structures and surrounds vessels without compressing their lumina (Fig. 13) [2, 46]. Histologically, it is a well-circumscribed mass made up of vascular spaces of variable size. The stroma is composed of collagen fiber and fibrous tissue and its walls can contain focal accumulation of lymphoid tissue.

The lymphangioma is classified into three categories depending on the size of the vascular spaces: capillary (or simple), cavernous and cystic. The last two categories are the only ones found in the retroperitoneal area in less than 5% of cases [47].

The tumor shows no particular preference for any specific age or sex. Its location in the retroperitoneum more often affects older children or adults.

The mass grows in a benign manner and can sometimes reach such sizes as to cause compression on the adjacent structures (Fig. 13). It can provoke a range of symptoms that go from abdominal pain and enlargement, fever, fatigue, weight loss and hematuria to acute abdomen. Other clinical manifestations can be linked to complications arising in the mass such as infection, hemorrhage, torsion or rupture. Lastly, it can be found by chance in asymptomatic patients during examinations for other clinical reasons.

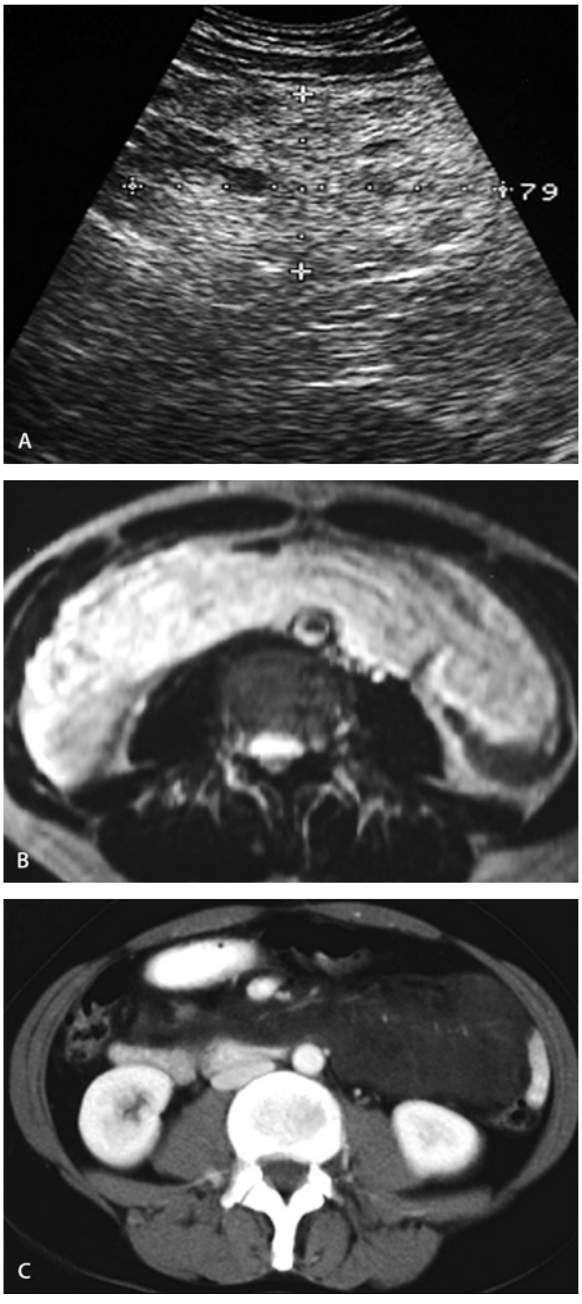

Fig. 13A–C. Lymphangioma. US (**A**) shows a voluminous hyperechoic mass with well-defined margins. The mass appears considerably hyperintense in the T2-weighted (**B**) axial scan and notably hypodense with multicyclic margins at the CT examination after CM administration (**C**). The lesion, without mass effect, stretches along the mesenteric root, where it circumscribes the mesenteric vessels. These findings should give rise to the suspicion of lymphangioma

Diagnosis is quite easy with imaging. Plain film of the abdomen can be useful in recognizing complications such as dislocation of intestinal loops or obstruction. US and CT are very sensitive and relatively specific in evaluating the cystic variant of this mass. US examinations demonstrate the internal structure of the lesion with its typically well-defined margins. If it is of the cystic type, it can have a uni- or multilocular aspect and at the subsequent US controls, it shows progressive growth, wall thickening and septa, and the fluid content becomes increasingly echoic (Fig. 13A) [46].

CT confirms the US findings and gives further information on the tumor's size, composition, extent and its relationship with the surrounding anatomic structures. Sometimes at CT, the lymphangioma has a high lipidic content, mimicking a lipoma (Figs. 13c, 14) [48]. The cystic lymphangioma appears as a well-circumscribed cystic mass and has a homogeneous aspect with liquid-type toning (Fig. 14). Septa, all of similar thickness, are often found [47].

MR, thanks to its ability to directly acquire multiplanar images, delineates the relationship of the mass more precisely, especially with the skeletal system, also demonstrating the particular signal characteristics, which are considerably higher in the T2-weighted sequences (Fig. 13B) [47]. After CM administration, there is minimal contrast enhancement [2].

The differential diagnosis is made mainly with cystic or apparently cystic forms in the retroperitoneum area such as cysts and pseudocysts, hematomas, abscesses and lymphocele; with tumor-like lesions, such as lymphangioleiomyoma, which differentiates histologically from lymphangioma due to the presence of smooth muscle elements; with liposarcoma, leiomyosarcoma, fibrosarcoma and teratoma, which may have a cystic-like aspect. It should be remembered that sometimes, some retroperitoneal metastatic lymph nodes may have a cystic aspect [47].

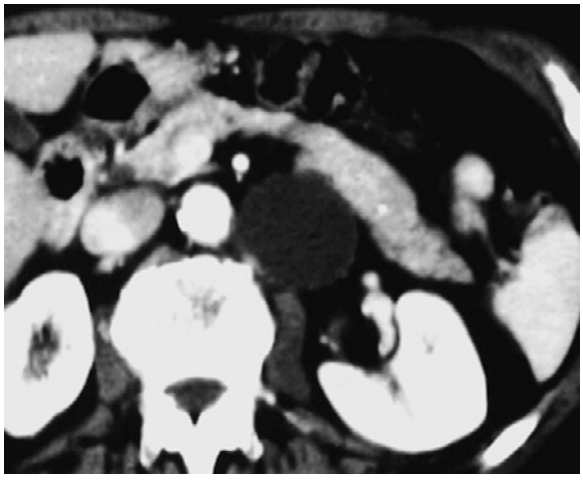

Fig. 14. Cystic lymphangioma. CT examination in the contrast-enhanced phase. A mass with lobulated morphology, notably hypodense after CM administration can be seen lying both in front and behind the body and tail of the pancreas. The appearance can mimic a lipoma (see Fig. 7)

From a therapeutic point of view, the lymphangioma is surgically removed and has an excellent prognosis with total resection [46]. Otherwise it tends to recur [47].

The angiosarcoma is a rare tumor of mesodermic origin originating from atypical endothelial cells. The most common sites found are the skin, soft tissues, liver, spleen and upper air tracts. Location in the retroperitoneal area is rather infrequent [49]. It occurs in advanced age. Clinical manifestations, mainly abdominal pain, are linked to organ compression or displacement. In some cases urinary and/or hematuria symptoms may appear.

The tumor's histologic aspect can vary from that of a well-differentiated angiosarcomatous pattern to that of a poorly differentiated solid pattern. The mass comprises small or medium-sized blood vessels that widely infiltrate the fibroadipose tissue and the bordering irregular vascular spaces. It also has a capsule.

US imaging is useful for identifying the lesion but not for classifying it. In fact, it shows a heterogeneous hypoechogenic mass. CT confirms the presence, location, size, internal consistency and extent of the tumor. Furthermore, it evaluates the presence of distant metastases. Nevertheless, it cannot establish the tumor's origin. The CT findings are of a solid mass with a heterogeneous content, well-defined margins and irregular enhancement after intravenous CM administration [49].

MR sequences show an isointense mass compared to the muscular tissue in T1-weighted images, with a high signal intensity in T2-weighted images. The tumor enhances inhomogeneously in fat-suppressed T1-weighted sequences after intravenous administration of gadolinium-DTPA. This evaluation confirms the vascular nature of the mass. The MR angiographic (MRA) examination is also very informative regarding this aspect, as it assesses the true vascularity of the mass [49]. The signal characteristics of the lesion are however, identical to those of other PRTs.

The angiosarcoma enters into differential diagnosis with tumor and nontumoral pathologies. The former are represented by lymphoma, hypervascular liposarcoma, leiomyosarcoma, metastases of renal cell carcinoma, choriocarcinoma, endothelioma, hemangiopericytoma and Kaposi's sarcoma. The following can be found within the nontumoral pathologies: retroperitoneal fibrosis, pancreatitis, aortic aneurysm, and retroperitoneal fluid accumulations (blood, abscess, lymphocele, urinoma).

Neural Tumors

Retroperitoneal neural tumors also originate from the central nervous system or are associated with it. They are therefore not included in the WHO classification of soft tissue. However, bearing in mind the site and the imaging aspects, as well as the problems in differential diagnosis that these tumors create, they are included in this work. Two types of tumors are considered: those originating from the nerves and those originating from support (Schwann) cells. The first category includes benign masses (ganglioneuroma) and malignant ones (neuroblastoma and ganglioneuroblastoma). The second group also includes benign forms (neurofibroma and schwannoma), infrequent in the retroperitoneum, and malignant forms (malignant schwannoma). Tumors originating in the nerves derive from primordial neural cells that migrate toward the sympathetic ganglions and the suprarenal gland medullary.

The ganglioneuroma is a benign mass of the peripheral and central nervous system. It develops from mature ganglion cells, and is the most mature form among the autonomous nervous system masses. It occurs in children and young adults (the majority of cases occur before the age of 20), with a slight prevalence for females. The main site of origin is the posterior mediastinum followed by the retroperitoneal space. This type of tumor is benign, its growth is slow but expansive, with progressive mass effect and involvement of the adjacent structures. It can extend to the spine, but this is not very common [50].

The ganglioneuroma can originate from the transformation of a neuroblastoma or a ganglioneuroblastoma through a maturing process that can be spontaneous or induced by radio-chemotherapeutic treatment. In fact, tumors originating from nerves are expressions of three developmental stages of the cancerous process itself. Neuroblastomas are made up of immature neuroblasts, while ganglioneuroblastomas are composed of a mixture of neuroblasts and mature ganglion cells. Lastly, ganglioneuromas, as stated above, are composed of mature ganglion cells and Schwann cells.

The ganglioneuroma appears as a rounded or oval mass with clear margins, and is usually well-circumscribed by a capsule. Its diameter is generally around 10 cm but in some cases can reach 50 cm. The mass has an abundant myxoid matrix, which raises suspicions of its diagnosis at imaging, especially MR [2, 26, 50], and it frequently contains calcifications. As it is generally hormonally inactive, the mass often remains asymptomatic for a long time due to its slow growth and can be detected as a palpable abdominal mass and/or with the nonspecific complaint of abdominal pain, encopresis and diarrhea, depending on its location and size [51, 52].

US imaging shows a solid, homogeneous mass whose echotexture is similar or inferior to that of hepatic or splenic parenchymas (Fig. 15A) [53]. At plain CT it has low density and is moderately enhanced after intravenous CM administration (Fig. 15B). This finding is due to the histopathologic abundance of myxoid matrix and the relatively low ganglion cell component that make up the mass. CT therefore leads to a differential diagnosis in terms of neuroblastomas and pheochromocytomas, which usually demonstrate a high concentration of CM. Moreover, CT imaging is more sensitive in identifying any calcifications that US and MR did not recognize (Fig. 15b). This finding can lead to the differentiation between a ganglioneuroma and its malignant form, the neuroblastoma. This is the most important differential diagnosis within the area of retroperitoneal tumors in children and young adults [50].

In T1-weighted MR images, the mass has a homogeneously low signal intensity (the same as muscle tissue) (Fig. 3B) unless the mass contains hemorrhagic areas or an adipose component, which then give an intermediate signal intensity in T1. In T2-weighted images, the mass has a high signal intensity (like fluids), in relation to the myxoid component (Fig. 3A). After injecting CM, the T1-weighted images gradually show a homogenous marked enhancement of the mass (Fig. 3B–D). When compared, the histological findings and the imaging aspect correlate well (Fig. 15). Endocrinologically active masses are rare and are found almost exclusively in children. The literature reports only two adult cases. The childhood forms describe a high urinary excretion of catecholamine metabolites (vanilmandelic acid and homovanillic acid) and high plasmatic levels of adrenalin and dopamine [51].

In the functioning masses found in adults, there was a moderate increase in plasmatic and urinary levels of norepinephrine and dopamine. Since the literature reports cases of malignant transformation of ganglioneuromas, it is necessary to make an early diagnosis, completely remove the mass surgically and then carry out a long postoperative follow-up [52]. The prognosis is generally good, as the tumor does not usually recur after surgical resection.

The neuroblastoma is a rare tumor in adults, while it is one of the most common malignant pathologies in children, holding third place after leukemias and brain tumors [54, 55]. The most common locations are the adrenals (48%), the retroperitoneum (32%), the kidneys (10%), and it can also be found in the mediastinum, the cervical and sacral region and, since the tumor originates along the sympathetic ganglion chain, the Zuckerkandl organ and the adrenal medullary.

Histologically, the neuroblastoma is composed of small rounded cells with hyperchromatic nuclei and poor cytoplasm, positive for neuron-specific enolase (NSE) and synaptophysin. These elements make up various types of totipotent cells of the neural crest in different stages of development. The neuroblastoma is highly

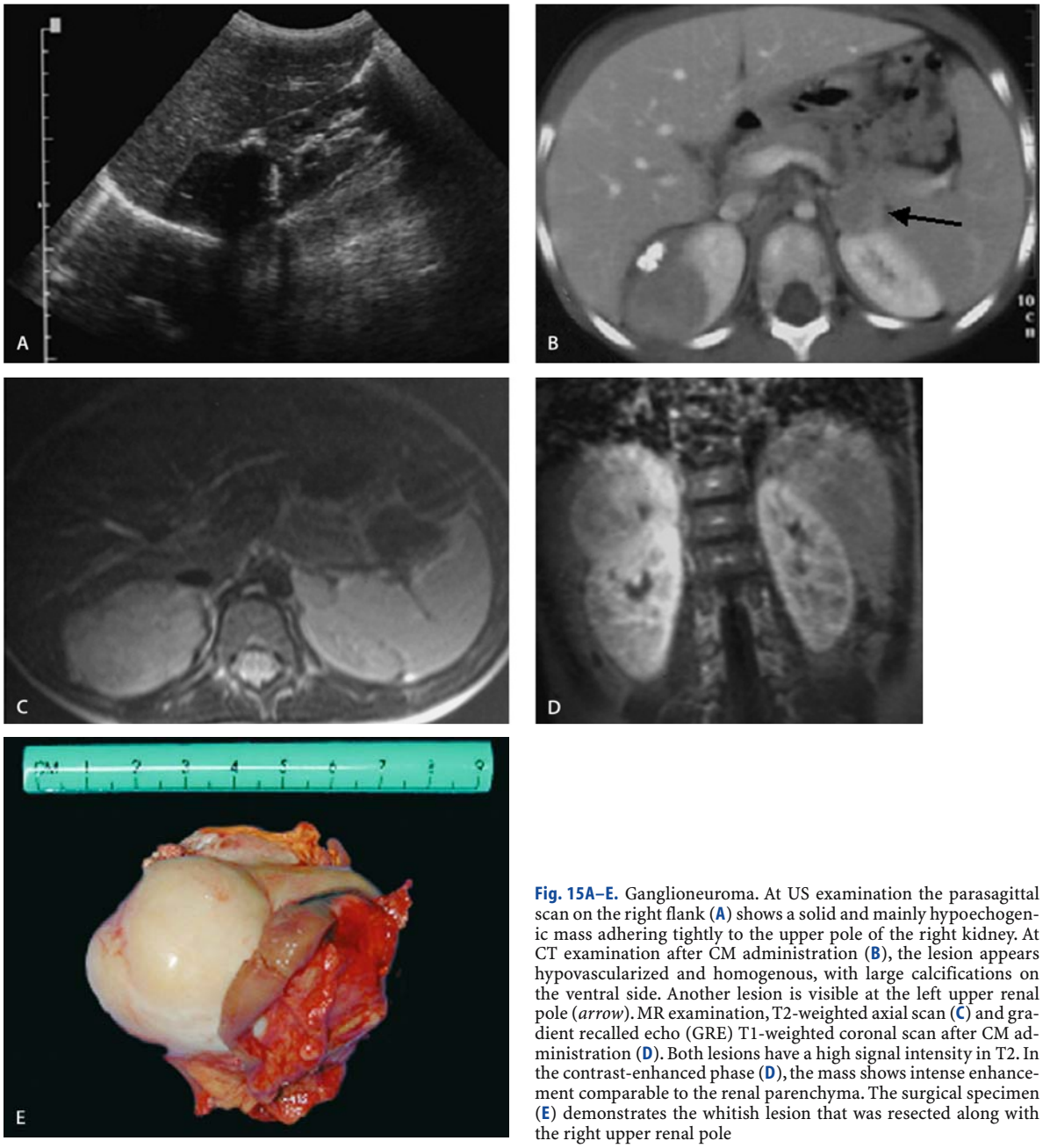

Fig. 15A–E. Ganglioneuroma. At US examination the parasagittal scan on the right flank (**A**) shows a solid and mainly hypoechogenic mass adhering tightly to the upper pole of the right kidney. At CT examination after CM administration (**B**), the lesion appears hypovascularized and homogenous, with large calcifications on the ventral side. Another lesion is visible at the left upper renal pole (*arrow*). MR examination, T2-weighted axial scan (**C**) and gradient recalled echo (GRE) T1-weighted coronal scan after CM administration (**D**). Both lesions have a high signal intensity in T2. In the contrast-enhanced phase (**D**), the mass shows intense enhancement comparable to the renal parenchyma. The surgical specimen (**E**) demonstrates the whitish lesion that was resected along with the right upper renal pole

malignant and in most cases, there are already bone, lymph node, hepatic and skin metastases at the moment of diagnosis.

The tumor's clinical manifestation has nonspecific symptoms such as fever, general indisposition and pain caused by the growth of the mass. In rare cases, the tumor has created an obstructive jaundice [54].

The US findings for this tumor are of a hypoechoic and normally large mass. This examination can be carried out as a preliminary study of the mass for evaluating any involvement of the biliary system by recognizing dilation of the intrahepatic biliary tracts and the gallbladder [54].

At CT, the mass appears large (about 6–8 cm in diameter), lobular and covered by a thin capsule. It is common to find intratumoral calcifications, which can sometimes also be seen at ultrasound. Intravenous CM administration produces a low-density nonspecific pattern. T1-weighted MR images show a mass with low signal intensity, which in T2-weighted images presents

transition toward high signal intensity. From the above description, is it evident that US, CT and MR are not able to make a definite differential diagnosis between a neuroblastoma and other malignant tumors.

Therefore other evaluations are necessary to reach a definitive diagnosis such as an immunohistochemical analysis for neuron-specific enolase (NSE) and synaptophysin and the dosage of a specific neuroblastoma marker, i.e., vanilmandelic acid (VMA) in the urine.

Neuroblastoma cells can give rise to the production of catecholamine, but usually only an increase in their inactive urinary metabolite level is found [54].

The plexiform neurofibroma appears as an intricate network of cancerous fronds with a serpiginous appearance along a nerve branch or its branches [56, 57]. Microscopically, it is composed of a chaotic series of Schwann cells dispersed in an extracellular matrix made of mucopolysaccharides and collagen.

Plexiform retroperitoneal neurofibromas are described in adolescents or young adult patients. Typically they are bilateral and symmetrical masses in the paraspinal or presacral area. With their elongated and cylindrical aspect, they extend into the neural foramen.

At CT, the mass appears with a low homogeneous toning after intravenous contrast medium administration. It sometimes mimics a lymphangioma (Fig. 16). The finding can be attributed to the intratumoral presence of adipose tissue, cystic degeneration and the presence of myxoid matrix. Less frequently, these lesions can contain calcifications and/or demonstrate, after CM administration, a serpiginous or peripheral enhancement. The tumor does not usually recur after radical surgical resection [56].

The benign Schwannoma is also known as neurinoma or neurilemmoma. This is a solitary, slow-growing benign tumor that develops from Schwann cells. It can occur at any age but its incidence rate peaks between the 30s and 60s. In a few cases it can locate at the retroperitoneal level [58], representing approximately 1%–5% of all retroperitoneal masses [59]. There is no sex preference. Macroscopically, it appears as a rounded or oval mass in the paravertebral site or along the route of a nerve and is well encapsulated. It is grayish in color at dissection with irregular, degenerative, cystic and hemorrhagic aspects. At immunohistochemical examination, the benign schwannoma is positive for S-100, the neural protein that is found inside Schwann cells. It is sometimes possible to identify the originating nerve adhering closely to the tumoral capsule. It is not usually bigger than 5 cm in diameter, although it can be larger in the retroperitoneal location. Schwannomas are seldom multiple and in this case appear in subjects affected by von Recklinghausen's disease [57]. It rarely tends to become malignant, again seen mostly in cases of von Recklinghausen's disease [60]. The clinical aspect of the benign schwannoma is often represented by vague abdominal or low dorsal pain. In these cases, because of its location, the tumor can cause urethral obstruction. This mass enters into the differential diagnosis with pathologic processes that involve the structures adjacent to its site of origin: kidneys, suprarenal glands (tumoral processes), pancreas (cystic tumor), liver (tumor of the caudate lobe), psoas muscle (inflammation, hematoma, abscess, tumor) [59, 61].

When the formation is in its early stages, CT imaging shows a solid, homogeneous mass with a capsule. In the more advanced stage, a cystic-type aspect more commonly appears because of hemorrhage or necrosis. This is unlike other retroperitoneal tumors that usually show no cystic-type change, thus making the differential di-

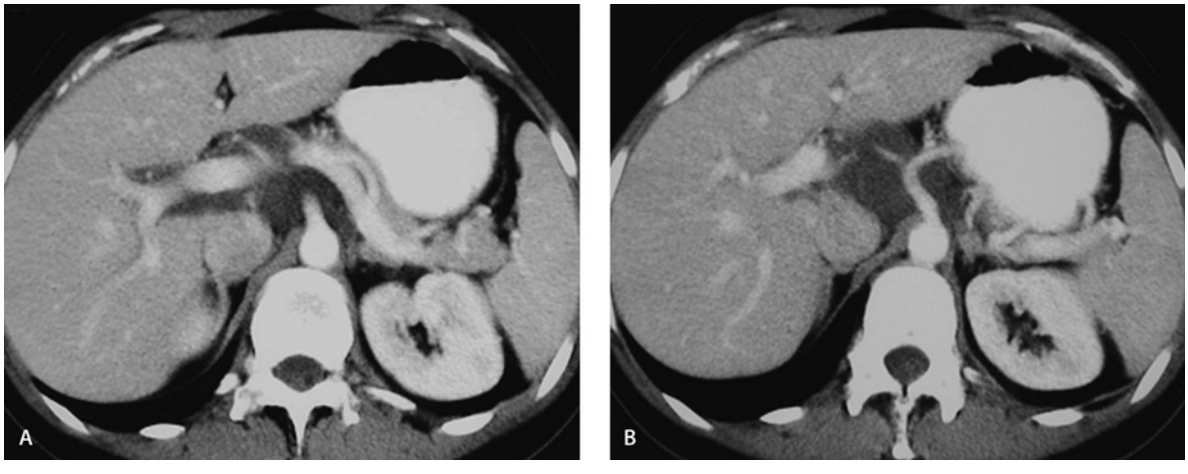

Fig. 16A, B. Multicentric neurofibroma mimicking a lymphangioma. CT examination after CM administration (**A**, **B**): axial scans at the level of the celiac trunk. An expansile hypodense mass, without mass effect, is appreciable surrounding the celiac branching and extending along the hepatoduodenal ligament

agnosis easier. CT images reproduce the heterogeneous character of a benign Schwannoma in the advanced stage less faithfully than MR sequences. In T1-weighted MR images, the lesion is usually hypointense or isointense, while in the T2-weighted sequences, it appears hyperintense (Fig. 17A). After injection of gadolinium, inhomogeneous areas inside the tumor enhance. This allows for a more definite characterization of the structural components of the tumor (Fig. 17B–D) [60]. MR imaging also helps to establish the tumor's relationship with the surrounding structures more precisely, thus leading to an effective resection (Fig. 17). Resection is the only efficient treatment [58].

The paraganglioma is formed by neural crest cells [62, 63]. In the retroperitoneum, about 20% of such tumors are located in the extra-adrenals area with the origin prevalently at the level of the Zuckerkandl organ. The paraganglioma can be associated with MEN IIA, bronchial or gastrointestinal carcinoid, von Hippel-Lindau syndrome and neurofibromatosis. The literature reports a predominance in males. The average age is about 40 years. They are usually functioning tumors, especially the benign lesions of suprarenal origin [64]. In the majority of cases (60%), they secrete epinephrine and norepinephrine.

Macroscopically, the paraganglioma appears as a brownish, partially encapsulated mass. Its natural history is variable. Retroperitoneal paragangliomas are potentially metastatic (20%–40%) [63]. Of adrenal originating tumors, 10%–15% are malignant and the percentage is even higher for aorticosympathetic paragangliomas. The histological aspect does not distinguish the benign forms from the malignant ones, as both have cellular pleomorphism and mitotic figures [64].

In general, the benign or functioning tumors are smaller than the malignant or nonfunctioning ones.

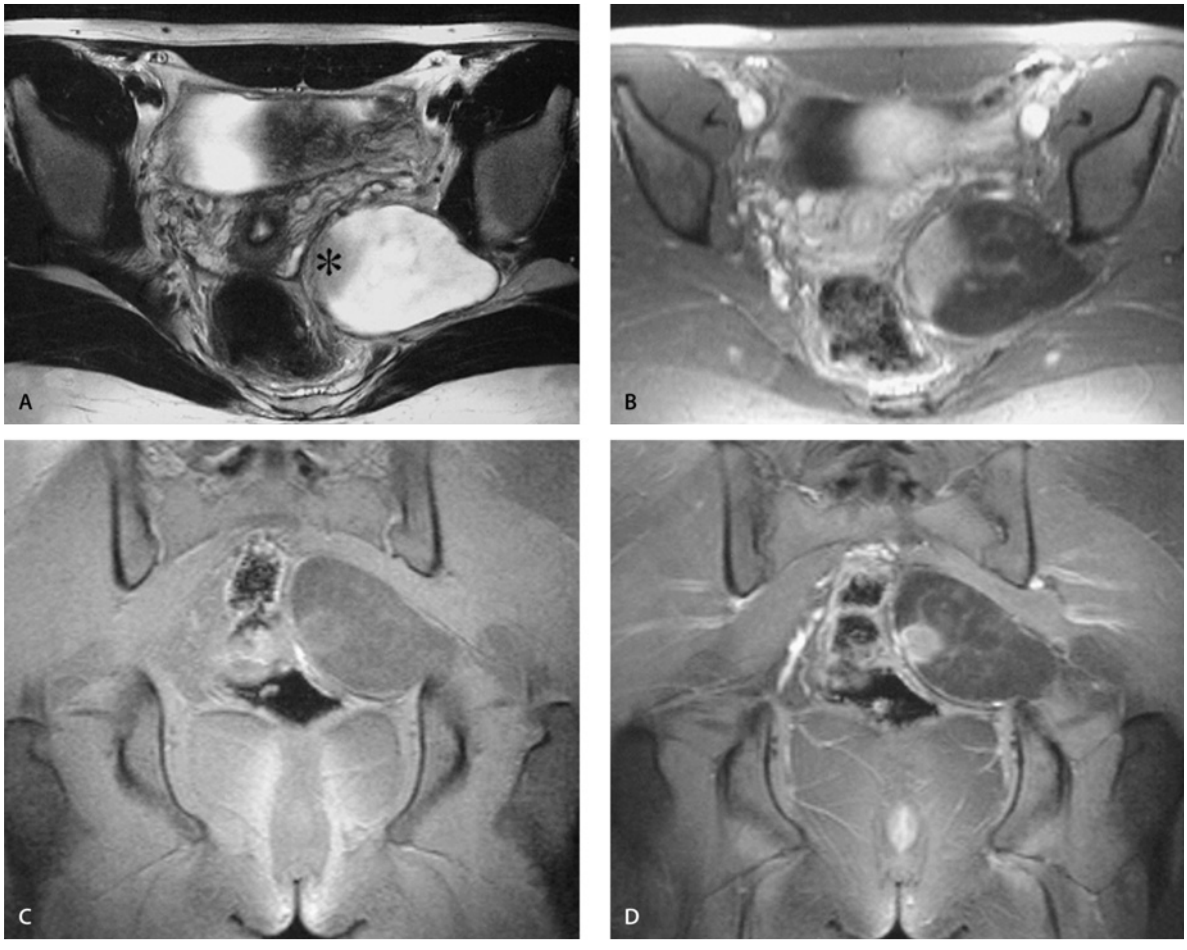

Fig. 17A–D. Benign Schwannoma extending into the left gluteal region through the major ischiatic foramen, MR examination. In the T2-weighted axial scan (**A**), the lesion appears quite hyperintense and well defined. A hypointense nodule is visible at the medial side of the lesion (*asterisk*). In the unenhanced GRE T1-weighted coronal scan (**B**), the lesion appears hypodense; at the medial side there is a dubious, slightly more intense nodular image which, after CM administration, shows intense enhancement in the axial (**C**) and coronal (**D**) scans. The piriform muscle is displaced cranially

However, there is no difference between the adrenal and extraadrenal lesions. The latter are more often malignant and invade the adjacent organs such as the liver, pancreas, intestine, lymph nodes and blood vessels. They metastasize in the bones, lungs, liver and heart.

Of all the imaging methods, CT has proved effective in demonstrating such tumors, finding the location, extent and nature (Fig. 18A, B). Furthermore, it is able to give information on resectability and the benign/malignant character of the lesion. The malignant forms are more commonly extra-adrenal, large and heterogeneous, with poorly defined margins and necrosis. The benign tumors are generally homogeneous with clear margins (Fig. 18). Up to 15% of retroperitoneal para-

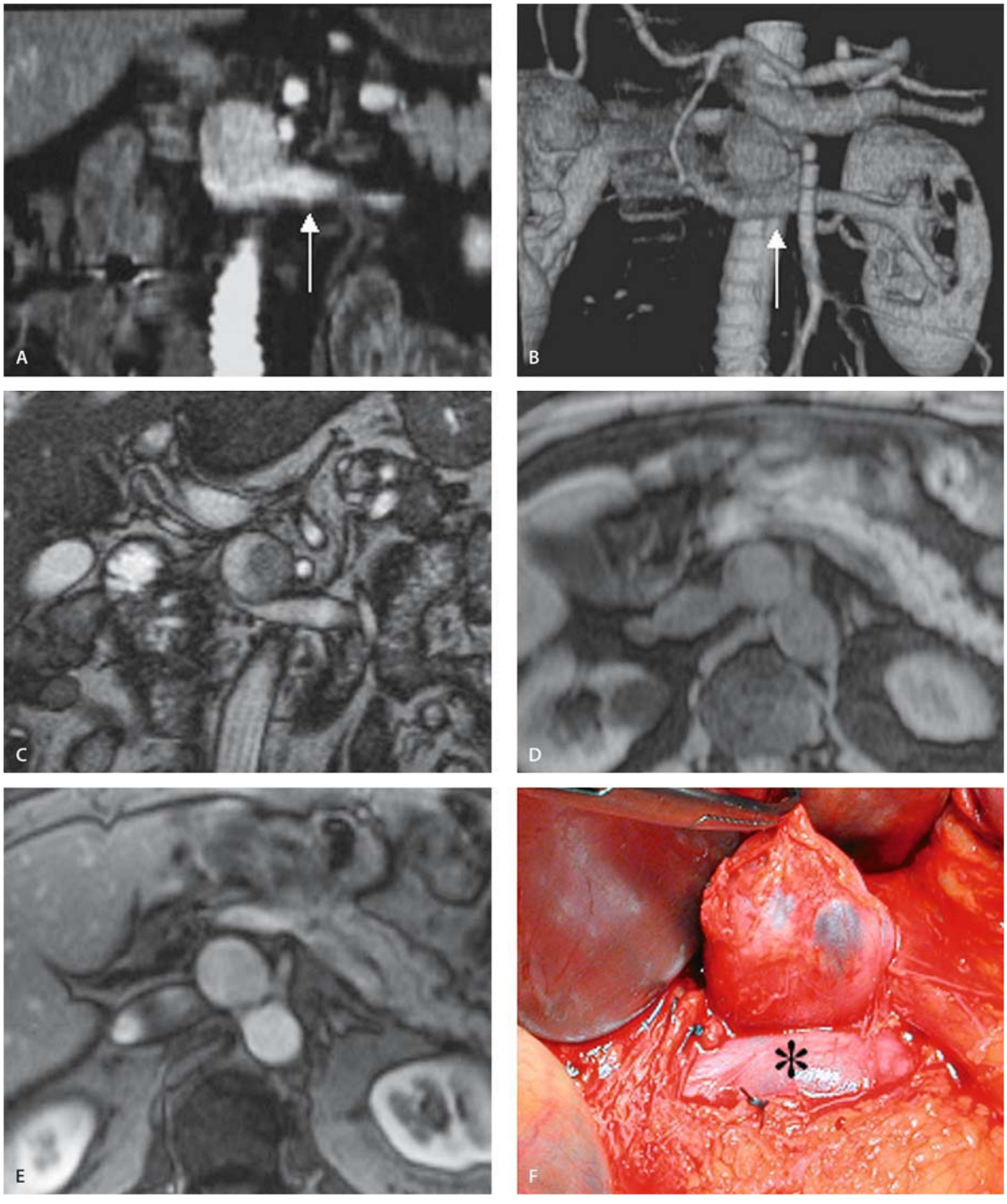

gangliomas contain punctate calcifications. Enhancement after CM administration is variable [64], but it is nevertheless usually high. The tumor's hypervascularization is associated with the frequent presence of hemorrhagic necrosis inside the lesion, which can be seen as fluid–fluid levels. This aspect can be recognized both with CT and MR imaging (Fig. 18C–E) [2, 64].

Extraskeletal Bone Tumors

Extraskeletal osteosarcomas account for 1%–2% of all soft tissue sarcomas and approximately 4% of all osteosarcomas [65–67]. When they are located in the retroperitoneum (17% of cases) they appear as a growing mass, are often large with calcified areas within and can cause swelling, and vague, nonspecific abdominal pain may or may not be present [65, 66, 68, 69].

Macroscopically, the extraskeletal sarcoma varies depending on the relative quantity of osteoid, bone and other components. It is made up of partially ossified solid areas and cystic areas where necrotic-hemorrhagic phenomena prevail. It is pseudoencapsulated or infiltrating and varies in size from 5 to 15 cm.

Histologically, it is common to find osteoid, chondroid and bony substance with a different representation of the osteoblastic, fibroblastic and chondroblastic elements. It has been observed that, in the presence of giant multinucleated cells of the osteoclast type, poor sinusoidal vascularization or intratumoral hemorrhage is frequently found [65, 70].

Conventional X-rays and CT both commonly highlight masses that contain a large quantity of osteoid and/or calcified material. Moreover, CT can evaluate the presence of low density areas, expressions of suspected necrosis or hemorrhage, and also whether or not the mass is well-outlined [68]. At bone scintigraphy, intense captation is demonstrated, as for lively osteoblastic activity [65, 68]. At angiography, the tumor is frequently highly vascularized [71].

MR can determine the size and the characteristics of the tumor very precisely. It can reveal cystic areas, hemorrhagic and necrotic zones and solid components, which correspond to the resected specimen, and it can also demonstrate the margins that, if clear, correspond to the pseudocapsule when examined pathologically. However, hemorrhage and necrosis can be found in other soft tissue sarcomas [68].

This tumor enters into the differential diagnosis with several benign and malignant processes that can produce bone or osteoid. The most important benign lesions are calcified posttraumatic hematoma and ossified myositis. Among the malignant forms are malignant fibrohistiocytoma with osteocartilaginous metaplasia, synovial sarcoma with calcifications, epithelioid sarcoma, liposarcoma and many other mesenchymal and epithelial tumors that can have bone or osteoid formations within them [65, 67, 68, 71]. Nevertheless, the absence of osteoid or calcified material, which could be visible radiologically within a soft tissue mass, should not stop the radiologist from suspecting extraskeletal osteosarcoma, because there are reports in the literature of some cases where such findings were not found radiologically. In these cases, the differential diagnosis is directed toward other sarcomas that do not contain bony and osteoid tissue such as myxoid liposarcoma, synovial sarcoma, malignant fibrohistiocytoma and extraskeletal myxoid chondrosarcoma [68].

The prognosis of extraskeletal osteosarcoma is rather severe. Almost all patients die following recurrence and/or metastases (pulmonary, hepatic, lymph node, bone) within 2–3 years of the operation, but relapse is, in most cases, very quick (a few months after surgery). The size of the tumor (<5 vs ≥5 cm) is a very important prognostic factor since retroperitoneal tumors or tumors that arise inside the abdomen tend to be very large and total resection of the mass is very difficult [65, 67].

Unclassified Tumors

Unclassified retroperitoneal tumors are masses whose origin and histologic differentiation is uncertain or undefined.

The peripheral primitive neuroectodermal tumor (PPNT) and Ewing's extraskeletal sarcoma are rare malignant tumors of poorly understood histogenesis, whose cells have a varied morphology and irregular nuclei. It is thought that they represent the same type of tumor but with a different level of neuroendocrine differentiation (the PPNT represents the well-differentiated form and Ewing's sarcoma the undifferentiated). In 90% of cases, they occur before the age of 30 and have a preference for males. The clinical symptoms at the beginning are pain, swelling, fever and weight loss. The most typical sites of origin are the lower limbs, the paraverte-

Fig. 18A–F. Paraganglioma. CT examination after CM administration: MPR reconstruction in the coronal plane (**A**) and maximum-intensity-projection (MIP) reconstruction (**B**). A hypervascular, rounded and clearly defined lesion is recognizable displacing the left renal vein downward (*arrow*). MR examination, fast imaging with steady-state precision (true FISP) coronal (**C**) sequence, unenhanced axial GRE T1 (**D**) and axial GRE T1 after CM administration (**E**). The lesion appears inhomogeneously hyperintense and well defined in (**C**). It is intensely bright in the contrast-enhanced phase (**E**). At surgery (**F**) it is easily separable from the left renal vein (*asterisk*)

bral regions, the thoracic wall and the retroperitoneum. Ewing's extraskeletal sarcoma accounts for 4% of all sarcomas in childhood [72].

Macroscopically, the PPNT and Ewing's sarcoma appear lobular and well circumscribed. They sometimes have irregular margins and a rather inhomogeneous content due to the presence of necrotic-hemorrhagic and cystic areas. They can reach considerable dimensions of up to 40 cm in diameter. Microscopically, they are made up of small, rounded cells with a round nucleus and are rich in periodic acid Schiff (PAS)-positive glycogen cytoplasm, organized in lamina [73]. Prognosis is severe since the occurrence of metastases and postsurgical relapse is high.

CT often shows an infiltrating paravertebral mass with internal calcifications [72]. MR, thanks to multiplanar acquisitions and the high level of tissue contrast between cancerous and adipose tissue, is the best imaging method for evaluating the spatial extent of the tumor (Fig. 19) [73].

The primitive retroperitoneal synovial sarcoma is a very rare and extremely malignant tumor with a high rate of relapse and mortality [74]. It is of mesenchymal origin and mainly affects children and young adults, with females being more at risk. The usual site of origin is periarticular, especially at the level of the lower limbs. The lesions are generally large, deeply located and grow rapidly. Clinical and objective findings are nonspecific [75]. Macroscopically, only the smaller masses have a pseudocapsule; the others are characterized by poorly defined and infiltrating margins. The internal content appears inhomogeneous with necrotic areas and irregular calcifications (present in 15%–20% of cases). When it arises at the retroperitoneal level, it usually does not present characteristics at imaging that are able to safely distinguish it from other mesenchymal tumors [74]. At US, the lesion has a mixed appearance (Fig. 20A). At CT (Fig. 20B, C), the lesion appears well bordered, solid and enhancement is irregular (Fig. 20C). MR can help with diagnosis. In fact, at MR the synovial sarcoma appears as a very large mass with an intermediate signal intensity in both T1- and T2-weighted sequences, with a heterogeneous signal pattern above all in T2, directly correlated with the considerable size of the tumor (bowl of fruit sign, Fig. 3F). After intravenously injecting gado-

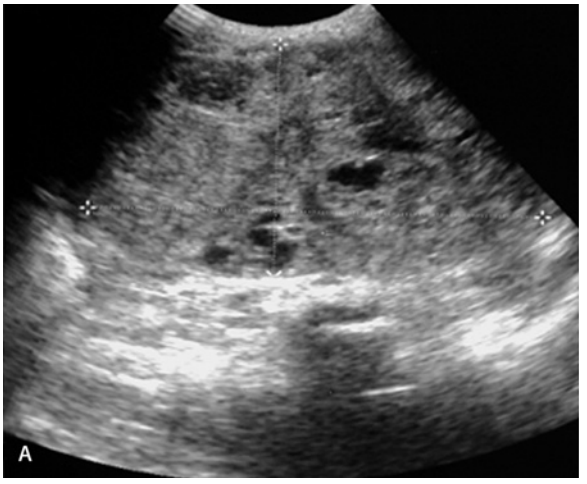

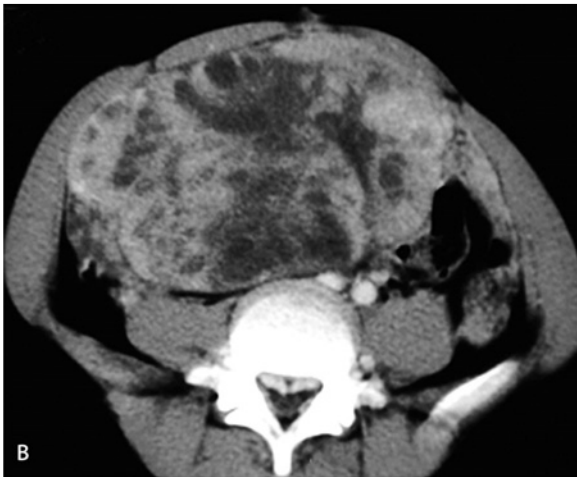

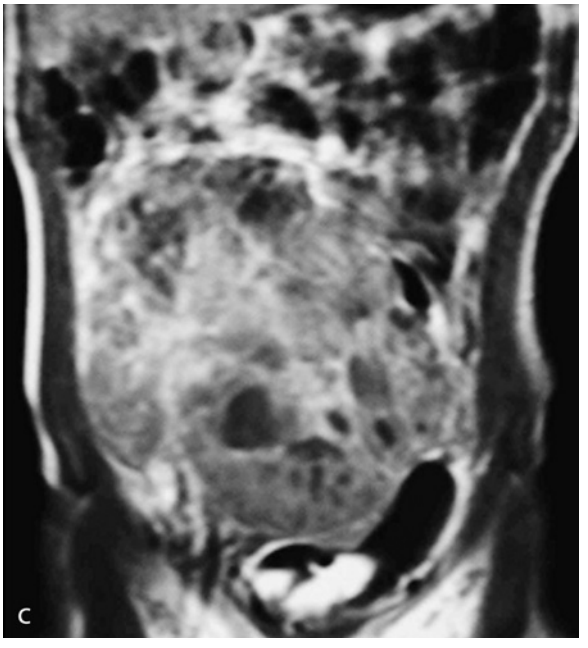

Fig. 19A–C. Ewing's sarcoma. In the US scan in the axial plane (**A**), a voluminous, mainly hyperechoic mass can be seen with a solid, irregular content. There are multiple hypodense areas within (necrotic). In the CT scan after CM administration (**B**), a voluminous hyperdense mass is visible, within which multiple hypodense areas are confirmed, corresponding to the hypointense areas visualized in the SE T1-weighted coronal MR scans after gadolinium administration (**C**)

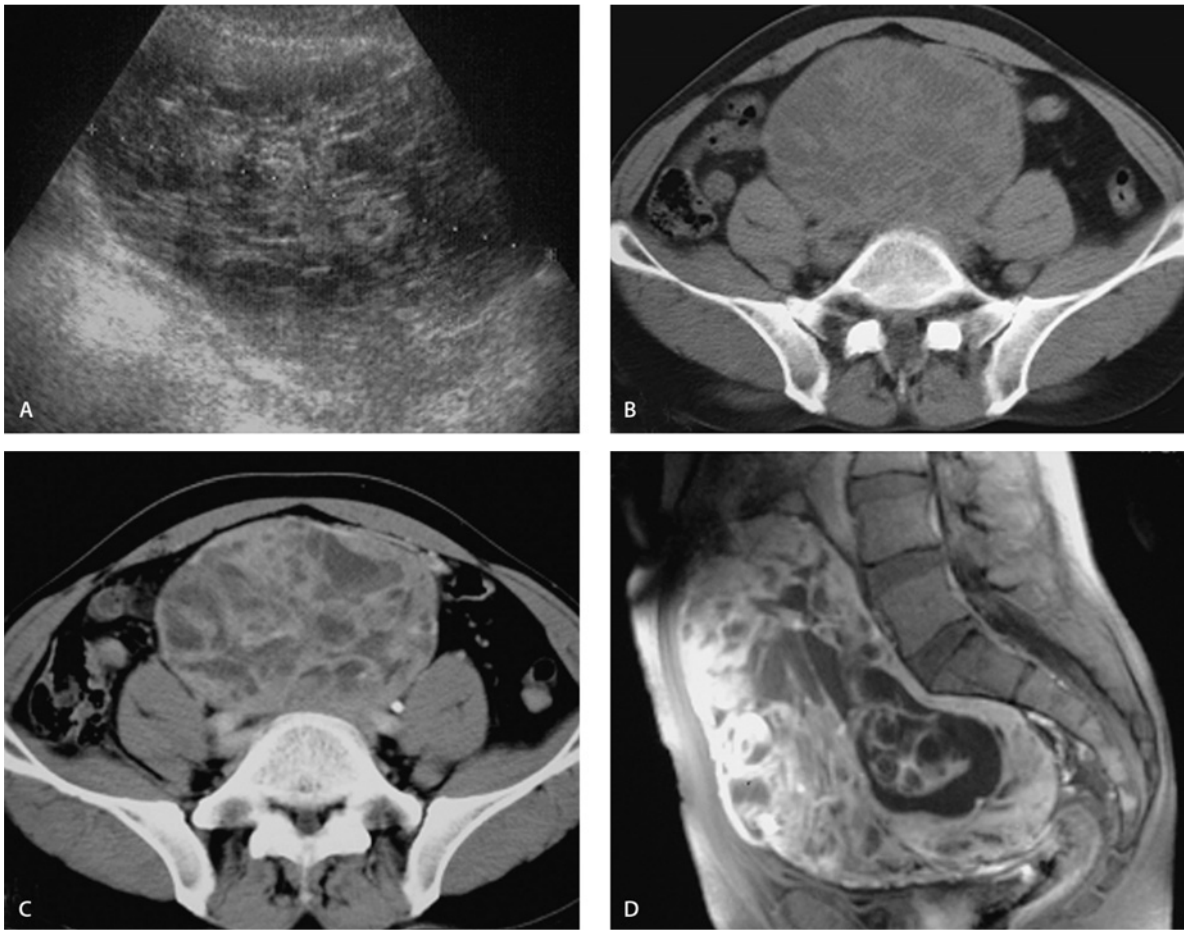

Fig. 20A–D. Synovial sarcoma. The US scan in the axial plane (**A**) shows a voluminous mass with irregular echogenic content due to the presence of minute transonic spaces within it (necrotic). At the CT examination before CM administration (**B**), the lesion appears irregularly isodense compared to the muscle. Its margins are rather clear. After CM administration (**C**), the lesion has an inhomogeneous enhancement, as demonstrated in the sagittal FS GRE T1-weighted scan (**D**)

linium, the synovial sarcoma shows an inhomogeneous enhancement (Fig. 20D). Moreover, the presence of hemorrhagic areas, of lesions with fluid content and hyper-, hypo- or iso-intense areas compared to the adipose tissue (the so-called triple-signal) in the T2 sequences, can suggest this diagnosis. MR is also able to highlight the sarcoma's invasion of soft tissues and contiguous bone in 21%–28% of cases [75].

Miscellaneous

Even if it does not strictly enter into the classification of PRTs, Castleman's disease is taken into consideration by virtue of its frequency and the characteristics that usually lead to its diagnosis. It is a rare lymphoproliferative syndrome that generally appears as a benign isolated mediastinal mass [76]. Histologically, it is characterized by a large vascular proliferation surrounding the normal lymphoid follicles. Two histologic patterns are distinguishable: hyaline vascular (85%–90%) and plasma cellular (10%–15%). The former is characterized by abnormal lymphoid follicles, numerous vessels and extensive fibrous septa. The latter has mature polyclonal plasma cells and few vessels.

Castleman's disease is ubiquitous, nevertheless it predominates at the lymph node stations. The local form is more frequent. It is a solitary mass, generally asymptomatic and nonfiltrating and causes compression on the surrounding organs. The most common site is the mediastinum (60%–70%). Abdominal forms are rare (10%–17%), the majority being in the retroperitoneum. Different hypotheses have been made on its pathogenesis: a cancerous anomaly in cellular differentiation, an immunologic disorder, a variety of hamartoma. It can be associated with paraneoplastic manifestations such as pemphigus, a recently defined autoimmune syndrome.

The histologic diagnosis of the lesion, essentially based on the cellular architecture, is quite difficult, and a biopsy can provide poor or sometimes erroneous information. At CT, the lesion shows clear margins and high vascularization, which is responsible for the high degree of enhancement [77].

MR evaluation of Castleman's disease has recently been described [76]. In T1-weighted sequences, the signal is isointense or slightly hyperintense compared to the muscle tissue and hypointense compared to the hepatic parenchyma. In T2-weighted sequences, the signal is variable but usually shows a considerable homogeneous hyperintensity. After administration of gadolinium, there is pronounced enhancement in the arterial phase that persists in the later sequences.

Calcifications, fibrous septa or vessels with linear aspects of hypointensity are sometimes recognizable within the mass. The presence of an extensive fibrous component produces a particularly heterogeneous signal, like the enhancement after CM administration.

The disease can be cured with total surgical resection as relapse is unusual. However, in some cases this can be hindered by the hypervascularity of the mass.

References

1. Serio G, Danieli D, Procacci C, Caudana R, Mangiante G, Nifosi F, Benetti R, Mongelli D (1983) Retroperitoneal tumors. Tactics, technics and surgical results. Chir Ital 35:3–37
2. Nishino M, Hayakawa K, Minami M, Yamamoto A, Ueda H, Takasu K (2003) Primary retroperitoneal neoplasms: CT and MR imaging findings with anatomic and pathologic diagnostic clues. Radiographics 23:45–57
3. D'Amico DF, Frego M (1994) I tumori retroperitoneali. In: Collana monografica della Società Italiana di Chirurgia (ed), . Collana monografica della Società Italiana di Chirurgia. Vol 2. Rome, pp 20–34
4. Ebbe M (1993) A 6 kg retroperitoneal liposarcoma in a 42-year-old woman. Scand J Urol Nephrol 27:409–412
5. Storm FK, Sondak V, Economou JS (1987) Sarcomas of the retroperitoneum. In: Eilber FR (ed) The soft tissue sarcomas. Grune & Stratton, , Orlando, pp 239–247
6. Tramontano R, Ponzio S, Fraccalini M, Fossati G (1998) Retroperitoneal tumors. Observations on 8 cases. Minerva Chir 53:539–541
7. Engelken JD, Ros P (1997) Retroperitoneal MR imaging. MRI Clin North Am 5:165–178
8. Heslin MJ, Smith JK (1999) Imaging of soft tissue sarcomas. Surg Oncol Clin North Am 8:91–107
9. Bautista N, Su W, O'Connell TX (2000) Retroperitoneal soft-tissue sarcomas: prognosis and treatment of primary and recurrent disease. Am Surg 66:832–836
10. Jaques DP, Coit DG, Brennan MF (1989) Soft tissue sarcomas of the retroperitoneum. In: Shiu MH, Brennan MF (eds) Surgical management of soft tissue sarcoma. Lea & Febiger, Philadelphhia, pp 12:157–169
11. Van Dalen T, Coebergh JWW, Casparie MK, Gimbrere CHF, Hoekstra HJ, Van Geel BN, Van Coevorden F, Hennipman A (2001) Soft tissue sarcoma: the predominant primary malignancy in the retroperitoneum. Sarcoma 5:5–8
12. Fletcher CDM, Unni KK, Mertens F (2002) Tumours of soft tissue and bone. WHO Classification of Tumours. IARC Press, Lyon
13. Pistolesi GF, Procacci C, Caudana R, Bergamo Andreis IA, Manera V, Recla M, Grasso C, Florio C (1984) CT criteria of the differential diagnosis in primary retroperitoneal masses. Eur J Radiol 4:127–138
14. Lane RH, Stephens DH, Reiman HM (1989) Primary retroperitoneal neoplasms: CT findings in 90 cases with clinical and pathologic correlation. AJR Am J Roentgenol 152:83–89
15. Nishimura H, Zhang Y, Ohkuma K, Uchida M, Hayabuchi N, Sun S (2001) MR imaging of soft-tissue masses of the extraperitoneal spaces. Radiographics 21:1141–1154
16. Sumi Y, Shindoh N, Komura S, Minowa O, Ozaki Y, Kyogoku S, Katayama H (2000) Paratesticular aggressive fibromatosis: CT findings. Abdom Imaging 25:210–212
17. Al Jadaan SA, Al Rabeeah A (1999) Mesenteric fibromatosis: case report and literature review. J Pediatr Surg 34:1130–1132
18. Einstein DM, Tagliabue JR, Desai RK (1991) Abdominal desmoids: CT findings in 25 patients. AJR Am J Roentgenol 157:275–279
19. Casillas J, Sais GJ, Greve JL, Iparraguirre MC, Morillo G (1991) Imaging of intra- and extra-abdominal desmoid tumors. Radiographics 11:959–968
20. Mantello MT, Haller JO, Marquis JR (1989) Sonography of abdominal desmoid tumors in adolescents. J Ultrasound Med 8:467–470
21. Ayuso JR, Garcia-Criado A, Caralt TM, Ayuso C, Torras A, Ribalta T (1999) Atypical retroperitoneal fibrosis: MRI findings. Eur Radiol 9:937–939
22. Braun J, Schuldes H, Berkefeld J, Zanella F, Jonas D, Usadel KH, Badenhoop K (2001) Panhypopituitarism associated with severe retroperitoneal fibrosis. Clin Endocrinol (Oxf) 54:273–276
23. Vivas I, Nicolas AI, Velazquez P, Elduayen B, Fernandez-Villa T, Martinez-Cuesta A (2000) Retroperitoneal fibrosis: typical and atypical manifestations. Br J Radiol 73:214–222
24. Jaques DP, Coit DG, Hajdu SI, Brennan MF (1990) Management of primary and recurrent soft-tissue sarcoma of the retroperitoneum. Ann Surg 212:51–59
25. Kempson RL, Fletcher CDM, Evans HL, Hendrickson MR, Sibley RK (2001) Atlas of tumor pathology. Tumors of the soft tissues. Armed Forced Institute of Pathology, Washington DC
26. Nishimura H, Zhang Y, Ohkuma K, Uchida M, Hayabuchi N, Sun S (2001) MR imaging of soft-tissue masses of the extraperitoneal spaces. Radiographics 21:1141–1154
27. August C, Holzhausen HJ, Zornig C, Harms D, Schroder S (1994) Plexiform fibrohistiocytic tumor. Histology, immunohistology and ultrastructure. Pathologe 15:49–53
28. Habermann CR, Nicolas V, Steiner P (1995) Magnetic resonance tomography diagnosis of plexiform fibrohistiocytic tumor. Aktuelle Radiol 5:243–245
29. Kransdorf MJ, Brancroft LW, Peterson JJ, Murphey MD, Foster WC, Temple HT (2002) Imaging of fatty tumors: distinction of lipoma and well-differentiated liposarcoma. Radiology 224:99–104
30. Hicks J, Dilley A, Patel D, Barrish J, Zhu SH, Brandt M (2001) Lipoblastoma and lipoblastomatosis in infancy and childhood: histopathologic, ultrastructural and cytogenetic features. Ultrastruct Pathol 25:321–333
31. Yalcin B, Öztûrk H, Kismet E, Deveci S, Centinkur0un S, Özcan O (2001) Giant retroperitoneal lipoma in a child. Pediatr Radiol 31:304
32. Sansom HE, Blunt DM, Moskovic EC (1999) Large retroperitoneal hibernoma-CT findings with pathologic correlation. Clin Radiol 54:625–627
33. Niedergethmann M, Hildenbrand R, Winkler M (2001) Monstrous, retroperitoneal liposarcoma – a case report. Swiss Surg 7:32–35
34. Israel GM, Bosniak MA, Slywotzky CM, Rosen RJ (2002) CT differentiation of large exophytic renal angiomyolipomas and perirenal liposarcomas. AJR Am J Roentgenol 179:769–773
35. Arkun R, Memis A, Akalin T, Emin Ustun E, Sabah D, Kandiloglu G (1997) Liposarcoma of soft tissue: MRI finding with pathologic correlation. Skeletal Radiol 26:167–172
36. Barile A, Zugaro L, Catalucci A, Caulo M, Di Cesare E, Splendiani A, Gallucci M, Masciocchi C (2002) Soft tissue liposarco-

ma: histological subtypes, MRI and CT findings. Radiol Med (Torino) 104:140–149
37. Ishida H, Naganuma H, Konno K, Sato M, Hamashima Y, Konno S, Watanabe S, asanuma Y, Ishida J (2000) Retroperitoneal liposarcoma: sonographic findings. Abdom Imaging 25: 554–558
38. Spiekerman M, Ford KL 3rd (1999) Aunt Minnie's corner. Well-differentiated retroperitoneal liposarcoma. J Comput Assist Tomogr 23:806
39. Ylagan LR, Bhalla S (2001) Fine needle aspiration cytology of a dedifferentiated liposarcoma: report of a case with histologic and immunohistochemical follow-up. Acta Cytol 45: 641–644
40. Kurugoglu S, Ogut G, Mihmanli I, Korman U, Durak H (2002) Abdominal leiomyosarcomas: radiologic appearances at various locations. Eur Radiol 12:2933–2942
41. La Fienza A, Alberici E, Meloni G, Preda L, Campani R (2000) Extraperitoneal pelvic leiomyosarcoma. MR findings in a case. Clin Imaging 24:224–226
42. Shindo S, Matsumoto H, Ogata K, Katahira S, Kojima A, Iyori K, Ishimoto T, Kobayashi M, Tada Y, Suzuki T, Itakura J, Iizuka H, Matsumoto H (2002) Surgical treatment of retroperitoneal leiomyosarcoma invading the inferior vena cava: report of three cases. Surg Today 32:929–933
43. Szèkely E, Kulka J, Miklòs I, Kaliszky P (2000) Leiomyosarcomas of the great vessels. Pathol Oncol Res 6:233–236
44. Hemant D, Krantikumar R, Amita J, Chawla A, Ranjeet N (2001) Primary leiomyosarcoma of inferior vena cava, a rare entity: imaging features. Australas Radiol 45:448–451
45. Kunieda K, Saji S, Kuwabara I, Watanabe A, Katoh M, Sugiyama Y, Shimokawa K (2000) Rapid growth of a retroperitoneal rhabdomyosarcoma following right hemicolectomy for ascending colon cancer: report of a case. Surg Today 30: 372–375
46. Konen O, Rathaus V, Dlugy E, Freud E, Kessler A, Shapiro M, Horev G (2002) Childhood abdominal cystic lymphangioma. Pediatr Radiol 32:88–94
47. Bonhomme A, Broeders A, Oyen RH, Stas M, De Wever I, Baert AL (2001) Cystic lymphangioma of the retroperitoneum. Clin Radiol 56:156–8
48. Friedman AC, Hartman DS, Sherman J, Lautin EM, Goldman M (1981) Computed tomography of abdominal fatty masses. Radiology 139:415–429
49. Scialpi M, Galasso C, Di Maggio A, Mancini A, Resta M, Angelelli G, Rotondo A (2001) Primary retroperitoneal angiosarcoma: MR imaging features. Eur Radiol 11:791–795
50. Scherer A, Niehues T, Egelbrecht V, Modder U (2001) Imaging diagnosis of retroperitoneal ganglioneuroma in childhood. Pediatr Radiol 31:106–110
51. Tosaka A, Ando M, Arisawa C, Okano T (1999) Endocrinologically active retroperitoneal ganglioneuroma with positive iodine-131-metaiodobenzylguanidine scintigraphy. Int J Urol 6 :471–474
52. Zhang Y, Nishimura H, Kato S, Fujimoto K, Ohkuma K, Kojima K, Uchida M, Hayabuchi N (2001) MRI of ganglioneuroma: histologic correlation study. J Comput Assist Tomogr 25: 617–623
53. Radin R, David CL, Goldfarb H, Francis IR (1997) Adrenal and extra-adrenal retroperitoneal ganglioneuroma: imaging findings in 13 adults. Radiology 202:703–707
54. Kawakami M, Koda M, Matsunaga N, Kishimoto Y, Shabana M, Kato H, Nishimuki E, Kojo H, Miura K, Kawasaki H (2001) Adult-type neuroblastoma originated in retroperitoneum beginning with obstructive jaundice. Clin Imaging 25:284–287
55. Lindner W, Behnisch W, Kunz U, Debatin KM, Pohlandt F (2001) Congenital neuroblastoma mimicking early onset sepsis. Eur J Pediatr 160:436–438
56. Fenton LZ, Foreman N, Wyatt-Ashmead J (2001) Diffuse, retroperitoneal mesenteric and intrahepatic periportal plexiform neurofibroma in a 5-year-old boy. Pediatr Radiol 31: 637–639
57. Sato M, Ishida H, Konno K, Komatsuda T, Hamashima Y, Naganuma H, Kon H, Watanabe S, Ishida J (2000) Abdominal involvement in neurofibromatosis 1: sonographic findings. Abdom Imaging 25:517–522
58. Baron JM, Hallal H, Jimenez M, Alguacil GF (2000) Retroperitoneal benign schwannoma. Gastroenterol Hepatol 23:460
59. Sharma SK, Koleski FC, Husain AN, Albala DM, Turk TMT (2002) Retroperitoneal schwannoma mimicking an adrenal lesion. World J Urol 20:232–233
60. Schindler OS, Dixon J, Case P (2002) Retroperitoneal giant schwannomas: report on two cases and review of the literature. J Orthop Surg (Hong Kong) 10:77–84
61. Kishi Y, Kajiwara S, Seta S, Kawauchi N, Suzuki T, Sasaki K (2002) Retroperitoneal schwannoma misdiagnosed as a psoas abscess: report of a case. Surg Today 32:849–852
62. Sonoda I, Kasuya K, Aoki T, Tsuchida A, Asami K, Inoue K, Ozawa T, Koyanagi Y (1999) Malignant paraganglioma metachronously recurring at short duration in different paraganglions: report of a case. Surg Today 29:769–772
63. Hruby G, Lehman M, Barton M, Peduto T (2000) Malignant retroperitoneal paraganglioma: case report and review of treatment options. Australas Radiol 44:478–482
64. Pui MH, Liu MJ, Guo Y, Chen YM (1999) Computed tomography of retroperitoneal paragangliomas. Australas Radiol 43: 303–306
65. Vulpio C, Destito C, Carlucci I, Mercuri M, Ruffini RA, Wiel Marin (1996) Extraskeletal retroperitoneal osteosarcoma. A case report and review of the literature. Minerva Chir 51: 1129–1133
66. Grignon DJ, Ayala AG, Carrasco CH, Rederick Ames A, Meis J (1989) Case report 532. Skeletal Radiol 18:147–151
67. Bane BL, Evans HL, Ro JY, Carrasco CH, Grignon DJ, Benjiamin RS, Ayala AG (1990) Extraskeletal osteosarcoma. A clinicopathologic review of 26 cases. Cancer 65:2762–2770
68. Doud TM, Moser RP Jr, Giudici MAI, Frauenhoffer EE, Maurer RJ (1991) Case report 704. Skeletal Radiol 20:628–632
69. Varma DGK, Ayala AG, Qun Guo S, Moulopoulos LA, Kim EE, Charnsangavej C (1993) MRI of extraskeletal osteosarcoma. J Comput Assist Tomogr 17:414–417
70. Allan CJ, Soule EH (1971) Osteogenic sarcoma of the somatic soft issues. Clinicopathologic study of 26 cases and review of literature. Cancer 27:1121–1133
71. Wesseling FJH, Tjon RTO, Tham A, Breed W, Klinkhamer PJJM, Ziekenhuis C (1990) Retroperitoneal extraskeletal osteosarcoma. AJR Am J Roentgenol 155:1139–1140
72. Modrego PJ, Pina MA (2001) Extraskeletal Ewing's sarcoma presenting with neurological symptoms. Report of two cases. Neurol Sci 22:257–259
73. Hatori M, Okada K, Nishida J, Kokubun S (2001) Periosteal Ewing's sarcoma. Radiological imaging and histological features. Arch Orthop Trauma Surg 121:594–597
74. Song H, Koh BH, Rhim H, Hong EK, Park YW (2002) Primary retroperitoneal synovial sarcoma: a case report. J Korean Med Sci 17:419–422
75. Narvàez JA, Narvàez J, Aguilera C, De Lama E, Portabella F (2001) MR imaging of synovial tumors and tumor like lesions. Eur Radiol 11:2549–2560
76. Irsutti M, Paul JL, Selves J, Railhac JJ (1999) Castleman disease: CT and MR imaging features of a retroperitoneal location in association with paraneoplastic pemphigus. Eur Radiol 9:1219–1221
77. Kaneko T, Takahashi S, Takeuchi T, Goto T, Kitamura T (2003) Castleman's disease in the retroperitoneal space. J Urol 169: 265–266

Part 6
Musculoskeletal Radiology

Radiologic-Pathologic Correlations of Bone Infection

Shah H.M. Khan, Johan L. Bloem

6.1

Contents

Introduction

Musculoskeletal infection is common in clinical practice. Infection of the musculoskeletal system provokes a response in the host that can be visualised in detail with current imaging techniques, in contrast to the insulting organism. The manner of the host's response is limited and is mainly aimed at containing the infection. Nevertheless, there is a vast variety of presentation seen on imaging reflecting the continuously shifting balance between host and organism, depending on the immune competence and maturity of the host on one hand, and the virulence of the organism on the other. Knowledge of this dynamic process is imperative to enable appropriate use of imaging techniques after taking into consideration the clinical findings and laboratory results. A good understanding of the various stages of musculoskeletal infection is essential to augment the interpretation of the vast amount of imaging information available to arrive at an accurate diagnosis and thereby institute timely and effective treatment to prevent destructive sequelae in the mature or developing skeleton.

In this chapter we aim to focus on the pathogenesis and radiologic–pathologic correlation and will use this as a perspective in explaining the role of the various imaging techniques in excluding or identifying infection and its mimics.

Pathophysiology

Osteomyelitis as a term was first used by Nelaton in 1844 and refers to infection of the bone and marrow, usually by pus-producing organisms [1]. It is commonly caused by bacteria but fungi, parasites and viruses are also putative agents.

Animal models have demonstrated the inherent resistance of bone to infection [2]. Infection tends to occur only when there are very large inoculates, trauma, or the presence of foreign bodies [3, 4]. The most common aetiological agent of osteomyelitis, *Staphylococcus aureus,* adheres to bone by expressing receptors (adhesins) for components of bone matrix (fibronectin, laminin, collagen, and bone sialoglycoprotein) [5] and cartilage [6]. *S. aureus* is also able to elaborate fibronectin-binding adhesins, which enables it to attach to surgically implanted devices in bone [7].

Although *S. aureus* is the commonest cause of osteomyelitis in all age groups, there are other organisms that play an important role in specific circumstances. In the neonates or infants, group B *streptococcus, E. coli* and *Haemophilus influenzae* are also common incriminating organisms. Gram-negative organisms are common pathogens in adults, particularly in intravenous drug abusers. Multiple organisms are frequently found when osteomyelitis develops by contiguous spread of infection from soft tissues. Postsurgical osteomyelitis in patients treated with preoperative antibiotics is typically caused by *S. epidermidis*.

There are four principal routes of infection of the osseous and articular structures. These are haematogenous, spread from a contiguous source, direct implantation and postoperative infection.

The vascular anatomy of bone plays an important role in pathogenesis of osteomyelitis. The vascular supply varies with age and determines the radiologic and pathologic features of osteomyelitis. Three different patterns are recognised. In the infant, some of the metaphyseal vessels penetrate the growth plate to supply the epiphysis. However, in the child over the age of 1 year and before the growth plate fuses, the metaphyseal and epiphyseal blood supply are distinct and are separated by the growth plate. After the fusion of the growth plate, the metaphyseal vessels are able to re-establish supply to the epiphysis. Therefore, infection in the infant and adult can extend into the epiphysis with potential of causing growth plate damage and growth arrest, as well as septic arthritis.

The course of osteomyelitis has been arbitrarily divided into acute, subacute and chronic stages according to the nature of onset and clinical features. On histology, the acute stage is associated with infiltration by polymorphonuclear cells and the chronic stage is dominated by lymphocytes and plasma cells (Fig. 1).

Acute haematogenous osteomyelitis occurs following bacteraemia with lodgement of the bacteria at the very vascular metaphyseal region of bones. It commonly occurs in children, particularly around the knee. Acute haematogenous osteomyelitis is relatively uncommon in healthy adults, but can occur in the immunocompromised or intravenous drug abusers. The metaphyses, especially around the knee, are predilection sites, probably because of rapid growth and trauma in children. At these sites the blood flow slows down and the macrophages have decreased phagocytic ability, which are conducive to proliferation of bacteria.

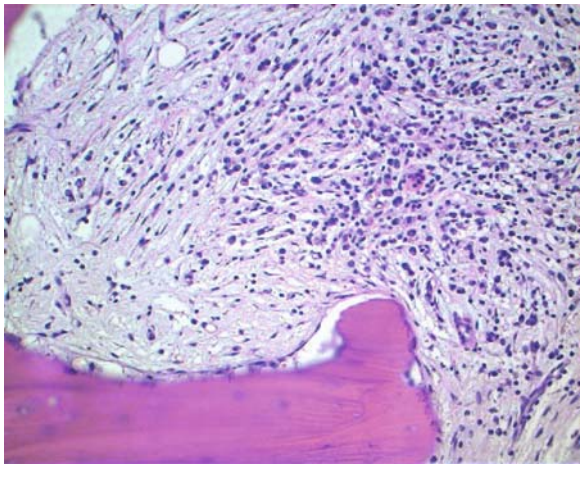

Fig. 1. Light micrograph showing chronic osteomyelitis. Note the presence of fibrosis of the marrow fields, with the absence of preexistent haematopoiesis. Aggregates of lymphocytes and plasma cells are present. The surrounding bone trabeculae show marked remodelling

With the onset of infection, an acute inflammatory response is elicited in the bone characterised by vascular engorgement, oedema and cellular infiltration by polymorphonuclear cells. The production of inflamma-

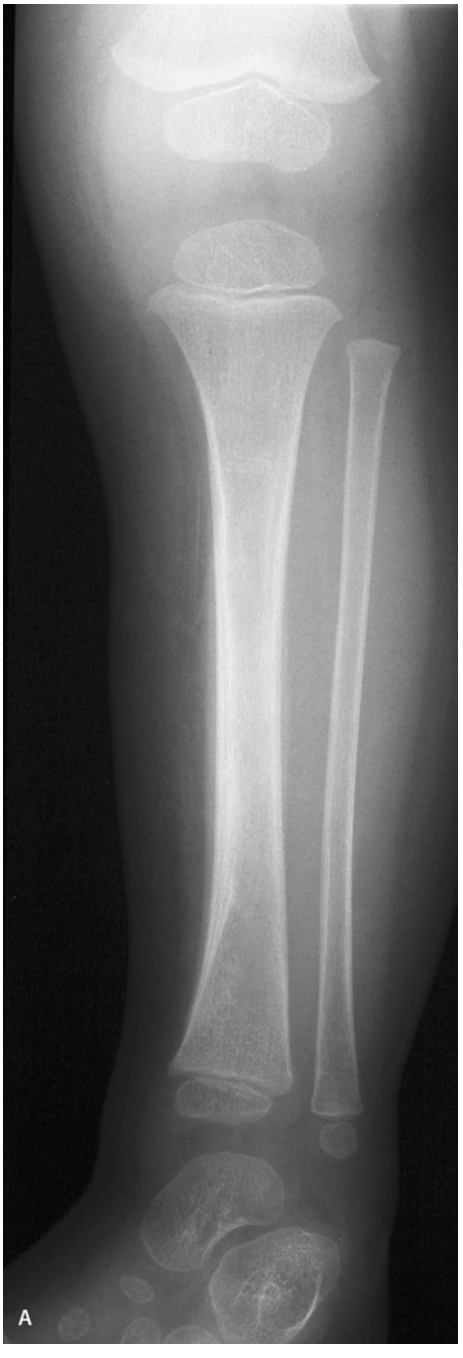

Fig. 2. A Frontal radiograph of the leg in a 13-month-old child with acute osteomyelitis, which shows florid lamellar periosteal new bone formation. **B**, **C** Sagittal T1-fat suppressed with Gd-chelate and axial fat-suppressed MR images, respectively, which exquisitely demonstrate the onion skin-like multiple layers of periosteal new bone formation

tory exudates raises the pressure within the inexpansile bone, compressing the vascular channels leading to extensive bone necrosis. The enzymes released by the bacteria, polymorphonuclear cells and dying tissues also contribute to the local bone marrow or cortical necrosis. The exudate extends across the network of Haversian and Volkmann canals to reach the cortex, which is thin at the distal metaphysis. Abscesses form at the cortex and elevate the periosteum, disrupting the blood supply to the external cortex. The pus may penetrate the periosteum and extend into the adjacent soft tissues, leading to single or multiple abscesses. Elevation of the periosteal membrane triggers periosteal ossification, which arises from the cambium (inner) layer of the periosteum. The periosteal new bone formation is referred to as involucrum, which partially or fully surrounds the infected bone. In the infant and child, the periosteum is loosely attached and can be easily peeled off, producing prominent periosteal elevation and exuberant involucrum formation (Fig. 2).

Soft tissue oedema and abscess formation are frequently seen earlier than osseous features in infants because of the loose periosteum. In contrast, the periosteum is firmly attached to the underlying cortex in adults, which leads to delayed appearance of the periosteal reaction. Therefore, subperiosteal abscesses and involucrum formation are also unusual in the adult. Interruption of the metaphyseal and periosteal blood supply may lead to extensive cortical necrosis with consequent formation of sequestrum in more severe cases. The sequestrum is a dead piece of bone bereft of vascular supply that potentially harbours the infective organism. As it is avascular, it appears dense on plain radiograph due to retention of mineralisation as opposed to the rest of the vascular bone, which may be osteopenic due to inflammation. The antibiotics are rendered ineffective in combating the bacteria residing within the sequestrum, as it is unable to permeate through to the avascular dead bone. Here the organism may lie dormant for years. Hence, for the treatment to be effective, it is very important to look for any evidence of a sequestrum and to remove it. These bacteria may produce recrudescence many years later with pus formation, which may discharge through defects in the involucrum, known as cloaca (Fig. 3). Abscesses may form in the soft tissue or communicate with the skin, discharging fragments of dead bone through a chronic sinus. The infection may follow a protracted course in chronic osteomyelitis that tends to weaken the bone by producing osseous atrophy and predisposing to pathological fracture.

Following adequate treatment and onset of healing process, granulation tissue forms in the marrow cavity to be subsequently replaced by fibrous or fatty tissues. The abscesses are transformed into cystic cavities.

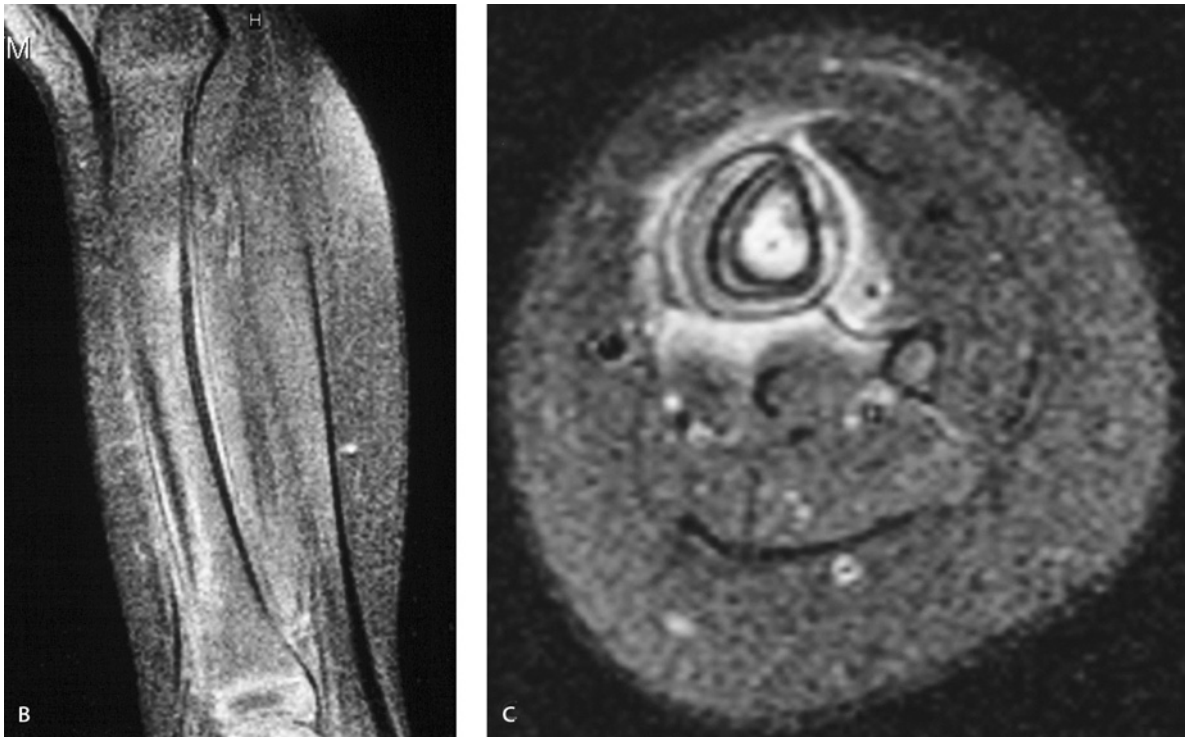

Fig. 2B, C

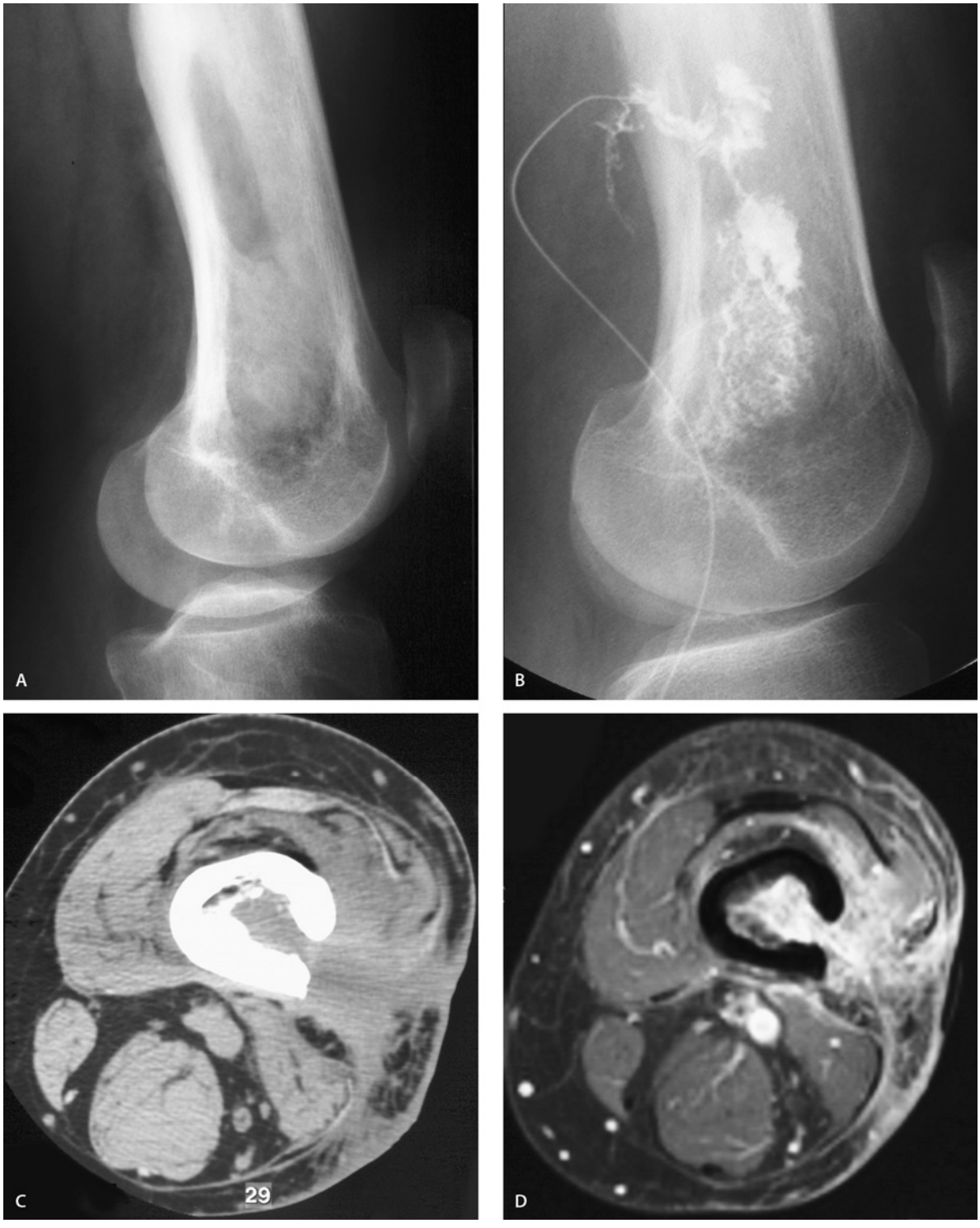

Fig. 3A–G. Chronic osteomyelitis in a 42-year-old man. **A** Lateral knee radiograph demonstrating lucency in the lower third of the femur with irregular dense area in the metaphysis consistent with a sequestrum. Solid periosteal new bone formation is also noted. **B** Sinogram through the cloaca demonstrating the tortuous tract extending into the medullary cavity. **C** Multislice CT axial sections through the distal femur demonstrating the cloaca with increased density in the adjacent soft tissue due to inflammation. **D, E** Axial fat-suppressed with Gd-chelate-enhanced MRI sequences at the same level as the CT and distally, demonstrating high-signal inflamed marrow and adjacent soft tissues and low signal abscess distally. **F, G** Multislice CT 3D reconstruction and comparable coronal STIR MR images, respectively. Solid periosteal new bone formation (involucrum) with extensive sequestrum associated with a cloaca on the lateral aspect is easily appreciated on the CT image. Intensely high signal abscess is noted within the medullary cavity on the MR image along with the low signal sequestrum

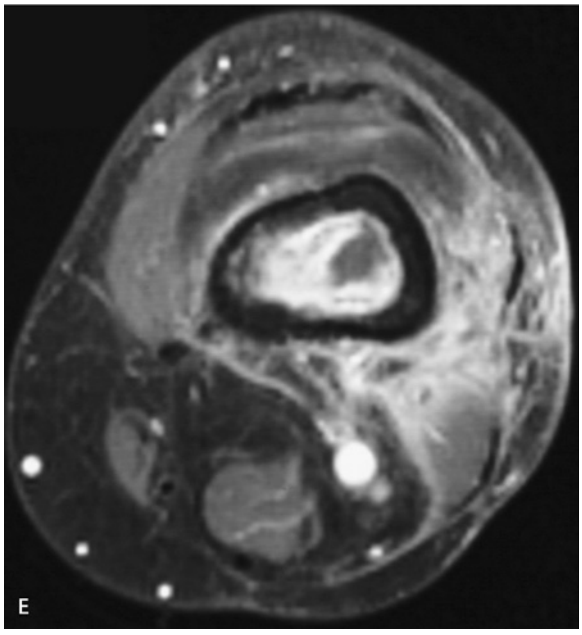

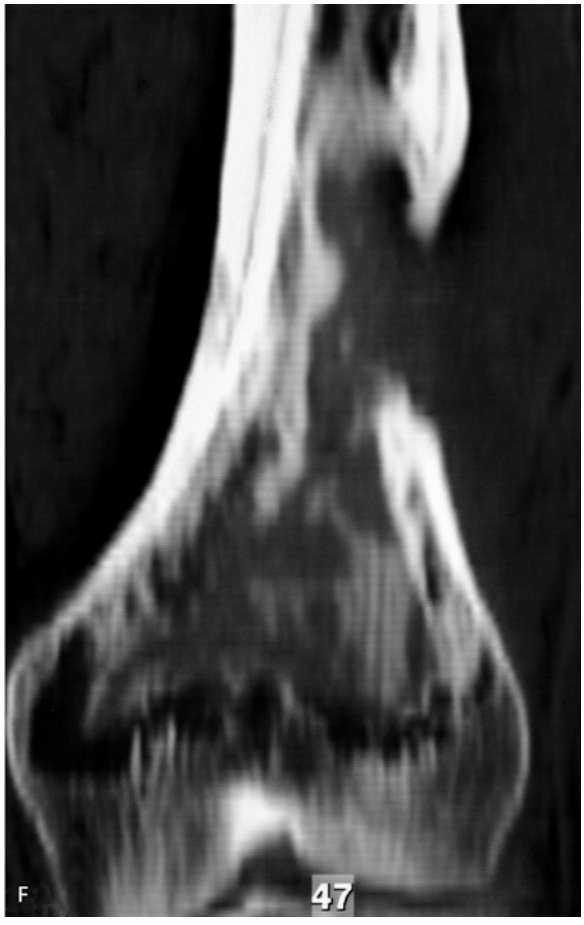

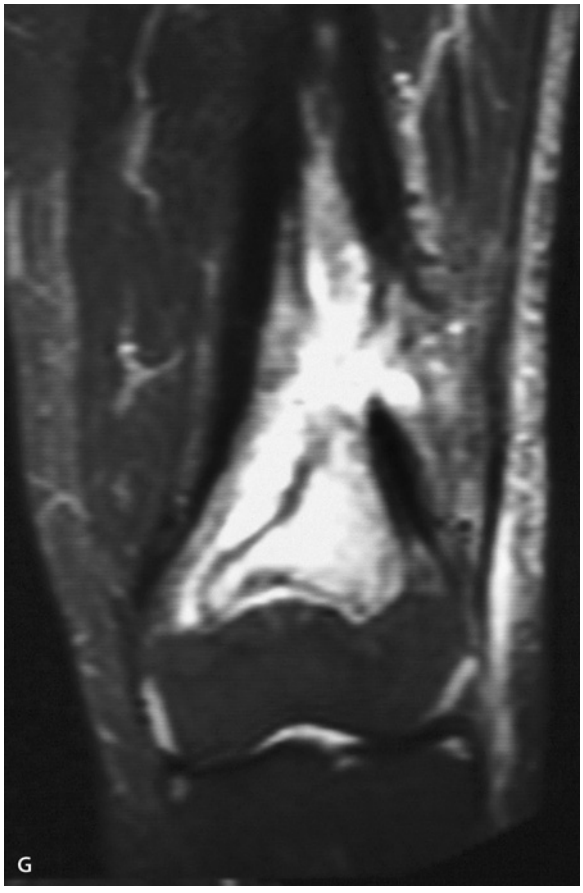

Fig. 3E–G

Radiological Features

Magnetic Resonance Imaging

The focus of infection in the bone demonstrates low signal intensity on T1-weighted images, and high signal intensity on T2-weighted and short tau inversion recovery (STIR) images. This is seen early in the disease process, reflecting the presence of hyperaemia, oedema and inflammatory cellular response. Radiographs are often negative at this stage since more than 60% of trabecular bone has to be destroyed before it can be detected.

MR is the imaging modality of choice in investigating bone marrow infection as it is able to accurately delineate the extent of the infection and also allows visualisation of sequelae such as necrotic areas of bone, soft tissue abscesses and sinus tracts [8]. MRI can evaluate cortical bone and sequestrum but CT is superior in assessing subtle changes. Normal cortical bone is represented as a signal void, whereas intracortical lesions almost invariably show areas of increased signal intensity relative to cortex on T2-weighted, STIR and Gd-chelate-enhanced images. Following disruption of cortex, facilitated by accompanying osteoporosis, the periosteum is elevated and periostitis and soft tissue involvement ensue. In this stage, high signal intensity on T2-weighted images is seen within the cortex and subperiosteally. This represents infectious material, unmineralised cellular periosteal reaction and elevated periosteum (onion skin appearance). This periosteal involvement is often better seen on MR than on radiographs. Mineralised periosteal reaction is seen as a solid or layered signal void area, whereas the nonmineralised cellular cambium layer of the periosteum has high signal intensity on T2-weighted images (Fig. 2).

Fat-suppressed contrast-enhanced imaging significantly increases the sensitivity (88%) and specificity (93%) in the diagnosis of osteomyelitis compared to three-phase bone scintigraphy and higher specificity than nonenhanced MR, particularly in complicated cases such as chronic osteomyelitis, postoperative state, and neuroarthropathy [9].

Radionuclide Imaging

Bone scintigraphy using ^{99}mTc-MDP(methylene diphosphonate) and ^{99}mTc-HMDP(hydromethylene diphosphonate) is quite sensitive in detecting osteomyelitis. Three-phase bone scan is usually carried out, consisting of angiogram, blood pool and delayed phases. Increased uptake is seen in all the three phases in osteomyelitis, reflecting the hyperaemia and increased bone turnover. However, this is not specific and may be seen in conditions such as fracture, treated osteomyelitis and diabetic neuroarthropathy. Photopenia may be seen in the presence of pus, very aggressive disease and impaired vascularity.

Radionuclide imaging is limited by poor resolution, which restricts the ability to accurately pinpoint the lesion. This may be overcome to a certain extent by employing SPECT scan. Nevertheless, bone scan is an important imaging modality in the work-up of patients suspected of having osteomyelitis. A negative scan can exclude osteomyelitis with a sensitivity that is greater than 90%. The sensitivity is lower in children and elderly patients [10].

The poor specificity can be increased by using ^{111}In-WBC scintigraphy, which plays a useful role in the investigation of chronic osteomyelitis and diabetic foot.

Preliminary studies using the PET (positron emission tomography) scan suggest immense potential in diagnosing bone infection and ability to differentiate it from other conditions. ^{18} FDG (fluorodeoxyglucose) is the agent commonly used in PET imaging, which behaves like glucose and accumulates at sites of inflammation due to increased glycolysis. Unlike bone scintigraphy, results can be obtained fairly rapidly with improved resolution and multiplanar capability.

Studies by De Winter et al. have found FDG PET to be accurate in 94% of cases, compared with 81% for combined bone and leukocyte scan, in diagnosis of musculoskeletal infections. It has the ability to distinguish areas of haematopoiesis in the axial skeleton from foci of infection, which are difficult to tell apart on current imaging modalities [11]. Guhlmann et al. have demonstrated immense promise in the imaging of chronic osteomyelitis, with sensitivity of 100% and specificity of 92% [12].

Computed Tomography

CT plays a valuable role in the imaging of osteomyelitis. It is able to accurately demonstrate sequestra, calcification and gas within bone and cortical destruction. One of the earliest findings seen on CT is presence of intramedullary gas associated with increased density of the marrow due to oedema. In chronic osteomyelitis, CT is able to show sequestra that may be concealed within densely sclerotic bone on a radiograph (Fig. 4).

With the advent of multislice CT with multiplanar reconstruction capability, CT plays a useful role in the imaging of infections involving the irregular bones and joints such as sternoclavicular joint, pelvis, and spine. It is particularly useful as image guidance enabling aspiration or biopsy [10].

However, CT is limited by inability to accurately distinguish between suppuration, reactive granulation tissue, oedema and fibrosis [13].

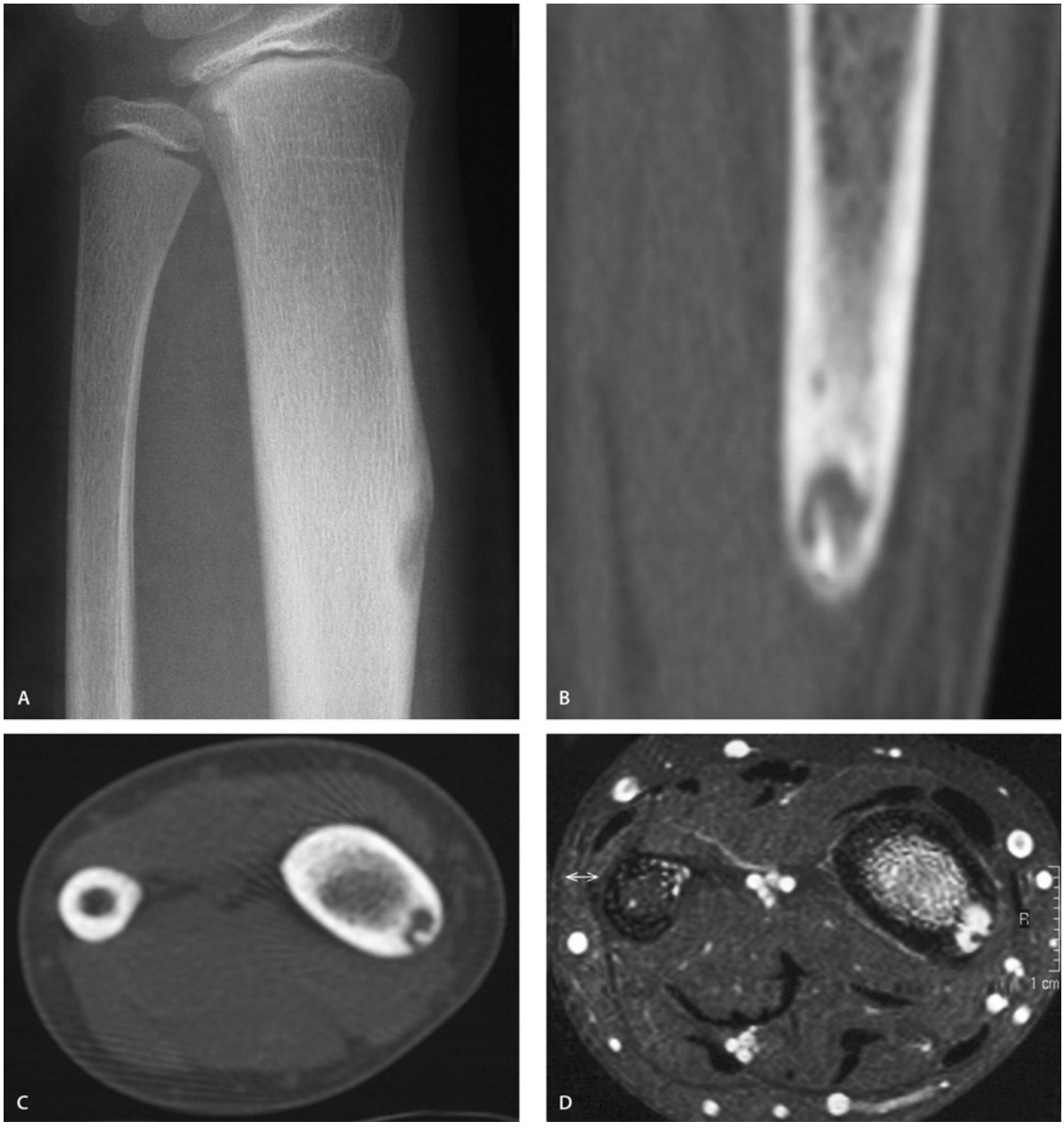

Fig. 4. A Frontal radiograph of the forearm in a 13-year-old male child with osteomyelitis showing a linear lucency in the midshaft of the radius with a subtle density within it, suggestive of a sequestrum. **B, C** CT sagittal reconstruction and axial section clearly display the linear sequestrum within the abscess cavity. The adjacent inflamed marrow is high density compared to the low-density fatty marrow visible in the ulna. **D** Axial T1-weighted fat-suppressed (SPIR) with Gd-chelate-enhanced MR image shows the low-signal sequestrum surrounded by high-signal abscess. Note that the sequestrum demonstrates no enhancement

Ultrasound

Ultrasound is a cheap and easily accessible non-ionising imaging modality that can be used to assess patients with suspected bone and soft tissue infections, particularly in diagnosis of soft tissue abscesses and joint effusions [14]. It plays a valuable role in cases where the diagnosis is inconclusive and can help assess the possible soft tissue causes of pain or swelling such as cellulitis, thrombophlebitis, bursitis, haematoma, tenosynovitis or subcutaneous abscess. The earliest sign of osteomyelitis seen on ultrasound may be deep soft tissue swelling and periosteal reaction adjacent to the affected bone [15]. Subperiosteal fluid collection in children or soft

tissue abscesses adjacent to infected bone in adults may be seen in clinically suspected cases of osteomyelitis [16].

In the diagnosis of osteomyelitis, ultrasound can be used in conjunction with other imaging modalities but plays an important role in enabling real-time guidance for aspiration or biopsy of effusions or abscesses.

Stages of Osteomyelitis

Acute Osteomyelitis

Radiographic evidence of significant osseous destruction is delayed for a period of 7–21 days. Bone scintigraphy and MR are able to demonstrate early changes. Focal deep soft tissue swelling in the metaphyseal region of infants and children may be the first radiographic sign. Effacement of soft tissue planes and muscle swelling, which spreads to involve the superficial muscles and subcutaneous tissue, is subsequently observed on radiographs, but easily appreciated on ultrasound. The degree of osseous change visible radiologically lags behind the actual pathology. Epiphyseal, metaphyseal or diaphyseal ill-defined radiolucencies corresponding to the osseous destruction are seen on radiographs of the mature skeleton. Endosteal scalloping, intracortical lucent regions or tunnelling and poorly defined subperiosteal bony defects are also seen. Mild periosteitis is usually associated but periosteal reaction is more prominently observed in the immature skeleton both on radiographs and US.

In the majority of cases, the clinical features, laboratory and radiological findings are enough to diagnose acute osteomyelitis and early treatment can be instituted. However, blood cultures are positive in only 50% of untreated acute haematogenous cases, but may obviate the need for bone biopsy. The pick-up rate on blood culture is lower in children than in adults.

Sometimes, the clinical features can be confusing and the pathological and radiological findings may be inconclusive. Eosinophilic granuloma and bone tumours such as Ewing sarcoma and sometimes osteosarcoma can mimic acute osteomyelitis. The clinical features and age groups are similar. Patients tend to be acutely ill and present with clinical and laboratory signs of infection. The affected limb is red, swollen and painful. Radiographs may show similar features of ill-defined osteolysis with periosteal reaction and soft tissue changes. In Ewing sarcoma, the periosteal reaction is less regular, and the soft tissue mass is typically more prominent than in the other two conditions.

Subacute Osteomyelitis

Following the acute phase, osteomyelitis is normally contained. The typical example at this stage is Brodie's abscess. The incriminatory agent is usually *S. aureus* and the abscess represents infection that has been localised either due to low virulence or good immune response. It is typically seen in the metaphysis of the distal tibia in young boys. The wall of the abscess is lined by granulation tissue that is surrounded by spongy bone eburnation, which is seen on radiographic examination as a lucent lesion with sclerotic rim.

The central abscess cavity is low signal on T1-weighted sequences but high on T2 and STIR sequences. The granulation tissue at the periphery of the abscess forms an inner ring, which has a slightly higher signal intensity than the abscess cavity on T1- and proton density-weighted images. It demonstrates intense enhancement following gadolinium-chelate administration and is difficult to appreciate on T2-weighted images because of the high signal intensity of the abscess (Fig. 5).

Therefore Gd-chelate-enhanced imaging is the only reliable MR method to diagnose or exclude osseous and soft tissue abscesses. An outer ring representing fibrotic bone reaction and sclerosis is seen in 93% of patients [17], that is low signal on both T1- and T2-weighted sequences. The peripheral halo is the result of the marrow oedema and inflammatory response, which is low signal on T1 and high signal on T2 and STIR images [18, 19]. The penumbra sign is observed in subacute osteomyelitis but not in tumours. It is the transition zone between the abscess and the sclerotic bone that is high signal on T2-weighted images and enhances following Gd-chelate administration [20]. Low signal intensity within soft tissue abscess may represent air or cellular debris.

A small intracortical abscess may be difficult to distinguish from osteoid osteoma. The central nidus in osteoid osteoma demonstrates enhancement unlike the sequestrum, which is low signal on all MR sequences. Abscess characteristically demonstrates the penumbra sign, but the marked reactive inflammatory response, seen as high signal intensity on T2-weighted MR images, favours diagnosis of osteoid osteoma.

Chronic Osteomyelitis

Following the subacute phase of Brodie's abscess, the phase of chronic osteomyelitis may be encountered. It results from either delayed or inadequate treatment of acute osteomyelitis, and occurs in about 15%–30% of patients.

In the subacute and chronic stages of osteomyelitis, considerable periosteal bone formation can surround the altered cortex, associated with increased number of

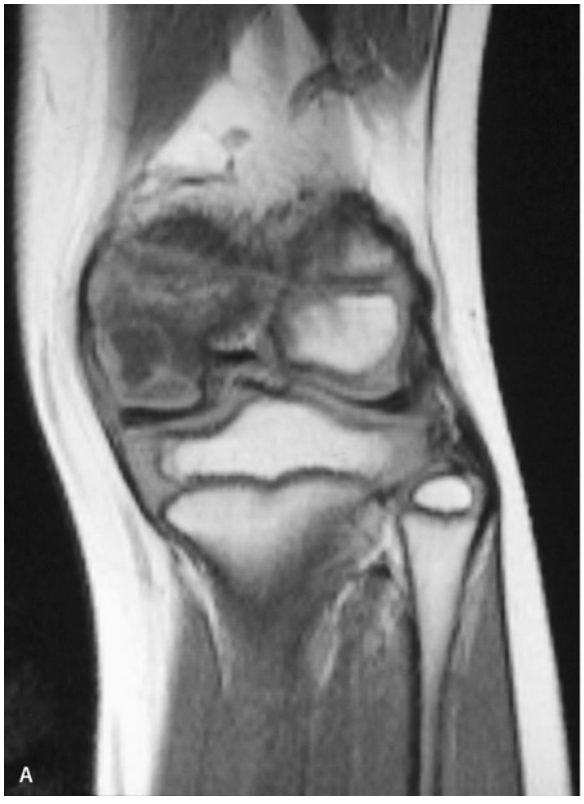

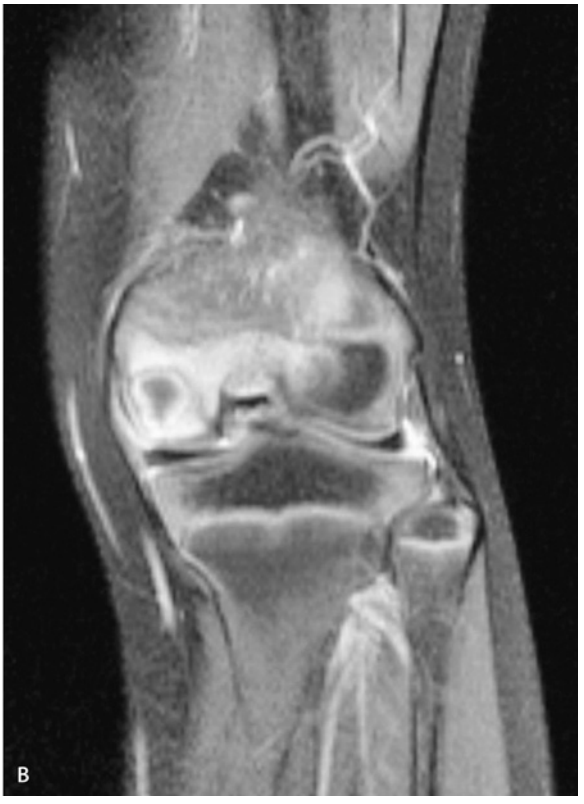

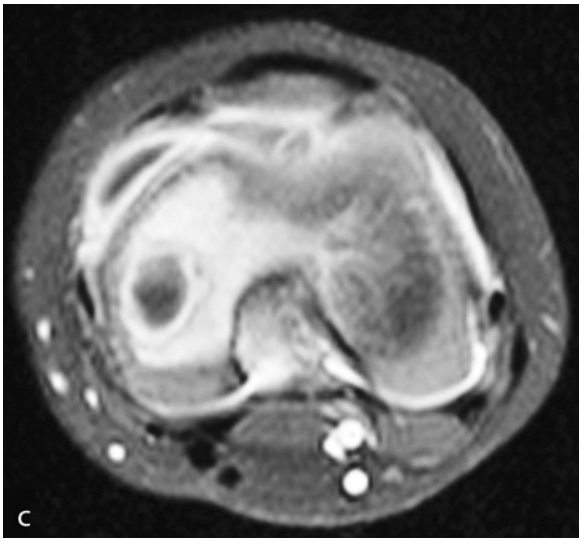

Fig. 5A–C. MRI of Brodie's abscess in a 5-year-old female child. **A** T1-weighted coronal MRI shows a low-signal area abscess in the medial femoral condyle with an intermediate signal ring due to the granulation tissue. Just external to this is a thin low-signal ring due to bony eburnation, surrounded by a diffuse low-signal area peripheral halo representing marrow oedema. **B, C** On the coronal and axial T1-weighted fat-suppressed images with Gd-chelate, marked enhancement of the granulation tissue is seen. This is referred to as the penumbra sign. The peripheral marrow oedema also demonstrates enhancement. The central abscess and the bony sclerosis do not exhibit any enhancement. Note the synovitis seen adjacent to the medial condyle of femur

spongy trabeculae in the affected marrow, as part of the healing response. This leads to extensive bony remodelling with considerable radiodensity and contour irregularity. Cystic changes may occur within the sclerotic area and sequestra are common.

In this stage, radiography as a rule is sufficient to make the diagnosis. However, sequestrum was visible in only 9% of cases in one series. The sensitivity increases with serial review of radiographs to 14% and specificity of 70% [21]. CT is superior to radiography and MR in visualising sequestra, marrow calcification and cortical destruction and may be useful in conjunction with MR. On MR sequestra characteristically appear as low signal intensity on all pulse sequences and do not exhibit enhancement following gadolinium-chelate administration (Fig. 4). Sinus tracts and cloacae appear as curvilinear high-signal areas on T2-weighted images and may demonstrate enhancement [17]. MR imaging is an

important tool in visualising abscesses that need surgical drainage.

Differentiating active from inactive chronic osteomyelitis can be extremely difficult. The extensive bony remodelling and osteosclerosis of the chronic osteomyelitis may obscure changes of reactivation. Radiographically, areas of new destruction, thin linear periostitis and sequestrations are indicative of reactivation. On CT and MR, abscess or sequestration also suggest activity. Preliminary studies using PET scan appear very promising. It is able to detect infection in remodelled bone with a sensitivity of 100% and specificity of 92% and the accuracy is not affected by the presence of orthopaedic devices [12].

Postoperative Infection

Internal fixation of fractures, intervertebral disc surgery, arthroplasty and various types of reconstructive procedures may be complicated by infection or septic arthritis. There is generally delay in diagnosis because the signs are masked by concomitant tissue trauma or the suppressive effect of prophylactic agents or a less virulent organism.

Unlike infection in an intact bone, where the production of the inflammatory exudates raises the intramedullary pressure, leading to widespread ischaemia and bone death, the pressure build up does not occur in postoperative bones as it has been decompressed by the operative procedure. The inflammatory response including periosteal new bone formation and sequestrum is not common in these cases. Tibia and femur are typical sites for infection after internal fixation and the hip and knee joints after arthroplasty.

Combination of radiography, scintigraphy, arthrography and joint aspiration are useful in diagnosis. Increasing osseous and cartilaginous destruction, periostitis, soft tissue swelling and exaggerated lucency around the prostheses may be seen in infection.

Diabetic Foot Osteomyelitis

Early diagnosis is particularly important in this group of patients, to prevent further progression of the disease and to reduce the rate of amputations. Diabetic angiopathy combined with neuropathy leads to tissue hypoxia and loss of sensation, allowing repetitive trauma and muscular atrophy. This results in generalised osteopenia, bone resorption and fragmentation along with foot deformity. The ischaemia predisposes the pedal skin to ulceration and the hyperglycaemia produces an excellent medium for the bacteria to flourish with consequent osteomyelitis in the underlying bone. The ulcers tend to occur at sites of pressure over bony prominences of the deformed foot. The commonest site is under the metatarsal heads (mainly the first and the fifth); the other sites include the tips of the toes, interphalangeal joints, calcaneus and over the malleoli. The ulcers tend to predominate in the forefoot but about one-fifth occur in the hindfoot. The sites of osteomyelitis are invariably adjacent to skin ulcers, consistent with spread of infection from soft tissue [22] (Fig. 6).

Septic arthritis is noted in one-third of diabetic patients with osteomyelitis, mainly involving the first and fifth metatarsophalangeal joints.

Plain radiographs should be the initial imaging investigation but they are the least sensitive for diagnosing pedal osteomyelitis [13]. The presence of focal osteolysis along with cortical disruption that is contiguous to soft tissue infection and ulceration are highly suggestive of osteomyelitis. However, bony osteopenia, fragmentation with increased density, and periosteal reaction are not discriminatory because these signs are also found secondary to neuroarthropathy. Sensitivity varies from 52%–93% and specificity from 50%–74% [23–25].

Bone scintigraphy has been found to have a mean sensitivity of 85%–93% and specificity of 43%–54% [26]. The high rate of false-positive results is due to neuroarthropathy, especially in the midfoot and hindfoot, cellulitis and periostitis secondary to soft tissue inflammation. ^{111}In-labelled leukocyte imaging has a higher specificity of 78% and is frequently used to diagnose osteomyelitis in patients with neuroarthropathy.

MR imaging is the most sensitive (approaching 100%) of all modalities for diagnosing osteomyelitis and has a higher specificity (greater than 81%) in most series [24, 25, 27, 28]. On T1-weighted images, the normal high fatty signal of the marrow is replaced by low signal in infection, which appears as high signal, in keeping with oedema, on T2-weighted and STIR sequences (Fig. 7). The STIR sequence has the highest sensitivity (96%) and negative predictive value (94%) and can thus be used to screen patients suspected of having osteomyelitis. Enhancement is noted on fat-suppressed T1-weighted Gd-chelate sequences and is specific in abscesses where rim enhancement is seen. Diffuse enhancement can be produced by other conditions such as fractures, tumours, inflammatory arthritis, neuroarthropathy, and postoperative changes. Nevertheless, the T1-weighted fat-suppressed gadolinium enhancement MR sequence has the highest specificity for osteomyelitis (88%) [9].

The primary signs of osteomyelitis may be equivocal or mimicked by conditions such as fracture, neuroarthropathy and technical factors such as inhomogeneous fat suppression due to bulk susceptibility and volume averaging of small bones of the foot. Diagnosis can be difficult, but there are other features that may be seen on MR imaging of diabetic foot that are indicative of osteomyelitis. These are referred to as secondary signs

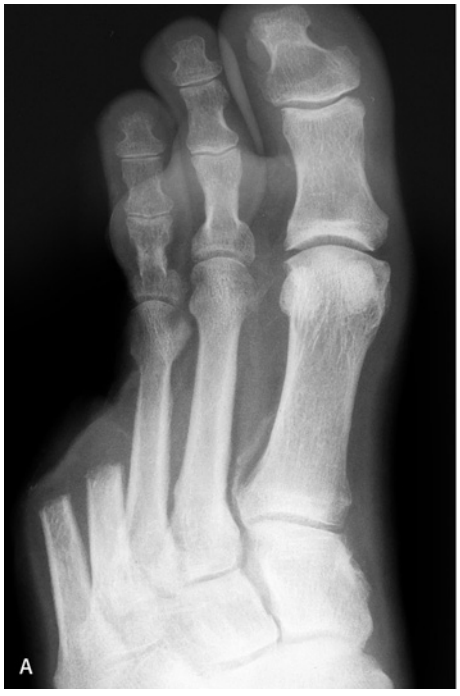

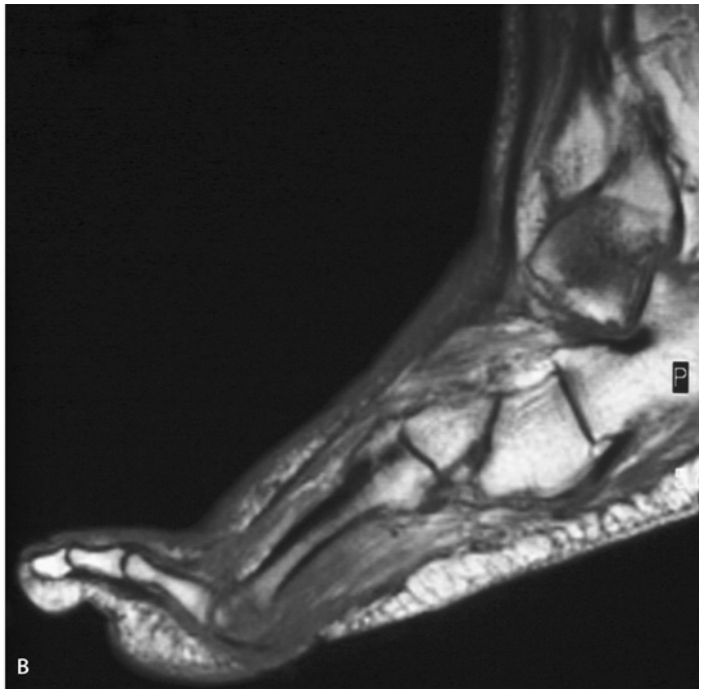

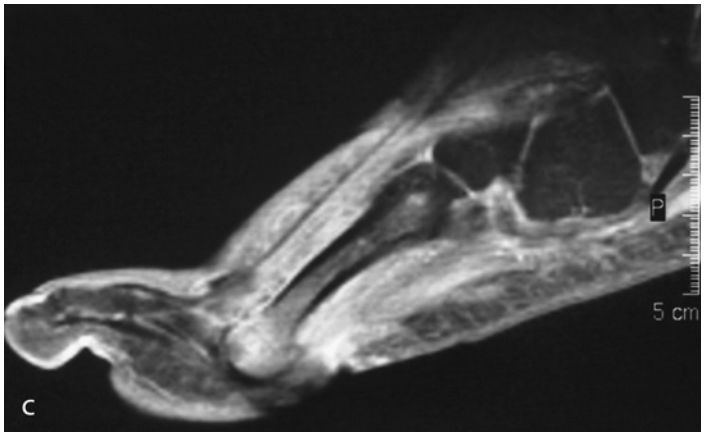

Fig. 6. A Plain radiograph of the foot in a 68-year-old diabetic patient. There is erosion of the third metatarsal head. Amputations of the 4th and 5th toe rays are noted due to previous osteomyelitis. Also note the calcified media of the digital artery that is commonly seen in diabetics. **B, C** Sagittal T1-weighted and T1-weighted fat-suppressed with Gd-chelate enhancement MR images, respectively. Low-signal area is seen in the head of the 3rd metatarsal on the T1 sagittal image, which demonstrates enhancement consistent with osteomyelitis. Note the adjacent deep skin ulcer

and include cellulitis, soft tissue mass, soft tissue abscess, sinus tract and cortical interruption, which are helpful in bolstering diagnostic confidence. Of these signs, the presence of sinus tract, cutaneous ulcer and cortical interruption had the highest positive predictive value for the presence of osteomyelitis [29].

MR readily demonstrates ulceration, oedema and localised fluid collections in the soft tissues, joints and tendon sheaths. MR findings are not infrequently nonspecific for osteomyelitis and need to be correlated with clinical examination and other imaging studies. In neuroarthropathy, almost all signs of osteomyelitis may be seen except abscesses, focal plantar ulcers and high signal intensity areas that are contiguous with cortical disruption. Usually low signal intensity is seen in both T1- and T2-weighted sequences in the bone marrow, indicative of osteosclerosis [13].

In diabetes, compromised vascular supply may mask areas of osteomyelitis and abscesses. A contrast-enhanced MR sequence is necessary to diagnose areas not demonstrating enhancement. These areas represent necrosis and gangrene and occur in about a quarter of cases with pedal infections. It is important to be aware of this possibility to enable accurate preoperative surgical planning with the aim of reducing damage of unaffected tissue [30].

In the acute phase, early institution of treatment with antibiotics following diagnosis with radiographs would obviate extensive imaging. Patients with extensive neuroarthropathy in diabetic foot may benefit from ^{111}In-

leukocyte-labelled scintigraphy. These measures make efficient use of scarce health resources.

However, despite its cost, the most efficient and cost-effective method of diagnosis for many patients with diabetic foot is MR imaging [31].

Septic Arthritis

Septic arthritis can result from haematogenous spread, contiguous bony osteomyelitis or direct inoculation following trauma. *Staphylococcus aureus* is the commonest cause of septic arthritis [32]. It is commonly seen in neonates, affecting the hip, knee and the ankle joints. Since there is no specific imaging to rule out early arthritis, puncture of the joint should be performed immediately when septic arthritis is included in the differential diagnosis.

Septic arthritis is a disabling disease that requires urgent diagnosis to prevent the sequelae of joint damage. Delayed diagnosis will result in rapid destruction of the cartilage due to the actions of the enzymes elaborated by the neutrophils, synovial cells and bacteria [33]. The synovial membrane becomes oedematous, and hypertrophic in response to bacterial infection. There is profuse synovial fluid production that is seen on plain radiograph as joint effusion and soft tissue swelling. Subsequently, marginal and central cartilage loss with joint space narrowing is evident. The hyperaemic joint is reflected by osteopenia on the radiograph. Ultimately, subchondral collapse and ankylosis results. Typical features of osteomyelitis with periostitis may be seen in the adjacent bones. In tuberculosis, marginal erosions with preservation of joint space and periarticular osteoporosis can be prominent.

MR imaging demonstrates synovial thickening, outpouchings and enhancement, due to increased permeability of inflamed vessel walls, perisynovial oedema and joint effusion [32, 34].

Conclusion

Usually, the diagnosis of osteomyelitis is straightforward, but the clinical and radiological findings may be conflicting and confusing. Even with the advancement of imaging technology, findings may remain inconclusive, particularly in complicated cases such as diabetic foot. A good understanding of the underlying pathophysiological process along with close correlation of radiologic and pathologic findings will augment diagnostic confidence and improve accuracy.

■ **Acknowledgements.** We thank Pancras Hogendoorn for providing histological correlation.

References

1. Resnick D, Niwayama G (2004) Osteomyelitis, septic arthritis, and soft tissue infection: mechanisms and situations. Diagnosis of bone and joint disorders. Saunders, Philadelphia, pp 2354–2418
2. Norden CW (1988) Lessons learned from animal-models of osteomyelitis. Rev Infect Dis 10:103–110
3. Belmatoug N, Cremieux AC, Bleton R, Volk A, SalehMghir A, Grossin M et al (1996) New model of experimental prosthetic joint infection due to methicillin-resistant *Staphylococcus aureus*: a microbiologic, histopathologic, and magnetic resonance imaging characterization. J Infect Dis 174:414–417
4. Zimmerli W, Lew PD, Waldvogel FA (1984) Pathogenesis of foreign-body infection – evidence for a local granulocyte defect. J Clin Invest 73:1191–1200
5. Herrmann M, Vaudaux PE, Pittet D, Auckenthaler R, Lew PD, Schumacher-Perdreau F et al (1988) Fibronectin, fibrinogen, and laminin act as mediators of adherence of clinical staphylococcal isolates to foreign material. J Infect Dis 158:693–701
6. Patti JM, Boles JO, Hook M (1993) Identification and biochemical characterization of the ligand binding domain of the collagen adhesin from *Staphylococcus aureus*. Biochemistry 32:11428–11435
7. Fischer B, Vaudaux P, Magnin M, el Mestikawy Y, Proctor RA, Lew DP et al (1996) Novel animal model for studying the molecular mechanisms of bacterial adhesion to bone-implanted metallic devices: role of fibronectin in *Staphylococcus aureus* adhesion. J Orthop Res 14:914–920
8. Chandnani VP, Beltran J, Morris CS, Khalil SN, Mueller CF, Burk JM et al (1990) Acute experimental osteomyelitis and abscesses – detection with MR imaging versus CT. Radiology 174:233–236
9. Morrison WB, Schweitzer ME, Bock GW, Mitchell DG, Hume EL, Pathria MN et al (1993) Diagnosis of osteomyelitis: utility of fat-suppressed contrast-enhanced MR imaging. Radiology 189:251–257
10. Sammak B, Abd EB, Al Shahed M, Hamilton D, Al Nabulsi J, Youssef B et al (1999) Osteomyelitis: a review of currently used imaging techniques. Eur Radiol 9:894–900
11. De Winter F, Vogelaers D, Gemmel F, Dierckx RA (2002) Promising role of 18-F-fluoro-D-deoxyglucose positron emission tomography in clinical infectious diseases. Eur J Clin Microbiol Infect Dis 21:247–257
12. Guhlmann A, Brecht-Krauss D, Suger G, Glatting G, Kotzerke J, Kinzl L et al (1998) Chronic osteomyelitis: detection with FDG PET and correlation with histopathologic findings. Radiology 206:749–754
13. Gold RH, Tong DJF, Crim JR, Seeger LL (1995) Imaging the diabetic foot. Skeletal Radiol 24:563–571
14. Bureau NJ, Chhem RK, Cardinal E (1999) Musculoskeletal infections: US manifestations. Radiographics 19:1585–1592
15. Mah ET, LeQuesne GW, Gent RJ, Paterson DC (1994) Ultrasonic signs of pelvic osteomyelitis in children. Pediatr Radiol 24:484–487
16. Abiri MM, Kirpekar M, Ablow RC (1989) Osteomyelitis: detection with US. Radiology 172:509–511
17. Tehranzadeh J, Wong E, Wang F, Sadighpour M (2001) Imaging of osteomyelitis in the mature skeleton. Radiol Clin North Am 39:223–250
18. Marui T, Yamamoto T, Akisue T, Nakatani T, Hitora T, Nagira K et al (2002) Subacute osteomyelitis of long bones: diagnostic usefulness of the "penumbra sign" on MRI. Clin Imaging 26:314–318
19. Marti-Bonmati L, Aparisi F, Poyatos C, Vilar J (1993) Brodie abscess: MR imaging appearance in 10 patients. J Magn Reson Imaging 3:543–546
20. Grey AC, Davies AM, Mangham DC, Grimer RJ, Ritchie DA (1998) The 'penumbra sign' on T1-weighted MR imaging in subacute osteomyelitis: frequency, cause and significance. Clin Radiol 53:587–592
21. Tumeh SS, Aliabadi P, Weissman BN, McNeil BJ (1987) Disease activity in osteomyelitis: role of radiography. Radiology 165:781–784

22. Ledermann HP, Morrison WB, Schweitzer ME (2002) MR image analysis of pedal osteomyelitis: distribution, patterns of spread, and frequency of associated ulceration and septic arthritis. Radiology 223:747–755
23. Seldin DW, Heiken JP, Feldman F, Alderson PO (1985) Effect of soft-tissue pathology on detection of pedal osteomyelitis in diabetics. J Nucl Med 26:988–993
24. Yuh WT, Corson JD, Baraniewski HM, Rezai K, Shamma AR, Kathol MH et al (1989) Osteomyelitis of the foot in diabetic patients: evaluation with plain film, 99mTc-MDP bone scintigraphy, and MR imaging. AJR Am J Roentgenol 152:795–800
25. Wang A, Weinstein D, Greenfield L, Chiu L, Chambers R, Stewart C et al (1990) MRI and diabetic foot infections. Magn Reson Imaging 8:805–809
26. Larcos G, Brown ML, Sutton RT (1991) Diagnosis of osteomyelitis of the foot in diabetic patients: value of 111In-leukocyte scintigraphy. AJR Am J Roentgenol 157:527–531
27. Crim JR, Seeger LL (1994) Imaging evaluation of osteomyelitis. Crit Rev Diagn Imaging 35:201–256
28. Weinstein D, Wang A, Chambers R, Stewart CA, Motz HA (1993) Evaluation of magnetic resonance imaging in the diagnosis of osteomyelitis in diabetic foot infections. Foot Ankle 14:18–22
29. Morrison WB, Schweitzer ME, Batte WG, Radack DP, Russel KM (1998) Osteomyelitis of the foot: relative importance of primary and secondary MR imaging signs. Radiology 207:625–632
30. Ledermann HP, Schweitzer ME, Morrison WB (2002) Nonenhancing tissue on MR imaging of pedal infection: characterization of necrotic tissue and associated limitations for diagnosis of osteomyelitis and abscess. AJR Am J Roentgenol 178:215–222
31. Morrison WB, Schweitzer ME, Wapner KL, Hecht PJ, Gannon FH, Behm WR (1995) Osteomyelitis in feet of diabetics: clinical accuracy, surgical utility, and cost-effectiveness of MR imaging. Radiology 196:557–564
32. Karchevsky M, Schweitzer ME, Morrison WB, Parellada JA (2004) MRI findings of septic arthritis and associated osteomyelitis in adults. AJR Am J Roentgenol 182:119–122
33. Fitzgerald RH, Kelly PJ (1995) Infections of the skeletal system. In: Howard RJ, Simmons RL (eds) Surgical infectious diseases. Appleton & Lange, London, pp 1207–1236
34. Hopkins KL, Li KC, Bergman G (1995) Gadolinium-DTPA-enhanced magnetic resonance imaging of musculoskeletal infectious processes. Skeletal Radiol 24:325–330

Bone Tumors

A. Mark Davies, David C. Mangham

6.2

Contents

Introduction

There are a large variety of tumors and tumor-like lesions arising in the musculoskeletal system. To the unwary observer they present a bewildering spectrum of radiographic appearances that can lead to misinterpretation and suboptimal management. Although primary malignancies are relatively rare they often pose an intriguing problem for the radiologist, particularly as the pathology is frequently equally challenging. Dramatic progress has been achieved over the past two decades in both the management and prognosis of musculoskeletal malignancies. Prior to this, early amputation followed by the rapid development of metastases was the typical scenario for most patients. The addition of chemotherapy to the surgical management of patients with, for example, conventional osteosarcoma, has improved the 5-year survival from less than 20% to 76% [1, 2]. Provided wide surgical margins are obtained, no difference is seen between the long-term survival of patients with amputation and those undergoing limb-salvage surgery [3].

During this period of improving outcome the imaging of musculoskeletal tumors has also undergone something of a revolution with the introduction of newer sophisticated techniques, albeit at a price. Despite these exciting technical developments, the cornerstone of musculoskeletal imaging remains the humble radiograph. In this chapter the interpretation of the radiograph and its value in patient management are stressed. In addition the case of imaging in surgical staging and follow up is reviewed. It is beyond the scope of this chapter to describe each tumor type in detail.

A close working relationship between radiologist and pathologist is ideal. Their different perspectives on the lesion in question are complementary. Frequently, there is complete agreement on the nature of the lesion in question. It is not unusual, however, for a correct diagnosis to be only possible by consensus. For example, the histological features of a biopsied giant cell tumor (GCT) of bone closely mimic the appearance of a brown tumor of hyperparathyroidism. The radiologist has the "big picture", enabling him/her to detect the presence or absence of signs of metabolic bone disease elsewhere in the skeleton. Conversely, radiography of an apparently typical lesion may turn out to be something completely different following pathological examination (Fig. 1).

Detection

The patient with a bone or soft tissue mass, irrespective of its nature, will typically present with either pain or swelling. Frequently, tumors, particularly around the knee, are initially misdiagnosed as an athletic injury [1]. The pain may be mild and intermittent initially but later becomes more severe and unremitting, particularly if it is a malignancy. Alternatively, a pathological fracture may be the precipitous presenting feature. Occasionally, a bone tumor, typically a benign lesion, can be an incidental radiographic finding.

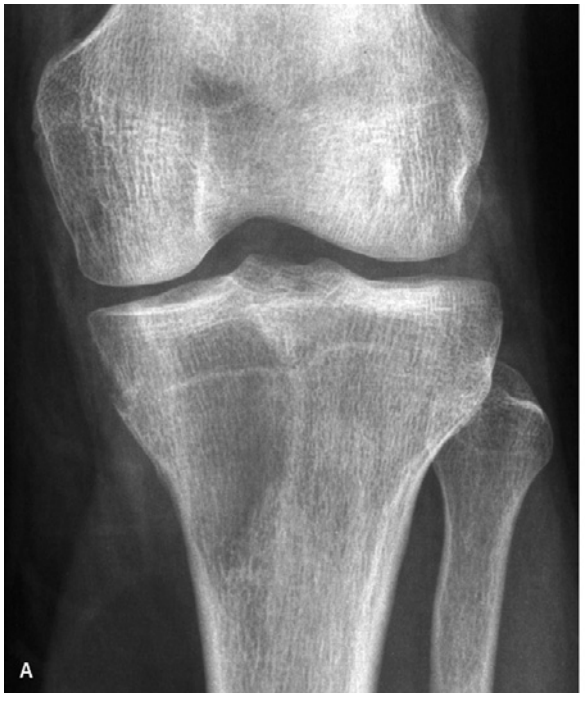

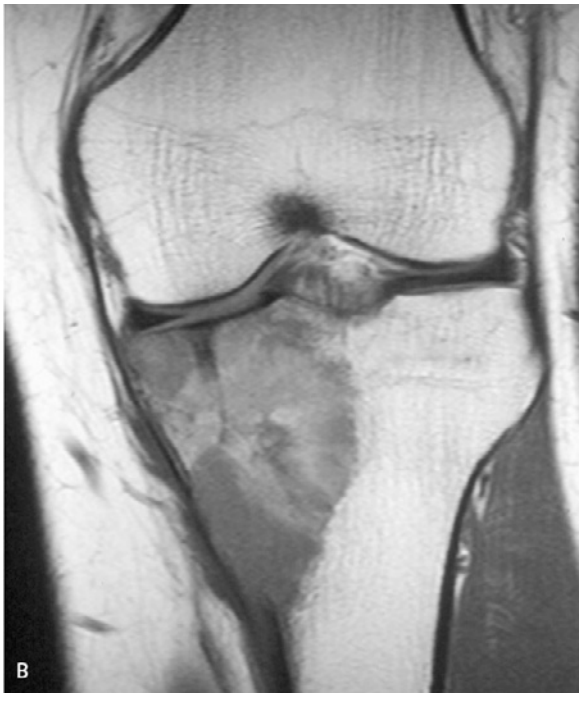

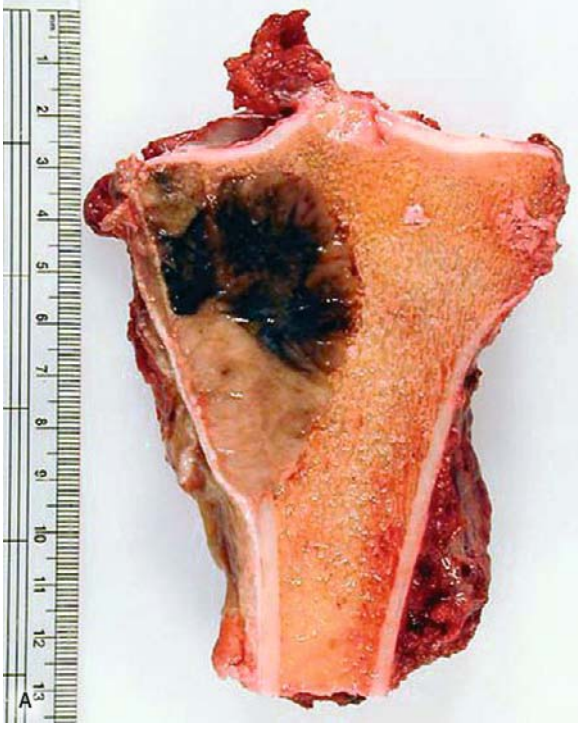

Fig. 1A–C. Melanoma metastasis in the proximal tibia in a 50 year old male. The radiographic appearances (**A**) resemble a GCT but the patients age favors a metastasis. The hyperintensity within the lesion on the unenhanced T1-weighted images (**B**) is due to the paramagnetic property of melanin. The precise intramedullary extent of the tumor is more clearly demonstrated on the MR image. The photograph of the pathological specimen (**C**) shows similar appearances to the MR image with the pigmentation of the melanin containing component

Despite newer imaging techniques, the radiograph is the preliminary and single most important imaging investigation. It remains cheap, easily obtainable and universally available. The radiologist and clinical ignore the value of the radiograph at their peril. Frequently, the diagnosis may be obvious to the trained eye and further imaging is then directed towards staging the lesion. Alternatively, if an abnormality is present on the film and the exact nature is not immediately apparent certain findings will indicate a differential diagnosis and other forms of imaging can then be employed to assist in making a more definitive radiological diagnosis. If the initial radiograph is normal, however, with persisting and increasing symptoms a repeat radiograph in due course may be indicated.

Early signs of a bone tumor and/or infection include all areas of ill-defined lysis or sclerosis, cortical destruction, periosteal new bone formation and soft tissue swelling. Bone lesions are frequently missed or overlooked on the initial radiograph. In a study performed at the authors' institution in approximately 20% of cases neither the clinician nor the radiologist at the referring center detected the bone tumor on the initial radiographs, although evidence was present on retrospective review of the films [5]. A number of features may improve the rate of detection. Attention to good radio-

graphic technique is essential. The fundamental prerequisite for skeletal radiology, that at least two views of an area are obtained, must be strictly adhered to. Often subtle signs of a lesion may be discernible on one view but not be visualized on the second. It is ironic that the more complex the bony anatomy, the fewer the projections are obtained. The prime example is the pelvis, where early lesions may be missed due to the curvature of the bones and can be obscured by the overlying soft tissues, bowel gas and vascular calcifications.

Careful scrutiny of the entire film including the periphery is necessary, and if an abnormality is seen at the edge of the film, further, more extensive views will be required. If the film is overexposed it should be viewed with a bright light or may even need to be repeated; not only the bone should be optimally seen, but also the soft tissues for assessment of density changes or displacement of tissue planes.

In the presence of a normal radiograph, referred pain needs to be considered, in which case further radiographs would be indicated. Hip joint pathology presenting with referred pain to the knee is a well-recognized entity in the child.

The pathological process may be well established even in the presence of a normal radiograph. At least 40–50% of trabecular bone must be destroyed before a discrete area of lucency can be seen on the radiographs [6, 7]. Erosion or destruction of the cortex is more readily apparent. A typical example is the vertebral metastasis. Classically, the first radiographic abnormality detected is destruction of the pedicle, by virtue of its small size and well defined cortex. Cross-sectional imaging has shown that the vast majority of these metastases arise within the vertebral body and that the pedicle is only involved secondarily [8]. However, the destruction of the trabecular bone within the vertebral body is frequently not visible on the initial radiographs. It is self-evident that the smaller the bone involved, with a greater proportion of cortical to medullary bone, the easier it will be to detect an abnormality on the radiographs.

On occasion, radiographically occult lesions can be detected by bone scintigraphy and/or magnetic resonance (MR) imaging. A typical example in this regard is the painful adolescent scoliosis due to an osteoid osteoma, the nature of which is not immediately obvious on the radiograph. An intense focus of increased activity/uptake on bone scintigraphy may suggest the diagnosis. Often, however, the high sensitivity of bone scintigraphy will highlight the site of pathology, but its lack of specificity means that other imaging, frequently retrospective review of the radiographs, will be required to establish the diagnosis. The high sensitivity of MR imaging for marrow abnormalities means it has to be interpreted with caution lest incidental findings are considered unduly significant.

Radiological Diagnosis

Once a skeletal abnormality has been detected, the next objective of imaging is to attempt to characterize the lesion and, in doing so, indicate an appropriate differential diagnosis to the referring clinician. At this stage important maximums that should be appreciated include not overtreating a benign lesion, not undertreating a malignant lesion and not misdirecting the approach to biopsy which might prejudice subsequent surgical management [9]. In drawing up a differential diagnosis for a particular case the radiologist must first have a knowledge of the different pathologies that may arise in the musculoskeletal system. While an understanding of the microscopic features is not required, it is self-evident that an entity will not appear in the differential diagnosis if the radiologist involved is unaware of its existence. Musculoskeletal tumors can best be categorized according to their tissue of origin and then into benign and malignant subtypes.

Before assessing the imaging the prudent radiologist should establish some basic facts regarding the patient. In recognizing the relevance of certain clinical details the differential diagnosis may then be significantly reduced even before the imaging is taken into account. Important factors to be noted include the following:

- **Age:** The age of the patient is arguably the single most useful piece of information as it frequently influences the differential diagnosis. Many musculoskeletal neoplasms exhibit a peak incidence at different ages. For osteosarcoma this is in the second and third decades. Osteosarcoma is, therefore, unlikely to be high in the differential diagnosis on a bone forming lesion in a middle-aged or elderly patient except in the presence of a pre-existing bone lesion such as Paget's disease. Metastases and myeloma should always be considered if a bone lesion is identified in a patient over 40 years of age. Similarly, metastatic neuroblastoma should be in the differential at 2 years of age or under. Conversely, a tumor arising in adolescence or early adult life is unlikely to be a metastasis.

- **Gender:** When looking at a large series of patients with a particular type of bone tumor it can be seen that many occur more commonly in boys. In the individual case this fact does not play a significant role in formulating the differential diagnosis.

- **Ethnic Origin:** Amongst the bone neoplasms, Ewing's sarcoma is unusual in that it is prevalent in Caucasians but is rarely seen in the Afro-Caribbean races. A number of non neoplastic bone conditions that may on occasion simulate neoplasia also show a racial predisposition, e.g. sickle cell, Gaucher's and Paget's diseases. It is only in isolated cases that the ethnic origin of

the patient provides a useful pointer to the diagnosis. Osseous TB can mimic a tumor and in the developed countries is more commonly seen in immigrants from the Asian subcontinent.

■ **Family History:** There is little evidence of a familial predisposition to the formation of musculoskeletal neoplasms in most instances. The exceptions are certain hereditary bone conditions which may be found in association with malignant change, e.g. diaphyseal aclasis.

■ **Previous Medical History:** Information that should be noted in all patients, whenever present, is a history of a prior malignancy or a pre-existing bone condition. If such relevant details are forthcoming it is important to establish if previous imaging exists and, if so, obtain sight of it for review with the contemporary imaging.

■ **Multiplicity:** It is critical early in the management of a patient to establish whether a lesion is solitary or multiple as it will influence the differential diagnosis. Frequently this question will not be definitively answered until the staging imaging is performed.

■ **Serology:** Abnormal serological tests, such as raised erythrocyte sedimentation rate (ESR) and white cell count, together with the examination findings of a hot swollen limb, are highly suggestive of a bone or soft tissue infection. Ewing's sarcoma however, is notorious for presenting with similar clinical and serological findings. The brown tumor of hyperparathyroidism may mimic a true bone tumor on imaging and histology. A raised serum calcium level should alert the clinician to the possibility of this diagnosis.

In establishing a perspective of the patient as a whole the factors detailed above should be taken in conjunction with one another, for example, age and multiplicity. Multiple bone lesions in the child will suggest a bone dysplasia, Langerhans cell histiocytosis (LCH), leukemia or metastatic neuroblastoma, whereas, in the adult, metastatic disease and myeloma are the most likely. It is at this stage that attention should now turn to the imaging. The radiograph remains the most accurate of all the imaging techniques currently available in determining the differential diagnosis of a bone lesion [10]. The radiologist may attempt a diagnosis from the radiograph in one of two ways. First, the so-called Aunt Minnie [10] or pattern recognition approach, which relies on familiarity with the typical overall appearances of a particular lesion. This is all very satisfactory if the mass under investigation is classical in appearance, but problems arise if the lesion has atypical features, arises at an unusual site or is mimicked by a differing pathology. The second, preferred approach, which might best be termed pattern analysis, relies on meticulous recognition of various radiographic signs [11, 12]. The analysis can be best illustrated by answering a series of five questions: Which bone is affected? Where in that bone is the lesion located? What is the tumor doing to the bone (pattern of destruction)? What form of periosteal reaction, if any, is present? What type of matrix materialization, if any, is present?

Site in Skeleton

Most bone tumors and infections occur around the knee and in the proximal humerus and as such little diagnostic information can be deduced from noting the affected bone in many cases. There are exceptions. Cartilage tumors of the hands and feet, while common, are almost invariably benign (Fig. 2). Both osteofibrous dysplasia and adamantinoma classically involve the diaphysis of the tibia and are extremely rare at any other site. Chordoma characteristically arises from the clivus or sacrum. Although many different tumors may arise in the bony spine, malignant lesions are found predominantly in the anterior part of the vertebra (body), while benign lesions are characteristically found in the posterior elements (neural arch). Most spinal infections, while developing in the vertebral endplate, will rapidly extend to involve the disc space, which is uncommon in neoplasia.

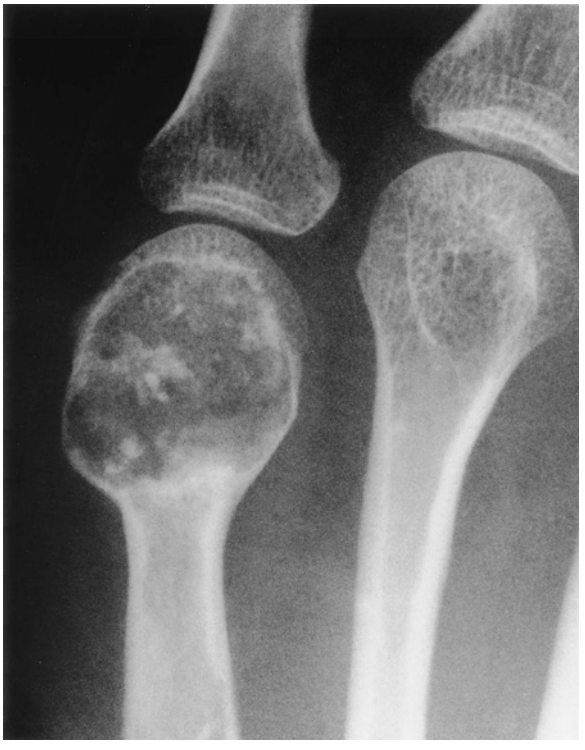

Fig. 2. Enchondroma, distal metacarpal, showing the typical cartilage matrix of popcorn calcification

Location in Bone

The site of the original bone tumor is an important parameter of diagnosis (Fig. 3) [13]. It reflects the site of greatest cellular activity. During the adolescent growth spurt the most active areas are the metaphyses around the knee and in the proximal humerus. Tumor originating from marrow cells may occur anywhere along the bone. Conventional osteosarcoma will tend, therefore, to originate in the metaphysis or metadiaphysis (Fig. 4), whereas Ewing's sarcoma will arise in the metaphysis or, more distinctively, in the diaphysis (Fig. 5). In the child the differential diagnosis of a lesion arising within an epiphysis can be realistically limited to chondroblastoma (Fig. 6), epiphyseal abscess (pyogenic or tuberculous) and rarely, LCH. Following skeletal fusion subarticular lesions, analogous in the adult to the epiphyseal lesions, include giant cell tumor (Fig. 7), clear cell chondrosarcoma (rare) and intraosseous ganglion. With the exception of epiphyseal abscess most osteomyelitis will arise within the metaphysis of a long bone, most commonly tibia and femur.

It can also be helpful to identify the origin of the tumor with respect to the transverse plane of the bone. Is the tumor central, eccentric or cortically based? For example, a simple bone cyst, fibrous dysplasia and Ewing's sarcoma will tend to be centrally located (Fig. 3). Giant cell tumor (Fig. 7), chondromyxoid fibroma and nonossifying fibroma (Fig. 8) are typically eccentric. Lesions

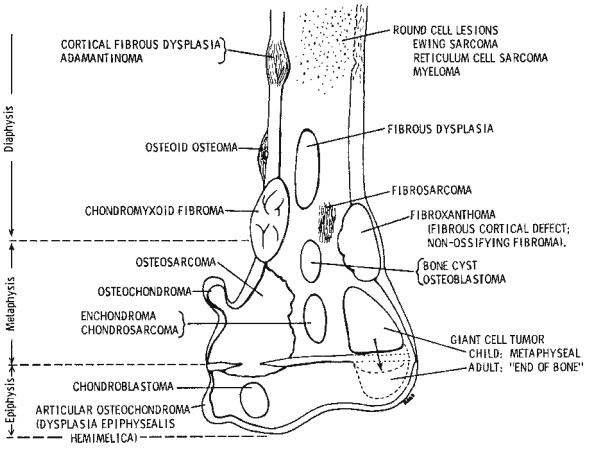

Fig. 3. A composite diagram of the sites of origin of primary bone neoplasms. (From [12], with permission)

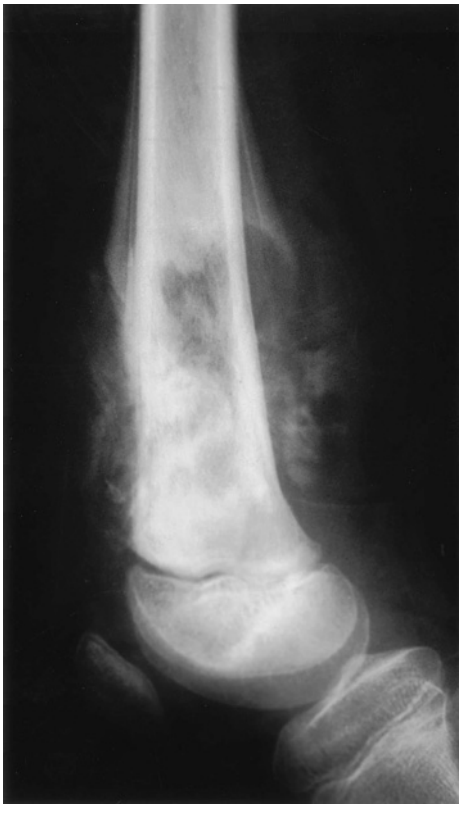

Fig. 4. Lateral radiograph of the knee of a 12-year-old female showing an extensive osteosarcoma of the distal femoral metaphysis. There is malignant osteoid mineralization with Codman's angles proximally and a spiculated periosteal reaction distally

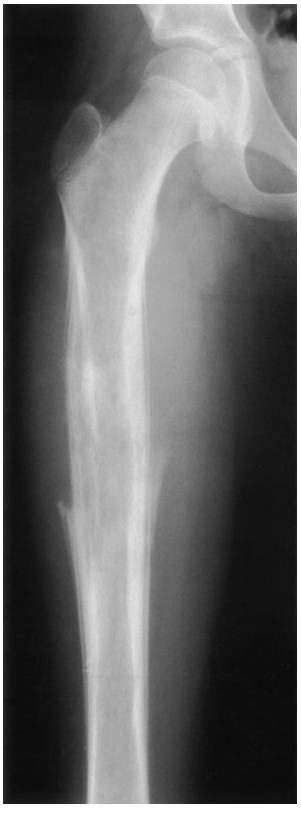

Fig. 5. Anteroposterior (AP) radiograph of the femur of a 9-year-old female showing the classic features of a Ewing's sarcoma: there is lamellar periosteal new bone formation with interruption distally (Codman's angles) against a background of permeative bone destruction

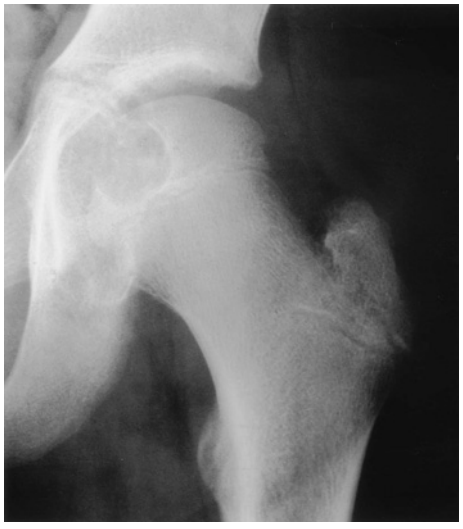

Fig. 6. AP radiograph of the hip of a 13-year-old male showing a rounded lytic lesion in the proximal femoral epiphysis typical of a chondroblastoma

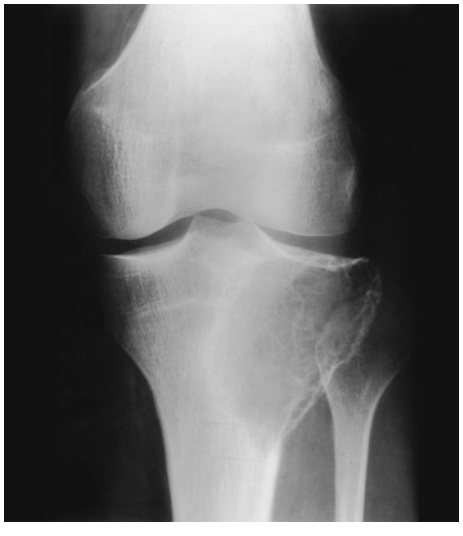

Fig. 7. AP radiograph of the knee of a 38-year-old male showing the typical lytic, subarticular, eccentric location of a giant cell tumor

that usually arise in an eccentric position may appear central if the tumor is particularly large or the involved bone is of a small caliber. There are numerous surface lesions of bone which are related to a greater or lesser extent to the cortex [14, 15]. A benign example if the periosteal or juxtacortical chondroma. Most of the malignant surface lesions of bone are the rarer forms of osteosarcoma, e.g. periosteal, high-grade surface and parosteal osteosarcoma (Fig. 9). 50% of parosteal osteosarcoma arise on the posterior surface of the distal femoral metaphysis.

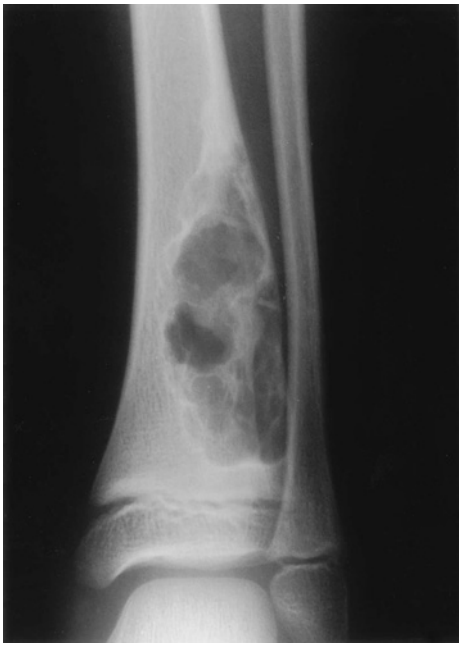

Fig. 8. AP radiograph of the distal tibia of a 6-year-old boy showing a lytic, eccentrically located lesion with geographic bone destruction (type IA) typical of a nonossifying fibroma

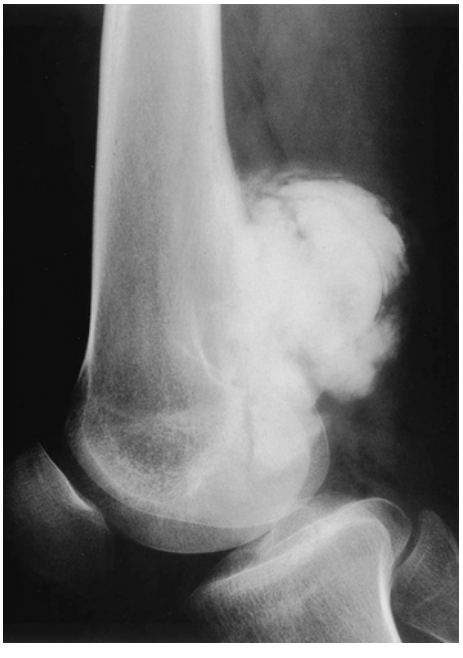

Fig. 9. Lateral radiograph of the distal femur of a 32-year-old female with ivory density mineralization on the posterior metaphysis typical of a parosteal osteosarcoma

Pattern of Bone Destruction

Analysis of the interface between tumor and host bone is a good indicator of the rate of growth in the lesion. A sharply marginated lesion usually denotes slower growth, than a nonmarginated lesion (Fig. 10). the faster the growth, the more aggressive the pattern of destruction and the wider the zone of transition between tumor and normal bone. Aggressivity per se does not conclusively indicate malignancy, but the malignant tumors tend to be faster growing than their benign counterparts. Classification of the different patterns of bone destruction has not been bettered since Lodwick's seminal work [11, 12, 16, 17]. Each pattern reflects a particular growth rate and thereby a differential diagnosis [13, 18]. It must be noted that any classification is artificial and that a series of bone tumors will exhibit a spectrum of bone destruction from well-to ill-defined.

Geographic bone destruction. In this pattern the growth rate is sufficiently indolent that the lesion will appear well marginated with a thin zone of transition. The geographic or type I pattern may be subdivided into IA, IB and IC depending on the appearance of the margin and the effect on the cortex (Fig. 10). Type IA, the slowest growing of all the lesions and thereby the least aggressive, is typified by a sclerotic margin (Fig. 8). The thicker the sclerosis the slower rate of growth. The vast majority of these lesions will prove to be benign. In type IB the lesion is well defined without the sclerotic margin (Fig. 7). While still slow-growing, the rate is

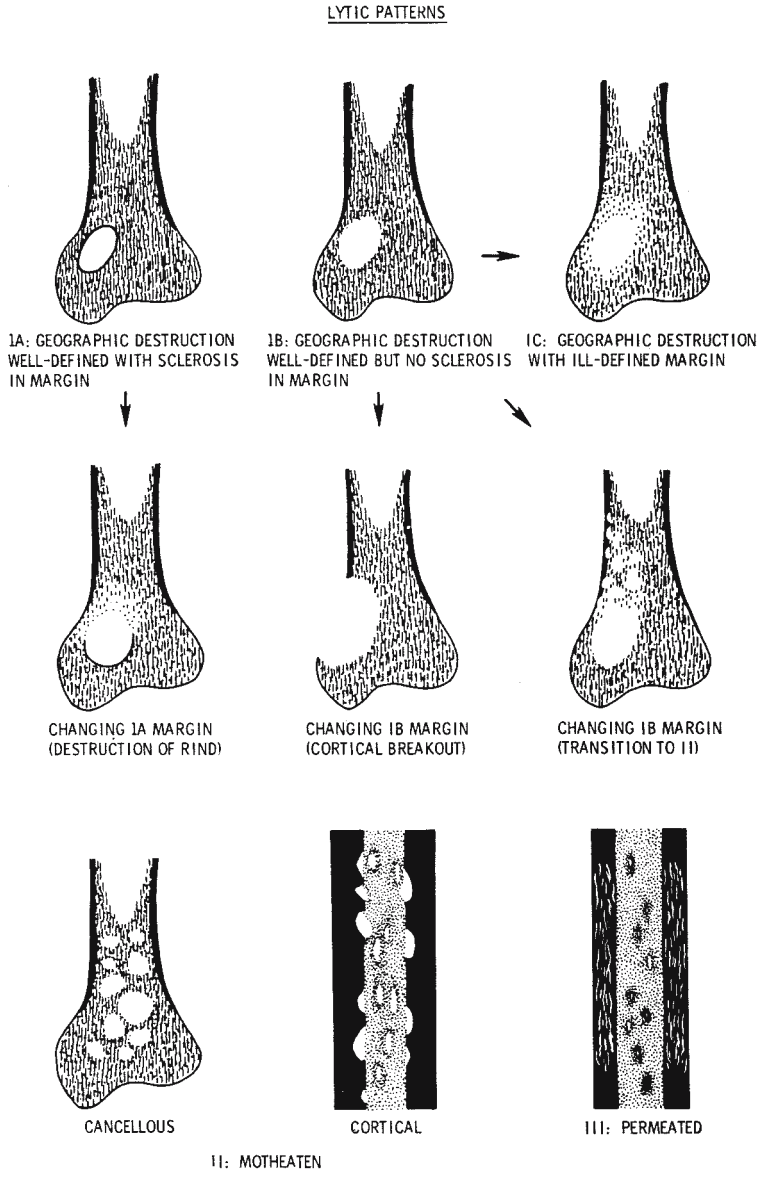

Fig. 10. Patterns of bone destruction and their margins. *Arrows* indicate the most frequent transitions or combinations of these margins. Transition implies increased activity and a greater probability of malignancy. (From [12], with permission)

slightly greater than type IA. Again, the majority of type IB lesions are benign, although some malignancies may on occasion demonstrate this pattern. In type IC the margin is less well defined, indicating a more aggressive pattern. The cortex is also destroyed. Few benign tumors exhibit a type IC pattern. The differential diagnosis in this situation includes giant cell tumor, malignant fibrous histiocytoma and lymphoma of bone.

Moth-eaten and permeative bone destruction. Moth-eaten (type II) and permeative (type III) patterns of bone destruction reflect the increasingly aggressive nature of these tumors compared with geographic lesions (Fig. 10). Again, this is a spectrum of change varying from multiple small areas of lysis to permeation, sometimes almost imperceptible radiographically, characterized by minute tiny cortical defects and a wide ill-defined zone of transition (Figs. 5, 11). The highly aggressive nature of these lesions does not allow the host bone sufficient time to react and produce a response [18]. Typically, malignancies, including metastasis, Ewing's sarcoma and osteosarcoma exhibit a moth-eaten or permeative appearance (Figs. 5, 11). Benign tumors in general do not show this pattern of bone destruction. Acute osteomyelitis may also give a moth-eaten pattern of bone destruction.

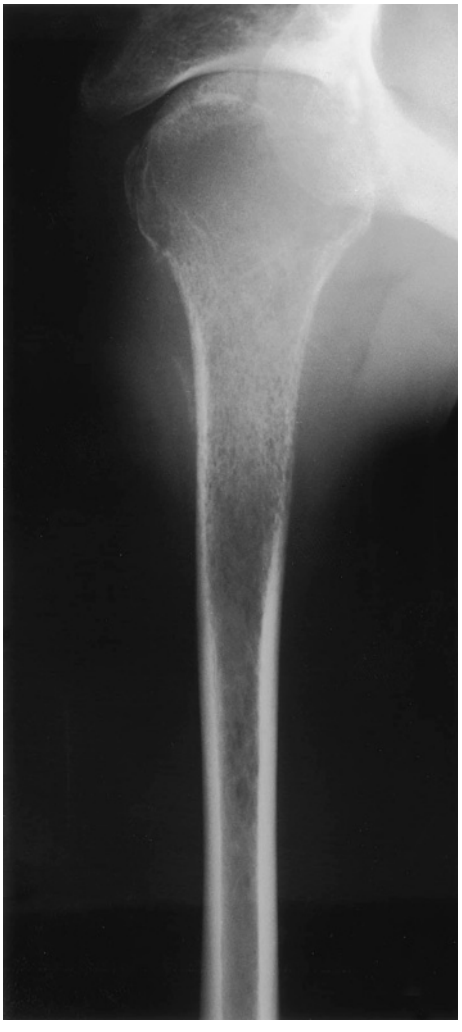

Fig. 11. AP radiograph of the humerus of a 22-year-old male showing an extensive Ewing's sarcoma. There is confluent lysis proximally and permeative bone destruction distally with a wide zone of transition

Periosteal Reaction

The periosteum is the thin layer of soft tissue with osteoblastic properties that lines the outer cortex of bone. It is normally radiolucent but will mineralize when the osteoid-producing cells of the inner cambium layer are stimulated by an adjacent osseous or paraosseous process. The rate of mineralization is partly dependent on the age of the patient. The younger the patient the more rapid the appearance of radiographic change and vice versa. Periosteal reaction, otherwise known as periosteal new bone formation, may occur in any condition which elevates the periosteum, whether it be blood, pus or tumor. The term "periostitis", favored in older texts, is best avoided as it infers an inflammatory etiology.

The appearance and nature of a periosteal reaction is frequently valuable in narrowing down the differential diagnosis of a bone tumor. A good, albeit complex, classification identified three broad categories; continuous, discontinuous or interrupted and complex (Fig. 12) [9, 19].

Continuous periosteal reaction. A continuous periosteal reaction may be observed with either an intact or a destroyed underlying cortex. In the latter the bone is said to be "expanded" but this is a misnomer as bone cannot be inflated like a balloon (Fig. 12) [19]. Nevertheless the term "cortical expansion" is well entrenched in common usage. It represents a relatively slow process by which endosteal bone resorption is balanced by periosteal new bone formation. In faster growing lesions the endosteal resorption will exceed periosteal apposition and a thin outer "shell" will be produced (Fig. 13). The thickness of this shell is an indicator of the rate of growth of the lesion but it is not a good discriminator of benign from malignant. Shells are typically found in benign lesions such as simple bone cyst, aneurysmal bone cyst (Fig. 13), chondromyxoid fibroma, fibrous dysplasia and giant cell tumor. They are also well recognized in "expansile" metastases of renal and thyroid origin and plasmacytoma. Additions to, rather than substitutes for, the original cortex occur with a continuous periosteal reaction with an intact cortex (Fig. 12). The periosteal reaction may be solid, a single lamella, lamellated or spiculated. The solid type implies the slow apposition of layers of new bone to the cortex, sometimes termed

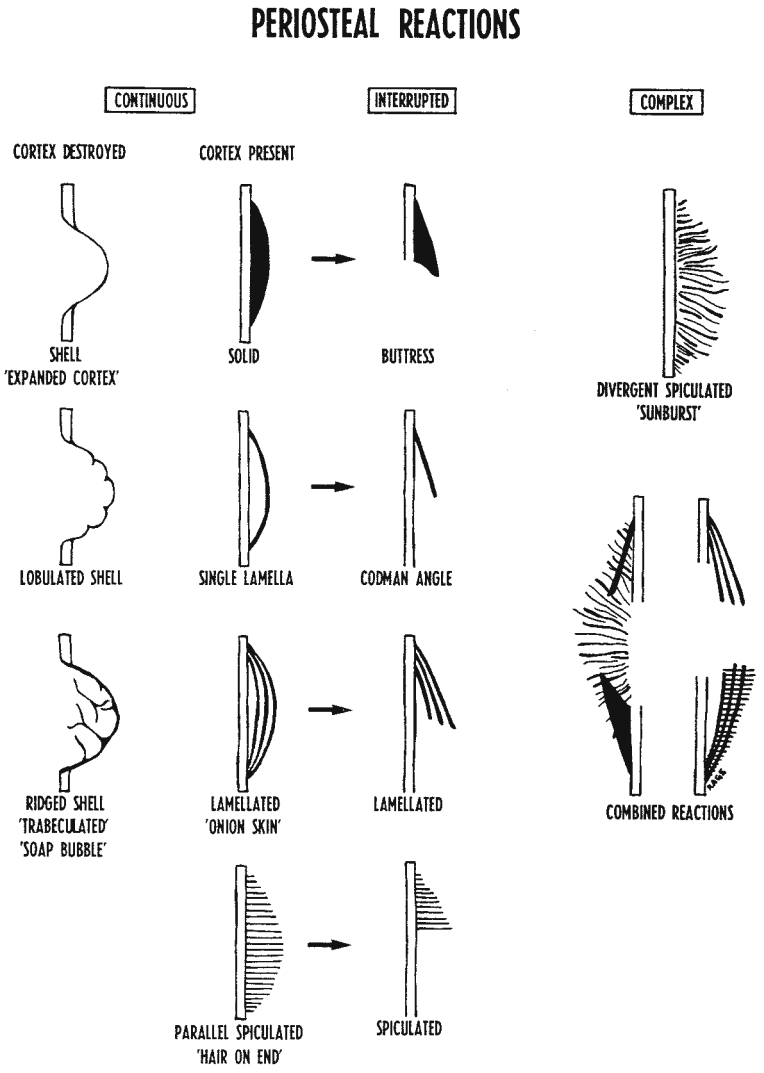

Fig. 12. Periosteal new bone patterns. The *arrows* indicate that the continuous reactions may be interrupted. (From [18], with permission)

"cortical thickening" or "cortical hyperostosis" [19]. It is seen in chondroma, central chondrosarcoma, and eccentrically in osteoid osteoma. If the solid periosteal reaction is extensive with an undulating quality the differential diagnosis includes chronic osteomyelitis, hypertrophic osteoarthropathy (Fig. 14), chronic lymphedema and varicosities.

A single lamellar periosteal reaction is formed by a thin radiodense line separated from the cortex by a narrow radiolucent zone (Fig. 15). It usually denotes a benign disorder and is frequently seen with traumatic and inflammatory conditions (Fig. 15). It should be appreciated that a periosteal reaction is a dynamic process and a single lamella may fill in to produce a solid appearance or go on to the addition of further lamellae. The lamellated periosteal reaction, otherwise known as onion-skin, is seen in Ewing's sarcoma (Fig. 5), osteosarcoma (Fig. 4), eosinophilic granuloma of the long bones in children and acute osteomyelitis.

A spiculated periosteal reaction occurs when the mineralization is oriented perpendicular to the cortex and denotes a more rapidly evolving process. It is typical of malignant tumors such as osteosarcoma and Ewing's sarcoma but may be seen in benign tumors such as meningioma, hemangioma of bone and non-neoplastic conditions such as thalassemia and thyroid acropachy. The location of a spiculated periosteal reaction significantly influences the differential diagnosis.

Discontinuous/interrupted periosteal reaction. In the interrupted periosteal reaction the mineralization has been breached in one of two ways (Fig. 12): either the process, usually a tumor, simply occupies the available space, or the rate of apposition is exceeded by resorption. Close attention should be paid to the margins of the periosteal reaction. Rapidly growing benign tumors may exhibit a peripheral wedge or buttress with a thin or even nonexistent shell. The buttress should be distinguished from the Codman angle which is the tri-

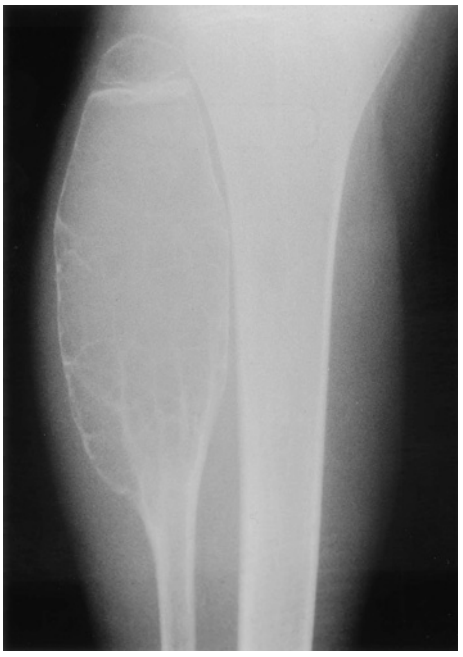

Fig. 13. AP radiograph of the proximal fibula of a 13-year-old male showing the typical expanded "shell" of an aneurysmal bone cyst

angular elevation of interrupted periosteum with one or more layers of new bone located at the periphery of the lesion (Figs. 4, 5) [20]. This pattern is suggestive, if not diagnostic, of malignancy as it may also be seen in osteomyelitis. In malignant bone tumors the site of interruption of a periosteal reaction is usually the area of maximum extraosseous tumor growth.

Combined/complex periosteal reaction. More than one pattern of periosteal reaction may be manifest in the same case and reflects the varying rate of growth at different sites in the lesion (Fig. 12). The divergent spiculated periosteal reaction, otherwise known as "sunburst," is a typical example of a complex pattern and is suggestive of osteosarcoma (Figs. 4, 16).

Matrix

A number of tumors produce a matrix, the intercellular substance, that can calcify or ossify. The radiodense foci should be differentiated from other causes of calcifications such as fracture callus, sclerotic response adjacent to a tumor, necrotic debris and dystrophic calcification. Radiodense tumor matrix is either osteoid or chondroid. The exception is fibrous dysplasia, where the collagenous matrix may be sufficiently dense to give a ground-glass appearance (Fig. 17).

Tumor osteoid is typified by solid (sharp-edged) or cloud to ivory-like (ill-defined edge) patterns (Figs. 4, 9, 18, 19) [21]. Tumor cartilage is variously described as

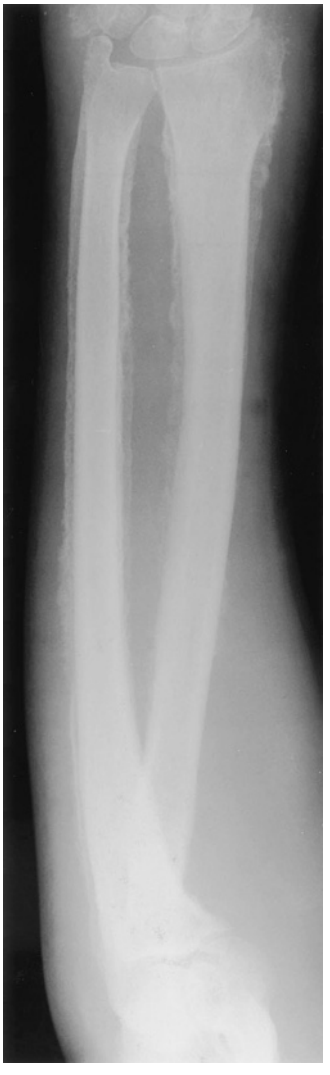

Fig. 14. Radiograph of the forearm bones of a 72-year-old male with a history of bronchial carcinoma showing florid periosteal new bone due to hypertrophic osteoarthropathy

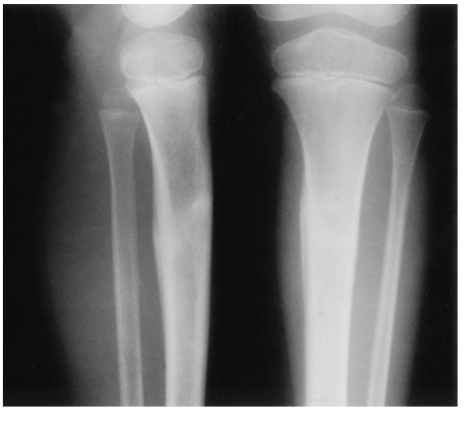

Fig. 15. AP and lateral radiographs of the tibia of a 7-year-old female showing the typical lamellar periosteal reaction of a tibial stress fracture which is frequently mistaken for a sarcoma

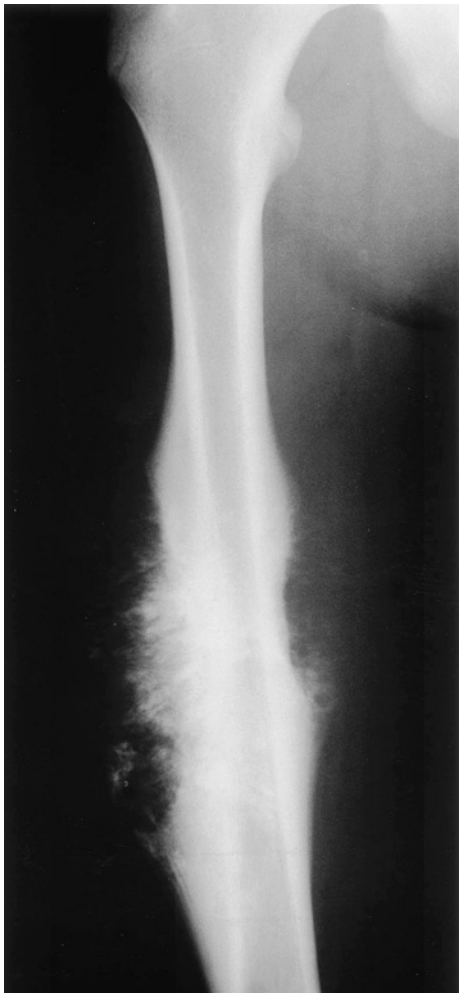

Fig. 16. AP radiograph of the femur of a 17-year-old male showing the spiculated periosteal new bone formation of a periosteal osteosarcoma

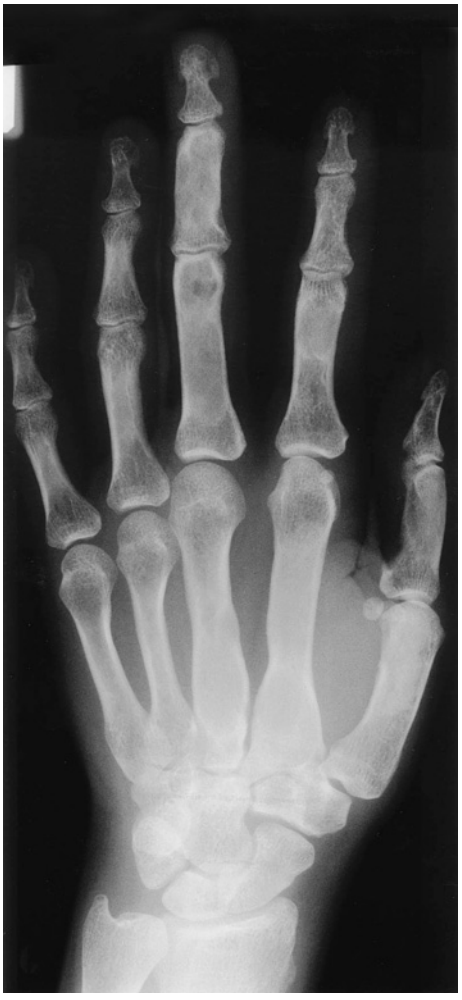

Fig. 17. Radiograph of the hand showing polyostotic fibrous dysplasia with the typical ground-glass matrix

stippled, flocculent, ring and arc and popcorn in appearance (Figs. 2, 18, 20) [21]. Identifying the pattern of matrix calcification will significantly reduce the differential diagnosis, but matrix per se has no influence as to whether the lesion is benign or malignant (Figs. 2, 20). The distribution can be helpful. For example, both enchondroma and medullary infarction may show calcification of a similar nature. The distribution is typically central in enchondroma (Fig. 2) and peripheral in medullary infarction.

CT and MR Imaging in Diagnosis

The principal role of CT and MR imaging in the management of the patient with a suspected bone tumor is in staging. In selected cases both techniques can be useful in establishing a differential diagnosis. The CT features that should be assessed are similar to those previously described when evaluating the radiographs. This reflects the fact that both are radiographic techniques relying on the attenuation of an X-ray source. Cortical breaching, soft tissue extension and faint mineralization are all more readily appreciated on CT scans than on radiographs. This is of particular value in complex anatomical areas such as the pelvis and spine. Although the physical basis of MR imaging is different, similar morphological information can be easily identified. The exception are the signal voids of fine mineralization which can be easily missed on MR imaging. Potentially misleading MR features that might suggest a sarcoma are prominent marrow edema and soft tissue edema. These are however common with osteoid osteoma, osteoblastoma, chondroblastoma, stress fractures and infection.

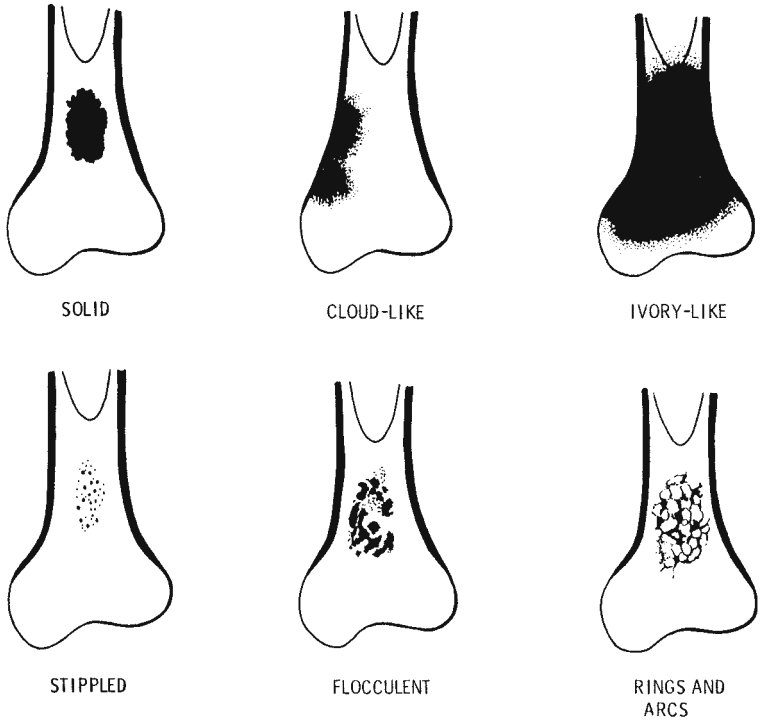

Fig. 18. Mineralized matrix patterns. Tumor osteoid (*top row*) appears as increased density with a solid (sharp-edged) or cloud to ivory-like (ill-defined edge) pattern. Tumor cartilage (*bottom row*) creates stippled, flocculent, and solid density patterns. Rings and arcs represent bony rims around tumor cartilage lobules. (From [20], with permission)

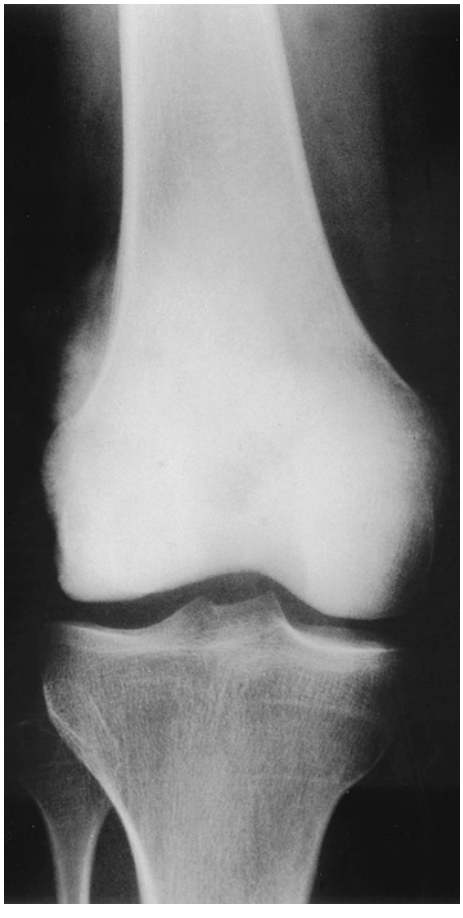

Fig. 19. AP radiograph of the knee of a 20-year-old male showing a sclerotic osteosarcoma of the distal femur indicated by the ivory-like tumor osteoid

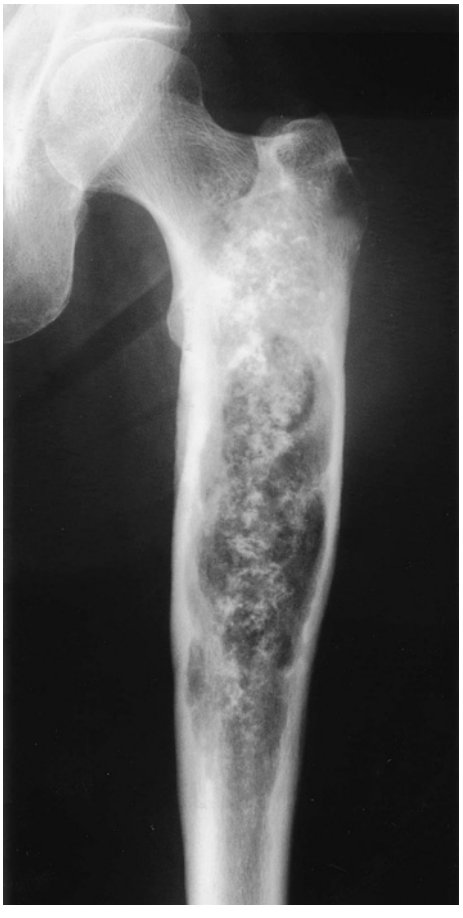

Fig. 20. AP radiograph of the proximal femur of a 64-year-old female showing an extensive central chondrosarcoma. The tumor is mildly expansile with endosteal scalloping and typical popcorn cartilage mineralization

The majority of tumors will have prolonged T1 and T2 relaxation times, thereby showing low to intermediate signal in T1-weighted and high signal on T2-weighted sequences. Close attention to the morphological and signal characteristics may on occasion yield additional diagnostic information. For example, hyperintensity on T1-weighted images within the lesion suggests subacute hemorrhage or the presence of paramagnetic material such as melanin (Fig. 1). Fluid-fluid levels are well demonstrated on both CT and MR imaging in a large number of different musculoskeletal conditions. In the immature skeleton with the appropriate radiographic appearances, fluid-fluid levels are most commonly seen in aneurysmal bone cysts (ABCs) (Fig. 21) [22]. The most important differential diagnosis in this situation is a telangiectatic osteosarcoma which frequently contains fluid-fluid levels.

Dynamic contrast-enhanced MR imaging has been used to differentiate benign from malignant bone lesions using the slope of the derived time-intensity curves [23]. Benign bone lesions tend to show a low slope as compared with the high or steep slope of malignant lesions. Although many of the studies show a highly statistically significant difference in the slope values of benign and malignant lesions, there is considerable overlap such that this technique is of limited value in routine practice. For example, highly vascularized or perfused lesions in children such as ABC, LCH, osteoid osteoma and acute osteomyelitis may all show slope values in the malignant tumor range.

Tumor Mimics

There is a large number of disparate bone conditions which can have similar imaging appearances to tumors. What constitutes a tumor mimic depends very much on the expertise of the individual reviewing the imaging. The majority can be classified as normal variants, post traumatic and inflammatory conditions. In the adolescent patient, stress fractures and chronic apophyseal avulsion injuries are frequently mistaken for an osseous malignancy (Fig. 15) [24, 25]. Acute osteomyelitis, at any age, but typically in children, will have an aggressive radiographic appearance thereby simulating malignancy.

There are a number of unrelated non-neoplastic or benign neoplastic lesions which, over the years, have been lumped together and given the term “don’t touch me lesions”. The radiographic diagnosis of these conditions to the experienced, is straightforward and further imaging and biopsy are not indicated in the majority of cases. This category includes fibrous cortical defect, bone island, small foci of fibrous dysplasia and the distal femoral cortical irregularity (periosteal desmoid).

Pathological Correlates

Not surprisingly, the features that are relied upon to help establish a radiological diagnosis or differential diagnosis (vide supra) are also employed by the pathologist when examining the gross and microscopic features of the biopsied, curetted or resected specimen. In addition, to help establish a diagnosis, the pathologist will rely on “high resolution” features that are not apparent to the radiologist e.g. cellular architectural formations, cytological features, mitotic rate etc. The affected bone, and the site of the lesion within bone, will only be apparent to the pathologist on an excised specimen. On curetted or biopsied bone lesions, it is essential that the pathologist be given this critical information.

The pattern of bone destruction seen radiologically can be appreciated pathologically. Enchondromas often show encasement by host bone (Fig. 22), other benign tumors (with the exception of hemangioma) show an abrupt transition from the lesion to reactive host bone. Malignant bone tumors show a permeative growth pattern with entrapment of lamellar (i.e. pre-existing) bone by the neoplasm.

Normal periosteum is composed of a thin covering of fibroblastic tissue which has an osteogenic (and sometimes chondrogenic) potential. It is composed of

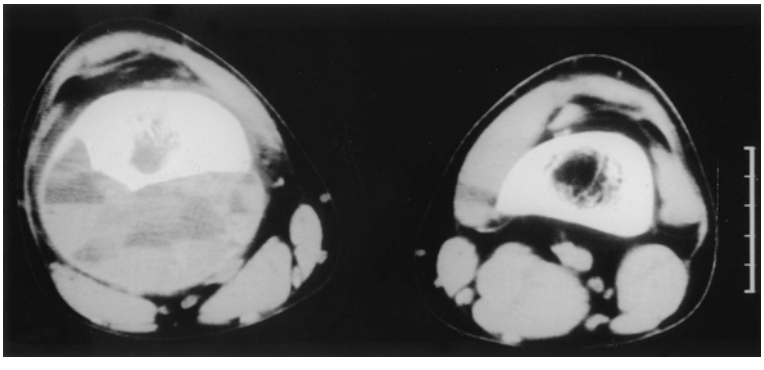

Fig. 21. Axial CT through the distal femora of a 19-year-old male. Lytic expansile lesion arising from the posterior aspect of the right femoral metaphysis containing multiple fluid-fluid levels typical of an aneurysmal bone cyst

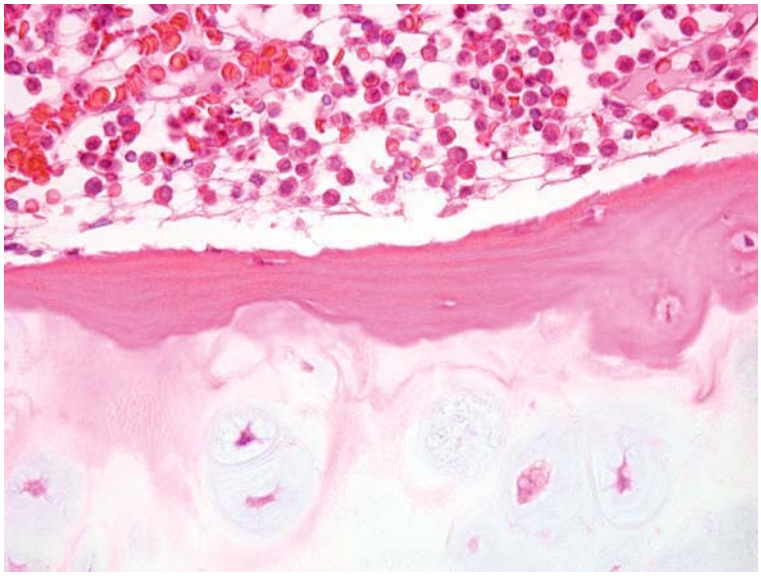

Fig. 22. Histological section of the edge of an enchondroma (hematoxylin & eosin, H&E) showing the features of "bony encasement". The tumor growth rate is so slow that there has been deposition of orderly, lamellar bone on the surface. Adjacent to the encasing bone is normal hematopoietic marrow

an inner cambium layer and an outer fibrous layer. The cambium layer is applied directly to the outer cortex and shares collagen fibers with cortical bone (so-called Sharpey's fibers) (Fig. 23). As such, subperiosteal lesions create and occupy a potential space. As indicated above, an elevated periosteum may be intact or disrupted (Fig. 24). In either case, elevation of the periosteum stimulates it to produce new bone. The patterns of new bone formation are discussed above (section 3.11). The histologic appearance of radiologically apparent matrix is predictable. Matrices that are apparent radiologically are due to calcification/mineralization seen in bone, cartilage and dystrophically calcified tissue.

Staging

Accurate surgical staging is a fundamental requisite of all oncological imaging. The staging system universally used for bone tumors is that adopted by the Musculoskeletal Tumor Society [26]. This assigns one of three grades according to the local extent of the tumor, presence or absence of metastases and the histological grade (Table 1). Classification of the first two features of the staging system relies entirely on imaging. However, the grade of the tumor is obviously determined by histological examination of the biopsy specimen and confirmed by review of the whole specimen following the defini-

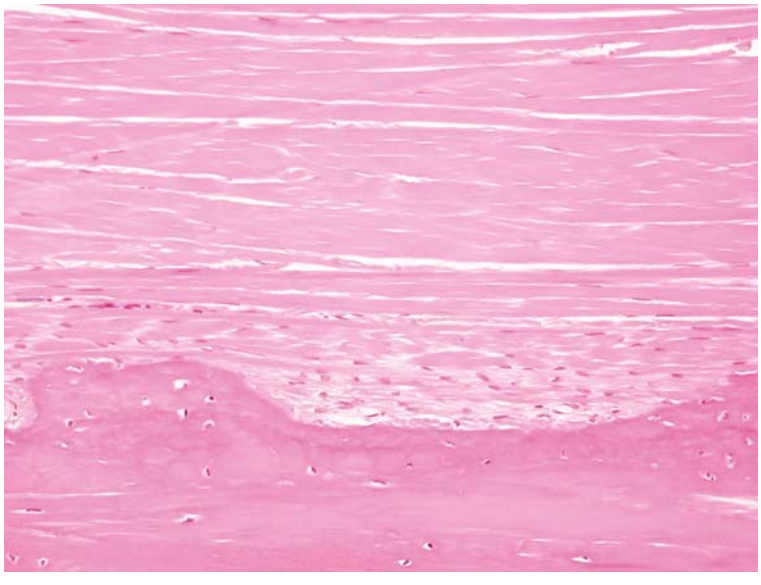

Fig. 23. Histological section of normal, relatively inactive periosteum (H&E). The outer fibrous layer is densely collagenous and relatively hypocellular. The inner cambium layer is more cellular and applied directly to the outer surface of the cortex

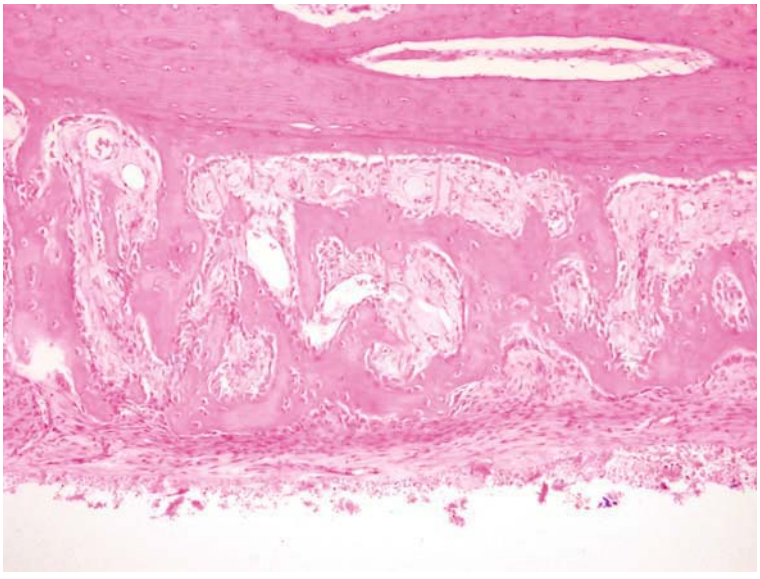

Fig. 24. Histological section of elevated periosteum (H&E). There are new trabeculae of woven bone between the cellular, elevated periosteum and the cortical lamellar bone. Any process that elevates periosteum will produce a similar effect

tive surgery. The value of a straight-forward staging system, such as this, is that it is easily applied, correlates well with prognosis and allows valid comparison of studies of differing treatments and treatment centers.

Determination of local tumor extent usually relies on MR imaging. One study has shown CT to be as good as MR imaging in staging [27], although there has been some doubt expressed as to whether the technique and quality of technology used in that multicenter study were strictly comparable [28]. However, where access to MR imaging remains limited, CT is an adequate alternative, albeit with significant radiation burden. The MR scan should preferably be performed before the biopsy as the trauma of the procedure may result in hemorrhage and edema which can exaggerate the true extent of the tumor. A T1-weighted sequence oriented along the long axis of the affected bone should be performed first as it offers excellent signal-to-noise ratio and resolution and is particularly sensitive to bone marrow changes (Figs. 1, 25A) [29]. It is used to define the extent of the tumor in bone. Further sequences should be performed at right angles to the first and, to give good resolution between the soft tissues and the tumor, should be a T2-weighted sequence with, if available, fat suppression. Alternatively, a STIR sequence may be preferred. The STIR sequence, due to its sensitivity to edema, will tend to overestimate the extent of a tumor both in bone and the surrounding soft tissues [30] Remaining sequences can be tailored to the particular case. The extent of the tumor in bone and soft tissue should be accurately measured and the relationship to the neurovascular structures and adjacent joint assessed.

It is important to include an anatomical reference point on at least one of the sequences in order that measurements of the tumor can be related to a relevant point. The adjacent joint margin will usually suffice for this purpose. A scale should be included on all hardcopy produced. Although small field of view scans ensure good demonstration of tumor details, a large field of view T1-weighted sequence should be included to confirm or exclude skip metastases (Fig. 25B). Gd-DTPA has little value in the initial staging [31]. It may help distinguish subsynovial spread from true joint invasion and a dynamic contrast-enhanced scan may be obtained at this stage as a baseline study for the subsequent assessment of tumor response to chemotherapy.

For exclusion/confirmation of pulmonary metastases, chest CT is required. The sensitivity of pulmonary CT has been improved with the introduction of spiral CT [32]. Overstaging with spiral CT is a potential hazard as up to 70% of solitary nodules less than 5 mm in diameter at initial presentation in children with solid extra-thoracic tumors may be benign [33].

Bone scintigraphy is used to exclude skeletal metastases. It is important to correlate scintigraphic abnormalities with radiographs of the relevant area. Scintigraphy can also be valuable in the detection of skip metastases (Fig. 25C). Skip metastases may not always be visible on scintigraphy, hence the value of MR imaging [34].

Table 1. Staging system of the musculoskeletal tumor society [26]

Stage	Description
IA	Low-grade intracompartmental lesion
IB	Low-grade extracompartmental lesion
IIA	High-grade intracompartmental lesion
IIB	High-grade extracompartmental lesion
III	Metastatic disease at presentation

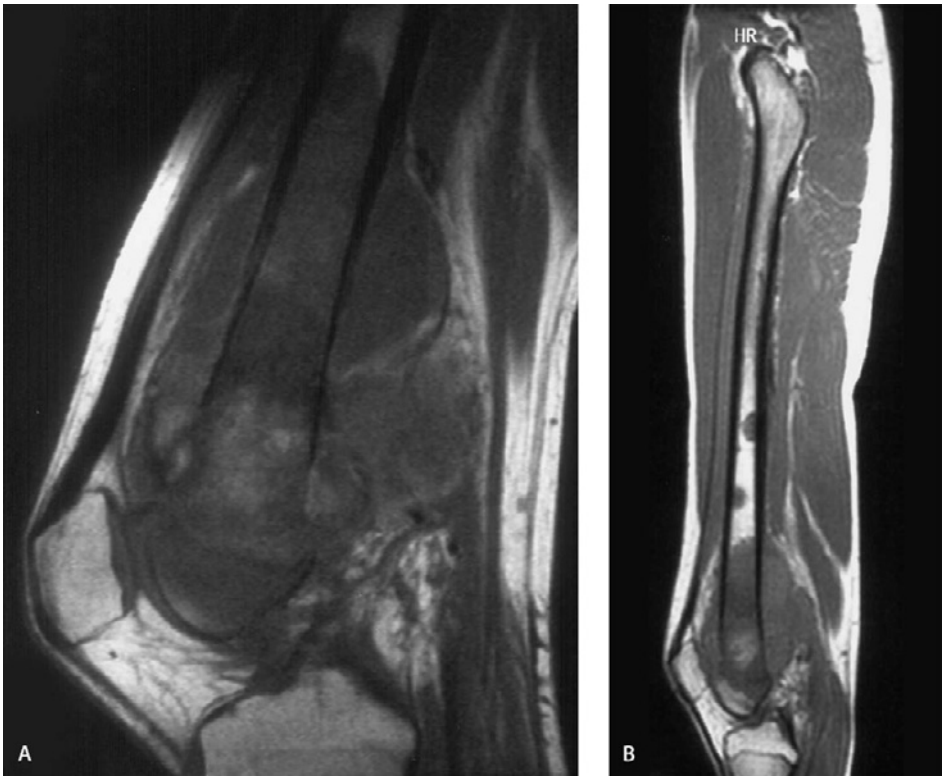

Fig. 25A–C. Osteosarcoma of the distal femur. The small field of view sagittal T1-W image (**A**) shows good detail of the primary tumour but fails to show the two more proximally located skip metastases evident on the large field of view sagittal T1-W images (**B**). Bone scintigraphy (**C**) shows increased activity both in the primary tumour and the two skip metastases

Biopsy

With the exception of the "don't touch me lesions", verification of the radiological diagnosis will require a biopsy to complete the staging prior to management decisions. Conventional fluoroscopy is usually adequate in most cases but CT fluoroscopy can be useful when biopsying small or relatively inaccessible lesions. Problems associated with biopsy occur up to 5-times more commonly when it is performed at the referring hospital rather than at the specialist treatment center [35]. Biopsy techniques vary between units. Some advocate fine needle aspiration, others needle biopsy or open biopsy. The expertise required applies as much to the pathologist interpreting the specimen as to the individual responsible for obtaining it. It is important that the biopsy tract is placed so that it will be fully excised at the time of definitive surgery.

Assessment of Tumor Response to Chemotherapy

Most patients with a biopsy-proven sarcoma of bone will be entered into one of the international adjuvant chemotherapy trials prior to undergoing definitive surgery. The exception is chondrosarcoma which is not sensitive to chemotherapy or radiotherapy. After a predetermined number of cycles of chemotherapy and immediately before surgery, the patient is re-staged with a MR scan of the primary tumor and a CT scan of the chest. This is to ensure that the stage of the tumor has not altered and that the planned surgery is still appropriate. Also, this is an opportunity to use imaging to assess the response of the tumor to the chemotherapy. Histological response to chemotherapy expressed as percentage necrosis is one of the most important prognostic indicators in both osteosarcoma and Ewing's sarcoma. Over the years all types of imaging have been used to estimate the response to chemotherapy.

Post-chemotherapeutic radiographic and CT findings do not consistently differentiate the good from poor responder [36]. For example, an increase in tumor volume may suggest a poor response but may also rep-

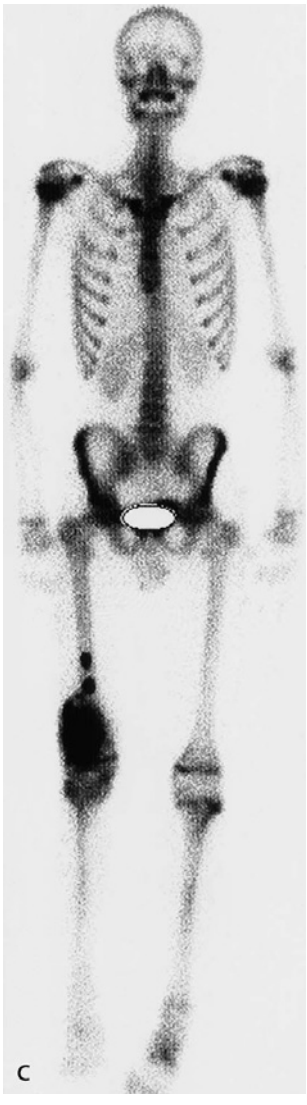

Fig. 25C.

resent hemorrhage secondary to necrosis in a responsive tumor [37].

If there is a significant extra-osseous component to the tumor, Doppler ultrasound can be used to monitor response [38]. This is potentially attractive in children as prolonged immobility is not required. However, the technique is operator dependent which may affect reproducibility of results on sequential scanning.

Scintigraphy using technetium-99m methylene diphosphonate, thallium-201, gallium-67 and FDG-PET scanning have all been advocated in the estimation of tumor response [36]. Inherent in all is the limited anatomical resolution and, with PET scanning, limited availability. To date, these techniques are largely reserved for research purposes.

Unenhanced MR imaging has a limited role. Increased or unchanged tumor volume and increased peritumoral edema after chemotherapy suggest a poor histological response in osteosarcoma and Ewing's sarcoma. Virtual obliteration of the extra-osseous component combined with a hypointense rim in Ewing's sarcoma usually indicates a good response. It is however, impossible to exclude small foci of viable tumor without contrast medium. Standard contrast-enhanced MR imaging is also of limited value as viable tumor, revascularized necrotic tissue, reactive hyperemia, etc. may all enhance. It is for this reason that much of the work on imaging assessment of sarcoma response to chemotherapy over the past decade has concentrated on dynamic contrast-enhanced MR imaging. A number of different techniques have been described but all rely on the underlying principle that viable tumor enhances rapidly (i.e. within seconds of the contrast medium arriving in the adjacent artery) whereas all other enhancing tissues take much longer. It is possible on the console of most modern scanners to plot a time/intensity curve showing the uptake of the contrast medium. By comparing the curve obtained before commencement of chemotherapy with that obtained after, the tumor response can be estimated. It should be noted that this is a time-consuming and costly exercise with numerous variables that directly influence patient management in few cases.

Follow-up

Assuming that the patients do not have stage III disease (i.e. metastases) either at presentation or developing during preoperative chemotherapy, they are closely monitored for evidence of local recurrence [39], metastatic disease [40] and complications of treatment.

Local recurrence is almost inevitable if the original resection margin was not wide. Recurrence may be detected on radiographs as a soft tissue mass with or without bone destruction. Locally recurrent bone sarcoma will usually occur within the soft tissues at the site of the initial surgery as the host bone will have been excised and replaced with a prosthesis. Detection on radiographs is easier if there is evidence of matrix mineralization. Recurrent tumors with the propensity to mineralise (i.e. osteosarcoma) will usually exhibit focally increased activity on scintigraphy, but it is rarely used for this purpose.

MR imaging is the technique of choice in the detection of early recurrence when local control may still be surgically achievable. While ultrasound does have some attractions [41], MR imaging will still be required for preoperative evaluation if a recurrence is identified (Fig. 26). Depending on the presence or absence of mineralization, most recurrences will show a high signal intensity mass on T2-weighted or STIR images. Diffuse high signal intensity is frequently seen shortly after surgery or can be prolonged following radiation therapy

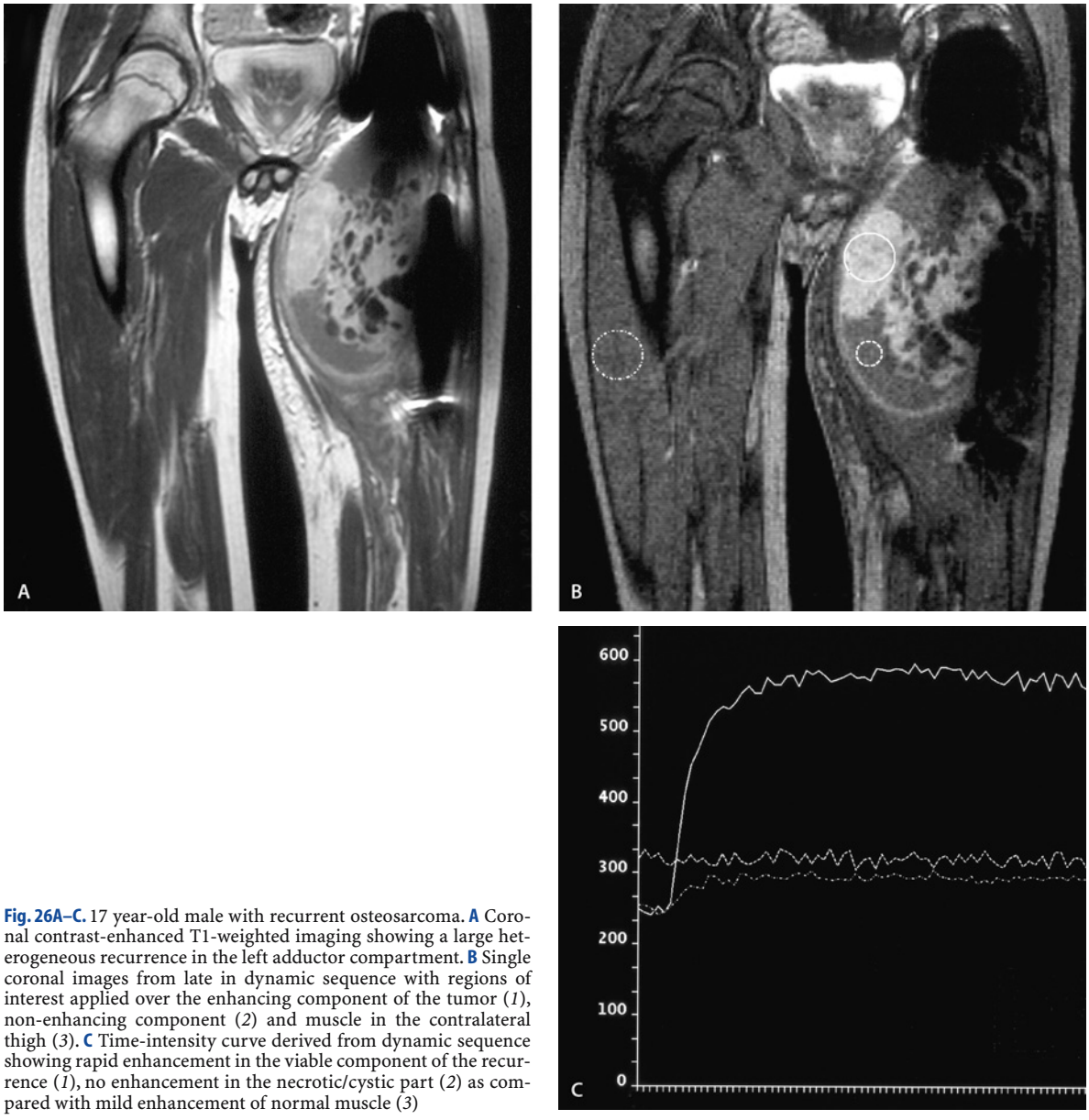

Fig. 26A–C. 17 year-old male with recurrent osteosarcoma. **A** Coronal contrast-enhanced T1-weighted imaging showing a large heterogeneous recurrence in the left adductor compartment. **B** Single coronal images from late in dynamic sequence with regions of interest applied over the enhancing component of the tumor (*1*), non-enhancing component (*2*) and muscle in the contralateral thigh (*3*). **C** Time-intensity curve derived from dynamic sequence showing rapid enhancement in the viable component of the recurrence (*1*), no enhancement in the necrotic/cystic part (*2*) as compared with mild enhancement of normal muscle (*3*)

[42]. Contrast medium may be required to distinguish enhancing recurrent tumor from seromas, hematomas etc.

It is generally accepted that it is usually the metastatic disease that will eventually kill the patient and not the primary tumor itself. It is for this reason that follow-up imaging is concentrated on the site where the metastases are likely to occur, namely the lungs. Chest radiographs are usually considered adequate. Serial chest CT scans are of doubtful value in view of the considerable radiation dose involved.

The natural history of osteosarcoma has been modified by chemotherapy in that up to 20% of those who develop metastases will first do so in bone prior to there being any evidence of pulmonary metastases. The prognosis for a patient with osseous metastases is so poor that serial follow-up scintigraphy is unlikely to modify the outcome. Scintigraphy is indicated should a patient on follow-up develop bone pain. Sarcoma metastases to other sites, such as the central nervous system and viscera, are uncommon and are usually a late manifestation of the disease [40].

It should be recognized that the prolonged medical and surgical management of a child with a sarcoma is not without risk of complications. Prostheses may become loose or infected or require replacement if the

child has outgrown the extended length of a growing prosthesis [43]. Allografts may also become infected and are prone to fracture. In the long-term follow-up of patients who received radiotherapy, pain or functional impairment within the radiation field should lead to consideration of bone necrosis or radiation-induced sarcoma.

Conclusions

Imaging, with all its different techniques, has a role in the management of the patient with a bone sarcoma from initial detection and diagnosis to follow-up after definitive surgery. No imaging investigation should be reported in isolation without knowledge of relevant clinical details and results of prior investigations. If the diagnosis is in doubt, the old adage biopsy the infection and culture the tumor is appropriate. The importance of the multidisciplinary approach in the management of bone sarcomas cannot be overemphasized.

References

1. Kropei D, Schiller C, Ritschl P, Saltzer-Kuntschik M, Kotz R (1991) The management of IIB osteosarcoma. Clin Orthop 270:40–44
2. Veth RP (1991) IIB osteosarcoma. Clinical management, local control and survival statistics -The Netherlands. Clin Orthop 270:67–73
3. Simon MA, Aschliman MA, Thomas N, Mankin HJ (1986) Limb salvage treatment versus amputation of osteosarcoma of the distal end of the femur. J Bone Joint Surg Am 68: 1331–1337
4. Muscolo DL,Ayerza MA, Mokino A, Costa-Paz M, Aponte-Tinao LA (2003) Tumors above the knee misdiagnosed as athletic injuries. J Bone Joint Surg Am:85:1209–1214
5. Grimer RJ, Sneath RS (1990) Diagnosing malignant bone tumors: editorial. J Bone Joint Surg Br 72:754–756
6. Ardran GM (1951) Bone destruction not demonstrable by radiography. Br J Radiol 24:107–109
7. Edelstyn GA, Gillespie PJ, Grebbel FS (1967) The radiological demonstration of osseous metastases: experimental observations. Clin Radiol 18:158–162
8. Algra PR, Heimans JJ, Valk J, Nauta JJ, Lachniet M, Kooten van B (1991) Do metastases in vertebra begin in the body or the pedicles? Am J Roentgenol 158:1275–1279
9. Moser RP, Madewell JE (1987) An approach to primary bone tumors. Radiol Clin North Am 25:1049–1093
10. Kricun ME (1983) Radiographic evaluation of solitary bone lesions. Orthop Clin North Am 14:39–64
11. Lodwick GS (1965) A probabilistic approach to the diagnosis of bone tumors. Radiol Clin North Am 3:487–497
12. Lodwick GS (1966) Solitary malignant tumors of bone: the application of predictor variables in diagnosis. Semin Roentgenol 1:293–313
13. Madewell JE, Ragsdale BD, Sweet DE (1981) Radiologic and pathologic analysis of solitary bone lesions. Part I: Internal margins. Radiol Clin North Am 19:715–748
14. Kenan S, Abdelwahab IF, Klein MJ, Herman G, Lewis MM (1993) Lesions of juxtacortical origin (surface lesions of bone). Skeletal Radiol 22:337–357
15. Seeger LL, Yao L, Eckardt JJ (1998) Surface lesions of bone. Radiology 206:17–33
16. Lodwick GS, Wilson AJ, Farrell C, Virtama P, Dittrich F (1980a) Determining growth rates of focal lesions of bone from radiographs. Radiology 134:577–583
17. Lodwick GS, Wilson AJ, Farrell C, Virtama P, Dittrich F (1980b) Estimating rate of growth in bone lesions: observer performance and error. Radiology 134:585–590
18. Kricun ME (1993) Parameters of diagnosis. In: Imaging of bone tumors. Saunders, Philadelphia, pp 2–45
19. Ragsdale BD, Madewell JE, Sweet DE (1981) Radiologic and pathologic analysis of solitary bone lesions. Part II. Periosteal reaction. Radiol Clin North Am 19:749–783
20. Codman EA (1926) Registry of bone sarcoma. Surg Gynecol Obstet 42:381–393
21. Sweet DE, Madewell JE, Ragsdale BD (1981) Radiologic and pathologic analysis of solitary bone lesions. Part III. Matrix patterns. Radiol Clin North Am 19:785–814
22. Davies AM, Cassar-Pullicino VN (1992) The incidence and significance of fluid-fluid levels on computed tomography of osseous lesions. Br J Radiol 65:193–198
23. Verstraete KL,De Beene Y, Roels H, Dierick A, Uyttendale D, Kunnen M (1994) Benign and malignant musculoskeletal lesions: dynamic contrast-enhanced MR imaging. Radiology 192:835–843
24. Davies AM, Evans N, Grimer RJ (1988) Fatigue fractures of the proximal tibia simulating malignancy. Br J Radiol 61:903–908
25. Davies AM, Carter SR, Grimer RJ, Sneath RS (1989) Fatigue fractures of the femoral diaphysis in the skeletally immature simulating malignancy. Br J Radiol 62:893–896
26. Enneking WF, Spanier SS, Goodman MA (1980) A system for the surgical staging of musculoskeletal sarcoma. Clin Orthop 153:10
27. Panicek DM, Gatsonis CG, Rosenthal DI, Seeger LL, Huvos AG, Moore SG, Caudry DJ, Palmer WE, McNeil BJ (1997) CT and MR imaging in the local staging of primary malignant musculoskeletal neoplasms: report of the radiology diagnostic oncology group. Radiology 202:237–246
28. Steinbach L (1998) CT and MR imaging in the local staging of primary malignant musculoskeletal neoplasms:comment. Sarcoma 2:57–58
29. Saifuddin A (2002) The accuracy of imaging in the local staging of appendicular osteosarcoma. Skeletal Radiol 31:191–201
30. Onikul E, Fletcher BD, Parham DM, Cheng (1996) Accuracy of MR imaging for estimating intraosseous extent of osteosarcoma. AJR Am.J. Roentgenology 167:1211–1215
31. Seeger L, Widoff BE, Bassett LW, Rosen G, Eckardt JJ, (1991) Preoperative evaluation of osteosarcoma: value of gadolinium dimeglimine-enhanced MR imaging. AJR Am J Roentgenol 157:347–351
32. Ginsberg MS, Panicek DM (2000) Subcentimetre pulmonary nodules detected in patients with sarcoma. Sarcoma 4:63–66
33. Grampp S. Bankier AA, Zoubek A, Wiesbauer P, Schrotb B, Henk CB, Grois N, Mostbeck GH (2000) Spiral CT of the lung in children with malignant extra-thoracic tumors: distribution of benign vs malignant pulmonary nodules. Eur Radiol 10:1318–1322
34. Bhagia SM, Grimer RJ, Davies AM, Mangham DC (1997) Scintigraphically negative skip metastases in osteosarcoma. Eur Radiol 7:1446–1448
35. Mankin HJ, Mankin CJ, Simon MA (1996) The hazards of biopsy revisited. J Bone Joint Surg Am 78:656–663
36. Shapeero LG, Vanel D (2000) Imaging of the response of high-grade osteosarcoma and Ewing sarcoma to chemotherapy with emphasis on dynamic contrast-enhanced MR imaging. Semin Musculoskeletal Radiol 4:137–146
37. Van der Woude, Bloem JL, Hogendoorn PCW (1998) Pre-operative evaluation and monitoring chemotherapy in patients with high-grade osteogenic and Ewing's sarcoma, review of current imaging modalities. Skeletal Radiol 27:57–71
38. Van der Woude HJ, Bloem JL, Van Oostayen JA, Nooy MA, Taminiau AH, Hermans J, Reynierse M (1995) Treatment of high-grade bone sarcomas with neoadjuvent chemotherapy: the utility of sequential color Doppler sonography in predicting histopathologic response. AJR Am J Roentgenol 165: 125–133

39. Davies AM, Vanel D (1998) Follow-up of musculoskeletal tumors. 1. Local recurrence. Eur Radiol 8:791–799
40. Bearcroft PWP, Davies AM (1999) Follow-up of musculoskeletal tumors. 2. Metastatic disease. Eur Radiol 9:192–200
41. Choi H, Varma DgK, Fornage BD, Kim EE, Johnston DA (1991) Soft-tissue sarcoma: MR imaging vs sonography for detection of local recurrence after surgery. Radiology 157:353–358
42. Richardson ML, Zink-Brody GC, Pattern RM, Koh WJ, Conrad EU (1996) MR characterization of post-irradiation soft tissue edema. Skeletal Radiol 25:537–543
43. Kaste SE, Neel MN, Rao BN, Thompson VF, Pratt CB (2001) Complications of limb-sparing procedures using endoprosthesis replacements about the knee for paediatric skeletal sarcomas. Paediatric Radiol 31:62–71

Arthritis

Iain Watt

6.3

Contents

Introduction

Arthritis is a major cause of debility in the world, particularly in the developed world, where increasing demands are made by ageing populations to retain full physical function in a pain-free fashion. Whilst attention has been focused on the inflammatory arthritides, most noticeably rheumatoid arthritis (RA), an increasing awareness of the significance of osteoarthritis has become noticeable in the last 5–10 years. This chapter will review the major pathological and radiological changes that occur in joints during disease and will attempt to refocus attention away from a pattern recognition approach to one of analysing the underlying pathological processes and repair mechanisms.

Clearly, arthritis may involve a single joint, a group of joints or it may be truly polyarticular. Whilst each of the categories carries its own differential diagnosis, from the point of view of any one involved joint, it matters not whether it is alone or one of many. Thus, all of the pertinent arthritides will be viewed from the perception of a single joint becoming abnormal.

It is important to remember that a joint is a complex organ comprising capsule, synovium, cartilage and bone [1]. Further, muscles, ligaments and tendons control and stabilise an individual joint. All of these structures interrelate either directly or indirectly by virtue of exudates or transudates. In addition, not all joints are the same. The majority of the important joints used in day-to-day living are true synovial joints, that is the capsule is lined with synovium and movement occurs by virtue of hyaline cartilage. Obvious examples of these include the knee and hip joints. Other joints are truly fibrous, as in a synostosis, and some fibrocartilaginous, for example the symphysis pubis. However, effectively most of the arthritides involve synovial joints and therefore this chapter will focus on them.

As indicated, a synovial joint comprises a number of important interrelated structures. Synovitis cannot occur in isolation without altering the quality of joint fluid, which in turn has an effect on hyaline cartilage and subchondral bone. However, for convenience of learning, it is easier to see the major structures within a joint as separate, each having its own group of pathologies, and then to refocus at the end on their interrelationships.

Synovium

Synovial tissue is truly remarkable. Essentially, it is only a few cells thick. This tissue lines all of our major articulations. It has a rich blood supply, receiving a substantial proportion of total cardiac output in a fine capillary network. The latter is unique in itself for it has no basement membrane and therefore ultrafiltrates plasma to form joint fluid. Thus, it is hardly surprising that small-molecular-weight substances readily make their way into joint fluid. Indeed, joint fluid dynamics are well es-

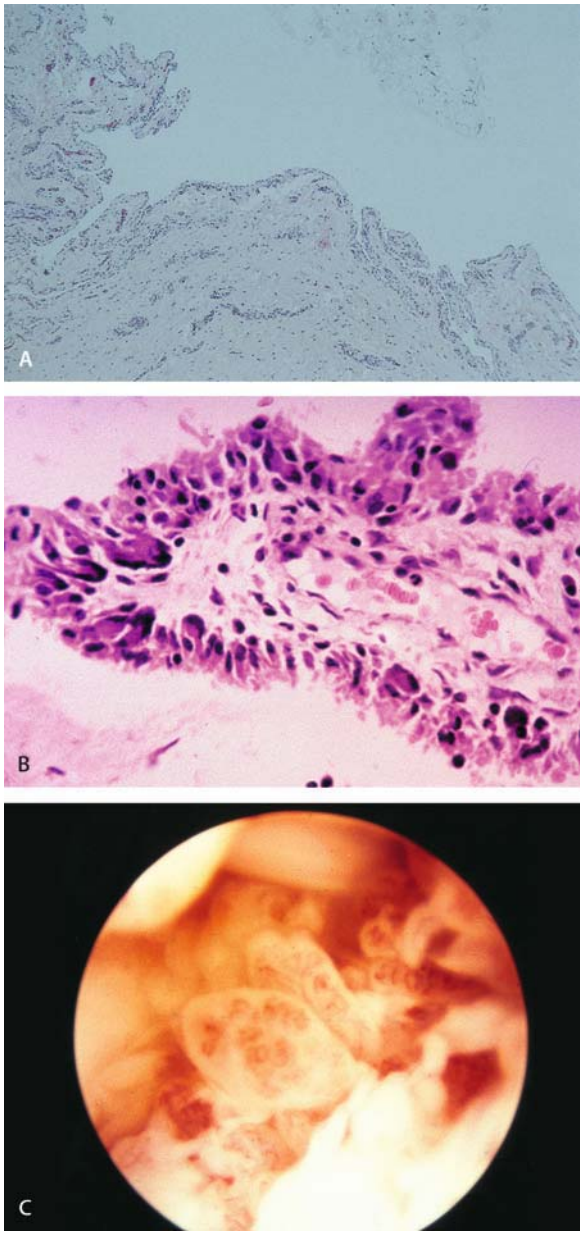

Fig. 1A–C. A Normal synovium. Note the simple, single layer of the surface cells and the convoluted pattern. The underlying connective tissue is loose, with no evidence of blood vessel enlargement or cellular infiltration. **B** Pathological synovium in rheumatoid disease. Note the folded, corrugated nature of the synovium, the thickness and the presence of giant cells. **C** The appearances at arthroscopy in rheumatoid disease. Note the papillary nature of the synovium and the redness due to hypervascularisation

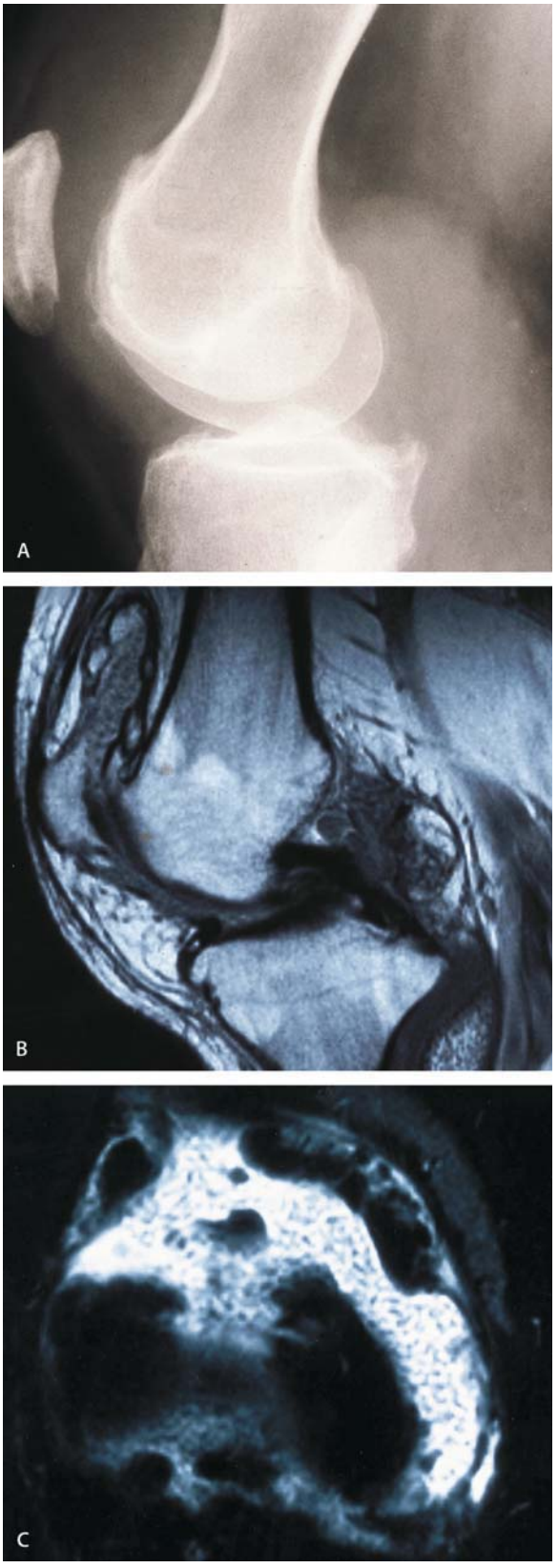

Fig. 2A–C. Synovial chondromatosis. **A** A lateral radiograph demonstrates obvious soft tissue swelling of the knee joint, the suprapatellar pouch is swollen, Hoffa's fat pad is displaced and a mass is present in the popliteal fossa. A so-called pressure erosion of the distal femur is also present, suggesting that the lesion is chronic. Note that the outline of the suprapatellar pouch is well defined, consistent with a non-inflammatory cause of synovitis. **B**, **C** MRI demonstrates numerous osteochondral loose bodies

tablished and depend on production of fluid by synovium and its subsequent resorption. The purpose of joint fluid is to lubricate the joint and to provide nutrition for hyaline cartilage. Cartilage (see "Hyaline Cartilage") is completely avascular and depends exclusively on synovial perfusion in the adult to provide chondrocytes with the necessary energy and raw materials. It is also remarkable that a tissue that is so richly vascularised with capillaries that have no basement membrane is so very rarely involved with metastatic disease. Further, granted the numerous showers of bacteria in blood, it can be argued that septic arthritis is also rare. The reason why synovium is so efficient at apparently being resistant to malignant cells and blood-borne bacteria is still a mystery.

Nonetheless, synovium is susceptible to inflammation. Inflammatory synovitis is characterised by thickening and oedema of synovium (Fig. 1). This results in the tissue becoming more richly perfused, congested and developing papillary folds. Numerous causes of synovitis are recognised, of which relatively few are relevant radiologically. This is because synovitis is not a particularly obvious radiological disorder. Thickened synovium does not occur immediately and many causes of transient synovitis are associated only with an increase in joint fluid production (joint effusion) rather than structural changes in synovium. Accordingly, the most obvious radiological feature of synovitis is a joint effusion. This may be obvious clinically by palpation, radiologically by soft tissue swelling on plain film (Fig. 2) or by other imaging modalities including ultrasound. In the appropriate clinical context, polyarticular synovitis may indicate the possible future evolution of an inflammatory disease such as rheumatoid arthritis. However, without development of erosion of bone no further specific radiological diagnosis is possible. Thus, the presence of soft tissue swelling is indicative of irritated synovium without being specific. The more inflamed the synovium, the less well defined the soft tissue outline will be radiographically (Fig. 3). Plain films cannot distinguish between joint fluid and synovial thickening.

Synovium may proliferate and change into pannus. However, it is by no means clear when a thickened and inflamed synovium metamorphoses into the chronic hypertrophied thick membranous tissue that we call pannus. Indeed, it is not clear whether this transition occurs at all, since pannus may represent an entirely different pathological change that does not require initial synovitis! Pannus itself is a heterogeneous tissue containing chronic inflammatory cells and areas of fibrosis and necrosis together with neovascularity. In some cas-

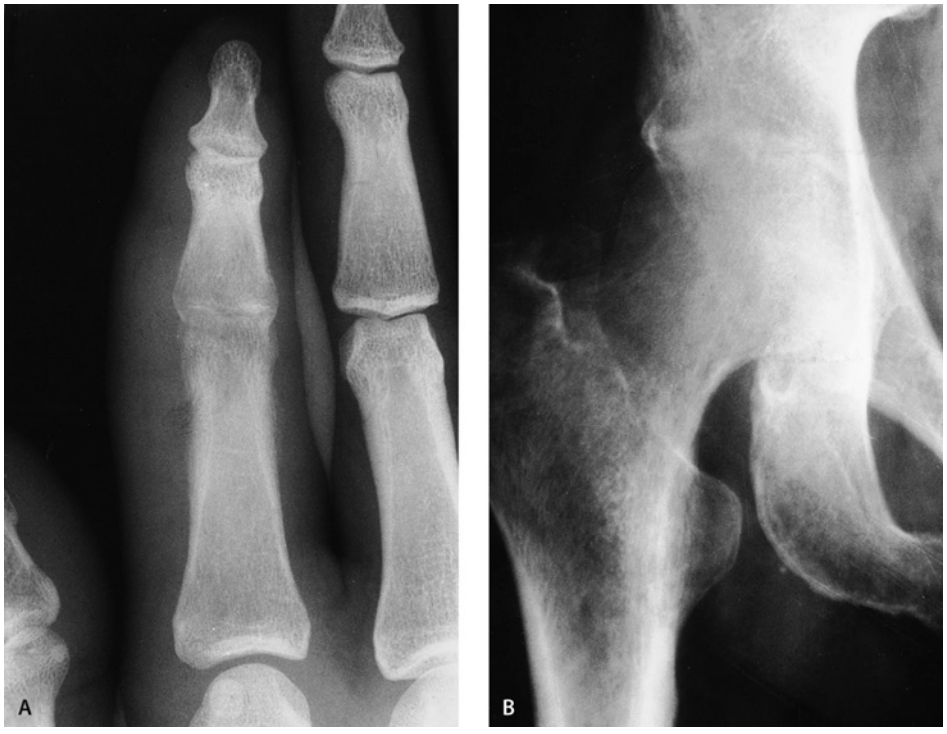

Fig. 3A, B. Septic arthritis. **A** Involving a proximal interphalangeal joint. Note the ill-defined soft tissue swelling, juxtaarticular osteopenia and complete loss of hyaline cartilage thickness. **B** At the hip joint, again the same features are present, but note also the complete loss of outline of the articular cortices of the femoral head and acetabulum

es, it may contain a number of giant cells. Indeed many authorities have likened the margin between pannus and bone to that which occurs between metastasis and bone. That is, there is an ischaemic zone with neovascularity and bone destruction products being produced by the synovium. Pannus may either be acute inflammatory or, once the disease process has burnt out, become thick fibrous tissue. Radiologically, the appearances of this tissue will vary considerably depending on the imaging modality employed.

Plain Films

In addition to soft tissue swelling, the hallmark of pannus is invasion of bone. This is described as erosion but de facto is a loss of cortical outline and trabecular detail. This will appear first in the bare area (Fig. 4) where synovium touches bone without intervening hyaline cartilage [2], the latter being relatively resistant to invasive pannus. It is important to remember that inflammatory tissue adjacent to bone may produce osteopenia on a radiograph simply because calcium has been leached out rather than because actual physical destruction has occurred. Such a process may account for some reports of healing erosions when recalcification of demineralised trabeculae has occurred. Nonetheless, in most instances eventual bone destruction does occur with trabecular disruption. In either circumstance the earliest plain film manifestation will be a loss of cortical outline at the bare area, producing the so-called dot dash or paint brush appearance as trabeculae appear to have no overlying cortex (Fig. 5). Biologically active synovitis is characterised by the development of an ill-defined erosion as well as soft tissue, whereas more stabilised burnt out disease may permit healing to occur and the margins of the erosions thus will be corticated and well defined (Fig. 6). In practical terms, rheumatoid erosions do not occur very early in disease evolution on plain X-rays. One may expect perhaps 30% of patients to show bone erosion by the end of their 1st year of illness, perhaps 60% at the end of year 2 [3]. Corticated and well-defined erosions will also occur where a focal mass lesion is present within synovium; a classic example is the tophaceous deposition of monosodium monourate (gout) (Fig. 7). Here chronically deposited crystals develop a mass lesion, which indent bone with secondary remodelling. Deposits of fat (as in multicentric reticulohistiocytosis or xanthomata) and even chronic granulomatous process such as tuberculosis may produce similar corticated erosions (caries sicca) (Fig. 8). The cortication clearly, therefore, represents chronicity.

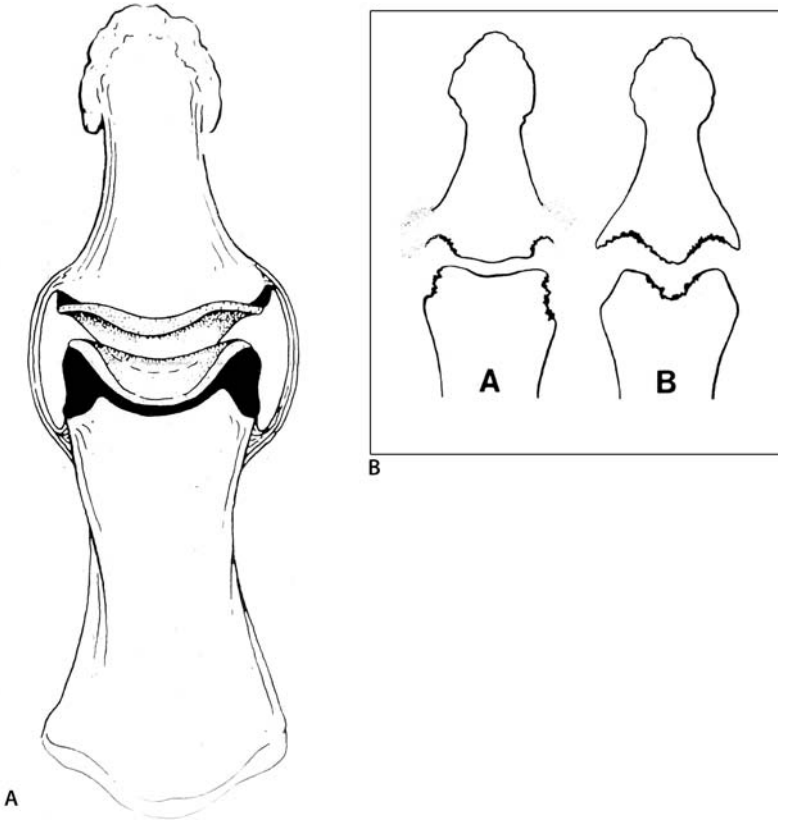

Fig. 4A, B. The concept of the bare area (derived from [2]). **A** The area at a terminal interphalangeal joint where synovium directly contacts bone and is not covered by cartilage is coloured in black. This area is known as the bare area and is where erosion occurs first in rheumatoid disease or psoriatic synovitis. **B** Difference between psoriatic arthritis (PSA) and erosive osteoarthritis (EOA). In **A** there is periarticular erosion with new bone formation, but normal articular surfaces, whereas in **B** there is clearly disease of the major articular surfaces (EOA)

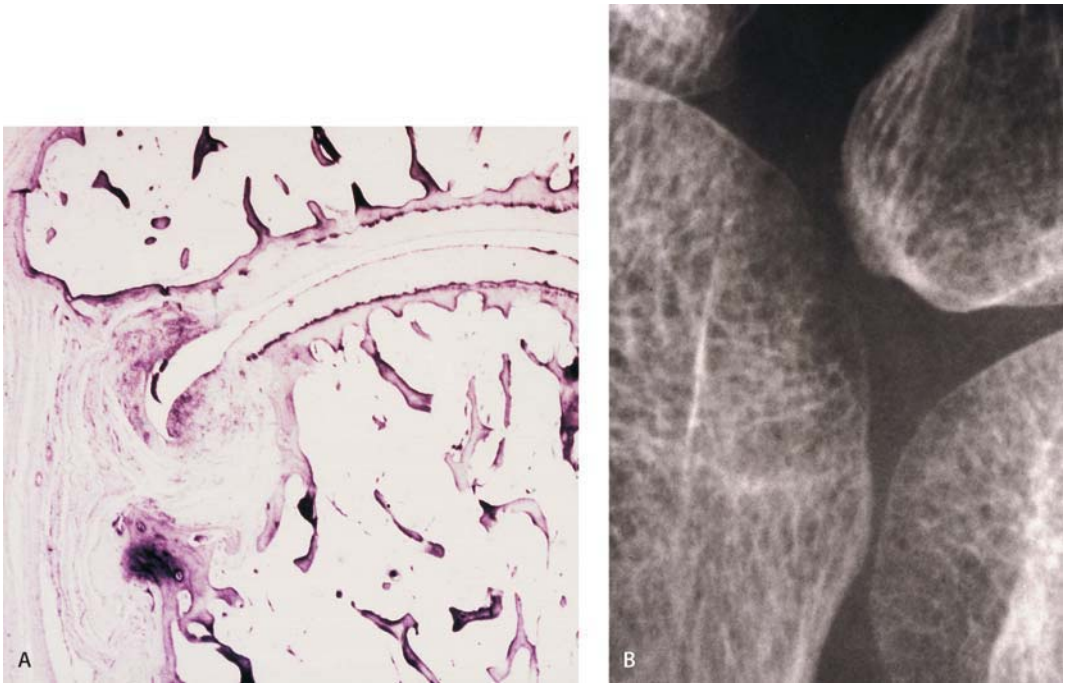

Fig. 5A, B. Rheumatoid erosions. **A** A localised radiograph demonstrates loss of resolution of the articular cortex of the bare area with uncovered trabeculae. **B** A histological specimen from a metacarpophalangeal joint shows invasion by pannus at the same site, the articular cartilage being essentially normal

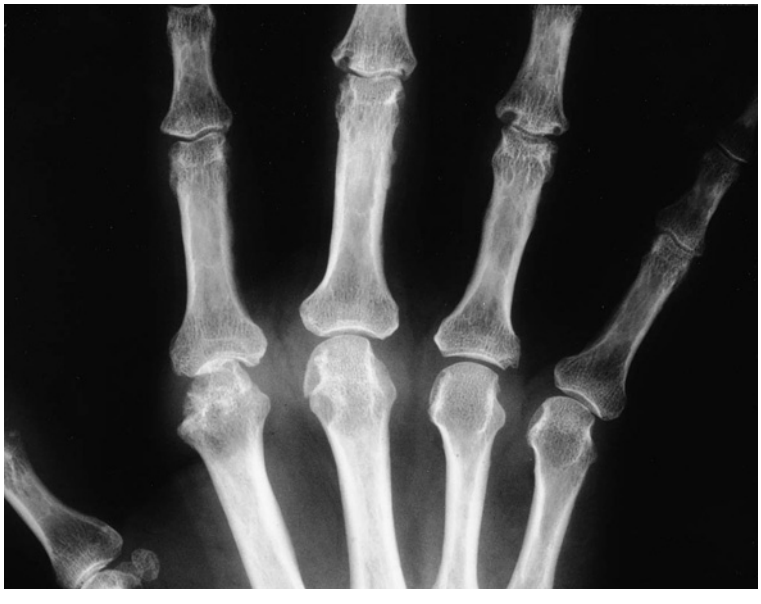

Fig. 6. Well-defined erosions in rheumatoid disease. Note active disease at the metacarpophalangeal joints, but corticated, well-defined lesions at the proximal interphalangeal joints with no evidence of active synovitis

Synovium, once thickened, may also contain an excess of iron (from chronic bleeding) or other high-atomic-number substances such as calcium (synovial chondromatosis, for example). Iron is the classic metal to be deposited in the chronic bleeding disorders, causes of which include haemophilia, Christmas disease and synovial haemangiomatosis. On plain film, this is characterised by diffuse opacification (Fig. 9). Pigmented villonodular synovitis (PVNS) also has the same effect and will produce well-defined periarticular erosions. However, this condition tends to be non-inflammatory, presenting with joint swelling typically involving the

Fig. 7A–C. Well-defined erosions in gout. **A** Classic tophi are demonstrated on the finger. **B** The effect on underlying bone is shown (a different patient). Note the eccentric soft tissue swelling, the well-defined periarticular erosions and the overhanging margin sign. **C** Palaeopathological specimens from Hadrian's Wall demonstrate typical gouty lesion in a Roman soldier

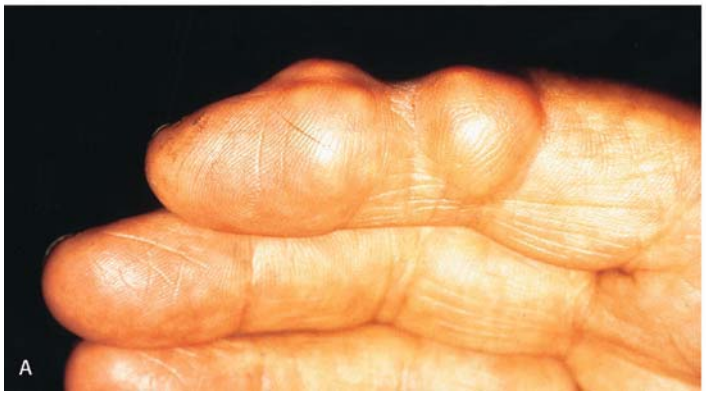

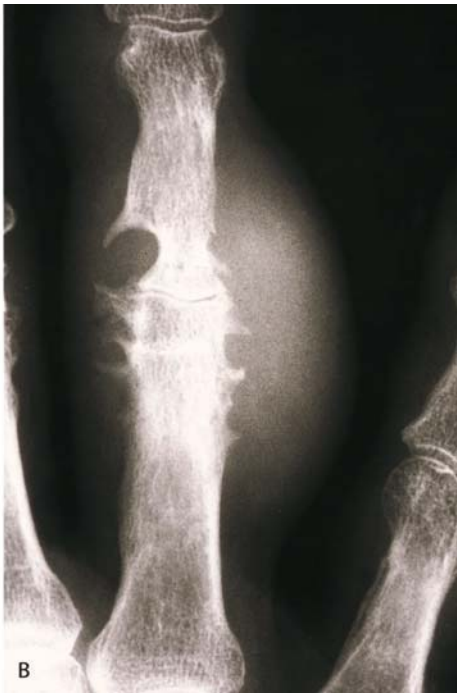

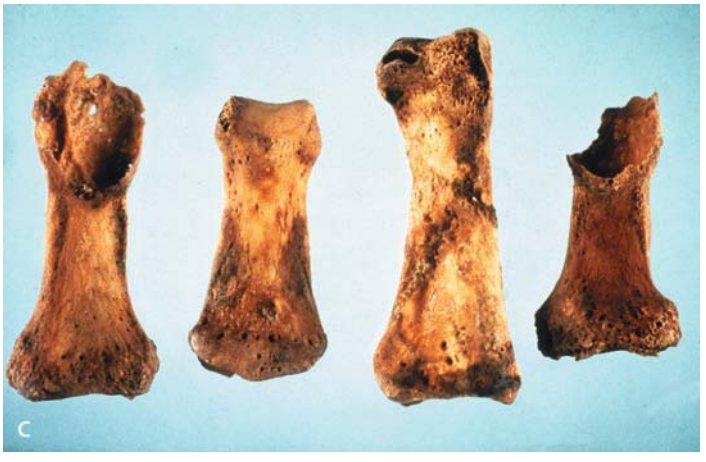

Fig. 8A, B. Well-defined erosions due to tuberculosis. **A** A typical caries sicca lesion is present. Note how well defined the erosive lesion is on the humeral head. **B** Typical pathology showing caseation and giant cells

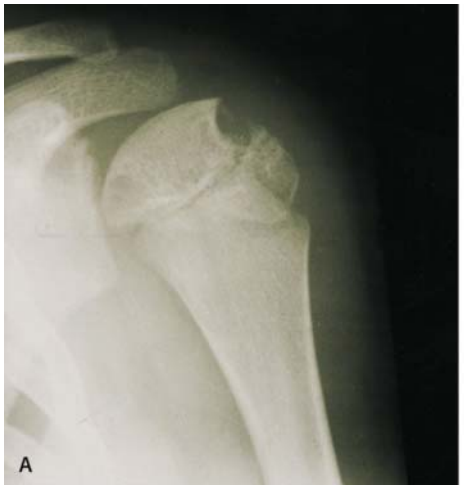

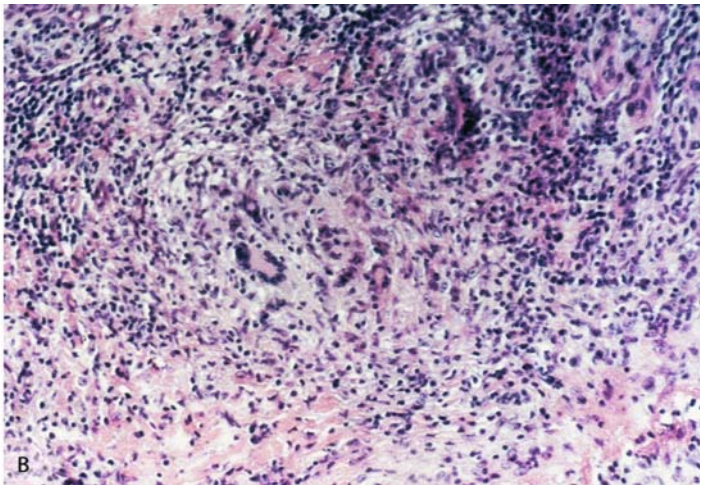

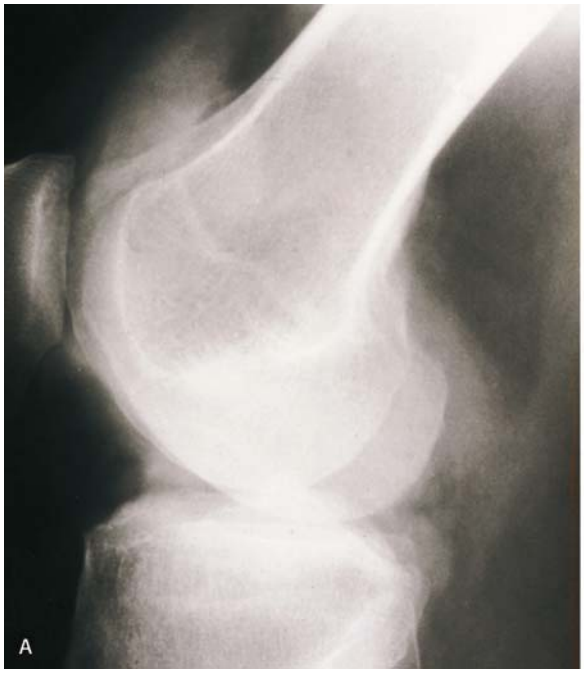

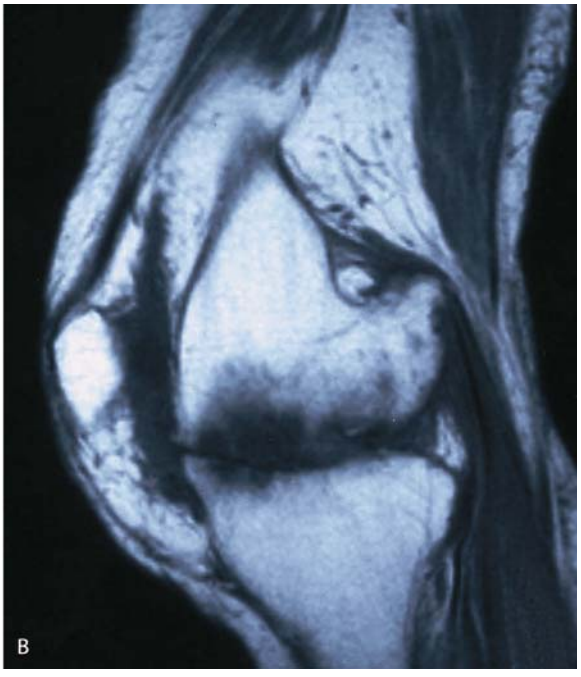

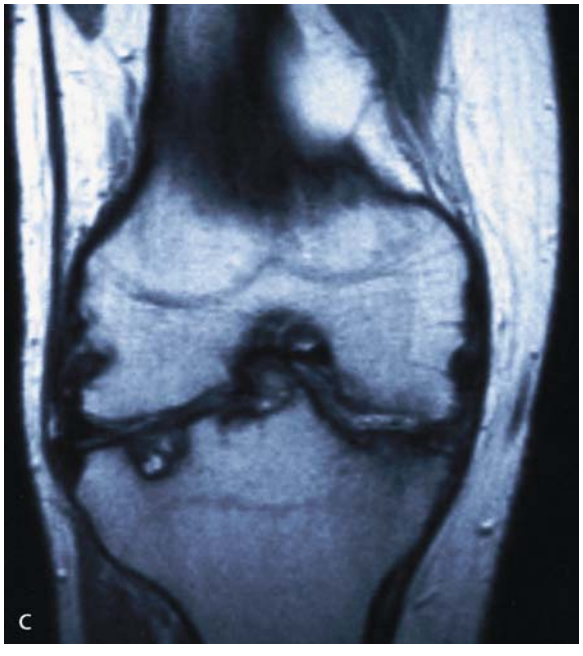

Fig. 9A–C. Haemophilia. **A** Note radiopaque synovium on the lateral radiograph of the knee due to repeated haemarthroses. **B, C** Typical features of haemophilic arthropathy are shown on MRI. The synovium is thick and low signal, consistent with iron overload. Note also that iron is present in the subchondral bone lesions. There is secondary osteoarthritis with loss of cartilage thickness and subchondral cysts

knee or the hip. The other radiopacity that may be helpful is calcification, as in synovial chondromatosis. Here, one may expect to see a ring or rings of calcification consistent with the cartilaginous bodies characteristic of this disorder (see below). Thus, in a patient presenting with an arthropathy characterised by well-defined erosions, the finding of a diffusely opaque synovium presents an important differential diagnostic sign. Pressure of bone will of course occur outside joints wherever synovium is found; hence, tendon sheaths and bursae may also be involved.

Scintigraphy

Any radiopharmaceutical that reflects vascularity will be abnormal in synovitis, hence a pertechnetate scan, or the blood phase of a bone scan. However, neither is specific. On occasion, patients will present with multiple joint pains and all clinical and laboratory investigations appear to be normal. Under these circumstances, a bone scan is an extremely sensitive means of excluding the probability of synovitis or arthritis. Once an inflammatory arthropathy is present, bone scans are severely limited since they cannot distinguish between the inflammatory changes of the synovitis and secondary subchondral bone changes associated with hyperaemia and remodelling. In these circumstances, it may be necessary to use an agent that marks the inflammatory process better, for example technetium-labelled nanocolloid (Fig. 10) or human immunoglobulin [4]. Gallium has been used, but it essentially labels white blood cells, so again is not discriminatory, since both inflammation and infection produce active scans. Labelled white blood cells are useful in infectious disease, but less so in

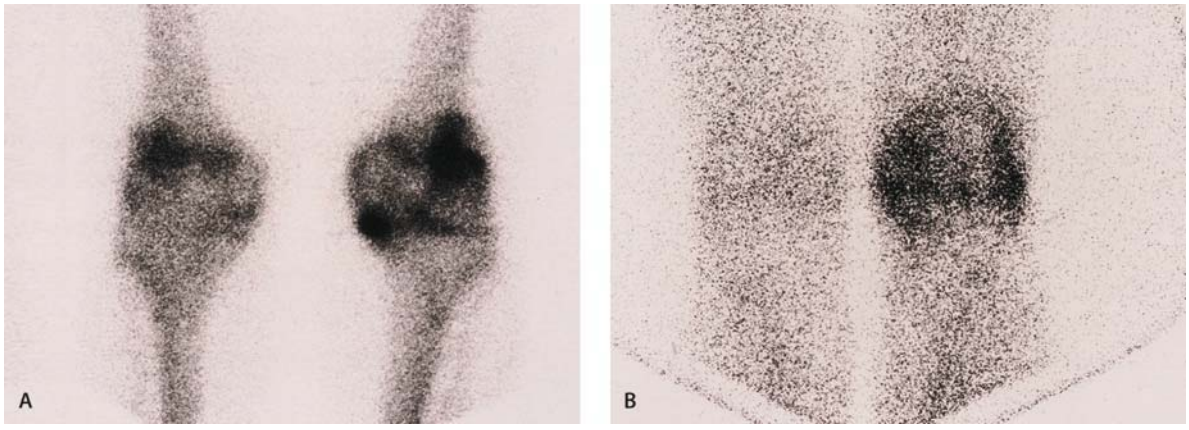

Fig. 10A, B. Scintigraphy in rheumatoid arthritis. **A** The late phase of a radionuclide bone scan shows a generalised increase in activity in the left knee (*right image*) due to mixture of rheumatoid synovitis and secondary osteoarthritis. **B** A nanocolloid scan clearly demonstrates the synovitis component

chronic infection when false negatives may occur. However, these scans too will be abnormal in some non-infectious inflammatory cases.

Magnetic Resonance Imaging

This has become the modality of choice in the evaluation of synovitis. The inflammatory changes are characterised, firstly, by increased water levels and thickness of the tissue. Hence on MRI one will see thick synovium, which shows high signal on T2 weighting or on STIR (short tau inversion recovery). Normal synovium is not readily visible on conventional MRI, although it can be seen on T2-weighted FLASH sequences and using magnetisation transfer contrast techniques. The increase in vascularisation and permeability can be demonstrated by gadolinium chelate-enhanced imaging (Fig. 11). The more inflammatory the synovium, the more permeable the tissue, the greater the vascularisation and hence the rate of accumulation of a gadolinium chelate following intravenous bolus injection. Not only is the rate of enhancement increased but also the peak enhancement. Because of normal joint dynamics in which joint fluid is produced rapidly by synovium, early (between 5 and 10 min) transudation of the gadolinium chelate occurs from synovium into joint fluid. This makes measurement of synovial thickness more difficult and limits the time available for image acquisition. However, this rapid transudation of contrast medium into joint fluid offers positive benefit insofar as indirect MRI arthrography can be performed by this route, and it offers as yet little explored means of indirectly assessing joint fluid dynamics.

Is there further information that may be gleaned from the dynamic acquisition of contrast-enhanced MRI in synovitis? Work suggests that whilst both the rate of enhancement and peak enhancement are valuable, it is the former that may reflect response to therapy and predict relapse [5]. Quantification of the mass of abnormal synovial tissue is also being explored, there being no "right" means at present. These are areas of importance in order to evaluate rapidly the effects of standard or novel therapy. A number of small studies have looked at response to standard agents, for example following intra-articular steroids. However, as synovitis and pannus may be different, and attract differing therapies, MRI has the ability to look for differential therapeutic responses [6].

Even pannus does not represent a single tissue type on MRI. Findings suggest a spectrum of pathology with some patients showing curvilinear thickening of synovium with uniform contrast medium enhancement, histologically correlating with simple inflammatory synovitis [7]. Others show eccentric areas of lobularity and nodularity that histologically correspond to inflammatory pannus. Tissue necrosis and fibrosis have occurred in others, resulting in a heterogeneous form of pannus that on MRI will show areas of enhancement and others of fibrosis. Eventually, pannus becomes a fibrous mass and the corresponding MRI images show a markedly reduced enhancement and the signal texture of fibrous tissue, which is low signal on most pulse sequences. Rich iron content in synovium is manifest by low signal (Fig. 9), the low signal becoming greater and more enhanced the longer the TR of the individual pulse sequence. This is to be expected in patients with chronic iron overload, particularly the bleeding disorders, and in amyloidosis.

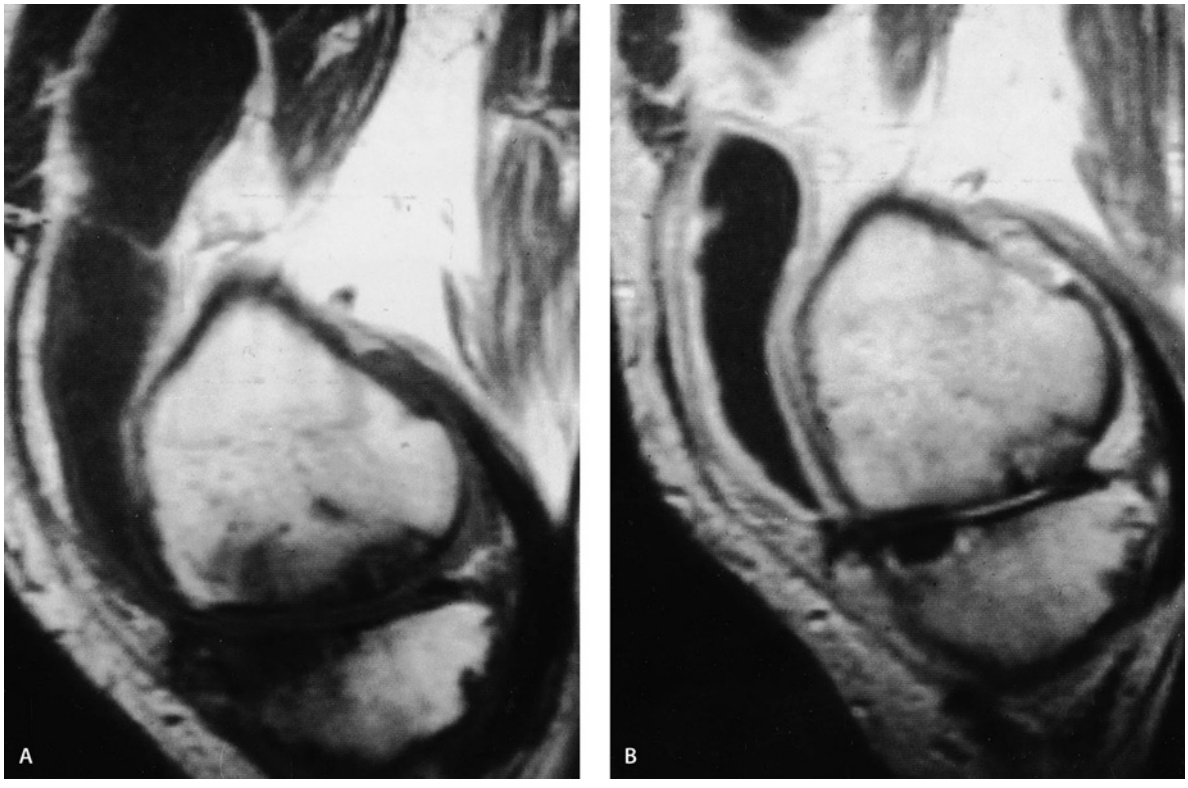

Fig. 11A, B. Rheumatoid arthritis on MRI. **A** Before intravenous contrast medium and **B** after intravenous contrast medium. Note the enhancing tissue due to thickened pannus can be clearly distinguished from joint fluid on the postcontrast medium images

Ultrasonography

This technology is enjoying resurgence, justifiably, and increasingly is being evaluated for the detection of synovitis and bone erosion. Ultrasound clearly demonstrates joint effusion and thickened synovium. It is an excellent technique for the demonstration of many soft tissue pathologies, especially tendon sheath and entheseal disease, as well as providing superb visualisation and guidance for interventional procedures. The question remains open as to the ability of ultrasound to reliably quantify degrees of inflammatory process and their response to therapy. Whilst some work is available on the demonstration of synovial vascularity, even using power Doppler relatively few larger vessels can be identified in thick synovium and vascularisation is difficult to reproducibly assess. Hence, the evaluation of resistive indices and therapy effects can be difficult. Some work suggests that erosion of bone is also detectable using ultrasound and that ultrasound may demonstrate more erosion than plain films. However, the practicality and reliable quantification of this investigation is still debatable.

Differential Diagnosis of Synovitis

In some diseases, inflammatory synovitis and invasive pannus are associated with new bone formation. This is a characteristic of the seronegative arthritides in particular psoriasis (PSA) and Reiter's syndrome. The new bone formation occurs actually in the erosions or adjacent to them (Fig. 12). The development of new bone formation is so unique to this group of disorders as to imply an entirely different aetiopathogenesis. Indeed, there are some suggestions from MRI studies that the disease process in PSA or Reiter's syndrome may originate outside the joint, in the capsule and ligaments, and that synovitis and intra-articular joint involvement may be secondary events [8]. Not all patients with PSA, as diagnosed clinically, have new bone formation. The question then is do these patients with a rash and an arthropathy have psoriatic arthritis or rheumatoid disease? Is the clinical diagnosis the gold standard or perhaps can MRI or even plain films diagnose the real arthritis of PSA?

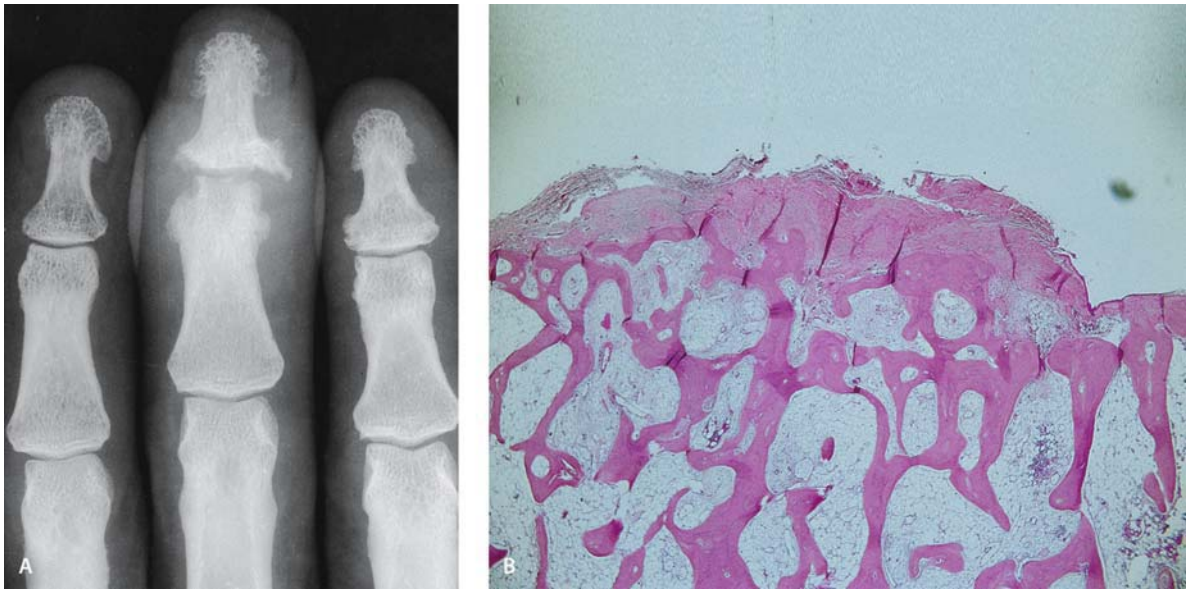

Fig. 12A, B. Proliferative new bone formation in erosions. **A** Typical psoriatic disease of the terminal interphalangeal joint. Note the symmetrical soft tissue swelling and the erosions at the bare areas, but in particular the development of new bone formation in association with the erosions. **B** A section of the femoral head from a patient with psoriasis. The articular cartilage has been destroyed, but note the fibrovascular invasive pannus overlying the articular surface, within which reactive bone formation is present

Tumours of Synovium

Synovial tumours are extremely rare. Indeed, that which is known as synovial sarcoma rarely, if ever, involves joints! Synovial sarcoma is so called because it is comprised of two cell lines reminiscent of the two primary cells occurring in synovium. There is no evidence, however, to suggest that it actually comes from that tissue. In addition to PVNS, summarised above, the other common benign synovial tissue tumours are synovial chondromatosis and the much rarer lipoma arborescens. The former is characterised by the development of metaplastic cartilage within synovium, the aetiology of which is totally unknown. The cartilaginous lesions enlarge and are shed, eventually acting as free intra-articular separate bodies within the joint. Enchondral ossification may occur in addition to calcification of the cartilage. The disease is characterised by proliferation following which a phase of budding or shedding of the lesions may occur and the final stage may be a residual hypovascular bald synovium. Clearly, the radiological hallmarks include soft tissue swelling, calcification characteristically, as in all cartilage-containing lesions, in the form of rings and separate multiple osteochondral bodies (Fig. 2). Lipoma arborescens is much less common, in which synovium develops frond-like fatty deposits demonstrated on plain films as intra-articular translucencies, often bathed in joint fluid due to the irritant effect of the lipoma.

Malignant tumours of synovium are extremely unusual. Primary sarcomas are very rare, metastasis virtually unheard of and transarticular spread of an adjacent bone or soft tissue tumour worthy of a case report!

Hyaline Cartilage

Hyaline cartilage is a truly unique tissue, yet it is comprised of relatively few components. A meshwork of collagen (collagen 2) fibres anchor into bone and extend perpendicular to the articular surface itself, where they radiate horizontally. The fibres are extremely tough and long living. At the bone-to-collagen interface, a curvy line of provisional calcification occurs, the so-called tidemark. Crammed into the spaces between the collagen fibres are substantially sized molecules of proteoglycan. These bottlebrush-like proteins exert a huge negative charge that avidly attracts water molecules. The pressure exerted within the collagen network is so large it cannot be reproduced readily in the experimental situation. The production of collagen and proteoglycan rests in the hands of chondrocytes arranged throughout cartilage in columns extending from the bone surface to the articular surface. Effectively, cartilage functions as an extremely effective avascular hydrodynamic cushion. Compression of the articular surface displaces water horizontally as the collagen network is compressed. Water may move through channels or leaves, previously

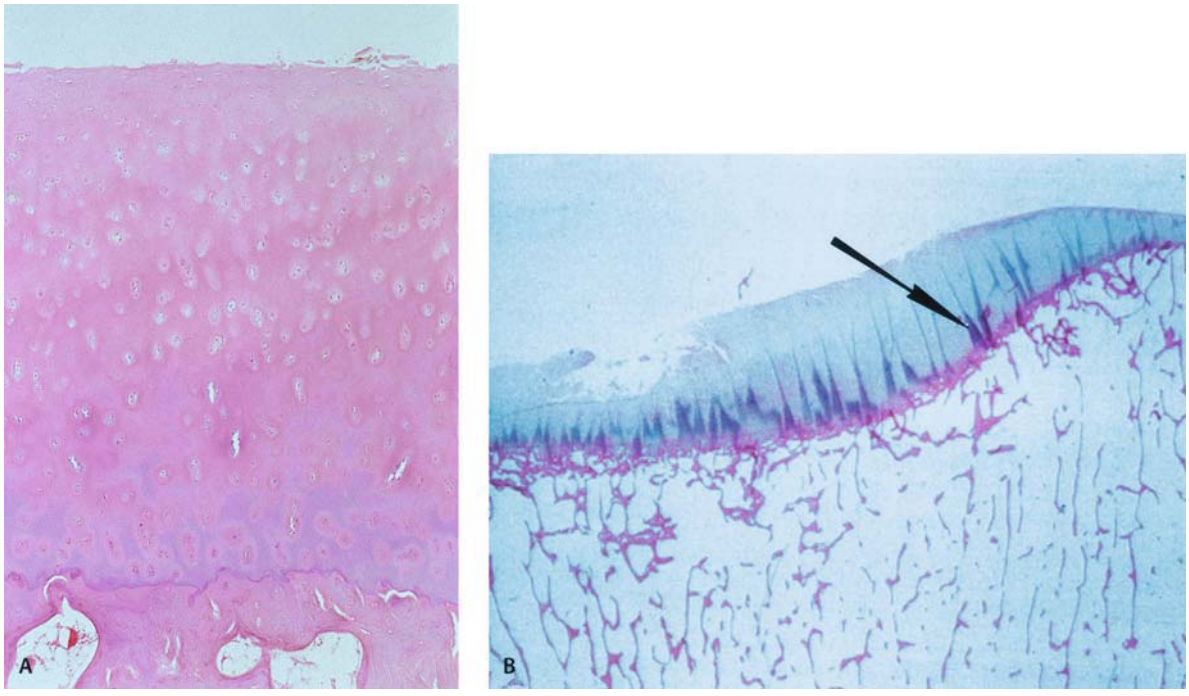

Fig. 13A, B. Hyaline cartilage. **A** Normal hyaline cartilage. A single zone of provisional calcification (tide mark) is present with chondrocytes arranged in neat columns and an even distribution of pink staining proteoglycan. **B** Striations are demonstrated within hyaline cartilage, corresponding to columns of proteoglycan and collagen, demonstrable on high-field MRI

unrecognised structures recently demonstrated by MRI [9] (Fig. 13). The water is redistributed within cartilage so that overall cartilage volume may not change. Once pressure is relieved from joint loading, water flows back attracted by the negative charge of the proteoglycans. Hyaline cartilage has neither a blood supply nor innervation. Nutrition depends purely on that provided by circulating synovial fluid.

Cartilage Pathology

Thinning

Cartilage radiologically can only do one of three things. It can grow thin, become thicker or calcify. Thinning of hyaline cartilage is a normal finding in the ageing population, with collagen networks beginning to wear and proteoglycan formation by chondrocytes becoming less efficient. Further, the proteoglycans themselves frequently have missing side branches or chains, reducing their ability to attract and retain water molecules. Cartilage thus becomes thinner in normal ageing individuals. Cartilage may also become thin because the proteoglycans contained within it become proteolysed. This is particularly the case in inflammatory synovitis or in septic arthritis where rapid destruction of proteoglycan and cartilage thinning occurs. This is reversible, however, if the chondrocytes remain alive and the collagen network is not disturbed. Once collagen has become involved, cartilage may swell because the proteoglycan molecules are no longer constrained. Once the articular surface of hyaline cartilage is disrupted, the collagen network is partially or focally destroyed. This cannot be repaired to normality: cartilage will fissure or ulcerate (Fig. 14). These lesions may extend down the tidemark between it and underlying subchondral bone. Such damaged cartilage is unstable, and because of the radiating superficial collagen network, a natural tendency exists for such lesions to gape apart. Joint fluid and debris are forced down to the tidemark that may result in areas of bone necrosis and the development of cystic intrusions or subchondral "cysts". To be accurate, these are not true cysts as they communicate to the joint surface and are not lined by a single cell layer. As radiologists, we misuse this word in joint disease.

Cartilage undergoes a series of repair mechanisms in order to attempt to restabilise a disrupted articular surface. These include the following mechanisms.

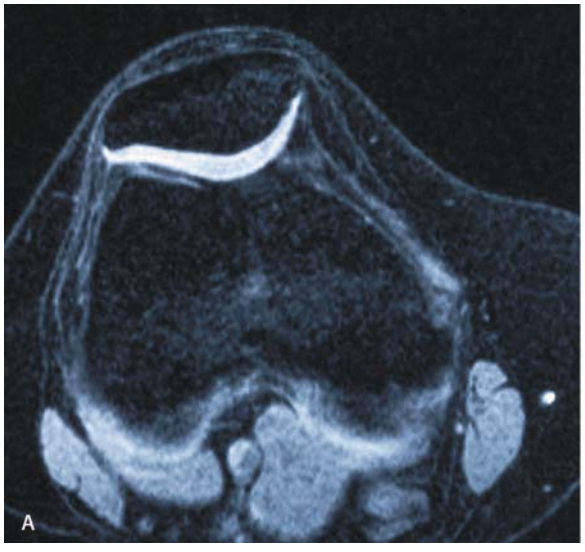

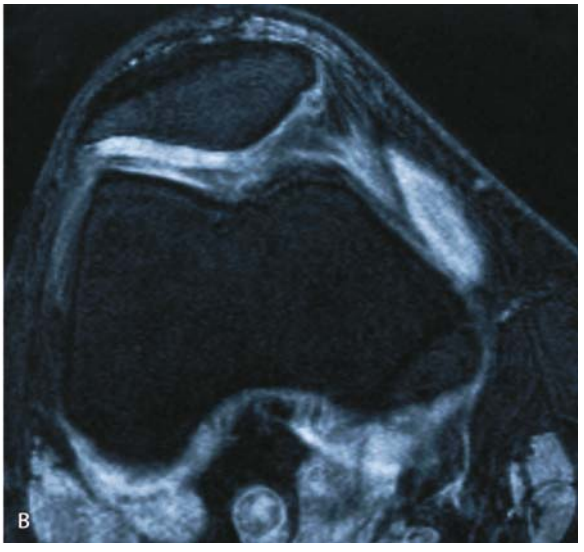

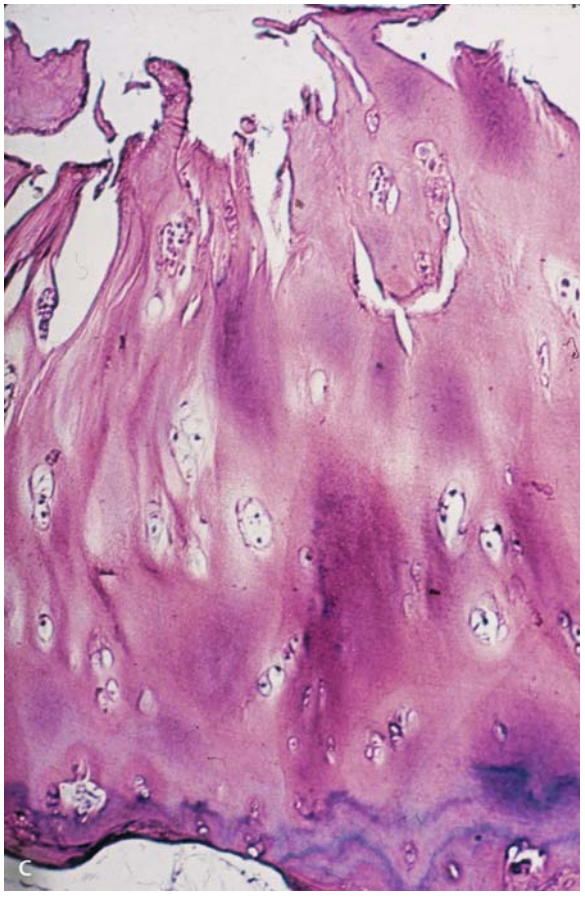

Fig. 14A–C. Hyaline cartilage. **A** Normal hyaline cartilage is shown on a gradient-echo T2-weighted 3DFT sequence at the patellofemoral joint. Compare and contrast this with **B**, which shows marked cartilage loss and fibrillation, particularly of the medial facet of the patella. **C** Typical histology of osteoarthritis. Note the cartilage irregularity, fissuring, abnormal columns of proliferating chondrocytes and multiple tidemarks

Osteophytes

Osteophytes develop initially at the margins of the joint on the hyaline cartilage – cortical bone interface. They are originally cartilaginous proliferations and hence should be called chondrophytes. In due course, these undergo enchondral ossification and are recognised on plain film as osteophytes. Tiny marginal osteophytes are thus a normal finding in an elderly population as cartilage thins and the joint becomes slightly unstable. Chondrophyte production is one of the earliest responses to joint instability, and thus may represent a normal healing response, rather than be disease. Large florid osteophytes are recognised as part of the process of osteoarthritis but may be considered a reparative phenomenon. When cartilage is extremely thin or fissured on articular surfaces, blood vessels may penetrate through the tidemark. These too may undergo enchondral ossification to produce so-called stud or surface osteophytes.

Multiple Tidemarks

The tidemark is the zone of calcification that glues hyaline cartilage onto subchondral bone. It is normally corrugated, effectively giving greater grip for the cartilage against bone when resisting sheering stresses. In osteoarthritis, as cartilage becomes destroyed, or as new cartilage is formed in the form of osteophytes, the tidemark is remoulded. Hence, one of the pathological features of osteoarthritis is the finding of multiple tidemarks (Fig. 15). Once bone has become exposed at an articular surface, one of two processes may occur. One

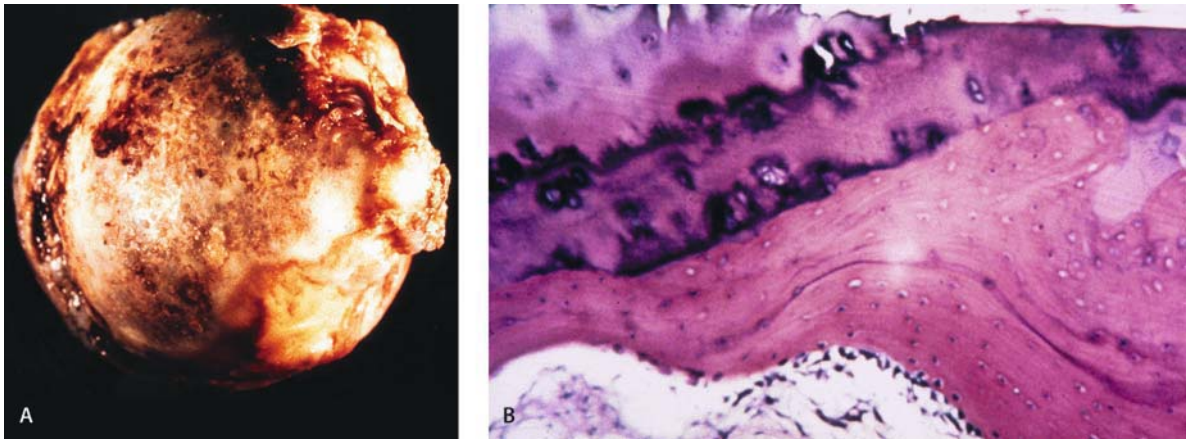

Fig. 15A, B. Osteoarthritis. **A** An excised femoral head demonstrates total loss of cartilage over the major articular surface and large chondrophytes on the margins due to hypertrophic cartilage. **B** Typical histology shows attrition and multiple tidemarks with subchondral new bone formation buttressing the diseased cartilage

may be perceived to be a repair mechanism, that is the development of dense sclerosis on the surface of bone, so-called eburnation. This may be associated with the development of deep grooves. These are found particularly at the knee or patellofemoral joint (Fig. 16), where they too may be thought to represent a means of stabilising the joint by providing it with "railway tracks". Unfortunately, these grooves are difficult to see on routine radiographs, but they are readily visible on skyline views of the patellofemoral joint, for example. The other

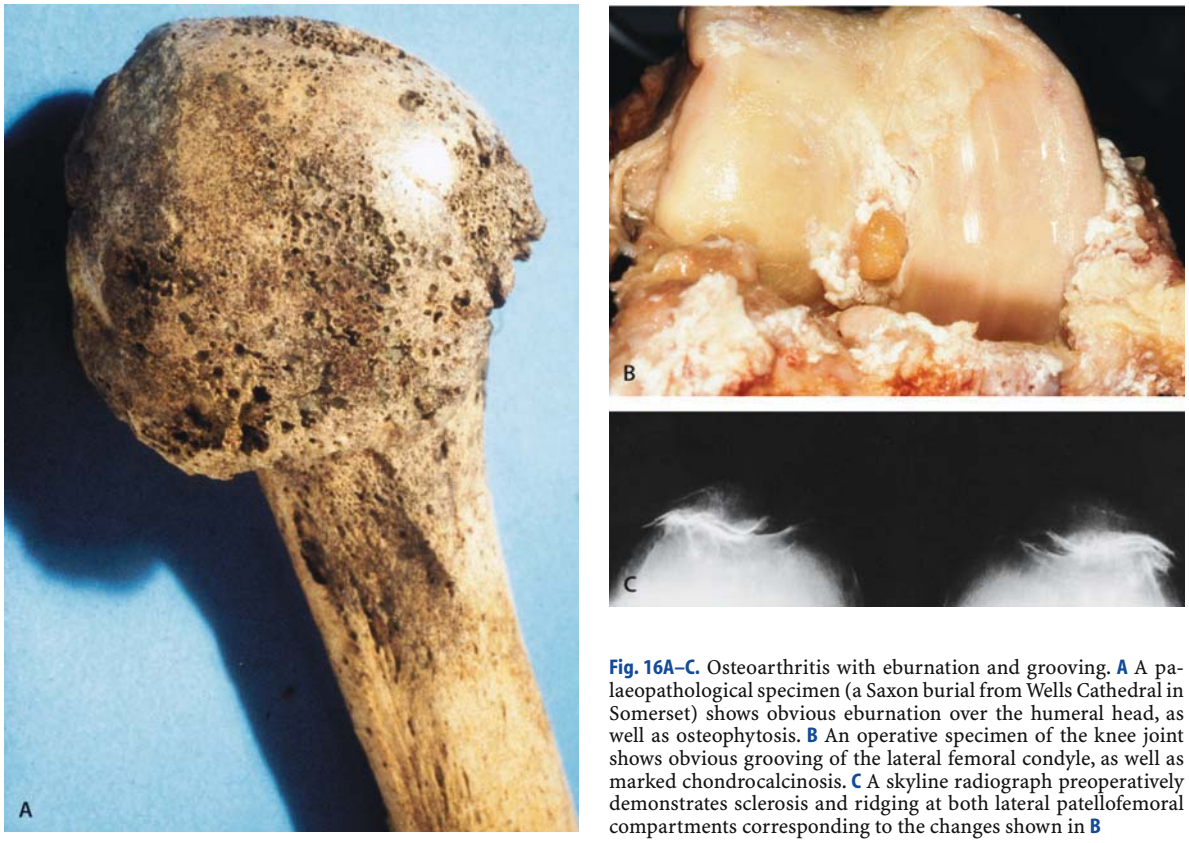

Fig. 16A–C. Osteoarthritis with eburnation and grooving. **A** A palaeopathological specimen (a Saxon burial from Wells Cathedral in Somerset) shows obvious eburnation over the humeral head, as well as osteophytosis. **B** An operative specimen of the knee joint shows obvious grooving of the lateral femoral condyle, as well as marked chondrocalcinosis. **C** A skyline radiograph preoperatively demonstrates sclerosis and ridging at both lateral patellofemoral compartments corresponding to the changes shown in **B**

process that may occur is trabecular failure, as subchondral bone is no longer being protected by a hydrodynamic cushion or by an eburnated articular surface. Radiologically, this is recognised as diffuse subchondral sclerosis. This represents trabecular collapse, fracturing and callus, and thus is a phase of joint failure.

Fibrocartilage

Some surface defects will fill in with fibrous tissue of cartilage origin. This occurs usually with focal defects, for example in the repair of a localised area of osteochondritis dissecans. On plain film, such a lesion cannot be seen, except via arthrography. Healed shallow defects can be seen on MRI, however, when low, abnormal signal in the defect is usual, reflecting the reduced water content of this tissue.

Bone Changes

Whilst synovitis produces an inflammatory milieu in joint fluid, which results in proteoglycan loss and overall cartilage thinning, hyperaemia of bone occurs also. As the result, bone may become softened and remoulded. An obvious example is the protrusio acetabuli seen in association with rheumatoid arthritis of the hip. In osteoarthritis, on the other hand, cartilage loss tends to be focal, repair may well occur at sites remote from the primary lesion, especially marginal osteophyte formation, and secondary subchondral bone changes are expected.

Thickening

Cartilage thickness may be increased in real terms in acromegaly, when it is one of the early manifestations of the disease. It is also thickened in myxedema and some mucopolysaccharidoses. It is incorrect to assume that thickened hyaline cartilage is necessarily a benefit. In fact, thicker cartilage is at risk of fissuring and fracture and promotes the development of osteoarthritis (Fig. 17). Cartilage may appear relatively thick also when extensive erosion is present. This occurs in the chronic, non-inflammatory synovial diseases, because in spite of erosion, cartilage has not been lysed. Consideration should be given to gout or PVNS, for example.

Calcification

Calcification in cartilage is extremely common and occurs with increasing age up to perhaps 40% of normal individuals at the age of 80. The crystal concerned is calcium pyrophosphate dihydrate (CPPD) and is almost certainly at least partly a by-product of metabolically active chondrocytes. Two types of pyrophosphate crystals have been described. Some occur about 50 μm below the articular surface at the site of tangential collagen fibres and are associated with surface fibrillation. The other type is larger aggregates that are thought to assist with short-term sheer loading [10]. CPPD crystals thus may actually be a deliberate part of a protective mechanism of hyaline cartilage under load and not the pathological process that they are frequently considered to be. Radiologically, CPPD deposition is recognised as

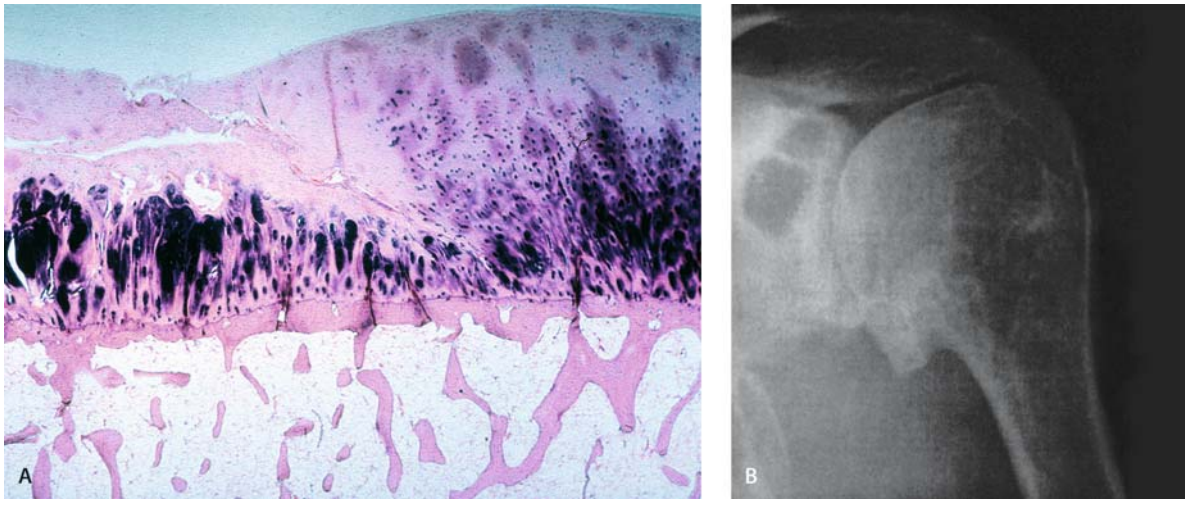

Fig. 17A, B. Acromegaly. **A** Typical histology reveals grossly thickened abnormal hyaline cartilage. Note the huge increase in number and size of the chondrocytes, their high metabolic rate (*dark staining*) and the fissuring occurring already. **B** Severe hypertrophic osteoarthritis of the shoulder in a patient with acromegaly. Note that the bone ends appear big and even now, joint space width appears increased, rather than diminished as might have been expected in idiopathic osteoarthritis

chondrocalcinosis and is typically found in those joints that also have fibrocartilages within them (Fig. 18), for example the knee (the menisci), the wrist (the triangular fibrocartilage) and the hips (the labrum). The relationship between fibrocartilage and hyaline cartilage is completely unknown.

Chondrocalcinosis occurs more frequently in a number of metabolic conditions, particularly those that involve iron, calcium or magnesium metabolism, since they are all closely interrelated. Episodes of crystal shedding do occur, when CPPD crystals are released into the joint and are associated with an inflammatory synovitis (pseudogout). The crystals of CPPD are almost certainly released because of shedding of the superficial layers of hyaline cartilage within which they are contained. However, episodes of pseudogout do not necessarily occur just because CPPD crystals are present. For example, pseudogout and osteoarthritis are unusual in hyperparathyroidism, whereas chondrocalcinosis is common. Data also suggest that the crystals shed during an episode of pseudogout are of a different type from those associated with hypertrophic osteoarthritis [11].

Very rarely, chondrocalcinosis is due to hydroxyapatite deposition. However, hydroxyapatite is found typically in periarticular tissues, for example in calcific periarthritis at the rotator cuff or the gluteal tendons (see below). Again, hydroxyapatite crystals are markedly inflammatory, producing acute synovitis. In rapidly destructive osteoarthritis (previously called analgesic hip or Milwaukee shoulder), the presence of hydroxyapatite in the joint largely reflects bone debris, although some

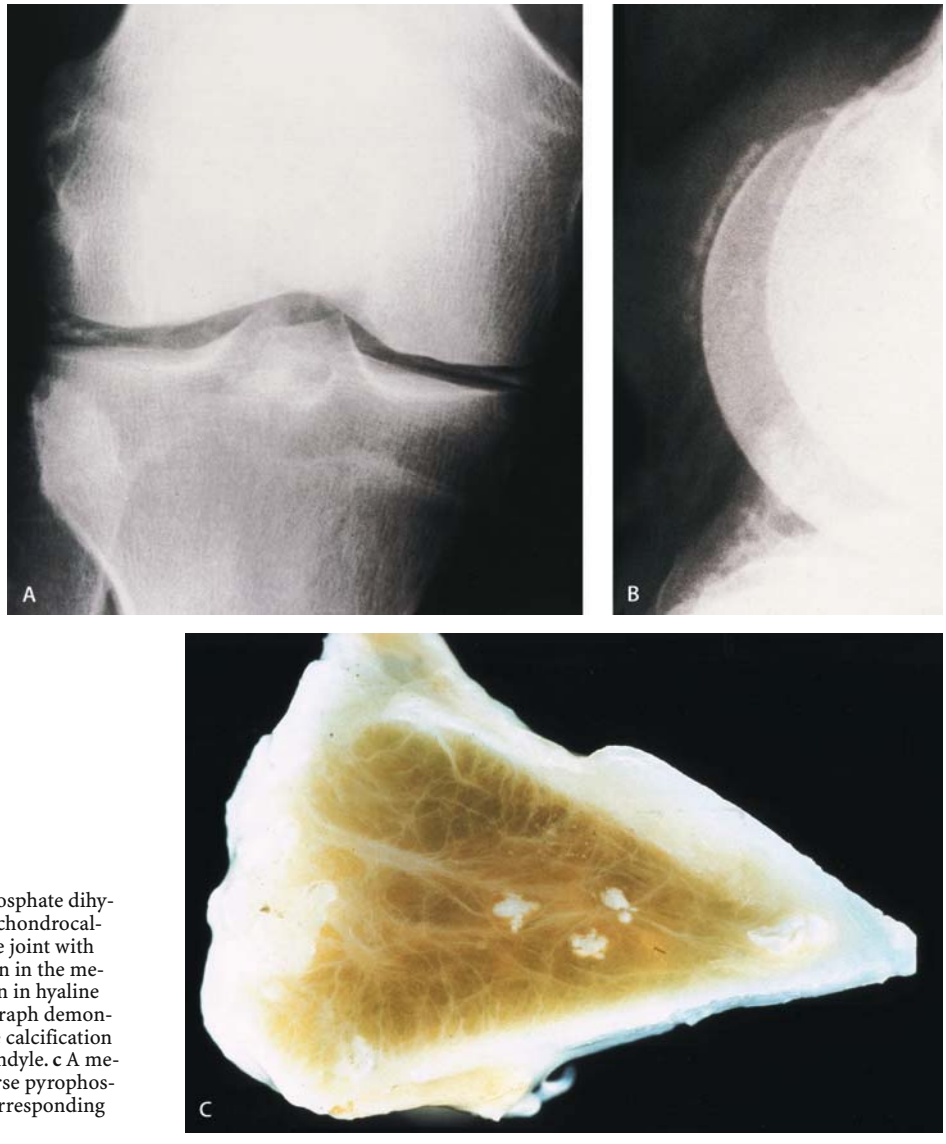

Fig. 18A–C. Calcium pyrophosphate dihydrate deposition. **A** Classic chondrocalcinosis is shown at the knee joint with coarse granular calcification in the menisci and linear calcification in hyaline cartilage. **B** A lateral radiograph demonstrates the hyaline cartilage calcification over the medial femoral condyle. **c** A meniscal specimen shows coarse pyrophosphate crystal deposition corresponding to **A**

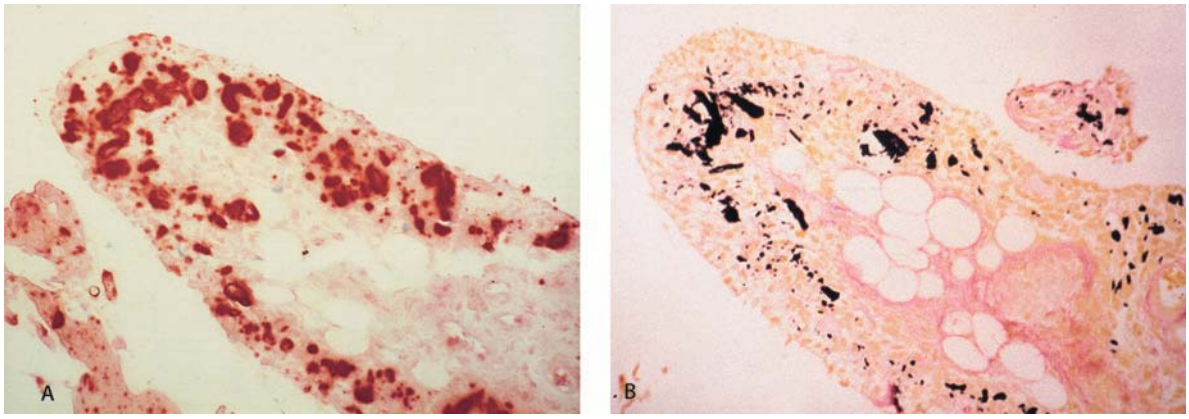

Fig. 19A, B. Hydroxyapatite deposition in destructive, atrophic osteoarthritis. An alizarin red stain of synovium (**A**) and a Van Gieson stain (**B**) show abundant hydroxyapatite deposition in synovium, as well as fragments of collagen, confirming a mixture of so-called bone dust and newly formed crystal deposits

of the crystals are newly formed (Fig. 19). There is thus an intimate interrelationship between the deposition of some crystals in cartilage and joints and what is happening in subchondral bone. Certainly, individuals who deposit CPPD (likely to be coming from active chondrocytes) tend to develop hypertrophic osteoarthritis and to have normal central bone density. Individuals whose joints fail rapidly, depositing hydroxyapatite, often have somewhat osteopenic skeletons. Thus it may well be that the way in which a joint responds to insult reflects the ability of bone to be formed generally throughout the skeleton (Fig. 20).

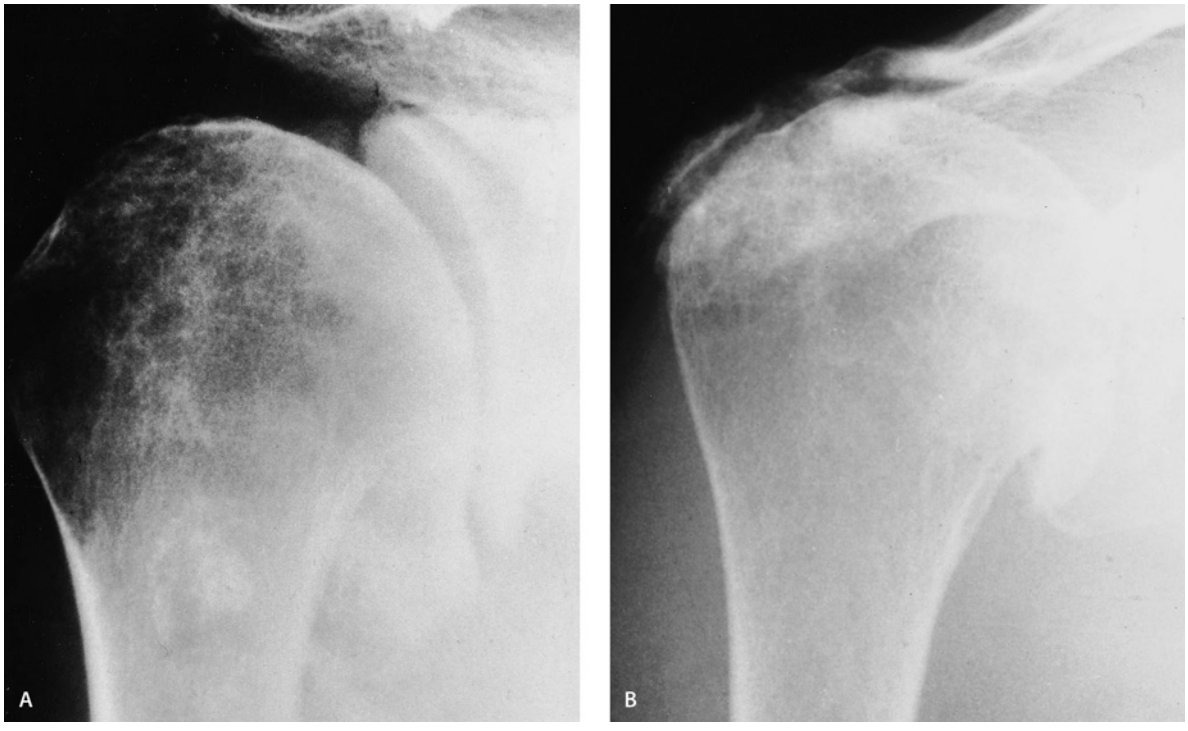

Fig. 20A, B. The spectrum of crystal associated arthritis. **A** Typical pyrophosphate arthropathy. Marked hypertrophic osteoarthritis with several separate osteochondral bodies occurring in a joint (the shoulder), which normally does not suffer from idiopathic osteoarthritis. Aspirated joint fluid contained abundant pyrophosphate crystals. **B** Rapidly destructive osteoarthritis of the shoulder. Note the effusion in the subdeltoid bursa, cephalic migration of the humeral head, attrition of the acromion and clavicle and the absence of osteophytosis. Joint fluid yielded abundant hydroxyapatite crystals

Pyrophosphate Arthropathy, Haemochromatosis and Other "Cystic" Arthritides

Some patients in whom CPPD is deposited also develop a hypertrophic osteoarthritis as explained in the preceding section. This is not always the case, and not every patient who has a hypertrophic form of osteoarthritis with multiple subchondral cysts will have pyrophosphate arthropathy or CPPD crystals detectable either on plain film or from joint aspiration. The presence of multiple cystic lesions across an articular surface should also suggest the possibility of haemochromatosis (Fig. 21A). This largely male disorder associated with iron dysmetabolism is characterised by multiple subchondral cysts and a destructive arthropathy. However, the histological process here is completely different. Instead of the multiple calcified tidemarks of osteoarthritis or pyrophosphate-associated osteoarthritis, the tidemark in haemochromatosis is straightened and flattened out [12] (Fig. 21B, C). The reason for this is not known, but the effect is that hyaline cartilage no longer can resist the sheer stresses suffered by the joint during movement. Consequently, hyaline cartilage peels off the articular surface and multiple subchondral radiolucencies are demonstrated on plain film. Because iron and calcium metabolism are related, patients with haemochromatosis frequently also have chondrocalcinosis due to the deposition of CPPD crystals, but the lesions created by sheering cartilage occur irrespective of whether or not CPPD crystals are also present. Similarly, cystic lesions are often a major feature of haemophilic arthropathy and the other bleeding disorders. The other rare disease associated with abnormal copper metabolism, Wilson's disease, is also characterised by multiple subchondral cystic lesions.

Radiological Assessment of Hyaline Cartilage

■ **Plain X-rays.** Plain films do not normally show hyaline cartilage, as it is not radiopaque. Further, the gap between the bone ends on plain film could contain any combination of joint fluid, hyaline cartilage, debris, menisci or whatever. In some joints, articular surfaces are held together by muscle and capsular tone, for example the ankle, metacarpophalangeal or hip joints. In others that are designed to be very mobile, for example the knee; weight-bearing films may be necessary in order to reliably demonstrate the inter-bone distance and from them infer hyaline cartilage thickness by opposing the joint surfaces under load. This is reliably the case in the medial compartment of the knee joint, but not the lateral. Demonstration of cartilage pathology is possible by employing contrast arthrography, but, by definition, this is an invasive procedure and may require CT to fully delineate areas of interest.

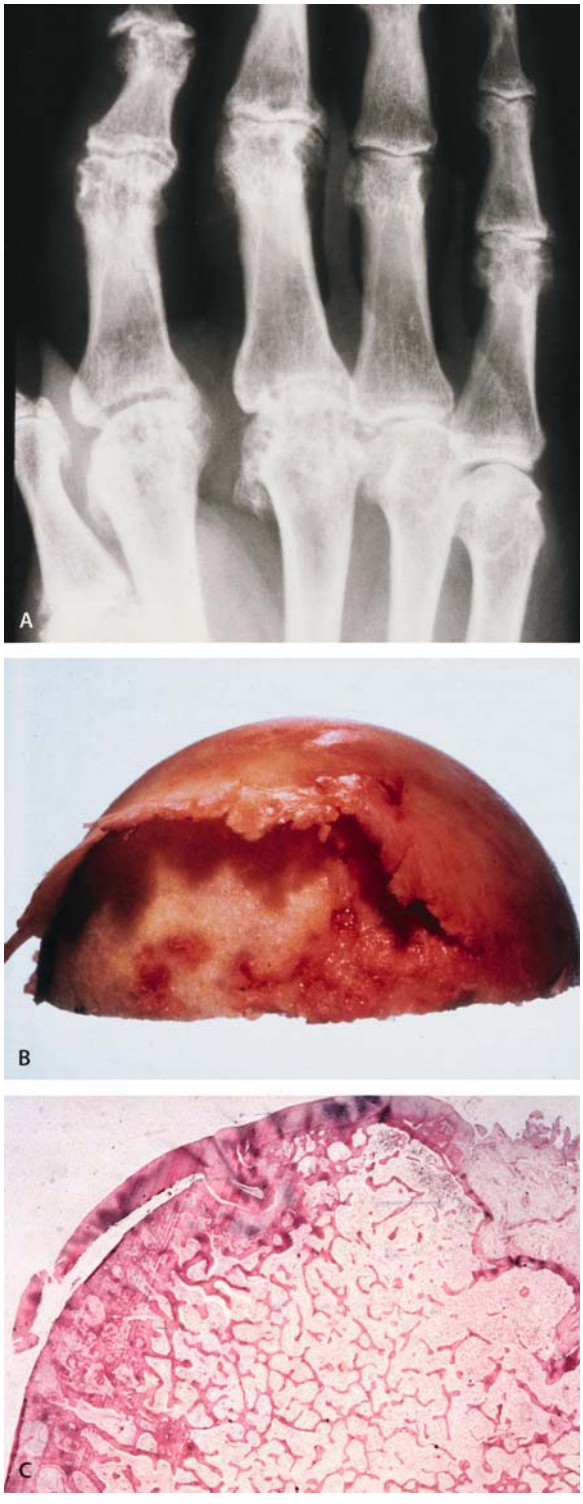

Fig. 21A–C. Haemochromatosis. **A** A radiograph of the hand demonstrates typical multiple small cystic lesions arranged in a subarticular position over the metacarpal heads. **B** A specimen from a femoral head shows hyaline cartilage peeling away from underlying bone due to straightening of the tidemark shown in **C**

■ **Ultrasonography.** Whilst this may demonstrate hyaline cartilage, it cannot do so over the main articular surfaces simply because no acoustic window exists between articular bony surfaces. Direct application of ultrasound probes during arthroscopy is being explored also. This method, whilst highly invasive, permits assessment of cartilage plasticity and thus softening in early degeneration.

■ **Magnetic Resonance Imaging.** This is now the prime means of assessing hyaline cartilage, mainly by using T2-weighted gradient echo 3DFT sequences (Fig. 14A, B). Hyaline cartilage may be shown to be a high-signal structure that is quantifiable, reliably, with roughly 3%–5% reproducibility. What exactly is being demonstrated, however, in terms of anatomy has been the subject of debate. A number of publications have suggested that the high-signal material is banded, each band roughly corresponding to a histological zone. Other authors have suggested, however, that this is spurious and subject to truncation artefacts, and that the only reliable means of assessing hyaline cartilage in detail is using spin-echo techniques. Publications have attempted to quantify hyaline cartilage in joints, mainly the knee. Results compared with histological quantification suggest about a 10% error rate [13, 14]. Recent research has indicated also that MRI may demonstrate a hitherto unrecognised ultrastructure within hyaline cartilage comprising striations of low-signal material presumed to represent collagen columns [9] (Fig. 13B). Hyaline cartilage close to bone, at the zone of provisional calcification, is also not demonstrated on clinical MRI scanners, as the presence of calcium needs such a short TR that it cannot be imaged on currently available clinical scanners. Nonetheless, MRI reliably will demonstrate both focal and generalised cartilage abnormalities. MRI demonstrates water content of hyaline cartilage on conventionally used pulse sequences. The collagen structure can be inferred on magnetisation transfer contrast but presently does not add practically to the assessment of cartilage itself. There are also theoretical means of imaging proteoglycan in vitro but not yet in vivo.

Summary

In arthritis cartilage may be thinned, because of the release of proteolytic enzymes and other substances by synovium. In this case, the inter-bone distance narrows and bone may soften. Cartilage may thicken because of acromegaly or other rare disorders. Focal ulceration of cartilage is difficult to visualise other than by using MRI or contrast-enhanced arthrography. Generalised cartilage loss can be assessed reliably by plain films supplemented by weight-bearing films where appropriate. Accurate assessment can also be made by MRI. Secondary reparative phenomena that originate in cartilage include osteophytosis. Subchondral bone response is probably under the influence of more generalised controllers of bone formation, hence may be linked with systemic disorders such as osteoporosis. Chondrocalcinosis is probably an overreaction by metabolically active chondrocytes in later life, although some CPPD crystals are a normal finding in weight-bearing cartilage. CPPD crystals are a marker of a hypertrophic bone response once joint damage has occurred and hydroxyapatite crystals, although rarely intra-articular, usually reflect a failing joint.

Enthesis Disorders

An enthesis is that site at which ligaments, tendons and other fibrous tissue are inserted into bone by the so-called Sharpey's fibres. Obviously, the purpose of capsule and ligaments is to provide stability for a joint that is tough, flexible and able to absorb sudden unexpected forces and tensions. In arthritis, two distinct subsets of enthesis disease can be recognised. The presence or absence of an inflammatory lesion at the enthesis itself differentiates them.

Erosive Enthesopathies

In some conditions, for example ankylosing spondylitis, an inflammatory lesion develops at the enthesis. This manifests itself in a number of ways. The first is erosion, typically found on the corner of a vertebral body or at a site where an enthesis is inserted into bone elsewhere, for example the os calcis. The erosion may be associated with soft tissue swelling, where it is possible to see this because of disturbed fat plains, for example at the os calcis (Achilles tendon or plantar fascia) or the patella (quadriceps tendon or patellar ligament). Secondly, the erosion is associated with new bone formation. In the case of ankylosing spondylitis in the spine, this forms adjacent to the erosion and eventually may cause intervertebral or interfacetal joint fusion. Bone proliferation is manifest also within the underlying bone itself, for example the so-called bright spot or Romanus lesion in a vertebra. Although ankylosing spondylitis (or ankylosing spondylitis associated with inflammatory bowel disease) is the classic cause of an erosive enthesitis PSA, Reiter's syndrome and Behçet's syndrome produce similar changes (Fig. 22). However, this latter group of diseases tends to produce lesions that are more asymmetric and the new bone formation in the spine may be coarser and less gracile.

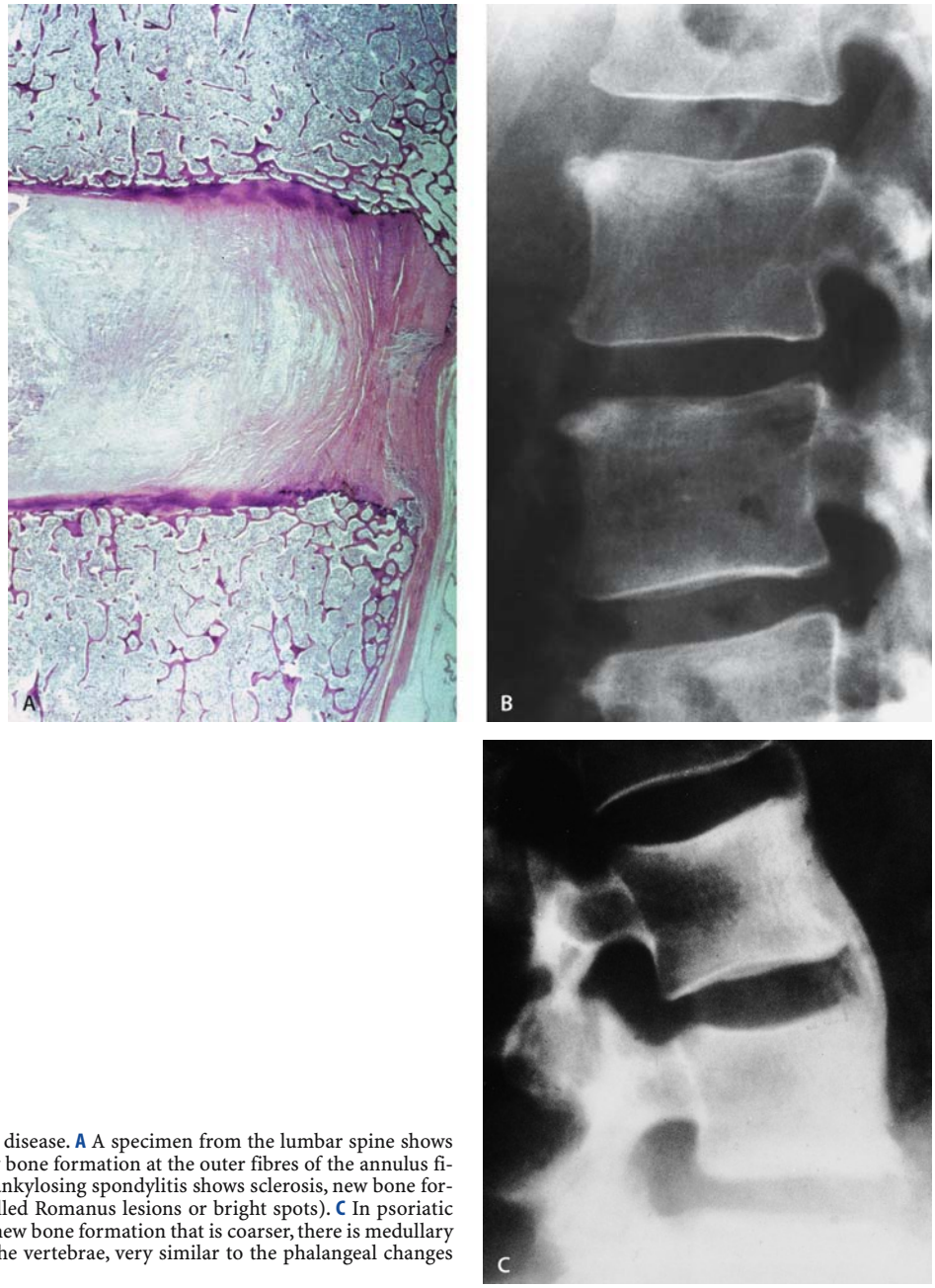

Fig. 22A–C. Erosive enthesis disease. **A** A specimen from the lumbar spine shows granulation tissue and new bone formation at the outer fibres of the annulus fibrosus. **B** A radiograph in ankylosing spondylitis shows sclerosis, new bone formation and erosion (so called Romanus lesions or bright spots). **C** In psoriatic spondylitis, in addition to new bone formation that is coarser, there is medullary sclerosis underlying it in the vertebrae, very similar to the phalangeal changes shown in Fig. 12a

Non-erosive Enthesopathies

New bone formation at the enthesis without erosion is very common by comparison. Probably the most common aetiology is chronic low-grade trauma, for example at the patella around the quadriceps mechanism or the os calcis with the Achilles tendon or plantar calcaneal spurs. Frequently the new bone formation occurs adjacent to tangentially inserted fibres. This may represent a chronic traction phenomenon. As indicated, however, these lesions are never associated with an erosive abnormality or with an obvious inflammatory change in the form of soft tissue swelling. Similarly, on MRI, such lesions will be shown not to have an inflammatory component, unlike ankylosing spondylitis and the group described above where enhancing tissue can be shown at the enthesis insertion as well as high signal on STIR. However, since both groups of disorders are associated with new bone formation, a bone scan using a bone-seeking radiopharmaceutical is non-discriminatory.

The most common cause of generalised enthesis ossification is Forestier's disease or DISH (diffuse idiopathic skeletal hyperostosis) [15]. Here generalised enthesis ossification occurs in fairly predictable sites: the thoracolumbar spine, particularly to the right of the thoracic spine, frequently unilateral (Fig. 23); around the muscle and ligament origins and insertions of the pelvis and the shoulders; the quadriceps mechanism; and the os calcis. Forestier's disease/DISH is associated with obesity, late-onset non-insulin-dependent diabetes and gout,

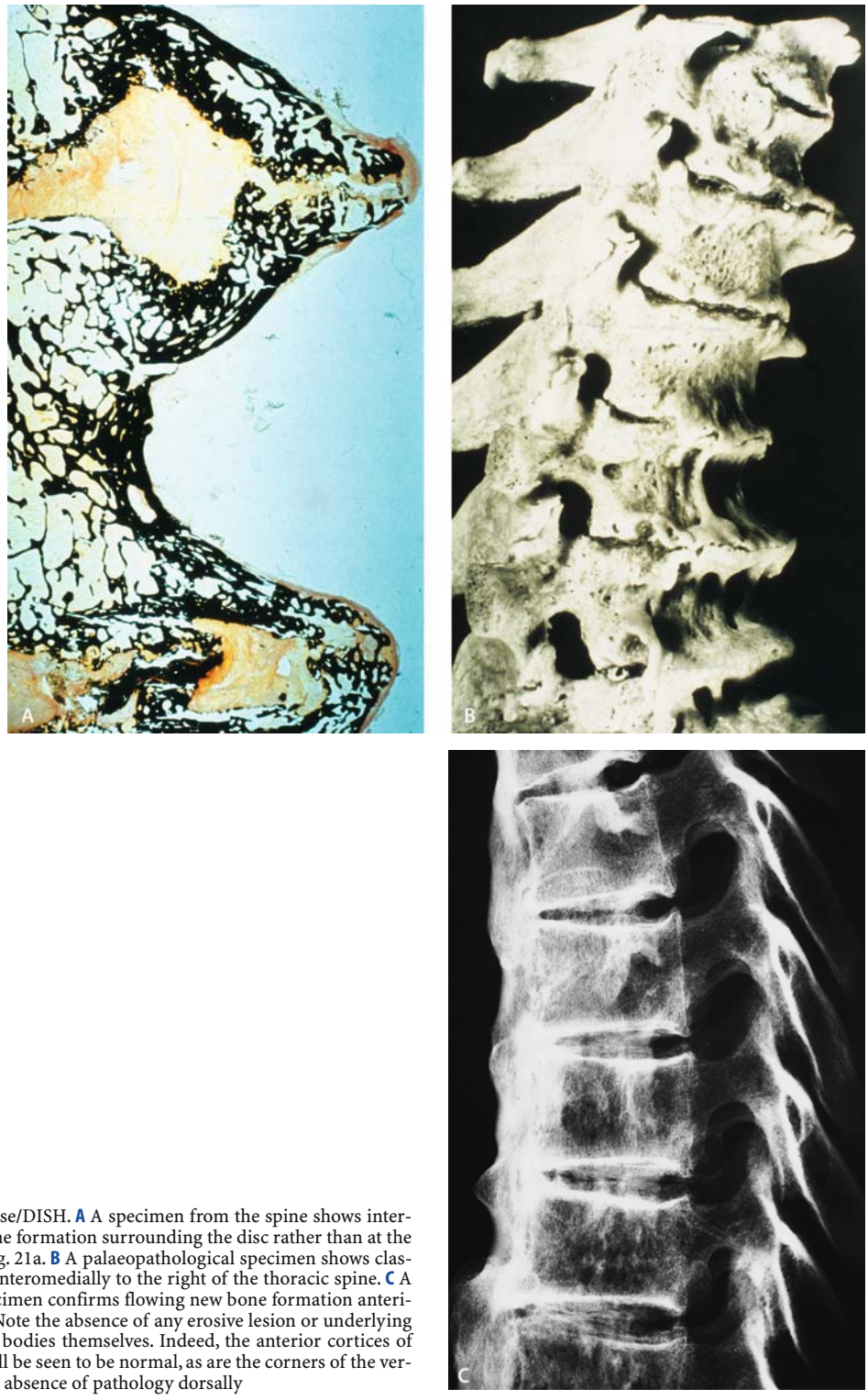

Fig. 23A–C. Forestier's disease/DISH. **A** A specimen from the spine shows interdigitating enthesis new bone formation surrounding the disc rather than at the corners of the disc as in Fig. 21a. **B** A palaeopathological specimen shows classic flowing osteophytosis anteromedially to the right of the thoracic spine. **C** A radiograph of another specimen confirms flowing new bone formation anteriorly in the thoracic spine. Note the absence of any erosive lesion or underlying pathology in the vertebral bodies themselves. Indeed, the anterior cortices of the vertebral bodies can still be seen to be normal, as are the corners of the vertebral bodies. Note also the absence of pathology dorsally

and probably represents a manifestation of a robust, somewhat overweight bone-forming individual. Indeed, if such individuals develop osteoarthritis they are frequently hypertrophic. Forestier's disease/DISH is not the only cause of enthesis new bone formation; others include obesity and age (presumably due to wear and tear) and fluorosis.

Calcific Periarthritis

This disorder occurs at the shoulder joint in 80% of cases. The next most common site is at the gluteal tendons. The lesion is characterised by fibrinoid necrosis within the tendon itself and the presence of freshly deposited hydroxyapatite crystals. In the case of the shoulder, this usually occurs in the rotator cuff, at the so-called critical or ischaemic zone. The aetiology is unknown, but most likely abnormal collagen breakdown products act as a focus for calcification to occur. In other words, the deposition of hydroxyapatite is passive rather than active. Radiologically this process is marked by obvious ill-defined soft tissue calcification. The older, more longstanding a lesion, the denser and more defined the calcification becomes. CPPD may be deposited also in the enthesis in those patients who are depositing a large quantity of the crystal, but this is usually linear and close to the enthesis rather than at critical or ischaemic zones.

Differentiation between the various types of erosive enthesis disease can be difficult. However, reference to the sacroiliac joints may be helpful. In ankylosing spondylitis, involvement is usually symmetrical, affecting both joints and the two major components of the joints, these being the mainly fibrous, amphiarthrodial compartment as well as the sliding, cartilaginous diarthrodial joint. The other group of diseases, that is, PSA, Reiter's syndrome and Behçet's syndrome, tend to be asymmetric and patchy. Forestier's disease/DISH may involve the sacroiliac joints also but characteristically causes non-erosive (by definition) anterior bridging new bone formation best visualised on a direct axial CT scan.

Summary

To summarise, disease of the enthesis occurs usually in the seronegative group, which involve the sacroiliac joints. Symmetrical erosive disease occurs in ankylosing spondylitis (with or without inflammatory bowel disease), whereas asymmetric involvement may occur with PSA, Reiter's syndrome and Behçet's syndrome. Non-erosive enthesis ossification is part of a generalised bone-forming character and is typified by Forestier's disease/DISH.

Drawing It All Together

It was emphasised at the outset that a joint is an organ within which are synovium, cartilage and bone and around which are entheses. Whilst it may assist understanding to separate these components, in practice they should be seen as interrelated in an integral unit. Osteoarthritis, for example, whilst predominantly a disease of cartilage and subchondral bone, is clearly associated with a joint effusion and low-grade synovitis. The latter no doubt contributes to the metabolic changes that occur. Similarly, although rheumatoid disease is predominantly a synovial disorder, the effects on subchondral bone and hyaline cartilage are undoubted. Some conditions clearly manifest themselves in more than one tissue within the joint organ. The classic example is PAO (pustular arthrosteitis) or SAPHO (synovitis, acne, pustulosis, hyperostosis and osteitis) syndrome [16]. Here bone proliferation almost certainly is associated with a chronic inflammatory disorder of as yet unknown aetiology. This manifests itself not only in bone, as mass lesions and chronic osteomyelitis, but also at the enthesis, with erosive coarse new bone formation, and in joints with features indistinguishable from PSA. What processes are occurring remain to be evaluated. This chapter has set out to encourage the reader to differentiate between arthritides, by distinguishing not disease entities but pathological processes. Medicine has a habit of pigeonholing and subdividing phenomena that are frequently the manifestations of disease processes rather than diseases themselves. For example, we have come to think of osteoarthritis as joint failure, manifest by subchondral cysts, sclerosis and osteophytosis. Yet in truth, these changes may themselves be manifestations of repair and the prime aetiology of osteoarthritis is unknown at present. Why does hyaline cartilage and subchondral bone fail in the first place? Worse, clinically PSA has been classified into various subsets, some of which include features indistinguishable from rheumatoid arthritis! MRI has shown two major subsets of disease in PSA [8]. In this series of patients, it was shown that half the patients had synovitis and erosion that were indistinguishable from rheumatoid arthritis. However, the other half exhibited changes that included capsular and pericapsular inflammatory changes: in other words showing features primarily of an enthesis disorder. Are these two very different manifestations the same disease? Clearly the answer has to be no! Do patients who have PSA and a rheumatoid arthritis-like manifestation have PSA, or do they have a skin disease called psoriasis and rheumatoid arthritis? These are the challenges that arise from analysing the appearances we see as radiologists rather than accepting patterns as diseases and then wondering why, on occasion, we cannot readily give a name to such a pattern.

References

1. Watt I (1997) Arthritis-basic differential diagnosis. Eur Radiol 7:344–351
2. Martel W, Stuck KJ, Dworin AM, Hylland RG (1980) Erosive osteoarthritis and psoriatic arthritis: a radiologic comparison in the hand, wrist and foot. Am J Roentgenol 134:125–135
3. Brook A, Corbett M (1977) Radiographic changes in early rheumatoid disease. Ann Rheum Dis 36:71–73
4. De Bois MHW, Arndt JW, Van der Velde EA et al (1994) Joint scintigraphy for quantification of synovitis with 99mTc-labelled human immunoglobulin G compared with late phase scintigraphy with 99mTc-labelled diphosphonate. Br J Rheumatol 33:67–73
5. Østergaard M, Stoltenberg M, Henriksen O, Lorenzen I (1996) Quantitative assessment of synovial inflammation by dynamic gadolinium-enhanced magnetic resonance imaging. A study on the effect of intra-articular methylprednisolone on the rate of early synovial enhancement. Br J Rheumatol 35:50–59
6. Creamer P, Keen M, Zananiri F, Waterton J, Maciewicz R, Dieppe P, Watt I (1997) Quantitative MRI of the knee: a method of measuring response to intra-articular therapies. Ann Rheum Dis 56:378–381
7. Jevtic V, Watt I, Rozman B et al (1993) Precontrast and postcontrast (Gd-DTPA) magnetic resonance imaging (MRI) of hand joints in patients with rheumatoid arthritis. Clin Radiol 48:176–181
8. Jevtic V, Watt I, Rozman B, Kos-Golja M, Demsar F, Jarh O (1995) Distinctive radiological features of small hand joints in rheumatoid arthritis and seronegative spondyloarthritis demonstrated by contrast enhanced (Gd-DTPA) magnetic resonance imaging. Skeletal Radiol 24:351–356
9. Foster JE, Maciewicz RA, Taberner J, Dieppe PA, Freemont AJ, Keen M, Watt I, Waterton JC (1999) Structural periodicity in human articular cartilage: comparison between magnetic resonance imaging and histological findings. Osteoarthritis Cartilage 7:480–485
10. Hayes A, Clift SE, Miles AW (1997) An investigation of the stress distribution generated in articular cartilage by crystal aggregates of varying material properties. Med Eng Phys 19:242–252
11. Swan A, Heywood B, Chapman B, Seward H, Dieppe P (1995) Evidence for a causal relationship between the structure, size and load of calcium pyrophosphate dihydrate crystals, and attacks of pseudogout. Ann Rheum Dis 54:825–830
12. Axford J, Bomford A, Revell P, Watt I, Williams R, Hamilton E (1991) Hip arthropathy in genetic haemochromatosis: radiographic and histologic features. Arthritis Rheum 34:357–361
13. Peterfy CF, van Dijke C, Janzen DL et al (1994) Quantification of articular cartilage in the knee with pulsed saturation transfer subtraction and fat-suppressed MR imaging: optimisation and validation. Radiology 192:485–491
14. Kladny B, Bail H, Swoboda B, Schiwy-Bochat H, Beyer WF, Weseloh G (1996) Cartilage thickness measurement in magnetic resonance imaging. Osteoarthritis Cartilage 4:181–186
15. Resnick D, Shaul SR, Robins JM (1975) Diffuse idiopathic skeletal hyperostosis (DISH): Forestier's disease with extraspinal manifestations. Radiology 115:513–524
16. Kasperczyk A, Freyschmidt J (1994) Pustulotic arthrosteitis: spectrum of bone lesions with palmoplantar pustulosis. Radiology 191:207–211

Nonneoplastic Disease of the Spine

Herwig Imhof

6.4

Contents

Introduction

Back pain and spinal diseases are the second most common problem that prompts patients to visit physicians. The increase in back disabilities surpassed all other cases tenfold between 1980 and 1990. In the same period, conventional radiography, bone scintigraphy, myelography and discography were supplemented by CT and MRI. In the last years PET was added. The wise use of all these different modalities is a great challenge.

Because back pain is a self-limiting disease in the majority of cases and its prevalence is so high, imaging of every patient with complaint would be very costly. Back pain does not follow the classic model of disease, in which symptoms closely correlate with imaging abnormalities. For example, roughly 80% of patients with low back pain may have no detectable abnormalities. Asymptomatic individuals, however, may be found to have striking findings on imaging studies. In many cases, radiology will serve only to rule out other serious conditions (such as neoplasm or infection), for accurate localization of disk herniation, and for surgical planning.

Spinal Degeneration

Pathophysiology

The disk consists of the annulus fibrosus, nucleus pulposus and porous, cartilaginous endplates (Fig. 1). It is an osmotic system, in which proteoglycans bind "free" water. The nucleus has a very high expansion power (6–8 atm osmotic swelling pressure) (Fig. 2). During

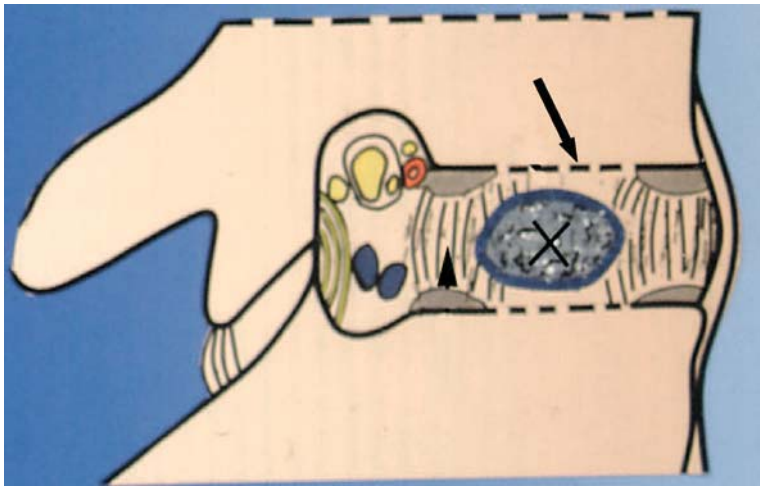

Fig. 1. Schematic drawing: lateral view of spine with disk, showing the nucleus pulposus (*x*), annulus fibrosus (*arrowhead*) and cartilaginous endplates (*arrow*)

Fig. 2. Vertebral disk specimen: swelling of the disk due to the osmotic swelling pressure of the proteoglycans

motion the normal eccentrically located nucleus pulposus seems to migrate anteriorly and posteriorly. During extension a posterior disk bulge is greatest. During relaxation the disk takes up water and attains its full size (preloading). This full-size disk stretches the accompanying ligaments (anterior and posterior longitudinal ligaments, etc.). Therefore the spine is an elastic rod. Loading of the spine leads to an elastic deformity of the spine, strengthening its physiological S-shaped lordosis and kyphosis [1–3].

During loading the disk becomes dehydrated, causing the accompanying ligaments to become loosened. The disk-height is reduced. The spine loses its homogenous elasticity. In turn, localized overloading of the disk and subchondral spinal endplates may take place.

The disk is only partially vascularized until the age of 4 years. Later on nourishment is based on fluid diffusion from the neighboring bony endplates and soft tissue (ligaments, etc.) (Fig. 3). Diffusion is enhanced by motion. Lack of motion over a long period of time leads to metabolic problems and inadequate nutrition. The frequency of this motion is also very important. Whole-body vibration frequencies of about 4–5 Hz may result in fluid stasis and metabolic problems within the disk [4].

Recurrent localized overloading – particularly in the lower lumbar and cervical spine – leads to tears in the annulus fibrosus (Fig. 4). The expansion power presses nucleus pulposus masses into these tears (internal disruption). In the worst case it leads to herniation, which could be either protrusion of nucleus material (with or without preservation of the overlying longitudinal structures) or disk extrusion (with obliteration of the overlying longitudinal structures). A herniation does not inevitably result in neurological symptoms. On the contrary, it is assumed that in older age groups (>50 years) the majority of disk herniations occur without any clinical symptoms. Moreover, it is well known that there may be a repair mechanism by fibrovascular tissue, which dissolves the protruded disk within 9–12 months. For this reason, among other things, without corresponding clinical symptoms the treatment of herniated disks is very conservative nowadays. The coming and going of disk herniations during life may represent the natural life of disks. Only in relatively rare cases they will develop clinical signs. On the other hand, in some cases the herniated disk loses the connection to the central part completely and shifts independently up – or downwards – in the spinal canal (sequestered disk) [5].

As a result of degenerative processes, tiny calcifications may develop within the disk (Fig. 5). As a sign of internal structure disruption with dissolution of gas

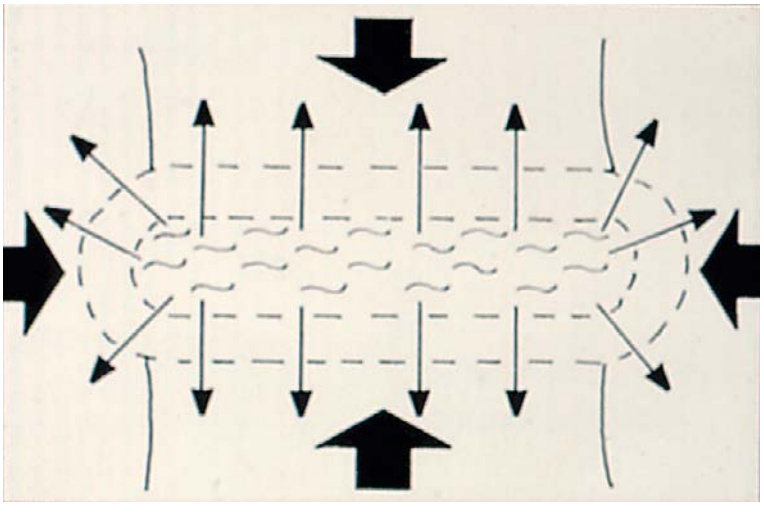

Fig. 3. Schematic drawing: compression and decompression of the disk with exchange of metabolic products during motion

(nitrogen) the so-called vacuum-phenomenon may be recognized [6].

A process very similar to that described in the anterior and posterior part of the disk may take place within the bony endplates. If these and the annulus fibers are weakened locally (e.g., in osteoporosis) the nucleus pulposus, because of its high internal pressure, will invade the bone resembling Schmorl's node. Active (symptomatic) Schmorl's node shows signs of inflammation and fracture healing (Fig. 6).

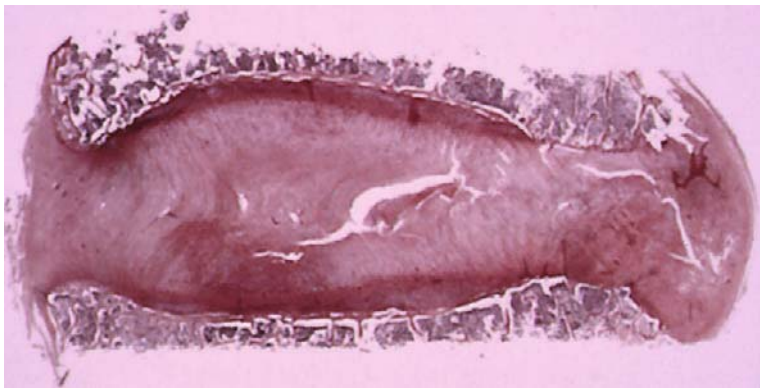

Fig. 4. Micromorphological sagittal cut with HE staining of a protruded disk with tears within the annulus fibrosus and nucleus pulposus

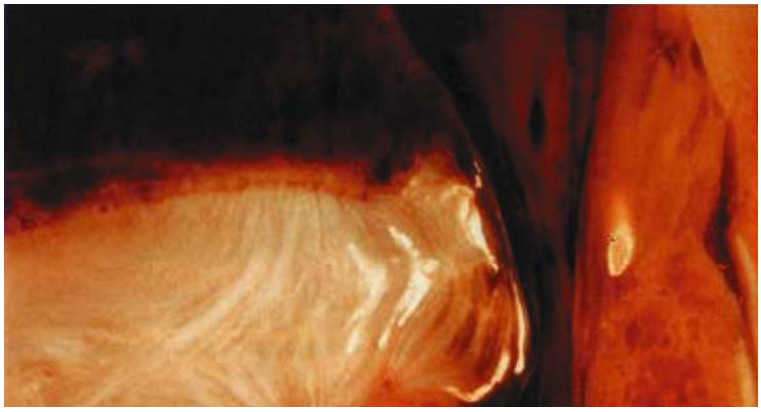

Fig. 5. Macromorphological sagittal cut of a lumbar spine specimen: calcification within the annulus and dorsal longitudinal ligament (chondrocalcinosis); minor dorsal herniation

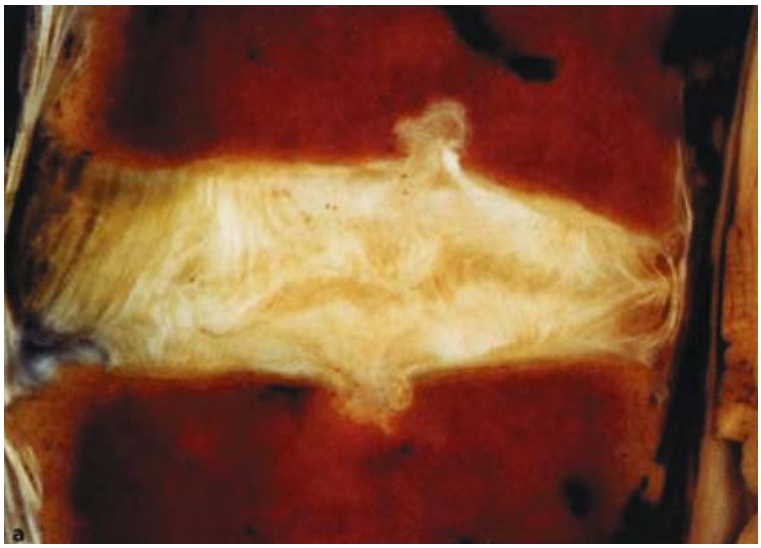

Fig. 6. Macromorphological sagittal cut of a lumbar spine specimen: herniation of disk tissue into the neighboring bone (Schmorl's nodes). The herniation is surrounded by sclerotic bone

Since the introduction of MRI into routine clinical imaging it has become well known that there are also degenerative changes within the bony endplates. Just as in synovial joints, this border region is damaged during overloading. This results probably in pain and activation of fibrovascular tissue, producing a pseudoinflammatory state representing stage I (Modic) degeneration. Today, it is assumed that the endplate fails before the injured annulus fails. Endplate failure seems to be the precursor to disk degeneration, since failure may disrupt disk nutritional pathways from the vertebra. Later on, this recurrent damages (stress) to the endplates leads to localized fatty conversion (stage II) (Fig. 7). Stage III is represented by the well-known subchondral calcifications (sclerosis). In Stages II and III the exchange of nutrients is increasingly reduced because of the further loss of fine vessels and endplate calcifications. The number of chondrocytes that support the disk will be diminished [1, 7].

As a side effect, it must be noted that the activated fibrovascular tissue of the endplates and surrounding soft tissue may grow into the disk, ending in neovascularization of the disk, particularly at the anterior and posterior part (Fig. 8).

Fig. 7. Macromorphological sagittal cut of a lumbar spine specimen: high-grade osteochondrosis with a central tear and fatty marry conversion, subchondrally

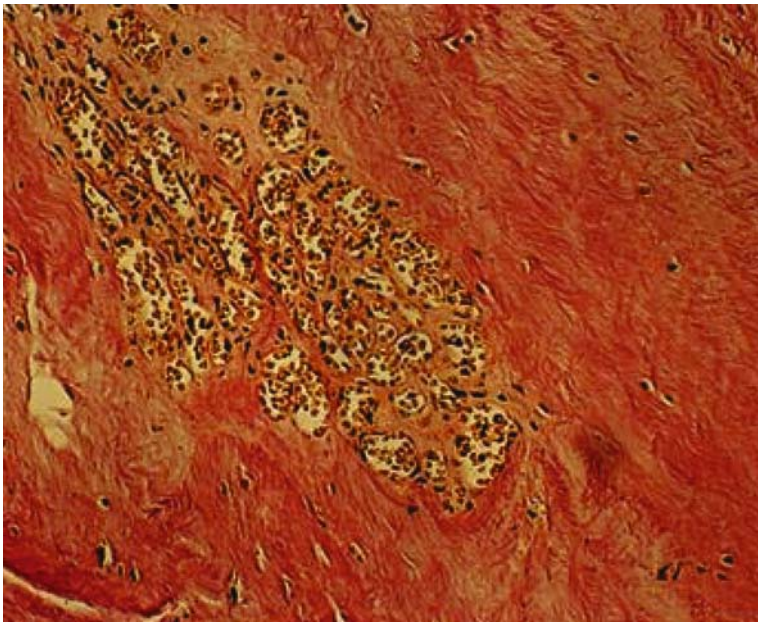

Fig. 8. Microscopic cut with Gieson staining: capillary invasion into the annulus fibers (revascularization of the disk)

During aging and degeneration the disk loses water. A healthy disk contains approximately 85% water, the rest being collagen and proteoglycans. Whether aging and degeneration are the same pathophysiological process is still unclear. However, there is no question that degeneration is mostly found in the aged population [8]. Given the loss of water in aging and degeneration, the water content drops to approximately 70%. The disk becomes more fibrous and disorganized, with loss of distinction between nucleus and annulus; the preloading of the accompanying ligaments is minor. While in the healthy, young spine loading takes place in the central part of the disk, this loading process is shifted peripherally to the annulus fibers in the chronically overloaded spine, leading to the above-described tears in the annulus. The spine as a whole becomes less elastic, the ligaments are looser. Local instability may develop, best visualized by in increasing retrolisthesis and spinal stenosis (Fig. 9). Local stress on the ligaments and instability itself leads to the formation of (traction) osteophytes. These prevent stress by restricting movement and restoring stability.

Following vascular invasion, progressive breakdown of the disk-tissue contents will result in their resorption. At this stage, the narrow space between the vertebral bodies will be occupied by a small amount of vascularized fibrous tissue, the neighboring bone becomes sclerotic. Frequently, the final stage of the resorption process is the spontaneous fusion of adjacent vertebral bodies (Fig. 10).

The intervertebral (facet) joints are typical synovial joints. They normally have a very thin corticalis laterally, which may even vanish in older people. Their degenerative changes are the same as in any other joint: cartilaginous and subchondral changes leading to cartilage edema, fibrillation and localized baldness, subchondral edema, cysts, sclerosis and effusion osteophytes and joint-space narrowing as well. A very typical marker for degenerative changes are synovial cysts. The innervation of the facet capsules is very rich. The angulation of the facet joints seems to be very important for the development of degeneration. The 3D orientation of the facet joint surfaces shows a gradual and characteristic change through each of the cervical, thoracic and lumbar spine regions. The kinematic constraints provided by the facet joints are particularly pronounced in the cervical spine, where there is marked coupling between lateral bending and axial torsion. In the thoracic spine they are organized like segmental socket joints. In the lumbar spine there is a great variation in the 3D orientation

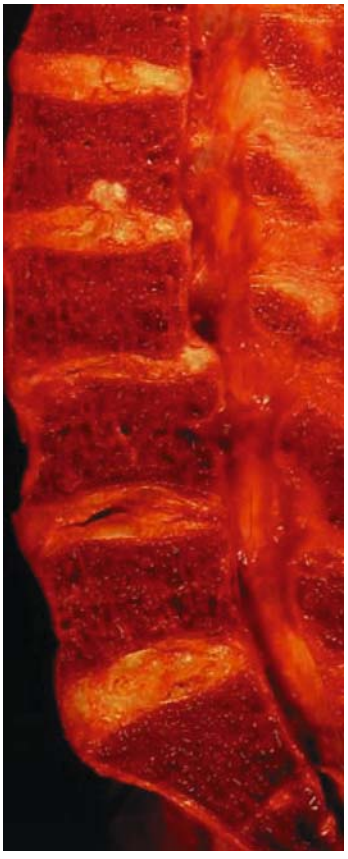

Fig. 9. Macromorphological sagittal cut of the lumbar spine: degenerative spondylolisthesis at L3/L4 with disk-space narrowing and a step formation between L3 and L4. Schmorl's node at L2

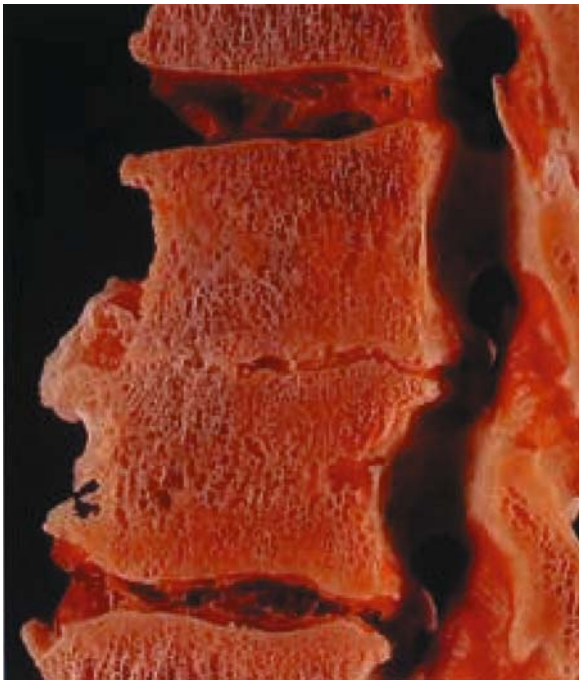

Fig. 10. Macerated lumbar spine (sagittal cut): bony fusion in severely degenerated disk

between sagittal and coronal orientation. While in the majority of cases, L1/L2 is more sagittally oriented, L4/L5 is in almost 90% frontally oriented: the former limits axial rotation, the latter flexion. It must be stressed that the surface of the facet joints is almost never flat, but arcuate (Fig. 11). Accordingly, the possible overloading depends in part on the positioning and surface of the facet joints. This is even aggravated if there is a asymmetry in the facet-plane orientation (tropism), which is found in approximately 30% of men and women. In such cases with a tropism of more than 5°, invariably a local overloading will take place during rotation (Fig. 12). It is therefore not surprising that in such cases annulus fissures are found unilaterally in 80% of all cases [4, 9, 10].

Facet joints and the disk share the load. In an upright position, 80% of the load is taken by the disk, 20% by the facet joint. In a flexed position the facet joint has to take over 50% of the load. The highest facet joint pressure develops under combined rotation, flexion, and compression. Reduction of disk height by 1 mm increases the facet-joint load by 36%, a 4-mm loss by 61%.

Spinal ligaments pass between each vertebra along the length of the spine and function to limit excessive joint motion. These ligaments include the anterior and posterior longitudinal ligaments, the ligamentum flavum, the inter- and so-called supraspinous ligaments, and the intratransverse ligaments. The facet-joint capsules and the annulus fibers also act as tension-bearing structures between the articular process. The anterior

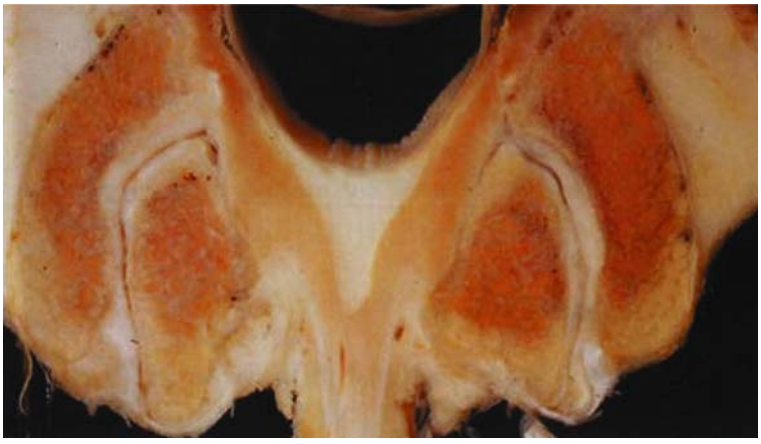

Fig. 11. Macromorphological cut (axially) through the facet joints: asymmetry of the joint surface (tropism). On the left side the articular cartilage is rarefied

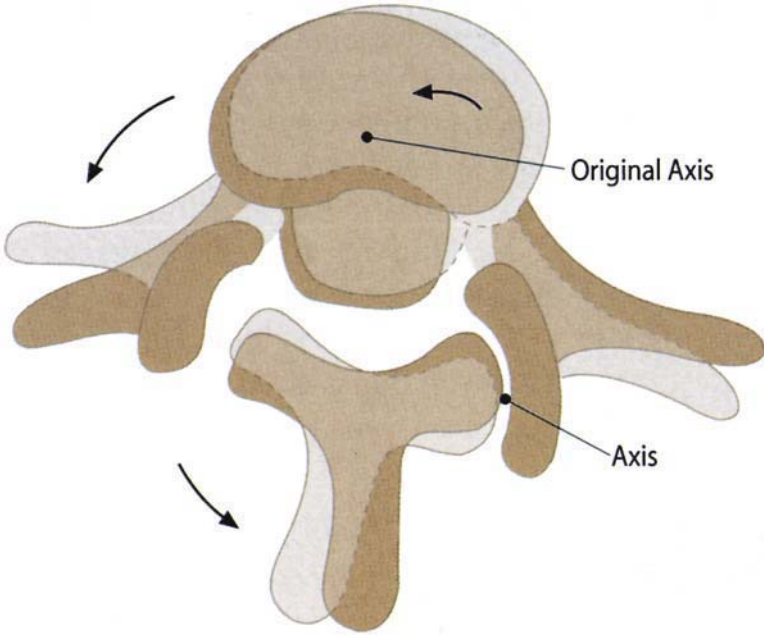

Fig. 12. Schematic drawing of the spine (axially) during rotation to the left side: there is a localized overloading in the right facet joint. The rotation is limited by the ligaments around the left facet joint and the annulus fibers

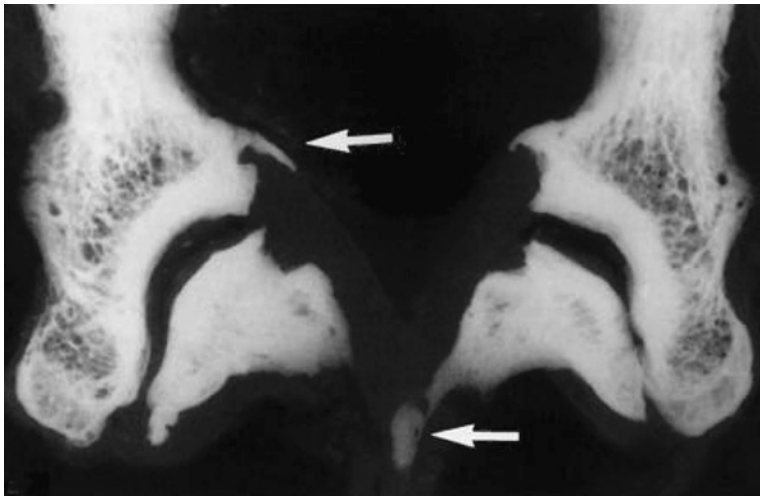

Fig. 13. Axial specimen radiography of lumbar facet joints: degenerative joint space narrowing with osteophytes (*arrows*). Typical calcification at the insertion of the left flaval ligament

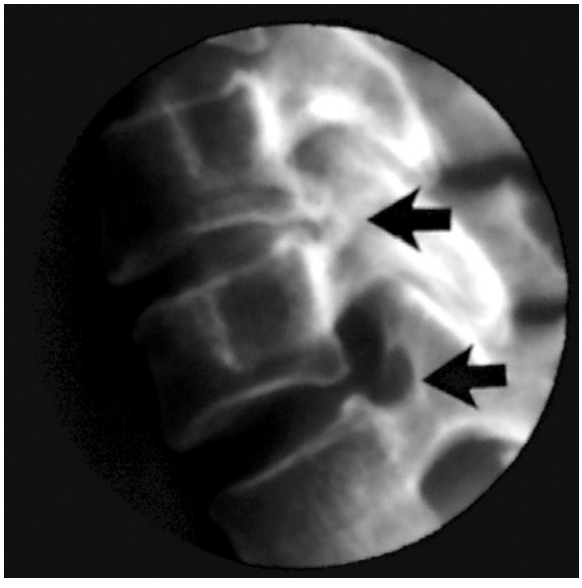

Fig. 14. Lateral conventional radiograph of the cervical spine: disk space narrowing and dorsal osteophytes with foraminal stenosis (*cranial arrow*). The calcified band crossing the foramen is a normal variation (*caudal arrow*)

longitudinal ligament is nonelastic and limits hyperextension and rotation. The posterior longitudinal ligament limits ventral flexion and lateral bending. The elastic flaval ligaments are very important for the preloading process and tend to calcify very early in life (Fig. 13). The interspinous ligaments limit ventral flexion and dorsal shifting. The so-called supraspinous ligament is actually not a ligament, but part of the fascia thoracolumbalis. The facet-joint capsules, particularly in the lumbar region limit shifting during rotation. All ligaments are extensively supplied by proprioceptors. They probably allow a direct coordination (activation) of the back muscles [3].

One of the major clinical questions is why pain is experienced in degenerative disease. Currently, it is thought that this is an acute decompensation in already damaged tissue. Critical points are possible bony stenoses and ligament problems: spinal canal stenosis with disk protrusion or extrusion and foraminal stenosis with osteophytes (Fig. 14) . Ligament – and capsular – lesions (e.g., overstretching) cause pain in about 70% of all cases. Subchondral bone marrow changes may also lead to pain (e.g., edema). Finally, disk tears themselves may provoke pain (internal disruption of the disk) by cytokines and macrophages [7].

Imaging

The basic imaging procedures are still conventional radiographs in two planes.

The first signs of incipient degeneration may be localized malalignments (retrolisthesis) with or without rotation of the vertebral body. Functional images (examination in maximal ante- and retroflexion or sidebending) can show abnormal localized mobility (Fig. 15). Later on, the disk spaces become narrowed (chondrosis) and subchondral sclerosis is seen (osteochondrosis) (Fig. 16). The disk height in the spine normally shows a progressive increase in height from cranially to caudally with the exception of C7/Th1 and L5/S1, which show normally a lower height than the vertebral body above. The facet joints also show narrowing and subchondral sclerosis with irregular surfaces. Osteophytes may develop near the disk laterally and anteriorly, rarely posteriorly, and at the facet joints as well. They are also signs of segmental instability [5, 11].

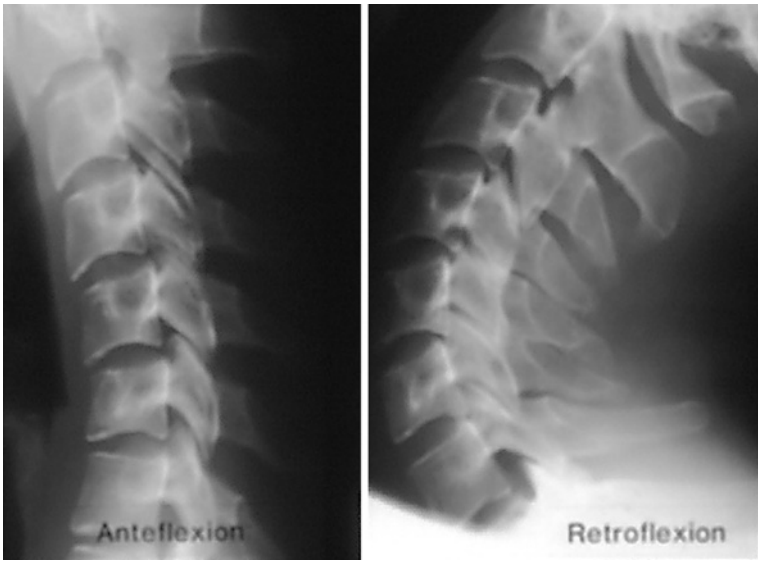

Fig. 15. Functional conventional radiographs of the cervical spine in maximal retro- and anteflexion: uniform and harmonious (smooth) flexion in all segments. The three lines (anterior vertebral body line, posterior vertebral body line, interlaminar junction line) must run parallel. There should be a tiling up of the vertebral bodies

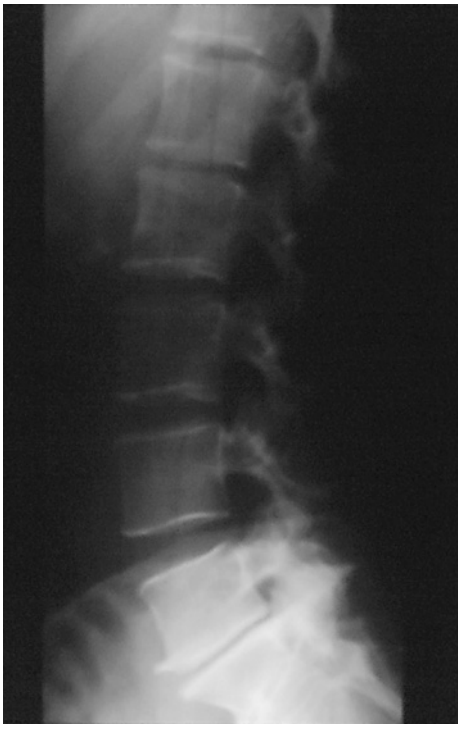

Fig. 16. Lateral conventional radiograph of the lumbar spine: osteochondrosis L5/S1 with disk space narrowing, subchondral sclerosis, and anterior osteophytes

As degeneration progresses, the disk height becomes significantly diminished, osteophytes become prominent, and the motion segments (disk + two complete vertebrae) become stable, but less mobile.

Discrete abnormalities within the facet joints may be best evaluated with CT (Fig. 17). CT also allows recognition of disk calcifications (Fig. 18) and gas (vacuum phenomenon) within the disk. The latter is one of the best signs of degeneration on conventional radiographs; the former may be found in aging and degeneration, but also in metabolic diseases (e.g., pyrophosphate disease, hyperparathyroidism, ochronosis, diffuse idiopathic skeletal hyperostosis, etc.).

Only in the lumbar spine is CT almost equal to MRI in visualization of disk bulging and herniation (protrusion and extrusion) (Fig. 19) [4]. A protrusion is a local-

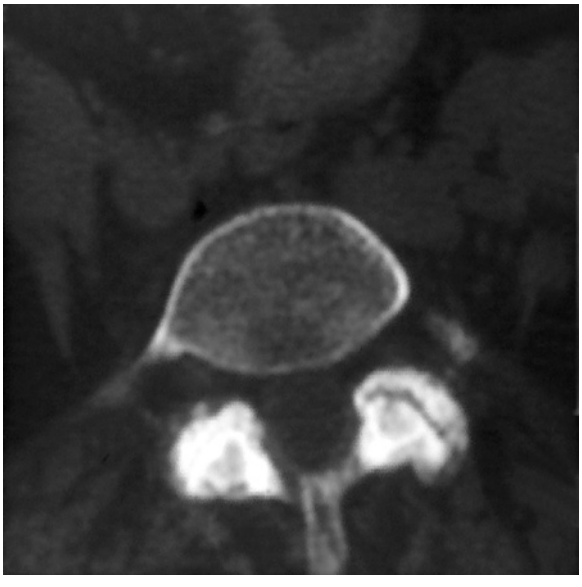

Fig. 17. Axial CT of the lumbar spine: severe degenerative changes in the facet joints with joint space narrowing, irregularity, osteophytes, and subchondral sclerosis. The angulations of the facet joints are asymmetrical (tropism)

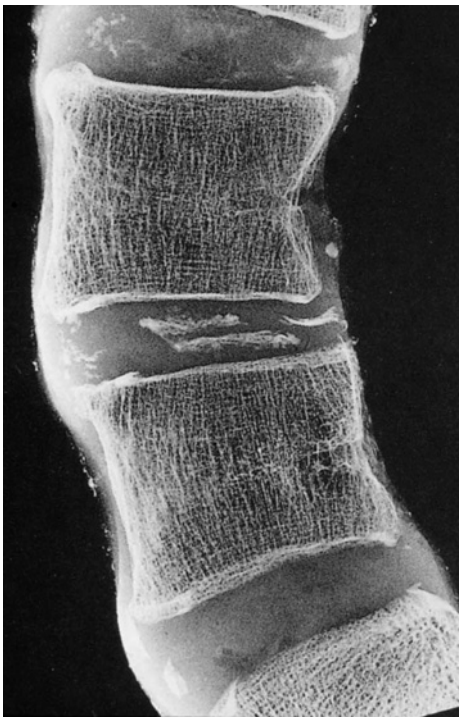

Fig. 18. Specimen lateral radiograph of the lumbar spine: disk calcifications with minor degenerative abnormalities

ized abnormality of disk contour wherein the base of the abnormality measured along the circumference of the disk is greater than the extension beyond the circumference, measured perpendicular to the base. An extrusion is a localized abnormality of disk contour wherein the base of abnormality is narrower than the extension beyond the circumference. A disk bulge is a generalized extension of the disk (at least 180°), usually limited to 3 mm [7].

It must be stressed that these definitions of protrusion, extrusion and bulge are strictly morphological, but pathoanatomically a bulge may have full-thickness annular fissures. Similarly, protrusions do not necessarily have intact outer annular fibers and extrusions may consist of a combination of nuclear and annular material. Clinically, there is in most cases no real relation between pain and morphology. Nevertheless, large compressive lesions (i.e., disk extrusions) are almost always symptomatic. The best surgical results are achieved when 1) a well-defined disorder is demonstrated by imaging studies and 2) imaging findings are closely correlated with the clinical history and physical findings.

CT directly outlines the herniated soft tissue masses, minimized epidural fat (lumbar spine) or subdural fluid space (cervical spine). It is important to distinguish far lateral from lateral and central extrusions, and calcified

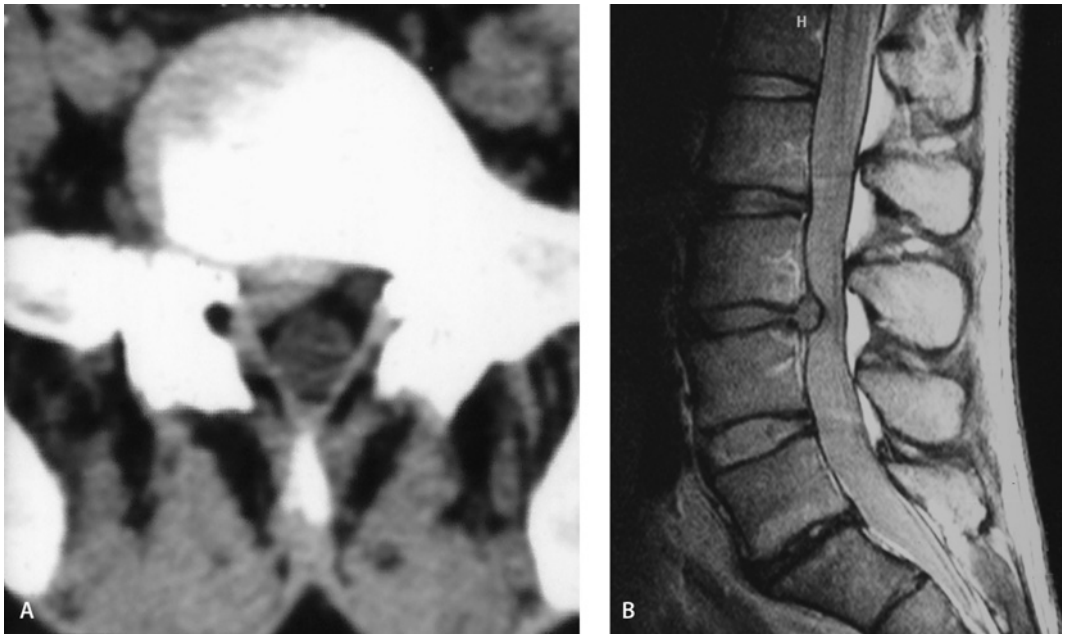

Fig. 19. **A** Axial CT of the lumbar spine: right lateral disk prolapse with obliteration of the epidural fat, but no compression of the dural sac. **B** Lateral MRI of the lumbar spine (spin density image): protrusion of the disk dorsally L3/L4 with preservation of the longitudinal ligament. Compression of the dural sac. Disk-space narrowing and minor reactive fatty marrow conversion

from uncalcified ones. The latter distinction may be particularly important before invasive treatment, since hard or calcified prolapses cannot dissolve. In some cases, the extruded disk loses its connection with the central part and becomes a sequestrum, which may move up or down in the spinal canal and be calcified or uncalcified (Fig. 20).

In the last few years, MRI has become the standard imaging method in many centers. It allows direct visualization of the disk itself. Because of its high water content, the nucleus pulposus is bright on T2-weighted images. With aging and degeneration, it gains a horizontal dark line (nucleus cleft), later becoming less bright until it reaches the same low intensity as the surrounding annulus fibrosus. Meanwhile, the size and height of the disk decline continuously (Fig. 21) [8, 12].

In acute stage I (Modic) the subchondral bone marrow and any active Schmorl's nodes are hyperintense on T2-weighted images (Fig. 22) and enhance after intravenous injection of contrast medium (Fig. 23). Stage II shows fatty subchondral intensities (hyperintense on T1- and T2-weighting). Finally, sclerosis (stage III) will show a low intensity signal in all sequences.

Disk bulging or herniation is seen directly, as described above in the paragraph on CT. The sign is encompassed by loss of epidural fat or subdural CSF

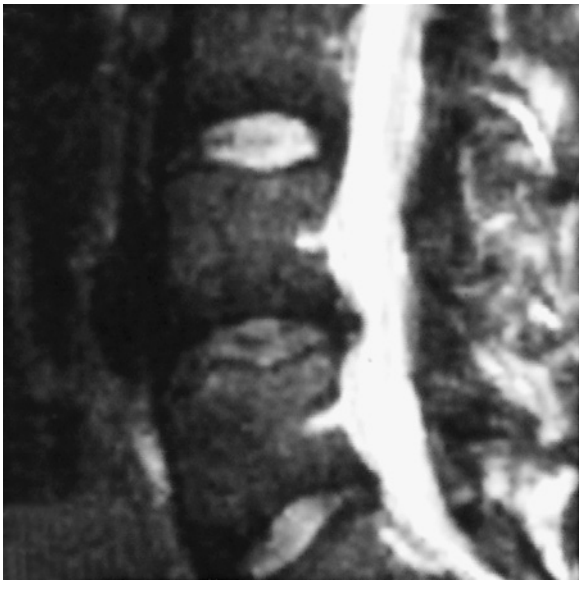

Fig. 21. Lateral T2-weighted MRI of the lumbar spine showing different stages of disk degeneration. Uppermost disk: disk has bright hyperintensity and a horizontal dark line (nucleus cleft). Middle disk: intensity of annulus fibrosus and nucleus pulposus is very low due to loss of water. The height of the disk is reduced. Lowermost disk: disk height is reduced, but there is still hyperintensity within the disk, probably also representing remaining expansion power

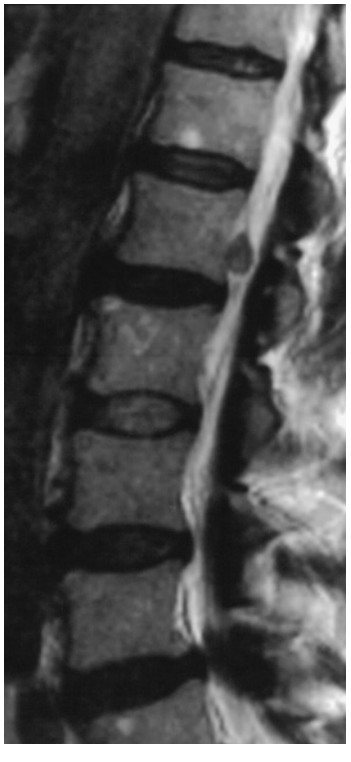

Fig. 20. Lateral MRI of the lumbar spine (spin density): low-density disk sequester at the height of the vertebral body L1

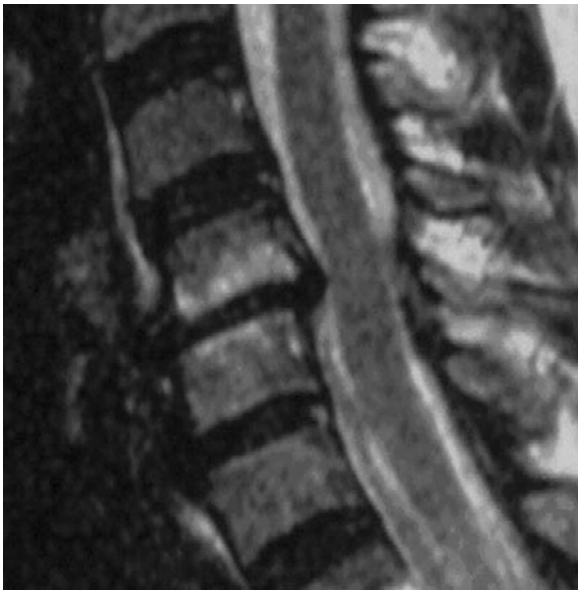

Fig. 22. Lateral T2-weighted MRI of the cervical spine showing stage I degeneration with subchondral bone marrow edema. Indentation of the dural sac is visible, minor retrolisthesis. The patient has severe pain

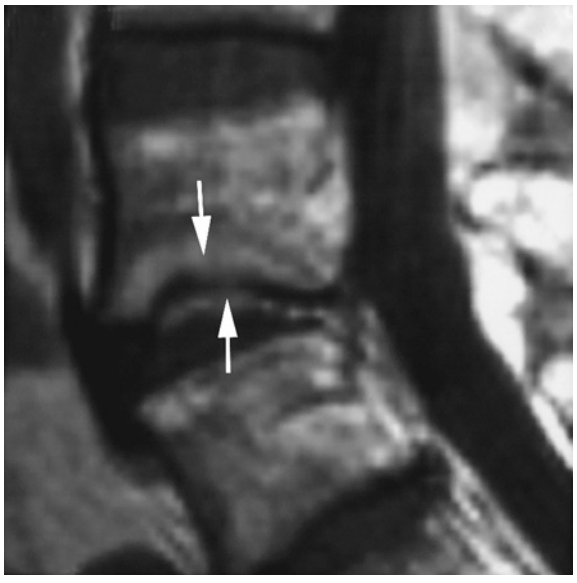

Fig. 23. Lateral T1-weighted MRI of the lumbar spine with contrast enhancement showing subchondral and linear disk contrast enhancement (*arrows*) due to (pseudoinflammatory) fibrovascular tissue in stage I degeneration (repair mechanism) with revascularization of the disk

space, obliteration of the longitudinal ligaments, and thickened epidural veins (Fig. 24). Direct compression of the medulla or nerve roots can be visualized. The majority of herniated disks shrink by more than 75%. The shrinkage occurs in the 1st month after symptoms start, as a result of hydration followed by quick dehydration. This process explains why some extruded disks appear bright on T2-weighted MR images early in the disease (Fig. 25). Only 8% of disk herniations enlarge. Extrusions and large protrusions have the highest rate of spontaneous shrinkage and symptom improvement.

Internal disk disruption is a controversial entity, the proponents of which believe that chronic lumbar back pain originates in the disk. The mechanism is thought to be leakage of the nucleus pulposus into the outer annulus or epidural space without frank herniation.

Postoperatively, in 15% of all cases patients have the same symptoms as before (failed back surgery syndrome). In these cases, the question arises of whether there is a recurrent or residual disk herniation or only scarring. By intravenous injection of contrast medium, MRI (CT as well, in the lumbar spine) can differentiate between the two: even if the operation is years in the past, scar will show an enhancement due to fibrovascular tissue and have no mass effect, whereas recurrent or residual disk prolapse will reveal no enhancement, but typically a mass effect. In some cases a recurrent or residual disk may be surrounded by scar tissue (Fig. 26). Epidural scarring is responsible for 24% of all failed back operations [14].

There is a high correlation between the extent of scarring and the severity of recurrent radicular pain. Less common causes of failed back syndrome are postoperative diskitis, arachnoiditis and instability.

CT myelography and discography are rarely used nowadays. MRI should give the same results in the vast majority of cases. Only in cases of unexplained back pain where localization is impossible, examinations

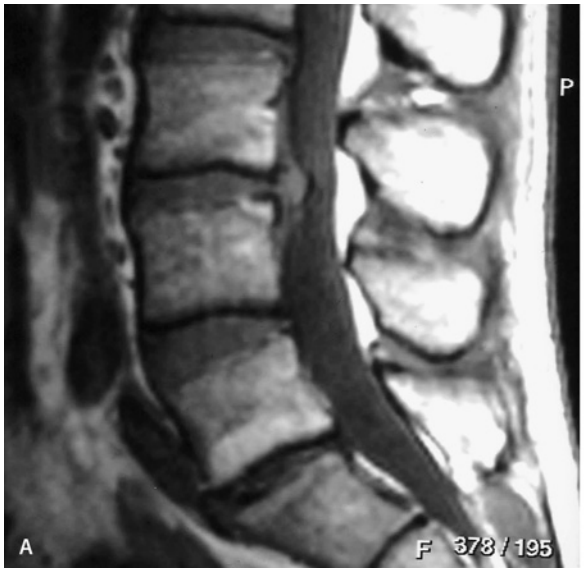

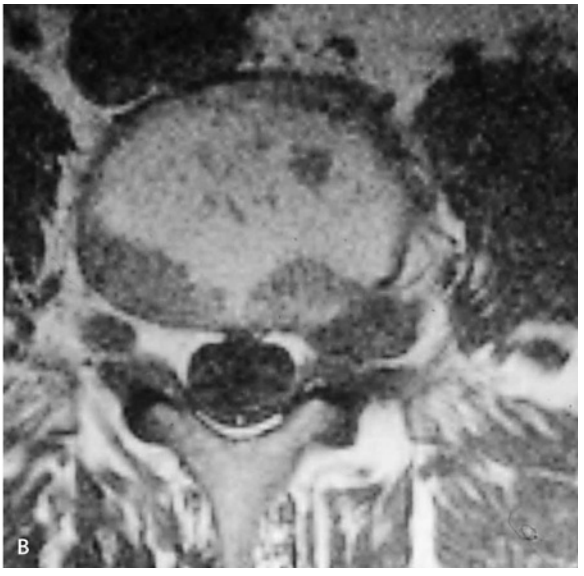

Fig. 24A, B. Lateral T1-weighted MRI of the lumbar spine. **A** Lateral: dorsal disk herniation at L3/L4 with localized fatty marrow conversion. Severe disk space narrowing with fatty marrow conversion at L5/S1. **B** Axial: left-sided low-intensity mass in the foramen representing a disk extrusion

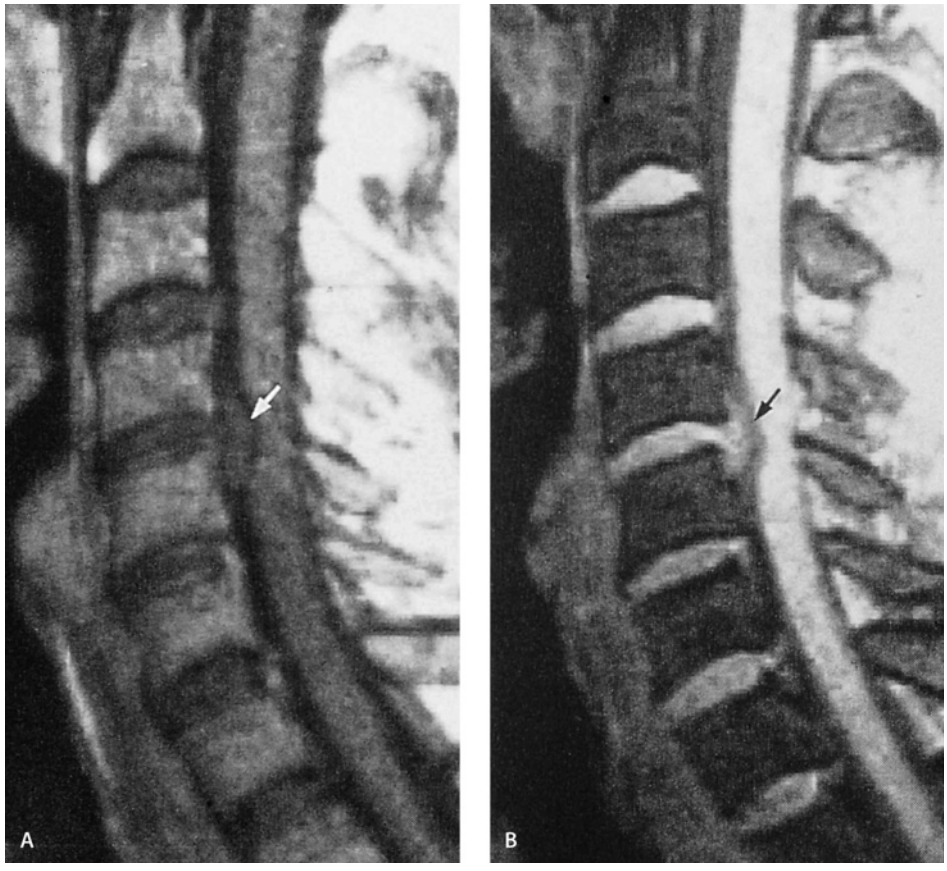

Fig. 25. A Lateral T1-weighted MRI of the cervical spine: low-intensity disk extrusion at C4/C5 with impression of the dural sac (*arrow*). **B** Lateral T2-weighted MRI of the cervical spine: the disk material is hyperintense (*arrow*)

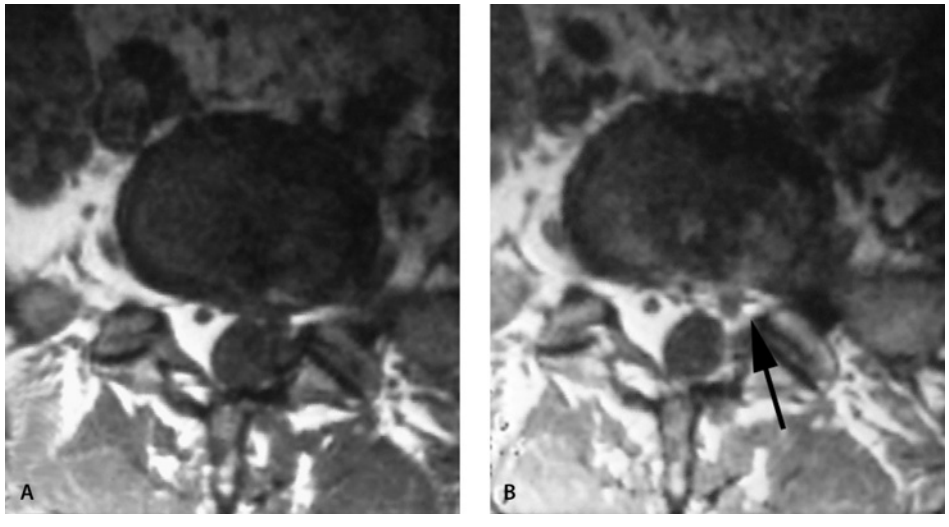

Fig. 26A, B. Postoperative axial T1-weighted MRI of the lumbar spine **A** before and **B** after injection of contrast medium. **A** Low-intensity mass within the left anterior epidural region. The nerve root cannot be distinguished. **B** Enhancement of the low-intensity mass except for the swollen nerve. *Arrow*: scar tissue

with spinal loading may reveal hidden abnormalities. Discography with pain-relieving drugs may discern symptomatic levels in cases of multiple-level disk disease.

Inflammation

Spondylitis is a rare disease, constituting only 1%–4% of all cases of osteomyelitis. It is more common in males (male:female ratio, 3:1). Typically, it is found in the older age group (60–80 years). Spondylitis is in most cases preceded by infections elsewhere in the body such as the respiratory system, genitourinary system, and the skin. Predisposing factors are diabetes mellitus, intravenous drug abuse, liver disease, kidney failure and conditions that suppress the immune system. Due to the insidious onset of the disease – particularly in granulomatous spondylitis – a delay in diagnosis is very common [13].

Pathophysiology

In the majority of cases the infectious process is transferred hematogenously by arteries or veins, rarely by direct continuous invasion. In recent years, cases the posttraumatic (postoperative) etiology have been increasing due to interventional procedures. The venous propagation is based on a retrograde flow in valveless veins within the abdomen or thorax (Batson plexus). Retrograde venous flow develops whenever the internal pressure within the thorax or abdomen is heightened [2].

Spondylitis can be divided into pyogenic and granulomatous. The most common isolated organism in pyogenic spondylitis is – unchanged for decades – *Staphylococcus aureus*, which accounts for 42%–84% of infections, followed by streptococcus, pseudomonas and *Escherichia*. In granulomatous spondylitis, the most frequently found causes are tuberculosis, fungi (histoplasmosis, aspergillosis), leprosy and parasites.

As anywhere in the body, a bacterial or viral embolus reaches a highly vascularized region where there is a local insult or immunosuppression (e.g., due to a microinfarction, trauma, etc.). Therefore the location of spondylitis is primarily based on vascularization, which is age-dependent. Until the age of 4 years, there are no end arteries in the vertebral body, only in the disk. Therefore newborns and children up to 4 years of age may primarily get diskitis. Older age groups have equatorial and metaphyseal end arteries, in which inflammation usually starts (Fig. 27). The infectious process is therefore located anteriorly, near the disk or centrally in the vertebral body. It may include the disk secondarily (spondylodiskitis). Simple diskitis may only be found in children or result from iatrogenic procedures. The vertebral arches are very rarely involved in an infectious process.

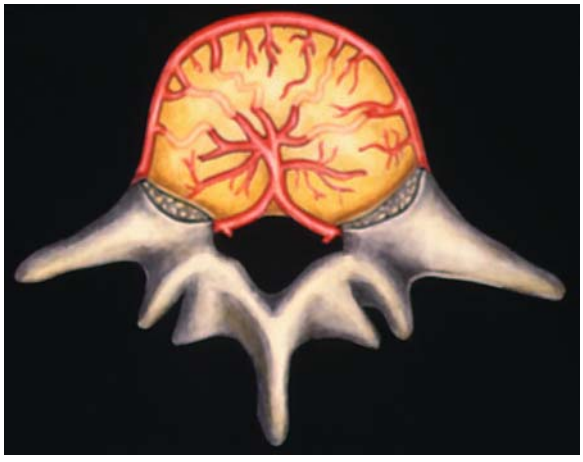

Fig. 27. Schematic drawing of the arteries of a vertebral body: up to the age of 4 years, all arteries are interconnected. In the adult and older children the arterial connections become obliterated (*dotted lines*) resulting in end arteries

Inflammatory processes may reveal different appearances due to individual differences in the velocity of infection and the reaction of bone and soft tissue. At first there is a bacteriemia (viremia) followed by localized edema, demineralization with reactive hyperemia, and demarcation by fibrovascular tissue. Repair starts from outside. Activation of osteoclasts and transformation of fibroblasts into osteoblasts leads to new bone formation (primitive bone with a high density). Granulomatous spondylitis may show in about 30% soft tissue calcification. Finally, there is complete healing with rebuilding of trabecular and cortical bone. In some cases, this last step does not take place. In such a case, the dense calcified bone remains unchanged.

Possible complications are abscesses, which may develop within the bone or near the spine. Dead bone within the abscess in the bone is called a sequestrum. The paraspinal abscess formation – particularly in tuberculosis – may involve surrounding soft tissue and spinal cord. In granulomatous spondylitis, several vertebral segments are typically involved. The propagation occurs preferentially in the anterior subligamentous zone (Fig. 28). In the worst case – particularly in granulomatous spondylitis – the disease may end up in severe kyphosis with eventual ankylosis (Pott's disease) [5, 13].

While in pyogenic spondylitis the infectious process may be localized in the lower lumbar spine or thoracolumbar transition, the granulomatous entity involves more commonly the lower half of the thoracic and the lumbar spine.

In about 10%–20% of all cases, acute spondylitis is transformed to chronic spondylitis (by definition, if there is not complete healing after 6 months), due to delayed diagnosis, insufficient treatment or inadequate

Fig. 28. Macromorphological sagittal cut of thoracic spine: infectious process located anterior of and near the disk with anterior subligamentous extension

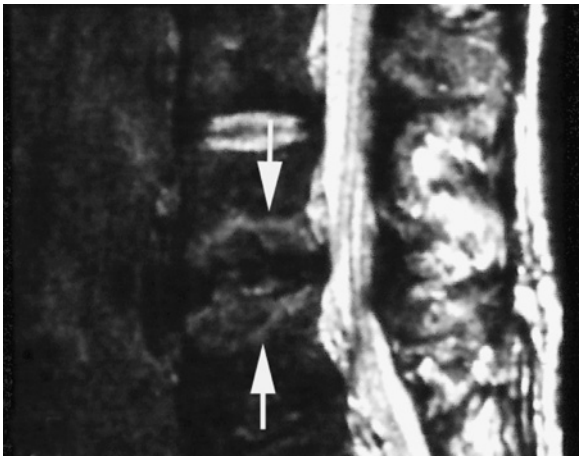

Fig. 29. Lateral T2-weighted MRI of the lumbar spine showing hyperintensity within the subchondral bone marrow, representing reactive edema in acute spondylitis

host defense. It is characterized by recurrent exacerbations of acute disease and insufficient healing. In many cases, it is the result of granulomatous, rarely of pyogenic spondylitis.

Imaging

Early diagnosis is possible using MRI. Hyperemia and the higher metabolic turnover of bone lead to localized T2 hyperintensity (edema) (Fig. 29) with contrast enhancement on T1-weighted images (hyperemia and reactive fibrovascular tissue). The T2-hyperintensity may involve the disk. The absence of the intranuclear cleft on T2-weighted images differentiates an infected disk from a well-hydrated, healthy disk. After injection of contrast medium, the disk, adjacent vertebral bodies, and involved paraspinal/epidural soft tissues are enhanced (Fig. 30). These typical (acute) findings may change to hypointensity when calcification starts (low-intensity bands).

Three-phase bone scan has a somewhat lower accuracy rate in acute pyogenic spondylitis in comparison to MRI. Moreover, it has a very low detail resolution: the anatomical details cannot be differentiated. Finally, it is also very time-consuming combined with radiation, additional disadvantage. However, in unclear chronic spondylitis disease, leukocyte bone scintigraphy or antigen scintigraphy may be an excellent problem solver.

In the last years positron emission tomography (PET) with FDG (18F-fluorodeoxyglucose) has increasingly been used in suspected spondylitis. In several publications, it proved useful for differentiation of degenerative and infectious endplate abnormalities found in MRI. While PET in a high percentage (>90%) of cases was positive in infectious disease, it remained normal in all degenerative processes, even in Modic I stage [15].

The first signs of spondylitis on standard radiographs are localized demineralization and narrowing of disk space with retrolisthesis. These abnormalities are found typically near the endplates and/or anteriorly (Fig. 31). In this stage, CT (conventional or spiral CT) could already reveal erosive changes within bony structures (Fig. 32) and soft tissue swelling.

Later on, reactive sclerosis develops from the outside and is the first sign of healing on conventional radiographs (Fig. 33). Finally, after some months normalization of all bony structures can be seen. In cases of complications, a sequestrum may develop (Fig. 34). Typically this is a central dense bone within a lytic lesion. The sequestrum looks more dense because the surrounding bone is porotic and the sequestrum itself may condense. In doubtful cases, CT is the method of choice to visualize these abnormalities [11].

MRI is the imaging modality of choice in early diagnosis or in unclear cases during treatment. Typically, in the acute phase it shows a localized hyperintensity on T2-weighted images (edema), which may involve the disk (spondylodiscitis). Later on there is localized con-

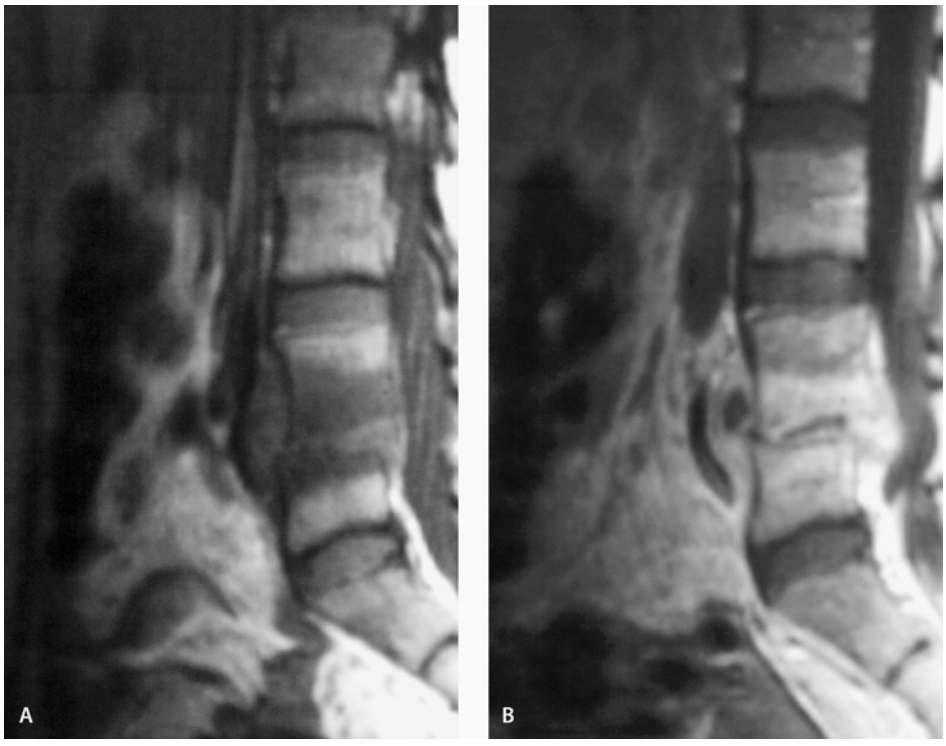

Fig. 30A, B. Lateral T1-weighted lumbar spine. **A** Before contrast medium injection and **B** after contrast medium injection. **A** There is a low-intensity lesion with soft tissue involvement of L4/L5. **B** Marked enhancement of the complete lesion

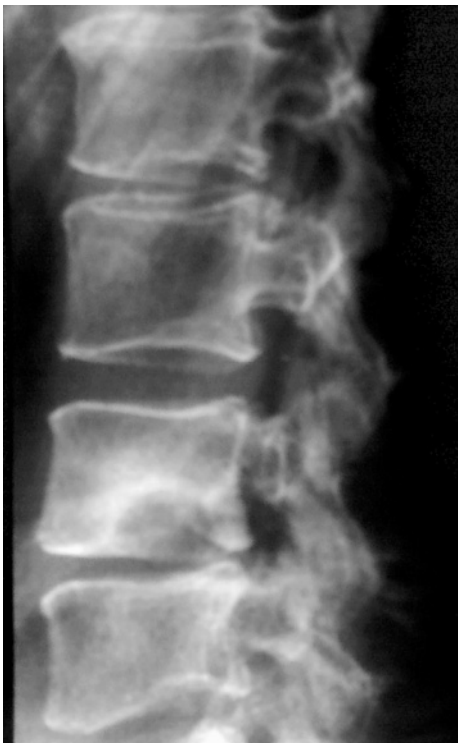

Fig. 31. Lateral conventional radiograph of the lumbar spine showing disk space narrowing with subchondral erosion dorsally and rim calcification in subacute spondylitis

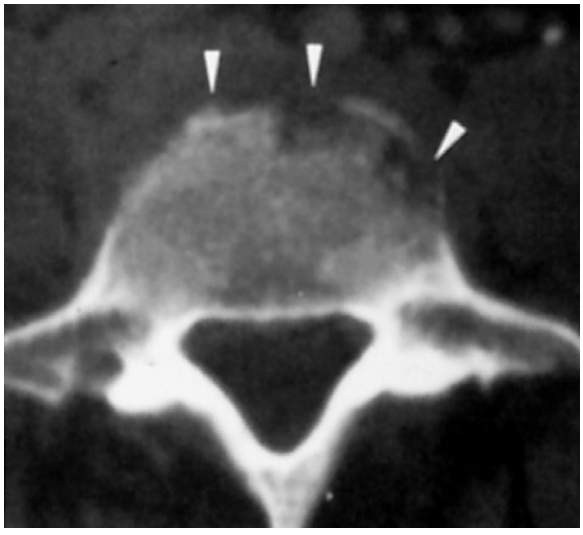

Fig. 32. Axial CT of the lumbar spine showing anterior erosions (*arrows*) with soft tissue swelling (*arrowhead*) in acute spondylitis

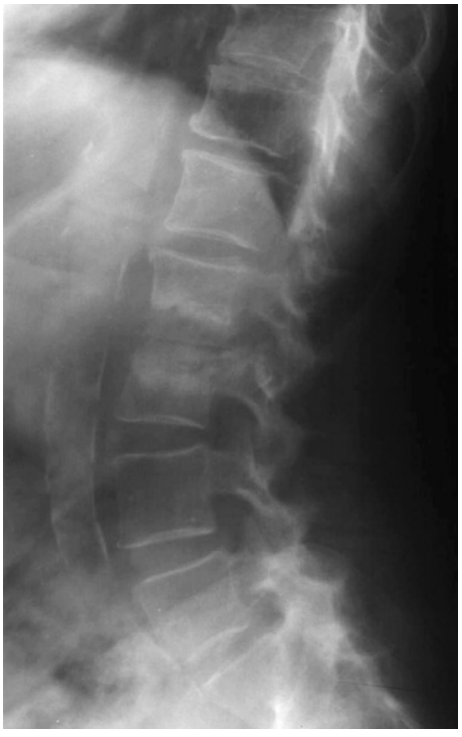

Fig. 33. Lateral radiograph of lumbar spine: inflammatory erosive changes between L2/L3 with sclerotic margins as first signs of healing

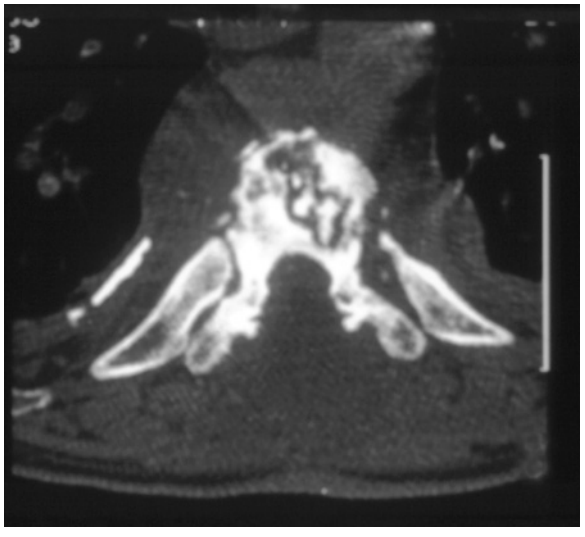

Fig. 34. Axial CT of the lumbar spine showing several calcifications (dense bone) within a lytic lesion representing multiple sequestra in an abscess

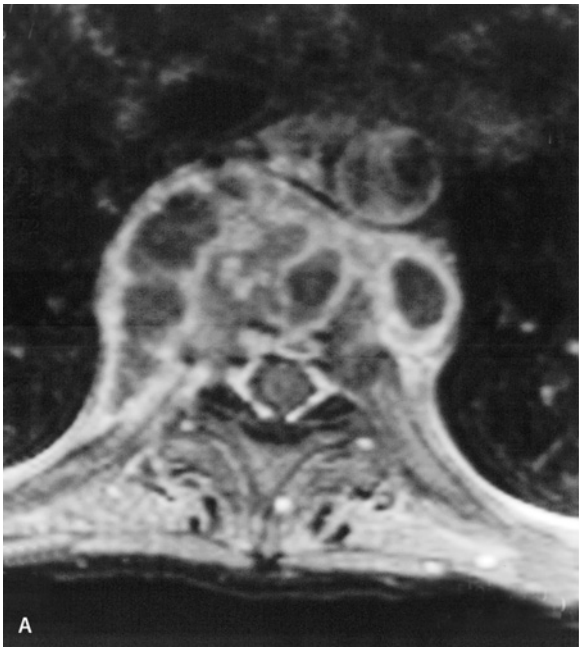

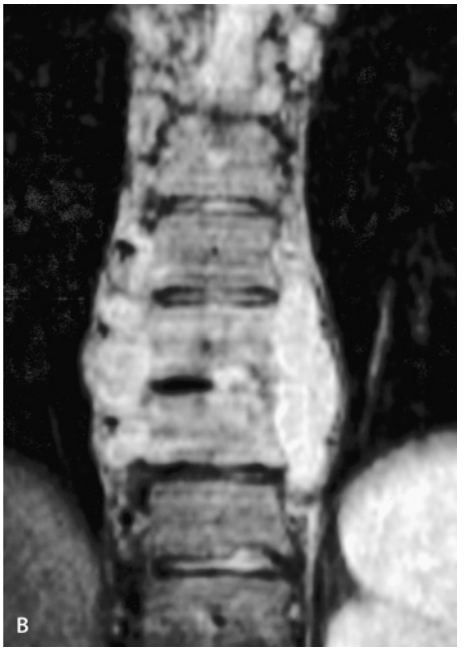

Fig. 35A, B. MRI of tuberculous spondylitis: **A** axial and **B** coronal, both after contrast medium application. **A** Hyperintense paraspinal soft tissue mass with multiple loculated, sharply outlined low-intensity lesions representing abscesses. **B** Paraspinal hyperintense soft tissue masses with multiple low intensities

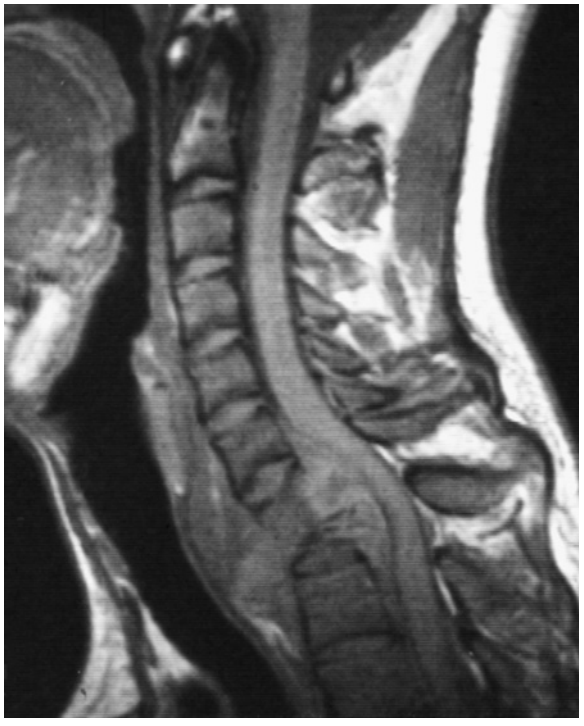

Fig. 36. Lateral T2-weighted MRI of the cervical spine: huge soft tissue mass at C7 with paraspinal and epidural extension. The disks seem to be preserved. Histology: lymphoma

trast enhancement on T1-weighted images starting from the outside. Finally, fatty marrow conversion takes places, which is also a marker of healing. Other signs of a favorable response to treatment are calcification on standard radiographs, reduction of edema and soft-tissue swelling and less enhancement after contrast medium injection.

Complications such as soft tissue and epidural abscesses are best seen with MRI or CT. Typically, a homogeneous fluid is found centrally, surrounded by soft tissue rim or irregular thickness. After contrast medium application, a rim enhancement is demonstrated (Fig. 35).

Granulomatous (tuberculous) spondylitis reveals the same basic imaging symptoms as pyogenic spondylitis, but progresses very slowly over months with minor clinical symptoms. Soft tissue swelling (with calcification) may be very prominent, and a huge soft tissue abscess may be found (e.g., psoas abscess, epidural abscess). Typically, tuberculous spondylitis can affect several neighboring vertebral bodies.

Rare pathogens of spondylitis are fungi or parasites. In fungal spondylitis, the imaging signs are very similar to those seen in tuberculosis. Parasitic spondylitis usually shows very typical findings (e.g., *Echinococcus* cyst).

Blastoma and granulomatous spondylitis may present a differential diagnostic problem. Characteristically, blastomas (except myeloma and chordoma) do not involve the disk, while spondylitis almost always does (Fig. 36).

Early cases of spondylitis and stage I degeneration (pseudoinflammation) may be another differential diagnostic problem. Typically in spondylitis, the disk is edematous (hyperintense on T2-weighted images), while in degeneration there are low intensities on T1- and T2-weighted images, or even gas. The disk space is narrowed.

Eventually FDG-PET could serve as a problem solver, as described above.

References

1. Modic TM, Masaryk TJ, Ross JS (1992) Magnetic resonance imaging of the spine. Year Book Medical, St Louis
2. Bullogh PG (1993) Spinal diseases. Gower Medical
3. Graichen H, Putz R (1999) Anatomische und funktionelle Aspekte von Brust- und Lendenwirbelsäule. Orthopäde 28: 424–431
4. Van Mow C, Mayes WC (1991) Basic orthopaedic biomechanics. Raven, New York
5. El-Khoury GY (2003) Essentials of musculo-skeletal imaging. Elsevier-Churchill Livingston, Philadelphia
6. Tiedjen K, Müller KM (2001) Pathologie der degenerativen Wirbelsäulenerkrankung. Springer, Berlin Heidelberg New York
7. Renfrew DL (2003) Atlas of spine imaging. Elsevier-Saunders, Philadelphia
8. Bohndorf K, Imhof H (2001) Musculoskeletal imaging. Thieme, Stuttgart
9. Bogduk N (2000) Klinische Anatomie von Lendenwirbelsäule und Sakrum. Springer, Berlin, Heidelberg New York
10. Puddu G, Giombini A, Selvanetti A (2001) Rehabilitation of sports injuries. Springer, Berlin Heidelberg New York
11. Resnick D, Niwayama G (1995) Diagnosis of bone and joint disorders. Saunders, Philadelphia
12. Gundry CR, Fritts HM (1997) Magnetic resonance imaging of the musculo-skeletal system – the spine (part 8). Clin Orthop Rel Res 338: 275–287
13. Vigorita VJ (1999) Orthopaedic pathology. Lippincott, Williams & Wilkins, Philadelphia
14. Vahlensieck M, Reiser M (2002) MRT des Bewegungsapparates. Thieme, Stuttgart
15. Stumpe KDM, Zanetti M, Weishaupt D, Hodler J, Boos N, von Schulthess GK (2002) FDG positron emission tomography for differentiation of degenerative and infectious endplate abnormalities in the lumbar spine detected on MR imaging. AJR Am J Roentgenol 179: 1151–1157

Radiology and Pathological Correlations of Bone Tumours of the Spine

Iain W. McCall

6.5

Contents

Introduction

There are a large number of tumour types that affect the musculoskeletal system reflecting the different cellular constituents of bone, bone marrow and of the associated tendons, ligaments and muscles. The incidence of tumour types varies in the spine compared to the appendicular skeleton, reflecting the persistence of haemopoietic marrow in the axial skeleton into adulthood and the epiphyseal growth activity in the appendicular skeleton of children. The embryological development of the spine from the notochord results in tumours specific to the spine and skull. The spine may also be indirectly affected by tumours developing in the spinal cord, meninges and nerve roots that pass through the spinal canal and foramina.

As with the appendicular skeleton, the incidence of differing tumours varies depending on patient age, with some lesions being primarily limited to the growing spine while others only present in the mature skeleton. The structural similarity of each level of the spine means that most tumours may occur at any level, although there are variations in the incidence in different sections. The vascularity of the spine and its increased haemopoietic activity also makes it a natural repository for malignant cells from other tumours so that the incidence of clinically manifest metastases is higher in the spine than in the appendicular skeleton. The high ratio of trabecula to cortical bone in comparison to the long bones also renders the vertebra biomechanically vulnerable to bone replacement by primary or metastatic tumour, resulting in collapse of the vertebral body. The thin cortical bone of the vertebral body is less able to restrain the tumour growth, with resultant expansion beyond the confines of the vertebra, which may result in compression of the adjacent spinal cord or nerve roots. Vertebral collapse may also limit the space within the spinal canal and foramina, resulting in clinically manifest neurological deficit. Vertebral collapse from trabecula fractures or tumour replacement of trabecula bone may also irritate pain nerve endings in the bone; backache is the most common presenting feature. In many cases, this is not specific but pain of severe and sudden onset or pain that is continuous and unrelieved by lying down or exercise is a clinical pointer to the presence of a spinal tumour. Occasionally the pain pattern has specific features, as with osteoid osteoma, but this is unusual.

Some spinal tumours are more common in specific parts of the vertebra, again reflecting the structural differences of the vertebral body and the posterior elements, which have a low marrow content and thicker cortical bone. However, tumour originating from one part of the vertebra will easily extend or invade another part, as there are no natural boundaries. Tumour extending into the lamina from the vertebral body must disrupt the pedicles, providing a very specific feature on the radiographs. This is important, as considerable trabecula destruction may occur within the vertebral body before it becomes visible on a radiograph.

Tumour extension from the vertebral body or posterior elements results in a para-vertebral or pre-vertebral mass of tumour which may invade or displace the adja-

cent tissue, becoming visible on the radiographs in the thoracic spine and to a lesser extent in the cervical spine due to the close proximity of the air-filled structures, which provide the necessary radiographic contrast with the tumour tissue.

Radiographs remain the initial investigation in most cases of suspected spinal tumour but magnetic resonance (MR) may be the appropriate first investigation in some instances, in particular in the demonstration of metastases in cases where a primary neoplasm is known or where neurological symptoms and signs are the presenting clinical features. MR is the most sensitive method to identify marrow replacement by tumour in the vertebral body but is less effective in identifying focal lesions in the cortical bone of the posterior elements. MR may also fail to identify the presence of calcification or ossification within a tumour and define the bone reaction at the margin of the tumour. While these may be evident on the radiographs, they are best identified on computed tomography (CT). Finally, isotope studies using bone seeking technetium-labelled methylene diphosphonate (^{99m}Tc-MDP) may identify occult bone lesions, although they are more accurate in lesions which are bone-producing and may not identify lesions which are purely destructive. They have the additional advantage of being able to examine the whole skeleton at one time, providing an opportunity to identify extensive metastatic involvement. Whole-body MR is available in some systems and although not widely used at the present time, its value is being actively investigated [1].

Tumours of the Haematopoietic System

Multiple Myeloma

Multiple myeloma is the most common primary malignant tumour involving the spine. It is rare before the age of 40 years and involves mainly the axial skeleton.

Pathologically the gross specimen shows either diffuse gelatinous red infiltration or tumour in a nodular pattern. Histologically, marrow becomes infiltrated with sheets of proliferating plasma cells and B cells. There is considerable pleomorphism of the nuclei and an increase in mitoses (Fig. 1). The B cells produce abnormal protein gammaglobulins with an increase in IgA and a decrease in IgG and IgM bands on serum protein electrophoresis. Light chain subunits of immunoglobulins, Bence-Jones protein, is excreted in the urine.

The proliferation of cells leads to a replacement of the trabeculae resulting in areas with no bone present (Fig. 1). These may extend into the pedicles but usually commence in the bodies. The resorption of bone may result in vertebral collapse and a soft tissue mass may extend beyond the margins of the vertebra and lead to narrowing of the spinal canal.

Radiographs may show generalised osteopaenia with a loss of sharpness of the trabeculae (Fig. 1), but well-defined lytic lesions without any surrounding sclerosis may be seen and these may be multiple (Fig. 1). The vertebral bodies are involved initially with pedicular involvement late in the disease process. Paravertebral masses may be seen and vertebral collapse may be present. CT will demonstrate the extensive bone loss without evidence of calcification or of residual fragments of bone (Fig. 2). Extensive destruction of cancellous bone contrasting with the relative preservation of cortical bone on CT is suggestive of myeloma in comparison with both cancellous and cortical destruction with metastases [2]. The extent of the soft tissue mass is also demonstrated on CT but is better visualised on MR, which demonstrates decreased signal on the T1-weighted sequences and increased signal on T2 and STIR. These features are not specific for myeloma and metastases will also produce a similar pattern. Soft tissue extension into the spinal canal may cause spinal cord or cauda equina compression. Radioisotope studies are of little value in myeloma, as there is no new bone formation, and although reduced uptake may be present, it is generalised and difficult to perceive.

Plasmacytoma

Plasmacytoma is a solitary lesion, which presents with localised pain but also may initially present with paraparesis or paraplegia. Pathologically it consists of plasma cells and may precede the onset of myeloma by up to 10 years. The histological appearance is similar to myeloma with large numbers of plasma cells, but the mitotic activity is less (Fig. 3).

Radiographically it may present as a solitary expanding lucent lesion in the vertebral body or posterior elements. MR is the investigation of choice. On T1 there is an expanding tumour of uniform intermediate intensity slightly higher than muscle, which has a well defined margin and may have a lobulated outline (Fig. 3). On T2 there is a uniform high signal intensity which is also present on the STIR sequence (Fig. 3). The spinal cord or cauda equina may be compressed by the mass. CT provides little additional information but confirms the absence of any surrounding bone production or sclerosis and any calcification in the tumour. Radioisotope studies may demonstrate a local loss of activity.

Lymphoma

Lymphoma can arise in lymphoreticular tissue anywhere in the body but the majority of cases of musculoskeletal lymphoma develop via secondary spread through haematogenous dissemination from nodal dis-

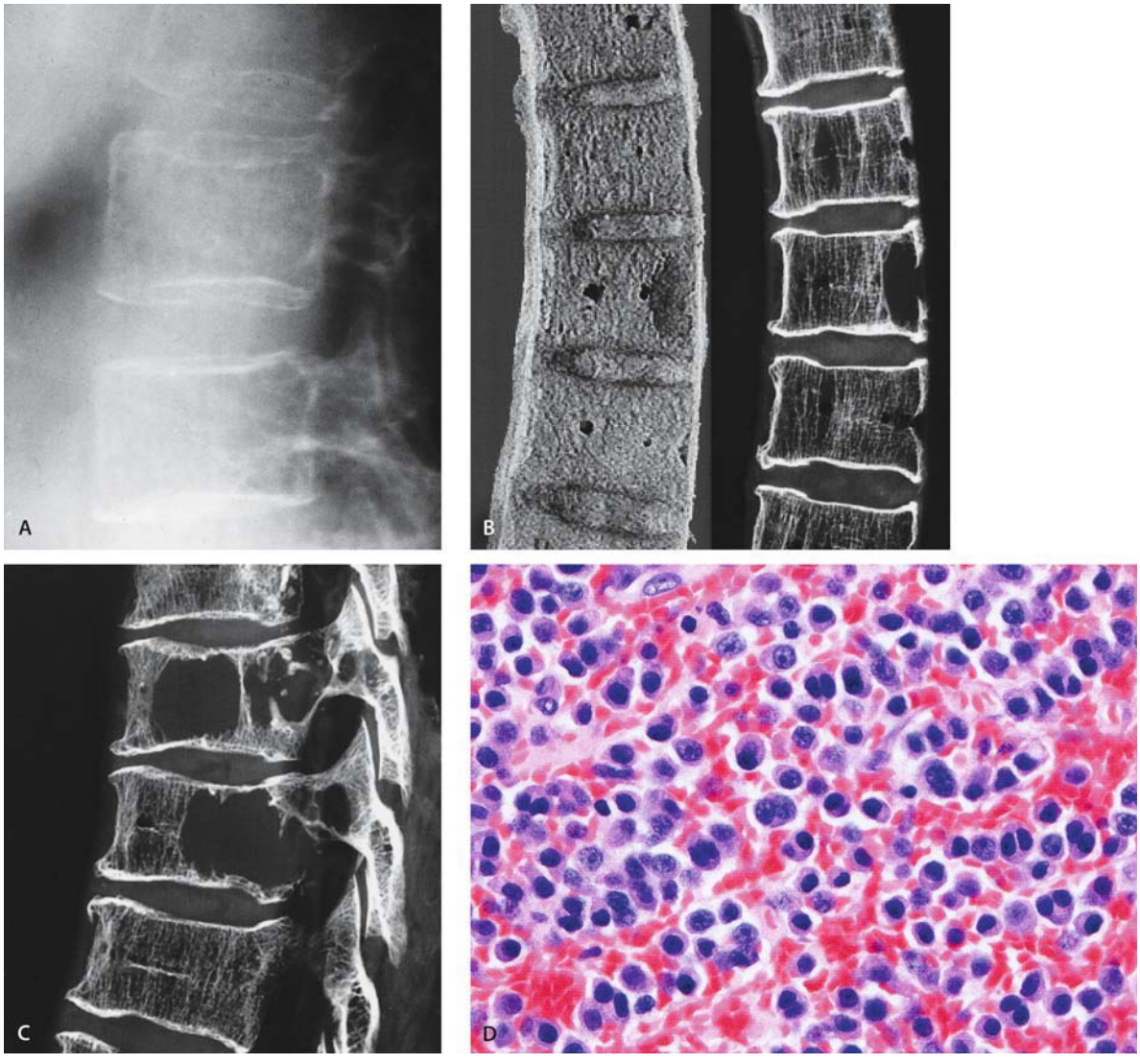

Fig. 1A–D. Multiple myeloma. **A** Lateral radiograph shows marked osteopaenia without evidence of expansion. **B** A gross specimen shows normal trabecular bone replaced by tumour. The margin is clearly defined but is irregular. The radiograph of the specimen shows a lucent area replacing the trabeculae without bone reaction at the margin. **C** Radiograph of a specimen with more extensive tumour replacement involving the pedicles and with destruction of the posterior vertebral wall. **D** Microscopy of myeloma shows sheets of plasma cells with atypical and pleomorphic nuclei

ease. Bone marrow biopsies performed on series of non-Hodgkin's lymphoma patients showed bone marrow involvement in between 18% and 23% of patients [3, 4]. Primary lymphoma of bone, which originates in bone with no evidence of disease elsewhere for at least 6 - months after diagnosis, accounts for less than 5% of all malignant bone tumours [5] and characteristically presents in older patients with 93% older than 20 years [6]. The extensive bone marrow of the spine makes it more likely to be the site of involvement by secondary osseous lymphoma rather than the appendicular skeleton [7], although primary non-Hodgkin's lymphoma typically arises in the diaphysis of long bones or in flat bones of the axial skeleton.

However, involvement may be limited to the epidural tissue or even the cord. Lymphoma is characterized pathologically by proliferation of cells native to lymphoid tissue including lymphocytes, histiocytes, and their precursors. Three types of lymphoma have been enumerated, namely B-cell, T-cell and Hodgkin's disease. Hodgkin's lymphoma is separated from all other forms by the presence of the pathological Reed-Sternberg giant cells. Histologically the tumour is made up of a diffuse cellular population of small round cells and

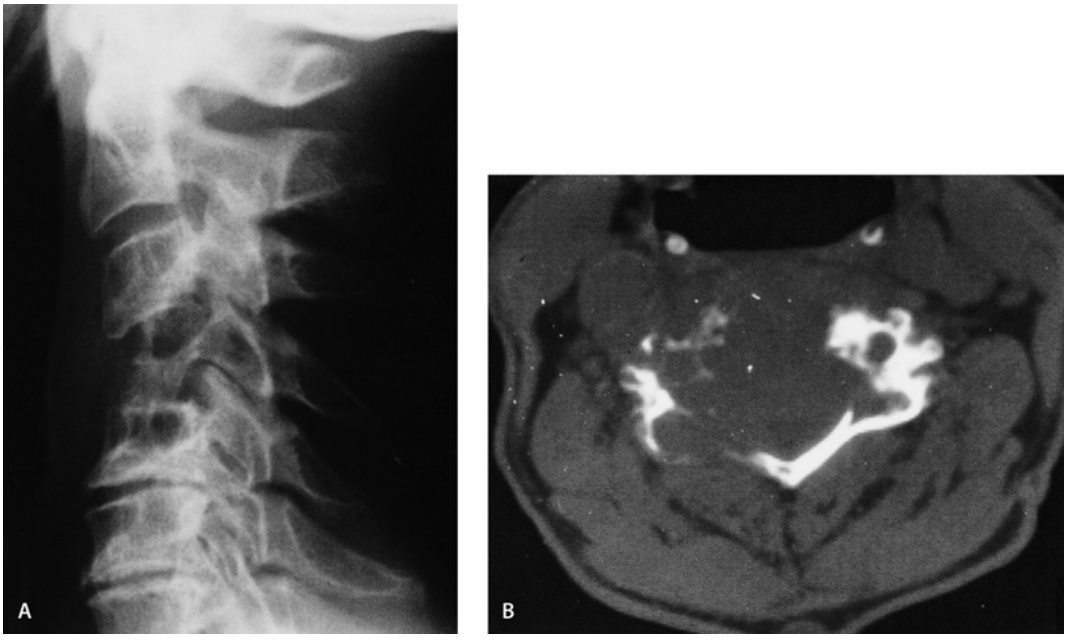

Fig. 2A, B. Multiple myeloma. **A** Lateral radiograph of the cervical spine showing destruction of C4 and C5 vertebral bodies with widening of the prevertebral soft tissue space. **B** CT of C4 shows a purely destructive lesion

large histiocytes that infiltrates between bone trabeculae and medullary fat (Fig. 4.). Immunohistochemical analysis shows that nearly all lymphomas will express common leukocyte antigen and B-cell markers CD20 and CD79a. Primary Hodgkin's lymphoma of bone is very rare, while secondary osseous involvement occurs in 10%–25% of patients with Hodgkin's lymphoma [5]. Primary bone lymphomas, most commonly, are large-cell or mixed small- and large-cell lymphomas of the B-cell lineage. Lesions in the vertebral body are initially destructive but may produce a bone reaction with woven bone laid down on the trabeculae.

Radiographic appearances in the vertebral body are either of a permeative osteolytic lesion or a mixed lytic and patchy sclerotic pattern of bone destruction with ill-defined margins to the lesions. There may be diffuse trabecula thickening, which may produce an appearance of general vertebral sclerosis (Fig. 4). Osteolytic or mixed sclerotic and osteolytic lesions form 90% of the cases. Lesions may be solitary in 30% of cases. The end plates are preserved. A soft tissue para-vertebral mass may be seen in the thoracic spine, and presentation may show on a chest radiograph as a hilar mass with widening of the mediastinum (Fig. 5). CT may be useful to demonstrate the sclerotic component of the tumour and the mixed osteolytic and sclerotic components (Fig. 4).

MR delineates diffuse low-signal areas within the marrow on T1-weighted sequences, which are high-signal on T2 and STIR. Vertebral collapse may be present and a soft tissue mass extending into the spinal canal, sometimes extensively through the epidural space, is commonly present and may result in cord compression (Fig. 4). Extensive paravertebral spread including the pleural space is well demonstrated on MR (Fig. 5). The appearance of lymphoma in some cases may be very similar to metastatic disease.

Metastases

Metastatic cancer is the most frequent malignant tumour of bone. The spine is a common site for metastases to bone due to its high marrow content, abundant blood supply and large sinusoidal channels. The most common tumours to metastasise are breast, lung, prostate, kidney, thyroid and colon, and the effect on bone is, to a certain extent, dependent on the source of the primary tumour. Metastases usually present with pain, which is often unremitting and persists at night, but in the spine, presentation with neurological features may occur as a result of either expansion of tumour mass to compress the cord or cauda equina or of secondary vertebral collapse from bone destruction. Metastases may also be discovered as part of the initial staging process of the primary tumour or on routine follow up examinations.

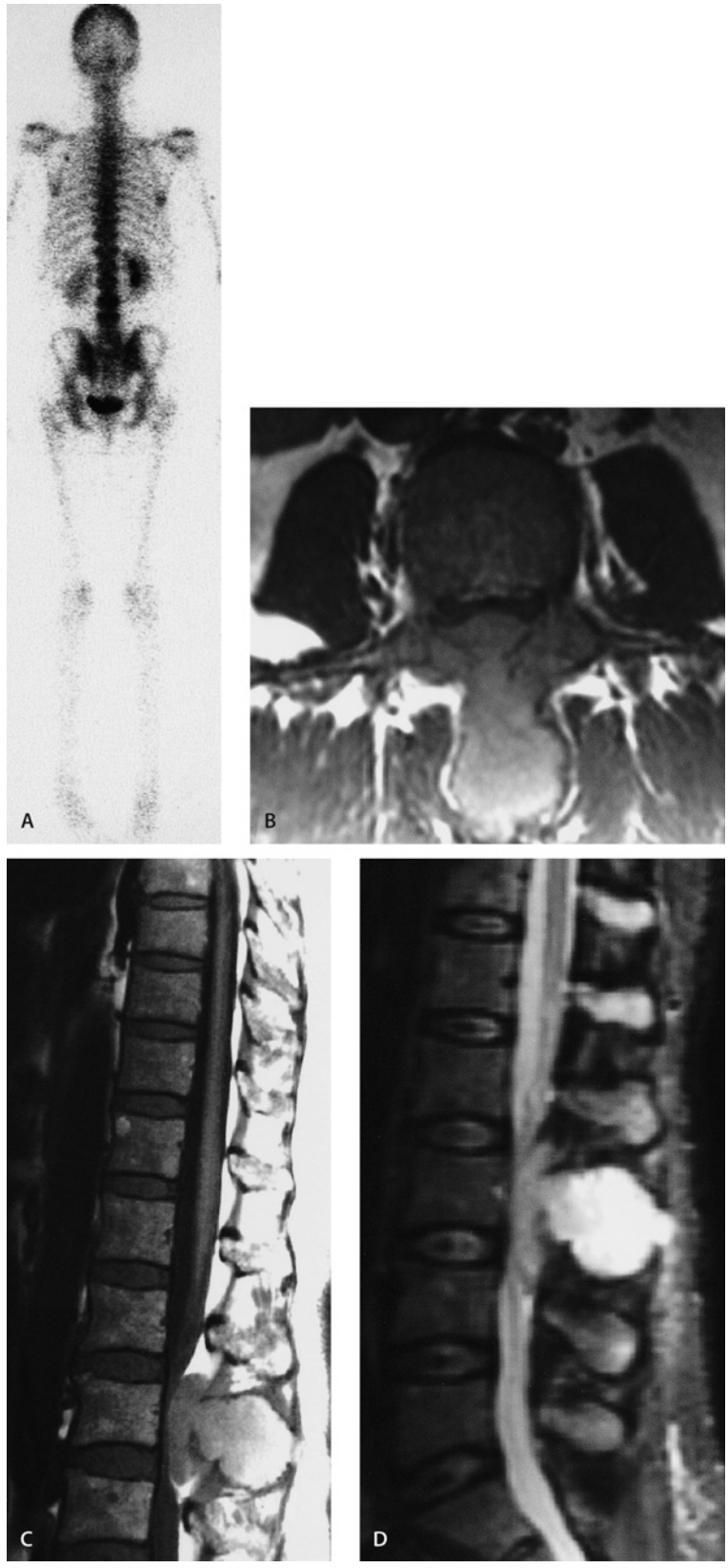

Fig. 3A–E. Plasmacytoma. **A** An initial whole-body Tc99m MDP study shows no evidence of abnormal isotope activity. **B** T1-weighted axial and **C** sagital sequences shows marked expansion of the spinous process with a thin persistent cortical outline, although tumour has broken through the inner lamina cortex. The tumour is intermediate signal and has extended along the epidural fat, remaining well defined. The cauda equina is markedly compressed. **D** STIR sagittal sequence shows the majority of the tumour as high signal intensity, although the tissue in the canal is more intermediate signal, which may in part be due to coil positioning. **E** Sheets of atypical plasma cells are demonstrated.

Fig. 3E

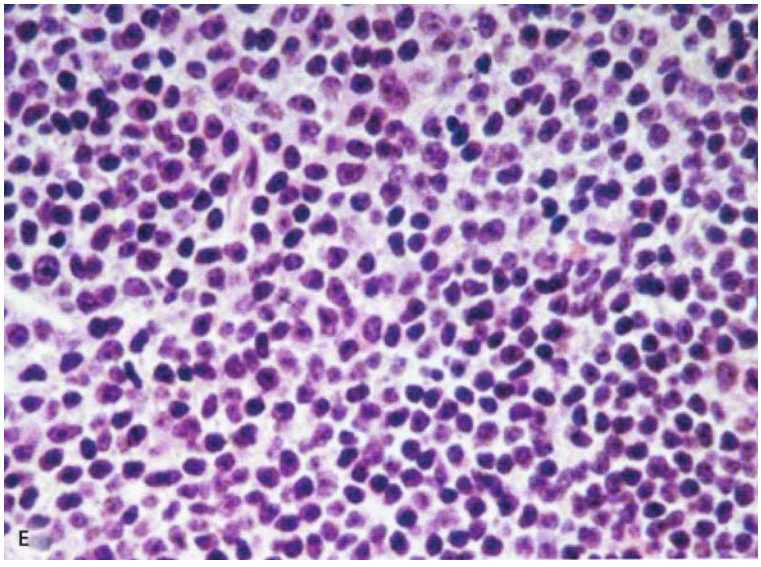

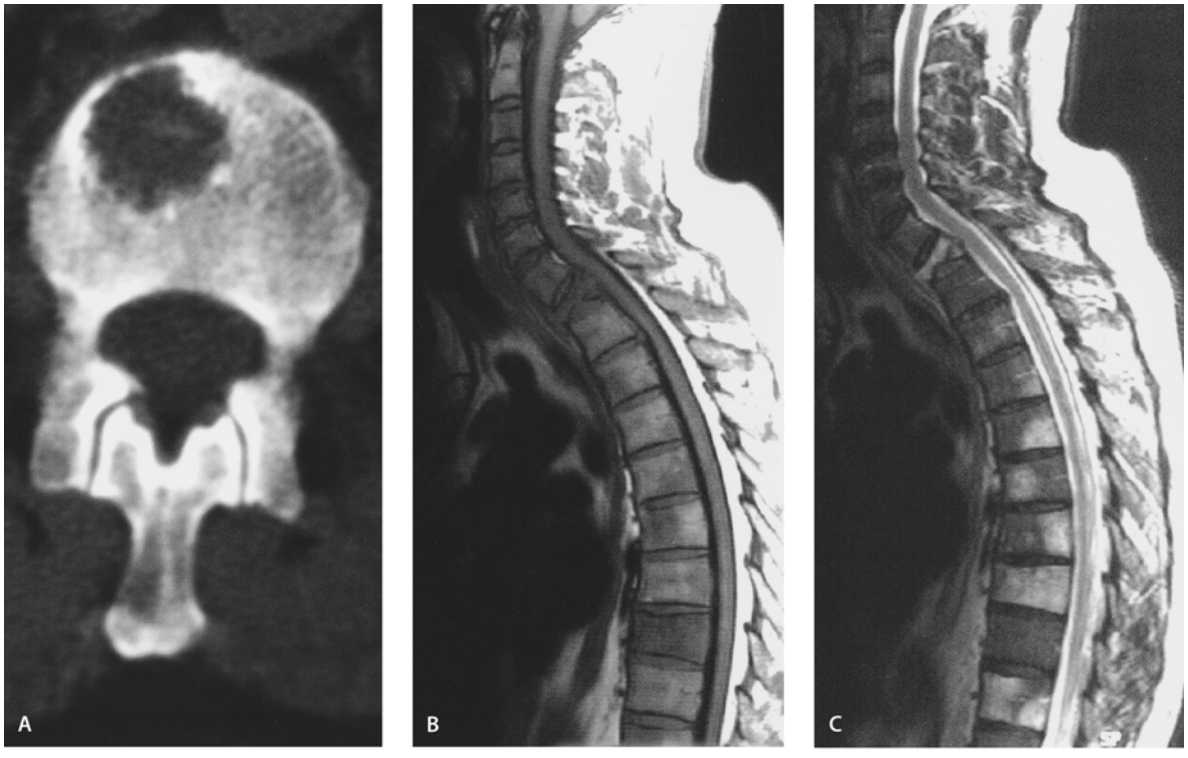

Fig. 4A–D. Hodgkin's lymphoma. **A** CT demonstrates an area of bone destruction in the thoracic vertebral body associated with other areas of sclerosis. **B** MR sagittal T1-weighted sequence demonstrates variable signal in multiple vertebra with low and intermediate signal. The body of the first thoracic vertebra has collapsed. **C** T2-weighted sequence shows multiple foci of high signal. **D** histology shows multiple small round cells and scattered large Hodgkin's cells

Fig. 5A–D. Non-Hodgkin's lymphoma. **A** Chest radiograph shows a mass overlying the right hilum. **B** CT demonstrates a large para-vertebral mass extending into the thoracic spinal canal. **C** MR in the coronal plane demonstrates the para-vertebral mass extending over five vertebral levels. A number of small foci of high signal are also seen in the vertebral bodies. **D** The T2-weighted axial study shows the displacement of the cord by the lymphoma mass

Fig. 4D

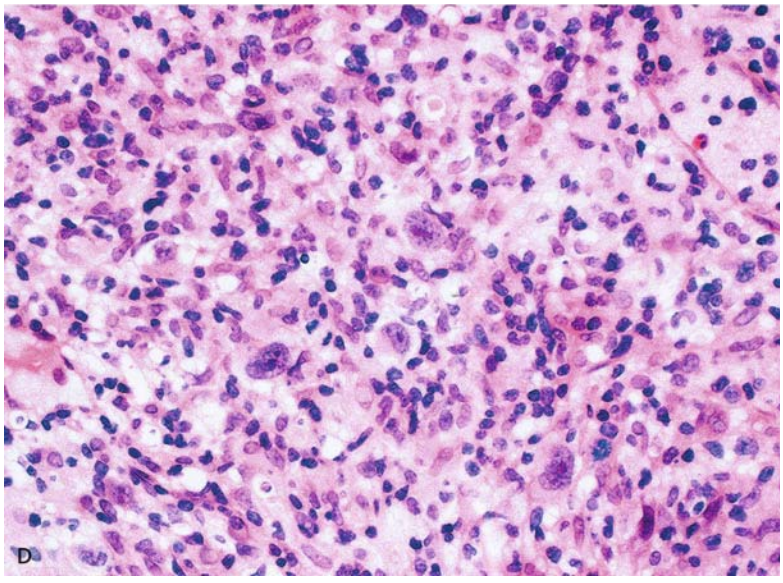

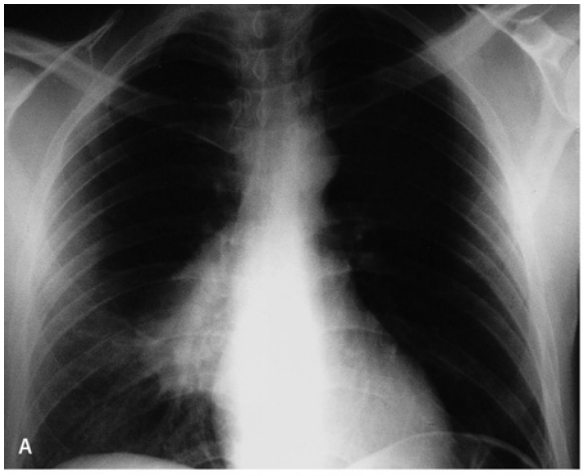

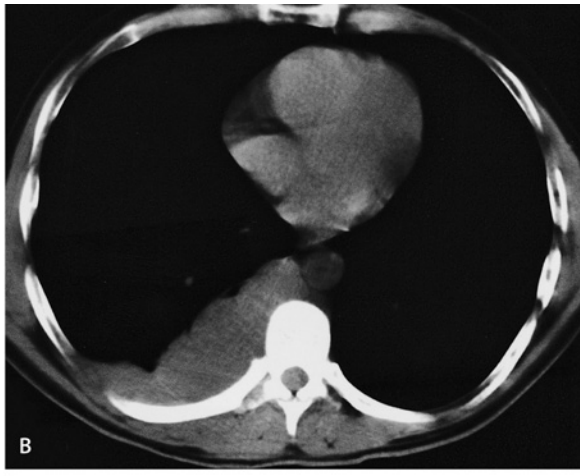

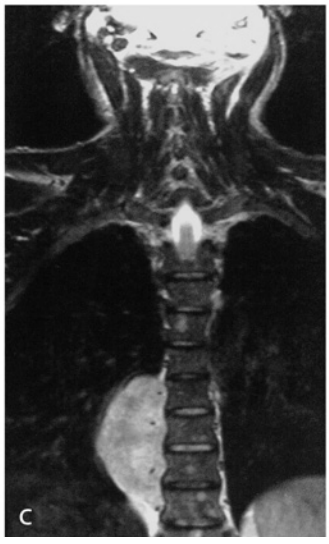

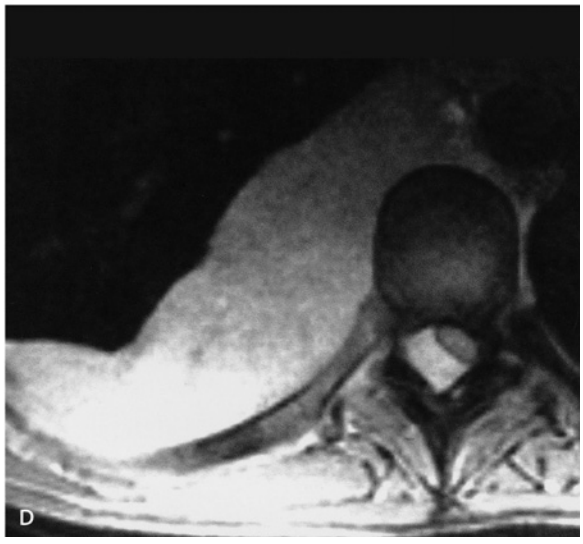

The metastasis may be the presenting feature of the disease, and biopsy of the metastasis may suggest the source of the primary tumour. Biopsy in the spine is most effectively undertaken using image-guided needles: many articles have confirmed the accuracy of this method. Both the core of tissue and any blood clot should be examined as the blood may exhibit evidence of cancer which crushed tissue precludes.

Microscopic identification of the primary site may be difficult if the tissue identifies poorly differentiated neoplasms. However, the presence of squamous pearls may be seen in well-differentiated tumours if they originate from squamous carcinoma and mucin-producing glands if they stem from adenocarcinoma. The clear cells of renal carcinoma may be easily identified (Fig. 6) but may be confused with chordoma or very rarely clear-cell chondrosarcoma.

Osteoblastic metastases produce reactive bone as fine spicules of woven bone adherent to the residual existing bone [8], and the spaces between are filled with tissue and malignant cells.

Radiological evaluation of metastatic disease in the spine is often initially undertaken with plain radiographs The lateral view may identify either increased or decreased bone density, which may be localised to a single vertebra or involve multiple levels. Decreased density may be difficult to appreciate and a substantial loss of trabecula bone may occur before it is visualised unless there is destruction of the cortical outline of the vertebra. Extensive loss of bone may result in vertebral collapse, which may be difficult to differentiate from osteoporotic collapse in some cases. The AP view is valuable to identify the presence of pedicle and lamina destruction, which will enable a malignant diagnosis to be suspected (Fig. 7). A para-vertebral soft tissue mass may also be seen in the thoracic spine, which assists in the differentiation from osteoporosis. Metastases may also be identified by using the bone-seeking isotope ^{99m}Tc MDP. Multiple sites of increased isotope uptake are strong indications of metastatic disease. Osteoporosis may also produce multiple sites of uptake due to fractures, but the pattern in the spine in osteoporosis is typical, with horizontal lines of activity, which do not extend beyond the outline of the vertebra. Paget's disease may also produce multiple sites of increased activity: correlation with radiographs is essential. Scintigraphy may also produce false-negative studies if the pattern is predominantly bone destruction without bone reaction, which may occur in breast and renal metastases; although an area of decreased activity may be visible (Fig. 7), it is often difficult to evaluate.

Computed tomography provides accurate demonstration of the sites of bone destruction or sclerosis and is valuable in guiding the biopsy needle to the most active site to increase the accuracy of histology. Magnetic resonance is now the most accurate method of identifying early spinal metastatic involvement. On T1-weighted sequences, the normal marrow fat is replaced by intermediate- or low-signal tissue which may involve a single vertebra or may be multiple (Fig. 7). On T2 there is increased signal intensity, which is greater on the STIR sequence as this sequence highlights the high-signal metastatic focus from the very low signal of the suppressed fat signal (Fig. 7). Whole-body STIR sequences are now advocated for the initial search for metastatic foci [9]. There is usually heterogeneous enhancement following gadolinium injection. Differentiation between metastatic and osteoporotic collapse on MR may occasionally be difficult if there is no paravertebral or epidural soft tissue mass. The presence of low-signal fracture lines beneath the end plate and partial preservation of normal fatty marrow in the vertebral body are features of osteoporotic collapse [10]. Diffusion MR imaging has also been found valuable in the differentiation [11].

The tumour may have expanded through the vertebral cortex either into the paravertebral tissue or into the epidural space, which may result in cord or nerve root compression. This is accurately identified on MR and the extent of the compression can be evaluated. Direct metastatic involvement of the cord and nerve roots may occur

Fig. 6A–G. Metastasis. **A** Lateral lumbar radiograph demonstrates destruction and partial collapse of L4 vertebra. **B** AP radiograph shows associated destruction of the pedicle. **C** ^{99m}Tc MDP study demonstrates a reduced L4 vertebral activity compared to other levels. **D** Sagittal T1-weighted sequence shows L4 replaced by low-signal tissue, which is high signal on T2. **E** Both sequences show the soft tissue mass expanding into the spinal canal. Further foci are seen in other lumbar vertebra. **F** Biopsy of the vertebra demonstrated the typical clear cells of renal metastases. **G** CT of the kidney demonstrates a mass in the left kidney consistent with a carcinoma

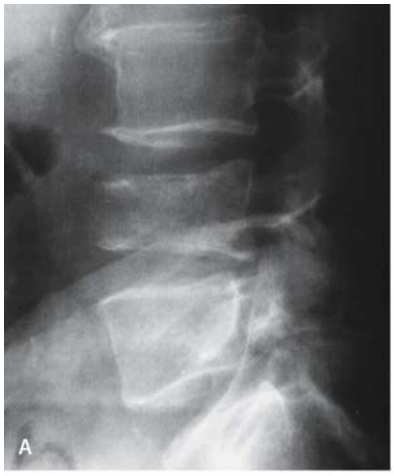
A

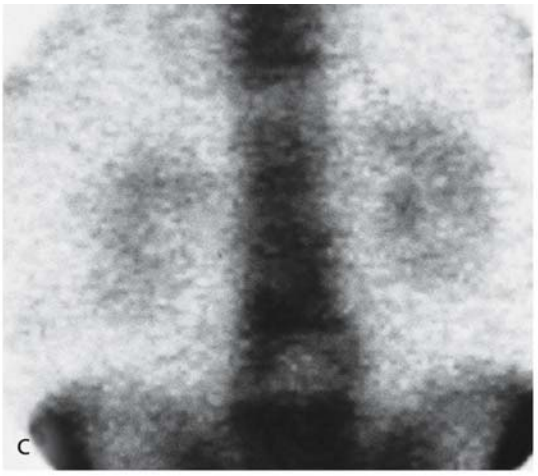
C

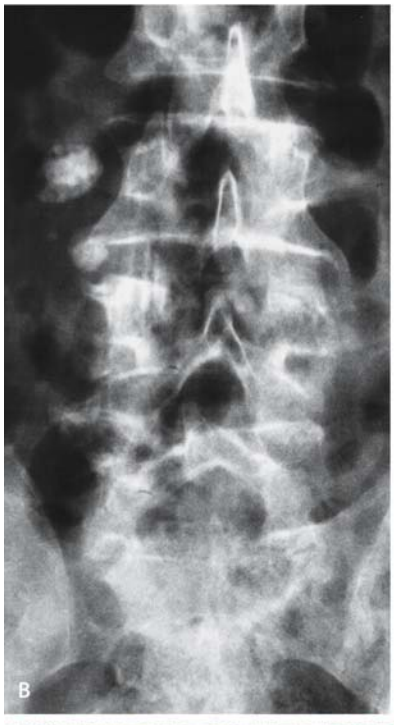
B

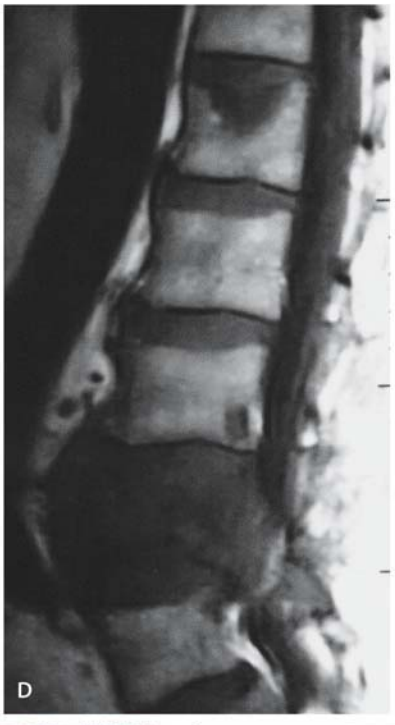
D

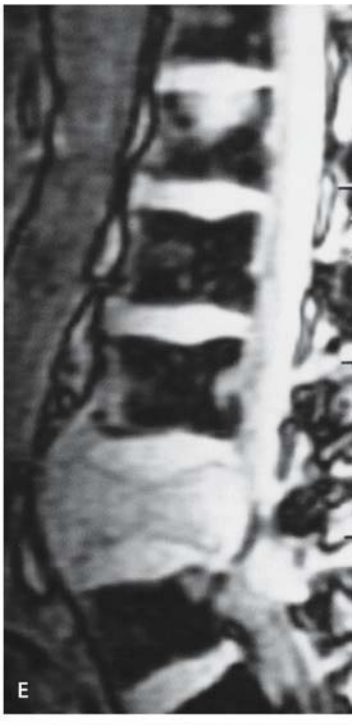
E

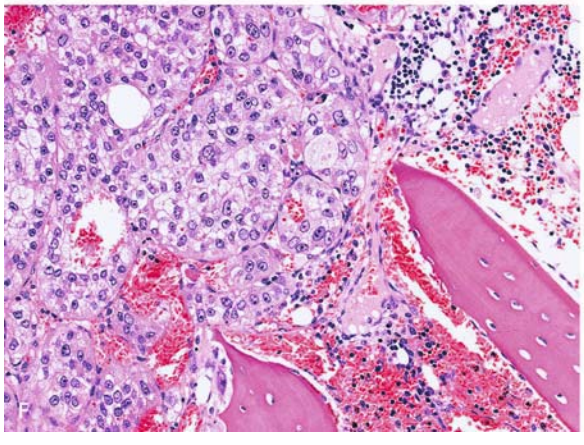
F

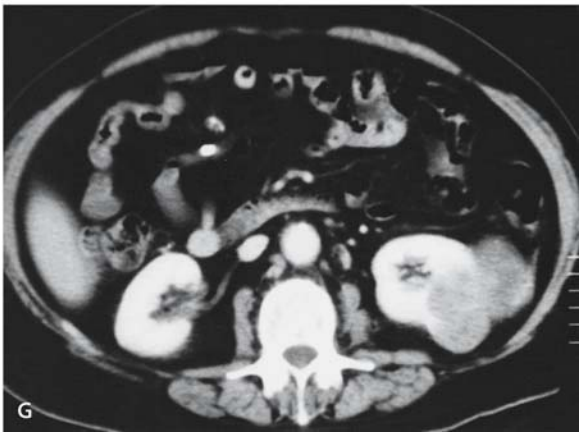
G

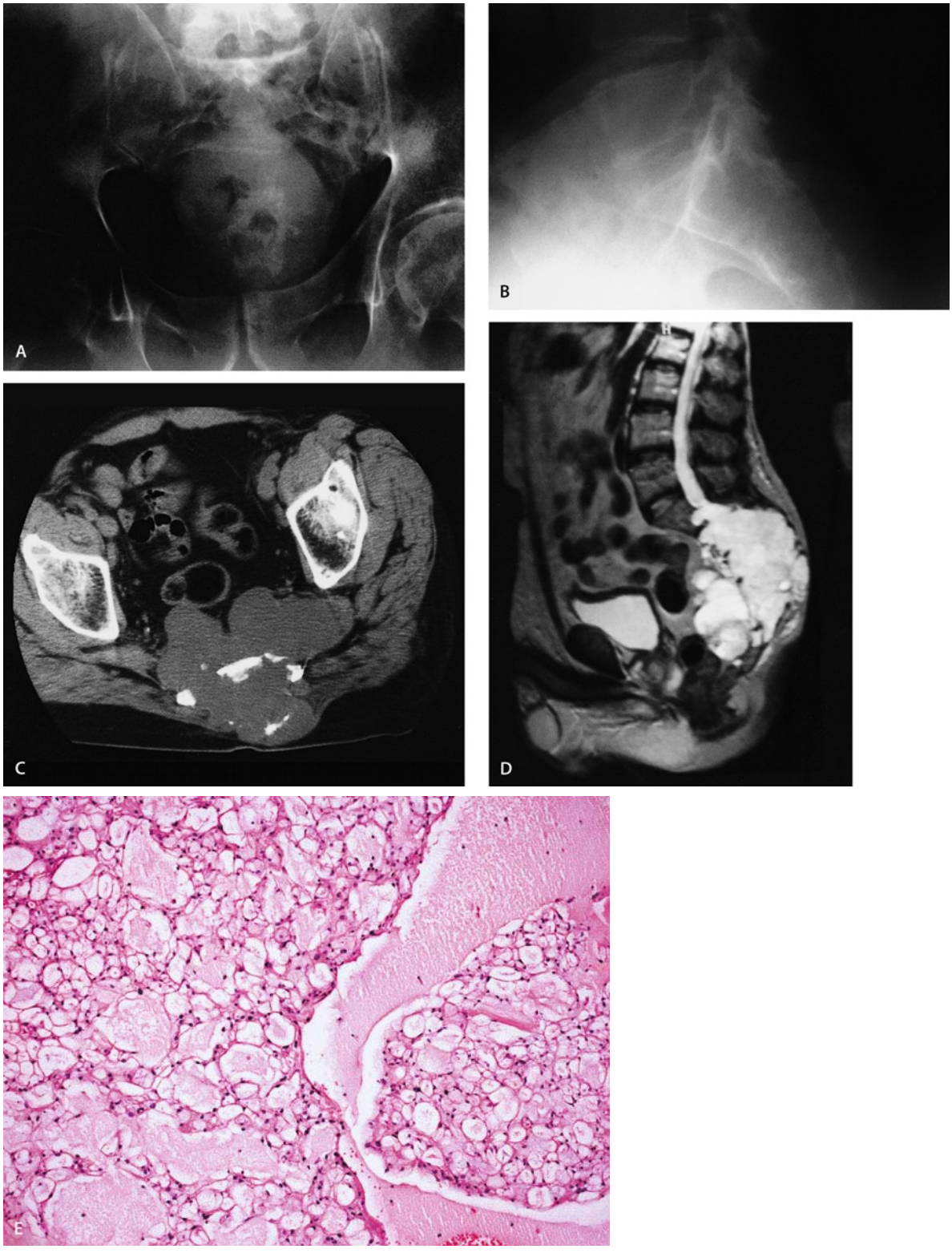

Fig. 7A–E. Chordoma. **A** Extensive destruction of the sacrum with loss of normal foraminal architecture in S3 and S4 is seen on the AP radiograph. The lateral view **B** shows destruction of the posterior vertebral wall and posterior elements of the sacral vertebra. **C** CT shows a large soft tissue attenuation mass destroying the sacrum and extending into the pelvic cavity. No evidence of calcification is seen in this lesion. **D** Sagittal T2-weighted sequence shows lobulated tumour with high signal. **E** Histology demonstrates cords and sheets of large, cohesive cells with abundant cytoplasm set in a myxoid matrix

Primary Tumours of the Spine

Chordoma

Chordoma arise from notochord remnants and are slow-growing malignant lesions. Approximately 60% affect the spine, the large majority being found in the sacrococcygeal region (50% of total), with a small proportion in the lumbar (7%) and cervical spine (5%). The remainder involve the spheno-occipital region. Over 80% of patients are over 50 years old and males are affected twice as commonly as females [12]. The symptoms are often insidious in onset and include pain, neurological signs, signs of rectal compression or a palpable mass. Microscopically the notochord tissue is somewhat similar to immature cartilage and is composed of oval cells with central nuclei and vacuolated cytoplasm embedded in an eosinophilic myxomatous stroma (Fig. 7). Chordoma may also exhibit cartilaginous differentiation with cartilage areas of various sizes. Dedifferentiated chordoma is rare, consisting of conventional chordoma and high-grade spindle cell or pleomorphic sarcoma. Macroscopically chordoma form a white, soft, multi-lobulated mass with a fibrous pseudocapsule. Fluid and gelatinous mucoid substance associated with recent and old haemorrhages and necrotic areas are found within the tumour. Fifty per cent show intratumoral calcification and sequestered bone fragments.

Radiographs show destruction of bone, and sacral lesions may extend across the sacroiliac joints, while vertebral lesions may also involve adjacent intervertebral discs.

CT shows a mostly lytic lesion (Fig. 7) and may have a low attenuation, probably related to the myxoid nature [13, 14]. Calcification in the soft tissue mass has been reported to be seen in 15%–18% of cases [15] but was not seen in any of the spinal cases in another series [16].

The vertebral body is most commonly involved with sparing of the posterior elements, but occasionally a large soft tissue component without vertebral bone involvement may be seen mimicking a neurogenic tumour and associated with enlargement of the neuroforamen [15]. Vertebral body involvement may be limited to one vertebra or to multilevel involvement. A soft tissue component which extends posteriorly into the epidural space is common. The presence of a concomitant soft tissue mass spanning several vertebral levels is highly characteristic for chordomas.

MR appearances are characterised by a lobulated mass with a low or isointense heterogeneous signal intensity to muscle on T1 with a high fluid-like signal intensity on T2 weighting due to the myxoid content [17] (Fig. 7). A low-signal-intensity pseudocapsule and thin interlesional septation are usually present [18]. After gadolinium contrast administration, almost all lesions show heterogeneous moderate enhancement, although some cases may have a ring or arc pattern [16] and others have rim enhancement, which may reflect the lobular nature of the lesions and possibly cartilaginous differentiation [19]. The characteristic sign of epidural involvement is the curtain sign on the axial images [20]. After gadolinium contrast administration, an epidural tail sign is seen on the sagittal images due to involvement of the posterior longitudinal ligament.

Primary Osteogenic Tumours

Osteoid Osteoma

These lesions are characteristically seen in children and young adults, with males affected twice as frequently as females, and present with localised pain which is worse at night and which may be relieved by aspirin. Although it most commonly occurs in the long bones, 5% of these lesions are in the spine and are found in the posterior elements of the vertebra. In the spine they may occasionally present as scoliosis with or without pain. Histological evaluation shows a focal lesion of highly vascular tissue with seams of osteoid tissue and immature woven bone lined with osteoblasts and osteoclasts. There is surrounding trabecular bone thickening with woven bone laid down on the lamellar bone of the trabeculae (Fig. 8).

Radiographic demonstration may be difficult with a localised increase in bone density overlying the pedicle or lamina (Fig. 8). However, there may be no discernible abnormality. Radioisotope studies show a focal area of marked increased activity on the bone phase and also the early blood pool phase. The role of scintigraphy is to guide the cross-sectional imaging systems, particularly CT to the area of interest [21]. CT is the most valuable method to demonstrate the actual lesion. There is a small lucency, which may have a central high attenuation due to mineralisation. There is surrounding sclerotic bone with some thickening of the lamina or pedicle (Fig. 8).

On MR the nidus may be difficult to visualise and may be seen better following the injection of intravenous gadolinium, particularly when fat suppression techniques are used [22]. The signal characteristics of individual osteoid osteomas varies depending on the amount of reactive bone surrounding the lesion and the degree of oedema [23]. There is decreased or intermediate signal in the posterior elements on T1-weighted sequences with increased signal around a low-signal nidus on T2-weighted and STIR sequences due to bone response and marrow oedema. The T2-weighted signal is variable depending on the age of the tumour, its vascularity and the presence of calcification. The axial plane is most useful in demonstrating the lesion and use of

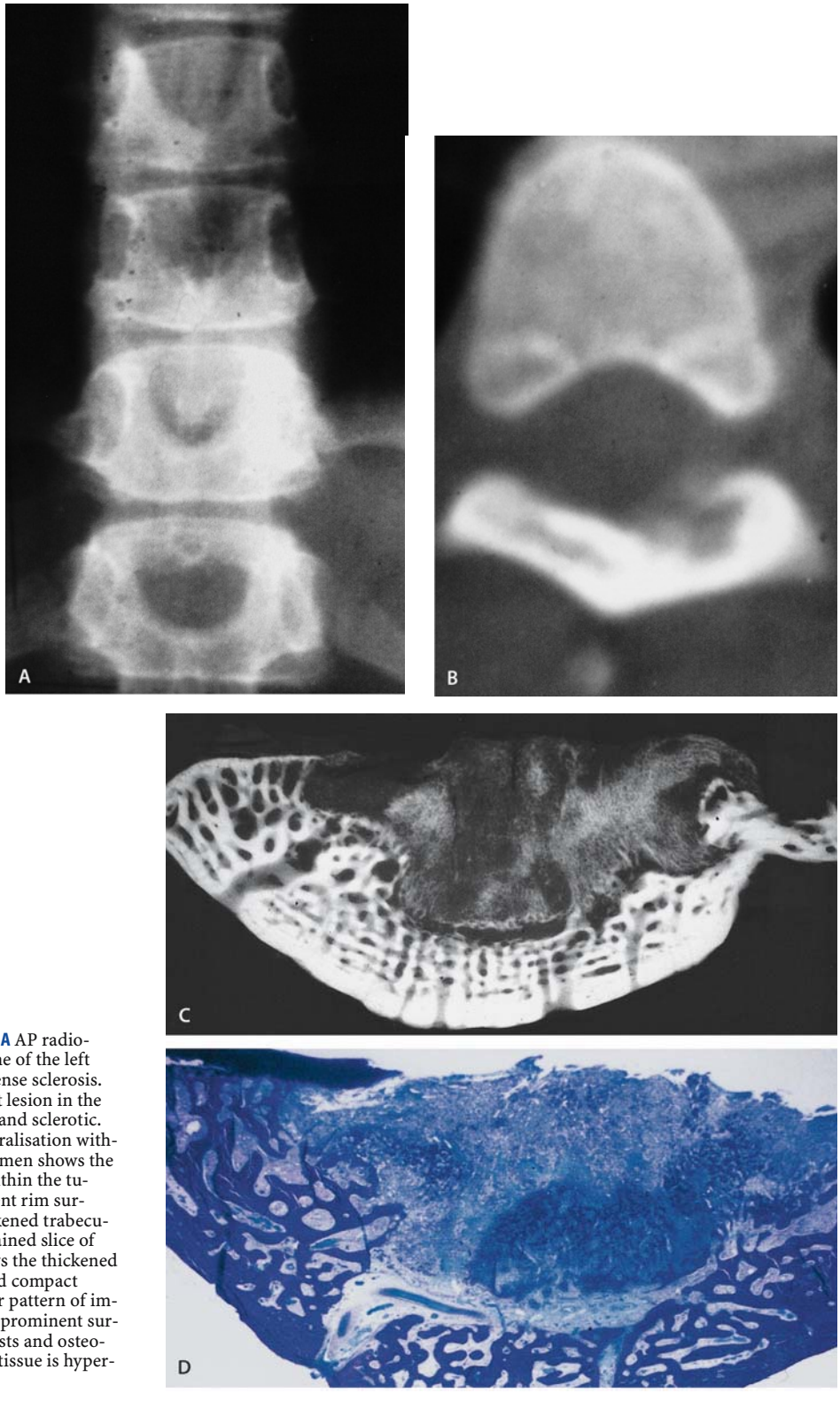

Fig. 8A–E. Osteoid osteoma. **A** AP radiograph shows that the outline of the left pedicle is obscured with dense sclerosis. **B** CT demonstrates a lucent lesion in the lamina which is thickened and sclerotic. The lucency contains mineralisation within it. **C** Radiograph of specimen shows the irregular mineralisation within the tumour which has a thin lucent rim surrounded by markedly thickened trabecular bone. **D** Macroscopic stained slice of the macroradiograph shows the thickened surrounding trabecular and compact bone. **E** Irregular trabecular pattern of immature woven bone with a prominent surface monolayer of osteoblasts and osteoclasts. The intratrabecular tissue is hypervascular reactive stroma

Fig. 8E

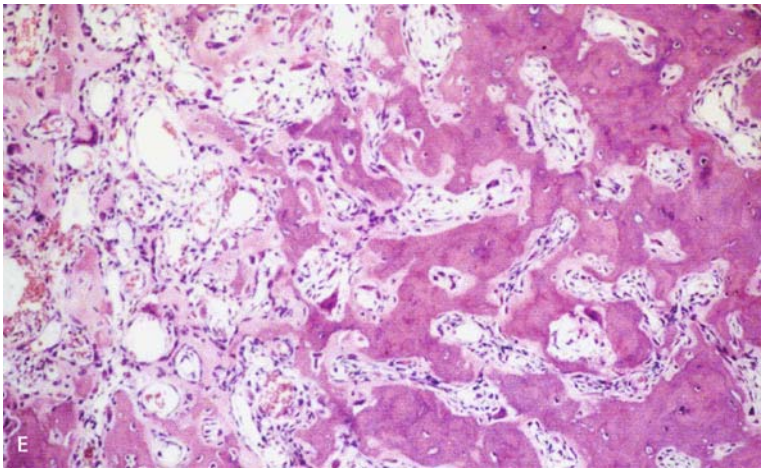

surface coils with a small field of view are more likely to characterise an osteoid osteoma [22].

Osteoblastoma

Osteoblastoma is a solitary benign osteoid and bone-forming neoplasm which contains many well-differentiated osteoblasts and osteoclasts and has a vascular stroma. They affect young adults and are usually painful but they may also present with a scoliosis; 30% occur in the spine and originate almost exclusively in the posterior elements, pedicles or transverse process. Some lesions are large and present with neurological symptoms due to cord or nerve root compression.

Macroscopically they are larger than osteoid osteomas, which rarely exceed 1 cm in diameter.

Microscopically they consist of a vascular spindle-cell stroma with abundant irregular bone and osteoid with abundant osteoblasts and osteoclasts on the bone surfaces.

This pathological appearance is similar to osteoid osteoma but the tissue pattern is less regular than osteoid osteoma [8]. They may result in compression of the spinal canal and cord and recur unless removed completely.

Radiographically the lesions are of varying lucency and degrees of mineralisation. They are usually well circumscribed without extensive surrounding bone reaction or sclerosis. They show very marked uptake of bone-seeking isotope and have a very well-defined outline on the isotope scan (Fig. 9).

They are best evaluated with CT (Fig. 9), which will show the size and outline and also the extent of invasion or encroachment on the spinal canal. Ossification of the ligamentum flavum associated with osteoblastoma has been reported and is best seen on CT [24].

Aneurysmal Bone Cyst

The spine is the site of involvement in primary aneurysmal bone cyst in 23% of cases [25], but secondary lesions arising in other tumours such as osteoblastoma are rare and only one case has been reported complicating fibrous dysplasia in the spine [26]. They most frequently involve the lumbar spine followed by the cervical, thoracic spine and sacrum [27]. The coccyx is not affected. Posterior elements are most commonly affected, although expansion into the vertebral body may occur and multiple vertebra may also be involved. Pathologically the lesions replace bone, with large blood-filled spaces surrounded by fibrous septa with giant cells connected to the host capillary network (Fig. 10). The walls of an aneurysmal bone cyst are usually soft and fibrous and internally there are separate spaces containing friable brownish blood clot. The cystic spaces are of varying sizes, and although containing blood, they are not lined with vascular endothelium. Focal or diffuse collections of haemosiderin or reactive foam cells and chronic inflammatory cells may be seen in the septa [8]. There may be foci of reactive bone.

Radiographs of the lesions show well-defined osteolytic areas with initially destruction of the posterior elements and pedicles. A soft tissue mass may be seen which is easy to define in the thoracic spine with widening of the para-vertebral shadow but is less obvious in the lumbar spine (Fig. 10). Extension into the vertebral body results in destruction with preservation of the disc space, and vertebral collapse may eventually occur with a local kyphosis. In the later stages of development, a cortical shell may be delineated, producing a soap bubble appearance.

CT and MR are essential diagnostic tools which define the tumour extent and determine whether the soft tissue mass margins are smooth and sharply defined.

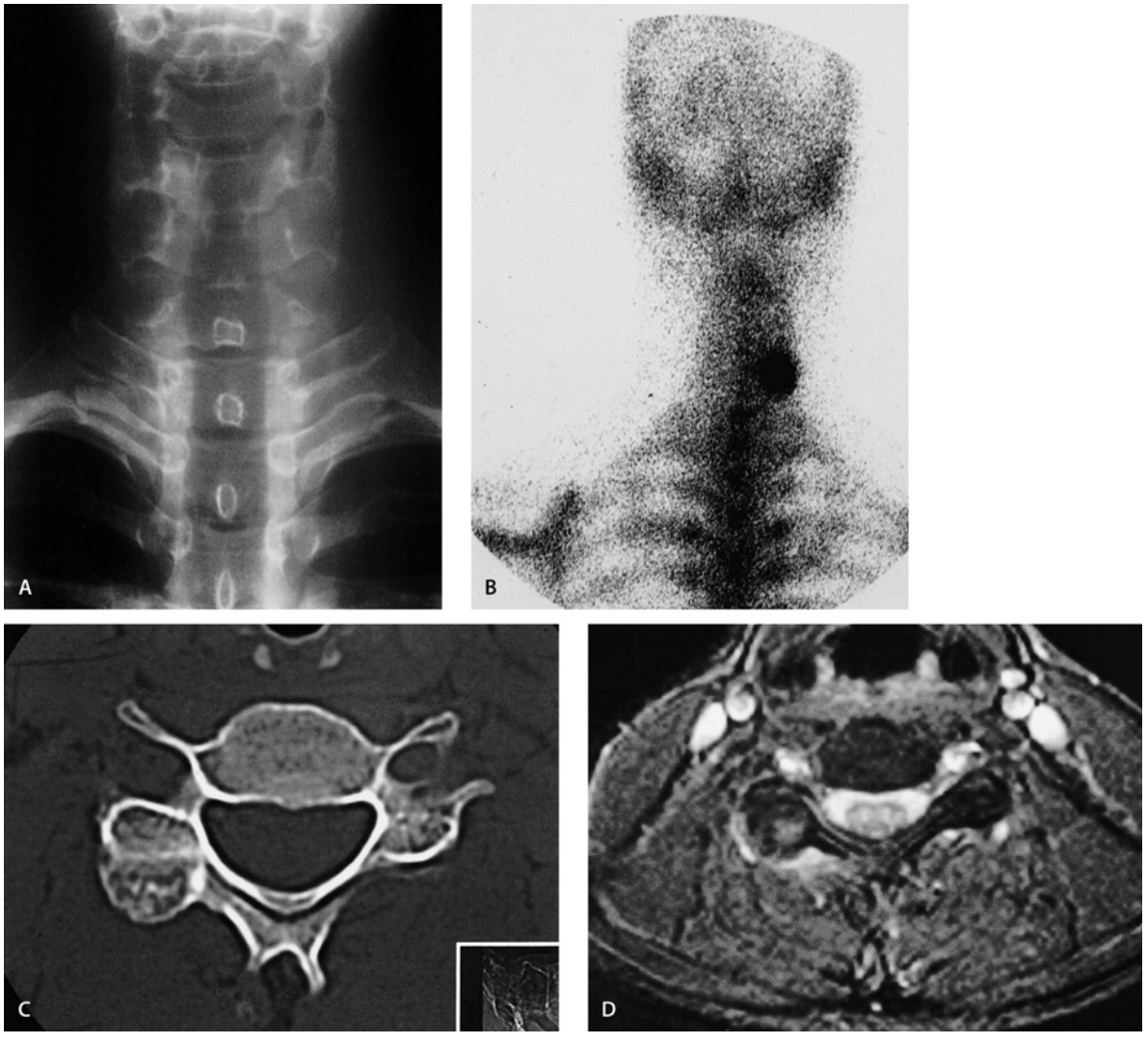

Fig. 9A–D. Osteoblastoma. **A** Lateral radiograph of the cervical spine appears normal. **B** ^{99m}Tc-MDP bone scan demonstrates a focal well-defined high-uptake focus in the cervical spine. **C** CT shows a well-defined tumour with mixed sclerosis and lucency involving the lateral mass of the cervical vertebra. **D** T2-weighted MR shows oedema around the mass

The soft tissue mass may show thin low-signal septa with a well-defined rim of low signal intensity on MR. The hallmark of the lesions is the presence fluid–fluid levels of low and high attenuation due to collection of blood and fat seen in 35% of cases on CT [28] (Fig. 10). MR identifies the fluid–fluid levels well on the T2-weighted sequences, and these blood fluid levels show high signal over intermediate signal. However, fluid–-fluid levels may be present in a number of tumours or pseudotumours and are not specific to aneurysmal bone cysts [29]. There is no evidence of calcification or bone production in the lesions.

Haemangioma

Intravertebral haemangioma are vascular hamartoma which are usually asymptomatic and the majority are found incidentally on plain radiographs or more frequently on MR. They are among the most frequently occurring spinal tumours and there has been a significant increase in the demonstration of haemangioma in recent years due to the increased use of MR, which identifies lesions very easily.

Symptoms when present are usually pain but rarely the haemangioma may increase in size, resulting in neurological symptoms due to root or cord compression.

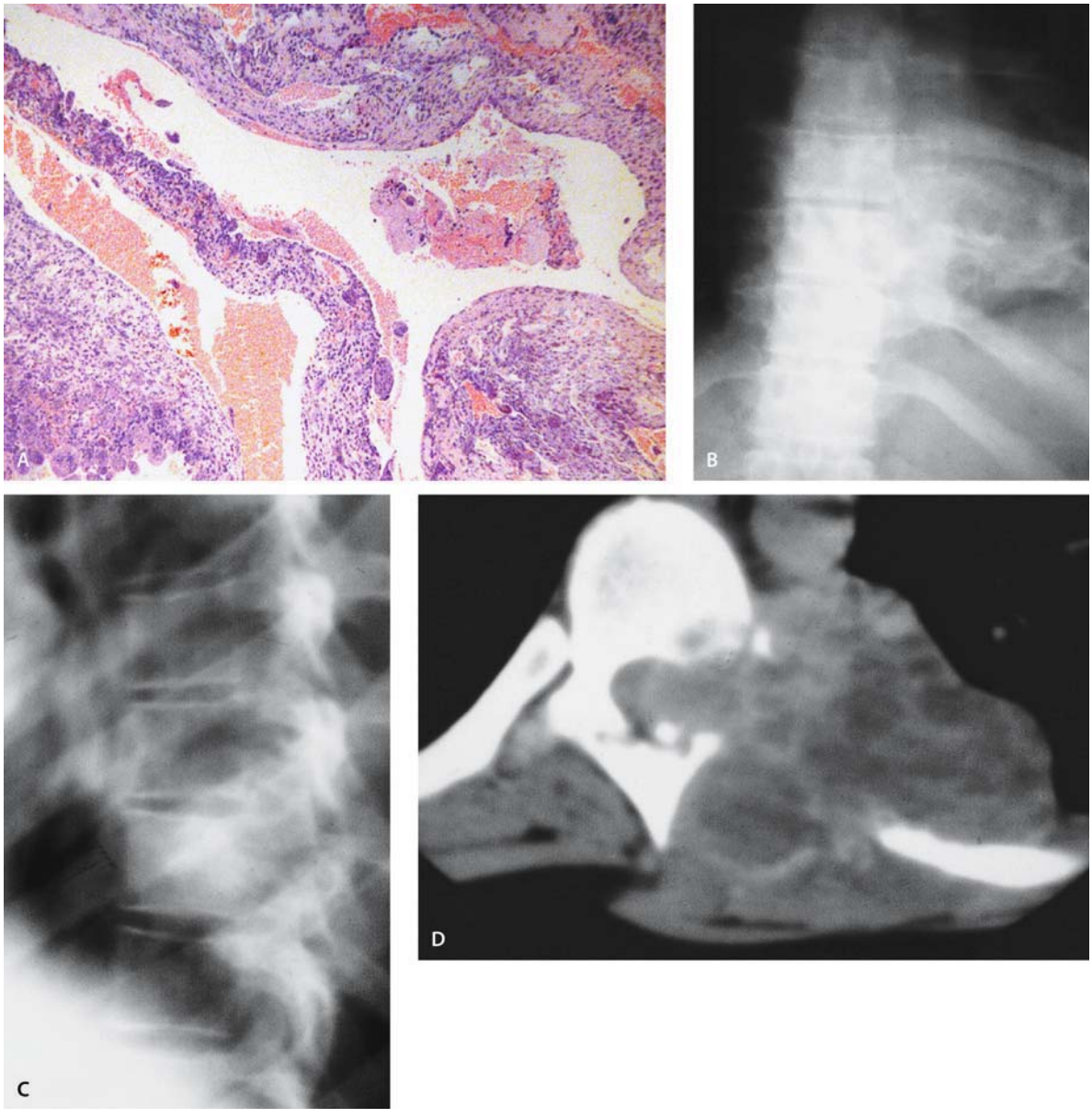

Fig. 10A–D. Aneurysmal bone cyst. A Low-powered H and E stain shows cystic cavities containing blood surrounded by septa containing multiple osteoclast-like giant cells, fibroblasts and vascular stroma. **B** AP and **C** lateral radiographs shows destruction of the pedicle and posterior wall of the vertebral body. There is also destruction of the adjacent rib. A large para-vertebral mass is present seen through the cardiac shadow on the AP view. The increased density of the vertebral body is due to the soft tissue mass superimposed on the vertebra. **D** Computed tomography demonstrates the large soft tissue mass which has destroyed the lamina, pedicle, adjacent rib and posterior vertebral wall. It is of variable attenuation with fluid–fluid levels within it. The soft tissue mass is displacing the cord within the spinal canal

They are most commonly in the thoracic spine and the lumbar spine, the cervical spine and sacrum are infrequent sites.

The gross pathological specimen appears as multiple small, dark red cavities with coarse bone trabeculae, which are well demarcated from the adjacent normal trabecular bone (Fig. 11). Histologically the cavities consist of walled cavernous blood vessels or proliferating capillaries lined with thin, flattened epithelium (Fig. 11).

Radiographically the appearances vary depending on the size of the lesion. The trabecular pattern may appear coarse and there is usually a decrease in bone density in the affected area, although some vertebra may

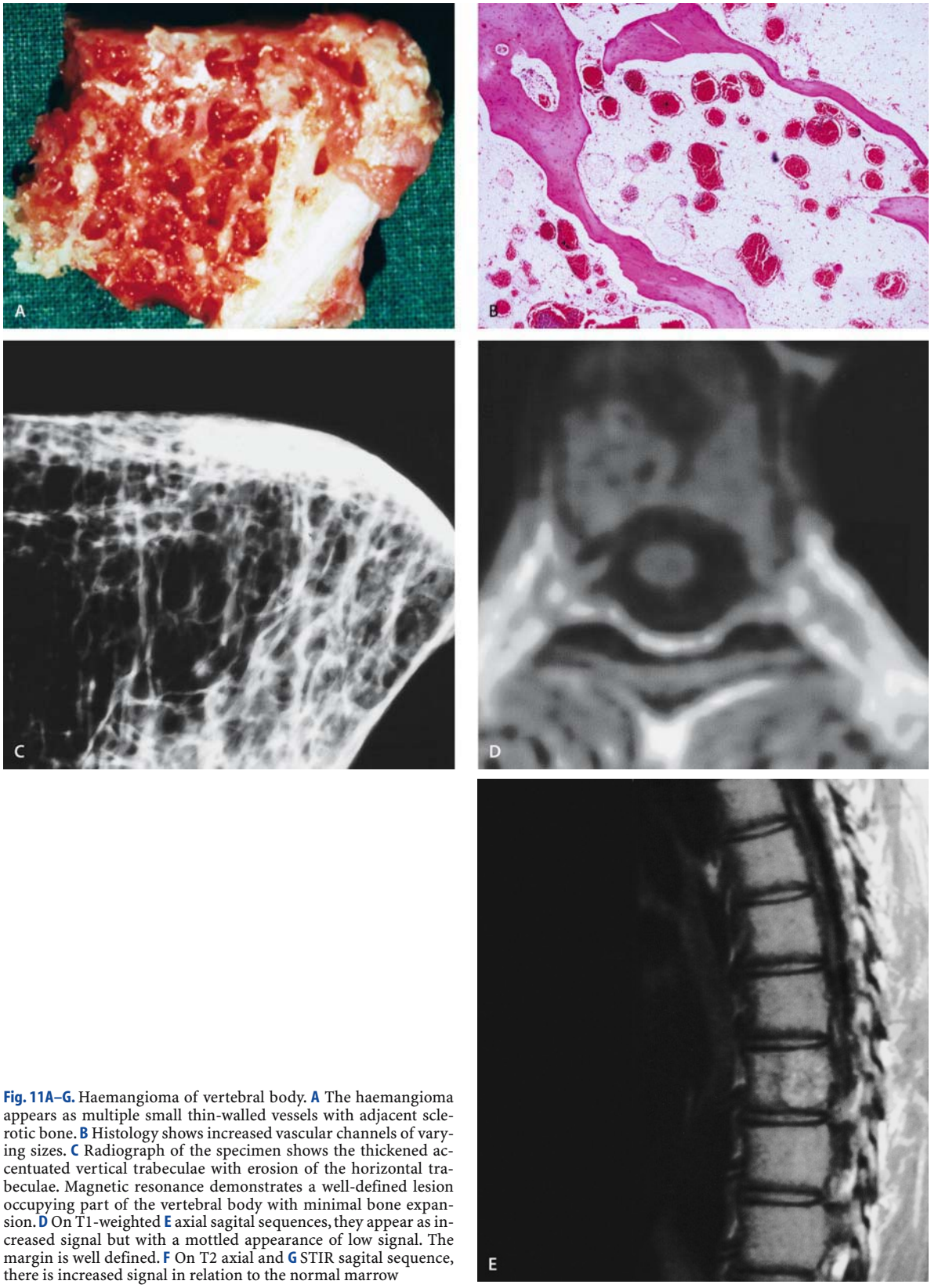

Fig. 11A–G. Haemangioma of vertebral body. **A** The haemangioma appears as multiple small thin-walled vessels with adjacent sclerotic bone. **B** Histology shows increased vascular channels of varying sizes. **C** Radiograph of the specimen shows the thickened accentuated vertical trabeculae with erosion of the horizontal trabeculae. Magnetic resonance demonstrates a well-defined lesion occupying part of the vertebral body with minimal bone expansion. **D** On T1-weighted **E** axial sagital sequences, they appear as increased signal but with a mottled appearance of low signal. The margin is well defined. **F** On T2 axial and **G** STIR sagital sequence, there is increased signal in relation to the normal marrow

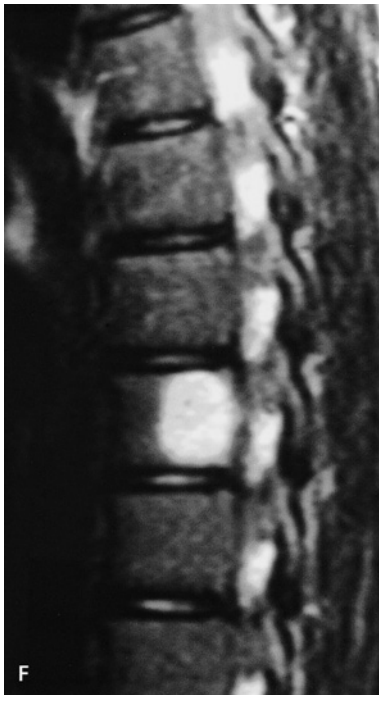

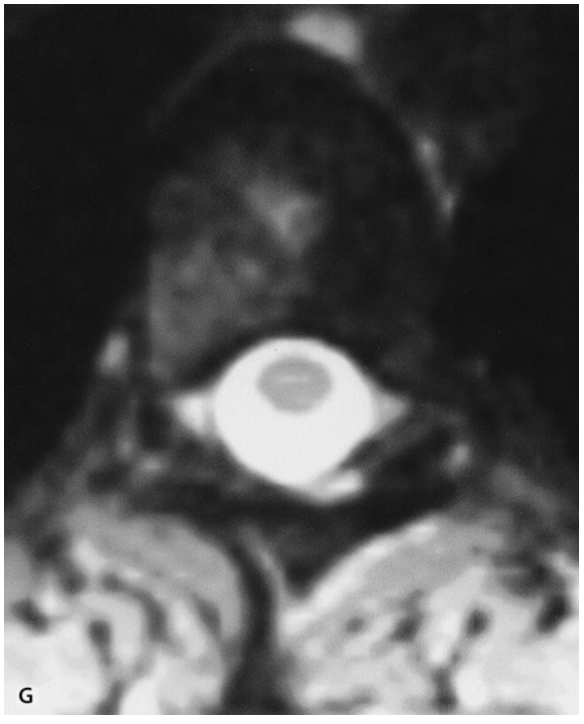

Fig. 11F, G.

appear to be increased in density [30] (Fig. 11). On axial CT, haemangiomas are low density due to fat, with punctate hyperdensities within the lesion due to the vertical bone struts seen in cross-section.

On MR, haemangiomas may have a variable appearance, with some lesions having a hyperintense signal on spin-echo T1-weighted sequences and intermediate signal on T2 weighting or intermediate intensity on T1 and high signal on T2 (Fig. 11). Lesions may be heterogeneous or homogeneous. The balance between the two different patterns depends on the relative proportion of adipocytes and of vessels and interstitial oedema [31]. Areas with high signal intensity on T1 and intermediate signal on T2 contained a larger proportion of surface marrow occupied by fat cells, while intermediate signal on T1 and high on T2 was similar to normal marrow but a larger proportion of surface area occupied by vessels and oedema, suggesting that the vascular component of the lesion is responsible for the high signal on T2 [31].

Rarely haemangiomas become aggressive, extending into the pedicles and posterior elements, causing expansion and breaking through the vertebral wall into the epidural space. Laredo et al. [32] found numerous packed, thin-walled vascular cavities and the absence of fatty replacement at histological analysis of compressive vertebral haemangioma

Eosinophilic Granuloma

These lesions are rare but are well recognised in the spine, representing 7.8%–15% of the total solitary eosinophilic granulomas [33] and are seen in children who present with pain, muscle spasm and may have a local kyphosis. A single vertebra is involved in half the cases and the thoracic spine is involved in 55% of cases, with the lumbar and cervical spine involved in similar proportions of the remainder [34]. Pathologically the vertebral body is involved with invasion of non-neoplastic proliferation of histiocytes, with a variable increase in polymorphs, lymphocytes and eosinophils (Fig. 12). The histiocytes have cytoplasmic organelles and Birbeck granules.

The classic feature on the radiograph is vertebral collapse, giving a vertebra plana with preservation of adjacent intervertebral disc (Fig. 12). Other characteristic findings include an absence of osteolytic areas, increased density of the vertebral body, preservation of the pedicles and neural arch, and absence of a paravertebral shadow [34]. The vertebra gradually regenerates with recovery of partial height, with a persistent dense line in the centre of the vertebra [33] (Fig. 12).

Giant Cell Tumours

Seven percent of giant cell tumours involve the spine, and the sacrum is affected in 90% of these cases [35]. The age range is similar for appendicular giant cell tumour and there is a higher incidence in women. Typically the lesion is osteolytic (Fig. 13), exhibiting cortical

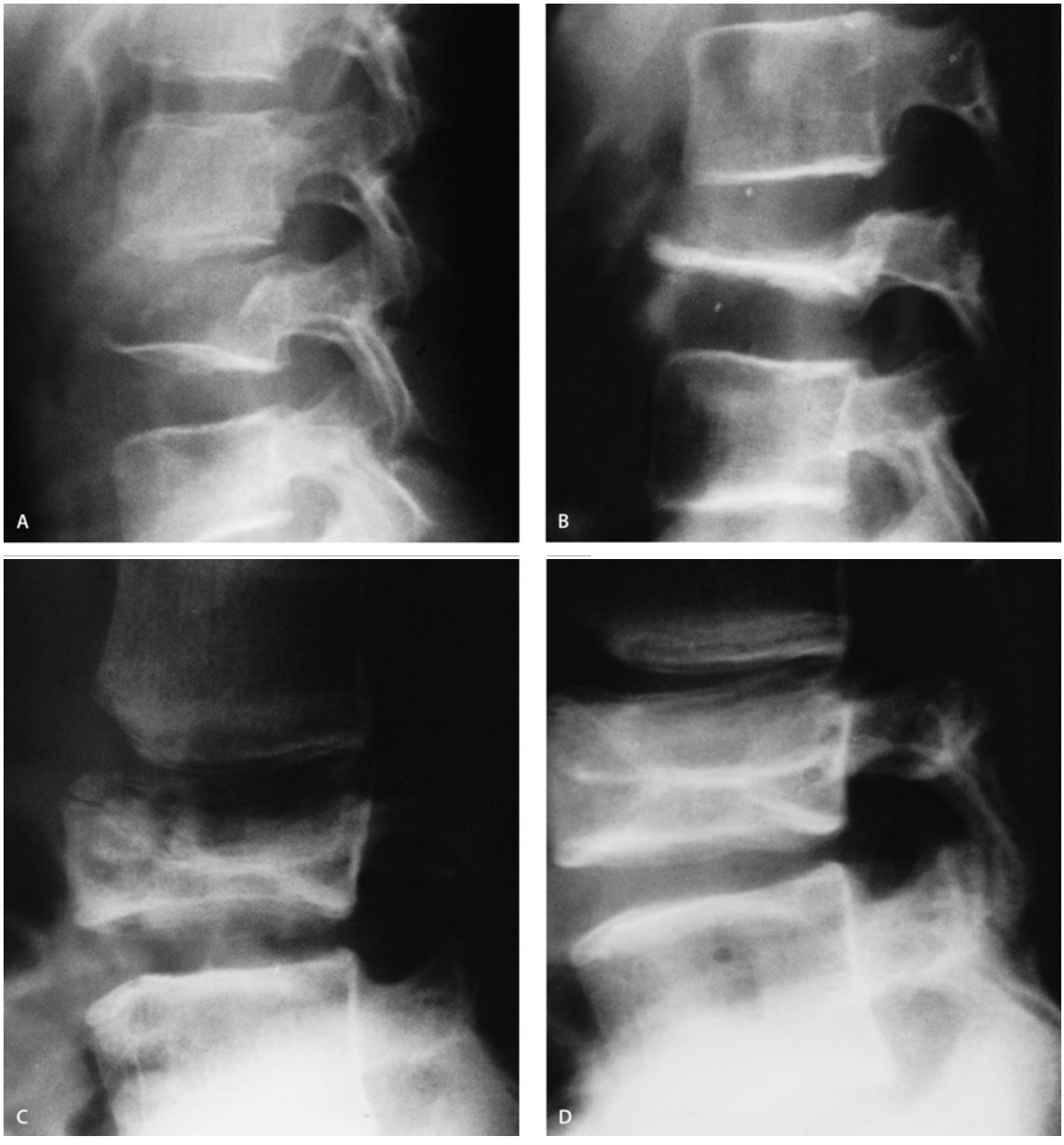

Fig. 12A–E. Eosinophilic granuloma. **A–D** Lateral radiographs of the spine show the stages of collapse and regeneration with the classical feature of vertebra plana followed by a partial re-growth of the vertebral body. **E** Histology shows numerous Langerhans cells with cleft-ed nuclei and variable distributed eosinophils and neutrophils

Fig. 13A–E. Giant cell tumour. **A** AP radiographs of the spine show an expanding destructive lesion in the T12 vertebral body with loss of the left pedicle and an adjacent paravertebral soft tissue mass. The inferior endplate remains visible but the superior end plate is destroyed. **B** CT demonstrates a large soft tissue tumour re-placing the vertebral body and pedicle with a septate appearance but without an outer cortical rim. **C** Axial MR images show inter-mediate signal on both T1- and (**D**) T2-weighted sequences with a low signal pseudocapsule. **E** Histology demonstrates the cellular nature of the lesion with mononuclear stromal cells, large multi-nucleated giant cells and poorly developed reactive bone.

Fig. 12C–E

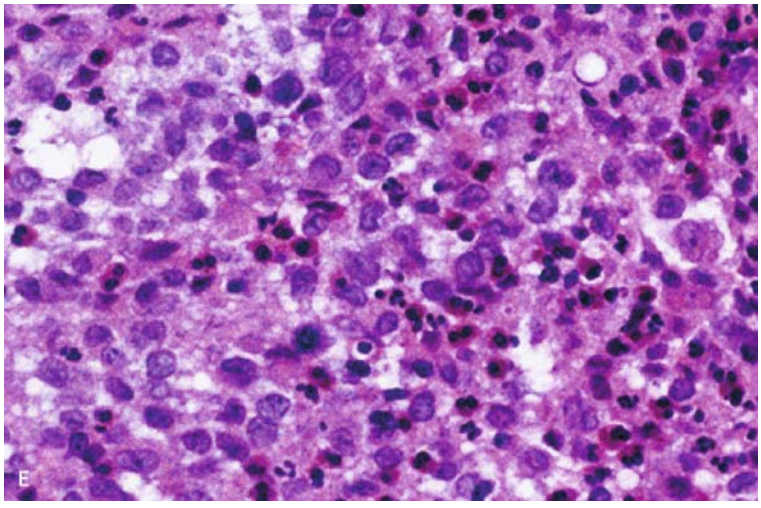

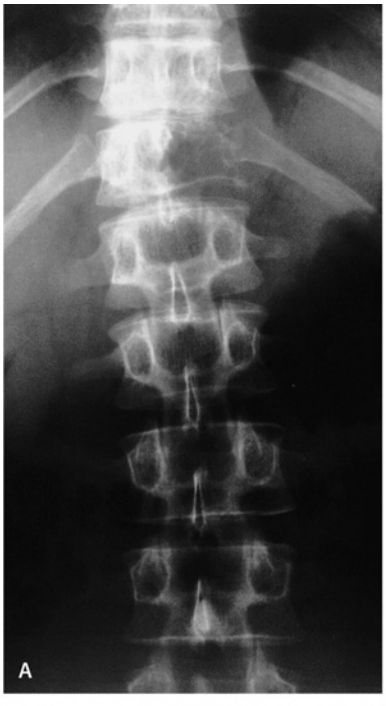

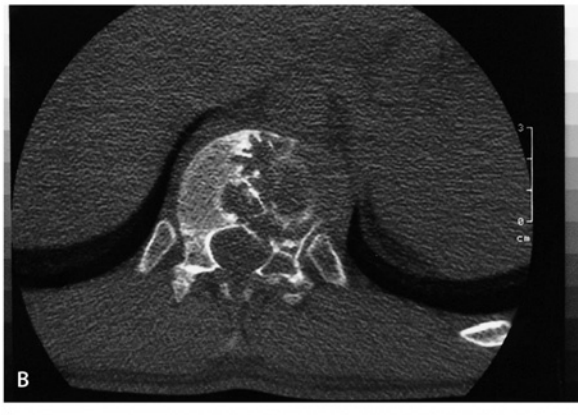

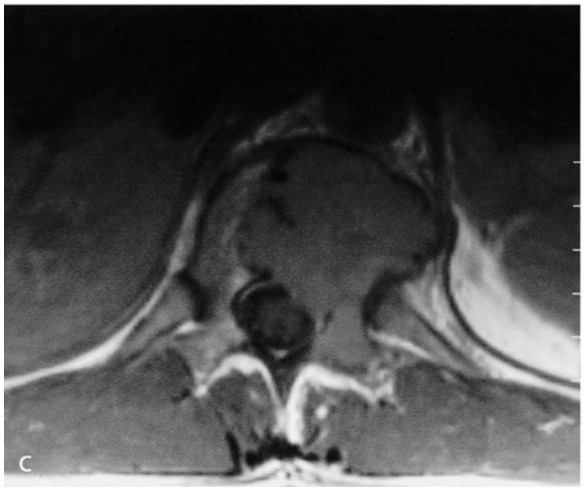

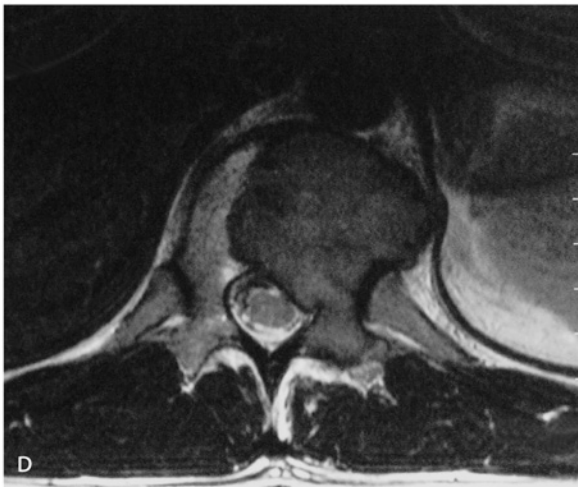

Fig. 13E

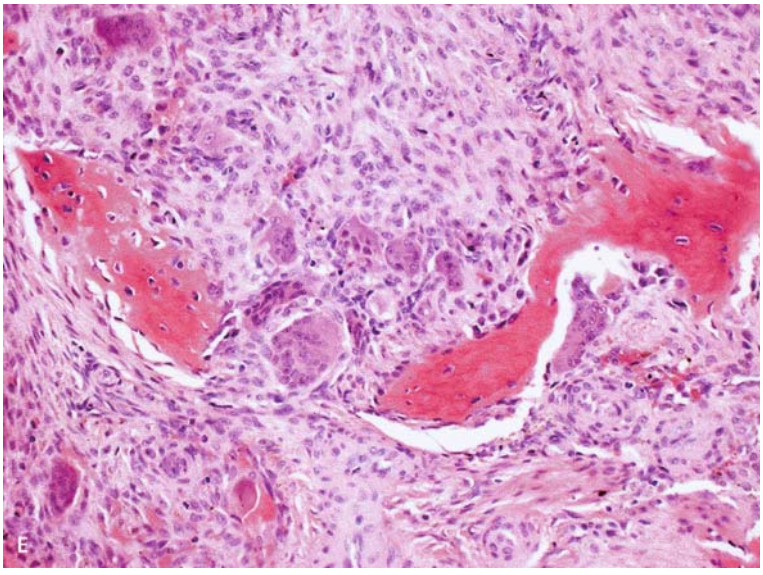

expansion, a cortical shell and with apparent bony septation. Sacral lesions may cross the sacroiliac joints, and vertebral lesions above the sacrum commonly involve both body and arch, with adjacent vertebral involvement also possible [36]. On MR, giant cell tumours exhibit a low to intermediate signal on T1-weighted images and also on T2 weighting (Fig. 13) in the majority of cases, probably due to the high collagen content and haemosiderin deposition [37]. Cystic areas, foci of haemorrhage, fluid–fluid levels and a peripheral low-signal pseudocapsule may be seen. The tissue appears relatively homogeneous and histologically is composed of mononuclear stromal cells that have a round or ovoid shape with relatively large nuclei and multinucleated giant cells dispersed evenly throughout the tissue. Foci of bone may also be present, particularly at the periphery of the tumour (Fig. 13)

Cartilage Tumours of the Spine

Chondroblastoma

These tumours are rare, constituting less than 1% of bone tumours and spinal involvement is only 1.4% of all chondroblastoma [38]. There is a predominance of males, and the vertebral lesions present clinically a decade later than its appendicular counterpart. Histologically they are characteristic of chondroblastoma with round and ovoid cells often mixed with a scattering of giant cells. There is an intercellular chondroid matrix in which lacelike deposits of calcium granules are observed. Some lesions may have cystic and haemorrhagic areas, which may cause confusion with aneurysmal bone cysts.

On imaging, vertebral chondroblastoma appear aggressive, with a large destructive bony lesion and a large soft tissue mass and significant spinal cord compression. Morphologically the imaging features suggest malignancy but calcification, which may be subtle and best demonstrated on CT, will point to the cartilaginous nature of the lesion. Bone oedema was not a feature of these lesions on MR. The imaging features may be similar to chondrosarcoma [39] but the age of presentation is completely different, with a range of 45–55 years

Chondrosarcoma

It has been reported that 3%–12% of chondrosarcoma arise in the spine [39, 40] and although rare, it is still the second most common primary malignant tumour of the spine after chordoma. It is an indolent slow-growing tumour, often revealed clinically because of adjacent neurological compression. Most spinal chondrosarcoma are of the exostotic type resulting from sarcomatous change of an osteochondroma. They are seen radiologically as a large calcified mass arising from the vertebral body of posterior elements and enlarge in the paraspinal soft tissue. The central part of the tumour is densely calcified with stippled, punctate irregular calcifications and typical rings and arcs [2]. CT and MR show the calcifications enclosed in a thick cap of sarcomatous cartilage. Destruction of underlying bone may be seen but is not always present.

Clear cell chondrosarcoma is a low-grade malignancy accounting for approximately 2% of all chondrosarcoma. It commonly involves the epiphysis and epi-metaphysis of long bones, but it has been reported in vertebra in a very small number of cases [40].

Histologically it is characterised by tumour cells with abundant clear cytoplasm and characteristic round, centrally placed nuclei arranged in a lobulated growth pattern. They contain variable amounts of hyaline cartilage, osteoid production, and focal cystic changes such as aneurysmal bone cyst formation may be present. However, bone formation and a cartilaginous component were absent or minimal in the reported spinal lesions [41].

CT demonstrates cortical destruction and soft tissue extension and the mass may be partially mineralised. Differentiation from osteoblastoma may be difficult.

Acknowledgements. I am grateful to Dr Charles Mangham for his assistance with the histological illustrations and guidance.

References

1. Kavanagh E, Smith C, Eustace S (2003) Whole body turbo STIR MR imaging: controversies and avenues for development. Eur Radiol 13:2196–2205
2. Laredo JD, El Quessar A, Bossard P, Vuillemin-Bodaghi V (2001) Vertebral tumours and pseudotumours. Radiol Clin North Am 39:137–163
3. Conlan MG, Bast M, Armitage JO et al (1990) Bone marrow involvement by non-Hodgkin's lymphoma: the clinical significance of morphologic discordance between the lymph node and bone marrow. J Clin Oncol 8: 1163–1172
4. Bennett JM, Cain KC, Glick JH et al (1986) The significance of bone marrow involvement in non-Hodgkin's lymphoma J Clin Oncol 4:1462–1469
5. Ostrowski M, Inwards C, Strickler JG et al (1999) Osseous Hodgkin's disease. Cancer 85:1166–1178
6. Parker BR, Marglin S, Castellino RA (1980) Skeletal manifestations of Hodgkins's disease and non-Hodgkin lymphoma. Semin Roentgenol 15:302–315
7. Braunstein EM, White SJ (1980) Non-Hodgkin lymphoma of bone. Radiology 135: 59–63
8. Bullough PG (1991) Atlas of orthopedic pathology with clinical and radiological correlations. 2nd edn. Gower Medical, New York
9. Walker R, Kessar P, Blanchard R et al (2000) Turbo STIR magnetic resonance imaging as a whole body screening tool for metastases in patients with breast carcinoma: preliminary clinical experience. J Magn Reson Imaging 11:343–350
10. Cuenod CA, Laredo JD, Chevret S et al (1996) Acute vertebral collapse due to osteoporosis or malignancy. Appearances on enhanced and gadolinium-enhanced MR images. Radiology 199:541–549
11. Baur A, Stabler A, Bruning R et al (1998) Diffusion-weighted MR imaging of bone marrow: differentiation of benign versus pathological fractures. Radiology 207:349–356
12. Bjornsson J, Wold LE, Ebersold MJ et al (1993) Chordoma of the mobile spine: a clinico-pathologic analysis of 40 patients. Cancer 71:735–740
13. Firooznia H, Pinto RS, Lin JP et al (1976) Chordoma: radiological evaluation of 20 cases. AJR 127:797–805
14. Rosenthal DI, Scott JA, Mankin HJ et al (1985) Sacrococcygeal chordoma: magnetic resonance imaging and computed tomography. AJR 145:143–147
15. Inci S, Palaoglu S, Erbengi A (1996) Low cervical chordoma: a case report. Spinal Cord 34:358–360
16. Smolders D, Wang X, Drevelengas A, Vanhoenaker E, De Schepper AM (2003) Value of MRI in the diagnosis of non-clival, non-sacral chordoma. Skeletal Radiol 32:343–350
17. Sze G, Uichanco LS, Brant-Zawadski MN et al (1988) Chordomas: MR imaging. Radiology 166:187–191
18. Murphy JM, Wallis F, Toland J, Toner M, Wilson GF (1998) CT and MRI appearances of a thoracic chordoma. Eur Radiol 8: 1677–1679
19. De Beuckeleer LH, De Schepper AM, Ramon F, Somville J (1995) Magnetic resonance imaging of cartilaginous tumours: a retrospective study of 79 patients. Eur J Radiol 21: 34–40
20. Kuker W, Thiex R, Friese S et al (2000) Spinal subdural and epidural hematomas: diagnostic and therapeutic aspects in acute and sub-acute cases. Acta Neurochir (Wien) 142: 777–785
21. Bottner F, Wortler K, Link T (2000) Osteoid osteoma (letter). J Bone Joint Surg Br 82B:306–307
22. Davies M, Cassar-Pullicino VN, Davies AM, McCall IW, Tyrrell PNM (2002) The diagnostic accuracy of MR in osteoid osteoma. Skeletal Radiol 31:559–569
23. Assoun J, Richardi G, Railhac JJ et al (1994) Osteoid osteoma: MR imaging versus CT. Radiology 191:217–223
24. Okuda S, Myoui A, Nakase T, Wada E, Yonenobu K, Yoshikawa H (2001) Ossification of the ligamentum flavum associated with osteoblastoma: a report of three cases. Skeletal Radiol 30:402–406
25. Adler CP (2000) Bone diseases: macroscopic, histological and radiological diagnosis of structural changes in the skeleton. Springer, Berlin Heidelberg New York, pp 318–321, 412–417
26. Lomasney M, Basu A, Demos TC, Laskin W (2003) Fibrous dysplasia complicated by aneurismal bone cyst formation affecting multiple cervical vertebrae. Skeletal Radiol 32: 533–536
27. Capanna R, Van Horn JR, Biagini R et al (1989) Aneurysmal bone cyst of the sacrum. Skeletal Radiol 18:109–113
28. Hudson TM (1984) Fluid levels in aneurysmal bone cysts: a CT feature. AJR 141:1001–1004
29. Tsai JC, Dalinka MK, Fallon MD et al (1990) Fluid-fluid level: a non-specific finding in tumours of bone and soft tissue. Radiology 175:779–782
30. Laredo JD, Reizine D, Bard M, Merland JJ, Tubiana JM (1986) Vertebral haemangiomas: radiologic evaluation. Radiology 161:183–189
31. Baudrez V, Galant C, Vande Berg BC (2001) Benign vertebral hemangioma: MR-histological correlation. Skeletal Radiol 30: 442–446
32. Laredo JD, Assouline E, Gelbert F, Wybier M, Merland JJ, Tubiana JM (1990) Vertebral hemangiomas: fat content as a sign of aggressiveness. Radiology 177:467–472
33. Canadell J, Villas C, Martinez-Denegri J et a (1986) Vertebral eosinophilic granuloma. Spine 11:767–769
34. Yeom JS, Lee CK, Shin HY et al (1999) Langerhans cell histiocytosis of the spine: analysis of twenty-three cases. Spine 24: 1740–1749
35. Bidwell JK, Young JW, Khalluff E (1987) Giant cell tumour of the spine: computed tomography appearance and review of the literature. J Comput Assist Tomogr 11:307–311
36. Hart RA, Boriani S, Biagini R et al (1997) A system for surgical staging and management of spine tumours: a clinical outcome study of giant cell tumours of the spine Spine 22 1773–1782; discussion, 1783
37. Aoki J, Tanikawa H, Ishii K et al (1996) MR findings indicative of haemosiderin in giant cell tumours of bone: frequency, cause and diagnostic significance. AJR 166:145–148
38. Ilaslan H, Sundaram M, Unni KK (2003) Vertebral chondroblastoma. Skeletal Radiol 32:66–71
39. Shives TC, McLeod RA, Unni KK, Schray MF (1990) Chondrosarcoma of the spine. J Bone Joint Surg Am 71:1158–1165
40. Camins MB, Duncan AW, Smith J et al (1978) Chondrosarcoma of the spine. Spine 3:202–209
41. Collins MS, Koyama T, Swee RG, Inwards CY (2003) Clear cell chondrosarcoma: radiographic, computed tomographic, and magnetic resonance findings in 34 patients with pathological correlation. Skeletal Radiol 32:687–694

Soft Tissue Tumors

Mark D. Murphey, Mark J. Kransdorf

6.6

Contents

Introduction

The goals of radiologic evaluation of soft tissue tumors are: (1) lesion detection, (2) identifying a specific diagnosis or reasonable differential diagnosis, and (3) lesion staging. Imaging of soft tissue tumors to achieve these goals has markedly evolved, improved, and expanded with the advent of computerized tomography (CT) and magnetic resonance imaging (MRI). Indeed, CT and particularly more recently MRI allow lesion detection and staging by delineating anatomic extent in all cases and relatively specific diagnosis in approximately 25%–50% of soft tissue tumors. We would suggest that evaluation of soft tissue tumors is now similar to bone tumors in that pathologic diagnosis should incorporate the imaging findings in the vast majority of cases. This is particularly true in large tumors where only a small amount of tissue may be available for pathologic review initially, and the question arises as to the true representation of the entire lesion. Our purpose is to provide a framework for the systematic approach to radiologic evaluation of soft tissue tumors. While our approach reviews multiple imaging modalities, we emphasize MRI, as it is generally considered the optimal radiologic tool in the evaluation of soft tissue tumors.

The annual incidence of benign soft tissue tumors has been estimated at 300 per 100,000 people, accounting for approximately 750,000–800,000 lesions in the United States [1, 2]. Thus, benign soft tissue tumors are relatively common lesions and outnumber malignant soft tissue tumors by a ratio to 100–150 to one [1, 2]. The National Cancer Institute figures of 1990 reveal 5,700 soft tissue malignancies annually in the United States resulting in 3,100 deaths [3].

While there are innumerable possible pathologic diagnoses for a soft tissue mass, more than 70% of benign tumors and 80% of malignant neoplasms are accounted for by eight diagnoses [4, 5]. In the series of 18,677, cases from the Armed Forces Institute of Pathology (AFIP) common benign soft tissue tumors include lipoma and its variants (16%), fibrous histiocytoma (13%), nodular fasciitis (11%), neurogenic neoplasm (10%), hemangioma (7%), fibromatosis (7%), and pigmented villonodular synovitis (PVNS)/giant cell tumor of tendon sheath (GCTTS) (4%) [4]. In addition, ganglia typically account for a large number of benign lesions, although due to a selection bias of the AFIP series as a secondary consultation, it represents only a small percentage of their cases. The AFIP review of 12,370 malignant soft tissue neoplasms reveals that common lesions include malignant fibrous histiocytoma (MFH)/fibrosarcoma (29%), liposarcoma 14%, nonspecific spindle cell sarcoma (12%), leiomyosarcoma (8%), malignant peripheral nerve sheath tumor (MPNST; 6%), dermatofibrosarcoma protuberans (DFSP; 6%) and synovial sarcoma (5%) [5].

Radiologic Evaluation

In our opinion and experience, the radiologic evaluation of a soft tissue tumor should *always* begin with radiographs. While helpful in only a small percentage of cases, certain features may be diagnostic and more dif-

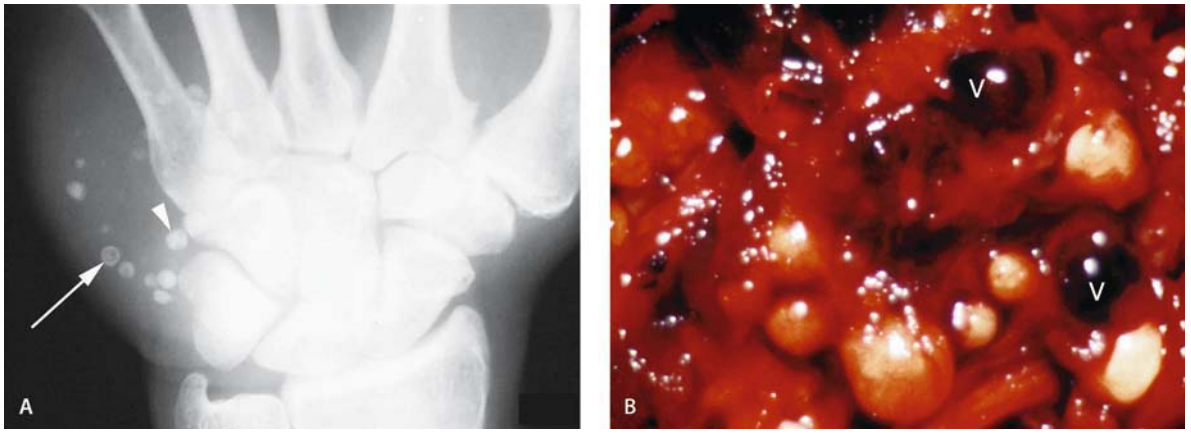

Fig. 1A, B. A 52-year-old man with hemangioma of hypothenar region of hand. **A** Radiograph shows multiple small, smooth, rounded calcifications (*arrow*), more opaque peripherally, characteristic of phleboliths. Small nonspecific calcifications are also seen (*arrowhead*). **B** Corresponding intraoperative photograph shows multiple phleboliths in large cavernous spaces (*v*) of the hemangioma

ficult to appreciate on advanced imaging (CT and MRI). Unfortunately, in this day and age of high tech imaging, this simple inexpensive study is at times forgotten and it cannot be predetermined in which cases radiographs will be critical for diagnosis. Radiographs may reveal that an apparent soft tissue mass is related to an underlying bone lesion such as an exostosis or posttraumatic deformity. Calcification of a soft tissue mass may be characteristic in hemangioma (Fig. 1), synovial chondromatosis or myositis ossificans (heterotopic bone formation). Calcification may also be nonspecific in appearance on radiographs, although its identification still limits differential considerations and is frequently associated with extraskeletal chondrosarcoma or osteosarcoma and synovial sarcoma. Finally, radiographs allow detection of underlying osseous involvement with periosteal reaction, cortical destruction and marrow invasion. In our experience, the common soft tissue sarcomas which reveal bone invasion are synovial sarcoma and MFH.

Nuclear Medicine

Scintigraphic evaluation does not play a primary role in evaluation of soft tissue masses. Benign and malignant soft tissue tumors, particularly more vascularized lesions, frequently reveal mild increased uptake of radionuclide on bone scintigraphy due to increased blood flow. In addition, lesions with mineralization may show more prominent radionuclide activity from the increased turnover of calcium and phosphate. Gallium scanning has been advocated to distinguish benign peripheral nerve sheath tumors (BPNST) from malignant peripheral nerve sheath tumor (MPNST), although evaluation has included only small numbers of patients [6]. Specifically, prominent gallium uptake is seen in MPNST as opposed to BPNST (neurilemmoma and neurofibroma) that demonstrate limited or no uptake. Thallium and positron emission tomographic (PET) studies have been used to assess response to treatment (radiation therapy and/or chemotherapy) as well as to evaluate possible tumor recurrence following surgical resection, although an in-depth discussion of this topic is beyond the scope of this discussion.

Angiography

In the past, angiographic evaluation of soft tissue tumors, particularly sarcomatous lesions, was relatively common to assess the degree of vascularity and serve as a surgical vascular road map. In addition, angiography was often used to evaluate the effect of preoperative therapy with response depicted as decreased vascularity as a result of hemorrhage and or necrosis. However, angiography has largely been supplanted by other imaging modalities such as CT or MR angiography (MRA). Embolization of soft tissue neoplasms may be performed via angiographic access as a method to decrease blood loss during surgical resection in lesions with prominent vascularity. Angiomatous lesions, particularly when diffuse or extensive (angiomatosis), may be embolized as the only method of treatment.

Fig. 2A–C. A 28-year-old woman with myxoid liposarcoma simulating a cystic mass. **A** Coronal T1-weighted and (**B**) T2-weighted MR images show a homogeneous mass (*arrows*) with low and high signal intensity, respectively, suggesting a cystic mass. **C** Ultrasound study reveals hypoechoic solid mass (*arrowheads*). Surgical resection revealed pathologic diagnosis of myxoid liposarcoma

CT, MRI, and Ultrasound

The advantages of CT and MRI in comparison to radiographs in evaluation of soft tissue tumors is primarily a function of their superior contrast resolution. In our opinion and experience, MRI is generally superior to CT in radiologic evaluation of soft tissue tumors because of its marked improvement in contrast resolution and multiplanar capabilities (Figs. 2–7). CT may be preferred if MRI is contraindicated as well as for masses in certain anatomic regions such as the periscapular area or chest or abdominal wall, where motion artifact can be problematic. In addition, CT is the modality choice to both detect and characterize calcification (chondroid or osteoid) in soft tissue tumors if radiographs are inadequate (given their subtle nature or obscuration by complex anatomy, particularly overlying osseous structures, i.e., the pelvis).

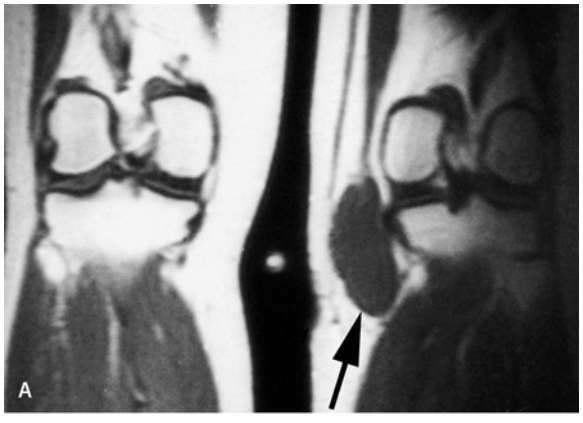

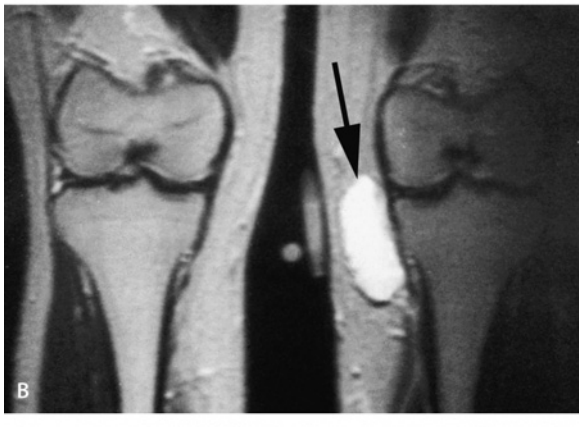

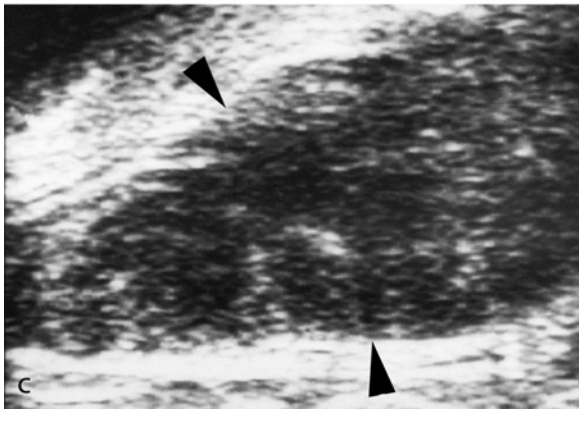

Placement of a marker over the soft tissue mass is helpful with both CT and MRI. This is particularly important for subcutaneous lipomas, which may be obscured by the surrounding normal fat. Patient positioning may also be important with both modalities, particularly again with superficial lesions so that the tumor is not compressed. A prone position may be required in patients with paraspinal or posterior extremity masses.

Soft tissue tumors should be imaged in at least two orthogonal planes by MRI. The axial plane is usually optimal for evaluation and both conventional T1-weighted and T2-weighted spin-echo MRI should be obtained. A second plane of imaging should also be performed either coronal (best for masses located medial or lateral in a compartment) or sagittal (best for masses located anterior or posterior in a compartment). Fat-suppressed T2-weighted or short tau inversion recovery (STIR) MR sequences are often employed in the second plane to increase the conspicuity of tumors in addition to T1-weighted images. Gradient-echo MR images may be used to accentuate magnetic susceptibility in identifying hemosiderin and depicting lesion-fat interfaces for neurovascular involvement.

The chosen field of view depends on lesion size and location. However, generally the smallest field of view that allows evaluation of the entire mass is preferable for MRI. Imaging of the contralateral side is more often helpful with CT as opposed to MRI related to the superior contrast resolution of the latter modality.

Intravenous contrast material can be administered for either CT or MRI in an attempt to improve the contrast resolution in evaluation of soft tissue tumors. In general, contrast is much more important for CT (several precontrast images should also be obtained for comparison) in differentiating soft tissue tumors from surrounding muscle because of its inferior contrast resolution. In contradistinction, lesion detection and delineation is typically easily evaluated on MRI without the need for intravenous contrast [7, 8]. However, an exception to this is seen with neoplasms that are highly necrotic, hemorrhagic or myxomatous. In these cases, intravenous contrast can be very informative in identification of areas of enhancing solid cellular tissue (Fig. 5). This becomes vital in directing biopsy to these solid areas that harbor diagnostic tissue for histologic evaluation as opposed to nondiagnostic regions of hemorrhage, necrosis and nonspecific myxoid tissue.

Ultrasound (US) is another imaging modality that can be used in the evaluation of soft tissue tumors. Advantages of US include its low cost, real-time scanning,

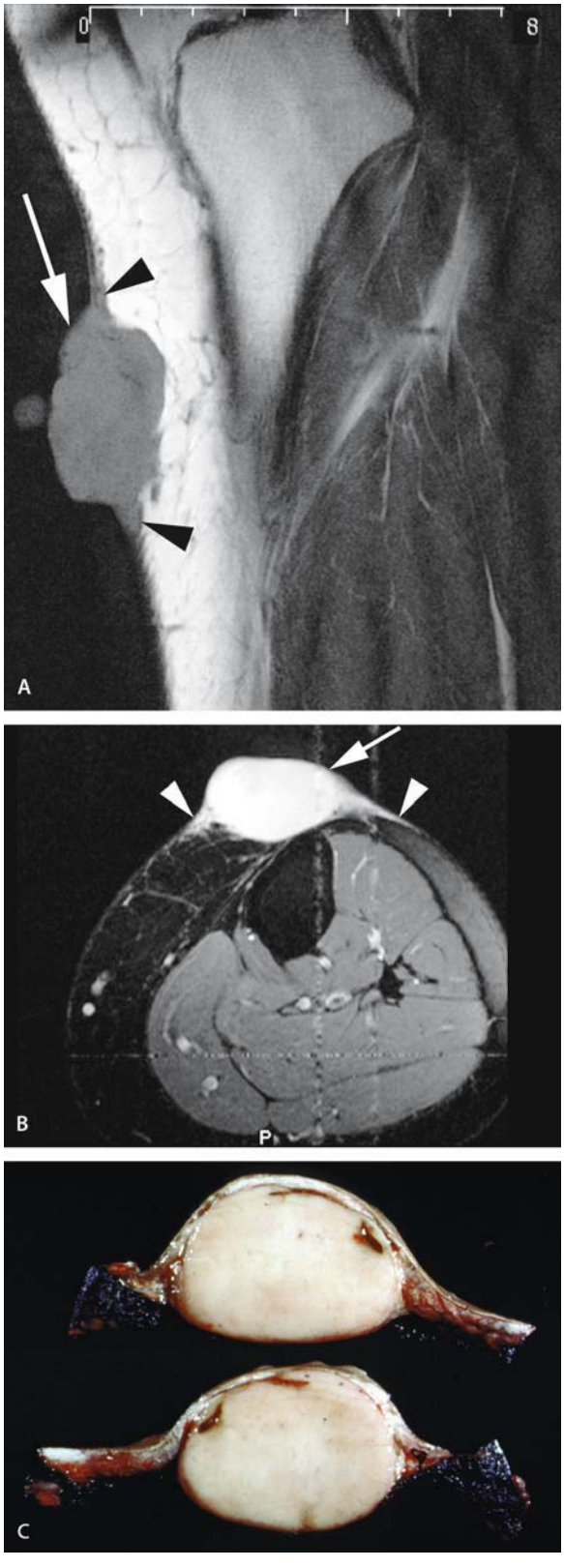

Fig. 3A–C. A 38-year-old man with a slowly enlarging subcutaneous mass involving the skin, representing dermatofibrosarcoma protuberans (DFSP). **A** Sagittal T1-weighted MR image shows a subcutaneous mass (*arrow*) protruding from and involving the skin. **B** Axial inversion recovery MR image reveals similar findings and high signal intensity in the mass (*arrow*). Linear extension along the skin (tail sign) (*arrowheads*) are also seen on both images. **C** Sectioned gross specimen demonstrates manifestations identical to that seen on MR imaging

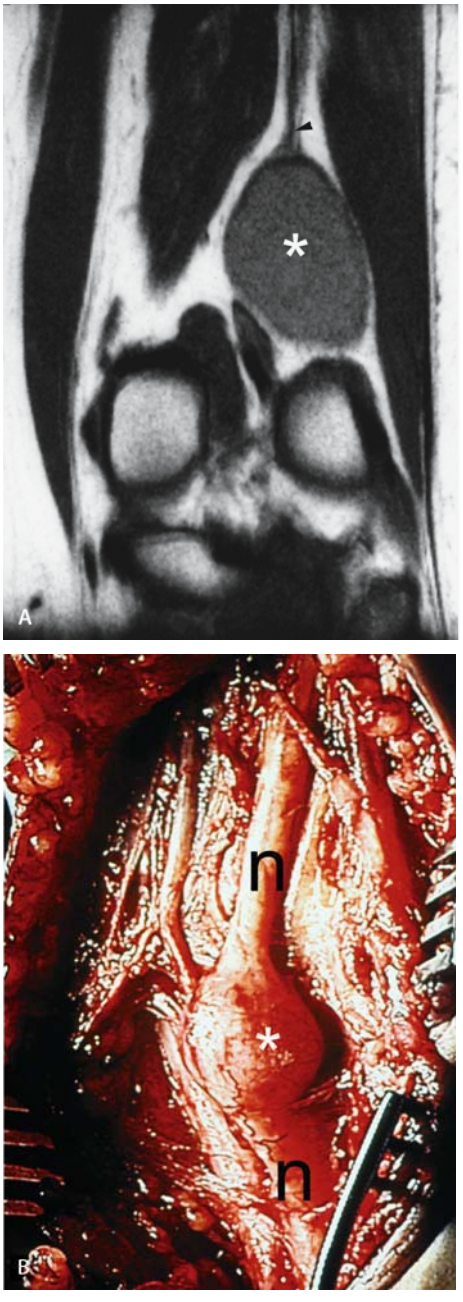

Fig. 4A, B. A 49-year-old woman with a slowly enlarging neurilemmoma of the posterior distal thigh. **A** Coronal T1-weighted MR image shows a deep intermuscular mass (*) surrounded by fat (split-fat sign). Linear tubular extension superiorly represents the entering sciatic nerve (*arrowhead*) and creates a fusiform shaped mass. **B** Intraoperative photograph demonstrates the neurilemmoma (*) as well as both the entering and exiting nerve (*n*)

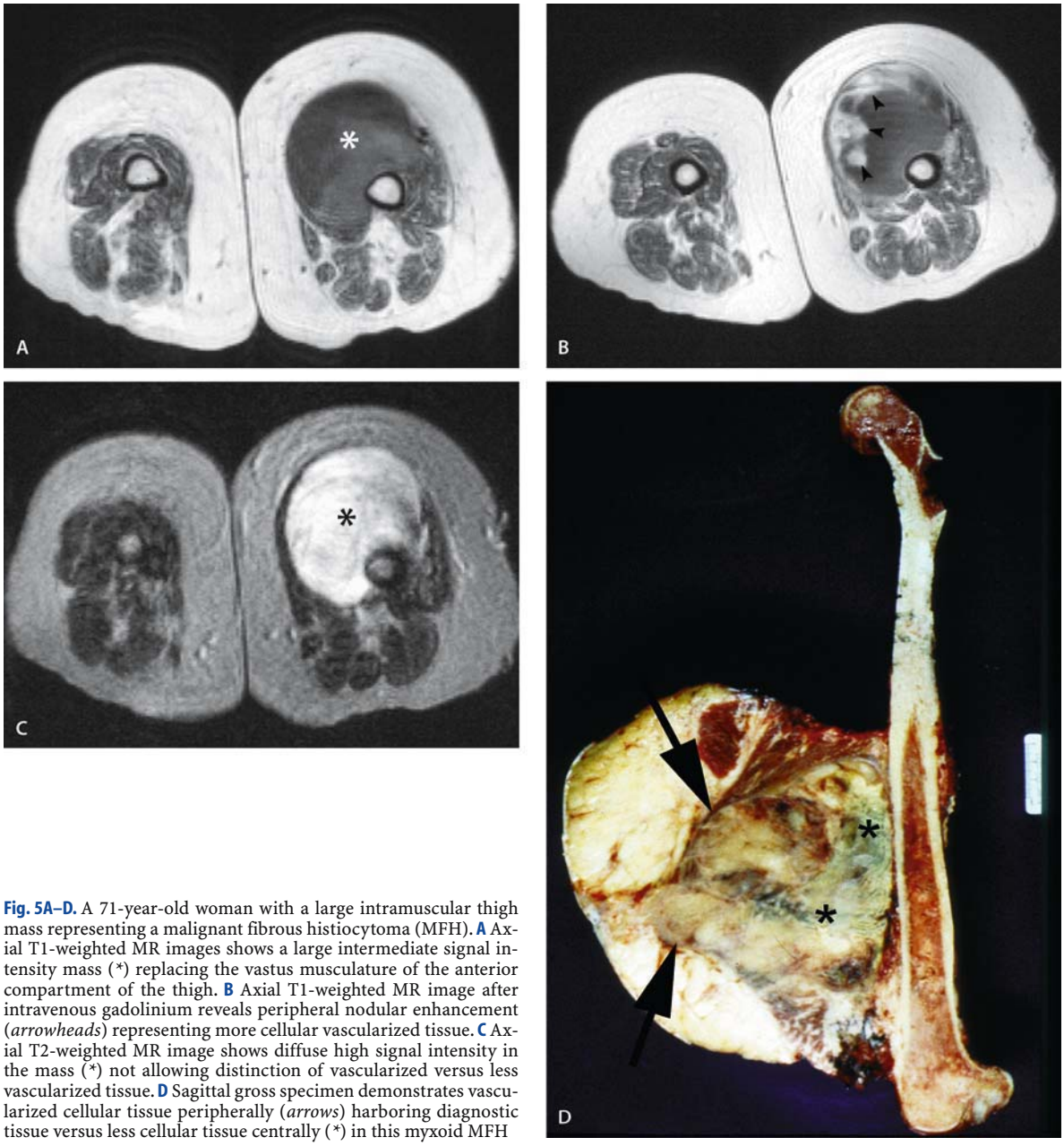

Fig. 5A–D. A 71-year-old woman with a large intramuscular thigh mass representing a malignant fibrous histiocytoma (MFH). **A** Axial T1-weighted MR images shows a large intermediate signal intensity mass (*) replacing the vastus musculature of the anterior compartment of the thigh. **B** Axial T1-weighted MR image after intravenous gadolinium reveals peripheral nodular enhancement (*arrowheads*) representing more cellular vascularized tissue. **C** Axial T2-weighted MR image shows diffuse high signal intensity in the mass (*) not allowing distinction of vascularized versus less vascularized tissue. **D** Sagittal gross specimen demonstrates vascularized cellular tissue peripherally (*arrows*) harboring diagnostic tissue versus less cellular tissue centrally (*) in this myxoid MFH

lack of ionizing radiation and lack of intravenous contrast. Subcutaneous lesions are often best evaluated by sonography because of their superficial location. Perhaps the most important use of US is in distinguishing a solid from a cystic soft tissue mass. This distinction is very important in differential diagnosis, and US, as in other organ systems, is quite adept at identifying truly cystic structures (anechoic with posterior acoustic enhancement), which include ganglion, synovial cyst, bursa, and abscess. In contradistinction, US demonstrates the solid consistency with internal echoes of other soft tissue tumors, including myxomas and myxoid neoplasms (i.e., myxoid liposarcoma), which on CT and or MRI may simulate a cyst because of their high intrinsic water content (Fig. 2). Doppler sonography can also be applied to assess lesion vascularity and response of neoplasm to preoperative chemotherapy and radiation therapy.

Despite the many advantages of US, there are also several disadvantages. This modality is very operator-dependent and relatively unusual examinations, such as for musculoskeletal tumors, often require physician scanning and a significant time commitment. Additionally, the field of view is often limited and large lesions

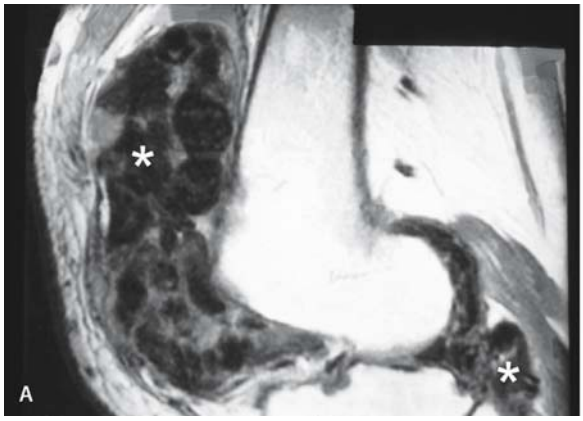

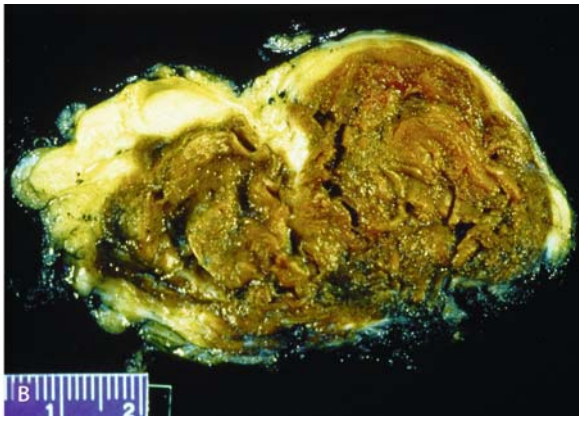

Fig. 6A, B. A 34-year-old woman with enlarging knee join mass resulting from involvement by pigmented villonodular synovitis (PVNS). **A** Sagittal proton density MR image shows massive involvement of the joint with tissue that demonstrates marked low signal (*). **B** Photograph of gross specimen of a representative piece of the intraarticular tissue reveals marked brown color related to extensive hemosiderin deposition causing the MR appearance characteristic of PVNS

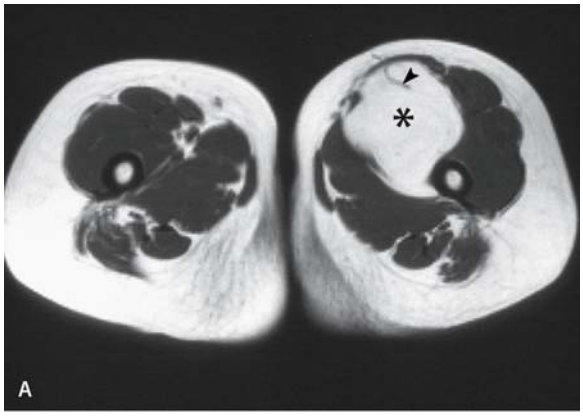

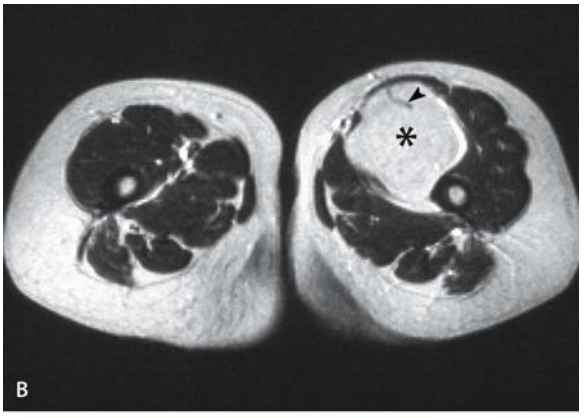

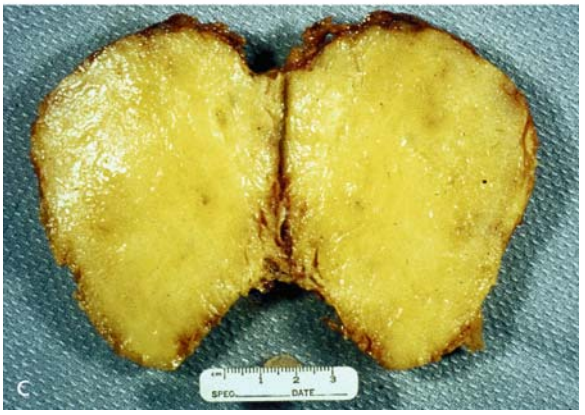

Fig. 7A–C. A 54-year-old woman with a long-standing anterior thigh mass representing a lipoma. **A** Axial T1-weighted and (**B**) T2-weighted MR images show a soft tissue mass (*) isointense with fat on all pulse sequences with single small septation anteriorly (*arrowhead*). **C** Sectioned gross specimen reveals monotonous yellow adipose tissue

may be difficult to assess entirely. While US is quite adept at evaluating superficial lesions, deep-seated lesions, particularly in complex areas of anatomy such as the pelvis, may be obscured by overlying bone. The contrast resolution of sonography is also inferior to that of MRI.

Staging

There are several staging systems (see Tables 1, 2) frequently used in evaluation of soft tissue sarcomas [9, 10]. However, all have in common the need for a close working relationship between the orthopedist, oncologist, radiologist and pathologist to appropriately stage lesions and guide treatment options. The treatment of choice for the vast majority of soft tissue sarcomas is surgical resection and limb salvage. Much of the information necessary, particularly the lesion extent and involvement of adjacent structures, to stage soft tissue tumors is obtained by imaging. Important features to assess include lesion extent (does the tumor cross a major fascial plane to involve more than one compartment), size (is the lesion larger than 5 cm, thus worsening prognosis for sarcomas), and identifying involvement of adjacent bone, joint, or neurovascular structures. Again, the multiplanar capabilities and superior contrast resolution of MRI make this the modality of choice in the assessment of most soft tissue tumors (particularly deep-seated lesions).

Table 1. Enneking staging of sarcomas of soft tissue and bone

Stage	Grade	Extent	Metastasis
IA	G1	T1	M0
IB	G1	T2	M0
IIA	G2	T1	M0
IIB	G2	T2	M0
III	G1–G2 G1–G2	T1 T2	M1 M1

G histologic grade; surgical grade: *G1*, low risk of metastasis, <25%; *G2*, high risk of metastasis, >25%. Site: *T1*, intracompartmental; *T2*, extracompartmental. Metastasis: *M0*, no regional or distant metastases; *M1*, regional or distant metastases present
Modified from [9]

Table 2. American joint commission staging protocol for sarcoma of soft tissue

Stage	Histologic grade (G)	Primary Tumor (T)	Regional lymph node (N)	Distant metastasis (M)
1A	1	1	0	0
1B	1	2	0	0
IIA	2	1	0	0
IIB	2	2	0	0
IIIA	3–4	1	0	0
IIIB	3–4	2	0	0
IVA	1–4	1–2	1	0
IVB	1–4	1–2	0–1	1

Histologic grade (*G*): *G1* well differentiated; *G2* moderately well differentiated; *G3–G4* poorly differentiated, undifferentiated. Primary tumor (*T*): *T1* tumor 5 cm or less in greatest dimension; *T2* tumor more than 5 cm in greatest dimension. Regional lymph nodes (*N*): *N0* no regional lymph node metastasis; *N1* regional lymph node metastasis. Distant metastasis (*M*): *M0* no distant metastasis; *M1* distant metastasis
Modified from [10]

Lesion Evaluation

In our opinion and experience, important features in the evaluation of soft tissue tumors are location, intrinsic imaging characteristics (including lesion size, margin and extent) and patient age.

Lesion Location

Lesion location (identical to bone tumors) is one of the most important clues to diagnosis. Specific anatomic distribution of various soft tissue tumors is available, although this information, in our opinion, is less helpful in general as compared to the compartment involved: subcutaneous, intermuscular, intramuscular, intraarticular/periarticular, and multiple lesions. There are exceptions to this concept: for example, a lesion deep to the scapular tip almost invariably represents an elastofibroma.

Subcutaneous masses are extremely common clinically. However, they are relatively infrequently evaluated by imaging because clinical evaluation is relatively easy (Fig. 3). In contradistinction, deep-seated soft tissue masses (intermuscular, intramuscular or intraarticular) are usually imaged because of inadequate clinical assessment. Common benign and malignant subcutaneous lesions are listed in Table 3.

Intermuscular soft tissue masses are usually surrounded by a rim of fat which we term the split-fat sign with the surrounding musculature draped around the lesion. This is best depicted by MRI but is also seen on CT (Fig. 4). It occurs because the deep intermuscular tissue is primarily composed of fat and soft tissue mass arising in this location maintains a rim of adipose tissue as it enlarges. In large lesions, the intermuscular location is often best determined by evaluating the superior and inferior aspect of the tumor. Common benign and malignant soft tissue tumors arising in the intermuscular space are listed in Table 3.

Soft tissue masses centered in muscle (intramuscular) replace the normal muscle texture signal intensity on MRI (Fig. 5). These lesions reveal surrounding muscle and typically lack a fat rim unless they involve an entire compartment. Common benign and malignant soft tissue tumors that arise in the intramuscular space are listed in Table 3.

Soft tissue masses that arise within or immediately adjacent to a joint have a relatively limited differential diagnosis. These lesions are usually benign. Synovial sarcoma is the most frequent malignancy, although it is rare to originate in a joint (5%–10% of cases) (Table 3).

Table 3. Soft tissue tumor location

Subcutaneous	Angiomatous lesions Benign fibrous histiocytoma DFSP (dermatofibrosarcoma protuberans) Granuloma annulare Leiomyosarcoma Lipoma Lymphoma MFH (malignant fibrous histiocytoma) Metastasis (especially melanoma) Myxoma Nodular fasciitis Skin appendage tumor
Intermuscular	Liposarcoma (myxoid and higher grade) Fibromatosis Ganglion Leiomyosarcoma Nodular fasciitis Neurogenic tumors Synovial cyst Synovial sarcoma
Intramuscular	Angiomatous lesions Lipoma MFH (malignant fibrous histiocytoma) Fibrosarcoma Myxoma Liposarcoma (well differentiated) Leiomyosarcoma/rhabdomyosarcoma Soft tissue Ewing sarcoma/PNET
Intraarticular/ Juxtaarticular	Lipoma arborescens Pigmented villonodular synovitis Synovial chondromatosis Giant cell tumor of tendon sheath Synovial cyst, bursa, ganglion Synovial hemangioma Tumoral calcinosis Synovial sarcoma Arthropathy

Intraarticular lesions often diffusely involve the joint, as seen with PVNS (Fig. 6), synovial chondromatosis and lipoma arborescens.

The detection of multiple soft tissue masses markedly restricts differential diagnosis. Lipomas are multiple in 5%–15% of patients [11, 12]. The fibromatosis and angiomatous lesions are multifocal in up to 20% of patients[1, 3, 13]. Patients with type 1 neurofibromatosis [NF 1] invariably reveal multiple neurogenic tumors and rapid enlargement of a lesion should be viewed as representing malignant degeneration to MPNST. Myxomas may be multiple in association with fibrous dysplasia (Mazabraud syndrome) [14]. Finally, metastases may be multifocal, particularly to the subcutaneous tissue (melanoma and breast) or rarely to muscle (bronchogenic carcinoma).

Intrinsic Imaging Characteristics

Intrinsic imaging characteristics of soft tissue masses that frequently suggest the diagnosis include signal intensity as well as the lesion morphology and shape. Detection of adipose tissue in a soft tissue mass limits the differential diagnosis to lipoma (Fig. 7), hibernoma, hemangioma and liposarcoma. Markedly low signal intensity on T2-weighted MRI may be related to rapidly flowing blood (arteriovenous hemangioma), calcification (extraskeletal osteosarcoma), hemosiderin (PVNS or GCTTS) (Fig. 6) or high collagen content (some cases of fibromatosis). Soft tissue masses demonstrating high water content on advanced imaging (CT, MRI or US) suggests a "cystic" lesion and restricts diagnostic possibilities to ganglion, bursa, abscess, liquefied hematoma, or myxoid neoplasm (Figs. 2, 5) (myxoma, myxoid liposarcoma or myxoid MFH).

Lesion shape and internal structure often reveal a characteristic imaging appearance of soft tissue masses reflecting the lesions gross morphology and histologic composition. Soft tissue tumors composed of serpentine channels and spaces invariably represent an angiomatous lesion. A fusiform shaped mass with entering and exiting tubular structure is caused by a neurogenic tumor (Fig. 4). Another characteristic sign of neurogenic neoplasm is the target sign on T2-weighted MRI with a rim of high signal peripherally and low signal centrally. Linear extension along fascial planes or skin (tail sign) is common in fibromatosis, nodular fasciitis and dermatofibrosarcoma protuberans (Fig. 3). Soft tissue neoplasms, both benign and malignant, usually have a relatively well-defined margin with little surrounding edema. This is related to the pseudocapsule surrounding many soft tissue neoplasms. In fact, prominent edema about a soft tissue mass (not previously treated with radiation or chemotherapy) should suggest a reactive or inflammatory process as opposed to neoplasm.

Patient age must also be considered in determining the order of differential diagnoses of a soft tissue mass just as with bone tumors. As an example, a soft tissue mass composed of a small amount of fat but largely containing tissue with a high water content (myxoid) in a patient over the age of 20 years almost certainly represents a myxoid liposarcoma. In marked contradistinction, the diagnosis of a soft tissue mass with identical imaging features in a 2-year-old would invariably be a lipoblastoma. Table 4 shows differential diagnosis in order of decreasing frequency for three age groups: children, young adults, and older adults.

Specific Lesions by Imaging

Overall specific diagnosis is possible in 20%–50% of soft tissue tumors [15–17]. In our opinion, this percentage will gradually increase with more experience and description of specific characteristics, particularly on MRI, although likely not beyond approximately 70%–80% of soft tissue masses.

Table 4. Soft tissue tumor differential by age (modified from [4, 5])

Child (<16 years)	
Benign	Malignant
Hemangioma	Fibrosarcoma/MFH
Fibromatosis	Synovial sarcoma
Fibrous histiocytoma	Rhabdomyosarcoma
Granuloma annulare	MPNST
Young adult (16–45 years)	
Benign	Malignant
Ganglion	MFH/Fibrosarcoma
Fibrous histiocytoma	Liposarcoma
Nodular fasciitis	Dermatofibrosarcoma protuberans (DFSP)
Neurogenic neoplasm (Neurilemmoma, neurofibroma)	Synovial sarcoma
Lipoma	MPNST
Hemangioma	
Older adult (46 years and up)	
Benign	Malignant
Ganglion	MFH/fibrosarcoma
Lipoma	Liposarcoma
Neurogenic neoplasm (neurilemmoma, neurofibroma)	Leiomyosarcoma
Fibrous histiocytoma	MPNST
Nodular fasciitis	DFSP
Myxoma	

Lipomatous Lesions

Soft tissue tumors containing significant amounts of fat are usually easily detected on CT or MRI because of the intrinsic appearance of these adipose regions is identical to subcutaneous fat. These lesions include lipoma, lipoblastoma, hibernoma, liposarcoma and their variants.

Imaging of lipomas typically reveals a mass with homogeneous adipose tissue and lesions in or between muscles are easily differentiated from surrounding tissue (Fig. 7). However, subcutaneous lipomas can be difficult to detect because of their location in surrounding adipose tissue with which they have an identical appearance. Identification of a thin surrounding pseudocapsule (low-signal MRI, muscle attenuation on CT) is necessary to distinguish these lesions from the background of subcutaneous fat. Nonlipomatous mesenchymal components are occasionally seen in lipomas, typically as small inconspicuous septa.

Lipoblastomas may be focal or diffusely infiltrative (lipoblastomatosis) and often reveal a predominantly fat-containing mass. However, in very young patients, myxoid components (showing high water content appearance) often predominate with only small elements of adipose tissue, simulating liposarcoma by imaging.

Hibernoma, reflective of its pathologic brown fat composition, shows imaging features similar to but not identical to fat. These lesions are generally more vascular than lipomas and can reveal prominent enhancement after intravenous contrast by CT or MRI.

The imaging of liposarcoma varies depending on the histologic subtype. Well-differentiated liposarcomas shows extensive areas identical to subcutaneous fat by CT and MRI. In fact, in some cases differentiation from lipoma similar to pathologic evaluation can be difficult. In general, well-differentiated liposarcoma demonstrates more nonlipomatous components than lipoma, particularly prominent septa, both in number and thickness, and in up to 10% of cases mineralization. Higher-grade liposarcomas (myxoid, round cell and pleomorphic), reflecting more anaplasia, reveal less adipose tissue by imaging. However, in our experience, focal areas of fat (usually <10% of the tumor) are seen in the vast majority of lesions (90%–95%) by MRI (superior to CT), suggesting the diagnosis. Myxoid liposarcomas are typically intermuscular lesions and their high water content histologically is reflected in much of the lesion showing a cyst-like appearance. In our experience, 5%–10% of cases of myxoid liposarcoma may suggest an entirely cystic lesion on CT or T1- and T2-weighted MRI, although intravenous contrast demonstrates diffuse or peripheral nodular enhancement and sonography also reveals evidence of a solid, not a cystic mass (Fig. 2).

Angiomatous Lesions

Angiomatous lesions include hemangioma, lymphangioma, angiomatosis (and angiomatous syndromes). Hemangioma is the most common of these lesions, accounting for 7% of all benign soft tissue tumors. It is the most frequent soft tissue neoplasm in infants and children.

Radiographs may reveal characteristic phleboliths, particularly in cavernous lesions (Fig. 1). However, it is the detection of serpentine vascular spaces and/or channels that is distinctive of hemangioma on CT, MRI or US, and these areas enhance after intravenous contrast. Intramuscular hemangiomas are most commonly evaluated radiologically and frequently reveal associated fat atrophy of muscle by MRI (superior to CT). In our experience, one or both of these findings allow diagnosis in the vast majority of hemangiomas and obviate biopsy in small lesions with limited symptoms. MRI and US can also identify areas of low blood flow (high signal on T2-weighted MRI and low resistance flow on Doppler US) vs high blood flow (flow void in T2-weighted MRI and high resistance flow on Doppler US). These features are important to direct treatment options.

Lymphangiomas are usually cavernous lesions that involve the head, neck or axilla in the first two years of life (50%–90%) [1]. The large unilocular or multilocular cystic spaces are well evaluated by CT, MRI or US. Interestingly 25% of lesions may show high signal on TI- and T2-weighted MRI related to the fat in the chylous fluid [6].

Angiomatosis and angiomatous syndromes represent diffuse infiltration of the soft tissues by hemangiomatous and/or lymphomatous tissue. Lesions are identical to that already described for solitary lesions but more extensive. Imaging is important to evaluate for visceral involvement which is associated with a worsened prognosis.

Neurogenic Tumors

Neurogenic tumors include traumatic and Morton neuroma, neurilemmoma (schwannoma), neurofibroma and MPNST. Advanced imaging features are frequently characteristic either by location and history (Morton or traumatic neuroma) or lesion morphology and shape related to a known nerve distribution. Radiographs, on the other hand, are either normal or show a nonspecific soft tissue mass.

Morton neuromas represent perineural fibrosis of the plantar digital nerve, not a true neoplasm. These lesions are painful and occur most commonly between the heads of the third and fourth or second and third metatarsals. MRI and US are the best modalities to detect these small soft tissue masses in this relatively specific location. Interestingly, they are often low signal on T2-weighting MR images and are usually more conspicuous of T1-weighting.

Traumatic neuromas, BPNST and MPNST are all suggested by their fusiform shape caused by the exiting and/or entering nerve (Fig. 4). MRI is superior to CT and US to depict this morphology owing to its multiplanar capabilities and contrast resolution. Associated findings include the target sign (CT and MRI), the fascicular sign (small circular regions within the lesion best on long TR MRI caused by nerve fascicles in the lesion), the split fat sign and associated muscle atrophy distal to the lesion (Fig. 4).

Differentiation of neurilemmoma (nerve eccentric to mass) from neurofibroma (nerve as an intimate part of the mass) is often difficult except in lesions of large nerves. Similarly, distinction of BPNST from MPNST can be perplexing. Imaging features that suggest MPNST include size (>5 cm), ill-defined margins, central necrosis, rapid growth and increased radionuclide uptake on gallium scans [6]. In addition, MPNSTs less frequently demonstrate intrinsic imaging features such as the target sign, fascicular sign, split-fat sign as compared to BPNSTs, reflecting their more aggressive growth and higher degree of anaplasia [6].

"Cystic" Masses

Soft tissue masses that can have an imaging appearance of cysts include synovial cyst, bursal fluid collection, ganglion, perilabral or meniscal cyst, hematoma, abscess, and myxomatous neoplasms. These lesions can all have a similar intrinsic appearance on noncontrast CT on MRI. CT shows low attenuation and MRI reveals low signal intensity on TI-weighting and very high signal on T2-weighting. US demonstrates an anechoic lesion with posterior acoustic enhancement. Clinical history and lesion location is very helpful in distinguishing these lesions.

Synovial cysts can occur about any joint, although the most frequent location is the popliteal region (Baker cyst). Identification of a neck extending toward the joint, typical location, and intrinsic characteristics usually allow diagnosis. Popliteal cysts may rupture and dissect into the calf causing pain. This often results in hemorrhage and a complex mass as opposed to a fluid filled noncomplicated Baker cyst. Recognition of the fusiform shape and prominent surrounding edema (caused by irritation of surrounding tissue) help distinguish these lesions.

Ganglia, unlike synovial cysts, are not lined by synovium but by fibrous tissue. Similar to synovial cysts, ganglia may be unilocular of multilocular. These lesions most frequently affect the wrist (70%) and are usually small (1–3 cm), intermuscular, adjacent to joints and occasionally intraarticular [3, 6]. US is often the easiest and least expensive modality to diagnose ganglia. Focal fluid collections arising from fluid extending through tears of labra and menisci were formally considered ganglia. However, currently these lesions are regarded as perilabral or meniscal cysts.

Liquefied hematoma and abscess formation often show a thick peripheral wall and clinical history is usually helpful. The wall of hematoma is often very low signal on all MR pulse sequences because of hemosiderin deposition. Abscess walls often reveal higher signal on T1-weighted MRI and may show linear extensions of a sinus tract.

Myxomatous neoplasms include myxoma, neurogenic neoplasm, liposarcoma, MFH and extraskeletal chondrosarcoma. While these lesions may simulate cysts, intravenous contrast reveals thick nodular peripheral or diffuse enhancement of variable degree. In contradistinction, truly cystic masses show thin peripheral and septal enhancement (Fig. 5). US may also help in that these lesions do not meet the criteria for a cyst (anechoic with posterior acoustic enhancement) usually showing internal echoes (Fig. 2).

Other Lesions with Specific Imaging Appearances

Elastofibroma represents a reactive process that can usually be diagnosed by its specific location of a mass deep to the scapular tip. It is a common lesion that can be recognized on 2% of CT chest examinations [3, 6]. Small streaks of fat may be seen on CT and MRI, and lesions typically show intermediate signal intensity on all MR images.

PVNS can be either focal (GCTTS) or diffuse and often has a characteristic imaging appearance on MRI. This is related to hemosiderin deposition and resultant marked low signal intensity on T2-weighted MRI as well as an intraarticular, bursal or tendon sheath location (Fig. 6).

Synovial chondromatosis also frequently reveals pathognomonic features with multiple intraarticular, bursal or tenosynovial chondral bodies. Uniform calcification of these innumerable fragments is best seen on radiographs or CT and can be difficult to detect by MRI when small. However, the extent of involvement is well evaluated on MRI with the nonmineralized chondroid metaplasia showing very high signal on T2-weighting because of the high water content of hyaline cartilage.

There are multiple types of fibromatosis that can involve the musculoskeletal system. These lesions are typically intermuscular and often reveal infiltrative margins, suggesting a malignant lesion. Imaging findings that suggest this diagnosis include lesion location (foot, hand, shoulder, chest, abdominal wall, and paraspinal locations), linear extension along fascia (fascial-tail sign), and prominent low signal intensity regions on T2-weighted MRI (particularly if band-like in appearance).

Nonspecific Soft Tissue Masses

Soft tissue masses with a nonspecific imaging appearance should be assessed for extent and staging. Imaging features of small size (<5 cm), defined margins, homogeneity, and lack of neurovascular encasement suggest a benign process. In contradistinction, large size (>5 cm), ill-defined margins, heterogeneity, and neurovascular or bone involvement suggest a malignant process. However, in our opinion, differentiation of benign vs malignant cannot be made with enough confidence to alter the need for biopsy. Benign lesions that can reveal aggressive characteristics simulating malignancy include hematoma, fibromatosis, reactive lymph nodes, abscess, and myositis ossificans. Malignant lesions that at times reveal indolent features simulating benign disease include synovial sarcoma and myxoid liposarcoma.

Conclusion

In summary, the role of imaging in evaluation of soft tissue tumors has markedly improved because of the advent of CT, US, and more recently MRI. Indeed the latter modality has particularly improved the goal of imaging that includes lesion detection, characterization, and staging. Relatively specific histologic diagnosis can be made by imaging characteristics in 25%–50% of lesions. We believe this will gradually increase over time with continuing experience. Soft tissue masses that often reveal pathognomonic imaging appearance include lipomatous lesions, angiomatous lesions, neurogenic tumors, "cystic" masses, elastofibroma, PVNS, synovial chondromatosis and the fibromatoses. In imaging evaluation of soft tissue tumors with a nonspecific imaging appearance, lesion extent remains a vital role of radiologic assessment but distinction of benign from malignant lesions is fraught with uncertainty. These nonspecific masses require biopsy to direct definitive treatment. Clinical evaluation and treatment of soft tissue masses must emphasize a team approach incorporating the combined skills of radiologists, pathologists, and orthopedic oncologists with the ultimate goal of improving patient management and outcome.

References

1. Enzinger FM, Weiss SW (1995) General considerations. In: Enzinger FM, Weiss SW (eds) Soft tissue tumors, 3rd edn. CV Mosby, St. Louis, pp 1–16
2. Mettlin C, Priore R, Rao U, Gamble D, Lane W, Murphy GP (1982) Results of the national soft-tissue sarcoma registry. Analysis of survival and prognostic factors. J Surg Oncology 19:224–227
3. Kransdorf MJ, Murphey MD (2000) Radiologic evaluation of soft-tissue masses: A current perspective. AJR Am J Roentgenol 175:575–587
4. Kransdorf MJ (1995) Benign soft-tissue tumors in a large referral population: distribution of diagnosis by age, sex and location. AJR Am J Roentgenol 164:395–402
5. Kransdorf MJ (1995) Malignant soft-tissue tumors in a large referral population: distribution of diagnoses by age, sex and location. AJR Am J Roentgenol 164:129–134
6. Kransdorf MJ, Murphey MD (eds) (1997) Imaging of soft tissue tumors. WB Saunders, Philadelphia
7. Sundaram M, McGuire MH, Herbold DR (1988) Magnetic resonance imaging of soft tissue masses: an evaluation of fifty-three histologically proven tumors. Magn Reson Imaging 6:237–248
8. Kransdorf MJ, Murphey MD (1997) The use of gadolinium in the MR evaluation of soft tissue tumors. Semin Ultrasound CT MR 18:251–268
9. Enneking WF, Spanier SS, Goodman MA (1980) A system for the surgical staging of musculoskeletal sarcoma. Clin Orthop 153:106–120
10. Arlen M. Marcone R (1992) Sarcoma management based on a standardized TNM classification. Semin Surg Oncol 8:98–103
11. Osment LS (1968) Cutaneous lipomas and lipomatosis. Surg Gynecol Obstet 127:129–132
12. Rydholm A, Berg NO (1983) Size, site and clinical incidence of lipoma. Factors in the differential diagnosis of lipoma and sarcoma. Acta Orthop Scand 54:929–934

13. Sundaram M, Duffrin H, McGuire MH, Vas W (1988) Synchronous multicentric desmoid tumors (aggressive fibromatosis) of the extremities. Skeletal Radiol 17:16–19
14. Sundaram M, McDonald DJ, Merenda G (1989) Intramuscular myxoma: a rare but important association with fibrous dysplasia of bone. AJR Am J Roentgenol 153:107–108
15. Kransdorf MJ, Jelinek JS, Moser et al (1989) Soft-tissue masses: diagnosis using MR imaging. AJR Am J Roentgenol 153: 541–547
16. Berquist TH, Ehman RL, King BF, Hodgman CG, Ilstrup DM (1990) Value of MR imaging in differentiating benign from malignant soft tissue masses: study of 95 lesions. AJR Am J Roentgenol 155:1251–1255
17. Crim JR, Seeger LL, Yao L, Chandnani V, Eckardt JJ (1992) Diagnosis of soft-tissue masses with MR imaging: can benign masses be differentiated from malignant ones? Radiology 185:581–586

Part 7
Breast Radiology

Invasive Breast Cancer

Ingvar Andersson

7.1

Contents

Introduction

Close collaboration between radiologists and pathologists is fundamental for the understanding of breast imaging, i.e., mammography, ultrasound and MRI. Many beginners in breast imaging find the histologic classifications cumbersome. However, the basics are quite simple and most students will find the increased understanding of breast pathology as reflected in imaging most stimulating.

There are several histologic classifications of breast cancer. One of the most widely used is the one proposed by Fisher et al. (Table 1) [1]. The dominating microscopic type in this classification is the infiltrating ductal carcinoma NOS (not otherwise specified), which accounts for about 70% of all breast cancers. About 10% is infiltrating lobular carcinoma. Medullary and mucinous carcinoma usually make up about 5% each. Tubular carcinoma represents 1%–5%. Other microscopic types are rare. Fisher's classification does not include carcinoma in situ.

The frequency of the various microscopic types may vary depending on several factors such as the availability of medical care, access to modern diagnostic techniques and whether breast cancer screening is prevalent in the population. This is illustrated by the frequency of the various histologic types of breast cancer in the invited and control groups of the Malmö Mammographic Screening Trial (Table 2) [2]. The main differences are a greater proportion of tubular carcinoma and ductal carcinoma in situ (DCIS) in the screened group.

Table 1. Microscopic classification of invasive breast carcinoma according to Fisher et al. 1975 [1]

a. Infiltrating duct carcinoma NOS
b. Lobular carcinoma
c. Medullary carcinoma with lymphoid infiltration
d. Mucinous carcinoma
e. Tubular carcinoma
f. Adenoid-cystic carcinoma
g. Papillary carcinoma
h. Carcinosarcoma
i. Paget's disease
j. Combinations

Table 2. Incidence of histologic types of breast cancer in the first round of the Malmö Mammographic Screening Trial

	Screened group (*n*=116)	Control group (*n*=238)
Invasive carcinoma		
Infiltrating ductal NOS	49%	65%
Tubular	22	7
Lobular	10	11
Medullary	1	7
Mucinous	1	2
Noninvasive carcinoma		
DCIS	14	5
LCIS	3	3

DCIS ductal carcinoma in situ, *LCIS* lobular carcinoma in situ

Ductal Carcinoma NOS

The term "ductal" refers to the fact that this type of breast cancer was thought to originate from ductal epithelium as opposed to lobular carcinoma, which was thought to start in the lobules. Nowadays, both types of cancer are believed to originate in the terminal lobular-ductal unit of the breast gland. Ductal carcinoma now refers to a malignant epithelial tumour growing in columns without the formation of organoid structures such as tubular or papillary structures.

The large group of ductal carcinoma NOS has been subdivided into two groups in some classifications, for instance, in the one proposed by Linell et al. [3] (Table 3, Figs. 1, 2). One of the two subgroups is characterized by

Table 3. Classification of breast carcinoma according to Linell et al. 1984 [3]

1. Noninvasive
   a. Ductal carcinoma in situ including Paget's disease of the nipple
   b. Lobular carcinoma in situ
2. Invasive
   a. Invasive ductal carcinoma (comedo type)
   b. Tubular and tubuloductal carcinoma
   c. Invasive lobular carcinoma
   d. Mucinous carcinoma
   e. Medullary carcinoma with lymphoid stroma infiltration
   f. Adenoid-cystic carcinoma
   g. Secretory carcinoma
   h. Lipid-rich carcinoma
   i. Carcinoid
   j. Metaplastic carcinoma
   k. Others

abundant fibrosis and is also called cancer with productive fibrosis, scirrhous carcinoma or stellate carcinoma. In the classification by Linell et al., it is called tubuloductal carcinoma. The general outline is irregular with spicules extending into the periphery.

The other subgroup of invasive ductal carcinoma has a different micro- and macroscopic appearance, with less fibrous stroma and a more circumscribed or knobby periphery. The cells are usually large and polymorphous. This subtype is called ductal carcinoma of the comedo type. "Comedo" means worm and refers to the worm-like structures that sometimes can be seen on the cut surface representing proliferating cancer cells and necrotic material, which fill the ducts of the in situ component. The necrotic material may undergo dystrophic

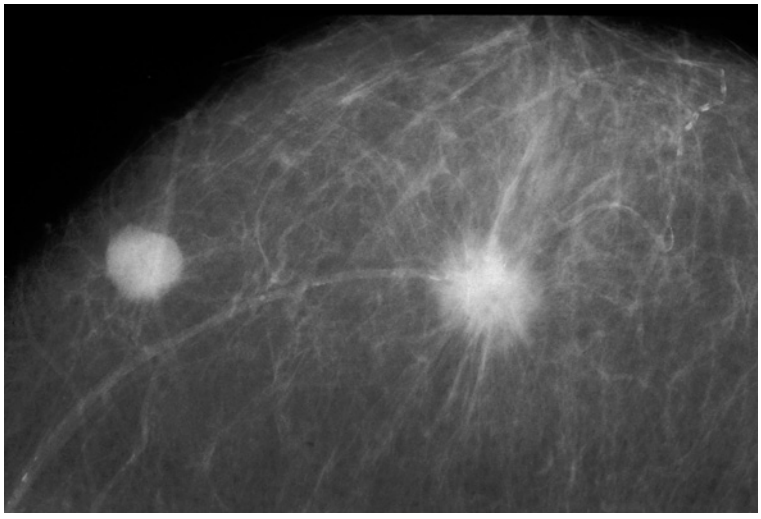

Fig. 1. A 64-year-old woman with two different morphologic types of ductal carcinoma: one spiculated and one circumscribed. On histopathologic examination, the spiculated tumour was found to be a 1.9-cm ductal invasive carcinoma, the centre of which consisted of hyaline connective tissue with abundant elastoid, Nottingham grade 2 and oestrogen receptor-positive. The circumscribed tumour was a 1.2-cm invasive ductal carcinoma growing in solid columns with less stroma and more pronounced nuclear atypia and mitoses, corresponding to Nottingham grade 3. Metastatic growth in two out of ten axillary lymph nodes

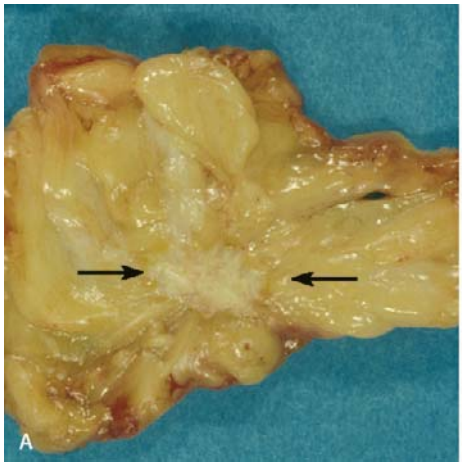

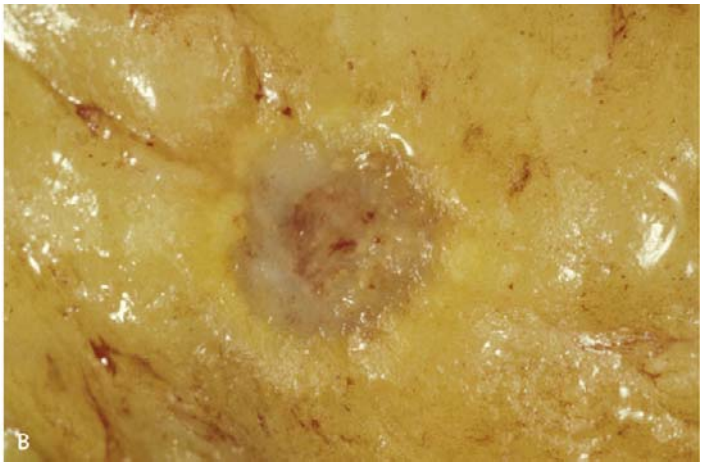

Fig. 2. A Specimen showing a greyish – white tumour with an irregular, spiculated outline (*arrows*). Microscopy showed an invasive ductal carcinoma with abundant fibrosis. **B** Specimen showing a more circumscribed tumour with moist, greyish red cut surface. Microscopic examination showed a ductal carcinoma of the comedo type. **C** Specimen showing comedones coming out of the cut surface (*arrows*)

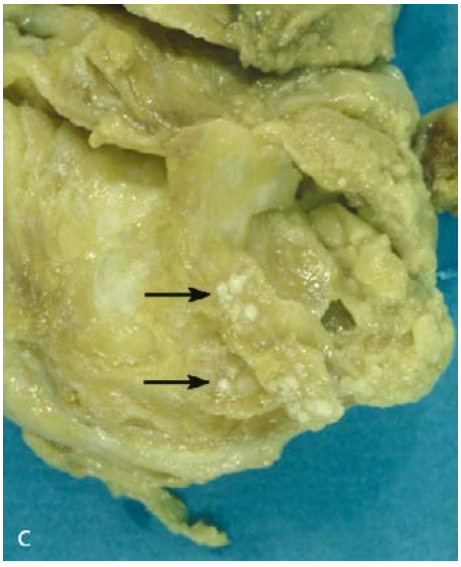

Fig. 2C

Table 4. Classification of breast carcinoma according to WHO 1981 [8]

1. Noninvasive
   a. Intraductal carcinoma
   b. Lobular carcinoma in situ
2. Invasive
   a. Invasive ductal carcinoma
   b. Invasive ductal carcinoma with a predominant intraductal component
   c. Invasive lobular carcinoma
   d. Mucinous carcinoma
   e. Medullary carcinoma
   f. Papillary carcinoma
   g. Tubular carcinoma
   h. Adenoid-cystic carcinoma
   i. Secretory (juvenile) carcinoma
   j. Apocrine carcinoma
   k. Carcinoma with metaplasia
   l. Others
3. Paget's disease of the nipple

calcification, which in the typical case can be seen on the mammogram as granular calcification with a linear arrangement (Fig. 6C).

The distinction between tubuloductal carcinoma and ductal carcinoma of the comedo type is of more than academic interest. Not only is the radiographic and microscopic morphology different, but also the biologic behaviour. It has been demonstrated that the spiculated type of carcinoma has a higher hormone receptor content than the carcinoma of the comedo type [4, 5].

Long-term follow-up has demonstrated a better prognosis for patients with tubuloductal carcinoma than for patients with ductal carcinoma of the comedo type, as classified according to Linell et al. [6].

It should be mentioned that a similar subgrouping of ductal carcinoma NOS was proposed by Foote and Stewart in their classification from the 1940s [7]. The WHO classification from 1981 (Table 4) [8] also has a somewhat similar subgrouping.

From a radiographic point of view, cancer with productive fibrosis is characterized by an irregular margin with spicules of varying length coming out of its periphery (Fig. 3). There may be a reactive thickening of the structures between the tumour and the nipple as well as of the nipple and areola and the skin overlying the tumour. There is often a process of shrinking, resulting in retraction of the nipple or the skin overlying the tumour. The thickening of these structures may be the result of reactive fibrosis or oedema only and does not necessarily imply that the cancer has spread to the skin or nipple.

One characteristic of scirrhous carcinoma that is sometimes seen on the mammogram is a relatively broad radiolucent zone surrounding the tumour

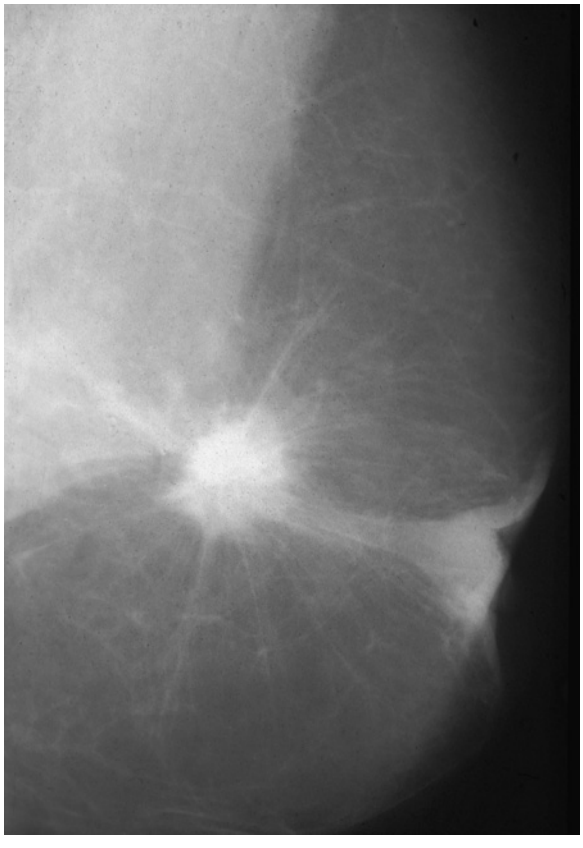

Fig. 3. Spiculated, ductal carcinoma with abundant reactive fibrosis and retraction of the pectoral muscle and the nipple/areolar complex, which is thickened. There was no tumour invasion of nipple or areola nor of the pectoral muscle

(Fig. 4). This is not to be confused with a so-called halo, which is a thin radiolucent zone seen around a well-circumscribed, usually benign tumour. In the specimen

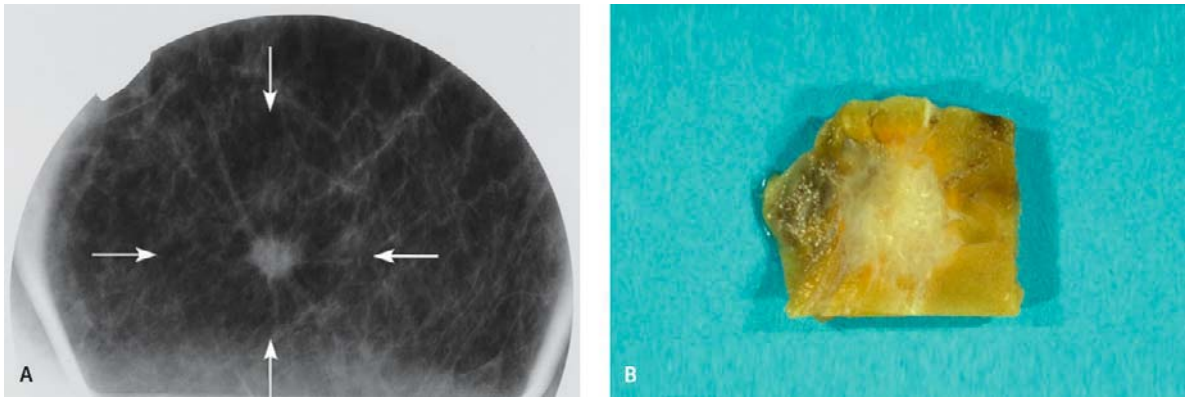

Fig. 4. A Spiculated tumour showing a broad radiolucent zone around the tumour (*arrows*). **B** Spiculated carcinoma of the ductal type surrounded by a yellow-orange zone

containing a scirrhous carcinoma, a peculiar zone of yellow-orange fat is sometimes seen around the tumour. Furthermore, on palpation this type of tumour is often larger than its radiographic size would suggest, sometimes to such an extent that it is very difficult to localize the tumour itself by palpation for appropriate biopsy needle aspiration of cytological material. In extreme cases, it may even be difficult to localize the cancer for surgical biopsy. In addition, the fibrosis within a tumour of this type may be quite abundant, which is another reason why it may be difficult to obtain representative material on needle biopsy of such a tumour.

The radiolucent zone described above, the peritumoral zone of yellow fat and the larger size on palpation may be interrelated, but the mechanism underlying these phenomena is not well understood.

On ultrasonography, a spiculated cancer is characterized by a so-called echogenic border, which is explained by the fibrous strands in the periphery of the tumour, mixed with other tissue components, resulting in a high reflectivity of the ultrasound beam (Fig. 5). Also, these tumours are usually hypoechoic in the centre due to a predominant fibrosis with few other tissue components.

Ductal carcinoma of the comedo type often presents radiographically as a poorly defined mass and may therefore be difficult to identify mammographically, especially if located in fibroglandular tissue (Fig. 6). Sometimes it may be more circumscribed or multinodular. However, also in such cases commonly there are areas of indistinctness or projections of the tumour into the surrounding tissue. Not infrequently, calcifications are seen in the tumour itself or in the surrounding tissue as an expression of DCIS. The calcifications may be of the typical comedo type mentioned above or nonspecific, depending on the presence or absence of necrosis and the growth pattern of the intraductal component (solid vs cribriform, papillary or mural). If extensive, the designation "ductal carcinoma with extensive intraductal component" has been used, which has been shown to imply a higher than average risk of recurrence after conservative surgery [9]. Because of the relative paucity of reactive fibrosis in ductal carcinoma of the comedo type, less reaction is seen in the surrounding tissue, including skin or nipple retraction.

There are many other interesting differences. One is the tendency of cancer of the comedo type to grow within the ducts of the nipple and to occasionally grow in the dermis of the nipple in the form of Paget's disease. On the other hand, when tubuloductal carcinoma grows in the nipple, it grows between the ducts rather than within the ducts and is never associated with Paget's disease of the nipple. The in situ component ac-

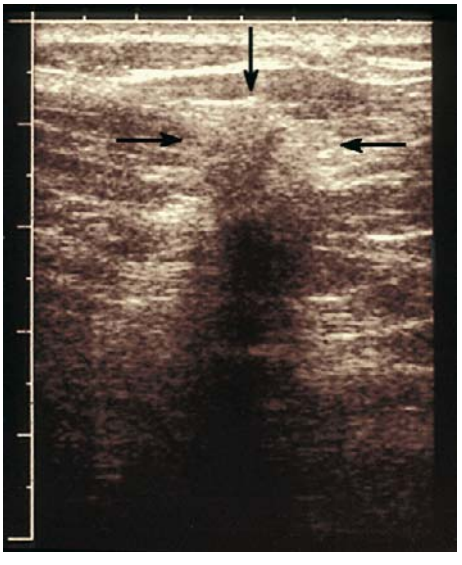

Fig. 5. Ultrasound examination showing an echogenic border (*arrows*) surrounding a hypoechoic centre, representing a spiculated ductal carcinoma

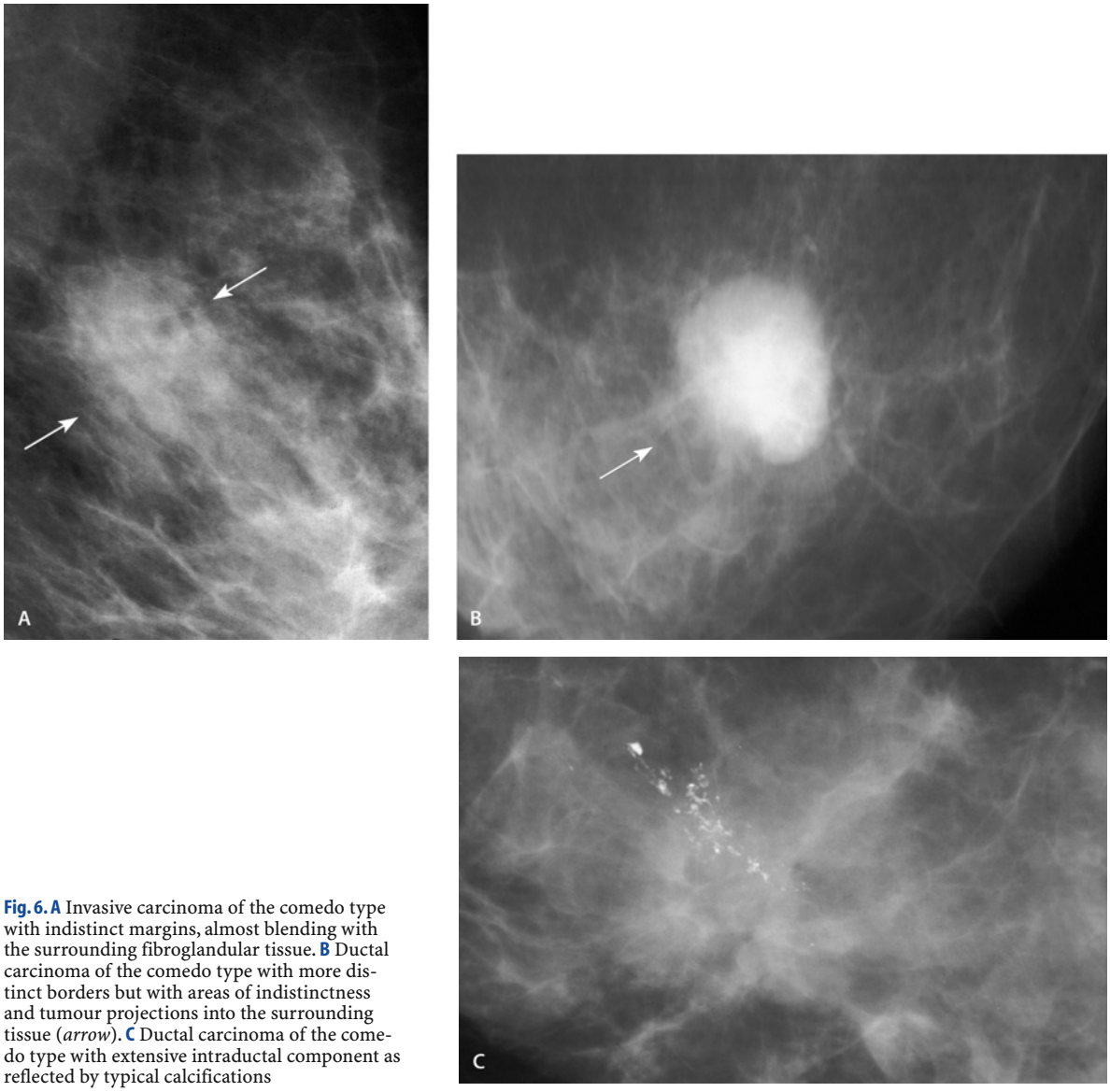

Fig. 6. A Invasive carcinoma of the comedo type with indistinct margins, almost blending with the surrounding fibroglandular tissue. **B** Ductal carcinoma of the comedo type with more distinct borders but with areas of indistinctness and tumour projections into the surrounding tissue (*arrow*). **C** Ductal carcinoma of the comedo type with extensive intraductal component as reflected by typical calcifications

companying tubuloductal carcinoma is almost always of cribriform or the papillary type.

Radiographically, Paget's disease may be seen as a nonspecific thickening of the nipple and areola, in addition to signs of invasive or noninvasive disease in the breast parenchyma. However, in as many as 50% of patients with Paget's disease findings may be negative radiographically [10].

In terms of histologic grading [11], the cancer of the comedo type also tends to be of a higher grade than the tubuloductal type of carcinoma. It has also been demonstrated by the Nottingham group that spiculated masses correlate with low histologic grade and absence of vascular invasion, while poorly defined masses and comedo-type calcifications correlate with high histologic grade and presence of vascular invasion [12].

Out of the less frequent histologic varieties, medullary carcinoma with lymphocytic infiltration and mucinous carcinoma present as circumscribed masses. (Fig. 7) Actually, medullary carcinoma and carcinoma of the comedo type may be related [13]. Intracystic carcinoma also belongs to this group.

On ultrasonography, medullary and mucinous carcinoma usually present as lobulated, well-circumscribed hypoechoic lesions with homogeneous internal echo pattern (Fig. 7). Sometimes posterior enhancement is seen.

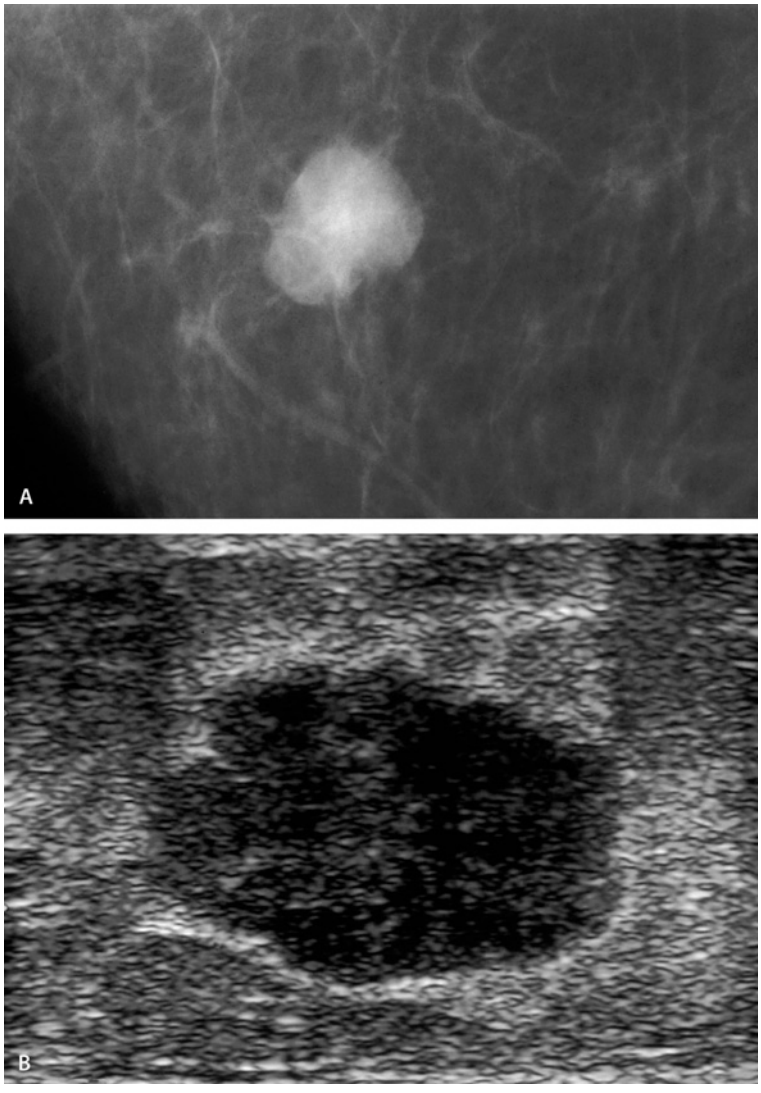

Fig. 7. A Mammogram showing a well-circumscribed slightly lobulated tumour. On microscopy, a medullary carcinoma with lymphoid infiltration was found. **B** Ultrasonography showing a well-circumscribed lobulated hypoechoic tumour with a suggestion of echo enhancement posterior to the tumour. Microscopy showed a medullary carcinoma with lymphoid infiltration

Tubular and Lobular Carcinoma

In addition to tubuloductal carcinoma, there are two histologic types of carcinoma that present as spiculated tumours: tubular carcinoma and lobular invasive carcinoma. The former is characterized by tubule formation and usually is small at presentation, axillary metastasis is relatively infrequent and the prognosis is excellent (Fig. 8). This type of carcinoma has many similarities with the so-called radial scar, which is a benign lesion, unrelated to surgical scars. Its aetiology is unclear, as is its relationship to tubular carcinoma. It is characterized by stellate configuration with a hyaline centre and retracted ducts and lobules often containing epithelial proliferations and sometimes DCIS. Radiographically, most radial scars have an ill-defined, sometimes radiolucent centre with long spicules. Many radial scars are indistinguishable from a small breast cancer (Fig. 9). Nonspecific calcifications are often seen adjacent to the lesion, representing epithelial proliferations/DCIS.

Lobular invasive carcinoma shows several gross morphologic patterns, some of which are very deceptive from a diagnostic point of view. In a 10-year series of lobular invasive carcinoma, 53% presented as a spiculated density that was usually easy to identify [14].

However, in 16% the main radiographic finding was architectural distortion and in another 11% either a poorly defined opacity or parenchymal asymmetry (Fig. 10). Not infrequently, lobular invasive carcinoma grows in multiple foci, which is reflected in the MR image (Fig. 10D). Furthermore, in 16% the mammogram was negative. The radiographic changes were frequently well seen in only one or two of the three standard views. This is a reflection of the fact that lobular invasive carci-

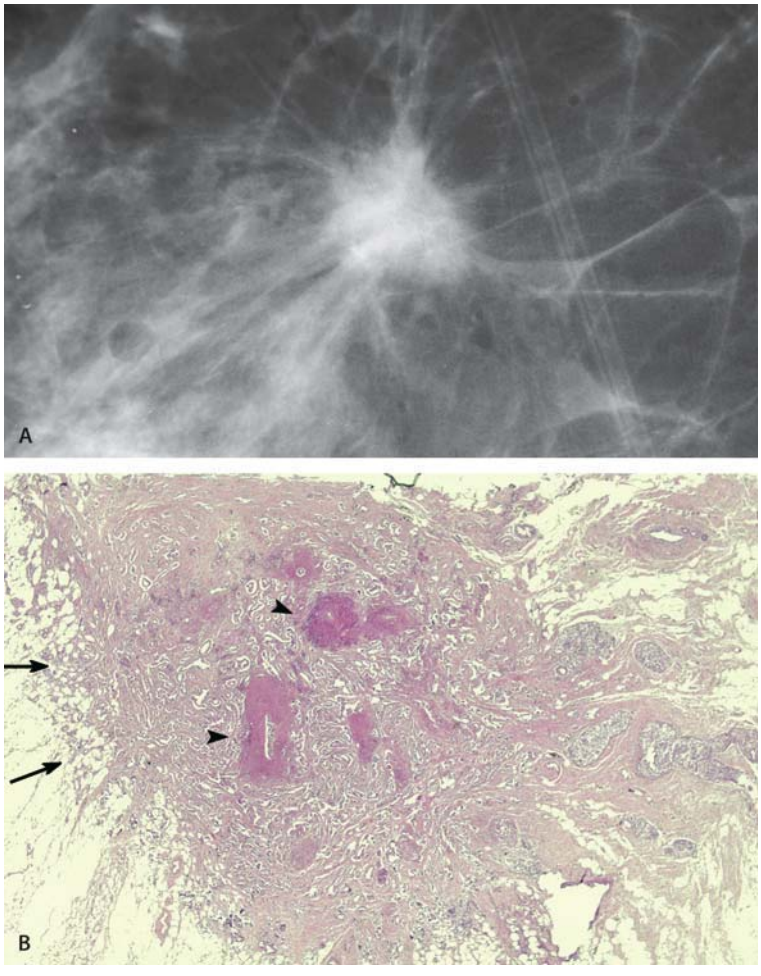

Fig. 8. A Screening detected, small, spiculated tumour. Microscopy showed a tubular carcinoma. **B** Specimen showing a spiculated tumour characterized by tubular structures infiltrating into fatty tissue (*arrows*) and also showing abundant elastoid tissue (*arrowheads*)

Fig. 9. A Radial scar simulating breast cancer. **B** Specimen showing a spiculated tumour simulating breast cancer. On microscopy, a radial scar was found

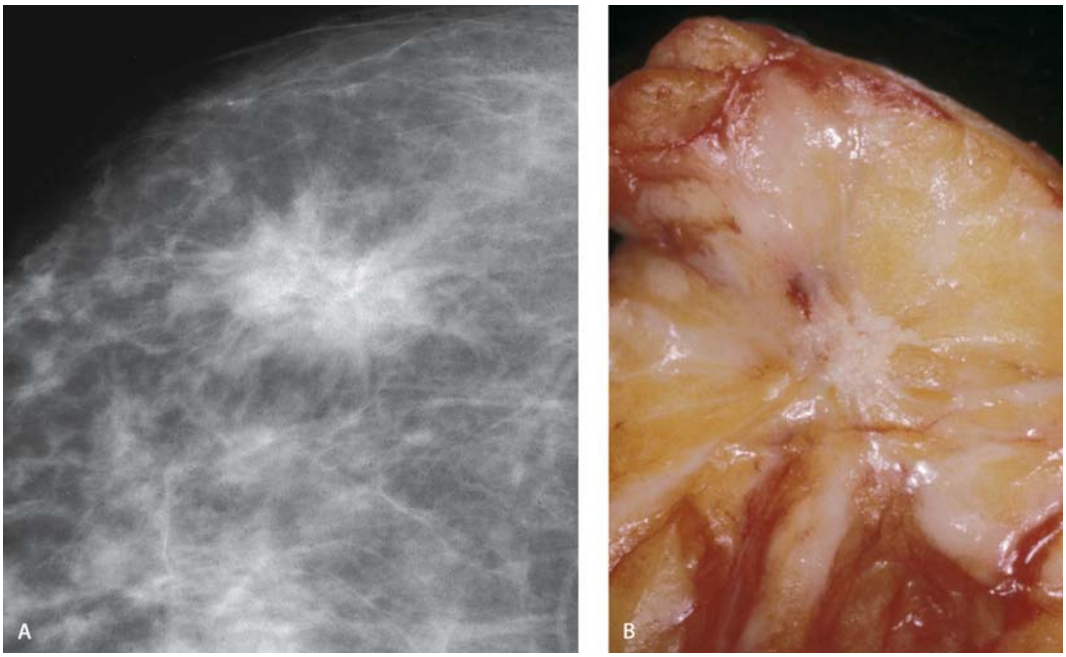

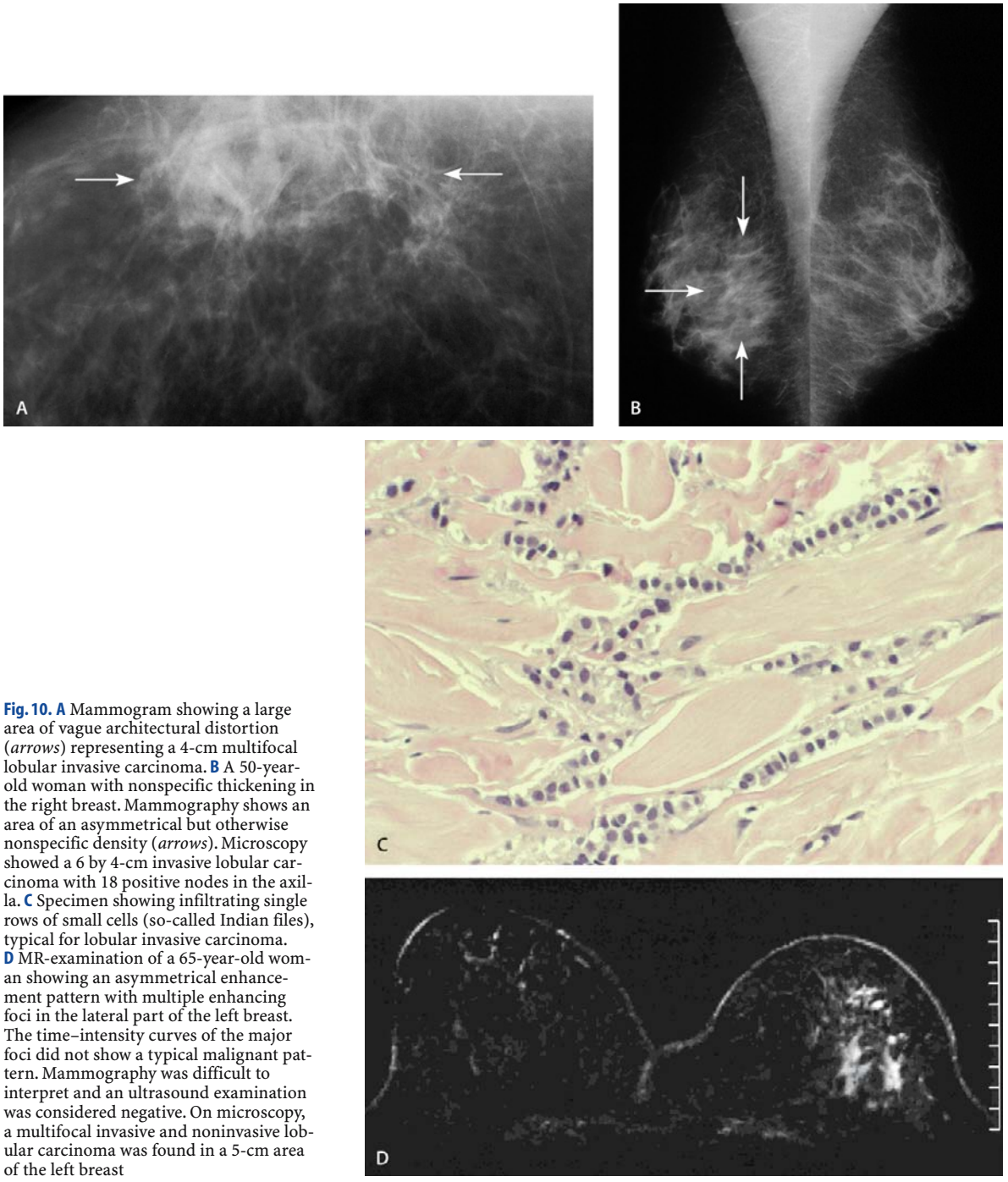

Fig. 10. A Mammogram showing a large area of vague architectural distortion (*arrows*) representing a 4-cm multifocal lobular invasive carcinoma. **B** A 50-year-old woman with nonspecific thickening in the right breast. Mammography shows an area of an asymmetrical but otherwise nonspecific density (*arrows*). Microscopy showed a 6 by 4-cm invasive lobular carcinoma with 18 positive nodes in the axilla. **C** Specimen showing infiltrating single rows of small cells (so-called Indian files), typical for lobular invasive carcinoma. **D** MR-examination of a 65-year-old woman showing an asymmetrical enhancement pattern with multiple enhancing foci in the lateral part of the left breast. The time–intensity curves of the major foci did not show a typical malignant pattern. Mammography was difficult to interpret and an ultrasound examination was considered negative. On microscopy, a multifocal invasive and noninvasive lobular carcinoma was found in a 5-cm area of the left breast

noma microscopically often grows in single rows of cells (so-called Indian files) that infiltrate the breast tissue without significantly changing the normal architecture. If there is only scarce reactive fibrosis and no solid growth of cancer cells, there may be no significant mass formation and no significant density on mammography. Also, on ultrasonography the findings may be subtle in the form of only slight architectural disruption of the normal anatomy and multiple small shadowing artefacts. Even on MRI lobular invasive carcinoma may not be detected or show an enhancement pattern mimicking benign lesions.

Rare Types

Carcinoma with metaplasia usually presents as circumscribed tumour. The metaplasia may be of varying forms, including squamous cells, spindle cells as well as colloid and osteoid patterns. The osteoid components may simulate calcifications on the mammogram (Fig. 11). Other rare types of breast carcinoma have no special traits on imaging.

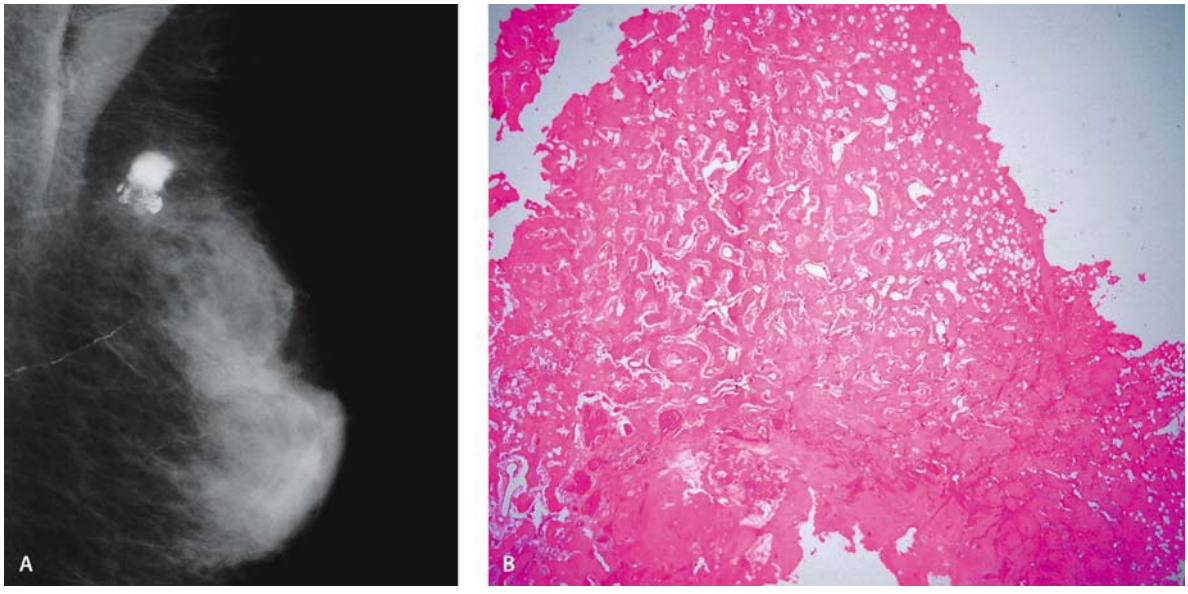

Fig. 11. A 72-year-old woman who had been treated for breast cancer 10 years prior to the present examination, which shows a new dense structure that might represent bone formation. **B** Microscopic section showing metaplastic carcinoma with cartilaginous and osseous metaplasia

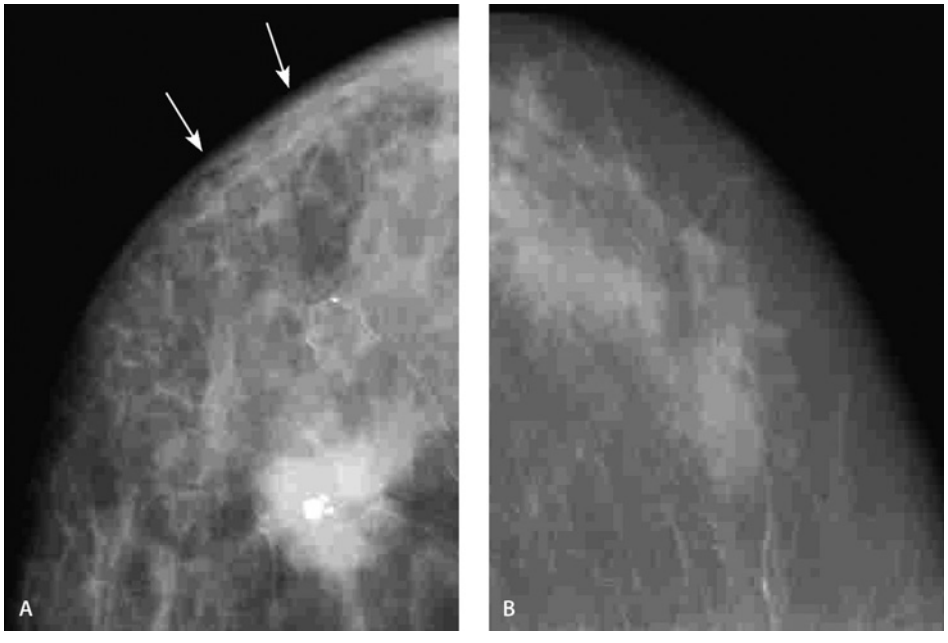

Fig. 12. A Oedema of the breast. Skin thickening and trabecular pattern in the subcutaneous tissue (*arrows*). Obvious tumour with malignant characteristics. On microscopy, a ductal carcinoma with angiolymphatic invasion was found. **B** Contralateral normal breast for comparison. The skin line is barely visible and the subcutaneous tissue shows homogeneous fat attenuation. **C** Ultrasonography showing dilated lymphatic channels (*arrowheads*) and skin thickening

Oedema of the Breast

Any highly malignant type of breast cancer may cause obstruction of the venolymphatic drainage either by angiolymphatic invasion in the breast and/or extensive metastatic disease in the axilla. The dominant radiographic findings are skin thickening, a trabecular pattern which is particularly obvious in the subcutaneous tissue and in addition a generally increased density in the breast tissue (Fig. 12). On ultrasonography, dilated lymphatics may be seen in the subcutaneous tissue in addition to skin thickening and increased echogenicity in the fatty tissue.

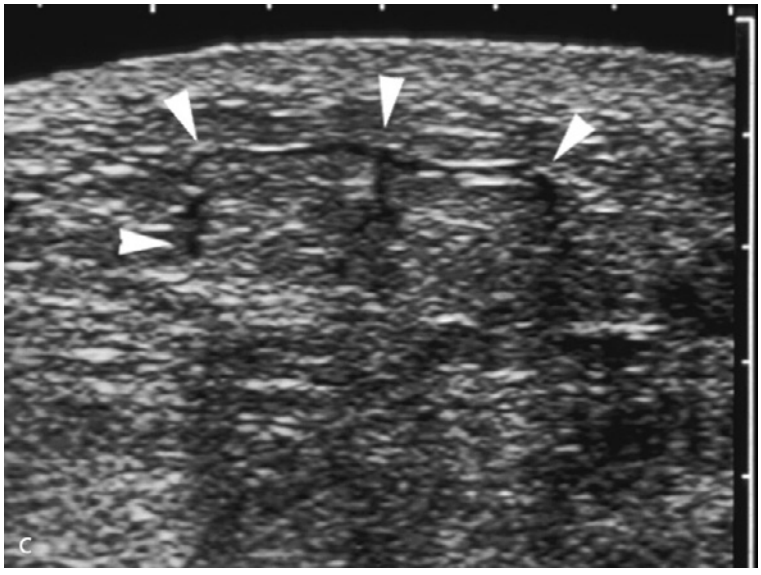

Fig. 12C

References

1. Fisher ER, Gregoria RM, Fisher B (1975) The pathology of invasive breast cancer. Cancer 36:1
2. Andersson I (1981) Radiographic screening for breast carcinoma. Acta Radiol Diagn 22:227
3. Linell F, Ljungberg O (1984) Atlas of breast pathology. Copenhagen, Munksgaard
4. Broberg A, Glas U, Gustafsson SA et al (1983) Relationship between mammographic pattern and estrogen receptor content in breast cancer. Breast Cancer Res Treat 3:201–207
5. Nielsen N, Poulson H (1985) Relation between mammographic findings and hormonal receptor content in breast cancer. AJR Am J Roentolgenol 145:501
6. Garne JP, Aspegren K, Linell F et al (1994) Primary prognostic factors in invasive breast cancer with special reference to ductal carcinoma and histologic malignancy grade. Cancer 73: 1438–1448
7. Foote FW, Stewart FW (1946) A histologic classification of carcinoma of the breast. Surgery 19:74–99
8. World Health Organization (1981) Histological typing of breast tumours. 2nd edn. International histological classification of tumours. No. 2. Geneva
9. Holland R, Connolly JL, Galman R, Mravunac M, Henriks J HCL, Verbeck ALM, Schmitt SJ, Silver B, Boyages J, Harris JR (1990) The presence of an extensive intraductal component following a limited excision correlates with prominent residual disease in the remainder of the breast. J Clin Oncol 8: 113–118
10. Ikeda DM, Helvie MA, Frank TS et al (1993) Paget disease of the nipple. Radiologic-pathologic correlation. Radiology 189: 89–94
11. Elston CW, Ellis IO (1991) Pathological prognostic factors in breast cancer. The value of histological grade in breast cancer: experience from a large study with long-term follow-up. Histopathology 19:403–410
12. De Nunzio MC, Evans AJ, Pinder SE et al (1997) Correlations between the mammographic features of screen detected invasive breast cancer and pathological prognostic factors. Breast 6:146
13. Linell F, Rank F (1989) Breast cancer. Dialogos, Lund
14. Hilleren DJ, Andersson I, Lindholm K et al (1991) Invasive lobular carcinoma. Mammographic findings in a ten year experience. Radiology 178:149–154

Breast Cancer: Early Detection

Ingrid Schreer, Jutta Lüttges

7.2

Contents

Introduction

The early diagnosis of breast cancer is the most important and challenging aspect of breast imaging. Early detection means detection in a preclinical detectable stage, preferably before dissemination. Data from the Swedish Two-County Study demonstrated that if tumors are diagnosed under 15 mm in diameter, the probability of axillary involvement is very low. The European protocol for breast cancer screening recommends that in organized screening programs the proportion of tumors less than 10 mm should be more than 50%, the rate of DCIS more than 20%.

The removal of these small invasive and noninvasive tumors requires two steps: a preoperative assessment involving exact localization and possibly marking of the lesion and postoperative specimen radiography to enable a precise correlation of the radiological and histopathological findings. This procedure is also mandatory when preoperative interventional assessment procedures are performed.

In eight randomized trials, mammography proved to be the most effective modality for detecting clinically occult breast cancer. The prerequisites of an organized screening program include (a) effective quality management, (b) experienced interpretation, (c) double reading, (d) correlation of histopathological and radiological findings and (e) documentation (sensitivity, specificity and accuracy).

To focus on the correlation between pathology and radiology, an interdisciplinary approach is essential in cases in which small invasive and noninvasive cancers are impalpable. If clinical signs are lacking, the images and the histopathological sections need to be correlated to ensure that a suspicious area is actually removed. Apart from the double diagnostic assessment in such cases, both pathologists and radiologists benefit from the close cooperation required and gain useful insights into both fields. It would be highly advisable to include such cooperation in the training of both radiologists and pathologists.

The following aspects will be discussed: detection of small invasive cancers, detection of ductal carcinoma in situ (DCIS), detection of high risk lesions and detection in high risk patients.

Detection of Small Invasive Cancers

Breast cancers smaller than 10 mm have a 20-year relapse rate of only 14% [2]. Invasive ductal carcinoma, not otherwise specified (NOS), is the largest group of malignant breast tumors. It constitutes 65%–80% of breast malignancies [1]. Mammography reveals a circumscribed density, mostly with an irregular, or not well-defined contour (Fig. 1). Sonographically, it corresponds to a hypoechogenic lesion with an irregular form, poorly outlined contour, acoustic shadowing and rupture of the surrounding parenchymal structures. The smaller the size of the mass, the more difficult it is to perform a contour analysis.

Diagnostic difficulties arise with both well-circumscribed and poorly outlined densities (≤15 mm). The diagnostic strategy depends on (a) the extent of the desired sensitivity and (b) the cost-effectiveness accepted by the health care system.

In the United States a benign to malignant ratio of 5–10:1 is accepted. This involves additional noninvasive

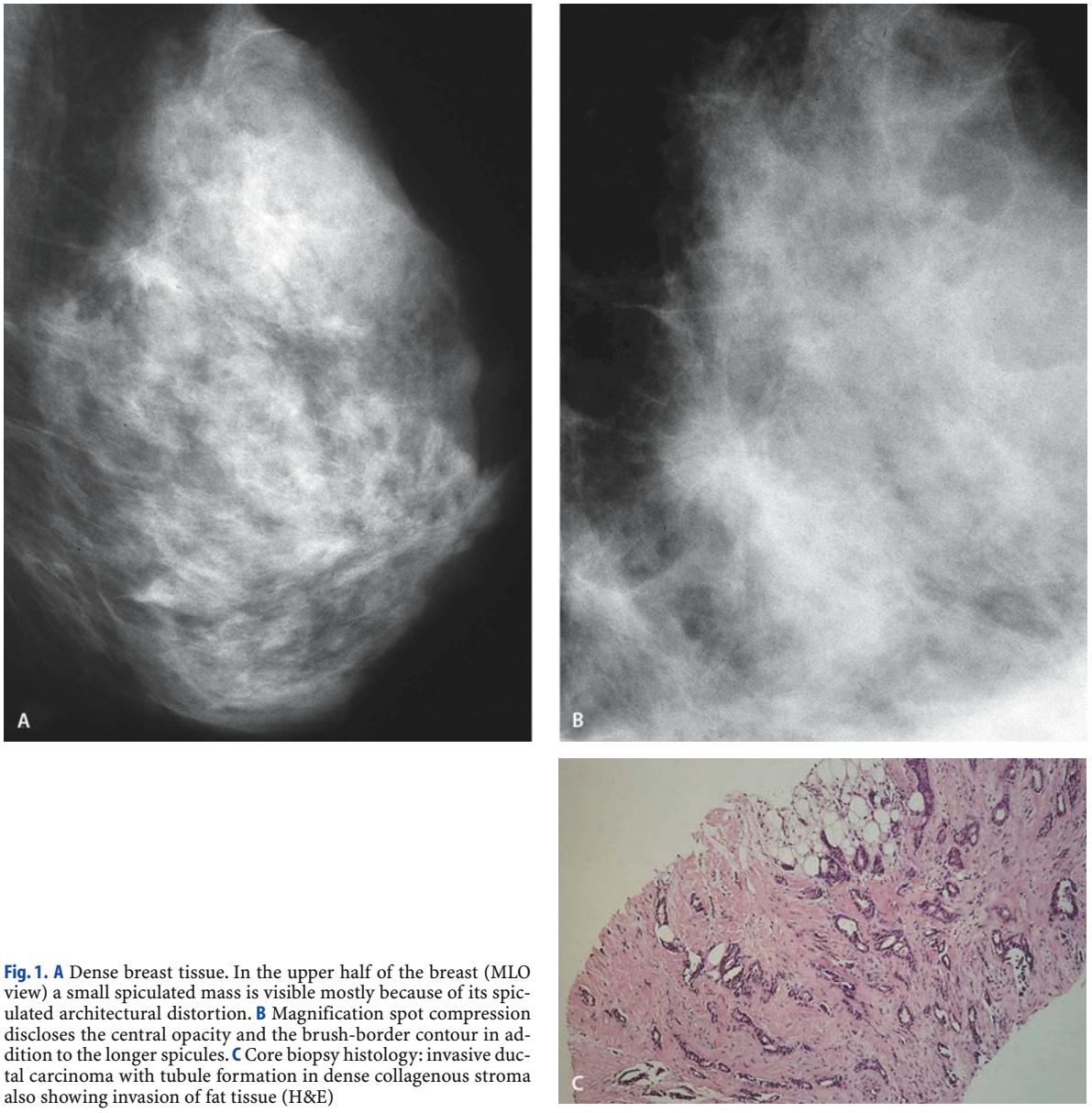

Fig. 1. A Dense breast tissue. In the upper half of the breast (MLO view) a small spiculated mass is visible mostly because of its spiculated architectural distortion. **B** Magnification spot compression discloses the central opacity and the brush-border contour in addition to the longer spicules. **C** Core biopsy histology: invasive ductal carcinoma with tubule formation in dense collagenous stroma also showing invasion of fat tissue (H&E)

and invasive work-up procedures. The risk of overlooking malignancies is minimized at the expense of a higher false-positive rate. In contrast, the European protocol restricts the assessment strategy for reasons of cost-effectiveness: in the Netherlands and Sweden, screening mammography is claimed to have a high positive predictive value (>0.6). High specificity, however, always results in lower sensitivity. A compromise between these two positions should be attempted for the benefit of early detection. The differential diagnosis of small poorly outlined densities (Figs. 2–5) encompasses nodular fibrosis, sclerosing papilloma, fibroadenoma and non-high-grade DCIS. Poorly outlined densities, if small in size, may be visible in only one view. Additional magnification with spot compression enables detection in the second view and makes margin definition easier and more reliable (poorly outlined in both views, discovery of spicules, brush-border appearance) (Fig. 1). The location must be defined in both views if histological information is needed (minimally invasive percutaneous core biopsy, vacuum biopsy, open biopsy).

High-resolution ultrasound also permits detection of a density only visible in one view. Additional information can be gained with this cross-sectional imaging technique, including the contour, form (depth/width ratio), echogenicity, echo texture and secondary phenomena, even for small nodular lesions.

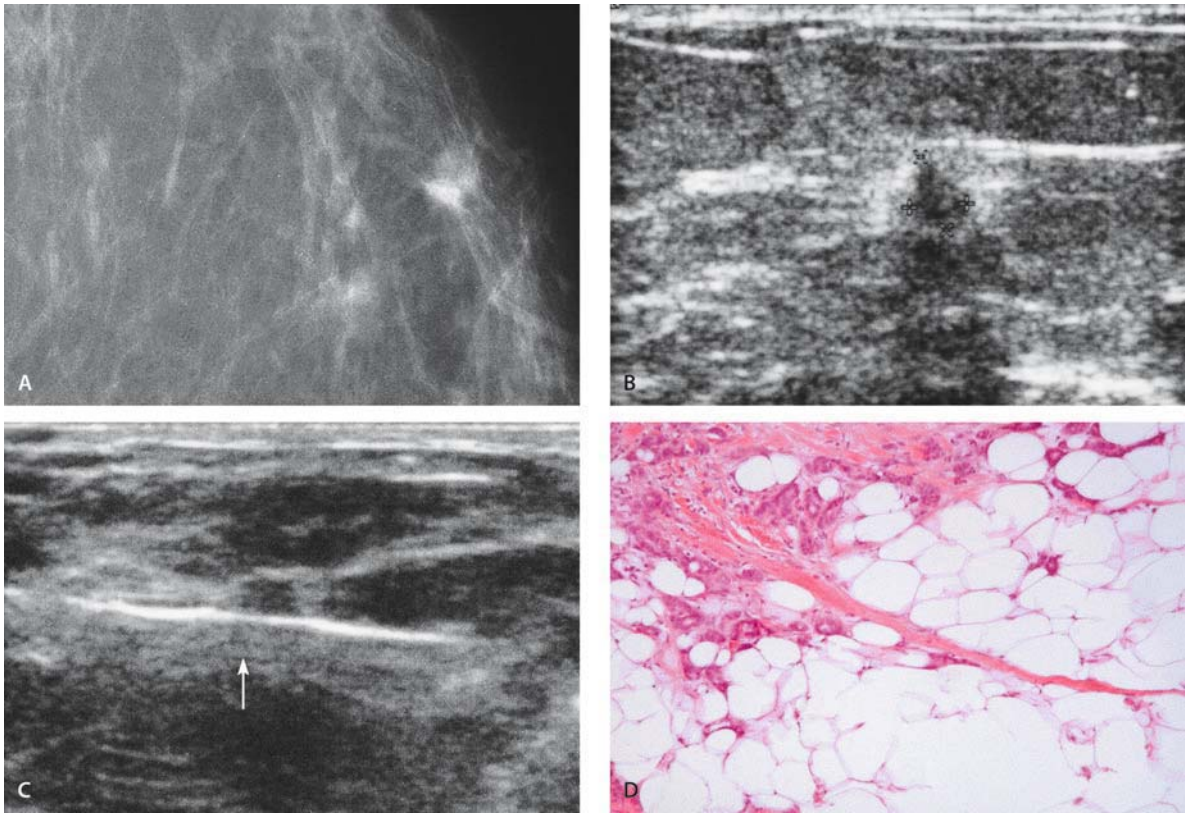

Fig. 2A–D. Differential diagnosis of small poorly outlined densities: invasive tubular carcinoma. **A** Small roundish lesion with spiculated contour, nonpalpable, in 9 o'clock position (cc view) of the right breast. **B** The lesion corresponds sonographically to a 3.7 × 5.1-mm hypoechoic lesion, irregular form and hyperechoic border. **C** Core cut biopsy, sonographically guided, documentation of the needle path. **D** Tubular carcinoma with fingerlike invasion of the surrounding fat and along fibrous septa appearing as spicules in radiography

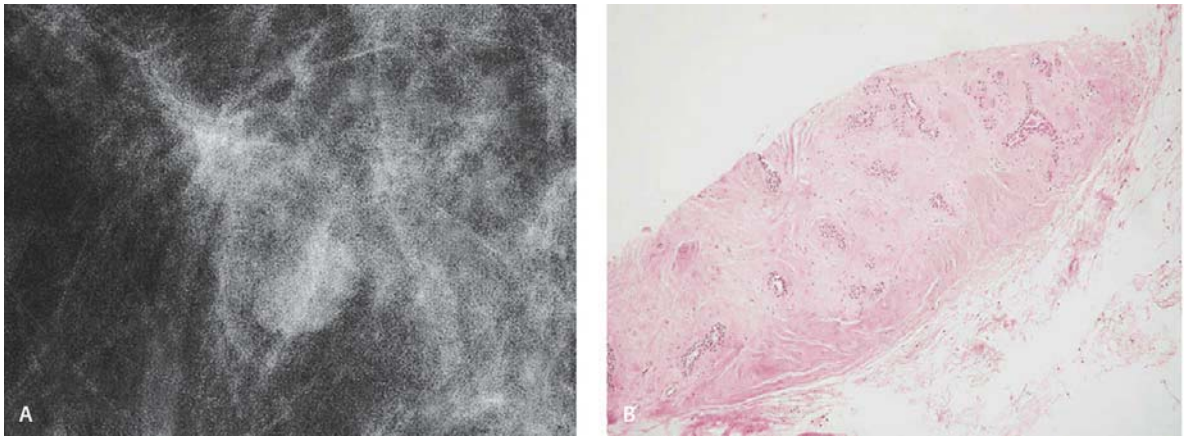

Fig. 3A, B. Differential diagnosis of small poorly outlined densities: Nodular fibrosis. **A** Partly well-outlined, partly poorly outlined density centrally in the right breast. **B** Nodular sclerosis

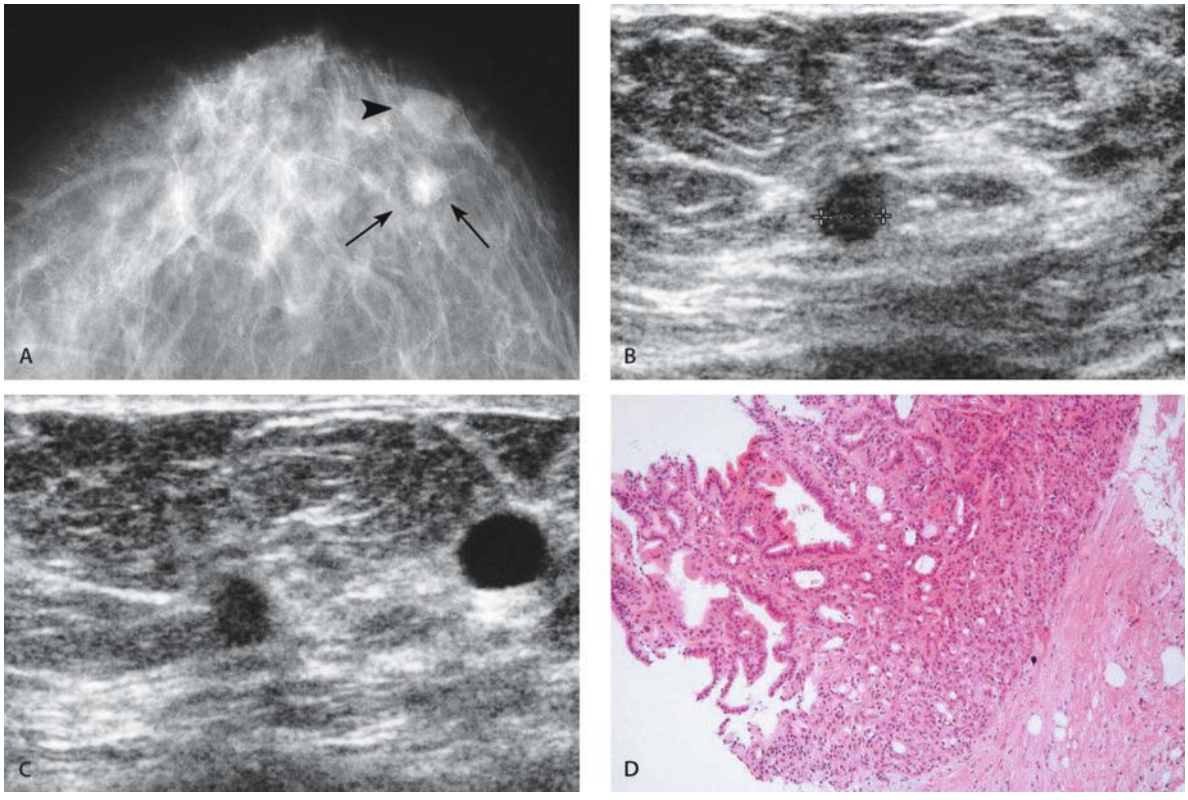

Fig. 4A–D. Differential diagnosis of small poorly outlined densities: Sclerosing papilloma. **A** A 5-mm lesion in the inner half of the left breast (*arrows*), ventrally another oval poorly outlined density (*arrowhead*). **B** On ultrasound a roundish, poorly outlined hypoechoic lesion, suspicious. **C** The ventrally located lesion corresponded to a cyst, the second one, also poorly outlined with ultrasound, hypoechoic, sonographically suspicious. **D** Intraductal papilloma with sclerosis and tubular component

The final diagnosis of a poorly outlined nonpalpable density after conducting a complete, problem-solving imaging examination may result in a recommendation for an open biopsy. During this process of localization, excision and specimen radiography (or specimen sonography), close correlation of pathological and radiological findings is indispensable. The radiologist is in charge of localizing the density as exactly as possible (cosmetic aspects, morbidity) on radiographic images of the specimen with or without magnification, preferably in two projections to provide additional information on size and margins. Particularly if large tissue samples have been obtained, it may be helpful to mark the suspicious area for the pathologist with a needle.

The pathologist must have access to the radiographic images of the specimen so that he can choose the appropriate area to study. He must also assess the distance between the tumor and the margin of the specimen and correlate the histopathological information with the imaging features. In a final interdisciplinary conference involving the surgeon, the radiologist and the pathologist, the diagnostic or therapeutic consequences should be determined.

The assessment of a nonpalpable well-circumscribed solitary lesion depends upon the individual risk situation (age, family history, prior breast-conserving therapy). The positive predictive value of a noncalcified, solid, nonpalpable mass with round, oval or lobular contour and circumscribed margins not obscured by adjacent tissue has been reported to be 1.8% [3]. It should be emphasized that these studies were based on specific interpretative criteria and included ultrasound examination and a comparison with prior mammograms, if available, before recommending periodic follow-up instead of an immediate biopsy. If a mammographically well-outlined lesion is palpable but sonographically not typical of a benign lesion [4] (ellipsoid, well-circumscribed, hypoechoic with edge shadowing, echogenic pseudocapsule) ultrasound-guided core needle biopsy for histological diagnosis is recommended. The targeting of sonographically detected solid lesion under 10 mm is a challenge and needs standardized technique and the use of high-end equipment by an experienced radiologist.

The radiologist should be aware of the possibility of multifocality, multicentricity and associated noninva-

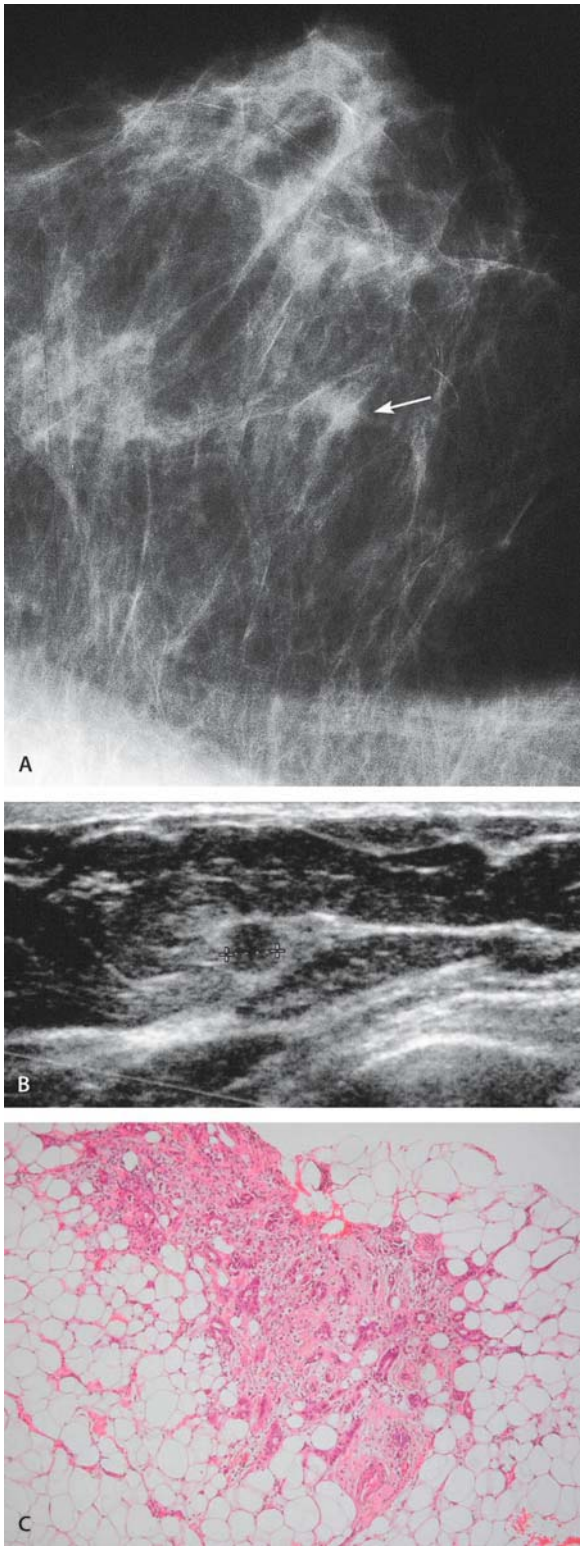

Fig. 5A, B. Differential diagnosis of small poorly outlined densities: Invasive ductal carcinoma. **A** Tiny density (MLO view) to small to define its contour. **B** Sonographically hypoechoic 4.3 mm measuring roundish lesion with discrete hyperechoic border. **C** Invasive ductal carcinoma (grade 2), 4 mm in diameter

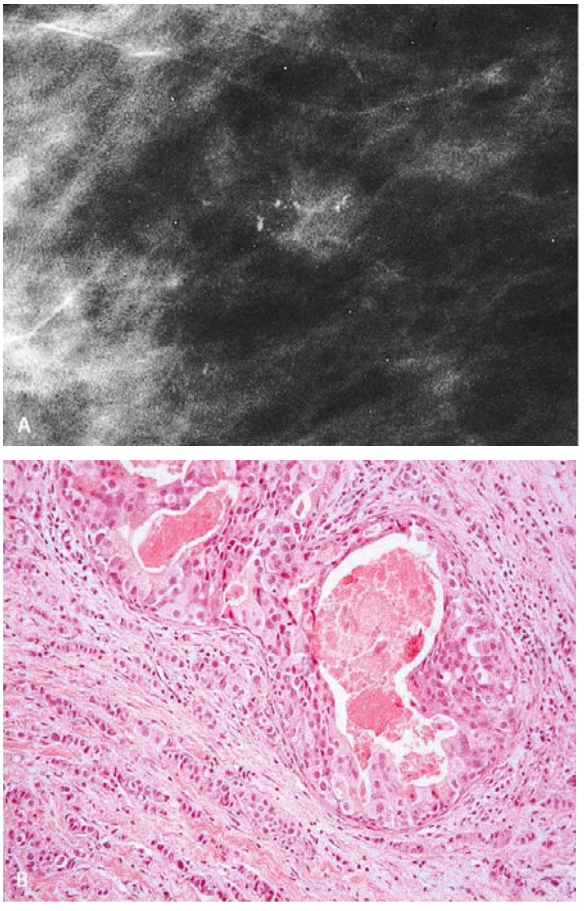

Fig. 6A, B. **A** Poorly outlined density combined with pleomorphic microcalcifications. **B** Ductal carcinoma in situ with adjacent invasive lobular carcinoma (grade 2)

sive components even in small cancers. In Fig. 8, a tiny microcalcification cluster close to the thoracic wall, completely separate from the small centrally located invasive cancer, turned out to be a DCIS. The patient required a mastectomy.

Very small invasive ductal or lobular carcinomas with a pronounced desmoplastic component and small tubular carcinomas display on mammography architectural distortion without a central mass (Fig. 9). Therefore they are indistinguishable from a radial scar (Fig. 10). In such cases neither mammography nor ultrasound is diagnostic. Open biopsy with preoperative localization is the only possibility to accurately distinguish these lesions. Core-needle biopsy and even vacuum-assisted core-needle biopsy are not recommended because of the risk of a sampling error. Moreover, it is impossible to accurately assess the extent of such lesions.

Asymmetry in a mammogram without palpable lesion often corresponds to an island of asymmetric nor-

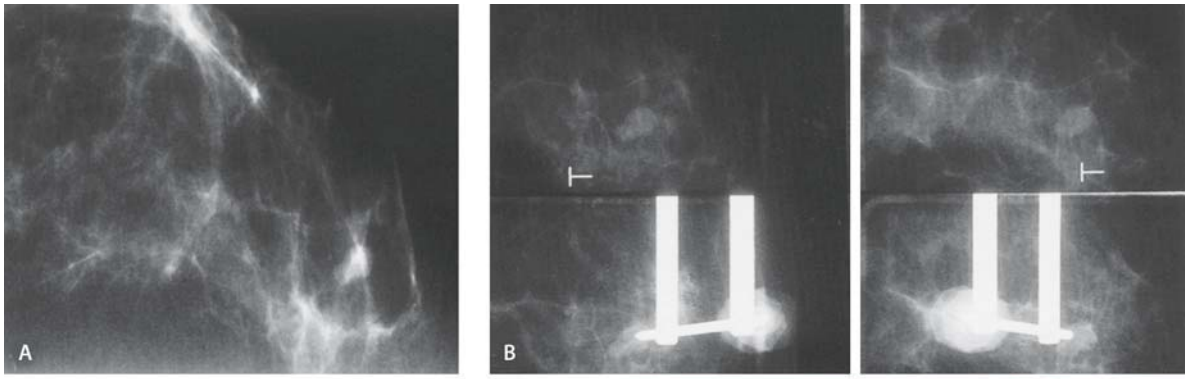
A
B

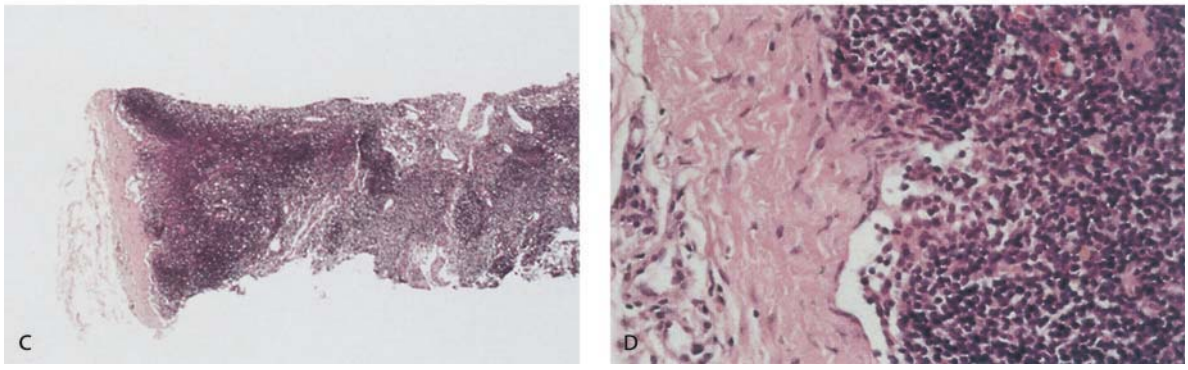
C
D

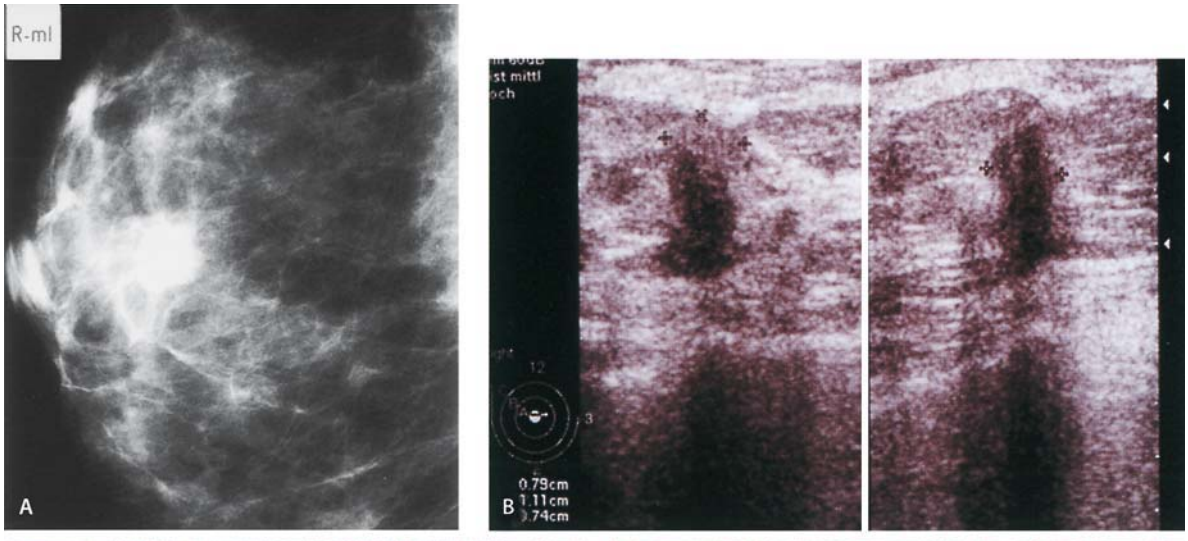
R-ml
A
0.79cm
1.11cm
B

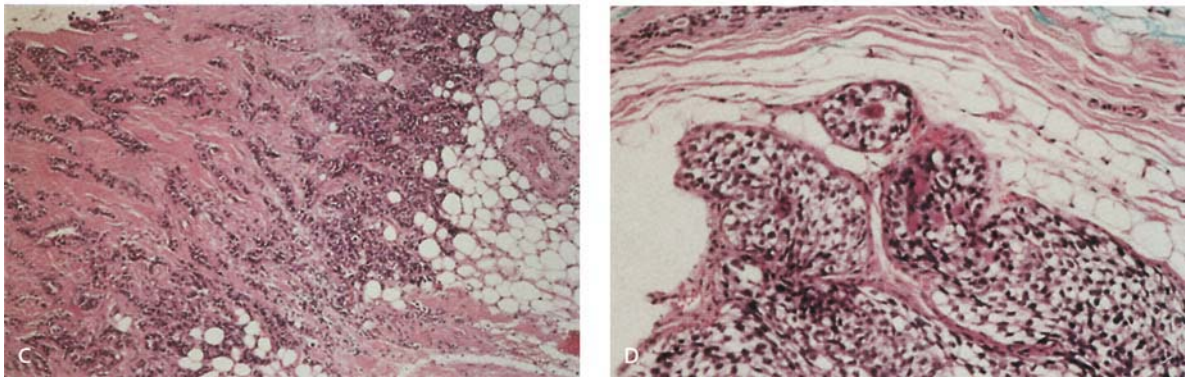
C
D

Fig. 7. A A 35-year-old woman with a high familial risk, worried and anxious about the newly detected well-circumscribed, sonographically not distinguishable density in her right breast. **B** Stereotactically guided core biopsy. **C** Core specimen histology: transnodular biopsy of a tiny intramammary lymph node with capsule formation and marginal sinus structure, no atypical cells (*left*, low magnification; *right*, high magnification)

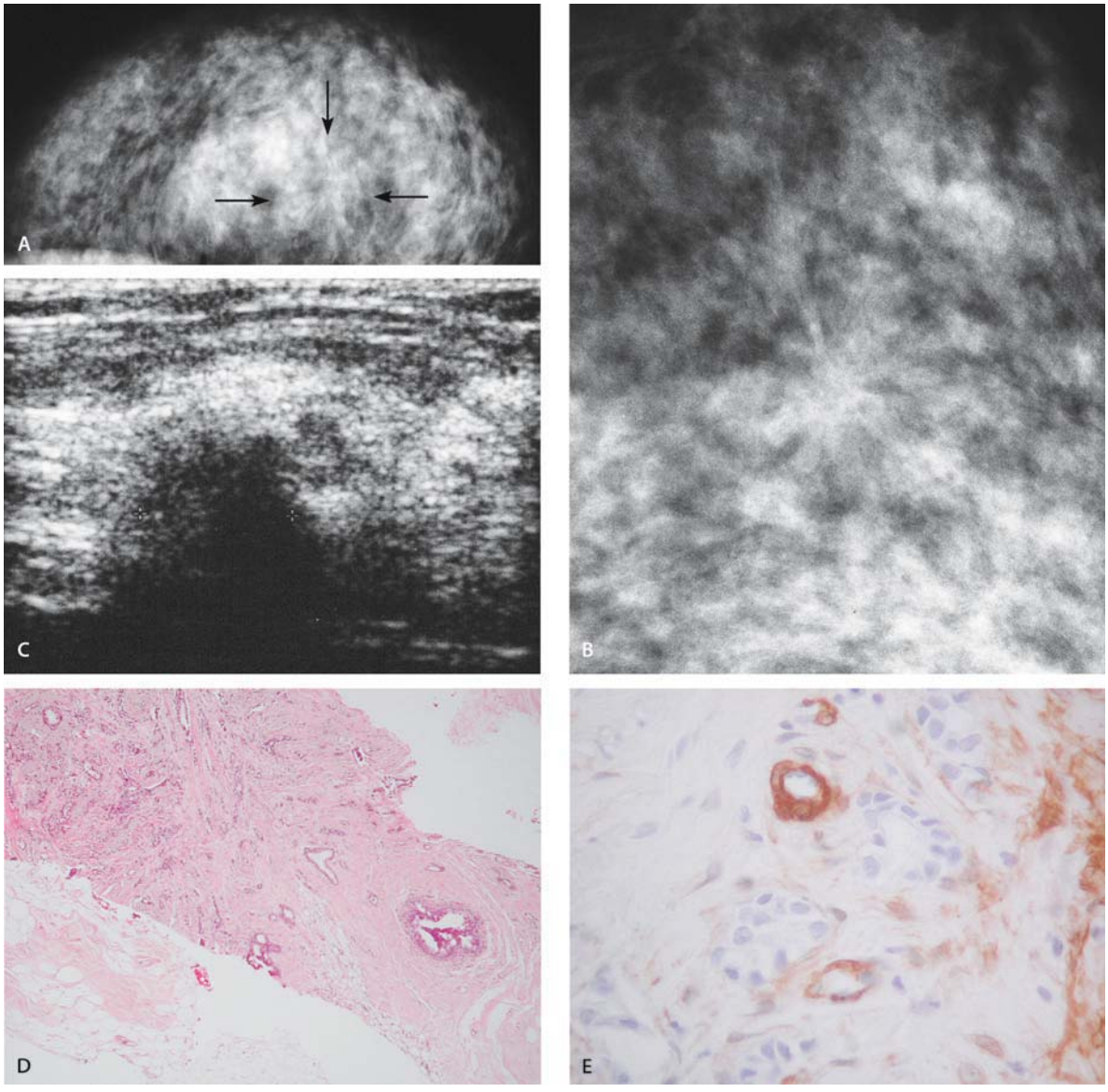

Fig. 9A–E. Differential diagnosis of architectural distortion: **A** Discrete star-like lesion (cc projection). **B** With spot compression magnification the architectural distortion becomes clearly visible within dense breast tissue. **C** On ultrasound a very suspicious hypoechoic lesion, poorly outlined with posterior acoustic shadowing. **D** Tubular lesion, radial appearance of the stroma (core biopsy). **E** Tubular carcinoma with lack of myoepithelial cells, immunohistochemical staining for actin

Fig. 8. A A 45-year-old woman ML mammogram demonstrates an ill-defined, highly suspicious central mass as well as a small cluster of pleomorphic microcalcifications close to the thoracic wall. Both lesions were localized, the density with sonographic guidance, the microcalcifications stereotactically guided. **B** High-resolution ultrasound: ill-defined hypoechoic lesion, posterior shadowing, highly suspicious. **C** Core biopsy: invasive ductal carcinoma with dense stroma and diffuse infiltration of adipose tissue (*left*). On the *right*, dilation of terminal duct segments by solid nests of atypical ductal cells with slight nuclear pleomorphism and broad, weakly eosinophilic to clear cytoplasm (biopsy)

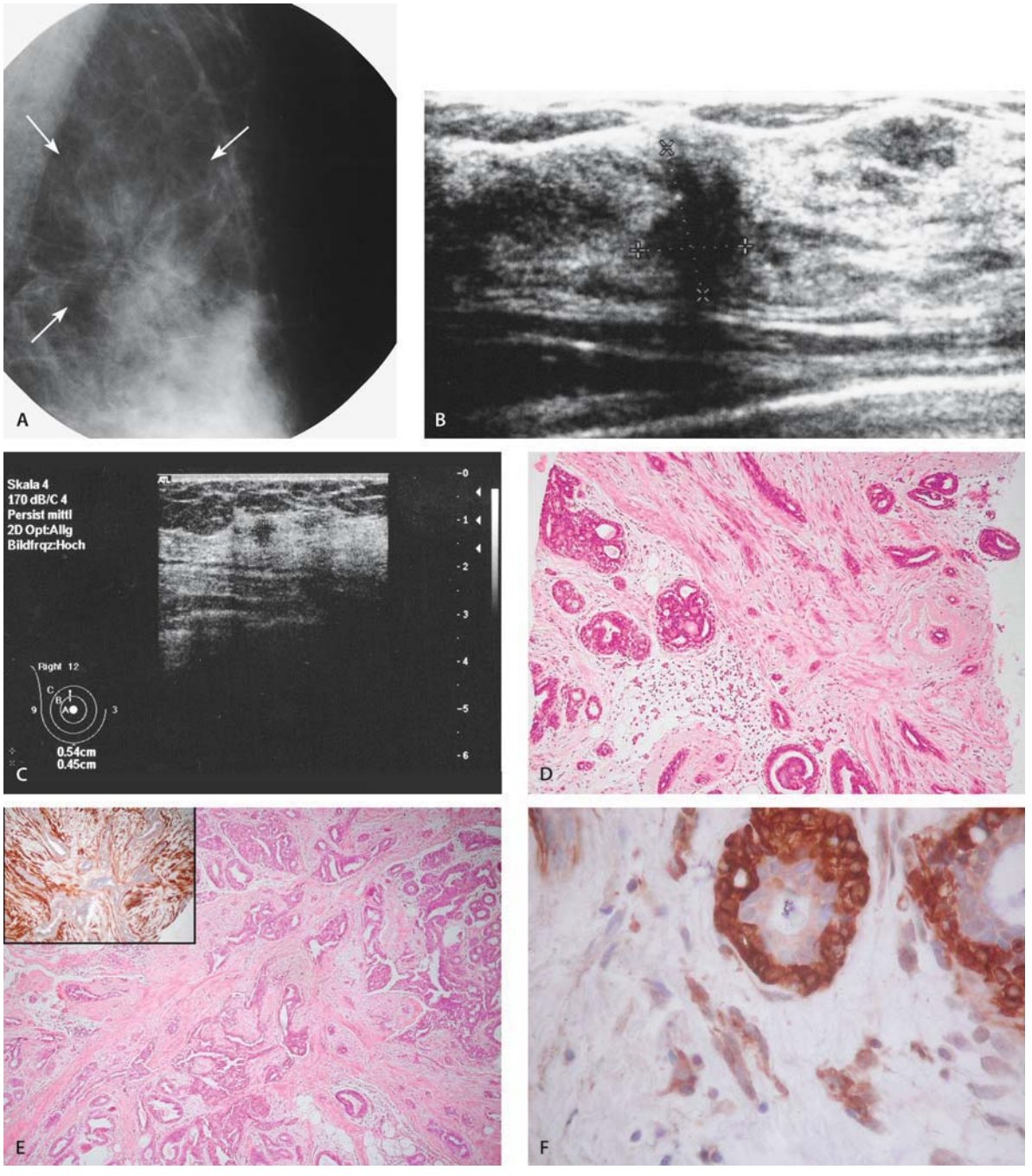

Fig. 10A–F. Architectural distortion: radial scars. **A** Star-like lesion without central density in the upper part of the left breast, impalpable. **B** No mammographic abnormality, but on ultrasound a small hypoechoic lesion with unsharp, partly radiating contour and posterior shadowing. **C** Only sonographically detected 5.4 × 4.5-mm hypoechoic lesion in 12 o'clock position of the right breast. **D** Tubular lesion, radial appearance of the stroma (core biopsy). **E** Resection specimen with radial scar (inset immunohistochemistry for actin). **F** Tubular lesion surrounded by myoepithelial cells, which are diagnostic of a radial scar, immunohistochemical staining for actin (*arrow*)

mal breast tissue. On the other hand, it can be a subtle sign of malignancy, especially if microcalcifications are visible under magnification spot compression, as was the case in the patient in Fig. 11. On open biopsy DCIS, atypical ductal hyperplasia and a radial scar were detected.

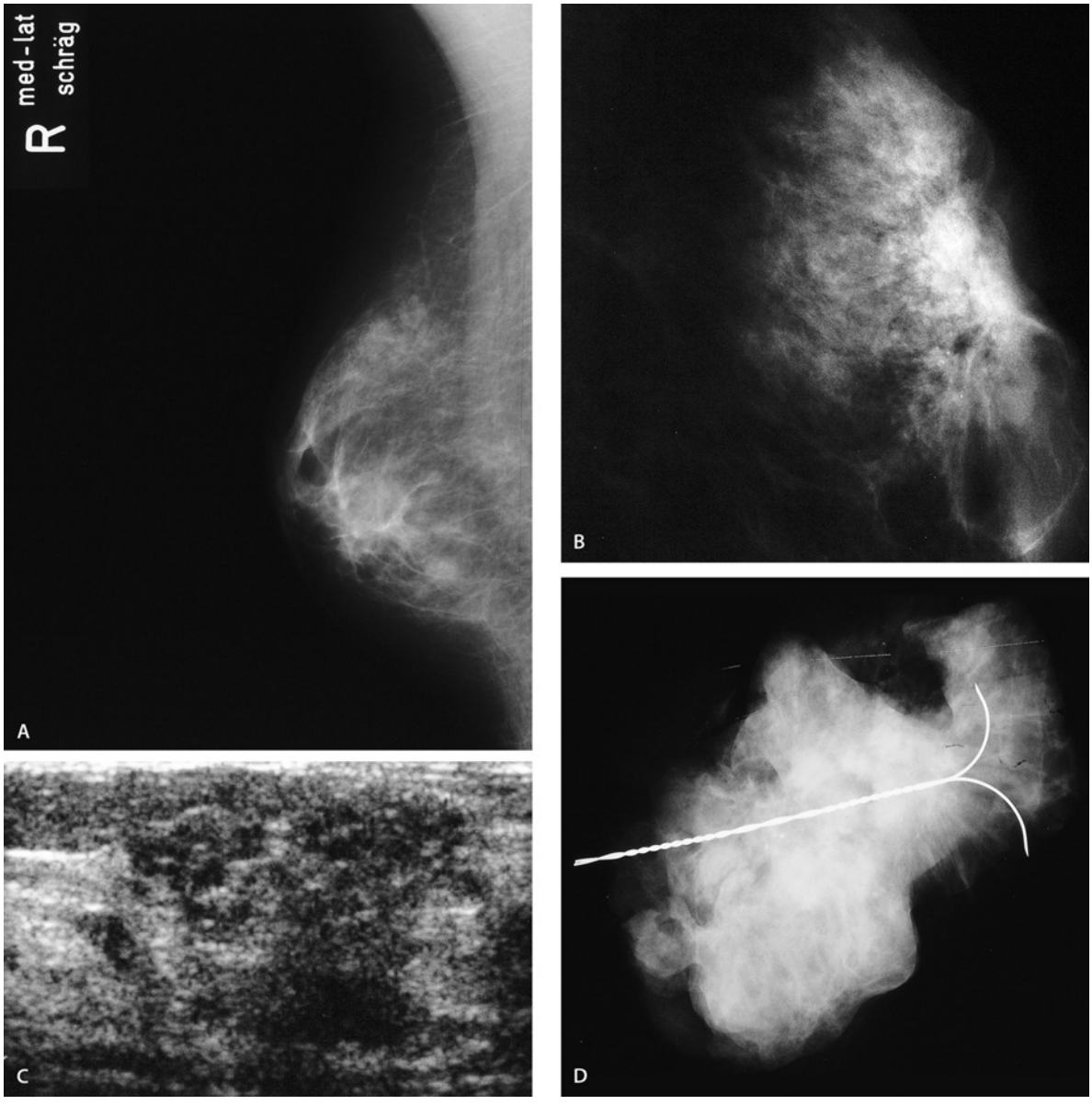

Fig. 11. A A 39-year-old woman with a focal asymmetry of the left breast, known for 4 years. The recent mammogram showed in addition an architectural distortion and a few noncharacteristic microcalcifications. **B** Spot compression magnification (ML view): architectural distortion within the asymmetric area together with a few pleomorphic microcalcifications. **C** Sonographically the region presented only microcystic parenchyma. **D** Specimen radiography detects clearly the radiating structure and microcalcifications along the localization wire. Histology: low-grade DCIS, ADH and radial scar

Detection of Ductal Carcinoma in Situ

DCIS encompasses a biologically heterogeneous group of lesions of varying malignant potential. The new WHO classification (2003) [5] distinguishes two main groups of precursor lesions of invasive breast cancer: (1) lobular neoplasia and (2) intraductal epithelial proliferations, the latter of which includes two subgroups. The usual ductal hyperplasia has been retained in this group, although it is regarded as a benign lesion and not accepted as a true precursor lesion (an example of an inconsistency in this WHO concept). True precursor lesions are ductal intraepithelial neoplasias of varying grades [1–3], with flat epithelial atypia and atypical ductal hyperplasia bearing the lowest risk and ductal carcinoma in situ, grade 3, the highest. Despite some inconsistencies, this new classification forms the basis for diagnosis, treatment and the evaluation of the prognosis.

Since the early 1990s, as the use of screening mammography has increased, both radiologists and pathologists have been confronted with problems concerning the diagnosis and morphological aspects that determine the prognosis of these lesions (nuclear grade, necrosis, size of lesion, architecture, cytonuclear grade and cytoarchitectural differentiation, cell size).

We refer to chapter 7.3 of this book concerning the typical morphological appearances and a detailed analysis of the correlation between different types of calcifications and histological subtypes of DCIS and would like to concentrate on three selected topics in which pathological–radiological correlation is especially crucial.

The Size of the Lesion

If DCIS presents with microcalcifications, the radiologist is responsible for estimating the extent of the lesion preoperatively. Two orthogonal magnification views with spot compression are the prerequisite. A significant correlation exists between mammographic appearance and histological findings. Tabár published a study [5] including 198 cases of DCIS with mammographic abnormalities, 88 of them (44%) cases of DCIS of high nuclear grade and 110 corresponding to intermediate or low nuclear grade. The high-grade lesions correlated with microcalcifications in 85% of cases (75/88) and with asymmetric densities in only 15% (13/88). The microcalcifications typically presented as casting type (95%) or crushed stone-like (47%) calcifications (Fig. 13A); a few (4%) showed powdery microcalcifications. This relation changes in the case of intermediate- and low-grade DCIS types in favor of crushed-stone (56%) and powdery (32%) calcifications, with a decrease in casting type microcalcifications (12%).

In general, the extent of typical ductal microcalcifications corresponds fairly well with the histological size of the lesion. Nevertheless, one must bear in mind that histologically malignant cells can be detected beyond the mammographically visible area of microcalcifications. Furthermore, this correlation is not as clear for cases of well-differentiated DCIS. Roundish clusters of powdery microcalcifications may be indistinguishable from the calcifications of a sclerosing adenosis.

Therefore the radiologist's task is to ascertain the extent of an excision (specimen radiography in two views with magnification to visualize the third dimension, to mark the one focus or multiple foci of calcifications within the specimen). Both the tissue specimen and the radiographic image should be sent to the pathologist. This is necessary for defining the area to be sectioned and indispensable for determining the size and answering the question of whether the microcalcifications are correlated with DCIS. Margin width seems to be the most reliable prognostic parameter of recurrence, independent of morphological determinants and irradiation [6].

Uncommon Features

Asymmetries and masses were mammographic features of intermediate- and low-grade DCIS in 20% of the Falun data [5]. Figure 16 shows an example of a mass,

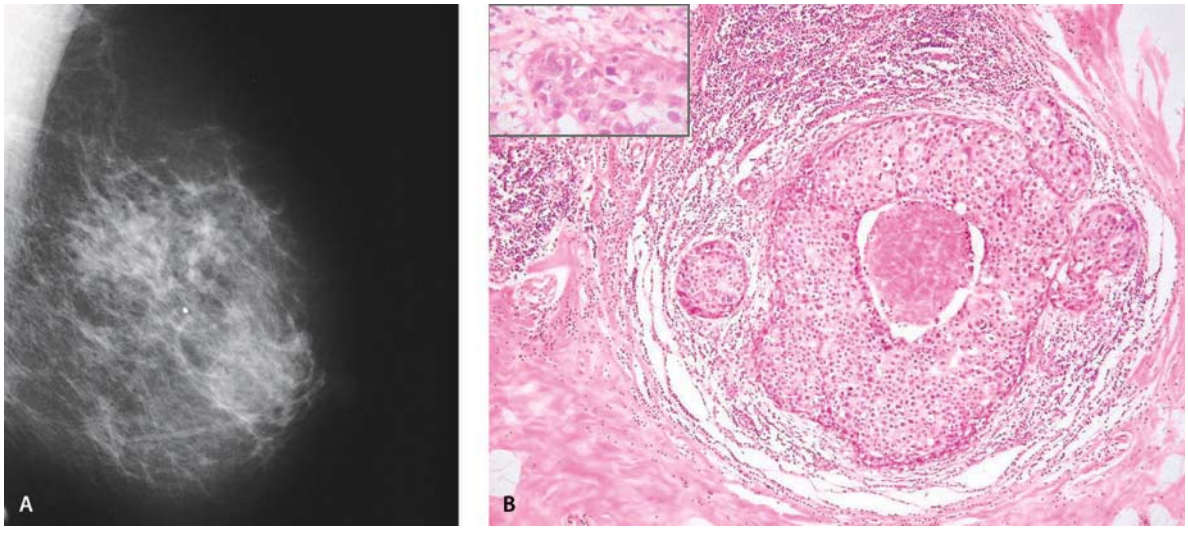

Fig. 12A, B. Area of asymmetric density in combination with structural asymmetry: vacuum-assisted core-needle biopsy revealed DCIS in all cores. In open biopsy, a microinvasive ductal carcinoma was additionally detected (pT1 mic pTis). **B** Ductal carcinoma in situ of high-grade malignancy with calcification and microinvasion (*inset*)

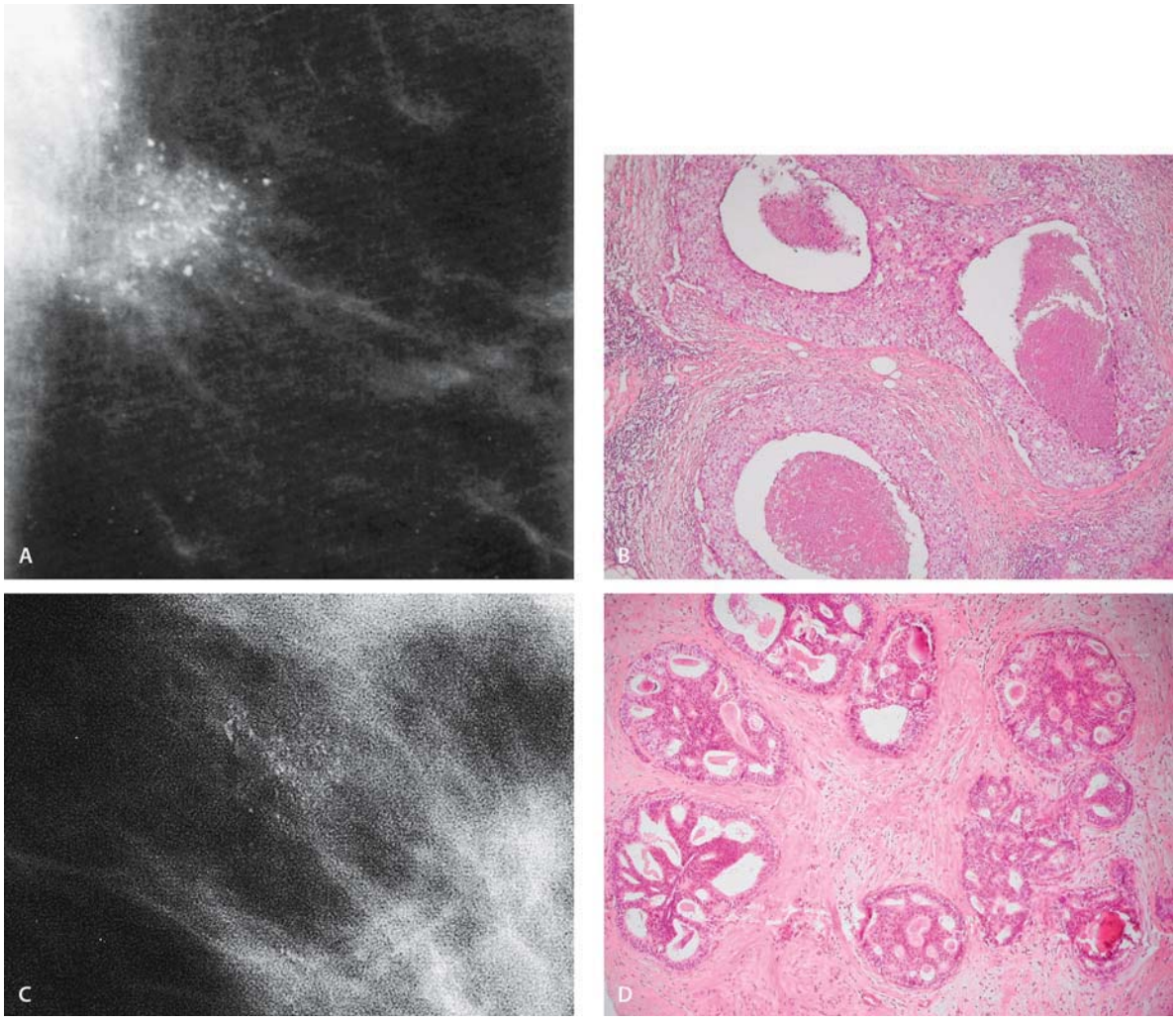

Fig. 13. A Segmental cluster of typically ductal microcalcifications (coarse, granular, pleomorphic, linear, branching) associated with diffusely denser tissue corresponding to high-grade DCIS. **B** Ductal carcinoma in situ of high-grade malignancy with dilatation of the ductal lumen and aggregated coarse calcifications. **C** Cluster of mostly fine granular, discretely pleomorphic microcalcifications: DCIS of intermediate grade. **D** Ductal carcinoma in situ of low-grade malignancy forming fine granular calcifications

which was invisible within the extremely dense tissue on mammography, but detectable on ultrasound as a hypoechoic, not well-outlined focal area. Two further examples of DCIS are demonstrated in Figs. 11 and 12.

Diagnosis and Size Determination of DCIS with Stereotactically Guided Vacuum-assisted Core-needle Biopsy

Vacuum-assisted large core biopsy has been shown to overcome the limitations of automated Tru-Cut core-needle biopsy for microcalcifications. Because it allows much larger contiguous specimens and more total tissue volume to be aspirated without additional morbidity, it has become the method of choice for assessing indeterminate clusters of microcalcifications. If these microcalcifications consist of an extremely small group, it can be completely removed by the vacuum-assisted device (Fig. 14A, B). Core specimen radiography with magnification and postbiopsy mammography should confirm that the entire lesion was removed.

The newly developed technique of vacuum-assisted biopsy is a powerful tool in diagnostic breast pathology. A relatively large amount of breast tissue can be obtained with this method, revealing the topography of the breast lesion. When the radiologist and the pathologist exchange information, however, some aspects have to be considered to optimize the diagnostic results. The tissue is gathered bit by bit using the circular movement

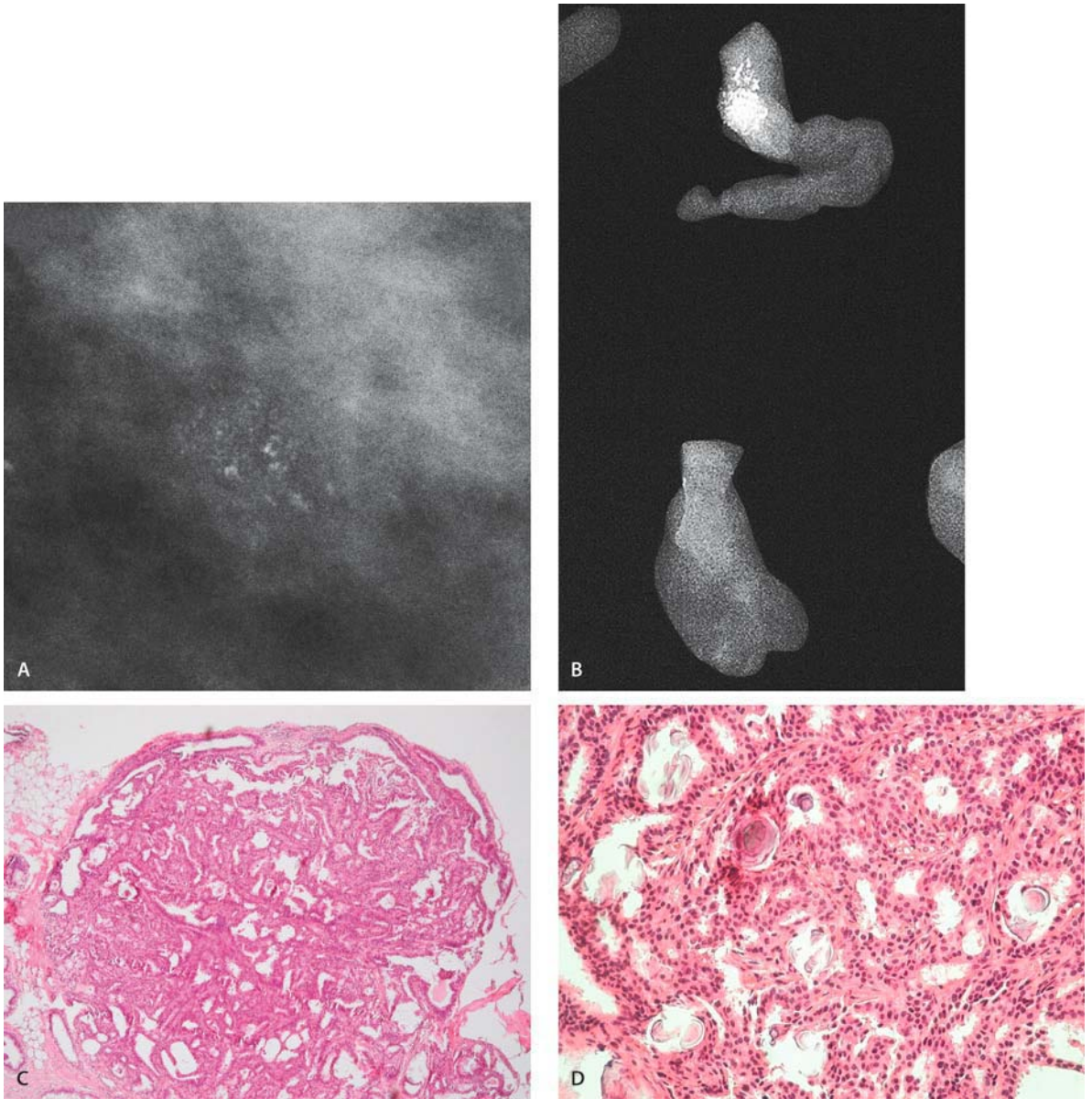

Fig. 14A–D. Differential diagnosis of BIRADS 4 – microcalcifications. **A** Cluster of granular calcification. **B** Specimen radiography: complete removal with vacuum biopsy. Histology, papillary hyperplasia. **C** Ductal papillary hyperplasia. **D** Higher magnification with microcalcification (*arrows*)

of the mammotome. Though not necessary, it is highly recommendable to number the different parts clockwise in the order of aspiration during the tissue embedding procedure, to reflect the topographical aspects of the lesions. It is important that each sample be sectioned and stained on the histological slides. Step sectioning in at least four steps is sufficient and most reliable. The radiographic image of the core specimen should only be submitted with the tissue if microcalcifications exist, so that the pathologist can estimate whether the calcifications seen histologically indeed correlate with the radiographic findings. It should be emphasized that only a minimum of training is necessary to diagnose microcalcifications accurately in core specimens.

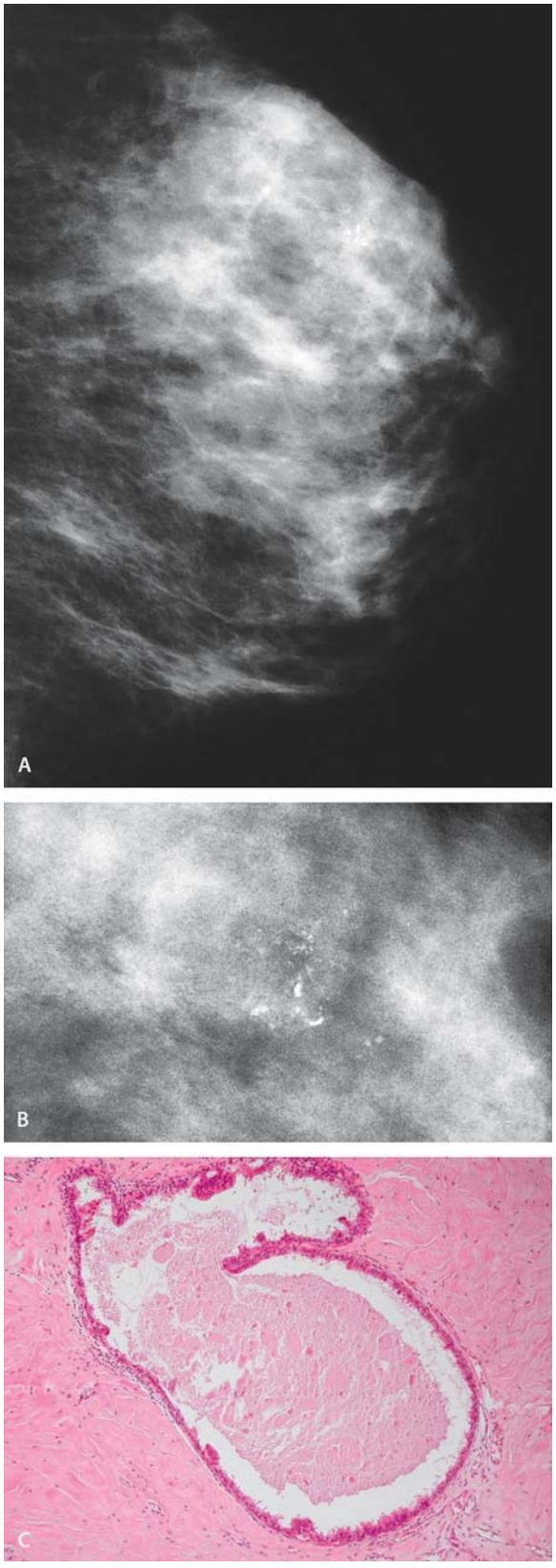

Detection of High-Risk Lesions (ADH, ALH, CLIS)

Page and Anderson [7] define DCIS as a combination of (a) a uniform population of cells, (b) smooth geometric spaces between cells of micropapillary formations with even cellular placement and (c) hyperchromatic nuclei.

Atypical ductal hyperplasia (ADH) is defined as a non-comedo DCIS [8] less than 2 mm in diameter. This definition, however, is still controversial.

ALH is characterized by changes similar to those in lobular carcinoma in situ (CLIS), which, however, do not fulfill all the requirements for a CLIS. ALH can involve both lobules and ducts.

In a study by Page and Dupont [9, 10], the risk of developing breast cancer for a women with ADH was highest in the first 10 years after a benign breast biopsy (RR, 9.8), and it fell to 3.6 after 10 years. The risk seems to be influenced by menopause status and family history.

In view of the promising results of two chemoprevention studies (NSABP-P1, MORE Study) [11–13], high-risk lesions diagnosed at such an early stage could have the option of being treated with chemoprevention.

Classification of proliferative breast lesions appears difficult and shows high interobserver variability. The prevalence of ADH in studies in which a biopsy was performed because of a palpable mass is 2%–4%. When performed because of microcalcifications, it increases to as much as 12%.

Whereas CLIS will always remain an incidental finding in mammography, ADH typically is combined with microcalcifications (Figs. 9, 10), but can also produce densities (Fig. 7).

No pathognomonic type of microcalcification exists for ADH lesions. With an increasing frequency of core biopsy for indeterminate microcalcifications, ADH will be detected more frequently. Automated devices produce underestimates of 36%–56%, because after more than five passes with a 14g-Tru-Cut needle, the tissue acquisition and the volume of tissue can be insufficient to permit a diagnosis of DCIS. With the vacuum-assisted device, which can excise larger volumes of tissue, this underestimation of ADH and DCIS can be reduced. However, the diagnosis of DCIS with early stromal invasion will remain difficult (Fig. 21B).

Fig. 15. A Triangular group of pleomorphic microcalcifications. **B** Magnification spot compression detects the pleomorphic particle form, even some casting-type calcifications are visible. Histology: fibrocystic disease. **C** Ectatic duct with fine granular microcalcifications

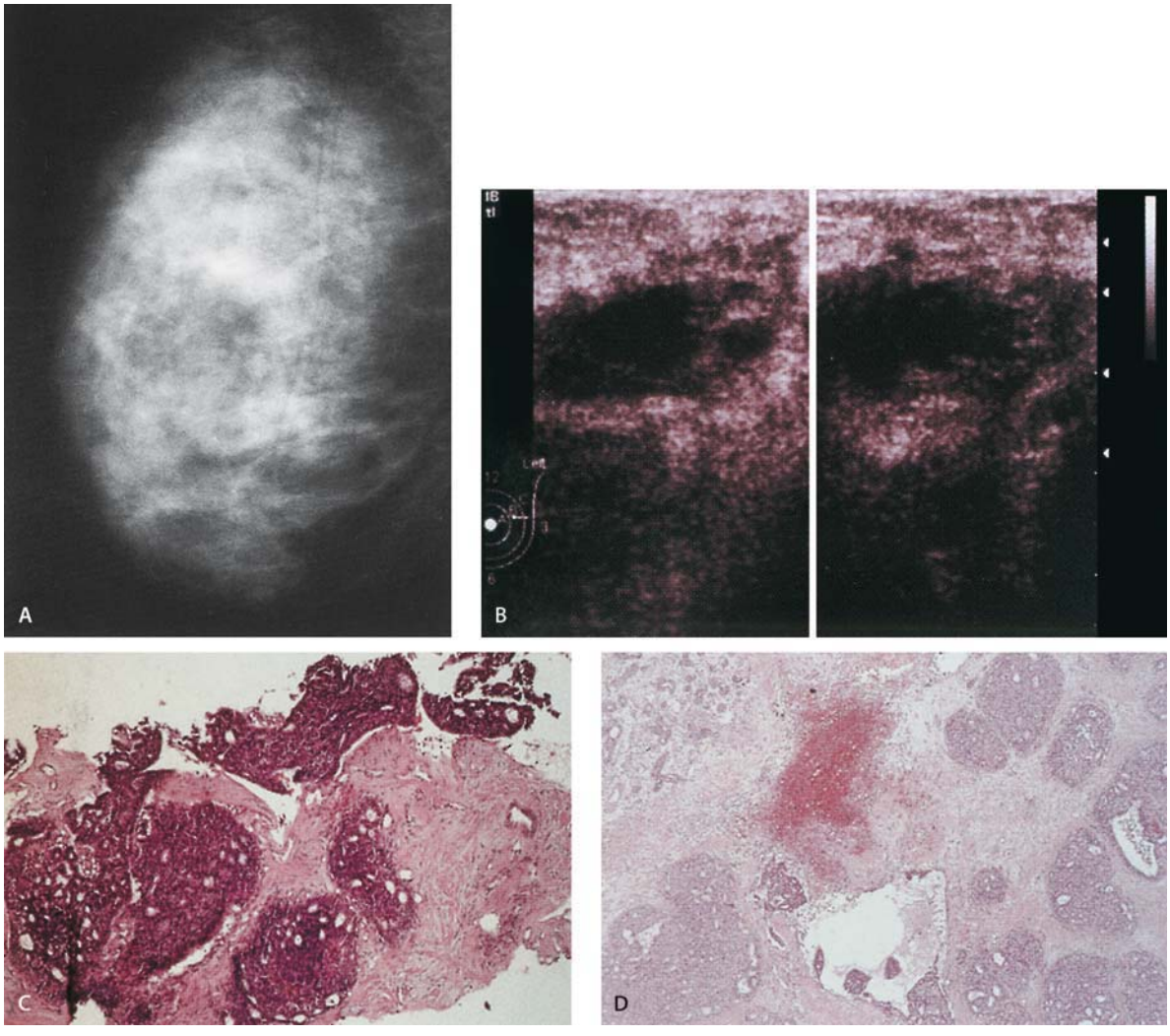

Fig. 16. **A** A 42-year-old woman without palpable findings. MLO view showing very dense breast tissue, the sonographically visible mass hidden by the dense parenchyma. **B** Ultrasound examination was added to gain further diagnostic information. An overall, ill-defined hypoechoic lesion with irregular borders was discovered. Tru-Cut core-needle biopsy revealed DCIS. **C** Core biopsy histology, dilation of several immediate adjacent ducts by mainly solid nests of ductal epithelium with minor cribriform component, overall appearance of solid tumor (DCIS). **D** Resection specimen: large defect and resulting hemorrhage with minimal remnants of the lesion

Early Detection in High-Risk Patients

Three options can be offered to women who are at especially high risk, (a) close surveillance, (b) prophylactic mastectomy and (c) chemoprevention.

Close surveillance is the most frequently chosen option. Consequently, diagnostic imaging strategies need to be developed and above all evaluated under study protocol conditions. The sensitivity of mammography may be limited, so that in the German study protocol (Consortium Hereditary Breast and Ovarian Cancer sponsored by the German Cancer Aid) regular high-resolution ultrasound examination (6-month intervals) and contrast-enhanced MRI (yearly) are additionally offered, starting at the age of 25.

If an abnormality is found by any of these imaging modalities, a complete work-up should be performed, including minimally invasive percutaneous core biopsy to detect breast cancer at as early a stage as possible.

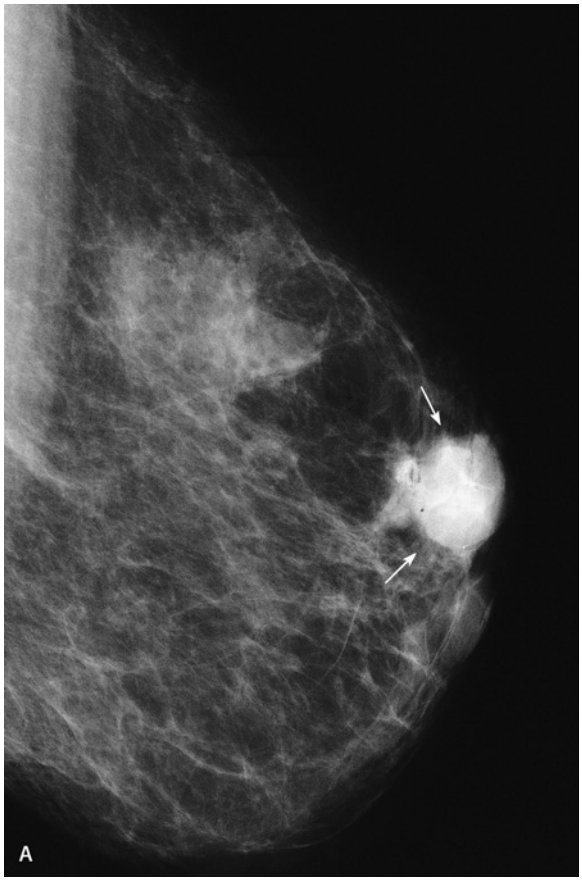

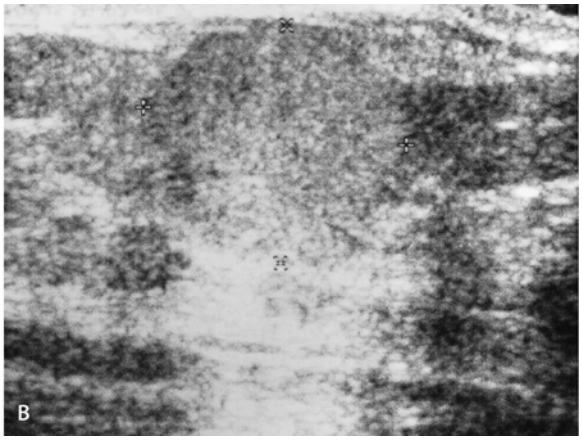

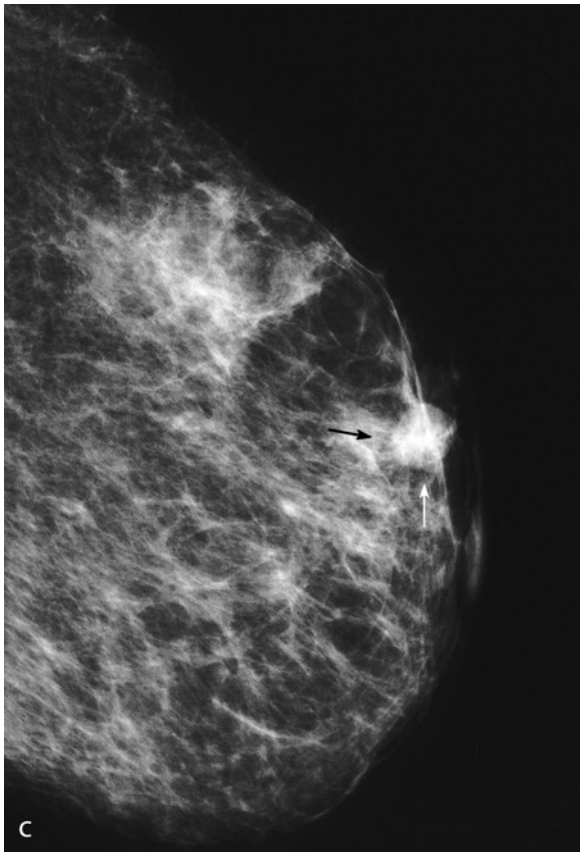

Fig. 17. A A 90-year-old woman, presenting with palpable mass of left breast. A poorly outlined density in 1 o'clock position. **B** On sonography the mass corresponds to a 1.72 × 1.57-cm hyperechoic roundish mass, poorly outlined, strong posterior echo enhancement. **C** Regression of the lesion after 6 months of Tamoxifen treatment

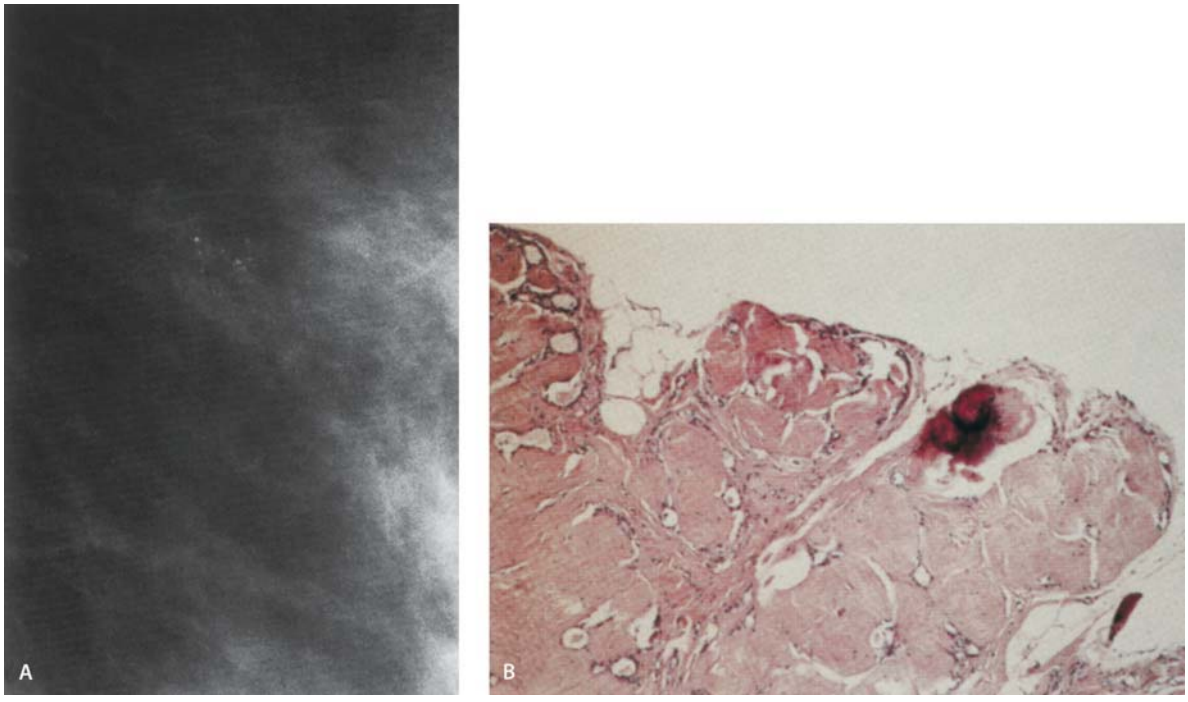

Fig. 18. A Mediolateral magnification view mammogram: tiny cluster of segmental distributed punctate and fine granular microcalcifications. Vacuum-assisted core biopsy was performed with complete removal of the cluster. **B** Histology: Fibroadenomatoid hyperplasia with dense collagenous stroma and calcifications

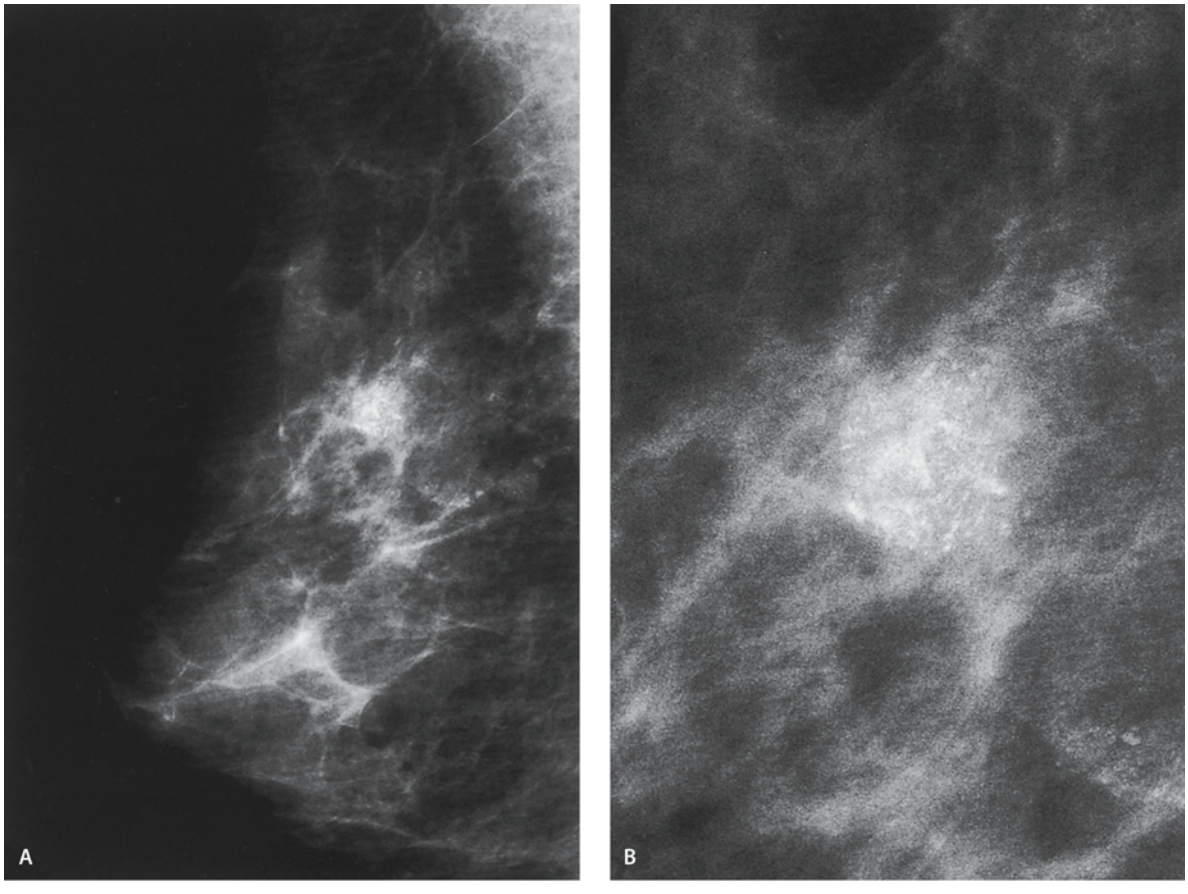

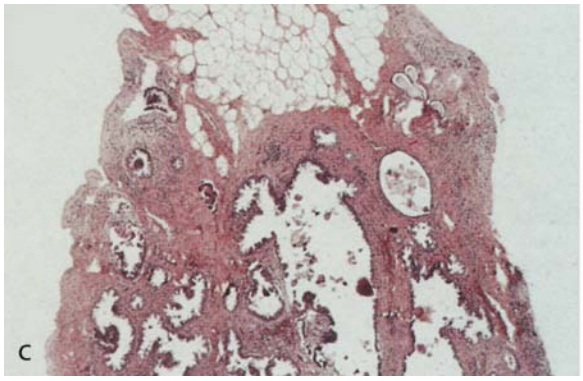

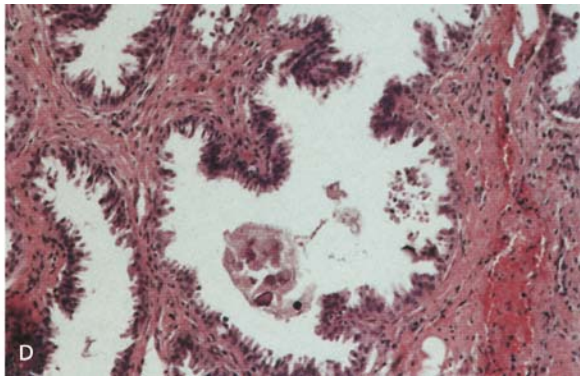

Fig. 19C, D

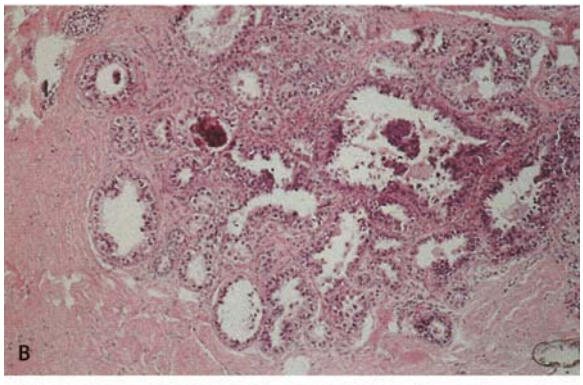

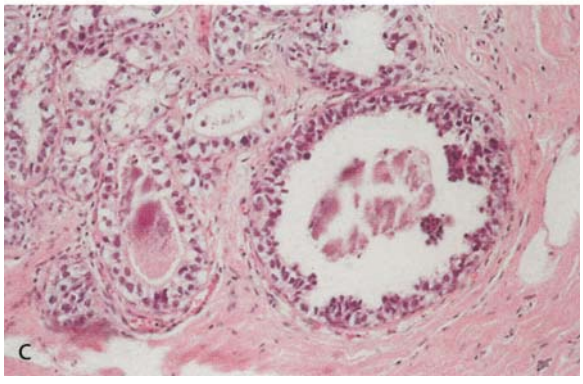

Fig. 20. **A** Mediolateral magnification view of a tiny cluster of coarse as well as punctate calcifications. Vacuum-assisted core biopsy removed the entire group. **B** Dilated ducts with papillary epithelial proliferation and various degrees of nuclear atypia. Extensive calcifications. *Left*, low magnification, *right*, high magnification

Fig. 19. **A** Multiple, round, not always well-circumscribed densities of different sizes in the upper half of the breast. **B** Magnification mammography (ML): granular, linear, pleomorphic and amorphic calcifications within the largest of the masses. Vacuum-assisted core biopsy was performed. **C** Histology: complex ductular lesion with papillary ductal epithelial proliferation and coarse ductal calcifications (*left*, low magnification; *right*, high magnification)

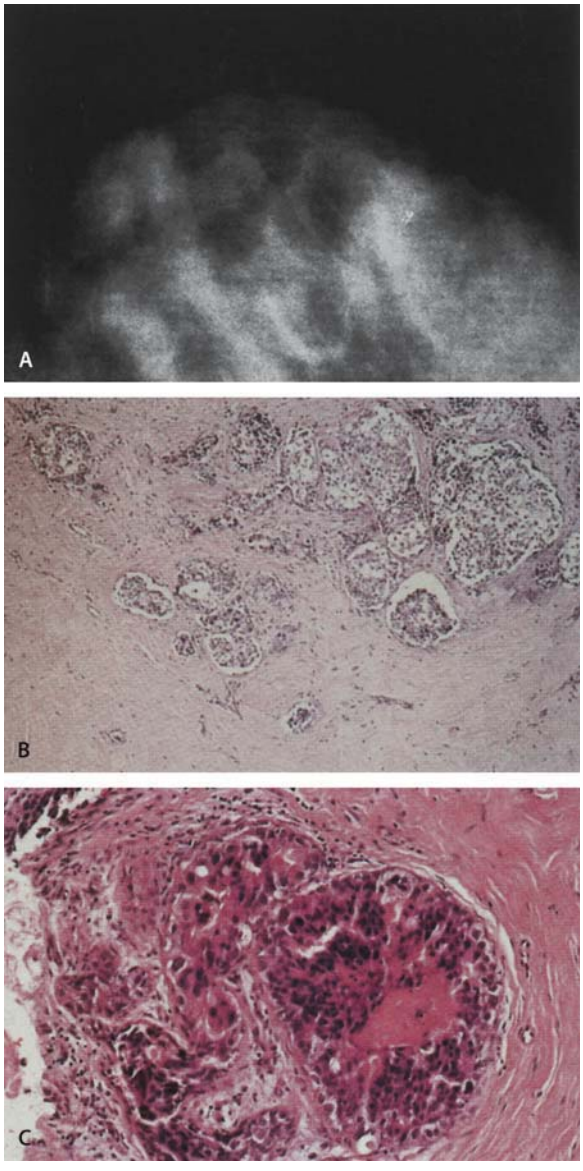

Fig. 21. A Tiny cluster of microcalcifications in the cc mammogram, composed of one v-shaped microcalcification and a few roundish ones. Work-up with vacuum-assisted core biopsy. **B** Histology: intraductal carcinoma with central calcifications and severe nuclear polymorphism (DCIS, high grade). (*left side*) Small invasive component of a ductal carcinoma in the vicinity of the DCIS (*right side*)

Conclusion

Early detection of breast cancer and histological-radiological correlation are intimately linked together, because small invasive and noninvasive cancers are typically nonpalpable. Additionally, borderline lesions exist that may be difficult to identify histologically within small tissue samples.

European quality standards recommend that more than 70% of all nonpalpable cancers should be confirmed histologically before definitive surgery. Therefore guidance with imaging is mandatory for preoperative core-needle or vacuum-assisted biopsy, for preoperative localization and specimen radiography. There are limitations to imaging-guided interventions related to the size, localization and type of lesion. Consequently, incorrect target selection, in case of stereotactically guided intervention, can result in a sampling error. This can be minimized by strict adherence to standardized performance protocols including close histological–radiological correlation at each step of the procedure. This interdisciplinary approach is a fundamental basis of a multidisciplinary concept for breast cancer centers.

References

1. Ellis IO, Galea M, Broughton N (1992) Pathological prognostic factors in breast cancer. II. Histological type. Relationship with survival in a large study with long-term follow-up. Histopathology 20:479–489
2. Rosen PP, Saigo PE, Braun DW (1989) Pathologic prognostic factors in stage I and stage II breast carcinoma: a study of 655 patients with a median follow-up of 18 years. J Clin Oncol 7:1239–1251
3. Sickles EA (1997) Management of lesions appearing probably benign at mammography. In: Friedrich M, Sickles EA (ed) Radiological diagnosis of breast diseases. Springer, Berlin Heidelberg New York, pp 167–172
4. Stavros AT, Thickmann D, Rapp CL et al (1995) Solid breast nodules: use of sonography to determine between benign and malignant nodules. Radiology 196:123–134
5. WHO Classifications of tumours (2003) Tumours of the breast and female genitale organs. IARC Press, Lyon
6. Tabàr L (1997) In: Silverstein MJ (ed) Ductal carcinoma in situ of the breast. Lippincott, Williams and Wilkins, Philadelphia
7. Silverstein MJ, Lagios MD, Groshen S, Waisman JR, Lewinsky BS, Matino S, Gamagami P, Colbum WJ (1999) The influence of margin with on local control of ductal carcinoma in situ of the breast. New Engl J Med 340:1455–1461
8. Page DL, Anderson TJ (1987) Diagnostic histopathology of the breast. New York Churchill Livingston
9. Tavassoli FA, Norris HF (1990) A comparison of long-term follow-up for atypical hyperplasia and intraductal hyperplasia of the breast. Cancer 65:518
10. Page DL, Dupont WD, Rogers L (1988) Ductal involvement by cells of a typical lobular hyperplasia: a long-term follow-up study of cancer risk. Human Pathol 19:201–207
11. Dupont WD, Page DL (1989) Relative risk of breast cancer varies with time and diagnosis of a typical hyperplasia. Human Pathol 20:723–725
12. Fisher B, Dignam J, Wolmark, Wickerham DL, Fisher ER, Mamounas E, Smith R, Begociv M, Dimitrov NV, Margolese RG, Kardinal CG, Kavanah MT, Fehrenbacher I, Oishi RH (1999) Tamoxifen in treatment of intraductal breast cancer: national surgical adjuvant breast an bowel project B-24 randomized controlled trial. Lancet 353:1993–2000
13. Wickerham DL, Costantino J, Fisher B, Kavanah M, Wolmark N (1999) Average annual rates of invasive an noninvasive breast cancer by history of LCIS and atypical hyperplasia for participants in the BCPT. Proc. ASCO 327
14. Cauley J, Krueger K, Eckert S, Muchmore D, Taylor Y, Scott T (1999) Raloxifen reduces breast cancer risk in postmenopausal women with osteoporosis, 40-month data from the MORE trial (Abstract #328). Proc ASCO

Breast Cancer: Correlations Between Imaging and Morphological Details

Edward Azavedo

7.3

Contents

Introduction

Breast cancer is the most common malignancy that can affect a woman during her lifetime. In Sweden it comprises 27% of all malignancies in women. During the last 30 years, the detection of breast cancers has shifted from palpable tumours in symptomatic women to impalpable tumours in asymptomatic women. This is mainly the result of the widespread use of imaging modalities, particularly mammography in mass screening programs [1].

Mammography is today the method of choice to screen healthy asymptomatic women for breast cancer and the immediate adjunct method is ultrasound technology. While mammography does detect small impalpable breast cancers, it also has the ability to detect abnormalities representing minor non-malignant but pathological changes. In this respect, the interpretation of imaging findings with correlation to morphological changes is mandatory to minimize harm and worries [2]. There are several typical imaging findings that can be correlated with morphological changes representing malignancies, and this knowledge is essential for further specific diagnostic interventions. Stereotaxic and ultrasound-guided interventions can provide us cells or tissue material for morphological assessment and these reports have to be consistent with the imaging diagnosis [3, 4].

Spiculated Densities

The most common type of screening-detected breast cancer is the spiculated lesion, with or without microcalcifications. This type of lesions corresponds to 61% of all screening-detected breast cancers in our screening experience [5]. Some of the typical imaging characteristics of cancers appearing as spiculated densities are:

a. Focal density that is higher than surrounding tissue
b. Spicula that are short, fine and concentric
c. Spicula that are seen at the border zone almost around the entire density
d. Spicula that do not cross the density under consideration

Details such as the increase in density correspond to an increased number of cells as compared to the surrounding tissue and the spicula correspond to the outward growth of a malignancy from the centre of the density. These details are shown in Figs. 1–4.

Ultrasound examinations of these tumours will show a solid lesion where some of the features such as echogenicity (hypoechoic or anechoic), contours (irregular margins), form (depth greater than width) are typical

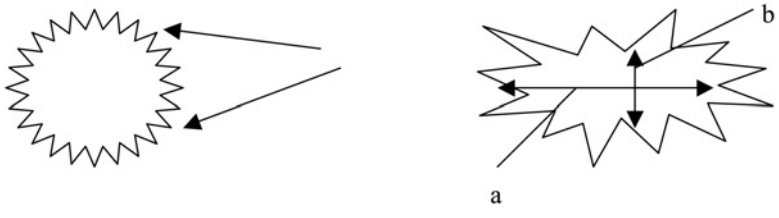

Fig. 1. Sketch of a spiculated density that shows concentric spicula and a sketch showing two different sizes of one and the same tumour

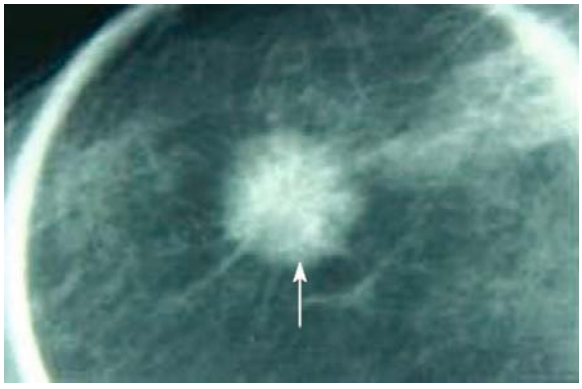

Fig. 2. Spiculated densities in a case of invasive carcinoma that shows fine, short and concentric spicula

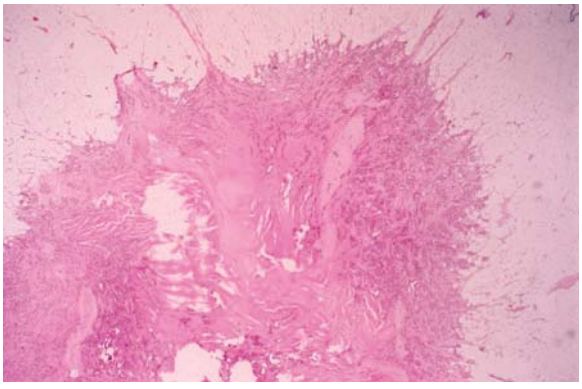

Fig. 4. Histopathology of an invasive carcinoma, a spiculated density on a mammogram, showing the outward-growing cancer cells that represent the fine and short spicula

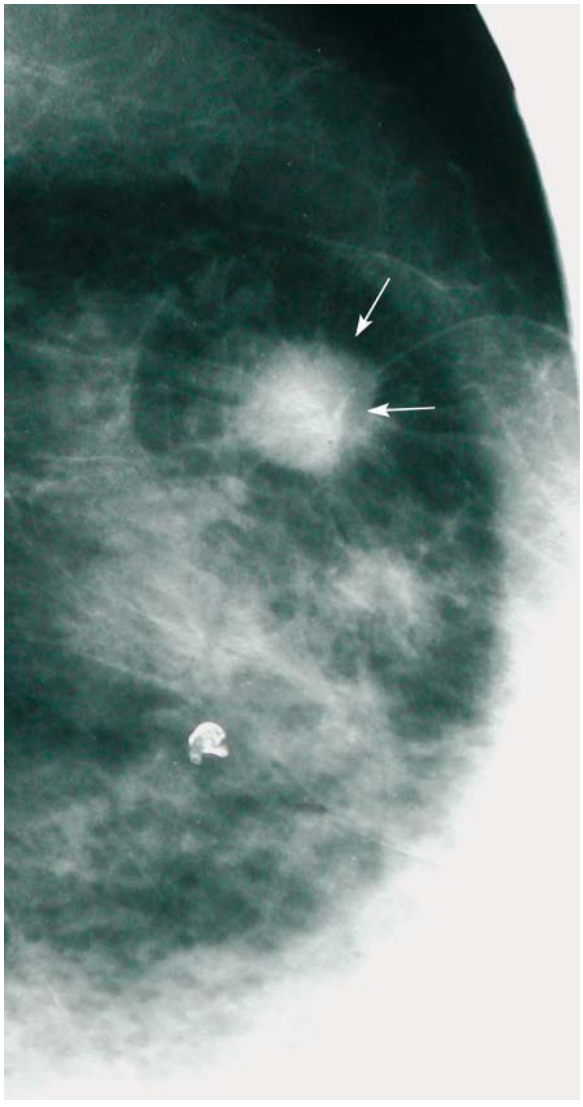

Fig. 3. Peritumoral corona (pseudoradiolucency)

for malignant lesions [6]. This appearance on sonography is rather typical for both spiculated densities and other kinds of invasive malignancies, even though some malignant tumours may show quite regular margins to the surrounding tissue.

Some indirect signs of malignancy often seen in conjunction with solid malignant lesions are pseudoradiolucency around a tumour and effects on the skin near a tumour. The pseudoradiolucency, also called peritumoral corona, is a radiolucent zone around a tumour, and this is usually seen when fat surrounds a tumour (Fig. 3). This peritumoral corona is different and should be distinguished from the halo sign around solid lesions with sharp margins that represent a benign lesion [7, 8]. Effects on the skin usually comprise skin thickening with folded and/or retracted skin near a malignant tumour, indicating contraction of tissue surrounding a tumour.

Developing Density

A developing density in a radiolucent area or an increasing density in an already dense background is another common phenomenon that should worry a breast imager. Transition from a radiolucent to a radiopaque area or a focal increase in density in an existing dense area should mean an increased number of cells until the contrary is proven. Ultrasound can rather easily differentiate a cystic from a non-cystic increase in density. A developing non-cystic density warrants action to find an explanation for the increase in density that in many a case may be a malignancy, even if benign changes such as fibrosing adenosis could be the correct diagnosis. Even if a developing non-cystic density lacks spicula, it is mandatory to assess the finding morphologically either with cytology or histology. When using only cytology, one must make sure that the needle positioning is

right and that the material obtained through fine needle aspiration (FNA) is adequate enough to make a cytological diagnosis. Lobular carcinomas that grow diffusely in a dense area may pose a challenge to a cytologist, since the number of epithelial cells obtained could be minimal due to the abundant fibrous background containing fibroblasts, collagen, etc. In addition, low-grade lobular carcinomas are often of the small cell type with very little cell atypia. Histological assessment with core biopsies could be a good complement or alternative in such situations. Rather typical lobular carcinomas are shown in Figs. 5 and 6.

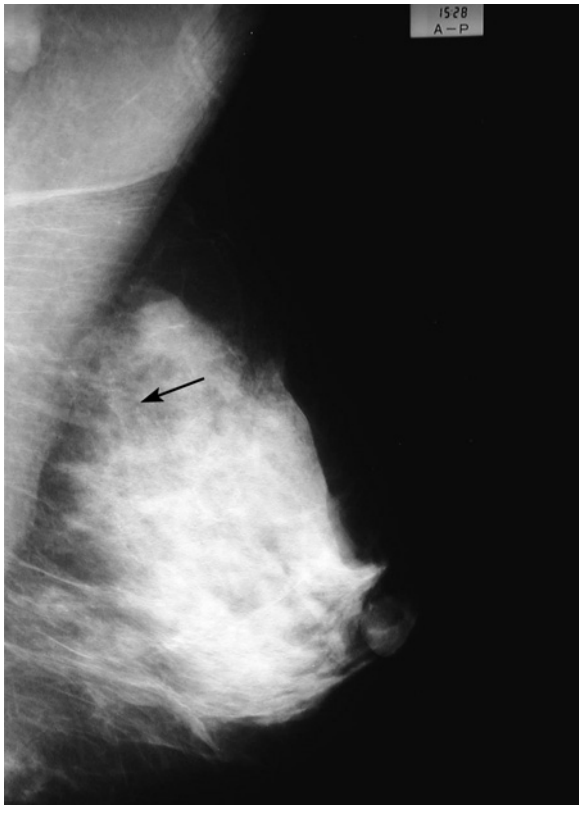

Fig. 5. A developing density in the upper outer quadrant representing a lobular carcinoma

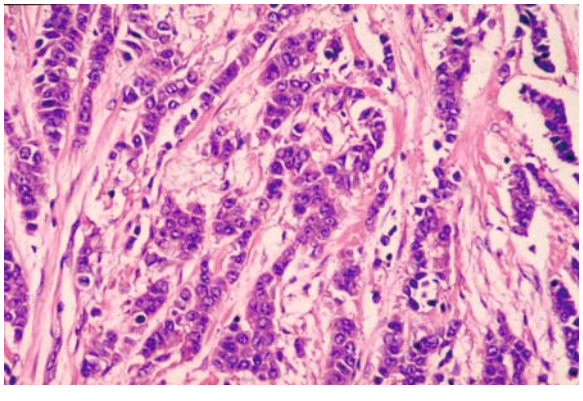

Fig. 6. Histopathology of a lobular carcinoma

Medullary and Mucinous Carcinomas

Medullary and mucinous carcinomas can show mixed features but appear as densities. Medullary carcinomas occur in less than 5% of all cases but are more common in younger women where the frequency can be up to 11% in women younger than 35 years of age [9]. On mammography they show up as round or oval uncalcified lesions, often with lobulated margins and homogeneous density. Mucinous carcinomas comprise about 4% of all breast cancers and are often seen in the elderly patients [10, 11]. Clinically, they could be soft and ill-defined but mammographically they are usually seen as rather well-defined densities.

Radiating Lesions Without a Central Density

In asymptomatic women, one can sometimes find radiating lesions that do not show a central density. These lesions can be very obvious in certain projections, while they may look different in other views. They also have radiating structures that are thicker and longer than the fine spicula in a spiculated density. Moreover, the thick and long radiating structures could be parallel, sometimes 2–3 cm long, and may have fatty tissue between them. Although these lesions might look like an invasive carcinoma at first sight, they are not palpable even when the size of the whole area is as big as 2–4 cm (Figs. 7, 8). These lesions, sometimes called black stars by some authors, usually represent a non-malignant pathological lesion that is called a radial scar. In our screening experience, the frequency of these lesions was 0.06%, but some authors report a much higher frequency [12]. The generally accepted management of these lesions is surgical excision, because even if the lesion is non-malignant in itself, there are reports that there could be a carcinoma associated with these lesions.

Radial scars have different names and are now generally considered as a variant of sclerosing adenosis [13]. They usually lack secondary signs involving the skin such as skin thickening and skin retraction.

Topographic and Other Characteristics of Breast Cancers

According to the literature and our own experience, we find that the majority (50%) of breast cancers occur in the upper outer quadrant, approximately 25% in central

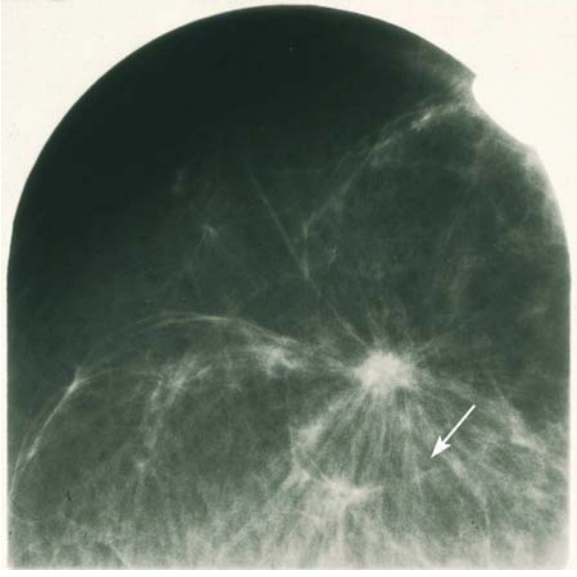

Fig. 7. A radiating lesion (stellate lesion) representing a radial scar. Note the thick and long spicula as compared to the fine spicula around a carcinoma

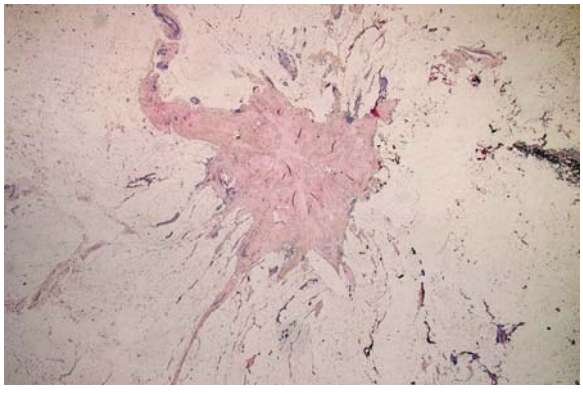

Fig. 8. Histopathology of a radial scar showing thick fibrous strands

areas around the nipple and around 5% in the lower inner quadrant [14, 15].

The more irregular the margins of a density are, the more suspicious it is of malignancy. The same is true the more lobulated a density is. The intensity of a density usually appears too high for its size when the density represents a malignancy.

The size of a lesion is crucial for correct clinical staging, which in turn is the basis for adequate management. In this respect, there could be quite widespread discrepancies between sizes as evaluated on imaging modalities and sizes recorded in clinical examinations and by pathologists. In general, the size of a lesion is not enough to differentiate a lesion between benign and malignant. Comparison between mammographic and ultrasound sizes with clinical examination could show differences. If and when there is a desmoplastic reaction around a tumour, then the clinical estimate of the size of that tumour could be bigger than the mammographic size. This is also true when a tumour is situated rather centrally because the surround tissue up to the skin on both sides of the tumour will probably make it feel bigger than its actual size in the breast. We can sometimes also see differences in tumour size as seen on a mammogram and ultrasound. In some cases a desmoplastic reaction may increase the mammographic size as compared to size on an ultrasound image, but it could also be the contrary when ultrasound can show diffuse infiltration around a mass, especially in dense breasts. The size of a tumour as measured on a surgical specimen will be the final figure that will form the basis for classification and management of a case. In an elongated or an oval tumour, the recorded size of the tumour on a surgical specimen could vary depending upon how the tumour was cut, and this may be discriminatory as compared to imaging modalities (Fig. 1). In many a case microscopic examination will reveal an extensive intraductal component that cannot always be evaluated on imaging modalities, and therefore the ultimate tumour size in these cases will be bigger on surgical specimens than the imaging modalities [16].

In general malignant disease increases with age and this is true even for breast cancers. Therefore even well-defined circumscribed densities should be considered as potentially malignant in postmenopausal women. Recent trends with increasing use of HRT in peri- and postmenopausal women can be a challenge to a breast imager, who may find focal increases in density secondary to the use of HRT [17]. This demands careful analysis of every single new density that is seen on mammograms of women using HRT.

Recent advances in studies regarding neoangiogenesis have shown that malignant tumours do need increased vascularization to feed growth. Histopathology can show increased vascularity with direct microscopy, and recent developments in immunohistopathology have shown that angiogenesis is quite a common factor seen and associated with malignancy. Some of these early signs can be seen with our imaging modalities that can pick-up neoangiogenesis [18].

In conclusion, breast imagers should have a regular multidisciplinary contact with surgeons, oncologists and especially pathologists for a better understanding and characterization of breast tumours.

References

1. Tabar L, Vitak B, Chen HH, Duffy SW, Yen MF, Chiang CF, Krusemo UB, Tot T, Smith RA (2000) The Swedish Two-County Trial twenty years later. Updated mortality results and new insights from long-term follow-up. Radiol Clin North Am 38: 625–651
2. Tot T, Tabar L, Dean PB (2000) The pressing need for better histologic-mammographic correlation of too many variations in normal breast anatomy. Virchows Arch 437: 338–344
3. Azavedo E, Svane G and Ringertz H (1991) The role of the radiologist in screening for non-palpable breast tumors in Sweden. Invest Radiol 26: 174–178
4. Azavedo E, Svane G and Auer G (1989) Stereotactic fine needle biopsy in 2594 mammographically detected non-palpable lesions. Lancet 1: 1033–1036
5. Azavedo E, Svane G (1991) Radiologic aspects of breast cancers detected through a breast cancer screening program. Eur J Radiol 13: 88–90
6. Stavros AT, Thickmann D, Rapp CL et al (1995) Solid breast nodules: use of sonography to determine between benign and malignant nodules. Radiology 196: 123–134
7. Wylie E (1993) Malignant disease. In: Tucker AK (ed) Text book of mammography. Churchill Livingstone, New York, pp 81–118
8. Gravelle H (1980) Mammography. In: Sutton D (ed) A textbook of radiology and imaging. Churchill Livingstone, New York, pp 1396–1410
9. Meyer JE, Amin E, Lindfor KK, Lipman JC, Stomper PC, Genest D (1989) Medullary carcinoma of the breast: mammographic and ultrasonic appearances. Radiology 170: 79–82
10. Haagensen CD (1986) Diseases of the breast. WB Saunders, Philadelphia
11. Page DL, Anderson TJ (1987) Diagnostic histopathology of the breast. Churchill Livingstone, New York
12. Azavedo E, Svane G (1992) Radial scars detected mammographically in a breast cancer screening programme. Eur J Radiol 15: 18–21
13. Tucker AK (1993) Text book of mammography. Churchill Livingstone, New York
14. Zuckerman HC (1986) The role of mammography in the diagnosis of breast cancer. In: Ariel I, Cleary JB (eds) Breast cancer diagnosis and treatment. McGraw-Hill, New York
15. O'Higgins N (1984) Malignant disease. In: Taylor S, Chisholm GD, O'Higgins N, Shields R (eds) Surgical management. Heinemann, London, p 609
16. Holland R, Hendriks JHCL, Verbeek ALM, Mravunac M, Schuurmans Stekhoven JH (1990) Extent, distribution and mammographic/histopathologic correlations of breast ductal carcinoma in situ. Lancet 335: 519–522
17. Lundström E, Christow A, Kersemaekers W, Svane G, Azavedo E, Söderqvist G, Mol-Arts M, Barkfeldt J, von Schoultz B (2002) Effects of Tibolone and continuous combined hormone replacement therapy on mammographic density. Am J Obstet Genecol 186: 717–22
18. Gamagami P (1996) Breast cancer angiogenesis. In: Atlas of mammography: New early signs in breast cancer. Blackwell Science, Oxford, pp 167–230

Subject Index

D

E

N